

ASM Handbook®

Volume 06A Welding Fundamentals and Processes

Prepared under the direction of the
ASM International Handbook Committee

Volume Editors

Thomas J. Lienert, Los Alamos National Laboratory
Sudarsanam Suresh Babu, The Ohio State University
Thomas A. Siewert, National Institute of Standards and Technology (retired)
Viola L. Acoff, The University of Alabama

Division Editors

Chris Conrady, Edison Welding Institute; **John Elmer**, Lawrence Livermore National Laboratory
Jerry Gould, Edison Welding Institute; **Patrick Hochanadel**, Los Alamos National Laboratory
Kenn Lachenberg, Sciaky Inc.; **Leijun Li**, Utah State University; **Howard Ludewig**, Caterpillar Inc.
Bruce Madigan, Montana Tech of The University of Montana; **Muralidhar Tumuluru**, US Steel Corporation
Norman Y. Zhou, University of Waterloo

ASM International Staff

Eileen DeGuire, Senior Content Developer; **Steve Lampman**, Content Developer
Susan Sellers, Editorial Assistant; **Ann Britton**, Editorial Assistant
Madrid Tramble, Senior Production Coordinator; **Patty Conti**, Production Coordinator
Diane Whitelaw, Production Coordinator; **Scott D. Henry**, Senior Manager, Content Development
Bonnie R. Sanders, Manager of Production

Editorial Assistance

Elizabeth Marquard
Beverly Musgrove
Buz Riley



The Materials
Information Society

Materials Park, Ohio 44073-0002
www.asminternational.org

Copyright © 2011
by
ASM International®
All rights reserved

No part of this book may be reproduced, stored in a retrieval system, or transmitted, in any form or by any means, electronic, mechanical, photocopying, recording, or otherwise, without the written permission of the copyright owner.

First printing, November 2011

This book is a collective effort involving hundreds of technical specialists. It brings together a wealth of information from worldwide sources to help scientists, engineers, and technicians solve current and long-range problems.

Great care is taken in the compilation and production of this Volume, but it should be made clear that NO WARRANTIES, EXPRESS OR IMPLIED, INCLUDING, WITHOUT LIMITATION, WARRANTIES OF MERCHANTABILITY OR FITNESS FOR A PARTICULAR PURPOSE, ARE GIVEN IN CONNECTION WITH THIS PUBLICATION. Although this information is believed to be accurate by ASM, ASM cannot guarantee that favorable results will be obtained from the use of this publication alone. This publication is intended for use by persons having technical skill, at their sole discretion and risk. Since the conditions of product or material use are outside of ASM's control, ASM assumes no liability or obligation in connection with any use of this information. No claim of any kind, whether as to products or information in this publication, and whether or not based on negligence, shall be greater in amount than the purchase price of this product or publication in respect of which damages are claimed. THE REMEDY HEREBY PROVIDED SHALL BE THE EXCLUSIVE AND SOLE REMEDY OF BUYER, AND IN NO EVENT SHALL EITHER PARTY BE LIABLE FOR SPECIAL, INDIRECT OR CONSEQUENTIAL DAMAGES WHETHER OR NOT CAUSED BY OR RESULTING FROM THE NEGLIGENCE OF SUCH PARTY. As with any material, evaluation of the material under end-use conditions prior to specification is essential. Therefore, specific testing under actual conditions is recommended.

Nothing contained in this book shall be construed as a grant of any right of manufacture, sale, use, or reproduction, in connection with any method, process, apparatus, product, composition, or system, whether or not covered by letters patent, copyright, or trademark, and nothing contained in this book shall be construed as a defense against any alleged infringement of letters patent, copyright, or trademark, or as a defense against liability for such infringement.

Comments, criticisms, and suggestions are invited, and should be forwarded to ASM International.

Library of Congress Cataloging-in-Publication Data

ASM International

ASM Handbook

Includes bibliographical references and indexes

Contents: v.1. Properties and selection—irons, steels, and high-performance alloys—v.2. Properties and selection—nonferrous alloys and special-purpose materials—[etc.]—v.22B. Metals Process Simulation

1. Metals—Handbooks, manuals, etc. 2. Metal-work—Handbooks, manuals, etc. I. ASM International. Handbook Committee. II. Metals Handbook.

TA459.M43 1990 620.1'6 90-115

SAN: 204-7586

ISBN-13: 978-1-61503-133-7

ISBN-10: 1-61503-133-2

ASM International®
Materials Park, OH 44073-0002
www.asminternational.org

Printed in the United States of America

Multiple copy reprints of individual articles are available from Technical Department, ASM International.

Foreword

From the efforts of volunteer editors, authors, and reviewers, this Volume 6A of the *ASM Handbook* series, provides updated and expanded coverage on the fundamentals and processes of welding technology, research, modeling and simulation. Welding and allied joining technologies are instrumental in the modern use of materials, and the many volunteers should be proud in this work to serve engineers, students, technicians, researchers, and others with authoritative, reliable reference information on welding fundamentals and processes.

Coverage of joining technologies continues to grow in the *ASM Handbook* series, and this Volume is the first of several Volumes devoted to the many new developments of materials joining. In this Volume, new coverage reflects the continued growth of solid-state welding processes and the expanded use of computer modeling in the simulation of welding processes. Procedure development, quality control, and process improvements are also emphasized for arc, resistance, and directed-energy beam welding.

ASM Handbooks are a cornerstone of ASM International, and this effort could not have been accomplished without the dedicated efforts of many volunteers. Our thanks are extended to the editors, listed on the title page, and the authors and reviewers given in the List of Contributors. We are grateful for the contribution of their time and expertise.

Mark F. Smith
President
ASM International

Stanley C. Theobald
Managing Director
ASM International

Preface

The ASM Handbook Volume 6A, *Welding Fundamentals & Processes*, represents the first of at least two volumes to be published on aspects of welding and joining. As indicated in the title, Volume 6A focuses on fundamental aspects of welding, and on the many welding processes. Volume 6B, planned for future publication, will concentrate on weldability and behavior of a range of alloys and materials.

As with the last edition of this Volume, the Volume Editors recognized that the researchers, engineers, technicians and students that will use this handbook have different needs with regard to their level of understanding. Accordingly, the sections of this handbook fall into two major categories. The sections on fundamentals provide in-depth background on the scientific principles associated with welding, while the sections on the various welding processes take a more practical approach. The Volume Editors have also tried to present a

comprehensive reference that can be of use to the diverse welding community.

All sections of the handbook have been reviewed to be sure that they reflect the current status of the technology. Many sections have been expanded, such as the sections on fundamentals, high-energy density, solid-state welding and especially weld modeling. New processes and process variations developed since the last printing of this Volume have been incorporated, including friction stir welding, magnetic pulse welding, hybrid processes, direct metal deposition, penetration enhancing fluxes and ultrasonic additive manufacturing. A section on safe practices has also been added.

We wish to thank our many colleagues who served as section editors and authors of the individual articles. This handbook would not have been possible without their efforts.

Thomas J. Lienert, Los Alamos National Laboratory

Sudarsanam Suresh Babu, The Ohio State University

Thomas A. Siewert, NIST (retired)

Viola L. Acoff, The University of Alabama

Contents

Fundamentals of Welding	1	Mass Transfer	83
An Overview of Joining Processes		Procedure Development	85
<i>Robert W. Messler, Jr.</i> ,	3	Fluid Flow Phenomena during Welding	
Need for Joining	3	<i>W. Zhang</i>	89
Forces and Interactions in Materials Joining	4	Mass Transport in the Arc	89
Mechanical Joining—Fastening and Integral		Gas Tungsten Arc Welding	89
Attachment	5	Deep-Penetration Electron Beam and Laser Welds	92
Adhesive Bonding	6	Gas Metal Arc Welding	93
Welding	7	Submerged Arc Welding	94
Brazing and Soldering	9	Transport Equations for Weld Fluid Flow	94
Variant and Hybrid Processes	10	Concluding Remarks	94
General Design Aspects	10	Fundamentals of Weld Solidification	
Summary	11	<i>John N. DuPont</i>	96
Overview of Welding Processes		Microstructural Features in Fusion Welds	96
<i>Robert W. Messler, Jr.</i> ,	13	Solidification Parameters	97
Classification of Welding Processes	13	Nucleation Considerations in Fusion Welding	97
Chemically Driven Fusion Welding	14	Grain Structure of Fusion Welds	99
Electric Arc Fusion Welding	16	Substructure Formation in Fusion Welds	100
Directed-Energy Fusion Welding Processes	21	Rapid Solidification Considerations	111
Nonfusion (Solid-State) Welding Processes	24	Dilution in Fusion Welding	
Brazing and Soldering	25	<i>John N. DuPont</i>	115
Fundamentals of Fusion Welding	27	Introduction	115
Welding Process Fundamentals		Dilution and Fusion Zone Composition	115
<i>Thomas W. Eagar and Aaron D. Mazzeo</i>	29	Influence of Welding Parameters on Dilution	117
Energy-Source Intensity	29	Influence of Dilution on Fusion-Zone Microstructure and	
Characterization and Modeling of the Heat Source		Properties	119
<i>S.S. Glickstein, E. Friedman, and R.P. Martukanitz</i>	35	Solid-State Transformations in Weldments	
Simplified Modeling of the Heat Source	36	<i>Mehran Maalekian</i>	122
Arc Welding	36	Special Factors Affecting Transformation Behavior in	
High-Energy-Density Welding	39	a Weldment	122
Resistance Spot Welding	40	Heat-Affected Zone of a Single-Pass Weld	123
Nature and Behavior of Fluxes Used for Welding		Fusion Zone of a Single-Pass Weld	129
<i>Wesley Wang and S. Liu</i>	43	Heat-Affected Zone in Multipass Weldments	134
Equilibrium Parameters	43	Fusion Zone in Multipass Weldments	137
Heat Flow in Fusion Welding		Weldments in Select Alloy Systems	137
<i>Chon L. Tsai</i>	55	Thermomechanical Effects of Fusion Welding	
Introduction	55	<i>P. Michaleris</i>	146
Mathematical Formulations	57	Formation of Residual Stress: Three-Bar	
Engineering Solutions and Empirical Correlation	58	Analogy	146
Parametric Effects	64	Mathematical Formulations	147
Thermophysical Properties of Selected Engineering		Residual Stress	149
Materials	65	Distortion	151
Factors Influencing Heat Flow in Fusion Welding		Residual Stresses and Distortion	
<i>Ole Runar Myhr and Øystein Grong</i>	67	<i>Koichi Masubuchi</i>	158
Introduction	67	Formation of Residual Stresses and Distortion	158
Analytical Solutions of the Thermal Field around Moving		Techniques for Measuring Residual Stresses	159
Point and Line Sources	68	Magnitude and Distribution of Residual Stresses in	
Numerical and Analytical Solutions of the Thermal		Weldments	160
Field in Complex Welding Operations	75	Effects of Residual Stresses and Distortion on the Service	
Acknowledgment	80	Behavior of Welded Structures	162
Transfer of Heat and Mass to the Base Metal in Gas		Thermal Treatments of Weldments	165
Metal Arc Welding		Fundamentals of Solid-State Welding	169
<i>Ian Harris</i>	82	Mechanisms of Bonding for Solid-State Welding	
Heat Transfer	83	Processes	
		<i>Jerry E. Gould</i>	171

Solid-State Welding Processes	171	Purpose of Qualification and Responsibility for the Task.	260
Mechanisms of Solid-State Bonding	171	Qualification of Welding Procedures	260
Extension of the Contacting Surfaces	172	Qualification of Welding Personnel	265
Separation of the Contaminated Areas	172	Qualification Documentation	265
Realignment of the Grain Structures for Bonding	174	General Design Considerations for Arc Welding Processes	
Thermal Dissolution of Oxides/Contaminants	175	<i>W.C. Mohr and O.W. Blodgett</i>	266
Breakdown of the Interfacial Structure	176	Nomenclature	266
Comparison of Solid-State Bonding Processes	176	Types of Joints	266
Summary	176	Types of Welds	267
Fundamentals of Friction Welding		Weld Joint Design	267
<i>D.D. Kautz</i>	179	Fillet Welds	269
Process Parameters	179	Groove Preparation Welds	270
Friction Welding Technology	180	Groove- and Fillet-Weld Combinations	271
Metallurgical Parameters	181	Edge Preparation	271
Fundamentals of Friction Stir Welding		Butt Joints	273
<i>P.S. De, N. Kumar, J.Q. Su, and R.S. Mishra</i>	186	Corner Joints, Flange Joints, and Plug Welds	274
Thermal Aspects	186	T-Joints and Joints for Specific Applications	275
Material Flow	188	Joints Made by Submerged Arc Welding	276
Friction	190	Power Sources for Arc Welding	
Defects	191	<i>Lee Allgood</i>	277
Strain and Strain Rate in FSW	195	Power Source Characteristics	277
Overall Microstructural Feature	196	Short Arc GMAW Power Sources	280
Fundamentals of Ultrasonic Welding		Multiple Arc (Multiple Operator) Power Sources	281
<i>Leijun Li and Chunbo (Sam) Zhang</i>	201	Power Source Selection Considerations	283
Models	202	Arc Welding Process Control	
Results	203	<i>Daniel A. Hartman, George E. Cook, R. Bruce Madigan, and</i>	
Fundamentals of Solid-State Resistance Welding		<i>David R. DeLapp</i>	285
<i>Jerry E. Gould</i>	209	Overview on Welding Process Control	285
Projection Welding	209	Control System Requirements	285
Bonding Mechanisms during Solid-State		System Parameters	286
Projection Welding	210	Sensing	287
Mechanical/Heat-Transfer Balances	210	Modeling	289
Effect of System Mechanical Dynamics on		Control of Arc Welding	290
Projection Welds	211	Shielding Gases for Arc Welding	296
Effect of Electrical Characteristics on Projection Welds	213	Basic Properties of a Shielding Gas	296
Geometric Effects	213	Shielding Gas Blends	297
Summary of Analysis	215	Shielding Gas Selection	297
Conclusions	215	Influence of Shielding Gas on Weld Mechanical Properties	300
Fundamentals of Diffusion Bonding	217	Shielding Gas and Fume Generation	300
Diffusion Bonding Process	217	Self-Shielded Flux Cored Arc Welding	301
Bonding Surfaces Containing Oxides	218	Shielded Metal Arc Welding	
Mechanism of Diffusion Bonding	218	<i>Steve Knostman</i>	302
Diffusion Bonding with Interface Aids	220	The SMAW Process	302
Nondestructive Evaluation of Solid-State Welds		Applications	303
<i>Jeong Na, Roger Spencer, Evgueni Todorov, Sean Gleeson,</i>		Electrodes	303
<i>and Perry White</i>	222	Weld Schedules and Procedures	304
Nondestructive Evaluation Fundamentals	222	Variations of the SMAW Process	306
Examples of NDE of Solid-State Welds	223	Underwater Welding	307
Mechanical Properties of Soft-Interlayer Solid-State Welds	230	Repair Welding	307
Microstructure of Interlayer Welds	230	Safety Considerations	307
Tensile Loading of Soft-Interlayer Welds	231	Gas Metal Arc Welding	
Shear Loading	235	<i>Chris Conrardy</i>	309
Multiaxial Loading	236	Principles of Operation	309
Environmentally Induced Failure of Interlayers	236	Process Parameters	312
Arc Welding Processes	239	Consumables	313
Introduction to Arc Welding	241	Equipment	314
Arc Welding Fundamentals	241	Process Variations	316
Historical Development of Arc Welding	243	Safety Considerations	317
Arc Physics of Gas Tungsten and Gas Metal Arc Welding		Plasma Gas Metal Arc Welding	
<i>Y.M. Zhang</i>	249	<i>Ian D. Harris</i>	318
Gas Tungsten Arc Physics	249	Equipment	318
Gas Metal Arc Physics	254	Procedure	319
Qualification of Welding Procedures and Personnel		Applications	319
<i>Harvey R. Castner</i>	260	Personnel	320
		Hybrid Laser Arc Welding	
		<i>Brian M. Victor</i>	321

Advantages and Limitations	321	Fixturing and Tooling for Stud Arc Welding	385
Applications and Operating Modes	321	Stud-Welding Quality Control, Qualification, and Inspection . .	388
Process Description	322	Stud-Welding Safety Precautions	390
Joint Designs	324	Capacitor Discharge Stud Welding	391
Equipment and Consumables	325	Applications	391
Sources of Defects	326	Equipment	392
Quality Control and Inspection	327	Personnel Responsibilities	392
Safety	327		
Flux Cored Arc Welding		Resistance Welding Processes	395
<i>Michael T. Merlo</i>	329	Introduction to Resistance Welding	397
Process Features	329	Types of Resistance Welds	398
Applications	330	Thermoelectric Effects	398
Equipment	330	Resistance Welding Power Supplies and Controls	
Base Metals	331	<i>Donald F. Maatz, Jr. and Tom Morrisett</i>	404
Electrode Manufacture	332	Heat Input	404
Electrode Diameters	333	Equipment	404
Electrode Classification	333	Resistance Spot Welding	
Submerged Arc Welding		<i>Murali D. Tumuluru</i>	409
<i>Lee E. Allgood</i>	335	Process Description	409
Principles of Operation	335	Equipment	411
Process Applications	336	Machine Construction	413
Automatic SAW Power Source and Equipment	337	Welding Electrodes	414
SAW Fluxes	337	Effect of Surface Condition on Welding	415
Electrodes for SAW	338	Evaluation Methods	416
Weld-Metal Considerations	339	Applications	419
SAW Process Parameters	339	Safety	421
Defects in SAW	341	Projection Welding	
Training and Safety	343	<i>Warren Peterson</i>	423
Gas Tungsten Arc Welding		Introduction	423
<i>Lee E. Allgood</i>	344	Application Advantages and Limitations	425
Applications	345	Material Property Effects	426
Principle of Operation	346	Specifications and Recommended Practices	427
Equipment	347	Process Fundamentals	427
GTAW Welding Procedures	351	Personnel	430
Safety When Using GTAW	353	Process Requirements	430
Acknowledgments	354	Sources of Defects	432
Gas Tungsten Arc Welding with Penetration-Enhancing Compounds		Quality Control and Inspection	432
<i>Ian D. Harris</i>	355	Safety	434
Principles of Operation	355	List of specifications	435
Advantages and Disadvantages	355	Resistance Seam Welding	
Equipment, Procedures, and Applications	356	<i>Robert Matteson</i>	438
Personnel	357	Process Applications	439
Plasma Arc Welding		Advantages and Limitations	439
<i>Ian D. Harris</i>	359	Fundamentals of Lap Seam Welding	441
Principles of Operation	359	Types of Seam Welds	444
Advantages and Disadvantages	360	Processing Equipment	444
Equipment	360	Weld Quality and Process Control	446
Applications	361	Flash Welding and Upset Welding	
Typical Components and Joints	362	<i>R. (Bob) Matteson</i>	448
Operations	363	Introduction	448
Electroslag and Electrode Gas Welding		Flash Butt Welding	448
<i>S.D. Brandi, S. Liu, and R.D. Thomas, Jr.</i>	365	Upset Welding	453
Fundamentals of the Electroslag Process	365	High-Frequency Welding	
Constitutive Equations for Welding Current, Voltage, and Travel Rate	368	<i>Menachem Kimchi</i>	456
Temperature Relations between the Slag Bath and Electrode in ESW	369	Fundamentals	457
ESW Thermal Cycles Equations	369	Advantages and Limitations	458
ESW Consumables	370	Applications	458
Metallurgical and Chemical Reactions	372	Equipment	459
Electroslag Process Development	373	Personnel	461
Electrode Gas Welding	374	Safety	461
Electroslag and Electrode Gas Process Applications	375	Inspection and Quality Control	461
Problems and Quality Control	376	Procedure Development and Practice Considerations for Resistance Welding	
Stud Arc Welding	380	<i>Murali D. Tumuluru, Hongyang Zhang, and R. (Bob) Matteson</i> . .	463
Process Overview	380	Spot Welding Variables	463

Seam Welding Procedure Development	473	Design of Laser Beam Weld Joints	570
Nonferrous Alloys	482	Laser Beam Weld Quality	572
Evaluation and Quality Control of Resistance-Welded Joints		Laser Beam Delivery Optics and Manufacturing Economics	
<i>Hongyan Zhang</i>	486	<i>Tim Webber</i>	580
Quality Attributes of Resistance Welds	486	Optics for Beam Delivery	580
Destructive Testing	489	Manufacturing Economics	583
Nondestructive Testing	495	Laser Deposition Processes	
High Energy Electron Beam and Laser Beam Welding	505	<i>J.O. Milewski and T. Palmer</i>	587
Introduction to High Energy Density Electron and		Laser Cladding	587
Laser Beam Welding		Near-Net Shape Processing	591
<i>J.W. Elmer, P.W. Hohanadel, K. Lachenberg, and T. Webber</i>	507	Laser Weld Quality Monitoring	
History of Electron Beams and Laser Beams	507	<i>Randolph Paura</i>	595
Properties of Electron and Laser Beams	509	Overview of Laser Welding	595
Comparison between Electron and Laser Beam		Process Variables	597
Welding	511	Real-Time or In-Process Monitoring	599
Electron Beam		Examples of Laser Weld Monitoring	601
Electron Beam Welding		Laser Cutting, Drilling, and Shock Peening	
<i>P.W. Hohanadel, J.W. Elmer, K. Lachenberg, P. Burgardt,</i>		<i>Charles Caristan</i>	606
<i>and D.D. Kautz</i>	514	Principles of Laser-Cutting Thermal Processes	606
Principles of Operation	514	Principles of Laser-Drilling Processes	619
Advantages	515	Principles of Laser Shock-Peening Processes	621
Limitations	516	Microjoining with Laser and Electron Beams	
Process Control	517	<i>Gerald A. Knorovsky</i>	625
Operation Sequence and Preparation	517	Definition—What Is a Microweld?	625
Weld Geometry	519	Microscale Physical Phenomena	625
Joint Design	519	Process Description	628
Electron Beam Welding Machines	519	Techniques and Applications	632
Safety	520	Future Trends	634
Design Considerations for Electron Beam Welding		Solid-State Welding Processes	639
<i>Kenn Lachenberg, Patrick Hohanadel, and John Elmer</i>	522	Procedure Development and Practice Considerations for	
Weld Geometry	522	Inertia and Direct-Drive Rotary Friction Welding	
Joint Design	524	<i>Tim Stotler</i>	641
Special Joints and Welds	526	Tooling	642
EBW in Vacuum	527	Procedure Qualifications	642
EBW in Nonvacuum	529	Process Monitoring and Control of Rotary Friction Welding	
Tooling/Fixturing	531	<i>Daniel A. Hartman and Thomas J. Lienert</i>	646
Welding of Thin Metal	531	Background	646
EBW of Thick Metal	532	System Parameters	647
Use of Filler Metal	533	Monitoring	648
EBW for Poorly Accessible Joints	534	Control	652
Design for Scanning/Joint Tracking	535	In-Process Quality Control	652
Electron Beam Welding as a Repair Method	536	Development of Welding Procedures for Friction Stir Welding	
EBW Process Control Plans, Codes, and Specifications	538	<i>Kevin J. Colligan</i>	654
Nontraditional Applications of Electron Beams		Procedure and Procedure Development Requirements	655
<i>Kenn Lachenberg, Scott Stecker, Karen Taminger, and</i>		Procedure Development	656
<i>Gary La Flamme</i>	540	Procedure Qualification	661
Electron Beam Near-Net Shape Processing	540	Friction Stir Welding Tool Designs	
Dynamic Beam Deflection Processing	544	<i>Carl D. Sorensen</i>	664
Quality Control of Electron Beams and Welds		Friction Stir Welding Tool Materials	664
<i>T.A. Palmer, P.W. Hohanadel, and K. Lachenberg</i>	548	Friction Stir Welding Tool Geometry	666
Process Control of Essential Variables	548	Predicting and Measuring Tool Performance	672
Beam Diagnostic Tools for Determining Beam Focus	549	Summary	673
Quality Control	554	Friction Surfacing	678
Laser Beam		Process Description	678
Laser Beam Welding		Equipment	679
<i>Tim Webber, Thomas Lieb, and J. Mazumder</i>	556	Applications	679
Laser Beam Welding Advantages and Limitations	556	Diffusion Bonding	682
Laser Beam Welding Fundamentals and Process		Process Variants	682
Physics	558	Diffusion Bonding of Metals	683
Process Selection	560	Diffusion Bonding of Oxide Ceramics (Ref 46)	685
Health and Safety	566	Explosion Welding	
Laser Beam Weld Design, Codes, and Quality Assessment		<i>Stephen Liu, John Banker, and Curtis Prothe</i>	690
<i>J. Mazumder, Tim Webber, and Randolph Paura</i>	570	Overview of Process Attributes	690

Procedure Development and Practice Considerations	691	Modeling of Thermal-Electrical-Mechanical Coupling in	
Weld Characteristics	695	Fusion Welding	
Manufacturing Process and Practice	697	A. <i>De</i>	789
Products and Applications	698	Thermal Analysis	789
Forge and Coextrusion Welding		Electrical Analysis	790
<i>Paul S. Korinko</i>	701	Discretization of Sheet-Electrode Geometry for Numerical	
Forge Welding	701	Modeling	790
Coextrusion Welding	702	In-Process Growth of Electrode-Sheet Contact	790
Magnetic Pulse Welding		Incorporation of Latent Heat	791
<i>Sachin D. Kore, J. Imbert, Y. Zhou, and M. Worswick</i>	704	Estimation of Contact Resistivity	791
Fundamental Theory	704	Results and Discussions	792
Equipment	705	Modeling of Metallurgical Microstructure Evolution in	
Magnetic Pulse Welding Process	706	Fusion Welding	
Process Parameters	707	<i>Ole Runar Myhr and Øystein Grong</i>	797
Mechanical Testing of Magnetic-Pulsed Welds	707	The Internal State Variable Approach	797
Metallurgical Characterization of Magnetic-Pulsed Welds	707	Isokinetic Microstructure Models	798
Applications	708	Complex Microstructure Models Describing the Evolution	
Safety Guidelines While Handling the MPW Setup	708	of a Particle Size Distribution	807
Summary	709	Microstructure Modeling in the Context of Engineering	
Cold Welding		Design	813
<i>Niels Bay</i>	711	Acknowledgments	817
Bonding Mechanisms and Theoretical Modeling of		Numerical Aspects of Modeling Welds	
Bond Strength	711	<i>John Goldak, Mahyar Asadi, and Lennart Karlsson</i>	819
Alternative Methods of Surface Preparation	712	Modeling of Welds	819
Quality Control	713	Geometry of Weld Models	820
Process Variants and Applications	713	Energy Equation and Heat Transfer	820
Roll Welding and Laser Roll Welding		Microstructure Evolution	825
<i>Muneharu Kutsuna</i>	717	Thermal Stress Analysis of Welds	826
Roll Welding	717	Fluid Flow in the Weld Pool	827
Laser Roll Welding	719	Acknowledgment	828
Laser Roll Welding of Dissimilar Metals	720	Modeling of Thermomechanical Phenomena in Fusion Welding	
Ultrasonic Welding		C. <i>Schwenk</i>	830
<i>Janet Devine</i>	725	Basic Principles and Heat Effects of Welding	830
Equipment and Process Parameters	725	Required Material Properties and Measurement	
Personnel Requirements	728	Techniques	831
Applications	729	Analysis of Material Properties Input Data	832
Ultrasonic Additive Manufacturing		Experimental Data for Validation of Thermal and	
<i>Karl Graff</i>	731	Mechanical Results	834
Process Fundamentals	731	Workflow for Thermomechanical Welding Simulation	835
Applications	733	Reference Information	843
Equipment and Procedures	734	Safe Welding Practices	
Material Properties in UAM	735	<i>American Welding Society</i>	845
Quality Control	739	Safety Management	845
Safety	740	Protection of the Work Area	846
Fundamentals of Weld Modeling	743	Personal Protective Equipment	848
Introduction to Integrated Weld Modeling		Protection Against Fumes and Gases	850
<i>Sudarsanam Suresh Babu</i>	745	Safe Handling of Compressed Gases	855
Process Modeling	746	Protection Against Electromagnetic Radiation	858
Microstructure Modeling	748	Electrical Safety	858
Performance Modeling	754	Fire Prevention and Protection	860
Access and Delivery of Integrated Weld Process Models	756	Explosion Prevention	861
Use of Optimization Methodologies	758	Process-Specific Safety Considerations	861
Concluding Remarks	759	Safety in Robotic Operations	866
Modeling of Heat and Mass Transfer in Fusion Welding		Welding Fuels and Shielding Gases	869
<i>Wei Zhang, Rohit Rai, Amit Kumar, and Igor V. Krivtsov</i>	766	Summary of Fusion Welding Processes	870
Important Considerations	766	Weldability of Ferrous and Nonferrous Alloys	874
Mathematical Description	767	Preheat and Postweld Heat Treatment Temperatures for	
Application to Fusion Welding Processes	775	Selected Steels	878
Mass Transfer in Weld Pool	780	Glossary of Terms	882
Reliability of Models	785	Abbreviations	892
Future Models	786	Metric Conversion Guide	895
		Index	897

Fundamentals of Welding

An Overview of Joining Processes 3	Overview of Welding Processes 13
Need for Joining. 3	Classification of Welding Processes 13
Forces and Interactions in Materials Joining 4	Chemically Driven Fusion Welding 14
Mechanical Joining—Fastening and Integral Attachment. 5	Electric Arc Fusion Welding 16
Adhesive Bonding 6	Directed-Energy Fusion Welding Processes 21
Welding. 7	Nonfusion (Solid-State) Welding Processes 24
Brazing and Soldering. 9	Brazing and Soldering. 25
Variant and Hybrid Processes. 10	
General Design Aspects. 10	
Summary 11	

An Overview of Joining Processes

Robert W. Messler, Jr., Rensselaer Polytechnic Institute

FEW ENGINEERING STRUCTURES start out as a single part, so joining is often the key process in the manufacture of devices or assemblies or the erection of structures. Its purpose is to keep the component parts of such devices, assemblies, or structures together with the required proximity, arrangement, orientation, and alignment to allow the overall device, assembly, or structure to perform its intended function(s) while resisting imposed loads. Since all components or parts are made from materials, such as metals, ceramics, or polymers/plastics (materials engineers prefer the term *polymers* rather than *plastics*, because the former properly distinguishes this fundamental type of material from metals and ceramics, while the latter refers to the property of easy permanent changes to the material shape), successful joining always requires an understanding of how such materials interact when brought into contact with one another. Once such interactions are understood, an engineer can choose among a variety of options for accomplishing joining, some of which rely solely on mechanical forces, some principally on chemical forces, and some principally on physical forces that have their origin in the natural attraction that arises between atoms or molecules. These different forces, in turn, give rise to mechanical joining using either supplemental fasteners or only the shape of the mating parts in a joint, to adhesive bonding using principally chemical forces arising from surface absorption between a chemical agent and the mating parts between which it is sandwiched, or to welding using the natural force of attraction between atoms and/or molecules. Beyond these basic categories of joining, there are some subtypes, some variants, and some combinations known as hybrids. Together, the various options for joining materials are as much an enabling technology as they are a pragmatic process for manufacture, construction, or repair.

Need for Joining

Assemblies are generally manufactured in-plant from fabricated detail parts using one or more joining processes, while structures are generally erected on-site from prefabricated

parts using one or more joining processes. There are instances where very small assemblies or structures are produced from either very small parts or components or directly when the materials comprising components are created at the same time the assembly or structure—typically known as a device—is created. In both cases, joining remains a key process to enable the creation of the device. Examples of very small assemblies employing joining are microelectromechanical systems (Fig. 1). An example of a device in which the components and the device are created simultaneously, but still involving joining, is solid-state microelectronic devices, such as transistors on silicon chips (Fig. 2).

The most obvious need for joining is to make things that are too large to make in one piece because of some inevitable limitation of the process by which those things could otherwise be made. Such limitations exist for all primary processes by which materials can be shaped into parts, including casting (of metals or ceramics, including cement and concrete); molding (of polymers); forging (of metals); rolling, drawing, or extruding (of metals, glasses, and some polymers); or powder compacting (of metals or ceramics). Related to this need is the need to make things that are too complex in shape, even though they may not be too large



Fig. 1 Microelectromechanical systems, such as the one shown here, also must be assembled, typically by mechanical interlocking. Such devices are typically made using techniques first developed for use in microelectronics; i.e., photoetching and deposition.

for the aforementioned primary processes to create. For example, the secondary process of machining can be used to create parts with complex shapes, although it is limited to parts no larger than the limits of the primary processes to produce the starting stock. Otherwise, machined detail parts must be joined to produce an assembly.

Another obvious need for joining is to create assemblies or structures in which the required functions are best achieved by mixing materials of different types, whether at a fundamental level (e.g., metal, ceramic, or polymer) or within a category (e.g., two different metals or alloys). An example of the former is the need to join glass to cement or concrete, to wood, or to metal to create a window in a structural wall. An example of the latter is the need to join pure copper to stainless steel to produce the clad bimetal starting stock for cookware with heat-dispersing bottoms.

Further optimization is often desired when using as much of a material starting stock as

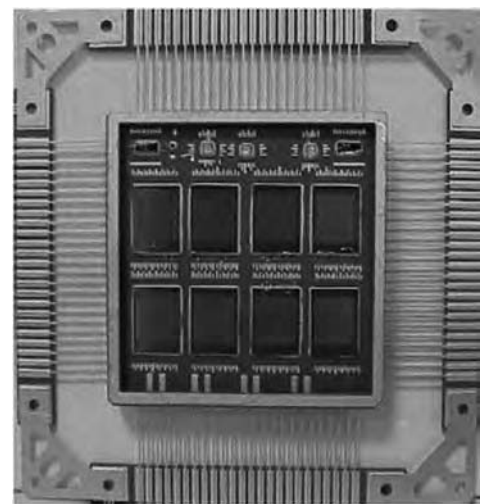


Fig. 2 Solid-state microelectronic devices, beginning at the silicon chip level, involve assembly, including by chemical (e.g., deposition and reaction), welding (e.g., die bonding and soldering), and mechanical (e.g., pressure contact) means. Here an assembled electrically erasable programmable read-only memory complementary metal oxide semiconductor device is shown.

4 / Fundamentals of Welding

Table 1 Reasons for and benefits of joining (by design goals)

Goal 1: Achieve functionality
<ul style="list-style-type: none">• To carry or transfer loads in an array of parts needing to act together without moving (i.e., a static structure)• To carry and transfer loads in an array of parts needing to act together by moving (i.e., a dynamic structure)• To achieve size and/or shape complexity beyond the limits of primary fabrication processes (e.g., casting, molding, forging, forming, powder processing, etc.)• To enable specific functionality demanding mixed materials• To allow structures to be portable (i.e., able to be moved to or from sites)• To allow disassembly for ultimate disposal• To impact damage tolerance in the structure beyond that inherent in the materials of construction (i.e., structural damage tolerance)
Goal 2: Facilitate manufacturability
<ul style="list-style-type: none">• To obtain structural efficiency through the use of built-up details and materials• To optimize choice and use of just the right materials in just the right place• To optimize material utilization (i.e., minimize scrap losses)• To overcome limitations on size and shape complexity from primary fabrication processes• To allow on-site erection or assembly of prefabricated details
Goal 3: Minimize costs
<ul style="list-style-type: none">• To allow optimal material selection and use (versus forcing compromise)• To maximize material utilization and minimize scrap losses• To keep the total weight of materials to a minimum (through structural efficiency)• To provide more cost-effective manufacturing alternatives (versus forcing a primary fabrication process to its limit)• To facilitate automation of assembly, for some methods• To allow maintenance, service, repair, or upgrade; all of which reduce life-cycle costs• To facilitate responsible disposal
Goal 4: Provide aesthetics
<ul style="list-style-type: none">• To enable application of veneers, facades, etc., different from the underlying structure• To allow complex shapes to be formed

Source: Ref 1

possible to minimize waste or scrap. Such improved utilization can be enabled by joining small pieces cut from large starting stock in such a way as to minimize waste (e.g., by nesting flat detail parts punched or otherwise cut from a sheet of metal) to create larger ones. This approach is used in the automobile industry with laser blanking (using pieces from different-gage sheet metal stock to create a patchwork part for forming into a body panel).

There are other reasons for joining that sometimes may be considered needs and other times may be considered benefits. These, as well as the aforementioned needs, are summarized in Table 1 and are discussed in the small number of references available on general approaches to joining listed in the Selected References at the end of this article.

Forces and Interactions in Materials Joining

The engineering options to join materials involve the application of mechanical, chemical, and/or physical forces that bind materials together. It also should be obvious from the preceding section that joining is not only valuable but sometimes an essential process for in-plant manufacturing and on-site construction. In addition, joining is (far more than may be realized or planned) an important process for

in-service repair. In fact, some of the greatest challenges to welding involve making repairs in parts or assemblies or structures that either were not created by welding in the first place or were created by welding but the identity of the metals or alloys of construction is no longer known.

Compatibility of Dissimilar Materials. Before looking at the various major options by which joining can be accomplished, first consider what forces allow two or more parts to be held together in a joint. To the materials engineer, the joining of two or more parts depends on what generic (if not specific) type of material is used for each of the different parts. Obviously, the shapes of the parts to be joined and the purpose of the joint are also important considerations; however, these factors are addressed after considering the fundamental issue of what types of materials are being joined together. After all, when different materials are joined together, the materials must be compatible with one another to form a properly functioning joint.

Compatibility of dissimilar materials involves chemical, physical, and mechanical interactions. First and foremost, the materials in a joint should be chemically compatible so that adverse reactions (e.g., galvanic corrosion) do not occur. Second, physical compatibility of joined materials is also required. For example, when service requires the joint to function

within some temperature range, it is critical to know if one material reacts to heat radically different than another material in the joint. If coefficients of thermal expansion differ by more than approximately 15 to 20% or if melting points are radically different, then this may adversely affect joint function within some temperature range. Third, mechanical compatibility is important, so that key properties of hardness, strength, or stiffness are not radically dissimilar. For example, large differences in mechanical properties may lead to performance problems, such as inordinate wear of one part by the other, intolerable stressing of one part compared to the other, or unacceptable deflection or lack of flexibility of one part versus the other.

Joining with Mechanical, Chemical, and Physical Forces. There are only three types of forces, from a fundamental standpoint, that can be used to hold two or more parts in contact against unwanted motion, regardless of the materials involved. These three are mechanical, chemical, and physical forces that arise from atomic-level attraction.

Mechanical forces arise from one part physically interfering with another part or parts because of their macroscopic shapes and microscopic surface roughness. At the macroscopic level, if the shapes of two or more abutting parts are such that one fits into—or nests within—the other(s), they are prevented from moving at least in some directions. In general, two solid bodies can move in any of three directions by translation, that is, in the x -, y -, or z -direction on a Cartesian coordinate system, or by rotation about the x -, y -, or z -axis of the Cartesian coordinate system. These six distinct types of relative motion are known as degrees of freedom, and thus, there are six degrees of freedom of motion in three-dimensional space: three in translation and three in rotation.

For example, if a protrusion on one part fits into a matching recess on the other, those two parts are prevented from sliding over one another under a shear force but are not prevented from separating from one another under tension. As seen in the next section, such interference can arise from either having a special part cause the mutual interference or by having the abutting parts themselves have shapes that mate to cause interference (Fig. 3). In both cases, strictly mechanical forces, and no atomic-level forces of any kind, operate to keep the parts together against unwanted movement in at least some directions.

Besides macroscopic-level interference caused by the shapes of mating parts, there is also always some degree of interference at the microscopic level due to surface asperities, that is, peaks and valleys. When two real surfaces, which are never perfectly smooth on an atomic scale, are in contact, the high and low points on one surface interact with the high and low points on the other surface. This microscopic mismatch between surfaces results in friction. Friction is what helps fasteners operate in mechanical joining.

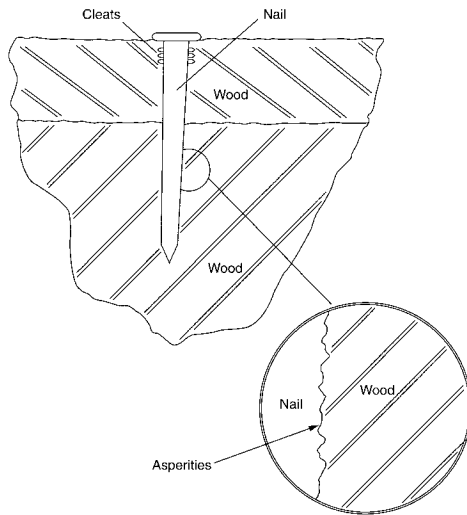


Fig. 3 Schematic illustration showing how interference at both macroscopic levels between parts and/or designed- and processed-in geometric features and at microscopic levels due to ever-present surface asperities leads to mechanical interlocking. Here the example of a nail driven into two pieces of stacked wood is shown. The nail interferes with the two pieces of wood to prevent shear between them, while the forged-in cleats as well as microscopic asperities on the nail surface prevent the nail from coming out of the wood.

The advantages of using mechanical forces to accomplish joining are:

- Materials being joined mechanically need not be similar, so long as they are either chemically compatible or are separated by an intermediate, insulating material.
- Parts joined mechanically can uniquely allow relative motion between mating parts in selected directions of translation and/or rotation, while not moving in other directions.
- Parts assembled mechanically can, uniquely, be intentionally disassembled. (By proper design, unintentional disassembly can be prevented.)
- Joints created by purely mechanical forces arrest propagating cracks in parts at the part-to-part interface, where there is no material continuity. (This imparts damage tolerance to the structural assembly.)
- The level of skill needed to perform mechanical joining is relatively low compared to other methods of joining (e.g., adhesive bonding and welding).
- Mechanical joining is easy to perform in-plant or on-site.
- Resulting joints can easily approach the strength of the joint elements.

The disadvantages of using mechanical forces to accomplish joining are:

- Mechanically, joints can loosen or disassemble unintentionally.
- Stress tends to concentrate at discrete points of mechanical fastening or attachment.

- Mechanical joints can leak fluids unless special precautions are taken (e.g., gaskets, sealants, etc.).
- The labor intensity associated with mechanical fastening is high.

Chemical forces arise principally from surface adsorption between a chemical agent and the materials (i.e., parts) being joined, although they can also arise from an actual chemical reaction between the agent and the part materials. In the former case, there is no adverse effect of the chemical agent on the part materials, and the forces of attraction giving rise to adhesion are relatively weak secondary bonding forces arising from the dipole nature of molecules comprising the chemical agent. In the latter case, there can be an adverse effect if either a weak or brittle boundary layer forms between the chemical agent and one or more of the parts in the joint. When chemical reactions occur, the forces giving rise to adhesion are usually strong primary bonding forces arising from the tendency of the atoms of most chemical elements to attract one another. In both cases, the chemical agent is known as an adhesive, while the base parts involved in the joint are known as adherends. The overall joining process is known as adhesive bonding. Figure 4 shows how adhesives develop strength at a joint.

Physical forces arise between atoms and, to a lesser extent, between molecules as a natural result of their structures. These physical forces, which are electromagnetic (actually, electrostatic) in their origin and character, are the basis for joining by welding as well as the subprocesses of brazing and soldering. In each case, actual atomic-level bonding (metallic, ionic, covalent bonding) results in very high joint strengths. The atoms of all of the elements except the inert gases exert a force of attraction on one another that increases as the distance between them decreases, resulting in the formation of bonded atom pairs. When very large numbers of (ideally, all) pairs of atoms across an interface between two materials form such bonds, the two materials are held together as if they were one, that is, forming a weld. The strength of the weld can easily approach the strength of the base materials involved in the joint.

As seen in the section “Welding” that follows the sections on mechanical joining and adhesive bonding, what needs to be accomplished to actually produce welds is to facilitate this natural process of bonding between atoms.

Mechanical Joining—Fastening and Integral Attachment

There are two ways in which interference can be caused to occur between parts comprising a joint produced by mechanical forces only:

- By using a supplemental part whose sole purpose is to cause such interference

- By using the shapes of the parts themselves to cause the interference

The former approach is known as mechanical fastening, with the special supplemental part being called a fastener. The latter approach is known as integral mechanical attachment, with the mating features being called attachment features. Interested readers are referred to some excellent references at the end of this article.

Mechanical joining, in one or the other of the two forms described, accounts for more than half of all the joining performed in the world every year. The fact that mechanical joining is simple, is available in diverse forms, works with all materials (metals, ceramics, cement and concrete, glass, polymers, wood, and composites) in virtually any combination, does nothing to alter the material properties in which it is accomplished, repeatedly produces joints with high structural integrity, allows intentional disassembly without damaging the parts, uniquely allows relative motion in controlled directions between joined parts, and is highly portable accounts for its tremendous popularity. However, despite all of this, there are other viable and important approaches to joining.

Mechanical fastening is possible using a number of well-known as well as several less obvious but still familiar methods. Examples of some well-known and/or familiar mechanical

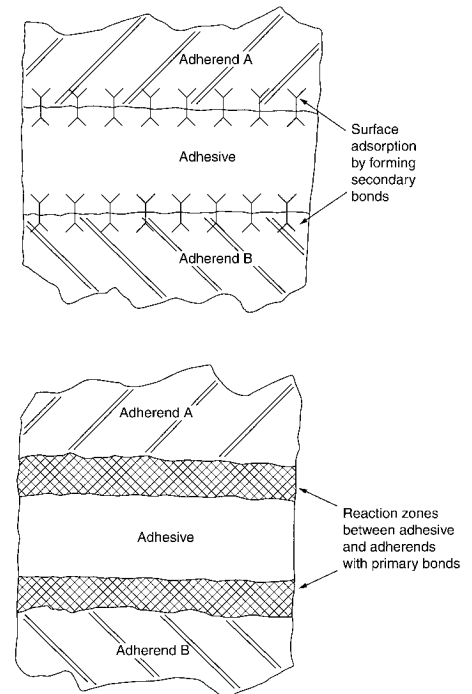


Fig. 4 Schematic illustration showing how either surface adsorption arising from the formation of secondary bonds between an adhesive and adherend(s) (top) or the formation of actual reaction zone(s) between the adhesive and adherend(s), in which primary chemical bonds are formed, contribute to adhesive bonding.

6 / Fundamentals of Welding

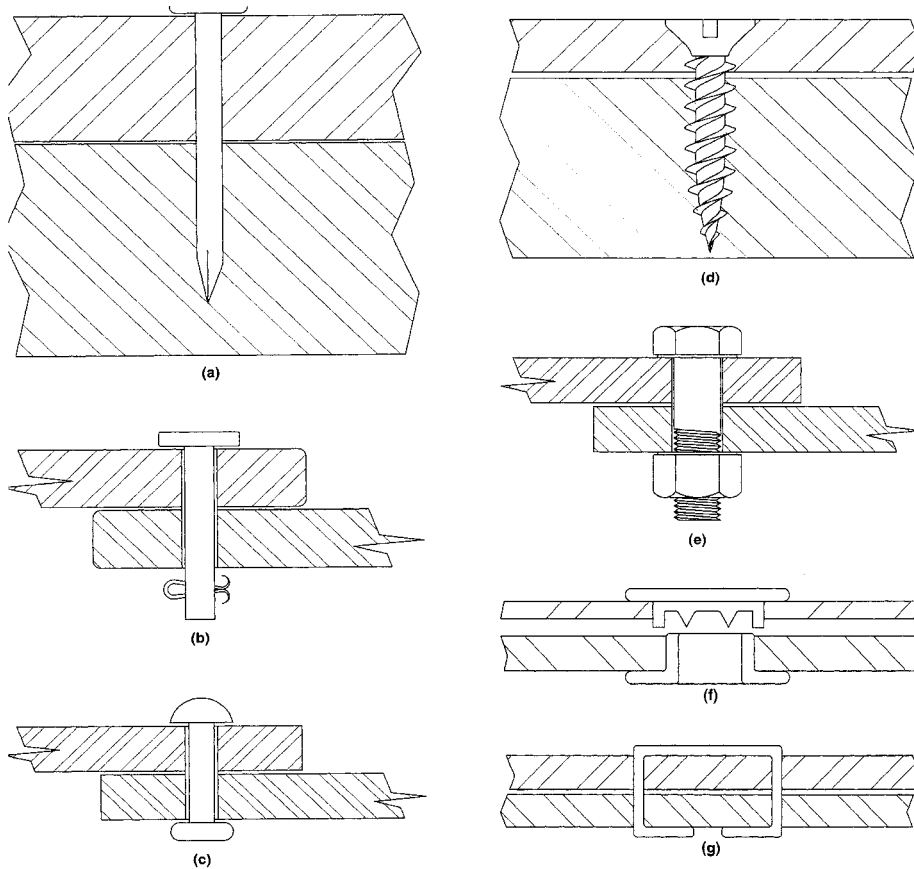


Fig. 5 Schematic illustration of some general mechanical fastening methods and fasteners, including (a) nail in wood, (b) metal pin (with locking Cotter pin) in metal, (c) upset rivet in metal, (d) self-tapping screw in wood, (e) nut and bolt in metal, (f) mating eyelets and grommets (commonly known as snaps) in fabric or leather, and (g) metal staple in paper, cardboard, or leather. Source: Ref 1

fastening methods and fasteners are shown in Fig. 5.

Well-known methods involve the use of metal nails, metal pins, metal or plastic rivets, metal self-tapping screws, threaded metal bolts and machine screws (either with internally threaded parts or with internally threaded metal nuts), metal or fabric washers, metal retaining clips and rings, metal eyelets and grommets (familarly known as metal snaps, as found on some leather garments and on jeans), and metal keys and keyways.

Less obvious but familiar methods include plastic, metal, or ceramic buttons and button-holes; metal or plastic zippers; metal staples; metal or polymeric stitches, lashings, splices, and knots in rope; and others. In each and every case, the sole purpose of the fastener as a part is to cause interference between the parts of the intended joint into which, or with which, they are employed. Once fastened, the joined parts are prevented from separating, at least in some directions of motion.

Mechanical fasteners vary in the specific way in which they are installed and in the way in which they resist applied forces. However, it is possible to fasten joints to achieve load-

carrying capability that equals or even exceeds that of the joint elements themselves. Joint efficiency, which is defined as the stress sustained in that feature or agent that actually allows joining divided by the stress carried in the adjoining structural members, can be high, typically close to or exceeding 100%. Fasteners allow assembled joints to be intentionally disassembled without damaging the joint elements. This said, care must be taken during both design and manufacturing/assembly to prevent unwanted, unintentional disassembly.

Integral Mechanical Attachment. Much older, and gaining popularity again, is the use of geometric features integral to the parts being assembled to cause mechanical joining. This method is known as integral mechanical attachment. Well-known examples include dovetail-and-groove joints in wood, crimps and hems in sheet metal, and so-called snap-fits in plastic or polymer parts.

Integral mechanical attachment, also referred to as integral interlocks, operates in one of three ways:

- By having the features and the parts of which they are a portion remain rigid

- By having the features deflect and then recover elastically against some relatively more rigid mating feature or part
- By being plastically deformed into parts once those parts are mated

The result is rigid interlocks (e.g., dovetail and grooves, machined ways and rails, molded threads on glass), elastic interlocks (e.g., snap-fit features such as cantilever hooks like those found on the lids of battery compartments on cell phones and torsion locks like those found on so-called child-proof plastic medicine bottles), and plastic interlocks (e.g., crimps, hems, stakes). As opposed to fasteners (which can be numerous in large assemblies such as nailed wood-frame houses or riveted aluminum alloy airliners), integral attachment features reduce part count and facilitate assembly, whether done manually or using automation. As such, they are receiving renewed interest in modern design and manufacturing.

Adhesive Bonding

Undoubtedly as old as mechanical joining using interlocking objects, another joining method is the use of naturally sticky substances to hold things together by adhesion. This is the basis of adhesive bonding. Even the earliest humans surely recognized the value of sticky plant and animal excretions (e.g., sap or pitch from trees and spittle from some beetles) and extracts (e.g., plant rubber and blood or fish glues) for joining animal skins, wood, and plant fibers. In its modern form, synthetic chemical agents, rather than naturally occurring ones, tend to dominate the joining process of adhesive bonding. However, regardless of their source, certain chemical agents have the ability to create adhesion between themselves and other materials and hence between virtually any two materials between which such agents are sandwiched. The underlying mechanism responsible for such adhesion is surface adsorption.

Surface adsorption involves the formation of relatively weak secondary bonds between at least some of the molecular species found in the chemical agent, known as an adhesive, and at least some of the molecular (or atomic) species found in the materials being joined, known as the adherends. Without going into great detail here, two possible types of such secondary bonding are van der Waals bonding and hydrogen bonding. In van der Waals bonding, certain of the molecules in the adhesive and certain of the molecules in the adherends induce dipoles in one another; creating positive and negative portions in one another. The result is that the positive portions of molecules in either the adhesive or one or both of the adherends are attracted to—and attract—the negative portions of the molecules in one or both of the adherends or the adhesive, creating bonded pairs across the joint interface. The result is

what is known as adhesion. In hydrogen bonding, hydrogen atoms in the adhesive serve as links or bridges to atoms or molecules in the adherends, creating bonding across the joint interface that tends to be stronger than that created by van der Waals bonding.

While weak compared to primary bonds, van der Waals bonding and hydrogen bonding still result in significant adhesion because such large numbers of submicroscopic bonds are created across macroscopic interfaces. In other words, while the shear (and particularly, peel) strength of adhesives (typically 20+ MPa, or less than 3000 psi) tends not to be impressive compared to the shear or tensile strengths of mechanical fasteners or welds (typically 135 to 700 MPa, or 20,000 to 100,000+ psi), the fact that adhesives are—or should be—applied over large areas allows adhesive-bonded joints to carry tremendous loads or forces. As an example, think about a square card table (36 by 36 in.) covered with soft, freshly chewed gum with a shear strength of 10 psi that is smeared over its entire surface. If such a table was turned upside down and pressed face-to-face with another such table, the force required to pull the two tables apart in shear would be almost 13,000 lb!

Because of the just-described principal mechanism for adhesion, that is, surface adsorption, successful adhesive bonding requires the joining of large surface areas. The larger the better! Once bonded, adhered joints perform best under shear stresses operating in the plane of the adhesive, as opposed to tensile forces or, worse, peel forces operating out of the plane of the adhesive. The result is that properly adhesive-bonded joints tend not to develop stress concentrations like fastened joints do, since applied loads or forces are spread over the large surface area of the bond layer, and areas of concentrated stresses can slip a little or redistribute the loads.

The relative advantages of adhesive bonding are:

- Spreading of applied forces over large areas to produce relatively low stresses
- Little or no stress concentration (except at the ends of overlapped or lapped joint elements, where peel can occur)
- Utility with a wide variety of materials (metals, ceramics, glasses, polymers, composites, wood, cement and concrete) in virtually any combination (so long as the adhesive is chemically compatible with each of the adherends involved in the joint)
- Little if any change to the chemical composition or microstructure, and thus the properties, of the adherends
- Sealing of joints against fluid intrusion or extrusion, that is, leakage
- Damping of shock loads and vibrations
- Blunting of cracks propagating within adherend(s)

Adhesive bonding is not without its shortcomings. Relative shortcomings or outright disadvantages include:

- Sensitivity to out-of-plane loads or stresses (e.g., peel or cleavage)
- Requirement of careful joint preparation
- Requirement of rigid process control for demanding applications
- Difficult inspection and virtually impossible repair of process-induced defects
- Extremely complicated stress analysis for critical applications
- Joint life that is sensitive to a wide variety of environmental factors, including temperature (not too high and not too low), moisture (not too high and not too low), cyclic changes in temperature or moisture (i.e., weathering), radiation (including ultraviolet), solvents, and various biological agents (e.g., mold, mildew, fungi, microbes, insects, and vermin)
- Limits to upper service temperature, especially for organic (polymeric) adhesives
- Protection of worker health from possible fumes, contact dermatitis, and so on

In fact, adhesives develop adhesion between adherends using more than just the chemical forces arising from surface adsorption, although true adhesives must always rely on this mechanism predominantly. Depending on the particular adhesive and on the particular adherend(s), three other mechanisms can—and often do—contribute to joint adhesion:

- Mechanical interlocking
- Diffusion
- Electrostatic attraction

Mechanical interlocking can arise when a soft, pliable adhesive fills in the nooks and crannies caused by the surface roughness (i.e., asperities) of all real surfaces. Adhesion is increased both by the dramatically increased surface area over which surface adsorption is occurring as well as from some locking of adhesive into nooks and crannies with re-entrant angles. Obviously, a contribution from mechanical interlocking arises when adherends are naturally porous or are artificially but intentionally roughened.

Diffusion can contribute to adhesion when some atomic migration occurs across the interface between the adhesive and one or both of the adherends. Such diffusion occurs when the adhesive is particularly fluid and the adherend(s) is (are) permeable, although solid-state diffusion can occur under other circumstances as well. A well-known example is how water-moistened glues or mucilage on postage stamps migrate into the spaces among the fibers of a paper envelope. Related to this type of diffusion is the entangling of the long-chain molecules making up polymers when one polymer is adhesively bonded to another using a polymeric adhesive or simply a solvent. A well-known example is how a polyvinyl chloride plastic patch is bonded to a polyvinyl chloride swimming pool liner once it has been softened with acetone in what is known as solvent cementing.

Finally, electrostatic forces of attraction (Coulomb forces) can arise in certain materials (i.e., adhesives and adherends) when charged particles (e.g., electrons and positive ions) separate within these materials by what is known as polarization. This mechanism tends to occur, if it occurs, in polymers and, to a far lesser extent, in glasses. A supposed manifestation of such an electrostatic contribution to adhesion is when transparent adhesive tape is stripped from a plastic part, and a static charge or even a static discharge occurs.

Figure 6 schematically illustrates the various mechanisms that can contribute to adhesion in adhesive bonding, one or more of which tends to operate with specific adhesives and adherends. Successful adhesive bonding requires proper joint design (to avoid out-of-plane peel or cleavage stresses in favor of pure shear stresses), proper joint preparation (which includes at least careful cleaning but also, often, preconditioning with what is known as a primer), proper adhesive selection for the adherend(s) being joined, and proper adhesive application and curing (which may involve drying or may involve setting with heat or ultraviolet radiation or a chemical catalyst). The interested reader is referred to any of several excellent references on adhesive bonding at the end of this article.

Welding

As mentioned earlier, welding is the natural consequence of bonds between atoms of all of the elements in the periodic table (except the inert gases). Atoms form bonds with one another, in certain combinations and in different specific ways. The upper portion of Fig. 7 shows schematic plots of the competing forces of attraction and repulsion that add algebraically (positive attraction forces to negative repulsion forces) to result in a zero net force at a particular spacing between atoms of similar or dissimilar types (i.e., elements) as they approach one another from what, to those atoms, seems like an infinite initial separation. Under normal circumstances (e.g., a relatively stress-free state), the atoms making up a solid material are separated from one another by this equilibrium interatomic spacing.

When atoms are involved, they are electrically neutral. As they approach one another, they induce a dipole in one another by having the center of positive charge associated with the nucleus displace from the center of negative charge associated with the surrounding orbiting electrons. Once this occurs, they attract one another with a greater and greater force as the distance between them continues to decrease. At some point, however, the negatively charged electrons orbiting in very large orbits (compared to the size of the positively charged nucleus) sense one another's presence and give rise to a repulsive force that builds more and more as the atoms move closer and closer together. In fact, the repulsive force increases

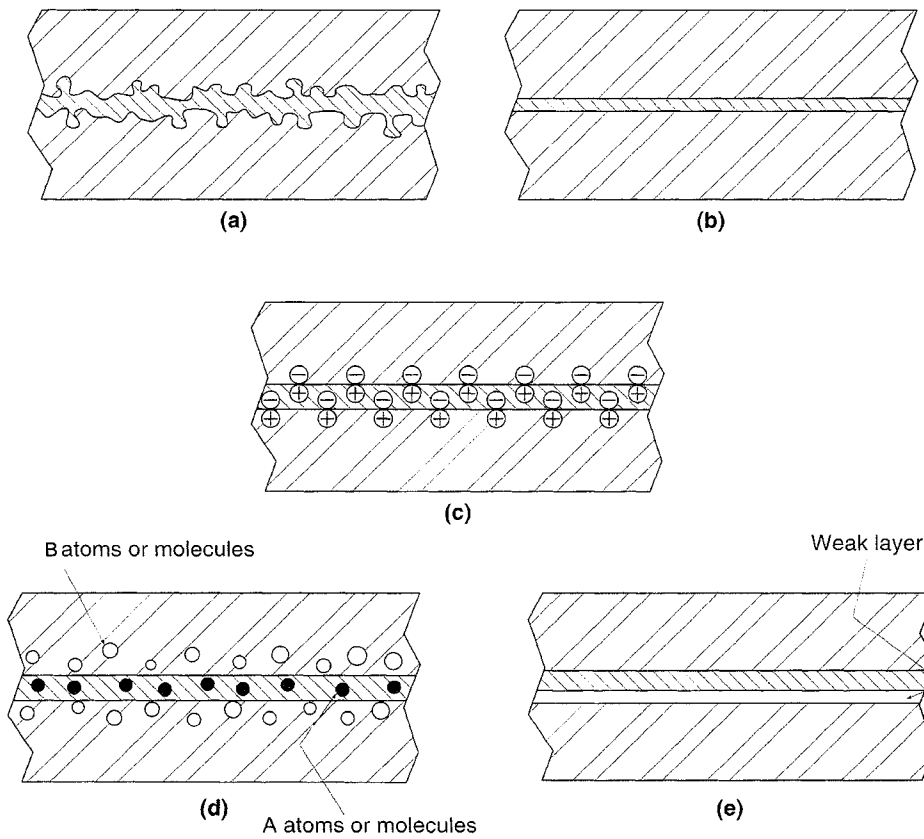


Fig. 6 Schematic illustration of the various mechanisms that can lead to adhesion during adhesive bonding, that is, (a) mechanical interlocking of adhesive into microscopic surface asperities, (b) secondary bonding from adsorption with proper wetting from surface energy effects, (c) electrostatic attraction from charge separation or polarization, and (d) diffusion of some atoms or molecules back and forth between adhesive and adherends. Also, (e) the formation of a weak boundary layer that can lead to the adhesive failure of joints. Source: Ref 1

faster than the attractive force. When the two competing forces are added, a curve of net force results, as shown in the upper portion of Fig. 7. At the point of separation where the attractive force and the repulsive force are equal but opposite, the net force is zero, and this separation is the natural bond length. The net attractive force over the distance the atoms move together adds up to form the bond energy.

So, even neutral atoms, by inducing dipoles in one another, approach one another under the resulting force of attraction until they come to a point where a rising force of repulsion caused by their outermost orbits (or shells) of electrons sensing one another comes into balance to result in a zero net force and, not incidentally, a minimum potential energy state. Once at this equilibrium interatomic spacing, the atoms bond with an energy given by the depth of the well in the net potential energy curve, that is, the binding energy or bond energy. The greater the depth of this well, the greater the strength of bonding, and hence, the greater the strength of the material mechanically (against fracture), thermally (against melting), and chemically (against reaction and,

particularly, corrosion). As a natural consequence of this behavior of all atoms (except those of the inert gases), given the opportunity, atoms of the same element or most different elements will come together and bond. In other words, they form a weld. Welding then is simply the process of enabling atoms to come together in very large numbers to do what they want to do naturally. However, there are some obstacles to be overcome to make welds in real, solid materials.

Two things about the surfaces of real, solid materials pose obstacles to the formation of a weld between two abutting pieces as a result of the natural tendency of the atoms of such materials to come together to their equilibrium interatomic spacing and form strong primary chemical bonds in very large numbers. The first, which is true of all solid materials regardless of their type (e.g., metal, ceramic, or polymer), is that real surfaces are far from smooth on an atomic scale. No matter how much effort is put into creating a smooth surface on a part, there are high and low points—hills and valleys, referred to earlier as asperities—that prevent all but a very small fraction of all the

atoms on the surface from coming into intimate enough contact to allow bond formation. Even for the most highly polished surface, the typical fraction of atoms that come into intimate contact is approximately 1 in every 10^6 to 10^8 . This means that even though strong primary atomic bonds form between these atoms, the overwhelming majority of atoms at the abutting surfaces do not come into close enough proximity to form bonds. Hence, the overall effect of such limited bonding is that the strength of the created weld is only approximately 1 one-millionth to about 1 one-billionth of the theoretical strength of the materials involved, not nearly enough to hold the pieces together under their own weight.

Figure 8 schematically illustrates how welds form naturally in ideal materials with perfectly smooth surfaces (in a and b) versus how such weld formation is hindered by the existence of surface asperities on the surfaces of real materials (in c). To increase the number of atoms on the abutting part surfaces that come into intimate contact, there are two options:

- Apply pressure to cause the contacting high points to deform plastically, bring more points into intimate contact, and form more bonds
- Add atoms to the gaps between the contacting high points to fill in those gaps and form more bonds

The easiest way to add atoms is in the form of a liquid, which can flow into the nooks and crannies, created by melting either the materials being joined or by adding a molten compatible filler material. The first bulleted option is the basis for nonfusion pressure welding, while the second bulleted option is the basis for fusion welding (both of which are described in the section “Classification of Welding Processes” in the article “Overview of Welding Processes” in this Volume).

The second thing about the surface of most real materials is that they are rarely clean at the atomic level. That is, the surface rarely consists of only atoms making up the base materials involved in what is to become the joint. Rather, the surfaces of most materials are contaminated by oxides or other tarnish layers, by adsorbed water and/or gases from the air, or, if the parts were not cleaned, by oils, greases, paint, and so on. These contaminants prevent atoms of the base materials from coming into intimate contact to form bonds and a weld.

Figure 8(d) schematically illustrates how the surfaces of real materials are covered with contaminants that prevent atoms of the base materials from coming together to form bonds. Figure 8(e to g) show how pressure can be used to overcome the obstacles of asperities and contamination of the surfaces of real materials to form a weld in the solid state. Not shown is how atoms could readily fill in the gaps between contacting high points by being added in the liquid state (i.e., as molten material) to

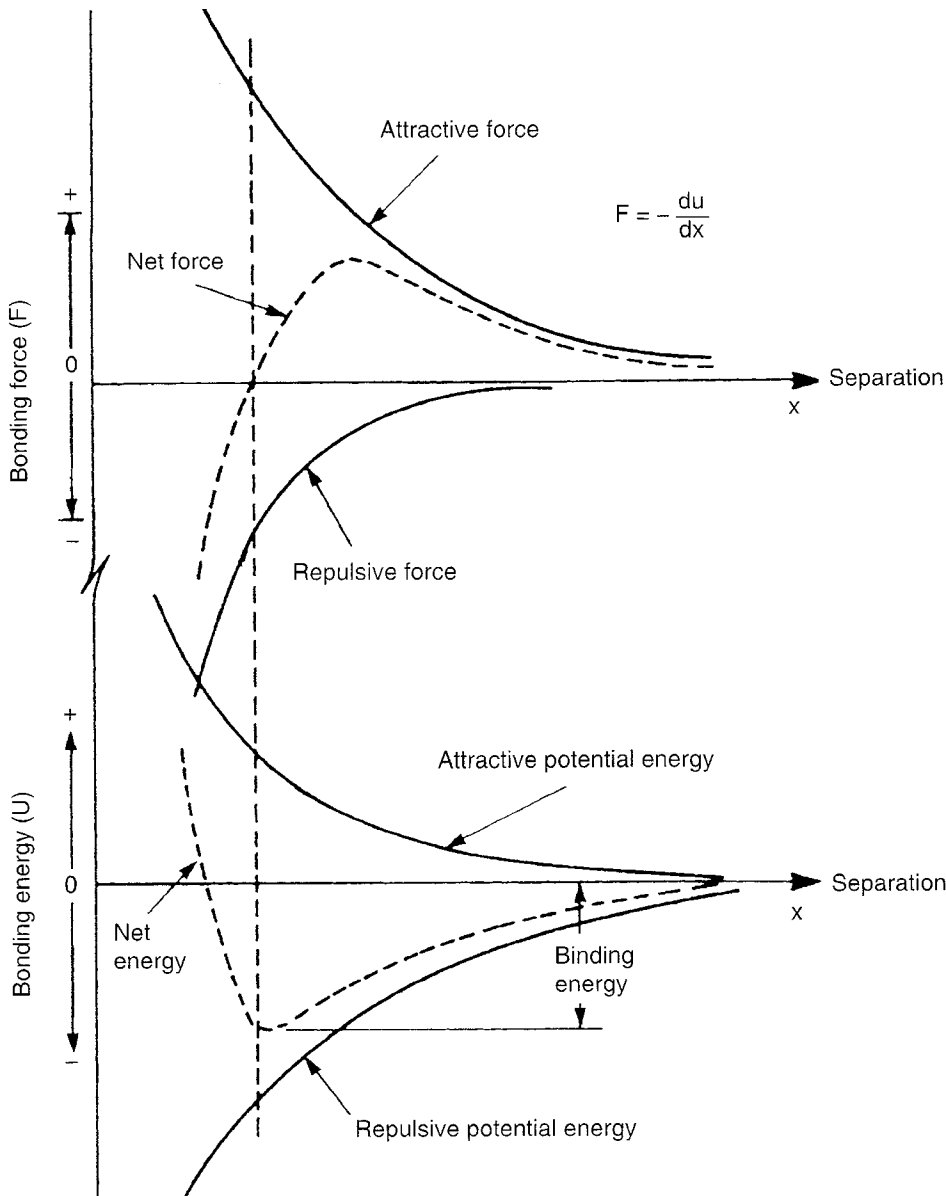


Fig. 7 Schematic plot of the forces (top) and potential energies (bottom) involved in atomic bond formation as the underlying mechanism of welding. Source: Ref 1

allow more bond formation. Obviously, the successful creating of welds with good properties is critically dependent on proper cleaning of the part surfaces prior to welding.

The advantages of welding include:

- Creation of joints that are permanent (as opposed to life-limited, as is the case with most adhesive-bonded joints, or possible to disassemble, as is the case for mechanical joints), precluding accidental disassembly or loosening
- Wide variety of process embodiments, to optimize selection for purpose
- Applicability to many materials within a fundamental material class, that is, within metals, ceramics, glasses, or thermoplastic polymers

- Amenability to either manual or automated operation
- General portability and suitability for use outdoors or indoors
- Creation of leaktight joints, if desired
- Achievement of excellent joint strength and efficiency

Advantages notwithstanding, there are some disadvantages, which include:

- Impossibility of disassembly without severely damaging parts, for any purpose (including recycling)
- Alteration of base material structure and disruption of base material properties by the heat associated with some process embodiments (especially involving fusion)

- Impossibility of joining fundamentally dissimilar materials (e.g., metals to glasses), although such joining can often be done using brazing or soldering
- Requirement of considerable operator skill and stringent process control for production of high-quality joints
- Relative high cost (compared to mechanical joining and adhesive bonding) due to required skills and labor intensity
- Possible high cost for capital equipment, especially for some automated processes

The real forte of welding is for joining metals, although the process can also be employed for joining similar or dissimilar glasses, for joining similar or dissimilar thermoplastic polymers, and for joining some ceramics (particularly oxide types). As such, because of the tremendous importance of metals, in general, and steels, in particular, to the technological advancement and economy of societies, welding is a particularly important joining process, accounting for more than 60% of the gross domestic product of industrialized countries.

Brazing and Soldering

Like welding, both brazing and soldering also form primary bonds (in metals, metallic bonds). Like welding processes, soldering and brazing also rely on interdiffusion between joined materials to form the soundest joints. Unlike fusion welding, however, neither brazing nor soldering requires—nor causes—any melting (or fusion) of the base materials. Rather, bond formation occurs between molten filler and the ever-solid substrates.

Both brazing and soldering involve the use of a filler material that melts at a temperature below that of the base material(s). The only difference between processes classified as brazing and those classified as soldering is that brazing fillers melt above 450 °C (840 °F), while solders melt below 450 °C (840 °F). These temperatures are actually quite arbitrary, because nothing special happens there, but melting of fillers at 450 °C has become the generally accepted break-point between the temperatures for soldering and brazing.

During brazing and soldering, the melting of filler materials is essential so that these molten fillers can:

- Wet the surface of the base materials (by lowering the surface energy of those base materials)
- Flow or spread over the surfaces of the base materials by capillary action, usually aided by separating base material parts between 0.05 and 0.2 mm (0.002 and 0.008 in.)
- Speed up needed interdiffusion

These criteria are different than those for the parent process of welding (which involves

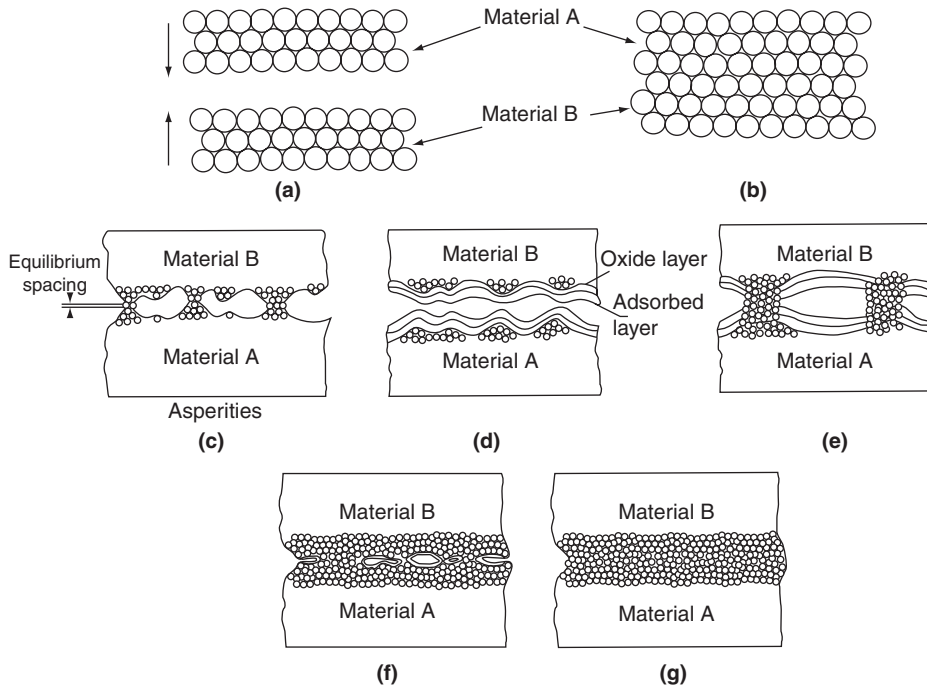


Fig. 8 Schematic illustration of the formation of welds as the result of two perfectly smooth and clean ideal materials versus two real materials. The ideal surfaces (a) before and (b) after being brought into intimate contact. The real surfaces always contain microscopic asperities (c) and usually are contaminated with tarnish layers and/or adsorbed gases or water (d), all of which inhibit bond formation between metal atoms. Application of pressure, with or without heat, leads to progressive formation of welds (e through g). Source: Ref 1

melting of base materials and/or interdiffusion between the base materials). For both, the fillers tend to be alloys with eutectic or near-eutectic compositions from alloy systems having eutectics.

Both brazing and soldering share the following advantages:

- There is minimal disruption of the base materials by operating at relatively low temperatures.
- Joining of fundamentally different materials (e.g., metals to ceramics and metals to glasses) can be done.
- The joint forms itself by the nature of the flow, wetting, and subsequent crystallization process, even when the heat and the braze or solder are not directed precisely to the places to be joined.
- The resulting joint tends to spread loading over large surfaces and performs better in shear, especially peel, rather than in tension.
- Considerable freedom is allowed in the dimensioning of joints, so that it is possible to obtain good results even if a variety of components are used on the same product.
- The brazed or soldered connections can be disconnected if necessary, thus facilitating repair.
- The equipment for both manual and machine brazing/soldering is relatively simple.
- The processes can be easily automated, offering the possibility of in-line

arrangements of brazing/soldering machines with other equipment.

Variant and Hybrid Processes

Besides the major joining options of mechanical joining (fastening or integral attachment), adhesive bonding, and welding (including brazing and soldering), there are some so-called variant processes that are difficult to place within any one of the aforementioned categories. There also are some interesting hybrid processes, which are combinations of the major and/or variant methods. In addition, some references, most notably, the *Welding Handbook* of the American Welding Society, tend to refer to the variant and hybrid processes mentioned here, as well as some other processes, such as thermal cutting and flame straightening or shaping, as allied processes (as described in the section “Classification of Welding Processes” in the article “Overview of Welding Processes” in this Volume). Both variant processes and hybrid processes are described only briefly here for completeness. The interested reader is encouraged to seek other references, such as those listed at the end of this article.

Two variant processes are braze welding and thermal spraying. Braze welding tends to fall between what is properly classified as fusion welding and what is properly classified as

brazing. Like brazing, it employs filler that melts below the temperature of the base material(s), but unlike brazing, and more like all forms of fusion welding, it does not rely on capillary attraction to cause the molten filler to distribute in the joint. Instead, the filler in braze welding is deposited in a prepared groove between the parts to be joined. Thermal spraying involves the heating and acceleration of metallic, ceramic, or even thermoplastic polymer feedstock converted into particulate form to cause those particles to adhere to a properly prepared substrate. The process can be used to restore lost material with relatively low heat input to the substrate or to apply coatings to resist wear or corrosion, provide traction, or provide lubricity. Heating and propulsion embodiments use electric arcs, plasmas, combusted fuel gases, or detonation of fuel gases.

Hybrid processes combine two different processes to obtain some particular benefit(s), often with some synergism. Examples include the combining of spot welding and adhesive bonding in weld bonding, the combining of welding and brazing in weld brazing, and the combining of riveting and adhesive bonding in rivet bonding. Similar hybrids have also been developed within welding, combining two different welding processes to obtain some benefit(s). A few examples include laser/gas tungsten arc, laser/gas metal arc, and laser/plasma arc.

General Design Aspects

The term *design for joining* refers to creating a mechanism that allows the fabrication of a joint that meets this service condition using a suitable joining process, at minimal cost. In this context, design for joining emphasizes how to design a joint or conduct a joining process so that components can be produced most efficiently and without defects. This involves selection and application of good design practices based on an understanding of process-related manufacturing aspects such as accessibility, quality, productivity, and overall manufacturing cost.

A good design uses the inherent advantages of the selected method of joining. For example, braze joints perform very well when subjected to shear loading but not when subjected to pure tensile loading. When using a brazing process to join parts, it would be beneficial to employ innovative design features that would convert a joint subjected to tensile loading to shear loading. For example, use of butt-lap joints instead of butt joints can provide a beneficial effect in flat parts and tubular sections.

The selection of an appropriate design to join parts is based on balancing several considerations related to the product and joining process. Product-related considerations include codes and standards, fitness for service, aesthetics, manufacturability, reparability, reliability, inspectability, safety, and unit cost of

fabrication. Considerations related to the joining process include material types and thicknesses, joint (part) geometry, joint location and accessibility, handling, jiggling and fixturing, distortion control, productivity, training, and initial investment.

Joint Design. The individual parts of a component meet at joints, and the term *joint design* often emphasizes design for meeting structural requirements, because the typical function of many joints is to transmit or distribute forces from one part to the other parts of an assembly. An ideal joint is one that effectively transmits forces among the joint members and throughout the assembly, meets all structural design requirements, and can still be produced at minimal cost.

The design or selection of appropriate joint type is determined primarily from the type of service loading. For example, butt joints are preferred over tee, corner, lap, or edge joints in components subjected to fatigue loading. Joints also must be designed to reduce stress concentration. Sharp changes in part geometry near the joint tend to increase stress concentration or notch effects. Smooth contours and rounded corners tend to reduce stress-concentration effects.

The specific joint design aspects, such as the size, length, and relative orientation of the joint, are based on stress calculations that are derived from an evaluation of service loads, properties of materials, properties of sections, and appropriate structural design requirements. Joint design also can have important process implications.

Orientation and Alignment. Designs that maintain the relative orientation and alignment of component parts save valuable time during fit-up and enhance the ability to produce a high-quality joint. For example, operations involving furnace brazing or diffusion bonding with interlayers benefit from such a type of joint design, because they also require preplacement of the brazing filler or the interlayer in the joint.

Joint Location and Accessibility. Joints obviously must allow proper access. Limited accessibility can reduce the overall quality and productivity, depending on the method of joining. In arc welding, for example, weld joint designs employ bevel angles and root openings to enhance accessibility to the welding torch (or electrode) and provide adequate weld penetration. The best bevel angles provide adequate accessibility while reducing the amount of weld metal required to complete the joint.

Unequal Section Thickness. When members of an assembly have unequal section thicknesses, joint designs should provide a smooth flow of stress patterns through the unequal sections. Modifications to the design may also be needed for process reasons. When making a fillet weld using an arc welding process, if thicknesses of the members are not greatly different, directing the arc toward the thicker member may produce acceptable penetration. However,

special designs for joining will be required when large differences in section thicknesses result in large differences in heat-dissipating capacities. When a thick member is arc welded to a thin member, the welding heat input (mainly current) needed to obtain a good penetration into the thick member is sometimes too much for the thin member and results in undercutting of the thin member and a poor weld. Similarly, if the proper amount of current for the thin member is used, the heat is insufficient to provide adequate fusion in the thick member, and again a poor weld results. Too little heat input can also cause underbead cracking in certain structural materials.

A widely applicable method of minimizing heat sink differential is to place a copper backing block against the thin member during fusion welding. The block serves as a chill, or heat sink, for the thin member. Another way to obtain equalized heating and smooth transfer of stress with unequal section thicknesses is to taper one or both members to obtain an equal width or thickness at the joint. Commonly, when two pipes of dissimilar internal diameter and wall thickness are to be joined, a convenient way is to introduce a “reducer” between the two pipes. One end of the reducer will have the same size and wall thickness as the larger pipe, while the other end of the reducer will have the same size and wall thickness as the smaller pipe.

Distortion Control. Design of an appropriate weld joint can also help reduce welding-related distortion. Fusion welding processes employ localized melting and solidification to join component parts, which can result in excessive thermal strains. These thermal strains are dependent on the type of material, the welding process, and the welding procedure. Reducing the overall length of the weld or the amount of weld metal that needs to be deposited to complete a joint reduces both residual stresses and distortion. For example, intermittent welding instead of continuous welding reduces the overall length of a weld. For more details on distortion of fusion-welded joints, see the article “Residual Stresses and Distortion” in this Volume.

Summary

Joining is key to the manufacture of large or complex devices or assemblies, the construction of large, complex structures, and the repair of parts, assemblies, or structures in service. It also allows materials to be mixed to optimum advantage and utilized for maximum economy.

There are basic joining methods that use purely mechanical forces arising from physical interference between (and possibly some interlocking between) parts, chemical forces arising from surface adsorption or outright reactions, and the physical forces arising from the natural tendency for the atoms of all but the inert gas elements to form strong atomic-level bonds. These lead to the generic options of mechanical

joining, adhesive bonding, and welding, including brazing and soldering.

Mechanical joining can be accomplished using special supplemental parts whose only purpose is to facilitate joining, known as fasteners, in mechanical fastening or simply using some geometric features of the parts themselves to create interference and interlocking. The greatest advantages of mechanical joining are utility with all materials in virtually any combination, with no degradation of material properties or microstructure, and the unique abilities to allow relative motion between joined parts (if desired) and allow intentional disassembly (if desired).

Adhesive bonding relies primarily on the development of secondary bond formation between a compatible chemical agent known as an adhesive and base materials known as adherends. Other contributions to overall joint strength, that is, adhesion, can come from mechanical interlocking, limited diffusion, or electrostatic attraction from polarization between the adhesive and the adherends. The major advantage of the process is load spreading, while the major limitation is always susceptibility to environmental degradation.

Welding arises from the natural tendency of the atoms of most elements in the periodic table (except the inert gases) to form one or more ionic, covalent, or metallic atomic-level bonds. By using either enough pressure to deform surface asperities that limit the number of points of intimate, atomic-level contact or by adding atoms from a molten material source to backfill gaps, welds rivaling the strength of the base materials is possible. Welding can be accomplished with the categories of metals, ceramics, glasses, and thermoplastic polymers but not between these classes. One of two subclassifications or subtypes of welding, either brazing or soldering, can be used to join dissimilar, as well as similar, combinations of materials.

Finally, there are some special variants and hybrids of the basic joining processes. Two important variants are braze welding and thermal spraying. Three hybrids are weld bonding, weld brazing, and rivet bonding.

REFERENCE

1. R.W. Messler, Jr., *Joining of Materials and Structures: From Pragmatic Process to Enabling Technology*, Butterworth-Heinemann/Elsevier, Burlington, MA, 2004, p 14, 112–113, 192, 290, 291

SELECTED REFERENCES

General materials

- W.F. Callister, Jr., *Materials Science and Engineering: An Introduction*, 7th ed., John Wiley & Sons, Inc., New York, NY, 2007
- R.W. Messler, Jr., *The Essence of Materials for Engineers*, Jones & Bartlett Learning, Sudbury MA, 2010

12 / Fundamentals of Welding

- J.F. Shackelford, *Introduction to Materials Science for Engineers*, 6th ed., 2004

General joining

- R.W. Messler, Jr., *Joining of Materials and Structures: From Pragmatic Process to Enabling Technology*, Butterworth-Heinemann/Elsevier, Burlington, MA, 2004
- R.O. Parmley, *Standard Handbook of Fastening & Joining*, 2nd ed., McGraw-Hill, New York, NY, 1989

Mechanical fastening

- A. Black, *Design of Mechanical Joints*, Marcel Dekker, New York, NY, 1990

- J.A. Speck, *Mechanical Fastening, Joining, and Assembly*, Marcel Dekker, New York, NY, 1997

Integral mechanical attachment

- R.W. Messler, Jr., *Integral Mechanical Attachment: A Resurgence of the Oldest Method of Joining*, Butterworth-Heinemann/Elsevier, Burlington, MA, 2006

Adhesive bonding

- *Adhesives and Sealants*, Vol 3, *Engineered Materials Handbook*, ASM International, 1990
- A.H. Landrock, *Adhesive Technology Handbook*, Noyes Publications, Park Ridge, NJ, 1985

Welding

- R.W. Messler, Jr., *Principles of Welding: Processes, Physics, Chemistry and Metallurgy*, John Wiley & Sons, New York, NY, 1999
- *Welding Handbook*, 8th ed., Vol 1–3, American Welding Society, Miami, FL, 1990–1993

Brazing and soldering

- D.M. Jacobson and G. Humpston, *Principles of Brazing*, ASM International, 2005
- G. Humpston and D.M. Jacobson, *Principles of Soldering*, ASM International, 2004

Overview of Welding Processes

Robert W. Messler, Jr., Rensselaer Polytechnic Institute

BECAUSE METALS AND ENGINEERING ALLOYS are used in more diverse applications than any other material, and because welding offers particular advantages for joining metals and alloys into structures wherein the joints are intended to be permanent, it is appropriate and important to survey the various ways in which welding can be performed. Welding processes can be fairly meaningfully and conveniently classified into those that achieve material continuity by melting the base metal without or with some filler metal or for those that achieve material continuity by causing plastic deformation through the application of pressure without or with some heat. The former are known as fusion welding processes, while the latter are known as nonfusion welding processes.

Once a decision is made that it is acceptable and advantageous to use fusion or not, it is important and beneficial to consider the type of energy source to be used to cause such melting or such plastic deformation, respectively. For fusion welding, chemical energy sources include combustion of fuel gas with oxygen (oxyfuel welding processes) and exothermic reaction of particulate metals and oxides (combustion synthesis welding processes), while electrical energy sources include arcs (arc welding processes), joule heating (resistance welding processes), or high-energy-density beams (radiant energy or beam welding processes). For solid-phase, nonfusion welding, mechanical energy sources predominate, including the use of pressure, friction, and solid-state diffusion, although the energy of chemical reactions can also be used for at least solid-state deposition processes.

It is also possible to produce joints between metals and even between metals and ceramics using two subtypes of welding known as brazing and soldering. In both, fillers that melt are used to create material continuity with base materials that do not melt, even at the interface. Brazing and soldering processes can be performed using a variety of chemical or electrical energy sources that are, not surprisingly, similar for these two low-temperature processes.

This article provides an overview on the classification of welding processes along with a brief overview of key process embodiments for joining by:

- Fusion welding with chemical sources for heating
- Fusion welding with electrical energy sources (arc welding or resistance welding)
- Fusion welding with directed energy sources (laser welding, electron beam welding)
- Nonfusion welding processes (regardless of the particular energy source, which is usually mechanical but can be chemical)
- Related subprocesses of brazing and soldering

Classification of Welding Processes

One of the advantages of welding processes for producing joints in metals and alloys is the diversity of specific process embodiments. This diversity maximizes the possibility of finding the right process for the right situation and application. However, at the same time, such diversity can seem confusing without some high-level scheme for classifying the various process methods or embodiments. Classification helps to divide processes into logical categories within which there are certain key similarities or certain important differences, and it relates major categories to one another to allow comparison of relative merits and shortcomings or penalties for specific application.

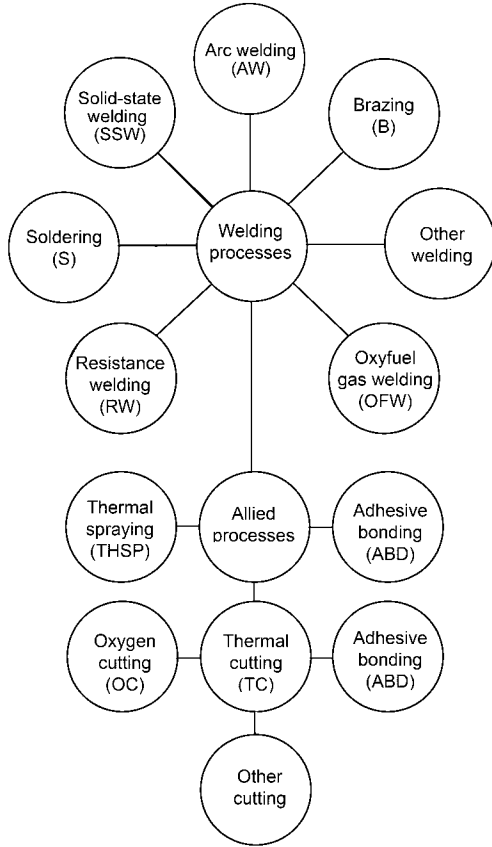
Figure 1 presents a master chart of welding and allied processes developed by the American Welding Society (AWS). It is useful for three things. First, it subdivides welding processes into major categories (e.g., arc welding, oxyfuel gas welding, resistance welding, etc.). Second, it shows the general relationship of so-called allied processes, which use similar energy sources (e.g., electric arcs and oxyfuel gas combustion) for related, thermally-based processes such as cutting and material thermal spraying. Third, it gives the AWS designation acronym for short-hand reference to a specific process (e.g., GMAW for gas metal arc welding).

While interesting, and offering some utility, this master chart fails to classify specific process embodiments within welding in such a

way as to make clear familial relationships in a hierarchical fashion; that is, it fails to provide a taxonomy. Widely used in biology and biological sciences, in that discipline, a taxonomy is an orderly classification of plants or animals according to their presumed natural relationships. First-generation parent-daughter, second-generation grandparent-granddaughter, as well as aunt-niece, cousin, and other relationships can be shown in taxonomies. When applied to classify inanimate things or, as in the case of welding, processes, a taxonomy helps with an understanding of the derivation of one process from another, with key similarities and differences, and even with the possible identification of “missing links” to stimulate invention or development.

Figure 2 presents a taxonomy of welding processes developed by the author. At the highest level of the taxonomy presented in Fig. 2, process embodiments are divided into pressure and nonpressure categories, while immediately below this level each of these is divided into nonfusion and fusion subtypes. The relationship of specific process embodiments to the fundamental ways in which welds can be created in real materials to overcome the obstacles to the establishment of material continuity is immediately obvious; that is, either pressure to cause plastic deformation or heat to cause melting can be used. Within the general subclassification of nonpressure welding processes that operate by relying on fusion, further subdivision into processes that rely on fusion of identical or virtually identical base and/or filler materials or of dissimilar base materials and fillers can be seen under headings of homogeneous (in the former case) and heterogeneous (in the latter case). Brazing and soldering appear under the heterogeneous subdivision. Further subclassifications consider use of filler or not (i.e., autogenous welding), as well as other key differences.

Not used in the taxonomy presented in Fig. 2 is the source of energy by fundamental type, that is, chemical energy, electrical energy, or mechanical energy. This notwithstanding, the classification shown tends to work quite well to understand the relationship among various process embodiments.



(a)

Group	Welding process	Letter designation
Arc welding	Carbon arc	CAW
	Electrode gas	EGW
	Flux-cored arc	FCAW
	Gas metal arc	GMAW
	Gas tungsten arc	GTAW
	Plasma arc	PAW
	Shielded metal arc	SMAW
	Stud arc	SW
Brazing	Diffusion brazing	DFB
	Dip brazing	DB
	Furnace brazing	IB
	Induction brazing	IRB
	Resistance brazing	RB
	Torch brazing	TB
	Oxyfuel gas welding	Oxyacetylene welding
Oxyhydrogen welding		OHW
Air acetylene		...
Pressure gas welding		PGW
Resistance welding	Flash welding	FW
	Projection welding	DFW
	Resistance seam welding	RSEW
	Resistance spot welding	RSW
	Upset welding	UW
Solid-state welding	Cold welding	CW
	Diffusion welding	DFW
	Explosion welding	EXW
	Forge welding	FOW
	Friction welding	FRW
	Hot pressure welding	HPW
	Roll welding	ROW
	Ultrasonic welding	USW
Soldering	Dip soldering	DS
	Furnace soldering	FS
	Induction soldering	IS
	Infrared soldering	IRS
	Iron soldering	INS
	Resistance soldering	RS
	Torch soldering	TS
	Wave soldering	WS
	Other welding processes	Electron beam
Electroslag		ESW
Flow		FLOW
Induction		IW
Laser beam		LBW
Percussion		PEW
Thermit		TW

(b)

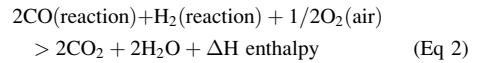
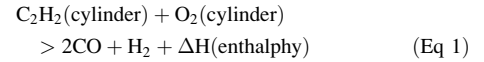
Fig. 1 (a) Master chart of welding and allied processes used by the American Welding Society (AWS). (b) List of the abbreviations used by the AWS for various welding, brazing, and soldering processes. Source: Ref 1

Chemically Driven Fusion Welding

There are two ways in which chemical energy can be harnessed to cause melting and enable fusion welding: combustion of a fuel gas in the presence of oxygen, and solid-phase reaction of certain powdered metals with certain other powdered metals, possibly with carbon, or with certain oxides of less-active metals. The former processes are called oxyfuel gas welding processes, while the latter are called combustion synthesis welding processes. Both, obviously, involve exothermic reactions. (In chemistry, an exothermic reaction or process is one that spontaneously produces or evolves heat as it occurs.)

Hydrocarbon gases, as well as plain hydrogen, can react with oxygen to combust. In

undergoing oxidation, hydrocarbon fuel gases form combustion products in two stages. In the first stage, during what is known as primary combustion, the hydrocarbon gas dissociates to form hydrogen gas and carbon monoxide as the first step in oxidation of the dissociated carbon. In the second stage, during what is known as secondary combustion, the hydrogen is oxidized to form water vapor, and the carbon monoxide is further oxidized to the final state of carbon dioxide. Each step, as shown subsequently for the example of the combustion of acetylene gas, C_2H_2 , is accompanied by the release of energy (known as enthalpy in thermodynamics and as the heat of combustion in chemistry) in the form of heat:



During primary combustion of the C_2H_2 contained in a pressurized cylinder (as a liquefied compressed gas) by oxygen contained in a pressurized cylinder (as a compressed gas), $\Delta H = 227 \text{ kJ/mol}$ of heat is released during the dissociation of the C_2H_2 at 15°C (50°F) to carbon and hydrogen, while the partial combustion (oxidation) of carbon to form carbon monoxide releases $\Delta H = 221 \text{ kJ/mol}$ of carbon. No combustion of the hydrogen takes place at this stage. During the second stage of combustion (i.e., secondary combustion), which occurs immediately after primary combustion in oxyfuel gas welding, the carbon monoxide and hydrogen react with oxygen from the surrounding air to release $\Delta H = 242 \text{ kJ/mol}$ of hydrogen and $\Delta H = 285 \text{ kJ/mol}$ of carbon monoxide, or $\Delta H = 570 \text{ kJ/mol}$ for the overall reaction (Eq 2). Considering the entire reaction, that is, primary and secondary combustion, approximately one-third of the total heat of combustion released comes from the primary combustion stage, and two-thirds comes from the secondary combustion stage.

When one looks at the combustion flame produced during oxyfuel gas welding, in general, and oxyacetylene welding, in particular, it appears as shown schematically in Fig. 3. There is a region right at the end of the gas torch where there is no flame, because combustion has not yet taken place. Beyond this colorless region is a distinct whitish-yellow to white inner cone in which primary combustion has taken place by the pressurized oxygen having been supplied to the pressurized fuel gas and the mixture having been ignited. Outside this inner cone is a blue to bluish-white outer flame in which secondary combustion has taken place when the products of partial combustion from the primary combustion region mix with oxygen from the surrounding air to further combust/oxidize. While only one-third of the total heat produced by the full combustion process is released in the primary combustion region (i.e., $\Delta H = 448 \text{ kJ/mol}$ out of $\Delta H = 1260 \text{ kJ/mol}$ for oxyacetylene welding), this region is actually hotter (that is, at a higher temperature) than the outermost secondary combustion region. The reason for this is that the density of the energy in the primary region is greater because this region is constrained by the surrounding region of secondary combustion. It is consistently true of all energy sources that the intensity of the source (which correlates to its peak temperature) is directly related to the density of the energy in that source. A familiar example is the concentration of sunlight by a magnifying glass to produce very high temperatures in the focused spot. For maximum heating,

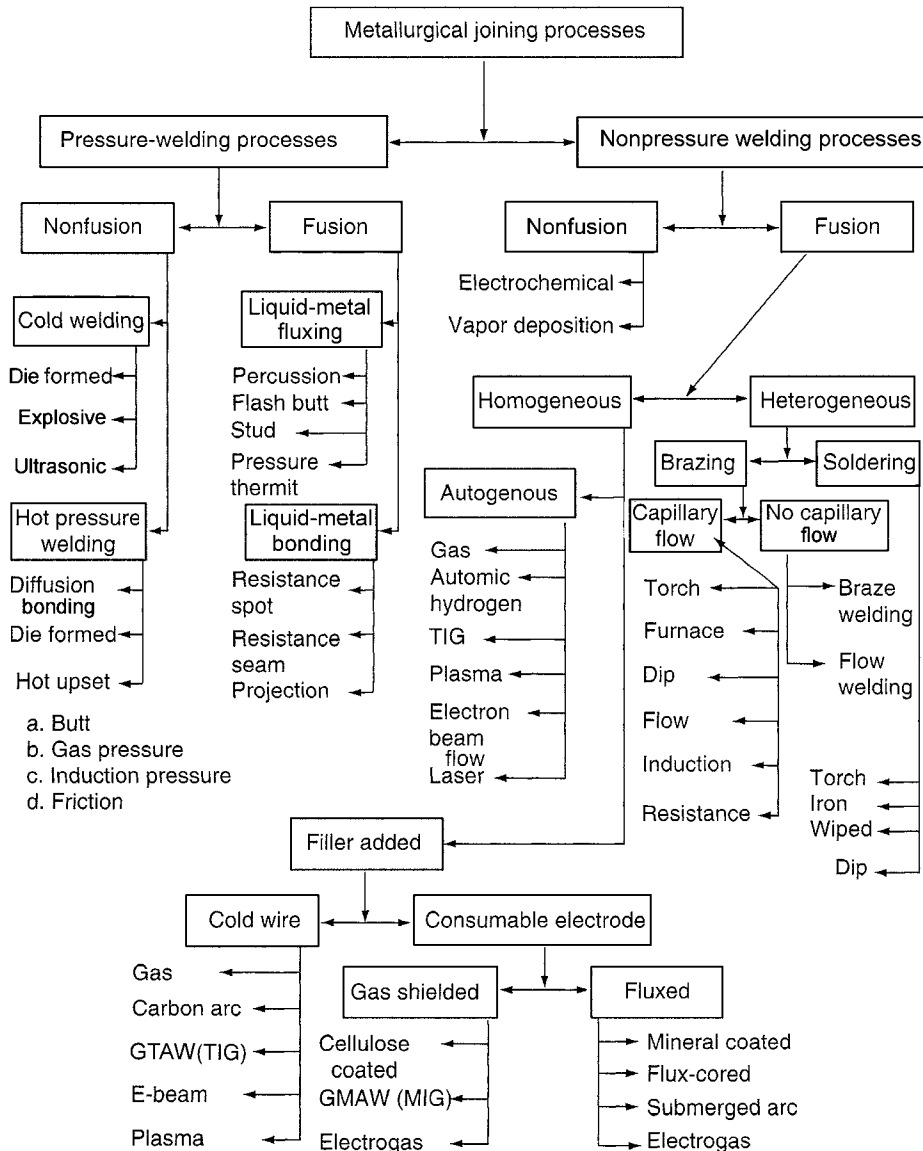


Fig. 2 Schematic representation of the overall taxonomy of welding processes. GTAW, gas tungsten arc welding; GMAW, gas metal arc welding; TIG, tungsten inert gas; MIG, metal inert gas. Source: Ref 2

whether for welding or for cutting, the tip of the inner cone should be played on the workpiece. It is possible to change the chemical nature and temperature of the flame in oxyfuel gas welding by adjusting the relative proportions (on a molar or volume basis) of oxygen and fuel gas being supplied through the torch (Fig. 4). When the ratio of fuel gas (in the case discussed previously, acetylene) to oxygen is balanced according to the chemical reaction in Eq 1, the flame is chemically neutral, that is, with neither a tendency to cause oxidation or reduction at the surface of the metal being heated/welded. This is the way an oxyfuel gas flame should be adjusted for most situations. If excess oxygen is supplied, the flame becomes oxidizing to the metal being heated/welded, and also hotter. This is the way an oxyfuel gas

flame should be adjusted either to burn off hydrocarbon contaminants (e.g., oil or grease) or to weld alloys in which one of the components has a high vapor pressure and is thus volatile and prone to loss during welding, or to cut metals. A prime example in welding is the risk for loss of zinc from brasses (i.e., copper-zinc alloys). If excess fuel gas (here, acetylene) is supplied, the flame becomes reducing to the metal being heated/welded, removing some oxides or tarnish layers to provide atomically clean metal. This is the way an oxyfuel gas flame should be adjusted for heating/welding metals or alloys that oxidize easily, such as aluminum alloys, magnesium alloys, or stainless steels (in which an ever-present corrosion-preventing oxide of chromium forms at the surface).

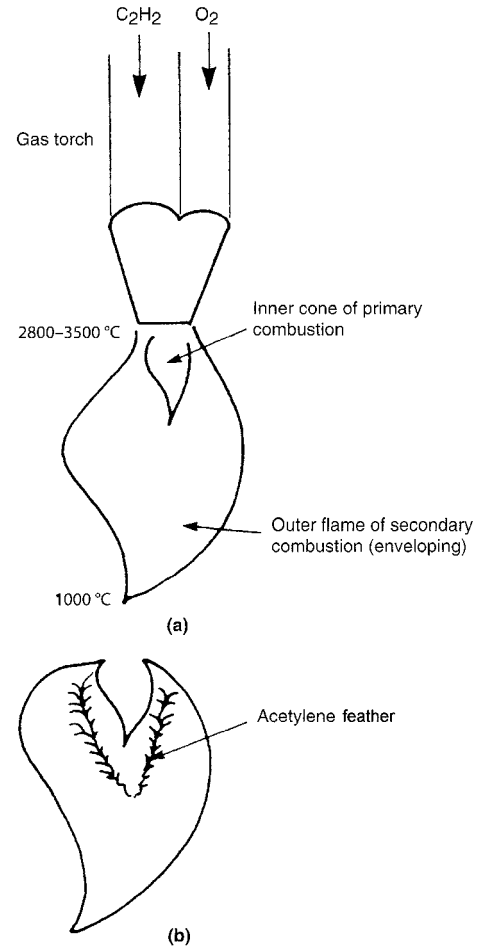


Fig. 3 Schematic illustration of a typical oxyfuel gas flame used in welding and cutting, here showing an oxyacetylene flame adjusted to be (a) neutral and (b) reducing. The primary and secondary regions of combustion are shown in (a), while the acetylene “feather” characteristic of a reducing flame is shown in (b). Source: Ref 2

To ignite the flame in oxyfuel gas welding, the fuel gas only should be turned on and ignited to produce a yellow, sooty flame. Oxygen should then be introduced by slowly opening the valve to the oxygen supply. The flame will become progressively less yellow and sooty and more blue to bluish-white and cleaner as more and more oxygen is mixed in. To turn off the flame, the fuel gas should be turned off first.

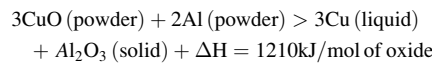
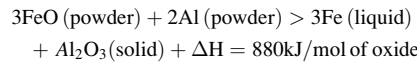
The neutral condition in an oxyacetylene flame, for example, can be found by turning the oxygen flow rate down until small bright-blue flecks (from unburned acetylene), known as acetylene feathers, appear around the inner cone. With excess acetylene, the flame is chemically reducing. By bringing the oxygen up to just make the acetylene feathers disappear, the flame is made chemically neutral. By increasing the oxygen flow rate above the level for a neutral flame, a chemically oxidizing flame is produced.

Oxyfuel gas welding offers easy portability but limited heating capacity in terms of peak temperatures attainable in the flame and thus limited ability to melt higher-melting-point metals and alloys. The process is used for heating, cutting, piecing, gouging, flame straightening or shaping, as well as welding or brazing metals. Table 1 lists the flame temperatures and other key features of various oxyfuel gas welding and allied processes.

The second way in which chemical reactions can be used to produce heat for welding or brazing is best known as thermit welding but which actually includes a wide variety of so-called aluminothermic reactions and, more recently, a variety of similar highly exothermic chemical reactions known as combustion synthesis reactions. What these have in common is that they all employ a highly exothermic chemical reaction between mixtures of finely divided (i.e., powdered or particulate) metals

(at least one of which is active or reactive), active metals and less-active-metal oxides, active metals and graphite, or active metals and less-active-metal nonoxide compounds (e.g., carbides, nitrides, silicon dioxide, etc.).

The aluminothermic reactions, which are the basis for thermit welding, involve the reaction between finely divided pure aluminum and a less-active-metal oxide, commonly either oxides of iron or copper. The former are used to weld iron-base alloys (principally carbon steels) and the latter to weld copper-base alloys (principally pure copper). Two (of approximately five) reactions are:



The thermit (or aluminothermic) reaction is carried out as shown in Fig. 4, in which the molten metal reaction product, being fluid and dense, runs down to the bottom of the reaction vessel or crucible to flow into a prepared joint and around joint members to form a weld upon solidification. As shown, welds can be made in either horizontally or vertically arranged joint members. Thermit welding has been used historically to weld steel reinforcing bars, steel railroad track rails (end-to-end), and large-cross-section electrical connections.

More recently, a wide variety of exothermic reactions have been studied and employed for producing refractory compounds (e.g., oxides, carbides, nitrides, silicides, borides, etc.) and, by using such compounds to cause bonding, to cause joining (predominantly by an exothermic brazing process, because there is seldom any melting of the base material) of ceramics to one another or to metals. These are collectively known as combustion synthesis reactions but are also referred to as self-propagating high-temperature synthesis reactions. The generic process has potential both for joining and for applying surfacing layers.

Electric Arc Fusion Welding

Electrical energy can be applied in various ways to heat up a material. For workpieces that are electrical conductors, the workpiece can be made part of the electric circuit with an electric power supply. Once part of the electric circuit, either electric current can be passed to the conductive workpiece through an arc from an electrode to the workpiece across a gap in a gas, or the electric current can be passed directly through the workpiece as an integral part of the circuit. Processes that use the former approach are called arc welding processes, while those that use the latter approach are called resistance welding processes. Another way of using electrons to heat a workpiece (whether an electrical conductor or not) is with a beam of intense, high-density electrons. These three basic ways are shown schematically in Fig. 5. Arc welding and resistance welding are described in this section, while electron beam welding is described in the next section,

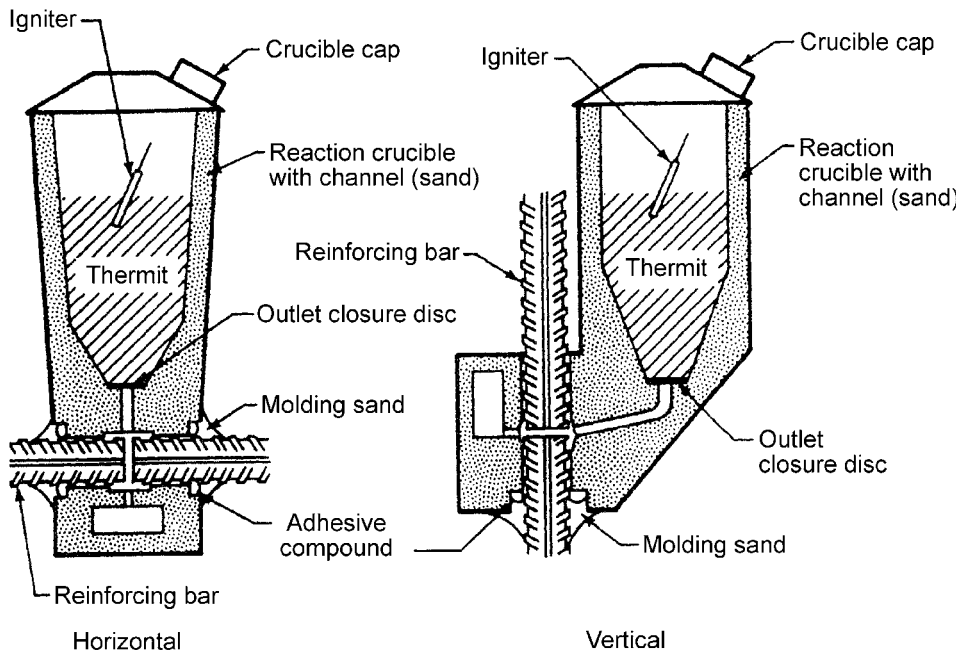


Fig. 4 Schematic illustrations showing the typical arrangements of the thermit process for welding concrete steel reinforcing bars, horizontally or vertically. Source: Ref 3

Table 1 Flame temperatures and other key features for various oxygen-fuel gas welding processes

Fuel gas	Formula	Specific gravity(a)	Volume-to-weight ratio(a)		Oxygen-to-fuel gas combustion ratio(b)	Flame temperature for oxygen(c)		Heat of combustion					
			Air = 1	m ³ /kg		ft ³ /lb	°C	°F	Primary		Secondary		Total
								MJ/m ³	Btu/ft ³	MJ/m ³	Btu/ft ³	MJ/m ³	Btu/ft ³
Acetylene	C ₂ H ₂	0.906	0.91	14.6	2.5	3087	5589	19	507	36	963	55	1470
Propane	C ₂ H ₆	1.52	0.54	8.7	5.0	2526	4579	10	255	94	2243	104	2498
Methylacetylene-propadiene (MPS)(d)	C ₃ H ₄	1.48	0.55	8.9	4.0	2927	5301	21	571	70	1889	91	2460
Propylene	C ₃ H ₆	1.48	0.55	8.9	4.5	2900	5250	16	438	73	1962	89	2400
Natural gas (methanol)	CH ₄	0.62	1.44	23.6	2.0	2538	4600	0.4	11	37	989	37	1000
Hydrogen	H ₂	0.07	11.77	188.7	0.5	2660	4820	12	325

(a) 15.6 °C (60 °F). (b) The volume units of oxygen required to completely burn a unit volume of fuel gas. A portion of the oxygen is obtained from the atmosphere. (c) The temperature of the neutral flame. (d) May contain significant amounts of saturated hydrocarbons. Source: Ref 4

“Directed-Energy Fusion Welding Processes,” along with laser beam welding.

Modes of Arc Welding

When electrons are forced to jump across a gap in a circuit made up of good (usually metal) electrical conductors, it does so in the form of an arc. The arc consists of negatively charged electrons moving through the gap between two electrodes at different electrical potentials, or voltages. One electrode (called the anode) is said to be positive with respect to the other,

while the electrode with the more negative electric potential is called the cathode. Electrons either are forced out of the cathode when it is heated (by thermal emission), or they are pulled from the cathode by the strong attractive force from the positive anode. A greater difference in the electrical potential between a cathode and an anode allows electrons to cross a larger gap between the two electrodes.

Electrons always move from negative to positive; however, in the long-established convention of a current, which is really the flow or flux of electrons from cathode to anode, the current flow is taken to occur from positive to

negative. When electrons flow across a gap in air or some other gaseous atmosphere, they can impact atoms within the air/gas gap and cause orbiting electrons to be ejected from those atoms. This ejection of electrons produces positive ions of the atoms in the air/gas gap. The resulting ions also move in the arc under the influence of the applied voltage (or potential difference), but toward the cathode. The net effect of an arc is the heating of the metal workpiece due to the impact of very fast-moving electrons and/or slower-moving ions (which have a much higher mass than electrons). Their kinetic energy is absorbed and converted to heat when the fast-moving electrons or slower-moving and heavier positive ions strike the workpiece surface.

Figure 6 schematically illustrates different modes of electric arc heating by either of two direct current polarities or by an alternating polarity. If the potential difference or voltage of the power supply is unchanging in polarity (i.e., the cathode remains the cathode and the anode remains the anode at all times that current is flowing), the electricity is said to be operating as direct current, or dc, mode. If the polarity is cycled back and forth, the electricity is said to be operating as alternating current, or ac.

With dc operation, the workpiece can be either positive relative to the electrode in the welding source, or it can be negative. The two modes of dc operation are typically referred to as follows:

- *Direct current straight polarity (DCSP)*: Arc heating when the workpiece is positive and the welding electrode is negative. This operating mode also is called dc electrode negative or dc-.
- *Direct current reverse polarity (DCRP)*: Arc heating when the workpiece is negative and the welding electrode is positive. This operating mode also is called dc electrode positive or dc+.

In ac operation, one-half of the voltage cycle operates as dc-/DCSP, while the other half operates as dc+/DCRP. In addition, it is possible to apply a small dc bias voltage on top of an ac voltage, thus shifting the half-cycles of the ac wave from being balanced between dc-/DCSP and dc+/DCRP. This accentuation of one or the other to affect the welding is described as DCSP versus DCRP. This ac arc welding mode is known as wave balance control.

The effect of these different operating modes on the shape of the resulting molten weld pool (shown in profile as a section across a weld produced by a moving heat source) is also shown in Fig. 6, as follows:

- Deep welds, with 70% of the heat of the arc found in the workpiece for the DCSP mode (left)
- In the DCRP mode (center), shallow welds and strong cleaning action at the workpiece

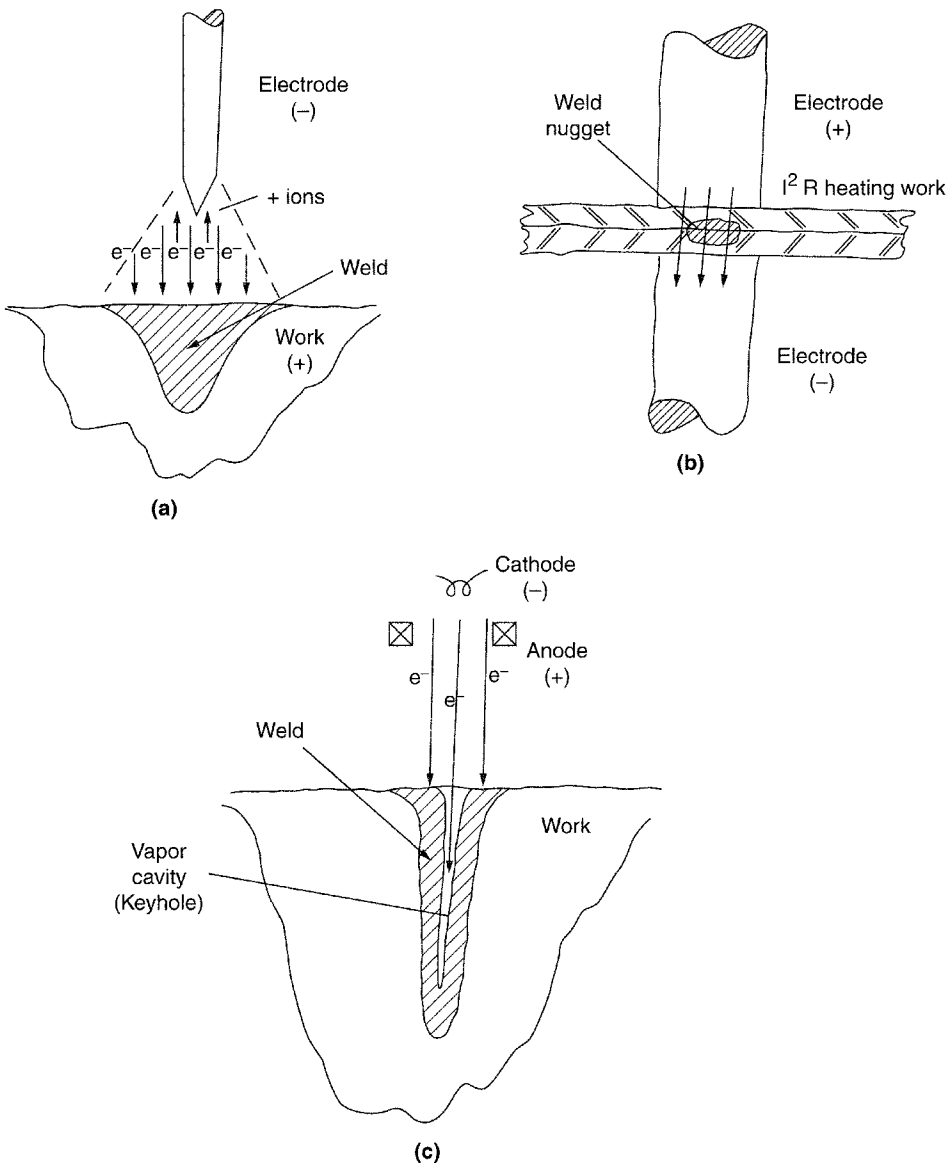


Fig. 5 Schematic illustrations of the three basic ways in which electrical energy, supplied by a power source, can be used to heat and fusion weld a metal, including (a) use of the kinetic energy of electrons and positive ions in an arc to bombard the workpiece and produce heat (in arc welding), (b) use of the resistance of a workpiece to the passage of current to produce Joule heating (in resistance welding), and (c) use of an intense, dense beam of either electrons or photons to bombard a workpiece and produce heat when the kinetic energy of the particles in the beam are stopped by the atoms in the workpiece material (in electron beam and laser beam welding, respectively)

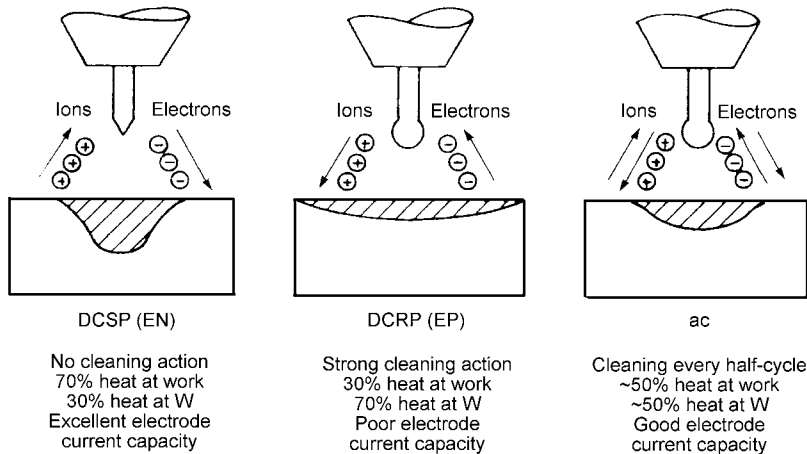


Fig. 6 Schematic illustration summarizing the characteristics of the various operating modes for gas tungsten arc welding. DCSP (EN), direct current straight polarity (electrode negative); DCRP (EP), direct current reverse polarity (electrode positive); ac, alternating current. Source: Ref 2

surface occurs from a scrubbing action by bombarding heavy ions, with 70% of the heat of the arc found in the welding electrode (center)

- In the ac mode (right), an intermediate profile is produced with some surface cleaning and fairly balanced distribution of heat from the arc in the welding electrode and in the workpiece.

Different arc welding processes, as described next, tend to run under different preferred operating modes.

Arc Welding Processes

The two broad subtypes of arc welding processes are those that employ nonconsumable electrodes and those that employ consumable electrodes. Non-consumable electrodes produce the arc and melt the base metal(s) of the workpiece(s) either without using a filler or by adding a filler wire to the molten weld pool. Consumable electrodes produce an arc and provide filler metal to the joint as they are consumed. Major modern types of nonconsumable electrode arc welding include:

- Gas tungsten arc welding (GTAW)
- Plasma arc welding (PAW)
- Stud arc or simply stud welding (SW)
- Magnetically-impelled arc butt welding (MIAB)

Major modern types of consumable electrode arc welding processes include:

- Gas metal arc welding (GMAW)
- Shielded metal arc welding (SMAW)
- Flux-cored arc welding (FCAW)
- Submerged arc welding (SAW)
- Electrode gas welding (EGW)
- Electroslag welding (ESW)

Only GTAW, PAW, GMAW, SMAW, FCAW, and SAW are described here. The

reader interested in other processes or desiring more details on the processes covered here should refer to the references listed at the end of this article or to other articles in the *ASM Handbook* series (as noted for each process described in the following).

Nonconsumable Electrode Arc Welding.

Gas tungsten arc welding and plasma arc welding are examples of processes that employ non-consumable electrodes. Both use a permanent electrode made from tungsten, the highest-melting-point metal (at 3410 °C, or 6170 °F), contained within the body of a torch designed to provide a protective shield of inert gas of argon or helium or a mixture of the two.

Electric current is delivered to the tungsten electrode through a cable by a copper contact tube. In GTAW, an arc is struck between the tungsten electrode and the workpiece, operating in either DCSP, DCRP, or ac. The heat produced melts the base metal in the workpiece and causes it to flow together with any other abutting and melted workpiece. Upon solidification, a weld is produced by this filler-free, autogenous process. Filler can be added in the form of a solid wire that is dipped into the molten weld pool as welding is taking place.

The inert shielding gas protects the tungsten electrode from oxidizing and, simultaneously, protects the molten weld pool and subsequent hot but rapidly cooling weld from undesirable oxidation. In plasma arc welding, the torch consists of an inner and an outer body. The inner body is made positive relative to the tungsten electrode so that an arc is established across the gap through which some argon is flowing. When the argon is heated and ionized, it expands greatly and, as a result of the increased pressure in this nozzle, produces an extremely hot and dense plasma or constricted arc. The plasma heats the workpiece to cause melting and produce a weld. More inert argon from the outer body of the torch provides shielding to the weld.

Figure 7 compares GTAW and PAW in schematic illustrations. Compared to GTAW, PAW produces deeper-penetrating welds, can operate at faster welding speeds, and is cleaner because of both the double-shielding and by preventing accidental touching of the tip of the tungsten electrode to the workpiece to cause contamination by tungsten. While GTAW can be operated in DCSP, DCRP, or ac modes, great care must be taken to prevent overheating and melting at the tip of the tungsten electrode by the heat being concentrated there in the DCRP mode. Plasma arc welding is operated almost exclusively in the DCSP mode. For more details, see the articles “Gas Tungsten Arc Welding” and “Plasma Arc Welding” in this Volume.

Consumable Electrode Arc Welding Processes. A gas-shielded cousin of GTAW is GMAW, in which a continuous solid-wire welding electrode is intended to be consumed to become filler metal for the weld. The process is operated in DCRP to take advantage of the concentration of heat at the tip of the welding wire electrode. As the wire melts, the molten metal transfers to the joint to contribute to the weld. Various inert or near-inert gases are used with GMAW, including argon, N₂, CO₂, and various combinations of these and, possibly small amounts of H₂ or even O₂ (1 to 2 vol%). The goal is to exclude the high percentages of N₂ and O₂ that comprise air and that lead to porosity and embrittlement. The advantage of GMAW is much higher deposition rates for welding, reaching ~5 kg (10+ lb) per hour or more.

Like all consumable electrode arc welding processes, GMAW can be operated to cause the molten metal produced at the tip of the consumable electrode to transfer to the workpiece by any of several modes, including globular, spray, and short-circuiting or dip transfer. Each has relative advantages and disadvantages (see the article “Gas Metal Arc Welding” in this Volume for more details).

The next two, very popular, forms of consumable electrode arc welding do not employ an inert shielding gas from a compressed gas source (i.e., a pressurized cylinder). Rather, they generate their own relatively protective (but not inert) shielding gas through the thermal decomposition of certain mineral ingredients contained in the fluxes found as either coatings on a fixed-length core wire (in SMAW) or within the core of a continuous tubular wire (in FCAW). In addition to the generation of a shielding gas, the flux coating on SMAW electrodes and the flux core in FCAW wires also can:

- Provide a supply of ions and electrons to facilitate arc initiation and prevent unwanted arc extinction
- Produce a molten flux that both metallurgically refines the molten metal in the weld pool and covers the weld pool and the newly formed weld to prevent unwanted oxidation
- Allow alloying additions to the core wire to adjust the composition of the deposited filler

and, occasionally, add iron powder to increase the deposition rate of iron-base fillers

Figure 8 compares the FCAW (Fig. 8a) and SMAW (Fig. 8b) processes in schematic illustrations. Both processes tend to be operated in the DCRP mode to take advantage of the arc heat being concentrated at the tip of the electrode to be consumed, but at least SMAW can be operated in DCRP or ac for some electrode types (or formulations). Because FCAW employs a continuous wire, welding productivity tends to be higher, as does the effectiveness

of shielding out-of-doors (because the shielding gas is generated at the core of the arc rather than near its surface).

The remaining major types of consumable electrode arc welding processes are intended for applications requiring very heavy metal deposition to weld thick sections or apply heavy overlays. These include SAW, EGW, and ESW. All tend to operate in DCRP using very high currents (often 1000+ A), very large-diameter filler wires (or multiple wires or even strip), and are mechanized rather than performed manually.

Figures 9 through 11 schematically illustrate SAW, EGW, and ESW, respectively. In SAW, a dry granular flux is used to cover the arc, hence the name submerged arc. Shielding comes from the protective molten flux and subsequent glasslike slag cover that forms on the weld pool and solidifying weld, respectively. Electro gas welding uses an inert gas for shielding, while ESW uses a molten slag produced by I^2R joule heating as current and molten droplets move through the molten slag layer, extinguishing the arc in the process. Submerged arc welding is restricted to welding in a horizontal plane, while EGW and ESW can be used out of position in a vertical plane as well.

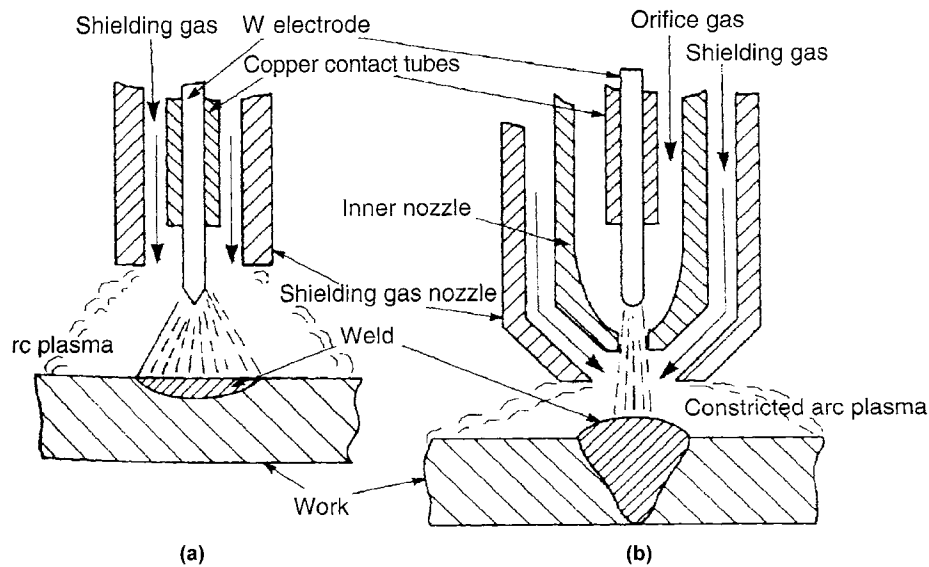


Fig. 7 Schematic illustration comparing (a) gas tungsten arc welding and (b) plasma arc welding processes. Source: Ref 2

Resistance Welding Processes

When electric currents flow through conductive materials (such as metals or alloys), there is some inherent resistance to the free flow of electrons through the conductor. The amount of resistance (R) is proportional to the inherent resistivity (ρ) of the material and the length (L) of the conductor, such that $R = \rho \times L/A$, where A is the cross-sectional area of the conductor. Electrical resistance is thus lowered when conductor cross section is increased.

The resistivity (ρ) of a material is a basic physical property, of which the inverse (or reciprocal) is the material electrical conductivity, designated by σ . Resistivity of a material depends on a number of factors, such as temperature, alloy content, and/or the number of crystal defects in the alloys. This can be understood by the general nature of a conductor. The atoms in the conductor vibrate at very high

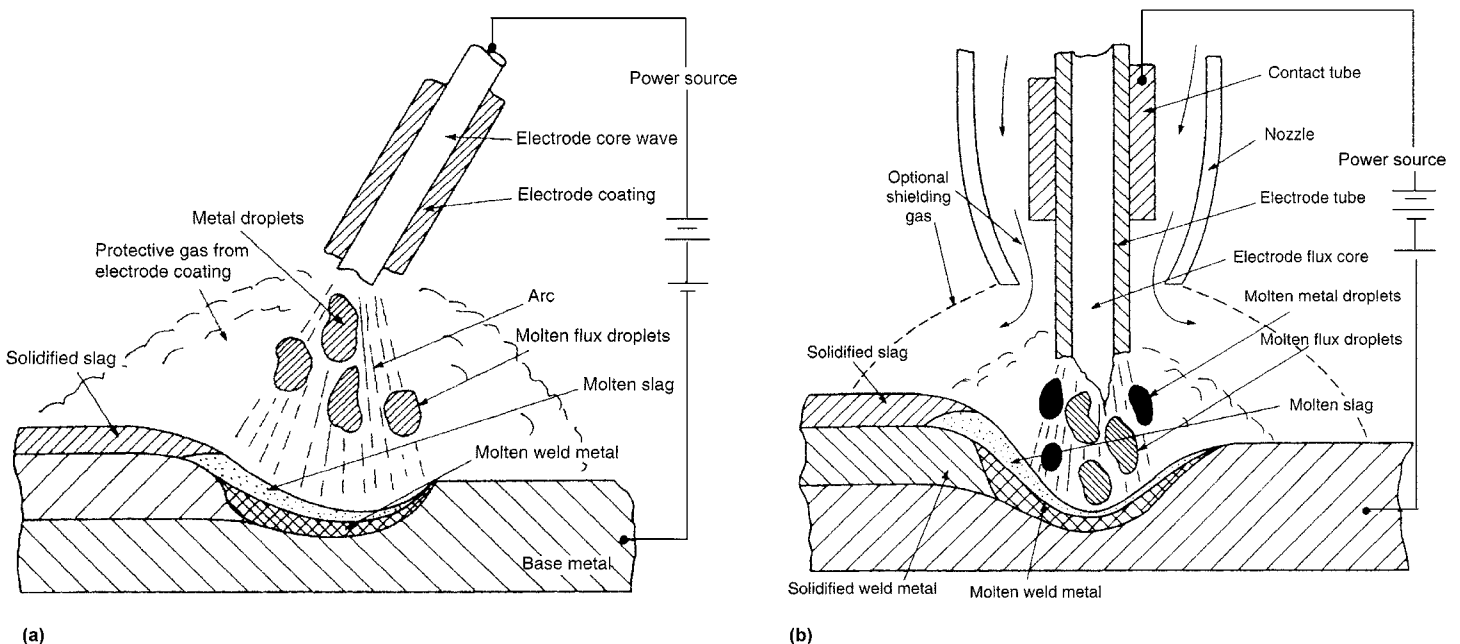


Fig. 8 Schematic illustration comparing (a) shielded metal arc welding and (b) flux-cored arc welding processes. Source: Ref 2

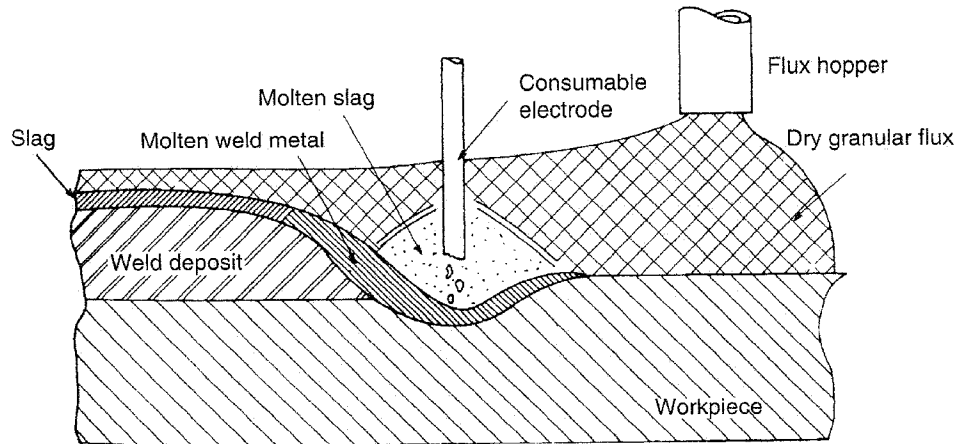


Fig. 9 Schematic illustration of the submerged arc welding process used for heavy deposition in plane (i.e., down-hand) only. Source: Ref 2

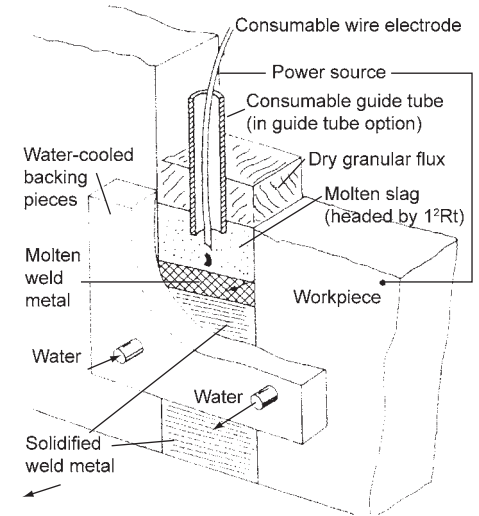


Fig. 11 Schematic illustration of the electroslag welding process used for heavy deposition welding in position or in a vertical plane using special tooling (as shown). Source: Ref 2

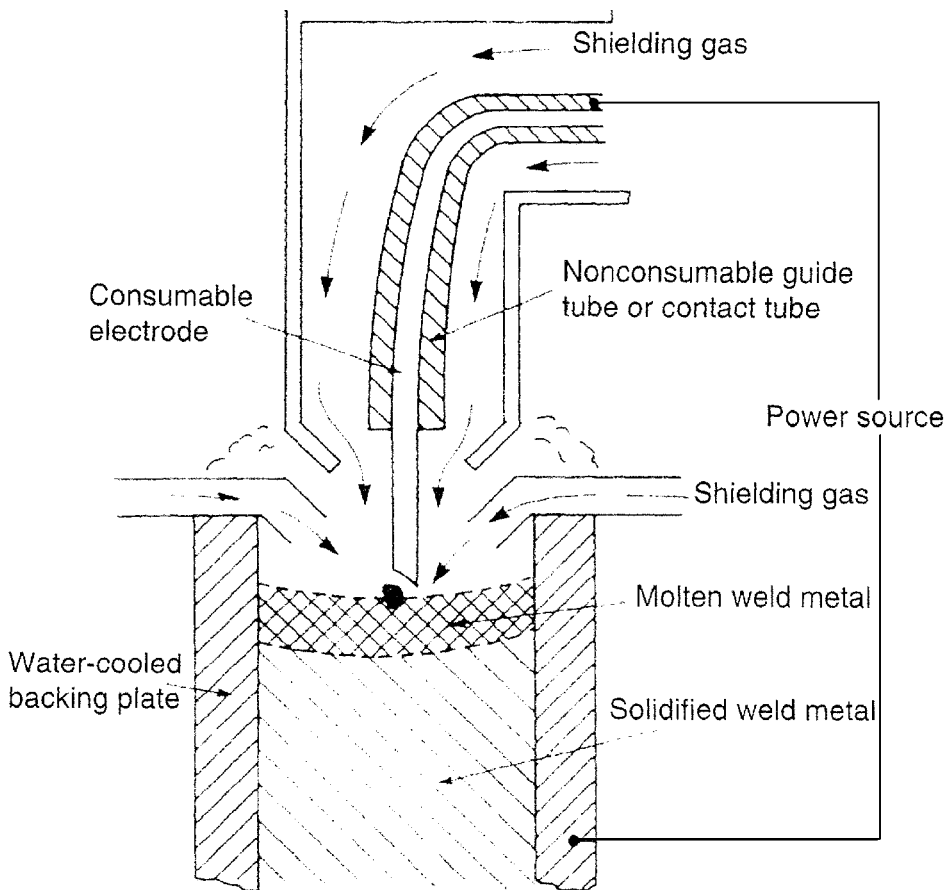


Fig. 10 Schematic illustration of the electrogas welding process used for heavy deposition welding in position or in a vertical plane using special tooling (as shown). Source: Ref 2

frequencies (albeit with very small amplitudes), and the crystal structures of metals also have imperfections in the arrangement of their atoms. These two factors have the effect of impeding electron flow, because the resulting perturbation of the electric field associated with the vibrating atoms and crystal imperfections of

the conductor gives rise to scattering of electrons. Thus, resistivity of a conductor becomes greater with an increase in temperature and/or with an increase in the number of crystal structure imperfections (caused by cold working, for example, or other factors). Conversely, there would be no impediment to the flow of free

electrons in a perfect crystal at absolute zero (-273°C), where the atoms do not vibrate. The resistance (R) of a physical circuit element also depends on the length of the element (L) and the cross-sectional area (A) through the relationship $R = \rho \times L/A$.

The result of current, I , flowing through a conductor with a resistance R is the production of heat Q given by I^2R in units of watts (with units of volt-amperes). This is known as joule heating and is the basis for resistance welding. It can essentially increase without limit if the current continues to flow such that the rate of I^2R heating exceeds the rate at which that heat can be dissipated by or from the conductor. For this reason, resistance welding processes are able to cause melting (or fusion) in any metal or alloy and can do so very quickly.

Figure 12 schematically illustrates one embodiment of resistance welding known as resistance spot welding (RSW). In it, sheets of metal are squeezed between copper electrodes, and a spot or nugget of molten metal is formed preferentially at the interface between the stacked sheets, where the contact resistance is the highest (so the I^2R heating is the greatest/fastest) and any cooling by heat extraction through the water-cooled electrodes is minimal.

Other methods of resistance welding include:

- *Resistance seam welding (RSEW)*: To produce overlapping spots to form a seam
- *Projection welding (PW)*: Where weld nuggets are localized at embossments or other raised portions (projections) of sheets being stacked
- *Percussion welding (PEW)*: Also known as capacitor-discharge welding, where a sudden discharge of electrical energy stored in a capacitor is used to produce a spot weld

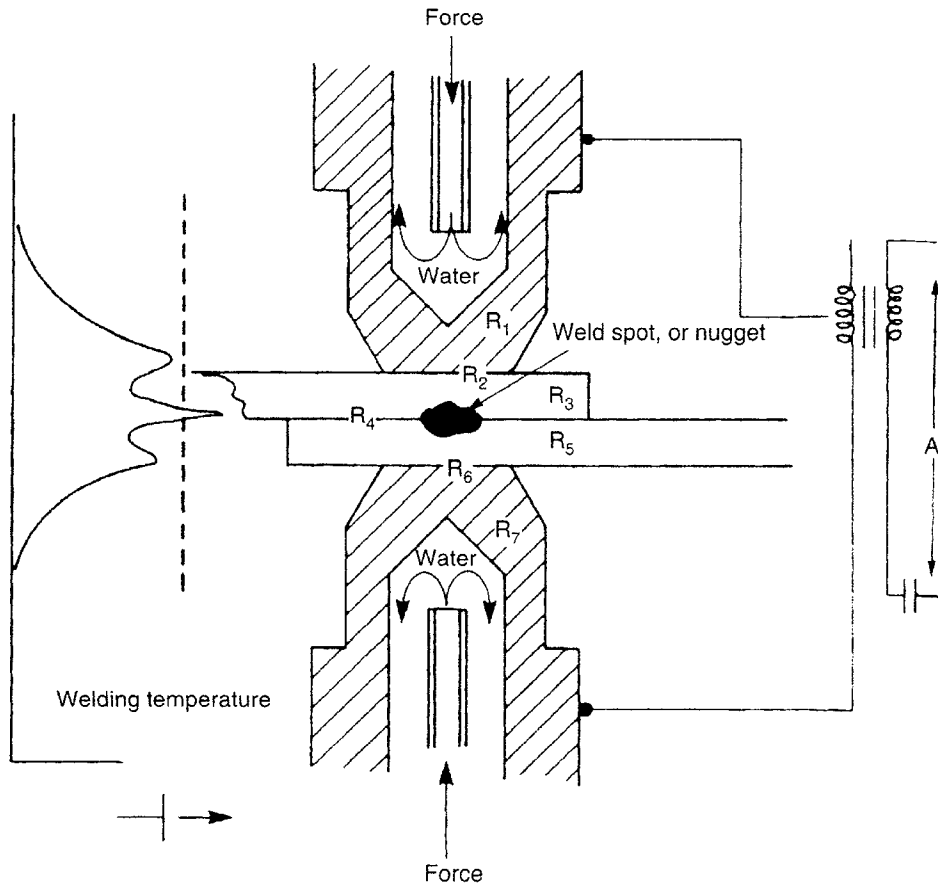


Fig. 12 Schematic illustration of the resistance spot welding process. Source: Ref 2

Another hybrid method involves welds to be formed when two parts are slowly brought into contact to first arc (across initial points of contact) and then heat by Joule (I^2R) heating. The weld is fully formed when the two parts are rammed together using an upsetting force. Two of these, with subtle differences in the sequence of heating and upsetting, are called flash welding (FW) and upset welding (UW).

Schematic illustrations of the RSEW and the PW processes are shown in Fig. 13. Figure 14 schematically illustrates the FW process. What all resistance welding processes share in common are very limited joint configurations (being limited to lap joints for RSW and PW, and butt welds for RSEW, PEW, FW, and UW) and high heating and postweld cooling rates. The latter makes these processes attractive for welding alloys prone to degradation from exposure to high temperatures for too long, as tends to occur with the arc welding processes.

Directed-Energy Fusion Welding Processes

Beams of directed energy are another method of heating for fusion welding (so that a supply

of atoms in a liquid state fills the gaps between the surfaces of the materials being joined). A beam of very fast-moving particles impinges upon a material and can cause rapid and intense heating in the immediate vicinity of the point of impingement. Heating of the workpiece occurs when the kinetic energy of the particles in the beam is converted into the thermal energy of atoms in the workpiece. The rate of heating is, in fact, so rapid that the generated heat does not have a chance to conduct very far away. As a result, the temperature of the material at the point of impingement rises extraordinarily rapidly to the melting point and then beyond the melting point to the boiling or vaporization point. Once (or when) this occurs, and the material literally vaporizes in the path of the high-energy-density beam, a vapor cavity forms what is known as a keyhole. Surrounding this vapor cavity is an annular column of molten metal. The keyhole mode occurs when the energy density of the heating source exceeds approximately 10^{10} to 10^{13} W/m^2 . For energy densities below approximately 10^9 W/m^2 , heating occurs by what is known as the melt-in mode or conduction mode. Arc welding processes typically operate at 5×10^6 to 5×10^8 W/m^2 energy densities. The PAW process is capable of operating in either mode, depending

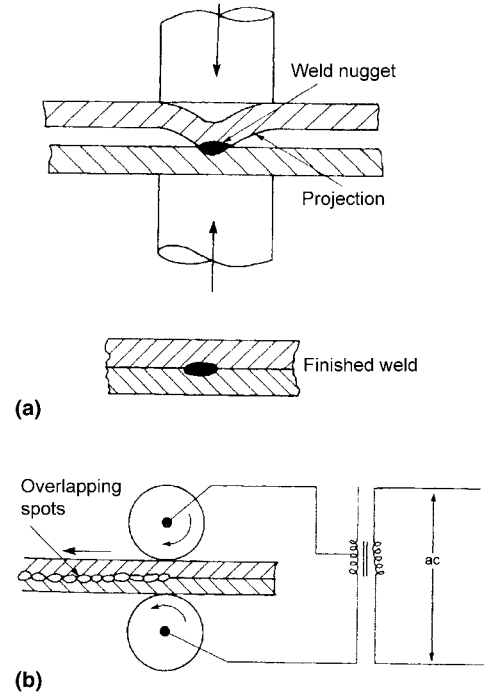


Fig. 13 Schematic illustration comparing the (a) resistance seam welding and (b) projection welding processes. Source: Ref 2

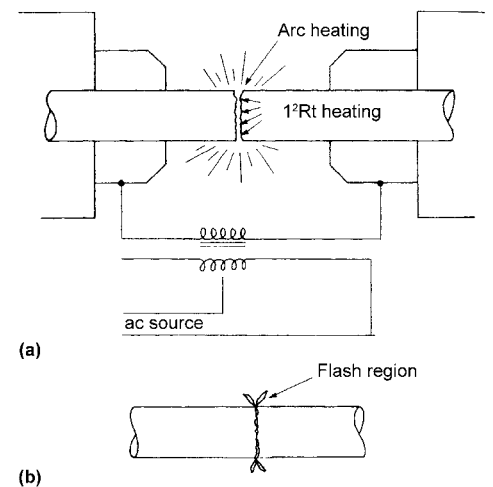


Fig. 14 Schematic illustration of (a) the flash welding process and (b) a typical as-welded flash weld. Source: Ref 2

on the current at which welding is being performed. Figure 15 schematically compares the melt-in (or conduction) and keyhole modes of welding for the PAW process, as an example.

As the beam energy source moves along (at the welding speed), the molten material surrounding the vapor cavity flows backward to the rear of the weld pool, links up by surface-tension forces, and fills the gap that was momentarily created by the moving vapor cavity or keyhole. Welding with beams of high-energy particles results in:

22 / Fundamentals of Welding

- Welds with a high aspect ratio (i.e., very deep relative to its width)
- Welds with a narrow heat-affected zone (because heating outside the weld is limited to a very narrow region)
- Very high welding velocities or speeds
- Little or no distortion from shrinkage of molten metal to solid metal or from thermal contraction of heated base metal in the heat-affected zone

The two methods of high-energy-density beam welding processes (or what are sometimes referred to as radiant energy beam welding processes) are electron-beam welding (EBW) and laser-beam welding (LBW) (Fig. 16). The former uses a dense beam of very fast-moving electrons thermally emitted from a cathode and accelerated over a potential of tens to hundreds of thousands of voltage, while the latter uses a dense beam of photons moving at the speed of light. To prevent the electrons from colliding with atoms or molecules in the atmosphere (and thus being scattered), the EBW method is almost always performed in a vacuum (typically 10^{-3} to 10^{-5} atm pressure). The LBW method can be performed in vacuum but is usually performed in an inert gas atmosphere, since photons are not scattered by atoms to any significant degree.

Electron beam welding is a high-energy-density fusion process that is accomplished by bombarding the joint to be welded with an intense (strongly focused) beam of electrons that have been accelerated up to velocities 0.3 to 0.7 times the speed of light at 25 to 200 kV, respectively. The instantaneous conversion of the kinetic energy of these electrons into thermal energy as they impact and penetrate into the workpiece on which they are impinging causes the weld-seam interface surfaces to melt and produces the weld-joint coalescence desired. Electron beam is applicable to any metal that can be arc welded; weld quality in most metals is equal to or superior to that produced by GTAW. Electron beam welding can also be used to weld some materials that cannot be welded by GTAW, such as certain ceramics.

Because the total kinetic energy of the electrons can be concentrated onto a small area on the workpiece, power densities as high as 10^8 W/cm² (10^7 W/in.²) can be obtained. That is higher than is possible with any other known continuous beam, including laser beams. The high-power density plus the extremely small intrinsic penetration of electrons in a solid workpiece results in almost instantaneous local melting and vaporization of the workpiece material. That characteristic distinguishes EBW from other welding methods in which the rate of melting is limited by thermal conduction.

As noted, one of the prime advantages of EBW is the ability to make welds that are deeper and narrower than arc welds, with a total heat input that is much lower than that required in arc welding. This ability to achieve a high

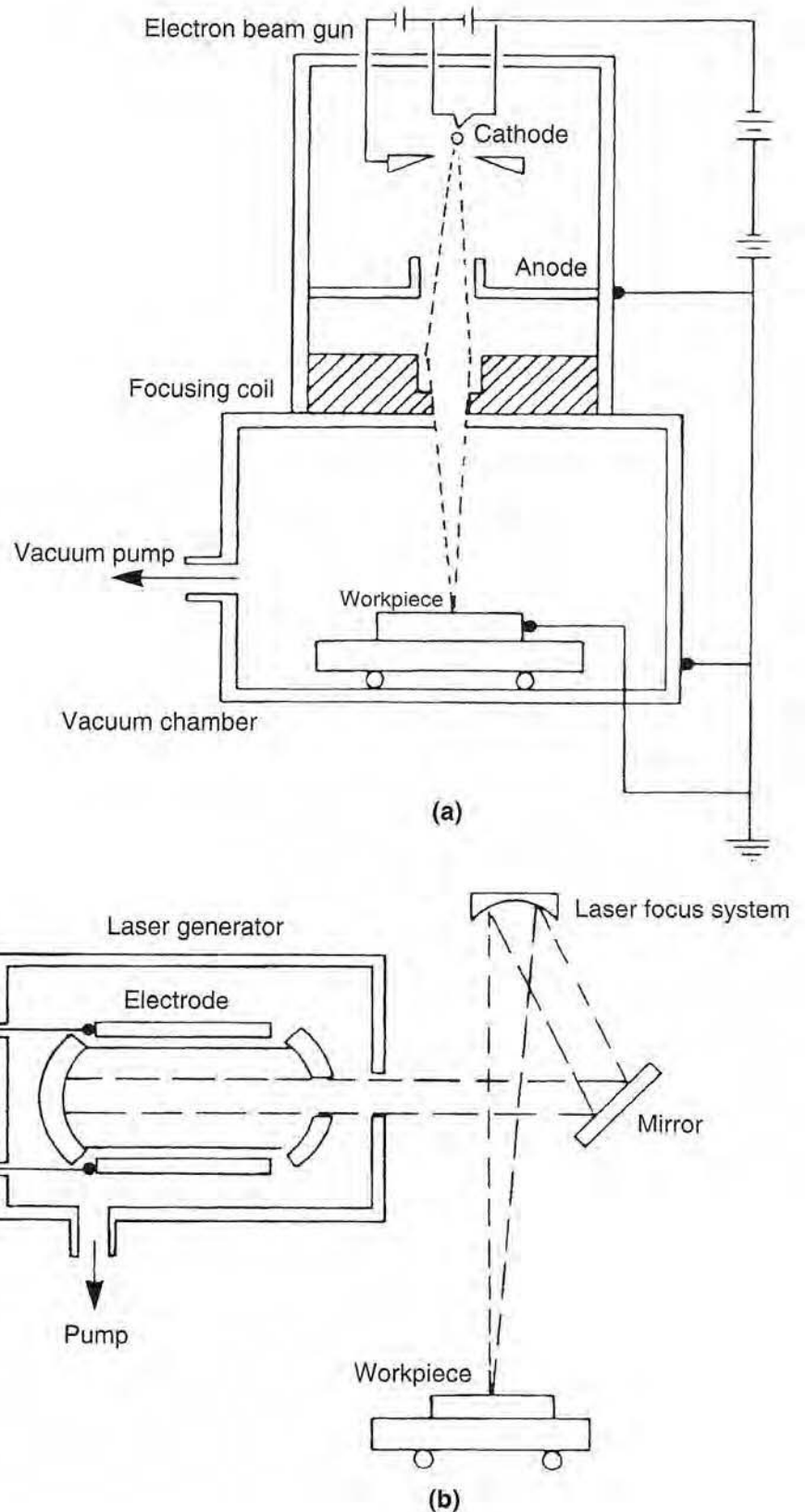


Fig. 15 Schematic illustration of the (a) melt-in or conduction versus (b) keyhole modes in high-energy-density welding processes, including plasma arc welding, electron beam welding, and laser beam welding.
Source: Ref 2

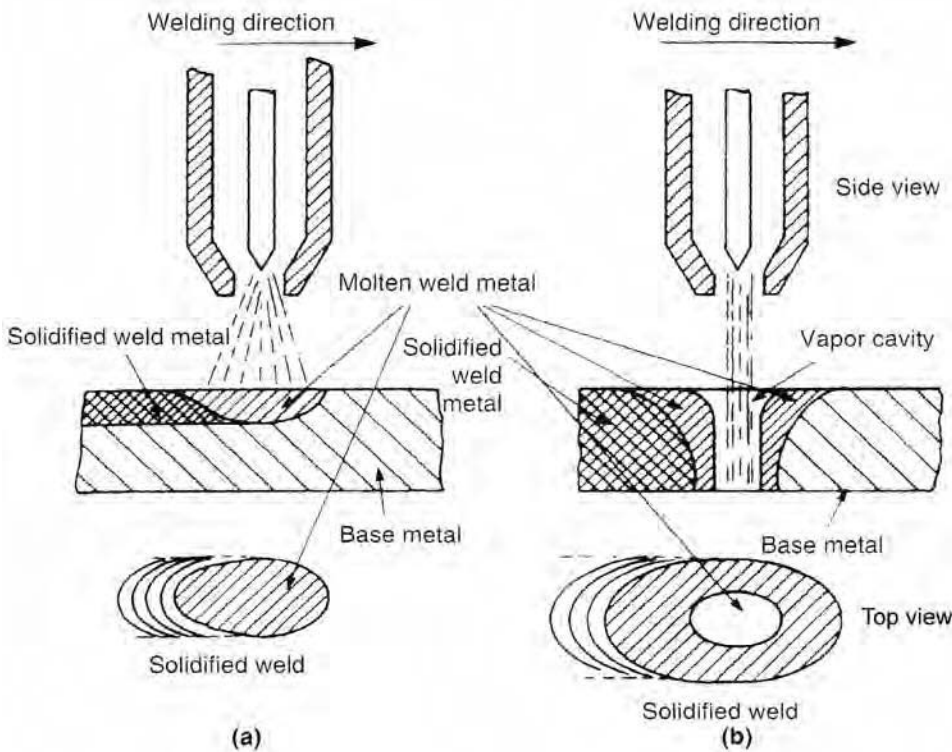


Fig. 16 Schematic illustrations of the (a) electron beam welding and (b) laser beam welding processes. The former is virtually always operated in a hard vacuum, while the latter can operate in air, in an inert gas atmosphere, or in vacuum. Source: Ref 2

weld depth-to-width ratio eliminates the need for multiple-pass welds, as is required in arc welding. The lower heat input results in a narrow workpiece heat-affected zone (HAZ) and noticeably fewer thermal effects on the workpiece.

In EBW, a high-purity vacuum environment can be used for welding, which results in freedom from impurities such as oxides and nitrides. The ability to employ higher weld speeds, due to the high melting rates associated with the concentrated heat source, reduces the time required to accomplish welding, thereby resulting in an increased productivity and higher energy efficiency for the process. Total energy conversion efficiency of EBW is approximately 65%, which is slightly higher than so-called conventional welding processes and much higher than other types of high-energy-density welding processes, such as LBW.

These EBW process can:

- Minimize distortion and shrinkage during welding
- Facilitate welding of most hardened or work-strengthened metals, frequently without significant deterioration of mechanical properties in the weld joint
- Facilitate welding in close proximity to heat-sensitive components or attachments
- Allow hermetic seal welding of evacuated enclosures while retaining a vacuum inside the component

- Permit welding of refractory metals, reactive metals, and combinations of many dissimilar metals that are not joinable by arc welding processes

The ability to project the electron beam a distance of over 510 mm (20 in.) under high-vacuum conditions, as well as the low end of medium-vacuum conditions, allows otherwise inaccessible welds to be completed.

Equipment costs for EBW generally are higher than those for conventional welding processes. The cost of joint preparation and tooling also is more than that encountered in arc welding processes, because the relatively small electron beam spot size that is used requires precise joint gap and position. The available vacuum chamber capacities are limited; workpiece size is limited, to some degree, by the size of the vacuum chamber employed. Consequently, the production rate (as well as unit cost) is affected by the need to pump down the chamber for each production load. However, when compared to other types of high-energy-density welding (such as LBW), production costs are not as high.

Laser beam welding uses a movable source of intense laser energy (with power densities on the order of 10^5 to 10^7 W/cm²). The word *laser* is the acronym for “light amplification by stimulated emission of radiation.” Lasers provide a source of very coherent radiation (such that radiating waves are highly

synchronized in terms of both frequency and phase), and the coherent nature of the laser beam allows it to be focused to a small spot, leading to high energy densities.

Laser systems had been used since the 1960s for making microwelds in electronic circuit boards, inside vacuum tubes, and in other specialized applications where conventional technology was unable to provide reliable joining. Until the 1970s, laser welding had been restricted to relatively thin materials and low speeds because of the limited continuous power available. High-power continuous-wave carbon dioxide (CO₂) and neodymium-doped yttrium-aluminum-garnet (Nd:YAG) lasers were subsequently developed with potential for deep-penetration welding.

The ability of the laser to generate a power density greater than 10^6 W/cm² (6×10^6 W/in.²) is a primary factor in establishing its potential for welding. Numerous experiments have shown that the laser permits precision (that is, high-quality) weld joints rivaled only by those made with an electron beam.

Laser welding offers the following advantages:

- Light is inertialess (hence, high processing speeds with very rapid stopping and starting become possible).
- Focused laser light provides high energy density.
- Laser welding can be used at room atmosphere.
- Difficult-to-weld materials (for example, titanium, quartz, etc.) can be joined.
- Workpieces do not need to be rigidly held.
- No electrode or filler materials are required.
- Narrow welds can be made.
- Precise welds (relative to position, diameter, and penetration) can be obtained. Welds with little or no contamination can be produced.
- The HAZ adjacent to the weld is very narrow.
- Intricate shapes can be cut or welded at high speed using automatically controlled light-deflection techniques.
- The laser beam can also be time shared.

Like EBW, precise part fit-up and alignment are much more critical in laser welding than in ordinary arc welding. The typical focal spot diameter for a laser beam ranges from 100 to 1000 μm (0.004 to 0.040 in.). Although laser welding equipment is much more expensive than power arc welding systems, laser welding can provide much higher throughput relative to conventional arc welding.

When the capital cost of LBW is compared to EBW, LBW can be a cost-effective option, because no vacuum enclosure is necessary for LBW. However, the penetration depth obtained in laser welding is less than that observed in EBW. For example, the maximum thickness of type 304 stainless steel plate that can be welded using a 77 kW CO₂ laser is on the order

of 50 mm (2 in.). In contrast, an EBW system can produce welds in type 304 stainless steel up to several inches in thickness, if EBW is done under a vacuum. The penetration depth of the EBW process extends only a relatively short distance under atmospheric pressure.

A laser beam, however, can be transmitted an appreciable distance through the atmosphere without serious attenuation or optical degradation because of its coherent nature. Laser beam welding thus offers an easily maneuverable, chemically clean, high-intensity, atmospheric welding process with narrow HAZ and subsequent low distortion. Peak penetration, p_{\max} , for LBW is defined by:

$$p_{\max} \propto P^{0.7}$$

where P is the power (in watts). In terms of weld width (w) and depth (d), both conduction-mode welding ($w/d \geq 1$) and deep-penetration welding ($w/d < 1$) can be obtained with lasers.

Nonfusion (Solid-State) Welding Processes

As described in the preceding article, "Overview of Material Joining Processes," the process of fusion (in which a supply of atoms, in the liquid state, fill the gaps between the limited number of points of intimate contact for the surfaces of real materials) is not the only way to achieve material continuity across a joint to produce a weld. The other option is to use pressure to deform these contacting high points and force more points into intimate contact. This is the basis for producing welds in the solid state in what is known and classified as nonfusion welding or solid-state welding.

The most common energy source for accomplishing nonfusion welding is mechanical and involves the application of pressure to cause either macroscopic or microscopic plastic deformation or to generate friction. Some solid-state welding methods that rely on pressure and macroscopic plastic deformation include:

- Cold welding
- Hot pressure welding
- Roll welding
- Explosion welding

Nonfusion methods using mechanical pressure also can rely on microscopic plastic deformation for solid-state welding. This includes most applications of explosion welding and some forms of diffusion welding (e.g., deformation diffusion welding).

Nonfusion welding processes also rely on energy sources other than mechanical pressure. For example, all forms of friction welding rely on frictional energy (although there is significant plastic deformation in some forms, such as friction stir welding and friction surfacing). Ultrasonic welding also involves the use of

frictional energy for solid-state welding. Nonfusion welding also can be accomplished without pressure of any significant degree by relying solely on solid-state diffusion, as in most forms of diffusion welding. Finally, there are some nonfusion methods that employ chemical reactions as a source of energy, often involving the formation of some reaction layer. These collectively fall under solid-state deposition welding.

Table 2 lists the eight major nonfusion welding processes along with variations within each. Table 3 lists the relative advantages and shortcomings of nonfusion welding processes, the two most notable being:

- Preservation of (or, at least, minimal disruption to) the original microstructure of the materials being joined
- Ability to join widely different materials, even between fundamental types (i.e., metals, ceramics, polymers) (because intermixing on a gross or macroscopic scale is not necessary)

Nonfusion pressure welding processes are based on the fact that most metals and alloys can almost always be plastically deformed; that is, they exhibit some degree of ductility. By applying pressure, the initial high points that come into intimate contact when joint elements are abutted are deformed, and more (less-high) points are brought into contact. Once high points come into contact, atoms move around (i.e., diffuse) in the solid state to attempt to increase the radius at the neck that is formed. The driving force of this mechanism is to reduce the area of free surface. Atoms at the surface of a material, whether solid or liquid, are at a higher energy than those in the interior, which are completely surrounded by other atoms making up the material.

This process can be continued for at least some time by applying greater and greater pressures, but it can absolutely be facilitated by applying some heat in addition to the deformation. By heating the base metals being pressure welded, three favorable things take place:

- The stress required to cause plastic deformation is lowered, as the strength of metals and alloys decreases with increasing temperature.
- The deforming metal is not able to strain harden, as thermal recovery processes take place.
- Atoms in each joint element migrate (i.e., diffuse) across the interface into the other joint element, tending to obliterate the interface.

When deformation is done below the recrystallization temperature of the material, the processes are known generically as cold welding. When it is done at temperatures above the recrystallization temperature, the processes are generically known as hot pressure welding. One form of pressure welding that can be performed cold or hot, or in between (i.e., warm), is roll welding. As shown schematically in

Table 2 List of the eight major nonfusion (solid-state) welding processes with variations within each

1. Cold welding	Press welding Forge welding Roll welding Toggle welding Hydrostatic impulse welding Shock-wave impulse welding
2. Hot pressure welding	Pressure gas welding Forge welding
3. Roll pressure welding	Hot, warm, or cold roll welding
4. Explosion welding	
5. Friction welding	Radial friction welding Orbital friction welding Rotational friction welding Direct-drive welding Inertia welding Angular (reciprocating) friction welding Linear (reciprocating) friction (or vibration) welding Friction stir welding Friction surfacing
6. Ultrasonic welding (USW)	Spot, ring, line, and seam USW Microminiature welding Microminiature thermosonic welding
7. Diffusion welding	Conventional diffusion welding Deformation diffusion welding Resistance diffusion welding Continuous seam diffusion welding Diffusion brazing Combined forming/welding Creep isostatic pressing Superplastic forming/diffusion bonding
8. Solid-state deposition welding	Electrochemical deposition Vapor deposition Chemical vapor deposition Chemical reaction bonding

Source: Ref 5

Fig. 17, this process squeezes two sheets of usually dissimilar metals or alloys together to form a clad bimetal. A well-known example is the roll welding of pure copper onto various stainless steels. Such bimetal feedstock is used for making high-end cookware with heat-dispersing bottoms as well as liners for electrochemical plating and processing tanks.

Diffusion Welding/Bonding. In diffusion welding, the only real need for pressure is to hold the parts to be welded in contact. The principal factor is the temperature at which the process is carried out, because atomic diffusion in the solid state increases exponentially with temperature. This means that the rate at which atoms move doubles with every 30 °C (50 °F) increase in temperature. It is easy to see that the rate of diffusion is increased many orders of magnitude (i.e., thousands to millions of

Table 3 Relative advantages and shortcomings of nonfusion welding processes

Advantages	Shortcomings
1. General absence of melting and thus solidification (so, structure is retained)	1. Stringent requirements for cleaning joint faying surfaces for some processes (e.g., CW, ROW, HPW, DFW, and solid-state deposition welding)
2. Low heat input (minimally disrupts microstructure)	2. Elaborate tooling is required for some processes (e.g., DFW)
3. Wide variety of process embodiments	3. Challenging inspection of joint quality
4. Applicable to many materials within a class as well as between classes (since there is little or no intermixing)	4. Repairing process-induced defects is difficult to impossible.
5. High joint efficiency is possible for many situations where the same cannot be said for fusion welding processes.	5. Processes require specialized equipment, are rarely portable, and almost always must be automated.

CW, cold welding; ROW, roll pressure welding; HPW, hot pressure welding; DFW, diffusion welding. Source: Ref 5

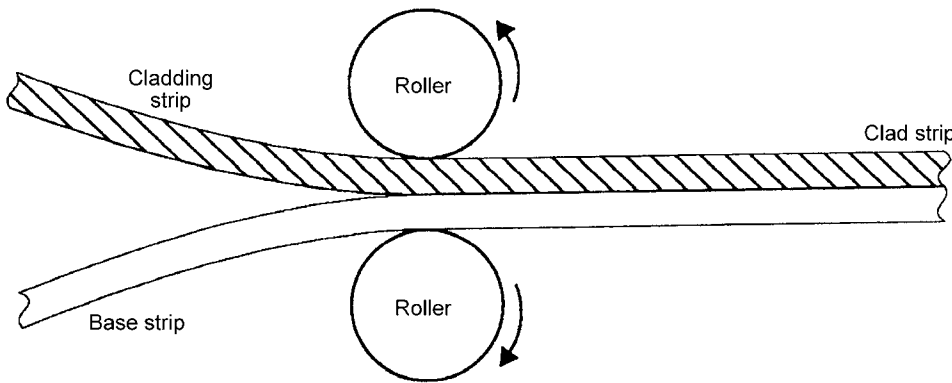


Fig. 17 Schematic illustration of the roll welding process producing clad metals or bimetal strips of sheet. Source: Ref 5

times faster). Once again, the driving force for diffusion to cause welding is the thermodynamic benefit of lowering the free surface area between materials.

Explosion Welding. An unusual nonfusion welding process is explosion welding. As shown schematically in Fig. 18, this process uses the detonation of high-velocity explosive charges to accelerate a prime component so that it slams into a base component. A weld is formed virtually instantaneously when microscopic surface asperities are deformed to bring virtually all of the atoms on both sides of the interface into intimate contact. As the prime component rushes toward the base component, the air between the two is expelled at supersonic velocities, which scrubs off any potentially weld-inhibiting tarnish layers. Examination of the metal in the vicinity of the newly formed weld (and prior interface) exhibits almost turbulent plastic flow over short dimensions in the thickness direction. The process tends to be used only for welding one thick, simply-shaped (often a plate) component to another.

Friction welding processes produce welds in essentially the same way as the just-described pressure welding processes. The main difference is that the plastic deformation occurs on a microscopic rather than a macroscopic scale. In fact, the origin of friction when one nonlubricated metal rubs over another is actually the occurrence of microwelding.

In all friction welding, it is necessary to move one part relative to the other while a squeezing force is being applied. This is what gives rise to the friction (as the force of friction is equal to the squeezing force times the coefficient of friction between the two materials/forms). The friction simultaneously generates heat at the interface and causes plastic deformation on a microscopic-length scale. Specific processes of friction welding (as shown in Table 2) include radial and orbital friction welding, direct-drive and inertia rotational friction welding, angular friction welding, and linear (reciprocating) or vibration friction welding.

Ultrasonic welding is also a friction welding process; however, the frequency of vibration between abutted parts is greater than 25 to 30 kHz (i.e., in the ultrasound region beyond human hearing), and the amplitudes of movement are very small. Ultrasonic welding has found its greatest usage in the welding of thermoplastics (i.e., those plastics that soften upon heating and stiffen upon cooling) under what is widely classified as plastics welding.

Solid-State Deposition Welding Processes. Finally, there are a few processes by which metals (as well as ceramics) can be joined in the solid state, that is, via a nonfusion process. While not often thought of as welding processes, they really are, because what is being accomplished is primary atomic bond formation by bringing atoms into intimate contact with

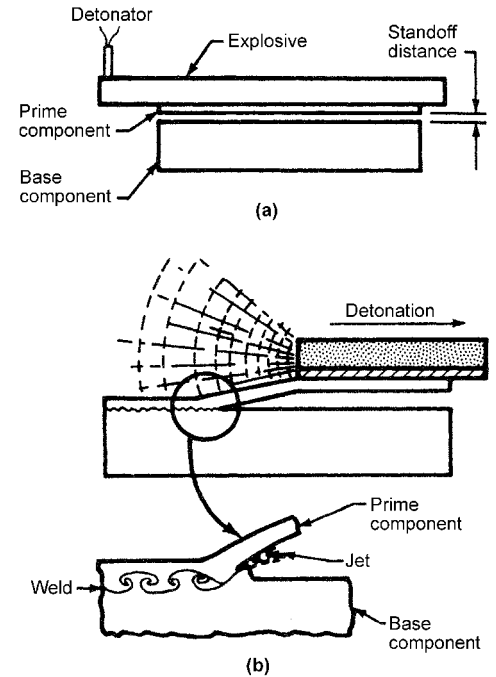


Fig. 18 Schematic illustration of the explosion welding process showing (a) the typical component arrangement and (b) the characteristic action between components during welding. Source: Ref 5

one another. Table 2 lists some of the more common examples of solid-state deposition welding processes.

Brazing and Soldering

Both brazing and soldering rely on primary bonding and on interdiffusion between joined materials to form the soundest joints, just as welding processes do. The difference is that neither brazing nor soldering involve any melting (or fusion) of the base materials. Rather, bond formation occurs between the ever-solid substrates and a molten filler metal with a melting point below that of the base materials. Specific embodiments within both brazing and soldering are remarkably similar in terms of the energy source used and the method of filler application, while they differ only in the melting point of fillers used. Table 4 lists a variety of the most common embodiments of brazing and soldering to allow comparisons to be made.

Brazing is a process for joining solid metals in close proximity (i.e., carefully gapped 0.025 to 0.125 mm, or 0.001 to 0.005 in.) by introducing a liquid metal that melts above 450 °C (840 °F). A sound brazed joint generally results when an appropriate filler alloy is selected, the parent metal surfaces are clean and remain clean during heating to the flow temperature of the brazing alloy, and a suitable joint design that allows capillary action is used.

Table 4 Comparison of the most common brazing and soldering process methods

	Brazing	Soldering
Chemical heat sources		
Gas torch	Torch brazing(a)	Torch soldering(a)
Gas furnace or oven	(Gas) furnace brazing	(Gas) oven soldering
Heat of condensation	Vapor-phase brazing	Condensation soldering
Exothermic reactions	Combustion synthesis(a)	Reaction soldering
Electrical heat sources		
Furnace or oven	(Electric) furnace brazing	(Electric) oven soldering
Molten salt	Chemical dip brazing	...
Molten metal	Molten metal dip brazing	Dip soldering
Induction	Induction brazing(a)	Induction soldering(a)
Infrared	Infrared brazing(a)	Infrared soldering(a)
White light	...	White light soldering(a)
Diffusion	Diffusion brazing	Reaction soldering
	Reaction brazing	
	Transient liquid-phase bonding	
Resistance	Resistance brazing	Resistance soldering
Laser	Laser beam brazing(a)	Laser beam soldering
Electron beam	Electron beam brazing(a)	...
Other	...	Iron soldering
		Wave soldering

(a) Localized vs. generalized heating

Strong, uniform, leakproof joints can be made rapidly, inexpensively, and even simultaneously. Joints that are inaccessible and parts that may not be joinable at all by other methods often can be joined by brazing. Complicated assemblies comprising thick and thin sections, odd shapes, and differing wrought and cast alloys can be turned into integral components by a single trip through a brazing furnace or a dip pot. Metal as thin as 0.01 mm (0.0004 in.) and as thick as 150 mm (6 in.) can be brazed.

The effective strength of a brazed joint is high. The nature of the interatomic (metallic) bond is such that even a simple joint, when properly designed and made, will have strength equal to or greater than that of the as-brazed parent metal.

The mere fact that brazing does not involve any substantial melting of the base metals may offer several advantages over other welding processes. It is generally possible to maintain closer assembly tolerances and to produce a cosmetically neater joint without costly secondary operations. Even more important, however, is that brazing makes it possible to join dissimilar metals (or metals to ceramics) that, because of metallurgical incompatibilities, cannot be joined by traditional fusion welding processes. (If the base metals do not have to be melted to be joined, it does not matter that they have widely different melting points. Therefore, steel can be brazed to copper as easily as to another steel.)

Brazing also generally produces less thermally induced distortion, or warping, than fusion welding. An entire part can be brought up to the same brazing temperature, thereby preventing the kind of localized heating that causes distortion in welding.

Finally, and perhaps most important to the manufacturing engineer, brazing readily lends itself to mass-production techniques. It is relatively easy to automate, because the application of heat does not have to be localized, as in fusion welding, and the application of filler metal is less critical. In fact, given the proper clearance conditions and heat, a brazed joint tends to "make itself" and is not dependent on operator skill, as are most fusion welding processes.

Automation is also simplified by the fact that there are many means of applying heat to the joint, including torches, furnaces, induction coils, electrical resistance, and dipping. Several joints in one assembly often can be produced in one multiple-braze operation during one heating cycle, further enhancing production automation.

Soldering is a joining process by which two substrates are bonded together using a filler metal (solder) with a liquidus temperature that does not exceed 450 °C (840 °F). The substrate materials remain solid during the bonding process. The solder is usually distributed between the properly fitted surfaces of the joint by capillary action.

The bond between solder and base metal is more than adhesion or mechanical attachment, although these do contribute to bond strength. Rather, the essential feature of the soldered joint is that a metallurgical bond is produced at the filler-metal/base-metal interface. The solder reacts with the base-metal surface and wets the metal by intermetallic compound formation. Upon solidification, the joint is held together by the same attraction, between adjacent atoms, that holds a piece of solid metal together. Even after the joint has completely solidified, diffusion between the base metal and the soldered joint continues for a while as the completed part cools. Mechanical properties of soldered joints therefore are generally related to, but not equivalent to, the mechanical properties of the soldering alloy.

Mass soldering by wave, drag, or dip machines has been a preferred method for making high-quality, reliable connections for many decades. Correctly controlled, soldering is one of the least expensive methods for fabricating electrical connections.

REFERENCES

1. R.L. O'Brien, Ed., *Jefferson's Welding Encyclopedia*, 18th ed., American Welding Society, Miami, FL, 1997, p 634
2. R.W. Messler, Jr., *Joining of Materials and Structures: From Pragmatic Process to Enabling Technology*, Butterworth-Heinemann/Elsevier, Burlington, MA, 2004, p 300, 301, 313, 315, 316, 320–324, 327–330
3. *Welding Processes*, Vol 2, *Welding Handbook*, 9th ed., American Welding Society, Miami, FL, 2004
4. R.L. O'Brien, Ed., *Welding Processes*, Vol 2, *Welding Handbook*, 8th ed., American Welding Society, 1991, p 354
5. R.W. Messler, Jr., *Principles of Welding: Processes, Physics, Chemistry and Metallurgy*, John Wiley & Sons, Inc., New York, NY, 1999, p 96, 97, 103, 104

SELECTED REFERENCES

- H.B. Cary and S.C. Helzer, *Modern Welding Technology*, 6th ed., Pearson Learning/Prentice-Hall, Upper Saddle River, NJ, 2005
- R.W. Messler, Jr., *Principles of Welding: Processes, Physics, Chemistry and Metallurgy*, John Wiley & Sons, New York, NY, 1999
- *Welding Processes*, Vol 2, *Welding Handbook*, 9th ed., American Welding Society, Miami, FL, 2004

Fundamentals of Fusion Welding

Welding Process Fundamentals	29	Transport Equations for Weld Fluid Flow	94
Energy-Source Intensity	29	Concluding Remarks	94
Characterization and Modeling of the Heat Source	35	Fundamentals of Weld Solidification	96
Simplified Modeling of the Heat Source	36	Microstructural Features in Fusion Welds	96
Arc Welding	36	Solidification Parameters	97
High-Energy-Density Welding	39	Nucleation Considerations in Fusion Welding	97
Resistance Spot Welding	40	Grain Structure of Fusion Welds	99
Nature and Behavior of Fluxes Used for Welding	43	Substructure Formation in Fusion Welds	100
Equilibrium Parameters	43	Rapid Solidification Considerations	111
Heat Flow in Fusion Welding	55	Dilution in Fusion Welding	115
Introduction	55	Introduction	115
Mathematical Formulations	57	Dilution and Fusion Zone Composition	115
Engineering Solutions and Empirical Correlation	58	Influence of Welding Parameters on Dilution	117
Parametric Effects	64	Influence of Dilution on Fusion-Zone Microstructure and Properties	119
Thermophysical Properties of Selected Engineering Materials	65	Solid-State Transformations in Weldments	122
Factors Influencing Heat Flow in Fusion Welding	67	Special Factors Affecting Transformation Behavior in a Weldment	122
Introduction	67	Heat-Affected Zone of a Single-Pass Weld	123
Analytical Solutions of the Thermal Field around Moving Point and Line Sources	68	Fusion Zone of a Single-Pass Weld	129
Numerical and Analytical Solutions of the Thermal Field in Complex Welding Operations	75	Heat-Affected Zone in Multipass Weldments	134
Acknowledgment	80	Fusion Zone in Multipass Weldments	137
Transfer of Heat and Mass to the Base Metal in Gas Metal Arc Welding	82	Weldments in Select Alloy Systems	137
Heat Transfer	83	Thermomechanical Effects of Fusion Welding	146
Mass Transfer	83	Formation of Residual Stress: Three-Bar Analogy	146
Procedure Development	85	Mathematical Formulations	147
Fluid Flow Phenomena during Welding	89	Residual Stress	149
Mass Transport in the Arc	89	Distortion	151
Gas Tungsten Arc Welding	89	Residual Stresses and Distortion	158
Deep-Penetration Electron Beam and Laser Welds	92	Formation of Residual Stresses and Distortion	158
Gas Metal Arc Welding	93	Techniques for Measuring Residual Stresses	159
Submerged Arc Welding	94	Magnitude and Distribution of Residual Stresses in Weldments	160
		Effects of Residual Stresses and Distortion on the Service Behavior of Welded Structures	162
		Thermal Treatments of Weldments	165

Welding Process Fundamentals*

Thomas W. Eagar and Aaron D. Mazzeo, Massachusetts Institute of Technology

WELDING AND JOINING processes are essential for the development of virtually every manufactured product. However, these processes often appear to consume greater fractions of the product cost and to create more of the production difficulties than may be expected. There are a number of reasons that explain this situation.

First, welding and joining are multifaceted, both in terms of process variations (such as fastening, adhesive bonding, soldering, brazing, arc welding, diffusion bonding, and resistance welding) and in the disciplines needed for problem solving (such as mechanics, materials science, physics, chemistry, and electronics). An engineer with unusually broad and deep training is required to bring these disciplines together and to apply them effectively to a variety of processes.

Second, welding or joining difficulties usually occur far into the manufacturing process, where the relative value of scrapped parts is high.

Third, a very large percentage of product failures occur at joints because they are usually located at the highest stress points of an assembly and are therefore the weakest parts of that assembly. Careful attention to weldment design and joining processes can produce great rewards in manufacturing economy and product reliability.

The purpose of this Section of the Volume is to discuss the fundamentals of fusion welding processes, with an emphasis on the underlying scientific principles.

Because there are many fusion welding processes, one of the greatest difficulties for the manufacturing engineer is to determine which process will produce acceptable properties at the lowest cost. There are no simple answers. Any change in the part geometry, material, value of the end product, or size of the production run, as well as the availability of joining equipment, can influence the choice of joining method. For small lots of complex parts, fastening may be preferable to welding,

whereas for long production runs, welds can be stronger and less expensive.

The perfect joint is indistinguishable from the material surrounding it. Although some processes, such as diffusion bonding, can achieve results that are very close to this ideal, they are either expensive or restricted to use with just a few materials. There is no universal process that performs adequately on all materials in all geometries. Nevertheless, virtually any material can be joined in some way, although joint properties equal to those of the bulk material cannot always be achieved.

The economics of joining a material may limit its usefulness. For example, aluminum is used extensively in aircraft manufacturing and can be joined by using adhesives or fasteners, or by welding. However, none of these processes has proven economical enough to allow the extensive replacement of steel by aluminum in the frames of nonluxury automobiles. An increased use of composites in aircrafts is limited by an inability to achieve adequate joint strength in the original product or to repair a product that has been in service.

It is essential that the manufacturing engineer work with the designer from the point of product conception to ensure that compatible materials, processes, and properties are selected for the final assembly. Often, the designer leaves the problem of joining the parts to the manufacturing engineer. This can cause an escalation in cost and a decrease in reliability. If the design has been planned carefully and the parts have been produced accurately, the joining process becomes much easier and cheaper, and both the quality and reliability of the product are enhanced.

Generally, any two solids will bond if their surfaces are brought into intimate contact. One factor that generally inhibits this contact is surface contamination. Any freshly produced surface exposed to the atmosphere will absorb oxygen, water vapor, carbon dioxide, and hydrocarbons very rapidly. If it is assumed that each molecule that hits the surface will be

absorbed, then the time-pressure value to produce a monolayer of contamination is approximately $0.001 \text{ Pa} \cdot \text{s}$ ($10^{-8} \text{ atm} \cdot \text{s}$). For example, at a pressure of 1 Pa (10^{-5} atm), the contamination time is 10^{-3} s , whereas at 0.1 MPa (1 atm), it is only $10 \times 10^{-9} \text{ s}$ (Ref 1).

In fusion welding, intimate interfacial contact is achieved by interposing a liquid of substantially similar composition as the base metal. If the surface contamination is soluble, then it is dissolved in the liquid. If it is insoluble, then it will float away from the liquid-solid interface.

Energy-Source Intensity

One distinguishing feature of all fusion welding processes is the intensity of the heat source used to create the molten condition. Virtually every concentrated heat source has been applied to the welding process. However, many of the characteristics of each type of heat source are determined by its intensity. For example, when considering a planar heat source diffusing into a very thick slab, the surface temperature will be a function of both the surface power density and the time.

Figure 1 shows how this temperature will vary on steel with power densities that range from 400 to 8000 W/cm^2 .

At the lower value, it takes less than a minute to melt the surface. If that heat source were a point on the flat surface, as shown in Fig. 2, then the heat flow would be divergent and not melt the steel. This shows the dramatic effect of divergent heat flow and the need for higher heat intensities when the heat source is a laser, an arc, or a point source compared to a planar heat source as developed in friction welding. Rather, the solid metal would be able to conduct away the heat as fast as it was being introduced. It is generally found that point heat-source power densities of approximately 1000 W/cm^2 are necessary to melt most metals.

* Updated and revised from T.W. Eagar, Energy Sources Used for Fusion Welding, *Welding, Brazing, and Soldering*, Vol 6, *ASM Handbook*, ASM International, 1993.

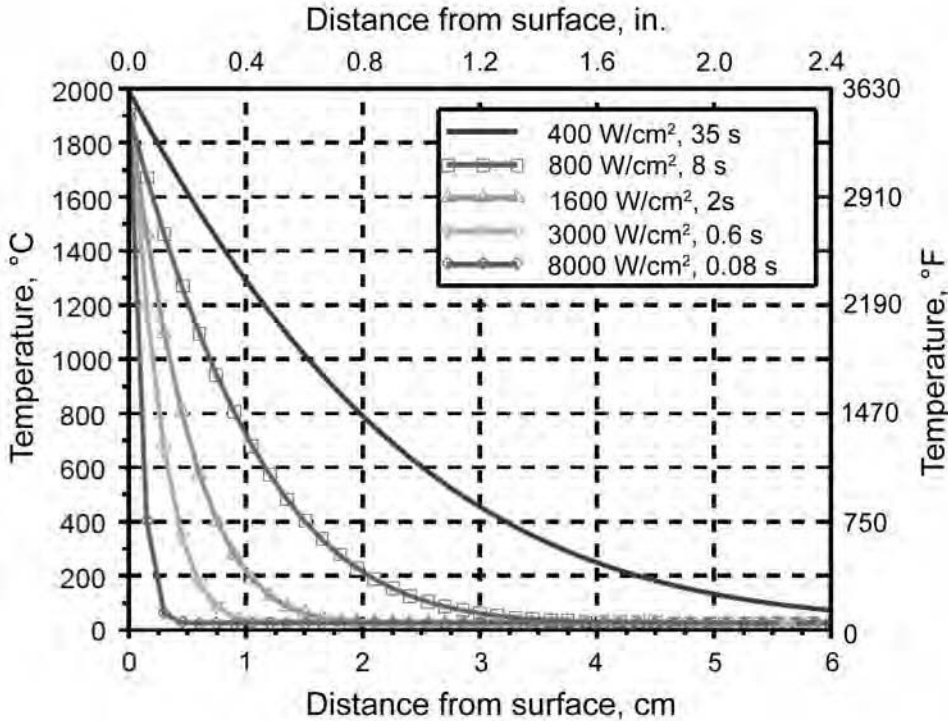


Fig. 1 Temperature distribution after a specific heating time in a thick steel plate heated uniformly on one surface as a function of applied heat intensity. Initial temperature of plate is 25 °C (77 °F), thermal conductivity is 50 W/m · K, specific heat capacity is 475 J/kg · K, density is 7800 kg/m³ (0.28 lb/in.³), and thermal diffusivity is 0.13 cm²/s.

At the other end of the power-density spectrum, heat intensities of 10⁶ or 10⁷ W/cm² will vaporize most metals within a few microseconds. At levels above these values, all of the solid that interacts with the heat source will be vaporized (resulting in hole drilling), and no fusion welding can occur. Thus, the heat sources for all fusion welding processes should have power densities between approximately 0.001 and 1 MW/cm². This power-density spectrum is shown in Fig. 3, along with the points at which common joining processes are employed (Ref 2, 3).

The fact that power density is inversely related to the interaction time of the heat source on the material is evident in Fig. 1. Because this represents a transient heat conduction problem, one can expect the heat to diffuse into the steel to a depth that increases as the square root of time, that is, from the Einstein equation:

$$x \sim \sqrt{\alpha t} \tag{Eq 1}$$

where x is the distance that the heat diffuses into the solid, in centimeters; α is the thermal diffusivity of the solid, in cm²/s; and t is the time in seconds. Tables 1 and 2 give the thermal diffusivities of common elements and common alloys, respectively. In addition, Table 3 shows how thermal diffusivity of materials can vary with temperature.

For the planar heat source on a steel surface, as represented by Fig. 1 and 4, the time in

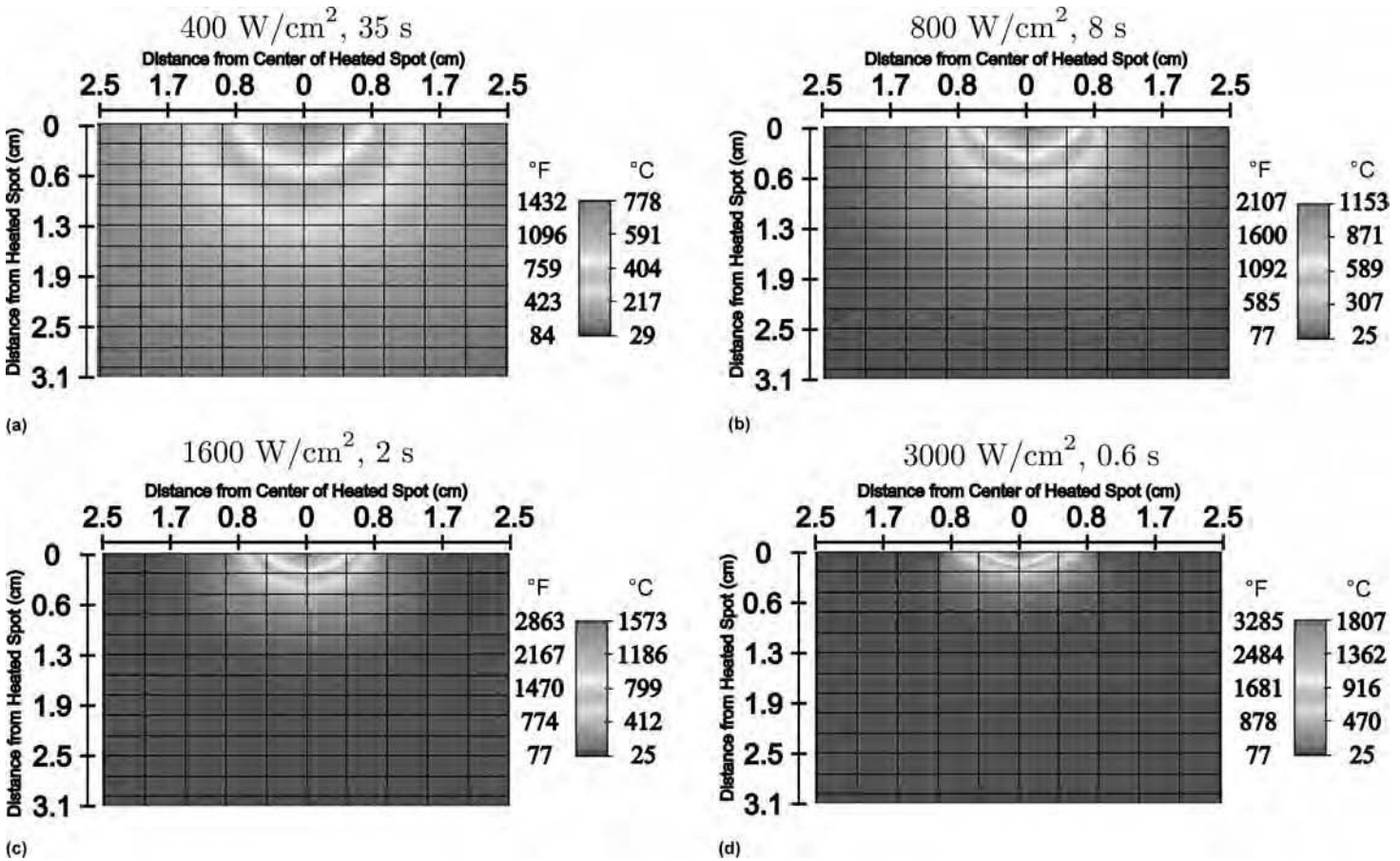


Fig. 2 Finite-element analysis temperature distribution results after a specific heating time in a thick steel plate heated over a 1 cm (0.4 in.) wide region on the top surface. Initial temperature of plate is 25 °C (77 °F), thermal conductivity is 50 W/m · K, specific heat capacity is 475 J/kg · K, density is 7800 kg/m³ (0.28 lb/in.³), and thermal diffusivity is 0.13 cm²/s. Images are magnified views of a 6.25 cm tall by 10 cm wide (2.5 in. tall by 4.0 in. wide) cross section.

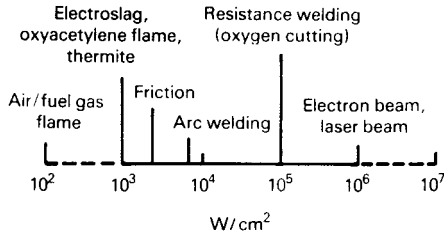


Fig. 3 Spectrum of practical heat intensities used for fusion welding

seconds for the heated surface temperature to increase by an amount ΔT is given by:

$$t = \pi k^2 (\Delta T)^2 / [4\alpha(H.I.)^2 \times 10^4] \quad \text{(Eq 2)}$$

where H.I. is the net heat intensity (in W/cm^2) transferred to the workpiece, k is the thermal conductivity (in $W/m \cdot K$) of the material, and α is the thermal diffusivity of the material (in cm^2/s) (Ref 8). The time in seconds to produce melting on the surface, t_m , is given by:

$$t_m = (1800/H.I.)^2 \quad \text{(Eq 3)}$$

where H.I. is the net heat intensity (in W/cm^2).

Equation 3 provides a rough estimate of the time required to produce melting and is based on the thermal diffusivity of steel. Materials with higher thermal diffusivities—or the use of a local point heat source (with divergence of heat flux) rather than a planar heat source—will increase the time to produce melting by a factor of up to 2 to 5 times. On the other hand, thin materials tend to heat more quickly.

If the time to melting is considered to be a characteristic interaction time, t_i , then the graph shown in Fig. 5 can be generated. Heat sources with power densities that are of the order of $1000 W/cm^2$, such as oxyacetylene flames or electroslag welding, require interaction times on the order of 1 s with steel, whereas laser and electron beams, at $1 MW/cm^2$, need interaction times on the order of only 1 μs . If this interaction time is divided into the heat-source diameter, d_H , then a maximum travel speed, V_{max} , is obtained for the welding process (Fig. 6).

The reason why welders begin their training with the oxyacetylene process should be clear: this process is inherently slow and does not require rapid response time to control the size of the weld puddle. Greater skill is needed to control the more-rapid fluctuations in arc processes, where the reaction time required is less than a second. The weld pool created by the high-heat-intensity processes, such as laser beam and electron beam welding, cannot be humanly controlled and must therefore be automated. This need to automate leads to increased capital costs. On an approximate basis, the heat intensity in W/cm^2 of a process can be substituted

Table 1 Thermal diffusivities of common elements from 20 to 100 °C (68 to 212 °F)

Element	Density		Heat capacity		Thermal conductivity		Thermal diffusivity	
	g/cm ³	lb/in. ³	J/kg · K	cal/g · °C	W/m · K	cal/cm · s · °C	mm ² /s	cm ² /s
Aluminum	2.699	0.098	900	0.215	221	0.53	91	0.91
Antimony	6.62	0.239	205	0.049	19	0.045	14	0.14
Beryllium	1.848	0.067	1880	0.45	147	0.35	42	0.42
Bismuth	9.80	0.354	123	0.0294	8	0.020	7	0.069
Cadmium	8.65	0.313	230	0.055	92	0.22	46	0.46
Carbon	2.25	0.081	691	0.165	24	0.057	15	0.15
Cobalt	8.85	0.320	414	0.099	69	0.165	19	0.188
Copper	8.96	0.324	385	0.092	394	0.941	114	1.14
Gallium	5.907	0.213	331	0.079	29–38	0.07–0.09	17	0.17
Germanium	5.323	0.192	306	0.073	59	0.14	36	0.36
Gold	19.32	0.698	131	0.0312	297	0.71	118	1.178
Hafnium	13.09	0.472	147	0.0351	22	0.053	12	0.12
Indium	7.31	0.264	239	0.057	24	0.057	14	0.137
Iridium	22.5	0.813	129	0.0307	59	0.14	20	0.20
Iron	7.87	0.284	460	0.11	75	0.18	21	0.208
Lead	11.36	0.410	129	0.0309	35	0.083	24	0.236
Magnesium	1.74	0.063	1025	0.245	154	0.367	86	0.86
Molybdenum	10.22	0.369	276	0.066	142	0.34	50	0.50
Nickel	8.902	0.322	440	0.105	92	0.22	23.5	0.235
Niobium	8.57	0.310	268	0.064	54	0.129	23.6	0.236
Palladium	12.02	0.434	244	0.0584	70	0.168	24	0.24
Platinum	21.45	0.775	131	0.0314	69	0.165	24.5	0.245
Plutonium	19.84	0.717	138	0.033	8	0.020	3.0	0.030
Rhodium	12.44	0.449	247	0.059	88	0.21	29	0.286
Silicon	2.33	0.084	678	0.162	84	0.20	53	0.53
Silver	10.49	0.379	234	0.0559	418	1.0	170	1.705
Sodium	0.9712	0.035	1235	0.295	134	0.32	112	1.12
Tantalum	16.6	0.600	142	0.034	54	0.130	23	0.23
Tin	7.2984	0.264	226	0.054	63	0.150	38	0.38
Titanium	4.507	0.163	519	0.124	22	0.052	9	0.092
Tungsten	19.3	0.697	138	0.033	166	0.397	62	0.62
Uranium	19.07	0.689	117	0.0279	30	0.071	13	0.13
Vanadium	6.1	0.22	498	0.119	31	0.074	10	0.10
Zinc	7.133	0.258	383	0.0915	113	0.27	41	0.41
Zirconium	6.489	0.234	280	0.067	21	0.050	12	0.12

Table 2 Thermal diffusivities of common alloys from 20 to 100 °C (68 to 212 °F)

Material names	Density		Heat capacity		Thermal conductivity		Thermal diffusivity		Ref
	g/cm ³	lb/in. ³	J/kg · K	cal/g · °C	W/m · K	cal/cm · s · °C	mm ² /s	cm ² /s	
Aluminum alloys									
1100 O temper	2.71	0.098	904	0.22	222	0.53	90.62	0.91	4
6061 O temper	2.7	0.098	896	0.21	180	0.43	74.4	0.74	4
7075 T6 temper	2.8	0.101	960	0.23	130	0.31	48.36	0.48	4
Copper alloys									
C22000 commercial bronze	8.8	0.318	376	0.09	189	0.45	57.12	0.57	4
C26000 cartridge brass	8.53	0.308	375	0.09	120	0.29	37.51	0.38	4
C46400 naval brass	8.41	0.304	380	0.09	116	0.28	36.3	0.36	4
C17000 beryllium copper	8.26	0.298	420	0.1	118	0.28	34.01	0.34	4
C60600 aluminum bronze	8.17	0.295	375	0.09	79.5	0.19	25.95	0.26	4
Magnesium alloys									
AZ61A	1.8	0.065	1050	0.25	80	0.19	42.33	0.42	4
AZ91	1.81	0.065	1050	0.25	72	0.17	37.88	0.38	4
Carbon steels									
AISI 1025	7.86	0.284	486	0.12	51.1	0.12	13.38	0.13	5, 6
Iron, carbon steel, 0.5% C	7.83	0.283	465	0.11	54	0.13	14.83	0.15	7
Iron, carbon steel, 1.0% C	7.8	0.282	473	0.11	43	0.1	11.65	0.12	7
Iron, carbon steel, 1.5% C	7.75	0.280	486	0.12	36	0.09	9.55	0.1	7
Stainless steels									
Type 301	8	0.289	500	0.12	16.2	0.04	4.05	0.04	5
Type 304	7.82	0.282	460	0.11	13.8	0.04	3.84	0.04	7
Type 316	8	0.289	500	0.12	16.2	0.04	4.05	0.04	5
Type 347	7.82	0.282	420	0.1	15	0.04	4.57	0.05	7
Type 410	7.8	0.282	460	0.11	24.9	0.06	6.94	0.07	5
Nickel-base alloys									
Nimonic 80A	8.16	0.295	460	0.11	8.7	0.02	2.32	0.02	5
Inconel 600	8.41	0.304	445	0.11	14.8	0.04	3.95	0.04	5
Titanium alloys									
6Al-4V	4.43	0.160	550	0.13	6.7	0.02	2.75	0.03	4, 6
Ti 5Al-2.5Sn	4.48	0.162	530	0.13	6.6	0.02	2.78	0.03	4, 6

Table 3 Temperature effects on thermal diffusivity

Material name	Density		Temperature		Heat capacity		Thermal conductivity		Estimated thermal diffusivity		Ref				
	g/cm ³	lb/in. ³	°C	°F	J/kg · K	cal/g · °C	W/m · K	cal/cm · s · °C	mm ² /s	cm ² /s					
Stainless steels															
Type 304	7.82	0.28	20	68	460	0.12	13.8	0.03	3.8	0.038	7				
			100	212								15	0.04	4.2	0.042
			200	390								17	0.04	4.7	0.047
			400	750								21	0.05	5.8	0.058
			600	1110								25	0.06	7.0	0.070
Type 347	7.82	0.28	20	68	420	0.10	15	0.04	4.6	0.046	7				
			100	212								16	0.04	4.9	0.049
			200	390								18	0.04	5.5	0.055
			400	750								20	0.04	6.1	0.061
			600	1110								23	0.05	7.0	0.070
Carbon steels															
Iron, carbon steel, 0.5% C	7.83	0.28	0	32	465	0.11	55	0.13	15.1	0.151	7				
			20	68								54	0.13	14.8	0.148
			100	212								52	0.12	14.3	0.143
			200	390								48	0.11	13.2	0.132
			400	750								42	0.10	11.5	0.115
AISI 1025	7.86	0.28	600	1110	486	0.12	51	0.12	9.6	0.096	7				
			100	212								51	0.12	13.4	0.134
			200	390								49	0.12	11.9	0.119
			300	570								46	0.11	10.4	0.104
			400	750								43	0.10	8.8	0.088
			500	930								39	0.09	7.3	0.073
			600	1110								36	0.09	5.9	0.059
			700	1290								32	0.08	3.6	0.036
			725	1337								30	0.07	2.7	0.027
775	1427	27	0.06	3.7	0.037										

Note: Some specific heat and conductivity values for AISI 1025 are estimated by two-point weighted averaging values from Ref 5.

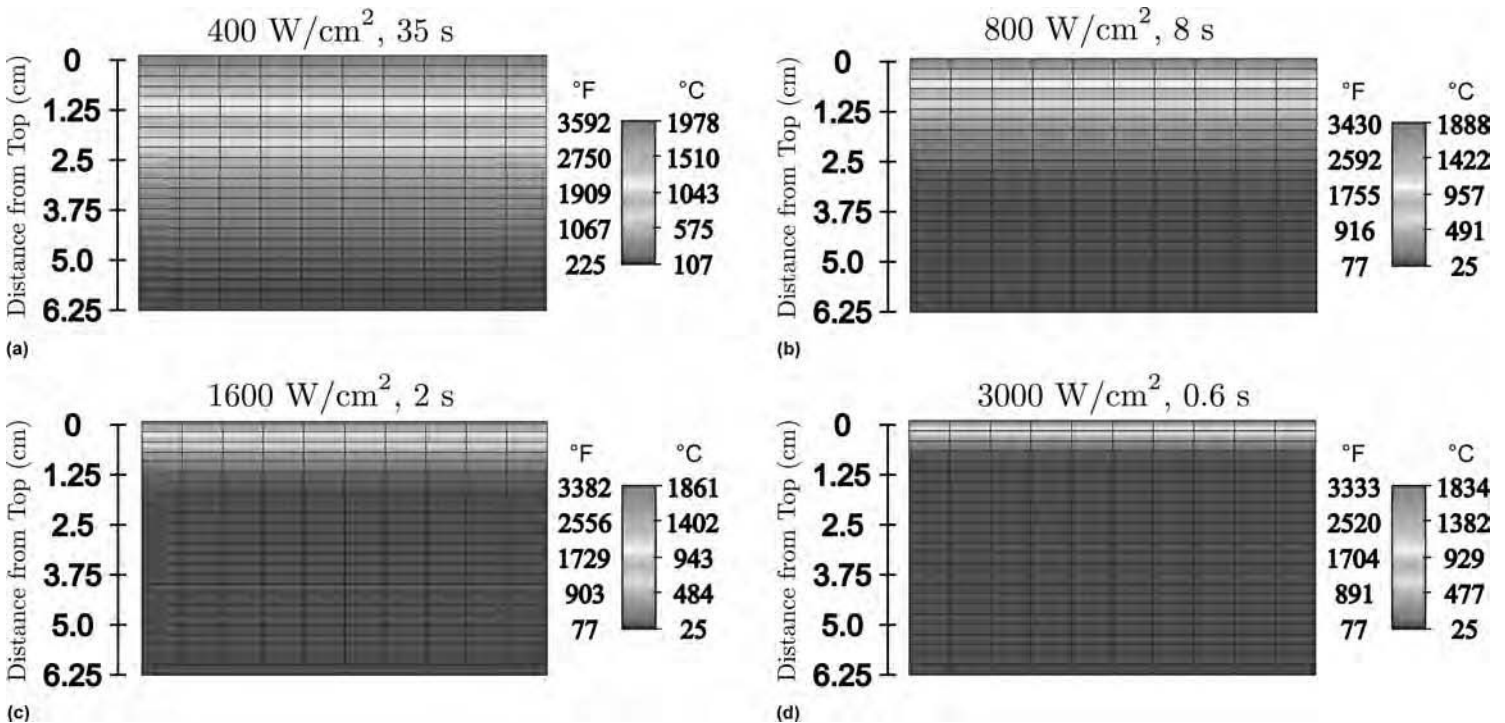


Fig. 4 Finite-element analysis temperature distribution results after a specific heating time in a thick steel plate heated uniformly on one surface as a function of applied heat intensity. Initial temperature of plate is 25 °C (77 °F), thermal conductivity is 50 W/m · K, specific heat capacity is 475 J/kg · K, density is 7800 kg/m³ (0.28 lb/in.³), and thermal diffusivity is 0.13 cm²/s.

with the dollar cost of the capital equipment. With reference to Fig. 3, the cost of oxyacetylene welding equipment is nearly \$1000, whereas a fully automated laser beam or electron beam

system can cost \$1 million. Note that the capital cost includes only the energy source, control system, fixturing, and materials handling equipment. It does not include operating,

maintenance, or inspection costs, which can vary widely depending on the specific application.

For constant total power, a decrease in the spot size will produce a squared increase in

the heat intensity. This is one of the reasons why the spot size decreases with increasing heat intensity (Fig. 6). It is easier to make the spot smaller than it is to increase the power rating of the equipment. In addition, only a small volume of material usually needs to be melted. If the spot size were kept constant and the input power were squared to obtain higher densities, then the volume of fused metal would increase dramatically, with no beneficial effect.

However, a decreasing spot size, coupled with a decreased interaction time at higher power densities, compounds the problem of controlling the higher-heat-intensity process. A shorter interaction time means that the sensors and controllers necessary for automation must operate at higher frequencies. The smaller spot size means that the positioning of the heat source must be even more precise, that is, on the order of the heat-source diameter, d_H . The control frequency must be greater than the travel velocity divided by the diameter of the heat source. For processes that operate near the maximum travel velocity, this is the inverse of the process interaction time, t_1 (Fig. 5).

Thus, not only must the high-heat-intensity processes be automated because of an inherently high travel speed, but the fixturing requirements become greater, and the control systems and sensors must have ever-higher frequency responses. These factors lead to increased costs, which is one reason that the very productive laser beam and electron beam

welding processes have not found wider use. The approximate productivity of selected welding processes, expressed as length of weld produced per second, to the relative capital cost of equipment is shown in Fig. 7.

Another important welding process parameter that is related to the power density of the heat source is the width of the heat-affected zone (HAZ). This zone is adjacent to the weld metal and is not melted itself but is structurally changed because of the heat of welding. Using the Einstein equation, the HAZ width can be estimated from the process interaction time and the thermal diffusivity of the material. This is shown in Fig. 8, with one slight modification. At levels above approximately 10^4 W/cm², the HAZ width becomes roughly constant. This is due to the fact that the HAZ grows during the heating stage at power densities that are below 10^4 W/cm², but at higher power densities it grows during the cooling cycle. Thus, at low power densities, the HAZ width is controlled by the interaction time, whereas at high power densities, the width is independent of the heat-source interaction time. In the latter case, the HAZ width grows during the cooling cycle as the heat of fusion is removed from the weld metal and is proportional to the fusion zone width.

The change of slope in Fig. 8 also represents the heat intensity at which the heat utilization efficiency of the process changes. At high heat intensities, nearly all of the heat is used to melt

the material, and little is wasted in preheating the surroundings. As heat intensity decreases, this efficiency is reduced. For arc welding, as little as half of the heat generated may enter the plate, and only 40% of this heat is used to fuse the metal. For oxyacetylene

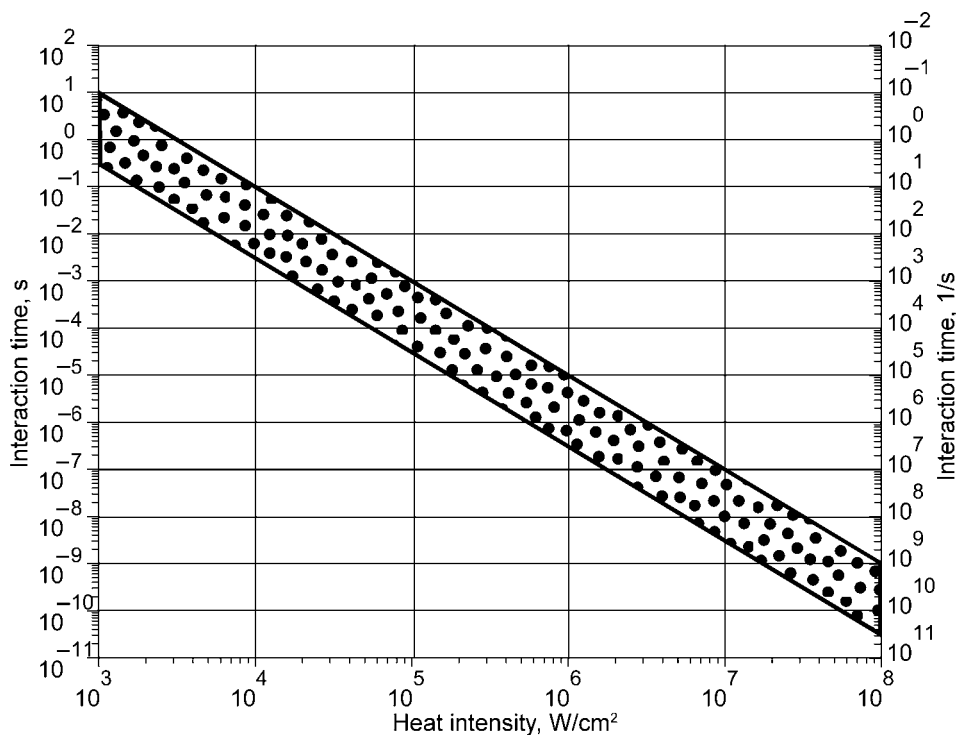


Fig. 5 Typical weld pool/heat source interaction times as a function of heat-source intensity. Materials with a high thermal diffusivity, such as copper or aluminum, would lie near the top of the band, whereas magnesium alloys and steels would lie in the middle. Titanium alloys, with very low thermal diffusivities, would lie near the bottom of the band.

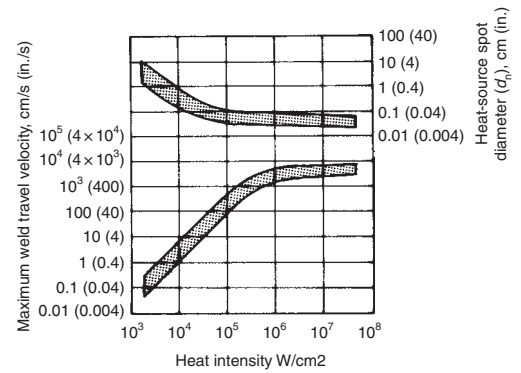


Fig. 6 Maximum weld travel velocity as a function of heat-source intensity based on typical heat-source spot diameters

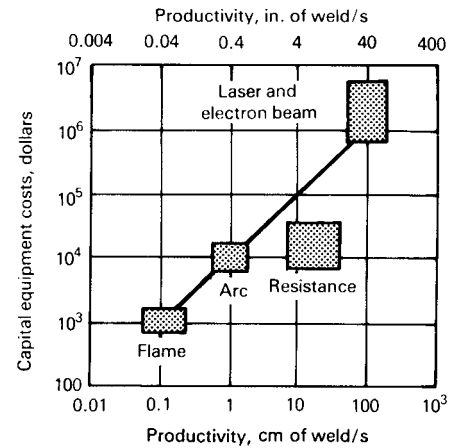


Fig. 7 Approximate relationship between capital cost of welding equipment and speed at which sheet metal joints can be produced

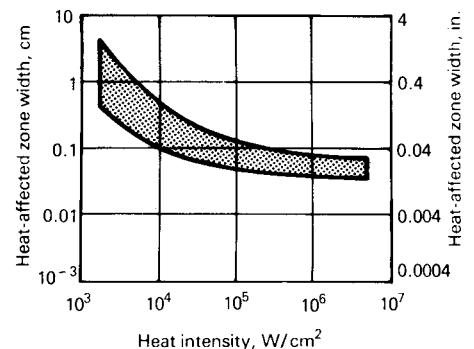


Fig. 8 Range of weld heat-affected zone widths as a function of heat-source intensity

welding, the heat entering the metal may be 10% or less of the total heat, and the heat necessary to fuse the metal may be less than 2% of the total heat.

A final point is that the heat intensity also controls the depth-to-width ratio of the molten pool. This value can vary from 0.1 for low-heat-intensity processes to more than 10 for high-heat-intensity processes.

It should now be evident that all fusion welding processes can be characterized generally by heat-source intensity. The properties of any new heat source can be estimated readily from the figures in this article. Nonetheless, it is useful to more fully understand each of the common welding heat sources, such as flames, arcs, laser beams, electron beams, and electrical resistance.

These are described in separate articles on fusion welding processes in this Volume.

REFERENCES

1. *Adhesion on Cold Welding of Materials in Space Environments*, Special Technical Publication 431, ASTM, 1967, p 105
2. D.M. Roessler, An Introduction to the Laser Processing of Materials, *The Industrial Laser Handbook*, D. Belforte and M. Levitt, Ed., PennWell Books, 1986, p 16–30
3. J.E. Anderson and E.F. Stresino, Heat Transfer from Flames Impinging on Flat and Cylindrical Surface, *J. Heat Transf.*, Vol 85, 1963, p 49–54
4. *Properties and Selection: Nonferrous Alloys and Special-Purpose Materials*, Vol 2, *ASM Handbook*, ASM International, 1990
5. *Properties and Selection: Irons, Steels, and High Performance Alloys*, Vol 1, *ASM Handbook*, ASM International, 1990
6. “Metallic Materials Properties Development and Standardization (MMPDS-04),” Battelle Memorial Institute, 2008
7. A. Bejan and A.D. Kraus, *Heat Transfer Handbook*, John Wiley & Sons, 2003
8. M.M Yovanovich, Conduction and Thermal Contact Resistances (Conductances), *Handbook of Heat Transfer*, 3rd ed., W. Rohsenow et al., Ed., McGraw-Hill Professional, 1998, p 3.27

Characterization and Modeling of the Heat Source*

S.S. Glickstein (retired) and E. Friedman (retired), Westinghouse Electric Corporation
R.P. Martukanitz, Applied Research Laboratory, Pennsylvania State University

THE HEAT THAT IS SUPPLIED TO THE WORKPIECE, which then is transferred within the workpiece to produce melting, forms the basis of every welding process. The heat-transfer process, or thermal cycle, in the weldment has many consequences, including the complex metallurgical changes that take place in the fusion zone, where the metal is melted and subsequently solidified, and in the adjacent heat-affected zone, where material is heated to temperatures that are below the melting point but are sufficiently high to produce changes in the microstructure and in mechanical properties.

Three types of energy are used primarily as direct heat sources for fusion welding: electric arcs, laser beams, and electron beams. Oxyfuel gas welding is also used occasionally, and internal joule heating arising from electrical resistance is also common for welding of thin material. However, fusion welding using internal joule heating, that is, resistance welding, does not involve the use of a direct heat source. The intensity or energy distribution associated with the direct heat sources may vary dramatically and, to a large degree, dictates the use of these heat sources for welding. The total amount of heat (Q) that is provided to the workpiece is measured in watts (W) and may be defined by the welding parameters, such as welding current times welding voltage for arc processes, or directly for laser beam welding, because laser output power is usually provided in watts. The amount of energy that the welding heat source provides per unit of cross-sectional area is referred to as the heat flux (q) and is defined in watts per square meter (W/m^2). A general portrayal of the heat flux associated with a direct welding source may be described by its energy distribution. Figure 1 illustrates the differences in energy distribution of various heat sources, as well as the melting patterns of

the base metal generally associated with these sources. As illustrated in the figure, the oxyfuel gas welding process is a diffuse or distributed heat source, whereas the laser beam and electron beam welding processes are defined as high-energy-density processes. The heat source of arc welding processes may be described as being between the diffuse and high-energy-density sources. Also as shown in Fig. 1, the distribution of energy within the heat source plays an important role in determining the potential fusion zone geometry. Although the distribution of energy during welding is of significance, another critical factor is the energy-transfer efficiency, the ratio of the amount of energy provided by the heat source to the quantity that is transferred to the base material. As with energy density, the four heat sources primarily used for fusion welding vary greatly as to their energy-transfer efficiencies.

Because of the important role the heat source plays during welding, the ability to accurately define the energy provided to the workpiece, as well as the amount transferred for welding, is of interest for theoretical as well as practical considerations. The description of the input-energy source is basic to any numerical modeling formulation designed to predict the outcome of the welding process. Both the magnitude and distribution of the source are fundamental and unique to each joining process, and the resultant output of any numerical model is therefore affected by the initial description of the heat source. An understanding of both the physics and the mathematical simulation of these sources is essential for characterizing the heat source. This article briefly reviews the physical phenomena that influence the input-energy distribution and discusses several simplified and detailed heat-source models

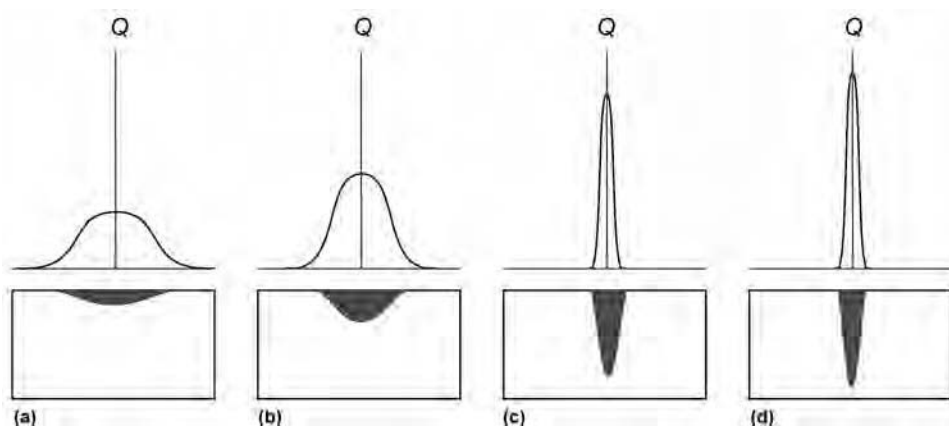


Fig. 1 Schematic of energy densities and melt patterns associated with various heat sources used for fusion joining. (a) Oxyfuel flame. (b) Gas tungsten arc. (c) Laser beam. (d) Electron beam. Q , total amount of heat

that have been used in the modeling of arc welding, high-energy-density welding, and resistance welding processes.

Simplified Modeling of the Heat Source

Analytical modeling of the welding heat source is generally complex, because of the nature of energy transfer to the workpiece, whether the source of that energy is an arc, a high-energy-density beam of electrons or laser light, or joule heating. For numerical modeling purposes, heat input to the weldment is usually applied as a distribution of surface flux, a distribution of heat generated internally, or a combination of both. Many analytical treatments, however, have sought to simplify the characterization of the heat source by assuming that the effective thermal energy supplied by the heat source is deposited in such a narrow band of material that it may be idealized mathematically as a point or a line source, depending on the geometry of the weldment (Ref 1). Heat input idealizations of this sort lend themselves to the derivation of closed-form welding temperature solutions and the avoidance of developing numerical finite-element or finite-difference models to calculate temperatures. These solutions are valid only for simple geometries and in regions removed from the fusion and heat-affected zones, where details of the distribution of heat input from the source and accurate representations of the thermal energy transferred from the weld bead to the rest of the weld joint are not important.

The fundamental simplified heat-source model is developed for a flat plate of infinite extent bounded by the planes $z = 0$ and $z = h$. Heat is input at a point that is either stationary or is moving at uniform speed, v , in the x -direction on the surface $z = 0$, so that at any time, t , the point source is located at $x = vt$ (Fig. 2). If the end effects that result from the initiation

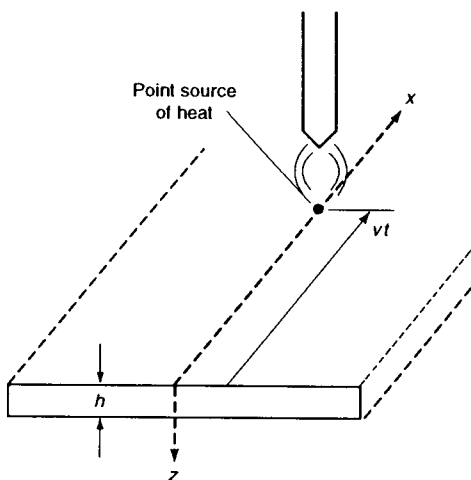


Fig. 2 Moving point source in infinite plate

or termination of the heat source or the finite dimensions of the weldment are neglected, then the resulting temperature distribution associated with the moving source is stationary with respect to a moving coordinate system, the origin of which coincides with the point of application of the heat source. This class of temperature response is termed quasi-stationary.

In general, for either a stationary or a moving point source, heat is conducted through the plate without hindrance until the insulating effect of the ideally adiabatic surface at $z = h$ is felt. For a sufficiently thick plate, the temperature rise at $z = h$ is so small that the solution for an infinitely thick plate, which is associated with a single source of heat, is applicable. For a moderately thick plate, the temperature rise at $z = h$ from the infinitely thick plate point-source solution is large enough to result in nonzero heat flow at $z = h$. An image source of the same strength applied at $z = 2h$ ensures that the surface $z = h$ is adiabatic. However, the image source produces nonzero heat flow at $z = 0$, and another image source applied at $z = -2h$ is now required to satisfy conditions at $z = 0$.

Carrying this imposition of image point sources of heat along ad infinitum (Fig. 3), an infinite distribution of image sources superposed with the original source at $z = 0$ yields the desired adiabatic conditions at both the $z = 0$ and $z = h$ surfaces. The temperature solution for this series of image sources is in the form of an infinite series (Ref 2), which converges more rapidly for thicker plates. The solution for the moderately thick plate applies to thin plates as well, but convergence of the infinite series would be extremely slow. As an

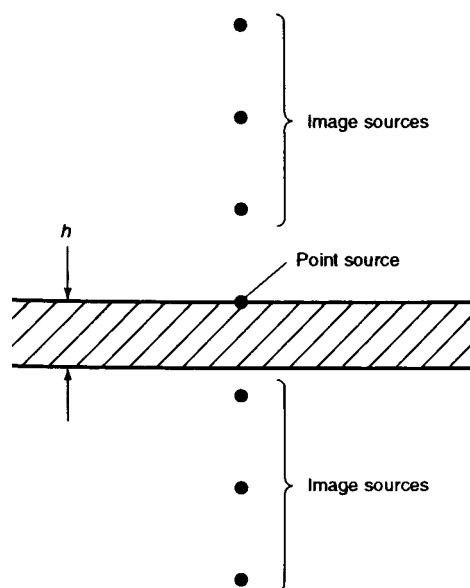


Fig. 3 Superposition of image sources in finite-thickness plate

alternative, the heat source can be applied as a line source distributed uniformly through the thickness (Ref 3). This simplified approach eliminates any variation of the temperature distribution through the thickness and is often used to model high-energy-density welding processes that result in the formation of a keyhole, as is discussed later.

Offshoots of these cases also have been developed. These include considerations of plates of finite width, in which case sets of image sources are needed to ensure adiabatic conditions at the edges (Ref 4); line sources of heat traveling on a circular path (Ref 5); and conditions that simulate either initiation or termination of the heat source (Ref 6). Variations of the moving point source approach have been employed (Ref 7) to calculate the temperatures needed for weld-induced residual stress calculations in piping.

Arc Welding

Gas Tungsten Arc Welding

Gas tungsten arc welding (GTAW) is the most frequently modeled arc welding process in which the heat source is a nonconsumable electrode. In the direct current electrode negative (DCEN) process, the pieces of material are joined together by energy that is transferred to the workpiece by four primary mechanisms (Ref 8):

- Kinetic energy of the electrons that constitute the arc current
- Heat of condensation of the electrons (work function) penetrating the solid work surface
- Radiation from the arc
- Thermal conduction from the arc plasma to the workpiece

The first two mechanisms constitute the major source of energy to the weldment (Ref 9). Also, because electrons are negatively charged, they inherently travel from the negative to the positive pole of the arc, and hence, welding polarity may have a large effect on the transfer of energy. Welding using direct current electrode negative (DCEN), such as with the gas tungsten arc process, utilizes the electrons traveling from the tungsten electrode to the positive workpiece to provide a fairly efficient transfer of energy to the base metal. Employing direct current electrode positive (DCEP), such as with gas metal arc welding, results in electrons being directed from the base metal to the positive consumable electrode with lower energy transfer to the workpiece. The use of variable polarity may be viewed as a compromise between DCEN and DCEP.

Because of the complicated nature in which energy is transferred from the arc, heat input to the weldment can be modeled by one of the point- or line-source approaches discussed in the preceding section of this article. If none of

these treatments is appropriate for the particular application, then a more realistic approach is to input the energy by a distribution of surface flux, a distribution of heat generated internally, or a combination of the two. If an internal heat distribution is confined to a thin layer of material adjacent to the heated surface, then the choice of heat-input model is immaterial (Ref 10). The magnitude of heat input to the workpiece is expressed simply as the product of what has traditionally been defined as the arc power (that is, the product of the voltage drop across the arc and the arc current) and the arc transfer efficiency, which account for energy losses from the arc.

Estimates of arc efficiency can be made by conducting calorimetry measurements, correlating computed temperatures with thermocouple readings from test welds, or using some other observable response to the welding thermal cycle. Because the voltage used is usually determined from measurements at some point within the power supply, estimates must be made to account for losses within the electrode and other parts of the system (Ref 11). Changes in welding process variables, such as shielding gas, electrode configuration, arc gap, and minor element additions to the arc, affect arc efficiency, as does the material that is being welded (Ref 12).

The magnitude of heat applied to the weldment surface may not be known with great accuracy, and the distribution of the heat input is even more uncertain. Input-energy distribution depends on factors related to the electrode and the physics of the arc, as well as on the interaction of the arc with the molten weld pool. For example, the arc characteristics and the depth-to-width ratio of the weld puddle will change as the vertex angle of the conical tip of the electrode is altered (Fig. 4). As the arc becomes more constricted, the heat source becomes more concentrated, thus increasing

weld penetration. Changes in heat-source distribution (that is, input current) will affect the electromagnetic forces in both the arc and the weld puddle, resulting in changes in weld-puddle motion, which can promote alterations in convection heat transfer within the weld puddle. Shielding gas composition and minor alloying elements also can influence the distribution of input energy.

When welding at low currents and high voltages, the perturbation of the weld-puddle surface may be considered to have a small effect on the heat-input distribution, and a model that considers heat to be applied as a surface flux is usually satisfactory. However, as the current increases (particularly when the arc voltage is small, indicating a short electrode-to-work surface distance), the arc jet can depress the weld-puddle surface and affect the configuration of the distribution on the surface of the weldment (Fig. 5). The effects of depressing the weld puddle can be accommodated empirically by postulating some or all of the heat from the arc to be deposited internally. However, the specification of an internal heat-generation distribution is more complex than that of a surface flux.

For models in which heat from the welding arc is postulated to be deposited on the surface of the weldment, the input energy is often assumed to be a radially symmetric, normally distributed surface flux at any instant in time (Ref 13). The heat flux provided by the source, q , can be expressed conveniently as an exponential, or Gaussian, function, such that:

$$q(r) = \left(\frac{3fQ}{\pi r'^2}\right) \exp\left[-3\left(\frac{r}{r'}\right)^2\right] \quad (\text{Eq 1})$$

where f is the bulk energy-transfer coefficient, Q is the magnitude of the heat input per unit time (Q being the product of the welding current and voltage for arc processes and laser

power for laser beam welding), r is the distance from the center of the heat source to the surface, and r' is a characteristic radial dimensional distribution parameter that defines the region in which 95% of the heat flux is deposited. In the limit as $r' \rightarrow 0$, the heat input becomes a point source of strength fQ on the surface. When using measured energy distributions for defining the spatial distribution of energy as a Gaussian function, it is appropriate to use the radius that provides an area under the distribution equal to $1-(1/e^3)$. However, for laser beam welding, the beam radius representing the usable energy is often reported as $1-(1/e^2)$, which represents 86.5% of the total energy.

The bulk energy-transfer coefficient, f , describes the total amount of energy that is transferred to the workpiece and is a measure of the transfer efficiency of the process. The energy-transfer coefficient may be estimated by determining the ratio of the total energy provided to the workpiece through calorimetry and the theoretical amount of energy that may be generated by the process, which, in the case of GTAW, is the product of the welding voltage and current. Although the efficiency depends on the material being welded and the specific process conditions, calorimetry measurements have yielded transfer coefficients for GTAW with DCEN of 0.7 to 0.9, whereas the transfer efficiency for GTAW of aluminum using alternating current has been measured to be between 0.3 and 0.4 (Ref 14–16).

Equation 1 describes the heat-input distribution from a stationary arc. The amount of heat transferred to the workpiece (fQ), the distribution parameter (r'), and the duration of heating are necessary to fully characterize the input energy. Figure 6 shows typical variations of the weld bead depth and width for stationary spot welds on 6.5 mm (0.25 in.) thick plates with both the distribution parameter and the duration of heating, t^* .

Other forms of the heat-input distribution also can be used. These include ramp, or triangular, distributions; uniform heat-input distributions over finite areas (for example, the area of the weld-puddle surface); or combinations of the two (that is, trapezoidal distributions).

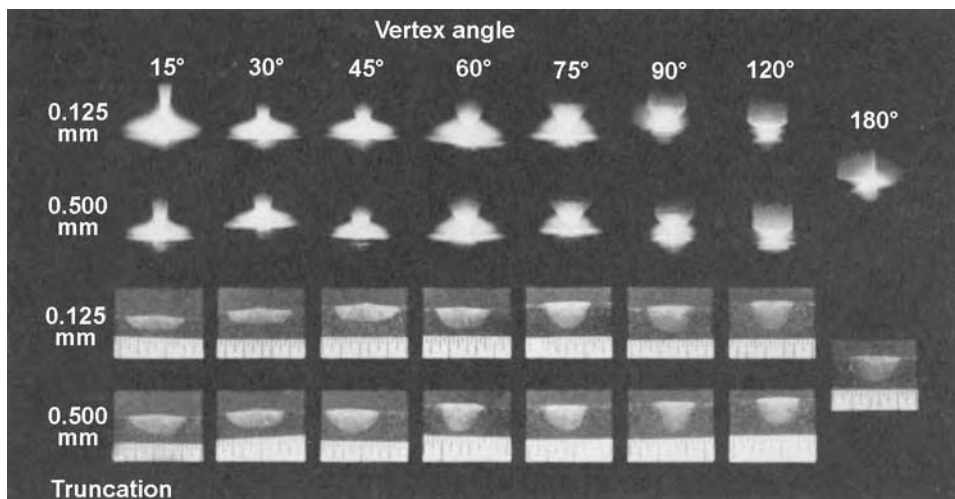


Fig. 4 Arc shape and weld bead geometry as a function of electrode tip angle in a pure argon shield for 2.38 mm (0.10 in.) diameter electrodes truncated to 0.125 and 0.500 mm (0.005 and 0.2 in.); arc gap, 1 mm (0.04 in.). Source: Ref 12

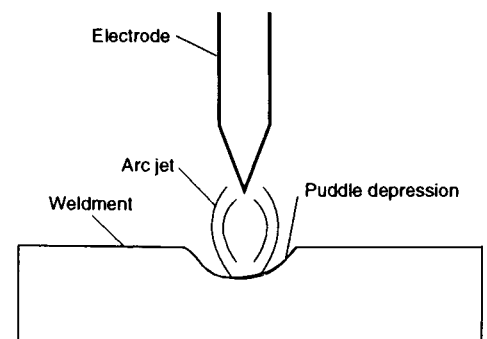


Fig. 5 Effect of arc jet on depression of weld pool

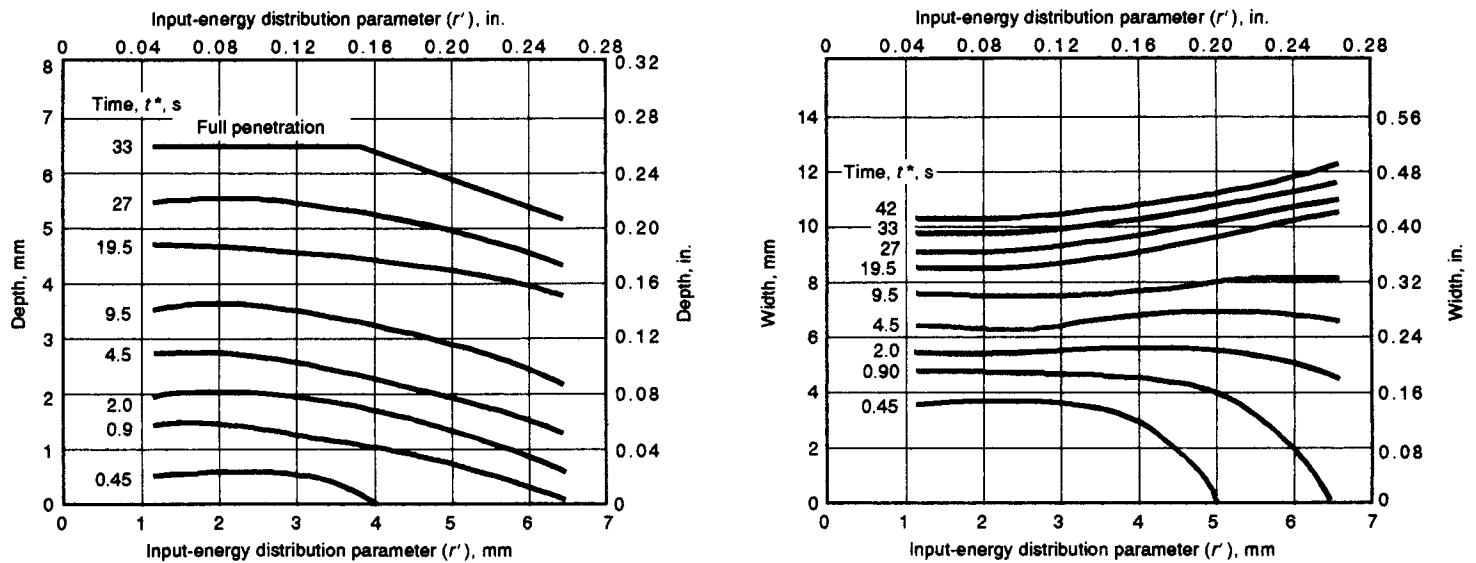


Fig. 6 Weld bead dimensions for different durations of heating, t^* , and input-energy distribution parameter, r' , with $Q_0 = 1060$ W. Source: Ref 10

The axisymmetric characterization of heat input for stationary arcs enables temperatures in the weldment to be calculated using axisymmetric thermal analysis methods, if the weldment geometry justifies such an analysis. On the other hand, if the heat source is moving, then the resultant flow of heat is three-dimensional; that is, temperature gradients develop through the thickness of the weldment, as well as in directions parallel to and transverse to the welding direction. If the weldment geometry is regular (for example, flat plate), then the heat source from the arc is moving at a constant, sufficiently high speed, v , and if end effects such as the starting and stopping of the arc are neglected, then transient two-dimensional thermal analyses at cross sections normal to the welding direction may be satisfactory (Ref 17). The heat input at a section transverse to the direction of arc travel is given by:

$$q(x, t) = \left(\frac{3fQ}{\pi r'^2} \right) \exp \left[-3 \left(\frac{x}{r'} \right)^2 \right] \exp \left[-3 \left(\frac{vt}{r'} \right)^2 \right] \quad (\text{Eq 2})$$

where x is the distance from the centerline of the weld, and t is the time measured from the moment the center of the heat source passes over the weld section being analyzed. The four heat-input parameters characterizing a moving arc (f , Q , r' , v) are embodied in this formulation. The inverse of the speed of a moving arc is akin to the duration, t^* , of a stationary arc, because a moving arc supplies a heat input, fQ/v , per unit length of weld, whereas a stationary arc provides a total amount of heat, fQt^* , to the weldment.

For models in which heat is deposited internally, rather than as a surface flux, the input energy can be assumed to be deposited within a spheroidal or ellipsoidal region that is similar in shape to the weld puddle. As described by

Ref 18, the heat input can be taken to vary exponentially as a Gaussian distribution in all directions within the ellipsoid. Thus, the energy-input distribution is completely specified by the dimensions of the ellipsoid. More elaborate models can be formulated by prescribing either double-ellipsoid heat-input regions that better match weld-puddle shape or conical regions of internal energy deposition. Regardless of the methodology chosen to characterize the distribution of the heat input, the geometric parameters of the distribution should be established, at this stage of computer-modeling development, by correlating calculated thermal-response characteristics, such as the weld bead and heat-affected zone dimensions, with measured values.

Gas Metal Arc Welding

Gas metal arc welding (GMAW) modeling is more complex than that of the GTAW process, because of the need to consider thermal energy that is transferred to the workpiece not only by mechanisms similar to those associated with the GTAW process but, more importantly, by heat contained in the molten metal drops that are transferred as filler metal from the consumable electrode wire to the workpiece. Refer to Ref 19 for additional details. Because the GMAW process uses DCEP, the heat associated with the kinetic energy of the electrons and the heat of condensation is now input to the electrode. The energy previously input to the weldment is replaced by the energy of positively charged ions, which contribute a much smaller amount of heat to the weldment.

In addition, the radiation and conduction via the arc plasma make minor contributions to the heat input to the weldment. The more-important source of heat is derived from the

mass of molten material and is related directly to both the temperature and the melting rate of the electrode wire. The melting rate of the electrode is governed primarily by joule heating and by arc heating similar to that of the GTAW process. The transfer of material to the workpiece can be globular, such that the metal is deposited in droplets, the diameters of which are greater than that of the electrode, or in a spray, in which mass is transferred to the weld puddle as droplets with diameters that are smaller than that of the electrode.

The thermal energy applied to the workpiece therefore consists of two sources: the arc energy distribution generated at the cathode area (workpiece) and the thermal energy of the metal drops transferred from the filler wire. The arc input energy has a significant effect on the width of the weld puddle and thus of the solidified weld bead, whereas the energy in the molten metal contributes significantly to the melting of the workpiece (Ref 20). Furthermore, the impingement of the metal drops on the puddle significantly affects the depth of penetration (Ref 21), because the impact of each drop causes a distinct indentation in the weld puddle, especially at high currents.

Modeling of the heat input from the GMAW process should generally include the effects of heat input from the filler-metal droplets, the addition of new weld material from the filler wire, and, in many cases, the significant indentation of the weld-puddle surface, as well as a spatially distributed heat flux on the surface to represent radiation energy from the arc and positive ion impingement. Accurate representations of these phenomena are so complex that alternate treatments are essential. In Ref 22, the heat input from the GMAW process was modeled as a Gaussian distribution and accounted for the energy necessary to melt the electrode wire.

In Ref 23, a model in which heat is input partly in the weld puddle and partly as a surface flux was developed. A more common approach is to model the addition of filler metal by “creating” new metal in an analytical model.

In finite-element treatments, for example, new metal is simulated by adding sets of elements to the model. For three-dimensional models, these elements can be introduced in distinct increments of time, whereas for a two-dimensional analysis of a cross section normal to the welding direction, a set of elements corresponding to a weld bead cross section can be created. More recently, the contour outlining the weld bead has been determined experimentally and then used as the starting boundary condition for the thermal modeling of welds. As an example, the boundary condition can be a time-dependent temperature that may reach or exceed the melting temperature of the material.

Other Arc Welding Processes

Shielded metal arc welding, submerged arc welding, and flux cored arc welding are other processes in which energy is transferred to the workpiece both from the arc and from an overheated consumable electrode. The previously outlined semiempirical methodology for simulating the heat input for the GMAW process also appears to be well suited for the flux welding processes, although the introduction of a slag layer, whether it develops from the melting and solidification of electrode-covering material or from a flux feeding tube, presents another factor to be considered when calculating weld-induced temperatures.

High-Energy-Density Welding

High-energy-density welding, such as laser beam or electron beam welding, may be described as the use of a high-intensity heat source capable of very small spatial distribution. These processes employ intense energy of the focused, or nearly focused, energy beam and result in energy intensities of between 10^5 and 10^7 W/cm². Under these conditions, temperatures developed at the beam and material interaction region are sufficient to cause vaporization. Based on a constant material and thickness, the process depends on the intensity distribution and travel velocity of the incident beam. At low intensities, such as with a relatively diffuse heat source, vaporization occurs over a wide region and at a significantly lower energy. At sufficiently high intensities, as with a relatively concentrated heat source, the central region of interaction between the beam and substrate exhibits a vapor cavity or keyhole containing evaporated atoms of the substrate and ionized gas. These conditions are illustrated for diffuse and concentrated intensity distributions in Fig. 7 and 8, respectively, and coarsely reflect the two primary conditions for beam

welding, that is, conduction- and keyhole-mode welding (Ref 24).

The obvious practical difference for the conditions represented in Fig. 7 and 8 is depth of penetration; however, many subtle distinctions are also present. It has been promulgated that laser beam welding in the conduction or keyhole mode is a discreet process dictated by the intensity distribution of the beam and certain properties of the material; consequently, inadequate coupling or energy transfer between the beam and the workpiece has been described as conduction-mode welding. In actuality, there exists a more gradual transition between the conditions shown in Fig. 7 and 8 based on the material thermal and physical properties as well as the intensity distribution of the source energy. Beam welding with inadequate energy required for sufficient evaporation results in a small amount of energy being transferred to the substrate and hence only a small amount of surface melting directly under the highest intensity. In the case of laser beam welding under this condition, the transfer of usable energy under this

situation is governed purely by Fresnel absorption, with the vast majority of optical energy being reflected from the surface.

The circumstances represented by the condition shown in Fig. 8 are vastly more complex than what has been described previously. In this case, the energy density required to establish and maintain the keyhole is significantly higher than that of the conduction mode and results in significant evaporation of the substrate and the formation of a plasma. Laser beam welding under these conditions results in enhanced absorption of the beam within the plasma by photon-induced acceleration of free electrons to a higher energy and temperature and the propagation of this energy by electron collision with atoms and ions. This mechanism is termed inverse bremsstrahlung, referring to the converse of photonic energy being produced from an accelerated electric charge (Ref 25, 26).

Figure 9 illustrates the shape of the source distributions for laser beams representing three basic fundamental transverse electromagnetic

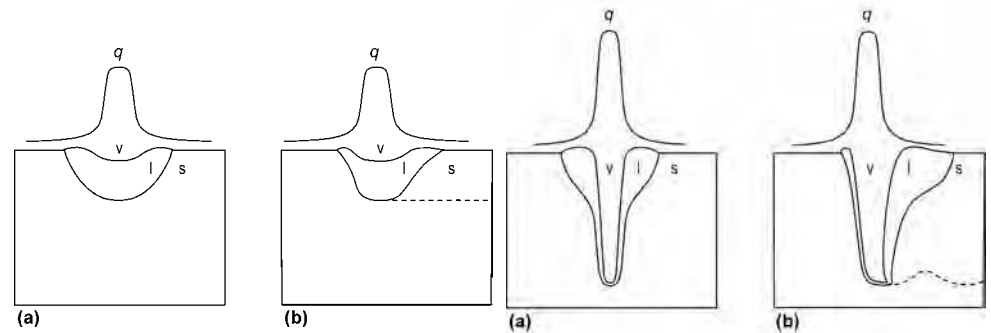


Fig. 7 Schematic of beam weld profiles for a diffuse Gaussian intensity distribution (q) showing the vapor or plasma (v), liquid (l), and solid (s) phases for orientations (a) transverse and (b) longitudinal to the workpiece with beam motion to the left. Source: Adapted from Ref 24

Fig. 8 Schematic of beam weld profiles for a concentrated Gaussian intensity distribution (q) showing the vapor or plasma (v), liquid (l), and solid (s) phases for orientations (a) transverse and (b) longitudinal to the workpiece with beam motion to the left. Source: Adapted from Ref 24

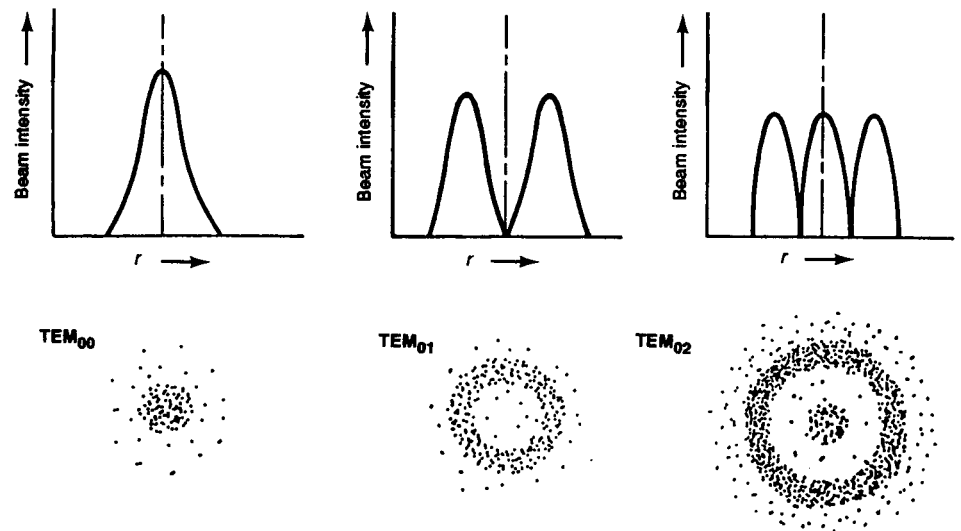


Fig. 9 Distribution of energy for laser beams representing three different transverse electromagnetic modes (TEM), with the horizontal axis showing increasing distance from the center of the heat source to the surface

modes. The fundamental transverse electromagnetic mode, TEM₀₀ (a Gaussian distribution), is often selected as the heat-input description for laser welding analysis. It is also assumed to be the source distribution for electron beam welding. The exact determination of the Gaussian width parameter, r' , depends on the optics of the laser or electron beam welding system. In many cases, a point source on the surface is an excellent approximation. In laser beam welding, if the energy is delivered via a fiber-optic system, such as with a neodymium: yttrium-aluminum-garnet or ytterbium-fiber laser, then the output source distribution is often described as a truncated Gaussian source distribution or "top hat" of specified width. Shown in Fig. 10 are measured distributions for ytterbium-fiber laser beams delivered through a fiber optic and representing Gaussian and top-hat energy distributions (Ref 27).

If a keyhole mode of welding is being formulated, then modeling of the input-energy distribution is complicated. Several different

formulations have been discussed in the literature. In the keyhole mode, the energy density is sufficiently high to cause material ablation near the center of the beam, resulting in beam penetration further into the weldment. A hole created in the material is maintained by equilibrium between vapor pressure in the keyhole, surface tension, and hydrodynamic pressure in the surrounding melt. The exact distribution of energy deposited in the hole is complicated and depends on the scattering and absorption of the beam through the weldment, as well as on the focal parameters of the system. Several different models have been used to simulate these conditions.

The simplest model for the keyhole mode of welding is that of a moving line source through the weldment (Ref 28). The appropriate solution of the heat equation was obtained by Rosenthal (Ref 29). The model does not describe the typically observed semicircular part of the weld cross section at the top, because it corresponds to a liquid region, the size of which does not vary through the

thickness of the workpiece. This simple model has been found to be very useful, however, in providing relations between such quantities as the power absorbed and the width of the weld.

A thermal analysis of the laser process has been derived for a Gaussian source moving at a constant velocity over a large range of conditions, from simple heat treating to deep-penetration welding (Ref 30). To obtain a more realistic weld shape, the simple line-source approach was modified (Ref 31) by adding a point source close to the surface of the workpiece to the line source distributed uniformly through the thickness. The line source models uniform absorption of heat by the workpiece with depth, whereas the point source corresponds to a much more concentrated region of absorption in the vicinity of the laser focus, which contrasts with the absorption from multiple reflections that occur in the main part of the keyhole. The temperature distribution from this combined-source model yields a vertical weld seam shape that reflects the general shape of that found from experimental investigations (Fig. 11).

A simple description of the input energy avoids the problem of defining the exact nature of the energy-transfer process in the keyhole itself. A more sophisticated model is necessary to characterize this effect. The attenuation of the laser beam in the vertical direction has been accounted for (Ref 32) by calculating the temperature at a depth, d , below the surface. If the temperature at depth d exceeds the boiling point of the material, then point d is deemed to be transparent. The incident power is then applied at a point below it, after suffering some absorption. This sequence continues through the substrate. The transparent grid points keep their high temperatures as if the keyhole were filled with a hot plasma.

This brief overview of several of the approaches used to model the high-energy-density welding process points out the difficulty in defining a unique methodology. Experimental data must be used for specific welding conditions to establish the overall approach, as well as the magnitude and distribution of the input source energy.

Resistance Spot Welding

The electrical resistance spot welding process for joining two materials at their common interface involves a complicated interaction of electrical, thermal, mechanical, metallurgical, and surface phenomena. Figure 12 is a simplified representation of the resistance spot welding process showing some essential features for producing a weld.

In this welding process, the faying surfaces of two or more workpieces are fused and joined at a spot by electric current flowing through the weldment (joule heating). The weldment is

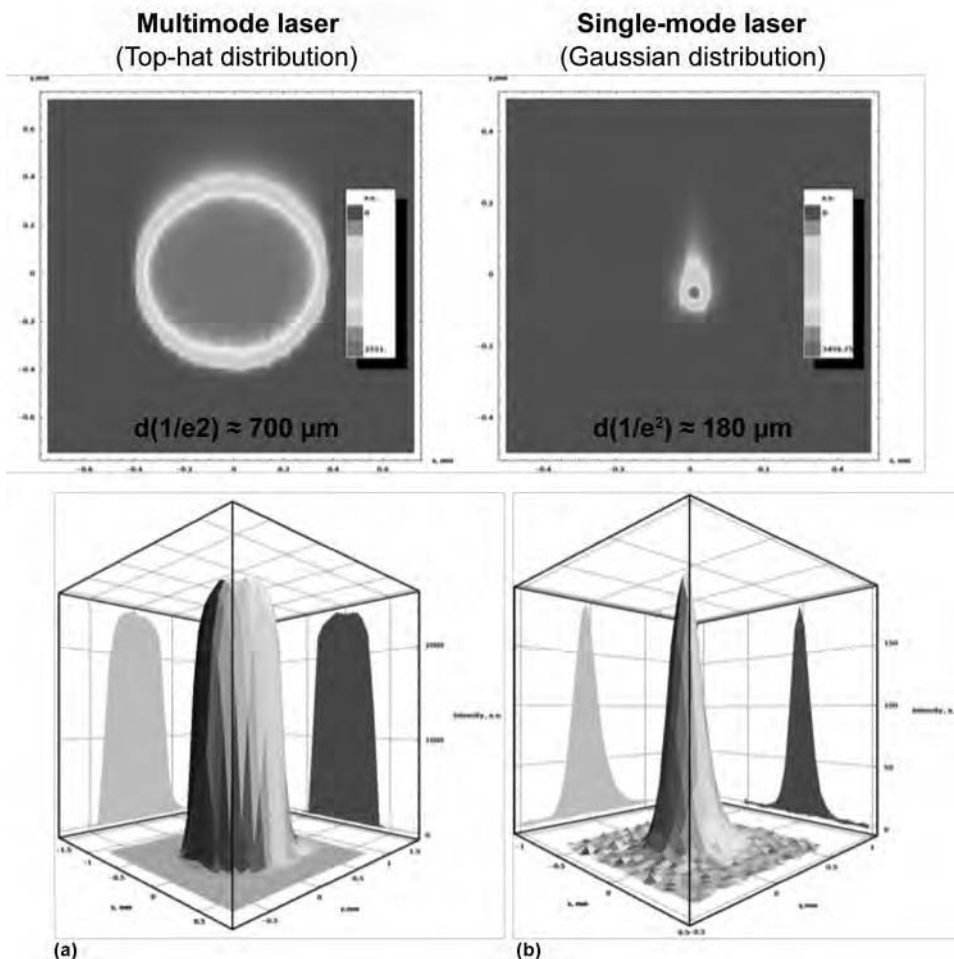


Fig. 10 Measured energy distributions for ytterbium-fiber lasers having (a) top-hat and (b) Gaussian energy distributions. Source: Ref 27

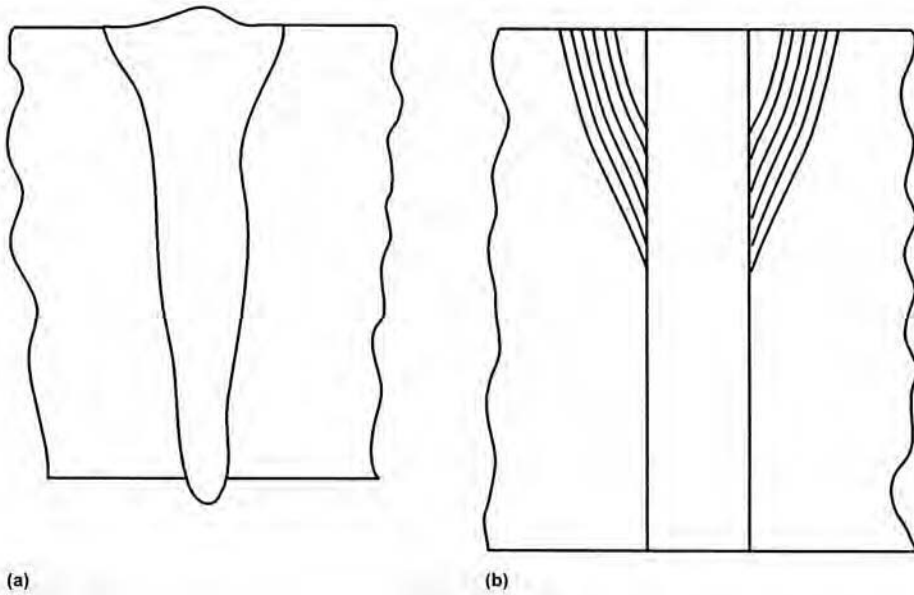


Fig. 11 Outlines of cross sections of (a) experimental and (b) calculated keyhole welds. Calculated results shown for several different point sources added to the line source. Source: Ref 31

actually held together by the compressive force exerted by the electrodes. Because the input energy in this weld process is due to joule heating, the spatial distribution of the current and the electrical resistance within the workpiece must be determined when modeling the heat source. Most importantly, the contact resistance at the surfaces of both the electrode and the workpiece, as well as the interfaces of the workpieces, must be established. The electrical contact resistance depends on the surface condition of the material, its hardness, the degree of oxidation, the amount and kind of impurities, as well as the apparent pressure at the surfaces and the temperature. The fact that these quantities are time dependent is another complication, because the joule heat source must be considered as a time-dependent parameter.

A detailed description of the process is presented in the article “Resistance Spot Welding” in this Volume. Literature reviews of the resistance spot welding process simulation are provided in Ref 33 and 34. The brief overview provided subsequently of some important findings in the literature on resistance welding highlights several points that must be considered when developing a model of the heat source.

In 1958, experimental and analytical investigations of the resistance spot welding process were performed (Ref 35). The researchers reported current density singularities at the outer rim of the contact area from theory and correlated this phenomenon with experimental results that showed heat concentration at the periphery. They concluded that the bulk of the material near the contact region was not heated appreciably by the flow of current through it but was heated indirectly by conduction from the

peripheral region of the contact area. However, further study indicated that the contact area plays a major role only in the early stages of weld-nugget formation. This fact reinforces the earlier remarks that the modeling of the heat source must consider not only the spatial distribution of the heat source but its time dependence.

Further reinforcing this idea, it was found (Ref 36) that in the beginning of the welding process, most of the voltage drop occurred at the interface between the electrode and the weldment and in the interface of the two workpieces (21 and 66%, respectively). The researchers determined that after six cycles from the instant that weldment fusion begins, most of the voltage drop takes place in the base metal (87%). This occurs because the interfacial resistance decreases as the temperature rises, which is due to melting at the interface, and because the resistivity of the base metal increases with increased temperature.

Complicating the modeling process is the unknown, but very important, contact diameter at the faying surface. This parameter depends on the geometry of the electrodes, the surface conditions, and, most importantly, the mechanical load applied by the electrode. Research (Ref 34) in modeling this process has used the diameter of the electrode face as the contact diameter between the electrode and the workpiece, but a slightly larger diameter is used to represent the contact diameter at the interface of the workpieces. Figures 13 and 14 show the current density and joule heating as functions of the nondimensional radius R/R_c , where R_c is the assumed contact radius.

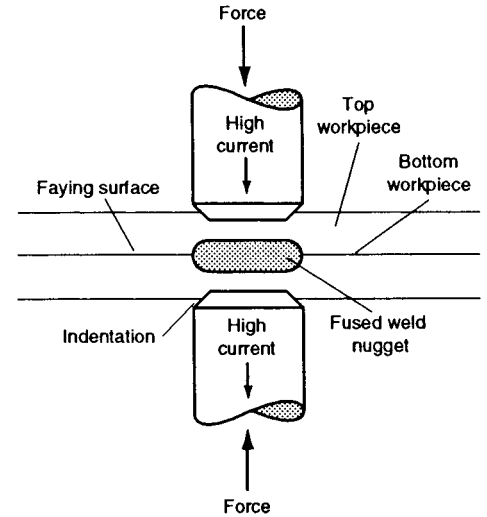


Fig. 12 Resistance spot welding process

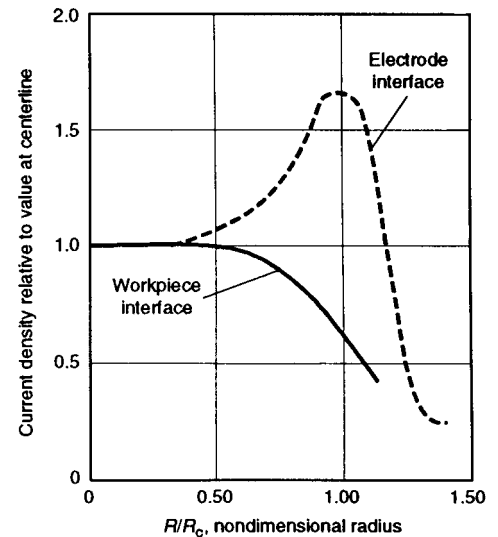


Fig. 13 Current density ratio versus nondimensional radius. Time, 2 cycles; R_c , radius of contact. Source: Ref 33

The authors of both Ref 33 and 34 stress the importance of developing a thermomechanical coupling model that will account for changes in resistance and current distributions during the welding process. This article has tried to point out that the input description of the heat source for resistance welding is extremely complicated. It depends on the electrode geometry, the weldment material, and the weldment surface condition, as well as the weld parameters (including the mechanical forces on the electrode) that must be considered as being time dependent.

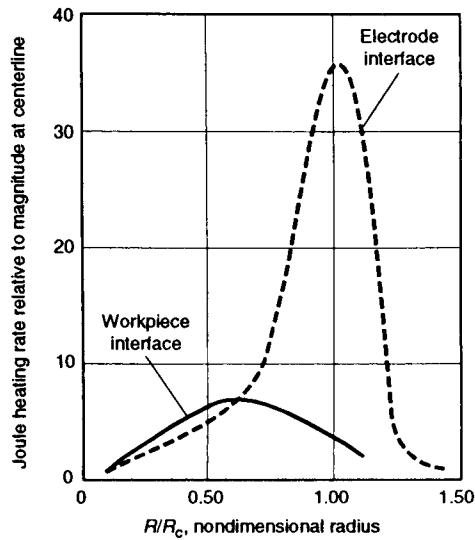


Fig. 14 Joule heating rate ratio versus nondimensional radius. Time, 2 cycles; R_c , radius of contact. Source: Ref 33

REFERENCES

- P.S. Myers, O.A. Uyehara, and G.L. Borman, Fundamentals of Heat Flow in Welding, *Weld. Res. Council Bull.*, No. 123, July 1967
- H.S. Carslaw and J.C. Jaeger, *Conduction of Heat in Solids*, Clarendon Press, London, 1959
- D. Rosenthal and R. Schmerber, Thermal Study of Arc Welding, *Weld. J. Res. Suppl.*, Vol 17 (No. 4), 1938, p 2s-8s
- D. Rosenthal, The Theory of Moving Sources of Heat and Its Application to Metal Treatments, *Trans. ASME.*, Vol 68, 1946, p 849-866
- W. Soedel and R. Cohen, Arc-Welding Temperatures in a Circular Disk Structure, *Weld. J. Res. Suppl.*, Vol 49 (No. 7), 1970, p 337s-340s
- T. Naka and K. Masubuchi, Temperature Distribution of Welded Plates, *J. Jpn. Weld. Soc.*, Vol 16 (No. 7 and 12), 1947, p 281-290 (Part I) and p 374-378 (Part II)
- E.F. Rybicki et al., A Finite-Element Model for Residual Stresses and Deflections in Girth-Butt Welded Pipes, *J. Pressure Vessel Technol. (Trans. ASME)*, Vol 100, Aug 1978, p 256-262
- P.A. Schoeck, An Investigation of the Anode Energy Balance of High Intensity Arcs in Argon, *Modern Developments in Heat Transfer*, Academic Press, 1963, p 353-400
- M.B.C. Quigley, P.H. Richards, D.T. Swift-Hook, and A.E.F. Gick, Heat Flow to the Workpiece from a TIG Welding Arc, *J. Phys. D: Appl. Phys.*, Vol 6, Dec 1973, p 2250-2259
- E. Friedman and S.S. Glickstein, An Investigation of the Thermal Response of Stationary Gas Tungsten-Arc Welds, *Weld. J. Res. Suppl.*, Vol 55 (No. 12), Dec 1976, p 408s-420s
- R.A. Chihoski, The Rationing of Power Between the Gas Tungsten Arc and Electrode, *Weld. J. Res. Suppl.*, Vol 49 (No. 2), Feb 1970, p 69s-82s
- J.F. Key, Anode/Cathode Geometry and Shielding Gas Interrelationships in GTAW, *Weld. J. Res. Suppl.*, Dec 1980, p 364-s
- V. Pavelic, R. Tanbakuchi, O.A. Uyehara, and P.S. Myers, Experimental and Computed Temperature Histories in Gas Tungsten-Arc Welding of Thin Plates, *Weld. J. Res. Suppl.*, Vol 48 (No. 7), 1969, p 295s-305s
- N.S. Tsai and T.W. Eager, Distribution of the Heat and Current Fluxes in Gas Tungsten Arcs, *Metall. Trans. B*, Vol 16 (No. 12), 1985
- S.S. Glickstein and E. Friedman, Weld Modeling Applications, *Weld. J.*, Vol 69 (No. 9), 1984, p 38-42
- H.B. Smartt, J.A. Stewart, and C.J. Einson, "Heat Transfer in Gas Tungsten Arc Welding," ASM Technology Series Paper 8511-011, ASM International
- E. Friedman, Thermomechanical Analysis of the Welding Process Using the Finite Element Method, *J. Pressure Vessel Technol. (Trans. ASME)*, Vol 97, Aug 1975, p 206-213
- J. Goldak et al., Computer Modeling of Heat Flow in Welds, *Metall. Trans. B*, Vol 17, Sept 1986, p 587-600
- J.H. Waszink and G.J.P.M. Van Den Heuval, Heat Generation and Heat Flow in the Filler Metal in GMA Welding, *Weld. J. Res. Suppl.*, Vol 61, Aug 1982, p 269s-282s
- W.G. Essers and R. Walter, Heat Transfer and Penetration Mechanisms with GMA and Plasma-GMA Welding, *Weld. J. Res. Suppl.*, Vol 60, Feb 1981, p 37s-42s
- K.C. Tsao and C.S. Wu, Fluid Flow and Heat Transfer in GMA Weld Pools, *Weld. J. Res. Suppl.*, Vol 67, March 1988, p 70s-75s
- P. Tekriwal and J. Mazumder, Finite Element Analysis of Three-Dimensional Transient Heat Transfer in GMA Welding, *Weld. J. Res. Suppl.*, Vol 67 (No. 7), 1988, p 150s-156s
- B.L. Josefson, Residual Stresses and Their Redistribution during Annealing of a Girth-Butt Welded Thin-Walled Pipe, *J. Pressure Vessel Technol. (Trans. ASME)*, Vol 104, Aug 1982, p 245-250
- R.P. Martukanitz, A Critical Review of Laser Beam Welding, *Proceedings of the International Symposium on Lasers and Applications in Science and Engineering*, Vol 5706, SPIE, 2005
- T.Y. Yang, W.L. Kruer, R.M. More, and A.B. Langdon, Absorption of Laser Light in Overdense Plasmas by Sheath Inverse Bremsstrahlung, *Phys. Plasmas*, Vol 2, 1995, p 3146-3154
- A. Poueyo-Verwaerde, B. Dabezies, and R. Fabbro, Thermal Coupling Inside the Keyhole during Welding Process, *Laser Materials Processing: Industrial and Microelectronics*, Vol 2207, SPIE, 1994, p 175-184
- S.M. Kelly, Applied Research Laboratory, Pennsylvania State University, personal communication, March 2011
- D.T. Swift-Hook and A.E.F. Gick, Penetration Welding with Lasers—Analytical Study Indicates That Present Laser Beam Welding Capabilities May Be Extended Tenfold, *Weld. J. Res. Suppl.*, Vol 52, 1973, p 492s-499s
- D. Rosenthal, Mathematical Theory of Heat Distribution during Welding and Cutting, *Weld. J. Res. Suppl.*, Vol 20, 1941, p 220s-234s
- H.E. Cline and T.R. Anthony, Heat Treating and Melting Material with a Scanning Laser or Electron Beam, *J. Appl. Phys.*, Vol 48 (No. 9), 1977, p 3895
- W.M. Steen, J. Dowden, M. Davis, and P. Kapadia, A Point and Line Source Model of Laser Keyhole Welding, *J. Phys. D: Appl. Phys.*, Vol 21, 1988, p 1255-1260
- J. Mazumder and W.M. Steen, Heat Transfer Model for CW Laser Material Processing, *J. Appl. Phys.*, Vol 51 (No. 2), 1980, p 941
- H.A. Nied, The Finite Element Modeling of the Resistance Spot Welding Process, *Weld. J. Res. Suppl.*, April 1984, p 123-s
- C.L. Tsai, O.A. Jammal, J.C. Papritan, and D.W. Dickinson, Modeling of Resistance Spot Weld Nugget Growth, *Weld. J. Res. Suppl.*, Feb 1992, p 47-s
- J.A. Greenwood and J.B.P. Williamson, Electrical Conduction in Solids—II. Theory of Temperature-Dependent Conductors, *Proc. R. Soc. (London)*, Vol 246, 1958, p 13-31
- H.S. Cho and Y.J. Cho, A Study of the Thermal Behavior in Resistance Spot Welding, *Weld. J. Res. Suppl.*, June 1989, p 236-s to 244-s

Nature and Behavior of Fluxes Used for Welding

Wesley Wang, ESAB Welding & Cutting Products
S. Liu, Colorado School of Mines

FLUXES are added to the welding environment to improve arc stability, to provide a slag, to add alloying elements, and to refine the weld pool (Ref 1, 2). Different ingredients in the flux system will provide the process with different pyrometallurgical characteristics and thus different weld-metal properties (Ref 3, 4). More specifically, a welding flux must:

- Stabilize the arc and control arc resistivity
- Provide slag with the proper melting temperature
- Provide low-density slag
- Permit the use of different types of current and polarity
- Add alloying elements
- Refine the weld pool (deoxidation and desulfurization)
- Provide proper viscosity for out-of-position welding
- Promote slag detachability
- Produce smooth weld contour
- Reduce spatter and fume

The slag that forms during welding covers the hot weld metal and protects it from the atmosphere. Welding slag consists of the glass-forming components of the flux, as well as inclusions that form in the weld pool, coalesce, rise, and become incorporated into the slag.

The need to improve flux formulation to achieve optimal weld metal composition, and ultimately improve the properties of weldments, has led to fundamental studies of weld pyrochemistry. Understanding the thermodynamic and kinetic factors that are prevalent at the electrode, in the arc column, and in the weld pool has led to more precise prediction of the final weld metal composition (Ref 5–15).

In addition, quality bead appearance, the ease of welding at different positions, as well as easy slag detachability are considerations for flux formulation.

Equilibrium Parameters

Equilibrium is not achieved during welding, because of the very large temperature and density

gradients, the short reaction times, and the large electric currents. Despite these expected departures from equilibrium, thermodynamic considerations can be used as a guide for constraining chemical reactions and mechanisms involved in welding (Ref 5, 7, 9). A common approach is to assume that extremely high temperatures and high surface-to-volume ratios allow thermodynamic equilibrium to be locally attained, in spite of the short reaction times available.

Further complicating the issue is the dependence on welding parameters of the chemical partitioning between the slag and the weld metal (Ref 3, 7). This dependence suggests that the pyrometallurgical reactions involved are influenced by the processes that occur at the electrode tip. As a specific example, the welding parameters affect metal-transfer mode and metal droplet size, which in turn alter the chemical kinetics. Nonetheless, thermodynamics will reveal the direction taken by the chemical reactions (but will not accurately predict weld-metal composition).

The effective slag-metal reaction temperature has been estimated (by pyrochemical analysis of slag-metal compositions) to be approximately 1900 °C (3450 °F), a temperature intermediate between that of the hot spot at the arc root (2300 °C, or 4170 °F) and the melting point of iron (1500 °C, or 2730 °F). Thus, during the droplet lifetime, the average temperature is effectively 1900 °C (2730 °F). During this period, oxygen from the hot spot reactions is distributed throughout the droplet, and that oxygen reacts with the metallic elements to form oxides; these products of oxidation pass into the slag, and the slag-metal reactions tend toward equilibrium. Despite shielding, some nitrogen may still be present in the arc. Thus, similar considerations presented previously for oxygen should be given to nitrogen as well. Estimates of the time for which the molten slag and molten metal are in contact range from 3 to 8 s. During the process, the gaseous phase in the arc cavity contacts the metal for an estimated 0.5 to 1.0 s.

Effect of Oxygen

The most important chemical reagent in controlling weld metal composition, and thus microstructure and properties, is oxygen (Ref 3, 4, 14, 16–19). Oxygen directly reacts with alloying elements to alter their effective roles by:

- Reducing hardenability
- Promoting porosity
- Producing inclusions

All three effects are significant to weld quality.

Oxygen is introduced into the weld pool at high temperatures by:

- The presence of oxide fluxes that dissociate in the arc
- The slag-metal reactions in the weld pool
- The oxides on the surface of baked metallic powders mixed with flux or on electrode
- The aspiration of atmosphere (air) into the arc.
- Lubricants on solid and composite (metal cored and flux cored) wires

Shielding gas may contain oxidizing reagents; examples of common industrial gases used in welding are 75Ar-25CO₂ or 100% CO₂. As a result, the weld metal oxygen can range from 100 to over 1000 ppm, depending on the type of welding consumable used.

The weld metal oxygen measured directly at the molten electrode tip has been reported to be as high as 1400 ppm. Individual droplets have been found to contain as much as 2000 ppm oxygen. There are two views concerning the genesis of the high oxygen content. One suggests that pyrochemical or electrochemical reactions (or both) provide oxygen to the electrode tip, and then further oxidation occurs within the droplet as it passes through the arc. The other view is that the high oxygen levels of the droplet represent the maximum buildup of oxygen in the electrode prior to detachment, with limited reaction during flight across the arc

to the weld pool. In either case, high oxygen concentrations are introduced into the weld pool by the welding process.

At the melting point of iron, the solubility of oxygen in pure liquid iron is approximately 1600 ppm at 100 kPa (1 atm) pressure. During solidification, oxygen solubility decreases to approximately 860 ppm at 1500 °C (2730 °F) in δ-Fe. Most of the alloying elements present in liquid steel reduce oxygen solubility through deoxidation equilibria. Steelmaking processes typically yield analytical oxygen levels ranging from 70 to 100 ppm. Welds typically pick up oxygen to levels of several hundred ppm, then deoxidize to oxygen levels of approximately 200 to 300 ppm. Deoxidation of the weld metal occurs in two separate steps, the first being the primary deoxidation of the weld pool (Ref 6). Secondary deoxidation occurs during solidification as solute concentrations increase within the intercellular or interdendritic regions. The secondary deoxidation will either form very small inclusions or will coat the interdendritically trapped primary inclusions.

The high oxygen concentrations added to the weld pool by the metal droplets significantly affect deoxidation. Figure 1 shows experimentally measured soluble oxygen concentrations for various deoxidants (solid lines), along with deoxidation curves predicted by the solubility products (broken lines). The experimental deviation is caused by interactions of the deoxidant with other alloy elements. If the oxygen and metallic element concentrations resulting from the welding process exceed the equilibrium concentration for a specific reaction, inclusions will result. The ability to form a specific inclusion will correspond directly to the position of the weld pool composition relative to the activity plot for this inclusion. Thus, the thermodynamic order for the formation of primary oxides would be $Al_2O_3 > Ti_2O_3 > SiO_2 > Cr_2O_4 > MnO$.

Inclusion Formation. Inclusions form as a result of reactions between metallic alloy elements and nonmetallic tramp elements, or by mechanical entrapment of nonmetallic slag or refractory particles. Inclusions may include:

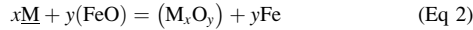
- Oxides
- Sulfides
- Nitrides
- Carbides
- Other compounds
- Multiple phases

Among these, oxides and complex oxides occur most frequently in the size range known to influence steel weld-metal microstructure.

Using only thermodynamic considerations in the analysis of slag-metal reactions, the following reactions may be considered as the ones that describe inclusion formation:



where the underlining of a component \bar{M} (\bar{O}) and the component \bar{O} (\bar{M}) indicate that \bar{M} and \bar{O} , respectively, are dissolved in the metal, and:



The equilibrium constants (K_1 and K_2) for the aforementioned two reactions are:

$$K_1 = \frac{(a_{M_xO_y})}{[a_M]^x [a_O]^y} \quad (\text{Eq 3})$$

where a_i is the activity, a function of the concentration, for component i , and:

$$K_2 = \frac{(a_{M_xO_y})}{[a_M]^x [a_{\text{FeO}}]^y} \quad (\text{Eq 4})$$

Equilibrium compositions for the weld deposit can be estimated with Eq 1 through 4 and can be used to predict trends for the weld pool pyrochemical reactions. The actual compositions may, however, differ from the calculated values due to the partitioning of alloying element

during cellular or dendritic solidification, commonly observed in steel weldments.

During solidification of a weld metal, solute elements segregate to the liquid at the solid/liquid interface, and the solute concentrations can reach high levels in the interdendritic regions, as suggested in Fig. 2. Neglecting solid diffusion, the solute composition in the liquid at the solid/liquid interface can be modeled (Ref 6) by the nonequilibrium lever rule, or Scheil equation:

$$C_L = C_0 f_L^{k-1} \quad (\text{Eq 5})$$

where C_0 is the bulk concentration in the weld pool, C_L is the solute concentration in the liquid at the interface, and k is the equilibrium partition ratio.

The equilibrium partition ratio, k , controls the direction and the extent of segregation. For most alloy elements in steel, the partition ratio is less than 1, and the element segregates to the interdendritic liquid.

Consider the deoxidation equilibrium as represented by the dissolution reaction for a complex oxide:

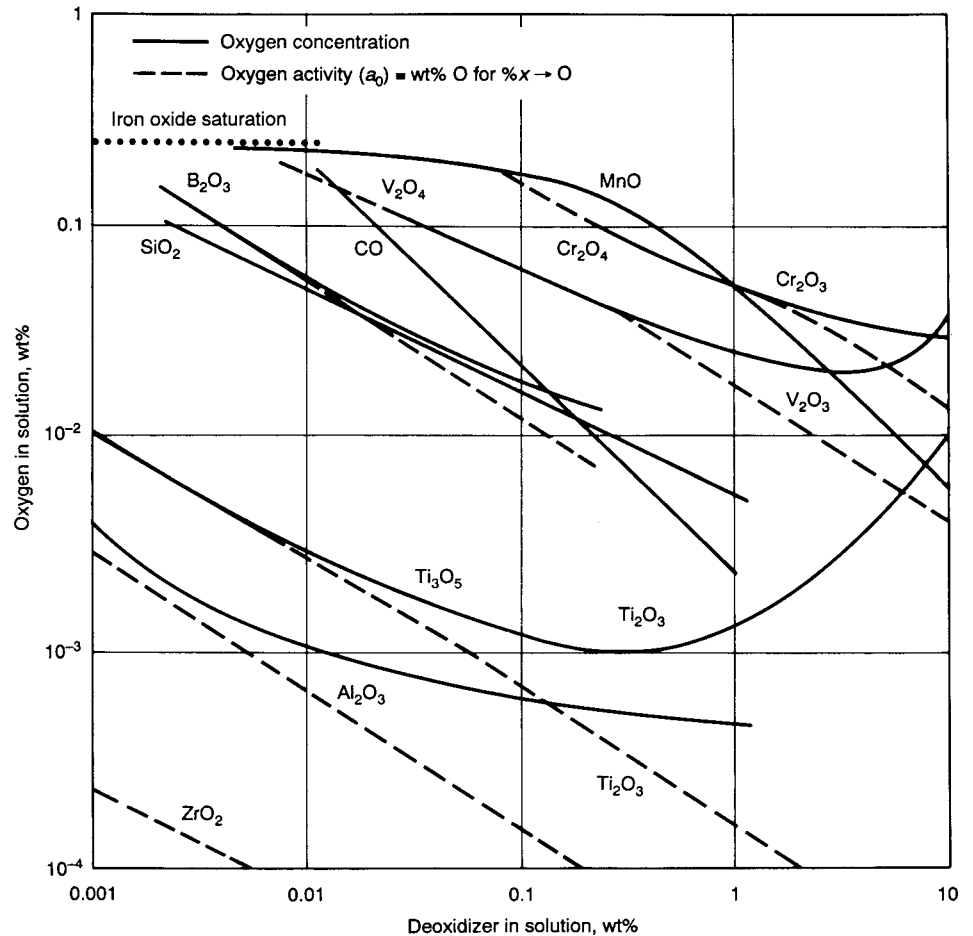


Fig. 1 Deoxidation equilibria in liquid iron alloys at 1600 °C (2910 °F). The broken lines show deoxidation equilibria predicted by solubility product calculations. The solid lines show experimentally determined soluble oxygen concentrations for various deoxidants. The experimental deviation is caused by variations in the activity coefficients with increasing deoxidant concentration. Source: Ref 20

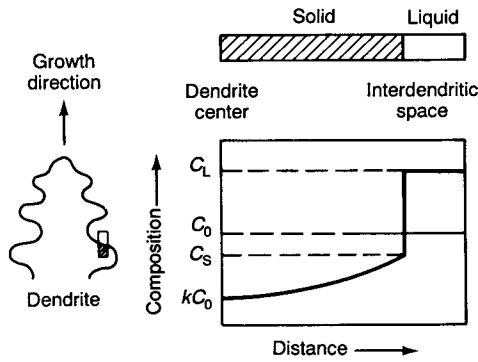
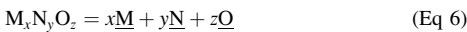


Fig. 2 Schematic showing the solid and liquid composition profiles modeled by Eq 5 based on the assumption that there is complete liquid diffusion and no solid diffusion. C_0 , the initial alloy composition; k , the partition ratio of the solid to liquid compositions on the equilibrium phase diagram; kC_0 , the initial composition of the solid; and C_S and C_L , the solid and liquid compositions, respectively, at the solidification interface. Source: Ref 4



The free energy change associated with the dissolution of the $M_xN_yO_z$ can be written as:

$$\Delta G = \Delta G^0 + RT \ln \frac{[M]^x[N]^y[O]^z}{[M_xN_yO_z]} \quad (\text{Eq 7})$$

where $[M]$, $[N]$, and $[O]$ are the solute activities in the liquid; and x , y , and z are the stoichiometric constants from Eq 6. The value $[M_xN_yO_z]$ is the activity for the specific inclusion and can be assumed to have a value of 1.

The ratio of the activities of the reactants to that of the oxide can be termed the activity quotient (Q):

$$Q = \frac{[M]^x[N]^y[O]^z}{[M_xN_yO_z]} \quad (\text{Eq 8})$$

With Eq 5 representing the extent of segregation, the solute activities in the interdendritic liquid can be written as:

$$[M] = [\gamma_M][M_0]f_L^{k_M-1} \quad (\text{Eq 9a})$$

$$[N] = [\gamma_N][N_0]f_L^{k_N-1} \quad (\text{Eq 9b})$$

$$[O] = [\gamma_O][O_0]f_L^{k_O-1} \quad (\text{Eq 9c})$$

In Eq 9(a to c), $[M_0]$, $[N_0]$, and $[O_0]$ are the bulk concentrations of M, N, and O in the melt; and $[\gamma_M]$, $[\gamma_N]$, and $[\gamma_O]$ are the activity coefficients for the solutes.

Substituting Eq 9(a to c) into Eq 8 gives the free energy as a function of the remaining liquid fraction:

$$\Delta G = \Delta G^0 + RT \ln \frac{[\gamma_M M_0 f_L^{k_M-1}]^x [\gamma_N N_0 f_L^{k_N-1}]^y [\gamma_O O_0 f_L^{k_O-1}]^z}{[M_x N_y O_z]} \quad (\text{Eq 10})$$

Equation 10 expresses the free energy driving force for oxide dissolution. The first term on the right side, ΔG^0 , represents standard equilibrium conditions. The second term represents the departure from equilibrium caused by changes in reactant concentrations or by segregation during solidification.

At equilibrium, the free energy driving force, ΔG , is zero, and the equilibrium concentrations can be found by equating the two terms on the right side of Eq 10. At equilibrium, the activity quotient becomes the equilibrium constant, K_{eq} :

$$\Delta G^0 = -RT \ln \frac{[M]^x[N]^y[O]^z}{[M_xN_yO_z]} = -RT \ln K_{eq} \quad (\text{Eq 11})$$

Inclusion precipitation is possible when the concentrations of oxygen and deoxidants exceed the equilibrium values for a particular oxide. This condition, known as precipitation index, can be expressed as the ratio of the activity quotient to the equilibrium coefficient:

$$\text{Precipitation index} = \frac{Q}{K_{eq}} \quad (\text{Eq 12})$$

A precipitation index less than unity indicates that the concentrations of oxygen and deoxidants are below the equilibrium value, and the precipitation of the inclusions will not occur. A value greater than 1.0 indicates that concentrations are sufficiently high for precipitation according to the methodology described previously. The compounds Al_2O_3 , Ti_2O_3 , and SiO_2 are some of the oxides that will form in a low-carbon low-alloy steel weld. Multiple reactions can occur, and different oxides may appear in the same weld when more than one of these deoxidizers is present.

Metal Transferability during Pyrochemical Reactions. The final weld-metal concentration for a particular element is made up of contributions from the filler wire, flux, and base metal; however, losses caused by the welding process vary for each element.

Delta Quantity. The nominal composition of each weld can be calculated considering just the dilution effect of the filler wire and base metal. The extent of loss or transfer of a specific element can be evaluated by a quantity, which expresses the difference between the analytical and the nominal composition of a weld. These quantities, designated delta quantity in this article, indicate the effect of the flux on element transfer during welding. A positive delta quantity indicates an elemental transfer from the flux to the weld metal. A negative delta quantity suggests an elemental loss from the weld pool to the slag. A null delta quantity for a specific element suggests an apparent equilibrium condition, in which the flux and slag content for that element are the same. Flux compositions with null delta-quantity behavior have been used to make equilibrium calculations and thus achieve a better understanding of the chemical reactions involved in welding (Ref 8). Investigators have also quantified elemental transfer by measuring similar neutral points (null delta quantity) for various flux systems and have developed a thermodynamic

model capable of predicting neutral points for some slag systems (Ref 10).

Arc Stabilizers. Arc welding fluxes are compositionally more complex than fluxes used in other metallurgical processes, such as steelmaking. Many of the additions to the flux are not designed to assist weld-metal refinement. Some additions are present to promote arc stability, generate plasma and protective gases, control viscosity, support out-of-position welding, ensure sufficient wetting at weld toes, and promote slag detachability.

The welding arc requires an inert or chemically reducing plasma and shielding gas that can be easily ionized. Additions must be made to the flux to achieve the necessary current-carrying capacity and to maintain arc stability. Specific additions will be necessary for the various modes of current (direct current, dc, or alternating current, ac) and polarity.

Alkali metal, zirconium, and titanium additions to the arc affect the ionization process and the ease with which the welding arc is reinitiated (reinitiation is required 50 to 60 times per second with ac welding). These additions come to the welding flux as feldspar (alkali aluminum silicates), rutile, lithium carbonate, titanium aluminate, and potassium oxalate, and they play an especially important role when welding either in the dc electrode negative (DCEN) mode or in ac mode. Arc stabilizers are also important in high-speed welding when the cathode and anode spots are less stable. These additions are part of the American Welding Society (AWS) classification of electrodes, as seen by the fourth digit (E XXXX) in the classification standard for steel electrodes for shielded metal arc welding (SMAW) given in Table 1. The electrodes designed to perform with ac mode or in the DCEN mode have been specified as containing high titania or alkali metal (potassium or sodium) additions. Special additions such as Li_2O have been used to achieve multipurpose results, for example, reducing the viscosity while increasing the arc stability.

Changes in Flux Composition with Delta Quantity. Figure 3 shows a transfer of manganese for welds made with SiO_2 - TiO_2 - CaO -1wt% Na_2O fluxes at constant 40 wt% SiO_2 content. These values vary widely, depending on other alloy concentrations. The data indicate that manganese loss to the slag is very high, and that the activity of manganese varies considerably with changes in the amount of titania in the flux. Note, however, that because of high vapor pressure, manganese loss due to vaporization is expected to be high as well. Manganese is very important to weld-metal hardenability and must be closely controlled to obtain the optimum weld microstructure. Controlling the weld-metal manganese concentration in the titania-containing flux systems would require strict compositional control of the welding flux to ensure the correct manganese concentration in the weld metal.

In the same system, the delta titanium showed a constant increase with increasing titania content of the flux (Fig. 4). Because of the large amounts of titania in the flux, it is not surprising that the welds show positive compositional deviations for titanium. These results also suggest that close control of the weld-metal

titanium content will require control limits of the TiO₂ content of the flux. The optimal titanium concentration in a steel weld metal regarding Charpy V-notch impact toughness is 350 to 400 ppm.

If the delta quantity changes rapidly with flux composition, it may be difficult to maintain specific weld-metal composition, microstructure, and properties with variation in flux composition. The magnitude of the delta

quantity for specific elements is most often not as serious a concern as a rapid change in the delta quantity with variations in flux chemistry and welding parameters. The magnitude of the delta quantity can be adjusted by altering the alloy content of the welding wire or the amount of ferro-additions to the flux. Thus, a suitable combination of wire, flux, and welding parameters should achieve negligibly small delta quantities of major alloying elements.

Shielding Gas. When the shielding gas that protects the weld pool comes from the flux, it is necessary to understand the decomposition of specific flux components. Two common shielding gas atmospheres from flux dissociation are hydrogen and CO/CO₂. The hydrogen gas can be produced by the decomposition of cellulose (wood flour or similar hydrocarbons). A CO/CO₂ atmosphere results from the decomposition of carbonates such as limestone (CaCO₃) or dolomite [CaMg(CO₃)₂]. Combustion of the carbonaceous contents in the cellulose in the arc will also result in CO/CO₂. The CO/CO₂ atmosphere can be balanced to provide a reducing (and thus protective) atmosphere.

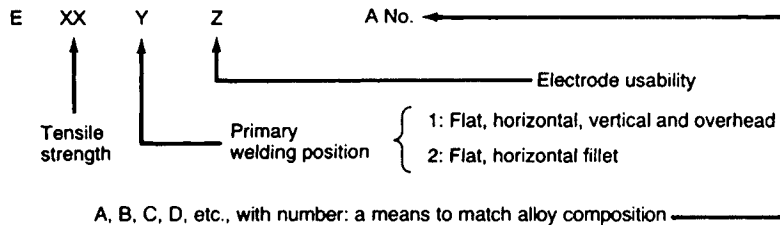
At high temperatures, CO₂ or CO will react with carbon to achieve equilibrium, which requires the presence of CO and CO₂. It is the relative amounts of CO and CO₂ that determine the reducing/oxidizing nature of the arc environment. The CO/CO₂ ratio also determines the recovery of specific alloying elements. Typical plasma atmospheres for both hydrogen-type and low-hydrogen-type electrodes are given in Table 2.

In submerged arc welding, the covering flux also produces the protective shielding gas and plasma. Other gaseous phases, including fluorine-bearing components, are also part of the plasma.

The effect of arc environment (for example, amounts of CO and CO₂) on weld-metal chemistry control for hyperbaric welding with a basic electrode is shown in Fig. 5.

Table 1 American Welding Society classification of selected shielded metal arc welding electrodes for welding mild and low-alloy steels

Electrode designation	Current and polarity(a)	Penetration	Arc stabilizers	% Fe
EXX10	DCEP	Deep	High cellulose-Na	0-10
EXXX1	ac, DCEP	Deep	High cellulose-K	0
EXXX2	ac, DCEP	Medium	High rutile-Na	0-10
EXXX3	ac, DCEP, DCEN	Light	High rutile-K	0-10
EXXX4	ac, DCEP, DCEN	Light	Rutile-iron powder	25-40
EXX24	ac, DCEP, DCEN	Light	Rutile-iron powder	50
EXXX5	DCEP	Medium	Low H-Na	0
EXXX6	ac, DCEP	Medium	Low H-K	0
EXX27	ac, DCEN, DCEP	Medium	Iron oxide-iron powder	50
EXXX8	ac, DCEP	Medium	Low hydrogen-iron powder	25-40
EXX28	ac, DCEP	Medium	Low hydrogen-iron powder	50



(a) DCEP, dc electrode positive; DCEN, dc electrode negative

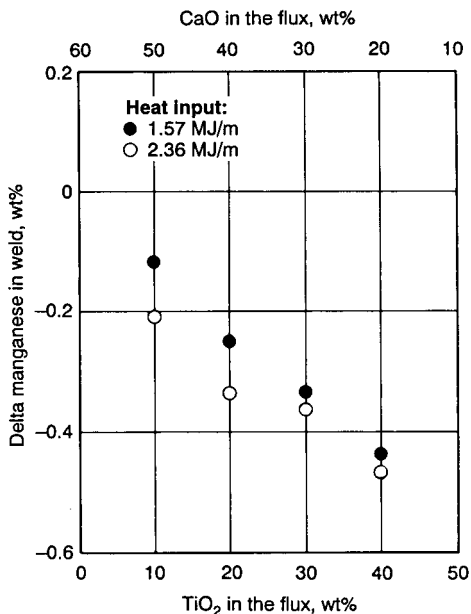


Fig. 3 Plot of changes in manganese content in the weld versus the variation in flux composition as a function of two heat inputs. The SiO₂ content was maintained at 40% throughout the flux cored arc welding process. Source: Ref 21

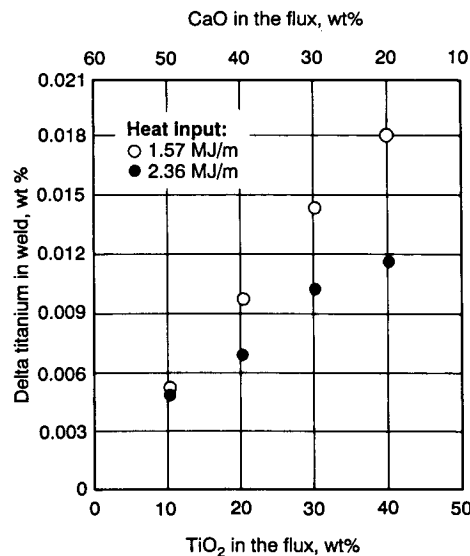


Fig. 4 Plot of changes in titanium content in the weld versus the variation in flux composition as a function of two heat inputs. The SiO₂ content was maintained at 40% throughout the flux cored arc welding process. Source: Ref 21

Table 2 Gas composition of welding arc obtained from specific types of welding electrodes

AWS designation	Type	Composition, wt%			
		H ₂ O	H ₂	CO ₂	CO
6010	Cellulosic	16	41	3	40
6015	Basic	2	2	19	77

Source: Ref 15

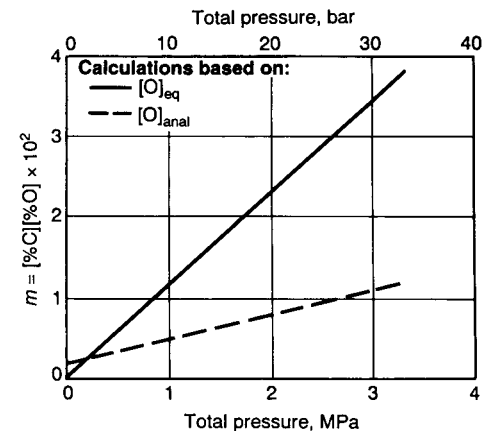


Fig. 5 Effect of pressure on the product $m = [\%C][\%O]$ for hyperbaric welding with a basic electrode. Source: Ref 12

The high-pressure welding allows evaluation of the CO reaction. Considering the CO reaction:



the law of mass action gives:

$$k = \frac{P_{CO}}{[C][O]} \quad (\text{Eq 14})$$

where [C] and [O] are the weld-metal carbon and oxygen contents, respectively. At equilibrium, the partial pressure of CO is directly related to the total pressure by Dalton's law.

In Fig. 5, two lines are indicated. The solid line plots the product of the weld-metal oxygen and carbon as a function of total pressure when the analytical weld-metal oxygen concentration, [%O]_{anal}, was used. The broken line indicates a similar relationship; however, in this case, the weld-metal oxygen concentration has been corrected for the displacement of oxygen because of the formation of manganese silicate inclusions during welding and its transport to the slag. The equilibrium oxygen content, [%O]_{eq}, in the liquid steel at high temperatures is then given by the following expression:

$$[%O]_{eq} = [%O]_{anal} + \frac{32}{28} \Delta[%Si] + \frac{16}{55} \Delta[%Mn] \quad (\text{Eq 15})$$

where Δ[%Si] and Δ[%Mn] represent the difference between the expected compositions of these elements (from knowledge of initial consumables and base plate compositions as well as dilution) and the actual compositions measured. The linearity of these lines in Fig. 5 is evidence of the strong influence of the CO reaction in arc welding.

The evidence of water reaction control for some electrodes (for example, cellulosic electrodes) can be seen in Fig. 6. With an increase in the degree of oxidation of the deposited metal, the weld-metal hydrogen content decreases (Ref 22). The relationship between weld-metal oxygen and hydrogen contents, as seen in Fig. 6, is consistent with the functional form expected from the law of mass action for an H₂O reaction. It is apparent that with increasing weld-metal oxygen content there is a significant reduction in weld-metal hydrogen. The hydrogen content of the deposited metal can be reduced by increasing the CaCO₃ content of the coating. With the ever-increasing requirements of weld-deposit properties and the increasing need for higher productivity, pyrochemistry will play an important role for flux formulation and weld property prediction.

Basicity Index

As indicated in the section "Metal Transferability during Pyrochemical Reactions" in this article, the transfer of alloying elements during welding depends strongly on the physical and chemical properties of the flux. The ability to correlate flux properties with weld-metal

chemical compositions and properties is essential to understand the interactions between weld metal and flux.

Because of the incomplete understanding of the thermodynamic properties of slags, the empirical concept of basicity has been applied to predict flux and weld properties. A basicity index, *BI*, for welding has been proposed:

$$BI = \frac{CaO + CaF_2 + MgO + K_2O + Na_2O + Li_2O + 1/2(MnO + FeO)}{SiO_2 + 1/2(Al_2O_3 + TiO_2 + ZrO_2)} \quad (\text{Eq 16})$$

where the chemical components are given in weight percent. When the basicity index for a given flux is less than 1, the flux is considered acidic. A flux with a *BI* between 1.0 and 1.2 can be classified as neutral. A flux with a *BI* greater than 1.2 is considered basic.

In general, the higher the basicity, the cleaner the weld with respect to nonmetallic inclusions (that is, lower weld-metal oxygen content) (Ref 23). Figure 7 illustrates the correlation between weld-metal oxygen and the basicity index for some flux systems. The weld-metal oxygen content drops significantly as the *BI* is increased to 1.2 and then remains relatively constant at approximately 250 ppm O. The correlation between weld-metal oxygen, which is an indirect indication of weld-metal toughness, and basicity is acceptable for some welding flux systems, especially those that are primarily based on CaO, MgO, and SiO₂. However, Eq 16 cannot be used to correlate the strength and toughness of welds made with high flux concentrations of Al₂O₃, TiO₂, ZrO₂, MnO, FeO, and CaF₂. Although numerous basicity formulas have been considered, none has been flexible enough to deal with high amphoteric oxide contents. There is still some concern over using this index (which was primarily conceived by

steelmakers for evaluating sulfur refinement) for predicting weld-metal oxygen, or for use as a general criterion for weld metal quality (Ref 7). Additionally, the *BI* does not consider the physical properties of the fluxes, nor does it explain the kinetics of the flux-metal reactions.

Basicity index has been used by the welding industry as a measure of expected weld-metal cleanliness and mechanical properties. Consequently, manufacturers of welding consumables have classified and advertised their fluxes with this index. It is believed that high basicity means high toughness, a quality of great interest to the engineer, while an acidic flux means excellent slag behavior, a characteristic of interest to the welder attempting to improve weld bead morphology and deposition rate. Table 3 classifies the various coating formulations for SMAW electrodes using the descriptors of cellulosic, basic, acid, and rutile (alternating current stabilizer and slag former).

Considerations of SMAW Formulation

Pyrochemical Kinetics during Welding.

The ability of a flux to refine as well as protect the weld pool is related to the mass transport processes in the flux. Under normal welding conditions, the flux should melt approximately 200 °C (360 °F) below that of the alloy for proper flux coverage, molten metal refinement, and for protection of the weld deposit. One of the most important physical properties of a flux is its slag viscosity, which not only governs the way the slag flows and covers the molten weld pool but also strongly affects the transport processes involved in pore removal, deoxidation, and retention of alloying additions. The chemical processing and refining by the flux to achieve a weld deposit with low concentrations of oxygen and sulfur and optimal concentration of hardenability agents (carbon, manganese, chromium, molybdenum, nickel, and so on)

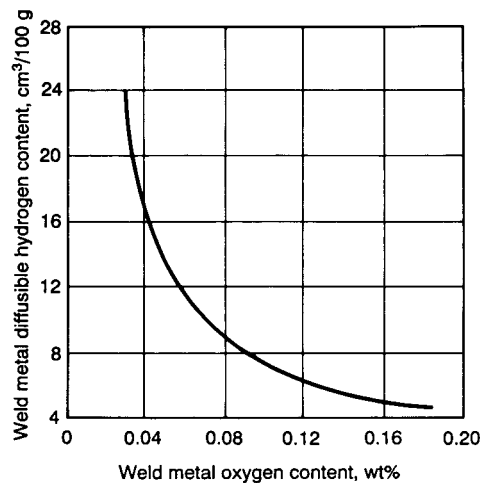


Fig. 6 Plot of weld-metal oxygen content versus weld-metal hydrogen content when welding with electrodes that contain chromium and niobium in their coating. Source: Ref 22

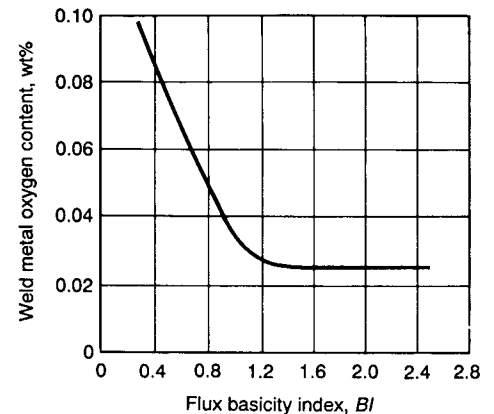


Fig. 7 Effect of weld-metal oxygen content on flux basicity index when using the submerged arc welding process. Source: Ref 23

may not be achieved unless slag viscosity is also adequate. The viscosity is strongly temperature-dependent, so the use of various heat inputs during welding may require different flux compositions to produce the matching slag viscosity. For simple ionic melts, the viscosity has been shown to follow an Arrhenius-type temperature dependence:

$$\eta = \eta_0 \exp\left(\frac{E_\eta}{RT}\right) \tag{Eq 17}$$

where η is the viscosity, η_0 is a system constant, E_η is the viscous activation energy, R is the gas constant, and T is the temperature.

For polymeric melts, Eq 17 often does not hold true. It has been shown that in certain cases a modified equation can be used:

$$\eta = \eta_0 \exp\left[\frac{E_\eta}{R(T - T_0)}\right] \tag{Eq 18}$$

where T_0 is a constant for a given flux composition. The presence of entrapped particulates tends to increase the slag viscosity. Slag viscosity is also affected by composition. The compositional dependence is commonly reported by considering E_η to be a function of composition at constant temperature.

The slag must be fluid enough so that it flows and covers the molten weld pool but must be viscous enough so that it does not run away from the molten metal and flow in front of the arc, leading to possible overlapping by the weld metal. (For overhead welding, surface tension becomes a primary factor because fluidity reduces coverage [opposite gravitational vector].) It has been reported that if the manganese silicate flux viscosity at 1450 °C (2640 °F) is above 0.7 Pa · s (7 P), a definite increase in weld surface pocking will occur. Pock marks have been associated with easily reducible oxides in the flux, which contribute oxygen to the weld pool. The weld pool reacts with carbon

to form carbon monoxide, which cannot be transported through a high-viscosity flux and is trapped at the liquid-metal/flux interface. The result is a weld metal surface blemished by surface defects or pocks. Because viscosity is sensitive to temperature and thus heat input, pocking can be the evidence that a flux formulated for high-current welding is being used at too low a current or too great a travel speed. The viscosity of most welding fluxes at 1400 °C (2550 °F) is in the range of 0.2 to 0.7 Pa · s (2 to 7 P).

Slag viscosity also affects the shape of the weld deposit and must be carefully controlled when covered electrodes are used out of position. The higher the slag viscosity, the greater the weld penetration will be in submerged arc welding. However, this benefit must be balanced, because if the viscosity is too high, the gaseous products cannot escape the weld pool, resulting in unacceptable porosity. This condition can be monitored by observing the density of pores trapped in the underside of the detached slag. Detached slags manifesting a honeycomb structure suggest a severe weld-metal porosity problem. This condition usually means that a given flux has experienced an insufficient heat input for the effective transport of gas through the slag.

Alloy Modification. Another required function of the welding consumables is to make alloy additions to the weld pool, usually in the form of powder metal or ferro-additions (Ref 1). Often, the composition of the wire that makes up the rod for the shielded metal arc electrode from a specific manufacturer is the same, regardless of the alloy to be welded. Alloying is achieved by powder metal additions to the flux coating. Manganese, silicon, chromium, niobium, and other alloying additions are adjusted in the weld pool by ferroalloy powder additions. Specially prepared alloy additions of Fe-50Si, Fe-80Mn, Fe-60Mn-30Si, and others are used. One concern in formulating

electrodes using ferro-additions is the alloying element recovery (that is, the amount of the element that is transferred across the arc and into the weld deposit). Values for the recovery of typical elements in steel welding are given in Table 4. The metal losses are either to the slag or to the fume.

Slipping and Binding Agents. In the case of SMAW electrodes, slipping agents are also added to the green flux formulation to improve the extrudability of the flux onto the rod (Ref 1). Glycerin, china clay, kaolin, talc, bentonite, and mica have all been used as slipping agents. Binding agents can be classified into two types. The first type comprises binders that bond the flux components to the rod without introducing a hydrogen source. These low-hydrogen binders include sodium silicate and potassium silicate. The second type of binding agent does function as a hydrogen source. The binders used for high-hydrogen electrodes can be organic in nature and include gum arabic, sugar, dextrine, and other specialized synthetic organic binders. Attempts are ongoing to identify and select nonconventional chemicals as binding agents

Table 4 Recovery of elements from selected electrode coverings

Alloy element	Form of material in electrode covering	Approximate recovery of element, wt%
Aluminum	Ferroaluminum	20
Boron	Ferroboron	2
Carbon	Graphite	75
Chromium	Ferrochromium	95
Niobium	Ferrocolumbium	70
Copper	Copper metal	100
Manganese	Ferromanganese	75
Molybdenum	Ferromolybdenum	97
Nickel	Electrolytic nickel	100
Silicon	Ferrosilicon	45
Titanium	Ferrotitanium	5
Vanadium	Ferrovanadium	80

Source: Ref 1

Table 3 Electrode coating formulations of selected shielded metal arc welding electrodes

Electrode		Coating formulation(a)											Comments
Type	AWS designation	Rutile	Cellulose	Quartz	Carbonates	Ferromanganese	Organics	Iron ore-manganese ore	Calcium carbonate	Complex silicates	Fluorspar	Ferroalloys	
Cellulosic	6010	20–60	10–50	15–30	0–15	5–10	Cellulose promotes gas shielding in the arc region. Hydrogen increases heat at weld. High hydrogen content (30–200 ppm). Deep penetration, fast-cooling weld
Rutile	6012	40–60	...	15–25	0–15	10–12	2–6	Slags mainly for slag shielding Relatively high hydrogen content (15–30 ppm). High inclusion content in weld deposit
	6013	20–40	...	15–25	5–25	1.4–14	0–5	
Acid-ore	6020	X	X	X	...	X	...	X	Relatively high hydrogen content. High slag content in weld metal
Basic	7015	0–10	...	0–5	20–50	...	20–40	5–10	Relatively low hydrogen levels (≤ 10 ppm), hence commonly used in welding low-alloy construction steels. Electrodes should be kept dry. Low inclusion content in weld deposit

X, data unavailable. Source: Ref 24

to substantially reduce hydrogen contents in weld metal.

Slag Formation. Slag, a mixture of glass and crystalline structure, must solidify on the already solidified weld deposit to protect the surface from oxidation during cooling. Specific physical properties are required of the slag. At 1G welding position, it could melt below the melting temperature of steel (~1450 °C, or 2640 °F), must have a density significantly less than steel to reduce slag entrapment in the weld deposit, must possess the proper viscosity in the temperature range of 1450 to 1550 °C (2640 to 2820 °F), and must easily detach from the weld deposit after welding.

Silicates, aluminates, and titanates are all primary slag formers. The high-valence cations of these compounds produce a bonding network that can promote glass formation. Most electrodes produce silicate or titanate slag. Silicates of such elements as manganese produce smooth and uniform glass deposits but also produce weld deposits that are relatively high in weld-metal oxygen content. These fluxes are said to range from acidic to neutral. The titanate and aluminate fluxes produce more rigid slag bead covering the weld. The result is generally a lower concentration of weld metal oxygen but a higher-viscosity slag. Aluminates and calcium-bearing compounds are common additions to basic fluxes for the submerged arc welding of high-toughness linepipe steels. Minerals used for slag formation include:

- Rutile
- Potassium titanate
- Ilmenite
- Alumina
- Silica flour
- Iron powder
- Fluorspar
- Feldspar
- Manganese dioxide

Asbestos (up to 50%) was used before the 1970s as a slag former but has since been removed from formulations by welding consumable manufacturers.

Slag Detachability. Slag removal is a serious productivity concern for steel fabricators. The relative ease of slag detachability influences the economic advantages of flux-related welding processes. Residual slag on the weld deposit promotes slag stringers in multipass weldments, limits the effective use of narrow-gap flux-related welding processes, and may reduce the corrosion resistance of the weldment. Welding flux formulators have modified flux compositions to alleviate or reduce this hindrance (Ref 25).

Poor slag removal has been reported to occur when the flux contains fluorite. Slags containing spinels (with $AO \cdot B_2O_3$ formula) generally have been found to attach tenaciously to the weld deposit. Slags with cordierite and $(Cr, Mn, Mg)O \cdot (Cr, Mn, Al)_2O_3$ -type spinel phases

have been reported to be difficult to remove from stainless steel weldments. It has also been reported that if $(CaO)_2SiO_2$, Cr_2TiO_5 , and $FeTiO_5$ are present, the slag readily detaches from the weld deposit (Ref 25). The compositional range for acceptable slag detachability has been reported for the $CaO \cdot CaF_2 \cdot SiO_2$ system and the $CaO \cdot TiO_2 \cdot SiO_2$ system. Easier slag removal has also been related to deoxidation with aluminum instead of titanium. Increasing the Al_2O_3 content in the flux has demonstrated improved detachability (Ref 25).

Types of Fluxes

After considering the large number of necessary requirements as described earlier, a welding flux must be carefully and deliberately formulated to achieve optimized performance. A number of different arc welding processes depend on welding fluxes. Each of these processes requires a different formulation.

SMAW Fluxes. The typical constituents and their functions in electrode coatings for the SMAW process are given in Table 5. It should be noted that the flux ingredients are based on additions of refined minerals of the earth. Natural minerals offer an economical method of keeping welding consumables at a reasonable cost. Table 6 presents the elemental content of these minerals. Table 7 gives the typical chemical compositions for flux coatings for three different SMAW electrodes.

Submerged Arc Welding (SAW). In the SAW process, the flux drops from a hopper onto the work such that the welding arc is submerged beneath the granular flux, producing an arc cavity that contains metal vapors, silicon monoxide, manganese oxide, gaseous fluorides, and other higher-vapor-pressure components of the flux. This arc welding process has been recognized as one that produces very little, if

any, fume. Submerged arc welding is limited mainly to the flat or horizontal position and requires significant setup time. It is very successful in manufacturing numerous similar parts and long-seam welding of heavy-section steel parts, such as producing welded steel pipe.

Submerged arc fluxes are made in three different forms:

- *Bonded fluxes* mix nonmetallic and ferro-additions with a low-temperature binder into mixtures of small particles.
- *Agglomerated fluxes* are similar to the bonded fluxes except that a ceramic glass binder, cured at high temperature, is used.
- *Fused fluxes* are made by pouring a homogeneous glass mixture of the proper flux composition into water, resulting in a frit.

Generally speaking, changing from bonded to agglomerated to fused fluxes improves control of the weld-metal composition, especially with respect to such impurities as hydrogen and oxygen.

There are seven types of submerged arc fluxes (Table 8). Flux classification according to basicity is the result of observed correlations between weld-metal oxygen concentration and flux composition. Table 9 gives some typical compositions for SAW fluxes.

Flux cored arc welding (FCAW) uses a hollow wire filled with flux reagents and ferro-additions. The two types of flux cored electrodes are gas-shielded flux cored electrodes and self-shielded flux cored electrodes (Ref 26). Table 10 gives typical chemical compositions for the three types of carbon-dioxide-shielded cored electrodes. Table 11 gives the typical chemical compositions for the four types of self-shielded flux cored electrodes.

There are two types of gas-shielded FCAW wires: ferrous and nonferrous. Ferrous wires, including carbon steel and stainless steels wires,

Table 5 Typical functions and compositions of constituents for selected mild steel shielded metal arc welding electrode coatings

Coating constituent	Function of constituent		Composition range of coating on electrode				
	Primary	Secondary	E6010, E6011	E6013	E7018	E7024	E7028
Cellulose	Shielding gas	...	25-40	2-12	...	1-5	...
Calcium carbonate	Shielding gas	Fluxing agent	...	0-5	15-30	0-5	0-5
Fluorspar	Slag former	Fluxing agent	15-30	...	5-10
Dolomite	Shielding gas	Fluxing agent	5-10
Titanium dioxide (rutile)	Slag former	Arc stabilizer	10-20	30-55	0-5	20-35	10-20
Potassium titanate	Arc stabilizer	Slag former	(a)	(a)	0-5	...	0-5
Feldspar	Slag former	Stabilizer	...	0-20	0-5	...	0-5
Mica	Extrusion	Stabilizer	...	0-15	...	0-5	...
Clay	Extrusion	Slag former	...	0-10
Silica	Slag former
Asbestos	Slag former	Extrusion	10-20
Manganese oxide	Slag former	Alloying
Iron oxide	Slag former
Iron powder	Deposition rate	Contact welding	25-40	40-55	40-55
Ferrosilicon	Deoxidizer	5-10	0-5	2-6
Ferromanganese	Alloying	Deoxidizer	5-10	5-10	2-6	5-10	2-6
Sodium silicate	Binder	Fluxing agent	20-30	5-10	0-5	0-10	0-5
Potassium silicate	Arc stabilizer	Binder	(b)	5-15(b)	5-10	0-10	0-5

(a) Replaces titanium dioxide (rutile) to permit use with alternating current. (b) Replaces sodium silicate to permit use with alternating current

are the dominant part of the gas-shielded FCAW wire family. The nonferrous wires include copper-nickel alloy, Inconel, and titanium wires. In addition to the gas-shielded FCAW wires,

gas-shielded metal cored wires that use iron powder as a predominant component in their cores also have carbon steel and stainless steel types.

Most self-shielded FCAW wires are carbon steel wires. There are only a few stainless steel FCAW wires designed for hardfacing, overlay, or repairing applications.

Considerations of FCAW Formulation.

The purpose of flux formulation is to achieve a successful welding process to produce acceptable weld beads that meet predetermined qualifications through the assistance of fluxes and the resultant slag. Flux cored arc welding requires a stable arc, friendly puddle handling, easy slag removal to yield a continuous bead with a smooth and compact profile, and a proper amount of transferred alloying elements. Therefore, a flux/slag system must be designed accordingly.

A successful flux formula consists of five essential groups of ingredients. Each group not only plays its own role but also interacts with the others. They can be categorized accordingly as follows.

Group I: Viscosity Controllers. During welding, the liquid slag is pushed away from the arc column. Most of the slag builds up behind the moving puddle. To minimize the exposure of liquid metal to the welding environment, the viscosity of the liquid slag must be controlled such that the liquid slag follows the moving puddle consistently and

in a timely manner. The viscosity can be reduced by breaking down the slag network (using Ca²⁺ and other metal ions in the titanate or silicate network) to facilitate the slag flow. Usually, a liquid slag with correct viscosity can achieve a desirable balance of surface tensions at the weld toe, that is, good wetting to produce a weld with smooth transition at the weld toe and flat reinforcement crown.

Group II: Network Builders. The slag network formers are the essential ingredients with respect to the integrity of the slag covering on a weld bead. They can form a two- or three-dimensional network. They can be oxides, such as rutile (TiO₂), iron oxide, silicates, and so on, and fluorides, including CaF₂, BaF₂, and so on. These network formers determine the nature of a slag system, forming either an oxide-type slag or a fluoride-type slag or a combined one. Rutile- or CaF₂-base flux systems are commonly used for gas-shielded flux cored wires, and the iron-oxide- or BaF₂-base flux systems are used for self-shielded flux cored wires.

Group III: Deposit Volume Controllers. Metal sheath, iron powder, and metal alloys are the major contributors to a weld-metal pool. The weight or volume of a liquid puddle can affect the welding process significantly. For instance, a carbon steel flux cored wire designed to have a significant amount of iron powder (for example, 50% iron powder in an

Table 6 Typical composition of common minerals used in SMAW electrode coatings

Mineral	Chemical composition
Ilmenite	FeO · TiO ₂
Talc	3MgO · 4SiO ₂ · H ₂ O
Bentonite	Complex Al, Mg, Ca, Fe hydroxides
Silica, quartz	SiO ₂
Cellulose	(C ₆ H ₁₀ O ₅) _x
Alumina	Al ₂ O ₃
Muscovite, mica(a)	K ₂ O · 3Al ₂ · 6SiO ₂ · 2H ₂ O
Actinolite	CaO · MgO · 2FeO · 4SiO ₂
Magnetite	Fe ₃ O ₄
Hematite	Fe ₂ O ₃
Rutile, titania	TiO ₂
Dolomite	MgO · CaO · (CO ₂) ₂
Fluorspar, fluorite	CaF ₂
Cryolite	Na ₃ AlF ₆
Lime	CaO
Limestone, calcite, marble	CaCO ₃
Zirconia	ZrO ₂
Feldspar(a)	K ₂ O · Al ₂ O ₃ · 6SiO ₂
Clay(a)	Al ₂ O ₃ · 2SiO ₂ · 2H ₂ O
Sodium silicate	SiO ₂ /Na ₂ O (ratio-3.22)
Potassium silicate	SiO ₂ /K ₂ O (ratio-2.11)
Chromic oxide	Cr ₂ O ₃

(a) Although these substances can have several chemical compositions, only typical composition is given. Source: Ref 1

Table 7 Chemical composition of coverings used in electrodes for shielded metal arc welding of mild steels and low-alloy steels

Description	Electrode AWS designation	Composition(a), wt%														
		CaO	TiO ₂	CaF ₂	SiO ₂	Al ₂ O ₃	MgO	Na ₃ AlF ₆	N ₂ O	FeO	Si	Mn	Fe	CO + Co ₂	Volatile matter	Moisture
High-cellulose, gas shielded	E6010	...	10.1	...	47.0	...	3.2	...	5.1	1.3	1.5	2.8	25.0	4.0
High-titanium gas-slag shield	E6012	...	46.0	...	23.6	5.0	2.0	...	2.4	7.0	1.5	2.5	5.0	2.0
Low-hydrogen iron powder	E7018	14.4	...	11.0	20.5	2.0	1.0	5.0	1.2	...	2.5	1.8	28.5	12.0	...	0.1

(a) After baking. Source: Ref 1

Table 8 Fluxes used for submerged arc welding applications

Flux type	Constituents	Basicity	Flux form	Advantages	Limitations	Comments
Manganese silicate	MnO + SiO ₂ > 50%	Acid	Fused	Moderate strength; tolerant to rust; fast welding speeds; high heat input; good storage	Limited use for multipass welding; use where no toughness requirement; high weld metal oxygen; increase in silicon on welding; low in carbon	Associated manganese gain; maximum current, 1100 A; higher welding speeds
Calcium-high silica	CaO + MgO + SiO ₂ > 60%	Acid	Agglomerated, fused	High welding current; tolerant to rust	Poor weld toughness; use where no toughness requirement; high weld metal oxygen	Differ in silicon gain; some capable of 2500 A; wires with high manganese
Calcium silicate-neutral	CaO + MgO + SiO ₂ > 60%	Neutral	Agglomerated, fused	Moderate strength and toughness; all current types; tolerant to rust; single- or multiple-pass weld
Calcium silicate-low silica	CaO + MgO + SiO ₂ > 60%	Basic	Agglomerated, fused	Good toughness with medium strength; fast welding speeds; less change in composition and lower oxygen	Not tolerant to rust; not used for multiwire welding	...
Aluminate basic	Al ₂ O ₃ + CaO + MgO > 45%; Al ₂ O ₃ > 20%	Basic	Agglomerated	Good strength and toughness in multipass welds; no change in carbon; loss of sulfur and silicon	Not tolerant to rust, limited to de electrode positive	Usually manganese gain; maximum current 1200 A; good mechanical properties
Alumina	Bauxite base	Neutral	Agglomerated, fused	Less change in weld composition and lower oxygen than for acid type; moderate to fast welding speeds
Basic fluoride	CaO + MgO + MnO + CaF ₂ > 50%; SiO ₂ ≤ 22%; CaF ₂ ≤ 15%	Basic	Agglomerated, fused	Very low oxygen; moderate to good low-temperature toughness	May present problems of slag detachability; may present problem of moisture pickup	Can be used with all wires, preferable dc welding; very good weld properties

FCAW wire formulation) can produce an overweighed weld pool. When this wire is used in an out-of-position application, the slag will not be able to support the puddle, resulting in an overflow or dripping of the liquid metal. Therefore, this type of wire is limited to the flat and down-hand welding position.

Fluorides are the most effective agents to increase the fluidity of liquid slag, along with their hydrogen-removal effect. However, if the liquid slag is too fluid, it tends to flow away from the liquid steel pool, losing its protection effect.

On the contrary, if a wire is overdesigned regarding flux volume, the resultant weld pool can be overcrowded with slag, causing slag inclusion and removal problems. Hence, it reduces the welding efficiency.

It should be noted that the volume of a liquid pool and the amount of alloying elements can also be adjusted by the weight percent fill of the flux core in a wire, provided there is a constant welding condition.

Group IV: Arc Energy and Stability Controllers. In addition to the welding current and voltage, arc energy can also be provided by the flux core ingredients to achieve smooth arc performance. During welding, a stable arc is critical to achieve high arc energy efficiency; otherwise, arc stoppage, erratic metal transfer, and so on can occur and dissipate the arc energy, resulting in poor welding. Arc stabilizers with low

dissociation energy and ionization potential, such as Na₂O and Li₂O, can produce a large amount of electric charge carriers to the arc column to establish a stable plasma. Deoxidizers such as aluminum and magnesium can react with oxide ingredients in the welding flux, resulting in thermite reactions and generating exothermic heat. Aluminum and magnesium are also strong nitride formers that can react with nitrogen in the atmosphere, releasing heat. In either case, the resultant heat will increase the arc energy, contributing to a more stable arc, which also helps the metal transfer and arc stability.

Group V: Slag Formers. Other than those chemicals in groups I through IV, the rest of the nonmetallic chemicals in a formula are slag formers. They are also important in a formula to provide a supplemental support to successful welding. For example, Fe₃O₄ can effectively reduce the surface tension of the liquid pool to improve the bead morphology. Being an acidic oxide, MnO is known to effectively improve the wetting. Quite a few of the slag formers have been patented as effective additives in various formulas.

Flux ingredients in a formula can interact with each other. Thus, their content should be carefully designed to achieve a balanced slag behavior. The interactions between the two groups of ingredients are quite complicated. In general, two opposite interactions may exist.

One is positive in that the interaction will facilitate and reinforce the discussed functions of the five groups. The second is negative in that the effects of one ingredient counteract those of the ingredients from a different group. Interactions are shown in Fig. 8. The solid arrows represent negative interactions, and the dashed arrows represent positive interactions.

Negative interactions include:

- *Group I → Group II:* Ingredients of Group I can effectively disrupt the networks built by Group II ingredients. For example, calcium and other metal ions can break down the networks of titanium oxide or silicon oxide, affecting the viscosity and coverage of the weld pool.
- *Group II → Group V:* Ingredients of group II tend to react with Group V ingredients to form compounds that subsequently solidify. Therefore, Group II ingredients reduce the amount of Group V ingredients in the uncombined form and weaken the effects of these ingredients on the liquid slag. A case in point is aluminum oxide (an ingredient of Group V), which is known to render the slag more refractory with its high melting point. However, titanium oxide (an ingredient of Group II) can react with it to produce aluminum titanate. Because Al₂TiO₅ has a melting point almost 700 °C (1260 °F) lower than that of aluminum oxide (Ref 27), the refractory effect from alumina in the presence of titanium oxide is weakened. Therefore, the amount of alumina must be increased accordingly to achieve the refractory effect on the slag.
- *Group V → Group III:* Ingredients of Group V can be refractory fluxes (such as aluminum and magnesium oxides) or those with melting points higher than or close to the melting point of steel. Together with other

Table 9 Typical compositions of submerged arc welding fluxes

Flux	Composition, wt%									Basicity index (BI)
	Al ₂ O ₃	SiO ₂	TiO ₂	MgO	CaF ₂	CaO	MnO	Na ₂ O	K ₂ O	
A	49.9	13.7	10.1	2.9	5.7	...	15.1	1.6	0.2	0.4
B	24.9	18.4	0.2	28.9	24.2	...	1.8	2.1	0.07	1.8
C	19.3	16.3	0.8	27.2	23.6	9.8	0.08	0.9	1.1	2.4
D	18.1	13.2	0.5	28.2	31.8	4.5	0.1	0.9	0.9	3.0
E	17.0	12.2	0.7	36.8	29.2	0.7	8.9	1.6	0.1	3.5

Table 10 Typical flux compositions of available CO₂ shielded FCAW electrodes

Electrode			Composition, wt%											
Type number	Description	AWS designation	SiO ₂	Al ₂ O ₃	TiO ₂	ZrO ₂	CaO	Na ₂ O	K ₂ O	CO ₂ (as carbonate)	C	Fe	Mn	CaF ₂
1	Titania (nonbasic)	E70T-1, E70T-2	21.0	2.1	40.5	...	0.7	1.6	1.4	0.5	0.6	20.1	15.8	...
2	Lime-titania (basic or neutral)	E70T-1	17.8	4.3	9.8	6.2	9.7	1.9	1.5	...	0.3	24.7	13.0	18.0
3	Lime (basic)	E70T-1, E70T-5	7.5	0.5	3.2	...	0.5	2.5	1.1	55.0	7.2	20.5

Source: Ref 26

Table 11 Typical flux compositions of available self-shielded FCAW electrodes

Electrode			Composition, wt%													
Type number	Description	AWS designation	SiO ₂	Al	Al ₂ O ₃	TiO ₂	CaO	MgO	K ₂ O	Na ₂ O	C	CO ₂ (as carbonate)	Fe	Mn	Ni	CaF ₂
1	Fluorspar-aluminum	E70T-4, E70T-7, E60T-8	0.5	15.4	12.6	0.4	0.2	1.2	0.4	0.4	3.0	...	63.5
2	Fluorspar-titania	E70T-3	3.6	1.9	...	20.6	...	4.5	0.6	0.1	0.6	0.6	50.0	4.5	...	22.0
3	Fluorspar-lime-titania	E70T-6	4.2	1.4	...	14.7	4.0	2.2	0.6	2.1	50.5	2.0	2.4	15.3
4	Fluorspar-lime	E70T-5	6.9	...	0.6	1.2	3.2	0.6	0.3	1.3	58.0	7.9	...	22.0

Source: Ref 26

slag components, these ingredients can effectively restrict the flow of liquid slag and liquid metal that is from Group III ingredients.

- *Group III* → *Group IV*: Ingredients of Group III absorb part of the arc energy to melt and incorporate into the weld pool. They can potentially consume a large amount of the arc energy contributed by Group IV ingredients, resulting in a cooler arc. A fluoride-base self-shielded flux cored wire is a good example of this interaction. The formation energy of CaF_2 and CaO are -290.3 and -151.8 Kcal/mol, respectively, in separation (Ref 28). In addition, CaF_2 has two fluorine atoms to be ionized, instead of one oxygen atom in CaO . As a result, CaF_2 (an ingredient of Group III) consumes more arc energy that is partially contributed by Group IV ingredients. It indeed confirms the observation that a fluoride-base flux cored wire has a “colder” arc than an oxide-base flux cored wire.
- *Group IV* → *Group I*: It is known that temperature is the strongest variable that affects viscosity. Group IV ingredients help increase arc energy. The increased arc energy can greatly reduce the slag viscosity. Note that chemical composition control alone, that is, reducing or controlling the amount of Group I ingredients, will not be effective to adjust the slag viscosity. It is observed that when an excessive amount of aluminum is added into a rutile-base formula, the heat from the thermite reactions will cause the molten slag to drip regardless of the amount of Group I ingredients present in the formula.

Positive interactions include:

- *Group I* → *Group III*: Ingredients of Group I can reduce the viscosity of liquid slag. As a result, the liquid slag can move around more easily, which relaxes the confinement of the liquid metal deposit covered by slag and facilitates the spreading out of the liquid metal. Note that the Group IV → Group I interaction is about the viscosity of slag, and the Group I to Group III interaction here concerns the fluidity of liquid metal and weld bead formation through the slag.
- *Group III* → *Group II*: Oxides from Group III ingredients can participate in the formation of Group II networks. For example, the iron oxide produced from the liquid steel can be used to build the slag network of a Fe_3O_4 -base slag system of a self-shielded flux cored wire.
- *Group II* → *Group IV*: Many slag network builders of Group II, such as rutile and silica, can stabilize the welding arc. They definitely support the work of Group IV ingredients.
- *Group IV* → *Group V*: Strong deoxidizers and denitriders, such as titanium and aluminum, can produce oxides and nitrides with high melting points. Those products from the oxidation and nitriding reactions join Group V ingredients to become a part of the group. As a result, the supplemental function of Group V ingredients, such as holding the liquid metal at out-of-position welding, can be reinforced.
- *Group V* → *Group I*: Ingredients of Group V are not pure chemicals. They usually have a certain amount of residual elements (calcium and other metal ions, for example) that

happen to be Group I ingredients. Those residues can work together with Group I ingredients to control the viscosity of liquid slag.

Due to the complex relationship among flux ingredients in a formula, the effects of every flux ingredient must be carefully weighed and balanced in order to have a well-behaved slag system. After the slag system is successfully established, alloying and microstructure management can help to achieve qualified mechanical properties, including yield and tensile strength, elongation, Charpy V-notch impact toughness, hardness, crack tip opening displacement, and so on.

An FCAW Electrode Formulation Example.

A basic E71T-5-type flux cored wire is commonly used on critical steel structures. Having inferior welding operability to a rutile-base E71T-1-type flux cored wire, it is not as popular as the rutile-base wire. Therefore, it is of importance to improve its welding performance to populate its application. Traditional basic wires use the CaF_2 - SiO_2 - CaO flux system to design formulas. Based on that, a matrix of chemical formulas is shown in Table 12.

It was found that wire 1 was hard to weld due to the high fluidity and mixing of the molten flux with the steel pool. However, the problem of fluidity and slag/metal mixing was gradually resolved from wires 2 to 5. Wire 5 just separated the molten slag from the steel pool. Also observed, the arc stability gradually improved from wires 1 to 5. It was obvious that CaO in wire 1 broke down the slag network too much to cause the fluidity problem to allow molten slag to flow into the steel pool. In other words, the action of Group I → Group II happened strongly here. Due to the poor slag behavior, the weld was extremely convex, and the slag was firmly attached on the bead surface. In addition, it seemed that the volume of liquid steel was too excessive to be fully covered by the slag. On the other hand, increasing the amount of Group IV ingredients, Li_2O in this case, apparently improved the arc stability.

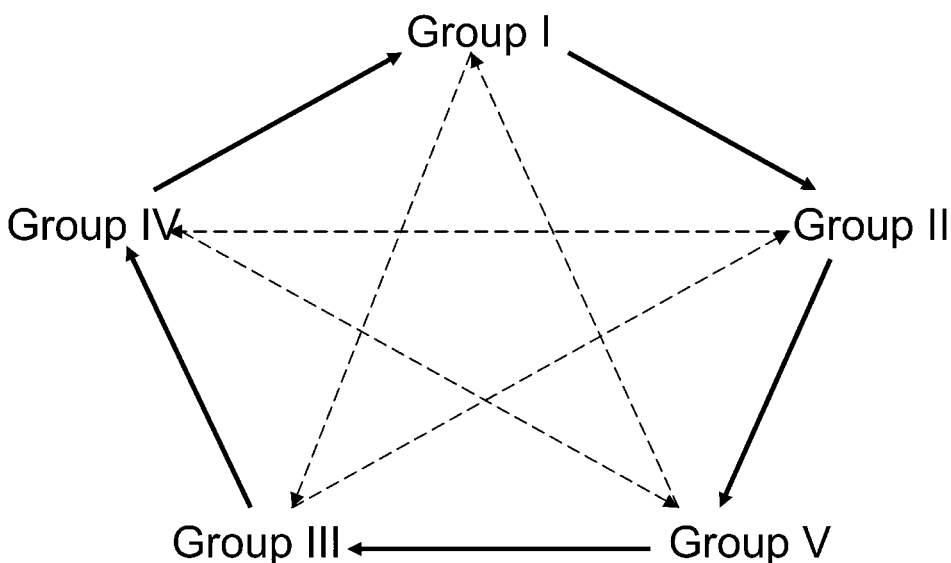


Fig. 8 Interactions between flux ingredients. The solid arrows represent negative interactions, and the dashed arrows represent positive interactions.

Table 12 Matrix of chemical formulas—phase I

Group	Ingredient	Wire 1	Wire 2	Wire 3	Wire 4	Wire 5
I	CaO	12.0	10.8	9.5	8.2	7.0
	SiO ₂	8.0	9.2	10.5	11.8	13.0
II	TiO ₂	9.8	9.8	9.8	9.8	9.8
	CaF ₂	20.8	20.8	20.8	20.8	20.8
III	Fe	34.9	34.9	34.9	34.9	34.9
	C	0.3	0.3	0.3	0.3	0.3
IV	Mn	7.2	7.2	7.2	7.2	7.2
	Na ₂ O	1.5	1.5	1.5	1.5	1.5
	K ₂ O	1.5	1.5	1.5	1.5	1.5
	Li ₂ O	0.0	0.4	0.75	1.1	1.5
	Al ₂ O ₃	1.0	1.0	1.0	1.0	1.0
V	ZrO ₂	1.5	1.5	1.5	1.5	1.5
	MgO	1.5	1.1	0.75	0.4	0.0
Total		100.0	100.0	100.0	100.0	100.0

To further improve the slag behavior, the weight percent of CaO should be reduced, and more Group II ingredients, SiO₂ and/or TiO₂, should be added to formulas. Hence, two new formulas were designed and presented in Table 13.

The formula of wire 6 increased the amount of Group II ingredient, that is SiO₂, to promote the formation of slag network and balance the negative interaction from the Group I ingredient, CaO. In addition, the amount of iron powder, that is, Group III ingredient, was reduced so that the liquid deposit could be fully covered by the slag. It was found that wire 6 produced good-looking beads. The weld bead was completely covered by the slag, and slag removal became much easier. However, the weld had porosities and wormholes, which indicated the need to reduce the oxygen content of the weld.

Instead of SiO₂, the formula of wire 7 increased the amount of TiO₂, a Group II ingredient, to develop the slag network. It also decreased the amount of CaO. As a result, the negative interaction of Group I → Group II was further depressed. To achieve a low oxygen content in the weld, metallic silicon, a Group IV ingredient, was used for deoxidation. In addition, the interaction of Group IV → Group I also suppressed the negative effect of CaO. The weight percent of iron powder was again reduced to facilitate a more complete reaction of deoxidation in the weld pool. A moderate increase of CaF₂ reduced the source of oxygen, which also benefitted the control of oxygen content in the weld. Considering the mechanical properties, carbon was deleted from the formula to avoid martensite in the weld.

An AWS plate was successfully welded by wire 7 at the 1G position. The slag was well behaved in terms of its flow, spreading, and removal. After passing x-ray examination, the plate was machined out to acquire standard samples for tension and Charpy V-notch impact tests. Detailed mechanical properties and chemical composition are shown in Table 14. Apparently, both the strength and Charpy V-notch

impact toughness failed the AWS A5.20 specification.

To increase both strength and impact toughness, more manganese was needed to promote the acicular ferrite, in addition to solid-solution strengthening by more silicon in the weld metal. On the other hand, from the viewpoint of slag adjustment, increasing the amount of CaF₂ by reducing the amount of oxides (TiO₂ and SiO₂) could reduce more oxygen in the wire. Therefore, wire 8 was formulated, as shown in Table 15.

Again, an AWS plate was successfully welded at the 1G position. The resultant mechanical properties and chemical composition passed the AWS A5.20 specification (Table 16).

Table 14 Mechanical properties and chemical composition of the weld metal made by wire 7

Item	Wire 7	AWS A5.20
C	0.03	0.12 max
Mn	0.75	1.75 max
Si	0.30	0.9 max
S	0.008	0.03 max
P	0.010	0.03 max
Yield strength, ksi	56	58 min
Ultimate tensile strength, ksi	66	70–95
Elongation, %	29	22
Charpy V-notch, -20 °F, ft-lb	15	20 min

Table 15 New chemical formula—phase III

Group	Ingredient	Wire 8
I	CaO	4.0
II	SiO ₂	2.7
	TiO ₂	21.0
III	CaF ₂	32.5
	Fe	20.0
IV	Si	5.5
	Mn	8.0
	Na ₂ O	1.5
	K ₂ O	1.2
	Li ₂ O	0.6
V	Al ₂ O ₃	1.0
	ZrO ₂	1.0
	MgO	1.0
	Total	100.0

Table 16 Mechanical properties and chemical composition of the weld metal made by wire 8

Item	Wire 8	AWS A5.20
C	0.03	0.12 max
Mn	0.90	1.75 max
Si	0.40	0.9 max
S	0.008	0.03 max
P	0.011	0.03 max
Yield strength, ksi	62	58 min
Ultimate tensile strength, ksi	72	70–95
Elongation, %	27	22
Charpy V-notch, -20 °F, ft-lb	90	20 min

Table 13 Matrix of chemical formulas—phase II

Group	Ingredient	Wire 6	Wire 7
I	CaO	12.2	4.0
II	SiO ₂	18.2	7.5
	TiO ₂	9.8	25.0
III	CaF ₂	20.3	26.5
	Fe	25.0	18.0
IV	C	0.3	...
	Si	...	5.0
	Mn	7.2	7.2
	Na ₂ O	1.5	1.5
	K ₂ O	1.5	1.2
	Li ₂ O	1.1	0.6
V	Al ₂ O ₃	1.0	1.0
	ZrO ₂	1.5	1.0
	MgO	0.4	1.5
	Total	100.0	100.0

REFERENCES

1. G.E. Linnert, Chapter 8, *Welding Metallurgy*, Vol 1, AWS, 1965, p 367–396
2. C.E. Jackson, Fluxes and Slags in Welding, *Weld. Res. Bull.*, No. 190, 1973
3. T. Lau, G.C. Weatherly, and A. McLean, The Sources of Oxygen and Nitrogen Contamination in Submerged Arc Welding Using CaO-Al₂O₃ Based Fluxes, *Weld. J.*, Vol 64 (No. 12), 1985, p 343s–347s
4. T.H. North, H.B. Bell, A. Nowicki, and I. Craig, Slag/Metal Interaction, Oxygen, and Toughness in Submerged Arc Welding, *Weld. J.*, Vol 57 (No. 3), 1978, p 63s–75s
5. N. Christensen and J. Chipman, Slag-Metal Interaction in Arc Welding, *Weld. Res. Bull.*, No. 15, Jan 1953, p 1–14
6. R.H. Frost, D.L. Olson, and S. Liu, Pyrochemical Evaluation of Weld Metal Inclusion Evolution, *Proc. Third Int. Conf. Trends in Welding*, ASM International, June 1992
7. C.A. Natalie, D.L. Olson, and M. Blander, Physical and Chemical Behavior of Welding Fluxes, *Ann. Rev. Mater. Sci.*, Vol 16, 1986, p 389–413
8. J.E. Indacochea, M. Blander, N. Christensen, and D.L. Olson, Chemical Reactions with FeO-MnO-SiO₂ Fluxes, *Metall. Trans. B*, Vol 16, 1985, p 237–245
9. U. Mitra and T.W. Eagar, Slag-Metal Reactions during Welding, *Metall. Trans. B*, Vol 22, 1991, p 65–100
10. C.S. Chai and T.W. Eagar, Slag-Metal Equilibrium during Submerged Arc Welding, *Metall. Trans. B*, Vol 12, 1981, p 539–547
11. N. Christensen, Metallurgical Aspects of Arc Welding, *Weld. J.*, Vol 27, 1949, p 373s–380s
12. O. Grong, D.L. Olson, and N. Christensen, Carbon Oxidation in Hyperbaric MMA Welding, *Met. Construct.*, Vol 17, Dec 1985, p 810R–814R
13. U. Mitra and T.W. Eagar, Slag-Metal Reactions during Submerged Arc Welding of Alloy Steels, *Metall. Trans. A*, Vol 15, 1984, p 217–227
14. T.W. Eagar, Sources of Weld Metal Oxygen Contamination during Submerged Arc Welding, *Weld. J.*, Vol 57, 1978, p 76s–80s
15. N. Christensen, *Welding Metallurgy, Lecture Notes*, NTH, 1979
16. O. Grong, T.A. Siewert, T.A. Martins, and D.L. Olson, A Model for the Silicon-Manganese Deoxidation of Steel Weld Metal, *Metall. Trans. A*, Vol 17 (No. 10), 1985, p 1797–1807
17. T.H. North, The Distribution of Manganese between Slag and Metal during Submerged Arc Welding, *Weld. Res. Abroad*, Vol 23 (No. 1), 1977, p 2–40
18. T. Boniszewski, Basic Fluxes and Deoxidation in Submerged Arc Welding of Steel, *Metall. Constr. Brit. Weld. J.*, Vol 6, 1974, p 128

54 / Fundamentals of Fusion Welding

19. L. Davis, *An Introduction to Welding Fluxes for Mild and Low Alloy Steels*, Welding Institute, 1981
20. *Making, Shaping and Treating of Steel*, United States Steel Corporation, 1984
21. P.S. Dunn, C.A. Natalie, and D.L. Olson, Sol-Gel Fluxes for Flux Cored Welding Consumables, *J. Mater. Energy Systems*, Vol 8 (No. 2), 1986, p 176–184
22. L.I. Sorokin and Z.A. Sidlin, The Effect of Alloying Elements and of Marble in an Electrode Coating on the Susceptibility of a Deposited Nickel Chrome Metal to Pore Formation, *Svar. Proizvod.*, No. 11, 1974, p 7–9
23. S.S. Tuliani, T. Boniszewski, and N.F. Eaton, Notch Toughness of Commercial Submerged Arc Weld Metal, *Weld. Met. Fabr.*, Vol 37 (No. 8), 1969, p 27
24. T.G.F. Gray, J. Spence, and T.H. North, *Rational Welding Design*, Butterworths, 1975
25. D.L. Olson, G.R. Edwards, and S.K. Marya, The Physical and Chemical Behavior Associated with Slag Detachability during Welding, *Ferrous Alloy Weldments*, Vol 67–70, Trans Tech, 1992, p 253–268
26. *Fumes and Gases in the Welding Environment*, AWS, 1979
27. E.M. Levin and H.F. McMurdie, *Phase Diagrams for Ceramists, 1975 Supplement* (Fig. 4150–4999), American Ceramic Society, 1975, p 134–135
28. C.T. Lynch, *Handbook of Materials Science*, Vol I, CRC Press, 1974

Heat Flow in Fusion Welding*

Chon L. Tsai, United Ship Design and Development Center

DURING FUSION WELDING, the thermal cycles produced by the moving heat source cause physical state changes, metallurgical phase transformation, and transient thermal stress and metal movement. After welding is completed, the finished product may contain physical discontinuities that are due to excessively rapid solidification, adverse microstructures that are due to inappropriate cooling, or residual stress and distortion that are due to the existence of incompatible plastic strains.

To analyze these problems, this article presents an analysis of welding heat flow, focusing on the heat flow in the fusion welding process. The primary objective of welding heat-flow modeling is to provide a mathematical tool for thermal data analysis, design iterations, or the systematic investigation of the thermal characteristics of any welding parameters. Exact comparisons with experimental measurements may not be feasible, unless some calibration through the experimental verification procedure is conducted.

Introduction

Welding Thermal Process. A physical model of a generic moving-source (i.e., electric arc, electron or laser beam) welding system is shown in Fig. 1. The welding heat source

moves at a constant speed along a straight path. The end result, after either initiating or terminating the heat source, is the formation of a transient thermal state in the weldment. At some point after heat-source initiation but before termination, the temperature distribution is stationary, or in thermal equilibrium, with respect to the moving coordinates. This is called a “quasi-steady” state. The origin of the moving coordinates coincides with the center of the heat source. The intense welding heat melts the metal and forms a molten pool. Some of the heat is conducted into the base metal and some is lost from either the heat column or the metal surface to the environment surrounding the weld. Three metallurgical zones are formed in the plate upon completion of the thermal cycle: the weld-metal (WM) zone, the heat-affected zone (HAZ), and the base-metal (BM) zone. The peak temperature and the subsequent cooling rates determine the HAZ structures, whereas the thermal gradients, the solidification rates, and the cooling rates at the liquid-solid pool boundary determine the solidification structure of the WM zone. The size and flow direction of the pool determines the amount of dilution and weld penetration. The material response in the temperature range near melting temperatures is primarily responsible for the metallurgical changes.

Two thermal states, quasi-stationary and transient, are associated with the welding process. The transient thermal response occurs during the source initiation and termination stages of welding, the latter of which is of greater metallurgical interest. Hot cracking usually begins in the transient zone, because of the nonequilibrium solidification of the base material. A crack that forms in the source-initiation stage may propagate along the weld if the solidification strains sufficiently multiply in the wake of the welding heat source. During source termination, the weld pool solidifies several times faster than the weld metal in the quasi-stationary state. Cracks usually appear in the weld crater and may propagate along the weld. Another dominant transient phenomenon occurs when a

short repair weld is made to a weldment. Rapid cooling results in a brittle HAZ structure and either causes cracking problems or creates a site for fatigue-crack initiation.

The quasi-stationary thermal state represents a steady thermal response of the weldment with respect to the moving heat source. The majority of the thermal expansion and shrinkage in the base material occurs during the quasi-stationary thermal cycles. Residual stress and weld distortion are caused by the incompatible inelastic strains that remain in the weldment after completion of the thermal cycle.

Relation to Welding Engineering Problems. To model and analyze the thermal process, an understanding of thermally-induced welding problems is important. A simplified modeling scheme, with adequate assumptions for specific problems, is possible for practical applications without using complex mathematical manipulations. The relationship between the thermal behavior of weldments and the metallurgy, control, and distortion associated with welding is summarized as follows.

Welding Metallurgy. As already noted, defective metallurgical structures in the HAZ and cracking in the WM usually occur under the transient thermal condition. Therefore, a transient thermal model is needed to analyze cracking and embrittlement problems. Proper welding techniques, such as using end tabs or current slope control, may be used to avoid the transient thermal effects.

To evaluate the various welding conditions for process qualification, the quasi-stationary thermal responses of the weld material must be analyzed. The minimum required amount of welding heat input within the allowable welding speed range must be determined in order to avoid rapid solidification and cooling of the weldment. Preheating may be necessary if the proper thermal conditions cannot be obtained under the specified welding procedure. A quasi-stationary thermal model is adequate for this type of analysis.

Hot cracking results from the combined effects of strain and metallurgy. The strain

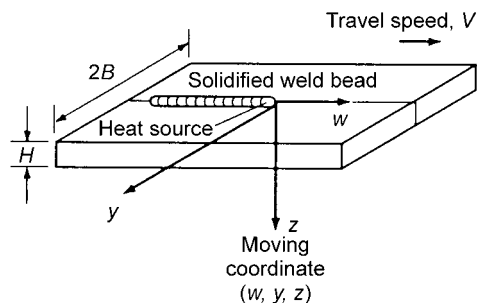


Fig. 1 Schematic of the welding thermal model

effect results from weld-metal displacement at near-melting temperatures, because of solidification shrinkage and weldment restraint. The metallurgical effect relates to the segregation of alloying elements and the formation of the eutectic during the high nonequilibrium solidification process. Using metallurgical theories, it is possible to determine the chemical segregation, the amounts and distributions of the eutectic, the magnitudes and directions of grain growth, and the weld-metal displacement at high temperatures. Using the heating and cooling rates, as well as the retention period predicted by modeling and analysis, hot-cracking tendencies can be determined. To analyze these tendencies, it is important to employ a more accurate numerical model that considers finite welding heat distribution, latent heat, and surface heat loss.

Welding Control. In-process welding control has been studied by researchers. Many of the investigations are aimed at developing sensing and control hardware. The link between weld-pool geometry and weld quality has also been extensively studied and developed in the past decade. For a new welding process or procedure development, transient heat-flow analyses may be used to correlate the melted surface, which is considered to be the primary control variable, to the weld thermal response in a time domain.

Welding Distortion. The temperature history and distortion caused by the welding thermal process creates nonlinear thermal strains in the weldment. Thermal stresses are induced if any incompatible strains exist in the weld. Plastic strains are formed when the thermal stresses are greater than the material yield stress. Incompatible plastic strains accumulate over the thermal process and result in residual stress and distortion of the final weldment. The material response in the lower temperature range during the cooling cycle is responsible for the residual stresses and weldment distortion. For this type of analysis, the temperature field away from the welding heat source is needed for the modeling of the heating and cooling cycle during and after welding. A quasi-stationary thermal model with a concentrated moving heat source can predict, with reasonable accuracy, the temperature information for the subsequent stress and distortion analysis.

Literature Review. Many investigators have analytically, numerically, and experimentally studied welding heat-flow modeling and analysis (Ref 1–18). The majority of the studies were concerned with the quasi-stationary thermal state. Boulton and Lance-Martin (Ref 1), Rosenthal and Schmerber (Ref 2), and Rykalin (Ref 3) independently obtained an analytical temperature solution for the quasi-stationary state using a point or line heat source moving along a straight line on a semiinfinite body. A solution for plates of finite thickness was later obtained by many investigators using the imaged heat-source method (Ref 3, 4). Tsai (Ref 5) developed an analytical solution for a

model that incorporated a welding heat source with a skewed Gaussian distribution and finite plate thickness. It was later called the finite source theory (Ref 6).

With the advancement of computer technology and the development of numerical techniques such as the finite-difference and finite-element methods, more exact welding thermal models were studied and additional phenomena were considered, including nonlinear thermal properties, finite heat-source distributions, latent heat, and various joint geometries. Tsai (Ref 5), Pavelic et al. (Ref 7), Kou (Ref 8), Kogan (Ref 9), and Ecer et al. (Ref 10) studied the simulation of the welding process using the finite-difference scheme. Hibbitt and Marcal (Ref 11), Friedman (Ref 12), and Paley and Hibbert (Ref 13) made some progress in welding simulation using the finite-element method.

Analytical solutions for transient welding heat flow in a plate were first studied by Naka (Ref 14), Rykalin (Ref 3), and Masubuchi and Kusuda (Ref 15) in the 1940s and 1950s. A point or line heat source, constant thermal properties, and adiabatic boundary conditions were assumed. Later, Tsai and Hou (Ref 16) extended the analytical solution to incorporate Gaussian heat distribution using the principle of superposition. The solution was used to investigate the effect of pulsed conditions on weld-pool formation and solidification without the consideration of latent heat and nonlinear thermal properties.

The analysis of the transient thermal behavior of weldments using numerical methods has been the focus of several investigations since 1980. Friedman (Ref 17) discussed the finite-element approach to the general transient thermal analysis of the welding process. Ecer et al. (Ref 10) developed a two-dimensional transient heat-flow model using a finite-difference scheme and a simulated pulsed-current gas tungsten arc welding process. Fan and Tsai (Ref 18) modeled the two-dimensional transient welding heat flow using a finite-element scheme to study the transient welding thermal behavior of the weldment. Frewin and Scott (Ref 19) studied a three-dimensional finite-element model of the heat flow during pulsed laser beam welding. Bonifaz (Ref 20) studied the transient thermal histories and sizes of fusion and heat-affected zones using the finite-element method, incorporating thermal efficiency in the heat-transfer analysis. DebRoy and David (Ref 21) conducted a more comprehensive review on the physical processes in fusion welding. Because of the complexity of fusion welding processes, solution of many important contemporary problems in fusion welding requires an interdisciplinary approach. Solution to the problems and issues requires science-based tailoring of composition, structure, and properties of the weld materials.

In the past two decades, the coupled heat transfer and viscous flow in a weld pool has been studied using the finite-element method by many investigators. Dilawari et al. (Ref 22)

studied two physical models for qualitative insights in the electrosag welding process using the finite-element method. It was revealed that the total weld heat may be reduced by 30% when the strip electrode was used in place of the wire electrode. McLay and Carey (Ref 23) studied the detailed structure of the flow circulation regions and layers, which incorporated the surface-tension-driven flow (Marangoni effect) and the moving phase boundary. More recently, many investigators developed three-dimensional numerical models to study the viscoplastic flow and temperature field in friction stir welding by solving the equations of conservation of mass, momentum, and energy. Nandan et al. (Ref 24, 25) determined the spatially variable non-Newtonian viscosity from the computed values of strain rate, temperature, and temperature-dependent material properties. The computed results showed that significant plastic flow occurs near the tool, where convective heat transfer is the main mechanism of heat transfer.

General Approach. The various modeling and analysis schemes summarized previously can be used to investigate the thermal process of different welding applications. With adequate assumptions, analytical solutions for the simplified model can be used to analyze welding problems that show a linear response to the heat source if the solutions are properly calibrated by experimental tests. Numerical solutions that incorporate nonlinear thermal characteristics of weldments are usually required for investigating the weld-pool growth or solidification behavior. Numerical solutions may also be necessary for metallurgical studies in the weld HAZ if the rapid cooling phenomenon is significant under an adverse welding environment, such as welding under water.

Thermally related welding problems can be categorized as:

- Solidification rates in the weld pool
- Cooling rates in the HAZ and its vicinity
- Thermally-induced strains in the general domain of the weldment

The domain of concern in the weld pool solidification is within the molten pool area, in which the arc (or other heat source) phenomena and the liquid stirring effect are significant. A convective heat-transfer model with a moving boundary at the melting temperature is needed to study the first category, and numerical schemes are usually required as well.

The HAZ is always bounded on one side by the liquid-solid interface during welding. This inner-boundary condition is the solidus temperature of the material. The liquid weld pool may be eliminated from thermal modeling if the interface could be identified. A conduction heat-transfer model would be sufficient for the analysis of the HAZ. Numerical methods are often employed, and very accurate results can be obtained.

The thermal strains caused by welding thermal cycles are due to the nonlinear temperature distribution in the general domain of the weldment. Because the temperature in the material near the welding heat source is high, very little stress can be accumulated from the thermal strains. This is due to low rigidity, that is, small modulus of elasticity and low yield strength. The domain for thermal strain study is less sensitive to the arc and fluid-flow phenomena and needs only a relatively simple thermal model. Analytical solutions with minor manipulations often provide satisfactory results.

In this article, only the analytical heat-flow solutions and their practical applications are addressed. The numerical conduction solutions and the convective models for fluid flow in a molten weld pool are not presented.

Mathematical Formulations

Conduction Equation. A diagram of the welding thermal model is shown in Fig. 1. The origin of the moving coordinates (w, y, z) is fixed at the center of the welding heat source. The coordinates move with the source at the same speed. The conduction equation for heat flow in the weldments is:

$$\nabla \cdot (\lambda \nabla \theta) + \rho C_p V \frac{\partial \theta}{\partial w} + \dot{Q} = \rho C_p \frac{\partial \theta}{\partial t} \quad (\text{Eq 1})$$

The initial condition is:

$$\theta = \theta_0, \text{ at } t = 0 \quad (\text{Eq 2})$$

and the generalized boundary condition is:

$$\lambda_w \frac{\partial \theta}{\partial w} \ell_w + \lambda_y \frac{\partial \theta}{\partial y} \ell_y + \lambda_z \frac{\partial \theta}{\partial z} \ell_z - \dot{q} + h(\theta - \theta_\infty) = 0 \quad (\text{Eq 3})$$

where ∇ is a differential operator; θ is the temperature ($^{\circ}\text{C}$); θ_∞ is the environmental temperature ($^{\circ}\text{C}$); θ_0 is the initial temperature ($^{\circ}\text{C}$); λ is the directional thermal conductivity in any coordinate system ($\text{J}/\text{mm} \cdot \text{s} \cdot ^{\circ}\text{C}$); $\lambda_w, \lambda_y,$ and λ_z are the respective orthotropic thermal conductivities ($\text{J}/\text{mm} \cdot \text{s} \cdot ^{\circ}\text{C}$) in the w -, y -, and z -directions (mm); ρ is density (g/mm^3); C_p is specific heat ($\text{J}/\text{g} \cdot ^{\circ}\text{C}$); h is the surface heat-loss coefficient ($\text{J}/\text{mm}^2 \cdot \text{s} \cdot ^{\circ}\text{C}$); $l_w, l_y,$ and l_z are the direction cosines of the boundary surface; \dot{Q} is the volumetric heat source ($\text{J}/\text{mm}^3 \cdot \text{s}$); \dot{q} is the surface heat source ($\text{J}/\text{mm}^2 \cdot \text{s}$); t is the elapsed time after initiation of the welding heat source (s); and V is the welding speed (mm/s). For materials with homogeneous thermal properties, the thermal conductivities become directional-independent ($\lambda_w = \lambda_y = \lambda_z = \lambda$) and can be factored out of the differential operators in Eq 1.

The volumetric heat source represents the joule heating in the weldment that is due to the electric current flow (or mechanical energy generation due to friction or plastic flow in friction or friction stir welding) within that conducting medium. The total energy of such

internal joule heating in welding is usually minimal, compared to the arc heat input. The majority of the energy is concentrated in a very small volume beneath the arc (Ref 5). In other words, a very high energy density generation exists in the weld pool, and it may have a significant effect on transient pool growth and solidification.

Heat-Source Formulation. The direction cosines on the surface that receives the heat flux from the welding source ($z = 0$) are $l_w = l_y = 0$ and $l_z = -1$. Within the significant heat-input area (to be defined later in this section), the heat-loss coefficient, h , is zero.

The distribution of the welding heat flux on the weldment surface can be characterized, in a general form, by a skewed Gaussian function (Ref 6):

$$\dot{q}(r, w) = \dot{q}_0 \exp\left(-Cr^2 - \frac{\beta V}{2\kappa} w\right) \quad (\text{Eq 4})$$

where β is a weight constant, κ is the thermal diffusivity of the base material (mm^2/s), C is a shape constant, \dot{q} is surface heat flux ($\text{J}/\text{mm}^2 \cdot \text{s}$) as a function of (r, w), \dot{q}_0 is heat flux ($\text{J}/\text{mm}^2 \cdot \text{s}$) at the source center, r is the radial coordinate from the source center (mm), and V is the welding speed (mm/s).

The weight constant, β , indicates the significance of the welding travel speed. A normal distribution of the welding heat flux is obtained if the weight constant is zero. For the conventional welding processes, a normal distribution is usually adequate for predicting thermal responses of a material.

In general, the total energy input to the weldment, which is a fraction of the total welding power generated by the welding machine, is the sum of the concentrated heat and the diffused heat (Ref 26). The concentrated heat is carried by the core of the energy transmission medium, for example, the arc plasma column. The diffused heat reaches the weld surface by radiation and convection energy transport from the core surface. The heat-flux distribution is a function of the proportional values between these two types of energy. The fraction of the total welding power reaching the weldment indicates the heating efficiency of the welding process, and the fraction percentage is defined as welding heat efficiency, η .

The shape constant, C , can be obtained in terms of the core diameter, D (mm), and the concentration factor, F . The concentration factor is defined as the ratio of the concentrated heat to the net energy reaching the weldment. The core diameter can be assumed to be the diameter of the plasma column in the arc welding process. The concentration factor and welding heat efficiency are not fully understood and have been subjected to manipulation during the mathematical analyses in order to obtain a better correlation with the experimental data.

Assuming a normal heat-flux model ($\beta = 0$), the core diameter and the concentrations factor are required to determine the shape

constant, C , and the heat flux at the source center, \dot{q}_0 . By integrating Eq 4 over the core heat area and the entire heat-input domain ($r = 0 \rightarrow \infty$), the shape factor can be determined by dividing the two integrals. The heat flux at the source center can then be determined from the second integral. The two constants are expressed as:

$$C = \frac{4\ell n[1/(1-F)]}{D^2} \quad (\text{Eq 5})$$

$$\frac{\dot{q}_0}{\dot{Q}} = \frac{C}{\pi} \quad (\text{Eq 6})$$

In the case of arc welding:

$$\frac{\dot{q}_0}{\eta EI} = \frac{C}{\pi} \quad (\text{Eq 7})$$

where E is the welding arc voltage (V), and I is the welding current (A).

For practical purposes, the welding heat source can be considered to be restricted within a circle of radius r_a (mm), where the heat flux drops to 1/100 of the center flux \dot{q}_0 . The radius of the significant heat-input area can be written as:

$$r_a = \sqrt{\frac{\ell n(100)}{C}} = \frac{2.146}{\sqrt{C}} \quad (\text{Eq 8})$$

Surface Heat Loss. The heat-loss coefficient, h ($\text{J}/\text{mm}^2 \cdot \text{s} \cdot ^{\circ}\text{C}$), represents both radiation and convection heat loss from the boundary surfaces outside the significant heat-input area. The formulation for both heat-loss mechanisms can be written as the radiation heat-loss coefficient (in air):

$$h_{\text{rad}} = \epsilon \sigma (\theta_w^4 - \theta_\infty^4) \quad (\text{Eq 9})$$

where ϵ is emissivity (e.g., 0.3 for an oxidized steel surface), σ is the Stefan-Boltzmann constant ($5.6704 \times 10^{-14} \text{ J}/\text{s} \cdot \text{mm}^2 \cdot \text{K}^4$, where K is the absolute temperature in $^{\circ}\text{C}$), θ_w is the surface temperature ($^{\circ}\text{C}$), and θ_∞ is the environmental temperature ($^{\circ}\text{C}$).

The natural convection heat-loss coefficient in air is in the range of $(5 \sim 25) \times 10^{-6}$ (Ref 27) and in water is in the range of 0.003 to 0.1 (Ref 28). The unit for both coefficients is in $\text{J}/\text{s} \cdot \text{mm}^2 \cdot ^{\circ}\text{C}$.

Natural convection is dominant at a temperature below $550 \text{ }^{\circ}\text{C}$ ($1020 \text{ }^{\circ}\text{F}$), whereas radiation becomes more important at temperatures above this level. The total heat-loss coefficient is the sum of radiation and convection. In underwater welding, heat losses are due primarily to heat transfer from the surface to the moving water environment. This motion is created by the rising gas column in the arc area (Ref 29), which is similar to a boiling heat-transfer phenomenon.

For an insulated surface, no heat transfer into or out of the surface is assumed. The

temperature gradient normal to the surface is zero and can be represented by:

$$\bar{n} \cdot \nabla \theta = 0 \quad (\text{Eq 10})$$

where \bar{n} is a unit vector normal to the surface and equals $(I_w^2 + I_y^2 + I_z^2)^{0.5}$.

Other Boundary Conditions. There are several other possible boundary conditions in welding heat-flow modeling that depend on the assumptions used for model simplification. One is the condition at infinity:

$$\theta = \theta_\infty \text{ or } \lim_{r \rightarrow \infty} \frac{\partial \theta}{\partial r} = 0 \quad (\text{Eq 11})$$

Another is the condition near the heat source. In the case of a line source for a thin plate:

$$-2\pi\lambda H \lim_{r \rightarrow 0} \frac{\partial \theta}{\partial r} = \eta EI \quad (\text{Eq 12})$$

where H is the plate thickness (mm).

In the case of a point source for a thick plate:

$$-2\pi\lambda \lim_{r \rightarrow 0} \left(r^2 \frac{\partial \theta}{\partial r} \right) = \eta EI \quad (\text{Eq 13})$$

In the case of a finite source for a thick plate (on a heating surface):

$$\bar{n} \cdot (-\lambda \nabla \theta) = \dot{q}(r); \quad r \leq r_a \quad (\text{Eq 14})$$

Another is represented by the conditions at the solid-liquid interface:

$$\theta_s = \theta_l = \theta_m \quad (\text{Eq 15})$$

$$[\bar{n} \cdot (\lambda \nabla \theta)]_s - [\bar{n} \cdot (\lambda \nabla \theta)]_l = \pm \rho_s L \frac{ds}{dt} \quad (\text{Eq 16})$$

where “+” indicates the melting process and “-” indicates the solidification process. The subscripts “s” and “l” indicate the temperature and the properties in a solid and liquid, respectively. The \bar{n} is a normal vector on the boundary surface or interface, r_a is the radius of the heat-input area (mm), L is the latent heat of the base material (J/g), and the subscript “m” represents the melting temperature of the base material.

Engineering Solutions and Empirical Correlation

General Solutions. The general (analytical) heat-flow solutions for fusion welding can be categorized by those appropriate for a thick plate, a thin plate, or a plate with finite thickness. In most cases, the boundary surfaces (except for the heat-input area) are assumed to be adiabatic, and the thermal properties are independent of temperature. The various metallurgical zones in the weldment are assumed to be homogeneous, and the thermal model is linear.

The solutions give the temperature for a specific point if the welding velocity, V , voltage, E , and current, I , as well as the physical properties of the plate material (ρ , λ , C_p) and the welding heat efficiency, η , are known. This specific point is defined by r and w in:

$$r = \sqrt{w^2 + y^2 + z^2} \quad (\text{Eq 17})$$

where $w = x - Vt$. The heat-flow solutions are not accurate at points near the welding arc because a point source or line source is assumed for thick and thin plates, respectively.

To approximate the transient temperature changes at the start and end of a weld, Fig. 2 shows a global coordinate system (x, y, z), the origin of which is fixed at the source initiation, where t_0 is the welding time and t_1 is the time after the welding heat-source termination. The temperature solutions at t_0 and t_1 are the temperature changes at the start and end of the weld, respectively.

The temperature solution for thick plate at the arc start location is:

$$\theta - \theta_0 = \frac{\eta EI}{2\pi\lambda V t_0} \quad (\text{Eq 18})$$

The quasi-stationary temperature distribution is:

$$\theta - \theta_0 = \frac{\eta EI}{2\pi\lambda r} \exp\left[\frac{-V(w+r)}{2\kappa}\right] \quad (\text{Eq 19})$$

At the arc termination location, the solution is:

$$\theta - \theta_0 = \frac{\eta EI}{2\pi\lambda V t_1} \quad (\text{Eq 20})$$

where κ is the thermal diffusivity, which is the ratio of thermal conductivity to the specific heat of the material:

$$\left(\kappa = \frac{\lambda}{\rho C_p}, \text{ mm}^2/\text{s}\right)$$

The transient time periods, t_0 and t_1 , are in the order of seconds for the common arc welding processes.

The temperature solution for thin plate at the arc start location is:

$$\theta - \theta_0 = \frac{\eta EI}{4\pi\lambda H} \exp\left(\frac{V^2 t_0}{2\kappa}\right) \cdot K_0\left(\frac{V^2 t_0}{2\kappa}\right) \quad (\text{Eq 21})$$

The quasi-stationary temperature distribution is:

$$\theta - \theta_0 = \frac{\eta EI}{2\pi\lambda H} \exp\left(\frac{-Vw}{2\kappa}\right) \cdot K_0\left(\frac{Vr}{2\kappa}\right) \quad (\text{Eq 22})$$

For the arc termination location, the solution is:

$$\theta - \theta_0 = \frac{\eta EI}{4\pi\lambda H} \exp\left(\frac{V^2 t_1}{2\kappa}\right) \cdot K_0\left(\frac{V^2 t_1}{2\kappa}\right) \quad (\text{Eq 23})$$

where K_0 is the modified Bessel function of the second kind of zeroth order, and ηEI is the welding heat-input rate.

Temperature for Plate with Finite Thickness. The image method enables the investigator to superimpose the solutions for an infinitely thick plate, the source of which is placed on imaginary surfaces until the proper boundary conditions on the plate surfaces are obtained. This method is based on the premise that if a solution satisfies the governing equation and the boundary conditions, then it must be not only a correct solution but the only solution (that is, the uniqueness of solution premise).

Using the image method, the solution for plates of finite thickness with adiabatic surfaces can be modified from the respective temperature solutions described previously.

Let $\phi_0(w, y, z, t)$ be the initial solution for an infinitely thick plate. The temperature solution for a finite thick plate can be obtained by superimposing the imaginary solutions $\phi_{mn}(w, y_m, z_n, t)$ and $\phi'_{mn}(w, y'_m, z'_n, t)$ to the initial solution, and this can be written in a general form as:

$$\theta - \theta_0 = -\phi_0(w, y, z, t) + \sum_{m=0}^{\infty} \sum_{n=0}^{\infty} [\phi_{mn}(w, y_m, z_n, t) + \phi'_{mn}(w, y'_m, z'_n, t)] \quad (\text{Eq 24})$$

where $y_m = 2mB - y$; $y'_m = 2mB + y$; $z_n = 2nH - z$; and $z'_n = 2nH + z$, in which B is the half width and H is the thickness of the plate. The subscripts m and n are integers that vary from zero to infinity.

For a plate with sufficient width (i.e., this is usually the case in a practical situation), the subscript m is zero. The solution will converge and reach the correct adiabatic surface condition in six to ten superposition steps (i.e., n value is up to 6 to 10), depending on the thickness of the plate. The two-dimensional solution (that is, thin plate) is generally used for any solution that requires more than ten superposition steps.

Equation 24 can be expressed as:

$$\theta - \theta_0 = -\frac{\eta EI \exp\left(\frac{-Vw}{2\kappa}\right)}{2\pi\lambda} \cdot \left\{ \frac{\exp\left(\frac{-Vr}{2\kappa}\right)}{r} + \sum_{n=1}^{\infty} \left[\frac{\exp\left(\frac{-Vr_{2n}}{2\kappa}\right)}{r_{2n}} + \frac{\exp\left(\frac{-Vr_{2n+1}}{2\kappa}\right)}{r_{2n+1}} \right] \right\} \quad (\text{Eq 25})$$

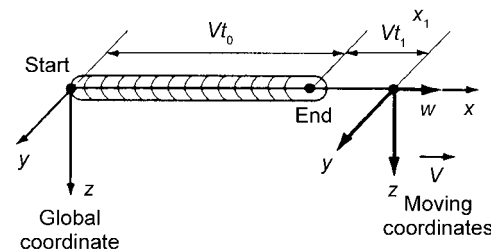


Fig. 2 Global and moving coordinate systems for welding heat conduction

where:

$$r_{2n} = \sqrt{w^2 + y^2 + (2nH - z)^2} \text{ and } r_{2n+1} = \sqrt{w^2 + y^2 + (2nH + z)^2} \quad (\text{Eq 26})$$

Cooling Rate. Frequently, it is desirable to know the cooling rate experienced at some location in a weldment to enable a prediction of the metallurgical structure in that area. A general methodology by which cooling-rate equations are obtained from the temperature-distribution equations is discussed as follows.

Recall that the moving coordinate w is defined by $w = x - Vt$. Using this definition, it is easily shown that:

$$\frac{\partial w}{\partial t} = -V \quad (\text{Eq 27})$$

Using the chain rule, the cooling-rate equation is:

$$\frac{\partial \theta}{\partial t} = -V \frac{\partial \theta}{\partial w} \quad (\text{Eq 28})$$

Because the temperature-distribution equations are a function of w and r , the cooling-rate equations can be obtained by differentiating the temperature-distribution equations with respect to w and multiplying by $-V$.

The cooling rate is defined as the slope of a tangent line drawn on the temperature-time curve. Because the cooling rate changes with temperature, when one speaks of a cooling rate, the specific temperature, θ_c , at which it occurs must also be given. In a weldment, the variable of interest is the cooling rate at the critical temperature that ultimately defines what type of metallurgical structure will result (if the material is heat treatable). For steels, this critical temperature is the "nose" of the continuous cooling transformation curve. At this temperature, the cooling rate determines if upper transformation products (pearlite, upper bainite) or lower transformation products (martensite, lower bainite) will form. For many steels, this critical temperature ranges from approximately 200 to 540 °C (400 to 1000 °F).

The cooling rate in a weldment is also a function of location, because the temperature varies with location during welding. To find a cooling-rate equation for the quasi-stationary state, the particular location in the weldment that is of interest and corresponds to the cooling temperature at a given distance from the heat source must be defined. The resulting cooling-rate equation will be applicable only to that location.

The differentiation, $\partial\theta/\partial w$, of either Eq 19 or 25, which is required to obtain the cooling-rate expression, will result in a function of w and r . The variable r can be written in terms of w if the location of interest is defined by a given set of values of y and z . This relationship for r , once formulated, can then be substituted into $\partial\theta/\partial w$, the result being a function of w alone.

To determine w corresponding to the critical temperature, θ_c , a temperature-distribution

equation is required (Eq 19 or 25). The aforementioned r - w relationship and temperature-distribution equation (Eq 19 or 25) where θ is equal to θ_c , critical temperature, are used to determine w . Then, w is substituted into the $d\theta/dw$ expression obtained previously. The end result will be an equation that defines the cooling rate for a particular location in the weldment, and, being a function of the critical temperature, the welding conditions and thermal conductivity of the base material.

To determine the cooling rate in a thick plate along the weld centerline (that is $y = 0$) for a particular critical temperature, the cooling-rate equation can be reduced to:

$$\left[\frac{\partial \theta}{\partial t} \right]_{\theta_c} = \frac{-2\pi\lambda V(\theta_c - \theta_0)^2}{\eta EI} \quad (\text{Eq 29})$$

This equation has been used to predict weld cooling rates in shop practices. Cooling rate is inversely proportional to heat input per unit weld length (that is, \dot{Q}/V) and is proportional to thermal conductivity and the critical temperature at which the cooling rate needs to be evaluated.

On the basis of experimental results, a cooling-rate equation was developed for the HAZ of low-carbon steel weldments (Ref 30). This equation considers the combined effects of plate thickness, H (in.), preheating temperature, θ_0 (°C), and welding conditions, and is given as:

$$\left[\frac{\partial \theta}{\partial t} \right]_{\text{HAZ}} = 0.35 \left\{ \left(\frac{\theta_c - \theta_0}{I/V} \right)^{1.7} \left[1 + \frac{2}{\pi} \tan^{-1} \left(\frac{H - H_0}{\alpha} \right) \right] \right\}^{0.8} \quad (\text{Eq 30})$$

The variables α and H_0 depend on the critical temperature of interest. Several values are given in Table 1.

The units used in Eq 30 are important, because the same units that were used in developing the equation must be employed in its application. The plate thickness, H , must be given in inches, and the travel speed, V , must be given in in./min (ipm). The temperatures θ_c and θ_0 must be given in °C, and the welding current, I , must be given in amperes. Using the correct units, the application of Eq 30 will result in a predicted cooling rate (°C/s) for the HAZ of a low-carbon steel weldment made by common arc welding processes.

For low-carbon steels welded by the shielded metal arc welding (SMAW), gas metal arc welding (GMAW), and submerged arc welding (SAW) processes, an empirical equation has been developed that correlates the weld-metal cooling rate at 538 °C (1000 °F) with a 95 to 150 °C (200 to 300 °F) preheat to the weld nugget area (Ref 31):

$$^{\circ}\text{C/s} = \left(\frac{2012}{\text{Nugget area}} \right)^{1.119} \quad (\text{Eq 31})$$

where the nugget area is in mm². For low-carbon steels, an empirical chart for determining nugget area for a given welding condition (Fig. 3) also has been developed (Ref 32).

Table 1 Selected critical temperature and corresponding values for α and H_0

Critical temperature, θ_c		H_0		α	
°C	°F	mm	in.	mm	in.
700	1290	9.9	0.39	2.0	0.08
540	1000	14.2	0.56	4.1	0.16
300	570	19.8	0.78	9.9	0.39

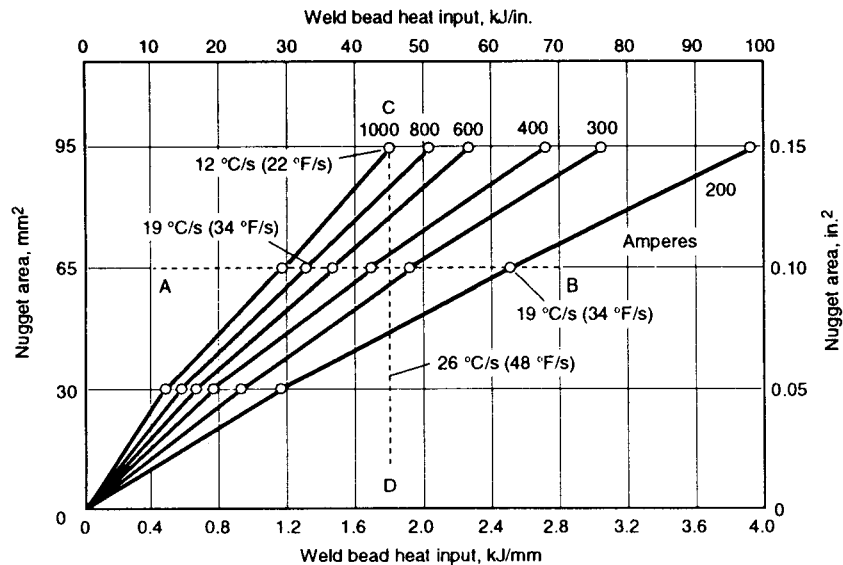


Fig. 3 Relation between nugget area, heat input, and current

The straight line drawn to connect the current and weld bead heat input (i.e., $\eta EI/V$) intersects the nugget area at the calculated value. The product of welding heat efficiency and arc voltage remains a rather constant value in arc welding. Therefore, weld nugget area and weld-metal cooling rate are influenced primarily by the welding current and speed. Welding voltage controls weld bead shape.

Peak Temperature. An equation to determine the peak temperature in a weldment at a given distance y from the weld centerline would enable the prediction of HAZ sizes as well as weld bead widths. The general concept of obtaining a peak-temperature equation, as well as some results that have been obtained, are discussed as follows.

Consider Fig. 4 and note that the maximum, or peak, temperature is given when $\partial\theta/\partial t = 0$. For the thick-plate model, the cooling rate can be obtained by differentiating Eq 19 and multiplying by $-V$:

$$\frac{\partial\theta}{\partial t} = -V \frac{\partial\theta}{\partial w} = \frac{-V\eta EI}{2\pi\lambda r} \exp\left[\frac{-V(w+r)}{2\kappa}\right] \left[\frac{-w}{r^2} - \frac{V}{2\kappa} \left(1 + \frac{w}{r}\right)\right] \quad (\text{Eq 32})$$

Clearly, the only way that $\partial\theta/\partial t$ can be equal to zero is if

$$\frac{-w}{r^2} - \frac{V}{2\kappa} \left(1 + \frac{w}{r}\right) = 0 \quad (\text{Eq 33})$$

Equation 33 describes the relationship that must exist between the two location variables, r and w , for the temperature at that point to be equal to the peak temperature. For a given y and z in thick plate, this equation can be solved together with the geometric fact that (Eq 17):

$$r = \sqrt{w^2 + y^2 + z^2}$$

for $w = w_p$ and $r = r_p$. The subscript "p" represents the corresponding peak-temperature location. If w_p and r_p are substituted into the temperature-distribution equation for thick plates (Eq 19), the peak temperature for a given y and z can be determined.

Such a solution for r and w is not explicitly possible, however, because the equations for r and w that result are not explicit. Consequently, iterative techniques are required, resulting in a solution that is both cumbersome and time-consuming.

One method of obtaining a simpler thick-plate peak-temperature equation is to assume that the heat input is from an instantaneous line on the surface of the plate, rather than from a moving point source (that is, $V \rightarrow \infty$). This allows the elimination of the time dependency in the peak-temperature evaluation. Using this assumption, the temperature distribution is given by:

$$\theta - \theta_0 = \frac{\eta EI}{2\pi\lambda t} \exp\left(\frac{-r^2}{4\kappa t}\right) \quad (\text{Eq 34})$$

Again, to find the peak-temperature location, $\partial\theta/\partial t$ is set equal to zero and the equation is solved for r . The result is:

$$\frac{r^2}{4\kappa t} = 1 \quad (\text{Eq 35})$$

Substituting Eq 35 into Eq 34 yields the peak-temperature expression, $\theta = \theta_p$, which is:

$$\frac{1}{(\theta_p - \theta_0)} = \frac{1}{\left(\frac{\eta EI}{V}\right)} \left(\frac{e\rho C_p \pi r^2}{2}\right) \quad (\text{Eq 36})$$

It has been found that Eq 36 gives results that are too high, but that the slope of $1/(\theta_p - \theta_0)$ versus r^2 is accurate. To rectify this situation, Eq 36 is forced to fit experimental results by specifying a known temperature/location condition (θ_r at r_r). When this is done, Eq 36 becomes:

$$\frac{1}{(\theta_p - \theta_0)} = \frac{[e\rho C_p \pi (r^2 - r_r^2)]}{2 \cdot \left(\frac{\eta EI}{V}\right)} + \frac{1}{(\theta_r - \theta_0)} \quad (\text{Eq 37})$$

where θ_r and r_r are the reference temperature and distance. If the peak temperature (θ_p) evaluation is restricted to locations on the plate surface ($z = 0$), then $r = y$; and if the reference temperature and distance are assumed to be the melting temperature and the distance from the weld centerline to the fusion boundary (one-half of the weld bead width), then Eq 37 can be written as:

$$\frac{1}{(\theta_p - \theta_0)} = \frac{e\rho C_p \pi \left[y^2 - \left(\frac{d}{2}\right)^2\right]}{2 \cdot \left(\frac{\eta EI}{V}\right)} + \frac{1}{(\theta_m - \theta_0)} \quad (\text{Eq 38})$$

where θ_m is the melting temperature, and d is the weld bead width. This equation gives the peak temperature θ_p in a thick plate at a distance y from the weld centerline.

Solidification Rate. The weld solidification structure can be determined by using the constitutional supercooling criterion. Three thermal parameters that influence the solidification structure are temperature gradient normal to the solid-liquid interface, G ($^{\circ}\text{C}/\text{mm}$), solidification rate of the interface, R (mm/s), and cooling rate at the interface, $\partial\theta/\partial t$, at melting temperature ($^{\circ}\text{C}/\text{s}$ and equal to the product of GR). The microstructure may change from being planar to being cellular, a columnar dendrite, or an equiaxial structure if the G/R ratio becomes smaller. The dendrite arm spacing will decrease as the cooling rate increases. The solidification structure becomes refined at higher cooling rates.

At a quasi-steady state, the weld pool solidifies at a rate that is equal to the component of the electrode travel speed normal to the solid-liquid interface. Therefore, the solidification rate varies along the solid-liquid interface from the electrode travel speed, at the weld trailing edge, to zero, at the maximum pool width. The temperature gradient and the cooling rate at the solid-liquid interface can be determined from Eq 19, 22, and 24.

Modified Temperature Solution. The temperature solutions have a singularity at the center of the heat source. This singularity causes the predicted temperatures to be inaccurate in the area surrounding the heat source. However, a condition exists in which the peak temperature along the weld bead edge, that is, the solid-liquid interface location at the maximum pool width, is the melting temperature of the material. Using this temperature condition as a boundary condition for the temperature solutions, Eq 19 and 22 can be modified as shown subsequently: For thin plate:

$$\theta - \theta_0 = B_z \exp\left(\frac{-Vw}{2\kappa}\right) K_0\left(\frac{Vr}{2\kappa}\right) \quad (\text{Eq 39})$$

where B_z is a heat-input constant to be determined from the weld bead width, d :

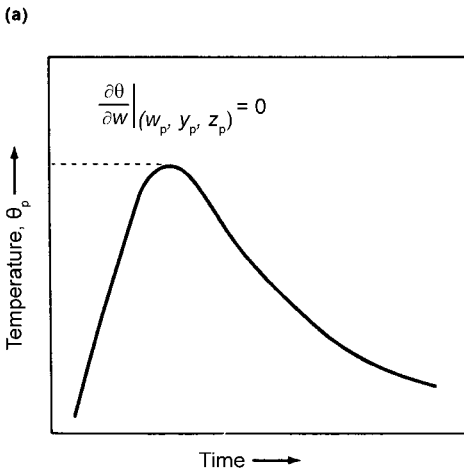
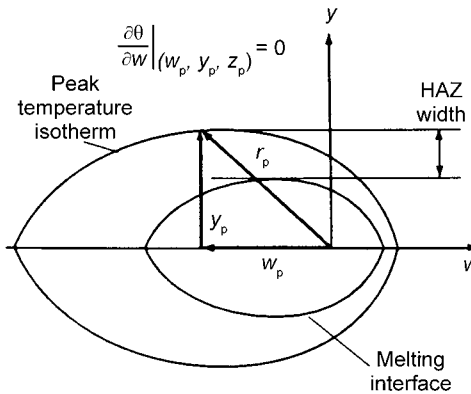


Fig. 4 Schematic showing peak temperature at (w_p, y_p, z_p) , with w_p to be determined for a given peak temperature value for a given (y_p, z_p) location. (a) Isotherms. HAZ, heat-affected zone. (b) Temperature history

$$B_z = \frac{(\theta_m - \theta_0) \exp\left(\frac{-Vr_B}{2\kappa}\right) \left[\frac{K_0(Vr_B/2\kappa)}{K_1(Vr_B/2\kappa)}\right]}{K_0\left(\frac{Vr_B}{2\kappa}\right)} \quad (\text{Eq 40})$$

with a bead width of:

$$d = 2r_B \sqrt{1 - \left[\frac{K_0(Vr_B/2\kappa)}{K_1(Vr_B/2\kappa)}\right]^2} \quad (\text{Eq 41})$$

For thick plate:

$$\theta - \theta_0 = B_z \frac{\exp[-V(w+r)/2\kappa]}{r} \quad (\text{Eq 42})$$

$$B_z = (\theta_m - \theta_0)r_B \exp\left(\frac{-Vr_B}{2\kappa}\right) \left[\frac{1}{1 + \left(\frac{2\kappa}{Vr_B}\right)} - 1 \right] \quad (\text{Eq 43})$$

with a bead width of:

$$d = 2r_B \sqrt{1 - \frac{1}{1 + \left(\frac{2\kappa}{Vr_B}\right)}} \quad (\text{Eq 44})$$

The welding heat input, \dot{Q} , is replaced by the heat-input parameter, B_z , which can be determined from measurement of the weld bead width, d . These equations can also be used to estimate the arc efficiency from the weld bead width.

A Practical Application of Heat-Flow Equations (Ref 33). The thermal condition in and near the weld metal must be established to control the metallurgical events in welding. The particular items of interests are the:

- Distribution of peak temperature in the HAZ
- Cooling rates in the weld metal and in the HAZ
- Solidification rate of the weld metal

Using aforementioned equations with some numerical values placed in them, several simple formulas are found in the published references. Although the following discussion focuses primarily on manual arc welding, certain general statements are applicable to all welding processes.

Peak Temperatures. The distribution of peak temperatures in the base metal adjacent to the weld is given by (Ref 34):

$$\frac{1}{\theta_p - \theta_0} = \frac{4.13\rho C_p H Y}{H_{net}} + \frac{1}{\theta_m - \theta_0} \quad (\text{Eq 45})$$

where θ_p is the peak temperature ($^{\circ}\text{C}$) at distance Y (mm) from the weld fusion boundary, θ_0 is the initial temperature ($^{\circ}\text{C}$), θ_m is the melting temperature ($^{\circ}\text{C}$), H_{net} is the net energy input equal to $\eta EI/V$ (J/mm), ρ is the density of the material (g/mm^3), C_p is the specific heat of solid metal ($\text{J}/\text{g} \cdot ^{\circ}\text{C}$), and H is the thickness of the base metal (mm).

Equation 45 can be used to determine the:

- Peak temperatures at specific locations in the HAZ
- Width of the HAZ
- Effect of preheat on the width of the HAZ

In addition, determination of the peak temperature at specific locations in the HAZ and the width of the HAZ can be obtained by the procedure described in the section "Engineering Solutions and Empirical Correlation" in this article.

Cooling Rate. Because the cooling rate varies with position and time, its calculation requires the careful specification of conditions. The most useful method is to determine the cooling rate on the weld centerline at the instant when the metal passes through a particular temperature of interest, θ_c . At a temperature well below melting, the cooling rate in the weld and in its immediate HAZ is substantially independent of position. For carbon and low-alloy steels, θ_c is the temperature near the pearlite "nose" temperature on the time-temperature transformation diagram. The value of $\theta_c = 550^{\circ}\text{C}$ (1020°F) is satisfactory for most steels, although not critical.

The cooling rate for thick plate (Ref 34) is:

$$R = \frac{2\pi\lambda(\theta_c - \theta_0)^2}{H_{net}} \quad (\text{Eq 46})$$

Equation 46 is comparable to Eq 29, which was obtained by the procedure described in the section "Cooling Rate" in this article. Adams (Ref 34) has developed a cooling-rate equation for thin plate along the centerline from Eq 24, which is:

$$R = 2\pi\lambda\rho C_p \left(\frac{H}{H_{net}}\right)^2 (\theta_c - \theta_0)^3 \quad (\text{Eq 47})$$

where R is the cooling rate ($^{\circ}\text{C}/\text{s}$) at a point on the weld centerline at just that moment when the point is cooling past the θ_c , ρC_p is the volumetric specific heat ($\text{J}/\text{mm}^3 \cdot ^{\circ}\text{C}$), and λ is the thermal conductivity of the base metal ($\text{J}/\text{mm} \cdot \text{s} \cdot ^{\circ}\text{C}$), respectively.

The dimensionless quantity τ , called the relative plate thickness, can be used to determine whether the plate is thick or thin:

$$\tau = H \cdot \sqrt{\frac{\rho C_p (\theta_c - \theta_0)}{H_{net}}} \quad (\text{Eq 48})$$

The relative plate thickness, τ , indicates a thermal balance between weld heat input and the material specific heat. The more energy input to the joint would lead to a more uniform temperature distribution through the plate thickness, which is analogous to a thinner plate condition. On the other hand, a smaller amount of weld heat input would cause deeper temperature slope through the thickness. The specific heat reduces the effect of heat input. In

practical situations, the thick-plate equation applies when τ is greater than 0.75, and the thin-plate equation applies when τ is less than that value.

Equations 46 and 47 are used to determine the cooling rate along the centerline for thick plate and thin plate, respectively. If one is interested in the cooling rate at the location at distance y from the centerline, iterative techniques should be used to solve the cooling rate. First, w and r can be obtained by iteration of the simultaneous equations, which consists of Eq 19 or 25, where θ equals θ_c and $r^2 = w^2 + y^2$, where y is given. Then, substitute w and r into the differentiation, $\partial\theta/\partial t = -V\partial\theta/\partial w$, from the temperature from Eq 19 or 25. The result will be the cooling rate for thick or thin plate located at y distance from the centerline:

$$\left[\frac{\partial\theta}{\partial t}\right]_{\theta_c}$$

In addition, the cooling rate for HAZ of low-carbon steel weldments can be obtained from Eq 30 directly.

Solidification Rate. The solidification rate can have a significant effect on metallurgical structure, properties, response to heat treatment, and soundness. The solidification time, S_t , of weld metal, measured in seconds, is:

$$S_t = \frac{LH_{net}}{2\pi\lambda\rho C_p(\theta_m - \theta_0)^2} \quad (\text{Eq 49})$$

where L is the heat of fusion (J/mm^3).

Example 1: Welding of 5 mm (0.2 in.) Thick Low-Carbon Steels. The thermal properties needed for heat-flow analysis are assumed to be:

Melting temperature (θ_m), $^{\circ}\text{C}$ ($^{\circ}\text{F}$)	1510 (2750)
Austenitization temperature, $^{\circ}\text{C}$ ($^{\circ}\text{F}$)	730 (1345)
Thermal conductivity (λ), $\text{W}/\text{m} \cdot \text{K}$ ($\text{J}/\text{mm} \cdot \text{s} \cdot ^{\circ}\text{C}$)	28 (0.028)
Volumetric specific heat (ρC_p), $\text{J}/\text{mm}^3 \cdot ^{\circ}\text{C}$	0.0044
Heat of fusion (L), J/mm^3	2

The welding condition is assumed to be:

Current (I), A	200
Arc voltage (E), V	20
Travel speed (V), mm/s (ipm)	5 (12)
Preheat (θ_0), $^{\circ}\text{C}$ ($^{\circ}\text{F}$)	25 (77)
Heat-transfer efficiency (η)	0.9
Net energy input, H_{net} , J/mm (kJ/in.)	720 (18.3)

Calculation of the HAZ Width. The value of Y at $\theta_p = 730^{\circ}\text{C}$ (1345°F) may be determined from Eq 45:

$$\frac{1}{730 - 25} = \frac{4.13(0.0044)5Y}{720} + \frac{1}{1510 - 25} \quad (\text{Eq 50})$$

resulting in a value for Y (the width of the HAZ) of 5.90 mm (0.23 in.).

In addition, the HAZ width can be obtained by the procedure described in the earlier section, "Peak Temperature" (relating to Eq 32 to 38). By substituting $w = w_p$, $r = r_p$, $y = y_p$, and $z = 0$ (on surface) into Eq 17 and 33, one respectively obtains:

$$r_p^2 = w_p^2 + y_p^2 \quad (\text{Eq 51})$$

$$\frac{-w_p}{r_p^2} - \frac{V}{2\kappa} \left(1 + \frac{w_p}{r_p} \right) = 0 \quad (\text{Eq 52})$$

Inserting $V = 5 \text{ mm/s}$, $\kappa = \lambda/\rho C_p = 0.028/0.0044 = 6.364 \text{ mm}^2/\text{s}$ into Eq 52:

$$\frac{-w_p}{r_p^2} = 0.393 \left(1 + \frac{w_p}{r_p} \right) \quad (\text{Eq 53})$$

From the temperature distribution equation (Eq 19) and $E = 20 \text{ V}$, $I = 200 \text{ A}$, $\eta = 0.9$, $\lambda = 0.028 \text{ J/mm} \cdot \text{s} \cdot \text{°C}$, $\theta_p = 730 \text{ °C}$, $\theta_0 = 25 \text{ °C}$, $V = 5 \text{ mm/s}$, $\kappa = \lambda/\rho C_p = 0.028/0.044 = 6.364 \text{ mm}^2/\text{s}$:

$$730 - 25 = \frac{0.9 \cdot 20 \cdot 200}{2\pi \cdot 0.028 r_p} \cdot \exp \left[\frac{-5(w_p + r_p)}{2 \cdot 0.028/0.0044} \right] \quad (\text{Eq 54})$$

$$-3.368 + \ln(r_p) = -0.393(w_p + r_p) \quad (\text{Eq 55})$$

Solving the simultaneous equations, Eq 53 and 55, the peak temperature location (r_p , w_p) is determined. The peak temperature of 730 °C boundary from the weld centerline (y_p) can be determined from Eq 51 using the obtained values of r_p and w_p . The final solution result showing the peak temperature of 730 °C location with respect to the moving arc center on the plate surface is at ($w_p = -10.51 \text{ mm}$, $y_p = 12.63 \text{ mm}$, $z_p = 0 \text{ mm}$).

To determine the HAZ width, the weld bead width or boundary of peak temperature of 1510 °C must be determined. The difference between the two distances to the weld centerline of two peak temperatures is the HAZ width (Y). Following the same mathematical procedure as used for 730 °C peak temperature location, the 1510 °C location can be determined, which is at ($w_p = -4.84 \text{ mm}$, $y_p = 6.68 \text{ mm}$, $z_p = 0 \text{ mm}$). The HAZ size $Y = 12.63 - 6.68 = 5.95 \text{ mm}$ (0.23 in.), which is less than 1% difference.

Effect of Tempering Temperature on Quenched and Tempered (Q&T) Steels. If the plate had been quenched and then tempered to 430 °C (810 °F), then any region heated above that temperature will have been "overtempered" and may exhibit modified properties. It would then be reasonable to consider the modified zone as being "heat affected," with its outer extremity located where $\theta_p = 430 \text{ °C}$ (810 °F):

$$\frac{1}{430 - 25} = \frac{4.13(0.0044)5Y_z}{720} + \frac{1}{1510 - 25} \quad (\text{Eq 56})$$

resulting in a value for Y of 14.23 mm (0.56 in.). Tempering to 430 °C increases the HAZ by 140%.

Effect of Preheating Temperature on Q&T Steels. Assume that the Q&T steel described previously was preheated to a temperature, θ_0 , of 200 °C (390 °F):

$$\frac{1}{430 - 25} = \frac{4.13(0.0044)5Y_z}{720} + \frac{1}{1510 - 200} \quad (\text{Eq 57})$$

resulting in a value for Y of 28.40 mm (1.12 in.). Preheating Q&T steel at 200 °C will double the HAZ size. Therefore, an upper limit on the preheating temperature is specified for Q&T steels in most of the welding codes.

Effect of Energy Input on Q&T Steels. Assume that the energy input into the Q&T steel (without preheating) increases 50% (that is, 1.08 kJ/mm , or 27.45 kJ/in.):

$$\frac{1}{430 - 25} = \frac{4.13(0.0044)5Y_z}{1080} + \frac{1}{1510 - 25} \quad (\text{Eq 58})$$

resulting in a value for Y of 21.34 mm (0.84 in.). Increasing the energy input by 50% will also increase HAZ by 50%.

Example 2: Welding of 6 mm (0.24 in.) Thick Low-Carbon Steels. The thermal properties needed for heat-flow analysis are assumed to be:

Melting temperature (θ_m), °C (°F)	1510 (2750)
Austenitization temperature, °C (°F)	730 (1345)
Thermal conductivity (λ), W/m · K (J/mm · s · °C)	28 (0.028)
Volumetric specific heat (ρC_p), J/mm ³ · °C	0.0044
Heat of fusion (L), J/mm ³	2

The welding condition is assumed to be:

Current (I), A	300
Arc voltage (E), V	25
Preheat (θ_0), °C (°F)	25 (77)
Heat-transfer efficiency (η)	0.9

Critical Cooling Rate at 550 °C (1022 °F) (θ_c). A critical cooling rate exists for each steel composition. If the actual cooling rate in the weld metal exceeds this critical value, then hard martensitic structures may develop in the HAZ, and there is a great risk of cracking under the influence of thermal stresses in the presence of hydrogen.

The best way to determine the critical cooling rate is to make a series of bead-on-plate weld passes in which all parameters, except the arc travel speed, are held constant. After the hardness tests on the weld passes deposited at travel speeds of 6, 7, 8, 9, and 10 mm/s (14, 17, 19, 21, and 24 ipm), it was found that at the latter two travel speeds, the weld HAZ had hardness exceeding the critical value (e.g., 350 HV). Therefore, the critical cooling rate was encountered at a travel speed of approximately 8 mm/s

(19 ipm). At this speed, the net energy input (i.e., the minimum requirement) is:

$$H_{\text{net}} = \frac{25(300)0.9}{8} = 844 \text{ J/mm} \quad (\text{Eq 59})$$

From Eq 48, the relative plate thickness is:

$$\tau = 6\sqrt{\frac{0.0044(550 - 25)}{844}} = 0.31 \text{ mm} \quad (\text{Eq 60})$$

Because τ is less than 0.75, the thin-plate equation (Eq 47) applies:

$$\frac{R}{2\pi\lambda} = 0.0044 \left(\frac{6}{844} \right)^2 (550 - 25)^3 = 32.20 \quad (\text{Eq 61})$$

resulting in R being equal to $2\pi(0.028)32.20$, which is equal to 5.7 °C/s (10.3 °F/s). This value is the maximum safe (critical) cooling rate for this steel, and the actual cooling rate cannot exceed this value.

Preheating Temperature Requirement. Although the critical cooling rate cannot be exceeded, in the actual welding operation a pre-heat can be used to reduce the cooling rate to 5.7 °C/s (10.3 °F/s).

Assume that the welding condition is:

Current (I), A	250
Arc voltage (E), V	25
Heat-transfer efficiency (η)	0.9
Travel velocity (V), mm/s (ipm)	7 (17)
Plate thickness (H), mm (in.)	9 (0.35)

The energy heat input, H_{net} , is:

$$H_{\text{net}} = \frac{25(250)0.9}{7} = 804 \text{ J/mm} \quad (\text{Eq 62})$$

Assuming that the thin-plate equation (Eq 47) applies:

$$\left(\frac{R}{2\pi\lambda} \right)_{\text{max}} = 32.20 = 0.0044 \left(\frac{9}{804} \right)^2 (550 - \theta_0)^3 \quad (\text{Eq 63})$$

resulting in a θ_0 of 162 °C (325 °F).

The relative plate thickness should be checked:

$$\tau = 9\sqrt{\frac{0.0044(550 - 162)}{804}} = 0.41 \quad (\text{Eq 64})$$

Because τ is less than 0.75, the thin-plate equation does apply. If the initial plate temperature is raised either to or above 162 °C (325 °F), then the cooling rate will not exceed 5.7 °C/s (10.3 °F/s). For this case, a minimum preheat temperature should be 162 °C (325 °F).

Equation 31 is an empirical equation for predicting the cooling rate in the weld bead. The nugget area can be determined from Fig. 3 using the weld bead heat input of 0.8 kJ/mm (20 kJ/in.), welding current of 250 A, and without preheating, which leads to an approximate value of 28 mm^2 (0.04 in.^2). The cooling rate calculated from Eq 31 is:

$$^{\circ}\text{C/s} = \left(\frac{2012}{28}\right)^{1.119} = 119 \text{ }^{\circ}\text{C/s} \quad (\text{Eq 65})$$

This cooling rate would be too high, and preheating must be used.

Effect of Joint Thickness. If the plate thickness increases from 9 to 25 mm (0.35 to 1 in.), but there is the same level of energy input, then the calculation of the required preheat temperature would be as follows. First, using the thin-plate equation (Eq 47):

$$\begin{aligned} \left(\frac{R}{2\pi\lambda}\right)_{\max} &= 32.2 \\ &= 0.0044 \left(\frac{25}{804}\right)^2 (550 - \theta_0)^3 \end{aligned} \quad (\text{Eq 66})$$

resulting in a value for θ_0 of 354 °C (669 °F).

The relative plate thickness, τ , should be checked:

$$\tau = 25 \sqrt{\frac{0.0044(550 - 354)}{804}} = 0.82 \quad (\text{Eq 67})$$

Because τ is greater than 0.75, the use of the thin-plate equation is inadequate. Using the thick-plate equation (Eq 46):

$$32.2 = \frac{(550 - \theta_0)^2}{804} \quad (\text{Eq 68})$$

resulting in a value for θ_0 of 389 °C (730 °F).

The relative plate thickness should be checked:

$$\tau = 25 \sqrt{\frac{0.0044(550 - 389)}{804}} = 0.74 \quad (\text{Eq 69})$$

Although τ is less than, but close to, 0.75, using the thick-plate equation is adequate. Therefore, the initial temperature should be raised to 389 °C (730 °F) by preheating to avoid exceeding the cooling rate of 5.7 °C/s (10.3 °F/s).

Now, if the plate thickness increases to 50 mm (2 in.), but there is the same level of energy input, then the thick-plate equation (Eq 46) applies and, again, the value for θ_0 is 389 °C (730 °F).

The relative plate thickness should be checked:

$$\tau = 50 \sqrt{\frac{0.0044(550 - 389)}{804}} = 1.48 \quad (\text{Eq 70})$$

Because τ is greater than 0.75, the use of the thick-plate equation is adequate.

Under some welding conditions, it is not necessary to reduce the cooling rate by using preheat. For example, if the plate thickness is 5 mm (0.2 in.) and there is the same level of energy input:

$$\begin{aligned} \left(\frac{R}{2\pi\lambda}\right)_{\max} &= 32.2 \\ &= 0.0044 \left(\frac{5}{804}\right)^2 (550 - \theta_0)^3 \end{aligned} \quad (\text{Eq 71})$$

resulting in a value for θ_0 of -24 °C (-11 °F). Therefore, using preheat is unnecessary.

Fillet-Welded Tee Joints. For a weld with a higher number of paths, as occurs in fillet-welded tee joints, it is sometimes necessary to modify the cooling-rate equation, because the cooling of a weld depends on the available paths for conducting heat into the surrounding cold base metal.

When joining 9 mm (0.35 in.) thick plate, where $H_{\text{net}} = 804 \text{ J/mm}$ (20.4 kJ/in.), and when there are three legs instead of two, the cooling-rate equation is modified by reducing the effective energy input by a factor of 2/3:

$$H_{\text{net}} = \frac{2}{3}(804) = 536 \text{ J/mm} \quad (\text{Eq 72})$$

Using the thin-plate equation (Eq 47):

$$\begin{aligned} \left(\frac{R}{2\pi\lambda}\right)_{\max} &= 32.2 \\ &= 0.0044 \left(\frac{9}{536}\right)^2 (550 - \theta_0)^3 \end{aligned} \quad (\text{Eq 73})$$

resulting in a value for θ_0 of 254 °C (490 °F).

The relative plate thickness should be checked:

$$\tau = 9 \sqrt{\frac{0.0044(550 - 254)}{536}} = 0.44 \quad (\text{Eq 74})$$

Because τ is less than 0.75, using the thin-plate equation is adequate. A higher preheat temperature is required for welding a tee joint because of the added cooling mass. The minimum preheat temperature should be increased from 162 to 254 °C (324 to 489 °F) when changing weld joint type from butt to tee of 9 mm (0.35 in.) plate thickness using the same amount of welding heat input.

Example 3: Cooling Rate for the Location at Distance y (mm) from the Centerline.

For a steel plate of 25 mm (1 in.) thickness (H), the welding condition is assumed to be:

Current, A	300
Arc voltage, V	25
Arc efficiency, η	1.00
Heat input (ηEI), kW (J/s)	7.5 (7500)
Travel speed (V), mm/s (ipm)	1.0 (2)
Preheat (θ_0), °C (°F)	20 (68)

The thermal properties needed for heat-flow analysis are assumed to be:

Melting temperature (θ_m), °C (°F)	1400 (2552)
Thermal conductivity (λ), W/m · K (J/mm · s · °C)	43.1 (0.0431)
Volumetric specific heat (ρC_p), J/mm ³ · °C	0.0037
Thermal diffusivity (κ), mm ² /s	11.65

Assume that one is interested in the critical cooling rate at the location on the surface ($z = 0$) at distance $y = 20$ mm from the centerline at the instant when the metal passes through the specific temperature of 615 °C (1140 °F). Initially, the relative plate thickness should be checked. From Eq 48, the relative plate thickness is:

$$\tau = 25 \sqrt{\frac{0.0037 \cdot (615 - 20)}{7500}} = 1.37 \quad (\text{Eq 75})$$

Because τ is greater than 0.75, this plate can be treated as a thick plate. Equation 32 should be used to calculate the cooling rate for thick plate at the location where the variables are w and r and at critical temperature $\theta = \theta_c$. To solve Eq 32, the value of w and r must be calculated first. From Eq 19, the temperature distribution of thick plate, and Eq 17, where $z = 0$, the following two simultaneous equations are obtained:

$$\begin{aligned} 615 - 20 &= \frac{7500}{2\pi(0.0431)r_p} \exp\left[\frac{-1 \cdot (w_p + r_p)}{2 \cdot 11.65}\right] \\ \text{and } r_p &= \sqrt{w_p^2 + 20^2} \end{aligned} \quad (\text{Eq 76})$$

The value of w_p and r_p can be solved by using iteration techniques to solve the aforementioned simultaneous equation. The result is that $w_p = -82.77$ mm and $r_p = 85.15$ mm.

Substituting w_p and r_p into Eq 34:

$$\begin{aligned} \left[\frac{\partial\theta}{\partial t}\right]_{\theta_c} &= -V \frac{\partial\theta}{\partial w} \\ &= \frac{-1 \cdot (7500)}{2\pi(0.0431)(85.15)} \\ &\quad \cdot \exp\left[\frac{-1 \cdot (-82.77 + 85.15)}{2(11.65)}\right] \\ &\quad \cdot \left[\frac{-(-82.77)}{85.15^2} - \frac{1.0}{2(11.65)}\right] \\ &\quad \cdot \left(1 + \frac{-82.77}{85.15}\right) \end{aligned} \quad (\text{Eq 77})$$

Therefore:

$$\left[\frac{\partial\theta}{\partial t}\right]_{\theta_c=615} = -3 \text{ }^{\circ}\text{C/s} \quad (\text{Eq 78})$$

From Eq 46 we can calculate the cooling rate along the centerline at the same temperature (615 °C, or 1140 °F):

$$R = \frac{2\pi(0.0431)(615 - 20)^2}{7500} = 12.8 \text{ }^{\circ}\text{C/s} \quad (\text{Eq 79})$$

Also from the empirical equation, Eq 30, one can calculate the cooling rate in the HAZ at a temperature of 615 °C (1140 °F):

$$\begin{aligned} \left[\frac{\partial\theta}{\partial t}\right]_{\theta_c=615} &= 0.35 \left\{ \left[\frac{615 - 20}{300/2} \right]^{1.7} \right. \\ &\quad \left. \left[1 + \frac{2}{\pi} \tan^{-1} \left(\frac{1.0 - 0.486}{0.125} \right) \right]^{0.8} \right\} \\ &= 3.7 \text{ }^{\circ}\text{C/s} \end{aligned} \quad (\text{Eq 80})$$

H_0 and α can be determined from Table 1, and using the linear interpolation method between the temperature differences, the values at 615 °C (1140 °F) are $H_0 = 0.486$ and $\alpha = 0.125$.

At the same temperature of 615 °C (1140 °F), the cooling rate at the centerline is approximately three times greater than the cooling rate at the location a distance $y = 20$ mm (0.8 in.) from the weld centerline. The predicted cooling rate at this location is close to the estimated cooling rate of the HAZ, using the empirical formula, under the given welding condition.

Example 4: Solidification Rate. A weld pass of 800 J/mm (20.3 kJ/in.) in net energy input is deposited on a low-carbon steel plate (using material properties shown in example 2 in this article). The initial temperature is 25 °C (77 °F). The solidification time in the weld pool (Eq 49) would be 0.94 s:

$$S_t = \frac{2(800)}{2\pi(0.028)(0.0044)(1510 - 25)^2} = 0.94 \text{ s} \quad (\text{Eq 81})$$

Parametric Effects

To show the effects of material property and welding condition on the temperature distribution of weldments, the welding of 304 stainless steel, low-carbon steel, and aluminum are

simulated for three different welding speeds: 1, 5, and 8 mm/s (2, 12, and 19 ipm). The thermal conductivity and thermal diffusivity of 304 stainless steel are 26 W/m · K (0.026 J/mm · s · °C) and 4.6 mm²/s (0.007 in.²/s), respectively. For low-carbon steel, the respective values are 50 W/m · K (0.050 J/mm · s · °C) and 7.5 mm²/s (0.012 in.²/s); whereas for aluminum, the respective values are 347 W/m · K (0.347 J/mm · s · °C) and 80 mm²/s (0.124 in.²/s). The heat input per unit weld length was kept constant, 4.2 kJ/s (1 kcal/s), for all cases. The parametric results are described as follows.

Effect of Material Type. Figures 5(a) to (c) depict the effect of thermal properties on isothermperature contours for a heat input of 4.2 kJ/s (1 kcal/s), and travel speeds of 1, 5, and 8 mm/s (2, 12, and 19 ipm). The temperature spreads over a larger area and causes a larger weld pool (larger weld bead) for low-conductivity material. The isothermperature contours also elongate more toward the back of the arc for low-conductivity material. For aluminum, a larger heat input would be required to obtain the same weld size as the stainless steel weldment.

Effect of Welding Speed. Figures 6(a) to (c) show the effect of welding speed on isothermperature contours. When the travel speed increases, the weld size decreases and the

isothermperature contours are more elongated toward the back of the arc. Larger heat inputs would be required for faster travel speeds in order to obtain the same weld size.

Figure 7 shows the effect of welding heat input on the peak temperature at two locations, 6.4 and 13 mm (¼ and ½ in.) from the weld centerline. (The material simulated in this illustration is low-carbon steel plate with a large thickness.) Within the practical range of welding conditions for the GMAW process of low-carbon steels, the peak temperature at both locations increases linearly, as the welding current increases, and decreases exponentially, with the travel speed. To increase welding current proportionally with travel speed for constant heat input per unit weld length (that is, $\dot{Q}/V = \text{constant}$), the peak temperature at two locations increases with the travel speed, which implies a larger weld size resulting from higher heat input. The welding current has a more significant effect on peak temperature than does the travel speed. However, the increase in peak temperature is more dominant at the 6.4 mm (¼ in.) location. The influence of proportional increase in welding current and travel speed on peak temperature diminishes as the distance from the weld centerline increases and when the travel speed becomes high.

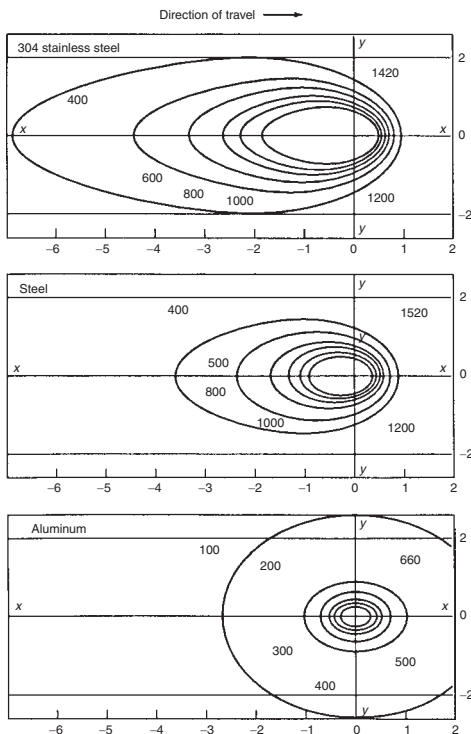


Fig. (5a) Effect of thermal property on isothermperature contours for a heat input of 4.2 kJ/s (1 kcal/s) at a welding speed, V , of 1 mm/s (2 ipm) and the respective thermal conductivities of each material (refer to text for values). Values for x and y are given in cm, and temperatures are given in °C.

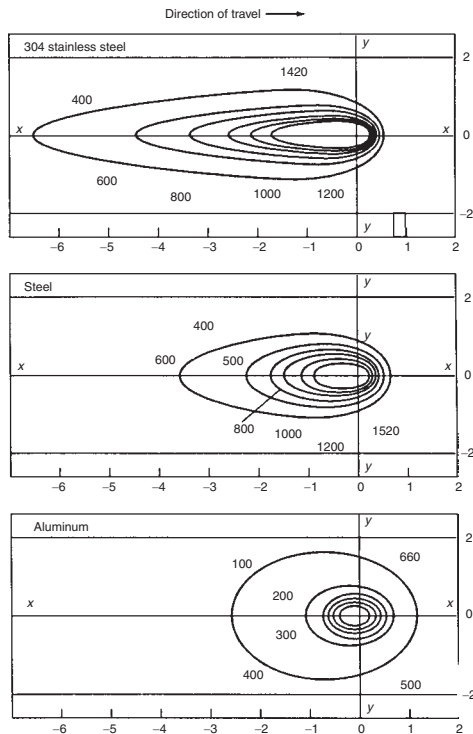


Fig. (5b) Effect of thermal property on isothermperature contours for a heat input of 4.2 kJ/s (1 kcal/s) at a welding speed, V , of 5 mm/s (12 ipm) and the respective thermal conductivities of each material (refer to text for values). Values for x and y are given in cm, and temperatures are given in °C.

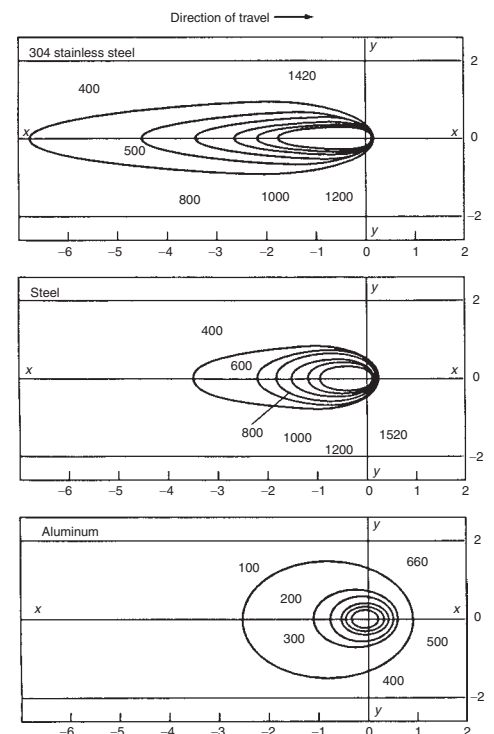


Fig. (5c) Effect of thermal property on isothermperature contours for a heat input of 4.2 kJ/s (1 kcal/s) at a welding speed, V , of 8 mm/s (19 ipm) and the respective thermal conductivities of each material (refer to text for values). Values for x and y are given in cm, and temperatures are given in °C.

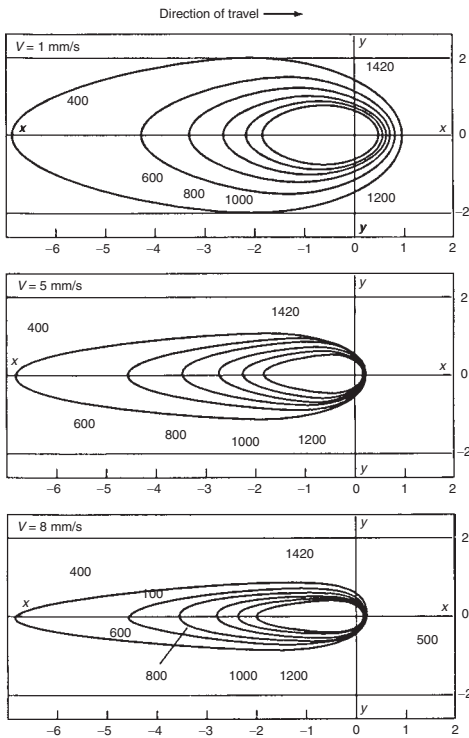


Fig. (6a) Effect of welding speed, V , on isotemperature contours of 304 stainless steel for 4.2 kJ/s (1 kcal/s) heat input

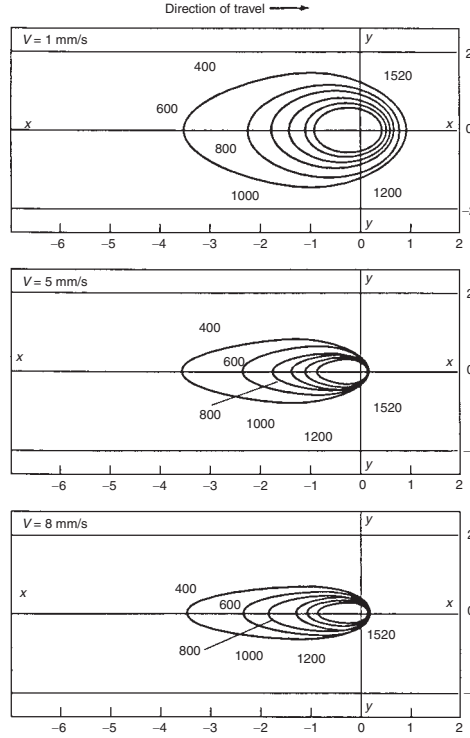


Fig. (6b) Effect of welding speed, V , on isotemperature contours of low-carbon steel for 4.2 kJ/s (1 kcal/s) heat input

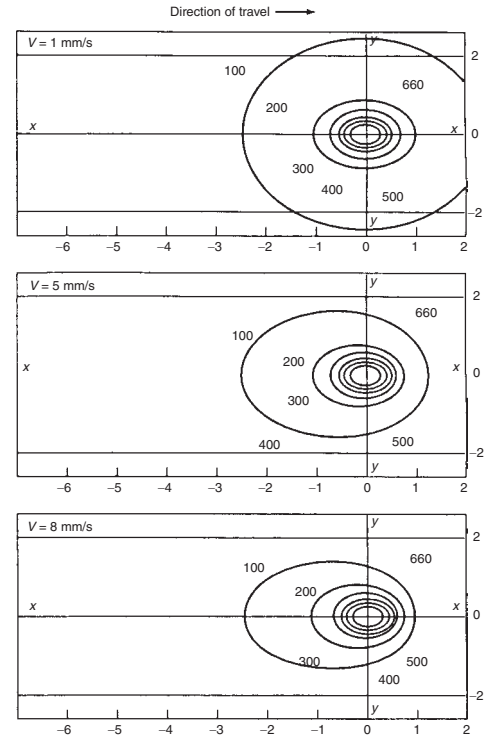


Fig. (6c) Effect of welding speed, V , on isotemperature contours of aluminum for 4.2 kJ/s (1 kcal/s) heat input

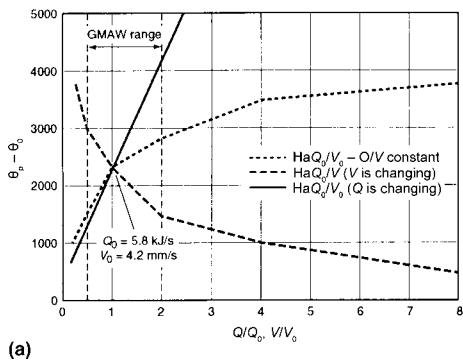
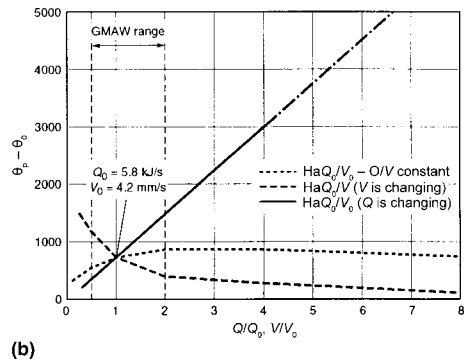


Fig. 7 Peak temperature determined by the point heat-source solution. (a) At 6.4 mm (1/4 in.) from the center. (b) At 13 mm (1/2 in.) from the center. GMAW, gas metal arc welding



Thermophysical Properties of Selected Engineering Materials

For the sake of convenience when using heat-flow equations, the thermal properties of selected engineering materials are provided in Table 2.

REFERENCES

1. N.S. Boulton and H.E. Lance-Martin, Residual Stresses in Arc Welded Plates, *Proc. Inst. Mech. Eng.*, Vol 33, 1986, p 295

2. D. Rosenthal and R. Schmerber, Thermal Study of Arc Welding, *Weld. J.*, Vol 17 (No. 4), 1983, p 2s
 3. N.N. Rykalin, "Calculations of Thermal Processes in Welding," Mashgiz, Moscow, 1951
 4. K. Masubuchi, *Analysis of Welded Structures*, Pergamon Press, 1980
 5. C.L. Tsai, "Parametric Study on Cooling Phenomena in Underwater Welding," Ph.D. thesis, MIT, 1977
 6. C.L. Tsai, Finite Source Theory, *Modeling of Casting and Welding Processes II*, Engineering Foundation Meeting, July

31-Aug 5, 1983, New England College (Henniker, NH), p 329
 7. R. Pavelic, R. Tanakuchi, O. Uyehara, and P. Myers, Experimental and Computed Temperature Histories in Gas Tungsten Arc Welding in Thin Plates, *Weld. J.*, Vol 48 (No. 7), 1969, p 295s
 8. S. Kou, 3-Dimensional Heat Flow during Fusion Welding, *Proc. of Metallurgical Society of AIME*, Aug 1980, p 129-138
 9. P.G. Kogan, The Temperature Field in the Weld Zone, *Ave. Svarka*, Vol 4 (No. 9), 1979, p 8
 10. G.M. Ecer, H.D. Downs, H.D. Brody, and M.A. Gokhale, Heat Flow Simulation of Pulsed Current Gas Tungsten Arc Welding, *Modeling of Casting and Welding Processes*, Engineering Foundation 1980 Meeting, Aug 3-8, 1980 (Rindge, NH), p 139-160
 11. H. Hibbitt and P. Marcal, A Numerical Thermomechanical Model for Welding and Subsequent Loading of a Fabricated Structure, *Comput. Struct.*, Vol 3, 1973, p 1145
 12. E. Friedman, Thermomechanical Analysis of the Welding Process Using Finite Element Methods, *Trans. ASME*, Aug 1975, p 206
 13. Z. Paley and P. Hibbert, Computation of Temperature in Actual Weld Design, *Weld. J.*, Vol 54 (No. 11), 1975, p 385s

Table 2 Thermal properties of selected engineering alloys

Alloy	Density (ρ), at 20 °C (68 °F), g/cm ³	Specific heat (C_p), at 20 °C (68 °F), kJ/kg · K	Thermal conductivity (λ) at 20 °C (68 °F), W/m · K	Coefficient of thermal expansion (β), at 20 °C (68 °F), 10 ⁻⁵ /°C
Carbon steel				
~0.5% C	7.833	0.465	54	1.474
~1.0% C	7.801	0.473	43	1.172
~1.5% C	7.753	0.486	36	0.970
Aluminum				
Al-Cu (94–96% Al, 3–5% Cu)	2.787	0.883	164	6.676
Al-Si (86.5% Al, 1% Cu)	2.659	0.867	137	5.933
Al-Si (78–80% Al, 20–22% Si)	2.627	0.854	161	7.172
Al-Mg-Si (97% Al, 1% Mg, 1% Si, 1% Mn)	2.707	0.892	177	7.311
Titanium	4.500	0.52	16	0.84

Alloy	Density (ρ), at 100 °C (212 °F), g/cm ³	Specific heat (C_p), at 0–100 °C (32–212 °F), kJ/kg · K	Thermal conductivity (κ) at 100 °C (212 °F), W/m · K	Coefficient of thermal expansion (α), at 0–538 °C (32–1000 °F), 10 ⁻⁵ /°C
Stainless steel				
Chromium-nickel austenitic	7.800–8.000	0.46–0.50	18.7–22.8	1.700–1.920
Chromium ferritic	7.800	0.46–0.50	24.4–26.3	1.120–1.210
Chromium martensitic	7.800	0.42–0.46	28.7	1.160–1.210
Carbon steel	7.800	0.48	60	1.17

14. T. Naka, Temperature Distribution during Welding, *J. Jpn. Weld. Soc.*, Vol 11 (No. 1), 1941, p 4
15. K. Masubuchi and T. Kusuda, Temperature Distribution of Welded Plates, *J. Jpn. Weld. Soc.*, Vol 22 (No. 5), 1953, p 14
16. C.L. Tsai and C.A. Hou, Theoretical Analysis of Weld Pool Behavior in the Pulsed Current GTAW Process, *Transport Phenomena in Materials Processing*, ASME Winter Annual Meeting, 1983
17. E. Friedman, "Finite Element Analysis of Arc Welding," Report WAPD-TM-1438, Department of Energy, 1980
18. J.S. Fan and C.L. Tsai, "Finite Element Analysis of Welding Thermal Behavior in Transient Conditions," 84-HT-80, ASME
19. M.R. Frewin and D.A. Scott, Finite Element Model of Pulsed Laser Welding, *Weld. J.*, Vol 78 (No. 1), 1999, p 15s–22s
20. E.A. Bonifaz, Finite Element Analysis of Heat Flow in Single-Pass Arc Welds, *Weld. J.*, Vol 79 (No. 5), 2000, p 121s–125s
21. T. DebRoy and S.A. David, Physical Processes in Fusion Welding, *Rev. Modern Physics*, Vol 67 (No. 1), 1995, p 85–112
22. J.H. Dilawari, T.W. Eagar, and J. Szekely, An Analysis of Heat and Fluid Flow Phenomena in Electroslag Welding, *Weld. J.*, Vol 54 (No. 9), 1975
23. R. McLay and G.F. Carey, Coupled Heat Transfer and Viscous Flow, and Magnetic Effects in Weld Pool Analysis, *Int. J. Numer. Methods Fluids*, Vol 9, 1989, p 713–730
24. R. Nandan, G.G. Roy, T.J. Lienert, and T. DebRoy, Numerical Modeling of 3D Plastic Flow and Heat Transfer during Friction Stir Welding of Stainless Steel, *Sci. Technol. Weld. Join.*, Vol 11 (No. 5), 2006, p 526–537
25. R. Nandan, G.G. Roy, T.J. Lienert, and T. DebRoy, Three-Dimensional Heat and Material Flow during Friction Stir Welding of Mild Steel, *Acta Mater.*, Vol 55, 2007, p 883–895
26. R.L. Apps and D.R. Milner, Heat Flow in Argon-Arc Welding, *Br. Weld. J.*, Vol 2 (No. 10), 1955, p 475
27. H.S. Carslaw and J.C. Jaeger, *Conduction of Heat in Solids*, Oxford Press
28. The Engineering ToolBox, section on convective heat transfer, www.engineering-toolbox.com
29. C.L. Tsai and J.H. Wu, "An Investigation of Heat Transport Phenomena in Underwater Welding," presented at the ASME Winter Annual Meeting (Miami Beach, FL), 1985
30. H. Kihara, H. Suzuki, and H. Tamura, *Researches on Weldable High-Strength Steels*, 60th Anniversary Series, Vol 1, Society of Naval Architects of Japan, Tokyo, 1957
31. C.E. Jackson, Department of Welding Engineering, The Ohio State University Lecture Note, 1977
32. C.E. Jackson and W.J. Goodwin, Effects of Variations in Welding Technique on the Transition Behavior of Welded Specimens—Part II, *Weld. J.*, May 1948, p 253-s to 266-s
33. Heat Flow in Welding, Ch 3, *Welding Handbook*, Vol 1, 7th ed., AWS, 1976
34. C.M. Adams, Jr., Cooling Rate and Peak Temperature in Fusion Welding, *Weld. J.*, Vol 37 (No. 5), 1958, p 210s–215s

Factors Influencing Heat Flow in Fusion Welding

Ole Runar Myhr, Hydro Aluminium and Norwegian University of Science and Technology
Øystein Grong, Norwegian University of Science and Technology

IN GENERAL, a quantitative analysis of metallurgical reactions in fusion welding requires detailed information about the weld thermal history. To obtain a broad overview of factors affecting heat flow in a real welding situation, the analytical modeling approach is preferable, because this makes it possible to derive relatively simple equations that provide the required background for an understanding of the temperature-time pattern. An important aspect of the approach is the use of dimensionless groups for a general outline of the temperature distribution (Ref 1). Although this practice inevitably increases the complexity of the mathematical treatment, it is a convenient way to reduce the total number of variables to an acceptable level and hence condense general information about the weld thermal program into two-dimensional maps or diagrams. Consequently, readers who are unfamiliar with the concept should accept the challenge and try to overcome the barrier associated with the use of such dimensionless groups in heat flow analyses.

Introduction

Fusion Welding Processes

Fusion welding is a collective term that includes the following processes (the terminology used here is in accordance with the American Welding Society's recommendations, Ref 2):

- Shielded metal arc welding (SMAW)
- Gas tungsten arc welding (GTAW)
- Gas metal arc welding (GMAW)
- Flux cored arc welding (FCAW)
- Submerged arc welding (SAW)
- Laser welding
- Electron beam welding (EBW)

Arc Efficiency Factors

In arc welding, which includes the first five processes listed previously, heat losses by

convection and radiation to the surroundings are taken into account by the efficiency factor, η , defined as:

$$\eta = q_0 / (IU) \quad (\text{Eq 1})$$

where q_0 is the net power received by the weldment (e.g., measured by calorimetry), I is the welding current (amperage), and U is the arc voltage. For SAW, the efficiency factor has been reported in the range of 90 to 98%; for SMAW and GMAW, from 65 to 85%; and for GTAW, from 22 to 75%, depending on polarity and materials (Ref 3). A summary of ranges is given in Table 1.

Thermal Properties of Some Metals and Alloys

A precondition for obtaining simple analytical solutions of Fourier's second law of heat conduction is that the thermal properties of the base material are constant and independent of temperature. The thermal properties in question are the thermal conductivity, λ , the thermal diffusivity, a , and the volumetric heat capacity, ρc . For most metals and alloys, λ , a , and ρc may vary significantly with temperature. In addition, the same thermal properties are also dependent upon the chemical composition and the thermal history of the base material, which further complicates the situation.

Table 2 Physical properties for some metals and alloys

Material	λ , W · mm ⁻¹ · °C ⁻¹	a , mm ² · s ⁻¹	ρc , J · mm ⁻³ · °C ⁻¹	T_m		$H_m - H_0(a)$, J · mm ⁻³	ΔH_m , J · mm ⁻³
				°C	°F		
Carbon steels	0.040	8	0.005	1520	2770	7.50	2.0
Low-alloy steels	0.025	5	0.005	1520	2770	7.50	2.0
High-alloy steels	0.020	4	0.005	1500	2730	7.40	2.0
Titanium alloys	0.030	10	0.003	1650	3000	4.89	1.4
Aluminum (>99% Al)	0.230	85	0.0027	660	1220	1.73	0.8
Al-Mg-Si alloys	0.167	62	0.0027	652	1205	1.71	0.8
Al-Mg alloys	0.149	55	0.0027	650	1200	1.70	0.8

(a) Does not include the latent heat of melting (ΔH_m). Source: Ref 1, based on data from Ref 5–8

By neglecting such effects in the heat flow models, several limitations are imposed on the applications of the analytical solutions. Nevertheless, experience has shown that these problems, to some extent, can be overcome by the choice of reasonable average values for λ , a , and ρc within a specific temperature range. Table 2 (Ref 5–8) contains a summary of relevant thermal properties for various metals and alloys, based on a critical review of literature data. It should be noted that the thermal data in Table 2 do not include a correction for heat consumed in melting of the parent material. Although the latent heat of melting is temporarily removed during fusion welding, experience has shown that this effect can be accounted for by calibrating the equations against a known isotherm (e.g., the

Table 1 Recommended arc efficiency factors for various welding processes

Welding process	Arc efficiency factor, η	
	Range	Mean
Submerged arc welding (steel)	0.91–0.99	0.95
Shielded metal arc welding (steel)	0.66–0.85	0.80
Gas metal arc welding (CO ₂ -steel)	0.75–0.93	0.85
Gas metal arc welding (Ar-steel)	0.66–0.70	0.70
Gas tungsten arc welding (Ar-steel)	0.25–0.75	0.40
Gas tungsten arc welding (He-Al)	0.55–0.80	0.60
Gas tungsten arc welding (Ar-Al)	0.22–0.46	0.40

Source: Ref 1, based on data from Ref 3, 4

fusion boundary). In practice, such corrections are done by adjusting the arc efficiency factor, η , until a good correlation is achieved between predictions and experiments.

Analytical Solutions of the Thermal Field around Moving Point and Line Sources

The purpose of this section is to review the classical models for the pseudo-steady-state temperature distribution around moving heat sources. The analytical solutions to the differential heat flow equation under conditions applicable to fusion welding were first presented by Rosenthal (Ref 9, 10), but the theory was later extended and refined by a number of other investigators (Ref 3, 11–13).

Thick-Plate Model

The thick-plate model consists of an isotropic semiinfinite body at initial temperature T_0 limited in one direction by a plane that is impermeable to heat. At time $t=0$, a point source of constant power, q_0 , starts on the surface at a given position, moving in the positive x -direction by a constant speed, v . The rise of temperature, $T-T_0$, in a point P at time t is then sought. The detailed mathematical derivation of the general thick-plate solution is given in Ref 1, 9, and 10. Here, only the resulting equations are presented and discussed.

General Solution. The general thick-plate solution describing the pseudo-steady-state temperature distribution for a moving-point heat source is given by (Ref 9, 10):

$$T - T_0 = \frac{q_0}{2\pi\lambda} \left(\frac{1}{R}\right) \exp\left(-\frac{v}{2a}(R+x)\right) \quad (\text{Eq 2})$$

This equation is often referred to as the Rosenthal thick-plate solution (Ref 9, 10) in honor of D. Rosenthal, who first derived the relation by solving the differential heat flow equation directly for the appropriate boundary conditions. The Rosenthal equation gives, with the limitations inherent in the assumptions, full information about the thermal conditions for point sources on heavy slabs and is thus a true three-dimensional model. A schematic representation of Eq 2 is shown in Fig. 1.

Simplified Solution for a Fast-Moving High-Power Source. It follows from Eq 2 that the isotherms behind the heat source become increasingly elongated as the power, q_0 , and the welding speed, v , increase. In the limiting case, when $q_0 \rightarrow \infty$, $v \rightarrow \infty$ and q_0/v remains finite, the isotherms will degenerate into surfaces that are parallel to the welding x -direction, as shown in Fig. 2 (Ref 1). Conduction of heat will then occur exclusively in the directions normal to the x -axis, meaning that the mode of heat flow becomes essentially two-dimensional (i.e., restricted to the y - z plane).

As shown by Rykalin (Ref 11), the solution is then given by the equation:

$$T - T_0 = \frac{q_0/v}{2\pi\lambda} \left(\frac{1}{t}\right) \exp\left(-\frac{(r^*)^2}{4at}\right) \quad (\text{Eq 3})$$

where r^* is the two-dimensional radius vector in the y - z plane.

Equation 3 represents the simplified solution for a fast-moving high-power source on a semi-infinite slab and is valid within a limited range of the more general Rosenthal equation for three-dimensional heat flow (Eq 2).

Thin-Plate Model

The thin-plate model considers a line source in a wide sheet of thickness d and initial temperature, T_0 . At time $t = 0$, the source starts to move at a constant speed, v , in the positive x -direction. The rise of temperature, $T-T_0$, in a point P at time t is then sought. Details of the mathematical derivation of the general thin-plate solution are given in Ref 1, 9, and 10.

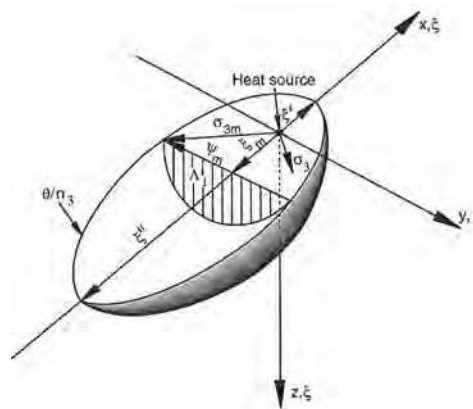


Fig. 1 Three-dimensional graphical representation of the Rosenthal thick-plate solution (schematic). Source: Ref 1

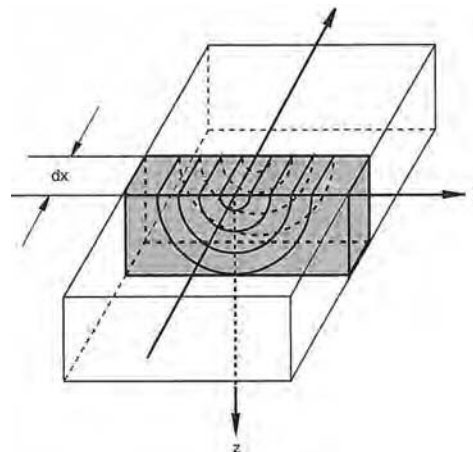


Fig. 2 Fast-moving high-power source on a semiinfinite slab. Source: Ref 1

General Solution. At pseudo-steady state, the general thin-plate solution reads:

$$T - T_0 = \frac{q_0/d}{2\pi\lambda} \exp\left(-\frac{vx}{2a}\right) K_0\left(\frac{vr}{2a}\right) \quad (\text{Eq 4})$$

where K_0 is the modified Bessel function of the second kind and zero order.

Equation 4 is often referred to as the Rosenthal thin-plate solution. It follows that this model is applicable to all types of welding processes (including electron beam, plasma arc, and laser welding), provided that a full through-thickness penetration is achieved in one pass. Under such conditions, the mode of heat flow will be essentially two-dimensional (i.e., restricted to the x - y plane). A graphical representation of Eq 4 is shown in Fig. 3 (Ref 1, 14).

Simplified Solution for a Fast-Moving High-Power Source. Similar to the conditions existing during thick-plate welding, the isotherms behind the heat source become increasingly elongated as the arc power, q_0 , and the welding speed, v , increase. In the limiting case, when $q_0 \rightarrow \infty$, $v \rightarrow \infty$, and q_0/v remains finite, the isotherms will degenerate into surfaces that are parallel to the welding x -direction, as shown in Fig. 4. Under such conditions, the mode of heat flow becomes essentially one-dimensional, which means that the temperature distribution is given by the following equation (Ref 11):

$$T - T_0 = \frac{q_0/vd}{\rho c(4\pi at)^{1/2}} \exp(-y^2/4at) \quad (\text{Eq 5})$$

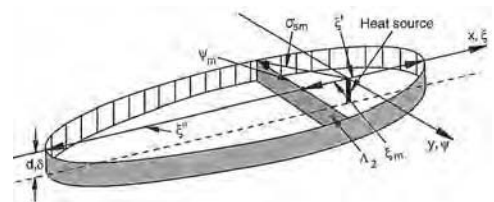


Fig. 3 Graphical representation of Rosenthal thin-plate solution (schematic). Source: Ref 1, 14

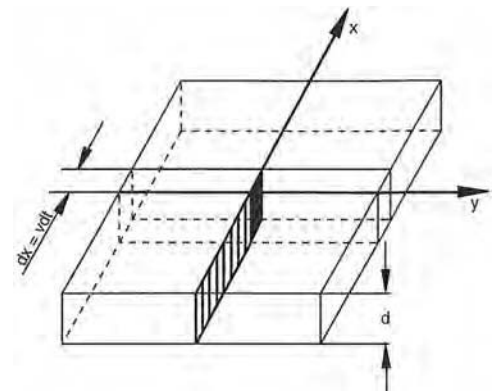


Fig. 4 Graphical representation of a fast-moving high-power source in a thin plate. Source: Ref 1

Equation 5 represents the simplified solution for a fast-moving high-power source in a thin sheet and is valid within a limited range of the more general Rosenthal equation for two-dimensional heat flow (Eq 4).

In situations where the inherent assumption of adiabatic plate surfaces is not fulfilled (e.g., due to the use of external heat sinks or forced air cooling), it is still possible to employ analytical solutions similar to the ones presented previously. However, this requires the introduction of an additional term in the constitutive equations containing the efficient heat-transfer coefficient, which, in a semiempirical manner, allows for transfer of heat across the plate surfaces to the surrounding cooling medium. Further details are given in Ref 11 to 13 and 15.

Medium-Thick-Plate Model

In a real welding situation, the assumption of three- or two-dimensional heat flow inherent in the Rosenthal equations is not always met because of variable temperature gradients in the through-thickness z -direction of the plate.

General Solution. The general medium-thick-plate model considers a point heat source moving at constant speed across a wide plate of finite thickness d . With the exception of certain special cases (e.g., watercooling of the back side of the plate), it is a reasonable approximation to assume that the plate surfaces are impermeable to heat. Thus, to maintain the net flux of heat through both boundaries equal to zero, it is necessary to account for mirror reflections of the source with respect to the planes of $z = 0$ and $z = d$. This can be done on the basis of the "method of images," as illustrated in Fig. 5.

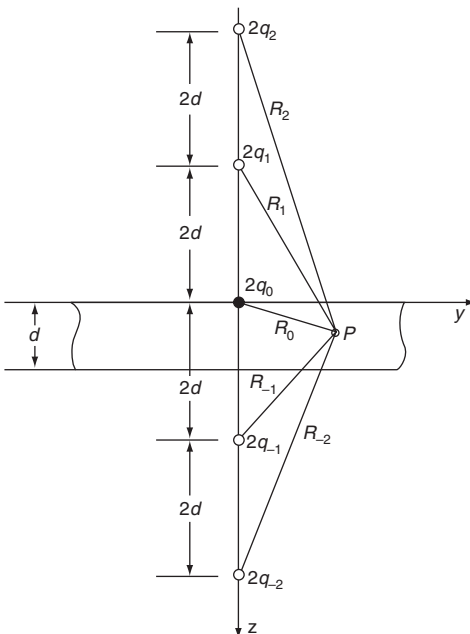


Fig. 5 Real and imaginary point sources on a medium-thick plate

By including all contributions from the imaginary sources $\dots 2q_{-2}, 2q_{-1}, 2q_1, 2q_2, \dots$ located symmetrically at distances $\pm 2id$ below and above the upper surface of the plate, the pseudo-steady temperature distribution is obtained in the form of a convergent series (Ref 10):

$$T - T_0 = \frac{q_0}{2\pi\lambda} \exp\left(-\frac{vx}{2a}\right) \sum_{i=-\infty}^{i=+\infty} \left(\frac{1}{R_i}\right) \exp\left(-\frac{vR_i}{2a}\right) \quad (\text{Eq 6})$$

where:

$$R_i = \sqrt{x^2 + y^2 + (z - 2id)^2}$$

In practice, the number of imaginary heat sources necessary to achieve the required accuracy depends on the chosen values of R_0 and $vd/2a$. It follows from Eq 6 that the thermal conditions will be similar to those in a thick plate close to the center of the weld. Moreover, Rosenthal (Ref 9, 10) has shown, on the basis of a Fourier-series expansion, that Eq 6 converges to the general thin-plate solution (Eq 4) for points located sufficiently far away from the source. However, at intermediate distances from the heat source, the pseudo-steady-state temperature distribution will deviate significantly from that observed in thick- or thin-plate welding because of variable temperature gradients in the through-thickness direction of the plate. This leads to a mixed mode of heat flow, which, in the following, is referred to as 2.5-dimensional (2.5-D). Within the 2.5-D "transition region," the thermal program is only defined by the medium-thick-plate solution (Eq 6).

Simplified Solution for a Fast-Moving High-Power Source. Also in the medium-thick-plate welding situation, a simplified solution exists in the limiting case when $q_0 \rightarrow \infty$, $v \rightarrow \infty$, and q_0/v remains finite. The isotherms will then degenerate into surfaces that are parallel to the welding x -direction, and conduction of heat will then occur exclusively in the directions normal to the x -axis. The pseudo-steady-state temperature distribution is then given by the following equation:

$$T - T_0 = \frac{q_0/v}{2\pi\lambda} \left(\frac{1}{t}\right) \sum_{i=-\infty}^{i=+\infty} \exp(-r_i^2/4at) \quad (\text{Eq 7})$$

where:

$$r_i = \sqrt{y^2 + (z - 2id)^2}$$

Note that Eq 7 is actually the simplified solution for a fast-moving high-power source in a thick plate (i.e., Eq 3) summed for each source. Within the validity range of this equation, the mode of heat flow is mixed (i.e., 1.5-dimensional), meaning that it is a special solution of the more general Eq 6.

General Outline of the Pseudo-Steady-State Temperature Distribution in Bead-on-Plate Welding

To obtain a general survey of the pseudo-steady-state temperature distribution, it is convenient to present the different solutions in a dimensionless form. The following parameters are defined for this purpose (Ref 1, 14):

- Dimensionless temperature:

$$\theta = \frac{T - T_0}{T_c - T_0} \quad (\text{Eq 8})$$

- Dimensionless operating parameter:

$$n_3 = \frac{q_0 v}{4\pi a^2 \rho c (T_c - T_0)} = \frac{q_0 v}{4\pi a^2 (H_c - H_0)} \quad (\text{Eq 9})$$

- Dimensionless plate thickness:

$$\delta = \frac{vd}{2a} \quad (\text{Eq 10})$$

- Dimensionless x -coordinate:

$$\xi = \frac{vx}{2a} \quad (\text{Eq 11})$$

- Dimensionless y -coordinate:

$$\psi = \frac{vy}{2a} \quad (\text{Eq 12})$$

- Dimensionless z -coordinate:

$$\zeta = \frac{vz}{2a} \quad (\text{Eq 13})$$

Isothermal Contours and Mode of Heat Flow

Because of the number of variables involved, it is not possible to present two-dimensional plots of the isotherms without first specifying the dimensionless plate thickness. Examples of calculated isotherms in different planes are shown in Fig. 6 and 7 for δ equal to 0.5 and 5, respectively. It is evident that an increase in the dimensionless plate thickness from 0.5 to 5 has a dramatic effect on the shape and position of the isothermal contours. However, to explain these observations in an adequate manner, it is necessary to condense the results into a two-dimensional diagram. As shown in Fig. 8, this can be done by plotting the calculated field boundaries at maximum width of the isotherms versus the parameters θ_p/n_3 and $vd/2a$, as described in Ref 1 and 14.

It is seen from Fig. 8 that a large plate thickness generally will favor three-dimensional heat flow. With decreasing values of θ_p/n_3 , the conditions for a fast-moving high-power source are approached before the transition from the thick-plate to the thin-plate solution occurs. In such cases, the isotherms at the bottom of the plate will be strongly elongated in the welding direction, ξ , and shifted to positions far behind

the heat source. The opposite is observed at small values of $vd/2a$, because a rapid equalization of the temperature gradient in the through-thickness direction of the plate will result in elliptical isotherms at both surfaces, located in an approximately equal distance from the heat source. In either case, the temperature at which the cross-sectional isotherms approach a semicircle or become parallel with the $\zeta(z)$ -axis can be obtained from Fig. 8 by reading-off the intercept between the line for the dimensionless plate thickness and the respective field boundaries.

Table 3 contains a summary of the various solutions for the pseudo-steady-state temperature distribution in bead-on-plate welding. Note that each special solution is valid within certain ranges of θ_p/n_3 and δ , as defined by the field boundaries in Fig. 8. In contrast, the general medium-thick-plate solution is always valid in the sense that it contains the five other solutions listed in Table 3.

Case Studies. Consider stringer bead GMAW on 12.5 mm (0.5 in.) thick plates of low-alloy steel and aluminum (i.e., an Al-Mg-Si alloy), respectively, under the conditions $E = 1.5$ kJ/mm and $\eta = 0.8$. Details of welding parameters for the four series involved are given in Table 4. Computed peak temperature contours in the transverse section of the welds are given in Fig. 9 and 10.

Aluminum Welding. Figures 9(a) and (b) reveal a strong influence of the welding speed on the shape and position of the cross-sectional isotherms at a constant gross heat input of 1.5 kJ/mm. It is evident that the extension of the fusion zone and the neighboring isotherms becomes considerably larger when the welding speed is increased from 2.5 to 5 mm/s (0.1 to 0.2 in./s). This effect can be attributed to an associated shift from elliptical to more elongated isotherms at the plate surfaces (Fig. 8), which reduces heat conduction in the welding direction. It follows from Fig. 8 that the upper left corner of the map represents the typical operating region for aluminum welding.

Because of the pertinent differences in the heat flow conditions, the temperature-time pattern will also vary significantly between series A1 and A2. Hence, in the case of aluminum welding, the usual procedure of reporting arc power and travel speed in terms of an equivalent heat input per unit length of bead is highly questionable, because this parameter does not define the weld thermal program. In general, the correct course would be to specify q_0 , v , and d and compare the weld thermal history on the basis of the dimensionless parameter n_3 and δ .

Steel Welding. If welding is performed on a steel plate of similar thickness, the operating region will be shifted to the lower right corner of Fig. 8. Under such conditions, the isotherms adjacent to the fusion boundary will be strongly elongated in the x-direction even at very low welding speeds (Fig. 7). This implies that the thermal program approaches a state

where the temperature distribution is uniquely defined by the net heat input ηE , corresponding to the limiting case of a fast-moving high-power source. As a result, the calculated shape

and width of the fusion boundary and neighboring isotherms are seen to be virtually independent of choice of q_0 and v , as illustrated in Fig. 10(a) and (b).

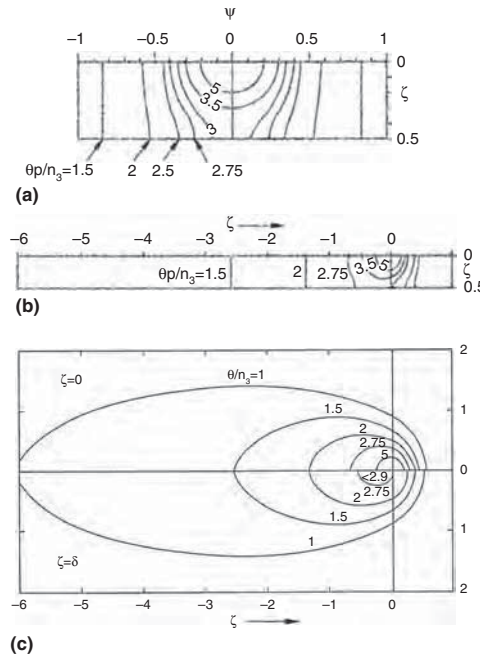


Fig. 6 Examples of computed isothermal contours in different sections for $\delta = 0.5$. (a) Cross section. (b) Longitudinal section. (c) Upper and lower surface of plate. Source: Ref 1, 14

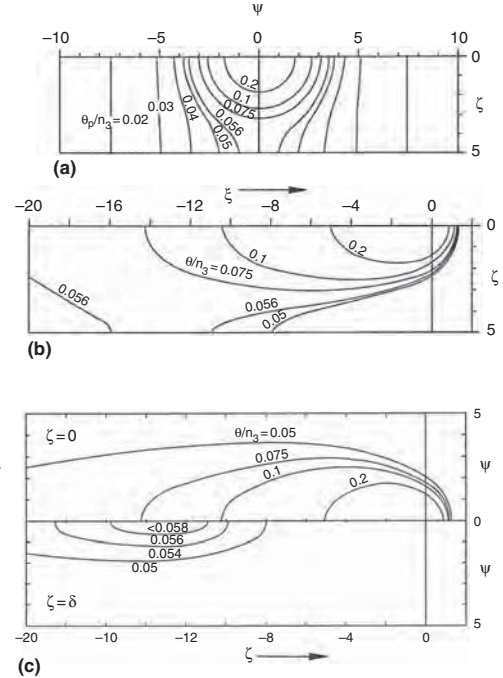


Fig. 7 Examples of computed isothermal contours in different sections for $\delta = 5$. (a) Cross section. (b) Longitudinal section. (c) Upper and lower surface of plate. Source: Ref 1, 14

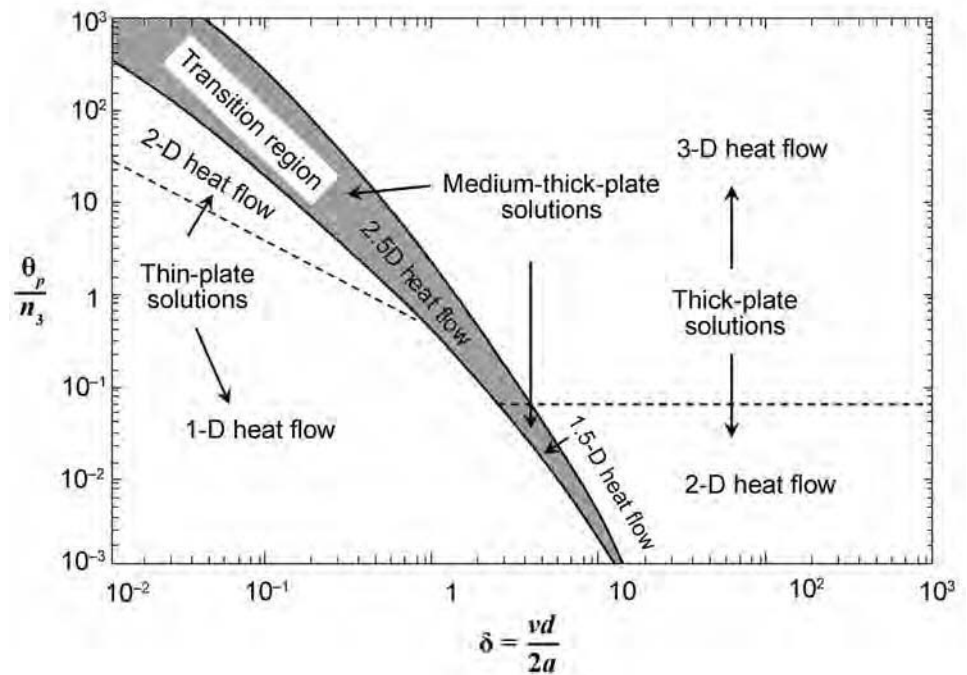


Fig. 8 Heat flow mechanism map showing calculated field boundaries in transverse direction ($\psi = \psi_0$) of plate versus θ_p/n_3 and $\delta = vd/2a$. From this map, the validity range of the various solutions listed in Table 3 can be evaluated.

Table 3 Summary of various analytical solutions for the pseudo-steady-state temperature distribution in bead-on-plate welding

Solution	Mode of heat flow	Equation		Source
		Standard form	Dimensionless form	
1. General medium-thick-plate solution	2.5-D heat flow	$1. T - T_0 = \frac{q_0}{2\pi\lambda} \exp\left(-\frac{vx}{2a}\right) \sum_{i=-\infty}^{i=+\infty} \left(\frac{1}{R_i}\right) \exp\left(-\frac{vR_i}{2a}\right)$	$\frac{\theta}{n_3} = \exp(-\xi) \sum_{i=-\infty}^{i=+\infty} \left(\frac{1}{\sigma_i}\right) \exp(-\sigma_i)$	Ref 1,10
	1.5-D heat flow	$2. T - T_0 = \frac{q_0/v}{2\pi\lambda} \left(\frac{1}{\tau}\right) \sum_{i=-\infty}^{i=+\infty} \exp(-r_i^2/4at)$	$\frac{\theta}{n_3} = \left(\frac{1}{\tau}\right) \sum_{i=-\infty}^{i=+\infty} \exp(-(\sigma_i)^2/2\tau)$	
3. General thick-plate solution	3-D heat flow	$3. T - T_0 = \frac{q_0}{2\pi\lambda} \left(\frac{1}{R}\right) \exp\left(-\frac{v}{2a}(R+x)\right)$	$\frac{\theta}{n_3} = \frac{1}{\sigma_3} \exp(-\sigma_3 - \xi)$	Ref 1,9,10
4. Special thick-plate solution	2-D heat flow	$4. T - T_0 = \frac{q_0/v}{2\pi\lambda} \left(\frac{1}{\tau}\right) \exp(-(r^*)^2/4at)$	$\frac{\theta}{n_3} = \left(\frac{1}{\tau}\right) \exp(-(\sigma_4)^2/2\tau)$	Ref 1,11
5. General thin-plate solution	2-D heat flow	$5. T - T_0 = \frac{q_0/d}{2\pi\lambda} \exp\left(-\frac{vx}{2a}\right) K_0\left(\frac{vz}{2a}\right)$	$\frac{\theta\theta}{n_3} = \exp(-\xi) K_0(\sigma_5)$	Ref 1,10
6. Special thin-plate solution	1-D heat flow	$6. T - T_0 = \frac{q_0/vd}{\rho c(4\pi at)^{1/2}} \exp(-y^2/4at)$	$\frac{\theta\theta}{n_3} = \sqrt{\frac{\pi}{2\tau}} \exp(-\psi^2/2\tau)$	Ref 1,11

Table 4 Operational conditions assumed in case studies

Material	Series	q_0 , W	v		d		E_s , kJ/mm	n_3	δ
			mm/s	in./s	mm	in.			
Al-Mg-Si alloy	A1	6000	5	0.2	12.5	0.5	1.5	0.36	0.50
	A2	3000	2.5	0.1	12.5	0.5	1.5	0.09	0.25
Low-alloy steel	S1	9600	8	0.3	12.5	0.5	1.5	32.6	10
	S2	4800	4	0.2	12.5	0.5	1.5	8.2	5

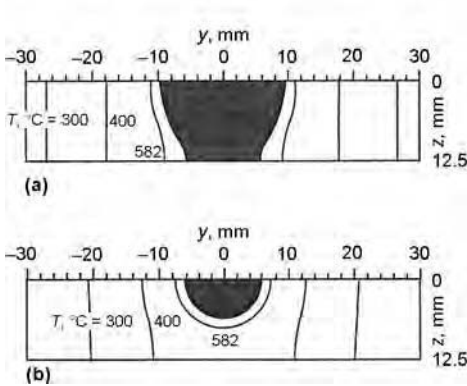


Fig. 9 Computed peak temperature contours in aluminum welding at pseudo-steady state. (a) Weld A1. (b) Weld A2. Black regions indicate fusion zone. Operational conditions as in Table 4. Source: Ref 1, 14

Analytical Solutions of the Thermal Field around Distributed Heat Sources

In some cases, it is also necessary to consider the important effects of heat distribution on the bead morphology and the resulting shape of the heat-affected zone (HAZ) isothermal contours.

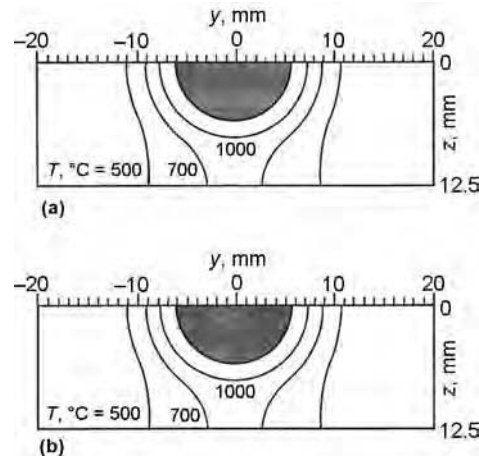


Fig. 10 Computed peak temperature contours in steel welding at pseudo-steady state. (a) Weld S1. (b) Weld S2. Black regions indicate fusion zone. Operational conditions as in Table 4. Source: Ref 1, 14

Of particular interest in this respect is the formation of the so-called weld crater/weld finger frequently observed in GMAW and SAW stringer bead weldments (Fig. 11). Although the nature of these phenomena is very complex,

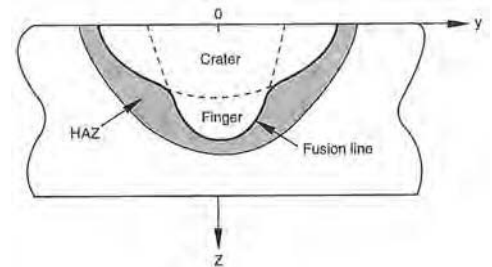


Fig. 11 Schematic diagram showing the weld crater/weld finger formation during stringer bead welding. HAZ, heat-affected zone. Source: Ref 1

they can readily be accounted for by applying an empirical correction for the effective heat distribution in the weld pool.

General Solution. The general model of Myhr and Grong is described in Ref 1. The heat distribution used to simulate the weld crater/weld finger formation is shown schematically in Fig. 12(a). Here, two discrete distributions of elementary point sources are considered, which extend in the y - and z -directions of the plate, respectively. The contribution from each source to the temperature rise in an arbitrary point P located within the plate is calculated on the basis of the "method of images," as shown in Fig. 12(b) and (c). For a heat source displaced in the y -direction (Fig. 12b), the temperature field is given by Eq 6:

$$T(q_a) = \frac{q_a}{2\pi\lambda} \exp\left(-\frac{vx}{2a}\right) \sum_{i=-\infty}^{i=+\infty} \left(\frac{1}{R_i}\right) \exp\left(-\frac{vR_i}{2a}\right) \quad (\text{Eq 14})$$

where:

$$R_i = \sqrt{x^2 + y^2 + (z - 2id)^2}$$

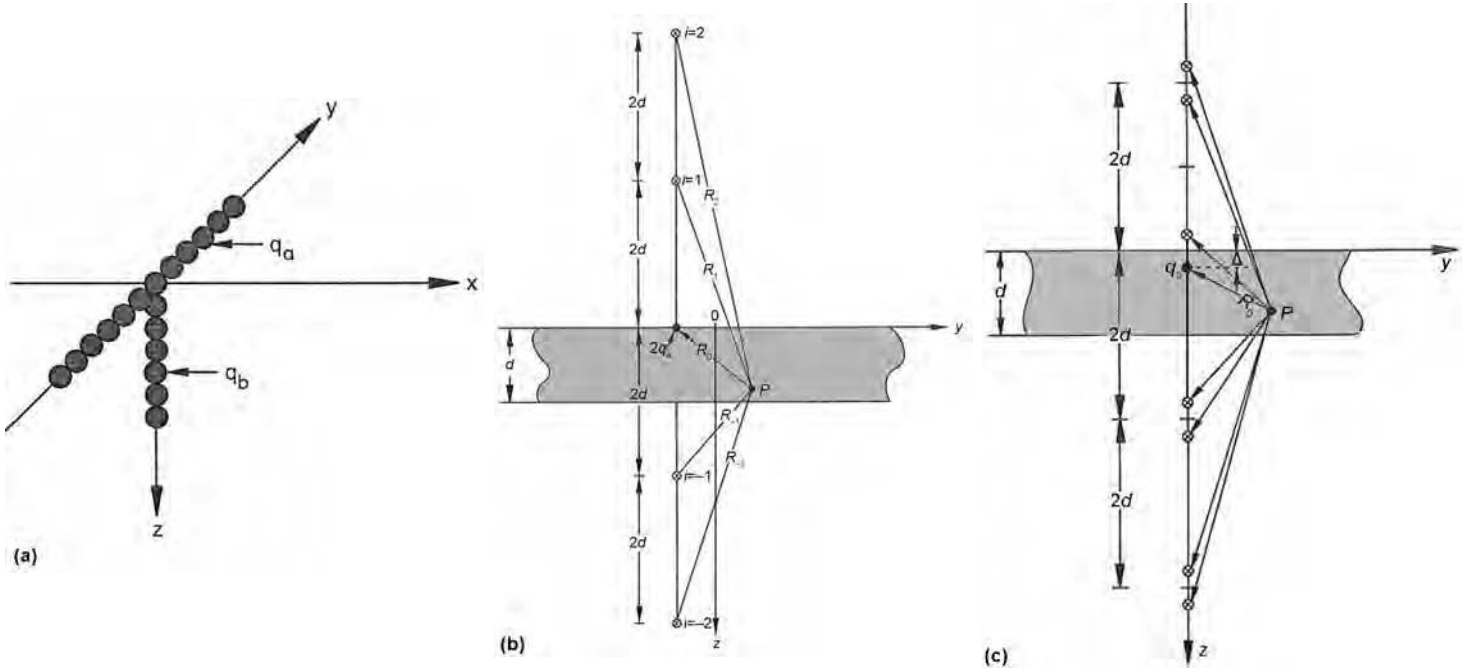


Fig. 12 General heat flow model for welding on medium-thick plates. (a) Physical representation of the heat distribution by elementary point sources. (b) Method for calculating the temperature field around an elementary point source displaced along the y -axis. (c) Method for calculating the temperature field around an elementary (submerged) point source displaced along the z -axis. Source: Ref 1

Similarly, for a submerged point source located along the z -axis (Fig. 12c):

$$T(q_b) = \frac{q_b}{4\pi\lambda} \exp\left(-\frac{vx}{2a}\right) \left[\sum_{j=-\infty}^{j=+\infty} \left(\frac{1}{R_j}\right) \exp\left(-\frac{vR_j}{2a}\right) + \sum_{k=-\infty}^{k=+\infty} \left(\frac{1}{R_k}\right) \exp\left(-\frac{vR_k}{2a}\right) \right] \quad (\text{Eq 15})$$

where:

$$R_j = \sqrt{x^2 + y^2 + (z - 2jd - \Delta)^2}$$

and

$$R_k = \sqrt{x^2 + y^2 + (z - 2kd + \Delta)^2}$$

Note that Eq 15 correctly reduces to Eq 14 when Δ approaches zero. The total temperature rise in point P is then obtained by superposition of the temperature fields from the different elementary heat sources, taking:

$$T(t) = T_0 + \sum_i [T(q_a^i) + T(q_b^i)] \quad (\text{Eq 16})$$

where:

$$q_0 = \sum_i (q_a^i + q_b^i) = \eta UI \quad (\text{Eq 17})$$

In practice, the heat distribution can be subdivided into a relatively small number of elementary point sources, and usually a total number of eight to ten sources is sufficient to obtain good results (i.e., smooth isothermal

contours). However, the relative strength of each heat source and their distribution along the y - and z -axes must be determined individually through trial and error by comparing the calculated shape of the fusion boundary with the real (measured) one.

Figure 13 shows the results from such calculations, carried out for a single-pass (bead-in-groove) gas metal arc steel weld. It is evident that the important effect of the weld crater/weld finger formation on the HAZ peak temperature distribution is adequately accounted for by the present model. A weakness of the model is, of course, that the shape and location of the fusion boundary must be determined experimentally before a prediction can be made.

Simplified Solution for a Fast-Moving High-Power Source. Similar to the situation described previously, a point heat source will clearly not be a good model when the heat source is supplied over a large area. Welding with a weaving technique and surfacing with strip electrodes are prime examples of this kind.

In the model of Grong and Christensen (Ref 16), the Rosenthal thick-plate solution is considered for the limiting case of a high arc power, q_0 , and a high welding speed, v , maintaining the ratio q_0/v within a range applicable to arc welding. Consider next a distributed heat source of net power density, $q_0/2L$, extending from $-L$ to $+L$ on either side of the weld centerline in the y -direction, as shown schematically in Fig. 14. It follows from Eq 3 that an infinitesimal source, dq_y , located between y' and $y' + dy'$ will cause a small rise of temperature in point P at time t as (Ref 16):

$$dT_{y'} = \left(\frac{dq_y/v}{2\pi\lambda}\right) \left(\frac{1}{t}\right) \exp\left[-\frac{(r')^2}{4at}\right] \quad (\text{Eq 18})$$

where:

$$r' = \sqrt{(y - y')^2 + z^2}, \quad dq_y = q_0 dy'/2L, \quad \text{and } \lambda = \rho c$$

Substituting:

$$u = (y - y')/\sqrt{4at}, \quad dy' = -du\sqrt{4at}$$

and integrating from $y' = -L$ to $y' = +L$ gives:

$$T - T_0 = \left(\frac{q_0/2vL}{\rho c\sqrt{\pi}}\right) \left(\frac{\exp(-z^2/4at)}{\sqrt{4at}}\right) \left[\operatorname{erf}\left(\frac{y+L}{\sqrt{4at}}\right) - \operatorname{erf}\left(\frac{y-L}{\sqrt{4at}}\right) \right] \quad (\text{Eq 19})$$

where $\operatorname{erf}(u)$ is the Gaussian error function.

General Outline of the Peak Temperature Distribution. Because of the complex nature of Eq 19, the variation of peak temperature with distance in the y - z plane can only be obtained by numerical or graphical methods. Accordingly, it is convenient to present the various solutions in a dimensionless form. The following parameters are defined for this purpose (Ref 1, 16):

- Dimensionless operating parameter:

$$n_w = \frac{q_0/2vL^2}{\sqrt{\pi}\rho c(T_c - T_0)} = \frac{q_0/2vL^2}{\sqrt{\pi}(H_c - H_0)} \quad (\text{Eq 20})$$

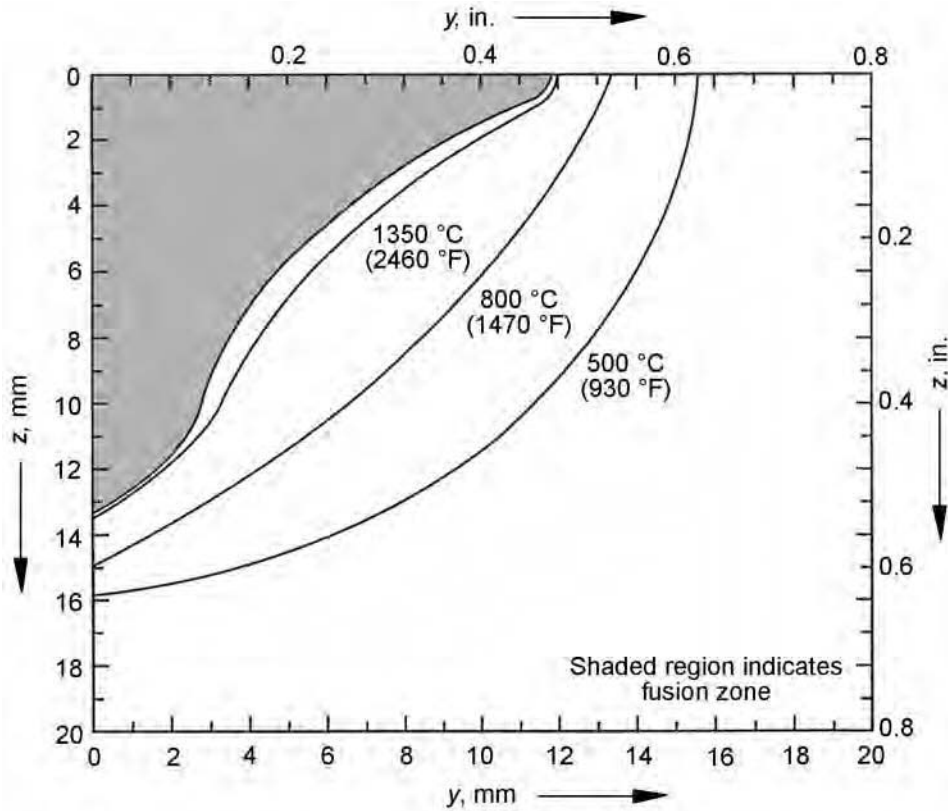


Fig. 13 Calculated peak temperature contours in the transverse section of a gas metal arc steel weldment. Operational conditions: $I = 450$ A, $U = 30$ V, $v = 2.6$ mm/s (0.1 in./s), $d = 50$ mm (2 in.). Source: Ref 1

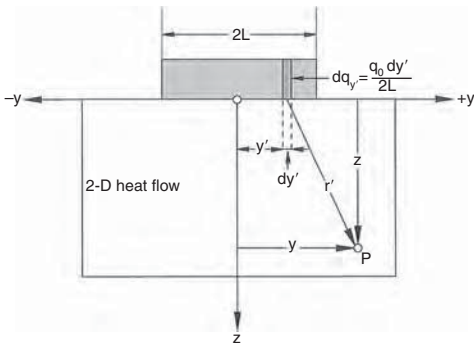


Fig. 14 Distributed heat source of net power density $q_0/2L$ on a semiinfinite body assuming two-dimensional heat flow. Source: Ref 1, 16

- Dimensionless time:

$$\tau_5 = \frac{\sqrt{4at}}{L} \quad (\text{Eq 21})$$

- Dimensionless y-coordinate:

$$\beta = \frac{y}{L} \quad (\text{Eq 22})$$

- Dimensionless z-coordinate:

$$\gamma = \frac{z}{L} \quad (\text{Eq 23})$$

Substituting these parameters into Eq 19 yields

$$\frac{\theta}{n_w} = \frac{1}{\tau_5} \exp\left[-\left(\frac{\gamma}{\tau_5}\right)^2\right] \left[\text{erf}\left(\frac{\beta+1}{\tau_5}\right) - \text{erf}\left(\frac{\beta-1}{\tau_5}\right) \right] \quad (\text{Eq 24})$$

where θ is the dimensionless temperature defined previously in Eq 8.

The variation of peak temperature, θ_p , with distance in the y - z plane has been numerically evaluated from Eq 24 for chosen values of β and γ (i.e., $\beta = 0$, $\beta = 3/4$, $\beta = 1$, and $\gamma = 0$). The results are presented graphically in Fig. 15 and 16 for the through-thickness ($z = z_m$) and the transverse ($y = y_m$) directions, respectively. These figures provide a systematic basis for calculating the shape of the weld pool and neighboring isotherms under various welding conditions.

In Fig. 17, the weld width-to-depth ratio has been computed and plotted for various combinations of n_w and θ_p . It is evident that the predicted width of the isotherms generally is much greater and the depth correspondingly smaller than that inferred from the point source model. Such deviations tend to become less pronounced with decreasing peak temperatures (i.e., increasing distance from the heat source). At very large values of n_w , the theoretical shape of the isotherms approaches that of a semicircle, which is characteristic of a point heat source.

Implications of the Heat Distribution. Figure 18 shows a graphical presentation of the calculated peak temperature contours for a gas metal arc steel weld deposition using a weaving technique. It is evident from these plots that the predicted shape of the isotherms, as evaluated from Eq 24, departs quite strongly from the semicircular contours required by a point heat source. Moreover, a closer inspection of Fig. 18 shows that inclusion of the heat distribution also gives rise to systematic variations in the weld thermal program along a specific isotherm, as evidenced by the steeper temperature gradient in the y -direction compared with the z -direction of the plate. This point is more clearly illustrated in Fig. 19, which compares the HAZ temperature-time program for the two extreme cases of $z = 0$ and $y = 0$, respectively. It follows from Fig. 19 that the retention time within the austenite regime is considerably longer in the latter case, although the cooling time from 800 to 500 °C (1470 to 930 °F), $\Delta t_{8/5}$, is reasonably similar. These results clearly underline the important difference between a point heat source and a distributed heat source as far as the weld thermal program is concerned.

Analytical Solution of the Thermal Field around a Moving Keyhole

The analytical keyhole model is shown in Fig. 20. In this case, the circular keyhole moves relative to the workpiece with a constant velocity of v . According to the assumptions, the diameter of the keyhole is equal to $2r_0$, and the wall temperature is equal to T_0 . At pseudo-steady state, the temperature distribution around the keyhole is given by (Ref 18):

$$\frac{T - T_0}{T_v - T_0} = \exp\left(-\frac{vr \cos \phi}{2a}\right) \sum_{n=0}^{\infty}$$

$$\varepsilon_n I_n\left(\frac{vr_0}{2a}\right) \frac{K_n\left(\frac{vr}{2a}\right)}{K_n\left(\frac{vr_0}{2a}\right)} \cos(n\phi) \quad (\text{Eq 25})$$

General Outline of the Temperature Distribution. For a general representation of the pseudo-steady-state temperature distribution, it is convenient to rewrite Eq 25 in a dimensionless form. The following parameters are defined for this purpose (Ref 17, 19):

$$\Omega = \frac{T - T_0}{T_v - T_0} \quad (\text{Eq 26})$$

$$\xi = \frac{vr \cos \phi}{2a} = \frac{vx}{2a} \quad (\text{Eq 27})$$

$$\kappa = \frac{vr_0}{2a} \quad (\text{Eq 28})$$

$$\sigma = \frac{vr}{2a} \quad (\text{Eq 29})$$

Analogy with the Line Source Solution

Hemmer and Grong (Ref 17) have further investigated the analogy between the key-hole solution and the line source solution to predict the penetration depth in electron beam welding (EBW). At pseudo-steady state, the temperature distribution around a moving line source is given by Eq 4. By replacing the plate thickness d with the penetration depth p , it reads:

$$T - T_0 = \frac{q_0/p}{2\pi\lambda} \exp\left(-\frac{vx}{2a}\right) K_0\left(\frac{vr}{2a}\right) \quad (\text{Eq 32})$$

Equation 32 can be written in a dimensionless form in terms of the following group variables (Ref 17):

$$n_2 = \frac{q_0/p}{2\pi\lambda(T_m - T_0)} = \frac{q_0/p}{2\pi a(H_m - H_0)} \quad (\text{Eq 33})$$

$$\theta = \frac{T - T_0}{T_m - T_0} \quad (\text{Eq 34})$$

where T_m now refers to the melting point (or liquidus temperature) of the base material. Substituting these parameters into Eq 32 gives:

$$\theta/n_2 = \exp(-\xi) K_0(\sigma) \quad (\text{Eq 35})$$

The half-width of the isotherms ψ_m can be found by differentiating Eq 35 with respect to ξ . Hence, ψ_m is also a unique function of the dimensionless operating parameter n_2 . In practice, this means that the penetration depth can be linked to the group variables Ω and κ by way of Eq 30 and 31.

Coupling of Models and Prediction of the Penetration Depth. Because of the analogy between the two solutions, they can be combined to obtain the set of master curves shown in Fig. 22. From these curves, the normalized (scaled) penetration depth can be read for various combinations of process parameters (i.e., v and $2r_0$) and material properties (i.e., a , T_m , and T_v). Conversion into real (metric) units is then carried out by way of Eq 33, using appropriate input data for the applied beam power, q_0 , and the heat content of the base material at the melting point, $H_m - H_0$.

It follows from Fig. 22 that the penetration depth in EBW is uniquely defined by three group variables: Ω , which includes the keyhole wall temperature, T_v ; n_2 , which includes the beam power density, q_0 ; and κ , which includes the electron beam diameter, $2r_0$, and the welding speed, v . In addition, the thermal properties of the base material come into play through the parameters λ , a , and T_m . Provided that all necessary input parameters are known, it has been shown that the penetration depth during EBW can be estimated with an accuracy of $\pm 25\%$ for titanium alloys and $\pm 15\%$ for both aluminum alloys and duplex stainless steels

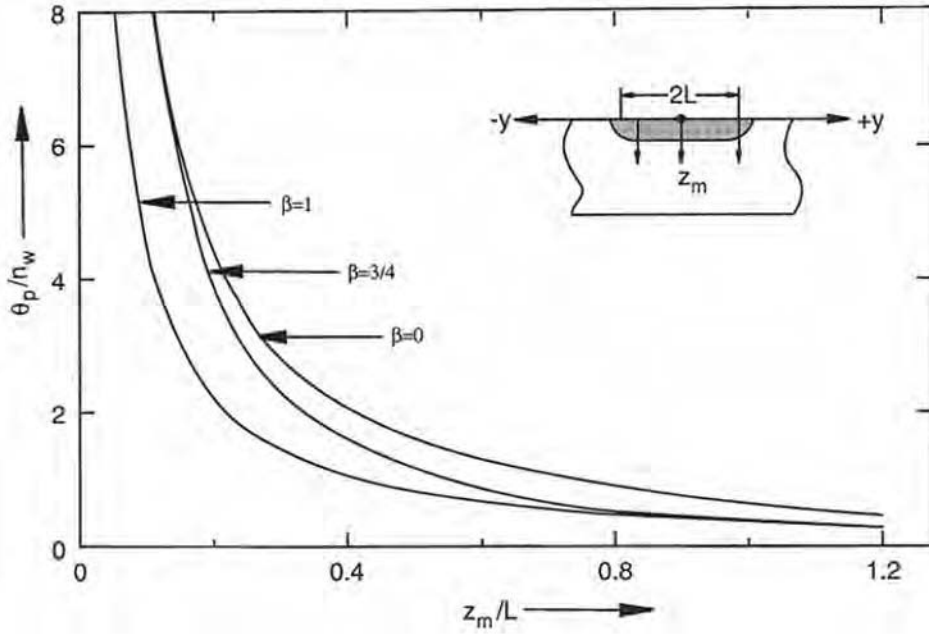


Fig. 15 Calculated peak temperature distribution in the through-thickness direction of the plate at various positions along the weld surface. Dimensionless parameters are defined in Eq 20 to 24. Source: Ref 1, 16

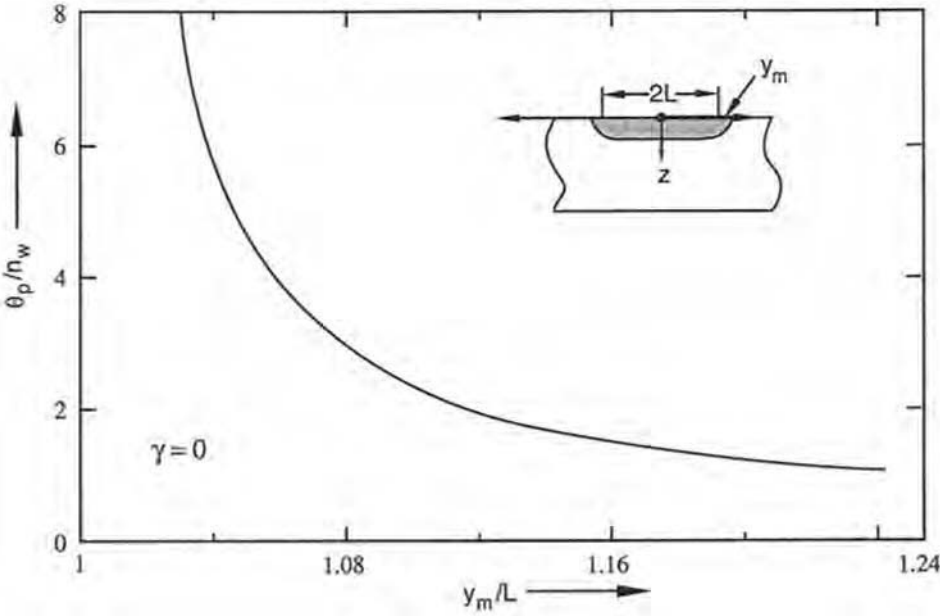


Fig. 16 Calculated peak temperature distribution in the transverse direction of the plate at position $\gamma(z) = 0$. Dimensionless parameters are defined in Eq 20 to 24. Source: Ref 1, 16

Substituting these parameters into Eq 25 gives:

$$\Omega = \exp(-\xi) \sum_{n=0}^{\infty} \varepsilon_n J_n(\kappa) \frac{K_n(\sigma)}{K_n(\kappa)} \cos(n\phi) \quad (\text{Eq 30})$$

In the cross section of the plate, the shape of the isotherms is characterized by their depth-to-width ratio. Referring to Fig. 21(a), the dimensionless half-width of the isotherms is given by:

$$\psi = \psi_m = \frac{vy}{2a} = \frac{vr \sin \phi}{4a} = \sigma \sin \phi \quad (\text{Eq 31})$$

The parameter ψ can be evaluated numerically from Eq 30 and 31 for various starting conditions. The results are summarized in Fig. 21(b) for a limited range of values of ψ and κ . It follows that ψ_m is uniquely defined by these two group variables.

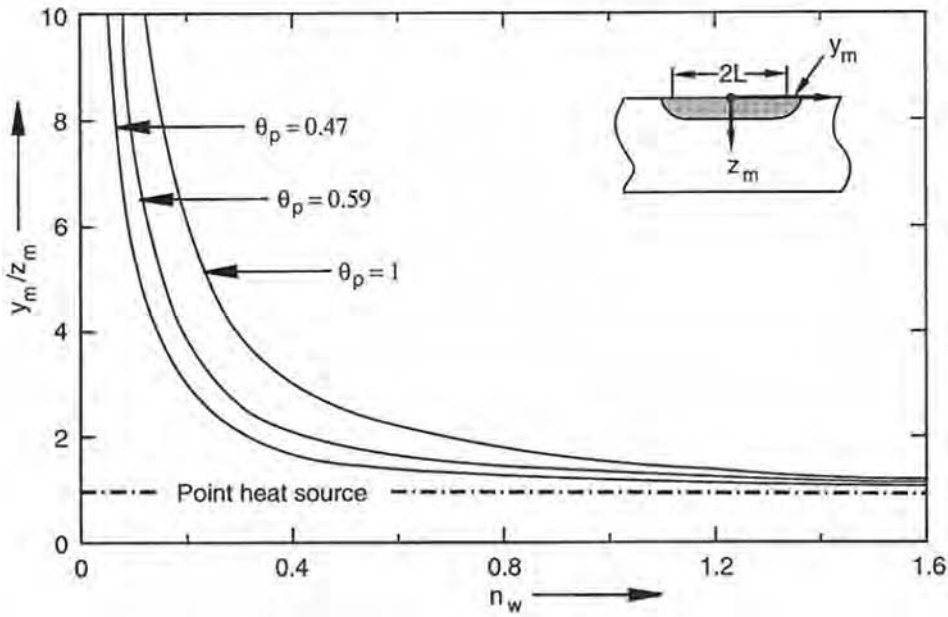


Fig. 17 Effects of n_w and θ_p on the weld width-to-depth ratio. Dimensionless parameters are defined in Eq 20 to 24. Source: Ref 1, 16

- Time-dependent welding speed and net heat input
- Continuous addition of filler material during welding (Ref 22–25)
- Gradual release of the latent heat of fusion between the solidus and liquidus temperatures during solidification (Ref 22–25)
- Weld-metal fluid flow (Ref 20, 26–28)

In the following, the importance of some of these additional factors is further evaluated and explored. However, the intention is not to cover all aspects of numerical simulations but rather to illustrate the similarities between the analytical and numerical approaches and the inherent limitations of the former one.

In the present case, the numerical simulations are carried out using the general-purpose finite-element code WELDSIM. The program accounts for all of the effects listed previously, except weld-metal fluid flow. A detailed description of the various components of the program is given in Ref 22 to 25.

Temperature-Dependent Material Properties

As previously stated in the section “Thermal Properties of Some Metals and Alloys,” a precondition for obtaining simple analytical solutions of Fourier’s second law of heat conduction is that the material properties of the base material are constant and independent of temperature. Because this assumption represents a crude oversimplification of the problem, it will, in certain cases, impose restrictions on the use of analytical solutions. In practice, however, their limitations are best illustrated by means of specific examples, based on a comparison with outputs from numerical simulations.

Effect of Latent Heat of Fusion. In numerical simulations, the latent heat of fusion, ΔH_m , can be readily included in the expression for the specific heat function, thereby allowing alloys with a freezing range to be simulated (Ref 20). This is not possible in the analytical case, where ΔH_m must either be included or ignored when calculating the dimensionless operating parameter n_3 based on Eq 9. Figure 23 shows how this affects the resulting peak temperature contours in conventional bead-on-plate steel welding. As expected, the isothermal zone widths are significantly smaller when the latent heat of fusion is accounted for in the analytical solutions compared to the situation where $\Delta H_m = 0$. This is in contrast to that observed in the numerical simulations, where the effect of ignoring or including the latent heat of fusion is seen to be small because the contribution, in a real welding situation, is just temporary and therefore less striking. Hence, the two different numerical simulations tend to yield the same isothermal zone widths with increasing distance from the weld centerline. These results are, in turn, almost identical to those obtained using the analytical model with $\Delta H_m = 0$.

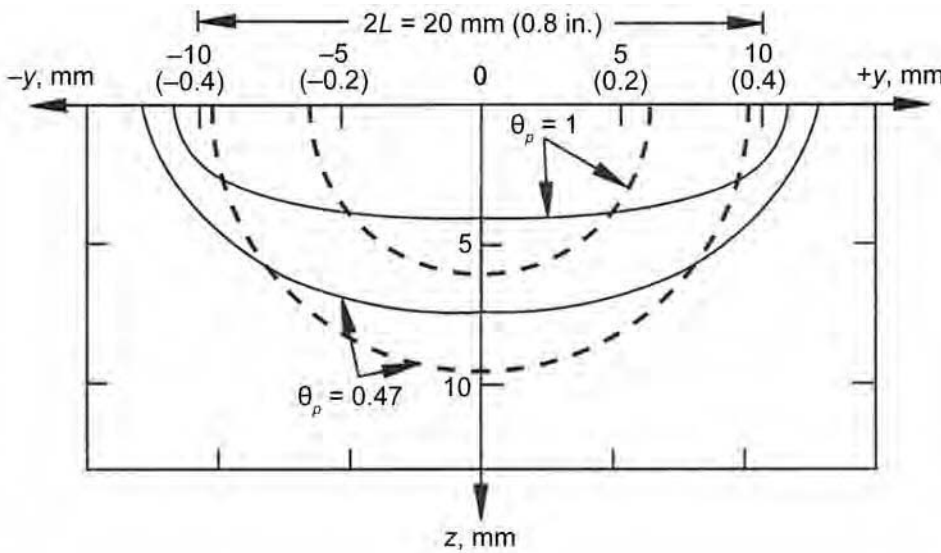


Fig. 18 Predicted shape of fusion boundary and A_{c1} isotherm during gas metal arc welding of steel with an oscillating electrode. Solid lines: distributed heat source; broken lines: point heat source. Operating conditions: $I = 315$ A, $U = 25$ V, $v = 5$ mm/s (0.2 in./s), $2L = 20$ mm (0.8 in.), $T_0 = 20$ °C (70 °F). Source: Ref 1

using the model of Hemmer and Grong (Ref 17).

Numerical and Analytical Solutions of the Thermal Field in Complex Welding Operations

Over the years, numerical simulation of heat flow phenomena in fusion welding has become more and more common and largely reduced the need for further developments of the

analytical solutions. This is because a number of important side effects can easily be accounted for in the numerical analyses without contributing to a significant increase in the computational efforts. These are:

- Complex geometries
- Advanced boundary conditions
- Temperature-dependent thermal properties (Ref 20)
- Realistic representation of the heat source (Ref 21)

Effects of Thermal Conductivity and Volumetric Heat Capacity. In addition, the analytical models assume that the thermal properties—thermal conductivity, λ , and volumetric heat capacity, ρc (and thus a)—are constant and independent of temperature. The justification of this simplifying assumption is further investigated in Fig. 24, based on a comparison with numerical simulations of the same peak temperature contours in ordinary bead-on-plate welding. It is evident from the figure that the use of temperature-dependent thermal properties has very little effect on the computed isothermal contours and that the analytical solutions give results that are in close agreement with those obtained in the numerical simulations. Hence, the assumption of constant thermal properties is deemed to be reasonable in most welding situations.

Start and Stop in Welding

During start and stop in welding, the assumption of pseudo-steady state is no longer valid, implying that transient effects will dominate. Although the mathematical treatment of the problem is complicated, both the heating and cooling case can be handled analytically, along the lines indicated in Ref 1.

Duration of the Transient Heating Period. For example, in thick-plate welding the duration of the transient heating period is determined by two group variables, that is, the dimensionless radius vector, σ_3 , and the dimensionless time, τ , defined as:

$$\sigma_3 = \frac{vR}{2a} \tag{Eq 36}$$

and

$$\tau = \frac{v^2 t}{2a} \tag{Eq 37}$$

Similarly, in thin-plate welding the governing length scale parameter is σ_5 , taking (Ref 1):

$$\sigma_5 = \frac{vr}{2a} \tag{Eq 38}$$

Equations 36 and 38 imply that a dimensionless distance may be “short” for one combination of welding speed, v , and thermal diffusivity, a , while the same position may represent a “long” distance for another combination of v and a . Similarly, Eq 37 shows that the dimensionless time τ may be “short” or “long” at a given number of seconds, depending on the ratio $v^2/2a$. Hence, transient effects during start and stop will be much more dominant in aluminum welding compared to steel welding, because of the pertinent difference in

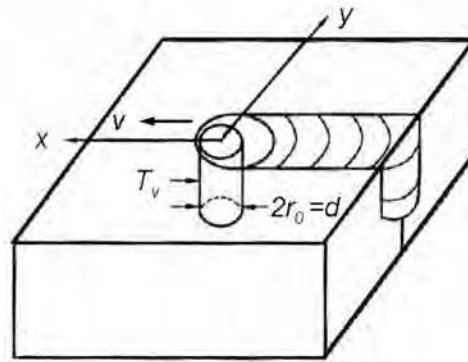
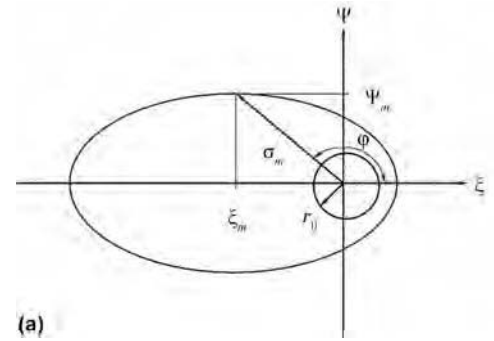
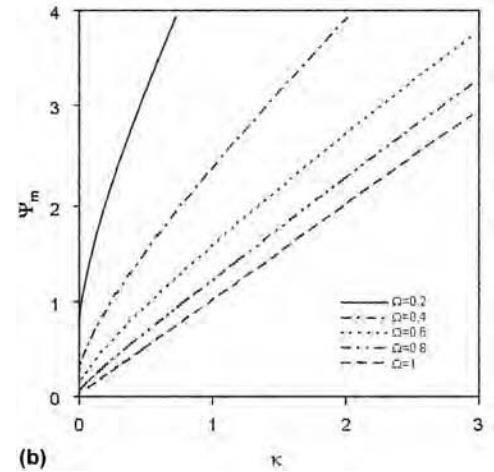


Fig. 20 Schematic representation of the analytical keyhole model showing the cylindrical cavity of constant surface temperature moving through the plate. Source: Ref 17



(a)



(b)

Fig. 21 Interrogation of Eq 30 and 31. (a) Coordinate system and definition of parameters. (b) Plots of ψ_m versus κ for various values of Ω . Source: Ref 17

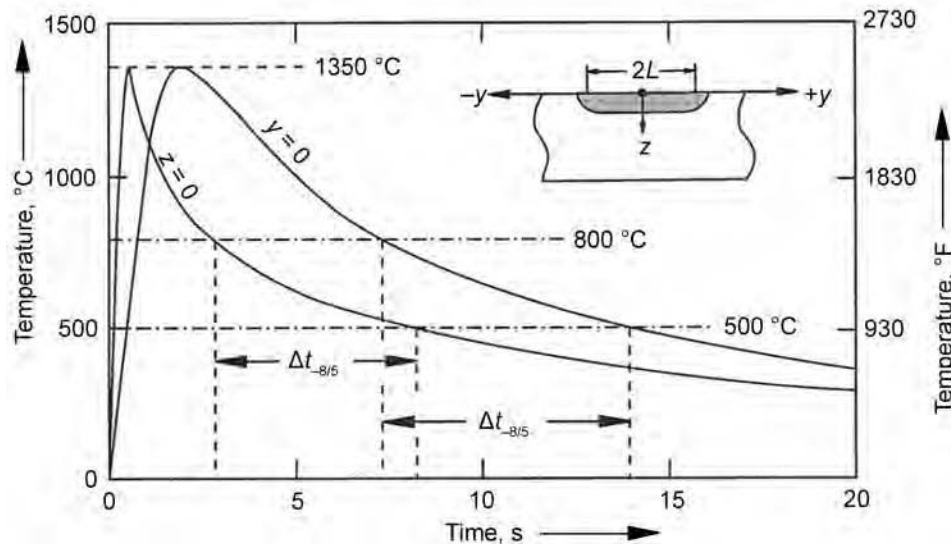


Fig. 19 Calculated heat-affected zone thermal cycles in positions $y = 0$ and $z = 0$. Operational conditions as in Fig. 18. Source: Ref 1

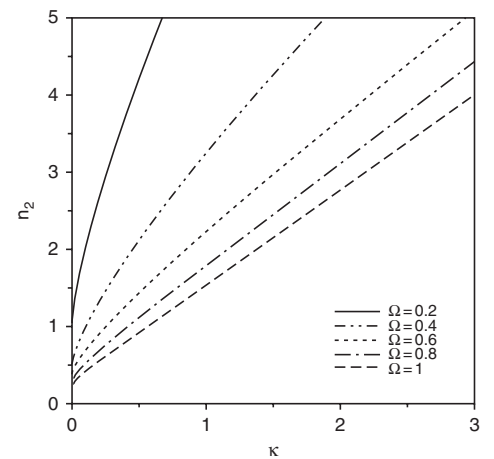


Fig. 22 Master curves for prediction of penetration depth during electron beam welding. Source: Ref 17

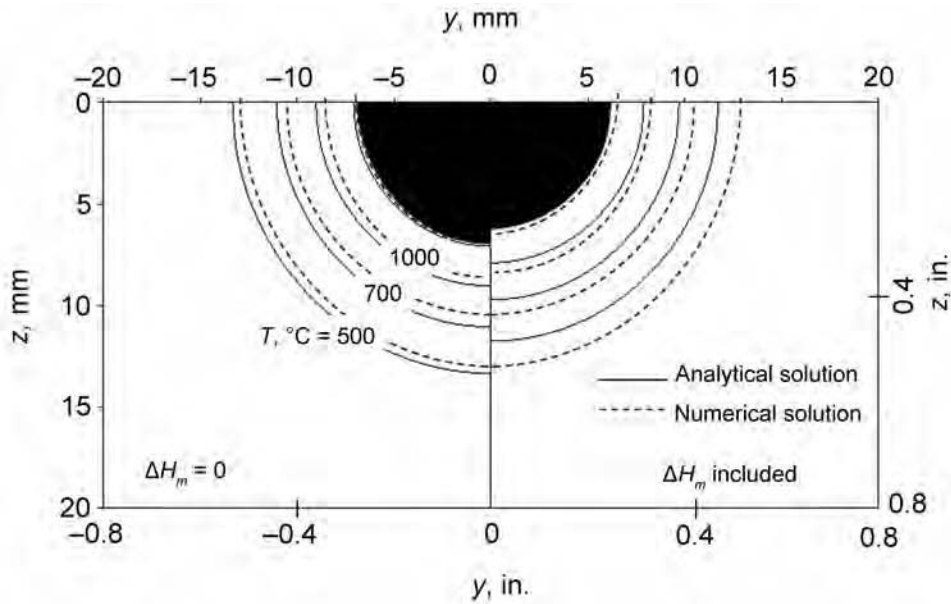


Fig. 23 Effect of the latent heat of fusion (melting) on the predicted peak temperature contours (500, 700, and 1000 °C, or 930, 1290, and 1830 °F) in conventional bead-on-plate steel welding. Solid and broken lines represent analytical and numerical calculations, respectively, whereas black regions indicate fusion zone. Operating conditions: $I = 280$ A, $U = 22$ V, $v = 2.5$ mm/s (0.1 in./s), $\eta = 0.8$, and $T_0 = 20$ °C (68 °F)

Aluminum Welding. Figure 25 shows how the isothermal contours in the weld cross section change with position from the start of the welding operation in series A1. A closer inspection of the figure reveals that the width of the isotherms continuously increases during the transient heating period. Even after 50 mm (2 in.) (referred to as the start position), pseudo-steady state has not yet been reached. This follows from a comparison between Fig. 25(b) and (c). Hence, the pseudo-steady-state solutions listed in Table 3 should not be applied to aluminum welding unless the welds are very long.

Steel Welding. Figure 26 shows corresponding results for steel welding (series S1). In this case, the width of the isotherms is almost identical at all three positions, indicating that pseudo-steady state has already been reached after a weld length of 20 mm (0.8 in.). Therefore, the pseudo-steady-state solutions are much more applicable to steel welding than aluminum welding because the time to reach saturation, in practice, is short when the thermal diffusivity is low, as in steel.

Groove Welding

Numerical simulation tools can also handle complex geometries and accurately represent most joint configurations of practical interest. The analytical models, on the other hand, are less flexible because they are, in principle, restricted to simple plate geometries. Still, their field of application can readily be extended to groove welding by proper adjustment of the net arc power without changing the underlying constitutive equations, as shown for the following geometries.

Simple Joint Geometries. By introducing a correction factor, f , in the models, which takes into account variations in the effective heat diffusion area, groove welding can readily be handled analytically. Taking f equal to 1 for ordinary bead-on-plate welding (b.o.p.), the net power of a groove weld can be defined as (Ref 1):

$$[q_0] = f[q_0]_{b.o.p.} \tag{Eq 39}$$

Recommended values of the correction factor f for some joint configurations are given in Fig. 27. For example, if q_0 in bead-on-plate welding is 4.93 kW, and groove welding is to be carried out under identical thermal conditions, Eq 39 implies that the net arc power in the analytical solutions should be adjusted as follows in each case:

- Welding in a V-groove ($\phi = 90^\circ$): $f = 2$, $[q_0] = 4.93/2 = 2.46$ kW
- Welding in an X-groove ($\phi = 90^\circ$): $f = 1$, $[q_0] = 4.93$ kW
- Welding of a T-joint: $f = 2/3$, $[q_0] = 4.93 \times (3/2) = 7.40$ kW

The resulting peak temperature contours, as calculated from numerical simulations

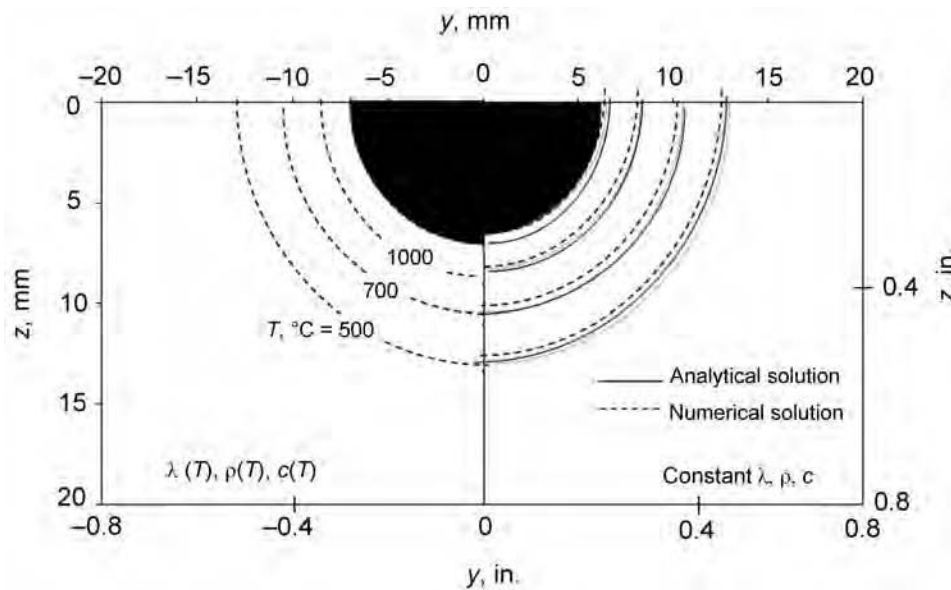


Fig. 24 Effect of thermal conductivity (λ) and volumetric heat capacity (ρc) on the predicted peak temperature contours (500, 700, and 1000 °C, or 930, 1290, and 1830 °F) in conventional bead-on-plate welding. Left side: temperature-dependent thermal properties; right side: constant thermal properties. Solid and broken lines represent analytical and numerical calculations, respectively, whereas black regions indicate fusion zone. Operational conditions: $I = 280$ A, $U = 22$ V, $v = 2.5$ mm/s (0.1 in./s), $\eta = 0.8$, and $T_0 = 20$ °C (68 °F)

the thermal properties of the two base materials (Table 2). This point is further elaborated in the case studies presented subsequently.

Case Studies. Consider the same examples presented previously in the section “Case Studies” under “Isothermal Contours and Mode of Heat Flow,” that is, stringer bead GMAW on 12.5 mm (0.5 in.) thick plates of

low-alloy steel and aluminum, respectively, under the conditions $E = 1.5$ kJ/mm and $\eta = 0.8$. Details of welding parameters are given in Table 4. Numerical methods shall be used to evaluate how the cross-sectional isotherms will evolve with time (i.e., change with position along the weld) in series A1 and S1, respectively.

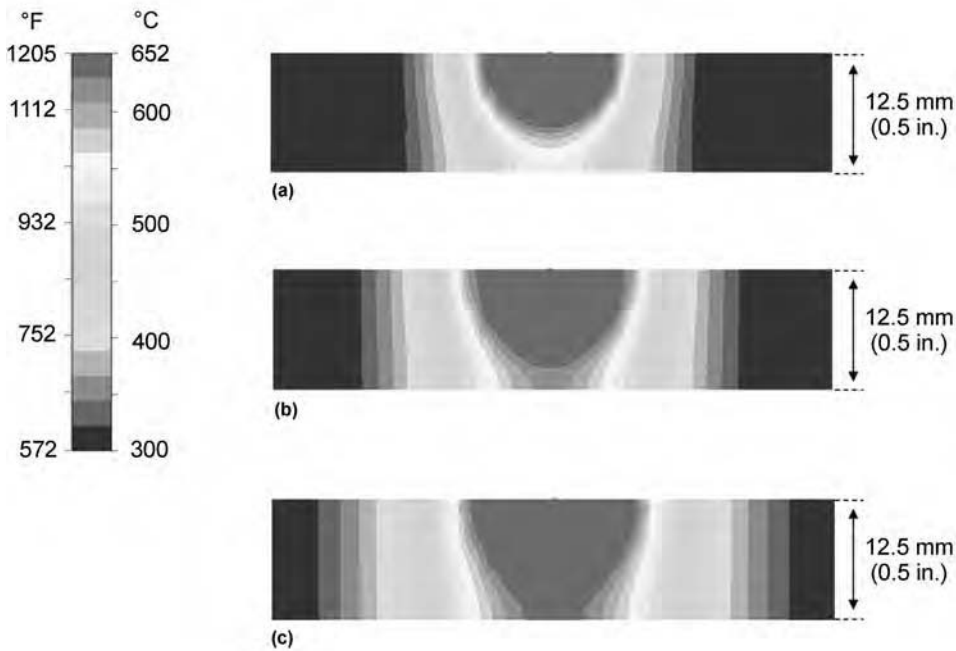


Fig. 25 Computed peak temperature contours in aluminum welding at various positions along the weld. Figures (a), (b), and (c) provide snapshots at positions 20, 50, and 150 mm (0.8, 2, and 6 in.) from the start of the weld, respectively. Operational conditions as for series A1 in Table 4

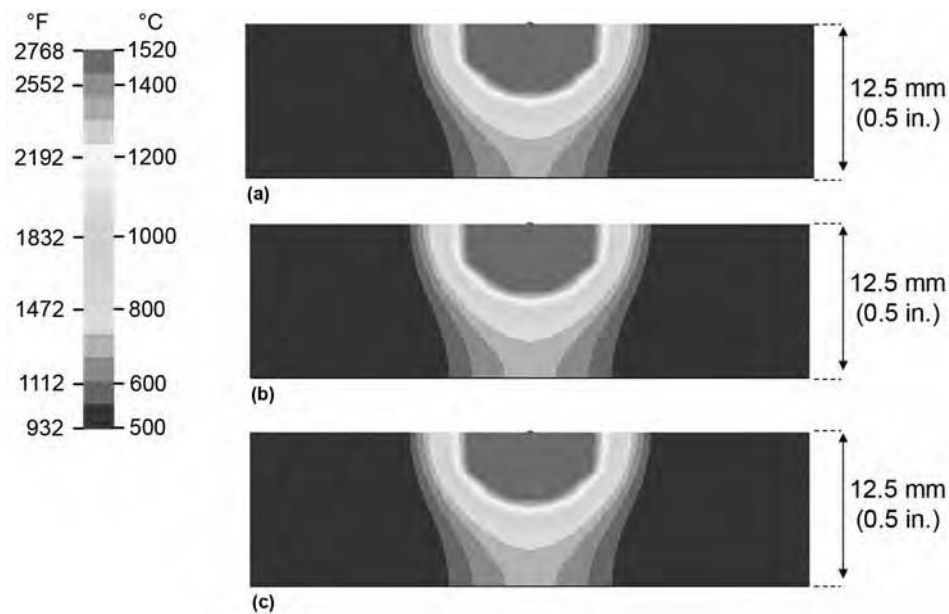


Fig. 26 Computed peak temperature contours in steel welding at various positions along the weld. Figures (a), (b), and (c) provide snapshots at positions 20, 50, and 150 mm (0.8, 2, and 6 in.) from the start of the weld, respectively. Operational conditions as for series S1 in Table 4

and the Rosenthal thick-plate solution (i.e., Eq 2), respectively, are shown in Fig. 28. As expected, both the width and the shape of the isotherms are seen to be identical in all four cases (i.e., they are all segments of the same circles). Moreover, it is interesting to note that the Rosenthal thick-plate solution

yields results that are very close to those obtained using more sophisticated numerical analyses. This is true as long as the welding conditions are comparable and correspond to pseudo-steady state, as discussed previously in the section “Start and Stop in Welding.”

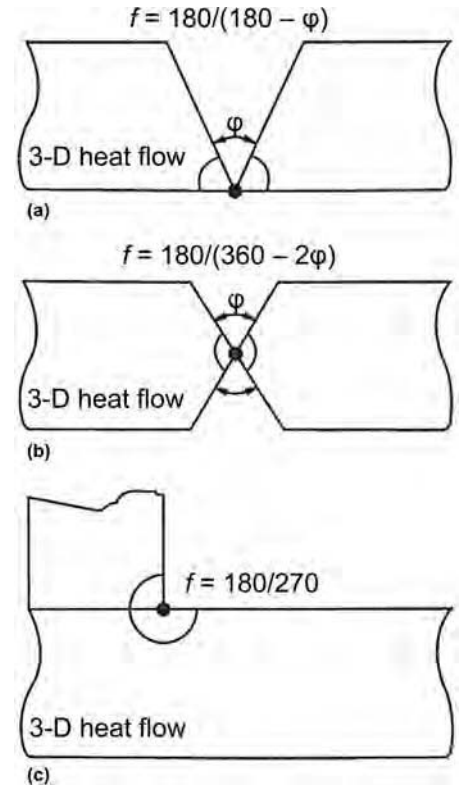


Fig. 27 Recommended correction factors, f , for some joint configurations. (a) Single V-groove. (b) Double V-groove. (c) T-joint. Source: Ref 1

Complex Joint Geometries. More complex joint geometries can only be handled by means of numerical methods. For example, the case shown in Fig. 29 is a good illustration of this, in which two aluminum plates of variable thickness, forming a T-joint, are joined using GMAW. Because of the high thermal conductivity of aluminum, the assumption of infinite plate thickness is not valid for any of the members. In the example, a filler material is also continuously deposited from a consumable electrode during welding. In the numerical simulation, this is accounted for by continuous activation of elements that are part of the weld reinforcement at material points that coincide with the instantaneous position of the moving heat source (Ref 22–25). None of these features can be handled analytically.

Advanced Boundary Conditions

Furthermore, the numerical modeling approach allows for the use of advanced boundary conditions, for example:

- Position- and temperature-dependent heat-transfer coefficients to represent forced-air cooling at defined positions
- Local heat sinks, such as a steel backing supporting the weld

The effect of using a steel backing in single-pass butt welding of aluminum is illustrated in

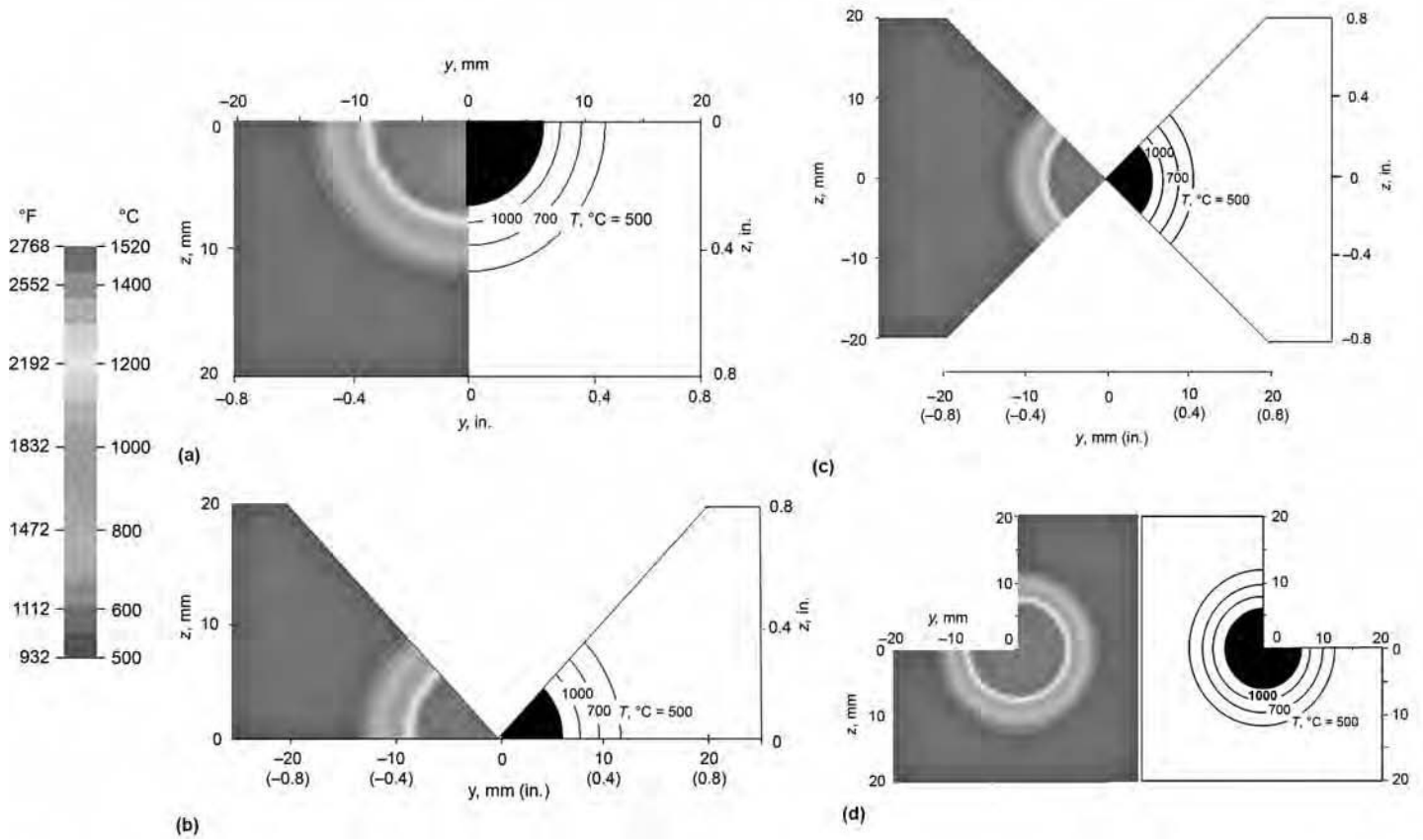


Fig. 28 Numerical and analytical calculations of peak temperature contours for various joint configurations in fusion welding of steel. (a) Bead-on-plate. (b) V-joint. (c) X-joint. (d) T-joint. Operational conditions: $I = 280$ A, $U = 22$ V, $v = 2.5$ mm/s (0.1 in./s), $\eta = 0.8$, and $T_0 = 20$ °C (68 °F)

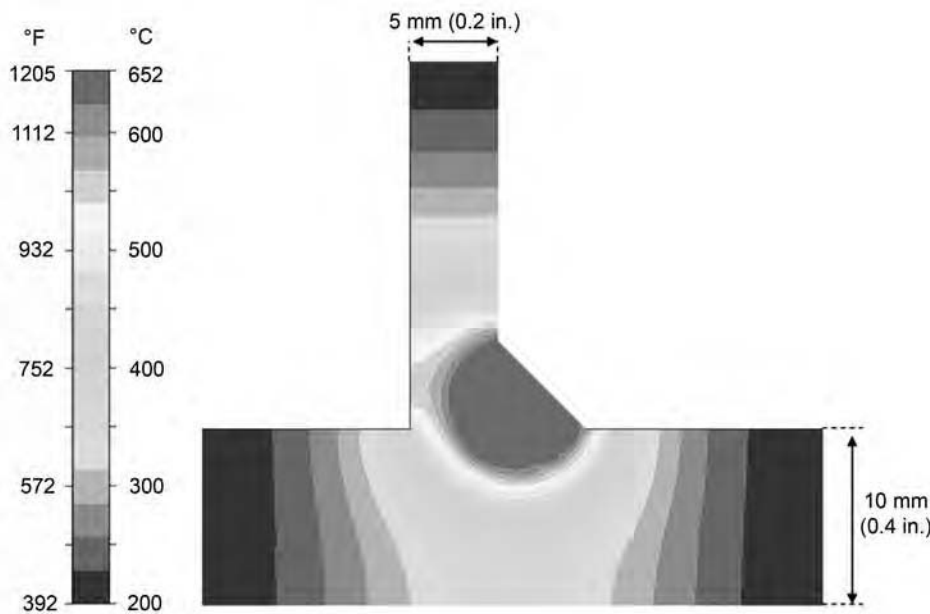


Fig. 29 Numerical calculations of peak temperature contours in gas metal arc welding of an aluminum T-joint with continuous addition of a filler material. Operational conditions: $I = 250$ A, $U = 20$ V, $v = 8.0$ mm/s (0.3 in./s), $\eta = 0.8$, and $T_0 = 20$ °C (68 °F)

Fig. 30. In these simulations, the heat-transfer coefficient, h , between the steel backing and the aluminum plate is varied systematically, keeping the plate thickness, d , the net arc power, q_0 , and the welding speed, v , constant and within a sensible range typical for gas metal arc butt welding of 2 mm (0.08 in.) thin aluminum plates. Specifically, Fig. 30 shows plots of the predicted isothermal contours in the cross section of the welds for three different cooling conditions: $h = 0$ (adiabatic surfaces—no heat loss to the surroundings), $h = 800 \text{ W} \cdot \text{m}^{-2} \cdot \text{°C}^{-1}$ (moderate pressure between the aluminum plate and the steel backing), and $h = \infty$ (full metallic contact between the aluminum plate and the steel backing). Although the thermal gradients in the transverse direction of the weld increase with increasing values of the heat-transfer coefficient, the predicted cross-sectional isotherms appear to be reasonably straight in the through-thickness direction of the plates. In addition, they are sufficiently elongated at the top and bottom of the plate surfaces to limit extensive heat diffusion in the welding direction in all three cases (not shown here). Hence, the use of a steel backing does not significantly alter the mode of heat flow within the HAZ of single-pass butt welds of sheet

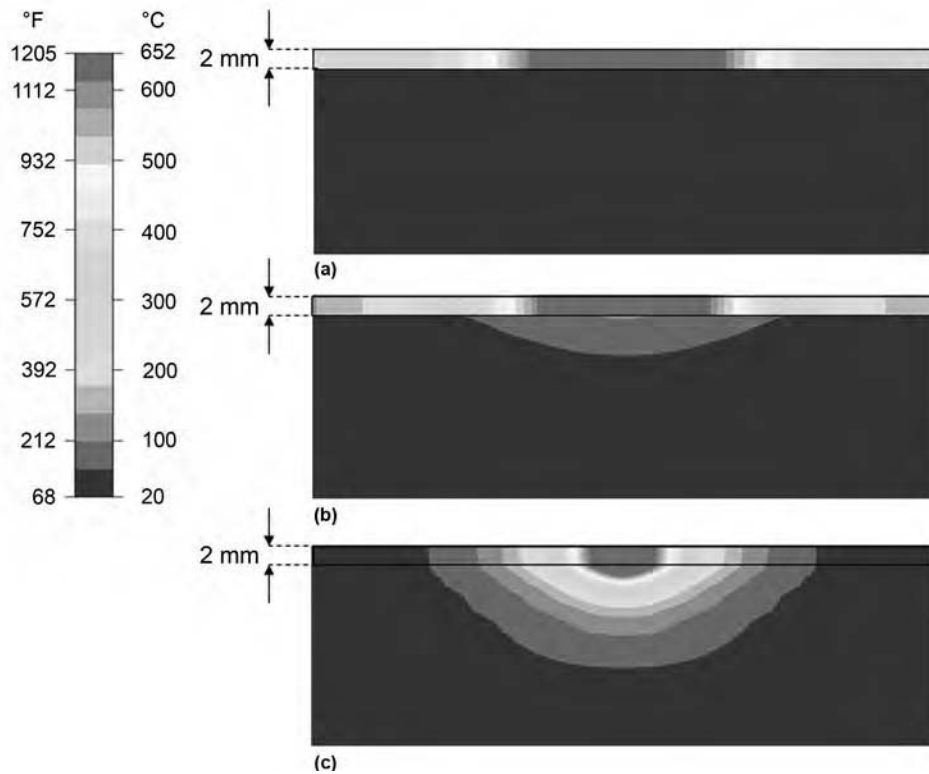


Fig. 30 Predicted isothermal contours in cross section of 2 mm (0.08 in.) thin aluminum plate with and without the use of a steel backing. Operational conditions: $q_0 = 2.4$ kW, $v = 15$ mm/s (0.6 in./s), and $d = 2$ mm (0.08 in.). (a) $h = 0$ (adiabatic surfaces—no heat loss to the surroundings). (b) $h = 800 \cdot \text{Wm}^{-2} \cdot ^\circ\text{C}^{-1}$ (moderate pressure between the aluminum plate and the steel backing). (c) $h = \infty$ (full metallic contact between the aluminum plate and the steel backing). Source: Ref 25

materials. This essentially means that the HAZ temperature-time pattern at pseudo-steady state is uniquely defined by the group variables q_0/vd when the actual values of the plate thickness, d , and the heat-transfer coefficient, h , between the aluminum plate and the steel backing are fixed.

Acknowledgment

The authors acknowledge the financial support provided by the Norwegian Research Council and Hydro Aluminium through SIM-Lab, the Centre for Research-Based Innovation at the Norwegian University of Science and Technology, Trondheim, Norway.

REFERENCES

- Ø. Grong, *Metallurgical Modelling of Welding*, 2nd ed., The Institute of Materials, London, 1997
- Welding Handbook*, 8th ed., Vol 2, American Welding Society, Miami, FL, 1991
- N. Christensen, V. de L. Davis, and K. Gjermundsen, Distribution of Temperatures in Arc Welding, *Brit. Weld. J.*, Vol 12, 1965, p 54–75
- S. Kou and Y. Le, Three-Dimensional Heat Flow and Solidification during the Autogeneous GTA Welding of Aluminium Plates, *Metall. Trans. A*, Vol 14, 1983, p 2245–2253
- Physical Constants of Some Commercial Steels at Selected Temperatures*, British Iron and Steel Research Association, Butterworths, London, 1953
- R. Hultgren, R.L. Orr, P.D. Anderson, and K.K. Kelly, *Selected Values of Thermodynamic Properties of Metals and Alloys*, J. Wiley & Sons, New York, 1963
- E. Griffiths, Ed., *J. Iron Steel Inst.*, Vol 154, 1946, p 83–121
- Properties and Selection: Nonferrous Alloys and Pure Metals*, Vol 2, *Metals Handbook*, 9th ed., American Society for Metals, 1979
- D. Rosenthal, Mathematical Theory of Heat Distribution during Welding and Cutting, *Weld. J.*, Vol 20, 1941, p 220s–234s
- D. Rosenthal, The Theory of Moving Sources of Heat and Its Application to Metal Treatments, *Trans. ASME*, Vol 68, 1946, p 849–866
- N.N. Rykalin, *Berechnung der Wärmevergange beim Schweissen*, VEB Verlag Technik, Berlin, 1953
- V.A. Karkhin, P.N. Homich, and V.G. Michailov, Models for Volume Heat Sources and Functional-Analytical Techniques for Calculating the Temperature Fields in Butt Welding, *Proc. Eighth Int. Seminar on Mathematical Modelling of Weld Phenomena*, Sept 2006 (Graz, Austria)
- D. Radaj, *Eigenspannungen und Verzug beim Schweißen*, Verlag für Schweißen und Verwandte Verfahren, DVS-Verl. GmbH, Düsseldorf, Germany, 2002, p 34–40
- O.R. Myhr and Ø. Grong, Dimensionless Maps for Heat Flow Analyses in Fusion Welding, *Acta Metall. Mater.*, Vol 38, 1990, p 449–460
- A. Pilipenko, “Computer Simulation of Residual Stress and Distortion of Thick Plates in Multi-Electrode Submerged Arc Welding. Their Mitigation Techniques,” Ph.D. thesis, Norwegian University of Science and Technology, Trondheim, Norway, 2001, p 71–75
- Ø. Grong and N. Christensen, Effects of Weaving on Temperature Distribution in Fusion Welding, *Mater. Sci. Technol.*, Vol 2, 1986, p 967–973
- H. Hemmer and Ø. Grong, Prediction of Penetration Depths during Electron Beam Welding, *Sci. Technol. Weld. Join.*, Vol 4 (No. 4), 1999, p 219–225
- T. Miyazaki and W.H. Giedt, Heat Transfer from an Elliptical Cylinder Moving Through an Infinite Plate Applied to Electron Beam Welding, *Int. J. Heat Mass Transf.*, Vol 25, 1982, p 807–814
- H. Hemmer, Ø. Grong, and S. Klokkehaug, A Process Model for the Heat-Affected Zone Microstructure Evolution in Duplex Stainless Steel Weldments, Part II: Application to Electron Beam Welding, *Metall. Trans. A*, Vol 31, March 2000, p 1035–1048
- T. Zacharia and S.A. David, Heat and Fluid Flow in Welding, *Mathematical Modelling of Weld Phenomena*, The Institute of Materials, London, England, 1993, p 3–23
- J. Goldak, A New Finite Element Model for Welding Heat Sources, *Metall. Trans. B*, Vol 15, 1984, p 299–305
- O.R. Myhr, S. Klokkehaug, H.G. Fjær, Ø. Grong, and A.O. Klukuken, Modelling of Microstructure Evolution, Residual Stresses and Deformations in 6082-T6 Aluminium Weldments, *Weld. J.*, Vol 77, July 1998, p 286–292
- O.R. Myhr, Ø. Grong, S. Klokkehaug, H.G. Fjær, and A.O. Klukuken, Process Model for Welding of Al-Mg-Si Extrusions, Part I: Precipitate Stability, *Sci. Technol. Weld. Join.*, Vol 2 (No. 6), 1997, p 245–254
- O.R. Myhr, H.G. Fjær, S. Klokkehaug, E. J. Holm, Ø. Grong, and A.O. Klukuken, WELDSIM—An Advanced Simulation Model for Aluminium Welding, *Proc. Ninth Int. Conf. on Computer*

- Technology in Welding*, Sept 1999 (Detroit, MI), p 52–63
25. O.R. Myhr and Ø. Grong, Novel Modelling Approach to Optimisation of Welding Conditions and Heat Treatment Schedules for Age Hardening Al Alloys, *Sci. Technol. Weld. Join.*, Vol 14 (No. 4), 2009, p 621–632
26. D.C. Weckman, Modelling Thermofluids Phenomena in Arc Welds, *Proc. Fifth Int. Conf. on Trends in Welding Research*, June 1998 (Georgia), American Welding Society, 1999, p 3–12
27. R. Rai, T.A. Palmer, J.W. Elmer, and T. DebRoy, Heat Transfer and Fluid Flow during Electron Beam Welding of 304l Stainless Steel Alloy, *Weld. J.*, Vol 88, 2009, p 54–61
28. T. DebRoy, H. Zhao, W. Zhang, and G.G. Roy, Weld Pool Heat and Fluid Flow in Probing Weldment Characteristics, *Mathematical Modelling of Weld Phenomena 6*, The Institute of Materials, Minerals and Mining, London, England, 2002, p 21–42

Transfer of Heat and Mass to the Base Metal in Gas Metal Arc Welding*

Ian Harris, Edison Welding Institute

HEAT AND MASS TRANSFER in arc welding is normally studied from the standpoint of the weld pool and heat-affected zone (HAZ); however, it is also instructive to examine heat and mass transfer from the arc to the base metal. This article describes the latter topic in terms of the gas metal arc welding (GMAW) process and provides practical information related to the development of welding procedures and the general operation of the process.

Welding procedures emphasize control of parameters such as electrode wire-feed speed (or current), arc voltage, welding travel speed, contact tip-to-workpiece distance, as well as welding current pulse parameters (peak and background current, and peak and background time, Fig. 1). It is therefore easy to overlook the fact that the process is ostensibly a source of heat and mass inputs to the weldment. Melting of the base metal, dilution of the filler metal, solidification of the weld bead, microstructural development in the weld bead and HAZ, and thermomechanical distortion and residual stresses all follow from the heat and mass inputs. The conventional parameters identified previously are variables that control the heat and mass inputs. An example of the relationship between the conventional parameters of electrode speed and welding speed to heat and mass transferred to the weldment is shown in Fig. 2 for certain conditions, as applied to the welding of thick-section steel.

The issues described in this article include the following:

- Total heat transferred to the base metal
- Partitioning of heat transfer between the arc and the molten electrode droplets
- Transfer modes of the droplets
- Role of the arc in droplet transfer
- Simple model for welding procedure development based on an understanding of heat and mass transfer to the base metal

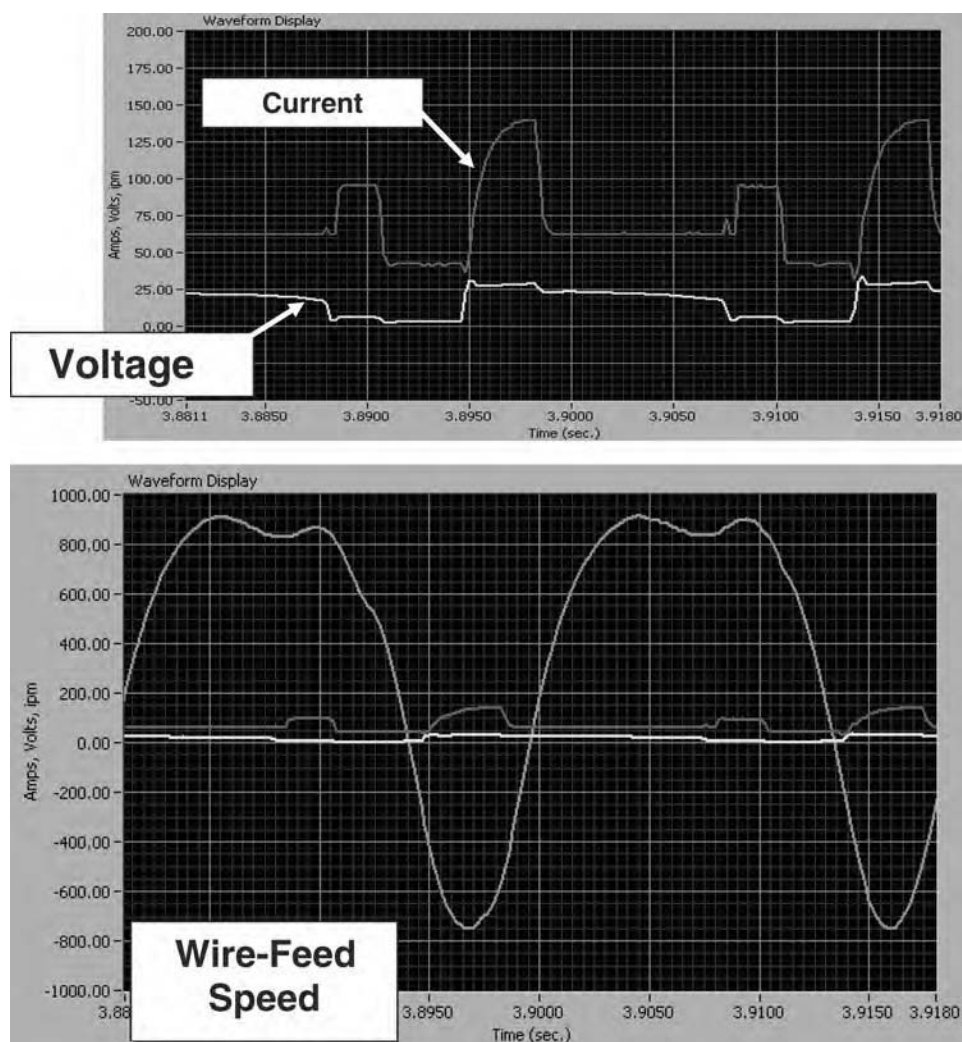


Fig. 1 Current, voltage, and wire-feed control for reciprocating wire-feed gas metal arc welding. Courtesy of Edison Welding Institute

* Revised from H.B. Smartt, Transfer of Heat and Mass to the Base Metal in Gas-Metal Arc Welding, *Welding, Brazing, and Soldering*, Vol 6, *ASM Handbook*, ASM International, 1993, p 25-29

Heat Transfer

The total transfer of heat, H (neglecting pre-heating), from the GMAW process to the weldment per unit time is given by:

$$H = \eta EI \tag{Eq 1}$$

where E is voltage, I is current, and η is the heat-transfer efficiency. The rate at which heat is transferred to the weldment per unit length of weld is given by:

$$H = \frac{\eta EI}{R} \tag{Eq 2}$$

where R is welding speed. Calorimeter-based heat-transfer experiments reveal that the heat-transfer efficiency for welding thick-section steel is nominally 80 to 90%, as indicated in Fig. 3. The total heat-transfer efficiency is altered somewhat by changing other parameters. For example, it increases slightly as the power supply open-circuit voltage is decreased (for a silicon-controlled rectifier-regulated power supply), and it increases slightly with increasing contact tube-to-base metal distance. However, 85% is a reasonable estimate for most conditions.

Partitioning of Heat Transfer. In the GMAW process, the molten droplets of electrode material carry a significant portion of the total heat transferred to the weld pool. This is seen in calorimetry experiments (Fig. 3), where the total heat-transfer efficiency of the GMAW process is partitioned into those portions associated with transfer by the arc and by the molten droplets. At low electrode speeds, approximately 60% of the total heat transferred is associated with the arc. As electrode speed increases, the fraction of total heat transferred associated with the droplets

increases, reaching nominally 50% at current levels in excess of approximately 220 A (that is, at approximately 230 mm/s, or 9.1 in./s, electrode speed) for the conditions used.

Mass Transfer

Droplet Transfer Modes. Although the International Institute of Welding (IIW) lists eight distinct metal-transfer modes (Ref 3), the modes commonly used in U.S. welding practice are short circuiting, globular, spray, streaming spray, and rotating spray. The mode terms *drop* and *repelled* used by the IIW are often referred to as *globular*, and the mode term *projected* is generally referred to as *spray*. The globular, spray, streaming, and short-circuiting transfer modes are shown in Fig. 4 to 7.

When all other parameters are held constant, the metal-transfer mode at the lowest wire-feed speed (and associated current level) is short circuit. As wire speed (and therefore current) increases, the mode changes rapidly from globular to spray. With an additional increase in wire speed (and current), spray transfer becomes streaming transfer. Figure 8 shows the droplet sizes during the transition from globular to spray to streaming transfer for direct and pulsed current welding. If an adequately high current, contact tube-to-base metal distance, and voltage exist, then rotating transfer, wherein the lower part of the electrode becomes molten over a considerable length and rotates in

a helical spiral under the influence of the magnetic field surrounding the arc, can occur. As it rotates, a controlled stream of droplets is transferred from the electrode tube to the weld pool over a relatively wide area. Additional increases in wire feed/current at low voltage shorten the arc length and, eventually, the wire stubs into the weld pool. In addition, with appropriate conditions (for example, carbon dioxide, argon-carbon dioxide mixtures, and helium-base shielding gases), droplets can be transferred directly, by surface tension forces, after contact of the drop with the weld pool, a condition called short-circuiting transfer.

In practical applications, the optimal transfer mode depends in part on the thickness of the base metal being welded. For example, very thin sections (in all positions) require the short-circuiting mode (with low current levels and appropriate settings of voltage and other operating parameters, including shielding gas composition). Thicker sections show best results with spray or streaming transfer. These transfer modes also produce high heat input, maximum penetration, and a high deposition rate. In welding steel, they are generally limited to welding that occurs in the flat position and the horizontal fillet position, except when pulsed current is used. Rotating transfer can be used in a deep groove in thick-section material. One- and two-pass heavy fillet welds are also a major area of application for this process variation.

Globular transfer (Fig. 4) involves a droplet that, generally, is much larger in diameter than

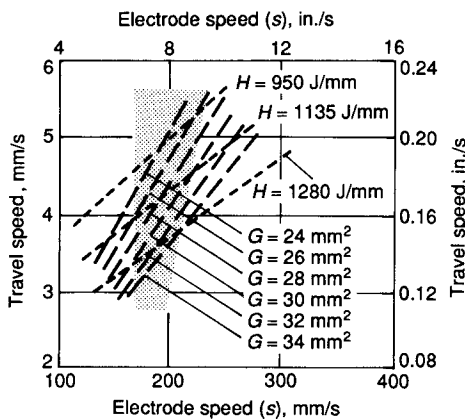


Fig. 2 Plot of welding speed versus electrode speed as a function of heat transfer per length of weld, H , and mass transfer expressed in terms of reinforcement, G . Power supply open-circuit voltage, E_0 , is 32 V; contact tube-to-base metal distance, C_T , is 15.9 mm (0.625 in.). Shaded area denotes region in which spray and streaming transfer modes occur; globular transfer occurs at lower electrode speeds, and electrode contacts the weld pool at higher electrode speeds. Source: Ref 1

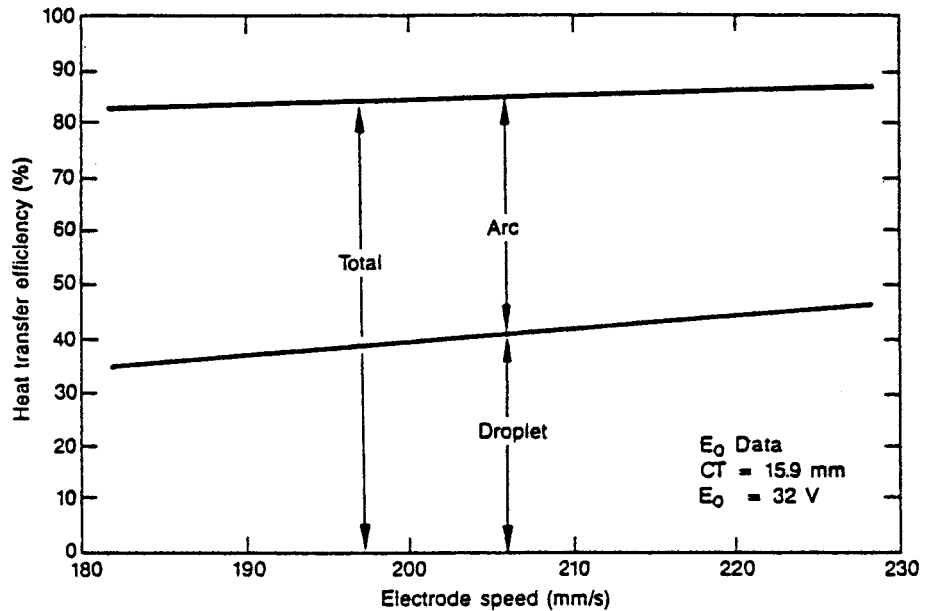


Fig. 3 Plot of heat-transfer efficiency to base metal versus electrode speed for 0.89 mm (0.035 in.) diameter steel electrode in an Ar-2% O_2 shield gas. Total heat-transfer efficiency is shown partitioned into arc and molten drop components. Power supply open-circuit voltage, E_0 , is 32 V; contact tube-to-base metal distance, C_T , is 15.9 mm (0.625 in.). Source: Ref 2

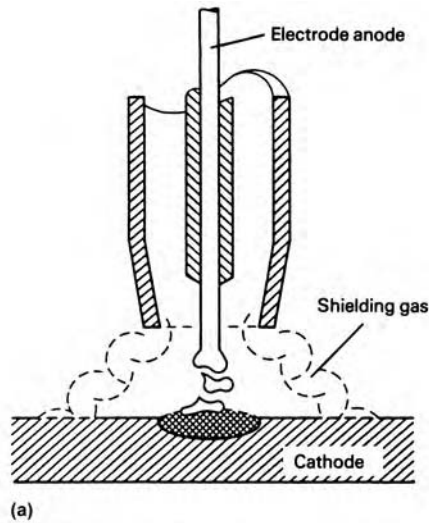


Fig. 4 Globular transfer mode in gas metal arc welding of steel. (a) Schematic showing transfer of electrode material globules onto cathode base metal. (b) High-speed photograph of globular metal transfer

the electrode wire. Globular transfer can involve a transfer rate of approximately 1 to 10 drops/s, and the arc has a soft, rounded appearance. Droplet detachment and transfer are mainly due to the gravitational force, which limits globular transfer to in-position welding. For spray transfer (Fig. 5), droplet and electrode diameters are roughly equivalent.

Spray transfer can involve 100 drops/s, and the arc noticeably contracts, or stiffens. Drops usually travel in-line down the center of the arc, but several drops may be in flight at the same instant.

In streaming transfer (Fig. 6), a well-developed liquid column extends from the solid electrode down into the arc and breaks into small droplets before contacting the weld pool (see the following discussion on spatter). Streaming transfer can involve 1000 drops/s, and the arc has a characteristic cone shape, as shown in Fig. 6.

In short-circuiting transfer, the arc is very short (Fig. 7a). During metal transfer, the

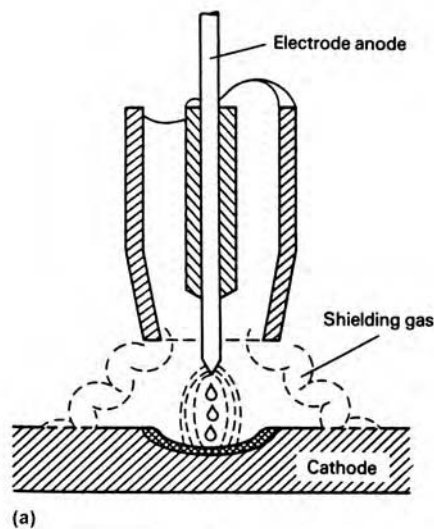


Fig. 5 Spray transfer mode in gas metal arc welding of steel. (a) Schematic showing transfer of electrode material droplets onto cathode base metal. (b) High-speed photograph of spray metal transfer mode

undetached molten droplet contacts the weld pool, shorting out the arc (Fig. 7b), which then extinguishes. Surface tension plays an important role in transferring the drop to the weld pool, but detachment of the drop from the electrode is due to electromagnetic pinch forces. Reignition of the arc in conventional short-circuit arc welding is violent (Fig. 7c), resulting in considerable spatter. Development of higher levels of electronic control of power sources has resulted in several additional variants of electronically controlled short-circuit transfer mode. In these cases, the arc reignition is controlled to very low current level, which significantly minimizes spatter generation. There are also reciprocating wire-feed systems from at least two manufacturers that control the wire feed in both forward and reversing motions. These systems, combined with electronic current control, are capable of eliminating spatter on arc reignition and even on initial arc strike (Ref 5) (Fig. 9).

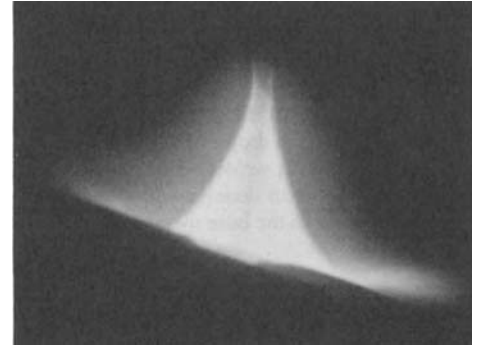


Fig. 6 High-speed photograph of streaming transfer mode in gas metal arc welding of steel

Systems involving two gas metal arcs in a single torch provide interesting additional challenges and opportunities to increase welding speed and deposition rate. These systems typically operate with current isolation and asynchronous pulsing (Fig. 10) of the welding arcs to avoid electrical interference and arc blow, which otherwise substantially destabilize the metal transfer. The arcs can be operated in pulse/constant-voltage (CV), CV/pulse, and pulse/pulse modes, depending on the desired arc characteristics, deposition rate, and welding position (Ref 5).

As seen in Fig. 8, the transition from one mode to another actually involves continuous variations in droplet size. Because the product of droplet volume and transfer rate equals the electrode melting rate (in appropriate dimensions), there is also a continuous variation in droplet transfer rate. Detailed experimental studies have shown that rapid, cyclic transition from globular to spray to globular and so on occurs in the transition region between globular and spray transfer (Ref 6). Although it is generally not possible for the welder to see droplet transfer events in the spray and streaming transfer modes (except under ideal conditions for spray transfer), the changes in arc shape and the associated changes in electrical and acoustic noise allow a trained welder to readily identify all of the transfer modes. The section "Electrical and Acoustic Signals" in this article describes this event more fully. Welding is increasingly mechanized, robotic, or deployed in methods other than manual (referred to as semiautomatic in GMAW because the wire is fed automatically). The skill sets of a good welder and/or welding engineer are still needed to set up and maintain the correct operation of the process, arguably more so because the intent is to increase productivity and throughput while maintaining an acceptably high level of weld quality.

Assuming that mass is conserved as welding occurs, the transverse cross-sectional area of the weld bead added to the weldment for a single weld pass, G , is given by:

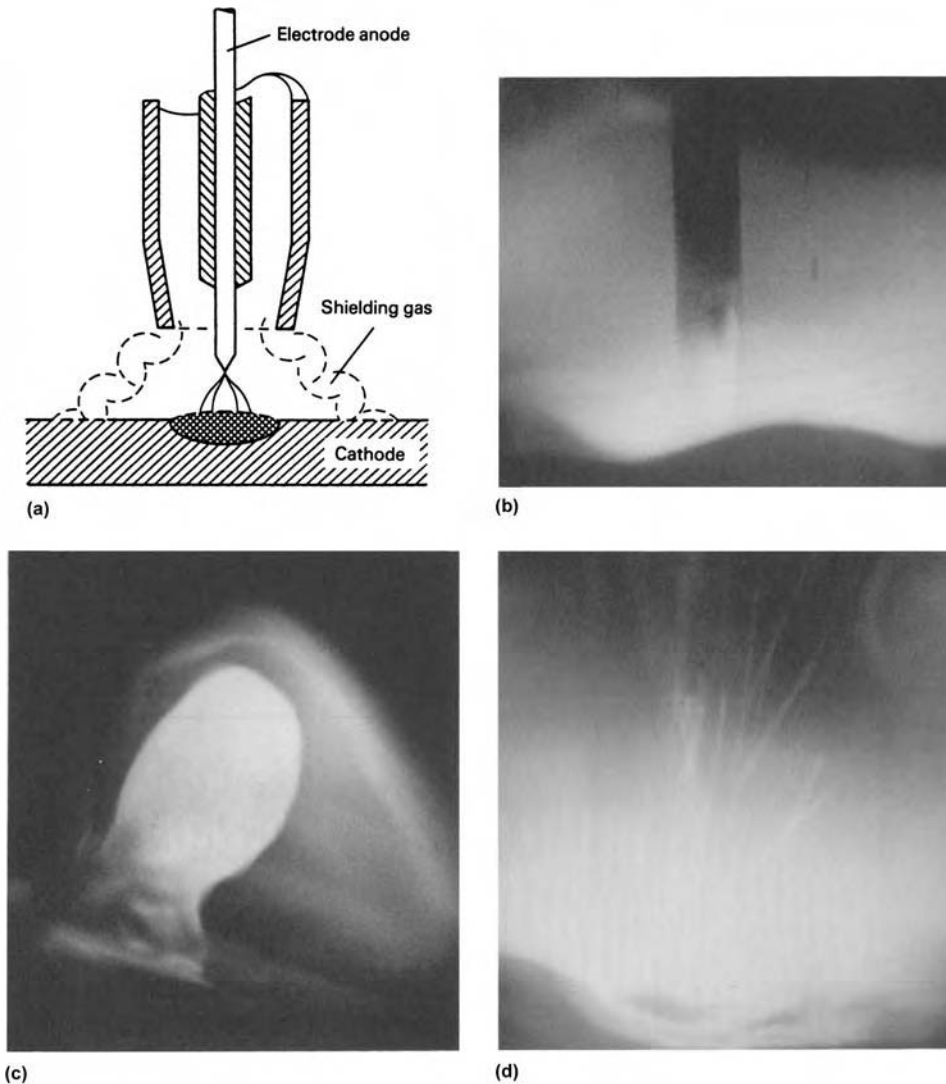


Fig. 7 Short-circuiting transfer mode in gas metal arc welding of steel. (a) Schematic showing transfer of electrode material by surface tension of weld pool onto cathode base metal. (b) High-speed photograph of material transfer when arc length is very short. (c) High-speed photograph of cyclic shorting of arc by the electrode during metal transfer to weld pool. (d) High-speed photograph of violent arc reignition with associated spatter

$$G = \frac{S \pi d^2}{R^4} \quad (\text{Eq 3})$$

where S is electrode speed, R is welding speed, and d is electrode diameter. For the spray and streaming transfer modes, the assumption that mass is conserved is reasonably good. However, because short circuiting and other conditions generate considerable spatter, the actual reinforcement will be slightly less than the value calculated by Eq 3.

Droplet Velocity and Temperature. In spray and streaming transfer, the droplets are accelerated rapidly through the arc to the weld pool. Velocities of 1 m/s (40 in./s) are typical, increasing with voltage (Fig. 11). Calorimetry-based experimental results indicate that steel droplets can reach temperatures of approximately 2600 K (4220 °F) (Ref 2). This explains

why the droplets transport one-half of the total heat transferred to the base metal.

A result of the activity of molten electrode droplets in heat transfer to the base metal is that they also play an important role in convective heat transport in the weld pool and thus in weld penetration (Ref 7). This can be seen in Fig. 12, a transverse cross section of a gas metal arc bead-on-plate weld on carbon steel. The region of deep penetration in the center of the weld bead is associated with the heat convected to the lower portion of the weld pool by the entering droplets.

Electrical and Acoustic Signals. As the droplets of molten metal detach from the electrode, an almost instantaneous change occurs in the electrode extension, which results in a sudden, although small, change in the electrical resistance between the contact tube and the base

metal. The results are spikes in the secondary circuit voltage and welding current, accompanied by pressure changes in the arc. Thus, both electrical and acoustic noise (Fig. 13) are generated by the GMAW process and are characteristic of the droplet transfer mode. The waveforms for globular transfer show prominent spikes associated with individual droplet transfer events. This can also be seen in Fig. 14, a plot of the computer-digitized current for a weld on carbon steel, where a change from globular to spray transfer has occurred at approximately 8 s into the weld. The power spectra of the current changes dramatically for the two transfer modes (Fig. 15), leading to a means of detecting transfer mode during welding.

Several specific techniques have been identified (Ref 9) for detecting the mode of metal transfer: Fourier transform, standard deviation, peak ratios, and integrated amplitude of the current and voltage signal. In a similar manner, spatter, lack of shielding gas, and contact tube wear can also be detected. Similar power spectra changes also occur in the secondary circuit voltage and acoustic noise. The change in acoustic noise allows the aural detection of the transfer mode. An experienced welder can readily hear, for example, the difference between globular and spray transfer.

Contact of the molten droplet with the weld pool, while the droplet is still attached to the electrode, also results in a sudden change in electrical resistance. This is important, because spatter is generally produced when this electrode-to-weld pool contact breaks. (Spatter can also be produced by rapid expansion of gas bubbles in the electrode as it melts.) The resulting electrical and acoustic noise can be used to detect that spatter is being produced.

Procedure Development

The preceding discussion leads to a logical approach toward selecting welding parameters during the development of welding procedures. First, given a nominal power supply arc voltage and contact tip-to-workpiece distance, the electrode wire-feed speed can be set to determine the welding current. It can be shown that:

$$S = \frac{4\eta GI}{H\pi d^2} (E_O + HI) \quad (\text{Eq 4})$$

where E_O is the power supply arc voltage. It is assumed that the proper selection of electrode type and shielding gas have been made, and that the electrode diameter is appropriate for the application, which, based on the number of shielding gases, wire types, and diameters available, is worth checking with a welding engineer.

Second, the arc voltage is adjusted to give either an acceptable arc length or electrode extension. The objective is to prevent either burnback (transfer of the arc to the contact tube) or spatter caused by shorting of the

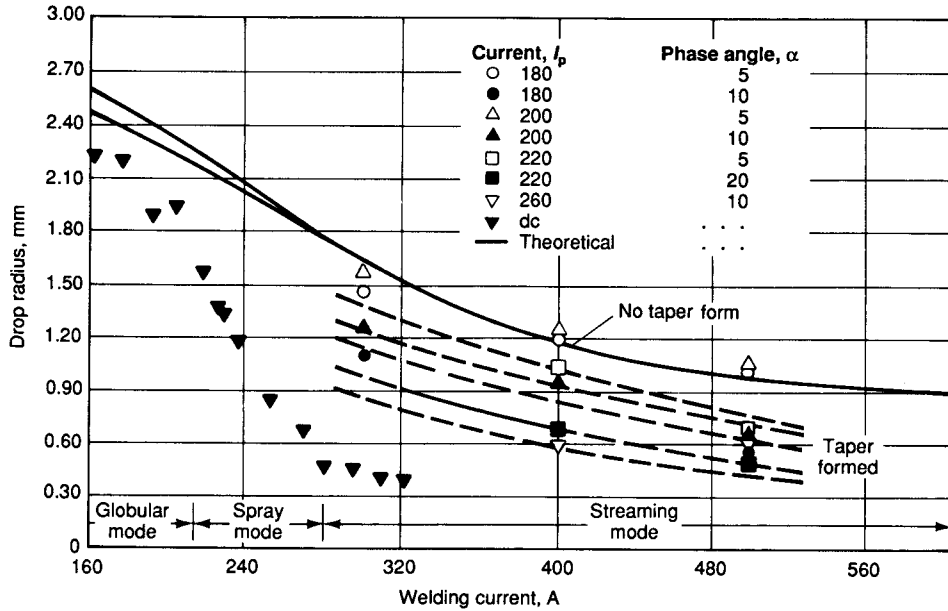


Fig. 8 Droplet sizes attainable under selected current pulsing conditions in gas metal arc welding of steel. Source: Ref 4

molten electrode droplets with the weld pool prior to detachment from the electrode. Fine adjustment of voltage may be necessary to obtain a clean start of the process, thus avoiding a short period of spatter or globular transfer following arc ignition. The combination of current and voltage for a given contact tip-to-workpiece distance determines the droplet transfer mode.

Third, the welding current determines the melting rate of the electrode. The electrode melting rate (\$M_{tp}\$) is a quadratic function of current (Ref 10):

$$M_{tp} = (C_1 + C_2A)I + C_3 \frac{LI^2}{A^i} \quad (\text{Eq 5})$$

where \$A\$ is the cross-sectional area of the electrode, and \$C_1, C_2, C_3\$, and \$i\$ are constants.

Another researcher (Ref 11) defines \$M_{tp}\$ by:

$$M_{tp} = C_4I + C_5 \frac{LI^2}{A} \quad (\text{Eq 6})$$

where \$C_4\$ and \$C_5\$ are constants.

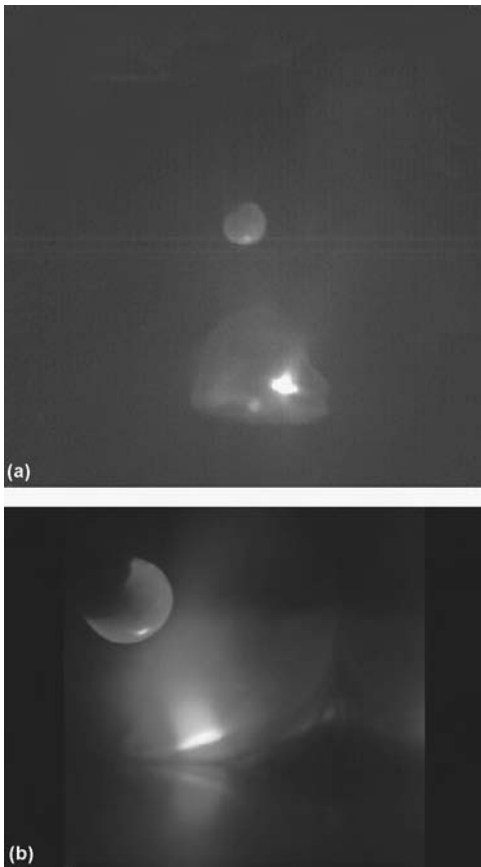


Fig. 9 (a) Pulsed gas metal arc welding of titanium; growing the metal droplet in the background current phase. (b) Reciprocating wire-feed gas metal arc welding; growing a droplet before transfer through short circuit. Courtesy of Edison Welding Institute

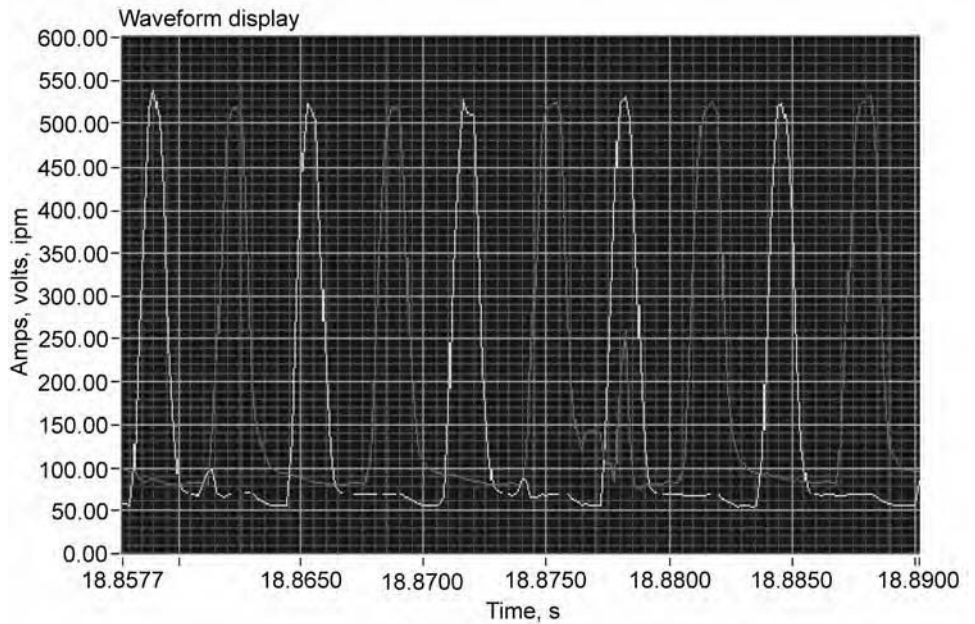


Fig. 10 Tandem gas metal arc welding current waveforms showing asynchronous current pulsing. Courtesy of Edison Welding Institute

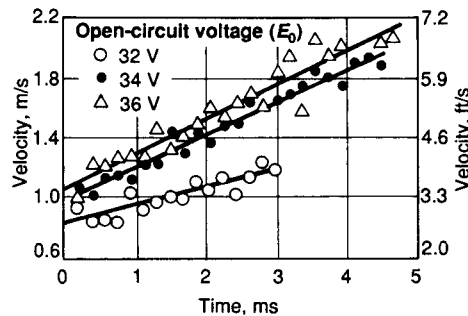


Fig. 11 Droplet velocities for spray transfer in gas metal arc welding of steel at three different open-circuit voltages. Source: Ref 6

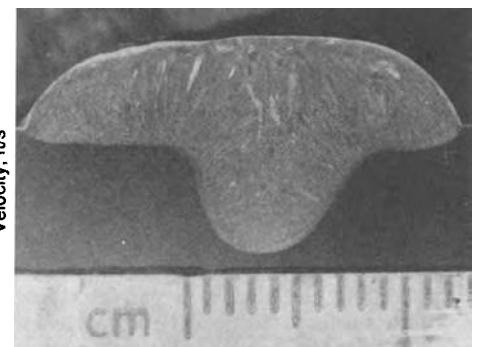


Fig. 12 Transverse cross section of gas metal arc bead-on-plate weld in carbon steel to show deep penetration in the weld bead center generated by molten electrode droplets

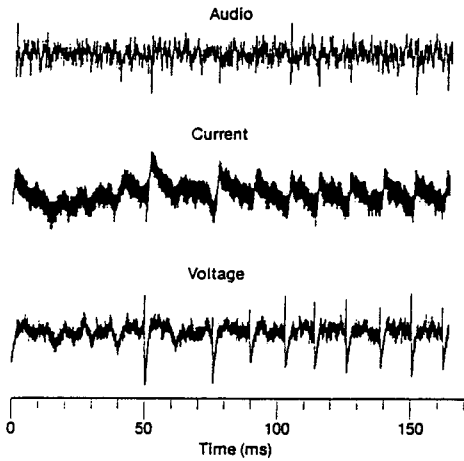


Fig. 13 Audio, current, and voltage during globular transfer in gas metal arc welding of steel. Source: Ref 8

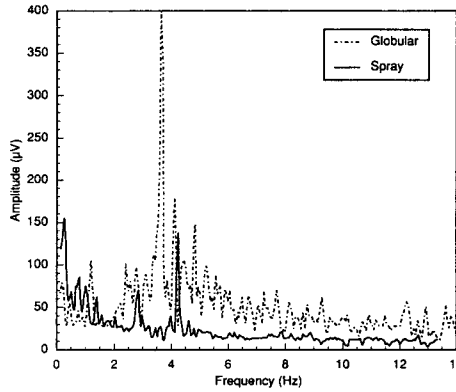


Fig. 15 Welding current power spectra for globular transfer and spray transfer modes during gas metal arc welding of steel. Source: Ref 1

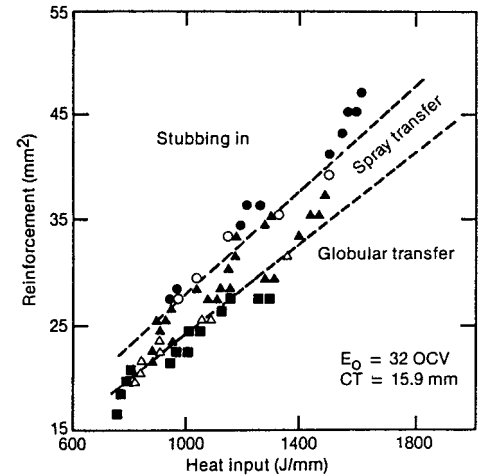


Fig. 16 Plot of reinforcement versus heat input to show parameters that favor spray transfer mode for gas metal arc welding of steel. Power supply open-circuit voltage, E_0 , is 32 V; contact tube-to-base metal distance, C_T , is 15.9 mm (0.625 in.).

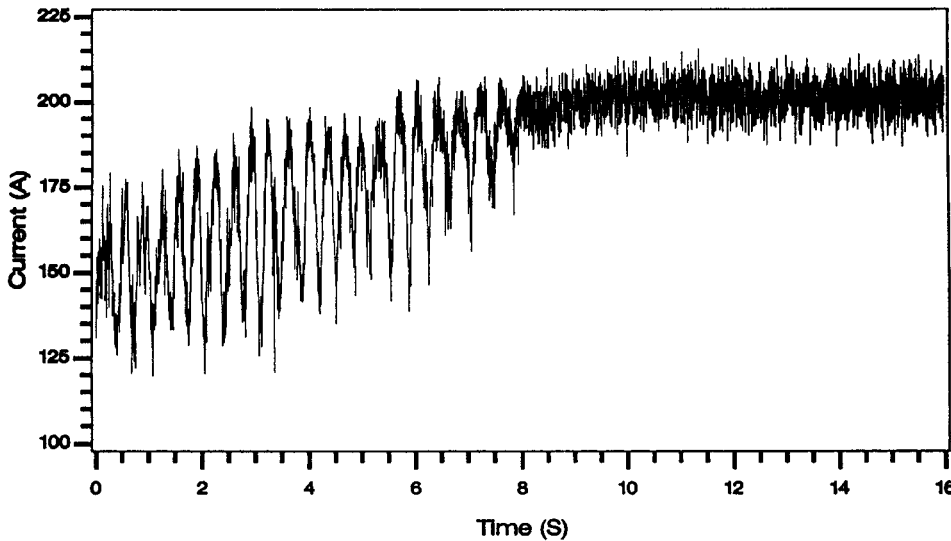


Fig. 14 Plot of digitized current versus time during a gas metal arc weld in carbon steel in which a transition from globular to spray transfer occurred (at $\sim t = 8$ s) as current was increased. Source: Ref 1

Given a desired melting rate, the welding travel speed is set to obtain the desired weld bead area. The welding current, arc voltage, and welding travel speed have all now been set, thus determining the heat input per length of weld ($H = \eta EI/R$).

It should be noted that it is actually possible to independently vary heat input and mass input (in terms of weld bead reinforcement) to the weld, over at least a small range. This is shown in Fig. 16, where the same data presented in Fig. 1 are replotted in terms of reinforcement as a function of heat input per length of weld.

The previous discussion on procedure development ignores second-order effects, such as the dependence of arc length on weld travel speed. It should also be realized that several iterations through the steps defined earlier may

be required for final parameter determination. Items such as the correct torch travel angle and work angle relative to the welding direction and the joint, including the weld position (flat, horizontal, vertical, overhead), are additional important factors when it comes to the performance and functionality of the weld and its acceptance. Proper power supply settings must be used, and code requirements must be met, typically in terms of both visual criteria (visual testing, liquid penetrant testing) and volumetric inspection (liquid penetrant testing, radiographic testing), depending on the welding specification and code requirements. Increasingly, data recorders and loggers are used for quality-assurance purposes and to alarm fault conditions to minimize scrap production that would otherwise increase in an automated, high-productivity environment.

REFERENCES

1. H.B. Smartt, Idaho National Engineering Laboratory, 1992
2. A.D. Watkins, "Heat Transfer Efficiency in Gas Metal Arc Welding," Master's thesis, University of Idaho, April 1989
3. J.F. Lancaster, *The Physics of Welding*, 2nd ed., International Institute of Welding, Pergamon Press, 1986, p 233
4. T.W. Eagar, D.E. Hardt, H.B. Smartt, and J.A. Johnson, Process Controllability in Gas Metal Arc Welding: Micro and Macroscopic Problems, *Proc. Eighth Symposium on Energy Sciences*, CONF-9005183, U.S. Department of Energy, Argonne National Laboratory, May 1990, p 51-67
5. I.D. Harris, "High Speed GMAW-P and Laser GMAW-P Hybrid Welding of Sheet Steel," Ph.D. thesis, Cranfield University, England, March 2009, p 237
6. D.E. Clark, C. Buhmaster, and H.B. Smartt, Droplet Transfer Mechanisms in GMAW, *Proc. Second International Conference on Trends in Welding Research* (Gatlinburg, TN), 1989
7. W.G. Essers and R. Walter, Heat Transfer and Penetration Mechanisms with GMA and Plasma-GMA Welding, *Weld. J.*, Vol 60 (No. 2), 1981, p 37-s to 42-s
8. J.A. Johnson, N.M. Carlson, and H.B. Smartt, Detection of Metal Transfer Mode in GMAW, *Proc. Second International Conference on Trends in Welding Research* (Gatlinburg, TN), 1989

88 / Fundamentals of Fusion Welding

9. G. Adam and T.A. Siewert, Sensing of GMAW Droplet Transfer Modes Using an ER100S-1 Electrode, *Weld. J.*, Vol 69 (No. 3), March 1990, p 103-s to 108-s
10. A. Lesnewich, Control of Melting Rate and Metal Transfer in Gas-Shielded Metal-Arc Welding, Part II—Control of Metal Transfer, *Weld. J.*, Vol 37 (No. 9), Sept 1958, p 418-s to 425-s
11. J.H. Waszink and G.J.P.M. Van den Heuvel, Heat Generation and Heat Flow in the Filler Metal in GMA Welding, *Weld. J.*, Vol 61 (No. 8), Aug 1982, p 269-s to 282-s

Fluid Flow Phenomena during Welding*

Updated by W. Zhang, Oak Ridge National Laboratory

MOLTEN WELD POOLS are dynamic. Liquid in the weld pool is acted on by several strong forces, which can result in high-velocity fluid motion. Fluid flow velocities exceeding 1 m/s (3.3 ft/s) have been observed in gas tungsten arc (GTA) welds under ordinary welding conditions, and higher velocities have been measured in submerged arc welds. Fluid flow is important because it affects weld shape and is related to the formation of a variety of weld defects. Moving liquid transports heat and often dominates heat transport in the weld pool. Because heat transport by mass flow depends on the direction and speed of fluid motion, weld pool shape can differ dramatically from that predicted by conductive heat flow. Temperature gradients are also altered by fluid flow, which can affect weld microstructure. A number of defects in GTA welds have been attributed to fluid flow or changes in fluid flow, including lack of penetration, top bead roughness, humped beads, finger penetration, and undercutting. Instabilities in the liquid film around the keyhole in electron beam and laser welds are responsible for the uneven penetration (spiking) characteristic of these types of welds.

Mass Transport in the Arc

High-velocity gas motion occurs in and around the arc during welding. The gas motion is partially due to shielding gas flow, but, more importantly, it is driven by electromagnetic forces associated with the arc itself. In gas metal arc (GMA) welds, liquid filler metal is also being transferred through the arc from the electrode to the workpiece. Both the mode and velocity of metal transfer have major effects on weld pool shape. Mass transport in and around the arc is important in GTA welding (GTAW) and even more so in GMA welding (GMAW). A detailed description of this phenomenon can be found in the articles on arc physics and metal transfer and weld behavior in this Volume; only the effects of this transport on the weld pool are discussed in this article.

Gas Tungsten Arc Welding

Most experimental and theoretical work on weld pool fluid flow and its effects has been directed toward GTAW. The motivation for much of this work was the observation of dramatically different weld pool shapes for GTA welds made using identical welding parameters on different heats of the same material with the same nominal composition. An extreme example of weld shape variability is shown in Fig. 1. Early observations of variable weld shape (often referred to as variable penetration) were not only an intellectual puzzle but also an indication of a growing practical problem. Gas tungsten arc welding is commonly used for high-precision, high-quality automated welding applications where reproducibility of weld shape or penetration is critical.

The possibility that fluid flow in the weld pool could alter weld shape has been recognized for many years. For example, in 1965 Christensen et al. (Ref 1) proposed that convection is partially responsible for weld pool shapes that deviate from those predicted by conduction solutions. The forces driving fluid flow in GTA weld pools have also been long known. The four primary driving forces are surface tension gradients, electromagnetic or Lorentz forces, buoyancy forces, and aerodynamic drag forces caused by passage of the arc plasma over the weld pool surface.

Surface-Tension-Driven Fluid Flow Model.

Surface tension gradients were first proposed by Ishizaki et al. (Ref 2) as potential driving forces for weld pool fluid flow. Surface-tension-driven fluid flow was first described by Thomson (Ref 3) in 1855, but the phenomenon is commonly called Marangoni convection from the work of Carlo Marangoni (Ref 4).

In 1982, Heiple and Roper (Ref 5) proposed that surface tension gradients are commonly the dominant forces driving fluid flow in GTA welds, and that these gradients could be drastically altered by very small concentrations of certain trace elements. Surface tension gradients exist on a weld pool surface because the surface tension is temperature dependent, and there are large temperature gradients on a weld pool surface. For pure metals and many alloys, the surface tension decreases as temperature increases; that is, the surface tension temperature coefficient is negative. For weld pools in such materials, the surface tension will be greatest on the coolest part of the pool surface at the edge, and lowest on the hottest part under the arc near the center of the pool. Such a surface tension gradient produces outward surface fluid flow, as shown schematically in Fig. 2 (a). This fluid flow pattern transfers heat efficiently from the hottest part of the weld pool (near the center) to the edge and produces a relatively wide and shallow weld.

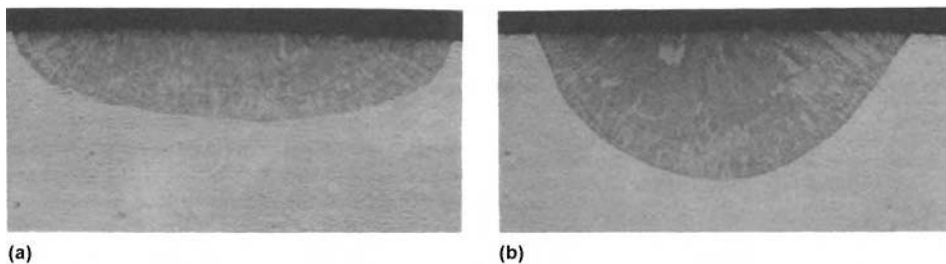


Fig. 1 Partial-penetration gas tungsten arc welds made under the same welding conditions on two heats of type 304L stainless steel having the same nominal composition. (a) 3 ppm S, $d/w = 0.2$. (b) 160 ppm S, $d/w = 0.40$. Original magnification: $9\times$

* Updated and revised from C.R. Heiple and P. Burgardt, "Fluid Flow Phenomena During Welding," *Welding, Brazing, and Soldering*, Vol 6, *ASM Handbook*, ASM International, 1993

Certain elements are surface active in molten metals; that is, they segregate to the surface of the solvent liquid metal and lower the magnitude of the surface tension, often drastically. Small concentrations of surface-active additions can also change the temperature dependence of the surface tension of the solvent metal or alloy so that, for a limited range of temperature above the melting point, the surface tension increases with increasing temperature. With a positive surface tension temperature coefficient, the surface tension will be highest near the center of the weld pool. Such a surface tension gradient will produce fluid flow inward along the surface of the weld pool and then down, as indicated schematically in Fig. 2(b). This fluid flow pattern transfers heat efficiently to the bottom of the weld pool and produces a relatively deep, narrow weld.

Experimental Observations. This physical model (i.e., surface-tension-driven fluid flow model) was developed and verified with a series of experiments in which stainless steel base metal was doped with low concentrations of various elements and the effect of the doping on weld pool shape measured. High-speed motion pictures of the weld pool surface suggested the fluid flow patterns indicated in Fig. 2. The addition of sulfur, oxygen, selenium, and tellurium to the stainless steel in low concentrations (less than 150 ppm) was shown to substantially increase GTA weld depth-to-width ratio (d/w). All these elements are known to be highly surface active in liquid iron. Measurements of the temperature dependence of the surface tension for steels with different GTA weld penetration characteristics produced an impressive correlation between a positive surface tension temperature coefficient arising from surface-active impurities and high d/w ratio welds (Fig. 3).

When additions were made to the weld pool of elements known to react with surface-active

elements already present in the steel to form compounds that are not surface active, the GTA weld d/w ratio decreased. Aluminum reacts with oxygen, producing wider, shallower welds in 21-6-9 stainless steel. Cerium reacts with both sulfur and oxygen, also producing lower d/w ratio welds. The effects of trace elements on weld shape have also been observed in a number of other alloys. These observations are summarized in Table 1.

The simple physical model illustrated in Fig. 2 has been remarkably successful in qualitatively explaining trace element effects. For example, changing GTAW conditions alters the magnitude and distribution of arc energy input to the weld, which in turn changes temperature gradients on the weld pool surface. From Fig. 2, a change in welding conditions that makes the center of the weld hotter, such as increasing current, should drive the existing fluid flow pattern more strongly. As shown in Fig. 4, increasing current improves the d/w ratio of steel doped with surface-active elements and reduces it for high-purity base metal. If the center of the weld becomes so hot that there is a region where the temperature coefficient of the surface tension is no longer positive, then the fluid flow pattern necessary for deep penetration is disrupted and the d/w ratio decreases. This effect is seen at high currents in Fig. 4. Similar results have been obtained for other welding parameters. The surface temperature at which the change from positive to negative surface tension temperature coefficient occurs for stainless steel is estimated by extrapolation in Fig. 3 to be approximately 2050 °C (3720 °F). Detailed thermodynamic calculations of the temperature dependence of the surface tension of iron-sulfur alloys predict that the transition from positive to negative dy/dT will occur at 2032 °C (3690 °F) for the high-sulfur alloy in Fig. 3. Recent spectrographic weld pool temperature measurements and numerical

simulations have indicated that this temperature can be exceeded in stainless steel GTA weld pools under normal welding conditions.

Sahoo et al. (Ref 8) analyzed the published data on interfacial tension of several binary systems, including iron-sulfur and iron-oxygen, and developed a formulation to satisfactorily describe the surface tension and its dependence on temperature and concentration for those systems. In particular, their formulation shows that the temperature coefficient of surface tension for iron-sulfur and iron-oxygen systems can change from negative to positive value as the temperature increases, which is consistent with that shown in Fig. 3.

The surface-tension-driven fluid flow model should be applicable to non-arc processes, provided the energy input distribution is similar to a GTA arc. This condition is satisfied for conduction-mode electron beam and laser welds. Dramatic increases in weld d/w ratio in selenium-doped zones in stainless steel have been observed for both traveling laser and electron beam conduction-mode welds. The weld shape changes were similar to those observed for GTA welds.

Conduction-mode electron beam welds can also be used to demonstrate that variations in weld shape with changes in welding parameters, as illustrated in Fig. 4, are not a result

Table 1 Effect to trace element impurities on GTA weld penetration of selected alloys

Alloy system	Trace element impurity	
	Increases weld penetration	Decreases weld penetration
Zirealloy-2	Chlorine	...
Iron-base alloys	Sulfur, oxygen, selenium(a), tellurium(a)	Calcium, aluminum, cerium(a), lanthanum(a), silicon(b), titanium(b)
Stainless steels 304, 316, 21-6-9, JBK-75		
AISI 8630		
2.5Cr-1Mo		
Nickel-base alloys	Sulfur	Oxygen
Inconel 600, 718		

(a) Uncommon impurities. (b) Effect negligible or uncertain

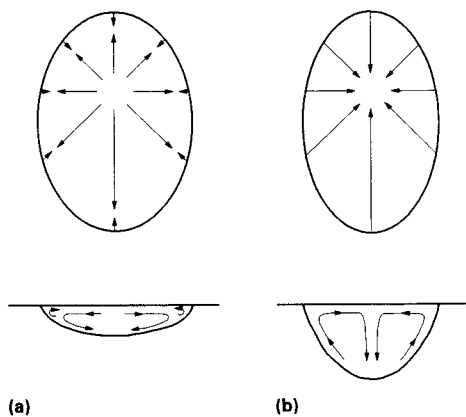


Fig. 2 Schematic showing surface fluid flow (top) and subsurface fluid flow (bottom) in the weld pool. (a) Negative surface tension temperature coefficient (pure material). (b) Positive surface tension temperature coefficient (surface-active elements present)

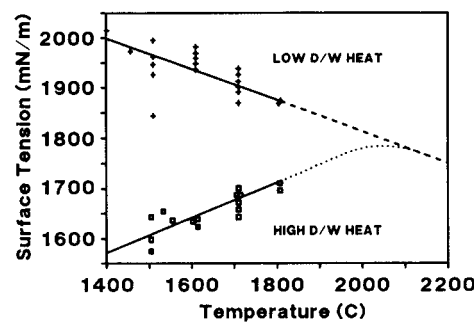


Fig. 3 Plot of surface tension versus temperature for two liquid steels. The data labeled "high d/w heat" are from material having approximately 160 ppm more sulfur than the material labeled "low d/w heat." The dashed lines indicate the expected behavior of the surface tension above the maximum temperature studied. Source: Ref 6

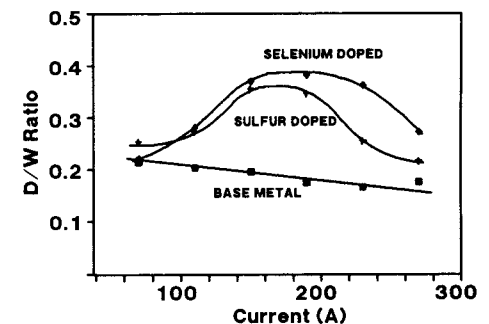


Fig. 4 Plot of weld d/w ratio versus weld current for the starting base metal (type 304 stainless steel with very low residual impurity content) as well as for zones doped with sulfur and selenium. Source: Ref 7

of some complex arc/weld pool interaction. One of the results of an investigation of the effect of changes in beam focus on weld shape in electron beam welds on low- and high-sulfur materials is shown in Fig. 5. The high-sulfur material exhibits a maximum in d/w ratio with increasing power density at a moderate power density away from sharp focus, which is analogous to that shown with increasing current in Fig. 4. (The low- and high-sulfur stainless steels have deep and nearly identical penetration near sharp focus. Near sharp focus, where the power density is high, penetration is by a keyhole mechanism in which average penetration is unrelated to surface-tension-driven fluid flow.) Measurements of the electron beam power-density distribution verified that there were no anomalous changes in the beam, such as a beam width maximum, with increasing peak power density. The d/w ratio maximum away from sharp focus is therefore proposed to originate from exactly the same mechanism as for increasing current with GTA welds.

Measurements of electron beam power distribution were made as a function of beam focus and were used to calculate the beam power density at the d/w maximum. The power density was also calculated at the d/w maximum for GTA welds. Calculation of weld pool surface temperatures using a traveling distributed heat-source model showed the central surface temperatures to be essentially identical at the d/w maxima for the electron beam and GTA processes. The calculated surface temperatures using the traveling distributed heat-source conduction approximation are much too high because, as indicated previously, most of the heat transport in the weld pool is by mass flow rather than by conduction. Nevertheless, the equality of the calculated weld pool peak temperatures at the d/w maxima provides strong confirmation that the mechanism responsible for the presence of the maximum in weld d/w with increasing input power density is independent of heat source and is not a result of an arc phenomenon.

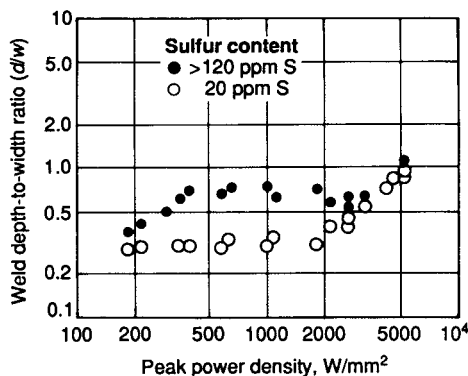


Fig. 5 Plot of electron beam weld pool ratio (d/w) versus electron beam power density for low-sulfur (20 ppm) and high-sulfur (>120 ppm) type 304L stainless steel. Keyhole formation begins at approximately 2×10^3 W/mm².

A final example of the success of the fluid flow model in explaining GTAW phenomena is provided by butt welding together two steels with large differences in weld penetration characteristics. The weld pool is not centered over the joint; rather, it is displaced toward the material with low d/w behavior (Ref 9), as indicated schematically in Fig. 6. The low d/w material has a low concentration of surface-active impurities and therefore a high surface tension. Thus, there is a net surface tension gradient across the weld pool toward the low d/w material, producing the fluid flow pattern and weld cross section indicated in Fig. 6. The actual fluid flow pattern is certain to be more complicated than that illustrated.

Numerical Simulations. Direct measurement of weld pool fluid flow is very difficult. Surface flow has been studied by observing the motion on the surface of slag or intentionally added particles, as has bulk flow in transparent liquid/solid systems using simulated welding heat sources. There are a number of numerical calculations of weld pool fluid flow and shape, the most comprehensive of which appears to be that of Zacharia et al. (Ref 10). These numerical fluid flow simulations agree in broad terms with the physical model illustrated in Fig. 2; however, they differ in detail with Fig. 2 and with one another. One result of the analysis of Zacharia is that the weld pool surface temperature reached in stationary welds exceeds that in traveling welds. Trace element effects should therefore be less pronounced in stationary welds, because a larger portion of the pool surface is above the temperature range where a positive surface tension temperature coefficient exists. This prediction is in agreement with experimental observations. A detailed review of recent numerical models of heat and mass transfer in the weld pool is provided in the article "Modeling of Heat and Mass Transfer in Fusion Welding" in this Volume.

Interactions. Experiments in which low concentrations of various elements have been added to the base metal have demonstrated clear changes in weld pool shape. However, when weld d/w ratio is plotted versus chemical analysis for numerous heats of material, considerable scatter is observed. A comparison of

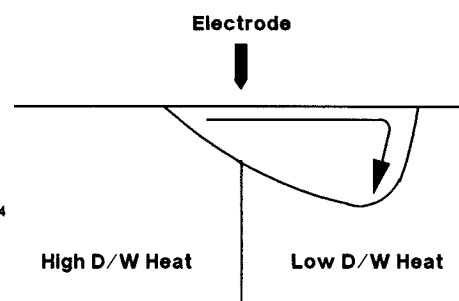


Fig. 6 Schematic showing typical fluid flow generated when butt welding two heats of material with different penetration characteristics. Source: Ref 9

weld d/w ratio in a standard weldability test versus sulfur content for approximately 200 lots of steel is shown in Fig. 7. There is a clear trend of increasing d/w with increasing sulfur, but the variability for a given sulfur content is substantial. Some of this variability is associated with imprecision in chemical analysis for sulfur and some with variations in oxygen content. However, it appears that much of the variability is related to interactions of the surface-active elements sulfur and oxygen with other components of the steel. Calcium is known to react with oxygen and, to a lesser extent, with sulfur to form stable compounds unlikely to be surface active. Aluminum and silicon also react with oxygen to form stable compounds. Thus, the amount of sulfur and oxygen available for segregation to the weld pool surface is a complicated function of the total weld pool chemistry.

There is an additional complication, illustrated in Fig. 8. When oxygen is added to the shielding gas, weld d/w ratio increases, passes through a maximum, and then declines with increasing oxygen content. Similar effects are seen with SO₂ additions. The surface of welds made with torch gas concentrations above the d/w maximum are heavily oxidized. A possible explanation for the decreasing d/w ratios at higher oxygen concentrations is that a liquid oxide film (slag) is formed on the weld pool surface, altering the surface tension gradients.

Oxygen can be added to the weld pool in other ways. Oxidizing the plate surface prior to welding adds oxygen to the weld pool and increases the weld d/w ratio. Wire brushing and grit blasting an originally clean surface increases both the surface oxide thickness and the surface area, thereby adding oxygen to the weld pool. The d/w ratio of JBK-75 stainless steel (a modification of ASTM A-286) GTA welds as a function of amount of wire brushing is similar in form to Fig. 8. Welds on plate brushed beyond the weld d/w maximum had extensive slag on the weld surface. The weld

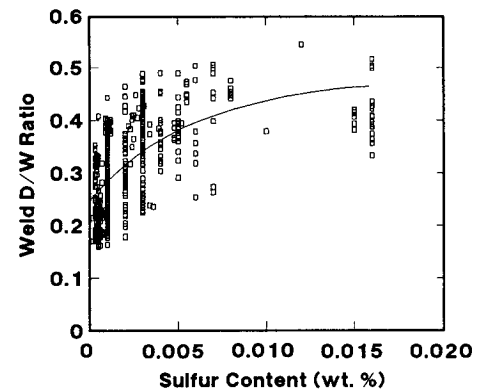


Fig. 7 Plot of weld d/w ratio versus sulfur content for approximately 200 heats of type 304L stainless steel. Each point is an average of multiple sulfur analyses and weld d/w ratio measurements. If single values are used, the scatter is greater. Source: Ref 11

d/w ratio on JBK-75 stainless steel appears to be particularly sensitive to oxygen additions. Similar wire-brushing experiments on type 304 stainless steel showed smaller effects.

Although the origin of the difference in sensitivity between JBK-75 and type 304 is not known, one possibility is indicated by surface tension measurements on iron-silicon alloys in contact with carbon dioxide. The effect of CO_2 on the surface tension was a strong function of silicon content. For low-silicon alloys, the surface tension dropped sharply when contacted with CO_2 . For alloys with more than 1.2% Si, the surface tension increased when contacted with CO_2 . The different behavior was attributed to differences in slag formation on the liquid metal surface. Thus, silicon appears to interfere with the ability of oxygen to produce a positive surface tension temperature coefficient on liquid iron. The JBK-75 stainless steel used in the wire-brushing experiments contained only 0.06% Si, and the 21-6-9 used for the torch gas experiment (Fig. 8) contained only 0.16% Si. Type 304 stainless steel typically contains more than 0.5% Si. Thus, the high sensitivity of JBK-75 to oxygen additions may be related to its unusually low silicon content. Reports in the literature on the effect of oxygen on GTA weld penetration have been somewhat variable; differences in weld pool silicon content may be partially responsible for this variability.

Effects of High Current. Electromagnetic (Lorentz) stirring of the weld pool becomes more important at higher currents. The direction of the Lorentz force produces the deep penetration fluid flow pattern indicated in Fig. 2(b). At sufficiently high current, the Lorentz force dominates other forces that drive fluid flow, and the effects of trace elements become less important. In addition, the plasma jet becomes stronger with increasing current and, at high enough currents, produces a significant depression of the weld pool surface. The plasma jet forces are resisted by surface tension forces on the weld pool. Halmoy (Ref 13) has shown

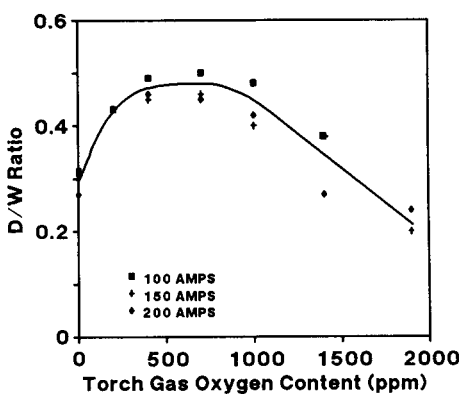


Fig. 8 Plot of weld d/w ratio versus oxygen concentration in the torch gas for tungsten arc bead-on-plate welds on 21-6-9 stainless steel. Source: Ref 12

that for a traveling weld, the radial pressure gradient from the plasma jet tends to transport liquid from the front to the rear of the weld (Fig. 9). For a sufficiently strong pressure gradient, p_B , the liquid level under the arc may be pushed down to the bottom of the pool, as shown in Fig. 9(c). High-speed motion pictures of the effect of sulfur additions on weld pool fluid flow in 21-6-9 stainless steel showed behavior similar to that in Fig. 9(c) after large sulfur additions. Sulfur additions substantially reduce the weld pool surface tension and thereby increase the effect of the plasma jet.

In addition, a surface depression almost certainly changes the energy distribution input to the weld pool by the arc compared with a flat weld pool surface. Finally, under some high-current conditions, a vortex has been observed near the center of weld pools.

Strategies for Controlling Poor and Variable Penetration. A number of techniques have been developed to reduce penetration variability and improve penetration. Sometimes the weld pool shift illustrated in Fig. 6, which occurs when heats with different penetration characteristics are welded together, can be minimized by very tight heat sinking. The sensitivity of weld shape to trace element differences is a function of welding parameters, as illustrated in Fig. 4 for current; thus, combinations of welding parameters can be chosen that minimize heat-to-heat penetration variability. For wire-fed joints, some joint designs are more tolerant of penetration variability than others. For example, joints with thinner, wider lands are less sensitive than narrower grooves with thicker lands.

Material control by selection or specification is another approach. It was originally anticipated that stainless steels with less than 20 ppm S would have poor, but consistent, penetration. However, the data illustrated in Fig. 7 demonstrate that penetration variability is substantial even at these very low sulfur levels. Stainless steels with more than approximately 100 ppm S generally have consistently good penetration. A related approach is to test incoming material for welding characteristics and then select material with desired welding behavior for critical applications.

Finally, the weld pool can be doped with enough surface-active elements to ensure good

penetration. Sulfur and oxygen are the most practical dopants for ferrous alloys. The addition of oxygen or sulfur dioxide to the torch shielding gas has been shown to improve penetration and reduce penetration variability; however, this approach presents several practical problems. Oxygen can also be added to the weld pool by oxidizing the weld joint or by otherwise increasing the oxygen content of the weld groove surface—by wire brushing, for example. Probably the most useful approach is to dope the weld pool in the wire-fed joints by using a special filler wire. A group of defense contractors had a special heat of type 380L stainless steel produced with a sulfur content in the range of 100 to 150 ppm. The heat was then converted into weld wire. Welds made with this wire on a variety of stainless steel base metals have exhibited consistent and good penetration.

Deep-Penetration Electron Beam and Laser Welds

Keyhole Formation. A fundamental difference between arc heat sources and electron or laser beam heat sources is that electron and laser beams are capable of delivering heat over a small area at much higher power densities. As the power density of the welding heat source is increased, the peak surface temperature of the weld pool rises. For many metals, vapor pressure rises nearly exponentially with temperature and becomes appreciable (above 4000 Pa, or 30 torr, for an electron beam operating in a vacuum) near $0.8 T_b$, where T_b is the material boiling point in degrees Kelvin. As the surface temperature approaches this value, the liquid surface under the power source is depressed by the vapor pressure. As the liquid moves away from the power source, the surface is depressed and a cavity is formed. This is the basic theory of keyhole formation by an electron or laser beam.

Fluid Flow in the Keyhole. The keyhole is a cavity having roughly the size and shape of the beam; that is, it is usually approximately cylindrical. Fluid flow in the thin layer around the cavity plays a major role in determining the behavior of deep-penetration, keyhole-mode electron beam and laser welds. The first flow

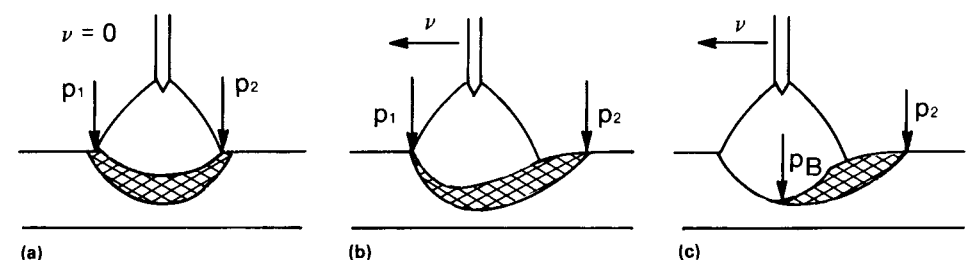


Fig. 9 Effect of arc pressure on the weld pool for stationary and traveling welds. (a) $v = 0$. (b) $v > 0$, with weak radial pressure gradient, p_1 . (c) $v > 0$, with strong radial pressure gradient, p_B . Source: Ref 13

required for a traveling weld is transport of metal melted at the front wall of the cavity to the rear (where it eventually solidifies). Because of the weld geometry, this liquid must move around the keyhole cavity as a thin, high-velocity layer on the walls of the cavity. The dominant driving force for this motion appears to be surface tension gradients. As in GTAW, these gradients arise because the surface tension is temperature dependent and there is a substantial temperature difference between the front and rear of the cavity.

Calculations of the fluid flow have been performed by Wei and Giedt (Ref 14). Their calculations for pure iron predict that liquid metal is moved from the front to the rear of a sharp focus keyhole in a film that is approximately 0.02 mm (0.0008 in.) thick and is moving at a velocity of approximately 250 mm/s (10 in./s). The fluid is driven by a temperature difference of approximately 400 °C (720 °F). These results are only nominal values from the calculations, but they change little with the assumptions used and are representative of electron beam welds in general.

There is an interesting potential problem with this model. As discussed previously, the surface tension temperature coefficient, $d\gamma/dT$, can be positive over a limited temperature range in steels and some other alloys if surface-active impurities are present in sufficient quantity. If $d\gamma/dT$ is positive, then it would appear that molten metal would not be transported around the cavity. The likely resolution of this difficulty is that the liquid dwells slightly longer in the front of the cavity and is heated by the beam above the temperature at which a transition to negative $d\gamma/dT$ occurs. Some perturbation of the normal fluid flow may occur under these circumstances. Effects of such a perturbation on weld characteristics appear to be uncommon. The only available evidence for such an effect comes from electron beam welds performed on a heat of type 304 stainless steel with very low residual impurity content, except for approximately 340 ppm S. These welds had very high porosity compared with identical welds in other heats of material.

Instability in Keyhole Fluid Flow. In addition to the steady-state flow of liquid around the keyhole, significant instability in the fluid motion has been seen. For example, Mara et al. (Ref 15) used side-view, self-illuminated x-ray films to show that the beam location shifts between full penetration and nearly zero penetration in an irregular fashion. High-speed x-ray photographs show that the variable penetration is caused by a lump of metal that sags into the keyhole from high up on the cavity rear wall. The sequence of events that creates weld penetration irregularity was analyzed by Tong and Giedt (Ref 16) and is illustrated schematically in Fig. 10. First, the beam forms a keyhole and produces a lump of very hot displaced metal at the top rear of the traveling cavity (Fig. 10a). After some period of time, the weld reaches the full penetration allowed by heat flow (Fig. 10b).

The lump of displaced metal is unstable and eventually falls into the cavity, partially filling it. The beam must now drill through this additional material. The sequence (a) to (c) in Fig. 10 occurs repeatedly, but irregularly, and produces weld penetration variability. When particularly severe, the irregular penetration is called spiking. Spiking also leads to a tendency for voids to become trapped in the root of the weld.

A mathematical model that is the basis for understanding this keyhole instability was developed by Giedt et al. (Ref 14, 16). Stability of the keyhole is basically a balance between vapor pressure, which keeps the cavity open, and surface tension, which tries to close the cavity. Vapor pressure and surface tension are both functions of temperature. Vapor pressure increases nearly exponentially with temperature for many materials, while surface tension generally decreases slowly with temperature. Because there is a substantial temperature gradient from the top to the bottom of the keyhole, both vapor pressure and surface tension vary with depth in the keyhole. Direct measurements of cavity wall temperatures for electron beam welds indicate that the temperature at the top is nearly equal to the melting temperature, while the temperature at the bottom is high enough that the vapor pressure there is large. In type 304 stainless steel, the temperature at the bottom of the cavity is approximately 1200 °C (2200 °F). The data indicate that the temperature profile is insensitive to welding variables and is determined primarily by material properties, that is, by the temperature where the vapor pressure exceeds approximately 1330 Pa (10 torr).

Based on temperature measurements of a typical keyhole, the vapor pressure decreases approximately exponentially with height from the bottom of the keyhole and approaches zero at the top of the keyhole. The vapor pressure is balanced primarily by surface tension. For pure iron and many other materials, the surface tension decreases approximately linearly

with temperature. Thus, the inward surface tension pressure increases slowly from the bottom to the top of the keyhole. The balance of vapor pressure and surface tension is such that the cavity is stable near the bottom, where the vapor pressure tending to expand the cavity exceeds the surface tension tending to collapse it. At the top, the cavity is unstable because the surface tension tending to collapse it exceeds the vapor pressure tending to expand it. Thus, the cavity will always tend to be filled by liquid originating from above some height, H , in the keyhole, the pressure crossover height. This cavity filling produces weld penetration irregularity, which is a consequence of the nature of the keyhole in deep-penetration welding. More recently, Matsunawa (Ref 17) studied the role of keyhole instability in porosity formation using high-speed x-radiography observations. It was found that cavity formation caused by keyhole fluctuation could be reduced or suppressed by stabilizing the keyhole. For example, controlled pulse modulation in continuous-wave laser welding can effectively reduce porosity formation by imposing forced oscillation of the keyhole.

Penetration irregularity is usually less severe if H (as measured from the top) is a small fraction of the keyhole depth. In such cases, the volume of the lump is small, and liquid tends to flow into the cavity relatively smoothly. If H is a large fraction of the keyhole depth, then the liquid lump has a relatively large volume, and when it falls into the keyhole at irregular times, it nearly fills the cavity and produces large penetration variations.

Gas Metal Arc Welding

Fluid flow certainly occurs in GMA weld pools, but reports on the details of its nature and effects are quite limited. In the spray transfer mode, the impact of the stream of droplets from the electrode on the weld pool forms a

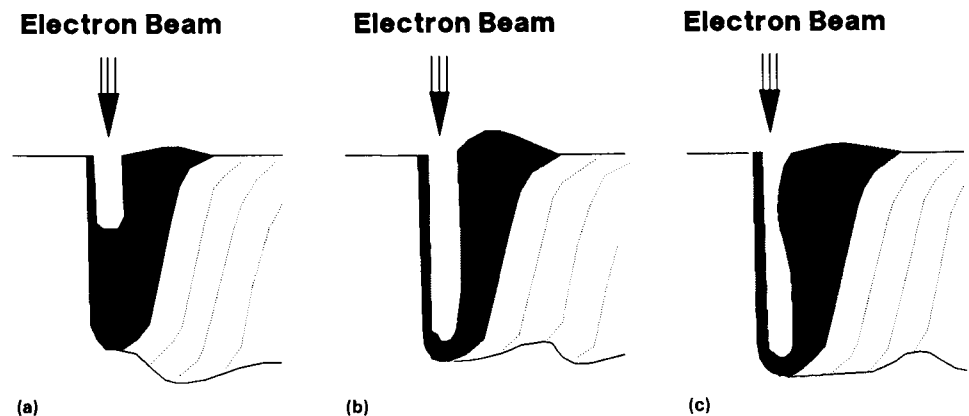


Fig. 10 Schematic showing keyhole instability. (a) Keyhole is formed by heat generated by electron beam. (b) Maximum penetration that can be produced by heat flow. (c) Liquid cools, causing impending collapse of displaced metal. The keyhole is filled by a lump of cooling material at the end of (c), which returns the keyhole to condition (a) to restart the sequence.

substantial depression or crater. This is the mechanism responsible for the typical finger-like penetration observed with argon as the torch gas. Thus, the depth of penetration is primarily dependent on the momentum of the stream of droplets. A plot of penetration versus the momentum of the droplet stream shows an excellent correlation (Fig. 11). Because the major force driving the droplets toward the weld is drag from the plasma jet, the kinematic viscosity (density times viscosity) of the shielding gas is important. For example, argon has a substantially higher kinematic viscosity than helium, so argon drives the droplet stream more effectively, resulting in a deeper, narrower penetration finger than with helium torch gas. The strength of the plasma jet can also be altered by changing the ambient pressure. For GMA welds on aluminum, Amson and Salter (Ref 19) saw a steady decrease in penetration with pressure until at 13,300 Pa (100 torr) there was essentially no penetration at all. Another way to modify the penetration depth is to spread the stream of droplets over the surface of the weld. This can be accomplished by applying a varying transverse magnetic field.

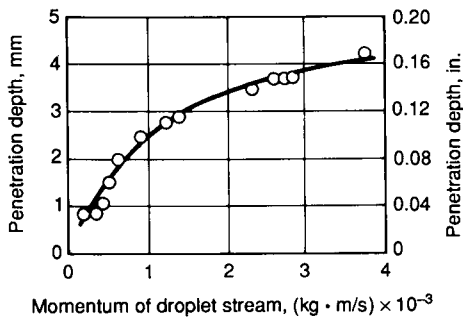


Fig. 11 Plot of gas metal arc weld penetration in mild steel for spray transfer mode versus momentum of droplet stream. Source: Ref 18

Submerged Arc Welding

Currents commonly employed in submerged arc welding are much higher than those used in GTAW or GMAW. Submerged arc welding currents often exceed 1000 A. Thus, the electromagnetic or Lorentz force combined with the tendency of the radial pressure gradient in the moving cavity to transport liquid to the rear of the cavity (Fig. 9) is likely the dominant force driving fluid flow. The generally accepted flow pattern is indicated schematically in Fig. 12. A cavity is formed at the front of the moving weld pool by arc pressure and by the momentum of drops from the rapidly melting electrode. Metal that is melted at the front of the pool flows underneath and on either side of the cavity. At the rear of the pool, the flow reverses and metal flows back toward the cavity along and near the surface. Flow velocities can be very high; Eichhorn and Engel (Ref 21) measured 4 m/s (13 ft/s) at 720 A. The flow pattern was derived from observations of the motion of marker elements, added to the weld pool, as determined from subsequent metallographic sections, and from the motion of radioactive tracer additions. The general features illustrated in Fig. 12 appear to be supported by x-ray fluoroscopy observations. Major perturbations in the indicated fluid flow have been demonstrated, including reversal of the flow direction. These perturbations have been associated with weld defects.

Transport Equations for Weld Fluid Flow

Although the aforementioned welding processes vary significantly in many aspects, such as welding equipment, the fluid flow phenomena during welding can be described mathematically by a common set of transport equations. The different fluid flow characteristics and resulting weld nugget shapes in those welding processes are largely attributed to the different boundary conditions and material states. The transport equations are available in many

standard textbooks, such as Ref 22. For incompressible laminar flow of Newtonian fluids, the transport equations are as follows:

$$\nabla \cdot \vec{v} = 0 \tag{Eq 1}$$

$$\rho \left(\frac{\partial \vec{v}}{\partial t} + \vec{v} \cdot \nabla \vec{v} \right) + = -\nabla p + \mu \nabla^2 \vec{v} + S_v \tag{Eq 2}$$

$$\rho \left(\frac{\partial h}{\partial t} + \nabla \cdot (\vec{v}h) \right) + = \nabla \cdot (kT) + S_h \tag{Eq 3}$$

where v is fluid velocity, ρ is density, t is time, p is pressure, μ is molten metal viscosity, h is sensible heat, k is thermal conductivity, T is temperature, and S_v and S_h are heat-source terms. The sensible heat is expressed as:

$$h = \int C_p dT$$

where C_p is the specific heat. Equations 1 through 3 are the continuity, moment conservation, and energy conservation equations, respectively. Detailed discussion on the solution of the transport equations and associated boundary conditions to calculate heat and mass transfer in the weld pool is provided elsewhere in this Volume (see, for example, the article “Factors Influencing Heat Flow in Fusion Welding” and the articles in the Section “Fundamentals of Weld Modeling”).

Concluding Remarks

This article is a modification of a previous article in an earlier edition of the ASM Handbook. In order to maintain the conformance with original authors, major parts of the article has been maintained to allow for contiguity. It is noted that significant progresses have been made recently towards understanding the fluid flow phenomena in arc plasma and weld pool. Examples include, the formation of unusual, wavy fusion boundaries caused by welding parameters and material properties (Ref 23); unsteady Marangoni flow in a molten pool consisting of immiscible dissimilar metals (Ref 24); welding of stainless steel plates containing different concentrations of sulfur (Ref 25); heat transfer and fluid flow during key-hole mode laser welding (Ref 26, 27); Formation of Humped Beads in High Speed Gas Metal Arc Welding due to Strong Backward Fluid Flow (Ref 28); unified model for stationary tungsten-inert-gas welding process taking into account the close interaction between the arc plasma and the weld pool (Ref 29); and direct visualization of Marangoni convection in a simulated transparent weld pool of NaNO_3 heated with a defocused CO_2 laser beam (Ref 30). Since the numerical modeling plays an essential role in gaining the understanding, details on these recent progresses are discussed in another article, which is focused on the modeling of fluid flow phenomena during welding.

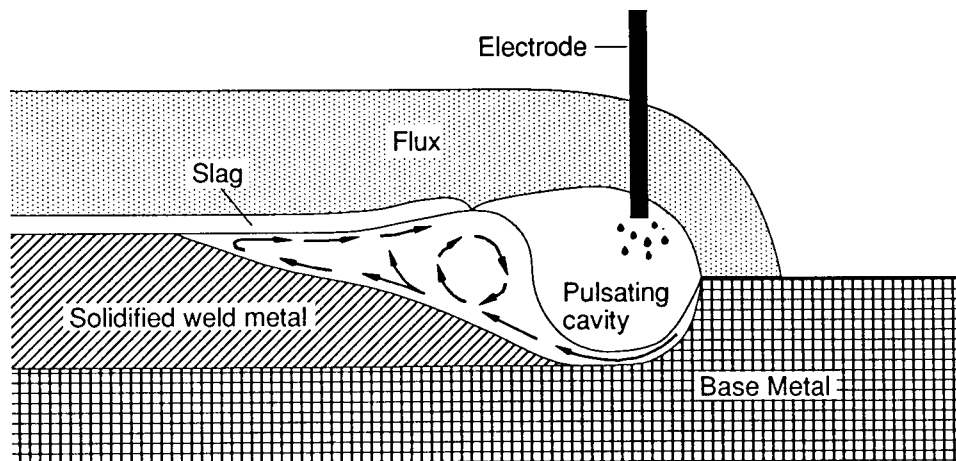


Fig. 12 Schematic showing typical flow pattern in a submerged arc weld pool. Source: Ref 20

REFERENCES

1. N. Christensen, V. de L. Davies, and K. Gjermundsen, Distribution of Temperatures in Arc Welding, *Br. Weld. J.*, Vol 12, 1965, p 54–75
2. K. Ishizaki, K. Murai, and Y. Kanbe, "Penetration in Arc Welding and Convection in Molten Metal," Document 77-66, Study Group 212, International Institute of Welding, 1966
3. J. Thomson, On Certain Curious Motions Observable at the Surfaces of Wine and Other Alcoholic Liquors, *Philos. Mag.*, Vol 10, 1855, p 330–333
4. C. Marangoni, Über die Ausbreitung der Tropfen einer Flüssigkeit auf der Oberfläche einer anderen, *Ann. Phys. Chem.*, Vol 143 (No. 7), 1871, p 337–354
5. C.R. Heiple and J.R. Roper, Mechanism for Minor Element Effect on GTA Fusion Zone Geometry, *Weld. J.*, Vol 61, 1982, p 97s–102s
6. B.J. Keene, K.C. Mills, and R.F. Brooks, Surface Properties of Liquid Metals and Their Effects on Weldability, *Mater. Sci. Technol.*, Vol 1, 1985, p 568–571
7. P. Burgardt and C.R. Heiple, Interaction between Impurities and Welding Parameters in Determining GTA Weld Shape, *Weld. J.*, Vol 65, 1986, p 150s–155s
8. P. Sahoo, T. DebRoy, and M.J. McNallan, Surface Tension of Binary Metal—Surface Active Solute Systems under Conditions Relevant to Welding Metallurgy, *Metall. Trans. B*, Vol 19, 1988, p 483–491
9. M.J. Tinkler, I. Grant, G. Mizuno, and C. Gluck, Welding 304L Stainless Steel Tubing Having Variable Penetration Characteristics, Paper 29, *The Effects of Residual, Impurity, and Micro-Alloying Elements on Weldability and Weld Properties*, P.H.M. Hart, Ed., The Welding Institute, Cambridge, 1984
10. T. Zacharia, S.A. David, J.M. Vitek, and T. DebRoy, Weld Pool Development during GTA and Laser Beam Welding of Type 304 Stainless Steel, Part 1—Theoretical Analysis, *Weld. J.*, Vol 68, 1989, p 499s–509s
11. P. Burgardt and R.D. Campbell, Chemistry Effects on Stainless Steel Weld Penetration, *Ferrous Alloy Weldments*, Trans Tech Publications, Switzerland, 1992, p 379–415
12. C.R. Heiple, P. Burgardt, and J.R. Roper, The Effect of Trace Elements on GTA Weld Penetration, *Modeling of Casting and Welding Processes II*, J.A. Dantzig and J.T. Berry, Ed., TMS-AIME, 1984, p 193–205
13. E. Halmoy, The Pressure of the Arc Acting on the Weld Pool, *Arc Physics and Weld Pool Behavior*, The Welding Institute, Cambridge, 1979, p 259–266
14. P.S. Wei and W.H. Giedt, Surface Tension Gradient-Driven Flow Around an Electron Beam Welding Cavity, *Weld. J.*, Vol 64, 1985, p 251s–259s
15. G.L. Mara, E.R. Funk, R.C. McMaster, and P.E. Pence, Penetration Mechanisms of Electron Beam Welding and the Spiking Phenomenon, *Weld. J.*, Vol 53, 1974, p 246s–251s
16. H. Tong and W.H. Giedt, A Dynamic Interpretation of Electron Beam Welding, *Weld. J.*, Vol 49, 1970, p 259s–266s
17. A. Matsunawa, Problems and Solutions in Deep Penetration Laser Welding, *Sci. Technol. Weld. Join.*, Vol 6, 2001, p 351–354
18. W.G. Essers and R. Walter, Heat Transfer and Penetration Mechanisms with GMA and Plasma-GMA Welding, *Weld. J.*, Vol 62, 1981, p 37s–42s
19. J.C. Amson and G.R. Salter, Analysis of the Gas-Shielded Consumable Metal-Arc Welding System, *Br. Weld. J.*, Vol 10, 1963, p 472–483
20. J.F. Lancaster, *The Physics of Welding*, International Institute of Welding, Pergamon Press, Oxford, 1984, p 243
21. F. Eichhorn and A. Engel, "Mass Transfer in the Weld Pool," Document 201-70, Study Group 212, International Institute of Welding, 1970
22. R.B. Bird, W.E. Stewart, and E.N. Lightfoot, *Transport Phenomena*, 1st ed., John Wiley & Sons, New York, 1960
23. A. Arora, G.G. Roy, and T. DebRoy, Unusual wavy weld pool boundary from dimensional analysis, *Scripta Materialia*, Vol 60, 2009, p 68–71
24. P.S. Wei and F.K. Chung, Unsteady Marangoni Flow in a Molten Pool When Welding Dissimilar Metals, *Metallurgical and Materials Transactions B*, Vol 31B, 2000, p 1387–1403B
25. S. Mishra, T.J. Lienert, M.Q. Johnson and T. DebRoy, An Experimental and Theoretical Study of Gas Tungsten Arc Welding of Stainless Steel Plates with Different Sulfur Concentrations, *Acta Materialia*, Vol 56, 2008, p 2133–2146
26. H. Ki, P.S. Mohanty, and J. Mazumder, Modeling of Laser Keyhole Welding. I. Mathematical Modeling, Numerical Methodology, Role of Recoil Pressure, Multiple Reflections, and Free Surface Evolution, *Metallurgical and Materials Transactions A*, Vol 33A, 2002, p 1817–1830A
27. R. Rai, J.W. Elmer, T.A. Palmer, and T. DebRoy, Heat Transfer and Fluid Flow during Keyhole Mode Laser Welding of Tantalum, Ti-6Al-4V, 304L stainless steel and vanadium, *Journal of Physics D, Applied Physics*, Vol 40, 2007, p 5753–5766
28. M.H. Cho and Dave F. Farson, Understanding Bead Hump Formation in Gas Metal Arc Welding Using a Numerical Simulation, *Metallurgical and Materials Transactions B*, Vol 38B, 2007, p 305–319
29. M. Tanaka, H. Terasaki, M. Ushio and J.J. Lowke, A Unified Numerical Modeling of Stationary Tungsten-Inert-Gas Welding Process, *Metallurgical and Materials Transactions A*, Vol 33A, 2002, p 2043–2052A
30. C. Limmaneevichitr and S. Kou, Visualization of Marangoni Convection in Simulated Weld Pools Containing a Surface Active Agent, *Welding Journal*, Vol 79, 2000, p 324s–330s

SELECTED REFERENCES

- P. Burgardt, Welding Variable Effects on Weld Shape in Electron Beam Welding of Steels, *Ferrous Alloy Weldments*, Trans Tech Publications, Switzerland, 1992, p 269–328
- P. Burgardt and R.D. Campbell, Chemistry Effects on Stainless Steel Weld Penetration, *Ferrous Alloy Weldments*, Trans Tech Publications, Switzerland, 1992, p 379–415
- C.R. Heiple and P. Burgardt, Penetration in GTA Welding, *Weldability of Materials*, R. A. Patterson and K.W. Mahin, Ed., ASM International, 1990, p 73–80
- C.R. Heiple and J.R. Roper, The Geometry of Gas Tungsten Arc, Gas Metal Arc, and Submerged Arc Weld Beads, *Welding: Theory and Practice*, D.L. Olson, R.D. Dixon, and A.L. Liby, Ed., North-Holland Elsevier Science Publishers, Amsterdam, 1990, 1–34
- K.C. Mills and B.J. Keene, Factors Affecting Variable Weld Penetration, *Int. Mater. Rev.*, Vol 35, 1990, p 185–216

Fundamentals of Weld Solidification

John N. DuPont, Lehigh University

MICROSTRUCTURAL EVOLUTION during solidification of the fusion zone represents one of the most important considerations for controlling the properties of welds. A wide range of microstructural features can form in the fusion zone, depending on the alloy composition, welding parameters, and resultant solidification conditions. The primary objective of this article is to review and apply fundamental solidification concepts for understanding microstructural evolution in fusion welds.

Microstructural Features in Fusion Welds

Figures 1 through 3 schematically demonstrate the important microstructural features that must be considered during solidification in fusion welds (Ref 1, 2). On a macroscopic scale, fusion welds can adopt a range of grain morphologies similar to castings (Fig. 1), in which columnar and equiaxed grains can potentially form during solidification. The final grain structure depends primarily on alloy composition and the heat-source travel speed. Although some of the concepts applicable to grain structure formation in castings apply to welds, there are also some unique differences. While the columnar and equiaxed zones can form in welds, the fine-grained chill zone at the mold wall represented by the fusion line is rarely observed in welds. Fundamental concepts associated with nucleation are needed to understand these differences. In addition, the solid/liquid interface in welds is typically curved and its rate of movement is controlled by the heat-source travel speed, which leads to differences in formation of the columnar zone within welds. These differences can be understood through application of competitive grain growth processes that occur during solidification.

On a microscopic scale, there can also be a wide range of substructural morphologies within the grains (Fig. 2), including planar (i.e., no substructure), cellular, columnar dendritic, and equiaxed dendritic. The type and relative extent of each substructural region is governed by the process of constitutional supercooling in which the liquid becomes

cooled below its liquidus temperature due to compositional gradients in the liquid. The extent of constitutional supercooling in the weld is determined by the alloy composition, welding parameters, and resultant solidification parameters. Lastly, the distribution of alloying elements and relative phase fractions within the substructure (Fig. 3) are also important microstructural features that strongly affect weld-metal properties. The particular example shown in Fig. 3 represents a case in which extensive residual microsegregation of alloying elements exists across a cellular substructure after nonequilibrium solidification. This microsegregation, in turn, produces a relatively high fraction of intercellular eutectic and associated secondary phase. The microsegregation behavior and concomitant amount of secondary phase that forms can each be understood with solute redistribution concepts. Lastly, dendrite tip undercooling can become important at high solidification rates associated with high-energy-density welding processes. Tip undercooling can lead to significant changes in the primary solidification mode, distribution of solute within the solid, and final phase fraction balance. Rapid solidification concepts are needed to understand these phenomena. All of these fundamental solidification concepts (nucleation, competitive grain growth, constitutional supercooling, solute redistribution, and

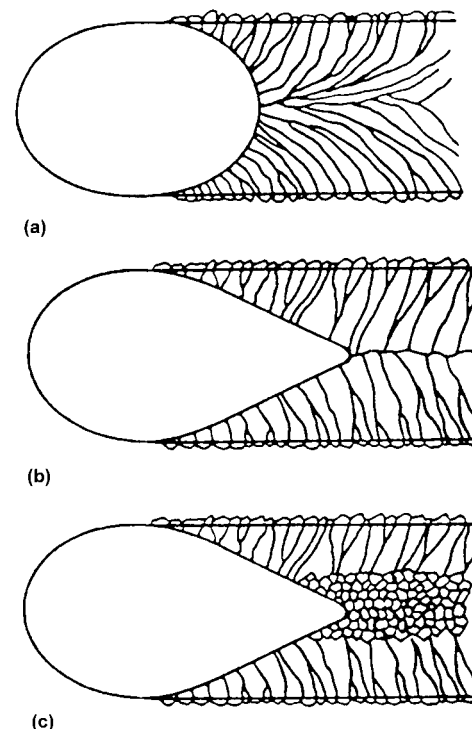


Fig. 1 Types of grain morphologies that can form in fusion welds

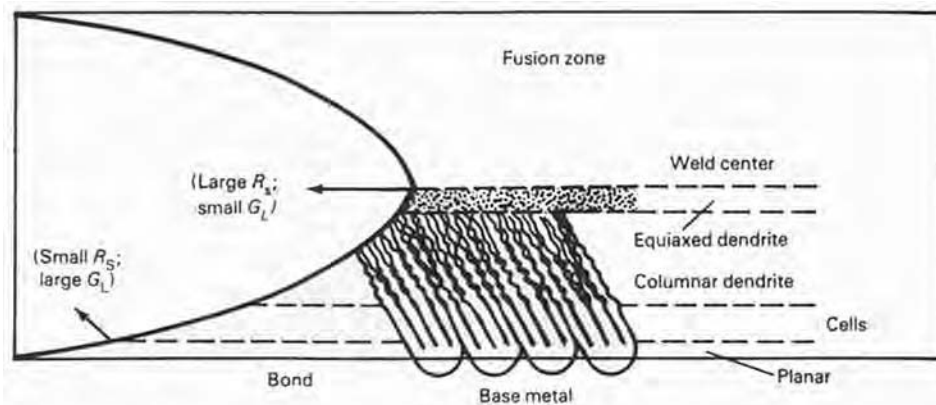


Fig. 2 Types of substructure morphologies that can form within the grains of fusion welds

rapid solidification) depend on the solidification parameters during welding. Thus, the important solidification parameters are briefly described, followed by detailed discussions and application of fundamental solidification concepts for understanding microstructural evolution.

Solidification Parameters

The temperature gradient (G), solid/liquid interface growth rate (R), and cooling rate (ϵ) are the important solidification parameters. These three parameters are related by:

$$\epsilon = GR \tag{Eq 1}$$

This simple relation is not always intuitive and can be understood more clearly with the help of Fig. 4. This figure shows a fixed temperature gradient moving from right to left at a rate R so that $t_1 > t_2$. At a fixed position x^* , the temperature is reduced from T_1 to T_2 within the time $t_1 - t_2$. In other words, the time it takes for a temperature reduction (i.e., the cooling rate) is governed by the rate of movement (R) of the temperature gradient (G) through space.

The solidification parameters are not controlled directly in fusion welding but are governed by the welding parameters. As explained in more detail subsequently, the growth rate is determined largely by the speed of the heat source and shape of the weld pool. The cooling rate and temperature gradient are controlled primarily by the heat input (HI), which is defined as:

$$HI = \frac{\eta P}{S} \tag{Eq 2}$$

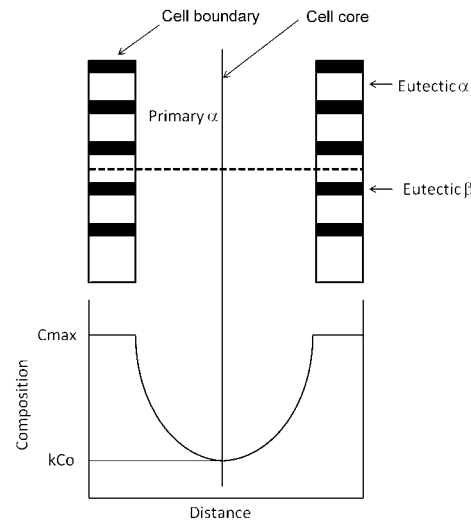


Fig. 3 Potential distribution of alloying elements and phase fractions that can form in fusion welds. Example shown is for a simple eutectic system that forms primary α phase and intercellular α/β eutectic under conditions of nonequilibrium solidification. Location of composition trace is across primary and eutectic α phase, as shown by horizontal dotted line.

where η is the heat-source transfer efficiency, P is the heat-source power, and S is the heat-source travel speed. The heat input represents the amount of energy delivered per unit length of weld. It should be noted that ϵ , G , and R cannot be represented by single values during solidification. Due to the complex nature of heat flow in the weld pool, the spatial distribution of temperature is not linear. Similarly, the value of R typically varies throughout the weld pool due to the change in growth directions between the solid/liquid interface and heat source. As a result, the values of ϵ , G , and R are functions of position and time. In general, the temperature gradient and cooling rate each decrease with increasing heat input. Detailed heat-flow equations can be used to quantify the influence of welding parameters on solidification parameters. Heat flow in welding is discussed in more detail in other articles in this Volume (see, for example, the article “Factors Influencing Heat Flow in Fusion Welding”).

Nucleation Considerations in Fusion Welding

Although the microstructures of castings and welds share some similarities, there are also some significant differences. For example, as shown schematically in Fig. 5 (Ref 3), castings typically exhibit a chill zone that consists of fine equiaxed grains which form near the mold wall. This zone forms as a result of nucleation at the mold/casting interface. This region is typically followed by a columnar zone and another equiaxed zone near the center of the casting. The columnar grain region and the central equiaxed grain zones can also form in fusion welds. However, the equiaxed grains associated with the chill zone generally do not form in fusion welds. The differences in these features can be understood with the application of

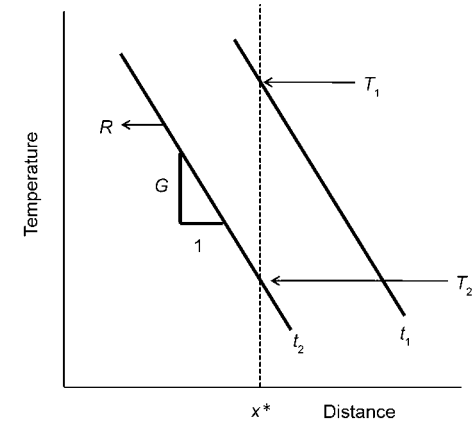


Fig. 4 Schematic illustration showing relation between temperature gradient (G), growth rate (R), and cooling rate. The cooling rate is controlled by the rate of movement of the temperature gradient.

nucleation theory, which is covered in this section.

Nucleation Theory

Figure 6 compares examples of homogeneous nucleation in a liquid (Fig. 6a, b) and heterogeneous nucleation on a preexisting mold wall (Fig. 6c, d). The change in free energy associated with homogeneous nucleation (ΔG_{hom}) is given by (Ref 4):

$$\Delta G_{\text{hom}} = -V_s \Delta G_v + A_{\text{SL}} \gamma_{\text{SL}} \tag{Eq 3}$$

where V_s is the volume of the nuclei, ΔG_v is the volume free-energy change associated with nucleation, A_{SL} is the solid/liquid interfacial area, and γ_{SL} is the solid/liquid interfacial energy. The volume free energy is the driving force for solidification and is shown schematically in Fig. 7(a), which shows the variation in volume free energy for the solid and liquid as a function of temperature. Note that $\Delta G_v = 0$ at the melting point, so there is no driving force for solidification at $T = T_m$. Thus, undercooling is generally required to drive the nucleation process. The interfacial energy is a positive contribution to the overall free-energy change and therefore works to oppose formation of the nucleus. The change in volume free energy with undercooling (ΔT) is given by:

$$\Delta G_v = \frac{L \Delta T}{T_m} \tag{Eq 4}$$

where L is the latent heat of fusion. A spherical nucleus is favored over other shapes because it provides the minimum surface area/volume ratio, thus providing the largest possible reduction in ΔG_{hom} by maximizing the negative $V_s \Delta G_v$ term and minimizing the positive $A_{\text{SL}} \gamma_{\text{SL}}$ term. For a spherical

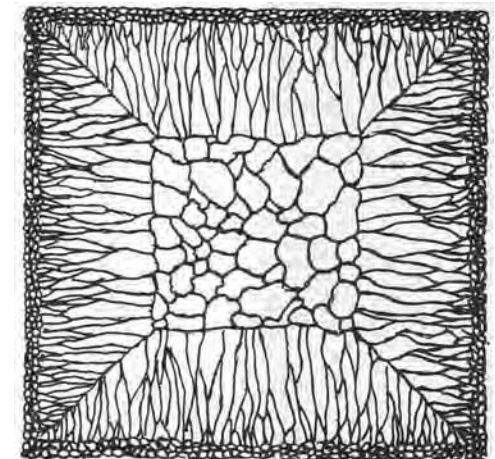


Fig. 5 Schematic illustration of grain structures that can form in castings, showing the chill zone near the mold wall, the columnar zone, and the equiaxed zone in the center of the casting. Source: Ref 3

nucleus of radius r , the free-energy change for homogeneous nucleation is given by:

$$\Delta G_{\text{hom}} = -\frac{4}{3}\pi r^3 \Delta G_v + 4\pi r^2 \gamma_{\text{SL}} \quad (\text{Eq 5})$$

Equation 5 is plotted in Fig. 7(b), which shows the individual contributions to ΔG_{hom} and the overall change in ΔG_{hom} . The overall change in ΔG_{hom} goes through a maximum, which describes the critical radius (r^*) at which point the reduction in ΔG_{hom} due to $-\frac{4}{3}\pi r^3 \Delta G_v$ begins to become larger than the increase in ΔG_{hom} associated with the $4\pi r^2 \gamma_{\text{SL}}$ term. A nucleus that forms with a radius smaller than r^* is unstable, because any further increase in the nuclei radius will produce an increase in ΔG_{hom} . Conversely, any nuclei that forms with a radius larger than r^* is stable, because further growth in the nuclei leads to an overall reduction in ΔG_{hom} . The maximum in ΔG_{hom} is denoted as ΔG^* and represents the activation energy associated with homogeneous nucleation. This condition is given by:

$$\frac{d\Delta G_{\text{hom}}}{dr} = -4\pi r^2 \Delta G_v + 8\pi r \gamma_{\text{SL}} = 0 \text{ at } r^* \quad (\text{Eq 6})$$

From which the following expressions can be derived for r^* and ΔG^* :

$$r^* = \frac{2\gamma_{\text{SL}}}{\Delta G_v} \quad (\text{Eq 7a})$$

$$\Delta G^* = \frac{16\pi\gamma_{\text{SL}}^3}{3(\Delta G_v)^2} \quad (\text{Eq 7b})$$

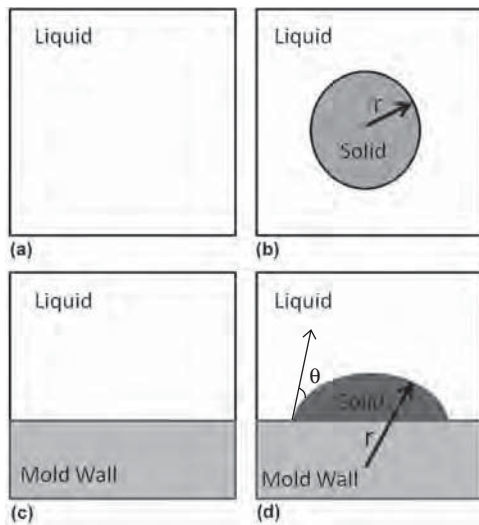


Fig. 6 Schematic illustrations of homogeneous (a and b) and heterogeneous (c and d) nucleation. Figures on the left are for a temperature above the melting point. Figures on the right are for a temperature below the melting point. The wetting angle, θ , is shown in (d).

Equations 7 and 4 can be combined to reveal the influence of undercooling on r^* and ΔG^* :

$$r^* = \left(\frac{2\gamma_{\text{SL}}}{L}\right) \frac{T_m}{\Delta T} \quad (\text{Eq 8a})$$

$$\Delta G^* = \left(\frac{16\pi\gamma_{\text{SL}}^3}{3L^2}\right) \left(\frac{T_m}{\Delta T}\right)^2 \quad (\text{Eq 8b})$$

Note that, according to Eq 8(a) and (b), r^* and ΔG^* are infinite when $\Delta T = 0$, indicating that nucleation cannot occur without some undercooling. The undercooling is needed so that the reduction in ΔG_{hom} due to the volume free-energy change (by way of Eq 4) is larger than that due to the increase in ΔG_{hom} associated with the interfacial energy term. Thus, r^* and ΔG^* each decrease with increased undercooling.

For heterogeneous nucleation on an existing mold wall, the overall free-energy change is given by (Ref 4):

$$\Delta G_{\text{het}} = -V_s \Delta G_v + A_{\text{SL}} \gamma_{\text{SL}} + A_{\text{SM}} (\gamma_{\text{SM}} - \gamma_{\text{LM}}) \quad (\text{Eq 9})$$

The first two terms are identical to those for homogeneous nucleation. The third term ($A_{\text{SM}} \gamma_{\text{SM}}$) represents the increase in overall free energy from formation of the solid/mold interface, while the fourth term ($A_{\text{SM}} \gamma_{\text{LM}}$) represents the reduction in overall free energy associated

with elimination of some of the liquid/mold interface due to formation of the nucleus. Note that the interfacial energy between two solids is typically less than that between a solid and a liquid. Thus, the $A_{\text{SM}}(\gamma_{\text{SM}} - \gamma_{\text{LM}})$ term is typically negative so the $\Delta G_{\text{het}} < \Delta G_{\text{hom}}$. The values of V_s , A_{SL} , and A_{SM} will depend on the shape of the nucleus as determined by the wetting angle, θ (Fig. 6d). The value of θ , in turn, is governed by the relative values of surface energies and is given by a force balance in the horizontal direction as:

$$\gamma_{\text{LM}} = \gamma_{\text{SM}} + \gamma_{\text{SL}} \cos \theta \quad (\text{Eq 10a})$$

$$\theta = \cos^{-1} \left(\frac{\gamma_{\text{LM}} - \gamma_{\text{SM}}}{\gamma_{\text{SL}}} \right) \quad (\text{Eq 10b})$$

Assuming the nucleus forms as a spherical cap, the values of A_{SL} , A_{SM} , and V_s are given by:

$$A_{\text{SL}} = 2\pi r^2 (1 - \cos \theta) \quad (\text{Eq 11a})$$

$$A_{\text{SM}} = \pi r^2 \sin^2 \theta \quad (\text{Eq 11b})$$

$$V_s = \pi r^3 (2 + \cos \theta) \frac{(1 - \cos \theta)^2}{3} \quad (\text{Eq 11c})$$

Equations 9 to 11 can be combined for an expression for ΔG_{het} :

$$\Delta G_{\text{het}} = \left(-\frac{4}{3}\pi r^3 \Delta G_v + 4\pi r^2 \gamma_{\text{SL}} \right) S(\theta) \quad (\text{Eq 12})$$

where:

$$S(\theta) = (2 + \cos \theta) \frac{(1 - \cos \theta)^2}{4} \quad (\text{Eq 13})$$

Note that $0^\circ \leq \theta \leq 180^\circ$ and $0 \leq S(\theta) \leq 1$. Thus, it is apparent that $\Delta G_{\text{het}} \leq \Delta G_{\text{hom}}$. This is shown schematically in Fig. 8. Low values of θ are an indication that the solid/mold interfacial energy is low so that the solid easily wets the mold wall. This leads to low values of $S(\theta)$ and reduced values of ΔG_{het} ; that is, nucleation is made easier for reduced values of γ_{SM} .

Application to Fusion Welding

Fusion welding represents a unique case that can be most easily understood by starting with Eq 10(b) and noting that the mold wall and the solid are identical, because the base metal acts as the mold in fusion welding. Thus, it can immediately be noted that fusion welding leads to the following conditions:

$$\gamma_{\text{SM}} = 0 \quad (\text{Eq 14a})$$

$$\gamma_{\text{LM}} = \gamma_{\text{SL}} \quad (\text{Eq 14b})$$

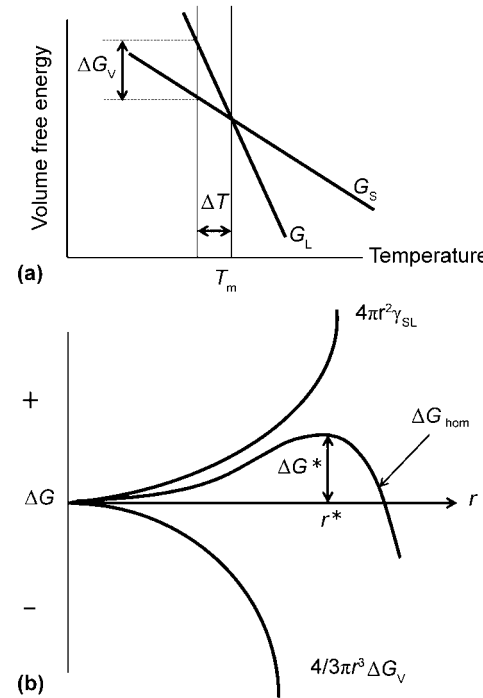


Fig. 7 (a) Variation in volume free-energy with temperature for the solid and liquid. (b) Variation in surface energy term, volume free-energy term, and ΔG_{hom} with nucleus radius for homogeneous nucleation

$$\theta = \cos^{-1} \left(\frac{\gamma_{SL}}{\gamma_{SL}} \right) = 0 \quad (\text{Eq 14c})$$

$$S(\theta = 0) = 0 \quad (\text{Eq 14d})$$

Thus, from Eq 12, the activation energy in fusion welding (ΔG_{fw}) for nucleation is given simply by $\Delta G_{fw} = 0$. This is compared to ΔG_{hom} and ΔG_{het} in Fig. 8. This can be interpreted by noting that the base-metal mold presents a perfect crystallographic match for growth of the solid fusion zone. Thus, there is no solid/mold interface in fusion welding due to this perfect crystallographic matching. An example of this in a fusion weld made with the electron beam process is shown in Fig. 9 (Ref 5). Note that there are no fine equiaxed grains at the fusion line, as often observed in the chill zone of castings. Instead, the weld-metal grains grow directly from the pre-existing base-metal grains. As a result, there is no barrier to formation of the solid. This condition is referred to as epitaxial growth, because growth occurs directly from the preexisting solid without the need for nucleation. Therefore, there is no undercooling required to initiate solidification at the fusion line, and solidification commences at the liquidus temperature of the alloy. It should be noted that undercooling can still occur near the weld centerline due to the process of constitutional supercooling, as explained in more detail later. This can lead to the formation of the central equiaxed zone often observed in fusion welds. Undercooling can also be required for nucleation of new phases during solidification.

Grain Structure of Fusion Welds

As described previously, the weld-metal grains will grow epitaxially from the preexisting base-metal grains. However, not all of these grains will be favorably oriented for continued growth. Two primary factors control the continued competitive growth of weld-metal grains:

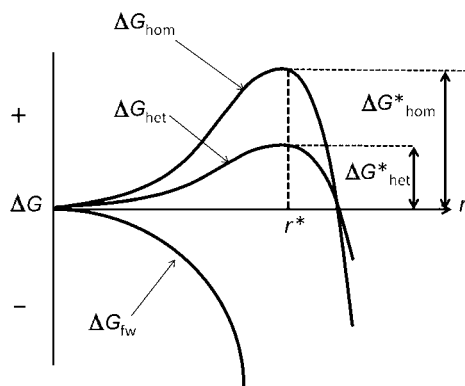


Fig. 8 Comparison of free-energy changes associated with homogeneous nucleation, heterogeneous nucleation, and fusion welding

- The grains tend to grow in a direction anti-parallel to the maximum direction for heat extraction.
- The solid will grow in the “easy-growth” crystallographic directions.

The first criterion results from the need to transport the latent heat of solidification down the temperature gradient into the cooler base metal. Because the temperature gradient is highest in a direction perpendicular to the solid/liquid interface, the resultant heat-flow rate is also highest in this direction. Thus, the grains tend to grow in a direction perpendicular to the solid/liquid interface. The second criterion results from the preferred crystallographic growth direction, which, for cubic metals, is along the [100] directions. By combining these two criteria, it can be seen that grains that have their easy-growth direction most closely aligned to the solid/liquid interface normal will be most favorably oriented to grow, thus crowding out less-favorably-oriented grains. This phenomenon accounts for the columnar grain zone that is often observed in castings, shown schematically in Fig. 5. In this case, the grains that nucleated near the mold wall and have their easy-growth direction aligned normal to the mold/casting interface outgrow the less-favorably-oriented grains, leading to the columnar region.

The situation is slightly more complex in fusion welding, because the pool shape produces a curved solid/liquid interface that is constantly in motion as it follows the heat source. This is shown schematically in Fig. 10 (Ref 6). Grains at the fusion line may initially be oriented in a favorable direction for growth, but their direction may become unfavorable as the curved solid/liquid interface changes its position. These grains may then eventually be overgrown by other grains that exhibit more favorable orientation for growth as the solid/liquid interface sweeps through the weld. An example of this is shown on a weld in nearly pure (99.96%) aluminum in Fig. 11(a) (Ref 7).

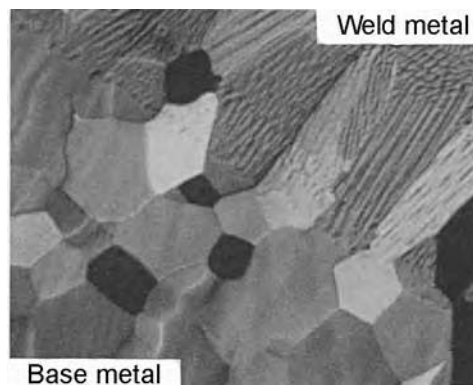


Fig. 9 Example of epitaxial growth from the fusion line in an electron beam weld of alloy C103. Original magnification: 400x. Source: Ref 5

As may be expected, the pool shape can have a strong influence on competitive grain growth and the resultant grain structure of the weld. In turn, the pool shape can be influenced by the welding parameters. At low-to-moderate heat-source travel speeds, the pool shape is generally elliptical and typically produces the grain structure pattern shown in Fig. 11(a). However, at higher travel speeds, the pool shape becomes elongated into a teardrop shape in which the solid/liquid interface is straight. This elongated shape is attributed to the low thermal gradient and high growth rate that exist at the weld centerline. The release of latent heat is proportional to the growth rate. Because the growth rate is highest at the weld centerline, the release rate of latent heat is also highest at the weld centerline. However, the temperature gradient is at a

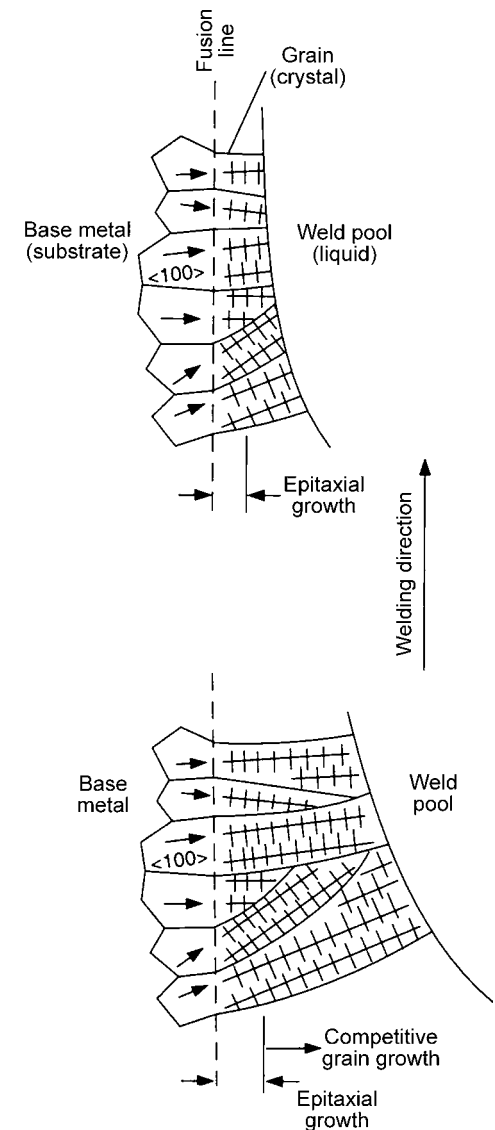


Fig. 10 Schematic illustrations of competitive grain growth in welds. (a) Early growth of grains near the fusion line. (b) Continued growth of favorably-oriented grains at a later time. Source: Ref 6

minimum at the weld centerline, so it is difficult to transport the latent heat away from the pool to permit solidification. This causes elongation of the pool near the weld centerline and leads to the teardrop shape. In this case, the direction of grain growth does not change (because the solid/liquid interface is no longer curved), and the grains grow straight toward the weld centerline until grains growing from each side of the weld intersect. This process typically leads to a centerline grain boundary, as shown in Fig. 11(b) (Ref 7).

Axial grains that grow along the direction of heat-source travel can also occasionally be observed in fusion welds. The various types of grain morphologies are summarized in Fig. 12 (Ref 6). Examples of grain structures produced with elliptical and teardrop-shaped weld pools were shown in Fig. 11. Figures 12(c) and (d) represent conditions in which an axial grain grows along the direction of the heat-source travel. These grains form in the region where the solid/liquid interface is generally perpendicular to the direction of heat-source travel, so that it becomes favorable for one or more grains to grow in this direction. The width of this zone can depend on the pool shape. The region of the interface that is perpendicular to the heat-source direction is relatively small in an elongated weld pool, so the width of axial grains will also be small. By comparison, this perpendicular region is relatively larger for an elliptical pool, so the axial grain region can also be larger.

The large columnar grains and the potential presence of centerline grain boundaries are generally undesirable from a weldability and mechanical property point of view. Centerline grain boundaries can often lead to solidification cracking associated with solidification shrinkage and low-melting-point films that become concentrated at the centerline. Fine, equiaxed grains are desired over coarse columnar grains for improvements in both cracking resistance and mechanical properties (at low temperature). One effective means for minimizing or eliminating the coarse columnar grains is through manipulation of the pool shape. Figure 13 shows an example of a weld in which the arc was oscillated at a frequency of 1 Hz in a direction normal to the heat-source travel (Ref 8). In this case, the continuously changing direction of the solid/liquid interface makes it difficult for the columnar grains to extend over large distances, thus providing a degree of grain refinement. Grain size reduction can also be achieved through the use of inoculants. This process takes advantage of heterogeneous nucleation (discussed previously) and liquid undercooling that occur due to constitutional supercooling. This topic is described in more detail in the next section.

Substructure Formation in Fusion Welds

As shown previously in Fig. 2, grains in welds typically exhibit various substructural

morphologies within the grains that can be cellular, columnar dendritic, or equiaxed dendritic. Cellular and columnar dendritic morphologies develop due to breakdown of the initially planar solid/liquid interface that forms at the fusion line, while equiaxed dendrites form by nucleation of solid in undercooled liquid, typically

near the weld centerline. Formation of these features can be understood with the concept of constitutional supercooling. The basics of this topic are described first, followed by application of the theory to understanding the substructure formation in fusion welds.

Constitutional Supercooling

As shown by the phase diagram in Fig. 14(a), formation of a solid leads to rejection of solute into the liquid. The extent of solute enrichment in the liquid progresses as solidification proceeds and the liquid composition follows the liquidus line. The solute rejected by the solid at the solid/liquid interface must be transported away from the interface by diffusion and/or convection in the liquid. If the solid/liquid interface growth rate is relatively high (which leads to a high rate of solute rejection) and/or the transport of solute into the liquid by diffusion or convection is low, then a solute boundary layer can develop in the liquid near the solid/liquid interface. Because solute enrichment leads to a reduction in the liquidus temperature (for an element that partitions to the liquid), it follows that the presence of a solute

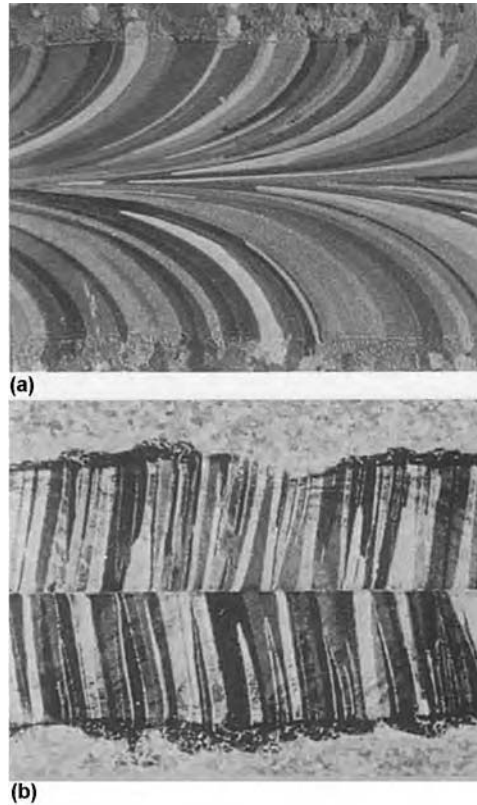


Fig. 11 Examples of (a) competitive grain growth and (b) a centerline grain boundary forming on a weld in 99.96 % Al. The weld in (a) was made at a welding speed of 250 mm/min (10 in./min). The weld in (b) was made at a welding speed of 1000 mm/min (40 in./min). Source: Ref 7

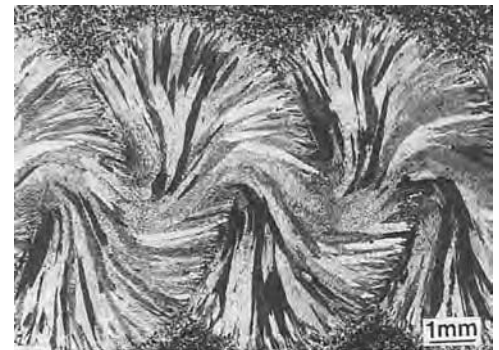


Fig. 13 Grain structure in a fusion weld of alloy 2014 made with transverse arc oscillation. Source: Ref 8

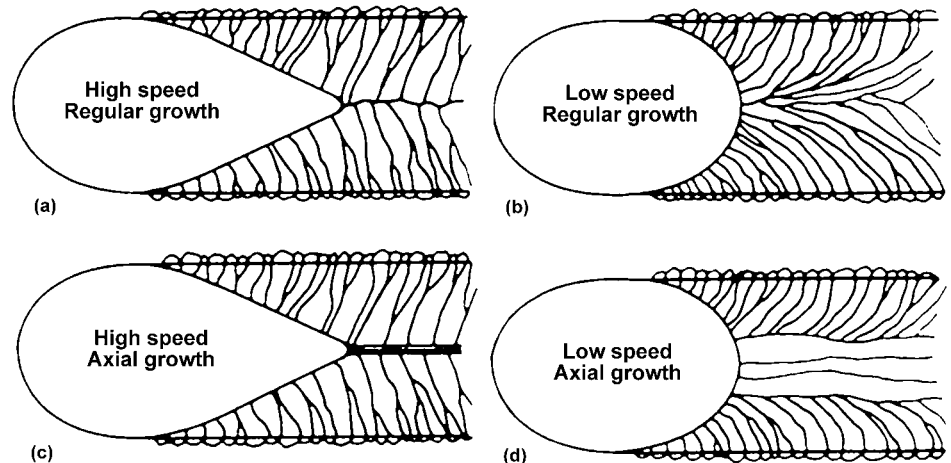


Fig. 12 Summary of various grain morphologies that can form from weld pools of different shapes. Source: Ref 6

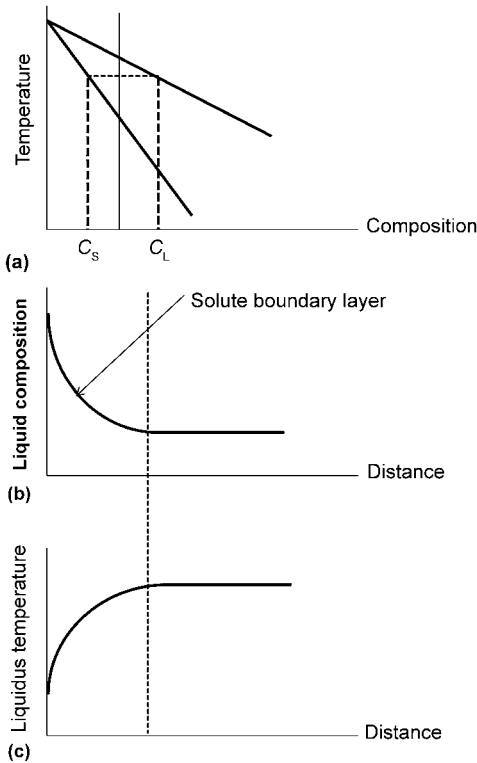


Fig. 14 Schematic illustration showing (a) solute enrichment in liquid during solidification, (b) formation of a solute boundary layer in the liquid, and (c) variation in liquidus temperature near the solid/liquid interface due to formation of the solute boundary layer

boundary layer leads to a gradient in the liquidus temperature near the solid/liquid interface. This is shown schematically in Fig. 14(b) and (c), where the liquidus temperature is relatively low at the solid/liquid interface due to the large amount of solute in the liquid at that point. The liquidus temperature gradually increases away from the interface as the solute concentration decreases. The liquidus temperature does not change outside the solute boundary layer.

Next, consider how the relative magnitudes of the liquidus temperature (T_L) gradient described previously (dT_L/dx) and the actual temperature (T_a) gradient (dT_a/dx) in the liquid affect the stability of a planar solid/liquid interface that forms as the alloy initially starts to solidify. Figure 15(a) shows the condition for a relatively steep temperature gradient such that $dT_a/dx > dT_L/dx$ in the liquid. The planar interface is moving to the right and develops protrusions during growth. Such protrusions can occur in practical situations due to interface pinning effects from inclusions in the liquid and/or differences in the rate of growth between neighboring grains that exhibit different crystallographic orientations relative to the solid/liquid interface (as described previously in the section about competitive grain growth). For this case in which $dT_a/dx > dT_L/dx$, the tip of the protrusion encounters liquid that is at a

temperature above the liquidus temperature of the alloy. Thus, the solid protrusion is not stable and melts back so that the planar interface remains stable. Under this condition, no substructure forms.

Figure 15(b) shows the case for a relatively low-temperature gradient in which $dT_a/dx < dT_L/dx$ in the liquid. In this case, the tips of the protrusions encounter liquid that is below the liquidus temperature of the alloy. This condition is referred to as constitutional supercooling because the liquid is cooled below its liquidus temperature due to constitutional variations within the liquid. Under this condition, the solid at the tips is stable because it is growing into liquid that is cooled below the liquidus temperature. In addition, because the growth rate of the solid is proportional to the undercooling, the growth rate at the tips will be higher than at the roots of the protrusions. As a result, the growth rate at the tips is faster than that at the roots, and the planar interface breaks down into a cellular interface. Note that solute redistribution in this case now occurs in three dimensions, and solute can build up at the cell boundaries as neighboring cells converge. Depending on the cooling rate and solute diffusivity in the solid, this local solute enrichment may persist after solidification (see the section “Solute Redistribution during Solidification” in this article for more details). The presence of the cell walls reflects differences in solute concentration that are revealed by etching. The condition for breakdown of the planar solid/liquid interface and concomitant formation of a cellular substructure is thus given by the condition at which $dT_a/dx < dT_L/dx$. This can be determined quantitatively by first developing an expression for the solute concentration gradient in the liquid (dC_L/dx) and then converting dC_L/dx into dT_L/dx via the phase diagram.

Assuming a linear solute gradient in the liquid, a mass balance about the solid/liquid interface is given by:

$$R(C_L - C_o) = -D_L \left(\frac{dC_L}{dx} \right) \quad (\text{Eq 15})$$

where C_L is the liquid composition at the solid/liquid interface, C_o is the nominal alloy composition, and D_L is the solute diffusivity in the liquid. The left side of Eq 15 represents the solute flux into the interface due to solute rejection by the solid, while the right side of Eq 15 represents the flux of solute down the gradient in the liquid (assuming a linear concentration gradient). At steady state, these two fluxes balance. For a phase diagram with a linear liquidus line, a given value of dC_L/dx produces a corresponding change in the liquidus temperature dT_L/dx that is given by:

$$\frac{dT_L}{dx} = m_L \left(\frac{dC_L}{dx} \right) \quad (\text{Eq 16})$$

where m_L is the liquidus slope. Combination of Eq 15 and 16 provides an expression for the constitutional criterion:

$$\frac{dT_a}{dx} < -\frac{Rm_L(C_L - C_o)}{D_L} \quad (\text{Eq 17})$$

The value of dT_a/dx is typically noted simply as G . At steady state, the value of C_L is given by $C_L = C_o/k$ (Ref 9), where k is the distribution coefficient given by $k = C_s/C_L$, where C_s is the solid composition. Thus, the expression for constitutional supercooling can be expressed as:

$$\frac{G}{R} < -\frac{m_L C_o (1 - k)}{k D_L} \quad (\text{Eq 18})$$

The parameters on the left are solidification parameters, while those on the right are parameters controlled by the alloy. The expression $m_L C_o (1 - k)/k$ represents the equilibrium solidification range of the alloy (ΔT_{eq}), so that the constitutional supercooling condition can also be written as:

$$\frac{G}{R} < -\frac{\Delta T_{eq}}{D_L} \quad (\text{Eq 19})$$

This condition represents the onset of undercooling and formation of a cellular substructure. Other substructural zones can form with increased undercooling. For example, the planar regions separating neighboring cells can undergo constitutional supercooling between the cells, thus leading to formation of columnar dendrites. With further undercooling, the liquid ahead of the dendritic interface can be supercooled to the point where nucleation can occur within the liquid, thus leading to formation of the equiaxed zone often observed in welds and castings and shown previously in Fig. 1(c) and Fig. 5. The equiaxed zone forms near the center of the weld or casting because the temperature gradient is the lowest at this location.

Examination of Eq 19 and reference to Fig. 15 indicate that supercooling is induced by low values of G and high values of R . The influence of G is readily apparent in Fig. 15, in which the extent of undercooling in the liquid increases as G decreases. The effect of R is to increase the concentration gradient in the liquid (Eq 15), which, in turn, increases the liquidus temperature gradient in the liquid. Thus, initial breakdown of the planar interface into a cellular one occurs at relatively high values of G/R . As G/R decreases, the substructural morphology can change from cellular to columnar dendritic to equiaxed dendritic. This is often summarized on a substructural diagram, as shown in Fig. 16.

Application to Fusion Welds

Fusion welds represent an interesting case of substructure formation because the values of G and R change continuously and in opposing directions around the solid/liquid interface within the weld pool. The value of G is relatively high at the fusion line because the molten pool is in contact with relatively cool base metal that has not been melted. The value of

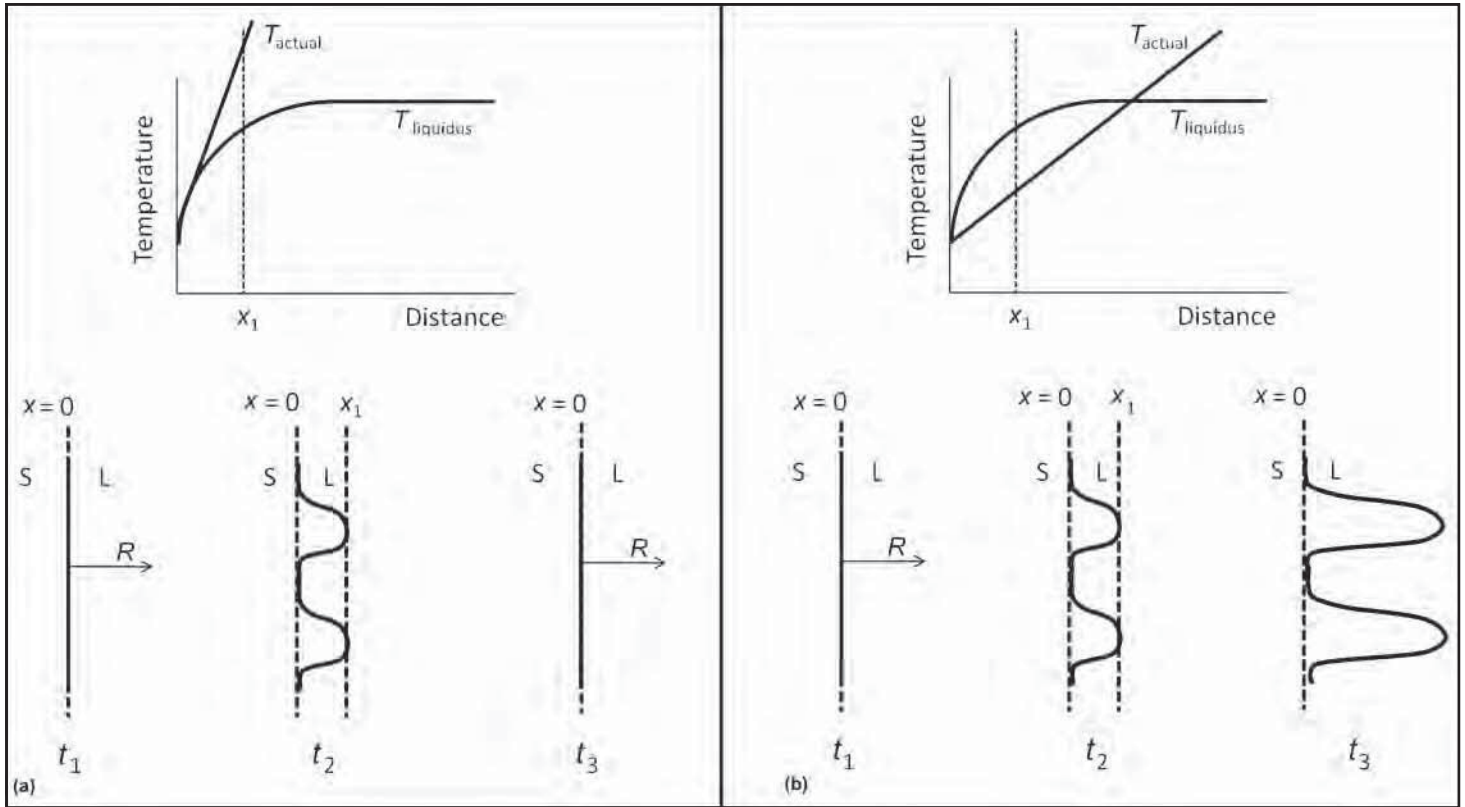


Fig. 15 Schematic illustrations showing (a) stability of a planar interface for a condition in which the actual temperature gradient in the liquid is greater than the liquidus temperature gradient and (b) breakdown of a planar interface for a condition in which the actual temperature gradient in the liquid is lower than the liquidus temperature gradient

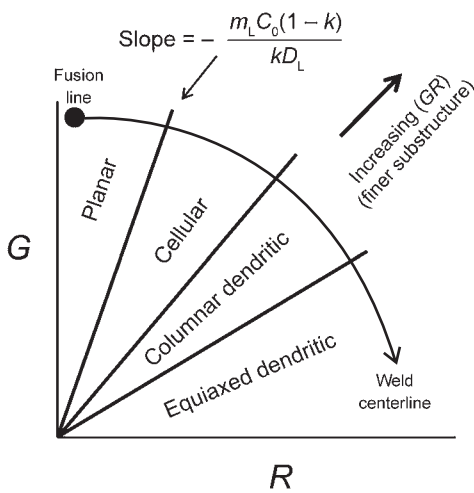


Fig. 16 Schematic illustration of a *G-R* diagram showing regions of various substructural morphologies

G decreases as the weld centerline is approached because the molten pool is in contact with resolidified weld metal that was already heated well above the liquidus temperature. An opposite trend exists for the growth rate. Figure 17 shows the relation between the heat-source travel speed (*S*) and growth rate (*R*) in terms of the angles α and β , where

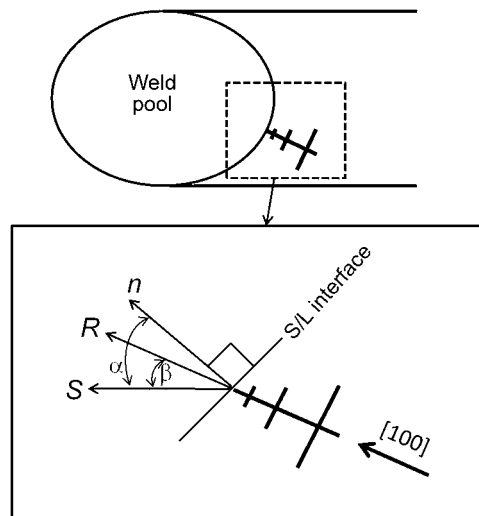


Fig. 17 Schematic illustration showing the relation between the heat-source travel speed (*S*) and growth rate (*R*) in terms of the angles α and β , where α represents the angle between the welding direction and normal to the solid/liquid interface, and β represents the angle between the welding direction and $[100]$ growth direction (for a cubic metal)

α represents the angle between the welding direction and normal to the solid/liquid interface, and β represents the angle between the welding direction and $[100]$ growth

direction (for a cubic metal). The growth rate *R* is given by:

$$R = \frac{S \cos \alpha}{\cos(\alpha - \beta)} \tag{Eq 20}$$

In many cases, the value of $(\alpha - \beta)$ is small so that $\cos(\alpha - \beta) \sim 1$, and the relation between the growth rate and heat-source travel speed is given simply as:

$$R = S \cos \alpha \tag{Eq 21}$$

From this it can be seen that $R \sim 0$ at the fusion line and $R \sim S$ at the weld centerline. Thus, the value of *G/R* is very high at the fusion line and decreases appreciably as the weld centerline is approached. This can be portrayed on the *G-R* diagram as shown in Fig. 16. As a result, the fusion zone initially forms as a planar interface, which breaks down into cellular and columnar dendritic morphologies as the centerline is approached. If enough undercooling is obtained, an equiaxed zone can form in the centerline of the weld. The relative positions of these substructural morphologies are shown schematically in Fig. 2. An example of the equiaxed zone is shown in Fig. 18 (Ref 2).

It is interesting to note that the planar zone typically occupies a very small fraction of the fusion zone. This suggests that the planar

solid/liquid interface is inherently unstable under most solidification conditions. This can be verified by direct application of Eq 18, and results of this for the aluminum-copper system are shown in Table 1. These results show the critical value of R required for breakdown of the solid/liquid interface for various values of G and C_o that may be encountered for typical G values representative of casting, arc welding, and laser welding. For these calculations, values of m_L (~ -3.3 °C/wt%) and k (~ 0.17) were obtained directly from the aluminum-copper phase diagram, and the value for solute diffusivity was taken as $D_L \sim 10^{-3}$ mm²/s. Note that the critical growth rates for constitutional supercooling are significantly lower than actual growth rates expected during solidification, thus verifying that a planar interface is inherently unstable. This implies that the initially planar interface growing from the fusion line will break down into a cellular one very quickly as the value of G/R decreases, which is indeed observed experimentally.

Columnar-to-Equiaxed Transition

The transition from cellular or columnar dendritic growth at the fusion line to heterogeneous nucleation near the weld centerline is often referred to as the columnar-to-equiaxed transition (CET). As discussed subsequently, the CET occurs due to the relatively large

constitutional undercooling near the weld centerline. In welds of polycrystalline alloys, the CET can be exploited for grain refinement. This is typically accomplished by adding inoculants to the weld to promote heterogeneous nucleation sites. The most effective inoculants are those that minimize the activation energy (ΔG_{het}^*) required for heterogeneous nucleation, so that nucleation can occur with minimal undercooling. Equation 9 can be used to provide some insight into effective inoculants, which, for heterogeneous nucleation on an inoculant, can be written as:

$$\Delta G_{het} = -V_s \Delta G_v + A_{SL} \gamma_{SL} + A_{SI} (\gamma_{SI} - \gamma_{LI}) \quad (\text{Eq 22})$$

This is identical to Eq 9, except that it is written for heterogeneous nucleation on an inoculant (I) rather than a mold wall (M). As previously discussed, the first two terms in Eq 22 are similar to those for homogeneous nucleation. The free-energy change associated with heterogeneous nucleation on an inoculant can be minimized by minimizing the interfacial energy between the solid and inoculant (γ_{SI}), so that the $A_{SI}(\gamma_{SI} - \gamma_{LI})$ term is as large and negative as possible. The inoculant/solid interfacial energy can be minimized by optimizing the crystallographic matching between the inoculant and solid. Common examples of inoculants include the use of titanium and zirconium in aluminum welds (Ref 10) and TiN in ferritic stainless steels (Ref 11).

Fusion Welding of Single Crystals

Nickel-base superalloy single crystals are often welded to rejuvenate worn blades or to repair miscast blades. Successful repair of these alloys requires preservation of the single-crystal structure during solidification of the weld pool by avoiding the CET. Constitutional supercooling has been supported as the CET mechanism by a wide range of experimental observations in studies conducted on single-crystal alloys using a variety of techniques, including autogenous laser surface melting (Ref 12–14), laser cladding (Ref 15), and electron beam welding (Ref 16). For example, studies on electron beam and pulsed laser beam welds of a single-crystal nickel-base superalloy PWA 1480 by David et al. showed that it was difficult to maintain the single-crystal structure during welding due to the formation of equiaxed stray grains. In contrast, similar experiments conducted on a relatively pure austenitic Fe-15Cr-15Ni stainless steel single crystal (Ref 17) demonstrated nearly perfect retention of the single-crystal nature in electron beam welds. The difference in these results can generally be attributed to the solute content of the different alloys. Although chromium and nickel segregate to the liquid during solidification, it is well known (Ref 18) that the equilibrium partition coefficients (k) for both chromium and nickel are close to unity, and they do not segregate strongly during solidification. This,

combined with the low level of other elements in the Fe-15Cr-15Ni alloy, minimizes the buildup of solute in the liquid during solidification. As a result, the liquidus temperature variation is minimized and provides a concomitant reduction in the level of constitutional supercooling in the liquid. Thus, the reduced level of solute segregation makes it easier to avoid the CET. In contrast, commercial single crystals require the addition of substitutional and interstitial alloying elements, many of which partition strongly during solidification. This leads to higher concentration gradients in the liquid and enhanced constitutional supercooling.

Hunt (Ref 19) was the first to develop an approximate analytical expression that described the CET. In that work, expressions for the nucleation rate were combined with dendrite growth undercooling equations to establish the condition for the CET. The type of growth that occurred was assumed to depend on the volume fraction of equiaxed grains that formed in the undercooled region when the advancing columnar front met the equiaxed grains. The structure was assumed to be fully columnar, and thus the CET was avoided, when the volume fraction of equiaxed grains was less than 0.0066. This led to the following condition for avoiding the CET:

$$G > 0.617(100N_o)^{1/3} \left[1 - \frac{(\Delta T_N)^3}{(\Delta T_c)^3} \right] \Delta T_c \quad (\text{Eq 23})$$

where G is the temperature gradient in the liquid, N_o is the total number of heterogeneous sites available for nucleation per unit volume, ΔT_N is the associated undercooling required for nucleation, and ΔT_c is the undercooling at the solid/liquid interface, which depends on the temperature gradient and growth rate. The value of ΔT_c can be calculated using dendrite growth undercooling models (Ref 20, 21). The practical difficulty in the application of Eq 23 lies in the ability to determine appropriate values of ΔT_N and N_o . Nevertheless, the model is useful because it was shown to correctly capture the observed effects of various factors on the CET, such as growth rate, temperature gradient, and alloy composition.

More recently, Gauman et al. (Ref 22) extended the analysis proposed by Hunt. The composition profile in the liquid was calculated directly using the appropriate solution of the diffusion equations for an isolated dendrite with a parabolic tip geometry. This was then used to determine the liquidus temperature profile (T_L). The actual local temperature profile in the liquid ($T_{q,z}$) was considered to be controlled by heat extraction through the solid and was determined through knowledge of the temperature gradient and dendrite tip temperature as determined by the Kurz, Giovanola, Trivedi (KGT) model (Ref 21). The actual undercooling (ΔT_z) at any location within the liquid is then given by:

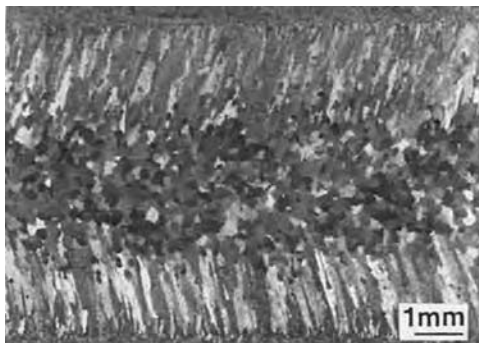


Fig. 18 Example of equiaxed zone in the centerline of a weld made with the gas tungsten arc welding process on 6061 aluminum. Source: Ref 2

Table 1 Constitutional supercooling calculations for the aluminum-copper system showing the critical growth rates required for breakdown of the solid/liquid interface for various values of G and C_o that may be encountered in casting, arc welding, and laser welding

C_o , wt% Cu	$G = 20$ °C/mm (casting)	$G = 200$ °C/mm (arc welding)	$G = 2000$ °C/mm (laser welding)
0.5	0.0024	0.024	0.24
2	0.0006	0.006	0.06
4	0.0003	0.003	0.03

$$\Delta T_z = T_z - T_{q,z} \tag{Eq 24}$$

Equiaxed grains will nucleate anywhere in this undercooled region where the actual undercooling is more than that required for nucleation, $\Delta T_z > \Delta T_N$. The critical volume fraction required for a fully equiaxed structure originally proposed by Hunt was used as the critical CET value.

Figure 19 shows an example of a microstructure selection map that was generated for the nickel-base single-crystal CMSX-4 using the approach described previously (Ref 12). The solid continuous line in the plot represents the transition between values of the solid/liquid interface growth rate and temperature gradient in the liquid that lead to the CET. A G - R combination below this line will result in columnar single-crystal growth, while combinations above this line lead to equiaxed growth and loss of the single-crystal structure. Material parameters required for calculation of the map were determined using a multicomponent thermodynamic database. The values of N_0 and ΔT_N were assumed to be $N_0 = 2 \times 10^{15}/m^3$ and $\Delta T_N = 2.5 \text{ }^\circ\text{C}$. An increase in the value of N_0 or a decrease in the value of ΔT_N will widen the range where equiaxed growth occurs. This map is useful in a practical sense because it identifies combinations of G and R that permit retention of the single-crystal structure during weld repair. The use of heat-flow equations can then be used to link R and G to the weld processing parameters, such as heat-source power, travel speed, and preheat temperature, in order to develop process-microstructure maps for successful weld repair.

Gauman et al. (Ref 12, 15) developed a simplified relationship between the temperature gradient, growth velocity, volume fraction of equiaxed grains (ϕ), and nuclei density (N_0) as:

$$\frac{G^n}{R} = a \cdot \left[\sqrt[3]{\frac{-4\pi N_0}{3 \ln(1-\phi)}} \cdot \frac{1}{n+1} \right]^n \tag{Eq 25}$$

where a and n are material constants that are determined by fitting calculations of the constitutional tip undercooling from the KGT model

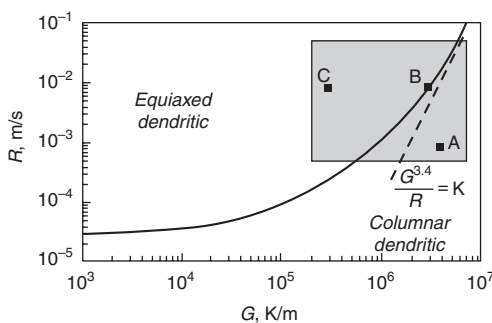


Fig. 19 Processing map for alloy CMSX-4 showing range of G - R conditions that produce columnar dendritic and equiaxed dendritic growth. Adapted from Ref 12

to an equation of the form $\Delta T = (aR)^{1/n}$. For CMSX-4, these values are $a = 1.25 \times 10^6 \text{ K}^{3.4}/\text{ms}$ and $n = 3.4$. This relation is valid under high-temperature gradient conditions in which the value of N_0 is most important for controlling nucleation and the value of ΔT_N can be ignored. Welds can be prepared under various values of G and R , and the resultant volume fraction of equiaxed grains (ϕ) can be directly measured on the weld cross sections. In this case, N_0 is the only unknown in Eq 25 and can thus be determined experimentally by fitting Eq 25 to the measured values of ϕ . For CMSX-4, this results in $N_0 = 2 \times 10^{15}/m^3$. When the original condition for a fully columnar microstructure proposed by Hunt is invoked ($\phi = 0.0066$), all values on the right side of Eq 25 are known and lead to the following condition for avoiding the CET:

$$\frac{G^n}{R} > K \tag{Eq 26}$$

where K is a material constant that depends on N_0 , ϕ , a , and n . For CMSX-4, $K = 2.7 \times 10^{24} \text{ K}^{3.4}m^{-4.4}s$. This approximate condition is shown as the dotted line in Fig. 19, and it can be seen that this approximation is more restrictive than the results obtained by the detailed calculations. However, Eq 25 is useful because it permits straightforward coupling of R and G to the weld processing parameters.

Figure 20 shows an example of a microstructure selection map for three different welds on alloy CMSX-4 (labeled "A," "B," and "C") prepared under different processing conditions. This plot shows the variation in the G^n/R ratio as a function of depth in the weld pool. As expected, the G^n/R ratio is highest at the fusion line (bottom of the weld) and decreases as the top of the weld is approached. The critical value for the CET of CMSX-4 is superimposed on the plot. Welds prepared under conditions in which the critical value of G^n/R remains below this critical value everywhere in the weld are expected to retain the single-crystal structure (e.g., weld A), while welds prepared with regions less than this value (e.g., welds B and C) will undergo the CET and lose the single-

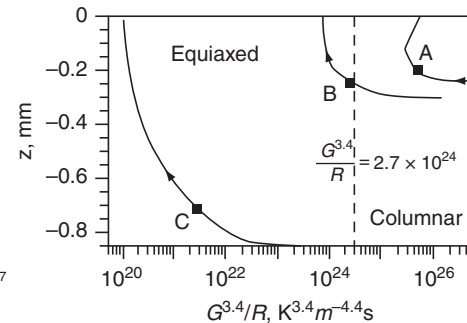


Fig. 20 Microstructure selection map for three different welds on alloy CMSX-4 (labeled "A," "B," and "C") prepared under different processing conditions. Source: Ref 12

crystal structure. Experimental identification of stray grains showed good agreement with the predictions of Fig. 20.

Figure 21 shows a process-microstructure map that was proposed to reveal semiquantitative relations between the important processing parameters of heat-source travel speed (V_b), power (P), and preheat temperature (T_0). This map was calculated using a single, integrated average of the G^n/R ratio to represent the variation in G and R that occurs with position in the melt pool. The region of high V_b and low P represents very low heat-input conditions that are insufficient to cause melting. At any travel speed, a reduction in power is beneficial, and this can be attributed to an increase in the temperature gradient. The results suggest that the effect of heat-source travel speed depends on the level of heat-source power. At low powers (i.e., $< \sim 550 \text{ W}$), the travel speed has no significant effect. Apparently, at this low power level, the gradient is high enough to avoid reaching the level of undercooling required for nucleation, regardless of the travel speed and resultant growth rate. At higher powers, the calculated results suggest that an increase in travel speed is deleterious to preserving the single-crystal columnar zone.

Experimental results generated to date generally confirm the expected influence of power described previously, but not travel speed. For example, Yoshihiro et al. (Ref 23) recently investigated the microstructure of welds on alloy CMSX-4 prepared over a wide range of powers and travel speeds using both the laser and gas tungsten arc (GTA) heat sources. A summary of their experimental results is shown in Fig. 22. They identified three types of morphologies: single crystals with directional dendrites that only grow in the [001] direction from the bottom of the weld, single crystals with disoriented dendrites, and welds with stray grains. The single-crystal welds with disoriented dendrites simply indicate the presence of dendrites that grew in directions orthogonal to the [001] direction. These results demonstrate that a reduction in power and increase in travel speed are always beneficial for preserving the single-crystal structure

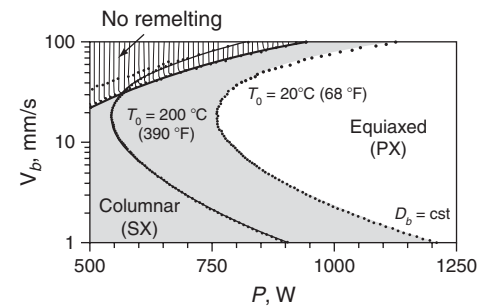


Fig. 21 Process-microstructure map for alloy CMSX-4 that reveals the semiquantitative relations between heat-source travel speed (V_b), power (P), preheat temperature (T_0), and the type of dendrite growth. Source: Ref 12

within the range of parameters investigated. The processing window for the GTA welds is slightly smaller than the laser welds. This is probably associated with the higher-intensity heat source of the laser that produces a higher temperature gradient.

Vitek (Ref 24) improved upon the model developed by Gauman et al. (Ref 12) that permitted a more in-depth analysis of the effect of travel speed. In the early model, the G''/R ratio was used as an indicator of stray grain formation, and a simple G''/R value was calculated at the centerline of the weld and averaged through the thickness. This neglects orientation effects of the solidification front and does not provide an accurate representation of stray grain tendency, because the fraction of stray grains does not vary linearly with G''/R . With the newer approach, the fraction of stray grains was determined directly at discrete positions in the weld pool and used to determine an area-weighted average of stray grains as an indicator of stray grain tendency. This improves the accuracy by accounting for the pool shape and variations in G and R around the pool.

Figure 23 shows the calculated variation in the weighted area fraction of stray grains in the weld ($\bar{\phi}_c$) as a function of welding speed for different weld powers. The tendency for stray grain formation decreases ($\bar{\phi}_c$ decreases) with a decrease in power and an increase in welding speed. Increasing travel speed is particularly advantageous. The only minor exception to this trend is observed at the lowest power and travel speed, where an increase in travel speed causes a small increase in $\bar{\phi}_c$ initially before $\bar{\phi}_c$ then decreases with increasing travel speed. These results indicate that, within this regime, the potential beneficial effect of the increase in temperature gradient produced by increasing travel speed is outweighed by the detrimental effect of an increase in growth rate that occurs with increasing travel speed. This can be understood by noting that the formation of stray grains depends on the G''/R ratio (where $n = 3.4$ for CMSX-4, for

example). Thus, stray grain formation is more sensitive to G than R . The anomalous effect of travel speed at low power has been attributed to changes in weld pool shape. At low powers and travel speeds, the weld pool shape is one in which the area susceptible to stray grain formation is a relatively large fraction of the total weld pool area. However, this trend is quickly diminished with further increases in travel speed.

Factors Affecting Substructural Scale. Dendrite spacing (λ) can have an important influence on the mechanical properties and time required for postweld homogenization treatments and therefore deserves some consideration. Kurz and Fisher (Ref 25) have proposed a geometrical model for primary dendrite spacing that leads to a relationship of the form:

$$\lambda \propto G^{-0.5}R^{-0.25} \quad (\text{Eq 27})$$

which suggests that R and G have different functional relationships on λ . Recall that G and R are related to the cooling rate through Eq 1. In most cases, dendrite spacing is related semiempirically to the cooling rate through an equation of the form:

$$\lambda = Ae^{-n} \quad (\text{Eq 28})$$

where A and n are material constants and typically $0.3 \leq n \leq 0.5$. Thus, dendrite spacing decreases with increasing cooling rate. This concept can be added to the G - R diagram shown previously in Fig. 16. Note that the ratio of G/R controls the type of substructure, while the quantity $GR (= \varepsilon)$ controls the substructural scale. As discussed previously, the cooling rate is inversely proportional to the heat input. Thus, high heat inputs lead to low cooling rates and large dendrite spacings in the weld; this has been observed experimentally in a number of alloy systems (Ref 26–28). It should also be noted that the cooling rate will vary throughout the weld due to changes in G and R , so that variations in λ within the fusion zone due to these changes are also expected.

Solute Redistribution during Solidification

Binary Models. Solute redistribution is an important topic because it controls both the distribution of alloying elements across the cellular/dendritic substructure and the type/amount of phases that form in the fusion zone during solidification. For many applications, solute redistribution can be effectively assessed with the aid of several simple models developed for binary alloys. These are reviewed first, followed by models developed for ternary alloys. Example application of the models to multicomponent alloys is also described, followed by a discussion on the application of thermodynamic models developed for multicomponent alloys.

There are various solute redistribution models available for binary alloys that account for such factors as solute diffusivity in the liquid and solid, dendrite tip undercooling, and coarsening. A good review on the subject is available in Ref 29. For many fusion welding applications, a large extent of solute redistribution behavior can be understood with the fairly simple equilibrium and nonequilibrium (Scheil) (Ref 30) models that account for the extreme cases of solute redistribution:

Equilibrium lever law :

$$C_s = \frac{kC_o}{(1-k)f_L + k} \quad (\text{Eq 29a})$$

$$C_L = \frac{C_o}{(1-k)f_L + k} \quad (\text{Eq 29b})$$

Nonequilibrium :

$$C_s = kC_o[1 - f_s]^{k-1} \quad (\text{Eq 30a})$$

$$C_L = C_o[f_L]^{k-1} \quad (\text{Eq 30b})$$

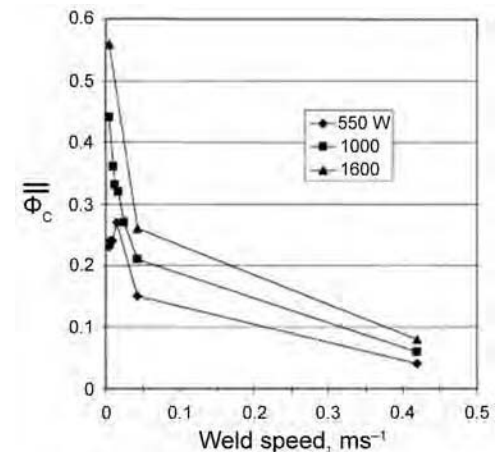


Fig. 23 Calculated variation in the weighted area fraction of stray grains in the weld as a function of welding speed for three different weld powers. Source: Ref 24

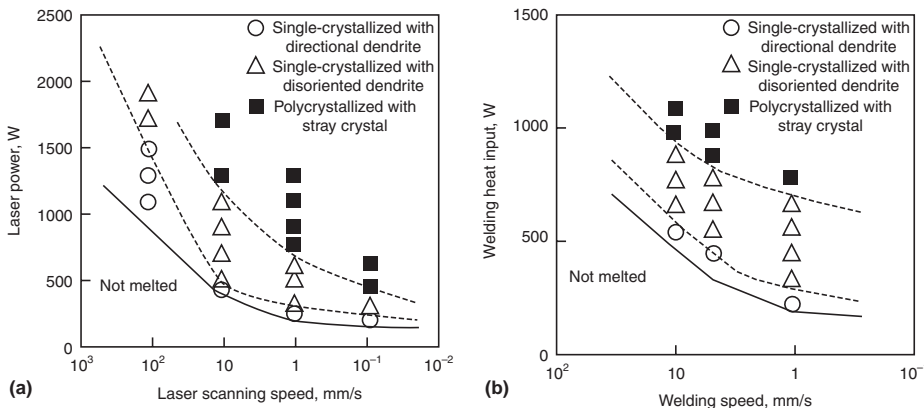


Fig. 22 Influence of heat-source power and travel speed on stray grain formation for alloy CMSX-4 for (a) laser welds and (b) gas tungsten arc welds. Source: Ref 23

where C_s and C_L are the solid and liquid compositions at the solid/liquid interface, C_o is the nominal alloy composition, f_s and f_L are the fraction solid and fraction liquid, and k is the equilibrium distribution coefficient, which is given by $k = C_s/C_L$. These expressions assume linear solidus and liquidus lines so that k is constant throughout solidification. The value of k is an important parameter because it describes the extent to which a particular element partitions between the solid and liquid. For $k < 1$, the solute partitions to the liquid, and the smaller the value of k , the more aggressive the partitioning to the liquid. For elements in which $k > 1$, the solute partitions to the solid during solidification.

The equilibrium lever law assumes complete diffusion in the liquid and solid during solidification, equilibrium at the solid/liquid interface, and no undercooling during growth. The nonequilibrium lever law (often referred to as the Scheil equation) carries similar conditions, except that diffusion in the solid is assumed to be negligible. These two cases represent the extreme conditions of residual microsegregation after solidification. The equilibrium lever law represents the case where there are no concentration gradients in the liquid or solid during solidification, and there is no residual microsegregation in the solid after solidification. In contrast, nonequilibrium conditions represent the most severe case of residual microsegregation in the solid after solidification because solid diffusivity is negligible.

As an example, consider a binary eutectic A-B system, shown in Fig. 24(a), that exhibits linear solidus and liquidus lines, a value of $k = 0.02$ (for solute element B), a eutectic composition of 20 wt% B, and a maximum solubility limit of 4 wt% B. Figures 24(b) and (c) show the variation in liquid composition during solidification under equilibrium and nonequilibrium conditions for two alloys: one below the maximum solid solubility with $C_o = 2$ wt% B and one above the maximum solid solubility with $C_o = 5$ wt% B. For the 2 wt% B alloy, the solidification conditions under each extreme are quite different. Under equilibrium conditions, the liquid composition never becomes enriched to the eutectic composition because solute in the solid is uniformly distributed and therefore capable of dissolving all the solute before the eutectic point is reached in the liquid. Note from Eq 29(b) that the maximum solute enrichment in the liquid for the equilibrium condition is given as C_o/k , which occurs when $f_L = 0$. In this case, $C_o/k < C_e$ (the eutectic composition). The resultant microstructure directly after solidification would simply consist of primary α with a uniform distribution of B. For the nonequilibrium case, the liquid composition will always become enriched to the eutectic point. Thus, directly below the eutectic temperature, the 2 wt% B alloy exhibits primary α with a concentration gradient and 0.06 weight fraction of the α/β eutectic when solidified under nonequilibrium conditions.

The two extreme solute redistribution behaviors for the 5 wt% B alloy are compared in Fig. 24(c). For the equilibrium case, the liquid composition will become enriched to the eutectic point because the nominal composition is above the maximum solid solubility. In other words, $C_o/k > C_e$. This eutectic reaction occurs when there is 0.06 weight fraction remaining liquid. Thus, the solidification microstructure directly after equilibrium solidification consists of primary α with a uniform distribution of B at the maximum solid solubility of 4 wt% and 0.06 weight fraction of the α/β eutectic. For the nonequilibrium case, the liquid composition is always higher at any stage during solidification (i.e., any particular value of f_L), because the solid does not dissolve as much solute. As a result, more liquid remains when the eutectic composition is reached (0.18 weight fraction), and more of the eutectic constituent forms in the solidification microstructure. The final alloy here exhibits primary α with a concentration gradient and 0.18 weight fraction of the α/β eutectic (three times the weight fraction of eutectic that formed for the equilibrium case). Figure 24(d) shows the corresponding solute profiles in the α solid phase after solidification for the 2 wt% B alloy. Under equilibrium conditions, there is simply primary α with a uniform distribution of 2 wt% B. For nonequilibrium conditions, the primary α phase exhibits a concentration gradient with a minimum of $kC_o = 0.4$ wt% B and a maximum at the solubility limit of 4 wt% B. The portion of solid that exhibits a uniform composition of 4 wt% B represents the eutectic α (the composition of the eutectic β is not shown).

Equations 30(a) and (b) have the interesting property that $C_L \rightarrow \infty$ as $f_L \rightarrow 0$ and $C_s \rightarrow \infty$ as $f_s \rightarrow 1$ (for $k < 1$), which indicates that the solid will always be enriched to the maximum solid solubility, while the liquid will always be enriched to the eutectic composition under nonequilibrium conditions. This can be attributed to the lack of diffusion in the primary α phase, which leads to the inability of all the solute to be incorporated into the primary phase. This can be understood by direct inspection of Fig. 24(d) and noting that the dissolved solute in the solid is given by the area under the $C_s - f_s$ curve. For the equilibrium case, the total dissolved solute is obviously 2 wt% B, which is the nominal value. However, the dissolved solute for the nonequilibrium case is always less than this due to the regions in the solid where $C_s < C_o$. In this case, the excess solute must be accommodated by formation of the eutectic constituent that contains the B-rich β phase.

Strictly speaking, it is important to note that the solute redistribution equations described in this section do not account for undercooling effects that can occur at the cell/dendrite tip during nonplanar solidification. Under high-energy-density welding processes that are operated at high travel speeds, this undercooling effect may become significant. This subject is discussed in more detail in the section "Rapid

Solidification Considerations" in this article. However, this effect is typically not significant under many moderate cooling-rate conditions typical of arc welding and high-energy-density processes operating at low heat-source travel speeds. In these cases, the models described for planar solidification can be applied on a local scale within a small volume element that encompasses a planar interface. An example

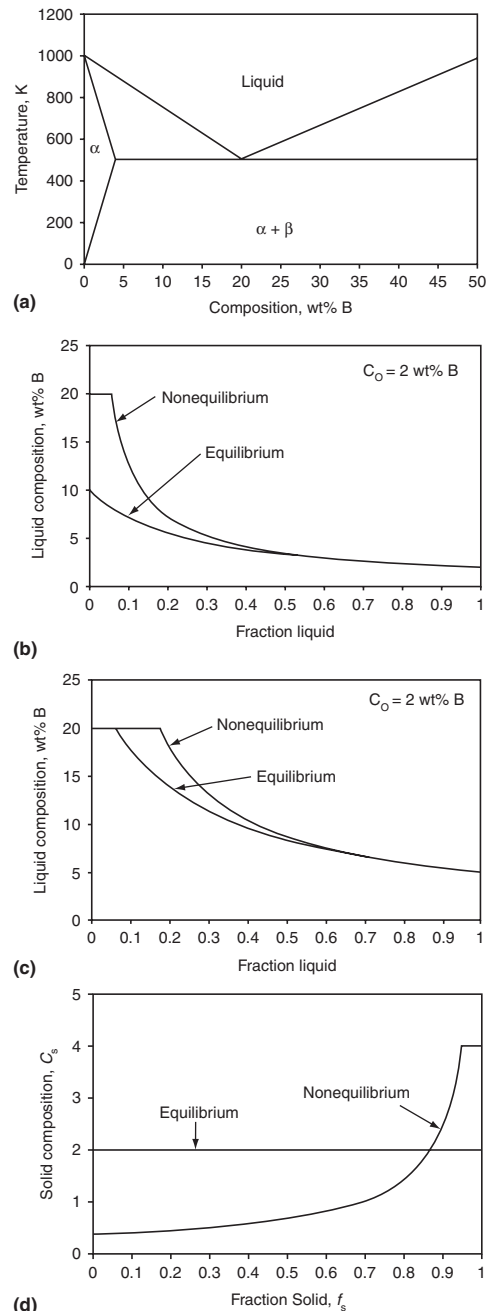


Fig. 24 Example of solute redistribution calculations for equilibrium and nonequilibrium conditions. (a) Hypothetical phase diagram. (b) Variation in liquid composition for $C_o = 2$ wt%. (c) Variation in liquid composition for $C_o = 5$ wt%. (d) Variation in solid composition for $C_o = 2$ wt%

of this is shown in Fig. 25 for cellular solidification. Here, the solidification process can be represented by the enclosed region shown and noting that solidification starts at the cell core (where $f_s = 0$) and finishes at the cell boundary when two cells meet ($f_s = 1$). The solute redistribution then occurs locally within the given volume element that exhibits an essentially planar interface between the liquid and solid.

The only difference that separates these two extreme cases of solute redistribution during solidification is the solute diffusivity in the solid. Thus, it is useful to consider the extent of solute diffusivity expected for a given set of parameters and resultant cooling rate. The Brody-Flemings model was the first attempt at taking back-diffusion into the solid into account during solidification and is given as (Ref 31):

$$C_s = kC_o \left[1 - \frac{f_s}{1 + \alpha k} \right]^{k-1} \quad (\text{Eq 31a})$$

$$C_L = C_o \left[1 - \frac{1 - f_L}{1 + \alpha k} \right]^{k-1} \quad (\text{Eq 31b})$$

$$\alpha = \frac{D_s t_f}{L^2} \quad (\text{Eq 31c})$$

The α parameter in Eq 31(c) is a dimensionless diffusion parameter, while D_s is the diffusivity of solute in the solid, t_f is the solidification time (cooling time between the liquidus and terminal solidus), and L is half the dendrite arm spacing. The $D_s t_f$ term in the numerator of Eq 31(c) essentially represents the distance that solute can diffuse in the solid during solidification, while the half dendrite arm spacing, L , represents the length of the concentration gradient. Thus, when $D_s t_f \ll L^2$, the solute is able to diffuse only a small fraction of the total gradient length, and solid-state diffusion will be insignificant. This represents the case in which $\alpha \approx 0$ and Eq 30 reduces to the Scheil equation. Clyne and Kurz (Ref 32) pointed out that Eq 31(a) and (b) do not reduce to the lever law as $\alpha \rightarrow \infty$. They proposed an alternate form of α that is given by:

$$\alpha' = \alpha \left[1 - \exp\left(-\frac{1}{\alpha}\right) \right] - 0.5 \exp\left(-\frac{1}{2\alpha}\right) \quad (\text{Eq 32})$$

Although this is not based on a physical model, use of α' correctly reduces Eq 31 to the lever law when $\alpha = \infty$ and to the Scheil equation when $\alpha = 0$. It should be noted that Kobayashi provided a more comprehensive model of solute diffusivity in the solid that can be used when more detailed calculations are required (Ref 33).

The potential for back-diffusion in the solid during fusion welding can be assessed by determination of the simple α parameter. The t_f and L terms in Eq 31(c) will each depend on the cooling rate of the weld (ϵ) via:

$$t_f = \frac{\Delta T}{\epsilon} \quad (\text{Eq 33})$$

$$L = \frac{\lambda}{2} = \frac{A\epsilon^{-n}}{2} \quad (\text{Eq 34})$$

where ΔT is the solidification temperature range, λ is the dendrite spacing, and A and n are material constants. (Equation 33 assumes a linear cooling rate through the solidification temperature range.) Thus, by knowing the solidification temperature range, cooling rate, and dendrite spacing/cooling rate relationship, the α parameter can be directly estimated as a function of cooling rate and the potential influence of solid-state diffusion can be determined.

Many studies have used these simple equations to explore the solidification behavior of welds in austenitic alloys. These studies have demonstrated that the solute redistribution behavior and resultant weld-metal microstructure are controlled primarily by the pertinent values of k and D_s for the alloying elements of interest. The value of D_s will control the potential for back-diffusion in the solid during solidification. Elements with very low k values can produce steep concentration gradients across the cellular or dendritic substructure of the weld. Table 2 shows an example that summarizes diffusivity data for many alloying elements in nickel (Ref 34). Upper bound values of α for each element can be calculated by determining D_s at the liquidus temperature, approximately 1350 °C (2460 °F) for many nickel alloys (Ref 35, 36), using a large but representative value of ΔT of 200 °C (360 °F) and reported values of $A = 32$ and $n = 0.31$ (Ref 37). Using these values, α can be calculated as a function of cooling rate and is shown in Fig. 26 for the substitutional alloying elements listed in Table 2. The values of A and n used here were for alloy 713. However, the values do not vary significantly among many nickel-base alloys (Ref 38). The α value decreases with increasing cooling rate due to the decrease in solidification time (t_f) with increasing cooling rate. More importantly, note that $\alpha \ll 1$ for all the elements considered under a wide range of cooling rates. The use of various values of ΔT , A , and n representative of other nickel-base alloys does not change this result significantly. It is also important to note that an upper bound value of D_s was calculated at a typical liquidus temperature of 1350 °C (2460 °F). The value of α can only decrease with the use of D_s values calculated at lower solidification temperatures.

These results clearly demonstrate that solid-state diffusion of substitutional alloying elements in austenitic alloys is insignificant during solidification of fusion welds. Experimental evidence has been published that supports these calculations for a variety of elements, including iron, chromium, niobium, molybdenum, and silicon (Ref 39, 40). In that work, dendrite core compositions were experimentally measured in

samples that were solidified under a wide range of cooling rates, including samples quenched during solidification and samples cooled at 0.2 °C/s and 650 °C/s. The dendrite core compositions were identical in all cases, indicating that solid-state diffusion is indeed negligible. In these cases, the simple form of Eq 30 can be used for quantitative calculations of final solute profiles and phase fractions. An example is provided later in this section.

Back-diffusion during weld solidification can be significant in body-centered cubic systems and for the diffusion of interstitial alloying

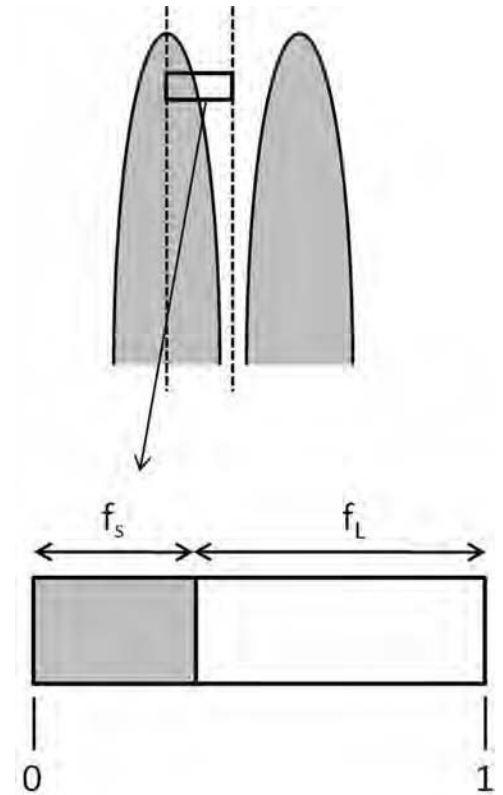


Fig. 25 Volume element for modeling solute redistribution during cellular solidification. The solidification process can be represented by the enclosed region shown and noting that solidification starts at the cell core (where $f_s = 0$) and finishes at the cell boundary when two cells meet ($f_s = 1$).

Table 2 Diffusion data for various alloying elements in nickel

Element	Diffusion coefficient (D_o), m^2/s	Activation energy (Q), kJ/mol
Fe	8.0×10^{-5}	255
Cr	1.1×10^{-4}	272
Co	1.4×10^{-4}	275
Nb	7.5×10^{-5}	264
Mo	1.0×10^{-4}	275
W	2.0×10^{-4}	299
Al	1.9×10^{-4}	268
Ti	4.1×10^{-4}	275
Cu	5.7×10^{-5}	258
C	8.0×10^{-6}	135

elements. For example, calculation of the α parameter for carbon in nickel will yield values that are significantly greater than unity. This is to be expected, because carbon diffuses by an interstitial mechanism and therefore exhibits diffusion rates that are orders of magnitude higher than the substitutional alloying elements. Evidence for this is reflected in the activation energy term (Q) for diffusion of carbon in nickel shown in Table 2. Note that Q for the substitutional alloying elements varies over a fairly narrow range of 255 to 299 kJ/mol, while the value for carbon is approximately half this at 135 kJ/mol.

Figure 27(a) shows calculated results for solute redistribution of carbon in nickel (Ref 39). In this figure, the solute redistribution behavior was calculated with Eq 31 and 32 using the temperature-dependent diffusion rate of carbon in nickel. Comparison is made between the nonequilibrium Scheil equation and the lever law. Note that the detailed results from the Clyne-Kurz model are essentially identical to that of the lever law, indicating that complete solid-state diffusion of carbon is expected in nickel-base alloys during solidification. A similar effect can be expected for nitrogen in nickel. This calculation was conducted for a cooling rate of 650 °C/s (1170 °F/s) through the solidification temperature range. Higher cooling rates typical of high-energy-density welding may alter this result and begin to limit carbon

diffusion in the solid. Aside from this possibility, these results demonstrate that carbon (and nitrogen) can be expected to exhibit complete diffusion in the solid during most welding conditions. Figure 27(b) shows a similar calculation for substitutional diffusion of titanium in a body-centered cubic Fe-10Al-5Cr alloy that was calculated using the detailed model proposed by Kobayashi (Ref 33, 41). These results are somewhat similar to those for carbon in nickel in that solid-state diffusion is essentially complete at moderate cooling rates. However, diffusion may become insignificant at very high cooling rates typical of high-energy-density processes. These results are meant to serve as example calculations that can be applied to understanding solute redistribution behavior in fusion welds of any alloy system when the pertinent alloy parameters are known.

For conditions in which solid-state diffusion is negligible, microsegregation will persist in the as-solidified weld (except for the case in which $k = 1$). An example of this is shown in Fig. 28 for fusion welds in a niobium-bearing superalloy (Ref 36, 42). The final degree of microsegregation can be assessed by direct determination of the k value for the element of interest, where the degree of microsegregation will increase with decreasing k value (for k values < 1). For example, the lowest concentration will occur at the dendrite core where solidification initiates. Direct inspection of Eq 30

indicates that, at the start of solidification when $f_s = 0$, the dendrite core composition (which is the first solid to form) is given by kC_0 .

Although the models described earlier were strictly developed for binary alloys, they can be used in a quantitative manner for multicomponent engineering alloys when the alloy properly mimics the solidification behavior of a binary system. An example is provided here by application of the simple binary Scheil equation to Ni-Cr-Mo-Gd alloys. A typical as-solidified microstructure of an alloy is shown in Fig. 29(a). These alloys exhibit γ dendrites and an interdendritic γ/Ni_5Gd eutectic-type constituent. Research (Ref 43, 44) has shown that gadolinium controls the solidification behavior of these alloys. In particular, the solidification temperature range and amount of terminal eutectic-type constituent that forms at the end of solidification are essentially dominated by the gadolinium concentration. Solidification of these alloys initiates at the liquidus temperature by the formation of primary γ -austenite. As solidification proceeds, the liquid becomes increasingly enriched in gadolinium until the liquid $\rightarrow \gamma + Ni_5Gd$ eutectic-type reaction is reached, at which point solidification is terminated.

This reaction sequence and temperature range is similar to that expected in the binary nickel-gadolinium system. Simple binary

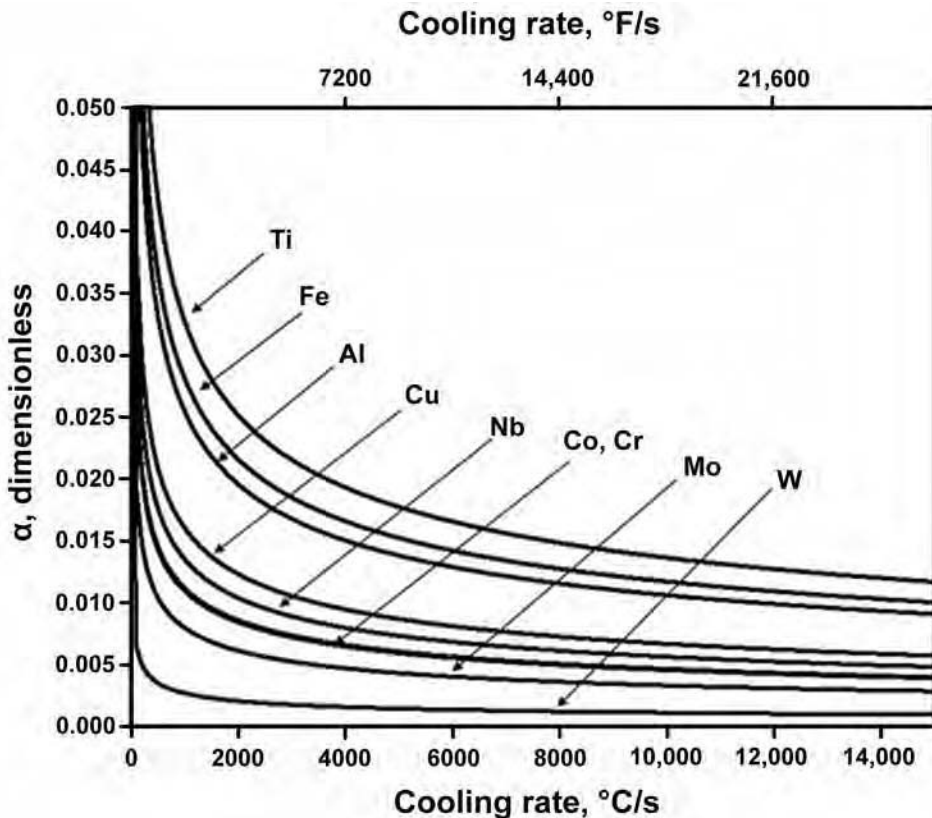
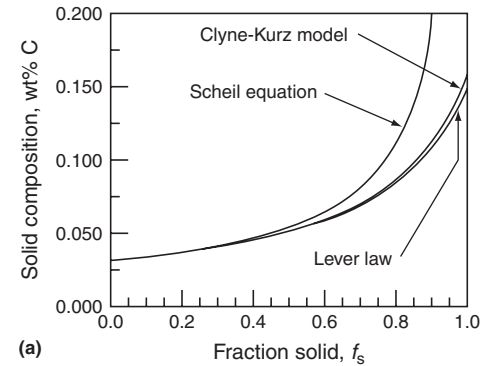
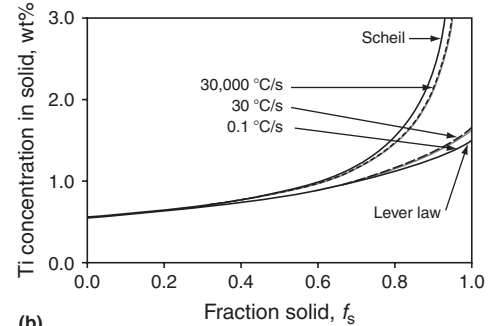


Fig. 26 Dimensionless α parameter as a function of cooling rate for a wide range of alloying elements in nickel



(a)



(b)

Fig. 27 Comparison of solute redistribution behavior. (a) Carbon in a nickel-base superalloy calculated using the lever law, Scheil equation, and Clyne-Kurz model. (b) Titanium in an Fe-10Al-5Cr-1.5Ti-0.4C alloy with varying cooling rates (calculated using the Kobayashi model) compared to the lever law and Scheil cases. Source: Ref 39

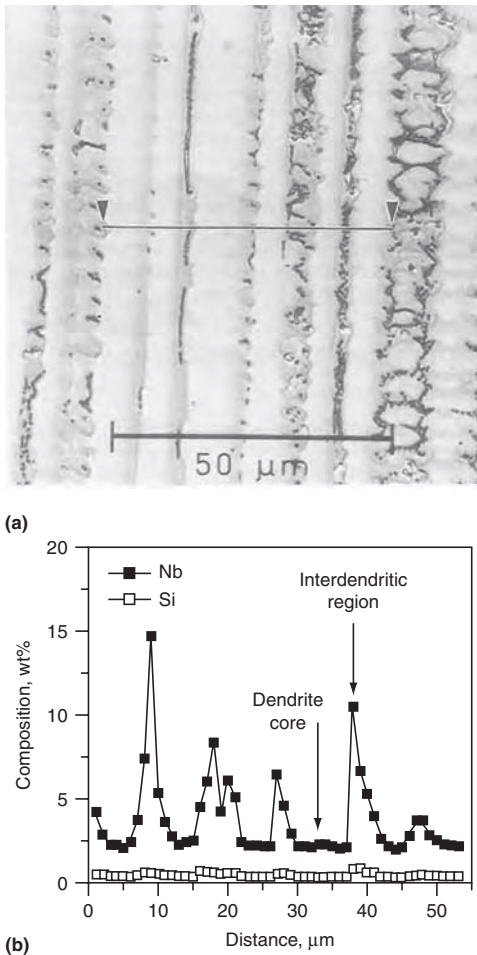


Fig. 28 Example of microsegregation in a weld of a niobium-bearing nickel-base superalloy. (a) Micrograph showing position of composition trace. (b) Corresponding electron probe microanalysis results showing niobium microsegregation. Source: Ref 36, 42

nickel-gadolinium alloys with less than approximately 13 wt% Gd exhibit a similar two-step solidification sequence consisting of primary austenite formation followed by a terminal eutectic reaction involving the $Ni_{17}Gd_2$ intermetallic at 1275 °C (2327 °F). By comparison, the multicomponent Ni-Cr-Mo-Gd alloys complete solidification at ~1258 °C (~2295 °F) by a terminal eutectic-type reaction involving the Ni_5Gd intermetallic. Thus, although the secondary phase within the terminal eutectic constituent is different in each case, the terminal reaction temperatures are very similar. As shown in Fig. 29(b), a pseudo-binary solidification diagram can be developed for this system that is similar to the phase diagram of a binary eutectic alloy. In this case, the solvent is represented by the Ni-Cr-Mo solid-solution γ -austenite phase, and gadolinium is treated as the solute element. The similarity of this γ -gadolinium binary system to a binary eutectic system is readily evident in several ways:

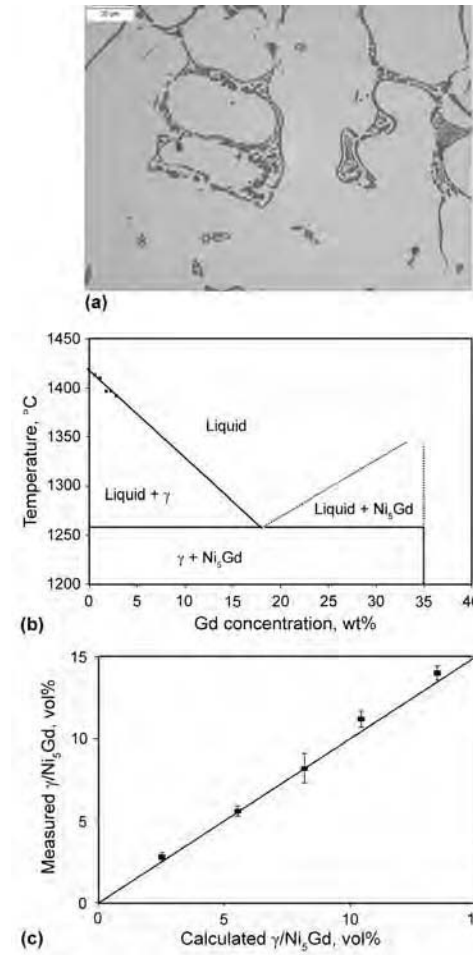


Fig. 29 (a) Microstructure of fusion weld on a Ni-Cr-Mo-Gd alloy. (b) Pseudo-binary phase diagram for the γ -gadolinium system. (c) Comparison of the measured and calculated γ/Ni_5Gd fraction eutectic from fusion welds made on alloys with various gadolinium concentrations. Source: Ref 44

- The as-solidified microstructure consists of primary γ dendrites surrounded by an inter-dendritic eutectic-type constituent in which the secondary phase in the eutectic is solute rich.
- The amount of eutectic-type constituent increases with increasing solute content.
- The proportional amount of each phase within the eutectic constituent is relatively insensitive to nominal solute content.

It was also observed that the eutectic temperature is not strongly dependent on the nominal gadolinium concentration. Key points of the diagram shown in Fig. 29(b) were determined with a combination of thermal analysis and quantitative microstructural characterization techniques. Figure 29(c) shows a comparison of the measured and calculated γ/Ni_5Gd fraction eutectic from fusion welds made on alloys with various gadolinium concentrations. In this plot, a comparison is made with the calculated

eutectic fraction using the simple Scheil equation. The Scheil equation can be used for eutectic fraction calculations by noting that, when $C_L = C_e$ (the eutectic composition), the remaining fraction liquid (f_L) transforms to fraction eutectic (f_e), so that:

$$f_e = \left(\frac{C_e}{C_0}\right)^{1/k-1} \quad (\text{Eq 35})$$

Good agreement is observed between the measured and calculated values. This supports the use of a pseudo-binary analog for modeling the solidification behavior of these alloys.

Ternary Models. The expressions derived earlier for binary alloys can be used quantitatively in multicomponent alloys when the alloy behaves like a binary system. However, many engineering alloys exhibit multiple reactions during solidification that occur over a range of temperatures and exhibit more than one eutectic constituent. Thus, they typically cannot be treated in a quantitative fashion with the simpler models described earlier. In this case, models for ternary alloys can be useful, and relatively simple solidification path equations can be derived for limiting cases of solute redistribution in ternary alloys. Two sets of solute redistribution equations are needed to fully describe the solidification paths of ternary alloys. The first set describes the variation in liquid composition and fraction liquid during the primary stage of solidification. These expressions can be used to identify if the liquid composition is enriched to a monovariant eutectic-type reaction and, if so, what type of reaction will occur and the fraction of total eutectic constituent that will form in the microstructure. The second set of expressions describes the variation in liquid composition and fraction liquid during the monovariant eutectic reaction. These expressions can be used to determine if the liquid composition is enriched to the ternary eutectic reaction and the fractions of both the monovariant and ternary eutectic constituents. Only the primary solidification path expressions are discussed here. More detailed information on the full ternary model can be found elsewhere (Ref 45).

For ternary solidification, three limiting cases can be identified based on the diffusivity of solute in the solid phases:

- Negligible diffusion of each solute in the solid phases, referred to as nonequilibrium solidification
- Negligible diffusion of one solute in the solid phases and infinitely fast diffusion of the other solute in the solid phases, referred to here as intermediate equilibrium.
- Infinite diffusion of each solute in the solid phases (equilibrium)

Expressions for the primary solidification paths for these three conditions are given by:

Equilibrium:

$$C_{LA} = \frac{C_{oA}}{\left(\frac{1-k_{zA}}{1-k_{zB}}\right)\left(\frac{C_{oB}-k_{zB}C_{LB}}{C_{LB}}\right) + k_{zA}} \quad (\text{Eq 36a})$$

Intermediate equilibrium:

$$C_{LA} = C_{oA} \left(\frac{C_{oB} - k_{zB}C_{LB}}{(1 - k_{zB})C_{LB}}\right)^{k_{zA}-1} \quad (\text{Eq 36b})$$

$$\text{Nonequilibrium: } C_{LA} = C_{oA} \left(\frac{C_{LB}}{C_{oB}}\right)^{\frac{k_{zA}-1}{k_{zB}-1}} \quad (\text{Eq 36c})$$

where f_L is the fraction liquid, C_{oj} is the nominal concentration of element j , C_{Lj} is the concentration of element j in the liquid, and k_{ij} is the equilibrium distribution coefficient for element j in phase i . When the liquid composition given by Eq 36 intersects a monovariant eutectic line, the remaining fraction liquid transforms to a binary-type eutectic and possibly the ternary eutectic. Thus, the value of f_L at the intersection point of the primary solidification path and monovariant eutectic line defines the total amount of eutectic in the microstructure. Details on the calculation procedure for determining this value are provided elsewhere (Ref 45). The difference among the three cases considered here is governed by the diffusivity of solutes in the solid phases. Thus, the condition that most closely describes the solidification behavior for an actual application can be determined by calculation of the α parameter for each of the solute elements of importance.

Figure 30 shows an example of primary solidification path calculations made for fusion welds on multicomponent superalloys that form the γ/NbC and γ/Laves eutectic-type constituents at the end of solidification (Ref 46). Although these alloys contain multiple elements, they can be treated as a pseudo-ternary $\gamma\text{-Nb-C}$ system. Niobium and carbon are treated as the important solute elements here because each element partitions aggressively to the liquid during solidification and leads to the formation of the niobium- and carbon-rich NbC phase and the niobium-rich Laves phase. For this system, niobium exhibits negligible diffusion, while carbon diffuses infinitely fast. Thus, Eq 36(b) was used for these calculations. Calculations are shown for alloys with similar niobium concentrations and various amounts of carbon. Note that the addition of carbon pushes the primary solidification path up into the carbon-rich side of the liquidus projection. The liquid composition must then “travel” a long distance down the γ/NbC eutectic line as the γ/NbC constituent forms. This accounts for the observed influence of carbon that leads to large amounts of the γ/NbC constituent in these alloys. It was also observed that carbon additions increase the start temperature of the $L \rightarrow \gamma + \text{NbC}$ reaction. This effect is not intuitive, because solute additions in which $k < 1$ (such

as carbon) typically lower reaction temperatures. The calculations demonstrate the reason for this effect. The dotted arrow near the γ/NbC eutectic line represents the direction of decreasing temperature (as determined through thermal analysis). Note that carbon additions drive the solidification path to the carbon-rich region of the diagram where the $L \rightarrow \gamma + \text{NbC}$ reaction is relatively high, thus accounting for the observed effect. Reasonable agreement was obtained between the measured and calculated volume fractions using these expressions (Ref 46).

Modeling of Multicomponent Alloys. The relatively simple models described previously are useful for assessing the solidification behavior of alloys that behave in a manner analogous to binary or ternary alloys. However, such approaches may be limited in some engineering alloys. Multicomponent thermodynamic and kinetic software is now available that can also be used for understanding solidification behavior in such systems, and a simple example is provided here. Figure 31(a) shows a light optical micrograph of a weld between a superaustenitic stainless steel (CN3MN) with ~6 wt% Mo and a nickel-base filler metal (IN686) with ~14 wt% Mo (Ref 47). This weld was prepared at the 21% dilution level. Welds in these alloys solidify with a primary $L \rightarrow \gamma$ solidification mode and then terminate solidification by a $L \rightarrow \gamma + \sigma$ reaction. Thus, the final weld microstructure consists of primary γ dendrites and interdendritic γ/σ eutectic. The σ phase is a molybdenum-rich phase. Welds made at low dilution levels (i.e., high molybdenum levels) would be expected to form relatively large fractions of the σ phase. However, as shown in Fig. 31(b), the σ -phase content does not change significantly with weld dilution level and associated nominal molybdenum concentration of the alloy. This immediately suggests that other factors besides the nominal concentration of molybdenum are also affecting the σ -phase content.

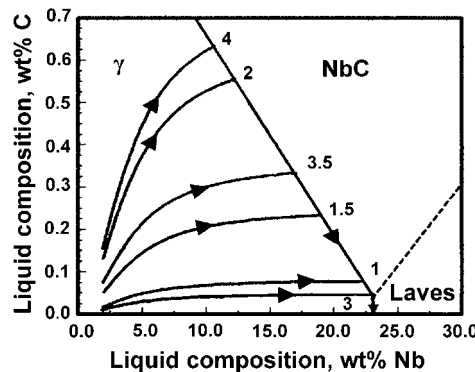


Fig. 30 Example of primary solidification path calculations made for fusion welds on multicomponent superalloys that form the γ/NbC and γ/Laves eutectic-type constituents at the end of solidification. Source: Ref 46

The σ -phase content is controlled by the amount of eutectic constituent that forms during the end of solidification. The fraction of eutectic is, in turn, controlled by the nominal alloy composition (C_o), eutectic composition (C_e), and distribution coefficient (k) for molybdenum (Eq 35). Note that the nickel and iron contents in the weld change appreciably with changes in dilution, and these changes in nickel and iron may affect the values of k and C_e . Figure 32(a) shows the variation in liquid composition during solidification using a multicomponent Scheil simulation with Thermocalc (Ref 48). The Scheil simulation is justified here because, as shown in Fig. 26, all the substitutional elements of interest are known to exhibit insignificant diffusion rates during solidification in austenite. Results are shown for welds at various dilution levels. Solidification starts at the nominal composition (C_o), which is controlled by the dilution level. The eutectic composition (C_e) is given by the inflection point where the eutectic reaction $L \rightarrow \gamma + \sigma$ begins. It is apparent that the eutectic composition decreases appreciably with increasing dilution. Figure 32 (b) shows the variation in the molybdenum partition coefficient (k) for the same dilution levels of interest. The partition coefficient for a given dilution does not vary significantly during solidification, but it increases slightly (from

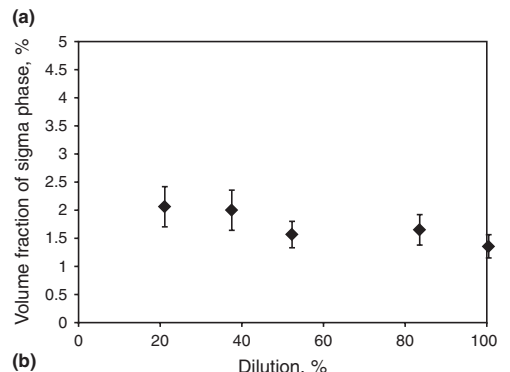
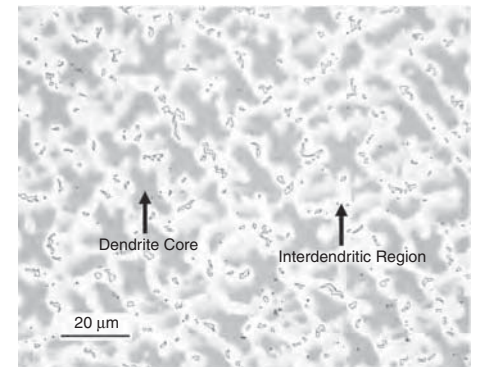


Fig. 31 (a) Light optical micrograph showing primary austenite and interdendritic σ phase that forms in a dissimilar weld between a superaustenitic stainless steel base metal and nickel-base filler metal. (b) Variation in σ -phase content with dilution. Source: Ref 47

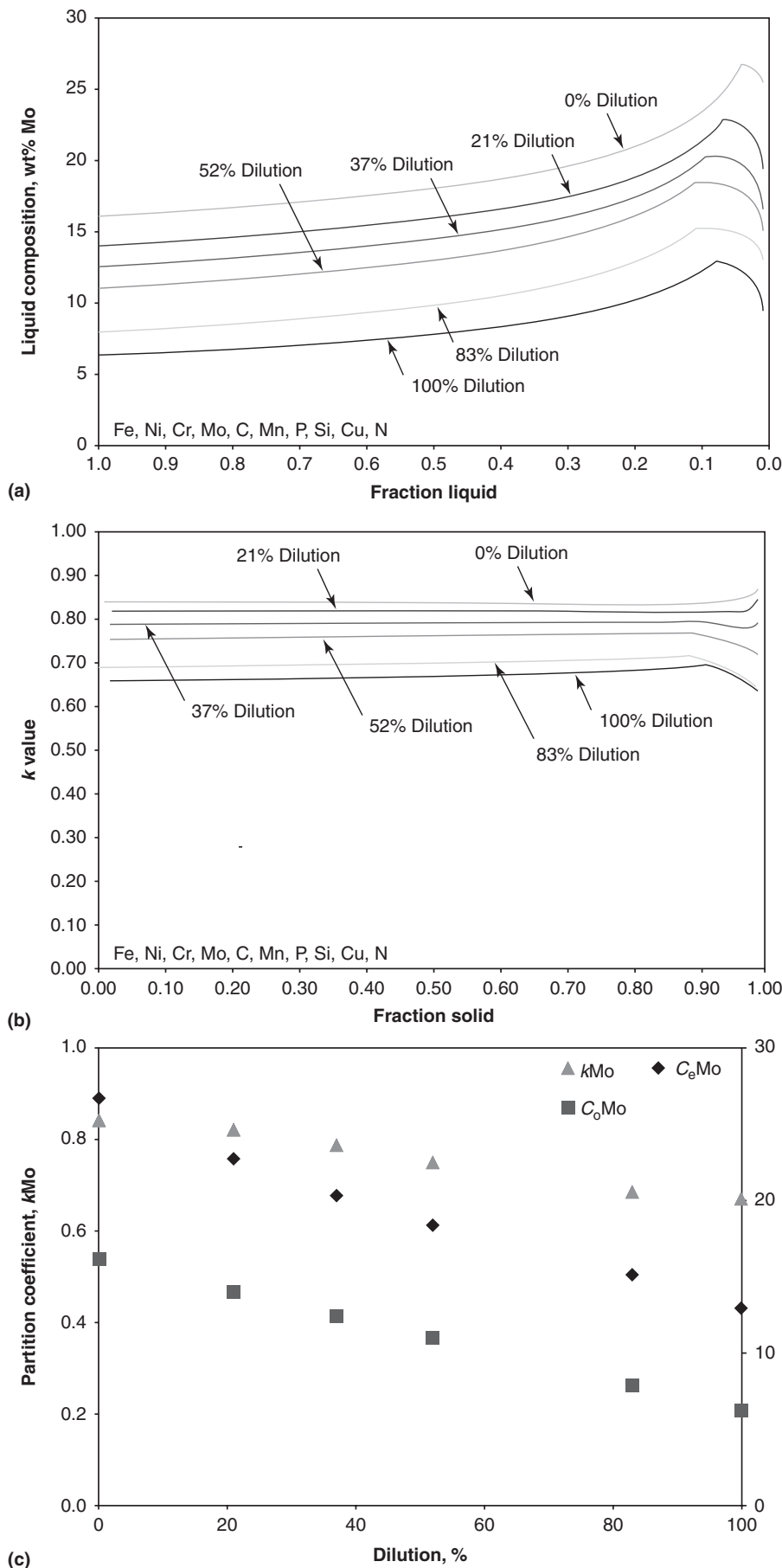


Fig. 32 Multicomponent Scheil calculations for fusion welds made between a superaustenitic stainless steel alloy and a nickel-base filler metal showing (a) variation in liquid composition with fraction liquid, (b) variation in k_{Mo} with fraction solid, and (c) variation in C_o , C_e , and k_{Mo} with dilution

~ 0.67 to 0.84) with decreasing dilution. Figure 32(c) summarizes the variations in C_o , C_e , and k as a function of dilution. An increase in C_o and a decrease in C_e and k will increase the fraction eutectic and resultant amount of secondary phase. These results demonstrate there are offsetting effects in these parameters that keep the σ -phase content relatively independent of the weld-metal composition. In other words, C_e and k each decrease with increasing dilution, which would, in itself, lead to an increase in fraction eutectic and amount of σ phase. However, these changes are offset by the decrease in nominal molybdenum concentration that occurs with increasing dilution. This accounts for the relatively constant σ -phase content observed in these welds.

The final σ -phase content will also depend on the maximum solid solubility of molybdenum in the austenite and σ phases. All of these factors can be accounted for with a complete multicomponent Scheil simulation. Table 3 shows the amount of σ phase calculated for all the dilution levels of interest. There is reasonable agreement between the measured and calculated amounts of σ phase. These results also carry important practical implications, because IN686 filler metal can be used at various dilution levels with minimal changes to the σ -phase content in the weld, which is beneficial from a solidification cracking and toughness standpoint.

Rapid Solidification Considerations

The conditions described previously ignore the effects of the nonplanar interface and solute buildup in the liquid on dendrite tip undercooling. Such factors can become important at high solidification rates associated with high-energy-density welding processes. These undercooling effects are shown schematically in Fig. 33. The liquidus and solidus lines for a planar interface (tip radius, $r = \infty$) are shown by the solid lines. Solute enrichment in the liquid at the solid/liquid interface results from solute rejection directly from the tip and diffusion down the solute gradient that exists between the cells. This local enrichment produces a reduction in the tip temperature, ΔT_C , as shown in Fig. 33. Undercooling is also produced by the surface energy effects due to the tip with a finite radius. In this case, the solidus and liquidus lines are depressed relative to those for an infinite

Table 3 Comparison of the percent σ values calculated using ThermoCalc and measured experimentally

Dilution, %	Calculated σ phase, %	Measured σ phase, %
100	1.9	1.4 ± 0.2
83	2.4	1.7 ± 0.3
52	2.3	1.6 ± 0.2
37	1.9	2.0 ± 0.4
21	1.4	2.1 ± 0.4

radius, as shown by the dotted lines. The corresponding undercooling associated with a finite tip radius is given by the ΔT_r term in Fig. 33. As a result of these two effects, the liquid temperature and composition can be changed significantly from (T_o, C_o) to (T_t, C_t) , as shown in the figure. Also note that this produces an increase in the dendrite core composition from kC_o to kC_t . This change in the operating point of the dendrite tip can have a significant effect on the stability of the primary solidification phase, the final distribution of solute in the solid, and the final phase distribution.

Different approaches have been used to solve the dendrite undercooling problem in order to determine the local tip temperature and composition. For example, Burden and Hunt (Ref 49) assumed that the dendrite tips grow with a radius that minimizes undercooling. This assumption was used to solve directly for the tip radius, which then provided a direct solution for the undercooling and resultant tip composition. However, this assumption does not capture the observed behavior in which a dendritic interface eventually reverts to a cellular and then planar interface at high solidification velocities. Note also that this reversion to a planar interface is not captured within the classical constitutional supercooling criteria (described previously), because the model neglects surface tension effects. At high solidification velocities, the cell spacing is decreased, which leads to an increase in the solid/liquid interfacial area. The increase in surface area helps accommodate the rapid rate of solute rejection required at high solidification velocities but also leads to increased surface energy. At very high velocities, the cellular interface is no longer energetically favorable, and a planar interface reappears.

The dendrite tip radius and solute redistribution around the tip are actually coupled, so that the assumption of a cell tip growing to minimize undercooling is not completely accurate. This condition has been considered in greater detail by Kurz et al. (Ref 21). In the KGT model, the tip radius is related to the temperature gradient and growth rate through the Peclet number (Pe) by:

$$R^2 \left[\frac{\pi^2 \Gamma}{Pe^2 D_1^2} \right] + R \left[\frac{m_1 C_o (1-k)}{D_1 [1 - (1-k)I(Pe)]} \right] + G = 0 \quad (\text{Eq 37})$$

where Γ is the Gibbs-Thomson parameter (ratio of specific solid/liquid interfacial energy to melting entropy), Pe is the Peclet number given by $Pe = Rr/2D_1$, and $I(Pe)$ is given by $I(Pe) = Pe \exp(Pe) E_1(Pe)$, where E_1 is the exponential integral function.

Direct solution of Eq 37 for the dendrite tip radius is not possible because Pe is defined in terms of both R and r . Thus, the expression must be solved numerically in which a wide range of Pe values are selected to determine $I(Pe)$, and then the quadratic Eq 37 is solved for R numerically. Once R is known, the dendrite radius is given by $r = 2PeD_1/R$. The

resultant tip temperature and composition are then given by:

$$C_t^* = \frac{C_o}{1 - (1-k)I(Pe)} \quad (\text{Eq 38})$$

$$T_t = T_o + m_1 C_t^* - \frac{2\Gamma}{r} \quad (\text{Eq 39})$$

As shown schematically in Fig. 33, this new “operating point” of the dendrite tip (i.e., the change in tip composition and temperature from (T_o, C_o) to (T_t, C_t)) also affects the subsequent solute redistribution because the new core composition is changed from kC_o to kC_t . Sarreal et al. (Ref 50) addressed this problem by assuming that undercooling at the dendrite tip is dissipated by forming a certain fraction of primary solid phase, f_s^o , that is given by the lever law at the undercooled temperature:

$$f_s^o = \frac{C_o - C_t^*}{C_t^* (k - 1)} \quad (\text{Eq 40})$$

Under conditions in which solute diffusion in the solid is negligible (which is often the case for substitutional alloying elements at high solidification velocities), the final fraction of eutectic that forms is then given by the modified form of the Scheil equation:

$$f_e = (1 - f_s^o) \left(\frac{C_e}{C_t^*} \right)^{\frac{1}{k-1}} \quad (\text{Eq 41})$$

Various levels of complexity can be accounted for with the KGT model. For example, D_1 and m_1 can each vary with temperature, while k can vary with both temperature and solidification velocity. At high solidification velocities, the value of $k \rightarrow 1$ due to solute trapping in the solid. This velocity dependence can be accounted for with the model proposed by Aziz (Ref 51) in which the effective distribution coefficient, k' , is given by:

$$k' = \frac{k + \frac{a_i R}{D}}{1 + \frac{a_i R}{D}} \quad (\text{Eq 42})$$

where a_i is related to the interatomic distance and is typically between 0.5 and 5 nm. Equation 42 has the form in which $k' = k$ at low values of R and $k' = 1$ at high R values.

Figure 34 shows example calculations of the KGT model for an Ag-5wt%Cu alloy. The results demonstrate how the tip radius (denoted as R in Fig. 34a), temperature, and core composition (C_s^* in Fig. 34c) change with increasing solidification velocity. The curves in Fig. 34(a) and (c) demonstrate how various assumptions about D_1 , m_1 , and k affect the results. Note that the dendrite radius initially decreases with increasing velocity but then rapidly increases and becomes infinite at high growth velocities. This is the condition in which a planar interface is restabilized. The

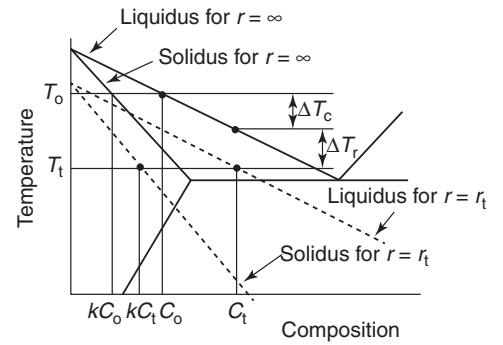


Fig. 33 Schematic illustration showing dendrite tip undercooling

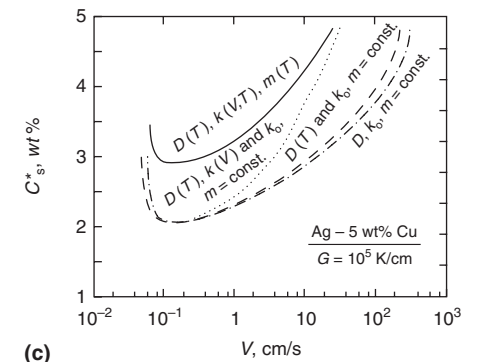
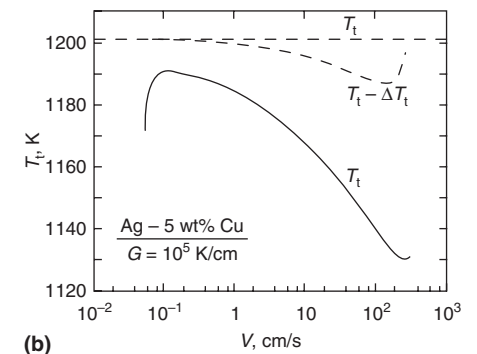
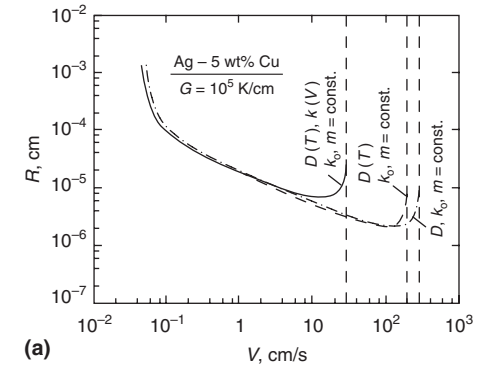


Fig. 34 Results from Kurz, Giovanola, Trivedi (KGT) model calculations showing variation in (a) dendrite radius, (b) dendrite tip temperature, and (c) cell core composition as a function of growth rate. Source: Ref 21

extent of undercooling at high velocities can be quite significant and can lead to subsequent enrichment in the cell core composition relative to that under ideal Scheil conditions (Fig. 34c). This effect provides one mechanism for reducing the extent of residual microsegregation that occurs in many alloys that exhibit low solute diffusivity in the solid.

Stainless steels represent an important group of engineering alloys in which dendrite tip undercooling can have a significant influence on the primary phase that forms. The composition of many commercial stainless steels is adjusted to induce primary delta-ferrite (δ) solidification. The delta-ferrite phase is desirable as the first solidification phase because it exhibits a higher solubility for tramp elements, such as phosphorus and sulfur. Thus, with primary ferrite solidification, more of the phosphorus and sulfur are kept in solution and avoid the low-melting-point phosphorus- and sulfur-rich phases that are known to aggravate solidification cracking. In contrast, the solubility for these tramp elements is relatively low in austenite (γ), and stainless steels that solidify as primary austenite are well known to be relatively sensitive to this form of cracking. Although some stainless steels have a nominal alloy composition that is designed to solidify as ferrite (under low solidification velocities), the nominal composition can lie close to the transition in primary solidification mode so that dendrite tip undercooling can cause a shift in the primary solidification mode at higher cooling rates.

Fukumoto and Kurz (Ref 52) used a multi-component form of the KGT model to predict how solidification velocity and resultant tip undercooling affects primary phase stability in stainless steels. In this work, interface response functions were developed by calculating the tip temperature of the δ and γ phases as a function of solidification velocity. An example calculation for an Fe-18Cr-11.3Ni (wt%) alloy solidified with a temperature gradient of 400 K/mm is shown in Fig. 35. The primary solidification phase is identified by noting that the phase with the highest tip temperature is the one that will solidify first. Note that, for this alloy and temperature gradient, a shift in the primary solidification mode is expected at a solidification rate of 3.2×10^{-2} m/s, and such shifts have been observed experimentally.

REFERENCES

1. T. Matsuda, T. Hashimoto, and T. Senda, *Trans. Natl. Res. Inst. Met. (Jpn.)*, Vol 11, 1969, p 43
2. S. Kou and Y. Le, *Metall. Trans. A*, Vol 19, 1988, p 1075–1082
3. T.F. Bower and M.C. Flemings, *Trans. AIME*, Vol 239, 1967, p 1620
4. D.A. Porter and K.E. Easterling, *Phase Transformations in Metals and Alloys*, 2nd ed., CRC Press, Boca Raton, FL, 1992
5. R.L. O'Brien, *Jefferson's Welding Encyclopedia*, 18th ed., American Welding Society, Miami, FL, 1997, p 316

6. S. Kou, *Welding Metallurgy*, 2nd ed., Wiley, Hoboken, NJ, 2003
7. Y. Arata, F. Matsuda, S. Mukae, and M. Katoh, *Trans. JWRI*, Vol 2, 1973, p 55
8. S. Kou and Y. Le, *Metall. Trans. A*, Vol 16, 1985, p 1345
9. M.C. Flemings, *Solidification Processing*, McGraw-Hill, New York, NY, 1974
10. B.P. Pearce and H.W. Kerr, *Metall. Trans. B*, Vol 12, 1981, p 479
11. J.C. Villafuerte and H.W. Kerr, *International Trends in Welding Science and Technology*, S.A. David and J.M. Vitek, Ed., ASM International, March 1993, p 189
12. M. Gauman, C. Bezencon, P. Canalis, and W. Kurz, *Acta Mater.*, Vol 49, 2001, p 1051–1062
13. S.L. Narasimhan, S.M. Copley, E.W. Van Stryland, and M. Bass, *Metall. Mater. Trans. A*, Vol 10, 1979, p 654–655
14. S. Yang, W. Huang, W. Liu, M. Zhong, and Y. Zhou, *Acta Mater.*, Vol 50, 2002, p 315–325
15. M. Gauman, S. Henry, F. Cleton, J.D. Wagniere, and W. Kurz, *Mater. Sci. Eng. A*, Vol 271, 1999, p 232–241
16. M. Rappaz, S.A. David, J.M. Vitek, and L.A. Boatner, *Metall. Mater. Trans. A*, Vol 20, 1989, p 1125–1138
17. J.M. Vitek, S.A. David, and L.A. Boatner, *Sci. Technol. Weld. Join.*, Vol 2, 1997, p 109–118
18. J.A. Brooks and A. Thompson, *Int. Mater. Rev.*, Vol 36, 1991, p 16–44
19. J.D. Hunt, *Mater. Sci. Eng. A*, Vol 65, 1983, p 75–83
20. M.H. Burden and J.D. Hunt, *J. Cryst. Growth*, Vol 22, 1974, p 109–116
21. W. Kurz, B. Giovanola, and R. Trivedi, *Acta Mater.*, Vol 34, 1986, p 823–830
22. M. Gauman, R. Trivedi, and W. Kurz, *Mater. Sci. Eng. A*, Vol 226, 1997, p 763–769
23. F. Yoshihiro, K. Saida, and K. Nishimoto, *Mater. Sci. Forum*, Vol 512, 2006, p 313–318
24. J.M. Vitek, *Acta Mater.*, Vol 53, 2005, p 53–67
25. W. Kurz and D.J. Fisher, *Fundamentals of Solidification*, Trans. Tech Publications, Switzerland, 1989
26. A. Munitz, *Metall. Mater. Trans. B*, Vol 16, 1985, p 149
27. J.A. Paul and T. DebRoy, *Rev. Modern Phys.*, Vol 67, 1995, p 85
28. S. Kou and Y. Le, *Metall. Mater. Trans. A*, Vol 13, 1982, p 1141
29. T.P. Battle, *Int. Mater. Rev.*, Vol 37, 1992, p 249–270
30. E. Scheil, *Z. Metallkd.*, Vol 34, 1942, p 70–77
31. H.D. Brody and M.C. Flemings, *Trans. AIME*, Vol 236, 1966, p 615–624
32. T.W. Clyne and W. Kurz, *Metall. Trans. A*, Vol 12, 1981, p 965–971

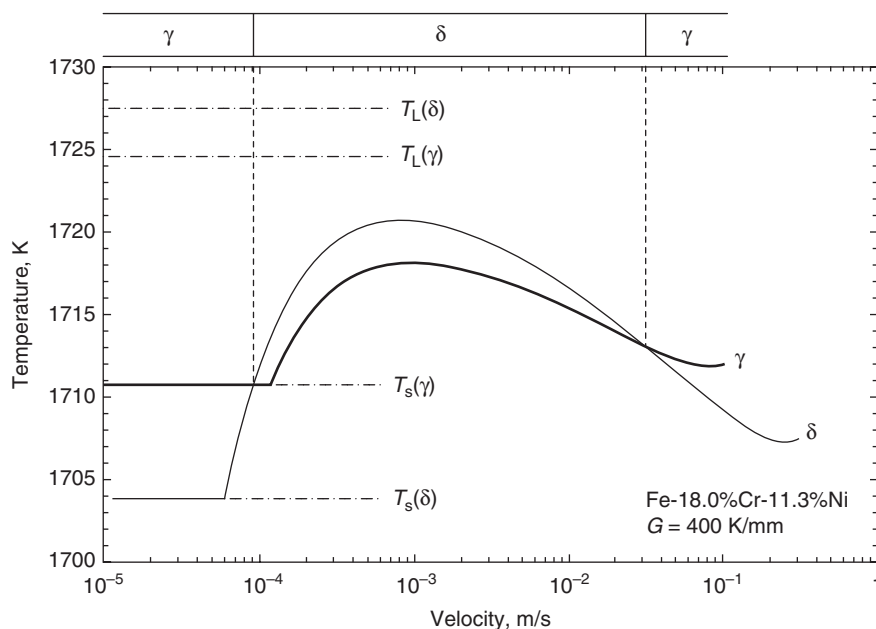


Fig. 35 Phase stability calculations for an Fe-18Cr-11.3Ni alloy solidified with a temperature gradient of 400 K/mm (290 °F/in.). The primary solidification phase is identified by noting that the phase with the highest tip temperature is the one that will solidify first. Source: Ref 52

33. S. Kobayashi, *Trans. ISIJ*, Vol 28, 1988, p 728–735
34. J.N. DuPont, J.C. Lippold, and S.D. Kiser, *Welding Metallurgy and Weldability of Nickel Base Alloys*, John Wiley & Sons, Hoboken, NJ, 2009
35. M.J. Cieslak, T.J. Headley, T. Kollie, and A.D. Romig, *Metall. Trans. A*, Vol 19, 1988, p 2319–2331
36. J.N. DuPont, C.V. Robino, A.R. Marder, M. R. Notis, and J.R. Michael, *Metall. Mater. Trans. A*, Vol 29, 1998, p 2785–2796
37. H. Joo and H. Takeuchi, *Tokai Daigaku Kiyo*, Vol 34, 1994, p 203–209
38. U. Heubner, M. Kohler, and B. Prinz, *Superalloys 1988*, Sept 18–22, 1988, TMS, Warrendale, PA, p 437–447
39. J.N. DuPont, C.V. Robino, and A.R. Marder, *Metal. Mater. Trans. A*, Vol 29, 1998, p 2797–2806
40. S.W. Banovic and J.N. DuPont, *Sci. Technol. Weld. Join.*, Vol 6, 2003, p 274–383
41. K.D. Adams and J.N. DuPont, *Metall. Mater. Trans. A*, Vol 41, 2010, p 194
42. M.J. Perricone and J.N. DuPont, *Metall. Mater. Trans. A*, Vol 37, 2005, p 1267–1289
43. J.N. DuPont and C.V. Robino, *Sci. Technol. Weld. Join.*, Vol 13, 2008, p 550–565
44. D.F. Susan, C.V. Robino, M.J. Minicozzi, and J.N. DuPont, *Metall. Mater. Trans. A*, Vol 37, 2006, p 2817–2826
45. J.N. DuPont, *Metall. Mater. Trans. A*, Vol 37, 2006, p 1937–1947
46. J.N. DuPont, C.V. Robino, and A.R. Marder, *Acta Mater.*, Vol 46, 1998, p 4781–4790
47. A. Stockdale, M.S. thesis, Lehigh University, Sept 2010
48. ThermoCalc S. 2008, ThermoCalc Software, Stockholm
49. M.H. Burden and J.D. Hunt, *J. Cryst. Growth*, Vol 22, 1974, p 109–116
50. J.A. Sarreal, *Metall. Trans. A*, Vol 17, 1986, p 2063–2073
51. M.J. Aziz, *J. Appl. Phys.*, Vol 53, 1982, p 1158
52. S. Fukumoto and W. Kurz, *ISIJ Int.*, Vol 37, 1997, p 677–684

Dilution in Fusion Welding

John N. DuPont, Lehigh University

Introduction

MANY APPLICATIONS EXIST in which alloys of differing compositions are joined by fusion welding. In these applications, the final fusion zone can potentially exhibit a composition that lies anywhere between that of each alloy. The final composition and corresponding microstructure and properties of the fusion zone will be determined by the dilution level. The dilution level is, in turn, strongly affected by the welding parameters. Thus, many dissimilar metal welding applications require careful control over the welding parameters and corresponding dilution level in order to produce welds with the proper microstructure and properties for the intended service. The objective of this article is to review the relation between dilution and bulk fusion-zone composition, describe the effect of welding parameters on dilution, and provide some typical examples of microstructure and property control in dissimilar weld applications.

Dilution and Fusion Zone Composition

Dilution can be understood with the schematic illustration provided in Fig. 1, which shows the amount of base metal melted (A_{bm}) and filler metal added (A_{fm}) in a typical fusion weld. The dilution is given by:

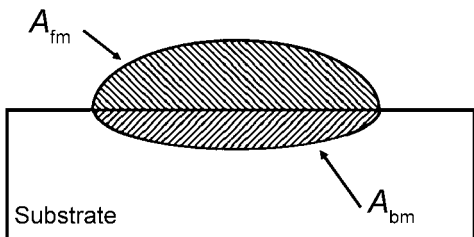


Fig. 1 Schematic illustration of dilution showing the amount of base metal melted (A_{bm}) and filler metal added (A_{fm}) in a typical fusion weld

$$D = \frac{A_{bm}}{A_{bm} + A_{fm}} \quad (\text{Eq 1})$$

Inspection of Eq 1 demonstrates that the dilution is simply a measure of the amount of base metal that mixes in with the fusion zone. In many applications, it is important to control the dilution level to provide the proper microstructure and properties for the intended service. For example, in cladding applications, the dilution is typically minimized in order to maintain the high alloy level and concomitant wear or corrosion resistance of the cladding. The concentration of any alloying element, i , in the fusion zone (C_{fz}^i) is determined by the dilution and concentrations of element i in the base metal (C_{bm}^i) and filler metal (C_{fm}^i) by:

$$C_{fz}^i = DC_{bm}^i + (1 - D)C_{fm}^i \quad (\text{Eq 2})$$

Equation 2 demonstrates that the weld-metal composition varies linearly with the dilution level. An example of Eq 2 is shown in Fig. 2, which shows the fusion-zone chromium concentration for a weld made on a carbon steel with no chromium ($C_{bm}^{Cr} = 0$) and a filler metal with 20 wt% Cr ($C_{fm}^{Cr} = 20$). Note that the fusion

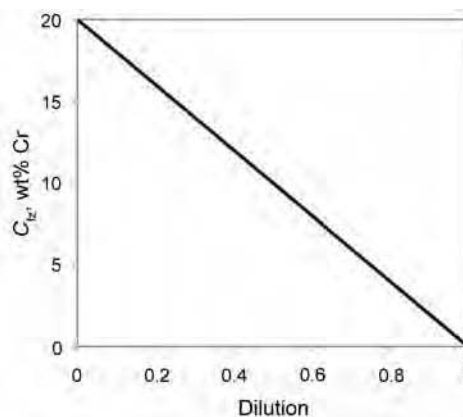


Fig. 2 Calculated fusion-zone chromium concentration as a function of dilution for a weld made on a carbon steel with no chromium and a filler metal with 20 wt% Cr

composition varies linearly from the filler-metal chromium concentration at 0 dilution to the base-metal chromium concentration at a dilution value of unity. It is important to note that a dilution value of 0 does not actually represent a fusion weld, because no base metal has melted. This condition would produce lack of fusion between the base metal and fusion zone. Thus, although attempts are often made to minimize dilution (depending on the application), it is important to note that some finite dilution is required to induce mixing between the base and filler metal in the molten state in order to form the weld. A dilution value of unity (or 100%) represents an autogenous weld in which no filler metal is added. Thus, it is not possible to achieve 100% dilution when a filler metal with a composition different than that of the base metal is used.

Equations 1 and 2 assume that the chemical composition of the weld can be determined based solely on geometric information (i.e., the amount of base metal melted and filler metal added). Recent measurements have verified that this is generally accurate. Figure 3 compares the weld-metal dilution determined from both geometric measurements and direct chemical composition measurements made by electron probe microanalysis (EPMA) (Ref 1). These data were obtained on fusion welds made between alloy AL-6XN (a superaustenitic stainless steel) and nickel-base alloys IN625 and IN622. Note that there is good agreement between the weld-metal compositions measured with each technique, thus confirming that the fusion-zone composition can generally be determined accurately with geometrical measurements and knowledge of the base-metal and filler-metal compositions.

It should be noted that other factors can change the final fusion-zone composition in ways that are not accounted for in the simple geometrical dilution equations described previously. For example, elemental losses due to evaporation from the pool surface can occur during welding and lead to a reduction in alloying content in the fusion zone. An example of this is provided in Fig. 4, which shows the manganese content of the base metal and the fusion

zone for welds made on manganese-containing stainless steels (Ref 2). Note that the manganese content in the fusion zone is appreciably lower than that of the base metal, and this has been attributed to the relatively high vapor pressure of manganese. Similar effects have been reported for losses of magnesium in aluminum-magnesium alloys, and evaporative losses can also occur from the surface of hot molten droplets in the gas metal arc welding process (Ref 3). The effect of these losses can be important when the alloying element of interest plays an important role in controlling the strength in the alloy (i.e., by solid-solution hardening or precipitation strengthening). Additives made to the weld beyond the filler metal can also affect the weld-metal composition,

such as the addition of active fluxes that are used to promote good penetration. Similarly, the liquid pool can sometimes dissolve elements from the shielding gas, such as oxygen and nitrogen (Ref 4). This can lead to relatively minor changes in alloy compositions, but these changes can often have significant effects on the weld-metal microstructure and properties. In high-energy-density welds made at high welding speeds, the melting and solidification occur very rapidly so that there is often not sufficient time for uniform mixing in the melt pool, and macrosegregation exists in the fusion zone. These factors must be considered on an individual basis when using the expressions for fusion-zone composition described previously.

It is also important to note that the fusion-zone composition given by Eq 2 assumes there is uniform mixing of alloying elements in the liquid state, so that the composition is uniform on a macroscopic scale. This is also found to be generally true due to the rather aggressive liquid mixing that occurs in the weld due to the various forces that lead to fluid flow (i.e., buoyancy force, Lorentz force, surface-tension-driven force, and force from the impinging arc plasma, Ref 5). Figure 5 shows EPMA composition profiles for iron, nickel, and chromium acquired from a weld made with 308 stainless steel filler metal on A36 carbon steel with the gas metal arc welding process (Ref 6). The composition trace was made from the top surface of the weld to the fusion line. An expanded view of the composition profile near the fusion line is provided in Fig. 5(b). Note that the weld is over 3 mm (0.1 in.) in length from the fusion line to the weld surface, and the partially mixed zone (PMZ) is a very small fraction of this length (~50 μm, or 0.002 in.). While the PMZ is always present near the fusion line of dissimilar welds, the width of this zone is generally small in relation to the fusion-zone size. There are instances where the PMZ can become appreciable in size. Figure 6 shows composition profiles for claddings in which commercially pure aluminum was deposited onto a carbon steel using the gas tungsten arc welding process (Ref 7). Each cladding was prepared at similar values of heat input but increasing filler-metal feed speed, the values of which are indicated in the figure caption. Note that the PMZ becomes an appreciable size of the fusion zone as the filler-metal speed is increased. This effect can become important in gas tungsten arc welds but is generally not expected in welds made with consumable electrode processes due to the more aggressive mixing that occurs from the molten droplet transfer.

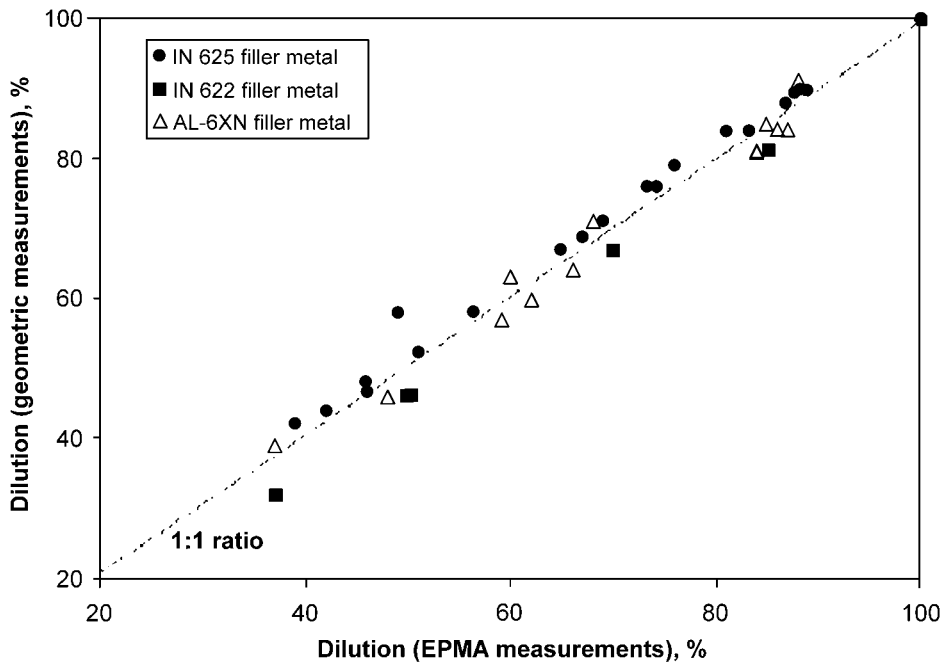


Fig. 3 Comparison of weld-metal dilution determined from geometric measurements and direct chemical composition measurements made by electron probe microanalysis (EPMA). Source: Ref 1

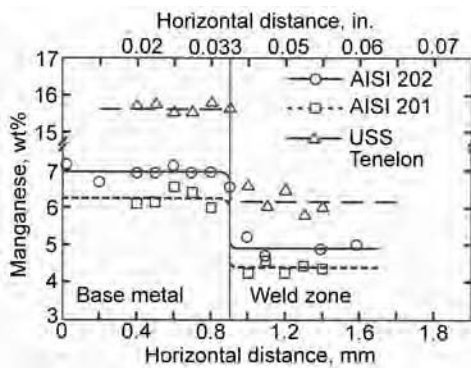


Fig. 4 Manganese content of the base metal and the fusion zone for welds made on manganese-containing stainless steels. Source: Ref 2

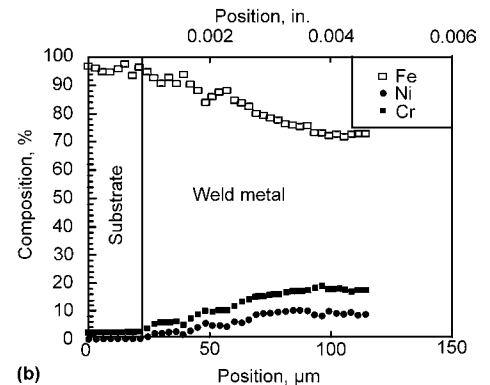
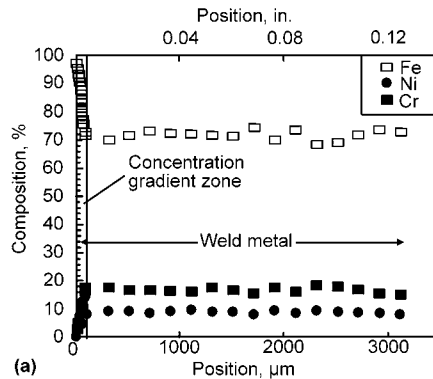


Fig. 5 Composition profiles for iron, nickel, and chromium acquired from a weld made with 308 stainless steel filler metal on A36 carbon steel with the gas metal arc welding process. Source: Ref 6

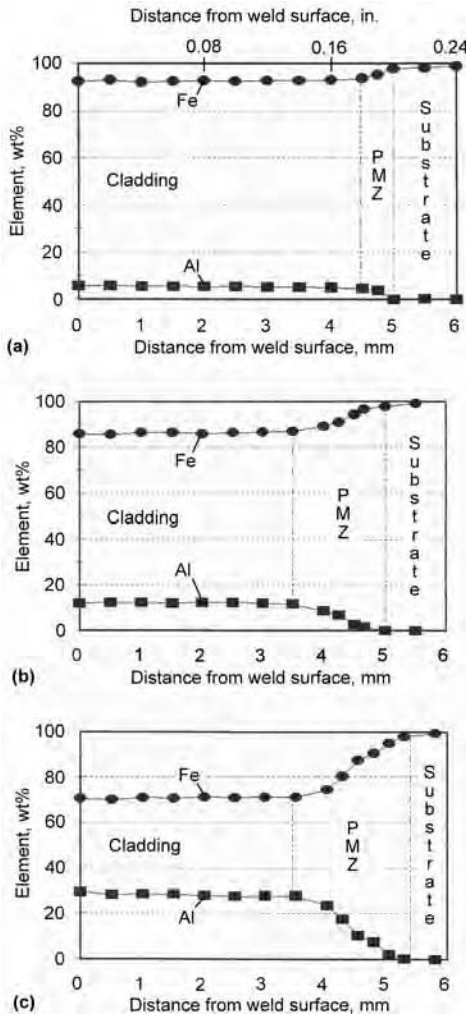


Fig. 6 Composition profiles for claddings in which commercially pure aluminum was deposited onto a carbon steel using the gas tungsten arc welding process at a fixed heat input with various filler-metal feed rates. (a) 15 mm/s (0.6 in./s). PMZ, partially mixed zone. (b) 30 mm/s (1.2 in./s). (c) 40 mm/s (1.6 in./s). Source: Ref 7

Influence of Welding Parameters on Dilution

The volumetric filler-metal feed rate (V_{fm}) and arc power (P) are the primary welding variables that control dilution. An example of this for gas tungsten arc welds made on alloy AL-6XN with IN625 filler metal is shown in Fig. 7. The plot shows a wide range of welds that were made at various values of filler-metal feed rate and arc power, and the number next to each data point represents the dilution level. The filler-metal feed rate controls the amount of filler metal added to the fusion zone, while the arc power generally controls the amount of base metal that is melted and mixed in with the fusion zone. For example, note in Fig. 7 that, for a fixed arc power, the dilution level decreases as the filler-metal feed rate increases. For a fixed arc power, the amount of melted

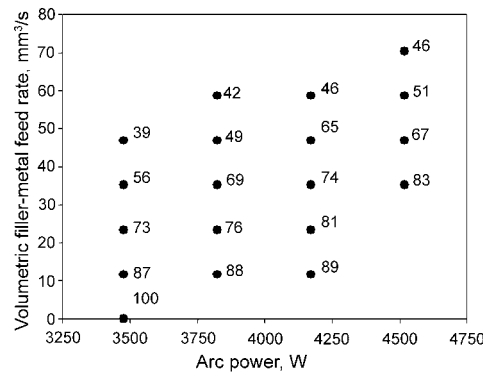


Fig. 7 Experimental matrix of fusion welds produced in which AL-6XN was the base metal and IN625 was the filler metal. Numbers to the right signify the dilution level.

base metal (i.e., the A_{bm} term in Eq 1) is fairly constant, but the increase in filler-metal feed rate causes the A_{fm} term to increase. As a result, the dilution decreases. Conversely, welds made with a fixed feed rate exhibit an increase in dilution with increasing arc power. In this case, the A_{fm} term is essentially constant, but the increase in arc power increases the amount of base metal melted, thus leading to an increase in the dilution level.

The qualitative effects of welding variables on dilution can be understood in a more quantitative fashion through the use of process efficiency factors. As shown in Fig. 1, dilution is typically determined by measurement of A_{fm} and A_{bm} using metallographic methods. However, dilution is actually the result of the volumetric quantities V_{fm} and V_{bm} , where V_{fm} is the volume of deposited filler metal and V_{bm} is the volume of melted base metal. These volumetric terms are simply reduced by one dimension into area terms when the sample is cross sectioned and the measurements of A_{fm} and A_{bm} are made. The assumption is made here that the cross-sectional areas do not vary along the length of the weld. Constant cross-sectional areas are produced along the weld length when the volumetric melting rate of the filler metal (V_{fm}) and the base metal (V_{bm}) are constant with travel speed. Under this assumption, dilution can also be expressed in terms of the volumetric melting rates of the base metal (V_{bm}) and the filler metal (V_{fm}) as:

$$D = \frac{V_{bm}}{V_{bm} + V_{fm}} \quad \text{(Eq 3)}$$

The volumetric melting rate of the filler metal is a controlled variable of the process. The implicit assumption in using the set value of volumetric filler-metal feed rate to represent the actual deposited volumetric filler-metal rate is that filler-metal losses due to spatter are negligible. An expression for V_{bm} can be obtained by considering a simplified balance of power

terms across the welding arc, which is facilitated by thermal efficiency factors (Ref 6, 8):

$$\eta_a \eta_m P = V_{fm} E_{fm} + V_{bm} E_{bm} \quad \text{(Eq 4)}$$

where η_a and η_m are the arc and melting efficiencies, respectively; P is the arc power; and E_{fm} and E_{bm} are the melting enthalpies of the filler metal and base metal, respectively. The left side of Eq 4 represents the melting power delivered by the arc, while the right side represents the power required for melting of the base metal and filler metal. The arc efficiency is essentially constant for a given process, while the melting efficiency can be estimated based on knowledge of the welding parameters (Ref 8). Thus, V_{bm} is the only unknown in Eq 4 and can be expressed as:

$$V_{bm} = \frac{\eta_a \eta_m P - V_{fm} E_{fm}}{E_{bm}} \quad \text{(Eq 5)}$$

Combining Eq 3 and 5 yields an expression for dilution in terms of the welding parameters, efficiency factors, and melting enthalpies of the filler metal and base metal:

$$D = \frac{1}{1 + \frac{\eta_a \eta_m P - V_{fm} E_{fm}}{V_{fm} E_{fm}}} \quad \text{(Eq 6)}$$

Note that both melting efficiency and dilution depend only on the volumetric quantities of the deposited filler metal and melted base metal. Thus, the shape of the weld does not need to be known to estimate these quantities.

It is interesting to note that the travel speed does not appear explicitly in Eq 6 when experience indicates that increases in travel speed will lead to increases in dilution (Ref 9). The relation between travel speed and dilution is readily apparent when the effect of travel speed on melting efficiency is considered. It is well known that increasing travel speed leads to an increase in the melting efficiency and a concomitant increase in the melting power (Ref 8). Inspection of Eq 5 indicates this will lead to an increase in V_{bm} with a corresponding increase in dilution. Therefore, the increase in dilution that is known to occur with travel speed is actually a direct result of the increase in melting efficiency.

Equation 6 demonstrates that dilution depends only on the ratio of volumetric filler-metal feed rate to melting power; that is, the individual values of V_{fm} and $\eta_a \eta_m P$ are not important. Figure 8 compares the measured and calculated dilution values as a function of the $V_{fm}/\eta_a \eta_m P$ ratio for dissimilar welds between alloy AL-6XN and IN625, and there is good agreement between the measured and calculated values. This validates the use of Eq 6 for estimating the weld-metal dilution from knowledge of the processing parameters, efficiency factors, and thermophysical properties and also demonstrates that dilution is generally controlled by the $V_{fm}/\eta_a \eta_m P$ ratio.

In many applications, it is often desirable to operate at high filler-metal feed rates (deposition rates) for economic reasons, while maintaining low dilution levels for corrosion resistance or avoidance of undesirable phase formation. In this regard, it is useful to develop a graphical display that reveals the effect of processing parameters on dilution. Equation 6 can be solved in terms of the deposition rate:

$$V_{fm} = \left(\frac{\gamma}{E_{bm} + \gamma E_{fm}} \right) \eta_a \eta_m P \tag{Eq 7}$$

$$\gamma = \frac{1}{D} - 1 \tag{Eq 8}$$

Equations 7 and 8 indicate that, for a given filler-metal/base-metal combination (i.e., E_{fm} and E_{bm} fixed), a plot of filler-metal feed rate (V_{fm}) against melting power ($\eta_a \eta_m P$) will yield various slopes that depend only on the dilution. An indication of the maximum filler-metal feed rate for a given melting power can be considered to be reached when the dilution is reduced to zero and the filler metal does not adequately fuse to the base metal. This occurs when the volumetric melting rate of the substrate is zero.

Figure 9 shows an example of a dilution diagram calculated for deposition of 308 stainless steel ($E_{fm} = 8.7 \text{ J/mm}^3$) onto A36 carbon steel ($E_{bm} = 10.5 \text{ J/mm}^3$). The filler-metal feed rate is plotted as a function of the melting power, and the slopes, which correspond to various calculated dilution levels, are plotted in 10% increments. Because the filler-metal/substrate combination is fixed here, the slopes are determined only by the dilution. A boundary between an inoperable range and an operable range is shown that describes the conditions for no dilution (i.e., a lack of fusion condition). Data for the submerged arc welding process are plotted on the diagram. The measured values of dilution are shown in the data points for comparison to the calculated isodilution lines, and the agreement is reasonable.

The effects of processing parameters are readily apparent on the diagram. For a fixed filler-metal feed rate, the dilution increases with increasing melting power. In this case, the extra melting power cannot be absorbed by the filler metal if the filler-metal feed rate is fixed, so the substrate absorbs the extra melting power, which results in an increase in the volumetric melting rate of the base metal and a concomitant increase in dilution. Note that a filler-metal feed rate of zero describes an autogenous weld that always has 100% dilution, as exhibited by the diagram. Conversely, for a given melting power, an increase in the filler-metal feed rate results in a decrease in dilution. In this case, additional filler metal is added without a significant change in the amount of melted base metal, leading to decreased dilution. When the filler-metal feed rate is increased beyond the

operable/inoperable boundary for a fixed melting power, the dilution reaches 0%, and lack of fusion is likely to result. The boundary between the inoperable and operable regimes simply represents the condition in which the

filler-metal feed rate is increased to the point in which all the melting power would be required to melt the filler metal, so that no power remains to melt the base metal. It is recognized that this somewhat oversimplifies

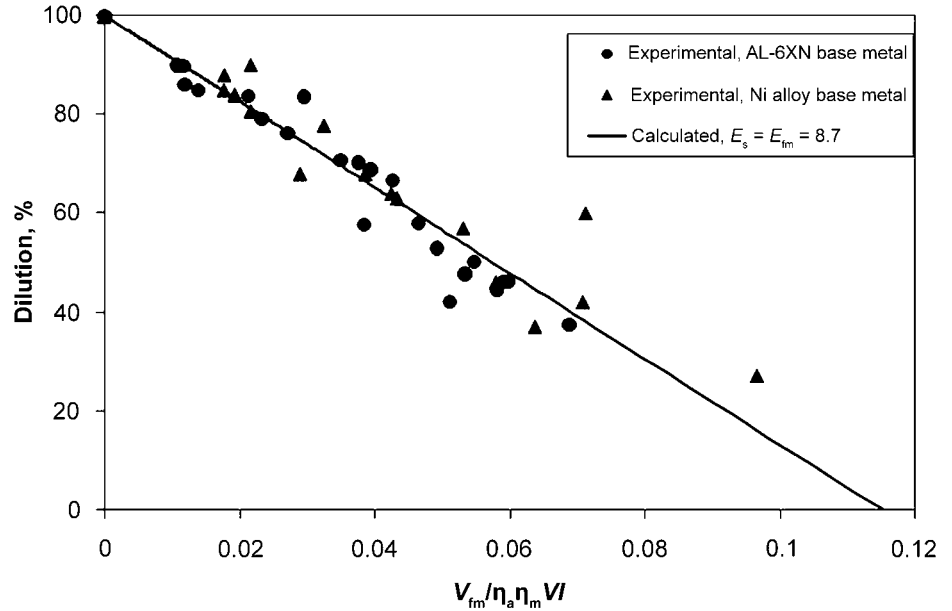


Fig. 8 Comparison of measured and calculated dilution values as a function of the $V_{fm} / \eta_a \eta_m P$ (where $P = VI$) ratio for dissimilar welds between alloy AL-6XN and IN625. Source: Ref 1

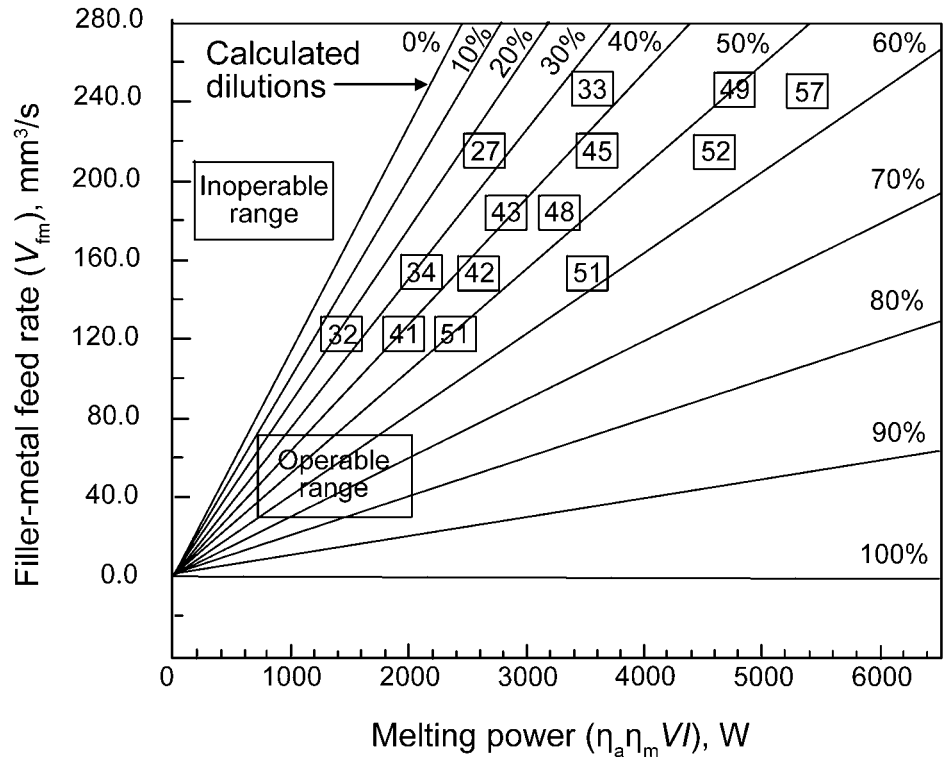


Fig. 9 Dilution diagram calculated for deposition of 308 stainless steel onto A36 carbon steel. Source: Ref 1

the problem, because it does not account for the relative rates of heat flow between the filler metal and base metal, but experimental results show this to be a reasonable approximation (Ref 10).

It should be recognized that the previous discussion pertains mainly to simple single-pass bead-on-plate welds. In more complex joint designs, other factors besides those described previously can also influence the dilution level. Figure 10 illustrates some examples. In an autogenous dissimilar weld, the placement of the heat source relative to the position of the seam in a square butt joint will influence the dilution, as shown in Fig. 10(a) and (b). In Fig. 10(a), the heat source is located to the left of the seam and will therefore melt more of alloy A, while Fig. 10(b) represents the reverse situation. In a multipass weld, the dilution can vary with position within the joint, as shown in Fig. 10(c). Here, the dilution may be high near the root of the weld, where a relatively large portion of base metal is melted. However, the dilution is minimized near the center of the cap pass, where the base-metal melting is minimized. Other welding parameter changes can also affect dilution. The heat balance and concomitant extent of melting between the electrode and base metal will be controlled by the polarity. For example, with the gas tungsten

arc welding process, a relatively deep weld pool will be created when the process is operated with electrode negative polarity, because a larger fraction of the thermal energy from the arc exists at the base metal. This will produce high dilution relative to electrode positive polarity, in which the weld pool is shallower due to a larger fraction of thermal energy at the electrode.

Influence of Dilution on Fusion-Zone Microstructure and Properties

The microstructure and corresponding properties of fusion welds are strongly controlled by the weld-metal composition. Wide variations in fusion-zone microstructure and properties are therefore possible in dissimilar welds that can exhibit large variations in dilution. Other articles in this Handbook provide detailed discussions on composition-microstructure-property relations in fusion welds that should be consulted when dissimilar welds are made between specific alloy systems. Only a few examples are provided here on common dissimilar welds of practical importance.

Deposition of Stainless Steel on Carbon or Low-Alloy Steel

Stainless steels are often deposited onto carbon and low-alloy steels for wear and/or corrosion resistance. In these applications, the final fusion-zone microstructure can be estimated fairly accurately with the Schaeffler diagram shown in Fig. 11. This diagram is used to estimate the final microstructure of steels and stainless steels based on the use of chromium equivalent (Cr_{eq}) and nickel equivalent (Ni_{eq}) values. Consider the deposition of 310 stainless steel with a typical composition of 0.05C-1.5Mn-25Cr-20Ni-0.5Si (all in weight percent) onto a low-alloy steel with a composition of 0.10C-1.0Mn-0.6Si-1.0Mo-2.25Cr. For the 310 stainless steel, $Cr_{eq} = 25.75$ and $Ni_{eq} = 22.25$. For the low-alloy steel, $Cr_{eq} = 4.15$ and $Ni_{eq} = 3.50$. These values are plotted on the diagram in Fig. 11. A fusion weld made between these two alloys can exhibit all possible Cr_{eq} and Ni_{eq} values that lie on a line connecting the two end points representing the individual alloys. Thus, depending on the dilution, the bulk fusion-zone microstructure can be fully austenitic, martensitic, or dual-phase martensite and austenite. A simple graphical procedure can be used to determine the dilution ranges that produce these corresponding microstructures. Note that the Cr_{eq} and Ni_{eq} values for 310 stainless steel represent 0% dilution, while the values for the low-alloy steel represent 100% dilution. The dilution level of any point along the line is given simply by the distance from the end point for 310 stainless steel to the point of interest, divided by the total distance of the line. For example, the phase boundary between the austenite and austenite plus martensite (A + M) regions occurs at 50% dilution, and the phase boundary between the A + M and martensite regions occurs at 67% dilution. These values are also noted on the diagram. This simple approach is convenient for setting dilution limits that are needed to produce a desired microstructure for a given application.

It should be noted that martensite will always form somewhere within the PMZ of dissimilar welds made between stainless steels and low-alloy or carbon steels. While the bulk Cr_{eq} and Ni_{eq} values of the fusion weld can be represented by any point along the line in Fig. 11, the PMZ will exhibit the entire range of Cr_{eq} and Ni_{eq} values that exist from the bulk weld to the low-alloy steel due to the composition gradients in the PMZ discussed previously. More detail on microstructural evolution near the fusion line of such dissimilar welds can be found in Ref 11 and 12.

Joining of Superaustenitic Stainless Steels

Another typical application of dissimilar welds involves the use of nickel-base filler metals (e.g., IN622, IN625, IN686) with

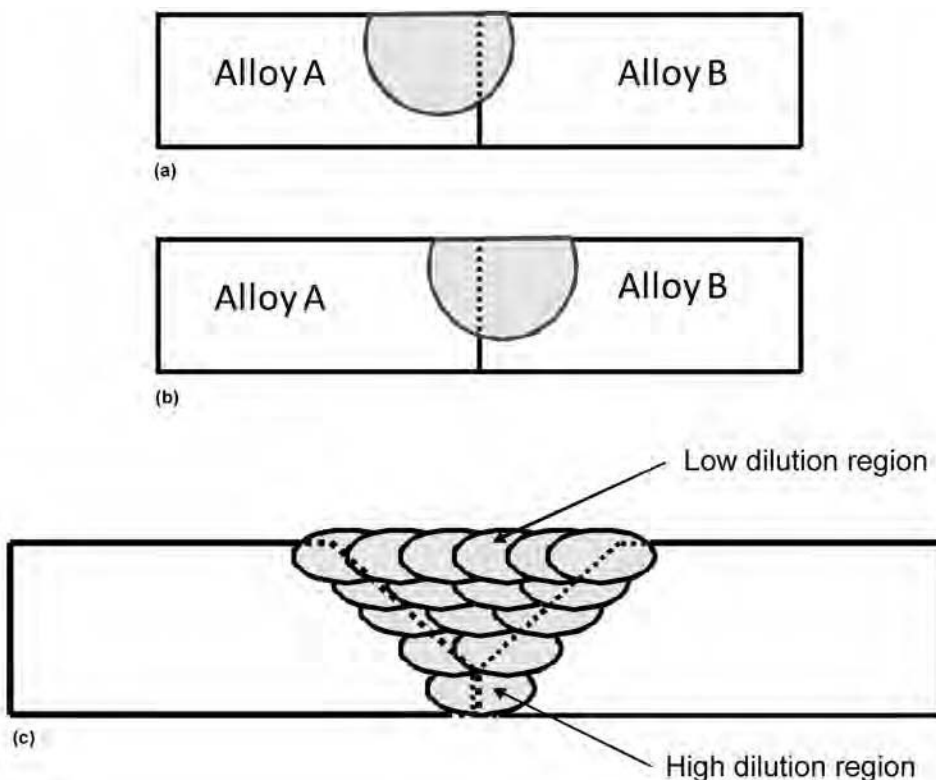


Fig. 10 Example of additional factors that can affect dilution. (a) and (b) Placement of the heat source relative to seam in a square butt weld. (c) Variation in dilution in a multipass butt weld

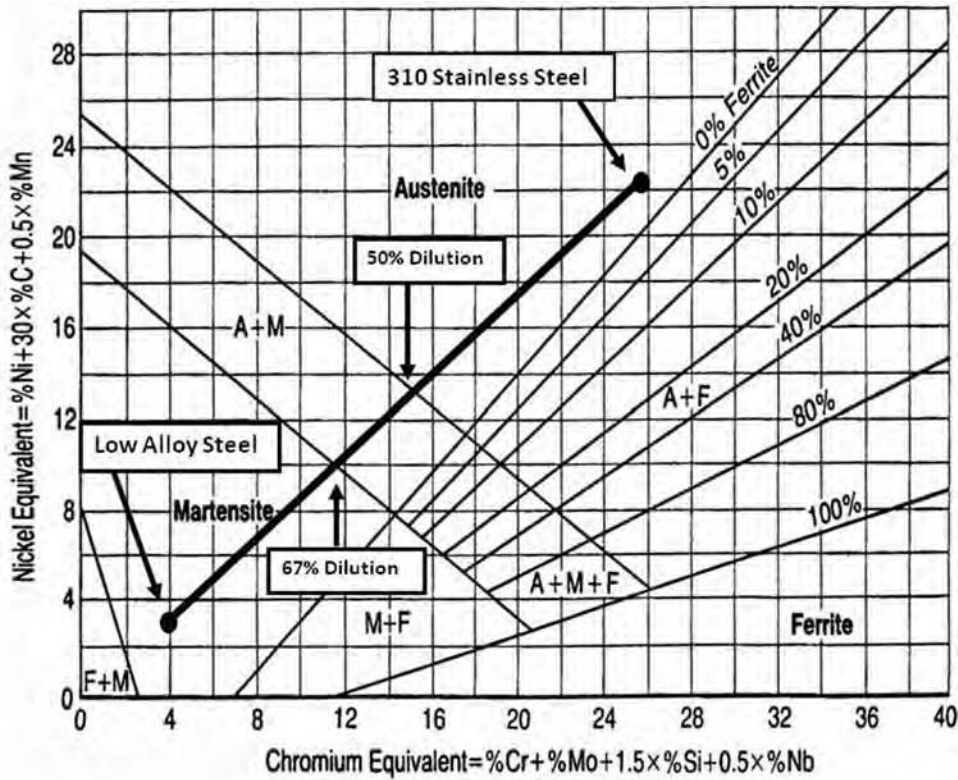


Fig. 11 Illustration of use of the Schaeffler diagram for estimating the microstructure for welds in which 310 stainless steel is deposited onto a low-alloy steel

relatively high molybdenum concentrations for joining of superaustenitic stainless steels. Superaustenitic stainless steels contain relatively high concentrations of nickel, chromium, nitrogen, and molybdenum for improved resistance to corrosion in a wide variety of aqueous media. However, the corrosion resistance of the weld can often be inferior to that of the base metal due to microsegregation of molybdenum (Ref 13). The microsegregation leaves the dendrite cores depleted in molybdenum, rendering them susceptible to accelerated corrosive attack (Ref 1, 13). In this case, nickel-base filler metals are used to enrich the molybdenum concentration of the weld as an aid to restoring the corrosion resistance. The use of nickel-base alloys does not prevent microsegregation of molybdenum, but the elevated molybdenum concentration in the weld helps counteract the negative effect due to microsegregation. For these applications, it is desirable to minimize the dilution level in order to maintain high concentrations of molybdenum in the weld zone for adequate corrosion resistance.

Figure 12 shows how dilution affects the corrosion resistance of welds made on alloy CN3MN (a cast superaustenitic stainless steel with a nominal molybdenum concentration of 6.2 wt%) using IN686 filler metal (approximately 16 wt% Mo). The plot shows the normalized mass loss as measured in the ASTM G48 test, which involves immersion in a 6 wt% solution of FeCl₃ at 75 °C (165 °F). The values next to each data point indicate the bulk molybdenum concentration in the weld. Also shown are the samples after each test in which the location of the weld and base metal are indicated. Note that, at the two highest dilution levels, the weight loss is relatively high, and extensive corrosion occurs in the weld. In contrast, dilution levels below approximately 50% lead to relatively low mass loss, and the weld exhibits less evidence of corrosion than the base metal. This improved corrosion resistance is attributed to the higher molybdenum concentration of the welds that were made with relatively low dilution values.

REFERENCES

1. S.W. Banovic, J.N. DuPont, and A.R. Marder, Dilution and Microsegregation in Dissimilar Metal Welds between Super Austenitic Stainless Steels and Ni Base Alloys, *Sci. Technol. Weld. Join.*, Vol 6 (No. 6), 2003, p 374–383, www.maney.co.uk/journals/stw and www.ingentaconnect.com/content/maney/stwj
2. T. DebRoy, *International Trends in Welding Science and Technology*, S.A. David and J.M. Vitek, Ed., ASM International, 1993, p 18
3. M. Pastor, H. Zhaq, R.P. Martukanitz, and T. DebRoy, *Weld. J.*, Vol 78, 1999, p 207s
4. Y.S. Sato, H. Kokawa, and T. Kumana, *International Trends in Welding Science*

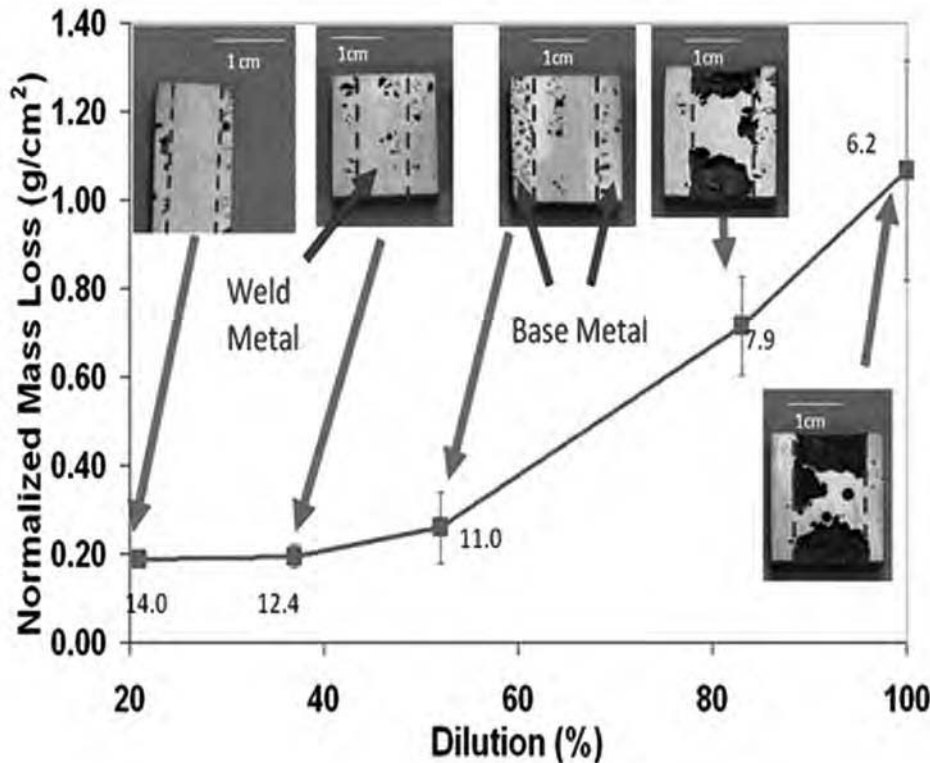


Fig. 12 Influence of dilution on the corrosion resistance of welds made on alloy CN3MN using IN686 filler metal

- and Technology*, S.A. David, J.M. Vitek, J. A. Johnson, H.B. Smartt, and T. DebRoy, Ed., ASM International, 1998, p 131
5. S. Kou, *Welding Metallurgy*, 2nd ed., John Wiley & Sons, 1993, p 97
 6. J.N. DuPont and A.R. Marder, Dilution in Single Pass Arc Welds, *Metall. Mater. Trans. B*, Vol 27, 1996, p 481–489
 7. S.W. Banovic, J.N. DuPont, and A.R. Marder, The Role of Aluminum on the Weldability and Sulfidation Behavior of Iron-Aluminum Claddings, *Weld. J.*, Vol 78, 1999, p 23s–30s
 8. J.N. DuPont and A.R. Marder, Thermal Efficiency of Arc Welding Processes, *Weld. J.*, Vol 74, Dec 1995, p 406s–416s
 9. Y.K. Oh, J.H. Devletian, and S.J. Chen, *Weld. J.*, Vol 69, 1990, p 37–44
 10. J.N. DuPont, On Optimization of the Powder Plasma Arc Surfacing Process, *Metall. Mater. Trans. B*, Vol 29, 1998, p 932–934
 11. J.N. DuPont and C.S. Kusko, Martensite Formation in Austenitic/Ferritic Dissimilar Alloy Welds, *Weld. J.*, Vol 86 (No. 2), Feb 2007, p 51s–54s
 12. T.W. Nelson, J.C. Lippold, and M.J. Mills, *Weld. J.*, Vol 78, 1999, p 329s
 13. A. Garner, How Stainless Steel Welds Corrode, *Met. Prog.*, Vol 127, 1985, p 31–34

Solid-State Transformations in Weldments*

Revised by Mehran Maalekian, The University of British Columbia

SOLID-STATE TRANSFORMATIONS occurring in a weld are highly nonequilibrium in nature and differ distinctly from those experienced during casting, thermomechanical processing, and heat treatment. This discussion primarily focuses on the welding metallurgy of fusion welding of steels and attempts to highlight the fundamental principles that form the basis of many of the recent developments in steels and consumables for welding. Accordingly, examples are largely drawn from the well-known and relatively well-studied case of ferritic steel weldments to illustrate the special physical metallurgical considerations brought about by the weld thermal cycles and by the welding environment. Because of space limitations, only a very brief discussion is included on welds in other alloy systems, such as stainless steels and aluminum-base, nickel-base, and titanium-base alloys.

The metallurgy of the welded joint can be classified into two main regions: the fusion zone (FZ) and the heat-affected zone (HAZ). A series of transformations occur during both heating and cooling, and every aspect of phase transformations in steel is relevant to the welding. The typical transformations that take place in the FZ during welding of, for instance, low-carbon steels are ferrite (α) \rightarrow austenite (γ) \rightarrow ferrite (δ) \rightarrow liquid \rightarrow ferrite (δ) \rightarrow austenite (γ) \rightarrow ferrite (α), while that of the HAZ is $\alpha \rightarrow \gamma \rightarrow \alpha$. During heating in the HAZ, austenite begins to form at the temperature Ac_1 , and it becomes fully austenitic at Ac_3 . (Ac_1 and Ac_3 are the temperatures at which austenite begins to form and is completely transformed from ferrite upon heating, respectively.) The austenite grains grow above Ac_3 , and during cooling the austenite starts to decompose into various microconstituents below the Ar_3 temperature (that is, the temperature at which austenite begins to decompose upon cooling) (Fig. 1). To describe the microstructural development

under nonequilibrium conditions in steels, a continuous cooling transformation (CCT) diagram (Fig. 2) is a convenient method. However, a conventional CCT diagram like the one shown in Fig. 2 cannot be used to accurately describe the transformation behavior in a weldment of the same material, because weld thermal cycles are very different from those used for generating conventional CCT diagrams.

Special Factors Affecting Transformation Behavior in a Weldment

Several aspects of the weld thermal cycle and weld segregation should be considered because of their effect on the transformation upon cooling:

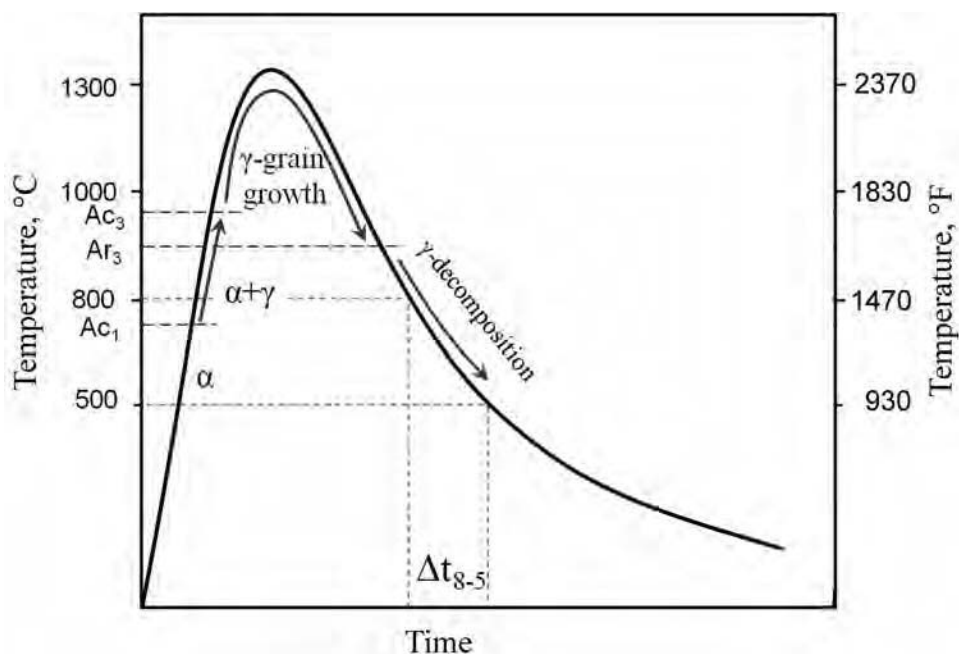


Fig. 1 Schematic illustration of typical microstructure history of the heat-affected zone that occurs during both heating and cooling of steel welds

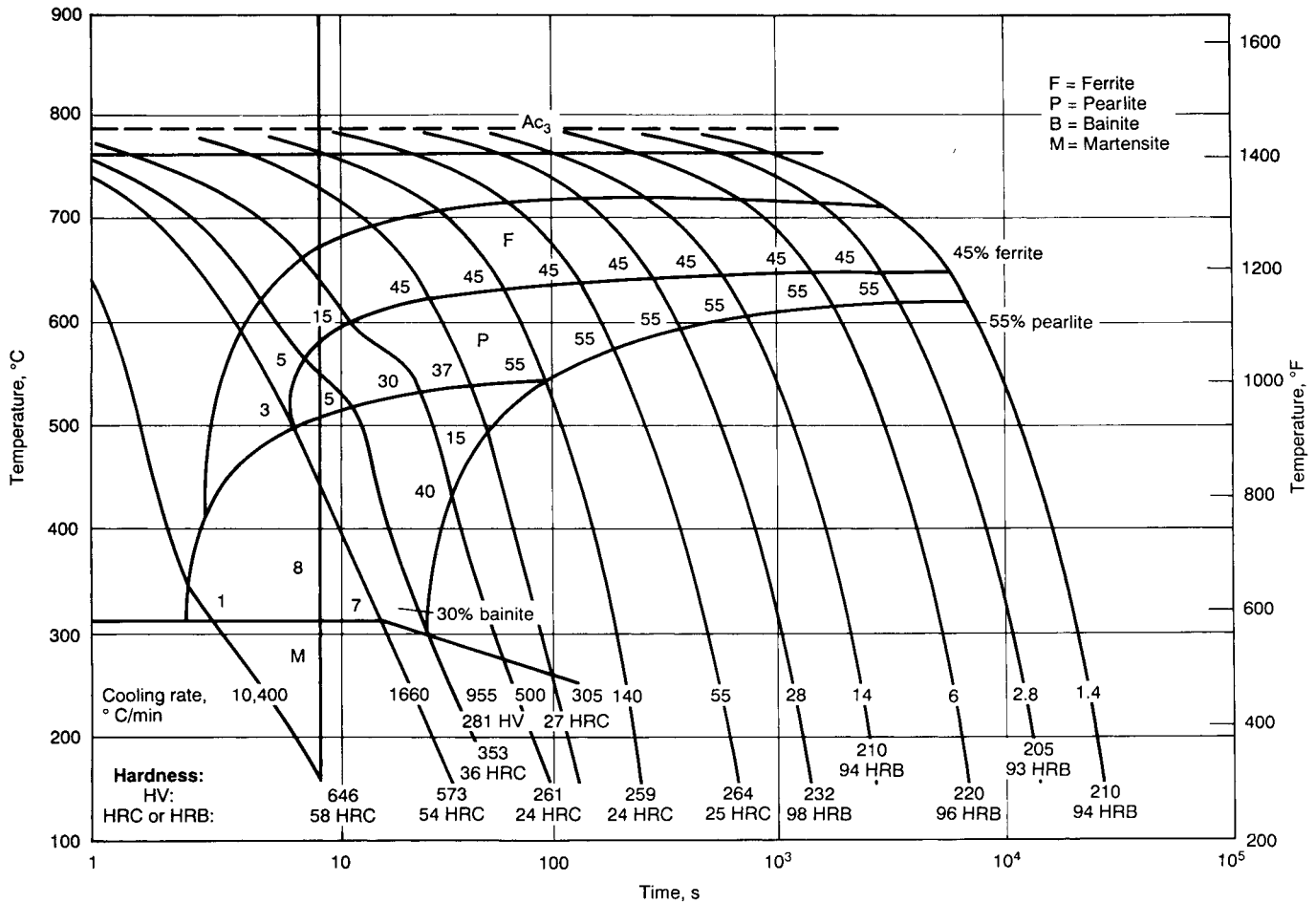


Fig. 2 Conventional continuous cooling transformation (CCT) diagram for AISI 1541 (0.39C-1.56Mn-0.21Si-0.24S-0.010P) plain carbon steel with ASTM number 8 grain size and austenitization at 980 °C (1800 °F). For each of the cooling curves in the plot (given in terms of °C/min), the transformation start and end temperatures given by the CCT curves, the amount of each transformation product, and the hardness of the final structure are shown. Ac_3 , 788 °C (1450 °F); Ac_1 , 716 °C (1321 °F). F, ferrite; P, pearlite; B, bainite; M, martensite. Source: Ref 1

- Peak temperatures reached in the HAZ can be very much higher than the Ac_3 temperature. The heating rates are very high, and the times spent at high temperature are of the order of only a few seconds.
- The temperature gradient in the HAZ is very steep, and this complicates the problem of studying in situ transformations in the HAZ during welding (Ref 1).
- During solidification of the weld metal, alloying and impurity elements tend to segregate extensively to the interdendritic or intercellular regions under the conditions of rapid cooling. Also, the pickup of elements such as oxygen by the molten weld pool leads to the entrapment of oxide inclusions in the solidified weld. These inclusions then serve as heterogeneous nucleation sites and can substantially influence the kinetics of subsequent solid-state transformations. Accordingly, the weld-metal transformation behavior is quite different from that of the base metal, even though the nominal

chemical composition has not been significantly changed by the welding process (Ref 2). Most of the CCT diagrams (applicable to the weld metal) have been generated by reheating the as-deposited weld metal (Ref 3). One of the limitations of these diagrams is that they are strictly applicable only to the high-temperature reheated zone of multipass welds, because the initial microstructure at high temperatures is not characteristic of that developed from the liquid phase.

- Welding may be carried out in several passes, and this may result in the superposition of several different heating and cooling cycles at one point, each of these cycles having the characteristics noted earlier.
- Solidification of the weld metal is accompanied by shrinkage, and the anisothermal conditions already emphasized cause deformation. The thermal cycles are therefore acting on metal that is subjected to mechanical stresses at the same time.

The essential differences between weld thermal cycles and the thermal cycles used for generating a conventional CCT diagram are summarized in Fig. 3. Thermal cycles for conventional CCT diagrams involve a slow heating rate, soak at a temperature just above the Ac_3 temperature, and subsequent cooling rates, whereas a much higher peak temperature and heating rate as well as a very short soaking time at peak temperature are characteristics of a weld thermal cycle. Owing to these significant differences (Fig. 3), a conventional CCT diagram can give only an approximate idea of the transformation behavior in the HAZ of a weldment.

Heat-Affected Zone of a Single-Pass Weld

Microstructural Zones. In the HAZ, the material is not melted, but the microstructure

and mechanical properties are altered by the heat of welding. There is a well-defined gradient of microstructure in the HAZ that can be divided into a number of subzones as a function of the distance from the fusion line, as illustrated in Fig. 4 for a carbon steel. Very high peak temperatures (T_p) in the regions immediately adjacent to the fusion line cause coarsening of the austenite (γ) grains, and this in turn increases the hardenability of this region relative to the other subzones. The slower the heating rate, the longer the retention time above Ac_3 and thus the more severe the grain growth becomes. As the peak temperature decreases with distance from the fusion line, the austenite

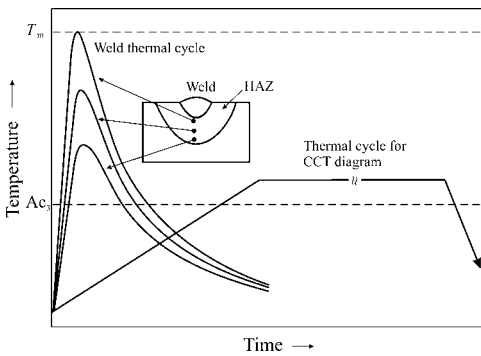


Fig. 3 Schematic showing differences between weld thermal cycle and thermal cycle used to generate a conventional continuous cooling transformation (CCT) diagram. Note the much higher heating rate, higher temperature, and shorter time above Ac_3 temperature for welding. HAZ, heat-affected zone

grain size decreases sharply. Regions of the HAZ further away from the fusion line become only partially austenitic during the heating. Owing to the increase in the solubility of carbon in austenite with decreasing temperature, the austenite that forms will have a rather high carbon concentration (Ref 5). The part that does not transform into austenite becomes tempered. Table 1 summarizes the temperature ranges for the variety of microstructural zones within the HAZ of steel welds. Because each of the subzones shown in Fig. 4 occurs in a small volume, it is difficult to study the transformation behavior of individual regions by in situ methods (Ref 2). It is more convenient to obtain information about the microstructural and property changes in the HAZ by weld simulation (Ref 4, 6). A thermal cycle simulator (TCS) is used to reproduce the thermal cycle corresponding to a point in the HAZ in a large volume that is convenient for mechanical testing. It is possible to program the required thermal cycle in the TCS so that the peak temperature and the cooling rate can be varied independently. A TCS can be used in conjunction with a high-speed dilatometer to study phase transformations in welding and to construct welding CCT diagrams. It is thus possible to obtain information about the microstructural changes in the HAZ for a wide range of welding parameters. Nevertheless, it should be borne in mind that weld thermal simulators, although very useful, have some limitations. For instance, because of the limited cooling capacity, extremely high cooling rates during electron and laser beam welding cannot be replicated. Moreover, the

temperature gradient in the specimen of the TCS is much lower than that in the HAZ near to the fusion boundary, which makes the specimen microstructure differ from the HAZ microstructure (Ref 7).

Peak Temperature-Cooling Time Diagrams. Figure 5 shows how a change in the peak temperature of the thermal cycle affects the CCT characteristics of a steel. The well-known effect of a larger γ grain size (caused by a higher peak temperature) in increasing the hardenability of the steel is seen. To present the information about the CCT behavior for a number of peak temperatures (Fig. 3, 4), it is more convenient to adopt the scheme shown in Fig. 6. In this peak temperature-cooling time (PTCT) diagram (Ref 8, 9), each point represents a weld thermal cycle with a peak temperature, T_p , given by the ordinate and the cooling time, Δt_{8-5} (that is, required for cooling from 800 to 500 °C, or 1470 to 930 °F, see Fig. 1), given by the abscissa. A microstructural constituent or a combination of two or more constituents is shown to occur over an area in the diagram. The upward slope in the boundary between two areas is consistent with the information presented earlier in Fig. 5 that the hardenability increases with an increase in the peak temperature of the thermal cycle. Hardness and C_v transition temperatures are also shown in the diagram, corresponding to different thermal cycles.

The CCT diagram shown in Fig. 5 is plotted with Δt_{8-5} as the abscissa instead of time, as in Fig. 2. The Δt_{8-5} is a popular measure in welding, probably because solid-state transformations during cooling occur between Ar_3 and martensite-start temperature, and in most steels Ar_3 is approximately 800 °C (1470 °F). However, historically, the practice of thinking in terms of a cooling time began when a need was recognized (Ref 10) to compare the CCT behavior of specimens subjected to different types of cooling curves—Jominy specimens; cylindrical bars cooled in air, water, or oil; dilatometer specimens cooled at a constant or a Newtonian rate (i.e., $T \propto e^{-t}$, where t is the time); and so on. Initially, the cooling rate at 704 °C (1300 °F) was used as a criterion to judge the equivalency of these specimens in terms of microstructure and hardness. Because transformation takes place at lower

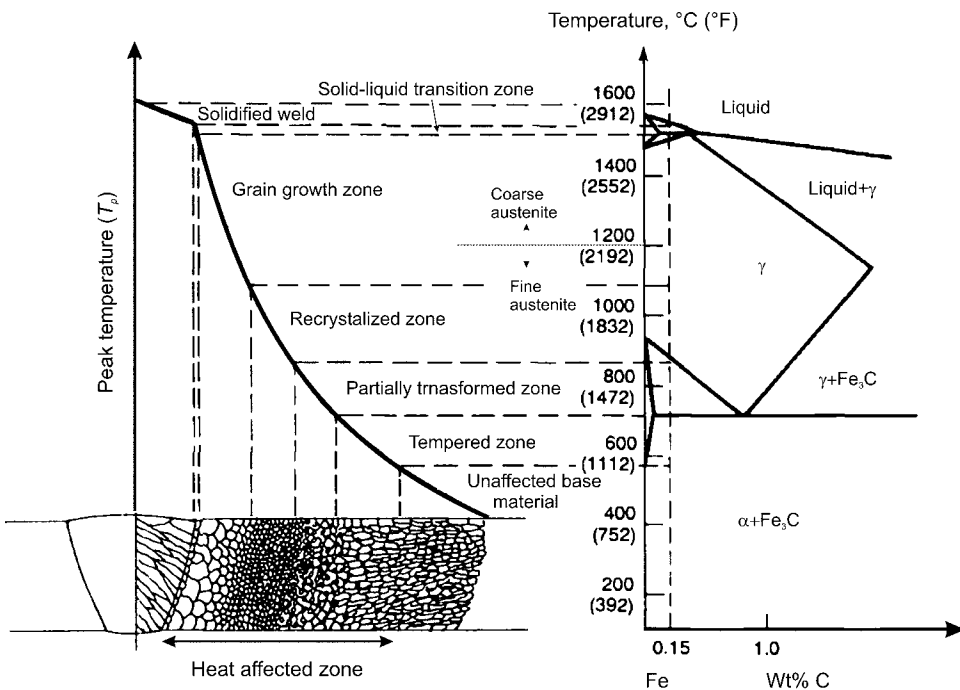


Fig. 4 Schematic illustration of the microstructural variation in the heat-affected zone of a carbon steel containing 0.15 wt% C. Source: Adapted from Ref 4

Table 1 Typical temperature ranges of the microstructural subzones within the heat-affected zone (HAZ) of steel welds

HAZ microstructure	Temperature range
Coarse-grained austenite	1500 °C > T_p > 1200 °C (2730 °F > T_p > 2190 °F)
Fine-grained austenite	1200 °C > T_p > Ac_3 (2190 °F > T_p > Ac_3)
Partially austenitized zone	Ac_3 > T_p > Ac_1
Tempered regions	Ac_1 > T_p

Source: Ref 5

temperatures in many steels, the half cooling time (Ref 10) was found to be a better equivalency criterion. The half cooling time was defined as the time to cool from A_{c3} to a temperature that lies midway between A_{c3} and room temperature. For the sake of general applicability, this was later modified to the $\Delta t_{8.5}$ criterion, and CCT diagrams began to be plotted with $\Delta t_{8.5}$ as the abscissa. It must be noted that using $\Delta t_{8.5}$ as an equivalency criterion is just an expedient solution that does not have strict theoretical justification (refer, for example, to the additivity principle in Ref 10).

A special significance of using $\Delta t_{8.5}$ as the abscissa in Fig. 6 is that it is almost constant (for $T_p > 900^\circ\text{C}$, or 1650°F) in the whole of the HAZ. This can be seen from Ref 4, where the expressions given for $\Delta t_{8.5}$ do not contain the distance from the weld centerline as a factor. The derivation of these expressions is based on the assumption that the time to cool to 800°C (1470°F) is far greater than the time to reach the peak temperature, so the $\Delta t_{8.5}$ can be taken to be the same for the whole of the weld and the HAZ. This assumption can be intuitively rationalized by observing that the

weld thermal cycles in Fig. 3 are such that the curves are approximately parallel below 800°C (1470°F). The constancy of $\Delta t_{8.5}$ in the HAZ means that the gradient in microstructure (in terms of the final transformation products from austenite) is mainly due to a variation in the peak temperature. By drawing a vertical line in Fig. 6 at a value of $\Delta t_{8.5}$ corresponding to a given heat input and preheating temperature, it is possible to obtain information about the type of microstructural gradient in the HAZ. A grasp of the changes in such properties as hardness and toughness can also be obtained from Fig. 6.

Continuous Heating Transformation Diagrams. The heating cycle in welding is also very important, because it influences the final microstructure and properties of the HAZ. For example, the heating rate to the peak temperature determines the degree of superheating, the rate of coarsening and dissolution temperature of carbides and nitrides, and the main proportion of austenite grain growth (Fig. 1, 4) (Ref 4). In fact, all of the aforementioned factors affect the degree of grain growth in the HAZ, which, in turn, will greatly influence the final properties of the weld.

The formation of austenite during heating is, in many respects, different from the transformations that occur during cooling. The formation of ferrite, for example, follows a "C-" curve kinetic form on a time-temperature transformation diagram. That is, the overall transformation rate goes through a maximum as a function of supercooling below the equilibrium temperature because of two opposing effects. As the temperature falls, the diffusion coefficient decreases, but the driving force for transformation increases (Ref 5). In contrast, during heating both the diffusion coefficient and the driving force increase with temperature. Thus, the overall rate of transformation increases continuously as the transformation temperature is raised, as shown in Fig. 7.

The heating rate in many welding processes can be very high, and considerable superheating may be required for the transformation to austenite on heating, because the A_{c1} and A_{c3} temperatures will be raised with an increase in the heating rate (Ref 11). For typical heating rates encountered in the region near the fusion line, the formation of austenite should be completed when the temperature has exceeded the A_{c3} by approximately 100°C (180°F) (Ref 5). This is seen in Fig. 8, a continuous heating transformation diagram, which is analogous to a CCT diagram. It is seen that grain growth begins only after the carbides have dissolved and after a homogeneous austenite (with respect to the distribution of carbon, at least) is formed.

Thermal Pinning. A fairly satisfactory correlation between real welds and simulation studies has been observed with respect to microstructure and property measurements. However, it has frequently been observed that the maximum austenite grain size in real welds is less than that in corresponding simulated

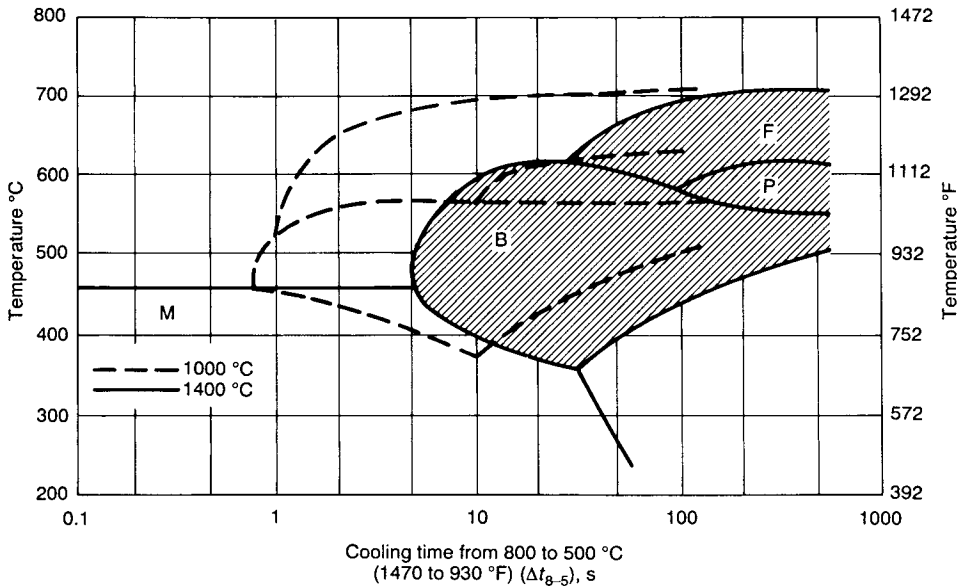


Fig. 5 Effect of a change in the peak temperature of the weld thermal cycle (from 1000 to 1400 °C, or 1830 to 2550 °F) on the continuous cooling transformation characteristics. M, martensite; B, bainite; F, ferrite; P, pearlite. Source: Ref 8

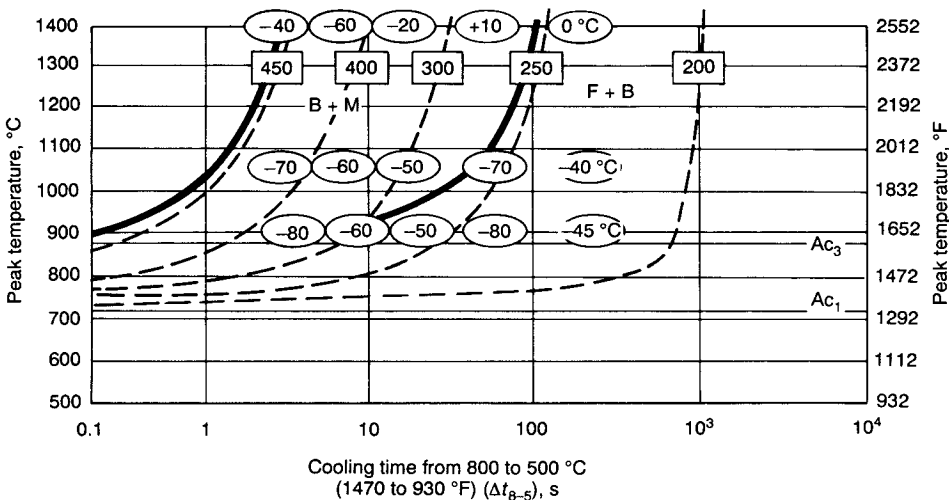


Fig. 6 Typical peak temperature versus cooling time diagram, showing the effects of these parameters of a weld thermal cycle on the final transformation products, on hardness, and on Charpy V-notch impact energy. B, bainite; M, martensite; F, ferrite. Figures in squares indicate the hardness (30 HV); figures in ovals indicate the 21 J (16 ft · lbf) transition temperatures for Charpy V-notch impact specimens subjected to a specific thermal cycle. Source: Ref 9

weld specimens (Ref 2, 4, 6). The reason is attributed to the very steep temperature gradient in the HAZ, especially near to the fusion line where the grains are coarsest, the temperature gradient is steepest, and the temperature can vary across a single grain, as first reported in the HAZ of a Cr-Mo-V steel (Ref 13). The phenomenon, termed thermal pinning, causes grains to grow nonuniformly, resulting in a shape change from, for example, equiaxed to pear shaped, as shown in Fig. 9(a) (Ref 4).

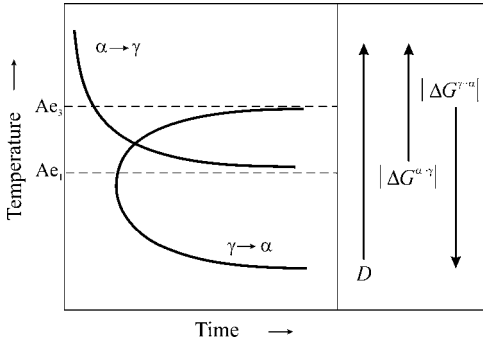


Fig. 7 Schematic comparison of the $\gamma \rightarrow \alpha$ transformation (time-temperature transformation curve) and the reverse $\alpha \rightarrow \gamma$ transformation. ΔG is the driving force, and D is the diffusion coefficient. Adapted from Ref 5

The corresponding increase in surface-to-volume ratio effectively represents an increase in energy, thereby neutralizing the reduction in energy present in normal grain growth. Another explanation for thermal pinning is that the steep temperature gradients cause the atomic mobility to vary across a large grain, resulting in different growth propensities in different parts of the grain (Ref 14). Under the simulation conditions, the austenite grains grow in all directions, and the constraint arising from the thermal pinning effect in real welds is difficult to capture and quantify. However, the problem has been modeled numerically using Monte Carlo simulation by subdividing the grains into many discrete small units, each with its own atomic mobility depending on the local temperature (Ref 14, 15). Figure 9(b) shows that the kinetics of grain growth at the HAZ with gradient heating are lower than that for bulk heating using an identical thermal cycle, thus indicating grain-boundary pinning in the HAZ due to thermal pinning. However, under the weld simulation condition, the austenite grains can grow in all directions, so the previous discussion shows that the PTCT diagram (along with property measurements, as in Fig. 6) can alert the user to the possibility of local brittle zones in actual weldments, and that any error in the property being assessed will be on the conservative side.

Austenite Grain Growth and Grain-Boundary Pinning. Grain size is of paramount importance in steels as a key factor in determining their strength and toughness. It also has immense impact on the vulnerability of an alloy to cold cracking and reheat cracking in welds (Ref 4). Austenite grain growth influences the kinetics of phase transformation and may promote the formation of martensite and bainite, with adverse effects on the fracture toughness of the weld (Fig. 5). Further, it has an important effect on the grain size in the weld metal where the grains are grown epitaxially from the HAZ. Figure 10 shows that the crystals of the weld deposit (columnar δ -ferrite) have derived from the grains of the parent metal at the fusion surface, that is, epitaxial growth. Thus, the grain growth in the HAZ not only affects strength and toughness but also influences the grain size of the weld.

Traditional ways of improving the strength of steels had been to increase the carbon and manganese content. However, such steels, even with their higher carbon equivalent (CE), did not possess adequate toughness and were prone to weld cracking. The weldability of steels, which is usually expressed in terms of CE, is poor if the CE exceeds 0.4 wt%, because of their increased tendency to form martensite.

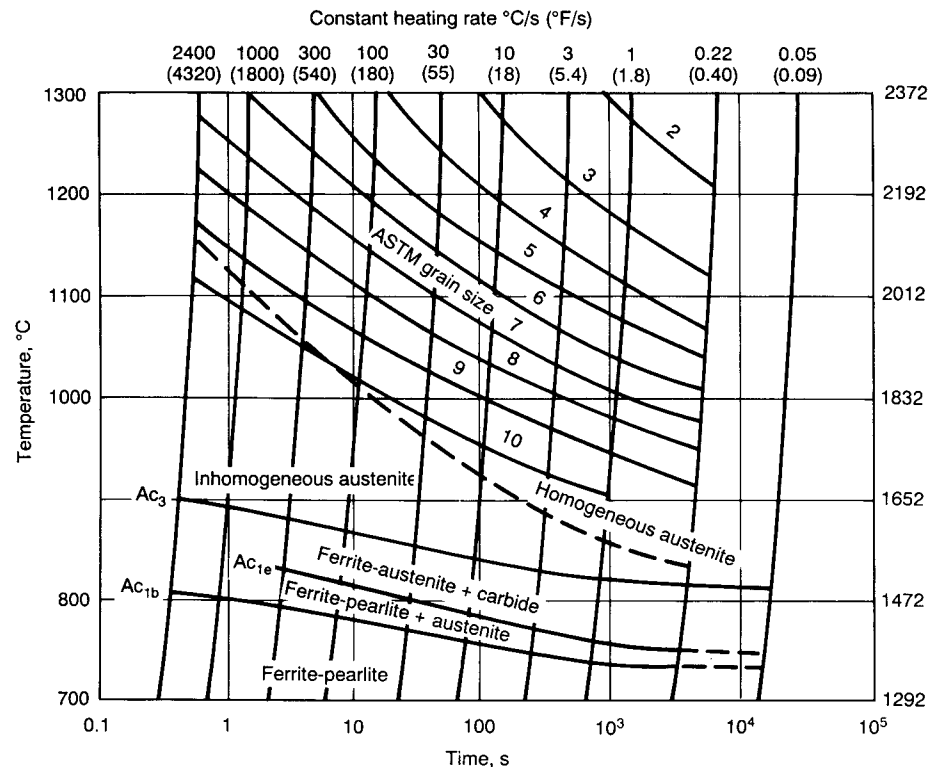


Fig. 8 Continuous heating transformation diagram for 34CrMo4 steel. In the region of homogeneous austenite there are lines of constant austenite grain size (ASTM numbers). Because of the measuring procedure, the diagrams can only be interpreted along lines of constant heating rate. To show the heating time more clearly, a time scale is added. Source: Ref 12

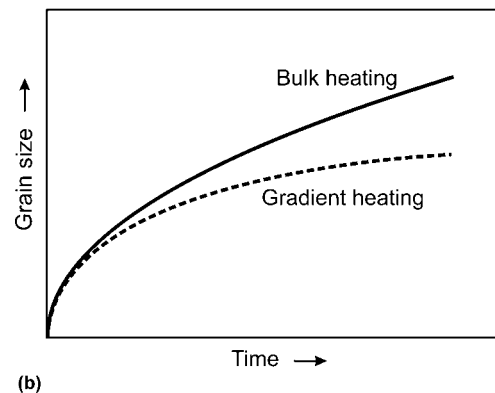
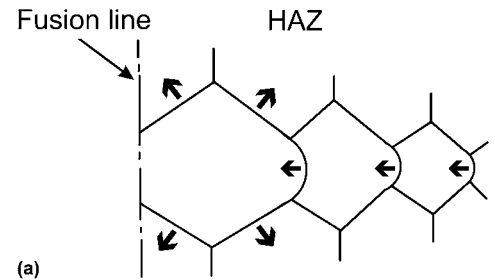


Fig. 9 (a) Steep temperature gradient in the heat-affected zone (HAZ) near the fusion line leads to a rapid change in grain size, which may tend to suppress grain growth due to grain shape changes. Arrows indicate direction of moving grain boundaries. Adapted from Ref 4. (b) Schematic kinetics of grain growth in the HAZ under steep temperature gradient (gradient heating) and corresponding uniform thermal cycle (bulk heating). The growth kinetics for the HAZ are much slower than that for the bulk heating. This can be seen in Ref 14 and 15.

Development of microalloyed or high-strength low-alloy (HSLA) steels through the last several decades made it possible to achieve higher strength levels with much lower carbon and manganese levels, thus improving weldability (Ref 16). In microalloyed steels, alloying additions are kept to a minimum, and higher strength is achieved primarily by a reduction in the grain size and by precipitation strengthening. A reduction in grain size is the only known method of increasing the strength and toughness at the same time. Because strengthening is obtained by other means, both carbon and the CE can be decreased and the susceptibility of HSLA steel to cold cracking thereby significantly reduced.

A fine ferrite grain size in these steels is achieved by controlled rolling in the austenitic condition (i.e., hot rolling). To obtain a fine austenite grain size before the $\gamma \rightarrow \alpha$ transformation, it is essential to add such grain-refining elements as niobium, titanium, vanadium, and aluminum. Such elements are strong carbide and nitride formers (except aluminum, which forms only nitrides); their addition to steels introduces fine precipitates to the austenitic matrix. The particles are usually found on grain boundaries, which are energetically more favorable formation sites. A short length of grain boundary is replaced by the precipitate, and the effective interfacial energy is lowered. When the grain boundary attempts to migrate away from the particles, the local energy increases, and a drag is exerted on the boundary by the particles. Therefore, the fine precipitates can pin the austenite grain boundaries and hinder grain coarsening (Fig. 11).

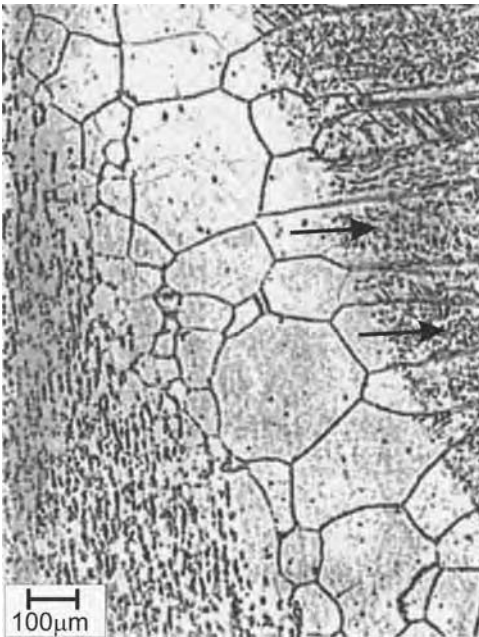


Fig. 10 Illustration of the epitaxial growth of columnar grains of the weld deposit from the fusion line of a stainless steel weld. After Honeycombe and Gooch, reprinted from Ref 5

In the HAZs of welds in these microalloyed steels, it is not possible to achieve the same optimal microstructure and microalloy precipitation obtained in the parent material by controlled thermomechanical processing. Because peak temperatures are much higher in the HAZ, the precipitate particles coarsen and dissolve, resulting in reduced pinning forces and therefore coarser austenite grains, as schematically shown in Fig. 11. This effect can be minimized by having precipitate particles that do not dissolve, even at higher temperatures. An idea of the stability of precipitate particles can be obtained from the solubility product shown in Fig. 12. It is seen that the nitrides compared with their respective carbides are more stable. Moreover, titanium nitride (TiN) has maximum stability, and this property has been used to advantage in many steels and has resulted in the development and extensive application of titanium technology (Ref 16). As shown in Fig. 13, the other carbides and nitrides are not as effective as titanium nitride in limiting the extent of grain coarsening; they play a bigger role during thermomechanical processing.

The austenite grain growth can be shown conveniently in the form of grain growth diagrams (Fig. 14), which illustrate contours of equal grain size as a function of the peak temperature and Δt_{8-5} (or input energy). In titanium-microalloyed steel (Fig. 14), it is seen that even in the presence of relatively stable

TiN precipitates, grain growth in the HAZ at high input energies can be considerable, which is attributed to the increase in the mean particle size, a process known as Ostwald ripening (Ref 16), as well as the partial dissolution of TiN. This means that it is not possible to stop, but only to limit, grain coarsening in the HAZ, especially in high-heat-input welds. This inevitable grain coarsening is actually used to advantage in titanium oxide steels (see the section "Titanium Oxide Steels" in this article). However, the grain growth can be made to cease after a certain time in the presence of a fine distribution of particles. Figure 15 shows that the limiting grain size (D_{lim}) is proportional to (r/f) with a constant of proportionality (k) that may be different for different materials. It also shows how a high volume fraction of fine precipitate particles is needed to maximize the pinning effect.

Unmixed and Partially Melted Zones in a Weldment. It is common to think of a single-pass weld as consisting of two zones: weld metal and HAZ. Careful metallographic examination has shown that a weld can, in fact, be divided into four regions (Fig. 16):

- *Composite zone:* A volume of base metal melted by the superheated filler metal experiences complete mixing to produce an alloy with nominal composition intermediate between that of the base metal and that of the filler metal.

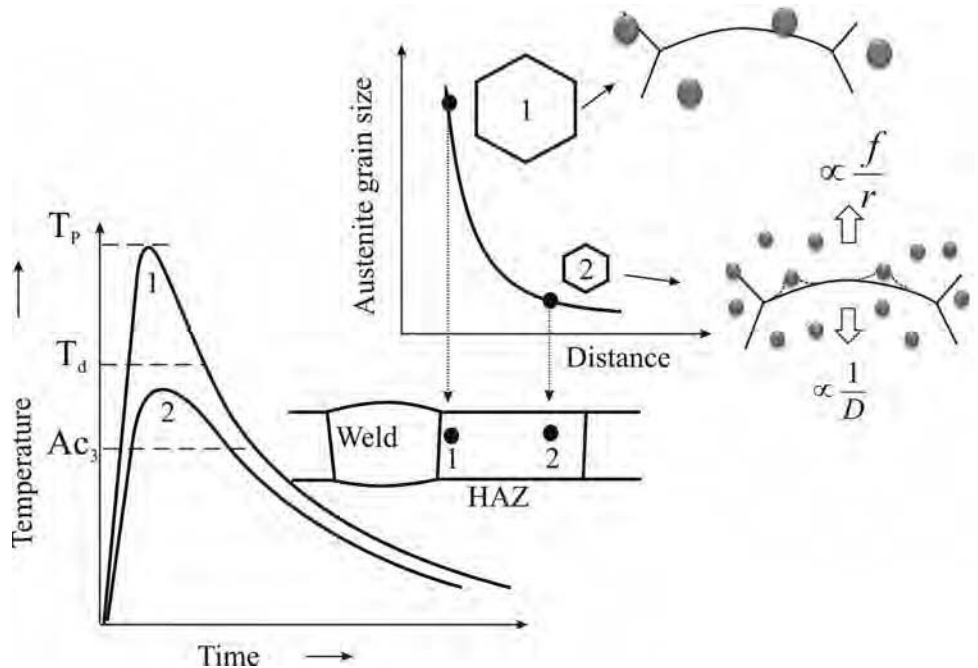


Fig. 11 Schematic illustration of austenite grain size in the heat-affected zone (HAZ) of microalloyed steel with second-phase particles as a function of distance from the fusion line and associated thermal cycle. The movement of grain boundaries driven from the reduction of total surface energy (proportional to the inverse of grain size, D) is hindered by the precipitates that exert a pinning force proportional to the ratio of precipitate volume fraction, f , to their size, r (i.e., f/r). At regions near the fusion line, where the temperature is well above the dissolution temperature of carbonitrides (T_d), profound grain growth can occur as a result of dissolution and/or coarsening of precipitates and subsequent reduction in particle pinning effect (compare positions 1 and 2 in the HAZ).

- *Unmixed zone*: Forms from the stagnant molten boundary-layer region (approximately 100 to 1000 μm, or 0.004 to 0.040 in., thick) at the outer extremities of the composite region. Because no mechanical mixing with the filler metal occurs here, the composition of the metal in this region is identical to that of the base metal, except for minor changes produced by diffusion.
- *Partially melted zone*: A region at the fusion boundary where the peak temperatures fall between the liquidus and solidus so that melting is incomplete
- *True heat-affected zone*: That portion of the base metal where all microstructural changes induced by welding occur in the solid state

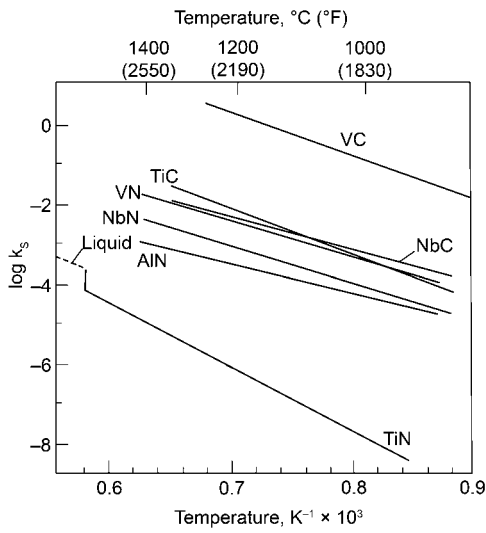


Fig. 12 Solubility products of carbides and nitrides in austenite. Adapted from Ref 17

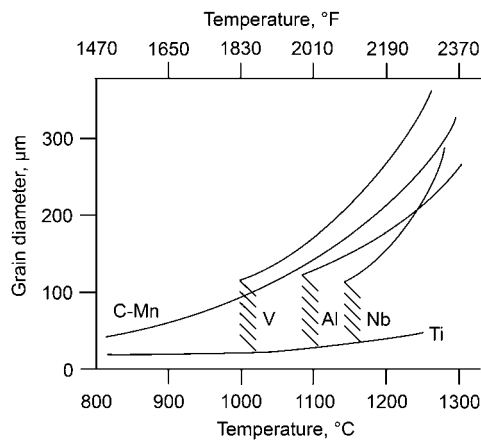


Fig. 13 Effects of various microalloying additions on the grain-coarsening temperature of austenite. Grain-coarsening temperatures depend on the microalloying level, nitrogen and/or carbon contents, and size of the precipitates. Titanium is the most efficient microalloying element for grain refining due to the extremely low solubility of titanium nitride in austenite. Source: Ref 18

The width of the partially melted zone can be extended by a phenomenon known as constitutional liquation (Ref 23), a phenomenon of localized melting due to a nonequilibrium distribution of phases during rapid heating, in which melting can occur even when the peak temperature is less than the solidus temperature. This can be understood by referring to a phase diagram for a simple binary system A and B (Fig. 17). Consider an alloy of composition C. Its equilibrium structures at temperatures T_1 , T_2 , T_3 , and T_4 are $\alpha + \beta$, α , α , and $L + \alpha$, respectively (Fig. 17a). On heating from room temperature to T_3 and holding at this temperature for a long time, the β particles will dissolve and give a homogeneous α of composition C. However, under conditions of rapid heating in the HAZ, the dissolution of β will give rise to a solute concentration gradient around each particle, as shown in Fig. 17(b). In the region surrounding each particle, the concentration of the solute B will correspond to that of liquid because, as the phase diagram shows, a liquid phase must exist between α and β at T_3 .

The partially melted zone is the region where liquation cracks have been known to occur in maraging steels, austenitic stainless steels, heat treatable aluminum alloys, and nickel-base

superalloys. It can also be a site where hydrogen-induced cracking is initiated (Ref 21, 22), both because it can act as a pipeline for the diffusion of hydrogen picked up by the molten weld metal and because such segregated regions have higher hardenability.

Although the phenomenon of constitutional liquation is usually discussed in connection with liquation cracking of aluminum- and nickel-base alloys (Ref 7, 23, 24), a more dramatic example can be found in the case of cast iron welds (Ref 25). Figure 18(a) illustrates the temperature range over which the formation of a partially melted zone in a cast iron may occur. Figure 18 (b) shows the microstructure of the HAZ in a cast iron weld deposited using a quench welding technique (Ref 26). This procedure involves welding without any preheat by intermittently depositing a series of small stringer beads and strictly maintaining the interpass temperature below approximately 80 °C (175 °F). The idea is to limit the size of the hard and brittle white iron colonies that form by constitutional liquation around the graphite nodules, and to make sure that they do not interconnect. By contrast, a procedure involving a preheat of approximately 200 °C (390 °F) can prevent the formation

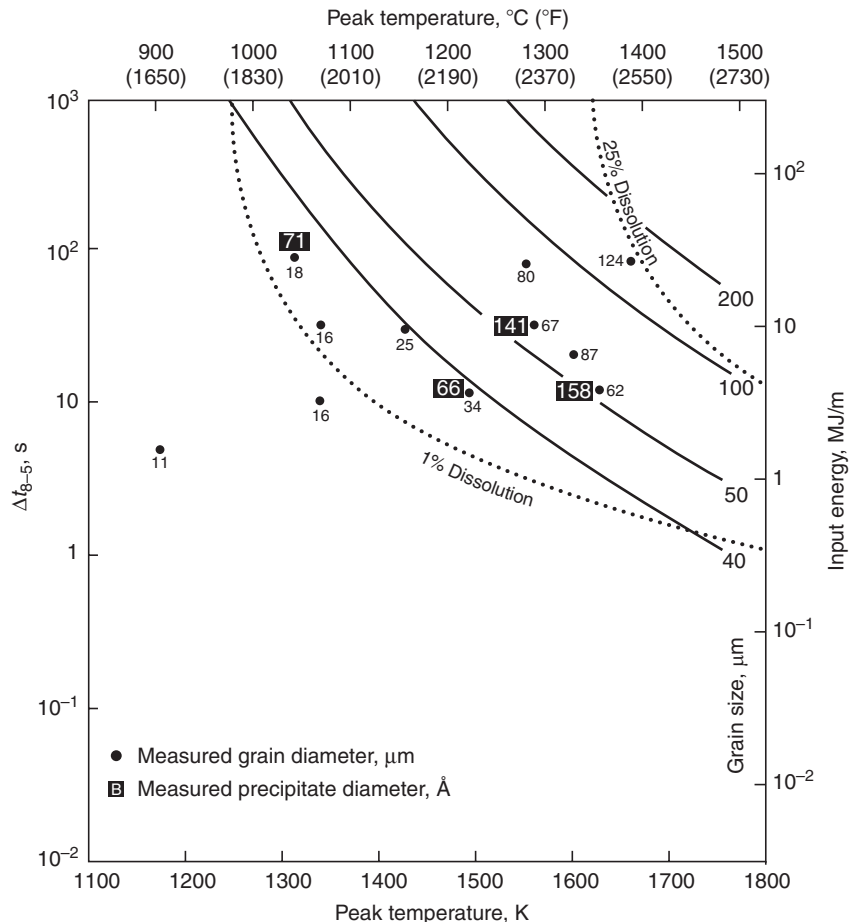


Fig. 14 Effect of peak temperature and precipitate (TiN) coarsening on austenite grain growth in the heat-affected zone of a titanium-microalloyed steel. The points in the diagram are experimental data, whereas the curves are calculated. Source: Ref 4

of martensite but not the formation of ledeburite (the structure of white iron). Because ledeburite forms at higher temperatures than martensite ($\approx 1100^\circ\text{C}$, or 2010°F), a much higher preheat temperature of approximately 600°C (1110°F) is required to reduce the cooling rate significantly and thereby prevent the formation of white iron. This high level of preheat is impractical. While cast iron appears to have been successfully welded with preheats of approximately 200°C (390°F), it has sometimes been found that weld repair is most effective when using the quench welding technique, by which it is possible to limit both the amount of ledeburite formed and the width of the HAZ.

Fusion Zone of a Single-Pass Weld

Transformations in Single-Pass Weld Metal. It is usually not necessary to select a filler metal that has exactly the same composition as the base metal; it is more important that the weld metal has the same strength and other properties (such as toughness or corrosion resistance). Because these properties are governed by the microstructure, it is important to understand the influence of different factors on phase

transformations in the weld metal. First, for a meaningful communication of the different features in a microstructure, the various phases and microconstituents must be identified using a system of nomenclature that is both widely accepted and well understood. In wrought steels, this need has been satisfied to a large degree by the Dubé scheme (Ref 27) for classifying the different morphologies of ferrite, as shown in Fig. 19. Similarly, confusion and controversy in the terminology for describing the microstructures in ferritic steel weld metals have been largely resolved by the classification scheme shown in Fig. 20. This scheme (Ref 28) was the result of several collaborative exercises undertaken under the auspices of the International Institute of Welding (IIW). It is worthwhile to note that the IIW approach to classifying microstructural elements is based on their appearance in the optical microscope. However, based on the knowledge of transformation behavior of various constituents, a different classification system has been proposed (Ref 29). Typical micrographs illustrating some of the microstructural constituents are shown in Fig. 21.

The transformation behavior in ferritic steel weld metals is best understood by first noting that ferrite is nucleated heterogeneously and that, for all practical purposes, it is necessary

to consider the competitive nucleation behavior only at grain boundaries and at inclusions. Figure 22 shows that inclusions must be larger than a certain size (0.2 to $0.5\ \mu\text{m}$, or 8 to $20\ \mu\text{in.}$, the typical size range of most weld-metal inclusions) for their potency as nucleation sites to reach a maximum. It also shows that nucleation of ferrite is always energetically more favorable at grain boundaries than at inclusions. Based on additional considerations, such as thermal contraction strains and lattice matching at inclusion-austenite-ferrite interfaces (not taken into account to obtain the results in Fig. 22), a discussion of why certain inclusions are more potent nucleation sites than others is found in Ref 3 and 30 to 32.

Broadly, the major factors affecting transformation behavior in ferritic steel weld metals are alloy composition, weld heat input (by its effect on γ grain size and $\Delta T_{(8-5)}$), oxygen content (that is, the inclusion content), and the nature of segregation in the weld metal. A typical weld CCT diagram is shown in Fig. 23. For the cooling curve shown in the figure, the first phase that forms is allotriomorphic ferrite, or grain-boundary ferrite in the IIW scheme. (The term *allotriomorphic* describes a particle of a phase that does not have a regular external shape; in

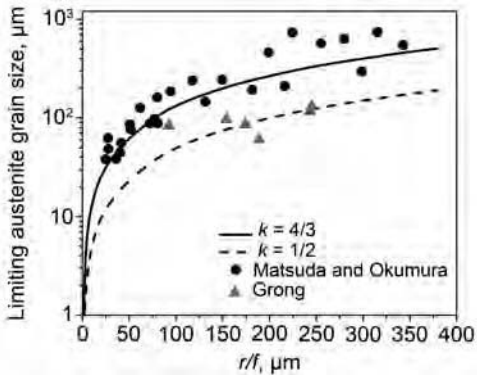


Fig. 15 Effect of particle radius (r) and volume fraction of precipitates (f) on the limiting (maximum) austenite grain size. The measured grain size data (symbols) reported for different steels (Ref 19, 20) are well represented by the equation $D_{\text{lim}} = k(r/f)$ (curves) using different k values.

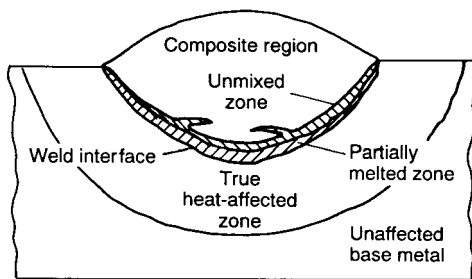
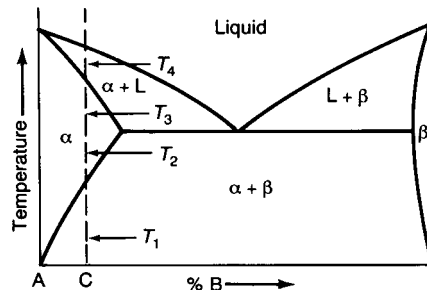
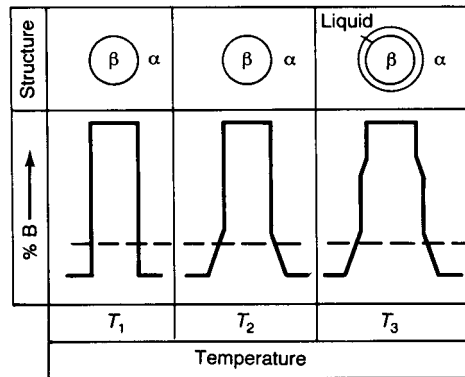


Fig. 16 Schematic showing the different discrete regions present in a single-pass weld. Source: Ref 21, 22

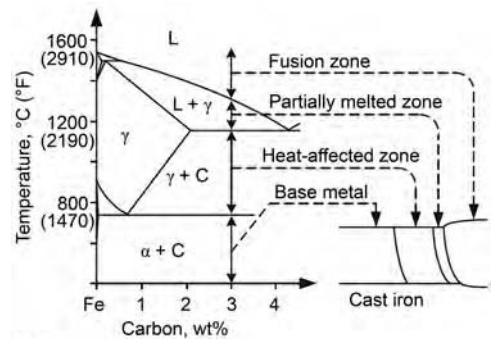


(a)



(b)

Fig. 17 Extension of partially melted zone by constitutional liquation. (a) Phase diagram for a simple binary alloy. (b) Structures and distribution of constituent B in alloy C at three temperatures shown in (a) when rapid heating is applied. Source: Ref 23



(a)



(b)

Fig. 18 (a) Schematic showing the location of the partially melted zone and associated phase diagram for a cast iron. Adapted from Ref 7. (b) White iron colonies obtained in the heat-affected zone of blackheart malleable iron welded using a quench welding technique with a nickel-base electrode. Original magnification: $180\times$. Source: Ref 26

the present context it means that ferrite grows on the grain-boundary surfaces and does not have a regular faceted shape reflecting the symmetry of its internal crystalline structure.) At lower temperatures, the mobility of the curved or random γ/α -allotriomorph boundaries decreases, and Widmanstätten side plates (ferrite side plates in the IIW scheme) form. Growth of these side plates is rapid because carbon is efficiently redistributed to the sides of the growing tips, thus avoiding solute pile-up problems. In addition, substitutional atoms do not diffuse during the growth of Widmanstätten ferrite.

After all the grain-boundary sites are saturated with allotriomorphic or Widmanstätten ferrite and their growth rate is not sufficient to extend to the interior of the grains, the nucleation of ferrite at inclusions within the γ grains becomes competitive. Acicular ferrite forms, a structure resulting from ferrite laths growing in different directions from inclusions and from laths already nucleated. Upon impingement, high-angle grain boundaries and a very fine dispersion of microphases are obtained between ferrite laths. *Microphases* in this context means the transformation structures resulting from the

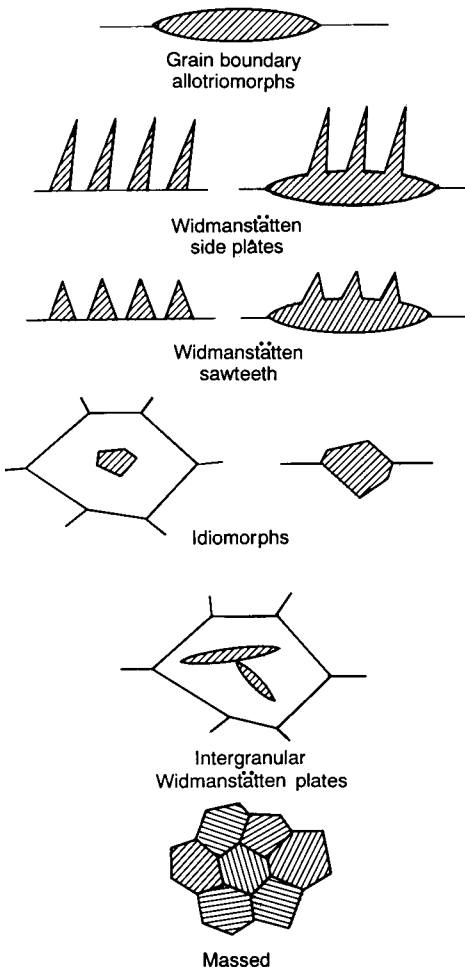
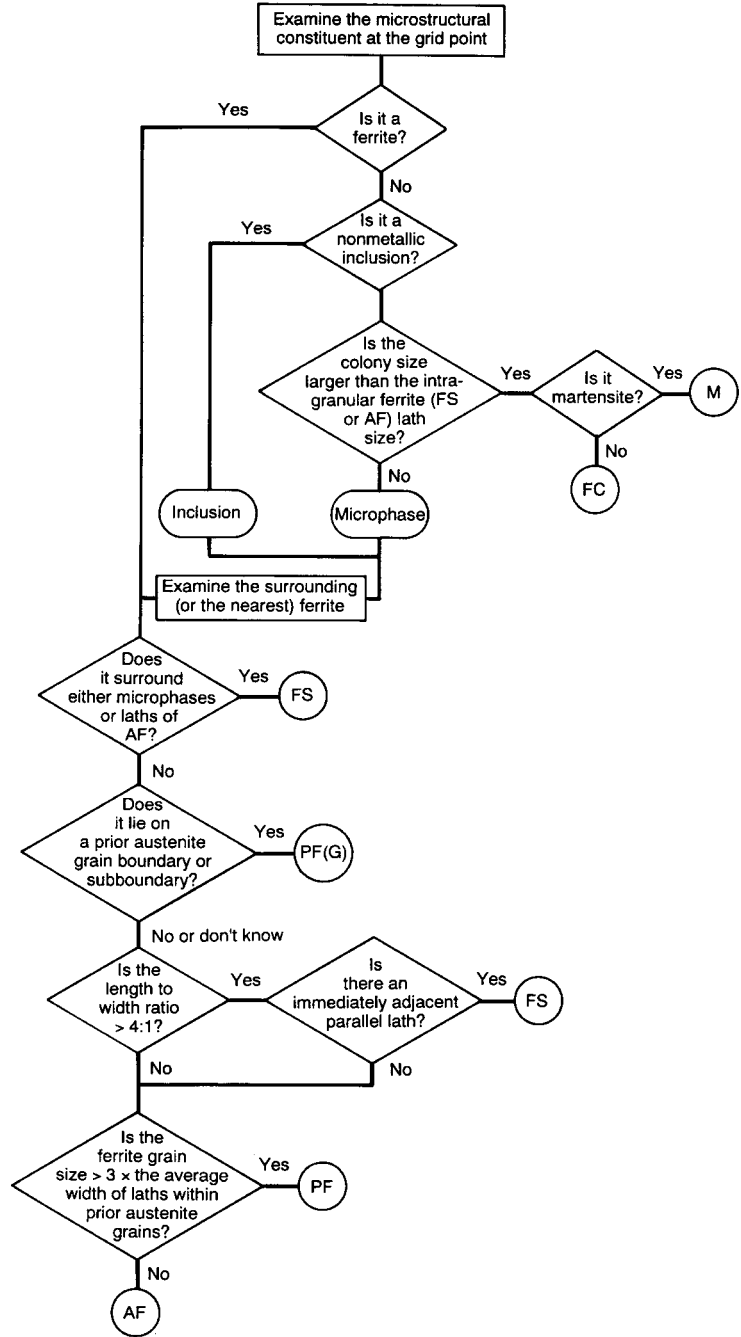


Fig. 19 Schematics showing the Dubé classification of ferrite morphologies. Source: Ref 27



Category	Abbreviation
Primary ferrite	PF
Grain-boundary ferrite	PF(G)
Intragranular polygonal ferrite	PF(I)
Ferrite with second phase	FS
Ferrite with nonaligned second phase	FS(NA)
Ferrite with aligned second phase	FS(A)
Ferrite side plates	FS(SP)
Bainite	FS(B)
Upper bainite	FS(UB)
Lower bainite	FS(LB)
Acicular ferrite	AF
Ferrite-carbide aggregate	FC
Pearlite	FC(P)
Martensite	M
Lath martensite	M(L)
Twin martensite	M(T)

Fig. 20 International Institute of Welding scheme for classifying microstructural constituents in ferritic steel weld metals with the optical microscope. Source: Ref 28

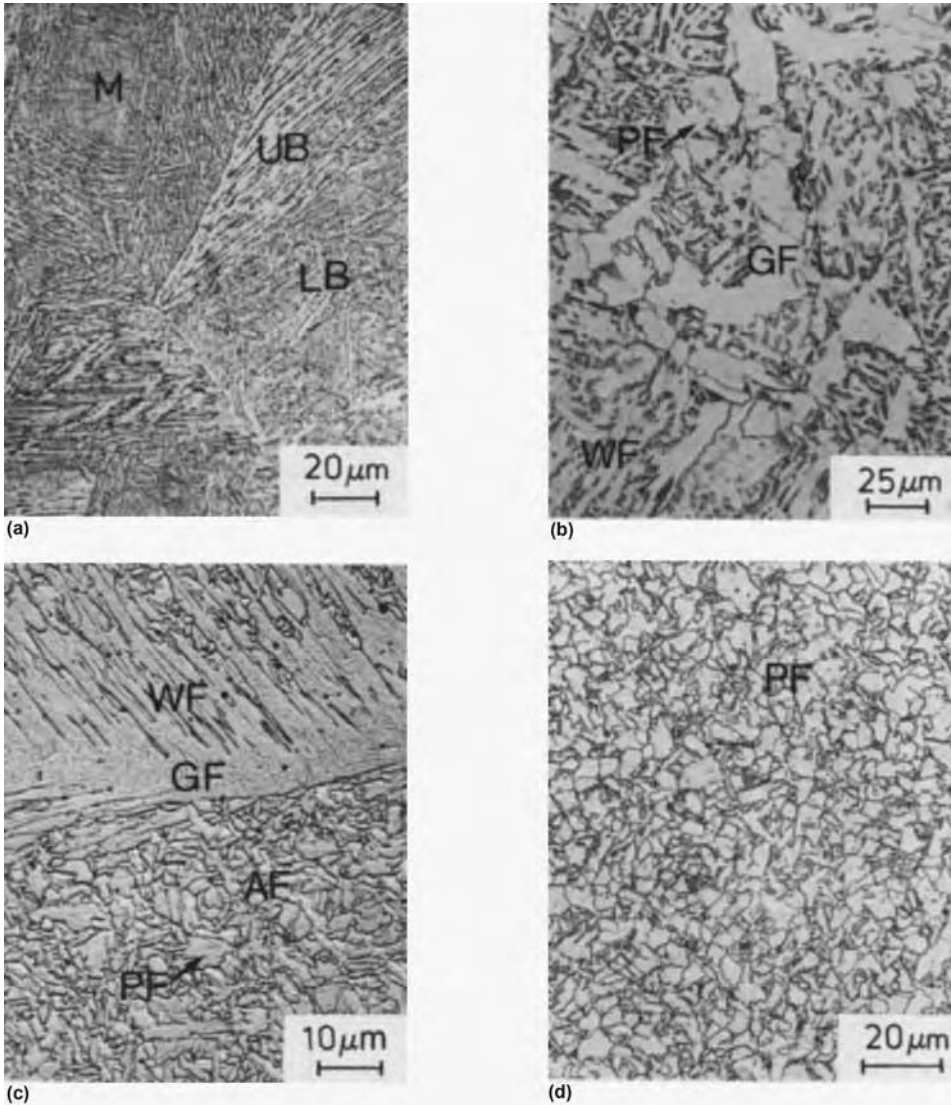


Fig. 21 Micrographs showing typical microstructures in low-alloy steel weld metal. (a) and (b) Coarse-grained heat-affected zone (low-heat-input welding). (c) As-deposited weld metal (low-heat-input welding). (d) Reheated weld metal (low-heat-input welding). M, martensite; UB, upper bainite; LB, lower bainite; PF, polygonal ferrite; GF, grain-boundary ferrite; WF, Widmanstätten ferrite; AF, acicular ferrite. Source: Ref 20

carbon-enriched regions between the ferrite laths; these could be the martensite-austenite constituent, bainite, or pearlite (see the section "Heat-Affected Zone in Multipass Weldments" in this article). An example of the microstructure of acicular ferrite is shown in Fig. 24. Acicular ferrite does not figure in the Dubé scheme because it is rarely observed in wrought steels. When the cooling rate is higher or when the inclusion content is very low, bainite can be nucleated directly at the γ grain boundaries. Bainite can form as upper or lower bainite; the difference between the two is illustrated in Fig. 25. Examination with transmission electron microscopy (TEM) is usually required for a firm identification of the type of bainite formed. In the case of the highest cooling rates, martensite is obtained.

Figure 26 shows the effect of alloying additions, Δt_{8-5} , oxygen content, and the γ grain size on the sequence and relative amounts of allotriomorphic ferrite, Widmanstätten ferrite, and bainite in the weld metal. Broadly, the trends shown can be understood in terms of the well-known observation that an increase in γ grain size, a decrease in inclusion content, and an increase in alloying additions will shift the CCT curves to lower temperatures and to longer times. While Fig. 26 can generally be interpreted by assuming that the individual factors act independently of each other, the transition from Fig. 26(b) to (a) with an increase in the inclusion content must be understood in terms of its effect of the γ grain size. It has been observed that the γ grain size decreases with an increase in the inclusion content, and this

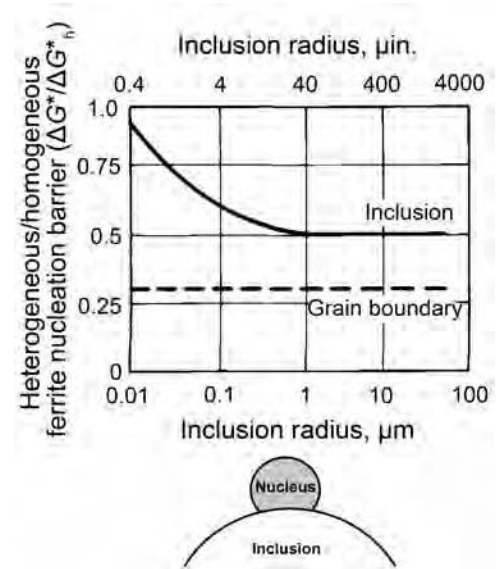


Fig. 22 Effect of particle radius on energy barrier to ferrite nucleation at inclusions, ΔG^* (heterogeneous), normalized relative to the homogeneous nucleation barrier, ΔG^*_h (homogeneous). Corresponding energy barrier to nucleation of ferrite at austenite grain boundaries is indicated by horizontal broken line. Adapted from Ref 4

decrease has been explained by the higher magnitude of pinning forces at higher inclusion contents (Ref 31). The smaller grain size implies a greater grain-boundary surface area, which increases the amount of grain-boundary ferrite and side plate structures formed at the expense of acicular ferrite in Fig. 26(a). The role of the initial formation or nonformation of allotriomorphic ferrite at γ grain boundaries in bringing about the transition from Fig. 26 (b) to (c) is discussed in the next section of this article.

Although the IIW classification is the result of a consensus viewpoint, some researchers (Ref 30) still feel that it places an exaggerated emphasis on morphological features observed with the light microscope. They believe that it is more important that the terminology reflect the mechanism of transformation (Ref 29). For example, it can be difficult to differentiate between Widmanstätten ferrite and upper bainite when using the light microscope, and both are identified as "FS" in the IIW classification. For a more fundamental understanding for a clear interpretation of the trends in microstructural development, it is essential to make a distinction between the two. In addition, the subclassification of grain-boundary ferrite in the IIW classification is not unequivocal in its meaning: It could refer to ferrite that forms by diffusion, to Widmanstätten ferrite, or to the ferrite in upper bainite. In contrast, the term *allotriomorphic ferrite* clearly identifies the mechanism by which it is formed. On the other hand, the IIW classification is easy to use and

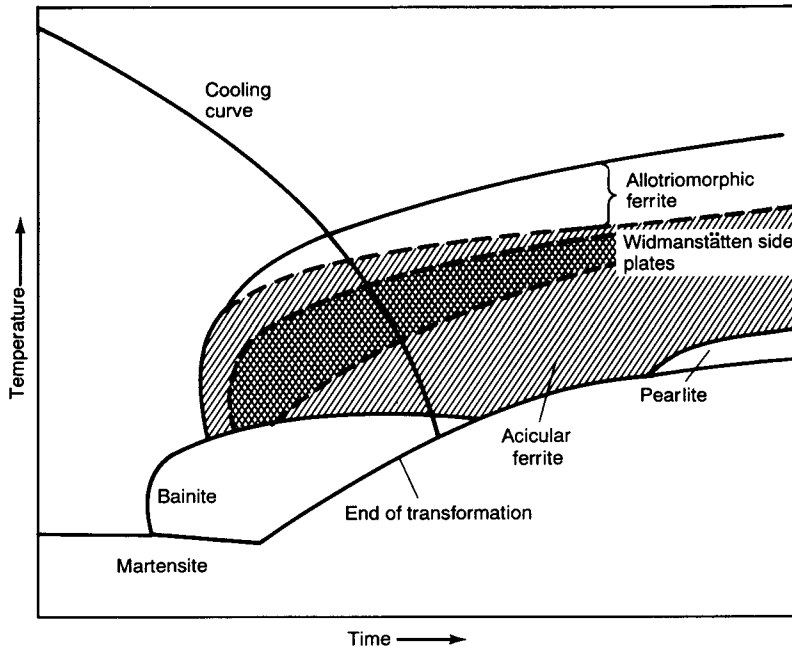


Fig. 23 Schematic of weld continuous cooling transformation diagram showing selected microstructures

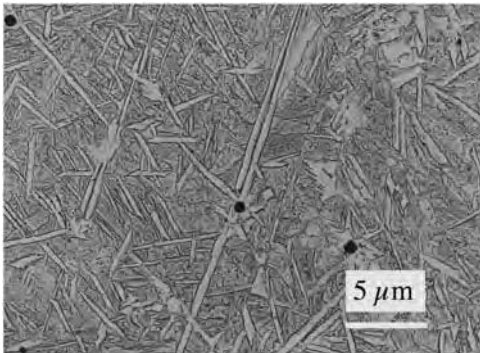


Fig. 24 Replica transmission electron micrograph showing acicular ferrite in a steel weld deposit. Source: Ref 30

allows a more detailed identification, either by judgment or by further TEM examination—for example, to determine whether FS is FS (SP) or FS(UB). At least it decreases the tendency for a wrong identification of the transformation mechanism with insufficient data. For a microstructure-toughness correlation, it is

sufficient to characterize the morphological features.

Sensitivity to Carbon. Small variations in carbon concentration can have a major influence on the microstructure of the welds, particularly because the carbon content of a weld is normally kept very low. It is seen from Fig. 27 that the sensitivity of growth kinetics of allotriomorphic and Widmanstätten ferrite to carbon becomes larger as the concentration of carbon decreases (Ref 30). The growth rate of ferrite increases sharply as the carbon concentration of the steel approaches its solubility in ferrite, because there is no need for the carbon to diffuse ahead of the austenite/ferrite interface since it can all be accommodated in the ferrite (Ref 30). Hence, the effect of carbon is expected to be greater when its concentration changes, for example, from 0.03 to 0.05 wt%, when compared with the change from 0.09 to 0.11 wt% (Fig. 27). Changes in mechanical properties reflect this behavior, the strength of low-carbon steels being very sensitive to the carbon concentration. Figure 28 illustrates that both microstructure and mechanical properties change more rapidly at low carbon concentrations.

The high sensitivity of the α/γ transformation to carbon at low concentrations leads to a corresponding decreased sensitivity to substitutional alloying elements. Carbon essentially controls the kinetics of transformation. Hence, for the weldability of steels that is often expressed in terms of carbon equivalent (CE), there are logically two popular formulas for the CE for low- and high-carbon weldable steels (Ref 5):

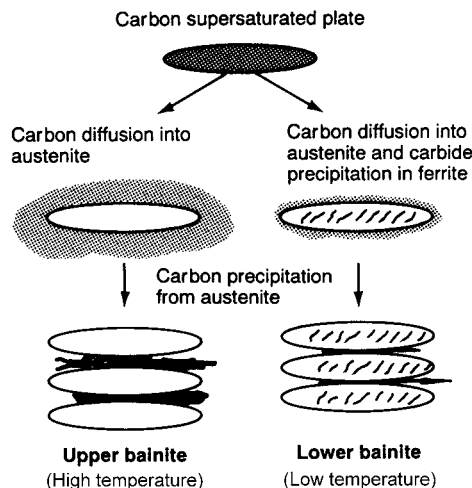


Fig. 25 Schematic showing the differences in the transformation mechanism for upper and lower bainite and the effect of these mechanisms on the final morphology. Source: Ref 30

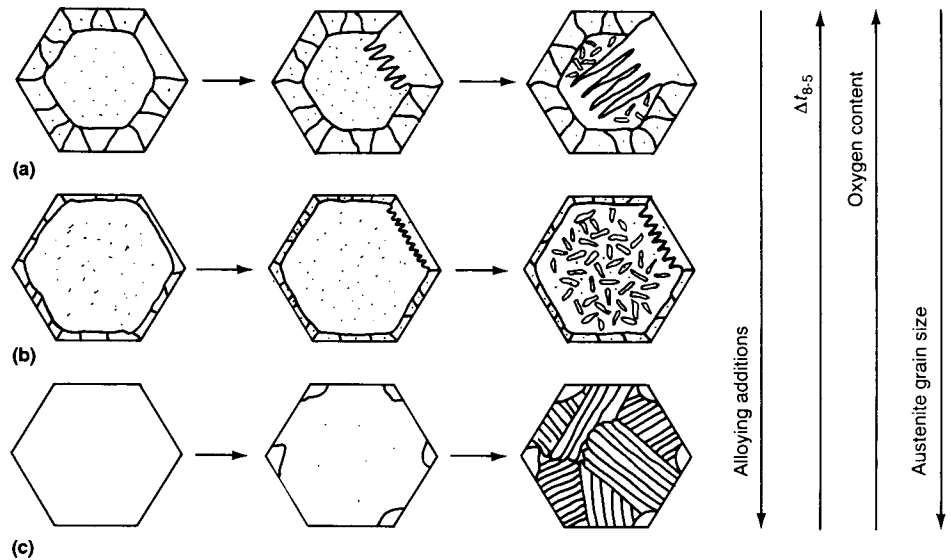


Fig. 26 Schematic showing the effect of alloy composition, $\Delta t_{b,5}$, oxygen content, and γ grain size on the development of microstructure in ferritic steel weld metals. The hexagons represent cross sections of columnar γ grains. (a) The γ grain boundaries become decorated first with a uniform, polycrystalline layer of allotriomorphic ferrite, followed by formation of Widmanstätten ferrite, and then by formation of acicular ferrite. (b) The growth rate of Widmanstätten ferrite is not sufficiently high to extend entirely across γ grains. Nucleation of ferrite at inclusions within the γ grains leads to an increase in the amount of acicular ferrite when compared with case (a). (c) The higher alloy content or the higher cooling rate suppresses the formation of allotriomorphic ferrite. This leaves the γ grain boundaries free to nucleate upper bainite. Source: Ref 30

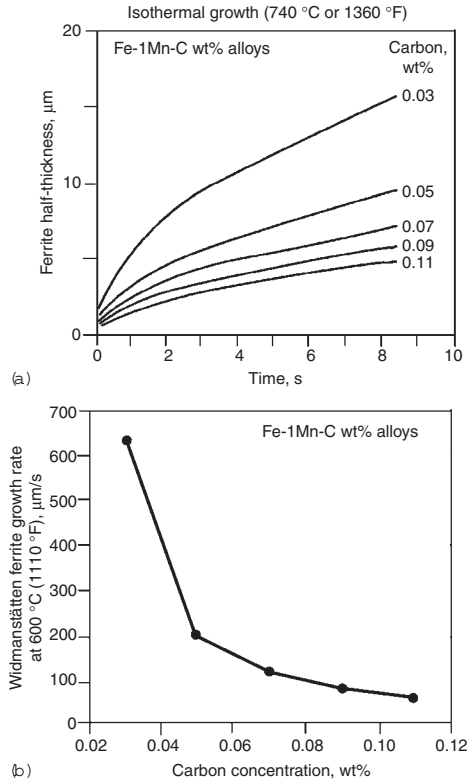


Fig. 27 (a) Diagram illustrating the calculated thickening of allotriomorphic ferrite during isothermal transformation. The growth kinetics become sensitive to carbon concentration as the latter approaches the solubility of carbon in the ferrite. (b) Calculated isothermal growth rate of Widman-

IIW > 0.18wt%C : CE

$$= C + \frac{\text{Mn} + \text{Si}}{6} + \frac{\text{Ni} + \text{Cu}}{15} + \frac{\text{Cr} + \text{Mo} + \text{V}}{5} \text{ wt\%} \quad (\text{Eq 1})$$

Ito-Besseyo < 0.18wt%C : CE

$$= C + \frac{\text{Si}}{30} + \frac{\text{Mn} + \text{Cu} + \text{Cr}}{20} + \frac{\text{Ni}}{60} + \frac{\text{Mo}}{15} + \frac{\text{V}}{10} + 5B \text{ wt\%} \quad (\text{Eq 2})$$

The second equation (Ito-Besseyo) has smaller coefficients for the substitutional solutes compared with the IIW equation. This is, as already stated, because at low carbon concentrations the kinetics of transformation are more sensitive to carbon content than to substitutional solutes.

Relating Weld-Metal Toughness to the Microstructure. A good insight into the subject of toughness in ferrite steel weld metal is obtained by examining the data shown in Fig. 29. It is seen from Fig. 29(a) that the upper-shelf Charpy V-notch (CVN) energy

monotonically decreases with an increase in oxygen content. In the upper-shelf temperature region, ductile fracture occurs by a process of microvoid coalescence, and because microvoids are initiated at the inclusion-matrix interface, the upper-shelf impact energy decreases with an increase in the inclusion content. In contrast, from Fig. 29(b) it is seen that an optimal inclusion content is required to obtain the lowest CVN transition temperature. The transition temperature is governed mainly by cleavage fracture, which in turn depends on how effectively a propagating cleavage crack is forced to change direction as it traverses the microstructure. At low inclusion contents, an upper bainitic structure is obtained, consisting of parallel platelets of ferrite (in a single packet) growing from the grain-boundary surfaces. With an optimal inclusion content, a predominantly acicular ferrite structure is obtained, in which the adjacent ferrite platelets tend to radiate in many different directions from the inclusion nucleation site. At higher inclusion contents, the amount of ferrite side plate structures increases, again having nearly parallel ferrite platelets. The highest toughness (that is, the lowest transition temperature) is obtained only in the “chaotic” microstructure of acicular ferrite, because it has the smallest effective ferrite grain size.

In recognition of the latter fact, most of the work in consumables development in the recent past has concentrated on increasing the amount of acicular ferrite in the microstructure. In line with the trends shown in Fig. 26(a) and (b), it has been found that decreasing the amount of grain-boundary ferrite and ferrite side plate structures increases the acicular ferrite content. This is shown more clearly in Fig. 30.

Recent work (Ref 30, 31, 33–35), however, has shown that a 100% acicular ferritic structure is neither desirable nor, in most cases, achievable. Figure 31(a), for example, shows that, depending on the weld metals, the maximum amount of acicular ferrite (~70 to 80%) is achieved at different oxygen concentrations. The acceleration of CCT diagrams owing to oxygen in the weld metal (Fig. 32) is consistent with the decrease in weld-metal hardness shown in Fig. 31(b). The role of oxides in providing additional heterogeneous nucleation sites is indicated by the fact that both bainite and ferrite regions are accelerated as the oxygen content is increased (Ref 35). In other words, the hardenability of the weld is lowered as the oxygen is increased. Figure 33 shows that the impact toughness peaks at approximately 70% acicular ferrite. This phenomenon was attributed to the formation of segregated bands of brittle microphases in the alloy compositions giving the highest acicular ferrite contents. Moreover, when the alloying additions are increased still further, the transformation behavior becomes such that allotriomorphic

ferrite formation is totally suppressed, leaving the γ grain boundaries free to nucleate upper bainite at lower temperatures (Fig. 26c). It appears that a small layer of allotriomorphic ferrite is essential to obtain high acicular ferrite contents. When it forms, it saturates the γ grain-boundary sites, and bainite nucleation at the γ/α -allotriomorphic interface is inhibited by the high carbon content there as a result of its rejection from the ferrite (Ref 30). Conditions are then favorable for intragranular nucleation at inclusion sites and thus the formation of acicular ferrite.

For the welding of steels with yield strengths less than 600 MPa (85 ksi), it has been possible to develop weld metals with matching strength and toughness by giving them high acicular ferrite contents. A yield strength of approximately 600 MPa (85 ksi) seems to be the ceiling for weld metals based on acicular ferrite. Attempting to obtain additional strength by additional alloying to increase the amount of solid-solution hardening and precipitation hardening, in fact, results only in increasing amounts of martensite and bainite, structures that are associated with a lower toughness. This phenomenon was observed in HSLA-100 steels, for example, where attempts to obtain a matching strength in the weld metal resulted in a drop in toughness (Ref 31, 37). It should be noted that a slightly undermatching weld metal (in terms of strength) appeared to be favorable. Thus, the already available lower-strength, high-toughness consumables having high acicular ferrite contents can be used for high-strength steels (Ref 38). These weld-metal compositions have an additional benefit in that they do not require the most stringent measures for avoiding hydrogen-induced cracking. Work on consumables development for high-strength steels is still in progress to match the base metal in strength and toughness (Ref 38–41).

Titanium Oxide Steels. In the discussion of the role of pinning by precipitate particles (for example, TiN) in limiting grain growth in the HAZ (in the section “Austenite Grain Growth and Grain-Boundary Pinning” in this article), it was pointed out that at high heat inputs, the particles dissolve and are not able to prevent coarse γ grains from forming. The low toughness in these coarse-grained regions is of some concern. The fact that a coarse γ grain size will lead to a higher acicular ferrite content (Fig. 26b) with improved toughness has been used to advantage in the development of titanium-oxide-containing steels (Ref 42, 43). The compound Ti_2O_3 is more stable than titanium nitride and does not dissolve, even at the highest heat inputs. The undissolved Ti_2O_3 particles do not stop grain growth, but their survival after the heating cycle means that they can be effective in nucleating acicular ferrite within the coarse γ grains. The precise

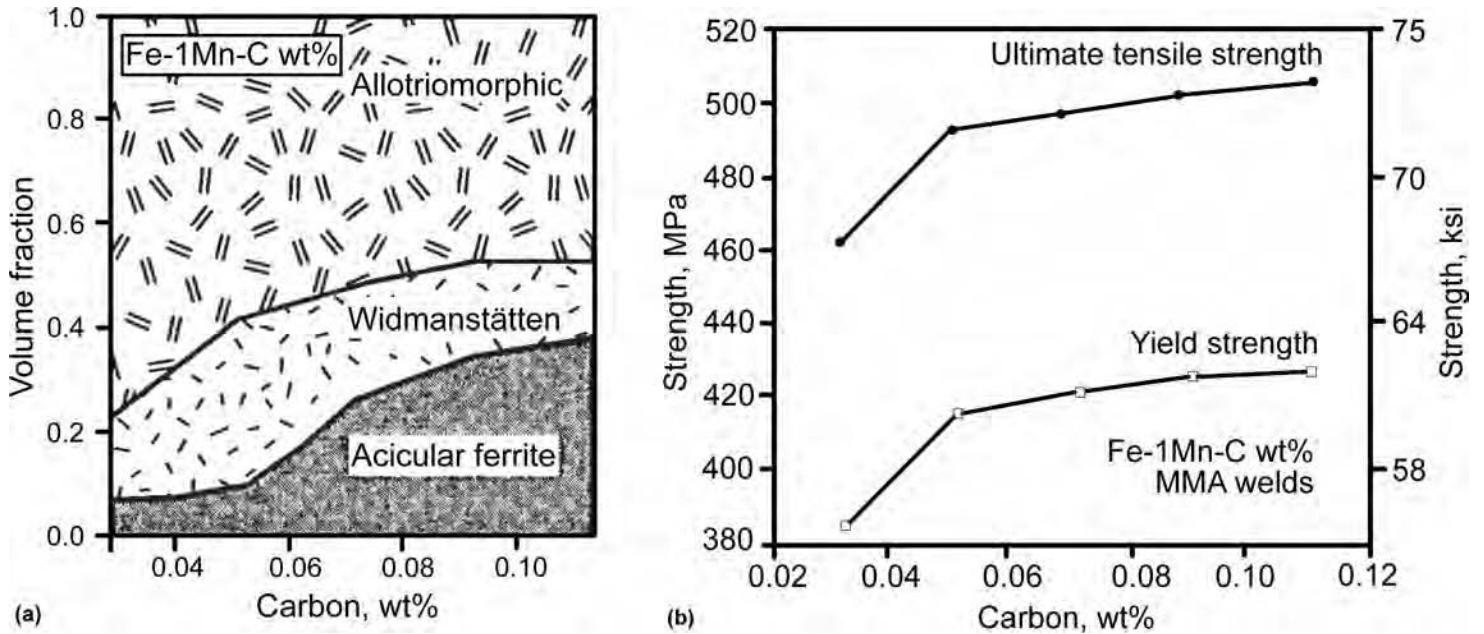


Fig. 28 Calculated variations in (a) microstructure (Ref 5) and (b) mechanical properties (adapted from Ref 5) as a function of carbon concentration in an Fe-1Mn-C wt% steel weld deposit using manual metal arc (MMA) welding (1 kJ/mm^{-1})

reasons why they are more effective than other undissolved inclusions (such as Al_2O_3) in nucleating acicular ferrite are not well understood (Ref 30). The improved HAZ microstructure and toughness obtained with titanium oxide steels over titanium nitride steels at high heat inputs are shown in Fig. 34 and 35, respectively.

Effect of Transformations on Transient Weld Stresses. The effect of transformations on weld stresses (and vice versa) is best illustrated by an old experiment known as the Satoh test (Ref 46). The method involves the cooling of a rigidly constrained steel tensile test sample from its austenitic state. During the test, the stress that accumulates is monitored. For uniaxial specimens using a HAZ simulation technique, the manner in which residual stress is accumulated during a weld thermal cycle was investigated for bainitic, martensitic, and stable austenitic steels (Ref 47). Initially, when a material is austenite at high temperature, its yield strength is low and only a small tensile stress can develop. On cooling, the tensile stress increases. When a phase transformation occurs, the resulting volume expansion opposes the contraction due to cooling and decreases the stress. When the transformation is complete, the tensile stress increases again (Fig. 36). As seen in Fig. 36, if the transformation occurs at a lower temperature (for example, in the case of 9CrMo steel), the magnitude of the final residual stress is less.

In contrast, the nontransforming austenitic steel exhibits a continuous increase in residual stress with decreasing temperature because of the thermal contraction of the constrained specimen. Moreover, the thermal expansion coefficient of austenite ($1.8 \times 10^{-6} / \text{K}$) is much larger than that of ferrite ($1.18 \times 10^{-6} / \text{K}$), and yet the slope of the line prior to transformation is smaller when compared with that after transformation is complete (Fig. 36) (Ref 48). This is because, at high temperatures, austenite has a low yield strength and can accommodate the thermal contraction by yielding. Ferrite is strong at low temperatures, so the slope of the stress/temperature curve is steeper.

By engineering the temperature regime over which phase changes occur, the pronounced effect of volume and shear strains of displacive transformation can be exploited to mitigate the development of welding residual stresses. In recent years, welding consumables with low austenite-to-martensite transformation temperatures (M_s) have been developed (Ref 49–51). By using the proposed welding electrodes that achieve M_s at or under 200°C (390°F) and martensite finish temperatures close to room temperature, it is possible to achieve near-zero or compressive residual stresses in the weld, as shown in Fig. 37. It has been shown that the fatigue limit of joints using the new low- M_s welding wire has been improved significantly (Ref 50). It should

be mentioned that the weld metal with fully martensitic structure is susceptible to hydrogen-induced cracking (HIC). This problem can be addressed by the use of a duplex martensite/retained austenite weld microstructure. Austenite can contribute by increasing the toughness and by minimizing the risk of HIC, because of the lower hardness and the higher hydrogen solubility of austenite compared to martensite. It has been shown that the resistance to cold cracking can be improved when the weld contains martensite with a small amount of retained austenite (Ref 41).

Heat-Affected Zone in Multipass Weldments

In the HAZ of a single-pass weld, the grain-coarsened zone (GC HAZ) is normally the region having the lowest toughness. Turning to a multipass weld, Fig. 38 (compare with Fig. 4) shows how the GC HAZ can be modified by subsequent passes and can be categorized into four regions, depending on the reheating temperature (Ref 52):

- *Subcritically reheated grain-coarsened (SCGC) zone:* The zone reheated below A_{c1}
- *Intercritically reheated grain-coarsened (ICGC) zone:* The zone reheated between A_{c1} and A_{c3}

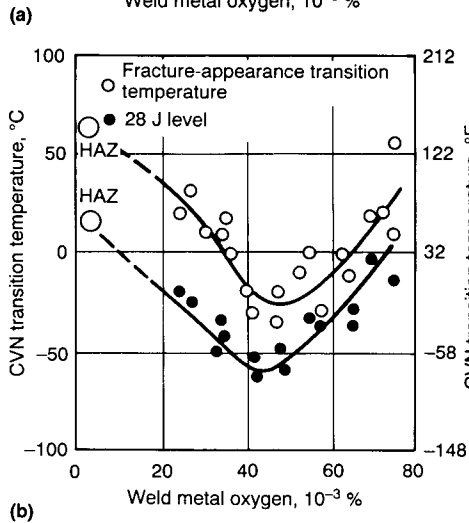
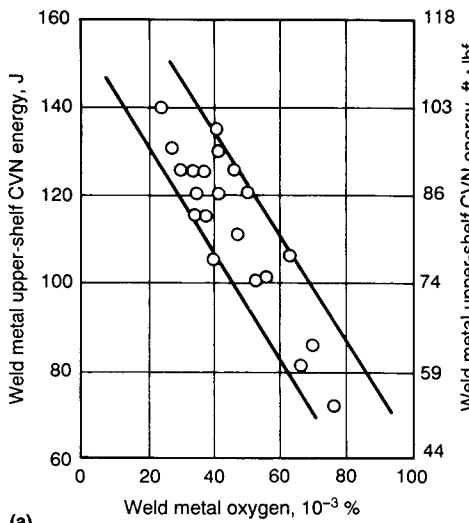


Fig. 29 Typical variation of selected weld-metal properties with oxygen content in ferritic steel weld metals. (a) Plot of Charpy V-notch (CVN) impact test upper-shelf energy versus oxygen content. (b) Plot of CVN transition temperature versus oxygen content. HAZ, heat-affected zone. Source: Ref 33

- *Supercritically reheated grain-refined (SCGR) zone:* The zone reheated above A_{c3} and below approximately 1200 °C (2190 °F)
- *Unaltered grain-coarsened (UAGC) zone:* The zone that is not reheated above approximately 200 °C (390 °F) or the zone that is again reheated above approximately 1200 °C (2190 °F)

Figure 39 shows how the crack tip opening displacement (CTOD) value of simulated specimens varies with the peak temperature of the second thermal cycle, T_{p2} ($T_{p1} = 1400$ °C, or 2550 °F). It is seen that the ICGC, UAGC, and SCGC regions have CTOD values less than approximately 0.1 mm (0.004 in.). Similar low values have been obtained by locating the crack tip in the CTOD tests at corresponding locations in the HAZ of actual multipass weldments. These low-toughness regions are commonly known as local brittle zones (LBZs).

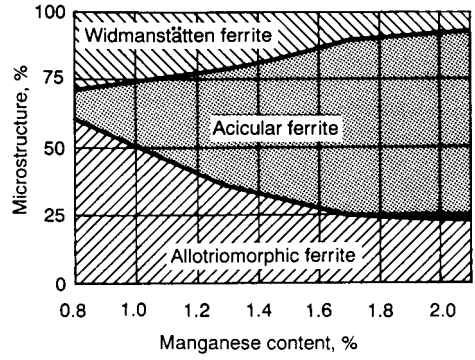


Fig. 30 Effect of manganese content of weld metal on the relative amounts of the microstructural constituents present. Carbon content maintained at 0.03%. Source: Ref 33

The low CTOD values have been obtained only in tests on modern structural steels, and no actual structural failure attributable to the LBZs has been reported so far (Ref 53). Because the structural significance of the low-toughness test results is still largely unresolved, the present conservative strategies are to choose a steel whose tendency to form LBZs is less and to choose a welding procedure by which the size of the LBZs can be reduced.

The ICGC HAZ usually has a lower toughness than the SCGC or UAGC regions, even though all of them have nearly the same γ grain size. This lower toughness is due to the higher amount of high-carbon martensite-austenite (M-A) constituent in the ICGC HAZ. When the GC HAZ is reheated to a temperature between A_{c1} and A_{c3} , austenite is nucleated at the high-carbon areas. Upon cooling, these local high-carbon areas can transform to give twinned martensite with very thin regions of retained austenite in between. (See Ref 54 for detailed metallographic procedures for identifying the M-A constituent.) The carbon content in the M-A islands can range from approximately 0.3 to 0.5% C. The significance of this is that, for a given nominal carbon content in the steel, the volume fraction of the M-A constituent will be much higher than it would be if most of the carbon formed carbides (by the lever rule). This fact will increase the number of crack nucleation sites and thereby contribute to the inferior toughness of ICGC HAZ. As is to be expected, the volume fraction of the M-A constituent also depends on the hardenability of the steel, which, in turn, depends on the alloying content. It has been shown that if the development of pearlitic microphases could be promoted instead of the development of M-A, by decreasing the alloy content, the toughness of the ICGC HAZ could be improved (Ref 55). However, this would have penalties in terms of achievement of parent plate strength. A more feasible solution would be to inhibit grain growth in the HAZ.

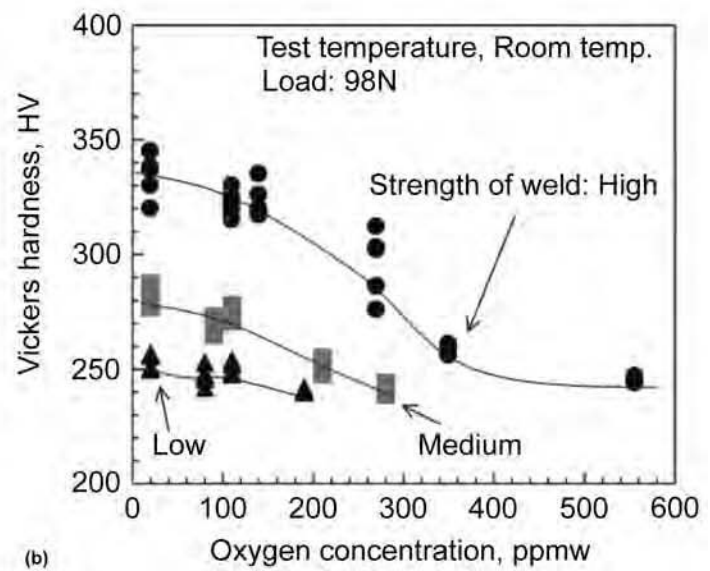
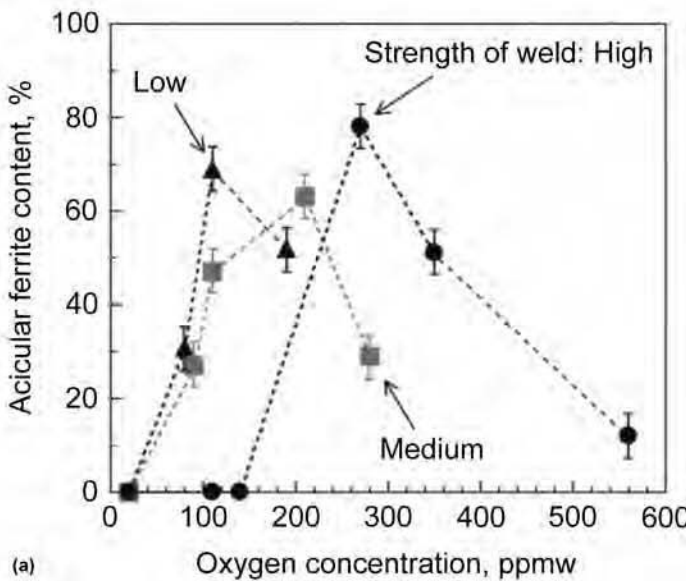


Fig. 31 (a) Acicular ferrite content as a function of oxygen concentration in low- (624 MPa, or 91 ksi), medium- (688 MPa, or 100 ksi), and high- (778 MPa, or 113 ksi) strength weld metals. (b) Effect of oxygen concentration on weld-metal hardness. ppmw, parts per million by weight. Adapted from Ref 35

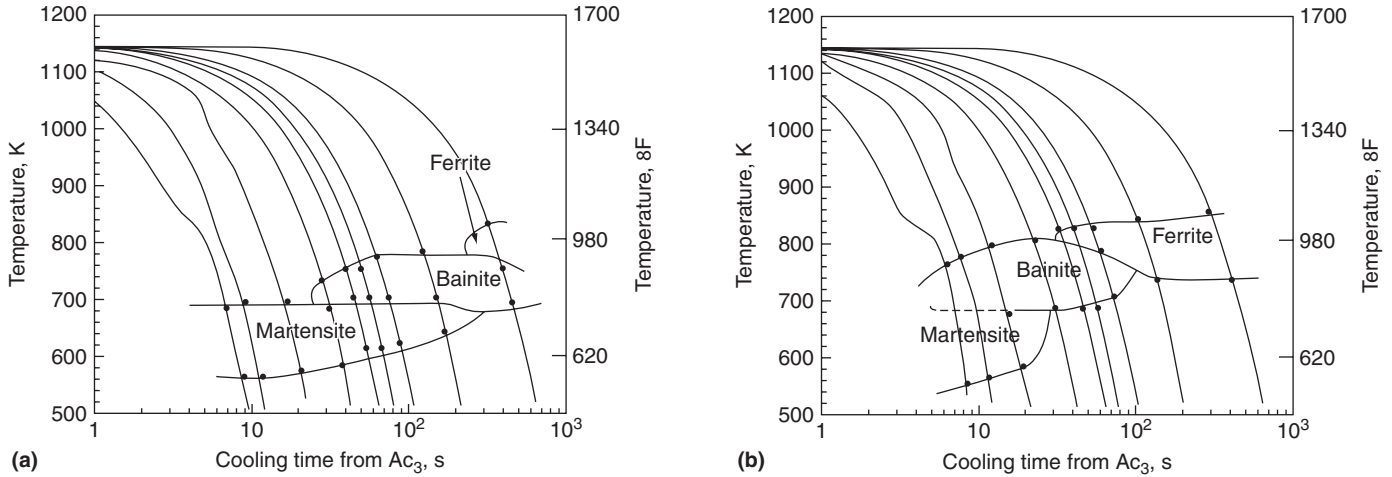


Fig. 32 Effect of oxygen concentration on continuous cooling transformation diagrams of a high-strength weld metal. (a) 20 parts per million by weight (ppmw) oxygen. (b) 350 ppmw oxygen. Adapted from Ref 35

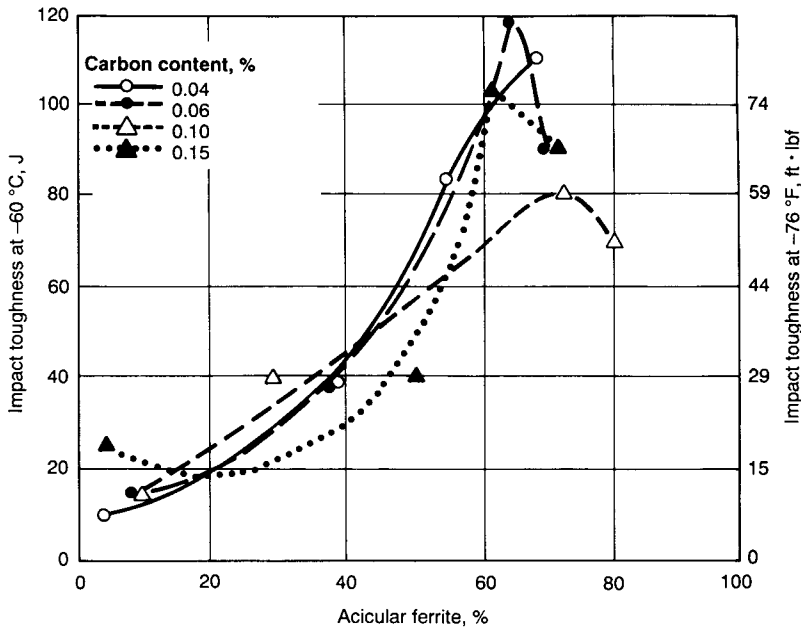


Fig. 33 Plot of impact energy versus acicular ferrite content for selected carbon contents at $-60\text{ }^{\circ}\text{C}$ ($-76\text{ }^{\circ}\text{F}$). Source: Ref 36

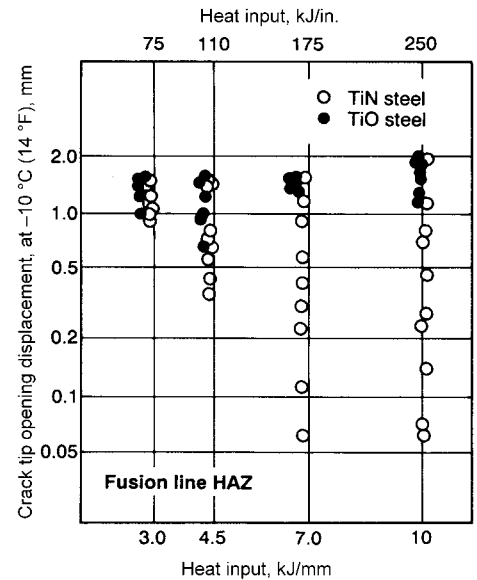


Fig. 35 Heat-affected zone (HAZ) toughness of titanium nitride and titanium oxide steels with 420 MPa (60 ksi) yield strength. Source: Ref 45

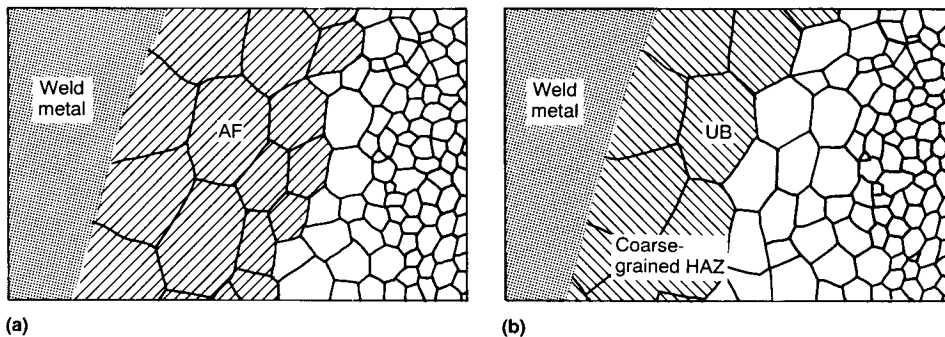


Fig. 34 Schematic showing heat-affected zone (HAZ) microstructure in selected high-heat-input welds. (a) Titanium oxide steel. (b) Titanium nitride steel. AF, acicular ferrite; UB, upper bainite. Source: Ref 44

The multipass welding procedure can alternatively be controlled to limit the size of the LBZs. Figure 40 shows how this can be done with a tandem three-wire high-current gas metal arc welding procedure by adjusting the distances between the three arcs. Special “temper-bead” procedures (Ref 57) have been developed for controlling the microstructure in the HAZ, and a need for these procedures arises in the following way. Low-alloy steel weldments for critical applications (for example, pressure vessels) require a postweld heat treatment (PWHT) in a furnace in order to temper the hard regions in the HAZ and relieve

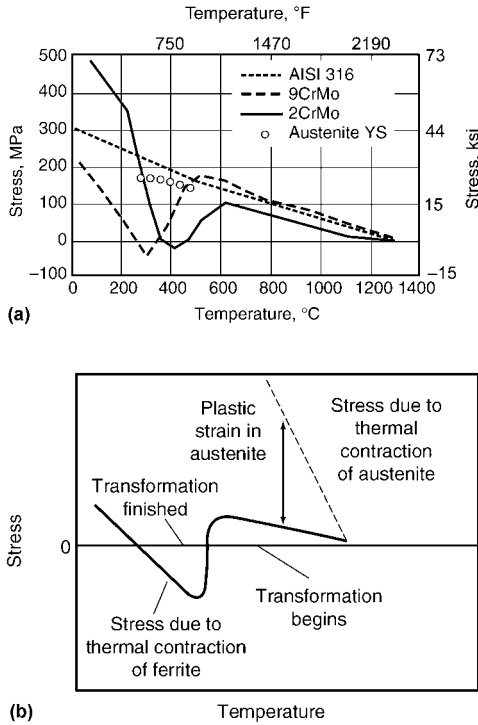


Fig. 36 (a) Axial stress accumulated in uniaxially constrained specimens during cooling of martensitic (9CrMo), bainitic (2CrMo), and austenitic (AISI 316) steels. Some experimental data are shown for yield strength (YS) of austenite in low-alloy steel. Adapted from Ref 47. (b) Schematic interpretation of the experiments shown in (a). Source: Ref 48

residual stresses. If on-site repairs become necessary after the component has been in service, PWHT is usually not feasible. The heat of the arc can then be used to achieve the tempering function of PWHT by suitable spatial positioning and sequencing of the individual passes. Grain refinement in the HAZ is also sought in order to increase the toughness and thereby offset the harmful effects of residual stresses that would remain in the absence of PWHT.

An example of a two-layer temper-bead procedure is shown in Fig. 41. The heat inputs of the first and second layer are carefully controlled, so that the heat from the second layer is used to refine the coarse-grained region in the HAZ of the base metal caused by the first layer. This idea can be extended one step further by using a pulsed gas tungsten arc welding procedure in which each pulse in a pulsed weldment successively refines and tempers the preceding pulse pitch region (Ref 11). The degree of microstructural refinement depends primarily on the welding speed and pulsing frequency, and these parameters can be controlled with great precision. In contrast,

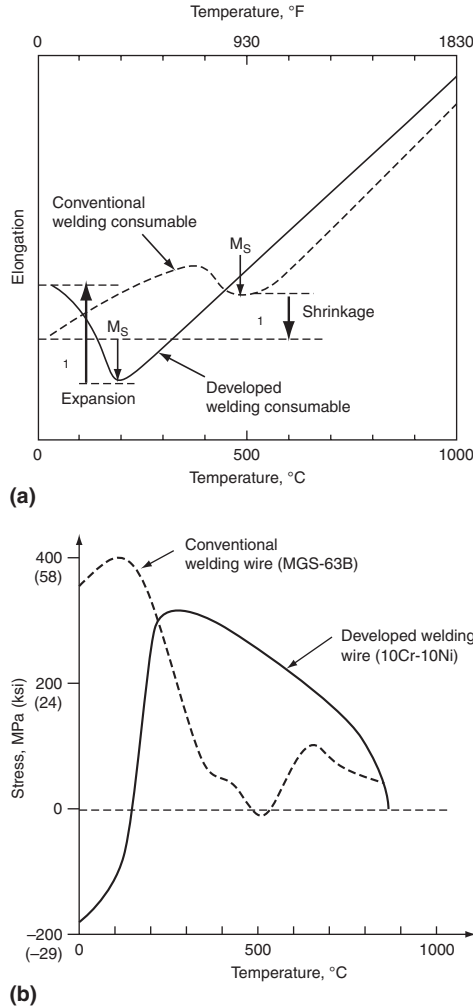


Fig. 37 Comparison between the low-transformation-temperature welding consumable and conventional steel wire. (a) Transformation strain developed during unconstrained cooling of welding

an important variable to be controlled in the temper-bead procedure is the weld-deposit height, and it is difficult to exercise the same degree of control on this variable. For this reason, it is argued that the maximum possible control on the microstructural changes in the repair weldment is possible with the pulsing procedure.

Fusion Zone in Multipass Weldments

In the weld metal of a multipass weld, reheating effects will lead to a gradient in microstructure similar to that in the HAZ. However, instead of a detailed classification, the multipass weld metal is usually considered to consist of just two regions (Fig. 42):

- *As-deposited or primary region:* Where the microstructure develops as the weld cools from the liquid phase to ambient temperature
- *Reheated or secondary region:* Where regions with the original primary microstructure are reheated to temperatures above the A_{c1} temperature. The tempered regions that are reheated to slightly lower temperatures are also generally considered to belong to this category.

The properties of the weld metal depend on the relative areas or volume fractions of the two regions, which, in turn, depend on the welding procedure; the properties are therefore procedure-specific. That is why it is necessary for welding procedures to be qualified according to codes and standards in addition to and separately from the qualification of consumables (for which a standard procedure is specified).

Weldments in Select Alloy Systems

Stainless Steels

It has long been known that solidification cracking can be avoided in austenitic stainless steel welds by having a small concentration of ferrite in them. Recent work has shown, however, that residual ferrite content at room temperature is no more than a symptom and that it is really the solidification mode (whether the weld metal solidifies as primary austenite or ferrite) that is the decisive criterion (Ref 58). It has been found that susceptibility to solidification cracking is least for a primary ferrite solidification mode (more specifically, when the solidification mode corresponds to the types shown in Fig. 43c and d). It is believed that low-melting-point liquid phases (formed by the segregation of impurities such as sulfur and phosphorus, for example) solidifying in the intercellular regions do not wet the δ - γ interphase boundaries as easily as they would δ - δ or γ - γ boundaries. In the ferritic-austenitic solidification mode (Fig. 43c, d), the δ - γ interphase boundary area is greater at temperatures just below the nominal solidus temperature, and this is the reason for a greater resistance to solidification cracking.

Information about the solidification mode can be obtained from the chemical composition of the weld metal by referring to the WRC-1992 diagram (Fig. 44a). It has been found that this diagram is more accurate than the Schaeffler (for duplex stainless steel welds) and Delong (for 300-series austenitic steel welds) diagrams developed earlier. These diagrams are strictly applicable only for the cooling rates obtained in manual metal arc (MMA) welding because the data for establishing the statistical correlations have been taken from MMA welds. The dotted lines in Fig. 44 are the demarcation

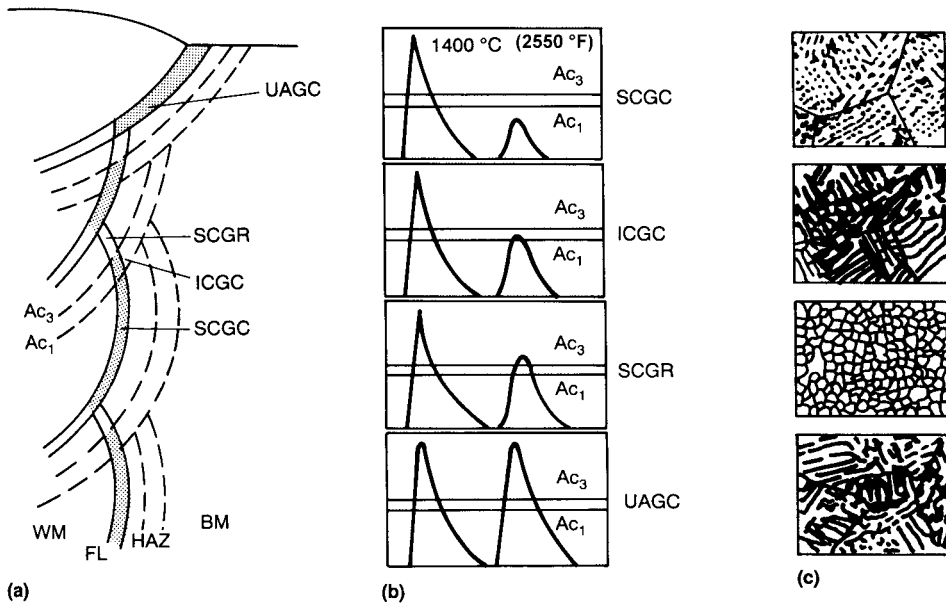


Fig. 38 Schematic showing the different subzones that can form in the coarse-grained region of the heat-affected zone (HAZ) in a multipass weld. (a) Position of subzones relative to base metal (BM) and weld metal (WM). FL, fusion line. (b) Plot of thermal cycles relative to A_{c3} and A_{c1} . (c) Microstructures at the different zones. See text for details. Source: Ref 52

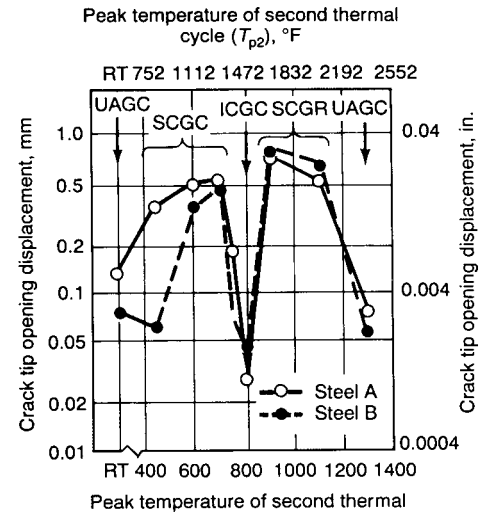


Fig. 39 Plot of crack tip opening displacement versus peak temperature of the second thermal cycle for simulated specimens subjected to a double thermal cycle. ($T_{p1} = 1400\text{ }^{\circ}\text{C} = 2550\text{ }^{\circ}\text{F}$; $\Delta t_{3.5} = 20\text{ s}$). The heat-affected zones (Fig. 38) corresponding to the simulation trials are also shown in the figure. Source: Ref 52

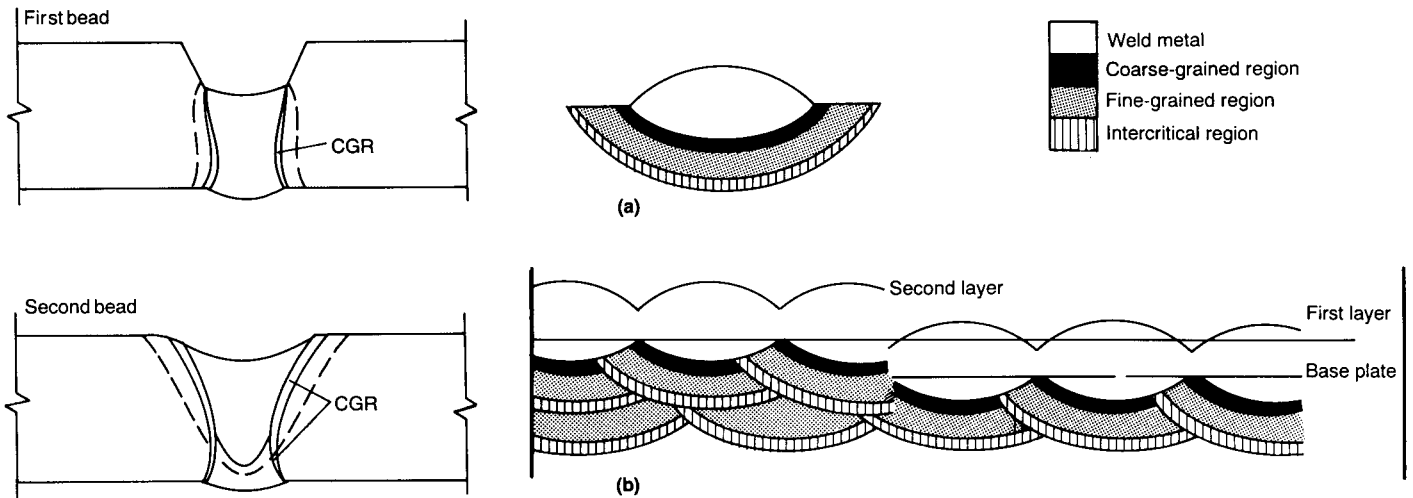


Fig. 41 Schematic showing a two-layer repair procedure. (a) Heat-affected areas of a single weld bead. (b) First layer causes coarse-grained regions to form in the heat-affected zone of the base metal (right portion of the figure). Deposition of the second layer refines these initial coarse-grained regions (left portion of the figure). Source: Ref 57

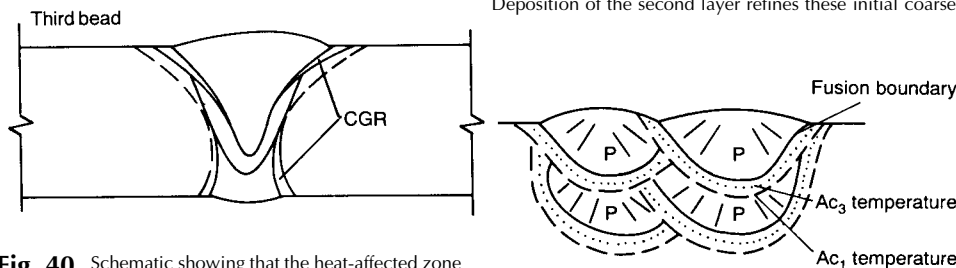


Fig. 40 Schematic showing that the heat-affected zone isotherms and the size and location of the coarse-grained region (CGR) can be controlled in a tandem three-wire high-current gas metal arc welding procedure. Grain refinement of initially formed coarse-grained regions is obtained by optimizing the distances between the three arcs. Source: Ref 56

Fig. 42 Primary (P) and re-austenitized regions in the weld-metal region of a multipass weld. The re-austenitized region is where the columnar structure is not clearly detected. Source: Ref 28

lines between the different solidification modes shown (that is, A, AF, FA, and F), corresponding to the types in Fig. 43(a to e), respectively. The AF-FA boundary in Fig. 44(a) (which, as discussed earlier, corresponds to the onset of cracking) intersects the iso-ferrite number lines at an angle. This is consistent with the findings of several investigators that the minimum ferrite content necessary to avoid hot cracking is different for different weld-metal compositions (that is, for weld metals deposited with E 316, E 308L, E 309, and so on).

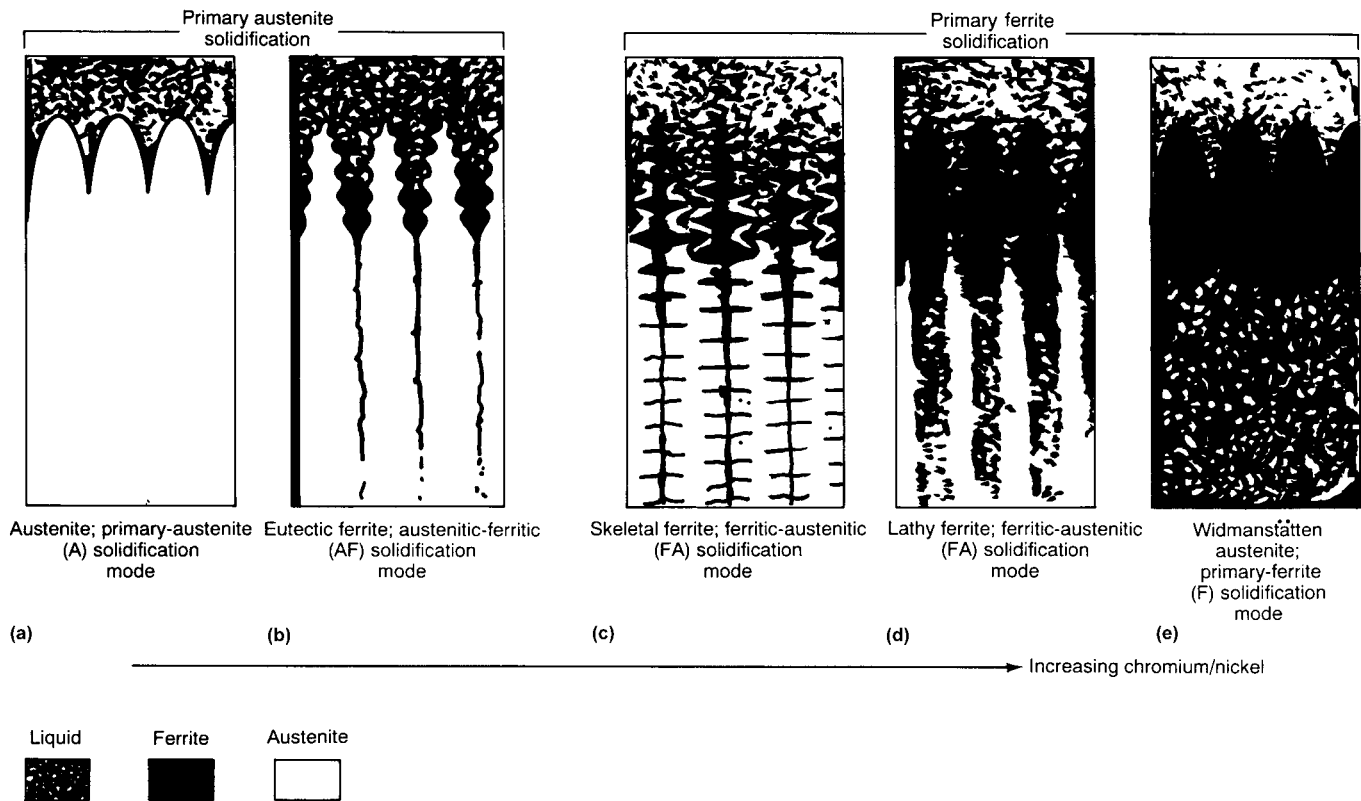


Fig. 43 Schematic showing solidification and transformation behavior resulting in a range of ferrite morphologies in austenitic stainless steel welds. Source: Ref 58

The utility of the WRC-1992 diagram has recently been expanded by adding martensite boundaries (Ref 60), as shown in Fig. 44(b). Using the modified WRC-1992 diagram, it is now possible to predict whether or not stainless steel clad layers, over nonalloy or low-alloy steel, will be free of martensite and will pass a 2T bend test (a bend test in which the bend specimen thickness, T , is twice the bending radius).

A discussion of weld decay due to sensitization and knife-line attack in the HAZ of austenitic stainless steels can be found in Ref 7, 61, and 62.

Aluminum Alloys

The main problems in the welding of heat treatable aluminum alloys are liquation cracking in the partially melted zone (PMZ) (see the section "Unmixed and Partially Melted Zones in a Weldment" in this article) and softening in the HAZ (Ref 7). Figure 45 shows, for example, the formation of liquation cracking in the PMZ of an aluminum alloy weld with partial penetration. A good discussion of how liquation cracking forms in aluminum alloys is found in Ref 63.

The softening in the HAZ means that the weld-joint strength can be reduced. Reasons for the softening can be understood by referring to Fig. 46. The parent material is assumed to be a 2000- or 6000-series aluminum alloy, artificially aged to contain the metastable phase of θ' (in aluminum-copper alloys), S' (in aluminum-copper-magnesium alloys), or β' (in aluminum-magnesium-silicon alloys). A very fine dispersion of precipitate particles is obtained in the parent material by a solution heat treatment followed by aging, and this is the reason for the high strength in the materials. Figure 46(b) shows that a gradient in hardness is obtained in the HAZ immediately after welding. At location 1, the high peak temperature causes the precipitate particles to go into solution, and the cooling rate is too high for reprecipitation. At locations 2 and 3, the precipitate particles partially dissolve and coarsen. After postweld artificial aging, fine precipitate particles are again formed at location 1, causing the hardness to increase to the level of the parent material. However, at locations 2 and 3, only a lower hardness can be obtained because of the formation of coarse precipitate particles. For increasing weld heat

inputs, the width of the softened zone increases. A good discussion of how the aforementioned phenomenon can be modeled is found in Ref 64.

Nickel-Base Superalloys

The high creep resistance of nickel-base superalloys makes them attractive for critical high-temperature applications such as gas turbines. Yet, it is this very characteristic that gives rise to the problem of strain age cracking in the weld HAZ (Ref 7, 24, 65). The high-temperature creep strength in the parent materials is obtained by forming fine precipitates of γ' ($\text{Ni}_3(\text{Al}, \text{Ti})$) or γ'' (Ni_3Nb) in them. In the region of the weld HAZ subjected to high peak temperatures, these precipitates dissolve, much as they do in aluminum alloys. After welding, the weldments are again solution heat treated and aged (note the difference between aluminum alloys and the nickel-base superalloys in this respect). The purposes of this treatment are to obtain the same uniform fine precipitation in the weld as in the parent material and to relieve the weld residual stresses.

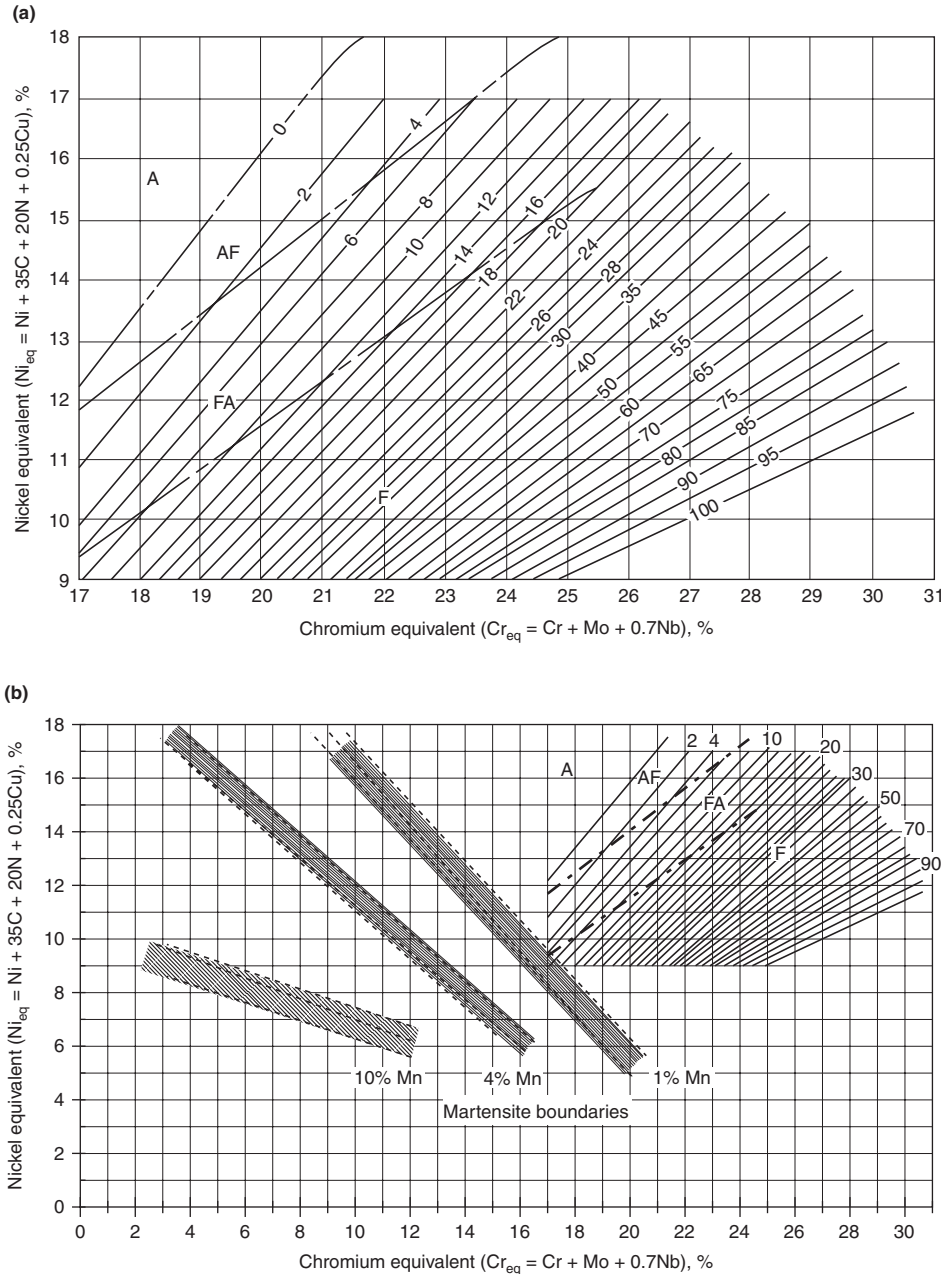


Fig. 44 (a) WRC-1992 diagram predicting ferrite content in stainless steels. Ferrite content is given by the ferrite number (FN), where 100 FN is approximately equal to 65 vol% ferrite. Boundaries denoting a change in solidification mode (A, AF, FA, and F in accordance with Fig. 43) are also shown (indicated by dotted lines). Source: Ref 59. (b) WRC-1992 diagram with martensite boundaries for 1, 4, and 10% Mn. Source: Ref 60

Normally (for example, in the case of low-alloy or carbon steel welds), PWHT in a furnace relieves the residual stresses because the yield stress at the PWHT temperature is very low. A residual stress greater than the yield stress cannot be supported, and stress relief is achieved by a process of creep and plastic deformation. This process is difficult in nickel-base superalloy weldments, however, because of their high creep strength and low creep

ductility. Reprecipitation in the solutionized regions of the HAZ (during the heating-up to the PWHT temperature) strengthens the matrix and does not allow any creep or plastic deformation (necessary for the relief of residual stress) to take place. Cracking can occur in this condition at the grain boundaries in the grain-coarsened region of the HAZ. Cracks initiated here have been known to run far into the base material. Figure 47 shows the development of

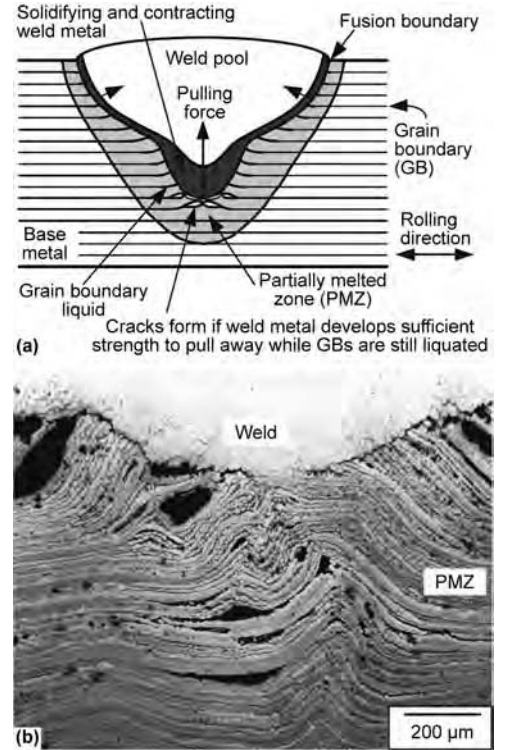


Fig. 45 Weld metal pulling and tearing the partially melted zone (PMZ). (a) Schematic showing the formation of liquation cracking in the PMZ of a partial-penetration gas metal arc weld of an aluminum alloy. The welding direction is perpendicular to the rolling direction. The weld metal in the papillary penetration solidifies rapidly. This pulls the PMZ that is weakened by grain-boundary (GB) liquation. (b) Microstructure near the weld root of 7075 aluminum made with filler wire of aluminum 1100. The weld metal pulls and tears the PMZ near the tip of the papillary penetration. Source: Ref 63

PWHT cracking. This problem is very difficult to solve, and the best solution has been found to be to switch over to materials such as Inconel 718 alloy that are inherently less susceptible to cracking, even though their creep strength is somewhat lower. Inconel 718 alloy contains γ'' precipitate, and the slow kinetics of precipitation in this alloy allow substantial stress relief to be achieved before precipitation increases the creep strength in the HAZ.

A more detailed discussion of the welding metallurgy and weldability of nickel-base superalloys can be found in Ref 24, 65, and 66.

Titanium Alloys

Titanium alloys find use in aerospace applications, pressure vessels, and so on because of their high strength-to-weight ratio, high corrosion resistance, and high fracture toughness. Pure titanium has two allotropic forms: low-temperature hexagonal close-packed (hcp) α phase and elevated-temperature body-centered

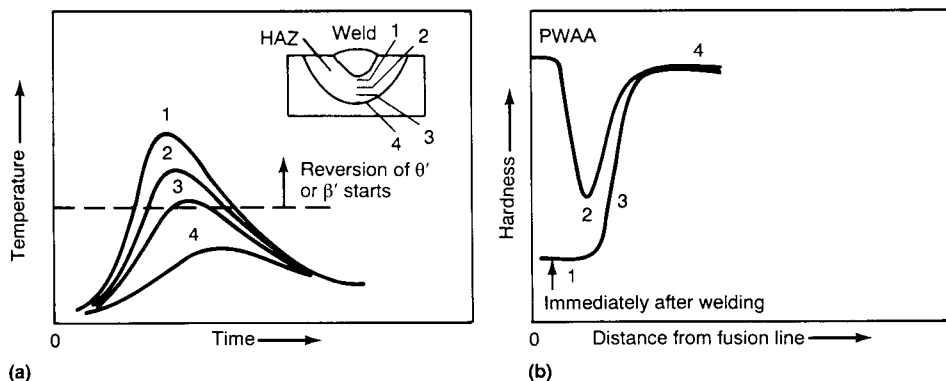


Fig. 46 Schematics showing the effect of weld thermal cycles on the softening in the heat-affected zone (HAZ) in age-hardenable aluminum alloys. (a) Thermal cycles in the HAZ (for corresponding locations in the weld, see inset). (b) HAZ hardness profiles before and after aging. PWAA, postweld artificial aging. Source: Ref 7

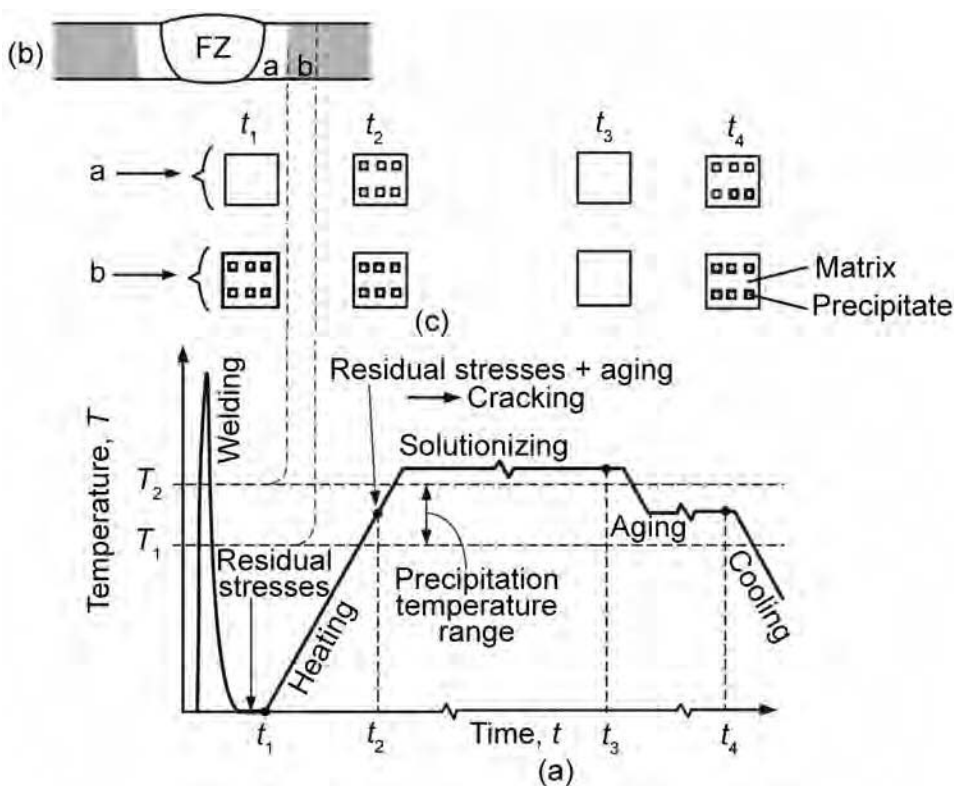


Fig. 47 Postweld heat treatment cracking in nickel-base alloys. (a) Thermal cycles during welding and heat treating. (b) Cross section of the weld showing fusion zone (FZ) and heat-affected zone. (c) Changes in microstructure. Adapted from Ref 7

cubic (bcc) β phase. Various alloying elements preferentially stabilize one or the other of these phases. As a result, titanium alloys are generally classified as α , $\alpha + \beta$, metastable β , and β alloys (Fig. 48).

The α alloys are not heat treatable (that is, it is not possible to obtain a significant increase

in strength and toughness by heat treatment), and they have the lowest strength of the four titanium alloy families. Interestingly, these alloys are thus considered to have excellent weldability—which means, in practice, that the weld thermal cycles cause no significant degradation in the properties of the weld and

HAZ relative to the parent material. Also, the $\beta \leftrightarrow \alpha$ transformation in the weld and near HAZ means that the extent of grain coarsening will not be as high as in other single-phase materials in which no phase transformation occurs upon heating or cooling, such as stabilized ferritic stainless steels (Ref 68), pure aluminum, and so on.

In the $\alpha + \beta$ alloys, a higher strength is obtained with a higher volume fraction of the β phase, which, in turn, is obtained with a higher β -stabilizing alloy content (Fig. 48). The effect of cooling rate on the phase transformations in two $\alpha + \beta$ alloys is shown schematically in Fig. 49. As in the case of steels, it is seen that the $\beta \leftrightarrow \alpha$ transformation can occur either by nucleation and growth at slower cooling rates or martensitically at higher cooling rates. The martensitic product in the lean $\alpha + \beta$ alloys has an hcp crystal structure (designated as α') or an orthorhombic one (designated as α'') in the β -stabilized $\alpha + \beta$ alloys. It is seen that the C-curve for the $\beta \leftrightarrow \alpha$ intergranular transformation is shifted to the right for alloys with increasing β -stabilizing alloy content, while that for the allotriomorphic α (more commonly referred to as grain-boundary, or GB, α) is relatively insensitive to alloy concentration (Ref 69). As a result, alloys that are fairly rich in β -stabilizing additions exhibit a stronger tendency to form a continuous network of GB α than do leaner $\alpha + \beta$ alloys.

The morphology of the α and β phases in the $\alpha + \beta$ base materials is strongly dependent on thermomechanical processing (TMP) and heat treatment, which are performed either in the β -phase field or in the two-phase $\alpha + \beta$ -phase field. When TMP is done in the $\alpha + \beta$ -phase field, the α that forms on cooling is continuously deformed. After recrystallization, a near-equiaxed α structure is obtained. Very little GB α is formed, because deformation introduces sufficient alternate heterogeneous nucleation sites in the form of dislocations. On the other hand, if TMP is done above the β -transus temperature (β -processing) and cooled, α forms at grain boundaries (giving GB α) and in the interior of grains as a Widmanstätten structure (also referred to as an acicular, lenticular, or basketweave structure). The microstructure in the weld and near the HAZ is closer to that obtained after β -processing.

Figure 50 shows the effect of $\alpha + \beta$ -processing and β -processing on the strength and toughness of $\alpha + \beta$ alloys with increasing β -stabilizing alloy content. At the lower strength levels obtained with a lower β -stabilizing alloy content (because of a lower volume fraction of β -phase present), the finer Widmanstätten structure obtained after β -processing has a higher toughness than the coarser structure obtained by $\alpha + \beta$ -processing. At

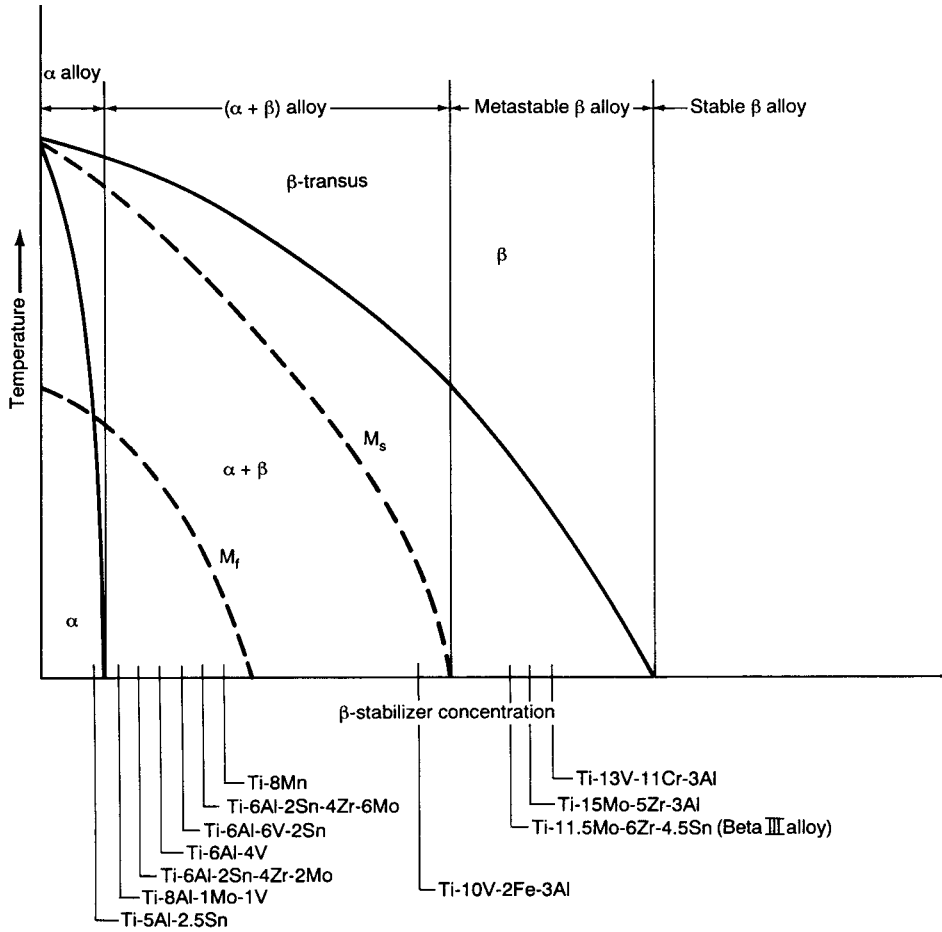


Fig. 48 Hypothetical β isomorphous phase diagram that shows relation between β -stabilizer solute content and titanium alloy family description. Selected common alloys are listed along the x-axis of the diagram based on their compositions. Source: Ref 67

higher strength levels, the trend reverses, with the $\alpha + \beta$ -processed structure having a higher toughness. This result can be understood in terms of the strength differences between GB α and the interior of the prior- β grains (Fig. 51). At lower strengths, when the grain interiors are relatively weak, the crack tip plastic zone is distributed between the GB α and the grain interiors. However, as the α -phase precipitates are refined by lower aging temperatures, as in the case of the metastable β alloys, the grain interiors are strengthened considerably. Under such circumstances, the cracks are essentially constrained to follow the GB α layer. This results in a contraction of the plastic zone, a reduction in the crack tip opening displacement for crack extension, and an attendant drop in the toughness.

The microstructures in the weld metal and the near HAZ (the region where the peak temperature exceeds the β -transus temperature) resemble those obtained after β -processing. This means that it is easier to obtain a matching toughness in the weld metal at the lower strength levels referred to in Fig. 50. However, even this result is made somewhat difficult to achieve by the coarser β grain size in the weld and HAZ. Grain coarsening in the HAZ induces coarse β grains to form in the weld too, because solidification in the weld metal occurs by epitaxial growth from the HAZ. The extent of grain coarsening is such that it is not uncommon to find a single columnar β grain traversing the entire thickness in gas tungsten arc welds on thin sheet (Ref 70). If high-energy-density welding processes are used (for example, electron beam welding or laser beam welding), it is possible to limit the extent of β grain coarsening. However, the high cooling rates in

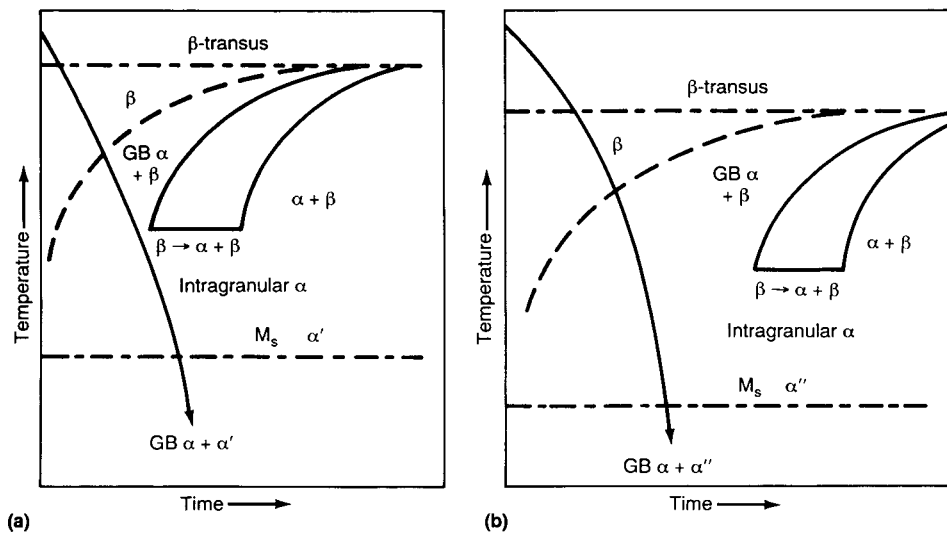


Fig. 49 Schematic continuous cooling transformation diagrams for two $\alpha + \beta$ titanium alloys with different β -stabilizer solute contents. (a) Lean $\alpha + \beta$ alloy (for example, Ti-6Al-4V). (b) $\alpha + \beta$ alloy (for example, Corona 5 [Ti-4.5Al-5Mo-1.5Cr]) richer in β -stabilizing solute content. GB, grain boundary

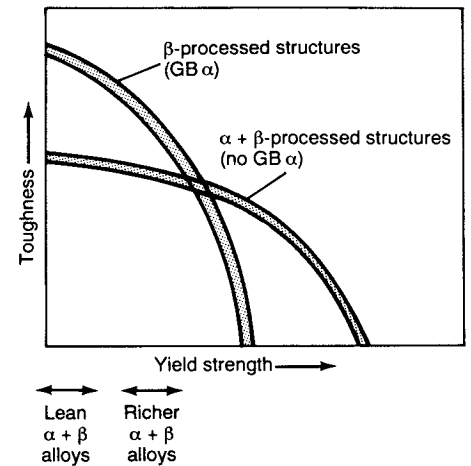


Fig. 50 Schematic plot of toughness versus yield strength for $\alpha + \beta$ - and β -processed structures. Approximate locations of lean (for example, Ti-6Al-4V) and richer β -stabilized $\alpha + \beta$ alloys (for example, Corona 5 [Ti-4.5Al-5Mo-1.5Cr]) are shown. GB, grain boundary. Source: Ref 69

the weld and HAZ will mean that a martensitic structure will be obtained.

To obtain adequate ductility and toughness, PWHT must be performed at temperatures close to the β -transus temperature. This can be a problem because the low strength at these

temperatures can cause sagging in large welded structures, and complex fixturing will be necessary to maintain dimensional tolerances. It can also be expensive, because inert gas shielding is required for almost the entire time of PWHT. (It is assumed in the present discussion that adequate care is taken to maintain proper shielding during welding.) Moreover, it can be difficult to increase the ductility in the weld metal and HAZ to a level equal to that in an $\alpha + \beta$ -processed base material (Fig. 52). The trends seen in Fig. 50 and 52 can be understood by noting that crack nucleation is more difficult in an equiaxed structure (because the strain concentration effects are less) and that the

plastic zone sizes are bigger (Table 2). This results in a higher tensile ductility. However, because crack propagation follows a less tortuous path, the toughness is lower. The reverse is true for a Widmanstätten structure (referred to as a lenticular structure in Table 2). Table 2 explains the apparently strange observation in titanium alloys that a structure having a high strength and toughness is not necessarily the one having a high tensile ductility. The implication of this observation for weldments is that, for many applications, it may be more important to optimize the welding and PWHT procedure with respect to the toughness than with respect to the ductility.

A more detailed discussion of the welding metallurgy of titanium alloys can be found in Ref 70, 72, and 73.

ACKNOWLEDGMENTS

The author would like to express his sincere gratitude to Professor Emeritus Horst Cerjak, Graz University of Technology, Austria, for the opportunity to contribute to this article and for his constant support and encouragement. The author would also like to thank Professor Bruno Buchmayr, University of Leoben, Austria, and Professor Sudarsanam Suresh Babu, The Ohio State University, for their encouragement.

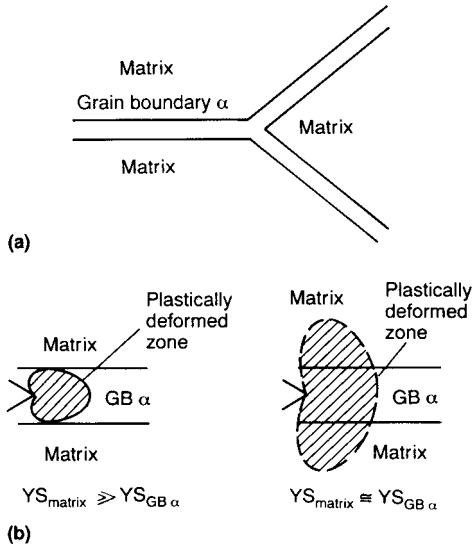


Fig. 51 Schematic showing the effect of the relative strengths of grain-boundary (GB) α and matrix on the plastic zone size. (a) GB α location relative to matrix. (b) Effect of plastic zone size on yield strengths of matrix and GB α . Source: Ref 69

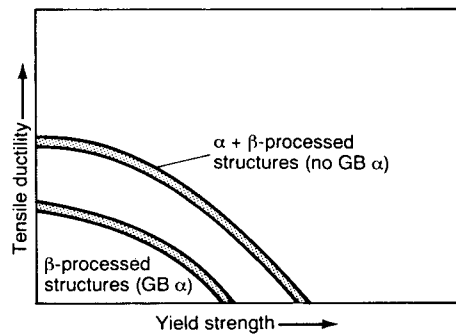


Fig. 52 Schematic plot of ductility versus strength for $\alpha + \beta$ - and β -processed structures. GB, grain boundary. Source: Ref 69

Table 2 Effect of morphological features of the microstructure on crack nucleation and propagation in $\alpha + \beta$ titanium alloys

Structure	Crack nucleation	Crack growth	Tensile ductility as a function of plastic zone size	Toughness as a function of crack propagation
Lenticular (Widmanstätten)	Easy	Difficult	<p>Small plastic zone Low ductility</p>	<p>Tortuous crack α-platelets High toughness</p>
Globular (equiaxed)	Difficult	Easy	<p>Large plastic zone High ductility</p>	<p>Nontortuous crack Void Globular α Low toughness</p>

Note: Voids initiated at the α - β interfaces are shown as black regions. Source: Ref 71

REFERENCES

1. *Atlas of Isothermal Transformation and Cooling Transformation Diagrams*, American Society for Metals, 1977
2. O.M. Akselsen and T. Simonsen, Techniques for Examining Transformation Behaviour in Weld Metal and HAZ—A State of Art Review, *Weld. World*, Vol 25 (No. 1/2), 1987, p 26–34
3. O. Grong and D.K. Matlock, Microstructural Development in Mild and Low Alloy Steel Weld Metals, *Int. Met. Rev.*, Vol 31 (No. 1), 1986, p 27–48
4. K. Easterling, *Introduction to the Physical Metallurgy of Welding*, 2nd ed., Butterworths-Heinemann, 1992
5. H.K.D.H. Bhadeshia and R.W.K. Honeycombe, *Steels Microstructure and Properties*, 3rd ed., Elsevier Ltd., 2006
6. *Weld Thermal Simulators for Research and Problem Solving*, The Welding Institute, United Kingdom, 1972
7. S. Kou, *Welding Metallurgy*, 2nd ed., John Wiley & Sons, 2003
8. C.F. Berkhout and P.H. Van Lent, The Use of Peak Temperature-Cooling Time Diagrams in the Welding of High Strength Steels, *Schweiss. Schneid.*, Vol 20 (No. 6), 1968, p 256–260 (in German)
9. Th.J. Van Adrichem and J. Kas, *Calculation, Measurement and Simulation of Weld Thermal Cycles*, Smitweld N.V., Nijmegen, The Netherlands
10. G.T. Eldis, A Critical Review of Data Sources for Isothermal Transformation and Continuous Cooling Transformation Diagrams, *Hardenability Concepts with Application to Steel*, D.V. Doane and J.S. Kirkaldy, Ed., TMS-AIME, 1978, p 126–157
11. P. Ravi Vishnu and K. Easterling, Phenomenological Modelling of Heat Flow and Microstructural Changes in Pulsed GTAW Welds of a QT Steel, *Mathematical Modelling of Weld Phenomena*, H. Cerjak and K. Easterling, Ed., The Institute of Metals, 1993
12. Verein Deutscher Eisenhüttenleute, Ed., *Steel—A Handbook for Materials Research and Engineering, Volume 1: Fundamentals*, Springer Verlag, 1992, p 175
13. P.J. Alberry, B. Chew, and W.K.C. Jones, Prior Austenite Grain Growth in Heat-Affected Zone of a 0.5Cr-Mo-V Steel, *Met. Technol.*, Vol 4, 1977, p 317–325
14. S. Mishra and T. DebRoy, Non-Isothermal Grain Growth in Metals and Alloys, *Mater. Sci. Technol.*, Vol 22, 2006, p 253–278
15. B. Radhakrishnan and T. Zacharia, Monte Carlo Simulation of Grain Boundary Pinning in the Weld Heat-Affected Zone, *Metall. Mater. Trans. A*, Vol 26, 1995, p 2123–2130
16. T. Gladman, *The Physical Metallurgy of Microalloyed Steels*, The Institute of Materials, 2002
17. R. Lagneborg, T. Siwecki, S. Zajac, and B. Hutchinson, The Role of Vanadium in Microalloyed Steels, *Scand. J. Metall.*, Vol 28, 1999, p 186–238
18. G.R. Speich, L.J. Cuddy, C.R. Gordon, and A.J. DeAredo, Formation of Ferrite from Control-Rolled Austenite, *Phase Transformation in Ferrous Alloys*, A.R. Marder and J.I. Goldstein, Ed., AIME, Warrendale, PA, 1984, p 314
19. S. Matsuda and N. Okumura, Effect of Distribution of Tin Precipitate Particles on the Austenite Grain Size of Low Carbon Low Alloys Steels, *Trans. ISIJ*, Vol 18, 1978, p 198
20. O. Grong, *Metallurgical Modeling of Welding*, 2nd ed., The Institute of Materials, 1997
21. W.F. Savage, E.F. Nippes, and E.S. Szekeres, A Study of Weld Interface Phenomena in a Low Alloy Steel, *Weld. J.*, Sept 1976, p 260s–268s
22. W.F. Savage, E.F. Nippes, and E.S. Szekeres, Hydrogen Induced Cold Cracking in a Low Alloy Steel, *Weld. J.*, Sept 1976, p 276s–283s
23. J.J. Pepe and W.F. Savage, Effects of Constitutional Liquation in 18-Ni Maraging Steel Weldments, *Weld. J.*, Sept 1967, p 411s–422s
24. W. Yeniscavitch, *Joining, Superalloys II*, C.T. Sims, N.S. Stoloff, and W.C. Hagel, Ed., John Wiley & Sons, 1987, p 495–516
25. E.E. Huccke and H. Udin, Welding Metallurgy of Nodular Cast Iron, *Weld. J.*, Aug 1953, p 378s–385s
26. E.N. Gregory and S.B. Jones, Welding Cast Irons, *Welding of Castings*, The Welding Institute, United Kingdom, 1977, p 145–156
27. L.E. Samuels, *Optical Microscopy of Carbon Steels*, American Society for Metals, 1980
28. “Guide to the Light Microscope Examination of Ferritic Steel Weld Metals,” Doc. IX-1533-88, International Institute of Welding, 1988
29. G. Thewlis, Classification and Quantification of Microstructures in Steels, *Mater. Sci. Technol.*, Vol 20, 2004, p 143–160
30. H.K.D.H. Bhadeshia and L.E. Svensson, Modelling the Evolution of Microstructure of Steel Weld Metal, *Mathematical Modelling of Weld Phenomena*, H. Cerjak and K. Easterling, Ed., The Institute of Materials, 1993
31. G.R. Edwards and S. Liu, Recent Developments in HSLA Steel Welding, *Advances in Welding Metallurgy, First U.S.-Japan Symposium*, American Welding Society and others, June 1990, p 215–293
32. S.S. Babu, The Mechanism of Acicular Ferrite in Weld Deposits, *Curr. Opin. Solid St. Mater. Sci.*, Vol 8, 2004, p 267–278
33. B. Ahlblom, “Oxygen and Its Role in Determining Weld Metal Microstructure and Toughness—A State of the Art Review,” Doc. IX-1322-84, International Institute of Welding, 1984
34. T. Koseki and G. Thewlis, Inclusion Assisted Microstructure Control in C-Mn and Low Alloy Steel Welds, *Mater. Sci. Technol.*, Vol 21, 2005, p 867–879
35. S. Terashima and H.K.D.H. Bhadeshia, Changes in Toughness at Low Oxygen Concentrations in Steel Weld Metals, *Sci. Technol. Weld. Join.*, Vol 11, 2006, p 509–516
36. L.-E. Svensson and B. Grefot, Microstructure and Impact Toughness of C-Mn Weld Metals, *Weld. J.*, Dec 1990, p 454s–461s
37. P.W. Holsberg and R.J. Wong, Welding of HSLA-100 Steel for Naval Applications, *Weldability of Materials*, R.A. Patterson and K.W. Mahin, Ed., ASM International, 1990
38. J.M.B. Losz and K.D. Challenger, Microstructure and Properties of a Copper Precipitation Strengthened HSLA Steel Weldment, *Recent Trends in Welding Science and Technology*, S.A. David and J.M. Vitek, Ed., ASM International, 1990
39. L.-E. Svensson, Consumables for Welding High Strength Steels, *Svetsaren*, Vol 54, 1999, p 29–33
40. W. Wang and S. Liu, Alloying and Microstructural Management in Developing SMAW Electrodes for HSLA-100 Steel, *Weld. J.*, Vol 81, 2002, p 132-s to 145-s
41. S. Zenitani, N. Hayakawa, J. Yamamoto, K. Hiraoka, Y. Morikage, T. Kubo, K. Yasuda, and K. Amano, Development of New Low Transformation Temperature Welding Consumable to Prevent Cold Cracking in High Strength Steel Welds, *Sci. Technol. Weld. Join.*, Vol 12, 2007, p 516–522
42. H. Homma, S. Ohkita, S. Matsuda, and K. Yamamoto, Improvements of HAZ Toughness in HSLA Steel by Introducing Finely Dispersed Ti-Oxide, *Weld. J.*, Oct 1987, p 301s–309s
43. N. Yurioka, Modern High Strength Steel in Japan, *Fifth International Symposium*, April 1990 (Tokyo), Japan Welding Society
44. H. Homma, S. Ohkita, S. Matsuda, and K. Yamamoto, Improvements of HAZ Toughness in HSLA Steel by Introducing Finely Dispersed Ti-Oxide, *Weld. J.*, Oct 1987, p 301s–309s
45. N. Yurioka, Modern High Strength Steel in Japan, *Fifth International Symposium*, April 1990 (Tokyo), Japan Welding Society
46. K. Satoh, Transient Thermal Stresses of Weld Heat-Affected Zone by Both-Ends-Fixed Bar Analogy, *Kovove Mater.*, Vol 8, 1970, p 569–587
47. W.K.C. Jones and P.J. Alberry, The Role of Phase Transformations in the Development of Residual Stresses during the Welding of Some Fast Reactor Steels, *Proc. Conf. Ferritic Steels for Fast Reactor*

- Steam Generators*, British Nuclear Energy Society, 1977
48. H.K.D.H. Bhadeshia, in *Handbook of Residual Stress and Deformation of Steel*, G. Totten, M. Howes, and T. Inoue, Ed., ASM International, 2002, p 3–10
 49. A. Ohta, O. Watanabe, K. Matsuoka, T. Shiga, S. Nishijima, Y. Maeda, and N. Suzuki, Fatigue Strength Improvement by Using Newly Developed Low Transformation Temperature Welding Material, *Weld. World*, Vol 43, 1999, p 38–42
 50. A. Ohta, K. Matsuoka, N.T. Nguyen, Y. Maeda, and N. Suzuki, Fatigue Strength Improvement of Lap Joints of Thin Steel Plate Using Low-Transformation-Temperature Welding Wire, *Weld. J.*, April 2003, p 78s–83s
 51. W.X. Wang, L.X. Huo, Y.F. Zhang, D.P. Wang, and H.Y. Jing, New Developed Welding Electrode for Improving the Fatigue Strength of Welded Joints, *J. Mater. Sci. Technol.*, Vol 18 (No. 6), 2002, p 527–531
 52. T. Haze and S. Aihara, Influence of Toughness and Size of Local Brittle Zones on HAZ Toughness of HSLA Steels, *Seventh International Conference on Offshore Mechanics and Arctic Engineering* (Houston, TX), 1988
 53. C.P. Royer, A User's Perspective on Heat Affected Zone Toughness, *Welding Metallurgy of Structural Steels*, J.Y. Koo, Ed., TMS-AIME, 1987
 54. F. Matsuda, Z. Li, P. Bernasovsky, K. Ishihara, and H. Okada, "An Investigation of the Behaviour of M-A Constituent in Simulated HAZ of HSLA Steels," Doc. IX-B-1591-90, International Institute of Welding, 1990
 55. P.L. Harrison and P.H.M. Hart, Relationships between HAZ Microstructure and CTOD Transition Behaviour in Multipass C-Mn Steel Welds, *Recent Trends in Welding Science and Technology*, S.A. David and J.M. Vitek, Ed., ASM International, 1990
 56. H. Onoe, J. Tanaka, and I. Watanabe, Japanese LNG Tanker Constructed Using a New Welding Process and Improved Al-Killed Steels, *Met. Constr.*, Jan 1979, p 26–31
 57. P.J. Alberry, Sensitivity Analysis of Half-Bead and Alternative GTAW Techniques, *Weld. J.*, Nov 1989, p 442s–451s
 58. J.A. Brooks and A.W. Thompson, Microstructural Development and Solidification Cracking Susceptibility of Austenitic Stainless Steel Welds, *Int. Mater. Rev.*, Vol 36 (No. 1), 1991
 59. D.J. Kotecki and T.A. Siewert, WRC-1992 Constitution Diagram for Stainless Steel Weld Metals: A Modification of the WRC-1988 Diagram, *Weld. J.*, May 1992, p 171s–178s
 60. D.J. Kotecki, A Martensite Boundary on the WRC-1992 Diagram, Part 2: The Effect of Manganese, *Weld. J.*, Dec 2000, p 346s–354s
 61. T.G. Gooch and D.C. Willingham, *Weld Decay in Austenitic Stainless Steels*, The Welding Institute, United Kingdom, 1975
 62. J.C. Lippold and D.J. Kotecki, *Welding Metallurgy and Weldability of Stainless Steels*, John Wiley & Sons, 2005
 63. C. Huang, G. Cao, and S. Kou, Liquefaction Cracking in Partial Penetration Aluminium Welds: Assessing Tendencies to Liquefy, Crack and Backfill, *Sci. Technol. Weld. Join.*, Vol 9 (No. 2), 2004, p 149–157
 64. H. Shercliff and M.F. Ashby, A Process Model for Age Hardening of Al Alloys—I. Model and II. Applications of the Model, *Acta Metall. Mater.*, Vol 38 (No. 10), 1990, p 1789–1812
 65. W.A. Owczarski, Process and Metallurgical Factors in Joining Superalloys and Other High Service Temperature Materials, *Physical Metallurgy of Joining*, R. Kosowski and M.E. Glicksman, Ed., TMS-AIME, 1980
 66. J.N. DuPont, J.C. Lippold, and S.D. Kiser, *Welding Metallurgy and Weldability of Nickel-Base Alloys*, John Wiley & Sons, Inc., 2009
 67. E.W. Collings, Introduction to Titanium Alloy Design, *Alloying*, J.L. Walter, M.R. Jackson, and C.T. Sims, Ed., ASM International, 1988, p 267
 68. C.R. Thomas and F.P.A. Robinson, Kinetics and Mechanism of Grain Growth during Welding in Niobium Stabilised 17% Chromium Stainless Steels, *Met. Technol.*, April 1978, p 133–138
 69. J.C. Williams and E.A. Starke, Jr., The Role of Thermomechanical Processing in Tailoring the Properties of Aluminum and Titanium Alloys, *Deformation, Processing and Structure*, G. Krauss, Ed., American Society for Metals, 1984, p 279–354
 70. W.A. Baeslack III, D.W. Becker, and F.H. Froes, Advances in Titanium Alloy Welding Metallurgy, *J. Met.*, May 1984, p 46–58
 71. J.P. Hirth and F.H. Froes, Interrelations between Fracture Toughness and Other Mechanical Properties in Titanium Alloys, *Metall. Trans. A*, Vol 8, July 1977, p 1165–1176
 72. C.G. Rhodes, Microscopy and Titanium Alloy Development, *Applied Metallography*, G.F. Vander Voort, Ed., Van Nostrand Reinhold, 1986
 73. W.A. Baeslack III, Metallography of Titanium Alloy Weldments, *Metallography and Interpretation of Weld Microstructures*, J.L. McCall, D.L. Olson, and I. LeMay, Ed., ASM International, 1987, p 23–60

SELECTED REFERENCES

- P.L. Harrison and R.A. Farrar, Application of Continuous Cooling Transformation Diagrams for Welding of Steels, *Int. Mater. Rev.*, Vol 34 (No. 1), 1989, p 35–51

Thermomechanical Effects of Fusion Welding

P. Michaleris, Pennsylvania State University

APPLICATION OF WELDING in fabricating large structures offers several advantages over mechanical joining methods, such as improved structural performance, weight and cost savings, and flexibility of design. However, welding induces residual stresses and distortion, which may result in loss of dimensional control, costly rework, and production delays. Welding may also introduce such defects as inclusions and lack of penetration, leading to reduced fatigue life.

Modeling of welding distortion and residual stress has been an active research area since the late 1970s. Some of the first publications in weld modeling include Ref 1 to 3. Significant research in the 1980s includes the development of the double-ellipsoid heat-input model by Goldak et al. (Ref 4) and the modeling of phase transformations (Ref 5–7). Most of the weld modeling in the 1970s and 1980s involved two-dimensional (2-D) models transverse to the welding direction using either plane-strain or generalized plane-strain conditions. These models demonstrated good correlations with experimental measurements for residual stress. However, these models were not capable of predicting the magnitudes of angular distortion (Ref 8) or of longitudinal buckling and bowing (Ref 9). Developments in weld modeling in the 1990s included the use of three-dimensional (3-D) moving-source models (Ref 10–12), the development of sensitivity formulations (Ref 13, 14), and the development of the applied plastic strain method (Ref 9, 15, 16). The 3-D moving-source models demonstrated the capability to model all distortion modes.

A detailed review of finite-element modeling for welding residual stress and distortion modeling is available in Ref 17 to 20. Typically, modeling of welding residual stress and distortion involves one-way coupled thermomechanical analyses. In thermal analysis, conductive heat transfer is considered through the use of empirical models that provide values for the applied welding heat input. Some researchers, in order to consider the effect of the convective heat flow in the molten metal, have used

artificially high thermal conductivity values for temperatures that exceed the melting point (Ref 11). However, this approach may lead to slower numerical convergence. In mechanical analysis, rate-independent elastoplastic material response is considered, using the results of the thermal analysis as thermal load. Both thermal and mechanical analyses are typically performed using the finite-element method in a Lagrangian reference frame. Although thermoelastoplastic modeling of welding is reportedly providing computed values of residual stress that agree closely with experimental measurements (Ref 15, 17–19), it is difficult to correlate the computed and measured fusion zones, especially for high-energy-intensity processes such as laser and hybrid welding (Ref 21–23).

Formation of Residual Stress: Three-Bar Analogy

The three-bar analogy is commonly used to illustrate the formation of welding residual stress. Figure 1 illustrates three bars of equal length connected at the ends. The shade of the bars correlates to their temperature, with dark representing hot and light representing cold.

The symbol S denotes their stress state. For thin plates, the stress correlates to the longitudinal stress component, and the middle bar corresponds to the welding region. The middle bar is considered to have a smaller diameter than the side bars, which correspond to the remaining part of the plate. Before welding, all bars are at room temperature and under zero stress (Fig. 1a). When the middle bar is heated (Fig. 1b), it expands and pulls along the side bars. The middle bar is under compression and the side bars are in tension. If the temperature is high, as in welding, the yield strength of the material drops, and the middle bar permanently deforms due to plasticity. When the middle bar returns to room temperature, it contracts. If the bar had not been connected (Fig. 1c) at room temperature, it would now be shorter than the side bars due to plastic deformation. However, because it is connected (Fig. 1d), it pushes the side bars into a state of compression. The middle bar is now in tension. Therefore, after welding, the welding region is expected to be in tension and the base material in compression. Figure 2 illustrates the computed temperatures and corresponding longitudinal stress across a plate before, during, and after welding (Ref 24). Before welding, the plate has zero stress. During welding, the welding region (center of the plate) is under compression and

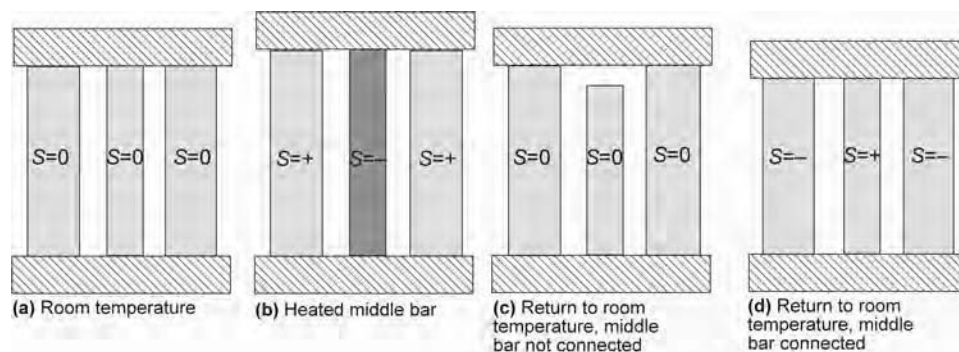


Fig. 1 Formation of welding residual stress

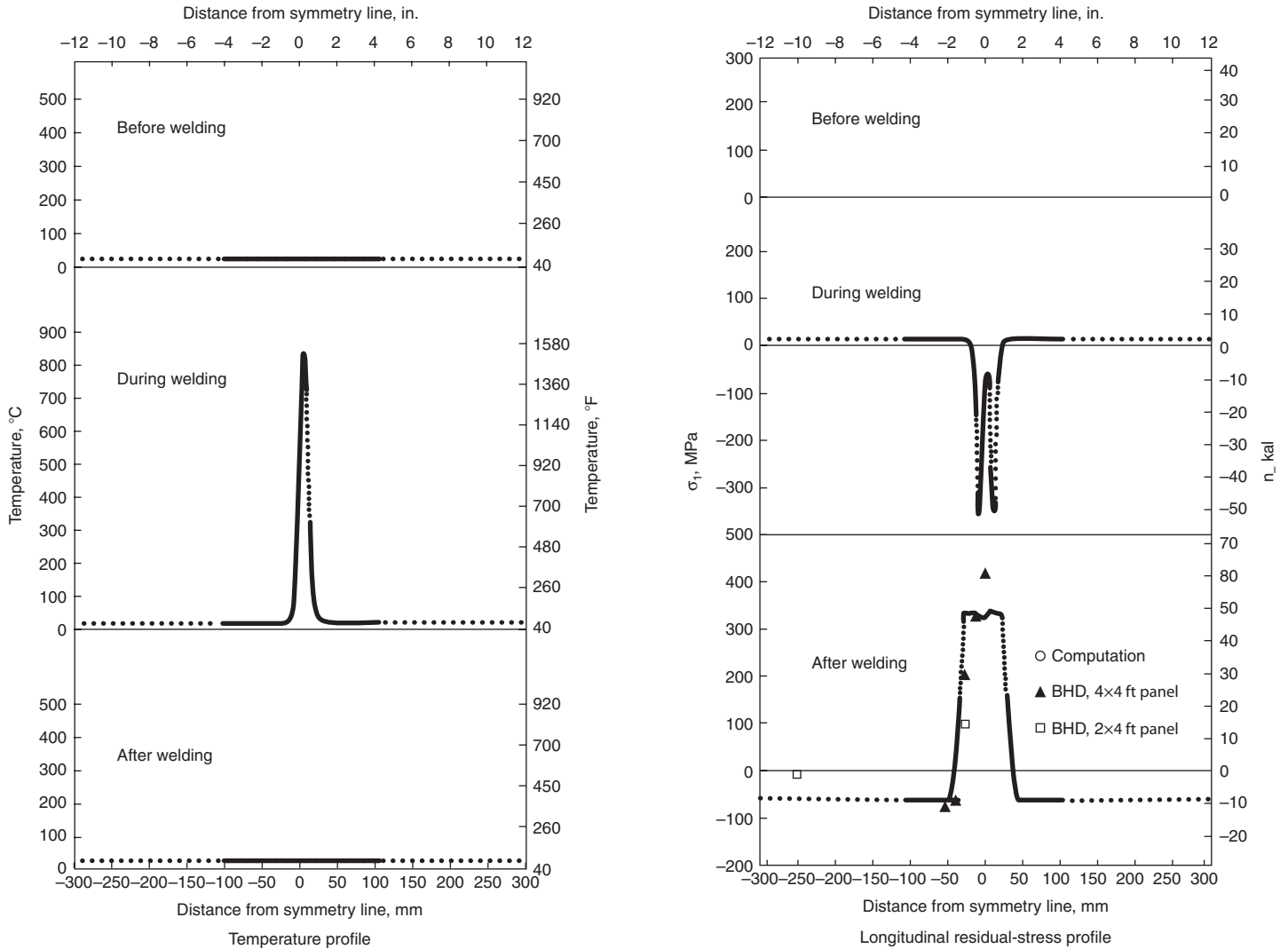


Fig. 2 Temperature and corresponding longitudinal residual stress before, during, and after welding. Source: Ref 24

the edges of the plate under tension. After cooling, the stresses reverse, resulting in tension at the welding region and compression elsewhere.

Volumetric solid-state phase transformations during the welding thermal cycle may also contribute to the generation of welding residual stress and consequently distortion (Ref 5, 7, 25–29). The section “Solid-State Transformations” in this article discusses the effect of solid-state phase transformation in further detail.

Mathematical Formulations

Thermal Transport

Thermal transport models of welding typically involve coupled heat and mass transfer and typically use computational fluid dynamics (CFD) solution methods in Eulerian reference frames (for more about fundamental principles of CFD, see Ref 30). A viscoplastic material

response is assumed in most thermal transport analyses of welding in order to eliminate the need for tracing and integrating the material response; this being the case, thermal transport analyses of welding compute the resulting residual stress to be zero. Such analyses have primarily been used to model the temperature field and physical shape of the weld pool (Ref 31–35), the interaction between arc and material (Ref 36), buoyancy, surface tension, and magneto-hydrodynamic effects (Ref 3).

Accurate material property data are lacking for metal alloys at extremely high temperatures (Ref 3). Currently, these material properties are available only in specific published cases (Ref 3). Parameters describing the arc (such as efficiency and other weighting factors) are also difficult to model accurately, as shown by the wide range of values chosen in studies for apparently similar conditions (Ref 31). Because of the difficulties of knowing all the material and arc variables in modeling, Mishra and

DebRoy introduced an identification method for these uncertain variables that combines experimental data with thermofluid modeling to obtain exceptional correlation with experimental data (Ref 31).

Thermal transport analyses of welding involve solving for the mass conservation, momentum balance, and energy balance simultaneously. The analysis is typically performed in a Eulerian reference frame centered on the welding torch, with material flowing through the control volume (Fig. 3). The analysis is further simplified by assuming steady-state conditions and thus eliminating dependence on time. The mass conservation equation (continuity equation) is given by:

$$\nabla \cdot (\rho v) = 0 \tag{Eq 1}$$

where ρ is the density, v is the velocity, and ∇ is the spatial gradient operator.

The conservation of momentum equation is as follows:

$$\nabla \cdot (\rho v) = -\nabla p + \nabla \cdot \boldsymbol{\sigma}' + \rho g \tag{Eq 2}$$

where p is the pressure, $\boldsymbol{\sigma}'$ is the deviatoric stress tensor, g is the acceleration due to gravity, and v is the velocity.

Newtonian material response is assumed, and the deviatoric stress, $\boldsymbol{\sigma}'$, is calculated as follows:

$$\sigma'_{ij} = \mu \left[\frac{\partial v_i}{\partial x_j} + \frac{\partial v_j}{\partial x_i} \right] \tag{Eq 3}$$

where μ is the viscosity.

The energy conservation equation is written in terms of enthalpy, H , as follows:

$$\nabla \cdot (\rho v H) = \nabla \cdot (k \nabla T) + Q \tag{Eq 4}$$

where k is the temperature-dependent thermal conductivity, and Q is the volumetric energy source.

As mentioned previously, the assumption of pure viscoplastic behavior (Eq 3) in thermal transport models of welding results in a computed value of zero residual stress, and the reason is shown in Eq 3. Once the velocity becomes zero, Eq 3 determines that the deviatoric stress is also zero. Computing residual stress requires modification of the constitutive model to account for the elastic component of stress, which depends on the deformation history of each particle. Furthermore, if material evolution (via, for example, hardening or transformations) is also to be considered in the computation of residual stress, the temperature, stress, strain, and internal variable history of each material particle must be computed. In a Eulerian reference frame, this computation can be accomplished by computing backward the streamline of each particle and then integrating the material evolution along the streamline (Ref 40–42). Another approach is to use a mixed finite-element analysis formulation and enforce the evolution in a weak form (Ref 43–46). Both approaches are quite specialized and require custom computer programming.

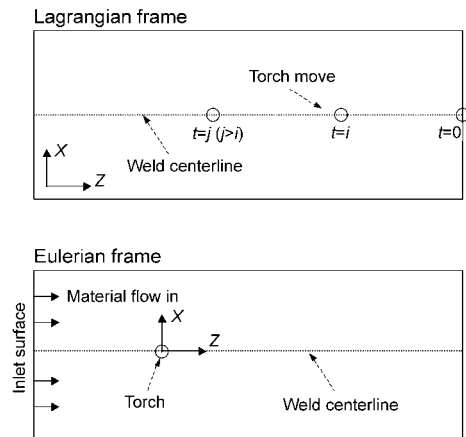


Fig. 3 Eulerian versus Lagrangian models in welding

Thermoelastoplasticity

Welding residual-stress analyses typically involve solving the energy and momentum balance sequentially in a Lagrangian reference frame. The material is attached to the mesh, and the welding torch travels with time (Fig. 3). The thermal analysis assumes conductive heat transfer only, but convective energy transfer is indirectly simulated by using artificially high thermal conductivity for temperatures above melting. The energy balance equation is as follows:

$$\rho C_p \frac{dT}{dt} = -\nabla \cdot \mathbf{q}(r,t) + Q(r,t) \tag{Eq 5}$$

where C_p is the specific heat capacity, T is the temperature, \mathbf{q} is the heat flux vector, t is the time, and r is the coordinate in the reference configuration.

The momentum balance equation is further simplified by assuming negligible inertia and body forces as follows:

$$\nabla \cdot \boldsymbol{\sigma} = 0 \tag{Eq 6}$$

where $\boldsymbol{\sigma}$ is the stress. Typically, a rate-independent elastoplastic material response is assumed in the mechanical analysis, allowing for the computation of residual stress due to plastic deformation during the welding heat cycle. Then, stress is computed as follows:

$$\boldsymbol{\sigma} = \mathbf{C} \boldsymbol{\varepsilon}_e \tag{Eq 7}$$

$$\boldsymbol{\varepsilon}_e = \boldsymbol{\varepsilon} - \boldsymbol{\varepsilon}_p - \boldsymbol{\varepsilon}_t - \boldsymbol{\varepsilon}_v - \boldsymbol{\varepsilon}_{tr} \tag{Eq 8}$$

$$\boldsymbol{\varepsilon}_p = \boldsymbol{\varepsilon}_q \cdot \mathbf{a}(\boldsymbol{\sigma}, \boldsymbol{\varepsilon}_q, T) \tag{Eq 9}$$

$$f = \sigma_e - \sigma_y \leq 0 \tag{Eq 10}$$

where T is temperature; \mathbf{C} is the material stiffness tensor; \mathbf{a} is the plastic flow vector; $\boldsymbol{\varepsilon}$, $\boldsymbol{\varepsilon}_p$, and $\boldsymbol{\varepsilon}_t$ are the total, plastic, and thermal strains, respectively; $\boldsymbol{\varepsilon}_q$ is the equivalent plastic strain; and $\boldsymbol{\varepsilon}_v$ and $\boldsymbol{\varepsilon}_{tr}$ are the volumetric change and transformation plasticity strain components, respectively (Ref 7, 28, 29). Equation 10 is the equation for isotropic hardening, where f is the yield function, σ_e is the von Mises stress, and σ_y is the yield stress. Active yielding occurs when $f = 0$.

The thermomechanical simulations of welding processes are further simplified by recognizing that the mechanical work is negligible compared to the heat input, and therefore, the unique coupling between thermal and mechanical behavior is the thermal expansion. On this understanding, a thermal simulation is performed first and a mechanical simulation afterward. However, when the components to be welded are unrestrained from rigid movements, large distortions may lead to a full thermomechanical coupling, because the fit-up and weld location may be altered (Ref 12).

Figure 4 illustrates a typical thermomechanical welding simulation. The welding conditions and joint configuration are the input to the thermal analysis, in which the heat flow, molten metal flow, and phase transformations are analyzed. The output from these analyses is the temperature history and microstructure. In the mechanical analysis, which may either follow or be coupled with the thermal analysis, the elastic-plastic deformation, creep, and transformation plasticity are analyzed. The distortion and residual stresses are the output of the mechanical analyses.

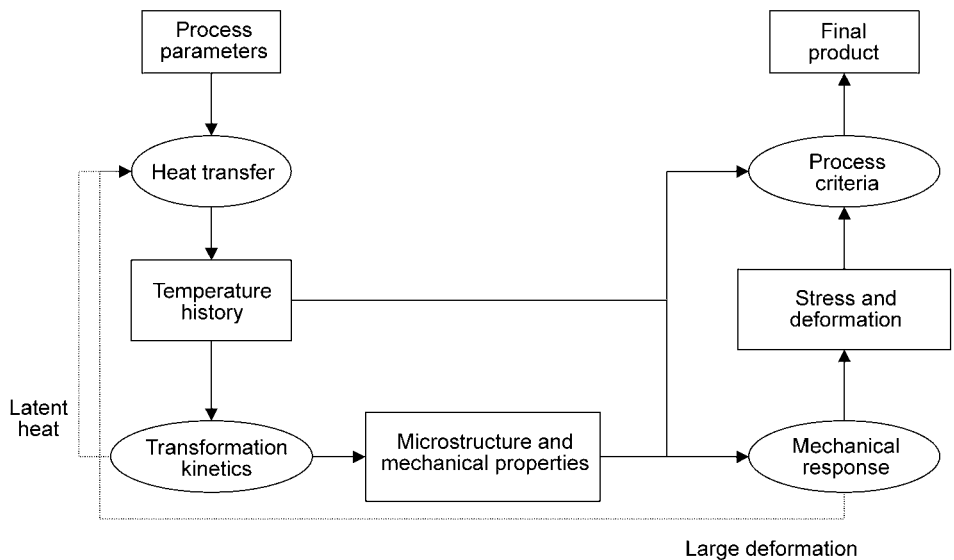


Fig. 4 Outline of thermomechanical weld modeling

Heat-Input Models

Depending on the process, different types of physics take place to generate the welding heat and fuse the material. For example, arc physics take place in arc welding, electric current flow takes place in arc and spot welding, and electron diffraction takes place in electron beam welding. Most commonly, in welding process modeling, the physics that account for the heat generation are not analyzed. Empirical heat-generation models are used instead.

A review of empirical models used to represent the heat generated in the welding process is presented in Ref 4 and 47 to 50. Early simulations of welding implemented simple point-and-line heat-source models as well as combinations of them (Ref 51–53). These simple heat-input models, in conjunction with the assumption of steady-state conditions and temperature-independent material properties, led to analytical solutions of the temperature field. These solutions provide a good approximation in regions far from the weld zone. However, the predicted infinite temperatures at the weld source are unrealistic. The availability of computational resources at low cost leads to the implementation of more accurate heat-input models for welding simulations. Papazoglou and Masubuchi (Ref 3) used a uniform density surface heat flux over the weld to simulate the welding heat input. Argyris et al. (Ref 2) and Tekriwal and Mazumder (Ref 11) used a surface heat flux with a Gaussian density distribution. Goldak et al. (Ref 4) proposed the double-ellipsoid heat-source model, where the heat generated by welding is simulated with a power density moving along with the torch. Other heat-input models impose a time-dependent temperature-boundary condition (frequently called ramp temperature-boundary condition) at selected points or regions of the weld pool (Ref 2, 54). The surface flux and volume heat-source models are directly derived from welding conditions and therefore are predictive. The ramp temperature models do not provide a direct relation to the actual weld parameters and thus require temperature measurements to determine the imposed conditions.

The most commonly used welding heat-input model is the double-ellipsoid model proposed by Goldak (Ref 4), in which the welding heat input is represented by a volumetric heat source, Q , as follows:

$$Q = \frac{6\sqrt{3}Q_w\eta f}{abc\pi\sqrt{\pi}} e^{-\left[\frac{3x^2}{a^2} + \frac{3y^2}{b^2} + \frac{3(z+vt)^2}{c^2}\right]} \quad (\text{W/mm}^3) \quad (\text{Eq 11})$$

where Q_w is the welding heat input; η is the welding efficiency; x , y , and z are the local coordinates of the double-ellipsoid model aligned with the weld fillet; a is the weld width; b is the weld penetration; c is the weld ellipsoid length; f is a scaling factor; v_w is the torch travel speed; and t is time. (Typically, different values are used for c and f in front of and

behind the weld.) An illustration of the energy density of the double-ellipsoid model is presented in Fig. 5.

Material Models

The rate-independent, deviatoric plasticity model with the von Mises yield condition and the associated flow rule has been used with success in many welding simulations (Ref 18). Some work has also used viscoplastic models (Ref 2, 55, 56) or combined rate-independent plasticity models at lower temperatures with viscoplastic models at higher temperatures (Ref 57). The hardening behavior at lower temperature is important in the computation of the residual stresses; the material near the weld undergoes cyclic loading, and choosing between isotropic or kinematic hardening will affect the stresses calculated from the model for this region (Ref 58).

For temperatures that exceed the melting point, the modulus of elasticity and yield limit have zero value. Viscous flow models are more appropriate at these temperatures. However, elastoplastic or elastoviscoplastic models may still be used in conjunction with a cut-off temperature. This technique is used for two reasons: The properties at high temperatures are usually unknown, and a too-soft weld metal in the model may cause numerical problems. In this technique, during the mechanical analysis, temperatures that exceed a cut-off value are reset to the cut-off temperature. An appropriate choice of cut-off temperature will not affect the residual stresses (Ref 3, 11, 18).

The very low value of yield strength along with the use of elastoplastic models may result in artificial hardening and lead to computed values that exceed the actual residual stresses. To account for the annealing effect that naturally occurs in metals, either a creep model may be used or all accumulated plastic strains may set to zero above a critical temperature (Ref 8).

Solid-State Transformations

Solid-phase transformations that occur during the thermal cycle produced by welding lead to irreversible plastic deformation known as transformation plasticity. This phenomenon can be driven either by volume change during phase transformations (Greenwood-Johnson effect) or by martensitic transformations in which, under external loading, martensite plates are formed with preferred orientation (Magee effect) (Ref 5, 7, 25–28). Oddy et al. (Ref 10, 59) decomposed the total strain into its elastic, plastic, thermal, volumetric change, and transformation plasticity (which is proportional to the deviatoric stress tensor) components. The authors report that transformation plasticity significantly affects longitudinal and transverse residual-stress distributions. Early work on weld modeling in which the thermal expansion coefficient is modified to take into account the

volumetric change during phase transformations is found in Ref 2 and 3. Argyris et al. (Ref 2) also modified the yield strength during cooling to reflect the formation of austenite, ferrite, and pearlite. From their numerical simulations, they conclude that the individual stress components are affected by the phase transformations during the heat cycle, but that the effects of phase transformations are dampened upon cooling of the weld. They also conclude that the equivalent von Mises stress is not affected by the phase transformations.

Multipass Welding

The simulation of multipass welding requires additional care (Ref 60). Early attempts involved lump weld passes (Ref 52, 53); however, this procedure should be performed with care (Ref 17). Two approaches, namely the use of quiet elements or inactive elements, are available for modeling of multipass welding. Quiet elements are present in the analysis but are given properties that prevent them from affecting the analysis. Inactive elements are not included at all until the corresponding filler material has been added. Both methods require special attention when large deformations occur. Quiet elements can accumulate excessive strains that must be reset during activation, and inactive elements can be severely distorted before activation, requiring the use of additional nodes and constraint equations. Both methods can give the same results (Ref 61). Methods and issues for obtaining correct sizes and shapes of the elements corresponding to the filler metal are described in Ref 60.

Residual Stress

In Michaleris et al. (Ref 15), the effectiveness of 2-D and 3-D small- and large-deformation analyses was investigated in the computation of welding distortion. Experimental testing was used for verification purposes. Fillet welding was performed on panels of various sizes, and residual-stress and distortion measurements were obtained and used as a

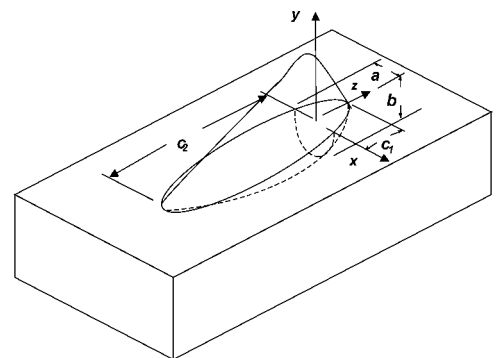


Fig. 5 Illustration of double-ellipsoid heat-input model. Source: Ref 4

benchmark to evaluate the accuracy of the various modeling methods. The panel thickness and welding conditions were kept the same in all experiments.

A schematic of the panel geometry and welding configuration is shown in Fig. 6. Three panels with dimensions (width by length) 255 by 255 mm (10 by 10 in.), 310 by 310 mm (12 by 12 in.), and 310 by 610 mm (12 by 24 in.) and a thickness of 3.2 mm (1/8 in.) are investigated. A stiffener with a height of 50 mm (2 in.) and thickness of 3.2 mm (1/8 in.) is fillet welded at the centerline of the panels.

255 by 255 mm (10 by 10 in.) Plate.

Figure 7 depicts the longitudinal residual-stress distribution for the 255 by 255 mm (10 by 10 in.) plate. Identical results are obtained for the longitudinal stress distribution from the small- and large-deformation analyses.

310 by 310 mm (12 by 12 in.) Plate.

Figure 8 shows the longitudinal residual-stress distribution computed using 2-D analysis (case B1) for a 310 mm (12 in.) wide panel. The 2-D analysis predicts constant compressive longitudinal stress away from the weld region. Figures 9 and 10 show the longitudinal residual-stress distribution computed using 3-D small- and large-deformation analyses, respectively. The large-deformation analysis shows slightly lower residual stress, which is attributed to relaxation due to buckling.

Longitudinal residual-stress measurements are carried out at seven locations along the transverse axis of the welded panel (Fig. 6). Figure 11 shows the comparison of the computed longitudinal residual stress and the experimental results along the transverse axis. The 2-D analysis cannot predict the longitudinal stress correctly at the ends of the plate. Both the 3-D small- and large-deformation analysis results compare well with the experimental results.

310 by 610 mm (12 by 24 in.) Plate.

Figures 12 and 13 show the distribution of longitudinal residual stress in the 310 by 610 mm (12 by 24 in.) plate computed by the 3-D small- (case C1) and 3-D large- (case C2) deformation

analyses, respectively. The plots show that the small-deformation analysis predicts a high compressive stress zone that stretches from a distance away from the weld centerline to the ends of the plate. The large-deformation analysis predicts a longitudinal stress distribution that is compressive away from the weld and decreases toward the ends. The difference is attributed to relaxation due to buckling.

Figure 14 compares the longitudinal residual-stress distribution along the transverse axis for the 2-D, 3-D small-, and 3-D large-deformation analyses with experimental results. The 3-D large-deformation analysis shows good correlation. The 2-D and the 3-D large-deformation analysis results are in close agreement but do not agree with the experimental results at the ends of the plate. The difference is attributed

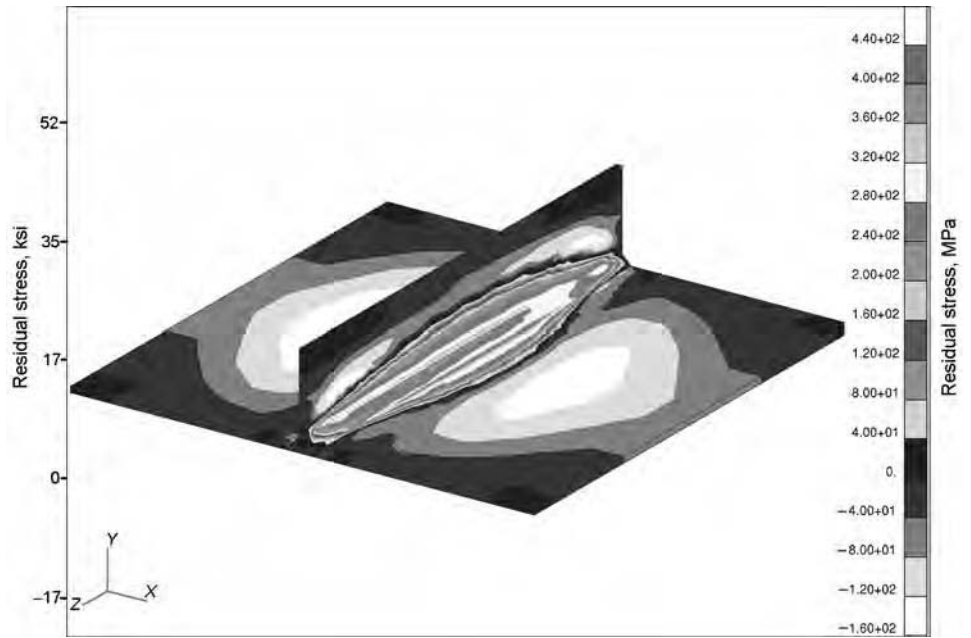


Fig. 7 Longitudinal residual-stress distribution predicted by three-dimensional small- and large-deformation analyses for 255 × 255 mm (10 × 10 in.) panel. Source: Ref 15

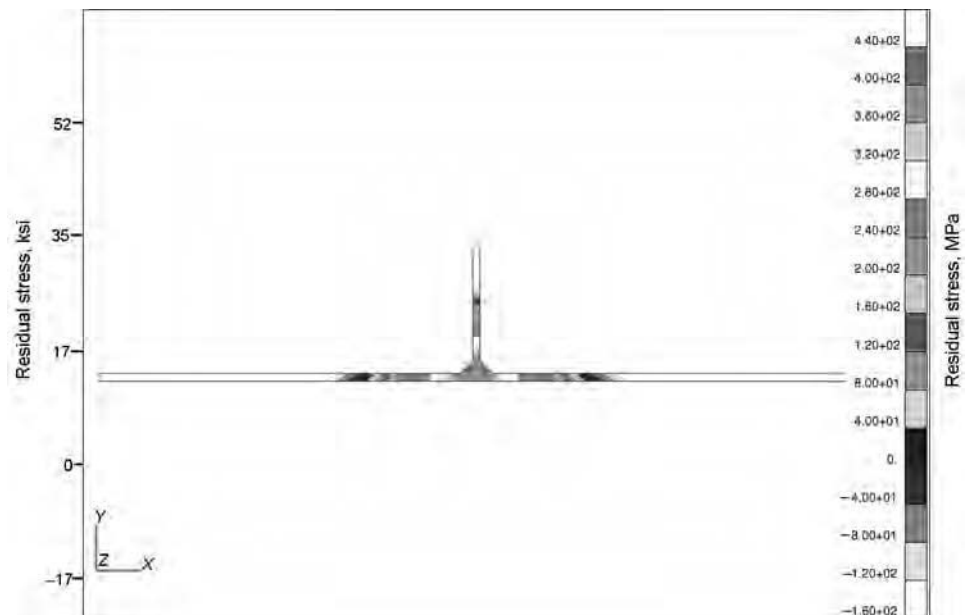


Fig. 8 Longitudinal residual-stress distribution computed by two-dimensional analysis for 310 mm (12 in.) wide panel. Source: Ref 15

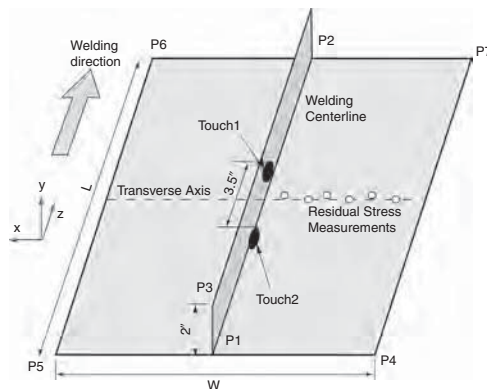


Fig. 6 Geometry and welding condition. Source: Ref 15

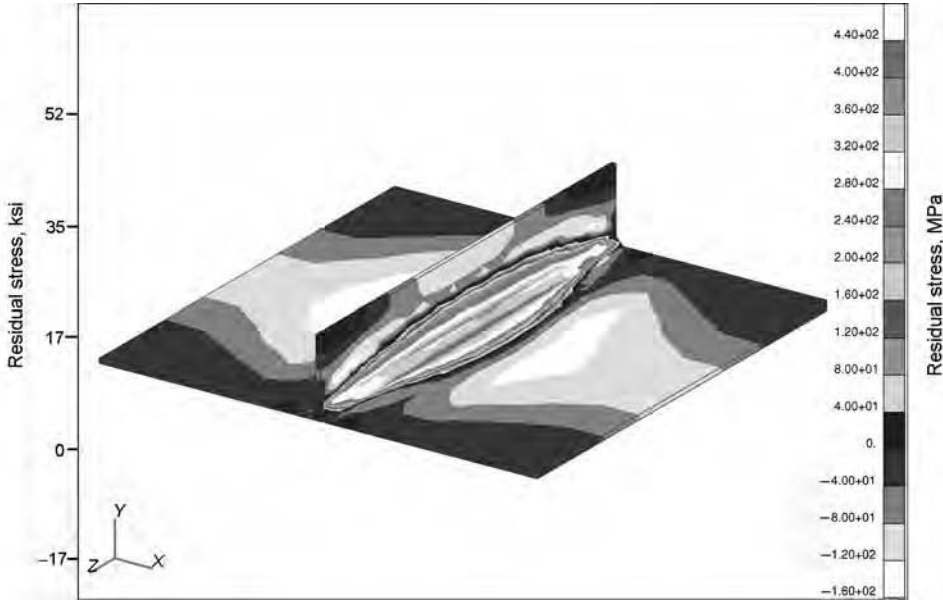


Fig. 9 Longitudinal residual-stress distribution computed by three-dimensional small-deformation analysis for 310 × 310 mm (12 × 12 in.) panel. Source: Ref 15

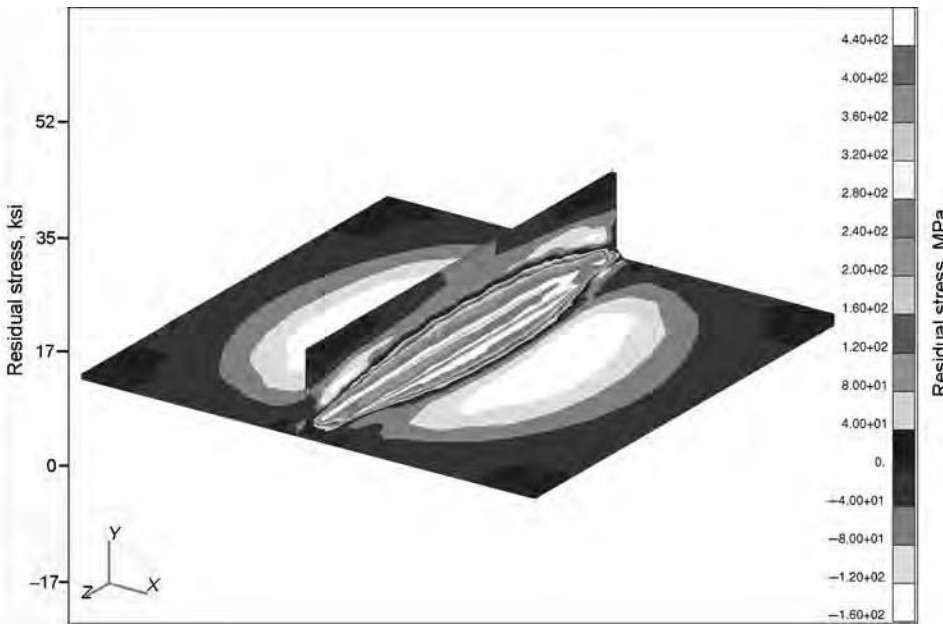


Fig. 10 Longitudinal residual-stress distribution computed by three-dimensional large-deformation analysis for 310 × 310 mm (12 × 12 in.) panel. Source: Ref 15

to stress relaxation due to buckling, which only the 3-D large-deformation analysis can capture.

Figure 15 shows the longitudinal residual-stress distribution along the transverse axis for 2-D and 3-D small-deformation analyses of models of varying lengths. The figure shows that the longitudinal stress distributions from the 2-D analysis approach the curve predicted by the 3-D small-deformation analysis as the panel becomes longer. This phenomenon is

attributed to the fact that the 3-D small-deformation analysis corresponds to the unstable equilibrium condition under no imperfections.

The following conclusions are drawn from Fig. 7 to 15 (Ref 15):

- The 3-D small-deformation analysis predicts correct values of longitudinal residual stress and distortion if there is no buckling. When buckling occurs, the 3-D small-deformation

analysis corresponds to the unstable equilibrium state.

- As panel length increases, the longitudinal stress distribution predicted by the 2-D analysis approaches a state corresponding to the unstable equilibrium state of long panels in the 3-D small-deformation results.
- The 3-D large-deformation analysis predicts the correct residual-stress distribution. It also captures end effects.

Distortion

Masubuchi (Ref 62) classified welding distortion into six types (modes), as illustrated in Fig. 16. In transverse shrinkage, the parts shrink transverse to the weld. Angular change is a distortion that manifests in fillet and butt welds, where the plates change angle as compared to the configuration prior to welding. In rotational distortion, the parts open as the welding progresses. In longitudinal shrinkage, the parts shrink in the welding direction. Welding-induced buckling is elastic instability caused by compressive residual stress. Longitudinal bending, also known as bowing or camber distortion, is bending caused by nonbalanced residual stresses with respect to the neutral axis of the part.

The welding distortion modes can be further classified into in-plane and out-of-plane modes. Transverse shrinkage, longitudinal shrinkage, and rotational distortion are in-plane modes, and buckling, longitudinal bending (bowing), and angular change are out-of-plane modes. In general, in-plane distortion is negligible in small parts and receives little attention. In large components (such as those used in shipbuilding), in-plane distortion can be significant, and manufacturers compensate by starting with bigger parts. Out-of-plane distortion modes are very common and sometimes difficult to control. When welding results in buckling distortion, the magnitude of distortion is very large, and distortion control methods should be implemented to remove the source of buckling. Structures with thick sections are more resistant to buckling and usually distort via the bowing and angular out-of-plane modes.

Most of the weld modeling in the 1970s and 1980s involved 2-D models transverse to the welding direction using either plane-strain or generalized plane-strain conditions. These models demonstrated good correlations with experimental measurements for residual stress. However, these models were not capable of predicting the magnitudes of angular distortion (Ref 8) or longitudinal buckling and bowing (Ref 9).

Large and complex structures such as ship panels generally have various types of welding-induced distortions, including angular deformation, longitudinal bending, and buckling. Conventional transient moving-source analyses on 3-D finite-element models, where millions of degrees of freedom and thousands

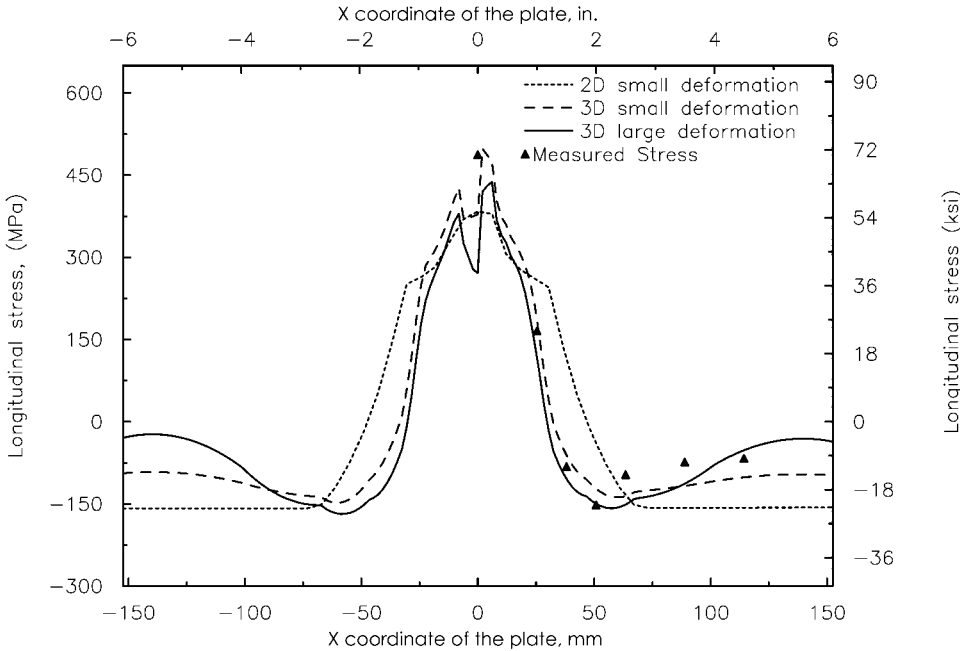


Fig. 11 Comparison of predicted longitudinal stress distribution with measured experimental stress values for 310 × 310 mm (12 × 12 in.) panel. Source: Ref 15

components were simplified as two normal components—longitudinal plastic strain and transverse plastic strain—and the shear components were neglected. They determined the plastic strain distributions by both empirical and analytical methods.

2-D/3-D Applied Plastic Strain Methods.

Michaleris et al. developed a 2-D/3-D applied plastic strain approach to capture welding-induced buckling distortion in large ship panels (Ref 9). Because the buckling was caused mainly by longitudinal stress, they mapped only the longitudinal plastic strain component. The plastic strain field was computed by a 2-D generalized plane-strain thermoelastoplastic welding simulation and was applied as a thermal load in a structural 3-D analysis. Solid elements were used in the structural analysis in Ref 9 and shell for the plates and truss for the welds in Ref 72. Michaleris et al. (Ref 9) report that the method can successfully predict buckling distortion. However, it does not account for angular distortion or welding sequencing effects.

The longitudinal component of plastic strain is applied as an orthotropic thermal load on the structural model. A unit thermal load is applied on the structural model, and then the load is scaled up by a factor γ computed as:

$$\gamma = \sigma_{res} / \sigma_1 \quad (\text{Eq 12})$$

where, σ_{res} is the computed residual stress in the 2-D model, and σ_1 is the stress resulting from the unit thermal load ($\Delta T_1 = -1.0$) in the structural model.

The structural analysis may consist of an eigenvalue analysis to compute the buckling stress and mode (Ref 73, 74):

$$\det(\mathbf{K} + \lambda_i \mathbf{K}_{G1}) = 0 \quad (\text{Eq 13})$$

where \mathbf{K}_{G1} is the nonlinear (stress stiffening) stress stiffness matrix for a unit negative thermal load applied in the weld region ($\Delta T_1 = -1.0$). In shell-truss models, the thermal load is applied to the truss elements only (Ref 72). The eigenvalues (λ_i) represent the multipliers (scaling factors) to the unit thermal load that will result in buckling. The structural analysis may also involve an incremental large-deformation analysis to compute the magnitude of distortion by applying a negative thermal load ($\Delta T = -\gamma$) at the weld region in the structural model.

A comparison of the 2-D/3-D applied plastic strain method and a direct 3-D thermoelastoplastic welding simulation against experimental measurements is presented in Ref 15. Figure 17 shows a 310 by 610 mm (12 by 24 in.) stiffened panel after welding. Excessive buckling distortion is visible. Figures 18 and 19 show the computed distortion using 3-D large-deformation thermoelastoplastic and 2-D/3-D applied plastic strain methods, respectively. Both analyses compute the buckling distortion accurately.

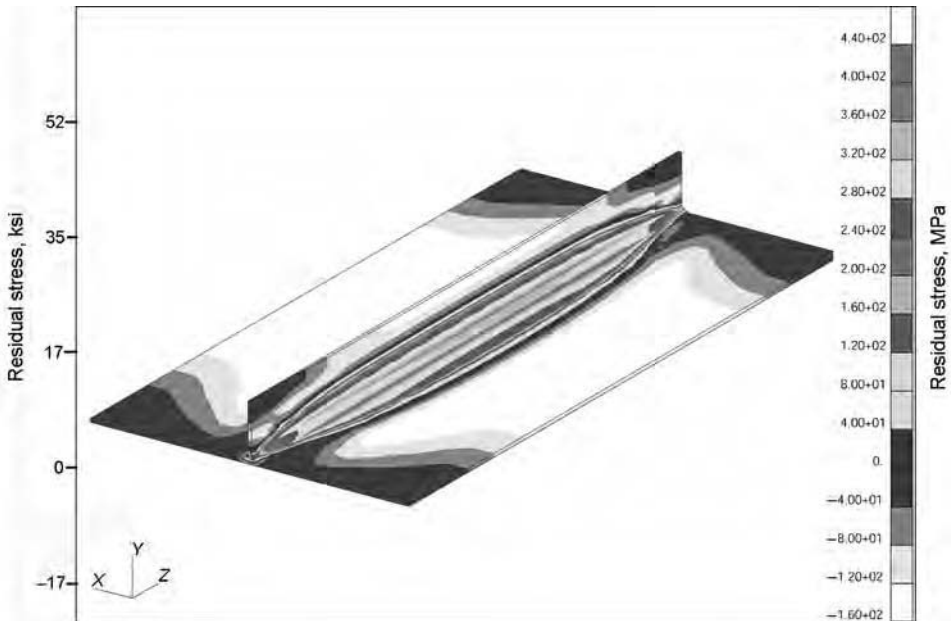


Fig. 12 Longitudinal residual-stress distribution computed by three-dimensional small-deformation analysis for 310 × 610 mm (12 × 24 in.) panel. Source: Ref 15

of time increments are involved, have been shown to be able to capture all types of welding distortions, but at great computational cost (Ref 63). A variety of simplified methods (inherent strain, applied plastic strain, fictitious loads) have been proposed over the years for modeling welding distortion in large structures (Ref 50).

Applied Plastic Strain Methods

The concept of applied plastic (inherent) strain was originally proposed by Ueda et al. (Ref 64) for determining the residual stresses and distortions of welded structures (Ref 65–71). In their approach, six plastic strain

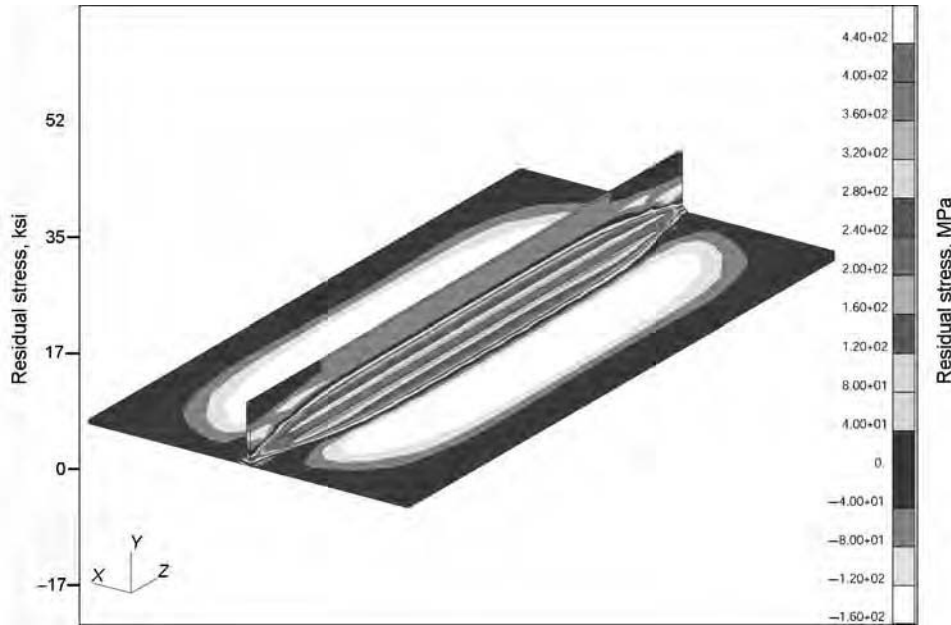


Fig. 13 Longitudinal residual-stress distribution computed by three-dimensional large-deformation analysis for 310 × 610 mm (12 × 24 in.) panel. Source: Ref 15

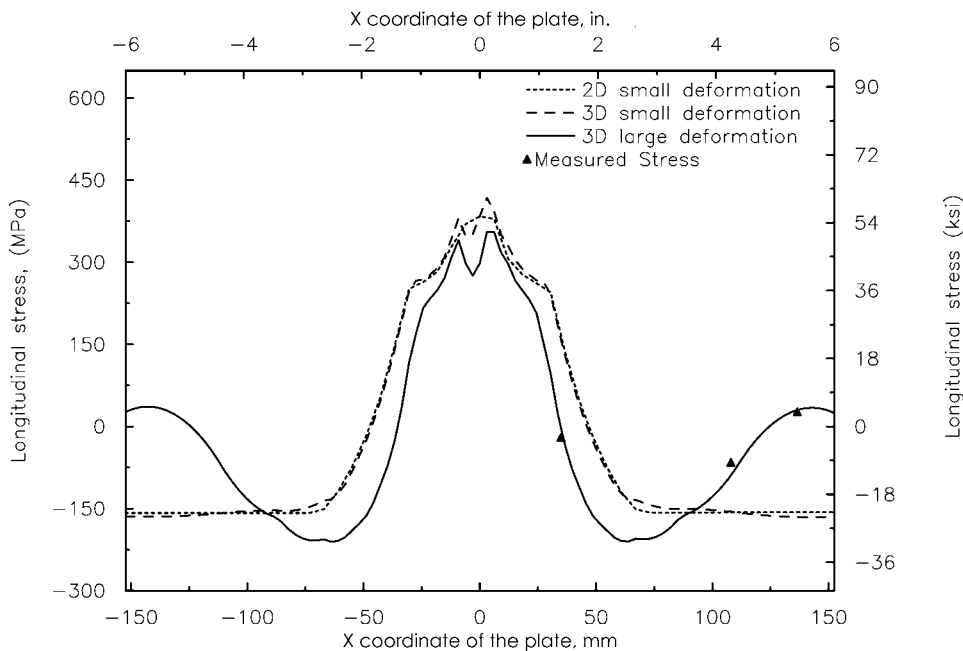


Fig. 14 Comparison of predicted longitudinal stress distribution with measured experimental stress values for 310 × 610 mm (12 × 24 in.) panel. Source: Ref 15

3-D/3-D Applied Plastic Strain Methods. Tsai et al. (Ref 75, 76) developed a 3-D plasticity-based applied approach to compute angular welding distortions in panels and T-joints. Their model demonstrated the relationship between cumulative plastic strains and angular distortions and reported that angular distortion is mainly induced by shear plastic strain (Ref 76, 77).

Michaleris et al. (Ref 16) developed a 3-D applied plastic strain method for computing welding distortion in large and complex structures. In this method, the six components of plastic strain of each weld are calculated in two steps. First, a 3-D moving-source analysis is performed on a small 3-D model with a shorter length, and then the plastic strain components of the small models are mapped and

superposed onto a large 3-D structural model to obtain the final distortion results. An interpolation algorithm was also developed for mapping between meshes with different densities. The effectiveness of the 3-D applied plastic strain method was evaluated by comparing to the distortion results from 3-D moving-source simulations. Figure 20 shows a comparison of the computed distortion using the applied plastic strain method and a direct moving-source thermoelastoplastic simulation on the entire structure. The numerical results show that the applied plastic strain method accounts for all distortion modes but is only qualitatively accurate for the prediction of angular distortion.

Effect of Initial Plate Straightness

The initial plate straightness can have a significant effect on the resulting welding distortion. Michaleris et al. (Ref 15) evaluated this effect using the applied plastic strain method by seeding the structural model with geometric imperfections of the first buckling mode, as follows:

$$x_i = x + \alpha_{imp} \cdot x_e \tag{Eq 14}$$

where x is the original node coordinates, x_i is the perturbed node coordinates, x_e is the normalized eigenmode solution for the first mode, and α_{imp} is the imperfection magnitude.

Figure 21 illustrates the computed buckling distortion for various magnitudes of imperfections for a 310 by 610 mm (12 by 24 in.) panel. The analyses show the computed buckling norm for increasing residual stress for several different values of imperfection magnitude, α_{imp} . For welds resulting in low residual stress (low magnitude of thermal load), the results are insensitive to imperfections. When the residual stress is close to the critical buckling stress, the onset of buckling is hastened, and its magnitude increases with increasing imperfection size. The critical thermal load computed by the eigenvalue analysis is illustrated in the figure by a vertical dotted line. At postbuckling residual stresses, there is no sensitivity. The results also demonstrate the highly nonlinear nature of distortion near the onset of buckling. A 10% change in the loading causes two to three times as great a change in distortion values.

2-D versus 3-D Analyses

Michaleris et al. (Ref 15) performed a comparison of 2-D, 3-D small-deformation, 3-D large-deformation, and 2-D/3-D decoupled applied plastic strain analyses for computing welding-induced distortion. Experimental out-of-plane distortion measurements were used as a reference. The following conclusions are drawn based on the results obtained:

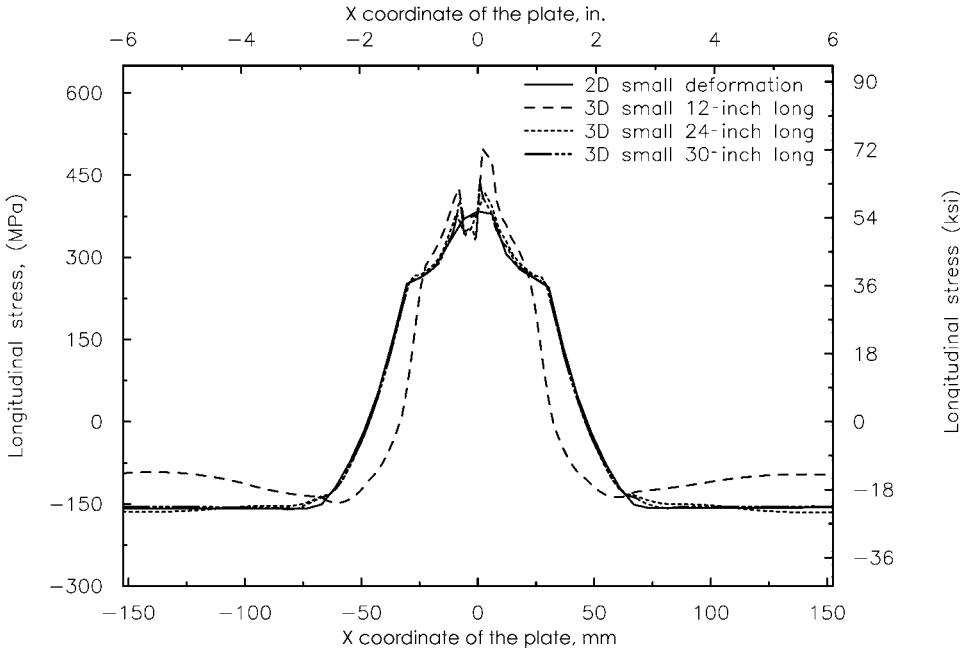


Fig. 15 Comparison of longitudinal stress predicted by two- and three-dimensional small-deformation analyses. Source: Ref 15

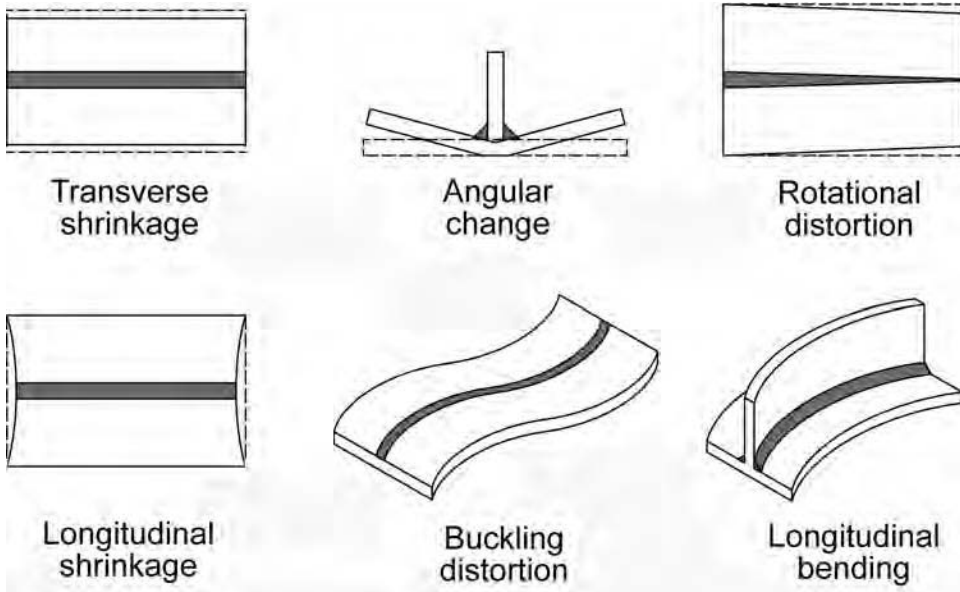


Fig. 16 Types of welding distortion. Source: Ref 62

- The 2-D generalized plane-strain analysis cannot capture welding distortion accurately. In thin plates, it does account for longitudinal buckling. In thick plates, it results in incorrect predictions of angular distortion.
- The 2-D/3-D applied plastic strain method predicts the onset and magnitude of buckling distortion accurately. However, it is not suitable for computing angular distortion.
- The 3-D large-deformation analysis predicts the correct magnitude of distortion in case of both angular and buckling distortion. It also captures end effects.
- Geometric or load imperfections are needed in large-deformation buckling analysis. In thermoelastoplastic analyses, the torch offset acts as load imperfection. Additional geometric imperfections are needed in the structural analyses of the applied plastic strain method.
- The distortion magnitude has a high sensitivity to the imperfection magnitude for residual stresses near the critical buckling stress.

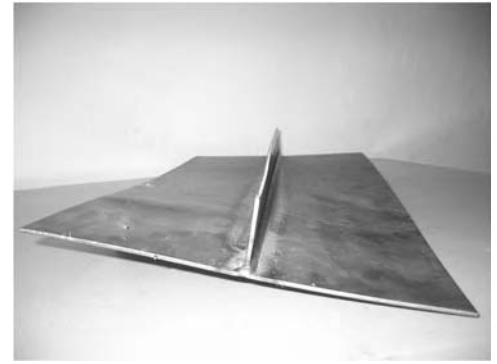


Fig. 17 Experimental 310 × 610 mm (12 × 24 in.) panel. Source: Ref 15

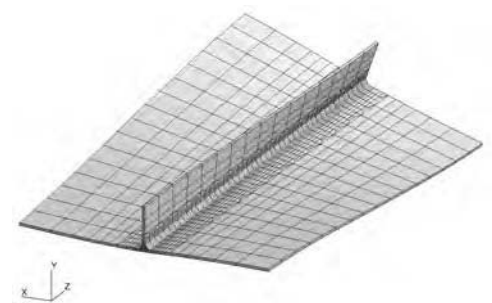


Fig. 18 Computed distortion by three-dimensional large-deformation analysis of a 310 × 610 mm (12 × 24 in.) panel. Original magnification: 2×. Source: Ref 15

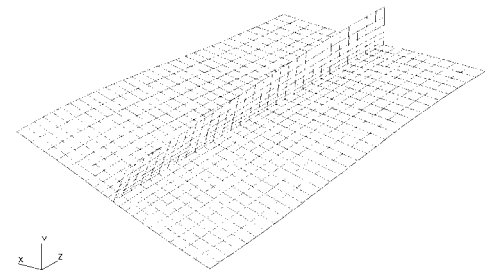


Fig. 19 Computed distortion by two- and three-dimensional decoupled analysis of a 310 × 610 mm (12 × 24 in.) panel. Original magnification: 2×. Source: Ref 15

- When buckling occurs, the residual stresses relax and reduce in magnitude.
- There are multiple equilibrium configurations in a buckled panel. In computational models, the configuration can be switched by switching the imperfection sign. The configuration of the experimental panels can be switched by applications of momentary external forces. Therefore, when buckling occurs, the buckling mode and absolute value of distortion magnitude are of significance.
- The 3-D large-deformation method becomes computationally very expensive as the problem size becomes large. Thus, the 2-D/3-D

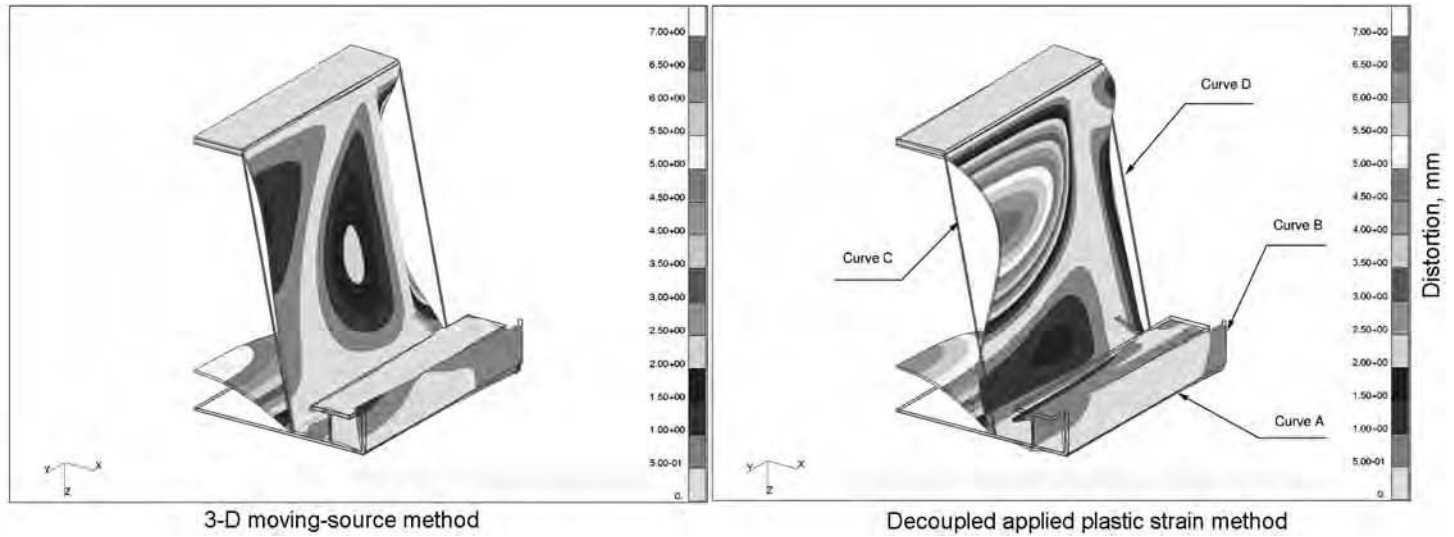


Fig. 20 Distortion results of the large structural model, large-deformation analysis. From Viewpoint 2. Original magnification: 50×

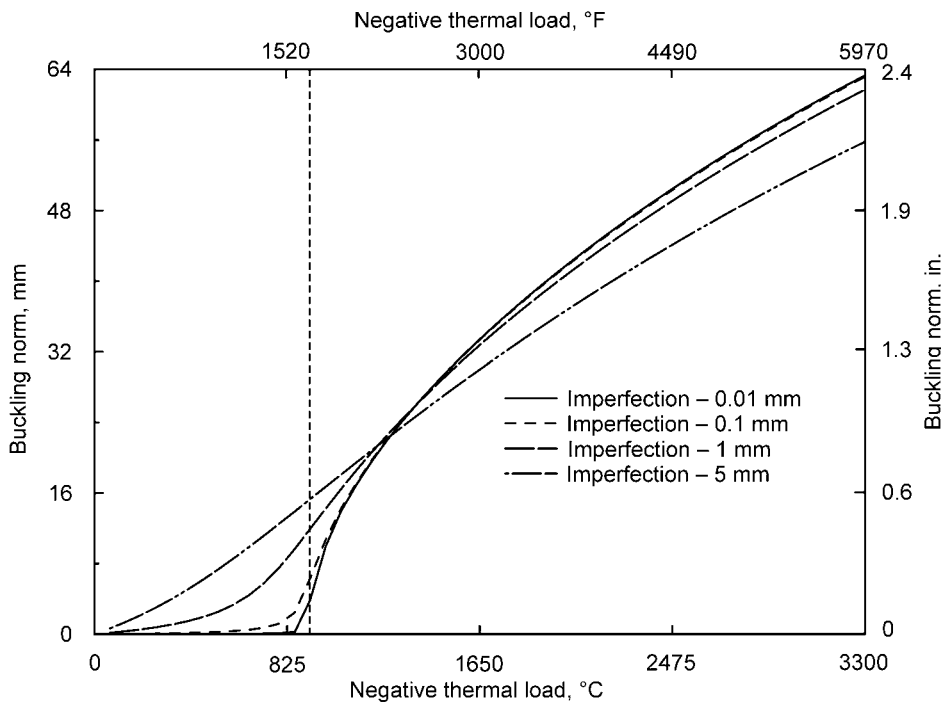


Fig. 21 Imperfection sensitivity for 310 × 610 mm (12 × 24 in.) plate. Source: Ref 15

applied plastic strain approach may be used as an effective tool to predict buckling-induced welding distortion instead of the 3-D large-deformation method.

REFERENCES

1. H. Hibbitt and P.V. Marcal, A Numerical, Thermo-Mechanical Model for the Welding and Subsequent Loading of a Fabricated Structure, *Comput. Struct.*, Vol 3, 1973, p 1145–1174

2. J.H. Argyris, J. Szimmat, and K.J. Willam, Computational Aspects of Welding Stress Analysis, *Comput. Methods Appl. Mech. Eng.*, Vol 33, 1982, p 635–666
3. V.J. Papazoglou and K. Masubuchi, Numerical Analysis of Thermal Stresses during Welding Including Phase Transformation Effects, *J. Pressure Vessel Technol.*, Vol 104, 1982, p 198–203
4. J. Goldak, A. Chakravarti, and M. Bibby, A New Finite Element Model for Welding Heat Sources, *Metall. Trans. B*, Vol 15, 1984, p 299–305

5. J.B. Leblond and J. Devaux, A New Kinetic Model for Anisothermal Metallurgical Transformations in Steels Including Effect of Austenite Grain Size, *Acta Metall.*, Vol 32 (No. 1), 1984, p 137–146
6. D.F. Watt, L. Coon, M.J. Bibby, J. Goldak, and C. Henwood, An Algorithm for Modeling Microstructural Development in Weld Heat-Affected Zones, *Acta Metall.*, Vol 36 (No. 11), 1988, p 3029–3035
7. C. Henwood, M. Bibby, J. Goldak, and D. Watt, Coupled Transient Heat Transfer-Microstructure Weld Computations, Part B, *Acta Metall.*, Vol 36 (No. 11), 1988, p 3037–3046
8. P. Michaleris, Z. Feng, and G. Campbell, Evaluation of 2D and 3D FEA Models for Predicting Residual Stress and Distortion, *Pressure Vessel and Piping Conference*, ASME, 1997, p 91–102
9. P. Michaleris and A. DeBicari, Prediction of Welding Distortion, *Weld. J.*, Vol 76 (No. 4), 1997, p 172–180
10. A.S. Oddy, J.A. Goldak, and J.M.J. McDill, Numerical Analysis of Transformation Plasticity in 3D Finite Element Analysis of Welds, *Eur. J. Mech., A/Solids*, Vol 9 (No. 3), 1990, p 253–263
11. P. Tekriwal and J. Mazumder, Transient and Residual Thermal Strain-Stress Analysis of GMAW, *J. Eng. Mater. Technol.*, Vol 113, 1991, p 336–343
12. S.B. Brown and H. Song, Implications of Three-Dimensional Numerical Simulations of Welding of Large Structures, *Weld. J.*, Vol 71 (No. 2), 1992, p 55s–62s
13. P. Michaleris, D.A. Tortorelli, and C.A. Vidal, Analysis and Optimization of Weakly Coupled Thermo-Elasto-Plastic Systems with Applications to Weldment Design, *Int. J. Numer. Methods Eng.*, Vol 38 (No. 8), 1995, p 1259–1285

14. P. Michaleris, J.A. Dantzig, and D.A. Tortorelli, Minimization of Welding Residual Stress and Distortion in Large Structures, *Weld. J.*, Vol 78 (No. 11), 1999, p 361–366s
15. P. Michaleris, L. Zhang, S.R. Bhide, and P. Marugabandhu, Evaluation of 2D, 3D and Applied Plastic Strain Methods for Predicting Buckling Welding Distortion and Residual Stress, *J. Sci. Technol. Weld.*, Vol 10, 2006, p 707–716
16. P. Michaleris, L. Zhang, and P. Marugabandhu, Evaluation of Applied Plastic Strain Methods for Welding Distortion Prediction, *J. Manuf. Sci. Eng.*, Vol 129, 2007, p 1000–1010
17. L.-E. Lindgren, Finite Element Modelling and Simulation of Welding, Part 1: Increased Complexity, *J. Therm. Stresses*, Vol 24, 2001, p 141–192
18. L.-E. Lindgren, Finite Element Modelling and Simulation of Welding, Part 2: Improved Material Modelling, *J. Therm. Stresses*, Vol 24, 2001, p 195–231
19. L.-E. Lindgren, Finite Element Modelling and Simulation of Welding, Part 3: Efficiency and Integration, *J. Therm. Stresses*, Vol 24, 2001, p 305–334
20. L.E. Lindgren and P. Michaleris, Modeling of Welding for Residual Stresses, *Handbook on Residual Stress*, Vol 2, J. Lu, Ed., SEM, 2005, p 47–67
21. M. Bugarewicz, “Modeling of High Energy Density Welding Processes to Predict Residual Stress and Distortion,” Ph.D. thesis, The Pennsylvania State University, University Park, PA, Dec 2006
22. E.W. Reutzel, S.M. Kelly, R.P. Martukanitz, M. Bugarewicz, and P. Michaleris, Laser-GMA Hybrid Welding: Process Monitoring and Thermal Modeling, *Fifth International Trends in Welding Research Conference Proceedings* (Pine Mountain, GA), ASM International, 2005, p 531–539
23. M. Bugarewicz, P. Michaleris, S. Kelly, and T. Reutzel, “Laser-GMA Hybrid Welding: Distortion Analysis and Design Optimization Modeling Techniques,” ICALCO (Miami, FL), 2005
24. P. Michaleris and X. Sun, Finite Element Analysis of Thermal Tensioning Techniques Mitigating Weld Buckling Distortion, *Weld. J.*, Vol 76 (No. 11), 1997, p 451–457
25. J.B. Leblond, G. Mottet, and J.C. Devaux, A Theoretical and Numerical Approach to the Plastic Behavior of Steels during Phase Transformations, Part I: Derivation of General Relations, *J. Mech. Phys. Solids*, Vol 34 (No. 4), 1985, p 395–409
26. J.B. Leblond, G. Mottet, and J.C. Devaux, A Theoretical and Numerical Approach to the Plastic Behaviour of Steels during Phase Transformations, Part 2: Study of Classical Plasticity for Ideal-Plastic Phases, *J. Mech. Phys. Solids*, Vol 34 (No. 4), 1986, p 411–432
27. J.B. Leblond, Mathematical Modelling of Transformation Plasticity in Steels, Part II: Coupling with Strain Hardening Phenomena, *Int. J. Plast.*, Vol 5, 1989, p 573–591
28. J. Leblond, Metallurgical and Mechanical Consequences of Phase Transformations in Numerical Simulations of Welding Processes, *Modeling in Welding, Hot Powder Forming, and Casting*, L. Karlsson, Ed., ASM International, 1997, p 61–89
29. A.S. Oddy, J.A. Goldak, and J.M.J. McDill, Numerical Analysis of Transformation Plasticity in 3D Finite Element Analysis of Welds, *Eur. J. Mech., A/Solids*, Vol 9, 1990, p 1–11
30. Numerical Methods for Casting Applications, *Casting*, Vol 15, *ASM Handbook*, ASM International, 2008, p 419–424
31. S. Mishra and T. DebRoy, A Heat-Transfer and Fluid-Flow Model to Obtain a Specific Weld Geometry Using Various Combinations of Welding Variables, *J. Appl. Phys.*, Vol 98, 2005, p 044902
32. Z. Yang, N. Chen, H.W. Ludewig, and Z. Cao, Virtual Welded-Joint Design by Coupling Thermal-Metallurgical-Mechanical Modeling, *Sixth International Trends in Welding Research Conference Proceedings* (Pine Mountain, GA), ASM International, 2003, p 861–866
33. G. Taylor, M. Hughes, N. Strusevich, and K. Pericleous, Finite Volume Methods Applied to the Computational Modelling of Welding Phenomena, *Second International Conference on CFD in the Minerals and Process Industries* (Melbourne, Australia), CSIRO, 1999, p 405–410
34. T. Zacharia, S.A. David, J.M. Vitek, and T. DebRoy, Weld Pool Development during GTA and Laser Beam Welding of Type 304 Stainless Steel, Part 1: Theoretical Analysis, *Weld. Res. Suppl.*, 1989, p S:499–509
35. C. Kim, W. Zhang, and T. Debroy, Modeling of Temperature Field and Solidified Surface Profile during Gas-Metal Arc Fillet Welding, *J. Appl. Phys.*, Vol 94 (No. 4), 2003, p 2667–2679
36. A. Mahrle, J. Schmidt, and D. Weiss, Simulation of Temperature Fields in Arc and Beam Welding, *Heat Mass Transf.*, Vol 36, 2000, p 117–126
37. T. Zacharia, A. Eraslan, D. Aldun, and S.A. David, Three-Dimensional Transient Model for Arc-Welding Process, *Metall. Trans. B*, Vol 20, 1989, p 645–659
38. J.J. Valencia and K.O. Yu, Chap. 6, *Modeling for Casting and Solidification Processing*, Marcel Dekker Inc., 2002, p 190
39. J. Goldak, J. Zhou, S. Tchernov, D. Downey, S. Wang, and B. He, Predicting Distortion and Residual Stress in Complex Welded Structures by Designers, *Seventh International Trends in Welding Research Conference Proceedings* (Pine Mountain, GA), ASM International, 2005, p 531–539
40. A. Agrawal and P.R. Dawson, A Comparison of Galerkin and Streamline Techniques for Integration Strains from an Eulerian Flow Field, *Int. J. Numer. Methods Eng.*, Vol 21, 1985, p 853–881
41. A. Bastier, M.H. Maitournam, K. Dang Van, and F. Roger, Steady State Thermo-mechanical Modelling of Friction Stir Welding, *Sci. Technol. Weld. Join.*, Vol 11 (No. 3), 2006, p 278–288
42. A. Bastier, M.H. Maitournam, F. Roger, and K. Dang Van, Modelling of the Residual State of Friction Stir Welded Plates, *J. Mater. Process. Technol.*, Vol 200, 2008, p 25–37
43. X. Qin and P. Michaleris, Thermo-Elasto-Visco-Plastic Modeling of Friction Stir Welding, *Sci. Technol. Weld.*, Vol 14, 2009, p 640–649
44. X. Qin, “Thermo-Elasto-Visco-Plastic Modeling of Friction Stir Welding in an Eulerian Reference Frame,” Ph.D. thesis, The Pennsylvania State University, 2009
45. X. Qin and P. Michaleris, Eulerian Elasto-Visco-Plastic Formulations for Residual Stress Prediction, *Int. J. Numer. Methods Eng.*, Vol 77, 2009, p 634–663
46. X. Qin and P. Michaleris, Eulerian Elasto-Visco-Plastic Formulations Based Directly on the Equilibrium Equation, *Int. J. Numer. Methods Eng.*, 2010, in review
47. J. Goldak, M. Bibby, J. Moore, R. House, and B. Patel, Computer Modeling of Heat Flows in Welds, *Metall. Trans. B*, Vol 17, 1986, p 587–600
48. J. Goldak, M. Gu, and E. Hughes, Steady State Thermal Analysis of Welds with Filler Metal Addition, *Can. Metall. Q.*, Vol 32 (No. 1), 1993, p 49–55
49. J.A. Goldak and M. Akhlaghi, *Computational Welding Mechanics*, Springer, 2005
50. D. Radaj, *Welding Residual Stresses and Distortion: Calculation and Measurement*, Woodhead Publishing, 2003
51. P.S. Myers, O.A. Uyshara, and G.L. Borman, Fundamentals of Heat Flow in Welding, *U.K. Weld. Res. Counc. Bull.*, No. 123, 1967
52. E.F. Rybicki and R.B. Stonesifer, Computation of Residual Stresses due to Multipass Welds in Piping Systems, *J. Press. Vessel Technol.*, Vol 101, 1979, p 149–154
53. E.F. Rybicki, D.W. Schmueser, R.B. Stonesifer, J.J. Groom, and H.W. Mishler, A Finite-Element Model for Residual Stresses and Deflections in Girth-Butt Welded Pipes, *J. Press. Vessel Technol.*, Vol 100, 1978, p 256–262
54. Y. Shim, Z. Feng, S. Lee, D.S. Kim, J. Jaeger, J.C. Papanitan, and C.L. Tsai, Determination of Residual Stress in Thick-Section Weldments, *Weld. J.*, Vol 71, 1992, p 305s–312s
55. O. Myhr, Modeling of Microstructure Evolution and Residual Stresses in Processing and Welding of 6082 and 7108 Aluminium

- Alloys, *Fifth International Conference on Trends in Welding Research* (Pine Mountain, GA), H.D. Brody and D. Apelian, Ed., ASM International, 1998
56. Z. Wang and T. Inoue, Viscoplastic Constitutive Relation Incorporating Phase Transformation—Application to Welding, *Mater. Sci. Technol.*, Vol 1, 1985, p 899–903
 57. J. Goldak, “Thermal Stress Analysis in Solids near the Liquid Region in Welds,” Mathematical Modelling of Weld Phenomena 3 (Graz, Austria), 1997
 58. D. Bammann and A. Ortega, The Influence of the Bauschinger Effect and Yield Definition on the Modeling of Welding Processes, *Sixth Int. Conf. on Modeling of Casting, Welding and Advance Solidification Processes* (Palm Coast, FL), T.S. Piwonka, V. Voller, and L. Katgerman, Ed., The Minerals & Materials Society, 1993, p 543–551
 59. A.S. Oddy and L.-E. Lindgren, Mechanical Modeling and Residual Stresses, *Modeling in Welding, Hot Powder Forming, and Casting*, L. Karlsson, Ed., ASM International, 1997, p 31–59
 60. L.-E. Lindgren and E. Hedblom, Modelling of Addition of Filler Material in Large Deformation Analysis of Multipass Welding, *Commun. Numer. Methods Eng.*, Vol 17 (No. 9), 2001, p 647–657
 61. L.-E. Lindgren, H. Runnemalm, and M.O. Nasstrom, Simulation of Multipass Welding of a Thick Plate, *Int. J. Numer. Methods Eng.*, Vol 44 (No. 9), 1999, p 1301–1316
 62. K. Masubuchi, *Analysis of Welded Structures*, Pergamon Press, Oxford, 1980
 63. J. Sun, “Modeling and Finite Element Analysis of Welding Distortion and Residual Stresses in Large and Complex Structures,” Ph.D. thesis, The Pennsylvania State University, University Park, PA, Aug 2005
 64. Y. Ueda, K. Fukuda, K. Nakacho, and S. Endo, A New Measuring Method of Residual Stresses with the Aid of Finite Element Method and Reliability of Estimated Values, *Trans. JWRI*, Vol 4 (No. 2), 1975, p 123–131
 65. Y. Ueda, Y.C. Kim, and M.G. Yuan, A Predictive Method of Welding Residual Stress Using Source of Residual Stress (Report 1), *Trans. JWRI*, Vol 18 (No. 1), 1989, p 135–141
 66. Y. Ueda and K. Fukuda, New Measuring Method of Three-Dimensional Residual Stresses in Long Welded Joints Using Inherent Strains as Parameters, *J. Eng. Mater. Technol.*, Vol 111, 1989, p 1–8
 67. Y. Ueda and M.G. Yuan, Prediction of Residual Stresses in Butt Welded Plates Using Inherent Strains, *J. Eng. Mater. Technol.*, Vol 115, 1993, p 417–423
 68. H. Murakawa, X.M. Zhong, and Y. Ueda, Buckling Behavior of Plates under Idealized Inherent Strain, *Trans. JWRI*, Vol 24 (No. 2), 1995, p 87–91
 69. H. Murakawa, N.X. Ma, Y. Ueda, and H. Maeda, FEM Analysis of 3D Welding Residual Stresses and Angular Distortion in T-Type Fillet Welds, *Trans. JWRI*, Vol 24 (No. 2), 1995, p 115–122
 70. M.G. Yuan and Y. Ueda, Prediction of Residual Stresses in Welded T- and I-Joints Using Inherent Strains, *J. Eng. Mater. Technol.*, Vol 118, 1993, p 229–234
 71. Y. Luo, M. Ishiyama, and H. Murakawa, Welding Deformation of Plates with Longitudinal Curvature, *Trans. JWRI*, Vol 28 (No. 2), 1999, p 57–65
 72. A. DeBiccari and P. Michaleris, Implementation of Analytical Tools for the Prediction and Control of Distortion in Thin Panel Structures, *Koichi Masubuchi: A Welding Research & Engineering Festschrift*, R.G. Morris, Ed., MIT Sea Grant Program (Cambridge, MA), 2000, p 73–96
 73. K.J. Bathe, *Finite Element Procedures*, Prentice-Hall, Inc., New Jersey, 1996
 74. R.D. Cook, D.S. Malkus, and M.E. Plesha, *Concepts and Applications of Finite Element Analysis*, John Wiley and Sons, Inc., New York, NY, 1988
 75. C.L. Tsai, S.C. Park, and W.T. Cheng, Welding Distortion of a Thin-Plate Panel Structure, *AWS Weld. J., Res. Suppl.*, Vol 78, 1999, p 156s–165s
 76. G.H. Jung and C.L. Tsai, Plasticity-Based Distortion Analysis for Fillet Welded Thin-Plate T-Joints, *Weld. J.*, Vol 83 (No. 6), 2004, p 177–187
 77. G.H. Jung, “Plasticity-Based Distortion Analysis for Fillet Welded Thin Plate T-Joints,” Ph.D., The Ohio State University, Columbus, OH, 2003

Residual Stresses and Distortion*

Koichi Masubuchi, Massachusetts Institute of Technology

COMPLEX THERMAL STRESSES occur in parts during welding due to the localized application of heat. Residual stresses and distortion remain after welding is completed. Transient thermal stresses, residual stresses, and distortion sometimes cause cracking and mismatching of joints. High tensile residual stresses in areas near the weld can cause premature failures of welded structures under certain conditions. Distortion, especially out-of-plane distortion, and compressive residual stresses in the base plate can reduce the buckling strength of a structural member subjected to compressive loading. Correction of unacceptable distortion is costly and, in some cases, impossible. The subjects related to residual stresses, distortion, and their consequences are too broad to be discussed in depth in this article. Those who need more detailed information are advised to refer to the references, especially Ref 1 to 8.

Formation of Residual Stresses and Distortion

Residual stresses, also referred to as internal stresses, initial stresses, inherent stresses, and locked-in stresses, are stresses that exist in a body after all external loads are removed. Residual stresses also occur when a body is subjected to nonuniform temperature changes; these stresses are called thermal stresses. The intensity of stress is usually expressed in load or force per unit area, such as newtons per square meter (N/m^2) or pascals (Pa), kilograms force per square millimeter (kg/mm^2), or pounds per square inch (psi).

Residual stresses in metal structures occur for many reasons during various manufacturing stages, including casting, rolling, bending, flame cutting, forging, machining, and grinding. Heat treatments at various stages also influence residual stresses. For example, quenching treatments produce residual stresses, while stress-relieving heat treatments may reduce such stresses. Areas in which residual stresses exist vary greatly—from microscopic areas to large sections of the metal structure. This article focuses primarily on macroscopic residual stresses. Residual stresses can be classified into two groups according to the mechanisms that produce them:

- Stresses produced by structural mismatch
- Stresses produced by an uneven distribution of nonelastic strains, including plastic and thermal strains

Thermal Stresses and Metal Movement during Welding

Because a weldment is locally heated by the welding heat source, the temperature distribution is not uniform and changes as welding progresses. During the welding thermal cycle, complex transient thermal stresses are produced in the weldment and the surrounding joint. The

weldment also undergoes shrinkage and deformation during solidification and cooling.

Thermal Stresses during Welding. Figure 1 schematically shows changes in temperature and resulting stresses that occur during welding by examining a bead-on-plate weld of a thin plate made along the x -axis. The welding arc, which is moving at a speed v , is presently located at the origin, O , as shown in Fig. 1(a). The area where plastic deformation occurs during the welding thermal cycle is shown by the shaded area, $M-M'$, in Fig. 1(a). The region where the metal is molten is indicated by the ellipse near O . The region outside the shaded area remains elastic throughout the entire welding thermal cycle.

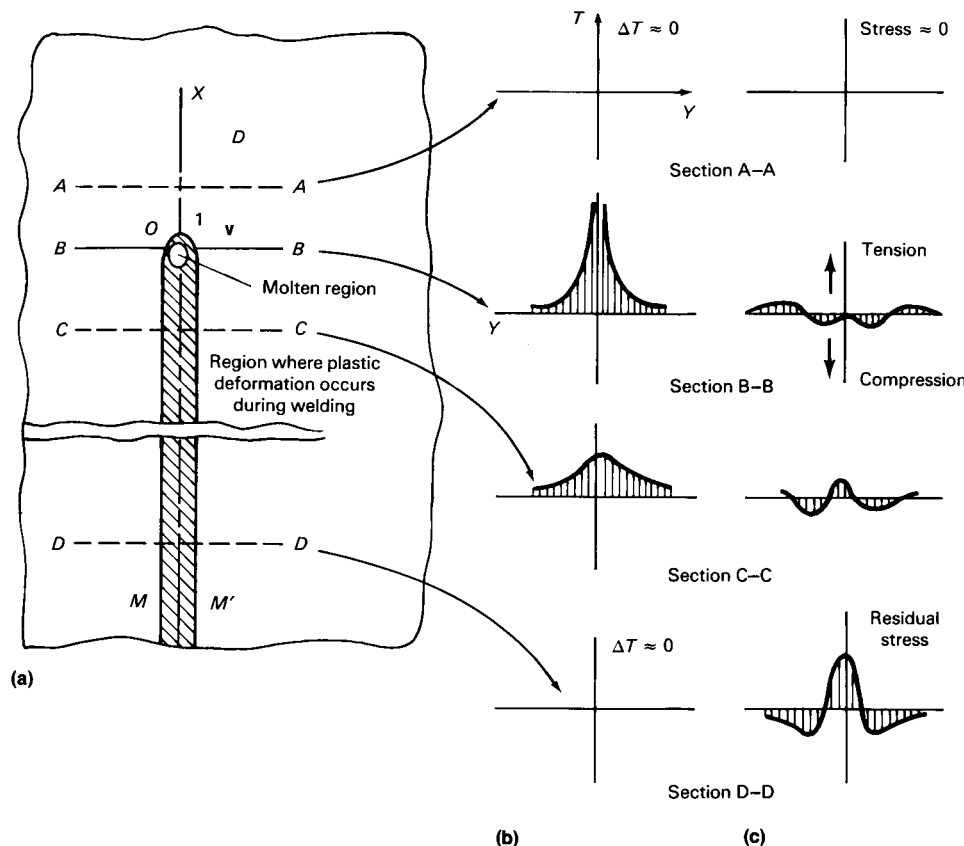


Fig. 1 Schematic representation of changes in temperature and stresses during welding. (a) Weld. (b) Temperature change. (c) Stress, σ_x . Stress distribution is shown in the plane stress condition. Therefore, stresses are regarded as being uniform in the thickness direction. Source: Welding Research Council

Temperature gradients along several cross sections through the weld bead path are indicated in Fig. 1(b). In the base metal ahead of the welding arc (denoted as section A-A), the slope of the temperature gradient due to welding ($\Delta T/\Delta Y$) is almost zero. However, along section B-B, which crosses the welding arc, the slope becomes very steep. Along section C-C, somewhat behind the welding arc, the slope becomes less steep. The slope of the temperature gradient due to welding once again approaches zero along section D-D, which is some distance behind the welding arc. Figure 1(c) shows the distribution of normal stress in the x -direction (σ_x) along the cross sections. Normal stress in the y -direction (σ_y) and shearing stress (τ_{xy}) also exist in a two-dimensional stress field. In a three-dimensional stress field, six stress components exist: σ_x , σ_y , σ_z , τ_{xy} , τ_{yz} , and τ_{zx} .

Figure 1(c) shows the distribution (along the y -axis) of normal stress in the x -direction (σ_x) due to welding (that is, thermal stress). Along section A-A, the stresses are almost zero. The stress distribution along section B-B is complicated. Beneath the welding arc, stresses are close to zero, because molten metal does not support shear loading. Moving away from the arc, stresses become compressive, because expansion of the metal surrounding the weld pool is restrained by the base metal. Because the temperatures of these areas are quite high, the yield stress of the material becomes quite low. In other words, a situation occurs in which stresses in these areas are as high as the yield stress of the base metal at corresponding temperatures. The magnitude of compressive stress passes through a maximum with increasing distance from the weld or with decreasing temperature. However, stresses occurring in regions farther away from the welding arc are tensile in nature and balance with compressive stresses in areas near the weld pool.

Figure 1(b) shows that along section C-C the weld-metal and base-metal regions have cooled. As they shrink, tensile stresses are caused in regions in and adjacent to the weld (Fig. 1c). As the distance from the weld increases, stresses become compressive. High tensile stresses exist along section D-D in and adjacent to the weld. Compressive stresses are produced in areas away from the weld.

Equilibrium Condition of Residual Stresses. Because residual stresses exist without external forces, the resultant force and the resultant moment produced by the residual stresses must vanish on any plane section:

$$\int \sigma \cdot dA = 0 \quad (\text{Eq 1})$$

$$\int dM = 0 \quad (\text{Eq 2})$$

where dA is area and dM is the resultant moment. Residual stress data must be checked in any experiment to ensure that they satisfy the above condition.

Metal Movement during Welding. During welding, the weldment undergoes shrinkage and deformation. The transient deformation,

or metal movement, is most evident when the weld line is away from the neutral axis of the weldment, causing a large amount of bending moment. Figure 2 schematically shows how a rectangular plate distorts when its longitudinal edge is heated by a welding arc or an oxyacetylene torch (for cutting, welding, or flame heating). Areas near the heat source, or the upper regions of the rectangular plate, are heated to higher temperatures and thus expand more than areas away from the heat source, or the lower regions of the plate. Therefore, the plate first deforms as shown by curve AB .

If all the parts of the material remained completely elastic during the entire thermal cycle, thermal stresses produced during the heating and cooling cycle would disappear when the temperature returned to the initial temperature. Deformation of the plate during the welding process would be indicated by curve $AB'C'D'$, resulting in no deformation after the thermal cycle. However, in most practical materials, plastic strains are produced in areas heated to elevated temperatures, causing plastic upsetting. The thermal stresses do not disappear when the temperature returns to the initial temperature, causing residual stresses. Transient deformation of the plate during heating and cooling is shown by curve $ABCD$. After the plate cools to the initial temperature, final deformation in the amount δ_f remains, which also is called distortion. The metal movement (that is, transient distortion or transient deformation) during welding and the distortion after welding is completed occur in opposite directions, generally with the same order of magnitude.

In summary, some basic characteristics of residual stresses and distortion are (Ref 9):

- The metal movement during welding (expansion) is opposite to the distortion that remains after welding.
- Although welding is completed in a short period (in a few minutes, for example), residual stresses and distortion take a relatively long time to develop completely (30 min to 1h)
- Because most of the nonelastic strains that cause residual stresses and distortions are produced during welding, necessary actions must be performed during welding to effectively control and reduce residual stresses and distortion.

Analyses of Residual Stresses and Distortion in Weldments

Residual stresses and distortion in welded structures have been recognized and studied since the 1930s. Analyses of these subjects require complex computation; therefore, most early studies were primarily empirical or limited to the analysis of simple cases. With the advancement of modern computers and computational techniques (for example, the finite-element and finite-difference method), a renewed effort has been made in recent years to study residual stresses and related phenomena. Therefore, it is now possible using computer programs to simulate the transient thermal stresses and metal movement during welding as

well as the residual stresses and distortion that remain after welding is completed (Ref 10–14). However, because these analysis methods are very complex, most are not practical for analyzing and controlling residual stresses and distortion in weldments.

Techniques for Measuring Residual Stresses

Many techniques have been used to measure residual stresses in metals (Ref 6, 15, 16). Table 1 lists most of the presently available measurement techniques and classifies them as follows:

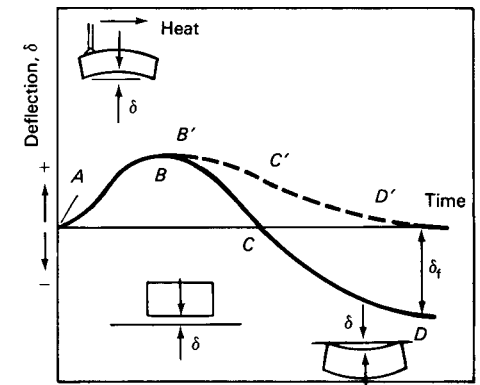


Fig. 2 Changes of deflection at the center of the lower edge of a rectangular plate due to heating by a heat source moving along the upper edge and subsequent cooling

Table 1 Classification of techniques for measuring residual stress

A-1 Stress-relaxation techniques using electric and mechanical strain gages	
Plate	Sectioning technique using electric resistance strain gages
	Gunnert technique
	Mathar-Soete drilling technique
	Stäblein successive milling technique
Solid cylinders and tubes	Heyn-Bauer successive machining technique
	Mesnager-Sachs boring-out technique
Three-dimensional solids	Gunnert drilling technique
	Rosenthal-Norton sectioning technique
A-2 Stress-relaxation techniques using apparatus other than electric and mechanical strain gages	
	Grid system-dividing technique
	Brittle coating-drilling technique
	Photoelastic coating-drilling technique
B X-ray diffraction techniques	
	X-ray film technique
	X-ray diffractometer technique
C Techniques using stress-sensitive properties	
Ultrasonic techniques	Polarized ultrasonic wave technique
	Ultrasonic attenuation technique
Hardness techniques	
D Cracking techniques	
	Hydrogen-induced cracking technique
	Stress-corrosion cracking technique

Source: Ref 17

- Stress-relaxation techniques
- X-ray diffraction techniques
- Techniques using stress-sensitive properties
- Cracking techniques

In the stress-relaxation technique, residual stress is determined by measuring the elastic-strain release that takes place when a specimen is cut into pieces or has a piece removed. In most cases, electric or mechanical gages are used for measuring this strain release (group A-1 in Table 1). A variety of such techniques exist (that is, there are many ways to section a specimen to determine residual stresses). Certain techniques are used to study stresses in a plate, while others are used for cylinders, tubes, or three-dimensional solids. Strain release caused by stress relaxation can also be determined by using grid systems, brittle coatings, or photoelastic coatings (group A-2 in Table 1). An inherent disadvantage of stress-relaxation techniques is that they are destructive (that is, the specimen must be partially or entirely sectioned). Nevertheless, the stress-relaxation techniques provide reliable quantitative data and are the most widely used method for measuring residual stresses in weldments.

In metals with crystalline structures, elastic strains can also be determined by using x-ray diffraction to measure the lattice parameter. Because the lattice parameter of a metal in the unstressed state is known or can be determined separately, elastic strain in the metal can be measured nondestructively without machining or drilling. Two methods are presently available: the x-ray film technique and the x-ray diffractometer technique. With x-ray diffraction, surface strains can be determined within a small area—for example, to a depth of 0.025 mm (0.001 in.) and a diameter of 0.0025 mm (0.0001 in.). Modern x-ray diffraction stress-measurement instrumentation can provide one complete measurement in time scales as short as a fraction of a second, and typically less than 1 min. However, x-ray diffraction techniques have some disadvantages. They are time-consuming, and they are not accurate, especially in situations where high temperatures have distorted the atomic structure of the material. Studies have recently been made using diffraction of neutrons, which can penetrate deeper into the metal than x-rays (Ref 18).

Attempts have been made to determine the residual stresses in metals by measuring their stress-sensitive properties. The following stress-measurement techniques have been proposed:

- Ultrasonic techniques, such as the polarized ultrasonic wave technique (which makes use of stress-induced changes in the angle of polarization of polarized ultrasonic waves) and the ultrasonic attenuation technique (which makes use of stress-induced changes in the rate of absorption of ultrasonic waves)
- Hardness techniques, which make use of stress-induced changes in hardness

However, none of these techniques has been developed beyond the laboratory stage, and

they have not been used successfully for the measurement of residual stresses in weldments.

Another technique developed for the study of residual stresses involves the close observation of cracks induced in the specimen by hydrogen embrittlement or stress-corrosion cracking (SCC). Cracking techniques are useful when studying residual stresses in complex structural models in which the distribution of residual stresses is complicated, but these techniques provide only qualitative, not quantitative, data.

Magnitude and Distribution of Residual Stresses in Weldments

A number of investigators have studied distributions of residual stresses in various types of weldments. Most of the data presented in this section relates to single welds as opposed to multipass welds. References 6 to 8 present detailed information.

Residual Welding Stresses, Reaction Stresses, and Stress Distributions in a Groove Weld. As stated earlier, residual stresses can be classified as (1) stresses produced by structural mismatch or displacement and (2) stresses produced by uneven distribution of nonelastic strains. The same method of classification is applicable to residual stresses in weldments: (1) reaction stresses caused when the weldment is restrained externally and (2) residual stresses produced in an unrestrained weldment.

Figure 3 shows a typical distribution of residual stresses in a groove weld. The significant stresses are those parallel to the weld direction, designated σ_x , which are usually called the longitudinal stresses, and those transverse to σ_x , designated σ_y , which are called the transverse stresses. The distribution of the longitudinal stress is shown in Fig. 3(b). Near the weld, tensile stresses of high magnitude are produced. These taper off quickly and become compressive at a distance equal to several times the width of the weld metal. The stress distribution is characterized by two parameters:

- The maximum stress at the weld region, σ_m
- The width of the tension zone of residual stress, b

The distribution of longitudinal residual stress, σ_x , can be approximated by:

$$\sigma_x(y) = \sigma_m \left[1 - \left(\frac{y}{b} \right)^2 \right] e^{-[1/2(y/b)^2]} \quad (\text{Eq 3})$$

Equation 3 satisfies the equilibrium conditions given in Eq 1 and 2.

Curve 1 of Fig. 3(c) shows the distribution of transverse stress, σ_y , along the length of the weld. In the center of the joint, tensile stresses of relatively low magnitude are produced. Compressive stresses are produced at the ends of the joint. If an external constraint is used to restrain the lateral contraction of the joint, approximately uniform tensile stresses along the weld are added, resulting in curve 2 of Fig. 3(c). However, an

external constraint has little influence on the distribution of residual stress (σ_x).

Residual Stresses in a Plug Weld. Figure 4 shows the distribution of both the theoretical and experimental residual stresses in a circular plug weld (Ref 19). Tensile stresses, as high as the yield stress of the material, are produced in both radial and tangential directions in the weld and adjacent areas. In areas away from the weld, radial stresses (σ_r) are tensile, and tangential stresses (σ_θ) are compressive; both stresses decrease with increasing distance from the weld (r).

Residual Stresses in a Welded Shape and a Column. Figure 5 shows typical distributions of residual stresses and distortion in various welded shapes (Ref 20). As shown in section xx of Fig. 5 (a), high tensile residual stresses are produced in areas near the weld, in the direction parallel to the weld line (axis). In the flange, longitudinal stresses are compressive (−) in areas away from the weld and tensile (+) in areas near the weld. Tensile stresses in areas near the upper edge of the web are caused by longitudinal bending distortion of the T-shape, which are caused by the longitudinal shrinkage of the weld. Angular distortion also is produced.

Figures 5(b) and 5(c) show typical distributions of residual stress in H-shapes (I-beams)

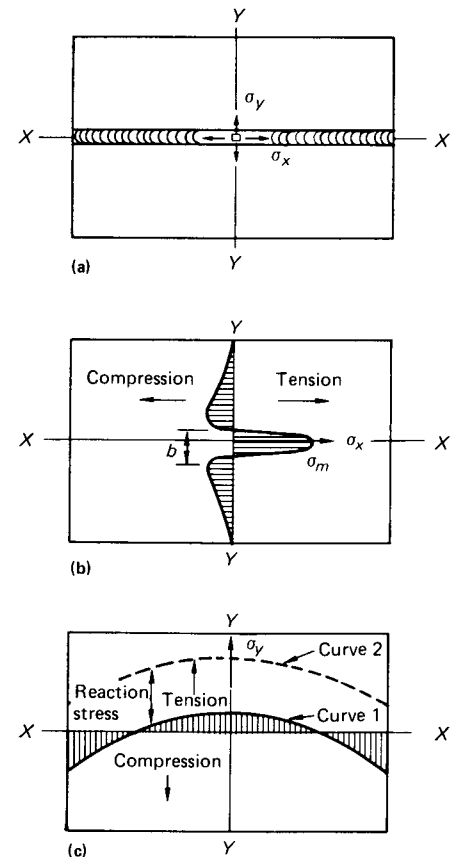


Fig. 3 Typical distributions of residual stresses in a groove weld. (a) Groove weld. (b) Distribution of σ_x along YY. (c) Distribution of σ_y along XX. Source: Welding Research Council

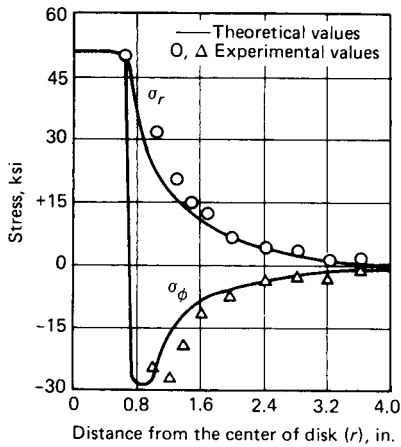
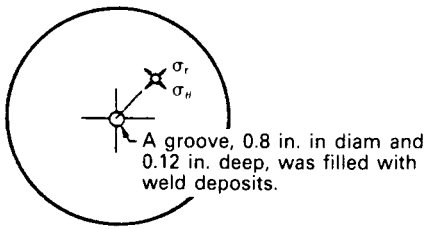


Fig. 4 Theoretical and experimental distributions of residual stresses in a plug weld

and in a welded box shape, respectively. Residual stresses are shown parallel to the weld line (axis); they are compressive in areas away from the welds and tensile in areas near the welds.

Residual Stresses in Weldments of Selected Materials. Distributions of residual stresses in welds in various metals are similar to those in low-carbon steel welds, discussed previously. In most cases, the maximum residual stresses are as high as the yield stress of the material. One exception is ultrahigh-strength steels, such as 4130, D-6a, and H13 (Ref 6). For such steels, peak values of residual stresses in some areas can be as high as the yield stress (or even higher in the case of triaxiality); however, average values of residual stresses in the weld metal are considerably lower than the yield stress.

Distortion in Weldments

Distortions found in fabricating structures are caused by three fundamental dimensional changes:

- Transverse shrinkage
- Longitudinal shrinkage parallel to the weld line
- Angular distortion around the weld line

These dimensional changes are shown in Fig. 6. The shrinkage and distortion that occur during fabrication of actual structures are far more complex than those shown in Fig. 6. For example, when longitudinal shrinkage occurs in a fillet joint,

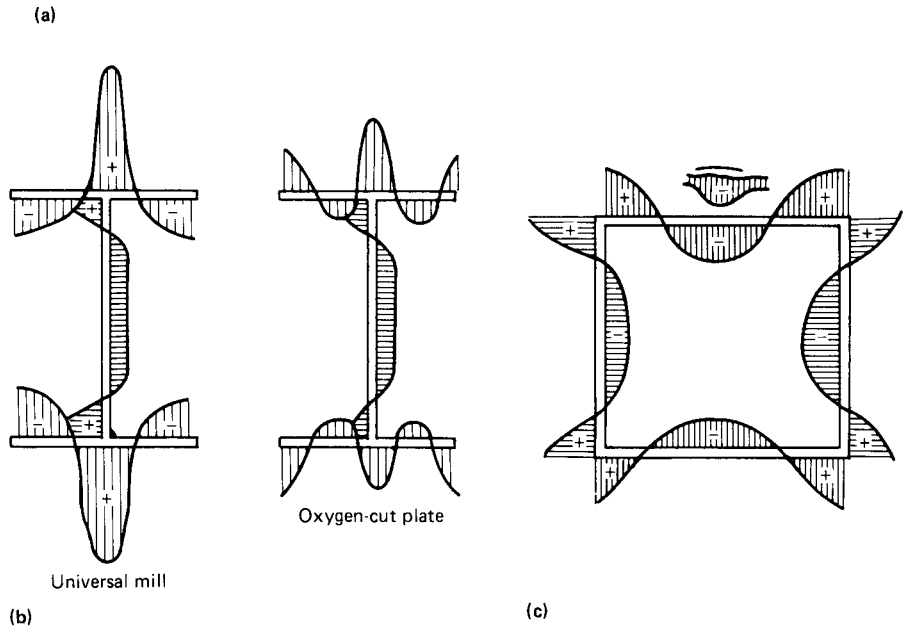
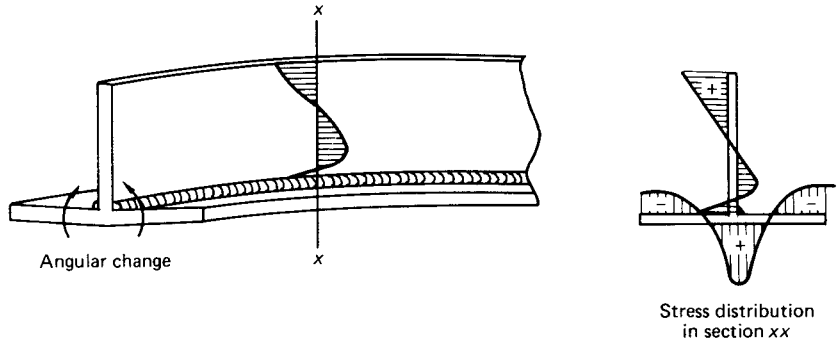


Fig. 5 Typical residual stresses in welded shapes. (a) T-shapes. (b) H-shapes. (c) Box shapes. Compressive stress, -; tensile strength, +

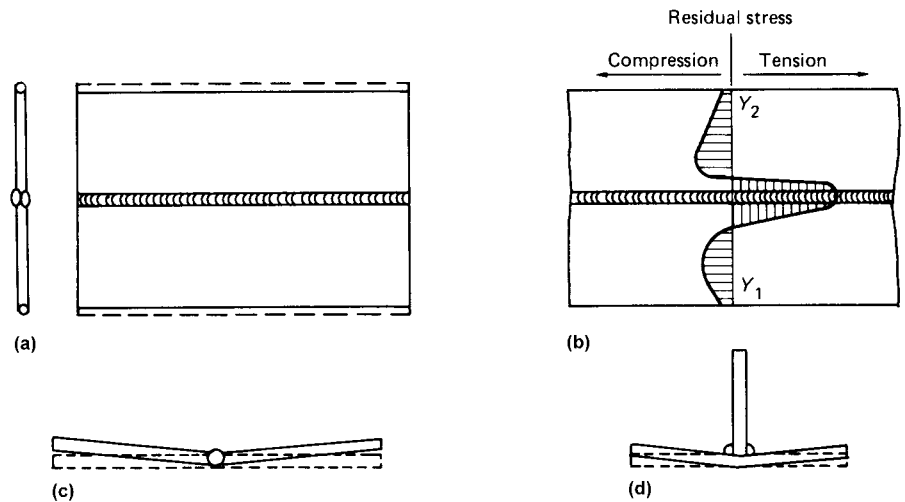


Fig. 6 Dimensional changes occurring in weldments. (a) Transverse shrinkage in a groove weld. (b) Longitudinal shrinkage in a groove weld. Distribution of longitudinal residual stress, σ_x , is also shown. (c) Angular change in a groove weld. (d) Angular change in a fillet weld. Source: Welding Research Council

the joint bends longitudinally unless the weld line is located along the neutral axis of the joint. A common structural element is a stiffened panel structure in which longitudinal and transverse stiffeners are fillet welded to a flat plate. Angular changes that occur in the fillet welds cause out-of-plane distortion in the plate, resulting in a shape which looks like a "hungry horse." Presented subsequently are brief discussions of:

- Transverse shrinkage of groove welds
- Angular distortion of groove welds
- Out-of-plane distortion caused by angular distortion of fillet welds
- Longitudinal distortion of built-up beams
- Buckling distortion

Transverse Shrinkage of Square-Groove Welds. In Fig. 6(a), shrinkage is uniform along the weld; however, transverse shrinkage that occurs in a groove weld, especially in a long groove weld, is not uniform and is typically much more complex. The major factors causing nonuniform transverse shrinkage in a groove weld are rotational distortion and joint restraint. When two separate planes are joined progressively from one end to the other, the plate edges of the unwelded portion of the joint move, causing a rotational distortion. This can be understood from Fig. 2. The rotational distortion is affected by welding conditions and the location of tack welds. In many practical joints, the degree of joint restraint is not uniform along the weld. Because the amount of transverse shrinkage is less when the joint is more severely restrained, nonuniform distribution of the magnitude of restraint results in an uneven distribution of transverse shrinkage.

Mechanisms of Transverse Shrinkage. The most important finding of mathematical analyses of mechanisms of transverse shrinkage is that the major portion of the transverse shrinkage of a groove joint is caused by contraction of the base plate adjacent to the weld. The base plate near the weld expands during welding. When the weld metal solidifies, the expanded base metal must shrink; this shrinkage accounts for the major part of transverse shrinkage. Shrinkage of the weld metal accounts for approximately 10% of the actual total shrinkage. Therefore, most formulas developed for computing transverse shrinkage of a square groove weld are composed of two parts:

- Shrinkage of the adjacent base plate
- Shrinkage of the weld metal

Transverse Shrinkage during Multipass Welding. Welding of a square-groove joint in a thick plate commonly requires a number of passes. Figure 7 shows how transverse shrinkage increases during multipass welding of a groove joint in 19 mm (3/4 in.) thick low-carbon steel plates. Shrinkage is pronounced during the early weld passes but diminishes during later passes because of the resistance to shrinkage that increases as the weld metal is increased. The effects of transverse shrinkage on various factors, including root opening, joint design,

electrode diameter, and degree of restraint, have been studied extensively (Ref 6).

Transverse Shrinkage in a Square-Groove Weld in Aluminum. As stated earlier, the major portion of transverse shrinkage of a square-groove weld is caused by contraction of the base plate adjacent to the weld. Compared with steel, aluminum has a much higher heat conductivity and coefficient of thermal expansion; therefore, transverse shrinkage of an aluminum groove weld is approximately three times greater than that of a steel groove weld of similar dimensions (Ref 6). Because the value of thermal conductivity of aluminum is much greater than that of steel, heat generated by the welding arc dissipates faster in aluminum than in steel, resulting in a broader heat-affected zone (HAZ) (Ref 7).

Angular Distortion of Groove Welds. In a groove weld, when transverse shrinkage is not uniform in the thickness direction, angular distortion often occurs. The angular change of a weld in a thick plate can be minimized by properly selecting the ratio of the size of the weld groove on the front surface to that of the back surface (Ref 6).

Out-of-Plane Distortion Caused by Angular Distortion in Fillet Welds. A stiffened panel composed of a flat plate with longitudinal and transverse stiffeners fillet welded to the plate is widely used for many structures. Angular changes that occur at fillet welds cause out-of-plane distortion of the flat plate (Ref 6). Figure 8 compares values of distortion at the panel center (δ_m) for steel and aluminum welded structures on the basis of the same fillet size (D_f) for selected plate thicknesses. Distortion in aluminum structures is less than in steel structures because the temperature distribution in the thickness direction is more uniform in an aluminum weld than in a steel weld (Ref 7).

Longitudinal Distortion of Built-Up Beams. Figure 9 compares values of longitudinal distortion expressed in terms of the radius of curvature of built-up beams in steel and aluminum. In this instance, aluminum welds distorted less than steel welds, perhaps because the temperature distribution in the z -direction is more uniform in an aluminum weld than in a steel weld.

Buckling Distortion. In any weldment, longitudinal residual stresses are compressive in areas away from the weld, as shown in Fig. 3. When the plate is thin, it may buckle due to these compressive residual stresses. Buckling distortion differs from bending distortion in that the amount of distortion in buckling is much greater. Also, there may be more than one stable deformed shape in buckling distortion. The most effective method for dealing with buckling distortion is prevention by proper selection of plate thickness, length of free span, and welding heat input.

When stiffeners are fillet welded to thin plate, the plate may buckle because of the compressive residual stresses that occur in the plate. Figure 10 shows relationships between distortion at the center of the panel and heat

input for square panels 500 mm (20 in.) long made with plates 4.6 to 10 mm (0.18 to 0.4 in.) thick. For example, in the case of a 500 by 500 mm (20 by 20 in.) panel with a plate 6 mm (0.24 in.) thick, the plate deflection increases suddenly when the heat input exceeds approximately 3700 cal/cm². This indicates that the critical heat input is approximately 3700 cal/cm². When the plate is 4.6 mm (0.18 in.) thick, this critical heat input is only approximately 2000 cal/cm². The following formula can be used to determine the critical heat input, H_{cr} , above which excessive buckling distortion occurs:

$$H_{cr} = \frac{Q}{t^3} \quad b \geq \sim 4 \times 10^5 \text{ cal/cm}^3 \quad (\text{Eq 4})$$

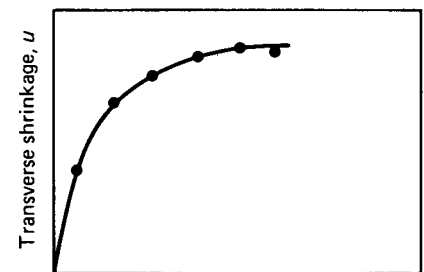
where b is the length of the panel, and t is the plate thickness, both in millimeters. The aforementioned parameter, H_{cr} , is also called the critical heat input index.

Effects of Residual Stresses and Distortion on the Service Behavior of Welded Structures

High tensile residual stresses in areas near the weld can cause premature failures of welded structures under certain conditions. Distortion, especially out-of-plane distortion, and compressive residual stresses in the base plate can reduce the buckling strength of a structural member subjected to compressive loading.

Changes in Residual Stresses

Changes in residual stresses when a groove-welded joint is subjected to tensile loading is shown in Fig. 11. Curve 0 shows the lateral distribution of longitudinal residual stresses in the as-welded condition. When uniform tensile stress, σ_1 , is applied, the stress distribution will be shown by curve 1. The stresses near the weld reach the yield stress, and most of the stress increase occurs in areas away from the weld. When the tensile applied stress increases to σ_2 , the stress distribution will be as shown by curve 2. As the level of



Weight of weld metal per unit weld length, w

Fig. 7 Increase of transverse shrinkage during multipass welding of a groove joint. Specimens were 19 mm (3/4 in.) thick low-carbon steel plates.

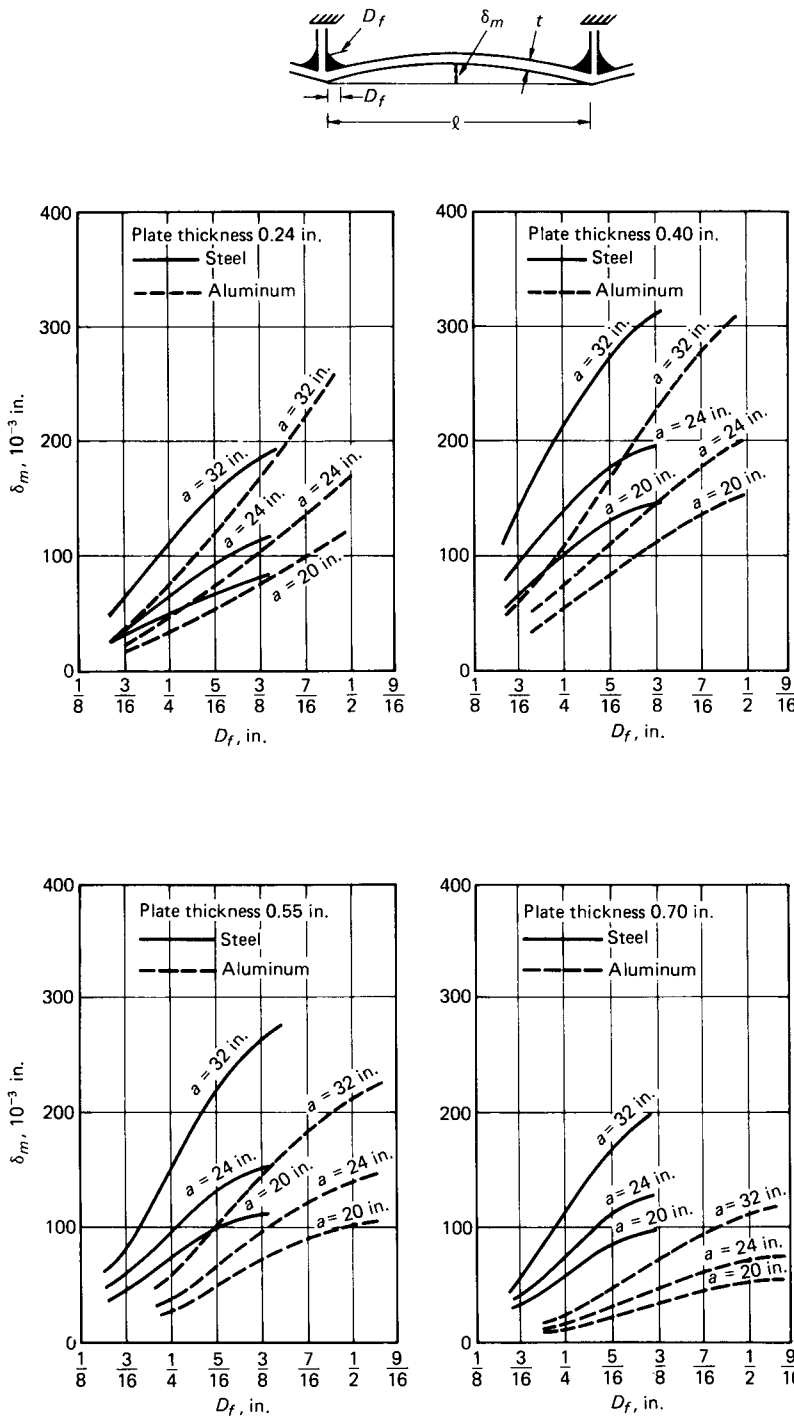


Fig. 8 Out-of-plane distortion (δ_m) as a function of plate thickness (t), span length (l), and the size of the fillet weld (D_f) for steel and aluminum. Relation of l to a in graphs: $a = l$

applied stress increases, the stress distribution across the weld becomes even more (that is, the effect of welding residual stresses on the stress distribution decreases). When the level of applied stress is further increased, general yielding takes place (that is, yielding occurs across the entire cross section). The stress distribution at general yielding is shown by curve 3. Beyond general

yielding, the effect of residual stress on the stress distribution virtually disappears.

The next consideration is the distribution of residual stresses after the tensile loads are released. Curve 1' shows the residual stress that remains after unloading when the tensile stress σ_1 is applied to the weld and then released. Curve 2' shows the residual stress distribution

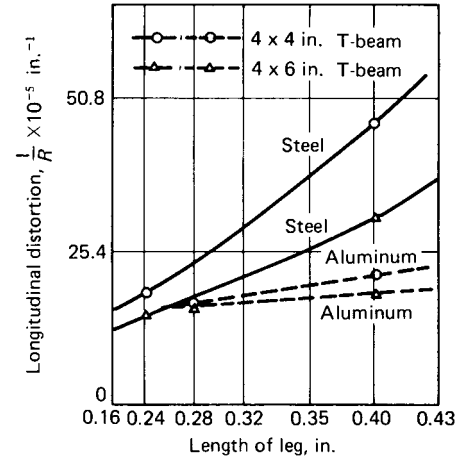
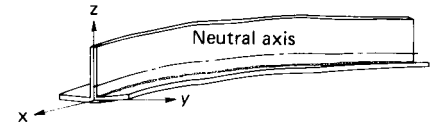


Fig. 9 Relationship between length of leg and curvature of longitudinal deflection in T-section beam. Source: Ref 6, 21

when the tensile stress σ_2 is applied and then released. Compared with the original residual stress distribution, curve 0, residual stress distributions after loading and unloading are less severe. As the level of loading increases, the residual stress distribution after unloading becomes more uniform (that is, the effect of welding residual stress on the overall stress distribution across the welded joint decreases). This phenomenon is called mechanical stress relieving.

Based on this analysis, the effects of residual welding stresses can be summarized as follows:

- The effect of residual welding stresses on the performance of welded structures is significant only for phenomena that occur under low applied stress, such as brittle fracture and SCC.
- As the level of applied stress increases, the effect of residual stresses decreases.
- The effect of residual stress on the performance of welded structures is negligible under applied stresses greater than the yield stress.
- The effect of residual stresses tends to decrease after repeated loading (that is, the reduction of residual stresses will be greater as the level of service load increases).

Effects of Residual Stresses on the Brittle Fracture of Welded Structures

Extensive studies have been conducted on the effects of residual stresses on the

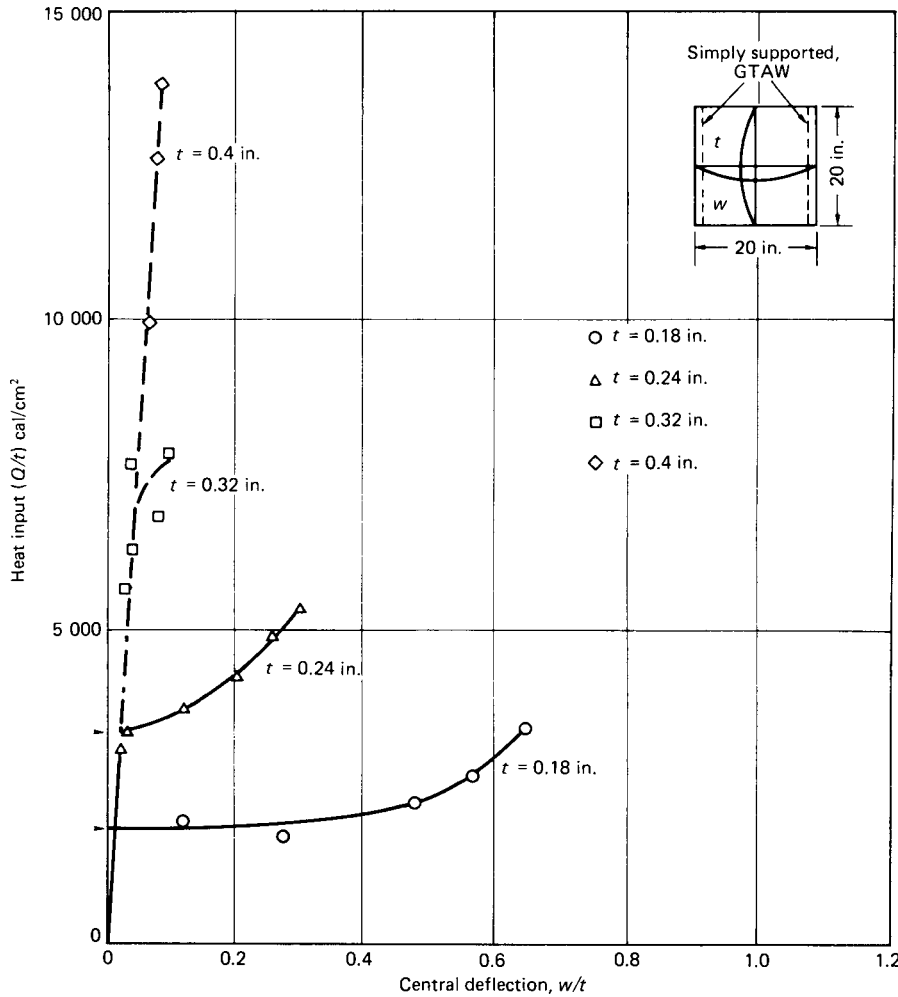


Fig. 10 Plot of heat input versus deflection for 500 × 500 mm (20 × 20 in.) low-carbon steel panels as a function of panel thickness

brittle fracture of welded steel constructions (Ref 6, 19). Investigators have observed differences between data obtained from brittle fractures in ships and other structures and experimental data obtained with notched specimens. Actual structural fractures were observed to occur at stresses far below the yield stress of the material; however, even when experimental test specimens contain very sharp cracks, the nominal applied fracture stress of a notched laboratory specimen is as high as the yield stress. A number of research studies have been carried out on low-applied-stress fractures of weldments in service. Under certain test conditions, complete fracture of a specimen occurred even though the magnitude of applied stress was considerably below the yield stress of the material.

Figure 12 shows the general fracture strength tendencies of welded low-carbon steel specimens at various temperatures and the effects of a sharp notch and residual stress on fracture strength (Ref 6, 23). When a specimen does not contain a sharp notch, fracture occurs

at the ultimate tensile strength of the material at the test temperature, as shown by curve *PQR*. When a specimen contains a sharp notch (but no residual stress), fracture occurs at the stresses shown by curve *PQST*. When the temperature is higher than the fracture transition temperature (T_f), a high-energy (shear-type) fracture occurs at high stress. When the temperature is below T_f , the fracture appearance changes to a low-energy (cleavage) type, and the stress at fracture decreases to near the yield stress.

These various fractures can occur when a notch is located in areas where high residual tensile stresses exist. At temperatures higher than T_f , fracture stress is equal to the ultimate tensile strength (curve *PQR*). Residual stress has no effect on fracture strength. At temperatures lower than T_f , but higher than the crack-arrest temperature (T_a), a crack may initiate at a low stress but will be arrested. At temperatures lower than T_a , one of two phenomena can occur, depending on the stress level at fracture initiation:

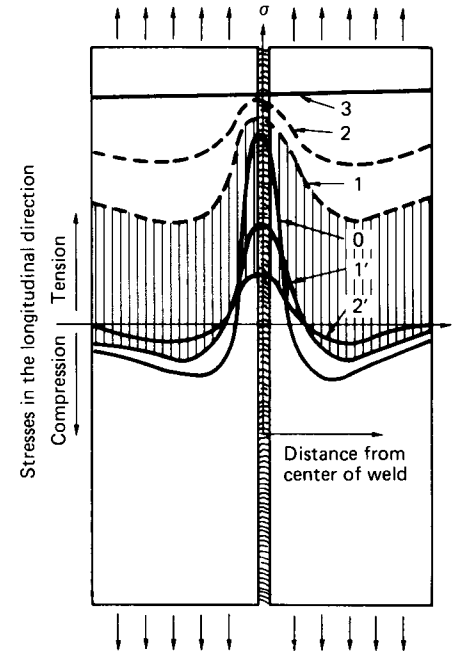


Fig. 11 Schematic showing distribution of stresses in a groove weld when uniform tensile loads are applied and the residual stresses that result after the loads are released. Curve 0, residual-stresses in the as-welded condition; curve 1, stress distribution at $\sigma = \sigma_y$; curve 2, stress distribution at $\sigma = \sigma_u$; curve 3, distribution of stresses at general yielding; curve 1', distribution of residual stress after $\sigma = \sigma_y$ is applied and then released; curve 2', distribution of residual stress after $\sigma = \sigma_u$ is applied and then released

- If the stress is below the critical stress (*VW*), the crack will be arrested after running a short distance; complete fracture will occur at the yield stress (*ST*).
- If the fracture initiation stress is higher than *VW*, complete fracture of the weldment will occur.

Effect of Stress-Relieving Treatments.

Residual stresses in weldments can be reduced by production of plastic deformation in proper amounts and distribution. This deformation can be applied mechanically, thermally, or by a combination of methods. In the most frequently used technique, called a stress-relieving treatment, a weldment is placed in a furnace or surrounded by local heaters for a certain period of time at a specific temperature, depending on the type of material and thickness, and then is cooled slowly. Typically, low-carbon steels are stress relieved at 595 to 650 °C (1100 to 1200 °F). Also, when a load is applied to a weldment, residual stresses are redistributed because of local plastic deformation. Residual stresses are reduced when the load is removed, as discussed previously (see Fig. 11).

In a series of tests, external loads were applied to different stress levels—50, 100, 150, 200, and 230 MPa (7, 15, 20, 30, and 35 ksi)—at 20 °C (68 °F), which was above the critical temperature for crack initiation (T_c).

The load was then reduced. After mechanical stress-relieving treatments, specimens were cooled to temperatures below $-30\text{ }^{\circ}\text{C}$ ($22\text{ }^{\circ}\text{F}$) and tensile loads were applied. For these specimens, fractures occurred only after the pre-loaded stresses were exceeded, even at this low temperature, as shown in Fig. 13(a). In another series of tests, specimens were thermally stress relieved by placing them in a furnace for 1 h at 320, 420, 520, and $620\text{ }^{\circ}\text{C}$ (610, 790, 970, and $1150\text{ }^{\circ}\text{F}$). Fracture stresses for these specimens were higher when welds were heat treated at higher temperatures, indicating that more stresses were relieved by heating at higher temperatures (see Fig. 13).

Effects of Residual Stresses on Fatigue Fracture of Welded Structures

Effects of residual stresses on the fatigue strength of weldments have been studied extensively (Ref 4, 25–27). Fatigue strength increases when a specimen has compressive residual stresses, especially on the specimen surface. Many investigators have reported that fatigue strength (the number of cycles to fracture under a given load, or the endurance limit) increased when the specimens had compressive residual stresses. Conversely, tensile surface residual stresses are expected to reduce fatigue strength. In conducting experiments to determine the effects of residual stresses on the fatigue strength of weldments, the surface conditions of specimens must be carefully considered. Because most fatigue cracks originate at the surface, surface smoothness is very important in obtaining high fatigue strength. For example, removing weld reinforcement, grinding surface irregularities, and other treatments are effective in reducing stress concentrations and increasing fatigue strength. In other words, although a specimen that has compressive residual stresses is expected to have a high fatigue strength, the specimen may yield poor results if it contains a sharp notch that initiates a fatigue crack.

Effects of Environment

Even without external loading, cracking can occur in weldments when the material is embrittled by exposure to certain environments and residual stresses are present. Stress-corrosion cracking is a brittle type of fracture that occurs in a material exposed to a certain environment; it should not be confused with other types of localized attack, such as pitting, galvanic attack, intergranular corrosion, or cavitation (Ref 1, 6, 27). Stress-corrosion cracking has been observed in a number of ferrous and nonferrous alloys exposed to certain environments (Table 2).

High-strength alloys are sensitive to atomic hydrogen. Many cracks in weldments are caused by hydrogen that is introduced

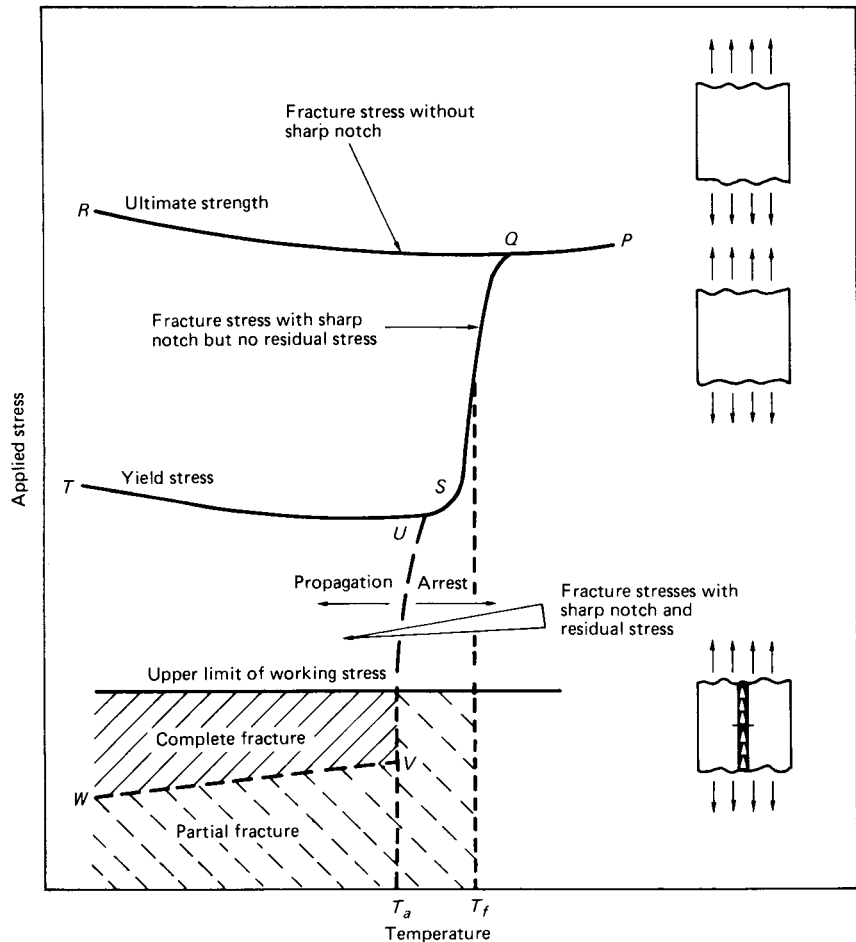


Fig. 12 Effects of sharp notch and residual stress on fracture strength. Source: Ref 22

during the welding process or that is present in the base metal. Hydrogen-induced cracking of weldments in various steels has been studied, and attempts have been made to develop a technique for determining the distribution of residual stresses in a weldment by observing the pattern of hydrogen-induced cracks (Ref 6).

Buckling Under Compressive Loading

Failures caused by instability or buckling sometimes occur in metal structures composed of slender bars or thin plates, when subjected to compressive axial loading, bending, or torsional loading. Residual compressive stresses decrease the buckling strength of a metal structure. In addition, out-of-shape (out-of-plane, out-of-circularity, and so forth) distortion caused by residual stresses also decreases buckling strength. Reference 6 discusses various subjects related to the effects of residual stresses and distortion on the buckling strength of structures of different shapes.

Thermal Treatments of Weldments

Thermal treatments are often necessary to maintain or restore the properties of base metal affected by the heat of welding. Thermal treatment may also affect the properties of the weld metal. The extent of changes in the properties of the base metal, weld metal, and HAZ are determined by several factors, including the soaking temperature, time, cooling rate, and material thickness. Further detailed information is available in Ref 7 and 8.

Preheat is the most common thermal treatment applied to weldments. Proper use of preheat can minimize residual stresses and distortion that would normally occur during welding as a result of lower thermal gradients around the weld. Preheat also has the beneficial effect in steels of reducing the tendency for the formation of a HAZ and weld-metal cracking.

Postweld Thermal Treatments. A properly executed postweld heat treatment results in uniform mechanical properties and reduced residual stresses. The effects of time at

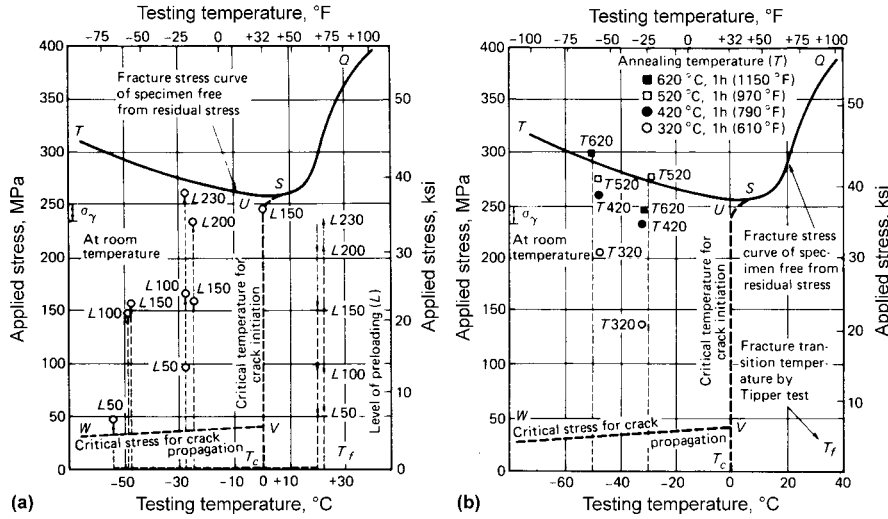


Fig. 13 Effects of stress-relieving treatments on brittle fracture characteristics of welded and notched wide plate specimens. (a) Effect of mechanical stress relieving. (b) Effect of thermal stress relieving. See Fig. 11 for explanations of curves QST and UVW. Source: Ref 24

Table 2 Environments that cause stress-corrosion cracking in selected ferrous and nonferrous alloys

Material	Environment
Aluminum alloys	NaCl-H ₂ O ₂ solutions
	NaCl solutions
	Sea water
Copper alloys	Air, water vapor
	Ammonia vapors and solutions
Gold alloys	Amines
	Water, water vapor
Inconel	FeCl ₃ solutions
	Acetic acid-salt solutions
Lead	Caustic soda solutions
	Lead acetate solutions
Magnesium alloys	NaCl-K ₂ CrO ₄ solutions
	Rural and coastal atmospheres
Monel	Distilled water
	Fused caustic soda
	Hydrofluoric acid
Nickel	Hydrofluosilicic acid
	Fused caustic soda
Ordinary steels	NaOH solutions
	NaOH-Na ₂ SiO ₃ solutions
	Calcium, ammonium, and sodium nitrate solutions
	Mixed acids (H ₂ SO ₄ -HNO ₃)
	HCN solutions
	Acidic H ₂ S solutions
	Sea water
	Molten Na-Pb alloys
	Acid chloride solutions such as MgCl ₂ and BaCl ₂
	NaCl-H ₂ O ₂ solutions
Stainless steels	Sea water
	H ₂ S
	NaOH-H ₂ S solutions
	Red fuming nitric acid
Titanium alloys	Salt solutions

Source: Ref 28

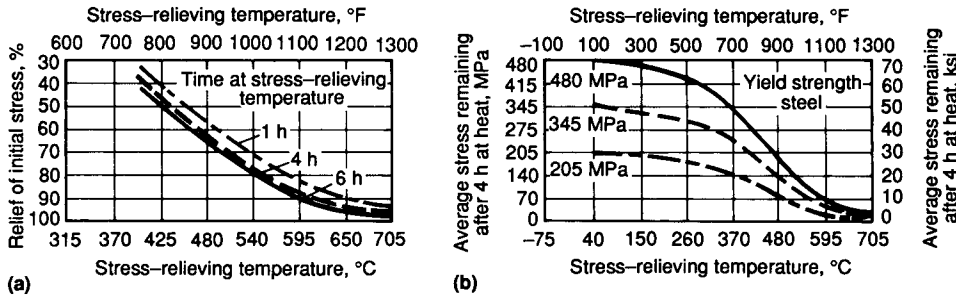


Fig. 14 Effect of temperature and time on stress relief. Time and temperature, 4 h

temperature and the stress-relieving temperature on residual stresses are shown in Fig. 14(a) and (b), respectively (Ref 8). When thick weldments require a postweld machining operation, a stress-relief treatment is usually necessary to achieve normal machining tolerance.

REFERENCES

- Z. Feng, Ed., *Processes and Mechanisms of Welding Residual Stress and Distortion*, Woodhead Publishing Limited 2005.
- J.A. Goldak, *Computational Welding Mechanics*, Springer, 2005.
- D. Radaj, *Heat Effects of Welding: Temperature Field, Residual Stress, Distortion*, Springer-Verlag, 1992
- P.J. Withers and H.K.D.H. Bhadeshia, Overview: Residual Stress, Part 1: Measurements Techniques, *Mater. Sci. Technol.*, Vol 17, April 2001, p 355–365

- P.J. Withers and H.K.D.H. Bhadeshia, Overview: Residual Stress, Part 2: Nature and Origin, *Mater. Sci. Technol.*, Vol 17, April 2001, p 366–374
- K. Masubuchi, *Analysis of Welded Structures—Residual Stresses, Distortion, and Their Consequences*, Pergamon Press, 1980
- K. Masubuchi, Residual Stresses and Distortion, *Welding, Brazing, and Soldering*, Vol 6, *Metals Handbook*, 9th ed., ASM, 1983, p 856–895
- K. Masubuchi, O.W. Blodgett, S. Matsui, E.P. Ross, and C.L. Tsai, Residual Stresses and Distortion, *Welding Technology*, Vol 1, *Welding Handbook*, 8th ed., AWS, 1987
- K. Masubuchi, Research Activities Examine Residual Stresses and Distortion in Welded Structures, *Weld. J.*, Vol 70 (No. 12), 1991, p 41–47
- L. Tall, Residual Stresses in Welded Plates—A Theoretical Study, *Weld. J.*, Vol 43 (No. 1), 1991, p 10s–23s
- H.D. Hibbit and P.V. Marcel, “A Numerical Thermomechanical Model for the

- Welding and Subsequent Loading of a Fabricated Structure,” NSRDC Contract N00014-67-A-019-0006, Tech. Rep. No. 2, Department of the Navy, March 1972
- T. Muraki, J.J. Bryan, and K. Masubuchi, Analysis of Thermal Stresses and Metal Movement During Welding—Part I: Analytical Study; Part II: Comparison of Experimental Data and Analytical Results, *J. Eng. Mater. Technol. (Trans. ASME)*, 1975, p 81–84, 85–91
- E.F. Rybicki et al., A Finite-Element Model for Residual Stresses and Deflection in Girth-Butt Welded Pipes, *J. Pressure Vessel Technol. (Trans. ASME)*, Vol 100, 1978, p 256–262
- P.O. Dexter and D. Pont, “Evaluation of Available Welding Simulation Software,” prepared for EPRI under Research Project C102-3 by Southwest Research Institute, May 1991
- R.G. Treuting, J.J. Lynch, H.B. Wishart, and D.G. Richards, *Residual Stress Measurements*, ASM, 1952
- K. Masubuchi, “Nondestructive Measurement of Residual Stresses in Metals and Metal Structures,” RSIC-410, Redstone Scientific Information Center, Redstone Arsenal, 1965

17. K. Masubuchi, Residual Stresses and Distortion, *Welding Handbook*, Vol 1, 7th ed., AWS, 1976
18. R.R. Hosbons, The Use of Neutron Diffraction to Determine Nondestructively the Residual Strain and Texture in Welds, *Recent Trends in Welding Science and Technology*, ASM International, 1989, p 103–106
19. H. Kihara, M. Watanabe, K. Masubuchi, and K. Satoh, *Researches on Welding Stresses and Shrinkage Distortion in Japan*, Vol 4, 60th Anniversary Series of the Society of Naval Architects of Japan, Tokyo, 1959
20. N.R. Nagaraja Rao, F.R. Esatuar, and K. Tall, Residual Stresses in Welded Shapes, *Weld. J.*, Vol 39 (No. 3), 1964, p 295–306s
21. G. Yamamoto, “Study of Longitudinal Distortion of Welded Beams,” M.S. thesis, Massachusetts Institute of Technology, May 1975
22. H. Kihara and K. Masubuchi, Effect of Residual Stress on Brittle Fracture, *Weld. J.*, Vol 38 (No. 4), 1959, p 159s–168s
23. W.J. Hall, H. Kihara, W. Soete, and A.A. Wells, *Brittle Fracture of Welded Plates*, Prentice-Hall, 1967
24. H. Kihara, K. Masubuchi, K. Iida, and H. Ohba, “Effect of Stress Relieving on Brittle Fracture Strength of Welded Steel Plate,” Document X-218-59, International Institute of Welding, London, 1959 (distributed in U. S. by AWS)
25. W.H. Munse, *Fatigue of Welded Steel Structures*, Welding Research Council, 1964
26. T.R. Gurney, *Fatigue of Welded Structures*, 2nd ed., Cambridge University Press, London, 1979
27. *Residual Stress Effects in Fatigue*, STP 776, ASTM, 1982
28. A.S. Tetelman and A.J. McEvily, Jr., *Fracture of Structural Materials*, John Wiley & Sons, 1967

SELECTED REFERENCES

- O.W. Blodgett, Types and Causes of Distortion in Welded Steel and Corrective Measures, *Weld. J.*, July 1960
- W.R. Osgood, *Residual Stresses in Metals and Metal Construction*, Reinhold Publishing, 1954

Fundamentals of Solid-State Welding

Mechanisms of Bonding for Solid-State Welding Processes . . .	171	Fundamentals of Solid-State Resistance Welding	209
Solid-State Welding Processes	171	Projection Welding	209
Mechanisms of Solid-State Bonding	171	Bonding Mechanisms during Solid-State Projection Welding . . .	210
Extension of the Contacting Surfaces	172	Mechanical/Heat-Transfer Balances	210
Separation of the Contaminated Areas.	172	Effect of System Mechanical Dynamics on Projection Welds . .	211
Realignment of the Grain Structures for Bonding	174	Effect of Electrical Characteristics on Projection Welds	213
Thermal Dissolution of Oxides/Contaminants.	175	Geometric Effects	213
Breakdown of the Interfacial Structure	176	Summary of Analysis	215
Comparison of Solid-State Bonding Processes	176	Conclusions	215
Summary	176		
Fundamentals of Friction Welding	179	Fundamentals of Diffusion Bonding	217
Process Parameters	179	Diffusion Bonding Process.	217
Friction Welding Technology	180	Bonding Surfaces Containing Oxides	218
Metallurgical Parameters	181	Mechanism of Diffusion Bonding	218
		Diffusion Bonding with Interface Aids	220
Fundamentals of Friction Stir Welding	186	Nondestructive Evaluation of Solid-State Welds	222
Thermal Aspects.	186	Nondestructive Evaluation Fundamentals.	222
Material Flow.	188	Examples of NDE of Solid-State Welds	223
Friction	190		
Defects	191	Mechanical Properties of Soft-Interlayer Solid-State Welds . .	230
Strain and Strain Rate in FSW	195	Microstructure of Interlayer Welds	230
Overall Microstructural Feature	196	Tensile Loading of Soft-Interlayer Welds	231
		Shear Loading	235
Fundamentals of Ultrasonic Welding	201	Multiaxial Loading	236
Models	202	Environmentally Induced Failure of Interlayers	236
Results	203		

Mechanisms of Bonding for Solid-State Welding Processes

Jerry E. Gould, Edison Welding Institute

SOLID-STATE WELDING PROCESSES encompass all the methods in which metallic bonding occurs without the presence of resolidified liquid metal. These processes range from cold methods (cold-pressure welding) to hot upset processes (forge processes) to diffusion processes (diffusion bonding). Typically, these processes take advantage of applied strain and/or heat to facilitate joining. Joining is largely the result of intimate intermetallic contact in the absence of local protective films.

This article focuses on the underlying mechanisms of bonding for these processes, with particular emphasis on mechanisms for the forge-type processes, while mechanisms for both the cold and the diffusion processes are considered in other articles. Specific mechanisms for different stages of these processes are identified and quantified using best-available theory. Further, these mechanisms are used to understand the roles of temperature and strain in facilitating bonding with these classes of joining technologies.

There are three categories of bonding mechanisms for the forge welding processes to be considered:

- Contaminant displacement/interatomic bonding
- Dissociation of retained oxides
- Decomposition of the interfacial structure

Modeling of contaminant displacement/interatomic bonding is largely taken from the cold-pressure literature and adapted to the forge welding processes. This modeling suggests that with increasing surface strain, bond strengths can asymptotically approach that of the base metal. The cold-pressure models can be adapted to forge welding processes by considering the role that the developing temperature field has on the distribution of strain. Generally, however, after the surface strain is applied (upset), there are still residual oxide particles trapped in the bondline, and thermal dissolution of these particles can further improve joint performance.

Thermal dissolution modeling has been adapted from the carbide dissolution (in steels) literature, with stability data collected from

the diffusion bonding literature. Resulting models show the importance of the size and distribution of the residual oxide particles, as well as the role of the thermal cycle.

Finally, the third underlying mechanism of forge welding processes is the decomposition of the interfacial structure. Following the forging required to displace contaminants, the bondline can be characterized as a highly dislocated, high-energy structure. Improvements in weld performance can be made by decomposing this structure and reducing the residual bondline strain energy. Decomposition can occur either by recovery or recrystallization, depending on the thermal cycle employed. There is evidence to suggest that decomposition by recrystallization gives better bond performance. Decomposition by recrystallization can be promoted by appropriate thermal cycles as well as appropriate distributions of strain following upsetting.

Solid-State Welding Processes

Solid-state welding processes are the oldest of welding processes, with the official American Welding Society definition of forge welding requiring an anvil and a hammer (Ref 1). Solid-state welding processes have proliferated, particularly over the last several decades, as new power systems have developed. General classifications of these processes include cold-pressure welding, externally heated hot-pressure processes, resistance processes, friction processes, arc-heated processes, and diffusion processes. In this article, mechanisms of bonding are described for those processes using both mechanically applied straining and heating. Detailed examinations of bonding mechanisms of the other processes are available in the literature. These include the cold-pressure welding processes (Ref 2–8) and the diffusion bonding processes (Ref 9–12). Specific variants of the other bonding processes are as follows:

- Externally heated hot-pressure processes
 - a. Forge welding
 - b. Gas pressure welding
 - c. Induction hot-pressure welding

- Resistance processes
 - a. Flash butt welding
 - b. Resistance butt welding
 - c. Projection welding
 - d. Mash seam welding
- Friction processes
 - a. Inertia welding
 - b. Continuous-drive friction welding
 - c. Linear friction welding
 - d. Friction stir welding
- Arc processes
 - a. Percussive welding
 - b. Magnetically impelled arc butt welding

These processes can be thought of as having two generally separable stages. These include a heating stage and an upsetting stage. As such, these welding methods can be generally classified as heat and forge processes. Distinctions between these processes then are largely in how heat and forging are applied. Inevitably, however, heat is first applied. Mechanistically, this heat is used for two purposes. First, heating the workpieces reduces the yield strengths of the base materials and permits forging to occur with high degrees of strain at reduced upsetting forces. Second, if heating is properly applied, upsetting creates high degrees of strain over a very localized area (at the bonding surface). Once the appropriate heating has been accomplished, forging (or upsetting) commences. Upsetting also has two major functions. These include collapsing asperities to create intimate contact, and displacing/dispersing protective oxides and films to facilitate metal-to-metal bonding. Residual heat content/heating is also considered advantageous, to further consolidate/homogenize the joint.

Mechanisms of Solid-State Bonding

To attempt to define the specific mechanisms of bonding for solid-state welding processes, it is first necessary to have an understanding about the microstructural and surface conditions of the workpieces planned for joining. On a microscopic scale, the surfaces for

bonding have been well categorized as irregular and covered with various oxide and contaminant films (Ref 2–12). In addition, there may be microstructural/compositional irregularities, which further complicate the joining process. A typical representation of the prebond surface condition is presented in Fig. 1. This surface is generally characterized as three layers: the base material, a layer of mechanically and/or chemically affected metal, and surface oxides/contaminant films.

There are a number of mechanisms that can proceed to form a bond between such surfaces. The most important of these is that asperities on the surfaces must be collapsed to form intimate contact between materials. In forge welding processes, creation of this intimate contact is done mechanically; that is, local yield stresses are exceeded on the contacting surfaces, and surface deformation is used to create the contact. For diffusion bonding processes (not covered extensively in this article), such surface collapse is done under relatively low forces and relies on creep and surface diffusional mechanisms to consolidate the surfaces.

Once the surfaces have come under intimate contact, bonding still cannot initiate until a number of other criteria are met. The most important of these is how oxide and surface contaminant films can be affected to allow intimate contact of the underlying virgin materials. Generally, there are two mechanisms for this. For forge welding processes, contaminant films can be broken up as a result of mechanical action. In addition, it is also possible to break down metal oxides by dissolution into the matrix. This is a mechanism particularly important in diffusion bonding (Ref 13) but also plays a role in other thermally assisted forge processes.

Even when base materials are in intimate contact, there are additional changes that must occur to facilitate an adequate joint. First, crystallographic matching across the boundary must occur (Ref 14). Obviously, most forge welding applications are between parent materials with randomly oriented grain structures, and so, this bond surface must take on the characteristic of a series of high-angle grain boundaries. Generation of this dislocation structure can occur mechanically (Ref 6) thermally (Ref 9, 10), or by a combination of the two. At this stage of the process, intimate solid-state bonding has undoubtedly occurred; however, the localized high-angle grain-boundary structure is

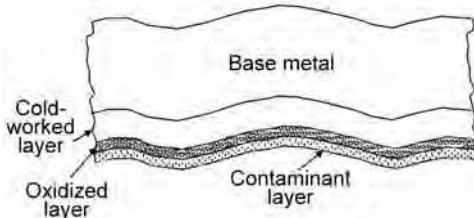


Fig. 1 Schematic representation of workpiece surface conditions in the prebonded state

relatively unstable and is unlikely to yield an adequate joint. As a result, the last stage of the process is to relieve these local bondline stresses, typically with some sort of thermal assist. Depending on the treatment, this local concentration of strain energy can result in a final bond structure ranging from local recovery to recrystallization (Ref 15).

As mentioned, these mechanisms collectively permit solid-state bonding between metallic materials, although not all mechanisms are used by all solid-state welding processes. Generally, these mechanisms, particularly as they operate within the group of forge welding processes, can be classified in three general areas. These include surface deformation mechanisms, contaminant dissolution mechanisms, and interfacial structure homogenization mechanisms. These are described in detail, including their direct relationship to the forge welding processes, in subsequent sections.

Contaminant Displacement/Interatomic Bonding. As briefly described previously, surface deformation mechanisms have two functions: to collapse surface asperities and to displace surface contaminants. It is of interest that the best information on the role of surface strain and its effect on the extent of solid-state bonding is available in the cold-pressure welding literature (Ref 2–8). Several authors have examined the roles of surface condition, mechanisms of interfacial breakdown, and degrees of subsequent bonding for cold-pressure welding applications. Collectively, initial bonding, related to surface straining, appears to progress through the following stages.

Extension of the Contacting Surfaces

For any bonding to occur, it is essential that contaminating oxides/films be disrupted. This is, of course, accomplished by application of contact surface strains. It is equally important, however, that surface oxides/films be in a condition in which they can be readily broken up when the surface strain is applied. Table 1 lists hardnesses for some common oxides. Of interest here is the difference between the hardnesses of the aluminum or copper oxides. Figure 2 shows some fractographs of bond surfaces for cold-pressure welds below critical bonding deformation for aluminum, copper, and silver. It is clear from these results that the aluminum oxide fails in a brittle manner, while the copper oxide fails in a shear manner.

Table 1 Representative hardnesses of some metal oxides at room temperature

Metal	Hardness, HV	Oxide	Hardness, HV
Al	15	Al ₂ O ₃	1800
Cu	40	Cu ₂ O	160
Ag	26	Ag ₂ O	135
Au	20

Source: Ref 6, Table 1

A more general plot showing the relationship between oxide/metal hardness ratio and required deformation for bonding is presented in Fig. 3. One method of improving the characteristics of surface film fracture is to locally cold work the base metal. It has been demonstrated that cold working the surface using scratch brushing both minimizes the extent of contaminant films and creates a local layer of heavily cold-worked material, which, on straining, can fracture and carry more ductile oxide films (Ref 6).

For most conventional forge welding processes, extension of the contacting surfaces is done with a combination of heat and force. For this stage of the process, local strain is the most important factor. However, how that strain is distributed is a strong function of how the thermal field is applied. Figure 4 shows some results from numerical simulations of the flash-butt welding process (Ref 16). This plot shows how contact surface strain is affected both by the amount of upset used and the level of flashing acceleration employed. Flashing acceleration directly controls the heat distribution in the workpiece, with higher flashing accelerations indicating steeper, higher thermal gradients (Ref 17, 18). For conductivity materials, particularly aluminum and copper, strain location provided simply by the thermal gradient is difficult. In such cases, pinch-off dies are recommended (Ref 19). Pinch-off dies simply use the constraint of the die (rather than the thermal profile) to create localization of forging. The function of pinch-off dies is shown schematically in Fig. 5.

Separation of the Contaminated Areas

It is established that the onset of bonding occurs with applied surface strain as surface contaminants are separated and virgin base materials are allowed to contact. Considerable work has been done, again largely in the cold-pressure welding area, attempting to quantify the separation of these contaminants and the resulting bond quality. In examining the role of contaminated surfaces, all workers agree that a critical strain must first be achieved that this surface ruptures (Ref 2–8). There are discrepancies, however, on how this rupture occurs. Mohamed and Washburn (Ref 6) suggest that separations of the two contaminated surfaces are unrelated, while Wright et al. (Ref 7) and later Bay (Ref 8) suggest that surface contaminants impinge on either side of the joining and therefore separate as pairs. Local bonding is then accomplished by extrusion of virgin material into the spaces between the separated contaminated surfaces. Each set of authors has developed models based on their assumption of interfacial breakdown. In each case, the underlying assumption is that the strength of the joint is a direct function of the fraction of

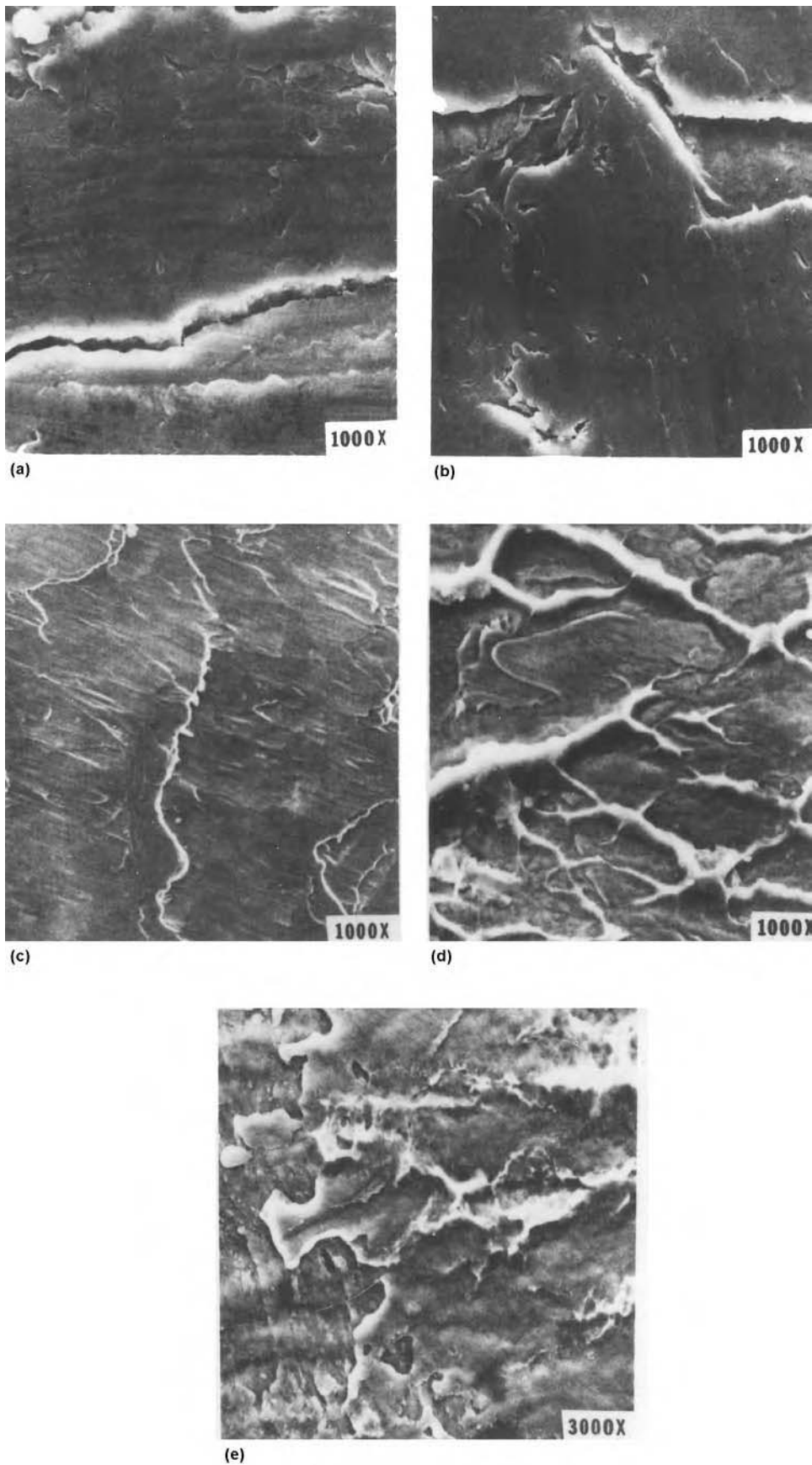


Fig. 2 Fractographs showing the faying surfaces of cold-pressure-welded aluminum, copper, and silver at subbonding strains. (a) Aluminum, 3% deformation. (b) Aluminum, 6% deformation. (c) Copper, 5% deformation. (d) Copper, 23% deformation. (e) Silver, 25% deformation. Source: Ref 6, Fig. 1

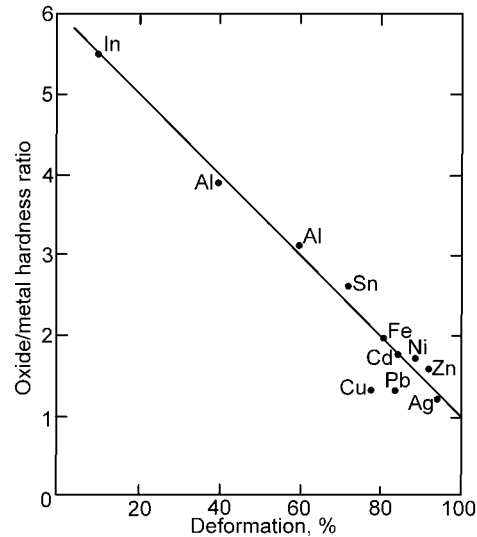


Fig. 3 Relationship between oxide/metal hardness ratio and the critical deformation for bonding during cold-pressure welding. Source: Ref 3

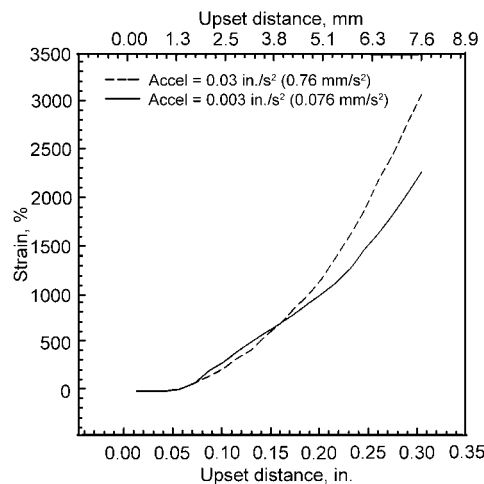


Fig. 4 Thermomechanical modeling results showing the relationship between flashing acceleration, upset distance, and contact surface strain for flash-butt welding mild steel

the bond area converted by actual base material/base material bonds.

The simplest of these models is that developed by Mohamed and Washburn (Ref 6). This model assumes a completely brittle contamination layer and no coordination of contaminants on either side of the bondline. The physical representation of this model is presented in Fig. 6. The resulting equation for strength is:

$$f = C \left(\frac{R}{R + 1} \right)^2 \quad (\text{Eq 1})$$

where f is the ratio of the joint strength to the parent material strength, R is the surface strain, and C is a constant to incorporate contaminant mismatches and contaminant hardness.

The model proposed by Wright et al. is slightly more complex. This model was generated for roll-bonding applications, so largely plain-strain conditions exist. The physical representation of this model is presented in Fig. 7. This model assumes matchup of contaminants across the bondline and attempts to account for a degree of prebonding deformation. The resulting equation for joint strength is:

$$f = C \left[1 - \frac{(1 - R_f)^2}{(1 - R_t)^2} \right] \quad (\text{Eq 2})$$

In this case, C is considered an empirical hardening factor, R_t is the threshold deformation for bonding, and R_f is the total deformation of the process. Equations 1 and 2 are similar, asymptotically approaching a maximum bond strength as the total deformation (R or R_f) approaches 1. The most complex analysis is provided by Bay. This model includes the effects of contaminant films and subsurface hardened layers and is diagramed in Fig. 8. The resulting equation for joint strength is:

$$f = (1 - \beta)Y \frac{p - p_e}{\sigma_o} + \beta \frac{Y - Y'}{1 - Y'} \frac{p}{\sigma_o} \quad (\text{Eq 3})$$

where f is now the ratio of weld tensile strength to base material tensile strength, β is the fraction area covered by contaminant films, p is the applied pressure, p_e is the threshold pressure

for bonding (extrusion pressure), and σ_o is the yield strength of the base material. Y and Y' are the surface exposure and threshold surface exposure, where the surface exposure is defined by:

$$Y = 1 - \frac{1}{1 + X} \quad (\text{Eq 4})$$

where X is the degree of expansion of the contact area.

These models, of course, show a greater degree of complexity, because a greater number of bonding factors are included. It is important to recall, however, that these models have been developed for cold-pressure processes, and these complexities may be more or less relevant for conventional forge welding processes. One factor of note is the extrusion pressure (described as p_e in Eq 3). This factor is included either directly or indirectly in each of these models. However, for conventional forge welding processes, extrusion pressures will fall dramatically with temperature and may be less of a factor. Also to be questioned is the role of subsurface cold-worked layers, which, in conventional forge welding processes, will probably anneal substantially before any macroscopic deformation occurs.

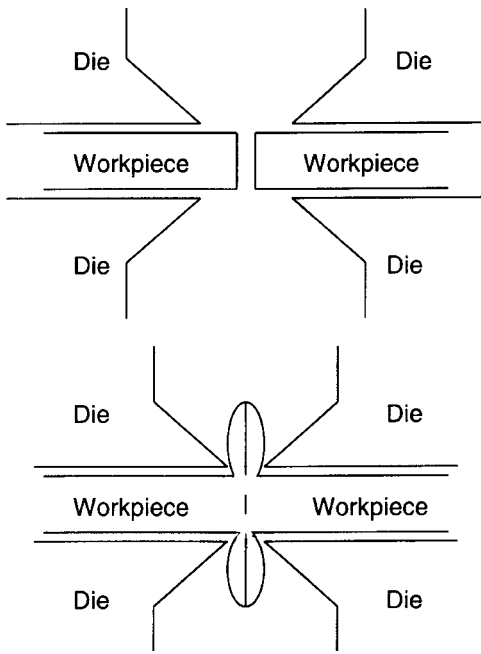


Fig. 5 Use of pinch-off dies in upset welding processes to localize strain

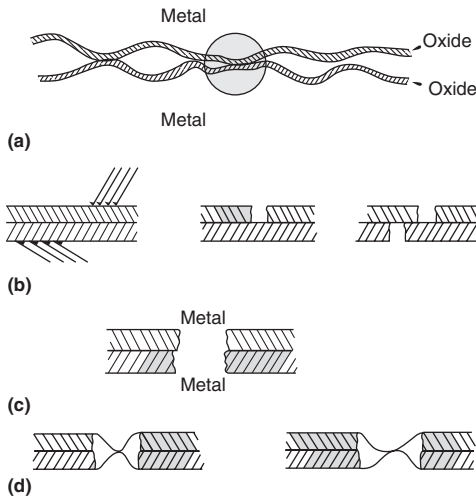


Fig. 6 Schematic illustration of interfacial breakup as proposed in the Mohamed and Washburn model. (a) Original interface. (b) Fracture of brittle oxide film. (c) First requirement for welding: formation of overlapped oxide-free metallic areas. (d) Second requirement for welding: extrusion of metal through the gaps created in the oxide and some relative shear displacement at the points of contact of oxide-free metal. Source: Ref 6

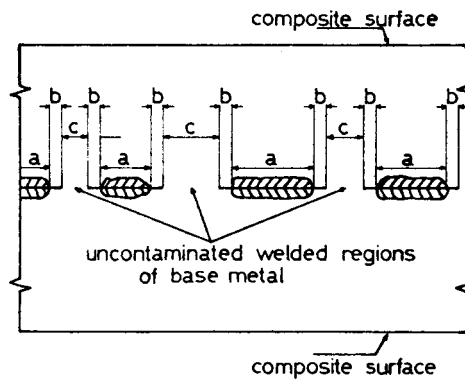


Fig. 7 Schematic illustration of interfacial breakup as proposed by Wright et al. Source: Ref 7

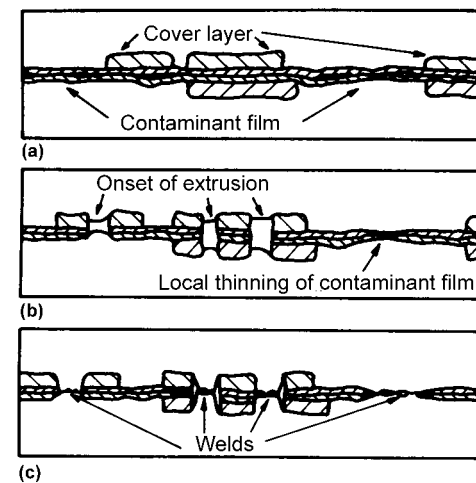


Fig. 8 Schematic illustration of interfacial breakup as proposed by Bay. (a) Interfacial surfaces. (b) Onset of extrusion and thinning of contaminant film. (c) Welds. Source: Ref 8

Realignment of the Grain Structures for Bonding

There is considerable evidence that crystallographic matchup across the bondline is also important at this stage of bonding (Ref 3, 6, 14). Detailed work (Ref 3) suggests that contact between similarly oriented close-packed or near-close-packed planes most readily bonds. For aluminum, (111) to (111) and (110) to (110) were found to bond readily, while (111) to (100) were found difficult to bond. However, most structural materials are polycrystalline, so such ideal crystallographic matchups are relatively uncommon. To accomplish bonding requires some localized crystallographic reorientation. The model here is the one of a series of grain boundaries. Grain boundaries can be thought of as a complex dislocation pileup, accommodating the misorientation between grains over a very small distance. The types of macroscopic surface strains and local intercontaminant extrusion described here are ideal sources for dislocation generation and undoubtedly contribute to the generation of this bondline structure. An example of this dislocated structure is presented in Fig. 9. This particular example is a resistance butt weld on steel, showing evidence of a residual bondline. This region is characterized by relatively high internal strain energy and may be a quality concern. Reactions of this region to the applied thermal fields typical of the forge welding processes are described in a subsequent section.

Thermal Dissolution of Oxides/Contaminants

The preceding discussion indicates the degrees to which bondline strain can be used to create a solid-state bond. However, implicit in that discussion and related modeling were two related facts: some level of contamination was always present in the joint area, and joint strengths could only asymptotically approach parent material strengths. The relationship here is straightforward. As long as contaminants exist in the joint, they reduce effective bond area and act as initiation sites for subsequent mechanical failures (Ref 20).

To achieve improved joint properties, particularly in industrial applications, some further reduction in the residual bondline contaminant content is advantageous. Fortunately, for many metallic systems, oxides are soluble in the matrix at elevated temperatures. The degree of solubility of a specific oxide in M_xO_y in a matrix of metal "A" at equilibrium can be defined by the solubility product:

$$K_{eq} = Z(C_M)^x(C_O)^y \quad (\text{Eq 5})$$

where K_{eq} is the equilibrium solubility product, C_M and C_O are the compositions of the metal "M" and oxygen in the matrix metal "A," and Z is a proportionality constant relevant to the activity coefficient. If the oxide is of the matrix metal, this expression reduces to:

$$K_{eq} = Z(C_O)^y \quad (\text{Eq 6})$$

with Z a different proportionality constant. This suggests that the solubility product is similarly a power function of the maximum soluble oxygen content in the base material. For oxides of the base materials, Eq 6 suggests that the solubility product can be estimated from the maximum solubility of oxygen in the matrix as taken from the appropriate phase diagram. In addition, the shape of the oxygen solvus provides some indication of the temperature dependence for the solubility product. In a similar manner, Eq 5 suggests that

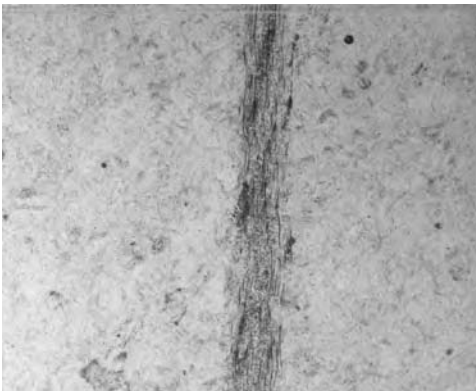


Fig. 9 Resistance butt weld on mild steel indicating a highly deformed zone down the bondline

the solubility product for non-base-material metal oxides relative to the base metal (as well as the temperature dependence) can also be estimated from the phase diagram. Here, the solubility product is estimated from the maximum solubilities of the secondary metal and oxygen in the base material.

If Raoultian behavior of oxygen in the base material is assumed, the proportionality constants in Eq 5 and 6 become equal to 1. Then, knowing the stoichiometry of the oxide present and using the appropriate phase diagram, approximate solubility products for some different metals can be done directly. Table 2 lists approximate solubility products for some standard engineering materials with their most common oxide. These solubility products are calculated for approximately bonding temperatures estimated for forge welding processes ($0.9 T_m$). Materials shown include aluminum, iron, and titanium. These solubility products cover approximately 30 orders of magnitude, indicating, on one extreme, the difficulty of dissolving aluminum oxide into an aluminum matrix as well as the relative ease with which titanium can dissolve its own oxide.

Similar calculations can be done for nonmatrix metal oxides. The approximately solubility product for Al_2O_3 on iron is calculated and compared to the similar calculation for the oxide of iron (Fe_2O_3) in Table 3. These calculations were done at the approximate bonding temperature for forge welding iron. In this case, the stoichiometry for the two oxides is similar ($x = 2, y = 3$), so the difference between the two solubility products is directly related to the solubility of the aluminum in the steel. This fact appears to account for the relatively low solubility of Al_2O_3 in iron.

Such solubility products and diffusivities of oxygen in the matrix have been used as a basis

Table 2 Estimated solubility products for oxides present on some common engineering materials assuming Raoultian behavior of oxygen in solution in the parent material

Metal	Oxide	K_{eq}
Al	Al_2O_3	3×10^{-29}
Fe	Fe_2O_3	1×10^{-15}
Ti	TiO_2	1×10^{-1}

Calculations are done for temperatures approximately representing bonding temperatures for forge welding processes ($0.9 T_m$) (internally generated).

Table 3 Comparison of solubility products for Al_2O_3 and Fe_2O_3 in an iron matrix at the appropriate bonding temperature for forge welding iron ($0.9 T_m$)

Base material	Oxide	K_{eq}
Fe	Al_2O_3	1.8×10^{-19}
Fe	Fe_2O_3	1.0×10^{-15}

Internally generated

for modeling oxide dissolution during diffusion bonding (Ref 21). However, this analysis was largely based on continuous oxide films and focused on the maximum thickness of these films for relatively long (diffusion bonding) heating cycles. Such an analysis does not take into account the breakup of the oxide film into discrete particles caused by the applied surface strain during forge welding processes, or the relatively short heating times.

A better analysis can parallel that done by Ashby and Easterling for the dissolution of carbide particles during welding (Ref 22). That analysis examines the dissolution of discrete particles. The approach used attempts to estimate the roles of both the solubility of the carbide constituents into the matrix and diffusion of these constituents away from the decomposing carbide. The approach is based on the assumption that distinct spherical particles can be dissociated completely into a volume of matrix with radius l . Further, the particle will dissociate into this volume at a locus of times and temperatures defined by:

$$l = (D^*t^*)^{1/2} \quad (\text{Eq 7})$$

where D^* and t^* are the combinations of the diffusivities (D , a function of temperature, defined at T^*) and times (t^*) over which the particle can be completely dissolved into the volume matrix defined by l . Combining this approach for examining the role of diffusion can be combined with an expression for the temperature dependence of the solubility product of the particle, to examine particle dissolution behavior. The discussions on solubility products for oxides detailed previously can be used to adapt these equations for oxide particle dissolution. The resulting governing equations include for base-metal oxide particles:

$$T_s = \frac{B}{A - \ln \left[\frac{(O)^y}{f} \right]} \quad (\text{Eq 8})$$

and for non-base-metal oxides:

$$T_s = \frac{B}{A - \ln \left[\frac{(M)^x(O)^y}{f} \right]} \quad (\text{Eq 9})$$

where T_s is the dissolution temperature, A and B are the temperature coefficients for the appropriate solubility product, and f is the matrix volume fraction affected by the decaying oxide, defined by:

$$f = \frac{1}{1 + \left[\frac{t}{\tau} \exp - \frac{Q_2}{R} \left(\frac{1}{T^*} - \frac{1}{T_s} \right) \right]^{3/2}} \quad (\text{Eq 10})$$

In this expression, Q_2 is the activation energy associated with the appropriate diffusivity (oxygen or metal + oxygen), and R is the ideal gas constant. With some estimate of t^* and T^* , Eq 10 combined with either Eq 8 or 9

(as appropriate) defines an implicit relationship between the time/temperature profile for the process and the degree of oxide dissolution.

In these expressions, t^* and T^* are direct functions of the oxide particle size and distribution. Values for these can presumably be estimated from the original distribution of oxides on the bonding surfaces and estimations of surface strain, as described previously.

From these equations, some qualitative estimate can be made of the role of both the degree of forging and time-temperature profile on bond quality. With increasing strain applied to the contacting surface, both particle size and density will inevitably fall. These factors reduce amounts of oxygen (and potentially second metal) that must be diffused and increase the kinetics of oxide dissolution. Extended heating (welding) times are important in that, again, diffusion is promoted. Increasing welding temperatures are not only advantageous for increasing rates of diffusion but also for increasing the solubility product for the dissolution reaction.

Breakdown of the Interfacial Structure

A third mechanism of bonding results from the decomposition of any interfacial structure. As described previously, straining of the bond surface, extrusion of material around residual oxide particles, and matching crystallographic structures across the bondline result in a highly dislocated bondline structure. This highly dislocated structure is of relatively high energy as well as planar. An example of such a highly dislocated bond is shown in Fig. 10. This structure obviously develops during straining the contact surface. However, the presence of various particulates from the contaminated bond surfaces may also stabilize this structure.

Decomposition of this structure is largely a thermally assisted process. To develop this highly dislocated structure, considerable energy for deformation is required. Much of this energy is stored in the interfacial structure itself. With varying degrees of activation

energy, this structure can quickly decompose to a lower energy variant. Parks (Ref 15) has done considerable work to understand the breakdown of contacting interfaces. In his work, he suggests two regimes for breakdown of this interfacial structure. These parallel the concepts of recovery and recrystallization. Recovery of the interface implies a realignment of the dislocated structure to reduce the overall strain energy of the system. This is typically done at relatively low temperatures, permitting only local movement of the dislocations that make up the boundary structure (Ref 23–25). During recovery, these dislocations realign themselves into dislocation cells. An example of such cells is shown in Fig. 11 (Ref 26). Parks found that very little effective bonding occurred if interfacial decomposition was limited to recovery. Rather, substantial bond strengths were found if higher annealing temperatures were used, resulting in bondline recrystallization. This is shown in Fig. 12. Recrystallization is essentially the nucleation and growth of new grains. Provided activation energies are high enough, this mechanism of interfacial decomposition shows the greatest reduction in bondline energy and is suggested by Parks as essential for forming high-integrity bonds.

During welding, residual stored energy (as local deformation) can play a role in the kinetics of recovery and/or recrystallization. Parks has demonstrated that actual bonding temperatures can be reduced depending on the degree of deformation in the material. Required recrystallization temperatures as a function of the degree of deformation for a range of materials are shown in Fig. 13.

Obviously, the extent to which this interfacial structure can decompose is a function of both the amount of strain applied and the temperature cycle experienced. Increasing amounts of strain (upset) obviously increase the amount of work in the material and promote subsequent breakdown of the interfacial structure. Time at temperature, however, provides the activation energy to allow this aspect of the bonding process to proceed. It is interesting from this discussion that greater levels of upset may permit bonding at shorter times and lower temperatures. However, in practice, extended times

and temperatures are almost always advantageous, permitting maximum homogenization of the joint microstructure.

Comparison of Solid-State Bonding Processes

The above discussion suggests that, in summary, solid state processes employ one or more of three mechanisms to accomplish bonding. These include disruption of contacting interfaces for nascent metal contact, diffusion related dissociation of residual contaminants, and breakdown of the remaining interfacial structure. These fundamental mechanisms, are driven by process mechanisms, specifically temperature, time, and deformation. Obviously, temperature and time both drive diffusion reactions (promoting both contaminant dissolution and breakdown of the interfacial structure), while deformation promotes interfacial disruption. This approach was used by Fenn (Ref 27). In the developed construct, Fenn created a ternary diagram with axes of temperature, time, and deformation. For this diagram, the axes are represented as conceptual fractional values. Here, temperature can be considered as the fraction of the absolute melting temperature, time as a dimensionless fraction, and deformation as the relative collapse of the two components. On this diagram, Fenn then placed hypothetical ranges for a number of solid state processes. The resulting diagram is shown in Fig. 14. Limits of the diagram include diffusion bonding (all time and temperature) and, cold welding (all deformation). Of note, most conventional solid state welding processes (flash welding, friction welding, upset (or forge) welding) fall toward the middle of the diagram, utilizing components of all the mechanisms described above. Of note, the diagram is not material specific. As a result, how individual processes fall on this diagram will be strongly affected by the substrate welded, shifting to match the specific combination of mechanisms most advantageous to individual material systems.

Summary

This article provides a systematic look at mechanisms of bond formation during solid-state (forge) welding processes. Discussions have been limited to those processes that can be characterized as having two stages: heating and forging. Explicitly excluded were those processes that do not use heating (cold-pressure welding processes) or forging (diffusion bonding processes). For the forge welding processes, three distinct mechanisms of bonding have been discussed. These include contaminant displacement/interatomic bonding, dissociation of retained oxides, and decomposition of the interfacial structure.

Contaminant Displacement/Interatomic Bonding. This mechanism of bonding relates to displacement of contaminants by local strain at the contacting surface. Displacement of these



Fig. 10 Interfacial structure on resistance-projection-welded mild steel

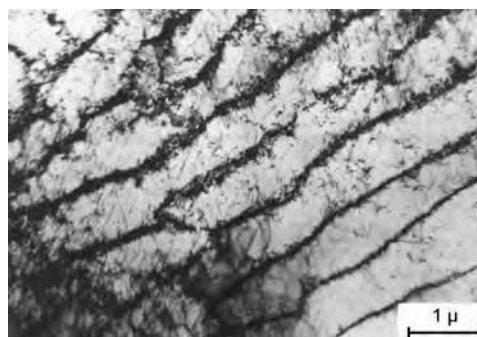


Fig. 11 Dislocation cells in a dynamically recovered iron microstructure. Source: Ref 26

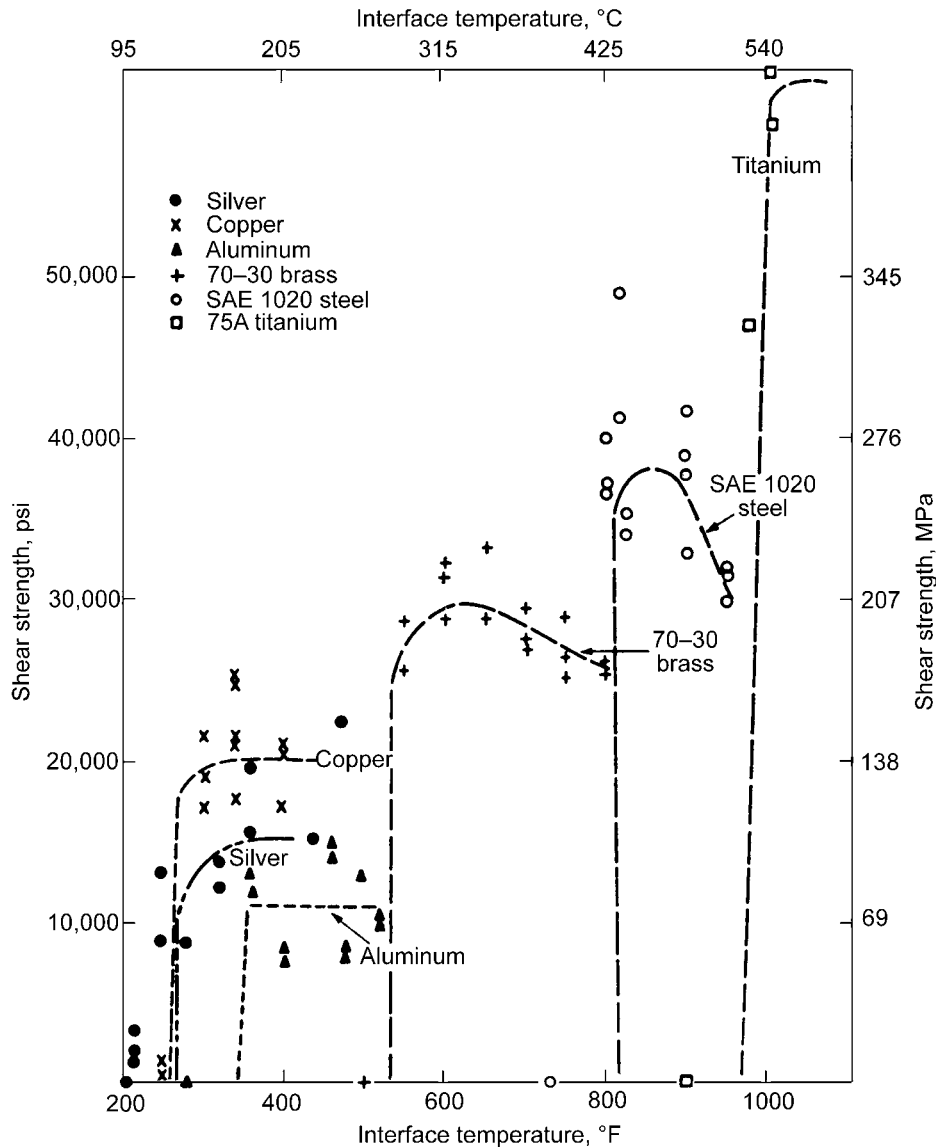


Fig. 12 Weld strengths as a function of annealing temperature for a range of materials. Source: Ref 15

contaminants allows exposure of clean surfaces for direct interatomic bonding. The basics for modeling this mechanism were largely taken from the cold-pressure literature. Although several models are available with increasing levels of complexity, all predict that bond strengths asymptotically approach that of the base metal with increasing surface strain. For the forge welding processes, the developed temperature distribution also plays a role, increasing metal plasticity, assisting in localizing strain at the bondline, and reducing required upset loads.

Thermal Dissolution of Oxides/Contaminants. The applied surface strains described previously permit considerable bonding but leave a residue of oxide/contaminant particles dispersed over the bond surface. As a mechanism for further facilitating bonding, many of

these particles can be thermally dissolved in the matrix. The relative solubility of specific types of particles can be assessed directly by examining solubility products between the constituent elements of the particle compared with solution in the base material. For base-material oxides, this solubility product is only a function of the solubility limit of oxygen in the matrix. This analysis was used to indicate relative stability of a range of base-metal oxides. This examination was extended, using previous work done for dissolution of carbide particles in steel, to examine the kinetics of dissolution. This analysis incorporates both solubility product and diffusivity factors. The results indicate the effects of residual oxide particle size as well as the role of the severity of the thermal cycle for dissolving these oxide particles.

Breakdown of the Interfacial Structure.

The side result of the first two mechanisms is a highly dislocated interfacial bond structure. This structure results largely from the application of bondline strain but can be stabilized by the presence of discrete oxide particles. This structure is of relatively high energy and can be a detriment to weld quality. Decomposition of this structure does improve bond quality. The mechanism of decomposition, however, depends on the thermal cycle employed. For relatively short or low-temperature cycles, the structure may only recover, resulting in a series of dislocation cells. At higher temperatures and longer times, recrystallization of the metal at the bondline can also occur. Some results suggest that recrystallization of the bondline structure results in better weld properties. Increasing stored energy at the bondline (caused by higher levels of strain) also appears to aid the kinetics of recrystallization and improve weld quality.

REFERENCES

1. "Standard Welding Terms and Definitions," ANSI/AWS A3.0-94, American Welding Society, Miami, FL, 1994
2. D.R. Miller and G.W. Rowe, Fundamentals of Solid Phase Welding, *Metall. Rev.*, Vol 28 (No. 7), 1962, p 433-480
3. R.F. Tylecote, Investigations on Pressure Welding, *Br. Weld. J.*, Vol 1 (No. 3), 1954, p 117-135
4. R.F. Tylecote, D. Howd, and J.E. Furmidge, The Influence of Surface Films on the Pressure Welding of Metals, *Br. Weld. J.*, Vol 5 (No. 1), 1958, p 21-38
5. L.R. Vaidyanath, M.G. Nicholas, and D.R. Milner, Pressure Welding by Rolling, *Br. Weld. J.*, Vol 6, 1959, p 13-38
6. H.A. Mohamed and J. Washburn, Mechanisms of Solid State Pressure Welding, *Weld. J. Res. Suppl.*, Vol 54 (No. 9), 1975, p 302s-310s
7. P.K. Wright, D.A. Snow, and C.K. Tay, Interfacial Conditions and Bond Strength in Cold Pressure Welding by Rolling, *Metals Technol.*, Vol 1, 1978, p 24-31
8. N. Bay, Mechanisms Producing Metallic Bonds in Cold Welding, *Weld. J. Res. Suppl.*, Vol 62 (No. 5), 1983, p 137s-142s
9. K. Inoue and Y. Takashi, Recent Void Shrinkage Models and Their Applicability to Diffusion Bonding, *Mater. Sci. Technol.*, Vol 8 (No. 11), 1992, p 953-964
10. Y. Takashi, K. Inoue, and K. Nishiguchi, Identifications of Void Shrinkage Mechanisms, *Acta Metall. Mater.*, Vol 41 (No. 11), 1993, p 3077-3084
11. T. Enjo, K. Ikeuchi, and N. Akikawa, Effect of Oxide Film on the Early Process of Diffusion Welding, *Trans. JWRI*, Vol 10 (No. 2), 1981, p 45-53
12. T. Enjo, K. Ikeuchi, and N. Akikawa, Effect of the Roughness of the Faying Surface on the Early Process of Diffusion

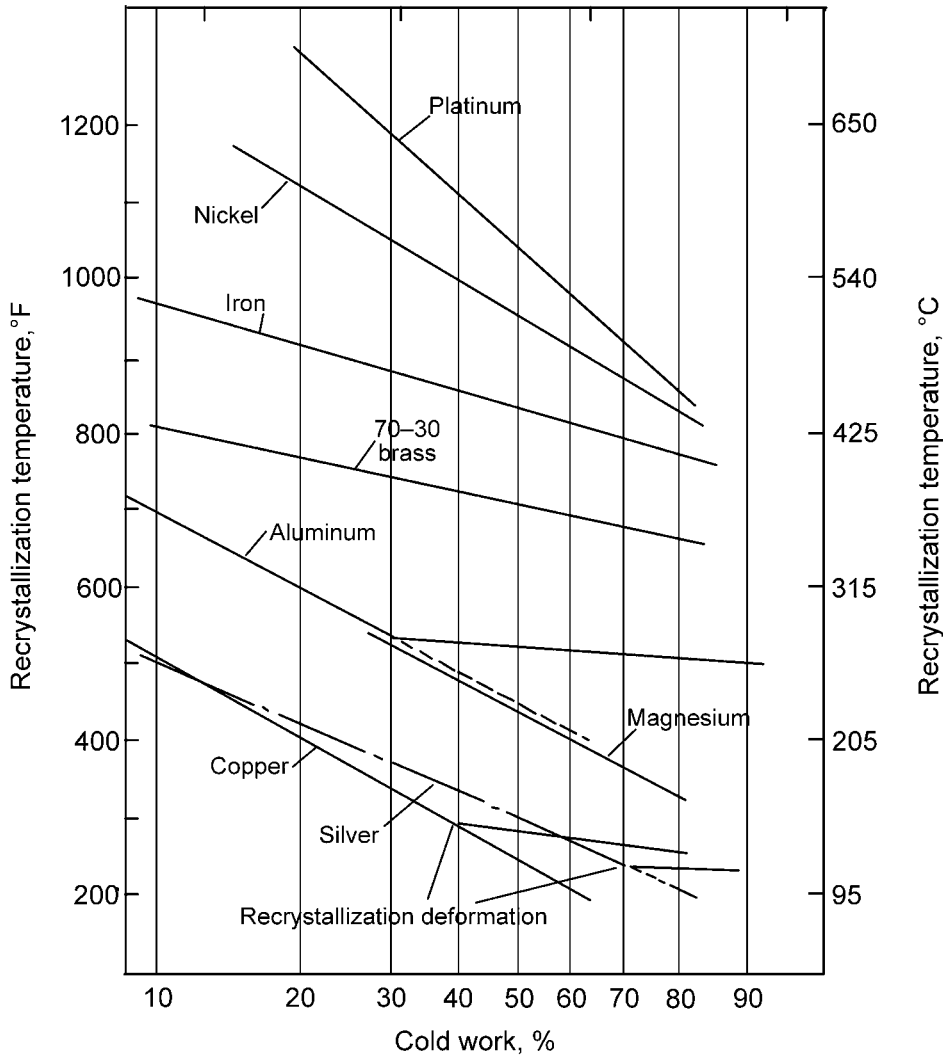


Fig. 13 Recrystallization temperatures as a function of degree of deformation for a range of materials. Source: Ref 15

Welding, *Trans. JWRI*, Vol 11 (No. 2), 1981, p 49-56

13. A. Nied, General Electric Company, Research and Development Center, Schenectady, NY, private communication, 1991
14. V.M. Zalkin, Theoretical Problems of Cold Pressure Bonding of Metals, *Svar. Proiz.*, Vol 11, 1982, p 41-42
15. J.M. Parks, Recrystallization Welding, *Weld. J. Res. Suppl.*, Vol 32 (No. 5), 1953, p 209s-222s
16. J.E. Gould and T.V. Stotler, "An Examination of Morphological Development during Flash Butt Welding," EWI Cooperative Research Report MR9602, 1996
17. E.F. Nippes, W.F. Savage, J.J. McCarthy, and S.S. Smith, Temperature Distribution during the Flash Welding of Steel, *Weld. J. Res. Suppl.*, Vol 30 (No. 12), 1951, p 585s-601s
18. E.F. Nippes, W.F. Savage, S.S. Smith, J.J. McCarthy, and G. Grotke, Temperature Distribution during the Flash Welding of Steel—Part II, *Weld. J. Res. Suppl.*, Vol 32 (No. 3), 1953, p 113s-122s
19. *Resistance Welding Manual*, 4th ed., Resistance Welding Manufacturers Association, Philadelphia, PA
20. W.F. Savage, Flash Welding—Process Variables and Weld Properties, *Weld. J. Res. Suppl.*, Vol 41 (No. 3), 1962, p 109s-119s
21. Z.A. Munir, A Theoretical Analysis of the Stability of Surface Oxides during Diffusion Welding of Metals, *Weld. J. Res. Suppl.*, Vol 62 (No. 12), 1983, p 333s-336s
22. M.F. Ashby and K.E. Easterling, A First Report on Diagrams for Grain Growth in Welds, *Acta Metall.*, Vol 30, 1982, p 1969-1978
23. J.D. Embury, A.S. Keh, and R.M. Fisher, Substructural Strengthening of Materials Subject to Large Plastic Strains, *Trans. Metall. Soc. AIME*, Vol 236 (No. 9), 1966, p 1252-1260
24. J.H. Cairns, J. Clough, M.A.P. Dewey, and J. Nutting, The Structure and Mechanical Properties of Heavily Deformed Copper, *J. Inst. Met.*, Vol 99, 1971, p 93-97
25. A.L. Wingrove, Some Aspects of Relating Structure to Properties of Heavily Deformed Copper, *J. Inst. Met.*, Vol 100, 1972, p 313-314
26. J.E. Pratt, Dislocation Substructure in Strain Cycled Copper as Influenced by Temperature, *Acta Metall.*, Vol 15 (No. 2), 1967, p 319-327
27. R. Fenn, "Solid phase welding—an old answer to new problems?" *Metallurgist and Materials Technologist*, Vol. 16 (No. 7): 1984, pp 341-342.

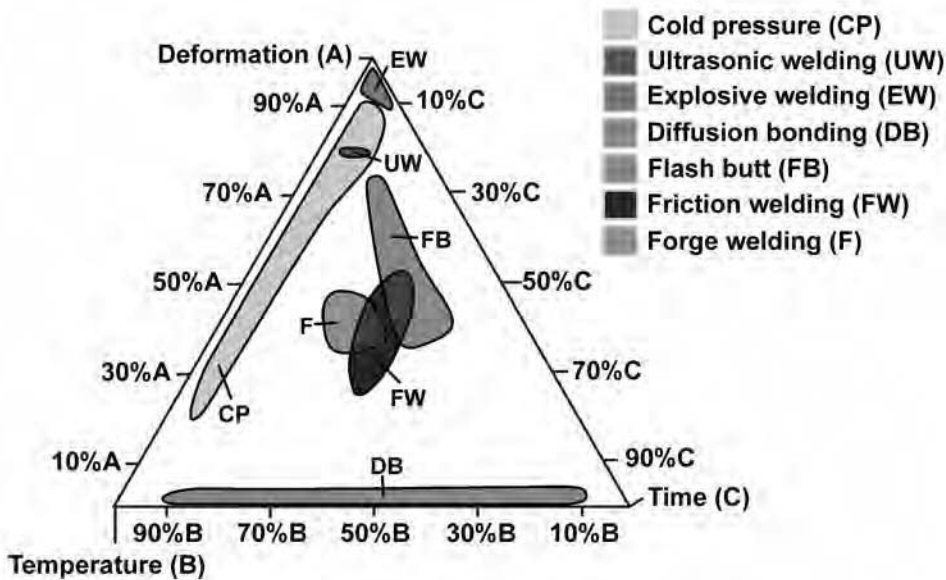


Fig. 14 Construct of time-temperature-pressure regimes of solid state welding processes proposed by Fenn (Ref 27). This diagram includes dimensionless values for temperature, time, and deformation, and contains suggested ranges for specific solid state processes.

Fundamentals of Friction Welding*

Revised by D.D. Kautz, Los Alamos National Laboratory

FRICION WELDING (FRW) is a solid-state welding process in which the heat for welding is produced by the relative motion of the two interfaces being joined. This method relies on the direct conversion of mechanical energy to thermal energy to form the weld, without the application of heat from any other source. Under normal conditions, no melting occurs at the interface.

Figure 1 shows a typical friction weld, in which a nonrotating workpiece is held in contact with a rotating workpiece under constant or gradually increasing pressure until the interface reaches the welding temperature. The rotational speed, the axial pressure, and the welding time are the principal variables that are controlled in order to provide the necessary combination of heat and pressure to form the weldment. These parameters are adjusted so that the interface is heated into the plastic temperature range where welding can take place. Once the interface is heated, axial pressure is used to bring the weld interfaces into intimate contact. During this last stage of the welding process, atomic diffusion occurs while the

interfaces are in contact, allowing a metallurgical bond to form between the two materials.

Friction welding involves heat generation through frictional abrasion (Ref 1–3), heat dissipation, plastic deformation, and chemical interdiffusion. The interrelation among these factors during FRW complicates development of predictive models for the friction welding process. However, from a qualitative standpoint, the process is well understood through empirical FRW studies that have been performed on a wide variety of materials. Five qualitative factors influence the quality of a friction weld (Ref 4):

- Relative velocity of the surfaces
- Applied pressure
- Surface temperature
- Bulk material properties
- Surface condition and presence of surface films

The first two factors are related to FRW, the last two are related to the properties of the materials being joined, while the temperature achieved is a combination of process parameters and material properties.

Commercial FRW applications employ a number of variations on the basic FRW concepts. These variations were developed to accommodate different part geometries and to produce different metallurgical effects (Ref 5) and are not discussed in this article.

Process Parameters

During FRW, the relative velocity, the applied pressure, and the duration of the force are the three variables that are controlled. The effect of these variables on weld quality is discussed for the two basic friction welding processes: direct-drive welding and inertia-drive welding. The surface temperature is the critical parameter for ensuring good welds and is dependent on the processing conditions and the materials being joined.

Although the surface temperature is not measured or directly controlled, the effects of insufficient or excessive temperature are generally apparent through visual examination of the finished weld. The bulk material properties and the condition of the surfaces being joined affect both the frictional forces and the forging characteristics of the materials being joined. These factors are discussed for the friction welding of both similar-material and dissimilar-material combinations.

Mechanisms of Friction Heating. The mechanism of heat generation during friction welding is complex. Studies in assessing the effective coefficients of friction for continuous-drive friction welding processes (Ref 6–8) have shown coefficient values considerably larger than normal values of sliding friction, typically found in the range of 0.15 to 0.3. These works define equilibrium coefficients of friction when friction welding steels as roughly equal to 2 over a wide range of processing conditions.

To understand the utility of this effective coefficient of friction and its suitability to the FSW process, it is useful to understand the variations in frictional behavior occurring during conventional friction welding. These mechanisms can be summarized from other works (Ref 7, 8). The typical coefficient of friction heating is diagrammed in Fig. 2. At the beginning of the process, the coefficient of friction is defined by the sliding friction, with values in the 0.15 to 0.30 range. Quickly, however, the contacting surface heats sufficiently to allow some instantaneous bonding, with subsequent shearing or tearing. This period of bonding and tearing is characterized by a rapidly rising coefficient of friction. It is during this period that the friction peak is often observed. The exact magnitude of this friction peak is difficult to characterize, because this stage of friction heating is so rapid.

During the friction peak stage, the very high effective coefficient of friction results in considerable generation of heat. This heat allows the material in the region of the bondline to

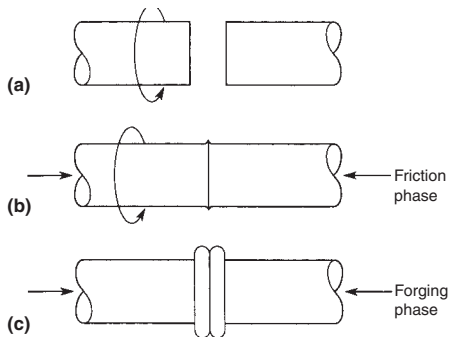


Fig. 1 Schematic showing fundamental steps in the friction welding process. (a) One workpiece is rotated, and the other workpiece is held stationary. (b) Both workpieces are brought together, and axial force is applied to begin the upsetting process. (c) Workpiece rotation is stopped, and the upsetting process is completed.

increasingly plasticize. The increasing thickness of the plastic layers then results in a final transition, during which bonding and shearing is replaced by a continuous working and recovery of the material. This is sometimes referred to as a viscoelastic condition. In this third stage, the effective coefficient of friction is defined by the temperature and extent of this plasticized region. During this time, the temperature profiles become relatively stable (Ref 7, 8), resulting in an equilibrium condition. It is in this stage that effective coefficients of friction in the range of 2 are observed.

The effectiveness of this model suggests that such equilibrium friction conditions exist between the tool and the workpiece. Given the highly differing plasticization temperatures between the steel tool and the aluminum workpiece, such equilibrium conditions must be restricted to the aluminum substrate. This can only occur if, in the preliminary stages of the process, aluminum is deposited onto the working surfaces of the tool. Once material is deposited onto the surface of the tool, the necessary plasticized region is now defined between this deposited material and the substrate itself. This is consistent with observations of aluminum deposits onto the surface of FSW tools (Ref 9). For FSW purposes, enhanced heat generation can be said to occur through metallurgical coupling between the tool and the workpiece.

It is clear that such metallurgical coupling brings into question the applicability of a coefficient of friction. In such cases, heat generation is more properly related to material working (Ref 10). However, for inclusion into the simplified modeling described in this work, an interpretive coefficient of friction term, incorporating these strain heat effects, is used. This means that the heating occurs only at the surface, which is reasonable, because the plastic deformation is very localized just beneath the shoulder.

Friction Welding Technology

There are two principal FRW methods: direct-drive welding and inertia-drive welding.

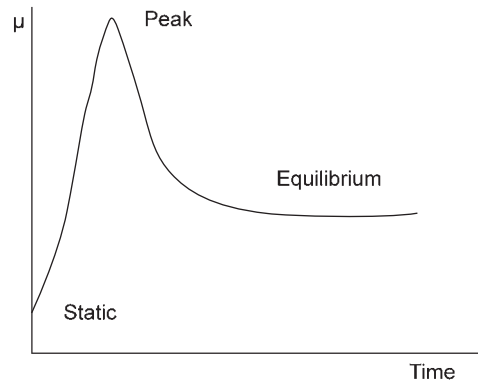


Fig. 2 Schematic representation of the coefficient of friction variations during direct-drive friction welding

Direct-drive FRW, sometimes called conventional friction welding, uses a motor running at constant speed to input energy to the weld. Inertia-drive friction welding, sometimes called flywheel friction welding, uses the energy stored in a flywheel to input energy to the weld. These two FRW technologies produce inherently different metallurgical effects at the joint interface.

Both FRW technologies can be applied through different types of relative motion to generate the friction necessary to form the weld. The most common FRW geometry is that shown in Fig. 1, in which one cylindrical component is held stationary and the other is rotated. However, in other methods, both components are rotated in opposite directions, or two stationary components are pushed against a rotating piece positioned between them. Additional forms of FRW, such as radial, orbital, and linear reciprocating motions, have been developed for special part geometries. These alternate methods are discussed elsewhere (Ref 5, 11).

Direct Drive Welding

In direct-drive FRW, a machine resembling a lathe is equipped with a brake and clutch, a means of applying and controlling axial pressure, and a weld-cycle timer and displacement controller. The operation of a direct-drive machine consists of a friction phase where heat is generated, a stopping phase where the rotation is terminated, and a forging phase where the pressure is applied to join the pieces. The relationships among the process variables are shown in Fig. 3, which plots the rotational speed and the axial pressure as a function of time for a typical weld. The time required to stop the spindle is also an important variable, because it affects the weld temperature and the timing of the forging force.

The forging phase starts at the instant when higher pressure (that is, a larger forging force)

is applied in the weld cycle. Thus, the forging phase actually starts during the stopping phase. In general, the larger forging force is applied (case 1) while the spindle is decelerating in the stopping phase (Fig. 3) or (case 2) after the spindle has stopped rotating at the end of the stopping phase. The difference between the two cases is the presence of a second friction peak. In case 1, the torque will rise again to reach a second peak before dropping. This produces a torsional force. In case 2, especially when the stopping phase is very short due to rapid braking, frictional torque does not rise but actually starts to decrease at the onset of the forging phase. In this case, there is no torsional force, and forging is affected only by the upsetting force.

The speed of rotation is the least sensitive process variable in that it can be varied over a wide range if heating time and pressure are properly controlled. For steels, the recommended peripheral velocity varies from 75 to 215 m/min (250 to 700 ft/min) (Ref 12). In general, higher speeds correspond to low weld heat inputs and are used to weld heat-sensitive materials such as hardenable steels.

The friction force is generally applied gradually to the weld to help overcome the initial contact-torque peak. For carbon steels, a friction pressure of approximately 70 MPa (10 ksi) at the interface area is required to form a good joint. After the drive motor is disengaged from the workpiece, the forging force is applied to complete the weld. Typical forging forces for carbon steel are of 140 MPa (20 ksi) at the weld interface.

Inertia-Drive Welding

The inertia-drive FRW method uses a similar type of machine except that the spindle holding the rotating piece is attached to a flywheel. The flywheel controls the energy input to the weld. The moment of inertia of the flywheel is an important variable that is adjusted by adding

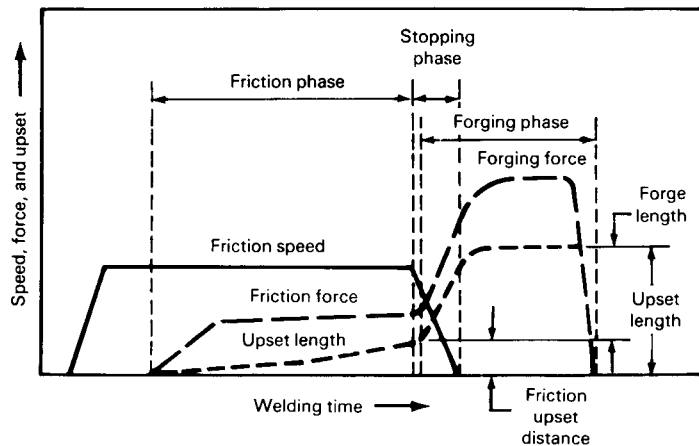


Fig. 3 Plot of selected parameters versus time relative to the three phases of the direct-drive friction welding process

or removing flywheel mass and diameter. The amount of energy stored in the flywheel is controlled by its speed. Once the spindle is at the correct speed, the drive system is disengaged, leaving a rotating flywheel mass. Axial pressure is then applied and held constant throughout the welding process. The applied pressure results in a decrease in the rotational speed, typically referred to as deceleration. In some cases, when the spindle has either nearly stopped or come to a complete stop, a higher forging force may be used.

Figure 4 illustrates the inertia-drive FRW process, which is similar to the direct-drive method in that the weld typically takes place in two stages: friction and forging. However, some weld schedules do not require a forging stage.

The major difference between the direct-drive and inertia-drive methods is the speed during the friction stage. In inertia welding, the speed continuously decreases during the friction stage, while in direct welding the speed remains constant.

The heat generated by the plastic deformation of materials at the faying surfaces during the forging phase, not the heat generated by friction in the friction phase, prevents rapid decrease of the temperature at the interface.

The process variables that control the characteristics of an inertia weld are the flywheel size (moment of inertia), the flywheel speed, and the axial pressure. The weld energy is related to the first two variables and is a fixed quantity once they have been determined. The kinetic energy in the flywheel at any time during the weld is given by:

$$E = \frac{S^2 \cdot I}{C}$$

where E is the energy (ft · lbf, or J), I is the moment of inertia (lb/ft², or kg/m²), S is the flywheel speed (rev/min), and C is a conversion constant that is equal to 5873 for English units or 182.4 for metric units.

The constant C is derived from:

$$E = \frac{1}{2}mv^2$$

where $v = \omega r$. Because $\omega = 2\pi S$, $v = 2\pi Sr$:

$$E = \frac{1}{2}m(2\pi)^2 S^2 r^2$$

$$E = \frac{1}{2}mr^2(2\pi)^2 S^2$$

Since $mr^2 = I$, the previous equation becomes:

$$E = \frac{1}{2}I(2\pi)^2 S^2$$

In SI units, the previous equation becomes:

$$E \left[\frac{\text{m}^2 \cdot \text{kg}}{\text{s}^2} \right] = \frac{1}{2}(2\pi)^2 S^2 \left[\frac{1}{\text{min}^2} \right] / [\text{m}^2 \cdot \text{kg}] \left[\frac{\text{min}}{60\text{s}} \right]^2$$

$$E = \frac{1}{2} \frac{(2\pi)^2}{60^2} S^2 I$$

$$E = \frac{I S^2}{C}$$

Solving for C in the previous equation:

$$C = \frac{2 \cdot 60^2}{(2\pi)^2}$$

$$= \frac{60^2}{2\pi^2}$$

$$= 182.378$$

The energy stored in the flywheel is proportional to its speed of rotation squared, S^2 . Therefore, a wide range of energy levels can be obtained without changing the flywheel to accommodate changes in part geometries. For large changes in the parts being joined, the capacity of an inertia welding machine can be modified by changing the flywheel moment of inertia if necessary.

Flywheel Energy. The moment of inertia of the flywheel is selected to produce both the desired amount of kinetic energy and the

desired amount of forging. Forging results from the characteristic increase in torque that occurs at the weld interface as the flywheel slows and comes to rest. This increased torque, in combination with the axial pressure, produces forging. Because forging begins at some critical velocity, the amount of forging depends on the amount of energy remaining in the flywheel, which is a linear function of the flywheel moment of inertia. Large, low-speed flywheels produce greater forging force than small, high-speed flywheels even though they contain the same amount of kinetic energy. Although small, medium, and large amounts of flywheel energy produce similar heating patterns, the amount of energy greatly affects the size and shape of the weld upset, as shown in Fig. 5(a) for similar-metal joints.

Peripheral Velocities. There is an optimum range of peripheral or linear surface velocities for each combination of metals being joined. For welding steel to steel, the recommended initial peripheral velocity ranges from 90 to 460 m/min (300 to 1500 ft/min). However, welds can be made at velocities as low as 85 m/min (275 ft/min). Figure 5(b) shows the effect of initial peripheral velocity on weld shape for similar-metal welds.

Axial Pressure versus Peripheral Velocities. The effect of varying the axial pressure is opposite to the effect of varying the velocity. Welds made at low axial pressure resemble welds made at medium velocity relative to the formation of weld upset and heat-affected zones (HAZ), as shown in Fig. 5(c). Excessive pressure produces a weld that has poor quality at the center and has a large amount of weld upset, similar to a weld made at a low velocity.

Metallurgical Parameters

Friction welding can be used to join a wide range of similar and dissimilar materials. Metals, ceramics, metal-matrix composites (MMCs), and polymers have been joined by FRW, and many of the dissimilar-metal combinations that cannot be joined by conventional fusion welding techniques are readily joined by FRW methods. This section summarizes some of the metals that have been joined by FRW and discusses the metallurgical considerations that govern the properties of the resulting weld.

Joining of Similar Materials

The two general requirements for forming good friction welds are, first, that the materials to be joined can be forged and, second, that the materials can generate friction at the weld interface. The first requirement eliminates similar-material welds in brittle materials such as ceramics, cast irons, and cemented carbides. However, ductile materials can sometimes be joined to these materials. The second

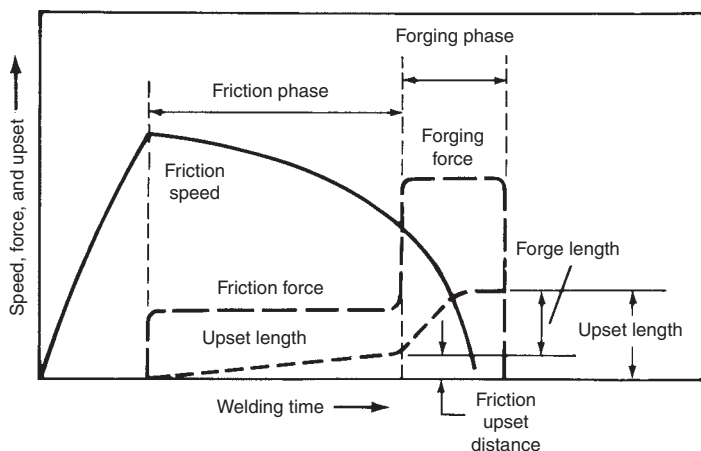


Fig. 4 Plot of selected parameters versus time relative to the two phases of the inertia-drive friction welding process

requirement eliminates materials that contain alloying additions that provide dry lubrication to the joint interface. Free-machining additives to steel, graphite-containing alloys such as cast iron, and lead alloys may be difficult to weld due to this requirement.

Almost all other metal alloys can be welded to themselves by FRW techniques. Table 1 summarizes a number of common similar-metal weld joints that have been made using inertia-

drive FRW. Metallic alloys known to form high-quality FRW joints include alloys based on aluminum, copper (copper-nickel, brass, bronze), iron (low-alloy steel, tool steel, stainless steel, maraging steel), nickel, titanium, tantalum, and many others (Ref 5, 11). Near full-strength metallurgical bonds can be produced for a very wide range of similar-metal alloy friction welds. The microstructure and mechanical properties of inertia-welded similar-metal

joints for the following alloys can be found in the sources listed:

Alloy	Ref
Low-alloy steels	13, 14
Austenitic stainless steels	15
Aluminum alloys	16-18
Titanium alloys	19

The relative ease of friction welding metals to themselves is related to the matching properties at the weld interface. Because the materials properties are matched, heat is distributed uniformly on both sides of the joint, and the deformation characteristics are identical on both sides of the joint. This results in symmetric welds with good properties. In general, the process variables do not vary significantly for different alloys within a given class of materials. However, there can be a significant variation in processing variables between different classes of materials (Table 1).

Because FRW generates localized heating at the interface, the HAZ is subject to rapid cooling due to heat transfer to the cold base metal. This rapid quenching may sufficiently alter the mechanical properties of the base metal in the HAZ region to require postweld heat treatment. For example, to restore ductility, stress relieving or tempering may be required to friction weld steels with hardenability greater than that of AISI 1035 (Ref 5, 11). In addition, age-hardenable alloys will lose strength in the HAZ during welding and may require postweld solution heat treating and/or postweld aging to restore their strength. Other alloys, such as those that obtain their strength from cold working, will lose strength in the HAZ of the weld, and their properties cannot be restored with postweld treatments.

Joining of Dissimilar Metals

While many similar-metal FRW joints are produced because of economic considerations, many dissimilar-metal FRW joints are produced because there are no alternative welding methods available. Examples of these types of joints include dissimilar-metal combinations with widely different melting points and

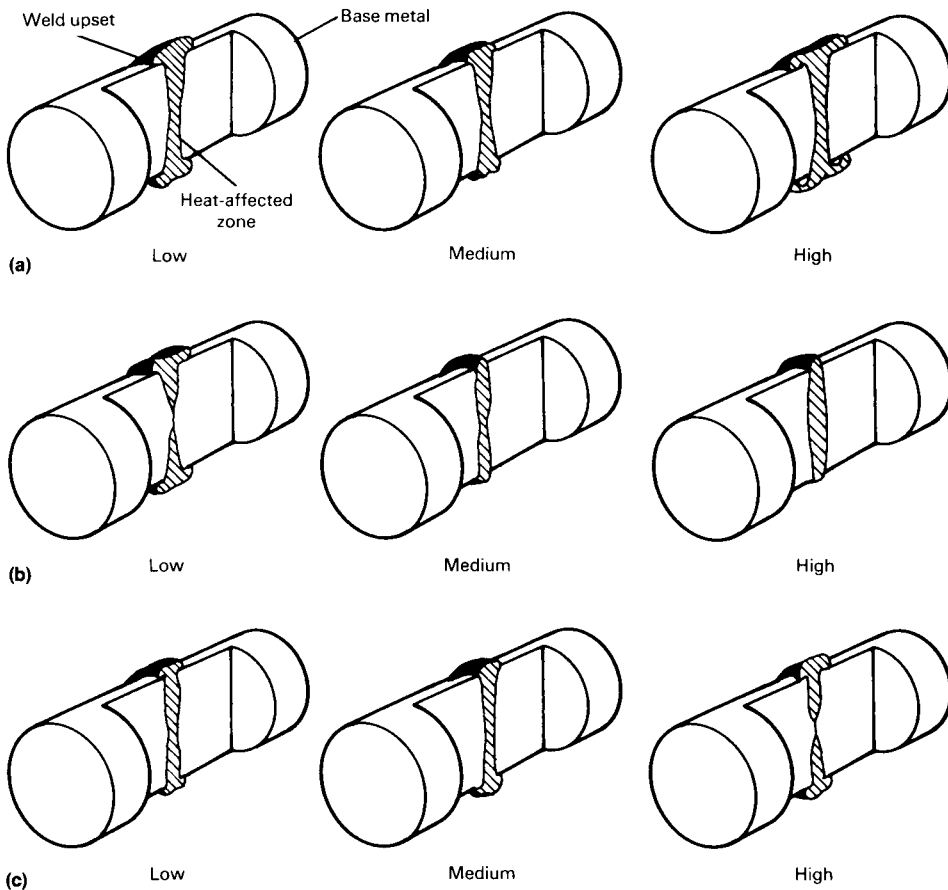


Fig. 5 Schematic showing effect of welding parameters on the finished weld nugget obtained when similar metals are welded using inertia-drive friction welding equipment. (a) Flywheel energy. (b) Initial peripheral velocity of workpiece. (c) Axial pressure. Source: Ref 12

Table 1 Parameters for inertia-drive friction welding of two 25 mm (1 in.) diameter bars made of similar metals

Work metal	Spindle speed, rev/min	Axial force		Flywheel size(a)		Weld energy		Metal loss(b)		Total time(c), s
		kN	lbf × 10 ³	kg · m ²	lb · ft ²	kJ	ft · lbf × 10 ³	mm	in.	
1018 steel	4600	53	12	0.28	6.7	33	24	2.5	0.10	2.0
1045 steel	4600	62	14	0.33	7.8	38	28	2.5	0.10	2.0
4140 steel	4600	67	15	0.35	8.3	41	30	2.5	0.10	2.0
Inconel 718	1500	220	50	5.48	130.0	68	50	3.8	0.15	3.0
Maraging steel	3000	90	20	0.84	20.0	41	30	2.5	0.10	2.5
Type 410 stainless	3000	80	18	0.84	20.0	41	30	2.5	0.10	2.5
Type 302 stainless	3500	80	18	0.59	14.0	41	30	2.5	0.10	2.5
Copper (commercially pure)	8000	22	5	0.04	1.0	14	10	3.8	0.15	0.5
Copper alloy 260 (cartridge brass, 70%)	7000	22	5	0.05	1.2	14	10	3.8	0.15	0.7
Titanium alloy, Ti-6Al-4V	6000	36	8	0.07	1.7	22	16	2.5	0.10	2.0
Aluminum alloy 1100	5700	27	6	0.11	2.7	20	15	3.8	0.15	1.0
Aluminum alloy 6061	5700	31	7	0.13	3.0	23	17	3.8	0.15	1.0

(a) Moment of inertia of the flywheel. (b) Total shortening of the workpieces during welding. (c) Sum of heating time plus welding time. Source: Ref 12

dissimilar-metal combinations that form incompatible phases when fusion welded. Table 2 gives parameters used for inertia welding several common dissimilar-material combinations.

Carbon Steels and Alloy Steels. In general, low- and medium-carbon steels are joined to each other under a wide range of conditions, and high-carbon steels are readily joined to alloy steels (Ref 12) using friction welding. High-speed tool steels are welded to alloy steel shanks for numerous machine-tool applications. Steel with carbon contents as high as 1.0%, such as 52100 steel, can be joined to lower-carbon alloys. Preweld heat treating may be required in some cases to better match the properties at the interface, and post-weld heat treatment may be required in some cases to temper the interface region of the high-carbon steel grades.

Stainless Steels to Other Selected Metals. Stainless steel alloys are comparatively easy to friction weld to other metals. For example, austenitic stainless steel to low-alloy steel (Ref 20), titanium and copper to stainless steel (Ref 21), and 1100 aluminum to stainless steel (Ref 22) are examples of transition joints that are made by FRW.

Titanium can be welded to stainless steel with extreme care (Ref 23), and other incompatible dissimilar combinations may be successfully welded using interlayer techniques (Ref 24). Figure 6 shows a micrograph of the interfacial region of an inertia weld between Monel 400 and 21-6-9 stainless steel. The joint properties are excellent, with plastic flow

occurring in Monel 400 before joint failure during bend testing.

Such transition joints can often be used as interlayers for the friction welding of incompatible materials. For example, it is difficult to weld 5083 aluminum directly to stainless steel. However, by first friction welding aluminum alloy 1100 to the stainless steel and machining the 1100 aluminum alloy back to an interlayer thickness of approximately 1 mm (0.04 in.), the 5083 aluminum alloy can be joined to the stainless steel via this 1100 interlayer with high joint efficiencies (Ref 25).

Figure 7(a) shows an example of an aluminum-base MMC that was friction welded to 1100 aluminum. The MMC is a 2024 aluminum alloy with 15 vol% Al_2O_3 particles. The interface region between these materials is shown at higher magnification in Fig. 7(b), where intermixing of both the materials is shown to occur.

Problems Common to Welding of Dissimilar Materials. In general, the same problems encountered when welding similar materials must be addressed when welding dissimilar materials. However, some problems are associated only with the welding of dissimilar materials or are greatly magnified during the welding of dissimilar materials. These factors include joint interfaces, low-melting phases, brittle phases, and different thermal expansions.

Joint Interfaces. While most similar-material welds are made with little concern for surface preparation, highly dissimilar-metal combinations are more sensitive. This happens for vari-

ous reasons. In stainless steel to aluminum alloy welds, the oxide surface that forms on the aluminum picks up contaminants such as water and hydrocarbons, forming extremely tenacious surface layers (Ref 26). If this layer is not removed prior to welding, poor structural welds may occur. In stainless steel to refractory metal alloy welds, the oxide on the faying surfaces again may contain contaminants such as water and hydrocarbons. The contaminants in this case are likely to alloy into the finished weldment. This alloying causes a reduction of structural integrity through the formation of low-melting or brittle phases at the weld interface.

Surface-treated interfaces frequently cause problems during FRW. Steels that have been carburized or nitrided, titanium alloys that have been nitrided, and other hardfaced alloys are difficult to friction weld due to the inherently low friction coefficient and low forgeability. The repeatability of welds made on materials with hard surface layers is difficult to characterize due to several factors, including coating thickness, coating quality, and physical properties of the coating. In most instances, weldability is improved if the surface-treated area is removed from the faying surface(s) before welding.

Low-Melting-Phase Formation. Some material combinations have very low-melting-point phases associated with mixing of constituents at the weld interface. The formation of these phases during the welding cycle is deleterious to the finished weld properties. Examples of combinations that fall into this category include

Table 2 Parameters for inertia-drive friction welding of two 25 mm (1 in.) diameter bars made of dissimilar metals

Work metal	Spindle speed, rev/min	Axial force		Flywheel size(a)		Weld energy		Metal loss(b)		Total time(c), s
		kN	lbf × 10 ³	kg · m ²	lb · ft ²	kJ	ft · lbf × 10 ³	mm	in.	
Copper to 1018 steel	8000	22	5	0.06	1.4	20	15	3.8	0.15	1.0
M2 tool steel to 1045 steel	3000	180	40	1.14	27.0	54	40	2.5	0.10	3.0
Nickel alloy 718 to 1045 steel	1500	180	40	5.48	130.0	68	50	3.8	0.15	2.5
Type 302 stainless to 1020 steel	3000	80	18	0.84	20.0	41	30	2.5	0.10	2.5
Sintered high-carbon steel to 1018	4600	53	12	0.35	8.3	41	30	2.5	0.10	2.5
Aluminum 6061 to type 302 stainless	5500	22	5	0.16	3.9	27	20	5.1	0.20	3.0
		67(d)	15(d)
Copper to aluminum alloy 1100	2000	33	7.5	0.46	11.0	10	7.5	5.1	0.20	1.0

(a) Moment of inertia of the flywheel. (b) Total shortening of the workpieces during welding. (c) Sum of heating time plus welding time. (d) The 22 kN (5000 lbf) force is applied during the heating stage of the weld; force is subsequently increased to 67 kN (15,000 lbf) near the end of the weld.

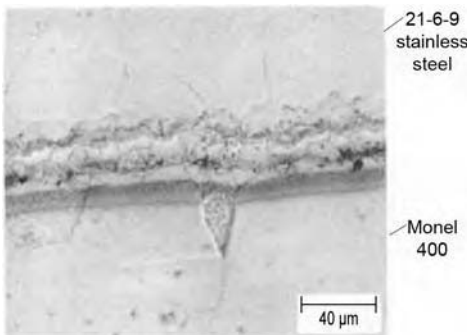


Fig. 6 Metallographic cross section of the interface of a Monel 400 to 21-6-9 stainless steel weld produced by inertia-drive friction welding. Note the fine grain size present at the interface.

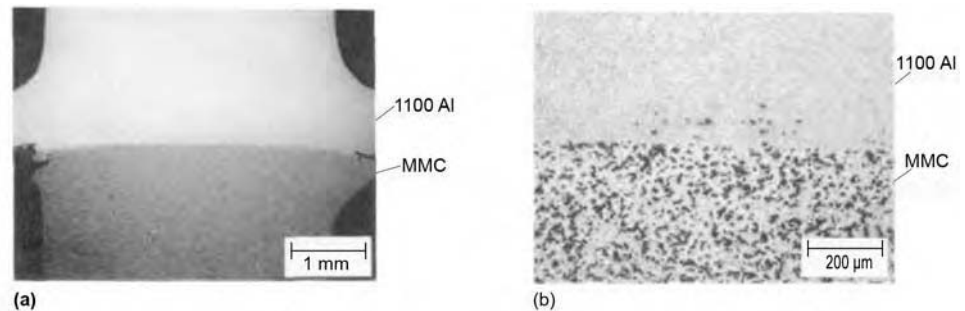


Fig. 7 (a) Cross section of the interface of a direct-drive friction weld joining 1100 aluminum to a 2024 aluminum alloy with 15 vol% Al_2O_3 particles. (b) Higher magnification of the same weld showing the excellent weld formed at the interface. MMC, metal-matrix composite

iron-base alloys to titanium alloys and aluminum alloys to magnesium alloys. Low-melting-point eutectics are found in both of these metallurgical systems, and great care must be exercised during parameter development to prevent the formation of liquid phases during the completion of successful welds.

Other weld combinations may be affected by contaminants at the weld interface. Examples include sulfur and phosphorus in iron-base alloys and bismuth in copper alloys. These contaminants may cause problems with hot shortness in very low concentrations. It is imperative that good cleaning practices be implemented when materials may have been contaminated with these elements or with material containing these elements.

Brittle-Phase Formation. Many materials, when combined, are susceptible to the formation of brittle phases. In some combinations, this occurs during the welding cycle; in others, service conditions after welding cause the problem. Two main reasons exist for brittle-phase formation in friction welds:

- Surface contaminants that embrittle the weld interface (see the section “Joint Interfaces” in this article)
- Formation of intermetallic phases between normal constituents of the alloys being welded

Intermetallic phase formation is common when welding refractory metal alloys to stainless steel alloys and in several other systems. In the case of stainless steels to refractory metals, σ phase or similar phases may occur at the interface upon welding. Proper weld procedure development reduces the amount of brittle phases that are formed but typically does not eliminate their formation completely.

Properly developed welds have satisfactory structural properties, because only small, non-continuous areas of the brittle phase are present at the weld interface. Figure 8(a) shows an inertia-drive welded joint between vanadium and 21-6-9 stainless steel. The interface is smooth and shows no areas of brittle phases. Electron microscopy techniques are needed to find the small areas of σ phase that could be present at the weld interface for this weld or for other deleterious phases in other material combinations.

Caution must be used when designing components for use at elevated-temperature extremes. In many instances, material combinations in which no brittle phases form during welding are susceptible to brittle-phase formation at the interface during high-temperature use. This is not a design issue when the welds are used for near-room-temperature applications. Figure 8(b) shows the vanadium to 21-6-9 stainless steel inertia-drive weld after a severe thermal cycle of 1000 °C (1830 °F) for 2 h with σ -phase and solid-solution growth at the weld interface. The thick layer next to the stainless steel is a solid solution of iron and vanadium. The thin layer next to the vanadium is σ phase and forms a continuous brittle fracture path across the weld interface.

Differential Thermal Expansion. Some material combinations are difficult to weld because of the large differences in thermal expansion. Low-expansion materials, such as refractory metals, ceramics, and low-expansion iron-nickel and iron-nickel-cobalt alloys, may fail or be highly stressed during cooling when welded to high-expansion material, such as austenitic stainless steels and nickel- and cobalt-base superalloys. Use of these combinations requires the designer to consider the large

stresses or metal fatigue developed within the fabricated structure if the welds are restrained when exposed to large temperature changes. Intermediate-expansion materials and multiple friction welds may be required to allow for the transition from high to low thermal expansion materials.

REFERENCES

1. T.H. Hazlet, *Fundamentals of Friction Welding, Source Book on Innovative Welding Processes*, American Society for Metals, 1981, p 11–36
2. F.P. Bowden and D. Tabor, *The Friction and Lubrication of Solids*, Part I, Oxford University Press, 1954
3. J. Goddard and H. Wilman, *A Theory of Friction and Wear during the Abrasion of Metals*, *Wear*, Vol 5, 1962
4. V.I. Vill, *Friction Welding of Metals*, translated from the Russian, American Welding Society, 1962
5. *Welding Handbook*, 8th ed., Vol 2, American Welding Society, 1991, p 739–763
6. R.L. Zaron and V.D. Voznesenskii, *Power and Heat Parameters of Friction Welds*, *Svarach Proviz.*, Vol 10, 1959, p 63–70
7. F.D. Duffin and A.S. Bahrani, *Friction Behavior of Mild Steel in Friction Welding*, *Wear*, Vol 26, 1973, p 53–74
8. A. Sluzalec, *Thermal Effects in Friction Welding*, *Int. J. Mech. Sci.*, Vol 32 (No. 6), 1990, p 467–478
9. C.J. Davies, *The Welding Institute*, Cambridge, U.K., unpublished research, 1995
10. T.J. Lienert, *The Ohio State University*, Columbus, OH, unpublished research, 1996
11. “Recommended Practices for Friction Welding,” ANSI/AWS C6.1–89, American Welding Society, 1989
12. *Welding, Brazing, and Soldering*, Vol 6, *Metals Handbook*, 9th ed., American Society for Metals, 1983
13. T.N. Hazlet, *Properties of Friction Welded Plain Carbon and Low Alloy Steels*, *Weld. J.*, Vol 41, 1962, p 49-s to 52-s
14. S.B. Dunkerton, *Toughness Properties of Friction Welds in Steels*, *Weld. J.*, Vol 65, 1986, p 193-s to 202-s
15. C. Lippold and B.C. Odegard, *Technical Note: Microstructural Evolution during Inertia Friction Welding of Austenitic Stainless Steels*, *Weld. J.*, Vol 63, 1984, p 35-s to 38-s
16. W.A. Baeslack III and K.S. Hagey, *Inertia Friction Welding of Rapidly Solidified Powder Metallurgy Aluminum*, *Weld. J.*, Vol 67, 1988, p 139-s to 149-s
17. H.H. Koo and W.A. Baeslack III, *Friction Welding of a Rapidly Solidified Al-Fe-V-Si Alloy*, *Weld. J.*, Vol 71, 1992, p 147-s to 169-s

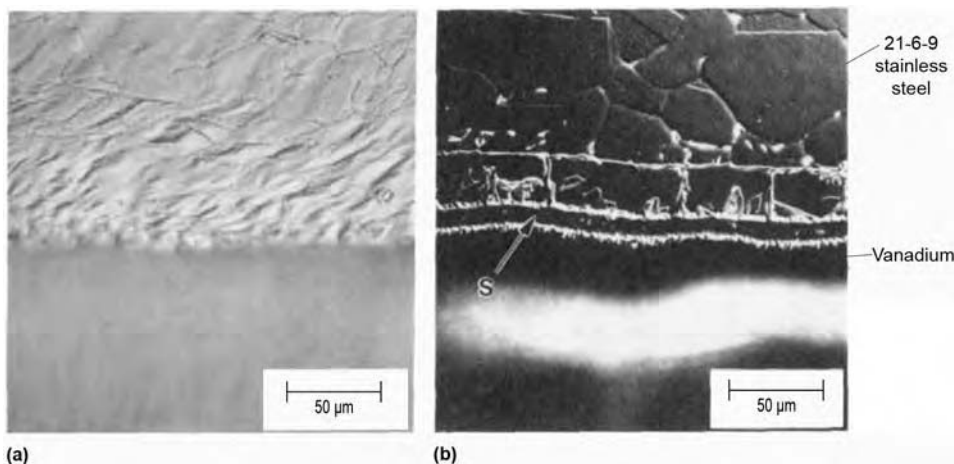


Fig. 8 Metallographic cross section of an inertia-drive friction welding joint between vanadium and a 21-6-9 stainless steel. Note the excellent weld quality at the interface. (a) Weld interface with no σ -phase growth. (b) Weld interface with σ -phase growth (indicated by “S”) and a solid-solution mixing caused by chemical diffusion after exposure to a 1000 °C (1830 °F) thermal cycle

18. K. Ogawa, H. Yamaguchi, T. Morimoto, K. Takemata, H. Sudo, and A. Hiratsuka, Shear Strength Characteristics of Aluminum Alloy Friction Welds, *Weld. J.*, Vol 5, 1991, p 860–866
19. C.G. Nessler et al., Friction Welding of Titanium Alloys, *Weld. J.*, Vol 50, 1971, p 379-s to 385-s
20. K.G.K. Murti and S. Sandaresan, Thermal Behavior of Austenitic-Ferritic Joints Made by Friction Welding, *Weld. J.*, Vol 64, 1985, p 327-s to 334-s
21. R.A. Bell, J.C. Lippold, and D.R. Adolphson, An Evaluation of Copper-Stainless Steel Friction Welds, *Weld. J.*, Vol 63, 1984, p 325-2 to 332-s
22. D. Yashan, S. Tsang, W.L. Johns, and M.W. Doughty, Inertia Friction Welding of 1100 Aluminum to Type 316 Stainless Steel, *Weld. J.*, Vol 66, 1987, p 27–37
23. M. Futamata and A. Fuji, Friction Welding of Titanium and SUS 304L Austenitic Stainless Steel, *Weld. Int.*, Vol 4, 1990, p 768–774
24. F. Sassani and J.R. Neelan, Friction Welding of Incompatible Materials, *Weld. J.*, Vol 67, 1988, p 264-s to 270-s
25. R. Armstrong, Lawrence Livermore National Laboratory, private communication and internal reports, 1991
26. *Properties and Selection: Nonferrous Alloys and Pure Metals*, Vol 2, *Metals Handbook*, 9th ed., American Society for Metals, 1979, p 204–209

Fundamentals of Friction Stir Welding

P.S. De, N. Kumar, J.Q. Su, and R.S. Mishra, Missouri University of Science and Technology

TRADITIONALLY, WELDING OF METALS AND ALLOYS has been a fusion-based process where a filler metal is used for joining. The approach, although applicable to a wide variety of commercial alloys, has its own specific limitations due to the nature of the process. As an example, high-strength precipitation-strengthened aluminum alloys are nonweldable by fusion techniques due to problems of liquation cracking and porosity. Friction stir welding (FSW) techniques, invented at The Welding Institute of the United Kingdom in 1991, have successfully overcome these drawbacks of fusion welding methods (Ref 1, 2). The concept is remarkably straightforward: a cylindrical tool with a pinlike attachment is rotated and slowly inserted into the rigidly clamped joint to be welded (Fig. 1a). The frictional and deformational effects due to the rotating tool surface in contact with the workpiece cause plasticization of the metals to be joined. Translational movement of the rotating tool (actual or relative to the workpiece) results in the mixing of plasticized metal volumes, leading to joining (Fig. 1b). Control of the FSW process is currently thought of in terms of process parameters and is not related directly to fundamental deformation mechanisms. Friction stir welding can be viewed as a deformation process used to join metals rather than a joining process that involves deformation.

Figure 2 shows the schematic section of a friction stir welded workpiece with its different zones after macroetching. The microstructural particulars are explained in more details later in this article. In this context, the advancing and retreating side of a friction stir weld needs further explanation. As already mentioned, during FSW the tool rotates as well as translates along the joint to be welded. Half of the weld, where the tool rotation direction has similar sense to the tool translation direction, is known as the advancing side of the weld. The other half, where the tool rotation direction is opposite to the tool translation direction, is known as the retreating side of the weld. The macrostructures in the advancing/retreating sides are significantly different, particularly in their shape and microstructure, and are explained later in this article. Subsequent sections present the link between deformation and FSW process parameters in more details.

Thermal Aspects

As previously indicated, FSW involves plastic deformation at high strain rates and elevated temperatures, with resultant microstructural changes leading to joining. The heat generated in FSW is primarily from two sources: frictional and plastic deformation. The frictional component is an outcome of the rotational movement of the tool shoulder and pin surfaces with respect to the stationary

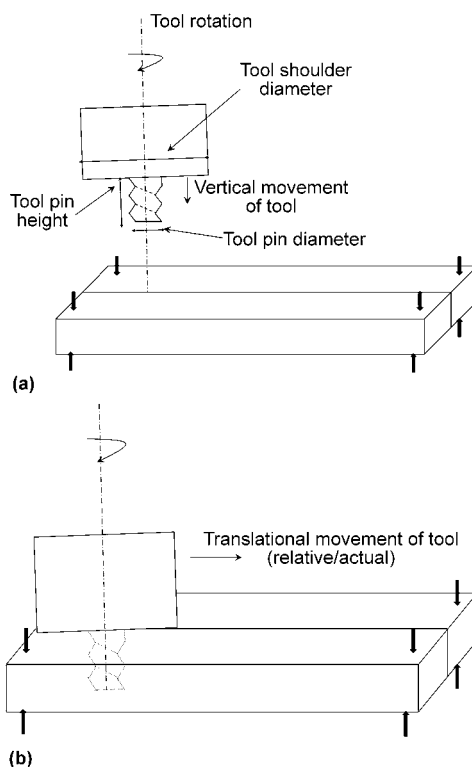


Fig. 1 (a) Schematic of a friction stir tool being inserted into the workpiece. The process is also sometimes called the plunge period of welding. The workpiece is clamped firmly to prevent any movement. The tool rotation direction and the pin thread handedness are adjusted such that material is pushed downward. (b) The tool fully plunged into the workpiece is moved along the seam while it is rotating, which consequently leads to welding due to mixing of metals in a plasticized state.

workpiece and is the primary heat source at the start of the process (i.e., the plunge period). The frictional heat generation causes a localized softening of the metal, which causes plastic deformation. During the pseudo-steady-state welding process, both frictional and plastic deformation contribute to the overall heat generation. Unlike other fusion welding techniques, in FSW no melting occurs (other than localized extreme parameters). In the next section, the results of experimental temperature measurements during FSW of various metals are summarized.

Temperature Measurement

The temperature generated during FSW is an important process variable and plays a vital role in determining the weld microstructure. Consequently, numerous experimental measurements of temperature around the weld zone have been reported. Figure 3 shows the peak temperatures measured around the welded region during a friction stir butt weld. It should be noted that no measurement in the actual welded region has been performed. This is primarily due to the experimental limitation imposed by the moving tool during the actual welding process. Table 1 summarizes a few examples of the maximum temperature measured in various metals during FSW, along with their locations (Ref 3–9). The first observation is that, regardless of the material welded, the temperatures measured were well below the

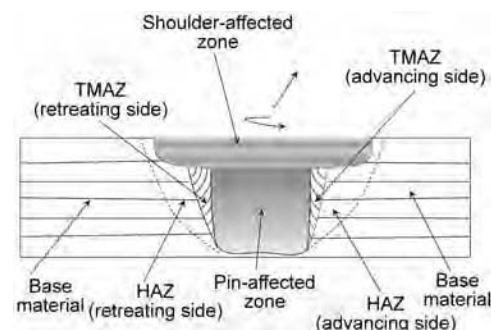


Fig. 2 Schematic macroetched section of a general friction stir welded microstructure with its different zones. TMAZ, thermomechanically affected zone; HAZ, heat-affected zone

solidus temperatures of the corresponding alloys. In addition, the microstructural features showed no obvious indication of melting. In fact, a detailed microstructural analysis of the weld nugget indicates the occurrence of a solid-state recrystallization type of phenomenon (see the section “Dynamic Recrystallization and Microstructural Evolution” in this article).

The temperatures reported in Table 1 were typical for the corresponding welding parameters. Thus, for the same welding setup, different FSW parameters result in different thermal cycles. Again, use of a different welding tool or weld backing plate will result in alterations of the thermal cycle. To predict and understand such changes, a thorough understanding of the factors controlling weld temperature is therefore essential. In the next sections, physical explanation of the heat input during FSW and the possible methods of their estimation are considered.

Heat-Source Estimation

Although heat-source estimation during FSW continues to be a topic of active research, this section covers the most common approaches adopted. One of the methods consists of measuring the power consumed by the machine during the welding process. Thus, Khandkar et al. (Ref 10) measured the torque and the

rotation rate during welding, from which the radial heat flux $\dot{q}(r)$ was calculated as:

$$\dot{q}(r) = \frac{P_{av}r}{\frac{2}{3}\pi R_{Shoulder}^3 + 2\pi R_{Pin}^2 H_{Pin}} \quad (Eq 1)$$

where P_{av} is the average power input calculated from the measured torque and rotation rate, $R_{Shoulder}$ is the shoulder radius, R_{Pin} is the pin radius, and H_{Pin} is the pin height. However, this method is limited by its inability to predict temperatures for unknown welding conditions. Moreover, the technique was based on the premise that heat generated during FSW was transferred fully to the workpiece, and it neglected any heat transferred to the tool and machine components. Schmidt and Hattel (Ref 11) proposed an alternative analytical model of heat generation where both the tool/workpiece contact condition and tool geometry were considered. According to this model, the total heat generated during the rotation of the tool can be expressed as:

$$Q_{total} = \frac{2}{3}\pi(\delta\tau_{yield} + (1 - \delta)\mu p) \cdot \omega \cdot [(R_{Shoulder}^3 - R_{Pin}^3)(1 + \tan \alpha) + 3R_{Pin}^3 H_{Pin}] \quad (Eq 2)$$

where δ is a dimensionless factor defining the contact conditions, τ_{yield} is the yield stress at the welding temperature and strain rates, μ is the

coefficient of friction, p is the contact pressure, ω is the tool rotation rate, and α is the tool shoulder cone angle. However, in this model Q_{total} is an implicit function of δ , τ_{yield} , μ , and p . Consequently, as in Eq 1, this restricts the prediction of weld temperature for cases where experimental measurements are unavailable (Ref 12). Because of the fully coupled thermomechanical nature of the friction stir process, temperature predictions for unknown weld conditions are possible only for models where both thermal and material flow equations are solved simultaneously. In fact, even in such coupled simulations, an appropriate model for heat generation is critical. A common approach adopted for this is an assumption that a finite fraction of the plastic work done during FSW is converted into heat. The plastic work done can then be calculated as:

$$\dot{q} = \beta \sigma \cdot \dot{\epsilon} \quad (Eq 3)$$

where β is the fraction of plastic work converted, σ is the stress, and $\dot{\epsilon}$ is the strain rate.

Alternatively, considering material to be a viscous fluid, the work done is calculated as a product of material viscosity (η) and strain rate and is given as:

$$\dot{q} = \beta \eta \cdot \dot{\epsilon} \quad (Eq 4)$$

The frictional heat contribution is generally regarded as a boundary condition and is expressed as:

$$\dot{q} = \mu p \dot{\gamma} \quad (Eq 5)$$

where $\dot{\gamma}$ is the slip rate, defined as the difference in velocity between tool surface and matrix. With a suitable heat-source model, the FSW temperatures can then be approximated using analytical/numerical methods.

Temperature Prediction: Analytical Approach

Any weld temperature prediction is based on the basic energy conservation equation, which can be schematically presented as (Ref 13):

$$\begin{aligned} \{ \text{Net rate of internal and kinetic energy stored} \} \\ = \{ \text{Net rate of internal and kinetic energy} \\ \text{flow by convection} \} \\ + \{ \text{Net rate of heat addition by conduction} \} \\ + \{ \text{Rate of heat generation} \} \end{aligned} \quad (Eq 6)$$

During FSW, the kinetic energy contribution is generally neglected, and the energy equation is adapted as:

$$\frac{\partial}{\partial t} \rho(C_p T) = -\vec{\nabla} \cdot \rho \vec{u}(C_p T) - \vec{\nabla} \cdot (k \vec{\nabla} T) + \dot{q} \quad (Eq 7)$$

where ρ is the material density, C_p is the specific heat capacity, T is the temperature, \vec{u} is the velocity, and k the thermal conductivity. Neglecting convective energy transport in Eq 7, analytical expressions for steady-state conditions can then be obtained by approximating the heat

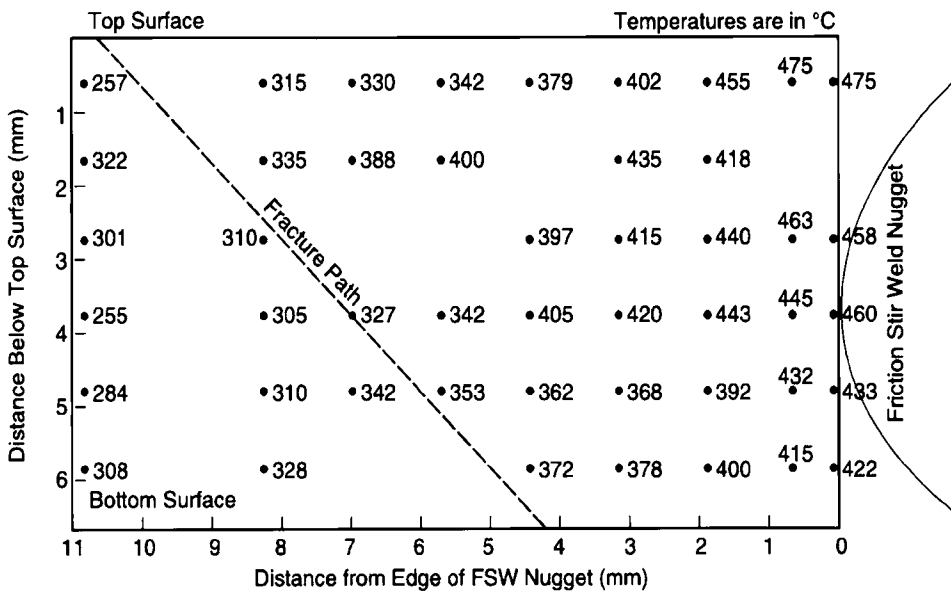


Fig. 3 Peak temperature distribution around the friction stir weld (FSW) region of a 6.35 mm (0.25 in.) thick butt-welded AA7075-T651 alloy. Source: Ref 3

Table 1 Summary of temperatures measured during friction stir welding of various metals

Serial	Alloy	Location measured	Temperature, K	Ref
1	AA6061-T6	Top surface and weld center	698	4
2	AA7075-T651	~0.6 mm (0.02 in.) below top adjacent to stir zone	748	3
3	AA6061-T6	...	810	5
4	AA1050	Close to stir zone bottom	583	6
5	AISI-1018	Shoulder-workpiece interface	1263	7
6	AA2195-T8	Adjacent to pin edge at plate middle	723	8
7	AZ-31	Measured in heat-affected zone	633	9

source as a line or point geometry. Thus, for point heat-source geometry, the pseudo-steady-state temperature distribution (Rosenthal's thick plate solution) is given as (Ref 14):

$$T - T_0 = \frac{q_0}{2\pi k} \left(\frac{1}{R} \right) \exp\left[-\frac{v}{2a}(R+x)\right] \quad (\text{Eq 8})$$

where T_0 is the initial plate temperature, v is the welding velocity, $a (= k/\rho C_p)$ is the thermal diffusivity, R is the distance from the source to the point of measurement, and x is the X -coordinate in the moving reference axis system (located at the source). For line heat-source geometry, the pseudo-steady-state temperature (Rosenthal's thin plate solution) distribution is given as (Ref 14):

$$T - T_0 = \frac{q_0/d}{2\pi k} \exp\left(\frac{vx}{2a}\right) K_0\left(\frac{vr}{2a}\right) \quad (\text{Eq 9})$$

where $K_0(vr/2a)$ is the modified Bessel function of the second kind and zero order. In fact, the first assessments of FSW temperature done by Gould and Feng (Ref 15) and Feng et al. (Ref 16) used Rosenthal's model. However, such analytical models are applicable only for very specific boundary conditions. Thus, in practical welding situations, heat loss through the tool and backing plate limits the applicability of such analytical models. In such instances, numerical solution to the problem is expected to give a better prediction. The next section discusses the results of such numerical models on FSW in more detail.

Temperature Prediction: Numerical Approach

As mentioned previously, a thorough analysis of temperature requires a simultaneous

solution of thermal and material flow equations. However, solving such coupled equations is exceedingly complex and is associated with specific limitations. In this section, temperature prediction by the solution of Eq 7 alone is discussed. The approach for such temperature prediction is based on numerical methods such as the finite-difference and finite-element methods.

However, subtle differences exist between the works of various authors. Thus, Song and Kovacevic (Ref 5) considered \dot{q} as a boundary condition with heat generation due to friction at the shoulder/matrix interfaces. Both friction and shear were considered to be the heat-generation source at the pin/matrix interface. The coefficient of friction was assumed to be a constant value (~ 0.4). On the other hand, Khandkar et al. (Ref 10) assumed the existence of a uniform shear stress at the entire tool/matrix interface. The total heat input was derived from the torque measurements obtained from actual FSW experiments. The simulated time-temperature profile obtained was then matched with the experimental data by assuming an appropriate conductance value of the base plate. Frigaard et al. (Ref 17) calculated the temperature profile by using an adjustable friction coefficient. The friction coefficient was adjusted such that the peak processing temperature never exceeded the liquation temperature. However, during the initial plunge period, the coefficient of friction was assumed to be a constant with an approximate value of 0.4. The pressure (P) during FSW was assumed to be constant. Similar simulations done by Khandkar and Khan (Ref 18) resulted in a friction factor value of only 0.15. As can be noted, although the predicted

temperature profiles matched with the measurements, the coefficient of friction assumed by various authors was inconsistent. The results clearly indicate that using friction as the sole heat-generation source is unrealistic and does not simulate the actual process occurring during FSW.

Material Flow

The discussion on thermal aspects of FSW and the variation in friction coefficients clearly indicates that plastic flow plays a crucial role during heat generation. In the next section, the experimental results on material flow during FSW are presented.

Experimental Aspects

Experiments on material flow in FSW can be categorized into two main groups: marker studies and dissimilar welding. In the marker studies, small, undissolvable material such as steel balls or SiC particles (in aluminum) are inserted in grooves machined along the welding path. The passage of the FSW tool and accompanying material flow displaces the markers, from which the material movement during FSW is reconstructed. In the dissimilar-welding technique, materials that etch differently are welded together, with the material flow reconstructed by postweld chemical etching. Alternatively, microtextural changes after FSW have also been used to understand the material movement. A more detailed discussion on texture evolution during FSW is given in the section "Texture" in this article. In Table 2, the results

Table 2 Summary of marker study results by various authors

Study type	Ref	Flow pattern
Steel shots in AA6061-T6 and AA7075-T6	19	(a) Steel shots affected by shoulder deposited chaotically and moved downward (b) Steel shots in pin front deposited continuously behind pin and moved up
AA5454-H32 marker in AA2195-T8	20	(a) Material stirring occurs only at shoulder-affected zone. (b) In pin-affected zone, material moves behind its original position. (c) For threaded pins, a secondary vertical flow exists.
Radioactive Ni tracer in AA2219-T8	21	Metal rotated around tool in a thin sliver just beneath shear surface ("wiping flow") in last-in/first-out mode.
Microtexture study in AA6063-T5	22	(a) Transverse weld section microtexture shows {111} planes as roughly parallel to pin surface. (b) The <110> directions were parallel to transverse direction. (c) Shear type of plastic flow along pin surface
Microtexture study in AA1100, AA6061-T6, and C458 alloy	23	(a) Dominant shear direction is aligned tangent to rotating tool. (b) Secondary shear direction along tool such that {111} planes are inclined 70° from the dominant shear direction
Cu foil along faying surface in AA6061-T6	24	(a) Advancing-side material deposits behind pin on advancing side. (b) Retreating-side material stays on retreating side. (c) Vortex movement within rotational zone associated with the pin
Microtexture study in AZ-61 alloy	25	(a) Prominent basal texture (0002) of base material traced an ellipsoid surrounding the pin column. (b) The effect was not noticed near the shoulder region. (c) Onion-ring structure and nugget shape associated with the elliptical trace of (0002) texture
Al-30vol%SiC and Al-20vol%W markers in AA7050 alloy	26	(a) Upward movement of material ahead of pin (b) Markers at advancing side distributed over a much wider region in the wake of weld compared to weld centerline (c) Downward movement of material due to tool threads
Microstructural studies on AA2024-T3/2524-T3	27	(a) Metallurgical bands (low-strain and high-strain alternating bands observed on etching) form, which correspond closely to tool marks. (b) Variation in secondary particle segregation and grain size along bands
Microstructure studies on AA2024-T3/2524-T3	28	(a) Strong correspondence between strain response and metallurgical bands (b) High-strain bands correspond to lower particle density, larger grain size. Reverse is true for lower-strain bands.
Textural studies on AA2195-T8 alloy	29	(a) The {111} planes are aligned with the tool rotation axis. (b) Randomly oriented grains in nugget
Cu as marker in AA2024-T3 alloys	30	(a) Average material flow velocity 0.1–0.3 times the tool rotation speed (b) Three different zones of rotation around the pin are proposed: rotation, transition, and deflection. (c) In rotational zone, material sticks to tool and undergoes multiple rotations.

of some marker and microtextural studies done in FSW have been summarized (Ref 19–33), and a typical example is presented in Fig. 4. The basic material flow characteristics obtained from experiments can therefore be summarized as follows (Ref 31):

- Near the shoulder region, material from the retreating side is dragged across the weld centerline and deposited on the advancing side.
- Material intersecting the pin travels around the retreating side and is deposited behind the tool, being moved backward from the original position by no more than one pin diameter, except for welds where shoulder flow dominates (e.g., in thin-sheet welding).
- Flow pattern similar to that of the shoulder is seen near the pin bottom, but on a much smaller scale.
- Tool runout can affect the material flow in addition to causing periodic variation in welding forces.

Although the aforementioned flow features were obtained mostly from FSW of aluminum alloys, similar studies on magnesium alloys and steels reveal identical material flow characteristics (Ref 25, 32). Therefore, the material flow characteristics mentioned previously holds true regardless of the crystal structure of the metal considered.

Another typical flow characteristic observed in FSW is the banded feature, which is observed on etching of FSW cross sections, as seen in Fig. 5 (see also the discussion on “onion rings” in the section “Cross Section of FSW Material” in this article). These bands are characterized by alternating microstructures with different grain and particle size distributions in the weld nugget, where the individual bands are separated by a distance equal to or less than the tool advance per revolution

(i.e., v/ω). Recent experiments by Yan et al. (Ref 35) indicate that the banding is associated with periodic oscillations in force that occur during each tool revolution in FSW and are unaffected by tool runout. However, at present no definite explanation for this periodic metallurgical feature is established, although broadly, material flow has been accepted to be behind its genesis.

Analytical Modeling

In this section, two analytical models, supplemented by experimental/numerical flow models, are described. In Nune’s (Ref 21) rotating plug model, the flow in the proximity of the tool pin was approximated by a rotating disc that is superimposed on a continuum moving at the speed of welding. The particle trajectory during FSW was therefore expressed as (Ref 21):

$$x^2 + \left(y + \frac{v}{\omega}\right)^2 = \text{Constant} \quad (\text{Eq 10})$$

The boundary of the rotating disc was considered to be a region of velocity discontinuity, that is, the shearing surface. Additionally, a vortex flow due to tool thread action was also incorporated where the radial velocity of material was assumed to vary sinusoidally with the weld depth. Although Nune’s (Ref 21) model partially simulated the material flow as observed by nickel tracer distribution, it is inapplicable for unthreaded tools and lacks physical explanation, particularly for the shoulder-affected region of FSW.

Schmidt and Hattel (Ref 36), on the other hand, proposed a two-dimensional analytical model to determine the material shear layer thickness located around the rotating tool (Fig. 6). This model explains the shear layer asymmetry observed in FSW experiments

and assimilates the rotation and transition zone concepts proposed by Guerra et al. (Ref 24). Schmidt et al. (Ref 30) further used this model to calculate the material flow velocity during FSW in a separate experimental paper published later. The width of the shear layer (w_θ) variation as a function of angle, θ (Fig. 6), calculated from the centerline of the weld (positive toward retreating side and negative toward advancing), was expressed as (Ref 36):

$$w_\theta = \frac{2R_{\text{pin}}v(\sin\theta + 1) + w_{\text{adv}}\omega}{\omega R_{\text{pin}} - v\sin\theta} \quad (\text{Eq 11})$$

Although the aforementioned analytical models provide valuable insight into the material flow mechanisms, they have a limited practical use. Consequently, numerical simulations are assuming a more significant role in extending the current understanding about the processes that occur during FSW.

Numerical Modeling

Standalone material flow models, although physically inaccurate, do provide significant insight into the process when done in tandem with experimental results. The mass and momentum balance equations form the basic building block for such simulations, where the mass balance equation is given as:

$$\frac{\partial \rho}{\partial t} = - \left[\frac{\partial(\rho u_x)}{\partial x} + \frac{\partial(\rho u_y)}{\partial y} + \frac{\partial(\rho u_z)}{\partial z} \right] \quad (\text{Eq 12})$$

with the density, ρ , remaining constant for all practical purposes. The momentum balance equation is expressed as (Ref 13):

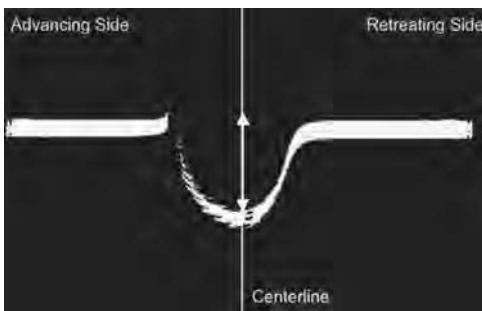


Fig. 4 Distribution showing the position of AA5454-O markers (white region) in AA2195-T8 alloy after the passage of friction stir tool pin. The markers placed perpendicular to the weld path moved backward by a distance equal to the chord length intersecting the pin circle, and oriented parallel to welding direction. The double arrow gives a measure of the pin diameter used. Source: Ref 31

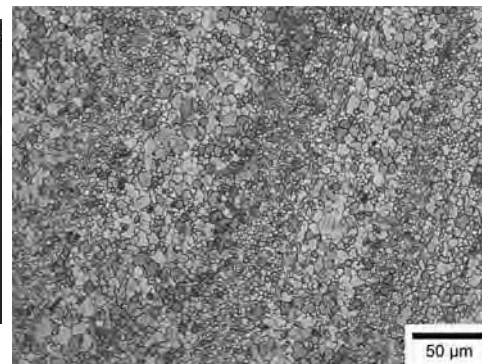


Fig. 5 Difference in grain size within the ring patterns observed in the horizontal-section microstructure of a bead-on-plate run of cast A356 alloy. The tool advance per revolution (APR) was 0.1 mm (0.004 in.). Note that the gap between the bands matches the APR from Ref 34.

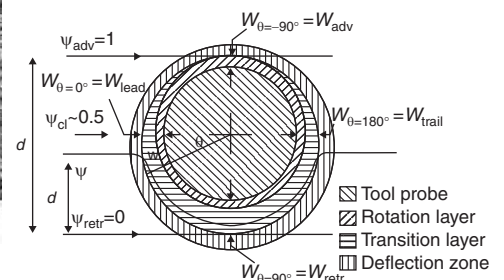


Fig. 6 Various layers in friction stir welding nugget as proposed by Schmidt and Hattel (Ref 36). The streamlines (ψ) of material flow are also depicted, along with the shear layer variation with θ . Source: Ref 30

$$\begin{aligned}
 & \{\text{Mass per unit volume times acceleration}\} \\
 & + \{\text{Pressure force on element per unit volume}\} \\
 & + \{\text{Viscous force on element per unit volume}\} \\
 & + \{\text{Gravitational force on element per unit volume}\} \\
 & + \{\text{Body forces}\} \qquad \qquad \qquad \text{(Eq 13)}
 \end{aligned}$$

Schmidt and Hattel (Ref 37) used a two-dimensional version of Eq 13 to model the material flow around the pin, where the material during FSW was assumed to follow a non-Newtonian power law equation. These simulations showed the presence of a rotational and transition zone, as proposed by Guerra et al. (Ref 24). Similar material flow simulations in two dimensions conducted by Xu et al. (Ref 38) used an adaptive Lagrangian-Eulerian technique (ALE) in combination with the experimental temperature measurements from a previous work. The results showed that material flow in FSW occurs along the retreating side, replicating the general flow feature observed during experiments. A complete understanding of material flow, however, requires three-dimensional simulations with simultaneous consideration of both thermal and material flow models. In the next section, a brief discussion on coupled modeling in FSW is presented.

Coupled Numerical Modeling

The principal intent of coupled numerical modeling using finite-element modeling (FEM) is to solve the energy and momentum partial differential equations (i.e., Eq 6 and 13) simultaneously. Depending on the approach taken, the heat source is modeled on the basis of Eq 3 and 5 or Eq 4 and 5. Thus, when material flow is considered to be a plastic deformation problem, Eq 3 and 5 are used, and when in the fluid dynamic approach, Eq 4 and 5 are adopted. However, in both cases, the stress response variation of the metal to changing temperatures and strain rate, that is, the choice of constitutive equation, determines the accuracy of the simulations.

Table 3 summarizes the constitutive equations adopted by various authors during FSW simulations, where the equation constants are obtained from isothermal hot compression experiments or torsion experiments. During hot compression experiments, the levels of strain achieved are much lower compared to those estimated for FSW. On the other hand, in torsion experiments, although levels of strains achieved are higher than in the hot compression case, the strain distribution is nonuniform, being highest at the surface and zero at the specimen center. Thus, the strain rate and temperature regimes during such experiments are significantly different from that of FSW, which introduces inherent uncertainties into the constitutive equations adopted.

Another important difference is the capability of the simulations to reproduce different welding defects (see the section “Simulation of Defect Formation” in this article) that occur during FSW. To understand the complexities of such simulation, the difference between Lagrangian and Eulerian representation in kinematics needs further

elucidation. In Lagrangian representation, the flow path of individually identifiable material volumes is traced with respect to their initial position. The Eulerian flow representation, on the other hand, tracks the material velocity at fixed locations in the space. Plastic deformation modeling uses the Lagrangian representation, while fluid dynamics modeling uses the Eulerian representation. In other words, the finite-element mesh during plastic deformation modeling distorts with the progression of the simulation, while in the fluid dynamics approach, the finite-element mesh remains undistorted. This, along with the contact surface requirements during FEM-based modeling, makes defect simulation using the fluid dynamics approach unachievable. Again, excessive mesh deformation during plastic-deformation-based FSW simulation creates numerical instabilities, causing Lagrangian representations to be inherently difficult to simulate. Currently, attempts are being made to address this issue by using more complex numerical methods, such as the ALE technique (Ref 39). In fact, Schmidt and Hattel (Ref 39) have shown that defect simulation using the ALE technique is numerically achievable (see the section “Simulation of Defect Formation” in this article). In Table 4, a summary of the different coupled numerical approaches used by various authors is presented.

Friction

As discussed previously, frictional heat generation is a major part of the FSW process.

Table 3 Constitutive models adopted in friction stir welding simulations published in literature.

Here, Z denotes the Zener-Holloman parameter, and σ , $\dot{\epsilon}$, and $\bar{\epsilon}$ are the average stress, strain rate, and strains, respectively. T_M is the melting point, and T_{ref} is a reference temperature. Remaining variables are material constants and are obtained experimentally.

Ref	Constitutive model used
39	$\sigma = (A + B[\dot{\epsilon}]^n) \left(1 + C \ln \frac{\dot{\epsilon}}{\dot{\epsilon}_0}\right) \left(1 - \left(\frac{T - T_{ref}}{T_M - T_{ref}}\right)^m\right)$
40	$\sigma(T, \dot{\epsilon}) = \frac{1}{2} \ln \left(\left[\frac{Z}{A}\right]^{1/n} + \left\{ \left[\frac{Z}{A}\right]^{2/n} + 1 \right\}^{1/2} \right)$
41	$\sigma_e = \frac{1}{2} \sinh^{-1} \left[\left(\frac{Z}{A}\right)^{1/n} \right]$
42	Extrapolation from experimental data
43	$\sigma = KT^A (\dot{\epsilon})^B (\bar{\epsilon})^C$
44	$\sigma_e = \frac{1}{2} \sinh^{-1} \left[\left(\frac{Z}{A}\right)^{1/n} \right]$
45	$Z = A(\sinh \alpha \sigma)^n$

Table 4 Summary of coupled simulations in friction stir welding as published in literature

Simulations are differentiated on the basis of modeling approach used: ALE, adaptive Lagrangian-Eulerian; CFD, computational fluid dynamics; and LM, Lagrangian method. The temperatures mentioned in column 4 are the peak simulation temperatures.

Ref	Approach	Material	Temperature, K	Other variables predicted
39	ALE	AA2024-T3	773	Deformation field, plunge force
40	CFD	AA6061-T4	Isothermal	Material flow, power, X-force
41	CFD	AA7075-T7	701	Material flow, pin forces
42	LM	AA6061-T6	773	Residual stress
43	LM	AA7075	731	Strain distribution, material flow
44	CFD	AISI-1018	1100	Strain rate, tool torque, material flow
45	CFD	AA5083 and AA7075-T6	1133	Material flow, transverse force, power

The frictional heat generated at the tool/work-piece interface is considered to be particularly important at the beginning of the process (plunge portion) and was also observed in the simulations of Schmidt and Hattel (Ref 39). According to Schmidt and Hattel’s simulation, during the pseudo-steady-state period of actual welding, the contribution of heat generated due to frictional forces decreases to ~25% of the total heat generated (Ref 39). Nonetheless, for accurate FSW process simulation, a proper assessment of frictional heat contribution is essential.

Frictional forces can be classified mainly into two types: Coulomb’s and constant shear. For Coulomb’s friction, the frictional force is expressed as:

$$\sigma = \mu p \qquad \qquad \qquad \text{(Eq 14)}$$

where μ is the Coulomb’s coefficient of friction, and p is the pressure applied. The frictional stress for the constant shear model is given as:

$$\sigma = m \frac{\sigma_0}{\sqrt{3}} \qquad \qquad \qquad \text{(Eq 15)}$$

where m is the friction factor, and σ_0 is the flow stress of the material. Schmidt and Hattel (Ref 11) proposed a modified description for the frictional forces during FSW, where three different conditions were assumed to exist. They are sticking condition, sliding condition, and partial sliding/sticking condition. A modified contact variable, δ , was proposed (see the

section “Heat-Source Estimation” in this article), which was defined as (Ref 11):

$$\delta = \frac{U_{\text{matrix}}}{U_{\text{tool}}} \quad (\text{Eq 16})$$

where U_{matrix} is the linear matrix velocity, and U_{tool} is the corresponding linear tool velocity at that position. This was subsequently used to develop an analytical model for heat generation in FSW (Eq 2). Thus, for the sliding condition, the value of m in Eq 15 is 0, while for sticking friction, m assumes a value of 1. It should be noted that in FSW, coefficient of friction values greater than 1 have also been reported. Colligan and Mishra (Ref 46) have reported coefficient of friction values as high as 1.3 (Fig. 7). This relates to the complexity of the frictional conditions during FSW. The experimental and theoretical approaches so far try to obtain or use a value of coefficient of friction for a particular run. However, the coefficient of friction would vary across the tool shoulder and pin surface because the pressure and temperature is location-specific. A fundamental understanding of this is lacking.

Defects

Improper processing leads to defects in the welded zone in all joining processes, and FSW is no exception. The defects have been found

in butt joints as well as lap joints. Material flow and heat-generation patterns have been attributed to the creation of defective welds. In this section, types of defects, processing parameters affecting the generation of these defects, and results of theoretical models and simulations to understand the formation and control of defects during FSW are discussed.

Types of Defects

Arbegas (Ref 47) reported various types of defects (wormhole or voids, lack of penetration, lack of fusion, surface lack of fill, root-flow defect, nugget collapse, surface galling, and scalloping), and representative examples of these are shown in Fig. 8. These defects are either flow related or geometric. Also shown in Fig. 8 is a processing map correlating the tool rotational rate and tool traverse speed and the impact of these parameters on the generation and control of these defects. In flow-related defects, processing of a material outside the processing window leads to defect generation due to unbalanced material flow. Improper tool selection, insufficient plunge depth, unequal thicknesses of joining materials, or improper seam tracking lead to geometric defect formation.

Among all, the most commonly encountered defects are voids, joint-line remnants, and improper root penetration (Ref 48). Voids have been reported to form on the advancing side of

the welds. Some of the voids formed during FSW are shown in Fig. 9. Figure 9(a) shows a predominantly surface-breaking void (Ref 49). A tunnel type of void is shown in Fig. 9(b) (Ref 50).

A joint-line remnant (JLR) defect is also termed a lazy “S” or zigzag line (Ref 51). If processing parameters or surface conditions at the interface of the materials being joined are such that, during processing, oxide layers cannot be disrupted, it leads to formation of a JLR. The oxide layers are present at the faying surface of the workpieces to be joined. A representative example is shown in Fig. 10 (Ref 48). Like other defects, JLR is also dependent on processing and geometric conditions.

Among many parameters, a considerably smaller pin height compared to the thickness of the plates to be joined and positioning of the tool relative to the joint interface are the main reasons for incomplete root penetration. Local thickness variation of plates may also lead to this defect (Ref 48).

Kim et al. (Ref 52) discussed three other types of defects: excess heat input resulting in flash formation, cavity- or groove-like defects, and abnormal stirring that leads to cavity formation. The groove and channel defects have also been reported by Chen et al. (Ref 53).

Parameters Affecting Defect Formation

Tool rotational rate, tool traverse speed, axial pressure, tool tilt angle, tool geometry, and gap between plates are a few important processing parameters determining the quality of the weld. Tool rotational rate affects the formation of defects in two ways. Low rotational rate causes lower heat input and hence less softening of the materials being joined, and very high rotational rate causes abnormal stirring. Kim et al. (Ref 52) have addressed these two aspects of the effects of rotational rate on the formation of weld defects. Figure 11 shows the effect of rotational rate on void formation. As can be noted, lower rotational rate led to insufficient heat input and resulted in defect formation. On increasing the rotational rate from 1250 to 1500 rpm and keeping the tool traverse speed the same (250 and 500 rpm) in the first two cases, sound FSW welds were obtained. On further increasing the rotational rate, defects appeared again due to abnormal stirring of the processed material. Kim et al. (Ref 52) suggested that the abnormal stirring was a result of a difference in temperatures between the upper and lower parts of the weld. In Fig. 11, the effect of axial pressure can be noted as well. For the defects arising due to insufficient heat input, increasing axial pressure reduced the size of the void. The effect of increase in axial pressure on the defects generated due to abnormal stirring was marginal.

In a study to show the effect of welding speed, Zhang et al. (Ref 54) changed welding speed from 40 mm/min (1.6 in./min) to 600

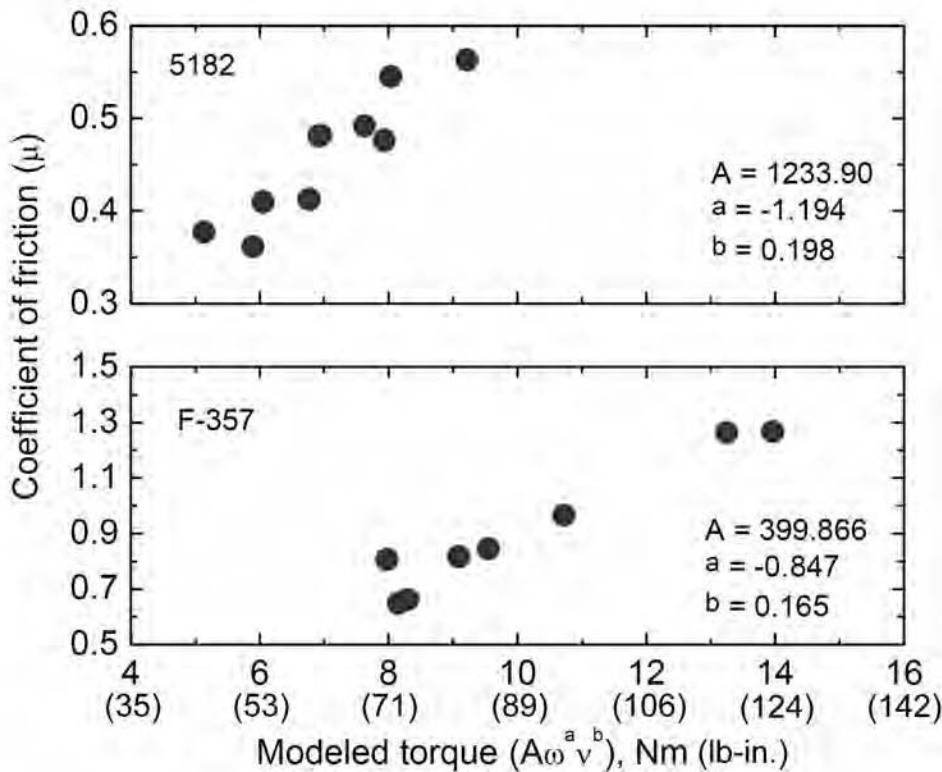


Fig. 7 Variation of coefficient of friction with torque for AA5182- and F-357-type aluminum alloys. Source: Ref 46

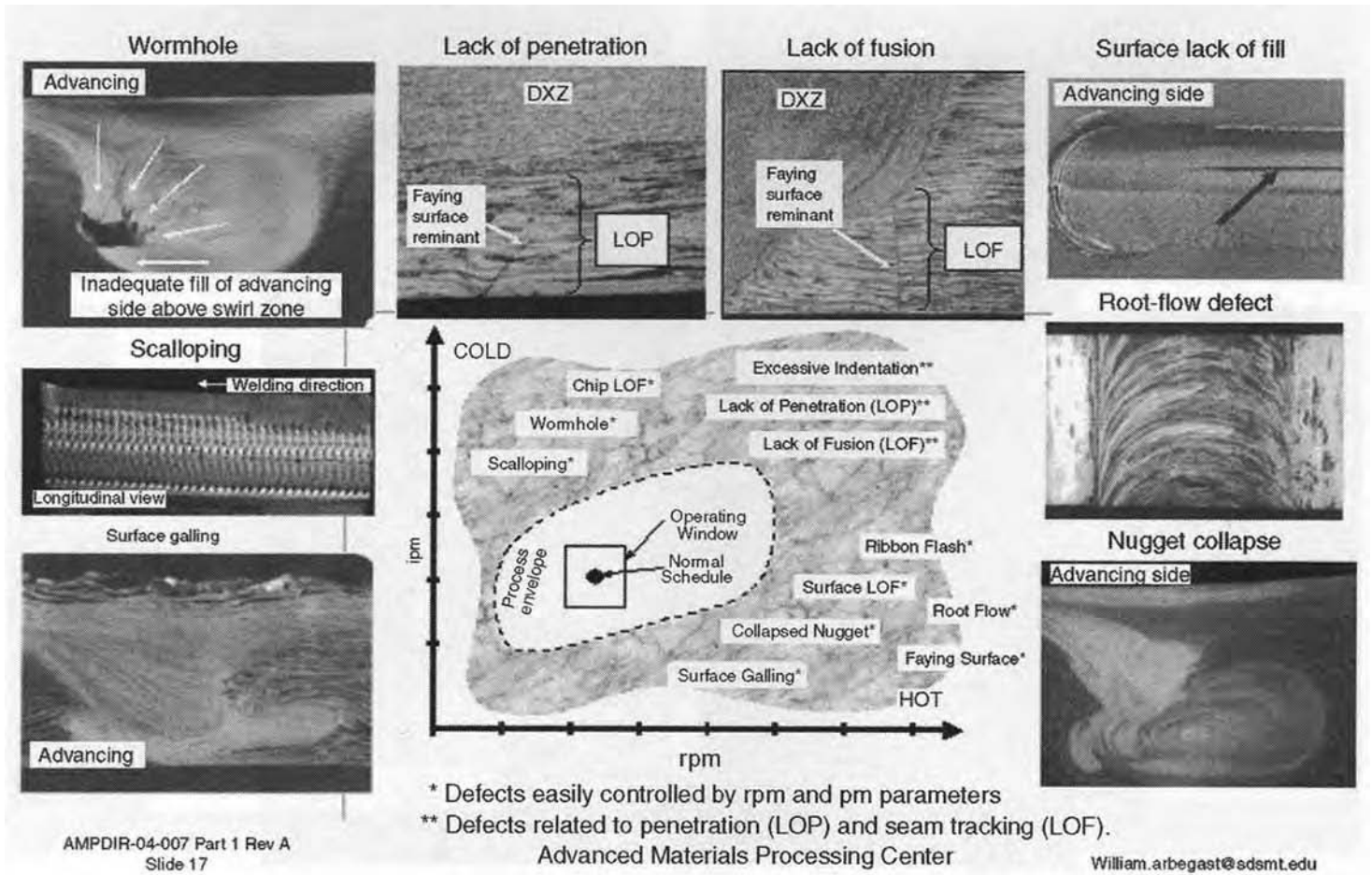


Fig. 8 Types of defects and process map (tool traverse rate vs. rotational rate) governing the process window. Source: Ref 47

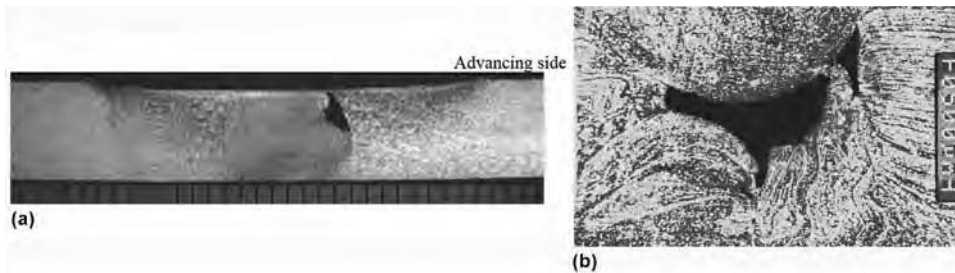


Fig. 9 (a) Surface-breaking void type of defect in a 2014Al alloy. Source: Ref 49. (b) Tunnel (void) defect formed in 5083Al-O alloy. Source: Ref 50

mm/min (24 in./min) at a constant rotation rate of 1000 rpm. The micrographs from their study demonstrating the effect of welding speed on defect formation are shown in Fig. 12. It can be noted that voids formed at a welding speed of 200 mm/min (8 in./min).

The effect of tool geometry has been studied by Elangovan and Balasubramanian (Ref 55, 56). Five different pin profiles (straight cylindrical, threaded cylindrical, tapered cylindrical, square, and triangle) were used by these

researchers, and the formation of a sound weld was discussed in terms of the effect of pin profiles on material flow. The material flow was explained on the basis of the relationship between the static and dynamic volume defining the zone of thermomechanically plasticized material flow. The effect of shoulder diameter on defect formation has also been addressed (Ref 55). Using a larger-diameter tool resulted in formation of sound welds due to sufficient heat input compared to tools with smaller diameters.

Tool tilt angle also has an influence on defect formation. Chen et al. (Ref 53) studied the effect of tool tilt angle on the formation of weld defects. The formation of groove-type defects was reported by these authors at a very small tool tilt angle (1°) on the advancing side of the weld. At a tool tilt angle of 3.5° , a sound weld formed. However, on further increase of the tilt angle $\geq 4.5^\circ$, void formation was observed again.

Leal and Loureiro (Ref 50) have studied the effect of alloys on the formation of defects. Three alloys, 5083-O, 2024-T3, and 6063-T6, were used in that study. Under the processing conditions used, 6063-T6 did not show any defects, whereas defects were observed in the remaining two alloys. This shows the link between the flow behavior of the material and defect formation.

Leonard and Lockyer (Ref 49) have shown the effect of the presence of joint gap on weld formation. A joint gap of 3.2 mm (0.13 in.), which corresponded to 50% of the plate thickness, resulted in a defective weld, and the presence of a cavity was reported on the advancing side of the weld.

Theoretical Models of Defect Formation

To develop a physical understanding of the defect formation process, efforts have been made to develop theoretical models by various researchers (Ref 52, 54, 57). Here, the model developed by Arbegast (Ref 57), based on a flow-partitioned deformation zone, is discussed. (Refer to Ref 52 and 54 for more details.)

Arbegast (Ref 57) divided the material flow process during FSW into four zones, as shown in Fig. 13. In accordance with this model, material passing through zone III on the retreating side is dragged toward the advancing side. It is interleaved with the material flowing from

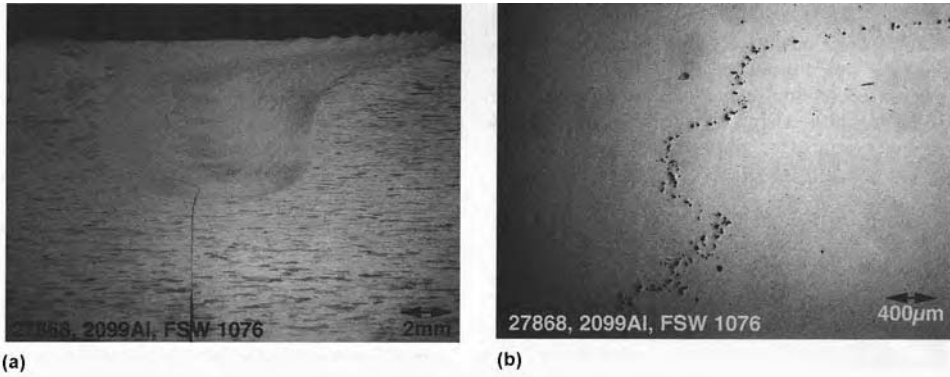


Fig. 10 (a) Macroscopic view of joint-line remnant defect. (b) Higher-magnification image showing the oxide particles dispersed in the processed zone. Source: Ref 48

ADC12, FSW, 4 mm (0.16 in.) thickness				
	6.9 kN	9.3 kN	11.8 kN	14.2 kN
Abnormal stirring				
	1750 rpm-250 mm/min (9.8 in./min)	1750 rpm-500 mm/min (20 in./min)	1500 rpm-750 mm/min (30 in./min)	1500 rpm-750 mm/min (30 in./min)
Sound FSW joints				
	1500 rpm-250 mm/min (9.8 in./min)	1500 rpm-500 mm/min (20 in./min)	1250 rpm-750 mm/min (30 in./min)	1250 rpm-750 mm/min (30 in./min)
				1000 rpm-750 mm/min (30 in./min)
Insufficient heat input				
	1250 rpm-250 mm/min (9.8 in./min)	1250 rpm-500 mm/min (20 in./min)	1000 rpm-750 mm/min (30 in./min)	750 rpm-750 mm/min (30 in./min)

Fig. 11 Effect of tool rotational rate on defect formation in friction stir welding (FSW). Additionally, the effect of axial pressure on defects can be noted. Source: Ref 52

the advancing side and is pushed vertically downward, entering zone I. Part of the material flowing in zone II may enter zone IV under the pin before entering into zone I from zone IV.

This model is based on the criterion of mass balance; material entering the cavity on the

trailing side created by the tool movement per revolution should be exactly balanced by the material flowing from the leading side of the tool. It was defined as the critical total mass flux of material, M_T^{cr} , and this is given as:

$$M_T^{cr} = \rho(\alpha \cdot \beta \cdot \phi^2)^{-1} \tag{Eq 17}$$

where ρ , α , β , and ϕ are the density of the material, the pin shape factor (mm^{-1}), the shoulder shape factor (mm^2), and the processing parameters (defined as tool rotational rate/tool traverse speed), respectively. For the extrusion zone, Eq 17 can be rewritten for a specific location (i) as:

$$M_T^{cr} = \sum \rho_i \left(\alpha \cdot \beta \cdot \left(\frac{\omega_i}{v_i} \right)^2 \right)^{-1} \tag{Eq 18}$$

In Eq 18, ω_i and v_i are the tool rotational rate and tool traverse speed, respectively. The whole process of welding is divided into three zones in terms of material flow: initial deformation zone (M_T^i), extrusion zone (M_T^e), and forging zone (M_T^f). The variables M_T^i , M_T^e , and M_T^f are given as:

$$M_T^i = M_I^i + M_{II}^i + M_{III}^i + M_{IV}^i = \sum_{j=I}^{IV} M_j^i \tag{Eq 19}$$

$$M_T^e = M_T^i + M_T^{XS} = \sum_{j=I}^{IV} M_j^i + \sum_{j=I}^{IV} M_j^{XS} \tag{Eq 20}$$

$$M_T^f = M_I^f + M_{II}^f + M_{III}^f + M_{IV}^f = \sum_{j=I}^{IV} M_j^f \tag{Eq 21}$$

For a defect-free weld, balanced material flow should take place, and this criterion is met when $M_T^f = M_T^{cr}$. For defect formation, $M_T^f < M_T^{cr}$. In such cases, $M_T^e = M_T^e + M_T^{wh}$ and M_T^{wh} is termed as wormhole mass deficiency and defined as:

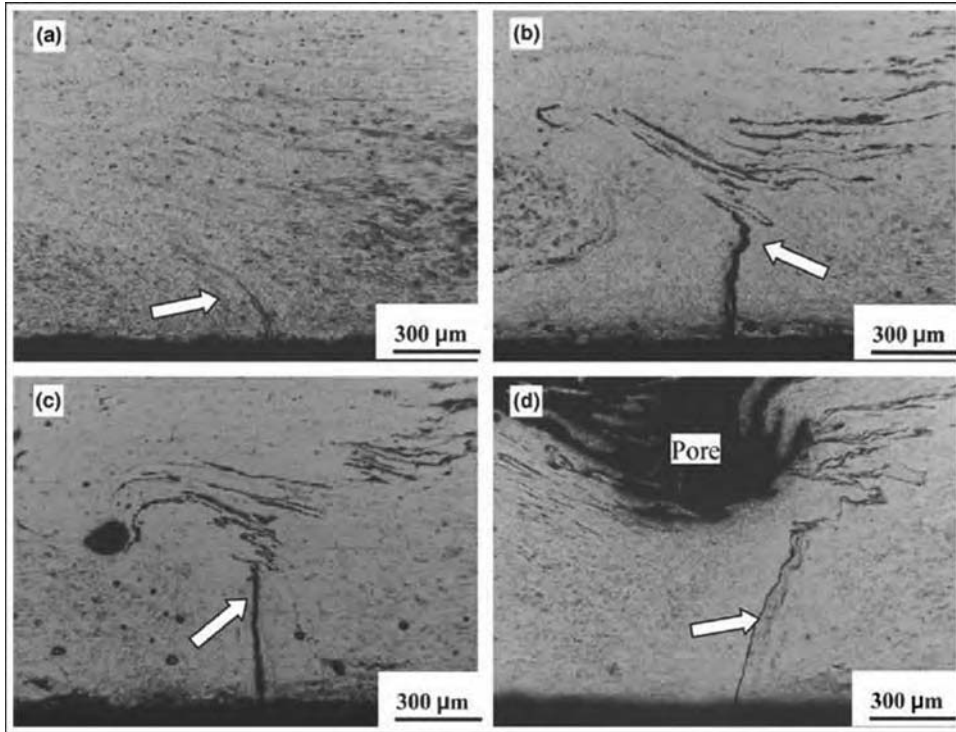


Fig. 12 Friction stir weld regions at tool traverse speed of (a) 40 mm/min (1.6 in./min), (b) 120 mm/min (4.7 in./min), (c) 150 mm/min (6.0 in./min), and (d) 200 mm/min (8.0 in./min). Processed region corresponding to 200 mm/min shows void. Source: Ref 54

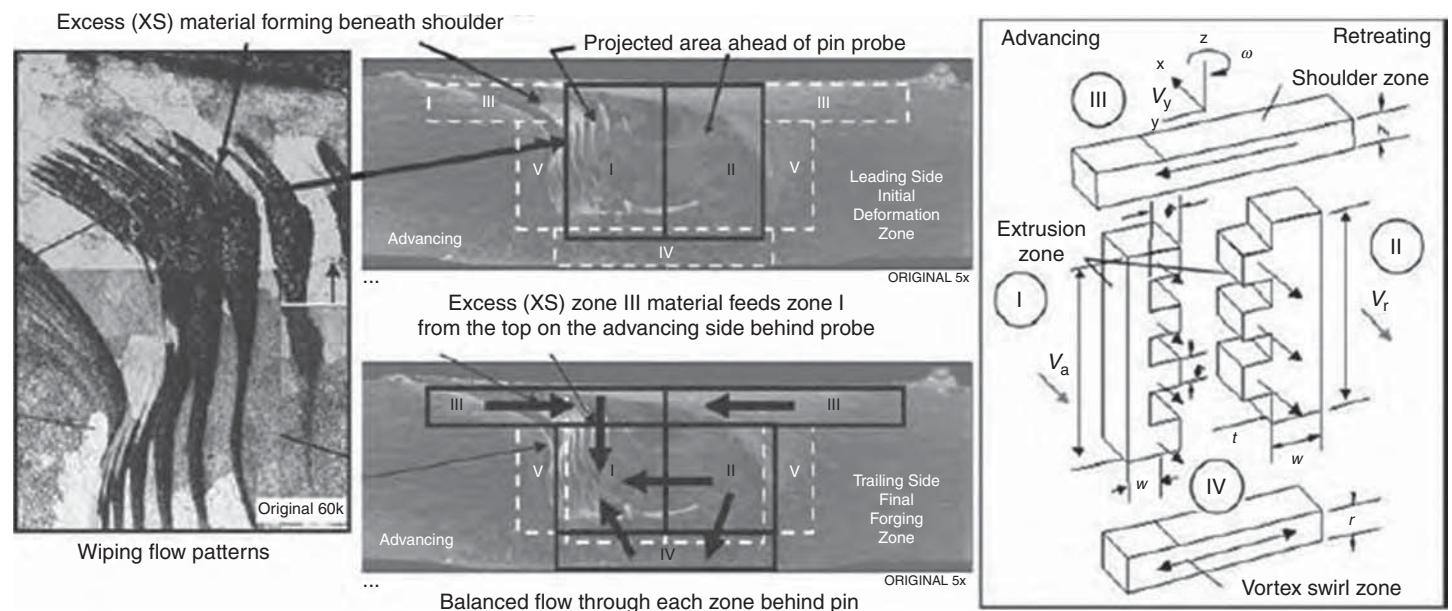


Fig. 13 Flow-partitioned zone model showing the flow of material during friction stir welding. Source: Ref 57

$$M_T^{wh} = M_T^{cr} - \sum_{j=1}^{IV} M_j^i - \sum_{j=1}^{IV} \psi_j(\alpha, \beta, \phi^2) \quad (\text{Eq 22})$$

where $\psi_j(\alpha, \beta, \phi^2)$ is an excess material factor that takes the excess material entering the extrusion zone into account. Hence, the flow-partitioned zone model represents formation of the defect in terms of an imbalance created by material flow from one zone to another.

Some of the defects shown in Fig. 8 can be explained using Arbegast's flow-partitioned model. Inadequate flow of materials to zone I from zones II, III, and/or IV would cause a third term on the right side of Eq 22 to be less than needed for mass balance. Consequently, it will result in formation of defects such as lack of fill, wormholes, or lack of consolidation. If there is very little or no flow of materials from zone II to zone IV, it will again create mass imbalance in zone IV and may result in a root-flow defect.

Simulation of Defect Formation

Despite availability of a large volume of experimental and theoretical data to understand the material flow during the FSW process, the exact nature of material flow is not known due to the complex nature of thermomechanical conditions during welding. Consequently, the formation of defects is not properly understood. Due to improved computational capability and the availability of commercial codes to simulate large deformation, efforts have been made to simulate the material flow process during FSW. Schmidt and Hattel (Ref 39) used fully coupled three-dimensional thermomechanical finite-element models using ABAQUS/Explicit to study the material flow during FSW. An ALE formulation and Johnson-Cook material model was used to model the system. The output of their simulation study leading to the prediction of void formation is shown in Fig. 14. It shows the formation of a void on the trailing side of the lower advancing side at the pin/matrix interface.

Strain and Strain Rate in FSW

For a severe plastic deformation process such as FSW, knowledge of the strain and strain rate experienced during processing is essential to understand the microstructural evolution. Such strain and strain-rate estimations have been carried out by various researchers using experimental, analytical, and simulation techniques. In some cases, a combined approach was also adopted. These efforts are summarized in Table 5.

A more simple and elegant way of estimating the strain and strain rates during FSW is the analytical approach, some of which is discussed further. Chang et al. (Ref 63) assumed the deformation process during FSW to be of the torsion type, which led to an expression for

strain rate. (Note: The texture observed after FSW is similar to torsional deformation; see the section "Texture" in this article.):

$$\dot{\epsilon} = \frac{\omega \pi r_e}{L_e} \quad (\text{Eq 23})$$

where r_e is the radius of the dynamically recrystallized zone, and L_e is the depth of the dynamically recrystallized zone. Long et al. (Ref 64) used the two-dimensional material flow field observed around the tool pin during experiments and simulations to propose a model for calculating strain and strain rate (Fig. 15). In this model, it was assumed that each streamline intersecting the pin on the leading side of the tool was transported to the trailing side at a position equal to the respective chord length. Based on this assumption, the expression to calculate strain in the FSW shear zone was given as:

$$\epsilon = \ln\left(\frac{l}{APR}\right) + \left| \ln\left(\frac{APR}{l}\right) \right| \quad (\text{Eq 24})$$

$$l = 2r \cos^{-1}\left(\frac{r-x}{r}\right) \quad (\text{Eq 25})$$

where APR is defined as the advance per revolution of the tool, l is the maximum stretched

length of a material in the shear zone of an initial length equal to APR, and r and x are the radius of the pin and the distance of the streamline from the retreating side of the tool, respectively. An estimate of the strain distribution in the processed zone for an APR = 0.5 mm/rev (0.02 in./rev) and a pin diameter of 10 mm (0.4 in.) is shown in Fig. 16 (Ref 64). It can be noted from Fig. 16 that, on the retreating side, strain is zero, while a maximum in strain is observed (in this case, ~8) on the advancing side. This is consistent with the experimental observations during FSW. A sharp transition from the base material to the advancing side of the processed zone and a gradual transition from the retreating side to the base metal are also observed. The average strain rate was calculated by obtaining the average strain from Eq 24 and 25, which was divided by the time per revolution (Ref 64). A typical result of this model is presented in Fig. 17.

The estimates for strain and strain rate discussed previously involve considerable simplification and assumptions. Hence, the actual strain and strain rate involved may be different from the values reported. A better understanding of the material flow process in the future is therefore expected to result in more comprehensive theoretical and computational models.

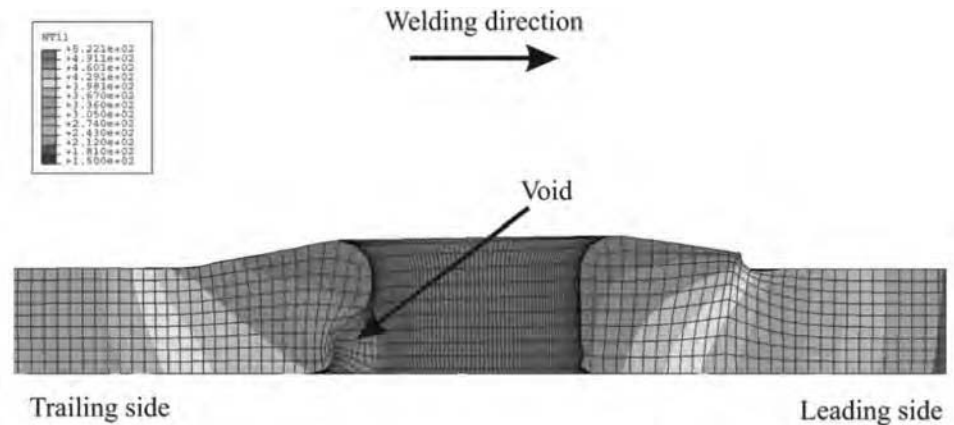


Fig. 14 Finite-element modeling in ABAQUS showing the formation of voids on the advancing trailing side of the weld. Source: Ref 39

Table 5 Summary of strain and strain rates during friction stir welding as reported in literature

Strain	Strain rate, s ⁻¹	Method	Ref
3.5	85	Dendrite rotation in thermomechanically affected zone (TMAZ)	58
...	10	Grain rotation in TMAZ	59
...	1-20	Extrapolated from Z and subgrain size relation	17
4.6	87	Modeling and marker methods	60
...	1.8	Plain-strain compression	61, 62
...	5-50	Analytical model	63
>10	~350	Analytical and numerical model	64
5-7	4-8	Numerical model	43, 65
10	9	Numerical model	66
...	30-100	Numerical model	44

Overall Microstructural Feature

Cross Section of FSW Material

The microstructure and its distribution produced during FSW are dependent on several factors. The contributing factors include alloy composition, initial material temper, welding parameter, tool geometry, and cooling rate. Based on microstructural characterization of grains and precipitates, a typical cross section of an FSW joint can be identified by three distinct zones: stirred (nugget) zone, thermomechanically affected zone (TMAZ), and heat-affected zone (HAZ) (Ref 67, 68). The HAZ is similar to that in conventional welds, although the maximum peak temperature is significantly lower than the solidus temperature. This zone experiences a thermal cycle but does not undergo any plastic deformation. Unique to the FSW process is the creation

of a transition zone, the TMAZ, between the HAZ and the nugget zone. The TMAZ experiences both temperature and deformation during FSW. The central stir region experiences the most severe deformation and is a consequence of the way in which a rotating tool deposits material from the front to the back of the weld. This region is usually referred to as the nugget zone (or weld nugget). Under some processing conditions, an “onion-ring” structure develops in the nugget zone. This has been linked to the nature of material flow during FSW (Ref 29, 69, 70). Depending on processing parameters, tool geometry, temperature of workpiece, and thermal conductivity of the material, various shapes of the nugget zone have been observed. Basically, the nugget zone can be classified into two types: a basin-shaped nugget that widens near the upper surface, and an elliptical nugget

(Ref 3, 71, 72). The interface between the nugget zone and the parent metal is relatively diffuse on the retreating side of the tool but quite sharp on the advancing side of the tool (Ref 73). Figure 18 shows the macroscopic features in a transverse section of an FSW 7075Al-T651 alloy.

The grain structure in the HAZ remains similar to the parent material. The TMAZ is characterized by a highly deformed structure. The grains of the original microstructure deform in this region in an upward flowing pattern around the nugget zone. Although the TMAZ undergoes plastic deformation, full recrystallization does not occur in this zone due to insufficient deformation strain. Grains in the TMAZ usually contain a high density of subboundaries (Ref 71). Within the nugget zone, intense plastic deformation at elevated temperatures during FSW results in generation of a recrystallized fine-grained microstructure. This region is also referred to as the dynamically recrystallized zone. It is well accepted that dynamic recrystallization during FSW results in generation of fine and equiaxed grains in the nugget zone. Figure 19 shows typical grain structures in different regions in an FSW 7050-T651 aluminum alloy. In some instances, where the dislocation recovery rate in a particular alloy is sufficiently high, the grain structure in the nugget region can remain unrecrystallized.

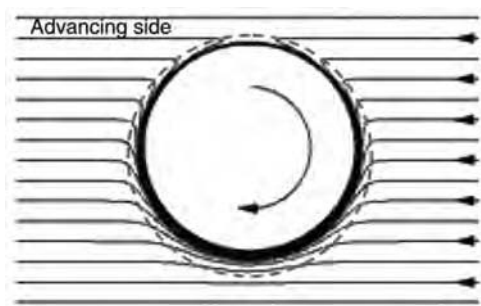


Fig. 15 Streamline flow field from two-dimensional computational fluid dynamics model representing material flow around a tool pin. Tool rotation is counterclockwise, and the tool moves from left to right. Source: Ref 31

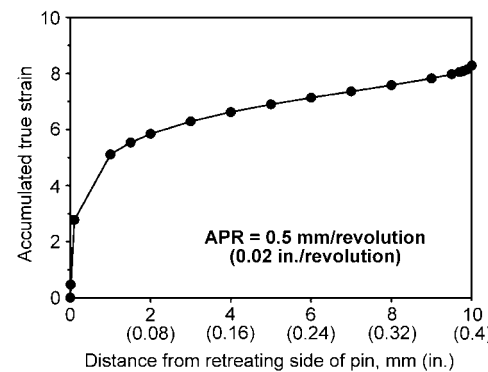


Fig. 16 Variation in strain from retreating side to advancing side for advance per revolution (APR) = 0.5 mm/rev (0.02 in./rev) ($\omega = 152$ rpm, $v = 0.27$ mm s⁻¹), tool pin diameter = 10 mm (0.4 in.), and tool pin height = 7.4 mm (0.3 in.). Source: Ref 64

Grain Size in the Nugget Zone

Grain size in the nugget zone in FSW materials can be affected by various factors, including processing parameters, tool geometry, composition of workpiece, temperature of the workpiece, vertical pressure, and active cooling. Typical recrystallized grain size in FSW aluminum and magnesium alloys is in the micrometer range, although ultrafine-grained microstructures (average grain size <1 μm) can be achieved by using external cooling or smaller tool geometries. Table 6 gives a summary of the grain size values obtained during FSW for a few aluminum and magnesium alloys.

Generally, FSW results in equiaxed fine-grained structures in the nugget zone. However, grain size is not uniform across the weld nugget. In FSW of aluminum alloys, the grain size tends to increase near the top of the weld zone, and it decreases with distance on either side of the weld-zone centerline. This corresponds roughly to the temperature variation within the weld zone (Ref 3, 105, 106). Figure 20 shows the distribution of the grain sizes in different locations of the nugget zone in FSW 7050Al (Ref 107). The average grain size ranges from 3.2 μm (126 μin.) at the bottom to 5.3 μm (207 μin.) at the top and 3.5 μm (138 μin.) from the retreating side to 5.1 μm (201 μin.) on the advancing side.

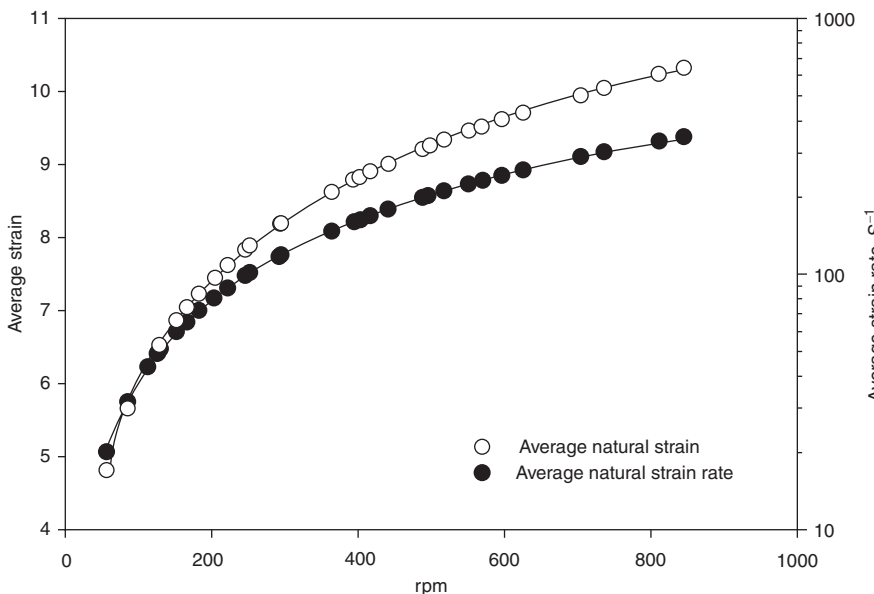


Fig. 17 Variation of average strain and strain rate as a function of tool rotational rate at $v = 1.27$ mm s⁻¹. Source: Ref 64

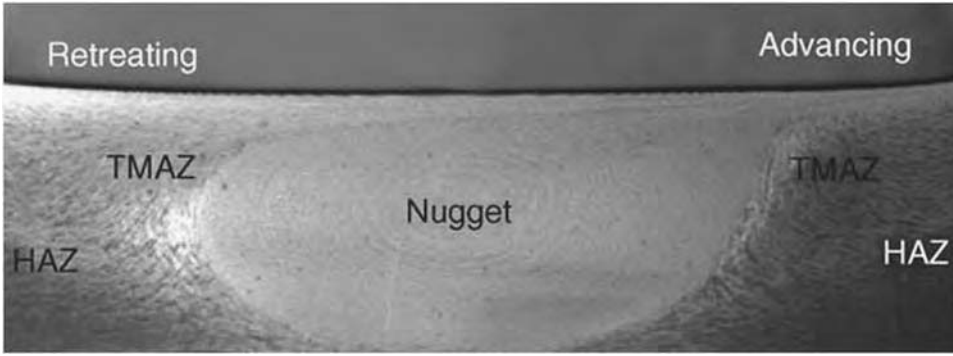


Fig. 18 Typical macrograph showing various microstructural zones in friction stir welded 7075Al-T651. TMAZ, thermomechanically affected zone; HAZ, heat-affected zone. Source: Ref 67

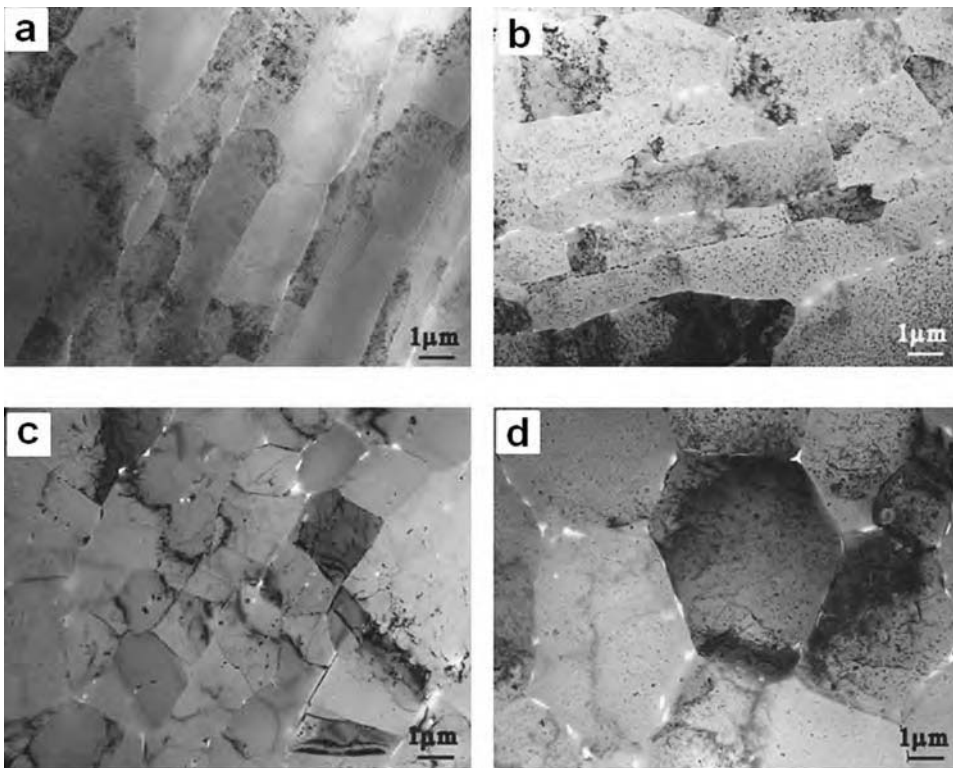


Fig. 19 Grain structure variations across friction stir welded 7050-T651 aluminum alloy. (a) Unaffected parent material. (b) Heat-affected zone. (c) Thermomechanically affected zone. (d) Nugget zone. Source: Ref 74

Table 6 Summary of grain size in nugget zone of friction stir welded aluminum and magnesium alloys

Material	Grain size		Ref
	μm	μin.	
7xxx	0.1–7.5	4–295	72, 74–78
6xxx	5.9–17.8	232–701	79–81
5xxx	3.5–6	138–236	82–84
2xxx	0.5–12	20–472	85–90
1xxx	0.5–20	20–787	6, 83, 91–93
Al-Cu-Mg-Ag-T6	5	197	94
Al-Li-Cu	9	354	59
Al-4Mg-1Zr	1.5	59	95
Al-Zn-Mg-6.7Sc	0.68	27	96
AZ31	0.085–50	3–1969	97–101
AZ91	15	591	102
Mg-6Al-3Ca-0.5Re-0.2Mn	0.9	35	103
Mg-5.5Y-4.3Zn	1	39	104

Precipitate Distribution

The temperature during FSW increases up to 400 to 550 °C (752 to 1022 °F) within the nugget zone in aluminum alloys (Ref 3, 6, 72, 79, 80, 108–111). The temperature gradually decreases from the nugget zone to the TMAZ to the HAZ. In the HAZ, the temperature rises above 250 °C (482 °F) for aluminum alloys (Ref 109), which exerts a significant effect on the precipitate structure. At such temperatures, precipitates in aluminum alloys can coarsen or dissolve into aluminum matrix, depending on alloy type and maximum temperature. Figure 21 shows the change of strengthening precipitates in an FSW 7050-T651 aluminum alloy (Ref 74). Precipitates in 7050-T651 base alloy predominantly consist of intragranular fine η' less than 50 nm (2 μin.), along with coarser η precipitates along grain boundaries. Following FSW, the precipitates coarsen and the precipitate-free zone increases in width along the grain boundary in the HAZ. In the TMAZ, strengthening precipitates underwent severe coarsening and partly dissolved, while a small amount of very fine η particles reprecipitated. The temperature in the nugget zone reaches the solution heat treatment temperature. Strengthening precipitates in this region go into solution and reprecipitate during cooling.

Texture

In FSW, each zone has a different thermomechanical history. What is even more complicated for FSW is that the nugget region consists of subdomains. For example, the top layer undergoes deformation by shoulder after the pin has passed through. In addition, depending on the tool rotation rate and traverse speed, the nugget region can contain ring patterns or other microstructural variations. Such deformation features can cause complex texture patterns in FSW materials. For example, in an FSW AA6063 alloy, the Goss orientation in the parent material changed to a shear texture component containing both {110} <001> and {114} <221> orientations, and these components rotated around the pin axis (Ref 22). Both these components were also observed in FSW AA1100 and AA6061 alloys, including the rotational aspect of the texture component from the advancing side to the retreating side (Ref 23). In FSW AA2195 alloy, B-fiber shear (torsion) textures were reported as the main textural components, with the shear plane normal and shear directions aligned approximately perpendicular to and tangential with the flow lines in the weld (Ref 112–114). It is also noted that in an FSW AA7075 alloy, no strong texture was detected (Ref 115). In general, the texture evolution in FSW of aluminum alloys can be classified into two types. One is a shear texture with easy slip plane(s) roughly parallel to the cylindrical pin surface. The other is the severe gradient in crystallographic texture through the

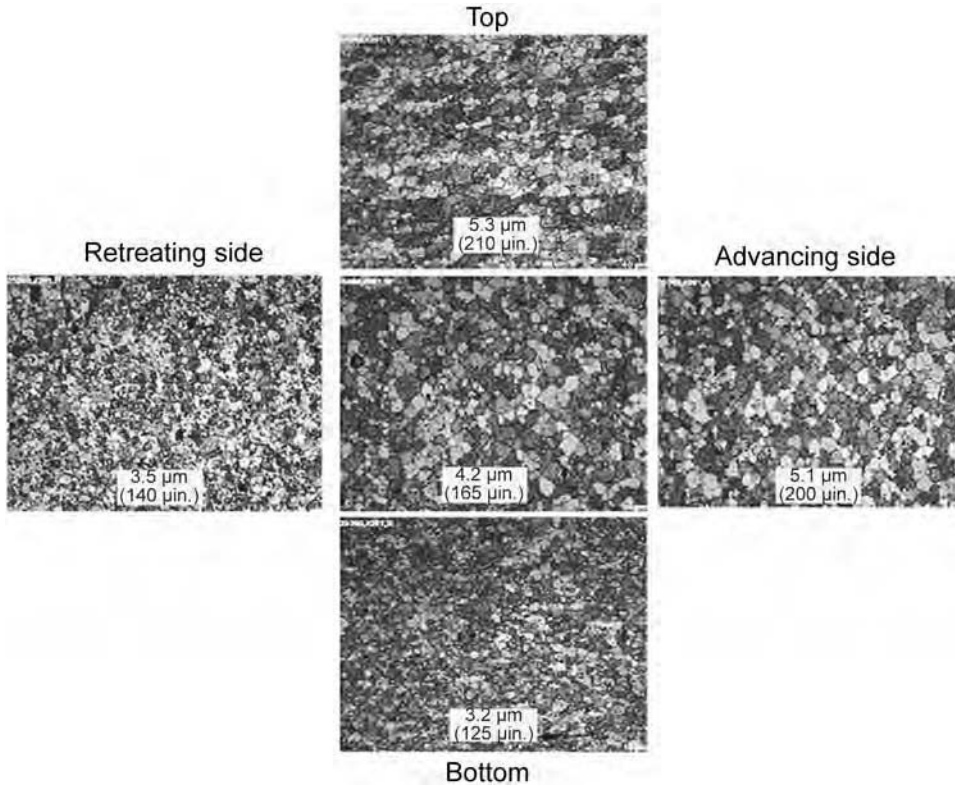


Fig. 20 Grain size distribution in various locations of a 7050Al weld nugget. Source: Ref 107

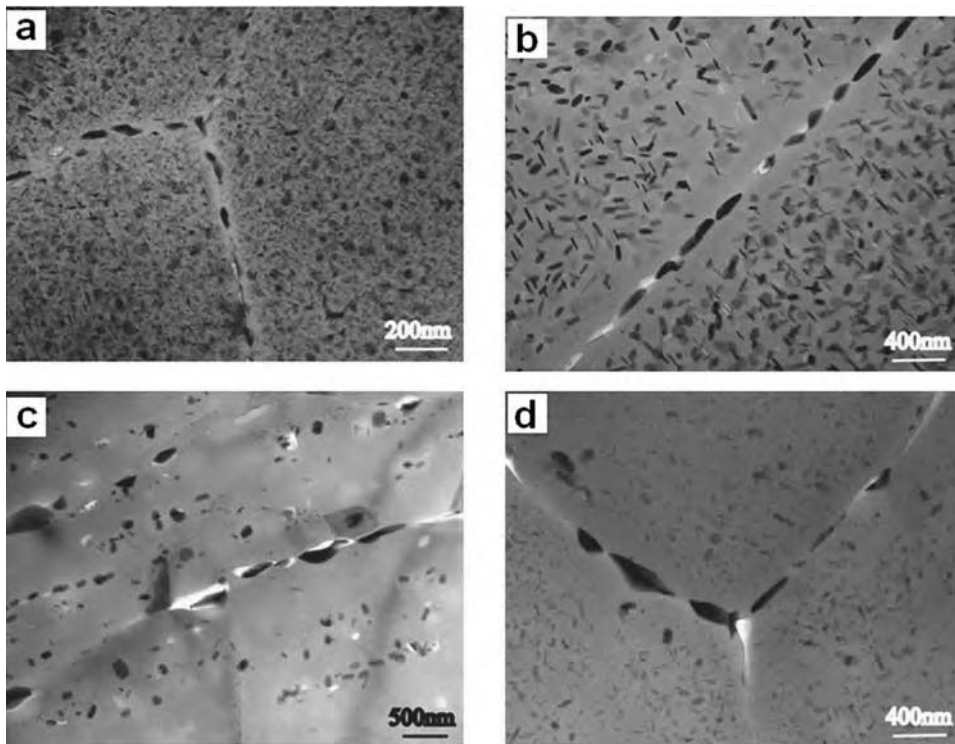


Fig. 21 Precipitate microstructures in a friction stir welded 7050Al-T651. (a) Base metal. (b) Heat-affected zone. (c) Thermomechanically affected zone. (d) Nugget zone. Source: Ref 74

thickness of the stir zone due to the complicated material flow. Severe plastic deformation has been considered as the main source for texture evolution during FSW.

Dynamic Recrystallization and Microstructural Evolution

Microstructural examinations of FSW aluminum alloys have shown a typically fine equiaxed grain structure in the stir zone. The fine-grained structure observed in the nugget has usually been attributed to dynamic recrystallization. Several recrystallization theories, including continuous dynamic recrystallization (CDRX) (Ref 59, 74, 81), discontinuous dynamic recrystallization (DDRX) (Ref 78, 80, 116), geometric dynamic recrystallization (Ref 17, 117), dynamic recrystallization in the adiabatic shear bands (Ref 118), and recrystallization via particle-stimulated nucleation (Ref 119) (which were developed to account for grain size control during conventional thermo-mechanical processing), have been used to explain the formation of grain structures during FSW/friction stir processing. In FSW Al-Li-Cu alloy (Ref 59), it was suggested that low-angle boundaries in the parent metal are replaced by high-angle boundaries in the nugget zone by means of a continuous rotation of the original low-angle boundaries during FSW. In this model, dislocation glide gives rise to a gradual relative rotation of adjacent subgrains. On the basis of microstructural observations in FSW 7050Al-T651 (Ref 74), it is proposed that the dynamic recrystallization in the nugget zone can be considered as CDRX on the basis of dynamic recovery. Subgrain growth associated with absorption of dislocation into the boundaries is the CDRX mechanism. Repeated absorption of dislocations into subgrain boundaries is the dominant mechanism for increasing the misorientation between adjacent subgrains during CDRX. Alternatively, DDRX has been proposed as an operative mechanism for the formation of very small grains in friction stir processed aluminum alloys. Using friction stir processing with rapid cooling, nanocrystalline structure was obtained in 7075Al and 7050Al-T76 alloys (Ref 78, 116). These recrystallized grains were significantly smaller than the pre-existing subgrains in the parent alloy and were identified as nonequilibrium in nature, predominantly high-angled, and relatively dislocation-free. Although the exact formation mechanism of the nanocrystalline structure is still not clear, the DDRX mechanism has been proposed for the nanostructure evolution (Ref 78).

During FSW, materials are heavily deformed at high temperatures. Material nearest to the tool pin experiences the largest strain and highest peak temperature. The resulting microstructures around the tool pin further evolve to form final grain structures under a thermomechanical deformation of decreasing strain, strain rate,

and temperature behind the pin tool. It is noted, however, that the formation of the final grain structure is unlikely to be a result of a single mechanism. In a study of friction stir processed 7075Al (Ref 120), multimechanisms, including DDRX, grain growth, dislocation introduction, dynamic recovery (DRV), and CDRX, were proposed to be inherent at different stages of microstructure evolution. The final grain structure contains of a range of microstructure/grains developed via different paths, either from initial recrystallized grains or subgrains formed from DRV. The grains have different densities of dislocations and are in various degrees of recovery. A complex microstructure evolution was also reported in FSW AZ31 magnesium alloy (Ref 101). The grain structure development was dictated not only by the texture evolution but also involved twinning, geometrical effects of strain, and limited discontinuous recrystallization.

REFERENCES

1. W.M. Thomas, E.D. Nicholas, J.C. Needham, M.G. Murch, P. Templesmith, and C.J. Dawes, G.B. Patent Application 9125978.8, Dec 1991
2. C. Dawes and W. Thomas, *TWI Bull.*, No. 6, Nov/Dec 1995, p 124
3. M.W. Mahoney, C.G. Rhodes, J.G. Flintoff, R.A. Spurling, and W.H. Bingel, *Metall. Trans. A*, Vol 29, 1998, p 1955–1964
4. L.E. Murr, G. Liu, and J.C. McClure, *J. Mater. Sci.*, Vol 33, 1998, p 1243–1251
5. M. Song and R. Kovacevic, *Int. J. Mach. Tools Manuf.*, Vol 43, 2003, p 605–615
6. Y.J. Kwon, N. Saito, and I. Shigematsu, *J. Mater. Sci. Lett.*, Vol 21, 2002, p 1473–1476
7. T.J. Lienert, W.L. Stellwag, Jr., B.B. Grimmer, and R.W. Warke, *Weld. Res.*, Jan 2003, p 1S–9S
8. Y.J. Chao, X. Qi, and W. Tang, *Trans. ASME*, Vol 125, 2003, p 138–145
9. L. Commin, M. Dumont, J.E. Masse, and L. Barrallier, *Acta Mater.*, Vol 57, 2009, p 326–334
10. M.Z.H. Khandkar, J.A. Khan, and A.P. Reynolds, *Sci. Tech. Weld. Join.*, Vol 8, 2003, p 165–174
11. H. Schmidt, J. Hattel, and J. Wert, *Model. Simul. Mater. Sci. Eng.*, Vol 12, 2004, p 143–157
12. H.B. Schmidt and J.H. Hattel, *Scr. Mater.*, Vol 58, 2008, p 332–337
13. B. Bird, W.E. Stewart, and E.N. Lightfoot, *Transport Phenomena*, John Wiley and Sons, 1994
14. Ø. Grong, *Metallurgical Modeling of Welding*, 2nd ed., The Institute of Materials, 1997
15. J.E. Gould and Z. Feng, *J. Mater. Process. Manuf. Sci.*, Vol 7, 1998, p 185–194
16. Z. Feng, J.E. Gould, and T.J. Lienert, *Hot Deformation of Aluminum Alloys II*, T.R. Bieler et al., Ed., TMS, Warrendale, PA, 1998, p 149–158
17. Ø. Frigaard, Ø. Grong, and O.T. Midling, *Metall. Mater. Trans. A*, Vol 32, 2001, p 1189–1200
18. M.Z.H. Khandkar and J.A. Khan, *J. Mater. Proc. Manuf. Sci.*, Vol 10, 2001, p 91–105
19. K. Colligan, *Weld. J.*, Vol 78, 1999, p 229S–237S
20. T.U. Seidel and A.P. Reynolds, *Metall. Mater. Trans. A*, Vol 32, 2001, p 2879–2884
21. A.C. Nunes, *Aluminum 2001*, p 235–248
22. Y.S. Sato, H. Kokawa, K. Ikeda, M. Enomoto, S. Jogan, and T. Hashimoto, *Metall. Mater. Trans. A*, Vol 32, 2001, p 941–948
23. D.P. Field, T.W. Nelson, Y. Hovanski, and K.V. Jata, *Metall. Mater. Trans. A*, Vol 32, 2001, p 2869–2877
24. M. Guerra, C. Schmidt, J.C. McClure, L. E. Murr, and A.C. Nunes, *Mater. Charac.*, Vol 49, 2003, p 95–101
25. S.H. Park, Y.S. Sato, and H. Kokawa, *Metall. Mater. Trans. A*, Vol 34, 2003, p 987–994
26. B. London, M. Mahoney, W. Bingel, M. Calabrese, R.H. Bossi, and D. Waldron, *FSW and P II*, K.V. Jata, M.W. Mahoney, R.S. Mishra, S.L. Semiatin, and T. Lienert, Ed., TMS, 2003
27. B. Yang, J. Yan, M.A. Sutton, and A.P. Reynolds, *Mater. Sci. Eng. A*, Vol 364, 2004, p 55–65
28. M.A. Sutton, B. Yang, A.P. Reynolds, and J. Yan, *Mater. Sci. Eng. A*, Vol 364, 2004, p 66–74
29. J.A. Schneider and A.C. Nunes, Jr., *Metall. Mater. Trans. A*, Vol 35, 2004, p 777–783
30. H.N.B. Schmidt, T.L. Dickerson, and J.H. Hattel, *Acta Mater.*, Vol 54, 2006, p 1199–1209
31. A.P. Reynolds, *Scr. Mater.*, Vol 58, 2008, p 338–342
32. S. Mironov, Y.S. Sato, and H. Kokawa, *Acta Mater.*, Vol 56, 2008, p 2602–2614
33. K. Kumar and S.V. Kailas, *Weld. Sci. Technol. Join.*, Vol 15, 2010, p 305–311
34. K. Kumar, Center for Friction Stir Processing, private communication
35. J.H. Yan, M.A. Sutton, and A.P. Reynolds, *Weld. Sci. Technol. Join.*, Vol 12, 2007, p 390–401
36. H. Schmidt and J. Hattel, *Friction Stir Welding and Processing III*, K.V. Jata, M.W. Mahoney, R.S. Mishra, and T.J. Lienert, Ed., TMS, 2005, p 205–211
37. H. Schmidt and J. Hattel, *Friction Stir Welding and Processing III*, K.V. Jata, M.W. Mahoney, R.S. Mishra, and T.J. Lienert, Ed., TMS, 2005, p 225–232
38. S. Xu, X. Deng, A.P. Reynolds, and T.U. Seidel, *Sci. Technol. Weld. Join.*, Vol 6, 2001, p 191–193
39. H. Schmidt and J. Hattel, *Model. Simul. Mater. Sci. Eng.*, Vol 13, 2005, p 77–93
40. T.U. Seidel and A.P. Reynolds, *Sci. Technol. Weld. Join.*, Vol 8, 2003, p 175–183
41. P. Ulysse, *Inter. J. Mach. Tool. Manuf.*, Vol 42, 2002, p 1549–1557
42. C.M. Chen and R. Kovacevic, *Inter. J. Mach. Tool. Manuf.*, Vol 43, 2003, p 1319–1326
43. G. Buffa, J. Hua, R. Shivpuri, and L. Fratini, *Mater. Sci. Eng. A*, Vol 419, 2006, p 389–396
44. R. Nandan, G.G. Roy, and T. DebRoy, *Metall. Mater. Trans. A*, Vol 37, 2006, p 1247–1259
45. P.A. Colegrove and H.R. Shercliff, *J. Mater. Proc. Technol.*, Vol 169, 2005, p 320–327
46. K.J. Colligan and R.S. Mishra, *Scr. Mater.*, Vol 58, 2008, p 327–331
47. W.J. Arbogast, Application of Friction Stir Welding and Related Technologies, *Friction Stir Welding and Processing*, R.S. Mishra and M.W. Mahoney, Ed., ASM International, 2007, p 273–308
48. C.B. Fuller, Friction Stir Tooling: Tool Materials and Design, *Friction Stir Welding and Processing*, R.S. Mishra and M.W. Mahoney, Ed., ASM International, 2007, p 7–35
49. A.J. Leonard and S.A. Lockyer, Flaws in Friction Stir Welds, *Proc. of Fourth International Friction Stir Welding Symposium* (Park City, UT), 2003
50. R. Leal and A. Loureiro, *Mater. Sci. Forum*, Vol 455–456, 2004, p 299–302
51. Y.S. Sato, F. Yamashita, Y. Sugiura, S.H. C. Park, and H. Kokawa, *Scr. Mater.*, Vol 50, 2004, p 365–369
52. Y.G. Kim, H. Fujii, T. Tsumura, T. Komazaki, and N. Nakata, *Mater. Sci. Eng. A*, Vol 415, 2006, p 250–254
53. H.-B. Chen, K. Yan, T. Lin, S.-B. Chen, C.-Y. Jiang, and Y. Zhao, *Mater. Sci. Eng. A*, Vol 433, 2006, p 64–69
54. H. Zhang, S.B. Lin, L. Wu, J.C. Feng, and S.L. Ma, *Mater. Des.*, Vol 27, 2006, p 805–809
55. K. Elangovan and V. Balasubramanian, *Mater. Des.*, Vol 29, 2008, p 362–373
56. K. Elangovan and V. Balasubramanian, *Mater. Sci. Eng. A*, Vol 459, 2007, p 7–18
57. W.J. Arbogast, *Scr. Mater.*, Vol 58, 2008, p 372–376
58. Z.W. Chen and S. Cui, *IOP Conference Series: Materials Science and Engineering*, Vol 4, 2009, p 012026
59. K.V. Jata and S.L. Semiatin, *Scr. Mater.*, Vol 43, 2000, p 743–749
60. S. Mukherjee and A.K. Ghosh, *Mater. Sci. Eng. A*, Vol 527, 2010, p 5130–5135
61. K. Masaki, Y.S. Sato, M. Maeda, and H. Kokawa, *Mater. Sci. Forum*, Vol 580–582, 2008, p 299–302
62. K. Masaki, Y.S. Sato, M. Maeda, and H. Kokawa, *Scr. Mater.*, Vol 58, 2008, p 355–360

63. C.I. Chang, C.J. Lee, and J.C. Huang, *Scr. Mater.*, Vol 51, 2004, p 509–514
64. T. Long, W. Tang, and A.P. Reynolds, *Sci. Technol. Weld. Join.*, Vol 12, 2007, p 311–317
65. G. Buffa, J. Hua, R. Shivpuri, and L. Fratini, *Mater. Sci. Eng. A*, Vol 419, 2006, p 381–388
66. A. Arora, Z. Zhang, A. De, and T. DebRoy, *Scr. Mater.*, Vol 61, 2009, p 863–866
67. R.S. Mishra and Z.Y. Ma, *Mater. Sci. Eng. R*, Vol 50, 2005, p 1–78
68. R. Nandan, T. DebRoy, and H.K.D.H. Bhadeshia, *Prog. Mater. Sci.*, Vol 53, 2008, p 980–1023
69. G. Baillias and C.D. Donne, *Materialprufung*, Vol 42, 2000, p 236–239
70. K.N. Krishnan, *Mater. Sci. Eng. A*, Vol 327, 2002, p 246–251
71. Y.S. Sato, H. Kokawa, M. Enmoto, and S. Jogan, *Metall. Mater. Trans. A*, Vol 30, 1999, p 2429–2437
72. C.G. Rhodes, M.W. Mahoney, W.H. Bingel, R.A. Spurling, and C.C. Bampton, *Scr. Mater.*, Vol 36, 1997, p 69–75
73. M. James and M. Mahoney, *Proceedings of the First International Symposium on Friction Stir Welding*, June 14–16, 1999 (Thousand Oaks, CA)
74. J.Q. Su, T.W. Nelson, R.S. Mishra, and M.W. Mahoney, *Acta Mater.*, Vol 51, 2003, p 713–729
75. Z.Y. Ma, R.S. Mishra, and M.W. Mahoney, *Acta Mater.*, Vol 50, 2002, p 4419–4430
76. K.A.A. Hassan, A.F. Norman, and P.B. Prangnell, *Mater. Sci. Forum*, Vol 396–402, 2002, p 1549–1554
77. I. Charit, R.S. Mishra, and M.W. Mahoney, *Scr. Mater.*, Vol 47, 2002, p 631–636
78. J.Q. Su, T.W. Nelson, and C.J. Sterling, *J. Mater. Res.*, Vol 18, 2003, p 1757–1760
79. G. Liu, L.E. Murr, C.S. Niou, J.C. McClure, and F.R. Vega, *Scr. Mater.*, Vol 37, 1997, p 355–361
80. Y.S. Sato, M. Urata, and H. Kokawa, *Metall. Mater. Trans. A*, Vol 33, 2002, p 625–635
81. B. Heinz and B. Skrotzki, *Metall. Mater. Trans. B*, Vol 33, 2002, p 489–498
82. G.S. Frankel and Z. Xia, *Corrosion*, Vol 55, 1999, p 139–150
83. Y.S. Sato, S.H.C. Park, and H. Kokawa, *Metall. Mater. Trans. A*, Vol 32, 2001, p 3023–3031
84. I. Charit, Z.Y. Ma, and R.S. Mishra, *Hot Deformation of Aluminum Alloys III*, Z. Jin, A. Beaudoin, T.A. Bieler, and B. Radhakrishnan, Ed., TMS, 2003, p 331–342
85. S. Benavides, Y. Li, L.E. Murr, D. Brown, J.C. McClure, *Scr. Mater.*, Vol 41, 1999, p 809–815
86. S.H. Kazi and L.E. Murr, *Friction Stir Welding and Processing*, K.V. Jata, M.W. Mahoney, R.S. Mishra, S.L. Semiatin, and D.P. Field, Ed., TMS, Warrendale, PA, 2001, p 139
87. H.G. Salem, A.P. Reynolds, and J.S. Lyons, *Scr. Mater.*, Vol 46, 2002, p 337–342
88. A.F. Norman, I. Brough, and P.B. Prangnell, *Mater. Sci. Forum*, Vol 331–337, 2000, p 1713–1718
89. I. Charit and R.S. Mishra, *Mater. Sci. Eng. A*, Vol 359, 2003, p 290–296
90. P.S. Pao, E. Lee, C.R. Feng, H.N. Jones, and D.W. Moon, *Friction Stir Welding and Processing II*, K.V. Jata, M.W. Mahoney, R.S. Mishra, S.L. Semiatin, and T. Lienert, Ed., TMS, Warrendale, PA, 2003, p 113
91. L.E. Murr, G. Liu, and J.C. McClure, *J. Mater. Sci. Lett.*, Vol 16, 1997, p 1801–1803
92. Y.J. Kwon, I. Shigematsu, and N. Saito, *Mater. Trans.*, Vol 44, 2003, p 1343–1350
93. Y.J. Kwon, I. Shigematsu, and N. Saito, *Scr. Mater.*, Vol 49, 2003, p 785–789
94. R. Braun and L. Litynska-Dobrzynska, *Mater. Sci. Forum*, Vol 396–402, 2002, p 1531–1536
95. Z.Y. Ma, R.S. Mishra, M.W. Mahoney, and R. Grimes, *Mater. Sci. Eng. A*, Vol 351, 2003, p 148–153
96. I. Charit and R.S. Mishra, *Ultrafine Grained Materials III*, Y.T. Zhu, T.G. Langdon, R.Z. Valiev, S.L. Semiatin, D. H. Shin, and T.C. Lowe, Ed., TMS, 2004
97. C.I. Chang, X.H. Du, and J.C. Huang, *Scr. Mater.*, Vol 59, 2008, p 356–359
98. J.A. Esparza, W.C. Davis, E.A. Trillo, and L.E. Murr, *J. Mater. Sci. Lett.*, Vol 21, 2002, p 917–920
99. W. Woo, H. Choo, M.B. Prime, Z. Feng, and B. Clausen, *Acta Mater.*, Vol 56, 2008, p 1701–1711
100. L. Commin, M. Dumont, J.-E. Masse, and L. Barrallier, *Acta Mater.*, Vol 57, 2009, p 326–334
101. U.F.H.R. Suhuddin, S. Mironov, Y.S. Sato, H. Kokawa, and C.-W. Lee, *Acta Mater.*, Vol 57, 2009, p 5406–5418
102. A.H. Feng and Z.Y. Ma, *Scr. Mater.*, Vol 56, 2007, p 397–400
103. M. Tsujikawa, S.W. Chung, T. Morishige, L.F. Chiang, Y. Takigawa, S. Oki, and K. Higashi, *Mater. Trans.*, Vol 48, 2007, p 618–621
104. D. Zhang, M. Suzuki, and K. Maruyama, *Mater. Sci. Forum*, Vol 539–543, 2007, p 3739–3744
105. L.E. Murr, Y. Li, R.D. Flores, E.A. Trillo, and J.C. McClure, *Mater. Res. Innovat.*, Vol 2, 1998, p 150–163
106. Y. Li, L.E. Murr, and J.C. McClure, *Mater. Sci. Eng. A*, Vol 271, 1999, p 213–223
107. M. Mahoney, R.S. Mishra, T. Nelson, J. Flintoff, R. Islamgaliev, and Y. Hovansky, *Friction Stir Welding and Processing*, K.V. Jata, M.W. Mahoney, R.S. Mishra, S.L. Semiatin, and D.P. Field, Ed., TMS, Warrendale, PA, 2001, p 183
108. L.E. Murr, G. Liu, and J.C. McClure, *J. Mater. Sci.*, Vol 33, 1998, p 1243–1251
109. Y.S. Sato, H. Kokawa, M. Enmoto, and S. Jogan, *Metall. Mater. Trans. A*, Vol 30, 1999, p 2429–2437
110. W. Tang, X. Guo, J.C. McClure, and L.E. Murr, *J. Mater. Process. Manuf. Sci.*, Vol 7, 1998, p 163–172
111. T. Hashimoto, S. Jogan, K. Nakata, Y.G. Kim, and M. Ushio, *Proceedings of the First International Symposium on Friction Stir Welding*, June 14–16, 1999 (Thousand Oaks, CA)
112. R.W. Fonda, J.F. Bingert, and K.J. Colligan, *Scr. Mater.*, Vol 51, 2004, p 243–248
113. R.W. Fonda and J.F. Bingert, *Scr. Mater.*, Vol 57, 2007, p 1052–1055
114. P.B. Prangnell and C.P. Heason, *Acta Mater.*, Vol 53, 2005, p 3179–3192
115. T. Shibayanagi and M. Naka, *Mater. Sci. Forum*, Vol 539–543, 2007, p 3769–3774
116. C.G. Rhodes, M.W. Mahoney, W.H. Bingel, and M. Calabrese, *Scr. Mater.*, Vol 48, 2003, p 1451–1455
117. K.A.A. Hassan, A.F. Norman, and P.B. Prangnell, *Proceedings of the Third International Symposium on Friction Stir Welding*, Sept 27–28, 2001 (Kobe, Japan)
118. L.E. Murr, E.A. Trillo, S. Pappu, and C. Kennedy, *J. Mater. Sci.*, Vol 37, 2002, p 3337–3360
119. T.R. McNelley, S. Swaminathan, and J.Q. Su, *Scr. Mater.*, Vol 58, 2008, p 349–354
120. J.Q. Su, T.W. Nelson, and C.J. Sterling, *Mater. Sci. Eng. A*, Vol 405, 2005, p 277–286

Fundamentals of Ultrasonic Welding

Leijun Li and Chunbo (Sam) Zhang, Utah State University

ULTRASONIC WELDING (UW), as a solid-state joining process, uses an ultrasonic energy source and pressure to induce oscillating shears between the faying surfaces to produce metallurgical bonds between a wide range of metal sheets (Ref 1, 2), thin foils (Ref 3), and wires. Besides joining metals, UW has been used to join semiconductors (Ref 4), plastics (Ref 5), glass (Ref 6), and ceramics (Ref 7). In contrast to fusion welding processes, UW has several inherent advantages (Ref 3, 8) derived from its solid-state process characteristics and has been used as a versatile joining method in the electronics, automotive, and aerospace industries since the 1950s.

Although numerous researchers have been studying the bonding mechanisms of UW for over 50 years, the process is still arguably the least understood welding process. Various mechanisms have been proposed for UW, including interdiffusion, recrystallization, plastic deformation, work hardening, breaking of contaminant, generation of heat by friction, and even melting (Ref 9, 10).

Diffusion has been observed at the interface between copper and aluminum welds for an extended period of welding time (Ref 11, 12). It has also been found that diffusion occurs along grain boundaries rather than in the bulk of the material in ultrasonic welding (Ref 13). Kreye et al. (Ref 14) examined the microstructure at the weld interface with transmission electron microscopy and claimed that the very small grain size observed in a thin layer could only be explained by melting and solidification. However, others (Ref 15, 16) concluded that neither diffusion nor recrystallization could be responsible for the joint formation of UW after comparing low-frequency vibration welding with UW of aluminum and examining the copper and soft iron UW. A great degree of plastic deformation and metal flow occur across the interface, and flow lines, evidence of extensive plastic deformation, are visible in the bond zone (Ref 17, 18). For the UW of aluminum foil, plastic flow occurs in a narrow interfacial zone approximately 10 to 20 μm (0.0004 to 0.0008 in.) in width (Ref 19). In this region, new subgrain structures form across the bond zone. When the relative motion at the beginning of the welding cycle cleans the surfaces

and plastically deforms asperities, micro-welds—areas in which the friction exceeds the flow stress level of the material and plastic metal flow has started—occur immediately between points of contact of the adjacent surfaces (Ref 9, 10, 20). Zhou et al. have used scanning electron microscopy to investigate the effects of process parameters on bond formation in thermosonic gold ball bonding on a copper substrate at ambient temperatures (Ref 21). They concluded that relative motion existed at the bonding interface as microslip at lower powers, transitioning into gross sliding at higher powers. Researchers in a variety of fields have observed that ultrasonic excitation of metals can produce an apparent reduction in the yield strength and an enhancement in the plastic flow behavior of metals (Ref 22, 23).

Due to the difficulties in definitively characterizing the UW process, the mechanism(s) for bond formation in the UW process are still under debate. The challenges for process measurement and instrumentation come from:

- The contact surface, where the bonding that occurs is invisible to observers
- The measurement devices or sensors, which tend to damage the contact surface and interfere with the bonding process
- The highly localized (a few micrometers) and transient (typically 20 kHz vibration) nature of ultrasonic bonding
- The necessity of a high spatial resolution (micrometer-scale vibration amplitude)

To overcome these obstacles and to gain insights into the UW process, numerous researchers have developed analytical (Ref 2, 17, 18) and numerical models (Ref 24–32).

During the last decade, UW has become a popular technique for joining thermoplastic polymers. Many studies were conducted in modeling the process. Senchenkov et al. (Ref 33, 34) studied the problem of vibrations and the dissipative heating of a viscoelastic prism by a waveguide. Benatar and Gutowski (Ref 35) modeled the UW of thermoplastics using a five-part model that included mechanics and vibration of the parts, viscoelastic heating, heat transfer, flow and wetting, and intermolecular diffusion. Roylance et al. (Ref 36)

outlined numerical simulation methods useful in understanding and developing UW for polymers. Verderber (Ref 37) implemented algorithms in an explicit finite-element (FE) analysis code applicable to the unique features of UW analysis. Senchenkov and Zhuk (Ref 38) studied the two-dimensional (2-D) problem of planar oscillations of plates under cyclic loading. The model developed was applied to the simulation of vibration of sonotrodes for UW of plastics. A similar study by Mikhailenko and Franovskii (Ref 39) proposed a two-dimensional FE model that linked thermo-electric processes in acoustic systems.

A recent combination of ultrasonic metal seam welding and computer numerical control milling has resulted in a new additive manufacturing process known as ultrasonic consolidation (UC). By continuously welding layers of metal foil to previously deposited material, during which the profile for each layer is created by contour milling, UC is able to build up complex, multifunctional, three-dimensional (3-D) objects. Objects with internal features, objects made up of multiple materials, and objects integrated with wiring, fiber optics, sensors, and instruments can thus be directly fabricated (Ref 3, 40, 41).

Numerical modeling of UW of metals and alloys began recently, with the development of emerging new technologies that employ UW in UC (Ref 3, 42, 43). Compared with UW of polymers, UW of metals seems to be more challenging to model. In metals, vibration and heat have effects on dislocation dynamics, metallurgical transformations, and associated variations in thermomechanical properties (Ref 44).

Gao and Doumanidis (Ref 17, 18) analyzed the mechanics of metal UW. They developed a 2-D, quasi-static/dynamic, elasto-plastic numerical model of the stress/strain field through FE analysis. In the study by de Vries (Ref 2), mechanics-based models were developed, along with a model for temperature generation and effect on mechanical properties of welded material. His models were capable of calculating the interface forces that were verified experimentally. Siddiq and Ghassemieh (Ref 31, 32) studied the changes in the friction work at the weld interface by simulating UW of metals based on a phenomenological material model, which incorporated both surface (friction) and volume (plasticity) “softening” effects.

Focusing on the contribution of friction to bond formation in UW, Zhang and Li developed a 3-D thermomechanical FE model (Ref 25). The model predicted a saturation of plastic deformation at the bond interface after a certain number of vibration cycles. Ding et al. (Ref 29, 30) analyzed deformation and stress distributions in the wire and bond pad during ultrasonic wire bonding using 2-D and 3-D FE models. A coupled temperature-displacement FE analysis performed by Huang and Ghassemieh (Ref 26) found the oscillation of stress in the substrate to lag behind the ultrasonic vibration by approximately 0.1 cycle of ultrasonic wave. Yadav and Domanidis (Ref 27) performed an FE analysis of two layers of aluminum foil subjected to certain welding conditions, with surface contact resistance calibrated by experiments. The results revealed a moderate temperature rise that was believed to be sufficient for metal bonding via vacancy diffusion. The fully coupling effects of thermal field (friction and plastic heat generation) and structural field (stress/strain, slide distance, and temperature-dependent material properties) were studied by Zhang and Li (Ref 24). In an effort to verify the model, plastic deformation was correlated with the bond area of welded joints.

Models

Governing Equations of Thermomechanical Processes

In modeling the UW process, the governing dynamic equation of displacement (u) for a linear structure (Ref 45) is:

$$[M]\{\ddot{u}\} + [C]\{\dot{u}\} + [K]\{u\} = \{L\} \quad (\text{Eq 1})$$

where (M) is the structural mass matrix, (C) is the structural damping matrix, (K) is the structural stiffness matrix, \ddot{u} is the nodal acceleration vector, \dot{u} is the nodal velocity vector, u is the nodal displacement vector, and $\{L\}$ is the applied load vector.

The basic constitutive equations between stress (σ) and strain (ϵ) are as follows:

$$\{\sigma\} = [D]\{\epsilon^{\text{el}}\} \quad (\text{Eq 2})$$

$$\{\epsilon^{\text{el}}\} = \{\epsilon\} - \{\epsilon^{\text{pl}}\} - \{\epsilon^{\text{th}}\} \quad (\text{Eq 3})$$

where $\{\sigma\}$ is the stress vector, (D) is the elastic stiffness matrix that is a function of temperature, $\{\epsilon^{\text{el}}\}$ is the elastic strain vector, $\{\epsilon\}$ is the total strain vector, $\{\epsilon^{\text{pl}}\}$ is the plastic strain vector, and $\{\epsilon^{\text{th}}\}$ is the thermal strain vector.

Conductive heat transfer can be considered using the following governing equation:

$$\rho c \left(\frac{\partial T}{\partial t} + (\vec{v} \cdot \nabla) T \right) = \dot{q} + \nabla \cdot ((\vec{K} \cdot \nabla) T) \quad (\text{Eq 4})$$

where ρ is the density, c is the specific heat, T is the temperature, t is the time, \vec{v} is the velocity vector for mass transport of heat, \dot{q} is the heat

generation rate per unit volume, \vec{K} is the conductivity vector, and:

$$\nabla = \frac{\partial}{\partial x} + \frac{\partial}{\partial y} + \frac{\partial}{\partial z}$$

Ultrasonic welding has been identified as a two-way coupled thermomechanical problem:

- The thermal field affects the mechanical field, because most of the material properties, such as modulus of elasticity, yield strength, and friction coefficient, are temperature sensitive.
- The mechanical field (friction and plastic deformation) generates heat, which affects the thermal field.

Therefore, modeling of the UW process demands a coupled-field analysis method. Because closed-form solutions for coupled-field equations are difficult to obtain, structural and thermal fields are generally treated separately in analytical modeling of UW (Ref 2, 17, 18).

Recently, commercial FE packages have expanded their capabilities in solving complex multiphysics problems. Many researchers found it convenient to study involved processes that are not solvable analytically. In the thermomechanical-coupled analysis, the FE matrix equation for mechanical and thermal fields, coupled by the thermoelastic constitutive equations, is (Ref 45):

$$\begin{aligned} & \begin{bmatrix} [M][0] \\ [0][0] \end{bmatrix} \begin{Bmatrix} \{\ddot{u}\} \\ \{\dot{T}\} \end{Bmatrix} + \begin{bmatrix} [C][0] \\ [C^{\text{th}}][C^{\text{t}}] \end{bmatrix} \begin{Bmatrix} \{\dot{u}\} \\ \{\dot{T}\} \end{Bmatrix} \\ & + \begin{bmatrix} [K][K^{\text{th}}] \\ [0][K^{\text{t}}] \end{bmatrix} \begin{Bmatrix} \{u\} \\ \{T\} \end{Bmatrix} \\ & = \begin{Bmatrix} \{L\} \\ \{Q\} \end{Bmatrix} \quad (\text{Eq 5}) \end{aligned}$$

where $[M]$ is the element mass matrix, $[C]$ is the element structural damping matrix, $[K]$ is the element stiffness matrix, $\{u\}$ is the displacement vector, $\{F\}$ is the sum of the element nodal force, $[C^{\text{t}}]$ is the element specific heat matrix, $[K^{\text{t}}]$ is the element diffusion conductivity matrix, $\{T\}$ is the temperature, $\{Q\}$ is the sum of the element heat-generation load and element convection surface heat-flow vectors, and $[K^{\text{th}}]$ is the element thermoelastic stiffness matrix:

$$([K^{\text{th}}]) = - \int_{\text{vol}} [B]^T \{ \beta \} \{ \nabla \{ N \} \}^T d\{\text{vol}\}$$

where $[B]$ is the strain-displacement matrix, N is the element shape function, and β is the vector of thermoelastic coefficients. For $[C^{\text{th}}]$, which is the element thermoelastic damping matrix, $[C^{\text{th}}] = -T_0[K^{\text{th}}]^T$, and T_0 is the absolute reference temperature.

Material Behavior in UW

Yield Rule and Plastic Deformation. The von Mises yield criterion has been widely applied in plastic analysis (Ref 24, 27). If the von Mises equivalent stress is lower than the material yield strength at temperature, the stress

state is elastic and no plastic strain is computed. If the stress exceeds the material yield strength, the plastic strain, ϵ^{pl} , is calculated by:

$$\{d\epsilon^{\text{pl}}\} = \lambda \left\{ \frac{\partial F}{\partial \sigma} \right\} \quad (\text{Eq 6})$$

where λ determines the amount of plastic straining, and F (yield function) is given by:

$$F = |\underline{\sigma} - \underline{\alpha}| - (\sigma^0 + R) = 0 \quad (\text{Eq 7})$$

where $\underline{\sigma}$ is the stress tensor, $\underline{\alpha}$ is the back stress tensor due to kinematic hardening, R is the isotropic hardening term, and σ^0 is the initial yield stress.

Thermomechanical Hardening Rules.

The nonlinear isotropic hardening rule was presented by Lemaitre and Chaboche (Ref 46) and Huber and Tsakmakis (Ref 47). The isotropic hardening (R), which describes the expansion of the yield surface, is defined as an exponential function of accumulated plastic strain:

$$R = A(1 - e^{-b\bar{\epsilon}^{\text{pl}}}) \quad (\text{Eq 8})$$

where $\bar{\epsilon}^{\text{pl}}$ is the equivalent plastic strain, while A and b are material parameters to be identified. A is the maximum change in the size of the yield surface, and b is the rate at which the size of the yield surface changes with changing plastic strains.

A nonlinear kinematic hardening rule proposed by Armstrong and Frederick (Ref 48) has been used to capture nonlinear hardening behavior and the smooth transition from elastic to plastic deformation. The evolution of back stress tensor ($\underline{\alpha}$) is given by:

$$\dot{\underline{\alpha}} = \frac{S}{\gamma} (\underline{\sigma} - \underline{\alpha}) \bar{\epsilon}^{\text{pl}} - \gamma \underline{\alpha} \bar{\epsilon}^{\text{pl}} \quad (\text{Eq 9})$$

where S and γ are the material parameters, which can be identified from cyclic testing. The γ term determines the rate at which the saturation value of kinematic hardening decreases with increasing plastic deformation. S is the kinematic shift of the yield surface.

Adopted from the hardening model by Johnson and Cook (Ref 49), the temperature term $(1 - T^m)$ can be embedded in the nonlinear isotropic and kinematic hardening model. The thermally modified nonlinear isotropic hardening law is given by:

$$R_{\text{th}} = A(1 - e^{-b\bar{\epsilon}^{\text{pl}}}) \cdot (1 - T^m) \quad (\text{Eq 10})$$

where m is a material parameter, and T is the nondimensional temperature given by:

$$T = \frac{T - T_{\text{transition}}}{T_{\text{melt}} - T_{\text{transition}}} \quad (\text{Eq 11})$$

Similarly, the modified nonlinear kinematic hardening law is given by:

$$\alpha_{th} = \alpha_{isothermal} (1 - T^m) \tag{Eq 12}$$

where $\alpha_{isothermal}$ is obtained from the numerical integration of Eq (Ref 50).

Siddiq and Ghassemieh (Ref 31, 32) introduced a phenomenological softening term, dependent on the ultrasonic energy density per unit time, in the isotropic and kinematic hardening terms (Eq 10 and 12). They have implemented these hardening models in user-defined ABAQUS subroutines and identified six parameters (Q, b, C, γ, m, d) using an inverse method from cyclic stress-strain data, thermal softening data, and acoustic (ultrasonic) softening data. The modified equations of isotropic and kinematic hardening are given by:

$$R_{ultrasonic} = R_{th} \cdot (1 - d \cdot E_{ultrasonic})^2 \tag{Eq 13}$$

$$\alpha_{ultrasonic} = \alpha_{th} \cdot (1 - d \cdot E_{ultrasonic})^2 \tag{Eq 14}$$

where R_{th} is defined in Eq 10, d must be identified from deformation behavior of the material in the presence of ultrasonic energy, $E_{ultrasonic}$ is the ultrasonic energy transferred from the sonotrode to the material, and α_{th} is defined in Eq 12.

Heat Generation in UW

Surface and Volume Heat Generation.

The ultrasonic mechanical energy, subsequently converted to thermal energy, can be determined by the local cyclic stress (σ), strain (ϵ), friction shear (τ_x), and component slip (e_x) near the faying interface. Heat is generated locally in the control volume, ($Q_v(x, y, z)$), by inelastic hysteresis and plastic deformation, and at the interface surfaces, ($Q_s(x, y)$), by friction during each cycle at the ultrasonic frequency, f , as shown in Fig. 1 (Ref 2, 27, 29):

$$Q_v(x, y, z) = f \oint \sigma_{eq}(\epsilon) d\epsilon_{eq} \tag{Eq 15}$$

$$Q_s(x, y) = f \oint \tau_x(\epsilon_x) de_x = N \oint \mu \sigma_z(\epsilon_x) de_x \tag{Eq 16}$$

where σ_{eq} and ϵ_{eq} are equivalent stress and strain, and σ_z is normal compressive stress.

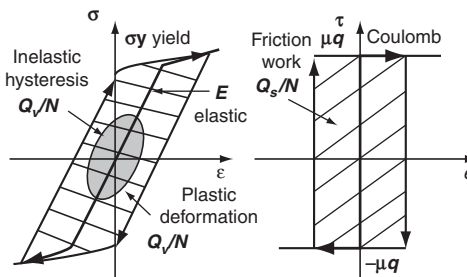


Fig. 1 Mechanical work done during each vibration cycle of ultrasonic welding. Source: Ref 27

The previous equations for calculating heat generation assume the mechanical state as a function of location only, without considering time and temperature influences. Zhang and Li (Ref 24) have proposed a plastic work rate (\dot{W}^{pl}), proportional to the plastic strain rate, to account for the effects of location, temperature, and time in UW:

$$\dot{W}^{pl}(x, y, z, t, T) = \sigma_j(x, y, z, t, T) \cdot \dot{\epsilon}_j^{pl}(x, y, z, t, T) \tag{Eq 17}$$

where $j = 1,2,3$. It is assumed that some of the plastic work converts to heat, while the rest is stored as energy of crystal defects accompanying plastic deformation. The fraction of the plastic work ($\dot{Q}^{pl}/\dot{W}^{pl}$) that is converted to thermoplastic heating (\dot{Q}^{pl}) is 0.33 for aluminum (Ref 51).

Friction Coefficient. As a friction-based welding process, there is no doubt that the friction coefficient at the faying interfaces plays a key role in UW by affecting the stress/strain state and surface heat generation. Gao and Domanidis (Ref 17) experimentally determined the friction-efficient history of aluminum 1100 foils during one cycle (Fig. 2). Zhang and Li (Ref 25) measured the aluminum-aluminum friction coefficient varying with temperature (Fig. 3) at a slide speed corresponding to UW conditions. Siddiq and Ghassemieh (Ref 31, 32) numerically described the friction coefficient varying with temperature and vibration cycle by curve-fitting the published experimental data. Based on Coulomb's friction law, the stick-slip contact condition can be identified with the relation of $|\tau_{fric}|$ and $\mu \cdot p$. If $|\tau_{fric}| < \mu \cdot p$, the friction is of the stick type, and if $|\tau_{fric}| = \mu \cdot p$, the friction is of the slip type.

Results

Vibration

The vibration of the sonotrode under a constant pressure produces a cyclic sliding at the bonding interface, along with periodic variation of the elastic/plastic strain/stress state, as

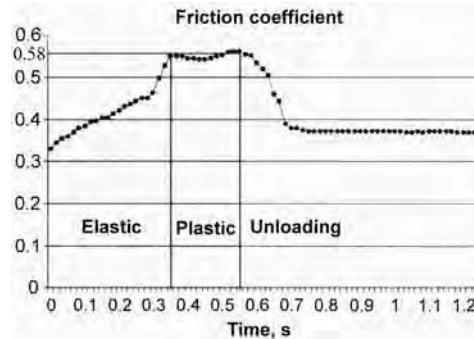


Fig. 2 Experimentally identified history of friction coefficient of aluminum 1100 foils during one cycle of weld. Source: Ref 17

illustrated in Fig. 4. The resultant shear stress at the interface is helpful to break the oxides/contaminants and to generate intimate contact between the faying surfaces. The overall effect of ultrasonic vibration of the bonding interface can be summarized by the so-called ‘‘acoustic softening’’ of metals. Based on a phenomenological model, the stress required to initiate metal plastic deformation decreased significantly with ultrasonic excitation. The material softening effect has been studied by evaluating the sonotrode displacement in the height direction, as illustrated in Fig. 5 (Ref 26). It is found

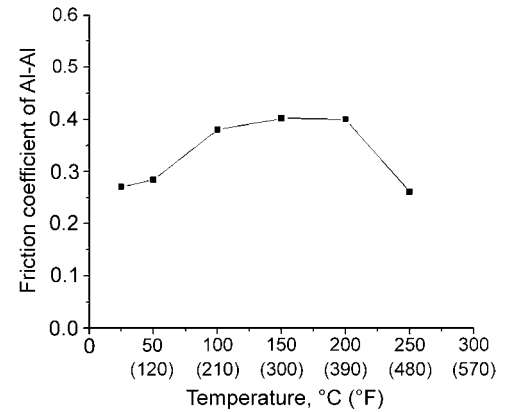


Fig. 3 Measured aluminum 3003-H18 friction coefficient varying with temperature. Source: Ref 25

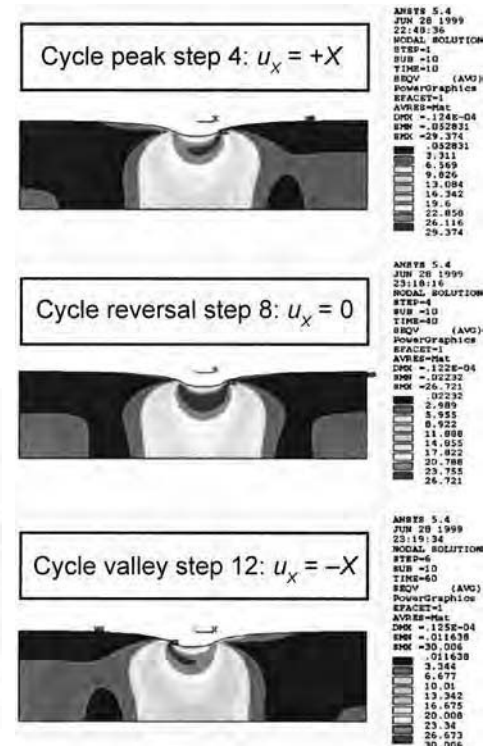


Fig. 4 Equivalent stress field, σ_{eq} , at three steps of one ultrasonic cycle. Source: Ref 17

that the sonotrode moves downward continuously during the entire UW process, under a constant load on the sonotrode. This softening effect becomes significant for a higher friction coefficient.

Friction

For those areas with the slipping contact condition, the shear stress results in the generation of friction heat. The friction work is affected by the vibration amplitude, as illustrated in Fig. 6, but has a nonlinear relation with the applied pressure. Higher pressure elevates the shear stress level but decreases both the overall slipping areas and distances of contact interface. Better ultrasonic bonds can be formed by greater friction work, because more ultrasonic energy is brought into the bonding interface. These results agree well with the experimental data of bond strength with amplitude and pressure (Ref 52).

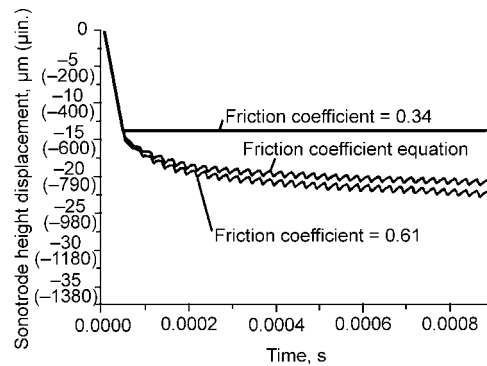


Fig. 5 Simulated displacements of the sonotrode versus time in height direction using different friction models. The external force applied on the sonotrode is 80 N (18 lb). The friction coefficient equation is defined as $\mu = E/p[\epsilon_{xx}(t) + \nu]$, where E and ν are the modulus and Poisson's ratio, respectively, and p is the constant pressure. Source: Ref 26

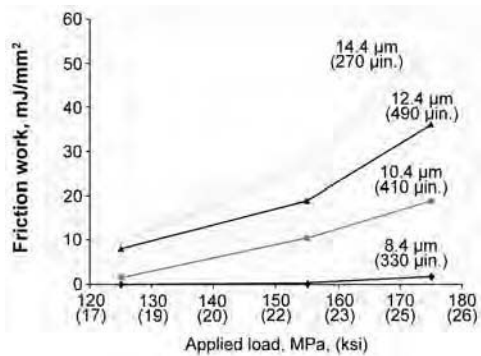


Fig. 6 Simulated friction work at foil/substrate interface. Velocity = 27.8 mm/s (1.1 in./s). Source: Ref 32

Temperature

Due to the heat generation from friction and plastic deformation, the temperature on the bonding interface increases during UW. Higher temperature occurs along the boundary of the foil/substrate contact area (Fig. 7). The generated heat can dissipate quickly across the entire contact surface for aluminum alloys. Some simulation results show the maximum temperature to be located at the foil/sonotrode interface (Fig. 8), resulting from severe plastic deformation. These simulation results seem to match the experimental observation of temperature measurement by high-speed thermal camera (Ref 2). The consequence of temperature rise is to reduce the stress state of the contact interface by decreasing the material properties and the friction coefficient. Thus, the friction work decreases with temperature rise, and the final

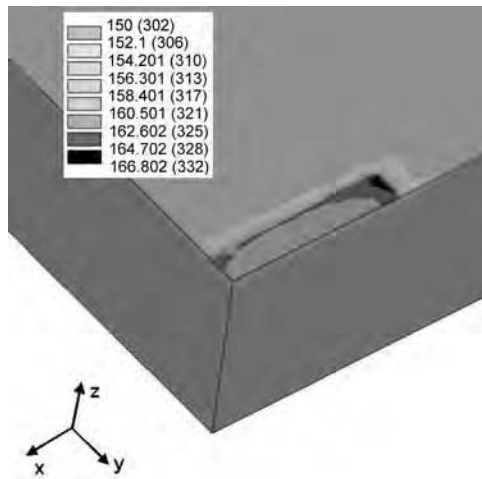


Fig. 7 Simulated three-dimensional temperature distribution at the 50th vibration cycle. Unit: °C (°F), 20 kHz frequency. Source: Ref 24

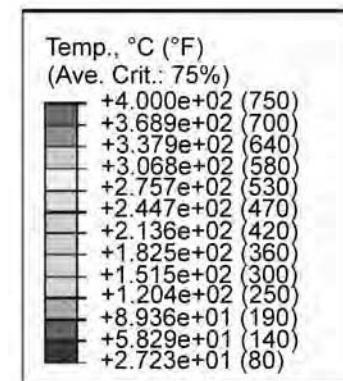


Fig. 8 Simulated temperature in the weld specimen. Amplitude = 8.4 μm (330 μin.), velocity = 27.8 mm/s (1.1 in./s), and pressure = 125 MPa (18 ksi). Source: Ref 32

temperature level is determined by the competition between friction and plastic deformation work. When only the friction heat generation is considered, the temperature rise is slowed down and seems to approach a steady state (Fig. 9). The increase of interface temperature is determined by $q_{friction} - q_{loss}$, where $q_{friction}$ is the friction heat-generation rate, and q_{loss} is the heat-dissipation rate by conduction. A balance between $q_{friction}$ and q_{loss} will be achieved eventually, because once the heat loss is greater than the friction heat generation and the interface temperature drops, the higher values of material properties in the lower temperature will automatically increase the $q_{friction}$ until a new thermal balance is achieved.

Plastic Deformation

A strong linear correlation between the plastic strain and bond area ratio, which reflects the bond strength level (Ref 52), is shown in Fig. 10. A large von Mises plastic strain will result in more bonded areas. Plastic

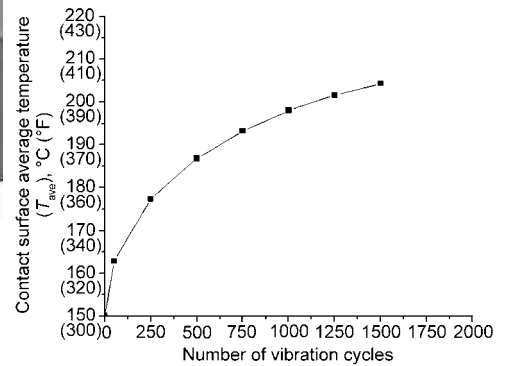


Fig. 9 Average temperature at the contact surface as a function of the vibration cycle (20 kHz frequency). Source: Ref 25

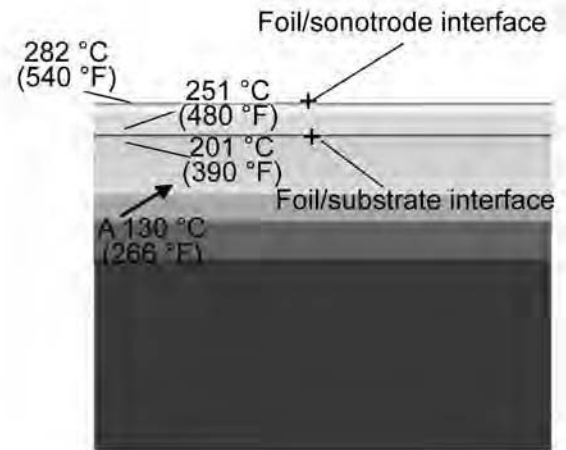


Fig. 8 Simulated temperature in the weld specimen. Amplitude = 8.4 μm (330 μin.), velocity = 27.8 mm/s (1.1 in./s), and pressure = 125 MPa (18 ksi). Source: Ref 32

deformation affects the bond formation in the following ways:

- It disperses the surface oxide layer.
- It generates heat to make the atoms more thermally active.
- It deforms the crystals and grains on the interfaces and generates a high dislocation density, which also provides potential energy for dynamic grain-boundary migration.

Therefore, the plastic deformation from the simulation model can be quantitatively correlated with the bonded area (bond strength) from experiments.

Another quantitative approach for building the relationship between the simulated and experimental data is to measure the dimension of dynamic recrystallized grains. From experiments, it is found that the crystals have been dynamically recrystallized into nanosized grains during processing (Fig. 11). From simulation data (Fig. 12), the plastic strain is relatively small at the beginning of bonding. The highest plastic strain occurs at the edge of the contact surface. Subsequently, the plastic deformation at the center of the contact surface exceeds the level of plastic strain at the edge and becomes the highest.

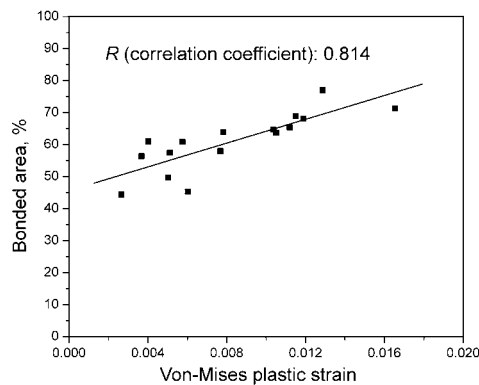


Fig. 10 Correlation of von Mises plastic strain and bonded area. Source: Ref 24

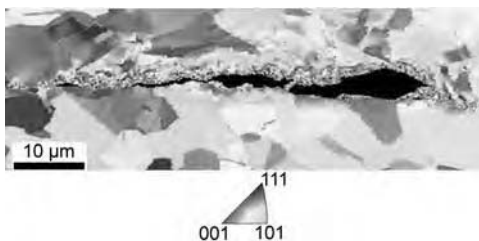


Fig. 11 Inverse pole figure of an unconsolidated portion of the nickel-nickel interface. Note the extremely fine grains that are present along the defect boundaries. Source: Ref 53

Bond Strength

The peeling test has been widely used to measure the bond strength of UW-made parts with laminated structure by examining the peak load (Ref 54). A novel push-pin-type test was developed as a general test for bond strength evaluation normal to bonded areas for laminated structures (Ref 52). This evaluation method includes both experiment—obtaining a load-displacement response—and elastic-plastic FE simulation, fitting the experimental load-displacement response by adjusting the material property coefficient for the bond zone to find the maximum stress normal to bonded areas from simulation results.

The bond strength is significantly influenced by process parameters. The bond strength

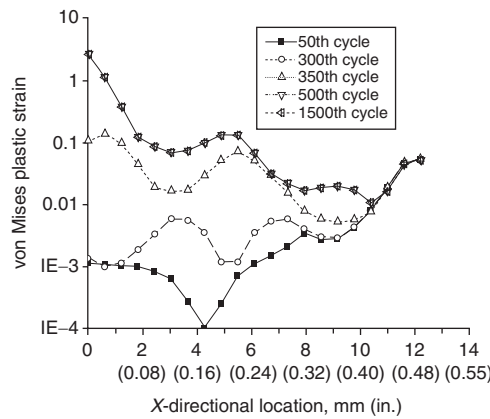


Fig. 12 Distribution of plastic strain as a function of location and vibration cycle. The X-direction is parallel to the sonotrode vibration direction. The origin is the center of the contact surface. Source: Ref 25

increases with the vibration amplitude and pre-heat temperature, decreases with the sonotrode traveling speed, but shows a nonlinear relation with normal pressure (Ref 52, 55). It is believed a high normal pressure will decrease bond strength, because the vibrational motion of the parts is constrained, and not enough friction heat will be generated. Indicators from both experiment and simulation are employed to predict the true bond strength. Linear weld density (LWD), defined as the length of the bonded interface divided by the total interface length under consideration (expressed in percentage), has a good linear relation with bond strength (Fig. 13), but a significant increase of LWD results in only a small increase in the bond strength. A 2-D experimental indicator, bond area percentage measured from the entire fracture surface, shows a more significant correlation with bond strength (Fig. 14). Friction

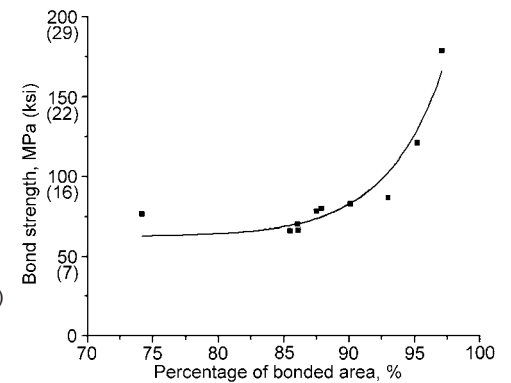


Fig. 14 Bond strength versus percentage of bonded area for aluminum 3003-H18. Source: Ref 52

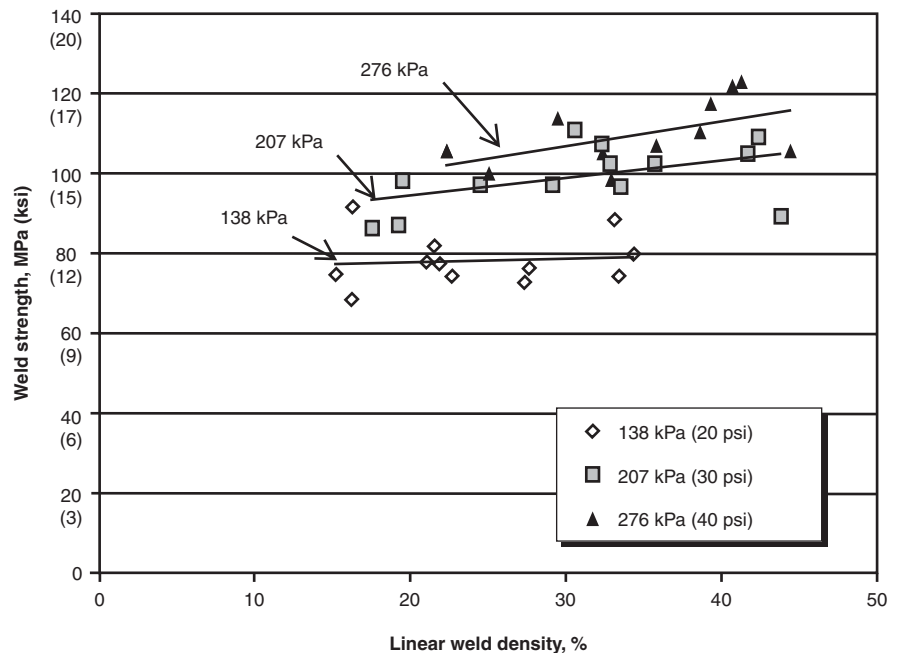


Fig. 13 Correlation of weld strength with linear weld density of welded aluminum 6061 specimens. Source: Ref 54

work and plastic deformation (Fig. 10) from simulation have also been used to estimate the bond strength of UW parts (Ref 24, 31, 52). The limitation of friction work as a bond strength indicator results from the neglect of contributions of plastic heat and vibration energy.

Geometry Effect (Height-to-Width Ratio of Build)

In ultrasonic consolidation, the geometry of buildup, specifically referring to the height-to-width ratio, influences the bond formation and results in different bond quality across the bonding interface and inside the substrate, although the same process parameters are used. The simulation shows that for a given vibration condition, with the increased substrate height, the amplitude of contact frictional strain decreases (Fig. 15), while that of contact interface displacement increases (Fig. 16). The reason for the decrease in the frictional stress at the contact interface for certain substrate heights is the complicated wave interference

occurring in the substrate (Ref 56). From experiments, parts with a height-to-width ratio of approximately 1.0 are not feasible to build (Ref 57). At this particular substrate height, the wave superposition produces a minimum interface relative displacement. The displacement on the contact interface is found to be a critical parameter for bond formation (Ref 25). The minimal displacement and relatively low friction stress are the reasons why a height-to-width ratio equal to 1.0 is a critical height for defects to occur in ultrasonic bonding. By using support materials for tall structures, resonant vibration of the UW part is constrained, and good bonding is possible. Figure 17 illustrates the cross-sectional view of a typical vibration pattern for a substrate with a height-to-width ratio of 1:1. The vibration pattern is believed to be closely related with those observed in fractography of ultrasonic welded joints (Fig. 18). The distribution of defects (unbonded areas) can be correlated with the saturated vibration patterns of strain/stress and displacement.

Mechanisms for Bond Formation

The temperature and microstructure of the bonding interface have been examined by researchers to identify the melting phenomenon in UW (Ref 2, 13, 58, 59). In most cases, no evidence of metal melting has been found. Diffusion has been observed at the interface between copper and aluminum welds for an extended period of welding time (Ref 11, 12). However, the relatively low temperature and short time during the rapid bonding process seems to make diffusion insignificant for bond formation. A very small grain size has been observed in a thin layer, and the interface region is believed to have experienced dynamic recrystallization (Ref 14, 53). The role of the recrystallization phenomenon in UW and its contribution to the ultrasonic bond is currently being investigated. Severe plastic deformation and metal turbulent flow occur across the interface, and flow lines, evidence of extensive plastic deformation, are visible in the bond zone (Ref 3, 17, 18). The severe, localized plastic

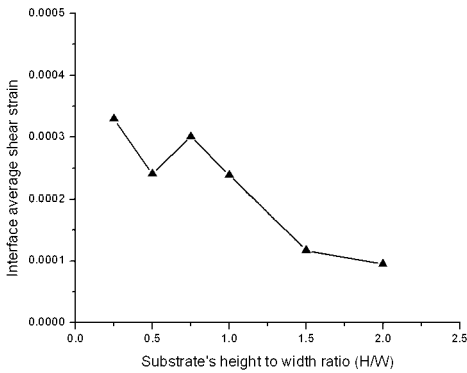


Fig. 15 Interface average shear strain versus height-to-width ratio at the 750th cycle (20 kHz frequency). Source: Ref 56

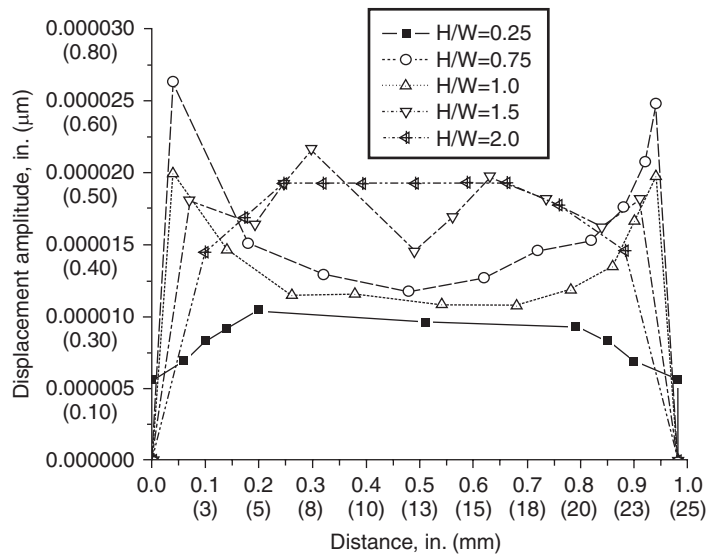


Fig. 16 Displacement amplitude at the 750th cycle for substrates with different height-to-width (H/W) ratios (20 kHz frequency). Source: Ref 56

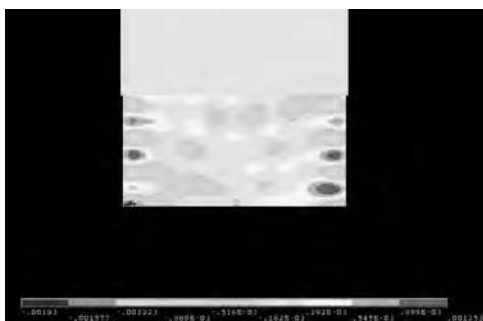


Fig. 17 Distribution of shear strain at the 750th cycle for a substrate with a height-to-width ratio (H/W) of 1.0. Source: Ref 56

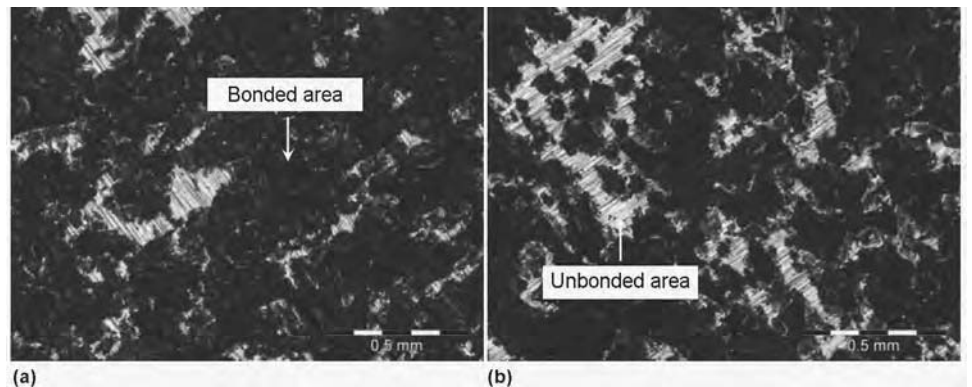


Fig. 18 Typical features of fractured surfaces. (a) 87.4% bonded. (b) 76.4% bonded. Source: Ref 24

deformation at the bond region is believed to be the major phenomenon in UW by establishing a metallurgical bond via atomic forces at those intimate contact areas (Ref 24, 53). Plastic deformation and metal flow at the bonded regions result in displacement of oxide films and flow of metal into the voids between the faying surfaces. Plastic deformation also provides the driving force for subsequent dynamic recrystallization, which may be the process through which the bond forms.

REFERENCES

1. T. Ueoka and J. Tsujino, Welding Characteristics of Aluminum and Copper Plate Specimens Welded by a 19 KHz Complex Vibration Ultrasonic Seam Welding System, *Jpn. J. Appl. Phys., Part 1*, Vol 41 (No. 5B), 2002, p 3237–3242
2. E. de Vries, “Mechanics and Mechanisms of Ultrasonic Metal Welding,” Ph.D. thesis, The Ohio State University, 2004
3. D.R. White, Ultrasonic Consolidation of Aluminum Tooling, *J. Adv. Mater. Proc.*, Vol 161, 2003, p 64–65
4. G.G. Harman and J. Albers, The Ultrasonic Welding Mechanism as Applied to Aluminum- and Gold-Wire Bonding in Microelectronics, *IEEE Trans. Parts, Hybrids, Packag.*, Vol 13 (No. 4), Dec 1977, p 406–412
5. D.A. Grewell, A Prototype “Expert” System for Ultrasonic Welding of Plastics, *Plast. Eng. (N. Y.)*, Vol 55, 1999, p 33–37
6. G. Wagner, F. Walther, T. Nebel, and D. Eifler, Glass/Glass Joints by Ultrasonic Welding, *Glass Technol.*, Vol 44, 2003, p 152–155
7. S.I. Matsuoka, Ultrasonic Welding of Ceramics/Metals Using Inserts, *J. Mater. Process. Technol.*, Vol 75 (No. 1–3), 1998, p 259–265
8. C.Y. Kong, R.C. Soar, and P.M. Dickens, An Investigation of the Control Parameters for Aluminum 3003 under Ultrasonic Consolidation, *Proc. Solid Freeform Fabrication Symposium* (Austin, TX), 2002, p 199–210
9. S. Ginzburg, A. Mitskevich, and Y. Nosov, Formation of the Joint in Ultrasonic Welding, *Weld. Prod.*, Vol 13 (No. 5), May 1967, p 45–47
10. U.I. Chang and J. Frisch, On Optimization of Some Parameters in Ultrasonic Metal Welding, *Weld. J.*, Vol 53 (No. 1), Jan 1974, p 24–35
11. W. Beyer, The Bonding Process in the Ultrasonic Welding of Metals, *Schweiss-technik*, Vol 19 (No. 1), Jan 1969, p 16–20
12. A. Watanabe, T. Yanagisawa, and S. Sunaga, The Effect of Oxide Film on the Strength of an Ultrasonically Welded Joint and Welding Process—Study of the Ultrasonic Welding of Dissimilar Metals (2nd Report), *Weld. Res. Abroad*, Vol 48 (No. 2), 2000, p 19
13. T. Hazlett and S. Ambekar, Additional Studies on Interface Temperatures and Bonding Mechanism of Ultrasonic Welds, *Weld. J.*, May 1970, p 196–200
14. H. Kreye, Melting Phenomena in Solid State Welding Processes, *Weld. J.*, Vol 56 (No. 5), May 1977, p 154–158
15. J. Harthoorn, “Ultrasonic Metal Welding,” Ph.D. thesis, Technical University Eindhoven, 1978
16. E. Heymann and B. Koehler, Influence of the Work Piece Preparation on Ultrasonic Welding, *ZIS-Mitteilungen*, Vol 11 (No. 1), Jan 1969, p 180–190
17. Y. Gao and C. Doumanidis, Mechanical Analysis of Ultrasonic Bonding for Rapid Prototyping, *J. Manuf. Sci. Eng. (Trans. ASME)*, Vol 124 (No. 2), 2002, p 426–434
18. C. Doumanidis and Y. Gao, Mechanical Modeling of Ultrasonic Welding, *Weld. J.*, Vol 83 (No. 4), 2004, p 140S–146S
19. D.R. White, Ultrasonic Consolidation of Aluminum Tooling, *Adv. Mater. Proc.*, Vol 161 (No. 1), 2003, p 64–65
20. A. Pfluger and X. Sideris, New Developments in Ultrasonic Welding, *Sampe Q.*, Vol 7 (No. 1), Oct 1975, p 9–19
21. Y. Zhou, X. Li, and N.J. Noolu, A Footprint Study of Bond Initiation in Gold Wire Crescent Bonding, *IEEE Trans. Component Packag. Technol.*, Vol 28 (No. 4), 2005, p 810–816
22. A. Eaves, Review of the Application of Ultrasonic Vibration to Deforming Metals, *Ultrasonics*, Vol 13 (No. 4), 1975, p 162–170
23. I. Hansson and A. Tholen, Plasticity due to Superimposed Macroscopic and Static Strains, *Ultrasonics*, Vol 16 (No. 2), 1978
24. C. Zhang and L. Li, A Coupled Thermal-Mechanical Analysis of Ultrasonic Bonding Mechanism, *Metall. Mater. Trans. B*, Vol 40, 2009, p 196–207
25. C. Zhang and L. Li, A Friction-Based Finite Element Analysis of Ultrasonic Consolidation, *Weld. J.*, Vol 87 (No. 7), 2008, p 187s–194s
26. C.J. Huang and E. Ghassemieh, 3D Coupled Thermomechanical Finite Element Analysis of Ultrasonic Consolidation, *Mater. Sci. Forum*, Vol 539–543, 2007, p 2651–2656
27. S. Yadav and C. Doumanidis, Thermomechanical Analysis of an Ultrasonic Rapid Manufacturing (URM) System, *J. Manuf. Proc.*, Vol 7 (No. 2), 2005, p 153–161
28. S. Elangovan, S. Semeer, and K. Prakasan, Temperature and Stress Distribution in Ultrasonic Metal Welding—An FEA-Based Study, *J. Mater. Proc. Technol.*, Vol 209, 2009, p 1143–1150
29. Y. Ding and J. Kim, Numerical Analysis of Ultrasonic Wire Bonding, Part 2: Effects of Bonding Parameters on Temperature Rise, *Microelectron. Reliab.*, Vol 48, 2008, p 149–157
30. Y. Ding, J. Kim, and P. Tong, Numerical Analysis of Ultrasonic Wire Bonding: Effects of Bonding Parameters on Contact Pressure and Frictional Energy, *Mech. Mater.*, Vol 38, 2006, p 11–24
31. A. Siddiq and E. Ghassemieh, Thermomechanical Analyses of Ultrasonic Welding Process Using Thermal and Acoustic Softening Effects, *Mech. Mater.*, Vol 40, 2008, p 982–1000
32. A. Siddiq and E. Ghassemieh, Theoretical and FE Analysis of Ultrasonic Welding of Aluminum Alloy 3003, *J. Manuf. Sci. Eng.*, Vol 131, 2009, p 041007
33. I.K. Senchenkov, O.V. Tarasenko, B.Y. Chernyak, V.I. Kozlov, and B.E. Frenkel, Acoustic Contact during the Ultrasonic Welding of Plastics, *Sov. Appl. Mech. (English translation of Prikl. Mekh.)*, Vol 23 (No. 2), 1987, p 159–165
34. I.K. Senchenkov, Vibrational Heating of a Nonlinearly Viscoelastic Rod Interacting with a Viscoelastic Element, *Sov. Appl. Mech. (English translation of Prikl. Mekh.)*, Vol 27 (No. 5), 1991, p 512–519
35. A. Benatar and T.G. Gutowski, Ultrasonic Welding of PEEK Graphite APC-2 Composites, *Polym. Eng. Sci.*, Vol 29 (No. 23), 1989, p 1705–1721
36. M. Roylance, J. Player, W. Zukas, and D. Roylance, Modeling of Ultrasonic Processing, *J. Appl. Polym. Sci.*, Vol 93 (No. 4), 2004, p 1609–1615
37. R.R. Verderber, Implementation of Algorithms for Modeling Ultrasonic Welding, *American Society of Mechanical Engineers, Pressure Vessels and Piping Division (Publication) PVP*, Vol 369, 1997, p 229–234
38. I.K. Senchenkov and Y.A. Zhuk, Modal Control of Planar Oscillation of Slotted Sonotrodes for Ultrasonic Welding of Plastics, *Int. Conf. Control of Oscillations and Chaos*, Vol 1, 1997, p 133–137
39. V.V. Mikhailenko and A.T. Franovskii, Numerical Modeling of Resonance Modes of the Oscillations of an Ultrasonic Electromechanical System with Automatic-Frequency Control, *Int. Appl. Mech.*, Vol 32 (No. 11), 1997, p 865–870
40. C.Y. Kong and R.C. Soar, Fabrication of Metal-Matrix Composites and Adaptive Composites Using Ultrasonic Consolidation Process, *Mater. Sci. Eng. A*, Vol 412, 2005, p 12–18
41. Y. Yang, J. Ram, and B. Stucker, An Experimental Determination of Optimum Processing Parameters for Al/SiC Metal Matrix Composites Made Using Ultrasonic Consolidation, *J. Eng. Mater. Technol. (Trans. ASME)*, Vol 129 (No. 4), 2007, p 538–549
42. J. Tsujino, T. Ueoka, T. Kashino, and F. Sugahara, Transverse and Torsional Complex Vibration Systems for Ultrasonic

- Seam Welding of Metal Plates, *Ultrasonics*, Vol 38, 2000, p 67–71
43. J. Tsujino and T. Ueoka, Welding Characteristics of Ultrasonic Seam Welding System Using a Complex Vibration Circular Disk Welding Tip, *Jpn. J. Appl. Physics, Part 1: Regular Papers and Short Notes and Review Papers*, Vol 39 (No. 5B), 2000, p 2990–2994
 44. A. Akay, Acoustics of Friction, *J. Acoust. Soc. Am.*, Vol 111 (No. 4), 2002, p 1525–1548
 45. Release 11.0 Documentation for ANSYS, ANSYS, Inc.
 46. J. Lemaitre and J.L. Chaboche, *Mechanics of Solid Materials*, Cambridge University Press, 1990
 47. N. Huber and C. Tsakmakis, Determination of Constitutive Properties from Spherical Indentation Data Using Neural Networks, Part II: Plasticity with Nonlinear Isotropic and Kinematic Hardening, *J. Mech. Phys. Solids*, Vol 47, 1999, p 1589–1607
 48. P.J. Armstrong and C.O. Frederick, “A Mathematical Representation of the Multi-axial Bauschinger Effect,” CEGB Report RD/B/N 731, 1966
 49. G.R. Johnson and W.H. Cook, Fracture Characteristics of Three Metals Subjected to Various Strains, Strain Rates, Temperatures and Pressures, *Eng. Fract. Mech.*, Vol 21, 1985, p 31–48
 50. ABAQUS, Abaqus version 6.5, online documentation, Hibbitt, Karlsson, & Sorenson Inc., 2006
 51. G. Ravichandran, A.J. Rosakis, J. Hodywany, and P. Rosakis, On the Conversion of Plastic Work into Heat during High-Strain-Rate Deformation, *AIP Conf. Proc.*, Vol 620 (No. 1), July 2002, p 557–562
 52. C. Zhang, A. Deceuster, and L. Li, A Method for Bond Strength Evaluation for Laminated Structures with Application to Ultrasonic Consolidation, *J. Mater. Eng. Perform.*, Vol 18 (No. 8), 2009, p 1124–1132
 53. Y. Yang, G.D. Janaki Ram, and B.E. Stucker, Bond Formation and Fiber Embedment during Ultrasonic Consolidation, *J. Mater. Proc. Technol.*, Vol 209, 2009, p 4915–4924
 54. C.Y. Kong, R.C. Soar, and P.M. Dickens, A Model for Welding Strength in Ultrasonically Consolidated Components, *Proc. Inst. Mech. Eng., Part C: J. Mech. Eng. Sci.*, Vol 219 (No. 1), 2005, p 83–91
 55. G.D. Janaki Ram, Y. Yang, and B.E. Stucker, Effect of Process Parameters on Bond Formation during Ultrasonic Consolidation of Aluminum Alloy 3003, *J. Manuf. Syst.*, Vol 25 (No. 3), 2006, p 221–238
 56. C. Zhang and L. Li, Effect of Substrate Dimensions on Dynamics of Ultrasonic Consolidation, *Ultrasonics*, Vol 50, 2010, p 811–825
 57. C. Robinson, C. Zhang, E. Siggard, J. Ram, B. Stucker, and L. Li, Maximum Height to Width Ratio of Freestanding Structures Built Using Ultrasonic Consolidation, *The 17th Solid Freeform Fabrication Symposium*, Aug 14–16, 2006 (Austin, TX), 2006
 58. P.C. Daniels, Ultrasonic Welding, *Ultrasonics*, Vol 3 (No. 4), 1965, p 190–196
 59. K. Joshi, The Formation of Ultrasonic Bonds between Metals, *Weld. J.*, Vol 50 (No. 12), Dec 1971, p 840–848

Fundamentals of Solid-State Resistance Welding

Jerry E. Gould, Edison Welding Institute

RESISTANCE WELDING PROCESSES are those which incorporate electric currents to facilitate Joule heating. This heating is then used to promote the metallurgical mechanisms that result in formation of a joint. The most common resistance processes nominally result in melting and resolidification of metal. These processes typically create weld “nuggets” as described in the article on “Resistance Welding” included in this volume. Joule (or resistance) heating can also be used to foster the necessary mechanisms for solid-state joining. Variants of solid-state resistance welding include flash-butt, upset-butt, mash-seam, etc. This article provides a fundamentals-based description of these approaches through one specific process variant. This is termed as solid-state resistance projection welding.

The underlying mechanisms of thermally assisted solid-state welding include displacement of bond line contaminants and thermal dissolution of contact surface oxides (see the article “Mechanisms of Bonding for Solid-State Welding Processes” in this Volume). Projection welding is a resistance welding process which uses geometric discontinuities to create highly localized heating. The approach can produce solid-state or fusion welds, and allows highly localized welds to be produced in predefined locations of components.

Solid-state projection welding is closely related to other solid-state processes, and it provides a good example in describing the mechanisms of solid-state welding with resistance heating. In this article, simple analytical tools are described to help understand the variety of mechanisms that occur during resistance projection welding. Factors relating to the quality of solid projection are discussed, including an explanation of the mechanisms of bonding for solid projection welding. This is followed by a review of how these mechanisms are affected by heat balance, current profile, mechanical characteristics of the welding equipment, and finally, the design of the projection itself.

The analysis is done in five parts, as described in the section “Summary of Analysis” in this article. It is shown that when projection welding is properly done, the results are solid state in character and incorporate both bond-line strain and thermal cycle components. Bond-line strain has the effect of disrupting surface contaminants and revealing the underlying clean material for bonding.

Projection Welding

Projection welding is one of the oldest variations of the resistance processes. Projection welding is defined by using a geometric feature as a current concentrator during resistance welding (Ref 1). The use of the projection allows highly localized welds in predefined locations based on the design of the component(s) (Ref 2). The resulting joints can be formed either as solid-state or fusion processes. Two categories of projections are typically used with these processes (Ref 2). These include embossed and solid projection welding.

Embossed projections are often used with sheet components. The projections are then stamped into one of the two components. Embossed projection welding has been studied extensively (Ref 3–7). These studies have included basic process dynamics (Ref 3), design guidelines for projections (Ref 3–6), process optimization studies (Ref 3–6), and the mechanics of bonding (Ref 3–7). Such welds using embossed projections accomplish bonding progressively, first through solid-state mechanisms and then through formation of weld nuggets.

These studies have shown that solid-state bonds can be accomplished at extremely short times (milliseconds), with weld nuggets forming at longer weld times (hundreds of milliseconds). With embossed projections, the maximum solid-state weld sizes are on the order of the projection size itself. Alternately,

if nuggets are allowed to grow, the weld size can exceed that of the projection by many times. These studies have led to the development of recommended practices for projection designs that are widely published (Ref 1, 8, 9).

Solid projection welding is used for machined or cold-headed components. This class of projection welding includes all those where the basic geometry of the components results in localized contact that can be used for current concentration (Ref 9). Geometries included in this class of projection welding vary widely. These include those with designed projections (e.g., annular projection welding) as well as those where the contact points are implied (edge projection welding, cross-wire welding). This class of projection welds (when done properly) typically results in solid-state joints (Ref 10–12). Because solid projection welding applications vary so broadly, there is little research or standardization for resulting designs. One area where some information is available is annular projection welds (Ref 10–12). These studies have evaluated projection designs for a number of different power supply types. Generally, the best weld quality is associated with balanced projection designs (forging will occur equally to the inside and outside diameters of the projection), and the projection will have a 90° included angle.

Projection welding is generally considered a reliable and robust process. However, given the variety of projection designs, the complexity of the stack-ups, and the number of material combinations with which the process is used, there are some chronic concerns. These include the presence of expulsion (melting and expelling of material), modes of projection collapse, consistency of the joint, and so on. The underlying causes of these problems can be multifold and include projection design, type of power supply used, mechanical system, and so on.

Bonding Mechanisms during Solid-State Projection Welding

As mentioned previously, solid projection welding generally results in solid-state joints. Fusion welds (indicated by the formation of a weld nugget) are not possible in these applications, because the solid projection geometry does not allow constraint of the weld nugget. Essentially, as the solid projection collapses, it must form laterally (or circumferentially). Because there are generally no provisions to allow flow of this displaced material, the individual component surfaces cannot make an enclosing contact, allowing formation of a weld nugget. Bonding, then, for solid projection welds is closely related to other solid-state processes. The mechanisms of solid-state bonding for thermally assisted processes are described in the article "Mechanisms of Bonding for Solid-State Welding Processes" in this Volume (Ref 13). During solid-state welding, two mechanisms predominate. These include surface disruption by the application of strain, and thermal dissolution of contact surface oxides.

Surface strain is an artifact of projection collapse. As the projection collapses, there is both deformation in that component as well as on the opposing surface. This deformation results in surface strains that act to disrupt the oxides resident on the contacting surfaces. As those oxides fracture, clean surface is exposed. Clean surfaces on the opposing parts, when brought into intimate contact, then share electrons and become bonded.

As suggested previously, the second mechanism of interest for projection welding is the thermal dissolution of any remaining oxides. Projection welding thermal cycles can be estimated from actual current flow times. These times range from a few to as many as several hundred milliseconds. Clearly, such short times require high temperatures for dissociation of residual oxides. This fact also suggests that degrees of residual oxides must be reduced through forging action (as described previously) for the mechanism to be effective. It is generally observed that both forging (i.e., surface strains) and thermal cycles (i.e., oxide dissociation) are required for effective projection welding.

A third mechanism is also often involved in solid projection welding. This mechanism is associated with localized melting and resolidification of metal. As mentioned earlier, melting is often associated with projection welding. Melting during solid projection welding is caused by overheating the part for the force applied. The balance between mechanical and thermal responses in projection welding is discussed in subsequent sections. When melting occurs, there is little constraint to contain this material. As a result, the liquid is typically both expelled (defined as weld expulsion) and retained along the bond line.

Liquid metal can be advantageous for projection welding, in that material solidifying along the bond line can facilitate a joint. This bonding mechanism is commonly used in percussion welding (Ref 14). Allowing such expulsion, however, has a number of drawbacks. One issue is the expelled metal itself. For projection welding applications, the resulting distribution of expelled material may be detrimental to the application (e.g., where sealing is required). In such cases, the lost material (due to localized melting) cannot be replaced in subsequent forging. This can result in porosity along the weld. In addition, a specific type of weld defect, so-called flat spots, can be related to this resolidified material.

The relationship between flat spots and liquid metal in otherwise solid-state welds has been well investigated with respect to flash butt welding (Ref 15–17). The problem is predominantly related to carbon segregation to this liquid material. Carbon at high temperatures is well known to segregate to liquid steel if it is present. The result is a local depletion of carbon from the working surfaces during processing. As forging occurs, the liquid is typically squeezed out. However, the thin layers of decarburized solid steel are then forged over the contact surface, leaving a so-called decarburized band across the interface. This band is typically only a few micrometers wide but can have hardnesses on the order of one-half that of the surrounding material.

Flat spots can then occur when there are residual discontinuities at the bond line. For the projection welding application, the most likely such discontinuities are residual oxides. Such discontinuities are inherently located in

this low-strength interface. The difference in yield strengths between the matrix and decarburized band can result in high triaxial stresses during cooling. Under such conditions, the defects can expand into planar cracks or so-called flat spots. These defects occur irregularly and can be the source of intermittent failures on projection-welded components.

Mechanical/Heat-Transfer Balances

Ideal projection welds show a number of underlying process characteristics. These include localized heating (and subsequent forging), stable applied forces to prevent expulsion, and a balanced forging profile. Achieving localized heating is typically a balance between the rates of heating and thermal conduction. Rapid heating rates (or alternately poor thermal conduction through the projection) result in steep thermal profiles in the projection itself. The temperature profile can be related to the forge depth through the temperature-dependent yield strength of the base material. A characteristic profile for 1015 steel is shown in Fig. 1 (Ref 18). This plot shows a rapid plunge in yield strength with increasing temperature. For an applied force, the band of material that is sufficiently soft to forge is clearly temperature dependent.

The thermal profile (and subsequently the forge depth) is strongly a function of both heating time and projection geometry. The latter is discussed in the section "Geometric Effects" in this article. The effect of heating time on the thermal profile can be estimated through a simple one-dimensional analysis. By looking

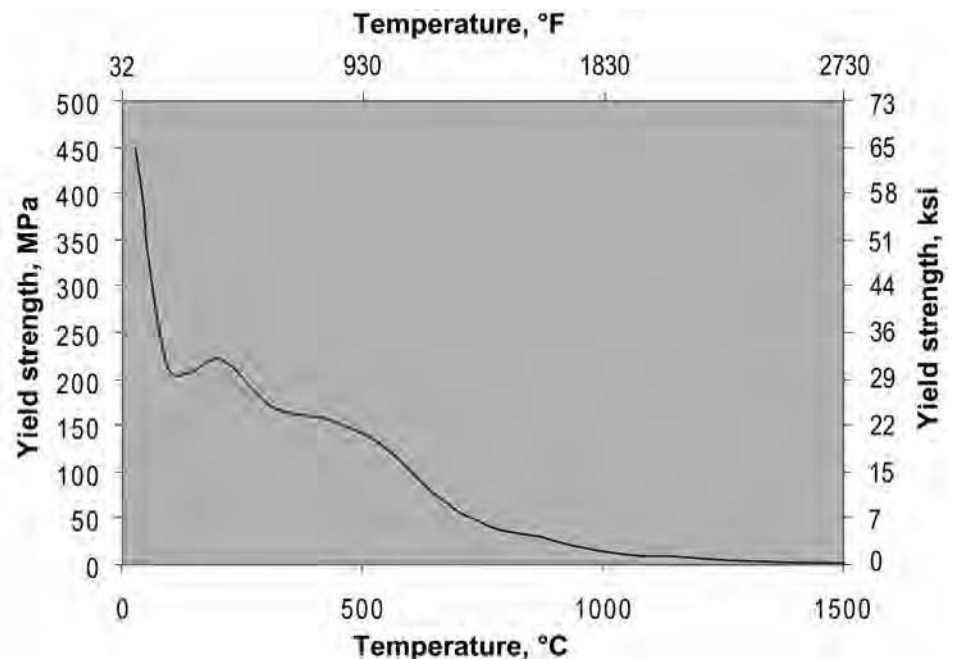


Fig. 1 Yield strength as a function of temperature for 1015 steel. Data taken from Ref 18

at essentially a straight-sided projection subjected to a heating pulse of duration t , the peak temperature profile in the part can be defined by the following equation (Ref 19):

$$T(x, t) = T_p - (T_p - T_o) \operatorname{erf}\left(\frac{x}{2\sqrt{\alpha t}}\right) \quad (\text{Eq 1})$$

where T_p and T_o are the peak (in the welding cycle) and room temperatures, respectively; α is the thermal diffusivity of the projection material; t is the effective width of the heat (weld) pulse; and x is the distance back into the projection. Characteristic results from this equation are shown in Fig. 2. This plot is based on a steel projection, using the thermal diffusivity at high temperatures ($\sim 0.1 \text{ mm}^2/\text{ms}$). These results show that for increasing heat pulse (weld) time, thermal gradients progressively decrease. Of particular interest is the effect such thermal gradients have on the forge depth in the projection. This can be assessed by determining the depth of material that is above some forging temperature in Fig. 2. Such a forge temperature for steels can be taken directly from Fig. 1. Here, it is estimated that $900 \text{ }^\circ\text{C}$ ($1650 \text{ }^\circ\text{F}$) is typical (although dependent on projection geometry and applied force) for forging this material. Using this as an approximate forging temperature, forge depths can then be taken directly from Fig. 2. These data have been replotted as forge depth as a function of heat time in Fig. 3.

For steep temperature profiles, the shallow forging depths suggest highly localized deformation. Such localized deformation implies progressively higher degrees of surface strain and improved weld quality. It is of note that processing requirements, particularly current on-times to achieve best surface strains, are contrary to those necessary for thermal dissolution of residual oxides along the bond line. That is, rapid thermal cycles tend to improve surface strains, while long times provide a good thermal profile for diffusion. Generally, balancing these two competing mechanisms is application dependent. Limited experimental data (Ref 10, 11, 20) show that biasing the process toward maximizing surface strains (short times, high currents) is typically beneficial. This is believed to be related to two factors. First, maximizing surface strains has the effect of minimizing the degree of residual oxides for thermal dissolution. It appears that shorter thermal cycles for dissociating fewer and smaller residual oxides is beneficial. Second, rapid thermal cycles reduce the tendency to form oxides on the surface of the projection prior to collapse. This appears again to reduce the size and distribution of these residual oxides, again minimizing the extent of the thermal cycle necessary for dissolution.

As mentioned, applied welding force may also be a concern. Low welding forces prohibit forging except at high temperatures. The effect, then, is twofold. First, because the difference between the forging and melting temperatures is reduced, unstable expulsion can result.

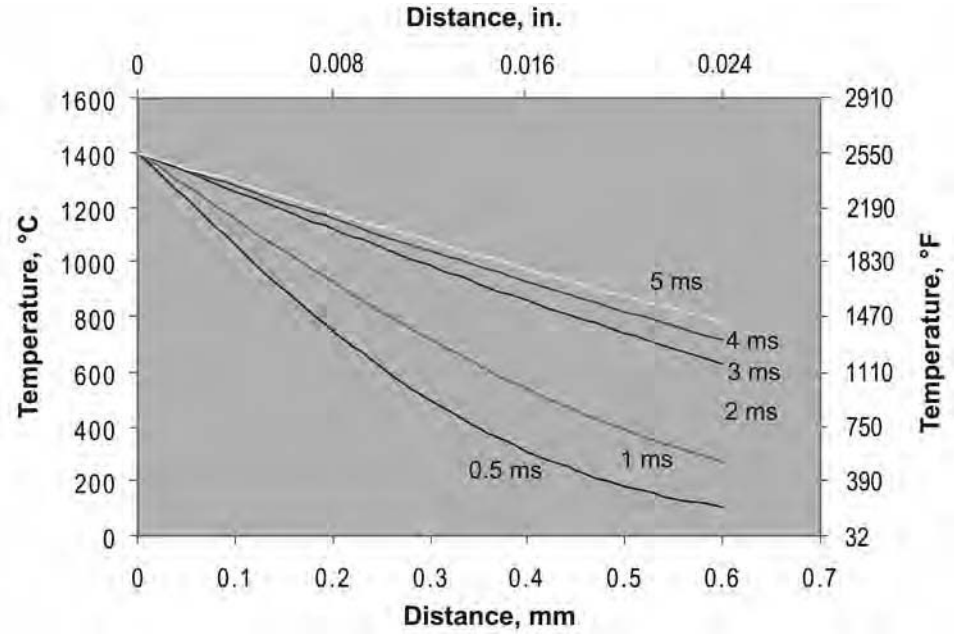


Fig. 2 Peak temperature profiles as a function of heat (weld) time for a straight-sided projection. Results are calculated from Eq 1.

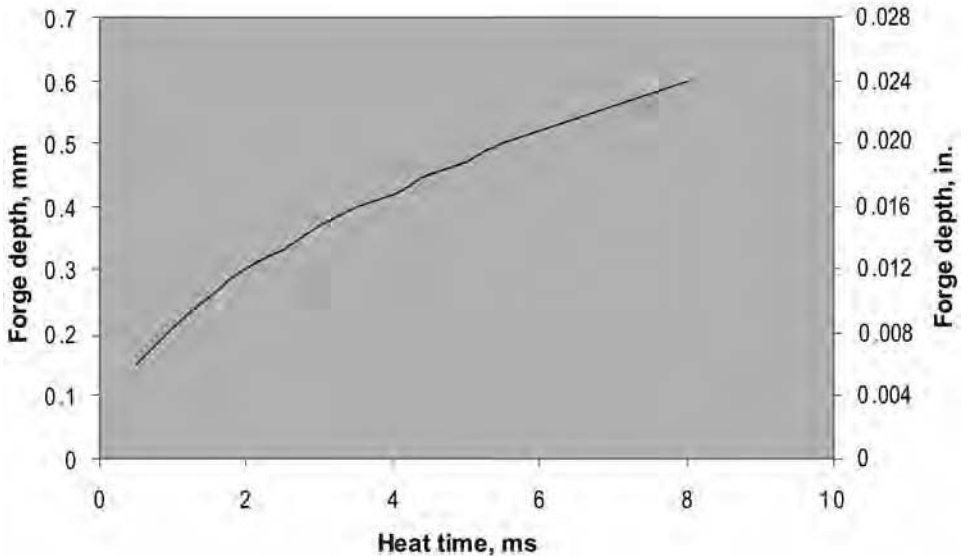


Fig. 3 Calculated forge depths on a straight-sided steel projection. Results are based on a $900 \text{ }^\circ\text{C}$ ($1650 \text{ }^\circ\text{F}$) forge temperature and the data shown in Fig. 2.

Second, because the interfacial temperatures are inherently higher, the driving forces for extended heat soak-back are increased. As a result, lower forces inherently result in shallower thermal gradients, with subsequent declines in weld quality. Similar problems are experienced with poor mechanical follow-up. The issue of mechanical follow-up is addressed in the next section. However, the implication of poor mechanical follow-up is a loss of welding force as the projection collapses. This dynamic variation in welding force has the same

influence as low welding force on such aspects as incidences of expulsion and reduced thermal gradients in the projection.

Effect of System Mechanical Dynamics on Projection Welds

As discussed previously, system mechanical dynamics play an important role in projection weld quality. Specifically, proper forging of

projections requires that the force consolidating the weld be maintained throughout the heating cycle. Otherwise, force dips will result, leading to heat soak and expulsion-related problems, as described in the previous section. The relationship between applied weld force, system mechanical inertia, collapse distance, and collapse time is demonstrated in the following equation (Ref 21):

$$\frac{W_{\text{head}}}{F_{\text{app}}} \leq \frac{g(f t)^2}{20x} \quad (\text{Eq 2})$$

where W_{head} is the weight of the welding head, F_{app} is the applied welding force, g is the acceleration due to gravity, t is the welding time, f is the fraction of the weld time over which projection collapse occurs, and x is the projection collapse distance. The equation is based on the assumptions of constant weld head acceleration, and that 95% of the applied welding force should be maintained for adequate welding. The results of this plot are presented graphically for a range of projection collapse distances, collapse times, and resultant head weight/applied force ratios in Fig. 4. This plot shows that for projection collapse times and distances on the order of 10 ms and 0.5 mm, respectively, the head weight must be less than 10% of the applied welding force. However, if for the same application the collapse time dropped to 5 ms, the critical head weight/applied force ratio would drop to 2.5%.

For larger-scale projection welding systems, the weld force is typically applied by a cylinder behind the ram and tooling. The weight of the

head then includes all those components. As a result $W_{\text{head}}/F_{\text{app}}$ can easily rise and fail the criterion described in Eq 2. This, however, can be compensated for by using so-called fast follow-up heads. These heads are spring loaded and act as a buffer between the main ram and the platen holding the electrode. Such springs can be made from steel (both coil and Bellville washer variations) or from various polymers. The use of these springs essentially reduces the moving weight in the process. In effect, the controlling head weight for Eq 2 then becomes that of the moving assembly below the springs. A typical fast follow-up head assembly is shown in Fig. 5. For this head, a spring is used for follow-up. In addition, the cavity holding the spring (in the center of the unit) is actually a bearing surface, providing alignment between the fast follow-up platen and the primary ram of the machine. With such an assembly, the moving weight in the system can be readily sized to match Eq 2.

Critical to any fast follow-up head is the design of the spring itself. The designs of such springs are usually bounded by geometric considerations and the required spring constant. The governing equation here is that for force supplied by a spring (Ref 22):

$$F_{\text{app}} = -kx_{\text{total}} \quad (\text{Eq 3})$$

where k is the spring constant, and x_{total} is the total displacement of the spring. This equation basically can be used to define spring collapse requirements to applied and relative forces. Similar to the analysis for mechanical follow-up, it is recommended that springs be designed

to maintain 95% of the applied weld force through the collapse distance of the projection. In terms of displacements, this can be expressed as:

$$\frac{x_{\text{precomp}} + x_{\text{comp}} - x}{x_{\text{precomp}} + x_{\text{comp}}} \geq 95\% \quad (\text{Eq 4})$$

where x_{precomp} and x_{comp} are the precompression (preload) and compression distances of the spring, and x is the collapse distance of the projection, as defined previously. Of note, $x_{\text{precomp}} + x_{\text{comp}}$ is equal to x_{total} in Eq 3. Also, x_{comp} must always be greater than x (with a margin) for the head to function properly. For steel springs, the constant k is a design characteristic of the unit. For polymer springs, this constant is defined by the modulus and the spring geometry through the following relationship:

$$k = E \frac{\text{area}}{L} \quad (\text{Eq 5})$$

In this equation, E is the material modulus, while L and “area” are the length and cross-sectional area of the spring itself. Springs for a specific application can then be designed iterating Eq 3 and 4 with the spring constant (for steel springs) or Eq 3 to 5 (for polymer springs). Heads are available in an array of configurations, matching both the requirements of the application and geometry of the welding equipment. When properly designed, projection welding mechanical systems can generally maintain 90% of the weld force throughout the projection collapse cycle.

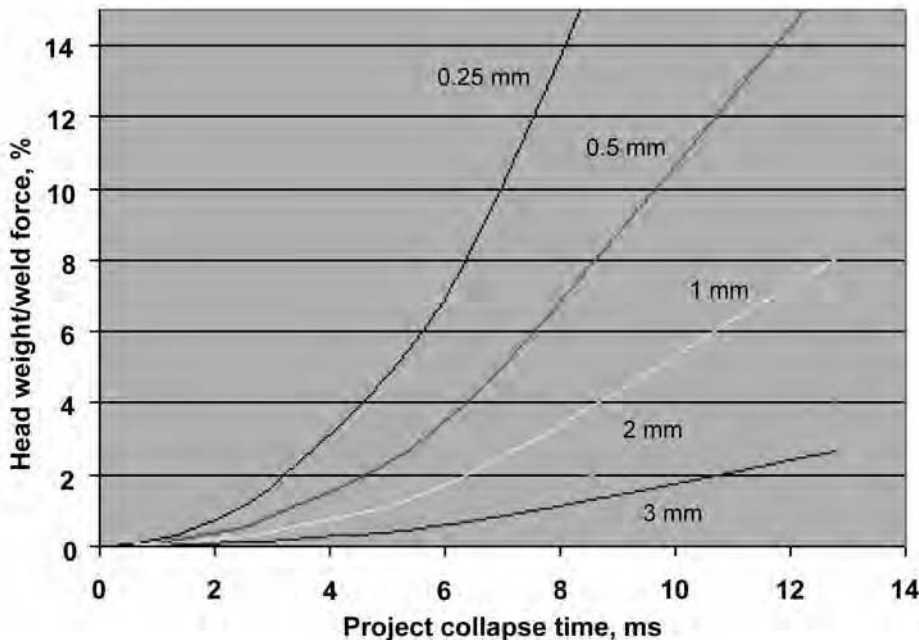


Fig. 4 Relationship between projection collapse distance, projection collapse time, and the head weight/weld force ratio

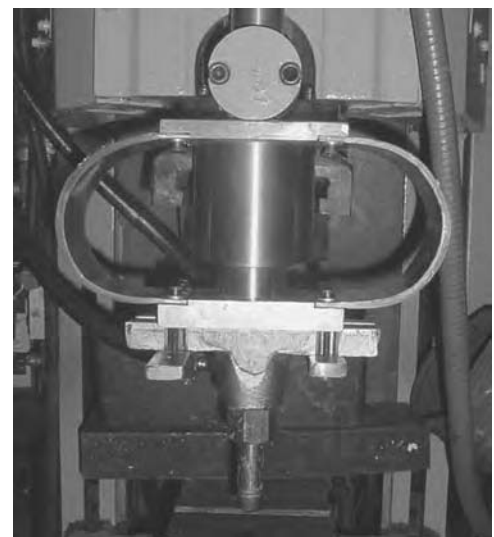


Fig. 5 Typical fast follow-up head for resistance welding. The spring is located in the body of the assembly. Note the shunts providing a current flow path around the spring.

Effect of Electrical Characteristics on Projection Welds

The thermal cycle of the projection welding process is, to a large degree, defined by the current waveform. As described previously, short cycles and fast rise times suggest localized deformation of the projection and improved weld quality. Longer weld cycles and faster rise times suggest more delocalized forging and subsequent reductions in quality. An example is provided here for the capacitive discharge (CD) variant of projection welding. While this is just one variant of power supplies used for this process, the analysis provides insight into how heat is generated for this class of welding methods. The schematic for the power circuit in CD welding systems is shown in Fig. 6. For operation, the switch on the left is used to charge the capacitor, while the switch on the right discharges the capacitor energy into the welding circuit. Characteristic values for the circuit include the capacitor charge voltage (V_c), the system capacitance (C), the turns ratio of the transformer (N), and the inductance and resistance of the secondary circuit (L_s and R_s). The L_s is usually defined by the secondary geometry (larger loops imply larger inductances), while the R_s is associated with the workpiece resistance. The secondary current waveform for this circuit is characterized in the following equations (Ref 23):

$$I_s(t) \approx V_c \sqrt{\frac{C}{L_s}} e^{-\zeta \omega t} \sin(\omega t) \tag{Eq 6}$$

where:

$$\omega = \frac{1}{N} \sqrt{\frac{1}{L_s C}} \tag{Eq 7}$$

and:

$$\zeta = \frac{NR_s}{2} \sqrt{\frac{C}{L_s}} \tag{Eq 8}$$

These equations are based on treating the secondary (output) as an inductance resistance capacitance circuit. The capacitance and charge voltage have been incorporated into these equations through the windings ratio expressions $V_s = V_c/N$ and $C_s = N^{1/2} C$, where V_s and C_s are the charge voltage and capacitance when reflected to the secondary of the transformer.

These equations allow current profiles to be estimated from process inputs (charge voltages), machine configurations (capacitances, transformer windings ratios), and workpiece arrangements (component resistances, secondary inductances). A characteristic waveform for a CD projection weld is shown in Fig. 7. This waveform was generated using conditions for a nominal 15 mm (0.6 in.) diameter steel annular projection weld. This included a capacitance of 2400 μ Fd, a charge voltage of 2000 V, a

transformer windings ratio of 100 to 1, a secondary inductance of 0.27 μ H, and a secondary resistance of 175 $\mu\Omega$. The waveform shows a characteristic shape, including a fast rise time and subsequent exponential decay of the current. For this waveform, the peak current obtained is approximately 70 kA, with an associated rise time of 2.3 ms.

Geometric Effects

As mentioned previously, solid projection welding can be accomplished with a wide variation of included geometries (Ref 10–12). As suggested by the results of the analyses provided earlier, the best designs of projections are those that optimize surface strains during welding. These projections are

typically geometrically symmetric, allowing uniform deformation in all unconstrained directions. For single-point projections, this is generally either a radiused or cone geometry. For annular projections, the desired cross-sectional geometry is typically an isosceles triangle. This triangle may also include a flat or radius at the tip. This projection is designed to forge equally to the inside and outside diameters of the component during welding.

For such projection designs, two variables are dominant. The first of these is the projection width. Projection widths are largely selected based on the strength requirements of the joint. Previous work (Ref 11) has based the width of the projection on the thickness of the opposing material in the application. This decision was largely based on achieving parent-material failure (in the opposing workpiece) during

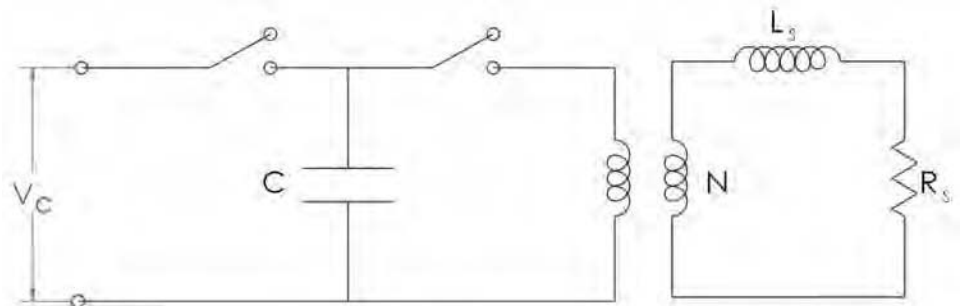


Fig. 6 Schematic representation of the power circuit for a capacitive discharge projection welding system. V_c , charge voltage; C , capacitance; N , windings ratio in the transformer; L_s , inductance in the secondary; R_s , resistance in the secondary

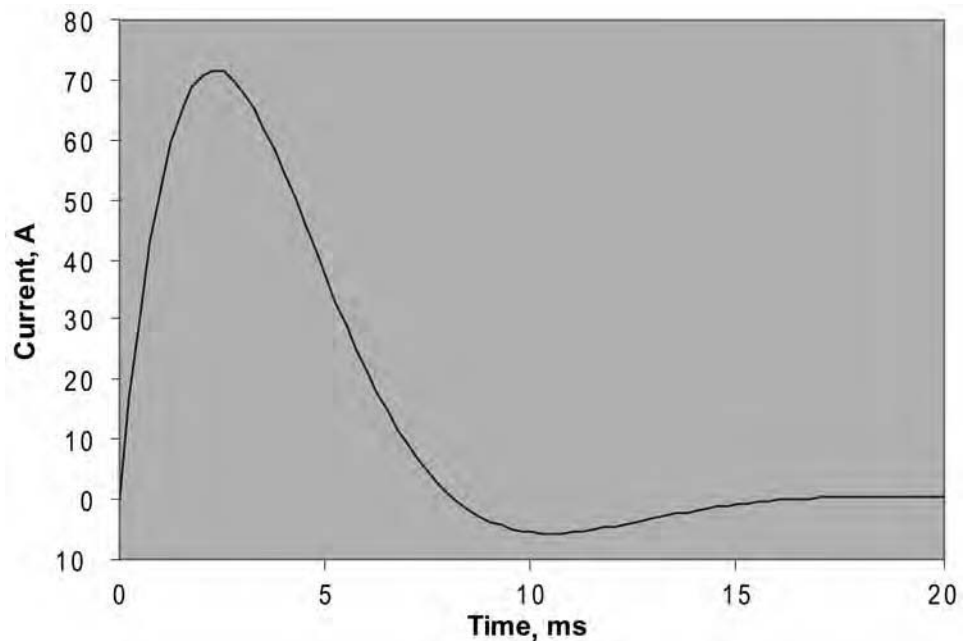


Fig. 7 Current waveform for a capacitive discharge projection welding system. Plot is generated using Eq 6 to 8, with a capacitance of 2400 μ Fd, a charge voltage of 2000 V, a transformer windings ratio of 100:1, a secondary inductance of 0.27 μ H, and a secondary resistance of 175 $\mu\Omega$.

destructive testing for welds on steels. The second of these is the included angle in the projection itself.

Included projection angle has effects on heat transfer during welding as well as the resultant profile of the forged material. The heat-transfer effects can be understood by conducting a simple one-dimensional thermal analysis incorporating the included angle of the projection. For simplicity, this analysis is conducted assuming steady-state conditions. In addition, it is assumed that the process is heat-sunk by the mass of the component at the base of the projection. The analysis here parallels that for truncated cone-style resistance welding electrodes (Ref 24). For an annular projection, the governing equation is then:

$$\frac{d^2T}{dx^2} + \frac{2 \tan \phi}{w + 2x \tan \phi} \frac{dT}{dx} = 0 \tag{Eq 9}$$

where ϕ is the included angle, w is the face width, and x is the distance back into the projection. Assuming a maximum temperature at the projection tip (similar to the approach used for Eq 1), the solution to this equation can be expressed as:

$$T = (T_p - T_o) \left[\frac{\ln \left(\frac{1 + \frac{2x}{w} \tan \phi}{1 + \frac{2h}{w} \tan \phi} \right)}{\ln \left(1 + \frac{2h}{w} \tan \phi \right)} \right] + T_o \tag{Eq 10}$$

where h is the height of the projection. Using this equation, the effect of the included projection angle on the resulting temperature profile is shown in Fig. 8. The plot is based on an annular projection with a 2 mm (0.08 in.) height and a 0.2 mm (0.008 in.) flat on the tip. As when examining the effects of heat (weld) time, a peak temperature at the projection tip of 1400 °C (2550 °F) is assumed. In general, the results show a progressively decreasing thermal gradient away from the projection tip. This is the result of change in projection cross section associated with the included angle. It is noted from this plot that the degree of heat penetration varies inversely with the included angle. That is, the narrowest included angles result in the deepest (into the projection) heat penetrations. This variation in heat penetration can again be used to examine the forge depths, as was done when considering heat (weld) times. These forge depths can be calculated by rearranging Eq 10. The resulting equation is:

$$x_f = \frac{w}{2 \tan \phi} \left[\left(1 + \frac{2h}{w} \tan \phi \right)^{1 - \frac{T_f - T_o}{T_p - T_o}} - 1 \right] \tag{Eq 11}$$

where x_f is the forge depth, and T_f is the forge temperature. Again, using a forge temperature of 900 °C (1650 °F), the variation in forge depths as a function of projection included angle is given in Fig. 9. The plot shows that the forge depth decreases monotonically with increasing angle. This again shows the heat-

sinking capability associated with changes in projection angle.

It has been documented that for annular projection welding, a 90° included angle appears to be optimal (Ref 11, 20). Both too-small (Ref 20) and too-large (Ref 11) included angles have been shown to be detrimental to weld performance. A too-small included angle inevitably leads to a too-wide forge zone. This, as described previously, leads to delocalized forging and reduced effective surface strains. The concerns with a too-large included angle

can be related to effective stresses during forging. Essentially, the increase in contact area during forging with a large included angle reduces effective stresses, limiting material deformation and effective strain.

Actual thermal cycles and forge depths are actually a combination of the effects of weld time and included projection angle. The effects have been described separately previously, with the time-based analysis done with a straight-sided projection and the geometric analysis done assuming steady-state conditions (long

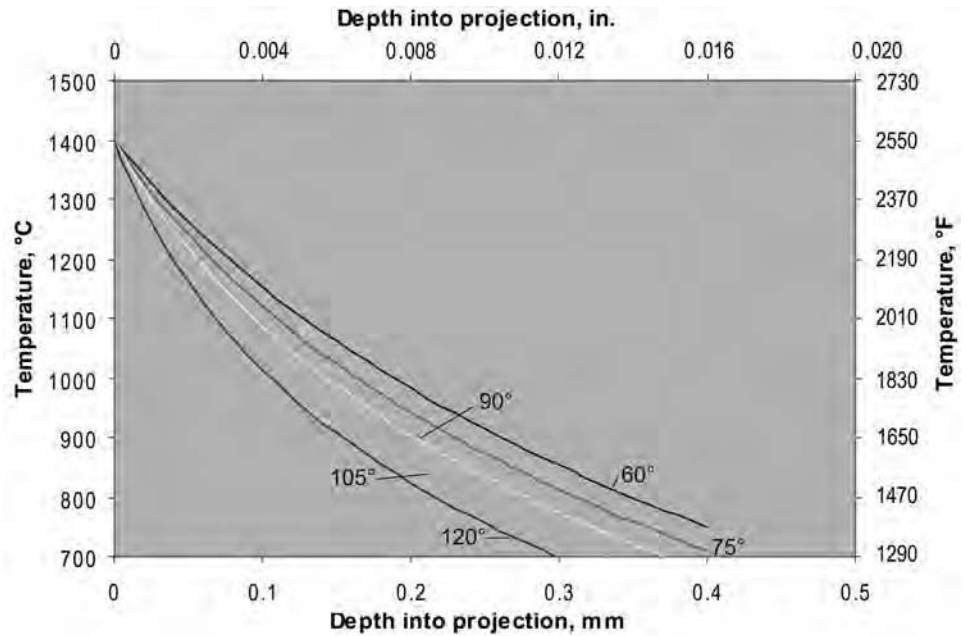


Fig. 8 Temperature profiles near the tip for an array of included projection angles. Data generated from Eq 10

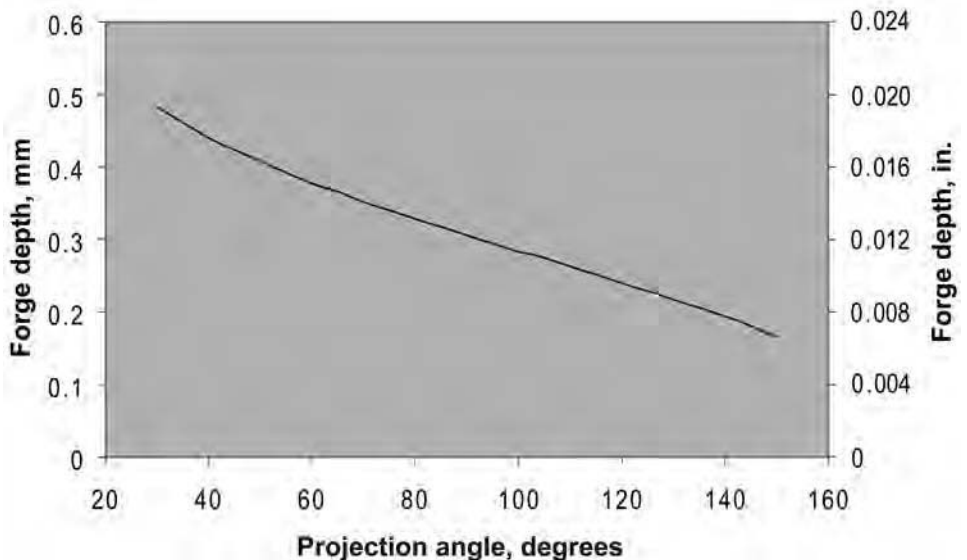


Fig. 9 Forge depth as a function of projection angle. Data generated from Eq 11, assuming a forge temperature of 900 °C (1650 °F)

heat times). Proper optimization requires balances of these two effects to achieve the best possible forging characteristic.

While the analysis done earlier assumes balanced projections, many applications use asymmetric profiles. Such asymmetric profiles tend to heat on the side with less material. This has been seen to result in, at a minimum, asymmetric set-down. This, in turn, has the effect of trapping material in the bond line, reducing weld quality. In addition, such asymmetric set-down can easily result in overheating on one side of the joint, resulting in expulsion. As mentioned earlier, expulsion is typically detrimental to solid projection welds, so joint quality is inevitably compromised. When using such unbalanced projections, shorter weld times tend to improve weld quality. This can be implied from Eq 1 as well as Fig. 2 and 3. Short weld times have the effect of minimizing thermal soak-backs (and forge depths), minimizing complex heating profiles associated with the specific projection design and the resultant quality variations. In general, however, balanced projection designs will yield better weld quality.

All the equations defining the temperature profiles for included-angle projections include flats at the tip. Flats at the tip are essential in these analyses, because a sharp tip implies a local heat-transfer discontinuity. Such a point contact would result in excessive current densities and essentially no heat flux into the projection. The second implication is that the tip of the component would reach temperature nearly instantaneously, causing follow-up problems for the application. In practice, no projection is absolutely sharp, in that the applied welding force would cause yielding at the tip. This would then dull the projection, creating a flat that matches the geometry and the applied welding force. In practice, flats are often used to compensate for follow-up in the welding machine. Recent work has shown that the use of a small flat (~0.2 mm, or 0.008 in.) can minimize weld defects and improve weld strengths, particularly for CD systems.

Finally, it is of note that annular projection welds are often made into holes (Ref 2, 9). These types of joints are referred to as edge-projection welds. Such welds use the geometry of the hole and component to imply a projection for resistance heating. Typical examples include a squared-off bar/tube into a tapered hole, and a tapered section into a straight hole. In both cases, the implied projection forges into and slides across the opposing working surface. The key factors described earlier for annular welds are equally valid for edge welds. These include mechanical balance of the (implied) projection, matching weld times to the desired set-down, and so on. One additional note is to address the motion of the projection across the mating surface. Generally, if the contact angle is too steep, the projection will experience too much lateral motion during forging. This has the effect of bringing contaminants into the

bond area (as the projection slides), reducing bond quality. As discussed earlier for unbalanced projections, shortening the weld times to minimize the forge depths can again be helpful in these applications.

Summary of Analysis

The foregoing analysis was done in five parts. First, efforts were made to define the basic mechanisms of bonding in projection welding. Thermal cycles can be used as a measure of oxide dissolution in the bond line. Basic theory, originally developed for particle dissolution during such thermal cycles, was reviewed in this context. It was noted that most studies suggest that surface-strain effects dominate those from thermal cycles in most projection welding applications. Some discussion was also provided regarding the influence of expulsion on subsequent weld quality.

The second stage of the analysis considered thermal and mechanical balances during projection welding. Thermal balances were analyzed by examining a defined heat pulse into a parallel-sided projection. From the resulting analysis, the concept of forge depth was defined. Forge depth compared the temperature-dependent yield strength to the thermal gradient in the projection. Generally, the greater the forge depth, the more delocalized the forging action and the lower the effective strains for bonding. The analysis showed that forge depths are strongly dependent on heat time. For projection welding, this is closely analogous to the current rise time. Narrower forge depths (with improved effective surface strains) are accomplished through shorter and shorter heat times. Short heat times, however, then require improved mechanical follow-up to prevent expulsion.

The third stage considered mechanical follow-up and related design issues. The relationships between forge distances, collapse times, welding forces, and necessary head weights were discussed, and a defining quantitative relationship was presented. This was followed by design criteria for spring-assisted fast follow-up systems.

The fourth step addressed current (and therefore heating) cycles associated with resistance projection welding. An example was provided by examining the CD process. A relationship was developed based on a simple inductance resistance capacitance circuit, combined with a constancy-of-energy relationship across the transformer. The resulting equations allowed details of the waveform to be predicted based on welding parameters (charge voltage) and process characteristics (system capacitances, transformer windings ratios, and both secondary resistances and impedances). Rise times from this analysis could be used to provide heating information for the various other analyses discussed in this work.

Finally, some consideration was given to the influences of projection geometry. A quantitative analysis was presented relating included projection angle, projection height, and the width of any flat on the projection tip to thermal profiles in the part during joining. These were then converted to forge depths using an approach similar to that described previously for heat times. These results suggest that wider included angles in the projection resulted in shallower forge depths. It is noted that previous experimental results suggested 90° as an optimal included angle for projection welding. At sharper projections, the wider forge depths correlated with reduced weld performance. For angles greater than 90°, it was speculated that the increase in projection cross section (with increasing forge depth) reduced stresses and effectively minimized any forging that would occur. This, in effect, again reduced weld performance. These results (collectively) were then discussed regarding nonsymmetric and edge-style projections. For such configurations, the use of short pulse times (with associated shallow forge depths) offered a way of mitigating the thermal imbalances associated with these designs.

Conclusions

In this work, the mechanisms of bonding for resistance projection welding have been examined in detail. These mechanisms were broken into several components. These included a review of the basic mechanisms of solid-state bonding, an analysis of the mechanical and heat-transfer characteristics of projection welding, assessments of weld head follow-up requirements, examinations of current waveforms, and influence of projection/workpiece geometries. Where possible, simplified mathematical solutions were developed to quantify the phenomena described. From these analyses, several conclusions were drawn:

- Bond-line quality is largely defined by contact surface strains and thermal cycles. Two metallurgical mechanisms are active during projection welding. These include surface strains for fracture and separation of oxide particles, and thermal cycles for particle dissolution. Surface strain effects appear to be dominant for achieving the best projection weld quality.
- Expulsion is generally detrimental to projection weld quality. Expulsion is the formation of liquid metal in the joint, and it implies poor welding practice. In particular, expulsion can lead to loss of metal in the weld and formation of soft zones. The former can lead to porosity and lack of bonding. The latter can cause softened layers along the bond line, leading to intermittent interfacial failures.
- Metal yield strengths typically decrease with increasing temperature and assist in

projection forging. In general, most metals show precipitous drops in yield strengths with increases in temperature. This softening with heating creates forge depths in the projection. These forge depths are defined by the temperature-dependent yield strength and the resulting thermal gradient in the projection.

- Forge depths during projection welding are a strong function of the heat pulse width. Longer heat pulse widths (or weld times) result in shallower thermal gradients in the projection. Such shallower thermal gradients increase forge depths and thus decrease effective strains at the bond line. This, in turn, can result in a reduction in weld quality.
- Proper mechanical follow-up is essential to achieving solid-state projection welds. Proper forging is accomplished by assuring that the applied force can be maintained at the contact surfaces throughout the welding process. This is accomplished by assuring that the weld head can accelerate at a sufficient rate to maintain force as the projection collapses. A criterion for head weight/weld force was developed based on the height of the projection and the effective collapse time.
- Application-specific spring-loaded fast follow-up heads can be defined through some simple design rules. Fast follow-up heads are typically designed with springs. The springs in these heads can be designed based on the load range of interest, the effective spring constant, and the availability of space within the welding machine.
- Current pulse profiles can be defined from process inputs and basic machine characteristics. Current pulse profiles can be defined by a simple analysis of the welding circuit. An example was provided for CD projection welding. Current response was calculated from basic process inputs (charge voltage) and machine characteristics (capacitance, transformer windings ratio, secondary inductance, and secondary resistance).
- Thermal profiles and effective forge depths are strongly affected by the projection design. Thermal profiles in projections during welding are strongly affected by local geometry, particularly the included projection angle. Results show that thermal gradients increase (and forge depths decrease) with increasing included projection angle. Experimental results have shown that weld quality does increase with included

projection angle, but only to a point. Above angles of 90°, the increase in contact area (with collapse of the projection) rapidly reduces the applied stresses (for a given weld force), minimizing deformation and surface strains and reducing joint quality.

- Rapid heat pulses can compensate for unbalanced and edge-style projection designs. Both heat pulse width and projection geometry affect forge depths in welded components. As the projection geometry becomes less optimal (unbalanced and edge-style projections), short pulse widths can be used to control effective temperature profiles and to create stabilized forging profiles.

REFERENCES

1. "Standard Welding Terms and Conditions," AWS A3.0:2001, American Welding Society, Miami, FL, 2001
2. J.E. Gould, Projection Welding, *Welding, Brazing, and Soldering*, Vol 6, *ASM Handbook*, ASM International, 1993, p 230–237
3. W.F. Hess and W.J. Childs, A Study of Projection Welding, *Weld. J. Res. Suppl.*, Vol 27 (No. 12), 1947, p 712s–713s
4. E.F. Nippes, J.M. Gerken, and J.M. Maciora, The Projection Welding of 0.010 and 0.020 Inch Steel Sheet, *Weld. J. Res. Suppl.*, Vol 29 (No. 9), 1950, p 41s–44s
5. E.F. Nippes and J.M. Gerken, Projection Welding of Steel in Heavy Gauges and Dissimilar Thicknesses, *Weld. J. Res. Suppl.*, Vol 31 (No. 3), 1952, p 113s–125s
6. J.F. Harris and J.J. Riley, Projection Welding Low Carbon Steel Using Embossed Projections, *Weld. J.*, Vol 40 (No. 4), 1961, p 363–376
7. J.E. Gould, D. Workman, and C. Raynes, An Examination of Projection Welding Coated Sheet Steels, *Sheet Metal Welding Conference VIII*, AWS Detroit Section, Detroit, MI, 1998
8. "Recommended Practice for Resistance Welding," AWS Document C1.1-66, American Welding Society, Miami, FL, 1966
9. *Resistance Welding Handbook*, RWMA, Philadelphia, PA, 1989
10. B. Girvin and J.E. Gould, Factors Affecting the Performance of Annular Projection Welds, *Sheet Metal Welding Conference VII*, AWS Detroit Section, Detroit, MI, 1996
11. B. Girvin and J.E. Gould, "Development of Projection Design Guidelines for Annular Projection Welding," EWI Cooperative Research Report MR9901, Edison Welding Institute, Columbus, OH, 1999
12. B. Girvin, J.E. Gould, and T. Stotler, "Characterization of Annular Projection Capacitive Discharge Welds," EWI Cooperative Research Report MR0113, Edison Welding Institute, Columbus, OH, 2001
13. J.E. Gould, Mechanisms of Bonding for Solid-State Welding Processes, *Joining of Advanced and Specialty Materials IV*, ASM International, 2002, p 89–97
14. R.D. Wilson, Rapid Solidification Joining of Silver Electrical Contact to Copper Conductors Using the Capacitor Discharge Welding Process, *11th Annual North American Welding Research Conference: Advances in Welding Technology*, Edison Welding Institute, Columbus, OH, 1995
15. B.A. Forostovets and A.S. Dem'Yanchuk, Chemical Heterogeneity in Flash Welds in Heavy Section Steel, *Avto. Svarka.*, No. 6, 1967, p 28–31
16. I.F. Squires and B. Met, Resistance Butt Welding of 0.8% Carbon Steel, *Br. Weld. J.*, Vol 15 (No. 12), 1968, p 610–620
17. V. Rieicansky and W. Lucas, Formation and Significance of Weld Line Defects in Flash Welded Mild Steel Tube and Bar, *Weld. Res. Int.*, Vol 4 (No. 4), 1974, p 1–27
18. G.V. Smith, "An Evaluation of the Elevated Temperature Tensile and Creep-Rupture Properties of Wrought Carbon Steel," ASTM Data Series DS 11S1, ASTM, Philadelphia, PA
19. J.P. Holman, *Heat Transfer*, 3rd ed., McGraw-Hill Book Company, New York, NY, 1972
20. J.E. Gould, "A Comparison of Power Supplies for Projection Welding Ball Joint Canister Shells," EWI Project Report 49133CSP, Edison Welding Institute, Columbus, OH, 2005
21. J.E. Gould, Recent Advances in Projection Welding, *EWI Insights*, Vol 18.2.1, 2005
22. E. Olberg, F.D. Jones, H.L. Horton, and H.H. Ryffel, *Machinery's Handbook*, 26th ed., Industrial Press, New York, 2000
23. R.J. Smith and R.C. Dorf, *Circuits, Systems, and Devices*, 5th ed., John Wiley & Sons, New York, NY, 1992
24. J.E. Gould and W. Peterson, Analytical Modeling of Electrode Wear Occurring during Resistance Spot Welding Galvanized Steels, *Sheet Metal Welding Conference XII*, AWS Detroit Section, Detroit, MI, 2006

Fundamentals of Diffusion Bonding*

DIFFUSION BONDING is only one of many solid-state joining processes wherein joining is accomplished without the need for a liquid interface (brazing) or the creation of a cast product via melting and resolidification (welding). In its most narrow definition, which is used to differentiate it from other joining processes such as deformation bonding or transient liquid-phase joining, diffusion bonding (DB) is a process that produces solid-state coalescence between two materials under the following conditions:

- Joining occurs at a temperature below the melting point, T_m , of the materials to be joined (usually $>1/2T_m$).
- Coalescence of contacting surfaces is produced with loads below those that would cause macroscopic deformation to the part.
- A bonding aid can be used, such as an interface foil or coating, to either facilitate bonding or prevent the creation of brittle phases between dissimilar materials, but the material should not produce a low-temperature liquid eutectic upon reaction with the materials to be joined.

Thus, diffusion bonding facilitates the joining of materials to produce components with no abrupt discontinuity in the microstructure and with a minimum of deformation. Within the confines of this definition, the DB process, in practice, is limited to either press or gas pressure or bonding approaches. It is also noted that the preferred term for this process, according to the American Welding Society, is diffusion *welding*. However, because diffusion *bonding* is used more commonly in industry, it is the term that is used in this article.

This article provides a qualitative summary of the theory of diffusion bonding, as distinguished from the mechanisms of other solid-state welding processes (see the article “Mechanisms of Bonding for Solid-State Welding Processes” in this Volume). Additional details on the fundamentals of diffusion bonding can be found in the article “Modeling of Diffusion Bonding” (Ref 1) and in the Selected References at the end of this article.

Applications details for both metals and oxide ceramics are in the article “Diffusion Bonding” in this Volume. It is also well established that diffusion bonding can be combined with superplastic forming (SPF); these processes are generally referred to as SPF/DB processes. Diffusion bonding in conjunction with superplastic forming is addressed in *ASM Handbook* articles “Superplastic Sheet Forming” (Ref 2) and “Forming of Titanium and Titanium Alloys” (Ref 3).

Diffusion Bonding Process

The DB process, that is, the application of pressure and temperature to an interface for a prescribed period of time, is generally considered complete when cavities fully close at the faying surfaces. Relative agreement is found for the mechanisms and sequence of events that lead to the collapse of interface voids, and the following discussion describes these metallurgical processes. Although this theoretical understanding of the DB process is universally applicable, it should be understood that parent metal strength is only approached for materials with surface conditions that do not have barriers to impede atomic bonding, such as the absence of surface oxides or adsorbed gases at the bonding interface.

In practice, oxide-free conditions exist only for a limited number of materials. Accordingly, the properties of real surfaces limit and impede the extent of diffusion bonding. The most notable exception is titanium alloys, which, at DB temperatures greater than 850 °C (1560 °F), can readily dissolve minor amounts of adsorbed gases and thin surface oxide films and diffuse them away from the bonding surfaces, so that they will not impede the formation of the required metallic bonds across the bond interface, as shown in Fig. 1(a). An example of a successful diffusion bond in a titanium alloy is illustrated in Fig. 1(b), where the integrity of the bonded interfaces was demonstrated with subsequent superplastic expansion without interface failure.

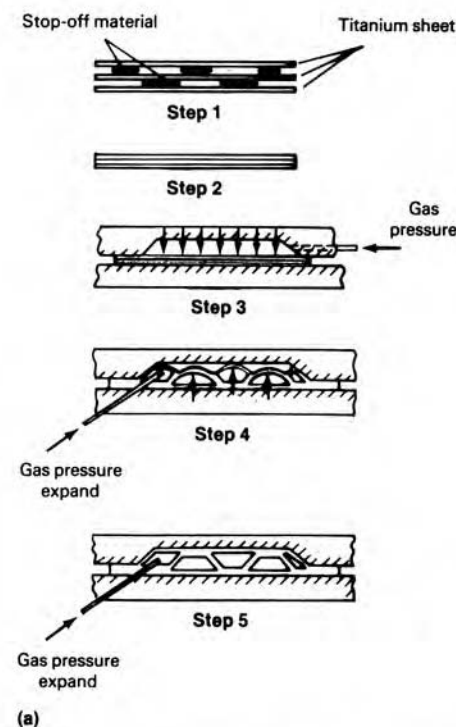


Fig. 1 Superplastic forming/diffusion bonding (SPF/DB) of titanium sheet. (a) Sequence of operations required to join three sheets of superplastic titanium alloy using the SPF/DB process. (b) Typical three-sheet titanium alloy component superplastically formed following diffusion bonding

* Reaffirmed in 2011 and reprinted from M.W. Mahoney and C.C. Bampton, Fundamentals of Diffusion Bonding, *Welding, Brazing, and Soldering*, Vol 6, *ASM Handbook*, ASM International, 1993, p 156-159

Similarly, the joining of silver at 200 °C (390 °F) requires no deformation to break up and disperse oxides, because silver oxide dissociates completely at 190 °C (375 °F). Above this temperature, silver dissolves its oxide and also scavenges many surface contaminants. Other examples of metals that have a high solubility for interstitial contaminants include tantalum, tungsten, copper, iron, zirconium, and niobium. Accordingly, this class of alloy is easiest to diffusion bond.

A second class of material, that is, metals and alloys that exhibit very low solubility for interstitials (such as aluminum-, iron-, nickel-, and cobalt-base alloys), is not readily diffusion bondable. Special consideration must be given to remove surface barriers to atomic diffusion prior to joining and subsequently prevent their reformation during the joining process. This is not an easy processing matter. Accordingly, the potential for high-strength bond interfaces for alloys with low interstitial solubility should be considered on an individual alloy basis.

Bonding Surfaces Containing Oxides

Diffusion bonding can be achieved for materials with adherent surface oxides, but the resultant interface strengths of these materials are considerably less than that measured for the parent material. Aluminum alloys are prime examples of this class of material. Research since 1960 has demonstrated only limited diffusion bond properties. Although interface strength can be increased for oxide-bearing materials, it requires considerable surface extension of the faying interfaces to create localized plastic flow of the metal and concurrent oxide breakage. This introduces an increased number of locations for metal-to-metal contact via plastic flow around or micro-extrusion through the broken oxide. In general, the oxide is not removed but is simply dispersed over a greater surface area in an enclosed environment, in which oxidation cannot recur. Thus, even with significant surface deformation, only a fraction of the interface area contributes to the strength of the bond. The proportion of oxide-free metallic area revealed is dependent on the relative hardness of the metal and its oxide film, as well as on the mechanical properties of the oxide. This type of bonding, although often considered as diffusion bonding, is better described as deformation bonding and does not fit within the strict definition of the low deformation associated with diffusion bonding.

Factors that affect the relative difficulty of diffusion bonding oxide-bearing surfaces include:

- *Surface roughness prior to welding:* A rougher surface will result in greater shear deformation.

- *Mechanical properties of the oxide:* The more brittle the oxide, the greater the dispersion for a given level of deformation.
- *Relative hardness of the metal and its oxide film:* Because plastic flow controls the amount of bonding area, large differences in their hardness should facilitate bonding.
- *Prestraining or work hardening of the material:* Initiation of bonding will occur at lower deformations for prestrained or work-hardened materials, and the degree of surface extension in the central region of the interface is considerably greater for cold-worked material. Thus, annealed material requires a larger total deformation before bonding will initiate.

It is clear that with the appropriate information, sufficient experiments can be performed to determine the diffusion bondability of most materials. Parent metal strength will not always be attained using the DB approach, particularly for materials with adherent oxides, but interface strength can be maximized if the fundamentals of the process are understood.

Mechanism of Diffusion Bonding

In diffusion bonding, the nature of the joining process is essentially the coalescence of two atomically clean solid surfaces. Complete coalescence comes about through a three-stage metallurgical sequence of events. Each stage, as shown in Fig. 2, is associated with a particular metallurgical mechanism that makes the dominant contribution to the bonding process. Consequently, the stages are not discretely defined but begin and end gradually, because the metallurgical mechanisms overlap in time. During the first stage, the contact area grows to a large fraction of the joint area by localized deformation of the contacting surface asperities. Factors such as surface roughness, yield strength, work hardening, temperature, and pressure are of primary importance during this stage of bonding. At the completion of this stage, the interface boundary is no longer a planar interface but consists of voids separated by areas of intimate contact. In these areas of contact, the joint becomes equivalent to a grain boundary between the grains on each surface. The first stage is usually of short duration for the common case of relatively high-pressure diffusion bonding.

During the second stage of joint formation, two changes occur simultaneously. All of the voids in the joints shrink, and most are eliminated. In addition, the interfacial grain boundary migrates out of the plane of the joint to a lower-energy equilibrium. Creep and diffusion mechanisms are important during the second stage of bonding and for most, if not all, practical applications, bonding would be considered essentially complete following this stage. As the boundary moves, any remaining voids are engulfed within grains where they are no longer

in contact with a grain boundary. During this third stage of bonding, the voids are very small and very likely have no impact on interface strength. Again, diffusional processes cause the shrinkage and elimination of voids, but the only possible diffusion path is now through the volume of the grains themselves.

Stage I—Microasperity Deformation

The nature of the starting surface is of considerable importance, because of the small macroscopic deformation allowed during diffusion bonding. A real surface is never perfectly clean or perfectly smooth, and the area of metal-to-metal contact between faying surfaces is a very small fraction of the area of joint contact. Contact is limited to a relatively few microasperities. At room temperature and under load, these asperities deform as long as the surface area of contact is such that the yield strength of the material is exceeded. The extent of this deformation is limited at room temperature and is even more limited for work-hardenable

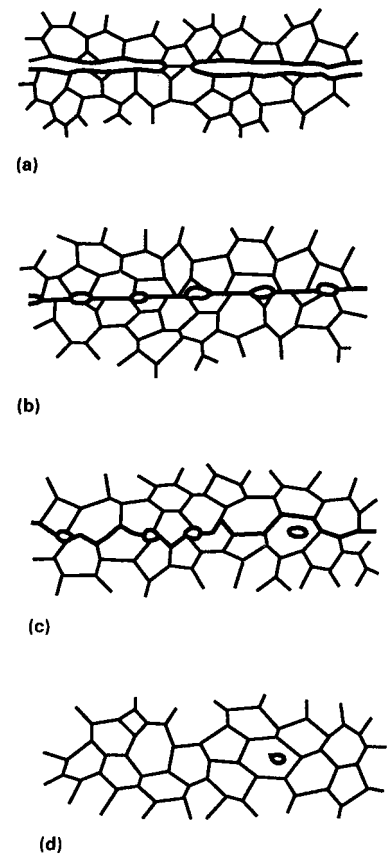


Fig. 2 Sequence of metallurgical stages in diffusion bonding process. (a) Initial contact: limited to a few asperities (room temperature). (b) First stage: deformation of surface asperities by plastic flow and creep. (c) Second stage: grain-boundary diffusion of atoms to the voids and grain-boundary migration. (d) Third stage: volume diffusion of atoms to the voids

materials. As temperature increases to the diffusion bonding temperature, the flow stress of the material decreases and additional asperity deformation occurs through plastic flow. Again, flow occurs until the area of contact increases to an extent that the yield strength of the material is exceeded. If the temperature is above the recrystallization temperature of the material, then work hardening is no longer a consideration. With time at temperature, creep mechanisms now control the rate of asperity deformation, and the area of contact or bond continues to grow. As the area of contact grows, the stress acting on the surface asperities decreases. Consequently, creep deformation progressively slows and diminishes in significance.

The contributions of temperature and pressure to both plastic and creep deformation during this initial stage of diffusion bonding are synergistic; that is, at higher temperatures, less pressure is required and vice versa. However, for any combination of temperature and pressure, bulk deformation to the part is limited to a small percentage (<2 to 3%). Ideally, at the completion of the first stage, the extent of asperity collapse should result in a planar area of contacting surfaces with individually dispersed voids. It is necessary to achieve this extent of contact in order to complete the final stages of diffusion bonding in a reasonable period of time.

For example, Fig. 3 illustrates the influence of pressure on the bond-line morphology for a titanium alloy. At lower pressures, where surface asperity deformation is less during the first stage of bonding, large voids remain at the interface, even after a reasonable time at temperature. Conversely with a higher applied pressure and a correspondingly greater initial

interface deformation, the bond interface becomes indistinguishable from the matrix alloy. It should be remembered that, by definition, very little bulk deformation is allowed and that only interface microdeformation contributes to the growth in contact area of the faying surfaces.

Surface Roughness. When considering the sequences in the stages of diffusion bonding, it is clear that the original surface finish plays a significant role in the time dependency for the completion of the different stages. The surfaces that are mated at the bond line are usually rather irregular, as a result of the machining or other surface-preparation steps. As shown in Fig. 4, the surface roughness can be viewed as a bimodal distribution of asperities; that is, small, short-wavelength asperities (surface roughness) arrange on larger, long-wavelength asperities (surfaces waviness).

It is expected that during the first bonding stage, a more uneven initial surface that is due to either roughness or waviness would produce more large voids than would a smooth initial surface. For example, as load is applied, asperities on rough surfaces will experience higher stresses on the points of contact. Plastic flow will occur at a lower load, and greater interface shear will occur. Although first-stage plastic flow and creep will create more localized interface deformation for a rough surface, fewer but larger voids will remain at the interface (the contact area should approach an equilibrium value independent of the initial surface roughness). In addition to size, the shape and curvature of the voids would be considerably different, with higher-aspect-ratio voids for the rougher starting surfaces. For the subsequent

diffusion-controlled collapse of interface voids during second-stage bonding, an initially rough surface will require a longer time or higher temperatures for the mass-transport processes to shrink and eliminate the voids.

Conversely, because real surfaces are not perfectly clean, some limited degree of interface deformation is necessary for the diffusion bonding of even oxide-free materials. Experimental evidence has demonstrated that even gold is not joined unless some shear displacement occurs as the two faying surfaces come into contact. It seems that the importance of the shear displacement, besides increasing the contact area, is that it destroys the continuity of any adsorbed oxygen layer that can contaminate the oxide-free area because of trapped air at the interface. Procedures as simple as wire brushing have been shown to be a particularly effective surface preparation. This can be partly attributed to the creation of rough layers on the surface.

Stage II—Diffusion-Controlled Mass Transport

The densification or collapse of interface cavities during the second stage of diffusion bonding is attributable to the lowering of the surface free energy by the decrease in surface area. This takes place with the formation of new, but lower-energy, solid-solid interfaces. Because the driving force is the same (reduction of surface energy) for all systems, the considerable differences in behavior in various types of systems are related to the different mechanisms of material transfer.

In diffusion bonding, a number of mass-transport processes are operative simultaneously, including time-dependent plastic flow, diffusion from the interface to the cavity via the lattice and the interface and grain boundaries, and diffusive flow around the surface of the void via the lattice and vapor phase. These different paths of mass transfer are illustrated in Fig. 5 and include:

- Plastic yielding that deforms an original contacting asperity
- Surface diffusion from a surface source to a neck
- Volume diffusion from a surface source to a neck
- Evaporation from a surface source to condensation at a neck

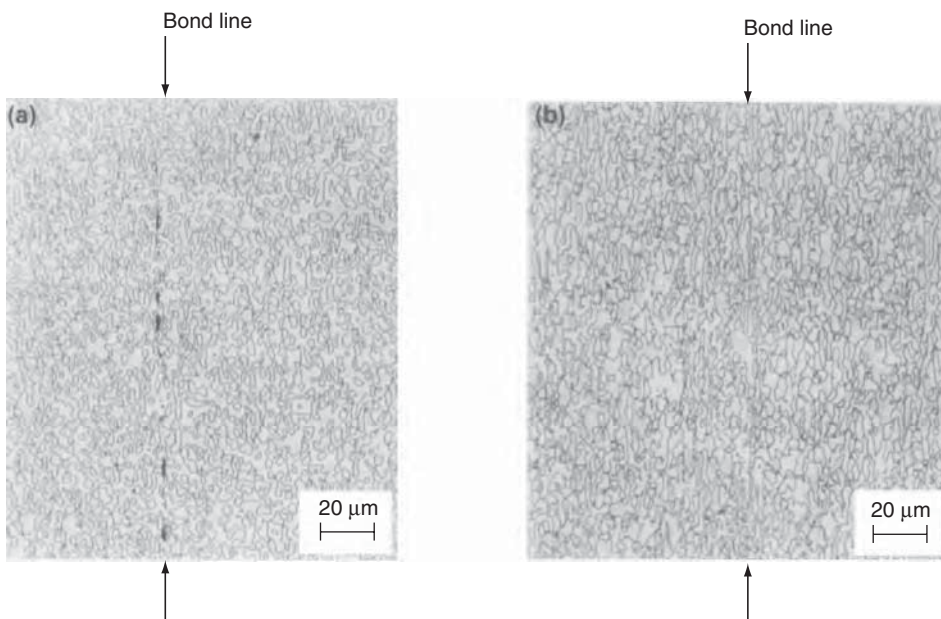


Fig. 3 Effect of pressure on the presence of voids at the bond interface of a titanium alloy diffusion bonded at temperatures of 980 °C (1795 °F) for 2 h. (a) Incomplete bond at 7.0 MPa (1.0 ksi). (b) Complete bond at 10.0 MPa (1.5 ksi)

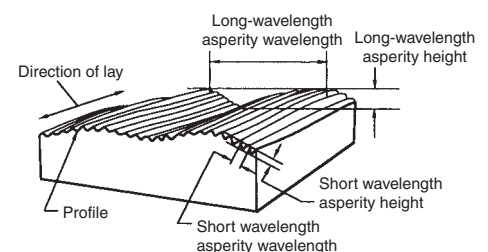


Fig. 4 Bimodal topography of mechanical surfaces

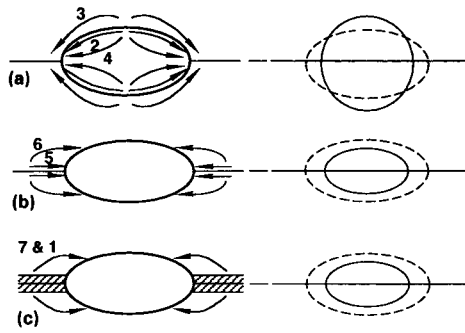


Fig. 5 Schematic of numerous paths of material transfer generated during the diffusion bonding process. (a) Surface source mechanisms. (b) Interface source mechanisms. (c) Bulk deformation mechanisms. See the text for specific mechanisms indicated by numbers shown in the schematic.

- Grain-boundary diffusion from an interfacial source to a neck
- Volume diffusion from an interfacial source to a neck
- Power-law creep

Although vapor transport and surface transport of matter change the shape of the void, they do not directly alter the volume. Thus, these transport paths have only a secondary influence on the rate of void collapse indirectly, through a change in void curvature. Only the transfer of matter from the matrix volume or from grain boundaries causes shrinkage and pore elimination. Thus, only the first two mechanisms, plastic flow and interface diffusion, actually reduce the volume of the interfacial voids. The dominance of either of these two processes is dependent on many inseparable factors, including material system, void geometry, microstructure, and bonding parameters.

When considering diffusion, evidence seems to suggest that the most efficient path for atom flow and counterdiffusing vacancies is along the interfacial grain boundary and along grain boundaries that intersect the void when the grain size is less than the pore size. Although the area of a grain boundary is small in comparison to the void surface, this high-diffusivity path has been shown to dominate. For example, bonding has been shown to be enhanced by first blasting the faying surfaces with chilled iron grit. This treatment promoted recrystallization and thus a finer grain size across the interface, creating additional high-diffusivity paths. In a related process (the sintering of Al_2O_3), porosity was shown to be eliminated next to grain boundaries, with residual porosity remaining at grain centers. Similarly, fine grain size, as exists in superplastic alloys, should create higher rates of void coalescence via grain-boundary diffusion. However, because the chemical potential driving force for grain-boundary diffusion mechanisms is partly dependent on the angle between the applied pressure and a particular grain boundary, its actual contribution will be dependent on its precise

orientation with respect to the applied pressure. The driving force will be maximal when the two are perpendicular and minimal when they are parallel.

Although there is insufficient evidence for generalization, evidence also exists to illustrate that diffusion is, at times, the rate-controlling factor for void coalescence. For example, maintaining temperature while removing pressure following the first bonding stage was shown to not significantly impede the joining process. The rate of void elimination was only slightly slower without the applied pressure. However, this change in rate could be due to either the lost contribution that deformation makes to void coalescence or a reduction in efficiency of the stress-enhanced grain-boundary contribution.

Stage III—Interface Migration

During the second stage of diffusion bonding, voids become much smaller and many are eliminated. Their grain-boundary pinning influence decreases, so that interfacial grain boundary migrates toward an equilibrium configuration, which is indistinguishable from the other grain boundaries in the microstructure. The driving force for the boundary migration is the reduction in grain-boundary area. The initially straight interfacial bond line becomes distorted with local penetrations of a few micrometers of one material into the other at triple points. As the boundary moves, any remaining voids become enclosed within grains where they are no longer in contact with a grain boundary. Diffusional processes continue to shrink and eliminate these cavities, but the diffusion path is now restricted to volume diffusion through the matrix lattice. Accordingly, the elimination of this final small volume of porosity would be likely to contribute an inordinate time to the bonding process for any interface strength benefits that may be achieved.

Diffusion Bonding with Interface Aids

Additional layers of material in the form of coatings or foils are often used as bonding aids for a variety of reasons. For example, an intermediate material can be used when joining dissimilar materials where a brittle intermetallic would otherwise form. In this case, the interfacial material would be selected for its compatibility with each of the materials to be joined and for its ability to prevent the creation of a brittle reaction layer. To promote diffusion in materials that contain elements with low diffusivities, the interfacial material should contain an element with a higher mobility than elements found in the joined materials. A common material for such applications is electroless nickel, which contains phosphorus. (Phosphorus has been shown to have a high diffusivity in other metallic systems.) However, caution should be exercised when

considering the addition of high-diffusivity elements, because of their potential for accumulation at grain boundaries and their resultant influence on mechanical properties.

Another approach is to add an interfacial material that will scavenge impurity elements at the interface and thus produce clean surfaces in situ. Materials with high solubilities for interstitial elements, such as titanium alloys, can be appropriate for this purpose. Because of the importance of localized plastic flow at the interface, a soft material addition can also be of benefit to maximize interfacial contact during the first bonding stage, where deformation mechanisms dominate.

With the addition of interfacial materials, geometric as well as metallurgical considerations become important. The mechanical strength of solid-state metallic bonds achieved with a thin interfacial layer of bonding material goes through a maximum, with decreasing joint thickness. For thick joints, tensile strength is directly related to the bulk properties of the interfacial layer material. As joint thickness decreases, the tensile strength of these joints increases, because of the matrix material restraint on the plastic flow of the interfacial layer. However, for very thin joints, the problems of surface roughness and cleanliness start to diminish the contact area and thus effectively reduce the joint tensile strength. Experimental studies should be performed for individual materials. In general, thicknesses of approximately 0.025 mm (0.00098 in.) yield maximum interface strengths.

REFERENCES

1. C.C. Bampton, Modeling of Diffusion Bonding, *Metals Process Simulation*, Vol 22B, *ASM Handbook*, ASM International, 2010, p 452–455
2. A.K. Ghosh and C.H. Hamilton, Superplastic Sheet Forming, *Metalworking: Sheet Forming*, Vol 14B, *ASM Handbook*, ASM International, 2006, p 345–366
3. J. Beal, R. Boyer, and D. Sanders, Forming of Titanium and Titanium Alloys, *Metalworking: Sheet Forming*, Vol 14B, *ASM Handbook*, ASM International, 2006, p 656–669

SELECTED REFERENCES

- B.M. Agers, The Mechanism of Small Tool Pressure Welding, *Brit. Weld. J.*, July 1964, p 313–319
- N. Brezds, Investigation of the Factors Determining the Tensile Strength of Brazed Joints, *Weld. Res. Supp.*, Nov 1954, p 545S–563S
- C.L. Cline, An Analytical and Experimental Study of Diffusion Bonding, *Weld. Res. Supp.*, Nov 1966, p 481S–489S
- R.L. Coble, Diffusion Models for Hot Pressing with Surface Energy and Pressure Effects as Driving Force, *J. Appl. Phys.*, Vol 41.12, 1970, p 4798–4807

- B. Derby and E.R. Wallach, Theoretical Model for Diffusion Bonding, *Met. Sci.*, Vol 16, Jan 1982, p 49–56
- B. Derby and E.R. Wallach, Diffusion Bonding: Development of Theoretical Model, *Met. Sci.*, Vol 18, 1984, p 427–431
- J.W. Dini, Use of Electrodeposition to Provide Coatings for Solid State Bonding, *Weld. J.*, Vol 61 (No. 11), Nov 1982, p 33–39
- G. Garmong, N.E. Paton, and A.S. Argon, Attainment of Full Interfacial Contact during Diffusion Bonding, *Met. Trans. A*, Vol 6, June 1975, p 1269–1279
- C.H. Hamilton, Pressure Requirements for Diffusion Bonding Titanium, *Titan. Sci. Technol.*, R.I. Jaffee and H.M. Burte, Ed., Plenum, 1973, p 625–647
- A. Hill and E.R. Wallach, Modeling Solid State Diffusion Bonding, *Acta Metall.*, Vol 37 (No. 9), Sept 1989, p 2425–2437
- W.H. King and W.A. Owczarski, Additional Studies on the Diffusion Welding of Titanium, *Weld. Res. Supp.*, Oct 1968, p 444S–450S
- H.A. Mohamed and J. Washburn, Mechanism of Solid State Pressure Welding, *Weld. Res. Supp.*, Sept 1975, p 302S–310S
- R. Pearce, Diffusion Bonding, *Proc. International Conference on Diffusion Bonding* (Cranfield, SIS), 1987
- J. Pilling, The Kinetics of Isostatic Diffusion Bonding in Superplastic Materials, *Mater. Sci. Eng.*, Vol 100, April 1988, p 137–144
- E.R. Wallach, Solid-State Diffusion Bonding of Metals, *Trans. JWRI*, Vol 17.1, 1988, p 135–148
- D.S. Wilkinson and M.F. Ashby, Pressure Sintering by Power Law Creep, *Acta Metall.*, Vol 23, 1975, p 1277–1285

Nondestructive Evaluation of Solid-State Welds

Jeong Na, Roger Spencer, Evgeni Todorov, Sean Gleeson, and Perry White, Edison Welding Institute

A NUMBER OF NONDESTRUCTIVE EVALUATION (NDE) methods, such as visual, liquid penetrant, magnetic particle, radiography, ultrasound, and eddy current, are available to detect flaws in solid materials. In general, the first three methods are for inspecting surface discontinuities such as cracks or cavities. For detection of surface and subsurface flaws, radiography, ultrasound, and eddy current are more suitable methods. Because most solid-state welds deal with internal flaws rather than surface-oriented ones, only radiography, ultrasound, and eddy current methods are discussed in this article. First, fundamental aspects of these three NDE methods are briefly described in terms of operation principles; second, some examples are discussed of NDE techniques performed on various types of flaws resulting from solid-state welding processes.

Nondestructive Evaluation Fundamentals

Radiography

Radiography is one of the most widely used volumetric NDE methods. This method is based on differential absorption of penetrating radiation by the material. X-rays or gamma rays are the two types of waves used for this process. The radiography method works well for detecting and sizing volumetric flaws such as pores, voids, and inclusions. With the radiographic method, it is possible to examine a wide variety of materials ranging from light to heavy elements, components of different sizes and shapes ranging from miniature electronics parts to large vessels, and different product forms such as castings, weldments, composites, and so on. For welding inspection applications, the rays pass through the weld and onto a sensitized film that is in direct contact with the back of the weld. When the film is developed, gas pockets, slag inclusions, cracks, or poor penetration are visible on the film. Conventional radiography, which uses x-ray machines or

radioactive isotopes such as iridium-192 and cobalt-60 for generating penetrating radiation, is used to record the internal flaws of the object on a radiographic film. Because of the danger of these rays, only qualified personnel are authorized to perform these tests.

As one of the recently developed radiography methods, digital x-ray radiography using cadmium telluride (CdTe) detectors provides the capability to detect small flaws that require very little inherent unsharpness. The main advantage of using a CdTe detector is its sensitivity when used with low-power microfocus generators (Ref 1). The following are some of the main advantages of digital radiography over conventional film radiography:

- Digital detectors require less radiation to create an image, typically only 1 to 4% of that normally required for a fine-grained, high-contrast, high-speed film (Ref 1).
- Image processing and computer-aided detection and diagnosis algorithms are available for image enhancement and analysis.
- The ability to transmit data to remote sites for consultation, review, or formal interpretation (Ref 2).
- Dark-room facilities are no longer required.
- There are no environmental issues with film and chemical disposal.

However, one of the biggest drawbacks with the radiography method over other NDE methods is the requirement for accessibility to both surfaces of the material to be tested.

Ultrasound

The ultrasonic method uses high-frequency sound waves to locate and measure flaws in welds. It can be used to inspect various materials such as metals, plastics, composites, ceramics, and others. This is an extremely sensitive method, and it can locate very fine surface and subsurface cracks as well as many other types of internal flaws. All types of joints can be tested. As the sound wave passes through the weld zone, flaws cause some of the sound energy to be

reflected back to the probe. By calibrating on known standards, the depth of flaws can be accurately determined. One of the advantages of the ultrasonic method is that only one side of the weld needs to be exposed for inspection.

The amount of ultrasonic energy reflected and transmitted through an interface can be related to the difference in the acoustic impedance, Z , which is defined by the multiplication of the density, ρ , of the medium and the sound velocity, v , in the medium, $Z = \rho \cdot v$. When an ultrasonic wave travels through an interface separated by two media having different acoustic impedances, Z_1 and Z_2 , as shown in Fig. 1, the reflection, R , and transmission, T , coefficients are defined by:

$$R = \left(\frac{Z_2 - Z_1}{Z_1 + Z_2} \right)^2 \quad (\text{Eq 1})$$

and

$$T = 1 - R \quad (\text{Eq 2})$$

where $Z_1 = \rho_1 \cdot v_1$ and $Z_2 = \rho_2 \cdot v_2$. As an example, for a longitudinal wave traveling in an aluminum alloy that interacts with a void filled with air, the reflection coefficient R is almost 1, because air has an acoustic impedance of $0.0004 \text{ g/cm}^2\text{-s}$ ($8 \times 10^{-4} \text{ lb/ft}^2\text{-s}$), while aluminum has approximately $17 \times 10^5 \text{ g/cm}^2\text{-s}$ ($35 \times 10^5 \text{ lb/ft}^2\text{-s}$). This means that the bigger the difference in the acoustic impedance, the stronger the reflection at the interface. This is why it is relatively easier

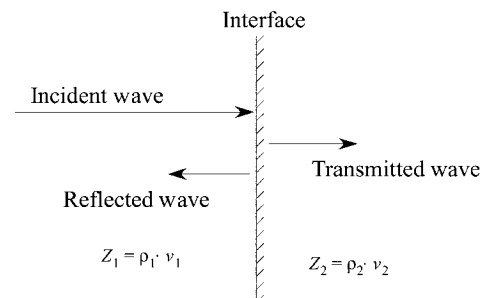


Fig. 1 Reflection and transmission of ultrasound at an interface separated by two different media

to detect voids in a solid material than it is to detect solid inclusions having an acoustic impedance value similar to the surrounding medium.

Other factors that must be considered when an ultrasonic technique is used are the frequency and the attenuation. In general, the minimum flaw size that would be detected by ultrasound is approximately one-half of the wavelength. The wavelength of ultrasound is determined by dividing the sound velocity of a material by the sound wave frequency; therefore, the higher the frequency, the smaller the flaw size that can be detected. However, a majority of materials have some levels of attenuation at a high frequency. The ultrasonic attenuation coefficient, α , represents how much ultrasonic energy is absorbed and scattered in the material. For metals, the value of α is proportional to the square of the frequency, that is, $\alpha \propto f^2$. It is common to consider both the minimum flaw size and the attenuation coefficient in the material at the frequency being considered. Especially for welded joints, the scattering portion of the attenuation due to a complex microstructure can be a major concern when a high-frequency signal is considered for a small flaw.

Recently, more advanced ultrasonic methods, such as linear phased array and matrix phased array, have been used for weld inspections. Phased array probes consist of multiple transducer elements within a single probe housing that can be grouped to form a desired aperture size and then pulsed in different timing sequences. By varying the timing sequences, the ultrasonic beam can be electronically scanned, steered, and focused to provide quicker coverage of a weld zone. Illustrations in Fig. 2 show how the linear phased array technique is used to focus or steer an ultrasonic beam for better detection. In both cases, the amount and sequence of delay in firing of each element determine the effects. For beam focusing, the midcentral section of the elements has more delay than the outer-edge elements, so the waves generated from the side elements converge into the central beam to create a focusing effect. In contrast, for the beam steering effect, one side of the elements has a longer delay time than the other side, as illustrated in Fig. 2(b). It is also possible to combine beam steering and beam focusing effects. This beam-manipulation capability with the linear phased array technique makes it possible to inspect parts and components with complicated geometries that are not easily inspected with conventional single-element transducers.

Eddy Current

The eddy current inspection method is based on the principle of electromagnetic induction, where eddy currents are induced in a conductive material when the material is placed in a changing magnetic field. It can be used for both ferrous and nonferrous materials. Usually, a drive coil carrying an alternating current induces a swirl of circulating electrical currents, called eddy currents, as shown in Fig. 3 (Ref 3). The eddy current

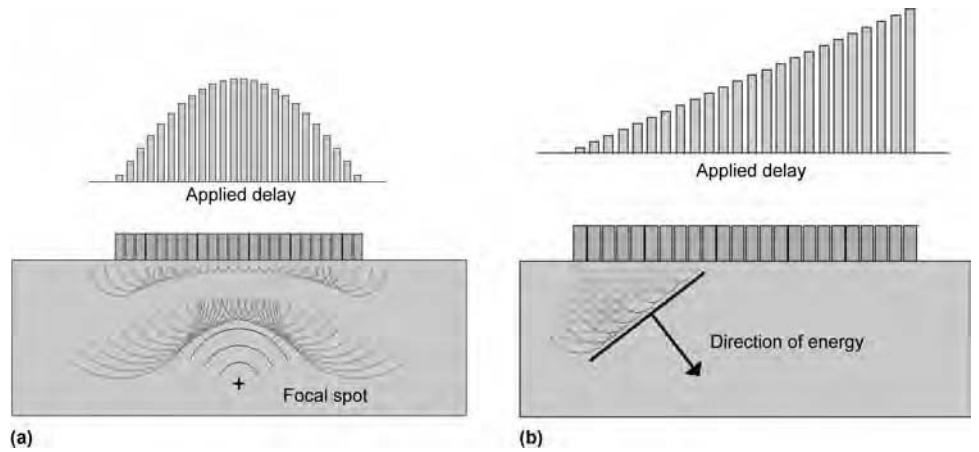


Fig. 2 (a) Beam focusing and (b) beam steering effects of a linear phased array

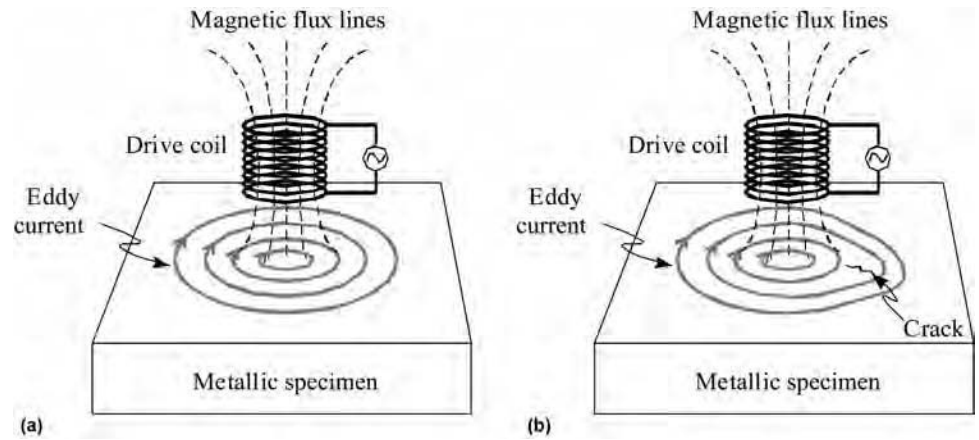


Fig. 3 Principle for inducing eddy currents in a conducting material. (a) Without defect. (b) With flaw

contours in the tested material are approximately similar in shape to the shape of the coil that generates the alternating field, especially on the material surface facing the coil. After eddy currents are induced in the material, a secondary magnetic field is formed to interact with the primary magnetic field of the drive coil. This mutual magnetic field interaction causes a change in the drive coil electrical impedance, which has two components: one is called the resistance, and the other is called the reactance. An eddy current instrument monitors and displays changes in the electrical impedance, which can be correlated to the surface or subsurface flaws in the specimen under test. The strength of eddy currents normally depends on the material electrical conductivity, magnetic permeability, frequency of drive signal, and distance between the coil and the material (referred to as the lift-off distance).

One of the most important parameters in the eddy current method is the depth of penetration, δ , as defined by:

$$\delta = \frac{1}{\sqrt{\pi f \mu_0 \mu_r \sigma}} \tag{Eq 3}$$

where f is the frequency of alternating current applied to the drive coil, μ_0 is the constant magnetic permeability of air or free space ($4\pi \times 10^{-7}$ H/m), μ_r is the relative magnetic permeability of the material, and σ is the electrical conductivity of the material. In general, the depth of penetration has a strong relationship with the detectability and sizing of flaws.

The eddy current techniques may be used to detect changes in metallurgical phase and chemical composition, hardness, residual stresses, and others that would affect the electrical conductivity and magnetic permeability distribution in the material (Ref 3). One of the main applications of eddy current is for surface and subsurface flaws and material discontinuities.

Examples of NDE of Solid-State Welds

Radiography (X-Ray)

One of the most common flaws resulting from solid-state welding processes is incomplete consolidation. For cold welding and

diffusion welding processes, cracks may also occur as a result of poor welds. A good example is an incomplete consolidation flaw in friction stir welding (FSW). This is a tunnel defect that forms at the intersection of the weld nugget, thermomechanically affected zone, and band of material running from the weld nugget toward the joint edge on the advancing side of the tool. These defects are attributable to a combination of welding parameters: insufficient or excessive rotational speed combined with a weak downward force. In such cases, the welded parts cannot be correctly stirred and mixed together, and hence, a tunnel, or so-called “wormhole,” is created, running along the entire weld (Ref 4). An x-ray image of a wormhole defect is shown in Fig. 4. In this case, the material was a 13 mm (0.5 in.) thick, 30 cm (12 in.) long high-strength low-alloy steel plate. A wormhole defect, shown as a dark line on the advancing side of the weld, was detected from the entering site to the exit site.

Because the size of flaws in diffusion bonding is determined by the scale of roughness and contaminations of the surfaces being bonded, both flatness and cleanliness influence the bond quality. Real-time radiography, coupled with a microfocus x-ray source and digital image enhancement, has been used to detect flaws in a diffusion-bonded titanium sample (Ref 5). Intentional voids 1 mm (0.04 in.) in size created by a high-melting oxide powder were successfully detected.

Ultrasound

A majority of solid-state welds are comprised of smooth, flat surfaces, where the most likely flaw would be located at the interface of the materials being joined. Because ultrasound is

sensitive to planar-type flaws, they provide a good reflecting surface for an incoming ultrasonic wave. This, in turn, makes them relatively easy to detect, provided the sound energy is reflected at an angle that allows reception by the receiving ultrasonic transducer(s).

If a pulse-echo technique, one of the conventional ultrasonic testing techniques, is used, the primary plane of the flaw must be oriented approximately perpendicular to the beam propagation direction, as shown in Fig. 5. When there is a discontinuity in the weld, the incoming wave reflects back at the discontinuity due to a strong impedance mismatch, and hence, the reflected signal appears early in time, as shown in the A-scan mode display on the left of the top illustration. Normally, multiple ultrasound reflections occur between the top surface of the specimen and the discontinuity, and hence, multiple peak signals would be displayed in the A-scan mode. Alternately, if there is no flaw in the weld, the incoming ultrasound continues its travel through the weld and reflects back at the opposite side of the material. The back surface reflection signal appears at a later time compared to the aforementioned defect signal, because of a longer propagation distance.

In situations where the sound beam cannot be aligned perpendicular to the flaws, an angle beam through-transmission (Fig. 6) or tandem pitch-catch (Fig. 7) technique may provide good detection. These techniques use two probes, with one probe transmitting and the other receiving. Precise placement of the probes is critical to assure proper coverage of the weld area. To obtain full inspection coverage, it is important to acquire data at different probe locations to inspect the full weld thickness. As an alternative to multiple probes and multiple probe positions, phased array probes could

be used to provide electronic beam steering and scanning (Fig. 8). For some applications, it may be necessary to inspect for cracking, porosity, or other flaws resulting from a joining process (Ref 6). In these cases, additional scans using pulse-echo angle beam shear waves or surface waves may be needed to detect certain types of flaws.

A related defect in FSW is incomplete penetration or lack of penetration (LOP), which can be a natural stress raiser from which a crack may propagate. An LOP defect can occur when the weld metal fails to penetrate the joint. As an example, a linear phased array NDE technique was used to detect an LOP defect in a friction stir weld of two aluminum plates. By using an angle beam wedge and a 5 MHz 60-element phased array probe, as shown in Fig. 9, shear wave conversion was achieved in the part. To increase the inspection zone, a sectorial scan was performed between angles 40 and 70°.

A corresponding snapshot image of the test result is shown in Fig. 10. It should be noted that the two images in Fig. 10, both D-scan and S-scan, are upside down when compared with the setup shown in Fig. 9. Because the sectorial scan data were collected with the reflected beam from the bottom surface of the part, the images appear to be upside down when reconstructed. As indicated in the D-scan image, the bottom of the part (root side) shows up on the top portion of the image, while the top surface of the part shows up on the bottom portion of the image. The situation is the same with the S-scan image; the top of the weld is on the bottom portion of the image, while the root area is on the top. A-scan data in Fig. 10 show a strong ultrasonic signal reflection at the bottom of the weld root. Macro sections depicted in Fig. 11 show the corresponding LOP defect near the bottom of the weld.

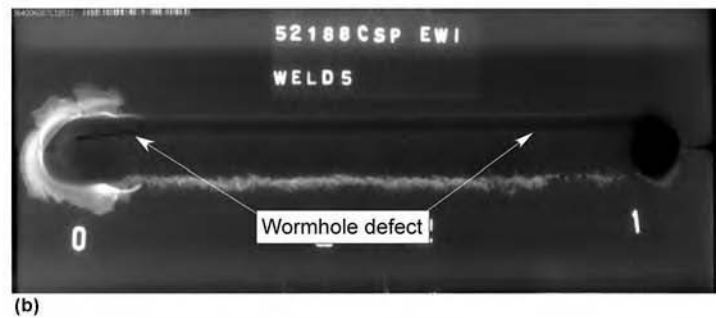
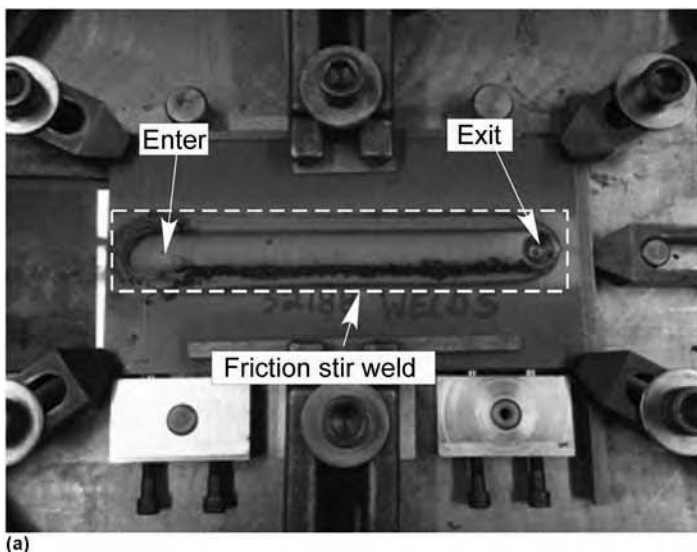


Fig. 4 (a) Friction stir weld on a high-strength low-alloy steel plate part. (b) Corresponding x-ray image showing a long wormhole defect along the advancing side of the weld. Courtesy of GE

Different ultrasonic NDE techniques have been discussed extensively by Nagy and Adler in connection with the evaluation of similar and dissimilar inertia and friction welds (Ref 7). The main conclusion they drew from the results of the study was that the great variety of solid-state bonding technologies,

material combinations, defect types, bond-quality considerations, and quantitative parameters made it necessary to evaluate the feasibility of any particular ultrasonic technique on a case-by-case basis. They also concluded that similar joints were much easier to interrogate for gross defects, but such defects were more common in

dissimilar joints. A symmetric reflection technique was introduced to detect weak flaws in the strongly reflecting interface region of dissimilar solid-state bonds. Depending on the accuracy of the reflection measurement, the detection threshold for interface imperfections was improved by approximately a factor of 10. In this way, even apparently flawless interfaces were also able to be characterized in a quantitative way by using an effective softening (or hardening) parameter.

Another specific problem associated with inertia and friction welds studied by Nagy and Adler was the so-called cold weld effect. Frequency analysis was introduced to assess interface conditions in this particular case, where conventional ultrasonic interrogation would often be less sensitive. The slope of the reflected spectrum was shown to be closely correlated to welding pressure and interface temperature. They suggested that the technique may be useful to monitor these welding process parameters. Finally, frequency analysis was used to study the sandwich-like layered structure of similar inertia welds. The ultrasonic technique proved to accurately predict the characteristic thickness of the interface layer, a principal macrostructure parameter closely related to bond quality. No frequency analysis study was reported for dissimilar bonds.

Flaws resulting from diffusion and inertia bonds are influenced by several manufacturing

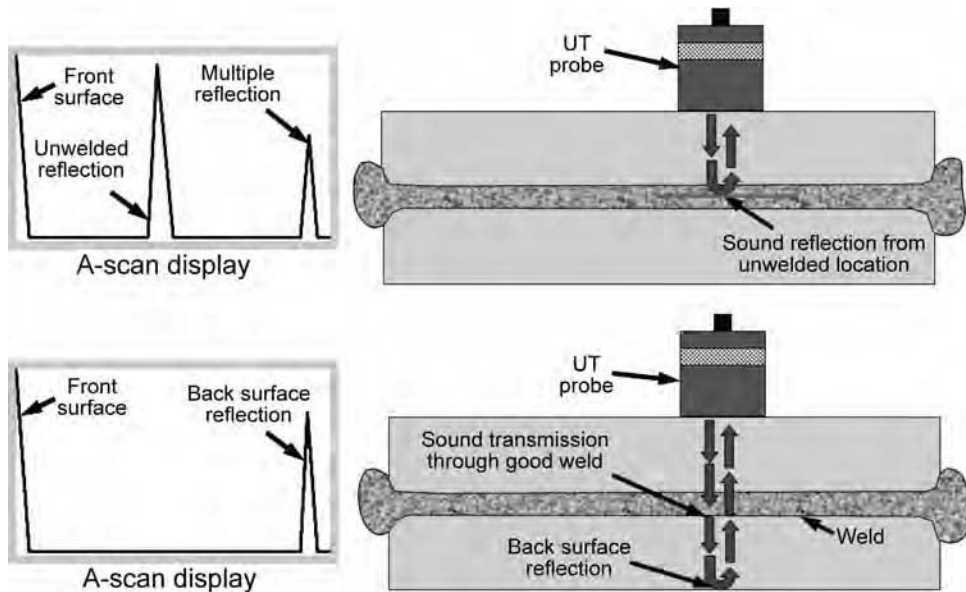


Fig. 5 Ultrasonic pulse-echo technique for a solid-state weld examination. UT, ultrasonic testing

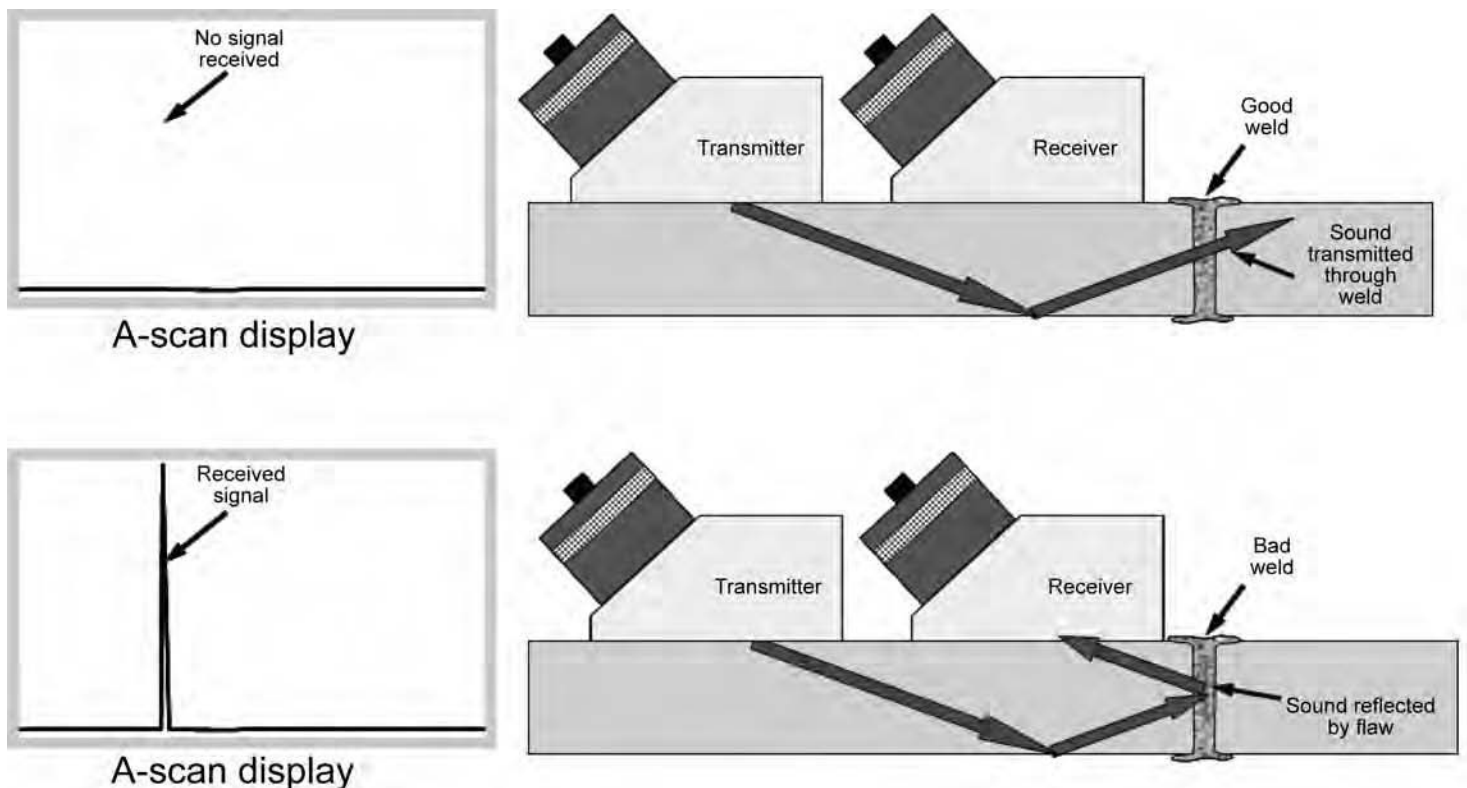


Fig. 6 Through-transmission pitch-catch technique

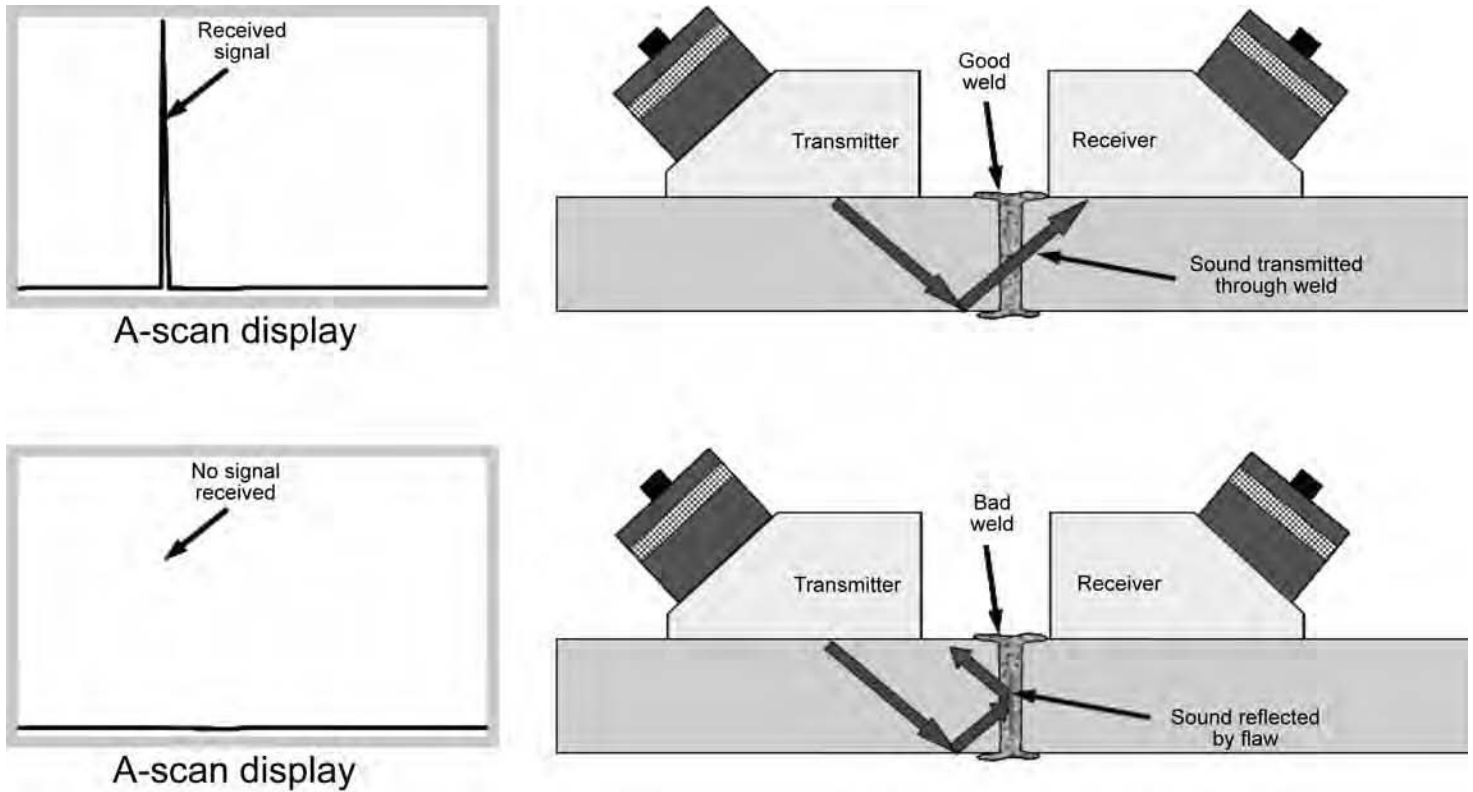


Fig. 7 Tandem pitch-catch technique

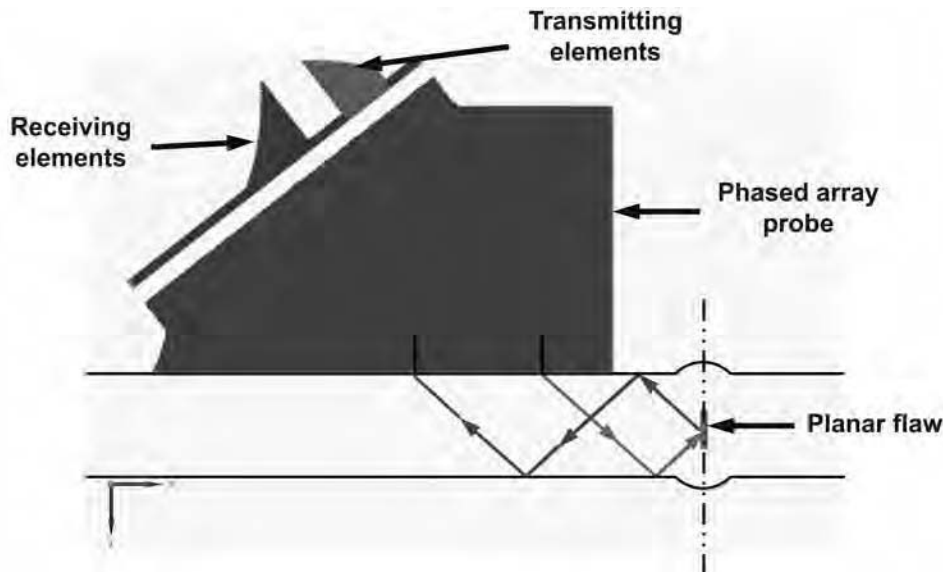


Fig. 8 Tandem pitch-catch technique using a linear phased array probe

variables, such as part geometry, part fit-up, surface finish, surface contamination, as well as bonding conditions such as time, temperature, and force. An ultrasonic C-scan inspection technique interrogating the bonding plane has been developed by combining a data-reduction technique with pattern-recognition algorithms (Ref 8, 9). A set of inertia-bonded copper-to-

stainless steel samples showed a good correlation with the bond strengths and the C-scan procedure, while diffusion-bonded copper-to-stainless steel and stainless steel-to-stainless steel samples did not show a reliable test result.

A planar distribution of flaws in diffusion-bonded IN100 aircraft engine rotor material has been investigated by using an ultrasonic

wave-scattering theory based on a quasi-static model (Ref 10, 11). Comparison to exact elasto-dynamic solutions and experimental results confirmed that the wave-scattering approach can provide a useful nondestructive inspection technique as well as a tool for fracture mechanics studies.

Various ultrasonic techniques, such as the time-of-flight diffraction (TOFD) technique, scanning acoustic microscopy (SAM), ultrasonic spectroscopy, and the compound scanning technique, have been used to detect diffusion bond defects (Ref 5). The TOFD method showed a promising result for sizing defects, but the location of defects in the material influences the test results, particularly shallow defects for which weak defect signals are often obscured by the later interface signals. For the SAM method, a high-frequency ultrasonic signal above 50 MHz is often scattered by grain boundaries and causes an image-dappling effect, resulting in loss of information about the bond interface. The ultrasonic spectroscopy method uses a Fourier transformation of pulse signals in the frequency domain to identify the scattering feature of microscopic voids and clusters of such voids related to diffusion bonds. In the compound scanning method, focused transducers were used in water tanks to improve the signal-to-noise ratio over the grain-boundary scattering noise. This method proved to be a better approach compared to conventional immersion

techniques, but technical difficulties were found with the probe positioning and alignment when a short pulse is used.

An acoustic emission technique has been used to measure resistance projecting weld strength in Zircaloy-2, a nuclear reactor alloy, followed by various surface treatments (Ref 12). Based on the acoustic emission

counts during the weld process, it was found that tensile-shear weld strength for a range of welder settings and surface-quality variations could be correlated. The weld nugget or process zone was thought to be the primary source of acoustic emission. The magnitude of the acoustic emission count and weld strength level was considered to be related

to the amount of material in the process zone that is plastically deformed during the weld process.

Another ultrasonic method, based on the electromagnetic acoustic transduction technology, has been used to monitor weld quality of flash butt welding of steel coil (Ref 13). The on-line real-time monitoring system detects voids, laps, misalignment, and over/under trim conditions in the weld. Results of the inspection are immediately presented to the weld machine operator for disposition. The information is used to correct suspect weld joints when they occur and to avoid weld breakage in subsequent processing operations.

Eddy Current

A majority of the eddy-current-based NDE work on solid-state welds has been performed for flaws in friction stir welds (Ref 14–20). Instead of using a conventional single probe consisting of transmitting and receiving coils in the same housing, various specialized eddy current techniques have been adapted. One such example is an array eddy current probe having several coils configured in a two-dimensional planar format. An array probe can provide the advantage of covering a wide surface area with one pass, which helps minimize the lift-off variations. Considering the noise source in the eddy current method, having a small variation in the lift-off is a big advantage over many single-probe-based scan techniques. In many cases, advanced signal processing algorithms can be used to produce more intuitive and easy-to-interpret test results when compared to conventional scanning techniques. Model-based algorithms can be developed to use eddy current signal amplitude and phase information to plot the array data in terms of the material electrical conductivity. The conductivity data collected with an array technique have been used to correlate the eddy current measurement results with an LOP defect in a friction stir weld (Ref 15).

Other eddy current techniques, such as pulsed eddy current and specialized eddy current sensors, have been used to demonstrate flaw detection and electrical conductivity mapping, which can be correlated with hardness change on a friction stir weld surface (Ref 16–19). Carr et al. have used the high-temperature superconducting SQUID system to characterize the inertia welds of stainless steel (Ref 20).

Recent advances in computer hardware and software have made possible computer modeling and simulation to be employed for optimization and prediction of eddy current technique performance (Ref 21). The computer models allow fast and comprehensive eddy current procedure development with significantly reduced costs for specimens and representative flaws fabrication.

An example of array eddy-current-based NDE performed on a friction stir weld in an

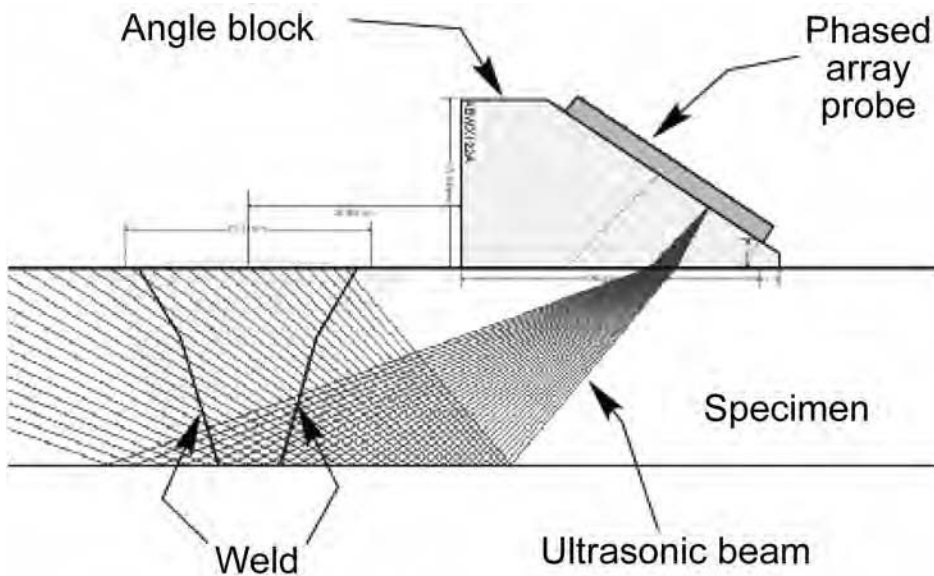


Fig. 9 Setup for the shear wave weld inspection technique with an angle beam wedge and a 5 MHz 60-element linear phased array probe

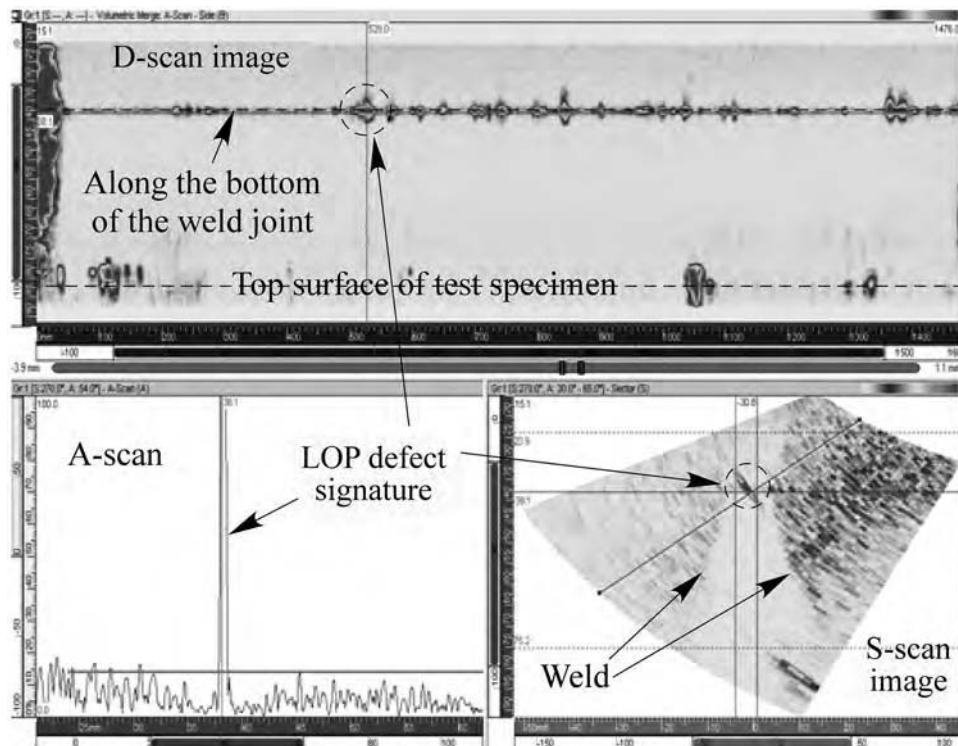


Fig. 10 Linear phased array results for a lack-of-penetration (LOP) defect in a friction stir weld part

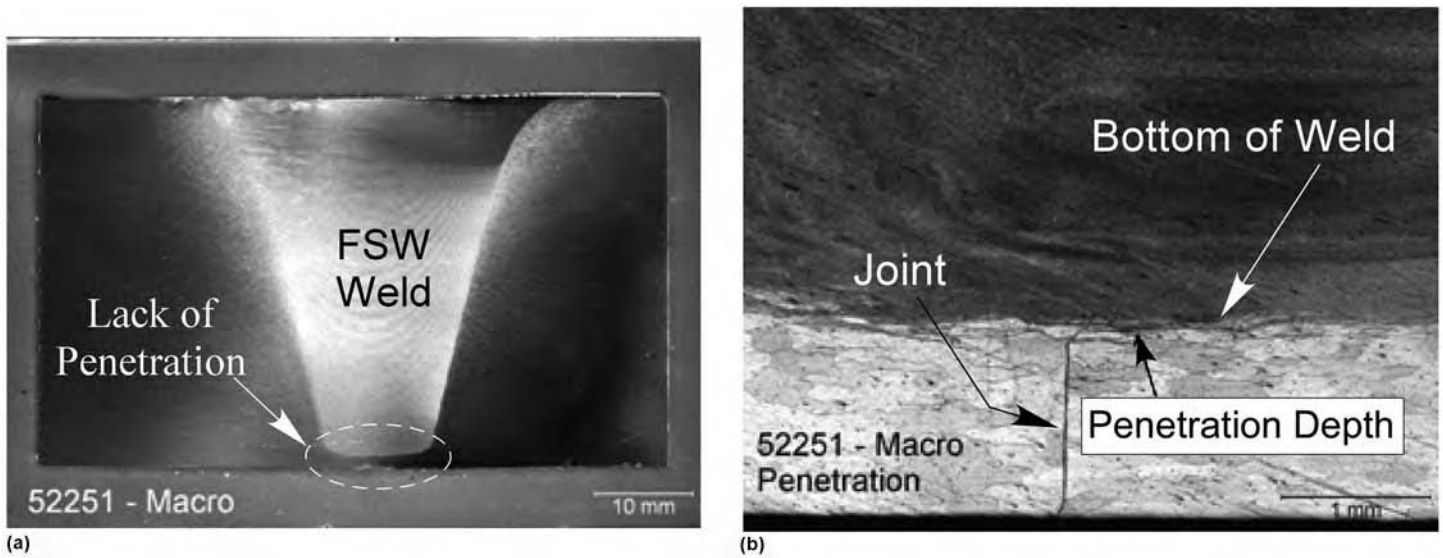


Fig. 11 Macro sections showing (a) lack-of-penetration (LOP) defect in a friction stir weld (FSW) aluminum part and (b) magnification (25×) of the LOP defect

aluminum part is shown in Fig. 12(a). For this test, a 32-element array probe was operated at 20 and 480 kHz, and the corresponding test results are shown in Fig. 12(b) and (c), respectively. It should be noted that the array sensor used for this particular specimen had a conformable front face made of a semiflexible polymer material to minimize lift-off noise on a slightly curved surface, as in this case.

The surface of the specimen was prepared to remove any irregularity as well as metal “lips” on the side section of the weld. Both C-scan images and isometric plots in Fig. 12(b) and (c) clearly show two groups of flaws. The biggest flaw, which was invisible on the surface, was detected along the central line of the weld near the tool exit site, location “B” in the images in Fig. 12(b) and (c). The other two lateral flaws, located at positions “A” and “C,” were detected along the advancing side of the weld. Another characteristic feature is the tool exit marks, as shown in the scan images. It may be caused by an increase in the electrical conductivity (possibly correlated to the hardness change), and it is clearly visible in an arc shape in the 20 kHz image. The same tool exit mark shown in the 480 kHz image is not as clear as in the 20 kHz case.

REFERENCES

1. B. Blakeley and K. Spartiotis, “Digital Radiography for the Inspection of Small Defects,” Paper presented at NDT 2005, Sept 2005 (Harrogate, U.K.)
2. Y. Ikeda and Y. Mizuta, Image Subtraction Method in Digital Radiography of

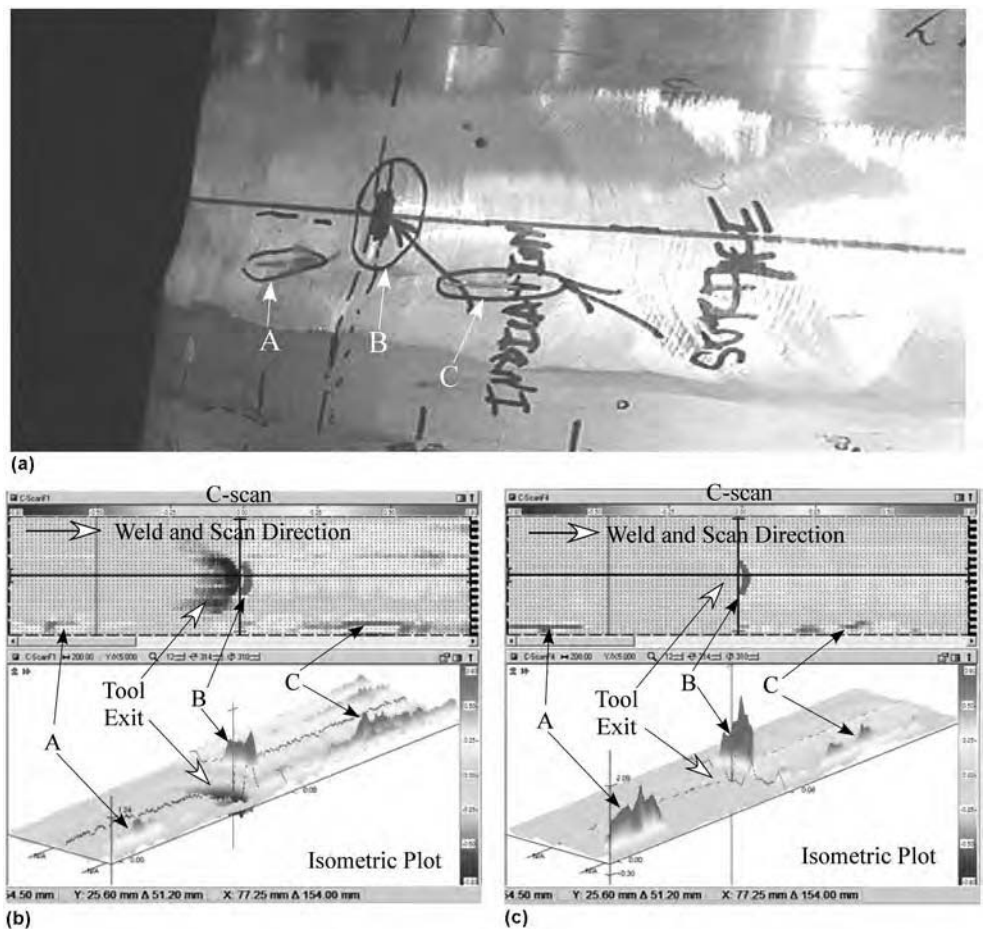


Fig. 12 Example of array eddy current examination for a friction stir weld in an aluminum plate. (a) Photo showing friction stir weld in an aluminum specimen with locations of flaws. (b) Test results at 20 kHz. (c) Test results at 480 kHz

- Welding, *Recent Advances in Nondestructive Evaluation Techniques for Material Science and Industries, Pressure Vessels and Piping Conference*, July 25–29, 2004, p 165–170
3. P. Moore, *Electromagnetic Testing*, Vol 5, *Nondestructive Testing Handbook*, 3rd ed., American Society for Nondestructive Testing, Columbus, OH, 2004
 4. P. Cavaliere, G. Campanile, F. Panella, and A. Squillace, Effect of Welding Parameters on Mechanical and Microstructural Properties of AA6056 Joints Produced by Friction Stir Welding, *J. Mater. Proc. Technol.*, Vol 180, 2006, p 263–270
 5. P. Kapranos and R. Priestner, NDE of Diffusion Bonds, *Metals and Mater.*, Vol 3 (No. 4), 1987, p 194–198
 6. S. Kleven, Ultrasonic Inspection of Explosion Welded Titanium Clad Plate, *Mater. Eval.*, May 1996
 7. P.B. Nagy and L. Adler, Ultrasonic NDE of Solid-State Bonds: Inertial and Friction Welds, *J. Nondestr. Eval.*, Vol 7 (No. 3–4), 1988
 8. G.H. Thomas and J.R. Spingarn, Ultrasonic Determination of Diffusion Bond Strength, *Review of Progress in Quantitative Nondestructive Evaluation*, Vol 3, D.O. Thompson and D.E. Chimenti, Ed., 1984, p 1243–1250
 9. G.H. Thomas and J.R. Spingarn, Ultrasonic Evaluation of Solid State Welds, *The World Conference on Nondestructive Testing*, Vol 2, 1985, p 925–932
 10. T.A. Gray, F.J. Margetan, and R.B. Thompson, Ultrasonic NDE Techniques for Integrally Fabricated Rotor, *Review of Progress in Quantitative Nondestructive Evaluation*, Vol 7, D.O. Thompson and D.E. Chimenti, Ed., 1988, p 1327–1334
 11. R.B. Thompson, O. Buck, D.K. Rebhein, F. J. Margetan, and T.A. Gray, Ultrasonic Nondestructive Evaluation of Solid State Bonds, *IEEE Ultrasonics Symposium*, 1989, p 1117–1123
 12. E.B. Schwenk and G.D. Shearer, Measuring Projection Weld Strength by Acoustic Emission, *Nondestr. Test.*, Vol 6 (No.1), 1973, p 29–33
 13. W.M. Latham, D.T. MacLauchlan, D.P. Geier, and D.D. Lang, EMAT Weld Inspection and Weld Machine Diagnostic System for Continuous Coil Processing Lines, *Proc. SPIE*, Vol 2948, 1996, p 252–258
 14. A. Lamarre, O. Dupuis, and M. Moles, Comprehensive Inspection of Friction Stir Welds Using Arrays, *Proceedings from Joining of Advanced and Specialty Materials*, Oct 2003 (Pittsburgh, PA), p 13–15; ASM International, 2004, p 96–103
 15. N. Goldfine, D. Grundy, V. Zilberstein, and D. Kinchen, Friction Stir Weld Inspection through Conductivity Imaging Using Shaped Field MWM-Arrays, *ASM Proceedings of the International Conference: Trends in Welding Research*, p 318–323; *Proceedings of the Sixth International Conference*, April 2002, ASM International, 2002, p 15–19
 16. C. Mandache, D. Laurent, A. Merati, and J. Mohammad, Pulsed Eddy Current Testing of Friction Stir Welds, *Mater. Eval.*, Vol 66 (No. 4), April 2008, p 382–386
 17. R.A. Smith, The Potential for Friction Stir Weld Inspection Using Transient Eddy Currents, *Insight*, Vol 47 (No. 3), March 2005, p 133–143
 18. L.S. Rosado, T.G. Santos, M. Piedade, P. M. Ramos, and P. Vilaca, Advanced Technique for Non-Destructive Testing of Friction Stir Welding of Metals, *Meas.: J. Int. Meas. Confed.*, Vol 43 (No. 8), Oct 2010, p 1021–1030
 19. T.G. Santos, P. Vilaca, and R.M. Miranda, Electrical Conductivity Field Analysis for Evaluation of FSW Joints in AA6013 and AA7075 Alloys, *J. Mater. Process. Technol.*, Vol 211 (No. 2), Feb 2011, p 174–180
 20. C. Carr, M.A. Espy, T.G. Abelin, and R.H. Kraus, Characterization of Stainless Steel Inertia Welds Using HTS SQUID NDE, *IEEE Trans. Appl. Supercond.*, Vol 15 (No. 2), June 2004, p 719–722
 21. E.I. Todorov, Parametric Studies and Optimization of Eddy Current Techniques through Computer Modeling, *Review of Progress in Quantitative Nondestructive Evaluation*, Vol 26, D.O. Thompson and D.E. Chimenti, Ed., 2006, p 249–256

Mechanical Properties of Soft-Interlayer Solid-State Welds*

THE UTILIZATION OF METAL INTERLAYERS for solid-state welding can be an appropriate joining method when brittle intermetallic compound formation, differential thermal contraction during cooling, or oxide dissociation and dissolution temperature preclude the use of conventional methods, such as fusion welding, brazing, and direct solid-state welding of the base metals. An interlayer can have the form of a foil (Ref 1–8), or it can be applied to one or both of the base metal surfaces by various coating methods, such as electrodeposition (Ref 1, 2, 4, 9), plasma spraying (Ref 2), or vapor-deposition methods.

Methods that utilize coated interlayers require a two-step joining procedure (coating and welding), as opposed to joints fabricated with foil interlayers, which may only require a single solid-state welding step. However, methods that utilize coated interlayers have the advantage of not requiring solid-state welding at the interface of the interlayer and base metal, as necessitated by the use of foil interlayers. The solid-state welding of some foil interlayer and base-metal combinations may require high temperatures and/or pressures, because of the high dissociation temperatures of the surface oxides, which may preclude or restrict their use (Ref 10–12).

Various base-metal combinations have been solid-state welded using coated silver as the interlayer metal. The principal advantage of silver as an interlayer for solid-state welding is that high-strength joints can be fabricated at relatively low temperatures (473 to 673 K) and pressures (100 to 200 MPa, or 15 to 30 ksi), because of the low dissociation temperature (<460 K) for silver oxide. Depending on the strength of the base metals and the method (hydrostatic or uniaxial stress) by which pressure is applied to the silver/silver interface, the joining process may result in variable deformation in the base metals. Because some plasticity in the base metal may be important to assist with intimate atomic contact across the interface, “soft” interlayers are often preferred.

Silver interlayers for solid-state welding are usually applied to one or both of the base metals by deposition using either electrodeposition (Ref 1, 13–17) or vacuum-coating methods. The vacuum-coating methods have included electron beam evaporation (Ref 18), hot-hollow cathode (HHC) evaporation (Ref 15, 19–26), ion plating using sputtering (Ref 27–29), and planar-magnetron (PM) sputtering (Ref 30–33).

Prior to deposition, the surface oxide layer may require removal from the base metal in order to achieve adequate adhesion of the silver. The surface oxide layer is usually removed by chemical- or sputter-etching methods. One advantage of vacuum coating over electrodeposition is the ability to sputter-etch the base metal in situ. This permits silver deposition with minimal recontamination of the oxygen on the base-metal surface (Ref 34).

Soft-interlayer solid-state welds that join stronger base metals have unique mechanical properties that are of fundamental interest and may be of critical importance to designers. These assemblies can be subjected to various applied stress states, such as tensile, where the load is applied perpendicular to the interlayer/base-metal interfaces, or shear, where the applied shear stress lies within the plane of the interlayer. Of course, in application, the interlayer may be subjected to a combination of applied tensile and shear loads. This is important because these types of welds are, mechanically, quite anisotropic. This includes the case where interlayers may be subjected to residual stresses from fabrication. The loading may be continually increasing, as with a conventional tensile test, or static, as with creep tests. Again, these behaviors are quite different.

Additionally, some interlayer/base-metal interfaces have been shown to be susceptible to stress-corrosion cracking when exposed to critical environments (Ref 35). The mechanical properties of soft-interlayer solid-state welds and the implications of these behaviors to service stress states and environments are

discussed in this article. It should be noted that although silver interlayers are emphasized, primarily because of their selection by previous researchers and industrial fabricators, the described trends appear to be completely consistent with joints that use other soft-interlayer metals.

Microstructure of Interlayer Welds

As-Deposited Coatings. A fine-grained (typically <1 μm , or 40 $\mu\text{in.}$, in diameter) columnar structure commonly forms in coatings that are vacuum deposited onto low-temperature substrates ($\sim 0.3 T_m$) using a low working-gas pressure (~ 1 Pa, or 1.5×10^{-4} psi). This type of structure has been reported previously in silver coatings fabricated for interlayer welding by HHC evaporation (Ref 20) and PM sputter deposition (Ref 30). The columns are perpendicular to the base-metal surface, and the axes of the columns are oriented perpendicular to a close-packed crystallographic direction. The columnar grains resulting from the PM sputter-deposition of silver often contain a high density of growth twins that are approximately 15 nm (0.6 $\mu\text{in.}$) thick (Ref 30).

Solid-State-Welded Interlayers. Figure 1 shows a solid-state-welded silver interlayer that is 150 μm (6 mils) thick between steel base metals after solid-state welding at 673 K (Ref 17). The silver interlayer typically consists of two types of structures: nonrecrystallized silver that has retained the columnar grains and fine microtwins of the as-deposited coating and silver that has recrystallized into large grains (>1 μm , or 0.04 in., in diameter) containing a high density of annealing twins. The solid-state-welded interfaces are generally free of any large voids, or nonbonded regions. In the case of rough base-metal surfaces, large voids can remain along the silver/silver interface.

* Reprinted from R.S. Rosen and M.E. Kassner, Mechanical Properties of Soft-Interlayer Solid-State Welds, *Welding, Brazing, and Soldering*, Vol 6, *ASM Handbook*, ASM International, 1993, p165–172

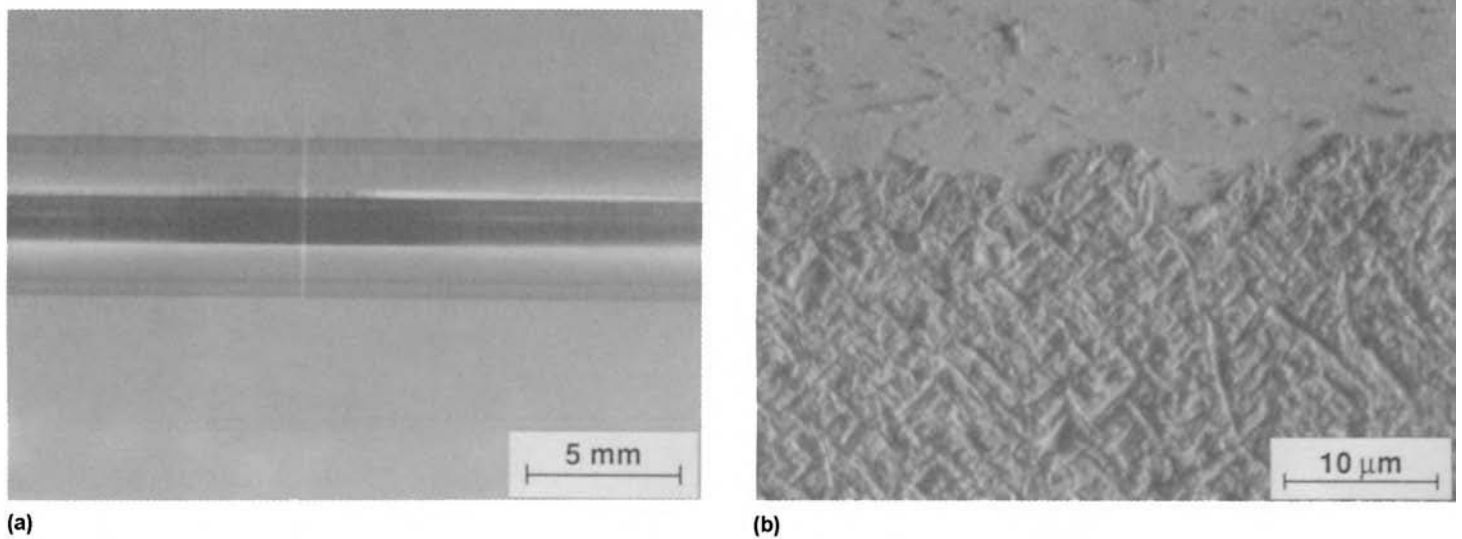


Fig. 1 (a) Optical photograph showing a 150 μm (6 mils), thick silver interlayer joining steel base metals and (b) optical micrograph of the solid-state-welded interface. Source: Ref 17

Tensile Loading of Soft-Interlayer Welds

Despite the relatively low strength of the interlayer material, it has long been known that thin (1 μm to 1 mm, or 40 μin. to 0.04 in.) interlayer welds or brazes between stronger base materials can have ultimate tensile strengths (UTS) that are much higher than that of the bulk interlayer material (Ref 36, 37). For example, the UTS of silver-interlayer solid-state welds between maraging steel base metals has been reported to be nearly 800 MPa (120 ksi) (Ref 32, 33), whereas the UTS of the bulk silver is only about 250 MPa (35 ksi) (Ref 38). The high tensile strength of the joint is due to the mechanical constraint provided by the stronger base metal, which restricts transverse contraction of the interlayer (Ref 36, 37, 39–45). The constraint establishes radial (triaxial) stresses that inhibit the development of shear stresses within the joint, thereby decreasing the effective, or von Mises, stress in the interlayer. This inhibits the plastic flow that leads to ductile fracture.

Effect of Interlayer Thickness on Stress.

The degree of mechanical constraint in the soft interlayer and the joint strength tend to increase with a decreasing thickness-to-diameter ratio, t/d , of the interlayer (Ref 36, 37, 39–42, 44, 46–53). Figure 2 summarizes the effect of t/d on the UTS of solid-state-welded silver interlayers fabricated using PM sputter deposition (Ref 30) and electrodeposition (Ref 15), compared with Ag-4Pd brazed interlayers (no hardening, because of the addition of palladium) (Ref 41). The UTS is shown to increase with a decreasing t/d ratio to about 0.002, below which only small strength increases can be expected. The higher UTS of sputter-deposited silver interlayers, compared with those utilizing

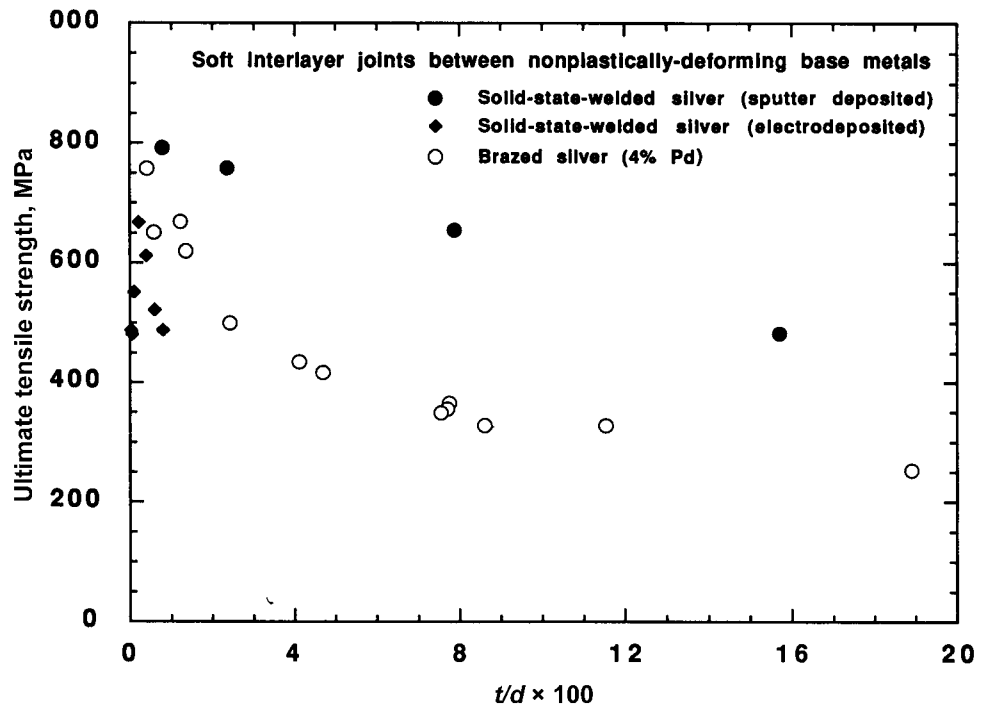


Fig. 2 Effect of interlayer thickness on ultimate tensile strength of solid-state-welded silver interlayers fabricated using planar-magnetron sputter deposition and electrodeposition, compared with Ag-4Pd brazed interlayers

electrodeposition or brazed-silver alloy, are discussed in the section “Effect of Interlayer Fabrication Method” in this article.

Although the tensile behavior of interlayer joints has been reasonably well understood qualitatively, particularly for thick interlayers, quantitative prediction has only recently been accomplished with finite-element method (FEM) codes. Orowan (Ref 36, 37) was perhaps the first to derive an analytical expression for

the radial (constraining) stress within the interlayer. It was proposed that:

$$\sigma_r = \frac{\sigma_y}{t} \left(\frac{d}{2} - r \right) \tag{Eq 1}$$

where σ_r is the radial stress, t is the thickness, d is the diameter, r is the radius, and σ_y is the yield stress of the interlayer. This equation

was originally derived by assuming ideal plastic behavior (that is, no strain hardening) of the interlayer and uniform plastic strain in the interlayer. Analytical attempts to account for strain hardening within the interlayer have led to modifications of Eq 1 that have, experimentally at least, provided reasonable correlation with upper bounds for UTS of soft-interlayer joints (Ref 41, 43, 48, 49).

More recently, FEM analyses (Ref 53, 54) reveal significant deviation from Eq 1. Figure 3(a) illustrates the effect of t/d on the radial stress distribution at the center plane for silver interlayer welds between nonplastically deforming base metals at a fixed applied tensile stress. These were determined from an FEM analysis that included the observed strain hardening of the interlayer metal and are plotted along with results predicted by Eq 1. This comparison shows that for large t/d ratios ("thick" interlayers), Eq 1 predicts qualitatively correct behavior for the radial stress distribution. However, for small t/d ratios ("thin" interlayers), the

FEM results indicate a relatively uniform and substantially lower stress distribution over most of the central portion of the interlayer than predicted by Eq 1. This is partly due to the simplifying assumptions in Eq 1, particularly that of a radially uniform strain state.

This effect is further illustrated in Fig. 3 (b), which shows the stress state in a strain-hardening silver interlayer at a small fixed t/d ratio. Although it is not shown, the effective (von Mises) stress, which measures the tendency to plastically deform, decreases with decreasing t/d , down to approximately 0.025. Hence, a decreasing t/d ratio increases the mechanical constraint in the interlayer such that a larger applied stress is needed to produce a given amount of plastic strain in the interlayer. Interestingly, and in contrast with Eq 1, the effective stress does not appear to substantially change with decreases in t/d that are less than approximately 0.025 (Ref 54). This is qualitatively consistent with the extrapolations of the solid-state-welded silver data in Fig. 2 (but not the braze data).

Early investigators (Ref 15, 40, 44, 45, 55) believed that this phenomenon was due only to discontinuities (solidification shrinkage cavities, surface flatness, and such) in very thin brazes and solid-state welds. Recent results (Ref 17, 30) of solid-state-welded interlayers fabricated using sputter-deposited silver onto lapped base metals (surface roughness of 0.03 μm , or 1.2 $\mu\text{in.}$) indicate that the modest increase (or plateau) in strength occurs even in the absence of preexisting voids that are common in thin brazes.

Interlayer Strain. Associated with the increased UTS of the constrained interlayers, compared to the UTS of the bulk or unconstrained interlayer metal, is a decreased plastic strain-to-failure, ϵ_f , of the interlayer. Early results (Ref 42) found that for brazed-silver interlayers joining elastically deforming base metals with a t/d ratio of 0.016, the ϵ_f is about 0.01. The results from specimens fabricated using solid-state welding of PM sputter-deposited silver interlayers, in which the base metals did not plastically deform, indicated plastic strains of only about 0.001 for a comparable t/d ratio of 0.024 (Ref 17, 33). The reason for the disparity is not clear. Perhaps the relatively large number of interfaces in the PM sputter-deposited interlayers (Ref 30, 33) led to higher cavity-nucleation rates. Other works do not appear to have made reliable attempts at determining the plastic strain-to-failure value. It should be emphasized that despite the relatively low plastic strain-to-failure, the fracture surface is that of a classic, ductile, microvoid-coalescence type of failure (Ref 33).

Time-Dependent Failure. It has been observed that at stresses substantially less than the UTS, delayed or time-dependent ductile fracture may occur. For at least the case of silver interlayers, decreases in the applied stress are associated with increased times-to-rupture, as indicated in Fig. 4. This figure shows that decreasing the t/d ratio (to about 0.02) and/or improving the base-metal surface finish (lapping) results in longer tensile creep-rupture times. Time-dependent failure is believed to be a consequence of cavity nucleation and/or growth (Ref 33), as is observed in short-term tensile tests that

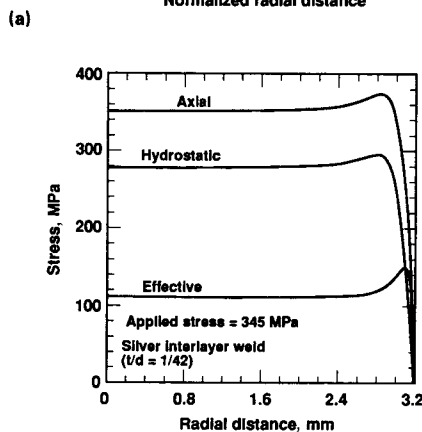
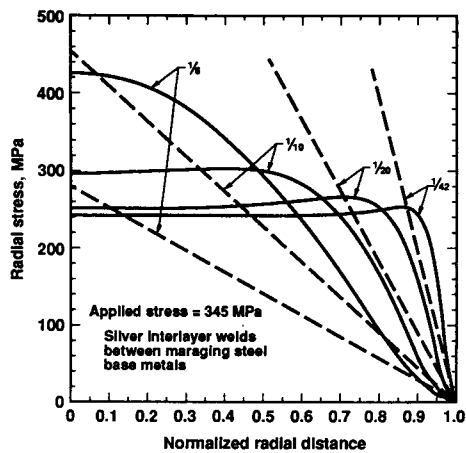


Fig. 3 Finite-element method analysis of the effect of t/d on the radial stress distribution at the center plane for silver interlayer welds between non-plastically deforming base metals at a fixed applied tensile stress. (a) Predictions of Eq 1 are given by dashed lines. (b) The stress state in a strain-hardening silver interlayer at a small fixed t/d ratio

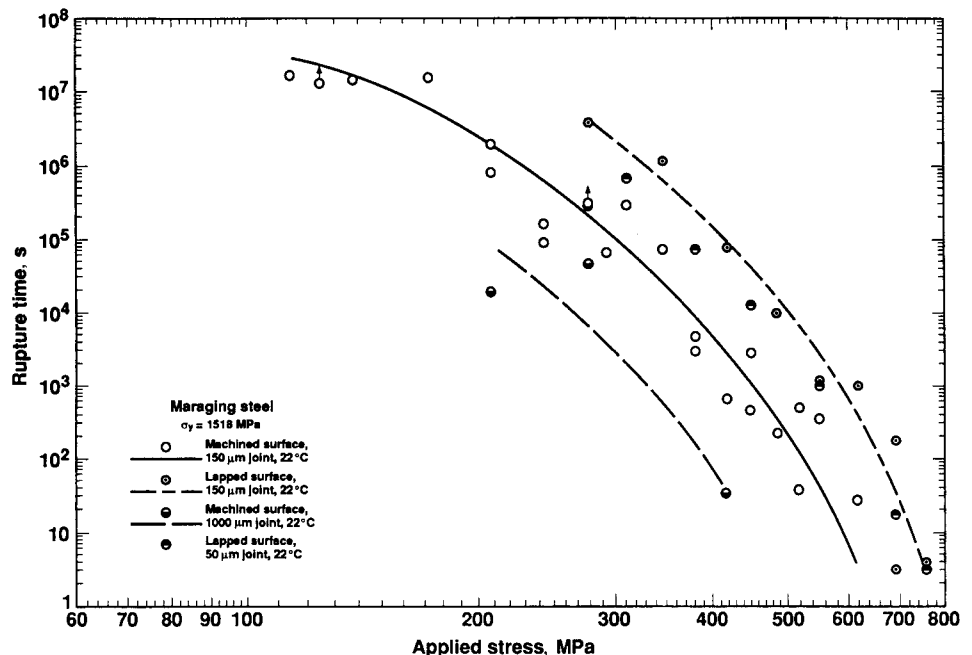


Fig. 4 Effect of interlayer thickness and base-metal surface finish on creep rupture of solid-state-welded silver joints between nonplastically deforming base metals

determine the UTS. For solid-state welds in which two coatings are joined, nucleation occurs principally at the silver/silver welded interface or the base-metal/silver-coated interface. The cavities appear to nucleate as a consequence of time-dependent plasticity within the interlayer. The cavities expand in diameter and final interlinkage, and failure appears to occur at relatively low “macroscopic” strains within the interlayer (for example, $\epsilon_f < 10^{-3}$).

Figure 5 shows scanning electron micrographs of a solid-state-welded silver interlayer joining steel base metals, loaded at the relatively low stress level of 207 MPa (30 ksi) (albeit, for a substantial fraction of the expected creep-rupture time). Some of the larger cavities consist of clusters of smaller ($< 0.5 \mu\text{m}$, or $200 \mu\text{in.}$, in diameter) microvoids. A typical fracture surface of a creep-rupture specimen is illustrated in Fig. 6. Naturally, the fracture surfaces appear identical to those of the short-term tests in which UTS values

were measured. It should be emphasized that, consistent with Fig. 2, as the interlayer metal strength increases, the strength of the weld joint increases. Similarly, as the interlayer metal creep resistance increases, the rupture times of the weld joint should increase. Hence, as reported for gold-nickel high-strength/creep-resistant interlayer brazes (Ref 56), time-dependent failure has not been observed over periods of about 1 year. Also, it appears that for silver brazes (Ref 33), time-dependent failure is observed but at increasingly longer times at decreasing stresses, perhaps because of differences in substructures, compared with solid-state-welded silver interlayers.

A nucleation-based theory has been proposed to explain the low plastic strain, time-dependent failures of soft-interlayer solid-state welds in which preexisting voids do not exist, and the base metal does not plastically deform. (Ref 17, 33, 57). Plastic deformation of the

interlayer, acting under the effective stress, causes cavity nucleation by dislocation pile-ups at interfaces. Nucleation continues with further creep of the interlayer, until the concentration of nuclei is sufficiently high to lead to instability in the material between the cavities. Coalescence by interlinkage or by uniform wall expansion (“growth”) then occurs. The point of instability between two small nanometer-sized cavities or nuclei separated by a few diameters or so may lead to subsequent rapid nucleation between the cavities, resulting in the formation of a single, larger cavity (as shown in Fig. 5). This process is repeated and eventually leads to the onset of final rupture, and gives the appearance of a classic, ductile, microvoid-coalescence type of fracture.

In contrast with this nucleation-based theory, other investigators (Ref 42) suggest that the macroscopic strain-to-failure is determined by the details of the uniform cavity expansion (growth). Here, once the cavities expand and come in proximity to other cavities, coalescence and ductile fracture occurs. In a creep experiment, according to the usual cavity-growth models, the rupture time is determined by the cavity growth rate or the speed of the expanding cavity wall. In the absence of vacancy-controlled growth, this speed is controlled by the macroscopic plastic strain rate. Therefore, the static (or creep) and dynamic (or quasi-static) failures of the thin interlayer welds should be, according to cavity-growth-based theories, related to the macroscopic strain in the interlayer. If steady-state plasticity is achieved throughout the silver interlayer material surrounding the cavities, then unstable cavity wall expansion may occur. However, since the macroscopic strains-to-failure are small ($\epsilon_f < 10^{-3}$), the time or strain up to the onset of final catastrophic failure (where a large ductile-dimple fracture surface begins to form) is not easily explained by a cavity-growth model in a strain-hardening material.

The silver-plasticity concept for rationalizing creep rupture is consistent with the temperature dependence of the time-to-rupture. The activation energy for the creep of silver at ambient and near-ambient temperatures for various substructures falls within the range of 50 to 71 kJ/mol (Ref 38, 58). The activation energy for the creep rupture of the solid-state-welded silver joints of Fig. 2, equal to 65 kJ/mol (Ref 33), falls within the range of activation energies for silver plasticity.

Effect of Base-Metal Properties. Time-dependent tensile fracture can be dramatically accelerated if there is creep, or time-dependent plasticity, of the base materials. Figure 7 shows the creep-rupture behavior of solid-state-welded silver interlayers ($t/d = 0.024$) joining one of two different strengths of type 304 stainless steel base metals: annealed or cold worked (Ref 17, 33). Interestingly, these base metals undergo time-dependent plasticity, or creep, at ambient temperatures at stresses that are less than the conventional yield stress of the metal.

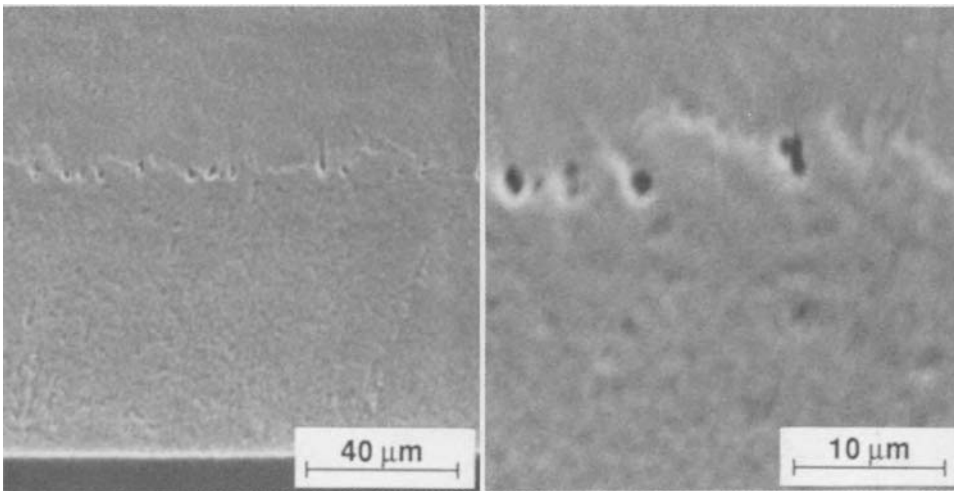


Fig. 5 Scanning electron micrographs showing solid-state-welded silver interlayer joining nonplastically deforming base metals, loaded at 207 MPa (30 ksi) ($\sim 1/3$ ultimate tensile strength) for a substantial fraction of the expected creep-rupture time

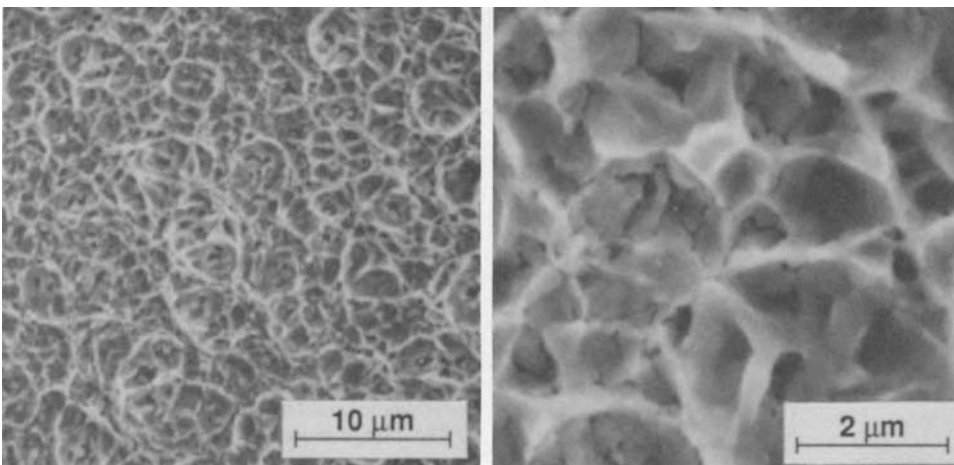


Fig. 6 Solid-state-welded silver interlayer fracture surface between lapped maraging steel base metals

Although the accumulated plastic strain in the creeping stainless steel is only about 0.001 to 0.01 at low stress levels, this nonetheless induces concomitant plastic strain within the interlayer that exceeds that which would occur within the interlayer in the absence of base-metal plasticity, resulting in shorter creep-rupture times. This behavior is consistent with previous reported data for creep ruptures of interlayers that join plastically deforming base metals (Ref 25, 26, 59, 60).

Finite-element analyses have confirmed that plasticity in the base metal allows the interlayer to plastically deform to a much greater extent than if the base metal deforms only elastically (Ref 54). This observation is important, because these small levels of time-dependent plasticity (0.001 to 0.01) are often observed, over time, in other structural metals and alloys at ambient temperature at stresses significantly below the conventionally defined yield stress. With an increase in test temperature, the stainless steel base-metal creep rate significantly increases and rupture times decrease. The activation energies for the creep rupture of silver interlayers between stainless steel base metals and for plastic flow in stainless steel are comparable, further suggesting that the temperature dependence of creep rupture is determined by creep plasticity in the stainless steel base metal. The transition from base-metal to interlayer-controlled creep rupture occurs at the "knee" of the cold-worked stainless steel data plot, at stress levels below which base-metal creep is negligible.

Figure 7 also shows the effect of base-metal surface finish, which is eventually coated, on the creep-rupture behavior of joints utilizing cold-worked type 304 stainless steel. Lapped cold-worked stainless steel base-metal specimens have longer rupture times than those of machined cold-worked stainless steel, as was the case with the maraging steel specimens. However, the increase in creep-rupture times of specimens utilizing lapped versus machined plastic base metals is only a factor of 5, which is considerably less than the increase of approximately 50 for specimens utilizing lapped versus machined elastic base metals. The difference between the increases in creep-rupture times for lapped plastic versus lapped elastic base-metal specimens may be due to the difference in failure processes. For the case of a plastic base metal, the strain in the silver is externally and uniformly imposed by the deformation of the base metal. For elastic base metals, plasticity is caused by the effective stress within the interlayer. It is believed that the heterogeneities along the solid-state-welded silver interface caused during the joining of the comparatively rough machined surfaces could result in regions that may be more resistant to plasticity than other regions. The heterogeneities at the solid-state-welded silver interface may be less significant in increasing the nucleation and coalescence rate of cavities in specimens utilizing plastic base metals than those utilizing elastic base metals, where the strain is indigenous to the interlayer, rather than being imposed by base-metal deformation.

Effect of Interlayer Fabrication Method. In general, the tensile strengths of PM sputter-deposited silver joints between various base metals have been reported to be equal to or greater than those utilizing other silver-coating methods and similar solid-state-welding parameters. For elastic base metals with lapped surfaces, PM sputter-deposited silver joint tensile strengths (Ref 30) of 758 and 793 MPa (110 and 115 ksi) using interlayers that are 150 and 50 μm (6 and 2 mils) thick, respectively, are comparable with HHC-deposited silver joints (758 MPa, or 110 ksi, using 10 μm , or 0.4 mil, thick interlayers) and greater than those of electrodeposited silver joints (669 MPa, or 97 ksi, using 25 μm , or 1 mil, thick interlayers) (Ref 15). However, the tensile strength values for silver-interlayer welds fabricated using these other two coating methods are achieved with considerably thinner interlayers, which have the advantage of greater plastic constraint produced by the base metals. For type 304 stainless steel (plastically deforming) base metals with machined surfaces and 150 μm (6 mils) thick joints, PM sputter-deposited silver joint tensile strengths (Ref 30) of 304 MPa (44 ksi) ($\sigma_{y,SS} = 221$ MPa, or 32 ksi) and 400 MPa (60 ksi) ($\sigma_{y,SS} = 359$ MPa, or 52 ksi) are comparable with electrodeposited silver joint strengths of 321 to 367 MPa (47 to 53 ksi) ($\sigma_{y,SS} = 296$ MPa, or 43 ksi) (Ref 16). For uranium (plastic) base metals with machined surfaces, the PM sputter-deposited silver joint tensile strength of 442 MPa (64 ksi) ($\sigma_{y,U} = 242$ MPa, or 35 ksi) (Ref 30) exceeds electrodeposited silver joint strengths of approximately 255 MPa (37 ksi) (despite the higher base-metal yield stress; $\sigma_{y,U} = 345$ MPa, or 50 ksi) and HHC-deposited silver joint strengths of 345 to 373 MPa (50 to 54 ksi) (Ref 16, 61). However, the lower joint strength using HHC-deposited silver (Ref 61) may have resulted from a lower solid-state welding pressure (138 MPa, or 20 ksi) and temperature (589 K) than those using PM sputter-deposited silver. The tensile strength of solid-state-welded silver joints between dissimilar metals, such as uranium ($\sigma_y = 345$ MPa, or 50 ksi) and type 304 stainless steel ($\sigma_y = 296$ MPa, or 45 ksi) fabricated using HHC deposition has been reported to average 442 MPa (64 ksi) (Ref 25). The tensile strength of electrodeposited silver joints between the same uranium and stainless steel base metals that were solid-state welded at the same pressure (207 MPa, or 30 ksi), temperature (873 K), and time (2 h) averaged only 345 MPa (50 ksi) (Ref 17, 30). Therefore, solid-state-welded silver joints fabricated using electrodeposition appear to be weaker than those fabricated using HHC deposition or PM sputter deposition.

Although there is only a limited amount of published test results of interlayer joint strengths fabricated by low-temperature solid-state welding of foils, it appears that interlayer/base-metal adhesion is difficult to achieve at temperatures below approximately $0.7 T_m$ of

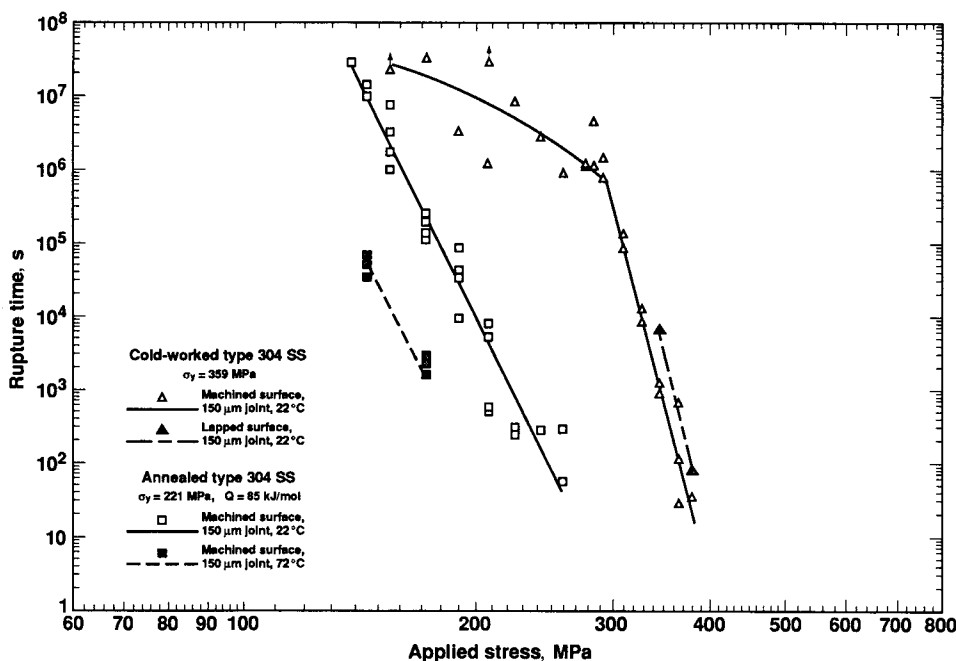


Fig. 7 Creep-rupture behavior of solid-state-welded silver interlayers ($t/d = 0.024$) joining one of two different strengths of type 304 stainless steel base metals (annealed or cold worked), both of which undergo time-dependent plasticity or creep at ambient temperatures at stresses less than the conventional yield stress of the metal

the interlayer. Tensile strengths of silver joints between alumina and type 321 stainless steel were reported to be only 40 MPa (5.8 ksi) when solid-state-welding parameters were 1073 K and 50 MPa (7.3 ksi) for 0.5 h (Ref 11). The investigators reported threshold solid-state-welding temperatures below which no measurable bonding was produced for each of the foils utilized (silver, aluminum, copper, and nickel). The threshold temperature to achieve solid-state welding of silver foils to alumina and type 321 stainless steel was reported to be 873 K (0.7 T_m of the silver), considerably higher than the temperature required to achieve solid-state welding of silver to itself (0.35 T_m) (Ref 18). Joint strengths of the previous interlayer fabrication processes were reported to be comparable (40 to 50 MPa, or 5.8 to 7.3 ksi) to those of silver foils (Ref 11). Tensile tests reported for silver-foil interlayers between type 304L stainless steel and Ti-6Al-4V alloy suggest that higher strengths may be achieved with coated interlayers than with foil interlayers (Ref 62). These joints were fabricated by solid-state welding a 125 μm (5 mils) thick silver foil between the base metals at 1153 K (0.94 T_m). The investigators (Ref 62) reported average joint strengths of 280 MPa (40 ksi). For annealed type 304 stainless steel and 150 μm (6 mils) thick joints fabricated using PM sputter deposition, the reported (Ref 30) tensile strength of 304 MPa (44 ksi) is higher, despite the higher base-metal yield stress of Ti-6Al-4V alloy used in the silver-foil study.

Shear Loading

Effect of Microstructure. The base metals provide relatively little mechanical constraint of the interlayer during shear loading (shear stress is parallel to the plane of the interlayer) and therefore reveal the mechanical behavior of the interlayer material itself. The behavior of the interlayer in shear can be converted to equivalent uniaxial tensile behavior using the von Mises stress and strain criteria:

$$\bar{\sigma} = \tau\sqrt{3}$$

$$\bar{\epsilon} = \gamma\sqrt{3}$$

where τ and γ are shear stress and strain, respectively. Effective (von Mises) stress-strain ($\bar{\sigma} - \bar{\epsilon}$) behavior for a 150 μm (6 mils) thick ($t/d = 0.024$) silver joint, fabricated using PM sputter-deposition (between maraging steel) and tested in torsion is shown in Fig. 8 (Ref 33), along with the reported results for bulk polycrystalline (annealed) silver (Ref 38). The yield stress ($\bar{\epsilon}_p = 0.2\%$) of the solid-state-welded joint is six times greater than the bulk-silver value, presumably because of the much more refined, twinned substructure. The strain-hardening rate, $d\bar{\sigma}_{\text{eff}}/d\bar{\epsilon}_{\text{eff}}$, at an effective stress of 100 MPa (15 ksi) is over nine times greater than bulk polycrystalline silver (Ref 38). The maximum interlayer stress is attained after a

strain of only 0.3 (99% of the maximum value is attained after a strain of only 0.1). Therefore, although the interlayer silver has a higher yield stress and strain hardens at a higher rate, it reaches essentially the same maximum stress as bulk silver at a substantially lower strain.

Differences in the maximum (steady-state) stress may result from two factors. First, the interlayer microstructure may not be identical to that of the bulk material. The second explanation is that slip (plasticity) is not isotropic. The plasticity is not isotropic. The plasticity is the result of dislocation activity on limited slip planes with specific Burgers vectors. The shear displacements of individual grains in the interlayer must generally be accommodated by neighboring grains. However, near the base metal, the accommodation is not possible, and additional slip systems may operate in the interlayer grains near the base metal, leading to greater local hardening and higher flow stresses. Torsion tests of solid-state-welded silver interlayers coated by HHC evaporation, using uranium-to-stainless steel base metals (Ref 26), showed similar increases in the yield stress and strain-hardening rates, compared with those of bulk-silver values. However, the steady-state stress of silver joints was approximately 25% higher than that of bulk silver, compared with 10% higher values for interlayers using PM sputter-deposited silver. One explanation for this difference may be the presence of HHC deposits, which may further raise the maximum, or steady-state, stress.

Time-Dependent Failure. Although not shown in Fig. 8, the plastic strain-to-failure in pure shear is very high ($\bar{\epsilon}_f = 5$ to 10) for thin, silver-interlayer specimens, just as for macroscopic, or bulk, silver specimens (Ref 33). This is nearly 4 orders of magnitude higher than for the case of tension. As previously discussed, cavity nucleation is promoted by the triaxial stress state established with simple uniaxial loading of constrained interlayers. The fact that torque saturates is consistent with the observation that some face-centered cubic metals, such as aluminum, copper, and silver (Ref 38), show a saturation in the flow stress. This fact is important because such saturations imply constant torque, or time-dependent, shear-stress failures. Figure 9 shows a comparison between the rupture time versus effective (von Mises) stress behavior in shear (Ref 26) (at torsional stresses less than the maximum of HHC-deposited-silver interlayers), compared with that of tension (Ref 17) (calculated using FEM analyses of PM sputter-deposited silver interlayers). The shear rupture times are longer than tensile rupture times at equivalent uniaxial stresses (calculated using the von Mises relation), consistent with the higher plastic strains-to-failure that are much higher for the torsion specimens ($\bar{\epsilon}_f > 5$) than for the tensile specimens ($\epsilon_f \sim 0.001$). The shorter rupture times for tensile joints are a direct result of the hydrostatic tensile stresses superimposed on the

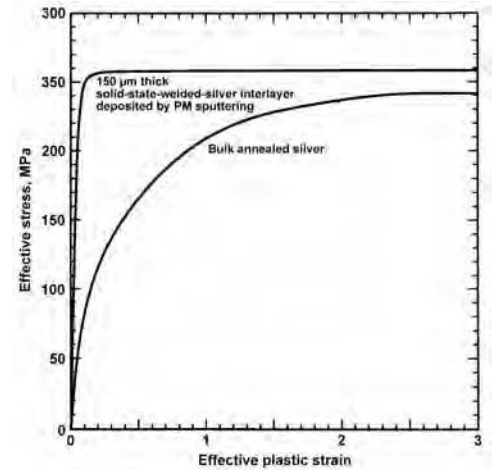


Fig. 8 Effective (von Mises) stress-strain behavior for a 150 μm (6 mils) thick silver interlayer ($t/d = 0.024$), fabricated using planar-magnetron (PM) sputter deposition, tested in torsion, along with results reported for bulk polycrystalline (annealed) silver

effective stresses caused by the mechanical constraint imposed by the base metal.

The change in steady-state strain-rate (or time-to-rupture, according to the Monkman-Grant relationship) with applied stress is predictable according to the steady-state stress exponent, n :

$$n = \left(\frac{\partial \ln \dot{\epsilon}}{\partial \ln \bar{\sigma}} \right)_i \quad (\text{Eq 2})$$

where n is about 30 for silver at ambient temperature (Ref 38). Naturally, the steady-state strain rate of the torsional specimens shown in Fig. 9 is less than the constant applied strain rate of the torsional specimens shown in Fig. 8. If the steady-state rate is not achievable in the interlayer metal, then time-dependent failure in shear is not expected to occur.

It is important to realize the consequence of the difference in plastic strains-to-failure between the constant shear-stress case and the constant tensile-stress case. For example, residual shear or tensile stresses may develop during fabrication of interlayer brazes or solid-state welds. This is particularly true in cases where dissimilar base materials are joined but have substantially different coefficients of thermal expansion. For thin interlayers subjected to residual shear stresses, the dimensions of the base metal and interlayer may be such that the stress is relaxed at strains less than the shear strain-to-failure. However, because the observed tensile strains-to-failure are small, creep rupture by residual tensile stresses is possible, provided a significant stress level exists. If the interlayer metal is resistant to time-dependent failure, then only the indirect implications of residual stress are important (for example, environmentally induced failure).

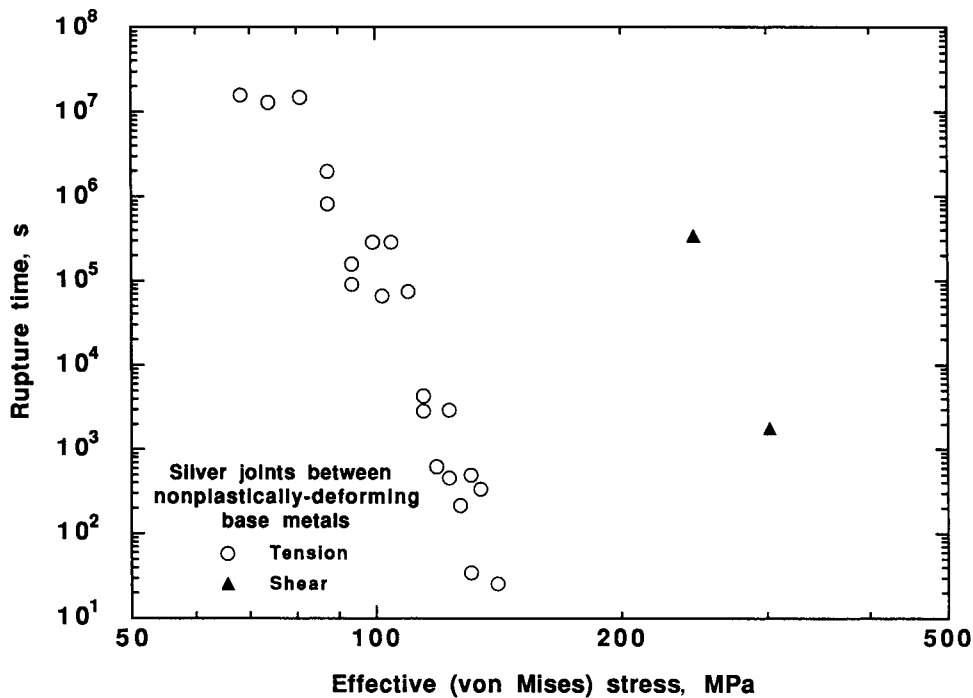


Fig. 9 Comparison between the rupture time versus effective (von Mises) stress behavior in shear, at torsional stresses less than the maximum of hot-hollow-cathode-deposited silver interlayers, compared with that of tension, calculated using finite-element method analyses of planar-magnetron sputter-deposited silver interlayers

Multiaxial Loading

As discussed earlier, in tension there is significant mechanical constraint by the base material, which tends to reduce the effective stress. In torsion, where the shear stress is parallel to the plane of the interlayer, there is no constraint, other than, perhaps, the relatively minor constraint associated with plastic strain incompatibilities between the interlayer and the base metal. It was also mentioned earlier that the equivalent uniaxial strain-to-failure for torsional deformation of soft-interlayer joints is roughly 4 orders of magnitude higher than the values for uniaxial tension, and the (effective) shear stress-to-failure is only about one-half the UTS. This suggests that the interlayers will behave anisotropically to imposed stresses. The mechanical properties of the intermediate cases of biaxial deformation are not readily interpolated between these limits. The authors have preliminary experimental evidence, for example, that low-strain ductile failures in thin interlayers may occur at particularly low stress levels and strains for cases where tensile loads are accompanied by in-plane shear stresses (Ref 63). This implies that some multiaxial residual stress states may render solid-state-welded interlayer joints substantially more vulnerable to failure than simple tensile-stress states, even though the “macroscopic” effective stress may be comparable, when calculated on the basis of the applied stress state in the base material away from the interlayer.

Environmentally Induced Failure of Interlayers

The interlayer/base-metal interfaces of some soft-interlayer welds appear particularly vulnerable to failure when exposed to external (corrosive) environments. For example, it is known that brazed silver interlayers between stainless steel are subject to galvanic corrosion in aqueous NaCl media (Ref 64, 65). When dissimilar base materials are joined, the potential for stress-corrosion cracking (SCC) exists if the joints are exposed simultaneously to some external (corrosive) environments and either shear or tensile stresses. If an interlayer is subjected to stress, then a determination of the vulnerability to SCC is appropriate. It was mentioned earlier that elevated-temperature joining using either solid-state or brazing processes may leave the joint under substantial residual stress, particularly in the case of dissimilar metals for which the coefficients of thermal expansion are significantly different. The authors have reported (Ref 35) that the uranium to type 304 stainless steel solid-state welds, fabricated using HHC-deposited silver interlayers (Ref 25, 26), are very susceptible to SCC. These silver solid-state welds were joined at 873 K, and the difference in thermal expansion coefficients leaves the joints of cylindrical specimens under significant residual shear stresses after cooling to ambient temperature. It was found that these residual stresses led to SCC at the uranium/silver interface in

air saturated with water vapor (100% relative humidity) (Ref 35). This cracking resulted in reduced tensile strengths and rupture times, when compared with those specimens tested in laboratory air (~40% relative humidity). Specimens subjected to the same 100% relative humidity in air in an unstressed state exhibited no loss in strength, even after lengthy exposure. This, of course, emphasizes the importance of considering the residual stresses as not only rendering the interlayer joints vulnerable to “pure mechanical” rupture but also to environmentally induced failures such as SCC, hydrogen embrittlement, and metal-induced embrittlement, if exposed to critical environments.

REFERENCES

1. J.T. Niemann, R.P. Sopher, and P.J. Rieppel, Diffusion Bonding Below 1000 °F, *Weld. J.*, Vol 37, 1958, p 337s–342s
2. I.M. Barta, Low Temperature Diffusion Bonding of Aluminum Alloys, *Weld. J.*, Vol 43, 1964, p 241s–247s
3. D. Hauser, P.A. Kammer, and J.H. Dedrick, Solid-State Welding of Aluminum, *Weld. J.*, Vol 46, 1967, p 11s–22s
4. P.A. Kammer, R.E. Monroe, and D.C. Martin, Further Studies of Diffusion Bonding Below 1000 °F, *Weld. J.*, Vol 48, 1969, p 116s–124s
5. Y. Iino and N. Taguchi, Interdiffusing Metals Layer Technique of Ceramic-Metal Bonding, *J. Mater. Sci. Lett.*, Vol 7 (No. 9), 1988, p 981–982
6. A. Urena, J.M.G.d. Salazar, and J. Quinones, Diffusion Bonding of Alumina to Steel Using Soft Copper Interlayer, *J. Mater. Sci.*, Vol 27, 1992, p 599–606
7. T. Yamada, K. Yokoi, and A. Kohno, Effect of Residual Stress on the Strength of Alumina-Steel Joint with Al-Si Interlayer, *J. Mater. Sci.*, Vol 25, 1990, p 2188–2192
8. M.G. Nicholas and R.M. Crispin, Diffusion Bonding Stainless Steel to Alumina Using Aluminum Interlayers, *J. Mater. Sci.*, Vol 17, 1982, p 3347–3360
9. C.L. Cline, An Analytical and Experimental Study of Diffusion Bonding, *Weld. J.*, Vol 45, 1966, p 481s–489s
10. A.T. D’Annessa, The Solid-State Bonding of Refractory Metals, *Weld. J.*, Vol 43, 1964, p 232s–240s
11. M.G. Nicholas and R.M. Crispin, Diffusion Bonding Ceramics with Ductile Metal Interlayers, *Proc. Int. Conf. Diffusion Bonding* (Cranfield, U.K.), 1987, p 173–182
12. B. Derby, Zirconia/Metal Diffusion Bonds, *Proc. Int. Conf. Diffusion Bonding* (Cranfield, U.K.), 1987, p 195–201
13. R.A. Morley and J. Caruso, The Diffusion Welding of 390 Aluminum Alloy Hydraulic Valve Bodies, *Weld. J.*, Vol 59 (No. 8), 1980, p 29–34

14. C.H. Crane, D.T. Lovell, W.A. Baginsky, and M.G. Olsen, Diffusion Welding of Dissimilar Metals, *Weld. J.*, Vol 46, 1967, p 23s–31s
15. M. O'Brien, C.R. Rice, and D.L. Olson, High Strength Diffusion Welding of Silver Coated Base Metals, *Weld. J.*, Vol 55 (No. 1), 1976, p 25–27
16. J.W. Dini, W.K. Kelley, W.C. Cowden, and E.M. Lopez, Use of Electrodeposited Silver as an Aid in Diffusion Welding, *Weld. J.*, Vol 63 (No. 1), 1983, p 26s–34s
17. R.S. Rosen, "Time-Dependent Failure of Silver Interlayer Welds," Ph.D. thesis, University of California, Davis, 1990
18. J.L. Knowles and T.H. Hazlett, High-Strength Low-Temperature Bonding of Beryllium and Other Metals, *Weld. J.*, Vol 49 (No. 7), 1970, p 301s–310s
19. P.S. McLeod and G. Mah, The Effect of Substrate Bias Voltage on the Bonding of Evaporated Silver Coatings, *J. Vac. Sci. Technol.*, Vol 11 (No. 1), 1974, p 119–121
20. G. Mah, P.S. McLeod, and D.G. Williams, Characterization of Silver Coatings Deposited from a Hollow Cathode Source, *J. Vac. Sci. Technol.*, Vol 11 (No. 4), 1974, p 663–665
21. D.G. Williams, Vacuum Coating with a Hollow Cathode Source, *J. Vac. Sci. Technol.*, Vol 11 (No. 1), 1974, p 374–377
22. E.R. Naimon, D. Vigil, J.P. Villegas, and L. Williams, Adhesion Study of Silver Films Deposited from a Hot Hollow-Cathode Source, *J. Vac. Sci. Technol.*, Vol 13 (No. 6), 1976, p 1131–1135
23. E.R. Naimon, J.H. Doyle, C.R. Rice, D. Vigil, and D.R. Walmsley, Diffusion Welding of Aluminum to Stainless Steel, *Weld. J.*, Vol 60 (No. 1), 1981, p 17–20
24. D.T. Larson and H.L. Draper, Characterization of the Be-Ag Interfacial Region of Silver Films Deposited Onto Beryllium Using a Hot Hollow Cathode Discharge, *Thin Solid Films*, Vol 107, 1983, p 327–334
25. R.S. Rosen, D.R. Walmsley, and Z.A. Munir, The Properties of Silver-Aided Diffusion Welds Between Uranium and Stainless Steel, *Weld. J.*, Vol 65 (No. 4), 1986, p 83s–92s
26. J.W. Elmer, M.E. Kassner, and R.S. Rosen, The Behavior of Silver-Aided Diffusion-Welded Joints under Tensile and Torsional Loads, *Weld. J.*, Vol 67 (No. 7), 1988, p 157s–162s
27. J. Harvey, P.G. Partridge, and A.M. Lurshy, Factors Affecting the Shear Strength of Solid State Diffusion Bonds Between Silver-Coated Clad Al-Zn-Mg Alloy (Aluminum Alloy 7010), *Mater. Sci. Eng.*, Vol 79, 1986, p 191–199
28. P.G. Partridge and D.V. Dunford, On the Testing of Diffusion-Bonded Overlap Joints Between Clad Al-Zn-Mg Alloy (7010) Sheet, *J. Mater. Sci.*, Vol 22, 1987, p 1597–1608
29. D.V. Dunford and P.G. Partridge, The Peel Strengths of Diffusion Bonded Joints Between Clad Al-Alloy Sheets, *J. Mater. Sci.*, Vol 22, 1987, p 1790–1798
30. R.S. Rosen and M.E. Kassner, Diffusion Welding of Silver Interlayers Coated onto Base Metals by Planar-Magnetron Sputtering, *J. Vac. Sci. Technol. A*, Vol 8 (No. 1), 1990, p. 19–29
31. M.E. Kassner, R.S. Rosen, G.A. Henshall, and W.E. King, Delayed Failure of Silver Aided Diffusion Welds Between Steel, *Proc. Second Int. Conf. Brazing, High Temperature Brazing, and Diffusion Welding*, German Welding Society, 1989, p 47–52
32. M.E. Kassner, R.S. Rosen, G.A. Henshall, and K.D. Challenger, Time-Dependent Failure of Silver-Interlayer Diffusion Welds Between Elastically-Deforming Base Metals, *Scr. Metall. Mater.*, Vol 24, 1990, p 587–592
33. M.E. Kassner, R.S. Rosen, and G.A. Henshall, Delayed Mechanical Failure of Silver-Interlayer Diffusion Bonds, *Metall. Trans. A*, Vol 21, 1990, p 3085–3100
34. P.G. Partridge and J. Harvey, "Process for the Diffusion Bonding of Aluminum Materials," U.K. patent application GB 2117691 A, 1983
35. R.S. Rosen, S. Beitscher, and M.E. Kassner, Stress Corrosion Cracking of Uranium-Silver Interfaces in Silver-Aided Diffusion Welds, *Int. Conf. Environment-Induced Cracking of Metals*, Vol 10, NACE, 1989, p 429–433
36. E. Orowan, Fracture and Strength of Solids, *Rep. Prog. Phys.*, Vol 12, 1948, p 185–231
37. E. Orowan, Fundamentals of Brittle Behavior of Metals, *Fatigue and Fracture of Metals*, John Wiley & Sons, 1952
38. M.E. Kassner, The Rate Dependence and Microstructure of High-Purity Silver Deformed to Large Strains Between 0.16 and 0.30 T_m , *Metall. Trans. A*, Vol 20, 1989, p 2001–2010
39. N. Bredz, Investigation of Factors Determining the Tensile Strength of Brazed Joints, *Weld. J.*, Vol 33, 1954, p 545s–563s
40. W.G. Moffatt and J. Wulff, Tensile Deformation and Fracture of Brazed Joints, *Weld. J.*, Vol 42, 1963, p 115s–125s
41. H.J. Saxton, A.J. West, and C.R. Barrett, Deformation and Failure of Brazed Joints—Macroscopic Considerations, *Metall. Trans.*, Vol 2, 1971, p 999–1007
42. A.J. West, H.J. Saxton, A.S. Tetelman, and C.R. Barrett, Deformation and Failure of Thin Brazed Joints—Microscopic Considerations, *Metall. Trans.*, Vol 2, 1971, p 1009–1017
43. E.P. Lautenschlager, B.C. Marker, B.K. Moore, and R. Wildes, Strength Mechanism of Dental Solder Joints, *J. Dent. Res.*, Vol 53, 1974, p 1361–1367
44. R.A. Musin, V.A. Antsiverov, Y.A. Belikov, Y.V. Lyamin, and A.N. Solokov, The Effects on the Strength of the Joint of the Thickness of the Soft Interlayer in Diffusion Welding, *Auto. Weld.*, Vol 32, 1979, p 38–40
45. R.M. Trimmer and A.T. Kuhn, The Strength of Silver-Brazed Steel Joints—A Review, *Brazing Soldering*, Vol 2, 1982, p 6–13
46. N. Bredz and H. Schwartzbart, Triaxial Tension Testing and The Brittle Fracture Strength of Metals, *Weld. J.*, Vol 53 (No. 12), 1956, p 610s–615s
47. W.G. Moffatt and J. Wulff, Strength of Silver Brazed Joints in Mild Steel, *Trans. AIME*, Vol 209 (No. 4), 1957, p 442–445
48. R.Z. Shron and O.A. Bakshi, The Problems of Gauging the Strengths of Welded Joints in Which There is a Soft Interlayer, *Weld. Prod.*, Vol 9, 1962, p 19–23
49. O.A. Bakshi and A.A. Shatov, The Stressed State in Welded Joints with Hard and Soft Interlayers, *Weld. Prod.*, Vol 13, 1966, p 13–19
50. V.S. Golovchenko and B.A. Golobov, The Use of Silver as an Intermediate Layer for Joining Titanium to Other Metals, *Weld. Prod.*, Vol 18, 1971, p 55–57
51. G.K. Kharchenko and A.I. Ignatenko, The Strength of Joints with a Thin Soft Interlayer, *Auto. Weld.*, Vol 21, 1968, p 33–35
52. W.M. Leher and H. Schwartzbart, Static and Fatigue Strength of Metals Subjected to Triaxial Stresses, Vol 60, 1960, p 610–626
53. E.A. Almond, D.K. Brown, G.J. Davies, and A.M. Cottended, Theoretical and Experimental Interlayered Butt Joints Tested in Tension, *Int. J. Mech. Sci.*, Vol 25 (No. 3), 1983, p 175–189
54. G.A. Henshall, R.S. Rosen, M.E. Kassner, and R.G. Whirley, Finite Element Analysis of Interlayer Welds Loaded in Tension, *Weld. J.*, Vol 69 (No. 9), 1990, p 337s–345s
55. H.J. Saxton, A.J. West, and C.R. Barrett, The Effect of Cooling Rate on the Strength of Brazed Joints, *Metall. Trans.*, Vol 2, 1971, p 1019–1028
56. M.C. Tolle and M.E. Kassner, Tensile Properties of Thin Au-Ni Brazes Between Strong Base Metals, *Scr. Metall. Mater.*, Vol 26, 1992, p 1281–1284
57. M.E. Kassner, M.C. Tolle, R.S. Rosen, G.A. Henshall, and J.W. Elmer, Recent Advances in Understanding the Mechanical Behavior of Constrained Thin Metals in Brazes and Solid-State Bonds, *The Metal Science of Joining*, M.J. Cieslak, Ed., TMS, 1992, p 223–232
58. R.W. Logan, R.G. Castro, and A.K. Mukherjee, Mechanical Properties of Silver at Low Temperatures, *Scr. Metall.*, Vol 17, 1983, p 63–66

238 / Fundamentals of Solid-State Welding

59. T.J. Moore and K.H. Holko, Solid-State Welding of TD-Nickel Bar, *Weld. J.*, Vol 49 (No. 9), 1970, p 395s–409s
60. R.S. Rosen, “An Investigation of the Properties of a Silver-Aided Solid-State Bond Between Uranium and Stainless Steel,” Report UCRL-53458, Lawrence Livermore National Laboratory, 1983
61. E.R. Naimon, R.G. Kurz, D. Vigil, and L. Williams, “Silver Films for Solid State Bonding,” Report RFP-3125, Rockwell International, 1981
62. Z. Nisenholtz, J. Mironi, and N. Nir, Diffusion Bonding of Stainless Steel 304L to Ti-6Al-4V Alloy, *Proc. Third Int. Conf. Iso-static Pressing* (London, U.K.), 1986
63. M.E. Kassner, Oregon State University, unpublished research, 1989
64. A.T. Kuhn and R.M. Trimmer, Review of the Aqueous Corrosion of Stainless Steel-Silver Brazed Joints, *Br. Corros. J.*, Vol 17 (No. 1), 1982, p 4–8
65. T. Takemoto and I. Okamoto, Effect of Composition on the Corrosion Behavior of Stainless Steels Brazed with Silver-Base Filler Metals, *Weld. J.*, Vol 64, 1984, p 300s–307s

Arc Welding Processes

Introduction to Arc Welding	241	Shielded Metal Arc Welding	302
Arc Welding Fundamentals	241	The SMAW Process	302
Historical Development of Arc Welding	243	Applications	303
Arc Physics of Gas Tungsten and Gas Metal Arc Welding	249	Electrodes	303
Gas Tungsten Arc Physics	249	Weld Schedules and Procedures	304
Gas Metal Arc Physics	254	Variations of the SMAW Process	306
Qualification of Welding Procedures and Personnel	260	Underwater Welding	307
Purpose of Qualification and Responsibility for the Task	260	Repair Welding	307
Qualification of Welding Procedures	260	Safety Considerations	307
Qualification of Welding Personnel	265	Gas Metal Arc Welding	309
Qualification Documentation	265	Principles of Operation	309
General Design Considerations for Arc Welding Processes	266	Process Parameters	312
Nomenclature	266	Consumables	313
Types of Joints	266	Equipment	314
Types of Welds	267	Process Variations	316
Weld Joint Design	267	Safety Considerations	317
Fillet Welds	269	Plasma Gas Metal Arc Welding	318
Groove Preparation Welds	270	Equipment	318
Groove- and Fillet-Weld Combinations	271	Procedure	319
Edge Preparation	271	Applications	319
Butt Joints	273	Personnel	320
Corner Joints, Flange Joints, and Plug Welds	274	Hybrid Laser Arc Welding	321
T-Joints and Joints for Specific Applications	275	Advantages and Limitations	321
Joints Made by Submerged Arc Welding	276	Applications and Operating Modes	321
Power Sources for Arc Welding	277	Process Description	322
Power Source Characteristics	277	Joint Designs	324
Short Arc GMAW Power Sources	280	Equipment and Consumables	325
Multiple Arc (Multiple Operator) Power Sources	281	Sources of Defects	326
Power Source Selection Considerations	283	Quality Control and Inspection	327
Arc Welding Process Control	285	Safety	327
Overview on Welding Process Control	285	Flux Cored Arc Welding	329
Control System Requirements	285	Process Features	329
System Parameters	286	Applications	330
Sensing	287	Equipment	330
Modeling	289	Base Metals	331
Control of Arc Welding	290	Electrode Manufacture	332
Shielding Gases for Arc Welding	296	Electrode Diameters	333
Basic Properties of a Shielding Gas	296	Electrode Classification	333
Shielding Gas Blends	297	Submerged Arc Welding	335
Shielding Gas Selection	297	Principles of Operation	335
Influence of Shielding Gas on Weld Mechanical Properties	300	Process Applications	336
Shielding Gas and Fume Generation	300	Automatic SAW Power Source and Equipment	337
Self-Shielded Flux Cored Arc Welding	301	SAW Fluxes	337
		Electrodes for SAW	338

Weld-Metal Considerations	339	Typical Components and Joints	362
SAW Process Parameters.	339	Operations	363
Defects in SAW	341		
Training and Safety	343	Electroslag and Electrogas Welding	365
Gas Tungsten Arc Welding	344	Fundamentals of the Electroslag Process	365
Applications.	345	Constitutive Equations for Welding Current, Voltage, and	
Principle of Operation.	346	Travel Rate.	368
Equipment	347	Temperature Relations between the Slag Bath and Electrode in ESW .	369
GTAW Welding Procedures.	351	ESW Thermal Cycles Equations.	369
Safety When Using GTAW	353	ESW Consumables	370
Acknowledgments.	354	Metallurgical and Chemical Reactions	372
		Electroslag Process Development	373
Gas Tungsten Arc Welding with Penetration-Enhancing		Electrogas Welding	374
Compounds	355	Electroslag and Electrogas Process Applications.	375
Principles of Operation	355	Problems and Quality Control	376
Advantages and Disadvantages.	355	Stud Arc Welding	380
Equipment, Procedures, and Applications	356	Process Overview	380
Personnel.	357	Fixturing and Tooling for Stud Arc Welding	385
		Stud-Welding Quality Control, Qualification, and Inspection . . .	388
Plasma Arc Welding	359	Stud-Welding Safety Precautions	390
Principles of Operation	359	Capacitor Discharge Stud Welding	391
Advantages and Disadvantages.	360	Applications.	391
Equipment	360	Equipment	392
Applications.	361	Personnel Responsibilities	392

Introduction to Arc Welding*

ARC WELDING is one of several fusion processes for joining metals. By the application of intense heat, metal at the joint between two parts is melted and caused to intermix directly or, more commonly, with an intermediate molten filler metal. Upon cooling and solidification, a metallurgical bond results. Since the joining is by intermixture of the substance of one part with the substance of the other part, with or without an intermediate of like substance, the final weldment has the potential for exhibiting at the joint the same strength properties as the metal of the parts. This is in sharp contrast to nonfusion processes of joining, such as soldering, brazing, or adhesive bonding, in which the mechanical and physical properties of the base materials cannot be duplicated at the joint.

In arc welding, the intense heat needed to melt metal is produced by an electric arc. The arc is formed between the work to be welded and an electrode that is manually or mechanically moved along the joint (or the work may be moved under a stationary electrode). The electrode may be a carbon or tungsten rod, of which the sole purpose is to carry the current and sustain the electric arc between its tip and the workpiece. Or, it may be a specially prepared rod or wire that not only conducts the current and sustains the arc but also melts and supplies filler metal to the joint. If the electrode is a carbon or tungsten rod and the joint requires filler-metal addition, that metal is supplied by a separately applied filler-metal rod or wire. However, most welding in the manufacture of steel products where filler metal is required is accomplished with the second type

of electrodes: those that supply filler metal as well as provide the conductor for carrying electric current.

This article introduces the fundamentals of arc welding, which is described in more detail in other articles on specific topics. This article also provides a brief summary of the history and early discoveries of arc welding. For many centuries, the only method man had for metallurgically joining metals was forge welding, a crude and cumbersome blacksmith-type operation in which heated metals were pounded or rammed together until they bonded. Then, within the span of a few years prior to 1900, three new processes came into existence. Arc welding and resistance welding were developed in the late 1880s and put to work in industry a few years later. Oxyacetylene welding was developed during the same period and was first used industrially in the early 1900s.

Today (2011), a wide variety of arc welding processes are used, as described further in separate articles. A general comparison of the most commonly used processes relative to some general application factors is summarized in Table 1. Although some of the ratings are subjective, they provide a general overview of the different processes. The general ratings encompass broad variation depending on application. For example, the rating of fair to excellent for FCAW in the field covers the broad range of alloys that might be used, and the difference between gas-shielded and self-shielded. Productivity (weld metal deposited per hour) is often a key factor, but the other factors in Table 1 also must be considered, as a minimum, when

selecting a welding process. Selection may involve a balance of productivity and weld quality, and each process has a number of conflicting advantages and limitations in specific situations.

Arc Welding Fundamentals

The basic arc welding circuit is illustrated in Fig. 1. An alternating current (ac) or direct current (dc) power source, fitted with whatever controls may be needed, is connected by a ground cable to the workpiece and by a "hot" cable to an electrode holder of some type, which makes electrical contact with the welding electrode.

When the circuit is energized and the electrode tip touched to the grounded workpiece

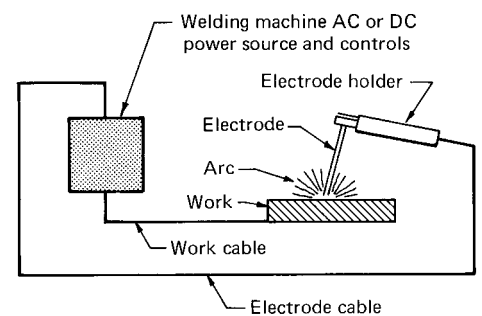


Fig. 1 Basic arc welding circuit. ac, alternating current; dc, direct current

Table 1 General application characteristics of selected arc welding processes

Parameter or characteristic	Process(a)					
	SMAW	GTAW	GMAW	FCAW	SAW	
Weld quality	Good	Excellent	Excellent	Good	Excellent	
Weld deposition rate	Fair	Poor	Good	Good	Excellent	
Field work	Excellent	Poor	Fair/good	Fair/good	Poor	
Equipment maintenance	Low	Low	Medium/high	Medium/high	Medium	
Smoke/fume emission	Medium/high	Low	Medium	Medium/high	Very low	
Heat input control	Good	Poor	Good	Good	Excellent	
Arc visibility and filler-metal placement	Good	Excellent	Satisfactory	Satisfactory	Not applicable(b)	
Variety of metals weldable	Excellent	Excellent	Good	Good	Fair	

(a) SMAW, shielded metal arc welding; GTAW, gas tungsten arc welding; GMAW, gas metal arc welding; FCAW, flux cored arc welding; SAW, submerged arc welding (b) Arc visibility is not applicable for SAW, as electrode placement is established prior to welding

*Adapted with permission from *The Procedure Handbook of Arc Welding*, 13th ed., The Lincoln Electric Company, 1995. Courtesy of The James F. Lincoln Arc Welding Foundation.

and then withdrawn and held close to the spot of contact, an arc is created across the gap. The arc produces a temperature of approximately 3590 °C (6500 °F) at the tip of the electrode, a temperature more than adequate for melting most metals. The heat produced melts the base metal in the vicinity of the arc and any filler metal supplied by the electrode or by a separately introduced rod or wire. A common pool of molten metal is produced, called a crater. This crater solidifies behind the electrode as it is moved along the joint being welded. The result is a fusion bond and the metallurgical unification of the workpieces.

What takes place immediately under the welding arc is similar to what happens in an electric furnace for metal production. Electrical furnace steels are premium grades; weld metal from steel electrodes is newly prepared electric-furnace steel and also premium grade. Properly executed welds are almost always superior in mechanical properties to the metals they join. In no other metals-joining process is the joint customarily stronger than the metals joined. However, the heat during arc welding also can cause various metallurgical effects in the weld metal and the adjacent base metal.

Arc Shielding

Joining metals with the heat of an electric arc, however, requires more than the moving of the electrode with respect to the weld joint. Metals at high temperatures are chemically reactive with the main constituents of air: oxygen and nitrogen. Should the metal in the molten pool come in contact with air, oxides and nitrides would be formed, which upon solidification of the molten pool would destroy the strength and toughness properties of the weld joint. For this reason, the various arc welding processes provide some means for covering the arc and the molten pool with a protective shield of gas, vapor, or slag. This is referred to as arc shielding. Arc shielding may be accomplished by various techniques, such as the use of vapor-generating and/or slag-forming coverings on filler-metal-type electrodes, the covering of the arc and molten pool with a separately applied inert gas, or a granular flux. The use of materials within the core of tubular electrodes also generates shielding vapors and slag.

Whatever the shielding method, the intent is to provide a blanket of gas, vapor, or slag that prevents or minimizes contact of the molten metal with air. The shielding method also affects the stability and other characteristics of the arc. When the shielding is produced by an electrode covering, by electrode core substances, or by separately applied granular flux, a fluxing or metal-improving function is usually also provided. Thus, the core materials in a flux cored electrode may supply a deoxidizing function as well as a shielding function. In submerged arc welding, the granular flux applied to the joint ahead of the arc may add

alloying elements to the molten pool as well as shielding it and the arc.

Figure 2 illustrates the shielding of the welding arc and molten pool with a covered "stick" electrode, the type of electrode used in most manual arc welding. The extruded covering on the filler-metal rod, under the heat of the arc, generates a gaseous shield that prevents air from contacting the molten metal. It also supplies ingredients that react with deleterious substances on the metals, such as oxides and salts, and chemically ties up these substances in a slag that, being lighter than the weld metal, rises to the top of the pool and crusts over the newly solidified metal. This slag, even after solidification, has a protective function; it minimizes contact of the very hot solidified metal with air until the temperature falls to a point where reaction of the metal with air is reduced.

While the main function of the arc is to supply heat, it has other functions that are important to the success of arc welding processes. It can be adjusted or controlled to transfer molten metal from the electrode to the work, to remove surface films, and to bring about complex gas-slag-metal reactions and various metallurgical changes. The arc itself is a very complex phenomenon that has been intensively studied. In-depth understanding of the physics of the welding arc is of little value to the welder, but some knowledge of its general characteristics is introduced in the following section, with more details given in the article "Arc Physics of Gas Tungsten and Gas Metal Arc Welding" in this Volume.

Nature of the Arc

An arc is an electric current flowing between two electrodes through an ionized column of gas, called a plasma. The space between the two electrodes or, in arc welding, the space between the electrode and the work can be divided into three areas of heat generation: the cathode, the anode, and the arc plasma (Fig. 3).

The welding arc is characterized by a high-current, low-voltage arc that requires a high concentration of electrons to carry the current. Negative electrons are emitted from the cathode and flow, along with the negative ions of the plasma, to the positive anode. Positive ions flow in the reverse direction. A negative ion is an atom that has picked up one or more electrons beyond the number needed to balance the positive charge on its nucleus, thus the negative charge. A positive ion is an atom that has lost one or more electrons, thus the positive charge. However, just as in a solid conductor, the principal flow of current in the arc is by electron travel.

Heat is generated in the cathode area mostly by the positive ions striking the surface of the cathode. Heat at the anode is generated mostly by the electrons. These have been accelerated as they pass through the plasma by the arc voltage, and they give up their energy as heat when striking the anode.

The plasma, or arc column, is a mixture of neutral and excited gas atoms. In the central column of the plasma, electrons, atoms, and ions are in accelerated motion and constantly colliding. The hottest part of the plasma is the central column, where the motion is most intense. The outer portion or the arc flame is somewhat cooler and consists of recombining gas molecules that were disassociated in the central column.

The distribution of heat or voltage drop in the three heat zones can be changed. Changing the arc length has the greatest effect on the arc plasma. Changing the shielding gas can change the heat balance between the anode and cathode. The addition of potassium salts to the plasma reduces the arc voltage because of increased ionization.

The difference in the heat generated between the anode and cathode can determine how certain types of arcs are used. For example, when gas tungsten arc welding of aluminum using argon gas, the electrode as a cathode (negative) can use approximately 10 times more current without melting than when used as an anode (positive). This indicates that more heat is generated at the anode than at the cathode. The submerged arc welding process generates more heat at the cathode rather than the anode, as

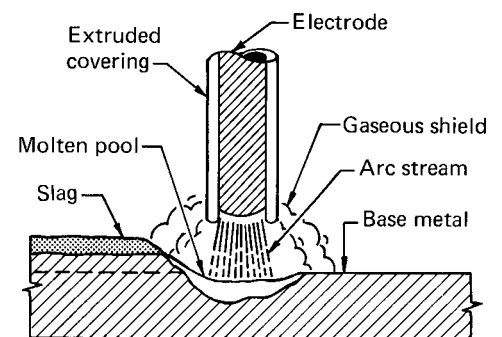


Fig. 2 The coating on a coated (stick) electrode provides a gaseous shield around the arc and a slag covering on the hot weld deposit.

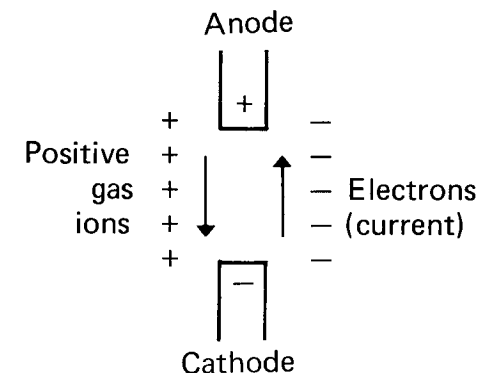


Fig. 3 Areas of heat generation in the arc

evidenced by the higher melt-off rate when the electrode is negative. The same is also true for EXX10 stick-electrode welding.

In welding, the arc not only provides the heat needed to melt the electrode and the base metal but, under certain conditions, must also supply the means to transport the molten metal from the tip of the electrode to the work. Several mechanisms for metal transfer exist. In one, the molten drop of metal touches the molten metal in the crater, and transfer is by surface tension. In another, the drop is ejected from the molten metal at the electrode tip by an electric pinch. It is ejected at high speed and maintains this speed unless slowed by gravitational forces. It may be accelerated by the plasma, as in the case of a pinched plasma arc. These forces are the ones that transfer the molten metal in overhead welding. In flat welding, gravity also is a significant force in metal transfer.

If the electrode is consumable, the tip melts under the heat of the arc, and molten droplets are detached and transported to the work through the arc column. Any arc welding system in which the electrode is melted off to become part of the weld is described as metal arc. If the electrode is refractory—carbon or tungsten—there are no molten droplets to be forced across the gap and onto the work. Filler metal is melted into the joint from a separate rod or wire.

More of the heat developed by the arc is transferred to the weld pool with consumable electrodes than with nonconsumable electrodes. This produces higher thermal efficiencies and narrower heat-affected zones. Typical thermal efficiencies for metal arc welding are in the range of 75 to 80% and for welding with nonconsumable electrodes, 50 to 60%.

Because there must be an ionized path to conduct electricity across a gap, the mere switching on of the welding current with a cold electrode posed over the work will not start the arc. The arc must first be ignited. This is accomplished either by supplying an initial voltage high enough to cause a discharge or by touching the electrode to the work and then withdrawing it as the contact area becomes heated. High-frequency spark discharges are frequently used for igniting gas-shielded arcs, but the most common method of striking an arc is the touch-and-withdraw method.

Arc welding may be done with dc, with the electrode either positive or negative, or with ac. The choice of current and polarity depends on the process, the type of electrode, the arc atmosphere, and the metal being welded. Whatever the current, it must be controlled to satisfy the variables—amperage and voltage—that are specified by the welding procedures.

Overcoming Current Limitations

The objective in commercial welding is to get the job done as fast as possible without sacrificing quality, so as to lessen the labor-time

costs of skilled workers. One way to speed the welding process would be to raise the current (use a higher amperage), because the faster the electrical energy can be induced in the weld joint, the faster will be the welding rate.

With manual stick-electrode welding, however, there is a practical limit to the current. The covered electrodes are from 23 to 46 cm (9 to 18 in.) long, and, if the current is raised too high, electrical resistance heating within the unused length of the electrode will become so great that the covering overheats and breaks down; that is, the covering ingredients react with each other or oxidize and do not function properly at the arc, or the coating simply falls off of the electrode. Also, the hot core wire increases the melt-off rate, and the arc characteristics change. The mechanics of stick-electrode welding are such that electrical contact with the electrode cannot be made immediately above the arc, a technique that would circumvent much of the resistance heating.

Not until the development of semiautomatic guns and automatic welding heads, which are fed by continuous-electrode wires, was there a way of solving the resistance-heating problem and thus making feasible the use of high currents to speed the welding process. In such guns and heads, electrical contact with the electrode is made close to the arc. The length between the tip of the electrode and the point of electrical contact is then inadequate for enough resistance heating to take place to overheat the electrode in advance of the arc, even with currents two or three times those usable with stick-electrode welding.

This solving of the point-of-contact problem and circumventing the effects of resistance heating in the electrode was a breakthrough that substantially lowered welding costs and increased the use of arc welding in industrial metals joining. In fact, through the ingenuity of welding equipment manufacturers, the resistance-heating effect has been put to work constructively in a technique known as long-stickout welding. Here, the length of electrode between the point of electrical contact in the welding gun or head and the arc is adjusted so that resistance heating almost, but not quite, overheats the protruding electrode. Thus, when a point on the electrode reaches the arc, the metal at that point is almost ready to melt. Thus, less arc heat is required to melt it, and, because of this, still higher welding deposition rates and speeds are possible.

Historical Development of Arc Welding

As noted, forge welding was the only method man had for metallurgically joining metals for many centuries. No one knows when man first learned to use forge welding. The working and hardening of steel—advanced arts that doubtless took centuries to evolve—were commonly

practiced 30 centuries ago in Greece. However, primitive tribes on different continents, and with no apparent means of communication, developed the same basic methods for smelting, shaping, and treating iron. Thus, the principles of welding probably were discovered, lost, and rediscovered repeatedly by ancient peoples.

By the time of the Renaissance, craftsmen were highly skilled in forge welding. Parts to be joined were shaped and then heated in a forge or furnace before being hammered, rolled, or pressed together. Vannoccio Biringuccio's *Pyrotechnia*, published in Venice in 1540, contains several references to such operations. Biringuccio was obviously intrigued by the process, because he wrote, "This seems to me an ingenious thing, little used, but of great usefulness."

For a few centuries thereafter, ordinary fire remained the principal source of heat for welding. The traveling tinker, a familiar figure on the dusty roads of the countryside, carried with him a small charcoal furnace for heating his irons. During this era, tinsmiths and other workers in metal often used the heat of burning gases to braze and solder.

Forge welding of iron developed into a recognized industry. However, the joining of large, heavy pieces required great skill and much labor, because they could be brought to the required temperature only if a fire were maintained around them. When the two parts were hot enough, they were forced together by various means and were often hung from cranes for this operation. The ends were struck repeatedly with a sledge hammer while the heat was maintained. Then, the work was withdrawn from the fire and finished on an anvil. Forge welding is still practiced today (2011) but to a very limited extent.

Just prior to 1900, three new processes changed the manner in which metals were joined together:

- Arc welding
- Resistance welding
- Oxyacetylene welding

Of these three new processes, arc welding has emerged as the most widely used and commercially important method. There is evidence that a Professor G. Lichtenberg may have joined metals by electric fusion as early as 1782 in Germany, but most accounts trace the history of electric welding to the discovery of the electric arc by Sir Humphrey Davy. In 1801, while experimenting with the infant science of electricity, Davy discovered that an arc could be created with a high-voltage electric circuit by bringing the two terminals near each other. This arc, which cast a bright light and gave off considerable heat, could be struck and maintained at will, and its length and intensity could be varied within limits determined by the circuit voltage and by the type of terminals used. Davy demonstrated the arc at the Royal Institute of England in 1808, where his discovery aroused a great deal of interest. For many years, however, it remained a scientific plaything; there appeared to be no practical use

for the phenomenon. In fact, Davy did not apply the term *arc* to his discovery until 20 years later.

After the discovery of the arc, the first person known to intentionally join metals by electric welding was an Englishman named Wilde. In the early 1860s, he melted together small pieces of iron, and, in 1865, he was granted a patent on his process—the first patent relating to electric welding.

The electric arc, however, remained of scientific interest only until 1881, when the carbon arc street lamp was introduced. Shortly thereafter, the electric furnace made its appearance in England. One of the earliest was installed in 1886 for the production of aluminum alloys. This particular application of the electric arc was an important step in the early development of the aluminum industry.

New Welding Methods Are Put to Work

Probably the first attempt to use the intense heat of the carbon arc for welding was made in 1881 when Auguste de Meritens used a carbon electrode to arc weld lead storage-battery plates. In this experiment, de Meritens connected the work to the positive pole of a current source and attached a carbon rod to the negative pole in such a manner that the distance between the rod and plate could be controlled. Some of the heat developed was lost to the surrounding air, but enough reached the plate to fuse the lead and join the parts. Other early efforts with arc welding employed carbon electrodes arranged similarly to the positions of electrodes in an arc lamp. The heat of the arc was deflected against the work by magnetic fields or by a jet of compressed air.

Two other scientists, Nikolas de Benardos and Stanislaw Olszewski, were interested in the de Meritens process and experimented with it. In 1885, they were issued a British patent for a welding process employing carbon electrodes (Fig. 4). A voltaic arc is formed by the approach of carbon to the part of the metal operated upon, the carbon usually forming the positive pole and the metal the other pole. The carbon, which may be solid or hollow, is fixed in an apparatus, one form of which is shown in Fig. 4. The frame “A,” having a jointed lever

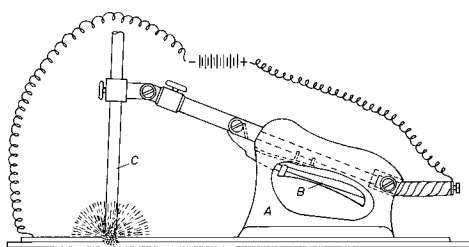


Fig. 4 Apparatus for applying a fused metallic coating for ornamental or other purposes in the British welding patent 12,984 issued to N. de Benardos and S. Olszewski on October 28, 1885. Layers of metal are formed by holding an insulated stick of metal in the electric arc. See text for description.

“B” to lower the carbon “C,” is insulated and supported on the plate or held in the hand. The frame may have wheels running on rails. The work may be supported on an insulated electrically connected plate.

Benardos, a Russian, also filed for a patent in his homeland. His application described a process in which the work was connected to a negative pole, and the carbon rod was fastened to the positive pole of a dc circuit. The rod was not fixed, as in de Meritens’ method, but was fitted with an insulated handle so that it could be manipulated by hand. This process was patented in 1887. Thus, Benardos is generally credited as the holder of the first patent on arc welding.

Benardos’ carbon arc process was put to work on a limited scale in England soon after it was developed. In 1887, a shop was using it to make tanks, casks, and iron garden furniture. In the 1890s, another English shop was welding wrought iron pipe up to a foot in diameter. In the United States, the Baldwin Locomotive Works established a shop in 1892, where carbon arc welding was used extensively for locomotive maintenance. In general, acceptance of the carbon arc process was slow, because the procedures used at that time introduced particles of carbon into the weld metal. These particles made the welded joint hard and brittle.

In the early days of arc welding, a bank of storage batteries was used as the power source (Fig. 5). Voltage could be controlled by the number of cells placed in series. Current could be controlled by the number of cells in parallel and by series resistors. The batteries were kept charged by dynamos or generators, powered by the shop steam engine or water wheel.

Two years after Benardos’ patent was granted, another Russian, N.G. Slavianoff, announced a process in which the carbon electrode was replaced by a metal rod. After an arc was struck, the rod gradually melted and added fused metal to the weld. In the same year, 1889, unaware of Slavianoff’s work, Charles Coffin was granted a U.S. patent on a similar metal arc welding process. (Coffin later became president of General Electric Company.)

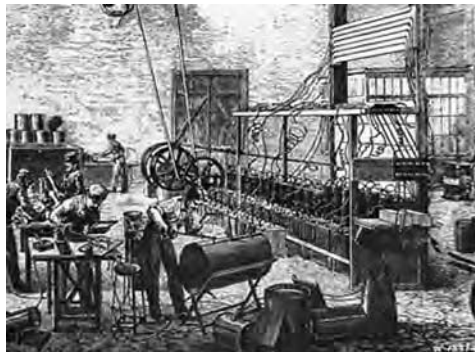


Fig. 5 Carbon arc welding shop of the late 1800s. The power source is a bank of batteries. Note the dynamo on the right.

The metal arc process simultaneously developed by Coffin and Slavianoff represented a giant step forward, because the metal electrode supplied not only fusing heat but also added additional filler metal necessary for the joint. In the carbon arc process, filler metal was supplied by excess metal along the weld line or by a metal rod held in the welder’s hand. Despite this advance in the technology, commercial application of the metal arc process in the following years was slow because satisfactory metal electrodes were not available.

Commercial Arc Welding Comes to America

Two Germans who had been working on the metal arc process in Europe came to the United States in 1907. They formed the Siemund-Wienzell Electric Welding Company and patented a metal arc welding method. A short time later, another German concern, Enderlein Electric Welding Company, also started operations in the United States. Then, a bit of intrigue was attempted. It is reported that Enderlein offered to ensure the validity of the Siemund-Wienzell patent by violating it, then putting up a weak defense when Siemund-Wienzell sued. The condition was that the two companies would then share the patent rights. Siemund-Wienzell refused the proposal. When Enderlein began using the process, the firm was promptly and sincerely sued.

In the suit, the patent holders were completely confounded when Enderlein introduced a copy of *Mechanics Handbook*, published in England in 1888. This handbook contained a woodcut unmistakably showing a shop using the metal arc process, and its publication date was before any patents had been issued. This revelation cast doubt on the validity of any patents on the process and, by so doing, opened the field of metal arc welding in the United States.

By 1917, there were four well-established manufacturers of arc welding equipment in the United States. One of these was The Lincoln Electric Company, which today (2011) is the world’s largest producer of arc welding equipment. Lincoln began experimenting with welding in 1902 and introduced its first machines in 1912 (Fig. 6).



Fig. 6 Portable arc welder of the early 1920s

Electrodes—The Key to Progress

In the early work with metal arc welding, it was apparent that the limiting factor was the electrode. The earliest electrodes were bare wire of Norway or Swedish iron, which produced brittle, weak welds. The arcs often overheated the weld metal, and the metal deposited by the electrode was embrittled by the reaction with the air. In an attempt to overcome these difficulties, researchers developed a number of electrodes that were lightly coated with various organic or mineral materials. Oscar Kjellborg of Sweden, who received a patent in 1907, is credited with being one of the pioneer developers of covered electrodes.

The coverings developed during this time did more to stabilize the arc than to shield or purify the weld metal. It was not until 1912, when Strohmenger obtained a U.S. patent for a heavily covered electrode, that industry had an electrode capable of producing weld metal with good mechanical properties. The early covered electrodes, however, were slow in gaining acceptance because of their cost. The covering process required expensive production operations, involving the application of fine aluminum wire and other materials.

The Impetus Onward—World War I

The first major increase in the use of welding occurred during World War I. The sudden need for large numbers of transport ships was a contributing factor. At the onset of the war, ships were built by the relatively slow process of riveting. Government officials realized that faster manufacturing methods were needed, and an Emergency Fleet Corporation was set up to find improved shipbuilding methods. Professor Comfort Adams of Harvard was asked to appoint a committee to investigate the problem, and in July 1917, the first committee meeting was held.

Many members of this committee were of the opinion that the key to increased production would be found in resistance welding, a process that had been invented in 1886 by Professor Elihu Thomson, a member of the committee. To gather background information, the committee visited England, where shipbuilders were using welding to some extent. There the committee discovered that it was arc, not resistance, welding that the British were using. Forced by gas shortages to curtail gas welding, England was using arc welding with both bare and covered metallic electrodes to produce bombs, mines, and torpedoes. The British had gone so far as to start construction of a ship with an all-welded hull.

The American committee returned as proponents of the arc welding method. The various supporters of gas and resistance welding, however, would not accept their findings at face value, and the subsequent debate included the relative merits of carbon and metal electrodes,

covered and bare-metal electrodes, and direct and alternating current.

During this discussion, a dramatic incident publicized the capabilities of arc welding. German ships interned in New York Harbor at the outbreak of the war had been scuttled by their crews so that the vessels could not be used in the Allied war effort. Damage was so extensive that revolutionary repair processes were clearly needed if the ships were to be put back into service without long delay. The Navy called in welding experts from two railroad companies, and these men recommended that repairs be made by arc welding. Most of the damaged components were subsequently repaired by this process, and the ships were rapidly returned to service. The potential of the process was clearly established.

In Europe, at approximately the same time, an all-welded cross-channel barge had been put in service. Also, the British launched their all-welded ship, the *Fulagar*, in 1920. Arc welding thus became an accepted process for shipbuilding.

The first application of arc welding to aircraft also occurred during World War I. Anthony Fokker, the Dutch airplane manufacturer, used the process to produce fuselages for some German fighter planes.

The Era of Slow Growth

In the years immediately following the war, applications for arc welding did not increase appreciably. In 1919, a patent was granted for a paper-covered electrode that did not leave a slag coating on the joint yet produced a tough, ductile weld. This welding electrode was used in 1925 to fabricate heavy pressure vessels for oil refineries. A three-span, 150 m (500 ft), all-welded bridge was erected in 1923 in Toronto, Canada. At approximately this time, manufacturers began to use arc welding increasingly for building storage tanks for fuel oil, gasoline, and petroleum distillates. An early application of large proportions was the construction of a million-gallon standpipe that stood 39 m (127 ft) high.

In 1928, the steel framework for the upper Carnegie Building in Cleveland, Ohio, was erected, using arc welding in a joint effort by The Austin Company and The Lincoln Electric Company (Fig. 7). Construction of this building brought out several important advances in construction techniques. No connection angles or plates were used at intersections, as commonly required with riveted assembly. Because welded lattice joists were used, piping could be concealed between floors. The building was 18 by 36 m (60 by 119 ft) and four stories high. The 115 tons of steel required was estimated to be 15% less than required for a riveted design. A factor contributing to this savings was the use of continuous beams, which permitted lighter beams and columns with no sacrifice in strength or rigidity.

In the 1920s, manufacturers were also using arc welding in the production of sheet steel fabrications, such as hot water tanks (Fig. 8), blower fans, air conduits, housings for machinery, and bases for machine tools. Foreseeing the potential, the arc welding industry began advocating the conversion of cast iron parts to welded assemblies.

In 1927, the development of an extrusion process for applying a covering to the metal core substantially lowered the cost of covered electrodes. These lower-cost electrodes proved to be one of the most significant developments in the evolution of arc welding. The extrusion process permitted varying the composition of the electrode covering to give desirable operating characteristics and meet specific application requirements. The shielded arc electrode, with its deoxidizers and protective gases and slag, became feasible.



Fig. 7 This building was erected in 1928 using arc welding and bare-wire electrodes.



Fig. 8 Early machine for welding the longitudinal seam in a hot water tank with an automatic carbon arc welding head.

Years of Rapid Advance

The applications for arc welding grew rapidly after 1929, and, by the onset of World War II, the process was becoming the dominant welding method. Prior to 1929, the largest undertaking involving welding was the construction of a 1.5 m (5 ft) diameter, 145 km (90 mile) pipeline for carrying water to cities east of San Francisco Bay. It was estimated that this pipeline would have leaked enough water to supply a city of 10,000 if riveted construction had been used. Leakage was minimal with welding.

In the 1930s, welding became increasingly important in shipbuilding (Fig. 9). The U.S. Navy, which had contributed much to welding research, turned to the process for practical reasons after the London Naval Treaty of 1930. This treaty imposed limits on the gross tonnages of the major navies of the world, and thereafter, the Navy often found welding advantageous to minimize weight and thereby maximize the firepower permitted by the tonnage restriction. For the same reason, the Germans used arc welding in their pocket battleships, three of which were launched from 1931 to 1934. Armor plate was difficult to weld, and the Germans developed a method for satisfactorily welding it.

In 1930, the first all-welded merchant ship was built in Charleston, South Carolina. This ship was the forerunner of the thousands of all-welded ships that were to be produced during World War II. Also in the 1930s, the U.S. Army became interested in welding, and a considerable amount of ordnance equipment was redesigned at the Watertown Arsenal for production by welding.

In approximately 1935, improved ac machines (or welders) were becoming available. These welders offered certain advantages, but ac arcs often proved difficult to maintain. To overcome this difficulty, producers of electrodes developed coverings that ionized more easily and thus stabilized the arc. Also during this decade, more stainless steels came into use in metalworking. These materials were relatively difficult to weld because hydrogen in the electrode coverings often caused porosity in the weld. Low-hydrogen electrode coverings were developed to overcome this difficulty.



Fig. 9 All-welded naval vessel that won a major award in a design competition in 1932.

Then, in the early 1940s, it was discovered that these low-hydrogen electrodes also provided good welds in armor plate. Stainless steel coverings were applied to low-alloy steel electrodes to further improve the quality of welded joints in armor plate.

During the 1930s, numerous attempts were made to bring some degree of mechanization with good shielding to the arc welding processes (Fig. 10). The early attempts at automatic welding were made with continuously-fed bare wire, with no shielding other than a thin slag flux that was sometimes painted on the workpiece. Shielding for automatic carbon arc welding was provided by passing a flux-impregnated paper string near the arc as it traveled along the seam. In 1932, an innovation was introduced. A heavy layer of flux was placed on the seam ahead of the carbon electrode. The heat of the arc melted the flux into a slag, which provided shielding. The development proved successful, and penstocks for the Tennessee Valley Authority project and water conduit for the Los Angeles Water Authority were welded by this precursor to the submerged-arc welding process.

Advances in welding fabrication also led to design innovations, such as the Hortonspheroids (Fig. 11). Chicago Bridge and Iron Company, after having invented the design, built



Fig. 10 Welding a steel beer barrel (1933)

many of these vessels between approximately 1930 and 1960 for storage of volatile liquids. The unique geometry makes the most efficient use of the steel shell plates by balancing the latitudinal and longitudinal membrane stresses. (Today, however, most of these vessels have been retired or derated from pressure service, because the unique geometry presents a challenge in the inspection and evaluation of vessel integrity.)

Use of a granular flux with a continuously-fed bare-steel electrode led to development in 1935 of the submerged arc process, which found its first major use in pipe fabrication and shipbuilding. A 159 m (521 ft) tanker was fabricated by this process in 1936. By 1940, the submerged arc process was well accepted but had proved practical primarily on steel plate over 6.3 mm ($\frac{1}{4}$ in.) thick. In approximately 1942, the process was improved to accommodate stock down to 2.4 mm ($\frac{3}{32}$ in.) thick and thus become feasible for automotive use and for general metal fabrication.

Hand-held, semiautomatic guns (Fig. 12) were developed for the submerged arc process in 1946. Voltage and current were controlled automatically, so that weld quality was uniform and results varied less with operator skill. Multiple arcs were introduced in 1948, primarily for manufacturing pipe with 6.3 to 12.7 mm ($\frac{1}{4}$ to $\frac{1}{2}$ in.) walls in diameters from 46 to 91 cm (18 to 36 in.). Subsequent improvements in submerged arc welding have been mainly in the areas of improved fluxes and more sophisticated welding equipment and controls.

One problem that continued to defy solution was the joining of the reactive metals aluminum and magnesium. Neither the submerged arc process nor covered electrodes provided enough shielding to adequately protect these metals from atmospheric contamination. To overcome this difficulty, welding engineers began to use bottled inert gases as shielding agents in the early 1930s. Later in that decade, successful gas-shielded processes powered by direct current (dc) began to emerge from the aircraft industry in response to a specific need to weld magnesium.

The first gas-shielded process employed a tungsten electrode and helium shielding gas



Fig. 11 Chicago Bridge and Iron Company Hortonspheroid of 80,000 barrel capacity in southern Texas (May 1940)

and became known as the the HeliArc process, as well as the gas tungsten-arc (GTA) or tungsten inert-gas (TIG) process. Initially, direct current and a positive electrode were used. It was found, however, that the tungsten electrode tended to overheat and transfer particles of tungsten to the weld unless a low current was used. Researchers then discovered that overheating could be avoided by making the electrode negative. This change proved satisfactory for welding stainless steel but still was not suitable for magnesium or aluminum. The next development was the use of ac with a high-frequency, high-voltage current superimposed over the basic welding current to stabilize the arc. This proved to be the solution to the problem of making good welded joints in aluminum and magnesium. In 1953, the tungsten arc process was modified by directing the arc through a nozzle, and the resulting method became known as the plasma arc process.

Postwar Developments Continue

The tungsten arc process proved unsatisfactory for welding thick sections of highly conductive materials because the workpieces tended to act as heat sinks. To overcome this difficulty, a consumable metal electrode was substituted for the nonconsumable tungsten electrode. The resulting process, announced in 1948, became known as gas metal arc (GMA) or metal inert-gas (MIG) welding. It proved successful for welding aluminum and was subsequently adapted for other nonferrous materials and for stainless and mild steels. About this time, studies showed that a more stable arc could be obtained by using gas mixtures instead of pure helium or argon.

An important development in manual covered-electrode welding also occurred in this era, namely, the use of iron powder in electrode coverings. One benefit of iron powder in the covering was a higher deposition rate and thus greater welding speed. Another was that the welder could simply drag the electrode along the seam without trying to hold it a fixed distance from the work. Thus, less skill was required, and proper welding technique could more easily be taught to beginners. The disadvantage of the iron powder in the covering was the high manufacturing cost. However, by 1953, advances in manufacturing technology and electrode design resulted in cost reductions that made possible the marketing of iron-powder electrodes at acceptable prices. The use of iron-powder electrodes became widespread.

As the gas metal arc and gas tungsten arc processes gained acceptance in the early 1950s, users found that shielding gases based on argon or helium were often too costly. To lower the material cost of the processes, researchers turned to one of the early developments in arc welding, using carbon dioxide gas as a shielding agent. John C. Lincoln, founder of The Lincoln Electric Company,

had applied for a patent on this idea in 1918. Refinements in both the process and equipment for welding steel using carbon dioxide as a shielding gas resulted in a low-cost process. This was immediately adopted by automotive shops and other metalworking plants for applications where the quality of the weld was not exceedingly critical.

One of the most significant developments of the period was the Innershield process, introduced by Lincoln Electric in 1958 for the welding of steel. Prior to its development, self-shielded processes derived protective gases from the decomposition of chemical coverings on the electrode. One could envision possibilities in mechanization with the covered electrode if it could be fed to the arc from a continuous coil. The coverings of such electrodes, however, tended to crack if wound into a coil, and also there was no practical way to feed electric current to a covered continuous electrode. Therefore, self-shielded electrodes as constituted could not be used with automatic or semiautomatic processes.

The Innershield process, also referred to as the self-shielded, flux cored arc welding process, solved the problem by incorporating the fluxing and shielding materials inside tubular filler-metal wire. The result was a self-shielded electrode that could be coiled and used with high-speed automatic and semiautomatic equipment. Some of the carbon-dioxide-shielded processes also began to employ a flux cored electrode at this time. The concept of a tubular electrode sheath to contain a powdered processing ingredients had been employed prior to 1958 but was limited to electrodes for surfacing applications.

In 1961, the Innershield electrode was introduced, providing exceptionally high deposition rates. This electrode, referred to as a fast-fill electrode, is widely used in semiautomatic welding (Fig. 13). Because heat input with the fast-fill electrode was considerably less than required by older types, the automatically-fed electrode holders, or welding guns, developed for its use did not require water cooling and thus were lightweight and easy to manipulate. The electrode produced welds that had good resistance to cracking and operational characteristics that lessened the amount of care required to fit up workpieces prior to welding.

When first introduced, the fast-fill electrode was limited to single-pass welds in the flat or horizontal positions. By 1962, fast-fill electrodes were available for multiple-pass welds. Thick plates could thus be welded at high deposition rates. In 1967, an all-position electrode was introduced that considerably broadened the application of the process. The American Welding Society has written specifications for flux cored electrodes. These specifications include both self-shielded electrodes and electrodes requiring gas shielding. These developments provided the means for enhancing the design of structures that exhibit cleaner lines,

lighter weight, lower cost, and an architectural appearance (Fig. 14–16).

As the arc welding processes reached a high level of development in the 1960s, research emphasis shifted somewhat. Producing reliable welds was unquestionable, but there was some difficulty in being able to determine whether a given weld made in the plant or field met the metallurgical standards for its particular application. Considerable attention was therefore focused on nondestructive testing,



Fig. 12 Four submerged arc passes are made inside the tower of this flame-gouged seam joining the head to the shell. A current of 400 A and a speed of 36 cm/min (14 in./min) were used.



Fig. 13 Splicing a column during the erection of a building in Los Angeles using the semiautomatic self-shielded, flux cored arc welding process



Fig. 14 Smooth, clean lines, without outside stiffeners carry a ramp on a sharp radius curve.



Fig. 15 Giant bridge girders fabricated by Allied Structural Steel for the Mississippi River crossing between Dresbach, Minnesota, and Onalaska, Wisconsin.



Fig. 16 San Francisco skyline showing a building with welded steel frames.

particularly ultrasonic, radiographic, magnetic particle, and dye penetrant techniques.

Researchers also exerted considerable effort on the development of new and emerging joining methods, such as laser welding and electron beam welding processes that use electricity but

do not employ an arc, as well as new forms of arc welding such as plasma arc welding. Although the newer processes do produce welds that were not previously possible, their limitations somewhat restrict their use to specialized applications.

Arc welding continues to serve as the primary means of metal joining. The flash, smoke, and sputter that emanated from the early European laboratories produced one of the most important processes of modern industry.

Arc Physics of Gas Tungsten and Gas Metal Arc Welding

Y.M. Zhang, University of Kentucky

THIS ARTICLE provides basic physics needed to understand two most widely used arc welding processes: gas tungsten arc welding (GTAW) and gas metal arc welding (GMAW). The GTAW part is an update from the article "Arc Physics of Gas-Tungsten Arc Welding" authored by J.F. Key (of EG&G Idaho, Inc.) and published in *Welding, Brazing, and Soldering*, Volume 6 of *ASM Handbook*, 1993. Treatments for general arcs, arcs in other specific arc welding processes, and arc physics in greater depths may be found in the Selected References listed at the end of this article and from other literature. A general description of arc welding processes is also given in the article "Overview of Welding Processes" in this Volume.

Gas Tungsten Arc Physics

The GTAW process is performed using a welding arc between a nonconsumable tungsten-base electrode and the workpieces to be joined. C.E. Jackson defined a welding arc as "a sustained electrical discharge through a high-temperature conducting plasma producing sufficient thermal energy so as to be useful for the joining of metals by fusion." This definition is a good foundation for the discussion that follows.

The physics of GTAW are fundamental to all arc processes and are more straightforward, because the complications of materials (for example, filler and flux) transferred through and interacting with the arc can be avoided. Geometrically, the arc discharge in GTAW is between a rod-shaped tungsten electrode and a planar-shaped electrode, that is, the workpiece.

Pure tungsten electrodes are less expensive and, possibly, more environmentally compatible than those with rare earth or other oxide additions. They are used for less critical welds, where tungsten contamination that could be caused by the molten electrode surface can be tolerated. They are also used for alternating current (ac) welding of aluminum, copper,

magnesium, and thin sections of low-alloy and stainless steels.

Analysis of the arc discharge is separated into electrode regions and the arc column. The electrode regions are confined to very small distances from the electrode surfaces, have very high electrical and thermal fields, and have much higher current density, because of the contraction of the arc to a small spot. As a result, electrode regions for both the cathode and the anode are difficult to analyze by diagnostic measurements and theoretical computation. This situation must be remedied for a thorough understanding of the process, because the process parameters control the arc discharge at the cathode, with the anode serving as the connection to ground. The arc column, on the other hand, is relatively easy to analyze but is important primarily as a means to deduce arc characteristics at the electrodes.

Polarity. The GTAW process generally uses a direct current (dc) arc, where the tungsten electrode has a negative polarity. The tungsten electrode thus becomes the cathode and the workpiece becomes the anode. The polarity is called straight polarity, or direct current electrode negative (DCEN).

Reverse polarity, or direct current electrode positive (DCEP), is literally the reverse of DCEN. The workpiece is the cathode and the tungsten electrode serves as the anode. Because most heat is generated at the anode in the GTAW process, DCEP is used for welding certain thin-section, low-melting-point materials when DCEN would be likely to cause excessive penetration or burn-through.

Either ac or DCEP is used for removing an oxide film from the surface of the weld pool or workpiece. This is particularly important in obtaining a sound joint in metals with a tenacious oxide, such as aluminum. The oxide film promotes emission during the half-cycle (ac) when the workpiece is negative polarity. As the oxide is depleted, the emission moves to a new location that has a high enough oxide content to sustain the discharge of electrons. The arc root or cathode spot where the emission

occurs is highly mobile in ac or DCEP and, as a result, the arc is much less stable than in DCEN.

Gas Shielding. In all cases, the arc and both electrodes are shielding by gas, usually an inert gas or a gas mixture. Argon and argon-helium mixtures are used most often, although argon-hydrogen mixtures are used for some applications. The GTAW process may simply use the arc to fuse the workpieces together without the addition of filler materials (autogenous), or filler may be added to the molten pool to fill grooves in thicker weldments. A reasonable understanding of welding arc fundamentals and the GTAW process requires a more thorough discussion of the electrode regions of the arc and the arc column.

Electrode Regions and Arc Column. The cathode and anode are similar in several respects. Both exhibit a voltage drop caused by a space charge that covers a very thin region over their surfaces, and the arc is significantly contracted on the surfaces. Figure 1 shows that the total arc voltage is partitioned between the electrode drops and arc column. The relative magnitude of these drops depends on welding parameters and electrode material.

The arc discharge requires a flow of electrons from the cathode through the arc column to the anode, regardless of polarity or whether ac or

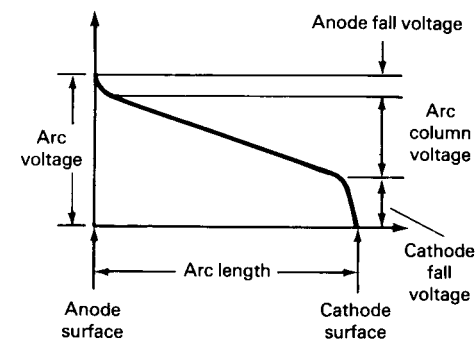


Fig. 1 Plot of relative arc voltage distribution versus relative arc length between electrodes

dc is used. Two cases of electron discharge at the cathode are discussed: thermionic emission and nonthermionic emission, also called cold cathode or field emission.

Thermionic emission results from joule heating (resistance) of the cathode by the imposed welding current until the electron energy at the cathode tip exceeds the work function (energy required to strip off an electron). This case applies to the general case of DCEN, where the tungsten electrode is the emitter, or cathode. Pure tungsten electrodes must be heated to their melting point to achieve thermionic emission. Once molten, the equilibrium tip shape becomes a hemisphere, and a stable arc results from uniform emission over this surface. Thoria (ThO₂), zirconia (ZrO₂), or ceria (CeO₂) are added to pure tungsten in amounts up to 2.2 wt% ThO₂, 0.4 wt% ZrO₂, or 3.0 wt% CeO₂ to lower the work function, which results in thermionic emission at lower temperatures and avoids melting the cathode tip. These electrodes typically have a ground conical tip, and thermionic emission is localized to a cathode spot. Thermionic emission creates a cloud of electrons, called a space charge, around the cathode. If a second electrode at a higher potential is nearby (the workpiece, in this case), then the electrons will flow to it, thus establishing the arc.

Nonthermionic, or field, emission creates an electron discharge with a very high electric field, typically exceeding 10⁹ V/m. This intense electric field literally pulls electrons out of a relatively cold or unheated cathode. This would not appear to be applicable to welding until one considers that for reverse polarity or DCEP, a condensation of positive ions from the arc column can build up in a very thin (1 nm, or 0.04 μin.) layer over the cathode surface, creating a very high localized electric field even though the cathode voltage drop may only amount to several volts.

An oxide layer, which is always present on the cathode surface in an actual weld, facilitates the discharge with a source of lower work-function electrons. When the oxide layer is very thin (on the order of one atom layer), emission occurs via a tunneling mechanism through the film to an emitting site. Thicker oxide films exhibit locally conducting spots at the end of filamentary channels through the oxide. Large currents flow in these channels, which are on the order of 100 nm (4 μin.) in diameter and have lifetimes of 0.001 to 1 μs.

The cathode cleaning action, which is one of the principal reasons to use DCEP or ac, results from stripping away the oxide film at the emitting sites by very small and intense jets of metal vapor and debris. It becomes obvious that a practical implication of the short lifetime of these cathode spots is a generally unstable arc that is due to the necessity of continual movement of the cathode spot to undepleted regions of oxide film. Arc instability is undesirable and DCEP or ac is only used when cathodic cleaning or the minimizing of heat input to the

workpiece is a higher priority than optimizing weld bead shape and location.

Anode. Welding process parameters (for example, current and voltage) control the arc discharge at the cathode. The electron flow enters the anode through the anode spot and constitutes 85% of the energy going into the weld pool, thus making current density the single most important welding parameter that determines pool shape. However, events at the anode can only be controlled indirectly by controlling the cathode. Anode spot stability does depend somewhat on shielding gas composition and the shape of the anode (that is, weld groove).

Current density and heat input measurements at the anode help to explain how process

parameters that are largely controlling events at the cathode will, in turn, influence the shape and melting rate of the weld pool. The relative contributions of heat transfer to the workpiece, in terms of the GTAW process, are shown in Fig. 2.

The Thomson effect represents the energy lost by electrons as they move from higher to lower temperatures. The sum of work function, Thomson effect, and anode fall gives an electron contribution to heat transfer of approximately 84%. The remaining 16% is due to thermal effects (that is, conduction, convection, and radiation). There are small heat losses from the pool that are due to evaporation of metal ions and radiation. Figure 3 shows that the

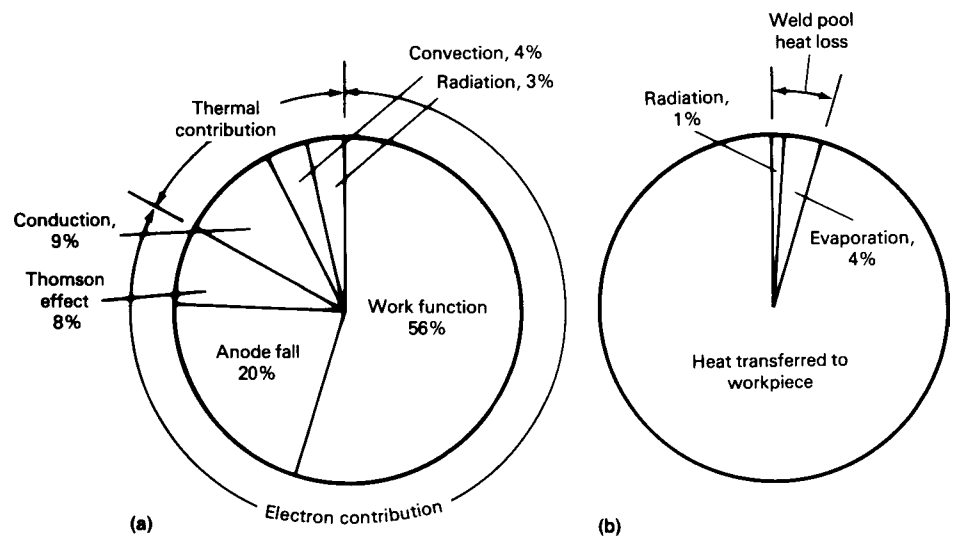


Fig. 2 Relative heat-transfer contributions to workpiece with gas tungsten arc welding. (a) Contribution of individual parameters to anode heat input. (b) Heat output at cathode (workpiece) relative to weld pool heat loss

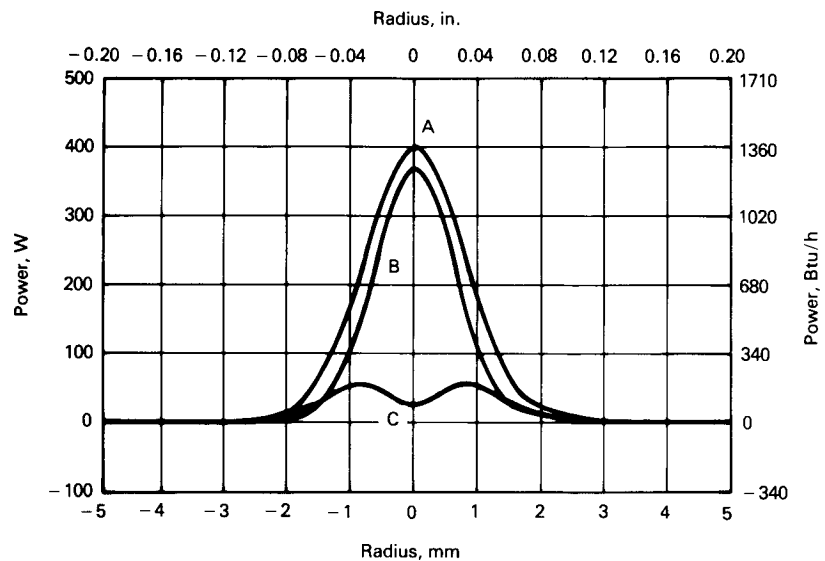


Fig. 3 Plot of electron and thermal contributions to heat transfer. A, total arc power (standard deviation, σ , of 0.8 mm, or 0.031 in.); B, electron contribution ($\sigma = 0.7$ mm, or 0.028 in.); C, thermal contribution. Weld parameters: current, 10 A; voltage, 10 V; time, 10 s; shielding gas, argon; electrode angle, 30°

energy distribution for this particular case approaches a Gaussian distribution (that is, normal distribution curve). High helium contents in the shielding gas have produced data that are typically better fit by a Lorentzian curve, indicating a narrower current density distribution (that is, a more-contracted arc at the anode spot).

Arc efficiency, in addition to those variables that have an effect on it, is an extremely important term in the heat-transfer analysis of welding. It gives the percentage of heat dissipated in the arc that actually is captured by the workpieces and is available for melting. Arc efficiency, as a function of all GTAW welding parameters and many materials, has been determined experimentally and found to be nominally 75%. The variables having the greatest effect on arc efficiency are arc voltage and anode material. For those variables, the effect is usually no more than $\pm 5\%$. Other parameters have a negligible effect.

Arc Column. The electron discharge between the electrodes partially ionizes the shielding gas in its path, thus making the arc column a conductor, or plasma. Overall, the arc column is neutral and is composed of electrons, positive gas and possibly metal ions, and neutral gas atoms.

Ironically, fundamental measurements of arc properties are most easily made in the arc column, although the actual effect of these properties on the electrode region of an actual weld must still be inferred. Nevertheless, it is useful to understand fundamentals of the arc that relate essential welding variables (for example, current, voltage, electrode gap, choice of shielding gas, and electrode shape) to arc temperature, current density distribution, and gas flow structure at the anode surface.

Effect of Cathode Tip Shape. For the general case of straight polarity, DCEN, the tip of the tungsten alloy cathode is ground to a point and then truncated somewhat to prevent the sharp tip from burning off and contaminating the weld. The included angle of the cone and the diameter of the truncation under some welding conditions have a significant effect on weld pool shape. Figure 4 shows examples of the effect of these two parameters on weld pool shape.

For a stationary spot-on-plate weld shielded by pure argon, the weld depth-to-width ratio increased with an increasing vertex angle up to 90° and with an increasing truncation diameter. The arc became less "bell shaped" and more "ball shaped" as the vertex angle or truncation diameter increased. These results should be a valid indication of the effect of cathode tip shape for pulsed current welding, which produces a series of overlapping spot welds.

A study of bead-on-plate welds (Fig. 5) made with constant current and velocity indicated a similar but less pronounced trend. These conditions produce a tear-drop molten pool shape when viewed from above, compared to a circular shape for spot or pulsed current welding.

Fluid and heat flow within the pool is less uniform front-to-rear in a tear-drop-shaped pool and probably has a greater influence on pool shape than electrode tip shape.

When the arc is used in a weld groove, the relative shapes of the cathode tip and the anode groove become more important. The arc discharge from the cathode will seek a path to ground with the lowest electrical resistance. For a stable arc properly centered in the groove (for example, a root pass), the shortest path to ground should be between the cathode tip and the bottom of the groove (Fig. 6). This will require the cathode vertex angle to be somewhat less than the included angle of the groove and/or a sufficiently wide groove to ensure that the shortest path to ground is from the cathode tip to the groove bottom and not, for example, from the electrode shoulder to the groove wall, as the case would be with a 90° electrode in a 10° narrow groove. Welding in a groove places a higher priority on arc stability and location than on maximum penetration.

To understand the effects of tip shape, temperature distributions in the plasma were measured. Figure 7 shows that as the cathode vertex angle increases, the plasma radius of the arc column increases at midgap and becomes more constricted near the anode. The quantitative interpretation of these results requires theoretical modeling, which has yet to be completed.

Effect of Shielding Gas Composition. The GTAW process typically uses either an inert gas, such as argon, or an inert gas mixture, such as argon and helium, to shield the arc and the weld from atmospheric contamination. Occasionally, a slightly reactive gas mixture, such as argon with up to 15 vol% H_2 , is used. (The 15 vol% limit is based on safety considerations.) Shielding gas composition has a rather strong effect on arc temperature distribution and, under certain conditions, a significant effect on weld pool shape.

Figure 8 shows how shielding gas affects arc voltage. The curves would all be displaced downward for shorter arc lengths, but the relative positions would be maintained. Figure 9 shows the effects of both cathode vertex angle and shielding gas composition on weld pool shape for spot-on-plate welds. Increasing additions of helium to argon show a remarkable increase in penetration when using a 30° vertex angle. However, the effect is much less evident when using a 90° vertex angle.

To understand these phenomena, arc temperature distributions for a variety of shielding gases and mixtures, electrode shapes, current, arc voltages (electrode gaps), and anode materials have been measured in order to clarify welding arc fundamentals. Welding arcs are composed of electrons, positive gas ions, and neutral gas atoms. Some measurement techniques give the temperature of one species (electrons), whereas other techniques give the

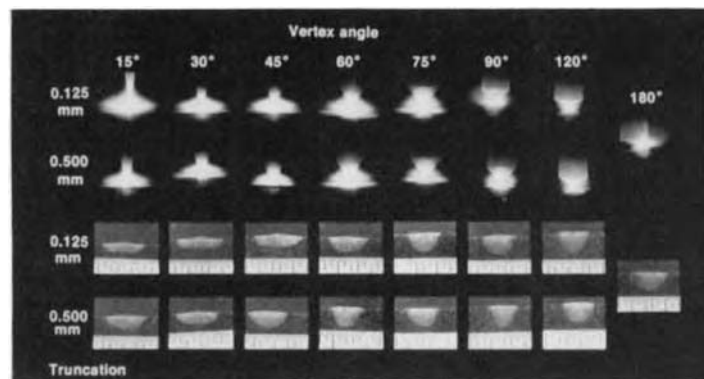


Fig. 4 Fusion zone profile for spot-on-plate welds as a function of electrode tip geometry using 100% Ar as a shielding gas. Weld parameters: current, 150 A; duration, 2 s

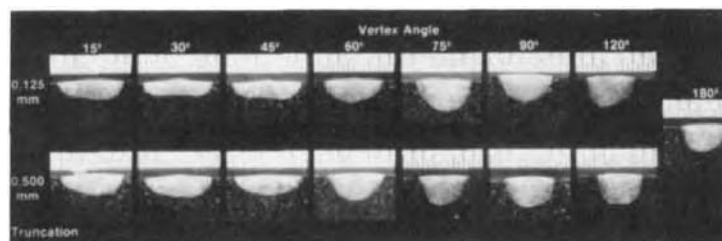


Fig. 5 Fusion zone profile for bead-on-plate welds as a function of electrode tip geometry using 100% Ar as a shielding gas. Weld parameters: current, 150 A; welding speed, 3 mm/s (0.12 in./s)

temperature of another species (neutral atoms). If the arc is in local thermodynamic equilibrium (LTE), all techniques should give the same temperature.

Although the assumption of LTE used to be considered completely valid, contemporary investigations have suggested that this is not always the case and that some of the older measurements may be somewhat in error. Absolute values of arc temperature are only needed to establish boundary conditions for detailed arc modeling of temperature-dependent properties. What is of more importance to the welding engineer or technologist is the relative effect of essential variables on heat input to the workpiece. Arc temperature measurement is one useful indication of how these variables affect the arc.

When compared to Fig. 7(a), Fig. 10 shows that large additions of helium to argon decrease peak temperatures slightly and increase the plasma diameter in the plasma column. The arc appears to become a broader and more isothermal heat source. The lower peak temperature is reasonable, because a combination of the high ionization potential of helium and relatively low currents of welding arcs gives

an arc column that is only slightly ionized. Figure 7 showed that a large vertex angle had a similar, but less pronounced, effect on arc temperature when adding helium to the shielding gas (that is, the axial peak temperature decreased and the plasma diameter increased).

Figure 11 shows that doubling the current from 150 to 300 A produces an increase in plasma diameter (that is, that portion of the arc above approximately 8000 K, or 13,900 °F). This effect occurs regardless of the shielding gas composition.

The arc length or gap between the electrodes is yet another process parameter that must be considered, especially for mechanized welding, where it can be kept reasonably constant. Because arc voltage increases roughly in proportion with arc length, longer arcs have higher arc voltages and consume more energy for the same current. However, this increased energy is generally lost through radiation to the environment surrounding the weld and does not effectively supply additional heat to the workpieces. Mechanized welding generally uses rather short arc lengths (2 to 3 mm, or 0.08 to 0.12 in.), whereas manual welding uses a longer arc length. Unfortunately, relationships that

establish a direct correlation between the temperature distribution in the arc column and the weld pool shape still have not been established, primarily because weld pool shape depends on other factors, such as compositionally dependent molten metal properties.

Flow Structure. Shielding gas is used to displace reactive gases in the atmosphere from the vicinity of the weld. Inert gases are preferred for the GTAW process, because they minimize unwanted gas-metal reactions with the workpieces. A uniform laminar flow of gas from the gas cup would be ideal and, in fact, is usually achieved as long as there is no welding arc. However, the arc discharge rapidly heats the gas in the arc column, and thermal expansion causes plasma jets. The lower temperature near the cathode tip in Fig. 11 is an indication of a jet pumping in cooler gas. This becomes an important factor at high currents, because these jets can depress the surface of the weld pool and alter heat transfer to it. The rapid gas expansion can cause the flow to deviate from laminar and, in extreme cases, the flow can become turbulent. Turbulence tends to mix atmospheric contaminants into the arc, often where they can do the most harm: at the surface

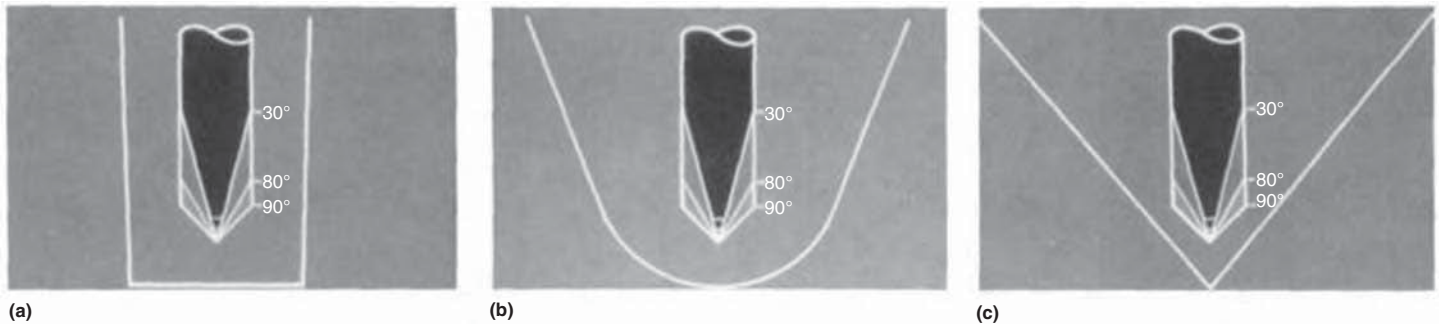


Fig. 6 Effects of electrode tip geometry on the path length to ground in weld grooves of various shapes. (a) 75° V-groove. (b) 40° U-groove. (c) 10° narrow groove

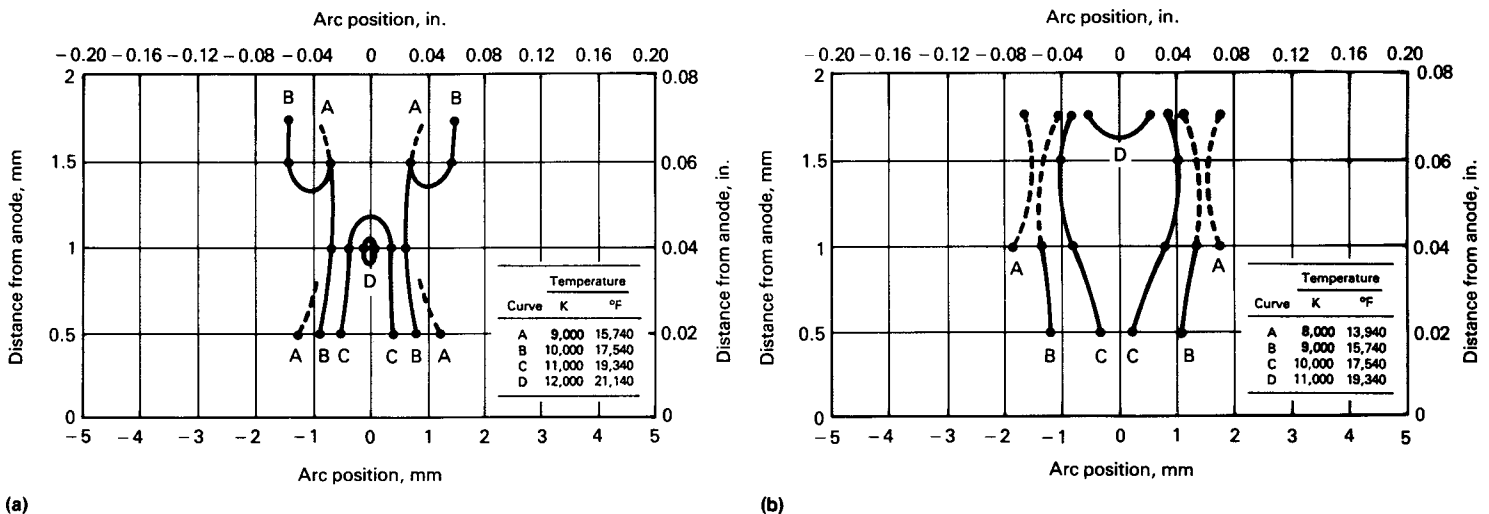


Fig. 7 Effect of vertex angle on gas tungsten arc welding arc column temperature distribution with 100% Ar used as shielding gas. (a) 30° electrode vertex angle. (b) 90° electrode vertex angle. Welding current, 150 A

of the molten weld pool. Holographic interferometry and Schlieren photography have been used to characterize gas flow.

Figures 12 to 14 show examples of laminar and turbulent flow. The flow from a commercial-design gas cup for three current levels is shown in Fig. 12. Laminar flow occurs where the fringes are generally straight and parallel. Turbulent flow is indicated by very wavy or circular fringes. Increasing current tends to make the laminar region somewhat broader and thicker, effectively increasing the area shielded from atmospheric contamination.

Figures 13 and 14 result from experiments with gas cup shapes that were designed to improve shielding. Figure 13 shows that a converging cone would be a very poor choice for the GTAW process, as indicated by the very small area of laminar flow and the extreme turbulence in the surrounding region.

Figure 14 is a venturi shape, which provides a large laminar flow region for all current levels and excellent shielding. This design may be somewhat better than commercial designs, but weld contamination studies should be conducted to verify this possibility.

Arc Length Control. As mentioned earlier, the arc length or gap between the electrodes is an important process parameter that must be considered. In particular, the distribution of the arc (thus arc force and heat distributions) is also determined by the arc length together with the arc current. Unlike the tungsten shape and flow gas that can be easily controlled, the arc length fluctuates and needs to be controlled for precision joining, where GTAW has its advantages.

The most convenient way to control the arc length is to use the arc voltage as a feedback of the arc length. This is because a change in the arc length would result in the same change in the arc column.

In a first-order approximation, the voltage of the arc column is considered to be proportional to the arc length (length of the arc column), and the voltage drops at the anode and cathode are considered to be constant for the given shielding gas and workpiece material. Hence, the change in the arc voltage is considered to be proportional to the change in the arc length, and controlling the arc length at a constant would be the same as controlling the arc voltage at a constant.

For precision sensing and control of arc length, especially when the arc length is small or the current may change, the aforementioned first-order approximation may not always be sufficient. The complexity has been demonstrated through the following:

- For the same arc length, the voltage of a tungsten-copper arc in argon decreases rapidly before the current increases to 50 A and decreases significantly before the current increases to 100 A (Ref 1).
- When the current is the same, the arc voltage decreases before the arc length increases to approximately 1 mm (0.04 in.) and then increases gradually when the arc length further increases (Ref 2, 3).

To use the arc voltage, V , as a precision feedback/measurement of the arc length, l , studies are needed for the particular anode (workpiece) to measure the arc voltage at different currents and arc lengths in order to establish an accurate model for the specific material being welded:

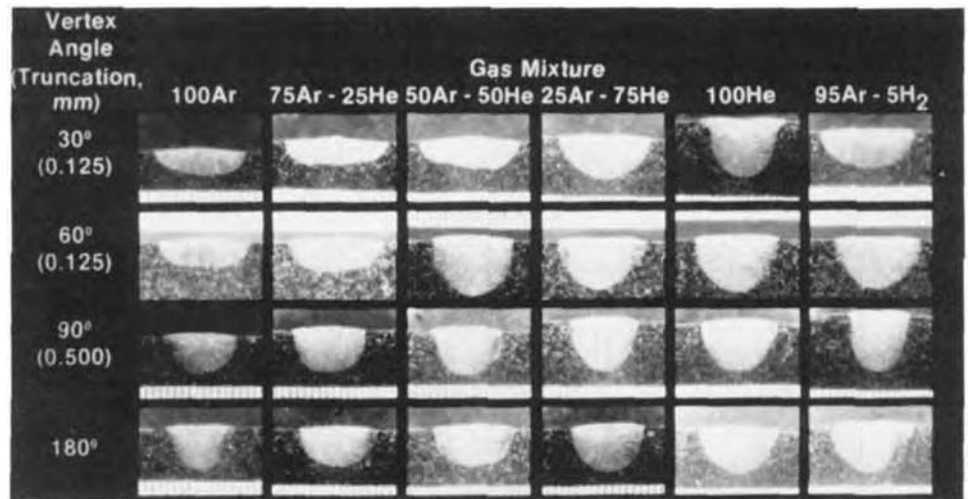


Fig. 9 Effect of electrode tip geometry and shielding gas composition on weld pool shape for spot-on-plate welds. Welding parameters: current, 150 A; duration, 2 s

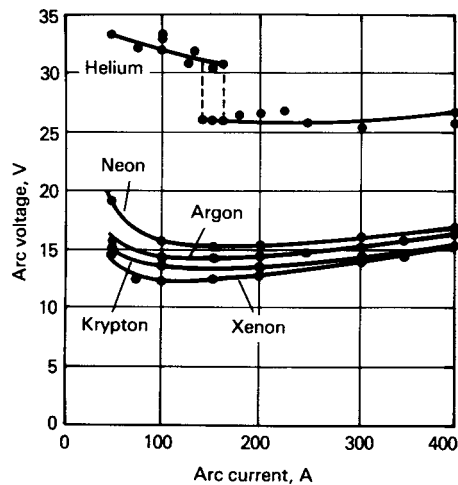


Fig. 8 Plot of arc voltage versus arc current for selected inert shielding gases. Welding parameters: anode, titanium; cathode, tungsten; polarity, direct current electrode negative; arc length, 12.7 mm (0.050 in.)

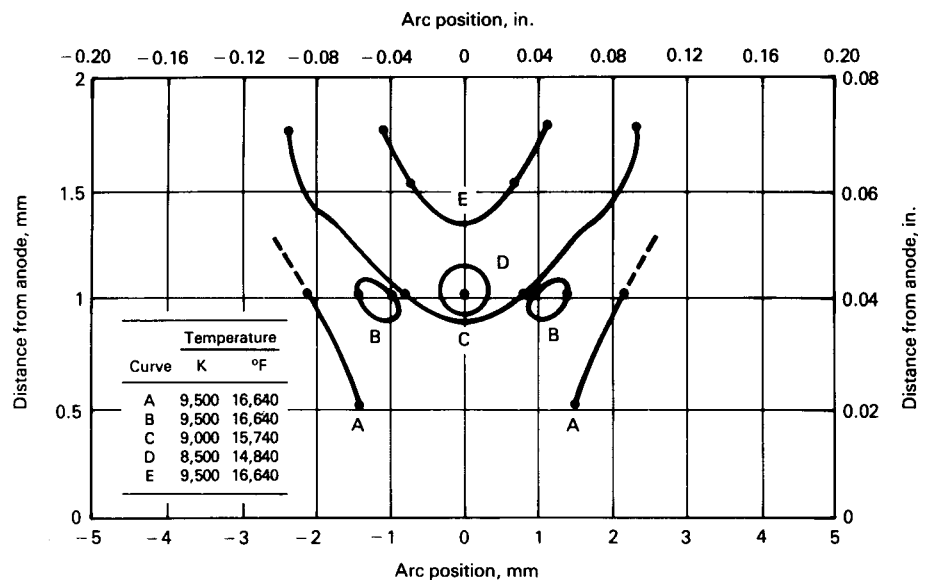


Fig. 10 Plot of gas tungsten arc welding arc column temperature distribution as a function of anode distance and arc position. Welding parameters: electrode vertex angle, 30°; current, 150 A; shielding gas, 10Ar-90He

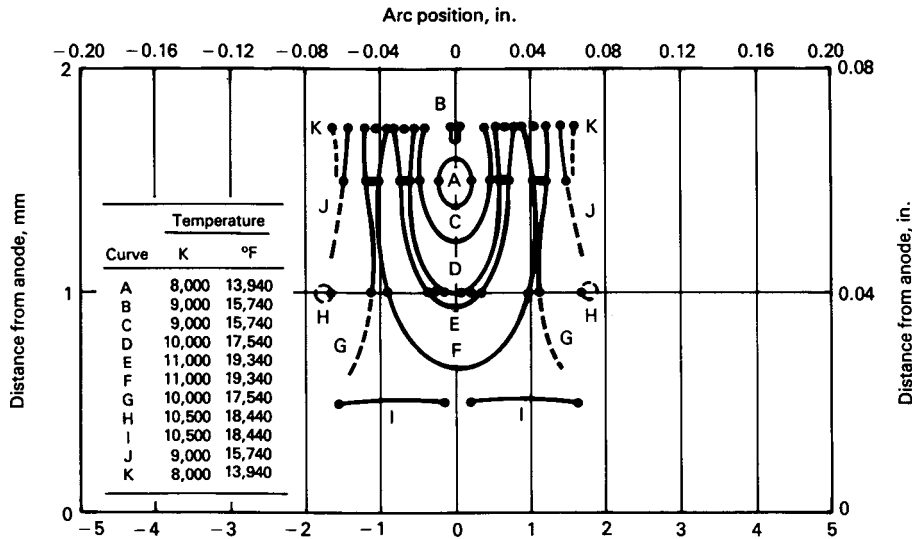


Fig. 11 Plot of gas tungsten arc welding arc column temperature distribution relative to anode distance and arc position. Welding parameters: electrode vertex angle, 30°; current, 300 A; shielding gas, 100% Ar



Fig. 14 Effect of geometry on venturi gas cup laminar and turbulent flow as detected by real-time holographic interferometry

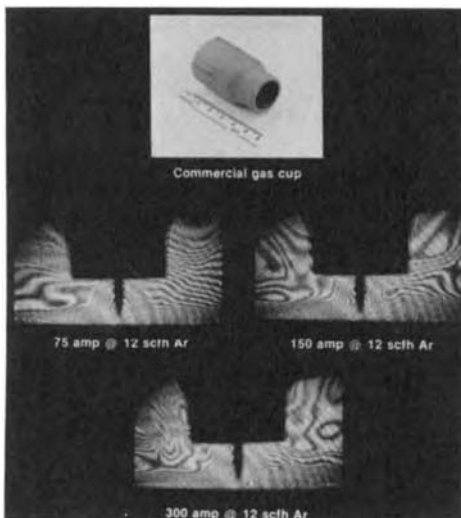


Fig. 12 Effect of geometry on commercial gas cup laminar and turbulent flow as detected by real-time holographic interferometry

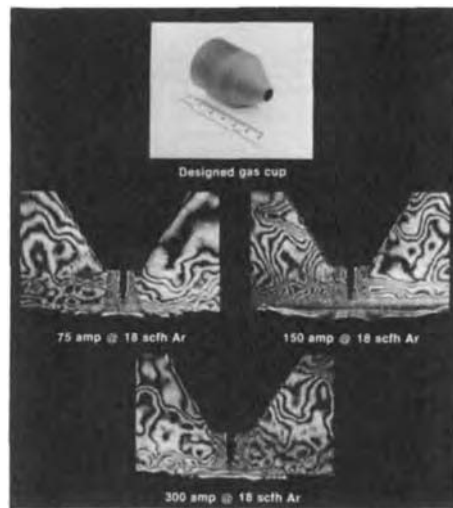


Fig. 13 Effect of geometry on converging cone cup laminar and turbulent flow as detected by real-time holographic interferometry

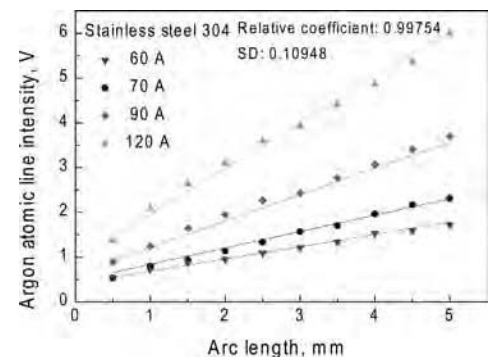


Fig. 15 Argon atomic line intensity versus arc length

$$I = f(V, I) \tag{Eq 1}$$

where I is the current. However, despite the possibility that such a model may be established and the model is deterministic, it is likely that this model will be nonlinear, as has been demonstrated in the previously referenced studies.

In the previous studies, because of the lack of capabilities to measure the weld pool surface, the arc length was difficult to accurately measure, and the gap between the tungsten and the unmelted workpiece was typically used as the measurement of the arc length. When the arc length is small and the welding current is large (such that the difference between the weld pool surface and the

workpiece surface is large), the arc length should be measured more accurately. To this end, technology recently developed to measure the three-dimensional weld pool surface may be used (Ref 4).

The nonlinearity issue seen in Eq 1 may be overcome by replacing the arc voltage using an argon atomic line intensity (Ref 5). Figure 15 shows the linear relationship between argon atomic line intensity and arc length. Ideal linear relationships are found in the entire arc length range that is typically used. Of course, the measurement of the line intensity requires the use of an optical-electric sensor with a band-pass filter, and it is more complex than the measurement of the arc voltage.

Gas Metal Arc Physics

The gas metal arc welding (GMAW) process is performed using a welding arc established in a shielding gas between a continuously-fed consumable wire electrode and the workpieces or base metal to be joined. Part of the shielding gas that is continuously supplied around the wire is ionized to form the arc column and to establish the arc; the rest surrounds the arc and molten metal to shield them from the atmosphere. The most widely used variant of GMAW is flux cored arc welding, where the wire electrode is solid metal and cored with flux of specific chemical powders.

The most fundamental difference between GMAW and GTAW is the presence of the metal-transfer process; that is, the consumable electrode must be melted and the liquid metal of the melted consumable wire must transfer from the electrode into the pool being formed by molten metal from the workpieces and

electrode. Both the melting of the electrode and how the melted electrode metal detaches from the electrode into the weld pool play fundamental roles in determining the behavior of the arc, the quality of the resultant welds, and the productivity of the process.

The detachment of the melted electrode is controlled by forces acting on the liquid droplet formed by the melted electrode. Of these forces, the electromagnetic force often plays a dominant role in determining the mode of the metal-transfer process and how the detachment is completed. The primary variable that controls the electromagnetic force is the welding current, while other factors such as electrode diameter, shielding gas, polarity, and so on also affect the electromagnetic force, but they are not conveniently adjusted during welding.

Another fundamental difference between GMAW and GTAW is that the material of the electrode varies with the application, because it will be melted and transferred into the base metal to become part of the weld metal. Also, the electrons are emitted from the material being welded in typical direct current electrode positive GMAW applications. Because the material that emits the electrons varies with application, the cathode voltage varies from application to application. Further, the electrons tend to emit from areas of lower electron voltage in the weld pool, the location of the cathode in relation to the anode (wire tip) may change, and the arc column may not always be straight if the reduction in the voltage for electron emission is greater than the increase in the arc column voltage. Because the location of the area of lower electron voltage in relation to the wire tip may change during welding, the arc (path, column, distribution) may be subject to change. In particular, because of cyclic changes in the arc length due to metal-transfer variations, the arc length in GMAW typically must be long enough to tolerate these periodic changes. This increased length of the arc also promotes the change of the arc. As a result, the arc voltage fluctuates in addition to the periodic change. For constant voltage (CV) power supplies, the current also fluctuates accordingly. Such fluctuations make it more difficult to sense by use of the arc signals than in GTAW.

The GMAW process generally uses a dc arc, where the electrode wire has a positive polarity. The wire thus becomes the anode and the workpiece becomes the cathode. The polarity is called reverse polarity, or DCEP. The purpose of DCEP is to detach the droplets formed by the melted wire. This is because the component of the electromagnetic force generated by the current along the wire axis direction typically has the same direction as the current in argon-rich gases. Hence, when the current flows away from the droplet, the electromagnetic force is a detaching force. Further, DCEP can remove oxide films from the surface of the weld pool or workpiece. The oxide film promotes emission. As the oxide is depleted, the emission moves to a new location that has sufficient

oxide content to sustain the discharge of electrons. The arc root or cathode spot where the emission occurs is highly mobile. Together with the oscillation of the weld pool surface caused by impact from the detached droplets, the arc is typically not completely stable. The arc voltage fluctuates, and for CV power supply the fluctuation in the arc voltage will cause the current to fluctuate.

In DCEP, the wire is primarily melted by the anode heat whose power is IV_{anode} , where I is the welding current, and V_{anode} is the anode voltage. The heat directly imposed on the workpiece by the arc is IV_{cathode} . For GMAW applications, the workpiece and wire are similar materials, and the $V_{\text{cathode}}/V_{\text{anode}}$ ratio is approximately 2 (Ref 6). Hence, if GMAW is performed using straight polarity, the wire is expected to be melted at double speed, so the deposition speed is doubled. That is, straight polarity helps GMAW to increase the deposition rate or reduce the heat input. However, in DCEN, the electromagnetic forces prevent the droplet from being detached. Hence, variable polarity or ac GMAW has been proposed that uses DCEN to speed the wire melting and DCEP to detach the droplet.

In all cases, the arc and both electrodes are shielded by gas, usually an inert gas, a gas mixture, or pure CO_2 . The inert gas is typically argon, and the gas mixture is Ar- O_2 or Ar- CO_2 . A gas mixture is used to improve the penetration capability and weld bead, and pure CO_2 is used for reduced costs and increased deposition and arc temperature.

A reasonable understanding of welding arc fundamentals and the GMAW process requires a more thorough discussion of electrode melting and droplet detachment/metal transfer, including the physics and physics-based controls.

Wire Melting. In GMAW (Fig. 16), a consumable wire is fed to the contact tube, which is typically connected to the positive terminal of the power supply. A shielding gas is supplied to surround the wire and is restricted by the nozzle to deliver to the local area that surrounds the wire. When the wire touches the negatively charged workpiece (connected to the negative terminal of the power supply), the tip of the wire is rapidly melted, forming a gap between the wire and the workpiece, and an arc is ignited across this gap. The anode of the arc directly melts the wire, and melted metal forms a droplet at the tip of the wire. The formation and detachment of the droplet is typically referred to as the metal-transfer process.

Before droplet detachment and metal transfer are analyzed, the melting of the wire in GMAW must be understood. Basically, the wire is melted by the anode and resistive heat, which are proportional to the current and its square, respectively. However, the resistive heat also depends on the length of the wire extension (E). The heat that melts the wire is often simplified as:

$$Q_{\text{wire}} = IV_{\text{anode}} + \left(\frac{\rho}{A}\right)EI^2 \quad (\text{Eq 2})$$

where ρ is the resistivity of the wire material, and A is the cross-sectional area of the wire. In a first-order approximation, ρ is treated as a constant. If greater accuracy is needed, the dependence of resistivity on temperature, that is, $\rho(T)$ and $\partial\rho(T)/\partial T \neq 0$, can be considered, and an equivalent resistivity can be calculated as the average resistivity over the wire extension to replace the constant resistivity in Eq 2:

$$\bar{\rho} = \left(\int_0^E \rho(T(\tau))d\tau\right)/E \quad (\text{Eq 3})$$

However, a more accurate calculation of this equivalent resistivity requires the following:

- $\rho(T)$, the dependence of resistivity on temperature for the given wire material
- $T(\tau)$, the dependence of temperature on position τ ($0 \leq \tau \leq E$) in the wire extension for the given wire material, diameter, current, and wire extension

One may find that extremely high precision for the heat that melts the wire is often not required because the temperature in the liquid droplet is not uniform, and the average temperature of the droplets changes with the current and droplet volume in addition to other metal parameters. Hence, the wire metal melt cannot be accurately determined from the heat.

Arc Length/Voltage Control. The length of the arc column from the droplet to the cathode on the weld pool surface is the arc length. The welding voltage is the sum of the voltage drop on the wire extension, the anode voltage drop, the arc column voltage, and the cathode voltage. The arc length is an approximate indicator for the distance from the wire tip to the weld pool surface and must be controlled at an appropriate level to prevent unintentional

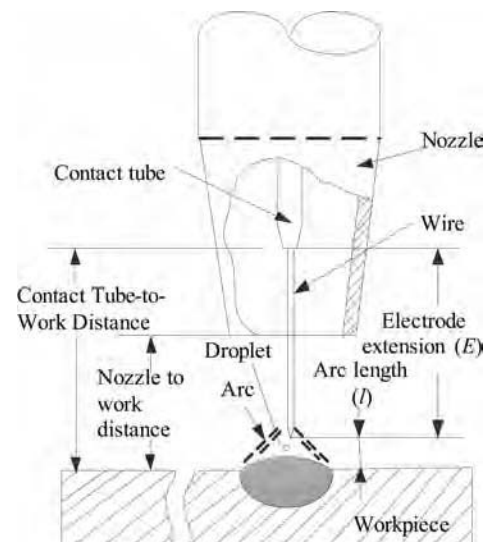


Fig. 16 Illustration of gas metal arc welding processes

short-circuiting (too short an arc length) or burning of the contact tube (too long an arc length). To this end, the arc length must be feedback controlled. Because the voltage drop on the wire extension is typically much smaller than the arc column voltage, and the cathode and anode voltage drops are both approximately constant, the arc column voltage can be approximately controlled by controlling the welding voltage.

The major parameter that determines the arc column voltage is the arc length, although the welding current also affects the arc column voltage. A first-order approximation is:

$$V = V_0 + kl \tag{Eq 4}$$

where $V_0 = V_{\text{anode}} + V_{\text{cathode}} + V_{\text{wire}}$ and k are both considered constant, although V_{wire} and k are both current-dependent and V_{wire} is also wire-extension-dependent. Hence, the welding voltage can be used to indicate the arc length, and the control of the arc length can be converted into the control of the welding voltage, which can be easily measured.

The arc length control is based on the following melting-feeding balance equation:

$$\frac{dl}{dt} \approx c_1 Q_{\text{wire}} - v_f \tag{Eq 5a}$$

or

$$\frac{dV}{dt} \approx k(c_1 Q_{\text{wire}} - v_f) \tag{Eq 5b}$$

where v_f is the nominal wire feed speed, and c_1 is a constant that depends on wire material, diameter, and droplet temperature.

When the contact-tube-to-work distance suddenly increases, the arc length immediately increases, such that the welding voltage also increases immediately. In this case, the feedback control system will reduce the voltage, and the needed dV/dt is negative. Based on Eq 5(b), Q_{wire} must decrease. From Eq 2, the current must be reduced. Once the current decreases, $dV/dt < 0$ will be realized, and the voltage will decrease.

Metal Transfer. The wire is continuously melted, but the metal melted from the wire may not transfer continuously/immediately into the base metal/weld pool. Instead, it accumulates at the tip of the wire to form a droplet, primarily because of the surface tension at the droplet (liquid)/wire (solid) interface that functions as a retaining force for the droplet. The metal-transfer process is often loosely used to refer to the entire process associated with wire melting, droplet formation and detachment, and merging with the base metal. Droplet detachment is specifically referred to in this section.

The droplet is transferred into the base metal through three major modes/types described subsequently: short-circuiting, globular, and spray transfer. There are two major established theories for when and how the droplet is detached: pinch instability and static force balance.

Detailed discussion and application of either theory to determine when and how the droplet is detached is beyond the scope of this article. This article only introduces the principle of static force balance.

When applying the static force balance theory, all forces imposed on the droplet are projected to the axis of the wire and are categorized into detaching forces (pointing away from the liquid-solid interface) and retaining forces (pointing toward the liquid-solid interface). In typical cases (an argon-rich shielding gas and DCEP), the major detaching forces are the electromagnetic force, which can be considered to approximately increase quadratically with the current, and the gravitational force, which increases proportionally with the mass of the accumulated mass in the droplet; the major retaining force is the surface tension at the liquid-solid interface, along with some supportive force from the momentum of electrons and ions. For a given wire material and diameter, the surface tension is approximately fixed, and the major parameters that determine when and how the droplet is detached are the welding current and arc length:

- Short-circuiting transfer is characterized by the occurrence of short-circuiting between the droplet and weld pool. When the wire feed speed is low, such that the current needed to melt the wire is small, the electromagnetic force will be small. Unless a condition exists for the droplet to grow to a level such that its gravitational force, together with the electromagnetic force,

exceeds the surface tension, the droplet will touch/short-circuit with the weld pool before transferring into the weld pool. Figure 17 shows a typical short-circuiting metal-transfer process. It is found that much spatter may be generated in this process.

- Globular transfer is characterized by relatively large droplets whose diameters are significantly greater than that of the wire. Two conditions are needed for this to occur: the arc length, l (Fig. 16), is sufficient to allow the droplet to grow to a diameter that is significantly larger than that of the wire, and the current is relatively small, such that the corresponding electromagnetic force is not sufficient to form a competent detaching force that exceeds the surface tension without a droplet of relatively large diameter to provide a sufficient gravitational force. Two typical globular transfers are shown in Fig. 18.
- In spray transfer, if the current is sufficient that the detaching electromagnetic force is close to or exceeds the retaining surface tension, the droplet will detach without a need for additional gravitational force. The diameters of the droplets will thus be similar to (drop spray) or much smaller than that of the wire. Figure 19 shows a typical drop spray metal transfer.

The occurrence of spray transfer is primarily determined by the current level for the given wire diameter and material, and the arc length, l , is irrelevant as long as it is not extremely short. The current level that determines if a

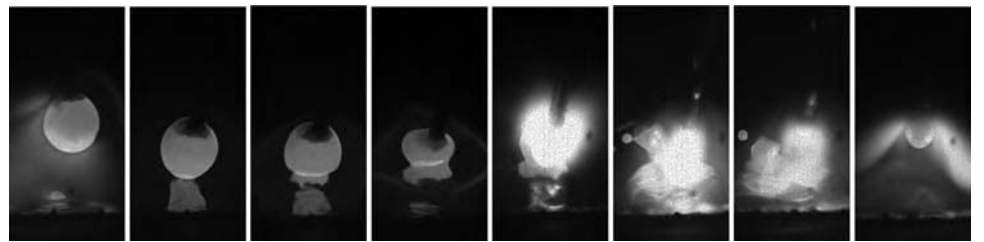


Fig. 17 Typical short-circuiting metal-transfer process

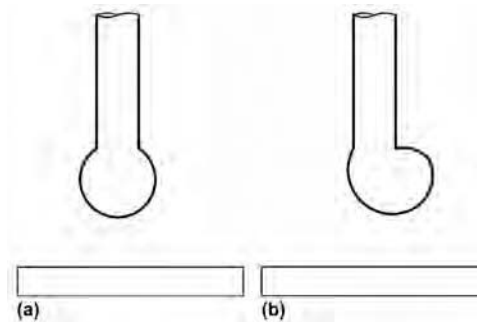


Fig. 18 Schematic of typical globular metal transfer. (a) Axial globular transfer. (b) Nonaxial globular transfer

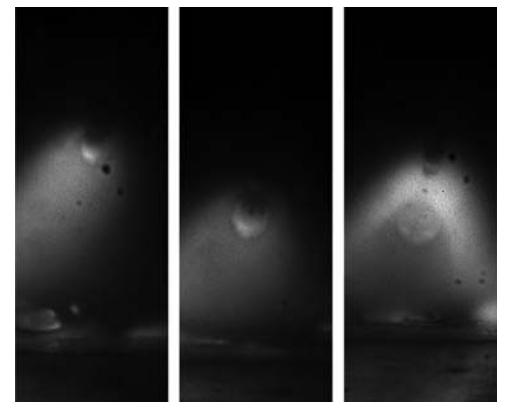


Fig. 19 Typical drop spray metal transfer

spray transfer could occur is referred to as the transition current, I_t , and it is approximately 230 A for steel wire of 1.2 mm (0.05 in.) diameter. At $I < I_t$, the gravitational force will play a role in providing sufficient detaching force. If I is sufficient, globular transfer theoretically could occur at any $I < I_t$, and the diameter (volume) of the droplets detached decreases as I increases; otherwise, short-circuiting would occur. For a given I , the transfer tends to change from short-circuiting to globular as I increases.

Static Force Balance and Arc Climb. The wire is continuously melted, but the resultant droplet typically detaches from the wire and transfers into the base metal discontinuously. The static force balance can be a good start to understanding the metal-transfer process.

The major forces acting on the droplet include gravitational force, electromagnetic force (Lorentz force), aerodynamic drag force, surface tension, and momentum force. The force due to gravity can be expressed as:

$$F_g = m_d g = \frac{4}{3} \pi r_d^3 \rho g \quad (\text{Eq 6})$$

where m_d is the mass of the droplet, r_d is the droplet radius, ρ is the droplet density, and g is the acceleration of the gravity. The surface tension is given as:

$$F_\sigma = 2\pi R\sigma \quad (\text{Eq 7})$$

where R is the electrode radius, while σ is the surface tension coefficient. The aerodynamic drag force can be expressed as:

$$F_d = \frac{1}{2} C_d A_d \rho_p v_p^2 \quad (\text{Eq 8})$$

where C_d is the aerodynamic drag coefficient, A_d is the area of the drop seen from above, and ρ_p and v_p are the density and fluid velocity of the plasma, respectively. The momentum force can be expressed as:

$$F_m = v_s \dot{m}_d \quad (\text{Eq 9})$$

where v_s is the wire feed speed, and \dot{m}_d is the change of the droplet mass. The electromagnetic force, F_{em} , is given by:

$$F_{em} = \frac{\mu_0 I^2}{4\pi} \left(\frac{1}{2} + \ln \frac{r_i}{r_u} \right) \quad (\text{Eq 10})$$

where μ_0 is the magnetic permeability, I is the welding current, r_i is the exit radius of the current path, and r_u is the entry radius of the current path; r_i and r_u are related with the process of the droplet status. Before the droplet starts to be detached, r_u is the same as the radius of the wire and is thus a constant. However, once the droplet is being detached, r_u decreases. The increase of F_{em} thus accelerates the detachment of the droplet. In the conventional GMAW process, the droplet is not detached when the retaining force, F_σ , is still sufficient to balance the detaching force, F_τ :

$$F_\tau = F_g + F_d + F_m + F_{em} \quad (\text{Eq 11})$$

During the metal-transfer process, the major variables that affect the detaching force are the droplet mass and the current, as can be seen from Eq 6 to 10. Because the surface tension is the major retaining force and it is fixed for the given wire, the droplet can only be detached either by waiting for the droplet to grow into a larger size, such that the gravitational force is sufficient to break the balance; waiting for the droplet to touch the weld pool, such that an additional detaching force—surface tension between the droplet and weld pool—is added; or by increasing the current to increase the electromagnetic force.

The phenomenon of the transition current implies that the effect of the electromagnetic force as the detaching force changes rapidly around the transition current. The rapid increase of the electromagnetic force reduces the dependence on the gravitational force to overcome the surface tension at the liquid-solid interface on the wire tip. Such a rapid increase in the electromagnetic force at detaching is due to the rapid climb of the arc (anode) from the bottom of the droplet toward the neck of the droplet (the solid-liquid interface). The climb of the arc increases the exit radius of the current in Eq 10. When the arc climbs rapidly as the current increases, the exit radius of the current in Eq 10 increases rapidly, such that the required gravitational force component is much smaller. (Figure 20 demonstrates the arc climb phenomenon.) As a result, the diameter of the droplet decreases rapidly in the narrow range around the transition current, from being much larger than that of the wire to being much smaller than that of the wire.

Metal-Transfer Control. Metal transfer plays a critical role in determining the quality of the welds produced. In conventional GMAW with a continuous waveform CV power supply, the continuous waveform current is dictated by the wire feed speed. If the wire feed speed is large, such that the resultant current is higher than the transition current, that is, $I \geq I_t$, the droplets are automatically detached smoothly at relatively small diameters as spray transfer, and the metal transfer is typically not an issue of concern unless the current is extremely high, producing a rotating transfer. However, if $I < I_t$ is required, the metal transfer could cause problems. If the arc length is long, the large droplets pending at the tip of the wire would wander about the wire axis and cause not only an arc instability but also uncertainties in the travel direction of the detached droplet. Droplets thus merge into the weld pool at different locations, forming irregular weld beads. If the arc length is short, resulting in short-circuiting transfers, spatters would be produced. Hence, a continuous waveform current is typically not used in the large current range $I < I_t$. A number of methods have been developed to control the metal-transfer process if the needed current is smaller than the transition current.

Pulsed Arc Control. This is a method to achieve the desired spray transfer over a wide range of average current by using a square waveform with a background current, $I_b < I_t$, to maintain the arc and a peak current, $I_p \geq I_t$, to detach the droplet, as shown in Fig. 21. The applications of GMAW that require different levels of heat input are thus greatly extended.

Surface Tension Transfer (STT, Lincoln Electric). This technology was developed from an understanding of phenomena associated with short-circuiting transfer. By detecting the progress of the short-circuiting process, the current waveform is controlled/optimized differently in different metal-transfer stages to minimize the production of spatters. Figure 22 shows its typical current waveform.

Cold Metal Transfer (CMT). Gas metal arc welding typically feeds the wire forward continuously by using a motor (wire feeder) at a distance from the welding torch to minimize the weight being carried and to maximize the torch accessibility. The CMT uses a second motor installed close to the torch to draw the wire back after the droplet touches the weld pool. As a result, the droplet can be successfully separated from the solid wire and transferred into the weld pool, and the arc is re-established during the separation process, as shown in Fig. 23. During the separation and arc re-establishment, the current is controlled at a minimal level to minimize the production of spatter.

Double-Electrode GMAW. In conventional GMAW, the current melts the wire. By adding a bypass electrode and bypass loop (Fig. 24), such that part of the current passes through the bypass loop, there will be two cathodes, one on the base metal and another on the bypass electrode. The current flowing to the workpiece becomes lower than the melting current. As a result, the arc root on the wire becomes more distributed, and the spray transfer is achieved with a base-metal current much smaller than the transition current (Ref 7).

Heat Input Control. Many GMAW applications require that a certain amount of metal be deposited into the workpiece with a minimal heat input. This problem can be posed as

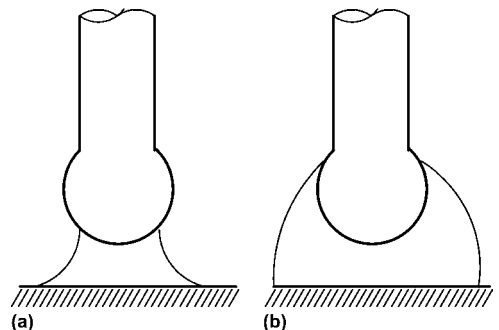


Fig. 20 Arc climb phenomenon. (a) Below transition current. (b) Above transition current

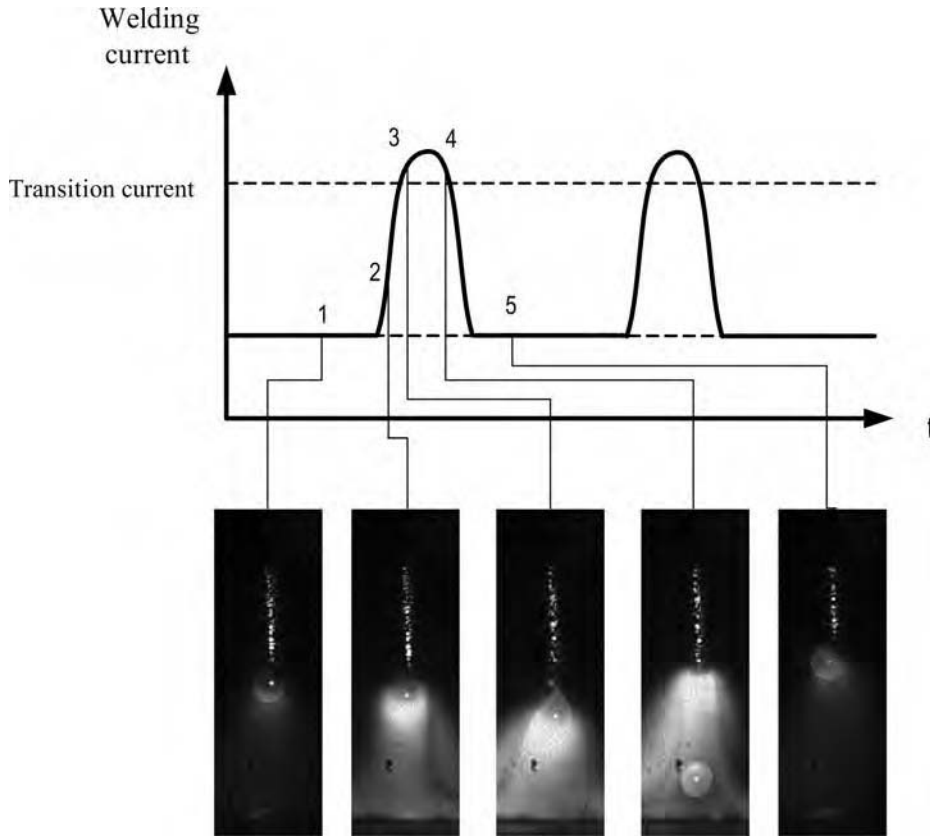


Fig. 21 Typical pulsed gas metal arc welding process

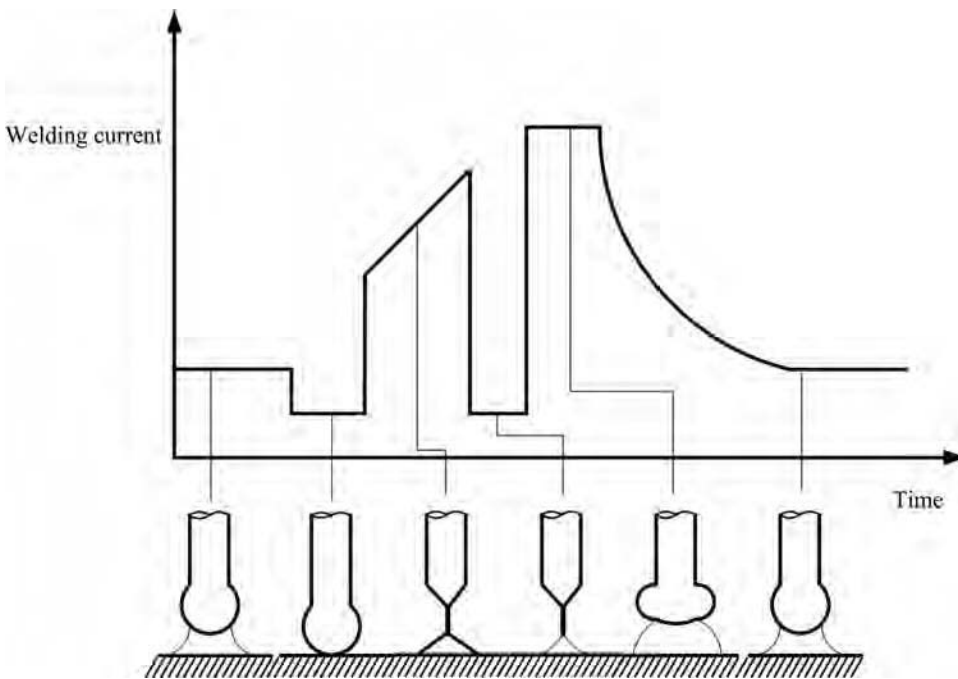


Fig. 22 Schematic of surface tension transfer process and current waveform

achieving a maximum efficiency ratio, defined as the effective heat over heat input ratio:

$$\lambda = H_e/H \tag{Eq 12}$$

where H is the heat input into the workpiece, and the effective heat, H_e , is the heat that melts the wire.

This can be simplified by omitting the arc column heat and resistive heat. In conventional direct current electrode positive GMAW:

$$H_e = V_a I/v \tag{Eq 13}$$

$$H = (V_a + V_c)I/v \tag{Eq 14}$$

where V_a is the anode voltage drop, V_c is the cathode voltage drop, and v is the travel speed. Their ratio is:

$$\lambda = V_a/(V_a + V_c) \tag{Eq 15}$$

In GMAW, the materials of the wire and base metal are similar, and $V_c \approx 2V_a$ (Ref 6). Hence, for conventional direct current electrode positive GMAW, the efficiency ratio is approximately 33%.

In direct current electrode negative GMAW:

$$H_e = V_c I/v \tag{Eq 16}$$

$$H = (V_a + V_c)I/v \tag{Eq 17}$$

The efficiency ratio is approximately 66%. However, in electrode negative (EN) mode, the electromagnetic force prevents the droplet from being detached. To resolve this issue, the polarity can be switched between EN and electrode positive (EP), such that the efficiency ratio is increased using EN but the droplet is detached using EP. The resultant processes are variable-polarity GMAW and ac GMAW.

In double-electrode GMAW, if the bypass electrode is nonconsumable, such as a tungsten:

$$H_e = V_a I/v \tag{Eq 18}$$

$$H = (V_a I + V_c I_{bm})/v \tag{Eq 19}$$

where I_{bm} is the base-metal current, and the melting current $I = I_{bp} + I_{bm}$, that is, the sum of the base-metal current and bypass current. The efficiency ratio is:

$$\lambda \approx I/(I + 2I_{bm}) \tag{Eq 20}$$

If $I_{bp} = I_{bm}$, then $\lambda = 50\%$. If $I_{bp} = 4I_{bm}$, then $\lambda = 5/7 = 71\%$.

For consumable double-electrode GMAW where the bypass electrode is a wire:

$$H_e = (V_a I + V_c I_{bp})/v \tag{Eq 21}$$

$$H = (V_a + V_c)I/v \tag{Eq 22}$$

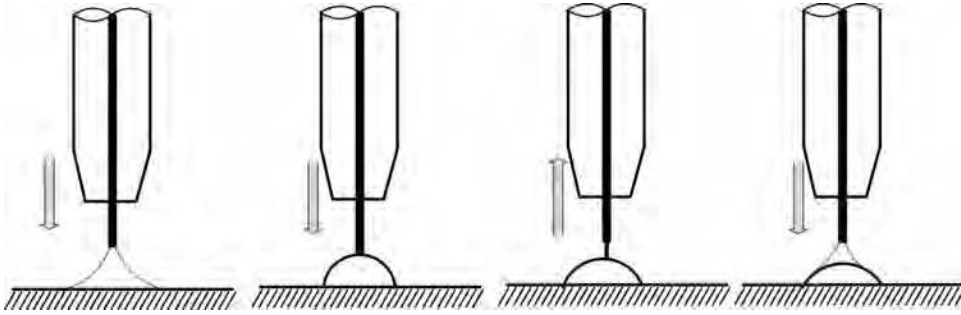


Fig. 23 Cold metal-transfer process (metal inert gas/metal active gas dip-transfer arc process). Courtesy of Fronius USA LLC, 2007

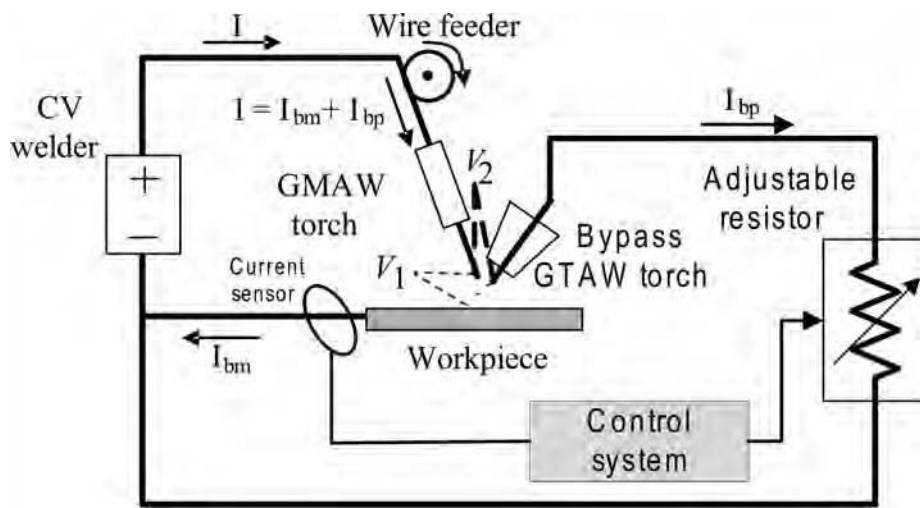


Fig. 24 Nonconsumable double-electrode gas metal arc welding (GMAW). GTAW, gas tungsten arc welding

The efficiency ratio is:

$$\lambda \approx 33\% + \left(\frac{2}{3}\right) \left(\frac{I_{bp}}{I}\right) \quad (\text{Eq 23})$$

If $I_{bp} = I_{bm}$, then $\lambda = 66\%$. If $I_{bp} = 4I_{bm}$, then $\lambda = 86\%$.

REFERENCES

1. K. Goldman, *Electric Arcs in Argon*, *Physics of the Welding Arc*, Institute of Welding, London, 1966
2. K. Ando and J. Nishikawa, "Studies on Anode and Cathode Energy of TIG Arc," IIW Document 211-158-68, 1968
3. J.F. Lancaster, Energy Distribution in Argon-Shielded Welding Arcs, *Br. Weld. J.*, Vol 1, 1954, p 412-416
4. H.S. Song and Y.M. Zhang, Measurement and Analysis of Three-Dimensional

Specular Gas Tungsten Arc Weld Pool Surface, *Weld. J.*, Vol 87 (No. 4), 2008, p 85s-95s

5. P.J. Li and Y.M. Zhang, Analysis of Arc Light Mechanism and Its Application in Sensing of GTAW Process, *Weld. J.*, Vol 79 (No. 9), 2000, p 252s-260s
6. E.J. Soderstrom, K.M. Scott, and P.F. Mendez, Calorimetric Measurement of Droplet Temperature in GMAW, *Weld. J. Res. Suppl.*, Vol 90, 2011, p 77-s to 84-s
7. K.H. Li and Y.M. Zhang, Metal Transfer in Double-Electrode Gas Metal Arc Welding, *J. Manuf. Sci. Eng. (Trans. ASME)*, Vol 129 (No. 6), 2007, p 991-999

SELECTED REFERENCES

- M. Amin, Pulse Current Parameters for Arc Stability and Controlled Metal Transfer in

Arc Welding, Met. Constr., Vol 15, 1983, p 272-278

- J.H. Choi, J. Lee, and C.D. Yoo, Dynamic Force Balance Model for Metal Transfer Analysis in Arc Welding, *J. Phys. D, Appl. Phys.*, Vol 34 (No. 17), 2001, p 2658-2664
- C.E. Jackson, The Science of Arc Welding, *Weld. J.*, Vol 39, 1960, p 129s-140s, 177s-190s, 225s-230s
- J.F. Key, Arc Physics of Gas-Tungsten Arc Welding, *Welding, Brazing, and Soldering*, Vol 6, *ASM Handbook*, ASM International, 1993, p 30-35
- J.F. Key, J.W. Chan, and M.E. McIlwain, Process Variable Influence on Arc Temperature Distribution, *Weld. J./Weld. Res. Suppl.*, Vol 62 (No. 7), 1983, p 179-s to 184-s
- Y.S. Kim, "Metal Transfer in Gas Metal Arc Welding," Ph.D. dissertation, MIT, Cambridge, MA, 1998
- J.F. Lancaster, Ed., *The Physics of Welding*, 2nd ed., International Institute of Welding, Pergamon Press, 1986
- K.H. Li, J.S. Chen, and Y.M. Zhang, Double-Electrode GMAW Process and Control, *Weld. J.*, Vol 86 (No. 8), 2007, p 231s-237s
- K.H. Li and Y.M. Zhang, Consumable Double-Electrode GMAW Part I: The Process, *Weld. J.*, Vol 87 (No. 1), 2008, p 11s-17s
- P.J. Modenesi, C.M.D. Starling, and T.I. Reis, Wire Melting Phenomena in Gas Metal Arc Welding, *Sci. Technol. Weld. Joining*, Vol 10 (No. 5), 2005, p 610-616
- C.G. Pickin and K. Young, Evaluation of Cold Metal Transfer (CMT) Process for Welding Aluminum Alloy, *Sci. Technol. Weld. Joining*, Vol 11 (No. 5), 2006, p 583-585
- "Process of Surface Tension Transfer," <http://content.lincolnelectric.com/pdfs/products/literature/nx220.pdf>
- S. Rhee and E. Kannatey-Asibu, Analysis of Arc Pressure Effect on Metal Transfer in Gas-Metal Arc-Welding, *J. Appl. Phys.*, Vol 70 (No. 9), 1991, p 5068-5075
- M. Richardson, P.W. Bucknall, and I. Stares, The Inference of Power Source Dynamics on Wire Melting, *Weld. J.*, Vol 73 (No. 2), 1994, p 32s-37s
- E.K. Stava, System and Method of Short Circuiting Arc Welding, U.S. Patent 5,148,001, 1992
- E.K. Stava, Short Circuit Arc Welder and Method of Controlling Same, U.S. Patent 6,501,049, 2002
- J.S. Thomsen, Control of Pulsed Gas Metal Arc Welding, *Int. J. Model. Identif. Control*, Vol 1 (No. 2), 2004, p 115-125
- Q.L. Wang and P.J. Li, Arc Light Sensing of Droplet Transfer and Its Analysis in Pulsed GMAW Process, *Weld. J.*, Vol 76 (No. 11), 1997, p 458s-469s

Qualification of Welding Procedures and Personnel

Harvey R. Castner, Edison Welding Institute

QUALIFICATION of welding procedures and personnel is an important step to assure the quality and performance of any welded component or structure. These qualifications confirm that the welding procedure will meet design requirements and that personnel are competent to produce welds that meet the expected quality levels. These are the reasons that welding codes, standards, and fabrication documents require the qualification of welding procedures and personnel. This article summarizes common welding procedure and personnel qualification variables and test methods. The reader is referred to the specific code, standard, or specification for the detailed qualification requirements that govern their particular application.

Several widely recognized codes and standards address qualification of welding procedures and personnel, including:

- Section IX of the American Society of Mechanical Engineers (ASME) “Boiler and Pressure Vessel Code”
- AWS B2.1, “Standard for Welding Procedure and Performance Qualification”
- NAVSEA Technical Publication S9074-AQ-GIB-010/248, “Requirements for Welding and Brazing Procedure and Performance Qualification”

Many other codes and standards include welding procedure and performance qualification requirements, for example:

- AWS D1.1, “Structural Welding Code—Steel”
- AWS D1.5, “Bridge Welding Code”
- API 1104, “Standard for Welding Pipelines and Related Facilities”

Purpose of Qualification and Responsibility for the Task

Fabricators, manufacturers, and contractors are responsible for the selection, definition, and control of the welding procedures they

use and the personnel who use them. This control normally includes the preparation of detailed written instructions known as welding procedure specifications (WPS)—or just welding procedure—and the qualification of both welding procedures and personnel. The purpose of qualifying a welding procedure is to demonstrate that the resulting welds will meet prescribed quality standards and have the requisite mechanical properties for the intended application. The qualification of personnel demonstrates their ability to produce welds that meet the quality requirements using the prescribed welding procedure.

Some fabrication codes and standards (for example, AWS D1.1) permit the use of a prequalified WPS that is within specified guidelines for materials, joint designs, processes, and methods. Other codes and standards (ASME “Boiler and Pressure Vessel Code Section IX”) permit the use of American Welding Society (AWS) Standard Welding Procedure Specifications. However, the majority of WPSs must be qualified by the user. The use of standard or prequalified procedures does not lessen the responsibility of the fabricator or contractor to ensure that the welding procedures are satisfactory for the application.

In all cases, all the important process variables must be documented in a welding procedure specification. A sample WPS form is shown in Fig. 1. If these variables change, then a new WPS may have to be prepared to reflect these changes. Whether the WPS must be requalified when revised depends on which variables are being revised. The qualification standard will identify which changes require requalification.

Qualification of Welding Procedures

Procedure qualification involves demonstrating that welds made using the procedure meet minimum soundness and mechanical property requirements. This is accomplished by

preparing, examining, and testing a qualification test weldment as well as documenting the results on a procedure qualification record (PQR). The most common method of procedure qualification involves welding a test weldment that is specifically designed for this purpose and testing it as described by the applicable code or standard. Some codes and standards permit qualification of procedures by testing special or prototype welds. The fabricator, manufacturer, or contractor must supervise and control the preparation of the qualification test welds.

The PQR documents the details of the welding variables used to prepare the qualification test weldment as well as the results of its inspection and testing. The sample form shown in Fig. 1 can be used for the PQR document along with the test results. The application of a WPS that is prepared based on the PQR is limited by the details of the test specimen and ranges of variables used in the test. For example, the range of base-metal thicknesses over which the procedure can be used is determined by the thickness of the qualification test specimen. Other variables in the WPS, such as preheat and interpass temperature or welding heat input, also may be limited by the ranges of the variables used for qualification.

While another organization may assist in the removal and assessment of test specimens, the contractor or fabricator is ultimately responsible for the procedure qualification tests, the results of these tests, and the control and application of the procedures in production. A single welding procedure qualification test may support a number of WPSs, or a single WPS may be supported by several procedure qualifications.

Types of Qualification Tests

Welding procedure qualification tests can be categorized as either standard or special tests. Standard procedure qualification test weldments represent the type of weld and weld joint that are to be used in production. Special welding

WELDING PROCEDURE SPECIFICATION (WPS) Yes **PREQUALIFIED** **QUALIFIED BY TESTING** **or PROCEDURE QUALIFICATION RECORDS (PQR)** Yes

Identification # _____
 Revision _____ Date _____ By _____
 Authorized by _____ Date _____
 Type—Manual _____ Semiautomatic _____
 Mechanized Automatic

Company Name _____
 Welding Process(es) _____
 Supporting PQR No.(s) _____

JOINT DESIGN USED
 Type: _____
 Single _____ Double Weld
 Backing: Yes No
 Backing Material: _____
 Root Opening _____ Root Face Dimension _____
 Groove Angle: _____ Radius (J-U) _____
 Back Gouging: Yes No Method _____

POSITION
 Position of Groove: _____ Fillet: _____
 Vertical Progression: Up Down

ELECTRICAL CHARACTERISTICS
 Transfer Mode (GMAW) _____ Short-Circuiting
 Globular Spray
 Current: AC _____ DCEP _____ DCEN Pulsed
 Power Source: CC CV
 Other _____
 Tungsten Electrode (GTAW)
 Size: _____
 Type: _____

TECHNIQUE
 Stringer or Weave Bead: _____
 Multi-pass or Single Pass (per side) _____
 Number of Electrodes _____
 Electrode Spacing _____ Longitudinal _____
 Lateral _____ Angle _____
 Contact Tube to Work Distance _____
 Peening _____
 Interpass Cleaning: _____

POSTWELD HEAT TREATMENT
 Temp. _____
 Time _____

BASE METALS
 Material Spec. _____
 Type or Grade _____
 Thickness: Groove _____ Fillet _____
 Diameter (Pipe) _____

FILLER METALS
 AWS Specification _____
 AWS Classification _____

SHIELDING
 Flux _____ Gas _____
 Composition _____
 Electrode-Flux (Class) _____ Flow Rate _____
 Gas Cup Size _____

PREHEAT
 Preheat Temp., Min. _____
 Interpass Temp., Min. _____ Max. _____

Pass or Weld Layer(s)	Process	Filler Metals		Current		Volts	Travel Speed	Joint Details
		Class	Diam.	Type & Polarity	Amps or Wire Feed Speed			

Procedure Qualification Record (PQR) # _____
Test Results

TENSILE TEST

Specimen No.	Width	Thickness	Area	Ultimate Tensile Load, lb	Ultimate Unit Stress, psi	Character of Failure and Location

GUIDED BEND TEST

Specimen No.	Type of Bend	Result	Remarks

VISUAL INSPECTION
 Appearance _____
 Undercut _____
 Piping porosity _____
 Convexity _____
 Test date _____
 Witnessed by _____

Radiographic-ultrasonic examination
 RT report no.: _____ Result _____
 UT report no.: _____ Result _____

FILLET WELD TEST RESULTS
 Minimum size multiple pass _____ Maximum size single pass _____
 Macroetch _____ Macroetch _____
 1. _____ 3. _____ 1. _____ 3. _____
 2. _____ 2. _____

Other Tests
 All-weld-metal tension test
 Tensile strength, psi _____
 Yield point/strength, psi _____
 Elongation in 2 in, % _____
 Laboratory test no. _____

Welder's name _____ Clock no. _____ Stamp no. _____
 Tests conducted by _____ Laboratory _____
 Test number _____
 Per _____

We, the undersigned, certify that the statements in this record are correct and that the test welds were prepared, welded, and tested in conformance with the requirements of Clause 4 of AWS D1.1/D1.1M, (_____) *Structural Welding Code—Steel*, (year) _____

Signed _____
 Manufacturer or Contractor
 By _____
 Title _____
 Date _____

Fig. 1 Welding procedure specification form. Source: Ref 1

procedure qualification tests use the specified welding procedure to fabricate prototype structures or mock-up components that are then subjected to loads that simulate the actual conditions encountered in service.

Groove-welded butt joints in plate and pipe are shown in Fig. 2 and 3, respectively, as examples of standard test weldments. Two examples of fillet welds in T-joints are shown in Fig. 4. Fillet welds can also be deposited on lap, corner, or edge joints. A partial penetration weld in a T-joint is shown in Fig. 5, whereas a plug weld test specimen is shown in Fig. 6. The latter could be a slot weld as well, and a similar weldment could be used for spot welds.

Resistance spot and seam welds are typically made on lap joints. Other test weldments are appropriate for friction, laser beam, electron beam, and stud welding or for cladding and surfacing weld deposits. The thickness of test weldments should be selected after considering the thickness of materials used in actual fabrications and the thickness limitations of the fabrication code or standard. The length and width of the test weldment should be sufficient to permit removal of the necessary test specimens.

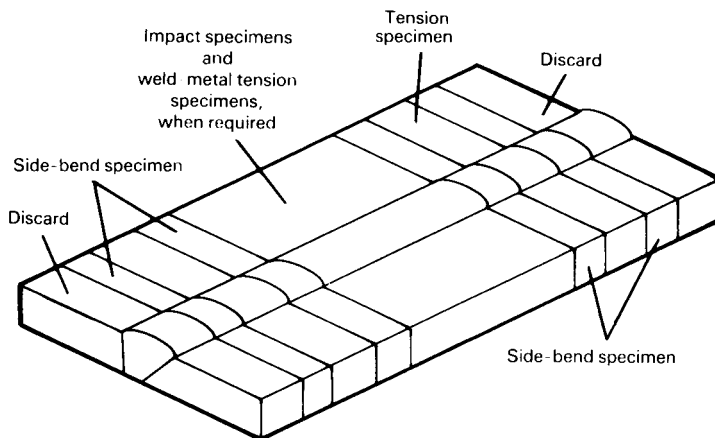


Fig. 2 Typical location of test specimens from groove welds in butt-joint test plate

After the test weldment is prepared and welded using the methods that are detailed in the PQR, it is examined and tested to the requirements of the applicable qualification code or standard. Standard tests include visual,

metallurgical, and nondestructive examinations, chemical analysis, and tests to determine mechanical properties. The mechanical property tests can include tension, bend, torque, nick-break, shear, peel, and hardness tests, as

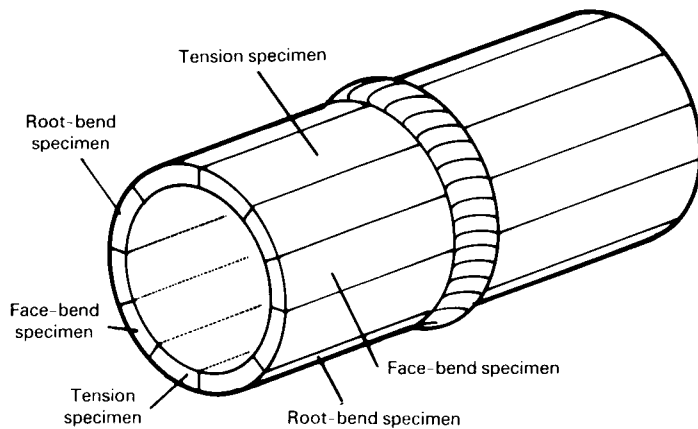


Fig. 3 Typical location of test specimens from groove welds in butt-joint pipe test

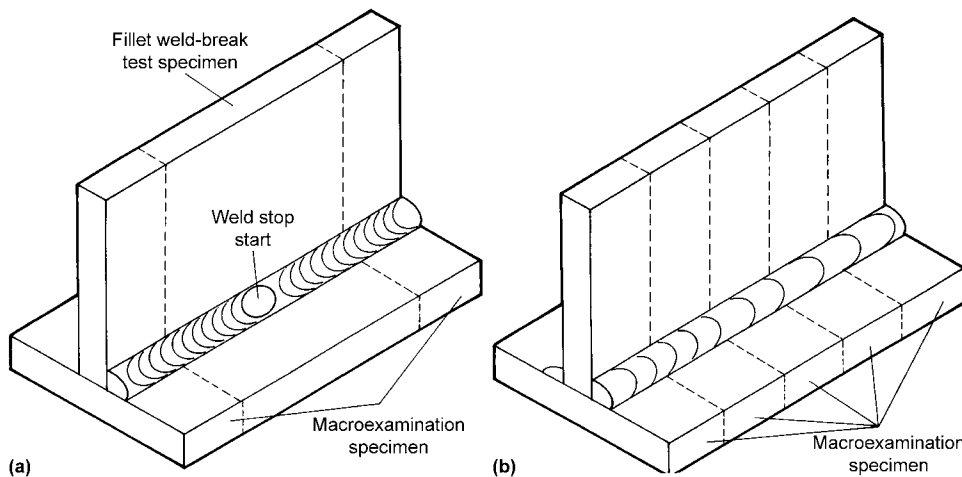


Fig. 4 Two examples of T-joint weldments for fillet weld qualification. (a) Fillet weld on one side of T-joint. (b) Fillet weld on both sides of T-joint

well as tests to determine impact (Charpy test) toughness or perhaps plane-strain (K_{Ic}) or plane-stress (K_{Ic}) fracture toughness.

Although the use of standard tests to qualify a WPS demonstrates the ability of the procedure to produce sound welds that meet the minimum required properties, these tests may not ensure that the welding procedure is suitable for all applications. Standard test plates are relatively small and are normally welded under laboratory, rather than production, conditions.

Special Qualification Tests. Codes and standards may permit the qualification of welding procedures by testing special or prototype welds. In other cases, the code, standard, designer, owner, or operator of the welded structure or component may require additional special qualification tests to establish the acceptability of a welding procedure. Special tests may involve welding mock-up or prototype structures and then subjecting these structures to loads that simulate the actual conditions encountered in service. Tests can

include static or dynamic loads, corrosive environments, high temperatures, shock, impact loading, or other tests. After load testing, the structure can also be tested destructively; welds can be sectioned and the cross sections examined for proper penetration, bead placement, and profile. Testing of roll-over protection structures is an example of a special test.

Standard Qualification Tests

Tests for Full-Penetration Groove Welds. Typical tests for full-penetration groove welds include tension, bend, and impact (Charpy) toughness tests. It is also common to subject weldments to chemical analysis, hardness tests, and macroexaminations of weld cross sections. Figures 2 and 3 indicate the location of tension and bend specimens in plate and pipe test weldments, respectively. Figure 7 shows the configuration of tension and bend specimens. The details of specimen size, orientation, removal,

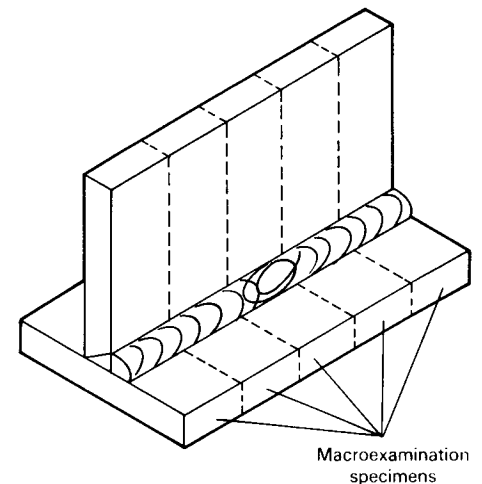


Fig. 5 Partial-penetration weld specimen

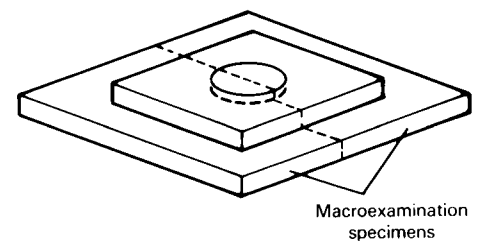


Fig. 6 Plug weld specimen

testing, and acceptance are provided in the welding code or standard or by references to ASTM International test standards or AWS B4.0, "Standard Methods for Mechanical Testing of Welds."

Tension Tests. Transverse tension tests are performed on full-penetration groove welds to determine the tensile strength of the weld region. The specimens can be full-section or reduced-section rectangular or round specimens (Fig. 7). Multiple tension specimens may be needed to test the entire thickness of plates that are more than 25 mm (1 in.) thick, as shown in Fig. 8. The acceptance of tension test results is normally based on a tensile strength that is either equal to or greater than the minimum specified tensile strength of the base metal being welded. If the weld metal has a lower specified strength than the base metal, then the tension test must exceed the specified minimum tensile strength of the weld metal. Some codes permit the strength of the tension specimen to be 5% below the specified minimum tensile strength of the base metal if the specimen breaks outside of the weld or fusion line. If all-weld-metal tension tests are required, then round specimens are typically removed from the center of the weld and oriented parallel to the weld axis.

Guided-Bend Tests. Bend tests are performed to verify the soundness and ductility of the weld and the heat-affected zone (HAZ). Figures 2, 3, and 8 show bend specimens that are typically oriented transverse to the weld axis, with the center of the weld in the center of the specimen. Face-bend and root-bend specimens are typically specified for base-metal thicknesses of less than 9.5 mm (0.375 in.). These specimens place either the face of the weld (face-bend) or the root of the weld (root-bend) on the convex side of the bend specimen. Side-bend specimens, taken through the thickness of the test weldment, are required for thicker test plates in order to test the entire weld cross section. Test weldments that are more than 38 mm (1.5 in.) thick may require multiple side-bend specimens to ensure that the entire weld thickness is tested (Fig. 8).

Under some circumstances, longitudinal bends are removed with their length parallel to the axis of the weld. Longitudinal-bend specimens are used for welds between dissimilar metals where there is a large difference in bend properties between the two base metals or between the weld metal and the base metal.

Guided-bend specimens are forced into a specified curvature (Fig. 7) by either applying a load to a plunger or forming the specimen around a fixed mandrel. The width and thickness of the specimen and the radius of the plunger or mandrel are designed to produce a minimum specified elongation in the outer surface of the specimen. It is important to follow the recommendations for specimen dimensions, because width and thickness influence test performance. The most common bend specimen for steel welds is 9.5 mm (0.375 in.) thick and

is formed around a 20 mm (0.75 in.) radius to yield 20% elongation in the outer surface of the specimen. Larger bend radii are permitted to match the lower ductility of some base metals or weld metals. Acceptable bend specimens must not fracture or have cracks or other open defects that exceed a specified maximum size (usually 3.2 mm, or 0.125 in.) on their convex surface.

Impact Toughness Tests. Charpy V-notch impact tests are often used to measure the fracture toughness of weld metals and HAZs. Charpy V-notch specimens are usually removed from the weld metal and HAZ, with the notch oriented normal to the surface. One face of the V-notch specimen is located within 1.6 mm (0.06 in.) of the surface of the material. Thick materials require additional specimens at subsurface locations. When permitted, subsized impact specimens can be used for thin materials that do not permit the removal of standard specimens. The number of specimens, their location and orientation, and the test temperature are determined by the design requirements or material specifications. Acceptance criteria may be a minimum specified absorbed energy in joules (ft-lbf), a minimum percentage of shear fracture appearance, or a minimum specified lateral expansion opposite the notch. The applicable code or standard should be consulted for test conditions and acceptance criteria for subsized specimens.

The assessment of toughness, in terms of dynamic tear or plane-strain fracture properties, using compact-tension or crack tip opening displacement specimens may be required for some welding procedures. Drop-weight tests are sometimes used to determine the minimum nil-ductility transition temperature for ferritic steel weld metal and HAZs. Codes and specifications describe how specimens should be

removed from the weld metal and HAZs to permit the measurement of each of these fracture toughness properties.

Tests for Fillet Welds, Partial-Penetration Groove Welds, and Spot and Plug Welds.

The procedure qualification of fillet welds typically involves T-joint test weldments, similar to those shown in Fig. 4. Some codes and specifications permit lap joints, corner joints, or other joint configurations that represent the actual joint used in production.

Procedures for partial-penetration groove welds can be qualified by making test weldments that represent the joint used for the application. Figure 5 shows a T-joint test weldment for a partial-penetration groove weld. Figure 6 shows the configuration of the test weldment for the qualification of plug or slot welds.

Completed fillet, partial-penetration, and plug or slot weldments are usually examined visually and tested to ensure that they meet the acceptance requirements of the weld-quality specification. These welds do not normally lend themselves to mechanical property testing, although tension-shear tests and weld-break tests can be conducted on them. The required mechanical properties must be determined from a standard groove-weld test. Macrosections are removed to verify root penetration.

Figures 4 and 5 show how macroexamination specimens are removed from fillet or partial-penetration welds. Figure 6 illustrates how plug or slot welds are cut through their center to produce macroetch specimens. The faces of macroetch specimens are ground smooth, etched, and then examined. Acceptable welds must have:

- The designated weld size and profile
- Fusion to the root of the joint
- No cracks

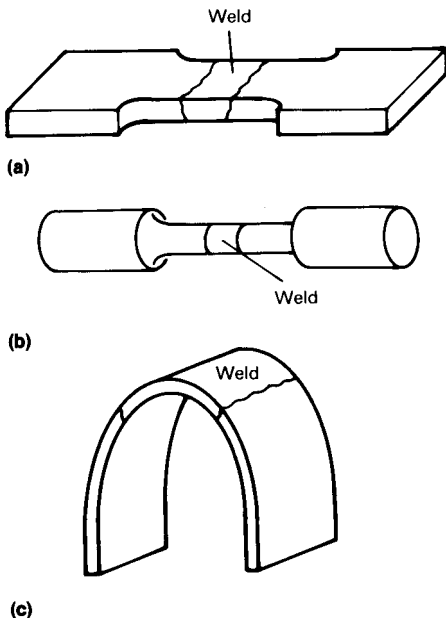


Fig. 7 Tension and bend specimens for testing of full-penetration groove welds. (a) Reduced-section tension specimen. (b) Round tension specimen. (c) Bend specimen

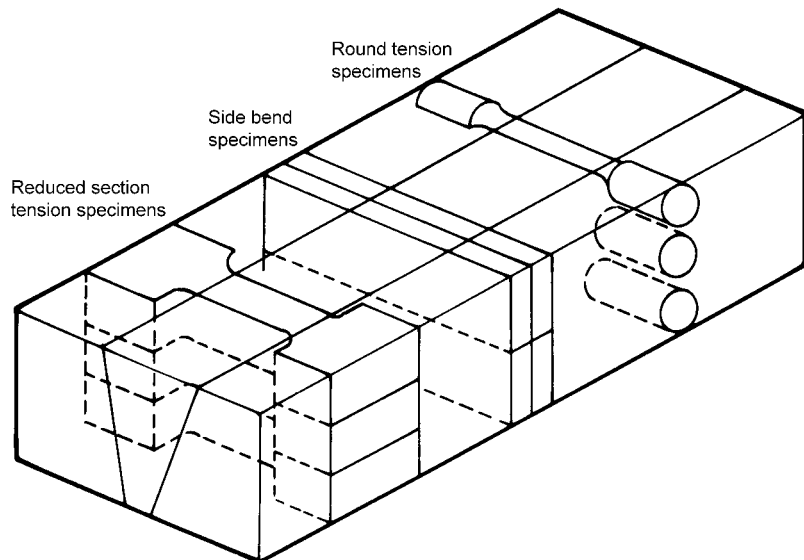


Fig. 8 Removal of multiple bends and tension specimens from thick test plates

- Complete fusion between adjacent layers of weld metal, as well as between weld metal and base metal

Shear tests can also be used to measure the strength of fillet, partial-penetration, plug, or slot welds. Usually, acceptable shear strength is at least 60% of the minimum specified tensile strength of the base metal.

Weld-break tests also may be required for fillet and partial-penetration welds. These specimens are removed from the weld, as shown in Fig. 4, and loaded so that the root of the weld is in tension until the specimen fractures or bends flat upon itself. Acceptance is determined by examining the fractured surface for complete fusion, the required depth of penetration, and porosity and inclusion levels that do not exceed a specified maximum size. The specimen is also acceptable if it bends flat upon itself without fracturing.

Procedure qualification tests for arc and resistance spot welds include tension-shear, torsion, peel, and hardness tests, as well as macroexaminations. Tension, torsion, and peel test specimens are examined to determine the location of failure and the size and soundness of the weld nugget.

Tests for Stud Welds. The qualification of stud welding procedures can involve welding and testing multiple specimens for each diameter, welding position, and geometry to be qualified. Sectioning and macroexamination can determine whether or not the welds and HAZs have the proper fusion and are free of cracks. Bend tests for stud welds involve bending the stud through a minimum angle (for example, 30°) and then bending it back to the original position. An alternative test is to bend the studs by hammering them flat onto the test plate. The bent studs must be free of visible separation or fracture. Stud welds also are tested by applying torque or tension loads.

Tests for Weld Cladding and Surfacing. The qualification of weld cladding procedures can involve liquid penetrant testing, chemical analysis of the deposit, macroexamination of cross sections, and bend tests. The qualification for hard-surfacing welding procedures can include hardness tests in addition to chemical analysis of the deposit and macroexamination of cross sections.

Limitations on Procedure Qualification. A new welding procedure must be qualified if it differs significantly from another qualified procedure. The application range of a welding procedure qualification is determined by placing limits on the welding variables specified in the procedure. Codes and standards define these limiting variables as essential variables, essential elements, or qualification variables. A welding procedure must be requalified if changes in these variables exceed specified limits.

Supplementary essential variables are the variables that affect notch toughness. Supplementary

variables become essential variables when notch toughness tests are required.

Nonessential variables are the remaining variables contained in the WPS that can be changed without requiring requalification. An essential variable for one process may be nonessential for another process.

Although there are differences in how codes and standards define essential variables, the variables described as follows are considered to be essential by most codes and standards.

Welding Process. A change of welding process will require requalification, because the process has a significant effect on the mechanical properties and metallurgical structure of the weld.

Base Metal. Changing from one base-metal type or thickness to another can affect weldability as well as the metallurgical and mechanical properties of the weld. Changes in base metals also can cause differences in weld penetration and weld fusion characteristics for certain welding processes. Therefore, significant changes in base-metal type, composition, heat treatment, or processing will require requalification.

Codes and standards group together base metals that have similar weldability characteristics, metallurgical properties, chemical compositions, or mechanical properties. The grouping of base metals reduces the number of required qualifications by allowing the qualification of a procedure on one of the materials in the group to qualify the procedure for use on the other base metals in that group. Changing to a base metal of another group requires requalification.

Separate welding procedure qualifications are typically required for pipe and plate. While a procedure qualification on pipe may also cover plate, a procedure qualification on plate may be restricted to welding plates and large-diameter pipes. Limitations also are placed on metal thickness for procedure qualification. Base-metal thickness influences cooling rate and therefore metallurgical and mechanical properties. The composition of a metal may also change with thickness. Most codes permit qualification on one thickness of test specimen to cover a range of base-metal thicknesses. Some codes require qualification on the exact thickness of metal that is to be used for production welds. Other codes require qualification on the thinnest and thickest metals that are used in production.

Filler Metal. Filler metals and welding electrodes with similar chemical compositions and operating characteristics also are grouped together for the purposes of procedure qualification. Grouping reduces the number of qualifications that must be done by allowing the qualification of one of the filler metals in the group to also qualify the others in that group. Ferrous filler metals can be grouped by both chemical composition and usability. The addition or deletion of a filler metal, supplementary filler metal, or consumable insert is an essential variable for arc welding processes.

Position is not an essential variable for some codes and standards, while other specifications allow qualification in one position to cover qualification in another position. Welding position usually is an essential variable for procedures requiring notch toughness testing.

Joint design is an essential variable for some processes and applications but not for others. Weld joint design should be an essential variable for processes where changes to the joint affect metallurgical structures and weld properties. Examples of these processes include stud, laser beam, electron beam, and friction welding.

Electrical Characteristics. Variations in the type of welding current (alternating or direct, for arc welds) or in polarity normally require requalification. A small change in welding current or voltage within limits permitted by the document does not typically require requalification. The results of more than one PQR can be used to support the acceptable performance of the range of variables for a given WPS. Procedures meeting notch toughness requirements may limit changes in electrical characteristics and travel speed through limits on weld heat input. The use of current pulsation and the pulse parameters may be essential variables. For example, beam current or beam power are essential variables for both laser beam and electron beam welding. Use of pulsed welding current is an essential variable for gas tungsten arc welding and gas metal arc welding in some codes or standards.

Shielding. The use and the composition of a shielding gas are essential variables for gas shielded arc welding, friction welding, and laser beam welding processes.

Preheat and Interpass Temperatures. Significant changes in preheat or interpass temperatures will affect properties and therefore will require requalification. Codes and standards differ on the size of the change in temperature that is permitted. Some codes limit changes to a maximum of 14 °C (25 °F), whereas others permit an increase or decrease of up to 56 °C (100 °F) before requalification is required.

Postweld Heat Treatment. The use of postweld heat treatment requires qualification that includes the heat treatment. The applicable code or standard should be consulted regarding changes in the postweld heat treatment temperature or time at temperature that requires requalification.

Other variables that affect the soundness, metallurgical structure, or mechanical properties of the weld are essential or qualification variables. These variables depend on the welding process being used. Examples of these variables include:

- Changing from a stringer to a weave bead, or changing the direction of welding for vertical arc welding procedures
- Changes in electrode composition or configuration for resistance welding

- Changes in filament type, size, or shape and in gun-to-work distance for electron beam welding
- Changes in focal length, focus position, or spot size for laser beam welding
- Changes in energy, applied loads, or the amount of upset for friction welding

Qualification of Welding Personnel

The employer is responsible for assuring that their personnel are trained and qualified to the specific requirements of the codes, specifications, or fabrication documents under which work is to be performed. Welding personnel, including welders, tack welders, and welding operators, are qualified by demonstrating their ability to produce welds that meet minimum requirements for soundness and quality. Qualification of personnel is also referred to as performance qualification.

Welding personnel are qualified by welding a test plate while following a welding procedure specification and having the test plate examined to determine its acceptability. Some standards permit qualification of personnel by examination of workmanship samples or production welds. Critical applications may require the welder to produce special welds that simulate the actual conditions encountered during fabrication. Training, knowledge tests, and visual acuity are part of the requirements of some specifications.

Performance Qualification Tests. The test specimens, types of tests, and variables that govern personnel qualification are based on the level of knowledge or skill required for the task and those variables that have an effect on the ability of the individual to produce sound welds. Therefore, personnel that are qualified only to produce tack welds or fillet welds do not have to demonstrate the same skill levels as those qualified for out-of-position pipe welding. Welding operators are qualified to produce welds using the mechanized, automated, or robotic equipment and the welding procedure specification that they intend to use.

Qualification using standard tests involves the individual preparing the test weld using the WPS and having the weld tested according to the requirements of the code or standard being used. These requirements typically include visual and nondestructive examination and/or the removal of specimens for mechanical property or other tests. Guided-bend tests, fillet weld-break tests, and macroexamination of weld cross sections are typical types of tests performed on performance qualification welds. These tests are similar or identical to those described previously for qualification of welding procedures. Many codes and standards permit radiographic tests to be substituted for guided-bend testing for performance qualification, since

the issue being examined is the welder's ability to produce a sound weld.

Limitations on Performance Qualification.

Variables that determine the limits of performance qualification include the welding process; base-metal type, composition, and thickness; type of weld; use of weld backing; a change in welding position to a more difficult position; changes in uphill or downhill progression for vertical-position welding; and a change in the filler-metal operating characteristics grouping.

Process. Use of each welding process requires specific knowledge and skills that make it essential that a welder is tested on the welding process to be used in fabrication. There are also certain changes within a process that affect usability and require requalification, such as the use of short-circuit metal transfer or pulsed welding current.

Base Metal. Similar to welding procedure qualification, changing from one base-metal grouping to another often requires requalification since the base metal can affect the filler metal used, weld penetration, and fusion characteristics. Codes and standards permit qualification on one base-metal group to allow personnel to weld metals in similar groups. The type and thickness of the base metal also are essential variables for performance qualification. Pipe, sheet, and plate may require different welding abilities or techniques that need to be verified by testing. Specific limits must be considered during performance qualification for welding of small-diameter pipes and heavy-thickness materials.

Weld Type. Producing fillet welds or groove welds can require different levels of skill, and therefore, qualification for groove welds is tested differently than qualification of an individual that will only produce fillet welds. The deletion of backing from a groove weld joint also requires requalification of individuals that have previously been qualified only on joints with backing.

Position. Welding in the vertical or overhead positions or welding pipe in the horizontal-fixed position requires greater skill than flat-position welding. Normally, a performance test in the more difficult position also qualifies for less demanding positions. A change in the direction of weld progression from uphill to downhill or vice versa requires requalification.

Filler Metal. A change to a filler metal from another operating characteristics group (F-number) usually requires requalification of the individual. There are some instances where qualification on one filler-metal group also qualifies the individual on other similar groups. The addition or deletion of a filler metal, supplementary filler metal, or consumable insert is an essential variable for arc welding processes.

Maintenance of Qualification. Failure to maintain their qualification or to demonstrate

competence can result in an individual having to requalify their ability to perform a welding operation. Once the welder or welding operator has passed a performance qualification test, they must continue to use the qualified skills in order to maintain their qualified status. Maintenance of personnel qualification requires verification that the individual has used the welding process during a period of time that is specified as every six months by some codes and standards or three months by others. Qualification of an individual can be revoked if their ability to produce satisfactory welds comes into question.

Qualification Documentation

Record keeping of procedure and performance qualification is an essential part of the responsibility of the activity (fabricator, manufacturer, and contractor) that uses welding procedures and employs welding personnel. Documentation includes preparation and maintenance of the WPS that defines the variables and methods to be used for welding. A PQR is used to document the actual welding variables that are used for the procedure qualification test weldment as well as the results of the tests of this weldment. Performance qualification test records are used to document the preparation, inspection, and testing of the performance qualification test. The activity also needs to record the use of a process by their qualified personnel in order to maintain their qualified status. The manufacturer or contractor should have these records available for review by customers or authorized inspectors.

REFERENCES

1. "Structural Welding Code—Steel," AWS D1.1, American Welding Society

SELECTED REFERENCES

- "Requirements for Welding and Brazing Procedure and Performance Qualification," NAVSEA Technical Publication S9074-AQ-GIB-010/248, Naval Sea Systems Command, U.S. Department of the Navy
- "Standard for Welding Procedure and Performance Qualification," AWS B2.1, American Welding Society
- "Standard Methods for Mechanical Testing of Welds," ANSI/AWS B4.0, American Welding Society
- "Structural Welding Code—Steel," AWS D1.1, American Welding Society
- "Welding and Brazing Qualifications, Boiler and Pressure Vessel Code," ASME B&PVC-IX, American Society of Mechanical Engineers
- *Welding Handbook*, American Welding Society

General Design Considerations for Arc Welding Processes

W.C. Mohr, Edison Welding Institute,
 O.W. Blodgett, The Lincoln Electric Company

A WELD JOINT serves to transfer the stresses between the joined members and throughout the welded assembly. The type of loading and service of the weldment influences the selection of a joint design and how forces and loads at different points are transmitted to different areas throughout the weldment.

Joint types describe how the members meet, and the names of different joint types are butt, T, corner, lap, and edge. The selected weld also may or may not require preparation in the form of a groove to permit proper access to the root of the joint. Several methods of joint preparation include machining, chipping, shearing, grinding, gas cutting, gas gouging, or air carbon arc gouging, which may be used to create single- or double-bevel, V-, J-, or U-grooves.

No preparation is needed for a square groove weld. The members can be abutted in the same plane. If there is zero root opening, the weld arc essentially fuses the members together. Usually, very little or no weld metal bridges the weld members, although some weld metal or reinforcement may be left on the top and bottom surfaces. Similarly, fillet welds, which join pieces perpendicular to each other, can be used on T-joints without preparation. The welds and the fusion into both members join the two pieces.

Groove preparations are often necessary, however, for successful welding of various corner, T-, and butt-joint applications. Frequently required with larger metal thicknesses, these weld preparations ensure that the welding heat and weld metal reach and fuse the root of the joint.

Nomenclature

Terminology describing various joints and welds is often confused. Types of welds and joints recognized by the American Welding Society (AWS) are illustrated in Fig. 1. Note that joints are the junctions where the members join, and welds are the mechanisms (groove or preparation) that complete joints. Figure 2 shows applications of some single-bevel and single-V welds on T- and corner joints.

Although precise nomenclature to differentiate between welds and joints is desirable, engineers will probably continue to use the terms interchangeably. For example, although Fig. 16 (discussed later) is technically a joint made with two partial-penetration double-bevel groove welds, the joint is referred to as a partial-penetration double-bevel groove joint. Thus, in this article as well as other practical applications, the terms *joint* and *weld* are used interchangeably to describe how a joint is constructed.

Types of Joints

Butt joints are joints between two abutting members lying approximately in the same plane. Although they may be welded with no preparation, butt joints are often grooved, especially with thicker and heavier plate.

Butt joints are preferable in uses where continuity of section is desired, such as fusion-welded joints in sheet or plate for pressure vessels, pipelines, decking, tanks, and similar construction applications. Generally, when the

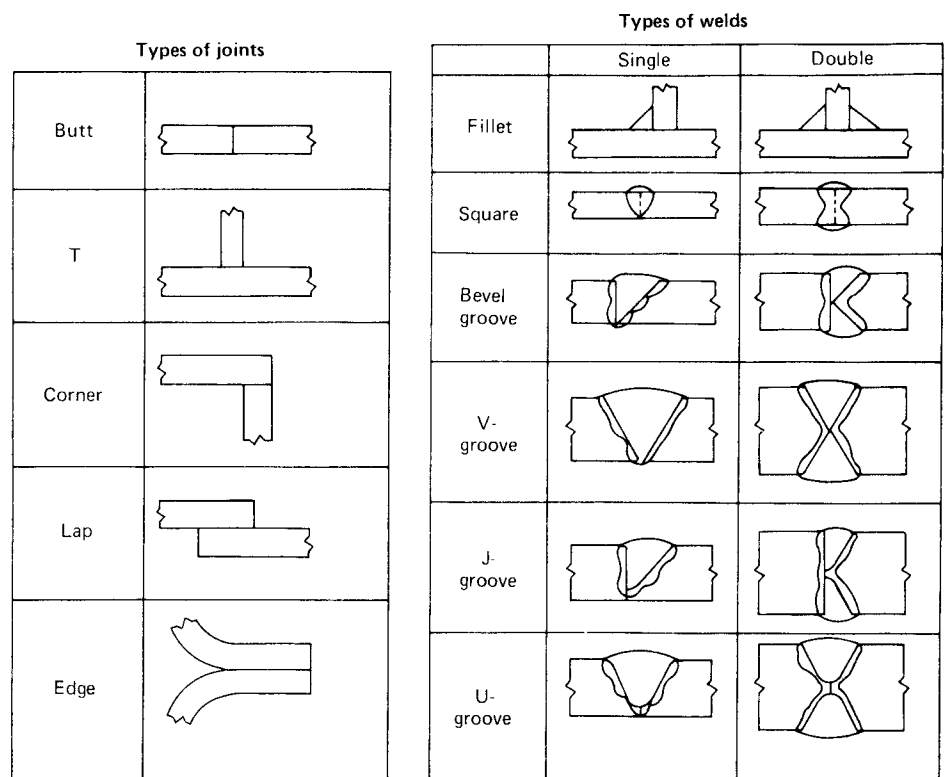


Fig. 1 Types of joints and welds

metal thickness exceeds approximately 6 mm (1/4 in.), the butt joint requires grooving to prevent a lack of fusion from weakening the weld.

T-joints are joints in which the members are positioned in the form of a "T." They are well suited for no-preparation fillet welds, but in thick material the preparation welds, such as the single-bevel in Fig. 2, may be necessary.

T-joints are frequently used in production of fabricated weldments, welded machinery components, attachment of flanges and plate stiffeners to webs of girders, and assembly of rolled section and tubular building structures. Fillet-welded T-joints should not be used for fusion welding with ordinary gas or arc welding of containers because corrosive solids may be trapped in the unwelded area between the members.

Corner joints are joints between members located at approximately right angles to each other that meet in the form of an "L." Typical applications are the same as those for T-joints.

Figure 3 shows various corner joints with fillet and preparation welds. The corner-to-corner joint (Fig. 3a) is difficult to assemble because neither plate can be supported by the other. A small electrode with low welding current must be used to prevent the first welding pass from melting through. This joint requires a large amount of weld metal. In contrast, the corner joint in Fig. 3(b) is simple to assemble, does not melt through easily, and requires half the amount of weld metal. Half the weld size is also used when welding the identical joint with two welds, one outside and the other inside (Fig. 3c), a design that has the same total throat as Fig. 3(a).

With thick plates, a partial-penetration groove weld (Fig. 3d) is often used in a corner joint. This weld requires beveling. For a deeper weld, a J-groove preparation may be chosen instead of a bevel (Fig. 3e). Another possibility, the fillet weld in Fig. 3(f), is inconspicuous and makes a neat and economical corner.

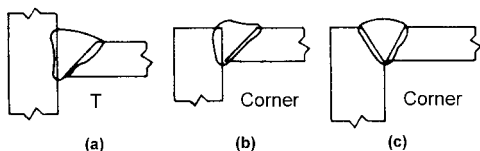


Fig. 2 Welds in T- and corner joints. (a) and (b) Single-bevel welds. (c) Single-V-groove weld

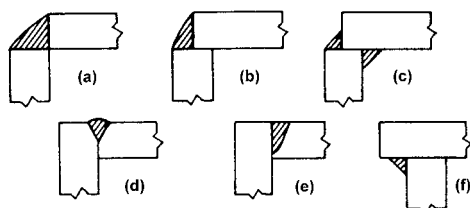


Fig. 3 Corner joints. (a), (b), (c), and (f) Fillet welds. (d) V-groove weld. (e) J-groove weld

Lap joints are joints made with two overlapping members. They do not require edge preparation. Lap joints are necessary for use in seam and spot welding of sheet metals.

Edge joints are joints between the edges of two or more parallel or nearly parallel members. They may not require the addition of filler metal for welding and are frequently used to join thin turned-out edges, such as those formed where the sides of a container meet.

Types of Welds

Fillet welds are welds approximately triangular in cross section, joining two surfaces essentially at right angles to each other in a lap, T-, or corner joint. Fillet welds require no preparation and are the most common type of weld used in structural work.

Square groove welds are welds in which the abutting surfaces are square (0° included angle). Because welding from one side makes penetration difficult, the double-square weld is used frequently to ensure the strength of the weld. Sometimes the root of the weld is opened and a backing bar is used. The purpose of a backing material, which is placed at the root of the weld joint, is to support the molten weld metal.

Bevel groove welds are welds in which only one member is beveled. The bevel angle (material removed by cutting) is measured between the prepared edge of a member and a plane perpendicular to the surface of the other member. Single-bevel groove preparations are widely used because they are easily prepared by oxyfuel gas cutting. They are well suited for corner and T-joints (Fig. 2), as well as butt joints 6 mm (1/4 in.) in thickness and greater. Double-bevel grooves are recommended, if welding from both sides is possible, when metal is 19 mm (3/4 in.) or thicker, because these grooves produce less distortion of the welded parts and reduce weld-metal requirements by approximately half.

V-groove welds are welds in which the total included angle of the groove between the members to be joined is the sum of the two bevel angles. Similar to single-bevel groove welds, single-V-groove welds are widely used because they are easily prepared by oxyfuel gas cutting. Figure 2 shows a single-V weld in a corner joint. These groove preparations are also used extensively in edge preparations for butt joints 6 mm (1/4 in.) in thickness and greater. The advantages of double-V bevel grooves are the same as those for double-bevel grooves.

J-groove welds are welds made in J-shaped grooves between the two members to be welded. Single-J-grooves are well suited for butt, corner (Fig. 3e), and T-joints. The advantages of double-J-groove preparations are the same as for double-bevel grooves.

U-groove welds are welds made in U-shaped grooves between two members to be

welded. Because of the rounded base, larger electrodes can be used with narrower groove angles than for V-groove welds. The U-groove preparations can be prepared by air carbon arc gouging or by machining, which yields more uniform grooves. Because J-grooves and U-grooves require at least 3 mm (1/8 in.) root face and 6 mm (1/4 in.) radius at the root of the joint, the material must be more than 9 mm (3/8 in.) thick for this joint to be used. The advantages of double-U-groove welds are the same as those for double-bevel welds.

Weld Joint Design

The first consideration in the design of a weld joint is its ability to transfer load; the second is cost. The ideal weld joint is one that can handle the loads imposed, usually with a substantial safety margin, and still be produced at minimal cost.

Therefore, once the type of joint has been selected primarily on the basis of load requirements, the choice of weld to complete the joint should be determined by the effects of the structural design and layout on weld metal, accessibility, and preparation requirements—variables that directly influence the cost of the weld joint. There may be other factors, such as distortion and fatigue resistance, that enter into the decision. Design factors can also be important in the prevention of defects such as incomplete fusion, solidification cracking, or lamellar tearing.

Weld Metal. In general, joint and weld types specified should require the least amount of filler metal to avoid unnecessary expense. The size of the weld should always be designed with reference to the size of the thinner member. The joint cannot be made any stronger by matching the weld size to the thicker member, which would require a greater amount of weld metal.

In the design stage, joints that create extremely deep grooves should be avoided, because these require more filler metal. Deep-penetration welding processes, such as submerged arc welding, especially automatic welding, reduce the volume of weld metal needed. Because greater thickness of plate can be welded, use of these methods may reduce the cost of groove preparations.

If groove welds are required, minimum root openings and included angle should be used to reduce the filler metal required. The use of double- instead of single-groove welds on thick plate where welding from both sides is feasible decreases the total filler metal.

To prevent waste of weld metal, welding specifications should avoid the unnecessary use of continuous welds. Welding everything that touches may have no engineering advantages yet increases the amount of weld metal used. Where sealing is required, other methods of postweld sealing can be preferred.

When joining high-strength materials, cost can be minimized by specifying the use of

high-strength weld metal only where required for primary load-carrying welds, in cases where alternate and lower-cost materials are compatible.

Accessibility. An important factor in the design of a weld joint is the accessibility of the members to be welded. The welder needs space to manipulate the electrode when making the weld. Frequently, what appears straightforward on the drawing board may be impractical in the shop or very costly to produce. As a rough estimate, there should be 200 mm (8 in.) above the weld cap to manipulate the electrode or torch and freedom to angle the arc toward either side of the joint by approximately 10°.

Distortion. There are several modes of welding distortion that can change the shape of the finished weldment. These are more severe with larger amounts of weld metal, larger amounts of heat input, and welds further from the center of the thickness of the parts being joined. These same parameters also increase the variability of distortion. Groove welds can be advantageous over fillet welds because they can reduce all of these parameters related to distortion. However, as earlier distortion builds up during progressive construction, it may become more difficult to control the gaps in groove welding, and fillet welding may need to be used.

Fatigue. Detail geometry and joint configuration are the most important variables affecting the fatigue life of a structural detail. Discontinuities associated with a weld detail can behave as preexisting cracks and serve as the initiation site (s) for further fatigue crack propagation. Fatigue cracks tend to grow from local stress concentrations, such as the weld edge on the surface or the weld root of a fillet weld.

The joint designs with poorest fatigue resistance are the nonsymmetrical types, such as strap, tee, and lap joints in which large secondary stresses are also developed. Poor fatigue resistance is also observed in non-load-carrying attachments or reinforcements to a plate strictly due to the stress-concentration effect of those attachments. Bevel welds are usually superior; lack of fusion and incomplete penetration problems often occur in fillet welds or square joints. Size effects must also be considered, because fatigue results obtained from small-scale specimens demonstrate distinctly higher fatigue limits than those obtained in full-scale sections.

The precise location and the magnitude of stress concentration in welded joints depend on the design of the joint and on the direction of the load. Some examples of stress concentrations in butt welds and fillet welds are given in Fig. 4. Concentration of stress at the toes of the weld may initiate cracking, even if the weld does not carry any load. Indeed, the weld toe is often the primary location for fatigue cracking in joints that have good root penetration. In situations where the root penetration is poor or the root gap is excessive, or in load-carrying

fillet welds where the weld throat is insufficient, the root area can become the region of highest stress concentration. Fatigue cracks in these situations start from the root of the weld and generally propagate through the weld (Fig. 5).

Standard methods are available for assessment of the acceptable fatigue stresses in welded structures. The preference for one type of weld joint over another may be affected by the need to prevent fatigue cracking. Groove welds can usually be made with lower stress concentrations than fillet welds. Moving weld ends to low-stress areas can also improve fatigue resistance.

Design Aspects in Prevention of Defects Associated with Arc Welds. Welded joints may include various types of discontinuities, some of which may be considered as defects if the discontinuity is an unacceptable condition for joint performance. The types of discontinuities may be divided into three broad classifications: design related, welding process related, and metallurgical. Design-related discontinuities include problems with design or structural details, choice of the wrong type of weld joint for a given application, or undesirable changes in cross section. Process-related discontinuities include lack of fusion, lack of penetration, porosity, shrinkage voids, inclusion, or other process effects. Metallurgical discontinuities include various types of cracking phenomena (e.g., lamellar tearing, solidification cracking) and the nonuniform distribution (segregation) or concentration of impurities or alloying elements during weld solidification.

The observed occurrence of discontinuities and their relative amounts depend on several factors, including the welding process used, process parameters, the type of weld made, the joint design and fit-up obtained, the material used, and the working and environmental conditions. Typical types of process-related discontinuities are discussed in other articles on specific arc welding processes. However, joint design can be a factor in preventing or reducing the likelihood of some types of metallurgical defects, such as solidification cracks and lamellar tearing.

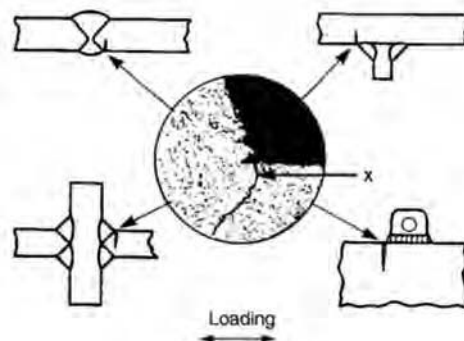


Fig. 4 Examples of stress concentrations in welded joints

Solidification cracks occur in the fusion zone near the end of solidification. Simplistically, they result from the inability of the semisolid material to accommodate the thermal shrinkage strains associated with weld solidification and cooling. Cracks then form at susceptible sites to relieve the accumulating strain. Susceptible sites are interfaces, such as solidification grain boundaries and interdendritic regions that are at least partially wetted.

Solidification cracking requires both a sufficient amount of mechanical restraint (strain) and a susceptible microstructure. Alloys with a wide solidification temperature range are more susceptible to solidification cracking than alloys that solidify over a narrow temperature range. Simply described, this is because accumulated thermal strain is proportional to the temperature range over which a material solidifies. This temperature range is determined primarily by chemical composition.

The development of shrinkage strains, and the rate at which the strain is applied, also influences the ability of an alloy to solidify without cracking. Because of the limited quantitative understanding of strain development in a solidifying weld, the practical approach taken to minimize the mechanical factor is to reduce the overall weld restraint through judicious joint design and appropriate choice of welding parameters. A simple way to minimize the restraint on a solidifying weld joint is to keep the joint gap to a minimum by designing hardware with good fit-up. Another approach, particularly attractive for small parts, is to design the weld joint as a standing edge.

Lamellar tearing is cracking that occurs beneath welds. It is found in rolled steel plate weldments. It is associated with nonmetallic inclusions such as oxides, sulfides, and silicates that are elongated in the direction of rolling. The net result of these inclusions is a decrease in the through-thickness ductility. The crack originates internally because of tensile strains produced by the contraction of the weld metal and the surrounding heat-affected zone (HAZ) during cooling.

The tearing always lies within the base metal, generally outside the HAZ and parallel to the weld fusion boundary. The problem is caused by welds that subject the base metal to tensile loads in the z-, or through-thickness, direction of the rolled steel. Occasionally, the tearing comes to the surface of the metal but

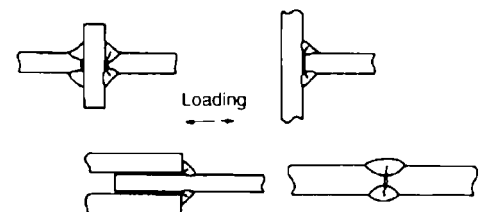


Fig. 5 Fatigue cracking from the weld root

more commonly remains under the weld (Fig. 6) and is detectable only by ultrasonic testing.

Thicker, higher-strength materials appear to be more susceptible. However, the phenomenon affects only a very small percentage of steel plates. The problem can be avoided by proper attention to joint details. In T-joints (Fig. 6), double-fillet welds appear to be less susceptible than full-penetration welds. Also, balanced welds on both sides of the joint appear to present less risk than large, single-sided welds. In corner joints, common in box columns, lamellar tearing can be readily detected on the exposed edge of the plate (Fig. 7a). The problem can be overcome by placing the bevel for the joint on the edge of the plate that would exhibit the tearing rather than on the other plate (Fig. 7b). Butt joints rarely exhibit lamellar tearing, because weld shrinkage does not set up a tensile stress in the through-thickness direction of the plates.

Fillet Welds

A fillet weld is measured by the leg size (ω) of the largest right triangle that may be inscribed within the cross-sectional area (Fig. 8). Although the actual leg of the fillet weld is defined by the distance from the root of the joint (the point where the members are closest before welding)

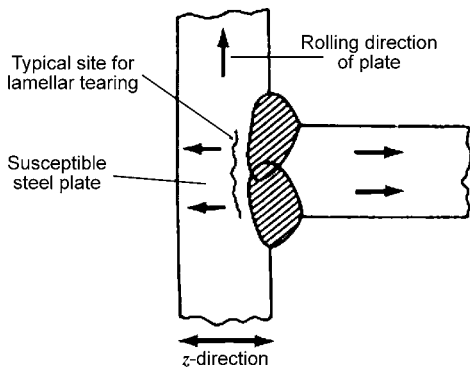


Fig. 6 Typical location for lamellar tearing in a T-joint. Stress across the plate thickness (the z-direction) occurs from strains that develop from weld-metal shrinkage in the joint. Lamellar separation is roughly parallel to the fusion line. Lamellar tearing can be prevented when the rolling direction of the plate is oriented perpendicular to the fusion line.

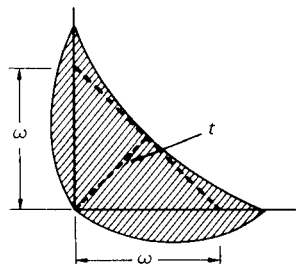


Fig. 8 Leg size (ω) of a fillet weld. t , throat

to the toe, which is the junction of the weld face and base metal, the leg size of the weld may be shorter than the leg in a concave fillet, as shown in Fig. 8. The leg size (ω) is equal to the side of a right triangle but does not extend from root to toe of the weld. Unequal leg size should be avoided, because the longer leg adds nothing to strength but does add to cost.

For efficient weld filler-metal use, the convexity of the fillet weld should be minimized. The 45° flat fillet, very slightly convex, achieves maximum strength and economy.

Throat Size. The shortest distance between the root of the joint and the face of the diagrammatical weld, or the throat (Fig. 8), is a better index of strength of a weld than leg size. It is along this throat (t) that the allowable stress over the minimum thickness is actually applied. The leg size (ω) of a fillet weld simply provides this throat.

Weld Size. Table 1 provides two basic methods of sizing fillet welds, with the first based on achieving the full strength of the adjacent members and the second based on the peak loadings. While the examples here are for steel, the same ideas apply to other arc-welded materials. The limit considered is the shear strength of the fillet weld material considered to be 30% of the minimum ultimate strength required for the weld metal.

When sizing fillet welds, the direction of loading should be considered. Extensive test

data have shown a 50% increase in weld strength under transverse versus parallel loading. However, a weld under transverse loading has less deformation capacity than a weld under parallel loading. So, when accounting for loading direction in a group of welds, both the angle of load on the weld element of interest and the angle of load on the element with the lowest capacity should be considered. AWS D1.1 has three methods for doing this calculation, using equations, tabular data, and graphs.

At one time, two 45° fillet welds that had legs equal to three-fourths of the plate thickness were considered to develop the full strength of the plate for either transverse or parallel loading, assuming that the weld metal was equivalent to the base metal and average penetration was obtained. Originally, calculations for full-strength welds were based on thinner plate welded on both sides, with the welds extending full length. Although this ratio of 0.75 is true for the old values of E60 weld metal and A 7 low-carbon steel prior to 1969, these values are not necessarily applicable when working with the wide range of steels and weld-metal strength levels available today (2011). Table 2 shows how the full-strength factor varies with weld-metal and plate strength levels for a number of steel grades. Suggested factors for the weld size in relation to plate thickness in rigidity or non-full-strength designs are also given.

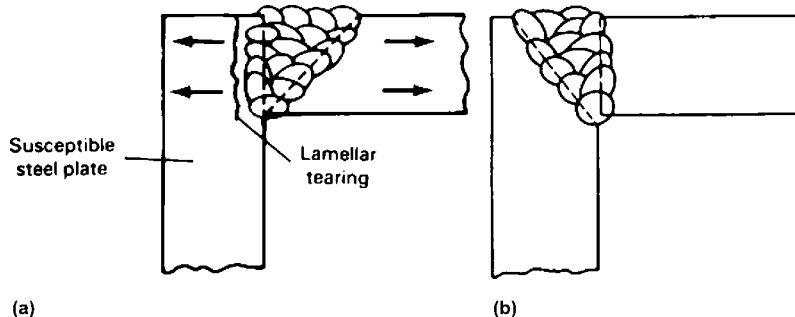


Fig. 7 Corner joint. (a) Lamellar tearing surfaces at the exposed plate edge. (b) Redesigned joint

Table 1 Allowable unit forces on fillet welds

Leg size, mm	E70 or equivalent		Leg size, in.	E70 or equivalent	
	Longitudinal load, N/mm	Transverse load, N/mm		Longitudinal load, 10 ³ lbf/in.	Transverse load, 10 ³ lbf/in.
2	205	307	1/16	0.93	1.39
3	307	461	1/8	1.86	2.78
4	410	614	3/16	2.78	4.18
5	512	768	1/4	3.71	5.56
6	614	921	5/16	4.64	6.96
8	819	1229	3/8	5.56	8.35
10	1024	1536	7/16	6.50	9.75
12	1229	1843	1/2	7.42	11.14
14	1433	2150	5/8	9.28	13.92
16	1638	2457	3/4	11.14	16.71
18	1843	2765	7/8	12.99	19.49
20	2048	3072	1	14.85	22.28
22	2253	3379			
25	2560	3840			

Weld Placement. In addition to sizing, the placement of welds in the most effective load-carrying positions can conserve weld metal. Welds that carry uniform loads along their length can carry much greater loads for the same weld size as welds that have part of their length loaded very lightly. A common example of this is a weld of a connection in bending where welds across the neutral axis must be much larger or longer to carry the same loading as welds remote from the bending neutral axis. Therefore, selection of the most effective weld position facilitates the use of smaller welds.

Comparison of Fillet and Groove Welds. Cost is the major consideration in the choice between fillet or groove welds. Although simple fillet-welded joints are the easiest to make, they may require excessive weld filler metal for larger sizes. The fillet welds in Fig. 9(a) are easy to apply and require no special plate preparation. Because these welds can be made with large-diameter electrodes using high welding currents, the deposition rate is high. However, the amount of weld metal increases in relation to the square of the leg size.

The double-bevel groove welds in Fig. 9(b) have approximately one-half the weld area of the fillet welds (Fig. 9a) but require extra preparation and the use of smaller-diameter electrodes with lower welding currents to place the

initial pass without melt-through. As plate thickness increases, this initial low-deposition region becomes a less important factor, and the higher cost factor (preparation and operation expenses) decreases in significance.

One means of deciding at what point in plate thickness double-bevel groove welds become less costly than fillet welds is from analysis of the cost of welding, cutting, and assembling. By reading upward from the plate thickness in Fig. 10, the relative costs of fillet welds or double-bevel welds of 45° or 60° can be determined. Thus, for smaller plate sizes, the 45° double-bevel groove weld is more expensive, but as plate thickness increases, the cost of fillet welds is higher. The accuracy of this technique depends on the accuracy of the cost data used in constructing the curves.

The single-bevel groove weld in Fig. 9(c) requires approximately the same amount of weld metal as the fillet welds in Fig. 9(a). Thus, there is no apparent economic advantage. There are some disadvantages, however. The single-bevel joint requires bevel preparation and, initially, a lower deposition rate at the root of the joint. From a design standpoint, the single-bevel groove weld offers a more direct transfer of force through the joint, which provides better service under fatigue loading.

Although the full-strength fillet welds (Fig. 9a) would be sufficient, some codes have

lower allowable limits for fillet welds and may require a leg size equal to the plate thickness. In those cases, the cost of the fillet-welded joint may exceed the cost of the single-bevel groove in thicker plates. Also, if the joint is positioned so that the weld can be made in the flat position, a single-bevel groove weld would be less expensive than fillet welds, because one of the fillets would have to be made in the overhead position, a costly operation (Fig. 11).

Groove Preparation Welds

The important design considerations for groove-weld selection are the depth of groove included angle, root opening, root face, and radius at root. Both complete joint penetration and partial joint penetration groove welds can be designed. The included angle, which is the angle of the groove weld, and the root opening, which is the portion of the joint before welding where the weld members are closest, are directly related. The root opening should be increased as the included angle decreases (Fig. 12) to allow for electrode access. The root face of a groove preparation, which helps to prevent melt-through at the root opening, is the portion of a weld groove face that is adjacent to the root of the joint. The radius at the root (groove radius) is the radius used to form the shape of a J- or V-groove joint.

Included angles vary from 20 to 60° (Fig. 12). Generally, the smaller the included angle, the less weld metal is required. The included angle and root opening must be sufficient to

Table 2 Weld size factors for full-strength and rigidity fillet welds

Steel ASTM grade	Yield strength of base metal		Strength level of weld metal			
	MPa	ksi	E70	E80	E90	E100
Full strength			Ratio of weld leg length to plate thickness for double-longitudinal fillet welds at full plate strength			
A36	248	36	0.56
A572-50	345	50	0.76
A572-65	448	65	1.00	0.86	0.77	...
A514	690	100	1.52	1.33	1.18	1.06
Rigidity design			Ratio of weld leg length to plate thickness for double-longitudinal fillet welds at half plate strength			
A36	248	36	0.28
A572-50	345	50	0.38
A572-65	448	65	0.49	0.43	0.38	...
A514	690	100	0.76	0.66	0.59	0.53

$$A = (\text{two welds}) \left(\frac{1}{2} \times \omega^2 \right) \\ = 2 \times \left[\frac{1}{2} \times \left(\frac{3}{4} t \right)^2 \right] \\ = 0.5625 \text{ in.}^2$$

$$A = (\text{two welds}) \left(\frac{1}{2} \right) \left(\frac{t}{2} \right)^2 \\ = \frac{t^2}{4} \\ = 0.250 \text{ in.}^2$$

$$A = (\text{one weld}) \left(\frac{1}{2} \times t^2 \right) \\ = \frac{t^2}{2} \\ = 0.500 \text{ in.}^2$$

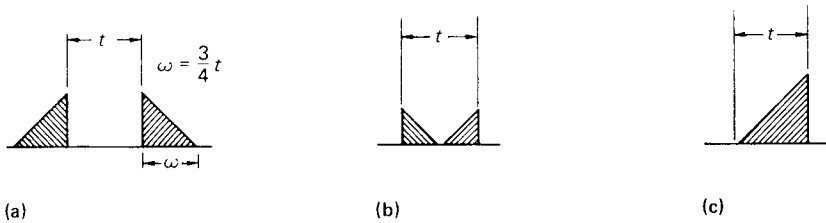


Fig. 9 Comparison of fillet and bevel-groove welds. ω is the leg size of the fillet weld in inches = 19.1 mm (¾ in.); A is the cross-sectional area of the weld in square inches = ½ ω²; t is the plate thickness in inches = 25.4 mm (1.0 in.) (a) Fillet welds. (b) Double-bevel groove weld. (c) Single-bevel groove weld.

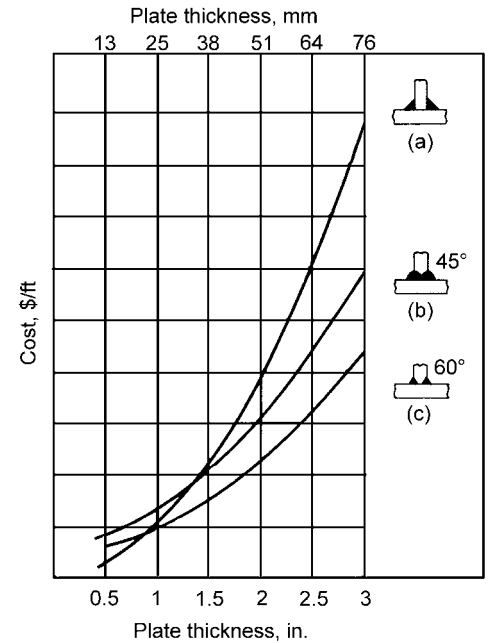


Fig. 10 Relative cost of welds having the full strength of the plate. (a) Fillet welds. (b) 45° double-bevel groove welds. (c) 60° double-bevel groove welds

permit the electrode access to the root of the joint and to ensure good fusion to the side walls with multiple passes. All four preparations in Fig. 12 are acceptable; all are conducive to good welding procedure and good weld quality. Therefore, selection usually depends on root opening and joint preparation, which directly affect weld cost (pounds of metal required).

Although the smaller included angle apparently requires less weld metal, it also requires a wider root opening. The wider root opening may defeat any savings achieved by the need for less metal in a narrower included angle, particularly in thinner plates. Thus, with 16 mm (5/8 in.) plate, a 60° included angle in a double-bevel joint, with its 3 mm (1/8 in.) root opening, is more economical than a 20° included angle with a 13 mm (1/2 in.) root opening. However, with 53 mm (2 in.) plate, the same combinations of root opening and bevel angle make the 20° included angle the choice, with less weld metal than the 60° angle.

Root openings are the separations between the members to be joined and provide electrode access to the root of the joint. The smaller the angle of bevel, the larger the root opening must be to obtain good fusion at the root.

If the root opening is too small, root fusion is more difficult to obtain, and smaller electrodes must be used, thus slowing the welding process. If the root opening is too large, weld quality does not suffer with use of a backing bar, but more weld metal is required, thus increasing welding cost and tending to increase distortion.

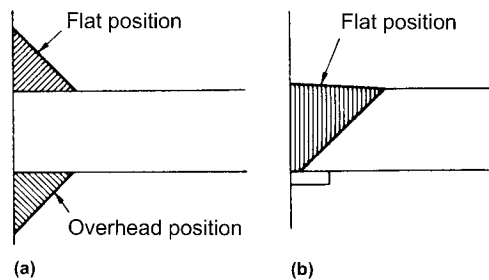


Fig. 11 Comparison of welds in the flat position in a T-joint. Fillet welds (a) are more expensive than a single-bevel groove joint (b) because of the overhead weld required.

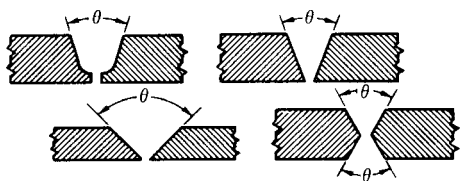


Fig. 12 Relationship of included angle size to the root opening

Bevel angles, because they affect the size of the root opening, also affect accessibility to all parts of the joint and the quality of fusion throughout the entire weld cross section. Accessibility can be improved by compromising between maximum bevel and minimum root opening. As in Fig. 13, the importance of maintaining proper electrode angle in confined quarters may affect the angle of bevel. The minimum recommended bevel for the conditions in Fig. 13 is 45°.

Double-groove weld joints reduce the amount of weld filler metal required for single-groove preparations by approximately half (Fig. 14). The decreased welding reduces distortion and facilitates alternating weld passes on each side of the joint, which further reduce distortion, at the cost of moving the welder or the part to switch sides.

Joint preparation after assembly has not always been considered acceptable. This practice—assembly and tackup before gouge preparation of V-grooves for welding—is practical and less costly in certain applications. V-groove joints for complete- and partial-penetration welds may be made prior to or after fitting.

Groove- and Fillet-Weld Combinations

Combinations of partial-penetration groove welds and fillet welds, such as those shown in Fig. 15, are used for many joints. The AWS prequalified, single-bevel groove T-joint, for example, is shown reinforced with a fillet weld.

Combination Double-Bevel Groove and Fillet Welds. The combination weld joint in Fig. 16 is welded using a partial-penetration double-bevel groove weld and two fillet welds. The plates are beveled to 60° on both sides to give a bevel whose depth is at least 29% of the thickness of the plate (0.29t). After the

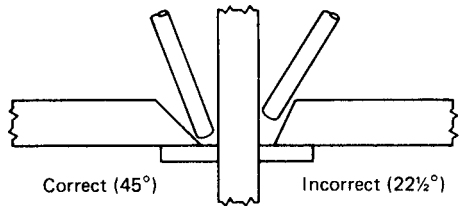


Fig. 13 Relationship of electrode angle on bevel angle

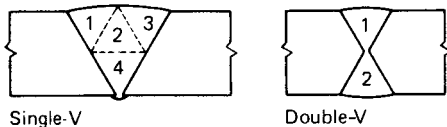


Fig. 14 Comparison of weld metal required for single- and double-V-groove weld joints

grooves are filled, they are reinforced with fillet welds of equal cross-sectional area and shape. This joint has a strength equal to that of the plate. These partial-penetration double-bevel groove joints have 57.8% of the weld metal of full-strength fillet welds. Although they require joint preparation, the 60° angles allow the use of large electrodes and high welding current.

Comparison of Single-Bevel Groove, Fillet, and Combination Welds. When full-strength fillet welds are not required in the design, savings can often be achieved by using partial-penetration groove welds. A 45° partial-penetration single-bevel groove weld with a 25 mm (1 in.) throat requires only one-half the weld area needed for a fillet weld. For smaller welds, however, this weld may not be as economical as the same-strength fillet weld, because of the cost of edge preparation and the need to use a smaller electrode and lower current on the initial pass.

Throat Size. Similar to the use of the minimum throat for fillet or partial-penetration groove welds, the minimum throat is used for designing a partial-penetration combination groove weld. As Fig. 17 shows, the allowable unit force for a combination weld is not the sum of the allowable unit forces for each portion of the combination weld, which would result in a total throat larger than the actual.

Edge Preparation

When considering whether to construct the weld joint using any of the groove welds—bevel, V-, J-, or U-groove—the cost of preparing the plate and weldment handling must be weighed



Fig. 15 Combination groove- and fillet-welded joints

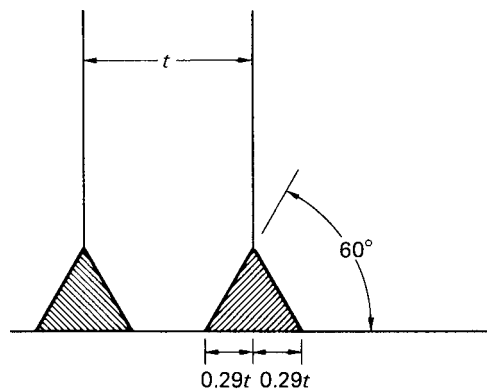


Fig. 16 Partial-penetration double-bevel groove joint. t, plate thickness. Depth of bevel is 29% of plate thickness.

against the savings in weld metal or other advantages of the groove-preparation welds.

Methods of cutting the groove-weld preparations include machining, chipping, shearing, grinding, flame (gas) cutting, gas gouging, and air carbon arc gouging. The choice of the most economical means depends on factors such as the type of material, section characteristics, quality required, and available equipment.

Edge preparations are cut into the weld member using flame cutting, shearing, sawing, punch-press blanking, nibbling, or cutoff machining (for bar and tube stock). In addition to cost, selection of the appropriate cutting operation depends on the quality of the edge for fit-up and whether a bevel is needed.

Because they are easily prepared by gas cutting, bevel and V-groove welds are more widely used. Although they offer the advantages of less weld filler metal and a more accessible work area, J- and U-groove preparations are not as applicable because they usually require machining or air carbon arc gouging, more costly methods of edge preparation. Thus, the bevel-groove preparation with a backing bar may be more economical than a J- or V-groove. If a plate planer is available, however, J- or V-groove preparations are often specified because of reduced weld-metal requirements.

For single-bevel and single-V-groove preparations, single-tip flame-cutting torches are used because only one cut is necessary. Double-bevel or double-V-groove preparations are usually made with multiple-tip flame-cutting

torches, which facilitate completion of the cut in one pass of the cutting machine.

Root faces on edge preparations provide additional thicknesses of metal to minimize melt-through, the tendency of the weld metal to pass through the root opening during welding. Feather-edge preparations, which provide only minimal thickness at the root opening, are more prone to melt-through than weld joints with root faces, especially if the gap becomes too large, and they require more weld filler metal to fill the joint.

A root face is more difficult to obtain than a feather edge. A feather edge can be achieved by one cut with a torch, while a root face usually requires two cuts or possibly a torch cut plus machining. If a 100% weld is required, a root face usually requires back gouging. When welding into a backing bar, root faces are not used because they decrease fusion at the root of the joint into the bar.

Spacer bars may be required to prevent melt-through when very large root openings are used on double-grooved joints (Fig. 18d). A wide gap may be unavoidable for practical reasons, such as difficulty in pulling the parts together for desired fit-up.

The metal spacer bar serves as a backing and maintains root opening throughout the course of the welding operation. When using a spacer bar, the joint must be back gouged to sound metal before the second side is welded.

Backing bars, another edge preparation frequently required when the root opening is

excessively large, are also used when welding must be done from one side (Fig. 18). Composed of metal, weld metal, or nonmetal, a backing bar is placed under or behind a joint to enhance the quality of the weld at the root. The bar usually remains in place after welding, becoming an integral part of the joint.

Steel backing bar material should conform to the base metal, maintaining a close contact with both edges to avoid trapped slag at the root of the weld joint. Feather edges are recommended on the weld members for best performance of backing bars in ensuring weld quality. To hold the backing bar in place, short intermittent tack welds should be used, preferably staggered to reduce any initial restraint of the joint (Fig. 19).

Back gouging, or removal of metal at the weld root, is often necessary to eliminate fusion defects at the root face when a butt weld is made without a backing bar. Without back gouging, penetration (the distance weld metal and fusion extend into a joint) may be incomplete (Fig. 20). Proper back gouging extends deep enough to expose sound weld metal and creates a contour that provides complete accessibility to the electrode (Fig. 21). Means of back gouging include grinding, chipping, and gouging. The most economical method, gouging, also leaves an ideal contour for subsequent beads.

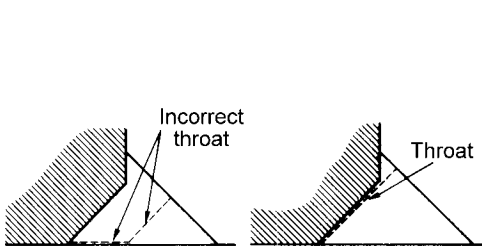


Fig. 17 Determination of minimum throat

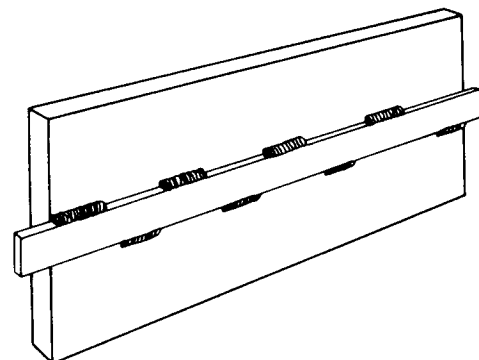


Fig. 19 Use of short intermittent tack welds to secure backing bars

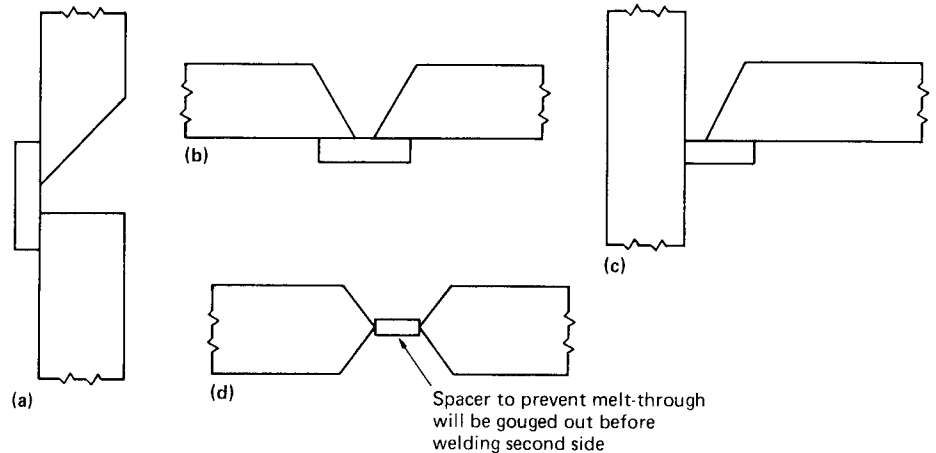


Fig. 18 Welding edge preparations for wide root openings. (a), (b), and (c) Backing bars. (d) Spacer bar

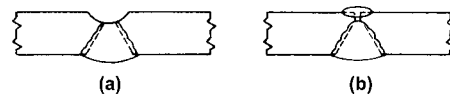


Fig. 20 Use of back gouging for complete penetration. (a) Complete penetration of weld with back gouging. (b) Incomplete penetration of weld prior to back gouging

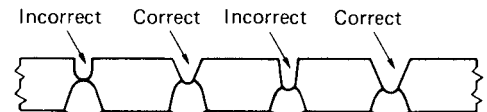


Fig. 21 Depth and contour of back gouging

Appendix: Recommended Proportions of Grooves for Arc Welding

Butt Joints

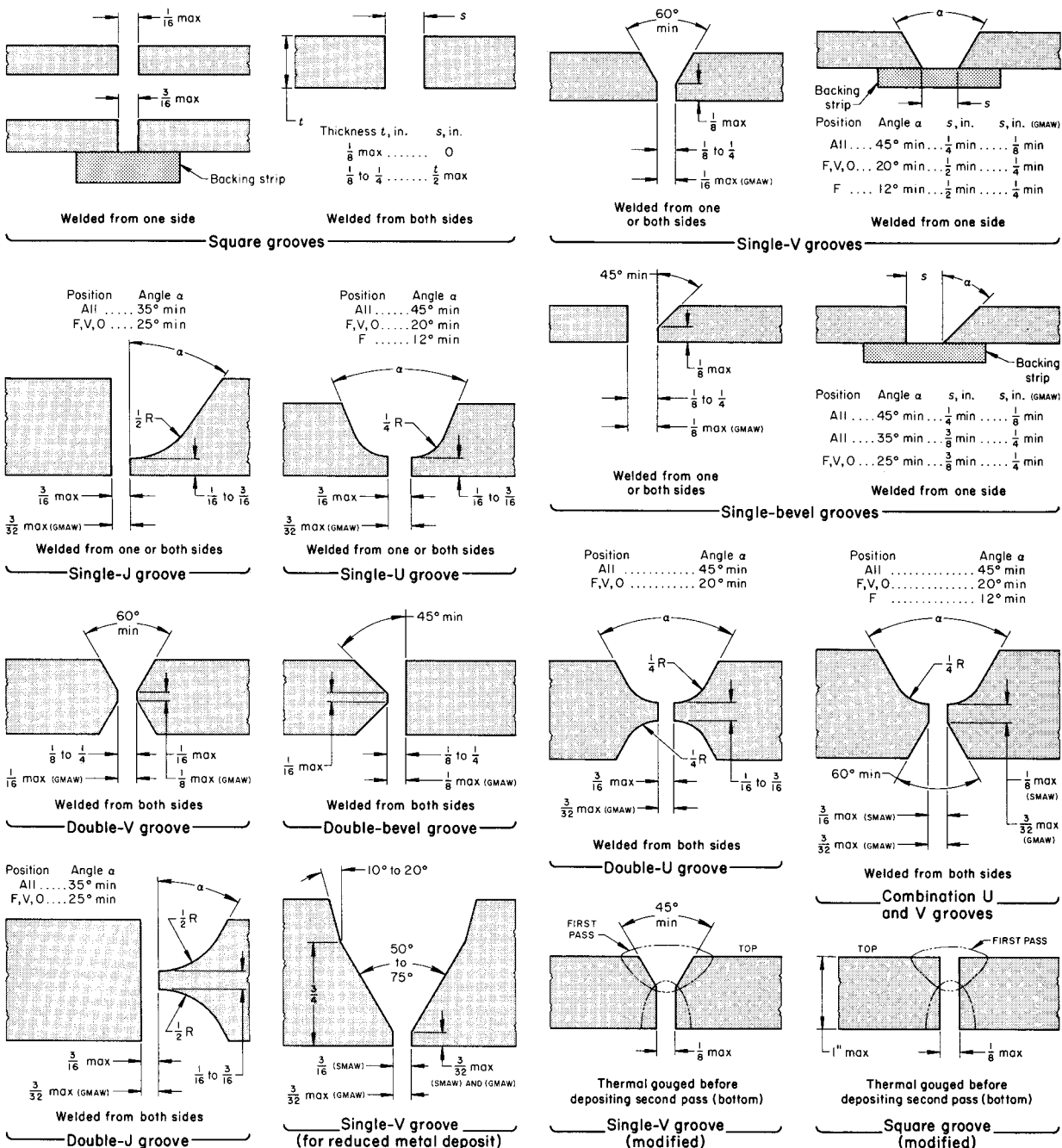


Fig. 22 Recommended proportions of grooves for butt joints. Made by shielded metal arc welding, gas metal arc welding, gas tungsten arc welding, flux cored arc welding, and oxyfuel gas welding (except pressure gas welding). Dimensions that apply to gas metal arc welding only are noted.

Corner Joints, Flange Joints, and Plug Welds

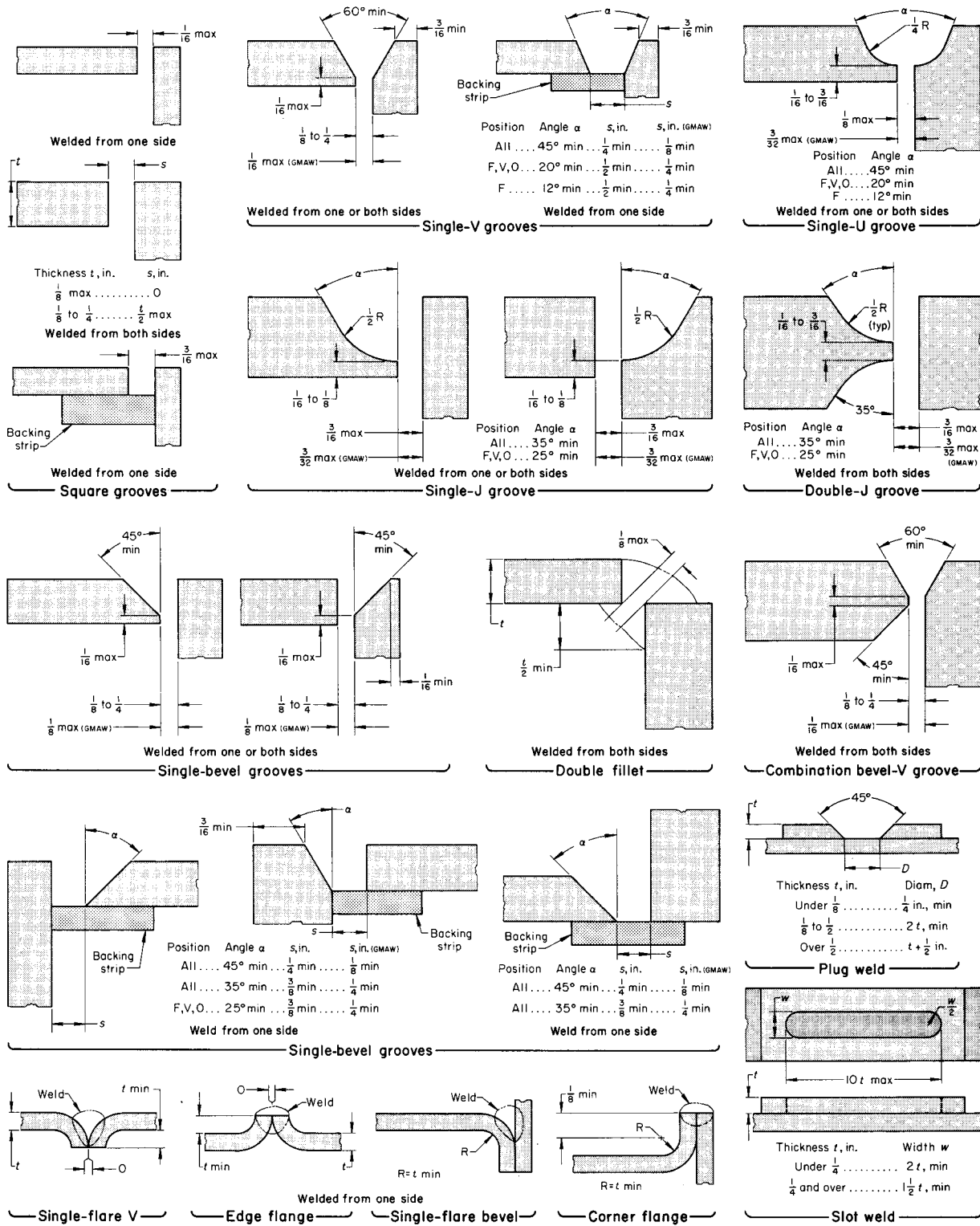


Fig. 23 Recommended proportions of grooves for corner and flange joints and plug welds. Made by shielded metal arc welding, gas metal arc welding, flux cored arc welding, and oxyfuel gas welding (except pressure gas welding). Dimensions that apply to gas metal arc welding only are noted.

T-Joints and Joints for Specific Applications

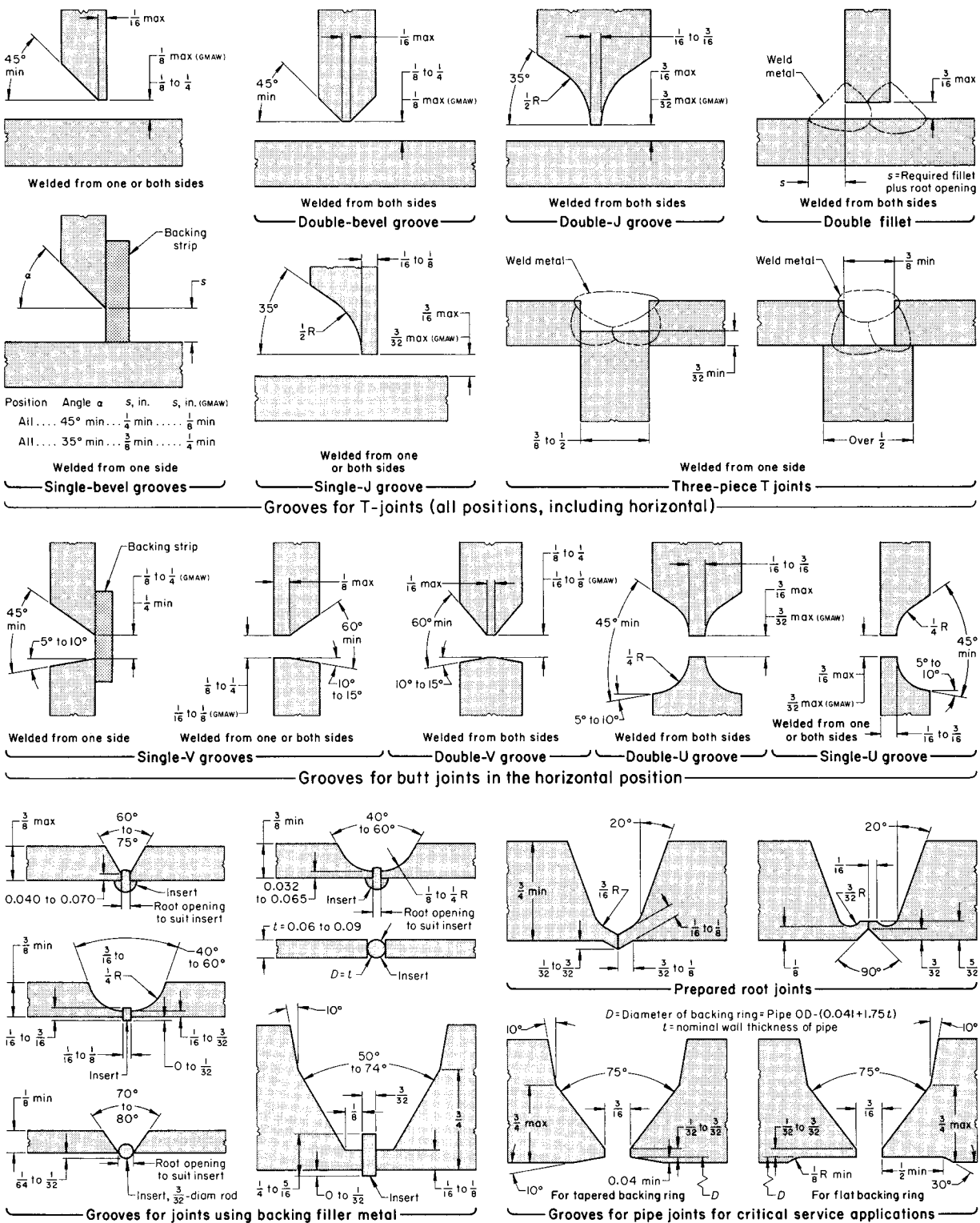


Fig. 24 Recommended proportions of grooves for T-joints and joints for specific applications. Made by shielded metal arc welding, gas metal arc welding, gas tungsten arc welding, and oxyfuel gas welding (except pressure gas welding). Dimensions for specific welding processes are noted.

Power Sources for Arc Welding

Lee Allgood, The Lincoln Electric Company

POWER SOURCES for the major arc welding methods are discussed in this article. The characteristics and technology of power sources are discussed along with suggested criteria for assuring that a power source selection can safely deliver the desired output and yield long service life when properly used. Arc welding consists of a number of distinct processes that require specific types of electrical power (amps \times volts) for the welding of many different materials in various thicknesses, joint configurations, and welding position. Therefore, there are a number of different types of power sources (welders) available.

Power Source Characteristics

Electric arc welding encompasses various methods, which are introduced in the article "Overview of Welding Processes" in this Volume and are covered in more detail in separate articles for each method. The methods of arc welding include:

- Shielded metal arc welding (SMAW)
- Gas tungsten arc welding (GTAW)
- Flux cored arc welding (FCAW) with some type of gas shielding or without requiring gas shielding
- Gas metal arc welding (GMAW) with short arc, spray arc, or pulsed arc modes of operation, as described subsequently
- Submerged arc welding (SAW) using direct current (dc), the most common, or alternating current (ac), with some operations using a number of independent arcs working in a tandem configuration (each arc requiring its

own power source) or two electrodes arranged together, with power from a common welder (power source)

- Plasma arc welding (PAW)

The type of current and voltage suitable for each of these processes is shown in Table 1. The power source output characteristics for all of these welding methods may be loosely described as constant current, constant voltage, and waveform control. As noted, GMAW also includes three different modes of operation. Short arc GMAW is loosely defined as using an arc voltage less than 24 V. (See the section "Short Arc GMAW Power Sources" in this article.) Spray arc GMAW usually involves arc voltages above 24 V and uses an argon-base shielding gas mixture. Pulsed arc, or waveform-controlled arc, operation may involve both short arc and spray arc in some form of controlled manner.

Typical volt-amp output curves are shown in Fig. 1 to 5. Figure 1 is typical of constant current welders primarily designed for manual stick electrode welding (SMAW). Setting the power source for maximum open-circuit voltage results in a very steep output curve, as shown by "A." This allows minimum current change but a relatively large voltage change, which is desirable for out-of-position welding with smaller-sized electrodes. Curve "B" allows a relatively large change in welding current as the arc length is manipulated during welding. This can be beneficial when welding in the flat and horizontal positions using larger electrodes. Most dc SAW uses constant current, especially for larger-sized single-pass welds.

Although the term *constant voltage* is used to describe the amps-volts relationship of the

power sources used for a number of arc welding methods, the output does vary somewhat as current increases (Fig. 2). Curve "A" in Fig. 2 is a common output used for the FCAW methods and is nearly a flat curve. Curve "B" is typical of the output used for GMAW. This curve usually droops 3 to 4 V per 100 A. This is sometimes referred to as slope control. Curve "C" is seldom used any longer but is designed to rise slightly as current increases, thus offsetting the effects of internal power source and cable heating at higher currents when welding with FCAW processes.

Waveform-controlled welding (Fig. 3) is also known as pulse welding (PW) but with some significant differences that enhance the process. Earlier welders for PW usually had a fixed number of pulses per second and permitted adjusting only the peak and background currents. Present-day PW machines permit changing the shape and frequency of the pulse. By doing this, optimum arc characteristics can be established for welding any type of material, using any appropriate type of gas and providing optimum control when welding thin or thick material while using small- or large-diameter electrodes. Some

Table 1 Type of current and voltage suitable for each arc welding process

Type of current and voltage(a)	Type of welding(b)						
	SMAW	GTAW	FCAW/gas	FCAW/no gas	GMAW	SAW	PAW
Constant current dc	X	X	X	X
Constant current ac	X	X	X	...
Constant voltage dc	X	X	X	X	...
ac square wave	...	X	X	...
ac custom sine wave	...	X
Waveform dc	X	...	X

(a) dc, direct current; ac, alternating current. (b) SMAW, shielded metal arc welding; GTAW, gas tungsten arc welding; FCAW, flux cored arc welding; GMAW, gas metal arc welding; SAW, submerged arc welding; PAW, plasma arc welding

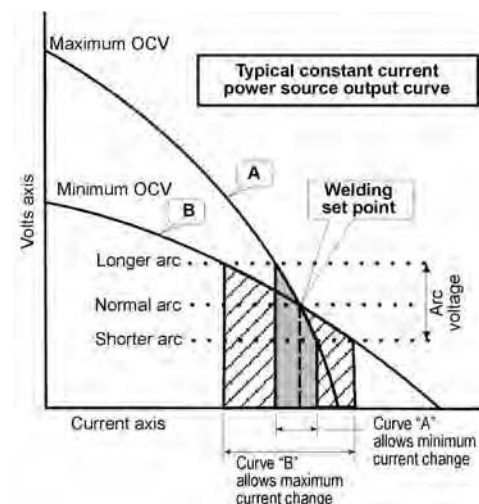


Fig. 1 This is typical of constant current welders primarily designed for manual stick electrode welding (shielded metal arc welding). OCV, open-circuit voltage

machines allow altering the waveform by using a number of external controls. Other machines can incorporate a library of predetermined, optimized waveforms. These are then accessed by a relatively simple external control. Today (2011), most of these machines incorporate advanced inverter technology.

Conventional sinusoidal ac welding (Fig. 4) has been and still is a very important type of current used for arc welding. It is the dominate type used for small, limited-input SMAW machines. In larger, industrial-sized machines, it is usually included as an option along with dc output. With larger-sized electrodes, ac virtually eliminates magnetic interference with the arc (arc blow) and is the preferred choice. Alternating current was, and largely still is, the preferred method by which aluminum and its alloys are GTA welded. Alternating current has traditionally been used for SAW applications where arc blow is a problem with dc or where larger-sized electrodes are used at high current. Multiple electrode configurations necessitate the use of ac. The use of ac with single-electrode SAW has sometimes been limited, especially on short-length welds, because of difficulty with arc starting.

Some square-wave-type power supplies (Fig. 5) have been built as specialized machines

specifically for GTAW for some time. The use of newer inverter technology has permitted the building of powerful machines designed primarily for SAW. These machines do not exhibit the arc striking problem mentioned in the Fig. 4 discussion. Arc stability is further enhanced because significantly less time is spent transitioning from positive voltage to negative voltage. Frequency from 0 (dc) to 80 Hz is easily accomplished by using external controls. This has been shown to have beneficial effects when welding different material thicknesses. These machines are usually software controlled and also provide rapid responses to changes in the weld puddle. The wave may be unbalanced to favor the positive side for increased penetration or to favor the negative side to increase deposition rate (Fig. 5b, c).

While there is some commonality in the power source output requirements between these processes, each process has many unique requirements. The type and thickness of material to be welded, size and type of electrode, shielding type, position of welding, and the weld joint influence how a particular power source will perform. More detailed information on each of these processes is available in other articles of this Handbook as well as from several other sources (Ref 1–3).

One common requirement is that the power source be designed to deliver the required power—current and voltage—at a sufficiently sustained rate to satisfy the job requirements. Sustained rate is expressed by percent duty cycle. Duty cycle (Ref 4) is the time a power source must operate at rated load within a 10 min period, expressed as a percentage, and not to exceed a stated temperature rise from a specified ambient temperature.

Power sources with single-phase ac input voltage are common and are available with outputs of ac only as well as ac/dc output. Welders with ac output are available in a wide range of output sizes from 80 to 1500 A. The ac/dc voltage output welders are usually available from 250 to 500 A output ratings. Typical schematic diagrams are illustrated in Fig. 6 to 8.

The dc current output is usually achieved by placing a rectifier in the secondary circuit of the power transformer, as shown in Fig. 7. These machines are primarily used for SMAW with ac or dc welding. Machines of this general size are readily available.

Power sources in the range of 175 to 350 A ac and ac/dc outputs and configured with additional controls suitable for GTAW welding are available. The smaller-sized machines, 80 to 250 A ac output type, are commonly used in

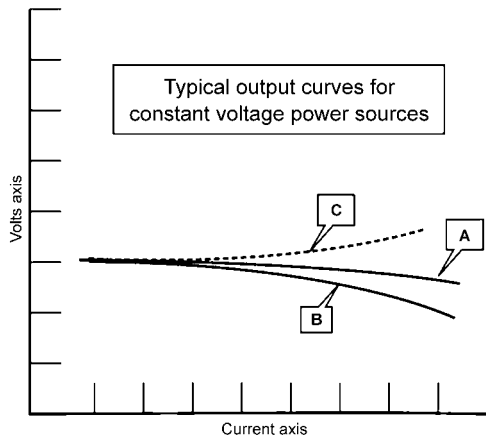


Fig. 2 Output variation of constant voltage supply as current increases

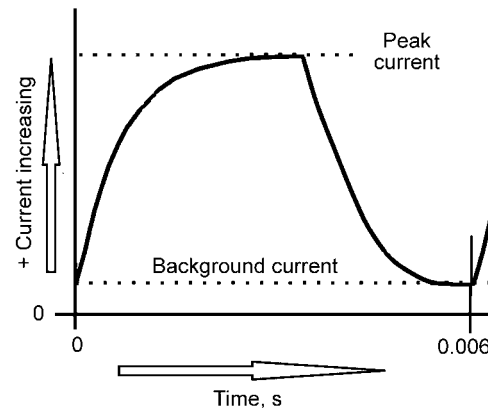


Fig. 3 Waveform-controlled pulse welding

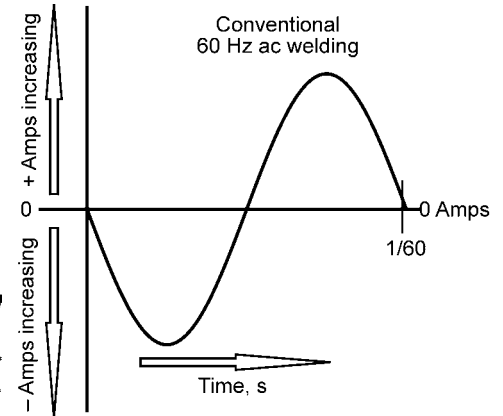


Fig. 4 Conventional sinusoidal alternating current (ac) for arc welding

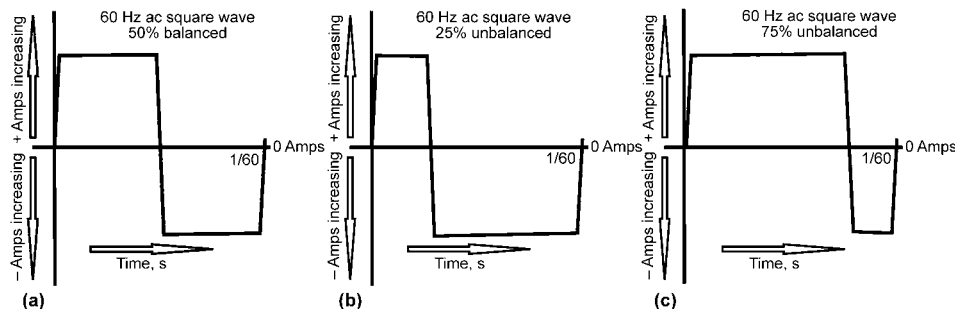


Fig. 5 Some square-wave-type power supplies

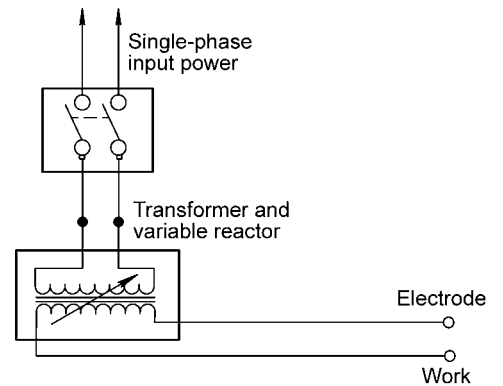


Fig. 6 Typical small, single-phase, alternating current output transformer welder

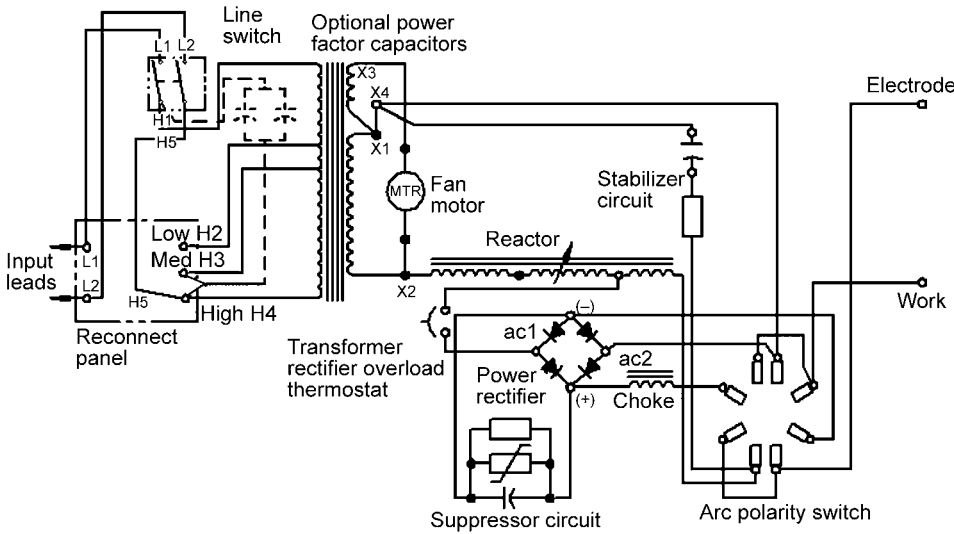


Fig. 7 Single-phase, alternating current/direct current, constant current welder

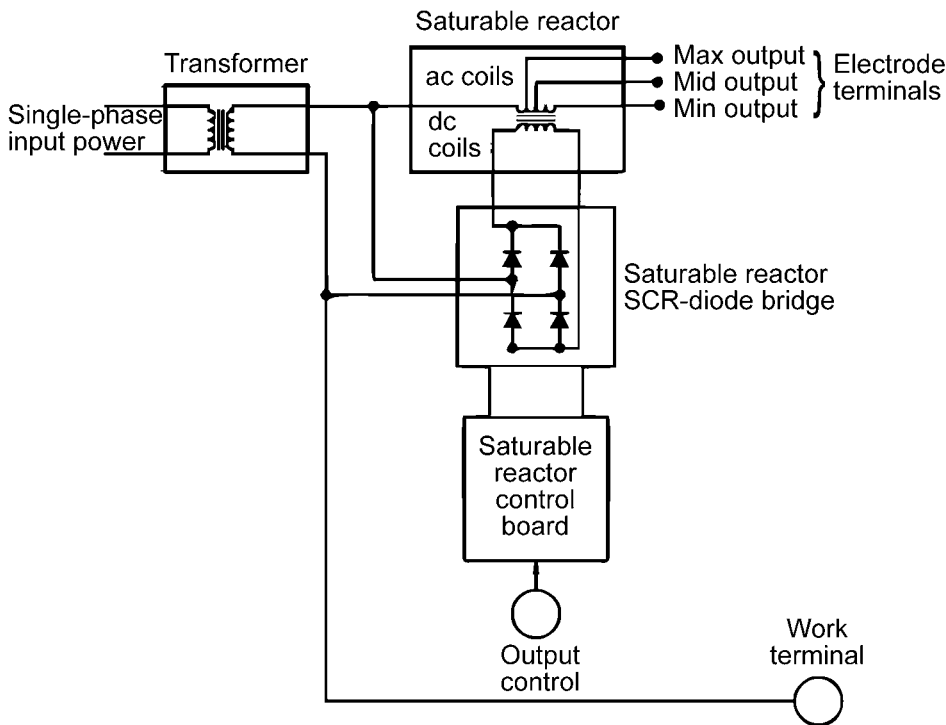


Fig. 8 Large-output, alternating current (ac), single-phase welder. dc, direct current; SCR, silicon-controlled rectifier

small machine shops, schools, maintenance departments, and by consumers. The smallest of these machines (80 to 225 A output rated) are usually designed to operate on 230 V, single-phase input and are rated at a 20% duty cycle. There are some machines rated at 80 A output that will operate on 120 V single-phase input. These machines have very limited output and duty cycle.

When a number of single-phase welders are connected to a single-phase power system or

to the same phase lines of a three-phase system, the supply line current draw will be the sum of the input current for each connected machine. If a number of machines are connected to the same phase of a three-phase system, significant line imbalance can occur. This can result in requiring larger supply lines and, perhaps, increased utility power costs. (See the section "Other Operational Costs" in this article.) The solution to this, whenever possible, is to establish groups of three machines and then connect

each machine in a group to a different pair of phase lines, as shown in Fig. 9. In group "A," the sum of the input current for each of the welders is drawn from lines L2-L3. In group "B," the current draw is balanced across all three input lines. The current draw for each line is 1.73 times the line draw for each welder.

There are also single-phase input, silicon-controlled rectifier, constant voltage dc output machines that are integrated with built-in wire feeders for FCAW and GMAW. These usually have a limited duty cycle at rated amperage and voltage but are adequate for many production welding applications involving smaller-diameter electrodes.

Three-phase input machines are the most commonly used machines for industrial applications today (2011). They are available as:

- Constant current machines for SMAW, GTAW, SAW, and PAW
- Constant voltage machines for FCAW and GMAW
- Combination constant current/constant voltage machines based on rated output that are well suited for SMAW, GMAW, and SAW

These machines are usually available in rated output sizes ranging from 250 to 1500 A. Typical electrical schematic drawings for this group are shown in Fig. 10 to 12.

Inverter-based power sources began to appear in about 1980 as a solution to requests for increased portability and to allow the operator ready access to controlling welding current at the point of use, especially on large construction sites. Inverter-based welders have become increasingly important and can be made to produce excellent output characteristics for SMAW, FCAW, GMAW, GTAW, and SAW. Most are configured for a specific process or combination of processes:

- SMAW
- SMAW, GMAW, FCAW
- GMAW and FCAW
- GTAW
- SAW

Inverter-based welders are available in output sizes ranging from 100 to 1000 A. The conversion from input voltage frequency (60 or 50 Hz) to high frequency (20 KHz or more) facilitates transforming the line voltage to welding voltage with transformers that are more efficient, smaller, and much lighter in weight than conventional step-down transformers. The lower voltage is then rectified and filtered to provide a smooth dc output. Figure 13 is a basic diagram of a three-phase input inverter. Figure 14 visually compares a typical 275 A rated inverter unit to a conventional 250 A ac/dc welder. Figure 15 illustrates a visual size comparison between a 400 A constant current/constant voltage (CC/CV) transformer welder and a 450 A inverter-based CC/CV welder.

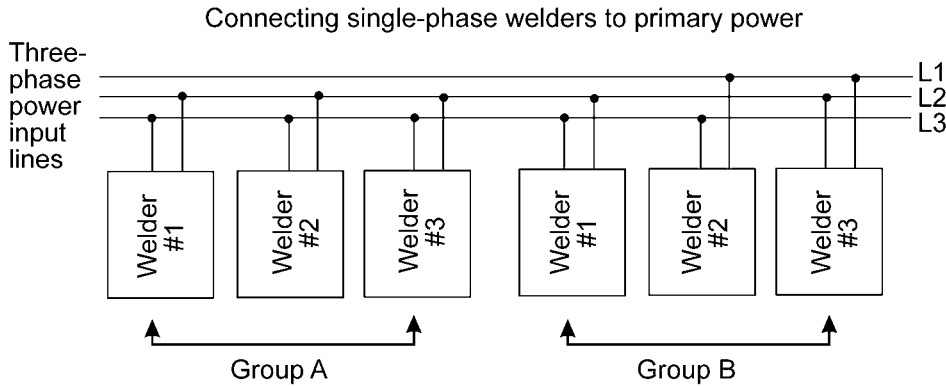


Fig. 9 Groups of three machines with connections to different pairs of phase lines. Each group consists of three single-phase welders with the same input current rating.

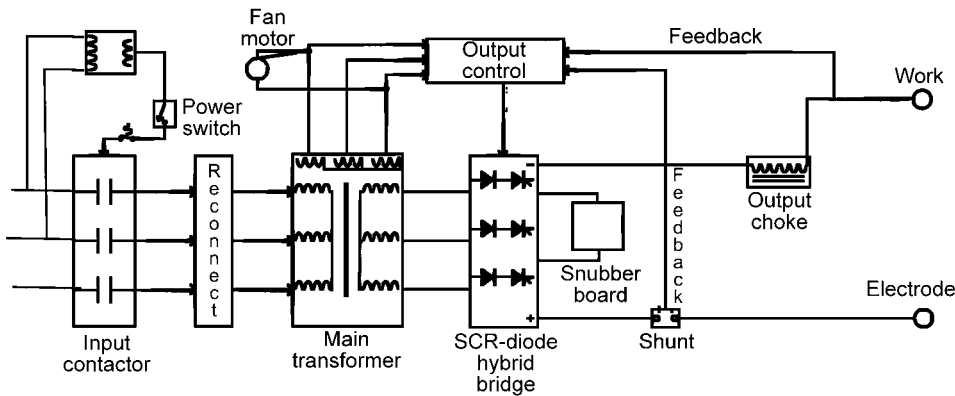


Fig. 10 Three-phase, constant current, direct current welder. SCR, silicon-controlled rectifier

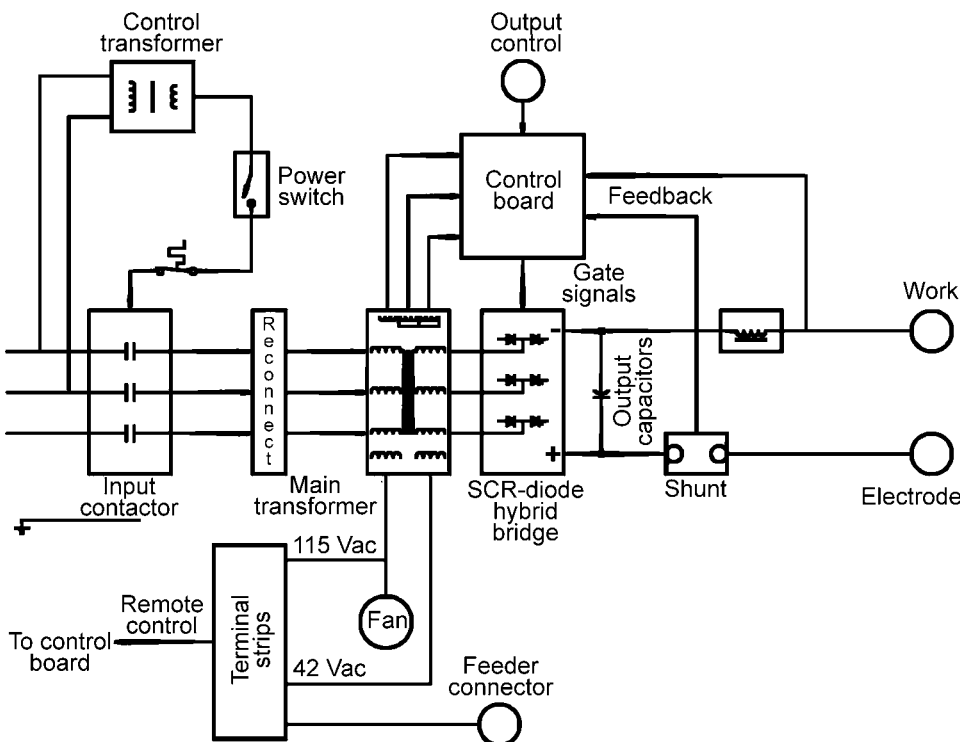


Fig. 11 Three-phase, constant voltage welder. SCR, silicon-controlled rectifier

Some of the smaller-rated units are designed so that they will operate on either three-phase or single-phase input voltage.

The versatility of inverter technology with solid-state electronics makes it possible for the designer to include many features with appropriate output characteristics within a single machine. Specific arc dynamics can be studied and replicated for all processes. For this reason, it is highly recommended that manufacturer's specifications be carefully reviewed.

Power Source Efficiency. The efficiency of a power source is a major factor in determining the cost to operate the welder. Figure 16 is a graphical comparison of the major power source groups. There are no specific industrial standard values for a power source, so each manufacturer's specifications should be checked. Typically, a power source will be more efficient as the output load approaches its rated value. The actual energy cost will be a combination of time at load and time at idle.

Other Operational Costs. There is another consideration in determining the cost of operation of a particular machine and that is the power factor of the unit. Power factor is related to the amount of current drawn from the power line in excess of what is needed to supply the operational energy. Power factor is usually expressed as a percentage number. The lower the number, the greater the current demand on the input line. It is not uncommon for power companies to impose an extra charge for systems operating below some fixed value. Poor power factor may also require heavier-gauge input wiring. One source for further information about power factor and operating costs is available from Cos Phi Inc. (Ref 5).

Short Arc GMAW Power Sources

Short arc welding is a method within the GMAW process, and it requires power sources with specific output characteristics. Traditionally, GMAW short arc (GMAW-S) power supplies used a CV transformer with varying means to control the magnitude of short-circuit current, usually using fixed or variable slope (Fig. 2 and 17) and fixed or variable inductance to control the rate of current response (Fig. 18). As inductance is increased, the rate of current change from short-circuit current to operating current is slowed. Properly adjusted, this provides increased fluidity in the weld puddle and results in improved weld appearance and reduced spatter.

Hybrid inverter power sources have been developed that cannot be classified as either true CC or CV power sources. Instead, they deliver current of a suitable waveform that uses continuous feedback information to control the short-circuiting dynamics. As with pulsed GMAW welding, the frequency of shorting may be set to optimize the arc. These power sources are ideally suited for the GMAW-S process.

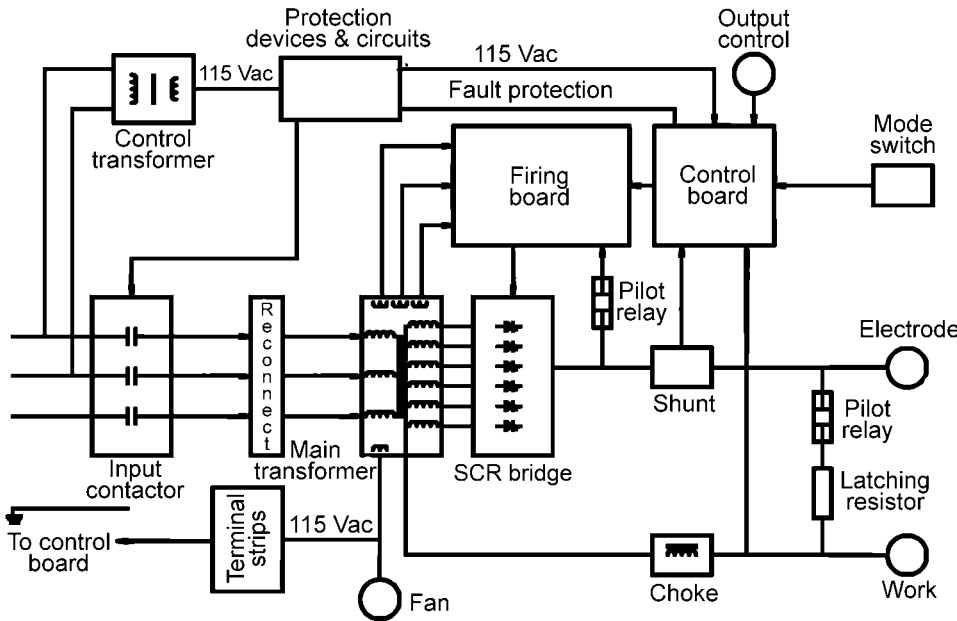


Fig. 12 Three-phase, constant current/variable voltage, direct current power source. SCR, silicon-controlled rectifier

inbred from years of welding experience. Typically, these machines offer a source of auxiliary dc power. This is suitable for temporary lighting or for universal voltage-powered hand tools. These machines are usually available in output rating sizes from 200 through 600 A with various duty cycles.

Alternator generators with rectified power output have largely replaced dc generator machines. In combination with solid-state component technology configured to operate in switch mode, these machines can be suitable for most of the welding processes. They are available with dc output and CC/CV welding modes. While engine power is still the limiting factor in establishing maximum welding current output at rated voltage, many of these machines have engines that permit nameplate rating at 100% output duty cycle.

Some machines are manufactured to offer other significant capabilities that allow them to function as portable generators, including:

- 120 V single-phase ac output
- 240 V single-phase ac output
- 240 V three-phase ac output

Machines offering any or all of these capabilities usually include appropriate connection plugs, circuit breakers, fuses, or ground fault circuit interrupter devices. Output frequency is regulated so that they may be used for true emergency power.

There are a few machines that also include a built-in air compressor. The pressure and cubic feet per minute output is suitable for most air-driven portable tools and carbon arc scarfing. Because of the versatility and wide choices within this family, manufacturer's specifications should be carefully considered.

Figure 19 is a schematic of a typical machine in this group, providing both three-phase and single-phase ac auxiliary output.

Multiple Arc (Multiple Operator) Power Sources

These actually represent a welding system rather than a single power source. Typically, one central power supply provides the output to a number of independent welding locations. These units are of special interest for welding projects that require a number of welding arcs within close proximity to each other, such as large construction projects, power plant and chemical plant turnaround, large offshore drilling platforms, and so on. There are two systems in common use:

- Resistance grid
- Multiple dc positive welders using dc switch-mode converters

Resistance grid systems generally are suitable only for SMAW and carbon arc air

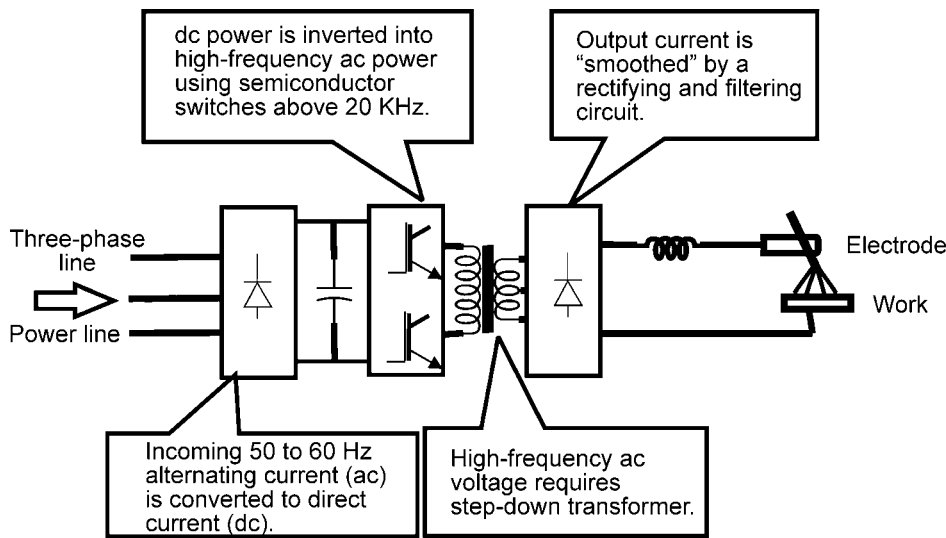


Fig. 13 Basic inverter diagram

Engine-powered welders have long been the power source of choice and still are today (2011) when portable welding power is needed. These machines are available from 125 to 600 A ratings. They may be powered by:

- Air-cooled engines
- Water-cooled gasoline engines
- Water- and/or air-cooled diesel engines

There are three fundamental types of engine-powered welders: generator, alternator, and alternator rectified.

The pure alternator output machines are usually small, air-cooled, engine-powered, limited-output machines of low duty cycle

that provide only for SMAW. These machines usually deliver only ac or dc. They usually provide a source of 120 or 240 V single-phase auxiliary power. The waveform of the auxiliary power may not be well regulated; therefore, it is not a substitute for a comparably sized power generator for use with sensitive electronic equipment and appliances but is amply suited for emergency power lighting and electric tools. Maximum output is usually limited by available engine horsepower.

The dc generator machines have been in use for years and are still preferred by some welding operators for demanding SMAW applications. This is largely a preferential legacy



Rectifier
250 A, 30% duty cycle
69 cm (27 in.) high, 48 cm (19 in.) wide,
55 cm (21.5 in.) deep
159 kg (350 lb)



Inverter
275 A, 60% duty cycle
34.5 cm (13.6 in.) high, 23 cm
(9.0 in.) wide, 51 cm (20.25 in.) deep
25 kg (54.5 lb)

Fig. 14 Size comparison: shielded metal arc welding transformer versus an inverter

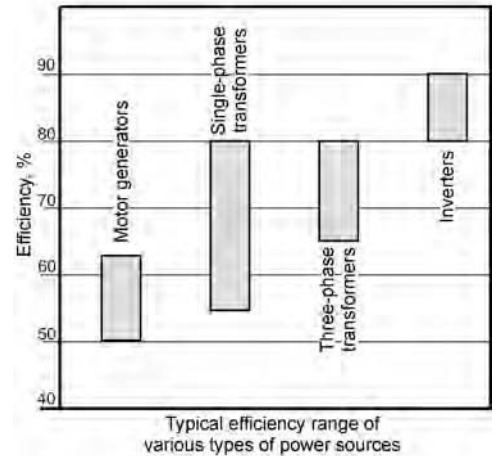


Fig. 16 Typical efficiency range of different types of power sources

scarfing. The power source is usually a three-phase, 100% duty cycle, dc constant voltage, 80 V output welder. Welding is accomplished by connecting individual resistance grid boxes across the power source welder output. The arc polarity dc+ must be the same for all attached units. A typical block diagram is shown in Fig. 20.

This system is inherently inefficient because the welding arc is usually in the range of 18 to 30 V. A 25 V, 150 A welding arc requires 3.75 kW of energy, but the power source must deliver 80 V at 150 A or 12 kW of energy. This amounts to an output power efficiency of only 26.6%. The efficiency of the power source itself would bring this efficiency down a bit more.

Multiple dc+ Welders. This system incorporates solid-state technology to permit SMAW, FCAW, GMAW, and carbon arc air scarfing. Unlike the resistance grid system, any constant current welder with an ample current output rating may be used. The connected units use advanced solid-state technology known as buck converters or choppers operating in switch mode (Fig. 21).

Each individual unit incorporates a power-off, CV output, CC output switch. All of the units connected to the main power source do not need to be welding with the same process. The individual units are usually rated for continuous output at 350 A, 34 V dc+. The number of units that can be connected and used is dependent on the rated kilowatt output capacity of the power supply. This can be approximately calculated using the formula:

$$\begin{aligned} \text{Power source capacity (Volts} \times \text{Amps)} \\ = 1.1 \times \text{Number of units} \times (\text{Volts} \times \text{Amps}) \end{aligned}$$

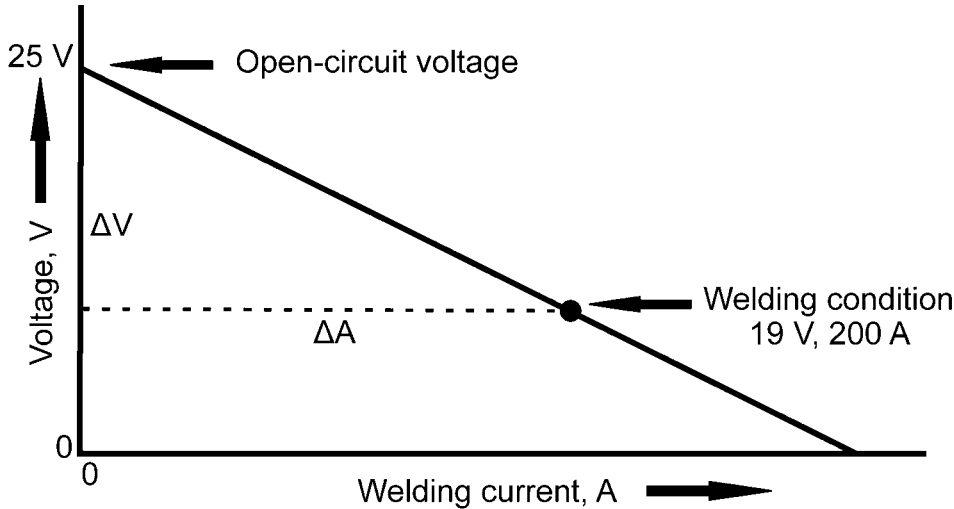
It is unlikely that all units will be operating at any one time or that all will be using the same output settings. Some units may be operating



Multiprocess CC/CV 400 A transformer welder
213 kg (470 lb)

Multiprocess CC/CV 450 A inverter welder
57 kg (125 lb)

Fig. 15 Size comparison: transformer versus inverter. CC/CV, constant current/constant voltage



$$\frac{\Delta V}{\Delta A} = \frac{25 \text{ V} - 19 \text{ V}}{200 \text{ A}} = \frac{6 \text{ V}}{200 \text{ A}} = \frac{3 \text{ V}}{100 \text{ A}} = \text{Slope}$$

Fig. 17 Fixed slope control of short-circuit current. Source: Ref 9

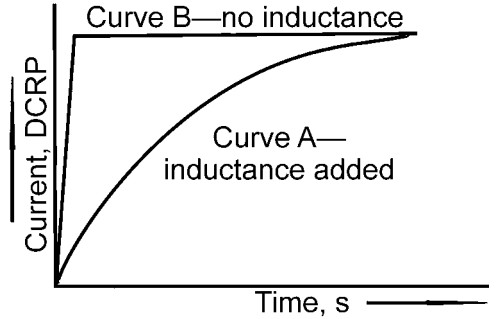


Fig. 18 Fixed or variable inductance control of current response. DCRP, direct current reverse polarity. Source: MIG/MAG Welding Guide, MIG C4.200, The Lincoln Electric Company

in the SMAW mode and others in FCAW. For this reason, the aforementioned formula should be considered a conservative estimate. Figure 22 illustrates a typical unit setup. All connected units operate with the electrode positive. The advantage with this is that the operator has almost any process readily available with fully presettable current and voltage output. Operator units may be paralleled for high current output to permit carbon arc air scarfing or resistance heating.

Power Source Selection Considerations

A welding machine should deliver the desired output, provide adequate service life durability, and be safe to use when properly installed and operated. The following items are some considerations when selecting a power source for desired output and adequate service life durability are:

- Duty cycle (Ref 4) that the power source must operate
- Electrical installation and wiring requirements
- Output capability of the power source
- Servicing and identification information
- Safety in use of properly installed and operated machines

Reference 6 identifies basic equipment characteristics to be included on the nameplate of the machine:

- Manufacturer's type designation and/or identification number
- Maximum open-circuit voltage
- Rated load volts
- Rated load amperes
- Duty cycle at rated load
- Maximum rated speed of generator in revolutions per minute at no load (for engine-powered machines)
- Rated frequency(s) of power supply
- Number of phases of power supply
- Rated input voltage(s) of power supply

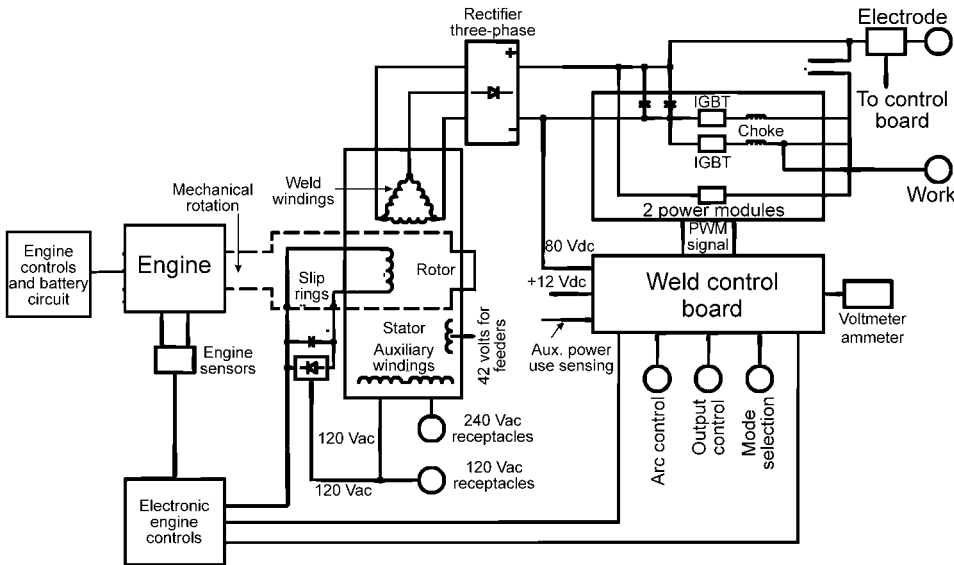


Fig. 19 Constant current/variable voltage alternator welder, with alternating current auxiliary output

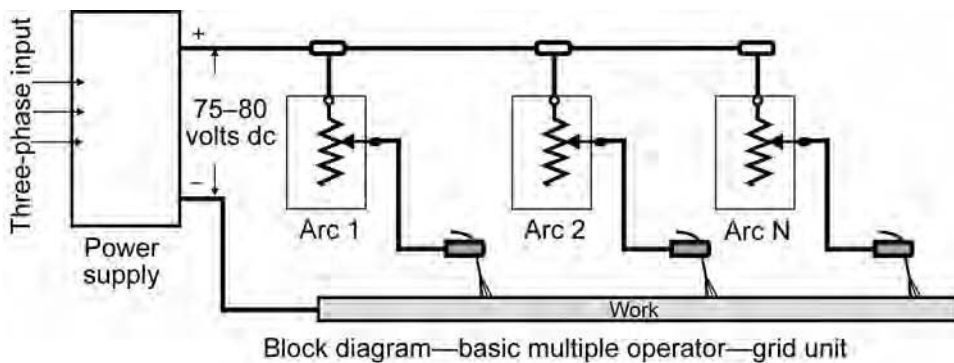


Fig. 20 Connection of individual resistance grid boxes across the power source

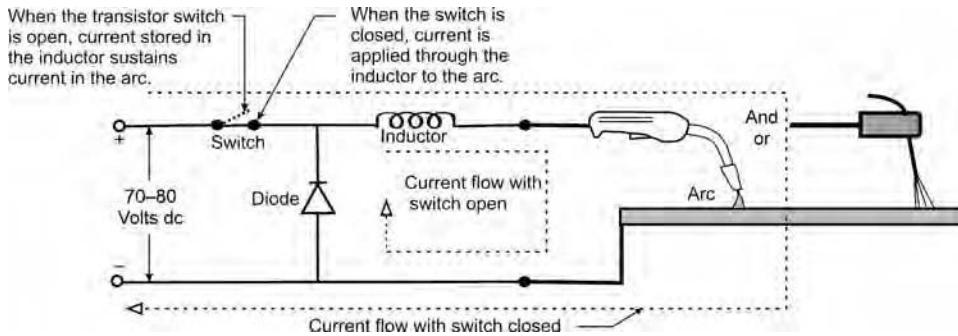


Fig. 21 Schematic of solid-state circuit of choppers operating in switch mode

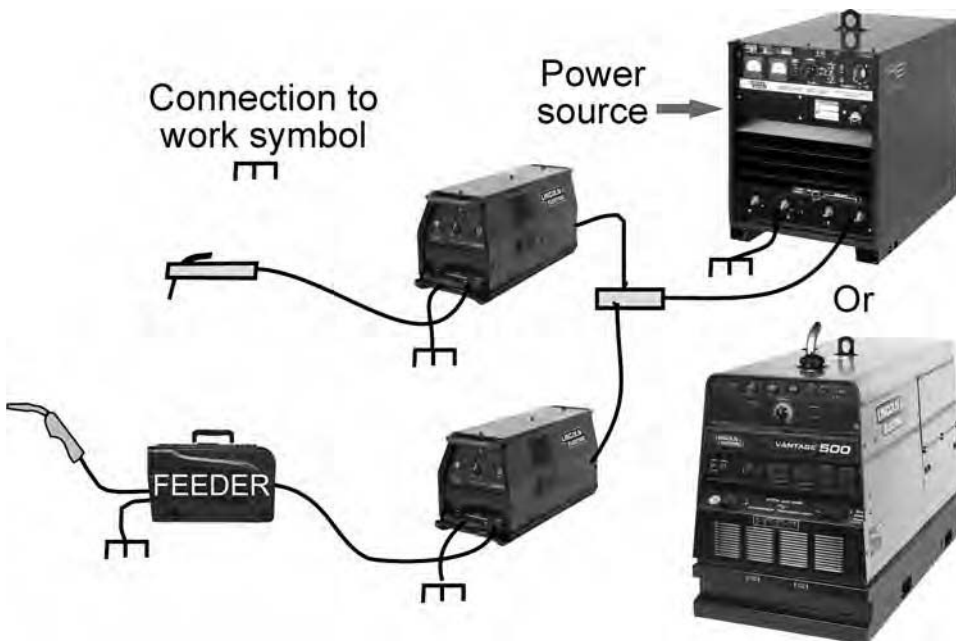


Fig. 22 Multiple-arc, multiple-process system

In the United States, electric-powered machines should be installed in accordance with the National Electrical Code. National Fire Protection Association (NFPA) 70, Article 630 (Ref 7) describes installation requirements. It is possible that local electrical codes may impose more rigorous requirements than the National Electrical Code. Installations outside the United States should be in compliance with local codes or regulations.

The operating environment of a power source requires careful consideration, such as whether it will be subjected to weather elements, whether workers and operators will be in close proximity to the power source (creating possible welding spatter or grinding particles), and whether the welder may be subjected to falling

or blowing foreign material. Standards for various levels of protection have been developed by the International Electrotechnical Commission (IEC) (Ref 8). Standards IEC 60529 (Ref 10) and IEC 60934-1 classify the various degrees of protection provided by electrical enclosures from intrusion of solid objects (including body parts such as hands and fingers), accidental contact, and water as follows.

A welder designed for indoor use should have a protection rating of at least IP21S. Welders that are to be used outdoors should at least meet the requirements of IP23S. In these designations:

- The first digit indicates the level of protection that the enclosure provides against

access to hazardous parts (e.g., electrical conductors, moving parts) and the ingress of solid foreign objects.

- The second digit indicates protection of the equipment inside the enclosure against harmful ingress of water.
- The ending designator letter “S” indicates moving devices are standing still or stationary during water testing.

For example, in the aforementioned rating of IP21S, the “2” designates protection from the ingress of fingers or similar objects greater than 12.5 mm (0.5 in.), and the “1” designates protection from vertical dripping of water. A “3” designates protection from spraying water. The rating IP23S is for storing welders out of doors but not intended to be used outdoors during precipitation unless otherwise sheltered. An abbreviated presentation of these ratings may be found at http://wikipedia.org/wiki/IP_code.

For guidance on safe installation and use of arc-welding equipment, welders should be used and welding should be done at least following the safe practice recommendations of AWS/ANSI Z49.1, “Safety in Welding, Cutting, and Allied Processes” (Ref 9), and the article “Safe Welding Practices” in this Volume.

REFERENCES

1. *Welding Handbook*, Vol 1, American Welding Society, Miami, FL
2. *Welding Handbook*, Vol 2, American Welding Society, Miami, FL
3. *The Procedure Handbook of Arc Welding*, 13th ed., The Lincoln Electric Company, Cleveland, OH
4. “NEMA EW-1 (2004) Electric Arc Welding Power Sources,” National Electrical Manufacturers Association, Rosslyn, VA, www.nema.org
5. Cos Phi Inc., Goderich, Ontario, www.cosphi.com/ebooks/
6. “NEMA EW-1 (2004) Electric Arc Welding Power Sources,” Section 5, National Electrical Manufacturers Association, p 19–24
7. “National Electrical Code,” NFPA 70, National Fire Protection Association, Quincy, MA, www.nfpa.org
8. International Electrotechnical Commission Regional Centre for North America, Worcester, MA
9. “Safety in Welding, Cutting, and Allied Processes,” AWS/ANSI Z49, American Welding Society, Miami, FL
10. Standard IEC 60529, ANSI/IEC, National Electrical Manufacturers Association, Rosslyn, VA

Arc Welding Process Control

Daniel A. Hartman, Manufacturing Behavioral Science
George E. Cook, Vanderbilt University
R. Bruce Madigan, Montana Tech of the University of Montana
David R. DeLapp, Vanderbilt University

WELDING is a complex, multidisciplinary process in which both intelligent and conventional control techniques have been successfully applied to mechanized welding systems in an attempt to control one or two system parameters, such as penetration, bead width, heat-affected zone, or cooling rate. However, to develop significantly higher degrees of autonomy, a weld controller must be able to regulate a number of functions of the welding process over an extended period of time and under varying process conditions and disturbances. Advances in the fields of artificial intelligence, operations research, sensor networks, and distributed control, improvements in network bandwidth and computational performance, and the availability of low-cost sensors and single-board computers offer the opportunity for collaboratively monitoring and controlling as many relevant process parameters as possible to achieve more robust, highly autonomous, general weld process controllers.

Although great strides continue to be made in the research community, the flexibility and judgment of a human welder has yet to be transferred successfully to a mechanical system. This article provides an overview of the research associated with the development of closed-loop feedback control of the arc welding process.

Overview on Welding Process Control

In a typical manual arc welding situation, a human welder can observe the sights, hear the sounds, and sense the reactive forces from the welding process. Using this feedback information, a welder can assess the welding process with respect to its desired state, make minor changes in the weld parameters under his/her immediate control (e.g., weld current, voltage, travel speed and electrode orientation with respect to the joint path), and maintain proper torch orientation and distance in an effort to control the desired state of the weld. Adapting these sensory inputs to machine control and making the appropriate decisions is a challenging task.

The human operator makes decisions based primarily on past learned experience. For instance, when a weld is performed in the vertical position, a seasoned welder knows that when the weld pool gets too large the liquid will run out of the pool, leaving a crater. Acquiring the skill and knowledge to perform complicated tasks, such as full-penetration vertical-up or overhead welds, is the result of countless hours of practice through acquired rule-of-thumb techniques. Explaining this knowledge involving precise visual cues to another person or to a knowledge engineer is difficult.

Most welding automation techniques did not evolve from traditional manual methods. Instead, control engineers have applied conventional quantitative techniques of system analysis through the use of difference, differential, and integral equations to model and control the mechanized aspects of welding. Applications involving through-the-arc sensing, such as arc voltage control and seam tracking, have met with a great amount of success, and they have found their way into commercial use and have been successfully used in industry (Ref 1–3). The sensing technique is low cost, reliable, and nonintrusive. Both of these automated solutions are mechanistic, governed by electromagnetic laws, and employ a single-input, single-output controller. These laws are well understood and are therefore strategically and efficiently applied to both the sensor feedback information and to the control laws within the closed-loop feedback path. In short, their success is directly correlated to their relative simplicity, inherent robustness, and adequate performance in a production environment.

More complex systems, such as bead geometry or penetration control, are well-understood phenomena that can be accurately modeled from a theoretical standpoint, but the computational complexity of the numerical models and the multiple-input, multiple-output nature of the required control laws have precluded their integration into mainstream commercial weld process controllers. Yet, the ability of a skilled human welder to assess and control bead geometry, for example, is not due

to a fundamental understanding of the laws of physics. Instead of applying a mechanistic approach to the control of the weld pool, a seasoned welder applies a more humanistic approach in which the feedback information is not based on precision and formal truths but rather on imprecision and partial truths. Fully automated welding robots will require a marriage between mechanistic approaches for phenomena that are physically well understood and mathematically feasible for both sensors and control algorithms and heuristic approaches for phenomena that are otherwise difficult or impractical to implement using conventional control techniques due to the required complexity resulting in a diminished accuracy.

Control System Requirements

Careful consideration of the power density of the heat source, the interaction time of the heat source on the weldment, and the effective spot size of the heat source must be thoroughly understood in order to design a weld process controller. In general, a heat intensity of approximately 10^3 W/cm² is required to melt most metals (Ref 4). Below this heat intensity, the solid metal can be expected to conduct heat away as fast as it is being introduced. On the other hand, a heat intensity of 10^6 or 10^7 W/cm² will cause vaporization of most metals within a few microseconds, thus preventing any fusion welding from occurring. Most fusion welding processes therefore lie between approximately 10^3 and 10^6 W/cm².

Examples of welding processes that are characteristic of the low end of this range include oxyacetylene welding, electroslag welding, and thermit welding. The high end of the power density range of welding is occupied by laser beam welding and electron beam welding. The various arc welding processes encompass the midrange of the heat source power densities.

The interaction time required to produce melting determines the appropriate bandwidth of the controller. For continuous welding, the interaction time is proportional to the spot

diameter divided by the travel speed. The minimum interaction time required to produce melting can be estimated from the relation for a planar heat source given by (Ref 4):

$$t_m = \left[\frac{K}{Pd} \right]^2 \tag{Eq 1}$$

where p_d is the heat intensity (W/cm^2), and K is a function of the thermal conductivity and thermal diffusivity of the material.

Figure 1 illustrates the relationship between the weld pool-heat source interaction time and the heat intensity. Eagar (Ref 4) states that materials such as copper or aluminum in which the thermal diffusivity is relatively high will lie on

the high end of the band, whereas materials such as steel, nickel alloys, or titanium will lie in the middle of the band. Uranium and ceramics in which the thermal diffusivity is relatively low will lie on the bottom of the band.

System Parameters

The arc welding process is a tightly coupled system which is composed of the arc; the power source, sometimes a wire feeder, and accessories; any tooling, fixtures, and positioning system; any consumables; and the part itself. Decoupling such a complicated system is extremely difficult. However, mapping the arc welding process as a parameter space can help identify aspects of the process that need to be explored in terms of process variability that can adversely impact product quality. Figure 2 illustrates how the arc welding process can be separated into process and product attributes and follows the guidance provided in Ref 5. Process attributes are those aspects of the process that the welding engineer has control over. They include the indirect weld parameters (IWP), preselected parameters, workpiece parameters, and other influential aspects of the process. The product attributes, or direct weld parameters (DWP), represent the characteristics of the postwelded product.

The weld quality is characterized by the direct weld parameters and is affected to varying degrees by the coupled effects of the process attributes. Indirect weld parameters are parameters that can be modified in-process as part of an open- or closed-loop control procedure, while the preselected parameters remain fixed during the process, for example, the electrode type, size, and tip geometry, the torch nozzle size, and the shielding gas type. Finally, other factors that can affect weld quality include clamping, heat sinks such as tack welds, heat buildup, backing, and impurities that may be found within the material, electrode, or shielding gas.

Once the preselected parameters are properly chosen, the quality of the weld can be controlled through proper selection and modification of the IWP. In general, the welding process presents the control engineer with two principal problems:

- In most cases, the relationship between the IWP and the DWP are nonlinear.
- The variables are highly coupled.

The job of the welding engineer is to determine a set of IWP (usually in a laboratory environment) that will produce the desired DWP. If the production floor conditions do not differ too much from the laboratory conditions and the process and environmental variability is kept to a minimum, then the welding operation can be expected to satisfy the postprocess quality inspection procedures. Otherwise, human or computer intervention must provide the necessary feedback to make corrective actions in the welding equipment settings.

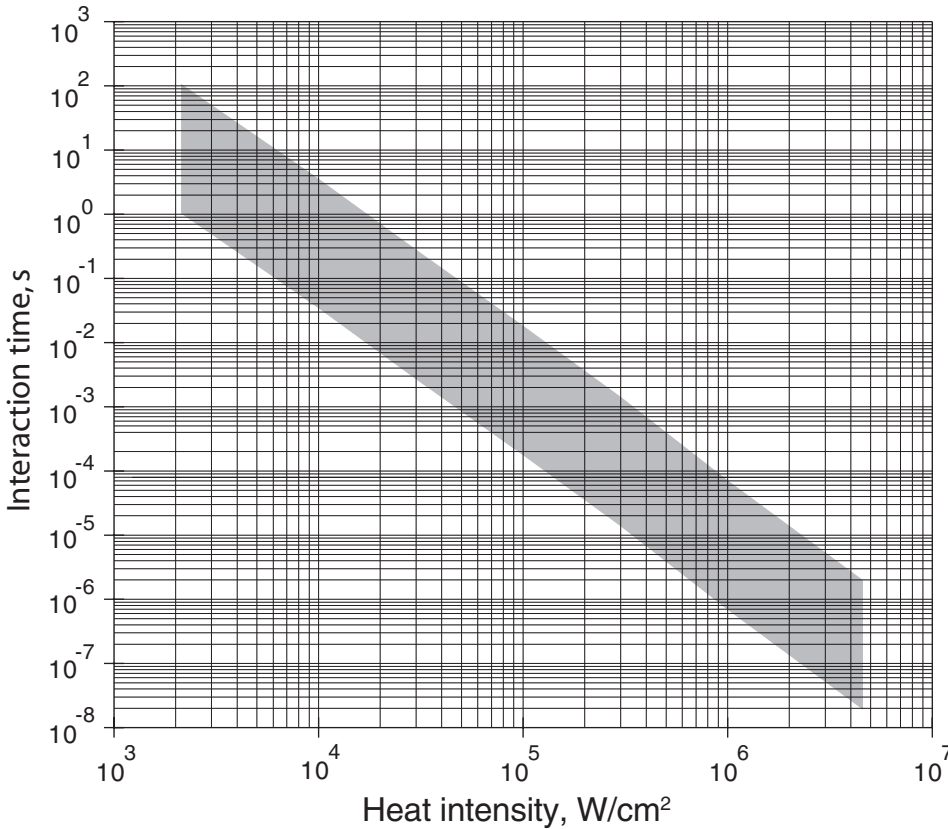


Fig. 1 Typical weld pool-heat source interaction time. Source: Ref 4

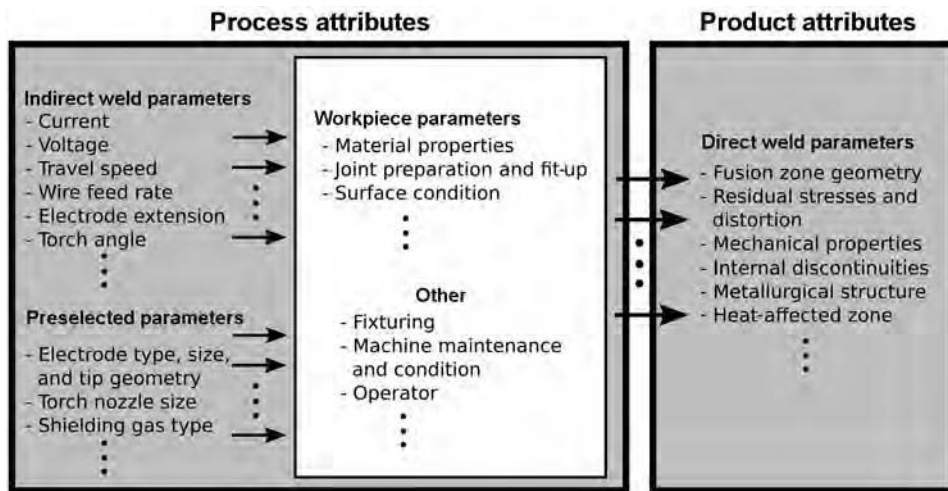


Fig. 2 The arc welding process can be separated into process and product attributes. The process attributes include those aspects of the process that the engineer has control over. The product attributes represent characteristics of the postwelded product.

A feasible solution is to sense the DWP of interest, compare the sensed variables with the desired variables, and adjust the IWP in real-time to reduce the error between the desired and sensed DWP. For a multiple-input, multiple-output and highly-coupled manufacturing process such as arc welding, the previously described approach usually involves a multivariable controller. The controller requires both dynamic and steady-state process models. The models must be computable in real-time, although they do not need to be as globally accurate as a computationally-intensive numeric model.

Successful implementation of a closed-loop feedback control system for arc welding requires sensing, modeling, and control. Each of these is discussed in the following sections.

Sensing

Directly sensing the DWP of interest provides the most robust feedback to a closed-loop control system. However, in certain cases, directly sensing many of the DWP associated with arc welding is impractical and/or infeasible in a production environment. Therefore, indirect sensing techniques are employed where a sensor is coupled with a model to “indirectly” sense, or infer, the DWP of interest. The following sections provide an overview of the more commonly applied sensing techniques for arc welding control.

Arc Sensing

Arc sensing (also commonly referred to as through-the-arc sensing) monitors the change in current (constant voltage power sources) or voltage (constant current and pulsed current power sources) in the arc. Systems employing arc sensors rely on the principle that the resistance between the welding torch electrode and the workpiece is a function of the distance separating the two. The obvious advantage of arc sensing is the use of the arc itself as a sensor. This reduces costs and avoids the technical challenges associated with instrumenting external sensors in or around the harsh environment of the welding arc. Active research and successful applications involving through-the-arc sensing date back over 40 years (Ref 6).

Arc sensing has been instrumental in achieving robust mechanized and robotic automation by providing joint tracking, bead width control, torch height control, and torch orientation. The sensing technique has been applied successfully to both consumable and nonconsumable arc welding processes. The feedback mechanism relies primarily on the voltage drop in the arc column as a rough order prediction of arc length (Ref 7). The voltage-arc length characteristic has been successfully employed in arc voltage control systems where the welding engineer specifies a desired arc voltage and a servomotor is used to vertically adjust the welding torch height with respect to the workpiece

surface (Ref 8). The arc-voltage length relationship has also been applied to joint tracking and width control in which the torch oscillates back and forth across the joint (Ref 8–11).

Rotating arc sensors, using either mechanical or electromagnetic oscillation, have been investigated to improve the sensitivity and responsiveness over conventional torch weaving methods (Ref 12). Recently, an electromagnetic arc oscillation system was developed for narrow-groove gas metal arc welding (GMAW) to achieve uniform sidewall penetration and provide feedback for an automatic joint tracking system (Ref 13). A mechanized arc rotation sensor was employed in Ref 14 to detect the end points of joints during GMAW of fillet welds. Robotic torch orientation detection and control is demonstrated in Ref 15 where a high-speed rotational arc sensor provides feedback of the deviation and inclination of the welding gun with respect to the workpiece surface.

Detection of surface contaminants on the workpiece and/or the electrode was accomplished in Ref 16 where the authors demonstrated that the electrical arc signals vary as a function of contaminants on the workpiece and/or electrode. Through-the-arc sensing of gas metal arc weld quality was also demonstrated in Ref 17 to 19. The characteristic changes in the current and voltage records were correlated to weld process instabilities such as loss of shielding gas, contact tip wear, change in contact-tube-to-work distance, and variations in the welding procedure that may induce changes in the droplet-transfer mode. A real-time monitoring system was developed that measures process stability and infers weld quality. In Ref 20, a process signature using arc voltage and wire feed rate is established to monitor arc start instability and estimate the amount of spatter generated during the unstable arcing period during GMAW.

The voltage-arc length characteristic has also been used to monitor the metal-transfer mode and droplet detachment during GMAW. Johnson et al. have demonstrated a correlation between the perturbations in the electrical arc signal with droplet transfer (Ref 21). Using high-speed video that is correlated with the arc voltage and current traces, they were able to detect the droplet detachment and to distinguish between the three transfer modes: globular, spray, and streaming. Using features of the arc signal, an artificial neural network was developed to estimate the spatter rate during GMAW short-circuit transfer mode (Ref 22).

Recently, the decreasing cost of titanium and its high strength-to-weight ratio, combined with its excellent corrosion-resistant properties, make it an ideal candidate for many chemical, marine, and military applications. Research into pulsed-current GMAW of titanium offers the potential for lower heat-input fabrication without the typical occurrence of spatter found in globular transfer. Active control of the waveform during pulsed-current GMAW of titanium has been demonstrated by Zhang et al. (Ref 23, 24). Spatter-free, one-drop-per-pulse metal transfer is

achieved by ensuring that the electromagnetic force that is generated by the detachment pulse is in phase with the downward oscillatory motion of the undetached droplet.

A method for detecting contact tube wear in GMAW is presented in Ref 25. The approach calculates a “wear parameter” that is based on the integral from 0.3 to 4 Hz of the power spectral density of the voltage or current. Real-time monitoring of the wear parameter during welding can predict the onset of tube wear when the parameter begins to grow nonlinearly or exceeds a predetermined threshold.

Weld pool oscillation sensing as a means of indirectly assessing the depth of penetration in an autogenous gas tungsten arc weld was first proposed by Hardt et al. (Ref 26). Originally recognized by Cheever and Howden (Ref 27) and later investigated further by Kotecki et al. (Ref 28), the authors were able to empirically verify that the pool’s natural resonant frequency increased as the pool’s radius decreased. The coupled sensing and modeling technique is founded upon the premise that the weld puddle oscillations are a function of the external force, the properties of the molten region, the surface tension, and the shape of the container. Determining the depth of penetration using the natural resonant frequency of the pool vibrations involves exciting the pool into motion, sensing the weld pool oscillations, and modeling the relationship between the frequency and the pool geometry. Through-the-arc voltage sensing can detect small fluctuations in the arc voltage as an indicator of weld pool surface displacement. Renwick and Richardson (Ref 29) and later Madigan et al. (Ref 30) used the alternating current component of the arc voltage as an indicator of pool oscillations. Other research attempts followed that improved upon the excitation and sensing techniques and extended the modeling fidelity (Ref 31–36).

Optical—Nonimaging and Imaging Optics

The arc light radiation and the resulting diffuse and specular reflections from the molten weld pool, the mass transfer, and the workpiece can provide valuable insight into the behavior and state of the welding process. Researchers have attempted to capture the dynamics of the welding process optically through both imaging and nonimaging techniques. Illumination comes from either the arc itself or an auxiliary high-intensity light source, for example, laser. Nonimaging and imaging optics are discussed in the following two sections.

Nonimaging optics are concerned with the capture of light radiation but without the intent to form an image of the source. Examples of nonimaging optical devices for monitoring an arc welding process include fiber optics and/or nonimaging lenses that are coupled with a photosensor, for example, photodiodes or photomultipliers. Although the arc light spectrum encompasses the

visible, ultraviolet, and infrared, the photosensor can be chosen to be more sensitive to one area of the spectrum, depending upon the need. A typical arc light sensor consists of a glass fiber bundle shrouded in some sort of light-limiting tube (such as a copper tube) that is pointed at the welding arc or the weld pool surface.

Several research efforts have investigated a more robust method of detecting changes in the arc length using the amount of light emitted by the arc as an improvement over arc voltage control (Ref 37) and as a method of sensing weld pool vibrations (Ref 38–43). Better sensitivity to fluctuations in the arc length using arc light rather than arc voltage can be attributed to the fact that most of the arc light is produced in the arc column, whereas only a minor amount of the arc voltage drop is from the arc column (Ref 41). A novel control system was demonstrated by Madigan (Ref 44) that relied on the arc light to monitor and control both the droplet frequency and the arc length during GMAW.

Although the sensitivity of monitoring pool oscillations using arc light is improved over arc voltage, the averaging effect of the pool motion over its entire surface remains as an obstacle. An alternative optical method for assessing pool oscillations relies on the specular reflections of arc light from the pool's mirrorlike surface (Ref 45–47). Unlike the previous optical methods that sense diffuse arc light emitted from the arc column, the optical probe is positioned approximately 45° to the workpiece in an effort to collect specular reflections from the arc and the electrode, as illustrated in Fig. 3. A novel excitation method (Ref 46) and modeling approach (Ref 45) are integrated in an effort to provide real-time closed-loop control of partial- and full-penetration welding conditions (Ref 47).

Imaging optics are concerned with the optical reconstruction of a light source. In welding control systems, imaging optics are typically

applied to the capture and reconstruction of the fusion zone geometry, the workpiece and joint geometry, or the mass transfer. Although vision-based systems have a long history of being employed as diagnostic tools in laboratory environments (Ref 27, 28, 48, 49), the continued advances in computational capabilities and reduction in cost have recently led to an increase in the research and application of vision-based systems for closed-loop control.

One of the first optical tracking systems was a coaxial viewing system developed by Richardson (Ref 50). The vision system is integrated inside the welding torch to detect the edges of the weld pool for process monitoring, joint tracking, and weld pool control. Pietrzak (Ref 51) also applied a coaxial vision-based system in which the weld pool width was monitored and controlled as a first-order approximation to the depth of penetration.

Due to the difficult optical environment that is caused by arc glare, welding spatter, and fume, most commercially successful joint tracking systems employ an auxiliary light source. Therefore, a number of optical tracking systems make use of a projected laser stripe to provide structured lighting that permits three-dimensional profiling of the joint (Ref 52, 53). However, improvements in the performance of vision-based platforms and the application of sophisticated image processing routines have enabled joint tracking without the external light source (Ref 54, 55). Xue has demonstrated a vision-based system for joint tracking GMAW that relies on the arc itself as an illumination source (Ref 56). A high-speed, vision-based spatter classification and contamination detection system is presented in Ref 57.

Using a digital camera imaging system, a penetration control technique has been developed during root pass welding of an open butt joint (Ref 58). The digital camera is positioned

in front of the torch at an angle of approximately 10 to 20° from a line tangent to the workpiece. A frontal view of the weld is obtained such that penetration can be viewed directly from the weld contour line. Penetration can therefore be directly monitored and controlled. This method is only applicable to the root pass with an open joint and provides no information during subsequent fill passes.

A novel, dual-camera backside and topside sensing system was developed to monitor the root opening during pulsed gas tungsten arc welding (GTAW) with filler metal (Ref 59). The system uses a neural network to predict the backside width and topside height and control the wire feed rate and the pulse duty cycle to compensate for root-opening variability.

Through the use of an elaborate laser-enhanced stroboscopic video system (Ref 60), the geometrical appearance of the weld pool has been extensively studied (Ref 61–63) as a means of monitoring and controlling weld joint penetration. Previous research contends that important information such as weld defects and penetration are contained in the surface deformation of the weld pool during GTAW and GMAW processes (Ref 64, 65). Therefore, the authors set out to investigate the possible application of monitoring and controlling weld penetration through pool surface shape. In particular, the weld pool area (two-dimensional shape) and three-dimensional surface can provide varying degrees of accuracy for controlling the weld process. However, when they are used in combination, the authors found that an improvement in maintaining both desired penetration and mechanical properties is achieved. The researchers employed artificial neural networks to emulate the human operator ability to extract weld quality information, in particular, penetration, from the shape of the weld pool. Additional efforts followed that have extended upon the previously described principles (Ref 66–68).

A novel imaging system to monitor the solidification and surface flow of autogenous gas tungsten arc weld pools is presented in Ref 69 and 70. The system was designed to investigate the formation of weld surface ripples. The authors present a theory of ripple formation that is based on solidification mode instability during columnar dendritic solidification (Ref 71).

Other Measurements

Temperature measurements involve either a direct contact method using thermocouples or a noncontact method employing either an infrared (IR) point source or a vision-based digital IR camera. Temperature distribution sensing methods involve certain disadvantages. Thermocouples, in particular, require intimate contact with the weldment at all times, while IR systems require calibration for differences in the thermal emissivity of the workpiece. In GTAW, accurate IR temperature measurements can be further hampered by interfering radiation from the arc

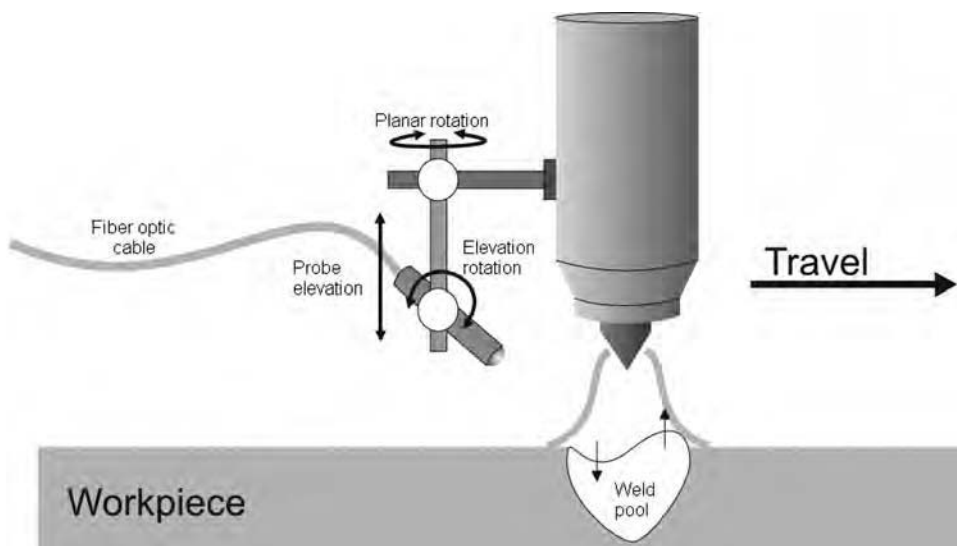


Fig. 3 A nonimaging optical probe can be used to collect arc light from an arc welding process. The probe can be elevated and rotated depending on the light source of interest

and the tungsten electrode (Ref 72). Finally, unlike IR sensors, which typically have a fast response time, contact temperature transducers such as thermocouples tend to have a slow response time (Ref 73), thus preventing them from being incorporated into a real-time feedback control system.

Monitoring the temperature distribution around the weld can infer many attributes of the welding process that can be applied to automated control. Thermally-based weld penetration estimation has been investigated using both contact (Ref 74–76) and noncontact-based sensing methods (Ref 72, 77–79). Independent of the sensor employed, thermally-based depth estimation requires a heat-transfer model in the closed-loop feedback path in order to address time-varying welding conditions. Consequently, controller accuracy depends on the accuracy of the sensor and the thermal model. Various research efforts have investigated the effects on the weld bead shape, penetration in particular, from the magnitude of heat input from the arc, the distribution of heat input over the surface of the weldment, and the duration of heat input (Ref 80–84). The effect of plate thickness, thermal properties, and operating variables (of the welding process) on the thermal phenomena, such as the cooling rate and the peak temperature distribution, must be thoroughly understood in order for a thermal model to accurately assess, and control, the weld bead geometry. Consequently, the process parameters, such as material thickness, thermal conductivity, and material composition, must be known a priori. The accuracy of the model predictions depends on the type of model employed and the accuracy of selecting various parameters. Furthermore, model parameters such as arc efficiency and distribution are only first-order approximations and therefore result in potential ambiguities or uncertainties in the ability of the model to accurately predict penetration.

In addition to penetration assessment methods, other potential applications to automated control involve sensing discontinuities (Ref 85), seam tracking (Ref 86), and cooling-rate measurements (Ref 87, 88).

Acoustical Signals. The airborne acoustical signals generated by the welding arc are a principal source of feedback for manual welders (Ref 89). Research into airborne acoustics as a means of inferring weld quality date back to the late 1960s (Ref 90) and are founded upon the principle that sound pressure variations occur due to changes in the electrical power of the arc column (Ref 91). Changes in the electrical power of the arc can be manifested by the effects of variation in gas flow, welding speed, welding current or voltage, and arc length or by the behavior of the molten weld pool, mass transfer, or heat source to material interaction. Therefore, the audio signal is a natural feedback mechanism for evaluating process stability, detecting defects in situ, and automated control.

The use of acoustical signals generated by GMAW for detection of metal-transfer mode

is presented in Ref 21. In Ref 92, Grad et al. identified that the main source of acoustic waves in GMAW short-circuit metal-transfer mode is arc reignition. Using airborne acoustics, the authors were able to assess process stability and detect welding conditions that lead to welding defects. Similar efforts are presented in Ref 93 to 97. The arc sound was also used in GTAW for monitoring welding quality (Ref 98), while acoustic arc length control was demonstrated in Ref 99.

Ultrasonic Techniques. Postweld inspection using ultrasonic techniques has been an effective and proven method for locating internal flaws such as discontinuities, cracks, slag inclusions, and porosity of a welded joint. Capable of working on all materials, ultrasonic testing is extremely sensitive, allowing it to detect exceptionally small flaws. Based upon an established technology, several researchers have applied ultrasonic techniques to weld penetration measurement for feedback control (Ref 100–103). The use of ultrasonics for weld process sensing has the potential to detect weld pool geometry and discontinuities in real-time. However, to be useful in a production system, a means must be developed for injecting and receiving the ultrasound with noncontact sensors. A noncontact system was developed that combined a laser array generation source and an electromagnetic acoustic transducer receiver (Ref 104, 105). Similar to other external sensing methods, movement of the sensor must be synchronized with the torch motion. Finally,

large temperature gradients within the heat-affected zone can reflect ultrasonic waves, thus limiting the quality and accuracy of measuring the weld pool dimensions.

Arc Tracer Spectroscopy. The use of arc tracer spectroscopy to determine root penetration during pulsed autogenous GTAW from the top-side of the workpiece is demonstrated in Ref 106. Although access to the back of the plate is necessary in order to attach tracer elements for spectroscopy detection, topside penetration sensing is accomplished and demonstrated in both the 2G position as well as in orbital welding. Penetration defects were determined by comparing predetermined root penetration spectroscopy to the current workpiece spectroscopy.

Modeling

There are at least two roles for models in a generic nonadaptive weld process controller. First, a model can be used in defining the initial equipment parameters of the process. The welder specifies the desired DWP, such as weld bead width and/or penetration, and the model is then used to arrive at suitable IWP, such as welding current and/or travel speed. Secondly, a model can be operated in parallel with the actual process and provide predictions of the DWP that cannot be measured directly in real-time. For example, a weld model can provide the controller with an estimate of the weld bead penetration. Figure 4 illustrates the application

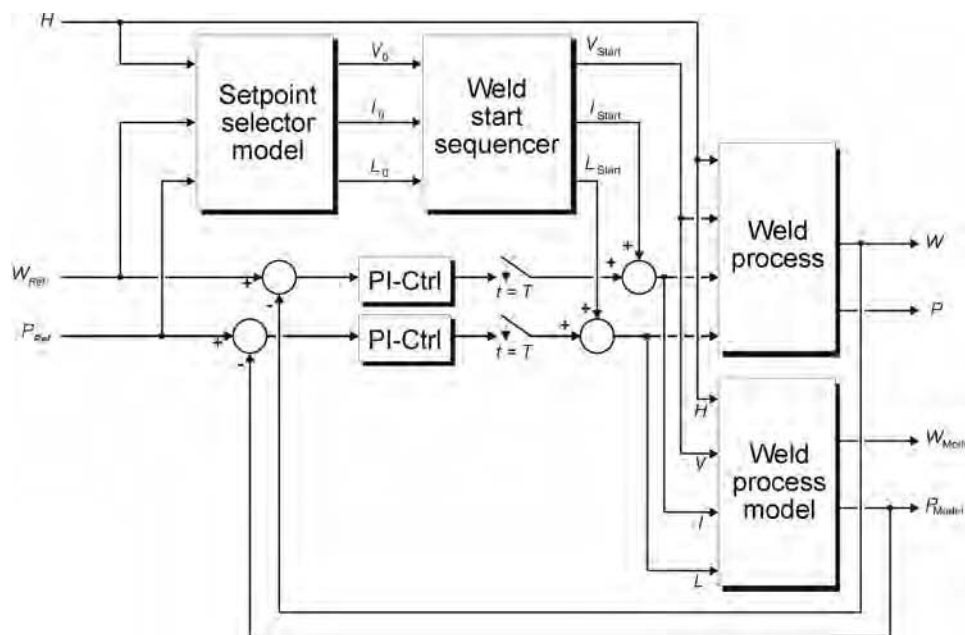


Fig. 4 An example closed-loop control system employs both a setpoint selector model and a steady-state weld process model. The desired bead width, W_{Ref} , and penetration, P_{Ref} , are specified by the user. These parameters, as well as the workpiece thickness, H , are fed to a setpoint selector model, which yields the nominal travel speed, current, and arc length (v_0 , i_0 , and L_0 , respectively). Upon reaching steady state, the closed-loop control is enacted. The bead width from the process is monitored in real-time, while penetration is estimated. The measured bead width and the estimated penetration are subtracted from the respective reference values, processed through proportional-plus-integral controllers, and added to the final values obtained from the setpoint sequencer. Source: Ref 107

of both models within the context of a closed-loop control system for GTAW bead width and depth of penetration (Ref 107).

A distinguishing characteristic of process models used for control purposes is they must be computed in real-time. This rules out many of the more exact numerical models that have been developed using finite-element and finite-difference methods. While simpler models may lack the precision and the fidelity of a numerical solution, they provide the necessary real-time responsiveness for automation of mechanized and robotic systems.

Weld process models are either derived from the fundamental physics of heat transfer, or they are constructed from empirical data. The models derived from heat-transfer physics frequently assume that the arc can be modeled as a heat source of a given form (a point source, a disk-shaped source of heat, etc.), and then the laws of heat conduction are applied to calculate the temperatures at various points in the workpiece (Ref 80, 81, 84, 108). The analytical derivations usually require significant simplifications, such as assuming that the workpiece is either infinitely thick or of a specific shape and that the thermal properties of the molten pool are homogeneous and the same as those of the solid base metal. As a result, physics-based models can be fairly inaccurate for open-loop control (Ref 109).

An alternative to a physics-based model is an empirically-derived model (Ref 110–112). These models may simply consist of one or more equations relating the DWP to the IWP and are derived by obtaining a best fit of experimental data to the given equations. In such cases, the models are derived without any consideration of the underlying physics of the process.

A number of weld process models can be placed between the two extremes of a purely physics-based model and an empirically-derived model. Frequently, physics-based models are derived using the necessary approximations, and then various “empirical constants” and other unspecified variables are tuned until the model adequately agrees with experimental welding data. By the same token, empirical models frequently use pieces of general knowledge of the process, derived from the underlying physics. Therefore, the physics-based and the empirical models bookend the opposite extremes in weld modeling.

Neural networks are an alternative to formal analytical techniques. Empirical in nature, neural network models are not governed by the physics of the process. Instead, they rely on the input and output relationships of the training data to define the weight matrix within a sophisticated pattern-mapping architecture. The advantages of neural models include relative accuracy and broad generality across many different problem domains. In particular, if the training data are general enough and span the entire range of process parameters, then the resulting model can capture the complexity

of the process, including nonlinearities and parameter cross couplings (Ref 107, 113–115).

Neural network model development is usually much simpler than other analytical alternatives. A neural model tailors itself to the training data. Speed is also a benefit. In a real-time control loop, a feed-forward neural model is relatively fast, because the input data are only propagated once through the network. Finally, neural networks can learn when new training instances become available. When compared to other control modeling methodologies, neural networks also have certain drawbacks. The most notable one is a lack of a comprehensive model that reflects the physics of the process. Finally, relating the qualitative effects of the networks structure or parameters to the process parameters is usually impossible.

Control of Arc Welding

Although an extensive amount of research has investigated multivariable feedback control of the fusion process, most commercial applications of control for arc welding have thus far been largely focused on the control of one, or at most two, parameters of the process. The control techniques for these parameters have usually been limited to classical feedback control, based on the assumptions of linear and time-invariant behavior of the controlled systems. Examples of such control schemes include voltage and current control of the welding power source, control of the arc voltage through adjustment of the arc length, and other isolated single-variable control applications.

The following sections discuss some of the research and development activities that attempt to extend the commercial, state-of-the-art welding process controllers.

Adaptive Control. The highly nonlinear relationships that generally exist between the direct and indirect weld parameters require a feedback control system with self-tuning capabilities. A feedback control system that has this added ability to modify its control law, for example, through modifications of gains and/or time constants, in response to changes in the process being controlled is formally known as an adaptive controller. (The term *adaptive control* that is widely used in industry refers to a system that automatically determines changes in process conditions and directs the equipment to take appropriate action. From an open-loop perspective, this approach does appear “adaptive” in nature; this is simply known as feedback control, whereas adaptive control is feedback control with the added capability of self-adjustment.) Assuming localized linearity, an adaptive controller can be used to change the controller characteristics in response to changes in the operating domain. An adaptive controller provides the robustness to maintain stable control over the entire operating range of the process.

Adaptive control algorithms have been developed for the nonlinear operating regions

of the arc-voltage length relationship to ensure a more robust and stable control system throughout the entire operating region (Ref 116, 117). In fusion welding, the time constant and gain of a linear controller for weld geometry regulation are highly dependent upon the welding conditions, for example, torch speed, arc length, material thickness, and material properties. Suzuki et al. demonstrate the advantages and benefits of an adaptive controller over a traditional linear controller for bead width control during GTAW (Ref 118).

Intelligent Control. Researchers working in the field of intelligent control typically derive an approach to solving a control problem that is inspired by the decision-making process in humans and other biological systems. Certain approaches are heuristic in format, and most turn out to be nonlinear and possibly adaptive. Unlike conventional methods in which stability is proven, verification that the approach is successful is commonly determined by simulation or by experimental evaluation. The relative advantages and disadvantages of using an intelligent method over a conventional method or over another intelligent method are difficult to assess due to the lack of a clear and objective set of evaluation criteria.

The tools used for artificial intelligence depend upon the application. Four of the most commonly applied intelligent tools are neural networks, expert systems, fuzzy logic, and genetic algorithms. Neural networks and genetic algorithms operate on unstructured data in the form of numbers, usually normalized between 0 and 1. Expert systems excel through the use of rules that operate on structured data in the form of words or symbols. Fuzzy logic can work well with both structured and unstructured data in the form of both symbols and numbers.

Methods of evaluating the performance of a controller using various techniques are complicated. When considering different techniques, Passino (Ref 119) suggests evaluating the following attributes of the system:

- Time-domain performance analysis, including stability and performance measures such as rise-time, overshoot, and steady-state error
- Simplicity of the design method
- Ease of understanding the approach
- Lead-time to design and implementation
- Ease of implementation

The development of a self-organizing, fuzzy logic weld penetration controller was presented in (Ref 120). The adaptive controller was modeled after expert human welding knowledge and tuned online to automatically adjust the sensitivities to its membership functions according to the current welding conditions. The single-input, single-output fuzzy logic controller relies on simple heuristics to capture the nonlinear, time-varying, asymmetric thermal relationship of the arc welding process. The translation from

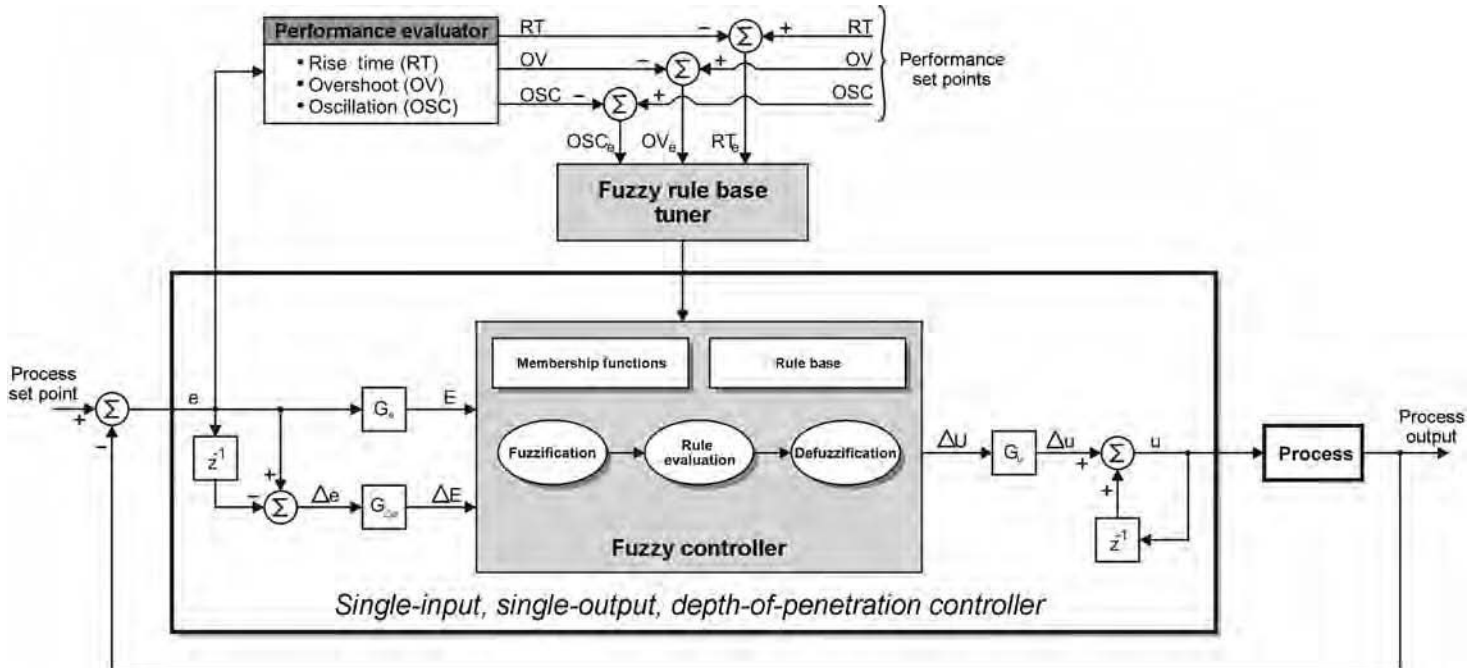


Fig. 5 A self-organizing fuzzy logic controller for depth-of-penetration control.

an expert's knowledge to a set of fuzzy variables and rules inevitably results in a generalized, yet nonoptimal, control rule base and therefore requires tuning to optimize the transient and steady-state performance under process-specific conditions. Figure 5 illustrates the controller and performance supervisor. The approach avoids the time-consuming, unsystematic, and error-prone manual tuning that is considered by some to be the greatest drawback to using fuzzy logic for control purposes. The performance tuner exploits the fundamental advantage of fuzzy systems by incorporating a vague, yet intuitive, human-based model of the system.

Multivariable Control. The welding control applications mentioned in the previous sections are usually adequate for their specific purposes, that is, to maintain one or two system parameters at predefined values. These traditional schemes, however, are not easily applicable to the more complex task of directly controlling multiple outputs of the process through the available equipment parameters, that is, controlling the DWP in terms of the IWP (Ref 5).

Cook et al. (Ref 107) have described a multivariable weld process control system that makes use of a model to estimate one of two DWP(s) controlled. The system, shown in Fig. 4, was configured to accept weld bead width and weld penetration as its two inputs. The system used width sensing, while penetration was estimated using a forward process model acting in parallel to the actual process. Conventional time-based up-sloping/down-sloping was used for weld initiation and termination, and an inverse process model was used

to provide initial weld IWPs (following up-slope) to the weld start sequencer. Using the layout in Fig. 4, the desired bead width and penetration are specified by the user as W_0 and P_0 , respectively. These parameters, as well as the workpiece thickness, H , are routed to a neural network setpoint selector (inverse process model), which produces the nominal travel speed, current, and arc length (v_0 , I_0 , and L_0 , respectively). Arc initiation and stabilization are controlled in an open-loop fashion by the weld start sequencer. Given the desired equipment parameters, the arc is typically initiated and established at a relatively low current, with the other equipment parameters set at some nominal value. Once the arc has been established, the equipment parameters are ramped to the setpoint values specified by the neural network. When the setpoint values have been reached, at time $\tau = T$, the closed-loop process control is enacted. The bead width was measured in real-time, while a real-time, neural network penetration predictor (forward process model) was run in parallel with the process to yield estimates of the penetration. The measured bead width and the estimated penetration are subtracted from the respective reference values, processed through proportional-plus-integral controllers, and added to the final values obtained from the setpoint sequencer.

Controlling a single or multivariable system is not a trivial task without an adequate quantitative model. In the case of arc welding, relationships between the various process inputs and outputs are not well defined. Furthermore, the process variables are coupled (that is, any given input parameter affects more than one

output parameter), and, in general, the welding processes are nonlinear (that is, the output parameters are not adequately described in terms of a linear combination of the input parameters and their time derivatives). All of these facts add to the difficulty of designing a general weld controller using conventional multivariable control.

Distributed, Hierarchical Control. An alternative to conventional multivariable control is a distributed, hierarchical control architecture. Decoupling of the process is accomplished through a loosely-coupled and hierarchical network of supervisors that oversee the application of successful one- and two-parameter conventional, adaptive, and intelligent controllers. The supervisors work together toward a common goal and achieve modularity, while increasing reliability and decreasing complexity.

Autonomy and multivariable control is achieved through the use of high-level, intelligent, decision-making techniques that supervise low-level, real-time control methodologies. Relevant information about the process that is typically overlooked or generalized upon in a conventional mathematical approach to control design can be incorporated more formally and logically using a collection of intelligent supervisory components. Communication, synchronization, and supervision are therefore critical in order to guarantee that the system will satisfy an overall or global goal.

A network architecture that facilitates communication permits integration of distributed components through a communication layer and maintains system integrity by preventing

deadlock. Equally important is an architecture that can help manage a diversity of decision-making processes. Cooperation, collaboration, and supervision between various agents is necessary in order to address resource management, conflict resolution, controller tuning, scheduling, and crisis and contingency management. Furthermore, the control system must be capable of interacting with a human expert or other system in order to generate goals, assess capabilities of the system, monitor overall performance, and alert the operator when human intervention is necessary.

A proposed architecture for an intelligent, multivariable, autonomous weld controller for arc welding is proposed in Fig. 6 and evolves from established conventional welding control systems by adding intelligent components (Ref 121). In addition to interfacing with sensors and other hardware, the execution layer is responsible for executing low-level numeric signal processing and control routines, process parameters identification routines, and failure identification routines. Essentially, the execution layer is responsible for individual control algorithms and monitoring techniques of the

physical process. The coordination level tunes, schedules, supervises, and redesigns the execution-level functions; performs crisis and contingency management; plans and coordinates execution-level tasks; and executes heuristic-type functions. Finally, the management level supervises all lower-level functions, allows humans or other systems access to relevant process monitoring and control information, and performs high-level learning about the user and the lower-level functions.

The intelligent supervisory agents in the coordination level would be responsible for managing multiple, concurrent, and often conflicting goals that are associated with the process of joining two components. The execution-level control elements would still execute low-level control algorithms (such as proportional, integral, or derivative functions, adaptive control, and intelligent methods) that provide accurate and fast response times, while an automated supervisory module can mimic a human welder's expert supervision of the welding process by incorporating this intuitive knowledge into a set of fuzzy rules.

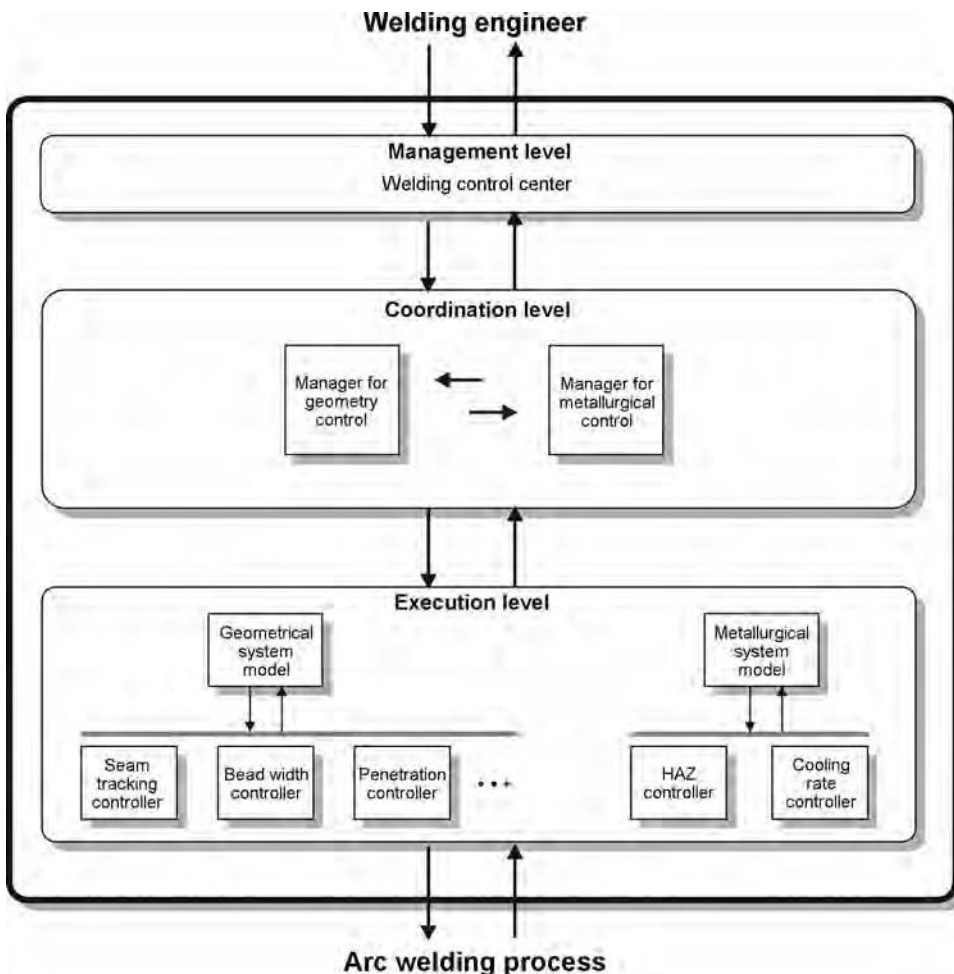


Fig. 6 Intelligent autonomous weld controller. HAZ, heat-affected zone

REFERENCES

1. R.B. Madigan, Ways to Keep Torches in Seams, *Weld. Des. Fabr.*, Oct 1987, p 48–50
2. B. Butler, Joint Tracking Automation Triples Propane Cylinder Production, *Weld. J.*, Vol 71 (No. 8), Aug 1992, p 61–63
3. Joint Tracking Robot System Transforms Company's Welding Production, *Weld. J.*, Vol 73 (No. 3), March 1994, p 68–69
4. T.W. Eagar, The Physics and Chemistry of Welding Processes, *Advances in Welding Science and Technology, Proceedings of an International Conference on Trends in Welding Research*, S.A. David, Ed., May 18–22, 1986 (Gatlinburg, TN), ASM International, p 291–298
5. G.E. Cook, Feedback and Adaptive Control in Automated Arc Welding Systems, *Met. Constr.*, Vol 13 (No. 9), Sept 1981, p 551–556
6. E.P. Vilkas, Automation of Gas Tungsten-Arc Welding Process, *Weld. J.*, Vol 45 (No. 5), May 1966, p 410–416
7. J.E. Lancaster, *The Physics of Welding*, 2nd ed., Pergamon Press, Oxford, U.K., 1986
8. G.E. Cook, Robotic Arc Welding: Research in Sensory Feedback Control, *IEEE Trans. Ind. Electron.*, Vol IE-30 (No. 3), 1983, p 252–268
9. R.W. Richardson, Seam Tracking Sensors—Improvements All the Time, *Weld. Des. Fabr.*, Sept 1982, p 77–82
10. G.E. Cook and P.C. Levick, Advances in Through-the-Arc Sensing for Adaptive Control, *Developments and Innovations for Improved Welding Production*, The Welding Institute, Cambridge, England, Sept 1983, p PII-1 to PII-9
11. G.E. Cook, K. Andersen, K.R. Fernandez, M.E. Shepard, and A.M. Wells, Jr., Electric Arc Sensing for Robot Positioning Control, *International Trends in Manufacturing Technology—Robotic Welding*, J.D. Lane, Ed., IFS (publications), London, U.K., 1987, p 181–216
12. R.V. Hughes and R.P. Walduck, Electromagnetic Arc Path Control in Robot Plasma Welding, *Int. J. Adv. Manuf. Technol.*, Vol 1 (No. 1), Sept 1985, p 9–25
13. Y.H. Kang and S.J. Na, Characteristics of Welding and Arc Signal in Narrow Groove Gas Metal Arc Welding Using Electromagnetic Arc Oscillation, *Weld. J.*, Vol 82 (No. 5), May 2003, p 93s–99s
14. W.-S. Yoo, Y.-H. Shi, J.-T. Kim, and S.J. Na, End Point Detection of Fillet Weld Using Mechanized Rotating Arc Sensor in GMAW, *Weld. J.*, Vol 85 (No. 8), Aug 2006, p 180s–187s
15. Y.F. Gao, H. Zhang, and Z.W. Mao, Welding Gun Inclination Detection and Curved Fillet Weld Joint Tracking, *Weld. J.*, Vol 88 (No. 3), March 2009, p 45s–53s

16. G.E. Cook and M.J. Scheid, Detection of Surface Contaminants by Computerized Arc Signal Analysis, *66th Annual AWS Convention, Abstracts of Papers*, May 1985 (Las Vegas, NV), p 223–225
17. T.A. Siewert, R.B. Madigan, T.P. Quinn, and M.A. Mornis, Through-the-Arc Sensing for Monitoring Arc Welding, *International Trends in Welding Science and Technology, Proceedings of the Third International Conference on Trends in Welding Research*, S.A. David and J.M. Vitek, Ed., June 1–5, 1992 (Gatlinburg, TN), ASM International, p 1037–1040
18. T.A. Siewert, R.B. Madigan, T.P. Quinn, and M.A. Mornis, Through-the-Arc Sensing for Measuring Gas Metal Arc Weld Quality in Real Time, *Mater. Eval.*, Nov 1992, p 1314–1318
19. T.P. Quinn, R.B. Madigan, C.B. Smith, and E.G. Blachowiak, Weld Defect Decisions Using Through-the-Arc Sensor Data, NIST Special Publication 923, *Seventh International Conference on Computer Technology in Welding*, T. Siewert, Ed., July 8–11, 1997 (San Francisco, CA), National Institute of Standards and Technology, p 496–502
20. U. Ersoy, S.J. Hu, and E. Kannatey-Asibu, Observation of Arc Start Instability and Spatter Generation in GMAW, *Weld. J.*, Vol 87 (No. 2), Feb 2008, p 51s–56s
21. J.A. Johnson, N.M. Carlson, and H.B. Smartt, Detection of Metal-Transfer Mode in GMAW, *Recent Trends in Welding Science and Technology, Proceedings of the Second International Conference on Trends in Welding Research*, S.A. David and J.M. Vitek, Ed., May 14–18, 1989 (Gatlinburg, TN), ASM International
22. M.J. Kang, Y. Kim, S. Ahn, and S. Rhee, Spatter Rate Estimation in the Short-Circuit Transfer Region of GMAW, *Weld. J.*, Vol 82 (No. 9), Sept 2003, p 238s–247s
23. Y.M. Zhang, E. Liguio, and R. Kovacevic, Active Metal Transfer Control by Monitoring Excited Droplet Oscillation, *Weld. J.*, Vol 77 (No. 9), Sept 1998, p 388s–395s
24. Y.M. Zhang and P.J. Li, Modified Active Control of Metal Transfer and Pulsed GMAW of Titanium, *Weld. J.*, Vol 80 (No. 2), Feb 2001, p 51s–61s
25. T.P. Quinn, R.B. Madigan, M.A. Mornis, and T.A. Siewert, Contact Tube Wear Detection in Gas Metal Arc Welding, *Weld. J.*, Vol 74 (No. 4), April 1995, p 115s–120s
26. D.E. Hardt, K.M. Masubichi, H.M. Panyter, E. Unkel, J. Converti, and M. Zachsenhouse, Improvement of Fusion Welding Through Modeling, Measurement, and Real-Time Control, *International Conference on Welding Technology for Energy Applications*, May 1982 (Gatlinburg, TN), p 281–299
27. D.L. Cheever and D.G. Howden, Technical Note: Nature of Weld Surface Ripples, *Weld. J.*, Vol 48 (No. 4), April 1969, p 179s–180s
28. D.J. Kotecki, D.L. Cheever, and D.G. Howden, Mechanism of Ripple Formation during Weld Solidification, *Weld. J.*, Vol 51 (No. 8), Aug 1972, p 386s–391s
29. R.J. Renwick and R.W. Richardson, Experimental Investigation of GTA Weld Pool Oscillations, *Weld. J.*, Vol 62 (No. 2), Feb 1983, p 29s–35s
30. R.B. Madigan, R.J. Renwick, D.E. Farson, and R.W. Richardson, Computer-Based Control of Full Penetration GTA Welds Using Pool Oscillation Sensing, *International Conference on Computer Technology in Welding*, The Welding Institute, Cambridge, U.K., 1986, p 165–174
31. C.D. Sorensen, “Digital Signal Processing as a Diagnostic Tool for Gas Tungsten Arc Welding,” Ph.D. dissertation, Massachusetts Institute of Technology, Department of Materials Science, 1985
32. R.B. Madigan, “Control of Full Penetration GTA Weld Size by Weld Pool Oscillation Sensing,” M.S. thesis, The Ohio State University, Department of Welding Engineering, 1985
33. H.W. Ludewig, “An IBM-PC Based GTAW Penetration Control Using a Fast Fourier Transform for Weld Pool Oscillation Frequency Detection,” M.S. thesis, The Ohio State University, Department of Welding Engineering, 1988
34. Y.H. Xiao and G. den Ouden, A Study of GTA Weld Pool Oscillation, *Weld. J.*, Vol 69 (No. 8), Aug 1990, p 289s–293s
35. Q.L. Wang, C.L. Yang, and Z. Geng, Separately Excited Resonance Phenomenon of the Weld Pool and Its Application, *Weld. J.*, Vol 72 (No. 9), Sept 1993, p 455s–462s
36. A.J.R. Aendenrooier and G. den Ouden, Weld Pool Oscillation during Pulsed GTA Welding, *Trends in Welding Research, Proceedings of the Fourth International Conference*, H.B. Smartt, J.A. Johnson, and S.A. David, Ed., June 5–8, 1995 (Gatlinburg, TN), ASM International, p 733–737
37. R.W. Richardson and E.S. Edwards, Controlling GT Arc Length from Arc Light Emissions, *Trends in Welding Research, Proceedings of the Fourth International Conference*, H.B. Smartt, J.A. Johnson, and S.A. David, Ed., June 5–8, 1995 (Gatlinburg, TN), ASM International, p 715–720
38. R.D. Lillquist and A.W. Case, Jr., “Method and Apparatus for Measuring Weld Penetration in An Arc Welding Process,” U.S. Patent 4,711,986, General Electric Company, Schenectady, NY, Dec 8, 1987
39. A.S. Tarn and D.E. Hardt, Weld Pool Impedance for Pool Geometry Measurement: Stationary and Nonstationary Pools, *Trans. ASME: J. Dynamic Sys., Measure. Control*, Vol III (No. 4), April 1989, p 545–553
40. R.T. Deam, Weldpool Frequency: A New Way to Define a Weld Procedure, *Recent Trends in Welding Science and Technology, Proceedings of the Second International Conference on Trends in Welding Research*, S.A. David and J.M. Vitek, Ed., May 14–18, 1989 (Gatlinburg, TN), ASM International, p 967–971
41. C.D. Yoo and R.W. Richardson, An Experimental Study on Sensitivity and Signal Characteristics of Weld Pool Oscillation, *Trans. Jpn. Weld. Soc.*, Vol 24 (No. 2), Oct 1993, p 54–62
42. D.M. Barborak, “Development and Test of a System for the Study of Weld Pool Oscillation Sensing,” M.S. thesis, The Ohio State University, Department of Welding Engineering, 1995
43. S.D. Stecker, “Characterization and Application of Weld Pool Oscillation Phenomenon for Penetration Control of Gas Tungsten Arc Welding,” M.S. thesis, The Ohio State University, Department of Welding Engineering, 1996
44. R.B. Madigan, “Control of Gas Metal Arc Welding Using Arc Light Sensing,” Ph.D. dissertation, Colorado School of Mines, May 1994
45. R.J. Barnett, “Sensor Development for Multi-Parameter Control of Gas Tungsten Arc Welding,” Ph.D. dissertation, Vanderbilt University, May 1993
46. K. Andersen, “Synchronous Weld Pool Oscillation for Monitoring and Control,” Ph.D. dissertation, Vanderbilt University, May 1993
47. D.A. Hartman, D.R. Delapp, R.J. Barnett, and G.E. Cook, A Neural Network/Fuzzy Logic System for Weld Penetration Control, *Trends in Welding Research, Proceedings of the Fifth International Conference*, H.B. Smartt, L.A. Johnson, and S.A. David, Ed., June 1–5, 1998 (Callaway Gardens, GA), ASM International, p 1096–1101
48. L.A. Jones, T.W. Eagar, and J.H. Lang, Investigations of Drop Detachment Control in Gas Metal Arc Welding, *International Trends in Welding Science and Technology, Proceedings of the Third International Conference on Trends in Welding Research*, S.A. David and J.M. Vitek, Ed., June 1–5, 1992 (Gatlinburg, TN), ASM International, p 1009–1013
49. L.A. Jones, T.W. Eagar, and J.H. Lang, Images of a Steel Electrode in Ar-2%O₂ Shielding during Constant Current Gas Metal Arc Welding, *Weld. J.*, Vol 77 (No. 4), April 1998, p 135s–141s
50. R.W. Richardson, D.A. Gutow, R.A. Anderson, and D.F. Farson, Coaxial Arc Weld Pool Viewing for Process Monitoring and Control, *Weld. J.*, Vol 63 (No. 3), March 1984, p 43–50

51. K.A. Pietrzak and S.M. Packer, Vision-Based Weld Pool Width Control, *Trans. ASME: J. Eng. Ind.*, Vol 116 (No. 1), Feb 1994, p 86–92
52. R. Vires, A Laser Based Vision System for Arc Welding Automation, *Conference on Advances in Automation for Precision Arc Welding*, Dec 2–3 1987 (Columbus, OH), Edison Welding Institute
53. J.P. Huissoon and D.L. Strauss, Seam Tracking Control of Robotic Arc Welding Systems, *Trends in Welding Research, Proceedings of the Fourth International Conference*, H.B. Smartt, J.A. Johnson, and S.A. David, Ed., June 5–8, 1995 (Gatlinburg, TN), ASM International, p 695–700
54. J.S. Kim, Y.T. Son, H.S. Cho, and K.I. Koh, A Robust Method for Vision-Based Seam Tracking in Robotic Arc Welding, *Proceedings of the 1995 IEEE International Symposium on Intelligent Control*, Aug 1995 (Monterey, CA), p 363–368
55. H.-C. Kuo and L.-J. Wu, An Image Tracking System for Welded Seams Using Fuzzy Logic, *J. Mater. Proc. Technol.*, Vol 120 (No. 1), 2002, p 169–185
56. F.X. Xue, L.L. Zhang, Y.H. Peng, and L. Jia, A Wavelet Transform-Based Approach for Joint Tracking in Gas Metal Arc Welding, *Weld. J.*, Vol 86 (No. 4), April 2007, p 90s–96s
57. G. Schwab, J.P.H. Steele, and T.L. Vincent, Vision-Based Spatter Classification and Contaminant Detection System, *Weld. J.*, Vol 88 (No. 6), June 2009, p 121s–130s
58. F. Nadeau, P. Fafard, G. Patenaude, and J. Tremblay, “Method and Apparatus for Controlling Root Pass Penetration in Open Butt Joints,” U.S. Patent 4,733,051, Canadian Patents and Development Limited, Ottawa, Canada, March 22, 1988
59. G.J. Zhang, S.B. Chen, and L. Wu, Intelligent Control of Pulsed GTAW with Filler Metal, *Weld. J.*, Vol 84 (No. 1), Jan 2005, p 9s–16s
60. T. Hoffman, Real-Time Imaging for Process Control, *Adv. Mater. Proc.*, Vol 140 (No. 3), Sept 1991, p 37–40
61. Y.M. Zhang, L. Li, and R. Kovacevic, Monitoring of Weld Pool Appearance for Penetration Control, *Trends in Welding Research, Proceedings of the Fourth International Conference*, H.B. Smartt, J. A. Johnson, and S.A. David, Ed., June 5–8, 1995 (Gatlinburg, TN), ASM International, p 683–688
62. R. Kovacevic and Y.M. Zhang, Sensing Free Surface of Arc Weld Pool Using Specular Reflection: Principle and Analysis, *J. Eng. Manuf., Proc. Part B*, Vol 210 (No. B6), 1996, p 553–564
63. R. Kovacevic and Y.M. Zhang, Monitoring of Weld Joint Penetration Based on Weld Pool Geometrical Appearance, *Weld. J.*, Vol 75 (No. 10), Oct 1996, p 317s–329s
64. M.L. Lin and T.W. Eagar, Influence of Arc Pressure on Weld Pool Geometry, *Weld. J.*, Vol 64 (No. 6), June 1985, p 163s–169s
65. S.I. Rokhlin and A.C. Guu, A Study of Arc Force, Pool Depression, and Weld Penetration during Gas Tungsten Arc Welding, *Weld. J.*, Vol 72 (No. 8), Aug 1993, p 381s–390s
66. C. Balfour, J.S. Smith, and A.I. Al-Shammaá, A Novel Edge Feature Correlation Algorithm for Real-Time Computer Vision-Based Molten Weld Pool Measurements, *Weld. J.*, Vol 85 (No. 1), Jan 2006, p 1s–8s
67. H.S. Song and Y.M. Zhang, Image Processing for Measurement of Three-Dimensional GTA Weld Pool Surface, *Weld. J.*, Vol 86 (No. 10), Oct 2007, p 323s–330s
68. H.S. Song and Y.M. Zhang, Error Analysis of a Three-Dimensional GTA Weld Pool Surface Measurement System, *Weld. J.*, Vol 88 (No. 7), July 2009, p 141s–148s
69. D.R. Delapp, R.J. Barnett, G.E. Cook, A.M. Strauss, and D.A. Hartman, An Investigation into the Local Solidification Rate of the GTA Weld Pool, *Trends in Welding Research, Proceedings of the Fifth International Conference*, H.B. Smartt, J.A. Johnson, and S.A. David, Ed., June 1–5, 1998 (Callaway Gardens, GA), ASM International, p 400–404
70. D.R. DeLapp, D.A. Hartman, G.E. Cook, A.M. Strauss, and R.J. Barnett, Development of a GTAW Observation System, *Trends in Welding Research, Proceedings of the Fifth International Conference*, H. B. Smartt, J.A. Johnson, and S.A. David, Ed., June 1–5, 1998 (Callaway Gardens, GA), ASM International, p 405–409
71. D.R. Delapp, “Observations of Solidification and Surface Flow on Autogenous Gas Tungsten Arc Weld Pools,” Ph.D. dissertation, Vanderbilt University, Aug 2005
72. D. Farson, R.W. Richardson, and X. Li, Infrared Measurement of Base Metal Temperature in Gas Tungsten Arc Welding, *Weld. J.*, Vol 77 (No. 9), Sept 1998, p 396s–401s
73. E.O. Doebelin, *Measurement Systems: Application and Design*, 3rd ed., McGraw-Hill, New York, NY, 1983
74. J.B. Song and D.E. Hardt, Closed-Loop Control of Weld Pool Depth Using a Thermally Based Depth Estimator, *Weld. J.*, Vol 72 (No. 10), Oct 1993, p 471s–478s
75. W.M. McCampbell, G.E. Cook, L.E. Nordholt, and G.J. Merrick, The Development of a Weld Intelligence System, *Weld. J.*, Vol 45 (No. 3), March 1966, p 139s–144s
76. B.E. Bates and D.E. Hardt, A Real-Time Calibrated Thermal Model for Closed-Loop Weld Bead Geometry Control, *Trans. ASME: J. Dynamic Sys., Measure. Control*, Vol 107 (No. 1), March 1985, p 25–33
77. P. Banderjee, Infrared Sensing for On-Line Weld Geometry Monitoring and Control, *Trans. ASME: J. Eng. Ind.*, Vol 117 (No. 3), Aug 1995, p 323–330
78. W. Chen and B.A. Chin, Monitoring Joint Penetration Using Infrared Sensing Techniques, *Weld. J.*, Vol 69 (No. 5), May 1990, p 180s–185s
79. H.E. Beardsley, Y.M. Zhang, and R. Kovacevic, Infrared Sensing of Full Penetration State in Gas Tungsten Arc Welding, *Int. J. Mach. Tools Manuf.*, Vol 34 (No. 8), Nov 1994, p 1079–1090
80. D. Rosenthal, Mathematical Theory of Heat Distribution during Welding and Cutting, *Weld. J.*, Vol 20 (No. 5), May 1941, p 220s–234s
81. D. Rosenthal, The Theory of Moving Sources of Heat and Its Application to Metal Treatments, *Trans. ASME*, Vol 68, Nov 1946, p 849–866
82. P. Jhaveri, W.G. Moffatt, and C.M. Adams, Jr., The Effect of Plate Thickness and Radiation on Heat Flow in Welding and Cutting, *Weld. J.*, Vol 41 (No. 1), Jan 1962, p 12s–16s
83. E. Friedman and S.S. Glickstein, An Investigation of the Thermal Response of Stationary Gas Tungsten Arc Welds, *Weld. J.*, Vol 55 (No. 12), Dec 1976, p 408s–420s
84. A.C. Nunes, Jr., An Extended Rosenthal Weld Model, *Weld. J.*, Vol 62 (No. 6), June 1983, p 165s–170s
85. B.A. Chin, N.H. Madsen, and J.S. Goodling, Infrared Thermography for Sensing the Arc Welding Process, *Weld. J.*, Vol 62 (No. 9), Sept 1983, p 227s–234s
86. S. Nagarajan, W.H. Chen, and B.A. Chin, Infrared Sensing for Adaptive Arc Welding, *Weld. J.*, Vol 68 (No. 11), Nov 1989, p 462s–466s
87. W.E. Lukens and R.A. Morris, Infrared Temperature Sensing of Cooling Rates for Arc Welding Control, *Weld. J.*, Vol 61 (No. 1), Jan 1982, p 27s–33s
88. C.J. Einerson, H.B. Smartt, J.A. Johnson, P.L. Taylor, and K.L. Moore, Development of an Intelligent System for Cooling Rate and Fill Control in GMAW, *International Trends in Welding Science and Technology, Proceedings of the Third International Conference on Trends in Welding Research*, S.A. David and J.M. Vitek, Ed., June 1–5, 1992 (Gatlinburg, TN), ASM International, p 853–857
89. A.F. Manz, Welding Arc Sounds, *Weld. J.*, Vol 60 (No. 5), May 1981, p 23
90. W.D. Jolly, Acoustic Emission Exposes Cracks during Welding, *Weld. J.*, Vol 48 (No. 1), Jan 1969, p 21–27
91. M.G. Drouet and E. Nadeau, Pressure Waves Due to Arcing Faults in a

- Substation, *IEEE Trans. Power Apparatus Sys.*, Vol. PAS-98 (No. 5), Sept 1979, p 1632–1635
92. L. Grad, J. Grum, I. Polajnar, and J.M. Siabe, Feasibility Study of Acoustic Signals for On-Line Monitoring in Short Circuit Gas Metal Arc Welding, *Int. J. Mach. Tools Manuf.*, Vol 44 (No. 5), April 2004, p 555–561
 93. M. Cudinal and C. Prezelj, Evaluation of the Sound Signal Based on the Welding Current in the Gas Metal Arc Welding Process, *Proc. Instit. Mech. Eng., Part C: J. Mech. Eng. Sci.*, Vol 217 (No. 5), 2003, p 483–494
 94. J. Tam and J. Huissoon, Developing Psycho-Acoustic Experiments in Gas Metal Arc Welding, *Proceedings of the 2005 IEEE International Conference on Mechatronics and Automation*, Vol 2, July 29–Aug 1, 2005 (Niagara Falls, Ontario, Canada), p 1112–1117
 95. A.S. Roca, H.C. Fals, J.B. Fernández, E.J. Macías, and E.S. Aden, New Stability Index for Short Circuit Transfer Mode in GMAW Process Using Acoustic Emission Signals, *Sci. Technol. Weld. Join.*, Vol 12 (No. 5), July 2007, p 460–466
 96. A.S. Roca, H.C. Fals, J.B. Fernández, E.J. Macías, and M.P. de la Parte, Artificial Neural Networks and Acoustic Emission Applied to Stability Analysis in Gas Metal Arc Welding, *Sci. Technol. Weld. Join.*, Vol 14 (No. 2), Feb 2009, p 117–124
 97. A.S. Roca, H.C. Fals, J.B. Fernández, E.S. Aden, and E.J. Macías, Stability Analysis of the Gas Metal Arc Welding Process Based on Acoustic Emission Technique, *Weld. Int.*, Vol 23 (No. 3), March 2009, p 173–180
 98. J.E. Wang, B. Chen, H.B. Chen, and S.B. Chen, Analysis of Arc Sound Characteristics for Gas Tungsten Argon Welding, *Sens. Rev.*, Vol 29 (No. 3), 2009, p 240–249
 99. P. Kaskinen and G. Mueller, Acoustic Arc Length Control, *Advances in Welding Science and Technology, Proceedings of an International Conference on Trends in Welding Research*, S.A. David, Ed., May 18–22, 1986 (Gatlinburg, TN), ASM International, p 763–765
 100. D.E. Hardt and J.M. Katz, Ultrasonic Measurement of Weld Penetration, *Weld. J.*, Vol 63 (No. 9), Sept 1984, p 273s–281s
 101. R. Fenn, Ultrasonic Monitoring and Control during Arc Welding, *Weld. J.*, Vol 64 (No. 9), Sept 1985, p 18–22
 102. N.M. Carlson and J.A. Johnson, Ultrasonic Sensing of Weld Pool Penetration, *Weld. J.*, Vol 67 (No. 11), Nov 1988, p 239s–246s
 103. N.M. Carlson, J.A. Johnson, and D.C. Kunerth, Control of GMAW: Detection of Discontinuities in the Weld Pool, *Weld. J.*, Vol 69 (No. 7), July 1990, p 257s–263s
 104. G.M. Graham and I.C. Ume, Automated System for Laser Ultrasonic Sensing of Weld Penetration, *AIM Proceedings of the 1997 First IEEE/ASME International Conference on Advanced Intelligent Mechatronics*, June 16–20 1997 (Tokyo, Japan), p 59
 105. A. Kita and I.C. Ume, Measuring On-Line and Off-Line Noncontact Ultrasound Time of Flight Weld Penetration Depth, *Weld. J.*, Vol 86 (No. 1), Jan 2007, p 9s–17s
 106. M. Hoffmeister, S. Dietrich, and G. Huismann, Front Face Controlled Root Penetration by Arc Tracer Diagnostics in TIG Welding of Duplex Stainless Steel Pipes, *International Trends in Welding Science and Technology, Proceedings of the Third International Conference on Trends in Welding Research*, S.A. David and J.M. Vitek, Ed., June 1–5, 1992 (Gatlinburg, TN), ASM International, p 927–930
 107. G.E. Cook and K. Andersen, Weld Modeling and Control Using Artificial Neural Networks, *IEEE Trans. Ind. Appl.*, Vol 31 (No. 6), Nov–Dec 1995, p 1484–1491
 108. N. Tsai, “Heat Distribution and Weld Bead Geometry,” Ph.D. dissertation, Massachusetts Institute of Technology, Department of Materials Science, 1983
 109. H.B. Smartt, C.J. Einerson, A.D. Watkins, and R.A. Morris, Gas Metal Arc Process Sensing and Control, *Advances in Welding Science and Technology, Proceedings of an International Conference on Trends in Welding Research*, S.A. David, Ed., May 18–22, 1986 (Gatlinburg, TN), ASM International, p 461–465
 110. C.E. Jackson and A.E. Shrubbsall, Control of Penetration and Melting Ratio with Welding Technique, *Weld. J.*, Vol 32 (No. 4), April 1953, p 172s–178s
 111. G.R. Salter and J. Doherty, Procedure Selection for Arc Welding, *Met. Constr.*, Vol 13 (No. 9), Sept 1981, p 544–550
 112. J.C. McGlone, Weld Bead Geometry Prediction—A Review, *Met. Constr.*, Vol 14 (No. 7), 1982, p 378–384
 113. K. Andersen, K. Ramaswamy, G. Karsai, and G.E. Cook, A Novel Approach Toward Relationships between Process Variables and Weld Geometry, *Recent Trends in Welding Science and Technology, Proceedings of the Second International Conference on Trends in Welding Research*, S.A. David and J.M. Vitek, Ed., May 14–18, 1989 (Gatlinburg, TN), ASM International
 114. K. Andersen, G.E. Cook, J.F. Springfield, and R.J. Barnett, Applications of Artificial Neural Networks for Arc Welding, *Proceedings of the Artificial Neural Networks in Engineering Conference*, C.H. Dagli, Ed., Nov 10–13, 1991 (St. Louis, MO), ASME Press, p 717–727
 115. G.E. Cook, R.J. Barnett, D.A. Hartman, and A.M. Strauss, Neural Network Systems Techniques in Weld Modeling and Control, *Computer-Aided Design, Engineering, and Manufacturing: Systems Techniques and Applications, Volume VI, Manufacturing Systems Processes*, C.T. Leondes, Ed., CRC Press, Boca Raton, FL, 2000, p 7-1 to 7-23
 116. J.B. Bjorgvinsson, G.E. Cook, and K. Andersen, Microprocessor-Based Arc Voltage Control for Gas Tungsten Arc Welding Using Gain Scheduling, *IEEE Trans. Ind. Appl.*, Vol 29 (No. 2), March–April 1993, p 250–255
 117. P. Koseyaporn, G.E. Cook, and A.M. Strauss, Adaptive Voltage Control in Fusion Arc Welding, *IEEE Trans. Ind. Appl.*, Vol 36 (No. 5), Sept–Oct 2000, p 1300–1307
 118. A. Suzuki, D.E. Hardt, and L. Valvani, Application of Adaptive Control Theory to On-Line GTA Weld Geometry Regulation, *Trans. ASME: J. Dynamic Sys. Measure. Control*, Vol 113 (No. 1), March 1991, p 93–103
 119. K.M. Passino, Toward Bridging the Perceived Gap between Conventional Control and Intelligent Control, *Intelligent Control Systems: Theory and Applications*, M.M. Gupta and N.K. Sinha, Ed., IEEE Press, New York, NY, 1996, p 3–27
 120. D.A. Hartman, D.R. Delapp, G.E. Cook, and R.J. Barnett, Intelligent Control in Arc Welding, *Smart Engineering System Design: Neural Networks, Fuzzy Logic, Evolutionary Programming, Complex Systems and Data Mining*, C.H. Dagli, J. Ghosh, A.L. Buczak, O. Ersoy, and M.J. Embrechts, Ed., Nov 7–10, 1999 (New York, NY), ASME Press, p 715–725
 121. K.M. Passino, Intelligent Control for Autonomous Systems, *IEEE Spectrum*, Vol 32 (No. 6), June 1995, p 55–62

Shielding Gases for Arc Welding*

THE SHIELDING GAS used in a welding process has a significant influence on the overall performance of the welding system. Its primary function is to protect the molten metal from atmospheric nitrogen and oxygen as the weld pool is being formed. The shielding gas also promotes a stable arc and uniform metal transfer. In gas metal arc welding (GMAW) and flux cored arc welding (FCAW), the gas used has a substantial influence on the form of metal transfer during welding. This, in turn, affects the efficiency, quality, and overall operator acceptance of the welding operation.

The shielding gas interacts with the base material and with the filler material, if any, to produce the basic strength, toughness, and corrosion resistance of the weld. It can also affect the weld-bead shape and the penetration pattern.

Understanding the basic properties of a shielding gas will aid in the selection of the right shielding gas or gases for a welding application. Use of the best gas blend will improve the quality and may reduce the overall cost of the welding operation as well.

Basic Properties of a Shielding Gas

The controlled electrical discharge known as the welding arc is formed and sustained by the establishment of a conductive medium called the arc plasma. This plasma consists of ionized gas, molten metals, slags, vapors, and gaseous atoms and molecules. The formation and structure of the arc plasma is dependent on the properties of the shielding gases used for welding. Table 1 lists the basic properties of gases used for welding (Ref 1).

The ionization potential is the energy, expressed in electron volts, necessary to remove an electron from a gas atom—making it an ion, or an electrically charged gas atom. All other factors held constant, the value of the ionization potential decreases as the molecular weight of the gas increases. Arc starting and arc stability are greatly influenced by the ionization potentials of the component shielding gases used in the welding process. A gas with a low ionization potential, such as argon,

Table 1 Properties of shielding gases used for welding

Gas	Chemical symbol	Molecular weight	Specific gravity(a)	Density		Ionization potential	
				g/L	g/ft ³	aJ(b)	eV
Argon	Ar	39.95	1.38	1.784	0.1114	2.52	15.7
Carbon dioxide	CO ₂	44.01	1.53	1.978	0.1235	2.26	14.4
Helium	He	4.00	0.1368	0.178	0.0111	3.92	24.5
Hydrogen	H ₂	2.016	0.0695	0.090	0.0056	2.16	13.5
Nitrogen	N ₂	28.01	0.967	12.5	0.782	2.32	14.5
Oxygen	O ₂	32.00	1.105	1.43	0.0892	2.11	13.2

(a) At 100 kPa (1 atm) and 0 °C (32 °F); air = 1. (b) 10⁻¹⁸ J. Source: Ref 1

can easily turn atoms into ions. Helium, with its significantly higher ionization potential, produces a harder-to-start, less stable arc.

Although other factors are involved in sustaining the plasma, the respective energy levels required to ionize these gases must be maintained; as a consequence, the arc voltage is directly influenced. For equivalent arc lengths and welding currents, the voltage obtained with helium is appreciably higher than it is with argon. This translates into more available heat input to the base material with helium than with argon.

The thermal conductivity of a gas is a measure of how well it is able to conduct heat. It influences the radial heat loss from the center to the periphery of the arc column as well as heat transfer between the plasma and the liquid metal. Argon, which has a low thermal conductivity, produces an arc that has two zones: a narrow hot core and a considerably cooler outer zone. The penetration profile of the weld fusion area then exhibits a narrow “finger” at the root and a wider top. A gas with a high thermal conductivity conducts heat outward from the core; this results in a wider, hotter arc core. This type of heat distribution occurs with helium, argon-hydrogen, and argon/carbon dioxide blends; it gives a more even distribution of heat to the work surface and produces a wider fusion area.

Dissociation and Recombination. Shielding gases such as carbon dioxide, hydrogen, and oxygen are multiatom molecules. When heated to high temperatures within the arc plasma, these gases break down, or dissociate, into their component atoms. They are then at least partially ionized, producing free electrons and current flow. As the dissociated gas comes into contact with the relatively cool work

surface, the atoms recombine and release heat at that point. This heat of recombination causes multiatomic gases to behave as if they have a higher thermal conductivity, similar to that of helium. Dissociation and recombination do not occur with gases, such as argon, that consist of a single atom. Thus, at the same arc temperature, the heat generated at the work surface can be considerably greater with gases such as carbon dioxide and hydrogen.

Reactivity/Oxidation Potential. The oxidizing nature of the shielding gas affects both welding performance and the properties of the resultant weld deposit. Argon and helium are completely nonreactive, or inert, and thus have no direct chemical effect on the weld metal. Oxidizing or active gases, such as CO₂ and oxygen, will react with elements in the filler metal or baseplate and will form a slag on the surface of the weld deposit. The loss of elements, such as manganese and silicon, from steel can affect the quality and cost of the weldment produced. Both weld strength and toughness generally decline as the oxidizing nature of the shielding gas increases.

Additions of reactive gases such as oxygen or carbon dioxide enhance the stability of the arc and affect the type of metal transfer obtained. Metal droplet size is decreased, and the number of droplets transferred per unit time increases as the level of oxygen in the shielding gas increases. Oxygen reduces the molten weld-bead surface tension, promoting better bead wetting and higher welding travel speeds. Small additions of CO₂ work in a similar manner.

The surface tension between the molten metal and its surrounding atmosphere has a pronounced influence on bead shape. If the surface

energy is high, a convex, irregular bead will result. Low values promote flatter beads with minimal susceptibility for undercutting.

Pure argon is generally associated with high interfacial energy, producing a sluggish weld puddle and high, crowned bead. The addition of a small amount of a reactive gas, such as oxygen, lowers this surface tension and promotes fluidity and better wetting of the base material; it does this without creating excessive oxidation of the weld metal.

Gas Purity. Some metals, such as carbon steel and copper, have a relatively high tolerance for contaminants in the shielding gas; others, such as aluminum and magnesium, are fairly sensitive to particular contaminants. Still others, such as titanium and zirconium, have an extremely low tolerance for any foreign constituent in the shielding gas.

Depending on the metal being welded and the welding process used, very small quantities of gas impurities can significantly affect welding speed, weld surface appearance, weld bead solidification, and porosity levels. The effects of any given impurity are wide ranging, but weld quality and eventual fitness for purpose are major areas of concern.

There is always a possibility that the gas, as delivered, is contaminated; however, it is far more likely that impurities will enter somewhere between the supply and the end-use points. For this reason, properly designed piping systems and high-quality hose are recommended for use with welding shielding gases. Typical industry minimum purity levels for welding gases are listed in Table 2 (Ref 1).

Gas density is the weight of the gas per unit volume. Density is one of the chief factors that influence shielding gas effectiveness. Basically, gases heavier than air, such as argon and carbon dioxide, require lower flow rates in use than do the lighter gases, such as helium, to ensure adequate protection of the weld puddle.

Shielding Gas Blends

To obtain a shielding gas that is suited to a specific application, a mix of gases is generally

needed. Each basic gas contributes certain characteristics to the performance of the overall mix. Some gas blends have relatively specific areas of application and limited operating ranges; others can be used on many materials under a variety of welding conditions. Each component of the blend brings with it properties that are supplemented by the others to produce an enhanced level of performance.

Argon is inert or unreactive with respect to the materials present in the welding electrode. With its low ionization potential, argon promotes easy arc starting and stable arc operation. Its lower thermal conductivity promotes the development of axial "spray" transfer in certain forms of GMAW. It is also used in applications where base material distortion must be controlled or where good gap-bridging ability is required.

Helium. Unlike argon, helium is lighter than air and has a low density. Like argon, it is chemically inert and does not react with other elements or compounds. Because of its high thermal conductivity and high ionization potential, more heat is transferred to the base material, thus enhancing the penetration characteristics of the arc. In many applications, it also allows higher weld travel speeds to be obtained. Because of its higher cost, helium is frequently combined with argon or argon mixtures to enhance the overall performance of the blend while minimizing its cost.

Oxygen combines with almost all known elements except rare and inert gases; it vigorously supports combustion. Small amounts of oxygen are added to some inert mixtures to improve the stability of the welding arc developed as well as to increase the fluidity of the weld puddle.

In the spray-transfer mode of GMAW, small additions of oxygen enhance the range over which this spatterless form of welding can be performed. The droplet size decreases and the number of drops transferred per unit time increases as oxygen is added to the blend.

Carbon dioxide is a reactive gas that is commonly used alone in certain types of GMAW. Oxidation of the base material and any filler electrode occurs readily. Carbon dioxide is

added to argon blends to improve arc stability, enhance penetration, and improve weld puddle flow characteristics. The higher thermal conductivity of carbon dioxide (because of the dissociation and recombination of its component parts) transfers more heat to the base material than does argon alone. A broader penetration pattern versus argon is obtained; however, base material distortion and lack of gap-bridging ability are possible problems.

Hydrogen is the lightest known element and is a flammable gas. Explosive mixtures can be formed when certain concentrations of hydrogen are mixed with oxygen or air. It is added to inert gases to increase the heat input to the base material or for operations involving cutting and gouging. Because some materials are especially sensitive to hydrogen-related contamination, its use is generally limited to special applications, such as the joining of stainless steels, and to plasma arc cutting and gouging.

Nitrogen is generally considered to be inert except at high temperatures. At arc welding temperatures, it will react with some metals (e.g., aluminum, magnesium, steel, and titanium), so it is not used as a primary shielding gas. It can be used with other gases for some welding applications (e.g., copper) and is also widely used in plasma cutting.

Shielding Gas Selection

In most welding applications, more than one shielding gas or gas blend can be used successfully. For example, there is no one optimal gas blend for joining carbon steels, but a considerable array of mixes are available depending on the specific requirements of the application. For some processes, such as gas tungsten arc welding and plasma arc welding, the choices may be somewhat limited by the nature of the electrodes used and the materials being welded. However, for applications involving GMAW, a multitude of blends can be selected from when carbon steels are being joined. Determination of the best blend depends on a number of specific job-related needs.

Accuracy of Gas Blends

The accuracy with which gases are blended is a function of the way in which they are supplied. If the source of the gas is a high-pressure cylinder, the following generally applies:

1. $\pm 10\%$ relative, minor component (Ref 2)
2. $\pm 0.5\%$ absolute for concentrations up to 5%; $\pm 10\%$ relative for concentrations between 5 and 50% (Ref 3)

For example, the mix accuracy of an Ar-2O₂ blend would be Ar/1.8–2.2O₂ (method 1) or Ar/1.5–2.5O₂ (method 2). A blend of Ar-25CO₂ would yield Ar/22.5–27.5CO₂ by either method of calculation.

Table 2 Typical gases purity and moisture content of shielding

Gas	Product state	Minimum purity, %	Maximum moisture(a), ppm	Approximate dewpoint at maximum moisture content	
				°C	°F
Argon	Gas	99.995	10	-60	-77
	Liquid	99.997	6	-64	-83
Carbon dioxide	Gas	99.5	19	-51	-60
	Liquid	99.8	50	-58	-73
Helium	Gas	99.95	32	-51	-61
	Liquid	99.995	3	-69	-92
Hydrogen	Gas	99.95	8	-63	-80
	Liquid	99.995	5	-65	-86
Nitrogen	Gas	99.7	32	-51	-61
	Liquid	99.997	5	-65	-86
Oxygen	Industrial	99.5	50	-48	-54
	Liquid	99.5	6	-64	-83

(a) Moisture specifications are measured at full cylinder pressure, the pressure at which the cylinder is analyzed. Source: Ref 1

When gas cylinders are properly filled with the appropriate blend, the components of that mixture will not separate unless the temperature of the environment is reduced far below normal working temperatures. If the gases are supplied from a liquid source, such as a bulk tank, the accuracy of the blend is a function of the mixing equipment used, but most likely falls within the $\pm 10\%$ minor component range.

Shielding Gases for GMAW

By far, the largest number of gas blends have been developed for GMAW, especially for joining carbon steel. These can be roughly divided into four categories: pure gases, argon-oxygen mixes, argon/carbon dioxide mixes, and three-part gas blends composed of either argon, helium, oxygen, carbon dioxide, or hydrogen. Table 3 contains suggestions for shielding gas selection based on material type, thickness, and mode of metal transfer.

Argon. Pure argon is generally used on nonferrous base metal, such as aluminum, nickel, copper, and magnesium alloys, and on reactive metals, such as titanium. Argon provides excellent arc stability, penetration, and bead profile when joining these materials. Its low ionization potential results in easy arc starting. Argon produces a constricted arc column with high current density, which concentrates the arc energy over a small area; deep, fingerlike penetration results.

Carbon Dioxide. A reactive gas, carbon dioxide is generally used only for joining carbon steel. It is readily available and relatively inexpensive. Because CO_2 will not support spray transfer, deposition efficiency is lower and spatter and fume levels are higher than with argon blends. Weld bead surfaces are more oxidized and irregular in shape. The higher ionization potential of CO_2 and its characteristic dissociation upon heating provide greater weld fusion and penetration while still achieving acceptable mechanical properties.

Helium. Because of its higher thermal conductivity, helium can provide additional heat input to the base material while still maintaining an inert atmosphere. Wetting action, depth of fusion, and travel speed can be improved over comparable argon levels. This advantage is most frequently used in the welding of heavier sections of aluminum, magnesium, and copper alloys.

Argon-Oxygen. The addition of a small amount of oxygen to argon greatly stabilizes the welding arc, increases the filler-metal droplet rate, lowers the spray transition current, and influences bead shape. The weld pool is more fluid and stays molten longer, allowing the metal to flow out toward the edges of the weld (Fig. 1a).

The most common blends contain 1, 2, 5, or 8% O_2 in argon. Increasing oxygen improves arc stability and makes higher travel speeds possible by enhanced puddle fluidity. Some

increased alloy loss and a greater chance of undercut occur as the oxygen level is increased, especially beyond 5%.

Argon/carbon dioxide blends are primarily used for carbon and low-alloy steels and have limited use for stainless steels. The addition of CO_2 to argon produces results similar to the addition of oxygen, but it also broadens the penetration pattern as the CO_2 content is increased (Fig. 1b). Above a range of 18 to 20% CO_2 , spraylike transfer can no longer be obtained; short-circuiting/globular transfer with somewhat increased spatter levels is found from this point up to approximately 50% CO_2 in argon.

The most common blends for spray transfer are argon plus 5, 8, 10, or 13 to 18% CO_2 . With increased CO_2 content, the more fluid weld puddle permits higher weld travel speeds.

Mixes with higher carbon dioxide levels can also be used for short-circuiting transfer—commonly, argon plus 20 or 25% CO_2 . Mixtures in this range provide an optimal droplet frequency for minimum spatter when small-diameter (0.9 and 1.2 mm, or 0.035 and 0.045 in.) wire is used.

Argon-Helium. Helium is often mixed with argon to obtain the advantages of both gases. These blends are primarily used for nonferrous base materials, such as aluminum, copper, and nickel alloys. Helium increases the heat input to the base material and thus is used for joining thick, thermally conductive plates. As the helium percentage increases, the arc voltage, spatter, and weld width-to-depth ratio increase (Fig. 1c).

The most common blends contain 25, 50, or 75% He in argon. The highest percentage of helium is used for joining thick (>50 mm, or 2 in.) plate material, especially aluminum and copper. Higher travel speeds can be obtained using helium-enhanced blends.

Three-Gas Blends. Mixtures containing three gas components are versatile because of their ability to operate in short-circuiting, globular, and spray-transfer modes. These blends are generally proprietary, and manufacturers' recommendations should be followed for their proper use.

Argon/Oxygen/Carbon Dioxide. Blends of argon, carbon dioxide, and oxygen are generally used to join carbon and alloy steels.

Argon/Helium/Carbon Dioxide. Helium and carbon dioxide additions to argon increase the heat input to the base metal, which improves wetting, puddle fluidity, and weld bead profile. With helium plus CO_2 additions less than 40%, good spray transfer is obtained for carbon and low-alloy steel welding. Some increase in tolerance of base material surface contamination is also noted.

When the helium content exceeds 50 to 60%, transfer is restricted to short-circuiting and globular. Blends in which the CO_2 content is relatively low ($\leq 5\%$) are generally used for the joining of stainless steels without any loss in corrosion resistance.

Argon/Carbon Dioxide/Hydrogen. Three-part blends of this design are intended for the joining of austenitic stainless steel in the spray or short-circuiting transfer modes. Because of the addition of hydrogen, these blends should not be used for carbon steel. The carbon dioxide and hydrogen increase the heat input to the base material and improve bead shape characteristics, as well as promote higher welding travel speeds.

Shielding Gas Selection for FCAW

Carbon Dioxide. The majority of large-diameter (>1.6 mm, or $> \frac{1}{8}$ in.) wires that use a shielding gas use carbon dioxide. Some smaller-diameter wires are formulated to operate in 100% CO_2 . The arcs are generally stable and provide a globular transfer over the usable operating range. Good performance over rust and mill scale on the plate surface is obtained with these large-diameter wires and CO_2 shielding.

Argon/Carbon Dioxide. A significant number of small-diameter (≤ 1.6 mm, or $\frac{1}{8}$ in.) cored wires are shielded with blends of argon with 15 to 50% CO_2 . These blends provide better out-of-position weld puddle control versus that of CO_2 . To obtain the best performance from a particular cored wire, check the manufacturer's product literature for the recommended gas blend.

Shielding Gas Selection for GTAW

Argon. The most commonly used gas for GTAW, argon exhibits low thermal conductivity, which produces a narrow, constricted arc column; this allows greater variations in arc length with minimal influence on arc power or weld bead shape. Its low ionization potential provides good arc-starting characteristics and good arc stability using the direct current electrode negative (DCEN) power connection plus superior arc cleaning action and bead appearance when alternating current (ac) power is used. Argon is the most commonly selected gas for DCEN welding of most materials and ac manual welding of aluminum.

Helium. The high thermal conductivity and ionization potential of helium make it suitable for the high-current joining of heavy sections of heat-conductive materials such as aluminum. Helium increases the penetration of the weld as well as its width. It also allows the use of higher weld travel speeds.

Argon-Helium. Blends of argon and helium are selected to increase the heat input to the base material while maintaining favorable arc stability and superior arc-starting characteristics. Blends of 25, 50, and 75% He in argon are commonly used.

Argon-Hydrogen. Hydrogen is added to argon to enhance its thermal properties. The slightly reducing atmosphere improves weld

Table 3 Recommended shielding gas selection for gas metal arc welding

Material	Thickness		Transfer mode	Recommended shielding gas	Advantages and limitations		
	mm	in.					
Carbon steel	<2.0	<0.080	Short circuiting	Ar-25CO ₂	Good penetration and distortion control to reduce potential burnthrough		
				Ar-15CO ₂			
	2.0–3.2	0.080–0.125	Short circuiting	Ar-8CO ₂	Higher deposition rates without burnthrough; minimum distortion and spatter; good puddle control for out-of-position welding		
				Ar-15CO ₂			
				Ar-25CO ₂			
	>3.2	>0.125	Short circuiting	Ar-15CO ₂	High welding speeds; good penetration and puddle control; applicable for out-of-position welds		
				Ar-25CO ₂			
				Globular	Ar-25CO ₂	Suitable for high-current and high-speed welding; deep penetration and fast travel speeds but with greater burnthrough potential	
					CO ₂		
				Conventional spray arc	Ar-1O ₂	Good arc stability; produces a more fluid puddle as O ₂ increases; good coalescence and bead contour; good weld appearance and puddle control	
Ar-2O ₂							
Ar-5CO ₂							
Ar-8CO ₂							
Ar-10CO ₂							
Ar-15CO ₂							
Pulsed spray				Ar-CO ₂ -O ₂ blends	Used for both gage and out-of-position weldments; achieves good pulsed spray stability over a wide range of arc characteristics and deposition ranges		
				Argon-5CO ₂			
	Ar-He-CO ₂ blends						
Alloy steel	All sizes	Short circuiting	Ar-8CO ₂	High welding speeds; good penetration and puddle control; applicable for out-of-position welds; suitable for high-current and high-speed welding			
			Ar-15CO ₂				
			Ar-CO ₂ -O ₂ blend				
		Spray arc (high-current density and rotational)	Ar-2O ₂	Reduces undercutting; higher deposition rates and improved bead wetting; deep penetration and good mechanical properties			
			Ar-5O ₂				
			Ar-CO ₂ -O ₂ blends				
		Pulsed spray	Ar-He-CO ₂ blends	Used for both light-gage and heavy out-of-position weldments; achieves good pulsed spray stability over a wide range of arc characteristics and deposition ranges			
			Ar-5CO ₂				
		Stainless steel, copper, nickel, and Cu-Ni alloys	All sizes	Short-circuiting transfer	Ar-He-CO ₂ blends	Low CO ₂ contents in helium mix minimize carbon pickup, which can cause intergranular corrosion with some alloys; helium improves wetting action; CO ₂ contents >5% should be used with caution on some alloys; applicable for all-position welding	
					He-Ar-CO ₂ blends		
Ar-1O ₂							
Spray arc	Ar-2O ₂			Good arc stability; produces a fluid but controllable weld puddle; good coalescence and bead contour; minimizes undercutting on heavier thicknesses			
	Ar-He-CO ₂ blends						
Pulsed spray	Ar-1O ₂			Used for both light-gage and heavy out-of-position weldments; achieves good pulsed spray stability over a wide range of arc characteristics and deposition ranges			
	Ar-2O ₂						
	Ar-He-CO ₂ blends						
Aluminum, titanium, and other reactive metals	≤13			≤½ in.	Spray arc	Argon	Best metal transfer, arc stability, and plate cleaning; little or no spatter; removes oxides when used with direct current electrode positive (reverse polarity)
					Spray arc	75He-25Ar	
	>13	>½ in.	Spray arc	50He-50Ar	High heat input; produces fluid puddle, flat bead contour, and deep penetration; minimizes porosity		
			Pulsed spray	Helium	High heat input; good for mechanized welding and overhead; applicable to heavy-section welding		
			Pulsed spray	50He-25Ar	Good wetting; good puddle control		

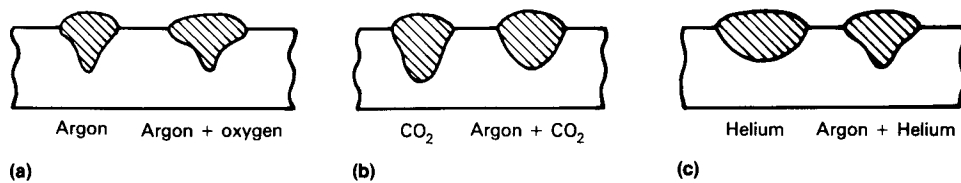


Fig. 1 Effect of shielding gas blends on weld profile using direct current electrode positive. (a) Argon versus argon-oxygen. (b) Carbon dioxide versus argon/carbon dioxide. (c) Helium versus argon-helium. Source: Ref 4

puddle wetting and reduces some surface oxides to produce a cleaner weld surface. To minimize problems associated with arc starting, additions of hydrogen are generally limited to 5 to 15%. These blends are primarily used to join some stainless steels, nickel, and nickel alloys. These mixtures should not be used to join alloy steels; delayed weld cracking may result.

Argon/2–5H₂ is used in manual welding applications on materials thicker than 1.6 mm (⅝ in.). Additions of 10 to 15% H₂ are used in

mechanized applications, such as those found in the manufacture of stainless steel tubing.

Warning: Special safety precautions are required when mixing argon and hydrogen. Do not attempt to mix argon and hydrogen from separate cylinders. Always purchase ready-mixed hydrogen blends from a qualified supplier.

Shielding Gas Selection for Plasma Arc Welding

The physical configuration of the plasma arc welding (PAW) system requires the use of two gases: a “plasma” or orifice gas and a shielding gas. The primary role of the plasma gas, which exits the torch through the center orifice, is to control arc characteristics and shield the electrode. The shielding gas, introduced around the periphery of the arc, shields or protects the weld area. In many applications, the shielding gas is also partially ionized to enhance the performance of the plasma gas.

Low-Current (<100 A) PAW. Argon is the preferred plasma gas for low-current PAW because of its low ionization potential, which ensures easy and reliable arc starting. Argon-helium mixtures are used for some applications

requiring higher heat inputs. The choice of the shielding gas depends on the type and thickness of the base material. Recommendations can be found in Table 4.

High-Current (≥100 A) PAW. The choice of gas used for high-current PAW also depends on the material to be welded. In almost all cases, the shielding gas is the same as the orifice gas. Again, argon is suitable for welding all metals, but it does not necessarily produce optimal results. Depending on the welding mode used (keyhole or melt-in), the optimal gas blend will vary. Table 4 lists gases recommended on the basis of materials joined.

Influence of Shielding Gas on Weld Mechanical Properties

The mechanical properties of a weld are dependent on specific characteristics of the shielding gas. When the gas blend is totally inert, the effects are less pronounced and are derived more indirectly. In this case, the shielding gas affects penetration and solidification, which can influence the microstructure of the resulting weld.

When the shielding gas contains active components, such as oxygen or carbon dioxide, the influence is direct and more substantial. The

oxygen potential of the shielding gas influences the amount of surface slag, the fume emission rate, the fluidity of the weld puddle, and the mechanical properties (both strength and toughness) of the weld metal. A number of empirical formulas have been developed to estimate the oxygen potential of a gas blend (Ref 5); the differences lie in their treatment of the CO₂ component of the gas mix. Because parameters other than gas composition can affect the oxygen level of the weld metal (e.g., welding speed), most of the recently developed formulas are also welding parameter and material specific. Their importance centers on how the oxidation potential is linked to elemental loss of silicon and manganese in the weld metal, to weld-metal oxygen content, and to weld mechanical properties.

Because a relatively complex relationship exists between the loss of alloying elements, the composition of the shielding gas, and the mechanical properties of the resulting weld metal, it is difficult to select an optimal gas blend that will work well with all types of wires. This influence is most noticeable in the GMAW of carbon steel. Figure 2 (Ref 5) and Table 5 (Ref 6) illustrate the effect of the shielding gas on impact strength and tensile strength. In general, as the oxidation potential of the shielding gas increases, the toughness and the tensile strength of the weld deposit decrease. Because of their lower oxidizing gas content, argon blends will generally produce weld properties superior to those obtained by shielding with CO₂ only. There appears to be an “optimal” oxygen content, because too low an oxygen level can also be detrimental to toughness.

Shielding Gas and Fume Generation

The shielding gas used in solid and flux cored wire welding affects the rate at which fumes are produced during welding, as well as

Table 4 Recommended guidelines for selecting plasma arc welding (PAW) shielding gases

Material	Thickness		Mode of penetration	
	mm	in.	Keyhole technique(a)	Melt-in technique(b)
Low-current PAW(c)				
Aluminum copper	<1.6	<1/16	Not recommended	Argon Helium
	≥1.6	≤1/16	Helium	Helium
Carbon steel	<1.6	<1/16	Not recommended	Argon Helium 75Ar-25He
	≥1.6	≥1/16	Argon 75He-25Ar	Argon 75He-25Ar
Low-alloy steel	<1.6	<1/16	Not recommended	Argon Helium Ar-1.5H ₂
	≥1.6	≥1/16	Argon 75He-25Ar Ar-1.5H ₂	Argon Helium Ar-1.5H ₂
Stainless steel, nickel alloys	<1.6	<1/16	Argon 75He-25Ar Ar-1.5H ₂	Argon Helium Ar-1.5H ₂
	≥1.6	≥1/16	Argon 75He-25Ar Ar-1.5H ₂	Argon Helium Ar-1.5H ₂
High-current PAW(d)				
Aluminum	<6.4	<1/4	Argon	Argon 75He-25Ar
	≥6.4	≥1/4	Helium	Helium 75He-25Ar
Copper	<2.4	<3/32	Not recommended	Helium
Carbon steel; low-alloy steel	<3.2	<1/8	Argon	Argon 75He-25Ar
	≥3.2	≥1/8	Argon	Argon
Stainless steel; nickel alloys	<3.2	<1/8	Argon Ar-5H ₂	Argon
	≤3.2	≥1/8	Argon Ar-5H ₂	75He-25Ar

(a) Properly balanced gas flow rates produce complete joint penetration by forming a small weld pool with a hole penetrating completely through the base metal. As the plasma torch is moved, metal melted by the arc is forced to flow around the plasma steam, producing the “keyhole” to the rear where the weld pool is formed and solidified. (b) Conventional fusion welding similar to that done with gas tungsten arc welding. (c) Gas selections shown are for shielding gas only. Orifice gas in all cases is argon. (d) Gas selections shown are for both the orifice and shielding gas. Source: Ref 1

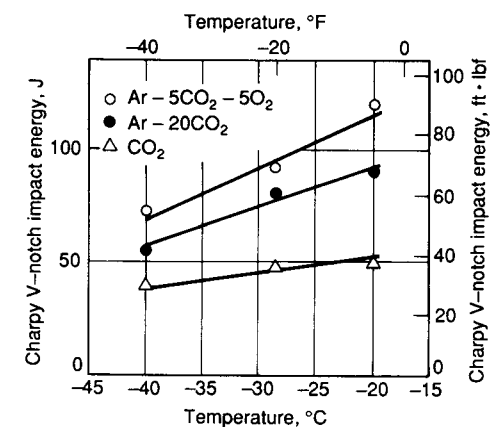


Fig. 2 Plot of weld-metal impact energy versus test temperature as a function of shielding gas composition. Source: Ref 5

Table 5 Effect of shielding gas on carbon, manganese, and silicon losses and on weld strength values

Shielding gas(a)	Ultimate tensile strength		Yield strength		Elongation, %	Weld-metal composition(b), %		
	MPa	ksi	MPa	ksi		C	Mn	Si
Ar-10CO ₂	640	92.9	544	79.0	25.7	0.09	1.43	0.72
Ar-18CO ₂	620	90.0	522	75.8	26.8	0.09	1.37	0.70
Ar-5CO ₂ -4O ₂	610	88.5	472	68.5	28.1	0.08	1.32	0.67
Ar-25CO ₂	601	87.2	505	73.3	29.3	0.09	1.30	0.65
Ar-12O ₂	591	85.8	510	74.0	27.5	0.06	1.20	0.60
CO ₂	594	86.2	487	70.7	27.8	0.10	1.21	0.62

(a) Gases listed in order of increasing oxidation potential. (b) Base wire composition: 0.115% C, 1.53% Mn, 0.98% Si. Source: Ref 6

the composition of the fumes. The type of shielding gas also affects the composition of the pollutant gases in the welding area. The fumes and gases generated in some welding applications impact health and safety; therefore, it is important for the user to review the Material Safety Data Sheets and precautionary labeling provided by the manufacturers and suppliers of welding consumables. Welding safety and health information can also be found in this Handbook and in ANSI Z49.1, "Safety in Welding and Cutting."

Fume generation rates are generally highest when CO₂ shielding is used. Inert gas blends containing CO₂ produce higher fume levels than those containing only oxygen additions. For solid wire welding at the same weld-metal deposition rate, argon blends typically generate significantly less fumes than when CO₂ only is used (Ref 7–9). Figure 3 (Ref 10) illustrates the dependence of the fume generation rate on shielding gas composition as a function of current level in GMAW. Similar trends can be seen when using gas-shielded flux cored wires.

Pollutant gases must be considered when arc welding. The gases of greatest interest are carbon monoxide, ozone, and nitrogen oxides. When CO₂ is used for shielding in confined spaces, CO can be a potential problem. Ozone can be a concern when high-energy gas-shielded welding is conducted, particularly on aluminum and stainless steel plate. It is produced in the immediate arc area as well as in the surrounding environment. Oxides of nitrogen can be present in some plasma welding and cutting applications (Ref 11).

Self-Shielded Flux Cored Arc Welding

The self-shielded flux cored wire welding process employs a continuous wire electrode that requires no external shielding. These cored wires generate protective shielding gases from components in the core material similar to those found in coated electrodes. The unique feature of this class of consumables is that they rely only partly on the exclusion of air from the molten electrode and weld pool to produce a quality deposit. In addition to deoxidizers, they contain denitrifiers to react with nitrogen that may be entrained in the molten metal. The less a given consumable relies on shielding and the more it relies on "killing" to control nitrogen and produce sound weld metal, the less that consumable will be affected by cross air currents and side winds.

Through careful control of welding parameters and the proper balance of core constituents, good-quality weld metal can be obtained under poor welding conditions. Self-shielded flux cored wires are especially suited to welding outdoors, where it is difficult to provide acceptable external gas shielding. Both light- and heavy-gage materials have been successfully joined with these electrodes.

REFERENCES

1. N.E. Larson and W.F. Meredith, *Shielding Gas Selection Manual*, Union Carbide Industrial Gases Technology Corp., 1990, p 10, 11, 18, 19, 30–32
2. "Specification for Shielding Gases," AWS A5.32-9X, July 1991 (draft)

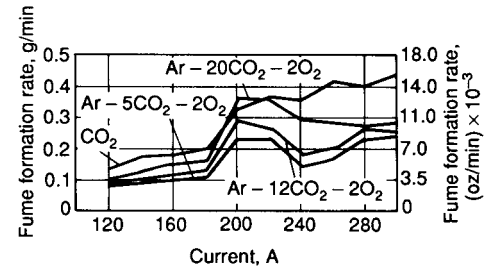


Fig. 3 Plot of fume formation rate versus current for mild steel solid wire using selected shielding gases. Source: Ref 10

3. "Gases for Gas-Shielded Arc Welding and Cutting," European Standard EN 439, Dec 1990 (draft)
4. H.B. Cary, *Modern Welding Technology*, 2nd ed., Prentice-Hall, 1989
5. N. Stenbacka and K.A. Persson, Shielding Gases for Gas Metal Arc Welding, *Weld. J.*, Vol 68, Nov 1989, p 41–47
6. H.U. Pomaska, "Shielding Gases for Arc Welding and Cutting," Sonderdruck 48, Linde AG, Linde Technische Gases, Holriegelskreuth, Germany
7. R.F. Heile and D.C. Hill, Particulate Fume Generation in Arc Welding Processes, *Weld. J.*, Vol 54, July 1975, p 201s–210s
8. H. Press and W. Florian, Contribution on the Formation of Toxic Substances in Gas Shielded Arc Welding and Determination of Desired Exhaustion Capacity, *IIW Proceedings of Colloquium on Welding and Health*, July 1980 (Portugal)
9. B. Haas, Influence of Process Specific Welding Parameters in Fume Generation in Solid Wire, GMA/Mag Welding, *IIW Proceedings of Colloquium on Welding Safety and Health*, July 1980 (Portugal)
10. D.E. Hilton and P.N. Plumridge, Particulate Fume Generation during GMAW and GTAW, *Weld. Met. Fabr.*, Vol 59 (No. 10), Dec 1991, p 555–560
11. N. Jenkins, J. Moreton, P.J. Oakley, and S. M. Stevens, *Welding Fumes Sources, Characteristics, Control*, Vol 2, The Welding Institute, Cambridge, United Kingdom, 1981, p 272

Shielded Metal Arc Welding*

Revised by Steve Knostman, Hobart Brothers Company

SHIELDED METAL ARC WELDING (SMAW), commonly called stick or covered electrode welding, is a manual welding process whereby an arc is generated between a flux-covered consumable electrode and the workpiece. The filler metal is deposited from the electrode and uses the decomposition of the flux covering to generate a shielding gas and to provide fluxing elements to protect the molten weld-metal droplets and the weld pool. This welding process has its origins in the 1800s, but it was not until the early 1900s that coverings for these electrodes began to be developed. In the 1930s, this method of welding began to grow in popularity and retains an important role in the welding industry. Shielded metal arc welding is one of the most used of various electric arc welding processes.

The SMAW Process

The important features of the SMAW process are shown in Fig. 1. The arc is initiated by momentarily touching or “scratching” the electrode on the base metal. The resulting arc melts both the base metal and the tip of the welding electrode. The molten electrode metal/flux is transferred across the arc (by arc forces) to the base-metal pool, where it becomes the weld deposit covered by the protective, less-dense slag from the electrode covering.

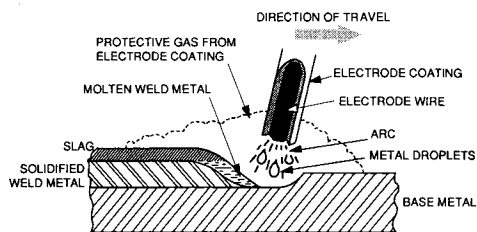


Fig. 1 Shielded metal arc welding process

Advantages and Limitations. The SMAW process is the simplest, in terms of equipment requirements, but it is, perhaps, the most difficult in terms of welder training and skill-level requirements. Although welder skill level is a concern, most new welders start as “stick welders” and develop the necessary skills through training and experience. The equipment investment is relatively small, and welding electrodes (except for the very reactive metals, such as titanium, magnesium, and others) are available for virtually all manufacturing, construction, or maintenance applications. Specific electrodes can be selected depending upon base-metal requirements and can be formulated to match specific base-metal requirements if necessary. Shielded metal arc welding has the greatest flexibility of all the welding processes. It can be used to weld both ferrous and nonferrous metals, it can be used in all positions (flat, vertical, horizontal, and overhead), with virtually all base-metal thicknesses (1.6 mm, or 1/16 in., and greater), in areas sensitive to wind and drafts, and in areas of limited accessibility, which is a very important capability.

Because the SMAW process is basically a manual process, the skill level of the welder is of paramount importance in obtaining an acceptable weld. The welder duty cycle is generally low, because of the built-in work break, which occurs after each electrode is consumed and requires replacement. In addition to replacing the electrode when the arc is stopped (broken), the welder may “chip” or remove slag and clean it away from the starting and welding area with a wire brush to allow the proper deposition of the subsequent weld. This electrode replacement and cleaning operation occurs many times during the work day (about every 2 min, or the time it generally takes to consume an electrode). This stopping, chipping, wire brushing, and electrode replacement prevents the welder from attaining an operator factor, or duty cycle, that is much greater than 25%.

Weld Quality. The quality of the weld depends on the design and accessibility of the joint, as well as on the electrode, the technique, and the skill of the welder. If joint details vary greatly from established design details, then a lower-quality weld can result. Other factors that also reduce quality are improper interbead cleaning, poor location of individual weld beads within the joint, and various problems with individual electrodes, including partially missing flux (chipped ends), core wires that are not centered within the flux covering, and covered ends (coating covering the strike end of the electrode). Overall, welds of excellent quality can be obtained with the SMAW process, as demonstrated by its use in naval ship repairs and off-shore oil jack-up rigs, nuclear power plants, and high-pressure oil/gas pipeline construction.

Base-Metal Thickness. The SMAW process can be used on thicknesses above 1.6 mm (1/16 in.) to an unlimited thickness. The thinner materials require a skilled welder, tight fit-up, and the proper small-diameter welding electrode. Welding position also is important when determining the minimum plate thicknesses that can be welded. Flat-position butt welds and horizontal fillet welds are generally considered the easiest to weld. Out-of-position welding (vertical, overhead) requires greater skill.

Welding Circuit. The circuit diagram for the SMAW process is shown in Fig. 2. The equipment consists of a power source, electrode holder, and welding cables that connect the power source to the electrode holder and the workpiece. Alternating current (ac), or direct current, electrode negative (DCEN), or direct current, electrode positive (DCEP) can be used, depending on the electrode coating characteristics. The DCEN source is also called dc straight polarity, whereas the DCEP source is also called dc reverse polarity.

Equipment. The welding machine, or power source, is the crux of the SMAW process. Its primary purpose is to provide electrical power

* Revised from R.H. Juers, Shielded Metal Arc Welding, *Welding, Brazing, and Soldering*, Vol 6, *ASM Handbook*, ASM International, 1993, p175–179.

of the proper current and voltage to maintain a controllable and stable welding arc. Its output characteristics must be of the constant current type. SMAW electrodes operate within the range from 25 to 500 A. The electrode producer should suggest a narrow optimum range for each size and type of electrode. Operating arc voltage varies between 15 and 35 V.

The electrode holder, which is held by the welder, firmly grips the electrode and transmits the welding current to it. Electrode holders are available in several designs, such as the pincher type and the collet, or twist, type, shown in Fig. 3. Each style has its proponents, and the selection is usually a personal preference. Electrode holders are designated by their current capacity. Selection factors, such as the current rating, duty cycle, maximum electrode size, and cable size, are shown in Table 1. The most lightweight holder that will accommodate the required electrode size is usually desired.

All electrode holders should be fully insulated. Because they are used in proximity to the arc and are exposed to high heat, they will deteriorate rapidly. It is extremely important to inspect and maintain electrode holders to ensure that they retain their current-carrying efficiency, their insulating qualities, and their electrode gripping action. Manufacturers supply spare parts so that the holders can be rebuilt and maintained for safe and efficient operation.

Certain pieces of auxiliary equipment can be used with the SMAW process, such as low-voltage control circuits, which enable the relatively high open-circuit voltage to be cut off until the electrode touches the workpiece. Other items include remote-control switches for the contactors, remote-control current-adjusting devices, and engine idling controllers for engine-driven power sources.

Applications

Most manufacturing operations that require welding will strive to use the mechanized processes that offer greater productivity, higher quality, and therefore more cost-effective production. For these reasons, the SMAW process has been replaced where possible. However, the simplicity and ability of the SMAW process to achieve welds in areas of restricted accessibility means that it still finds considerable use in certain situations and applications. Heavy construction, such as shipbuilding, and welding “in the field,” away from many support services that would provide shielding gas, cooling water, and other necessities, rely on the SMAW process to a great extent.

Although the SMAW process finds wide application for welding virtually all steels and many of the nonferrous alloys, it is primarily used to join steels. This family of materials includes low-carbon or mild steels, low-alloy steels, high-strength steels, quenched and tempered steels, high-alloy steels, stainless steels, and many of the cast irons. The SMAW process is also used to join nickel and its alloys and, to a lesser degree, copper and its alloys. It can be, but rarely is, used for welding aluminum.

In addition to joining metals, the SMAW process is frequently used for the protective surfacing of base metals. The surfacing deposit can be applied for the purpose of corrosion control or wear resistance (hard surfacing).

Electrodes

The electrodes used in the SMAW process have many different compositions of core wire and a wide variety of flux-covering types and weights. Standard electrode diameters of the core wire range from 1.6 to 8 mm (1/16 to 5/16 in.). Electrode length usually ranges from 230 to 455 mm (9 to 18 in.); the shorter lengths are associated with the smaller-diameter electrodes. A bare, uncoated end of the electrode (the grip end) is provided for making electrical contact in the electrode holder.

The coating on the electrode has numerous functions. It provides:

- Gas (normally, carbon dioxide), from the decomposition of certain coating ingredients to shield the arc and weld zone from the atmosphere
- Deoxidizers, for scavenging and purifying the deposited weld metal
- Slag formers, to protect the deposited weld metal from atmospheric oxidation and to help shape the weld bead
- Ionizing elements, to make the arc more stable and to operate with alternating current
- Alloying elements, to provide special characteristics to the weld deposit
- Iron powder, in certain electrodes, to increase productivity for welding ferrous metals

The American Welding Society (AWS) has established a system for identifying and classifying the different types of welding electrodes. All SMAW electrodes have the prefix letter “E” to indicate welding electrode. The symbols that follow the prefix are based on criteria that best describe the welding capabilities of the electrode metal. These criteria include chemical composition of the deposited weld metal, weld-metal mechanical properties, certain process parameters, or combinations of all factors.

The condition of the electrode coating is important to the quality of shielded metal arc welds. There are two general types of coatings: one is a cellulose type, which breaks down in the arc to produce hydrogen; the other is a cellulose-free coating that produces very low hydrogen levels. The first type of electrode coating is used when hydrogen in moderate amounts is acceptable for welds on noncritical structures. Electrodes with cellulose-type coatings have also been used when fast-freeze and good penetration characteristics are desirable and when hydrogen is controlled by preheat requirements (see the section “Preheating” in this article).

The second type of electrode coating is used for welds on structures for which even small amounts of hydrogen are not tolerable. The low-hydrogen electrode coatings are hygroscopic and pick up moisture from the atmosphere, particularly if the relative humidity is high. This occurs especially if the electrodes

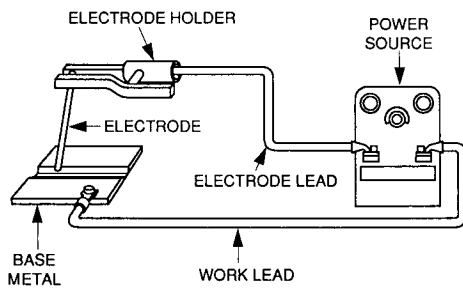


Fig. 2 Shielded metal arc circuit diagram

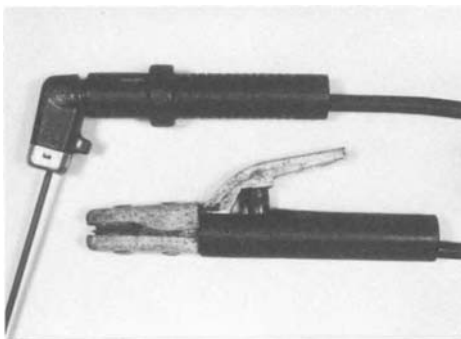


Fig. 3 Shielded metal arc welding electrode holders

Table 1 Size and capacity of electrode holders

Electrode holder	Rating		Maximum electrode size		Maximum cable size
	Maximum current, A	Duty cycle, %	mm	in.	
Small	100	50	3.2	1/8	1
	200	50	4.0	5/32	1/0
Medium	300	60	5.5	7/32	2/0
Large	400	60	6.4	1/4	3/0
Extra large	500	75	7.9	5/16	4/0
	600	75	9.5	3/8	4/0

are exposed to the air for more than 2 to 4 h. Moisture or other hydrogen-containing compounds in the coating are dissociated by the arc temperature, and the resulting atomic hydrogen is readily dissolved in the weld puddle.

Mild and Low-Alloy Steel-Covered Electrodes. The prefix used to identify these electrodes is followed by a number series that indicates minimum strength level, position capability, and type of covering and welding current. Table 2 explains how the number series is used in AWS A5.1, the specification for carbon steel electrodes for SMAW, and AWS A5.5, the specification for low-alloy steel electrodes. The first two digits after the “E” in the E6010 electrode designate a tensile strength of at least 430 MPa (60 ksi) for the deposited metal in the as-welded condition. The third digit indicates the position in which satisfactory welds can be made with the electrode. Thus, the “1” in E6010, for example, means that the electrode is satisfactory for use in all positions (flat, vertical, horizontal, and overhead). The “2” in E6020 indicates that the electrode is suitable for the flat position and horizontal fillets. The last digit or last two digits, taken together, indicate the applicable current type to be used and the type of covering on the electrode.

If electrodes have been exposed to moisture, low-hydrogen-covered electrodes, such as E7015, E7016, and E7018 for SMAW, must be baked at 230 to 260 °C (450 to 500 °F) for at least 2 h prior to welding. Higher-strength

electrodes (such as E8018, E9018, and E10018) must be dried at 370 to 430 °C (700 to 800 °F).

Stainless Steel-Covered Electrodes. The three-digit number that follows the prefix “E” indicates the chemical composition. In addition, letters or numbers can be used to indicate composition modifications or position usability. The specification AWS A5.4 identifies and classifies covered corrosion-resisting chromium and chromium-nickel steel welding electrodes.

Nickel and Copper Alloys. The designations for nonferrous product classifications, such as nickel and nickel alloys in AWS A5.11 and copper and copper alloys in AWS A5.6, follow the prefix with a list of chemical element abbreviations that are significant in identifying product composition, such as ENiCu, ENiCrFe, ECuSi, and ECuNi.

Surfacing Welding Electrodes. The designations for these products are contained in specifications AWS A5.13 and A5.21. They are very similar to the system used to identify nonferrous electrodes.

Aluminum and Aluminum Alloys. The specification for aluminum and aluminum alloy arc welding electrodes, AWS A5.3, uses the “E” prefix to indicate a covered electrode, followed by a series of numbers that identify the chemical composition that is equivalent to Aluminum Association alloy designations (for example, E1100, E3003, and E4043).

Suffix symbols are used in various classifications. The AWS A5.5 specification for low-

alloy filler metals uses suffixes such as -A1, -B2, -B2L, and -C1 to indicate chemical compositions. Table 3 identifies the weld deposit chemical composition associated with a number of suffixes found on low-alloy electrodes. The classifications for nonferrous products in the AWS A5.6 specification for copper alloys and in the AWS A5.11 specification for nickel alloys list a letter or number suffix that indicates position in a series of similar alloy groupings. A similar suffix pattern is also used in the AWS A5.13 and AWS A5.21 specifications for surfacing welding electrodes. Covered stainless steel electrodes employ a number, -15, -16, -17, or -26 as a suffix to identify usability. The -15 suffix indicates that the electrode is designed for all-position operation using DCEP electrical current. The -16 or -17 suffix indicates all-position operation with either ac or DCEP. The -26 suffix is designed for flat and horizontal fillet welding, and manufacturers should be contacted for operating currents.

Deposition Rates. The melting rate of the electrode is directly related to the welding current. The current density in the electrode increases with higher current, which increases the melting rate, which, in turn, increases the deposition rate.

The electrode coating also affects deposition rate. The iron powder types are designed to have higher deposition rates and therefore greater productivity. Figure 4 shows the expected deposition rate versus amperage for various electrodes at a 100% duty cycle. (The actual deposition rate will be considerably less. Deposition rate is a function of the duty cycle, which is affected by the time spent changing the electrodes, cleaning slag off of the weld, etc.) Electrode size and therefore usable current range are determined by the base-metal thickness, welding position, welder skill level, and joint details.

Weld Schedules and Procedures

Welding schedules are tables of operating parameters that will provide high-quality welds under normal conditions. Strict welding schedules are not as important for the manual SMAW process as they are for semiautomatic and automatic welding for several reasons. First, in a manual welding process, the welder controls conditions by arc manipulation, which achieves better control than any of the other arc welding processes. The welder also directly controls the arc voltage and travel speed and, indirectly, the welding current.

Second, meter readings are rarely used in the SMAW process for the duplication of jobs. It is generally considered that the recommended welding current ranges given in Table 4 for the different types of electrodes are sufficient for most operations. The settings provide a good starting point when first welding on a new application, although they are not necessarily the only welding settings that can be used

Table 2 Carbon and low-alloy steel-covered electrode identification system

AWS classification(a)	Minimum tensile strength		Minimum yield strength		Minimum elongation, %
	MPa	ksi	MPa	ksi	
E60XX	414	60	331	48	17–22(b)
E70XX	482–517(b)	70–75(b)	393–414(b)	57–60(b)	17–22(b)
E80XX	550	80	460–550(b)	67–80(b)	16–24(b)
E90XX	620	90	530–620(b)	77–90(b)	14–24(b)
E100XX	690	100	600–689(b)	87–100(b)	13–20(b)
E110XX	760	110	670–760(b)	97–110(b)	15–20(b)
E120XX	830	120	740–830(b)	107–120(b)	14–18(b)

Classification(c)	Flat position	Horizontal position	Vertical position	Overhead position
EXXIX	Yes	Yes	Yes	Yes
EXX2X	Yes	Fillet	No	No
EXX4X	Yes	Yes	Down	Yes

Classification(d)	Current(e)	Arc	Penetration	Covering/slag	Approximate iron powder(f), %
EXX10	DCEP	Digging	Deep	Cellulose/sodium	0–10
EXXX1	ac and DCEP	Digging	Deep	Cellulose/potassium	0
EXXX2	ac and DCEN	Medium	Medium	Rutile/sodium	0–10
EXXX3	ac and dc	Light	Light	Rutile/potassium	0–10
EXXX4	ac and dc	Light	Light	Rutile/iron powder	25–40
EXXX5	DCEP	Medium	Medium	Low hydrogen/sodium	0
EXXX6	ac or DCEP	Medium	Medium	Low hydrogen/potassium	0
EXXX8	ac or DCEP	Medium	Medium	Low hydrogen/iron powder	25–40
EXX20	ac or dc	Medium	Medium	Iron oxide/sodium	0
EXX24	ac or dc	Light	Light	Rutile/iron powder	50
EXX27	ac or dc	Medium	Medium	Iron oxide/iron powder	50
EXX28	ac or DCEP	Medium	Medium	Low hydrogen/iron powder	50

(a) First two or three digits indicate tensile strength in units of ksi and other mechanical properties (mechanical property requirements vary within each classification). (b) Minimum depends on electrode classification. Check AWS A5.1 and A5.5 for the various electrode classes. (c) Third (or fourth (second-to-last) digit indicates the welding position that can be used. (d) Last digit indicates usability of the electrode. (e) DCEP, direct current, electrode positive; ac, alternating current; DCEN, direct current, electrode negative; dc, direct current. (f) Iron powder percentage based on weight of the covering

Table 3 Suffix symbols and corresponding compositions for low-alloy steel-covered electrodes

Suffix(a)	Composition, %												
	C	Mn	Si	P	S	Ni	Cr	Mo	V	Cu	Al	Nb (Cb)	N
A1	0.12	0.6–1.0(b)	0.40–0.80(b)	0.03	0.03	0.40–0.65
B1	0.05–0.12	0.90	0.60–0.80(b)	0.03	0.03	...	0.40–0.65	0.40–0.65
B2L	0.05	0.90	0.60–1.00(b)	0.03	0.03	...	1.00–1.50	0.40–0.65
B2	0.05–0.12	0.90	0.60–0.80(b)	0.03	0.03	...	1.00–1.50	0.40–0.65
B3L	0.05	0.90	0.80–1.00(b)	0.03	0.03	...	2.00–2.50	0.90–1.20
B3	0.05–0.12	0.90	0.60–1.00(b)	0.03	0.03	...	2.00–2.50	0.90–1.20
B4L	0.05	0.90	1.00	0.03	0.03	...	1.75–2.25	0.40–0.65
B5	0.07–0.15	0.40–0.70	0.30–0.60	0.03	0.03	...	0.40–0.60	1.00–1.25	0.05
B6	0.05–0.10	1.0	0.90	0.03	0.03	0.40	4.0–6.0	0.45–0.65
B6L	0.05	1.0	0.90	0.03	0.03	0.40	4.0–6.0	0.45–0.65
B7	0.05–0.10	1.0	0.90	0.03	0.03	0.40	6.0–8.0	0.45–0.65
B7L	0.05	1.0	0.90	0.03	0.03	0.40	6.0–8.0	0.45–0.65
B8	0.05–0.10	1.0	0.90	0.03	0.03	0.40	8.0–10.5	0.85–1.20
B8L	0.05	1.0	0.90	0.03	0.03	0.40	8.0–10.5	0.85–1.20
B9	0.08–0.13	1.20	0.30	0.01	0.01	0.80	8.0–10.5	0.85–1.20	0.15–0.30	0.25	0.04	0.02–0.10	0.02–0.07
C1	0.12	1.25	0.60–0.80(b)	0.03	0.03	2.00–2.75
C1L	0.05	1.25	0.50	0.03	0.03	2.00–2.75
C2	0.12	1.25	0.60–0.80(b)	0.03	0.03	3.00–3.75
C2L	0.05	1.25	0.50	0.03	0.03	3.00–3.75
C3	0.12	0.40–1.25	0.80	0.03	0.03	0.80–1.10	0.15	0.35	0.05
C3L	0.08	0.40–1.40	0.50	0.03	0.03	0.80–1.10	0.15	0.35	0.05
C4	0.10	1.25	0.60–0.80(b)	0.03	0.03	1.10–2.00
C5L	0.05	0.40–1.00	0.50	0.03	0.03	6.00–7.25
NM1	0.10	0.80–1.25	0.60	0.02	0.02	0.80–1.10	0.10	0.40–0.65	0.02	0.10	0.05
D1	0.12	1.00–1.75	0.60–0.80(b)	0.03	0.03	0.90	...	0.25–0.45
D2	0.15	1.65–2.00	0.60–0.80(b)	0.03	0.03	0.90	...	0.25–0.45
D3	0.12	1.00–1.80	0.60–0.80(b)	0.03	0.03	0.90	...	0.40–0.65
G	...	1.0 min	0.80 min	0.03	0.03	0.50 min	0.30 min	0.20 min	0.10 min	0.20 min
M(c)	0.10	0.60–2.25(b)	0.60–0.80(b)	0.015–0.030(b)	0.012–0.030(b)	1.25–3.80(b)	0.15–1.50(b)	0.20–0.55(b)	0.05
P1	0.20	1.20	0.60	0.03	0.03	1.00	0.30	0.50	0.10
P2	0.12	0.90–1.70	0.80	0.03	0.03	1.00	0.20	0.50	0.05
W1	0.12	0.40–0.70	0.40–0.70	0.025	0.025	0.20–0.40	0.15–0.30	...	0.08	0.30–0.60
W2	0.12	0.50–1.30	0.35–0.80	0.03	0.03	0.40–0.80	0.45–0.70	0.30–0.75

(a) The suffix indicates the chemical composition of the weld-metal deposit. (b) Amount depends on electrode classification. Single values indicate maximum; check AWS A5.5 for the various electrode classes. (c) There are several different M classes; M classifications are intended to conform to military specifications.

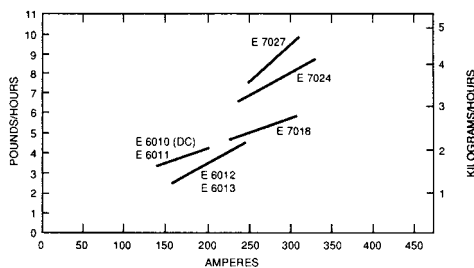


Fig. 4 Deposition rate versus amperes for various electrodes

under every condition. For example, for high-production work, the current settings could be increased considerably over those shown. Factors such as weld appearance, welding position, and welder skill also allow variations from the settings.

Welder Training. The SMAW process generally requires a high degree of welder skill to consistently produce quality welds. As a result, many training programs emphasize the SMAW process because of the arc manipulation skills developed by the welder. This acquired skill level makes the training on other processes much easier.

The exact content of a training program will vary, depending on the specific application of

the process. The complexity of the parts to be welded and the governing codes or specifications involved also dictate the length of the training program. For example, because a pipe welder would need more skill than a tack welder, the length of his training program would be greater.

The job title of arc welder (DOT 810.384-014) describes a person whose responsibility is to weld together many components. This job includes setting up the machine and part to be welded, striking the arc and guiding it along the joint, and performing such duties as chipping, grinding, and slag removal. The welder should be able to:

- Weld in all positions
- Pass employer performance tests
- Meet certification standards of governmental agencies or professional and technical associations

A tack welder (DOT 810.684-010) makes short beads at specific points to hold the parts in place for final welding. The tack welder also performs the duties of fitter helper.

A combination welder (DOT 819-384-010) welds metal parts together to either fabricate or repair assemblies. The combination welder is able to produce gas welds and electric arc welds and to perform flame-cutting operations.

The welder portion of the pipefitter description (DOT 862.381-018) must weld the pipe joint after it has been assembled and tacked in place.

Procedures. There is a definite relationship between the welding current, the size of the welding electrodes, and the welding position. These parameters must be selected to ensure that the welder has the molten weld-metal pool under complete control at all times. If the pool becomes too large, then it becomes unmanageable, perhaps allowing molten metal to run out, particularly during out-of-position welding. The welder should maintain the steady frying and crackling sound that comes with the use of correct procedures. Both the shape of the molten pool and the movement of the metal at the rear of the pool serve as guides in checking weld quality. The ripples produced on the bead should be uniform and have good side tie-in with no undercut or excessive reinforcement. The following factors are essential for maintaining high-quality welding.

Correct Electrode Type. It is important to select the proper electrode for each job. The selection should be based on the type of base metal, expected service, and mechanical properties required.

Correct Electrode Size. The choice of electrode size should depend on the type of electrode, welding position, joint preparation, base-metal thickness, and welder skill.

Table 4 Typical amperage ranges for selected shielded metal arc welding electrodes

Electrode diameter		E6010 and E6011	E6012	E6013	E6020	E6022	E6027 and E7027	E7014	E7015, E7016, and E7016-1	E7018 and E7018-1	E7024-1, E7024, and E7028	E7048
mm	in.											
1.6	1/16	...	20-40	20-40
2.0	5/64	...	25-60	25-60
2.4(a)	3/32	40-80	35-85	45-90	80-125	65-110	70-100	100-145	...
3.2	1/8	75-125	80-140	80-130	100-150	110-160	125-185	110-160	100-150	115-165	140-190	80-140
4.0	5/32	110-170	110-190	105-180	130-190	140-190	160-240	150-210	140-200	150-220	180-250	150-220
4.8	3/16	140-215	140-240	150-230	175-250	170-400	210-300	200-275	180-255	200-275	230-305	210-270
5.6	7/32	170-250	200-320	210-300	225-310	370-520	250-350	260-340	240-320	260-340	275-365	...
6.4	1/4	210-320	250-400	250-350	275-375	...	300-420	330-415	300-390	315-400	335-430	...
8.0(a)	5/16(a)	275-425	300-500	320-430	340-450	...	375-475	390-500	375-475	375-470	400-525	...

(a) These diameters are not manufactured in the E7028 classification.

Correct Current. If the current is too high, then the electrode melts too fast and the molten pool becomes large, irregular, and difficult to control. Current that is too low will not provide enough heat to melt the base metal, causing the molten pool to be sluggish, with a high, irregular, ropey weld bead. It should also be noted that the electrode has inherent current limits. If the current is too high, then the core wire overheats and the coating cracks. If the current is too low, then there is insufficient heat to maintain the arc and form the protective gas shield.

Correct Arc Length. If an arc is too long, then the metal melts off the electrode in large globules that wobble from side to side, resulting in a wide and irregular weld bead with considerable spatter and, possibly, porosity and mechanical property degradation. If the arc is too short, then it has insufficient heat to melt the base metal and electrode, which often results in the electrode sticking to the work.

Correct Travel Speed. A speed that is too fast allows the weld pool to freeze before impurities and gases can escape, and the bead will be narrow and inadequate in size. When the speed is too slow, the metal piles up and the bead is larger than required.

Correct Electrode Angle. In fillet welding and deep-groove welding, the electrode angle is particularly important. When making a fillet weld, the electrode should be held so that it bisects the angle between the plates and is perpendicular to the line of the weld. When undercut occurs in the vertical member, the angle should be lowered and the arc directed toward the vertical member.

Correct Arc Manipulation. When weaving is used, the width of the weave and the pause at the ends of the weave become important. The welder must pause at each end of the weave to allow adequate fill buildup and fusion to occur. The welder should also quickly move across the center of the weld, because heating is more concentrated in the center than at the edges.

Breaking the Arc. Before an arc is broken, it is important to know whether it will be reestablished with the next electrode and the weld continued or whether it is the end of a weld

pass. If welding is to continue, then the crater should remain and the arc quickly broken. If it is the end of a weld pass, then the arc should not be broken until the crater has filled.

Correct Interbead Cleaning. Proper interbead cleaning to remove slag and any spatter is essential to the production of high-quality welds. Proper cleaning prevents slag inclusions, lack-of-fusion defects, and porosity.

Preheating. Hydrogen levels in the weld can be reduced by preheating, such that rapidly diffusing hydrogen atoms escape from the weld surface. At approximately 250 °C (480 °F), no hydrogen-induced cracking of steels is possible, because hydrogen diffuses so rapidly that it will not segregate at the tips of the discontinuities or stress concentrations. The level of preheat or other precaution necessary to avoid cracking will depend on which region (weld metal or heat-affected zone) is more sensitive.

Variations of the SMAW Process

Gravity Welding. Gravity feed is considered to be an automatic method of applying the SMAW process. It uses a relatively low-cost mechanism that includes an electrode holder attached to a bracket, which slides down an inclined bar arranged along the line of weld. Special electrodes with a heavy coating are maintained in contact with the workpiece by the weight of the electrode holder and electrode. Once the process is started, it continues automatically until the electrode has burned to a short stub, whereupon the bracket and electrode holder are automatically kicked up to break the arc. One welder can operate several gravity feeders at the same time (Fig. 5). This increases productivity, reduces welder fatigue, and requires less-skilled welders, all of which result in substantial savings in welder labor costs. Table 5 compares the deposition rate, based on pounds per hour, when using one electrode manually versus two, three, four, or five gravity feeders.

Although gravity-fed SMAW was investigated in the United States, England, and the Scandinavian countries in the late 1940s and early 1950s, credit must be given to the

**Fig. 5** Gravity feeders being used on ship subassemblies**Table 5** Comparison of deposition rates for conventional shielded metal arc welding and multi-arc gravity-fed welding

Data are for making 7.9 mm (5/16 in.) fillet welds using E6027 electrodes.

Method	Deposition rate, lb/h
Manual, one arc	9
Gravity, two arcs	17
Gravity, three arcs	26
Gravity, four arcs	34
Gravity, five arcs	43

Japanese shipbuilders for perfecting and using the process on a large scale in the early 1960s. The gravity welding process is being used in shipyards, railroad car shops, and barge yards throughout the world. It has reasonable acceptance in applications where large amounts of horizontal fillet welds must be made in a relatively small area.

Firecracker welding is an automatic method by which shielded metal arc welds are made using a long electrode with an electrically non-conductive coating. Human involvement is not required after the arc is initiated. A firecracker weld is generally positioned in the flat position. The welding electrode is placed in the joint, and a retaining bar is placed over it. The arc is started by shorting the end of the electrode to the workpiece. The arc length is controlled by the coating thickness. As the arc

travels along the stationary electrode, the electrode melts and makes a deposit on the metal immediately underneath. Once the arc is started, the process proceeds to completion automatically. Electrodes that are up to 1 m (39 in.) long and have a core diameter of 5, 6, or 8 mm (0.20, 0.24, or 0.32 in.) have been used. Both alternating and direct current have been applied, and the former may be preferred, because of arc blow problems associated with direct current.

Underwater Welding

Underwater welding began during World War I when the British naval force used it to make temporary repairs to leaking rivets on ship hulls. The introduction of covered electrodes enabled successful underwater welding and the production of welds having approximately 80% of the strength and 40% of the ductility of similar welds made in air.

Underwater welding can be subdivided into two major categories: welding in a wet environment and welding in a dry protective environment (Ref 1). When underwater arc welding is conducted directly in the water, the SMAW process is usually used, although more recently flux cored arc welding has been used as well. Wet underwater welding has been demonstrated to be an acceptable repair technique at depths of 100 m (330 ft). However, wet welds have been made on carbon steel structures at depths as low as 200 m (660 ft).

Welding that is performed in a dry but high-pressure (hyperbaric) environment requires the construction of a chamber around the weld zone to create the dry habitat. The cost of hyperbaric welding is therefore much higher than that of wet welding. The setting up and tearing down of equipment can be very expensive in a deep-sea environment. Additionally, hyperbaric welding exhibits low mobility. Each fabrication situation often requires a customized setup. Both the gas metal arc welding (GMAW) and gas tungsten arc welding (GTAW) processes can be used in hyperbaric welding, unlike wet welding.

For both wet and dry underwater arc welding, the process is done with increased pressure of 0.1 MPa (1 bar) for each 10 m (33 ft) increase in depth. The influences of water depth (pressure) on arc behavior are similar for both wet welding and hyperbaric welding (Ref 2–4). The major difference is the cooling rate during wet welding, which affects the nature of the weld-metal phase transformation. The cooling time ($\Delta t_{8/5}$) is in the range of 8 to 16 s for cooling from 800 to 500 °C (1470 to 930 °F) during surface welding by SMAW. In contrast, a typical wet-welding procedure by SMAW has cooling-time ($\Delta t_{8/5}$) values between 1 and 6 s, depending on heat input (0.8 to 3.6 kJ/mm) and plate thickness (Ref 5–7). The greater cooling rate produces significant amounts of heat-affected zone (HAZ) martensite in nearly all low-carbon steels. As the carbon

equivalent (CE) of these steels approaches a value of 0.40 wt%, the fusion-line hardness usually exceeds 400 on the Vickers scale (98 N, or 10 kgf), where:

$$CE = \%C + \frac{\%Mn}{6} + \frac{\%(Cr + Mo + V)}{5} + \frac{\%(Ni + Cu)}{15} \quad (\text{Eq 1})$$

As the martensite content increases in the coarse-grained HAZ, the susceptibility to hydrogen cracking becomes a measurable concern. Because of the somewhat diminished weld properties, this SMAW application is generally restricted to salvage operations or underwater repair work.

Wet Welding. The relatively poor quality of welds made in a wet environment is due primarily to the problem of heat transfer, welder visibility, and the presence of hydrogen in the arc atmosphere during the welding operation. When the base metal and the arc area are surrounded entirely by water, there is little temperature or heat buildup of the base metal at the weld, nor is preheating possible. This creates a weld-metal quench effect, which traps higher amounts of hydrogen and also produces a weld solidification structure with reduced toughness and ductility. Both conditions contribute to the weld-metal cracking tendency experienced when welding steels underwater. Another disadvantage is the restricted visibility, which is due to the equipment and the existing local contaminants in the water, as well as those generated by the welding arc. Under the most ideal conditions, welds produced in wet environments using covered electrodes have rougher beads and poorer mechanical properties than those produced in air. They are used when no other option exists.

The covered electrodes used for wet welding must be waterproofed prior to underwater use. This can be done by wrapping them with waterproof tape or by dipping them in special sodium silicate mixes and allowing them to dry.

Dry Welding. The dry environment enables the production of high-quality welds that meet all code quality requirements. The SMAW process is not very popular for welding in the dry environment, because large amounts of smoke and fumes are produced. An extensive air-moving, filtering, and refrigeration system must be employed when the SMAW process is used, because a dry-environment area will quickly fill with the welding fumes, making it impossible for the welder to see that weld area and to function. For this reason, the GTAW and GMAW processes have broader use in dry welding applications.

Repair Welding

Depending on the specific application, all of the common welding processes can be used for repair welding:

- Shielded metal arc welding (SMAW)
- Gas metal arc welding (GMAW)
- Gas tungsten arc welding (GTAW)
- Submerged arc welding (SAW)
- Plasma arc welding (PAW)

For general repairs, the SMAW process still enjoys the widest range of applications for out-of-position welding and for short runs, especially when time is critical and when readily portable equipment is used. For the highest-quality welds, the GTAW and PAW processes find the widest application. For long runs or when a large amount of weld metal must be deposited and mechanization is feasible, the SAW process or, to a lesser extent, the GMAW process, is used.

When selecting a welding process, a number of factors must be considered in balancing productivity and weld quality. Productivity of each process can be ranked in terms of its deposition rate, but productivity is usually not an important consideration on most repair jobs. Some general comparisons are given in Table 6, but sometimes selection can be difficult because each process has a number of conflicting advantages and limitations in specific situations in terms of:

- Base-metal type
- Joint design and thickness
- Welding position
- Environmental conditions
- Equipment availability

Safety Considerations

The SMAW process, like all open arc welding processes, has a number of potential hazards. To alert welders about these safety concerns, all SMAW electrode containers carry a warning label that identifies the three most common safety hazards in these terms:

- Electric shock can kill.
 - Do not permit electrically live parts or electrodes to contact skin...or your clothing or gloves if they are wet.
 - Insulate yourself from work and ground.
- Fumes and gases can be dangerous to your health.
 - Keep fumes and gases from your breathing zone and general area.
 - Keep your head out of fumes.
 - Use enough ventilation or exhaust, or both, at the arc.
- Arc rays can injure eyes and burn skin.
 - Wear correct eye, ear, and body protection.

In addition to the general warnings on the container, further detailed information relating to safety is contained in ANSI/AWS Z49.1, "Safety in Welding and Cutting." The information described as follows is intended to expand

Table 6 Rating of selected welding processes as a function of weld parameters and characteristics

Parameter or characteristic	Process				
	SMAW	GTAW	GMAW	FCAW	SAW
Weld quality	Good	Excellent	Excellent	Good	Excellent
Weld deposition rate	Fair	Poor	Good	Good	Excellent
Field work	Excellent	Poor	Fair	Excellent	Poor
Equipment maintenance	Low	Low	Medium	Medium	Medium
Smoke/fume emission	High	Low	Medium	High	Very low
Heat input control	Excellent	Poor	Good	Good	Satisfactory
Arc visibility and filler-metal placement	Good	Excellent	Satisfactory	Satisfactory	Poor
Variety of metals weldable	Excellent	Excellent	Good	Good	Fair

SMAW, shielded metal arc welding; GTAW, gas tungsten arc welding; GMAW, gas metal arc welding; FCAW, flux cored arc welding; SAW, submerged arc welding

Table 7 Recommended filter lens shades used in shielded metal arc welding

Electrode diameter		Lens shade No.
mm	in.	
1.6	1/16	10
2.4	3/32	
3.2	1/8	
4.0	5/32	
4.8	3/16	12
5.6	7/32	
6.4	1/4	
7.9	5/16	14
9.5	3/8	

Source: Ref 8

on the general warnings and should be particularly useful for SMAW welders.

First, the filter plates installed within welding shields must be capable of stopping the harmful levels of infrared, ultraviolet, and visible light rays originating in the arc. Filter plates are now able to absorb 99% or more of the infrared and ultraviolet rays from the arc. The shade of the filter plate suggested for use with SMAW electrodes is given in Table 7.

Second, in addition to protecting himself, the welder must also be aware of others in the area who need protection, which can usually be provided by portable screens. The failure of those working around the arc to use adequate protection can result in eye burn, which is similar to sunburn and is extremely painful for a period of up to 48 h. Usually, eye burn does not permanently injure the eyes, but it can cause intense pain. A physician should be

consulted in the case of severe arc burn, regardless of whether it involves the skin or the eyes.

Third, the welding area must be adequately ventilated because of the heavy concentrations of smoke and fumes generated in the SMAW process. If welding is being performed in confined spaces with poor ventilation, such as in a tank, an external air supply in the form of a mask or special helmet may be required. In addition, a second person should be stationed at the tank manhole to provide any necessary assistance. Special ventilation is required when welding stainless steels or metals coated with copper, zinc, lead, or cadmium, because of the toxic nature of these fumes.

Fourth, cables with frayed or cracked insulation and faulty or badly worn connections can cause electrical short circuits and electrical shocks to personnel. When it is necessary to weld in a damp or wet area, the welder should wear rubber boots and stand on a dry, insulated platform.

REFERENCES

1. C.L. Tsai and K. Masubuchi, Interpretive Report on Underwater Welding, *Weld. Res. Counc. Bull.*, Vol 224, 1977, p 1–37
2. C.E. Grubbs and O.W. Seth, "Multipass All Position Wet Welding, A New Underwater Tool," OTC 1620, Offshore Technology Conference (Houston, TX), 1972
3. K. Masubuchi, Underwater Factors Affecting Welding Metallurgy, *Proc. Conf. Underwater Welding of Offshore Platforms and Pipelines*, AWS, 1980, p 81–98
4. N.M. Madator, Influence of the Parameters of the Underwater Welding Process on the Intensity of Metallurgical Reactions, *Weld. Res. Abroad*, Vol 3, 1972, p 63
5. N. Christensen, The Metallurgy of Underwater Welding, *Underwater Welding*, Pergamon Press, 1983, p 71–79
6. A. Hausi and Y. Suga, On Cooling of Underwater Welds, *Trans. Jpn. Weld. Soc.*, Vol 2 (No. 1), 1980
7. C.L. Tsai and K. Masubuchi, Mechanisms of Rapid Cooling in Underwater Welding, *Appl. Ocean Res.*, Vol 1 (No. 2), 1979, p 99–110
8. "Safety in Welding and Cutting," ANSI/AWS Z49.1, American Welding Society

SELECTED REFERENCES

- H.B. Cary, *Modern Welding Technology*, 2nd ed., Prentice-Hall, 1989
- "Filler Metal Comparison Charts," AWS FMC-89, American Welding Society
- R.J. Sacks and E.R. Bohnart, *Welding Principles and Practices*, 3rd ed., McGraw Hill
- "Safety in Welding and Cutting," ANSI/AWS Z49.1, American Welding Society
- "Technical Guide for Shielded Metal Arc Welding," Hobart Brothers Co.

Gas Metal Arc Welding

Chris Conrardy, Edison Welding Institute

GAS METAL ARC WELDING (GMAW) employs an electric arc established between a consumable wire electrode and the workpiece to be joined. Heat from the electric arc melts the continuously fed metal wire and the metal workpiece surface to deposit a weld bead. An externally supplied gas or gas mixture acts to shield the arc and molten weld pool from the atmosphere.

While *gas metal arc welding* is the standard terminology recognized by the American Welding Society (in accordance with ANSI/AWS A3.0-2010), the process is also commonly referred to as metal inert gas welding, because early applications employed a chemically inert shielding gas. Flux cored arc welding (FCAW) is a similar process but is differentiated from GMAW by the use of a tubular wire containing flux and may or may not require an externally supplied shielding gas.

Since its commercial introduction in 1948, GMAW consumables and equipment have continued to evolve and expand the range of applications. Today (2011), there are many equipment and consumable options suitable for a broad range of materials and applications. Materials include a variety of steel, stainless steel, aluminum, nickel, copper, magnesium, and titanium alloys. Applications range from welding of thin sheet to thick-section plate, pipe, forgings, and castings as well as cladding, hardfacing, and additive manufacturing. To achieve the desired results for a particular application, it is important to employ a suitable welding procedure, including wire and gas consumable types, equipment type, weld joint preparation, and welding process parameters.

Advantages. The flexibility and productivity of GMAW make the process a popular choice for many applications, and it is particularly well suited to high-production welding applications. Other advantages include:

- Continuous wire feeding allows long weld beads to be deposited without stopping. Welding speed and deposition rates are typically several times higher than gas tungsten arc welding (GTAW) or shielded metal arc welding (SMAW).
- GMAW can be implemented as a semiautomatic (i.e., handheld), mechanized, or

automatic operation and is the most widely used robotic arc welding process. When used as a semiautomatic process, less skill is typically required as compared with manual GTAW or SMAW.

- Unlike submerged arc welding (SAW), GMAW can be used in all positions with proper welding procedures.
- Unlike SAW and FCAW, GMAW does not produce a heavy slag or require postweld slag-removal operations.
- GMAW generally produces less smoke and fumes than SMAW or FCAW processes.
- There are many GMAW process variations that provide additional advantages for specific applications.

Limitations. As with any welding process, GMAW has limitations that restrict its use:

- Continuous wire feeding and externally supplied shielding gas makes the process equipment more complex, less portable, and requires more routine maintenance as compared with SMAW.
- Disruption of the shielding gas coverage, wire feeding problems, or improper gun maintenance can affect weld quality. Outdoor usage may require protection from air drafts that can disrupt proper shielding gas coverage.
- Accessibility is limited by the close proximity of the gun nozzle to the workpiece (generally less than 20 mm, or 0.8 in.) in order to maintain proper shielding gas coverage and wire stickout.
- Depending on the welding procedure and consumables used, GMAW can produce spatter that may adhere to the workpiece, welding gun, or part tooling.
- GMAW is generally less precise than GTAW and generally has lower deposition rates than SAW, although recent GMAW equipment advancements are reducing these limitations.
- Operator acceptance can be reduced by the higher GMAW gun weight relative to SMAW and greater radiated arc light intensity compared with SMAW, FCAW, or SAW.

Principles of Operation

A common GMAW process configuration is shown in Fig. 1. A basic GMAW system includes a welding power source, wire spool, wire feed unit, gas supply and delivery equipment, welding gun, workpiece, and electrical leads to connect the power source to the workpiece and gun. A wire electrode is continuously fed from a wire spool through a contact tube in the welding gun. Conventional GMAW employs direct current electrode positive (DCEP) polarity. The contact tip (also called a contact tube) creates an electrical contact to apply a voltage to the wire from the welding power source. The welding power source is also connected to the workpiece such that an electrical circuit is completed and current flows when the wire contacts the workpiece. Current flow causes a high-temperature electric arc to be established between the wire and the workpiece which melts the wire as it is continuously fed into the arc. The arc also melts the workpiece surface, forming a weld pool comprised of molten material from both the wire and the workpiece. An externally supplied shielding gas is directed through the gas nozzle to protect the molten weld pool and arc from atmospheric contamination and to influence the arc and weld pool characteristics.

Arc Length Regulation. Arc length has important effects on the process stability, weld shape, and weld integrity. An advantage of GMAW is self-regulation of the arc length in response to reasonable variations in the distance between the gas nozzle and the workpiece (called the standoff distance). In its most common configuration, the GMAW power source is designed to maintain a balance between wire feed and wire melting, such that a constant arc length is automatically maintained as the standoff distance is varied. This automatic arc length regulation is one reason semiautomatic GMAW generally requires lower skill as compared with SMAW or GTAW. Automatic arc length regulation is most commonly achieved through control of the welding current (amperage) to maintain a constant voltage. Arc voltage is directly related to arc length, so maintaining constant voltage results in a consistent arc length.

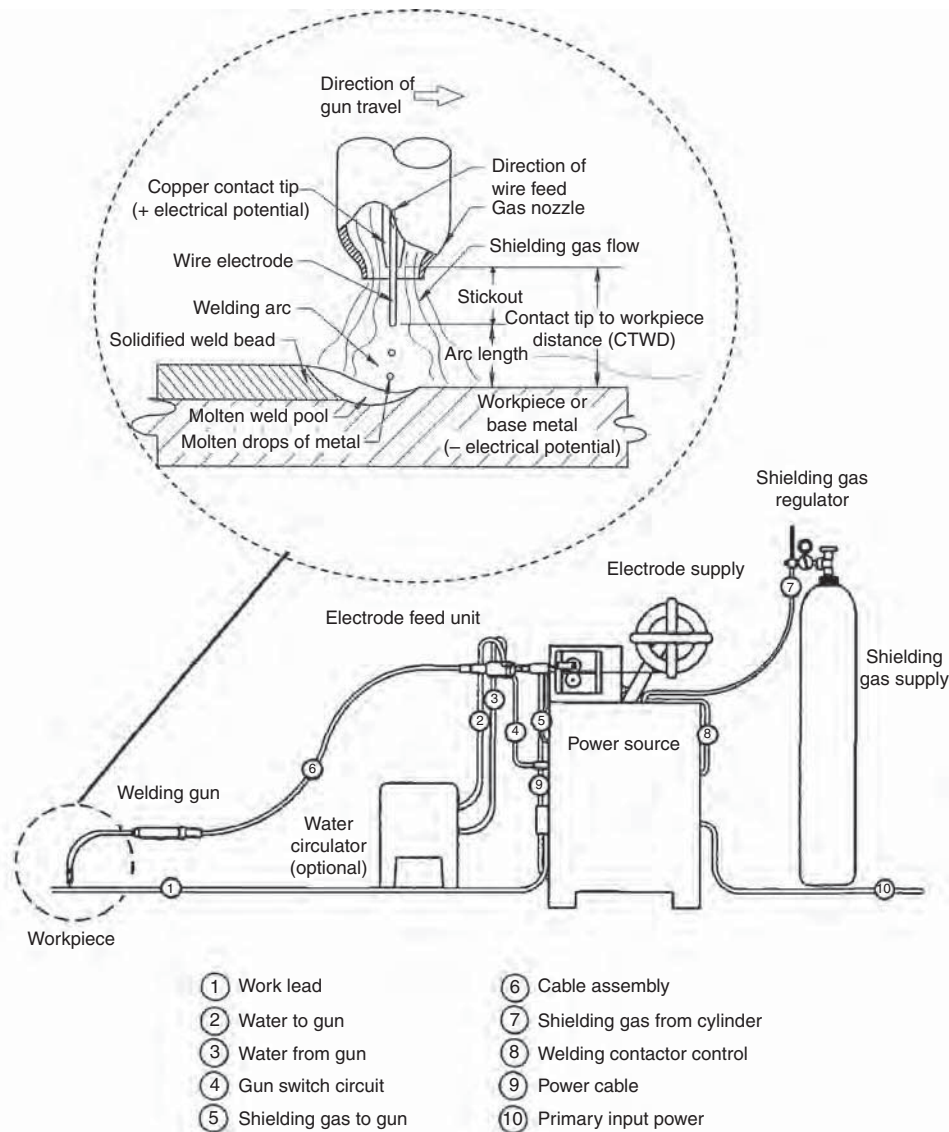


Fig. 1 Typical gas metal arc welding equipment configuration

The welding current determines the rate at which the wire melts and thereby affects the arc length. When the standoff distance is increased and the arc voltage begins to rise, the power source lowers the average welding current to reduce the wire melting rate and thereby return the voltage and arc length to the desired level. Conversely, reducing the standoff distance increases the current and wire melting rate to keep voltage and arc length constant.

Modes of Metal Transfer. The GMAW electrode continuously melts off at the same rate at which it is fed into the arc to maintain a consistent arc length. The mechanism by which the molten metal is transferred from the end of the electrode to the workpiece (called the mode of metal transfer) has significant effects on the weld characteristics. The three most commonly used modes of metal transfer are short-circuiting transfer, globular transfer,

and spray transfer. The mode that is obtained depends on a number of factors, including:

- Electrode and shielding gas compositions
- Electrode diameter
- Welding current and voltage levels
- Electrical polarity
- Power source output waveform and control methods
- Electrical extension of the wire beyond the contact tip

Short-circuiting transfer occurs at the lowest range of GMAW current and voltage levels and is typically employed with the smallest range of wire diameters. The low heat input produces a small, fast-freezing weld pool that is generally suited for joining thin sections, for out-of-position welding, and for bridging large root openings. The low heat input also results in

relatively little base-metal melting, which can contribute to incomplete fusion defects when welding thick sections. For this reason, short-circuit gas metal arc welding is restricted for some applications.

Figure 2 illustrates conventional short-circuiting transfer. When the arc initiates, the tip of the wire melts. As the wire advances, the molten tip contacts the weld pool, and the metal is transferred from the electrode to the workpiece. Metal transfer occurs only during the period when the electrode is in contact with the weld pool and not across the arc gap. When short circuiting begins, the welding current rises rapidly, which acts to pinch off the molten metal from the wire, thereby reestablishing the arc. The stability of the metal transfer depends on the rate and level of current rise. The current increase must be high enough to promote metal transfer yet not so high that violent separation and excessive spattering occurs.

The welding power source design and settings largely determine the current output and the stability of the transfer. In conventional constant voltage power sources, the open-circuit voltage and inductance of the power source affect the current level and rate of current rise. The optimum inductance setting depends on the electrical impedance of the welding circuit and the wire melting characteristics. More recent power source innovations employ sophisticated control methods to optimize the current output, metal-transfer stability, and fusion characteristics. Rather than rely on the natural electrical response of the power source transformer, these systems sense the arc and short-circuiting characteristics and actively control the current and voltage waveform output. In some cases, welding current and voltage control is synchronized with wire feed pulsation. The result is improved process stability and an expansion of the process capabilities beyond what is achievable with conventional short-circuiting transfer, as is discussed in the section “Process Variations” later in this article.

The choice of shielding gas influences the operating characteristics of the arc, weld metal wetting, and weld penetration. For example, when welding steels with conventional power sources, carbon dioxide shielding gas allows for deeper penetration and improved fusion characteristics but generally produces more spatter than inert shielding gases such as argon. Mixtures of carbon dioxide and argon can be used to achieve a compromise between weld penetration and spatter generation. Advanced controls employed by some modern power sources minimize spatter even when using carbon dioxide shielding gases.

Globular transfer occurs at current and voltage levels that are higher than used for short-circuiting transfer. This mode is characterized by large, irregular drops of molten metal that form on the end of the wire before transferring across the arc. Figure 3 illustrates globular transfer. The cycle starts with a drop forming on the end of the wire. As the wire continues

to melt, the drop grows until it is large enough to detach. If the arc length is too short, the drop may occasionally bridge the gap between the wire and pool, creating a short-circuit condition. The short circuit superheats the drop, causing it to explode and produce spatter. Because gravity is a significant contributor to the drop detachment and transfer, use of the globular mode of metal transfer is generally limited to the flat position.

The welding current and voltage ranges that produce globular transfer depend on the consumables used. For steel electrodes and substantially inert shielding gases, axial globular transfer occurs at current and voltage levels that are slightly higher than that used for short-circuiting transfer. With carbon dioxide shielding, however, this mode occurs up to very high current levels. Carbon dioxide shielding produces a randomly directed globular transfer when the welding current and voltage values are significantly higher than that used for short-circuiting transfer. Although severe spatter conditions may result with conventional arc lengths, carbon dioxide is still the most widely used

shielding gas for welding steel with the globular transfer mode. The spatter can be controlled to some extent by “burying” the arc below the base-metal surface, using high currents and relatively low voltages, as illustrated in Fig. 4. In this case, the high arc force depresses the weld pool surface to create a cavity that contains the spatter. This condition results in deep weld penetration but can produce poor weld metal wetting and excessive weld reinforcement. Recent advances in welding power source control technology have improved the arc stability and expanded the usable range with carbon dioxide shielding gas.

Spray transfer occurs at the highest current and voltage levels of the three modes. In spray transfer, small drops of metal stream from the end of the electrode and are axially accelerated across the arc gap with little or no spatter. The drops are typically smaller than the wire diameter and form at frequencies of over 100 times per second. Spray transfer is most easily recognized by the pointed appearance of the end of the wire electrode and the bright metal vapor arc core, as illustrated in

Fig. 5. If the arc length is sufficiently long, short circuits are avoided, resulting in very little spatter.

Spray transfer requires use of DCEP polarity and a welding current level that is above a critical value called the transition current. At current levels below the transition current, transfer occurs in globular mode. The transition current level depends on the wire chemistry, wire diameter, shielding gas composition, and, to a lesser extent, the electrode stickout beyond the contact tip. Transition currents for various diameters and shielding gas compositions are provided in Table 1. The table shows that transition current increases with wire diameter and with shielding gas CO₂ content for mild steels. For high CO₂ concentrations, a stable spray transfer cannot be achieved under normal usage conditions.

The spray transfer mode results in a highly directed stream of discrete drops that are dominated by arc forces that overcome the effects of gravity. This allows spray transfer to be used in any position with proper procedures. Another characteristic of spray transfer is the “finger” weld penetration produced directly under the electrode tip. The depth of this penetration is related to the current density and travel angle, with higher current levels and drag angles producing the greatest penetration. While increased penetration is often desirable, excessively deep and narrow finger penetration may be difficult to align with the weld joint and can lead to root defects such as cracking or porosity in some materials.

Spray transfer is often preferred for welding thick sections in the flat position due to the low spatter, high productivity, and good fusion characteristics. However, the high current levels can be problematic for welding thin materials or for welding out of position. For thin materials, the deep penetration can result in excessive root reinforcement or burn-through. Also, the large, fluid weld pool produced with high wire feed speeds and high average power levels can be difficult or impossible to control when welding in the vertical or overhead positions.

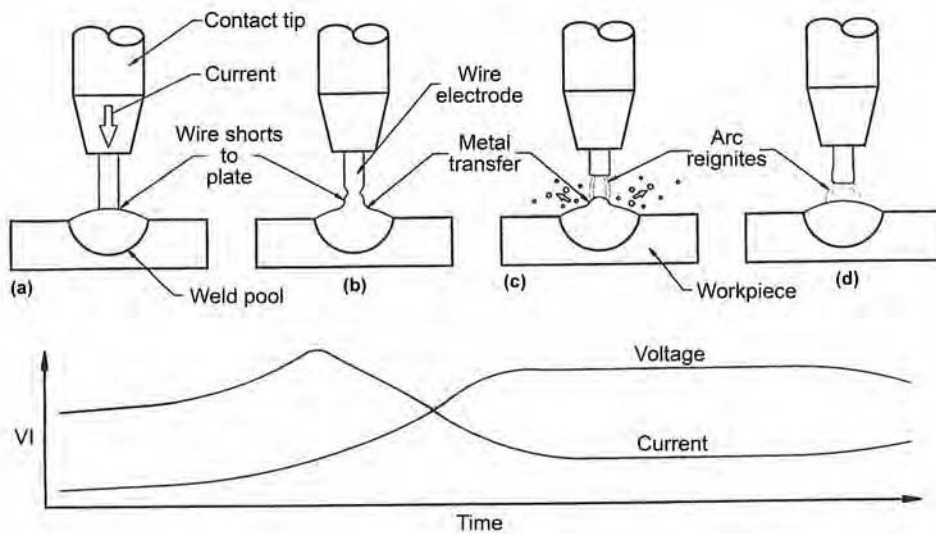


Fig. 2 Short-circuiting transfer

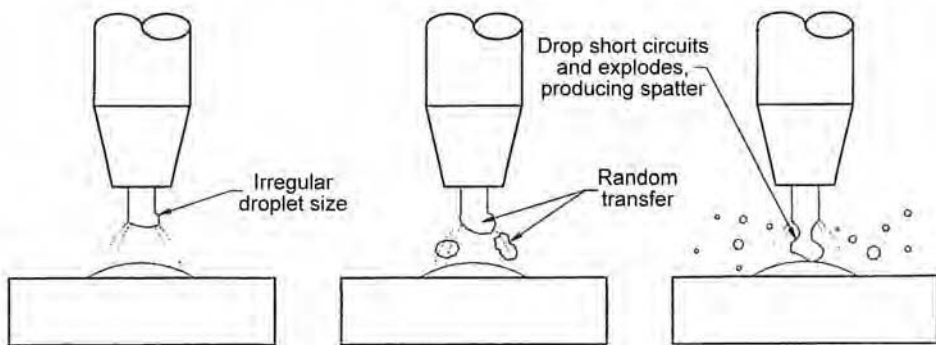


Fig. 3 Globular transfer

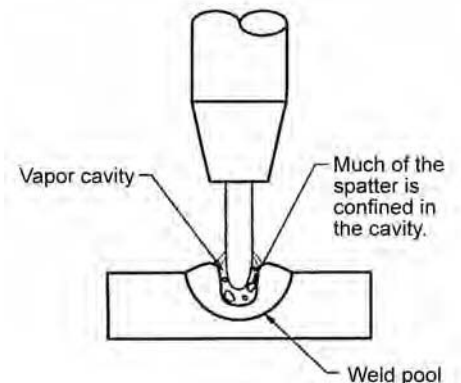


Fig. 4 Buried-arc technique

Pulsed spray is a variation of spray transfer in which the welding power is cycled from a low level to a high level, at which point spray transfer is attained. The lower average power allows pulsed gas metal arc welding to be used on thinner materials and provides better out-of-position operability than conventional spray transfer. A specially designed power source is employed to produce the pulsed output power. Figure 6 is a simple example of a pulse waveform. In this example, the current is raised to a high peak level exceeding the spray transition current for a short period of time (typically a few

milliseconds), then dropped to a low background level for the rest of the cycle. The peak pulse causes a drop of metal to be detached and propelled across the arc. The background period maintains the arc and melts the end of the wire. The cycle repeats up to several hundred times per second. The result is a stable, low-spatter spray transfer at average welding power levels significantly below that which is required for conventional spray transfer. Pulse spray waveforms may be designed to produce one drop per pulse, with the drop size similar to the wire diameter, as shown in Fig. 7.

Power source manufacturers tailor their pulse waveforms to provide preferred operation characteristics for given electrode material, diameter, and shielding gas combinations. In some cases, complex multilevel waveforms are developed for specific applications. The power source output waveforms also adapt for changes in wire feed speed setting, voltage trim setting, or stickout distance. This synergic adaptation may involve changing pulse frequency or levels to maintain the proper arc length and stable spray transfer over a wide range of operating conditions.

Process Parameters

The important variables of the GMAW process that affect weld penetration, bead shape, arc stability, productivity, and overall weld quality are:

- *Welding consumables:* Shielding gas composition, wire electrode type, diameter, and other physical attributes
- *Equipment settings:* Shielding gas flow rate, wire feed speed, polarity, voltage, pulsing conditions
- *Gun manipulation:* Standoff distance, travel speed, travel angle, work angle, weave, welding position and progression
- *Dependent variables:* Welding current, mode of metal transfer

Knowledge and control of these variables are essential to consistently produce welds of satisfactory quality. Because they are not completely independent of each other, changing one variable generally requires changing one or more of the others to produce the desired results. The selection is further complicated by the fact that the optimal settings are specific to the application, including the type and thickness of base metal, joint geometry, weld performance requirements, and so on. Thus, no single set of parameters provides optimum results in every case. Furthermore, there are additional parameters related to specific GMAW process variations. The following describes the effects of some of the more important parameters of conventional GMAW.

Welding current is considered a dependent variable because it is not directly set when a constant voltage power source is used but rather is a function of other process variables, such as wire feed speed, wire diameter, and standoff distance. Current varies in a direct relationship to wire feed speed and diameter and in an inverse relationship to standoff distance. For example, Fig. 8 illustrates the nonlinear relationship between wire feed speed and current for selected steel electrode diameters. These relationships exist because the power source welding current output varies dramatically with slight changes in arc voltage (arc length). Welding current level has important impacts on the process. Welding current can

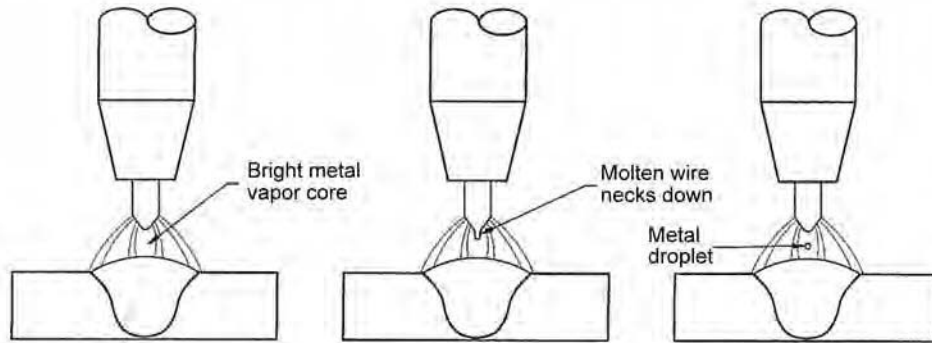


Fig. 5 Spray transfer

Table 1 Globular-to-spray transition currents

Electrode diameter		Shielding gas	Transition current, A
mm	in.		
0.89	0.035	98% Ar + 2% O ₂	165
1.14	0.045	98% Ar + 2% O ₂	220
1.57	0.062	98% Ar + 2% O ₂	275
0.89	0.035	92% Ar + 8% CO ₂	175
1.14	0.045	92% Ar + 8% CO ₂	225
1.57	0.062	92% Ar + 8% CO ₂	290
0.89	0.035	85% Ar + 15% CO ₂	180
1.14	0.045	85% Ar + 15% CO ₂	240
1.57	0.062	85% Ar + 15% CO ₂	295
0.89	0.035	80% Ar + 20% CO ₂	195
1.14	0.045	80% Ar + 20% CO ₂	255
1.57	0.062	80% Ar + 20% CO ₂	345

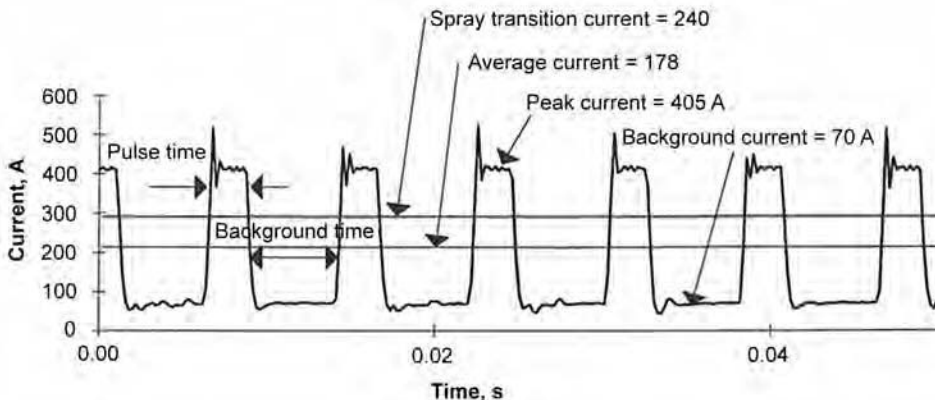


Fig. 6 Example of welding current waveform for pulsed gas metal arc welding

affect weld penetration, fusion characteristics, weld shape, and metal-transfer mode.

Polarity describes the electrical connection of the welding gun in relation to the terminals of the direct current welding power source. When the gun lead is connected to the positive terminal, the polarity is designated direct current electrode positive (DCEP). The vast majority of GMAW applications employ DCEP polarity, because it provides for a more stable arc, improved metal transfer, lower spatter, improved bead profile, and better penetration than direct current electrode negative (DCEN) polarity. Although relatively uncommon, a recent process variation employs variable polarity, switching rapidly between DCEP and DCEN, to tailor weld penetration and deposition rate for particular applications.

Arc voltage directly affects arc length. When all other variables are held constant, an increase in arc voltage setting will result in a longer arc. The specific power source voltage value to produce a given arc length depends on a number of factors, such as the shielding gas composition, wire feed speed, and standoff distance. Although control of arc length is more important, voltage is more easily monitored and is typically specified in welding procedures. An increase in arc length (increased voltage) tends to flatten the weld bead and increase the width of the fusion zone. Excessively long arc length can cause porosity, spatter, undercut, and poor weld shape when welding out of position. Reduced arc length tends to produce a narrower bead with a higher crown. Insufficient voltage can result in excessive short circuiting, arc instabilities, and spatter.

Travel speed is the rate at which the arc is moved along the weld joint. When all other conditions are constant, penetration is maximized at an intermediate travel speed that allows the arc energy to be directed onto the weld joint at the leading edge of the weld pool. At very slow speeds, the weld pool flows ahead of the arc, which reduces base-metal heating and hence penetration. As the travel speed is increased, the arc acts more directly on the base metal. However, further increases in travel speed impart less thermal energy to the base metal, and penetration is reduced. As travel speed is increased further, there is a tendency toward undercutting and weld bead humping. To some extent, the onset of these problems can be delayed by using a push angle along with an optimized arc length.

Travel angle is the orientation of the electrode with respect to the direction of travel. A push angle is the angle when the electrode is pointing toward the direction of travel, and a drag angle is the angle when the electrode is pointing away from the direction of travel. A drag travel angle that ranges from 5 to 15° (from perpendicular) provides maximum penetration and a narrow, convex surface. More common practice is to use a push travel angle, which provides better visibility for the operator and a weld with a flatter surface profile. For some materials, such as aluminum, a leading angle is preferred because it provides arc cleaning of base-metal oxides ahead of the molten pool, which promotes wetting and reduces base-metal oxidation.

Electrode extension is the distance between the last point of electrical contact with the contact tip and the end of the electrode. An increase in electrical extension increases electrical resistive heating of the electrode, which contributes to a greater electrode melting rate. Excessive electrode extension can reduce penetration and produce a narrow, crowned weld bead. The optimum electrode extension is generally in the range of 6 to 13 mm (0.25 to 0.5 in.) for short-circuiting transfer and 13 to 25 mm (0.5 to 1.0 in.) for globular or spray transfer.

Consumables

Proper electrode and shielding gas selection is essential to the success of any welding procedure. The electrode chemical composition is selected to achieve the desired weld-metal properties. For example, electrodes are typically specified to produce a minimum tensile strength. Other characteristics of interest may include toughness, corrosion resistance, color match, or compatibility with the base material. The composition may include deoxidizers and other agents to compensate for reactions in the

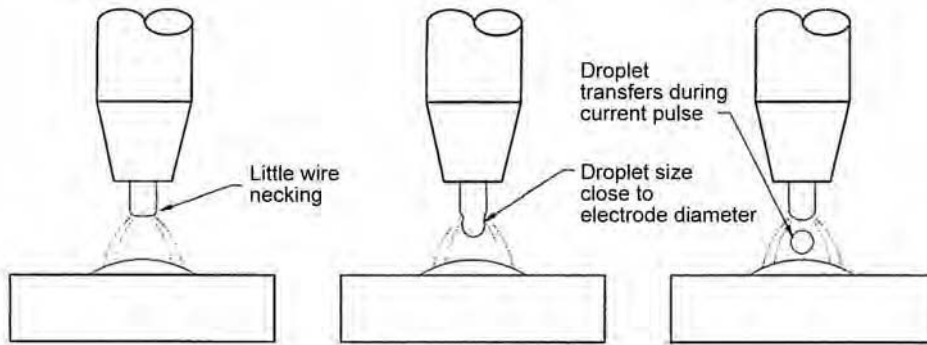


Fig. 7 Typical pulsed spray transfer

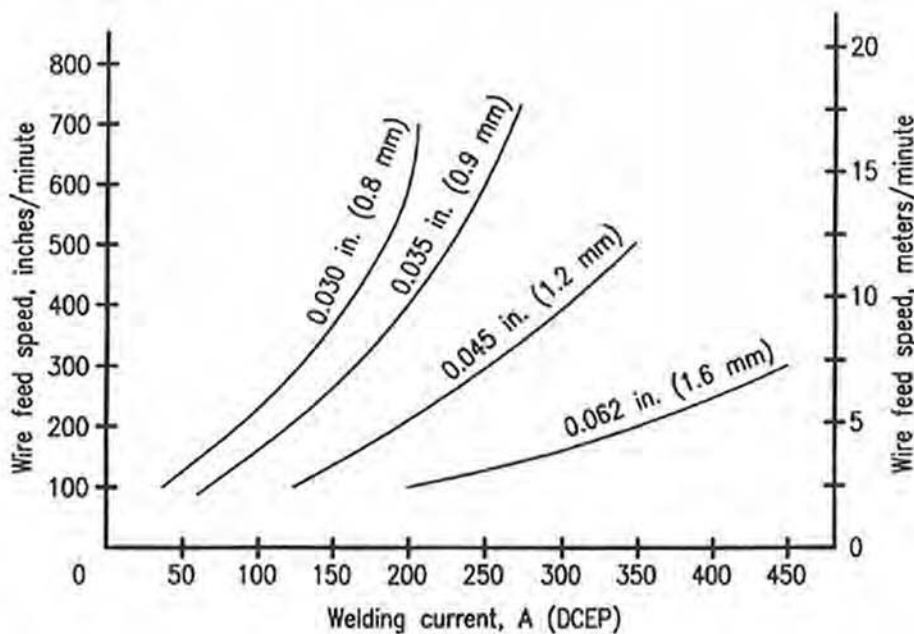


Fig. 8 Typical relationship between wire feed speed and welding current for several steel electrode diameters. DCEP, direct current electrode positive

welding arc and to influence arc stability, weld-metal fluidity, and wetting.

For steel electrodes, higher levels of silicon and manganese tend to produce a more fluid weld pool with better wetting and a flatter weld bead. Excessive fluidity, however, makes out-of-position welding difficult. Most applications employ filler metals of similar composition to that of the base metal. Gas metal arc braze welding, however, involves use of an electrode composition that has a significantly lower melting point than that of the base material, such as a copper alloy electrode used with a steel base material. Braze welding may be employed in situations where it is desirable to minimize base-metal melting, such as the sheet metal example in Fig. 9.

The electrode diameter is selected depending on the current range to be used for a given application. Table 2 illustrates typical current ranges for different steel wire diameters. The larger electrodes use higher current levels; however, the usable current ranges overlap to some degree. A larger electrode requires higher minimum current than a smaller electrode for the same metal-transfer characteristics. Higher currents produce greater electrode melting and larger, more fluid weld deposits. In general, smaller wire diameters are best for welding thin materials and for out-of-position welding, where lower current levels are preferred. Larger electrodes are generally preferred for applications requiring high deposition rates and deep penetration.

The electrode physical characteristics, including surface finish and straightness, are also important considerations. Electrode specifications establish requirements to ensure that users receive a uniform product that feeds smoothly. This includes having uniform winding on the spool or coil; smooth, clean surface finish; uniform diameter; and prescribed cast



Fig. 9 Cross section of a gas metal arc braze weld on sheet metal. Courtesy of Edison Welding Institute

Table 2 Typical current ranges for different wire diameters

Electrode diameter		Useable current range, A
mm	in.	
0.9	0.035	60–280
1.2	0.045	125–380
1.6	0.062	275–475

and helix. Cast and helix refer to the straightness, determined by laying a single coil of wire on a flat surface. A coil diameter that is too small (cast) or shows an excessive lift from the flat surface (helix) may cause wire feeding problems or excessive contact tip wear.

The shielding gas composition is selected to protect the molten metal and to affect the arc characteristics, mode of metal transfer, depth of fusion, weld bead profile, welding speed, and cleaning action. Figure 10 illustrates typical bead shape effects with various shielding gas compositions. Inert gases, such as argon and helium, are commonly used, as is the active gas carbon dioxide. It is also common to use mixtures of these gases and to employ small additions of oxygen.

Equipment

The major components of a GMAW installation include a welding gun, shielding gas supply, electrode feed unit, power source, and associated controls.

The welding gun provides electrical current to the electrode, directs the electrode to the workpiece, and directs the shielding gas to the weld area. A power cable electrically connects the gun to the power source. Different types of guns have been designed for many varied applications, ranging from light-duty guns for semiautomatic (handheld) applications to

heavy-duty guns for high-current automated applications. Light-duty guns are designed to be cooled by the surrounding air; however, as current requirements increase, a water-cooled gun may be needed. Figure 11 illustrates a typical air-cooled semiautomatic gun configuration. Guns are rated based on current-carrying capacity to operate continuously for a set period of time. Current ratings are often specified using CO₂ shielding gas and must be reduced if inert shielding is used.

The contact tip, which is usually made of copper or a copper alloy, both directs the electrode toward the work and transfers power to the electrode. Proper functioning of the contact tip is critical to the GMAW process operation. The electrode must feed easily through the contact tip while maintaining a consistent electrical contact point. Hesitation in wire feeding or variation in the contact point can create arc variations and instabilities. To achieve consistent operation, the contact tip hole is slightly larger than the wire diameter being used. The wire sliding through the tip causes wear, which can enlarge and elongate the hole. Spatter can also adhere to the tip and affect the proper operation. Routine maintenance should be performed to check and replace worn or damaged tips. Contact tip life can be affected by many factors, including the welding conditions, electrode surface condition, electrode straightness, tip design, and gun design.

The gas nozzle directs an even-flowing column of shielding gas into the weld zone to protect the molten weld metal from atmospheric contamination. Nozzle size is selected according to the application, with larger nozzles used when high-current welding produces a large weld puddle, and small nozzles used for low-current and short-circuit welding. Depending on the welding conditions, spatter can accumulate on the nozzle and disrupt the flow of shielding gas, necessitating periodic nozzle cleaning. When welding reactive materials, such as titanium, a trailing shield may also be used to protect the solidified weld bead during cooling.

The shielding gas supply system provides a constant pressure and flow rate of shielding

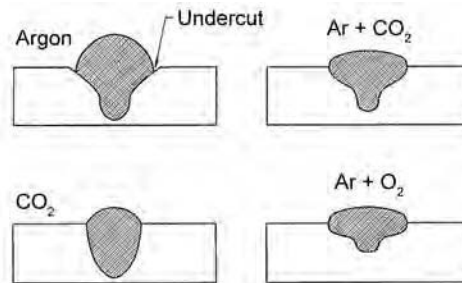


Fig. 10 Effect of shielding gas type on weld penetration and shape for steel

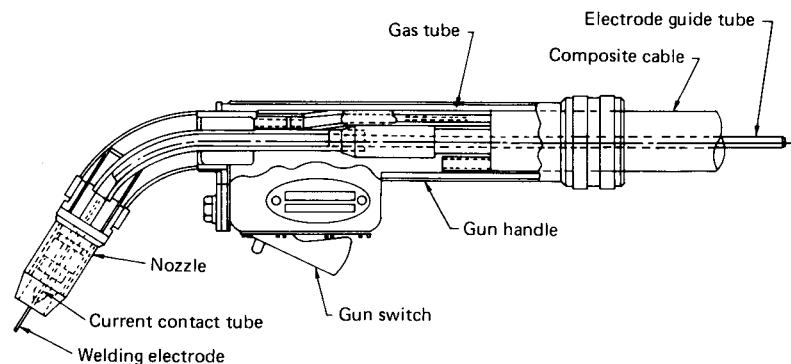


Fig. 11 Typical air-cooled semiautomatic gun configuration

gas during welding. The shielding gas source can be a high-pressure cylinder, a liquid-filled cylinder, or a bulk-liquid tank. The type and size of the gas storage source depend on economic considerations that are based on shielding gas consumption rates. Gas mixtures are available in cylinders, or mixing devices can be used to produce the desired mixtures on site. The regulator reduces the source gas pressure to constant working pressure, regardless of variations at the source. A gas flow meter, which is calibrated for the specific gas mixture, is often used to ensure a consistent gas flow rate. Hoses are used to transmit the gas from the source to the gun. Gas supply system connections should be periodically checked to ensure that they are leak-free to prevent intrusion of air into the shielding gas.

The electrode source must provide a large volume of electrode material that can be readily fed to the gun to ensure maximum process efficiency and stable operation. The source is usually in the form of a spool or coil that can hold from 7 to 27 kg (15 to 60 lb) of wire that has been wound to allow free feeding without kinks or tangles. Small spools of 0.45 to 0.9 kg (1 to 2 lb) are used for spool-type guns (Fig. 12). Large spools of up to 115 kg (250 lb) are also available, and material can be provided in drums of 340 to 455 kg (750 to 1000 lb). These large sources are often used with high-volume automated applications to allow long periods of continuous operation without stopping. For automated applications requiring precise weld wire positioning, a wire straightener may be placed between the electrode source and electrode feed unit to reduce the electrode cast.

The electrode feed unit, or wire feeder, consists of an electric motor, drive rolls, and accessories for maintaining electrode alignment and drive roll pressure (Fig. 13). The motor provides the mechanical energy to pull the electrode from the source and push it through the gun and to the work. The feed unit can be an integral part of the gun, as is the case with spool-type guns. Dual-feed (push-pull) units include a pull feeder in the gun and a separate push feeder near the electrode supply. Spool guns and dual-feed units are useful for feeding soft electrodes, such as aluminum, which are difficult to push through a conduit to the gun.

The feed motor is connected through a gear reducer to a set of wire feed rolls that transfer

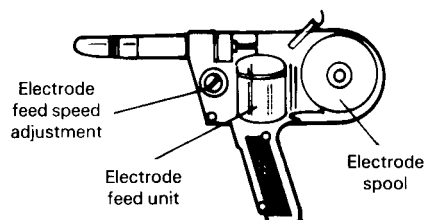


Fig. 12 Semiautomatic spool gun

mechanical energy to the electrode. Various types of drive rolls are available, including knurled, U-groove, V-groove, and flat. Selection of the proper roll type and pressure is important to ensure proper feeding of the electrode without damaging the electrode surface and creating debris that can clog the gun or liner. Knurled rolls are often used with harder materials, such as steel, to avoid slippage of the wire with minimal roll pressure. The U- or V-groove rolls are often used with softer electrode materials, to allow the electrode to be gripped without deformation. Flat rolls can be used in combination with U- or V-grooves for smaller-diameter electrodes.

The electrode conduit and liner direct the electrode from the feed rolls to the gun and contact tip. The conduit/liner diameter and materials are selected to provide support to the electrode while allowing it to slide freely without hesitation, which is important to maintaining arc instability and contact tip life. A steel liner is often recommended when using hard electrode materials such as steel. Other materials, such as nylon or other synthetic polymers, are often recommended for softer electrode materials, such as aluminum. Wire liners can wear or collect debris from the wire surface, resulting in increased sliding friction. A preventative maintenance program should include periodic inspection and replacement of wire liners when necessary.

The welding power source provides the electrical power that is delivered to the electrode and workpiece to produce the arc. Output voltage levels typically range from 15 to 80 V. Depending on the application, output current

levels can range from under 100 A to well over 500 A. Because the vast majority of GMAW applications use DCEP polarity, the positive welding lead is usually connected to the gun and the negative lead to the workpiece. The input power can be either a utility line (single or three phase, 120 to 480 V) for fixed installations, or an internal combustion engine with a generator for field applications. Power conversion technology has evolved from transformer-rectifier designs to inverter designs, which allow smaller and lighter power sources for equivalent output ratings. These newer designs also allow sophisticated control of the output waveforms for particular applications.

Output characteristics can be either constant current or, more commonly, constant voltage, also known as constant potential. A conventional constant voltage power source compensates/maintains a constant arc length when the contact-tip-to-workpiece distance varies by changing the output current and hence the electrode burn-off rate. Power source manufacturers have also developed many types of power source output waveforms and control strategies. Pulse-spray power source waveforms are tailored to specific electrode type, diameter, feed speed, and gas composition. The pulse waveform is automatically adjusted in response to changes in electrode feed speed or contact-tip-to-workpiece distance. This may involve changing pulse frequency, background current, or other waveform characteristics. Power sources have also been developed for short-circuiting transfer, again tailoring the output waveform to achieve desired arc characteristics.

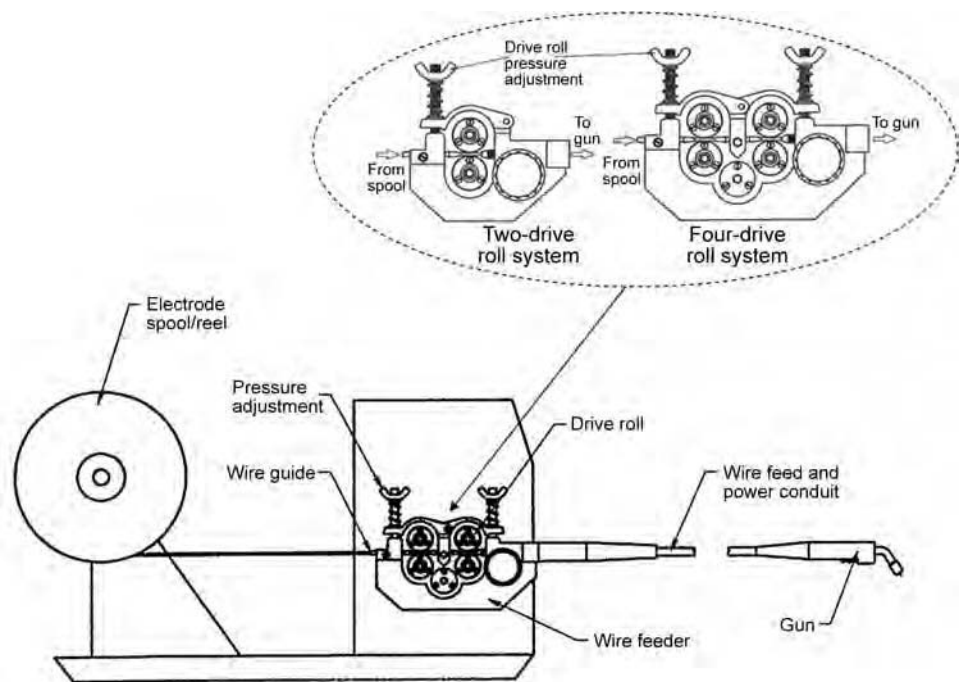


Fig. 13 Typical wire feeder and drive roll configuration

Welding controls are used to set the wire feed speed, voltage, and other process parameters. Power source settings and controls are a function of the power source type. Conventional constant voltage power sources have an electrode feed speed setting (which also determines the current) and a voltage setting (which affects the arc length). Power sources intended for short-circuiting transfer may have inductance and slope settings. Pulse synergic power sources often have electrode/gas selections to choose from and provide arc voltage trim adjustments. The location of the controls varies by power source type and application. Control settings can be found on wire feeders, power sources, or located remotely for ease of adjustment. Automated GMAW applications often involve a separate welding controller that coordinates power source parameters with motion control.

Process Variations

The advent of computer-based controls in combination with improved power conversion technologies has contributed to significant GMAW innovations with particular benefits for specific applications. The following briefly describes some of these variations.

Tandem GMAW makes use of two electrodes and two welding arcs in close proximity, which together produce a single weld pool (Fig. 14). This process variation makes use of two coordinated welding power sources and electrode feed units connected to a gun having two contact tips. Each arc may be separately adjusted to achieve the desired arc stability, penetration, and fill characteristics. This configuration allows significantly increased welding deposition rates and travel speeds as compared with conventional single-electrode GMAW. Tandem GMAW is generally limited to mechanized or automated implementations and is most commonly applied in the flat position, although it can be used for out-of-position welding with the proper welding procedures.

Reciprocating wire feed short-circuit GMAW involves varying the electrode feed speed and direction in coordination with control of welding current and voltage levels. Similar to conventional short-circuiting transfer, this process variation has an arcing phase where the end of

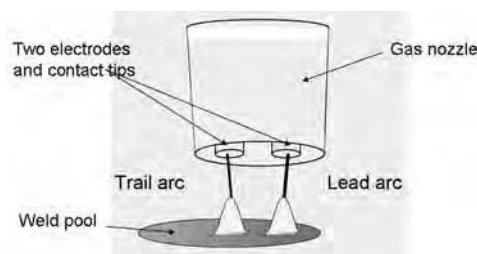


Fig. 14 Tandem gas metal arc welding uses two electrodes in close proximity.

the electrode melts and a shorting phase where the metal is transferred. Unlike conventional short-circuit welding, this process variation does not rely on a sudden rise in welding current to pinch off the molten metal. Rather, the electrode is advanced and retracted many times each second, allowing a single drop of material to be precisely deposited during each cycle. Because the welding current can be lowered during the shorting phase, spatter can be virtually eliminated. The net result is a low-spatter means to produce precise deposits, such as in Fig. 15.

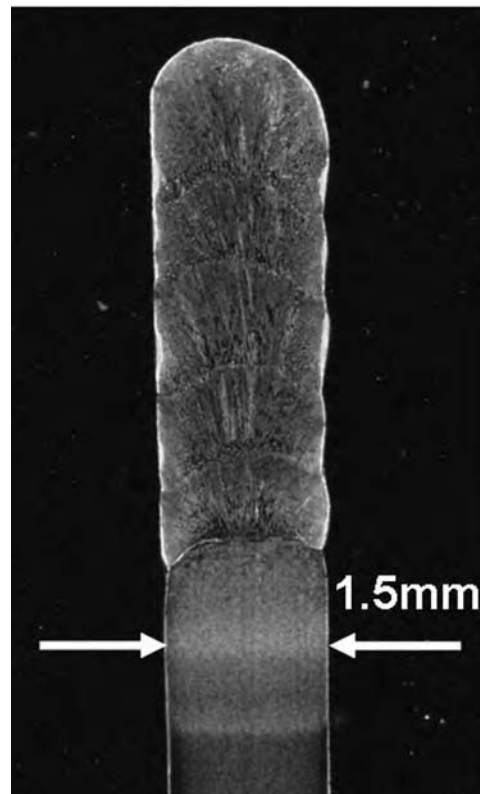


Fig. 15 Reciprocating wire feeding gas metal arc welding can produce precise deposits, such as this edge buildup on stainless steel. Courtesy of Edison Welding Institute

Variable polarity GMAW makes use of a specially designed welding power source that rapidly switches polarity to control drop transfer, deposition rate, and base-metal penetration. Figure 16 illustrates a variable polarity waveform with a portion of the cycle spent on electrode negative (DCEN) polarity and a portion of the cycle spent on electrode positive (DCEP) polarity. Arc stability is maintained by the rapid switching between electrode positive and electrode negative polarities, such that the arc does not extinguish during the instantaneous zero-current condition. As Fig. 17 shows, polarity has a dramatic effect on weld penetration. During the DCEN polarity portion, most of the arc energy is directed toward electrode melting, allowing higher deposition rates and reduced penetration. During the DCEP polarity portion, the majority of arc energy goes to base-metal melting and penetration. Thus, increasing the proportion of the time spent on DCEN reduces base-metal penetration and increases deposition rate. Drop transfer also occurs during the DCEP portion, so the output waveform determines the drop size and transfer frequency.

Hybrid laser GMAW is a process variation in which laser beam delivery optics are integrated with a GMAW gun. Higher productivities are possible than conventional GMAW, as the laser beam provides added penetration and stabilizes the GMAW process at higher travel speeds. Figure 18 illustrates the greater penetration possible with hybrid laser GMAW. Better tolerance to joint fit-up variations are possible than with conventional laser welding, because GMAW provides added fill and alloying. The arc and laser are in close proximity, such that the laser keyhole and GMAW weld pool interact. This process variation may be operated either with the laser beam leading or the GMAW torch leading.

Hybrid plasma GMAW involves combining a plasma arc welding torch with GMAW. The plasma arc welding torch provides additional base-metal heat input to improve wetting or penetration. This technique has been applied to improve weld profile and speed for braze welding applications.

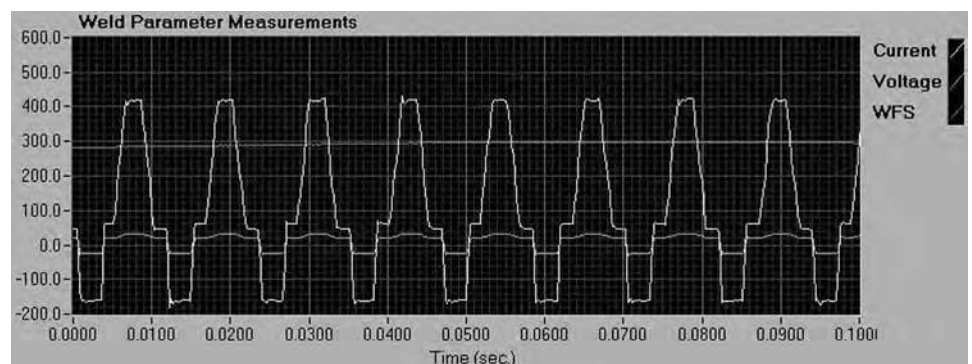


Fig. 16 Example of variable polarity gas metal arc welding output waveform. Courtesy of Edison Welding Institute

Narrow-groove GMAW makes use of specialized joint configurations to efficiently weld heavy sections with minimal distortion. Figure 19 illustrates a typical narrow-groove joint configuration. Narrow-groove GMAW requires the contact tip to reach down into the bottom of the joint to deposit each successive weld pass. To provide access, shielding gas is delivered with ancillary devices rather than a conventional gas nozzle. Special precautions are necessary to ensure the electrode is positioned to achieve proper side wall fusion. Several approaches have been developed to achieve side wall fusion, including tandem GMAW with each arc directed to one sidewall, and rotating contact tip, which directs the electrode to the sidewall. Figure 19 is an example of a narrow-groove weld in 125 mm (5 in.) thick plate produced at over 9 kg/hr (20 lb/hr) using a combination of tandem and electrode rotation.

Safety Considerations

The major hazards of concern during GMAW are inhalation of fumes and gases, electrical shock, and eye or skin injury from arc light radiation and hot spatter.

The type and amount of fumes and gases present during welding depend on the shielding gas type, electrode being used, the alloy being welded, and the presence of any coatings on

the base material. To guard against potential hazards, a welder should keep his head out of the fume plume. Ventilation is always required, and special precautions should be followed when welding in confined spaces where gases or fumes can collect. Fume sampling can be used to assess potential hazards. In some cases, respirators may be warranted to protect welders from hazardous fumes and gases.

Electric shock can result from exposure to high open-circuit voltages of GMAW power sources. All electrical equipment and the workpiece must be connected to an approved electrical ground. Cables should be of sufficient size to carry the maximum current required. Insulation should be protected from cuts and abrasion, and the cable should not come into contact with lubricants or other fluids that may cause deterioration. Work areas, equipment, and clothing must be kept dry at all times. The welder should be well insulated, wearing dry gloves, rubber-soled shoes, and standing on a dry board or platform while welding.

Radiant arc light, especially in the ultraviolet wavelength, is intense during GMAW. GMAW can also produce significant amounts of hot metal spatter. To protect eyes from injury, the proper filter shade should be used for the welding current level. Approved safety glasses should always be worn with GMAW to protect against hot spatter. Skin should also be protected from continuous exposure to the arc light

and hot spatter. The high-intensity ultraviolet radiation can cause rapid deterioration of cotton clothing. Leather, wool, and metal-coated cloth will better withstand exposure to arc radiation and protect skin. Ear protection both prevents exposure to excessive noise in the work area and can prevent spatter from entering the ear.

Conventional fire prevention requirements should be followed, such as removal of combustibles from the work area. Sparks and spatter can travel long distances, so care must be taken to minimize the start of a fire at locations removed from the welding operation. For further information, see the guidelines set forth in the National Fire Protection Association Standard NFPA No. 51B, "Fire Prevention during Welding, Cutting, and Other Hot Work."

Care should be exercised in the handling, storage, and use of cylinders containing high-pressure and liquefied gases. Cylinders should be secured with chains or straps during handling and use. Approved pressure-reducing regulators should be used to provide constant, controllable working pressure for the equipment in use. Lubricants or pipe fitting compounds should not be used for making connections, because they can interfere with the regulating equipment, and, in the case of oxygen service, they can contribute to a catastrophic fire. For further safety information, see ANSI/AWS Z49.1, "Safety in Welding and Cutting and Allied Processes."

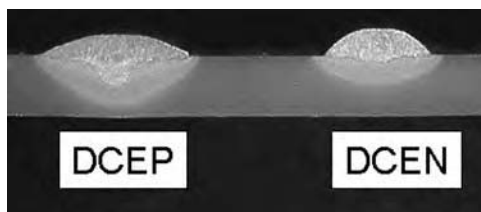


Fig. 17 Electrode positive polarity produces greater penetration than electrode negative polarity. DCEP, direct current electrode positive; DCEN, direct current electrode negative. Courtesy of Edison Welding Institute

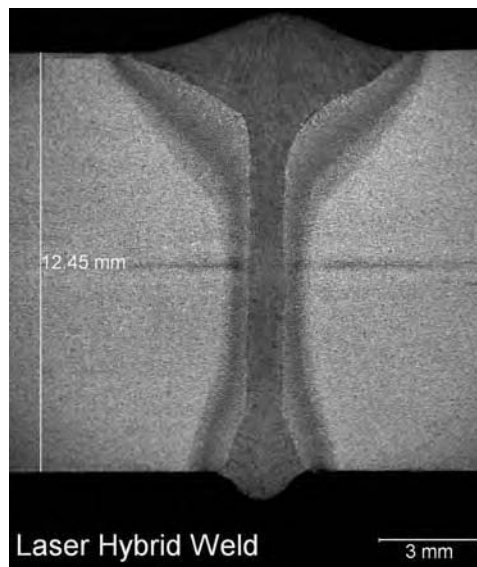


Fig. 18 Hybrid laser gas metal arc welding cross section. Courtesy of Edison Welding Institute

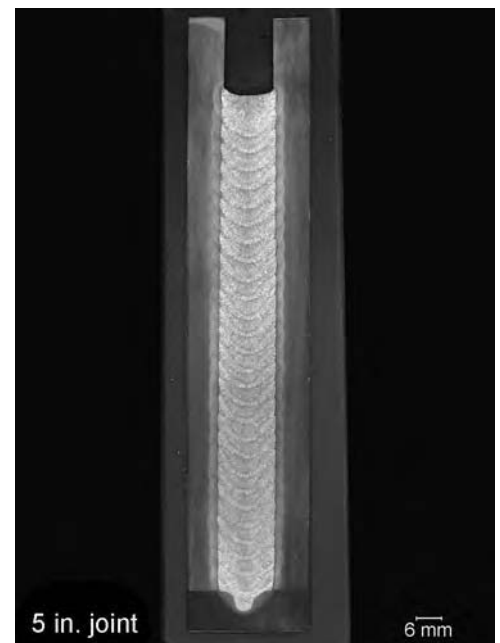


Fig. 19 Narrow-groove gas metal arc welding deposit. Courtesy of Edison Welding Institute

Plasma Gas Metal Arc Welding*

Revised by Ian D. Harris, Edison Welding Institute

PLASMA GAS METAL ARC WELDING (GMAW), also known as plasma metal inert gas (MIG) welding, was invented at the Philips Research Laboratories in Eindhoven, Netherlands, in approximately 1969 (Ref 1). The process can be defined as a combination of plasma arc welding (PAW) and GMAW within a single torch, where a filler wire is fed through the plasma nozzle orifice. Although originally referred to as plasma-MIG welding, the preferred term is plasma-GMAW. The process can be used for both welding and surfacing.

The plasma-GMAW process is illustrated in Fig. 1. Separate power supplies are used for the PAW and the GMAW elements of the equipment (for descriptions of PAW and GMAW, see the articles "Plasma Arc Welding" and "Gas Metal Arc Welding" in this Volume). An arc is struck between the tungsten electrode and the workpiece in a similar fashion to that of a PAW system. The filler wire can be fed to the plasma arc, either with or without the GMAW arc established. Without power supplied to the filler wire, the system can be operated as a PAW system with concentric feed of filler wire. Later versions of the system incorporated an

annular electrode to replace the offset tungsten electrode in the welding torch. A new configuration of hybrid plasma-GMAW is available, with in-line rather than concentric configuration of the two heat sources, and is also described briefly in the "Gas Metal Arc Welding" article.

The equipment can be operated either with a single power source, effectively as a PAW system with concentric filler wire feed, or with two power sources, for the plasma-GMAW operation. The polarity of the tungsten electrode is direct current electrode negative, as is that of the GMAW part of the system. The heat of the plasma arc is sufficient to achieve good metal-transfer stability for the GMAW element, despite the fact that when this process is used separately, it is almost always used in a direct current electrode positive mode. The filler wire is heated by the constricted plasma arc, as well as by the cathode heating of its own arc, and by resistance heating along the wire extension. Therefore, the melting and deposition rates of the wire are higher than the rates achieved by heating with either arc alone.

Metal transfer is governed not only by plasma streaming but also by arc forces between the wire tip and the workpiece. Because the metal droplets are totally enclosed by the plasma stream, spray transfer takes place even though the GMAW element operates on negative polarity.

Advantages and Disadvantages. The advantages of the plasma-GMAW process include deposition rates and joint completion rates that are higher than those of the conventional GMAW process. The independent control of the plasma arc and current to the filler wire leads to more control of metal deposition. This capability can yield improved productivity and good flexibility for controlling heat input and arc characteristics in both welding and surfacing operations. Good control of dilution is achieved by running the system without any power applied to the filler wire. Metal-transfer stability is increased, compared to that of the conventional GMAW process, and results in lower spatter levels. The cleaning action of the plasma arc results in lower porosity in

aluminum alloys, compared to that of the conventional GMAW process.

Disadvantages include the capital cost of two power sources (although there are systems that are designed to operate with one), the greater complexity of the torch, and the increased maintenance time and cost associated with this complexity. With two power sources, more welding parameters must be set up, compared to the conventional GMAW process.

Equipment

As noted earlier, the basic equipment includes a power source for the plasma arc and a power source for the GMAW part of the system. A special torch incorporating both a contact tip for the GMAW element and a cathode for the PAW element is required. The initial design incorporated an offset tungsten electrode, as well as a concentric conduit and contact tip for the delivery of the consumable wire (Fig. 1). A later design incorporated a concentric cathode for the plasma arc (Fig. 2).

The plasma-GMAW torch can be readily fitted to existing welding equipment, such as side beams and welding carriages, to replace the GMAW process in mechanized welding operations.

Power Sources. A constant-current power source with a high-frequency circuit to initiate the pilot arc is used for the plasma arc component of the system. The power source for the GMAW component can be used as a constant-voltage or a constant-current rectifier. Power sources have welding currents that typically range from 40 to 200 A for the plasma arc and from 60 to 300 A for the GMAW element at 100% duty cycle. However, equipment with welding currents up to 800 A is available and can be used for surfacing applications.

Welding Torches. A special torch with a concentric cathode for the plasma arc and a concentric conduit and contact tip for the delivery of the consumable wire is required (Fig. 2). A water-cooled copper alloy nozzle is

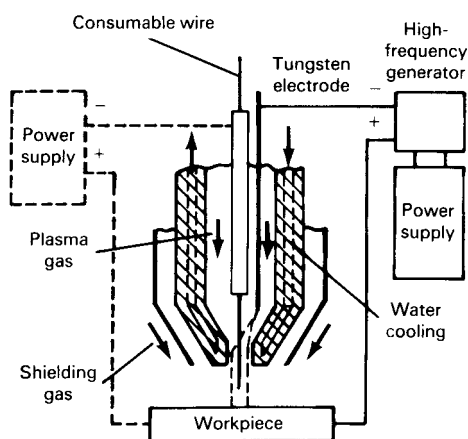


Fig. 1 Schematic of plasma gas metal arc welding equipment. Source: Ref 1

used to constrict the arc and to form a collimated plasma jet that exits the nozzle orifice. A plasma orifice gas and a focusing gas from the same supply are used; the latter is delivered via channels between the plasma welding electrode and the constricting nozzle. The focusing gas results in greater arc constriction and arc stability and prolongs the life of the constricting nozzle by creating a boundary gas layer between the nozzle orifice and the plasma arc. The contact tip, plasma cathode, and the constricting nozzle are all directly water cooled to provide 100% duty cycle at the typical welding currents identified in the preceding section, "Power Sources."

Shielding Gases. Three shielding gases are used: one for the plasma (orifice) gas, one to provide additional arc constriction and arc stability, and one for supplementary shielding. The plasma gas and the focusing gas are usually argon, because an inert gas is required to prevent oxidation of the PAW electrode. The supplementary shielding gas can be argon, argon-oxygen, argon-carbon dioxide, or argon-hydrogen, depending on the nature of the workpiece being welded or, in the case of a surfacing operation, on the material being deposited. Argon is used when welding aluminum alloys, whereas argon-oxygen and argon-carbon dioxide are used when welding steels. Argon-hydrogen is used when welding stainless steels or when surfacing with them.

Procedure

Process Operating Procedure. The plasma arc is ignited using a pilot arc in a fashion similar to that of a PAW system. The main arc is transferred from the electrode to the workpiece, and the plasma jet passes through the nozzle orifice. The system can be operated in this way, with the

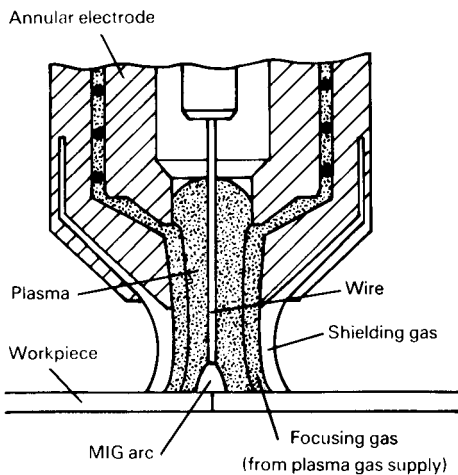


Fig. 2 Schematic of modern plasma gas metal arc welding torch with annular plasma arc welding electrode and additional (focusing) gas stream. Source: Ref 1

concentric cold wire being fed through the axis of the torch. A higher melting rate is achieved when power is applied to the wire through the contact tip and when both arcs are run simultaneously. The higher energy imparted to the wire by the plasma arc results in an increased wire deposition rate (Table 1). In this operating mode, deposition rates higher than those typical of the GMAW process can be achieved.

Inspection and Weld Quality Control.

Inspection requirements are similar to those of other arc welding or surfacing operations. Visual, ultrasonic, and radiographic inspection techniques are most appropriate. The dual action of the GMAW and plasma arcs results in weld quality that is sometimes higher than that achieved by the GMAW process alone. This is particularly true for aluminum alloys, because the cleaning action of the plasma arc often results in reduced porosity.

Quality control requires monitoring the welding parameters for both power sources, as well as monitoring the wire feed. In addition, the condition of the nozzle orifice (that is, the wear and concentricity of the orifice) should be monitored.

Troubleshooting. The relatively complex nature of the welding torch involves increased maintenance time. Erosion of the copper alloy nozzle orifice will cause a change in the arc shape and will affect the weld profile. Therefore, the nozzle should be checked periodically.

Applications

Material Types. The plasma-GMAW process is suitable for welding a wide variety of materials. The high heat energy supplied by the plasma and gas metal arcs makes the process suitable for high-melting-point materials, such as tungsten and molybdenum. The most common application is welding aluminum sheet and plate. Wear-resistant steels are used with the process in hardfacing applications. Austenitic stainless steels, such as types 308, 309, and 347, as well as nickel alloys, such as alloy 625, are used in cladding applications. Both solid and flux cored wires

(Ref 3) can be employed for welding and surfacing, although most applications involve solid wires.

Industries. The plasma-GMAW welding process has been used for the deposition of corrosion-resisting stainless steel and nickel-base alloys in the offshore industry, for the general fabrication of silos and tank trailers made from aluminum alloys (Ref 2), and for hardfacing applications in the excavation equipment industry as well as the dredging and offshore industries.

Typical Components and Joints. The plasma-GMAW process is suitable for welding of joints and for surfacing operations. The wide range of heat inputs available by choosing how to apply current to the consumable electrode provides additional flexibility for surfacing operations, compared to the range of heat inputs available with an external wire feed using the GTAW/PAW or the conventional GMAW process.

Single-V butt joints are commonly used for the plasma-GMAW welding of plate. A full-penetration weld can be made in a single pass on a 9.5 mm (0.375 in.) thick mild steel plate when operating the plasma and gas metal arcs simultaneously. This compares to three passes when just the PAW process is used. One would expect the same joint to require two or three passes for the conventional GMAW process.

When butt welding aluminum alloy sheet and plate in thicknesses ranging from 4.6 to 6.1 mm (0.18 to 0.24 in.), single-pass welds can be made at travel speeds that are more than twice as fast as when the GMAW process is used alone (Table 2). Welding of aluminum plate 10 mm (0.39 in.) thick in a single pass without edge preparation has been reported (Ref 4). The wire feed rate and melting rate were 14.5 m/min (571 in./min) and 80 g/min (2.82 oz/min), respectively, for the 1.6 mm (0.06 in.) diameter welding wire using the plasma-GMAW process. Lower porosity levels are achieved with the plasma-GMAW process because of the cleaning action of the plasma arc. When using mild steel and stainless steel, the plasma-GMAW process can make butt welds

Table 1 Comparison of filler wire melting rates for plasma gas metal arc welding (GMAW) with and without the GMAW arc

Mild steel filler wire; plasma gas, argon; shielding gas, 89% Ar + 6% CO₂ + 5% O₂

Plasma arc current, A	Plasma arc voltage, V	Filler wire current, A	GMAW arc voltage, V	Diameter of filler wire		Melting rate of filler wire	
				mm	in.	g/min	oz/min
110	29	0.9	0.04	22	0.78
135	30	0.9	0.04	28	0.99
160	32	0.9	0.04	33	1.16
190	34	0.9	0.04	40	1.41
190	37	100	31	1.2	0.05	85	3.0
190	38	150	32	1.2	0.05	130	4.6

Source: Ref 1

Table 2 Comparison of welding speeds for gas metal arc welding (GMAW) and plasma-GMAW welding of aluminum and steel

Parameter	Material				
	AlMg4.5Mn			Steel	
	GMAW	Plasma-GMAW	Plasma-GMAW	GMAW	Plasma-GMAW
Sheet thickness, mm (in.)	4.6 (0.18)	4.6 (0.18)	5.1 (0.20)	4.1 (0.16)	4.1 (0.16)
Wire diameter, mm (in.)	1.6 (0.063)	1.6 (0.063)	1.6 (0.063)	1.2 (0.047)	1.2 (0.047)
GMAW current, A	280–300	200	280	250	280
Plasma current, A	...	200	200	...	200
Wire feed speed, m/min (in./min)	8.1 (320)	10.9 (430)	10.9 (430)	5.1 (200)	11.4 (450)
Welding speed, m/min (in./min)	0.4 (16)	1.1 (43)	0.97 (38)	0.51 (20)	0.97(38)

Source: Ref 2

Table 3 Weld surfacing parameters for stainless steel deposits on mild steel using plasma gas metal arc welding (GMAW) with flux cored wires

	GMAW welding current, A	GMAW welding voltage, V	Plasma welding current, A	Plasma welding voltage, V	Welding speed		Deposition rate		Inner wire stickout		Dilution, %	Ferrite No.
					mm/min	in./min	kg/h	lb/h	mm	in.		
Undiluted weld metal	300	39	150	44	110	4.4	10	22	35	1.4	...	15, 12, 13
PZ 6400 (347) surfacing	200	31	150	40	80	3.2	6.6	14.6	55	2.2	8.6	12
PZ 6410 (308) surfacing	300	44	150	46	140	5.6	13	28.7	55	2.2	13.8	5.5
PZ 6415 (309) surfacing	400	50	150	51	190	7.6	20	44	55	2.2	9.7	6.5

Source: Ref 3

comparable to those made with the GMAW process alone at almost twice the travel speed (Table 2).

The hardfacing of dredging equipment with martensitic steel was made more productive by using the plasma-GMAW process, rather than the conventional GMAW

process. Higher deposition rates were achieved, resulting in reduced labor costs for the semiautomatic welding operation. Deposition rates of up to 20 kg/h (44 lb/h) can be achieved by plasma-GMAW surfacing of mild steel with stainless steel flux cored wires (Table 3).

Personnel

Skill Level and Training. The plasma-GMAW process can be used for semiautomatic, mechanized, or automated operation. It requires a skill level comparable to that of the conventional GMAW process, although additional parameters must be set for the plasma arc. Most welding and surfacing activities are carried out with mechanized equipment. When welding parameters are set, operation is similar to that of the GMAW process.

Health and safety issues are similar to those of other arc welding processes. Electric shock, eye protection, burns, ultraviolet radiation, and fume exposure are typical concerns. The plasma-GMAW process generates more radiant heat than the conventional GMAW process.

REFERENCES

1. W.G. Essers, A.C.H.G. Liefkens, and G.W. Tichelaar, Plasma-MIG Welding, *Proc. Conf. Advances in Welding Processes*, The Welding Institute, 1971, p 216–219
2. J.D. Swart, Plasma-MIG Boosts Tank Trailer Output, *Weld. Des. Fabr.*, Feb 1983, p 54, 55, 59
3. F. Eichhorn and E. Van Gaeve, Advantageous Surfacing with Plasma-MIG Using Cored Wires, *Proc. First Int. Conf. Surface Engineering*, The Welding Institute, 1986, p 99–110
4. H.-M. Gao, B. Yan, and W. Lin, Comparison between Plasma-MIG and MIG Procedures on 5A06 Aluminum Alloy, Fifth International Conference on Physical and Numerical Simulation of Materials Processing (ICPNS'07), Oct 23–27, 2007; *Mater. Sci. Forum*, Vol 575–578, Part 2, 2008, p 1382–1388

Hybrid Laser Arc Welding

Brian M. Victor, Edison Welding Institute

HYBRID LASER ARC WELDING (HLAW), also known as laser hybrid welding or simply hybrid welding, is a metal joining process that combines laser beam welding (LBW) and arc welding in the same weld pool. The concept of HLAW was first introduced in the 1970s as “arc-augmented laser welding” that combined LBW with gas tungsten arc welding (GTAW) (Ref 1). Since then, arc processes including GTAW, gas metal arc welding (GMAW), and plasma arc welding have been used; however, GMAW has become the most popular arc process for HLAW. Historically, high-power continuous-wave lasers such as carbon dioxide (CO₂) gas lasers and solid-state neodymium-doped yttrium-aluminum-garnet (Nd:YAG) lasers have been used for HLAW. With advancements in the performance of other solid-state technologies, fiber lasers, thin-disk lasers, and semiconductor diode lasers are increasingly used for HLAW.

Advantages and Limitations

Advantages. Hybrid laser arc welding is a high-productivity welding process that typically combines GMAW with LBW in the same weld pool. This process is used with mechanized or automated welding applications. These process combinations result in a synergy that incorporates the benefits of each individual process. Hybrid laser arc welding can offer the following advantages:

- The high energy density from the laser process can provide deep weld penetration and high processing speeds.
- With appropriate parameters, HLAW can be performed in all welding positions.
- Hybrid laser arc welding can provide lower heat input and less distortion than conventional arc welding.
- Hybrid laser arc welding can produce narrow welds with small heat-affected zones.
- Because of the deep-penetration capability, HLAW can enable less filler-metal usage for a given material thickness or reduce the number of passes required for a multipass joint.
- Filler material from the GMAW process can provide alloying additions and joint filling that is not possible with autogenous laser welding.

- Hybrid laser arc welding has a greater tolerance to joint gaps than autogenous laser welding.
- The laser component of the HLAW process can maintain a consistent weld pool at high processing speeds and reduce weld humping.
- Hybrid laser arc welding is applicable to a wide range of metal alloy systems.
- For reactive metals such as titanium and zirconium, the laser can provide stabilization of the arc welding process.
- Full-penetration HLAW can be performed without a backing material or consumable insert. In some cases, full-penetration HLAW of steel can be performed without root shielding gas.
- Because HLAW is an automated process, precise welds (relative to alignment, width, and penetration) can be obtained.

Limitations. Although HLAW is a productive and advantageous welding process, there are certain limitations that restrict its use:

- Precise alignment and strict part fit-up are required to maintain weld consistency and quality with HLAW.
- Hybrid laser arc welding is only used in mechanized or automated applications.
- Because of the small focal spot diameter of the laser beam, thick-section butt joints with a gap exceeding 1 mm (0.039 in.) are difficult to weld with the HLAW process.
- Due to the low heat input and fast cooling rates produced by HLAW, mechanical properties of the as-welded condition may, in some cases, be poorer than mechanical properties from arc welding processes with higher heat inputs.
- Although combined laser arc processing has been studied for decades, the HLAW process has had limited implementation in production manufacturing until recently. This short history may be an obstacle for implementing HLAW in applications already using established welding processes.
- Due to the expensive laser equipment, capital cost for HLAW systems can be 10 to 50 times higher than conventional automated GMAW systems.
- Compared to conventional arc welding processes, additional safety measures are necessary with HLAW to protect personnel from laser hazards.

Applications and Operating Modes

Hybrid laser arc welding can be used to weld a wide range of metals, including steel, stainless steel, nickel, titanium, aluminum, copper, and other alloy systems. With the high-productivity advantages of HLAW and the broad range of alloys that can be welded, many industries currently using GMAW or submerged arc welding (SAW) could benefit from hybrid welding. The HLAW process is suitable for applications where a productivity increase can justify the high capital cost of an automated hybrid welding system. These can be high-volume production applications or low-volume applications that require an extensive amount of welding. The HLAW process can increase productivity by providing faster processing speeds or deeper penetration.

Thin-section applications, such as automotive components, can benefit from HLAW by an increase in welding speed and a reduction in filler-metal usage (Ref 2). Lap and fillet joints of steel or aluminum sheet metal can be welded at speeds on the order of 4 to 14 m/min (160 to 550 in./min) without humping or lack-of-fusion defects (Ref 2, 3).

Hybrid laser arc welding can also provide an increase in productivity for thick-section welding. In thick-section applications, HLAW can produce deep-penetration welds at travel speeds on the order of 1 to 3 m/min (40 to 120 in./min). In this case, the increase in productivity is generated by deeper weld penetration rather than a drastic increase in travel speed. Using a 30 kW ytterbium-fiber laser, full-penetration HLAW of a 28 mm (1.10 in.) square butt joint has been completed in a single pass (Ref 4). Applications such as oil and gas transmission pipelines, wind turbine towers, prefabricated steel beams, nuclear components, ship structures, heavy vehicles, construction and mining equipment, and rail cars are some example applications that can benefit from the deep penetration of the HLAW process (Ref 5–7). By generating deep weld penetration at productive travel speeds, HLAW can reduce the number of weld passes or decrease weld distortion, compared to GMAW and SAW (Ref 8). To date, the most widely known production application of thick-section HLAW is in the shipbuilding industry.

In 2002, Meyer Werft GmbH in Papenburg, Germany, implemented HLAW for production welding of steel panels and stiffeners for commercial cruise ship fabrication. Using a 12 kW CO₂ laser combined with a 450 A GMAW system, steel plates 6 mm (0.24 in.) thick were welded at speeds of 2.5 to 3.0 m/min (98 to 118 in./min), and 15 mm (0.59 in.) plates were welded in a single pass at 1.2 m/min (47 in./min). By moving to the one-sided, single-pass HLAW process, Meyer shipyard reported welding speeds three times faster than GMAW or SAW and reduced filler-wire usage by an estimated 80%. In addition, HLAW produced less weld distortion and eliminated post-weld flattening processes at Meyer (Ref 9). Hybrid laser arc welding systems using high-power fiber lasers have also been developed for the shipbuilding industry (Ref 10).

Process Description

Hybrid laser arc welding most often combines LBW with GMAW in a common weld pool (Fig. 1). In HLAW applications, the GMAW process is always used to add filler metal to the weld. However, the laser process can be used for multiple purposes, depending on the laser power density (W/cm²) at the work surface.

The applications of the HLAW process can be divided into two groups based on the mechanism for which the laser is used. One is a stabilization mode, where the laser is used to augment the GMAW process without providing a significant increase in penetration or speed. The other is a penetration mode, where the laser generates a keyhole in the metal, providing both deep penetration and high processing speeds. These two modes are described in the section “Modes of Operation” in this article.

In addition, the major process variables for either mode of operation include three sets of welding parameters: the variables for the independent LBW and GMAW processes and welding variables that are specific to the HLAW process. The process variables specific to HLAW are:

- Travel speed (typically from 1 to 3 m/min, or 40 to 120 in./min)
- Process orientation
- Process separation

These parameters of the HLAW process are discussed in the section “Hybrid Laser Welding Parameters” in this article, while specific variables for the LBW process (discussed in other articles in this Volume) include:

- Laser power (typically from 200 W to 20 kW)
- Diameter of the focused laser beam (spot size typically 0.2 to 1 mm, or 0.008 to 0.39 in.)

The variables for GMAW, as discussed in the article “Gas Metal Arc Welding” in this Volume, include:

- Arc current, voltage, and polarity
- Wire feed speed
- Electrode diameter and composition
- Electrode extension (contact tip-to-work distance)
- Shielding gas composition

Other variables, such as base-metal composition, joint design, part fit-up, GMAW torch angle, shielding gas flow rate, laser wavelength, position of the laser focus with respect to the work surface, and preheat temperature, can play important roles in hybrid welding but are variables usually defined by the application or the available equipment. For HLAW with other arc processes, the GMAW variables would be replaced by the variables of the alternative arc process. The process separation, or distance between the laser and arc, would remain a critical variable regardless of the arc process used.

Modes of Operation

Stabilization-Mode HLAW. As noted, this mode of hybrid laser welding augments the GMAW process without providing a significant increase in penetration or speed. This mode is sometimes referred to as laser-assisted arc

welding. The method of augmentation can be different depending on the material being welded and the laser power density used. For reactive metals such as titanium and zirconium, the laser can be used to provide arc stabilization. As little as 200 W can stabilize the cathode spot during pulsed GMAW of titanium (Ref 11). For welding steel, stainless steel, nickel, and aluminum alloys, a low-power-density laser spot can be used to produce a wide, shallow weld pool ahead of the GMAW process to stabilize the filler-metal deposition. In this case, the laser process is used to increase the wetting angle of the deposited metal and produce a smooth weld bead. This technique can be used to prevent weld humping at fast travel speeds, increase weld toe angles, improve side-wall fusion in groove welds, or enhance attachment of deposited metal when welding out of position (Ref 12).

Using a low-power-density laser beam for stabilized-mode hybrid welding can provide technical benefits in unique applications. However, this mode of HLAW is usually cost-prohibitive for most production manufacturing applications. Laser equipment is much more expensive than arc welding equipment in terms of price per unit of output power (cost per watt). If the expensive laser equipment is used for stabilization rather than drastically increasing productivity (speed or penetration), the return on investment for a hybrid welding system may not be attractive.

Penetration-Mode HLAW. To fully utilize the benefits of an expensive laser system, HLAW is conducted primarily in penetration mode. This is sometimes referred to as arc-assisted laser welding. In penetration-mode HLAW, the laser generates a keyhole in the metal. Both deep penetration and high processing speeds can be achieved with keyhole laser welding.

A keyhole is formed when a laser beam with sufficiently high power density causes melting and vaporization of the base metal. As the metal is vaporized, it rapidly expands and pushes away from the substrate. This expansion exerts a reactive force on the melted substrate called the evaporative recoil force. This recoil force pushes the melted metal away to form a depression. The melted metal is continually pushed out until the depression has formed into a deep keyhole.

The keyhole can be partially or fully through the thickness of the metal. In the steady-state condition after the keyhole is established, continual vaporization of the bottom and walls of the keyhole holds it open against the forces of surface tension and gravity. The relationship of laser power density and travel speed dictates the penetration and width of the keyhole for a given base metal. Power densities on the order of 10⁶ to 10⁸ W/cm² are typical for keyhole laser welding.

Hybrid Laser Welding Parameters

Knowledge of each variable and the ability to precisely control them are necessary to consistently

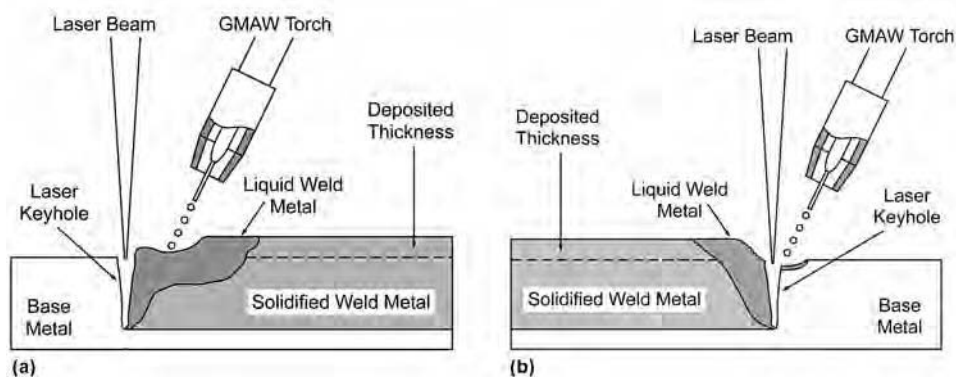


Fig. 1 Schematic of hybrid laser arc welding process orientations. (a) Laser leading. (b) Arc leading. GMAW, gas metal arc welding

produce hybrid welds with the desired quality. These variables can produce competing effects on the weld attributes, and balancing the performance of each variable is essential to successful hybrid welding. Table 1 lists the general effects of each HLAW variable on hybrid weld attributes. The effects listed are typical for welding butt joints over 6 mm (0.24 in.) thick or for welding thinner sections at travel speeds above 3 m/min (120 in./min).

Travel Speed. Hybrid laser arc welding is applicable over a wide range of travel speeds. Generally, the determining factor for welding speed is the productivity requirement. As travel speed increases, hybrid weld penetration will decrease. To maintain the required weld penetration at increasing travel speeds, more laser power and an increased rate of filler-metal deposition is required. If the existing laser equipment is limited in power, then a compromise must be made among travel speed, laser power, and weld penetration.

At travel speeds on the order of 4 m/min (160 in./min) or greater, joint-filling capabilities from the GMAW system can be limited. Gas metal arc welding systems are inherently limited to a maximum current output. For a given electrode diameter, there is a maximum wire feed speed at the maximum current rating of the GMAW power supply. This limitation can lead to insufficient filler-metal addition at faster travel speeds. If the required reinforcement or fillet size cannot be met for a given travel speed due to the limitations of the GMAW power supply, the travel speed, GMAW source, wire diameter, joint design, or the number of passes must be reevaluated. Additional GMAW torches with separate power supplies and wire feeders could be used to overcome deposition limitations.

Process Orientation. The HLAW process can be oriented in two directions: arc leading or laser leading. The GMAW process can be positioned behind or in front of the traveling laser keyhole. If the GMAW process travels behind the laser beam, the HLAW process orientation is referred to as laser leading. If the GMAW process travels ahead of the laser, the HLAW process orientation is referred to as arc leading. Figure 1 illustrates the laser-leading and arc-leading process orientations.

The main difference between the two orientations is the angle of the GMAW torch with

respect to the direction of travel. Torch angle can have an effect on the deposited GMAW bead. In the laser-leading HLAW configuration, the GMAW torch is traveling behind the laser beam, positioned at a “push angle.” In the arc-leading configuration, the torch is at a “drag angle,” traveling in front of the laser beam. This difference in torch angle can produce different weld surface geometries. In the laser-leading orientation, the deposited weld bead is relatively wide and flat, with large weld toe angles. With arc leading, the deposited weld bead is more narrow and convex, with sharper weld toe angles. Torch angle can be adjusted for each process orientation, but there is a limitation to how close the torch can be positioned to the beam axis, due to the beam convergence angle and obstructions from the laser-focusing optic assembly. Alternatively, the laser beam axis can be tilted while the GMAW torch is positioned normal to the work.

Another reported difference between the two process orientations is in penetration. If the laser beam is positioned in the arc depression of the GMAW process, the arc-leading configuration can provide slightly more penetration for HLAW. However, there is conflicting data reporting that the laser-leading process provides deeper penetration. In either case, the reported gain in penetration is generally considered insignificant for most manufacturing applications.

Process Separation. A key variable for HLAW is the process separation, or distance between the two welding processes. This is also known as the beam-to-wire distance or process spacing. Process separation can affect the solidification morphology and microstructure of a hybrid weld. Increasing the process separation will eventually separate the two processes into separate weld pools. Even if the weld pools of the two processes appear to be connected on the weld surface, a metallographic cross section of the hybrid weld can show that the fusion profiles from each process may have solidified separately within the thickness of the joint. This separate solidification can affect the weld microstructure and composition gradient of the GMAW filler metal through the thickness of the joint. Changing the process separation can also have an effect on the energy concentration of the hybrid process, affecting weld penetration, spatter generation, and root bead

profile in full-penetration welding. Process separation for HLAW is typically between 0 and 6 mm (0 and 0.24 in.), depending on the material, laser power, process orientation, and travel speed.

Laser Power. The relationship of laser power and focused beam diameter determines the laser power density. In penetration-mode HLAW, laser power density has the greatest effect on weld penetration. For most structural metals, approximately 1 kW of laser power is needed to provide 1 mm (0.039 in.) of penetration at a travel speed of 2.0 m/min (79 in./min). This estimate depends on the absorptivity of material being welded for a given laser wavelength and the diameter of the focused laser beam. For example, when welding low-carbon steel with a 10 kW laser, a full-penetration hybrid weld can be produced at 2.3 m/min (90 in./min) on a 9.5 mm (0.375 in.) square butt joint with no gap. Spot sizes larger than 600 μm (0.024 in.) can reduce the power density and require more laser power to penetrate a given thickness.

The depth and diameter of the keyhole are determined by the laser power and focused spot size, respectively. Large focused spot sizes, greater than 600 μm (0.024 in.), produce large-diameter keyholes with less penetration for a given laser power. Small-diameter spots, typically 100 to 600 μm (0.004 to 0.024 in.), are used more often in HLAW to generate narrow keyholes and produce welds with high aspect ratios (depth to width). Figure 2 is a video still of a steel hybrid bead-on-plate weld using 1.1 mm (0.045 in.) diameter wire. The image shows that the keyhole diameter is relatively small in respect to the width of the weld pool. This is because the GMAW process drives the weld width at the top surface of the material. Through the thickness of the material, the weld width is similar to the keyhole width. Figure 3 is a cross section of a penetration-mode hybrid weld conducted on a 12.45 mm (0.490 in.) carbon steel square butt joint. This weld was performed with 10 kW of laser power, a 333 μm (0.013 in.) laser spot size, and an 8.9 m/min (350 in./min) wire feed speed for a 1.1 mm (0.045 in.) diameter steel wire at a travel speed of 1.52 m/min (60 in./min). Note that the fusion zone resembles the superposition of a GMAW weld profile and a laser weld profile.

Table 1 Effects of hybrid laser arc welding process variables on weld attributes

Welding variable to change	Desired change in weld attribute							
	Penetration		Deposition		Cap bead width		Root bead width	
	Increase	Decrease	Increase	Decrease	Increase	Decrease	Increase	Decrease
Travel speed	Decrease	Increase	Decrease	Increase	Decrease	Increase	Decrease	Increase
Laser power	Increase	Decrease	No effect	No effect	Minor effect	Minor effect	Minor effect	Minor effect
Laser spot size	Decrease	Increase	No effect	No effect	Minor effect	Minor effect	Increase	Decrease
Wire feed speed and arc current	Minor effect	Minor effect	Increase	Decrease	Minor effect	Minor effect	No effect	No effect
Arc voltage	No effect	No effect	No effect	No effect	Increase	Decrease	No effect	No effect
Wire diameter	Minor effect	Minor effect	Decrease	Increase	Minor effect	Minor effect	No effect	No effect
Process orientation	Minor effect	Minor effect	No effect	No effect	Laser leading	Arc leading	Minor effect	Minor effect
Process separation	Minor effect	Minor effect	No effect	No effect	Minor effect	Minor effect	Decrease	Increase

Shielding Gas. The primary function of the shielding gas is to protect the molten weld metal from the surrounding atmosphere. Shielding gas for HLAW should be selected based on the material being welded; however, additional considerations are necessary based on the laser wavelength and the desired GMAW arc characteristics.

During LBW with a CO₂ laser, the vapor plume or plasma generated by the laser process can absorb and scatter the laser beam. This interference can cause a loss in weld penetration. Therefore, when hybrid welding with a CO₂ laser, it is necessary to remove or suppress the plume with gas usually containing some percentage of helium. In some cases, this can be done with gas delivered by the GMAW torch. In other cases, a secondary plume-suppression gas may be necessary. When hybrid welding with solid-state lasers such as Nd:YAG, fiber, thin-disk, or diode lasers, the shorter wavelengths are not significantly affected by the vapor plume, and a secondary gas for plume suppression is usually not necessary.

Shielding gas delivered from the GMAW torch is generally sufficient to protect the molten weld metal from the surrounding atmosphere. In some cases, a second gas trailing the welding process is needed to shield the weld as it cools. A trail shield device is generally used when welding reactive metals such as titanium or in applications where discoloration due to surface oxidation is unacceptable.

For the GMAW process, the shielding gas plays an additional role in determining weld profile, arc characteristics, and mode of metal transfer. Inert gases, active gases, and blends of the two can be used for HLAW. (For information about shielding gas compositions and which gases to use for specific applications, see the article “Shielding Gases for Arc Welding” in this Volume.)

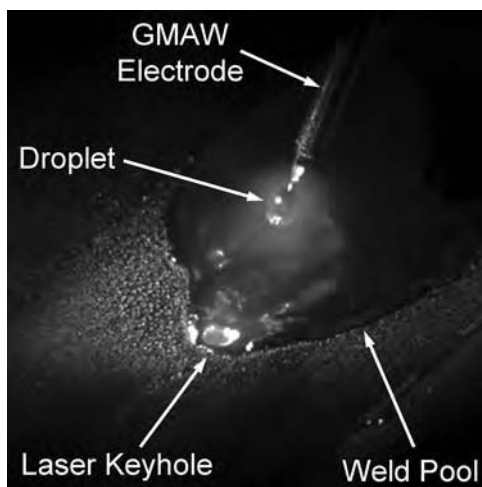


Fig. 2 In-process video image of penetration-mode hybrid laser arc welding on steel. GMAW, gas metal arc welding. Courtesy of Edison Welding Institute

Gas Metal Arc Welding Current, Voltage, and Polarity. Depending on the arc current, electrode diameter, electrode extension, and shielding gas composition used for the GMAW process, three general modes of metal transfer can be achieved: short-circuiting, globular, and spray transfer. Due to the fast travel speeds used in penetration-mode HLAW, spray transfer or pulsed GMAW are typically used. In pulsed mode, the GMAW power supply provides a controlled electrical output that pulses the welding current to detach individual droplets with each peak current pulse. Because of the advanced control provided by newer GMAW power supply technologies, most HLAW applications now use pulsed GMAW sources. However, spray transfer can be used to produce higher arc heat input for fast travel speed applications.

Arc voltage can be adjusted to increase or decrease the arc length. A longer arc length generally produces a wider melt width at the top surface of the weld. However, a long arc length can allow the deposited metal to wander from the weld centerline at fast travel speeds. A short arc length constricts the arc and limits weld pool width, reducing the wander of the deposited bead at high speeds.

The polarity of the GMAW system can be changed to affect the heat balance between the electrode and the work. However, the vast majority of GMAW and HLAW applications use direct current electrode positive (DCEP) polarity. The DCEP for GMAW provides good arc stability and low spatter generation. Direct current electrode negative and variable polarity (alternating current) have been tested with HLAW but have had limited commercial acceptance.

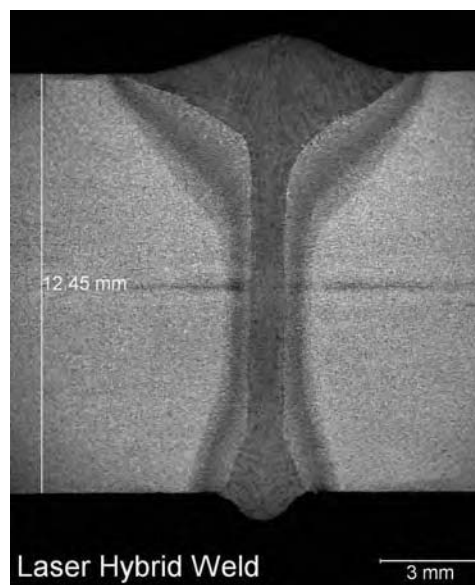


Fig. 3 Cross section of hybrid laser arc welding on a carbon steel square butt joint. Courtesy of Edison Welding Institute

Wire Feed Speed. The consumable GMAW electrode is fed into the welding process at a predetermined speed. This wire feed speed is selected to provide a specific volume of deposited metal for joint filling, gap bridging, or producing the required reinforcement at the cap and root of the weld. With conventional GMAW power supplies (constant voltage), wire feed speed and arc voltage are set while the power supply adjusts arc current and electrode melt rate to maintain a constant arc length. With modern pulsed GMAW power supplies (constant current), a waveform is designed for a specific wire feed speed. The pulsed waveform dictates the arc current that affects droplet frequency, droplet size, and arc voltage targets. If the wire feed speed is increased, the amplitude of the pulsed waveform is synergistically increased.

Joint Designs

Many joint designs can be welded with HLAW, including butt, groove, lap, flange, and fillet joints. Using the appropriate parameters, hybrid welding can be conducted in all welding positions. Hybrid laser arc welding can be performed on linear joints, circumferential joints, or two- and three-dimensional curvilinear joints. Figure 4 illustrates example joint designs for HLAW.

The primary difference in joint design between HLAW and conventional welding processes is that HLAW can provide both joint filling and deep penetration into the base metal. Typically in arc welding, a groove is prepared and then filled with molten metal deposited by the process. In autogenous laser welding, a square butt joint with no groove preparation is welded by penetrating through the joint thickness and fusing the two base metals together. The HLAW process is applicable to both methods of joint fusion.

A multipass V-groove joint that was previously welded with conventional GMAW could be redesigned as a single-pass HLAW joint.

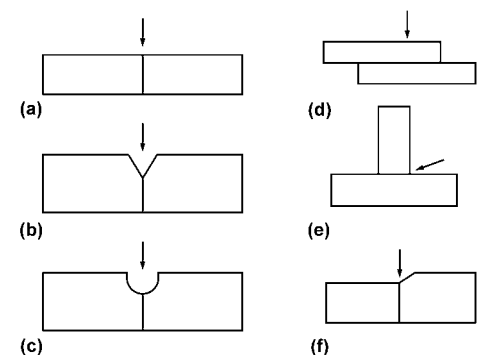


Fig. 4 Example joint designs for hybrid laser arc welding. (a) Square butt. (b) V-groove. (c) U-groove. (d) Lap weld. (e) Fillet weld. (f) Dissimilar-thickness joint

By using the high energy density of the laser process, HLAW can penetrate a square butt joint in a single pass while adding filler metal to produce positive weld reinforcement. To maximize productivity gains with HLAW, the weld joint should be designed to use the available laser power and maximize penetration or travel speed while maintaining weld quality.

Because the majority of the HLAW penetration is produced by the laser, HLAW is best suited as a root-pass process for thick-section multipass operations. After the root has been fused, subsequent passes with penetration-mode HLAW will only remelt and solidify the existing root weld. The only joint filling provided by the HLAW process is the deposition from the GMAW process. If the available laser power is unable to weld the entire joint thickness in a single pass, the joint should be designed to use a deep-penetration HLAW root pass, with subsequent fill passes using a different process (Fig. 4b, c).

The limitations on part geometries that can be welded with HLAW are based primarily on the limitations of the motion system and the access to the joint. For some applications, the combined size of the laser beam and GMAW torch can be too large to fit into tight corners or inside small-diameter pipes. Due to the required process separation length, turning sharp corners with the HLAW process should be avoided. To maintain consistent quality around a sharp corner, intersecting welds could overlap at the corner. Alternatively, the hybrid weld head can be designed to have a mechanized axis that rotates the GMAW torch about the laser beam.

In penetration-mode HLAW, small changes in the repeatability of the joint can have a large effect on weld quality. A variation in joint thickness, a mismatch in height between the two parts, a gap in the joint, or misalignment with the weld path can all affect the quality of the weld. To minimize the effects on weld quality, the consistency of the weld joint preparation should be strictly controlled.

Joint Gap. Fluctuations as little as 0.25 mm (0.010 in.) in the joint gap can require adjustments in weld parameters for deep-penetration HLAW. As the gap increases, maintaining weld stability with HLAW is challenging. Gap sizes above 1.0 mm (0.039 in.) are difficult to weld in a single pass for joints 6 mm (0.24 in.) or thicker. When welding on any gap, small variations in process separation or other welding parameters can have a large impact on weld quality.

Ideally, there should be no gap in the joint, because this is the easiest condition to prepare and keep consistent along the length of the joint. However, hybrid welding on a joint with no gap can cause poor mixing of the filler metal through the thickness of the joint (Ref 13). When a gap is present, more filler metal reaches the root of the joint, but higher wire feed speeds are required to fill the volume of the gap. Welding can be performed on a joint with a designed

gap; however, ensuring that the prefabricated gap remains constant may be difficult.

Joint Mismatch. In a butt or groove joint, mismatch is the measured distance between the top surfaces of the two parts being welded. This is also called vertical mismatch or high-low. Mismatch is common in the pipe-welding industry due to out-of-roundness or eccentricity between the two pipes to be welded. In penetration-mode HLAW for a full-penetration weld, the cap of the weld can generally tolerate a large amount of mismatch because of the deposited metal from the GMAW process. However, the weld bead is relatively small at the root, and the ability to bridge a mismatch is limited. Hybrid welding of joints with a mismatch greater than 2 mm (0.079 in.) is difficult for full-penetration welding of thick sections.

Joint Thickness. The total joint thickness that can be penetrated is determined by the laser power. For a zero-gap joint, the effective throat of a finished weld is approximately the sum of the laser penetration and the deposited thickness provided by the GMAW process. To maximize the effective throat that can be produced with HLAW, the weld joint is usually designed to have a root face or land thickness that is appropriate for the available laser power. The remaining thickness of the joint can be filled by the GMAW deposition.

Dissimilar joint thicknesses can be welded with the HLAW process (Fig. 4f). If the difference in thickness is small, 2 mm (0.079 in.) or less, a bevel preparation of the thicker section may not be necessary. Usually in dissimilar-thickness joints, the mismatch should be set at the cap of the weld rather than the root. At the cap, there is a larger weld pool and therefore more tolerance to mismatch geometries. At the root, there is a limited amount of molten metal to bridge the transition between the dissimilar thicknesses.

Even when welding similar thicknesses, the actual base-metal thicknesses can vary in production. A small increase in part thickness can require more laser power to maintain full penetration. The HLAW parameters and equipment must be designed to accommodate thickness variations that can be seen in production.

Equipment and Consumables

There are four major components of an HLAW system: the laser source, the GMAW source, the hybrid welding head, and the motion system. The consumables used for HLAW are the same as the consumables used in the individual laser and GMAW processes.

Laser Sources

Continuous-wave lasers are most often used for HLAW because they generate a constant laser power for the duration of the weld. The laser source is selected based on power and

wavelength. The output power capability is chosen based on the desired weld penetration for a given application. Travel speed, power density, base-metal absorptivity, and joint design can also affect the determination of laser power.

Multiple factors influence the selection of the laser wavelength. Table 2 lists the wavelengths of common high-power laser technologies that can be used for HLAW. Semiconductor diode lasers can also be used for HLAW; however, the output power and beam quality of diode lasers is currently not suitable for deep-penetration hybrid welding applications.

Carbon dioxide (CO₂) lasers produce a wavelength of 10.6 μm and must be transmitted to the work by reflective optics. Because CO₂ lasers are limited to reflective optic delivery, HLAW applications using CO₂ lasers are typically limited to linear welds on gantry-style motion equipment. Carbon dioxide lasers can have wall-plug efficiencies exceeding 10% and can have high output powers. Carbon dioxide lasers are typically on the order of 20 kW or less for welding applications but can be focused to small spot sizes to provide high power densities.

Solid-state lasers, including Nd:YAG, ytterbium-fiber, thin-disk, and diode lasers, produce wavelengths near 1 μm . The shorter wavelength allows solid-state lasers to be transmitted through flexible fiber optic cables to the work. Fiber optic delivery enables hybrid welding of complex contours and flexibility for welding multiple-part designs.

The Nd:YAG lasers are typically limited to 6 kW or less in output power. Due to the inherent characteristics of the technology, Nd:YAG lasers exhibit poor beam quality and therefore have limited power density. Lamp-pumped Nd:YAG lasers have wall-plug efficiencies (electrical-to-optical power efficiency) of less than 5%; however, diode-pumped models have better efficiency.

Fiber and disk lasers are also referred to as high-brightness lasers due to the excellent beam quality and high power densities they can produce. Both technologies can generate output powers above 20 kW and are excellent laser sources for HLAW. Both fiber and disk lasers are diode-pumped and have wall-plug efficiencies exceeding 25%. Fiber and disk lasers have become the most cost-effective high-power lasers in terms of price per watt and

Table 2 Wavelengths of various high-power laser technologies used for hybrid laser arc welding

Laser type	Wavelength, μm
CO ₂	10.6
Ytterbium fiber	1.070
Disk (ytterbium: yttrium-aluminum-garnet, or YAG)	1.030
Neodymium:YAG	1.064

maintenance costs. As the efficiency of pump diodes continues to increase, the overall efficiency of diode-pumped solid-state lasers will continue to increase.

Gas Metal Arc Welding Sources

Modern pulsed GMAW power supplies are typically used in most HLAW applications. Pulsed GMAW sources enable advanced control of arc stability, arc length, metal transfer, droplet size, droplet frequency, and spatter generation. Modern digital power supplies also enable intimate integration with the controllers of automated motion systems that are typically used for HLAW.

Due to the fast travel speeds used for HLAW, wire feed speeds and average current levels may be higher than typical GMAW applications. For this reason, the GMAW system should be capable of the maximum wire feed speed and current rating for the desired HLAW application. Because of the high average current used in HLAW, considerable heat is generated in the GMAW torch. In addition to the heat produced by the arc, the GMAW torch receives additional heat radiated by the laser process. To reduce damage from the heat generated during hybrid welding, the GMAW torch should be water cooled.

Push-type wire feeders are conventionally used for GMAW and HLAW. Push-pull wire feed systems that use drive rolls at the wire feeder and in the torch were conventionally used for soft electrode materials such as aluminum. Because push-pull feed systems offer increased control and consistency, they are being used more often in HLAW applications for both stiff and soft electrode types, including steel, stainless steel, aluminum, nickel, and titanium.

Hybrid Welding Head

The processing head for HLAW is a combination of laser-focusing optics and a GMAW torch.

Laser-Focusing Optics. The focusing optics should be selected to produce the desired spot size at the work. The optical assembly can consist of reflective or transmissive optics. In both cases, the lenses or mirrors are very sensitive to contamination. Dust, dirt, fingerprints, scratches, or other sources of contamination on the optical surfaces can cause a loss in transmitted laser power, an increase in the focused spot diameter, a change in power distribution, a shift in the focal position, or a combination of these effects. A transmissive cover window or debris shield is typically used to protect the optic assembly from contamination. A compressed air cross-jet, or air knife, is also used between the work and the optics to protect the cover window from weld spatter and fume.

In addition to spot size, the standoff distance of the focusing optic should be considered when choosing welding optics. If a longer focal

length focusing lens is selected, the expensive optic assembly will be farther from weld spatter. However, longer focusing optics generate a larger spot size. Larger spot sizes have lower power densities and produce less weld penetration or slower travel speeds. This trade-off must be managed to provide sufficient weld productivity while reducing the risk of damaging the expensive laser optics. Focal lengths of 200 to 300 mm (7.87 to 11.81 in.) are typical for HLAW.

Gas Metal Arc Welding Torch. The water-cooled GMAW torch should be capable of handling the appropriate current rating for the desired application. The contact tips, liner, and other consumables should be selected for the appropriate filler-metal alloy and wire diameter. If a small process separation (beam-to-wire distance) is used for HLAW, the GMAW nozzle may need to be modified so that the laser beam does not strike the nozzle. Alterations to the gas nozzle should be kept to a minimum so that the flow of the shielding gas is not significantly disrupted. If a large process separation is used, the GMAW gas nozzle does not need to be modified.

Because process separation, torch angle, electrode extension, and alignment of the two processes are critical, the method of mounting the GMAW torch with respect to the laser beam is critical. Off-the-shelf hybrid processing heads can be purchased that incorporate both the optics and the torch into one assembly. Custom hybrid welding heads can also be assembled by combining standard laser-focusing optics to a standard GMAW torch with a custom mounting bracket.

Whether custom-built or commercially purchased, the components of the hybrid welding head should have certain degrees of freedom. Based on the application, the GMAW torch angle and work angle can be fixed or variable relative to the beam. The torch should be able to move laterally to align with the beam along the weld joint, vertically to adjust the electrode extension relative to the beam focus, and horizontally to adjust the process separation from the beam axis. These adjustments can be manual or mechanized. The overall assembly should be rigid and capable of withstanding the travel speed, acceleration, and changes in position that may be used during processing.

Motion Systems

The motion systems that can be used for HLAW are dictated by the application. For linear welding, a linear beam or gantry system can be used. For complex geometries, a six-axis robot is generally used. In pipe-welding applications, the hybrid head could be mounted on a track system to traverse around the circumference of the pipe. The part or the hybrid welding head can be moved to achieve welding motion. In all cases, the dynamic accuracy and path repeatability of the motion system are significant variables. In particular, the standoff

distance of the hybrid welding head and alignment with the joint are critical for HLAW.

Hybrid Laser Arc Welding Consumables

Consumable Parts. The GMAW consumables include contact tips, gas nozzles, liner, guide tubes, and drive rolls. For different wire diameters, the contact tips, liner, guide tubes, and drive rolls should be changed. The contact tips should be changed periodically as the internal bore is eroded by the moving electrode. The internal bore of the contact tip is important because the wire must feed smoothly through the tube while making good electrical contact. As the bore of the contact tip wears away, poor electrical contact can result in erratic arc characteristics.

For welding with steel wire, a spiral steel liner is typically used to guide the wire through the torch cable. For soft wires such as aluminum, nylon or synthetic fluorine-containing resin liners are used. When welding with titanium wire, graphite liners are used to reduce contamination of the weld.

The primary consumables of the laser system are the cover windows that protect the focusing optic assembly from contamination and weld spatter. Other consumables depend on the type of laser source used for HLAW.

Filler-Metal Consumables. The chemical composition of the consumable GMAW electrode must be properly selected to achieve the desired properties in the hybrid weld metal. Of particular note with HLAW is that the heat input is typically lower than GMAW, and the cooling rate is much faster than conventional arc welding processes. This means that HLAW can significantly affect the solid-state transformations in the weld zone and that an acceptable electrode composition for GMAW applications may not always be acceptable for the fast cooling rate of the HLAW process, particularly in high-strength steels or other alloys with high hardenability.

For deep-penetration HLAW with little or no joint gap, the dilution of filler metal may not be homogeneous through the thickness of the joint. In some cases, weld-metal composition can be primarily filler metal near the cap of the weld and primarily base metal near the root. Knowledge of the heat input, cooling rate, and filler-metal dilution from the HLAW process and their effects on weld-metal microstructure is essential to producing high-quality HLAW welds.

Sources of Defects

Typical defects for HLAW are porosity, undercut, concavity, root humping (root bead instability), incomplete fusion, and incomplete penetration. Other defects can occur but are driven more by the application (joint design, alloy selection, travel speed, and cooling rate) than by the nature of the process.

Porosity. Assuming there is no source of contamination (oxidation, oil, foreign metals, weld

surface, joint interface, wire surface, shielding gas), porosity is generally attributed to the keyhole laser process used in penetration-mode HLAW. The keyhole is a column of metal vapor surrounded by the liquid weld metal. Turbulence in the keyhole can introduce gas pores into the molten weld. Aluminum and titanium are particularly susceptible to weld porosity from the HLAW process.

Partial-penetration HLAW occurs when welding in penetration mode but not fully penetrating through the joint thickness. Partial-penetration HLAW is highly susceptible to internal weld porosity due to instability at the root of the keyhole. Porosity caused by keyhole instability is typically seen in the bottom half of a partial-penetration HLAW cross section. To reduce the occurrence of porosity from keyhole instability, the weld can be redesigned to fully penetrate the joint thickness. Full-penetration welds are less likely to have porosity from keyhole instability. Increasing the spot diameter or modulating the laser power has been shown to reduce porosity from keyhole instability in partial-penetration laser welding.

Undercut and Concavity. Geometric defects such as undercut and concavity are typically caused by a gap in the joint that could not be filled by the deposited wire. Undercut at the toes of the weld surface can also occur due to the high travel speeds. In full-penetration welding, the molten weld can drop through the joint. This results in concavity or undercut at the top surface and excessive root reinforcement on the back surface of the weld.

Root Humping. In full-penetration HLAW of steel, improper welding parameters can result in irregularities in the profile of the root bead. This defect typically appears as a longitudinal humping profile at the weld root on the back side of the joint. This defect most often occurs in steel, but it has been seen in stainless steel, nickel, and titanium alloys as well. The physical phenomena that cause this defect are not fully understood; however, increasing the laser power reestablishes a stable full-penetration keyhole and eliminates the root-humping defect. Root-humping defects usually coincide with undercut or concavity defects at the weld cap.

Incomplete Fusion. Deep-penetration hybrid welds generally have very narrow weld profiles. Small deviations in joint alignment can cause the laser beam to miss the weld joint and result in an incomplete fusion defect. This can be a particularly troubling defect because the weld may appear to have complete fusion from a visual inspection of the top and bottom surfaces, but in the center of the thickness, the weld may not fuse the entire joint.

Incomplete Penetration. If there is a loss in laser power or an unexpected increase in the joint thickness, the hybrid weld may not fully penetrate the thickness, resulting in an incomplete-penetration defect. Loss in laser power or changes in the power distribution are usually the causes for incomplete penetration.

Contamination of the cover window or other optical surfaces can cause changes in laser power density at the work. The gas nozzle, air knife, or GMAW torch can clip the beam and reduce the laser power that reaches the work. If the process spacing has been reduced to zero, the deposited droplets from the GMAW process can impinge on the keyhole and decrease penetration depth.

Quality Control and Inspection

Hybrid laser arc welding is an automated process that requires strict controls on repeatability of the parts and of the welding system. To ensure the parts are repeatable, upstream processes should be addressed to accommodate the HLAW process. Improving upstream preparation of the parts and weld joints will only improve the productivity gains possible with HLAW.

Even with strict control on upstream processes, weld joint preparations are never perfect. To adjust for variations in joint fit-up, gap, and mismatch, real-time seam tracking and joint sensing should be implemented. With advanced control systems, the welding parameters and joint alignment can be adjusted on-the-fly to compensate for the variations in the joint. If a complex control system is not feasible, a path check could be conducted with a camera system coaxial to the laser beam to verify the joint alignment prior to welding.

To ensure consistent weld quality and penetration, periodic laser power measurements should be conducted. Scheduled preventative maintenance should be conducted on the GMAW and laser systems to ensure optimal working condition. Periodic inspection should also be conducted on the welded parts to ensure weld quality.

Inspection by destructive analysis could evaluate fusion profile, hardness, tensile strength, fatigue performance, or impact toughness of the hybrid weldment. Inspection by nondestructive evaluation (NDE) could search for centerline defects, incomplete fusion, porosity, solidification cracking, and incomplete penetration. The NDE methods typically used for HLAW are radiographic testing and ultrasonic testing.

Safety

The greatest safety concerns are from the laser welding equipment. Because high-power laser beams are invisible to the human eye, the hazards may not be readily apparent to inexperienced personnel. With exposed laser beams, personnel may be exposed and permanently injured before the existence of the hazard is even recognized. For this reason the American National Standards Institute specification ANSI Z136.1, "Safe Use of Lasers" (latest edition), requires that each facility using lasers designate an individual as the laser safety officer. This individual should be familiar with laser safety, ANSI Z136.1, and

potential hazards at the designated facility. Special precautions must also be taken to protect personnel from arc welding hazards.

Training. Employers of facilities using HLAW are responsible for providing training to all operators, engineers, technicians, maintenance, and service personnel. ANSI Z136.1 requires that training in the potential hazards and control measures be provided to all personnel involved in laser use. ANSI Z136.1 provides a model safety training program in Appendix D of the standard. Refer to the article "Safe Welding Practices" in this Volume and ANSI Z136.1, "Safe Use of Lasers," for more information on training.

Electrical Hazards. Both laser equipment and GMAW equipment employ high voltages and currents capable of lethal shock. Only qualified and authorized personnel should install and service equipment with the appropriate procedures, tools, and protective equipment. Refer to the article "Safe Welding Practices" in this Volume for more information on electrical hazards.

Eye Hazards. Eye injury is readily caused by laser beams. With laser beams operating in the visible or near-infrared spectrum, a 5 mW beam can inflict permanent retinal damage. Proper safety precautions must be taken to protect personnel from direct, scattered, reflected, and diffuse laser radiation. Depending on the laser wavelength employed, different safety measures and personal protective equipment are required. Consult ANSI Z136.1 for the appropriate safety measures for specific laser wavelengths.

The GMAW process produces intense visible and ultraviolet (UV) light. Appropriate protective equipment is required to protect personnel from this intense radiation generated by the electric arc. Eye protection is required for each of the welding processes used in HLAW to protect personnel from both laser and arc radiation. Refer to the article "Safe Welding Practices" in this Volume and ANSI Z136.1, "Safe Use of Lasers," for more information on eye hazards.

Skin Hazards. Skin exposure to the primary laser beam can result in severe burns and must be prevented by safety enclosures and operator training. There is no personal protective equipment rated to protect personnel from direct exposure to the primary beam. Enclosures should be designed to prevent operators or spectators from placing any body part near the beam path. Unless a sufficient enclosure is constructed, exposure to reflected and scattered laser light is possible. Intense UV light produced by the GMAW process can cause skin damage. Spatter and hot metal parts are burn hazards for HLAW personnel. Refer to the article "Safe Welding Practices" in this Volume for more information on skin hazards.

Fume Hazards. Both the laser and GMAW processes produce welding fumes. Fume hazards are dependent on base-metal composition, filler-metal composition, shielding gas composition, and welding parameters. Welders, operators, spectators, and other personnel in the welding area must be protected from overexposure to

fumes and gases produced during welding. Refer to the article "Safe Welding Practices" in this Volume for more information on fume hazards for various welding applications.

REFERENCES

1. W.M. Steen and M. Eboo, Arc Augmented Laser Welding, *Met. Constr.*, Vol 11, July 1979, p 332–335
2. H. Staufer, Laser Hybrid Welding in the Automotive Industry, *Weld. J.*, Vol 86, Oct 2007, p 36–40
3. D. Petring, C. Fuhrmann, N. Wolf, and R. Poprawe, Investigations and Applications of Laser-Arc Hybrid Welding from Thin Sheets up to Heavy Section Components, *Proceedings ICALEO 2003: Processes for Laser Hybrid Welding*, Oct 2003 (Jacksonville, FL), Laser Institute of America, 2003, p 1–10
4. F. Vollertsen and S. Grunenwald, Defects and Process Tolerances in Welding of Thick Plates, *Proceedings ICALEO 2008: Laser Materials Processing Conference*, Oct 2008 (Temecula, CA), Laser Institute of America, 2008, p 489–497
5. D. Howse, R. Scudamore, and G. Booth, The Evolution of Yb Fibre Laser/MAG Hybrid Processing for Welding of Pipelines, *Proceedings 15th International Offshore and Polar Engineering Conference*, June 2005 (Seoul, Korea), The International Society of Offshore and Polar Engineers, 2005, p 90–95
6. J. Defalco, Practical Applications for Hybrid Laser Welding, *Weld. J.*, Vol 86, Oct 2007, p 47–51
7. J. Kristensen, Thick Plate CO₂-Laser/MAG Hybrid Welding of Steels, *IW Doc. IV-932-07, IAW Annual Meeting 2007*, p 1–13
8. S. Kelly, S. Brown, J. Tressler, R. Martukanitz, and M. Ludwig, Using Hybrid Laser-Arc Welding to Reduce Distortion in Ship Panels, *Weld. J.*, Vol 88, March 2009, p 32–36
9. R. Moller and S. Koczera, Shipyard Uses Laser-GMAW Hybrid Welding to Achieve One-Sided Welding, *Fabricator*, Vol 33, Nov 2003, p 49
10. U. Jasnau and A. Sumpf, Laser Hybrid Welding with High Power Fiber Laser—New Chances for Use of Laser Technology, *Hitsaus. Tekniikka*, May 2006, p 57–61
11. B.W. Shinn, D.F. Farson, and P.E. Denney, Control of Weld Bead Shape with the Hybrid Welding Process, *IW Doc. IV-879-05, IAW Annual Meeting 2005*, p 1–10
12. H.W. Choi, D.F. Farson, and M.H. Cho, Using a Hybrid Laser Plus GMAW Process for Controlling the Bead Humping Defect, *Weld. J.*, Vol 85, Aug 2006, p 174s–179s
13. A. Fellman and A. Salminen, Study of the Phenomena of Fiber Laser-MAG Hybrid Welding, *Proceedings ICALEO 2007: Laser Materials Processing Conference*, Oct 2007 (Orlando, FL), Laser Institute of America, 2007, p 871–880

SELECTED REFERENCES

- C. Bagger and F. Olsen, Review of Laser Hybrid Welding, *J. Laser Appl.*, Vol 17 (No. 1), Feb 2005, p 2–14
- D. Rasmussen and L. Dubourg, Hybrid Laser-GMAW Welding of Aluminum Alloys: A Review, *Proceedings Seventh International Conference on Trends in Welding Research*, May 2005 (Pine Mountain, GA), ASM International, 2006, p 133–142
- "Safe Use of Lasers," ANSI Z136.1, American National Standards Institute

Flux Cored Arc Welding*

Revised by Michael T. Merlo, RevWires LLC, a Heico Wire Group Company

FLUX CORED ARC WELDING (FCAW) was introduced in 1957 to 1958 by two different manufacturers in the United States, and it represented the first improvement in continuous welding over the solid wire gas metal arc welding (GMAW). The same equipment and process variables employed in GMAW were used by the FCAW process. A unique engineering breakthrough in this process was the formation of a carbon steel tube around fluxing and alloying powders by filling the tube in the middle of its construction, closing it, and drawing it to a predetermined size.

In the early years, flux cored wires were manufactured with diameters of 3, 2.8, and 2.4 mm ($\frac{1}{8}$, $\frac{7}{64}$, $\frac{3}{32}$ in.) and were used for flat and horizontal welding positions only. There were two varieties of products made: one requiring gas shielding and one requiring no external gas shielding. The latter used denitrification to neutralize the effect of air intrusion (the "nitrogen boil"), and the former used the columnar flow of shielding gas to minimize air intrusion into the weld pool. In the late 1960s, smaller sizes were introduced, such as 2, 1.5, and 1.1 mm ($\frac{5}{64}$, $\frac{1}{16}$, and 0.045 in.) diameters. In the early 1970s, formulations were developed to allow welding in all positions, such as vertical up and overhead. This allowed flux cored wires to be used in applications formerly limited to covered electrodes and the shielded metal arc welding (SMAW) process.

Common shielding gases employed were carbon dioxide (CO_2) and a blend of 75%Ar-25% CO_2 . As manufacturing processes improved, both gas-shielded and self-shielded wires were introduced in diameters as small as 0.75 and 0.90 mm (0.030 and 0.035 in.). The gas-shielded products evolved to where formulations using gas blends of 85 to 90% Ar/balance CO_2 were designed and used in common applications.

Process Features

Flux cored welding electrodes are supplied in two distinct product types:

- Gas-shielded flux cored arc welding (FCAW-G) process
- Self-shielded flux cored arc welding (FCAW-S) process

The gas-shielded flux cored process (Fig. 1) uses an externally applied gas to assist in shielding the arc from oxygen and nitrogen in the atmosphere. The most deleterious effect of air intrusion is the nitrogen boil, wherein the insolubility of nitrogen in liquid steel causes it to boil out and create gross surface porosity. The columnar flow of shielding gas, typically CO_2 or blends of argon and CO_2 , protects the molten weld pool from atmosphere in the same manner as in the GMAW process. Additional protection from the intrusion of air is provided

by the fluxing and slag-forming powders within the core ingredients, which form a molten slag cover over the weld pool.

The use of CO_2 shielding gas leads to what is known as an active gas shielding (i.e., a gas that reacts with the elements in the molten puddle to form compounds). The effect of CO_2 shielding on the carbon content of the molten puddle is very unique. It can be carburizing or decarburizing. If the initial carbon content of the weld metal is low ($<0.05\%$), the CO_2 will carburize the molten puddle. If the initial carbon content of the weld metal is high ($>0.10\%$), the molten puddle will show a tendency to lose carbon. The use of CO_2 also promotes deeper weld bead penetration and a more fluid weld puddle from the exothermic reactions. The CO_2 disassociates

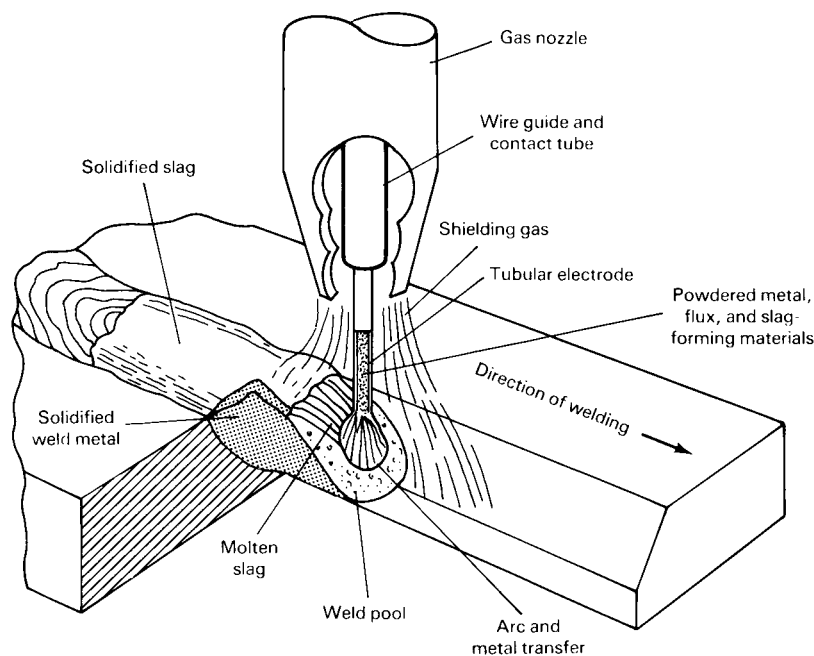


Fig. 1 Gas-shielded flux cored arc welding. Source: Ref 1

* Revised from D.W. Meyer, Flux-Cored Arc Welding, *Welding, Brazing and Soldering*, Vol 6, ASM Handbook, ASM International, 1993, p 886-889

($2\text{CO}_2 \rightarrow 2\text{Co} + \text{O}_2$) in the welding arc, and the O_2 reacts with the added deoxidizing elements within the tubular volume of the wire (as well as the iron in the base metal in steels).

Additives to the core ingredients can be used to stabilize the transfer, generate smaller droplets, and promote less spatter around the weldment. The use of argon with CO_2 , typically 75 to 80% Ar, provides an arc plasma with less heat of reaction (because of much less CO_2) and a lower-penetration weld bead. Argon (due to its higher energy of ionization) is more of a cooling gas than CO_2 ; hence, the weld pool solidifies much more quickly. The higher ionization promoted by argon stabilizes the welding arc, resulting in smaller droplet transfer and lower spatter levels. These blends also promote lower fume generation rates, because the addition of argon lowers the available oxygen from the CO_2 and reduces the amount of oxide formation, a key component of welding fume particles.

Argon blends are preferred for all-position welding, because the cooling effect of the argon promotes faster freezing of the weld pool; that, in turn, facilitates welding in the vertical up and overhead positions. Simultaneously, the fluxing and slag-forming agents in the core can be adjusted to assist in the freezing of the molten slag, further facilitating welding in all positions. Alloying agents, such as manganese, silicon, magnesium, and titanium, are added to the core ingredients for purposes of grain refinement, oxygen reduction, and strengthening of the weld deposit. Other alloys, such as nickel, chromium, molybdenum, and copper, can be added to produce higher-strength, low-alloy weld metal, which possesses improved strength and toughness properties over standard carbon steel weld metal.

Self-Shielded Flux Cored Arc Welding. In the FCAW-S process, alloying, slag-forming, and fluxing ingredients in the core protect the weld pool from atmospheric contamination, that is, the nitrogen boil. Because both oxygen and nitrogen can harm the weld pool by oxide contamination and porosity, respectively, different means of neutralization are employed. Combinations of lithium, magnesium, and aluminum, in elemental and chemical compound forms, either limit nitrogen solubility or combine with it to form nitrides, preventing the nitrogen boil. Elements such as manganese, magnesium, aluminum, and titanium are used to deoxidize the weld pool, combining with oxygen to form oxides that help form a protective slag covering the weld pool.

It should be noted that oxides of aluminum, along with nitrides of aluminum and magnesium, can be quite detrimental to the toughness of the resultant weld deposit. Several manufacturers have developed formulation technology that suppresses nitrogen solubility, reducing the residual level of aluminum oxides in the weld metal. These products have quite high levels of Charpy V-notch (CVN) impact toughness at subzero temperatures. There are also newer formulation technologies that provide all-position welding capability, in addition to

the high-CVN impact values. Unlike products from years ago that produced large droplet, or globular, transfer during welding, these newer products exhibit small droplet, spraylike transfer, facilitating all-position welding with lower spatter emission.

Advantages and Limitations. There are many advantages to the FCAW process. Both FCAW-G and FCAW-S provide the high productivity of continuous welding combined with the benefits afforded by the presence of slag-forming, fluxing, scavenging, and alloying agents. Advantages include but are not limited to:

- Higher deposition rates in all-position welding than SMAW or GMAW
- Less training and operator skill required than for GMAW or SMAW
- Simpler and more adaptable, in terms of welding equipment and positions, than submerged arc welding
- Deeper penetration than with SMAW; better sidewall penetration than GMAW
- More tolerant of rust, mill scale, and other oxide or hydrocarbon contaminants than GMAW

The specific advantage of high productivity with the FCAW process is the dominant basis for its use. However, the process does present some limitations that must be dealt with as a result of its high productivity. Some relative disadvantages are:

- Slag must be removed from the weld and properly disposed of.
- Fume generation rates, directly proportional to deposition rates, are higher than the lower-deposition-rate processes (GMAW and SMAW); fume extraction may be required.
- The process is not as portable as SMAW; shielding gas may be required, and suitcase feeders with a spool of wire may weigh up to 23 kg (50 lb).

Applications

Flux cored arc welding enjoys widespread use in many industries. Since its inception in 1957, the FCAW process has been adopted by virtually every industry seeking productivity and quality improvements in the welding operation. Both the FCAW-G and FCAW-S processes are used to fabricate structures from carbon and low-alloy steels. Both process variants are used for shop fabrication, but the FCAW-S process is preferred for field use. The acceptability of the FCAW process for structural use is illustrated by the fact that prequalified joints are included in the structural welding code of the American Welding Society (AWS).

Gas-shielded flux cored electrodes are commonly used to weld carbon, low-alloy steel, and stainless steels in the construction of

pressure vessels and piping for the chemical processing, petroleum refining, and power generation industries. In addition, flux cored electrodes are used to weld some nickel-base alloys.

Flux cored electrodes are also used in the automotive and heavy-equipment industries in the fabrication of frame members, axle housings, wheel rims, suspension components, and other parts. Small-diameter flux cored electrodes are used for automotive body repair.

Gas-shielded flux cored wires are used in the fabrication of mining machinery, off-road equipment, earth-moving machinery, pipe and superstructures for offshore drilling platforms, structural steel, water towers, oil storage tanks, military and commercial ships, rail cars, automobile components, hot water heaters, truck frames, wind towers, machine tools, automobile and truck wheels/rims, barges, farm machinery, and locomotives.

Self-shielded flux cored wires are used in many of the same applications but are also used for field erection of oil and gas pipelines, fabrication of high-rise structures, and welding of automobile body components. Because self-shielded electrodes have less penetration than the gas-shielded variety, they lend themselves quite readily to welding with minimal burn-through on lighter-gage steels, such as automotive body sections, various sheet metal applications, and certain structural joints.

Carbon steel flux cored electrodes are commonly used to weld grades of steel such as ASTM A516, A517, and A572, while the low-alloy types are used for low-temperature steels, such as ASTM A302 chromium-molybdenum steels, and high-strength steels, such as ASTM A514. Use of self-shielded electrodes has been dominant in field applications, such as pipeline construction and high-rise building construction, because gas-shielded electrodes require a shielding gas source near the welding arc. The use of gas cylinders in these instances has proved unwieldy, hence making self-shielded products the favorite choice.

Equipment

The FCAW process uses semiautomatic, mechanized, and fully automatic welding systems. The basic equipment includes a power supply, wire feed system, and welding gun. The required auxiliary equipment, such as shielding gas, depends on the process variant used and the degree of automation. The use of fume-removal equipment may be considered for welding applications indoors or in enclosed areas, as deemed necessary by safety and health professionals. Such systems should be designed for the specific application and area involved.

Typical semiautomatic equipment is shown in Fig. 2. The equipment used in the FCAW-G process is typically identical to GMAW equipment.

The recommended power supply for the semiautomatic FCAW process is a constant-voltage

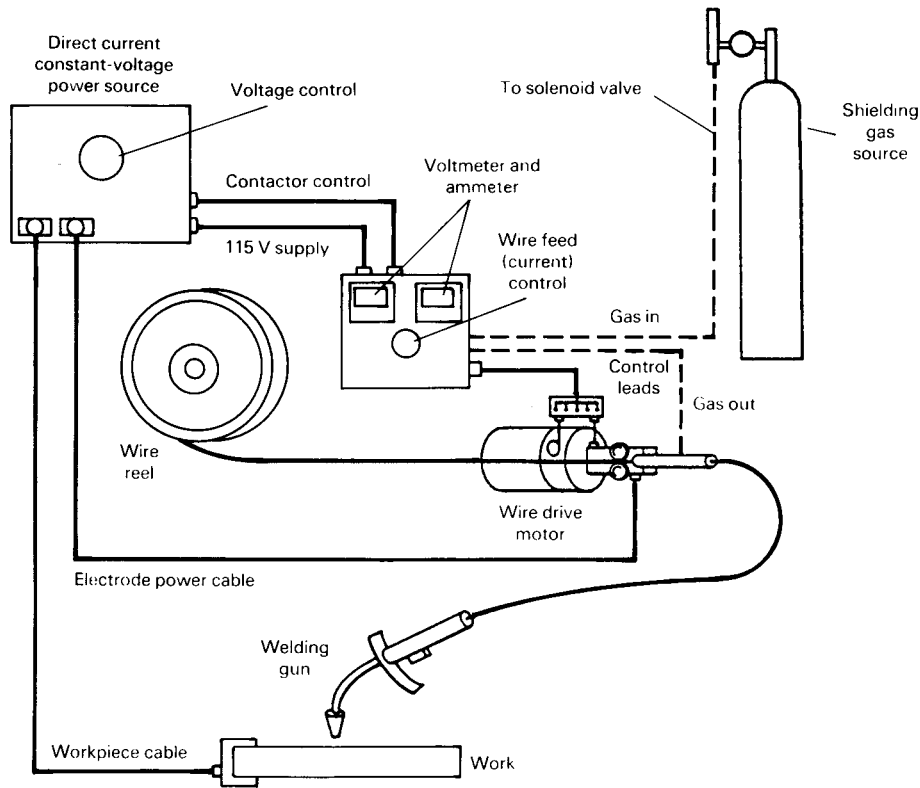


Fig. 2 Semiautomatic flux cored arc welding equipment. Source: Ref 1

direct current machine. Most power supplies used for semiautomatic FCAW have output ratings of 600 A or less. A power supply rated at 60% or more duty cycle is the best choice for most industrial applications, whereas a duty-cycle rating as low as 20% may be sufficient for maintenance and repair applications.

Constant-current power supplies are used in certain situations, such as field welding applications, where portable constant-current SMAW power supplies are readily available. The addition of a contactor and a voltage-sensing wire feeder makes this an adequate welding system. However, such a system is only recommended when the use of a constant-voltage system is not feasible, because constant-current systems produce an inherently less-stable welding arc than constant-voltage systems.

Wire feeders for constant-voltage FCAW systems are generally simple devices that provide a constant wire feed speed. The power supply provides sufficient current to maintain an arc at the voltage that is preset at the power supply. A change in wire feed speed results in a change in the welding current.

In a constant-current system, the wire feeder is somewhat more complex. The welding current is preset at the power supply. The wire feeder has a voltage-sensing feedback loop that allows it to adjust the wire feed speed to maintain the desired welding voltage. The wire feeder generally contains systems to close the contactor and open

the shielding gas solenoid valve (FCAW-G process only) when welding is started.

Because flux cored wires are easily deformed by excessive feed roll pressure, knurled feed rolls are generally used in the FCAW process. Some wire feeders use a single drive roll paired with an undriven pressure roll. Others have one or two pairs of drive rolls. It is generally believed that systems having two pairs of drive rolls require the least drive roll pressure to provide dependable feeding. Excessive pressure with smooth rolls can crush the wire to an oval shape, causing it to jam in the liner or the contact tip. Excessive pressure with knurled rolls can wear notches into the wire surface that carve a trough into the contact tip, causing feeding and electrical burnback problems.

Both air-cooled and water-cooled welding guns are used in the semiautomatic FCAW process. Air-cooled guns are generally preferred, because they are simpler to maintain, lighter in weight, and less bulky. Water-cooled guns may be required when welding currents over 500 A are used, especially when the shielding gas is rich in argon, because argon arcs radiate more heat to the gas cup on the gun. As a rule of thumb, the use of argon blends will typically reduce the current-carrying capacity of a gun by 50%, rendering a 400 A gun useful at a maximum of 200 A.

Air-cooled guns designed for gas-shielded welding should not be used for self-shielded

welding, because the gun depends on the flow of shielding gas for proper cooling. Although curved-neck guns are the most common, straight guns are used to a limited extent.

A trigger switch on the welding gun is closed to initiate wire feeding, welding current flow, and shielding gas flow. The electrode is delivered from the wire feeder to the gun through a flexible conduit. Standard conduit lengths are 3, 3.7, 4.6, and 7.7 m (10, 12, 15, and 25 ft). Other lengths may also be available.

Mechanized and automatic FCAW equipment is not substantially different from that used in the semiautomatic FCAW process. The power supply should be rated for 100% duty cycle. Power supplies capable of outputs up to 1000 A may be required for some applications. Constant-current systems are very seldom used for mechanized and automatic welding.

The wire feed system is separated into a drive motor assembly and a welding control device, the latter of which often has a system to automatically start the travel mechanism when wire feed, current flow, and shielding gas flow are initiated. The welding control device is often equipped with a voltmeter and ammeter, as well.

The welding gun in mechanized and automatic systems is often mounted directly to the drive motor assembly, eliminating the need for a conduit. The gun is usually straight, but curved-neck guns are also used. Both water- and air-cooled guns are used, depending on the welding current level and shielding gas.

Most of the commonly available air-cooled guns can be used at levels up to 500 A with CO₂ shielding gas. When argon-rich shielding gas is used, the same gun may only be suitable for use at levels up to 300 A. Water-cooled guns are generally used at higher current levels.

Various travel mechanisms are used, depending on the applications. These mechanisms include side-beam carriages, tractor-type carriages, and robots.

Fume-Removal Equipment. In many cases, the amount of fumes generated by the FCAW process is sufficient to require fume-removal equipment. Although such equipment can be as simple as exhaust fans in the shop roof, additional local fume collection is often necessary. These systems can be either collection hoods (located above the welding gun) or fume-extractor guns. These guns are more efficient at collecting fumes but are heavier and more bulky than standard welding guns. To be effective, fume-collection hoods must be repositioned each time the welding location is moved.

Base Metals

Carbon and Low-Alloy Steels. Most carbon and low-alloy steels can be welded by the FCAW process if suitable electrodes are available and if the steels can accommodate the process. Steels for which electrodes are available include the following.

Electrode Diameters

Flux cored electrodes are produced in diameters ranging from 0.030 to 1/8 in. (0.8 to 3.2 mm). All-position electrodes are usually available in diameters of:

- 0.030 in. (0.8 mm)
- 0.035 in. (0.9 mm)
- 0.045 in. (1.2 mm)
- 0.052 in. (1.4 mm)
- 1/16 in. (1.6 mm)

Electrodes for flat and horizontal welding are usually available in diameters of:

- 1/16 in. (1.6 mm)
- 5/64 in. (2.0 mm)
- 3/32 in. (2.4 mm)
- 7/64 in. (2.8 mm)
- 1/8 in. (3.2 mm)

Other diameters are supplied through special purchasing agreements between end users and the manufacturers. The 0.030 and 0.035 in. (0.8 and 0.9 mm) diameters are typically made in the self-shielded versions, with gas-shielded, all-position, flux cored electrodes commonly marketed in the 0.045, 0.052, and 1/16 in. (1.2, 1.4, and 1.6 mm) diameters. These diameters lend themselves quite readily to all-position welding applications.

Electrode Classification

Carbon and Low-Alloy Steel Electrodes. Carbon steel flux cored electrodes are classified by AWS A5.20, "Specification for Carbon Steel Electrodes for Flux Cored Arc Welding." The layout of this classification system is defined

in Fig. 4; an "X" indicates a position where a designator would be. For example, the designator indicating minimum tensile strength can be a 6, to denote 60 ksi (415 MPa), or a 7, to denote 70 ksi (480 MPa). The assignment of the final designator depends on the shielding requirements and features of the electrode, as well as the recommended welding polarity. These are described in Table 2. The designations EXXT-G and EXXT-GS are designed to allow the classification of electrodes that are not covered by any of the other classifications. There are also optional supplemental designators, allowing the addition of a "J" for lowering the temperature of CVN testing requirements by 11 °C (20 °F) and for adding the diffusible hydrogen designator, which indicates the diffusible hydrogen level that the electrode meets, such as H2, H4, H8, and H16 (representing 2.0,

4.0, 8.0, and 16.0 mL of hydrogen per 100 g of weld metal).

Low-alloy steel electrodes are classified under AWS A5.29, "Specification for Low Alloy Steel Electrodes for Flux Cored Arc Welding." This specification uses a classification system very similar to that used in specification AWS A5.20, except that a chemical composition designator is added to the designation. An electrode classified according to this specification will have the form EXXTX-X. All of the positions before the dash have the same meaning as those in specification AWS A5.20. The position behind the dash is the chemical composition designator, which consists of a letter and a number. The same optional supplemental designators are used in AWS A5.29 as in A5.20. Therefore, it is possible to have a classification that looks like

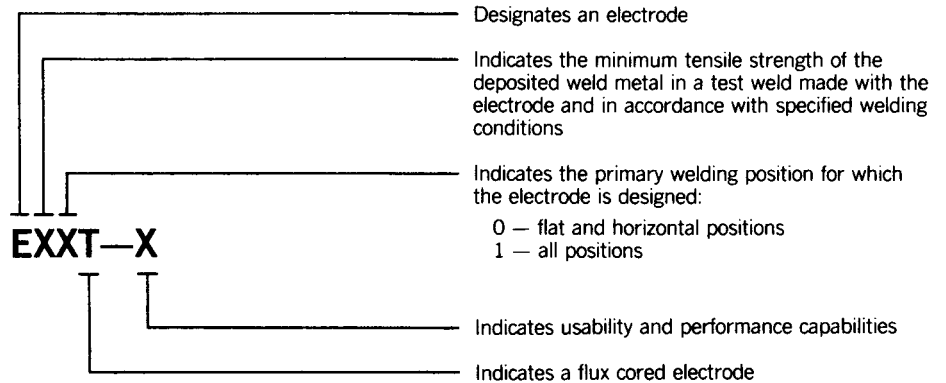


Fig. 4 Classification system for carbon steel flux cored electrodes. The letter "X" as used in this figure and in electrode classification designations in AWS specification A5.20-79 substitutes for specific designations indicated by this figure. Source: Ref 3

Table 2 Usability type designators for flux cored electrodes

Type(a)(b)	Shielding(c)	Single or multipass(d)	Transfer	Impact toughness requirement	Polarity(e)	Special characteristics
T-1	Gas	Multipass	Spraylike	20 ft · lbf at 0 °F (27 J at -18 °C)	DCEP	Low spatter, full slag coverage
T-2	Gas	Single	Spraylike	No requirement	DCEP	Low spatter, full slag coverage, high deoxidizers
T-3	Self	Single	Spraylike	No requirement	DCEP	High speed
T-4	Self	Multipass	Globular	No requirement	DCEP	High deposition, low penetration, crack resistant
T-5	Gas	Multipass	Globular	20 ft · lbf at -20 °F (27 J at -30 °C)	DCEP(f)	Improved toughness, crack resistant, thin slag
T-6	Self	Multipass	Spraylike	20 ft · lbf at -20 °F (27 J at -30 °C)	DCEP	Improved toughness, deep penetration
T-7	Self	Multipass	Globular	No requirement	DCEN	Crack resistant, good slag removal
T-8	Self	Multipass	Globular	20 ft · lbf at -20 °F (27 J at -30 °C)	DCEN	Improved toughness, crack resistant
T-9	Gas	Multipass	Spraylike	20 ft · lbf at -20 °F (27 J at -30 °C)	DCEP	Toughness requirements are at -20 instead of 0 °F (-30 instead of -18 °C).
T-10	Self	Single	Globular	No requirement	DCEN	High speed
T-11	Self	Multipass	Spraylike	No requirement	DCEN	General purpose
T-12	Gas	Multipass	Spraylike	20 ft · lbf at -20 °F (27 J at -30 °C)	DCEP	1.60 max Mn to meet ASME, enhanced toughness
T-13	Self	Multipass	Globular	No requirement	DCEN	Designed for aluminized and galvanized coated steels
T-14	Self	Multipass	Globular	No requirement	DCEN	Designed for thin-gage galvanized steels
T-G	Not specified	Multipass	Not specified	No requirement	Not specified	Not specified
T-GS	Not specified	Single	Not specified	No requirement	Not specified	Not specified

(a) A "C" designator is added when the electrode is designed for CO₂ shielding and an "M" designator when designed for Ar-CO₂ blends. (b) Addition of the "J" designator requires Charpy V-notch impact values to meet 20 ft · lbf (27 J) at -40 °F (-40 °C). (c) Gas-shielded electrodes are classified using CO₂ shielding; however, Ar-CO₂ mixtures are commonly used in practice. (d) Multipass electrodes are suitable for single-pass or multipass welding; single-pass electrodes are suitable for single-pass welding only. (e) DCEP, direct current electrode positive; DCEN, direct current electrode negative. (f) T-5 electrodes are classified using DCEP; however, they are sometimes used with DCEN in practice. Source: Ref 3

EXXTX-X J HX. The letter “X” that follows “EXXTX” denotes the alloy type of the electrode being classified, as follows:

Designator	Alloy type
A	Carbon-molybdenum steel
B	Chromium-molybdenum steel
Ni	Nickel steel
D	Manganese-molybdenum steel
W	Weathering steel
K	Other low-alloy steels
G	Not specified

Specification AWS A5.29 classifies only the EXXT1-X, EXXT4-X, EXXT5-X, and EXXT8-X electrode types, and the usability designator has the name meaning as that in specification A5.20. Minimum tensile strengths of up to 830 MPa (120 ksi) are included in specification AWS A5.29. Impact toughness requirements are based on the strength, usability, and chemical composition requirements of the electrode.

Stainless steel electrodes are classified under AWS A5.22, “Specification for Flux Cored Corrosion Resisting Chromium and Chromium-Nickel Steel Electrodes.” Classifications to this specification have the form EXXTX-X. The first three positions are the chemical composition designator, which corresponds to the American Iron and Steel Institute (AISI) designations (such as 308, 316, and 410) of steels having a similar composition. The final position is the shielding-type designator:

- T1 types are designed for use with CO₂.
- T-2 types are designed for use with Ar-2O₂ shielding gas.
- T-3 types are self-shielded.
- T-4 types are for use with 75 to 80% Ar/balance CO₂.

Also, a T-G type is included for electrodes that are not covered by the other shielding-type designators.

Nickel-Base Electrodes. A specification for nickel-base flux cored electrodes has been

published, AWS A5.34. Now that these products have their own classification document, flux cored nickel-base electrodes have found their way into many applications, such as cladding vessels for power generation, welding dissimilar metals on offshore platform components, and joining nickel-base materials to themselves on scrubbers and other highly corrosive weldments.

REFERENCES

1. *Welding Handbook*, 9th ed., Vol 2, American Welding Society, 2001
2. C.E. Jackson, “Fluxes and Slags in Welding,” WRC Bulletin 190, Welding Research Council
3. “Specification for Carbon Steel Electrodes for Flux Cored Arc Welding,” AWS A5.20-79, American Welding Society

Submerged Arc Welding

Lee E. Allgood, The Lincoln Electric Company

SUBMERGED ARC WELDING (SAW) is an arc welding process in which the arc is concealed beneath and shielded by a blanket of granular fusible material called flux that is placed over the joint area ahead of the arc. Filler metal is obtained primarily from an electrode wire that is continuously fed through the blanket of flux into the arc and pool of molten flux.

The distinguishing feature of submerged arc welding is the granular material (flux) that covers the weld area and prevents arc radiation, sparks, spatter, and fumes from escaping. The flux is of major importance in achieving the high deposition rates and high-quality weld deposit characteristics. In addition to shielding the arc from view, the flux provides a slag that protects the weld metal as it cools. The slag may also deoxidize and refine the weld metal, insulate the weld to reduce the cooling rate, and help to shape the weld contour. Figure 1 shows a schematic diagram of a typical submerged arc weld.

Principles of Operation

During welding, the heat of the arc melts some of the flux along with the tip of the continuously-fed electrode, as illustrated in Fig. 2. The tip of the electrode and the welding zone are surrounded and shielded by molten flux covered by a layer of unfused flux. The electrode is automatically held a short distance above the workpiece, with an arc between the electrode and the workpiece. As the electrode progresses along the joint, the lighter molten flux rises above the molten metal in the form of a slag. The slag then freezes over the newly solidified weld metal, continuing to protect the metal from possible contamination by nitrogen and oxygen while at elevated temperatures. After cooling and removing any unfused flux for reuse, the solidified slag may be easily removed from the weld.

Automatic welding generally uses electrodes ranging in diameter from 2.4 through 4.8 mm (3/32 through 3/16 in.), with 4 mm (5/32 in.) being perhaps the most commonly used size. Semiautomatic welding is limited in size to maintain flexibility of the cable through which the electrode is fed. The normal diameter for semiautomatic welding is between 1.6 and 2.4 mm (1/16 and 3/32 in.) with 2.0 mm (0.78 in.) being the most commonly used.

Advantages of SAW include:

- The process virtually eliminates weld spatter, thus simplifying weld cleaning.
- There is little or no arc radiation, eliminating the need for the operator to use a welder's helmet. It also eliminates surrounding-area weld flash, hence the need for protective screening.

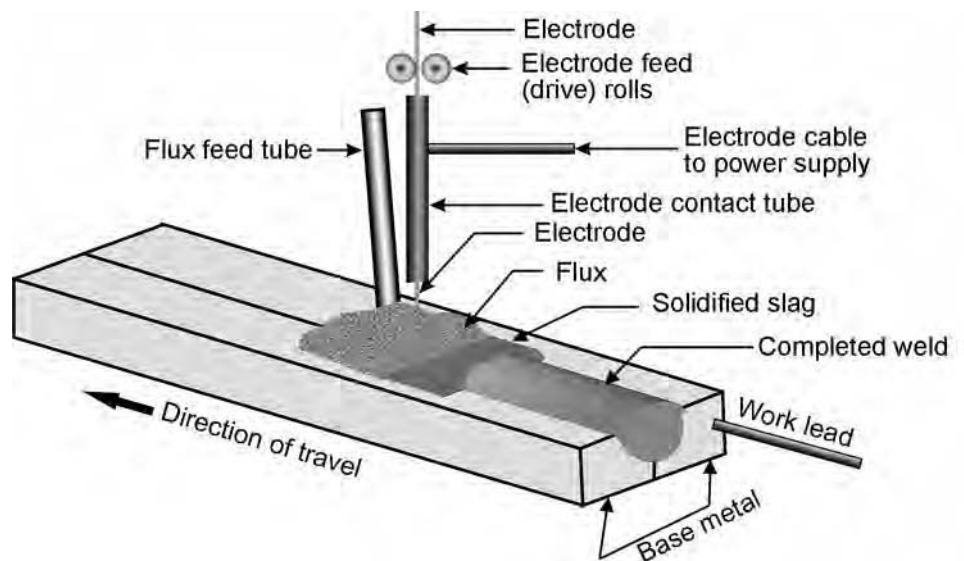


Fig. 1 Schematic of a typical submerged arc weld

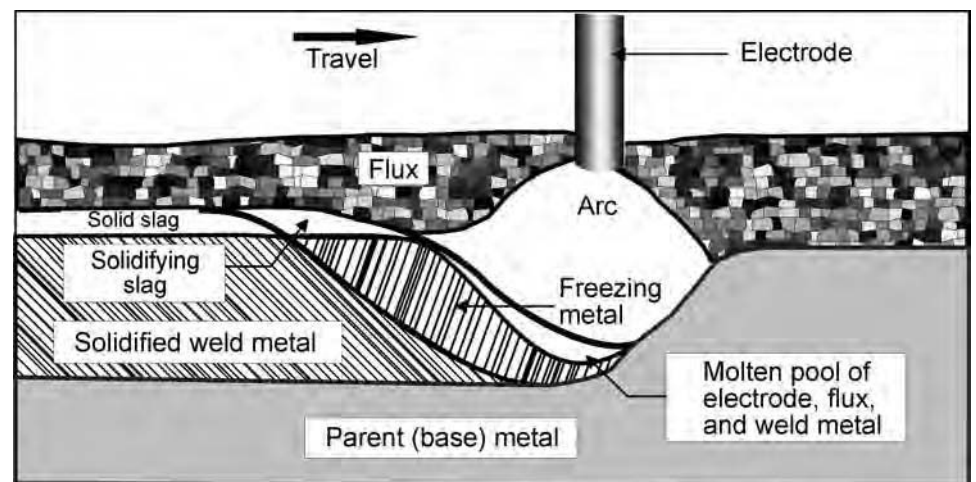


Fig. 2 Submerged arc weld pool schematic

- Submerged arc welding significantly reduces fume generation. In comparison to open-arc processes, virtually no fume is generated.
- The flux acts as a scavenger and deoxidizer to remove contaminants such as oxygen, nitrogen, and sulfur from the molten weld pool, thus helping to produce very clean weld deposits.
- Deposits that are low in hydrogen are readily achievable.
- Very high deposition rates are possible, thus significantly increasing welding speeds and reducing total arc times.
- High current density produces high arc penetration, allowing for reduced edge preparation. Figure 3 is a macrophotograph of a submerged arc weld produced with two plates that were square butted together with no edge bevel.
- Submerged arc welding is readily adapted to semiautomatic, machine automated, and fully automatic modes of operation.
- Multiple electrodes may be used in the same weld pool resulting in deposit rates unattainable by any other arc welding process.

Limitations of SAW include:

- Most welding is performed in the 1F, 2F, 1G, and to a limited extent, the 2G positions (Fig. 4, Ref 1).
- Slag must be removed from each pass (layer) in weld joints involving multiple weld passes, although this is no different than for most arc welding processes.
- High heat inputs for SAW somewhat unites the process to thicker materials, arbitrarily 6.4 mm (0.25 in.). Special conditions may allow welding thinner materials.
- Submerged arc welding is generally not suitable for welding nonferrous materials such as aluminum, magnesium, and their alloys.

Process Applications

If a steel is suitable for welding with gas metal arc welding, flux cored arc welding, or shielded metal arc welding, procedures likely can be developed to weld the steel with SAW (Ref 1). The main limitations of SAW are plate thickness and position. Because SAW is a high-heat-input and high-deposition-rate process, it

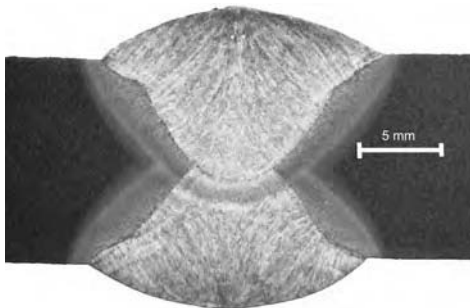


Fig. 3 Square-edge preparation on 12.5 mm (0.5 in.) plate

is generally used to weld thicker steels. Although the welding of 1.6 mm (0.062 in.) thick steel is possible, most SAW is done on plate over 6.4 mm (0.25 in.) thickness.

Types of Metals Submerged arc welding is most commonly used to join plain carbon steels. Low alloy and alloy steels can be readily welded with SAW if care is taken to properly control the heat input to prevent creating undesirable hardness in the heat-affected zone (HAZ). Alloy steels and heat treated steels can be welded using controlled heat input (Joules/min.) and interpass temperature procedures to avoid undesirable grain coarsening and/or cracking in the HAZ.

Heat input as well as interpass temperature control may be essential to developing specific mechanical properties in the weld deposit. Welding of stainless steels is possible and practical on many AISI grades of steel. However, it is not recommended for fully austenitic grades or where ferrite content is controlled to less than 4%. Silicon content may be considerably higher for other arc welding processes and may cause hot-short cracking in austenitic grades of material (Ref 1).

Industrial Uses for SAW. Submerged arc welding is ideally suited for any application involving long, continuous welds. The ability to readily weld thick plates, sometimes with simple joint configurations, makes SAW the method of choice for welding components or assemblies found in:

- Bridge girder fabrication
- Structural steel components
- Machinery components such as gear cases, gears, structural bases, hydraulic cylinder end-caps, and so on
- Shipbuilding
- Earthmoving, construction, and agricultural equipment
- Mining and mineral processing equipment
- Food processing equipment
- Pressure vessels
- Air receiver and compressed gas cylinders
- Pipe fabrication

Submerged arc welding is also suited for buildup and/or overlay with alloyed materials. Typical applications include steel mill and

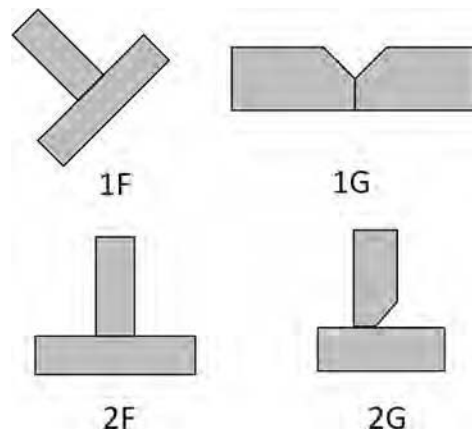


Fig. 4 Typical submerged arc welding positions

paper processing rolls, pressure vessel cladding, and hardfacing wear parts (Fig. 5). This is frequently done during fabrication of new components as well as the restoration to serviceability of worn components.

Joint Configurations. The most common weld deposits made with SAW are groove, fillet, lap, plug, joggle, and surfacing (buildup) deposits.

For groove or butt welds, the deep-penetration capability of SAW can play a role in specific joint selection. Plate up to 9.5 mm (0.38 in.) thick can be completely welded from one side using a square butt joint with an 0.8 mm (0.03 in.) root opening incorporating flux, copper, or ceramic backing. Plates in the thickness range from 6.4 to 19 mm (0.25 to 0.75 in.) that are square-edge butted with no gap may be welded without using backing by making one pass from each side, as shown in Fig. 3 (Ref 1).

Beveled joints may be used on any material 10 mm (0.38 in.) or greater. These joints may involve one pass from each side or multiple passes from either or both sides. When multiple passes are used, each pass should be such that slag is easily removed (Ref 1).

Fillet and lap welds with leg sizes up to 7.9 mm (0.31 in.) can readily be made in the horizontal 2F position (Fig. 6) using either semiautomatic or full-automatic methods. Welds larger than this can be made using multiple-pass techniques. In the flat (1F) position, it is possible to similarly produce welds of 12.7 mm (0.50 in.) leg size.

Submerged arc plug welds are made in the flat position only. The electrode is placed in the center of a prepared hole, and the arc is allowed to remain turned on until the hole is filled.

Ensuring High-Quality Welds. As with all arc welding processes, there are a number of steps that should be taken to produce high-quality welds. Make sure that the plate surfaces and the abutting surfaces to be welded are prepared such that:

- Organic materials including oil, grease, paint, and some paint primers are removed.
- Paint primers are kept uniform in thickness and as thin as possible.



Fig. 5 Submerged arc welding buildup on cylindrical object

- Rust in the weld area, especially red rust, is removed.
- The surfaces and abutting areas are free of moisture.
- Slag is removed from previous layers and any tack welds.
- Welding flux is clean and dry. This is very important when reusing unfused flux.
- An established welding procedure should be followed. This is especially important in repetitive work and mandatory to comply with most codes and standards, such as the American Society of Mechanical Engineers (ASME), the American Welding Society (AWS), and so on.
- A welding procedure should at least include electrode diameter, flux and electrode type, amperes and/or wire feed speed volts, type of current, travel speed and contact tip to work distance (CTWD), see (Fig. 7). This is sometimes referred to as electrical stick-out (ESO).
- Work should be securely grounded to the power source and, whenever possible, welding direction should be away from the ground.
- If preheating is required, the necessary temperature should be reached through the thickness of the section to be welded and (as a rule of thumb) at least 50 mm (two inches) on either side of the joint line.

Automatic SAW Power Source and Equipment

Power Supply. The power supplied to the contact tip may be direct current (dc) or alternating current (ac). Both dc and ac power have advantages and disadvantages.

In the United States, dc power has been the predominant type of power used for single-arc SAW. The dc power may be of a constant voltage or variable voltage (also known as constant current) type. In the past, both types have been supplied by motor generator or transformer

rectifier-type welders. More recently, inverter power sources have been designed for SAW. In Europe and the Far East, ac is more commonly used for single-arc SAW. In all cases, a suitable wire-feeding device is connected to the power supply. Figure 7 illustrates a simplified block diagram of a typical setup.

Advantages of the dc system include:

- Arc stability at both low and high travel speeds
- Better arc striking
- Usually uses three-phase input power, which keeps primary current draw balanced across each phase

Disadvantages of the dc system include:

- May encounter magnetic interference (arc blow), resulting in poor bead shape and possible porosity
- Multi electrode applications will create magnetic interference between themselves.

Advantages of the ac system include:

- Freedom from magnetic arc interference (arc blow)
- Higher deposition rates for the same current

Disadvantages of the ac system include:

- Arc ignition and arc instability may occur, especially at lower current settings. On a 60 Hz system, the arc extinguishes and reignites 60/s.
- May require voltages as high as 80 volts to insure acceptable arc ignition.
- Because these are single phase devices, larger input power lines are required.
- The high single-phase primary current draw can create significant supply line imbalances.
- Phasing and/or power sources for multiarc applications involve complex connections.
- Paralleling power sources for high current applications involves complex transformer connections.

Power Inverter Technology. Recent advances in power inverter technology, digital solid-state controls, and software control of power output have dramatically altered the nature of SAW power sources and related equipment. Figure 8 illustrates a modern power source, control unit, and wire drive.

These power sources differ from traditional motor generator or transformer-type power sources in the following ways:

- Three-phase power input is balanced at higher efficiencies irrespective of output mode.
- Either ac or dc power and constant current or constant voltage modes can be output from the same power source.
- Easy paralleling of power sources for high current outputs
- The ac output can be square wave, which increases arc stability (Fig. 9).
- To switch between ac and dc output, no external or internal wiring changes are required. Dc output may be either constant current or constant voltage.
- The ac output may be unbalanced, thus permitting controlled changes in penetration and deposit rate.
- The source is readily compatible with programmable logic controllers.

Control System Requirements. If constant voltage output is used, the wire is fed at a controlled, constant speed. The required welding current is determined based on the size of the electrode, the contact-tip-to-work distance, and the speed of the feeder. This is frequently the choice for small, high-travel-speed welds.

If constant current (variable voltage) output is used, the feeder monitors the arc voltage to adjust the wire feed speed and maintain a given arc length, while the power source maintains the desired current. This is usually the choice where large weld puddles are involved.

SAW Fluxes

Fluxes are described in several different ways, including method of manufacture, alloying effect, basicity index, and diffusible hydrogen potential.

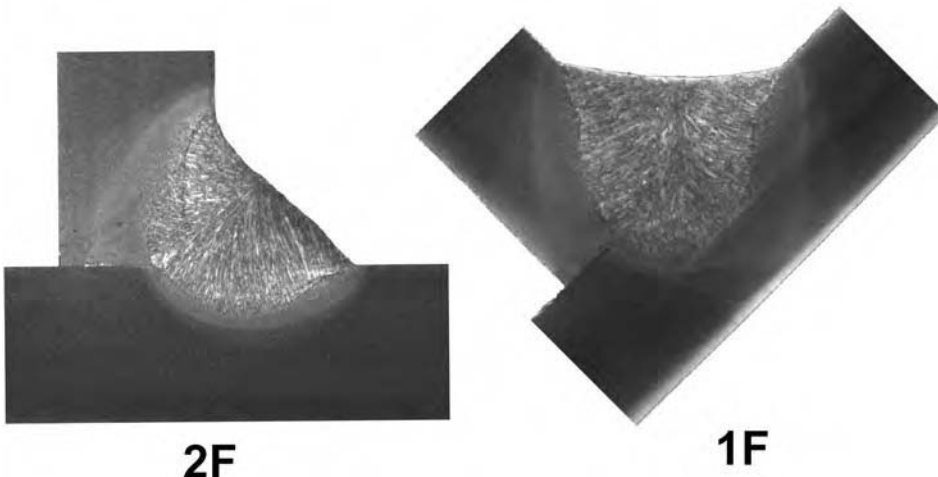


Fig. 6 Fillet welds, 8 mm (0.31 in.)

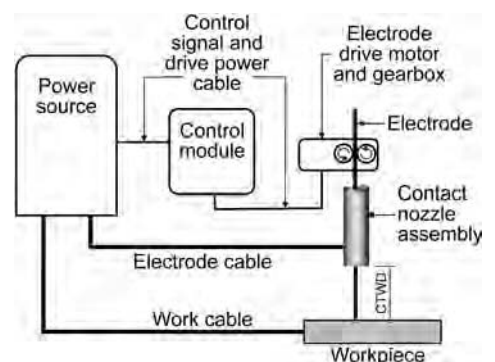


Fig. 7 Typical submerged arc welding equipment layout. CTWD, contact-tip-to-work distance

Fused fluxes are manufactured by melting, drying, and then grinding the raw materials. Agglomerated fluxes are manufactured by binding the raw materials together and heating them as a ceramic. Because of the lower manufacturing temperatures, agglomerated fluxes may contain alloys and high-melting compounds. Slag that has been produced by SAW is sometimes ground and used as a welding flux. Because of the inherent risks in this process, the usage is typically limited to overlay welding or less-critical applications. *Reground fluxes may require requalification to the appropriate material specification.* Fluxes can be produced over a wide range of particle sizes. Typically, smaller particle sizes are preferred for smaller welds, and larger particle sizes for larger weld puddles.

Fluxes may be categorized as active or neutral with regard to alloying weld metal. Active fluxes generally add alloy to a weld deposit and specifically may change the level of alloying based on the amount of flux that is melted with

respect to the electrode and base metal melted. They are particularly effective at resisting weld defects due to dirty steel and are mainly used for limited-pass welding. When using these fluxes, more care must be taken to keep welding conditions the same, because the amount of alloy deposited changes with the amount of flux melted. They are also known to increase the alloy level of multiple-pass welds as subsequent layers of weld metal are added.

Some fluxes contribute significant amounts of various alloys and are used for hardfacing and specific alloy steel applications. Other fluxes add chromium and are used to compensate for chromium that is lost during welding of stainless steels. Neutral fluxes are typically used for multiple-pass applications.

The neutral/active behavior of a given flux is expressed by the Wall neutrality number (N) (Ref 2, 3) and is defined by:

$$N = 100 \times (|\Delta\%Si| + |\Delta\%Mn|) \quad (\text{Eq 1})$$

where $|\Delta\%Si|$ is the absolute value of the change in the weight percent of silicon, and $|\Delta\%Mn|$ is the absolute value of the change in the weight percent of manganese when welds are made at 28 and 36 V. Fluxes that contribute alloying ingredients other than manganese and silicon are characterized by the expected composition or properties of the resulting weld metal.

Another common method used to describe submerged arc fluxes is the basicity index (BI). The basicity index is a measure of the ratio of strongly bound metallic oxides to weakly bound metallic oxides and roughly relates to the amount of oxygen in the weld metal. The Boniszewski basicity index (Ref 4) is defined by:

$$BI = \frac{(\text{CaO} + \text{CaF}_2 + \text{MgO} + \text{K}_2\text{O} + \text{Na}_2\text{O} + \text{Li}_2\text{O}) + \{\text{BaO} + \text{SrO} + 1/2(\text{MnO} + \text{FeO})\}}{\{\text{SiO}_2 + 1/2(\text{Al}_2\text{O}_3 + \text{TiO}_2 + \text{ZrO}_2)\}} \quad (\text{Eq 2})$$

Fluxes with a high basicity index (>2) generally produce weld metal with higher toughness properties in multiple-pass welds. Fluxes with a medium basicity index (1 to 2) generally produce weld metal with higher toughness in single-pass or two-run welds. Fluxes with a low basicity index (<1) are generally used where high impact toughness is not a requirement.

Fluxes exhibit more influence on submerged arc weld-metal hydrogen than do solid electrodes, so fluxes are sometimes classified in terms of the diffusible hydrogen of weld metal. Submerged arc weld metal can be produced with diffusible hydrogen levels of less than 2 mL/100 g to over 15 mL/100 g weld metal. Some fluxes must be dried prior to use to produce low weld-metal hydrogen values. Different welding fluxes will contain different amounts of moisture. Different welding fluxes will have different relationships between moisture in the flux and hydrogen in the weld. It is difficult to generalize this relationship, so the consumable manufacturer should be consulted with regard to appropriate flux storage and drying conditions.



Fig. 8 Inverter with digital control

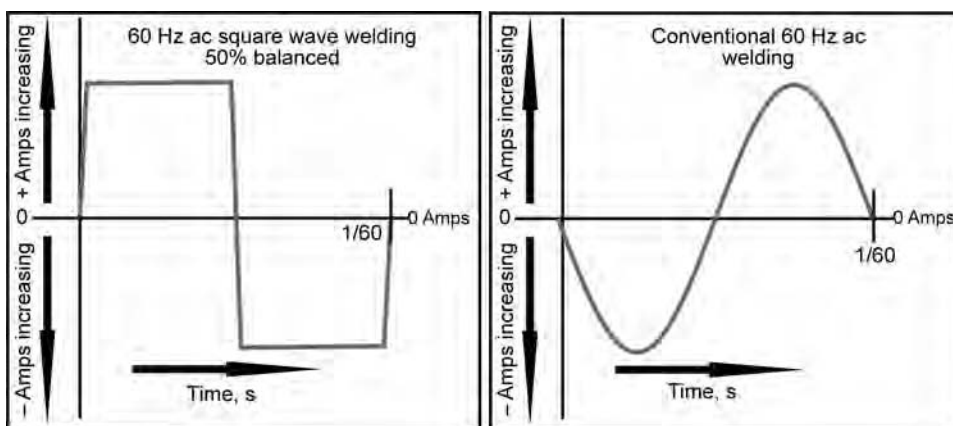


Fig. 9 Alternating current (ac) square wave and sine wave output

Electrodes for SAW

There are three different types of electrodes manufactured for SAW welding:

- **Solid:** These are drawn to specific sizes and are the most commonly used type. Solid electrodes are available for welding carbon steel, low-alloy steel, stainless steel, and nickel-base alloys. A thin copper coating is usually applied to the carbon steel electrodes to enhance atmospheric corrosion resistance and improve electrical contact. The most commonly used sizes range from 1.6 to 6.4 mm (0.062 to 0.25 in.).

- **Cored:** These are electrodes with a metallic sheath and a filling of metals and fluxing agents. They are often used to add alloy to a weld puddle to provide a specific weld-metal composition. Size availability ranges from 2 to 4 mm (0.078 to 0.156 in.).
- **Strip:** These are made from solid strip to an appropriate chemistry. They are available in widths from approximately 25 to 100 mm (1 to 4 in.). Thickness ranges are usually from 0.5 to 1.0 mm (0.02 to 0.04 in.). These electrodes are primarily used for cladding, buildup, overlaying, and hardfacing applications. The advantage of these electrodes is that low penetration and low dilution with parent plate (or previous layers) can be achieved at moderately high deposition rates. A major disadvantage is that special feeder drive rolls and contact nozzles are required.

Weld-Metal Considerations

A weld consists of melted parent plate and electrode and may also contain alloying elements from the flux. The weld-metal composition and mechanical properties are dependent on the welding procedure, the joint preparation, the consumables used, and any postweld heat treatment. Submerged arc weld metal is classified based on tensile strength, impact toughness, and sometimes chemical composition of the weld metal. Weld metal is classified based upon producing welds using specific procedures as detailed in

AWS specifications. Provision is made for classification by using either a multiple pass procedure or a two run procedure.

Classification of Multiple-Pass Plain Carbon Weld Metal. The classification of electrodes and fluxes for welding carbon steels is detailed in "Specification for Carbon Steel Electrodes and Fluxes for Submerged Arc Welding," ANSI/AWS A5.17 (Ref 2). The classification of solid electrodes is based on the chemical composition of the electrode. Flux is not classified alone but is based on the mechanical properties and diffusible hydrogen of weld metal produced with a given electrode. The classification system used to describe flux-electrode combinations for mild steel welding is shown in Fig. 10. References in that figure are to the appropriate figures and tables in AWS A5.17.

Classification of Multiple-Pass Low-Alloy Weld Metal. The classification of low-alloy steel welding electrodes and fluxes is detailed in "Specification for Low-Alloy Steel Electrodes and Fluxes for Submerged Arc Welding," ANSI/AWS A5.23 (Ref 3). The classification of solid electrodes is based on the chemical composition of the electrode. The classification of composite electrodes (cored wire) is based on weld deposit composition. Flux is not classified alone but is based on the mechanical properties, chemical composition, and diffusible hydrogen of the weld metal produced with a given electrode. The designator system for flux-electrode combinations of low-alloy steel is shown in Fig. 11. References in that figure are to the appropriate figures and tables in ANSI/AWS A5.23/A5.23M.

Classification of Two-Run Weld Metal.

The classification of submerged arc weld metal produced in the two-run welding method is also detailed in "Specification for Low-Alloy Steel Electrodes and Fluxes for Submerged Arc Welding," ANSI/AWS A5.23 (Ref 3). The classification of electrodes is identical to that for multipass welding. The classification of the flux-electrode combination is based on the mechanical properties and diffusible hydrogen of the weld metal produced using a specified two-run technique. The mechanical properties of a flux-electrode combination welded with a two-run technique will most often be very different than those obtained with a multipass welding technique. This is due to the reheating of the weld metal as subsequent weld passes are applied to the weldment. The designator system for flux-electrode combinations of low-alloy steel is shown in Fig. 12. References in that figure are to the appropriate figures and tables in ANSI/AWS A5.23/A5.23M.

Stainless Steel Electrodes for SAW. The requirements for classification of stainless steel electrodes are detailed in "Specification for Bare Stainless Steel Welding Electrodes and Rods," ANSI/AWS A5.9 (Ref 5). The classification of the filler metal is based on the chemical composition. There is no provision for classifying a flux-electrode combination in this specification.

Nickel and Nickel Alloy Electrodes. The requirements for classification of nickel and nickel alloy electrodes are detailed in "Specification for Nickel and Nickel Alloy Bare Welding Electrodes and Rods," ANSI/AWS A5.14 (Ref 6). The classification of the filler metal is based on the chemical composition. There is no provision for classifying a flux-electrode combination in this specification.

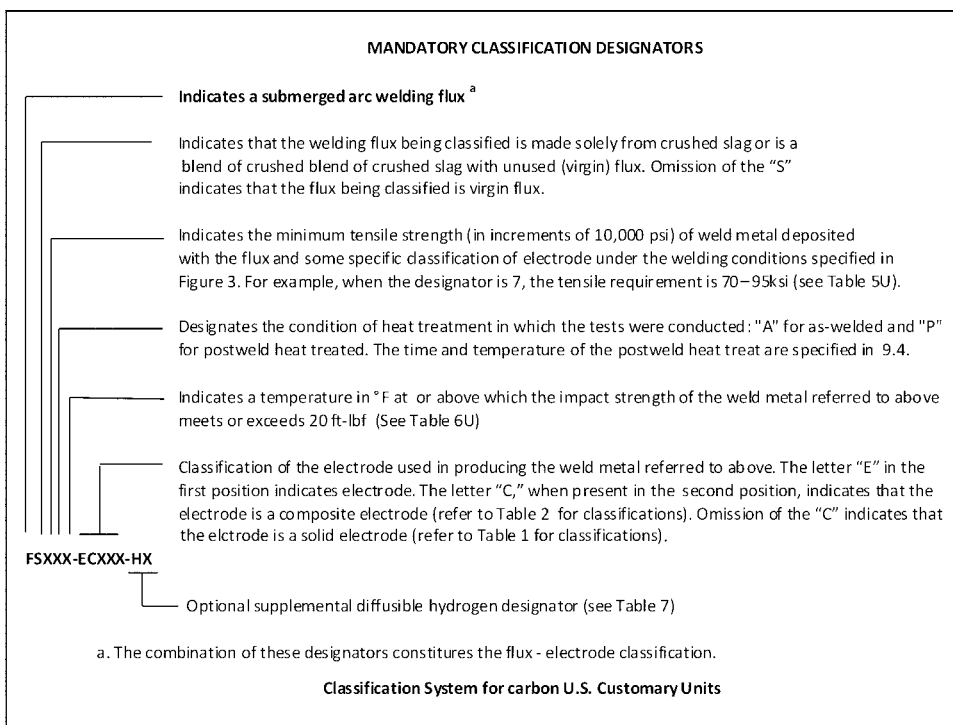


Fig. 10 Flux-electrode classification system for U.S. customary units. Source: Ref 2

SAW Process Parameters

In addition to the previously listed conditions for SAW, there are a number of considerations, including proper fit-up of the work and an appropriate welding procedure, that must be carefully controlled, just as with any automated arc welding process. The following is a discussion of several important factors.

Fit-Up of Work. Assembled parts to be welded should be fit-up accurately as specified to assure uniformity from assembly to assembly. Some key factors are:

- Whether fit-up of the workpieces is to be "tight" or with a specified gap, edge-preparation uniformity from piece to piece is important.
- Tack welding should be consistently uniform, and if a slag-forming process is used, the slag should be removed.
- Fixturing or clamping of the assembly should be sufficient to minimize distortion during welding and to establish a consistent weld.

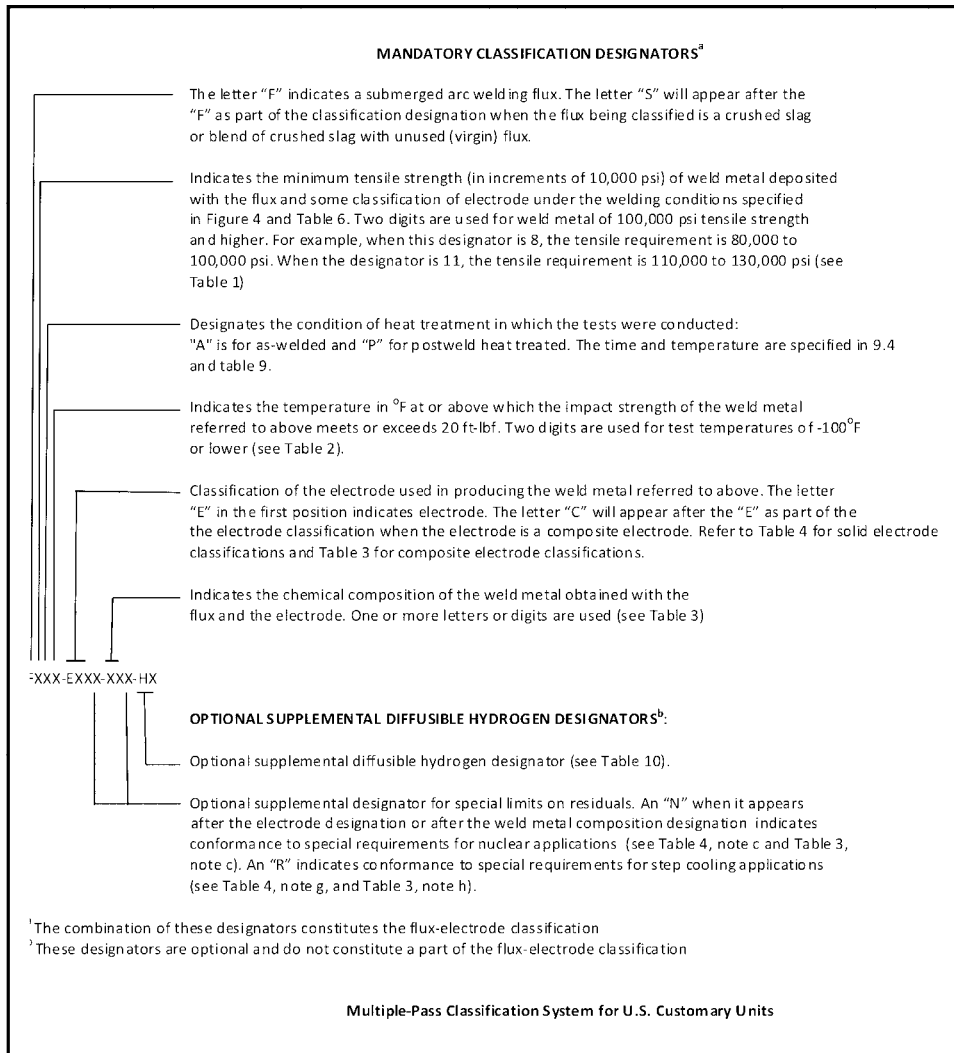


Fig. 11 Flux-electrode classification system for U.S. customary units. Source: Ref 3

- Travel motion alignment relative to the workpiece must be uniform. The use of automatic seam tracking may be beneficial for nonlinear seams.
- If groove welds are to be completely welded from one side, suitable joint backing is essential.

Welding Procedure Components. Appropriate welding procedure requires careful control of:

- Electrode-flux combination
- Electrode size
- Type of current (dc or ac)
- Current
- Voltage
- Type of voltage (variable or constant)
- Polarity if dc is used
- Frequency, balance, and offset if ac square wave is used
- Electrical stickout (ESO) (also referred to as contact-tip-to-work distance, Fig. 16)
- Travel speed
- Position of weld
- Number of passes
- Preheat and/or interpass temperature

These components act together with a joint design to constitute a specific welding procedure. Published procedures are available for many joint configurations and provide a good starting point for developing new welding procedures (Ref 1). Indiscriminant changes in any procedural component can result in a final weld that may not be acceptable in terms of serviceability or appearance. A brief description of the effects of some important procedural components follows.

Welding current has a direct influence on deposition rate, joint penetration, and the resulting internal and external bead shape. The type of current in conjunction with electrode size and ESO affects the deposition rate, penetration, and base-plate dilution. The effect of current variation on weld bead profiles is shown in Fig. 13. Welds made at excessively low

current (Fig. 13a) will tend to have little penetration and may result in a less stable arc. Welds made at excessively high current (Fig. 13b) will have deep penetration, high dilution, and an overall undesirable bead shape. Correct current (Fig. 13c) will produce a well-shaped bead.

The direction of current flow will also affect the weld bead profile. The current may be direct with the electrode positive (reverse polarity), electrode negative (straight polarity), sinusoidal ac, or variable polarity ac. When dc welding is the only choice available, electrode positive (dc +) is generally preferred for most applications because of greater arc stability. However, electrode negative (dc-) is used to increase deposition rate and reduce penetration. Electrode negative (dc-) is frequently used for fillet welding where joint penetration is undesirable or not needed. Because electrode negative (dc-) produces shallower penetration and therefore less base-plate dilution, it is often used for surfacing (buildup) applications.

Deposition rate for conventional alternating current is between that of dc straight and dc reverse polarity. Conventional ac (sine wave) alternating current is often used when welding current exceeds 1000 amps.

Alternating current is frequently used when arc blow is encountered, including in multiple-electrode applications.

Inverter and software-based power sources with digital control can provide a very stable square wave output that allows the user to control the percent of the cycle that is on the positive or the negative side. Referred to as percent balance, this allows for a significant increase in deposit rate over conventional ac sine wave output at equal amperes. An example of this increase is shown in Fig. 14 for a commonly used electrode size.

Arc Voltage. Like current, arc voltage will affect the bead shape and may affect the weld deposit composition when using active and alloy fluxes. Changes in voltage while holding the current constant can affect the resulting bead shape, as shown in Fig. 15. Excessively high voltage (Fig. 15b) will produce a hat-shaped weld, which has low resistance to cracking.

Setting voltage toward the high side will produce a longer arc length with a correspondingly wider, flatter bead with less penetration. However, when the voltage is excessively high, the weld bead appearance will mimic that of very low voltage. Lower voltages will shorten the arc length and increase penetration. Excessively low voltage will produce an unstable arc and a crowned bead as well as uneven surface contours (Fig. 15a).

Electrical stickout is variously referred to as ESO or contact-tip-to-work distance. It is the distance between the point at which current is input to the electrode and the work (Fig. 16). While not precisely correct, it is typically measured as the distance from the end of the electrode contact tip to the work surface or previous layer surface in multilayer welds.

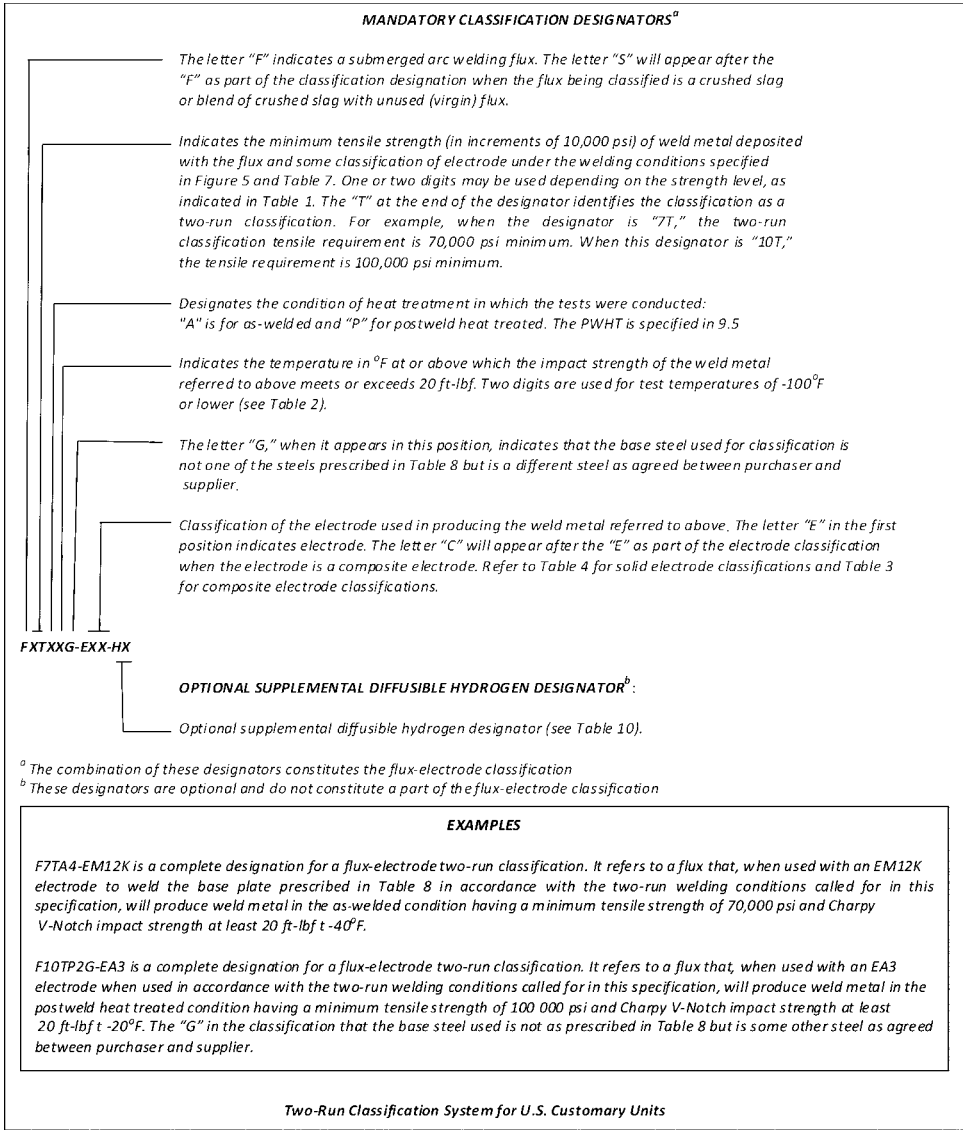


Fig. 12 Flux-electrode classification system for U.S. customary units. Source: Ref 3

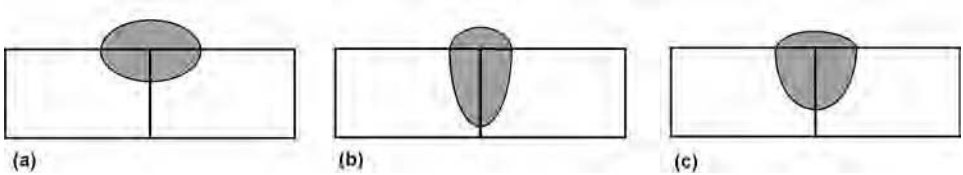


Fig. 13 Effect of welding current on bead shape

The current flowing in the electrode between the contact tube and the arc will cause some resistance heating, resulting in a voltage drop across that length of electrode. This resistance heating and subsequent voltage drop can be used to obtain higher deposition rates.

Normal electrode extension for solid SAW wire is approximately 7 to 12 times the electrode diameter. As this length increases, so does the amount of resistive heating and the melt-off

rate. This (I^2R) heating will create an increased drop in arc voltage and necessitate an increase in voltage output from the power source to maintain the desired voltage across the arc. Extending the electrode 20 to 30 times the diameter can increase deposition rates by more than 50% (Ref 1).

As the electrode is extended, keeping the electrode aligned to the weld seam can become a problem. Special insulated contact nozzles are

commercially available to keep the proper electrode alignment.

Travel Speed. With any given welding procedure, travel speed determines and controls the volume of weld metal deposited per incremental length. There are other effects from travel speed changes with an otherwise fixed welding procedure:

- Heat input is directly affected by travel speed and thus must be carefully considered when there are specific heat-input requirements.
- The proper travel speed will result in a good bead shape and slag removal. Travel speed also affects penetration.
- Excessively high travel speeds will promote a crowned weld bead as well as increase the tendency for undercut and porosity.
- Excessively slow travel speeds can cause an undesirable increase in the total weld puddle size. This can cause slag inclusions and wavy edges because the molten metal is not properly contained by the slag.

Figures 17 and 18 illustrate how the type of current and travel speed can interact to produce the same weld volumes. Voltages were adjusted as appropriate for the increase in deposit rate. Heat input for the three welds is within a 10% spread between the slowest- and highest-speed welds.

Flux depth should be just deep enough that the arc does not "flash through" the flux blanket. A flux blanket that is too thick can act as a dam and affect the overall bead appearance. In deep-groove welds, an excess amount of flux can result in a humped weld with poor fusion and trapped slag.

Too little flux will result in the arc flashing through the flux. This will result in poor weld surface appearance, arc instability, and may even cause weld porosity by allowing air to be drawn into the arc.

Defects in SAW

The fact that SAW is a high-heat-input process under a protective blanket of flux greatly decreases the chance of weld defects. However, defects such as lack of fusion, slag entrapment, solidification cracking, hydrogen cracking, or porosity can occur.

Insufficient Fusion and Slag Entrapment. Lack-of-fusion defects and slag entrapment are most commonly caused by improper bead placement or welding procedure. Improper placement can cause the weld metal to roll over and trap slag underneath. A crown-shaped bead caused by excessively high or low welding voltage may also contribute to slag entrapment and lack of fusion.

Solidification Cracking. Cracking along the center of the bead is usually due to improper bead shape, poor joint design, high joint restraint, or poor welding procedures. A bead width-to-depth ratio greater than 1 will decrease cracking tendencies (Fig. 19). If the weld bead is too deep,

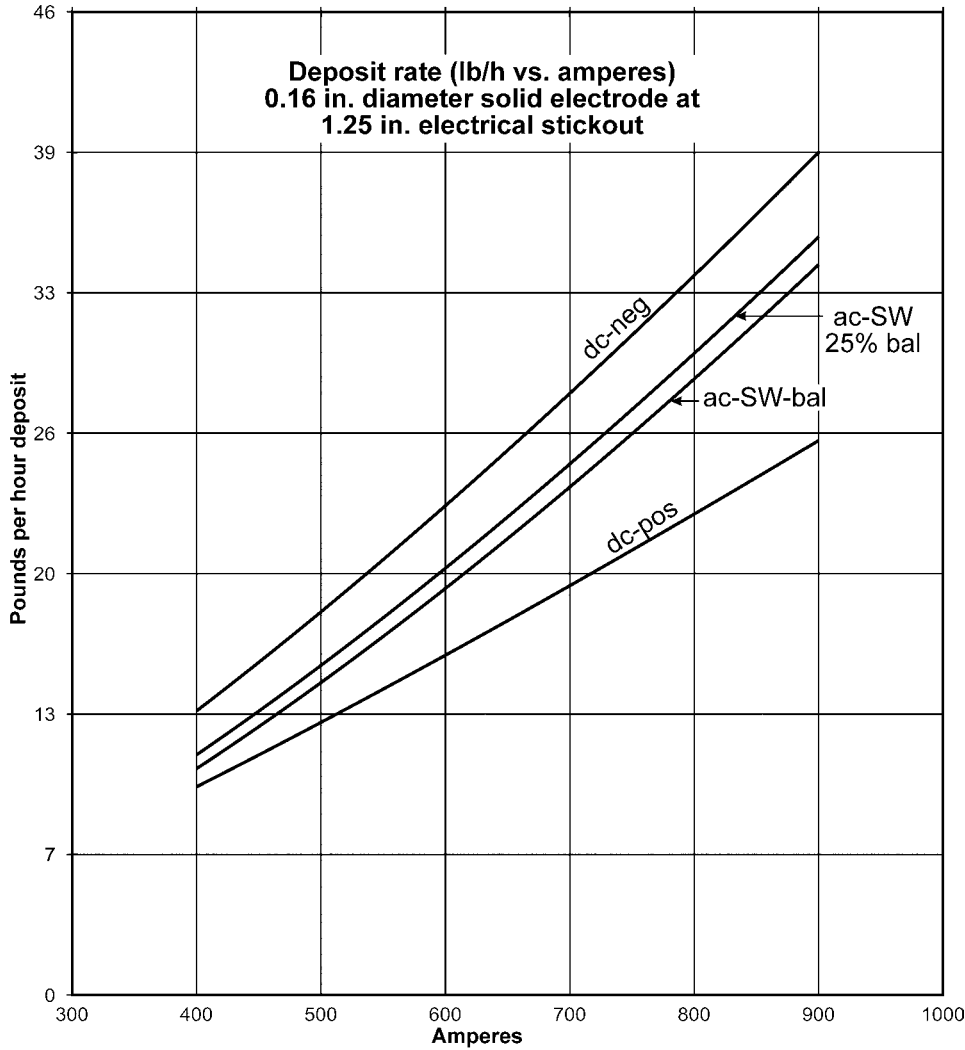


Fig. 14 Weld deposit rate versus current. ac-SW, alternating current-square wave; dc, direct current

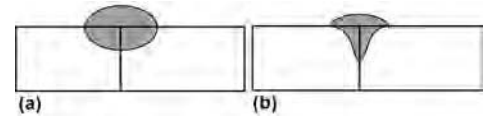


Fig. 15 Effect of voltage on bead shape

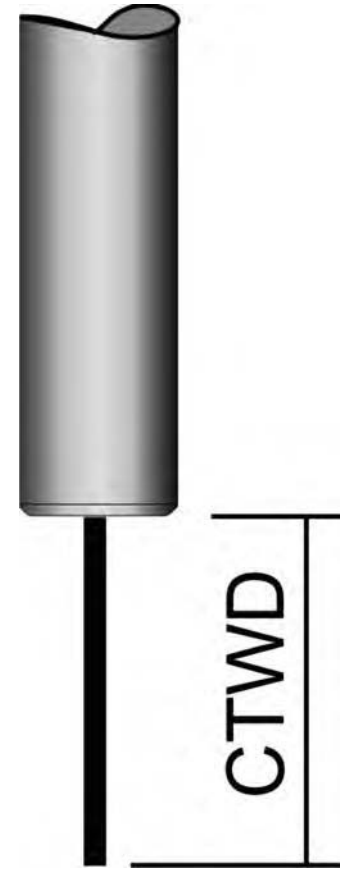
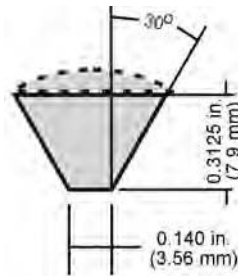


Fig. 16 Contact-tip-to-work distance (CTWD) or electrical stickout

increased shrinkage stresses related to solidification may cause centerline cracking. Joint design can also contribute to excessive shrinkage stresses and cracking. Because cracking is related to stresses in the weld, high-strength materials will have a greater tendency to crack. Therefore, special care must be taken to generate proper bead shape, preheat temperatures, and interpass temperatures, in addition to correct electrode and flux combinations, when welding these materials.

Hydrogen-Induced Cracking. Unlike solidification cracking, which appears immediately after welding, hydrogen cracking may occur from several hours to several days after welding has been completed. To minimize hydrogen cracking, all possible sources of hydrogen (for example, water, oil, grease, rust, thick primer paint, and dirt) present on the plate or joint should be removed. The flux, electrode, and



Groove-level full requires 0.340 lb/ft (0.505 kg/m) of deposited weld metal. Adding a cap of 5/8 × 1/16 in. (15.9 mm × 1.59 mm) requires an additional 0.089 lb/ft (0.132 kg.m) deposit.

Fig. 17 Prepared welding groove

plate should be clean and dry. Care should be taken to avoid moisture contamination of fluxes and electrodes. Fluxes and electrodes should be stored, handled, and redried, if necessary, as recommended by the consumable manufacturer.

Other considerations to reduce hydrogen-cracking tendency include:

- Electrodes with surface rust should not be used.
- Consumables designed to produce weld deposits that are very low in diffusible hydrogen should be considered, especially when welding high-strength steels.

- Follow proper preheat and interpass temperatures as well as postweld hold times and temperatures (Ref 1).
- Keep weld-metal layers as thin as possible, and allow as much time as possible for hydrogen to escape. Hydrogen escapes more readily with increasing time and temperature. Reduction of the distance that hydrogen must travel to escape will also assist in hydrogen removal from the weld metal.

Porosity caused by trapped gas is uncommon in SAW because of the protection provided by the flux. When porosity does occur, it may be in the form of internal porosity or visible holes on the weld bead surface. The gas bubbles that generate porosity originate either from a lack of protection from the atmosphere or from contaminants such as water, oil, grease, and dirt. To reduce porosity in SAW, in addition to proper flux coverage, all water, grease, dirt, and any other organic material should be removed from the plate and

the joint. Porosity that occurs at one end of the joint and becomes worse with subsequent passes may be caused by arc blow. Switching to ac polarity or changing the ground location may improve this situation. Occasionally, porosity can occur as the result of nitrogen being absorbed in plate edges prepared by plasma cutting. This problem can usually be eliminated by light grinding of the edges before welding.

Training and Safety

Welder Training. Submerged arc welding is an automatic or semiautomatic process carried out primarily in the flat or horizontal position with the arc obscured from view. Both forms of the process are largely controlled by welding procedure settings. The welder, or weld operator, is responsible for slight adjustments in equipment settings. Depending on the level and sophistication of fixturing, the welding operator may have to align the electrode to the

work and track the weld joint. Semiautomatic welding will require training to properly align the welding torch to the workpiece and to develop the skill to provide the appropriate travel speed.

A welder who is expected to establish welding procedures must understand how the various elements of a procedure interact with each other and influence the weld.

Workplace Health and Safety. Submerged arc welding has the advantage over other arc welding processes in that it is essentially devoid of arc radiation and smoke and fume generation. Nonetheless, good ventilation should be provided, and care should be taken in handling flux to avoid the generation of dust.

The heavy protective clothing and gear associated with open-arc processes is not required. Light protective clothing may be worn. Hot slag and flux can cause burns to exposed skin, as can contact with hot workpieces. Eye protection should be worn at all times.

Protection against electric shock should be provided by assuring that all equipment is properly installed and grounded. Welding cables should be maintained in good condition, with proper connections at each end. Specific practices as outlined in "Safety in Welding and Cutting and Allied Processes" (Ref 7) should always be followed.

Manufacturers' material safety data sheets should be carefully read and understood. *Note that there is one for the electrode and one for the flux.*

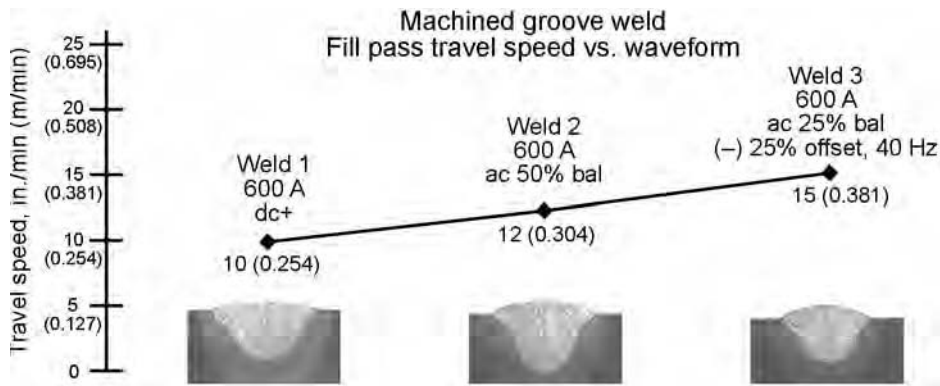


Fig. 18 Three identical weld volumes

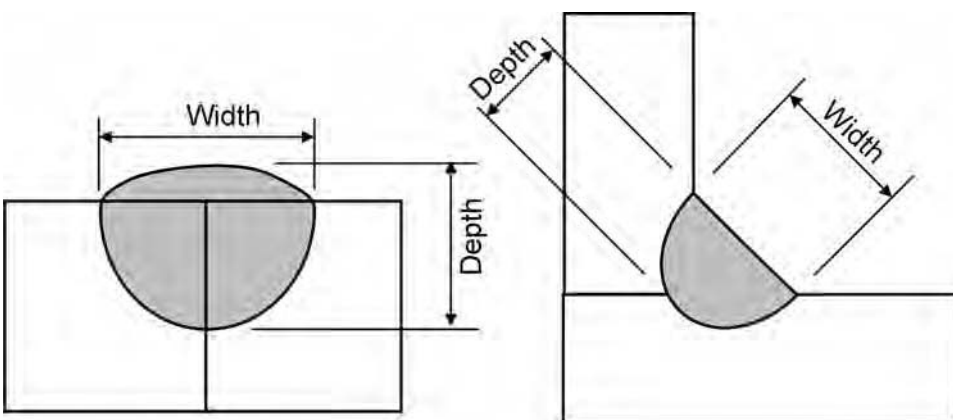


Fig. 19 Desirable bead shape

REFERENCES

1. *The Procedure Handbook of Arc Welding*, 13th ed., The Lincoln Electric Company, 1995, p 3.3-1 to 3.3-5, 6.1-12 to 6.1-19, 6.3-7 (Fig. 6.43), 6-3.28 to 6-3.72, 11.3-4 to 11.3-5
2. "Specification for Carbon Steel Electrodes and Fluxes for Submerged Arc Welding," ANSI/AWS A5.17/A5.17.17M-97 (R2007)
3. S.S. Tuliani, T. Boniszewski, and N.F. Eaton, Notch Toughness of Commercial Submerged Arc Weld Metal, *Weld. Met. Fabr.*, Vol 8, 1969, p 327-339
4. "Specification for Low-Alloy Steel Electrodes and Fluxes for Submerged Arc Welding," ANSI/AWS A5.23/A5.23M-2007
5. "Specification for Bare Stainless Steel Welding Electrodes and Rods," ANSI/AWS 5.9/A5.9M:2006
6. "Specification for Nickel and Nickel Alloy Bare Welding Electrodes and Rods," ANSI/AWS A5.14/A5.14M:2009
7. "Safety in Welding and Cutting and Allied Processes," ANSI Z49.1/AWS Z49.1, 2005

Gas Tungsten Arc Welding*

Lee E. Allgood, The Lincoln Electric Company

THE GAS TUNGSTEN ARC WELDING (GTAW) process was developed in the late 1930s when a need to weld magnesium became apparent. The GTAW process is also referred to as the tungsten inert gas (TIG) process and as Heliarc (Ref 3), the original registered trade name, and thus became commonly referred to as TIG welding.

The GTAW process derives the heat for welding from an electric arc established between a tungsten electrode and the part to be welded (also called the workpiece). The arc zone must be flooded with an inert gas to protect the tungsten electrode and molten metal from oxidation and to provide a conducting path for the arc current. In 1941, Russell Meredith and V.H. Pavlecka developed the first practical torch for holding a tungsten electrode and delivering an inert gas shield to protect the electrode, weld pool, and adjacent hot metal (Fig. 1). The inert gas is fed through a nozzle

surrounding the tungsten electrode, which provides a means of shielding the arc as it is moved along a weld joint. Torches used for higher currents are usually water cooled (Fig. 2).

The melting temperature necessary to weld materials in the GTAW process is obtained by maintaining an arc between a tungsten alloy electrode and the workpiece (Fig. 1, 3). Weld

pool temperatures can approach 2500 °C (4530 °F). The inert gas sustains the arc and protects the molten metal from atmospheric contamination. The inert gas is normally argon, helium, or a mixture of helium and argon. Although the process was developed with helium, argon soon became the most widely used shielding gas because of its lower cost, greater density, and smoother arc operation. Helium produces a higher-energy arc and so is still used for certain applications.

A typical setup for GTAW consists of an inert gas supply (argon, helium, or a mixture of these), including pressure regulators, flow meters, and hoses to deliver the gas to the arc. The gas(es) may be supplied from a cylinder(s) or liquid container(s). An illustration of a complete GTAW arrangement is shown in Fig. 4.

Gas tungsten arc welding may readily be automated for automatic, machine, or robotic welding (Fig. 5), but additional equipment is required, such as a means of mechanically moving the torch in relation to the work and feeding filler electrode into the weld pool. A fully automatic system may require a programmer consisting of a microprocessor to control weld current, travel speed, and filler electrode feed rate as well as a programmed travel path.

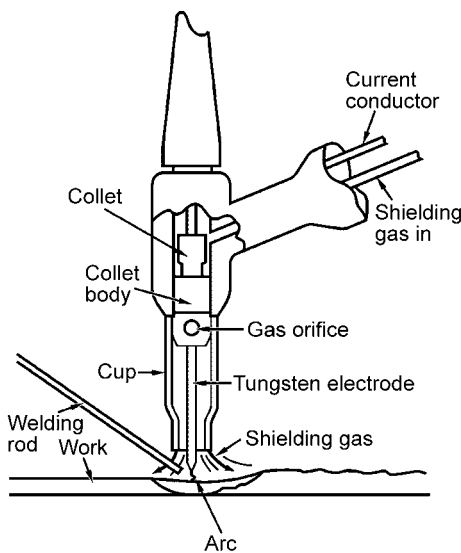


Fig. 1 Gas tungsten arc welding schematic

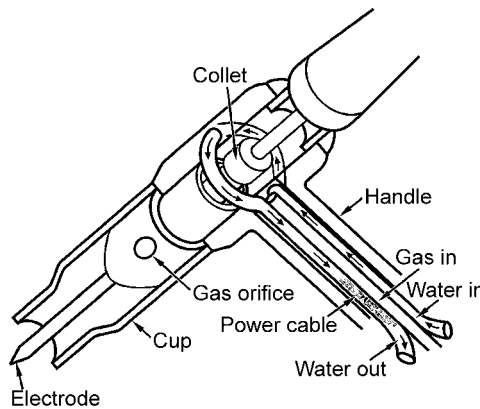


Fig. 2 Gas tungsten arc welding water-cooled torch



Fig. 3 Gas tungsten arc manual welding. Courtesy of Lynn Welding

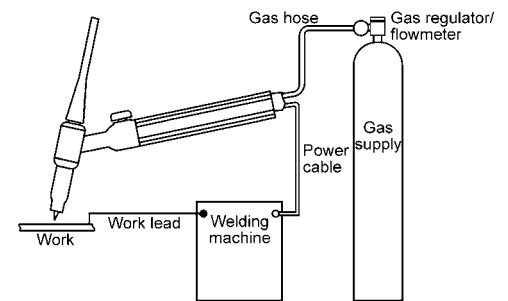


Fig. 4 Gas tungsten arc welding process schematic

* Adapted from Grant Ken-Hicken, Gas-Tungsten Arc Welding, *Welding, Brazing, and Soldering*, Vol 6, *ASM Handbook*, ASM International, 1993, p 190-194 (Ref 1), and with permission from The James F. Lincoln Arc Welding Foundation (Ref 2)

Applications

Various GTAW applications are shown in Fig. 6 and 7. Gas tungsten arc welding can be used for those alloys where high-quality welds and freedom from atmospheric contamination are critical. Examples of these are reactive and

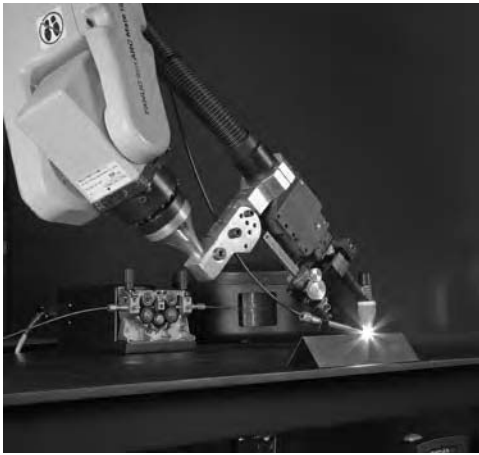


Fig. 5 Robotic welding. Note wire feed device supplying “cold” wire. Courtesy of The Lincoln Electric Company

refractory metals such as titanium, zirconium, and niobium, where very small amounts of oxygen, nitrogen, or hydrogen can reduce both the ductility and corrosion resistance. It can be used to join stainless steels (austenitic, ferritic, and martensitic types) and many nickel-base superalloys where high-quality welds are required. Both aluminum and magnesium alloys are readily weldable.

The GTAW process is well suited for welding thin sheet (Fig. 7c) and foil of all weldable metals because it can be controlled at the very low amperages (2 to 5 A) required for these thicknesses. Gas tungsten arc welding is an excellent process for root-pass welding with the application of consumable inserts or open-root techniques on pipe and tubing (Fig. 7). Gas tungsten arc welding should not be used for welding metals and alloys with very low melting points, such as tin-lead solders and zinc-base alloys, because the high temperature of the arc makes it difficult to control the weld puddle.

The GTAW process is especially suited when the highest weld quality is required. The operator has excellent control of heat input, and visibility is not limited by fumes or smoke from the process. Other advantages include (Ref 4):

- High-quality, low-distortion welds
- Free of the spatter associated with other methods

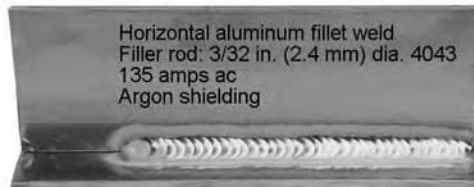
- Applicable with or without filler wire
- Applicable with a range of power supplies
- Suitable for almost all metals, including dissimilar ones
- Precise control of welding heat

Limitations of GTAW include (Ref 5):

- Lower deposition rates than consumable electrode arc welding processes
- Used manually, it requires slightly more welder dexterity and eye/hand coordination than gas metal arc welding or shielded metal arc welding for manual welding.
- Less economical than consumable electrode arc welding for thick sections greater than 9.5 mm (0.38 in.)
- Problematic in drafty environments because of possible difficulty in shielding the weld zone properly

Additional problems with the process may include:

- Possible tungsten inclusions if the electrode is allowed to contact the weld pool
- Contamination of the weld metal if proper shielding of the filler metal by the gas stream is not maintained
- Low tolerance for contaminants on filler or base metals



(a)



(b)



(c)



(d)



(e)



(f)

Fig. 6 Examples of gas tungsten arc welding applications. (a) Horizontal fillet welds. (b) Root-pass heavy wall pipe. (c, d) Aluminum alloy welds. (e) Titanium components welded in vacuum chamber. (f) Chromium-molybdenum steel component

- Contamination or porosity, caused by coolant leakage from water-cooled torches
- Arc blow or arc deflection, as with other processes when using direct current

Principle of Operation

In the GTAW process, an electric arc is established in an inert gas atmosphere between a tungsten electrode and the metal to be welded. The arc is surrounded by the inert gas, which may be argon, helium, or a mixture of these two. The heat developed in the arc is the product of the arc current times the arc voltage, where approximately 70% of the heat is generated at the positive terminal (anode) of the arc. Arc current is carried primarily by electrons (Fig. 8) that are emitted by the heated negative terminal (cathode) and obtained by ionization of the gas atoms. These electrons are attracted to the anode, where they generate approximately 70% of the arc heat. A smaller portion of the arc current is carried by positive gas ions that are attracted to the cathode, where they generate approximately 30% of the arc heat. The cathode loses heat by the emission of electrons, and this energy is transferred as heat when the electrons enter or interact with the anode. This is one reason why a significantly greater amount of heat is developed at the anode than at the cathode. Because the greater amount of heat is generated at the anode, the GTAW process is normally operated with the tungsten electrode or cathode negative (negative polarity) and the workpiece or anode

positive. This puts the heat where it is most needed, at the work.

Arc Polarity

The GTAW process can be operated in three different modes: electrode negative (straight polarity), electrode positive (reverse polarity), or alternating current (ac) (Fig. 9). In the electrode negative mode, the greatest amount of heat is developed at the work. For this reason, electrode negative (straight polarity) is used with GTAW for welding most metals. Electrode negative (straight polarity) has one disadvantage in that it does not provide cleaning action on the work surface. This is of little consequence for most metals, because their oxides decompose or melt under the heat of the arc so that deposited metal will wet the joint surfaces. However, the oxides of aluminum and magnesium are very stable and have melting points well above that of the metal. They are not removed by the arc heat and remain on the metal surface, restricting wetting, which, in turn, contributes to poor weld appearance.

In the electrode positive (reverse polarity) mode, cleaning action takes place on the work surface by impact of gas ions. This removes the thin oxide layer while the surface is under the cover of an inert gas, allowing molten metal to wet the surface before more oxide can form. The disadvantage of this mode is that the greater portion of heat is developed at the positive tungsten electrode and the smaller portion at the work. This means that to obtain the same heat at the work with electrode positive as with

electrode negative, the current must be increased by a factor of 2.3. This current increase, plus the fact that more heat is developed at the positive electrode, means that the electrode operating on positive polarity must dissipate approximately five times as much heat as an electrode operating on negative polarity. Usually, an electrode for positive polarity use is approximately four times the diameter of an electrode used for negative polarity. In the ac mode, the desirable features of both direct current (dc) modes are obtained at a reduced current level.

With GTAW-ac welding, the current flow goes to zero twice every cycle, and the arc must be restarted twice every cycle. When the electrode becomes negative, restarting occurs readily, but when the electrode becomes positive, restarting may be delayed, resulting in lower current. If the current does not start on the positive half-cycle, complete rectification occurs, and there will be no cleaning action. Continuous high frequency superimposed on the ac will assure that the arc is restarted early in each positive half-cycle to provide the cleaning action and minimize the unbalance. This is the reason that sine-wave-based GTAW power sources include a high-frequency generator.

When 60 Hz ac is used, cleaning is obtained on each positive polarity half-cycle, and some heat is developed at the work. The area cleaned on the positive polarity half-cycle will remain clean during the negative polarity half-cycle while shielded with inert gas. Most of the welding heat is delivered to the work during the negative polarity half-cycle. However, some power sources, when operated in the ac mode, must be modified when rectification occurs (as in the case of GTAW-ac of magnesium and aluminum).

Rectification and Cleaning Action with Alternating Current

When welding aluminum or magnesium with ac, an unbalanced wave form (Fig. 10) occurs because the hot tungsten electrode will emit electrons more readily than the clean metal surface. If this happens, more current will flow when the electrode is negative (Fig. 10), and



(a)



(b)



(c)



(d)

Fig. 7 Examples of gas tungsten arc welding application in welding tubular assemblies

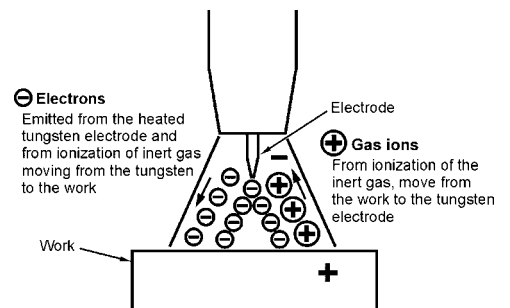


Fig. 8 Schematic of gas tungsten arc welding, direct current electrode negative

Current type	DCEN	DCEP	ac (balanced)
Electrode polarity	Negative	Positive	...
Electron and ion flow			
Penetration characteristics			
Oxide cleaning action	No	Yes	Yes — once every half cycle
Heat balance in the arc (approx.)	70% at work end 30% at electrode end	30% at work end 70% at electrode end	50% at work end 50% at electrode end
Penetration	Deep; narrow	Shallow; wide	Medium
Electrode capacity	Excellent e.g., 3.18 mm (1/8 in.)—400 A	Poor e.g., 6.35 mm (1/4 in.)—120 A	Good e.g., 3.18 mm (1/8 in.)—225 A

Fig. 9 Characteristics of current types for gas tungsten arc welding. DCEN, direct current electrode negative; DCEP, direct current electrode positive; ac, alternating current. Source: Ref 5

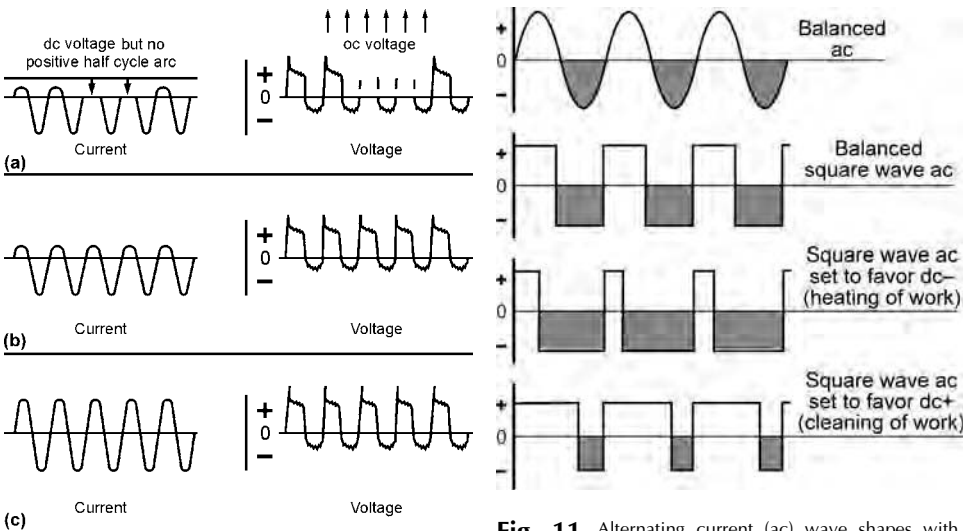


Fig. 10 Voltage and current wave forms for alternating current welding. (a) Partial and complete rectification. dc, direct current; oc, overcurrent. (b) With arc stabilization. (c) With current balancing. Source: Ref 5

rectification will occur. This causes the arc to look and audibly sound unstable.

Rectification will occur with older, sine-wave ac welding power supplies. More advanced GTAW machines include solid-state controls that allow adjusting the ac so as to favor either the positive or negative polarity half-cycle (Fig. 11). This feature is particularly useful

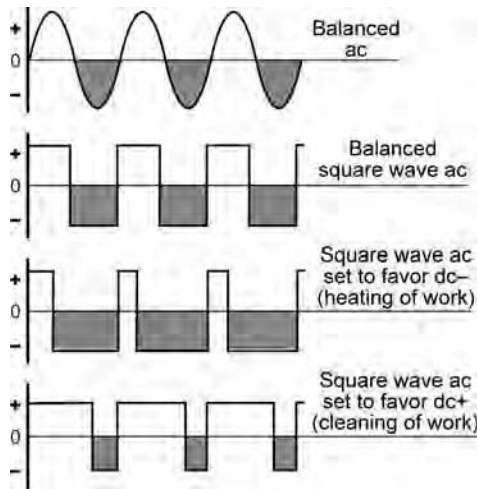


Fig. 11 Alternating current (ac) wave shapes with square-wave gas tungsten arc power supply. dc, direct current

when welding aluminum and magnesium, because the control can be set to favor the positive half-cycle for maximum cleaning. When the electrode is negative, more heat is generated in the weld pool where it is needed. The smaller amount of current when the electrode is positive is acceptable, as long as sufficient current flows to provide adequate cleaning of the surface. The lower current flow also means less heating of the tungsten electrode.

Some power sources also produce a square-wave ac rather than sinusoidal ac. When maximum cleaning is desired, the electrode positive mode is favored; when maximum heat is desired, the electrode negative mode is favored. In general, square-wave power sources are much less susceptible to arc rectification than sine-wave power sources, although it still sometimes occurs.

Equipment

Power Supplies

Power supplies for GTAW are usually of the constant-current type with a drooping (negative) volt-ampere curve (see the article “Arc Welding Power Supplies and Controls” in this Volume for more details on power sources in general and for inverters in particular). Saturable reactors and thyristor-controlled units are the most common. Advances in the electronics industry have readily been adapted by the welding community, resulting in sophisticated, lightweight power supplies. Transistorized dc power supplies are common. There are newer inverter-based power sources that will deliver dc, pulsed dc in addition to sine-wave ac, and square-wave ac. The output frequency can also be varied (Fig. 12). Higher frequencies can be beneficial in welding thin materials.

For many years, inverter power supplies were only capable of supplying dc. This limited the

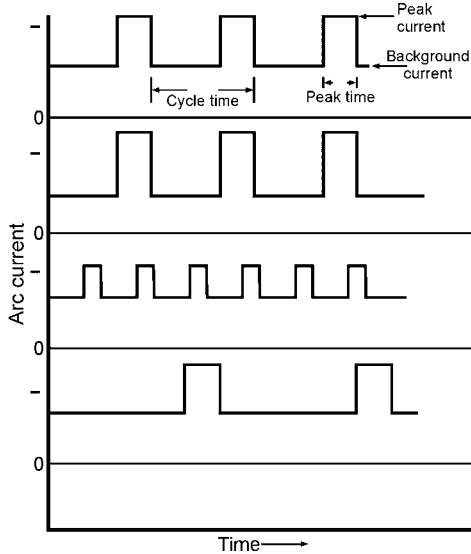


Fig. 12 Pulsed-wave shapes attainable with gas tungsten arc welding power supply

use of inverters for welding aluminum, which is normally gas tungsten arc welded using ac. By using two inverters running at opposite polarity and alternately switching them on and off, a pseudo-ac output is generated. Some inverters still generate ac in this manner. Today (2011), there are more sophisticated methods of generating ac. The ability to generate ac is what really makes the inverter suitable for welding aluminum using GTAW. The fact that the arc voltage never truly goes through zero means that the ac arc is much more stable than it was in the past.

Most inverter-based GTAW power supplies do not need the traditional high-frequency (HF) circuit, which had been added to improve arc initiation and arc stability. The elimination of continuous HF reduces the amount of radio-frequency interference generated by the power supply. In addition to having a very stable output, they also have faster response times than conventional silicon-controlled rectifier power supplies. Figure 13(a) illustrates the typical response of a thyristor-controlled welding

machine, while Fig. 13(b) shows an inverter-controlled arc welding machine.

The two figures show that the inverter-controlled machine reaches a steady-state output in approximately one-third the time of the thyristor-controlled machine, and without the typical starting current overrun and arc instability.

Advanced inverter-based machines also offer an additional major advantage. Figure 9 schematically shows typical penetration patterns for the three basic modes of GTAW: ac, dc negative, and dc positive. Advanced ac output inverter-type welders offer the additional ability to significantly alter the bead shape by adjusting the balance (Fig. 14a) or frequency of the balanced ac square wave (Fig. 14b).

Figure 15 illustrates an advanced 300 A rated ac/dc inverter. The compact size of 439 mm high by 269 mm wide by 620 mm deep (17.3 by 10.6 by 24 in.) and net weight of 34 kg (75 lb) make it highly suitable for portable as well as stationary use. Note that a graphical image of the output settings is displayed by this machine. This helps to simplify making output settings.

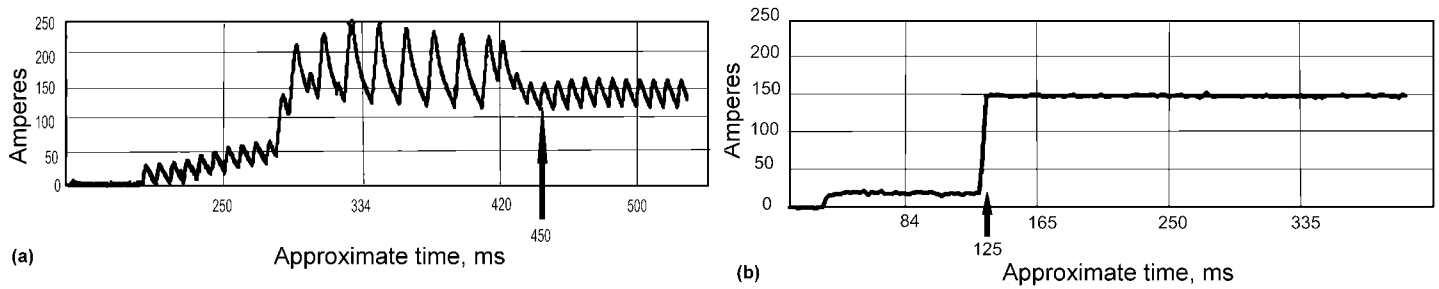


Fig. 13 Current profiles with (a) thyristor-controlled and (b) inverter-controlled welding machines

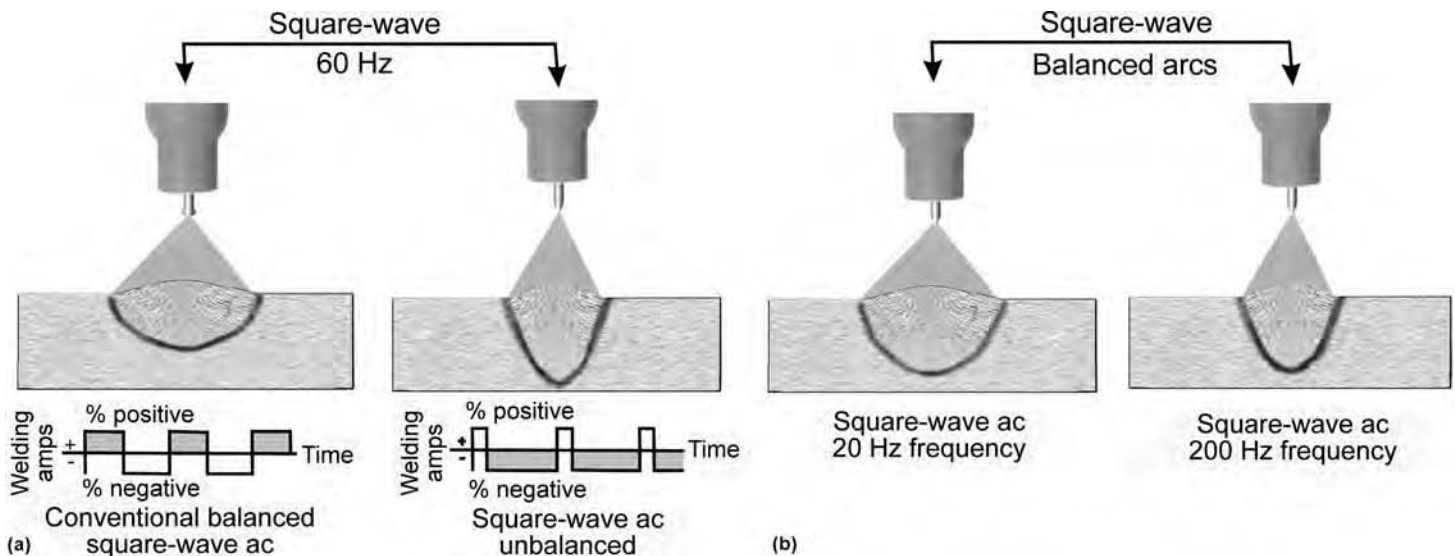


Fig. 14 Effect of alternating current (ac) waveform on weld profile. (a) Effect of altering balance. (b) Effect of altering frequency (with balanced square wave)

High Frequency. In GTAW, the term *high frequency* can have dual-usage meanings:

- The imposition of a separate high-frequency spark on the welding voltage
- On square-wave-output power sources, an ac output voltage greater than 60 Hz

Historically, the term is used to indicate that a separate high-frequency voltage is being generated and imposed on the welding circuit to enhance arc ignition, reignition, and stabilization. The frequency may be in the range of 20 MHz. Most machines have controls that permit continuously “on” operation or for initial arc starting only. The latter is useful to avoid having to bring the electrode into physical contact with the workpiece, which can cause tungsten contamination at the arc start point. In sine-wave ac output machines, continuous high-frequency operation is essential to assure arc stability by continuously assisting arc ignition as the sine-wave output approaches the zero point. This is essential to minimize or eliminate rectification when welding aluminum or magnesium (Fig. 10a). Some machines also permit adjusting the strength of the generated spark.

The imposed high frequency is usually generated by a spark-gap transformer. This may result in radiating signals that can interfere with radio, television, and electronic devices in general. *It is important that the manufacturer’s installation and grounding instructions be consulted and carefully followed.*

With advanced-design square-wave-output machines, the term is used to indicate that the ac output voltage frequency can be higher than 50 Hz. The output voltage frequency can usually be adjusted to anywhere from 20 to 300 Hz (Fig. 12, 14b). These machines also provide for a high-frequency spark for initiating the arc for the same reason as mentioned earlier. A major advantage of these machines is that continuous high frequency is not required to assure arc stability on ac, even when welding aluminum- or magnesium-base materials.

Torch Construction and Electrodes

The welding torch holds the tungsten electrode that conducts the current to the arc, and



Fig. 15 Advanced 300 A, alternating current/direct current inverter for gas tungsten arc welding

it provides a means of shielding the arc and molten metal. The major components of a typical welding torch are shown in Fig. 16.

Welding torches rated at less than 200 A are normally gas cooled (that is, the shielding gas flows around the conductor cable, providing the necessary cooling). Water-cooled torches are used for operation at higher welding currents and/or high arc-on times. Water-cooled torches are commonly used for mechanized, automatic, and robotic welding applications. The cooling water may be supplied to the torch from a recirculating system that uses a radiator or chiller to cool the recirculated water.

Electrode Selection. In selecting electrodes for GTAW, six factors must be considered: material to be welded, electrode material, size, tip shape, electrode holder, and nozzle to be used.

Electrodes for GTAW are typically available in diameters from 0.25 to 6 mm (0.010 to 0.250 in.) and in standard lengths ranging from 75 to 600 mm (3 to 24 in.). Electrodes are classified by the American Welding Society (Ref 6). The classifications are pure tungsten and tungsten alloys of thorium, cerium, lanthanum, or zirconium oxides (Table 1). All classified electrodes are color coded, as shown in Table 1.

Pure Tungsten (EWP). Pure tungsten electrodes (green), which are 99.5% pure, are the least expensive but also have the lowest current-carrying capacity on ac power, low resistance to contamination, and the highest

consumption rate. Pure tungsten is used primarily for ac welding.

Zirconia Tungsten (EWZr-1 and EWZr-8). Tungsten electrodes containing zirconia (brown and white, respectively) have properties between those of pure tungsten and thoriated tungsten electrodes regarding arc starting and current-carrying capacity. These electrodes are recommended for ac welding of aluminum over pure tungsten or thoriated electrodes.

Ceriated Tungsten (EWCe-2). Ceriated tungsten electrodes (gray) were introduced in the late 1980s. Ceriated tungsten electrodes operate well with either ac or dc polarity. These electrodes feature good starting and arc stability and also last longer than their thoriated tungsten counterparts.

Lanthanum Tungsten (EWLa-1, 1.5, and 2). Tungsten electrodes containing lanthanum (marked black, gold, and blue, respectively) have characteristics similar to ceriated tungsten. These tungsten electrodes can be used for both ac and dc applications. As the percentage of lanthanum increases, the arc stability, starting capability, and tip life improve. These electrodes can be used in place of thoriated tungsten with traditional and inverter-based power sources.

Thoriated Tungsten (EWTh-1 and 2). Tungsten electrodes containing 1% Th (yellow) or 2% Th (red) have greater electron emissivity than pure tungsten and therefore greater

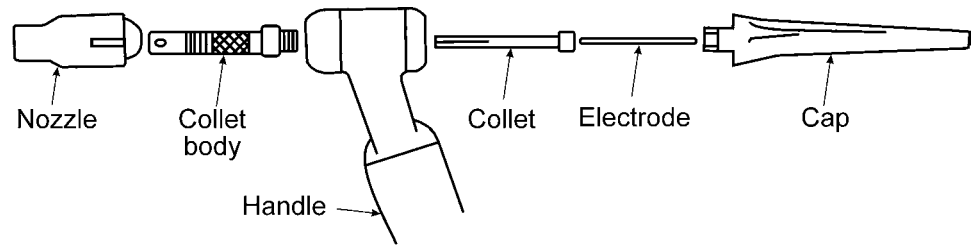


Fig. 16 Schematic showing exploded view of key components comprising a typical gas tungsten arc manual welding torch

Table 1 Chemical composition requirements for tungsten electrodes

Classification symbol (ISO 6848 classification)	Chemical composition requirements		Impurities, mass percent	Tungsten, mass percent	Color code and RGB color value(a)
	Principle oxide	Mass percent			
EWP (WP)	None	Not applicable	0.5 max	99.5	Green #008000
EWCe-2 (WCe20)	CeO ₂	1.8–2.2	0.5 max	bal	Gray (formerly orange) #808080
EWLa-1 (EWLa10)	La ₂ O ₃	0.8–2.2	0.5 max	bal	Black #000000
EWLa-1.5 (WLa 15)	La ₂ O ₃	1.3–1.7	0.5 max	bal	Gold #FFD700
EWLa-2 (WLa 20)	La ₂ O ₃	1.8–2.2	0.5 max	bal	Blue #0000FF
EWTh-1 (WTh10)	ThO ₂	0.8–1.2	0.5 max	bal	Yellow #FFFF00
EWTh-2 (WTh-2)	ThO ₂	1.7–2.2	0.5 max	bal	Red #FF0000
(WTh 30)	ThO ₂	2.8–3.2	0.5 max	bal	Violet #EE82EE
EWZr-1 (WZr3)	ZrO ₂	0.15–0.50	0.5 max	bal	Brown #A52A2A
EWZr-8 (WXr 8)	ZrO ₂	0.7–0.9	0.5 max	bal	White #FFFFFF
EWG	The manufacturer must identify all additions.	The manufacturer must state the nominal quantity of each addition.	0.5 max	bal	The manufacturer may select any color not already in use.

Note: Intentional addition of doping oxides other than indicated for a particular classification is prohibited. (a) Red, green, and blue (RGB) color values and color samples can be found at the following website: <http://msdn.microsoft.com/en-us/library/ms531197.aspx>. Source: Ref 6

current-carrying capacity and longer life. Arc starting is easier, and the arc is more stable, which helps make them more resistant to contamination from the base metal. They maintain a well-sharpened point when welding dc negative polarity. The most commonly used electrode is EWTh-2.

Caution with Thoriated Electrodes. Thorium (thoria) is a radioactive material. Appropriate safety precautions should be taken when using thoriated electrodes. The statement in Fig. 17 was developed by the International Institute of Welding Commission VIII on Health and Safety (Ref 7). The grindings from thoriated electrodes also may be considered as hazardous waste in some states, and disposal may be subject to environmental regulations.

Electrode Tip Shape. The electrode material, size, and tip shape (Fig. 18) will depend upon the welding application, material, thickness, type of joint, and quantity. Electrodes used for ac or electrode positive polarity will be of larger diameter than those used for electrode negative polarity. The shape of the electrode tip can affect the resulting weld shape. Electrodes with included angles from 30 to

120° are stable and give good weld penetration and depth-to-width ratios. Electrodes with smaller included angles (5 to 30°) are sometimes used for grooved weld joints to eliminate arcing to the part sidewalls. For aluminum, aluminum alloys, magnesium, and magnesium alloys, a hemispherical end shape may prove to be the most suitable (end radius equal to one-half the electrode diameter).

Shielding Gases

The original GTAW process used helium as the shielding gas for welding magnesium and aluminum. Today (2011), argon is the predominant shielding gas. Mixtures of the two are sometimes used for specific situations.

Argon is the least expensive of the inert gases used for shielding gas tungsten arc welds, which is only partially responsible for its widespread use. Argon has a low ionization potential (2.52×10^{-18} J, or 15.7 eV), making it easier to form an arc plasma than with other shielding gases. Argon is approximately 1.4 times heavier

than air, so it displaces air, resulting in excellent shielding of the molten weld pool.

Helium has an ionization potential of 3.92×10^{-18} J (24.5 eV), which results in more difficult arc initiation and requires operation at a higher arc voltage and hence higher heat input for a given current. This higher heat input can be very beneficial when welding copper, aluminum, and other high-conductivity materials. Helium shielding used with direct current electrode negative is very effective for welding thick aluminum.

Gas Purity. Most materials can be welded using a welding-grade torch gas with a purity of 99.995% or 50 ppm impurities. However, some reactive materials (for example, titanium, molybdenum, and tantalum) require that the contaminant level be less than 50 ppm. This may require certified gas purity or the use of gas filters and purifiers.

Gas Flow Rates. The density of argon is approximately 1.4 times that of air and 10 times that of helium. For this reason, argon is heavier and will blanket a weld area and be more resistant to cross drafts than helium. Helium, being much lighter than air, tends to rise rapidly and cause turbulence, which can bring air into the arc atmosphere. Because helium costs approximately three times as much as argon, and the required flow rate is two to three times that for argon, the cost of using helium as a shielding gas can be as much as nine times that of argon. Typical flow rates for argon are 9.4 to 14.2 L/min (20 to 30 ft³/min).

Backup Purge and Shielding the Weld. Protecting the molten weld pool from the atmosphere is very important in GTAW. Atmospheric contamination can result in weld cracks, porosity, scaling, and an unacceptable granular appearance. The gas cup on the welding torch is the primary outlet of shielding gas for most GTAW applications. Backside shielding is especially important on thin-material butt welds, fillet welds joining thin-walled tubing, and root-pass welds on pipe because the presence of oxygen can reduce weld-metal penetration and result in the effects mentioned previously. Copper backing bars and ceramics are sometimes used to hold shielding gas against the back surface of the molten weld

“Thorium oxides are found in thoriated tungsten electrodes up to 4.2% (ISO 6848-WT 40 electrode). Thorium is radioactive and may present hazards by external and internal exposure. If alternatives are technically feasible, they should be used.

“Several studies carried out on thoriated electrodes have shown that due to the type of radiation generated, external radiation risks—during storage, welding, or disposal of residues—are negligible under normal conditions of use.

“On the contrary, during the grinding of electrode tips there is generation of radioactive dust, with the risk of internal exposure. Consequently, it is necessary to use local exhaust ventilation to control the dust at the source, complemented, if necessary, by respiratory protective equipment. The risk of internal exposure during welding is considered negligible since the electrode is consumed at a very slow rate.

“Precautions must be taken in order to control any risks of exposure during the disposal of dust from grinding devices.

“The above statement is based on a considered view of the available reports. Commission VIII will continue to keep these aspects under review.”

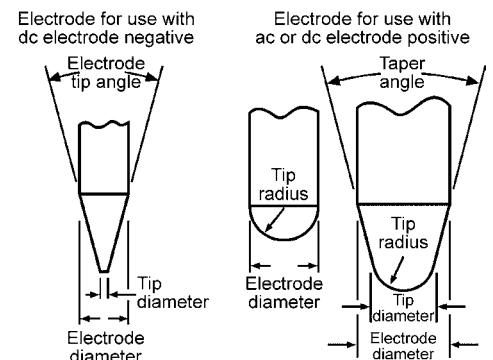


Fig. 17 CAUTION with thoriated electrodes. Statement of appropriate safety precautions when using thoriated electrodes, developed by the International Institute of Welding Commission VIII on Health and Safety. Source: Ref 7

Fig. 18 Electrode end shapes. ac, alternating current; dc, direct current

and support the molten underbead (Fig. 19). Reactive materials and special applications may require more elaborate shielding. This can be in the form of a simple trailing device (Fig. 20) that provides the inert shielding gas or may be as elaborate as a special welding chamber equipped with gas purifiers and analyzers or vacuum chambers. Note the absence of oxidation coloring on the titanium welds shown in Fig. 6(e). For repetitive parts that are automatically welded and where backside protection is not required, a trailing shield can be very effective. A trailing shield with backside protection may be required for some automated applications where currents and travel speeds may be higher.

Gas flow rate in a backup bar or closed tube can be fairly low because the space is small and enclosed; it may be approximately 2.4 L/min (5 ft³/h). Flow rate in a trailer shield may be equal to or greater than the flow rate in the torch, such as 9.4 to 23.6 L/h (20 to 50 ft³/h). Trailer shields may be curved to fit around circular joints.

Filler Metals for GTAW

In general, composition of the filler metal used for a specific GTAW procedure should match that of the material to be welded, especially if the filler material is readily available. The American Welding Society filler-metal specifications in Table 2 provide specific filler-metal requirements (Ref 8).

The thickness of the part to be welded will determine the need for filler-metal additions. Properly designed and prepared, lap welds, butt welds, and edge welds on material thinner than 2 mm (0.08 in.) may be autogenously welded without filler-metal additions. Autogenous welding of aluminum and magnesium is not generally recommended because there is a possibility of cracking, especially crater cracking. Filler metal, when needed, can be added

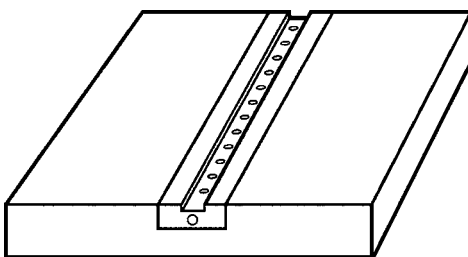


Fig. 19 Backup bar

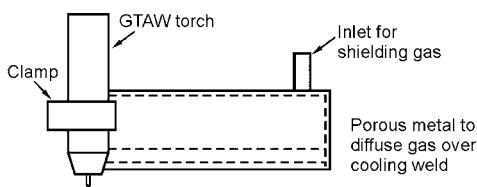


Fig. 20 Trailing shield. GTAW, gas tungsten arc welding

manually from straight lengths (Fig. 21) or automatically from a roll or coil. The filler metal is normally added cold. Filler metal may also be added by hot wire addition with automatic applications (Fig. 22).

Welding Inserts

The purpose of an insert is to preplace filler metal that will subsequently become part of the finished weld and therefore must be of a suitable material type. Welding inserts are used to produce a smooth, uniform backbead. The insert is normally a separate piece of material, although integral internal inserts are sometimes used. Smooth backbeads can be produced in a mechanized system or in manual systems when highly skilled welders are available. Inserts can be commercially obtained in several different configurations.

GTAW Welding Procedures

When a formal welding procedure specification record is required for a particular welded part to comply with specific agency requirements, such as the American Welding Society, American Society of Mechanical Engineers, or others, there are a number of selections and variables that must be considered. These include:

- Type and thickness of material
- Service requirement
- Joint design
- Position in which weld will be made
- Cleanliness of material to be welded
- Filler metal required if the weld is not autogenous
- Filler-metal diameter
- Tungsten type and diameter
- End shape of tungsten and end diameter
- Current type and amperes
- Arc voltage
- Composition of shielding gas
- Gas cup diameter
- Shielding gas flow rate

Table 2 Selection guide to American Welding Society (AWS) specifications for filler metal

AWS specification	Material to be welded
A5.18	Carbon steel
A5.28	Low-alloy steel
A5.9, A5.22	Stainless steel
A5.15	Cast iron
A5.14	Nickel alloys
A5.10	Aluminum alloys
A5.7	Copper alloys
A5.16	Titanium alloys
A5.24	Zirconium alloys
A5.19	Magnesium alloys
A5.21	Surfacing alloys
A5.30	Consumable inserts

Source: Ref 8

- Backside gas shield
- Travel speed

Current Range and Type

The useable current range for a given-sized electrode varies somewhat with the type of shielding gas, the type of equipment, and the type of current being used (Table 3) (Ref 6). The type of current used for specific GTAW applications is perhaps more important, with more choices than for other open-arc welding processes. Table 4 provides a helpful guide for current type selection.

GTAW Manipulation

As with any open-arc welding process, a skilled welder can easily make adjustments for some joint or part alignment issues that may occur, sometimes “on-the-fly” without having to stop and make setting changes. For critical, manual GTAW, some power sources permit remote current adjustment via a foot pedal or



Fig. 21 Typical manual electrode feeding

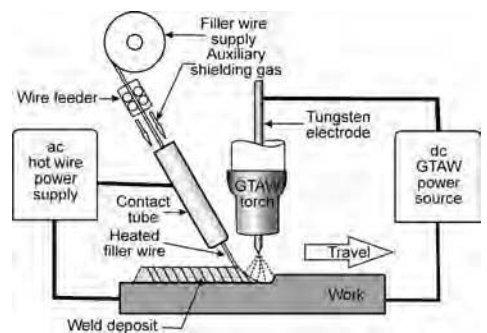


Fig. 22 Schematic of gas tungsten arc welding (GTAW) with hot wire feed. ac, alternating current; dc, direct current

Table 3 Approximate current ranges for tungsten electrodes depending on electrode diameter

Electrode diameter		Direct current, A				Alternating current, A	
		Electrode negative (-)		Electrode positive (+)		Pure tungsten	Tungsten with oxide additives
mm	in.	Pure tungsten	Tungsten with oxide additives	Pure tungsten	Tungsten with oxide additives		
0.25	0.010	Up to 15	Up to 15	Not applicable	Not applicable	Up to 15	Up to 15
0.30	...	Up to 15	Up to 15	Not applicable	Not applicable	Up to 15	Up to 15
0.50	0.020	2-20	2-20	Not applicable	Not applicable	2-15	2-15
1.0	0.040	10-75	10-75	Not applicable	Not applicable	15-55	15-70
1.5	0.060	60-150	60-150	10-20	10-20	45-90	60-125
1.6	...	60-150	60-150	10-20	10-20	45-90	60-125
2.0	...	75-180	100-200	15-25	15-25	65-125	85-160
2.4	0.093 (3/32)	120-220	150-250	15-30	15-30	80-140	120-210
2.5	...	130-230	170-250	17-30	17-30	80-140	120-210
3.0	...	150-300	210-310	20-35	20-35	140-180	140-230
3.2	0.125 (1/8)	160-310	225-330	20-35	20-35	150-190	150-250
4.0	0.156 (5/32)	275-450	350-480	35-50	35-50	180-260	240-350
4.8	0.187 (3/16)	380-600	480-650	50-70	50-70	240-350	330-450
5.0	...	400-625	500-675	50-70	50-70	240-350	330-460
6.3	...	550-875	650-950	65-100	65-100	300-450	430-575
6.4	0.250 (1/4)	575-900	750-1000	70-125	70-125	325-450	450-600
8.0	650-830
10.0

Note: If no value is given, no recommendation is available. The current values are based on the use of argon gas, and these values may vary depending on the type of shielding gas, type of equipment, and application. Source: Ref 6

Table 4 Suitability of gas tungsten arc welding current types for various materials

Metal to be welded	Alternating current(a)	DCEN(b)	DCEP(c)
Low-carbon steel:			
0.38-0.76 mm (0.015-0.030 in.)(a)	G(d)	E	NR
0.76-3.18 mm (0.030-0.125 in.)	NR	E	NR
High-carbon steel	G(d)	E	NR
Cast iron	G(d)	E	NR
Stainless steel	G(d)	E	NR
Heat-resistant alloys	G(d)	E	NR
Refractory metals	NR	E	NR
Aluminum alloys:			
≤0.64 mm (0.025 in.)	E	NR(e)	G
>0.64 mm (0.025 in.)	E	NR(e)	NR
Castings	E	NR(e)	NR
Beryllium	G(d)	E	NR
Copper and alloys:			
Brass	G(d)	E	NR
Deoxidized copper	NR	E	NR
Silicon bronze	NR	E	NR
Magnesium alloys:			
≤3.2 mm (0.125 in.)	E	NR(e)	G
≤4.8 mm (0.188 in.)	E	NR(e)	NR
Castings	E	NR(e)	NR
Silver	G(d)	E	NR
Titanium alloys	NR	E	NR

Note: E, excellent; G, good; NR, not recommended. (a) Stabilized and balanced. (b) Direct current electrode negative. (c) Direct current electrode positive. (d) Amperage should be approximately 25% higher than when DCEN is used. (e) Unless work is mechanically or chemically cleaned in the areas to be welded. Source: Ref 1

torch-mounted thumb-operated device. The welder's skills can also make some variations by controlling travel speed and/or manipulating the torch. Arc oscillation can be used in both manual and mechanized welding. The benefits in manual welding are basic to the control of the weld when adapting to changes in the weld joint and gap. In automated welding, the oscillation is typically produced by moving the entire welding torch mechanically and is preset to provide width of oscillation, rate, and dwell time at the end of each oscillation.

Filler-Metal Feeding

Most GTAW is accomplished by the welder manually feeding a straight length of filler electrode, as shown in Fig. 21. Even with manual GTAW, the filler electrode can be automatically power fed into the arc using special devices that can be incorporated and synchronized with the welding torch motion.

Mechanized or torch-mounted GTAW can incorporate either cold or hot wire feeding:

- *Cold wire*: Employs coiled wire fed from an independent wire feeder into the leading edge of the weld pool at a preset but adjustable rate. Figure 5 shows a setup using cold wire feeding. Note the wire supply, the feeder, and the feeding tip arrangement.
- *Hot wire*: Employs a heated filler metal to increase the deposition rate of the process. The wire is resistance heated to near the melting temperature and fed into the trailing edge of the weld pool. The higher deposition rates obtained with hot wire improve productivity. The process is suitable for making overlays as well as welds (Fig. 22).

Automatic and Robotic Welding

Generally, the factors that must be considered for manual GTAW also must be considered for automatic and robotic (A/R) GTAW. The main difference between manual and A/R GTAW is that travel speed, current, and wire feed rates can be greater for A/R welding. With higher travel speeds and higher current, the weld deposit would remain hot enough to oxidize after the torch passes, and for this reason, the use of a trailer shield is recommended for all materials. A trailer shield must be used with reactive and refractory metals such as titanium and niobium (columbium) and is strongly recommended with stainless steel and nickel- and cobalt-base alloys.

Successful A/R welding requires that parts be uniformly and consistently fit up from part to part. Only if this condition exists can the welding truly be automatically controlled. Weld programmers' programmable logic controllers and robotic controllers can control all the parametric functions for a GTAW application: arc current, voltage, travel speed, electrode feed

rate, and gas flow. These devices can be used to start and stop arc current, travel, wire feed, and gas flow and to control these items within fixed predetermined limits. These devices can also vary welding parameters along joints where thickness, type of joint, or other factors require a change. Most modern GTAW power supplies are capable of having current controlled by various external devices, thus allowing predetermined, multiple procedural changes.

Safety When Using GTAW

Gas tungsten arc welding is an electric arc welding process, just as are manual electrode, flux cored electrode, and gas metal arc welding, and therefore, as a minimum, the safe practices followed for these processes should be followed. There are three basic safety documents, and all personnel, welders, and supervisors alike should understand and be familiar with the safe practices discussed in these documents. These documents are:

- “Safety in Welding and Cutting,” ANSI Z49.1 (Ref 8)
- “Fire Prevention in the Use of Welding and Cutting Processes,” ANSI Z49.2 (Ref 8)
- “Safe Handling of Compressed Gases in Containers,” 11th ed., Compressed Gas Association (CGA) P-1 (Ref 9)

To protect personnel from injury or death, everyone must be aware of and understand all the possible hazards of arc welding and follow procedures and precautions to avoid these hazards. Just as for other open-arc welding processes, the possible hazards may be grouped into four categories:

- Electrical shock
- Fumes and gases
- Arc radiation
- Fire and explosion

With GTAW, there is a fifth potential hazard. If thoriated (thorium-base) electrodes are to be used, there is a potential for radioactive contamination, and all necessary precautions (Fig.17) should be strictly taken.

Electrical Shock

Electric shock can kill, and all personnel require protection from possible dangerous electrical shock:

- The electrode and work (or ground) circuits may be electrically “hot” when the welder is on. Never permit contact between “hot” parts of the circuits and bare skin or wet clothing. Use dry, hole-free gloves to insulate hands.
- Always insulate personnel from the work and ground by using dry insulation. When welding in damp locations, on metal floors,

gratings, or scaffolds, and when welding requires positions such as sitting or lying, make certain the insulation is dry and large enough to cover the full area of possible physical contact with work and ground.

- Always be sure the work cable makes a good electrical connection with the metal being welded. The connection should be as close as possible to the area being welded.
- Ground the work or metal to be welded using a good electrical connection.
- Maintain the welding torch, work clamp, welding cable, and welding machine in good electrical operating condition.
- Never dip the end of the torch in water to cool it. This can also crack the gas cup and contaminate the torch.
- Never simultaneously touch electrically “hot” parts of torches connected to two welders, because voltage between the two can be the total of the open-circuit voltage of both welders.
- When changing or installing electrodes in the GTAW torch, make sure the power is turned off at the welder.
- When working above floor level, provide protection against falling in the event of electric shock.
- Never allow GTAW with wet or damp gloves. They can allow shocks from the high frequency when it is being used.

Fumes and Gases

Welding may produce fumes and gases hazardous to health, and breathing these fumes and gases should be avoided. Precautions include:

- When welding, the welder should keep his head out of the fumes.
- Provide enough ventilation and/or exhaust at the arc to keep fumes and gases away from the breathing zone of the welder.
- When welding with consumables that require special or additional ventilation (such as those having significant amounts of manganese, chrome, etc.) or for welding on galvanized, lead-, or cadmium-plated steel and other metals that produce toxic fumes, local exhaust is recommended, and even greater care may be required, such as a fresh air supply to the welder by an air-supplied respirator.
- Do not allow welding in locations near chlorinated hydrocarbon vapors coming from degreasing, cleaning, or spraying operations. The heat and radiation of the arc can react with solvent vapors to form phosgene, a highly toxic gas, or other irritating products.
- Shielding gases used for arc welding can displace air and cause injury or death by suffocation. Always provide enough ventilation, *especially in confined areas*, to ensure that breathing air is safe.

- Everyone should read and understand the manufacturer’s instructions for the equipment and the consumables to be used, including material safety data sheets.

Arc Radiation

The total radiant energy produced by the GTAW process can be higher than that produced by the shielded metal arc welding process, because the quantity of welding fumes (smoke) produced is significantly lower and the arc is more exposed. Generally, the highest ultraviolet radiant energy intensities are produced when using an argon shielding gas and when welding on highly reflective materials such as aluminum. The range of suggested filter glass shades for GTAW, as presented in AWS/ANSI Z49.1, may be used as a guide (Ref 8):

Current range, A	Filter plate shade range number
0–50	8–10
50–150	8–12
150–500	10–14

The actual filter plate used will depend on the person and the location of the arc. It is recommended that the operator start with the darker shade and then go to lighter shades until the operation is sufficiently visible. However, do not go to a shade lighter than the lowest number for a given current range.

Dark leather or wool clothing (to reduce reflection that can cause ultraviolet burns to the face and neck underneath the helmet) is recommended for GTAW. The greater intensity of the ultraviolet radiation may cause rapid disintegration of cotton clothing (Fig. 21).

Provide adequate screening to protect other personnel, who may at times be close to the welding, from radiation exposure by using suitable screening.

Fire and Explosion

Remove fire hazards from the immediate area. If this is not possible, cover them to prevent any possible welding sparks from starting a fire. Remember that welding sparks and hot materials from welding can easily go through small cracks and openings to adjacent areas. Have a fire extinguisher readily available.

All personnel should read and follow the instructions on compressed gas cylinders, on associated equipment, and in the CGA publication P-1, “Precautions for Safe Handling of Compressed Gases in Cylinder” (Ref 9). Use only compressed gas cylinders containing the correct shielding gas for the process used and with properly operating regulators designed for the gas and pressure used. All hoses, fittings, and so on should be suitable for the application and maintained in good condition.

Always keep cylinders in an upright position and securely chained to a power source undercarriage or fixed support. Cylinders should be located:

- Away from areas where they may be struck or subjected to physical damage
- A safe distance from arc welding or cutting operations and any other source of heat, sparks, or flame

Never allow the electrode, electrode holder, or any other electrically “hot” parts to touch a cylinder.

The welder should keep his head and face away from the cylinder valve outlet when opening the cylinder valve. Valve protection caps should always be in place and hand tight, except when the cylinder is in use or connected for use.

Acknowledgments

Special thanks are given for the contributions from Lynn Welding of Newington, Conn.

(www.lynnwelding.com), and Innofab Source of Tempe, Ariz. (www.innofabsource.com). As with all welding processes, technology has advanced significantly from the 1993 edition of this Handbook. This article expands the excellent presentation made by Grant Ken-Hicken of the Sandia National Laboratory that appeared in the 1993 edition (Ref 1). Thanks are also given to The James F. Lincoln Arc Welding Foundation (Ref 2) for contributing much information to this article on GTAW.

REFERENCES

1. G. Ken-Hicken, Gas-Tungsten Arc Welding, *Welding, Brazing, and Soldering*, Vol 6, *ASM Handbook*, ASM International, 1993
2. *Gas Tungsten Arc Welding*, 2nd ed., The James F. Lincoln Arc Welding Foundation, Cleveland, OH, www.jlwf.org
3. Heliarc, registered trademark originally belonging to Linde Corporation and now ESAB
4. T. Myers, Why the Growing Interest in Gas Tungsten Arc Welding? *Fabricator*, Vol 22 (No. 9), Nov 1992, p 38–39
5. *Welding Handbook*, 8th ed., Vol 2, American Welding Society, 1991
6. “Specification for Tungsten and Oxide Dispersed Tungsten Electrodes for Arc Welding and Cutting,” AWS A5.12M/A5.12:2009 (ISO 6848:2004 MOD), American Welding Society, Miami, FL
7. Document VIII-1901-00 IIW-1496-00, International Institute of Welding, Cedex, France
8. American Welding Society, Miami, FL
9. Compressed Gas Association, Chantilly, VA

Gas Tungsten Arc Welding with Penetration-Enhancing Compounds

Ian D. Harris, Edison Welding Institute

GAS TUNGSTEN ARC WELDING (GTAW)—also referred to as the tungsten inert gas (TIG) process—is used in aerospace, power generation, oil and gas, and other industries for single-pass welds and the root passes of multiple-pass welds in sheet, plate, pipe, tube, fittings, and castings. The advantages of using the GTAW process include high-quality welds, precise control of welding parameters and heat input, and low equipment costs.

The productivity of GTAW is limited for many applications because of low deposition rates, shallow penetration (typically 3 mm, or $\frac{1}{8}$ in.), or inconsistent penetration caused by small variations of trace elements such as sulfur in the base material, especially in austenitic stainless steels (lower part of Fig. 1). To overcome these problems and reduce the cost of

fabrication and construction of a variety of products, the Edison Welding Institute (EWI) and the National Joint Council (Ref 1–3) developed compounds to enhance the penetration of the GTAW process. The EWI-trademarked process is DeepTIG for GTAW.

Penetration-enhanced GTAW processes have been referred to variously as Flux TIG, A-TIG, and GTAW with a penetration-enhancing compound (PEC). In all cases, the process uses a material that is not a flux but rather an oxide or mixture of oxides. Similar products are available in Canada (such as the Catalyst from Liburdi), Europe (originating from research at the Paton Welding Institute in Kiev, Ukraine, in the mid-1970s), and purportedly in India and China. Most are based on oxides, but little information on specific composition is available in the open literature. The EWI compounds are based on mixtures of oxides of silicon, titanium, and chromium, whereas the Catalyst from Liburdi is based on titanium oxide only. The U.S. patent (Ref 4) is held by EWI.

welding. A simple square-edged, closed-butt joint preparation is often used for the GTAW weld with a penetrating compound. In many applications, full penetration can be achieved with a square-edged, closed-butt joint, reducing joint preparation costs, filler material costs, heat input, distortion, and welding times. Thicker sections can be welded using a penetrating compound on a square-butt land for the root pass and the weld completed in a conventional groove preparation. The GTAW DeepTIG products are recommended for mechanized and orbital welding with and without filler metal. They also have proven useful in manual welding applications where maximum penetration is not required. Standard GTAW equipment, shielding and backing gases, and consumables are used. The DeepTIG compound is not intended to provide shielding for either the face or the root of the weld.

Advantages and Disadvantages

Shipbuilders and industrial users have confirmed the performance and cost benefits of using the penetration-enhanced GTAW process. For example, the GTAW-DeepTIG process increases weld penetration by as much as 300% for mechanized or automatic applications. The process also reduces heat-to-heat variation in penetration and distortion, based on achieving the desired penetration at a lower welding current. The DeepTIG process can also promote grain refinement in some alloys. The mechanical properties, weldability, corrosion resistance, and safe use of these fluxes have been extensively tested and found suitable for a wide range of applications. The penetration-enhanced GTAW process can reduce welding time by 50% in most applications. For example, typical application in stainless steels and nickel alloys that are welded manually in five passes may require only one or two passes using a GTAW with a penetrating compound. Welding times for these applications could be reduced from approximately 23 min for the manual

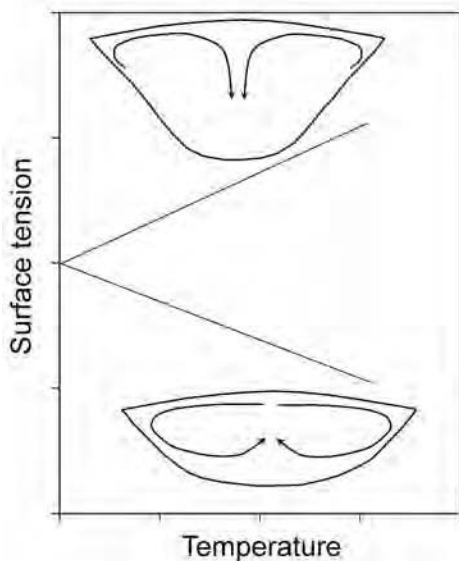


Fig. 1 Schematic of the mechanism of increased penetration (top) with penetration-enhancing compounds. There is a reversed weld-pool flow and increased penetration based on the higher surface tension.

Principles of Operation

The principles of operation are illustrated (Fig. 1) by the change of surface tension and fluid flow in the cross-sectional view of a weld pool resulting from the effect of active oxides in DeepTIG (or other PEC product). For simplicity, the DeepTIG name is principally used henceforth. The effect of the oxygen overwhelms the changes in penetration caused by sulfur, resulting in an inward fluid flow and increased surface tension, as shown in the upper part of Fig. 1. Penetration-enhancing compounds for GTAW can increase weld penetration by as much as 300% (Fig. 2) and produce consistent penetration regardless of heat-to-heat variations in base-metal composition.

The DeepTIG penetrating compound is a mixture of inorganic powders suspended in a volatile medium such as acetone or isopropyl alcohol. The mixture is applied to the base metal adjacent to the weld joint prior to

procedure to 3 min for a single-pass DeepTIG GTAW procedure.

Typical reasons for using a penetration-enhanced GTAW process include one or more of the following:

- High potential for reduced rejection rates
- Improved productivity
- High level of repeatability
- Reduced number of weld procedure specifications
- Reduced heat input and distortion compared to conventional GTAW
- Reduced joint preparation requirements
- Reduced wire consumption for making the weld

When the penetration-enhanced GTAW process is used for welding of austenitic and superaustenitic materials, there is little to no observable impact on microstructure morphology (Ref 5–8). Conversely, when used on duplex and superduplex stainless steels, the microstructure shifts to a finer prior-ferrite grain size with a larger volume fraction of austenite. One critical item noted following welding was that, for both duplex and superduplex, the weld-metal nitrogen content remained unchanged following welding. Typically, these alloys lose 10 to 30% of their nitrogen content during welding. Superduplex stainless steels welded in conjunction with penetrating compounds have been shown to exhibit improvements in both mechanical and corrosion properties. The use of commercially available oxide-based DeepTIG products for superduplex stainless steel yields a smaller observable (prior-ferrite) grain size when compared to welds produced without the use of penetration-enhanced GTAW.

Previous work (Ref 5–8) showed that the use of penetration-enhanced GTAW for various grades of duplex stainless steel grades offers a competitive advantage over that of conventional GTAW welding. In austenitic stainless steels (>95% austenite), for example, the use of DeepTIG increased penetration without affecting the primary solidification microstructure. In other stainless steels (~50% austenite), penetration was increased and weld quality was improved with a smaller prior- δ -ferrite grain size and a more consistent austenite/ferrite balance in the solidified weld metal. Some of the research suggests that this small grain size and austenite/ferrite balance occurs over a wide range of heat inputs, thus increasing the weldability window for duplex and superduplex alloys.

Preliminary welding procedures have been developed for full-penetration welds in 6 mm (0.25 in.) thick 300-series stainless steel square-butt joints. Faster travel speeds are possible by maintaining constant arc energy and maintaining a short arc length. To date, travel speeds have been tested up to 300 mm/min (12 in./min.) and used in the field up to 150 mm/min (6 in./min.). A residual slag that

typically remains on the top surface of the weld pool can be removed by grinding or mechanized wire brushing. The slag need not be removed prior to subsequent passes. This slag will float to the top of each subsequent pass and remain visible on the finished weldment. If the weld face appearance is important, slag removal is recommended prior to deposition of a cosmetic cap pass or deposition of subsequent passes in a multipass weld.

Equipment, Procedures, and Applications

Equipment. The welding equipment used for penetration-enhanced GTAW is the same as that used for conventional GTAW (Fig. 3). Maintenance of a short arc length (1.2 mm, or

0.050 in.) is critical to ensure maximum penetration during welding. Arc length is a critical variable in the repeatability of welds made with the penetration-enhanced GTAW products; hence, the use of arc voltage control and mechanized equipment is well recommended.

Penetrating compounds for GTAW are commercially available in kit form or in larger quantities. Kits include materials safety data-sheets and instructions on how to apply the penetrating compound to a joint. Also, the DeepTIG PEC is available from EWI in a wire that allows increased penetration by using a compound addition to the wire in a single product. This is currently available for stainless steels with an SS-7 core, yielding results similar to that shown in Fig. 4.

Procedure. Process operating procedure is very similar to that for conventional GTAW,

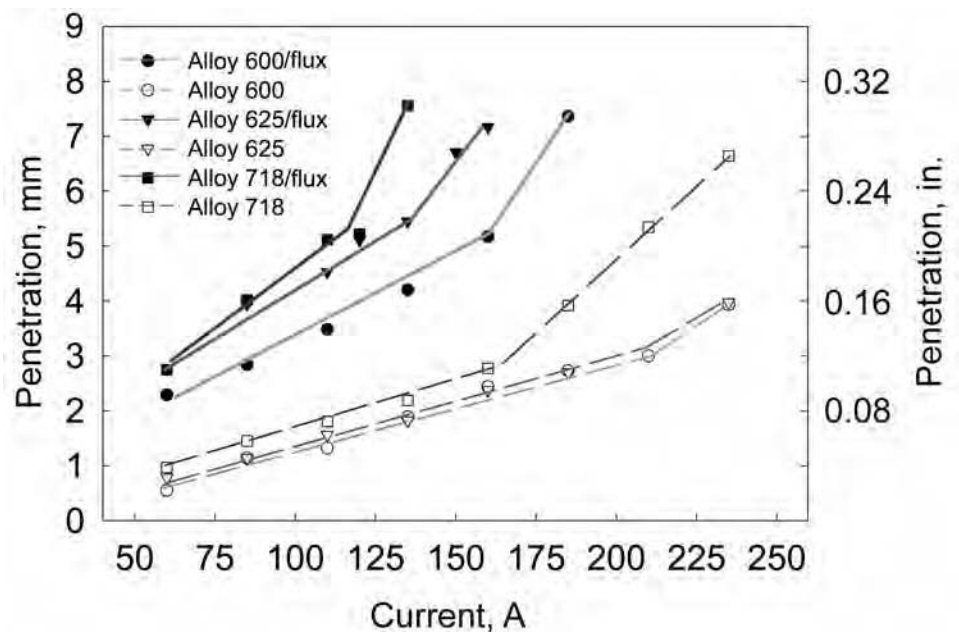


Fig. 2 Effect of welding current on penetration with and without the penetration-enhancing compound (DeepTIG, Edison Welding Institute)



Fig. 3 Penetration-enhancing compounds pasted onto the surface of a butt joint in a pipe for gas tungsten arc welding. Courtesy of the Edison Welding Institute

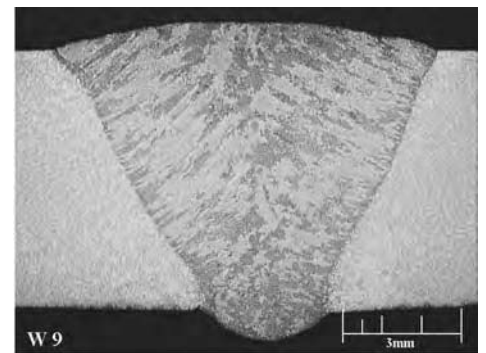


Fig. 4 A 6 mm (0.25 in.) thick type 304 stainless steel welded with penetration-enhanced gas tungsten arc welding (DeepTIG wire at 195 A). Courtesy of the Edison Welding Institute

and similar procedures are recommended. If a powder-based product is used, it should be applied using a carrier and mixed to a consistency that allows it to be easily applied to the joint when it is fit up. The product will not give the penetration increase desired if removed before welding, so care must be taken to avoid accidental contact before welding. With the product deployed in a wire, this is not a concern.

Inspection and weld quality control is very similar to conventional GTAW, and similar procedures are recommended. Troubleshooting is very similar to conventional GTAW, and similar procedures are recommended for the equipment used.

Applications. Penetrating compounds from EWI are available for the following joint materials:

- DeepTIG SS-7 for stainless steels (e.g., types 304, 316, 347, 409, 410, duplex, and superduplex)
- DeepTIG NI-139 for nickel-base alloys (e.g., alloys 600, 625, 690, 718, 800) (Fig. 5)
- DeepTIG CS-325 for carbon and low-alloy steels (e.g., A36, SA-178C, 2¼Cr-1Mo, X80)

Typical components and joints using the SS-7 penetrating compound in the GTAW of stainless steel include:

- Sterilization chambers and pressure vessels

- Coil ends joined together in steel production
- Nuclear fabrication
- Oil and gas (316L and duplex alloys 2205 and 2507) components such as umbilical center-tubes, plumbing on skids (injection pumps), hydraulic control panels, Christmas trees (plumbing)

The United States Navy has approved the use of the SS-7 product for GTAW of stainless steels. One shipbuilder is using penetration-enhanced GTAW to fabricate piping for Navy aircraft carriers and for commercial tankers. Another shipbuilder has used the SS-7 compound to improve the quality and reduce the costs of pipe welds on Navy destroyers.

A boiler manufacturer has used DeepTIG compounds for boiler tube production applications. An orbital GTAW equipment manufacturer uses the SS-7 compound for orbital GTAW of stainless steel tubing. Another manufacturer uses it for fabricating large medical instrument sterilizers. Another application is for fabrication of duplex and superduplex tubing (Fig. 6) for down-hole umbilicals associated with oil and gas equipment. Aerospace manufacturers and suppliers have used penetrating compounds for fabrication of various components.

Welds produced by GTAW with penetrating compounds perform commensurate to or better than conventional GTAW welds. Property improvements include:

- Increased strength
- Decreased volume of weld metal and heat-affected zone
- Increased corrosion resistance
- Improved bead shape and nugget size
- Improved austenite content in SAF 2507

- Smaller grain size in SAF 2507

In duplex and superduplex alloys, property improvements include:

- Improved microstructure, corrosion, and mechanical properties
- Weld metal retained a majority of the base-metal nitrogen
- Weld-metal properties exceeded industry requirements
- Refined primary delta grain size
- Small grains expand welding process window

The NI-139 compound is used in the aerospace industries for welding nickel-base alloys. One example is in turbine engine manufacture for nonrotating components (Fig. 7).

Boiler tube and pipe applications include welding carbon and alloy steels with the CS-325 compound. One example is a turbine barrel (Fig. 8).

Personnel

Skill level and training are the same as those for conventional GTAW, especially when mechanized or robotic welding is employed. The only significant difference is a short arc length, preferably with arc voltage control (AVC). The use of AVC makes the technique a little more difficult to achieve when welding manually, and the deeper weld pool requires more vigilance for the welder to control.

Health and safety issues are the same as those for GTAW. Electric shock, eye protection, burns, ultraviolet radiation, and fume exposure are typical concerns. A minor amount

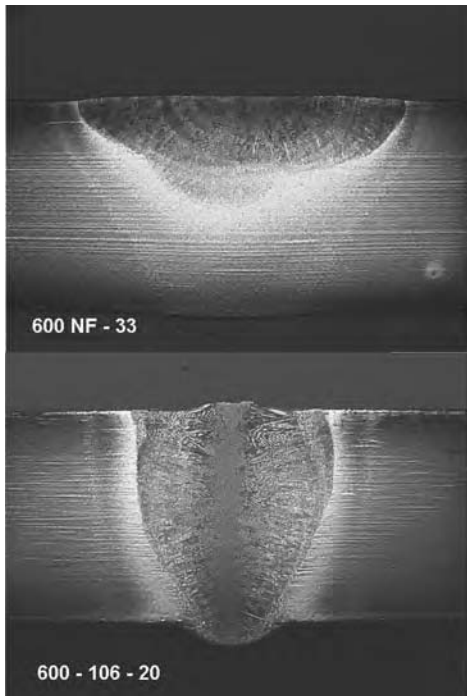


Fig. 5 Illustration of penetration increase on nickel alloy 600; 185 A, 9.5 V, 75 mm/min (3 in./min) travel speed. Without (top) and with (bottom) DeepTIG. Courtesy of the Edison Welding Institute

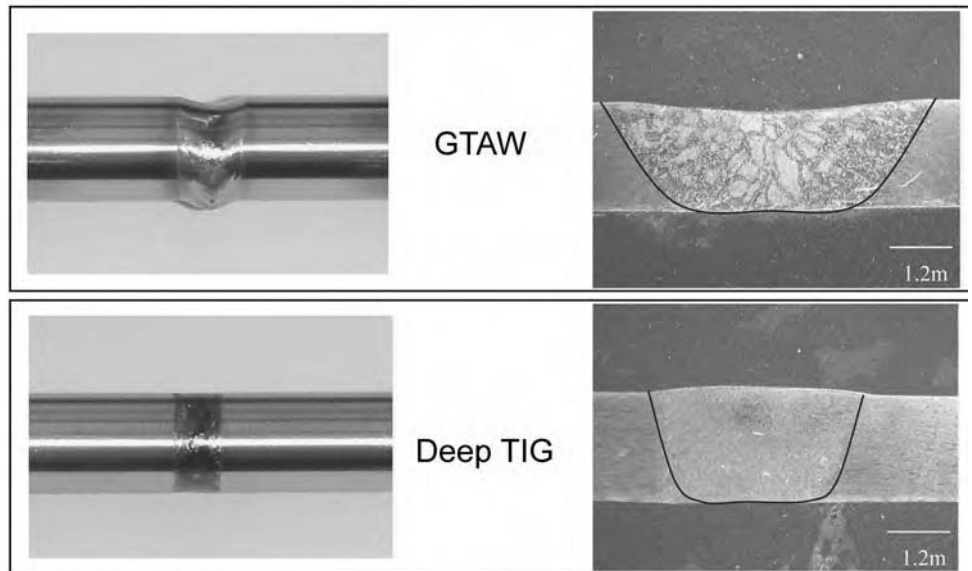


Fig. 6 Use of DeepTIG on thin-walled 2205 duplex tubing to reduce sagging from low depth-to-width ratio. GTAW, gas tungsten arc welding. Courtesy of the Edison Welding Institute and Sandvik



Fig. 7 Turbine rear frame in alloy 718 fabricated using DeepTIG. Courtesy of the Edison Welding Institute and GE

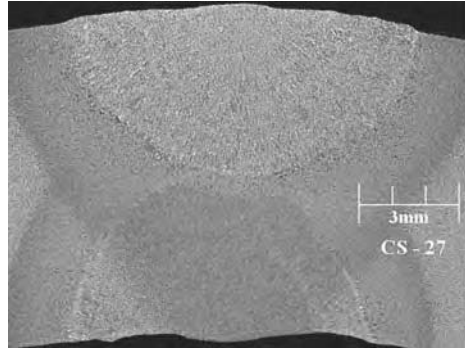


Fig. 8 Two-sided weld in a steel turbine barrel (prior to machining operation). Courtesy of the Edison Welding Institute

of fume generation will occur with the use of the compounds. Appropriate measures should be considered to reduce welder exposure to welding fumes. ANSI Z49.1-99, *Safety in Welding, Cutting, and Allied Processes*, should be reviewed before welding.

REFERENCES

1. U.S. Patent 5804972, filed 1996, granted Sept 1998
2. T. Paskell, M. Johnson, and W. Lin, "Development, Evaluation, and Deployment of Fluxes for GTAW That Increases Weld Penetration in Austenitic Stainless Steels, Carbon-Manganese Steels, and Copper-Nickel Alloys," Navy Joining Center Report NJC TDL 93-06, Columbus, OH, July 24, 1997
3. C.D. Lundin et al., "Gas Tungsten Arc Welding Flux for Increased Penetration Properties Characterization," University of Tennessee final project report, Project NJC TL 94-0038, June 1996
4. R. Richardson and P.G. Kirchheimer, "Mechanisms of Enhanced Penetration with Gas Tungsten Arc Welding," The Ohio State University Final Project Report, NJC TL 94-2048, March 1996
5. N.D. Ames, M.Q. Johnson, and M. Holmquist, "Orbital Welding of Small-Bore Super Duplex Tube Using GTAW Flux," Duplex Stainless Steel Conference, Oct 20, 2000 (Venice)
6. N.D. Ames, M. Ramberg, M.Q. Johnson, and T. Johns, "Comparison of Austenitic, Super Austenitic and Super Duplex Weld Properties Produced Using GTAW Flux," Stainless Steel World America 2002, Feb 12, 2002
7. N.D. Ames, M.Q. Johnson, and J.C. Lippold, "Effect of GTAW Flux on the Microstructure and Properties of Austenitic, Super Austenitic and Super Duplex Stainless Steel Welds," Trends in Welding Research 2002, April 15, 2002
8. N.D. Ames, C. Frye, and K. Larsen, "Improved Corrosion Resistance of Super Duplex Weldments," Stainless Steel World America 2004, Oct 20, 2004

Plasma Arc Welding

Ian D. Harris, Edison Welding Institute

PLASMA ARC WELDING (PAW) can be defined as a gas-shielded arc welding process where the coalescence of metals is achieved via the heat transferred by an arc that is created between a tungsten electrode and a workpiece. The arc is constricted by a copper alloy nozzle orifice to form a highly collimated arc column (Fig. 1). The plasma is formed through the ionization of a portion of the plasma (orifice) gas. The process can be operated with or without a filler-wire addition.

Principles of Operation

Once the equipment is set up and the welding sequence is initiated, the plasma and shielding gases are switched on. A pilot arc is then struck between a tungsten alloy electrode and the copper alloy nozzle within the torch (non-transferred arc mode), usually by applying a high-frequency open-circuit voltage. When the torch is brought in close proximity to the workpiece or when the selected welding current is initiated, the arc is transferred from the electrode to the workpiece through the orifice in the copper alloy nozzle (transferred arc mode), at which point a weld pool is formed (Fig. 1).

The PAW process can be used in two distinct operating modes, often described as the melt-in mode and the keyhole mode:

- *The melt-in-mode* refers to a weld pool similar to that which typically forms in the gas tungsten arc welding (GTAW) process, where a bowl-shaped portion of the workpiece material that is under the arc is melted.
- *In the keyhole mode*, the arc fully penetrates the workpiece material, forming a nominally concentric hole, or keyhole, through the thickness. The molten weld metal flows around the arc and resolidifies behind the keyhole as the torch traverses the workpiece.

Current and Operating Modes

The PAW process uses three current modes: microplasma (melt-in mode), medium-current

plasma (melt-in mode), and keyhole plasma (keyhole mode). This categorization is primarily based on the level of welding current. The microplasma mode is usually defined in the current range from 0.1 to 15 A. The medium-current plasma mode ranges from 15 to 100 A. The keyhole plasma mode is above 100 A. There is a certain degree of overlap between these current ranges. For example, keyholing can be achieved at 70 A on a 2 mm (0.08 in.) sheet. Equipment is available for welding currents up to 500 A, although a 300 A maximum is typical. Microplasma and medium-current melt-in modes are used for material up to 3 mm (0.12, or 1/8, in.) thick, whereas the keyhole plasma mode is used for greater thicknesses and higher travel speeds.

In addition to operating in a continuous and steady direct current electrode negative (DCEN) mode, the PAW process can be carried out using DCEN pulsed current, as well as in the variable polarity mode, which uses both direct current electrode positive (DCEP) and electrode negative polarity switching. The pulsed-current mode (both DCEN and DCEP/DCEP) is most often used when current levels (typically, above 100 A) are employed for keyhole plasma welding. Pulsing the current widens the tolerance region of acceptance welding parameters, primarily by further

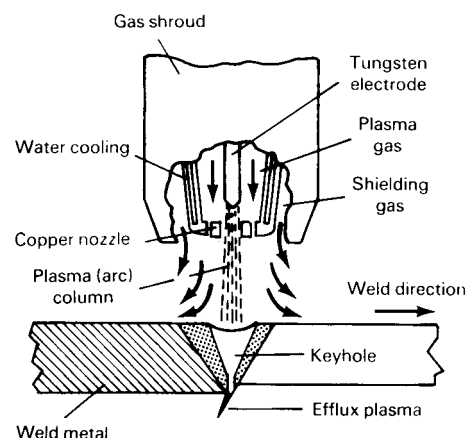


Fig. 1 Plasma arc welding process, showing constriction of the arc by a copper nozzle and a keyhole through the plate

stabilizing the formation of the keyhole itself (Fig. 2).

The electrode positive component of the variable polarity plasma arc (VPPA) welding process promotes cathode etching of the tenacious surface oxide film when welding aluminum alloys, allowing good flow characteristics and consistent bead shape. Pulsing times are typically 20 ms for the electrode negative component and 3 ms for the electrode positive polarity. The VPPA welding process is used very effectively in specialized aerospace applications.

The PAW process is generally applied when the high penetration of the keyhole welding mode can be exploited to minimize the number of welding passes and hence welding time. The time saved can reduce the direct labor element of the welding operation. At the other end of the scale, the microplasma operating mode is used to weld small, thin-section components (as low as 0.025 mm, or 1 mil, thick), where the high arc constriction and low welding

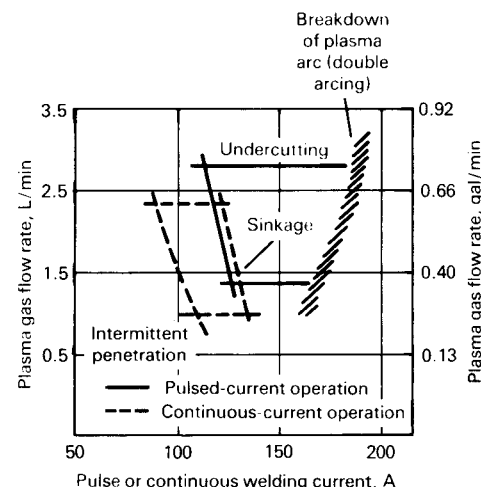


Fig. 2 Tolerance to variation in welding current and plasma gas flow rate in pulsed- and continuous-current keyhole welding; boundaries show the welding parameter combinations at which specific defects are likely to occur. Welding parameters: nozzle bore, 2.36 mm (0.0929 in.); electrode diameter, 4.8 mm (0.19 in.)

current can be beneficial in controlling heat input and distortion.

Advantages and Disadvantages

The advantages of the PAW process are primarily intrinsic to the keyhole mode of operation, because greater thicknesses of metal can be penetrated in a single pass, compared with other processes, such as GTAW. This greater amount of penetration allows a reduced amount of joint preparation. In some materials, for example, a square-grooved butt joint preparation can be used for thicknesses up to 12 mm (0.5 in.). The process can produce high weld integrity (similar to GTAW) while minimizing weld passes and hence welding times and labor costs. The columnar shape of the arc results in a greater tolerance to variations in torch standoff distance, when compared with the conical arc shape of a GTAW arc. The tungsten electrode used in the PAW process is protected from contamination by the constricting nozzle (Fig. 1). The longer arc length allows better viewing of the weld pool, which is important in manual welding.

Disadvantages include the greater capital equipment cost, when compared with its main rival, the GTAW process. Although high arc constriction achieves higher penetration, it also reduces the tolerance of the process to joint gaps and misalignment, when compared with the broader, conical arc of the GTAW process. The greater complexity of the PAW torch design and the greater number of parts requires more scheduled maintenance. The accurate set-back of the electrode tip, with respect to the nozzle orifice, is required to maintain consistent results. However, this task is facilitated by a general-purpose tool designed for nozzle removal and replacement and for electrode set-back adjustment.

Equipment

A basic PAW system consists of a power source, a plasma control console, a water cooler, a welding torch, and a gas supply system for the plasma and shielding gases (Fig. 3).

The power source, which supplies the main power for the welding system, is usually supplemented with a sequence controller and control console. The sequence controller sequences the timing of gas flow, arc initiation, main welding current control, and any up-slope and down-slope parameters. In its simplest form, the plasma control console controls the gas flow for plasma and shielding gases from separate flowmeters and incorporates the high-frequency pilot arc initiation circuit. The welding torch can be manual or mechanized and is water cooled to avoid torch overheating and to maximize component life.

In most PAW installations, plasma and shielding gases are supplied from separate gas cylinders, although bulk gas can readily be

used. The gas supply is usually routed through the plasma control console, where the individual flow rates are set by the operator.

The power source should be of a constant-current design. Transistorized power sources are most common, although inverter power supplies are also available. It should have a minimum open-circuit voltage of 80 V to ensure the reliable initiation and transfer of the main arc current. The power source can be adjusted for welding current, and it should have the capability to adjust the up slope and down slope of the current. It may be equipped with thumbwheels or potentiometers to select the parameters for pulse current operation, that is, peak and background current levels, as well as peak and background times.

Welding Torches

Like those of the other arc welding processes, PAW torches are available in a range of sizes for different power ratings and in manual and mechanized versions. The design principles are the same in each case. A tungsten alloy electrode is held in a collet within the torch body. To avoid one of the most common defects in plasma torches, it is critical to hold concentricity between the tungsten electrode and the orifice in the design and manufacture of the torch. The electrode assembly is set inside a plenum chamber and the plasma gas is supplied to this chamber. A threaded copper alloy nozzle forms the front of this chamber

and contains the nozzle orifice that is used to constrict the plasma arc. A shielding gas nozzle, usually of an insulating ceramic material, is threaded onto the front end of the torch and surrounds the constricting nozzle, creating an annulus through which the shielding gas is supplied. The torch is connected electrically to the power source, and the electrode forms the negative pole of the circuit for direct current welding. The gas hoses that supply the plasma and shielding gases and the water hoses that supply and remove water from the torch are all connected to the torch body or handle. These hoses are enclosed in a flexible sheath that extends from the torch to the components of the welding system.

Most constricting nozzles have a single orifice in the center. However, multiple-nozzle orifices can be used with higher-power torches to achieve further arc constriction. The most common version of this type of nozzle has a central orifice flanked by a smaller orifice on each side. The common centerline of the three orifices is arranged at 90° to the weld line during operation.

Electrodes

The nonconsumable electrode employed is usually a 2% thoriated tungsten electrode, that is, tungsten with 2% thorium oxide. The electrode specification is covered in AWS A5.12-92. The electrode size is selected according to the welding current level that will be used.

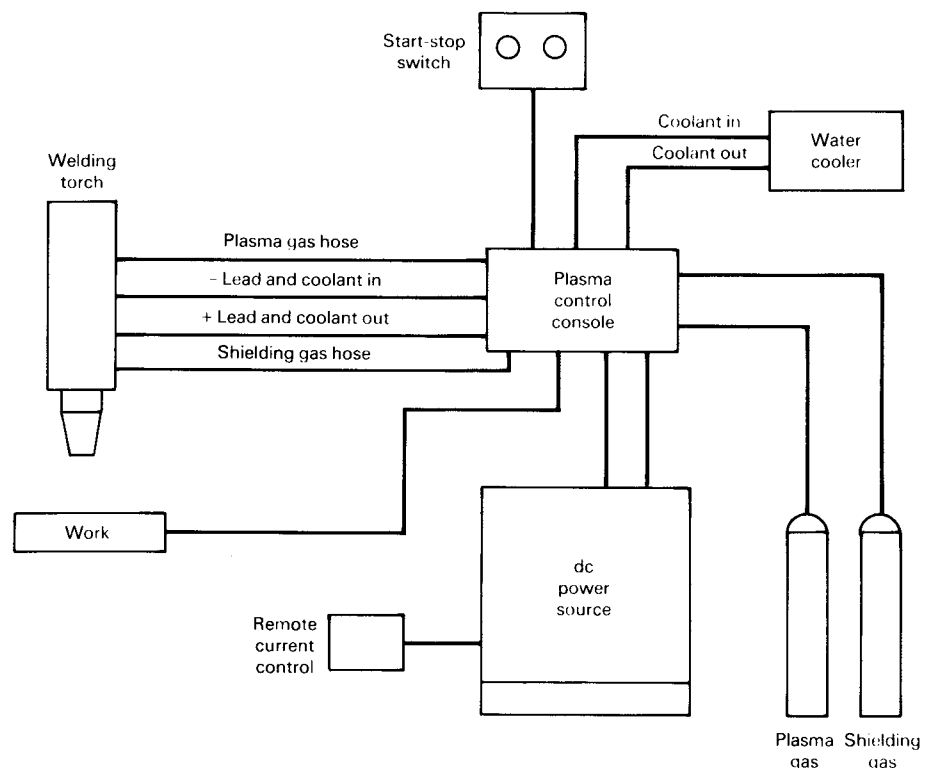


Fig. 3 Typical equipment for plasma arc welding. dc, direct current

The electrode is ground with a tapered point on the end, the angle of which depends on the selected welding current level. Electrode sizes and tip angles for a range of welding current levels are shown in Table 1.

Tungsten electrodes that contain oxides of rare-earth elements in place of the thorium oxide can also be used. These electrodes have been shown to have greater tip life. However, they are more expensive and their usefulness in plasma arc welding may be limited because of the high level of protection provided to the electrode tip preparation by the nozzle. In low-current microplasma welding applications, their better emissivity provides easier arc transfer and better overall performance.

If a finer wire is required, to fit the joint or to avoid undercut at the weld toes, then wires suitable for gas-shielded arc welding (for example, those used for GTAW) should be employed. The appropriate American Welding Society specification series is AWS A5.XX.

Plasma (Orifice) and Shielding Gases

The plasma gas is used to generate the arc, whereas the shielding gas is used to provide the weld pool with supplementary shielding from atmospheric contamination while it solidifies and cools. The plasma gas is almost always argon. Gas properties affect both weld shape and quality. Flow rates, particularly of the plasma gas, are also important, because they control the extent of plasma constriction. The flow rate can vary from 0.1 L/min (0.026 gal/min) for

microplasma welding up to 10 L/min (2.6 gal/min) for keyhole plasma welding. Considerable care is needed to regulate the gas flow rate if keyhole closure is required, because the flow rate must be sloped out to 1 to 2 L/min (0.26 to 0.52 gal/min) within approximately 1 s. Gas flow control is best achieved by electronic means.

The design and current rating of welding torches are based on argon plasma gas. Argon provides effective shielding, being heavier than air, and is cheaper than helium. Shielding gas selection is based on the type of base metal (Table 2).

Helium and argon-helium mixtures can be used as shielding gases to increase the thermal conductivity of the gas and hence the heating effect on the weld pool. Helium results in wider weld pools than argon, because it produces a higher arc voltage. Hydrogen additions to argon shielding gas tend to promote slightly narrower weld pools through arc constriction and achieve a very clean weld pool appearance, because it is a reducing gas. Although helium and hydrogen can be added to argon in the shielding gas to give higher heat input, the use of gases with higher heat contents in the plasma gas can result in torch overheating and potential damage.

Applications

The PAW process is commonly used to weld stainless steels in a wide range of thicknesses. The process can also be used with carbon and alloy steels, aluminum alloys, titanium alloys,

copper and nickel alloys, and more specialized materials, such as zirconium and tantalum. The thicknesses that can be welded in a single pass range from 0.025 mm (1 mil) for microplasma applications to 12.5 mm (0.5 in.) for the VPPA welding of aluminum. Direct current pulsing can be used on most materials.

The PAW process is often carried out in an autogenous mode, that is, without filler wire. When edge beveling is used, a filler wire is required to complete the joint. A filler wire can also be used with the keyhole mode of operation to avoid undercut at high welding speeds. Wire composition depends on that of the parent materials in the joint. The same continuous-wound wire that is used in GTAW operations is suitable.

The industries that use the PAW process can be categorized as those that weld thin-section sheet using microplasma or medium-current plasma welding and those that weld plate using keyhole plasma welding.

A wide range of small devices and assemblies made from thin stainless steel sheet, including bellows assemblies and associated fittings, are welded using the microplasma operating mode. The narrow weld bead that can be produced provides sheet-metal fabrications with a good cosmetic appearance. Furthermore, the high welding speed that can be achieved, coupled with the good tolerance to stand-off variations resulting from the columnar nature of the arc, makes the process attractive for high-volume production work.

Microplasma, as well as medium-current plasma modes, can be used to spot weld guide wires and lamp filaments, as well as in other applications that require highly repetitive autogenous welds. This type of application allows a user to limit the number of high-frequency arc starts that would be required with tungsten inert gas welding.

Keyhole plasma welding is extensively used to weld stainless steel pipe and tankage. The process is applied to individual strokes from plate to make stainless steel vessels in

Table 1 Maximum current for plasma welding with selected electrode diameter, vertex angle, and nozzle bore diameter

Maximum current, A	Electrode diam		Vertex angle, degrees	Plasma(a)				Shielding(b)			
	mm	in.		Nozzle bore diam		Flow rate		Shroud diam		Flow rate	
				mm	in.	L/min	gal/min	mm	in.	L/min	gal/min
Microplasma											
Torch rating, 20 A 5											
5	1.0	0.04	15	0.8	0.03	0.2	0.05	8	0.32	4-7	1-1.8
10	0.8	0.03	0.3	0.08
20	1.0	0.04	0.5	0.13
Medium current											
Torch rating, 100 A											
30	2.4	0.10	30	0.79	0.03	0.47	0.12	12	0.48	4-7	1-1.8
50	1.17	0.05	0.71	0.19
75	1.57	0.06	0.94	0.25
100	2.06	0.08	1.18	0.31
Torch rating, 200 A											
50	4.8	0.19	30	1.17	0.05	0.71	0.19	17	0.68	4-12	1-3.2
100	1.57	0.06	0.94	0.25
160	2.36	0.09	1.42	0.38
200	3.20	0.13	1.65	0.44
Torch rating, 400 A											
180	3.2	0.13	60(c)	2.82	0.11	2.4	0.63	18	0.72	20-35	5.3-9.2
200	2.82(c)	0.11(c)	2.5	0.66
High current											
Torch rating, 400 A											
250	4.8	0.19	60(c)	3.45(d)	0.14	3.0	0.79	20-35	5.3-9.2
300	3.45(d)	0.14(d)	3.5	0.92
350	3.96(d)	0.16(d)	4.1	1.08

(a) Argon plasma gas. (b) Argon and Ar-5H₂ shielding gas. (c) Electrode tip blunted to 1 mm (0.04 in.) diameter. (d) Multiport nozzle

Table 2 Plasma and shielding gas compositions

Material	Plasma gas		Shielding gas
	Plasma gas	Shielding gas	
Mild steel	Argon	Argon	Argon-2-5% H ₂ (a)
Low-alloy steels	Argon	Argon	Argon-2-5% H ₂
Austenitic stainless steel	Argon	Argon	Helium(a)
Nickel and nickel alloy	Argon	Argon	Argon-2-5% H ₂ (a)
Titanium	Argon	Argon	75He-25Ar(a)
Aluminum and aluminum alloys	Argon	Argon	Helium(a)
Copper and copper alloys	Argon	Argon	75He-25Ar(a)

(a) Also used

the food and chemical processing industries. Circumferential welding of strakes also can be used to create these products. Longitudinal seam welds in stainless steel pipe with wall thickness of ≥ 3 mm (≥ 0.12 in.) are ideally suited to keyhole plasma welding, because joint preparation is minimized and single-pass welding can be consistently achieved without the use of weld-backing devices. Pipes with wall thickness greater than 5 to 6 mm (0.20 to 0.24 in.) employ the keyhole mode of operation for the root pass. Depending on the material type and wall thickness, melt-mode PAW, GTAW, gas metal arc welding (GMAW), or submerged arc welding (SAW) are used to complete the joint. High-alloy composition piping is similarly manufactured.

The manufacturing of stainless steel tube from strip was one of the first applications of the PAW process. Because the process can reliably produce full-penetration welds without the use of backing, it is extensively used on tube mills, because a lack of access precludes welding from the inside.

The VPPA welding process has been very effective for welding large space shuttle orbiter sections of aluminum alloys, particularly the external fuel tank. The cathodic cleaning action of the electrode positive portion of the current cycle breaks up tenacious surface oxide film on the aluminum. The process can be used on thicknesses up to 12.5 mm (0.5 in.) with square-grooved butt joints, and it can be used for the root pass on thicker sections with edge beveling. It is anticipated that this technique will be extensively employed in building aluminum alloys structures in a modular space station.

Typical Components and Joints

The most common joint configuration used with the PAW process is a butt joint. The microplasma mode is used with overlapped butt (microlap) joints and with joints that have integral weld metal as a result of flanged, butted edges on very thin metals (Table 3). Corner joints with edge welds are also commonly welded using the microplasma and medium-current modes. An example is shown for thin-walled type 304 stainless steel tubing (Fig. 4) with edge welds between tubes with a wall thickness of less than 0.5 mm (0.020 in.).

Because the keyhole operating mode fully penetrates the workpiece, it is used exclusively on square-grooved butt joints and single-V joints with a root face (Table 3). For square-grooved butt joint preparation, the thickness that can be welded in a single pass depends on the fluid flow characteristics of the workpiece material for a given heat input from the plasma torch. Thus, alloys of titanium and zirconium can be butt welded with square-grooved preparation at greater thicknesses than steels and stainless steels. Generally, it is an industry-accepted practice to use square-grooved preparation without edge beveling for stainless steels up to 6 mm (0.24 in.) in thickness.

A 4 or 5 mm (0.16 or 0.20 in.) root face and a single-V preparation, usually with a 60° included angle, are used on steels thicker than 6 mm (0.24 in.) (Table 4). The root is welded in the keyhole mode, and the rest of the joint is completed with a filler wire addition by melt-mode PAW, GTAW, GMAW, or SAW, depending on the material type, joint volume to be filled, and the mechanical property requirements

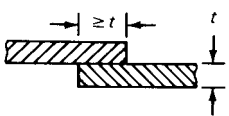
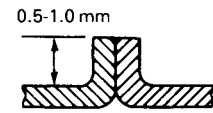

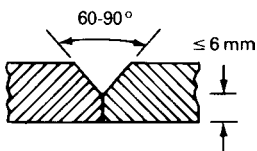
of the joint. An example is shown for 8 mm (0.3 in.) thick type 304L stainless steel (Fig. 5).

In the PAW process, fixturing for part fit-up is more critical than it is for the GTAW process, primarily because of the narrower, more-constricted arc in PAW. The backing bar design and shielding gas techniques employed for GTAW are appropriate for microplasma and medium-current modes. During keyhole welding, however, the arc passes right through the workpiece, forming an efflux plasma (Fig. 1) that normally extends 10 mm (0.4 in.) below the back face of the joint. This characteristic must be accommodated when designing backing systems. Failure to allow sufficient gap can result in turbulence in the efflux plasma, causing weld pool disturbance and porosity.

When welding longitudinal seams in tube or pipe, the weld can be started and stopped on run-on and run-off tabs, precluding the need for keyhole closure. However, when using the keyhole mode on circumferential seams of vessels or on butt joints in tubes or pipes, the keyhole will overlap the start of the weld to produce a complete joint. Keyhole closure without porosity has been an area of difficulty, particularly when butt welding tubes, and it represented an important concern for more-widespread use of the process. Modern electronic controls for simultaneous reduction in gas flow and current slope-out provide a more reliable method for keyhole closure.

Plasma arc welding with wire feed is also a suitable process to rebuild parts or produce parts in a layer-by-layer method known as additive manufacturing. The process can be used to add features to existing parts or to produce a whole new part, a generic example of which is shown in Fig. 6.

Table 3 Joint configurations for plasma welding sheet and tubular components

Thickness range		Joint type	Joint configuration	Process variant	No. of runs	Comments
mm	in.					
0.5–1.0	0.02–0.04	Micro-lap		Microplasma	1	Edges fully fused to produce additional weld metal; good clamping essential
0.5–1.5	0.02–0.06	Flanged edge		Microplasma	1	Edges fully fused to produce additional weld metal
3.0–6.0	0.12–0.24	Square but		Keyhole plasma	1	Grooved backing bar required to prevent disturbance of the efflux plasma. Additional (cosmetic) run using melt mode may be employed
6.0–15	0.24–0.60	Single-V butt		Keyhole plasma	2 or more	Keyhole technique used for root run only. Joint completed with the melt mode plus filler wire

Operations

Procedures

Process Operating Procedure. Welding parameters, such as welding current, arc voltage, travel speed (for mechanized/automatic operation), and plasma and shielding gas flow

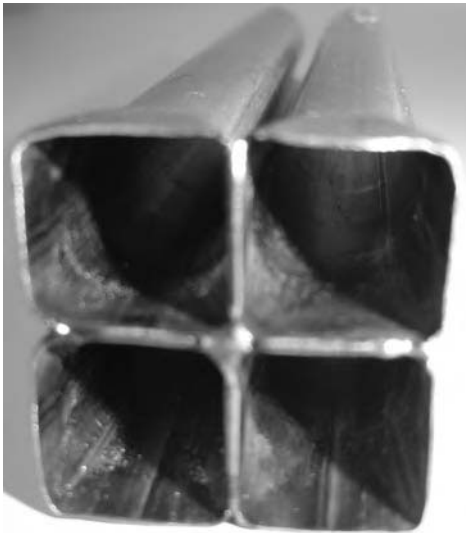


Fig. 4 Edge joints in thin type 304 stainless steel tubes. Courtesy of Edison Welding Institute

rates, are set by the procedure and implemented by the welder. Torch parameters include the correct electrode vertex angle and set-back distance, as well as the correct orifice diameter for the welding current level.

The operating sequence for the PAW process was described in the section “Principles of Operation” at the beginning of this article. After the weld pool or keyhole is formed, the torch is traversed across the workpiece at the preset welding speed. Welding is terminated by the down slope of the welding current, with simultaneous sloping of the plasma gas flow rate if keyhole welding and keyhole closure are desired. Slope control for the keyhole mode is shown in Fig. 7.

Most PAW is done in a mechanized or automated operation that does not require much operator intervention, except initially to set the parameters and to position the workpiece and torch. When current pulsing and keyhole closure operations are involved, numerous parameters must be set, which requires strict attention to detail, accurate part fit-up, and careful alignment of the torch relative to the joint.

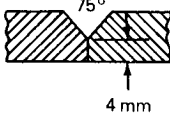
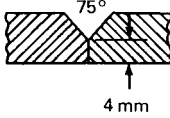
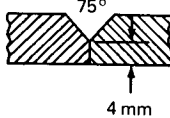

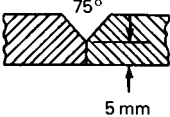
Inspection and Weld Quality Control. All of the common nondestructive evaluation techniques are applicable to plasma arc welds. Radiography and ultrasonic inspection are the most common techniques used. The fact that most plasma arc welding is carried out in the

keyhole mode means that there is a penetration bead on the root side of the joint. Visual inspection for full penetration, as well as for correct width and profile of both the penetration bead and the weld surface profile, can readily be accomplished. Smooth, even underbeads can be achieved through good procedure development with tolerances improved through current pulsing.

Troubleshooting. When troubleshooting a PAW operation, all of the previously defined basic parameters of the welding schedule should be checked. Welding discontinuities can result from incorrect electrode set-back or from a worn or damaged nozzle orifice. The concentricity of the diameter of the nozzle orifice and the alignment of the electrode and nozzle orifice are very important. Worn nozzles should be replaced. The condition of the tungsten electrode tip should also be checked.

An undercut is one of the most common defects in the PAW process. Depending on material type, thickness, and preset welding parameters, a two-sided undercut can occur above certain threshold welding speeds. This can only be eliminated by increasing welding current. A one-sided undercut can result from misalignment of the torch, the electrode/orifice and multiport nozzles, or from the mismatched fit-up of the workpieces. Correct alignment is essential.

Table 4 Keyhole plasma welding conditions for pipe prefabrication in type 304L/316L stainless steel

Tube diam		Thickness		Edge preparation	Welding current, A	Welding speed		Gas flow						Filler wire feed rate (1.0 mm diam)	
mm	in.	mm	in.			m/min	ft/min	Plasma gas, argon		Shielding gas, argon + hydrogen		Backing gas		m/min	ft/min
								L/min	gal/min	L/min	gal/min	L/min	gal/min		
60	2.4	7.5	0.30		160-100	0.22	0.72	4.5	0.13	18	4.8	10	2.6
					140-90	0.22	0.72	1.5	0.40	18	4.8	10	2.6	1.10	3.6
114(a)	4.6(a)	12	0.48		160-100	0.18	0.59	4.5	1.2	18	4.8	10	2.6	1.10	3.6
168(a)	6.7(a)	14	0.56		190-120	0.14	0.46	6	1.6	18	4.8	15	4.0
510 or 710	20.4 or 28.4	6	0.24		180	0.22	0.72	5	1.3	18	4.8	30	6.6	1.10	3.6
1000(b)	40(b)	12	0.48		270	0.21	0.69	7	1.8	25	6.6	30	6.6

(a) Welded thickness, 5 mm (0.20 in.). (b) Welded thickness, 6 mm (0.24 in.).

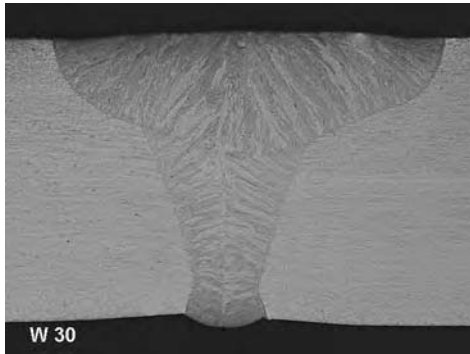


Fig. 5 Butt joint using keyhole plasma arc welding root pass and gas tungsten arc welding fill pass. Courtesy of Edison Welding Institute



Fig. 6 Layers of weld metal produced using plasma arc welding with wire feed to produce a new part feature. Courtesy of Edison Welding Institute

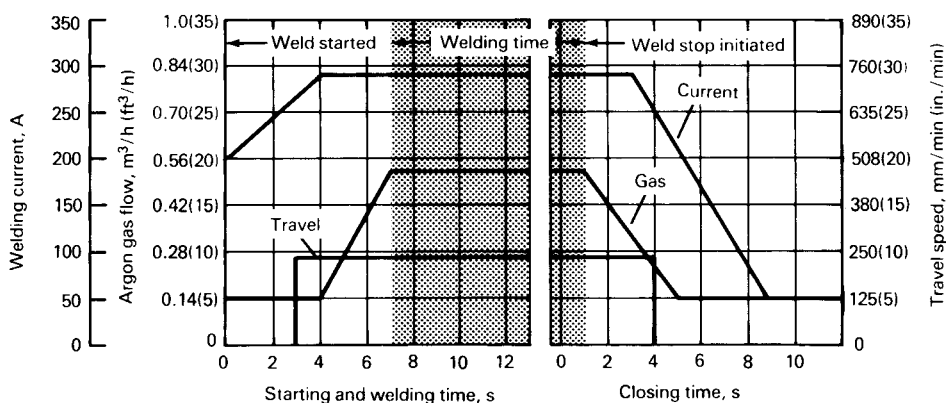


Fig. 7 Typical slope control pattern for welding current and plasma gas flow when starting and closing a keyhole; example is for 9.5 mm (3/8 in.) thick steel

Personnel Requirements

The skill level and training requirements for the PAW process are generally similar to those for the GTAW process. When manual welding, the columnar nature of the plasma arc allows

greater variation of the torch-to-workpiece distance without altering the size and shape of the weld pool. The fact that the electrode is protected from contamination by the nozzle means that tungsten contamination and tungsten inclusions in the weld metal are more readily

avoided than they are in the GTAW process. From the viewpoint of an operator, disadvantages include the greater complexity of the torch, in terms of nozzle orifice and electrode set-back considerations, and the correct setting of two gases (plasma and shielding gas).

When mechanized welding is carried out, which is usually the case for the keyhole mode, the operator is required to set a greater number of parameters (compared to GTAW), particularly if current pulsing and keyhole closure operations are required. Specific operator training is required for pulsed keyhole operation, and particularly for VPPA operations, which are usually carried out in the vertical position, welding upward, and thus require a high level of operator competence. Computerization of welding parameter selection is the trend for VPPA welding and other mechanized or automated PAW operations.

The health and safety issues related to the PAW process are very similar to those of other gas-shielded arc welding processes, especially GTAW. These include electrical shock; electromagnetic radiation hazards, particularly ultraviolet radiation; burns from hot metal parts; and welding fumes and gases, including ozone. Precautions must be taken to capture grinding dust when preparing tungsten electrodes. The volume of welding fumes produced is low and is similar to that produced by the GTAW process. Hexavalent chromium and ozone are concerns when welding stainless steels and aluminum alloys, respectively. Like the GTAW process, the low level of general welding fumes associated with PAW results in a comparatively higher level of ozone. However, the rapid decay of ozone within a short distance of the arc, coupled with the high degree of mechanization and automation typical of the keyhole plasma welding operation, means that operator exposure is generally very low. The microplasma mode, which is more commonly used manually, employs such low current levels that fume and ozone levels are very low.

Electroslag and Electrogas Welding*

Revised by S.D. Brandi, Escola de Politecnica da USP; S. Liu, Colorado School of Mines; and R.D. Thomas, Jr., R.D. Thomas and Company

ELECTROSLAG WELDING AND ELECTROGAS WELDING are two related procedures that are presently used to weld thick-section materials in the vertical or near-vertical position between retaining shoes. Primarily applied for joining steels of thicknesses over 50 mm (2 in.), electroslag welding (ESW) involves high energy input relative to other welding processes, resulting in generally inferior mechanical properties, specifically lower toughness of the heat-affected zone (HAZ). However, the high deposition rate and relatively low cost of the process make it attractive for heavy structural fabrication. The as-welded properties of electrogas welding (EGW), usually applied to steels under 50 mm (2 in.), are generally superior to those of electroslag welds, and the process is commonly applied to the field erection of storage vessels and other less critical structures.

Electroslag welding is a vertical welding process producing coalescence with molten slag that melts the filler metal and the surface of the work to be welded. Confined by cooling shoes, the molten weld pool is shielded by the molten slag, which moves along the full cross section of the joint as welding progresses. The conductive slag is maintained in a molten condition by its resistance to electric current passing between the electrode and the work (Ref 1). Electroslag welding can be considered a progressive melting and casting process in which the heat of a bath of molten flux is used to melt the filler metal and the edges of the plates to be welded. Electric arc occurs only at the beginning of the process, and once a molten bath is achieved, the arc is extinguished. During the process, flux is added periodically or continuously to maintain an adequate slag covering over the pool of molten metal. Two or more retaining shoes hold the molten metal in place until it has solidified. In normal operation with a constant potential power source, the electrode melts off while dipping only partly through the flux bath and gathers in the molten metal puddle. In the case of low-carbon steel,

the temperature of the bath is reported to be in the vicinity of 1925 °C (3500 °F), while the surface temperature is approximately 1650 °C (3000 °F) (Ref 2). The major process variables are welding current and voltage. Welding current is directly responsible for the electrode melt rate, while voltage influences the base-metal penetration and weld bead width. Both variables are sensitive to the physical properties of the welding flux, such as electrical resistivity and fluidity.

Electrogas welding is a method of gas metal arc welding (if a solid wire is used) or flux cored arc welding (if a tubular wire is used), wherein an external gas is supplied to shield the arc and molding shoes are used to confine the molten weld metal for vertical-position welding (Ref 2). Electrogas welding may or may not use an added flux. In the solid wire process, CO₂ shielding gas is commonly used and no flux is added. With the flux cored process, the core ingredients provide a small amount of flux to form a thin deposit of slag between the weld and the shoes. Self-shielding electrodes eliminate the need for external shielding gas. A major difference

between ESW and EGW is that the former relies on slag conduction to carry the welding current and the latter uses arc conduction. Despite the differences, similarities between ESW and EGW in terms of equipment, joint preparation, and welding procedures are such that they can be grouped into one category and described as allied processes.

Fundamentals of the Electroslag Process

Heat Flow Conditions

Electroslag welding is quite similar to in situ casting, with large volumes of molten metal and high heat content. When compared with other arc welding processes, electroslag welds have a long thermal cycle with very slow cooling rate. Electroslag welding generally consumes from 100 to 200 kJ/mm (2500 to 5000 kJ/in.), as compared to 10 to 40 kJ/mm (25 to 1000 kJ/in.) found in most arc welding processes. Figure 1 shows a typical thermal cycle

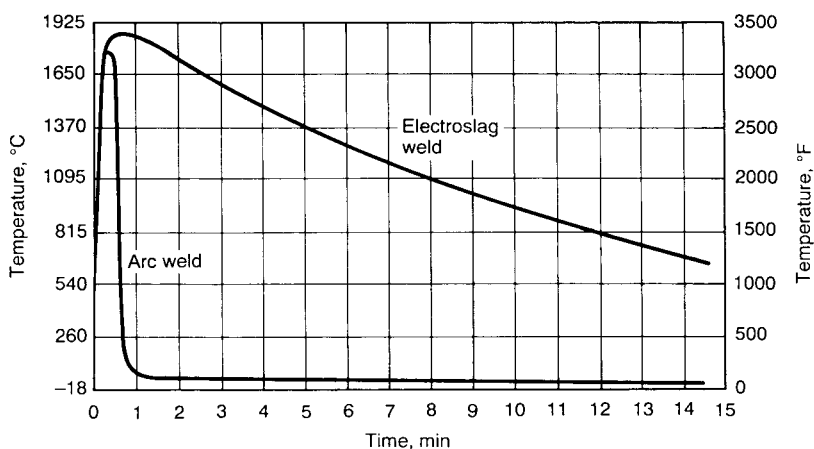


Fig. 1 Typical thermal cycle of an electroslag weld bath relative to that of an arc welding pool

* Adapted from R.D. Thomas, Jr., and S. Liu, Interpretive Report on Electroslag, Electrogas, and Related Processes, *Welding Research Council Bulletin*, No. 338, Nov 1988. Used with permission of the Welding Research Council

of an electroslag weld bath compared with that of an arc welding pool. As a consequence of the thermal experience, weld-metal solidification in ESW is extremely slow, resulting in a coarse primary solidification structure. The heat absorbed into the base metal also creates an extremely large HAZ (Fig. 2).

A heat balance diagram of a typical electroslag weld (Fig. 3) illustrates that approximately 60% of the heat is absorbed by the workpart,

close to 25% of the total heat is expended in the melting of the electrode, and approximately 10% of the heat is used to superheat the molten metal (Ref 3). The amount of heat extracted by the cooling shoes varies, depending on the thickness of the plate and on the welding conditions. In the welding of steel plates 90 mm (3.5 in.) thick, less than 10% of the heat of the molten slag and metal pool is transferred to the cooling shoes. In thinner plates, however, the

cooling shoes play a more significant role in the heat balance.

Mathematical models are used to estimate the three-dimensional temperature field in the slag, metal pool, and base-metal regions in an electroslag weldment, and to predict HAZ size and grain growth in the HAZ. Figure 4 shows an example of the calculated temperature distribution for a base plate 25.4 mm (1 in.) thick, 470 mm (18.5 in.) long, and 610 mm (24 in.) wide, at the time that corresponds to half the total time required for completion of the weld (Ref 4). The maximum temperatures reached in the slag and weld pool were 1960 and 1630 °C (3550 and 2960 °F), respectively. The temperature distribution in a weldment along planes parallel and normal to the parent plate surface can also be represented in the form of isometric temperature plots (Fig. 5).

The energy balance in the slag phase is summarized in Table 1. A major portion of the heat generated in the slag layer was transferred to the cooling shoes (36.1%). Approximately 22 and 15% of the heat was used in base-metal heating and electrode melting, respectively. The heat-generating patterns are highly sensitive to the geometric location of the electrode in the slag. With careful control of the process variables (such as gap distance and convective flow suppression) by external application of the electromagnetic field, reductions of two or three times the usual heat input could be practical.

To distribute the energy uniformly across the thickness of the weldment, empirical rules have been developed (Table 2) to determine the preferred number of electrodes, the wire spacing, and the traverse (oscillation) distance (Fig. 6). Oscillation speeds depend on the plate thickness, usually allowing a traverse time of 3 to 5 s; a dwell time at the end of each traverse ensures adequate penetration at the plate edges.

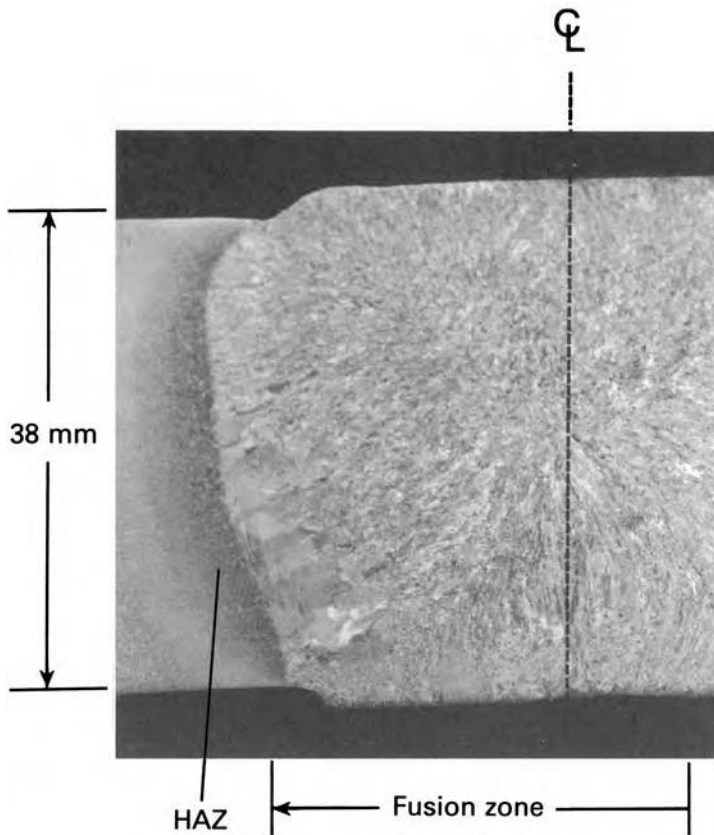


Fig. 2 Macrograph showing fusion zone and heat-affected zone (HAZ) in an electroslag weldment

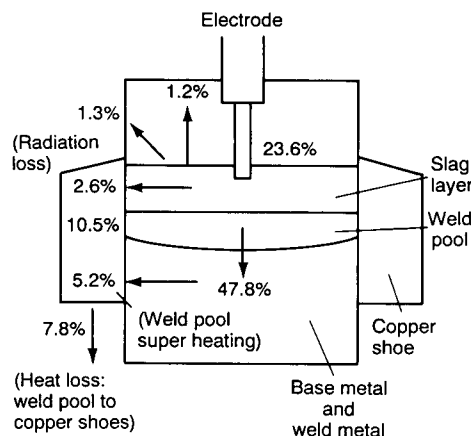


Fig. 3 Heat balance diagram of a typical electroslag weldment. Source: Ref 3

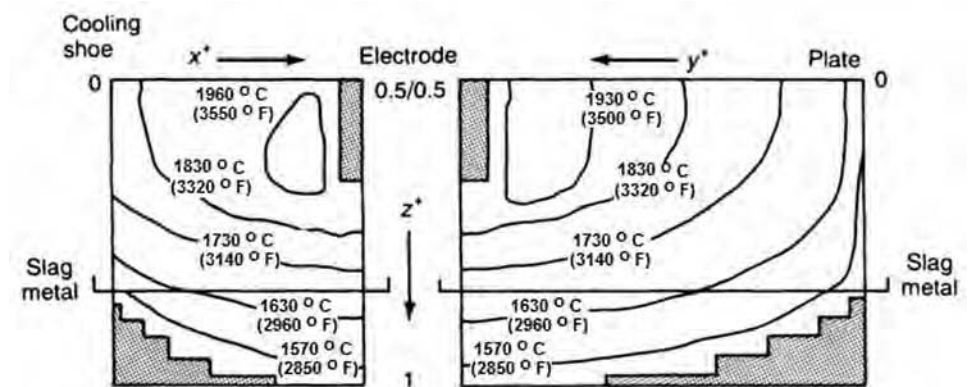


Fig. 4 Calculated temperature distribution of an electroslag weldment showing three-dimensional temperature field in the slag, metal pool, and base metal. Source: Ref 4

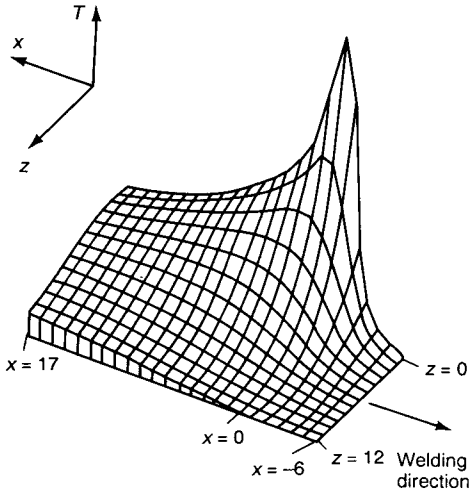


Fig. 5 Isometric three-dimensional temperature distribution in an electroslag weldment allowing improved visualization of the temperature profile. Source: Ref 5

Table 1 Energy balance in the slag phase of electroslag welding

Parameter(a)	Energy dissipated, %
Heat transfer from slag:	
To copper shoe	36.10
To base plates	20.22
To liquid metal	8.71
Heat used to heat the electrode to its melting point	15.26
Heat required:	
To melt the electrode	4.07
To heat flux cooling on the consumable guide	1.84
Heat carried by liquid metal drops	2.04
Radiation loss from the slag surface	1.75
Electrochemical loss	10.00

(a) Actual width of the slag pool, 0.044 mm (0.0017 in.); current, 534 A; other conditions are the same as those presented in Table 2. Source: Ref 5

Metal Transfer and Weld Pool Morphology

The droplet transfer rate and the length of time each droplet is in contact with the slag layer profoundly affect the chemical composition and the metallurgical properties of the weld pool.

Droplet Formation. In steady-state operation, the molten filler metal transfers into the weld pool in a globular mode. Current and voltage oscillograms indicate that despite the droplet size decrease observed with increasing voltage, welding current has no significant effect on the size of the droplets. Rather, the length of time that a droplet is in contact with the slag layer decreases considerably with increasing current. On the other hand, the length of time a droplet is in contact with the layer of slag increases with voltage, because

Table 2 Effect of joint geometry on multiple-wire butt electroslag welding

Steel plate thickness		Number of wires	Oscillation	Square butt gap opening	
mm	in.			mm	in.
19-75	¾-3	1	No	22-32	¾-1¼
25-130	1-5	1	Yes	32-35	1¼-1¾
75-150	3-6	2	No	32-35	1¼-1¾
75-280	3-11	2	Yes	32-35	1¼-1¾
130-535	5-21	3	Yes	35	1¾

Source: Ref 6

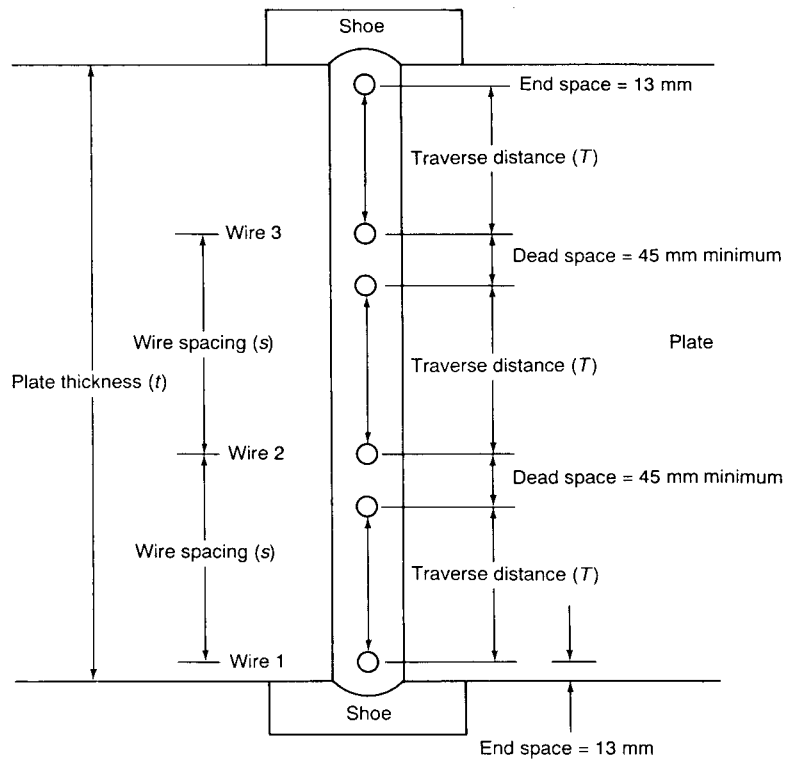


Fig. 6 Wire spacing diagram for multiple-electrode electroslag welding incorporating oscillation for better energy distribution across the thickness of the weldment. Source: Ref 6

the electrode tip is further away from the molten metal pool. The extent of interaction between a metal droplet and the slag layer determines the chemical composition of the weld pool.

Weld Pool Morphology. In an electroslag weldment, solidification begins at the fusion line, surfaces adjacent to the retaining shoes, and progresses toward the center of the weld. Because the process is continuous in a vertical or near-vertical-up position, solidification also progresses from the bottom toward the top part of the joint. The angles at which the columnar grains meet at the center of the weld depend on the shape of the weld pool, which can be described by the weld pool form factor. Form factor is defined as the ratio between the width, *w*, and the maximum depth, *h*, of the pool (Fig. 7). Welds having a high form factor (>2.0) will have grains meeting at an acute angle at the center line, while welds with a

low form factor (<1.0) will solidify with grains meeting at an obtuse angle. Low form factor is highly undesirable because of the potential accumulation of residual elements at the center of the weld joint. High welding current usually results in a low form factor, while low welding current usually results in a high form factor and shallow metal pool. High voltage promotes shallow pools and low voltage. Figure 7 shows two examples of different pool morphologies and form factors as a function of the welding current and voltage.

An additional factor controlling the weld puddle morphology is the welding flux conductivity. Actually, the bulk of the electrical energy is converted into thermal energy in a thin layer of the slag contiguous to the electrode tip, which acts as the heat source in ESW (Ref 3). High-conductivity fluxes generate less heat and result in less base-metal penetration and shallower weld pools.

Out-of-Position (Nonvertical) ESW

Electroslag welding has been successfully done in joints that are inclined from the vertical position. The stability of the process and the quality of the weld joint are both functions of the angle of inclination. Weld morphology, including penetration, HAZ, and weld-metal microstructure, is sensitive to the welding parameters. Preferential thermal radiation heating of the upper weld surface is considered the cause of asymmetric penetration and HAZ geometry (Ref 7).

Weld Pool Penetration and Magnetic Field Coupling

Magnetic field is not generally applied in ESW. For electroslag overlays, however, some use of magnetic field to promote fluid flow and to drive the molten slag layer from the hotter region to the colder region to eliminate undercutting has been reported (Ref 8). However, the effect of magnetic stirring, which induced convective fluid motion in the weld pool and disrupted the solidification and growth of the columnar dendrites, can be seen in Fig. 8 (Ref 9, 10). Mechanical vibration on electroslag

weld pools generally does not cause significant microstructural modification. However, some refinement of the as-deposited grains can result when the slag/molten metal interface is disturbed. The use of a quartz-shielded electrode guide tube as an extended stirrer has been reported to form a deeper weld pool, with the form factor decreasing from 3 to 1.5 (Ref 11, 12). Other techniques for refining weld-metal microstructures include ultrasonic cavitation and the use of chemical inoculators.

Constitutive Equations for Welding Current, Voltage, and Travel Rate

The power input per unit length of a weld is the primary variable that influences the degree of base-metal melting, the amount of filler-metal deposition, and the thermal history of the weldment. In ESW, current and travel speed are not independent variables, as in the other arc welding processes. For a constant voltage power supply, the current and power are both functions of the resistance of the slag pool. Hence, they are functions of the electrode feed rate, the mechanics of electrode melting, and the nature of the electrical and thermal transport at the electrode/slag interface. To control the welding process, a constitutive equation has been proposed (Ref 13):

$$I = BW^{1/2}V^{1/3} \tag{Eq 1}$$

where I is the welding current, W is the electrode feed rate, V is the welding voltage, and B is a proportionality constant. Equation 1 expresses the functional relationship between the various process variables and has the primary objective of selecting a voltage and current range that provides sufficient energy input for base plate penetration without excessive overheating of the HAZ. The relation can be empirically determined from Fig. 9. The total energy input per unit area of weld surface, E , can also be determined:

$$E = B \frac{L_g}{2\pi r^2(L+g)} \cdot \frac{V^{5/3}}{I} \tag{Eq 2}$$

where L is the width of the base plate, g is the root gap opening, and r is the radius of the welding electrode. Note also that this equation takes into consideration the electrode-to-joint geometry, which is related to the electrical and thermal transport in the process.

Unlike arc welding processes, in which an increase in current results in greater energy input and deeper penetration, the reverse occurs in ESW. An increase in current requires an increase in electrode burn-off rate, which increases the welding speed and decreases the energy input per unit area of weld. An excessive increase in the current at constant voltage, however, can shift the process from penetration to no penetration of the base plate. The process control boundaries for ESW can be easily developed (Fig. 10). Boundaries A through D enclose an operating space that exhibits good process stability and base-metal melting. Outside the indicated boundary, the process often appears to operate well but with inadequate base-metal penetration (Ref 13).

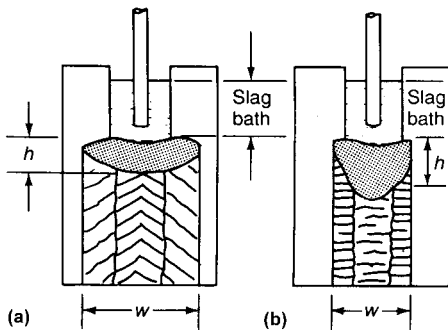
A change in electrode geometry and nature (cored) may result in a different constitutive equation (Ref 9, 15):

$$I = B'W^{0.35}V^{1.63} \tag{Eq 3}$$

where B' is the proportionality constant. The total energy input, E , is:

$$E = B' \frac{L_g - 2w_g t_g}{[L + (g - 2t_g)](w_e t_e)} \cdot \frac{V^4}{I^2} \tag{Eq 4}$$

where w_g is the width of the consumable plate guide, t_g is the thickness of the consumable plate guide, w_e is the width of the consumable electrode, and t_e is the thickness of the consumable electrode.



Effect of welding parameters on weld metal pool shape

Parameter	Effect of parameter increase on weld-metal pool dimension(a)		
	Pool width (w)	Pool depth (h)	Form factor (F = w/h)
Current or wire-feed speed:			
Low values	A	A	B
High values	D	A	D
Voltage	A	B	A
Slag pool depth	D	B	D
Root opening	A	C	A

(a) A, increase; B, slight increase; C, no change; D, decrease

Fig. 7 Effect of increase in welding parameters on weld pool form factor. (a) Optimum weld pool dimensions (shallow weld pool, high form factor, acute angle between grains). (b) Undesirable weld pool dimensions (deep weld pool, low form factor, obtuse angle between grains). Source: Ref 6



(a)



(b)

Fig. 8 Macrograph showing effect of superimposed magnetic field on electroslag weldments. (a) Field present. (b) Field absent. Original magnification: both 1.6x. Source: Ref 9

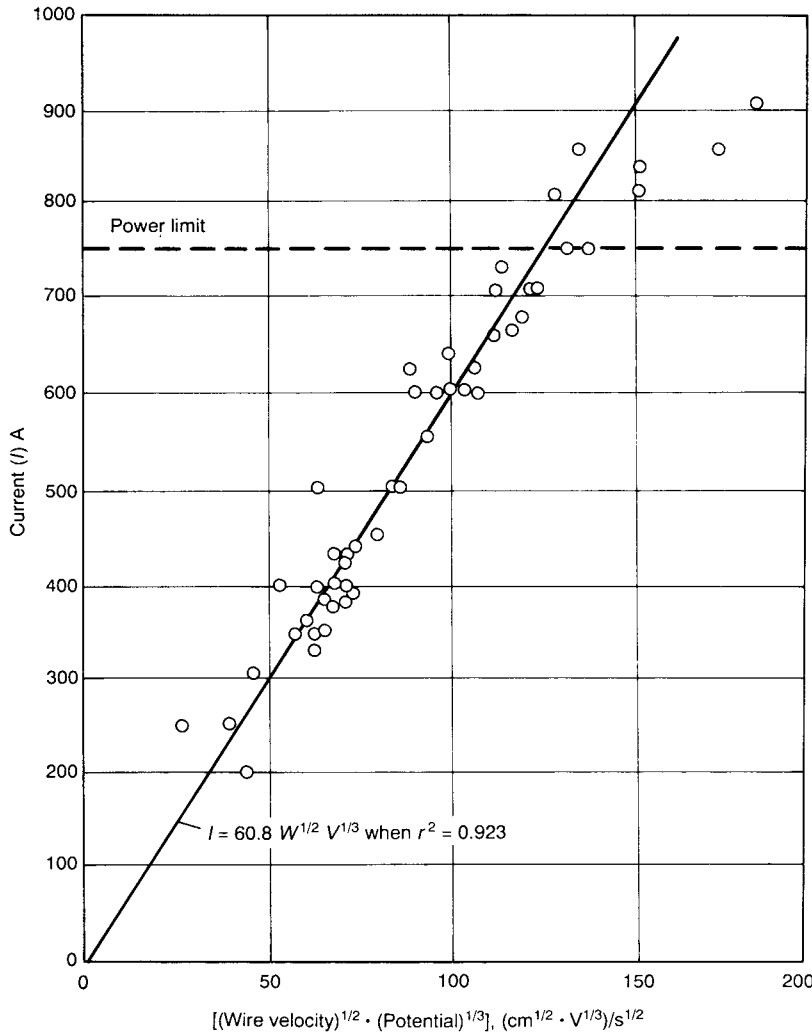


Fig. 9 Functional relation among welding current (I), potential (V), and wire-feed rate (W) for electroslag welding of 2¼Cr-1Mo steel. Line indicates value of $I = BW^{1/2}V^{1/3}$ for $B = 60.8$ and $r = 0.923$. Source: Ref 14

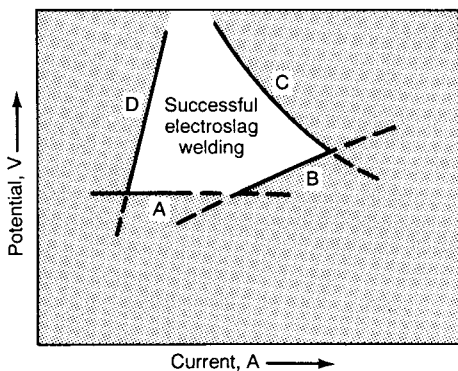


Fig. 10 Operating parameter window for electroslag welding. Boundary A represents the voltage threshold for parent plate fusion at low power inputs. Boundary B represents the constitutive equation for adequate penetration at high power levels. Boundary C represents the maximum power output of the welding power supply. Boundary D represents the limit of electrode feed rate at which the wire electrode melts by ohmic heating. Source: Ref 14

Temperature Relations between the Slag Bath and Electrode in ESW

Because the electrode is partially immersed in the slag bath, the current density presents a maximum value at the electrode tip and decreases substantially in the direction of the metal pool and the slag bath free surface. Therefore, heat is transferred to the periphery of the slag bath and to the periphery of the metal pool.

Experimental evidence (Ref 3) showed that metal droplets were heated to a temperature higher than the slag. Assuming only the heat transfer from the melted slag to the electrode wire, the temperature at the electrode tip, assuming a non-preheated electrode, can be calculated:

$$T_e = T_s \left[1 - \exp\left(-\frac{2\alpha S_{wet}}{c\gamma rW}\right) \right] \tag{Eq 5}$$

where T_e is the electrode temperature, T_s is the slag temperature, S_{wet} is the wet stickout (electrode depth into the slag bath), α is the heat-transfer coefficient, $c\gamma$ is the volumetric specific heat, r is the distance from the heat source, and W is the wire feed rate.

Figure 11 presents a plot of a carbon steel electrode tip temperature change as a function of the slag bath temperature and wet stickout for an electrode feed rate of 220 m/h (722 ft/h). In Fig. 11, an increase in the wet electrode stickout augments the electrode tip temperature for a constant slag temperature. An ESW usual wet stickout is 2 cm (0.79 in.) for a 2 mm (0.08 in.) electrode diameter. For this electrode stickout, the electrode tip temperature increases when the slag temperature is increased. In this condition, the electrode is heated but below the melting temperature.

Figure 12 depicts the electrode tip temperature as a function of electrode feed rate and slag temperature for a wet stickout of 2 cm (0.79 in.). Melting of the electrode is possible only for a slag temperature higher than 2000 °C (3632 °F) and an electrode feed rate below 80 m/h (260 ft/h) (for a slag temperature of 2200 °C, or 3992 °F), considering a carbon steel melting temperature of 1450 °C (2642 °F).

The results of Fig. 11 and 12 indicate the presence of another electrode heating mechanism, Joule heating. In this case, and neglecting the effect of heat conductivity along the wire and the heat transfer between wire and slag, the equation for the electrode temperature is (Ref 3):

$$T_e = \frac{i^2 \rho_e S}{c\gamma W} \tag{Eq 6}$$

$$S = S_{dry} + S_{wet} \tag{Eq 7}$$

where i is the current density, S is the total stickout, S_{dry} is the dry stickout (distance between electrode contact and the slag bath surface), and ρ_e is the electrode electric resistivity.

Figure 13 presents the effect of Joule heating of a 2 mm (0.08 in.) electrode wire diameter and a 2 cm (0.79 in.) wet stickout for different electrode feed rates.

ESW Thermal Cycles Equations

A quasi-stationary (pseudostationary) temperature field for an ESW can be achieved according to (Ref 3):

$$t_{qs} > \sqrt{\frac{7.5ar}{v_{welding}^3}} \tag{Eq 8}$$

where t_{qs} is the time to achieve a quasi-stationary state in a distance, r , and a is thermal diffusivity.

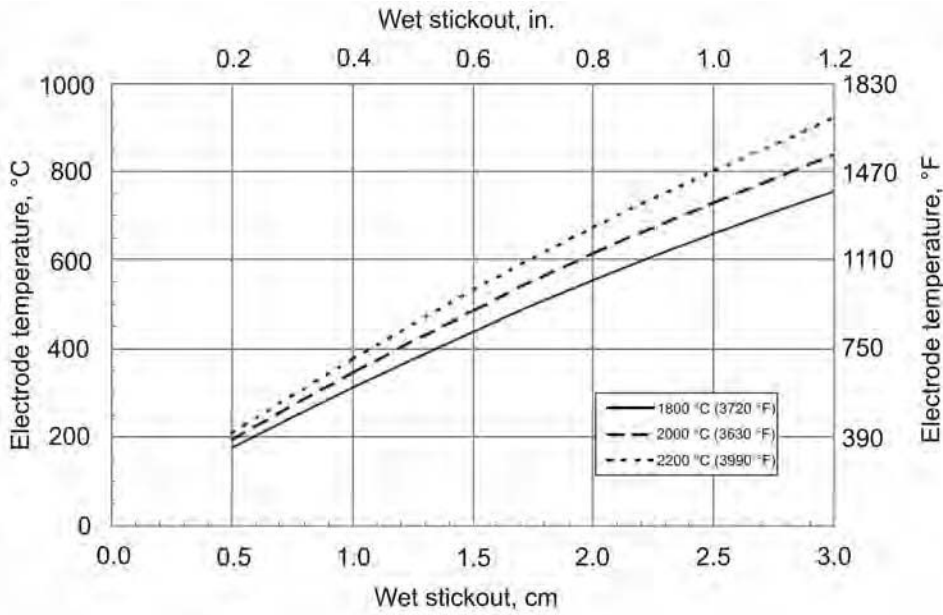


Fig. 11 Electrode temperature in a slag bath using a constant electrode feed rate (220 m/h, or 722 ft/h) and three different slag temperatures

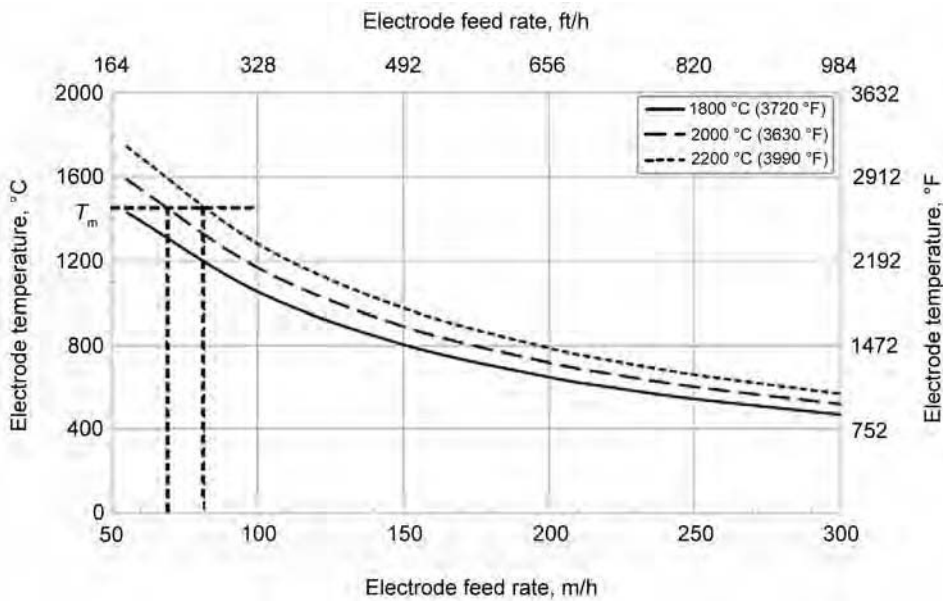


Fig. 12 Electrode temperature in a slag bath using a constant wet stickout of 2 cm (0.8 in.) and different electrode feed rates for three different slag temperatures. Electrode diameter: 2 mm (0.08 in.)

With this time and the welding speed, is it possible to calculate the distance from the beginning of welding where a quasi-stationary condition is achieved. This information is important to the:

- Shape and size of the weld-metal pool and, consequently, the solidification conditions and fusion zone microstructure
- Repeatability of thermal cycles in the HAZ, which means a constant microstructure for a fixed distance along the weld length and, consequently, constant mechanical properties for each point

- One maximum temperature field, which determines residual stresses and distortion
- Three heat sources, distributed and aligned in a linear geometry and traveling slowly, are used to simulate ESW thermal cycles. These three heat sources are located in:
- q_1 : Located at the surface of the slag bath and the atmosphere and is responsible for approximately 25% of the total heat input
 - q_2 : Located in the middle of the slag bath and is responsible for approximately 50% of the total heat input

- q_3 : Located in the middle of the metal pool and is responsible for approximately 25% of the total heat input

The temperature at a point of interest in the HAZ y -distance from the weld centerline is calculated (Ref 3):

$$T(x, t) = T_0 + \sum_{i=1}^3 \left(\frac{q_i}{2\pi\lambda h} \exp\left(-\frac{v_{\text{welding}}^2 t_i}{2a}\right) K_0\left(r_i \sqrt{\frac{v_{\text{welding}}^2}{4a^2} + \frac{b}{a}}\right) \right) \quad (\text{Eq 9})$$

$$q_i = \frac{\eta V_i I_i}{v_{\text{welding}}} \quad (\text{Eq 10})$$

$$r_i = \sqrt{\left(y - \frac{b}{2}\right)^2 + v_{\text{welding}}^2 t_i^2} \quad (\text{Eq 11})$$

where T_0 is the initial plate temperature (preheat temperature); q_i is the heat input of wire i ; λ is the thermal conductivity; h is the plate thickness; t is the time when a given heat source (number of electrodes) traverses the cross section containing the point of interest; a is the thermal diffusivity; $K_0(u)$ is the second-kind, zero-order Bessel function; v_{welding} is the welding travel speed; η is the thermal-transfer coefficient; r_i is the distance of heat source i to the point of interest in the HAZ; y is the distance from the weld centerline; and b is the root gap.

Figure 14 shows two carbon steel thermal cycles calculated by assuming $q_1 = q_3 = 0$, plate thickness of 50 mm (2 in.), root gap of 24 mm (0.9 in.), $I = 480$ A, $V = 35$ V, and $v_{\text{welding}} = 0.02$ cm/s (0.008 in./s).

ESW Consumables

ESW Fluxes

Similar to the fluxes used in other welding processes, ESW fluxes are formulated to refine the weld metal, to coat the surface of the retaining shoes and the completed weld metal, and to protect the molten metal from oxidation. However, several physical and chemical properties distinguish ESW fluxes from the others used in arc welding. Electroslag welding fluxes are invariably fused, rather than agglomerated. Compared with the arc welding fluxes, fluxes for ESW are higher in resistivity, because the arc is extinguished soon after the process becomes stable. Sometimes, an agglomerated starting flux with high conductivity is used to initiate the process and form the weld pool. After that, a running flux of high resistivity is added to generate heat for melting the filler metal and to maintain steady welding operation. In fact, for high-current welding the use of starting flux is often omitted.

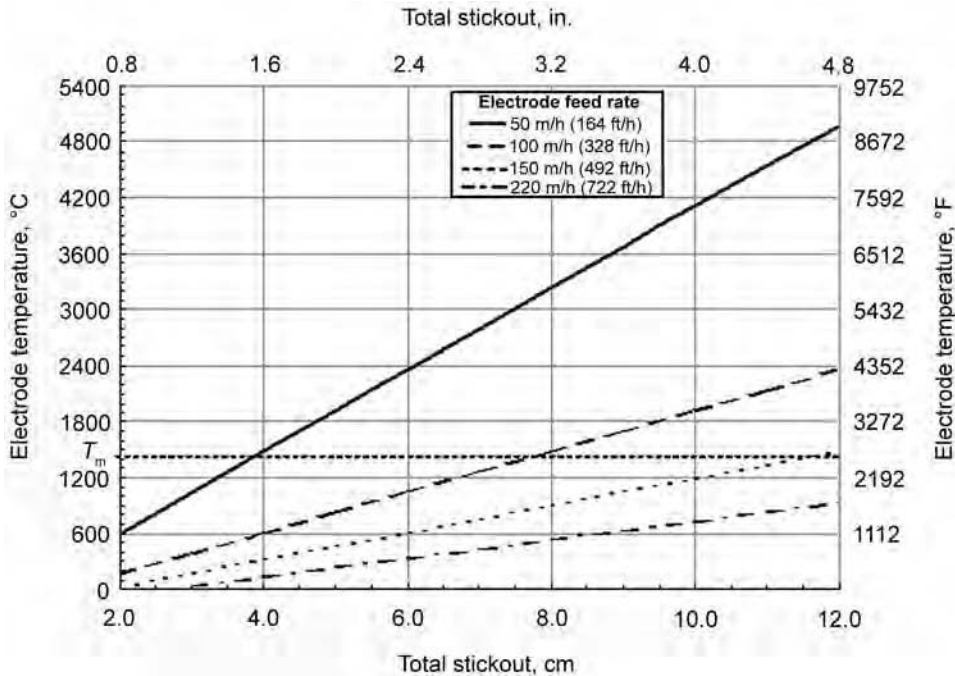


Fig. 13 Electrode temperature due to Joule heating. Wet stickout of 2 cm (0.8 in.) and a 2 mm (0.08 in.) electrode diameter

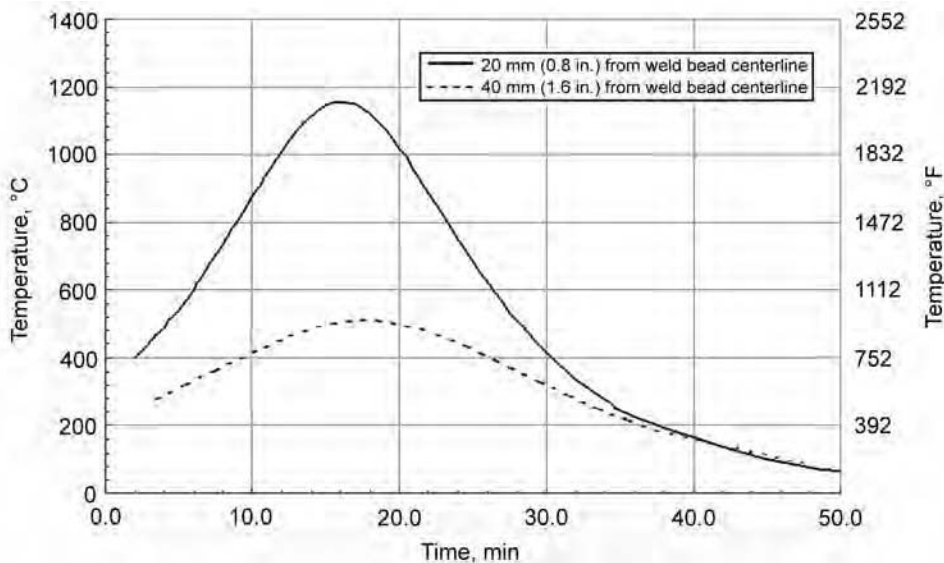


Fig. 14 Thermal cycles calculated by Eq 9 for two distances. Plate thickness of 50 mm (2 in.); root gap of 24 mm (0.9 in.); $I = 480$ A; $V = 35$ V; $v_{\text{welding}} = 0.02$ cm/s (0.008 in./s)

A typical running flux for low-carbon steels has the following composition (Ref 11):

Constituent	Content, wt%
SiO ₂	25
MnO	10
CaF ₂	15
Al ₂ O ₃	25
CaO	15
MgO	10

Electrical Resistivity. A flux of high resistance (or low conductivity) will draw less current, resulting in a colder weld pool and lower base-metal penetration. It will also allow the wire to drive deeper into the pool. On the other hand, a flux of low resistance may draw excessive current, raising the temperature of the bath until the process stabilizes with a shorter electrode extension. However, if resistance is too

low, then arcing may occur between the electrode and the slag bath surface, especially at higher voltages. This condition is aggravated in fluxes that show steeply increasing conductivity with rising temperature. In terms of process conditions, lower slag resistivity may result in operation at lower voltage.

Fluidity. In addition to its heat-generating ability, the molten slag must also have sufficient fluidity to cause rapid convection and good circulation, needed to distribute heat throughout the weld joint. Fluidity of a slag depends mainly on its chemical composition and operating temperature. The melting point of a flux must be below that of the base metal for weld pool refining, and its boiling temperature must be higher than the operating temperature to avoid loss by vaporization. Any preferential loss (of one or more ingredients) will alter the bath composition, which may greatly change the slag fluidity and electrical conductivity, resulting in improper shielding. If the composition of the fluxes is altered during operation, the change in energy imparted to the slag may cause an increase in temperature and in conductivity during welding of long seams, which may give rise to arcing on the top surface of the slag bath.

Low fluidity will tend to trap slag inclusions in the weld metal; excessive fluidity will cause leakage through the small space between the work and the retaining shoes. For joining thin plates, higher-fluidity fluxes are desirable to obtain good circulation in the relatively small bath.

Metallurgical Compatibility. Finally, the slag should be metallurgically compatible with the alloy being welded. For steel welding, the fluxes are generally mixed oxides of silicon, manganese, titanium, calcium, magnesium, and aluminum (Ref 1). These oxide components play an important role in the shielding and refining of the weld pool. Calcium fluoride (CaF₂) is added to basic oxides or silicate systems to achieve the proper resistivity and fluidity. Increasing CaF₂ decreases viscosity, melting point, and resistivity. Additions of TiO₂ also decrease resistivity, while Al₂O₃ increases it. However, TiO₂ also increases slag viscosity (Ref 2, 3). Special applications, such as inclusion control or sulfur removal, may require the addition of rare-earth compounds (Ref 16).

Slag detachability after weld-metal solidification is not a major problem in ESW. The addition of large quantities of TiO₂, however, will often result in difficult slag removal. Fluoride additions generally improve slag detachability.

ESW Electrodes

Various ESW techniques are available, depending on the type of electrodes and the feeding mechanism. The electrodes can be solid

wires, tubular flux cored wires, large-section solid electrodes, and large-section cored electrodes. The guides or nozzles can be consumable or nonconsumable. The conventional method uses nonconsumable guides (also known as snorkels), which are maintained approximately 50 to 75 mm (2.0 to 3.0 in.) above the molten flux. In this case, a mobile feeding head is used and is raised vertically to match the weld pool travel speed. If the electrode feeding mechanism is stationary, then the nozzle will be "consumed," becoming part of the weld metal when it is reached by the slag pool. Accordingly, the materials used in consumable guides generally match the chemical composition of the electrode or base metal. A consumable guide can either be a thin-walled tube or an assembly of plates or rods with conduits to feed the electrode wire. Fin-shaped guide tubes are prepared by welding webs to circular-section guide tubes to obtain more uniform weld pool heating (Ref 1, 3, 6). Among the different types of electrodes, only the wire type and the large-section cored electrodes require the use of nozzles for delivering the electrode into the root gap. Bare guides sometimes need insulation along their lateral surfaces if they cannot be precisely aligned within the weld joint. One solution is to insert insulating plugs at critical locations in the assembly. Flux-coated consumable nozzles are available to minimize the problem of insulating the electrode assembly. Figure 15 shows several shapes of electrodes and guides used in ESW.

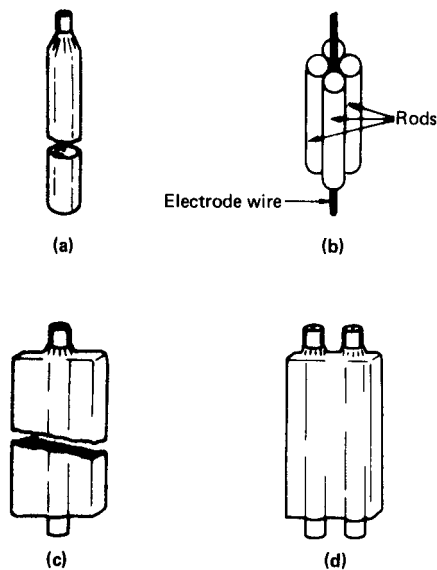


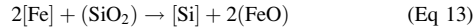
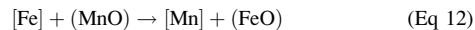
Fig. 15 Selected electrodes and guides (nozzles) used in electroslag welding. (a) Single flux-covered tube. (b) Cluster of rods taped together. (c) Flux-covered

Metallurgical and Chemical Reactions

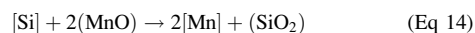
Fusion Zone Compositional Effects

In ESW of carbon and low-alloy steels, the major reactions involve manganese, silicon, carbon, and impurities such as oxygen, sulfur, and phosphorus. In the welding of high-alloy steels, reactions involving chromium, titanium, aluminum, and other elements are important. The extent and control of reactions are determined mainly by the concentrations of the elements in the liquid metal and by the concentrations of their oxides in the slag. The temperature in the reaction zone, the metal droplet/slag surface area, and the duration of contact between the molten metal and slag are other factors that affect the final weld-metal composition. The concentration of elements in the metal and slag is determined by the electrode wire and flux compositions and by the renewal of the slag pool (that is, the frequency with which the make-up flux is added to the pool).

Thermochemistry. In the case of slags containing high MnO and SiO₂, the reactions between the metal and slag can be described as:

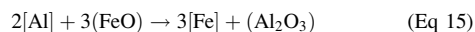


In Eq 12 and 13, $[M]$ and (NO) represent the activities of the metal M in the weld pool and of the oxide of element N in the slag layer. However, for all practical purposes, concentrations of the metallic element and oxide can be used instead of their activities in thermodynamic calculations. When electrodes containing high silicon are used, the reduction of manganese oxide by silicon must also be taken into account:



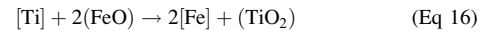
The lower the temperature, the more intense the reaction between manganese oxide and silicon. Changes in welding conditions, such as power input and temperature distribution, will have a definite effect on the recovery of alloying elements.

Like silicon, aluminum is often employed as a deoxidizer for steels and, to a lesser degree, as a microalloying element. The deoxidation reaction is:



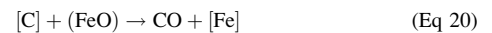
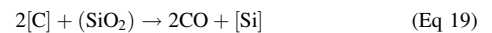
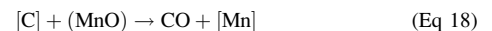
The reaction of aluminum with nitrogen is also important because it has a strong affinity for dissolved nitrogen in the weld pool and because aluminum nitride is responsible for the pinning of grain boundaries and grain growth control.

Titanium is widely used to alloy and modify steels. In welding, it is oxidized by the slag:



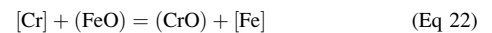
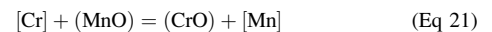
Similar to aluminum, titanium also reacts with carbon, nitrogen, and oxygen to form TiN, TiC, Ti(C,N), TiO, and TiO₂ particles that may remain trapped in the weld metal, moderating excessive grain growth.

The oxidation of carbon may take place as a result of carbon reacting with dissolved oxygen and metal oxides in the liquid metal:



Other minor constituents, such as vanadium and niobium, are oxidized by the slag at the expense of FeO to form a series of oxides, such as VO, V₂O₅, NbO, and Nb₂O₅.

When ESW is used to surface machine parts, metal-cored tubular wire electrodes are often used to provide high contents of alloy elements, such as chromium, molybdenum, vanadium, or titanium, in the deposited metal. When silicate fluxes are used, the oxidation of chromium takes place according to the following main reactions:



The welding consumables (fluxes and welding electrodes) and base metal are the major contributors of tramp elements, such as sulfur and phosphorus, to the weld pool. In addition, the temperature and welding conditions in ESW are not optimal for dephosphorization. As a result, increased migration of phosphorus from the slag to the weld pool occurs not only at the initiation of the weld but also at points where the electroslag process is resumed after an interruption. Sulfur in carbon steel welds is considerably more dangerous than phosphorus because it is the main cause of hot cracking. More recently, desulfurization slags with approximately 60 to 85 wt% CaF₂ and 15 to 40 wt% CaO have been adopted in ESW. Substantial desulfurization can also be achieved when carbon is added to a lime-fluorspar system.

There is also indication that in ESW the slag bath receives oxygen continuously from the surrounding atmosphere. With higher oxygen potential, the slag will also tend to oxidize the

weld metal. Therefore, some modified electroslag processes include an inert gas cover on top of the slag layer to ensure a more deoxidized weld pool.

Electrochemistry. In addition to the thermochemistry of the process, electrochemistry plays an important role in ESW (Ref 17, 18). Because the anode and cathode reactions all occur in one pool, the weight of electrode melted is approximately equal to the weight recovered in the weld pool. Current efficiency can then be expressed as a function of electrode melted and element concentration change. Anodic current efficiency data show that the bulk of the current at the anode is carried by the oxidation reactions of iron, chromium, manganese, and silicon (Ref 19), which also indicates that electrochemical reactions account for a large fraction of the charges transferred. The major charge-carrying reactions at the cathode are the reductions of iron, aluminum, chromium, manganese, and silicon cations from the flux. Furthermore, the current efficiencies for electrochemical reactions involving chromium, manganese, silicon, molybdenum, oxygen, and aluminum increase with increasing current density. The concentration changes are directly proportional to the welding current and to the current efficiency for the reactions, and they are inversely proportional to the electrode melt rate.

Weld-Metal Inclusions

Due to the almost "equilibrium" operating conditions of ESW as compared with other arc welding processes, inclusion separation is expected to be more complete. The larger volume of molten metal, less turbulent weld pool, slower cooling, and slower solidification rate in ESW contribute to a cleaner weld metal with relatively few submicron-sized inclusions.

Solidification Structure

The morphology of steel electroslag weld deposits was first characterized and summarized by Paton (Fig. 16). Yu et al. (Ref 20) further characterized the solidification substructure of low-carbon structural steel electroslag weldments and related them to the weld pool form factor:

- *Group 1:* Transition from cellular to columnar dendrites occurs at a short distance from the fusion line. Welds from this group show shallow molten metal pools with high form factor.
- *Group 2:* Cellular-to-columnar dendrite transition occurs further away from the fusion line, with a fine columnar grain zone at the center of the weld.
- *Group 3:* Characterized by a shallow angle of inclination (approximately 10°) between the columnar grains and the fusion line. The transition from dendritic to columnar

dendrites occurs close to the centerline of the weld. The grains meet at the center at an obtuse angle.

- *Group 4:* Dendritic-to-columnar dendrite transition occurs close to the centerline, with equiaxed grains at the center of the weld.

The deep pools and low form factor generally found in groups 3 and 4 welds are also responsible for the high sensitivity to centerline cracking and radial hot cracking of these welds.

Solid-State Transformations

The cooling rate of an electroslag weld metal is so much slower than those of other welding processes that reasonably coarse microstructures are found. During the austenite-to-ferrite transformation, primary ferrite and grain-boundary ferrite are the principal constituents, along with carbides, mostly in the form of pearlite. In low-alloy steels, acicular ferrite, martensite, bainite, and retained austenite can be found only in those welds that have considerable amounts of alloying ingredients.

Electroslag Process Development

High-Productivity Electroslag Processes

Responding to the technological challenge of the need for a large volume of deposited metal and low heat input, many high-speed ESW techniques have been developed (Ref 9–12, 15, 21–25). There have been essentially two approaches:

- Narrowing the gap to decrease the volume of metal deposited (thereby shortening the time needed to form the weld joint)
- Increasing the welding speed

With either approach, the productivity is increased and the heat can be distributed throughout a longer section of the weld.

With respect to the narrow-gap approach, the extent of gap cross-sectional area reductions is limited by the stability of the process and the size of the electrode and guide tube. Too narrow a gap may cause arcing between the electrode and the base metal. Solid flux blocks may be inserted at regular intervals to avoid arcing between a solid strip electrode in a thin-channel consumable guide and the base metal. Gaps as small as 12 mm ($\frac{1}{2}$ in.) have been reported (Ref 26). Narrow-gap welding, however, can result in higher base-metal dilution.

The use of powdered filler metal has been reported to increase the deposition rate in ESW (to over 24 kg/h, or 53 lb/h) with reduction in the specific heat input and to refine the weld-metal and HAZ microstructure. The supply of metal powder (ferrous, mainly) to the weld metal can be obtained by a flow of argon gas (Fig. 17). Welding speed as high as 230 mm (9 in.) per minute has been reported. Notch impact testing results measured with samples taken 1 to 2 mm (0.04 to 0.08 in.) from the fusion line showed good Charpy impact toughness.

Metal powder cored strip electrode for consumable guide ESW has also been used (Ref 9, 17). The average weld deposition rate is approximately two to three times higher than the solid wire process, over 38 kg/h (85 lb/h). The specific heat input of these welds was lower, at 0.8 kJ/mm^2 (520 kJ/in.^2). Rather than

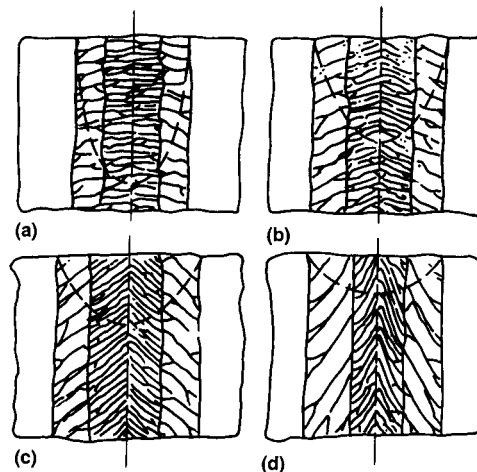


Fig. 16 Electroslag weld-metal solidification structure according to the variation of the orientation and the thickness of the columnar grains zone. (a) Group 1. (b) Group 2. (c) Group 3. (d) Group 4. See text for details. Source: Ref 3

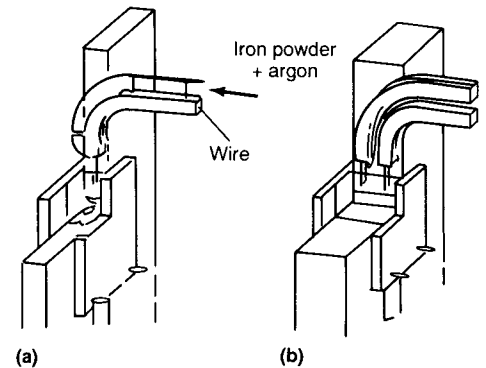


Fig. 17 Equipment setup for square-grooved high-speed welding with metal powder addition. (a) Plate thickness of 10 to 40 mm (0.375 to 1.56 in.). (b) Plate thickness of 40 to 100 mm (1.56 to 4 in.). Source: Ref 24

add metal powder to increase the deposition rate and absorb the excess thermal energy in the molten metal bath, a separate filler wire can be used (Ref 27). This is shown in Fig. 18. This setup resembles the feeding of a cold wire into plasma arc welding or gas tungsten arc welding processes. Not only is the productivity of the process increased, but the HAZ width is also reduced.

Narrow-Gap Improved Electroslag Welding

Narrow-gap improved electroslag welding (NGI-ESW) is a variant process of standard ESW with the aim of improving the toughness of the fusion zone and HAZ, the productivity, and the soundness of the weld bead. Compared to the range of process variables between both welding processes, for a 5 cm (2 in.) thick steel plate, NGI-ESW presents lower root opening (approximately 40%), higher welding current (67% more), higher welding speed (approximately twice the speed of standard ESW), and lower welding heat input (75% less energy per length) (Ref 28–34).

Similar to standard ESW, a molten slag and a molten welding pool are created, but in this case, the weld-metal dilution is approximately 50%. The consumable guide and the insulators, when melted, are mixed with the welding and slag pools, respectively. An ESW neutral fused flux is used, with controlled oxygen content in the weld metal (180 to 200 ppm). The consumable guide is made of low-carbon steel to improve the soundness of the weld bead. The filler metals used in NGI-ESW are metal-cored wires, according to AWS 5.25 ESW filler-metal specification.

The consumable guide in NGI-ESW is designed to distribute heat in a more uniform way. Usually, it has two shapes: the standard, with a cylindrical-type shape, and the sandwich,

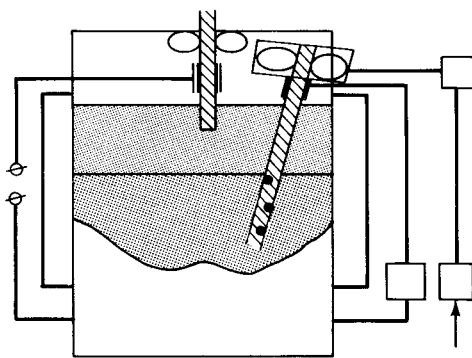


Fig. 18 Schematic of electroslag welding process using separate filler wire to increase deposition rate and absorb excess thermal energy in molten metal bath. Source: Ref 28

with a rectangular shape (Ref 34). These two shapes are presented in Fig. 19.

The consumable guide shape is important to uniform heat flow and also deposition rate and weld bead soundness, in particular, lack of fusion. Figure 20 compares the effect of two consumable guide shapes in the uniformity of heat flow (presented by arrows and two isothermals) and in the presence of cold spots, which generate a lack of fusion. The standard EWS shape is more prone to a lack of fusion when compared to NGI-ESW.

The NGI-ESW process presents reduced sensitivity to weld imperfections and improved toughness in the HAZ. These goals are achieved with higher productivity and substantial cost savings (Ref 34).

Electroslag Surfacing

Surfacing by means of weld overlays has a long history. Electroslag surfacing can be done in either the vertical or flat position. Where the area to be surfaced is small relative to the base metal, vertical electroslag surfacing is usually used. Adapting the vertical orientation of ESW to produce composite metallic structures involves replacing one of the parent-metal plates with a water-cooled mold. An interesting application is tool steel ingots that are given a soft steel electroslag-welded deposit on each end to facilitate the rolling operation.

For large areas, such as plates for tube sheets or cylindrical pressure vessels, electroslag surfacing is conducted in the flat position. Excellent process stability is one of the characteristics of the process. Even with electrodes as wide as 150 mm (6 in.), the quality of the surface weld is still comparable to that of welds produced by other processes. To minimize the undercutting problem and improve bead smoothness, Kawasaki Steel (Ref 6) developed the Maglay process, which uses an external magnetic field to control the flow of molten slag and metal. Dilution can also be controlled, to less than 10%. Forsberg (Ref 28) reports the development of a similar process, which uses strips of 60 to 90 mm (2.4 to 3.5 in.) width

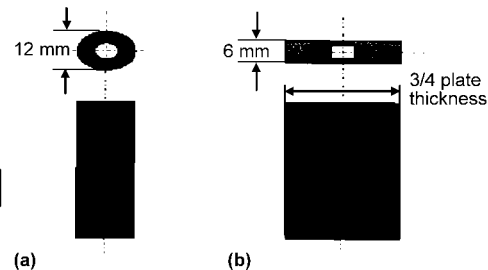


Fig. 19 Example of consumable guide designs for a steel plate. (a) Standard type for standard electroslag welding. (b) Sandwich type for narrow-gap improved electroslag welding. Source: Ref 34

and emphasizes the higher deposition rate and lower dilution ratio.

Electrogas Welding

Electrogas welding can be classified as a gas metal arc welding process. It was introduced in the early 1960s to perform single-pass welding of relatively thin plates in the vertical position. As shown in Fig. 21, the process is very similar to ESW, with the exception of the presence of an arc and the weld pool shielding mechanism (Ref 6). In most cases, shielding gas is used together with a bare or flux cored wire to provide a shielding gas on top of the molten pool of slag and weld metal. Self-shielded flux cored wires are often used without a separate gas shield. The production rate can be as high as 34 kg/h (75 lb/h), depending on the joint configuration and plate size. Special flux cored wires that contain fewer slagging ingredients must be formulated for EGW, because slag buildup on the molten weld-metal surface can affect arc stability and cause slag entrapment. The thicker the plate being welded, the less flux needed. When bare wire is used, small amounts of granular flux are usually added at the start. The slag needed for protection is produced from the deoxidizers in the electrode wire. For steel welding, the most common shielding gas is carbon dioxide. Additions of argon (75 to 80 vol%) to carbon dioxide seem to improve the arc stability and weld-metal properties. Flow rates are usually of the order of 14 to 19 L/min (30 to 40 ft³/h).

Heavy aluminum weldments are produced by EGW using argon-helium gas shielding with flow rates of 28 to 38 L/min (60 to 80 ft³/h).

In addition to its higher deposition rate, EGW presents the advantages of lower heat

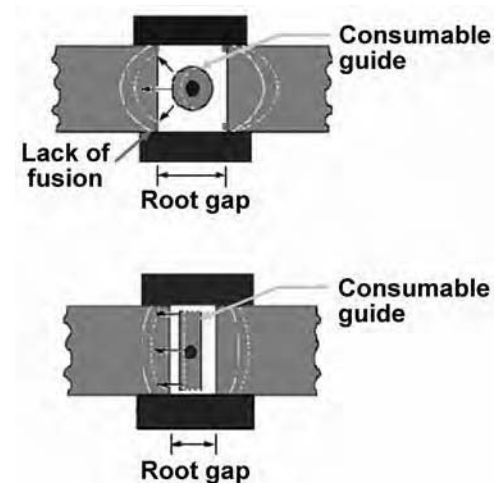


Fig. 20 Example of consumable guide designs for a steel plate. (a) Standard type for standard electroslag welding. (b) Sandwich type for narrow-gap improved electroslag welding. Source: Ref 34

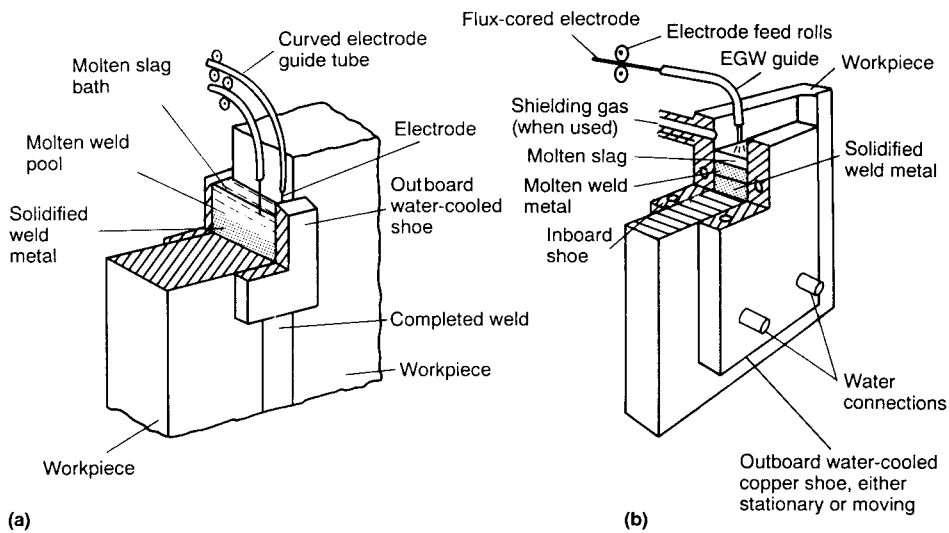


Fig. 21 Schematics comparing primary components of two vertical welding processes in which molten weld pools are confined by cooling shoes. (a) Electroslag welding. (b) Electrogas welding (EGW)

input, more refined microstructure, and improved HAZ properties. Consequently, post-weld heat treatment is not mandatory in many EGW applications. The process also offers easy restarting if the weld is interrupted (complicated in ESW). However, as the thickness of a plate increases, the shielding gas often fails to cover the entire joint area, leading to unacceptable porosity. Thick plates favor the choice of ESW because electroslag welds exhibit fewer inclusions and defects.

Multipass ESW and EGW

The metallurgical problems encountered in single-pass electroslag and electrogas processes can be largely overcome by multipass welding. An example is a thick steel square-butt electroslag weld joint with a fixed copper chill bar or water-cooled copper tube inserted at midwall, and a weld being produced with a moving shoe on one side. The copper chill is then removed, and the opposite side is welded. In practice, however, several problems may appear. One is related to the removal of the copper chill, gripped by the shrinkage that occurs during the first weld pass. Another is the problem of ensuring penetration by the second pass into the first pass. Unless the plate edges are machined and carefully fitted up, slag leakage may also occur.

Reference 29 reports the use of a copper chill bar that penetrated to the root of one side of a double V-joint preparation while EGW proceeded from the opposite side. An alternative method is to manually deposit the root pass, to avoid the problem of close fit-up tolerances needed for complete penetration. Where welding can only be approached from one side,

conventional backing bars are used, and the copper shoe protrudes into the joint to mold the initial pass, followed by the surface pass deposited in the conventional manner. This technique is satisfactory for EGW, but slag retention in the cavity formed by the protruding shoe and the base plates is a challenge in the electroslag process.

The consumable nozzle electroslag process can be used to make a multipass electroslag weld with a pass from each side. A tightly fitted spacer bar is placed at midwall. The electroslag weld pass from the first side partially penetrates the spacer bar, and the second pass from the opposite side consumes the remaining spacer and penetrates the first pass.

These process modifications do not solve the problem of the wide HAZ on the surface of the plates being welded, because toughness and fatigue properties at or near the outer surface of a weld are essential for the integrity and performance of the structure.

Electroslag and Electrogas Process Applications

Carbon and Low-Alloy Steels

The joining of heavy-section steels is the most common application of both ESW and EGW. As previously stated, ESW is commonly done on plates of thickness 50 mm (2 in.) and greater. In fact, economy is greatly increased if the section thickness is greater than 100 mm (4 in.). The range of application of EGW is between 9.5 and 75 mm (0.375 and 3 in.). When compared with arc welding processes, minimum distortion, vertical position, and

minimum joint penetration are the major advantages. Typical applications include fabrication of pressure vessels, nuclear components, power generation equipment, rolling mills, heavy presses, bridges, ships, and oil drilling rigs (Ref 30). Other structural applications reported are blast furnace shells (carbon steel) and a wind tunnel structure (HY-100 steel) (Ref 31, 32).

Structural Steels

A considerable number of highway bridges were fabricated using ESW prior to its ban in bridge construction. Some failures have been attributed to defects such as hydrogen cracking, lack of fusion, low HAZ fatigue properties, and so on. However, properly made welds were found to meet the radiographic standards required for impact and fatigue loading of structural members (Ref 33). In the case of low-alloy steels for structural applications, austenitizing postweld heat treatments have been considered necessary for electroslag welds. However, when proper attention is given to consumable (flux and electrode) selection, a stress-relieving heat treatment is generally sufficient to obtain good impact properties (Ref 34).

Shipbuilding. Electroslag and electrogas welding can be used for the welding of components and for on-ship welding. One application is the propeller shaft bracket assembly for natural gas and oil tankers. Stem frame parts, heavy rudderstock plates, longitudinal and vertical hull stiffeners, and shaft struts are often electroslag welded (Ref 35).

Pressure Vessels. Thick-wall pressure vessels used in the chemical, power generating, petroleum, and marine industries are manufactured using ESW. Plates are rolled to form the shell of the pressure vessel, and the longitudinal seam created is then welded. Lifting lugs on the vessels, nozzles, and branch pipes are also electroslag welded to thick-walled vessels. Due to the high heat input, the welding practice must be critically controlled. Where code requirements are specified, a normalizing heat treatment is also performed.

Penetrating members, such as nozzles and pipe fittings, are often costly to weld into thick-wall pressure vessels by conventional processes. A unique method employing both welding and casting techniques has been proposed by Norcross (Ref 36). A cylindrical water-cooled mold is tightly affixed to the outside surface of the vessel, and weld metal is cast in place. The hole of the nozzle is then machined to provide an opening into the vessel, at the end of which pipes or other attachments can be easily welded (Fig. 22). Even large-diameter penetrating members can be made by this method, by casting hollow cylinders after first tapering the vessel wall to allow the

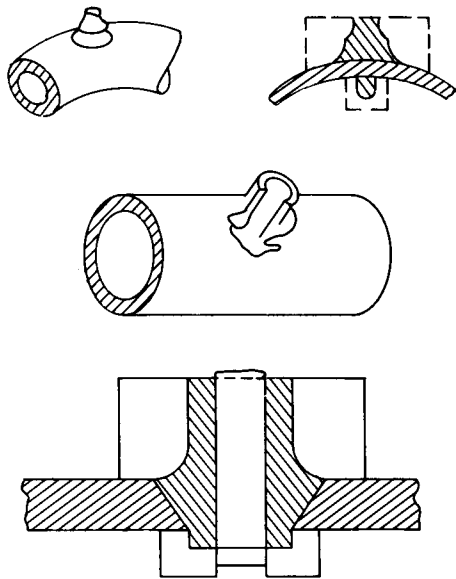


Fig. 22 Application of electroslag welding to incorporate penetrating members such as nozzles onto thick-wall pressure vessels. Source: Ref 38

starting zone of the electroslag weld to be machined away (Ref 37, 38).

Heavy Machinery. Large presses and machine tools are often manufactured from plates that are larger than the mills can produce, so ESW is used to join large plates together. Motor frames, press frames, gear blanks, turbine rings, crane rails, and crusher bodies are some of the common applications. In the transmission pipeline industries, ball valves and stop-gate valves are often electroslag welded.

Dissimilar Metal Joining

Electroslag remelting has been used to develop transition pieces for heavy-wall steam piping where low-alloy chromium-molybdenum steel pipe is to be joined to austenitic stainless steel pipe. Two round ingots, one of the ferritic alloy and one of the austenitic stainless steel, are welded together to form the electrode for electroslag remelting. As the electrode is melted in the molten slag bath, the composition gradually changes from one to the other, depositing a graded alloy billet that is later pierced and formed into a transition piece (Ref 38–40).

Joining and Repairing of Castings

Electroslag welding is also used to weld cast components. Instead of producing a large casting, many small castings of lower cost and simpler fabrication are produced and welded together. One such application is described by Brosholen et al. (Ref 41) to construct a cast

steel propeller shaft bracket. Cast iron has been electroslag welded using a cored wire containing either white or gray cast iron powders and a graphite nozzle (Ref 42). Defective thick sections of cast steels can be repaired by ESW, by drilling a series of connecting holes into the defect zone. A close-fitting water-cooled copper mold is inserted in one of the drilled holes while welding proceeds in the adjacent hole. On completion of that weld, the mold is moved to the next hole before the molten slag has cooled, which allows ESW to start in the vacated hole (Ref 43, 44).

Tool and Die Surfacing and Welding

The slow thermal cycles involved in ESW are favorable for depositing hardenable alloys. For large forging hammers and forming dies, hard wear-resisting alloys can be spilled to the surface of a carbon steel backing using multiple electrodes and current-pulsing techniques (Ref 45–47).

Stainless Steel and Nickel-Base Alloys

Two halves of large 38 tonne (42 ton) cast stainless steel pumps for nuclear electric power facilities have been successfully joined by circumferential welding of their equatorial surfaces and have been qualified to rigid nuclear code requirements. As-welded electroslag welds in austenitic stainless steels were found to be insensitive to knife-line attack after sensitization for 1 to 5000 h at temperatures ranging from 450 to 750 °C (842 to 1382 °F) in tests (Ref 48). It has also been demonstrated that ESW is suitable for welding 25 mm (1 in.) thick alloy 600 plates and 25 mm (1 in.) and 114 mm (4.5 in.) thick plates of alloy 800. Matching filler metals and Inconel filler-metal 82 produced sound welds with excellent elevated-temperature strength and stress-rupture results. Because stainless steels and nickel-base alloys do not undergo allotropic transformations, electroslag welds do not require a high-temperature postweld heat treatment.

Aluminum

Both ESW and EGW have been used to join thick sections of aluminum. One such application is to join 240 mm (9.5 in.) thick electrical conductors (busbars). Instead of the typical copper shoes, graphite shoes are used to obtain satisfactory weld surfaces and edge penetration (Ref 49). Gagan et al. (Ref 50) reported erratic penetration encountered in ESW of thick-section aluminum due to the magnetic fields generated by the welding process, which required special shielding screens around the weld zone. The high conductivity of aluminum and the prompt formation of a refractive oxide are also of concern. High-fluoride-content fluxes and an inert gas shield in EGW typically produce good results in welding thick-section

aluminum. For ESW of aluminum containing 4.5 wt% Mg, the following flux has been suggested (Ref 51):

Constituent	Content, wt%
MgF ₂	1–30
MgCl ₂	5–60
LiF	5–60
KCl	5–6

As welding progresses, additions are made to the flux containing 30 wt% each of KCl, LiF, and MgCl₂, and 10 wt% MgF₂. This flux is reported to work well for ESW of aluminum with copper shoes (Ref 51).

Titanium

The reactivity of titanium requires that residual elements such as hydrogen, oxygen, and nitrogen be minimized in ESW. A slag bath high in halides and containing virtually no oxides, and an inert gas (argon) shield over the bath, are required. Plate electrodes seem to produce better results (Ref 3, 52). Commonly, fluxes are halide compounds based on CaF₂ with rare-earth additions to produce welds low in oxygen, nitrogen, and hydrogen. Devletian (Ref 53) reported that because the high resistivity of titanium promotes rapid ohmic heating of the titanium consumables, stable welding operation generally requires large-diameter electrodes for nonconsumable guide welding, and nozzles or guide plates for consumable guide welding.

Problems and Quality Control

Fusion Zone

As discussed earlier in the section “Solidification Structure” of this article, both cellular and columnar dendrites are observed in the solidification structure of an electroslag weldment. Particularly in the cases of welds with low form factor, in which the transition from cellular to columnar dendrites occurs close to the centerline of the weld and the grains meet at an obtuse angle, centerline cracking and radial hot cracking are more frequently observed. These defects can be attributed to the combined effects of temperature gradient, solidification rate, degree of restraint in fit-up of the weld, high welding speed, and low form factor. In general, a long, straight-sided columnar grain structure (the result of high welding speed) tends to be weaker under load than the more equiaxed and finer grain structure of a slow-speed weld. At the same time, the cellular structure may be coarser and higher in segregation for the case of low welding speed. Figure 23 shows a proposed mechanism of solidification cracking.

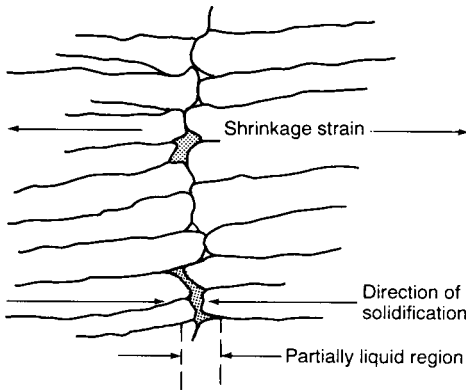


Fig. 23 Schematic indicating projected mechanism of solidification cracking in an electroslag weldment. Source: Ref 54, 55

Partially Melted Zone

Liquation cracking is associated with the melting of heavily segregated grain boundaries near the fusion line region. Carbon and manganese are the most common alloying elements involved in the formation of compounds such as (Mn,Fe)S that lower the melting temperature of the grain boundaries. Phosphorus, nitrogen, and boron are some of the other embrittling agents found in ferrous alloys. During cooling, residual stresses may build up and rupture these weakened boundaries. Under the slow heating and cooling conditions experienced by an electroslag weld, the susceptibility of a ferrous alloy to liquation cracking is increased. It has been reported that liquation cracks can be eliminated in heavy electroslag welds by microalloying the steels with cerium, titanium, and other elements to combine with sulfur and form small high-melting-point inclusions (Ref 56).

Temper Embrittlement

Thick-section 2.25Cr-1Mo steel plates used in pressure vessels for petroleum and chemical service at elevated temperatures are susceptible to temper embrittlement in service. The problem has been attributed to the presence of residual elements such as phosphorus and antimony. Bruscati (Ref 55) established an X factor to describe the effect of the residual elements:

$$X = \frac{10P + 5Sb + 4Sn + As}{100} \quad (\text{Eq 23})$$

where X is in parts per million. Acceptable weld-metal ductility can be obtained if the manganese and silicon contents and the X factor are low. Reduction of these elements can be achieved using basic fluxes. Another indicator, the Watanabe number, J , shows that welds and base metal are not susceptible to temper embrittlement if J is less than 200 (Ref 57):

$$J = (\text{Si} + \text{Mn})(\text{P} + \text{Sn}) \times 10^4 \quad (\text{Eq 24})$$

Hydrogen Cracking

Generally speaking, ESW is performed under perfect slag shielding conditions, and the rate of cooling of the weld metal is low. Therefore, the occurrence of hydrogen-induced cracking is minimal. However, under circumstances that require the use of a moist argillaceous material to prevent the slag from leaking out of the joint region, an atmosphere high in water vapor is present. Microcracks, and sometimes blowholes, may result in the weld metal. Grain-boundary separation, observed in some electroslag welds, can be completely eliminated by postweld heat treating at 300 °C (570 °F) immediately after welding, which indicates that by allowing hydrogen to diffuse out of the specimen, the integrity of the welds can be maintained. This effect is further evidenced by the higher cracking incidence at the bottom part of an electroslag weld. In addition, diffusible hydrogen content is high at a region close to the weld start, decreasing to a relatively constant value at short distances from the starting point. By increasing the depth of the pool, the cooling rate is reduced, and hydrogen escapes by diffusion before it causes damage (Ref 58).

Weld Distortion

When compared with welds produced using other processes, electroslag welds do not present significant distortion problems. Measurements show that both transverse and angular distortion are present and that the gap distance changes as welding progresses. However, the distortion is only of the order of 1 to 2%. Angular distortion occurs because of the rapid cooling of the welded portion of the joint, which tends to draw the parts together, reducing the gap distance. Material ahead of the weld is separated by a gap, so heating has no effect. Material in the weld is either liquid or so hot that it is soft. Neither can support much of a load. As the weld progresses, the very bottom of the weld (coldest metal) resists motion. A contraction of 3 mm (0.125 in.) at the top of a weld 1.3 m (4.3 ft) long is normal. This separation must be allowed during joint setup to avoid jamming the guides and disrupting the normal progress of welding. Parts to be joined must be fitted up so that the gap is wider at the top of the joint. For improved dimensional accuracy, welding must be done at the maximum travel speed attainable.

Postweld Heat Treatment. As discussed in the section "Solidification Structure" of this article, most of the as-welded electroslag weldments have very coarse as-cast structure in the weld metal and coarse grains in the HAZ. As a result, such electroslag weldments may not qualify for many critical applications.

For example, in the case of ferritic steels, normalizing is generally required to refine the weld-metal and HAZ structure. In the case of electroslag-welded nuclear transport flasks, normalizing is frequently followed by tempering (Ref 59). In some low-alloy steels, subcritical postweld heat treatments (for example, stress relief) may not be useful because they can be either detrimental or harmful to mechanical properties, particularly notch toughness. As an example, stress-relief 2.25Cr-1Mo steel weldments at 760 °C (1400 °F) significantly increased the fusion zone and HAZ toughness, but they coarsened the carbides in the base metal, reducing its toughness (Ref 60). Quenched and tempered material, when joined by ESW, must be heat treated after welding to obtain adequate mechanical strength in the weld and HAZ. Kapadia (Ref 61) examined the need to stress relieve components that will be exposed to fatigue loading and determined that in butt welds in the as-welded condition, the outside surfaces cool and contract before the center. Thus, compressive residual stresses are present, which improve fatigue life. Stress-relief heat treatments actually reduce this beneficial effect.

REFERENCES

1. Electroslag and Electroslag Welding, *AWS Welding Handbook*, Vol 2 (No. 7), AWS, 1978, p 226–260
2. H.C. Campbell, Electroslag, Electroslag, and Related Welding Processes, *WRC Bull.*, Vol 154, 1970
3. B. Paton, *Electroslag Welding and Surfacing*, Vol 1, MIR Publisher, Moscow, 1983
4. T. DebRoy, J. Szekely, and T. Eager, Heat Generation Patterns and Temperature Profiles in Electroslag Welding, *Metall. Trans. B*, Vol 11, 1980, p 593–605
5. R.H. Frost, J.E. Jones, and D.L. Olson, Electroslag Welding of Pressure Vessel Steels, *Electroslag Welding for Marine Applications*, Paper 2, U.S. Naval Academy, March 1985
6. "Electroslag Electroslag Tips & Techniques," Bulletin of Electrotherm Corp., 1973
7. J.E. Jones, D.L. Olson, and G.P. Martin, Metallurgical and Thermal Characteristics of Non-Vertical Electroslag Welding, *Weld. J.*, Vol 59 (No. 9), 1980, p 245s–254s
8. S. Nakano, N. Nishiyama, T. Hiro, and J. Tsuboi, Maglay Process—Electromagnetic Controlled Overlay Welding Process with ESW, *Kawasaki Steel Tech. Rep.*, Vol 2, 1981, p 31–42
9. S. Liu and C.T. Su, Grain Refinement in Electroslag Weldments by Metal Powder Addition, *Weld. J.*, Vol 68 (No. 4), 1989, p 132s–144s

10. C.T. Su, "High Speed Electroslag Welding," M.S. thesis, Pennsylvania State University, 1987
11. S. Venkataraman, J.H. Devletian, W.E. Wood, and D.G. Atteridge, Grain Refinement Dependence on Solidification and Solid State Reactions in Electroslag Welds, *Grain Refinement in Castings and Welds*, AIME, 1982, p 275–288
12. D.G. Atteridge, S. Venkataraman, and W.E. Wood, "Improving the Reliability and Integrity of Consumable Guide Electroslag Weldments in Bridge Structures," Research Report, Oregon Graduate Center, 1982
13. R.H. Frost, G.R. Edwards, and M.D. Rheinlander, A Constitutive Equation for the Critical Energy Input during Electroslag Welding, *Weld. J.*, Vol 60 (No. 1), 1981, p 12–62
14. S. Liu and C.T. Su, Performance Evaluation of a Metal Powder Cored Strip Electrode in High Speed Electroslag Welding, *Advances in Welding Science and Technology*, ASM International, 1986, p 401–412
15. R.D. Thomas, Jr., Corrosion Resistant Weld Overlays by the Dual Strip Process, *Brit. Weld. J.*, May 1966
16. A. Mitchell and G. Beynon, Electrochemical Reactions in the Electroslag Welding of Thick Walled Structures, *Avtom. Svarka*, Vol 6, 1965, p 32–37
17. A. Mitchell and G. Beynon, Electrochemical Reactions in the Electroslag Process, Ch. 2, *Bur. Mines Bull.*, 1976, p 669
18. M.E. Peover, Electroslag Remelting: A Review of Electrical and Electrochemical Aspects, *J. Inst. Met.*, Vol 100, 1972, p 97
19. R.H. Frost, D.L. Olson, and G.R. Edwards, "The Influence of Electrochemical Reactions on the Chemistry of the Electroslag Welding Process, *Modeling of Casting and Welding Processes II*, AIME, 1983, p 279–294
20. D. Yu, H. Ann, J.H. Devletian, and W.E. Wood, Solidification Study of Narrow-Gap Electroslag Welding, *Welding Research: The State of the Art*, E. Nippes and D. Ball, Ed., American Society for Metals, 1985, p 21–32
21. V.I. Avramenko, B.F. Lebedev, and V.I. Bozhko, Some Ways of Increasing the Productivity of Electroslag Welding, *Svar. Proizvod.*, Vol 10, 1973, p 16
22. S.A. Smirnov and L.A. Efimenko, Special Structural Features and Mechanical Properties of Electroslag Welded Joints Made Using Powdered Filler Metal, *Svt. Svarka*, Vol 9, 1973, p 46
23. F. Eichhorn and J. Rimmel, Situation of Research in Electroslag Welding—A Tendency of Further Development, *Ind. Weld. J.*, Vol 4, 1983, p 37
24. F. Eichhorn, J. Rimmel, and B. Wubbels, High Speed Electroslag Welding, *Weld. J.*, Vol 62 (No. 1), 1984, p 37
25. F. Eichhorn and J. Rimmel, "Efficient Fillet Welding in the Vertical Welding Position with Electrogas and Electroslag Welding Methods," Doc. XII-908-85, IIW, 1985
26. K. Watanabe, I. Sejima, S. Kokura, G. Taki, and H. Miyake, Problems and Improvement of Large Heat Input Electroslag Welding, *J. Jpn. Weld. Soc.*, 1975, p 519
27. B.F. Yakushin et al., Improving the Capacity of Electroslag Welded Joints for Resisting Hot Cracking, *Weld. Res. Abroad*, June/July 1984 (Translation from Russian by Automatic Welding, Oct 1982)
28. S. Forsberg, Resistance Electroslag (RES) Surfacing, *Weld. J.*, Vol 63 (No. 8), 1985, p 41–48
29. P.C. Arnold and D.C. Bertossa, Multiple Pass Automatic Vertical Welding, *Weld. J.*, Vol 45 (No. 8), 1966, p 651–660
30. D.J. Ellis and A.F. Gifford, Application of Electro-Slag and Consumable Guide Welding—Parts 1–6, *Met. Fabr.*, April–Nov 1973
31. H. Pass, The Electro-Slag Welding of a Blast Furnace Hearth Jacket, *Weld. Met. Fabr.*, Jan/Feb 1976
32. Electroslag Welding Helps to Restore Wind Tunnel, *Met. Progr.*, March 1976
33. J.S. Noel and A.A. Toprac, "Static, Fatigue, and Impact Strength of Electroslag Weldments," Research Report 157-1F, Research Project 3-5-71-157, Center for Highway Research, University of Texas, 1971
34. A.M. Makara et al., Electroslag Welding of Structural Steels without Normalizing, *Avtom. Svarka*, Vol 7, 1974, p 511–514
35. B. Howser, Application and Trends in Electroslag Welding in the United States, *Electroslag Welding for Marine Applications*, U.S. Naval Academy, March 1985, p 4-1
36. J.E. Norcross, Electroslag Developments, *FWP J.*, Vol 18 (No. 2), 1978, p 41–58
37. J.E. Norcross, Electroslag Boss and Process, U.S. Patent 4,130,931, Dec 1978
38. Electroslag Casting and Welding, British Patent 1,390,674, April 1975
39. D. Yapp and A.P. Bennett, Development of Electroslag-Melted Graded Transition Joints, *Welding Research Related to Power Plant*, Paper 34, Central Electricity Generating Board, Southampton, England, Sept 1972, p 464–481
40. A.P. Bennett, An Electrical Analogue of an Electroslag Remelting Operation Used as a Guide to Improved Control of the Process, *Met. Mater.*, April 1972, p 146–149
41. A. Brosholen, E. Skaud, and J.J. Vesser, Electroslag Welding of Large Castings for Ship Construction, *Weld. J.*, Vol 56 (No. 8), 1977, p 26–30
42. Y. Ishii, Electroslag Welding of Cast Iron, *Trans. Jpn. Weld. Soc.*, No. 2, Sept 1970, p 241–252
43. V.F. Yakovlev, P.I. Kovalkin, N.I. Evdokimov, M.G. Kozulin, and I.I. Sushchuck-Slyusarenko, Electroslag Welding of Steel Casting Defects, *Avtom. Svarka*, Vol 2, 1970, p 72
44. V.G. Svyynyuk, Electroslag Welding for Rectifying Defects in Cast Centrifugal Pump Wheels, *Autom. Weld.*, Vol 28 (No. 7), 1975, p 57–58
45. V.T. Arsenkin, V.G. Radchenko, and D.M. Likhohsherstov, The Electroslag Deposition of Die Steel on Carbon Steel, *Avtom. Svarka*, Vol 3, 1976, p 46–49
46. M.P. Ivanan et al., Electroslag Hardfacing of Beaters of Hammer Crushers, *Svar. Proizvod.*, Vol 7, 1974, p 48
47. Y.I. Gorbachev, E.A. Kovalevskii, and A.V. Matelev, Electroslag Welding of Die Steel, *Svar. Proizvod.*, Vol 11, 1984, p 12–13
48. N. Lehka, Problems Associated with the Corrosion of the Properties of Electroslag Welded Joints in Austenitic Steels of Increased Strength, *Zvrcske Spravy (Weld. News)*, Vol 26 (No. 3), 1976, p 61–68
49. P.M. Bartle, Development of an Electroslag Technique for Welding Thick Aluminum, *Weld. Inst. Res. Bull.*, Vol 12 (No. 3), 1971, p 67–71
50. Y.G. Gagen et al., Electroslag Welding of Aluminum Bus-Bars Located in the Zone of a Strong Magnetic Field, *Svar. Proizvod.*, Vol 12, 1972, p 19–21
51. Electroslag or Submerged Arc Welding of Aluminum or Its Alloys or Electroslag Remelting Aluminum, British Patent 1,544,248, April 1979
52. V.Y. Malin, Electroslag Welding of Titanium and Its Alloys, *Weld. J.*, Vol 64, Feb 1985, p 42–49
53. J.H. Devletian, Electroslag Welding of Non-Ferrous Metals—A Review, *Electroslag Welding for Marine Applications*, U.S. Naval Academy, 1985, p 3–1 to 3–32
54. K. Easterling, *Introduction to the Physical Metallurgy of Welding*, Butterworths, 1983
55. R. Bruscatto, Temper Embrittlement and Creep Embrittlement of 2-1/4Cr-1Mo Shielded Metal Arc Weld Deposits, *Weld. J.*, Vol 9 (No. 4), 1970, p 148s–156s
56. A.M. Makara, Y.Y. Kokalev, and I.V. Novikov, Liquidation Cracks in the HAZ in Structural Steels during Electroslag Welding, *Avtom. Svarka*, Vol 5, 1972, p 1–5
57. Y. Murakami, T. Namura, and J. Watanabe, *Heavy Section 2-1/4Cr-1Mo Steel for Hydrogenation Reactors*, STP 755, ASTM, 1982, p 383–417
58. T. Kunihiro and H. Nakajima, Micro-Cracking in Consumable-Nozzle Electroslag Weld Metal, *Significance of Defects*

- in Welded Structures*, Univ. Tokyo Press, 1973, p 105–109
59. S.S. Tuliani, K.S. Probert, and A.H. Briscoe, Fabrication of Electroslag Welded Magnox Fuel Transport Flasks, *Welding and Fabrication in the Nuclear Industry*, 1979, p 327–333
60. O. Serrano, G.E. Edwards, and R.H. Frost, A Comparison of As-Welded and Stress-Relieved 2-1/4Cr-1Mo Steel Electroslag Weldments: Microstructural and Properties, *The Application of 2-1/4Cr-1Mo Steel for Thick Wall Pressure Vessels*, ASTM, 1980
61. B.M. Kapadia, Influence of Residual Stress on Fatigue Crack Propagation in Electroslag Welds, *Fatigue Testing of Weldments*, STP 648, ASTM, 1977, p 244–260

Stud Arc Welding*

STUD ARC WELDING (SW), also known as arc stud welding, is a commonly used method for joining a metal stud, or fastener, to a metal workpiece. The process has been used as an alternative metal-fastening method since the 1940s. Millions of specially designed and manufactured metal studs are welded by this process every week in such diverse industries as construction, shipbuilding, automotive, and hard goods, as well as in miscellaneous industrial applications.

This article serves as a basic information source for those interested in accomplishing one-sided, no-hole attachment of metal fasteners. The SW process represents an alternative to other welding processes and is also a substitute for other fastening procedures, such as drilling and tapping, bolting, and self-tapping screws.

Process Overview

Stud arc welding is similar to many other welding processes, including arc and percussion welding, in that the base (weld end) of a specifically designed stud is joined to a base material by heating both parts with an arc that is drawn between the two. Equipment that is unique to this process regulates the arc length and arc dwell time. After an arc is struck, the stud weld end and the workpiece surface are brought to the proper temperature for joining and, after a controlled period of time, the two heated surfaces are brought together under pressure, creating a metallurgical bond capable of developing the full strength of the stud.

There are two basic types of stud arc welding, which are differentiated by the source of welding power. One type uses direct current (dc) power provided by a transformer/rectifier or a motor generator similar to that used in the shielded metal arc welding (SMAW) process. The second type uses power discharged from a capacitor storage bank. The process based on a dc power source is known as stud arc welding, whereas the process that utilizes capacitors is known as capacitor discharge stud welding (CDSW).

Both the SW and CDSW processes overlap in some areas of application. Generally, the SW process is used in applications that require similar stud and workpiece metals, the workpiece thickness is greater in relation to the stud diameter, and an accommodation

must be made for the stud flash (fillet). The term *flash* is preferred to the term *fillet*, because the metal that forms the flash during the stud arc welding process is expelled, rather than added, as occurs with other welding processes.

In contrast, the CDSW process is used extensively when welding to thin sheet metal and is used frequently with dissimilar workpiece and stud alloys. It is also used in cases where marks on the opposite side of the workpiece must be avoided or minimized. With this process, the stud diameter is limited to smaller sizes. The CDSW process is more fully described in the article "Capacitor Discharge Stud Welding" in this Volume. The factors on which process selection should be based are fastener size, base-metal thickness, base-metal composition, and reverse-side marking requirements (Table 1).

Equipment. As shown in Fig. 1, the basic equipment used for stud arc welding consists of a control system, which regulates the arc time and controls gun movement; a fixed or portable stud-welding gun, which holds the stud in position during the welding process to create the proper arc length and joining pressure; and connecting cables, which must be connected to a separate source of dc power. The other items that are needed to weld the workpiece are the studs themselves and ceramic arc shields, or ferrules. The equipment used for stud welding is comparable, in terms of size, portability, and ease of operation, to the equipment used in the SMAW process. Although the initial cost of stud-welding systems varies with the method selected, stud size, and productivity requirements, it is generally competitive with other fastening methods on an in-place or finished part cost basis.

A stud-welding control system that has been integrated in a transformer/rectifier power source is shown in Fig. 2. This type of equipment, which is the most widely used, is called a power/control system. It can weld studs with diameters up to 28.5 mm (1 1/8 in.). Either a single gun or dual guns can be used. Although a light-duty control system can weigh 11.3 kg (25 lb), the system shown in Fig. 2 weighs approximately 450 kg (1000 lb) and can be put on a wheeled cart for mobility.

A typical stud-welding gun (Fig. 3) is usually available in at least two sizes: standard duty, for

use with studs up to 16 mm (5/8 in.) in diameter, and heavy duty, for use on larger-diameter studs. The weight of the gun can vary from approximately 1.8 kg (4 lb), for a standard-duty gun, to 6.8 kg (15 lb), for heavy-duty models.

Table 1 Stud-welding process selection

Parameters	Stud arc welding	Capacitor discharge stud welding	
		Gap and contact methods	Drawn arc method
Stud shape			
Round	A	A	A
Square	A	A	A
Rectangular	A	A	A
Irregular	A	A	A
Stud diameter or area			
1.6 to 3.2 mm (1/16 to 1/8 in.)	D	A	A
3.2 to 6.4 mm (1/4 to 1/4 in.)	C	A	A
6.4 to 12.7 mm (1/4 to 1/2 in.)	A	B	B
12.7 to 25.4 mm (1/2 to 1 in.)	A	D	D
Up to 32.3 mm ² (0.05 in. ²)	C	A	A
Over 32.3 mm ² (0.05 in. ²)	A	D	D
Stud metal			
Carbon steel	A	A	A
Stainless steel	A	A	A
Alloy steel	B	C	C
Aluminum	B	A	A
Brass	C	A	D
Base metal			
Carbon steel	A	A	A
Stainless steel	A	A	A
Alloy steel	B	A	C
Aluminum	B	A	A
Brass	C	A	D
Base-metal thickness			
Under 0.4 mm (0.015 in.)	D	A	B
0.4 to 1.6 mm (0.015 to 0.062 in.)	C	A	A
1.6 to 3.2 mm (0.062 to 0.125 in.)	B	A	A
Over 3.2 mm (0.125 in.)	A	A	A
Strength criteria			
Heat effect on exposed surfaces	B	A	A
Weld fillet clearance	B	A	A
Strength of stud governs	A	A	A
Strength of base metal governs	A	A	A

A, applicable without special procedures or equipment; B, applicable with special techniques or for specific applications that justify preliminary trials or testing to develop welding procedure and technique; C, limited application; D, not recommended—welding methods not developed at this time. Source: Ref 1

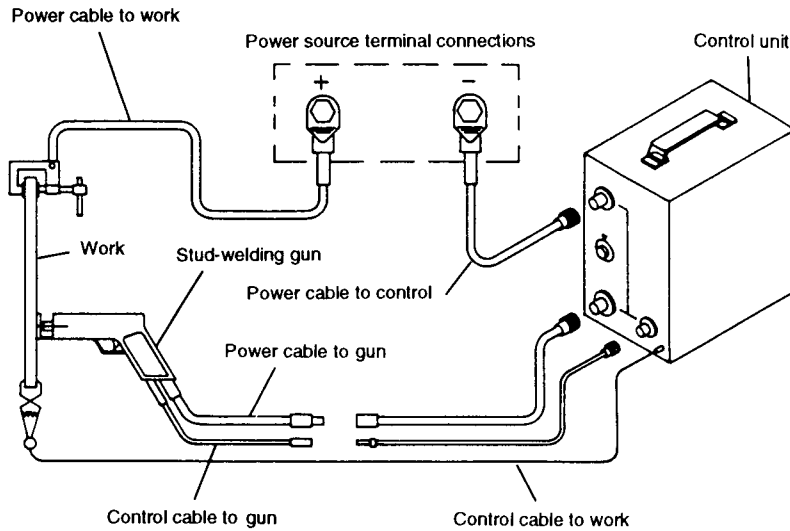


Fig. 1 Stud arc welding control system. The control system must be connected to a direct current power source for welding. In most applications, the stud (electrode) should be negative.

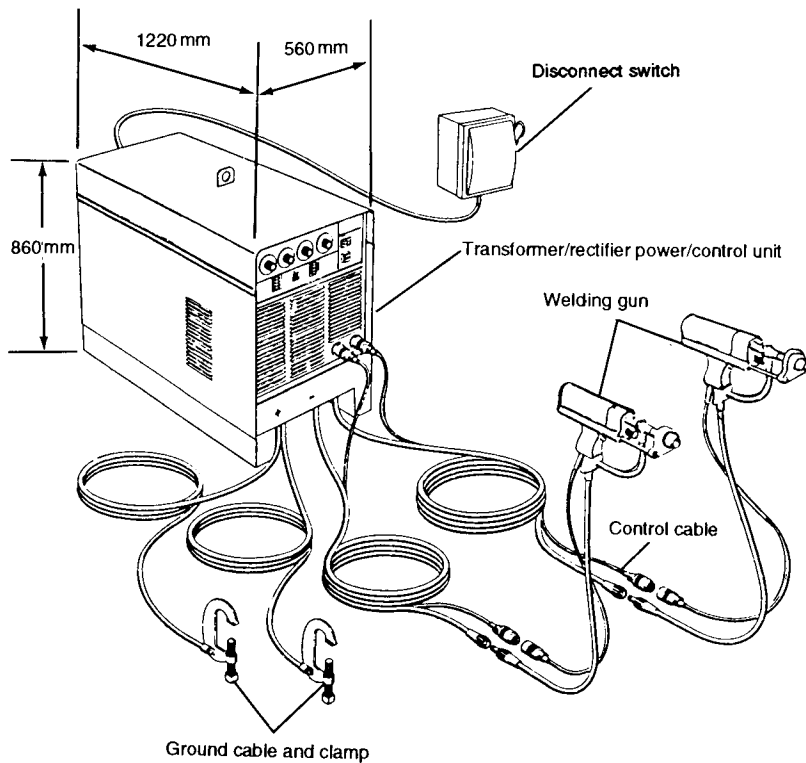


Fig. 2 Typical integrated power/control system for stud arc welding

Operation. The stud arc welding process utilizes the same principles as any other arc welding procedure. First, the stud, which acts as an electrode, is inserted into a chuck on the end of the gun, surrounded by a ceramic ferrule, and positioned against the workpiece (Fig. 4a). Next, the gun trigger is depressed, which starts

the automatic weld cycle by energizing a solenoid coil within the gun body that lifts the stud off the work and draws an arc. The arc melts the end of the stud and a portion of the workpiece (Fig. 4b). After a preset arc time (set on the control unit), the welding current is shut off and the solenoid is de-energized (Fig. 4c).

A main-spring in the gun forces the stud into the molten pool of metal, producing a full-strength weld, which is shown in Fig. 4(d) after the gun has been lifted off the stud and the ceramic ferrule removed. The result is a full-penetration, full-strength stud-to-workpiece weld, as shown in Fig. 5. This weld is similar to that obtained with other types of arc-welding processes.

Studs and Ferrules. With the exception of special processes, the stud arc welding of steel, stainless steel, and aluminum studs requires the use of a specifically designed weld stud and ceramic ferrule.

Studs. A wide range of studs are made by stud-welding manufacturers for the SW process. They vary in size and weld-base configuration, depending on the application requirements. The typical stud styles that are available include threaded, unthreaded, headed, and rectangular studs (Fig. 6). The steel stud diameters that are commonly welded using the SW process range from 2.7 to 25.4 mm (0.105 to 1.00 in.).

Full-strength welds result when using studs made from low-carbon steel that conforms to ASTM A-108 grades C-1010 through C-1020, although other steel grades can be used on a special-application qualified basis (Ref 2). Stainless steel studs are typically made from the austenitic series, including AISI 302, 302 HQ, 304, 305, 308, 309, 310, 316, 321, and 347, in both normal-carbon and low-carbon varieties. Stainless steel 303 is not an acceptable stud alloy. Aluminum studs are usually made from aluminum-magnesium alloys, including 5183, 5356, 5556, 5086, and 5456 (Ref 3).

Steel and stainless steel arc-welded studs that are larger than 6.4 mm (0.250 in.) in diameter use a welding flux to stabilize the welding arc and to deoxidize the weld area. The most commonly used flux is commercially pure aluminum, which is installed onto the weld end of the stud by thermal spraying, staking, or pressing a slug into a drilled hole in the end of the stud (Fig. 7). Studs that are 6.4 mm (0.250 in.) and under usually do not require fluxing.

Aluminum studs do not have to be flux loaded. Instead, the weld end of the stud has a conical or cylindrical tip that is shaped into the parent metal to help initiate the arc and control the arc length. To prevent the oxidation and embrittlement of the stud/plate weld zone during aluminum stud arc welding, the weld area is purged with an inert gas during the weld cycle. Argon gas is commonly used for this purpose, although helium also can be used. The typical gas flow rates for aluminum studs of various diameters are shown in Table 2.

When stud arc welding low-carbon and stainless steel studs, the stud (electrode) should be negative. Aluminum stud arc welding should be set up so that the stud is positive.

Obtaining a full-quality stud arc weld requires a sufficient amount of total energy

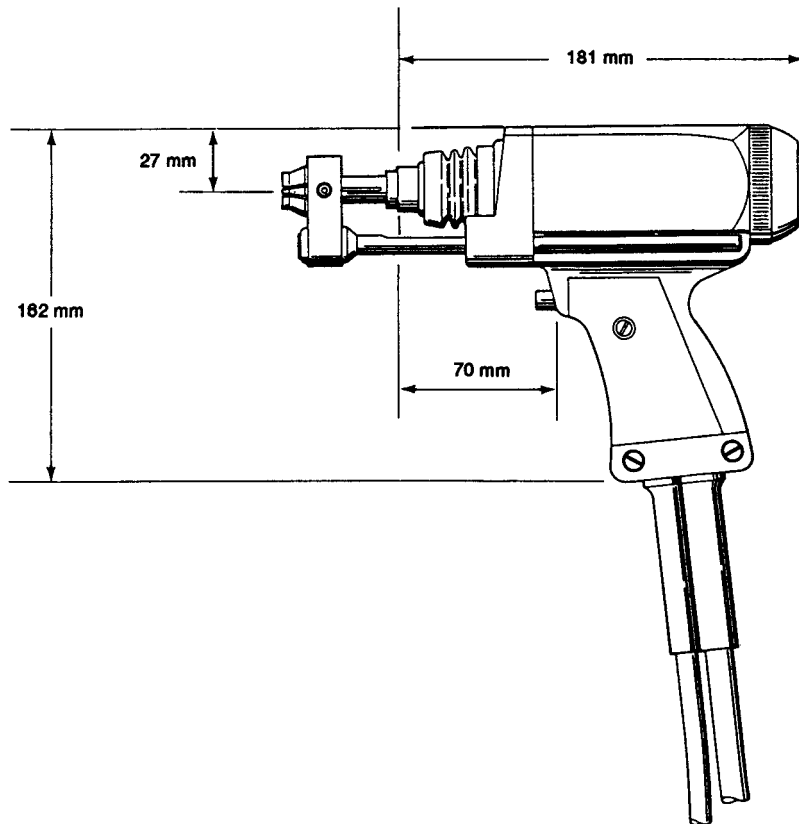


Fig. 3 Typical standard-duty gun for stud arc welding

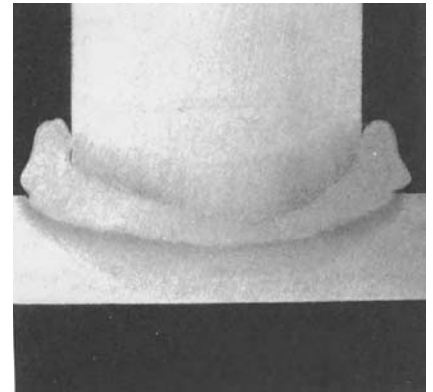


Fig. 5 Macrosection of low-carbon steel stud weld

settings for various SW stud diameters. The ideal settings in each weld position for a particular stud and workpiece should be established by beginning with typical settings and then varying them within the allowable range to meet the required conditions.

Typical settings are based on good weld conditions, such as a clean workpiece, good ground, and others. Also necessary is a proper dc power source, which should have the following characteristics:

- High open-circuit voltage (70 to 100 V)
- Rapid output current rise
- Drooping output volt-ampere curve
- High current output over a short time

Stud arc welding requires a very short weld time (Table 3), but a very high current input, when compared with other types of arc welding. Usually, the duty cycle for this process is much lower than that of other welding processes. Constant-voltage types of dc power sources are not suitable for stud welding. Many of the available dc power sources are acceptable for stud welding, including those supplied as integrated power/control systems by the stud-welding manufacturer. These integrated systems use both three-phase and single-phase incoming alternating current power. Both standard and special voltage units are available. Single-phase units are relatively low-cost, portable systems that are usually suitable for smaller-diameter (≤ 12.7 mm, or $\frac{1}{2}$ in.) stud arc welding. Three-phase units are preferred for larger-diameter studs, because they provide a balanced load on incoming power lines and have smoother arc characteristics. A transformer/rectifier power source, combined with an integral stud-welding control system, is shown in Fig. 2.

Weld cable length and cable size also can affect the total output of a power source. Basically, a larger welding cable size minimizes current loss that is due to cable length, resistance, and heating. Thus, when the distance from the power source to the gun increases significantly, or when the number and size of studs applied per minute are large, larger welding

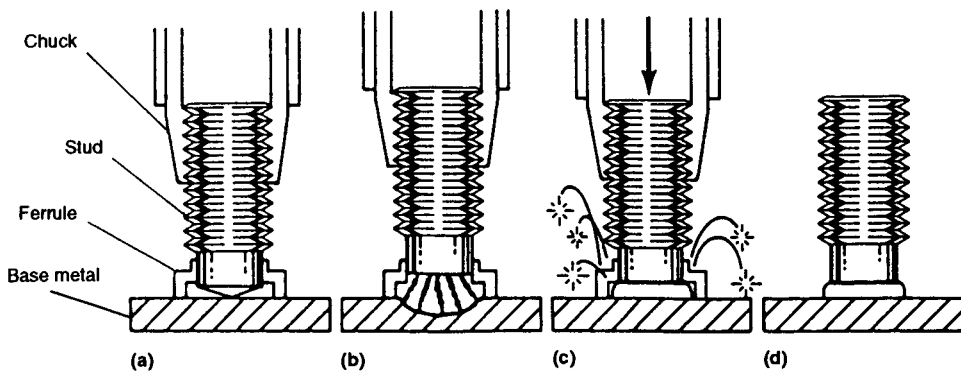


Fig. 4 Stud arc welding process. (a) Gun is properly positioned. (b) Trigger is depressed and stud is lifted, creating an arc. (c) Arcing period is completed and stud is plunged into molten pool of metal on base material. (d) Gun is withdrawn from welded stud and ferrule is removed.

input to the weld joint in order to produce melting and complete metallurgical bonding of the stud and workpiece. The energy input or weld current that is necessary depends on the stud diameter. Other parameters in the stud arc welding process are arc voltage, arc time, and plunge. Arc voltage is a function of the arc length, which is set as "lift," or the length the stud is drawn away from the workpiece during weld-cycle initiation. Plunge is the length of stud that extends past the end of the ceramic

ferrule and is available for melt-off during the weld cycle.

Studs are reduced in length during the weld cycle. Table 3 shows the typical reductions for steel and aluminum studs as a result of welding.

There is a range of setting combinations for all stud diameters. The same total energy input can be obtained by varying current input and arc time. For example, a low current input can be compensated for, to some extent, by increasing weld time. Table 3 also shows typical weld



Fig. 6 Common stud configurations for stud arc welding

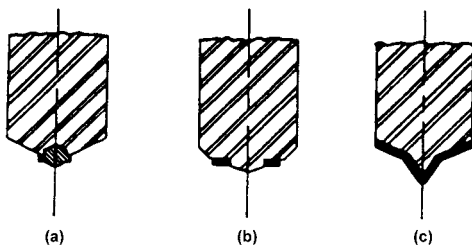


Fig. 7 Methods of flux loading studs. (a) Pressed in slug. (b) Staked on washer. (c) Coating

Table 2 Gas flow rates for aluminum stud arc welding

Stud weld base diameter		Shielding gas flow(a)	
mm	in.	L/min	ft ³ /h
6.4	¼	7.1	15
7.9	5/16	7.1	15
9.5	3/8	9.4	20
11.1	7/16	9.4	20
12.7	½	9.4	20

(a) Shielding gas, 99.95% pure argon

cables should be used. Smaller dc power sources suitable for stud arc welding can be wired in parallel to produce the necessary current range.

Ferrules, or ceramic arc shields, are used in most stud arc weld applications. They are available in a wide variety of sizes and shapes to fit specific stud base designs and applications. For example, there are specific designs for welding studs through metal deck, to the fillet or heel of an angle, to round pipes or bars, or in a vertical position. A ferrule is placed over every stud at the weld end, where it is held in place by a grip on the stud-welding gun. The ferrule is used only once and must be removed from the stud after welding is completed to allow the inspection of the completed weld. Typical ferrule configurations are shown in Fig. 8.

Ferrule design is important, because it controls certain functions during welding. For example:

- Vents on the bottom of the ferrule allow weld gases to escape from the weld area and restrict the inflow of air to minimize weld porosity and oxidation.
- The internal cavity of the ferrule confines and shapes the molten metal into a flash (fillet) around the stud periphery.
- Heat in the weld area is concentrated and contained.
- Flash and weld spatter are minimized.

Although the dimensions of the flash are controlled by the ferrule configuration, the flash diameter and height must be taken into consideration when designing mating parts. Manufacturer specifications on finished stud flash dimensions should be followed, and test welds should be made to establish part fit. Flash

Table 3 Typical stud welding settings

Stud base diameter	Length reduction	Downhand welding								Overhead welding								Vertical welding													
		mm		in.		Current, A	Time, s	Cycles	Lift, mm	Lift, in.	Plunge, mm	Plunge, in.	Current, A	Time, s	Cycles	Lift, mm	Lift, in.	Plunge, mm	Plunge, in.	Current, A	Time, s	Cycles	Lift, mm	Lift, in.	Plunge, mm	Plunge, in.					
Steel and stainless steel																															
4.8	0.187	3.2	0.125	300	0.15	8-9	1.6	0.062	3.2	0.125	300	0.15	8-9	1.6	0.062	3.2	0.125	300	0.15	8-9	1.6	0.062	3.2	0.125	450	0.17	10-12	1.6	0.062	3.2	0.125
6.4	0.25	3.2	0.125	450	0.17	10-12	1.6	0.062	3.2	0.125	450	0.15	10-12	1.6	0.062	3.2	0.125	450	0.17	10-12	1.6	0.062	3.2	0.125	500	0.25	15	1.6	0.062	3.2	0.125
7.9	0.312	3.2	0.125	500	0.25	15	1.6	0.062	3.2	0.125	500	0.25	15	1.6	0.062	3.2	0.125	500	0.25	15	1.6	0.062	3.2	0.125	600	0.33	20	1.6	0.062	3.2	0.125
9.5	0.375	3.2	0.125	550	0.33	20	1.6	0.062	3.2	0.125	550	0.33	20	1.6	0.062	3.2	0.125	600	0.33	20	1.6	0.062	3.2	0.125	750	0.33	20	1.6	0.062	3.2	0.125
11.1	0.437	3.2	0.125	675	0.42	25	1.6	0.062	3.2	0.125	675	0.42	25	1.6	0.062	3.2	0.125	750	0.33	20	1.6	0.062	3.2	0.125	875	0.47	28	1.6	0.062	3.2	0.125
12.7	0.500	4.8	0.125	800	0.55	33	1.6	0.062	3.2	0.125	800	0.55	33	1.6	0.062	3.2	0.125	875	0.47	28	1.6	0.062	3.2	0.125	1275	0.60	36	1.6	0.062	4.7	0.187(a)
15.9	0.625	4.8	0.187	1200	0.67	40	2.4	0.093	4.7	0.187	1200	0.67	40	2.4	0.093	4.7	0.187	1275	0.60	36	1.6	0.062	4.7	0.187(a)	1700	0.73	50	2.4	0.093	4.7	0.187(a)
19.1	0.750	4.8	0.187	1500	0.84	50-55	2.4	0.093	4.7	0.187	1500	0.84	50-55	2.4	0.093	4.7	0.187	1700	0.73	50	2.4	0.093	4.7	0.187(a)	Not recommended			Not recommended			
22.2	0.875	4.8	0.187	1700	1.00	60-65	3.2	0.125	6.4	0.250	1700	1.00	65	3.2	0.125	6.4	0.25				Not recommended			Not recommended							
25.4	1.000	6.4	0.250	1900	1.40	85	3.2	0.125	6.4	0.250	2050	1.40	72	3.2	0.125	6.4	0.25				Not recommended			Not recommended							
Aluminum(a)																															
4.8	0.187	3.2	0.125	150	0.25	15	2.4	0.093	3.2	0.125	150	0.25	15	2.4	0.093	3.2	0.125	180	0.20	12	2.4	0.093	3.2	0.125	225	0.30	18	2.4	0.093	3.2	0.125
6.4	0.250	3.2	0.125	200	0.40	24	2.4	0.093	3.2	0.125	200	0.40	24	2.4	0.093	3.2	0.125	275	0.40	24	2.4	0.093	3.2	0.125	350	0.60	36	3.2	0.125	3.2	0.125
7.9	0.312	3.2	0.125	250	0.50	30	2.4	0.093	3.2	0.125	250	0.50	30	2.4	0.093	3.2	0.125	350	0.60	36	3.2	0.125	3.2	0.125	430	0.70	42	3.2	0.125	3.9	0.156
9.5	0.375	3.2	0.125	325	0.65	39	3.2	0.125	3.2	0.125	325	0.65	39	2.4	0.093	3.2	0.125	430	0.70	42	3.2	0.125	3.9	0.156	460	0.80	48	3.2	0.125	4.7	0.187
11.1	0.437	3.2	0.125	400	0.80	48	3.2	0.125	3.9	0.156	400	0.80	48	3.9	0.156	3.9	0.156	475	0.80	48	3.2	0.125	4.7	0.187							
12.7	0.500	3.2	0.125	460	0.90	54	3.2	0.125	4.7	0.187	460	0.90	54	4.7	0.187	4.7	0.187	475	0.80	48	3.2	0.125	4.7	0.187							

(a) Stud arc welded aluminum studs require inert gas shielding; see Table 2.

dimensions can be accommodated by any of the five methods shown in Fig. 9.

The typical dimensions for flash clearance are shown in Table 4. It should be noted that the flash (fillet) of a stud weld is not the same as the fillet that is produced by conventional welding techniques. It may have areas of nonfusion on its vertical leg or shrink fissures, which have no adverse affect on weld strength or ductility (Ref 4). Consequently, it is not subject to

the profile and inspection criteria used for a conventional weld fillet.

Base Plate Material and Thickness. To obtain full strength, the stud arc welding of low-carbon steel, stainless steel, or aluminum studs should be made to a base material of sufficient thickness so that the stud fails in tension or torque, rather than by pulling a hole in the base-metal workpiece. In the case of stainless or low-carbon steel studs, the base-metal thick-

ness should be at least one-third that of the stud diameter. For aluminum studs, the aluminum base plate material should be at least half that of the stud diameter. Thinner base plates can be used if strength is not the primary design characteristic that is required. On thinner materials, the studs will pull a hole in the plate at strength levels below their maximum. If the plate is too thin, then the stud will burn a hole through it. The recommended base plate thickness for full-strength development and the minimum thicknesses required to prevent burning through the base plate are given in Table 5.

The most widely used combinations of base plate and stud materials are shown in Table 6. With low-carbon steel studs, no preheat or post-heat treatments are needed when welding to low-carbon steel or austenitic stainless steel base plate materials. As carbon content in the base plate increases into the medium range, heat treatment for stud welding may be required. Welding to high-carbon base plate is not suggested. When base plate/stud combinations are questionable, an application qualification test is suggested (Ref 5). Details on this procedure are provided in the section "Stud-Welding Quality Control, Qualification, and Inspection" in this article. For best results when welding stainless steel studs to low-carbon steel plate (especially) when working stress levels are very high or there are repetitive loading cycles), the studs should either be manufactured from annealed-in-process materials or postmanufacture annealed before use.

Good welding practice requires that the base plate material at the weld spot be cleaned. Common contaminants that can result in unsatisfactory welds if not removed include paint, heavy mill scale, heavy rust, oxidation, oil or grease, and plating, such as galvanizing and anodizing on aluminum. Removal methods vary according to the contaminant, the base material, and the end use. Wire brushing and grinding may be satisfactory on heavy structural steel but can be destructive to thin-gage metals or anodized aluminum, because they may reduce the thickness to a point where burn-through or less-than-full-strength welds result.

Suggested cleaning methods include grinding, wire brushing, or needle scaling on heavy materials; using solvents to clean grease and oil; and using a noncontaminating stainless wire brush or a nonmetallic foam disk to clean aluminum and milling. Because anodizing is difficult to remove from aluminum without reducing the metal thickness, consideration should be given to anodizing the base plate and stud after the welding operation.

Similarly, the weld end of the stud should be free from materials that would contaminate the weld, including paint, rust, galvanizing, and others. Studs cannot be coated with any nonconductive material that would interfere with the flow of welding current. Light copper flashing and nickel or chrome plating usually do not cause welding problems.

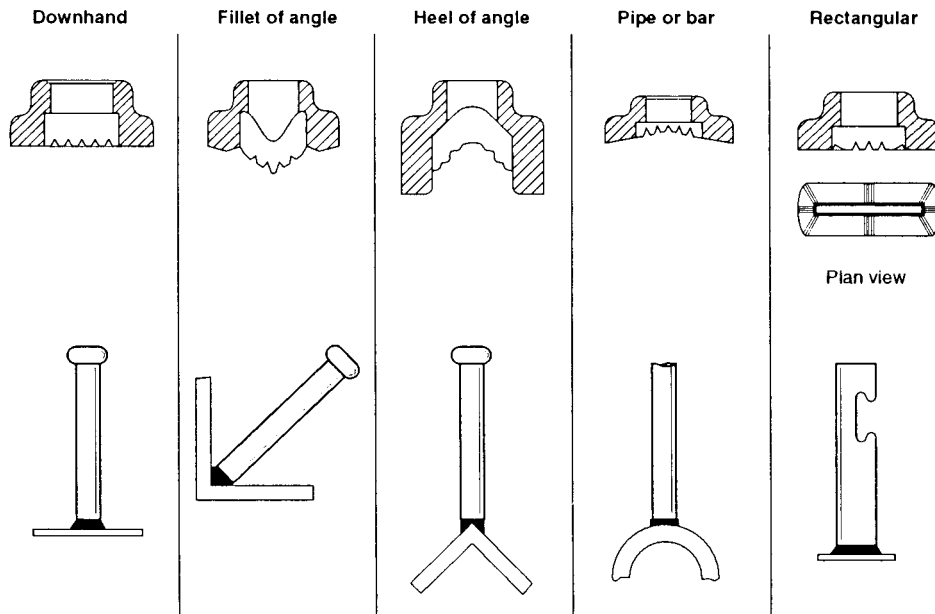


Fig. 8 Cross sections of ferrules showing some of the many varieties available for different stud base geometries, weld positions, and applications

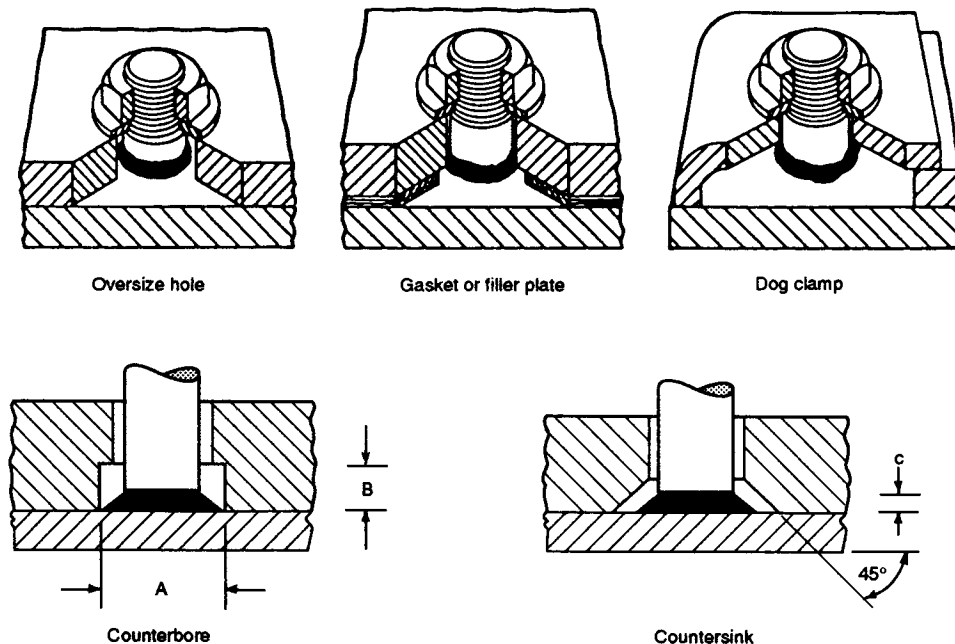


Fig. 9 Common methods for accommodating weld flash (fillet) with stud arc welds. Typical dimensions for A, B, and C are given in Table 4.

Table 4 Dimensions for counterbore and countersink weld flash clearance

A, B, and C are shown in Fig. 9.

Stud base diameter		Counterbore				90° countersink	
		A		B		C	
mm	in.	mm	in.	mm	in.	mm	in.
6.4	¼	11.1	0.437	3.2	0.125	3.2	0.125
7.9	⅜	12.7	0.500	3.2	0.125	3.2	0.125
9.5	½	15.1	0.593	3.2	0.125	3.2	0.125
11.1	⅞	16.7	0.656	4.7	0.187	3.2	0.125
12.7	1½	19.1	0.750	4.7	0.187	4.7	0.187
15.9	⅝	22.2	0.875	5.5	0.218	4.7	0.187
19.1	¾	28.6	1.125	7.9	0.312	4.7	0.187

Note: Dimensions can vary, depending on stud style and ceramic arc shield selected. Consult manufacturer for details

Table 5 Recommended base-metal thicknesses for stud arc welding

Stud base diameter		Steel base metal				Aluminum base metal			
		For full strength(a)		Minimum(b)		Without backup		Minimum with backup(c)	
mm	in.	mm	in.	mm	in.	mm	in.	mm	in.
4.8	⅜	1.59	0.062	0.91	0.036	3.18	0.125	3.18	0.125
6.4	¼	3.18	0.125	1.21	0.048	3.18	0.125	3.18	0.125
7.9	⅜	3.18	0.125	1.52	0.060	4.76	0.187	3.18	0.125
9.5	½	4.76	0.187	1.90	0.075	4.76	0.187	4.76	0.187
11.1	⅞	4.76	0.187	2.28	0.090	6.35	0.250	4.76	0.187
12.7	1½	4.76	0.187	3.04	0.120	6.35	0.250	6.35	0.250
15.9	⅝	6.35	0.250	3.68	0.145
19.1	¾	7.94	0.318	4.70	0.185
22.2	⅞	9.53	0.375	6.35	0.250
25.4	1	9.53	0.375	9.53	0.375

(a) Nearest commonly available base-metal thickness. (b) Steel without backup—will not develop full stud strength. (c) Metal backup required to prevent melt-through of base metal

Table 6 Typical combinations of base and stud metals for stud arc welding

Base metal	Stud metal
Low-carbon steel, AISI 1006 to 1022(a)	Low-carbon steel, AISI 1006 to 1020; stainless steel, 300 series
Stainless steel, 300 series(b), 405, 410, and 430	Low-carbon steel, AISI 1006 to 1020; stainless steel, 300 series
Aluminum alloys, 5000 series(c)	Aluminum alloys, 5000 series(c)

(a) Refer to ANSI/AWS D1.1-92, Table 4.1 (Groups I and II) for approved steels. (b) Except for the free-machining type 303 stainless steel. (c) Refer to ANSI/AWS D1.2-89, Table 7.1 and 7.4. Source: Ref 1

Because a high-amperage, short-time current is typical in the stud arc welding process, it is also important that the grounding spot(s) on the base material be clean, that the ground be tight, and that all cables be in good condition and have tight connections.

The position of the ground(s) also can influence stud-welding quality. This depends on the geometry of the base-metal shape and is the result of electromagnetic arc deflection, or arc blow (Ref 6). Occurrences are more common when studs are very near a free edge or are on long and narrow base plates, hollow pipe sections, or irregular peripheries, and can be corrected by moving the ground to a central position or using multiple grounds. Because

current flow is usually away from the ground toward the heavier or larger area of the base plate, arc blow is characterized by a lack of flash or fillet on the side of the stud nearer the edge, end, or smaller area.

Stud Strength. Fasteners will develop full material strength when they have been stud arc welded to compatible base plate alloys. Tables 7 to 9 show the tension and torque loads for various threaded stud diameters, based on minimum specified stud strengths (Ref 2, 3, and 6). For unthreaded stud fasteners, the yield strength and tensile or ultimate strength is calculated by:

$$\text{Yield strength} = A_s F_y$$

$$\text{Tensile strength} = A_s F_u$$

where A_s is the area of the stud shank (in.²), F_y is the specified stud material yield strength (minimum psi), and F_u is the specified stud material ultimate strength (minimum psi).

For threaded studs, the area is based on the mean effective thread area, which is calculated by:

$$A_s = 0.7854 [D - (0.9743/N)]^2$$

where D is the nominal diameter of the stud, and N is the number of threads per inch.

Process Variations and Special Equipment. There are several specific applications

that lend themselves to special variations of the stud arc welding technique. One application is the welding of studs to thin base materials that are less than the minimum thicknesses listed in Table 5. Although full weld base strength is usually not achieved, the resulting strength level is suitable for the application loadings involved. This process variation, which is called short-cycle stud arc welding, does not use a ceramic ferrule. Instead, higher weld current is used with very short times, which minimizes penetration of the stud into the base plate. Normally, this variation is used with stud diameters ≤ 9.5 mm (≤ 0.375 in.) in situations where backside marking is not considered detrimental.

The second special process is gas-shielded arc welding, which also does not use a ceramic ferrule. Instead, the stud-welding area is shielded by an inert gas, usually argon. This process can be used with both steel and aluminum but is more widely used with the latter material. The welding variables fall into a very narrow range, and conditions for application usually include tight tolerances and a tightly controlled setup. Consequently, the stud arc welding equipment most often consists of a fixed-gun production unit. A typical application is the welding of aluminum studs with special end configurations to aluminum kitchen utensils.

Special equipment is frequently used with the short-cycle and/or gas-shielded arc welding processes, because the application parameters must be tightly controlled and involve large quantities of studs applied in a production environment. Equipment manufacturers assemble many types of special equipment for production-line use. The equipment can be used with automatic stud feed, automatic stud and ferrule feed, computer-programmed indexing, robotic stud-welding guns, and other mechanisms. A typical automated stud arc welding production unit is shown in Fig. 10. A unit can involve simple, column-mounted, single-gun systems or sophisticated, multigun, multiple-feed units that cost thousands of dollars.

Fixturing and Tooling for Stud Arc Welding

Regardless of the stud-welding method employed, certain “expendable” accessories are required. These include such items as a chuck or collet to hold the particular stud being welded, a ferrule grip for the fastener, a foot that holds the ferrule grip, legs that attach to the gun and adjust to accommodate various stud lengths, and other minor items. The operating life of these items is variable, depending on the care and maintenance they receive. For example, a chuck may last for 5000 to 25,000 welds. Legs last indefinitely, whereas ferrule grips and feet usually have a shorter usage life.

Table 7 Mechanical properties of low-carbon steel stud arc welded fasteners

Fasteners have 380 MPa (55 ksi) minimum ultimate strength and 345 MPa (50 ksi) minimum yield strength.

Stud thread diameter(a)	Mean effective thread area(b)		Yield tensile load(c)		Ultimate tensile load		Yield torque(d)		Ultimate torque		Ultimate shear load(e)	
	mm ²	in. ²	kN	lbf	kN	lbf	J	ft · lbf	J	ft · lbf	kN	lbf
10-24 UNC	11	0.017	3.8	850	4.2	935	3.6	32(f)	4.0	35.1(f)	3.1	701
10-32 UNF	13	0.020	4.4	1,000	4.9	1,100	4.3	38(f)	4.7	41.3(f)	3.7	825
¼-20 UNC	21	0.032	7.1	1,600	7.8	1,760	9.1	6.7	9.9	7.3	5.9	1,320
¼-28 UNF	23	0.036	8.0	1,800	8.8	1,980	10.2	7.5	11.3	8.3	6.6	1,485
⅝-18 UNC	34	0.052	11.6	2,600	12.7	2,860	18.4	13.6	20.2	14.9	9.5	2,145
⅝-24 UNF	37	0.058	12.9	2,900	14.2	3,190	20.5	15.1	22.5	16.6	10.6	2,393
⅜-16 UNC	50	0.078	17.3	3,900	19.1	4,290	33.1	24.4	36.3	26.8	14.3	3,218
⅜-24 UNF	57	0.088	19.6	4,400	21.5	4,840	37.3	27.5	41.1	30.3	16.1	3,630
7/16-14 UNC	68	0.106	23.6	5,300	25.9	5,830	52.3	38.6	57.6	42.5	19.5	4,373
7/16-20 UNF	76	0.118	26.2	5,900	28.9	6,490	58.3	43.0	64.1	47.3	21.7	4,868
½-13 UNC	92	0.142	31.6	7,100	34.7	7,810	80.3	59.2	88.3	65.1	26.0	5,856
½-20 UNF	103	0.160	35.6	8,000	39.1	8,800	90.4	66.7	99.4	73.3	29.4	6,600
⅝-11 UNC	146	0.226	50.3	11,300	55.3	12,430	159.6	117.7	175.5	129.5	41.5	9,323
⅝-18 UNF	165	0.255	56.7	12,750	62.4	14,025	180.1	132.8	198.1	146.1	46.8	10,519
¾-10 UNC	215	0.334	74.3	16,700	81.7	18,370	283.1	208.8	311.3	229.6	61.3	13,778
¾-16 UNF	240	0.372	82.7	18,600	91.0	20,460	315.2	232.5	346.8	255.8	68.3	15,345
7/8-9 UNC	298	0.462	102.8	23,100	112.8	25,355	456.8	336.9	501.4	369.8	84.6	19,017
7/8-14 UNF	328	0.509	113.2	25,450	124.5	27,995	503.1	371.1	553.6	408.3	93.4	20,996
1-8 UNC	391	0.606	134.8	30,300	148.0	33,275	684.7	505.0	751.9	554.6	111.0	24,956
1-14 UNF	437	0.678	150.8	33,900	165.9	37,290	766.0	565.0	842.6	621.5	124.4	27,967

(a) UNC, unified coarse thread series; UNF, unified fine thread series. (b) Mean effective thread area is based on a mean full diameter midway between minor and pitch thread diameters. (c) In practice, a stud should not be used at or higher than yield load. A factor of safety should be applied, and 60% of yield is commonly used, although other values may be used at discretion of user. (d) Torque figures are based on the assumption that excessive thread deformation has not affected the proportional range of torque/tension relationship. An average torque coefficient of 0.20 was used in these calculations. (e) Shear load is based upon 0.75 times ultimate load. The user should apply an appropriate safety factor to these figures. (f) Value given in in. · lbf

Table 8 Mechanical properties of stainless steel stud arc welded fasteners

Fasteners have 520 MPa (75 ksi) minimum ultimate strength and 205 MPa (30 ksi) minimum yield strength.

Stud thread diameter(a)	Mean effective thread area(b)		Yield tensile load(c)		Ultimate tensile load		Yield torque(d)		Ultimate torque		Ultimate shear load(e)	
	mm ²	in. ²	kN	lbf	kN	lbf	J	ft · lbf	J	ft · lbf	kN	lbf
10-24 UNC	11	0.017	2.3	510	5.7	1,275	2.2	19.1(f)	5.4	47.8(f)	4.3	956
10-32 UNF	13	0.020	2.7	600	6.7	1,500	2.5	22.5(f)	6.4	56.3(f)	5.0	1,125
¼-20 UNC	21	0.032	4.3	960	10.7	2,400	5.4	4.0	13.6	10.0	8.0	1,800
¼-28 UNF	23	0.036	4.8	1,080	12.0	2,700	6.1	4.5	15.3	11.3	9.0	2,025
⅝-18 UNC	34	0.052	6.9	1,560	17.3	3,900	11.0	8.1	27.5	20.3	13.0	2,925
⅝-24 UNF	37	0.058	7.7	1,740	19.3	4,350	12.3	9.1	30.6	22.6	14.5	3,263
⅜-16 UNC	50	0.078	10.4	2,340	26.0	5,850	19.8	14.6	49.6	36.6	19.5	4,388
⅜-24 UNF	57	0.088	11.7	2,640	29.4	6,600	22.4	16.5	56.0	41.3	22.0	4,950
7/16-14 UNC	68	0.106	14.1	3,180	35.4	7,950	31.5	23.2	78.6	58.0	26.5	5,963
7/16-20 UNF	76	0.118	15.7	3,540	39.4	8,850	35.0	25.8	87.4	64.5	29.5	6,638
½-13 UNC	92	0.142	18.9	4,260	47.4	10,650	48.1	35.5	120.4	88.8	35.5	7,988
½-20 UNF	103	0.160	21.4	4,800	53.4	12,000	54.2	40.0	135.6	100.0	40.0	9,000
⅝-11 UNC	146	0.226	30.2	6,780	75.4	16,950	95.7	70.6	239.4	176.6	56.5	12,713
⅝-18 UNF	165	0.255	34.0	7,650	85.1	19,125	108.1	79.7	270.1	199.2	63.8	14,344
¾-10 UNC	215	0.334	44.6	10,020	111.4	25,050	169.9	125.3	424.5	313.1	83.6	18,788
¾-16 UNF	240	0.372	49.6	11,160	124.1	27,900	189.1	139.5	472.9	348.8	93.1	20,925
7/8-9 UNC	298	0.462	61.7	13,860	154.1	34,650	274.0	202.1	685.1	505.3	115.6	25,988
7/8-14 UNF	328	0.509	67.9	15,270	169.8	38,175	301.9	222.7	754.8	556.7	127.4	28,631
1-8 UNC	391	0.606	80.9	18,180	202.2	45,450	410.8	303.0	1027.0	757.5	151.6	34,088
1-14 UNF	437	0.678	90.5	20,340	226.2	50,850	459.6	339.0	1149.0	847.5	169.6	38,138

(a) UNC, unified coarse thread series; UNF, unified fine thread series. (b) Mean effective thread area is based on a mean full diameter midway between minor and pitch thread diameters. (c) In practice, a stud should not be used at or higher than yield load. A factor of safety should be applied, and 60% of yield is commonly used, although other values may be used at the discretion of user. (d) Torque figures are based on the assumption that excessive thread deformation has not affected the proportional range of torque/tension relationship. An average torque coefficient of 0.20 was used in these calculations. (e) Shear load is based upon 0.75 times ultimate load. The user should apply an appropriate safety factor to these figures. (f) Value given in in. · lbf

Accessories are relatively in-expensive items that should be planned for when preparing budgetary estimates on any given project.

The extent and sophistication of tooling for stud welding reflects the required production rate and the total number of studs to be welded. Locating the stud arc welding centers can be as simple as laying out the workpiece and center punching the locations either directly or through a template, as shown in Fig. 11. The studs are then placed in the punch marks, the

stud-welding gun is held vertically, and the weld is initiated. Although operator skill is a factor, careful welders can achieve a perpendicularity of $\pm 5^\circ$ and a location tolerance of approximately 1.2 mm (0.046 in.). Often, the cover plate in a base plate/cover plate assembly can be used as the template for marking.

A permanent template becomes more practical when an increasing number of studs are to be welded on repetitive locations. Stud arc welded fasteners can be welded directly

through temperature-resistant material which should be spaced off the work by 1.65 to 6.35 mm (0.065 to 0.250 in.) to allow expelled weld gases and weld spatter to escape without restriction, which could adversely affect weld quality. This type of template arrangement is shown in Fig. 12. Note that the template holes are drilled slightly larger than the outside dimension of the ceramic ferrule. Before the template is prepared, it is good practice to consult the manufacturer specifications for the

Table 9 Mechanical properties of aluminum stud arc welded fasteners

Fasteners have 290 MPa (42 ksi) minimum ultimate strength and 205 MPa (30 ksi) minimum yield strength.

Stud thread diameter(a)	Mean effective thread area(b)		Yield tensile load(e)		Ultimate tensile load		Yield torque(d)		Ultimate torque		Ultimate shear load(e)	
	mm ²	in. ²	kN	lbf	kN	lbf	J	ft · lbf	J	ft · lbf	kN	lbf
10-24 UNC	11	0.017	2.3	510	3.2	714	2.2	19.1(f)	3.0	26.8(f)	1.9	428
10-32 UNF	13	0.020	2.7	600	3.9	840	2.5	22.5(f)	3.6	31.5(f)	2.2	504
¼-20 UNC	21	0.032	4.3	960	6.0	1344	5.4	4.0	7.6	5.6	3.6	806
¼-28 UNF	23	0.036	4.8	1080	6.7	1512	6.1	4.5	8.5	6.3	4.0	907
⅝-18 UNC	34	0.052	6.9	1560	9.7	2184	11.0	8.1	15.5	11.4	5.8	1310
⅝-24 UNF	37	0.058	7.7	1740	10.8	2436	12.3	9.1	17.2	12.7	6.5	1462
⅜-16 UNC	50	0.078	10.4	2340	14.6	3276	19.8	14.6	27.8	20.5	8.7	1966
⅜-24 UNF	57	0.088	11.7	2640	16.4	3696	22.3	16.5	31.3	23.1	9.6	2218
7/16-14 UNC	68	0.106	14.1	3180	19.8	4452	31.5	23.2	44.1	32.5	11.9	2671
7/16-20 UNF	76	0.118	15.7	3540	22.0	4956	35.0	25.8	48.9	36.1	13.2	2974
½-13 UNC	92	0.142	18.9	4260	26.5	5964	48.1	35.5	67.4	49.7	15.9	3578
½-20 UNF	103	0.160	21.4	4800	29.9	6720	54.2	40.0	75.9	56.0	17.9	4032

(a) UNC, unified coarse thread series; UNF, unified fine thread series. (b) Mean effective thread area is based on a mean full diameter midway between minor and pitch thread diameters. (c) In practice, a stud should not be used at or higher than yield load. A factor of safety should be applied, and 60% of yield is commonly used, although other values may be used at discretion of user. (d) Torque figures are based on the assumption that excessive thread deformation has not affected the proportional range of torque/tension relationship. An average torque coefficient of 0.20 was used in these calculations. (e) Shear load is based on 0.60 times ultimate load. The user should apply an appropriate safety factor to these figures. (f) Value given in in. · lbf

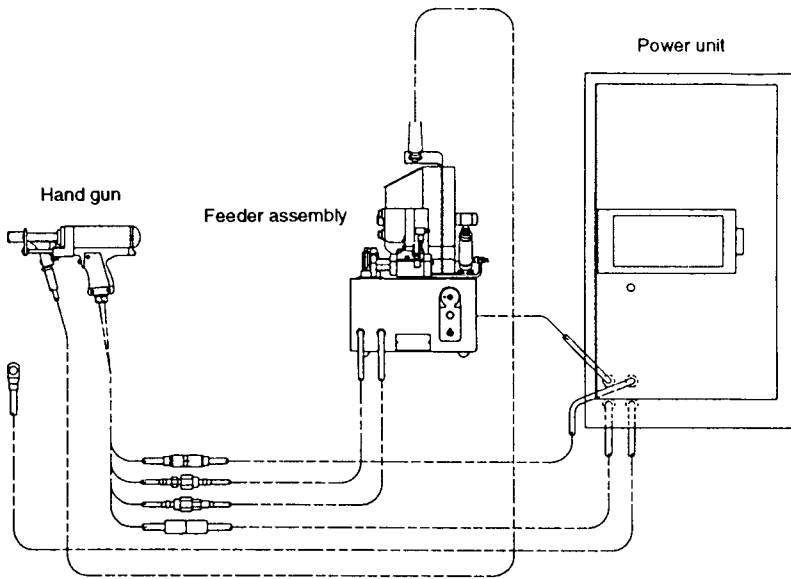


Fig. 10 Typical automatic stud-feed hand-gun system for portable operation using templates or fixtures on the workpiece

ceramic ferrule dimensions to be used with the stud being welded. Location accuracy, in this case, can be as tight as ± 0.78 mm (± 0.031 in.).

Even greater accuracy can be obtained, both in the vertical and horizontal directions, by adapting the template hole to fit a drill jig bushing tightly and by inserting the template adapter (or a ferrule tube adapter) through the bushing to the workpiece. The ferrule tube adapter also can be used for welding down into deeply drilled holes or into tight-fit areas (Fig. 13).

With closely spaced studs, the foot grip is sometimes modified so that after welding the initial stud at a center-punched location, the foot can be held against the reference stud to weld the next or adjacent stud on the required spacing.

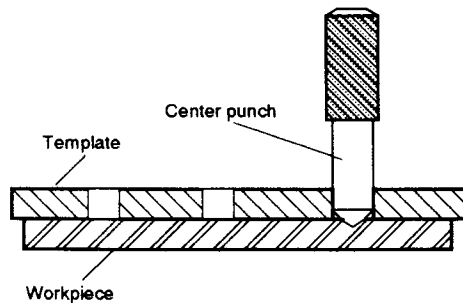


Fig. 11 Center punching base material through a template

The verticality of the weld stud can be ensured by several methods. The most accurate is obviously a fixed gun on a slide mechanism

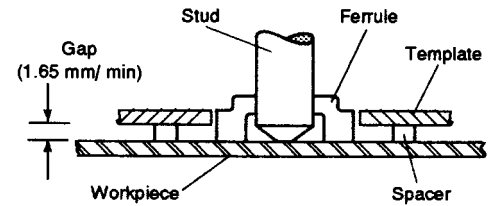


Fig. 12 Welding through a template using a ferrule with stud arc welding fasteners

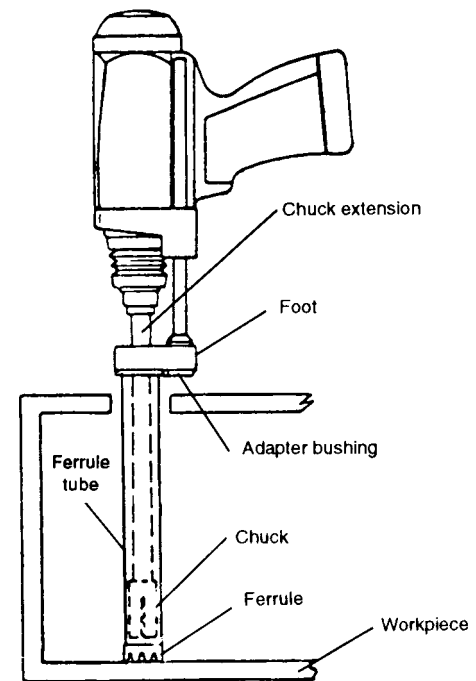


Fig. 13 Portable stud arc welding gun equipped with accessories for welding studs through or into a drilled or formed hole

of the type used for automatic-feed, high-production work. This type is also the most expensive. A portable gun can be mounted on a machine slide or drill press by fabricating a bracket (Fig. 14) in cases where production quantities do not justify the expense of automatic equipment.

Other methods of ensuring verticality are to use a bushing-type template, a bubble level mounted on the rear of the gun, or a bipod foot arrangement, as shown in Fig. 15. With the stud and ferrule acting as one fixed point, the two bipod screws are adjusted to obtain perpendicularity. Vertical variations that are less than $\pm 1^\circ$ can be achieved with proper accessories and adjustments.

A wide range of accessories is available for welding studs of different lengths or for welding studs into areas with limited access. Two widely used special accessories are shown in Fig. 16 and 17. For unusual situations, the manufacturer should be consulted to suggest or, possibly, design stud-welding accessories.

Stud-Welding Quality Control, Qualification, and Inspection

Because of its broad use for many years and the relative simplicity of its applications, stud welding in the downhand position is considered to be a prequalified procedure; that is, it is only necessary to weld two studs satisfactorily in the downhand position to qualify both the process and the operator. The two qualification studs can be bend tested, torque tested, or tension tested. The physical test is satisfactory if no failure occurs in the weld or the heat-affected zone.

Stud-welding code requirements (for example, Ref 2 and 7) define the necessary tests for prequalified stud welding to the flat or downhand position, as well as other positions. The limit on the flat position is defined as 0 to 15° slope on the surface to which the stud is applied. Beyond 15° , a ten-stud test is required. Again, each of the ten studs in the nonflat position must be bend, tensile, or torque tested. Bend testing is 90° from the original axis, whereas torque and tension testing are conducted until failure. Failure must occur in the stud shank or in the work-piece material, not in the weld or the heat-affected zone. All failures require retesting. Satisfactory testing qualifies the welder and the process.

Typical bend, torque, and tensile testing setups are shown in Fig. 18 to 20. Qualification records, including stud drawings, ceramic arc

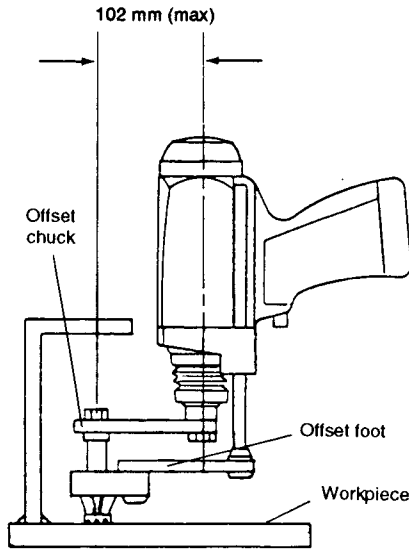


Fig. 16 Typical offset assembly used when stud arc welded fasteners must be welded below an obstruction

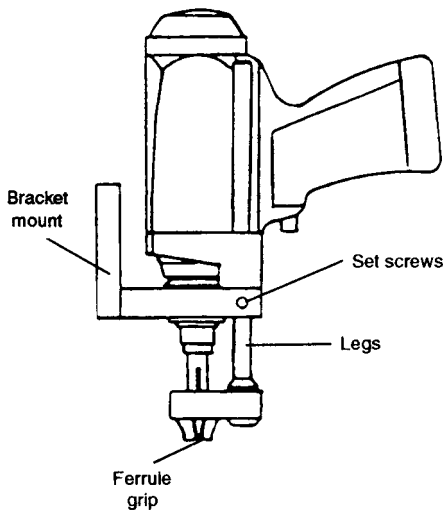


Fig. 14 Inexpensive method of mounting portable hand gun to machine slide or drill press to obtain fixed-position accuracy

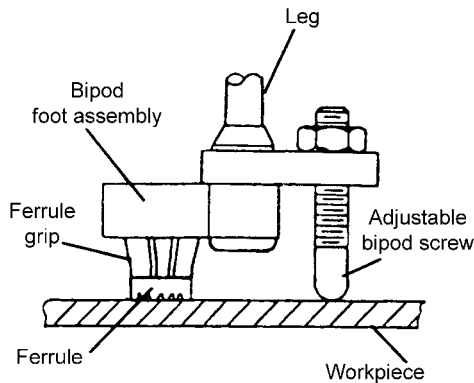


Fig. 15 Use of an adjustable bipod foot assembly to provide three-point contact, ensuring perpendicularity of stud to workpiece

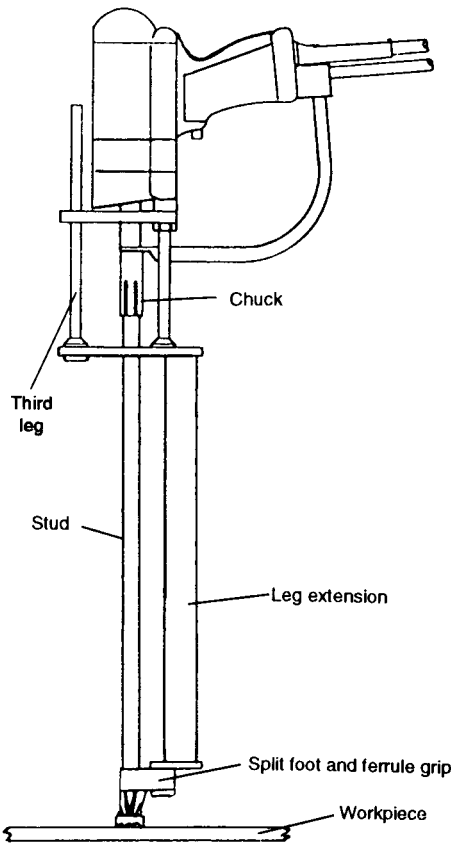


Fig. 17 Typical leg-extension accessory for welding long studs (up to 1.83 m, or 6 ft). Note the use of a split foot and ferrule grip; the gun does not have to be stripped the full length of the stud when the stud is welded.

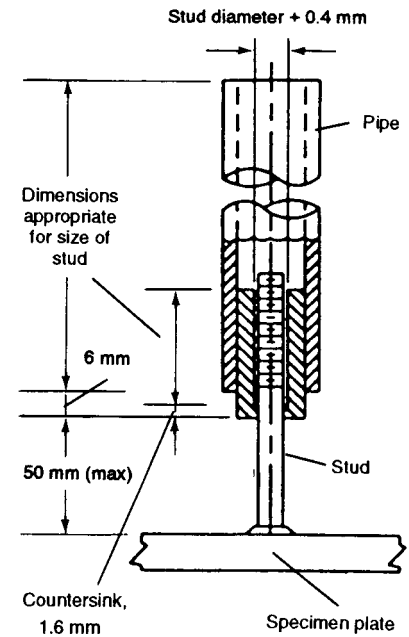


Fig. 18 Typical bend testing setup. Studs that must undergo application qualification should be bend 90° without weld failure (15° for aluminum studs). Testing for preproduction or testing during production for inspection purposes requires bend testing to 30° from original position (15° for aluminum studs). For threaded studs, torque testing in accordance with Fig. 19 should be used. Source: Ref 2

shield drawings (if used), weld settings, and position, should be kept.

Either two-stud or ten-stud testing should be conducted on a production piece or on a separate piece of the same type and thickness ($\pm 25\%$) of material that will be used in the application, in the same position in which the studs will actually be applied.

In addition to physical testing, the studs that are welded for qualification also must be visually inspected, whether there are two or ten. Visual inspection consists of verifying that a full 360° weld flash (fillet) is formed around the stud base. There should be no gaps or

undercuts in the flash or in the wetted area. As mentioned previously, flash can be irregular in both height and evenness and it can contain shrinkage fissures or cracks. Because flash is expelled, not deposited, metal, it should not be subject to the usual inspection criteria for a weld fillet.

The final visual inspection should be a measurement of the after-weld length. With stud arc welding, the after-weld length of the stud will be shorter by the lengths shown in Table 3. A consistent after-weld length, combined with acceptable visual inspection and physical testing, are assurances of satisfactory welds. Figure 21 shows typical stud arc weld appearances for both acceptable and problematic welds.

Passing the two-stud preproduction or the ten-stud application qualification test approves the procedure and operator. Production stud welding is then allowed to proceed. However, at the start of each new production period, a two-stud test is again required before production can begin. Similarly, a change in stud diameter, equipment, settings, or operator requires requalification.

During production, welding inspection and testing should be used on a continuous basis to confirm acceptable quality. This can be done on a reasonable number of studs, depending on the welding conditions and stud appearance. After the visual inspection of all stud welds,

physical testing of at least one weld per hundred is usually suggested. Any weld that does not show a full 360° flash or wetness should be tested. Welds without a full flash can be repair welded, but repaired welds are also required to be physically tested.

In the case of unthreaded studs, the quality inspection test can be to bend 15°. The studs can be straightened after testing, if required. Threaded studs can be subjected to a torque test to approximately 80% of the yield torque load, rather than a bend test. Failure in the weld or heat-affected zone is cause to reject the weld being tested. Failure also requires that the quantity of studs welded from the previous test to the present test be carefully inspected for weld deficiencies. Additional tests may be necessary to confirm weld quality.

If the quality inspection test studs must be straightened for end use, then they should be returned to the vertical position by using a bending tool. Continuous slow pressure should be applied during the straightening process.

Temperature at the time of stud welding and during stud testing is an influential parameter. Stud welding should not be conducted at temperatures below $-18\text{ }^{\circ}\text{C}$ ($0\text{ }^{\circ}\text{F}$). When the temperature is below $0\text{ }^{\circ}\text{C}$ ($32\text{ }^{\circ}\text{F}$), one additional stud per hundred welded should be tested to verify weld quality. Below $10\text{ }^{\circ}\text{C}$ ($50\text{ }^{\circ}\text{F}$), welded studs should be tested using the bending tool, rather than by hammer testing. In colder

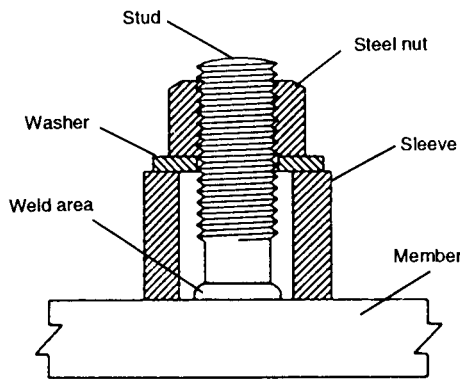


Fig. 19 Typical torque testing arrangement. Studs that must undergo application qualification or preproduction testing should be torqued to destruction without failure in the weld. Proof torque testing during inspection of threaded studs should be applied at 60 to 66% of the yield torque load for the stud size testing. Refer to Tables 7 to 9. Source: Ref 2

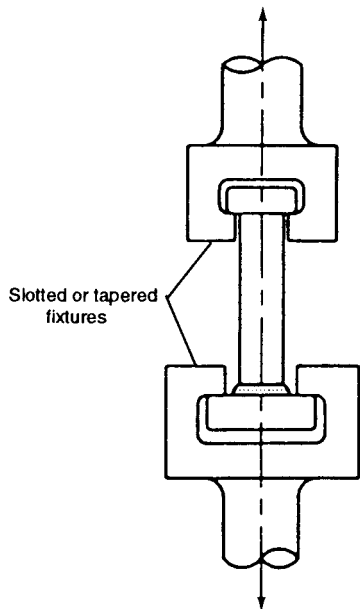


Fig. 20 Typical tension test fixture. For qualification of application or preproduction testing, either bend or torque testing can be substituted for tension testing.

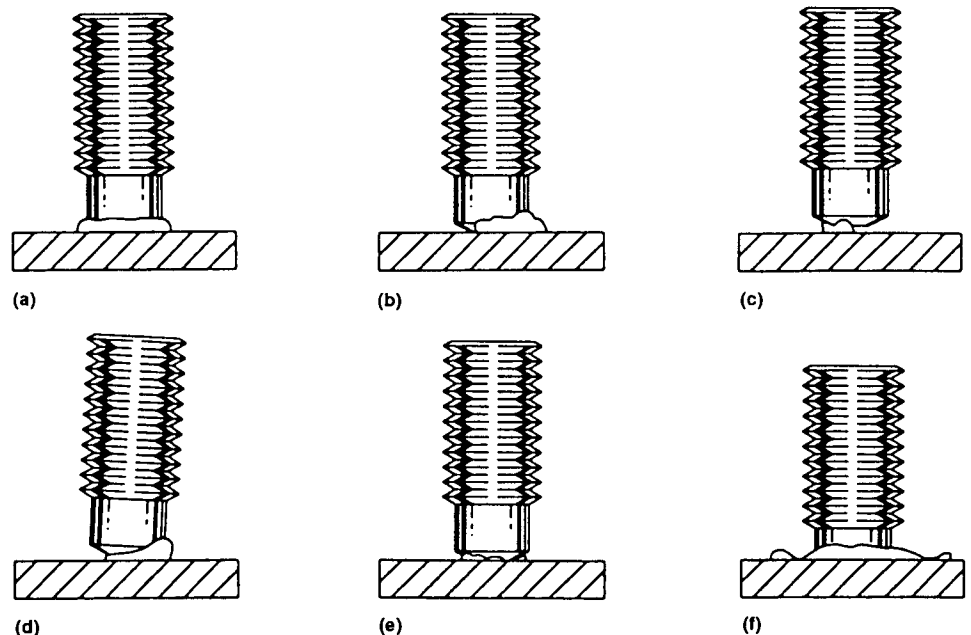


Fig. 21 Stud arc weld characteristics for satisfactory and unsatisfactory welds. (a) Satisfactory; good flash formation, wetting entire periphery of stud base. (b) Unsatisfactory; plunge too short, not enough material allowed for burn-off. Stud must project an adequate length beyond the ferrule. This condition can also be caused by bad grounding practice. (c) Unsatisfactory; hang up caused by inadequate arc length lift or by misalignment of stud, restricting free movement. (d) Unsatisfactory; misalignment of stud by poor gun position. (e) Unsatisfactory; cold weld, resulting in nonuniform or incomplete flash around stud periphery. (f) Unsatisfactory; hot weld, where molten material is expelled violently from weld, resulting in poor flash formation

welding temperature conditions, threaded studs should always be tested by torque, rather than by bending. Impact testing at low temperature produces brittle failures. This is not a function of weld quality but of the ambient temperature at the time of welding and testing. Data resulting from extensive tests conducted on studs welded and tested at various temperatures have shown that it is the temperature and manner of testing that influences the failure mode, rather than the temperature at the time of welding (Ref 8).

Another factor, besides temperature, that can affect weld quality is cleanliness of the weld area. Although stud arc welding does provide some cleaning action during welding, it is not sufficient to remove heavy contaminants. Coatings or rust on studs also can cause poor welds. Plating, except for a copper flash, nickel plating, or chromium plating, should be removed from the stud end prior to welding. This includes such materials as paint, zinc, and cadmium. Stud arc welded fasteners are usually capped during plating so that the weld end is left clean.

The plating or contaminant removal methods should be compatible with the base-material thickness and composition. For example, a heavy paint or rust cover on thick structural steel can be removed by grinding, needle scaling, sand blasting, or chipping, and the weld surface will still be acceptable for stud welding. Stainless steel, brass, aluminum; or other polished surfaces should be cleaned with appropriate solvents or other cleaning methods that will not destroy the material finish or contaminate the weld area. For example, a carbon-steel wire wheel or brush should not be used to clean stainless steel or aluminum-base material.

Studs and ferrules should be kept clean and dry prior to welding. Although cold conditions will not adversely affect either, they should be protected from exposure to adverse weather conditions, high humidity, marine atmospheres, and other extremes. When ferrules absorb water, the steam generated during the welding process can cause very poor welds and excessive weld spatter. Ferrules exposed to moisture should be oven dried at a temperature between 101 and 120 °C (215 and 250 °F) for 2 h before use.

The condition of weld cables, connections, and ground clamps can affect weld quality. These items should be checked frequently and either repaired or replaced, so that the cables are not frayed, connections are tight and clean, and ground clamps are properly functioning. Ground clamps should be tightly connected to the work-piece or work platen and attached to areas that have been cleaned of all deleterious materials that would prevent good current flow.

Stud-Welding Safety Precautions

Any welding process can be dangerous if proper safety precautions are not followed.

Equipment should be properly installed according to the directions of the manufacturer and maintained in good condition. Operators should be thoroughly trained in the use of the stud-welding process. They also should be familiar with the installation, operation, and maintenance procedures for the equipment being used.

Electrical shock is a potential cause of injury or death. Stud-welding systems should be properly installed and grounded using electrical connections made according to national (Ref 9) and local code guidelines.

Neither operators nor anyone else in the welding area should ever touch live electrical parts, or weld in wet areas, or wear wet gloves or clothing. In addition, all workers should ensure that they are insulated from shock.

All electric cables and connections should be kept in good condition. They should be inspected on a regular basis and frayed sections, broken insulation, or broken connectors should be repaired or replaced at once. Stud welding frequently uses long cable lengths, particularly on construction sites, where the cables are subject to abuse by tow-motors, trucks, material storage, or foot traffic. It should be ensured that these conditions do not result in cable damage.

Although weld spatter and arc flash are minimal with the stud-welding process, they do occur and precautions should be taken. All combustible or volatile materials should be removed from the weld area so that sparks or spatter cannot reach them. Gas cylinders should be stored and secured properly and checked to ensure that they do not contact any electrical cables in the welding circuit. Proper protective clothing should be worn, including boots, aprons, and gloves, as necessary. Eye protection is always necessary. Eye glasses with spectacle frames, side shields, and lenses with shade number three absorption filters should be worn by the operator at all times (Ref 10). Helpers or workers within 1.5 m (5 ft) of the weld area also should wear clear safety glasses with side shields. Fire-suppression equipment should be available in or adjacent to the weld area for immediate use in emergencies.

Ventilation of the welding area is necessary. Fumes from welding and cleaning materials, such as solvents, as well as paints, epoxies, and galvanizing or other coatings, can be harmful. Ventilation can be either forced or natural, depending on the job conditions. Material suppliers should provide material safety data sheets on any items being used in the welding area, and proper precautions for potentially dangerous contents should be followed.

Pinch points where fingers or hands can be caught should be avoided during material handling or where moving parts are involved in the welding process.

The instructions of the manufacturer should be followed when maintaining and servicing

the stud-welding equipment. If possible, all electric supplies should be disconnected and locked out during maintenance or troubleshooting work.

Finally, certain welding operations produce elevated noise levels during the weld cycle. Operators and other workers near the equipment should use hearing protection that can adequately protect them, in accordance with Ref 11.

REFERENCES

1. "Recommended Practices for Stud Welding," ANSI/AWS C5.4, AWS
2. "Structural Welding Code—Steel," ANSI/AWS D1.1, Section 7, "Stud Welding," AWS
3. "Structural Welding Code—Aluminum," ANSI/AWS D1.2, AWS
4. "Structural Welding Code—Steel," ANSI/AWS D1.1, Section 7, "Stud Welding," Footnote 27, AWS
5. "Structural Welding Code—Steel," ANSI/AWS D1.1, Section 7, "Stud Welding," Paragraph 7.6, AWS
6. W.A. Baeslack, G. Fayer, S. Ream, and C.E. Jackson, Quality Control in Arc Stud Welding, *Weld. J.*, Nov 1975, p 789–798
7. "Welded Steel Construction (Metal Arc Welding), Standard W59," Canadian Standards Association
8. D.J. Laurie Kennedy, Stud Welding at Low Temperatures, *Can. J. Civil Eng.*, Vol 7, 1980, p 442–455
9. "National Electrical Code," NFPA-70, National Fire Protection Association
10. "Safe Practice for Occupation and Educational Eye and Face Protection," Z87.1, ANSI
11. "Welding, Cutting, and Brazing," Standard 29CFR, Part 1910, Occupational Safety and Health Administration

SELECTED REFERENCES

- "Design and Application Hand Book for Light Gauge Metalworking," Publication CD-92, TRW Nelson Stud Welding Division, 1992
- "Industrial Design Data—Nelson Stud Welding Process," Publication MB-12-86, TRW Nelson Stud Welding Division
- "Safety in Welding and Cutting," ANSI/AWS Z49.1, AWS
- T.E. Shoup, "Stud Welding," Bulletin 214, Welding Research Council, April 1976
- Stud Welding, Chapter 9, *Welding Handbook*, 8th ed., AWS, 1990
- "Tooling Techniques for Stud Welding," TRW Nelson Stud Welding Division

Capacitor Discharge Stud Welding*

CAPACITOR DISCHARGE STUD WELDING is a stud arc welding process in which the tip of the stud melts almost instantly when energy stored in capacitors is discharged through it. The three basic modes of capacitor discharge (CD) stud welding are initial-gap welding, initial-contact welding, and drawn-arc welding. Figure 1 shows current-versus-time curves for the three process variations.

The initial-gap mode (Fig. 2) is begun with the stud held away from the work surface by the welding head. At the beginning of the weld cycle, the stud is forced against the work surface, melting the tip, the face of the stud, and the adjoining work surface upon contact with the work surface. The weld is completed using the gun forces (i.e., spring pressure or air pressure) to plunge the stud into the molten materials, forming a strong welded bond between the stud and the work surface. The weld cycle time (Fig. 1) for this process is from 4 to 6 ms, and the penetration of the weld zone into the work surface is normally from 0.10 to 0.15 mm (0.004 to 0.006 in.).

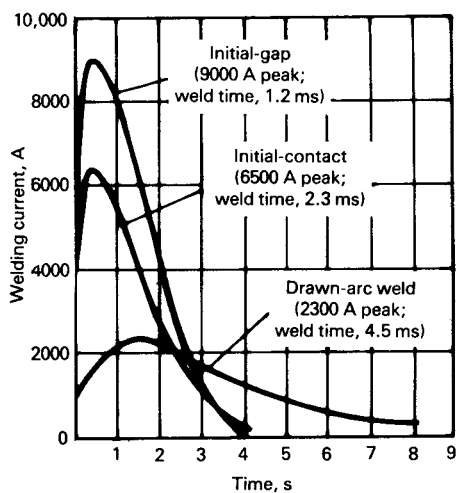


Fig. 1 Typical current-versus-time curves for the three capacitor discharge stud welding methods. Source: Ref 1

The initial-contact mode (Fig. 3) begins with the weld stud in contact with the work surface. The weld cycle is initiated with a surge of current that disintegrates the weld tip, thus melting the stud face area and the work surface that it immediately contacts. The stud is forced into the molten material, forming a strong homogeneous weld. This process has a weld cycle time of approximately 6 ms, much like the gap process.

The drawn-arc mode (Fig. 4) begins with the stud in contact with the work surface. When the weld cycle is initiated, a current surge is applied to the weld tip and the stud is retracted from the work surface, drawing an arc that melts the face of the stud and the work surface directly beneath it. The stud is then plunged into the molten pool of material, forming a welded connection. The weld cycle time for this process is longer than for the other two processes, and the heat-affected zone is thicker than it is in the preceding two processes.

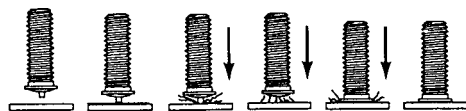


Fig. 2 Initial-gap capacitor discharge stud welding. See text for explanation. Source: Ref 1

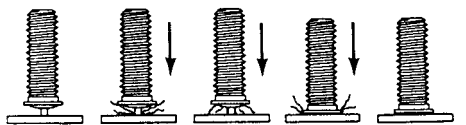


Fig. 3 Initial-contact capacitor discharge stud welding. See text for explanation. Source: Ref 1

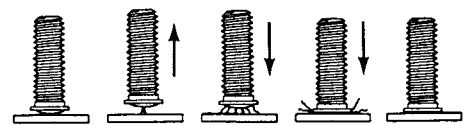


Fig. 4 Drawn-arc capacitor discharge stud welding. See text for explanation. Source: Ref 1

Advantages and Disadvantages. A major reason for using the CD stud-welding process is that it provides a strong welded fastener with either a minimum or no reverse side marking of the work material. Another reason is that it is cost-effective, especially for small-diameter fasteners. This process also allows fasteners to be welded to very thin sections of work material, as well as to thick sections (as thick as necessary), with reliable results. Furthermore, the process allows the welding of many dissimilar material combinations, such as aluminum studs to zinc die castings. The disadvantages of using the CD process are the limited stud diameters available and the fact that the work surface must be clean of mill scale, dirt, oxidation products, and oil.

Applications

The CD process is normally used for fastener sizes of 4-40 through 1/4-20, with lengths from 6.4 to 38.1 mm (1/4 to 1.5 in.). Although there are limited uses of 1/16-18 and 3/8-16 diameter studs in special applications, only the more-common stud diameters are considered in this article. The work material thickness can typically range from 0.25 mm (0.010 in.) to as thick as the application requires. The determining factors for making successful welds are the stud diameter, the materials being used, the strength required, and the amount of allowable reverse side marking. See Table 1 for guidance on the expected strength parameters.

The stud and workpiece materials can be common low-carbon steel, stainless steel, or aluminum. Also used are medium-carbon steel, lead-free brass and copper, Inconel, titanium, René 41, zirconium, gold, silver, and platinum. Table 2 shows some of the more popular combinations of materials. Various studs and plate materials can be combined, except when aluminum-base material is used.

Capacitor discharge stud welding is used in many industries in a large variety of applications because it is one of the most versatile and reliable processes available. The food processing industry uses this process on stainless steel utensils and machinery, aluminum

Table 1 Standard capacitor discharge stud fastener load strengths

Stud material	Stud size	Maximum fastening torque(a)		Ultimate tensile load		Maximum shear load	
		N·m	lbf·in.	kN	lbf	kN	lbf
Low-carbon copper-flashed steel	6-32	0.7	6	2.2	500	1.7	375
	8-32	1.4	12	3.4	765	2.6	575
	10-24	1.6	14	4.3	960	3.2	720
	¼-20	4.9	43	7.8	1750	5.8	1300
	⅝-18	8.1	72	12.9	2900	9.8	2200
Stainless steel (type 304)	⅜-16	11.9	106	19.1	4300	14.6	3250
	6-32	1.1	10	3.5	790	2.6	590
	8-32	2.3	20	5.6	1260	4.1	940
	10-24	2.6	23	6.8	1530	5.2	1150
	¼-20	8.5	75	12.8	2880	9.6	2160
Aluminum alloy (5000 series)	⅝-18	14.2	126	16.7	3750	12.5	2800
	⅜-16	20.0	186	21.6	4850	16.0	3600
	6-32	0.40	3.5	1.7	375	1.0	235
	8-32	0.85	7.5	2.6	585	1.6	365
	10-24	1.13	10	3.3	735	2.0	460
Brass (70-30 and 65-35)	¼-20	4.5	40	6.0	1360	3.8	850
	⅝-18	7.9	70	10.2	2300	6.2	1400
	⅜-16	9.1	81	15.1	3400	9.3	2100
	½-13	15.8	140	25.0	5500	13.4	3000
	6-32	0.9	8	2.7	600	1.7	390
	8-32	1.8	16	3.8	860	2.5	560
	10-24	2.09	18.5	4.6	1040	3.0	680
	¼-20	6.9	61	8.7	1950	5.7	1275
	⅝-18	11.5	102	14.6	3280	9.5	2140
	⅜-16	16.9	150	21.4	4800	14.1	3160

(a) These values should develop fastener tension to slightly less than yield point and should be used only as a guide; basic specifications shown above cover typical mechanical property values.

Table 2 Welding capabilities of capacitor discharge stud fasteners

Base material	Stud material			
	Mild steel (types 1008, 1010)	Stainless steel (types 304, 305)	Aluminum (5356, 6061)	Brass (70-30, 65-35)
Mild steel (1006 through 1030)	Excellent	Excellent	...	Excellent
Medium-carbon steel (1030 through 1050)	Good(a)	Good(a)	...	Good(a)
Galvanized sheet duct or decking	Good(a)	Good(a)
Structural steel	Good(a)	Good(a)	...	Excellent
Stainless steel (types 405, 410, 430, and 300 series, except 303)	Excellent	Excellent	...	Excellent
Lead-free brass, electrolytic copper, lead-free rolled copper	Excellent	Excellent	...	Excellent
Most aluminum alloys of the 1000, 3000, 5000, and 6000 series(b)	Excellent	...
Die-cast zinc alloys	Good(a)	Good(a)	Excellent	Good(a)

(a) Generally full-strength results, depending on the combination of stud size and base metal. (b) Other materials, such as 7000-series aluminum, titanium alloys, Inconel, and so on, can be welded under specified conditions.

cookware, and appliances. The aerospace industry applies the process to aircraft engines, aircraft parts and instrument areas, and components for outer space vehicles. The appliance industry uses CD welding for its cabinets, trims, and other components. The building industry uses it for doors, facia, subassemblies, and other exposed finished areas. The insulation industry uses it in securing insulation to heating and air conditioning duct work, as well as on apparatus at power plants, schools, and other major buildings. The automotive industry uses the process to secure trim and various components to cars and trucks. The ship-building industry uses it in fabricating components in

ship kitchens, in insulation applications aboard ship, and in other areas where components and instruments must be secured. The electrical industry uses this process when securing components inside various controllers and equipment, as well as in trim parts for cabinets. The sign industry uses it on both structural and component members of large and small signs.

Equipment

The equipment used for CD stud welding can be either portable or stationary production-type

units. The portable units consist of the basic controller that uses standard 110 V alternating current (ac) power input to charge the capacitors and a lightweight gun-shaped tool used for placing and welding the fasteners. The production-type units typically require 240/480 V ac three-phase incoming power and a compressed air supply. The production units are normally used for higher rates of productivity, close-tolerance work (down to ±0.13 mm, or 0.005 in.), critical reverse side marking requirements, automatic stud feeding, automatic feeding of the part to be welded, automatic location of the stud on the part, and exotic materials.

The production rate of portable equipment normally ranges from 4 to 6 studs/min, depending on the application. Material handling and other factors could cause this rate to be either slower or faster. The production rates for the permanent production equipment can range from 3 to 20 studs/min, depending on the application, special requirements, and tooling.

When the initial-gap or initial-contact modes of stud welding are used, welds are made on all materials without the use of shielding gases or ceramic arc shields. When using the drawn-arc mode while working with aluminum, a shielding gas would be necessary. This mode is also less flexible when working with exotic materials.

Personnel Responsibilities

The CD stud-welding process is easy to operate and maintain. The operator must first ensure that his unit is connected to the proper incoming voltage. The operator then determines whether the weld gun is connected to the negative and the ground is connected to the positive. Straight polarity is used for welding in nearly all applications. The operator places a given diameter of fastener into the stud gun. The gun is then placed on the work surface. The operator closes the trigger of the gun and the welding process begins. After the welding process is completed, the operator lifts the gun off the welded stud.

The operator needs to inspect the welds to ensure that the settings were correct. The controller voltage, which is set according to the recommendations of the equipment manufacturer, depends on the material and diameter of the fastener to be welded, as well as on the thickness and type of base material being used.

There are also other parameters that should be considered. If it is desirable to reduce spatter and smoky conditions in the weld area, then wetting the weld area with a wetting agent just prior to making the weld is recommended. If a wetting agent is used, then it is best to add a few drops of liquid hand soap to a pint of plain water and to spray or brush the solution into the

weld area. This will produce a clean weld with reduced, if not eliminated, spatter in the weld area. However, the noise of welding increases when a wet weld is made.

Weld inspection is normally done by bending the fastener by applying either a torque or tensile force to it. If a tensile force is applied, then care should be given to the diameter of the hole used to secure the plate material. A hole that is as small as possible should be used to accommodate the flange of the stud. If a large hole is used, the tensile factors may be reduced, because the plate material could yield prematurely. Prior to production welding,

it is recommended that sample welds be made on similar materials and tested to destruction. During production, operators should visually inspect the welds periodically. If weld inconsistency occurs, the process should cease, and the cause should be determined and eliminated.

A common occurrence that contributes to inconsistency is movement of the plate material during the short weld cycle. This can occur when working with materials that are less than 3.2 mm (0.125 in.) thick. There should not be a gap between the workpiece and the backup material of the fixture or table being used.

Proper fixtures and attention to their clamping system can alleviate this problem.

REFERENCE

1. H.A. Chambers, C. Champney, B.C. Hobson, and C.C. Pease, *Arc Stud Welding, Welding Handbook*, 9th ed., Vol 2, Welding Processes, Part 1, 2004

SELECTED REFERENCE

- *Recommended Practices for Stud Welding*, C5.4-84, AWS

Resistance Welding Processes

Introduction to Resistance Welding	397	Resistance Seam Welding	438
Types of Resistance Welds	398	Process Applications	439
Thermoelectric Effects	398	Advantages and Limitations	439
Resistance Welding Power Supplies and Controls	404	Fundamentals of Lap Seam Welding	441
Heat Input	404	Types of Seam Welds	444
Equipment	404	Processing Equipment	444
Resistance Spot Welding	409	Weld Quality and Process Control	446
Process Description	409	Flash Welding and Upset Welding	448
Equipment	411	Introduction	448
Machine Construction	413	Flash Butt Welding	448
Welding Electrodes	414	Upset Welding	453
Effect of Surface Condition on Welding	415	High-Frequency Welding	456
Evaluation Methods	416	Fundamentals	457
Applications	419	Advantages and Limitations	458
Safety	421	Applications	458
Projection Welding	423	Equipment	459
Introduction	423	Personnel	461
Application Advantages and Limitations	425	Safety	461
Material Property Effects	426	Inspection and Quality Control	461
Specifications and Recommended Practices	427	Procedure Development and Practice Considerations for	
Process Fundamentals	427	Resistance Welding	463
Personnel	430	Spot Welding Variables	463
Process Requirements	430	Seam Welding Procedure Development	473
Sources of Defects	432	Nonferrous Alloys	482
Quality Control and Inspection	432	Evaluation and Quality Control of Resistance-Welded Joints .	486
Safety	434	Quality Attributes of Resistance Welds	486
List of specifications	435	Destructive Testing	489
		Nondestructive Testing	495

Introduction to Resistance Welding

RESISTANCE WELDING (RW), invented in 1886 by Professor Elihu Thomson, is conceptually one of the simplest and most commonplace of welding processes. When an electric current flows through a conductive material, such as a pure metal or alloy, there is some inherent resistance to the free flow of electrons through the conductor. Mathematically stated, the thermal power (dQ/dt) produced when current (I) flows through a conductor of resistance R is given by $dQ/dt = I^2R$, where the unit of power is watts (or Joules/second). This production of thermal energy is formally known as Joule heating, or informally as I^2R heating. The process is most commonly used to weld two overlapping sheets or plates.

In a resistance weld, the local rate of Joule heating exceeds the rate at which heat can be dissipated by or from the workpieces being joined. The resulting increase in temperature may cause melting or merely heat the parts sufficiently to allow forging them together into a solid-state weld. In practice, a pair of electrodes clamps the workpieces together under controlled pressure. The electrodes conduct electrical current to the workpieces from the power supply, promote good local contact between the workpieces (both mechanical and electrical), and precisely constrict the flow of current to the joint location. The electrode pressure also acts to contain any molten metal produced at the joint location, impeding it from being expelled from the joint, which would result in gross porosity. Finally, the electrodes (which may be water cooled) extract the welding heat, promoting rapid cooling of the joint.

Resistance welding encompasses many variations on the basic theme of local Joule heating while an external pressure is applied. This article introduces some aspects of the most generally applied RW processes, followed by separate articles on specific RW processes, power supplies, procedure development, and quality control. In addition, while the dominant heating mechanism in all RW processes is Joule heating, there are also some secondary thermoelectric effects that may apply in specific instances (see the section “Overlooked Fundamentals of Resistance Welding” in this article).

Resistance Welding Processes

William Mohr, Edison Welding Institute

As noted previously, the rate of heat production (dQ/dt) during Joule heating is proportional to I^2R . The resistance depends on the material and is also a function of temperature. The electrical resistivity of metals and alloys usually increases greatly when they are heated. For instance, the resistivity of steel can increase by a factor of 10 or more from room temperature to 800 °C (1470 °F). So, passing current through a locally hot material tends to further heat the hottest regions. Because current flow is necessary to the process, highly resistive materials, such as ceramics, are not good candidates for RW (as explained by Ohm’s law in the form $I = E/R$). Such materials require lethal voltages to generate sufficient current. Low-resistivity materials, such as copper, where excessive current is required for sufficient heating, are also not good candidates for RW.

Pressure is applied even before the current is activated to ensure good electrical contact between the workpieces. Accurate control and timing of the electric current and application of pressure is an essential feature of RW. The actual temperature rise at the joint depends on the interrelationship of the three variables: current (squared), resistance (as a function of temperature and position), and the time duration of current flow. These variables are further affected by:

- Cooling effect of the electrodes
- Effect of electrode follow-up behavior on resistance (at the various interfaces)
- Effect of current shunting, where the current flow takes another path rather than through the desired weld area

An example of current shunting can occur when a thick section is being welded to a thinner section by indirect spot welding (see the article “Resistance Spot Welding” in this Volume). Current shunting also can occur through nearby previous welds when welds are close together. As the second weld heats up with an increase of

resistance, more of the current preferentially can go through the previous weld, which has a lower resistance through the section.

During RW, initial electrical heating typically occurs due to the higher resistance of the interface between the parts to be joined, rather than the base metals or the electrodes or the connections of the electrodes to the base metal. This resistance can come from surface roughness between the parts or from surface coatings. In some processes, the resistance can be provided by the shape of the parts to be joined or, rarely, by the resistance of one of the base metals.

Resistance-welded joints require cooler metal around the heated area to restrain the expansion of the hot area, whether or not it becomes molten. The strength of the bond also depends on the cleanliness of the mating surfaces, although the process is more tolerant of the presence of oxide layers and contaminants than other welding processes. Resistance welding processes require specialized machinery, but they have the major advantages of not requiring filler metals, shielding gases, or flux.

The three major RW processes are resistance spot welding, resistance seam welding, and projection welding. Other methods of RW include:

- Upset welding is a solid-state variation of RW. Rather than fusion (melting followed by coalescence), the primary method of creating a joint during upset welding is on forging (“upsetting”) with some resistance heating to improve plastic deformation during upsetting.
- Flash welding creates the heat for welding at the faying surfaces of the joint not only by resistance to the flow of electric current but also by arcing (“flashing”) across the interface (see the article “Flash and Upset Welding” in this Volume).
- Capacitor discharge stud welding, where a stud serves as a weld member, is a process similar to flash welding.
- High-frequency RW concentrates the surface current of the part to heat the base metal and cause the coalescence of metal.

These processes are described in more detail in separate articles in this Volume.

Types of Resistance Welds

Resistance welds must allow for the passage of electrical current to provide heating of the interface to be joined and for force to constrain the heated material and form the bond as it cools. This section briefly reviews some of the general design aspects of resistance-welded joints. Most of the processes discussed as follows are used for lap joints, where the weld joins faces of the material rather than edges.

Spot welds are most easily made between identical materials of the same thickness, employing identical electrodes on both sides, because this allows the heating to be symmetrically generated in each workpiece. Symmetrical heat balance such as this is advantageous because it locates the center of the molten zone on the interface between the sheets.

Spot welds can be made in series with more than two sheets joined in a single event. This requires attention to the surface condition of the faying surfaces to get the resistance at each of the multiple interfaces to be broadly similar. Welding of more than two sheet layers is most easily performed with thinner outside sheets and a thicker center sheet, because the heating profile at the two interfaces between thin-thick sections would be more uniform (see the article "Resistance Spot Welding" in this Volume for a schematic of the temperature profile across a spot weld).

When RW of workpieces that are not inherently heat balanced, the electrode combination can be changed to localize the heat more toward one side of the stack. Effects can be obtained from using a larger-diameter electrode on one side or a higher-conductivity material on that side. Another process change that can also improve the situation includes heating the joint more rapidly (to increase the heating effect of the interfacial resistance over that of the bulk resistance of the workpieces).

It is often desirable to minimize the visible effect of the spot weld on one of the surfaces. The use of a larger electrode for that side or dividing the job of providing mechanical force and electrical current contact between two locations can be used for this (see the article "Resistance Spot Welding" in this Volume).

Seam welds provide fluid-tight lap welds that are often used for pressurized vessels with mild internal pressure, such as exhaust system catalytic converters for vehicles. They are created as a series of overlapping spot weld nuggets, with each nugget cooling before the following nugget is initiated.

Parameters that affect weld quality and integrity of resistance seam welds are the materials to be joined, their thicknesses, the overlap distance, the electrode width, and the access available for the electrodes. The electrodes are usually copper alloy disks or wheels, which roll along the intended seam, although a variation with conventional cylindrical spot welding electrodes has also been used (stitch welding). The required workpiece clamping force is provided by the electrodes rather than through

separate fixtures. The axis of rotation of one wheel may be slightly nonparallel to allow clearance of adjacent members, but the difference should not be more than 6° , and the contact surface will still need to be parallel to the surface of the workpiece it contacts.

The presence of adjacent spot weld nuggets allows much of the current to be shunted through the previous spots, so the welding parameters for seam welding tend to have much higher current pulses than spot welding, with other parameters such as electrode force changed to compensate for this.

Projection welds localize the heating for RW at the contact between the workpieces by employing a small raised bump or projection on one of the members being joined. This has an advantage compared to conventional spot welding for welding materials with low contact resistance, such as galvanized sheets and copper alloys, or in cases where the heat balance is severely skewed away from the faying surface, such as when one of the materials is much thicker than the other. Projections are usually placed in the thicker of two dissimilar pieces, on the basis that the thicker piece will be more difficult to melt at the faying surface.

The projection must be designed to remain raised during the initial heating phase of welding but soften and compress or collapse by the end of the welding cycle. Projection design is thus connected with the design of the heating cycle. The low elevated-temperature strength of aluminum alloys tends to make them unsuitable for projection welding.

For sheets, the spherical dome projection punched into the sheet is most common. Thicker parts will usually have machined projections, although they can be punched in moderate thicknesses. For some applications, such as crossed wires, the configuration of the mating parts already provides a sufficient projection.

Designs with extended or multiple projections can be used, even providing a continuous length of weld for pressure-retaining components. In circularly symmetric geometries, an annular projection may be used for its ability to provide a single-shot, fully circumferential joint, such as hermetic cans for transistors.

When using extended or multiple projections, the fit-up tolerance must be tightened so that all of the projection areas can participate equally.

Butt Welds. Resistance welding can be used to create butt joints rather than lap joints, using processes such as flash welding, upset welding, and high-frequency induction (HFI) welding, as is widely used for the production of welded tube. All of these processes require electrical heating and displacing the two sides of the joint toward one another.

Material will often be extruded at and near the bond line during resistance butt welding. Many applications require the removal of this flash, for instance, by a cutting operation just after completion of welding.

Design of the preweld geometry in these processes requires a determination of the shortening

between the current-carrying clamps to achieve the desired final dimensions of the welded component. The components of this shortening are the loss of material directly at the bond line (the material extruded into the flash) and the upsetting and thickening of the adjacent base metal. Flash welding, in particular, has a significant fraction of shortening occurring by loss of material at the bond line. An estimate of flash weld shortening for steels, both in tubular and bar form, is provided in Ref 1.

Some welding processes add plastic deformation processes after butt welding to provide an accurate size and shape to the final component. For instance, HFI tube will commonly be sized to an accurate outer diameter after welding.

Overlooked Fundamentals of Resistance Welding*

G.A. Knorovsky, Sandia National Laboratories

Much knowledge has been accumulated concerning many aspects of RW since its invention by Elihu Thomson in 1886. This work discusses two factors that have not been well documented in the standard reference texts. As noted earlier, the principal heat source in RW is Joule (I^2R) heating. However, there are other heating effects that may also occur during RW. The second factor discussed in this section is the effect of the current pulse on the subsequent motion of the welding head (the so-called electrode "follow" behavior). While both of these effects are often unimportant, they may become critical when the RW process is being applied at its limits. Examples taken from sheet metal and microwelding applications are given.

Thermoelectric Effects

Although Joule (I^2R) heating is the predominant heating mechanism acting in RW, two types of thermoelectric effects may also be operative: the Peltier effect and the Thomson effect. To combine all three effects, two different situations are examined: one typical of an industrial sheet-metal-type weld and one typical of an electrical interconnection.

Peltier Effect. The Peltier effect occurs when the flow of current through a bimetallic junction causes energy to be absorbed or released at that junction. The Peltier effect is the inverse of the more widely known thermocouple (Seebeck) effect, where temperature difference between the ends of a bimetallic pair of conductors

* Adapted from Overlooked Fundamentals of Resistance Welding, *The Metals Science of Joining*, 1992

causes an electric potential difference to occur. The Peltier effect is associated with changes in potential energy due to the different energy levels of conduction electrons within the two materials. When a conduction electron changes energy levels, it gains or loses potential energy.

Kinetic energy of the electrons is essentially constant, because it is governed by the (current) flow. The potential energy, gained or lost from the different energy levels of two materials, is converted into a thermal effect. Mathematically, the thermal effect from the Peltier-effect heat is expressed as:

$$dQ_p/dt = -\Pi_{ab}J$$

where dQ_p/dt is the rate of heat released (i.e., the thermal power) per unit area due to current flow from material "a" to material "b." The symbol Π_{ab} is the Peltier coefficient for current flow from material "a" to material "b." J is the current density (in units of amperes/unit area, as opposed to I , given in amperes).

In the Peltier effect, note that the heat effect can be either positive (release) or negative (absorption), depending on the direction of current flow. This is distinct from the Joule heating effect (dQ_j/dt), which is based on the square of current density (J^2), such that thermal energy is only positive ($dQ_j/dt = J^2\rho$) and therefore released. The release or absorption of some thermal energy, depending on current flow direction in the Peltier effect, is the explanation why direct current resistance welds are sometimes polarity sensitive (Ref 2). It also offers an explanation as to why one electrode usually wears faster than its nominally identical counterelectrode.

The Peltier coefficient is related to the Seebeck coefficient (the proportionality constant $S_{ab} = dV/dT$), which relates output voltage (V) to hot versus cold junction temperature difference (in degrees Kelvin) for a thermocouple of materials "a" and "b" by:

$$\Pi_{ab} = TS_{ab}$$

Hence, the Peltier effect tends to be more important at higher temperatures. Finally, while the Peltier coefficient for a bimetal pair is governed by both members of the junction, data are compiled for individual materials. The paired material coefficient is obtained by subtracting values of the individual material coefficients:

$$S_{ab} = S_b - S_a$$

Data are available (Ref 3) for pure materials, thermocouple materials, and other materials where the thermoelectric coefficients have been used to measure solid-state phenomena (dilute magnetic alloys). Unfortunately, thermoelectric data are not available for many commonly resistance-welded materials, such as aluminum alloys and stainless steels.

The Thomson effect (named after William Thomson, Lord Kelvin, not Elihu Thomson) is similar to the Peltier effect but instead acts in a single conductor and refers to heat absorbed or

released when electric current flows through a conductor that contains a temperature gradient. The explanation of these effects lies in the conservation of energy and how the energy levels of conduction electrons vary with location (such as when crossing a bimetallic interface, in the case of the Peltier effect) and temperature.

The Thomson effect is governed by:

$$dQ_t/dt = -\mu J\nabla T$$

where dQ_t/dt is the rate of heat release per unit volume, μ is the Thomson coefficient, J is the current density (a vector), and ∇T is the temperature gradient (also a vector). Absorption of heat (dQ_t/dt negative) occurs if the current flow and thermal gradient vectors are parallel and μ is positive.

Of the three thermoelectric-effect coefficients, the Thomson coefficient is the only one that can be measured directly for a single material. The three thermoelectric coefficients can be shown to be interrelated by:

$$\mu = T dS/dT$$

$$\Pi = TS$$

where T is the absolute temperature. Note that these relationships of the Thomson coefficient to the other thermoelectric coefficients (which really are only measurable in pairs), allow values of S and Π for single materials to be tabulated without arbitrarily defining one material to be of zero potential.

Relative Contributions of Joule, Peltier, and Thomson Effects. Given these three effects, what are their relative contributions for typical RW scenarios? Because the Peltier effect is two dimensional and the Joule and Thomson effects are three dimensional, it is difficult to compare all three directly. It is possible to compare the Joule and Thomson effects, because they can be combined into a single equation relating rate of heat production per unit volume to current:

$$dQ/dt = \rho J^2 - \mu J \cdot \nabla T$$

or alternatively:

$$dQ/dt = J(\rho J - \mu \nabla T)$$

Typical values of ρ range from ~ 1 to ~ 100 $\mu\Omega\text{cm}$ for metals (Ref 4), with copper at room temperature having a value of 1.6 and iron at 1000 °C (1830 °F) having a value of 110 (data beyond 1000 °C are hard to obtain). With typical welding currents, J has values in the range of 10 to 100 kA/cm^2 (Ref 5), and the product ρJ would then tend to range between 0.01 and 10 V/cm . Likewise, the absolute value of μ typically ranges from approximately 1.5 to 35 $\mu\text{V/K}$, while the temperature gradient (∇T) ranges from 0 to approximately 50,000 K/cm , and the product can vary from zero to ~ 1.5 V/cm .

Comparing the relative sizes of these two products, it is seen that under certain circumstances

the Joule heating can overwhelm the Thomson heating (or cooling), while in others the two can be comparable in magnitude. Because the Thomson coefficient (μ) and resistivity (ρ) are both of approximately the same magnitudes for common metals, whichever of the two is larger—current density or thermal gradient—will determine which effect predominates. Another important consideration is that both effects cause voltage drops, which must be isolated when trying to measure apparent resistance across a weld. In symmetrical geometries with differential measurements, the Thomson effect voltage should cancel; however, the Peltier effect may cause asymmetrical thermal gradients in apparently symmetrical geometries.

To compare the Joule and Peltier effects, it is necessary to realize that the Peltier heat is not a function of the volume of the material that the current is flowing through. That is, if a given current density flows through two sheets of steel, one of which is 10 cm (4 in.) thick and the other 1 cm (0.4 in.), the Joule heat released will be 10 times as great in the former. On the other hand, if the two sheets are different materials and a Peltier effect occurs, it will be the same no matter how thick the materials are. Thus, a good comparison between Joule and Peltier heating is to find the thickness of materials needed to release the same amount of energy via either mechanism. This is expressed by the equality:

$$|dQ_p/dt \text{ (in J/cm}^2\text{-s)}| = dQ_j/dt \text{ (in J/cm}^3\text{-s)}\Delta z$$

where Δz is the overall couple thickness in centimeters, or alternatively:

$$|\Pi_{ab}J| = J^2(\rho_a\Delta z_a + \rho_b\Delta z_b) = J^2(\rho_a + \rho_b)\Delta z/2$$

where the subscripts refer to the two materials in the couple (each of equal thickness), and thus:

$$\Pi_{ab} = J(\rho_a + \rho_b)\Delta z/2$$

and finally:

$$\Delta z = 2 \Pi_{ab}/[J(\rho_a + \rho_b)]$$

Picking a couple made of iron-copper, at 0 and 1000 °C (32 and 1830 °F) the appropriate constants and calculated Δz values are compiled in Table 1.

It is seen that while the thicknesses calculated are small, they are nonnegligible. Also, the thickness is inversely proportional to current density. For the example chosen, it appears that the effect decreases at elevated temperatures; this is not necessarily always the case. As a counterexample, choose a nickel-molybdenum couple, both of which have relatively large (and opposite sign) Peltier coefficients. The appropriate constants and calculated Δz values are compiled in Table 2. At 1000 °C (1830 °F), the Peltier heat for this couple is approximately twice as important as at 0 °C (32 °F). Again, note that the Peltier effect coefficient has units of a voltage, and it too can lead to measurement errors in nonsymmetrical situations.

Example 1 (Automotive). As an example illustrating all three effects, consider the case where two sheets of 1 mm (0.04 in.) thick low-carbon steel are to be joined. This is typical of an industrial sheet-metal-type weld (although a direct current power supply is assumed, rather than the more typical alternating current).

The Resistance Welder Manufacturers' Association's (RWMA) recommended practice (Ref 6) suggests an electrode contact spot of 0.635 cm (0.25 in.) diameter, 10 cycles of weld current of 9500 A, use of RWMA class 2 electrodes, and 2200 N (500 lbf) electrode force. This corresponds to a current density of 30,000 A/cm². There are no data for the thermoelectric coefficients of class 2 electrode material, so the data for pure copper are used. Similarly, the data for pure iron instead of low-carbon steel are used. In Fig. 1 and Table 3, values of heat generation are calculated for volumes of 1 cm² (0.16 in.²) cross section of the appropriate thickness. Only the left half of the weld geometry is pictured. The right half should be symmetric for the Joule effect and antisymmetric for the Peltier and Thomson effects. Temperature distributions are assumed, and calculations of heat effects are made at three points in time during the weld.

At the beginning of the weld (Fig. 1), the initial temperature is uniform at 0 °C (32 °F). At the start of melting, a linear temperature distribution exists between the central temperature at 1500 °C (2730 °F) and the electrode/material interface at 200 °C (390 °F). This then reduces linearly to 0 °C (32 °F) in the electrode material over a distance of 6.35 mm (0.25 in.). At the end of current flow, the melting isotherm is located ¾ of the part thickness from the centerline (the fusion zone is considered to be isothermal at 1500 °C, or 2730 °F), the electrode/material interface is at 400 °C (750 °F), and a linear temperature gradient exists between these points. The electrode material is again assumed

to cool linearly with a distance to 0 °C (32 °F) over 6.35 mm (0.25 in.).

The temperatures chosen at the electrode/part interface correspond to available data (Ref 7). Positive current is assumed to flow from left to right. A negative sign in Table 3 implies that heat is absorbed; positive indicates that heat is generated. The actual values used for the Thomson and Joule coefficients are averages over the temperature ranges applicable. If the coefficient was not well behaved (i.e., not continuous), an interval over which an average value was computed is noted. Wherever a calculation temperature exceeds 1000 °C (1830 °F), it has been extrapolated by curve fitting (except for the resistivity of iron).

Note that the signs of all Peltier and Thomson terms are reversed on the other side of the center line (C_l) and that there is no Peltier effect at the iron/iron interface. Also note that because of the nonmonotonic temperature dependencies of the Peltier and Thomson coefficients of iron, the Peltier and Thomson heat effect behave in a complex manner with temperature. Observing the results in Table 3, it is clear that the Joule effect is quite dominant under all conditions, with the thermoelectric effects never constituting more than a relatively small fraction of the overall heat production. From the viewpoint of efficiency, it is interesting to note that at the beginning of the weld, more heat is generated in the electrodes than in the weldment. (This is why RW electrodes are often water cooled.)

Example 2 (Battery Terminal). Another example, typical of an electrical interconnection, is a 0.1 mm (0.004 in.) nickel ribbon being joined to a 3 mm (0.12 in.) diameter by 4 mm (0.16 in.) high molybdenum terminal pin (typical of a long-life, lithium-containing, D-sized battery). Experiments designed to develop a weld schedule for this connection suggest that a current of 1800 A through an electrode

contact spot 2 mm (0.08 in.) in diameter (~60,000 A/cm²) for a time period of 20 ms will yield successful welds. A molybdenum electrode (negative polarity) contacts the nickel ribbon, and a copper alloy electrode contacts the molybdenum pin. An electrode force of 50 N (11 lbf) is used.

Because the weld geometry is not symmetrical, the entire geometrical sequence is shown in Table 4. Again, the values of power are calculated per cm² cross section of appropriate length, with temperatures assumed as follows. Initially, a uniform temperature of 0 °C (32 °F) exists; at the start of melting, the nickel/molybdenum weld interface is at 1450 °C (2640 °F), while the molybdenum/nickel electrode interface is at 1000 °C (1830 °F), and the molybdenum/copper weld interface is at 425 °C (795 °F) (the electrodes linearly cool to 0 °C over a distance of 5 mm, or 0.2 in.). At the end of current flow, melting has propagated from the nickel/molybdenum interface into the nickel ribbon to a distance of 0.075 mm (0.003 in.), the molybdenum/nickel electrode interface is at 1300 °C (2370 °F), and the molybdenum/copper electrode remains at 425 °C (795 °F). Interpolations between the points given are linear (Fig. 2), and the values calculated refer to averaged coefficients over the temperature ranges where gradients exist. Wherever a calculation temperature exceeds 1000 °C (1830 °F), it has been extrapolated by curve fitting (except for the resistivity of molybdenum). These simplified assumptions are based on some finite-difference calculations

Table 1 Resistivities, Peltier coefficients, and calculated equivalent Joule heat thickness for iron-copper couple

Metal	Coefficient					
	At 0 °C (32 °F)			At 1000 °C (1830 °F)		
	ρ, μΩcm	Π, μV	Δz, cm	ρ, μΩcm	Π, μV	Δz, cm
Fe	8.59	3,986	...	112	-8,020	...
Cu	1.56	467	...	9.3	8,990	...
10,000 J, A/cm ²	0.07	0.028
100,000 J, A/cm ²	0.007	0.0028

Table 2 Resistivities, Peltier coefficients, and calculated equivalent Joule heat thickness for nickel-molybdenum couple

Metal	Coefficient					
	At 0 °C (32 °F)			At 1000 °C (1830 °F)		
	ρ, μΩcm	Π, μV	Δz, cm	ρ, μΩcm	Π, μV	Δz, cm
Ni	6.4	-4,870	...	48.1	-48,100	...
Mo	4.6	1,256	...	16.1	20,500	...
10,000 J, A/cm ²	0.11	0.21
100,000 J, A/cm ²	0.01	0.02

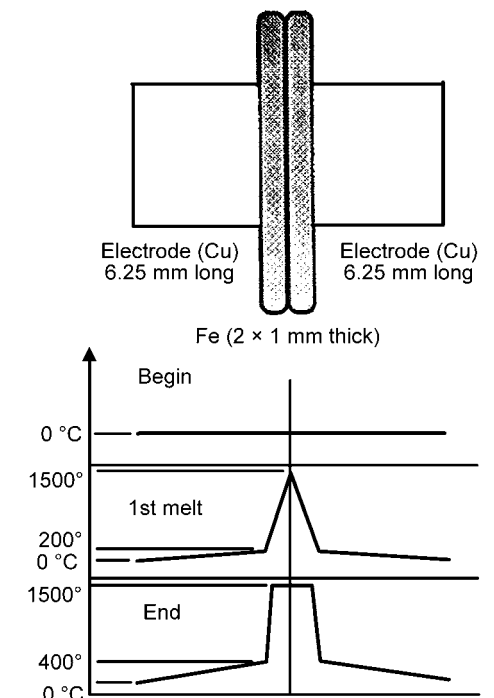


Fig. 1 Example 1 geometry and thermal profiles

(Ref 8), which were qualitatively verified by metallography.

In comparison with example 1, these calculations are quite different. First, in contrast to the automotive sheet steel, where the electrodes were generally much better conductors than the weldment, here one of the electrodes dissipates nearly as much heat as the molybdenum terminal. This is not surprising, because it is the same material, sees approximately the same temperature range, and is about the same length. The data in Table 4 are not normalized for the electrodes and terminal pin versus the nickel ribbon (5, 4, and 0.1 mm, or 0.20, 0.16, and 0.004 in., respectively), which makes it hard to see that the Peltier and Thomson effects are really quite significant in this case. Dividing the electrode entries by 50 and the terminal pin entries by 40 does this, allowing the heating contributions to be compared on an equivolume basis. Such a comparison is fair only at the beginning, because otherwise the resistivity change with temperature is not correctly factored in.

The resistivity values used to calculate the electrode and terminal entries in Table 4 were averaged over the temperature intervals shown in Fig. 2, while the temperatures at the nickel/molybdenum and molybdenum/nickel interfaces are much higher, and hence, the resistivity

used to calculate the Joule effect heating should be higher. For the case of molybdenum, the resistivity changes by approximately an order of magnitude between 0 and 1450 °C (32 and 2640 °F). A reasonable comparison for the first melt and end values can then be made by multiplying the “begin” value by the resistivity change, with temperature divided by the thickness disparity, 10×/50× (or 10×/40× for the terminal) to see the Joule heating effect of molybdenum at temperatures near the melting point of nickel. For example, at the end of the weld, it is calculated that approximately 1850 J/s of heat are being supplied by Joule heating in a 0.1 mm (0.004 in.) thickness of the molybdenum electrode and terminal on either side of the nickel ribbon. The nickel ribbon itself is providing 6400 J/s of heat at the ribbon/terminal interface and 5600 J/s of cooling at the electrode/ribbon interface. It is clear that this will have a substantial effect on the thermal balance. The Thomson effect is also significant compared to Joule heating before the thermal gradients in the nickel ribbon begin to diminish.

Effect of the Interfacial Resistance. The interfacial resistance must also be considered to complete the analysis. Data from Ref 5 suggest that the surface contact resistivity for copper alloy versus mild steel at room temperature

is on the order of $7.7 \times 10^{-4} \Omega/\text{cm}^2$ ($1.25 \times 10^{-4} \Omega/\text{in.}^2$). This suggests that the initial heating rate at the surface (per cm^2) for example 1 is on the order of 700,000 J/s! This resistance would correspond to that of an iron bar of 1 cm^2 (0.16 in.^2) area nearly 90 cm (35 in.) long. Clearly, this rate cannot be sustained for long, because the surface asperities that constrict the current and are the main cause of surface resistivity will rapidly heat and collapse, causing the surface resistivity to drop to a small value.

Nevertheless, it is clear that the early stages of heating are overwhelmingly controlled by surface resistance. The nickel-to-molybdenum weld finite-difference calculations mentioned earlier that incorporated the Joule and Peltier effects also incorporated a surface resistivity term. These results, plotted in Fig. 3, clearly demonstrate the importance of both the surface resistance and the Peltier effect. Temperature-dependent physical properties were used, except that the Seebeck coefficient (which controls the Peltier coefficient) was held constant at an average value. Additionally, the surface resistivity (chosen as $100 \mu\Omega/\text{cm}^2$) was set to zero when the interface warmed to half the homologous melting point.

The calculated interfacial temperatures (both weld and electrode) show clearly that the initial temperature rise is independent of the polarity chosen, but that subsequent to reaching the melting temperature, the Peltier effect becomes evident. It was found that after the initial transient, the weld interface temperature for the wrong choice of polarity was less than the electrode interface temperature.

Electrode “Follow” Behavior

The second neglected fundamental discussed here deals with the requirements for assuring good electrode “follow” behavior. Normally, the recommended design to achieve good follow behavior involves the use of low-inertia welding heads. In reality, because an RW head acts like a sprung mass, much like an automobile suspension system, a more complicated specification involving damping is necessary.

Table 3 Calculated relative powers of thermoelectric and Joule effects for example 1

Effect	Time	Location: C _L			
		Cu electrode	Interface	Fe	
				Solid	Liquid
Joule	Begin	890 J/s	...	770	...
	1st melt	960	...	3800	0
	End	1670	...	1710	7500
Peltier	Begin	...	-105
	1st melt	...	-34
	End	...	157
Thomson	Begin	0	...	0	...
	1st melt	-12	...	176 (200–577 °C)	0
				-195 (577–910 °C)	...
				-157 (910–1500 °C)	...
				31 (400–577 °C)	0
End	-30	...	-195 (577–910 °C)	...	
				-157 (910–1500 °C)	...

Table 4 Calculated relative powers of thermoelectric and Joule effects for example 2

Phenomenon	Time	Location							
		Mo electrode	Interface	Ni		Weld interface	Mo	Interface	Cu electrode
				Solid	Liquid				
Joule effect	Begin	9300 J/s	...	230	7,400	...	2,800
	1st melt	33,000	...	2,000	43,000	...	5,600
	End	41,000	...	530	1,650	...	43,000	...	5,600
Peltier effect	Begin	...	-370	370	...	-47	...
	1st melt	...	-4100	6,400	...	-450	...
	End	...	-5600	6,400	...	-450	...
Thomson effect	Begin	0	...	0	0	...	0
	1st melt	400 (0<T<760)	...	-780	-370 (425<T<760)	...	-70
				-90	...	1360	
				(760<T<1000)	...	(760<T<1450)	
				(1000<T<1300)	...	(1300<T<1450)	
End	400 (0<T<760)	...	-220	-370 (425<T<760)	...	-70	
						1360			
						(760<T<1450)			

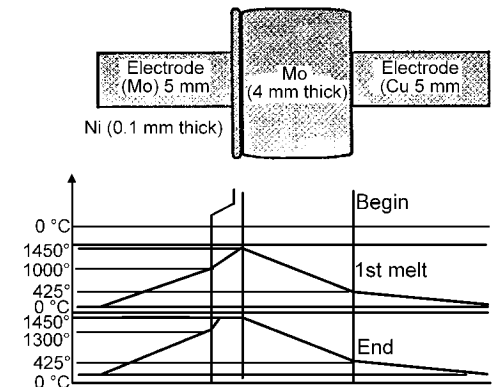


Fig. 2 Example 2 geometry and thermal profiles

An appropriate analogy would be driving a high-performance sports car on a bumpy road with its shock absorbers (dampers) removed. With this automotive analogy in mind, it is clear that a low inertia is an insufficient design requirement for acceptable follow in resistance weld head design.

The dynamic model of a resistance weld head is illustrated in the simplified schematic of Fig. 4, showing the various masses, springs, and bearings. For complex real systems, analytical calculation of the motion of a given point or points is a complex and time-consuming procedure, even using available powerful finite-element analysis programs. Indeed, sometimes the best procedure is to perform an experimental modal analysis, and use the results to understand the various motions possible, their resonant frequencies, and their relative importance. This procedure, while involved, is greatly facilitated by the computerized analysis and modeling procedures now available to vibration specialists.

Modal analyses on small welding heads were far less common, certainly when the resistance welders commonly used in industry were developed. However, by examining the dynamic behavior of a simple linear single-degree-of-freedom spring-mass-damper system, considerable insight can be gained into the behavior of more complex systems. The mathematical analysis of such a system is well developed and tractable yet exhibits much of the character of the behavior of more complex systems. It is often observed that in multiple-degree-of-freedom systems, the lowest-order modes are dominant.

There are two important regimes in vibration analysis: forced and free. Forced vibration refers to a regime where the system is driven by a periodic external force. If the periodic force is sinusoidal, this is referred to as harmonic motion. An alternating-current-type welder, where current pulses occur at periodic intervals, would exemplify this regime. Free

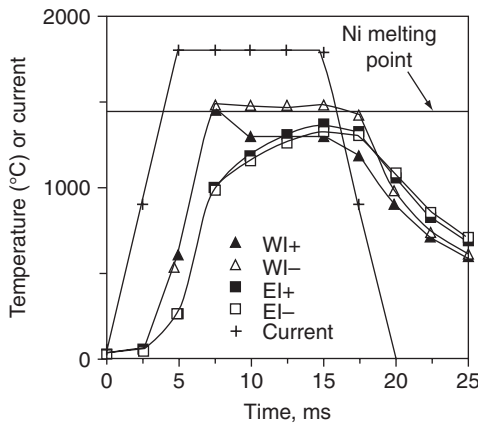


Fig. 3 Calculated temperatures at weld interface (WI) and electrode interfaces (EI) for geometry shown in Fig. 2 as a function of molybdenum electrode polarity

vibration refers to a situation where the system is given some initial stimulus to which it responds. A capacitive discharge or direct current welder is more characteristic of this type.

Referring to the simple single-degree-of-freedom system, the simplest type of free vibration to analyze is one where the system is removed from equilibrium (by stretching or compressing the spring) and then released. The solution of Newton's second law of motion in the form:

$$m \cdot (d^2x/dt^2) + b \cdot (dx/dt) + k \cdot x = 0$$

where m is mass, b is the damping coefficient, k is the spring constant, and subject to the appropriate boundary conditions, will describe how the system evolves with time. Many elementary texts on differential equations, for example Ref 9, use this as an introductory example of Laplace transformation solution methods.

The behavior of the system under conditions of underdamping, critical damping, and overdamping is shown in Fig. 5. While the rate of return to the equilibrium condition is fastest for the underdamped case, in many cases the oscillation is undesirable. For an undamped system, sinusoidal oscillation takes place at the so-called natural frequency of the system, which is given by:

$$f_a = (1/2\pi) \cdot (k/m)^{0.5}$$

For cases where less than a critical amount of damping takes place, oscillatory behavior still takes place, but the system eventually returns to equilibrium, and the damped natural frequency is slightly modified by the damping term:

$$f_d = f_n(1 - \zeta^2)^{0.5}$$

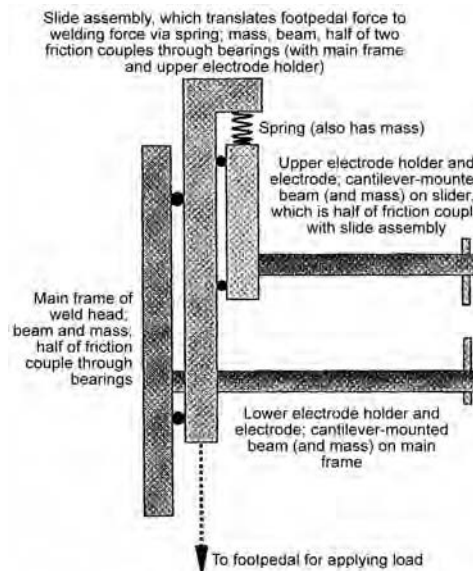


Fig. 4 Schematic of typical small resistance weld head

where $\zeta = b/(2[k/m]^{0.5})$. It can be shown that the logarithm of the ratio of successive amplitudes (the so-called logarithmic decrement; $\delta = \ln(\Delta x_i/\Delta x_{i+1})$, where Δx_i is the peak displacement from equilibrium for swing "i" in a given direction) can be used to conveniently measure the damping in a system via the equation:

$$\delta = \ln(\Delta x_i/\Delta x_{i+1}) = 2\pi\zeta/[(1 - \zeta^2)^{0.5}]$$

which simplifies to $\delta = 2\pi\zeta$ for $\zeta \sim 0.3$ or less.

When the critical amount of damping is present ($\zeta = 1$), oscillatory motion ceases, the system returns to equilibrium in the shortest period of time, and the natural frequency concept becomes irrelevant. Higher values of damping merely slow the return to equilibrium. Measurement of a typical small RW head in the author's laboratory gave a value of $\zeta \sim 0.09$.

The next most complex step involves shocking a system initially at equilibrium. If the shock involves applying a step function force (F_0), it may be shown (Ref 10) that the system responds as shown in Fig. 6. This situation is very close to what happens in a resistance welder, except that the force applied by the thermal expansion of the sample is not a square wave, and it decays to zero after some period of time. The ordinate of Fig. 6 is expressed in multiples of the equilibrium static displacement that the step force would produce. For insufficient damping, the dynamic response is nearly twice the static displacement that should result.

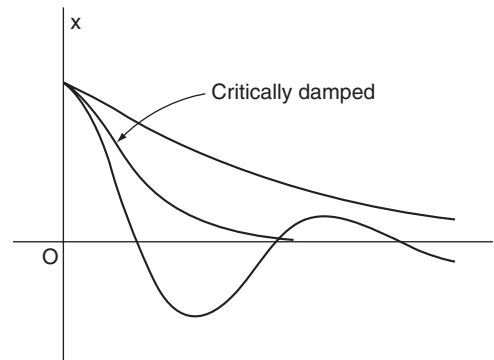


Fig. 5 Free response of system with variable damping. Upper curve is overdamped; oscillatory curve is underdamped.

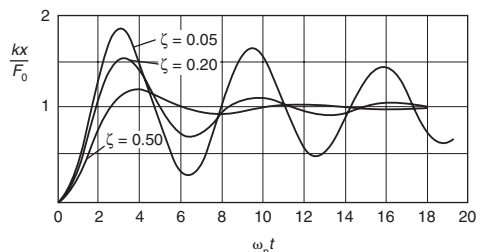


Fig. 6 Time response of system to step function load F_0 applied at time zero. ω_n is $2\pi f_n$.

Another important method of displaying the resulting displacement of a system that has been shocked is the response spectrum curve. This shows the maximum displacement that will occur sometime during the response of an undamped single-degree-of-freedom system (although it does not show actual displacement versus time) as the time of application of the shock varies with respect to the natural period (inverse of the natural frequency) of the system. The response spectrum diagram of a half-cycle sinusoid is shown in Fig. 7. It is clear that in order to respond in an accurate manner (i.e., near the static response value or ordinate = 1), one must choose a value of $t/\tau_n > 2.3$. The value where $t/\tau_n = 1/3$ apparently gives the correct response magnitude, but it is delayed in time, with the response being achieved long after the shock is over.

The implication of these diagrams (an excellent compilation is given in Ref 11 along with actual time response curves) is that the time of application of the shock must be long with comparison to the natural period of response of the system. Furthermore, gentler shocks are more accurately followed, and the effect of damping is generally positive in controlling the overshoot of the system (as long as it is not excessive).

It has been known for many years in the field of camshaft design that the third derivative of displacement (sometimes called the "jerk") must be controlled (Ref 12) in order to have a positionally accurate motion control not prone to excessive vibration. (By making the assumptions of uniform I^2R heating and R linearly increasing with temperature, it is possible to relate expansion versus time to current versus time, from which it can be shown that the initial third derivative of the displacement is proportional to the square of the slope of current versus time.)

Also important is a cam ramp time that is long in comparison to the natural period of the cam follower mechanism, and a cam that is stiff enough to resist the force applied to it by the follower. Poor dynamic design of a cam and follower can lead to follower "jumping" or loss of control, even when the spring-loaded follower should be able to accelerate fast enough to follow the nominal acceleration profile of

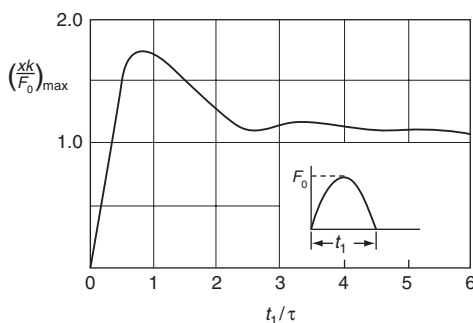


Fig. 7 Response spectrum diagram to half-sine force input (shown inset). τ is the natural period of the system.

the cam. One other desirable feature is that enough damping must be present to damp out any vibrations generated before the system has to actuate again (i.e., during the dwell time when the cam is not actively controlling the motion of the follower).

Returning to RW, capacitive-discharge-type power supplies provide a very difficult shock load for a mechanical system to follow. From measurements made on a typical small welding head, the compliance and mass of the upper arm and its mounting slide result in a calculated natural frequency of only 25 Hz. However, this assumes that the slide carrying the upper electrode can actually move during the period of the weld. If one assumes a cantilever mount (i.e., the slide mount essentially remains motionless during the force application period) and relies on the elastic deflection of the electrode arm to follow the part expansion, then the natural frequency calculated from beam theory (Ref 10) is approximately 2.5 kHz. For a load application period of a few (1 to 5) milliseconds, this gives a ratio of t/τ_n of $(0.001 \text{ to } 0.005)/(1/2500) = 2.5 \text{ to } 12.5$, which is excellent—excellent, that is, for a gentle half-sinusoid load profile (or the even gentler classical cycloidal motion typical of camshafts). However, the deflection that must be accommodated by elastic bending of the electrode holder will cause the opposed electrodes to lose parallelism (similar to a rocker-type head, which the slide-type head was supposed to improve upon) and hence promote spatter because of nonuniform loading of the pressurized molten zone.

Even though forced vibrations have not been discussed, it is clear that for alternating-current-type power supplies, the natural mechanical response frequency of the system must not be too near twice the power frequency or any of its harmonics if a resonance situation is to be avoided. It is unfortunate that silicon-controlled rectifiers do not chop the tails off of sinusoidal current pulses rather than the beginnings, because chopped alternating current pulses are clearly not a gentle load to follow. Fortunately, each one is a relatively small contribution to the overall heat input.

To summarize, it is recommended that RW power supply and head designers should take a page from the book of camshaft designers. They should attempt to better tailor the electrical pulse (and the expansion resulting) to the capabilities of the mechanical system that must control it. Additionally, the effect of damping on the mechanical response of a resistance weld head needs to be further investigated if the initial measurements of it are indicative of general practice.

ACKNOWLEDGMENTS

In this work on certain important but often overlooked aspects of RW, the author of this

section would like to acknowledge, in particular, the assistance of A.J. Russo, for performing finite-difference calculations incorporating the Peltier and Thomson effects, and Arlo R. Nord, for conducting experimental modal vibration testing and analysis of small resistance weld heads. Sandia National Laboratories is a multi-program laboratory managed and operated by Sandia Corporation, a wholly-owned subsidiary of Lockheed Martin Corporation, for the U.S. Department of Energy's National Nuclear Security Administration under contract DE-AC04-94AL85000.

REFERENCES

1. "Recommended Practices for Resistance Welding," AWS C1.1, American Welding Society, 2000
2. S. Scholz, An Investigation of the Influence of the Peltier Effect on Resistance Welds, *Z. Angewand. Phys.*, Vol 12 (No. 3), 1960, p 111–117
3. F.J. Blatt, P.A. Schroeder, C.L. Foiles, and D. Greig, *Thermoelectric Power of Metals*, Plenum Press, New York, NY, 1976
4. K.-H. Hellwege and O. Madelung, Ed., *Numerical Data and Functional Relationships in Science and Technology*, Landolt-Bornstein, New Series, Group III; *Crystal and Solid State Physics*, Vol 15, *Metals: Electronic Transport Phenomena*, Springer-Verlag, Berlin, 1982
5. H. Udin, E.R. Funk, and J. Wulff, *Welding for Engineers*, John Wiley and Sons, Inc., New York, NY, 1954
6. D. Giroux et al., Ed., *Resistance Welding Manual*, 4th ed., Resistance Welder Manufacturers' Association, Philadelphia, PA, 1989
7. E.W. Kim and T.J. Eager, Measurement of Transient Temperature Response during Resistance Spot Welding, *Weld. J. Res. Suppl.*, Vol 86 (No. 8), 1989, p 303-s to 312-s
8. A.J. Russo, Sandia National Laboratories, Albuquerque, NM, private communications, July–Dec 1988
9. E.D. Rainville, *Elementary Differential Equations*, 3rd ed., The Macmillan Co., New York, NY, 1964, p 212–224
10. W.T. Thomson, *Theory of Vibration with Applications*, 3rd ed., Prentice Hall, Englewood Cliffs, NJ, 1988, p 92
11. C.M. Harris and C.E. Crede, Chap. 8, *Shock and Vibration Handbook*, 2nd ed., McGraw-Hill Book Co., New York, NY, 1976
12. M.P. Koster, *Vibrations of Cam Mechanisms*, The Macmillan Press, Ltd., London, 1974

SELECTED REFERENCES

- L.P. Connor, Ed., *Welding Handbook*, Vol 2, 8th ed., American Welding Society, Miami, FL, 1991

Resistance Welding Power Supplies and Controls

Donald F. Maatz, Jr. and Tom Morrisett, RoMan Engineering Services

HEAT DURING RESISTANCE WELDING is generated by the flow of electrical current through the parts being joined. The main process variables are welding current, welding time, electrode force, and electrode material and design. High welding currents are required to resistance heat and melt the base metal in a very short time. The time to make a single resistance weld is usually less than 1 s. For example, a typical practice for welding two pieces of 1.6 mm (1/16 in.) mild steel sheet requires a current of approximately 12,000 A and a time of 1/4 s, while 3.2 mm (1/8 in.) sheet requires approximately 19,000 A and 1/2 s.

The function of the direct current (dc) power source or alternating current (ac) transformer for resistance welding is to deliver a predetermined amplitude of current to the welding electrodes that are clamping the workpiece. Current flows from the power source to one electrode, through the workpiece to the opposing electrode, and returns to the power source. The electrodes concentrate current into a small, usually circular area. The flow of this constricted current generates heat, concentrated largely at the interface(s) of the workpiece details to be joined.

Heat Input

The rate of heating must be sufficiently intense to cause local electrode/workpiece interface melting. The opposed electrodes apply a pressure and, when sufficient melting has been achieved, the current is interrupted. Electrode force is maintained while the molten metal solidifies, producing a sound, strong weld.

If both the local resistance of the workpiece and the welding current magnitude were constant, then the total quantity of heat, Q , developed in the workpiece would be given (in joules) by:

$$Q = I^2 R t$$

(Eq 1)

where I is the effective value of current in amperes, R is the resistance of the workpiece in ohms, and t is the duration of flow of current in seconds.

However, the resistance is not constant. Contact resistances decrease in magnitude, and the bulk resistance of the work column increases as its temperature rises. Furthermore, resistance variations of the workpiece may cause variations in the current amplitude, depending on the nature of the power source. Under these circumstances, the total quantity of heat, Q , is given by:

$$Q = \int_0^t i^2 r \cdot dt$$

(Eq 2)

where i is the instantaneous value of current expressed as a function of time, and r is the instantaneous resistance that is changing with time, t .

Equipment

Equipment Selection. The design of resistance welding machines resembles that of a "C" frame press (Fig. 1). The power source

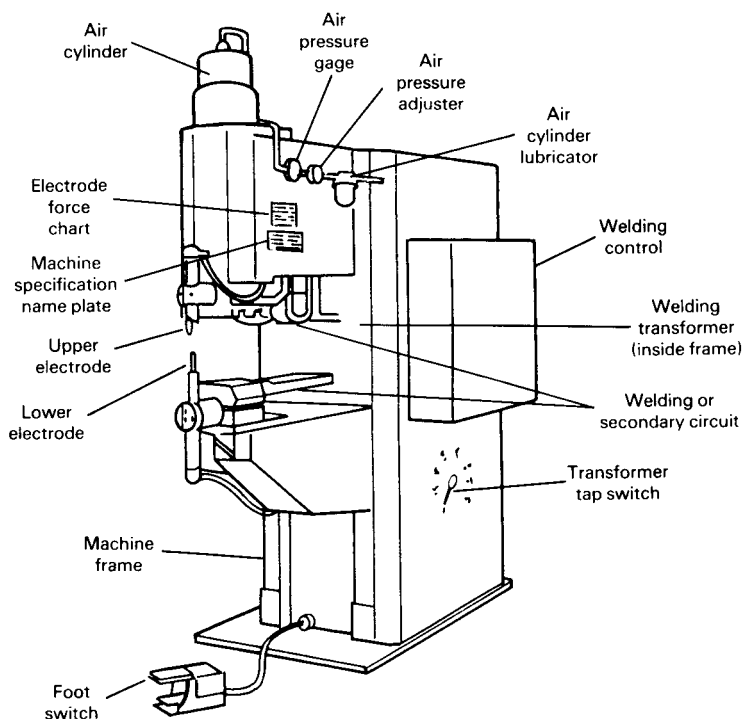


Fig. 1 Schematic showing primary components of a resistance welding machine

transformer secondary winding is connected to the electrodes on cantilevered arms, one of which provides for adjustable electrode force. Throat depth is the distance from the frame to the electrodes. Throat gap is the vertical distance between the two parallel secondary conductors. The total area of the secondary circuit (throat depth times throat gap, also known as the loop area) exerts a profound influence on output performance of an ac-operated welder. Any increase in inductance, whether due to geometry or magnetic materials within the secondary, will degrade performance and lower the power factor. Direct-current-operated welders are less susceptible to the loop area circuit inductance but nevertheless exhibit limited inductance effects.

The input to resistance welding power sources is usually 230 or 460 V utility power delivering single-phase or three-phase ac at 60 Hz. All systems require transformers to step down the line voltage to a relatively low value, with a proportional increase in current. The simplest systems consist of a transformer connected to single-phase power. More advanced sources produce a dc welding current through secondary rectification.

Single-Phase Systems. A single-phase system is shown in Fig. 2. The expected waveforms and current paths are also shown in this figure. Early single-phase systems employed ignitron tubes rather than silicon-controlled rectifiers (SCRs). The SCR began replacing ignitrons in the automotive industry as early as the late 1960s. By the 1970s, feedback systems for single-phase ac welders were available. A block

diagram for a single-phase ac welder with a feedback system is shown in Fig. 3. The earliest systems only employed local manual adjustment and were not available with remote adjustability, because this capability came about only after plantwide networks came into widespread usage. These early controls featured feedback systems that were based on an electronic signal feedback, such as the so-called dynamic resistance of the workpiece during welding, or simply systems that maintained a constant current or voltage at the workpiece. Later systems included the ability to "close the loop" around electrode displacement and other mechanical signals as well as the previously available electronic signals.

Older Rectification Systems. Single-phase dc systems have long been available. Figure 4 shows such a system and its expected waveforms for current and voltage at several places within the circuitry. These systems are based on ac weld controls, with the direct current brought about by rectification at the secondary of the welding transformer. The output current from this approach provided a direct current with a large "ac ripple," as also shown in Fig. 4. Welders with high secondary inductance provide lower ac ripple.

In primary rectification systems, a special three-phase transformer is designed with a very large iron core. Each dc pulse is limited in duration, and each is reversed in polarity to prevent saturation of the core. In the majority of applications, a weld is produced by a single impulse of direct current. For heavy gages, a pulsation

welding strategy consisting of a series of dc impulses of alternating polarity is separated by "cool time." The result is a very low-frequency alternating current. Hence, the term *frequency converter* is commonly applied to this type of power source. Figure 5 shows a three-phase half-wave primary rectified power source.

Secondary rectification systems are available in single-phase full-wave, three-phase half-wave, and three-phase full-wave forms; the latter is most commonly used. Three-phase full-wave systems consist of three single-phase transformers (or one three-phase transformer), with rectifiers connected to the secondary windings (Fig. 6). With this system, current pulse time is limited only by thermal considerations, and polarity is fixed.

The energy efficiency of a resistance welder depends on the efficiency of delivered energy at the electrodes. Energy is dissipated in the form of heat, because of resistance in the conductors. The current, I , which produces the heat of welding, is simply the secondary voltage divided by the total machine impedance, Z , plus that of the weld:

$$I = \frac{E}{Z} \quad (\text{Eq 3})$$

where Z is the vector sum of the resistance and the reactance:

$$Z = \sqrt{R^2 + X^2} = \sqrt{R^2 + (\omega L)^2} \quad (\text{Eq 4})$$

where R is the total resistance of the circuit, and $X = \omega L$ is the total reactance of the circuit (where ω equals $2\pi f$, where f is frequency, and L is the inductance).

Resistance welders designed for single-phase utility power are lowest in investment cost but highest in energy cost. The high-magnitude alternating current results in large inductive losses and a low power factor. Three-phase primary rectification and three-phase full-wave secondary rectification power sources reduce the power demand to approximately one-half and operate at a higher power factor.

The rapidly pulsing weld zone temperature inherent with a single-phase source is least desirable from a welding standpoint. In addition, copper electrodes deform from clamping impact, force, and heat, causing the occurrence of "mushrooming" (an increase in electrode contact area), which lowers current density. Mushrooming also reduces resistance in the current path. The welding current will increase because current is controlled indirectly in resistance welding machines by adjusting secondary voltage (that is, increasing or decreasing conduction time). See Fig. 7 for an example of changing conduction time. From Eq 3, a decrease in impedance causes an increase in the current. Therefore, all resistance in the work path influences the current magnitude produced by a given secondary voltage. This influence is small if total system impedance is high but significant if the system impedance is low.

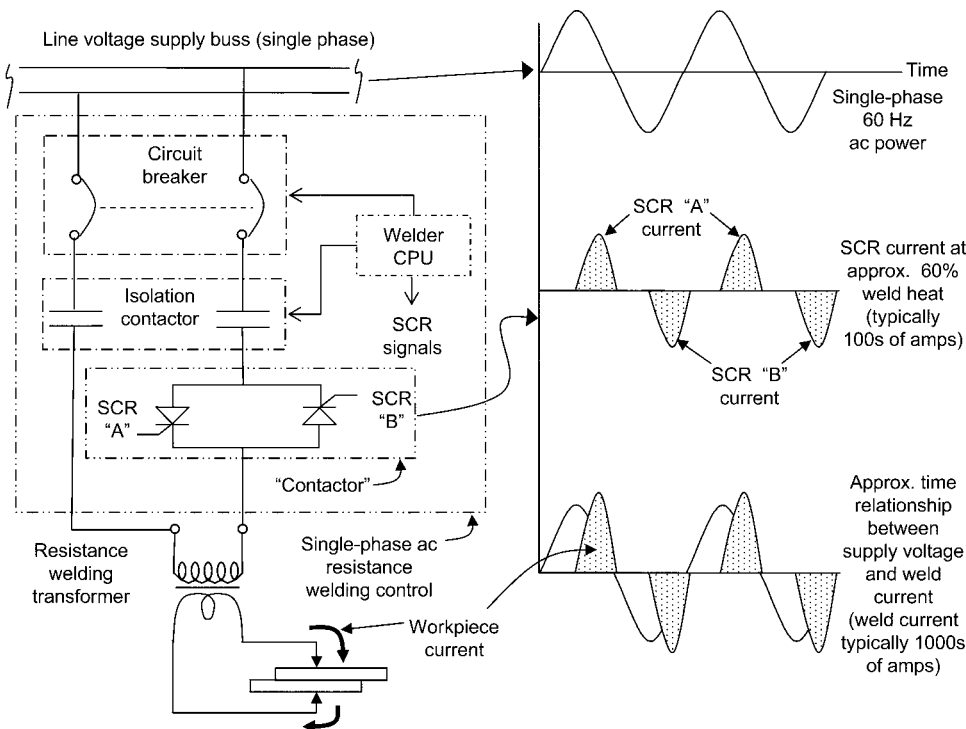


Fig. 2 Schematic for a single-phase alternating current (ac) resistance welding control without feedback. CPU, central processing unit; SCR, silicon-controlled rectifier

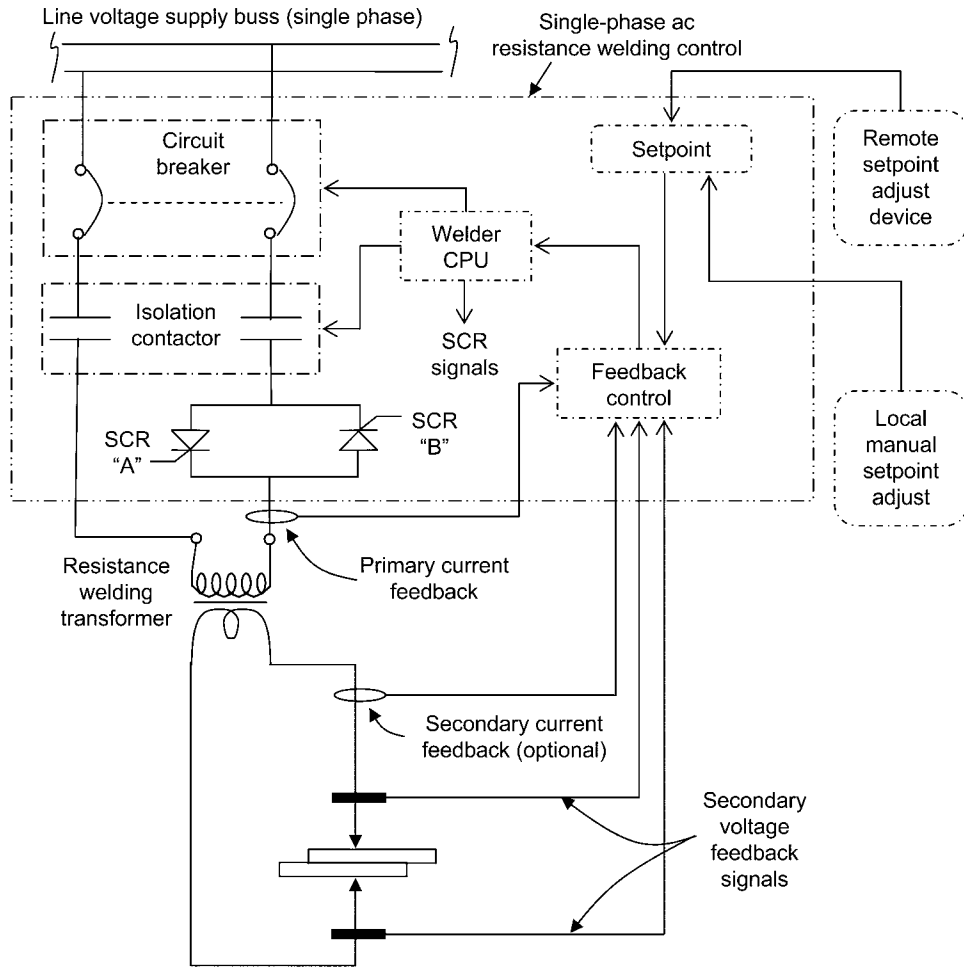


Fig. 3 Schematic for a single-phase alternating current (ac) resistance welding control with feedback. CPU, central processing unit; SCR, silicon-controlled rectifier

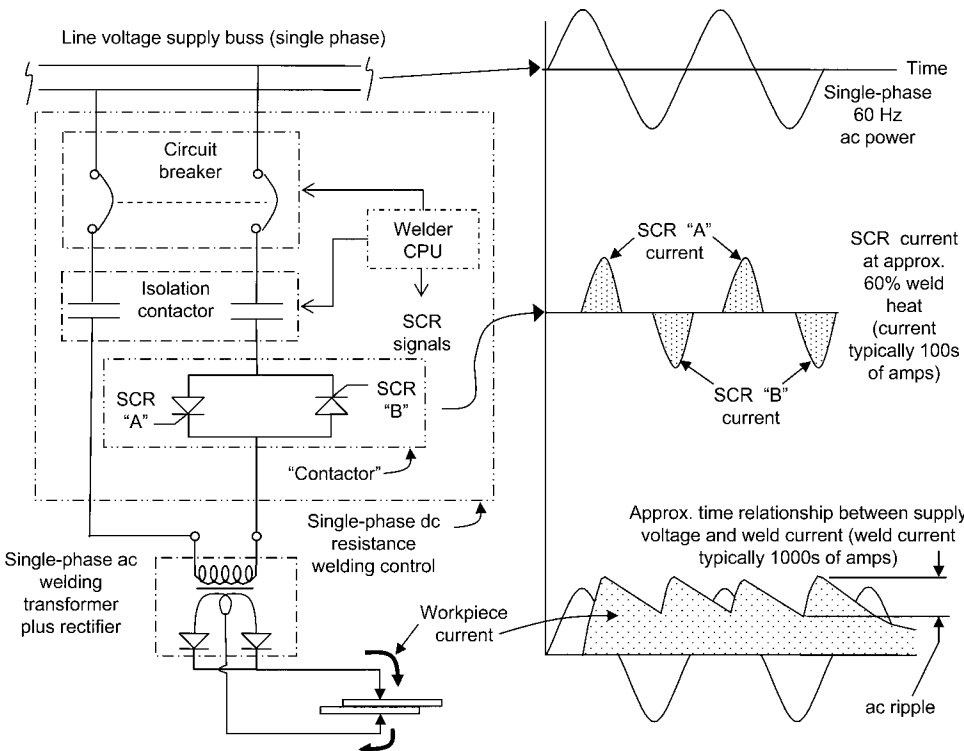


Fig. 4 Schematic for a single-phase direct current (dc) resistance welding control with feedback. ac, alternating current; CPU, central processing unit; SCR, silicon-controlled rectifier

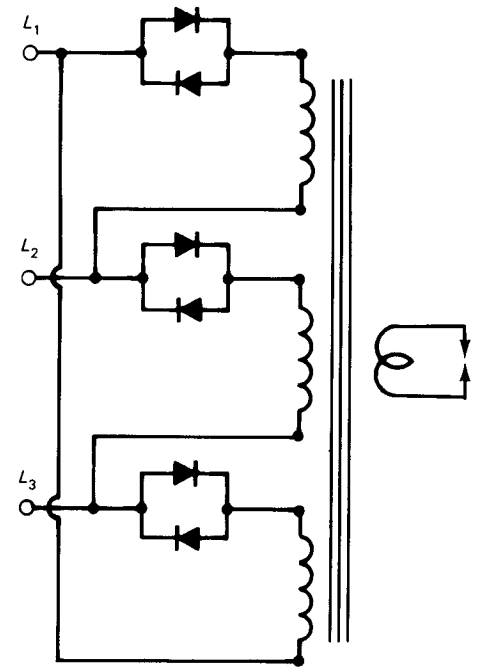


Fig. 5 Circuit diagram of three-phase half-wave resistance welding power source with primary rectification

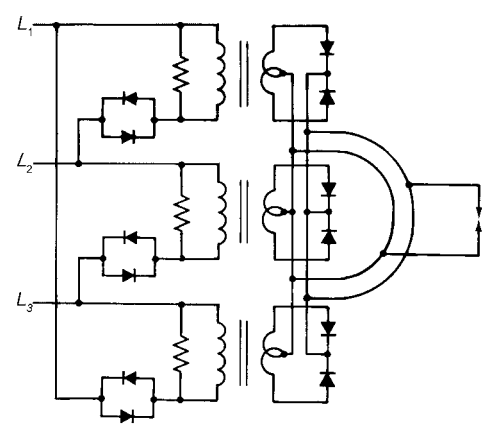


Fig. 6 Circuit diagram of three-phase full-wave resistance welding power source with secondary rectification

A three-phase primary rectification system exhibits the greatest degree of this self-compensating effect, followed to a somewhat lesser degree by the three-phase secondary rectification category.

Finally, a thermoelectric effect is associated with passing current from a copper alloy electrode to a workpiece of a given material. This phenomenon is important when welding aluminum or magnesium alloys with a single impulse. Reversing the current polarity for each successive weld, an inherent characteristic of the three-phase primary rectification system, provides the maximum electrode life between dressings.

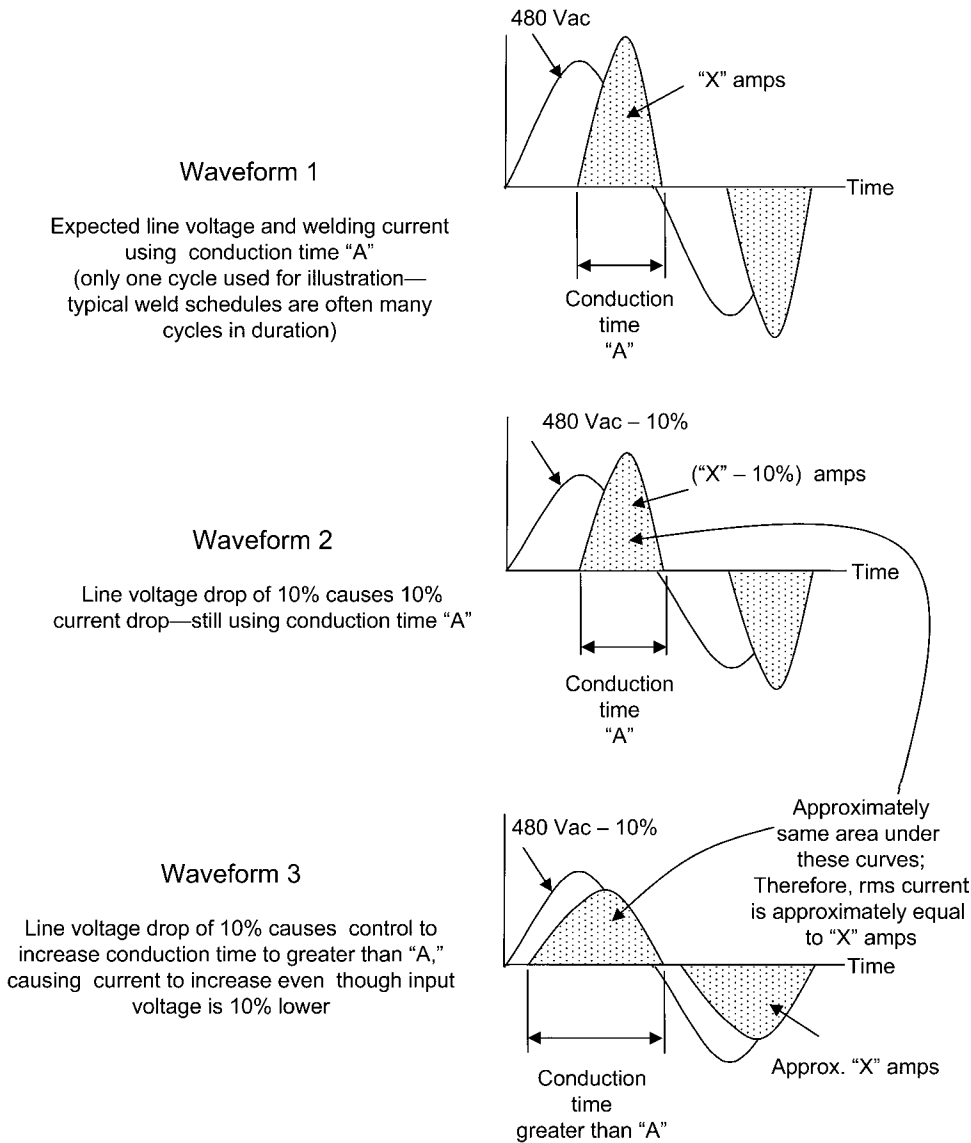


Fig. 7 Automatic voltage compensation example. Vac, volts alternating current; rms, root mean square

Newer Systems. Since the early-to-mid-1980s, newer technology has appeared that has transformed resistance welding control. Automatic voltage compensation (AVC, but known by many names) was one of the earliest feedback-type systems to be applied to large numbers of welding controls. Voltage compensation enables the welding control to take action when the input line voltage to the welder varies during the period welding is to be performed. Waveform 1 of Fig. 7 portrays the expected welding situation, where line voltage is shown as being 480 Vac, and the weld current driven in the welding transformer secondary is assumed to be "X" amperes. Waveform 2 shows an assumed instantaneous line voltage drop of 10%, resulting in weld current also dropping 10%. The AVC capability of a weld control monitors the input voltage and, in the

event of a short- or long-term voltage change, compensates for a loss (or rise) in anticipated welding current magnitude by changing the time period during which primary current is conducted through the welding transformer. In waveforms 1 and 2, the assumed conduction time is "A," meaning that for each half-cycle of weld time, the device that conducts current into the primary of the welding transformer will be on for a period equal to time "A." In waveform 3, the weld control, sensing the drop in input voltage, has increased this time to a level greater than "A," resulting in a longer half-cycle current duration but with a peak current level less than had been observed in waveform 1. The purpose of increasing the conduction time is to provide a root mean square (rms) current in waveform 3 that is equal to the rms current in waveform 1. In practice, this means that

the area under the current waveforms in waveform 1 and waveform 3 have equal areas.

By the mid-1980s, medium-frequency direct current (MFDC) controls were available. These controls provide direct current rather than the heretofore typical alternating welding current (Fig. 8). The MFDC name refers to the fact that a medium frequency (400 to 1200 Hz) is derived from the rectified three-phase power lines by using an inverter to generate an ac waveform. The medium-frequency waveform is then supplied to a specially wound welding transformer, which itself has a rectified secondary output, thus providing a dc welding current. Figure 8 shows the waveforms associated with each section of an MFDC welder.

Typically, MFDC welding controls also incorporate a feedback mechanism called constant current (CC) control. The CC responds to the actual current measurement in either the welding transformer primary or secondary circuit and can respond to dynamic changes in welding loop ac impedance (resistance to current flow in an ac circuit) or resistance in a dc welding loop. The AVC can monitor and respond only to the welding controls input voltage and is more limited in scope than the CC feedback system.

The CC level is usually entered into the weld control by the user as a setpoint. The setpoint can be manually entered but may be remotely entered by supervisory equipment, such as a programmable controller, robots, or other digital control systems/networks. The CC feedback system functions by comparing either the primary or secondary welding transformer current with the desired current setpoint (Fig. 9). If the measured weld current is below the control setpoint current level, the control automatically increases the output to force the measured current to match the setpoint current. Various weld control manufacturers use different software algorithms to achieve this result, and algorithms vary from relatively simple to rather complex.

The advantage of CC lies in the fact that power developed in the weld varies at the square of the welding current level. Therefore, a 10% drop from the required welding current level, if not corrected, will result in a 19% drop in weld power.

Constant current may also be used on ac weld controls, but the method suffers somewhat due to the limitations imposed by 60 Hz weld current adjustment. Typically, several weld cycles (16.67 ms per cycle at 60 Hz) must be measured prior to taking current modification action, and if the weld time is short (say 6 to 7 cycles), there is little time over which the control can compensate the measured current to match the setpoint current. Aggressive control action, such as attempting to achieve the desired current in a limited number of cycles, may cause overshoot (i.e., weld current in excess of the setpoint level) and hunting, where the weld current oscillates above and below the setpoint level. A nonaggressive algorithm may result in not achieving parity between current

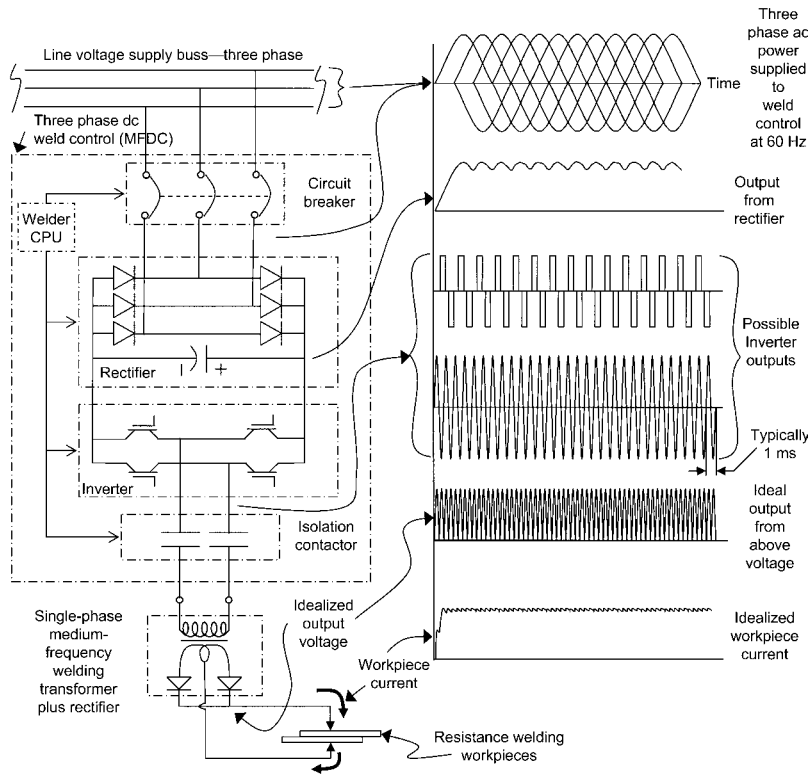


Fig. 8 Medium-frequency direct current (MFDC) resistance welding control block diagram and waveforms without feedback. CPU, central processing unit; ac, alternating current

measurement and setpoint within the weld time used to perform the weld. Because each weld control supplier typically has a proprietary method for adjusting their CC algorithm, minor differences in response may be expected.

Duty Cycle. Resistance welding is inherently an intermittent process with a series of very short current periods followed by “off” or “cool” periods. Therefore, this type of power source is rated on a 50% duty cycle and a 1 min integrating period. The relationship between kVA rating at 50% duty cycle and kVA demand at actual duty cycle is as follows:

$$kVA_{50\%} = kVA_{Demand} \sqrt{2 \cdot (D.C.)} \quad (Eq 5)$$

where D.C. is the duty cycle in percent, entered in the form of a decimal. Duty cycle is defined by:

$$D.C. = \frac{N \cdot T}{60 \cdot f} \quad (Eq 6)$$

where N is the number of welds per minute, T is the weld time in cycles, and f is the frequency in hertz.

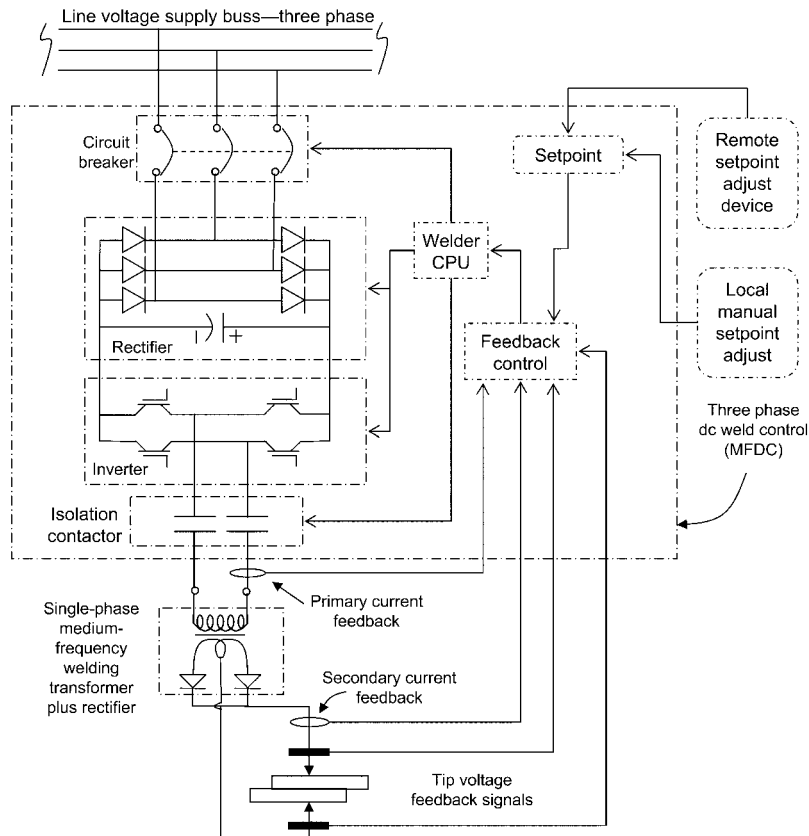


Fig. 9 Medium-frequency direct current (MFDC) resistance welding control with feedback. CPU, central processing unit

Resistance Spot Welding

Murali D. Tumuluru, United States Steel Corporation

RESISTANCE SPOT WELDING (RSW) is a process in which faying surfaces are joined in one or more spots by the heat generated by resistance to the flow of electric current through workpieces that are held together under force by electrodes. The contacting surfaces in the region of current concentration are heated by a short-time pulse of low-voltage, high-amperage current to form a fused nugget of weld metal (Fig. 1). When the flow of current ceases, the electrode force is maintained while the weld metal rapidly cools and solidifies. The electrodes are retracted after each weld, which usually is completed in a fraction of a second.

In RSW, the weld nugget (melted and resolidified region) forms at the faying surfaces (Fig. 1) but does not extend completely to the outer surfaces. The weld should be at a sufficient distance from the edge of the workpiece (edge distance) so that there is enough base metal to withstand the electrode force and to ensure that the local distortion during welding does not allow expulsion of metal from the weld.

Resistance spot welding is a common form of resistance welding. Most ferrous alloys can be resistance spot welded if the appropriate equipment is used with suitable welding conditions. This is particularly true for thin sheet or strip steel products, whether uncoated or coated. Weldability and the thickness of the metals joined are key factors in determining whether two materials can be resistance spot

welded. Many nonferrous alloys can be resistance spot welded also, as indicated in Table 1.

Spot welding is the most widely used joining technique for the assembly of sheet metal products, such as automotive body-in-white assemblies, domestic appliances, furniture, building products, enclosures, and, to a limited extent, aircraft components. Many assemblies of two or more sheet metal stampings that do not require gastight or liquidtight joints can be more economically joined by high-speed RSW than by mechanical methods. Containers frequently are spot welded. The attachment of braces, brackets, pads, or clips to formed sheet metal parts such as cases, covers, bases, or trays is another common application of RSW.

Major advantages of spot welding include high operating speeds and suitability for automation and inclusion in high-production assembly lines as well as other manufacturing operations. Repetitive spot welding can be carried out by the use of robots, as is commonly done in automotive assembly plants. With automatic control of current, timing, and electrode force, sound spot welds can be produced consistently at high production rates and low unit labor costs using semiskilled operators. However, RSW is primarily used for sheet products generally ranging in thickness from 0.7 to 3 mm (0.03 to 0.12 in.). For RSW, accessibility from both sides of the joint is essential to be able to hold the workpieces and pass current

for welding. On-line nondestructive testing of resistance spot welds is still unreliable, and methods for nondestructive testing of joints are still evolving.

Process Description

The four basic resistance welding processes (spot, projection, seam, and flash welding) are

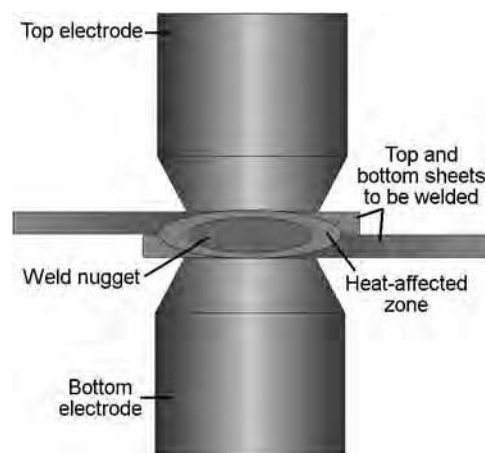


Fig. 1 Cross-sectional sketch of resistance spot welding of two sheets

Table 1 Relative weldability ratings of selected metal and alloy combinations used for resistance spot welding operations

A, excellent; B, good; C, fair; D, poor; E, very poor; F, impractical

Metals	Aluminum	Stainless steel	Brass	Copper	Galvanized iron	Steel	Lead	Monel	Nickel	Nichrome	Tinplate	Zinc	Phosphor bronze	Nickel silver	Terneplate
Aluminum	B	E	D	E	C	...	E	D	D	D	C	C	C	F	C
Stainless steel	F	A	E	E	B	A	F	C	C	C	B	F	D	D	B
Brass	D	E	C	D	D	D	F	C	C	C	D	E	C	C	D
Copper	E	E	D	F	E	E	E	D	D	D	E	E	C	C	E
Galvanized iron	C	B	D	E	B	B	D	C	C	C	B	C	D	E	B
Steel	D	A	D	E	B	A	E	C	C	C	B	F	C	D	A
Lead	E	F	F	E	D	E	C	E	E	E	...	C	E	E	D
Monel	D	C	C	D	C	C	E	A	B	B	C	F	C	B	C
Nickel	D	C	C	D	C	C	E	B	A	B	C	F	C	B	C
Nichrome	D	C	C	D	C	C	E	B	B	A	C	F	D	B	C
Tinplate	C	B	D	E	B	B	...	C	C	C	C	C	D	D	C
Zinc	C	E	E	E	C	F	C	F	F	F	C	C	D	F	C
Phosphor bronze	C	D	C	C	D	C	E	C	C	D	D	D	B	B	D
Nickel silver	F	D	C	C	E	D	E	B	B	B	D	F	B	A	D
Terneplate	C	B	D	E	B	A	D	C	C	C	C	C	D	D	B

based on electrical resistance to build up the heat necessary to produce a weld. For a given current, the amount of heating is proportional to the electrical resistance (R) of the conductor, as shown in Fig. 2. Heating is greatest at the interface of the two surfaces being joined, because the resistance at the interface (R_i) is larger than the resistance of the metal (R_m) or at the surface contact resistance (R_c) between the metal and electrode. Heating of metals also typically increases resistivity and thus promotes more rapid heating.

In spot welding, the size and shape of the electrodes determine the size, shape, and

position of the weld nugget. For example, if the two electrodes have identical face diameter between two workpieces of equal thickness, the weld nugget forms exactly at the interface between the workpieces, and electrode indentation is equal on both sides (Fig. 3a). In contrast, if the upper electrode face has a large, flat area compared to the lower electrode face, current density on the top surface is reduced. This reduces the heating effect of the top electrode and concentrates the center of heating and the resultant weld nugget toward the smaller electrode face (Fig. 3b). Such a weld nugget may be appropriate if the top surface were an

appearance piece requiring minimum electrode indentation.

In another situation, heat imbalance is used to improve welds on workpieces of unequal thickness (Fig. 4). The lower electrode face is smaller than the upper, which ensures that the weld nugget will grow into the thinner workpiece. Without such imbalance, the nugget may grow entirely in the thicker of the two workpieces. Thus, various methods of spot welding are available to ensure solid welds despite the configuration of the workpieces.

The simplest type of spot weld is a direct, single-spot weld (Fig. 5). In a direct weld, the

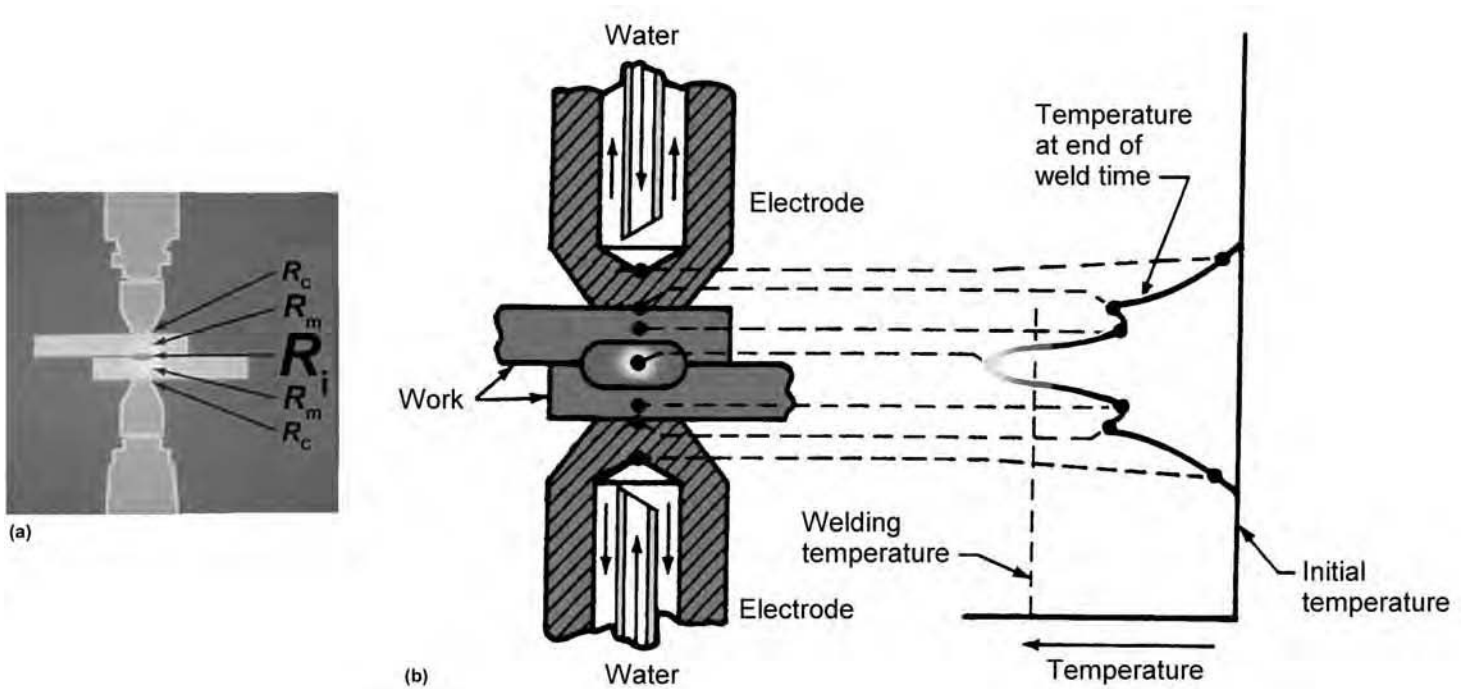


Fig. 2 Resistance and heating profiles in spot welding. (a) The larger resistance at the interface (R_i) results in (b) greater heating and melting for a fusion weld at the interface between the two workpieces. R_c , surface contact resistance; R_m , resistance of the metal

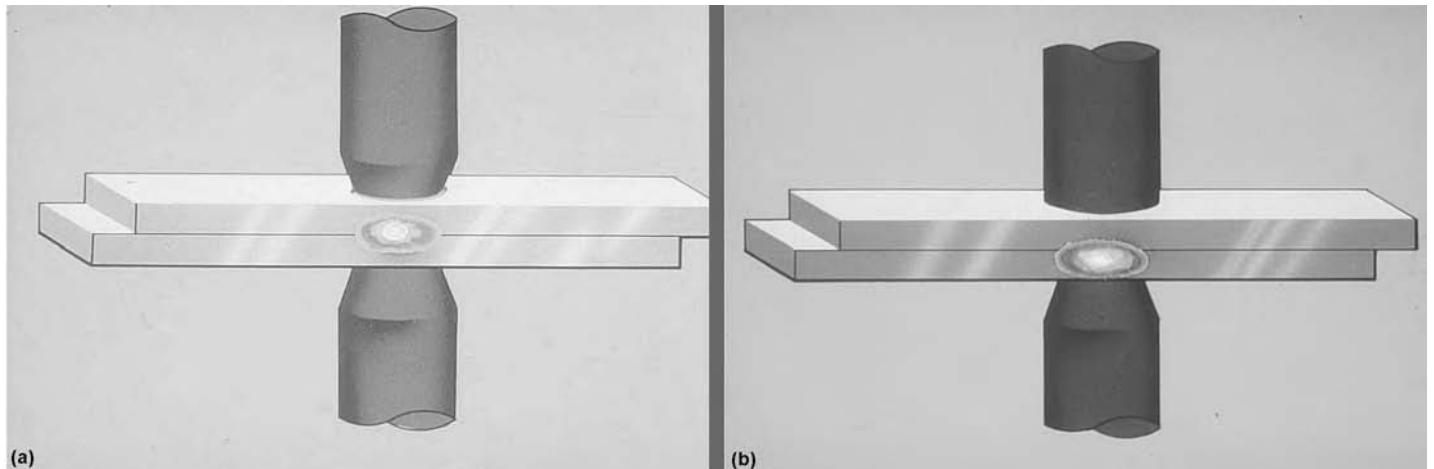


Fig. 3 Effect of electrode diameter on locations of heating zone. (a) Heating zone at midway between electrodes of equal diameter. (b) Heating zone concentrated toward the smaller-diameter electrode

welding current flows from the transformer to the electrode, through the weld to the second electrode, then back to the transformer. If the electrode cannot reach the bottom side of a workpiece, the one side of the transformer or an electrode may be connected to a mandrel or shunt bar, as shown in Fig. 5(b) and (c).

A series of direct spot welds also can be done when the two electrodes are connected to opposite ends of the transformer secondary but both contact the same workpiece (Fig. 6). Two welds are formed simultaneously with the same weld current. The current flows from one weld to the other through a copper shunt bar located below the lower workpiece. Series spot welds are done if the welding guns cannot reach the bottom side of a workpiece.

The disadvantage of a series weld occurs when the thicker section acts as the shunt (Fig. 6b) in dissimilar gage joining. Sixteen-gage steel sheet (1.52 mm, or 0.0598 in.) or heavier metal conducts too much of the secondary current through the top sheet, never allowing it to reach the weld interface to form a weld. This shunt current creates undesirable surface heating at the electrodes. Series welding is appropriate only for steel sheet metal of 18 gage (1.2 mm, or 0.0473 in.) or less. Therefore, when the top sheet is sixteen gage or heavier, indirect welding is used (Fig. 7). The heat balance during indirect welding is not as good as that in direct welding, but the method avoids the critical imbalance of series welding.

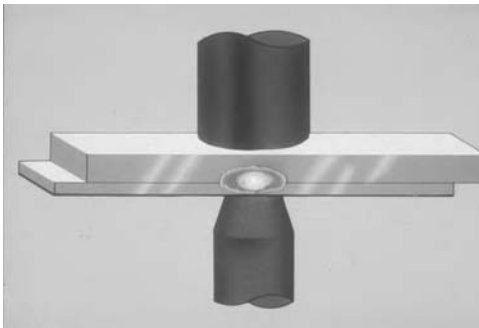


Fig. 4 Smaller electrode diameter to concentrate welding zone closer to a thinner section

Equipment

The equipment needed for RSW can be simple and inexpensive or complex and costly, depending on the degree of automation. Spot welding machines are composed of three principal elements:

- **Electrical circuit:** Consists of a welding transformer, tap switch, and a secondary circuit
- **Control circuit:** Initiates and times the duration of current flow and regulates the welding current
- **Mechanical system:** Consists of the frame, fixtures, and other devices that hold and clamp the workpiece and apply the welding force

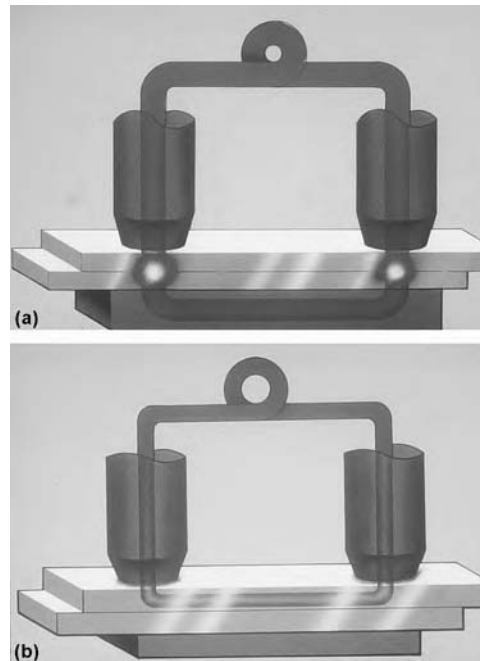


Fig. 6 Series direct spot weld. (a) Good conduction through the shunt and formation of two welds. (b) Current shunting in heavier-gage top section, which prevents weld formation and causes overheating at the contact points of the two electrodes

Specifications for resistance welding equipment have been standardized by the Resistance Welding Manufacturers Alliance (RWMA), which is a subcommittee of the American Welding Society. The RWMA also issues specifications for resistance welding equipment.

The transformer used in direct energy resistance delivers the power to the workpiece by changing the input high-voltage, low-amperage, alternating current (ac) in the primary winding to a low-voltage, high-amperage current in the secondary winding (Fig. 8a). This system forms the basis of pedestal, or gun-type, welding machines, where the output of the secondary transformer is applied directly to the welding electrodes.

More complex secondary circuits and electrode configurations are for making single or multiple welds with multiwelder machines (see subsequent information). Multiwelder machines are used in various high-production industries, such as automotive or appliance and sheet metal assembly (Fig. 9). To minimize the size and cost of multiwelders, transformers can be designed with two or more secondary circuits supplied from the same primary circuit. This design is achieved by using transformers in which the primary current is supplied to two or more separate secondary windings.

Split or multiple secondary transformers are generally used to produce four or more welds at the same time. One controller is used for control of the timing and current supplied to the electrode, which means that it is not possible, under these circumstances, to achieve individual control or setting of the welding conditions for each pair of welding electrodes. Difficulties can arise in optimizing the necessary welding conditions to maximize the electrode life for each welding station under these conditions. In addition, the possibility exists for developing shunt currents, or an out-of-balance welding current, between each secondary circuit.

Power Supplies. Midfrequency direct current (MFDC) is the newest type of power source being used in the resistance welding industry. The frequency used in an MFDC power source is normally 1000 to 1200 Hz. The transformer secondary has diodes that

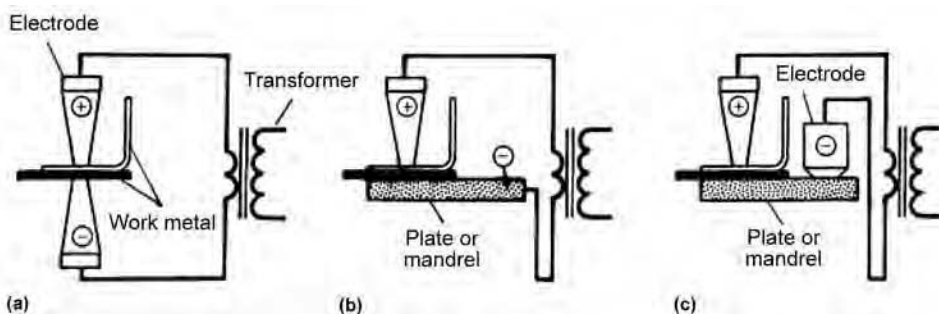


Fig. 5 Direct spot welding of single welds. (a) Electrodes directly above and below the weld zone. (b, c) Direct weld with conduction through a platen

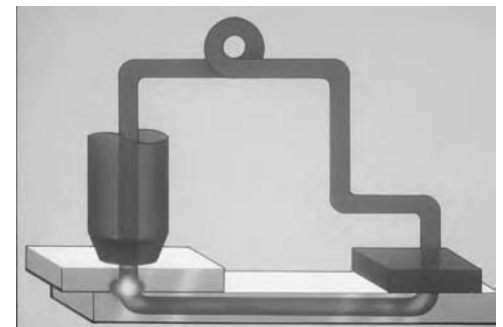
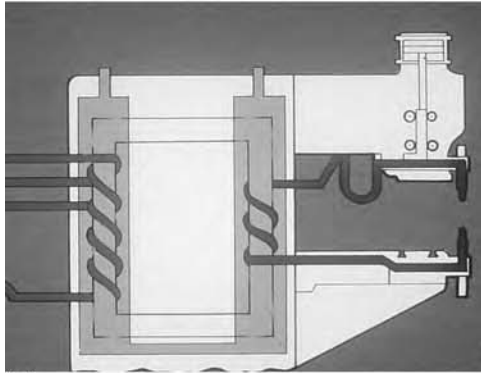


Fig. 7 Indirect spot weld. Current flows along the length of the bottom section (rather than through it, as in the case of direct spot welds).

convert current to 1000 to 1200 Hz direct current (dc) for welding. This type of power source was developed to reduce the size of the welding transformer, so that it could be incorporated into a welding gun that would go on the end of a robot. The reduction in the transformer size allows smaller robots to be used and improves the electrical efficiency over a standard 60 Hz ac power source. The improved electrical efficiency accounts for the popularity of MFDC power sources, especially in countries where



(a)



(b)

Fig. 8 Pedestal spot welder. (a) Schematic of primary and secondary transformer coils. (b) General-purpose welder (Resistance Welding Manufacturers Alliance size 0) with welding current up to approximately 35,000 A and step switch to provide various secondary voltages. Courtesy of R. Matteson, Taylor Winfield Technologies

power is expensive. The higher frequency makes better use of the transformer core, resulting in smaller-sized (therefore lighter) transformers.

An advantage of MFDC power sources is that the welding control cuts the waveform at a higher frequency. This allows for adjustment in the firing angle 20 times more often than in a 60 Hz system. The disadvantages of MFDC power sources are high cost and power limitations, both of which are improving every year. Seam welding is now becoming possible where spot welding had been the capability from a duty-cycle standpoint.

Secondary Impedance. The electrical characteristics of a spot welding machine are best defined in terms of their effect on the impedance of the secondary circuit. The latter is composed of two components:

- *Reactance:* Determined primarily by the depth and height of the throat of the machine and the amount of steel in the throat. Another critical factor is the frequency of the applied current.
- *Resistance:* Depends on the length and cross section of the conductors. Conductor material and operating temperature must also be considered.

Cables can be classified into three types: air-cooled jumper cables, water-cooled jumper cables, and kickless cables. In any application, it is necessary to ensure that the type and dimensions of cables are chosen to achieve the best balance between the total circuit resistance and the electrode life to be obtained with a multiple spot welder.

Single-Weld Configurations

Most pedestal and portable gun-welding machines employ direct welding, where the current flows directly through the welding electrodes and the workpiece to produce a single weld. In areas of difficult access, indirect welding may be necessary. Indirect welding is generally used when welding is carried out using either stationary or indexing welding guns and when access to the sheets being welded is limited to one side. In this case, the backing electrode generally consists of a large bar or platen, and the welding current flows from one side of the transformer secondary to the active electrode, through the welded area, and then along the platen/bar electrode or connecting jumper cable to the dummy electrode, which is connected to the other leg of the transformer secondary.

Higher welding currents are generally necessary when using dummy welding guns, which can lead to a shorter electrode life. The extent to which larger currents are required depends largely on the distance between the welding electrode and the dummy return electrode. In a multi-welder, this distance can be either fixed or variable, depending on whether a stationary or indexing head is used. Both types of welding heads can lead to losses due to stray current paths and extensive shunting of the current through jigs and fixtures. These factors must be considered in any design concept for a multiwelder station.

Two-Weld Configurations

Because of the need to minimize the number of transformers and the overall size and cost of



Fig. 9 Multigun welder with small double- and triple-piston air-operated guns and compact package transformers. Courtesy of R. Matteson, Taylor Winfield Technologies

a multiwelder, it is necessary to use configurations whereby two welds are made in one stroke of an electrode. Parallel, series, or push-pull welding configurations are used for this purpose.

In parallel welding, two or more direct welds, usually closely spaced, are made simultaneously with all upper electrodes connected to one side of the transformer and all bottom electrodes connected to the other side of the transformer (Fig. 10). Parallel welding has the advantage of lower shunt currents, thereby allowing shorter interweld spacings to be used. However, if two or more circuits are fed from a common transformer secondary winding, the current in each circuit will not be equal unless the impedances of each circuit are identical. This is often difficult to achieve in practice, and the electrode life obtained can therefore be different for each of the electrode pairs connected to the same transformer.

Series and Push-Pull Welding. As noted, two simultaneous welds can also be produced by means of series welding in which the secondary circuit is connected to two contoured electrodes that contact the workpiece from the same side, and a current backup bar/platen is used on the reverse side (Fig. 6a). Series spot welding circuitry ordinarily requires a large secondary loop because of the need for conducting the welding current around the large working area.

When direct welds are needed in the center of a deep workpiece, a set of transformers is used in a push-pull configuration (Fig. 11). The upper set of transformers matches the lower set, and it eliminates the need for long cable loops to the electrodes, resulting in lower secondary impedance. A longer electrode life can be obtained in push-pull welding compared to series welding.

It should also be noted that current shunting (Fig. 6b) between the electrodes occurs in both series and push-pull welding configurations, but to a lower extent in the latter. The magnitude of the shunt currents depends on interelectrode

distance and the type of material being welded. In all cases, current shunting will lead to a lower electrode life when welding zinc-coated steels, due to the need to use higher welding currents to compensate for the shunt currents (this can also lead to additional electrode sticking problems) and to the rapid falloff in weld size that occurs under conditions where current compensation is insufficient or nonexistent.

To some extent, the effects of both high secondary circuit impedance and current shunting can be overcome by using a constant-current facility fitted into the welding machine control circuit, but there is a limit to the effectiveness of these controls in a production situation. In addition, dc welding systems can be used in which secondary inductance/reactance effects are minimized. However, the effectiveness of using dc depends on the method used to develop the dc waveform and on the extent of the superimposed ac ripple on the dc waveform.

Machine Construction

Welding operations in highly automated production lines are based primarily on multiple spot welders and robotic cells. In addition, manual welding operations can be used to manufacture either subassemblies, which are fed into the main production/assembly lines, or, in many instances, finished products. These differing end uses require welding machines of varying designs and characteristics. The RSW machines can be divided into three basic types:

- Pedestal-type welding machines
- Portable welding guns
- Multiple spot welding machines incorporating lightweight gun welding units

Pedestal-type welding machines form the basis of most resistance spot or projection welding operations. Standard machines are either of the rocker arm type, as determined by the rocker action of the moving upper

electrode arm, or stationary, direct-acting machines. The latter outnumber the former because rocker arm machines are difficult to align due to the movement of the electrode in an arc motion. As the electrode wears, various skidding actions can be created between the upper and lower welding electrodes, depending on the extent of the electrode wear. This can change the point at which the electrodes meet relative to the fulcrum point of the moving arm. If the electrodes meet at a point above the fulcrum point, they have a tendency to slide outward from the machine. On the other hand, if the electrodes meet on a line below the fulcrum of the moving arm, the electrodes show a tendency to slide inward toward the machine. These relative movements can be different between the top and bottom electrodes, a consequence of which is a reduction in electrode life, particularly if welding coated steels. Other advantages of direct-acting machines include a lower electrode assembly mass, faster "followup" during welding, and a degree of rigidity that is impossible to obtain with an ordinary rocker arm machine. Press-type direct-acting machines have an upper electrode and welding head that move vertically in a straight line. The welding head is guided in bearings or guideways of sufficient proportion to withstand the offset loads imposed upon them. All of these factors tend to increase the electrode life obtained in a particular welding cell.

Portable welding guns are used in RSW when it is impractical or inconvenient to transport the work to the machine. The portable welding gun consists of water-cooled electrode holders, an air or hydraulic actuating cylinder, hand grips, and an initiating switch. The gun usually is suspended from an adjustable balancing unit, and the welding force is supplied by an air cylinder. Because of the high secondary losses of portable machines, transformers used in these machines have a secondary voltage two to four times as great as the voltage of transformers used in stationary machines of equal rating.

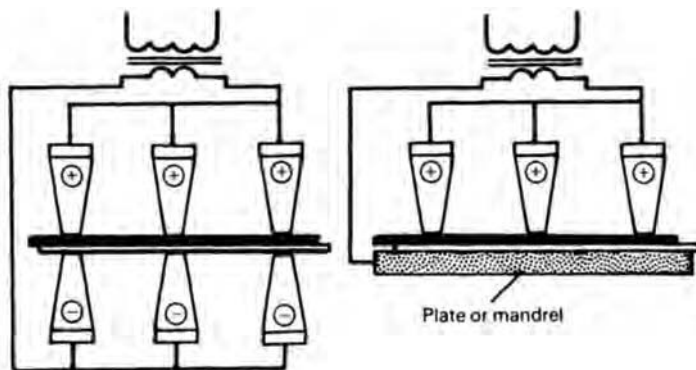


Fig. 10 Parallel welding for multiple spot welds with one transformer connected to multiple electrodes

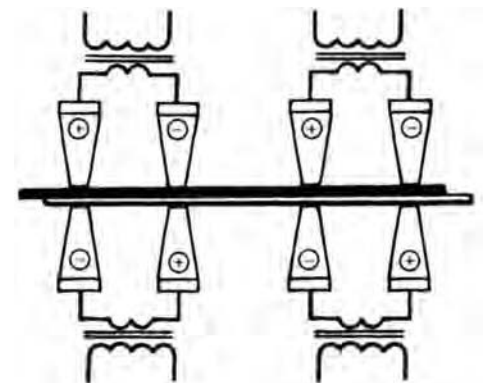


Fig. 11 Two sets of push-pull transformer arrangements for direct spot welding

Welding current is transmitted between the transformer terminals and gun terminals through a secondary cable, usually of the low-impedance or kickless type. The reactance of this type of cable is near zero, which results in a high power factor and reduced kilovolt-ampere demand. For safety reasons, the current initiating switch is usually operated at low voltage. Recent developments in encapsulated transformers and high-speed fail-safe devices enable the transformer to be integral with the welding gun. This results in lower secondary losses and is particularly preferred in robotic applications.

Gun welders typical of portable manually operated and robotic welding cells can be classified into two basic types:

- S-type (scissors)
- J-type (direct action or C/J type)

Two important features that influence the performance of these types of welding guns are the rate of force buildup and the extent to which the arms of the gun deflect under load. These features characterize the welding gun in terms of rigidity and the mechanics involved in their operation. An S-type gun uses a lever action to transmit the force applied by the cylinder head to the welding electrodes. However, due to an unbalanced pivot point, the force measured at the electrodes is less than that applied at the cylinder. With J-type welding guns, the force applied by the pneumatic cylinder is transmitted directly to the welding electrode. The rigidity of the framework of the welding gun is characterized by the extent to which the electrode arms deflect on application of the electrode force. This is an important factor in determining weld quality and the amount of skidding that can occur between the two welding electrodes. It should be noted that extensive skidding can lead to elliptical welds and/or decreased electrode life.

Welding guns are typically actuated by pneumatic cylinders. The electrodes move the entire range of the cylinder when the gun opens and closes. Clamping force is normally controlled by a pressure regulator, and the electrode force is measured using load cells. Pneumatic guns typically have two cylinders; one is used for short opening and the other creates a full opening between the top and the bottom electrodes.

The new trend in welding guns is the use of motor-controlled servo guns. The servo gun can provide a predetermined electrode opening anywhere in the full range of gun travel. Electrode force can be programmed to any desired value during a welding cycle or can be varied from weld to weld and different material-thickness stackups. Pneumatic guns close at full clamping force, which creates a high impact force on the electrode tips. The servo gun controls the rate at which the electrodes come together. The servo gun can also ramp up to the clamping force at a predetermined rate

that can be programmed. This controlled movement of the electrode lessens the impact between the electrode and parts to be welded, thereby extending the electrode life. This is perhaps one big reason that automotive manufacturers have started using servo guns. Another advantage of servo guns is that they make it possible to use a combination of multicurrent and electrode force control. This makes it possible to control the heat input into the base materials, thereby achieving fusion between the sheets and, at the same time, preventing weld-metal expulsion. The use of multistep force control has made it possible to weld advanced high-strength steels (minimum tensile strength >590 MPa, or 85 ksi) and combinations of high- and low-strength steels as well as sheets of dissimilar thickness (Ref 1).

Welding Electrodes

Electrodes in RSW perform the following major functions:

- Conduct the welding current to the workpieces
- Transmit the amount of force needed to the workpieces in the weld area to produce a satisfactory weld
- Rapidly dissipate the heat from the weld zone

During the welding operation, the electrodes are subject to great compressive stresses at elevated temperature and must be frequently dressed and periodically replaced. Because the current conducted to the workpieces must remain localized within a fixed area, the electrodes must resist these stresses without excessive deformation or mushrooming. The electrode force, in addition to forging the heated workpieces together, influences the passage of current to the localized area.

Maintenance. The shape, dimensions, and surface condition of the electrode tips or contact surfaces are important for consistent weld quality in RSW. The shape and dimensions of electrode tips are affected by mechanical wear and deformation, or mushrooming, at a rate depending on tip material and design, operating temperatures, rates of heating and cooling (thermal shock), and welding force.

Alloying between the electrode tip and the work metal can greatly increase the rate of deterioration of the electrode tip. Deterioration is especially rapid when copper alloy electrodes are used in welding work metal coated with tin, zinc, or aluminum, which alloy readily with the electrode metal.

Careful attention to electrode tip condition is needed to avoid such defects as weak or missed welds, irregularly shaped welds, erratic indentation, burning or discoloration of the work surface, surface melting, and electrode deposits on the work surface. Electrode tips should be

dressed and replaced at scheduled intervals. Preventive maintenance is particularly important when multiple electrode holders are used to ensure uniformity of resistance of each spot.

Materials for RSW electrodes should have sufficiently high thermal and electrical conductivities and sufficiently low contact resistance to prevent burning of the workpiece surface or alloying at the electrode face. In addition, the electrode should have adequate strength to resist deformation at operating pressures and temperatures. Because the part of the electrode that contacts the workpiece becomes heated to high temperatures during welding, hardness and annealing temperatures must also be considered. Electrode materials for RSW have been classified by the RWMA (Ref 2) and in International Standards Organization (ISO) standard ISO 5821 (Ref 3).

When welding two sheets of thickness up to 3 mm (1/8 in.) using truncated cone-type electrodes, the electrode tip diameter should be determined from:

$$d_2 = \sqrt{t} \quad (\text{Eq 1})$$

where d_2 is the initial tip diameter (in millimeters), and t is the thickness (in millimeters) of the sheet in contact with the electrode. When using truncated cone electrodes, the initial or set-up weld diameter should be equal to the diameter of the electrode tip:

$$d = d_2 = 5\sqrt{t} \quad (\text{Eq 2})$$

where d is the weld diameter (in millimeters). When welding two sheets of dissimilar thicknesses, the electrode dimensions and the required weld size should be specified appropriate to the thinner sheet thickness. In the case of three thicknesses, the second-thinnest sheet should be used.

When using domed or pointed electrodes, Eq 1 may not apply, and the electrode dimensions will depend on accessibility and flange width. In this case, the electrode tip dimensions and welding conditions should be chosen to give an initial weld diameter as specified in Eq 2. Where a pad or mandrel is used as the second electrode, its surface must be maintained to match the profile of the work.

During normal production, electrodes tend to mushroom, leading to an increase in electrode tip size. According to trends in automotive industry practice and international standards, the diameter of at least one of the electrode tips should not normally be allowed to increase above a value that results in a reduction greater than 30% from the starting weld diameter during a production run. This is equivalent to an increase in the electrode diameter to $1.3d$. When this diameter has been reached, the electrode should be replaced or redressed to its original size and contour. To maintain weld integrity, it is important to maintain weld shape and size and to prevent electrode mushrooming

(widening of the electrode face). A direct relationship exists between the weld size and the weld strength, with the strength increasing as the weld size is increased. Electrode mushrooming happens with use and is accelerated by the use of higher electrode forces required to successfully weld high-strength steels. To maintain weld size above the minimum required value (typically taken as four times the square root of the thickness of the sheets being welded), electrodes should be frequently dressed. It has become a common practice with many automotive companies to dress the electrodes after every 30 welds. Another practice for maintaining weld size is to use current steppers. The current steppers allow for a gradual increase in welding current, typically after every 200 welds, to maintain constant current density at the electrode-sheet interface. The drawback of the use of steppers is that this practice assumes a certain electrode tip life and preprograms current increase at regular intervals. The use of frequent electrode tip dressing is a more efficient way to maintain consistent weld size than the use of current steppers. Many fabricators, especially in automotive body fabrication, have resorted to the practice of frequent electrode tip dressing to improve weld quality and reliability of manufacturing practice.

Electrode shapes have been standardized by the RWMA. Figure 12 shows the six standard face or nose shapes, identified by letters "A" through "F" (Ref 2). Electrodes with type A (pointed) tips are used in applications for which full-diameter tips are too wide. Type D (eccentric, formerly called offset) face is used in corners or close to upturned flanges. Special tools are available for dressing the electrode faces, either in or out of the welding machine. It should be noted that electrode shape classification in accordance with ISO 5821 (Ref 3) is totally different from that in the RWMA classification. Due to the increased globalization of procurement by various companies, the use of the ISO standard for specifying electrode shapes is becoming popular.

The dome-shaped electrode (type B) and the truncated cone (type E) are commonly used in the automotive industry. The present trend is to use the dome-shaped electrodes. The reason for the popularity of dome-shaped electrodes is that they tend to stabilize quickly when welding coated steels and thus produce a consistent weld size soon after stabilization. To compensate for changes in weld size when making welds with new electrodes, especially when welding coated steels, a weld-size stabilization procedure is typically employed during laboratory evaluation of weldability of steels. The stabilization procedure conditions the electrode faces, thus stabilizing the weld size and promoting reproducible test results. The electrode stabilization procedure consists of adjusting the welding current as needed to maintain a specified or desired weld size.

Electrode Coolant Parameters. Generally, it is recommended that the water flow to the electrodes be a minimum of 4 L/min (1.1 gal/min) for welding two uncoated steel sheets of thickness up to and including 3.0 mm ($\frac{1}{8}$ in.). Higher flow rates are recommended when welding coated steels. The internal water cooling feed tube should be arranged to ensure that the water impinges onto the back working face of the electrode. The distance between the back and the working face of the electrode should not exceed the values given in the appropriate ISO or RWMA standard. The inlet water temperature should not exceed 20 °C (70 °F), and the outlet temperature should not exceed 30 °C (85 °F). To maintain these temperature levels, the electrode cooling water supply should be independent of transformer and thyristor water cooling circuits. Separate water circuits should be used for both top and bottom electrodes. Insufficient water cooling can cause degradation of the electrode, and copper from the electrode can melt and enter the steel substrate. The presence of molten copper in contact with the steel substrate can cause what is known as liquid metal embrittlement cracking. This type of cracking occurs along prior-austenite grain boundaries in steel and lowers the weld integrity.

Effect of Surface Condition on Welding

The workpieces to be welded or, at a minimum, the faying surfaces should be cleaned to ensure that the welds are free of inclusions. Dirt, scale, rust, and oxide film that may come in contact with the electrodes should be removed or reduced to ensure good surface appearance of the welds. Also, removal of foreign substances from workpiece surfaces reduces electrode pickup and consequently increases electrode life.

Effect of Oil Coatings. Thin coatings of oil on cold rolled or hot rolled pickled and oiled steel have little effect on the quality of spot welds. Excessive amounts of oil should be wiped off or removed in a degreasing operation. The oil itself may not be detrimental to the weld, but the dirt and other contaminants adhering to the oil may cause poor welds.

Effect of Rust, Scale, or Oxide. Steel coated with rust, scale, or thermally produced black or blue oxide finishes can be resistance spot welded in production, but the quality and consistency of welds is lower than on steel from which these coatings have been removed. Thin films that have low and uniform electrical resistance have the smallest effect on welding. Steel that is coated with extremely thick and nonuniform mill scale may not be weldable on a practical production basis without first removing the scale (Ref 4).

Steel on which uniform but heavy mill scale or oxide coatings are present can be welded in production by applying low-to-medium current in a series of pulsations at fairly high electrode pressure. The electrical conductivity of mill scale or oxide increases with temperature, and these coatings become fairly good conductors when red hot. Because of the variable time needed to break through the coating and establish current flow, manual timing gives more satisfactory results than automatic timing.

When metal having heavy scale or oxide coatings is welded, much or all of the scale or coating on the faying surfaces remains in the welds, regardless of current, surface resistance, or electrode pressure. These inclusions in the weld metal can cause voids, blowholes, and other internal defects that may sometimes be difficult to detect.

Surface Preparation. A film of dirt or oil can be removed from the surfaces of the workpieces by vapor degreasers and chemical baths; however, careful hand wiping of the surfaces to be spot welded may be sufficient. Oxide films can be removed by mechanical methods; the action must be severe enough to cut through the film but must not be so severe as to cause the formation of a rough or scratched surface.

Where it is impractical to use pickled or cold rolled steel, the surfaces to be welded can be machined, ground, or wire brushed far enough back from the edge of the workpiece to clear the electrodes, or for a distance equal to the overlap. Heating to elevated temperatures in a

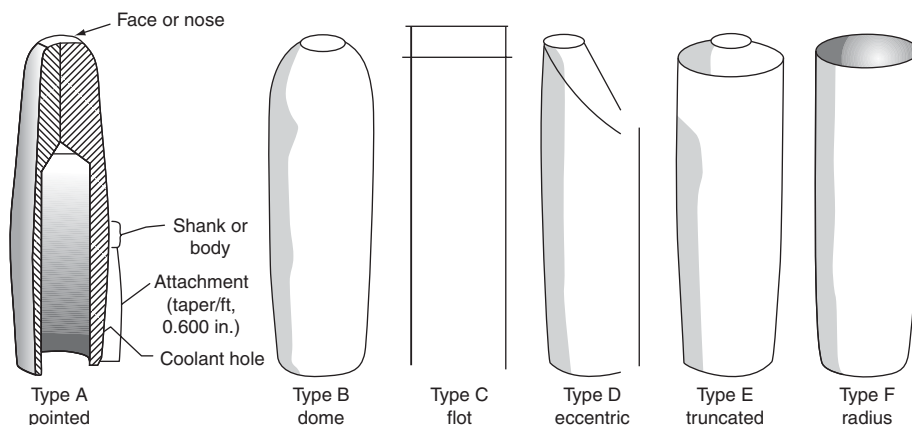


Fig. 12 Standard electrode face and nose shapes. Type D was formerly called offset.

reducing atmosphere is also an acceptable cleaning method for some metals.

Abrasive blast cleaning methods using sand, coarse grit, or shot usually are not satisfactory because particles of sand or scale are left embedded in the surface. Fine, sharp steel grit is satisfactory in some applications.

Evaluation Methods

Several tests are generally used to characterize the RSW behavior of steels and the integrity of spot welds. These include the welding current range determination, metallographic characterization of the weld and heat-affected zone microstructures, and microhardness and weld tensile tests (Ref 5, 6). Metallographic characterization and tensile tests are destructive tests intended to evaluate weld integrity as well. Visual examination and ultrasonic examination are nondestructive methods to evaluate weld integrity.

This section is a brief review of test methods as they pertain to the RSW method. A more detailed description of weld integrity criteria and test methods is provided in the article [5C] in this Volume on weld quality and evaluation methods.

Welding Behavior Evaluation

Welding current range is a useful parameter to assess the weldability of materials, particularly of steels. The current range is useful because it provides a range of welding currents over which welds with buttons of acceptable size can be produced. Welding current is the difference between the welding current required to produce a minimum weld size (I_{\min}) and the current that causes expulsion of weld metal (I_{\max}). Typically, the minimum weld size is defined as:

$$4\sqrt{t}$$

where t is the nominal sheet thickness. This parameter for minimum weld size is generally used in the automotive and steel industries.

The procedure to determine current range is described in detail in Ref 7. Test coupons measuring 140 by 50 mm (5.5 by 2.0 in.) are used in the current range determination. The coupons are overlapped by 25 mm (1.0 in.), and a shunt or anchor weld is made on one side of each coupon pair. On the other side, 35 mm (1.4 in.) from the edge, test welds are made. The test welds are peeled open, and the weld sizes are determined using calipers.

Current ranges are obtained by first determining the lowest welding current that produced the minimum acceptable weld size. Then, the current is gradually increased at typically 100 A increments, until weld-metal expulsion results. The difference between the current at the minimum weld size and the current at the expulsion weld size gives the current range.

The broader the current range exhibited by a material, the more robust the useful welding current range for the material. Note that the occurrence of weld-metal expulsion results in a loss of weld metal and reduces the weld size. This, in turn, lowers the load-bearing capability of the weld. Therefore, weld-metal expulsion should be avoided to maintain weld integrity.

Figure 13 shows a plot between welding current and the weld sizes for three grades of dual-phase steels. Dual-phase steels are a class of new advanced high-strength steel (AHSS) grades that have been developed for automotive applications to help automakers improve occupant protection and fuel economy. Dual-phase steels are considered AHSS to distinguish them from the conventional high-strength steels (HSS) or high-strength, low-alloy (HSLA) steels. The HSS types include HSLA steels and carbon-manganese steels of tensile strength up to 440 MPa (65 ksi). While the use of AHSS was nonexistent until 2001, it is anticipated that AHSS use in automotive bodies will climb to 50% by 2015 (Ref 8).

A welding force of 4.2 kN (944 lbf) was used for 590 MPa (86 ksi) steel (refers to the minimum tensile strength of the steel), while 5.3 kN (1192 lbf) was used for the 780 and 980 MPa (113 and 142 ksi) steels. Figure 13 shows that a current range of 2.2 kA was obtained for the 590 and 780 MPa grades and 2.5 kA for the 980 MPa grade. These current ranges are considered broad and show that there is a wide current range to successfully weld these dual-phase steels.

Metallographic characterization of weld and heat-affected zone (HAZ) microstructures is performed to examine the microstructural constituents as well as to look for the presence of any imperfections, such as voids or cracks.

Voids can be caused by entrapped gases from the coatings or by shrinkage cavities from rapid solidification. Shrinkage voids generally tend to be small and innocuous. They are typically seen near the center area of the weld nugget, which is the last area to solidify. They are generally not believed to affect the service performance of welds as determined by tensile strength.

Microhardness traverses are done on weld cross sections to look for uniformity of properties and the type of microstructural constituents. For example, the presence of martensite in steels shows higher hardness in HSS compared to regions in the HAZ that may show softer ferrite and bainitic constituents. Microhardness traverses are generally intended for informational purposes and not for weld acceptance or rejection. A typical weld microhardness traverse is done across the weld to cover as many indentations in the weld and HAZ as possible (Fig. 14). Depending on the hardness of the weld and HAZ, indentations can be placed as close as 0.4 mm (0.016 in.) apart.

Weld Integrity

Two types of weld tension tests are typically done to assess the weld tensile strength (Ref 7). One is called the cross-tension test. In cross-tension tests, two test strips are positioned normal to each other, and a spot weld is made at the center of the overlapped region. In the cross-tension test, a tensile load is applied on the weld in a direction normal to the weld. The other weld tensile test is the shear-tension test (sometimes referred to as the lap-shear test). In this test, two sheet samples, typically measuring 140 mm (5.5 in.) long by 60 mm (2.4 in.) wide, are overlapped by 45 mm

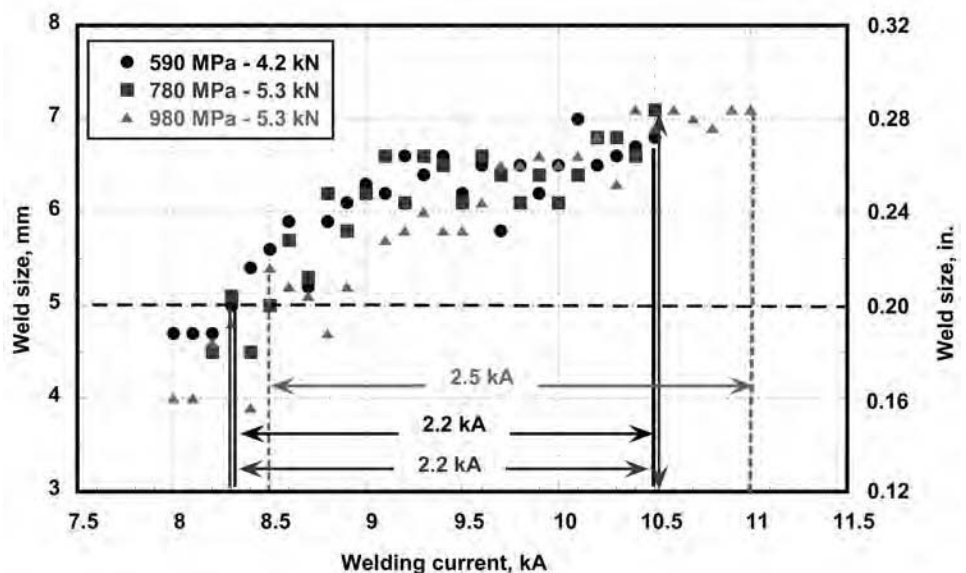


Fig. 13 Welding current range plot for three hot dipped galvanized dual-phase steels. Source: Ref 6

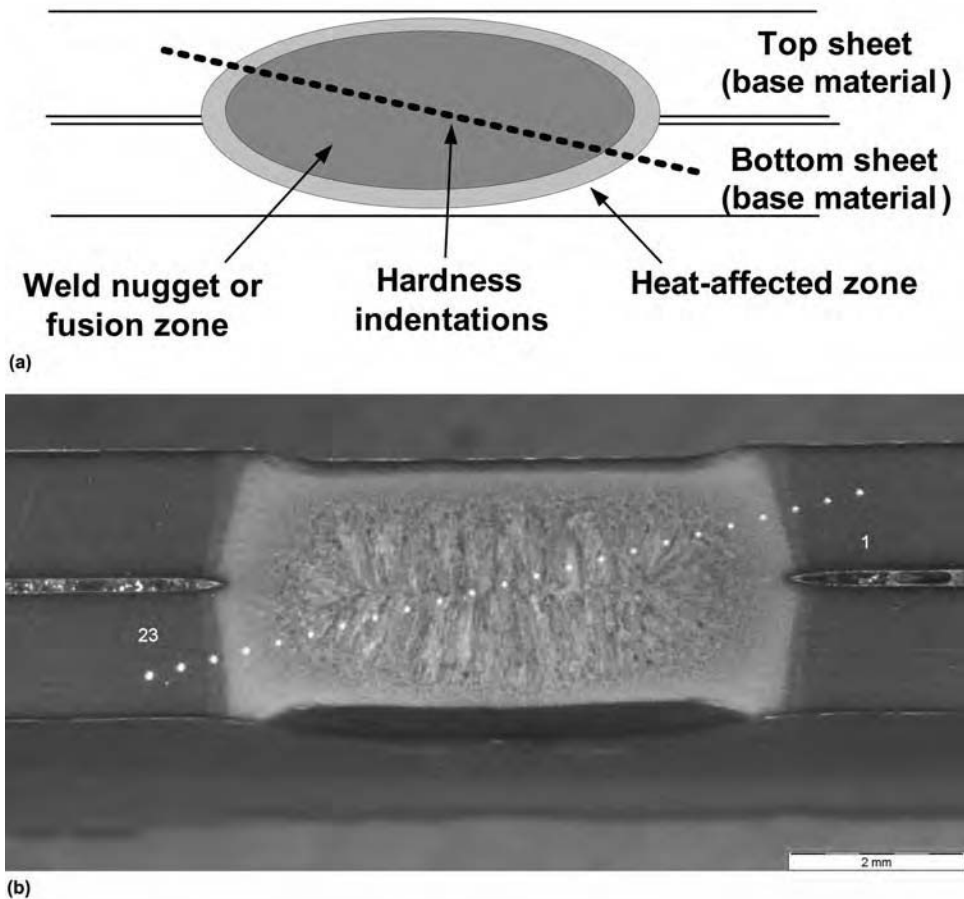


Fig. 14 Microhardness traverse across the weld, heat-affected zone, and unaffected base materials. (a) Schematic of a weld cross section. (b) Typical cross section

(1.8 in.) and joined with a single spot weld located at the center of the overlapped region. Schematics showing the test coupon dimensions and layout are presented in Fig. 15. The sample is then pulled in tension.

The parameters monitored in weld shear- and cross-tension tests are the peak load to failure (termed the weld strength), energy absorbed at peak load, total energy absorbed, and failure mode. Spot weld strength (or the peak force required for the weld to fail) is influenced by the weld size, as can be seen in Fig. 16.

Figure 16 shows the relationship between weld size and weld strength for 780 MPa (113 ksi) dual-phase steel. It can be seen that as the weld size is increased, both the shear-tension strength (STS) and cross-tension strength (CTS) also increased. Thus, it is important to maintain as large a weld size as possible without achieving weld expulsion. Other factors that influence the STS are the sheet thickness and the base material strength. Generally, as the sheet thickness and base material strength increase, both the STS and CTS also increase. However, CTS is not

conclusively found to be influenced by the base material strength (Ref 9). From Fig. 16 it is also apparent that the STS is much higher than the CTS at any given weld size. This suggests that the method of loading the weld influences the load required to fail the weld.

Energy absorbed in failure can also be monitored during the weld tensile tests. The energy absorbed for failure is strongly influenced by the type of test. The total deformation of the sample prior to failure in the cross-tension test, for instance, is much greater than that in the shear-tension test. As a result, in samples having the same sheet thickness, weld diameter, and material properties, the energy absorbed is greater for the cross-tension than the shear-tension test. When welds fail by pullout mode, the energy absorbed is much higher than when the welds fail interfacially. This is because the total deformation that occurs in the sample is always greater when a pullout failure occurs compared to when an interfacial failure occurs. However, caution should be exercised in evaluating energy-absorbed data in STS tests because

tensile samples during the test undergo significant rotation when failure occurs by button pull-out, and they transfer part of the applied load onto the base material. Therefore, it is important to understand the limitation in interpreting the energy-absorbed-to-failure data in STS.

There are two different failure modes that are generally observed in weld tension and peel tests, namely, interfacial fractures and full button pullout (Fig. 17). In the interfacial fracture, the weld fails at the interface of the two sheets, leaving half of the weld nugget in one sheet and half in the other. In the full button pullout, fracture occurs in the base metal or in the weld HAZ at the perimeter of the weld. In this failure mode, the weld nugget is completely torn from one of the sheets, with the weld remaining intact. It is also possible to obtain a combination of the two failure modes in which a portion of the nugget is pulled out of one of the sheets and the rest of the weld nugget shears at the interface. All of the various fracture morphologies that can be seen in resistance spot welds are provided in Ref 9. Notice from Fig. 16 that the welds failed interfacially up to 6 mm (0.24 in.). Above 6 mm weld size, the failure mode in the shear-tension test was by button pullout. In the case of the cross-tension test, all weld sizes yielded button pullout fractures.

Visual examination can detect the acceptability of weld shape, electrode indentation into the base material surrounding the weld, weld location, weld appearance, expulsion of weld metal, and surface cracking. A resistance spot weld may be circular or oval in shape. In the case of oval-shaped welds, the aspect ratio (the ratio of major dimension to minor dimension) should be 2.0 or less. Note that surface appearance is not always a reliable indicator of spot weld quality, because shunting and other causes of insufficient heating or inadequate penetration usually leave no visible effects on the workpiece. Therefore, other methods of weld evaluation must be pursued.

Welds should be placed at proper locations in accordance with the applicable drawings. Overlapping or closely spaced welds are not acceptable. It is recommended that welds should have an electrode indentation depth of less than 30%. Indentation is measured as a ratio of the electrode indentation depth to the thickness of the base material (Fig. 18).

Criteria for Acceptable Weld Integrity. Acceptable weld integrity criteria generally vary significantly among manufacturers and industries. Therefore, each fabricator should establish its own weld acceptance criteria, frequency of testing, and methods to test spot welds in consultation with the end users of fabricated parts. Attributes such as minimum acceptable weld size, weld strength, and indentation should be discussed. Methods of weld testing should be agreed upon between fabricators and end users. It should be noted

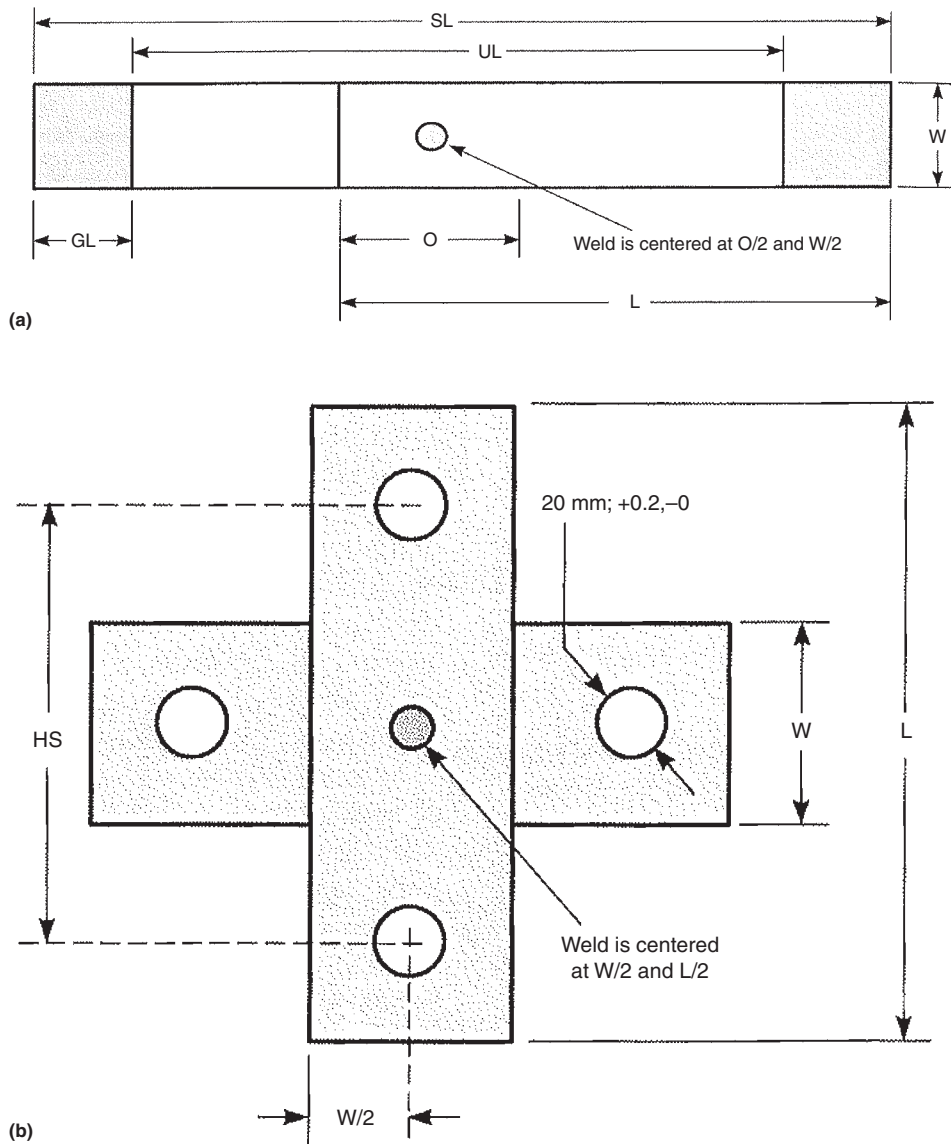


Fig. 15 Schematics showing the dimensions and layout of (a) shear-tension and (b) cross-tension test samples. Source: Ref 7

Sheet thickness		Coupon length (L)		Width (W)		Overlap (O)		Sample length (SL)		Unclamped length (UL)		Gripped length (GL)	
mm	in.	mm	in.	mm	in.	mm	in.	mm	in.	mm	in.	mm	in.
0.60-1.29	0.024-0.050	105	4.12	45	1.8	35	1.4	175	6.90	95	3.7	40	1.6
1.30-3.00	0.051-0.12	138	5.44	60	2.4	45	1.8	230	9.06	105	4.14	62.5	2.46

Length (L)		Width (W)		Overlap (O)		Hole spacing (HS)	
mm	in.	mm	in.	mm	in.	mm	in.
150	6.0	50	2.0	50	2.0	100	4.0

that not all methods of weld testing need to be performed to judge weld integrity for acceptance. It is suggested that, at a minimum, visual inspection be performed to ensure that welds are of acceptable quality. However, as noted previously, visual inspection

has limitations in checking weld integrity and is not always a reliable indicator of weld quality. Generally, destructive tests such as metallographic testing and tensile testing are performed prior to establishing welding parameters that provide acceptable welds.

These tests can be repeated at some intervals for verification of weld integrity.

For RSW purposes, steel grades can be classified into four groups depending on their strength (Table 2). Groups 3 and 4 are considered AHSS.

Spot weld strength is higher for groups 3 and 4 HSS and AHSS than that of the low- and plain carbon steels (group 1) for a given weld size. In the evaluation of weld tension test results in spot welds, it is generally believed, especially in the automotive industry, that an interfacial shear failure is indicative of poor weld integrity. This has generally been true for low-strength steels (tensile strength equal to or less than 350 MPa, or 51 ksi—group 1 in Table 2) in which interfacial failure is normally associated with insufficient fusion or some sort of weld imperfection, such as gross porosity. However, recent work on interfacial fractures in shear-tension tests of AHSS indicated there is a critical sheet thickness above which the expected failure mode could transition from pullout fracture to interfacial fracture. In an analysis by Radakovic and Tumuluru (Ref 11), it was shown that as the strength of the steel increases, the fracture toughness of the weld required to avoid interfacial failure must also increase. Therefore, despite higher load-carrying capacity, due to their high hardness, the welds in HSS may exhibit interfacial fractures. Tensile testing showed that the load-carrying capacity of the samples that failed via interfacial fracture was found to be more than 90% of the load associated with a full button pullout. This indicated that the load-bearing capacity of the welds is not affected by the fracture mode. Therefore, the mode of failure should not be the only criterion used to judge the quality of spot welds. The load-bearing capacity of the weld should be the primary focus in the evaluation of the shear-tension test results in AHSS. With the increased use of these steels in automotive bodies, it is important to understand their fracture behavior in shear-tension tests so that welds, otherwise sound, are not rejected solely based on fracture appearance. It is important to note that partial buttons (plugs) or interfacial fractures do not necessarily characterize a failed spot weld in AHSS. Interfacial fractures may be typical of smaller weld sizes in low-strength (tensile strength less than 300 MPa, or 44 ksi) steels or in all weld sizes in AHSS.

In-Line Destructive Weld Testing. The use of pneumatic chisels to peel welded panels is generally practiced for checking the weld integrity of resistance spot welds during product testing. This is often done on production lines. However, in HSS, especially AHSS, this type of on-line product testing may produce fracture through the weld during destructive chisel testing. Fracture through the weld becomes more common as the sheet thickness and base material strength increase and can mislead inspecting personnel to classify the welds as

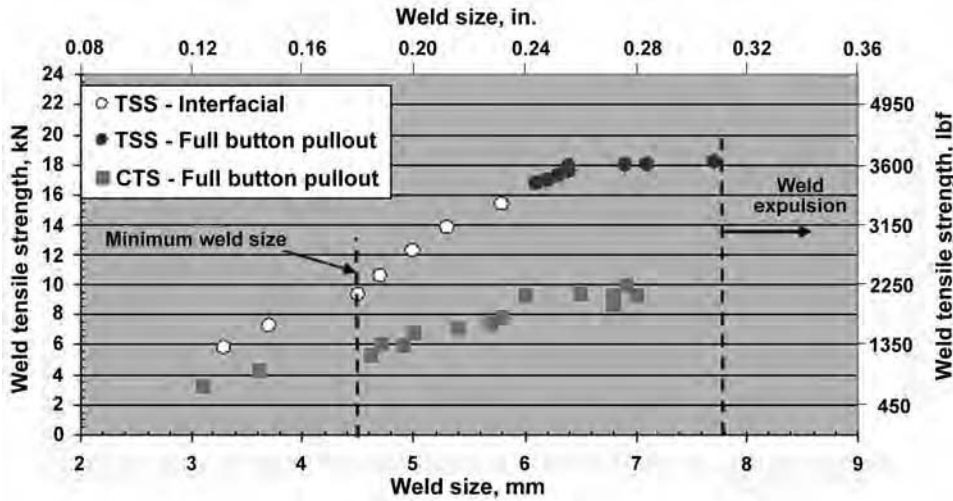


Fig. 16 Plot of weld shear- and cross-tension strengths as a function of weld size. TSS, tensile shear strength; CTS, cross-tension strength

Table 2 Steel classification for resistance spot weld purposes

Group	Minimum tensile strength		Typical products(a)
	MPa	ksi	
1	<350	<51	Mild 140/270 BH 180/300 BH 210/320 BH 240/340 BH 260/370
2	350–500	51–73	HSLA 280/350 HSLA 350/450 DP 300/500 DP 350/600 TRIP 350/600 DP 500/800 TRIP 500/800 CP 700/800
3	>500–800	>73–116	DP 700/1000 Mart 950/1200 Mart 1150/1400 Mart 1250/1520
4	>800	>116	

(a) Mild: mild steel; BH: bake-hardenable steel; HSLA: high-strength, low-alloy steel; DP: dual-phase steel; TRIP: transformation-induced plasticity steel; CP: complex-phase steel; Mart: martensitic steel. Source: Ref 12

defective. Weld-metal fracture may accompany significant distortion of the metal immediately adjacent to the weld during destructive peel testing. Under these conditions, resultant weld fracture may not accurately predict service life of the joint. Therefore, proper judgment should be exercised when evaluating the results of in-line chisel tests.

Ultrasonic testing of spot welds has recently gained acceptance with some manufacturers. However, because the method relies heavily on operator judgment, proper interpretation of the results is essential for obtaining a reliable evaluation. This method still needs further development before it can replace destructive weld testing completely. Several on-line real-time systems to monitor resistance welds are

currently available and are being used in some weld fabrication shops.

Applications

The workpiece thickness and the weldability of the metals are key factors in determining whether two materials can be resistance spot welded. As noted in the article “Introduction to Resistance Welding” in this Volume, the thickness of mating parts in spot welding is crucial to the heat balance. Thicknesses differing by more than a factor of 4 to 1 become difficult to weld even in favorable material combinations. Spot welds are most easily made between matching materials of the same thickness,

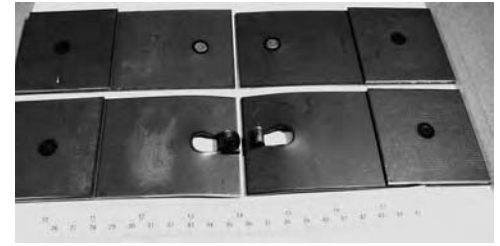


Fig. 17 Photograph showing the two types of weld fracture commonly observed in weld shear-tension tests. Source: Ref 10 with permission

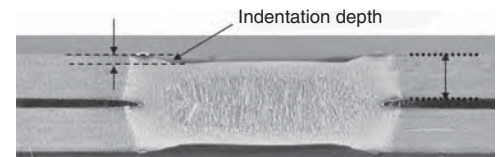


Fig. 18 Photograph of a weld cross section showing the method of measuring electrode indentation

because this matching allows the heating to be directed uniformly to both base materials.

Spot welding of specific alloys is described in the article “Procedure Development for Resistance Spot and Seam Welding” in this Volume. Many combinations of ductile metals and alloys can be spot welded. Table 1 lists some combinations that have been successfully welded. Many other combinations may also be satisfactorily welded. Copper and silver are difficult to weld, but they may be welded by the use of a low-conductivity electrode. Copper alloys are more commonly resistance brazed. In many applications, the weldability of copper is increased if it has a tinned surface.

Spot Welding of Uncoated Steels. Plain, low-carbon steels, which include interstitial-free steels with tensile strengths typically less than 300 MPa (44 ksi), can be satisfactorily welded using the RSW method over a wide range of time, current, and electrode force parameters. Practices recommended for spot welding SAW 1010 steel have been issued by the RWMA (Ref 2). These data can serve as starting points to establish suitable weld schedules. However, these data may require modification, depending on the type of welding machine, its dynamic properties, the pneumatic characteristics, the characteristics of the secondary circuit, the electrode shape, and the specific grade of steel being welded. Sufficient squeeze time should be chosen to enable the electrode force to build up to its preset value. This is particularly true for pneumatic guns that require time to build up the required electrode force. For lightweight gun welders with limited force

capability, the electrode force values are reduced up to 30% for sheet thicknesses greater than 1.6 mm (1/8 in.). The welding current must be adjusted accordingly. For welding sheets of dissimilar thickness, welding conditions may be based on the thinner sheet, or on the second-thinnest sheet when welding three sheets of different thicknesses.

Groups 1 and 2 are readily weldable using the RSW process, groups 3 and 4 require certain precautions to achieve acceptable welds. For welding of HSLA or AHSS grades (listed under groups 3 and 4 in Table 2), the following general guidelines are suggested as a starting point to develop specific weld schedules (Ref 12). Due to differences in steelmaking practices between various steel manufacturers, users should develop their own welding schedules (combinations of parameters) based on the specific composition of the steel grades being welded:

- Increase the electrode force by 20% or more than that used for similar-thickness low-strength steel.
- Increase the weld time, as appropriate.
- Try a multipulse welding schedule (several pulses of welding current and/or electrode pressure).
- Use a larger-diameter electrode tip than suggested for welding a similar-thickness low-strength, low-carbon steel.

The AHSS generally require less welding current and higher electrode force compared to low-strength plain carbon steels (group 1), because AHSS grades have higher electrical resistivity. This is due to the fact that these grades of steel contain higher amounts of alloying elements, such as manganese, chromium, and molybdenum, to develop the required strength. All of these elements increase the resistivity of steels. Therefore, welding current levels for AHSS are not increased and may even need to be reduced, depending on material chemical composition. The AHSS grades require higher electrode forces for equivalent thickness of low-carbon steels so as to decrease the resistivity at the sheet interface to control the heat generation.

An important precaution that should be followed when welding AHSS is that weld-metal expulsion should be avoided. Weld-metal expulsion is highly undesirable because it causes loss of weld metal, which, in turn, can lower the weld size, thereby reducing the weld strength. Expulsion is typically caused by the use of excessively high current or a misfit between parts to be welded, the latter being more common in industrial applications. Therefore, expulsion can be avoided by using welding current below the expulsion limit for the thickness and grade of steel being welded and ensuring that part fit-up is tight, without any gaps at the sheet interface.

Plain low-carbon steels with tensile strength up to 300 MPa (44 ksi) are readily weldable

using the RSW process. These steels can be obtained from a number of suppliers, with reasonable certainty of only minor variations in welding behavior. This is because these grades of steel contain only small amounts of carbon (generally less than 0.03%) and no other alloying elements as intentional additions. On the other hand, HSLA and AHSS grades of steels can have significant differences in composition between various steel suppliers, because these grades are typically specified by strength levels and total elongation, not composition. This is done to enable steelmakers to choose suitable compositions to produce the required strength and ductility levels based on their mill capabilities. Therefore, compositional variations between various steelmakers may require users to modify weld schedules to suit the specific composition being welded.

Spot Welding of Zinc-Coated Steels. The present trend in the automotive industry toward the use of larger amounts of zinc-coated steels in automotive assemblies required the users to know how these coatings affect the welding requirements. Coated steels offer additional resistance to the flow of current, on top of that offered by the substrates being welded, and therefore generally require lower welding current than uncoated steels. Caution should be exercised when welding coated steels because fumes containing zinc vapor are emitted. Provision should be made to extract the fumes safely. Welding of zinc-coated steels should be done in well-ventilated areas.

Two types of coatings are generally applied to steel sheets used in the automotive industry, namely, galvanized and galvanized coatings (Ref 13). Galvanized coatings contain essentially pure zinc with approximately 0.3 to 0.6 wt% Al. The term *galvanized* comes from the galvanic protection that zinc provides to steel substrate when exposed to a corroding medium. Two methods by which zinc coatings are applied to steel substrate are the hot dipping method and the electrodeposition method. The pure zinc coating is called the galvanized coating, and the zinc-iron alloy coating is called the galvanized coating. In the case of the hot dipping process of coating steels, a hot dipped galvanized (HDGA) coating is obtained by additional heating of the zinc-coated steel at 450 to 590 °C (840 to 1100 °F) immediately after the steel exits the molten zinc bath. This additional heating allows iron from the substrate to diffuse into the coating. Due to the diffusion of iron and the alloying with zinc, the final coating contains approximately 90% Zn and 10% Fe. Due to the alloying of zinc in the coating with diffused iron, there is no free zinc present in the galvanized coating. Galvanized coatings contain less aluminum, approximately 0.15 to 0.4 wt%, than the hot dipped galvanized (HDGI) coatings. These coatings can be applied by either a hot dipping process or electrodeposition. The coating thickness ranges from approximately 6 to 8 μm (0.24 to

0.32 mils) for galvanized coatings to approximately 12 to 14 μm (0.47 to 0.55 mils) for galvanized coatings.

Examination of the welding behavior of an AHSS grade of steel coated with 70/70 g/m² HDGI and 42/42 g/m² HDGA (steels coated on both sides)—“coating weights that are currently used in the automotive industry”—showed that the welding behavior was similar between the two coatings (Ref 13). One difference noted between the two coatings was that HDGA required lower welding current to form the minimum weld size. This may not be an advantage in the industry, given the current practice of frequent electrode tip dressing. Further, the type of coating had no effect on the weld shear-tension or cross-tension strength. The weld strength is controlled by the steel substrate.

Welding conditions can be easily optimized when using pedestal-type welding machines; however, this may not be the case in body-in-white assembly, where a combination of multiple spot welders and robotic cells are more commonly used. Such operations are susceptible to poor fit-up of parts, access problems, and electrode configurations that give rise to electrode skidding and expulsion. Consequently, the welding parameters may need to be adjusted to compensate for such situations. In many instances, one welding gun is used to weld a range of sheet thickness combinations or even a variety of material combinations in a particular part.

In these circumstances, the electrode life obtained may be lower than that derived using optimized welding conditions. For example, the electrode life obtained can depend greatly on the type of welding gun used (Fig. 19) or the angle of approach of the electrode. When multiple spot welding machines are used, it is essential that all welding machines are balanced electrically and that the same air pressure is supplied to each station. Electrode shape and configuration, water cooling arrangements, and electrode dressing schedules must be optimized. The last item is most important, because satisfactory weld quality can only be provided when the necessary electrode condition and shape are maintained over a production run. It is again stressed that frequent electrode tip dressing is highly recommended to maintain acceptable weld quality (hence integrity), especially when welding coated AHSS grades.

Water cooling is also a critical element of welding machine maintenance, because insufficient water cooling during welding can degrade the copper from the electrode and cause copper to melt and deposit onto the part surface. When this happens, molten copper can penetrate the steel substrate and cause liquid metal embrittlement cracking.

Weldability of Steels in Spot Welding. In HSS, several alloying elements are added to achieve the required strength levels. These alloying elements not only strengthen steels but affect other properties as well. Weldability

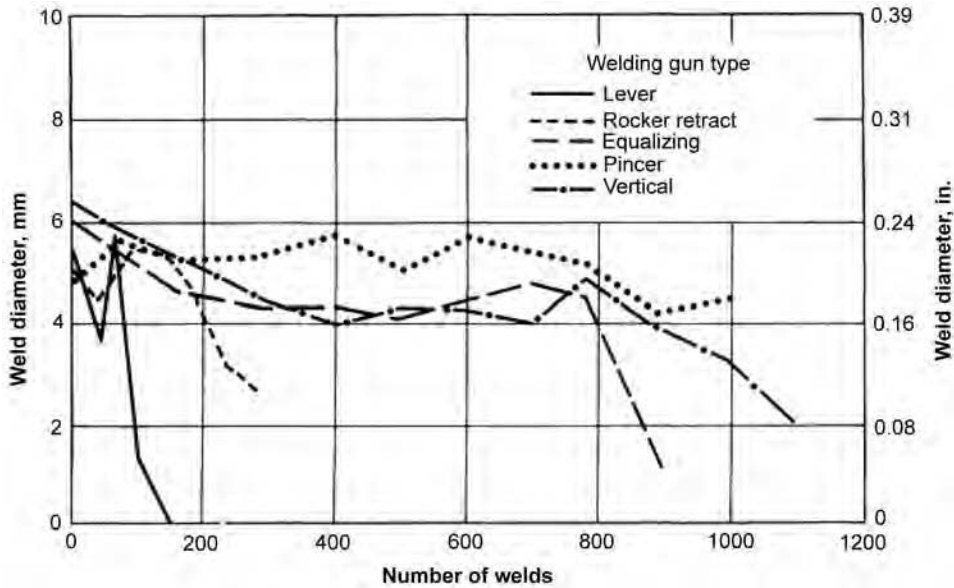


Fig. 19 Effect of resistance spot welding electrode gun type on electrode life for selected steels and alloys

is one important property of steels that is influenced by the addition of alloying elements. Weldability of a given grade of steel is generally described using the term *carbon equivalent* (C_{eq}). This term expresses the cumulative effect of various alloying elements on weldability. Most C_{eq} formulae contain such alloying elements as carbon, manganese, silicon, sulfur, and phosphorus that have significant influence on weldability (Ref 14). Most equations developed to predict the weldability behavior of steels in spot-welded applications are designed to provide an estimate of the weld zone hardness and shear- and cross-tension strengths of spot welds.

While there are several formulae for expressing C_{eq} of steels, there is no universally accepted, one single formula for expressing the weldability of steels in RSW applications. As a result, users must find a formula that best suits their application. It should be noted that C_{eq} should be used only as a general guide to assess weldability of steels. Assigning specific maximum values for accepting steels is not advisable.

Among all the elements used for alloying steels, carbon has the most effect on weldability of steels. Increases in base material carbon content increase the resultant weld hardness and weld shear-tension strength. However, increasing carbon content may reduce the useful welding current ranges of steels. A concern existed about the occurrence of weld interfacial fractures as the carbon content in steel is increased. This caused users to impose limits on maximum allowable carbon and C_{eq} . However, recent research has shown (Ref 11) that interfacial fractures are the expected mode of failure in AHSS, and that welds failing interfacially require more than 90% of the load necessary

to cause failure by button pullout. This means that occurrence of interfacial fractures should not cause concern about the load-bearing capability of spot welds in AHSS, and that fracture mode is not a good indicator of weld integrity, especially in AHSS grades.

Other alloying elements, such as manganese and silicon, do not have a significant effect on the welding behavior or welding current range in steels. However, increases in these two elements cause the resultant weld and HAZ hardness to increase. As mentioned earlier, an increase in weld and HAZ hardness causes the peak load in STS to also increase.

Weldability of Aluminum Alloys in Spot Welding. Most of the commercial aluminum alloys produced in sheet form can be spot welded, provided that suitable welding equipment is used. Because of the low electrical resistance of aluminum alloys, considerably higher welding currents are required relative to welding mild steel. In addition, the narrow plastic range between softening and melting means that welding forces, time, and current must be closely controlled. For consistent weld quality, it is essential that the tenacious surface oxide films are removed by mechanical or chemical techniques prior to welding.

To minimize the likelihood of cracking or porosity in the weld, careful control of the electrode force is necessary. If the force is applied too soon, the welding current may be insufficient due to a premature loss of contact resistance. Thus, correct initiation of the force relative to the current is essential. Dual force schedules are frequently used; therefore, a low-inertia welding head can be beneficial because it allows a more effective buildup of force to its final level.

Because of the higher secondary currents required when welding aluminum alloys, direct current secondary rectified or frequency converter welding machines are favored, particularly if high-quality welds are required (such as in aircraft applications).

Safety

As with any welding process, all necessary safety precautions should be followed to avoid injury to personnel and property and to prevent fires. Please consult Ref 15 and 16 for safety considerations required for welding operators. Safety considerations specific to RSW have been summarized in Ref 17. Some of the hazards in RSW are provided here for information purposes and include the following. Operators should be made aware of these and provided with adequate personal protective equipment to guard against injury and damage to equipment, building, and parts:

- Flying sparks from expulsion during welding can cause fire and explosion.
- Flying sparks can cause burn or injury to eyes and skin if operators are not protected properly.
- Because RSW is done primarily on sheet metal products that tend to have sharp edges, operators should be aware of cutting hazards. Cut-resistant gloves should be used when handling sheet metal.
- Electric shock can result from damaged cables and wiring.
- Equipment maintenance should only be done by authorized personnel after disconnecting all sources of energy, including electricity, compressed air, and water. Operators should be cognizant of potential energy in the system.
- Handling hot metal or welded parts can cause burns.
- Moving electrodes in RSW create pinch points. Extreme caution should be used when inserting or removing parts after welding.
- Fumes from spot welding on parts coated with paints or corrosion-resistant coatings can create fumes that cause inhalation hazards.

To avoid some of these hazards, operators should wear safety goggles or a face shield and not weld near flammable liquids or gases. Operators should wear dry insulating gloves (cut resistant when handling sharp objects) to prevent burns and cuts. Most important of all is to keep hands and fingers away from moving parts. Keep all protective guards in place. It is also important to ensure that there is adequate ventilation. Operators should familiarize themselves with the Material Safety Data Sheets for all materials, coatings, gases, and cleaners they handle.

DISCLAIMER

The material in this paper is intended for general information only. Any use of this material in relation to any specific application should be based on independent examination and verification of its unrestricted availability for such use and a determination of suitability for the application by professionally qualified personnel. No license under any patents or other proprietary interest is implied by the publication of this article. Those making use of or relying upon the material assume all risks and liabilities arising from such use or reliance.

REFERENCES

1. R. Ikedia, Y. Okita, and M. Ono, Development of New Resistance Spot Welding Process for Three Sheet Joints Using Electrode Force Control, *Fifth International Seminar on Advances in Resistance Welding*, Sept 24–26, 2008 (Toronto, Canada), W. Zhang and N. Scotchmer, Ed., Huys Industries, Weston, Canada
2. *Resistance Welding Manual*, 4th ed., Resistance Welder Manufacturers Alliance, 1989
3. "Resistance Spot Welding Electrode Caps," ISO 5821, TISO/TC 44/SC 6, International Organization for Standardization, 2007
4. D.W. Dickinson and T.V. Natale, SAE Paper 810353, Feb 1981
5. M. Tumuluru, "A Comparative Examination of the Resistance Spot Welding Behavior of Two Advanced High Strength Steels," SAE Technical Paper 2006-01-1214, presented at the SAE Congress (Detroit, MI), 2006
6. M. Tumuluru, An Overview of the Resistance Spot Welding of Coated High Strength Dual Phase Steels, *Weld. J.*, Vol 85, Aug 2006, p 31–37
7. "Recommended Practices for Test Methods for Evaluating the Resistance Spot Welding Behavior of Automotive Sheet Steel Materials," AWS Specification D8.9M-2002, American Welding Society, Miami, FL
8. M. Mehrkens, "Advanced High Strength Steel Technology in Porche Cayenne," paper presented at Great Designs in Steel—2004, Feb 2004, American Iron and Steel Institute, Southfield, MI
9. "Specification for Automotive Weld Quality—Resistance Spot Welding," ANSI/AWS D8.1-2007, American Welding Society, 2007
10. M. Tumuluru, Effects of Baking on the Structure and Properties of Resistance Welds in 780 MPa Dual Phase and TRIP Steels, *Weld. J.*, Vol 89 (No. 5), 2010, p 91s–100s
11. D.J. Radakovic and M. Tumuluru, Predicting Resistance Spot Weld Failure Modes in Shear Tension Tests, *Weld. J.*, Vol 87 (No. 4), 2008, p 96S–105S
12. *Advanced High Strength Steel (AHSS) Application Guidelines*, Version 4.1, Section 3—Joining, WorldAutoSteel, June 2009, www.worldautosteel.org
13. M. Tumuluru, The Effects of Coatings on the Resistance Spot Welding Behavior of 780 MPa Dual Phase Steel, *Weld. J.*, Vol 86, June 2008, p 161S–169S
14. H. Oikawa, T. Sakiyama, T. Ishikawa, G. Murayama, and Y. Takahashi, "Resistance Spot Weldability of High Strength Steels Sheets for Automobiles," Nippon Steel Technical Report 95, 2007
15. Occupational Safety and Health Administration (OSHA), Code of Federal Regulations, Title 29 Labor, Chapter XVII, Parts 1900 to 1910, Order No. 869-019-00111-5, Superintendent of Documents, U.S. Government Printing Office, Washington, D.C.
16. "Safety in Welding, Cutting, and Allied Processes," ANSI Z49.1, available from American Welding Society, Miami, FL
17. R.B. Hrisch, Making Resistance Spot Welding Safer, *Weld. J.*, Feb 2007, p 32–37

Projection Welding

Warren Peterson, Edison Welding Institute

PROJECTION WELDING is a variation of resistance welding in which current flow is concentrated at the point of contact with a local geometric extension of one (or both) of the parts being welded. These extensions, or projections, are used to concentrate heat generation. The process typically uses lower forces and shorter welding times than similar applications without projections. Typically, large, flat-faced electrodes (Fig. 1) are used against the projection.

Introduction

Projection welding is often used in the most difficult resistance welding applications; for instance, applications with significant thickness mismatches or those involving several close-spaced simultaneous welds can be projection welded. Compared to standard resistance welding applications, modification of the weld

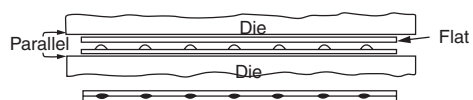
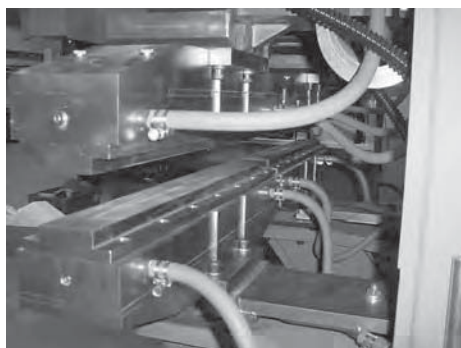


Fig. 1 Typical example of equipment and schematic for resistance projection welding. Tooling is platen mounted and consists of water-cooled copper blocks, welding die inserts, and locators. Courtesy of Taylor-Winfield Technologies, Inc.

schedule or welding equipment for projection welding may be needed to achieve optimal results.

Types of Projections

Projection welding applications are generally categorized as either embossed-projection welding or solid-projection welding. Variations of these are shown in Fig. 2 and 3. Joint configurations for embossed- and solid-projection types range from sheet-to-sheet joints, to cross-wire welds, to annular attachments, to nut welds, to weld screws, to ball-sheet joints, and so on.

Embossed-projection welding is generally a sheet-to-sheet joining process in which a projection is stamped onto one of the sheets to be joined. Then, resistance welding is conducted on a stack of sheets. Initially, weld current is

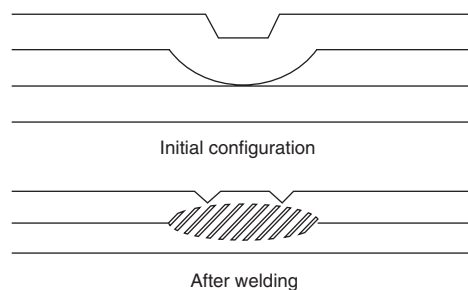


Fig. 2 Typical stacked configuration for embossed-projection welding of sheet

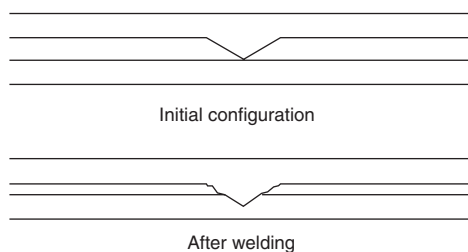


Fig. 3 Typical configuration for solid-projection welding

concentrated at the contact point and within the walls of the projection. Due to rapid joule heating of the projection, the projection collapses into the original sheet early in the process. However, during projection collapse, the contacting area breaks up the oxides on the surface, promoting continued current flow through the joint area. The increase in bulk resistivity promotes continued resistance heating at this location. In the traditional usage of the process, weld development proceeds as a conventional resistance weld, forming a fused weld nugget. In an alternate usage, the strain and heat developed during the preceding projection collapse develops a solid-state metallurgical bond at the faying interface, without producing a molten nugget between the sheets. These two approaches may require different projection geometries, welding parameters, or equipment. The advantages of each variant are addressed later.

The projection geometry for most embossed-projection welding applications typically involves discrete dimples stamped in the sheets. An annular-projection geometry is also common, forming a continuous circular dimple in the one of the sheets. This geometry increases the load required to mechanically collapse the projection. Consequently, annular projections are typically used for projection welding very thin-gage sheet.

Solid-projection welding requires that the projection be forged or machined onto one of the two components. Then, during resistance welding, the contact point and the projection itself experience preferential heating. In this case, the projection does not simply collapse, as in embossed-projection welding. Rather, the projection collapses by penetrating into the surface of the opposing material and by extrusion of metal to the periphery of the joint. Compared with embossed-projection welding, the traditional approach produces solid-state joints, rather than forming a fusion zone at the weld interface. The actual joints are caused by a combination of material forging and diffusion bonding, similar to resistance butt and flash butt welding.

Compared to embossed-projection welding, solid-projection welding involves a considerably

wider range of process variants used in production applications. Some of the common geometric variations of solid-projection welding are described as follows.

Annular-Projection Welds. One of the most common applications of solid-projection welding is to attach either tubular components or members with circular bases to flat substrates. This is commonly accomplished by annular-projection welding, in which a projection is machined onto the circular base or the end of the tubular section. Then, resistance welding is conducted to set the projection into the substrate. A typical weld geometry is shown in Fig. 4(g). Annular-projection welding generally provides high-integrity joints and can be used for leak-tight applications.

Cross-wire welding is a variation of solid-projection welding in which the projection is formed at the contact point of two crossing wires. The geometry for cross-wire welding is shown in Fig. 4(n). Upon resistance welding, heat is maximized at the location of the wire-wire contact, and the parts are subsequently forged together. Depending on the application, either highly localized joints (minimal forging) or heavily forged joints can be made in wire diameters commonly between 1.5 to 13.0 mm (0.06 to 0.51 in.). In some applications, cross-wire welding is conducted at rates up to 30 welds/second.

Projection Weld Nuts/Studs/Screws. Weld nuts represent an application of solid-projection welding in which the projections occur as extensions of material from the face of the nut, stud, or screw head. Typically, the weld faces contain three, four, or six projections, or feet, spaced around the nut, stud, or screw periphery. During welding, all of the projections are attached simultaneously. Examples of weld nut geometries are shown in Fig. 4(k and m).

Edge-to-sheet welds are typically a cross between embossed- and solid-projection welding. They are used to attach the end of a sheet to the flat face of an opposing component (Fig. 4f). The projections are generally stamped into the face of the attaching sheet. During welding, full local projection collapse occurs; however, bonding is strictly solid state (see the article “Fundamentals of Solid-State Resistance Welding” in this Volume).

Resistance mash welds (Fig. 5) create a narrow forge-type joint formed between two overlapping sheets. The sheet overlap distance is normally equal to between 0.5 to 2 times the thickness of the thinner sheet. Typically, flat bar-shaped electrodes cover the length of the overlapped joint. This is similar to mash seam welding which involves electrode wheels with flat or radiused profiles (see the article “Resistance Seam Welding” in this Volume). Substantial clamping force (at least twice the electrode force) is required to fixture the sheets against separation during welding. High clamping forces are required due to resistance to the wedgelike action created during the

forging process. Weld current is conducted through the narrow overlap, which causes the metal to heat and forge in the production of a solid-state bond.

Pin-and-Tenon Welds. Pin-and-tenon projection geometry (Fig. 4j) is a type of annular projection that produces a solid-state weld between a machined face (typically at 45°)

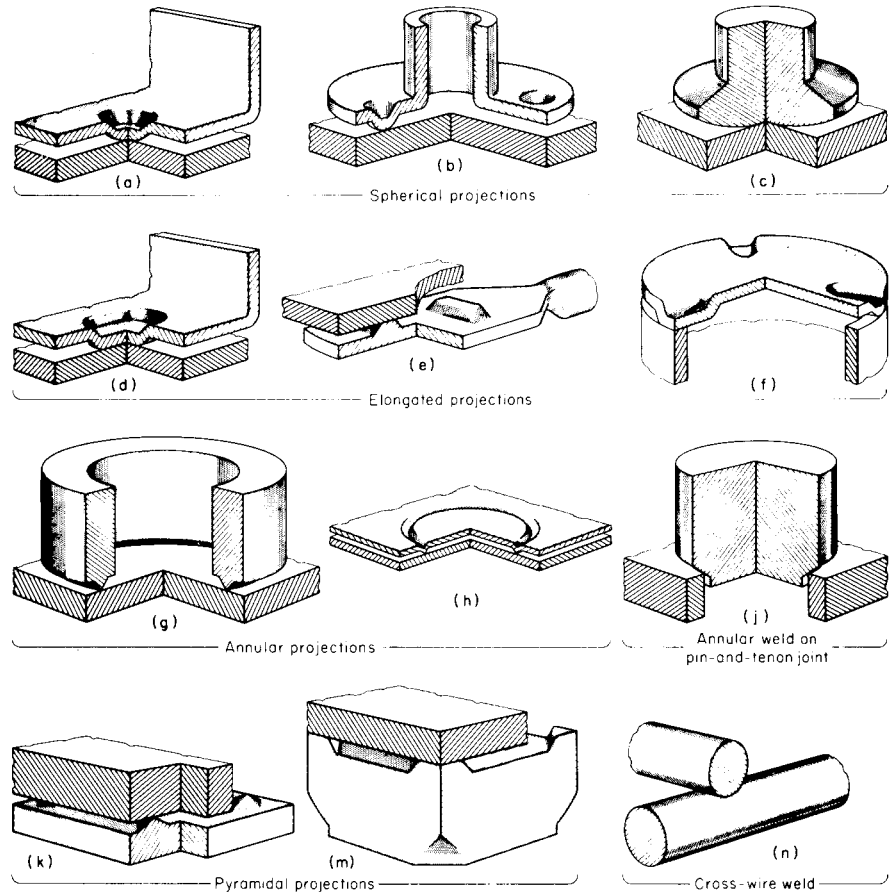


Fig. 4 Examples of embossed- and solid-projection welds

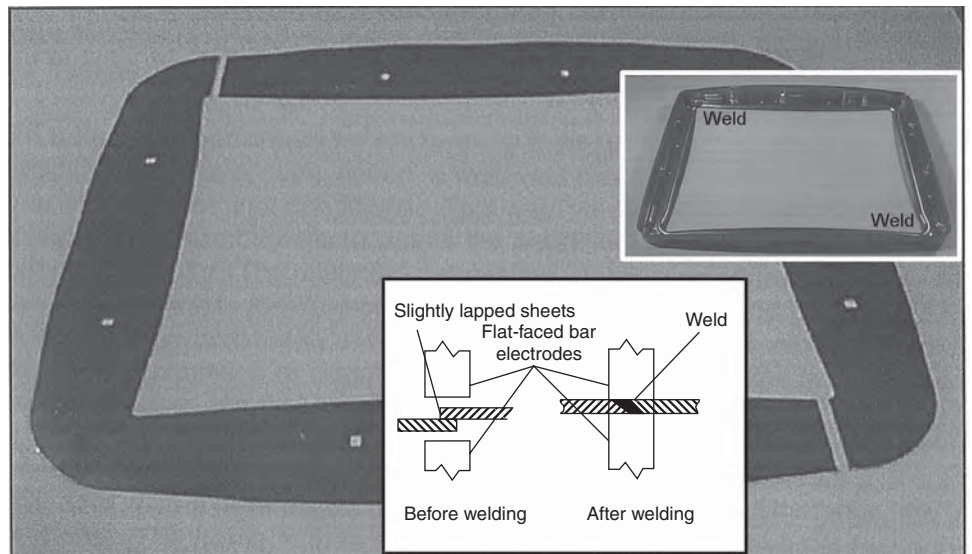


Fig. 5 Example of resistance mash weld. This application used flat-faced bar electrodes. Courtesy of Edison Welding Institutel

and the square corner of the opposing part. This is a common joint involving thick components where the wall of the pin does not deform inward during welding (approximately a 3.2 mm, or 0.125 in., minimum wall thickness is required).

Ball-to-Sheet Welds. The ball-to-sheet weld joint (Fig. 6) creates an annular solid-state weld between a hole placed in the sheet and the contacting circumference of a ball bearing. The diameters of the hole and the ball bearing should be selected to produce an approximate 90° included angle relative to the center of the ball bearing. Similar to the other forms of

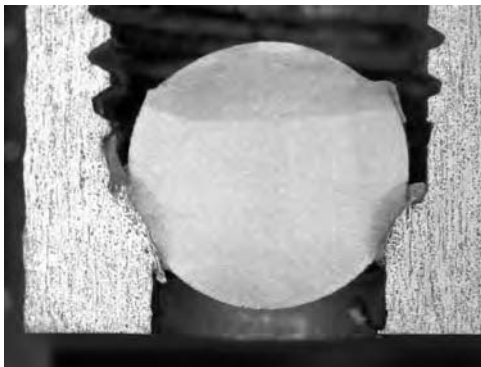


Fig. 6 Example of ball-to-sheet weld. The ball bearing is larger than the hole it is being welded into. Courtesy of Edison Welding Institute

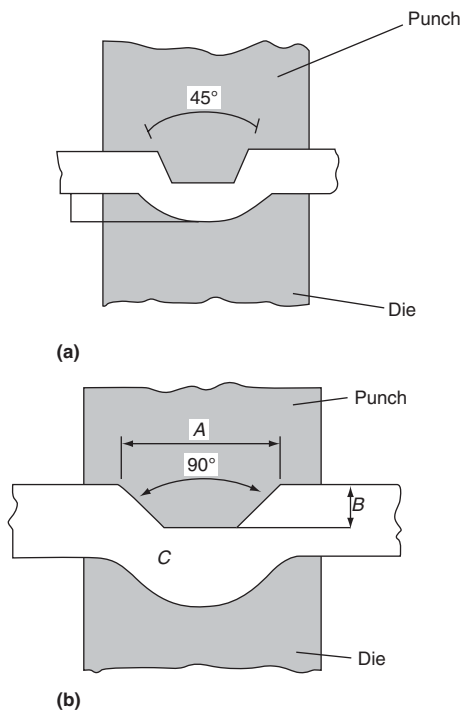


Fig. 7 Examples of coined embossed-projection designs. Source: American Welding Society and International Institute of Welding recommended projection designs, circa 1950s

annular-projection welding, the joint is generally air- and liquid-tight.

History

Embossed-Projection Welding. Projection welding was used prior to World War II; however, most of the systematic development work performed on embossed-projection welding occurred in the 1940s and 1950s on uncoated sheet. While there were many approaches to forming embossed projections described in the literature, eventually two basic types of projections were commonly investigated in the 1950s and 1960s: coined (American Welding Society, or AWS, and International Institute of Welding recommended practices) and formed (Harris and Riley, and Humpage) projection designs. Examples are shown in Fig. 7 and 8. The coined-projection styles were produced by coining between matching die sets, while the formed type projections were made by limited pushing of the sheet into an open die cavity using a punch. The formed type is subject to thinning and splitting during forming. The coined projection is thicker and stiffer. While the crush resistance of the two projection types differed, good welds could be produced with either, using optimized conditions.

Today (2011), the coined-projection designs are the most common in the United States. Originally, the primary use for projection

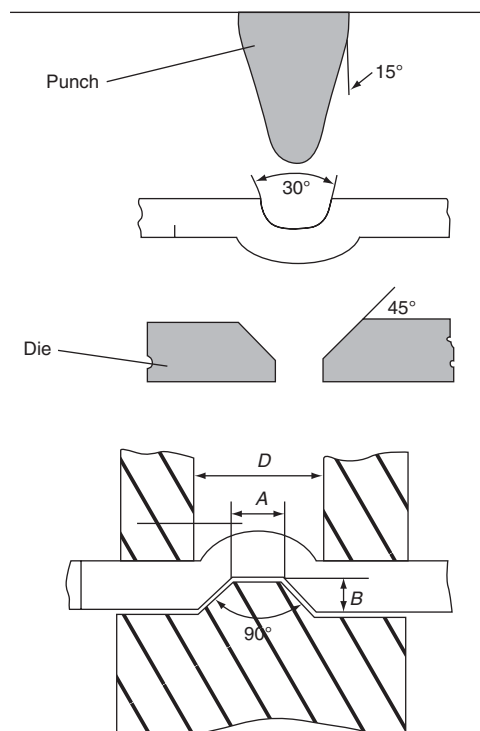


Fig. 8 Examples of formed embossed-projection designs. Source: Ref 1

welding was a means of enhancing the formation of conventional resistance weld nuggets between the sheets. Used in this way, the projection acted as a means of locating the molten weld nugget. As such, the weld times and electrode forces were somewhat similar to conventional spot welding parameters. Initial expulsion of metal during projection welding, caused by excessively rapid heating and collapse of the projection during welding, was commonly controlled through the use of weld current upslope and adjustments of electrode force.

Solid-Projection Welding. Many forms of solid-projection welding were also used prior to World War II. Due to the varied forms of solid-projection welding, there were fewer examples of systematic work defining standard projection geometries and welding parameters. Many of the solid-projection welding applications in the literature indicate the need for rapid electrode followup. This is necessary to maintain weld metal integrity and to reduce accelerated electrode wear caused by a transient loss or reduction in electrode contact during welding.

Modern Projection Welding. With continued advancements in technology and usage, the application of projection welding has widened over the years to recognize both fused weld nuggets and solid-state bond formation as legitimate modes of projection welding. A mix of fusion and solid-state welds is used in embossed-projection weld applications. However, most solid-projection weld applications are produced as solid state bonds, with a few exceptions. Some of the drivers toward the conversion from the fusion weld mode to the solid-state weld mode may be the reduced cycle time required for solid-state weld formation. Unfortunately, there is little distinction between weld schedules developed around fusion weld formation and those promoting solid-state bonding. Without clear delineations between these modes, wide variations regarding projection geometries, weld equipment requirements, and welding parameters for embossed- and solid-projection welding applications are observed in the literature.

Application Advantages and Limitations

The primary advantages of all resistance welding processes are the relatively low unit costs and the applicability to high-volume mass production environments. Typical production costs for projection welding include the additional expense of producing the projections and ensuring that the electrodes are properly located over the projections. These costs are offset by the relatively low capital and consumable costs and low maintenance requirements typical of most projection welding applications.

The advantages of projection welding are related to the ability of the process to create highly localized weld joints. This is manifested in a number of ways.

Projection welding allows multiple welds to be made simultaneously in the same station. For instance, in one application, 12 simultaneous welds are produced on a large automotive exhaust clamp. These are made in less time than required for the production of a single conventional spot weld. Similarly, embossed-projection welding is highly adaptable to the joining of multiple-sheet stacks.

Projection welding can be used in a wide range of hard-to-weld metal applications. For example, pure copper can be resistance mash welded with a narrow material overlap (IT) using a weld-and-forge technique. Other examples include welding of attachments to resulfurized free-machining components. If welded very quickly, solidification cracking can be avoided through the formation of a solid-state bond at the interface. Because no melting occurs and the forged joint generates little heat outside the contacting interface, sulfur generally does not form extensive compositionally-driven melting within the heat-affected zone (HAZ) of the welded component.

Projection welding can be used over a wide range of allowable thickness mismatches. Generally, traditional resistance welding is considered adaptable to sheet thickness variations of less than 3 to 1. However, with projection welding, there is no limit to the difference in component thicknesses.

Embossed-projection welding can be used to avoid external marking of sheet surfaces. For example, because flat electrodes are used and short weld times are used, the process is very effective at localizing heat at the faying interface and minimizing the residual heat produced on the outside surfaces.

Solid-projection welding can also be used to produce hermetic seals. Annular-projection welds are often used to seal the housing of glass-filled electrical connectors against an enclosure. Due to the very short heating cycle and moderately low electrode forces required, a projection welding can be successfully produced without significant thermal expansion of the housing and cracking of the glass.

Limitations. The limitations of the projection-welding process are largely related to the need for proper projection design and any modifications to existing resistance spot welding (RSW) equipment that may be required for optimal performance. Other limitations of projection welding include:

- Forming of one or more projections on one of the workpieces may require extra operations, unless the parts are press formed to design shape.
- When several welds are made at once with the same electrode, alignment of the work and dimensions (particularly height) of the

projections must be held to close tolerances to obtain consistent weld quality.

- When making simultaneous projection welds, the projection layout will be dictated by the shunt current paths, which may not coincide with the desired location.
- Because two parts are moving relative to each other during the welding process, proper gaging is difficult.

Material Property Effects

Solid-projection welds are essentially strain-assisted diffusion bonds (Ref 2). Because the projections typically collapse at very high temperatures (generally, within several hundred °C of the melting point), bonding can occur within the very limited available time (usually, less than 1 s).

Not surprisingly, some of the material-related factors that affect diffusion bonding also affect solid-projection welding. The most notable of these is the ability of the metal to dissolve its own oxide, such as titanium and copper. As a result, materials that do not energetically favor solid solubility of oxygen within the metal at forging temperatures, rather than the formation of the oxide at temperature, such as aluminum, will be relatively difficult to projection weld.

The strength-temperature relationship also affects projection weldability. Materials that maintain their strengths at relatively high temperatures permit substantial heating before projection collapse and a loss of strain localization. This heat then becomes available to promote diffusion after collapse of the projection. Conversely, metals exhibiting a rapid deterioration of strength at elevated temperatures cause premature projection collapse. This results in a rapid reduction in the current density, lowering welding temperatures, which slows diffusion and prohibits bonding.

Bulk resistivity also plays a role in projection welding, but to a lesser degree. Increased bulk resistivity can reduce the effectiveness of the projection as a current concentrator. Because the yield strength of most metals decreases with temperature, metals with high bulk resistivity develop heat within the projection quickly, which promotes premature collapse. This is seen as a tendency toward delocalized heating and general, rather than local, collapse of the projection. As a result, high-resistivity materials are more difficult to projection weld without appropriately altering the projection geometry.

Projection Welding of Steels. Uncoated and scale-free mild steels are usually easily projection welded. Uncoated mild steels have moderate levels of contact resistance and a moderate capacity to adsorb oxides, making them relatively easy to bond. However, metallic-coated mild steels (galvanized, aluminized, etc.) are more difficult to weld because the

coatings act as a barrier to bond formation and must be dispersed from the weld location during welding. Additionally, typical coatings have low resistivity that increases the current required to weld and promotes general yielding of the projection. Typical embossed-projection designs applied to coated sheet steels result in the direct shunting of current to the opposing sheet once the projection is nearly fully collapsed and contact between the respective coating interfaces occurs. Consequently, projection welds in galvanized steels generally require a customized projection, generally taller and narrower than standard projection designs. Sometimes, reduced electrode face diameters are also used to further concentrate current during resistance welding.

There are different concerns in projection welding high-strength steels. Projection welding, like other resistance welding processes, produces high cooling rates. Depending on the carbon content of the base metal, the hardness of the weld and the near HAZ can be very high. Additionally, these joints are often under high constraint. These conditions can lead to a loss of weld ductility and strength perpendicular to the sheet surface if postweld heat treatment is not used. Commonly, this is done by using an in situ tempering current pulse. The second current impulse is applied only after the weld and HAZ have cooled below the martensite finish temperature and without releasing the electrodes. Only proper adjustment of the magnitude of the temper current level will produce the desired improvement in weld toughness properties. Insufficient or excessive temper currents will not result in improved performance.

High-strength steels can also have relatively high electrical resistivities. This may lead to accelerated projection collapse and may require a customized projection design for best performance. Generally, a slight increase in projection height and a reduction in the base diameter are sufficient to accommodate the accelerated projection collapse compared to similar projections produced on mild steel.

Projection Welding of Aluminum and Aluminum Alloys. Aluminum and aluminum-base alloys can be very difficult to projection weld. The aluminum oxide is so tenacious that solid-projection welding, in particular, is nearly impossible by using traditional projection designs. The high initial electrical resistance of the aluminum oxide promotes surface expulsion at the projection tip. This expulsion may help remove the oxide at the initial contact location, but more extensive expulsion will harm weld quality.

In addition, it is very difficult to localize heat during the projection welding of aluminum alloys, because they soften at low temperatures. This is especially true for embossed projections. The characteristic rapid softening of the projection mandates the use of very short weld times, high currents, and low electrode force.

Rapid electrode followup head designs must be incorporated into the welding equipment. Special embossed-projection designs, with accompanying fast followup equipment, have been developed to accommodate the rapid softening and collapse characteristics of aluminum projections. Because the aluminum oxide is very stable, extensive deformation of the projection and the part surface is required to fracture and locally disperse the oxides prior to bond formation. However, weld consistency should be carefully evaluated.

Projection Welding of Copper and Copper Alloys. Projection welding is commonly applied to copper and copper-base alloys. In many applications, projections are virtually required for resistance welding, because of the generally high conductivity of these materials. In any case, projection welding must be performed very rapidly to localize heat at the faying interface. The projection should be designed to resist rapid collapse, similar to those made in aluminum.

Because electrical resistivity and strength at elevated temperatures are generally proportional, the ease of projection welding copper alloys can usually be ranked by their electrical conductivity. For alloys with relatively low electrical conductivity, heating of the contacting surfaces can be accomplished relatively easily while those of high conductivity may be very difficult. Similar to projection welding aluminum, the rapid softening of projections made in copper alloys requires very short weld times, high currents, low electrode force, and rapid electrode followup head designs incorporated into the welding equipment. However, different from welding aluminum, copper easily adsorbs its own oxide and therefore does not require the same extensive deformation to achieve bonding.

Electrodes for projection welding copper are often made of copper alloys. Some electrode sticking may occur, mandating frequent dressing. Water cooling is necessary to reduce sticking and maintain the electrode surface. In some cases, either pure or sintered refractory metals are used to avoid sticking issues. However, the refractory metal electrodes generate heat, which may promote rapid projection collapse and deterioration of weldability. Refractory electrodes are preferred in other cases, such as joining or consolidating the ends of stranded wires.

Copper alloys containing significant amounts of zinc can produce violent expulsion of metal due to the vaporization of zinc during welding. These alloys require weld schedules with short weld times and higher electrode forces. Custom projection designs may be required.

Other Metals. Low-alloy nickel-base alloys are ideal materials for projection welding, because they readily dissolve their own oxides and have adequate strength-temperature and resistivity properties. Stainless steels and higher-alloy nickel-base materials become slightly more difficult to weld because of the

formation of more-stable chromium oxide, increased high-temperature properties, and higher resistivities.

Conventional titanium alloys are relatively difficult to projection weld. Although titanium readily dissolves its own oxide, its high resistivity and low forging temperature generally cause premature collapse of the projection.

Specifications and Recommended Practices

Several recommended weld schedules and practices for the projection welding of various materials are given in the AWS publication C1.1M/C1.1:2000, "Recommended Practices for Resistance Welding." These schedules may be used as starting conditions for development of specific welding applications. This recommended practice also covers the shear and cross-tension testing method for resistance welds.

Other information sources include the current edition of the *Resistance Welding Manual*, published by the Resistance Welder Manufacturers Association, with recommended practices for projection welding and electrode materials. Several European specifications and recommended practices also can be used to define resistance projection welding applications (see the list at the end of this article along with other AWS specifications).

Automotive manufacturers have proprietary specifications and welding requirements for projection welding. These often follow other published guidelines. While not specifically called out, test methods and procedures for determining resistance spot weldability for automotive applications are defined in AWS D8.9:2002. Weld quality characteristics of individual welds may be defined by the applicable measures detailed in specification AWS D8.1M:2007. In 2007, AMS-W-6858A (2000)

and MIL-W-6858D (1992) were replaced by AWS D17.2.

Process Fundamentals

As previously mentioned, two modes (embossed and solid) of projection welding are often possible. When embossed-projection welding is used as a spot weld initiator, relatively long weld times are used to generate the bulk resistive heat at the joint interface necessary for melting to occur. Figure 9 shows the stages of projection collapse and weld nugget development in embossed projections. Early in the weld cycle, the projection serves to enhance the initial contact resistance and locate the weld at the faying interface (Fig. 9a). Unless conveyed away by thermal conduction, the initial heat generated through collapse of the projection is retained within the weld area (Fig. 9b). Further resistive heating of the bulk metal occurs with continued current flow (Fig. 9c). With sufficient energy input, a molten weld nugget will form (Fig. 9d). Generally, the weld nugget diameter will not exceed the base diameter of the projection. Used in this way, the projection acts as a heat balance technique to localize the molten weld nugget with respect to the faying interface location. Because of its similarity to the method of heating used in standard resistance welding applications, projection weld schedules that result in a molten weld nugget will often use somewhat similar values for weld time, electrode force, and so on compared to similar RSW applications. This mode is generally used only for embossed-projection welding.

Alternately, the projection can produce a solid-state bond at the faying interface, similar to the flash butt welding processes. In this case, little or no melting occurs throughout the weld cycle. The objective of this mode of welding is to produce a metallurgical bond through

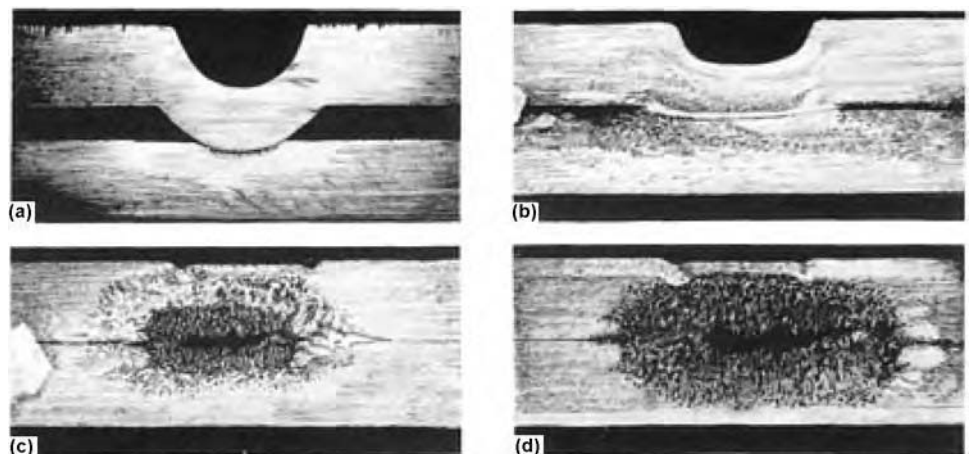


Fig. 9 Stages of projection weld collapse and nugget formation. (a) Initial condition. (b) Solid-state weld formed after 20% of total weld time. (c) Region of incipient melting after 70% of weld time. (d) Complete weld nugget at 100% of weld time

heating and collapse of the projection. The weld is formed by the appropriate combination of strain, heat, pressure, and time developed at the faying interface (Fig. 9b). During heating of the projection, the surfaces of both the contacting portions of the projection and the workpiece soften and strain, resulting in a breakup of oxides at the faying interface. For some materials, the elevated temperatures allow adsorption of some of these metal oxide fragments, depending on the solubility of the oxides within the solid metal at elevated temperatures. Deformation of the metals at the faying interface exposes metallurgically clean surfaces under intimate contact at elevated temperature and pressure. In appropriate combinations, these conditions promote bonding, provided they exist for a sufficient length of time. In some cases, a very thin transient liquid film may form early in the heating cycle. If formed, this liquid is quickly expelled or squeezed from the joint, taking with it the metal oxides that act as barriers to bond formation. This mode of projection welding uses very short weld times and high weld currents and requires equipment with good mechanical followup of the electrode.

The extent of projection collapse is limited by the establishment of mechanical equilibrium at elevated temperature and is determined by the projection design and applied electrode force. The solid-state welding mode is used primarily for solid-projection and some embossed-projection welding applications. This is especially true of metals with good electrical conductivity or when producing a molten nugget would result in an adverse metallurgical condition or when the required weld cycle time is relatively short.

Equipment

Resistance projection welding equipment may require specific modifications compared to common RSW equipment, such as the use of low-mass (inertia) weld heads. The approach rate of the head should not cause damage to the projection tip beyond that provided by the applied electrode force. A “soft” approach rate can improve weld consistency. Because the nature of projection welding is to direct current flow to the desired weld locations, there is considerably more flexibility in tooling. Conventional spot welding practice requires electrodes of specific sizes and shapes in order to localize current for welding. Projection welding uses large, flat-faced electrodes.

Additionally, projection welding equipment uses straight-acting force systems on pedestal welders, weld guns, or similar welding machines. A typical pedestal welder suitable for general-purpose projection and spot welding is illustrated in Fig. 10. Rocker-arm-type welders are generally not used. The type of force system significantly affects the mechanical electrode followup characteristics of the machine, depending on the masses of the moving components. Examples of the force systems used on projection

welding machines include pneumatic, hydraulic, “air-over-oil,” and other forms of mechanical-driven systems, such as cam operations. Pneumatic systems can provide fast response to projection moment, depending on the size of the orifices, the masses involved, and an ample supply of air. An air accumulator may be necessary to stabilize the supply pressure. Generally, hydraulic and air-over-oil systems provide slow electrode followup response. However, these may be adequate for the fusion mode of projection welding. Alternately, a separate fast followup head can be placed in line with the electrodes. Mechanical systems can provide very fast electrode followup characteristics, depending on the cam design. Servo guns may not be appropriate for projection welding. The displacement or force feedback systems that are used may not respond fast enough to match the rapid collapse of the projection during welding.

Electrode Followup. Projection welding requires high compliance or the rapid response of the loading system. This is necessary because projection welding requires the collapse of a projection, which, in turn, requires some motion of the welding head. If the followup of the welding head is insufficient, then a local loss of force will occur, potentially causing catastrophic overheating of the contacting surfaces and expulsion of metal from the joint. This causes porosity, cracking, or accelerated electrode wear. Therefore, projection welding systems typically use “fast followup” heads (Fig. 11), which consist of relatively low-inertia (mass) head components and mechanisms to maintain a nominally constant force. The head shown in Fig. 12 uses a relatively low-volume diaphragm assembly and a spring to maintain

this force on the components. Most systems, however, use either these low-volume diaphragm assemblies or springs to accomplish fast followup.

Calculating the dynamic response of the welding machine depends on the sum of the masses of the electrode, holder, and other moving components of the welder, as well as the applied electrode force and friction in the moving components. Figure 13 can be used as a guide to determine the maximum moving mass for a given level of electrode force. Generally, the sum of the moving masses should be less than 1% of the applied electrode force.

Welder Stiffness and Electrode Parallelism. The welding machine should have sufficient stiffness so that the upper electrode can remain parallel to the welding surface throughout the weld cycle. A loss of parallelism will result in expulsion during welding or poor weld quality when multiple projections are welded simultaneously. The upper and lower portions of the welder frame are sometimes tied together to improve mechanical stiffness and maintain parallelism of the electrodes. Similarly, the welded component should have sufficient stiffness, and the weld surface should be sufficiently backed up to avoid flexure of the part during welding.

Power Supply Types. Several types of weld power supplies can be used for projection welding. Standard alternating current (ac) weld power supplies are often used. These can be used in full-cycle and half-cycle operation. Traditional resistance welding equipment controls on full cycles (both positive and negative “half-cycles”) of the ac current waveform. This type of current is best used for the fusion



Fig. 10 Typical general-purpose projection and spot welder

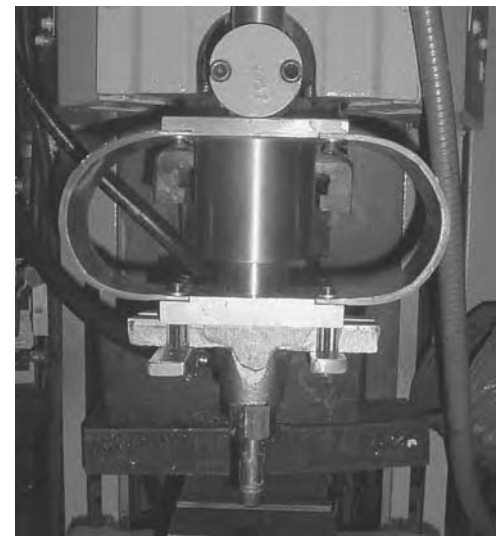


Fig. 11 Typical fast followup head for resistance welding. The spring is located in the body of the assembly. Note the shunts providing a current flow path around the spring. Courtesy of Edison Welding Institute

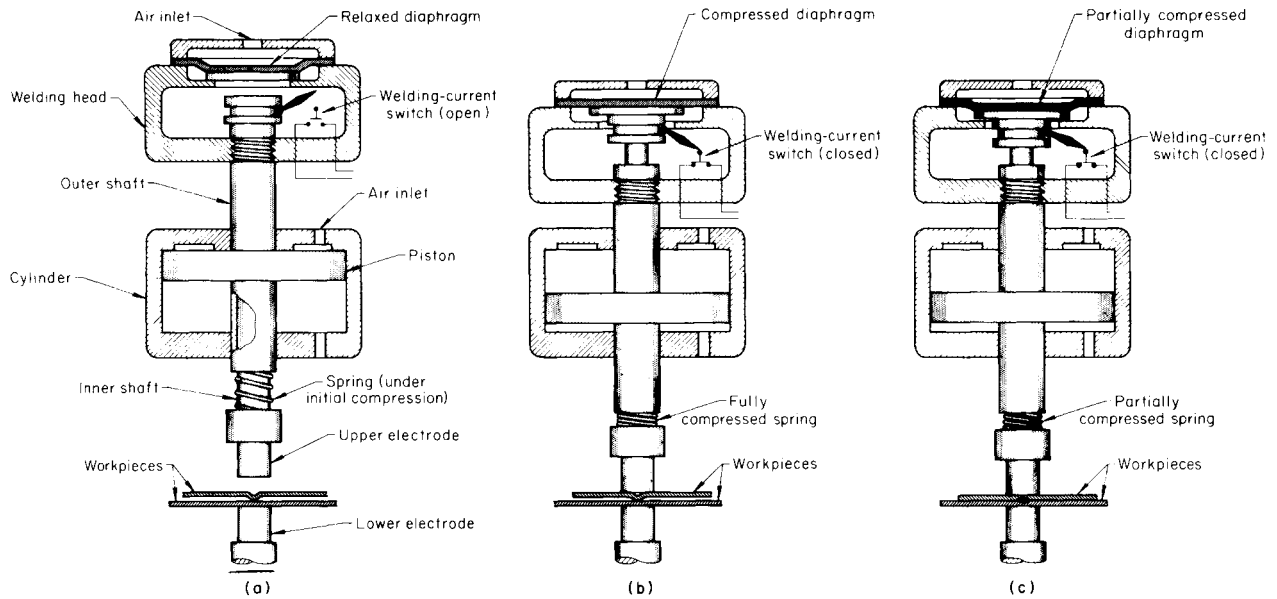


Fig. 12 Typical fast followup (low-inertia) head for projection welding. (a) In open position. (b) In position for squeezing and heating the projection. (c) At instant of projection collapse and start of nugget formation

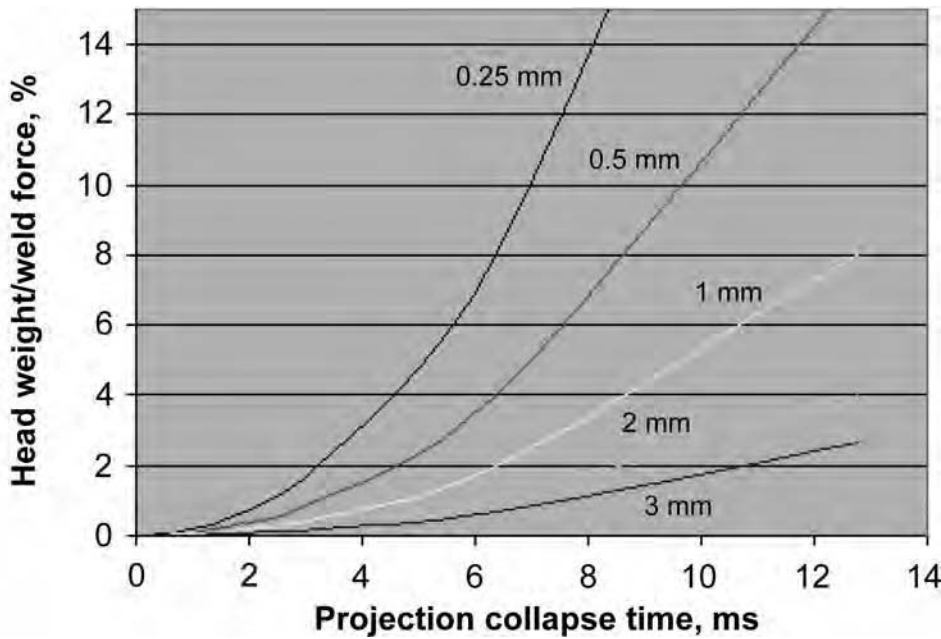


Fig. 13 Relationship between projection collapse distance, projection collapse time, and the head weight-to-weld force ratio. Courtesy of Edison Welding Institute

projection weld mode. The weld controller should be operated in constant voltage current mode rather than in constant secondary current mode. Constant current mode increases variability in weld quality for projection welding. This is because the dynamic resistance constantly changes during projection collapse, and adjustments to the weld current made

from feedback from the controller cannot be performed rapidly enough to maintain weld consistency, especially for the solid-state welding mode. Half-cycle ac weld power supplies are used in conjunction with high secondary voltage transformers to produce a very short-duration, single-impulse weld current. This effectively makes these welders a direct current

(dc)-type power supply. A stacked core transformer is recommended for these applications. These are usually used with the solid-state welding mode.

There are several types of dc power supplies. These include primary rectified dc, secondary rectified dc, midfrequency dc (MFDC), capacitive discharge, and other types of dc power sources. The dc-type power supplies do not usually exhibit the high peak currents associated with ac waveforms and therefore reduce the levels of expulsion observed during welding. As they have become more powerful, MFDC-type power supplies have rapidly replaced many types of traditional dc-type power supplies. The time to peak current is an important characteristic of dc-type power supplies. The solid-state mode of welding generally operates best with fast welding times, dictating a fast current rise time to peak current. The capacitive discharge type of dc power supplies produces a very fast rising current pulse. In some applications involving dissimilar metals, the polarity of the power should be checked to ensure that appropriate heat balance is maintained in the joint. The size and resistance of the secondary loop also influences current rise time.

Electrodes. Projection welding is typically done with large, flat electrodes. In most applications, tooling is simply shaped to match the contour of the part in the contacting location. The electrodes should be machined to produce flat parallel faces. Electrode parallelism should be checked when installed and prepared in the welding machine and when refractory-faced electrodes are used on only one side of the joint.

Personnel

Like all resistance welding processes, projection welding processes often use automated equipment, since the expertise level required to operate the equipment is relatively low. Generally, the skill levels and the health and safety issues are identical to those of conventional RSW. An area in which expertise is beneficial is the attention to detail by the operator. Resistance welding is subject to variations in setup conditions, and projection welding may be extraordinarily sensitive to setup variations in situations where the placement of projections is critical.

With limited expertise, operators or supervisory staff can visually inspect the characteristics of the process and the welds themselves to identify improper setups, as well as maintenance needs. These quality-assurance efforts, which fall under the auspices of total quality management or total quality joining, can be established with a minimum of on-line training and experience.

Process Requirements

The geometry of the projection is critical for many applications. The projection shape, base diameter, and height should be defined for optimal performance. A poorly designed projection may not be weldable in some applications. The projection should have appropriate symmetry and not be placed on the edge of the component face.

The projection shape should be selected to produce a controlled dynamic mechanical collapse, under the applied electrode force, such that the current density at the faying interface can be managed during heating and forging of the projection. Tall and slender projections tend to buckle during deformation, explode during welding, or are too stiff to promote the strain needed for bond formation. Short and wide projections tend to flatten rapidly at the contacting face and therefore provide insufficient current concentration during welding to heat or strain the faying interface for bonding.

Selecting a projection with the proper relationship between the projection height and base diameter will produce heat and strain at the faying interface, which encourages bond formation. Sometimes, an initial flat is placed on the top of the projection to avoid premature flashing during the initial surge of weld current. However, the width or diameter of this flat should be minimized because it reduces the strain developed at the projection tip.

The slope of the projection sides will govern the increase in contact area during projection collapse. The increase in conduction area should be proportional to the rate of the rising slope of the current impulse (dynamic current density), and the projection height should be sufficiently tall to develop the strain needed to

bond within the heating time allotted for the process. Similarly, if multiple projections are made simultaneously, then the projection heights should be tightly controlled. The projection geometry can be optimized for specific metals, coatings, or the mechanical performance of specific welding machines.

Tables of parameters for embossed-welding projection can be found for joining many types of metals. These should be examined in reference to the projection welding mode. This is most often indicated by weld time and electrode force specified. Weld times similar to those of RSW are used for the fusion weld mode of projection welding, but much shorter weld times are used for the solid-state mode. Weld current upslopes are usually not used for the solid-state mode of projection welding. Tabulated weld parameters for various materials are discussed as follows. Most of these are consistent with the fusion weld mode for the embossed projection designs.

Steel Embossed-Projection Welding

The embossed-projection welding of heavy-, intermediate-, and thin-gage sheet mild steel, as well as welds between dissimilar thickness joints, is described as follows.

Heavy-Gage Sheet Steels. The projection welding of heavy-gage steels, which involves an embossed-projection welding process, has many of the characteristics of solid-projection welding, particularly in its early stages, because of the thickness of the sheet.

In addition to defining the geometry of the projection, projection designs should provide an annular relief for projection material that is forged to the side during welding. Projection and die geometries for steels that range from 3.12 to 6.22 mm (0.123 to 0.245 in.) are shown in Table 1. The process requirements for forming these welds are given in Table 2. All welding schedules described in this article are single-pulse welding schedules.

Slope control is sometimes recommended to prevent preflashing of the projection upon initiation of the welding current or when the inertia of the welder is excessive. The application of a forge force is also recommended to alleviate weld porosity. Electrode or die wear may also be a concern, as it is in the spot welding of heavy-section steels. In such applications, pulsation welding schedules may be recommended.

Intermediate-Gage Sheet Steels. The projection welding of steels ranging in gage from 0.56 to 3.43 mm (0.022 to 0.135 in.), using single-point projections with single-impulse welding schedules, is well established. Projection-stamping die designs are given in Table 3, whereas process requirements are given in Table 4. Lower forces and shorter welding times are required, when compared with the conventional spot welding of these gages.

Thin-Gage Sheet. The projection welding of thin-gage steel sheet (<0.50 mm, or 0.020 in.) differs significantly from the projection welding of intermediate-gage sheet in that single-point projections become mechanically unstable. It also becomes increasingly difficult to use single-point projections to make adequate-sized welds. Therefore, annular projections are typically recommended for thin-gage steel. Table 5 provides the annular-projection weld geometry, as well as the required process conditions.

Dissimilar-Thickness Joints. As previously noted, the projection welding process is ideally suited for the joining of sheets of widely disparate thickness. When fabricating such joints, the best practice is to place the projection on the thicker sheet, where possible, using the projection design that is appropriate for the thinner sheet. This is done because the projection has the effect of concentrating the heat at the contact surface, regardless of the thicknesses of the sheets being joined. As a result, selecting conditions based on the thinner sheet has the effect of sizing the weld for that (attached) material.

Steel Solid-Projection Welding

Solid-projection welding of steels that are described as follows includes annular, nut, and cross-wire projection configurations.

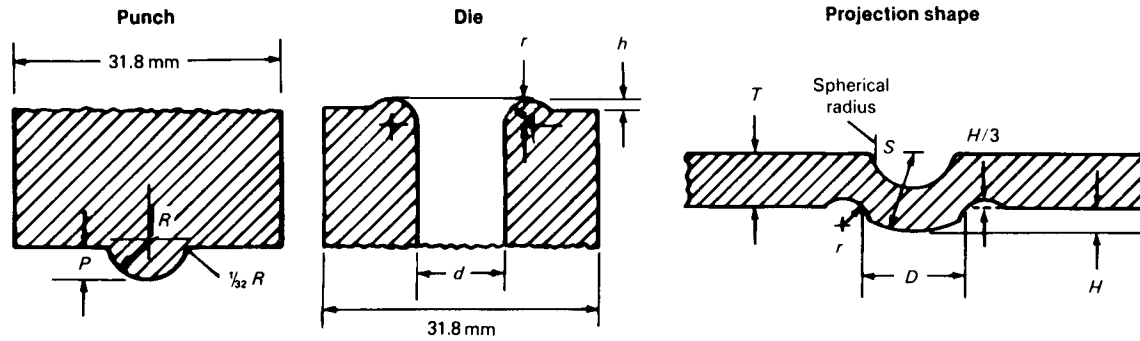
Annular-Projection Welding. Neither specific projection designs nor process conditions for annular-projection welding are well established. There is a general consensus on the use of 90° included angle triangular cross section projections in sizes that are scaled to the thickness of the opposing sheet. Typical practice includes approximately 4.5 to 8.9 kN (1000 to 2000 lbf) of force per linear inch (or 25 mm) of projection, as shown in Table 6. Weld times for annular projections for diameters ranging from 6.4 to 25 mm (0.25 to 1.0 in.) usually range from a single cycle to approximately 10 cycles. Typically, shorter welding times result in more-robust processing conditions. Maximum welding times are often limited by concerns over thermal damage to the base metal.

The best annular-projection design will recess the base diameter of the projection from the outside diameter of the part. Reasons for this are shown in Fig. 14. Projection designs that extend to the outside diameter of the part have the potential for unstable projection collapse, which can result in the formation of an incipient notch at the outside diameter of the part and an increase in the incidence of weld-related failures.

Larger-diameter annular-projection welds cause a problem in attaining the proper heat balance around the periphery of the projection. Typically, the side of the projection that is toward the throat of the machine will heat preferentially for two reasons. First, the shortest conductive (and highest current flow) path is

Table 1 Projection and die geometries for welding a range of heavy-gage steels

Data are for tool steel hardened to 50–52 HRC.



USS gage No.	Material thickness (T)		Projection						Punch				Die					
			Height (H), $\pm 2\%$		Diameter (D), $\pm 5\%$		Radius (S)		Radius (R), $\pm 0.1\text{ mm}$ ($\pm 0.005\text{ in.}$)		Height (P), $\pm 2\%$		Hole diameter (d), $\pm 0.1\text{ mm}$ ($\pm 0.005\text{ in.}$)		Recess radius (r), $r = S/3$		Recess height (h), $h = H/3$	
	mm	in.	mm	in.	mm	in.	mm	in.	mm	in.	mm	in.	mm	in.	mm	in.	mm	in.
11	3.12	0.123	1.47	0.058	6.86	0.270	4.98	0.196	2.39	0.094	1.91	0.075	5.61	0.221	1.65	0.065	0.483	0.019
10	3.42	0.135	1.57	0.062	7.62	0.300	5.46	0.215	2.77	0.109	2.06	0.081	6.35	0.250	1.83	0.072	0.508	0.020
9	3.88	0.153	1.63	0.064	8.38	0.330	5.97	0.235	3.18	0.125	2.16	0.085	6.86	0.270	1.98	0.078	0.533	0.021
8	4.17	0.164	1.73	0.068	9.14	0.360	6.30	0.248	3.58	0.141	2.31	0.091	7.54	0.297	2.11	0.083	0.584	0.023
7	4.54	0.179	2.03	0.080	9.90	0.390	6.96	0.274	3.96	0.156	2.64	0.104	8.33	0.328	2.31	0.091	0.686	0.027
6	4.95	0.195	2.13	0.084	10.4	0.410	7.26	0.286	3.96	0.156	2.82	0.111	8.59	0.338	2.41	0.095	0.711	0.028
5	5.33	0.210	2.28	0.090	11.2	0.440	7.75	0.305	4.75	0.187	3.05	0.120	9.09	0.358	2.57	0.101	0.762	0.030
4	5.72	0.225	2.54	0.100	11.9	0.470	8.26	0.325	4.75	0.187	3.35	0.132	9.35	0.368	2.74	0.108	0.838	0.033
3	6.22	0.245	2.84	0.112	13.5	0.530	9.27	0.365	4.75	0.187	3.76	0.146	10.3	0.406	3.07	0.121	0.940	0.037

Source: Ref 3

Table 2 Process requirements for projection welding of a range of heavy-gage low-carbon steels

USS gage No.	Projection size					Minimum										Upslope time(d), cycles	Weld time(d), cycles	Welding current(e), A	Tensile-shear strength(f)		
	Thickness(a)(b)		Diameter		Height		Minimum spacing, centerline to centerline				Minimum contact overlap		Electrode force weld(c)		Electrode force forge				MPa	ksi	
	mm	in.	mm	in.	mm	in.	mm	in.	mm	in.	MN	lbf	MN	lbf							
Schedule A: Welding normal-sized welds																					
9	3.89	0.153	8.38	0.330	1.57	0.062	44.5	1.75	22.9	0.9	8.9	2000	17.8	4000	15	60	15,400	52	7.5		
8	4.17	0.164	8.89	0.350	1.73	0.068	45.7	1.80	24.1	0.95	10.2	2300	20.5	4600	15	70	16,100	56	8.1		
7	4.55	0.179	9.91	0.390	2.03	0.080	48.3	1.90	25.4	1.0	11.7	2630	23.4	5260	20	82	17,400	66	9.5		
6	4.95	0.195	1.04	0.410	2.13	0.084	50.8	2.00	26.7	1.05	13.0	2930	26.1	5860	20	98	18,800	78	11.3		
5	5.33	0.210	1.12	0.440	2.34	0.092	53.3	2.10	29.2	1.15	14.2	3180	28.3	6360	25	112	20,200	86	12.5		
4	5.72	0.225	1.19	0.470	2.54	0.100	33.0	1.30	30.5	1.20	16.1	3610	32.1	7220	25	126	21,500	103	15.0		
3	6.22	0.245	1.35	0.530	2.84	0.112	63.5	2.50	33.0	1.30	17.4	3900	34.7	7800	30	145	23,300	119	17.3		
Schedule B: Welding small-sized welds																					
9	3.89	0.153	6.86	0.270	1.47	0.058	40.6	1.60	19.1	0.75	6.2	1400	12.5	2800	15	60	11,100	35	5.1		
8	4.17	0.164	7.37	0.290	1.57	0.062	41.9	1.65	20.3	0.80	6.3	1425	12.7	2850	15	70	11,800	38	5.5		
7	4.55	0.179	7.87	0.310	1.70	0.067	43.2	1.70	21.6	0.85	6.7	1500	13.4	3000	20	82	12,800	45	6.5		
6	4.95	0.195	8.38	0.330	1.83	0.072	44.5	1.75	22.9	0.90	7.1	1600	14.2	3200	20	98	13,900	53	7.7		
5	5.33	0.210	8.89	0.350	1.96	0.077	45.7	1.80	24.1	0.95	7.7	1730	15.4	3460	25	112	14,900	59	8.5		
4	5.72	0.225	9.40	0.370	2.08	0.082	48.3	1.90	25.4	1.00	8.3	1870	16.6	3740	25	126	16,000	72	10.4		
3	6.22	0.245	9.91	0.390	2.24	0.088	53.3	2.10	27.9	1.10	9.3	2100	18.7	4200	30	145	17,300	83	12.0		

(a) Low-carbon steel, SAE 1005–1010, 290–380 MPa (42–55 ksi) ultimate tensile strength. (b) Surface of steel may be oiled lightly but free from grease, scale, and dirt. (c) On single-force welds, use only weld force as electrode force. Electrode force contains no factor to further form poorly made parts. (d) Based on 60 Hz. (e) Starting values shown are based on experience of Resistance Welder Manufacturers Association member companies. (f) Tensile-shear strength per projection depends on the joint design. Source: Ref 3

along the inside of the throat, including the inboard side of the projection. Second, there is an inductive “skin” effect associated with alternating-current machines, which tends to concentrate current along the inside of the welder throat. Intermediate-diameter projections have

been successfully welded using direct current, because it minimizes the skin effect and appears to allow better heat balance.

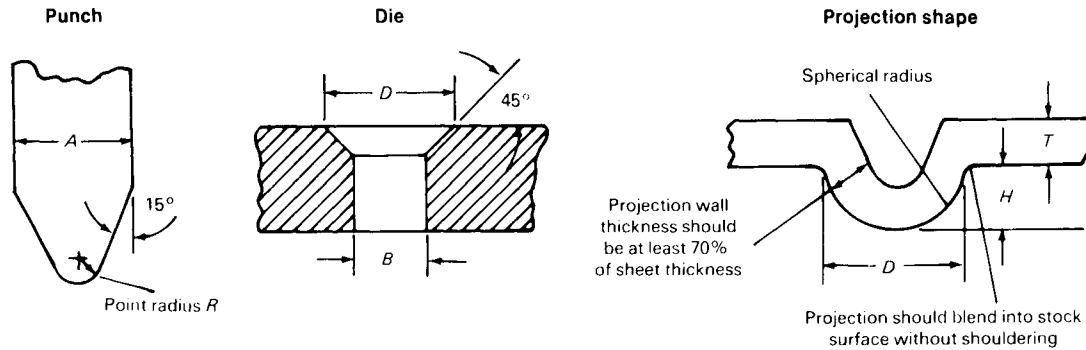
Larger-diameter projections may require dual-throat machines, which have dual transformers located on opposite sides of the

workpiece. Each has its own “throat.” The effect is to balance the resistive/inductive effects, allowing the welding of very large-diameter projections.

Nut Welding. Specific criteria for the design of weld nut projections, as well as appropriate

Table 3 Projection and die geometries for welding a range of intermediate-gage steels to make spherical projections

Data are for tool steel hardened to 50–52 HRC.



USS gage no.	Projection						Punch				Die			
	Material thickness (T)		Height (H), +2%		Diameter (D), +5%		Diameter (A)		Point radius (R), +0.05 mm (+0.002 in.)		Hole diameter (B), +0.1 mm (+0.005 in.)		Chamber diameter (D)	
	mm	in.	mm	in.	mm	in.	mm	in.	mm	in.	mm	in.	mm	in.
25–21	0.56–0.86	0.022–0.034	0.64	0.025	2.3	0.090	9.53	0.375	0.79	0.031	1.93	0.076	2.29	0.090
20–19	0.91–1.1	0.036–0.043	0.89	0.035	2.8	0.110	9.53	0.375	1.19	0.047	2.26	0.089	2.79	0.110
18–17	1.2–1.4	0.049–0.054	0.97	0.038	3.6	0.140	9.53	0.375	1.19	0.047	2.64	0.104	3.56	0.140
16–15	1.5–1.7	0.061–0.067	1.1	0.042	3.8	0.150	9.53	0.375	1.57	0.062	3.05	0.120	3.81	0.150
14	1.9	0.077	1.2	0.048	4.6	0.180	9.53	0.375	1.57	0.062	3.66	0.144	4.57	0.180
13	2.3	0.092	1.3	0.050	5.3	0.210	12.7	0.500	1.98	0.078	4.37	0.172	5.33	0.210
12	2.72	0.107	1.4	0.055	6.1	0.240	12.7	0.500	1.98	0.078	4.98	0.196	6.10	0.240
11	3.12	0.123	1.5	0.058	6.9	0.270	12.7	0.500	2.39	0.094	5.61	0.221	6.86	0.270
10	3.43	0.135	1.6	0.062	7.6	0.300	12.7	0.500	2.77	0.109	6.35	0.250	7.62	0.300

Source: Ref 3

processing conditions, are not well established. The weld current should be set to relatively high values, with weld times set to relatively short values. The weld current and time should be adjusted to achieve bonding while avoiding expulsion. Too high of an electrode force will produce inconsistent results, while too little force will promote expulsion.

There is a general consensus that the ideal number of projections on a weld nut is three, because it is assumed that all three will contact the opposing surface when the electrode force is applied, if the projections are of the same height and if the electrodes are aligned properly.

The actual design of the welding projections is not well established, although 90° included-angle square pyramidal, truncated cone, and hemispherical projections are common. When changing from one projection design to another, the height-to-base diameter ratio of the projection should roughly be maintained. Projection dimensions are nominally scaled according to the opposing sheet. Designs for embossed projections of the appropriate sheet size can be used as a guideline. The projections should be symmetric and not placed on the edges of the weld nut.

Cross-Wire Welding. The process conditions for the cross-wire welding of a range of wire thicknesses are given in Table 7. The conditions are usually specified in terms of requirements to achieve a certain level of compression set-down for the wires. Set-down is defined in Fig. 15. In general, joint strength increases as

the degree of set-down increases. The defined process conditions are for mild steels. Higher-strength materials, such as stainless steels or nickel-base alloys, will require higher forces and longer welding times to promote wire collapse and diffusion across the bond line.

Sources of Defects

The most common defects in projection welding include lack of bonding, cracking, holes, porosity, and cratering from metal expelled from the projection base. Lack of bonding (Fig. 16) is the result of insufficient heat to produce a fusion weld nugget or insufficient heat generated during projection collapse to produce bonding. Most often this is due to improper projection designs or imbalances in weld current levels, weld times, and electrode forces. Cracking, holes, and porosity (Fig. 17) can occur in projection welding from causes similar to RSW. This includes high hardness of the weld or HAZ, low-melting constituents in the weld metal, expulsion, and so on. Expulsion (Fig. 18) is often caused by excessive current, insufficient electrode force, inadequate electrode force followup, improper projection design, or excessive weld time.

Electrode wear can also deteriorate weld quality. Repeated welding operations can cause pitting, electrode contamination, or erosion of the electrode face. These can alter the heat generated at the electrode face or reduce the

effectiveness of projection collapse. Pitting or contamination can alter the heat generated at the electrode surface. For thermally conductive materials, increases in heat generated at the electrode interface can diffuse into the projection and soften it, causing premature collapse. Alternatively, electrode face contamination can reduce the heat generated at the faying interface or change the heat balance of the joint, resulting in a loss of weld quality. Locally deep erosion of the electrode face can reduce the available projection collapse distance during welding and reduce bond quality. Electrode wear can be reduced by improving the flow of coolant (water) through the electrodes and by electrode dressing. Accelerated electrode wear can also be caused by insufficient squeeze and hold times, electrode geometry, followup characteristics, and the quality of the refractory used on the electrode face.

Excessive weld current can produce a number of undesirable effects. Expulsion can also contaminate the threads on a weld nut application or make a fluid-carrying device unusable. It can cause surface marking on show surfaces. Incidental contact between the components (Fig. 19) during projection welding can shunt weld current and cause expulsion away from the intended weld location.

Quality Control and Inspection

There are many tests that can be used to validate projection weld quality. These tests

Table 4 Process requirements for projection welding of a range of intermediate-gage low-carbon steels



Configuration(a)	USS gage No.	Projection size						Minimum spacing centerline to centerline		Minimum contact overlap	
		Material thickness		Diameter		Height		mm	in.	mm	in.
		mm	in.	mm	in.	mm	in.				
A	25	0.559	0.022	2.29	0.090	0.635	0.025	9.65	0.38	6.35	0.25
B	23	0.711	0.028	2.29	0.090	0.635	0.025	9.65	0.38	6.35	0.25
C	21	0.864	0.034	2.79	0.110	0.889	0.035	12.7	0.50	9.65	0.38
D	19	1.09	0.043	2.79	0.110	0.889	0.035	12.7	0.50	9.65	0.38
E	18	1.24	0.049	3.56	0.140	0.965	0.038	19.1	0.75	12.7	0.50
F	16	1.55	0.061	3.81	0.150	1.07	0.042	19.1	0.75	12.7	0.50
G	14	1.96	0.077	4.57	0.180	1.22	0.048	22.4	0.88	12.7	0.50
H	13	2.34	0.092	5.33	0.210	1.27	0.050	26.9	1.06	15.7	0.62
I	12	2.72	0.107	6.10	0.240	1.40	0.055	31.8	1.25	19.1	0.75
J	11	3.12	0.123	6.86	0.270	1.47	0.058	38.1	1.50	20.6	0.81
K	10	3.43	0.135	7.62	0.300	1.57	0.062	41.4	1.63	22.4	0.88

Data are for SAE 1005–1010 steels with ultimate tensile strengths ranging from 290–380 MPa (42–55 ksi). Surface of steel may be oiled lightly but must be free from grease, scale, and dirt.

Configuration(a)	Weld time(b), cycles	Electrode force(c)		Welding current(d), A	Tensile-shear strength(e)	
		kN	lbf		kN	KIP
Welding schedule A (for single projection)(f)						
A	3	0.67	150	4,400	1.65	0.37
B	3	0.87	195	5,500	2.22	0.50
C	3	1.1	240	6,600	3.11	0.70
D	5	1.5	330	8,000	4.71	1.06
E	8	1.8	400	8,800	5.78	1.30
F	10	2.4	550	10,300	8.01	1.80
G	14	3.6	800	11,850	10.79	2.43
H	16	4.5	1020	13,150	14.46	3.25
I	19	5.6	1250	14,100	17.12	3.85
J	22	6.7	1500	14,850	21.35	4.80
K	24	7.3	1650	15,300	24.46	5.50
Welding schedule B (for 1–3 projections), each projection(g)						
A	6	0.67	150	3,850	1.45	0.33
B	6	0.67	150	4,450	1.89	0.43
C	6	0.67	150	5,100	2.34	0.53
D	10	0.93	210	6,000	3.89	0.88
E	16	1.2	270	6,500	4.89	1.10
F	20	1.6	365	7,650	7.01	1.58
G	28	2.4	530	8,850	9.56	2.15
H	32	3.0	680	9,750	12.45	2.80
I	38	3.7	830	10,600	15.35	3.45
J	45	4.5	1000	11,300	18.68	4.20
K	48	4.9	1100	11,850	21.57	4.85
Welding schedule C (for ≥3 projections), each projection(h)						
A	6	0.36	80	2900	1.29	0.29
B	8	0.45	100	3300	1.51	0.34
C	11	0.56	125	3800	1.89	0.43
D	15	0.71	160	4300	3.20	0.72
E	19	0.98	220	4600	3.89	0.88
F	25	1.5	330	5400	5.45	1.23
G	34	2.1	470	6400	7.78	1.75
H	42	2.7	610	7200	10.34	2.33
I	50	3.3	740	8300	12.90	2.90
J	60	4.0	900	9200	16.01	3.60
K	66	4.5	1000	9900	18.90	4.25

(a) Configuration designations are for the purposes of this table only. (b) Based on 60 Hz. (c) Electrode force contains no factor to further form poorly made parts. (d) Starting values shown are based on experience of Resistance Welder Manufacturers Association member companies. (e) Tensile-shear strength per projection depends on the joint design. (f) Schedule A is usable for welding more than one projection if current is decreased, but excessive weld expulsion may result and power demand will be greater than that for schedule B or C. (g) Schedule B is usable for welding more than three projections, but some weld expulsion may result, and power demand will be greater than that for schedule C. (h) Schedule C is usable for welding less than three projections with weld current increased approximately 15% and possible objectionable final sheet separation. Source: Ref 3

measure the strength, ductility, performance, or integrity of the bond.

Shear- or normal-type tensile tests (Fig. 20) can be performed, typical of other RSW applications. These tests can be applied to coupons or actual components in orientations representative of part performance. It provides a good measure of weld strength, but in some cases, it may not accurately describe weld ductility.

The peel test (Fig. 21) is frequently used on the shop floor to assess weld quality. It provides a qualitative assessment of weld ductility and strength.

The pushoff test (Fig. 22) is often the best test for defining weld quality of annular-projection or multiprojection welded components. It consists of pushing or pulling the welded component from the part in an orientation normal to the sample surface. The peak load and/or displacement is recorded. Interpretation of the fracture appearance also provides significant clues to weld performance or quality. Usually, the pushoff test is much more discriminating than the torque test.

The torque test (Fig. 23) is widely used on welded nut and similar configurations. Like the shear or tensile test, the torque test also places the weld under a shear-type load. However, the torque values commonly applied are representative of the part usage rather than its loading capacity. Additionally, this test does not assess the ductility of the weld. Because of the limited test torques often used and the orientation of the stresses, the torque test should be used as a proof test method. Other tests should be used to develop the production weld schedules.

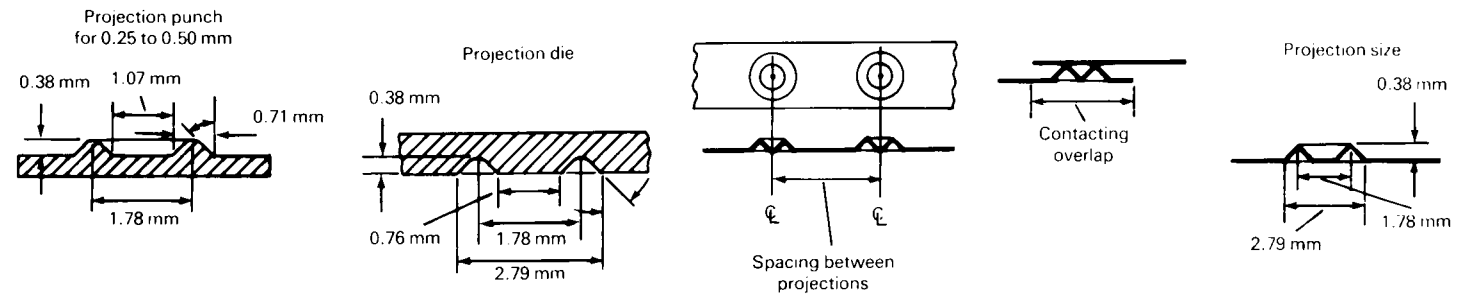
Metallographic inspection is a common method to assess bond line quality. Other metallurgical features (hardness distribution, grain size, etc.) of the weld can also be assessed. While it does not provide numerical values or assess the whole weld, metallurgical inspections can be invaluable for interpreting other test results.

The current range test is actually a set of test results that measure weld quality over a range of weld currents. When used as a quality measure in conjunction with changes to projection geometry, an optimal projection geometry can be defined for a specific application.

Projection set-down (Fig. 24) can be a useful indicator of weld quality, when it has been correlated with weld performance using some other weld quality test method. It is nondestructive and often can be used in feedback control schemes.

Feedback controller systems are available that can monitor weld voltage and current to compute dynamic resistance. Displacement of the weld head can also be monitored. This measure can often be directly related to weld quality. To be effective, the monitored displacement must measure the projection set-down. Displacement measurements within the fast followup head can be used to characterize the dynamic force applied to single projections. Displacement of the upper ram can be used to identify stiction (dynamic friction) issues with the welder.

Table 5 Projection designs and process requirements for annular-projection welding of thin-gage low-carbon steel



USS gage No.	Thickness(a)(b)		Minimum spacing centerline to centerline		Minimum contact overlap		Weld time(c), cycles	Electrode force(d)		Welding current(e), A	Tensile-shear strength each projection(f)			
	mm	in.	mm	in.	mm	in.		N	lbf		One		Two or more	
31	0.279	0.011	7.87	0.31	6.35	0.25	6	490	110	5200	1.3	0.19	1.0	0.14
26	0.483	0.019	7.87	0.31	6.35	0.25	6	1000	225	5400	2.8	0.40	1.9	0.28

(a) SAE 1010, low-carbon steel, 290–380 MPa (42–55 ksi) ultimate tensile strength. (b) Surface of steel may be oiled lightly but must be free from grease, scale, and dirt. (c) Based on 60 Hz. (d) Electrode force contains no factor to further form poorly made parts. (e) Starting values shown are based on experience of Resistance Welder Manufacturers Association member companies. (f) Approximate strength per projection depends on joint design. Source: Ref 3

Table 6 Projection design and process requirements for 90° included-angle solid annular projections

Sheet thickness		Projection height		Distance of projection base from edge		Projection base width		Electrode force		Weld current	
mm	in.	mm	in.	mm	in.	mm	in.	N/mm	lb/in.	KA/mm	KA/in.
0.76	0.03	0.51	0.02	0.13	0.005	1.02	0.040	128	731	356	14
1.02	0.04	0.61	0.02	0.15	0.006	1.22	0.048	158	900	356	14
1.27	0.05	0.71	0.03	0.18	0.007	1.42	0.056	184	1050	381	15
1.52	0.06	0.81	0.03	0.20	0.008	1.63	0.064	207	1181	381	15
1.78	0.07	1.02	0.04	0.25	0.010	2.03	0.080	263	1500	381	15
2.03	0.08	1.22	0.05	0.30	0.012	2.44	0.096	315	1800	406	16
2.29	0.09	1.42	0.06	0.36	0.014	2.84	0.112	368	2100	406	16
2.54	0.10	1.63	0.06	0.41	0.016	3.25	0.128	420	2400	432	17
3.18	0.13	1.83	0.07	0.46	0.018	3.66	0.144	473	2700	432	17
3.81	0.15	2.13	0.08	0.53	0.021	4.27	0.168	552	3150	457	18
4.45	0.18	2.44	0.10	0.61	0.024	4.88	0.192	630	3600	508	20
5.08	0.20	2.74	0.11	0.69	0.027	5.49	0.216	709	4050	559	22
5.72	0.23	3.05	0.12	0.76	0.030	6.10	0.240	788	4500	610	24
6.35	0.25	3.35	0.13	0.84	0.033	6.71	0.264	867	4950	660	26

Source: Edison Welding Institute

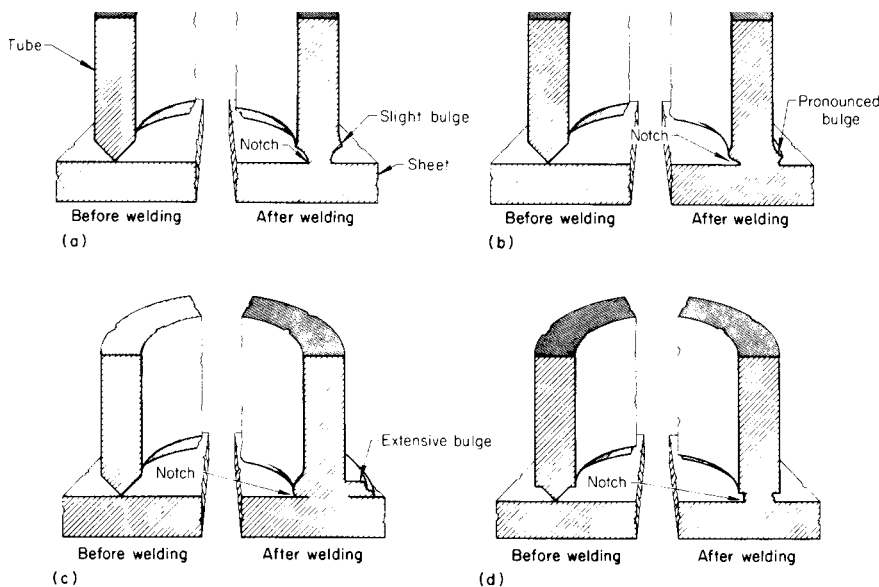


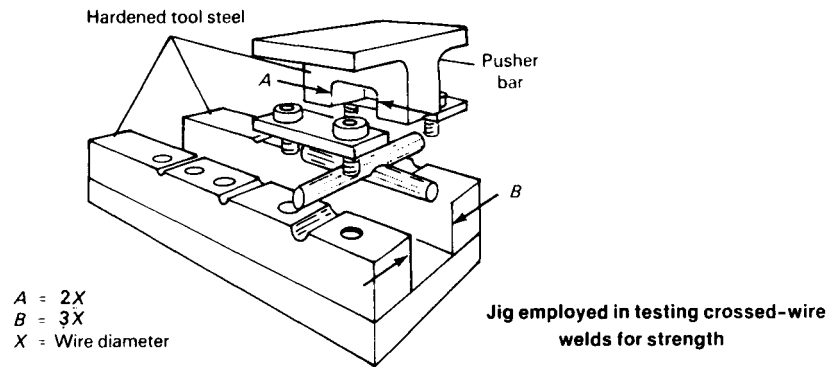
Fig. 14 Characteristics of projection collapse during annular-projection welding with different base widths. (a) Short weld time, full-width projection. (b) Correct weld time, full-width projection. (c) Excessive weld time, full-width projection. (d) Correct weld time, reduced-width projection

Safety

Safety concerns on projection welding are similar to those for other resistance welding processes. Concerns over pinching and crushing hazards, sharp metal edges, hazardous fumes, metal expulsion, hot work, electrical grounding and shock hazards, and other issues are identical because the welding equipment and base materials are very similar.

Personal safety equipment includes protective eyewear, gloves, wrist and arm guards, and so on. The welding machines can be further guarded in a number of ways. Some of these include two hand initiation switches, light curtains, barrier guards and locks, various other proximity sensors, electrical continuity monitoring, ground fault current relays, and so on. These are common to other forms of resistance welding.

Table 7 Process requirements for cross-wire welding of hot- and cold-drawn steel wires in a range of thicknesses



Wire diameter		Weld time(a), cycles	Cold-drawn wire			Weld strength			Hot-drawn wire			Weld strength	
mm	in.		kN	lbf	Welding current(b), A	MPa	ksi	Weld time(a), cycles	kN	lbf	Welding current(b), A	MPa	ksi
15% set-down													
0.63	1/16	5	0.45	100	600	3.1	0.45	5	0.45	100	600	2.4	0.35
3.18	1/8	10	0.56	125	1,800	6.8	0.98	10	0.56	125	1,850	5.2	0.75
4.76	3/16	17	1.60	360	3,300	13.8	2.0	17	1.60	360	3,500	10.3	1.5
6.35	1/4	23	2.58	580	4,500	25.5	3.7	23	2.58	580	4,900	19.3	2.8
7.94	5/16	30	3.67	825	6,200	35.2	5.1	30	3.67	825	6,600	31.7	4.6
9.53	3/8	40	4.90	1,100	7,400	46.2	6.7	40	4.90	1,100	7,700	42.7	6.2
11.1	7/16	50	6.22	1,400	9,300	66.2	9.6	50	6.22	1,400	10,000	60.7	8.8
12.7	1/2	60	7.57	1,700	10,300	84.1	12.2	60	7.57	1,700	11,000	79.3	11.5
30% set-down													
0.63	1/16	5	0.67	150	800	3.4	0.500	5	0.67	150	800	2.8	0.40
3.18	1/8	10	1.16	260	2,650	7.6	1.1	10	1.16	260	2,770	5.9	0.85
4.76	3/16	17	2.67	600	5,000	16.5	2.4	17	2.67	600	5,100	11.7	1.7
6.35	1/4	23	3.78	850	6,700	29.0	4.2	23	3.78	850	7,100	20.7	3.0
7.94	5/16	30	6.45	1,450	9,300	42.1	6.1	30	6.45	1,450	9,600	34.5	5.0
9.53	3/8	40	9.17	2,060	11,300	57.9	8.4	40	9.17	2,060	11,800	46.9	6.8
11.1	7/16	50	12.9	2,900	13,800	77.9	11.3	50	12.9	2,900	14,000	66.2	9.6
12.7	1/2	60	15.1	3,400	15,800	93.8	13.6	60	15.1	3,400	16,500	85.5	12.4
50% set-down													
0.63	1/16	5	0.89	200	1,000	3.8	0.55	5	0.89	200	1,000	3.1	0.45
3.18	1/8	10	1.56	350	3,400	9.0	1.3	10	1.56	350	3,500	6.2	0.90
4.76	3/16	17	3.34	750	6,000	17.2	2.5	17	3.34	750	6,300	12.4	1.8
6.35	1/4	23	5.52	1,240	8,600	30.3	4.4	23	5.52	1,240	9,000	21.4	3.1
7.94	5/16	30	8.90	2,000	11,400	44.8	6.5	30	8.90	2,000	12,000	36.5	5.3
9.53	3/8	40	13.4	3,000	14,400	60.7	8.8	40	13.4	3,000	14,900	49.6	7.2
11.1	7/16	50	19.8	4,450	17,400	82.1	11.9	50	19.8	4,450	18,000	70.3	10.2
12.7	1/2	60	23.6	5,300	21,000	100.7	14.6	60	23.6	5,300	22,000	89.6	13.0

(a) 60 Hz. (b) Starting values shown are based on experience of Resistance Welder Manufacturers Association member companies. Source: Ref 3

List of specifications

- AMS-W-6858A (2000) or MIL-W-6858D (1992), "Welding, Resistance: Spot and Seam," replaced by AWS D17.2
- AWS C1.1M/C1.1:2000, "Recommended Practices for Resistance Welding"
- AWS C1.4M/C1.4:2009, "Specification for Resistance Welding of Carbon and Low-Alloy Steels"
- AWS C1.5:2009, "Specification for the Qualification of Resistance Welding Technicians"
- AWS D8.1M:2007, "Specification for Automotive Weld Quality—Resistance Spot Welding of Steel"
- AWS D8.6:2005, "Specification for Automotive Resistance Spot Welding Electrodes"
- AWS D8.9:2002, "Recommended Practices for Test Methods for Evaluating Resistance Spot Welding Behavior of Automotive Sheet Steel Materials"
- AWS D17.2:2007, "Specification for Resistance Welding for Aerospace Applications"
- BS 7670, "Steel Nuts and Bolts for Resistance Projection Welding"
- EN 28167 (ISO 8167:1989), "Projections for Resistance Welding"
- EN ISO 14270, "Specimen Dimensions and Procedure for Mechanized Peel Testing Resistance Spot, Seam, and Embossed Projection Welds"
- EN ISO 14271:2001, "Vickers Hardness Testing of Resistance Spot, Projection, and Seam Welds (Low Load and Microhardness)"

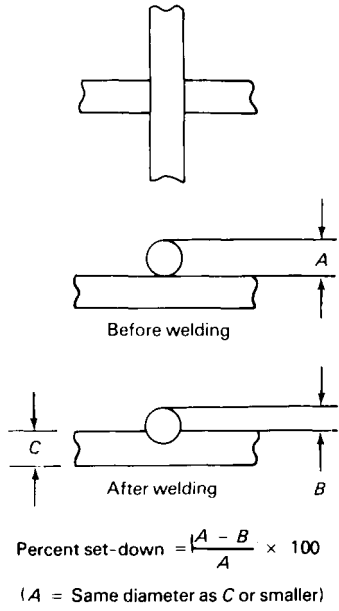


Fig. 15 Illustration of cross-wire weld and set-down measurement

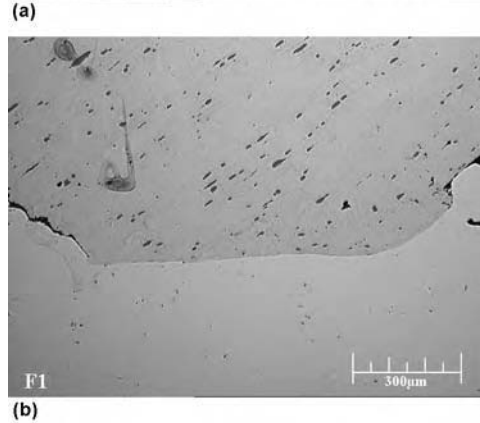
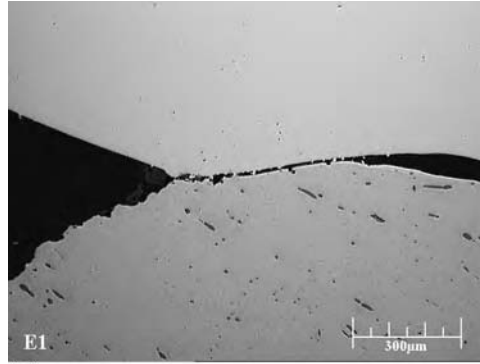


Fig. 16 Weld micrographs showing (a) lack of bonding features and (b) good bonding. Courtesy of Edison Welding Institute

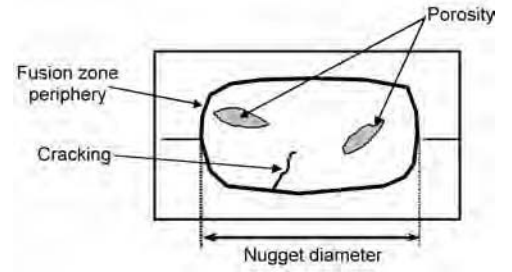


Fig. 17 Typical cracking and porosity metallographic features. Extracted and edited from AWS D8.1 drawing

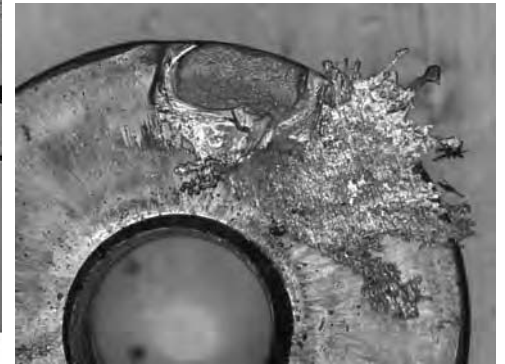


Fig. 18 Example of expulsion during projection welding

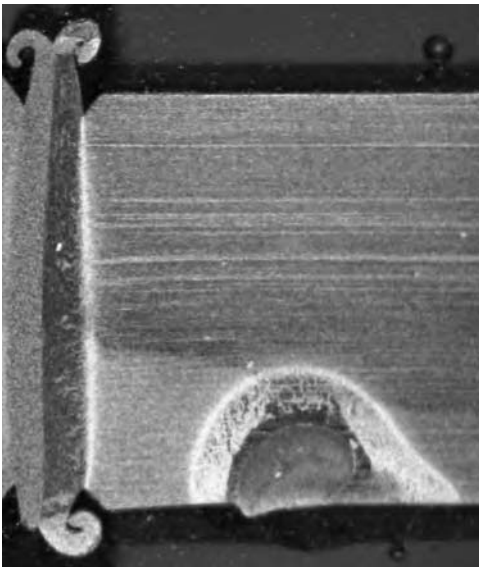


Fig. 19 Example of burning of adjacent components due to incidental contact during welding. Courtesy of Edison Welding Institute

Sheet thickness		Coupon length (L)(a)		Coupon width (W)(b)		Overlap (O)(b)		Sample length (SL)(a)		Unclamped length (UL)(b)		Gripped length (GL)(a)	
mm	in.	mm	in.	mm	in.	mm	in.	mm	in.	mm	in.	mm	in.
0.60–1.29	0.02–0.05	105	4.1	45	1.8	35	1.4	175	6.9	95	3.7	40	1.6
1.30–3.00	0.05–0.12	138	5.4	60	2.4	45	1.8	230	9.1	105	4.1	62.5	2.5

(a) May be increased to accommodate gripping fixtures. (b) Tolerance: ±1 mm (0.04 in.)

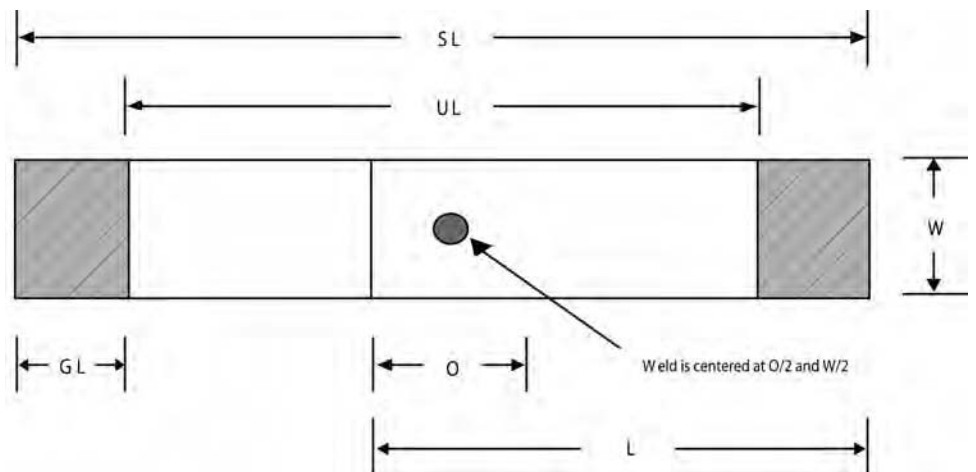


Fig. 20 Example of tensile-shear test coupon. Source: AWS D8.9F

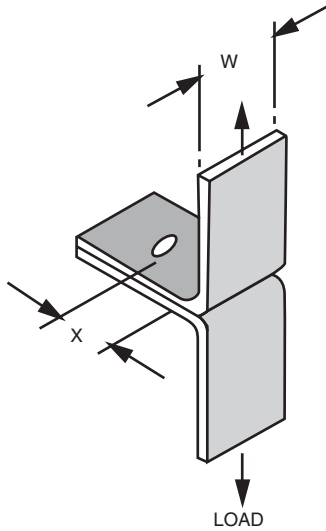


Fig. 21 Example of coach peel test coupon



Fig. 22 Example of pushoff test coupon on a projection weld nut. The bottom support has been cut away to show nut placement. The test measures the peak load to weld failure. Courtesy of Edison Welding Institute



Fig. 24 Example of projection set-down measurement. Courtesy of Edison Welding Institute

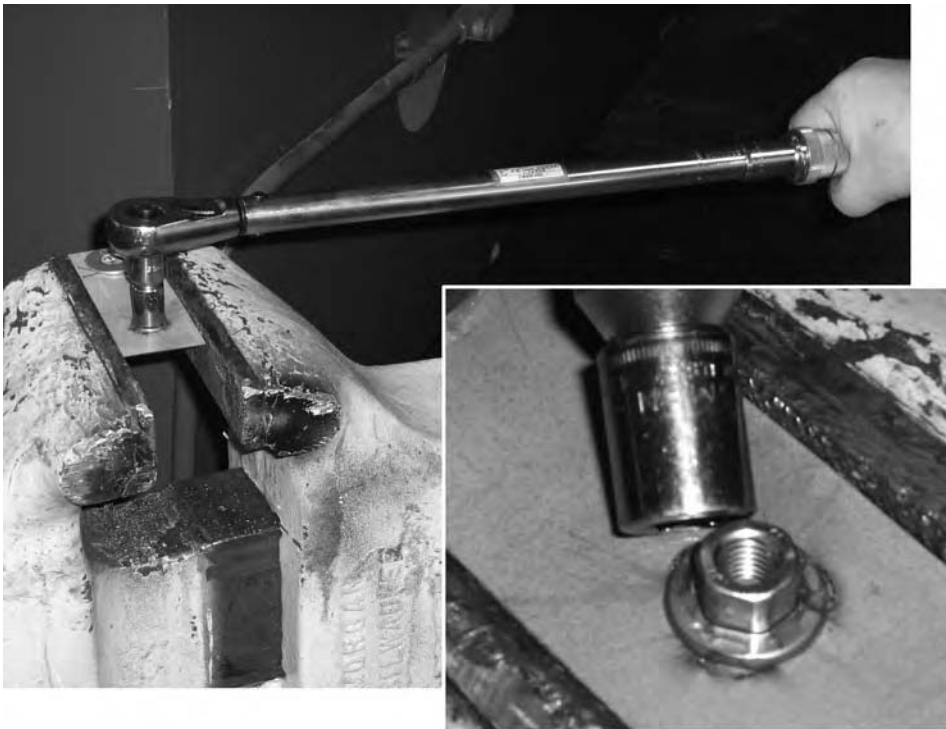


Fig. 23 Example of torque test being performed. The weld is proof tested to a specific torque value. Courtesy of Edison Welding Institute

- EN ISO 14272:2002, “Specimen Dimensions and Procedure for Cross Tension Testing Resistance Spot and Embossed Projection Welds”
- EN ISO 14273:2001, “Specimen Dimensions and Procedure for Shear Testing Resistance Spot, Seam, and Embossed Projection Welds”

- EN ISO 14327:2004, “Resistance Welding—Procedure for Determining the Weldability Lobe for Resistance Spot, Projection, and Seam Welding”
- EN ISO 14329:2003, “Resistance Welding—Destructive Testing of Welds—Failure Types and Geometric Measurements for Resistance Spot, Seam, and Projection Welds”
- EN ISO 15614-12:2004, “Specification and Qualification of Welding Procedures for Metallic Materials—Welding Procedure Test—Part 12: Spot, Seam, and Projection Welding”
- EN ISO 18278-1:2004, “Resistance Welding—Weldability—Parts 1 and 2: Assessment of Weldability for Spot, Seam, and Projection Welding of Metallic Materials”
- ISO 10447:2006, “Welding—Peel and Chisel Testing of Resistance Spot, Projection, and Seam Welds”
- ISO 16432:2006, “Resistance Welding—Procedure for Projection Welding of Uncoated and Coated Low Carbon Steels Using Embossed Projection(s)”

REFERENCES

1. J.F. Harris and J.J. Riley, Projection Welding Low-Carbon Steel Using Embossed Projections, *Weld. J.*, April 1961, p 363–375
2. *Resistance Welding Manual*, Resistance Welder Manufacturers Association
3. D. Beneteau, Ed., *Resistance Welding Manual*, 4th ed., G.H. Buchanan Co., 1989

Resistance Seam Welding

Robert Matteson, Taylor-Winfield Technologies

SEAM WELDING, as defined by the American Welding Society, is "A resistance welding process wherein coalescence is produced by the heat obtained from resistance to the flow of electric current through the work parts held together under pressure by circular electrodes. The resulting weld is a series of overlapping spot welds made progressively along a joint by rotating the electrodes."

Seam welding machines are capable of making two types of lap joint. A continuous, pressure-tight joint (Fig. 1a) is produced on the overlapped materials by continuously rotating electrodes with a welding current that is interrupted regularly to achieve the effect of overlapping spot welds. An interrupted current is not required on some thin materials. On these, a continuous welding current will produce a good-quality continuously fused seam weld.

A seam welder is also capable of producing a row of spot welds that do not overlap (Fig. 1b). While not actually seam welding, this roll spot welding operation can be accomplished on standard seam welder machines and is a useful production technique where a pressure-tight joint is not required. These lap seam welding techniques are the most simple and most readily accomplished in production. Where justified by final product appearance, another method is mash seam welding (Fig. 2), sometimes called narrow-lap welding. Mash seam welds are produced by overlapping two sheets, with work metal compressed at the joint.

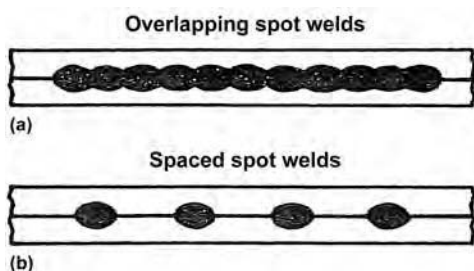


Fig. 1 Types of lap joints. (a) Pressure-tight joint. (b) Nonpressure-tight joint

A variety of workpiece/wheel configurations are possible (Fig. 3). In mash seam welding, electrode shape may be flat or contoured (radiused), depending on the thickness of the sheet. Wide-faced wheels with flat cross-sectional shape should not be used in mash seam welding of materials thinner than 1.0 mm (0.04 in.), while wheels with a contoured edge (Fig. 2c) are used on materials thinner than 1.0 mm (0.04 in.) or on thicker sheet. The radius of the electrode contour is about 100

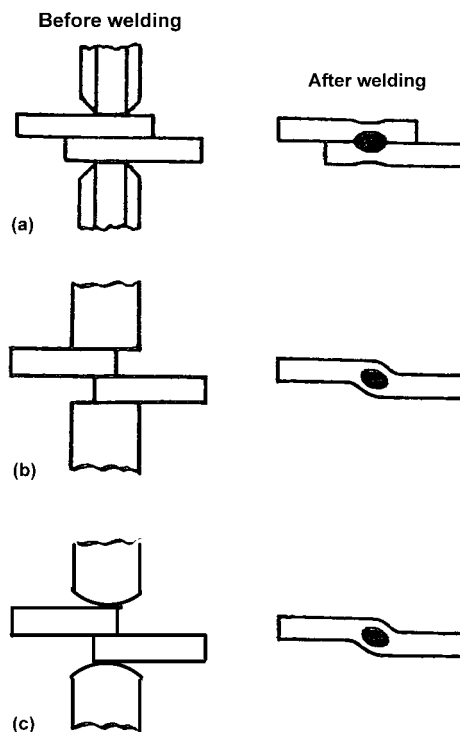


Fig. 2 (a) Lap seam weld, (b) mash seam weld with flat electrodes, and (c) mash seam weld with radiused (contoured) electrodes. Flat electrodes in mash seam welding should not be used when sheet thickness is less than 1mm (0.040 in.). Radiused electrodes can be used for sheet thicker than 1mm with the electrode radius of curvature about 100 times the sheet thickness.

times sheet thickness. Metal finish seam welding (Fig. 3c) uses a chamfered electrode wheel, and one side of the joint is mashed down while the other side of the joint has a smooth, flat finish. Overlap is greater than for mash seam welding, and higher current amperages and electrode forces are also required.

Two rotating circular electrode wheels are often used to apply current, force, and cooling to the work metal. When two electrode wheels are used, one or both wheels are driven, either by a direct drive of the wheel axles or by a knurl drive that contacts the peripheral surface of the electrode wheel (Fig. 4). For some applications, the electrode wheels idle while the workpiece is driven. Other electrode systems for seam welding may use one wheel and one flat bar-type electrode (Fig. 5), or a wire-feed system in which a copper wire is fed into a groove on the wheel.

Electrode wire seam welding (Fig. 6) is a patented process that requires an intermediate wire electrode between each wheel electrode and the workpiece. The electrode wire seam welding process is used almost exclusively for seam welding of tin mill products to fabricate cans. The copper wire travels around the wheel electrodes at the welding speed. The circular or flat cross-section of copper wire electrode provides a continuously renewed surface, but it is not consumed in the welding operation. This wire-feed process continuously provides a new copper surface for contact with the work metal and is often used on coated materials. In tin mill products, the tin build-up which would occur on a copper wheel electrode is thus avoided. The process requires specially designed welding systems. The seam welds may be made with two wheel electrodes, or one wheel electrode and a mandrel electrode.

In seam welding, a series of spot welds is made without retracting the electrode wheels or releasing the electrode force between spots. The electrode wheels may rotate either continuously or intermittently. Weld speed, current magnitude, current waveform, cooling system, and the electrode parameters of force, shape, and diameter are all related and must be carefully selected to optimize the process and produce the highest-quality weld.

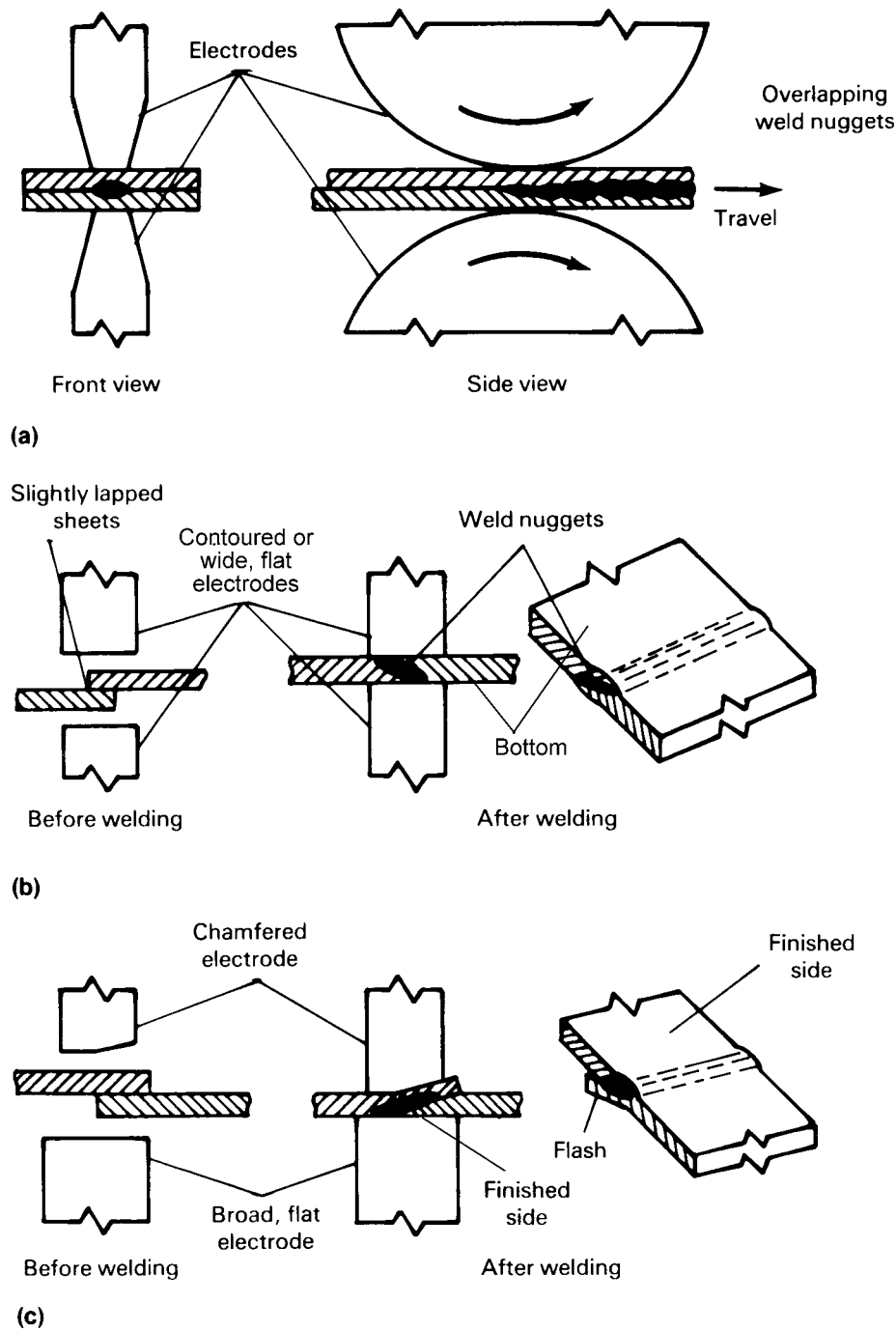


Fig. 3 Basic configuration of joints and resultant welds formed in resistance seam welding. (a) Lap seam welding. (b) Mash seam welding. (c) Finish seam with chamfered electrode. (d) Electrode wire seam welding.

Process Applications

Lap Seam Weld. Lap seams (Fig. 1a) are popular in automotive applications, such as automotive fuel tanks, catalytic converters, mufflers, and roof joints, as well as in nonautomotive applications, such as furnace heat exchangers, water tanks, and certain types of can making (Fig. 7c). Lap seam welding of multiple stackups and dissimilar thicknesses is also possible.

Mash Seam Weld. The process of mash seam welding is a variation of lap seam welding, where the overlap of the sheet is minimized to produce a weld that can be minimized in overthickness both by the welding process and by a subsequent planish (rolling) operation. This process is used in welding drums, barrels, and coils of steel in processing lines.

In a mash seam joint (Fig. 2b, 3b), the two sheets overlap by approximately one to two times

the sheet thickness. The weld area is forged or mashed down to an overthickness 5 to 25% greater than a single sheet thickness. Depending on the amount of overlap, much of the thickness reduction can occur during welding, and some occurs during planishing. With narrow overlap (in the range of $1 \times$ thickness of one of the sheets), it is possible to produce practically no “hump” in the as-welded condition.

It is necessary to have some amount of overthickness so the current path can be controlled, because the electrode wheels in mash seam welding can be wide and flat-edged. If flat (infinite radius) electrodes are used, especially on thin materials, wear grooves in the electrodes allow the electrodes to touch parent material outside the weld overlap, and current can flow that does not pass through the weld. Radiused (contoured) wheels are used to prevent current shunting when welding thin materials (materials less than 1.0 mm, or 0.04 in., thick, as previously noted).

Surface appearance and thickness can be improved through the use of hard steel planishing wheels to cold work the joint before or after welding. There always has been a need to minimize the overthickness of the welded seam in processing lines. One of the early ways to achieve this was to preplanish the edges of overlapped sheets, retract the overlap somewhat but not entirely, weld, and postplanish. The preplanish produced a taper on both edges of the overlap. Retraction then did two things:

- It meant welding thinner sheet edges together.
- It provided a region for the mashed materials to escape to.

This process was the basis of the Prep/Lap welder (Taylor-Winfield Technologies) provided in over 100 galvanizing lines from 1965 until 2000. Generally, this technique was used with commercial- and drawing-quality sheet steels that do not exhibit significant work hardening with the preplanish operation.

Typical applications of mash seam welding include drums, buckets, vacuum-jacketed bottles, aerosol cans, water tanks, and steel mill coil joining. Sheets of dissimilar thicknesses and/or coatings have been successfully mash seam welded. This development has created a whole new set of applications in tailored blank manufacturing, primarily for automotive use (see the *ASM Handbook* article “Forming of Steel Tailor-Welded Blanks” in Ref 1).

Advantages and Limitations

Advantages of seam welding, compared to resistance spot welding, projection welding, and laser welding, are:

- Gas-tight or liquid-tight joints can be produced (not possible with spot welding or projection welding).
- Seam width may be less than the diameter of spot welds, because the electrode contour

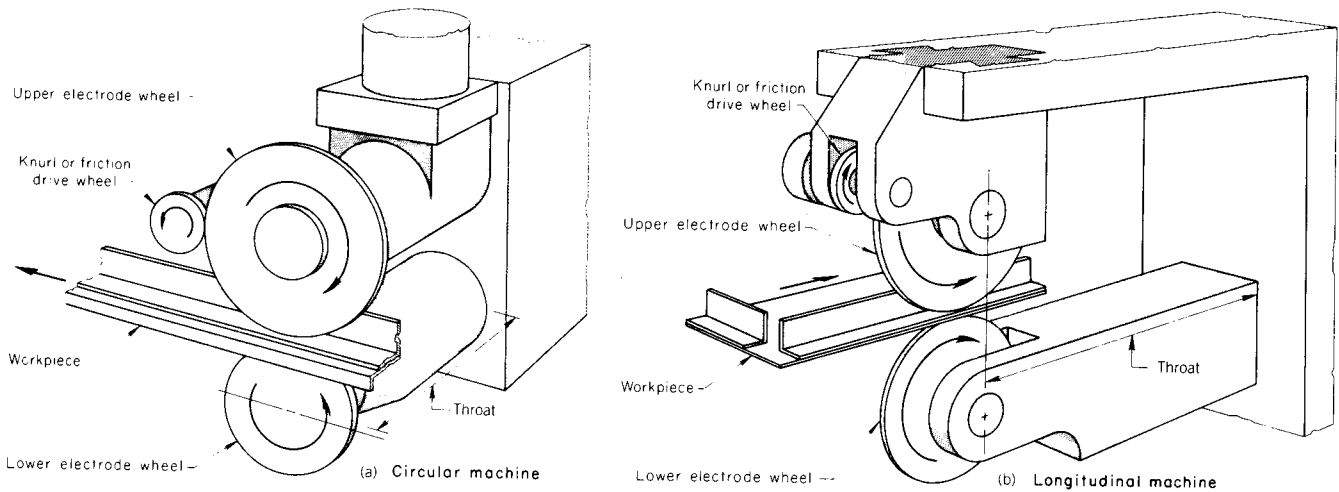


Fig. 4 Position of electrode wheels relative to throat on resistance seam welding machines

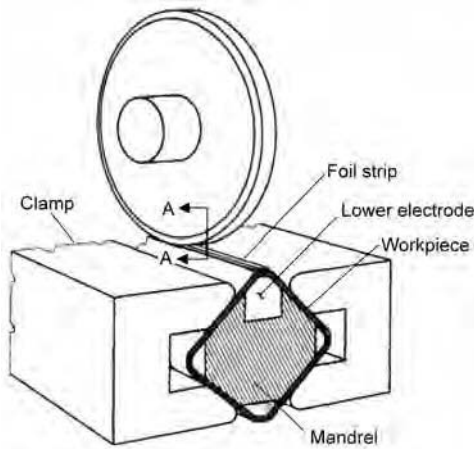


Fig. 5 Seam welding with single wheel and lower electrode

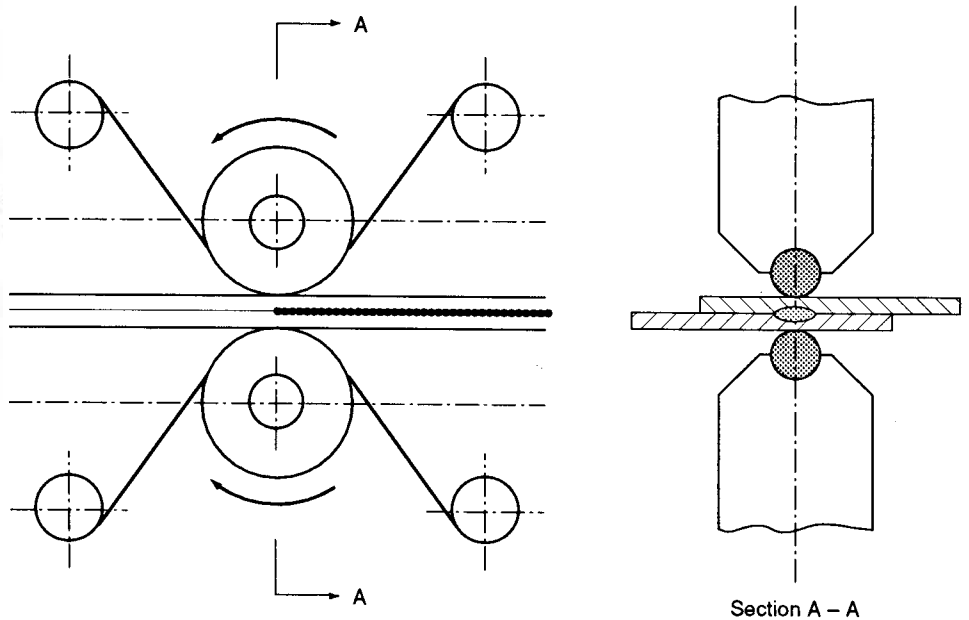


Fig. 6 Typical setup for an electrode wire seam welding process showing positions of wire relative to grooved wheel

- can be continuously dressed and is therefore of a stable shape.
- High-speed welding (especially on thin stock) is possible.
 - Coated steels are generally more weldable using seam welding than spot welding, because coating residue can be continuously removed from the electrode wheels if special provisions are made. Often, seam weld wheels that are used to weld coated materials are driven with another drive that simultaneously removes the buildup from the electrode. Also, large-diameter electrodes on coil-welding applications only rotate a few times per weld. This allows time between welds for electrode cleaning.
 - Coated steels are generally more weldable using seam welding than laser welding, because coating volatility is minimized by the intense pressure field in the weld zone.
 - Resistance seam welding is not particularly fitup-sensitive as compared to some other production-line methods, such as laser welding.

- The hardness of resistance seam welds made with air cooling is less than that of laser welds (120 HV versus 250 HV, respectively, for drawing-quality bare steel, and 170 HV versus 300 HV, respectively, for organic-coated drawing-quality steel).

Limitations of seam welding, apart from those it shares with spot welding and projection welding, are:

- Welds must ordinarily proceed in a single plane or on a uniformly curved surface. For special cases, multiplane welding has been achieved using a tilting welding head. The

radius of curvature connecting the planes must be sufficiently large.

- Obstructions along the path of the electrode wheel must be avoided or compensated for in the design of the wheel.
- Material handling must not induce extraneous forces into the fragile, molten weld zone during welding.
- Sharp corner radii or abrupt changes in contour along the path of the electrode wheel must be avoided (Table 1). Sharp corner radii or abrupt changes in contour will produce wheel wear and deposit copper on the weld surface, which is not desirable because it can lead to weld failure.

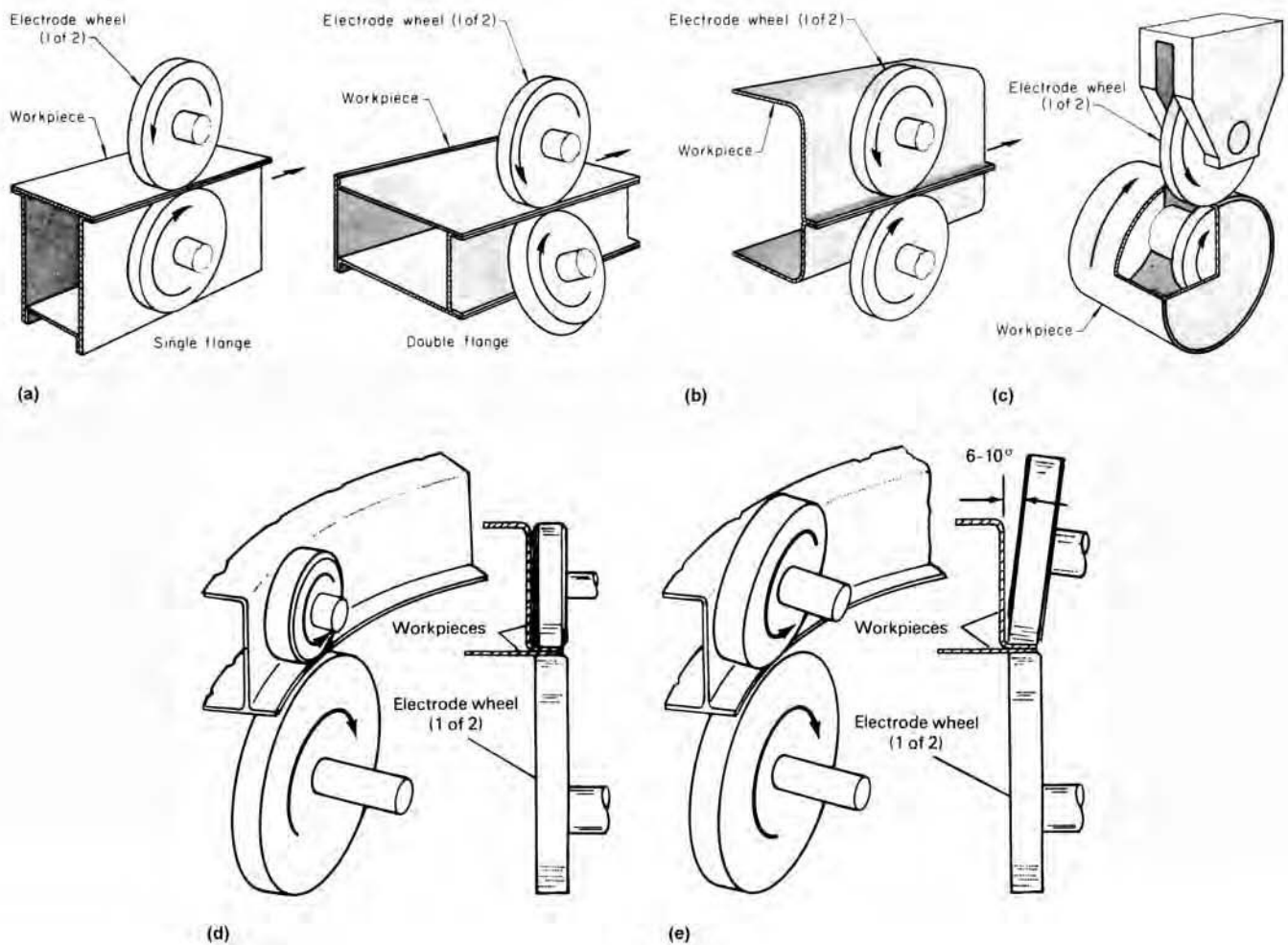


Fig. 7 Arrangement of electrode wheels relative to workpiece for selected flange-joint lap seam welds. (a) Single and double flange. (b) Two-member outward flange. (c) Two-member inward flange. (d) Small upper electrode wheel to avoid sidewall interference. (e) Canted large-diameter wheel to avoid sidewall interference

- Fatigue life of resistance seam welds is usually shorter than that of welds made by other seam welding methods.

The length of seams made in a longitudinal seam welding machine is limited by the throat depth of the machine (Fig. 4b). Current shunting through the weld, or a change in electrical impedance caused by the movement of the product inside the throat of the machine, can require current compensation (or constant current) as welding proceeds. Components using multiple crossing seam welds can be quality-sensitive at the weld intersections.

External water cooling of the electrodes and the weld zone may be required for high-speed welding. (Under high-speed conditions, the weld nuggets are still molten as they leave the pressure field of the wheels.) External cooling may add tooling cost for water containment and water removal from the parts after welding.

Materials requiring postweld heat and temper can be seam welded with special

considerations. Chromates and insulating lacquer coatings are not resistance seam weldable, because chrome-coated or lacquered materials are not readily weldable.

Fundamentals of Lap Seam Welding

The article "Resistance Spot Welding" in this Volume describes basic principles that are also generally applicable to seam welding. Certain concepts from resistance spot welding apply to resistance seam welding, because seam welding generally consists of a series of overlapping spot welds. The analog is that spot welding parameters depend on three key variables: current, the duration of current flow, and sheet thickness.

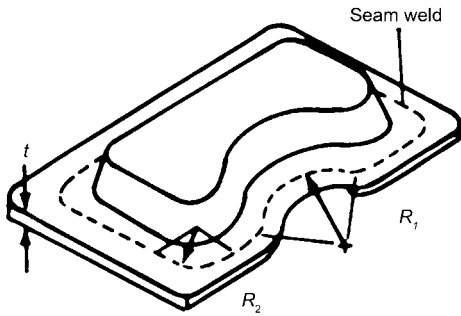
Likewise, there is a range of welding parameters for suitable seam welding—except that welding speed is a key parameter in seam welding (as opposed to the time of current flow in spot welding). For a given section thickness, the range of suitable current becomes more

narrow with higher welding speeds (Fig. 8). For example, the upper limit of current is defined by the onset of weld splash, while the minimum limit is the current necessary to develop a continuous seam weld.

The optimal weld speed may be identified experimentally as the speed with the widest current range for making good welds. Good welds are nominally free of typical metallurgical discontinuities (for example, surface cracks, gross lack of fusion at the weld interface, or surface melting eruptions). Additional discussion on developing the optimal welding lobe (such as in Fig. 8) for different thicknesses of sheet is included in the article "Procedure Development for Resistance Welding" in this Volume.

It is important to note that the current range of seam welding is widened by the judicious use of pulsed current to form distinct nuggets. Impulse profiles of 25 to 33% off-times are commonly used. Impulses contain off-time for the electrodes to draw heat away from the weld

Table 1 Recommended minimum radii of curvature for seam-welded aluminum and steel components



Base material	Minimum radius			
	Inside radius, R_1		Outside radius, R_2	
	mm	in.	mm	in.
Aluminum	250	10	75	3
Steel	150	6	50(a)	2(a)
			57(b)	2¼(b)
			64(c)	2½(c)
			75(d)	3(d)

(a) $0.8 \text{ mm} \leq t \leq 1.3 \text{ mm}$ ($0.031 \text{ in.} \leq t \leq 0.051 \text{ in.}$). (b) $t \leq 1.6 \text{ mm}$ ($t \leq 0.063 \text{ in.}$). (c) $t \leq 2.0 \text{ mm}$ ($t \leq 0.079 \text{ in.}$). (d) $t \leq 3.0 \text{ mm}$ ($t \leq 0.12 \text{ in.}$). Source: Ref 2

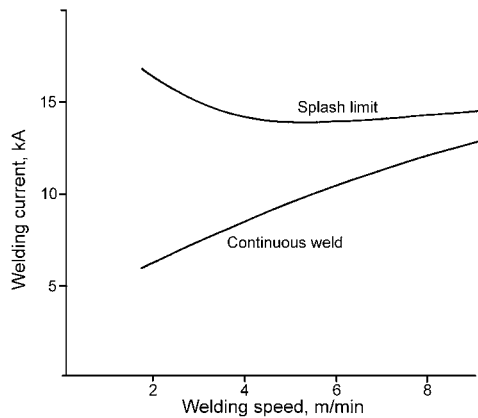


Fig. 8 Typical weldability lobe for seam welding of mild steel sheet (1.2 mm, or 0.05 in., thick) with alternating current. Source: Ref 3

surface. Therefore, the occurrence of surface discontinuities is lessened. In addition, off-time allows heat to redistribute itself within the weld, away from local hot spots.

Hot spots are places within the weld where thermal spikes may be occurring due to a relatively high local resistance, a nonuniform current density, a multiple stackup, or a stackup of unequal sheets. Hot spots are especially common along the weld interface when welding either thick plates or prepainted sheets. Hot spots on the outside surface of a weld occur naturally with unequal sheet thicknesses (on the thin side) or when welding is faster than permitted. On the other hand, hot spots can also occur within the sheet bulk, if due to erratic time distribution of current during on-time. Bulk hot spots begin to occur when welding near the maximum speed for a material, because current is actually not applied uniformly throughout the on-time, and time is required for the resulting nonuniform heat pattern to redistribute itself (Fig. 9).

The ideal impulse shape under high-speed conditions would seem to be a square wave (Fig. 10a). Because typical industrial power sources can only approximate this shape (Fig. 10b), it is worthwhile to accurately record the waveform of the actual secondary current in order to monitor its shape and stability during welding. Current range is greater in impulse mode than in nonimpulse (continuous-current) mode. The extra range seems to provide more robust penetration under difficult welding conditions, such as when intersecting other welds or turning corners with the seam.

One of the disadvantages of seam welding relative to spot welding is that solidification of the weld nugget occurs after the weld metal leaves the pressure field of the electrode wheels. Thus, if there is a large separating force on the weld before it freezes, it can come apart as it leaves the wheels. This postweld separation has been called “unzipping” or “alligatoring.” Impulses effectively cure this problem because the off-times create a modulating penetration profile (Fig. 11), providing cool tack joints between the molten spots.

It is desirable from a process control standpoint to select an impulse schedule that will produce nuggets of nearly equal length and width, in conjunction with the other parameters used (speed, wheel diameter, wheel width, and power source).

When welding dissimilar thicknesses, on-time must not be greater than the optimal weld time for the thinnest outer sheet (TOS). Mathematically:

$$t = 4(0.0292)(TOS)^2 \tag{Eq 1}$$

where TOS is in millimeters.

One way to satisfy the weld-time needs of both total stackup and TOS for thick-thin welding is to raise the number of nuggets (n) in the weld zone to 2 or 3. The goal here is to weld for the proper total time, but to do it with pulses of on-time no greater than dictated by Eq 1. To increase n , one must carefully consider the electrode wheels as well as the impulse schedule. Even when taking advantage of pulsation, it may become impossible to

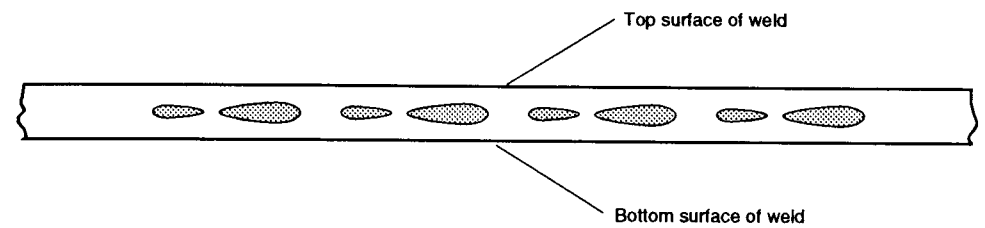


Fig. 9 Schematic showing lengthwise sectional view of the weld centerline of a lap seam joint with irregular nugget shapes. The lack of uniformity in the shape of the nuggets is attributable to an irregular pulse shape that does not provide sufficient time for heat flow to blend together the doublets.

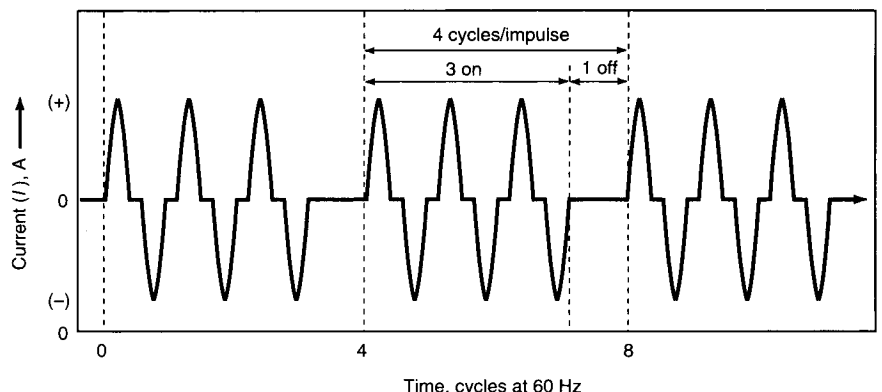
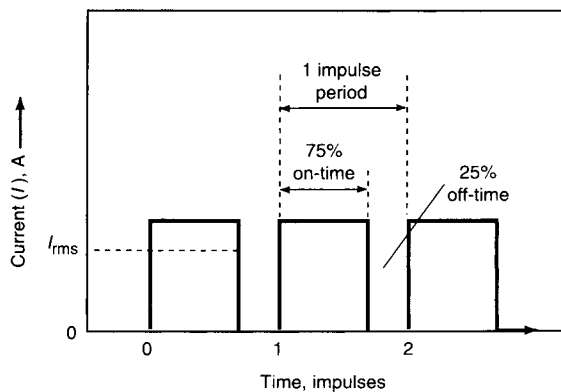


Fig. 10 Weld current profiles for seam welding. (a) Ideal impulse shape. On-time is 75% of impulse period, while off-time is 25% of impulse period. (b) Actual impulse shape is typically complex and nonideal. In this specific case, impulses are from an alternating current single-phase (3 on/1 off) current source.

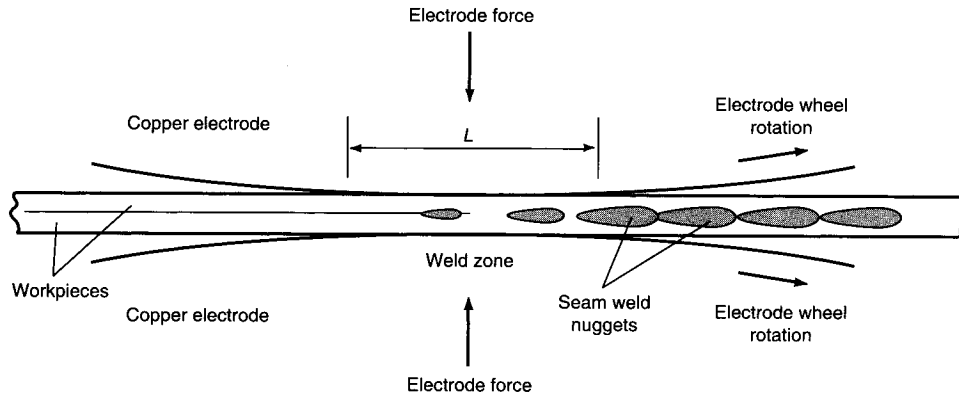


Fig. 11 Schematic showing lengthwise sectional view of proper nugget development in the weld zone of a pulsed lap seam weld. The length of the contact head footprint, L , is sufficient to contain three nuggets under the wheel.

seam weld extremely dissimilar thicknesses without damaging the thinnest outer sheet. This difficulty should become pronounced for thickness ratios above approximately 3 to 1, which is the general limit for thickness ratios.

Wheel Geometry, Weld Force, and Wheel Maintenance

The primary role of wheel geometry and force in seam welding is to control the dimensions of the weld zone or the size of the footprint that the wheel makes on the workpiece while welding. The length of the footprint, L , is an important factor in determining weld time. The variable L is primarily controlled by wheel diameter, force, and current. (As either force or current is increased, the wheel will sink deeper into the work, and L will increase.)

It can be worthwhile to measure or estimate L . This has been done experimentally using special voltage probes on the electrodes and by an optical silhouette method (Ref 4). A less accurate (but simpler) method is to read the heat pattern at the beginning and end of the weld, to estimate the number of nuggets (n) under the wheel at any one time. For bare steel, n can be as low as 1. However, the weldability of coated materials and dissimilar thicknesses improves when n is as high as 2 or 3 (Fig. 11). Keep in mind that the contact length will decrease somewhat as the wheel wears to a smaller diameter. (Normally, this change should not be of concern, except possibly when welding beyond the theoretical top speed for a material combination.)

Footprint width is best matched with impulse length, d , to produce nearly round nuggets. Width, however, is of secondary importance to impulse length.

A transverse radius on the wheel generally improves the welding range, because under high current conditions, it automatically reduces current density by sinking further into the work.

Under given electrode conditions, increasing weld force improves the welding range for speed and helps control cracking.

It is generally true that the current range improves with higher wheel pressure, until longitudinal splits begin to occur at seam starts or stops. On the other hand, at low force, transverse surface cracks may result at the upper end of the current range, especially on coated steels. A good rule of thumb is to weld at 80% of the seam-splitting force, or less. In addition, it may be helpful to de-energize the weld force except while welding, so as not to cause undue wheel wear.

For the highest-quality joints, it may be necessary to lightly machine the wheels as they are used, to maintain a constant edge profile. The types of wheel dressing tools are:

- Scrapers to remove contamination when welding coated materials
- Width cutters to remove mushroomed copper and to control wheel width
- Knurlers (Fig. 4) to maintain the transverse profile on the wheel and drive the wheels as needed
- Conditioners, which are essentially rollers with a reverse mask shape to roll the electrode into its correct shape. The conditioners have the distinct advantage of hardening the copper alloy of the electrode, which improves the wheel life without changing the electrical properties.

If wheel maintenance on the machine is not feasible, the wheels can be removed and redressed off-line. Alternatively, the wire-electrode seam welding process provides a constant wheel condition (Fig. 6) and thus eliminates the need for continuous wheel dressing.

Cooling the Weld

The weld cooling system is very important for process control of seam welding. Its primary role is to minimize thermal damage to the outer

surfaces of the weld while the weld interface is being heated above the melting point. The key elements in the success of the weld cooling system are:

- Electrode material (thermal or electrical conductivity)
- Electrode transverse shape (radius profile is best)
- Electrode cleanliness (should be dressed free from pickup of nonconducting coatings)
- Electrode cooling system
- Cooling water applied directly to the weld (if applicable), termed flood cooling

Cooling water for seam welding wheels can be either internal or external. Internal cooling systems cool the wheel but not the weld. The key advantage of internal cooling is that the process is dry; the workpiece, the machine, and the operator stay dry. The cost of installing floor drains and water-containment facilities is avoided. Neither is it necessary to remove water from inside the workpiece (as in the case of automotive fuel tanks). However, internally cooled wheels may cost more due to additional machining costs. Thus, operating costs for internal cooling may be higher than for external cooling. Some internal systems do not directly cool the wheel but only the wheel shaft.

On the other hand, with external cooling, spray nozzles are aimed with some precision at the workpiece-wheel separation point. The benefits of external cooling include:

- Thermal damage to the weld surface and any coatings is reduced, so that weldability is improved.
- Weld distortion is reduced.
- Fume emission is reduced.
- Wheel cleanliness improves, because water is directly applied to the hottest point on the wheel, producing a quench/cleaning action on the wheel surface.
- Weld hardness will increase, adding strength to the weld under certain loading conditions, such as crush loading. (*Some quench-sensitive materials may not allow external cooling.*)

In welding bare steel, rust-preventive water solutions are sometimes used.

Metals Welded

Most low-carbon, high-carbon, low-alloy, and stainless steels and many coated steels above approximately 0.15% carbon equivalent (CE) tend to form areas of hard martensite upon cooling. For steel sheet products, the following CE formula is used:

$$CE = C + (Mn + Cu + Cr)/20 + Si/30 + Ni/60 + Mo/15 + V/10 + 5B$$

In critical applications, the welds may require postweld tempering to reduce the hardness and

brittleness. In some cases, this can be done in the welding machine. Tempering can also be done in a furnace or by induction heating.

Aluminum and aluminum alloys can be wide-lap seam welded but not mash seam welded, due to their narrow plastic range. Nickel and nickel alloys can also be seam welded, but seam welding is not recommended for copper and high-copper alloys. Compatible combinations of dissimilar metals and alloys can also be seam welded. For additional information on the seam welding of stainless steel, aluminum alloys, and copper alloys, see the article "Procedure Development for Resistance Welding" in this Volume.

Types of Seam Welds

Several types of resistance seam welds can be made:

- Lap seam welds joining overlapping flat sheets
- Flange-joint lap seam welds with at least one flange overlapping the mating piece (Fig. 7a)
- Foil lap seam welds, in which an alloy metal foil is placed at the weld interface
- Mash seam welds with work metal compressed at the joint to reduce joint thickness (Fig. 2b)

In addition, both low-frequency and high-frequency induction and resistance welding are used for butt welding strip stock into tubes and other shapes.

Lap Seam Welds

The most common type of seam weld is a simple lap seam in which the pieces to be welded are lapped sufficiently to prevent the sheet edges from becoming part of the weld (Fig. 2a). Applications include sealing of cans and tanks in which liquid-tight or gas-tight joints are needed.

Flange-joint lap seam welds are used in joining assemblies having one straight member and one outward-flanged member at the joint to be welded (for example, the duct in Fig. 7a) or assemblies with two outward-flanged members (for example, the automotive gasoline tanks in Fig. 7b). Common applications include containers with out-turned bottoms or tops, and ducts or structural parts with out-turned sides. Unless the workpiece length is less than the usable throat depth of a longitudinal machine, seam welds of this type are made on a circular machine.

Often, container ends are dished for added strength, and one or both electrode wheels must be mounted at an angle to clear the workpiece. Wheel diameter limitations may also necessitate setting a wheel at an angle (Fig. 7a, right view).

Flange-joint seam welds can also be used for welding assemblies in which the flanges face

inward at the joint (Fig. 7c). However, to reduce overhang of the arm supporting the lower electrode or to reduce the required throat depth of the machine, the length of the workpiece should be kept to a minimum. If the lower electrode support is small, too much overhang can result in excessive deflection of the support and thus cause inconsistent weld quality because of force variation.

Mash Seam Welds

Mash seam welds are produced by overlapping two sheets by an amount ranging from one to two times the sheet thickness and applying electrode force and current. The resulting overthickness is 5 to 25%.

The joint itself acts as a current localizer, as in projection welding, because the overlap is thicker than either sheet by itself. Because the wheels are wide, the transverse position of the joint on the wheels can be oscillated as needed to prevent a groove from forming on the wheels and to increase the period between wheel dressings.

Careful selection of an impulse weld schedule will result in higher penetration and greater joint strength, although the "bumpy" appearance of a weld made with pulsating current may not meet product requirements. Cosmetic mash seam welds can be made with nonpulsed (continuous) current.

Because sheet overlap is a critical parameter, workpieces must be rigidly and accurately clamped or tack welded to prevent lateral motion during welding. Clamp distance is highly important and is related to stock thickness. On continuously fed, moving-part setups and thin-metal processes (where clamp distance would be too small), clamps may not be feasible. In these cases, a Z-bar and nosedpiece tooling arrangement is used to help position the edges to be welded.

In applications in which the mashed surface must be as flat and burr-free as possible after welding to facilitate porcelain enameling and to present a good appearance, a bar-type electrode is used against the surface to be enameled, and an electrode wheel is used against the other surface. The bar-type electrode may require periodic dressing to avoid excessive grooving and subsequent loss of current density. When a premium-finish appearance is required, the weld can be ground or roll planished to remove surface imperfections.

In steel coil joining, it is sometimes desirable for the final thickness of the mash seam weld to be similar to the single sheet thickness. To minimize the thickness gain from welding, pre- and/or postweld planishing rolls are used. These rolls are hard steel wheels, typically 100 mm (4 in.) in diameter and 20 mm (0.75 in.) in width. Planishing rolls are typically loaded to 22 kN (5000 lbf) or to twice the weld wheel force, to cold work the weld. In this way the overthickness may be held to as little as 5% on low-carbon steels and as much as

25% on dual-phase and transformation-induced plasticity grades. Also, the overlap may be retracted slightly after the preweld planish to further limit overthickness.

The highest-quality mash seam welds are made in low-carbon steels and stainless steels. The process is widely used in the manufacture of refrigerators, stoves, laundry equipment, and other products that receive porcelain enamel coatings. Mash seams are gaining popularity in automotive applications for creating tailored blanks that reduce weight and material loss in certain large stampings (for example, body sides and doors), reduce manufacturing complexity, and reduce the number of components and welds required to make finished automotive subassemblies.

Because of their narrow plastic range, nonferrous metals generally cannot be mash seam welded.

Processing Equipment

A seam welding machine is similar in construction to a spot welding machine, except that one or two electrode wheels are substituted for the spot welding electrodes. Power sources used for seam welding are similar to those used for spot welding. They usually consist of a welding transformer, with a tap switch in the primary circuit, driven by a silicon-controlled rectifier switching system and a secondary circuit with electrodes for transferring the welding current to the work metal.

Controls for seam welding are generally similar to those for spot welding, except for differences related to the relative motion of the work and the electrodes. Most modern weld timers are capable of generating impulse weld schedules for seam welding. (Higher impulse frequencies for welding thin stock can be obtained using special high-frequency systems, although complete machine redesign may be necessary due to transformer and throat area limitations that are directed by the frequency.) Tap switches and a phase-shift heat control are used as in spot welding for changing the transformer output current. In theory, direct feedback current regulation would be a desirable feature in seam welding, and some work has been done to develop and improve this.

Seam Welding Machines

In general, seam welding is done in a press-type resistance welding machine. Most seam welding machines are powered by alternating current, either three phase or single phase; some are designed for use with direct current, which includes medium-frequency direct current. Stored-energy seam welding machines have been built, but this type finds little use. Direct current frequency converter power supplies are used to tailor custom pulsation schedules.

Equipment for seam welding must be capable of:

- Delivering low-voltage, high-amperage current
- Supporting the electrodes and workpiece and applying the electrode force
- Moving the workpiece and/or driving the electrodes
- Regulating, timing, and sequencing the application of the welding current, force, and cooling water (if applied)
- Careful part handling, such that extraneous forces are not imposed during welding
- Provide cooling for forced-cooling systems or electrode cooling for indirect-cooled seam welding

Electrode Force and Support. The upper electrode wheel is mounted to, and insulated from, the operating head. The head, which is actuated by a direct-acting air or hydraulic cylinder, applies the electrode force. The lower electrode is either a wheel, a platen, or a mandrel and is mounted on a supporting arm, table, or knee. This lower support can be made adjustable for applications in which the work metals must be maintained at a constant level above the floor.

Electrode or Workpiece Drives. Workpieces are moved by rotating the electrodes with knurl or friction drive, by direct drive of the wheel shaft, by a driven workpiece and idling wheels, or by clamping the workpieces to a bar electrode and moving the bar electrode (Fig. 5).

Weld travel tends to be continuous on thin steel sheets (less than 1.7 mm, or 0.067 in.), whereas it is intermittent on thick sheets (greater than 3.0 mm, or 0.118 in.). The need for intermittent weld travel arises from the longer weld-time requirements of thick steel.

Knurl Drive versus Friction Drive. In a knurl drive or friction drive, one or both of the electrodes are rotated by a knurl or friction wheel on the peripheral surface of the electrode wheel, to provide nearly constant linear speed regardless of the diameter of the electrode wheel. The knurl drive, which has ridges or beads on the drive wheel to aid in turning the electrode, minimizes slippage and is more positive than the friction drive, in which the turning surface of the drive wheel is smooth. The knurled wheel also removes some of the pickup from the electrode wheels. A knurl drive is used when welding coated metals, such as galvanized steel and terneplate, in any application in which the electrodes are likely to pick up material from the work metal, and for scaled stock that cannot be precleaned. A knurl drive usually is not employed if good cosmetic appearance of the weld is important. Knurl or friction drives can be used only with electrode wheels large enough in diameter to allow clearance.

Gear drive is used if small-diameter electrode wheels cannot be driven by the use of knurled or friction wheels because of interference, or if the application cannot tolerate an electrode wheel that has been roughened by a knurled drive roll. With gear drive, in which

the mounting shaft of the electrode wheel is driven, the speed of welding decreases as the wheel wears down.

In a standard seam welding machine, interference may exist at some minimum distance between electrode wheel centers. If one wheel must be small to clear the workpiece, the other must be correspondingly large. If the ratio of the electrode wheel diameters is greater than 2 to 1, the smaller wheel should be driven, to minimize slippage. Welding speed can be kept constant in spite of wheel wear by a variable-speed gear-driven mechanism.

Movable Carriages. When a mandrel or a platen is used as the lower electrode (Fig. 5), the operating head carrying the upper electrode may be mounted in a carriage. The carriage is moved by an air or hydraulic cylinder, or by a motor-driven screw, and thus the upper electrode is passed over both the workpiece and the lower electrode. The upper electrode is free-wheeling, but it may be equipped with an idling knurl or conditioner wheel for dressing. Sometimes it is necessary to use a high-slip drive to assist on thin materials, to prevent wrinkling. In some machines, the workpiece is clamped to a bar-type lower electrode and moved under an idling fixed-position upper electrode wheel.

Types of Machines. There are four basic types of resistance seam weld machines: circular, longitudinal, universal, and portable.

Circular. The axis of rotation of the electrode wheels is at right angles to the front of the machine (Fig. 4a). This type of machine is used for circular work, such as for welding the heads on containers and for flat work requiring long seams. Head pivot capability for welding on an inclined plane is optional.

Longitudinal. The axis of rotation of the electrode wheels is parallel to the front of the machine (Fig. 4b), and throat depth is typically 300 to 915 mm (12 to 36 in.). This type of machine is used for welding short longitudinal seams in containers, for attaching pieces to containers, for coil joining, and for similar work. Machines with traveling heads or traveling electrodes, in which a mandrel or a platen is used for the lower electrode, are normally of the longitudinal type.

Universal. A swivel-type head and interchangeable lower arms allow the axis of rotation of the electrode wheels to be set either at right angles or parallel to the front of the machine.

Portable. The workpiece is clamped in a fixture, and a portable welding head is moved over the seam, either manually or by using a robot. This type of machine is used when the workpiece is too bulky to be handled by a regular machine or when it is more efficient to move the welding head rather than the workpiece. This type of machine is sometimes used for joining the roof and body sides on automobiles. The portable welding head is moved by motor-driven wheels, and an air cylinder mechanism provides the electrode force.

Selection of Electrodes

Alloy type and wheel configuration are the primary factors that determine electrode selection.

Class 1 Copper. Electrode wheels made of Resistance Welder Manufacturers Association (RWMA) class 1 copper (RWMA No. 1.16200) have been used for seam welding of aluminum and magnesium alloys, galvanized steel, and tin-plated steel. The minimum electrical conductivity of class 1 copper is 80% International Annealed Copper Standard (IACS). Recently, this material has been replaced by hot-forged and heat treated RWMA class 2 copper in the overaged condition (RWMA No. 1.18200). With adequate cooling and proper parameters, the high electrical and thermal conductivities of this material keep the electrode-workpiece interface at a temperature below the point where metallurgical discontinuities are formed near the weld surface.

Class 2 Copper. Seam welding of low-carbon and low-alloy steel is usually done with electrodes made of hot-forged and heat treated RWMA class 2 copper (RWMA No. 2.18200). Minimum conductivity is 75% IACS. Minimum hardness is typically 65 HRB. Class 2 also works well with all types of coated steel, but the metallurgical optimization of weld parameters and provisions for wheel maintenance are critical to the success of welding coated steels. For longer electrode life, premium class 2 wheels are available in the 20% cold-worked form, where a minimum hardness of 75 HRB may be specified. Cold-worked wheels show no appreciable loss of conductivity over the forged class 2 material; however, because the wheel surface is heated above annealing temperature during welding, it is necessary to continuously condition the wheel to maintain the cold-worked hardness. This is usually done with a conditioning roll shaped to the reverse image of the wheel shape and pressed against the rotating electrode.

Class 20 copper (RWMA No. 20.15760) is also used for electrode wheels, with properties similar to those of class 2 premium wheels. Class 20 wheels are made using a powder metallurgy process that produces a pure copper product, dispersion-strengthened with alumina. The alumina adds hot strength and tends to reduce pickup during welding of coated steels.

Class 3 copper (RWMA No. 3.17510) is sometimes used for seam welding materials with lower electrical conductivities, such as stainless steel, Nichrome, and Monel alloys. However, class 3 is used with special ventilation only because of the health hazard of atmospheric beryllium when welding or machining with class 3 material. (Beryllium-free class 3 alloy RWMA 3.18000 is also available.) Class 3 wheels have lower electrical conductivity (45% IACS), so they tend to run hot.

Sizes and Shapes. Electrode wheels range in diameter from 50 to 610 mm (2 to 24 in.). Popular sizes range from 100 to 305 mm

(4 to 12 in.), with widths from 6 to 19 mm (¼ to ¾ in.). Edge contours may be flat, radiused, beveled flat, or angled. In lap seam welding, weld quality seems to be easiest to control with a radius edge, as discussed previously. The need for nonradius contours is usually a matter of cosmetic appearance, or due to a tool access limitation. Mash seam welders use a flat-edge or radiused wheel, depending on sheet thickness (Fig. 3b).

Weld Quality and Process Control

It is best to design the entire process around proven weld parameters that have been metalurgically validated on workpieces very similar to actual production parts. Sensitive parts of the weld typically are starts, stops, corners, adjacent shunt paths, intersecting seams, and areas of poor metal fit. On coated metal, parameters should be flexible enough to handle normal coating variations. General troubleshooting information is summarized in Table 2.

To select starting weld parameters, use the guidelines presented in the section “Fundamentals of Lap Seam Welding” in this article and a welding schedule similar to that in Table 3. See also the article “Procedure Development for Resistance Welding” in this Volume for additional coverage on welding parameters. Working values should be chosen that are not too near the extreme limits of the material, the weld tool, or the plant facilities. To make leak-tight seams, weld spots should have approximately equal length and width. Ideally, the same welding parameters should be used for the entire length of the weld. Also, establish production procedures for maintenance of electrode wheels and cooling sprays (if applicable). Check process parameters against required values frequently, and make adjustments and repairs as needed.

The quality of resulting welds can be verified using chisel tests, Olsen ball tests, metallographic sections, pressure tests, or fatigue tests, depending on product requirements. Record target values for speed, force, pulsation,

and water cooling (if applicable). Record tap setting and lower and upper root mean square secondary current limits for acceptable weld quality. Record the actual secondary current waveform to see that it is acceptable (as in Fig. 10) and consistent throughout the weld. Process changes should be made only on the basis of data.

Nondestructive testing (for example, resistivity, ultrasonic testing, dye penetrant, magnetic particle, or eddy current) may be useful in some low-volume testing applications. However, such techniques should come into use only after the optimal parameters are verified metallographically and the process is well understood. In many instances, much can be observed from the external appearance of a lap seam weld, provided the weld surface is not planished or scarfed after welding.

Coated Steels. For a process that has been properly set up and optimized as described previously in this article, the difference in parameters between coated and uncoated steel lies mainly in weld current. Steels with low-melting

Table 2 Troubleshooting in resistance seam welding

Trouble	Cause	Remedy
Hot metal “squirts” out between the parts being welded.....	Welding current is too high. Welding force is too low for current used. Overlap is too small. Welded parts do not fit properly. Sequence is incorrect, allowing welding current flow without electrode force.	Lower transformer tap switch one step, or decrease heat dial setting. Increase air pressure in operating cylinder. Redesign parts with proper overlap and correct forming operations. Correct sequence by adjustment of electrical controls, pressure switch, or speed-control air valves.
Heating is uneven.....	Overlap is too small. Welded parts do not fit properly.	Redesign parts with proper overlap and correct forming operations.
Parts burned and pitted, or steel adheres to electrodes	Electrode face width is too small or not correctly shaped. Welding electrode is made of copper alloy having too much electrical resistance. Surfaces of welded parts are covered with excessive scale, dirt, or foreign matter. Flow of cooling water is too weak or not directed at weld. Welding speed is too fast for thick-nesses of steel being welded.	Reshape electrode to proper face width. Substitute an electrode of higher conductivity. Degrease parts or pickle them to remove grease, scale, and dirt. Increase quantity of cooling water, and properly direct it. Decrease the revolutions per minute of the electrodes.
Work does not weld at all.....	Welder settings have not been changed from those for welding thinner sheets.	Reset welding variables for thicker sheets.
Heat decreases as weld progresses	Magnetic material is being fed into the welder throat and reducing the welding current.	Use additional current-regulating control, or weld one-half length of joint, reverse, and weld other half.

Table 3 Recommended practice for seam welding of 1010 low-carbon steel

Data are for material free of scale, oxide, paint, grease, and oil. Welding conditions determined by thickness of thinnest outside piece.

Thickness (t) of thinnest outside piece(a)		Electrode dimensions						Net electrode force		Welding speed				Minimum contacting overlap(c)		
		Wheel width (W)(b)		Face width (w) (b)		Heat time, cycles (60 Hz)	Cool time (pressure tight), cycles (60 Hz)			mm/ min	in./ min	Welds per mm	Welds per in.			Approximate welding current, A
mm	in.	mm	in.	mm	in.			kN	lbf							
0.25	0.010	9.5	¾	4.8	⅜	1.8	400	2	1	200	80	0.60	15	8,000	9.5	¾
0.53	0.021	9.5	¾	4.8	⅜	2.5	550	2	2	190	75	0.48	12	11,000	11	⅞
0.80	0.031	13	½	6.4	¼	3.1	700	3	2	185	72	0.40	10	13,000	13	½
1.02	0.040	13	½	6.4	¼	4.0	900	3	3	170	67	0.36	9	15,000	13	½
1.27	0.050	13	½	7.9	⅝	4.7	1050	4	3	165	65	0.32	8	16,500	14	⅞
1.57	0.062	13	½	7.9	⅝	5.3	1200	4	4	160	63	0.28	7	17,500	16	¾
1.98	0.078	16	¾	9.5	¾	6.7	1500	6	5	140	55	0.24	6	19,000	17.5	1 1/16
2.39	0.094	16	¾	11	⅞	7.6	1700	7	6	125	50	0.24	6	20,000	19	¾
2.77	0.109	19	¾	13	½	8.7	1950	9	6	120	48	0.20	5	21,000	20.5	1 3/16
3.18	0.125	19	¾	13	½	9.8	2200	10	7	115	45	0.20	5	22,000	22	⅞

(a) Data for total thickness of pile-up not exceeding 4t. Maximum ratio between thicknesses, 3 to 1. (b) For RWMA class 2 electrode material (minimum conductivity, 75% IACS; maximum hardness, 75 HRB). Wheel width is overall width of a flat-faced wheel or of a wheel with a 75 mm (3 in.) radius face; face width is that of the contacting surface of flat-faced wheels. (c) For larger assemblies, minimum contacting overlap indicated should be increased 30%.

metallic coatings require more current than uncoated steels. Organic-coated steels require approximately the same current as uncoated steels (although the current range for making good welds will be smaller for the organic-coated steels). Some coatings (for example, zinc and aluminum) are particularly active at the electrode-workpiece interface. For these surface-active coatings, speed, force, and pulsation are selected to keep the surface temperature of the weld below the point where metallurgical discontinuities are developed. Diligent maintenance of the wheel condition and the cooling system cannot be overstated for sensitive applications.

REFERENCES

1. Forming of Steel Tailor-Welded Blanks, *Metalworking: Sheet Forming*, Vol 14B, *ASM Handbook*, ASM International, 2006, p 539–546
2. J.G. Bralla, Ed., *Handbook of Product Design for Manufacturing*, McGraw-Hill, 1986

3. W.W. Waddell, “High Speed Resistance Seam Welding of Uncoated and Coated Steels,” EUR 11550 EN, Commission of the European Communities, 1988
4. T. Yamamoto and T. Okuda, Fundamental Study on Weld Formation Phenomena of High Speed Lap Seam Welding, 3rd Report: Voltage Across Electrodes and Current Flow Area of Plate Surface, *Yosetsu Gakkaishi*, Vol 46 (No. 10), 1977, p 748–753 (in Japanese)

SELECTED REFERENCES

- Y. Adonyi, Resistance Seam Welding of Enameling Quality Steel Sheet, *Proc. Porcelain Enamel Institute Technical Forum*, Vol 52, 1990, p 729–748
- M.J. Karagoulis and M.A. Pusateri, Seam Welding and Pre-Painted Fuel Tanks at General Motors, *Proc. Sheet Metal Welding Conf. II*, American Welding Society, Oct 1986
- C.A. Leffel, “An Investigation into the Resistance Seam Weldability of Coated Steels,” Master’s thesis, The Ohio State University, 1990

- A.A. Mazaev and G.V. Nazarov, Effect of the Form of the Welding Pulse on Heating of the Weld Zone in One-Side Resistance Spot and Seam Welding, *Fiz. Khim. Obrab. Mater.*, Vol 17 (No. 5), 1983, p 125–131 (UDC 621.791.762.5 is in English)
- “Recommended Practices for Resistance Welding,” AWS C1.1, American Welding Society
- A.W. Schueler, Resistance Seam Welding, *Weld. Res. Counc. Bull.*, Vol 225, April 1977
- Soudronic LTD literature, Briarcliff Manor, NY
- K. Torii, Y. Kadano, and Y. Tamura, A Study on the Defects in Seam Welds of Metal Coated Steel Sheets, *Trans. Jpn. Weld. Soc.*, Vol 2 (No. 1), 1971, p 77–85
- S.A. Westgate, “The High Speed Resistance Seam Welding of Nominally 1.2 mm Low Carbon Steel Sheets,” Doc. 240/1984, British Welding Institute, 1984
- N.T. Williams, D.E. Thomas, and K. Wood, High Speed Seam Welding of Tinplate Cans, Parts I and III, *Met. Constr.*, April 1977, p 157–160; May 1977, p 406–408

Flash Welding and Upset Welding

R. (Bob) Matteson, Taylor-Winfield Technologies, Inc.

FLASH WELDING, also called flash butt welding, is a resistance welding process in which a butt joint weld is produced by a flashing action and by the application of pressure. In basic terms, it is a melting and a forging process. The pieces to be joined are suitably heated by many electrical arcs at the joining interface until the pieces are sufficiently hot to perform an upset, thereby forging the pieces together. The process is capable of producing welded joints with strengths equal to those of the parent materials. Flash welding is used to join metallic parts that have similar cross sections, in terms of size and shape. The process lends itself to joining nearly all grades of steel, aluminum, brass, and copper parts, in addition to selected dissimilar materials.

Introduction

Figure 1 is a schematic representation of a typical flash-welding operation. Flash butt welding has been in existence for 100 years or so, originally developed by Elihu Thompson. Generally, one of the metal pieces to be joined is held in a stationary clamp and the other is held in a movable clamp. Voltage is applied between the clamps during the flashing and often during the upset period as well. Clamping ensures good electrical contact between the current-carrying dies and the workpiece and prevents the parts from slipping during the upsetting action.

Flash welding is rapid and economical, and when properly executed, welds of uniform high quality are produced. Over the years, many improvements have been incorporated into the process, which have resulted in dimensional stability of the final assembly of pieces, removal of the external upset material, soundness of the final assembly, and other improvements. The process is used to join rails for railroads, coils of steel for processing in pickle and cold reduction lines, automotive parts, rings for aircraft engines, band-saw blades, and a wide variety of parts.

Flash welding can be used for joining many ferrous and nonferrous alloys and combinations of dissimilar metals. In addition to low-carbon steels, metals that are flash welded on a production basis include low-alloy steels, tool steels, stainless steels, aluminum alloys, magnesium

alloys, nickel alloys, and copper alloys. The joining process is fairly forgiving, which has produced a wide range of methods for the flashing rate that manufacturers of the equipment have argued is better than other flashing rate schemes.

Actually, on many materials, especially on low-carbon steels, the flashing rates may differ between different manufacturers and still produce satisfactory results. However, with the advent of advanced high-strength steels (AHSS), the heating rate during flashing and upsetting has a significant effect on the characteristics of the weld. These steels are referred to as AHSS materials and are classified into this category if the ultimate material strength exceeds 420 MPa (61 ksi). It is the introduction of AHSS materials that led to the current method of flash butt welding. Especially in the cases where the final product is repeatedly flexed, stressed, or bent, the current method imparts superior weld characteristics that cannot be achieved with other methods.

Upset welding (Fig. 1b) is a similar process to flash welding, because it uses much the same equipment and control features. However, in upset welding, the process does not produce flashing. The parts to be welded are held tightly together in clamps while voltage is applied. When the interface between the two parts is sufficiently heated to the correct temperature profile, upset occurs. Generally in upset welding, less material is lost as compared to flash welding. Upset welding is slightly less forgiving than flash welding because the loading of the parts must be more accurate. Both processes produce similar final results and are described in this article.

Flash Butt Welding

The four basic steps in flash welding are shown in Fig. 2. It is a variation of resistance welding, where arcing (flashing) is used to supply the major portion of the initial heat for the formation of a butt weld. The major difference between the temperature pattern developed in flash welding and that developed in resistance welding is that flash welding produces a much steeper thermal gradient. This steep thermal gradient, combined with the resulting

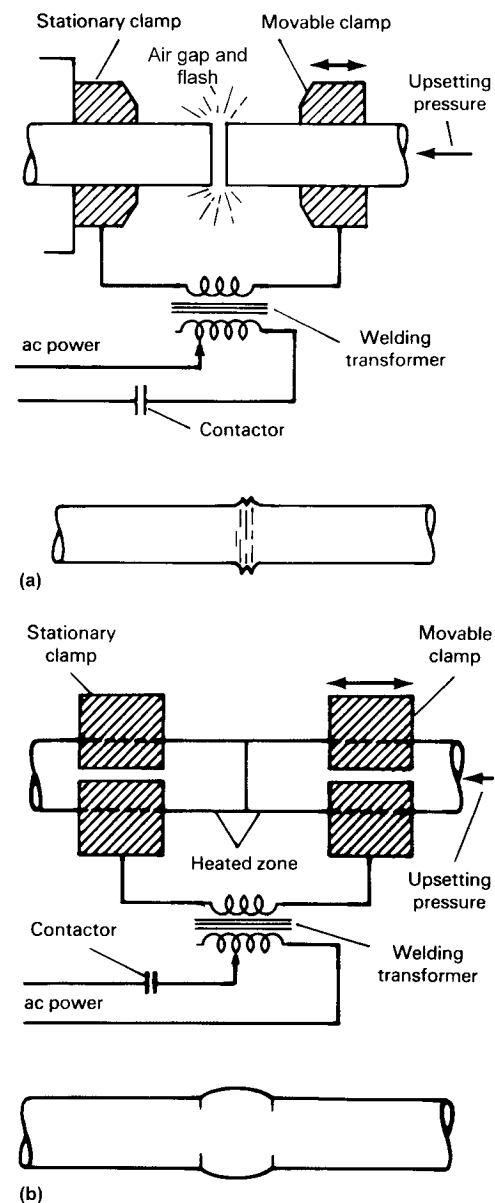


Fig. 1 Flash and upset welding process features (top) with typical profiles of resulting joints (bottom). (a) In flash welding, heating from an arc occurs before the upsetting operation is initiated. (b) In the upset welding process, electric current is applied while the pieces are pressed together.

characteristic upset pattern, enables flash welding to accommodate a much greater variety of materials and shapes than can be welded by resistance welding. Once the proper temperature-distribution pattern has been established, the abutting surfaces are rapidly forced together.

Three distinct peaks are characteristic of flash welds (Fig. 3). The two peaks on either side of the weld line represent the material displaced by the upsetting action; the center peak is the molten metal extruded out of the weld, including oxides or contaminants formed during heating. During the flashing action, craters are formed that contain molten metal and possibly oxides. If the energy input that produces the flashing is properly controlled, these oxides should be expelled with the flashing molten-metal particles that give the process its name. When the upsetting force is then applied, most of the impurities not expelled by the flashing are expelled with plastically deformed upset metal. Any nonmetallics that are not expelled usually remain at the fusion line, with little apparent depth back into the base metal on either side. Most static and fatigue failures that occur in flash welds originate at such discontinuities. These discontinuities normally have little effect on static strength but can measurably reduce fatigue life. Excessive energy input and insufficient upsetting force or travel speed are the most common causes of such inclusions.

Flash welding is commonly used to join sections of metals and alloys in production quantities. Materials with cross sections ranging from 65 to 13,000 mm² (0.1 to 20 in.²) are commonly flash welded. The process is also used to manufacture components of solid and tubular shape, in addition to strips and complex configurations. Flash welding is commonly used to weld rings that range in diameter from a few inches (Fig. 4)

to as much as 4.6 m (15 ft) (Fig. 5). The aircraft engine industry uses flash-welded rings made from heat-resistant materials in accordance with military specifications for jet aircraft.

Other flash-welding applications include:

- Chain links
- Transmission bands
- Automotive flywheel ring gears
- Strips that are joined for continuous processing lines
- Wire and bar drawing operations for continuous stamping press feed lines
- Roll form lines
- Aircraft landing gear
- Tube and rod eye clevises
- Band-saw blades (Fig. 6)
- Drill extensions using two different materials
- Miter joints for automotive and home window frames

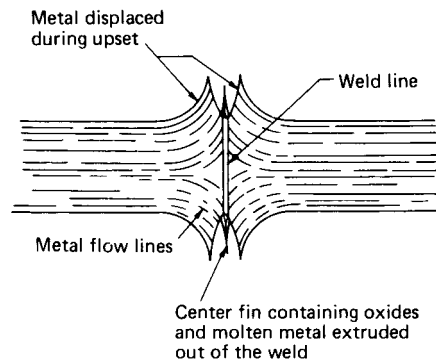


Fig. 3 Schematic showing cross-sectional view of typical peaks and flow lines generated in a flash weld

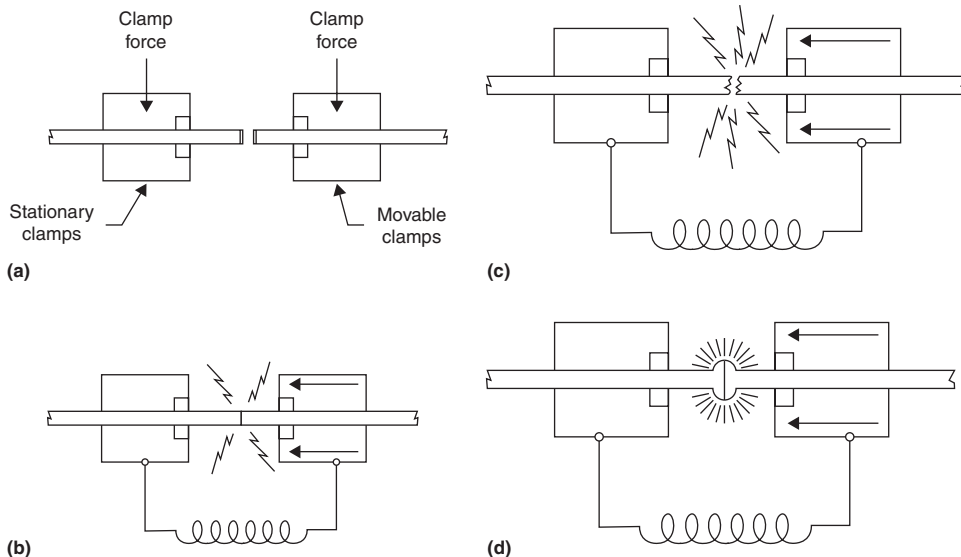


Fig. 2 The basic steps of flash welding. (a) Position and clamp parts. (b) Apply flashing voltage and start platen motion. (c) Flash. (d) Upset and terminate

- Crankshaft counterweights
- Aluminum-to-copper electrical transition for power transmission
- Anodes used in aluminum smelters
- Railroad rails, especially for high-speed trains

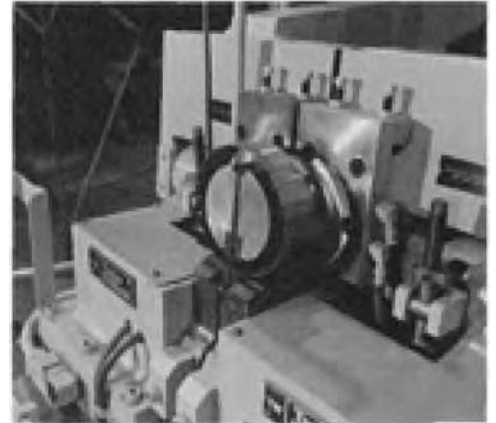


Fig. 4 Flash-welding machine used to fabricate a coiled steel strip into a small-diameter ring with a flange

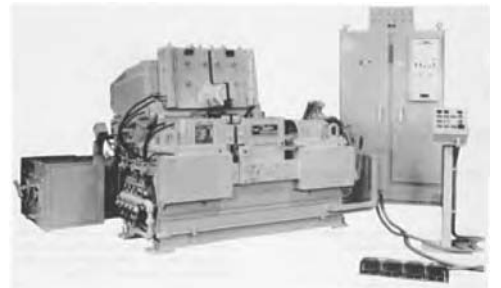


Fig. 5 Flash-welding machine with capacity to weld rings up to 4.6 m (15 ft) in diameter

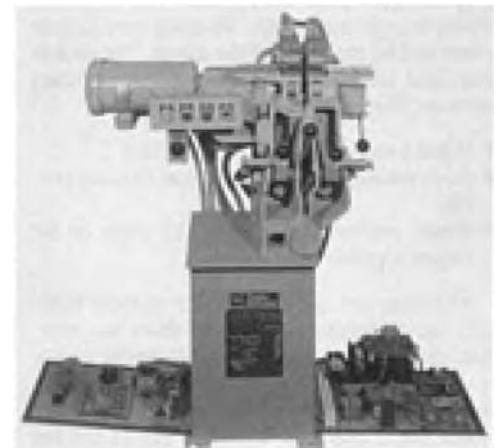


Fig. 6 Flash-welding machine installation equipped to weld band-saw blades

Process Steps in Flash Welding

Preweld Preparation. Parts that are flash welded come in a variety of forms, including forgings; rolled or extruded bar; sheet, strip, or plate; ring preforms; and castings. As a minimum precaution, the ends of the workpiece that are clamped on the current-conducting die must be free from dirt, scale, surface oxidation, and grease. The ends of the workpiece that extend into the weld zone must be free from any contamination that could react with the base metal at the high temperatures developed during welding.

Preweld cleaning of the workpieces at the die contact area also is important to ensure proper current flow and prevent local overheating of the workpiece surface. Because of the high current densities, hot spots can develop between the current-conducting dies and the workpiece if insufficient electrical contact is made. These localized hot spots are called die burns. Surface coatings (plated metal, conversion coating, or anodized coating) should not be present before welding, because they result in weld-area contamination or die burns. Oxides and foreign particles also can cause small pits in the surface as they overheat and burn into the workpiece. Loose scale and grease also may cause the parts to slip during upsetting.

Common cleaning techniques include abrading the surfaces by grinding, grit blasting, or wire brushing; pickling or chemical descaling; and vapor degreasing. In some cases, the ends of the workpiece must be machined or ground to fit the dies, particularly in welding of rough forgings or castings. Also, a chamfer may be required on the ends of the workpiece to initiate flashing action. Die burns, upset slippage, and inferior welds may be caused by poor fit-up between the current-conducting dies and the workpiece.

Burnoff. After the parts are clamped in the welding machine and the welding power is activated, the abutting surfaces are brought together for a brief period of violent flashing. This phase of the welding sequence is called burnoff. It serves the function of squaring off the abutting surfaces and compensates for inconsistencies in end preparation.

Preheating is a resistive heating phase of the welding process in which the heat is generated by the electrical resistance of the workpieces. It is accomplished by bringing the workpieces together under light pressure, creating a short circuit. The pressure must be great enough to prevent flashing but not so great that workpieces are prematurely welded.

In practice, preheating is performed in a cyclic manner; workpieces are brought together briefly, then separated for a brief period to allow the heat generated to diffuse into them. This sequence is repeated several times. Fully automatic machines perform this function, thus eliminating operator variables.

Flashing Stage. The primary purpose of flashing is to generate enough heat to produce a plastic zone that permits adequate upsetting. The rate of energy input must be in proper

proportion to the travel of the platen or movable die, so that constant flashing is maintained until the appropriate amount of metal is flashed off and the required plastic zone is obtained.

When the ends of the workpiece are brought together under light pressure, an electrical short circuit is established through the material. Because the abutting surfaces are not perfectly matched, the short-circuit current flows across the joint only at a few small contact areas. The large amount of current flowing through a relatively small area causes very rapid heating to the melting point. Heating is so rapid and intense that molten metal is expelled (flashed off) from the joint area. Following this expulsion, a brief period of arcing occurs. Arcing is not sustained due to the low voltages employed. Studies have shown that stable flashing can be maintained with as low as 2½ to 3 V, but typically the flashing voltage for alternating-current machines is from 5 to 10 V.

After the expulsion of molten metal and subsequent arcing, small craters are formed on the ends of the abutting surfaces. The pieces are steadily advanced toward one another, and other short circuits are formed and additional molten metal is expelled. This process continues as random melting, arcing, and expulsion occur over the entire cross-sectional surface. During flashing, many active areas are in various stages of this sequence (Fig. 7). Flashing surfaces act as heat sources, and the steep thermal profile is established primarily from these heat sources. Temperatures of the flashes are at or above the melting point of the material and are progressively lower as distance progresses from the flashing surface toward the clamp.

In general, the flashing rate in flash butt welding has been achieved by using motor-driven cams, analog computers, or digital computers to create position-versus-time profiles. Each of these systems either advances the movable platen and clamp directly or through the use of hydraulic systems. The hydraulic systems can incorporate proportional valves, servo valves, or indirect control of follow valves. Regardless of the method used to advance the movable plate during flashing, the process achieves similar final results. The analog and digital systems have allowed platen position to be determined by such controls as constant input power (kVA), constant acceleration, elliptical acceleration, or natural log acceleration. These schemes are adjusted to prevent deleterious effects such as freezing (solid interface mating) during the flash weld interval.

Upsetting (Forging) Stage. Bonding takes place during the upsetting action. Table 1 gives typical upsetting pressures for numerous classes of alloys. During upsetting, some metal must be extruded from the weld zone to remove slag and other inclusions not expelled during flashing. The extruded metal should extend beyond the cross-sectional boundaries of the workpiece to ensure that maximum amounts of slag and inclusions are removed when the weld upset is removed during subsequent trimming.

When the weld upset is removed, no evidence of the weld should remain. Porosity near the outer surface on an etched section of the weld, or a crevice around the workpiece after the weld upset has been removed, indicates incomplete bonding because of either insufficient upsetting force or insufficient plasticity during upsetting.

A large upset produced by an excessive upsetting force can be detrimental to weld quality, can waste metal, and indicates that most of the plastic metal has been extruded, requiring bonding to take place in metal where plasticity may not have been sufficient to ensure a good weld.

Postweld Heat Treatment. When welding materials with high carbon equivalents, it may be important to heat the weld to the austenitizing temperature and slow-cool to prevent the formation of martensite. This can be done by unclamping the part, opening the dies to the full-open position, reclamping with the weld in the center between the clamps, and applying short bursts of current to reheat the area.

Processing Equipment

Flash-welding machines are a horizontal press-transformer combination, which consists of a low-impedance welding transformer, a stationary platen, and a movable platen with clamping dies to position and hold the workpieces. The seven major components include:

- A machine bed that has a fixed platen attached to it, as well as a set of electrically insulated ways that support a movable platen

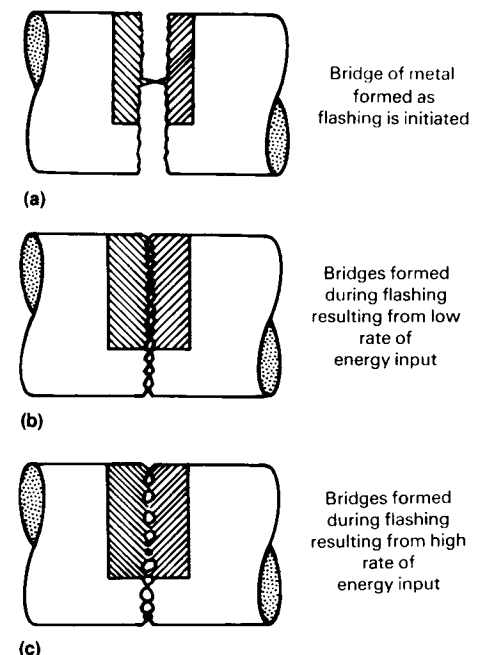


Fig. 7 Growth of contact points produced by energy input during flash welding

- A movable platen, which is generally mounted on the electrically insulated ways that are attached to the machine bed
- Two clamping assemblies, one of which is rigidly attached to each platen to both align and hold the parts to be welded in place
- Equipment for controlling the motion of the movable platen
- A welding transformer with adjustable taps
- Controls and monitors for machine functions
- A vent/flash catcher, which is incorporated to collect any fumes and excess flash materials to ensure operator comfort and safety and to maintain the cleanliness of the work area

Flash-welding machines may be manual, semi-automatic, or fully automatic. With manual operation, the operator controls the speed of the platen from the time flashing is initiated until the upset is completed. In semiautomatic operation, the

operator manually initiates flashing and then actuates an automatic cycle that completes the weld. In fully automatic operation, after the operator initiates the welding sequence, a fully automatic cycle can be used through the use of position-indicating devices and timers. Values for the various welding parameters are preselected by the operator. Automatic feedback control is used in some applications. These fully adaptive circuits vary from current to voltage feedback circuits, and data are obtained to control the welding sequences.

Various types of electrical, air, or hydraulic systems may be used for controls during flashing and upsetting. An example is illustrated in Fig. 8. The movable platen of a flash welder can be driven by a number of different methods. The simplest type often uses a cam that is motor driven through a gear box. Flashing time is then controlled by the speed of the motor. The cam is machined to produce the desired flashing cam curve profile, including the:

Table 1 Recommended upsetting pressures for flash welding of selected alloys

Strength classification	Upset pressure		Alloys	
	MPa	ksi	SAE designation	Others
Low forging	69	10	1020, 1112, 1315	High-strength low-alloy steels
Medium forging	103	15	1045, 1065, 1335, 3135, 4130, 4140, 8620, 8630	...
High forging	172	25	4340, 4640, 300M	Tool steels, titanium, aluminum
Extra-high forging	241	35	A-286, 19-9 DL	Nickel-base alloys(a)

(a) Materials exhibiting extra-high compressive strength at elevated temperatures

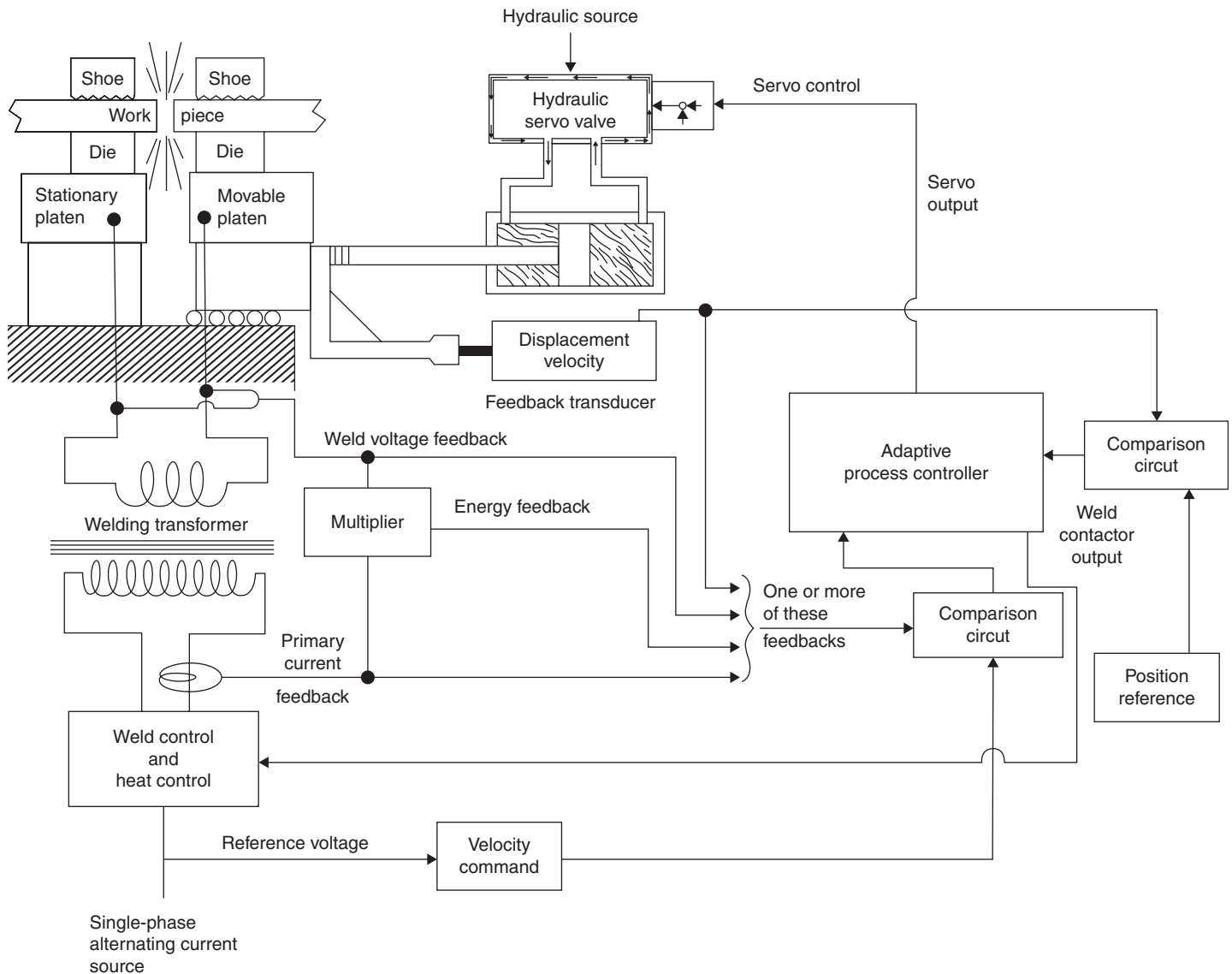


Fig. 8 Flow diagram showing adaptive controls used to control and monitor flash-welding process

- Initial burnoff region of linear flash
- Accelerating curve for the actual flashing profile (Fig. 9)
- Upset portion that causes the parts to be forged together after flashing

Machines that are either larger or more complex use hydraulic cylinders to drive the movable platen and to incorporate hydraulic servo systems. Although it is possible to use a servo valve to directly control the position of the platen via a hydraulic cylinder, this is not the preferred method, because contamination by the oil is extremely difficult to prevent. The better approach is to use a hydraulic servo actuator, in which the servo valve operates on its own refined oil system and the oil that circulates through the platen cylinder is derived from another hydraulic source. This approach has been shown to be more reliable and more accurate and to vastly improve servo valve life.

Controls and Auxiliary Equipment. Electrical controls on flash-welding equipment are designed to sequence the machine, control the weld current, and precisely control the platen position during flashing and upsetting. These controls often comprise programmable controllers, welding current controllers, and either motor or servo valve controllers. Silicon-controlled rectifier (SCR) contactors (solid-state switches) are used as the devices to control the flow of welding current from the power lines to the welding transformer. Older machines used ignitrons for this purpose, but SCRs have fully replaced them in recent years. Preheat and post-heat cycles are often required procedures in

flash-welding operations; timers with phase-shift heat control are used to accomplish these important functions.

Power Sources. The most common source of power for flash welders is single-phase alternating current (ac) power. Flash-welding transformers are kVA rated at 50% duty cycle. If an extremely large demand current is required and an adequate single-phase ac source is not available, then ac to direct current conversion is employed using a three-phase transformer/rectifier. The most frequently used rectifier systems are the three-phase half-wave and three-phase full-wave types, often supplied as a six-phase star configuration. In actual practice, no discernible differences in the weld produced by these two rectifier systems can be detected.

State-of-the Art Welding Unit Components. Devices that monitor and control selected process parameters are commonly incorporated into the latest flash-welding units.

A *linear ramp preflashing approach rate* is usually built into the flashing cam and minimizes any tendency of the weld to freeze at the beginning of flashing. The term *flashing cam* is used regardless of whether the cam is a motor-driven machined cam or if the position curve is generated electronically.

Natural Log Flashing Curves. Numerous technical articles have been published on what constitutes the best flashing curve. Although engineers are divided on this issue, it has been shown that the use of natural log curves results in significantly better welds than are produced using any other curve. The natural log system conforms to the natural heat-transfer

characteristics of the metal being welded, thereby creating a flashing progression that parallels the development of heat at the interface with a natural log gradient toward the clamp.

Natural log flashing curves are shown in Fig. 9. In this illustration, four values of natural log curves are shown, with exponent numbers of one to four. The curves with low exponent numbers are typically used on low-carbon materials because the starting travel rate is fairly fast and the final travel rate is slightly accelerated. The curves with high exponent numbers, three or four, are used for welding high-strength, low-alloy and AHSS materials because they require a slower starting rate and a higher final rate to develop flashing and to achieve the correct temperature profile for upsetting all of the material.

Ramp Turn-On of SCRs. Not to be confused with the linear approach ramp, this control device slowly and progressively turns on the SCRs at the beginning of the flashing cycle. Because the magnetic condition of a weld transformer may be unknown at the end of a previous weld, the ramp turn-on device is used to restore the transformer to a known condition. This greatly extends the life of the transformer itself, in addition to the SCR contactor, because it avoids the high inrush of current that would have occurred when the next weld was initiated.

No Phase Shift during Flashing. This control feature ensures that full voltage will be applied to the dies whenever flashing conditions are present, except during the ramp turn-on interval. A phase shift can reduce the average voltage but does not reduce the peak voltage. During the phase-delay period of the voltage waveform, the platen continues to travel forward until a peak voltage is suddenly applied, causing violent flashing and deep cratering. Although the pyrotechnics of a phase-shift flashing action can be quite impressive, the resulting weld will be a disaster. The best flashing action is relatively subdued and produces flash particles of significantly lower intensity and size.

The oxygen-depletion system used in this process is a patented method of combusting the oxygen that would otherwise exist in the weld interface region. In actual use, the oxygen-depletion system does more than remove oxygen. By heating the gases in the interface region, the ionization voltage is reduced, and higher flashing currents can be sustained at relatively low flashing voltages.

Clamping Dies and Fixtures. The materials commonly used for clamping dies are Resistance Welder Manufacturers Association (RWMA) class 3 and hardened tool steels such as H11, L6, and O1. Bronze and other copper-base electrode materials can be used in some applications. The die half (upper or lower) that conducts the current usually is made of a copper-base material. The other half is made of the same copper-base material or of hardened steel.

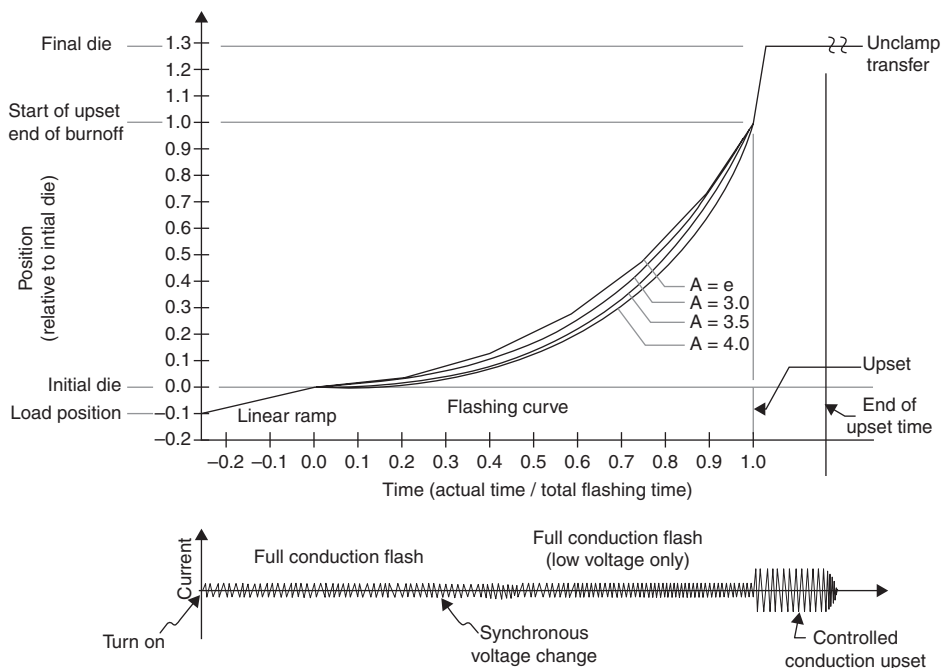


Fig. 9 Exponential flashing curves with related current

Generally, the shape of the clamping-die surface is such that the die encompasses almost the entire workpiece surface. The required area of clamping-die contact depends on the current needed for heating the workpiece and the pressure needed for holding it. Semicircular dies are used where the line contact provided by V-shaped dies gives insufficient surface for the current to flow without burning the workpiece, or for holding the workpiece without marking it. Table 2 gives the minimum lengths of clamping dies for welding rounds, tubing, and other sections of various diameters or minimum dimensions; these data are for welding steels of low or medium forging strength.

Failure Origins in Flash Welds

Porosity. Insufficient upsetting force or travel may leave porous areas of cast metal in the weld. Excessive electrical energy input can also lead to porosity by the formation of large craters by the expulsion of molten metal. Where large-diameter pieces are to be joined, one end face should be slightly chamfered so as to start the flashing at the center of the cross section. This helps to avoid trapping of particles in the weld.

Incomplete Fusion. Inadequate heating results in incomplete fusion, but it may also result from an upsetting travel that is so slow that the metal does not become sufficiently plastic to forge properly during upsetting. Another cause of inadequate heating can be the shunting of electrical current around the closed side of a ring to be flash welded; sufficient current may be bypassed to make flashing difficult, even resulting in a melt-through of the closed side of the ring.

Poor Weld Contours. Whenever heating is not uniform over the intended joint, an unfavorable temperature gradient is established that contributes to misalignment after welding. If parts are not properly aligned by the dies, they may slip past each other during upsetting, creating a lap instead of a proper weld. Workpieces of different cross sections that have not been adjusted in design to achieve a good heat balance, such as tubes of different diameters or wall thicknesses, may slide (telescope) over each other and create a poor-quality weld.

The internal flash and upset metal formed in flash welding of tubes or pipe are normally not removed (often, they cannot be), which leaves a reinforcement with two sharp notches adjacent to the fusion line. These notches act as stress raisers that, under cyclic loading, reduce the fatigue strength. They also restrict fluid flow and can serve as barriers to streamline fluid movement concentration-cell sites for corrosion.

Hot Cracks. Alloys that possess low ductility over a temperature range below the melting point may be susceptible to hot cracking. Such alloys are more difficult to flash weld but can usually be welded if the most favorable welding conditions are selected. Tension obviously should be avoided, and because the rim of the upset metal is in circumferential tension as upsetting progresses, it may be necessary to keep the upsetting force to the minimum acceptable. In such an operation, some cracks are likely to form that are shallow enough to allow complete removal when the upset metal is machined away. Precise coordination of current cessation and upsetting travel are important, and the joint should be under moderate compression during cooling.

Cold Cracks. Insufficient heat during upsetting or excessive upsetting travel causes colder metal to be forced into the weld zone. The metal cracks transversely to the weld line in the upset zone. This effect is also encountered in the flash welding of hardenable steels, because of the mass quench provided by the remainder of the workpiece. The use of a slow cooling rate, as well as heat treatment following welding, alleviates transformation stresses that could cause cracking under service loads.

Upset Welding*

Upset welding is a resistance welding process using both heat and deformation to form a weld. Pressure is applied before heating is started and is maintained throughout the heating period (Fig. 1b). As noted, the equipment used for upset welding is very similar to that used for flash welding. Upset welding differs from flash welding in that the parts are clamped in the welding machine, and force is applied to

bring the parts tightly together. High-amperage current is then passed through the joint, which heats the abutting surfaces. When they have been heated to a suitable forging temperature, an upsetting force is applied and the current is stopped.

The high temperature of the work at the abutting surfaces, plus the high pressure, causes coalescence to take place. After cooling, the force is released and the weld is completed. There is no arc or flash in upset welding. The area at the joint is usually enlarged over its original dimension. It can be used only if the parts to be welded are equal in cross-sectional area. For upset welding of large parts, the peak power drawn from the electrical supply may be a disadvantage.

Upset welding typically results in solid-state welds (no melting at the joint). The deformation at the weld joint provides intimate contact between clean adjoining surfaces, allowing formation of strong metallurgical bonds. If any melting does occur during upset welding, the molten metal is typically extruded out of the weld joint area.

A wide variety of shapes and materials can be joined using upset welding in either a single-pulse or continuous mode. Wire, bar, strip, and tubing can be joined end to end with a single pulse of welding current. Seams on pipe or tubing can be joined using continuous upset welding by feeding a coiled strip into a set of forming rolls, resistance heating the edges with wheel electrodes, and applying a force to upset the edges together.

Upset welds have similar characteristics to inertia friction welds, which are also solid-state welds. The amount of deformation is usually less for upset welds, and the deformation can be more precisely controlled using upset welding. For example, a pipe butt weld made using inertia friction welding will have a large upset on both the inside and outside, whereas an

* Adapted from W.R. Kanne, Jr., Upset Welding, *Welding, Brazing, and Soldering*, Vol 6, *ASM Handbook*, ASM International, 1993, p 249–251

Table 2 Minimum lengths of clamping dies, with and without backup, for flash welding selected diameters of workpieces made from steels of low or medium forging strength

Workpiece diameter(a)		Minimum length of clamping die				Workpiece diameter(a)		Minimum length of clamping die with backup		Workpiece diameter(a)		Minimum length of clamping die with backup	
mm	in.	With backup		Without backup(b)		mm	in.	mm	in.	mm	in.	mm	in.
6.35, 7.92	0.250, 0.312	9.53	0.375	25.4	1.00	50.8	2.00	31.8	1.25	152	6.00	82.3	3.25
9.53	0.375	9.53	0.375	38.1	1.50	63.5	2.50	44.5	1.75	165	6.50	88.9	3.50
12.70	0.500	9.53	0.375	44.5	1.75	76.2	3.00	50.8	2.00	178	7.00	95.3	3.75
19.05	0.750	12.70	0.500	50.8	2.00	88.9	3.50	57.2	2.25	191	7.50	102	4.00
25.40	1.000	19.05	0.750	63.5	2.50	102	4.00	63.5	2.50	203	8.00	108	4.25
38.10	1.50	25.40	1.000	76.2	3.00	114	4.50	69.9	2.75	216	8.50	114	4.50
						127	5.00	69.9	2.75	229	9.00	121	4.75
						140	5.50	76.2	3.00	241	9.50	127	5.00

(a) Diameter of rounds or tubing, or minimum dimension of other sections. (b) Backup is recommended for all workpiece diameters or minimum dimensions over 38.1 mm (1.50 in.).

upset weld can be controlled, through joint design and welding parameters, to have essentially no internal upset (Fig. 10).

The metallurgical structure of the weld area is that of a hot-worked material with a good diffusion bond across the weld interface, as can be seen in Fig. 10. This microstructure results in higher strength in the weld area than can be achieved for fusion welds (Fig. 11). With solid-state welds, there is difficulty in good nondestructive testing techniques to determine the quality of solid-state bonds. Normally, control of process variables is sufficient to ensure quality. Nondestructive methods, such as ultrasonics, are being applied to solid-state welds for determination of bond quality (see the article “Nondestructive Evaluation for Solid-State Welding” in this Volume).

Solid-state upset welding has advantages compared to typical fusion welding processes. These advantages are due to the simplicity of the welding process and the resulting solid-state weld microstructure. These advantages include:

- *Speed:* The upset welding process is fast (usually less than 1 s).
- *Ease of control:* The process has only three primary variables (current, force, and time).
- *Fewer defects:* Typical fusion welding defects, such as porosity, missed joints, incomplete fusion, spatter, and solidification cracking, do not occur in upset welds.
- *Enhanced weld properties:* The metallurgical properties of the weld metal and heat-affected zone in upset welds are those of hot-worked material. In other words, the strength of the weld zone is not reduced to that of an annealed structure, as in fusion welds.
- *Simplicity of equipment:* Upset welding equipment is not complex, involves no

rotating parts, and requires minimal maintenance.

- *Less-strict composition requirements:* Minor alloying elements do not affect upset weld quality, and thus, attention to alloy composition for weldability can be eliminated.
- *Ability to join difficult-to-weld materials:* Alloys normally considered unweldable can be joined by upset welding. For example, a variety of stainless steels (including A-286), superalloys (including thoria-dispersed nickel), refractory metals (including

tungsten), grade 2 titanium, and aluminum alloys (including 2024) have been successfully upset welded.

The effect of welding conditions, other than the basic parameters of force, current, and time, is generally minimal. Surface roughness usually has little effect, because it is overshadowed by the deformation that takes place during welding. Surface cleanliness and welding atmosphere may or may not be important, depending on the amount of deformation that

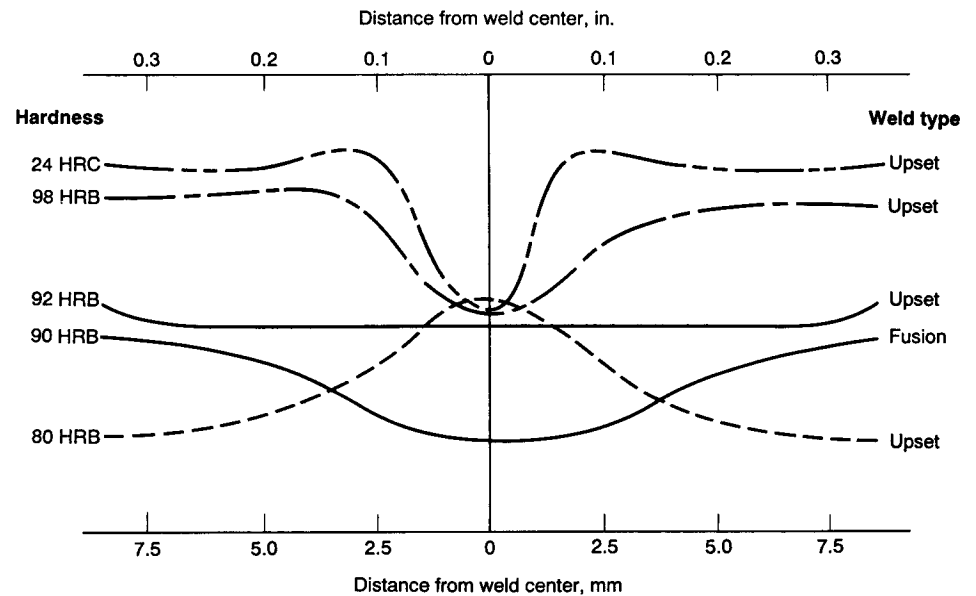


Fig. 11 Hardness across upset welds and in materials of various strengths compared to fusion weld hardness. Note that the weld area hardness (and therefore strength) is greater for the upset welds than for the fusion weld.

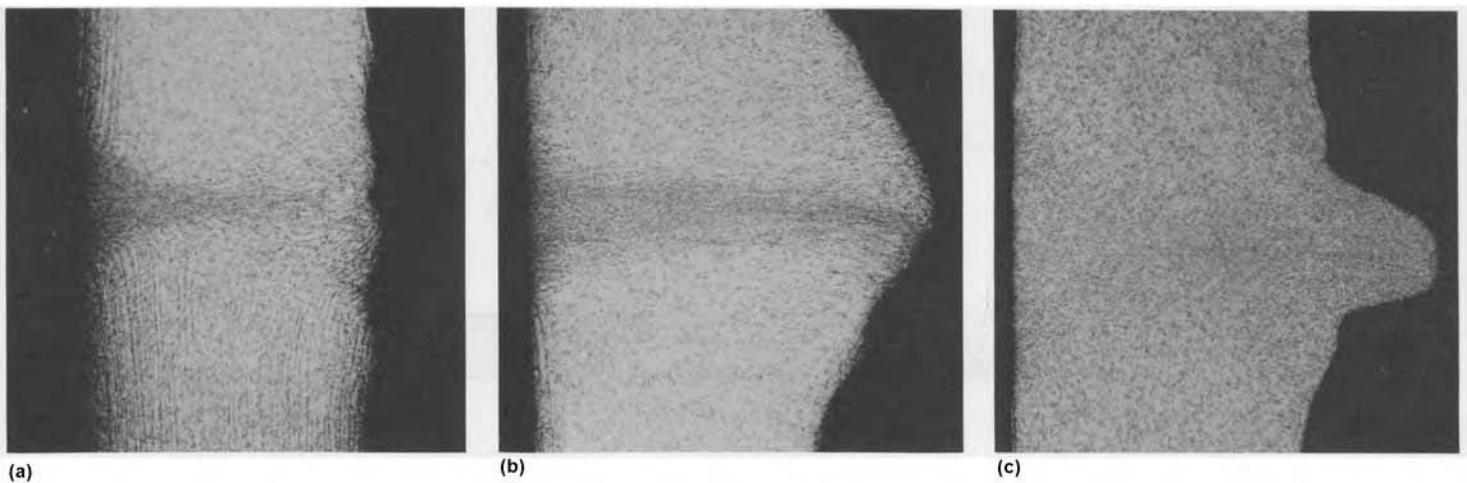


Fig. 10 Upset weld configurations in butt welds of pipe with an outside diameter of 25 mm (1 in.) and a wall of 3 mm (0.1 in.). Upset has been machined from the outside surface (on left). The internal upset configuration was controlled by adjusting weld parameters and joint design. (a) Minimum upset. (b) Large upset. (c) Narrow upset at low force. Courtesy of Westinghouse Savannah River Company

occurs to break up any oxide present before, or formed during, welding.

Plug welds are a type of upset weld that requires little fixturing. Plug welds up to 125 mm (5 in.) in diameter are used to seal the fill holes of canisters employed in the long-term disposal of high-activity nuclear waste. The canisters, which are made from 304L stainless steel, are 610 mm (24 in.) in diameter and 3 m (118 in.) in height. The plug configuration is shown in Fig. 12 relative to the hole of the canister being plugged. The considerable upsetting that occurs during the welding process results in a solid-state weld. Typically, these welds are made using pressure of 300 kN (75,000 lbf) with 230,000 A current applied for 1.5 s. The resulting welds have the high reliability required for long-term containment of radioactive material.

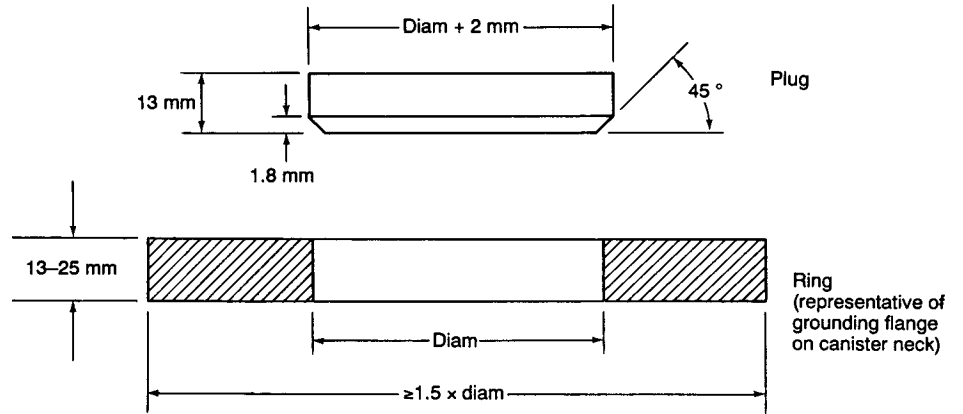


Fig. 12 Upset plug weld for canister closure

High-Frequency Welding*

Revised by Menachem Kimchi, Edison Welding Institute

HIGH-FREQUENCY RESISTANCE WELDING (HFRW) is a resistance welding process that uses high-frequency currents to concentrate the welding heat at the desired location. The heat generated by the electrical resistance of the workpiece to high-frequency currents produces the coalescence of metals, and an upsetting force usually is applied to produce a forged weld. High-frequency resistance welding is an automated process and is not adaptable to manual welding.

High-frequency resistance welding was developed during the late 1940s and early 1950s to fill the need for high-integrity butt joints and seam welds in pipe and tubing. The progressive development of this technology (Table 1) has served as the basis for the modern high-speed pipe and tube welding systems in current use. In this continuous process, high-frequency current is concentrated in the formed strip edges and generates rapid heating in a small volume of metal at the weld interface. Pressure rolls are then used to force the edges together to produce a solid-state weld (Fig. 1).

The principal application of high-frequency welding continues to be in the manufacture of seam-welded pipe and tube. The process is also used in the manufacture of products such as spiral-fin boiler tubes, closed roll form shapes, and welded structural beams. Other examples of manufacturing applications are the welding of the metal shielding layer that surrounds high-frequency coaxial cable, the manufacture of butt joints in strip material and for solar panels, and for the butt joints in pipe and tube production. In the production of welded tube and pipe, HFRW mills operate at very high speeds, generally ranging from 15 to 152 m/min (50 to 500 ft/min), depending on material diameter and thickness. Application sizes range from hypodermic needles to pipelines.

The tubemaking incorporates the simplest method of controlling high-frequency currents, that is, the generation of an edge “V.” High-frequency currents can be supplied to the welding process or workpiece by using either an induction coil (known as high-frequency induction welding) or electrical contacts (known as high-frequency resistance welding). The edge “V” is a series component of the circuit (Fig. 2).

Because of proximity and skin effects, current flow is concentrated across the full face width of the strip edges, resulting in controlled surface heating and subsequent welding. In this process, a coil of strip material is first formed into a longi-

tudinal hollow on a forming mill. The two edges of the strip are then high-frequency welded and squeezed together to form a continuous welded seam. As a result of squeezing or upsetting, some of the material from the butting faces

Table 1 Historical overview of high-frequency welding of pipe and tubing

1940 to 1950—Butt joints

Welds in butt joints were made with 10 kHz motor-generator power sources equipped with induction coils that could be opened for removal from the pipe or tube after the weld was formed. A municipal utility was the first to use mobile high-frequency welding equipment in the streets of New York City for the welding of butt joints in pipe. Pipes as large as 305 mm (12 in.) in diameter with wall thicknesses up to 8 mm (5/16 in.) were welded. The pipe ends were fitted and pressed together, then were induction heated to the forge-welding temperature in approximately 60s.

1949—Forge welding of continuous seams

The first high-frequency induction welding system was introduced for the continuous forge welding of the longitudinal seam in small steel tubes. The system used a 10 kHz motor generator equipped with a split-return induction coil suspended over the seam, similar to those used for continuously normalizing the weld seam in pipe welding. These systems were operated for many years but had the disadvantage of heating a large portion of the pipe.

1952—Induction welding of continuous seams

Thomas Crawford tested the continuous induction welding of longitudinal seams in various metal tubes, including some with electrical cable inside, using the induction welding process. Tests were made at an electrical frequency of 400 kHz and used an induction coil surrounding the tube. This technique for the seam welding of pipe and tube was highly successful and continues to be employed for pipe with outside diameters up to 406 mm (16 in.).

1952—Butt, lap, and T-joints

Wallace Rudd and Robert Stanton invented a high-frequency contact welding process for welding a large variety of continuous joints. The Rudd and Stanton system operated at 400 kHz and introduced the high-frequency welding current directly into the workpiece by means of sliding contacts. The sliding contacts permitted the production of butt joints, lap joints, and T-joints in pipe, strip, and structural products.

1954—Continuous seam welding

Successful tests were made for welding the longitudinal seam in aluminum tubing, leading to the introduction of the first commercial welding of aluminum irrigation tubing. This high-frequency welding equipment used motor-generator sets with a maximum output frequency of approximately 10 kHz. By the early 1960s, these systems had been superseded by high-frequency vacuum tube oscillators that typically operated at approximately 400 kHz.

1986—Solid-state induction welding

The first solid-state induction welding machine was installed and operated at the Société Meusienne in France. This equipment operated at a welding frequency of approximately 100 kHz.

1990—Solid-state inverter power sources

Solid-state inverters replaced vacuum-tube oscillators in many new equipment installations during the 1990s. These units were more easily configured to operate at a variety of welding frequencies between 80 and 800 kHz. Experience, supported by mathematical theory, showed that selecting the correct welding frequency could greatly improve weld quality, improve mill yield for difficult-to-weld metals, and adapt the properties of the weld to the specific application. Seams in pipes up to 660 mm (26 in.) in diameter were welded using solid-state inverter power sources operating between 80 and 150 kHz with power outputs of up to 1800 kW.

2000s—Selectable-parameter power sources

High-frequency welding power sources with selectable parameters became available that allowed the continuous adjustment of the parameters of this process. This increased the range of pipe and tube products that could be produced by a single tube mill.

Source: Ref 1

* Revised from W. Smith and J. Roberts, High-Frequency Welding, *Welding, Brazing, and Soldering*, Vol 6, *ASM Handbook*, ASM International, 1993, p 252–253, with content adapted from High-Frequency Welding, Chapter 5, *Welding Handbook*, Vol 3, *Welding Processes, Part 2*, American Welding Society, 2007, p 160–181 with permission



Fig. 1 Coil and pressure rolls in high-frequency seam welding of a tube

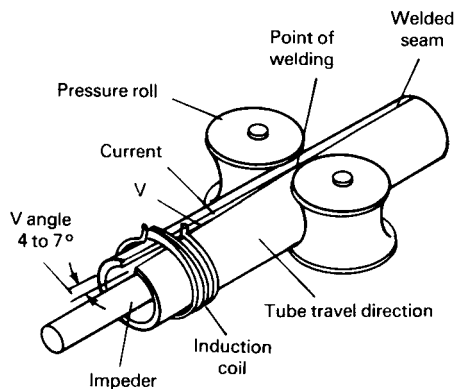


Fig. 2 Schematic of high-frequency induction welding apparatus for joining a tube seam

flows outward both at the outer and the inner diameters of a pipe or tube. This material, sometimes called flash or an upset, is usually trimmed by skiving knives. This is a good practice, but sometimes the flash on the inner diameter is rolled back into the material, instead of trimming.

Fundamentals

High-frequency current has certain characteristics that make it useful for welding. Unlike direct current or low-frequency alternating current, high-frequency current tends to flow at high densities along surfaces (skin effect) and seeks adjacent parallel surfaces for its return path (proximity effect). This means that the heating can be efficiently concentrated and focused to the surfaces where it is needed.

As noted, nearly all high-frequency welding processes involve surface bonding by some mechanical force that squeezes the materials together. This procedure helps produce a high-quality weld by squeezing out residual oxides and molten metal, which are detrimental to weld integrity. The removal of any molten metal from the weld zone is beneficial because it eliminates

the potentially harmful effects associated with cast structures, such as lower fracture toughness and poorer corrosion resistance.

There are two basic process variations of HFRW: contact resistance welding and induction welding. Both variations use high-frequency current to produce the heat for welding. In HFRW, the electrical contacts physically touch the workpiece when current is conducted through the workpiece. During induction welding, the current is induced in the workpiece by magnetic coupling with an external induction coil. There is no physical contact with the workpiece. Both methods rely on the properties of high-frequency electricity and thermal conduction, which determine the distribution of heat in the workpieces.

High-frequency contact welding and high-frequency induction welding are used to weld products made from coil, flat, or tubular stock with a constant joint symmetry throughout the length of the weld. Table 2 lists typical welding parameters for high-frequency seam welds and butt joints by induction and contact welding. Recommendations are shown for various metals and product forms.

Figure 3 illustrates basic joint designs used in high-frequency welding. Figures 3(a) and (b) are butt seam welds; Fig. 3(c) is a mash seam weld produced with a mandrel, or backside/inside bar. Figure 3(d) is a butt joint design in strip metal, and Fig. 3(e) shows a T-joint. Figures 3(f) and (g) are examples of helical pipe and spiral-fin tube joint designs. Figure 3(h) is an example of a seam weld in a closed roll shape; Fig. 3(j) illustrates a butt joint in pipe, showing the placement of the coil. Figure 3(k) shows a butt joint in bar stock.

High-frequency current in metal conductors tends to flow at the surface of the metal at a relatively shallow depth that becomes shallower as the electrical frequency of the power source is increased. This commonly is called the skin effect. The depth of electrical current penetration into the surface of the conductor is a function of electrical resistivity and magnetic permeability, the values of which depend on temperature. Thus, the depth of penetration also is a function of the temperature of the material. In most metals, the electrical resistivity increases with temperature; as the temperature of the weld area increases, so does the depth of penetration.

Metals that are magnetic at room temperature lose the magnetic properties above the Curie temperature. When this happens, the depth of penetration increases drastically in the portion of metal that is above the Curie temperature while remaining much shallower in the metal that is below the Curie temperature. When these effects are combined in steel heated at a frequency of 400 kHz, the depth of current penetration is 0.05 mm (0.002 in.) at room temperature, while it is 0.8 mm (0.03 in.) at 800 °C (1470 °F). The depth of current penetration for several metals as a function of frequency is shown in Fig. 4.

The second important physical effect governing the high-frequency welding process is thermal conduction of the heat generated by the electric currents in the workpiece. Control of

the thermal conduction and the penetration depth provides control of the depth of heating in the metal. Because thermal conduction is a time-dependent process, the depth to which the heat will conduct depends on the welding speed and the length of the electrical current path in the workpiece. If the current path is shortened or the welding speed is increased, the heat generated by the electric current in the workpiece will be more concentrated and intense. However, if the current path is lengthened or the welding speed is reduced, the heat generated by the electric current will be dispersed and less intense. The effect of thermal conduction is especially important when welding metals with high thermal conductivity, such as copper or aluminum. It is not possible to weld these materials if the current path is too long or the welding speed is too slow. Changing the electrical frequency of the high-frequency current can compensate for changes in welding speed or the length of the weld path, and the choice of frequency, welding speed, and path length can adapt the shape of the heat-affected zone (HAZ) to optimize the properties of the weld metal for a particular application.

It should be noted that the high-frequency current path at the surface of the workpiece is controlled by how close it is, or its proximity to its own return path. This phenomenon, called the proximity effect, is illustrated in Fig. 5. The proximity effect becomes more pronounced as the frequency is increased. Increased frequency reduces the penetration depth by confining the current to a shallower and narrower path. This property is illustrated in Fig. 6(a) and (b), where current patterns are shown for workpieces with the same geometry when the frequency of the electric current is 60 Hz and 10 kHz.

Referring to Fig. 6, a 60 Hz current in the steel plate flows in the opposite direction of the current flowing in the adjacent proximity conductor. In this case, the size and shape of the proximity conductor have negligible effect on the distribution of current in the steel plate. This example also shows that penetration at 60 Hz is deep compared to the thickness of the plate. As a result, the current flows fairly uniformly throughout the cross section of the plate. When the 10 kHz current is applied to the same system, the current flowing in the steel plate is confined to a relatively narrow band immediately beneath the proximity conductor. This narrow band is the path of lowest inductive reactance for the current in the plate. The shape and magnetic surroundings of the proximity conductor have a considerable effect on the distribution of the current in the steel plate but have no effect on the depth of penetration.

Controlling the concentration of current in a workpiece can achieve extremely high heating rates and high temperatures in a localized area, thereby heating only the region of the workpiece to be welded. By controlling the relative position of the surfaces to be welded, the heat can be positioned at the weld interface where it is needed without excessively heating the rest of the metal. The effect of changing the spacing and geometry

Table 2 Typical high-frequency welding parameters

Process and application	Metal	Principal workpiece dimension		Thickness		Welding speed		Welding power source range, kW	Welding frequency, kHz
		mm	in.	mm	in.	m/min	ft/min		
Induction seam welding: pipe and tube	Low-carbon steel (can be aluminum or zinc coated)	Outside diameter: 10–75	Outside diameter: 0.4–3	Wall thickness: 0.6–2	Wall thickness: 0.025–0.080	25–300	80–1000	50–500	300–400
	Carbon steel less than 0.05% C (can be aluminum or zinc coated)	Outside diameter: 50–200	Outside diameter: 2–8	Wall thickness: 1.5–12.7	Wall thickness: 0.060–0.5	20–150	60–500	200–1000	200–400
	Carbon steel less than 0.05% C	Outside diameter: 150–400	Outside diameter: 6–16	Wall thickness: 2–12.7	Wall thickness: 0.080–0.5	15–90	50–300	400–1200	150–300
Contact seam welding: pipe and tube	Low-carbon steel (can be aluminum or zinc coated)	Outside diameter: 10–75	Outside diameter: 0.4–3	Wall thickness: 0.6–2	Wall thickness: 0.025–0.080	25–300	80–1000	50–350	300–400
	Carbon steel less than 0.05% C (can be aluminum or zinc coated)	Outside diameter: 50–200	Outside diameter: 2–8	Wall thickness: 1.5–12.7	Wall thickness: 0.060–0.5	20–150	60–500	150–450	300–400
	Carbon steel less than 0.05% C	Outside diameter: 150–400	Outside diameter: 6–16	Wall thickness: 2–12.7	Wall thickness: 0.080–0.5	15–90	50–300	250–600	200–400
Induction seam welding: pipe and tube	Stainless steel	Outside diameter: 10–75	Outside diameter: 0.4–3	Wall thickness: 0.6–2	Wall thickness: 0.025–0.080	10–90	30–300	50–300	250–300
	Aluminum	Outside diameter: 10–38	Outside diameter: 0.4–1.5	Wall thickness: 0.3–1	Wall thickness: 0.010–0.040	40–150	120–500	50–150	400–800
	Copper	Outside diameter: 10–75	Outside diameter: 0.4–3	Wall thickness: 0.3–2	Wall thickness: 0.010–0.080	40–150	120–500	50–300	400–600
Induction welding: butt joints in pipe and tube	Low-carbon steel	Outside diameter: Up to 300	Outside diameter: Up to 12	Wall thickness: 2–12	Wall thickness: 0.08–0.5	10–60 s/joint		100–500	1–10
Induction welding: butt joints in beams	Low-carbon steel	Height: 75–500 Width: 50–300	Height: 3–20 Width: 2–12	Web thickness: 2–10 Flange thickness: 3–12	Web thickness: 0.080–0.375 Flange thickness: 0.125–0.5	10–40	30–120	100–350	200–400
Induction welding: spiral-fin boiler tubes	Low-carbon steel, stainless steel, or in combination	Outside diameter: 25–75	Outside diameter: 1–3	Wall thickness: To 10	Wall thickness: To 0.374	10–40	30–120	100–350	300–400

Source: Ref 1

of the conductors is shown in Fig. 6(c). The closer proximity conductor develops a more confined current path. A rectangular proximity conductor with the narrow edge at the same distance from the steel plate as the close round conductor exhibits a broader current distribution in the plate. If a magnetic core were placed around the proximity conductor, the current would be further concentrated and heating would take place directly below the proximity conductor, as shown in the figure.

If the two conductors, with currents flowing in opposite directions, are metal sheets placed edge to edge in a plane with a small gap between them, the proximity effect will cause the current to concentrate at the two adjacent edges, thus causing them to heat. The skin effect will confine the currents to a shallow depth at those edges. This is the situation that characterizes all high-frequency welding applications.

Advantages and Limitations

The advantages of high-frequency welding are that it is well suited for high-speed welding and can weld a large range of product sizes

and materials. Weld quality is not particularly sensitive to the presence of air, and special atmospheres are usually not needed. Weld quality is relatively (but not completely) tolerant of surface oxides and contamination. The disadvantages of high-frequency welding are that it is not well suited for low welding speeds and small-scale operations where welding is done by hand. High-frequency welding must be done continuously; continuous welds cannot be made in stop/start operations because a discontinuity in the weld will usually occur.

Because the concentrated high-frequency current heats only a small volume of metal at the weld interface, the process can produce welds at very high welding speeds and with high energy efficiency. High-frequency resistance welding can be accomplished with a much lower current and less power than is required for low-frequency or direct-current resistance welding. Welds are produced with a very narrow and controllable HAZ and with superfluid cast structures. This often eliminates the need for postweld heat treatment in tube production.

Oxidation and discoloration of the metal and distortion of the workpiece are minimal.

Discoloration may be further reduced by the choice of welding frequency.

Maximum speeds normally are limited by mechanical considerations of material handling, forming, and cutting. Minimum speeds are limited by material properties, excessive thermal conduction such that the heat dissipates from the weld area before bringing it to sufficient temperature, and weld quality requirements.

The fit-up of the surfaces to be joined and the manner in which they are brought together are important if high-quality welds are to be produced. However, high-frequency welding is far more tolerant in this regard than some other processes.

Flux or shielding gas are almost never used but can be introduced into the weld area for joining highly reactive metals such as titanium or for certain grades of stainless steel.

Applications

A wide range of commonly used metals can be joined by high-frequency welding. Materials that can be successfully high-frequency welded

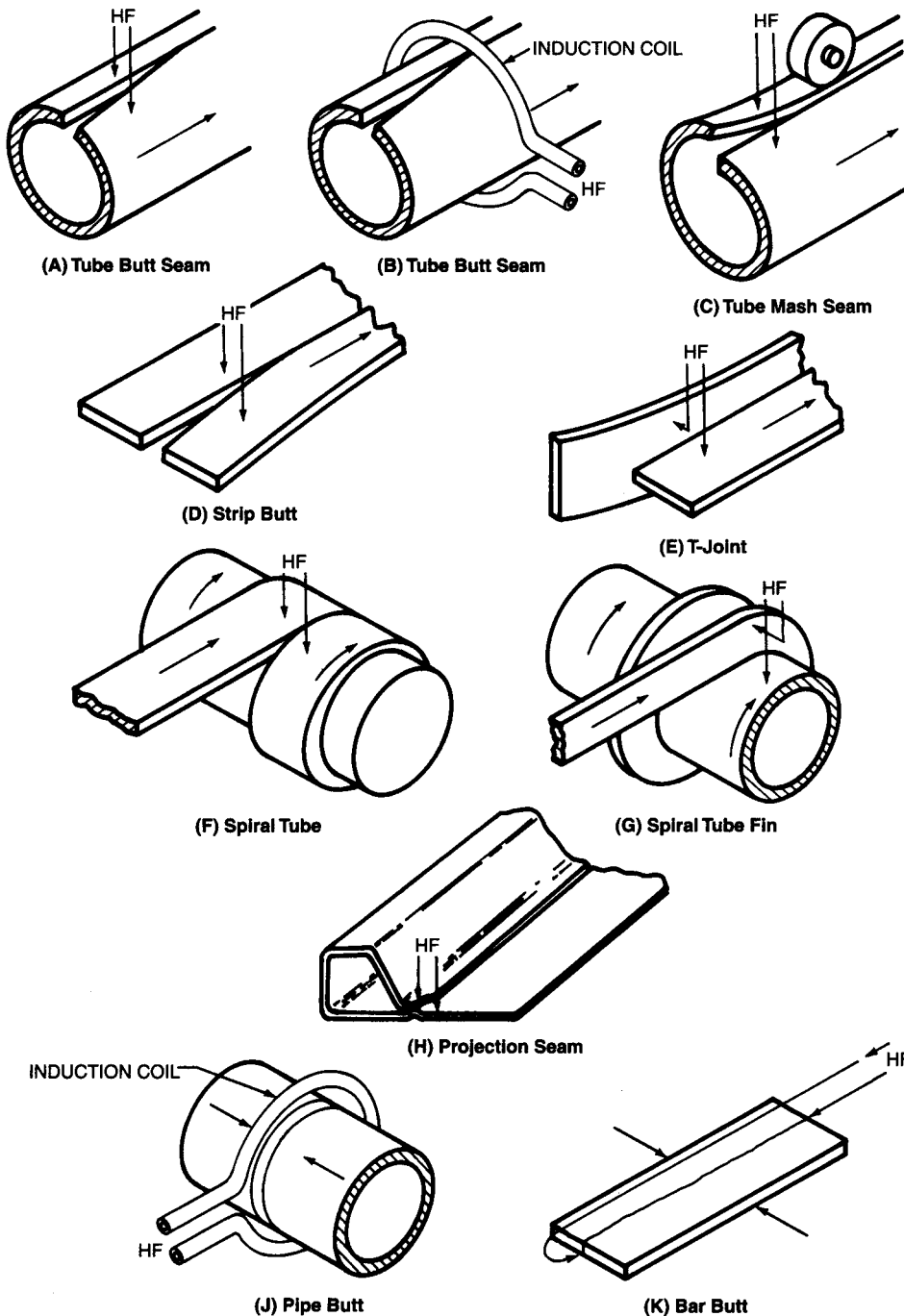


Fig. 3 Basic joint designs for high-frequency welds in pipe, tube, sheet, and bar stock. Source: Ref 1

into tube and pipe include carbon steels, stainless steels, aluminum, copper, brass, and titanium. Exceptions are materials that are unstable at welding temperatures, have a negligible hot-work capability, or experience property deterioration that cannot be subsequently recovered. Where necessary, a gas shield can be provided for reactive metals. Tube or pipe sizes fabricated by high-frequency welding range in size from 13 to 1220 mm (½ to 48 in.) in diameter.

High-frequency welding is most suitable in applications that involve the continuous edge, or butt, joining of metals. The largest single use of high-frequency welding is in the manufacture of tube and pipe. High-frequency welding is useful in the manufacture of certain types of heat-exchanger tube, where the edge of a rectangular strip is continuously welded onto the outside diameter of a tube to form a cooling fin. The fin can be welded around the tube in a spiral configuration (Fig. 7), or it can be straight

and parallel to the pipe axis. The greatest volume of heat-exchanger tube is made with low-carbon steel for both the tube and fins. However, other alloy combinations are growing in use, such as low-carbon steel fins on both stainless steel and chromium/molybdenum alloy steel tubes, stainless steel fins on low-carbon steel and stainless steel tubes, and aluminum fins on cupronickel tube.

High-frequency welding can also be used for the production of structural shapes, such as T-sections and I- and H-beams. The specific shape is constructed by welding rectangular strips together to produce the desired configuration. A heating "V" is established as the strip materials are brought together.

The end, or butt, welding of metal strip is another application in which high-frequency welding can be used. Single lengths of strip are welded to form a hoop that is subsequently formed into products such as wheel rims. High-frequency butt welding is also used to make long, continuous lengths of strip by butt welding together a series of shorter lengths. This is done for certain manufacturing processes that require strip material longer than that which is commercially available.

Equipment

Units for producing power for high-frequency welding include solid-state inverters (and perhaps some vacuum-tube oscillators still in operation). Depending on the application, frequency requirements can vary from 100 to 700 kHz, whereas power requirements vary from 30 to 1000 kW. Solid-state inverters produce frequencies ranging from 100 to 400 kHz. Vacuum-tube oscillators are available in frequencies up to 700 kHz. Because of their improved efficiency, solid-state units are replacing vacuum-tube units when frequency requirements permit.

Water-cooled copper conductors are used to carry the power to the coil or contacts. These conductors must be of minimum length and closely spaced to minimize impedance losses. The use of induction coils or electrical contacts to deliver high-frequency power to the workpiece has specific advantages and disadvantages.

Induction coils are commonly used in applications where the geometry of the workpiece can act as a closed circuit to pick up the induced power (for example, the welding of tube). The advantages of an induction coil are that it is generally more convenient to use and requires less maintenance than contacts. Because the coils do not contact the workpiece, they leave no marks or scratches. Induction coils are usually made from a water-cooled copper conductor that has one to three turns.

The delivery of high-frequency power through electrical contacts is more efficient than that through the use of coils because the power can be more directly and efficiently distributed to the weld area. The disadvantages of contacts are

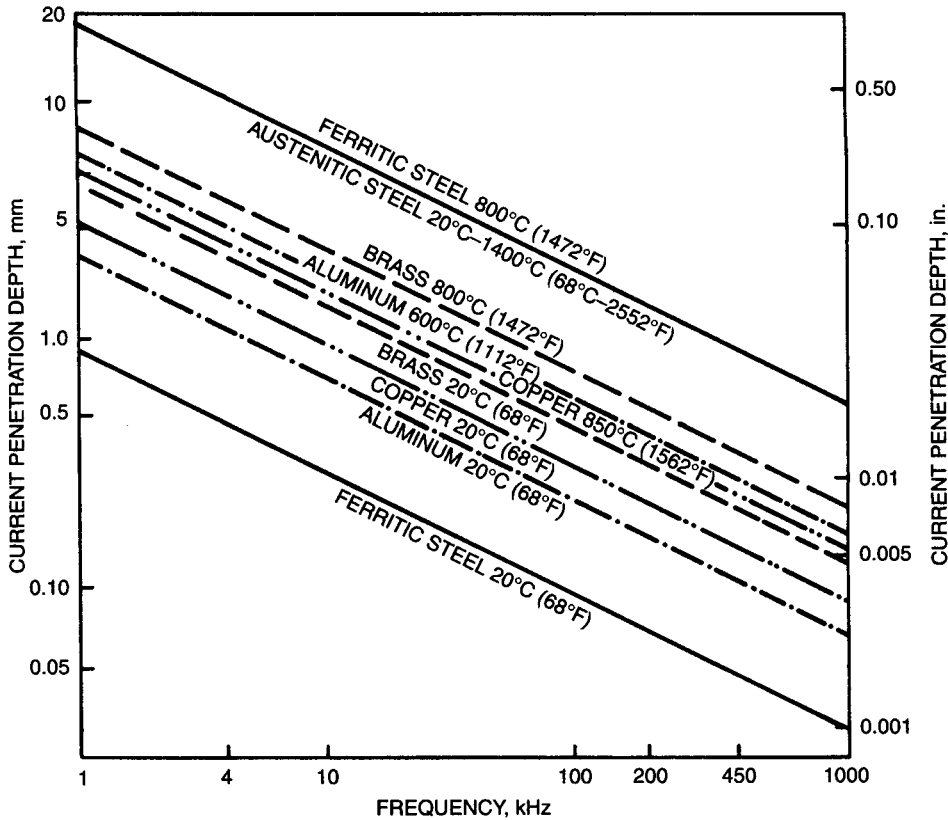


Fig. 4 Effect of frequency on depth of penetration. Source: Ref 1

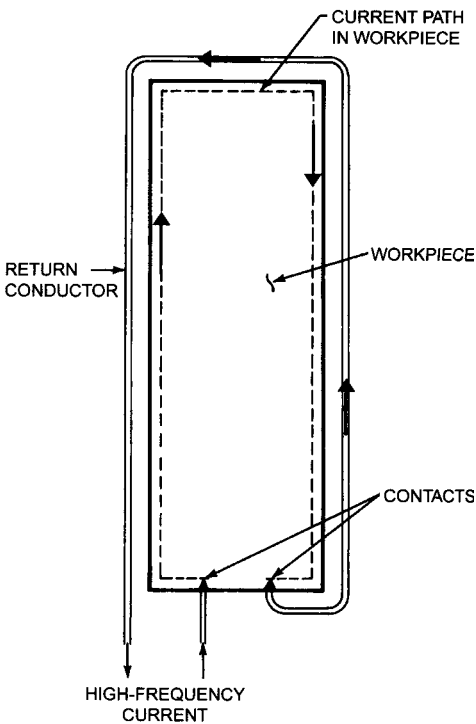


Fig. 5 Restriction of flow path of high-frequency current by proximity effect of the return conductor

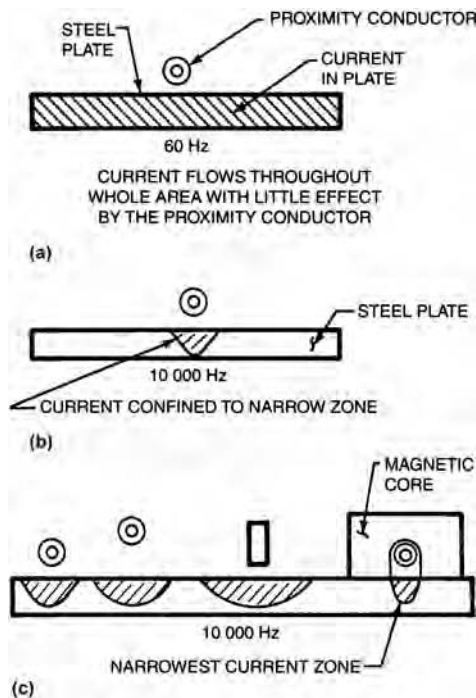


Fig. 6 Depth and distribution of current adjacent to various conductors

that they wear out, require periodic replacement, and can scratch, mar, or leave deposits on the surface of a workpiece, which can be objectionable in some cases. The presence of surface scale on base material can affect the current transfer from the contacts to the substrate.

In the production of tube and pipe, induction coils are usually used to make the smaller diameters (<305 mm, or 12 in.) because their advantages outweigh the loss of efficiency. Contacts are generally used for larger diameters because of their greater efficiency. Contacts are also used in structural shapes and fin heat-exchanger tubes, as well as for end welding, because induction coils cannot induce the current densities necessary for welding.

Impeders are used to improve welding efficiency in tube and pipe production. Impeders that consist of one or more water-cooled cores of ferrite material are placed inside the tube parallel to and under the weld area. The reason for this is the existence of a power-dissipating circuit loop consisting of the inside surface of the tube being welded. The impeder increases the inductive impedance of this path, which bypasses the weld zone. The positioning may vary for a given application based on experience. The impeder is generally positioned so that it extends approximately 1.5 to 3 mm (1/16 to 1/8 in.) beyond the apex of the "V" and the equivalent of one to two workpiece diameters upstream of the induction coil or contacts (Ref 2). Impeders are particularly important when a mandrel must be run through the workpiece in the weld area to perform an inside weld bead treatment (such as inside bead scarfing or bead rolling). Impeders are generally not required when welding a large-diameter workpiece with a high-frequency contact welding process (Ref 2).



Fig. 7 Manufacturing a spiral-fin tube using high-frequency welding

During operation, impeders efficiency is affected by temperature and degrades over time during welding. This reduction in efficiency during operation causes a drop in weld temperature and thus may affect quality by increasing the likelihood of producing cold welds. Corrections include either some periodic replacement of impeders and/or adjustment of the input power level to maintain a sufficient weld temperature.

Personnel

A considerable amount of on-the-job training is required for new operators of high-frequency welding equipment, as would be the case in any other mill process. High-frequency welding is a high-speed and, usually, high-volume process that often operates in conjunction with precision forming and handling equipment. The operating speed of tube mills ranges from 30 to 240 m/min (100 to 800 ft/min). A tube must be precisely formed prior to welding. Therefore, an operator must be familiar with both the operation of the welding equipment and the associated mechanical equipment for the forming or handling of the metal. Troubleshooting and repair of the welding equipment generally require specially trained personnel and are often conducted by the manufacturer. Improved and simplified systems for speed and/or power and weld temperature control are reducing the operator dependence of the process.

Safety

Serious consideration must be given to the health and safety of welding operators, maintenance personnel, and other workers in the area of the welding operations. Good engineering practice must be followed in the design, construction, installation, operation, and maintenance of equipment, controls, power

supplies, and tooling to conform to federal, state, and local safety regulations and industry standards.

Because high-frequency welding power sources are electrical devices, they require all the usual precautions in handling and repairing such equipment. Voltages, which range from 400 to 30,000 V, can be either low or high frequency and may be lethal. To prevent injury, proper care and safety precautions should be taken while working on high-frequency systems and generators. Modern units are equipped with safety interlocks on access doors, as well as automatic safety grounding devices that prevent unsafe operation of the equipment. The equipment should not be operated when panels or high-voltage covers have been removed or when interlocks and grounding devices have been blocked.

High-frequency, high-voltage leads must be encased in grounded metal ductwork to ensure safety and to minimize electromagnetic radiation. Induction coils and contact systems should always be properly grounded for operator protection. Grounding lines should be kept short to minimize inductive reactance. Injuries from high-frequency power, especially at the upper range of welding frequencies, tend to produce severe, local, surface tissue damage. Care should be taken that the magnetic field from the output system, particularly the output transformer, does not heat adjacent metallic sections by induction.

The high-frequency power source must also conform to the requirements of the Federal Communications Commission (FCC) as stated in Title 47, Part 15 concerning the radio-frequency emissions from industrial, scientific, and medical sources. Responsibility for complying with FCC standards is undertaken by the power-source manufacturer and does not pose a problem for the end user of the equipment, if the power source is installed following the manufacturer's recommendations. Information manuals provided by the manufacturers of equipment must be consulted, and

recommendations for safe practices must be strictly followed.

High-frequency currents are more difficult to ground than low-frequency currents, and ground lines should be as short as possible to minimize inductive reactance. All leads between the power source and the contacts or induction coil should be totally enclosed in an insulated or grounded structure and constructed in a way that minimizes electromagnetic interference. Also, care should be taken to prevent the high-frequency magnetic field around the coil and leads from induction heating of the adjacent metal mill components.

The weld area should be protected so that operating personnel cannot come in contact with any exposed contacts or induction coils while these devices are energized. Injuries to personnel from direct contact with high-frequency voltages, especially at the upper range of welding frequencies, may produce severe local tissue damage. The design, construction, installation, operation, and maintenance of the equipment, controls, power sources, and tooling should conform to the requirements of the United States Department of Labor in Occupational Safety and Health Standards for General Industry, (29) CFR Part 1910, Subpart Q. The American Welding Society document "Safety in Welding, Cutting, and Allied Processes," ANSI Z49.1: 2005, covers safe practices specifically for the welding industry.

Inspection and Quality Control

Although the quality of the weld can be very high with the HFRW process, a few weld-related quality problems exist. Modern nondestructive evaluation (NDE) techniques, such as eddy current and ultrasonic inspection, are commonly used to detect open-seam conditions such as cracks. However, the major problem that remains undetected is a condition referred

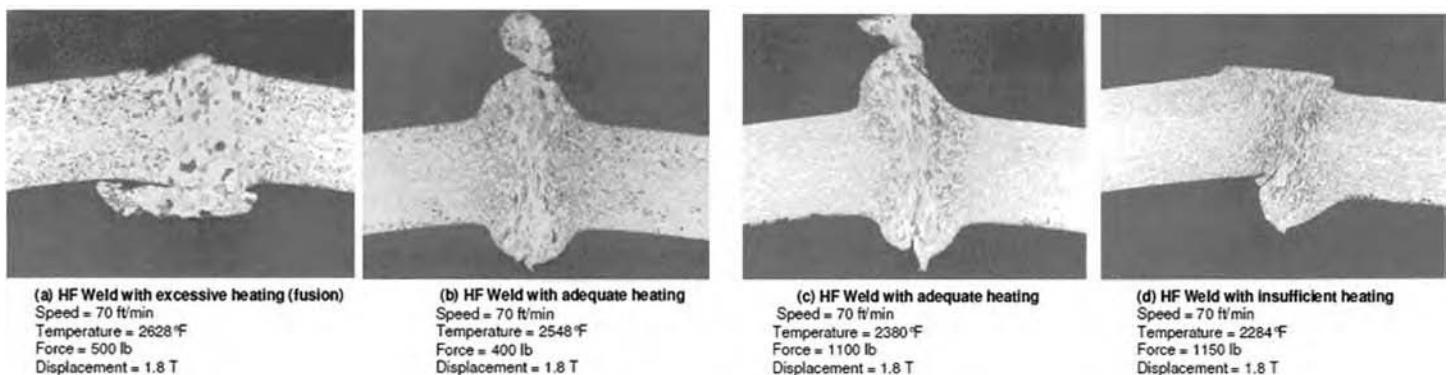


Fig. 8 Cross sections from welds of type 409 stainless steel tubes after high-frequency (HF) welding at different temperatures. (a) Excessive weld temperature results in melting and a fusion zone. (b) and (c) Good welds with sufficient heating and formation of a sound solid-state weld. (d) Insufficient heating results in a cold weld without a complete solid-state bond.

to as cold weld (also called paste or stuck weld) that is the result of improper welding parameters. Today's inspection and NDE techniques cannot always detect the cold-weld condition. This condition is difficult to detect because it visually appears to be a good weld. It is also difficult to detect by ultrasonic test methods if the defect is thin, filled with oxide scale, and short in length. A cold weld is usually welding-process-related and is typically revealed during mechanical testing or in service as a fracture or splitting along the weld seam.

New quality-control methodologies and monitoring techniques are being applied to HFRW mills, resulting in significant reduction and elimination of weld quality problems related to premature weld seam failures due to a cold-weld condition. Full-scale testing is done to generate production mill process windows for a range of critical welding variables, such

as temperature, squeeze force, displacement, and mill speed. Monitoring the welding parameters is done with traditional data-acquisition sensors and systems.

Monitoring of the resultant weld seam shape, size, and characteristics is also performed using a noncontact (laser) optical technology to make measurements of the surface profile of the prewelded and just-welded tube surface. These profile images are compiled from three-dimensional surface topography data that can be analyzed, enabling precise measurement of surface conditions and defects. Optimum welding parameters for a specific mill are correlated to laser-based profile images of the weld bead (upset geometry). The laser profile images can then be used to determine the quality of the welds as they are being made. A final step is to use the laser monitoring technique for feedback to control and maintain the optimum welding parameters

during welding, ensuring robust, high-quality tube and pipe.

Weld cross sections in Fig. 8 are from 409 stainless steel tubing welded at different temperatures. The welds shown in Fig. 8(b) and (c) are sound solid-state welds. An excessively high welding temperature (Fig. 8a) results in a fusion zone, while insufficient heating (Fig. 8d) results in a cold weld.

REFERENCES

1. High-Frequency Welding, *Welding Handbook*, Vol 3, *Welding Processes, Part 2*, American Welding Society, 2007, p 160–181
2. M. Kimchi, W. Peterson, P.F. Scott, and R.D. Czerski, High-Frequency Welding, *AWS Welding Handbook*, 9th ed., Vol 3, *Welding Processes, Part 2*, American Welding Society, 2007, p 159–182

Procedure Development and Practice Considerations for Resistance Welding

Murali D. Tumuluru, United States Steel Corporation
Hongyang Zhang, University of Toledo
R. (Bob) Matteson, Taylor Winfield Technologies

A GOOD WELDING PROCEDURE is essential to achieve acceptable-quality welds. To develop such a procedure, users must have a clear understanding of the effect of welding variables on the welding process. In resistance welding, the three key variables that affect the weld quality are the welding current, the electrode force, and the welding time (Ref 1, 2). An understanding of their role in weld formation will help in choosing the appropriate welding parameter combination. The effect of each of these variables is described subsequently. Much of the discussion is applicable to both spot and seam welding. In the first half of this article, variables, as they relate to spot welding, are presented. The second part of this article covers seam welding procedure development.

Spot Welding Variables

This section describes the significance of the three variables (welding current, electrode force, and welding time) that affect the resistance spot welding process. In addition, the effects of weld spacing as well as the effect of surface preparation on weld quality are presented. The process fundamentals of resistance spot welding are described in the article "Resistance Spot Welding" in this Volume.

Welding Current

Welding current is perhaps the most influential welding parameter that controls the heating at the sheet-to-sheet interface and hence the weld nugget (melted and solidified region) development and formation. Both alternating current (ac) and direct current (dc) are used in resistance spot welding. The ac and dc currents possess distinctive characteristics in both the total heating and the heat input rate, and their effects on weld formation and weld quality are different.

The common electric current waveforms are shown in Fig. 1. The single-phase ac current waveform is strongly affected by the resistance and reactance of the welding loop. As seen in Fig. 1(a), the electric current does not reach the designated value immediately after it is switched on. Rather, it is delayed by the impedance for approximately three cycles. Such a delay is also observed in single-phase dc (Fig. 1b), three-phase dc (Fig. 1c), and midfrequency direct current (MFDC) (Fig. 1d) current waveforms for the same reason. In addition, there are moments of time in which the electric current ceases flowing in Fig. 1(a), resulting in cooling in the weld stack-up. Because of the alternating nature of a single-phase ac current, the heating rate fluctuates between zero and its peak, and the heat provided may be insufficient for welding metals with high thermal conductivities, such as aluminum alloys. In spite of this shortcoming of ac transformers, they are widely used in the sheet metal industry because of their simplicity and low cost. Satisfactory results have been achieved in steel welding using such transformers.

To supply continuous heating, direct current has been used in various forms. The simplest one is a single-phase dc, as shown in Fig. 1(b). The moments when the current ceases flowing are significantly reduced, yet large current ripples still exist, meaning a fluctuating heating rate. An improvement to this is the three-phase dc, which fluctuates in a very narrow range (Fig. 1c). The MFDC transformers, which are gaining their market share, eliminate the rippling effect (Fig. 1d) and provide the necessary continuous heating needed for welding metals of high electrical and thermal conductivities. Even for steel welding, the advantages of MFDC are obvious. Shown in Fig. 2, the welds made on an interstitial-free steel using an MFDC and a single-phase ac have different shape and volume (Ref 4). More fusion is observed in the MFDC welds at both welding stages than in the ac welds. In addition, the

annular shape of the welds made using the ac in the figure could be the result of "skin effect," which is the phenomenon that an alternating electric current tends to flow on the outer part of a conductor. The concentration of electric current on the outer portion of the electric contact at the faying interface generates more heat at the periphery than the center of a weld. More discussion on the influence of skin effect on welding can be found in Ref 3. In ac welds, the current distribution can also be affected by the "throat effect," where the current tends to travel along the inside path, or throat, of the circuit. While generally not harmful, this effect can be observed in the weld nugget shape.

In resistance welding, the heat developed is proportional to the resistance in the electric circuit, which, in turn, is inversely proportional to the contact area. During welding, the contact area between the sheets is not constant, because it is enlarged as electrodes deteriorate through metallurgical alloying and mechanical deformation at the electrode-sheet interfaces. Weld quality is compromised if the electric current density drops due to electrode enlargement (or mushrooming) to a lower level than is originally set. Frequent electrode dressing is a very effective method to eliminate electrode tip size changes, thereby maintaining a constant current density. Another practical approach to address electrode tip face changes is the use of current steppers, which is common in production environments. The basic idea in current stepping is to maintain the level of current density so that sufficient heat is generated. The stepping algorithm can be derived both experimentally and analytically. The changes needed in electric current as a function of the increase in electrode face area are plotted in Fig. 3 (Ref 3). Because a larger weld is formed with a stepped-up current, more electrode force is needed to contain the liquid nugget. The changes in electrode force to maintain the pressure level are exactly the same as those for the current, as shown in the figure. The use of frequent electrode tip

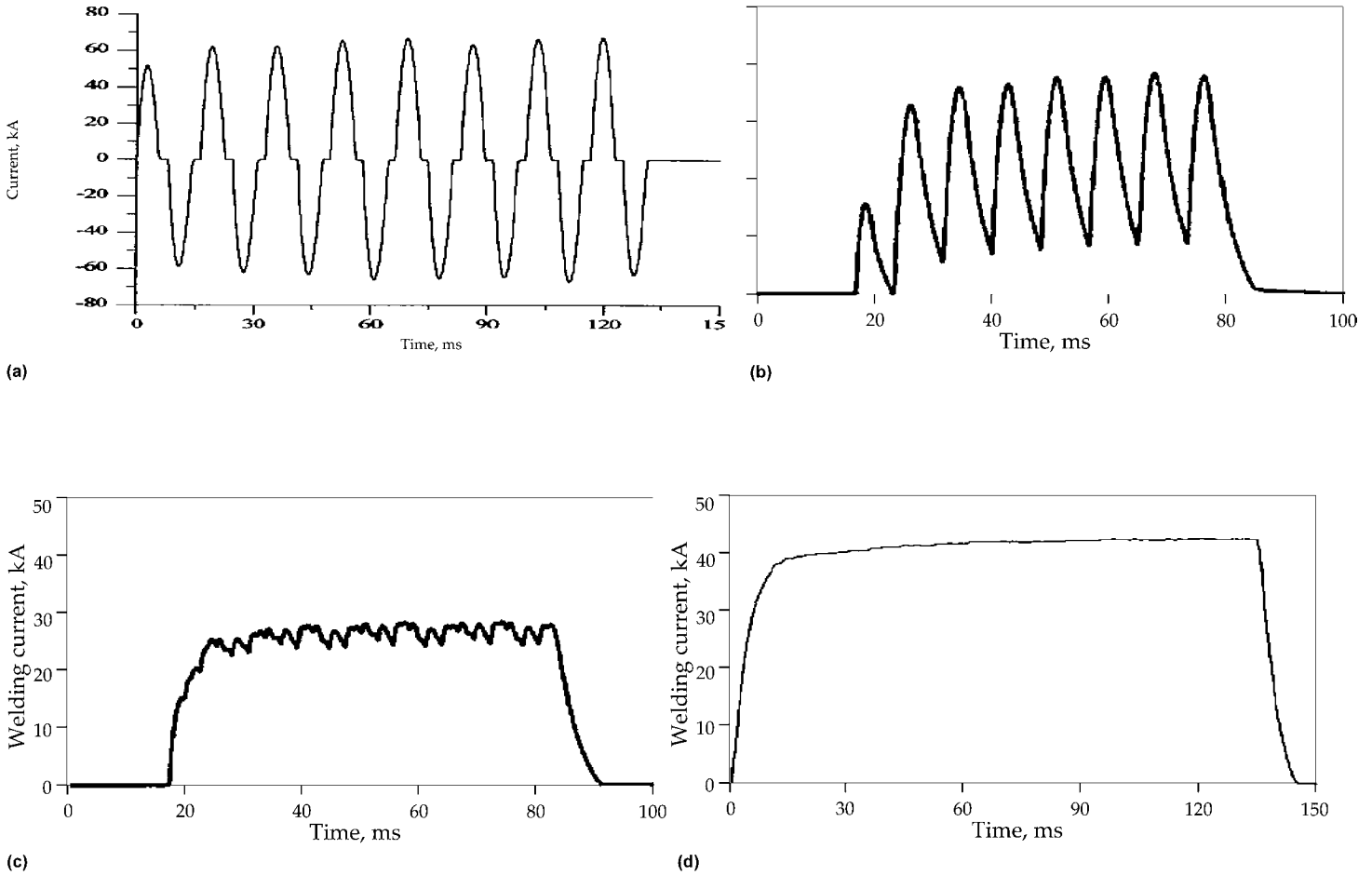


Fig. 1 Measured waveforms of welding current for resistance spot welding. (a) Single-phase alternating current. (b) Single-phase direct current. (c) Three-phase direct current. (d) Medium-frequency direct current. Source: Ref 3

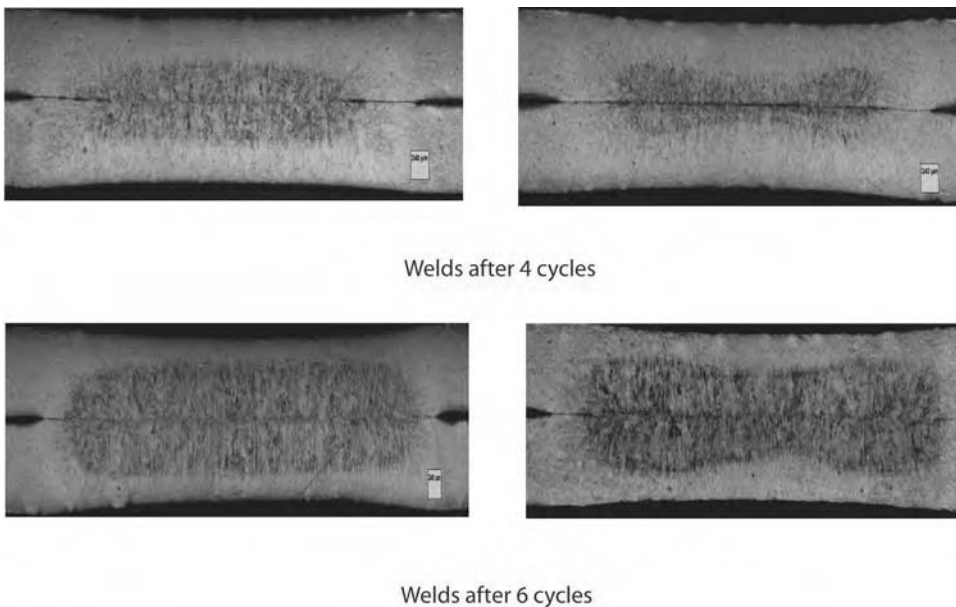


Fig. 2 Cross sections of interstitial-free steel welds made using midfrequency direct current (left) and alternating current (right) at different welding stages. Source: Ref 4

dressing is a much more efficient way to maintain constant current density than the use of current steppers. More automotive manufacturers have switched to the use of frequent electrode tip dressing to maintain consistent weld quality.

Welding or Electrode Force

Welding force, or electrode force, is the force applied to the workpieces by the electrodes during the welding cycle. Electrode force, usually measured and expressed as a static value, is a dynamic force in operation and is affected by the friction and inertia of the moving parts of the welding machine.

The workpieces to be spot welded must be held tightly together at the indented location of the weld to allow passage of current. Because increasing the electrode force decreases the contact resistance of the workpieces and therefore decreases the total heat generated between the faying surfaces of the workpieces by the welding current, electrode force should not be excessive.

The electrode force must be compatible with a welding current that is within the capacity of

the equipment and must permit the use of a welding time long enough to be reproducible. Also, the workpieces must be in reasonably intimate contact at the weld area without excessive electrode force. If the workpieces are deformed so that contact is not intimate in the weld zone, an excessively high force may be needed to overcome the deformation. Variations in weld strength and quality often result from the variations in electrode force required to bring the workpieces into proper contact, especially in the spot welding of stampings, formed workpieces, or thick sections of work metal. This is especially true when welding high-strength, low-alloy steels. Because of the high strength of these materials, they have considerably higher springback and thus require higher electrode forces than plain carbon steel. Sometimes, a squeeze time longer than that normally used is needed to force the

workpieces together. Also, because of the possibility of springback, hold time must be sufficiently long to permit solidification of the weld metal when the workpieces are still held together by the electrodes.

Because variations in electrode force cause changes in interfacial resistance and therefore heating, variations in electrode force can cause changes in the size and location of the lobe curves and current level, as seen in Fig. 4. Increased electrode force shifts the curves to higher current levels. This shift in the lobe curve indicates that weld current and weld time combinations which produce acceptable weld nuggets at one electrode force may no longer produce acceptable weld nuggets at the new electrode force. Thus, care should be taken when making electrode force changes, especially in alloys that have a limited acceptable weld current range, such as some of the

more difficult HSLA steels with yield strengths above 690 MPa (100 ksi).

Pound-force (lbf) and kilo-Newton (kN = 10^3 N) are the commonly used units for electrode force in resistance welding. Occasionally, deca-Newton or deka-Newton (daN = 10^1 N) are also used. The electrode force is a strong function of the drive mechanism. A pneumatic-cylinder-driven welding machine may produce a fluctuating electrode force during the application of electric current, resulting from the expansion/contraction of the weldment stack-up. Depending on the cylinder size, compressed air supply, and lubrication/alignment of the moving part of the welder, the electrodes may or may not respond to and follow the contraction of the weld, to provide a forging force. In addition, combined pneumatic and hydraulic cylinders have been used to supply a forging force to the weld. Servo-motor-driven welders have been developed that provide the opportunity of adjusting the electrode force during welding, in coordination with electric current. For instance, a sequential profiling of electric current and forging force has been realized on an electric servo welding gun (Ref 6). In the study by Grimes (Ref 5), the effect of forging force on weld quality was demonstrated. In Fig. 5, the electrode force was ramped up during welding by as much as twice the original force level, to suppress internal void/porosity formation. Satisfactory results were obtained.

Electrode force is also critical in controlling expulsion, an important process affecting weld quality. In a study on suppressing expulsion in welding an aluminum alloy AA5754, the critical level of electrode force was derived based on considering the interaction among the mechanical, thermal, and metallurgical processes during welding, as shown in Fig. 6 (Ref 7). The predicted electrode force levels were verified by experiments, and good agreement was achieved.

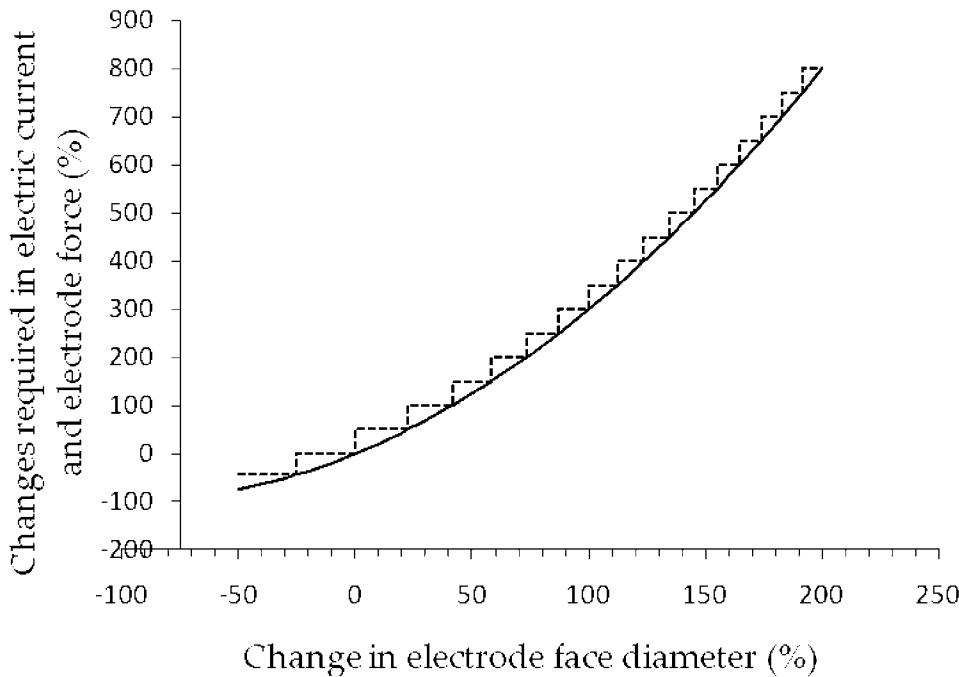


Fig. 3 Changes needed in electric current and electrode force as a function of the change in electrode face diameter

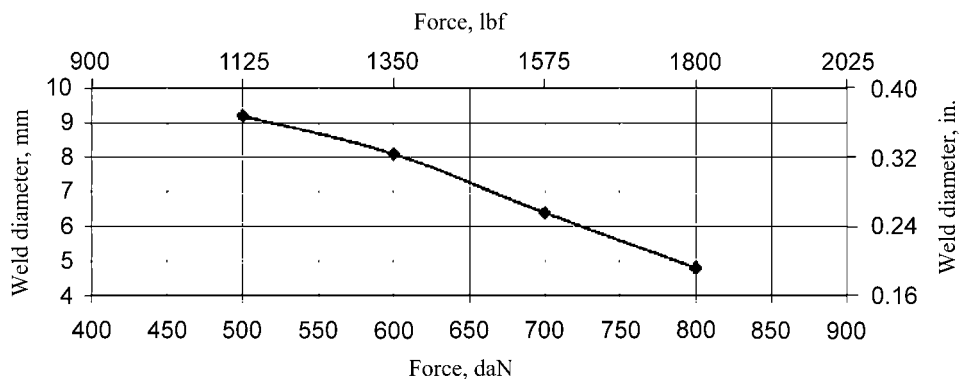


Fig. 4 Weld diameter vs. electrode force in welding an aluminum alloy. Source: Ref 5

Weld Time

Weld time (the duration of passing the welding current) is generally divided into several parts.

Squeeze time is an interval of delay between closing of the initiating switch and application of the welding current. It provides time for the solenoid-actuated head cylinder valve to operate and for the welding head to bring the upper electrode in contact with the workpiece and to develop full electrode force. This time must be sufficient to ensure that the parts have maintained intimate contact. On a 228 mm (9 in.) diameter cylinder, operated at 276 kPa (40 psi), it can take 120 cycles to develop full electrode force.

Weld time is the interval during which the welding current flows through the circuit. On many HSLA steels, a slightly longer weld time than normally applied for plain carbon steel has been noted to broaden the lobe curve and thus increase acceptable weld current ranges.

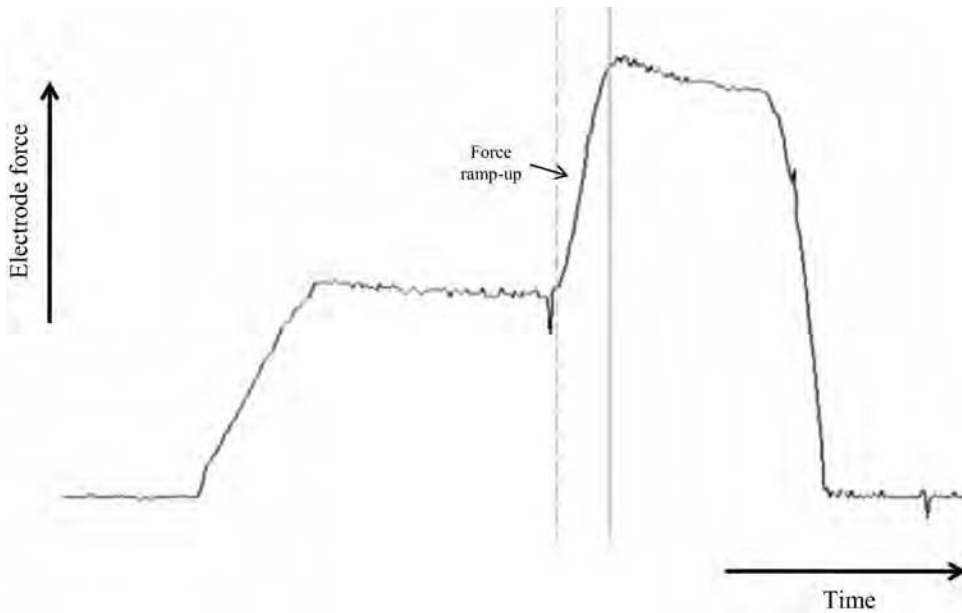


Fig. 5 Electrode force profile during welding with a forging force provided by an electric-servo motor. Adapted from Ref 5

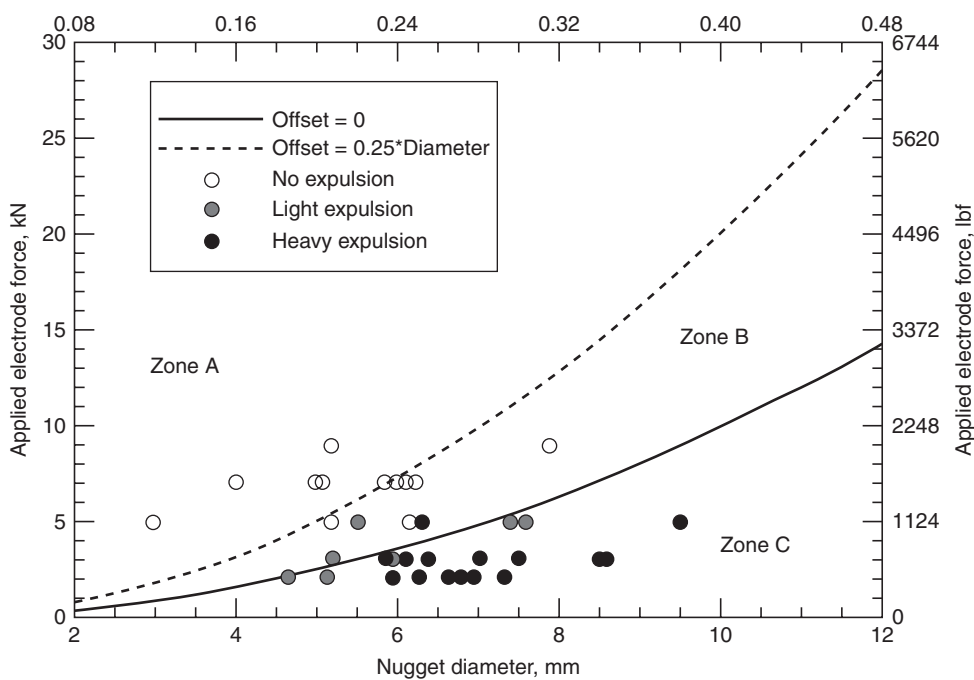


Fig. 6 Electrode force needed to suppress expulsion in welding AA5754. Source: Ref 7

Upslope time is a period of time when the weld current is deliberately ramped up from an initial value to the weld current value. This function is used often on multiple projections to reduce the possibility of destroying the projections that first make contact.

Hold time is the interval during which, after the welding current is off, the electrode force is held on the workpiece until the metal of the spot weld has solidified. Some HSLA materials

are hold-time sensitive. With hold times as great as 30 to 60 cycles ($\frac{1}{2}$ to 1 s), these materials tend to experience interfacial tearing when peel tested.

Off time is the interval from the end of the hold time until the beginning of the squeeze time for the next cycle. In an automatic cycle, off time is the time needed to retract the electrodes and to index, remove, or reposition the work. In manual operation, it is not fixed as a

maximum period by the control equipment but depends on time taken by the operator to start a new cycle. Upslope time permits the welding current to be increased over several cycles from a low value to that needed for welding, instead of having the full welding current applied instantly. A low initial or welding current reduces or prevents expulsion of metal, or spitting, when the current is first applied. Upslope control is used for welding at high current values and for welding scaly stock as well as most kinds of plated metals.

Downslope time permits the welding current to decay gradually to a low value instead of ending suddenly, and it helps to produce good welds in some types of heat treatable metals by lengthening the cooling time gradient. It is rarely needed in welding low-carbon steel, particularly if the carbon content does not exceed 0.15%, but is used when cooling rate must be limited, as in welding hardenable steels. Downslope can also be used to reset the core flux in the welding transformer to obtain uniform magnetic conditions of the transformer.

Effect of Surface Finish

In spot welding of assemblies that are to be porcelain enameled or painted, or are to receive other decorative surface finishes, the surface condition and close fit of parts after welding are as important as weld strength. Excessive indentation, overheating of the outside surfaces, spatter, and crevices interfere with the finishing operations and must be avoided.

Welding schedules and conditions must be selected that produce a weld of adequate strength with a minimum of indentation and minimum evidence of heating. This requires a uniform welding procedure that is best obtained with automatic control of current, time, and force. Electrode faces should be dressed at regular intervals, before they have worn so much that unsatisfactory spot welds are produced. Workpieces should be cleaned thoroughly before welding.

Effect of Weld Spacing on Heating

Shunting occurs when a second spot weld is made so close to the first one that the welding current can flow either through the metal at the first weld or through the metal between the electrodes at the point of the second weld. The welding current flows in inverse proportion to the resistance of the two paths. Division of current depends chiefly on the ratio of resistance of the base metal to interface resistance at the point of the second weld.

When making a second and following spot welds, the metal between the electrodes becomes a divided circuit; part of the current travels through the metal to the previously made spot weld, while the remainder travels through the metal between the electrode faces at the point of the second weld. If the distance

to the first spot weld is great enough, the resistance of the path through the first spot weld, compared to that directly through the metal, is high, and the shunting effect can be neglected. If the distance to the first spot weld is short, a significant fraction of the current is shunted through the first spot weld.

As the temperature of the metal between the electrode tips rises, the resistance at that point increases, thus adding to the shunting effect. Metals having high electrical resistivity are less influenced by the shunting effect than are low-resistivity metals.

The minimum spacing of spot welds in low-carbon steel workpieces depends on stock thickness, diameter of the fused zone, and cleanliness of the faying surfaces. The minimum recommended weld spacing for low-carbon, medium-carbon, and low-alloy steels is given in Tables 1 to 3. Welds can be made at less-than-recommended minimum spacing without significant shunting by using higher current and electrode force, shorter weld time, and fast follow-up.

If spot welds are made too close to the edge of a sheet or flange, there is an insufficient volume of base metal to withstand electrode pressure and heating. This results in a reduction in the effective force along the edge and uneven heating, causing the hot metal to be expelled from the

weld. When spot welds are made too close to an upright flange or sidewall, arcing may occur between the electrode and workpiece, or there may be a poor fit at the faying surface because of the bend radius. If large-diameter electrodes are needed because of the metal thickness, eccentric, or offset, faces may be used.

The minimum contacting overlap between two pieces of metal depends somewhat on the metal thickness, which, in turn, governs the electrode diameter and diameter of the fused zone. The minimum overlaps for low-carbon, medium-carbon, and low-alloy steels are given in Tables 1 to 4.

Development of Welding Schedules

A typical sequence of steps for determining the satisfactory conditions for spot welding is described as follows. The usual criteria for satisfactory welds in steps 1 to 4 are penetration, nugget diameter and indentation suitable for the application, and the absence of porosity, cracks, excessive expulsion, and gross imperfections:

1. *Make a preliminary selection of electrode force:* This is completed for the work to be welded and the electrodes to be used. Tables of recommended practices, such as Tables 4

to 7, provide starting points for this selection, as well as guidance in choosing preliminary values of current, weld time, and hold time for making trial welds to verify or correct this preliminary selection of electrode force.

2. *Establish the weld time and hold time:* This is done by evaluating trial welds made at several levels of current for each of a number of combinations of weld time and hold time. Squeeze time is not critical in welding trials and is usually set at a convenient value that is long enough to allow for a wide range of test conditions.
3. *Select electrode force:* Using the established combination of weld time and hold time, make welds at several different current levels, using a number of values of electrode force to cover a wide range of force.
4. *Select the welding current:* Using the established weld time, hold time, and electrode force, make test welds at current levels that cover a wide range of amperage.
5. *Verify selection of conditions:* Make trial runs under the welding conditions established by steps 1 to 4, to verify these selections as well as to establish reference data on weld quality and reliability for use in process control. A more complete evaluation than for steps 1 to 4 is performed at this stage.

Table 1 Weld spacing and edge distances for electrode endurance test samples

Sheet thickness		Weld spacing		Edge distance		Edge distance optional sample	
mm	in.	mm	in.	mm	in.	mm	in.
0.60–0.69	0.024–0.027	14	0.55	19	0.75	14	0.55
0.70–0.89	0.028–0.035	15	0.59	20	0.79	15	0.59
0.90–1.29	0.035–0.051	18	0.71	23	0.91	18	0.71
1.30–1.69	0.051–0.067	21	0.83	26	1.02	21	0.83
1.70–2.09	0.067–0.082	24	0.95	29	1.14	24	0.95
2.10–3.00	0.083–0.118	27	1.06	32	1.26	27	1.06

Source: AWS D8.9M

Table 2 Weld spacing from standard guidance

Determining sheet thickness		Standard spot weld spacing		Minimum spot spacing with weld schedule for each spot	
mm	in.	mm	in.	mm	in.
0.65–1.09	0.026–0.043	19	0.75	13	0.5
1.10–1.39	0.043–0.055	25	0.99	13	0.5
1.40–1.59	0.056–0.063	36	1.42	13	0.5
1.60–1.79	0.063–0.071	38	1.50	13	0.5
1.80–2.09	0.071–0.082	45	1.77	19	0.75
2.10–2.49	0.174–0.098	51	2.01	19	0.75
2.50–2.79	0.099–0.110	53	2.09	19	0.75
2.80–3.50	0.110–0.138	64	2.52	19	0.75

Source: GM GWS-1A

Table 3 Standard flange dimensions as a function of adjacent corner configuration

Flange angle, degrees	Bend radius, mm (in.)							
	1.0–1.5 (0.04–0.06)	1.6–2.0 (0.06–0.08)	2.1–2.5 (0.08–0.10)	2.6–3.0 (0.10–0.12)	3.1–3.5 (0.12–0.14)	3.6–4.0 (0.14–0.16)	4.1–4.2 (0.16–0.17)	≥4.3 (0.17)
120	13	13	13	13	13	12	12	12
110	14	14	13	13	13	13	12	12
100	15	14	14	14	13	13	12	12
90	15	15	14	14	13	13	13	12

Source: GM GWS-1A

Table 4 Recommended practices for single-impulse resistance spot welding of 1010 steel with class 2 electrodes(a)

Thickness of thinnest outside piece (t), in.(b)	Electrode dimensions		Net electrode force, lbf	Weld time, cycles (60 cps)	Welding current (approx.), A	Contacting overlap (min), in.	Weld spacing(d) (min), in.	Nugget diameter (approx.), in.	Breaking load (min) in shear, lb, for work metal with tensile strength of:	
	Body diameter, in.	Face diameter, in.(c)							Less than 70 ksi	70 ksi or more
0.010	3/8	1/8	200	4	4,000	3/8	1/4	0.10	130	180
0.021	3/8	3/16	300	6	6,500	7/16	3/8	0.13	320	440
0.031	3/8	3/16	400	8	8,000	7/16	1/2	0.16	570	800
0.040	1/2	1/4	500	10	9,500	1/2	3/4	0.19	920	1200
0.050	1/2	1/4	650	12	10,500	9/16	7/8	0.22	1350	...
0.062	1/2	1/4	800	14	12,000	5/8	1	0.25	1850	...
0.078	3/8	5/16	1100	17	14,000	11/16	1 1/4	0.29	2700	...
0.094	3/8	5/16	1300	20	15,500	3/4	1 1/2	0.31	3450	...
0.109	3/8	3/8	1600	23	17,500	13/16	1 3/4	0.32	4150	...
0.125	7/8	3/8	1800	26	19,000	7/8	1 3/4	0.33	5000	...

(a) Steel should be free from scale, oxides, paint, grease, and oil. (b) Thickness of thinnest outside piece (t) determines welding conditions. Data are for total thickness of pile-up not exceeding 4t; maximum ratio between two thickness, 3 to 1. (c) For type A, D, and E faces. Body diameters apply also to type F electrodes with 3 in. spherical-radius face. (d) Center-to-center spacing for two pieces for which no special precautions need to be taken to compensate for shunted-current effect of adjacent welds; for three pieces, increase spacings here by 30%. Source: Recommended Practices for Resistance Welding, AWS C1.1

Table 5 Recommended practices for single-impulse resistance spot welding and postheating of medium-carbon and low-alloy steels with class 2 electrodes(a)

Steel to be welded	Thickness (t) of each piece, in.(c)	Dimensions of upper and lower electrodes			Net electrode force (weld and temper), lbf	Time, cycles (60 cps)			Welding current (approx), A	Tempering current, % of welding current	Contacting overlap (min), in.	Weld spacing (min) (d), in.	Nugget diameter (approx.), in.	Breaking load (min) of weld, lb		Ratio, tensile to shear breaking load, %
		Body diameter, in.	Face diameter, in.	Face radius, in.		Weld	Quench	Temper						In shear	In tension	
1020 HR	0.040	3/8	1/4	6	1475	6	17	6	16,000	90	1/2	1	0.23	1 360	920	68
1035 HR	0.040	3/8	1/4	6	1475	6	20	6	14,200	91	1/2	1	0.22	1 560	520	33
1045 HR	0.040	3/8	1/4	6	1475	6	24	6	13,800	88	1/2	1	0.21	2 000	680	34
4130 HR	0.040	3/8	1/4	6	1475	6	18	6	13,000	90	1/2	1	0.22	2 120	640	30
4340 N&T	0.031	3/8	3/16	6	900	4	12	4	8,250	84	7/16	3/4	0.16	1 084	290	27
	0.062	3/4	5/16	6	2000	10	45	10	13,900	77	3/8	1 1/2	0.27	3 840	1440	37
	0.125	1	3/8	10	5500	45	240	90	21,800	88	7/8	2 1/2	0.55	13 680	4000	29
8630 N&T	0.031	1/2	3/16	6	800	4	12	4	8,650	88	7/16	3/4	0.16	1 220	524	43
	0.062	3/8	5/16	6	1800	10	36	10	12,800	83	3/8	1 1/2	0.27	4 240	2200	52
	0.125	1	3/8	10	4500	45	210	90	21,800	84	7/8	2 1/2	0.55	13 200	4500	34
8715 N&T	0.018	1/2	1/8	6	350	3	4	3	3,900	85	7/16	3/8	0.10	400	200	50
	0.062	3/8	5/16	6	1600	10	28	10	12,250	85	3/8	1 1/2	0.27	3 300	1800	55
	0.125	1	3/8	10	4500	45	180	90	22,700	85	7/8	2 1/2	0.55	12 760	4500	35

(a) Steel to be welded should be pickled, or otherwise cleaned, to obtain a surface contact resistance not exceeding 200 microhms. (b) HR, hot rolled; N&T, normalized and tempered. (c) Welding conditions are for joining two pieces of equal thickness, each of thickness t. (d) Minimum spacing for which no special precautions are needed to compensate for shunted-current effect of adjacent welds. Source: Recommended Practices for Resistance Welding, AWS C1.1.

Table 6 Recommended practices for multiple-impulse resistance spot welding of 1010 steel with class 2 electrodes(a)

Thicknesses of steel to be joined, in.		Electrode dimensions		Net electrode force, lbf	Single welds	Weld time, impulses(c)		Welding current (approx.), A	Contacting overlap (min), in.	Nugget diameter (min), in.	Breaking load (min) in shear(d), lb
						1-2 in.	2-4 in.				
1/8	1/8	1	7/16	1800	3	5	4	18,000	7/8	3/8	5,000
1/8	3/16	1	7/16	1800	3	5	4	18,000	7/8	3/8	5,000
1/8	1/4	1	7/16	1800	3	5	4	18,000	7/8	3/8	5,000
3/16	3/16	1 1/4	1/2	1950	6	20	14	19,500	1 1/8	9/16	10,000
3/16	1/4	1 1/4	1/2	1950	6	20	14	19,500	1 1/8	9/16	10,000
3/16	5/16	1 1/4	1/2	1950	6	20	14	19,500	1 1/8	9/16	10,000
1/4	1/4	1 1/4	9/16	2150	12	24	18	21,500	1 3/8	3/4	15,000
1/4	5/16	1 1/4	9/16	2150	12	24	18	21,500	1 3/8	3/4	15,000
5/16	5/16	1 1/2	3/8	2400	15	30	23	24,000	1 1/2	7/8	20,000

(a) Steel should be free from scale, oxides, paint, grease, and oil. (b) For type A, D, and E faces. Body diameters apply also to type F electrodes with 3 in. spherical-radius face. (c) Each impulse consists of 20 cycles on (heating) and 5 cycles off (cooling), at 60 cycles per second. (d) For steel with a tensile strength of less than 70 ksi. Source: Recommended Practices for Resistance Welding, AWS C1.1

These five steps not only determine optimum values for each of the welding variables but also establish ranges of satisfactory values for them and the criticality of each variable. The sequence of steps followed in setting up a resistance spot welding schedule may vary, depending on special aspects of the equipment or the work, the extent of experience with similar types of work, and requirements imposed by the purchaser or applicable specifications. When adjustment of welding conditions is needed at the start of or during production runs, the adjustment is usually made on weld time, hold time, or current, whichever is most convenient and effective.

Welding Machine

Many of the electrical and mechanical characteristics of a welding machine have a significant influence on the welding process and weld quality. Limited research has been conducted in this regard, primarily because of the difficulties in altering a welding machine mechanical and electrical features, especially in a systematic manner. The electrical characteristics of a welding machine are determined by the transformer, the

electrical cables, and the secondary loop. The mechanical aspects of a welding machine usually refer to the machine stiffness, friction, and moving mass. They interact with a welding process through affecting the electrode force and electrode follow-up characteristics (Ref 3), and their effects can be summarized in the following.

Machine Stiffness. The direct reflection of the effect of machine stiffness is the electrode force characteristics. In general it was found that high machine stiffness is beneficial to expulsion prevention and tensile-shear strength of the welds (Ref 8). As shown in Fig. 7, a higher stiffness results in a higher electrode force during welding than a lower stiffness, given the preset values of the electrode force being equal. A stiff welder also reduces electrode misalignment, resulting in less electrode wear and improved weld quality.

Friction primarily affects the follow-up behavior of the electrodes of a welder during welding. A well-lubricated and aligned guide-way of a welding machine allows the electrodes to move in when the weld contracts during cooling. This is critical in suppressing solidification cracks/voids by providing the necessary

forging force. Figure 8 clearly shows the effect of machine friction on the microstructure of welds. Without additional friction, the forging force provided by the electrodes created a dense structure (Fig. 8a), while the weld made with additional friction shows a large solidification void due to a lack of forging force. The welds made without additional friction also show slightly higher strength than those with additional friction.

Moving mass affects the touching behavior of a welder, and a weld stack-up tends to vibrate more if the moving mass is small than a welder with more moving mass. This in general does not affect the welding process or the weld quality, if the electric current is switched on after vibration stops. The dynamic force imposed by a moving mass on the weldment during welding is generally too low to make a noticeable impact.

In addition to these factors, the responses of the mechanical system to the welder control should also be understood. For instance, the actual squeeze time of electrodes can be significantly different from the input (Ref 3), which may have certain implications on weld quality, especially with short welding cycle time.

Table 7 Conditions for resistance spot welding of 1010 steel, with and without zinc coating(a)

Welding condition(b)	Steel 0.040 in. thick		Steel 0.125 in. thick	
	Zinc coated(c)	Uncoated	Zinc coated(c)	Uncoated
Weld times, cycles (60 cps)	13	10	42	26
Welding current, A	14,000	9500	20,000	19,000
Electrode force, lbf	650	500	2000	1800
Minimum welding space, in.	0.75	0.75	2	1.75
Nugget diameter, in.	0.21	0.19	0.48	0.33
Minimum contacting overlap, in.	3/8	1/2	1 1/8	7/8

(a) Data for zinc-coated steel are from AWS CL3, "Recommended Practices for Resistance Welding Coated Low Carbon Steels." Data for uncoated steel are from Table 4 in this article. All data are for welding with class 2 electrodes. (b) For joining two sheets of steel in each of the two thicknesses. (c) Coated with 1.25 oz of zinc per square foot of sheet size

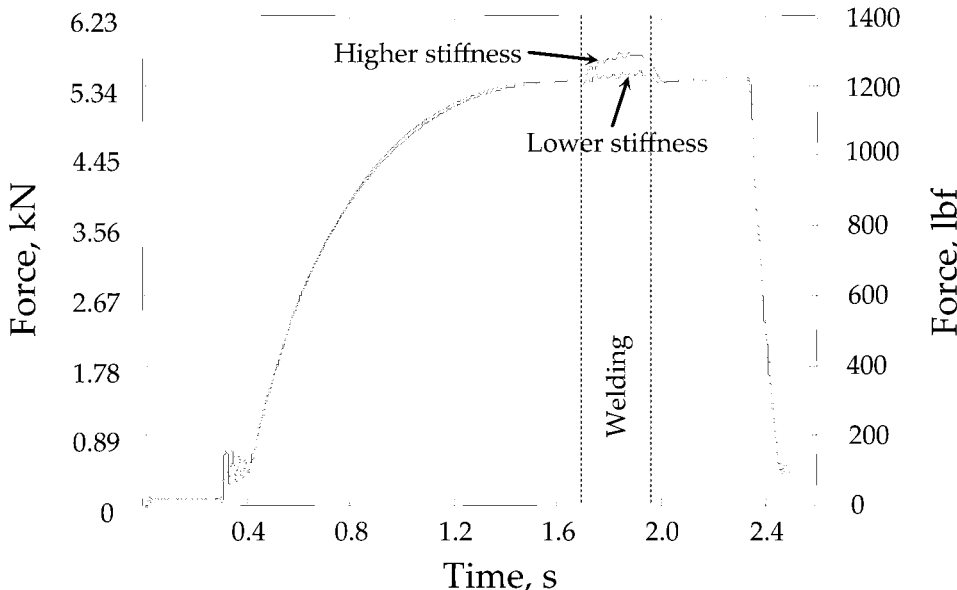


Fig. 7 Electrode forces under different welding machine stiffnesses. Source: Ref 3

Use of Weld Lobe Diagrams

The welding parameters, that is, welding current, time, and electrode force, all affect the weld formation and weld quality, as discussed previously. However, the values of these welding parameters must be decided together, not individually. Weld lobe diagrams are an efficient and most common means of dealing with both individual and interaction effects of various welding parameters in resistance welding.

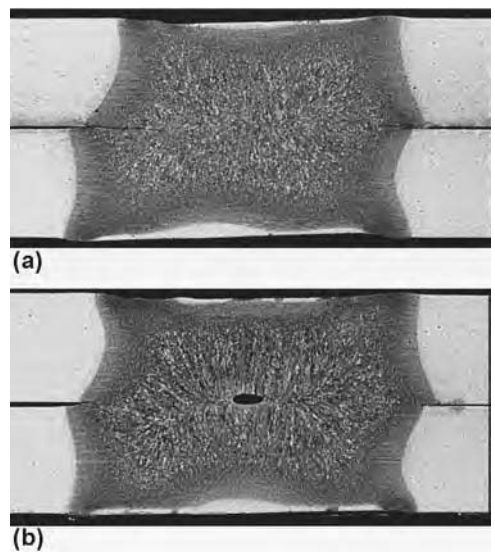


Fig. 8 Cross sections of welds made using machines with different frictions on a 1.7 mm (0.067 in.) steel. Source: Ref 8

A typical lobe diagram demonstrates how, together, the electric current and welding time affect the formation of minimum-sized welds and the occurrence of expulsion. These two limits divide the current-time domain into three regions, as shown in a schematic of a lobe diagram in Fig. 9. When the time is too short or the welding current too low, the heat generated is not sufficient to form an acceptable-sized weld. Another extreme case is when the heat is excessive, produced either by long welding time or high current; then expulsion or even electrode sticking could occur. In the middle is the region in which the current-weld time combinations produce acceptable welds without expulsion. The width of this region defines the

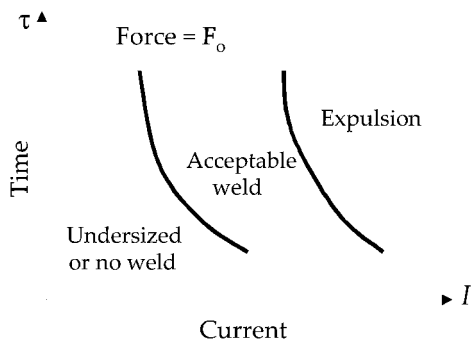


Fig. 9 Schematic of a lobe diagram

window of operation. A large or wide operation window is obviously preferred, because small fluctuations in welding parameters will not affect the welding process, or create an undesirable weld.

There are standard procedures, such as that recommended by the American Welding Society (AWS/SAE D8.9M, Ref 9), which can be followed to develop weld lobes. The weld lobes are material (in chemistry and thickness) dependent. Other process variables, such as electrode force, may have a significant influence on the shape and location of a lobe. For example, Fig. 10 is a three-dimensional lobe diagram for low-carbon steel showing the effect of electrode force. There are three classes of weldability lobes: A, B, and C. The class A lobe has a wider current-time window for suitable welds than class B or C lobes.

Figure 11 is the current-time plot for the class A, B, and C weldability lobes in Fig. 10. Note that the Resistance Welder Manufacturers Association (RWMA) chart schedule is outside the lobe boundaries. This is occurring more frequently, because current steelmaking practices of low-carbon steel are different than when the original RWMA schedules were developed. Current steelmaking practices, with electric arc melting and ladle metallurgy treatment, offer better composition control than in the past.

Influence of Process Variables on Weld Lobes. A weld lobe is defined by the boundaries of minimum and maximum currents at

specific welding times. The shape, size, and location of the boundaries and therefore the lobe are affected by a number of process-related variables.

Electrode Size and Condition. The electrode size determines the current density and pressure distribution at the interfaces and therefore the weld formation and expulsion. Large-sized electrodes require large welding current to produce sufficient heat or heating rate, which raises the minimum limit in a lobe diagram. For a fixed electrode force, a large electrode means low pressure, which is favored by expulsion and lowers the maximum current. Other electrode conditions, such as electrode wear and the face geometry of electrode caps, may also change the mechanical and electrical aspects of welding and the lobe diagrams.

Electrode Alignment. A weld lobe shift caused by electrode misalignment was reported by Karagoulis (Ref 10). The alignment of electrodes, either axially or angularly, affects the contact area for electrical current and mechanical pressure at the interfaces. The current density may be raised because of electrode misalignment, which promotes weld nugget formation and lowers the minimum current limit. On the other hand, the concentrated heating due to high electric current density and the reduced containment on the liquid nugget from the electrode make expulsion easier to occur. Therefore, the maximum current limit is reduced as well, resulting in a shift to the left of a lobe.

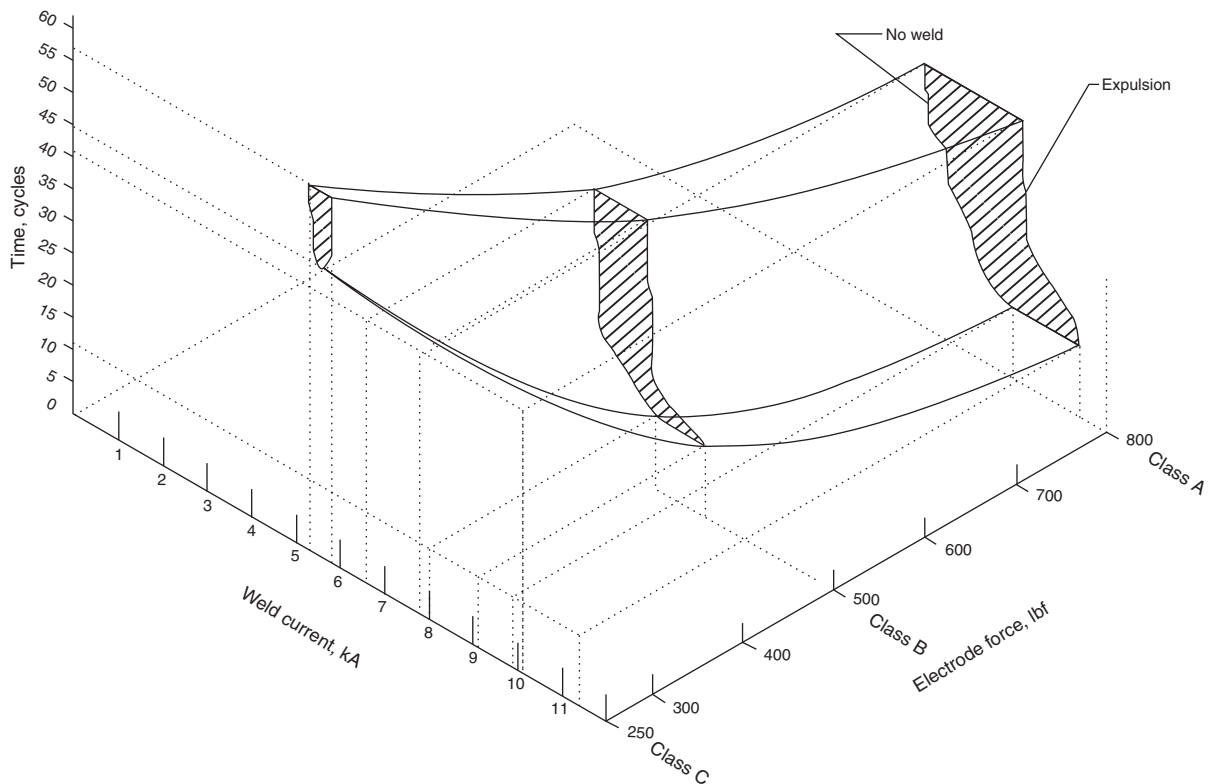


Fig. 10 Three-dimensional lobe diagram showing the effect of electrode force on suitable range of welding current and time in spot welding low-carbon steel

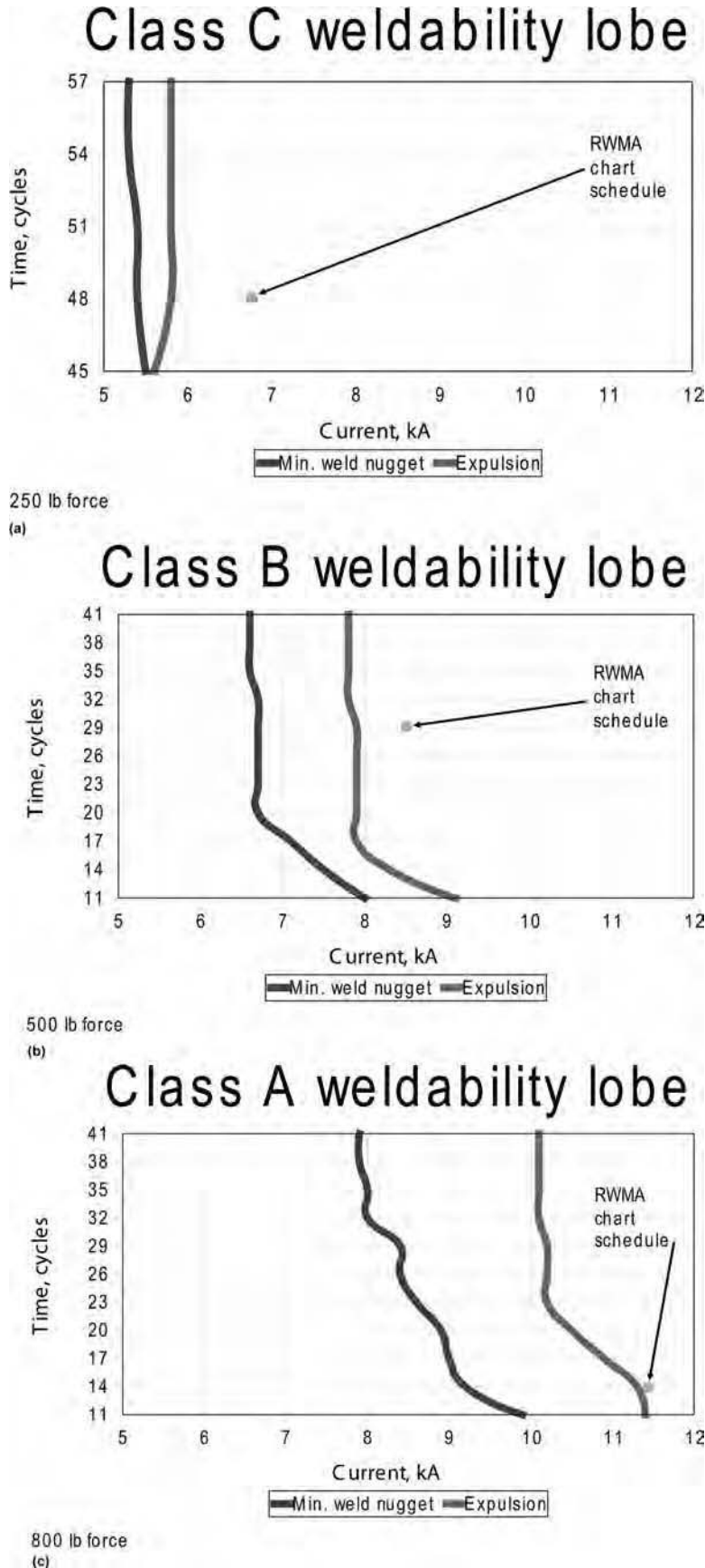


Fig. 11 Class A, B, and C weldability lobes for spot welding 16-gauge (1.6 mm, or 0.062 in.) low-carbon steel (Fig. 10). See text for discussion on Resistance Welder Manufacturers Association (RWMA) chart values outside the weldability lobes.

Part Fit-Up. The sheet fit-up condition affects the weld formation and expulsion in the same way as electrodes and electrode alignment. A poor fit-up condition may promote weld formation as well as expulsion and moves the weld lobe to the left. In addition, the electrode force needed to overcome the gap between the sheets with an abnormal fit-up condition is larger than in a normal situation, and therefore, the dependence of a weld lobe on electrode force is affected by part fit-up.

Electrical Impedance. The electrical characteristics, such as resistance and reactance of a welding setup, affect the heat input and therefore the weld formation and expulsion. Such an influence is complicated, especially when other process variables are involved. It was reported that the weld lobes become narrower and the boundaries steeper when adhesives were used in weld bonding (Ref 11). The changes in the shape and size of weld lobes are a result of the changes in the resistance of the weld stack-up because of the use of adhesives.

Electric Current Waveform. The effect of welding current profile on a weld lobe diagram is obvious. Welding that uses a steady, not a rippling, current supply is preferred, because the heating process is easier to control. The weld formation starts at an earlier stage when using an MFDC than an ac, which lowers the minimum current in a lobe diagram. In a comparative study of zinc-coated steels, it was found that expulsion is delayed when switching from a single-phase ac to an MFDC (Ref 4).

Electrode Force. It has been concluded by many researchers that varying an electrode force could lead to changes in the position, size, and shape of a lobe, as reported in the work by Kaiser et al. (Ref 12), for instance. In general, increasing electrode force often means a wider process window (Ref 13). More discussion is needed on the influence of electrode force on weld lobe diagrams.

The process abnormalities affect the weld lobes as well as the weld quality. In a statistical analysis by Li (Ref 14), several process variables were altered to create abnormal welding conditions. The weld lobes, characterized by the weld window location (the center of the current window, $\frac{1}{2}(I_{min} + I_{max})$), and the window width ($I_{max} - I_{min}$), were found to be a strong function of electrode size and welding time and a weak function of electrode force, fit-up, and axial and angular misalignment. In general, abnormal process conditions significantly reduce the current range, while the electrode force increases the window size. The experiment was conducted on 0.8 mm (0.03 in.) hot-dipped galvanized drawing steel, using a single-phase ac welder. Some of the conclusions of this study could be different for welding with different setups.

Effect of Electrode Force. The electrode force is usually fixed at a certain level when developing a lobe diagram. Therefore, the role of electrode force in a lobe diagram is often overlooked. In fact, the electrode force directly determines the mechanical and electrical

contact at the faying interface, which, in turn, affects the weld formation and expulsion processes. The electrical contact resistance at the faying interface is inversely proportional to the pressure and size of the contact area created by the electrode force. Therefore, increasing electrode force often delays weld nugget formation as the result of less Joule heating. Because the electrode force plays a major role in suppressing expulsion, large electrode force is beneficial for preventing expulsion. In general, both the current of minimum weld and the expulsion current are pushed up with an increased electrode, and, in most cases, the current range for making welds of a desired size without expulsion, or the operation window, is also enlarged. In welding a DP600 steel, it was found that increasing electrode force both widens the current range and moves the lobe to the right, as shown in Fig. 12 (Ref 15).

In addition to the magnitude of electrode force, the lobe diagrams are also strongly affected by the profile of electrode force. In a study comparing the influence of two different electrode driving mechanisms, Grimes (Ref 5) studied the difference in weld formation when welding with a pneumatic cylinder-driven and an electric servo-motor-driven pedestal welder. The servo motor welder was able to supply a forging force during welding, and experiments have shown that such a forging force not only helps reduce porosity in a weldment but also lowers the welding current required for forming a weld. Figure 13 shows a significant reduction in welding current when welding aluminum alloy sheets using a servo welder, compared to that using a welder with a pneumatic cylinder. The nominal electrode force is 300 daN (675 lbf) in both cases, while the servo welder supplies a 600 daN (1350 lbf) forging force at the end of welding. Therefore, welding with a forging force helps lower the minimum current in a lobe diagram. An electrode force with a forging component is also expected to raise the expulsion current, because electrode force is largely responsible for containing the liquid

metal in the nugget from being ejected. The effect of forging force on expulsion may diminish when expulsion occurs in the early stage of welding, as often observed in aluminum welding (Ref 16). In conclusion, welding with a forging action may lower the minimum welding current and raise the expulsion limit, as well as enlarge the current range or operation window.

Probabilistic Boundaries in Lobe Diagrams. In lobe diagrams, both the minimum weld current and the expulsion limit are usually expressed as lines with definite values. However, such limits are rarely used in practical welding directly. These boundaries, in fact, are affected by a number of uncontrollable random variables, and they are more of a probabilistic than deterministic nature. Many process variables, such as electrode condition, surface condition, sheet fit-up, and so on, have effects on weld formation

and expulsion. Therefore, a lobe diagram should be derived considering the uncertainty in obtaining a weld of specific size, or the occurrence of expulsion, through a standard statistical process. In the work by Zhang, et al. (Ref 17), the expulsion boundary was presented as a current range with limits corresponding to the chances of expulsion, for example, 0 and 100%.

In Fig. 14, the probabilities of expulsion of 0.05 and 0.95 are presented as the maximum current limit for a drawing steel. Such a limit, or a range for the expulsion boundary, is a strong function of welding time and electrode force. It is also clear from this figure that treating the expulsion boundary as a definitive line does not reflect the probabilistic nature of expulsion. Ideally, both the maximum and the minimum current boundaries should be determined, in terms of probabilities, through a

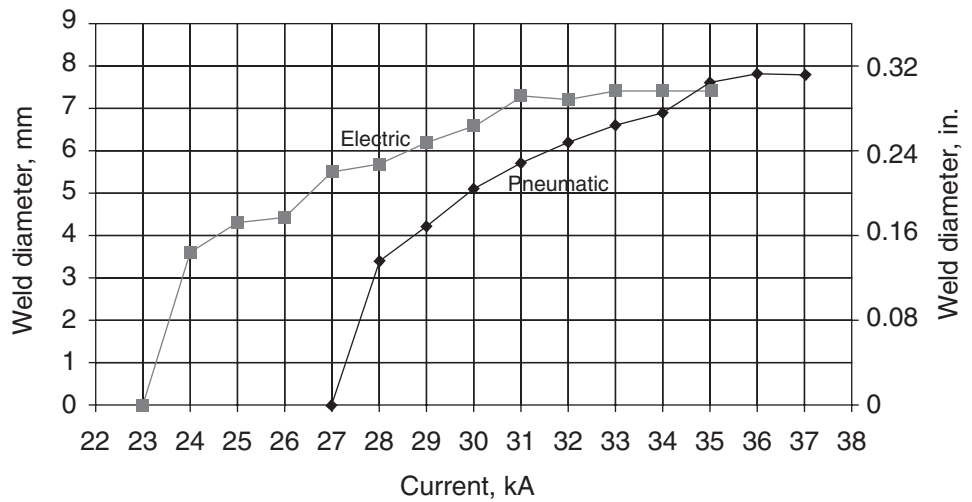


Fig. 13 Weld formation of 1.1 to 1.5 mm (0.04 to 0.06 in.) aluminum sheet stack-ups using a pneumatic and a servo pedestal welder. Source: Ref 5

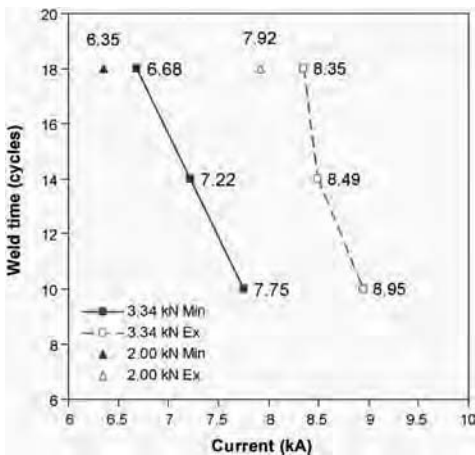


Fig. 12 Lobe diagrams for welding a DP600 steel. Source: Ref 15

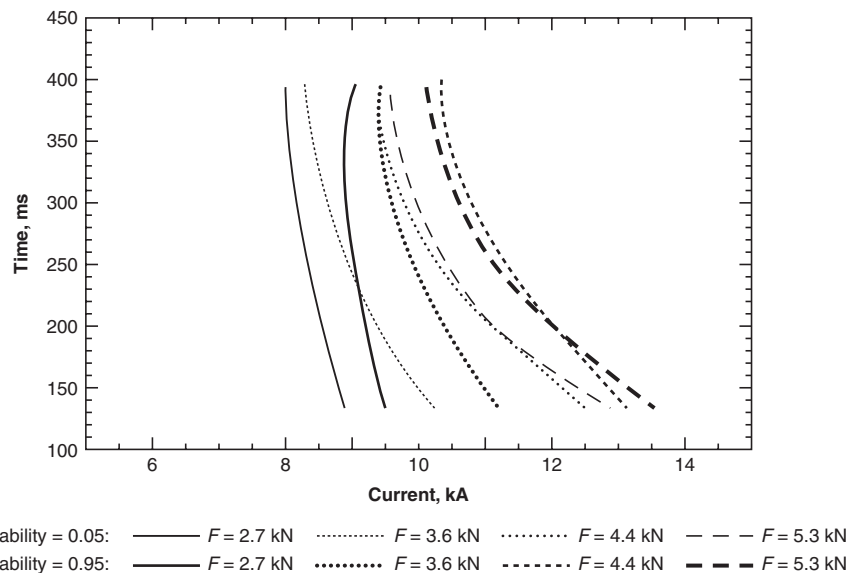


Fig. 14 Expulsion probabilities in welding a drawing steel under various levels of electrode force. Source: Ref 17

systematic statistical procedure. However, this may be difficult in practice because of the large amount of experiments involved in developing these boundaries.

Three-Dimensional (3-D) Lobe Diagrams. The boundaries of minimum-sized weld and expulsion of a lobe diagram are commonly expressed in terms of the combinations of welding time and current only, at a fixed electrode force. Three-dimensional lobe diagrams, such as the one in Fig. 10, can be used to show the effects of electrode force on the current-time weldability lobes. A higher force increases the range of welding current and time window for suitable welds (e.g., class A in Fig. 11).

The electrode force can be set high with low-carbon steels, so that the welding process may not be very sensitive to electrode force. However, lightweight materials such as aluminum or magnesium alloys are more sensitive to electrode force. Aluminum and magnesium usually experience large thermal expansion during heating and melting, and welding such materials depends strongly on the electrode force applied. When the electrode force is not treated as a variable, very limited information can be obtained on the interaction between the electrode force and other process variables. It is also difficult to optimize welding schedules without knowing the role the electrode force plays over a certain range, in weld formation and expulsion suppression. Therefore, it is of practical interest to consider the welding current, time, and electrode force together in developing welding schedules, that is, to construct 3-D lobe diagrams.

Most of the lobe diagrams incorporate the effect of electrode force by overlaying the lobes corresponding to different levels of electrode force in the same diagram. For instance, Fig. 12 shows the limits of minimum weld and expulsion under two electrode forces: 2.0 and 3.34 kN (Ref 15). Because only very limited levels of electrode force can be used in one lobe diagram, the electrode force is not treated in the same way as the other two, and its effect cannot be fully accounted for. A true 3-D lobe diagram presents the boundaries of minimum weld and expulsion as surfaces in a 3-D space of welding current, time, and electrode force. Using analytical expressions of expulsion probabilities developed through experiments for a drawing steel and two aluminum alloys (AA5754 and AA6111), Zhang (Ref 16) presented the surfaces of expulsion with the probabilities of 0.05 as the functions of all three welding process parameters in Fig. 15 to 17.

A probability of 0.05 represents a very small chance of expulsion, and therefore, the surfaces in the figures can be used as the limits of maximum-sized welds with a low risk of expulsion. As seen in the figures, different alloys have distinctive expulsion surfaces or characteristics. In general, low heat input, represented by low current and short time, has a low chance of expulsion when supplemented by a high electrode force. Expulsion in steel welding is contained if the combinations of current, time, and electrode force are located under the surface in Fig. 15. The risk of expulsion dramatically increases if the limit is

exceeded that is, when a combination of parameters located on the surface moves outward. Reducing welding current level and welding time and raising electrode force is efficient in avoiding expulsion in welding this steel. The difference between welding steels and welding aluminum alloys is evident by the drastically different expulsion surfaces in the 3-D lobe diagrams. The expulsion surface for AA6111 welding (Fig. 16) is less curved than that for welding the steel. The electrode force and welding current still affect the chance of expulsion, although to a smaller extent. Welding time is influential only when the electrode force is low, and it is virtually irrelevant under high electrode force. Similar observations are made on welding AA5754 (Fig. 17). In addition to the fact that the welding time has little effect on expulsion at both high and low electrode force levels, the expulsion exhibits very limited dependence on electrode force. The expulsion surface is very flat, and expulsion occurs once a critical value of welding current is reached.

Three-dimensional lobe diagrams present an opportunity for choosing all three welding parameters together, which is desirable in practice, especially when welding new materials on which not much practical experience is available. They also provide important information on the intrinsic nature of the sheet materials. For instance, the virtual independence of expulsion on welding time and electrode force exhibited in Fig. 17 for welding AA5754 implies that the liquid metal is ejected at a very early stage of welding (so varying welding time has little effect), and the volume of liquid metal may grow quickly to a level where expulsion cannot be effectively contained by electrode force. The difficulties and high cost associated with preparing the models of minimum-sized weld and expulsion for the limits in a 3-D lobe diagram, generated through a large experiment matrix, prohibit the use of 3-D lobe diagrams. Taking the probabilistic nature of the limits into consideration will make them more expensive to implement in practical welding.

Seam Welding Procedure Development

Seam welding produces coalescence by the heat obtained from resistance to the flow of electric current through the work parts held together under pressure by circular electrodes. Seam welding machines are capable of making two types of lap joint:

- continuous seam joint of overlapping materials from a series of overlapping spot welds made progressively along a joint by rotating the electrodes
- row of spot welds that do not overlap

Unless otherwise specified or required, the first method achieves a continuous, pressure-tight seam joint on fully overlapped sheet materials. The latter method, known as roll spot welding,

is not actually seam welding but is discussed at the end of this section, because it can be accomplished on standard seam welding machines.

During seam welding (Fig. 18), the electrodes continuously rotate while the welding current is interrupted regularly to achieve the effect of overlapping spot welds. On some thin materials, interrupted current is not required

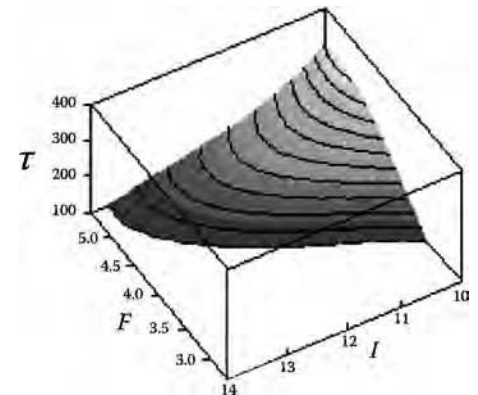


Fig. 15 Surface of expulsion with a probability of 0.5 for a drawing steel. Source: Ref 16

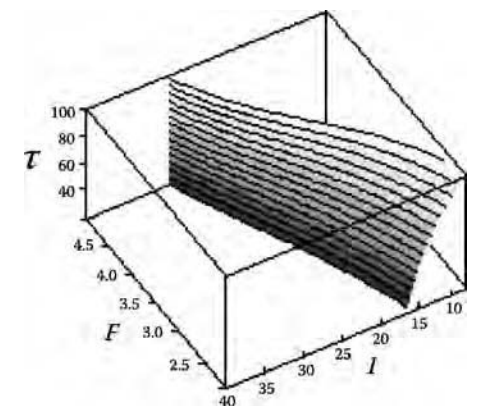


Fig. 16 Surface of expulsion with a probability of 0.5 for AA6111. Source: Ref 16

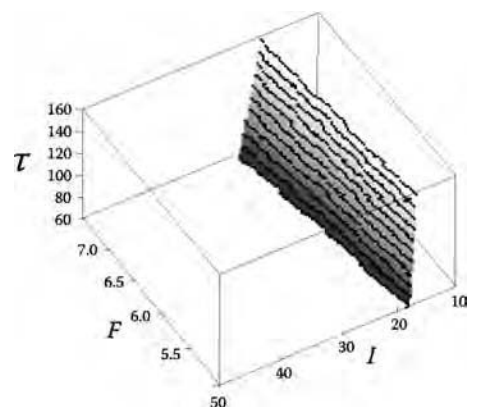


Fig. 17 Surface of expulsion with a probability of 0.5 for AA5754. Source: Ref 16

to produce a good-quality continuously fused seam. Another process variation is mash seam welding (see the article “Resistance Seam Welding” in this Volume). This process uses wide-faced welding wheels and a small, accurately gaged overlap of the sheet materials to be mash seam welded.

Seam welding is a proven production process, and its benefits are most readily achieved when product designers are aware of its characteristics and limitations. It is obviously impractical to set up charts that would cover all welding jobs and conditions, but this section provides some data tables for making

high-quality welds consistently, at maximum speed, and with the least maintenance of welding electrodes. However, it may be necessary to use other setups, because some applications may not require highest-quality welds, such as in difficult-to-reach places that need to be welded. The welding data tables are given as a good starting point, but other setups may be more suited for certain applications.

Seam Welding of Low-Carbon and Stainless Steels

Some of the general guidelines described earlier for spot welding are also applicable to seam welding and are highlighted for various typical low-carbon steels, such as SAE 1005, SAE 1010, SAE 1015, and so on, and for a group of chromium-nickel (austenitic) stainless steels classified as types 301, 302, 303, 304, 308, 309, 310, 316, 317, 321, 347, and 349. Applications involving ferritic and martensitic stainless steels must have special consideration, because the exact chemical composition and thickness of stock determine the practicability of seam welding.

Examples of seam welding parameters are summarized in Tables 8 to 10 for

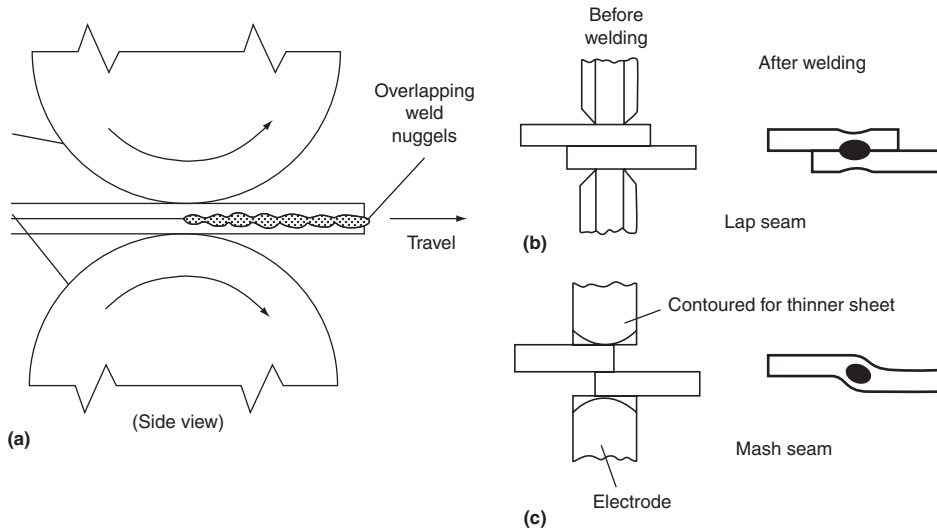


Fig. 18 Diagrams of seam and mash seam welding

Table 8 Seam welding low-carbon steel with interrupted current

Data common to all welding speeds										Pressure-tight joint (note 8)																	
Thickness of each of the two workpieces (note 1, 3)		Electrode width and shape (note 2, 9)		Electrode force (note b), lbf		Minimum contacting overlap <i>L</i> (note 4, 7)		Recommended maximum welding speeds				Recommended average welding speeds				Recommended minimum welding speeds				Roll spot welding Nonpressure-tight joint (note 10, 11)							
<i>T</i> , in.	US gage	Min. <i>d</i> , in.	Nor. <i>D</i> , in.	Min. Min.	Nor. Nor.	Use with min. <i>d</i> , in.	Use with max. <i>d</i> , in.	Heat time (note 5), cycles	Cool time (note 5), cycles	Welding speed in./min	Welds per in.	Welding current, kA	Heat time (note 5), cycles	Cool time (note 5), cycles	Welding speed, in./min	Welds per in.	Welding current, kA	Heat time (note 5), cycles	Cool time (note 5), cycles	Welding speed, in./min	Welds per in.	Welding current, kA	Heat time (note 5), cycles	Welding speed, in./min	Welding current, kA		
0.010	32	1/8	3/16	3/8	400	400	1/4	3/8	1	1	116	15.5	11.5	2	1	80	15	8	2	3	49	14.5	7.5	2	480	200	100
0.021	25	3/32	3/16	3/8	460	550	3/16	7/16	2	1	107	11	12.5	2	2	75	12	11	3	3	45	13	9	2	425	185	90
0.030	22	5/32	1/4	1/2	530	700	5/16	1/2	2	1	103	11.5	15	3	2	72	10	13	2	3	42	14	12	3	370	180	85
0.036	20	3/16	1/4	1/2	600	900	3/8	1/2	2	2	98	9	18.3	3	3	67	9	15	2	4	39	15.5	13.5	3	310	170	80
0.048	18	7/32	3/16	1/2	700	1050	7/16	5/8	2	2	95	9.5	20	4	3	65	8	16.5	4	4	37	12	14	4	250	160	75
0.060	16	1/2	3/16	1/2	750	1200	7/16	5/8	3	1	91	10	21	4	4	63	7	17.5	4	4	36	12.5	15.4	4	190	150	70
0.075	14	1/4	3/8	3/8	980	1500	1/2	11/16	3	1	85	10.5	22	6	5	55	6	20	6	6	30	10	16	5	170	140	60
0.090	13	1/4	7/16	3/8	1010	1700	1/2	3/4	4	2	80	7.5	23	7	6	50	5.5	21	6	6	27	11	17	6	160	120	55
0.105	12	5/32	1/2	3/4	1120	1950	5/16	13/16	4	2	75	6	25	9	6	48	5	22	6	6	25	12	18.5	6	150	100	50
0.120	11	3/16	1/2	3/4	1240	2200	3/8	7/8	4	2	70	8.5	27.5	11	7	45	4.5	23	6	6	23	13	21	6	140	90	45

Notes:

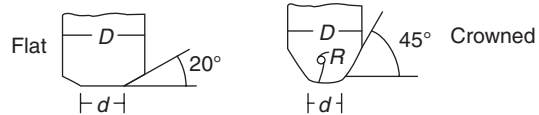
- Low-carbon steel is hot rolled, pickled, and lightly oiled, with an ultimate tensile strength similar to steel (SAE 1005–SAE 1010) (42–45 ksi).
- Electrode material is RWMA class 2 alloy.
- Surface of steel is lightly oiled but free from grease, scale, or dirt.
-



- Heat and cool times are indicated in cycles of 60-cycle frequency.
- Electrode force does not provide for force to press ill-fitting parts together.
- For large assemblies, minimum contacting overlap should be increased by 30% for ease of guiding.

Source: Ref 18

- Large assemblies should be welded at the slower speeds for ease of handling and guiding.
- Electrode face may be flat or crowned (for best weld appearance), as shown:

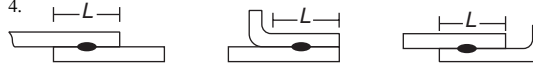


- Welding current is about 10% higher than shown for pressure-tight joint at same weld speed.
- Adjust the cool time to give desired spot spacing.

Table 9 Seam welding low-carbon steel with full-wave continuous current

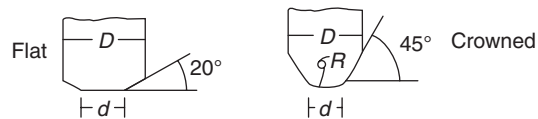
Data common to all welding speeds						Pressure-tight joint (note 8)							
						Recommended maximum welding speeds		Recommended average welding speeds		Recommended minimum welding speeds			
Thickness of each of the two workpieces (note 1, 3) T, in.	US gage	Electrode width and shape (note 2, 9)		Electrode force (note 6), lbf		Min. contacting overlap L (note 4, 7), in.	Welding speed, in./min	Welding current (note 5, 11), kA	Welding speed, in./min	Welding current (note 5, 11), kA	Welding speed in./min	Welding current (note 5, 11), kA	Recommended heat control range (note 10, 11)
		Min. d, in.	Min. D, in.	Min.	Norm.								
0.010	32	3/16	3/8	400	400	3/8	450	11.5	255	9	160	7	80-100
0.021	25	3/16	3/8	460	550	7/16	410	13	220	10.2	130	7.9	80-100
0.024	24	1/4	1/2	470	600	7/16	395	13.4	210	10.5	125	8.1	70-90
0.031	22	1/4	1/2	530	700	1/2	330	14.6	168	11.9	100	9.5	70-90
0.036	20	1/4	1/2	600	900	1/2	270	15.7	134	13	77	10.8	60-80
0.042	19	1/4	1/2	650	950	1/2	255	16.2	120	13.6	70	11.4	60-80
0.048	18	3/16	1/2	700	1050	7/16	202	16.9	100	14.4	58	12.2	50-70
0.062													
0.060	16	3/16	1/2	750	1200	7/16	142	18.5	72	16	41	13.8	50-70
0.075	14	3/8	1/2	980	1500	1 1/16	100	20.5	50	18	30	16	45-60

Notes:

1. Low-carbon steel is hot rolled, pickled, and lightly oiled with an ultimate tensile strength similar to steel (SAE 1005- SAE 1010) (42-45 ksi).
2. Electrode material is RWMA class 2 alloy.
3. Surface of steel is lightly oiled but free from grease, scale, or dirt.
4. 
5. Frequency of welding current is 60 cycles/s.
6. Electrode force does not provide for force to press ill-fitting parts together.
7. For large assemblies, minimum contacting over-lap should be increased by 30% for ease of guiding.

Source: Ref 18

8. Large assemblies should be welded at the slower speeds for ease of handling and guiding.
9. Electrode face may be flat or crowned (for best weld appearance), as shown:



10. Phase-shift heat control range is recommended to attain the best weld quality and appearance.
11. Since welder used on thicker materials must operate at "phased-back" current output, maximum full-wave current, output of welder must be approximately twice that of the welding current shown.

low-carbon steel and austenitic stainless steels. Further discussion is given in the section "Seam Welding Parameters" in this article. As noted, the welding data tables represent welding setups to make not only the highest-quality welds but also to make them most consistently, at maximum speed, and with the least maintenance of welding electrodes. It is these combinations of variables that are listed in the welding data tables. However, all factors must be given consideration before actual values are selected from the charts, because other setups may be needed for specific applications.

Surface Preparation. Low-carbon steel should be free from rust, mill scale, paint, heavy grease or oil to achieve high-quality seam welds. Steels with zinc, tin, or lead-coated surfaces are weldable. However, the electrodes need more frequent cleaning to maintain weld quality.

Steel grit blasting, grinding, or pickling are preferred methods for removing heavy scale or rust. A light film of thin oil to prevent the steel from rusting usually has no adverse effects on the weld, provided that dust has not been allowed to accumulate on the sheet surfaces during storage. If dirt has accumulated, it should be wiped off before welding.

As with carbon steels, stainless steels should be free from rust, scale, dirt, paint, heavy grease or oil for seam welding. Any satisfactory degreasing solution will remove grease and oil and thereby minimize the possibility of surface burning. Stainless steel sheet seldom has any surface scale on it. If scale is present, it can be removed by a 50% (by volume) solution of muriatic (hydrochloric) acid and water, heated to 60 to 65 °C (140 to 150 °F). Wash thoroughly in clean running water. The resulting dark "smutty" surface is cleaned by immersing in a solution of 20% (by volume) nitric acid. After the surface is clean, wash in hot water.

In some applications where the highest degree of weld quality and consistency is essential, it may be necessary to "immunize" or passivate the stainless steel before welding on a freshly machined, polished, or pickled article. A thin oxide film can be made to form rapidly and uniformly by dipping the stainless steel in a cold 20% nitric acid solution for approximately 30 min or warm (approximately 65 °C, or 150 °F) 20% nitric acid solution for approximately 10 min. This passivating treatment forms a thin protective coating of oxide. It also dissolves small particles of foreign material that may


have become lodged in the surface as a result of contact with forming tools or polishing wheels. These particles of common steel will rust and mar the stainless surface if not removed. While the aforementioned procedure allows very good welding results, it is not usually necessary before welding. By sending the welded assemblies through a similar treatment after welding, any discoloration will be removed and the appearance of the finished parts will be improved.

Part Fit-Up. Parts that are to be overlapped, or flanged and welded, should have enough overlap or flange width to prevent excessive burning of the edges of the parts by the welding heat or too much "spitting out" of hot metal. The welding data tables indicate the minimum width of overlap and flanges to make the best welds. For the welding of low-carbon steel with interrupted current timing, two sets of overlap dimensions are shown. With interrupted current timing, the larger dimension is preferred and should be used whenever the application permits. The smaller dimension will give reasonably good results, but it is imperative that guiding fixtures be used to make certain that the center of the electrode face rides over the center of the flange

Table 10 Seam welding stainless steel with interrupted current

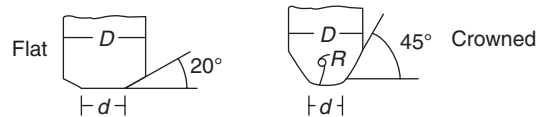
Data common to all welding speeds										Pressure-tight joint (Note 9)																	
Thickness of each of the two workpieces (note 1, 3)	Electrode width and shape (note 2, 12)	Electrode width and shape (note 2, 12)	Electrode force (note 6, 7) lbf	Min. contacting over-lap <i>L</i> (note 4, 8)	Recommended maximum welding speeds					Recommended average welding speeds					Recommended minimum welding speeds					Roll spot welding nonpressure-tight joint (note 10, 11)							
					Heat time (note 5), cycles	Cool time (note 5), cycles	Welding speed, in./min	Welds per in.	Welding current, kA	Heat time (note 5), cycles	Cool time (note 5), cycles	Welding speed, in./min	Welds per in.	Welding current, kA	Heat time (note 5), cycles	Cool time (note 5), cycles	Welding speed, in./min	Welds per in.	Welding current, kA	Heat time (note 5), cycles	Welding speed, in./min	Welds per in.	Welding current, kA				
0.006	38	1/8	3/8	1-1/2	3/16	300	300	1/4	1	1	90	20	6.3	2	1	60	20	4	2	2	44	20	3.6	2	180	120	50
0.008	35	3/16	3/8	1-1/2	3/16	330	350	1/4	1	1	90	20	6.4	2	1	60	18	4.6	2	3	40	18	4.15	2	180	120	80
0.010	32	3/16	3/8	1-1/2	3/16	375	400	1/4	1	1	90	20	6.6	2	2	60	16	5	3	2	44	16	4.5	3	180	120	80
0.012	30	3/16	1/8	1-1/2	1/4	425	450	3/16	2	1	80	15	6.8	3	2	55	15	5.6	3	3	40	15	5.05d	3	160	110	80
0.013	29	7/32	1/2	1-1/2	1/4	470	500	3/16	2	1	80	15	7.2	3	2	55	14	6.2	3	3	42	14	5.6	3	160	110	80
0.015	28	7/32	1/2	1-1/2	1/4	550	600	3/16	2	1	80	15	7.6	3	2	55	14	6.7	3	3	43	14	6	3	160	110	80
0.018	26	1/4	1/2	1-1/2	1/4	600	650	3/16	2	1	80	15	8.3	3	2	55	13	7.3	3	3	44	13	6.5	4	160	110	80
0.021	25	1/4	1/2	1-1/2	1/4	650	700	3/8	2	1	80	15	9	3	2	55	13	7.9	3	3	44	13	7.1	4	160	110	80
0.024	24	1/4	1/2	3	3/8	775	850	7/16	2	2	75	12	12	3	2	50	12	9.2	3	5	38	12	8.3	5	150	100	78
0.031	22	1/4	1/2	3	3/8	900	1000	7/16	2	2	75	12	13.5	3	3	50	12	10.6	3	5	38	12	9.6	5	150	100	75
0.036	20	1/4	1/2	3	3/8	1050	1300	1/2	3	2	70	10	14.5	3	4	47	11	13	3	6	36	11	12.3	6	140	94	70
0.048	18	3/16	1/2	3	1/2	1200	1600	3/8	3	2	65	11	15.5	4	4	45	10	14.2	4	6	36	10	13.5	7	130	90	65
0.060	16	3/16	1/2	3	1/2	1400	1850	3/8	3	2	60	12	16	4	5	40	10	15.1	4	6	36	10	14.5	8	120	80	60
0.067	15	3/16	1/2	3	3/8	1600	2150	11/16	4	3	58	9	16.4	4	5	40	9	15.9	4	8	34	9	15.7	10	116	80	55
0.075	14	3/8	3/8	3	3/8	1700	2300	11/16	4	3	56	9	16.8	4	6	40	9	16.5	4	9	31	9	16.5	10	112	80	50
0.090	13	7/16	3/8	3	3/8	1500	2550	3/4	5	3	55	8	17	5	5	40	9	16.6	5	8	31	9	16.6	12	110	80	40
0.105	12	1/2	3/4	3	3/4	1900	2950	13/16	5	3	53	8.5	17.3	5	7	38	8	16.8	5	12	27	8	16.8	14	106	76	30
0.120	11	1/2	3/4	3	3/4	2000	3300	7/8	5	4	50	8	18	5	6	38	8	17	6	13	24	8	17	15	100	76	25

Notes:

- Types of steel—301, 302, 303, 304, 308, 309, 310, 316, 317, 321, 347, and 349.
- Electrode material is RWMA class 3 alloy.
- Surface of steel is free from grease, scale, or dirt.
- 
- Heat and cool times are indicated in cycles of 60-cycle frequency.
- Electrode force does not provide for force to press ill-fitting parts together.
- Use maximum electrode force at maximum speed and when welding cold-worked material of 150 ksi or above ultimate tensile strength.
- For large assemblies, minimum contacting overlap should be increased by 30% for ease of guiding.

Source: Ref 18

- Large assemblies should be welded at the slower speeds for ease of handling and guiding.
- Welding current is about 10% higher than shown for pressure-tight joint at same weld speed.
- Adjust the cool time to give desired spot spacing.
- For best appearance, use radius-faced electrodes. Average application can be welded with flat-faced electrodes.



or overlap at all times. Slight runouts will cause pronounced spitting and deformation of the overlapped metal.

The amount of overlap dimension is associated with the electrode face width. If the smaller dimension of overlap is used, the smaller dimension of electrode face width should also be used, but the material thickness always determines the minimum electrode face and therefore the minimum overlap.

The range of welding speeds used with continuous current makes it inadvisable to reduce the overlap dimension from the indicated values, because of difficulty in guiding the work at such speeds. While smaller overlap dimensions would result in equally good welds, the design and operation of suitable guiding fixtures become difficult.

The overlap in seam welding is of great importance in making a satisfactory product.

If the application is such that the shape of the parts being welded makes it difficult for the operator to control the overlap in the seam welder, the overlap should be fixed by spot tacking. In this operation, the overlap is first established and held in some suitable manner until several spot welds are made along the line of the future seam weld. The spot welds fix the overlap so it will not change in seam welding because of warping, skidding, creeping, and so on.

While spot tacking can be done on the seam welder, with the welding electrodes preferably not rotating, it is better done on a spot welder assigned to the purpose. It is not unusual to have one spot welder in operation, spot tacking parts to be welded on several seam welding machines.

Parts should lie flat against each other where welds are to be made so that no force is required

from the electrodes to make the parts touch each other. The welder is not a forging machine, and improperly fitting parts will result in inconsistent and inferior welding, greater power demand, as well as excessive maintenance and replacement of the welding electrodes.

Seam welds in circular work require adequate inspection and close supervision to obtain the required conditions of good fit. Press fits or other types of assembly permitting intimate metal-to-metal contact around the entire circumference at the zone to be welded should be used if at all possible; otherwise, less than best-quality welds will result.

In many applications, it is necessary to weld along a continuous curve such as a flanged bottom to a cylindrical container. It is advisable to limit the minimum diameter to 100 mm (4 in.) to allow a suitable diameter of electrode and adequate working life. Smaller

diameters can be seam welded but require special consideration in selection of welding equipment electrode shapes and in welding technique.

The minimum advisable radius of seam welds around contoured corners (such as a gasoline tank) are:

- 50 mm (2 in.) radius for sheet steel gages of 22 through 18
- 60 mm (2¼ in.) radius for 16-gage steel
- 75 mm (3 in.) radius for sheet steel gages of 13 through 11

Electrode Drives. The best type of circular electrode drive for a specific application depends on the shape of the parts to be welded, the degree of surface marking that can be tolerated, and the surface condition of the steel.

Seam welding machines employ three types of electrode drive mechanisms: Knurl or friction roll drive, gear drive, and traveling head (or traveling fixture) drive, which uses idling weld wheels.

The knurl (or friction)-type drive has either the upper or lower (or both) rotating electrodes driven by a hardened steel contact wheel at the periphery of the electrode. The power-driven steel wheel usually has knurling on the engaging surfaces that cut into the face of the wheel or the sides of the wheel adjacent to the face. This type of drive has an advantage in that the peripheral speed of the electrode is independent of the electrode diameter. Hence, the speed remains constant as the electrode diameter changes. Also, both upper and lower wheels may be driven, and they will have the same peripheral speed, regardless of changes in electrode diameter during their useful life.

In the gear-driven type of machine, one electrode is usually driven by means of its gearing and the connected drive shaft. The other welding electrode idles and is turned by friction with the welded product between the electrodes. This drive is desirable in cases where the electrode face must be kept smooth to minimize marking of the product. Also, where space is limited in some welding products and small electrode diameters are required, the gear-driven design is mechanically more practical.

In the travel head type of welder, the head of the welder (with idling electrode wheel) is pushed or pulled over the work, which is clamped on a stationary fixture. A traveling fixture type of machine moves the work under or between stationary, idling electrodes. Traveling head seam welding machines are preferable when the welded product is large or difficult to manipulate through the welder. Traveling fixture type of machines are useful where the product must be accurately located or firmly clamped during the weld.

Gear drive is preferable for any required small electrode diameters and to minimize surface

marking on the welded product. Knurl drive is best to drive both electrodes, to automatically maintain the contour of the welding electrode, or to continuously knurl the electrode face. Knurl drive is desirable when welding coated materials such as template, galvanized, aluminized, or tin-plated steel.

Welding Machine Operation. The sequence most generally used is as follows:

1. Rotating electrodes set down on work
2. Force (pressure) on
3. Current on (current timing pattern starts)
4. Current off (end of weld, current flow is stopped)
5. Force (pressure) off
6. Rotating electrodes separate from work

Seam welding machines are usually built with control circuits to assure the proper sequence of operation, if all adjustments are properly made. The operation should be carefully checked to make sure that the proper sequence is obtained before turning on the welding current.

Seam Welding Electrodes

The welding electrodes must be of the proper material and shape and should be adequately water cooled. For welding low-carbon steel (Table 8), electrodes made of RWMA class 2 alloy usually give the best performance and life, while RWMA class 3 is recommended for welding of stainless steels.

The size and shape of the electrode is usually determined by the shape of the parts to be welded, the location of the welds, and the needs of the driving mechanism to keep the electrodes rotating. If welds are to be made on flanges, one edge of the electrode face is often made practically flush with the side of the electrode, allowing the face to weld the flange with the minimum degree of clearance.

From Table 10, it can be seen that radius-crowned electrodes are recommended when welding stainless steel. This selection is preferred for the best surface appearance, because the marking and indentation from the electrodes will be minimized. If electrode indentation is not objectionable, flat-faced electrodes of the same shape as those used for welding low-carbon steel are usable and will give good results.

The contour of the electrode will change in welding, and the contacting electrode face becomes wider and will eventually reach a point where the reduced unit welding current and unit force will not cause fusion. The faces should be redressed as often as necessary, and the best method of redressing is to put them in a lathe and machine them. Several sets should be available so that the redressing time does not reduce the production time of the welder. If radius-crowned faces are used, a

radius gage may be used for properly checking the contour to see that the correct radius is maintained.

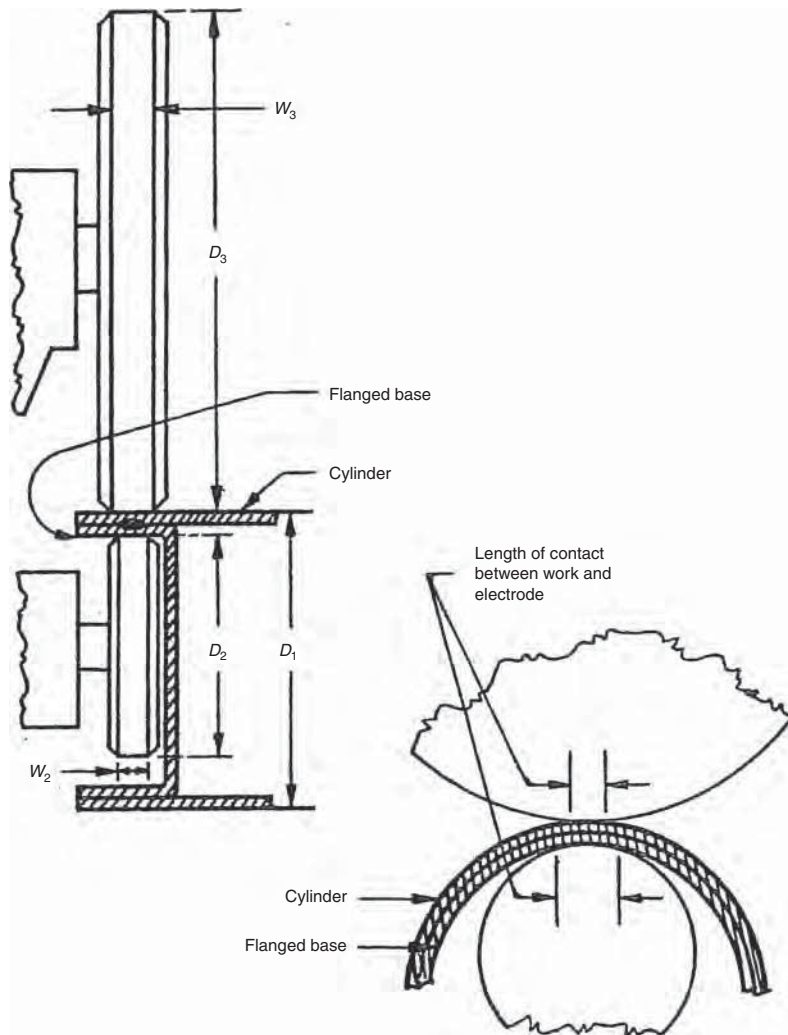
When the parts to be welded are of approximately equal thickness and it is desired to have as little surface marking as possible on one workpiece, the electrode in contact with the part to have a minimum of marking should have its face width at least 50% greater than the widths given in the welding data tables. The diameter of electrodes used in seam welding is determined principally by the application. Provide an adequate mass of copper alloy to prevent excessive temperature rise. Provide sufficient clearance to prevent the arms holding the welder bearings from interfering with the workpieces.

If the working conditions permit, the following sizes of electrodes are used:

- For light work (electrode forces up to 445 daN, or 1000 lbf), electrodes are usually 9.5 mm (¾ in.) wide and 178 mm (7 in.) in diameter.
- For medium work (electrode forces up to 890 daN, or 2000 lbf), electrodes are usually 13 mm (½ in.) wide and 203 mm (8 in.) in diameter.
- For heavy work (electrode forces up to 1335 daN, or 3000 lbf), electrodes are usually 19 mm (¾ in.) wide and 254 mm (10 in.) in diameter.

Some applications will necessitate using electrodes of different diameters. One electrode may be a small diameter to fit into the part being welded, and the other may be a large diameter to provide clearance between the horns of the welding machine carrying the bearings. As an example, select the case of a flange circular disc being welded into a cylindrical container of small diameter (Fig. 19). The electrode must pass into the bottom of the container, and, for the interests of adequate electrode life, it is made as large in diameter as possible. The outside electrode must be large in diameter to provide adequate work clearance. When the parts are assembled for welding, it will be noted that more metal is in contact with the smaller-diameter electrode. This metal will be cooled rapidly and will not reach welding temperature at the same time as the small area of metal in contact with the larger-diameter electrode, if the electrode face widths are equal. Consequently, to create a heat balance and prevent excessive surface marking of the metal in contact with the top electrode, the wheel face widths are varied (Fig. 19). The W_3 on the outside wheel is greater than the W_2 on the inside.

Seam welding machine electrodes can be internally water cooled if necessary, but this method is much less effective than the usual system of flooding water directly on the electrode and work. The cooling water is normally directed from four tubes to the point where the weld is being made. Continuously moving



Thickness of each workpiece	D_1 , in. min.	D_2 , in. min.	D_3 , in.	W_2 , in.	W_3 , in.
0.010	2	1 $\frac{3}{4}$	12	$\frac{1}{8}$	$\frac{1}{4}$
0.020	3	2 $\frac{3}{4}$	12	$\frac{1}{8}$	$\frac{1}{4}$
0.040	4	3 $\frac{3}{4}$	11	$\frac{3}{16}$	$\frac{1}{4}$
0.062	6	5 $\frac{3}{4}$	12	$\frac{3}{16}$	$\frac{3}{8}$
0.078	8	7 $\frac{3}{4}$	8	$\frac{3}{16}$	$\frac{3}{8}$
0.125	12	10	10	$\frac{5}{16}$	$\frac{3}{8}$

Fig. 19 Setup for seam welding a circular flange disc into a cylindrical container of small diameter

cold water thus cools the hottest part of the electrode and work on both the upper and lower surfaces of the weld. Water cooling promotes longer electrode life. Water cooling has other desirable effects. It quickly quenches the weld metal while considerable force is on the workpiece, thus making high rates of welding speed possible.

When welding coated materials such as galvanized or terne-coated steels, it is quite necessary to minimize pickup of the coating on the electrodes. The quenching action is also desirable when welding stainless steel in order to

minimize possible future corrosion of the steel due to the welding heat. In stainless steels of the chromium-nickel type (and not stabilized), there is a zone of temperature between 4425 and 815 °C (8000 and 1500 °F) in which carbide precipitation occurs. A proper application of cooling water keeps the time in this critical temperature range sufficiently short.

By having suitable water cooling, the warpage of the workpieces is minimized. It also allows easier handling of the parts, because the welding heat flows into the cooling water rather than into the parts themselves.

When welding two unequal thicknesses, the weld nugget will usually penetrate deeper into the thicker piece. By adjusting the flow of cooling water so that the thicker piece is cooled more thoroughly, the penetration into the thicker piece can be decreased while penetration into the thinner piece is increased. In other words, the flow of cooling water is adjusted to assist in compensating for the uneven heat balance condition created by the two unequal sheet thicknesses. The recommended welding technique is shown in Table 11.

A 5% (by volume) solution of borax in the cooling water will minimize the rusting of low-carbon steels. This solution should not be used as a cooling fluid in the welder transformer or internal cooling passages, because it may eventually clog such passages.

Seam Welding Parameters

Like spot welding, the formation and quality of seam welds depends on welding current, electrode force, and welding time. One key difference is that welding time is expressed as the speed of seam welding, based on the travel speed of the rotating electrodes. Like spot welding, these welding parameters must be decided together, because the quality of seam welds depends on the combined effects of welding current, electrode force, and welding speed.

Electrode force should be as high as is practical and will depend on the material thickness, the hardness of the material, the type of electrode material, size, and shape, as well as the mechanical and electrical capacity of the machine used. The welding force is usually applied by an air cylinder.


Table 8 gives recommended values to be used in the listed setups. It will be noted that two ranges are given for low-carbon steel seam welding using interrupted current timing. The lower range should be used with the minimum electrode face width. This combination should be selected only when the other combination cannot be used because of geometry of the parts, machine capacity, and so on. To weld under these conditions necessitates careful guidance of the workpieces and close control of welding variables. There must be no electrode force required to force the parts together before welding, and the work dragging load (tending to stop rotation of the electrodes) should be small.

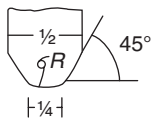
The higher welding force range should always be used when the parts have been previously cold worked. Higher force should also be used when welding takes place at the maximum recommended speed. The effect of electrode force on maximum welding speed is shown in Table 12 for mild steel. A 3-D lobe diagram is shown in Fig. 20.

Most modern welding machines are supplied with gages, charts, or tables to show the different welding forces for the various machine settings. Where such calibrations are not available, force gages can be used to

Table 11 Seam welding dissimilar thickness of low-carbon steel with interrupted current

Thickness (note 8), in.		Electrode force, lbf	Current, kA	Minimum contacting overlap, in.	Heat time, cycles	Cool time, cycles	Welding speed, in./min	Welds per in.
Thin sheet	Thick sheet							
0.031	0.075	600	16	1/2	3	2	72	10
0.031	0.075	800	22	1/2	2	1	142	8.5
0.031	0.048	800	17	1/2	3	2	72	10
0.031	0.048	800	20	1/2	2	1	142	8.5
0.048	0.075	1200	22	5/16	4	3	60	8.5
0.048	0.075	1200	22	5/16	3	1	120	7.5

- Notes:
1. Low-carbon steel is hot rolled, pickled, and lightly oiled with an ultimate tensile strength of similar to steel (SAE 1005 – SAE 1010) (42 – 45 ksi).
 2. Electrode material is RWMA class 2 alloy.
 3. Surface of steel is lightly oiled but free from grease, scale, or dirt.
 4. 
 5. Heat and cool times are indicated in cycles of 60-cycle frequency.
 6. Electrode force does not provide for force to press ill-fitting parts together.
 7. For large assemblies, minimum contacting overlap should be increased by 30% for ease of guiding.
 8. Large assemblies should be welded at the slower speeds for ease of handling and guiding.
 9. Electrode material—RWMA class 2 having shape of:



It is impossible to list all combinations of thicknesses—variables can be estimated as follows:
If thickness ratio is greater than 2 to 1, use variables indicated in Table 9 (for thinner sheet) except:

1. Increase electrode force by 15%.
2. Increase current by 30%.

If thickness ratio is less than 1.8 to 1, use variables indicated in Table 9 (for thinner sheet) except:

1. Use average of electrode force (normal).
2. Use average of welding current for the same approximate speed and timing pattern.

Source: Ref 18

Table 12 Effect of electrode force on maximum welding speeds attainable

Steel thickness, mm	Maximum welding speed, m/min					
	Narrow seam			Wide seam		
	Electrode force	ac	dc	Electrode force	ac	dc
0.75	3.0	...	8	3.5	6	4
	4.5	...	14	5.25	10	8
	6.0	...	16
1.2	4.0	10	4	2.4	4	4
	6.0	16	10	4.8	8	4
	8.0	16	14	7.2	8	8

ac, alternating current; dc, direct current. Source: Ref 19

measure such welding forces (under static conditions).

Welding Speed and Time. As noted, welding time during seam welding is controlled through the travel speed of the electrodes. Like spot welding, lobe diagrams are a common means of evaluating suitable parameters, except that welding speed (instead of welding time) is a variable in lobe diagrams for seam welding. Examples of lobes diagrams are shown for narrow seam weld (Fig. 21) and wide seam weld (Fig. 22) of low-carbon steel. Higher welding speeds narrow the processing window for suitable welds, as indicated in Fig. 21 and 22.

The time of heating during seam welding depends on whether continuous current or interrupted current (timed periodic impulses of current) is used. When continuous current is used, the welding current flows all or part of each half-cycle. An electronic or magnetic contactor permits the continuous current to flow during the complete time of each half-cycle, and transformer taps control the amount of current. Such current flow is designated as full-wave continuous current.

With the use of electronic contactors and phase-shifting heat control circuits, the continuous current can be made to flow only a portion of each half-cycle, and its magnitude

can be readily adjusted from 100 to 40% for a 220 V welding machine or from 100 to 20% for a 440 V welding machine. Such current flow is designated as phased-back continuous current.

Welding by the use of full-wave continuous current (supplied from a 60-cycle system) may be used if the stock thickness is 20 gage or less and the geometry of the work is such that welding speeds as indicated in Table 9 can be used. If the speeds must be much lower, phased-back continuous current is recommended.

With thicknesses of sheet above 1 mm (0.040 in.), welding with full-wave continuous current becomes less satisfactory. The surface appearance is poor, with deep ridges and occasional burned areas. Phased-back continuous current should be used to a material maximum of 0.2 mm (0.0075 in.) and is satisfactory under normal circumstances.

Variations in sheet surface cleanliness due to rust spots, and so on cause more trouble when continuous current is used than when the current is interrupted. Either full-wave continuous current or partial-wave continuous current may be used when making mash seam welds, depending on the thickness of the material.

Interrupted (periodic impulse) current is obtained by using an electronic current interrupter or timer. This interrupter allows current to flow for several cycles (heat time) and to stop flowing for several cycles (cool time) and thus repeats this heat-cool pattern as long as the control circuit is actuated and force is on the work. In commercial models of seam welding machine timers, the timing pattern of heat-cool is adjustable for a range of welding conditions.

The current flow or heat time is indicated in cycles (60 cycles per second, because this is the frequency of most power systems). If the heat time is 6 cycles, it means the current flows for exactly 6/60 or 1/10 of a second. The current cool time is indicated in a similar manner.

A pressure-tight joint will require a number of spots per inch to continuous fusion. The range is approximately 15 for 0.25 mm (0.010 in.) thick steel to 5 for 3.2 mm (0.125 in.) thick steel. In most cases, good welds result when the heat time is nearly equal to the cool time. Excessive welding speed will require a welding current so great that surface melting or burning of the material will result. Also, the excessive speed will cause the electrode to roll from the weld metal before it cools. This action results in erratic and inconsistent welding.

Electrode pickup occurs because the semi-molten material tends to adhere to the electrode. Increasing the kVA capacity of the welding transformer does not necessarily enable higher welding speeds.

If slow welding speeds are necessary (usually because of the shape of the work), the cool time should be increased to achieve proper weld spacing.

The number of welds per inch (or per centimeter) are calculated as follows:

$$N = \frac{60T}{(H + C)L} \text{ (for 60 cps frequency)}$$

where:

N is the number of impulses or spots per inch,

L is the length of the weld in inches (or centimeters),
 T is the time in seconds (to weld L),
 H is the heat time in cycles (current flow period), and
 C is the cool time in cycles between successive heat times. This equation may be transposed to:

$$H + C = (60T)/(NL)$$

Seam Welding Current. The welding current is the current that goes through the work and is measured in amperes. It is not usually practical to measure the welding current directly, so the current drawn by the welding machine from the shop power supply is measured and then multiplied by the welder transformer turns-ratio to obtain the welding current.

The turns-ratio for the various welder tap switch settings, if not in the manufacturer's instruction book, can be calculated by measuring the input (primary) voltage and dividing it by the measured output (secondary) voltage. It can also be obtained from the machine manufacturer.

With continuous timing, a standard ammeter can be used for measurement of primary current. With interrupted timing, the heat time is so short that accurate primary current readings cannot be measured with standard ammeters. The use of pointer-stop meters will accurately measure short-time welding currents of 3 cycles duration or longer.

As a general rule, the current is set as high as possible at the start of the weld to ensure, if possible, having enough current at the end of the weld. The degree of reduction of the welding current depends on the analysis of the material, the material thickness and shape of the parts, the area and shape of the welder throat opening, and the location of the work in the throat. Minimum current requirements for narrow and wide seam welds are compared in Table 13 for mild steel. Currents for mild steel are compared with high-strength steel in Table 14 and with coated steels in Table 15.

Many applications of seam welding are such that more magnetic material enters the throat of the welder as the weld progresses. This additional magnetic material in the welder secondary circuit reduces the welding current available. In longitudinal welding, this condition always exists. If it is not possible to obtain sufficient current at the end of the weld without excessive burning at the start of the weld, it is necessary to apply some form of current compensation. Suitable compensation controls can be incorporated in welding machines for magnetic materials. These controls are equipped with constant current, so they are not affected by magnetic circuit changes in the machine.

Seam Weld Testing

There are several methods of testing seam welds. The selection should depend on the final use of the welded product. The first rough check of a weld is easily performed by trying to tear the sheets apart by driving a chisel through the welded area. If the weld cannot be chiseled apart without tearing through the sheets, further tests may be made.

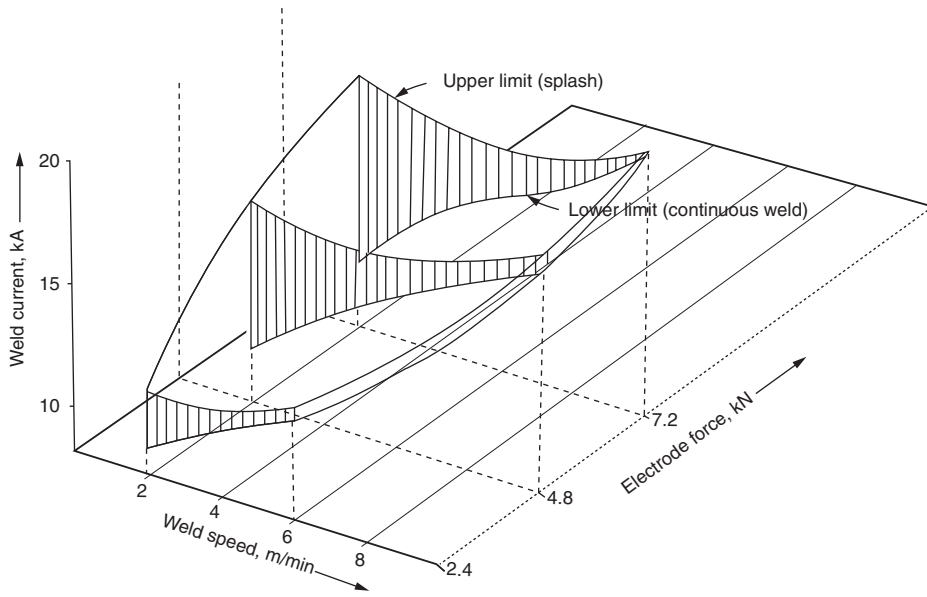


Fig. 20 Effect of electrode force on weldability lobes in seam welding of 1.2 mm (0.05 in.) thick mild steel (wide seam with alternating current). Source: Ref 19

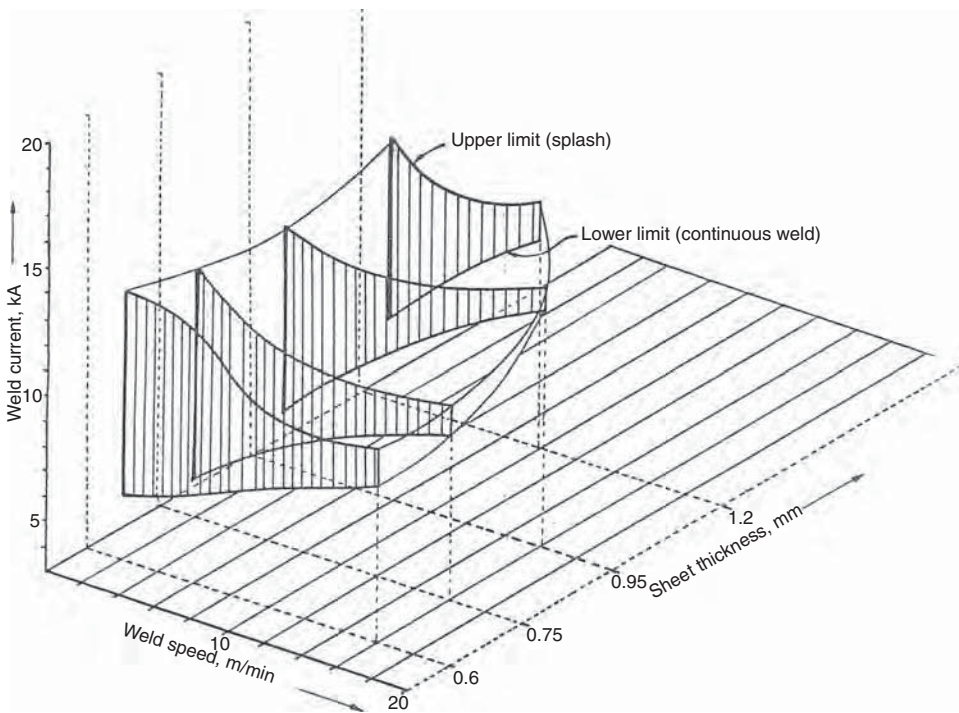


Fig. 21 Weldability lobes for narrow seam welding of a mild steel (alternating current). Source: Ref 19

A cross-sectional etch test to show the percent overlap of the fused nuggets, which should be approximately 20%, and the penetration of the fused zone into the sheets, which should be between 35 and 70% of the sheet thickness, is the normal metallurgical inspection test. The width of the weld depends primarily on the electrode face width and should be from 1½ to 3 times the stock thickness. If the weld width is too narrow and penetration is inadequate, physical strength will be sacrificed. If the weld width is too wide and penetration is

excessive, the weld center will be overheated. This causes excessive buckling, warpage, and poor appearance.

One of the more reliable tests is the pillow test, in which two sheets of convenient size, say 150 by 150 mm (6 by 6 in.), one of which has a pipe nipple welded to it, are seam welded completely around the edges and then subjected to hydrostatic pressure until failure takes place. Failure will usually occur on an inside edge of the seam, where the buckling due to expansion of the test sample is greatest.

After the welding schedule has been determined by the various types of test, production tests on containers can be satisfactorily made by subjecting each piece to air or gas pressure while submerged in water. A safe value of air pressure will disclose any leaks as rapidly as a much greater hydraulic pressure.

It is impractical to make seam welds without some indentation on one or both sides of the stock. Consequently, the stock thickness is reduced by the amount of indentation, causing some slight loss in strength. If the indentation is properly controlled, the welded joint will have a tensile strength of 80 to 100% of the parent metal.

Bearing Maintenance

A resistance seam welding machine bearing mechanism must transmit thousands of amperes from a stationary housing to a rotating shaft, on which is mounted the circular welding electrode. This bearing must also withstand heavy force and maintain proper electrode alignment.

Although journal-type bearings are more common, current collector types and needle bearing designs are frequently employed to achieve improved bearing alignment and to decrease maintenance requirements.

To ensure proper operation and reasonable life, adequate lubrication is necessary. Different bearing designs will require a particular type of lubricant and frequency of lubrication. Lubricant must be of a type to permit electrical current to flow freely. It is therefore important to precisely follow the maintenance recommendations of the welder manufacturer. Many bearing designs have built-in water cooling. In operation, water flow must be maintained to avoid excessive heating.

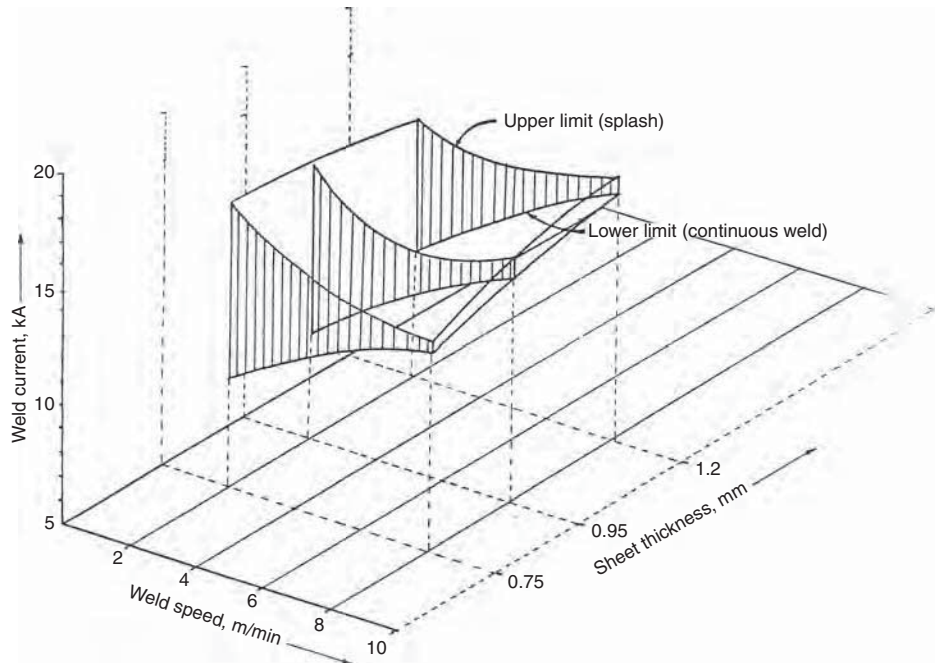


Fig. 22 Weldability lobes for wide seam welding of a mild steel (alternating current). Source: Ref 19

Table 13 Comparison of minimum current requirements for alternating current (ac) and direct current (dc) power supplies with narrow, wide, and mash seam welding

Mild steel thickness, mm	Narrow seam				Wide seam				Mash seam			
	ac, kA		dc, kA		ac, kA		dc, kA		ac, kA		dc, kA	
	2 m/min	6 m/min	2 m/min	6 m/min	2 m/min	6 m/min	2 m/min	6 m/min	2 m/min	6 m/min	2 m/min	6 m/min
0.60	5.25	6.25	4.0	4.25	6.75	6.75	5.0	6.0
0.75	4.75	6.5	4.5	5.25	9.5	12.75	7.0	10.25
0.95	5.5	7.25	5.0	5.5	8.5	13.0	7.25	9.25
1.2	6.5	9.25	4.5	6.75	10.25	14.25	8.5	12.25	11.5	12.25

Source: Ref 19

Table 14 Minimum and maximum welding currents for 1.2/1.4 mm (0.05/0.06 in.) thick mild and high-strength steels

Welding speed, m/min	Current parameter	Secondary current for steel type, kA			
		Mild steel	Rephosphorized	Niobium treated	Dual phase
2	Minimum	6.5 (6.0)	8.1 (7.0)	9.9 (5.9)	6.5 (6.0)
	Maximum	13.5	12.9	10.4	11.0
	Range	7 (7.5)	4.8 (5.9)	0.5 (4.5)	4.5 (5.0)
6	Minimum	9.25 (9.0)	8.7 (8.3)	9.9 (9.4)	9.0 (8.0)
	Maximum	11.75	11.0	10.3	9.6
	Range	2.5 (2.75)	2.3 (2.7)	0.4 (0.9)	0.6 (1.6)

Note: Minimum current refers to current for continuous weld plug; values in parentheses refer to current for stuck weld. Maximum current refers to current giving weld splash. Source: Ref 19

Other Methods

Mash Seam Welding. When the thickness through the finished weld must be a minimum, mash seam welding is used. A slight overlap of 1 to 1½ times the thickness of one workpiece is held by rigid external clamps or by tacking spot welds. Tacking spots should be close enough together to prevent the seam from opening up ahead of the electrodes, and the spot spacing will vary from 40 mm (1½ in.) on 0.5 mm (0.020 in.) material to approximately 75 mm (3 in.) on 2 mm (0.075 in.) material. The assembly is placed between two broad-faced flat electrodes, which forge the sheets together while welding them. The resulting thickness in the weld area is approximately 50% greater than one original sheet thickness. The process variables listed in Table 16 apply.

Mash seam welding is limited to low-carbon and coated steels of 13 gage (2.2 mm, or 0.090 in.) or less for most applications. Its use requires higher electrode maintenance than lap seam welding. It should not be used if lap seam welding is practical. Mash seam welding of stainless steel is not recommended, because the narrow plastic range of the material causes excessive burning and spitting, and the high hot-forging strength of the stainless steel causes excessive electrode wear, making the process impractical.

Roll Spot Welding. Seam welding machines are used for roll spot welding—making a series of spot welds with a gap between them. Roll spot welding is a useful production technique where a pressure-tight joint is not required.

Interrupted current timing must be used, and the spot spacing is determined by selecting the proper current cool time with relation to the welding speed. Tables 9 and 10 indicate a range of speeds for roll spot welding. This range is very flexible. Normally, the geometry of the work will allow selection of one of the three indicated ranges.

If a slower speed is desired, the minimum speed indicated for a pressure-tight joint can be used. No currents are indicated because they should be similar to the three ranges indicated

for pressure-tight joints. For example, if the welding speed is 100 in./min and spots are desired every 50 mm (2 in.) in 0.75 mm (0.030 in.) thick stock, the welding data table indicates the current heat time (H , in number of cycles) should be 3 cycles.

Proper cool time may be calculated by the formula:

$$H + C = (60T)/(NL) \text{ (at 60 cps)}$$

For example, with spot spacing of 50 mm (2 in.), N is ½. With a welding speed of 100 in./min, then L is 100 in. and T is 60 s. Heat time is 3 cycles, so calculating for cool time (C) to achieve proper spot spacing is as follows:

$$3 + C = (60 \times 60)/(1/2 \times 100) = 3600/50 = 72$$

$$C = 72 - 3 = 69 \text{ cycles}$$

Long cool times for intermittent seam welding may require the modification of standard seam weld timer ranges to obtain such times.

Nonferrous Alloys

Resistance spot, seam, projection, and upset welding are used to weld nonferrous sheet products. Suitability may vary depending on the work metal. For example, some of the coppers and copper alloys can be spot welded but not seam welded because of high conductivity, and not projection welded because of low compressive strength of the projections at elevated temperature.

Resistance welding of aluminum and copper alloys is common and discussed further. Titanium, nickel, and magnesium alloy sheets with thicknesses up to approximately 6 mm (¼ in.) are also welded by spot, seam, and projection resistance processes.

Aluminum and Its Alloys

Aluminum alloys, both of the non-heat-treatable and heat-treatable types, either wrought or

cast, can be resistance welded. Some of these alloys are welded more readily than others. Gas shielding may be required to maximize joint quality. Characteristics of aluminum alloys include comparatively high thermal and electrical conductivity, a relatively narrow plastic range (approximately 95 to 205 °C, or 200 to 400 °F, temperature differential between softening and melting), considerable shrinkage during cooling, a troublesome surface oxide, and an affinity for copper electrode materials.

Although aluminum alloys can be resistance spot and seam welded, some alloys or combinations of alloys have higher as-welded properties than others. Table 17 gives melting ranges, electrical and thermal conductivities, and resistance weldability of some wrought alloys and casting alloys.

Resistance welding is also done on Alclad products made by roll cladding some of the alloys listed in Table 17 with a thin layer of aluminum or aluminum alloy. Because this layer is anodic to the core alloy, it provides electrochemical protection for exposed areas of the core. Alclad alloys 2219, 3003, 3004, 6061, and 7075 have a cladding of alloy 7072, which contains 1% Zn; Alclad alloy 2014 has a cladding of alloy 6003 or sometimes alloy 6053, both of which contain approximately 1.2% Mg; and Alclad alloy 2024 has a cladding of alloy 1230, which contains a minimum of 99.3% Al.

The hardness of an alloy is one variable influencing weldability. Any alloy in the annealed condition (O temper) is more difficult to weld than the same alloy in a harder temper. In general, alloys in the softer tempers are much more susceptible to excessive indentation and sheet separation and to low or inconsistent weld strength. Greater deformation under the welding force causes an increase in the contact area and variations in the distribution of current and pressure. Therefore, welding of aluminum alloys in the annealed condition or in the softer tempers is not recommended without special electromechanical or electronic controls.

High-strength alloys such as 2024 and 7075 are easy to resistance weld but may require

Table 15 Comparison of minimum alternating current requirement for mild steel and coated steels

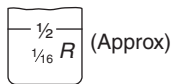
Welding speed, m/min	Minimum current for continuous weld plug(a)							
	0.75 mm mild steel	0.78 mm Al coated	0.75 mm terne (Pb/Sn)	0.85 mm hot dipped galvanized	0.78 mm electroplated zinc	0.88 mm iron-zinc	0.6 mm Galfan Zn-5% Al	0.7 mm Zalutite Zn-55% Al
2	4.75	10.75 (125)	9.75 (105)	9.25 (95)	7.75 (65)	11.0 (130)	9.0 (90)	10.75 (125)
4	6.0	10.5 (75)	10.5 (75)	10.5 (75)	8.5 (40)	11.0 (85)	10.5 (75)	10.5 (75)
6	6.5	10.5 (60)	13.0 (100)	11.75 (80)	9.5 (45)	11.25 (75)	11.0 (70)	10.75 (65)
8	7.25	11.0 (50)	13.5 (85)	12.75 (75)	11.0 (50)	12.5 (70)	11.0 (50)	10.75 (50)
10	7.75	11.5 (50)	13.75 (75)	14.5 (85)	12.5 (60)	13.5 (75)	11.5 (50)	11.5 (50)
Average increase in current compared to mild steel	kA	4.4	5.65	5.3	3.4	5.5	4.15	4.3
	%	70	90	80	50	80	65	75

(a) Values in parentheses refer to percentage increase compared to mild steel. Source: Ref 19

Table 16 Mash seam welding low-carbon steel with continuous current for pressure-tight joint

Thickness of each work piece (note 1, 3) in.	US gage	Electrode force, lbf	Initial overlap, in. (note 4)	Welding speed, in./min	Welding current (note 8)	Heat control range (note 7, 8)
0.021	25	600	0.031	160	10,500	70–90
0.030	22	900	0.046	130	13,000	70–90
0.036	20	1180	0.060	104	14,700	60–80
0.048	18	1500	0.075	80	16,000	50–70
0.060	16	1940	0.085	64	17,400	50–70
0.075	14	2500	0.097	55	19,000	45–60
0.090	13	3100	0.118	47	20,700	45–60

- Notes:
 1. Low-carbon steel is hot rolled, pickled, and lightly oiled. Ultimate strength is similar to steel (SAE 1005–1010) (42.5–45 ksi).
 2. Electrode material is RWMA class III. Electrode diameter from 8 to 12 in.



3. Surface of steel free from grease, scale, or dirt.
 4. Initial overlap must be closely controlled either by spot tacking prior to seam welding or by rigid clamping during seam welding.
 5. The final joint thickness will be about 150% of one sheet thickness.
 6. Degree of mashdown is equal on both sides.
 7. Phase-shift heat control range is recommended to attain the best weld quality and appearance.
 8. Since welder used on thicker materials must operate at phased-back current output, maximum full-wave current output of welder must be approximately twice that of the welding current shown.

applications of a forge pressure, because they are more susceptible to cracking and porosity than the lower-strength alloys.

Equipment. Best results in resistance welding of aluminum and its alloys are obtained by using a machine that has these features:

- Ability to handle high welding currents for short weld times
- Synchronous electronic controls for weld time and welding current
- Low-inertia welding head for rapid follow-up of electrode force
- Slope control (for single-phase welding machines)
- Multiple-electrode-force system to permit proper forging of the weld nugget and redressing of electrodes

Electrodes. Selection of electrode material and face shape, maintenance of the face, and cooling of the electrode are important in producing consistent spot and seam welds in aluminum alloys. The RWMA classes 1, 2, and 3 are used for welding aluminum alloys. These electrode materials have high electrical and thermal conductivities, which, combined with adequate cooling, help keep the temperature of the electrode below the temperature at which aluminum will alloy with copper and cause electrode pickup. Design of spot welding electrodes suitable for spot welding of aluminum includes both straight and offset electrodes. Straight electrodes should be used whenever possible, because deflection and skidding may occur with offset electrodes under

similar welding conditions. If offset electrodes are used, the amount of offset should be the minimum permitted by the shape of the assembly being welded. Electrodes should have the cooling-water hole within 9.5 mm (3/8 in.) of the face surface.

Copper and Its Alloys

Resistance spot welding is widely used for joining copper and copper alloys. Principal applications include welding sections up to approximately 1.50 mm (0.060 in.) thick, particularly those alloys with low electrical conductivities.

Many copper alloys with low conductivities can be seam welded easily. Coppers with a low weldability factor are difficult to seam weld. Projection welding is not recommended for copper or for most brasses. Bronzes can be projection welded with satisfactory results in many applications.

The resistance weldability of any copper alloy is inversely proportional to its electrical and thermal conductivities. Generally, alloys with lower conductivities are easier to weld. Compared with steel, most copper alloys require shorter weld time, lower electrode force, higher current, and different electrode materials that are compatible with the alloy being welded.

Welding Equipment. Single-phase and three-phase direct-energy and electrostatic stored-energy (capacitor-discharge) welding machines are used for resistance welding of copper and copper alloys. The addition of slope control to single-phase direct-energy welding

machines is not necessary for spot welding most copper alloys. In welding high-zinc brasses, the use of upslope can result in an increase of as much as 20% in weld strength. Downslope is not recommended for welding of any of the copper alloys.

Copper alloys are particularly sensitive to variations in welding conditions, and therefore, all direct-energy machines used for welding these alloys should be equipped with synchronous electronic controls, especially in applications requiring short weld times. These devices are capable of controlling weld time and welding current for repeated operations with extreme accuracy.

Electrodes. The current used for resistance welding of copper alloys is much higher than that used for welding low-carbon steel, and therefore, the electrode must have high electrical conductivity to minimize heat buildup. The RWMA class 1 electrode materials (typically tungsten or molybdenum alloys), containing copper and cadmium, are sometimes used for welding copper and high-conductivity brass and bronze. Class 2 materials, containing copper and chromium, are used on low-conductivity brass and bronze and the copper-nickel alloys. Class 3 materials are used in electrodes for seam welding.

Electrodes must be sufficiently water cooled to minimize sticking to the work metal and to prolong their life. Face contours must be carefully prepared, and the electrodes must be properly aligned for welding.

Coppers and copper alloys having electrical conductivity higher than approximately 30% IACS are the least well suited for resistance spot, projection, or seam welding, mainly because of severe electrode pickup.

Thin copper stock can be welded using electrodes faced with RWMA class 13 (tungsten) or class 14 (molybdenum), but surface appearance is poor and frequent electrode maintenance is required. A tinned coating on wire or sheet is helpful in welding copper.

Beryllium copper alloys can be resistance welded most successfully in thin gages. Spot welding produces satisfactory welds; seam welding is less successful. Projection welding is satisfactory, provided that the projections can be formed with the work metal in the annealed condition and without cracking the work metal around the projection. Close control of welding conditions is required for consistent weld size and joint strength.

Oxide films produced by heat treating must be removed to ensure low and consistent contact resistance. Work metals that have not been heated after rolling frequently need only degreasing before welding.

Low electrical conductivity (22% IACS for alloys C17000 and C17200) contributes to the weldability of beryllium copper alloys. However, they are more difficult to resistance weld than low-carbon steel. Alloy

Table 17 Melting ranges, electrical and thermal conductivities, and resistance weldability of common aluminum alloys

Wrought and casting alloys are identified by Aluminum Association designations.

Alloy and temper	Melting range		Electrical conductivity, %IACS(a)	Relative thermal conductivity(b),%	Resistance weldability(c)
	°C	°F			
Non-heat-treatable wrought aluminum alloys					
1350-H19	646–657	1195–1215	62	60	ST
1060-H18	646–657	1195–1215	61	57	ST
1100-H18	643–657	1190–1215	57	55	RW
3003-H18	643–654	1190–1210	40	39	RW
3004-H38	629–652	1165–1205	42	42	RW
5005-H38	632–652	1170–1205	52	51	RW
5050-H38	627–652	1160–1205	50	49	RW
5052-H38	593–649	1100–1200	35	35	RW
5083-H321	574–638	1065–1180	29	30	RW
5086-H34	584–640	1084–1184	31	32	RW
5154-H38	593–643	1100–1190	32	32	RW
5182-O	574–640	1065–1185	31	31	RW
5454-H34	602–646	1115–1195	34	34	RW
5456-H321	571–638	1060–1180	29	30	RW
Heat-treatable wrought aluminum alloys					
2014-T6	510–638	950–1180	40	39	ST
2024-T361	501–638	935–1180	30	31	ST
2036-T4	554–649	1030–1200	41	40	RW
2219-T37	543–643	1010–1190	28	29	ST
6009-T4	560–649	1040–1200	44	43	RW
6010-T4	585–649	1085–1200	39	38	RW
6061-T6	593–649	1100–1200	43	43	RW
6063-T6	615–654	1140–1210	53	51	RW
6101-T6	615–652	1140–1205	57	55	RW
7075-T6	477–638	890–1180	33	33	ST
Aluminum casting alloys					
413.0-F	574–582	1065–1080	31	32	LW
443.0-F	574–632	1065–1170	37	37	RW
308.0-F	521–613	970–1135	37	37	ST
238.0-F	507–599	945–1110	25	26	LW
513.0-F	579–638	1075–1180	34	34	ST
520.0-T4	449–604	840–1120	21	22	NR
333.0-T6	516–585	960–1085	29	30	ST
C355.0-T61	546–621	1015–1150	39	38	ST
356.0-T6	557–613	1035–1135	39	38	ST
712-F	604–643	1120–1190	40	39	RW

(a) International Annealed Copper Standard, volume basis at 20 °C (68 °F). For comparison, copper alloy 102 (oxygen-free copper) is 101% and low-carbon (1010) steel approximately 14%. (b) Based on copper alloy 102 as 100%, which has a thermal conductivity of 391 W/m · K (226 Btu/ft · h · °F) at 20 °C (68 °F). Low-carbon steel has a thermal conductivity of approximately 13% on this relative scale. (c) RW, readily weldable; ST, weldable in most applications but may require special techniques for specific applications; LW, limited weldability and usually requires special techniques; NR, welding not recommended

C17500 has an electrical conductivity of 45% IACS and is more difficult to resistance weld than higher-strength, lower-conductivity beryllium copper.

Low- and High-Zinc Brasses. The low-zinc brasses are difficult to weld, although easier than copper, and are subject to electrode pickup. Welds made in these brasses may lack strength, principally because of comparatively high electrical conductivity (32 to 56% IACS).

The high-zinc brasses have an electrical conductivity of 27 to 28% IACS and can be both spot and projection welded over a wide range of conditions. Electrode pickup can be a problem unless weld time, welding current, and electrode force are properly selected.

Excessive electrode pickup and blowthrough of the weld may occur when long weld times, high energy input, and low electrode forces are used. Yellow brasses (alloys C26800 and C27000) are less susceptible to electrode pickup than cartridge brass, except when long weld times and high energy input are used. Electrode force should be sufficient to prevent

arcng or expulsion of molten metal, to which these alloys are subject because of their 30 to 40% Zn content, which boils at approximately 905 °C (1665 °F). As shown in Table 18, the recommended electrode force, when using electrodes having a face diameter of 4.8 mm ($\frac{3}{16}$ in.), is approximately 1.8 kN (400 lbf).

Copper Nickels. The copper-nickel alloys have electrical conductivities of 4.5 to 11% IACS, are readily spot and seam welded with relatively low welding current, and generally do not alloy with the electrode material and cause electrode pickup.

Bronzes. The phosphor bronzes, except alloy C50500, which is not recommended for resistance spot and seam welding because of its high electrical conductivity (48% IACS), have relatively low electrical conductivity (11 to 20% IACS) and are readily spot and seam welded using low welding currents. Electrode pickup can be reduced by use of a type F (radius) electrode face and frequent redressing to keep the face clean and smooth. Hot shortness can be minimized by supporting the workpieces to prevent strain

during welding and by using a greater minimum overlap than recommended by the data in Table 19.

REFERENCES

1. *Resistance Welding Manual*, 3rd ed., Vol 1, Resistance Welder Manufacturers Association
2. *Resistance Welding—Theory and Use*, American Welding Society
3. T. Dupuy and D. Fardoux, “Spot Welding Zinc-Coated Steels with Medium-Frequency Direct Current,” Paper 1-2, SMWC IX, 2000
4. H. Zhang and J. Senkara, *Resistance Welding: Fundamentals and Applications*, 2nd ed., CRC/Taylor & Francis, 2011
5. P. Grimes, “Advantages of Using Servo Force Control When Resistance Welding Aluminum Sheet Metal,” Paper 6-2, SMWC XII, 2006
6. J.E. Gould, W. Peterson, and J. Cruz, “An Examination of Electric Servo-Guns for the Resistance Spot Welding of

Table 18 Guidelines for resistance spot welding of selected copper alloys

UNS No.	Alloy name	Weld time, cycles	Welding parameter(a)		Welding current, A
			Electrode force		
			kN	lbf	
C23000	Red brass	6	1.8	400	25,000
C24000	Low brass	6	1.8	400	24,000
C26000	Cartridge brass	4	1.8	400	25,000
C26800–C27000	Yellow brass	4	1.8	400	24,000
C28000	Muntz metal	4	1.8	400	21,000
C51000–C52400	Phosphor bronze	6	2.3	510	19,500
C62800	Aluminum bronze	4	2.3	510	21,000
C65100–C65500	Silicon bronze	6	1.8	400	16,500
C66700	Manganese brass	6	1.8	400	22,000
C68700	Aluminum brass	4	1.8	400	24,000
C69200	Silicon brass	6	2.3	510	22,000

(a) For spot welding 0.91 mm (0.036 in.) thick sheet using Resistance Welder Manufacturers Association (RWMA) type E electrodes with 4.8 mm (3/16 in.) diam face and 30° chamfer and made of RWMA class 1 material

Table 19 Guidelines for resistance spot welding of high-zinc brasses

Thickness of thinnest sheet		Minimum spot spacing		Minimum contacting overlap(a)		Shear load of joint	
mm	in.	mm	in.	mm	in.	kN	lbf
0.81	0.032	16	5/8	13	1/2	1.47	330
1.27	0.050	16	5/8	16	5/8	2.28	512
1.63	0.064	19	3/4	19	3/4	3.02	680
2.39	0.094	25	1	25	1	5.20	1168
3.18	0.125	38	1/2	32	1/4	8.33	1872

(a) Minimum edge distance is equal to one-half the contacting overlap.

11. R.M. Rivett and J.P. Hurley, "Weld Bonding of Zinc-Coated Sheet Steels," Paper A04, Proc. Sheet Metal Welding Conference IV, 1990
12. J.G. Kaiser, G.J. Dunn, and T.W. Eagar, The Effect of Electrical Resistance on Nugget Formation during Spot Welding, *Weld. J.*, Vol 61, 1982, p 167-s
13. J.E. Gould, M. Kimchi, C.A. Leffel, and D.W. Dickinson, "Resistance Seam Weldability of Coated Steels. Part I: Weldability Envelopes," Edison Weld. Inst. Res. Rep., No. MR9112, 1991
14. W. Li, "Monitoring and Diagnosis of Resistance Spot Welding Process," Ph.D. dissertation, University of Michigan, Ann Arbor, MI, 1999
15. C. Ma, D.L. Chen, S.D. Bhole, G. Boudreau, A. Lee, and E. Biro, Microstructure and Fracture Characteristics of Spot-Welded DP600 Steel, *Mater. Sci. Eng. A*, Vol 485, 2008, p 334–346
16. H. Zhang, Expulsion and Its Influence on Weld Quality, *Weld. J.*, Vol 78, 1999, p 373s
17. H. Zhang, J.S. Hu, J. Senkara, and S. Cheng, Statistical Analysis of Expulsion Limits in Resistance Spot Welding, *J. Manuf. Sci. Eng. (Trans. ASME)*, Vol 122, 2000, p 501
18. "Seam Welding Low-Carbon Steel and "Seam Welding Dissimilar Thicknesses of Low-Carbon Steel," Bulletin No. 23, Resistance Welder Manufacturers Association
19. N.T. Williams and W. Waddell, "High-Speed Resistance Seam Welding of Uncoated and Coated Steels," EUR 115550 EN, 1988

Complex Stack-Ups," Paper 5-6, SMWC XIV, 2010

7. J. Senkara, H. Zhang, and S.J. Hu, Expulsion Prediction in Resistance Spot Welding, *Weld. J.*, Vol 83 (No. 4), 2004, p 123-s to 132-s
8. H. Tang, W. Hou, S.J. Hu, and H. Zhang, Influence of Machine Mechanical Characteristics on RSW Process and Weld Quality, *Weld. J.*, Vol 82 (No. 5), 2003, p 116-s to 124-s

9. "Recommended Practices for Test Methods for Evaluating the Resistance Spot Welding Behavior of Automotive Sheet Steel Materials," AWS D8.9, draft, American Welding Society, Miami, FL, 2005
10. M.J. Karagoulis, "Control of Materials Processing Variables in Production Resistance Spot Welding," Paper B5, Proc. AWS Sheet Metal Welding Conf. V (Detroit, MI), 1992

Evaluation and Quality Control of Resistance-Welded Joints

Hongyan Zhang, University of Toledo

EVALUATING THE QUALITY of resistance welds is unique in several aspects. Unlike in fusion welding, where the joint is exposed and therefore can be visually inspected, a resistance weld is formed between two sheets. In the case of resistance spot welds, the geometric characteristic annular notch makes it a natural stress raiser in the edge of the weld nugget at the faying interfaces. Under loading, the stress concentration due to the geometry can promote cracking near the nugget, either in the heat-affected zone, which often results in a weld pullout, or along the original faying interface for an interfacial failure. The load-bearing capability of a resistance weld depends on the material, including the chemistry, strength, and sheet thickness, and the loading mode. In addition to the strength, other features of a weld, such as indentation depth, surface quality, and so on, are also considered as the quality attributes of a weld. The multifaceted nature of weld quality results in a large variety of quality definitions of spot welds, based on various aspects of the manufacturers' needs by the sheet metal industry and professional organizations.

The commonly used quality attributes, testing methods, and quality-control strategies in resistance spot welding are discussed in this article. First, some structural attributes of spot welds are presented. Commonly performed destructive and nondestructive evaluation methods also are presented in this article. Destructive evaluation is commonly conducted for both welding schedule development and quality assurance, where a certain percentage of the assembled parts are destructively tested in a manufacturing process. It has the advantages of being reliable and simple to perform, but the destroyed components generally cannot be reused, which represents a manufacturing cost. Nondestructive evaluation, on the other hand, can overcome the shortcomings of destructive evaluation methods, but the complexity and high cost of the testing devices and the skills required to perform such tests make it less attractive than it should be.

The quality of resistance welds also can be evaluated either during a welding process or after a weld is made. The in-process evaluation involves collecting process signals, and it has certain advantages, such as being nondestructive in general. The process signals, once they are correlated with weld quality, can be used to monitor a welding process. The controllable welding parameters, such as electric current, electrode force, and welding time, can be adjusted in a welding cycle to produce a quality weld. The off-line approach, on the other hand, is relatively easier to implement and therefore is more prevalent in practice, typically by destructive testing of the weld.

Quality Attributes of Resistance Welds

In this section, the structural attributes of spot welds are presented first. Some of them are purely cosmetic, and others have implications on the weld strength and hence its performance. The weld strength is measured through destructive testing, and the strengths of spot welds gathered from published works are compared for selected materials and tests. It is also attempted to correlate easily measurable weld geometric attributes with weld strength to form

the basis of using such attributes for weld quality. The industrial requirements for weld quality are presented at the end of this section.

Structural Attributes

A weld's quality is often described by its structural characteristic. Some of the structural attributes of a weld can be measured externally, and others can be revealed through destructive testing only.

Spot Welds. A spot weld contains a number of distinctive regions, as shown in Fig. 1.

Weld Nugget. In this region, the metal melts during heating and solidifies when the electric current is shut off. The microstructure of the nugget is more like that of a casting than of a rolled sheet, because it does not experience any cold work.

Heat-Affected Zone (HAZ). This region is adjacent to the weld nugget, in which the highest temperature during welding is below the melting temperature of the metallic grains, so they stay as a solid in the course of welding. However, certain solid-phase reactions may occur in this region, which may alter the structure and strength of this region. In addition, the region of the HAZ adjacent to the fusion line may experience grain-boundary melting, and it is termed the partial-melting zone.

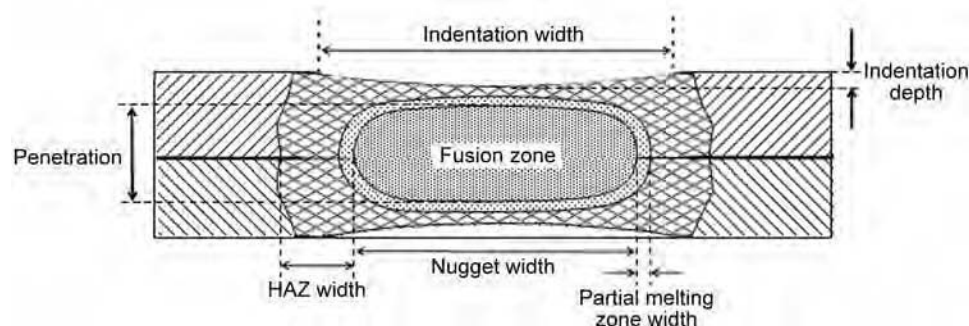


Fig. 1 Schematic of a spot weld. HAZ, heat-affected zone

Partial-Melting Zone. Although the temperature in the HAZ does not reach the melting temperature of the crystals of the metal, certain low-melting compounds at the grain boundaries may melt during welding. This region may exist in some metals and affect the structural integrity, such as in welding many aluminum and magnesium alloys. It may have minimal effect in welding most steels, if it even exists.

Base metal is the portion of a weld that does not experience metallurgical changes. The base metal adjacent to the HAZ is also influenced by the plastic deformation in the nugget and HAZ, and the base metal could be distorted. Such a distortion may affect the loading mode, and it also indicates the level of residual stresses in the weld.

Indentation Width and Depth. Because a weld indentation is directly related to the heating process and therefore the nugget formation, it is the most indicative index of weld quality that can be obtained without sectioning the weld or using nondestructive devices. As a matter of fact, many industrial companies have specific requirements for indentation in both width and depth. The indentation width is related to the area of heating or weld size, and its depth is a strong function of weld penetration. Because the indentation is a result of joule heating, its volume, approximated as a (hollow) cylinder, is related to total heat input and is used to measure the dimensions of the weld nugget. In certain cases, indentation has been successfully correlated with nugget size and weld strength. However, the correlation is strongly affected by material and processing factors, such as electrode cap size and shape. Therefore, it is still considered a qualitative measure of weld quality, and experience plays an important role in its use for quality measurement.

Typical Imperfections in Resistance Welds. Certain weld imperfections can be revealed directly by inspecting a weld externally. The commonly inspected imperfections are listed as follows, based on the observations of welding practitioners and researchers and on many resistance-welding-related standards and recommendations, such as AWS D8.7 (Ref 1):

1. Surface defects, including holes, cracks, and craters
2. Surface expulsion
3. Surface colorization
4. Excessive indentation
5. Excessive sheet separation and distortion
6. Edge weld
7. Insufficient weld spacing
8. Mislocated weld
9. Overlapped welds
10. Edge tears (only in seam welds)

Note that some of the listed imperfections are pertinent only to resistance spot welds and not seam welds. Seam welds, in most cases, tend to be continuous welds. For example, items 4, 7, and 9 are some of the attributes that generally pertain to spot welds.

A surface free of visible defects is always a requirement. Surface defects include cracks, burning holes, craters, and others abnormalities such as excessive indentation and so on. If the extent of these defects is limited to the surface only, they may have negligible effect on the strength. However, these defects very often are associated with internal defects and inferior weld nugget. For instance, the burning hole and the debris or whiskers shown in Fig. 2 are the result of localized overheating of the electrode-sheet contact interface, possibly due to the large contact resistance resulting from electrode deterioration. The adverse effects of these defects on weld quality are unquestionable. However, the influence of some surface defects may not be as obvious. The weld shown in Fig. 3(a) has fine surface cracks, and they appear to be insignificant. A cross section of the same weld, however, shows cracks extending through the thickness of the weld (Fig. 3b). In general, surface defects should be treated with care, understanding the possible existence of associated internal defects.

When the contact resistance at the electrode-sheet interface is high, excessive heating at the interface may melt the metal, which may be ejected under the electrode pressure. One example is shown in Fig. 4 (Ref 2). Similar to other surface defects, if such expulsion is limited to the surface, it may have little or no effect on weld strength. However, such an expulsion may be linked to other defects, for instance, a burning hole, as shown in the figure. Overheating related to surface expulsion is also the primary reason for electrode deterioration. Another sign of surface overheating is colorization of the weld surface. The temperature at the electrode-sheet interface is so high that the electrode surface is melted, leaving a trace of copper alloy on the surface of a weld. Because this is the result of melting of the electrode surface, rapid electrode wear may follow.

A weld can be severely distorted when the workpieces are improperly stacked and/or excessive heating or electrode force is applied. If a large gap exists between the sheets before welding, the sheets must be deformed by the electrodes to create the necessary contact at the faying interface for welding. Such a deformation is often aided by softening of the sheet material during heating. Even without poor fit-up of the sheets, a large electrode force or overheating may press the metal between the electrodes and force it to flow to the edges of the nugget around the faying interface. The distortion of spot welds is not a major concern from a cosmetic point of view if the weld is not located on the outer panel of a product such as an automobile. However, it has a quality implication in weld strength and overall dimensional stability. It may alter the loading mode of the weld and create a stress concentration that may not be anticipated. A severely distorted weld may significantly reduce the thickness of the metal that links the weld and the base metal and compromise the load-bearing

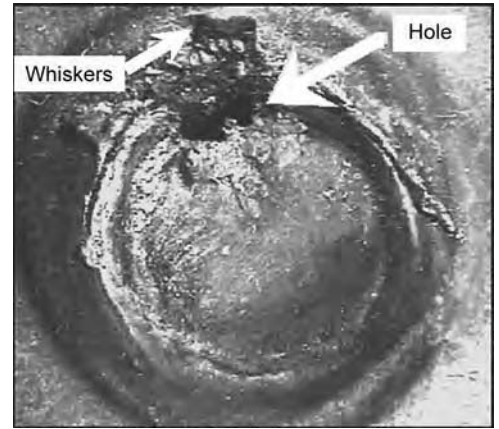


Fig. 2 Burning hole on the surface of a steel weld. Source: Ref 1

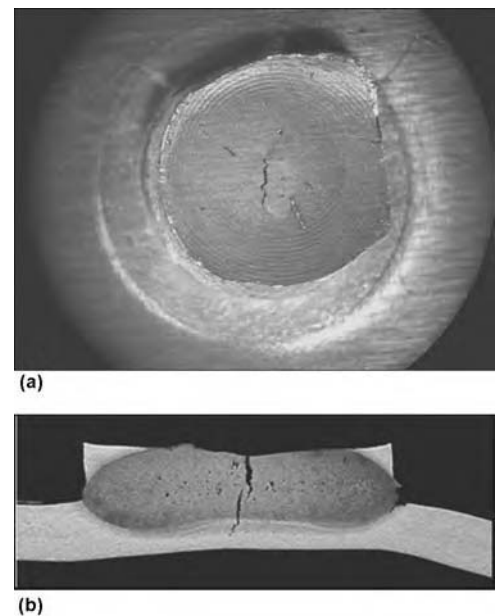


Fig. 3 Views of an AA6111 weld. (a) Top view of a peeled weld button. (b) Cross section of the same weld

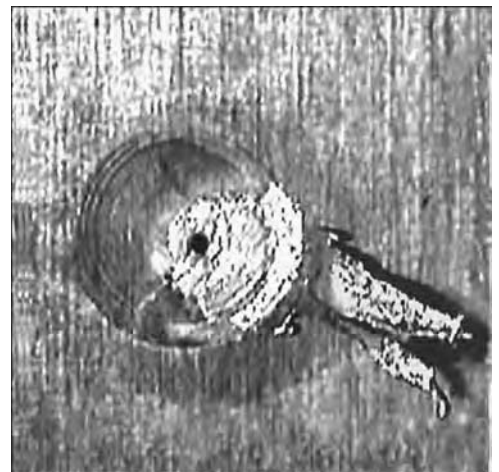


Fig. 4 Surface expulsion of an AA5754 weld. Source: Ref 2

capacity of the weld. In addition, the local distortions of individual welds may be accumulated and result in an out-of-specification structural component. There are significant efforts to reduce or control spot weld distortion to maintain dimensional stability of welded structures (Ref 3–5).

There are a number of quality attributes mainly related to design, maintenance, and execution of welding. If a weld is made too close to the edge of sheets, such as in the case of insufficient flange width, an edge weld may result (Fig. 5) in which the liquid metal is squeezed out to the edge of the sheets. Figure 6 shows welds made with insufficient spacing between the welds. The weld on the right was made after that on the left, using the same welding parameters, but its indentation is clearly smaller and shallower than that of the first weld. When making the second weld, part of the electric current is diverted by the first weld through a process called shunting, which effectively reduces the heat input in the second weld (Ref 6). Special attention is needed when performing weld repair in which insufficient weld spacing may be unavoidable. Higher electric current should be applied when adding a

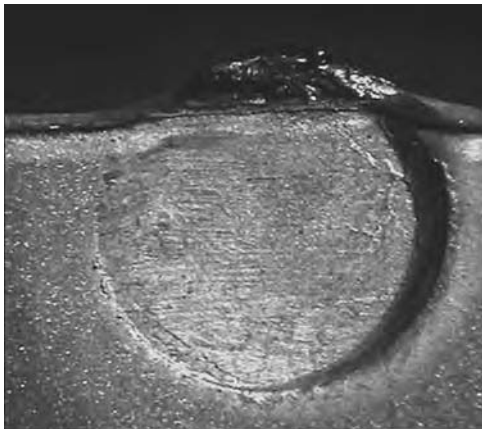


Fig. 5 Edge weld. Source: Ref 1

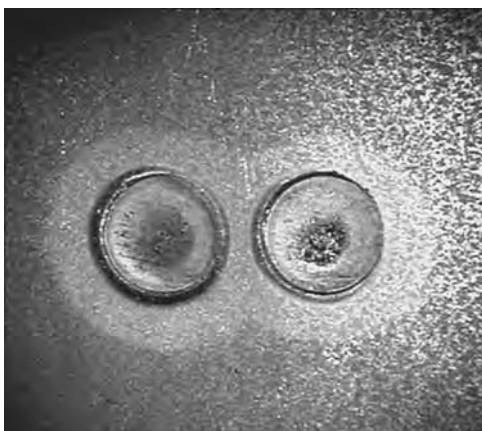


Fig. 6 Welds with insufficient spacing. Source: Ref 1

weld close to an existing weld. Welds may also be made at locations different from their designated places, and a malfunctioning welding robot may put two welds on top of each other, resulting in dislocated welds and overlapped welds.

Internal Characteristics. The internal characteristics of spot welds are usually revealed through metallographic examination of the weld cross section. The geometry and dimensions of various zones of spot welds are schematically shown in Fig. 1. The fusion zone is characterized by the nugget width and penetration. The nugget width may be different from the weld diameter, depending on the weld quality and testing method. The HAZ can be divided into two parts: a zone of solid-phase transformation near the base metal, and a partial-melting zone. It is beneficial to separate the partial-melting zone from the rest of the HAZ, because the metallurgical reactions in this zone are usually significantly different from those in the rest of the HAZ, and the implication for structure as well as weld quality should not be ignored. For instance, in welding aluminum alloy AA5754, it was found that liquation cracking may initiate from the molten grain boundaries in the HAZ next to the fusion zone, as seen in Fig. 7 (Ref 7).

In general, the following information can be obtained through metallographic examination of a spot-welded joint:

- Dimensions of various zones of a spot weld. These include the nugget width and height (penetration), width of the HAZ, and the extent of a possible partial-melting zone in the HAZ.
- Microstructures and phases of the regions. Because of the drastically different processing conditions of the base metal, the HAZ, and the nugget, their structures as well as properties can be significantly different.

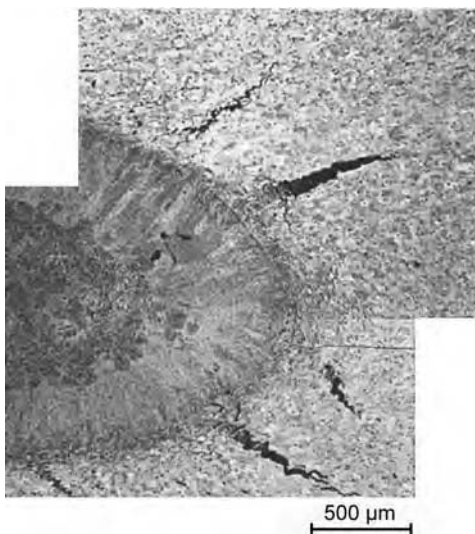


Fig. 7 Cracking in the heat-affected zone of an AA5754 weld near the fusion line. Source: Ref 7

- Discontinuities or imperfections. Solidification cracks and voids/pores may form in the nugget, and liquation cracking may occur in the partial-melting zone in the HAZ.
- Interfacial expulsion

The nugget, depicted as the fusion zone in Fig. 1, is clearly the most important part of a weld. Its geometry is usually described by the nugget width and penetration. Because a spot weld nugget is the joint that links the sheets, a large nugget width is preferred for load bearing. In addition, the height of the nugget, or penetration, is a direct indicator of the amount of heating, and therefore, a certain amount of penetration is required by most manufacturers. In most research on the strength of spot welds, the nugget size, or weld size, is linked to the load-bearing capability and other strength attributes, such as ductility. Because the formation of a weld nugget involves melting and solidification, defects such as liquation cracking and voids/pores may form in the nugget, in addition to significantly different microstructures from the HAZ and the base metal. In Fig. 8 (Ref 8), metallographic examination of a 590 MPa (85 ksi) dual-phase steel weld reveals a sizeable void as well as pores in the weld nugget. These are the direct result of a volume deficit caused by irreversible expansion and contraction during melting and solidification of the weld, due to expulsion, as evidenced by the remnants of the ejected and solidified metal at the faying interface near the nugget. There are also surface cracks, and one of them extends into and is connected with a pore in the nugget, through the HAZ along the grain boundaries. The structures of the weld nugget and the HAZ are significantly different from that of the base metal, as shown in the figure, and result from solidification and solid-phase transformations in the weld. The two typical phases, ferrite (body-centered cubic) and martensite (body-centered tetragonal), are observed in all of the regions. However, their morphologies, amounts, and distributions are drastically different. In the base metal, martensite is evenly distributed in a matrix of ferrite. The HAZ has more martensite, with its volume fraction increasing rapidly from the base metal to the fusion line, and the fusion zone is filled with martensite. Finer martensite and ferrite are observed in the HAZ, resulting from the repeated rapid heating-cooling cycles and the restricted grain growth in the region, as explained by the authors of Ref 8. Retained austenite and lower bainite are also observed in the region. In addition to the favorable chemistry for martensite formation in 590 dual-phase steel, the rapid cooling during resistance spot welding, estimated at a few thousands of degrees Celsius per second, plays an important role.

In addition to the structural difference in the HAZ from the base metal or the nugget, the unique location of the HAZ makes it an

influential factor in determining weld strength. Due to the characteristic geometry of a sharp notch near the nugget at the faying interfaces, a stress concentration may occur in the HAZ when a weld is loaded. The different material properties, such as yield strength and so on, in the HAZ from those in the nugget and base metal may enhance the stress concentration. As analyzed by Zhang and Senkara through finite-element modeling (Ref 6), the mechanical properties of the HAZ determine the performance of a weld. By varying the size, yield strength, ultimate tensile strength, and ductility of the nugget and HAZ of a weld, it was found that both the peak load and elongation of a weld increase with the nugget size, while changing the ductility and strength of the nugget has little effect. This can be primarily attributed to the fact that when loaded, the interior of a nugget is little stressed. On the other hand, the performance of a weld is very sensitive to the changes in the HAZ. Significant increases in peak load and elongation of a weld result from increases in the HAZ width, strength, and ductility.

Imperfections may also appear in the HAZ of a spot weld. Figure 9 (Ref 9) shows liquation cracking in the HAZ of a magnesium alloy AZ31D weld. The intergranular characteristics of the crack are the result of melting of intermetallic compounds such as $Mg_{17}Al_{12}$ at the grain boundaries. When the volume fraction of such low-melting compounds is sufficiently high, a network of liquid phases may exist in the HAZ surrounding the solid grains. Under thermal stresses during heating and cooling, the HAZ may be torn apart along such liquid grain boundaries. This has been observed in a number

of material systems, such as AA5754, AA6111 (Ref 10), AZ31B, and AZ91D (Ref 11).

Welding with expulsion is common on many production lines, because it is often used as an indicator of sufficient heating during welding. However, the loss of liquid metal during expulsion may create internal imperfections such as voids and cracks. In Fig. 10, large voids resulted from heavy expulsion in an AA5754 weld. There are several theories for the mechanisms of expulsion, and they are discussed in the book by Zhang and Senkara (Ref 12). The root cause of expulsion is the loss of containment of the liquid metal in the nugget, which imposes a large pressure onto its solid surrounding, that is, the HAZ. Because the pressure results from melting and thermal expansion of liquid metal, different materials have different tendencies for expulsion, due to their different thermal characteristics. Welding of aluminum and magnesium alloys is more prone to expulsion because of their higher volume expansion during melting than steels. As discussed by Zhang and others (Ref 2, 12), expulsion has an adverse effect on weld strength and should be avoided. Increasing the electrode force and lowering the welding current are two methods of suppressing expulsion.

Quality Requirements

Because the quality of spot welds is evaluated by their structural attributes and/or strengths in various tests, the requirements for weld quality are generally based on these two aspects as well. Almost all quality requirements, either by industrial companies or

professional organizations, contain certain provisions for weld size. An obvious advantage of using weld size as a required quantity is the close relationship between weld size and strength. Other geometric characteristics, such as penetration and so on, also appear as required weld attributes in various standards and recommendations. Because a weld is made for joining sheets together, a more meaningful weld-quality index is weld strength. However, the complexity in testing a welded joint and the large variance often associated with the testing results prevent the frequent performance of most types of tests, and only the peak load measured in a tensile-shear test is required for certain materials. In general, the measured strength of a weld, such as the peak load, is a function of the testing method and testing specimen geometry, in addition to the type of loading.

Destructive Testing

The quality of the weld is assessed by several quantitative and qualitative metrics from mechanical testing and/or by metallographic examination. Both techniques are destructive. In metallography, the weldment is sectioned for examination with a microscope. In mechanical testing, the weldment is loaded until the specimen fails.

Mechanical testing may be done manually or by mechanical loading with an instrumented device. In a manual test, the weld features, such as the weld shape and size, failure mode, and so on, are recorded. An instrumented test also

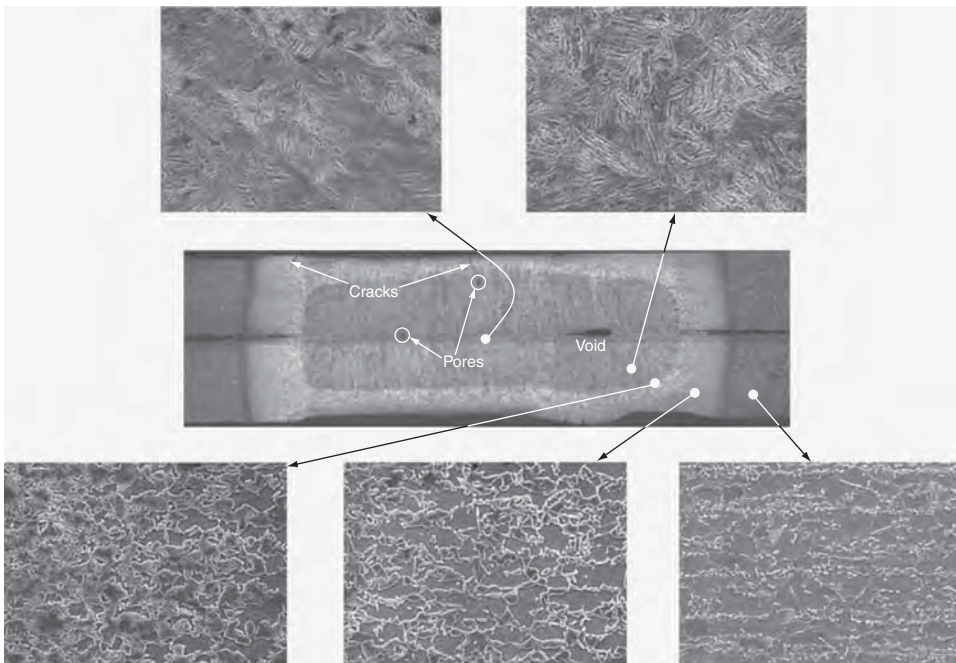


Fig. 8 Cross section and microstructures of a DP600 spot weld. Source: Ref 8

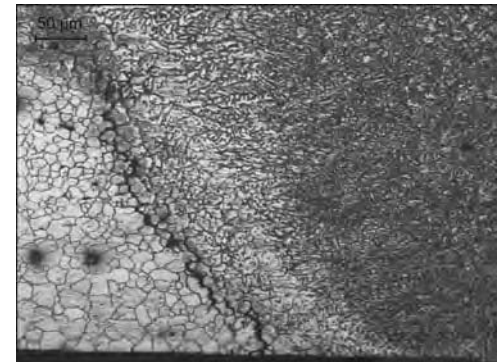


Fig. 9 Cracking in the heat-affected zone of an AZ31D spot weld. Source: Ref 9



Fig. 10 AA5754 weld with expulsion. Source: Ref 2

creates quantitative measures of weld strength, in addition to the observations from a manual test. Instrumented testing is necessary to quantitatively characterize weld strength.

Instrumented mechanical tests also can be classified into two groups: quasi-static tests and dynamic tests. In a quasi-static test, the load is applied slowly to minimize the influence of the load rate. In a dynamic test, the load rate is a process variable that is reported with the testing results. The load and displacement signals are commonly recorded for an instrumented test.

Manual Testing

Because weld size, shape, and failure mode revealed through a manual test are closely related to weld strength, manual testing is prevalent in both the production environment and laboratories. The commonly performed tests are:

- Chisel test
- Peel (roller) test
- Bend test
- Temperature monitoring of a seam weld

As illustrated in Fig. 11 for a chisel test, a chisel is forced into the gap at the faying interface between two adjacent welds until the weld fractures, which results in either a weld button or interfacial failure. This type of test is commonly performed on welded components when a peel test is impractical. Because of the constraint imposed by the neighboring welds, the load exerted by a chisel favors interfacial fracture rather than weld pullout. Therefore, an interfacial fracture obtained in a chisel test does not necessarily imply a substandard weld. An operator must be able to distinguish a

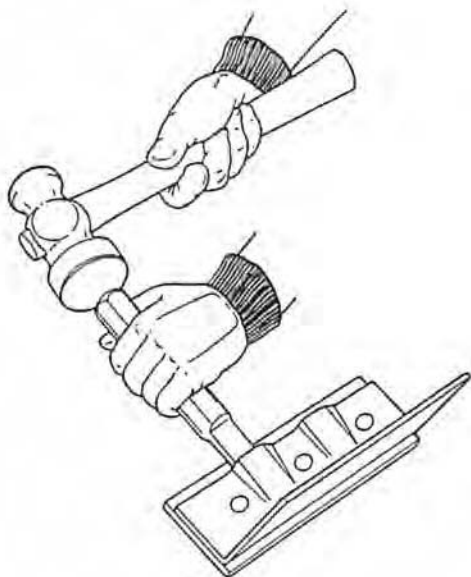


Fig. 11 Chisel test. Source: Ref 1

reasonable weld from a cold weld when an interfacial fracture mode is observed. Occasionally, a mechanized rather than a manual chisel test is performed in the production environment, especially when heavy-gage sheet welding is involved.

Another shop floor test is the peel test. It is usually performed using a hand tool, as shown in Fig. 12, and therefore, it is generally not applied to testing welds made on heavy-gage sheets. With one of the separated sheets gripped firmly, the other is rolled up to break the joint, either along the faying interfaces for a brittle weld, or leaving a weld button, usually on the gripped sheet. The fracture is recorded for the weld size, fracture mode, and so on. Certain experience is also required in performing a peel test, especially for the consistency of testing. Because the sheet must be rolled in the test, thick-gage or hard metals cannot be tested due to their high bending resistance.

A not-so-common manual test is the bend test. It is used to estimate the ductility of spot welds and to detect weld flaws, especially cracks. In the test, a section of three welds on a weld coupon is made by cutting from the center of the coupon along the longitudinal direction (Fig. 13). The specimen is bent to a certain angle and examined for cracks and other defects. The bend test is unique because the stress states in the weldment cannot be produced in other tests. Because the specimen is not uniform and the preparation process may not be consistent, a bend test is usually performed for visual inspection of weld quality only.

In the case of seam welds, an optical pyrometer is used to measure the temperature of the solidifying weld behind the welding electrode. A relationship between weld quality and measured temperature is established with trials. Generally, a temperature lower than an established optimal temperature is indicative of a cold weld, which results in poor fusion.

Generally, in all the tests, a load exerts certain crack-promoting stresses, either shear or tensile, on the nugget and HAZ of a spot weldment. The initiation and propagation of cracking depend on the stress level at a specific location and the material strength at the same location. The possible failure modes commonly observed in peel testing, along with the

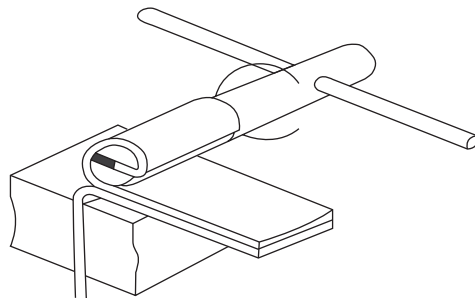


Fig. 12 Peel test. Source: Ref 1

evaluation procedure, are summarized in a chart in Fig. 14 (Ref 13). Although the failure modes are obtained in peel testing of spot welds, they are representative and contain all the typical observations for destructive evaluations. The quality interpretation of an interfacial fracture is often confusing. Certain tests and materials, such as impact testing and thick/stiff sheets, tend to produce interfacial failure even on a sound weld. As outlined in the figure, welds that fail with interfacial (including partial interfacial) fracture should be considered acceptable if there is fusion in the fractured weld area, with a size meeting the minimum weld requirements.

Quasi-Static Mechanical Tests

It is often desirable to generate uniform pure tensile or pure shear loading in material testing. In testing a spot-welded joint, however, such mode of loading is difficult to achieve because of the geometric characteristics of a spot-welded joint and the deformation/rotation of the specimens during testing. Various tests have been performed to measure the tensile, shear, or combined tensile and shear load-bearing capacity of spot welds. A more detailed description of the weld tensile tests is provided in the article "Resistance Spot Welding" in this Volume.

Cross-Tension Test. This test is intended to exert a normal tensile load to a weld. The specimen geometry and a typical mounting fixture are shown in Fig. 15 (Ref 14). Slippage of the specimen in the holding fixture may occur, and it changes the loading on the joint. Caution is also needed to minimize sheet distortion during testing. In addition, it may be difficult to prepare such a specimen with the weld properly

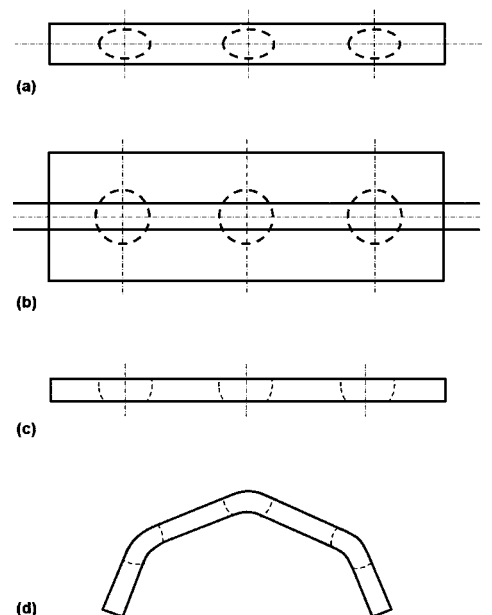


Fig. 13 Bend test. Source: Ref 12

**Resistance Spot Welding
peel test assessment flowchart**
Step 1. Perform peel test
Step 2. Measure fusion/button size.

Notes:

- (a) Weld size is greater than or equal to the minimum values specified.
- (b) Aspect ratio of the maximum dimension to the minimum dimension is less than 2 to one.
- (c) Measured in accordance with AWS D8.9
- (d) Measured dimension of fused area is greater than or equal to the minimum weld size specified.
- (e) Evidence of metal deformation due to the existence of a weld
- (f) Average diameter of through-sheet button plus partial thickness fracture is greater than or equal to the minimum weld size specified.

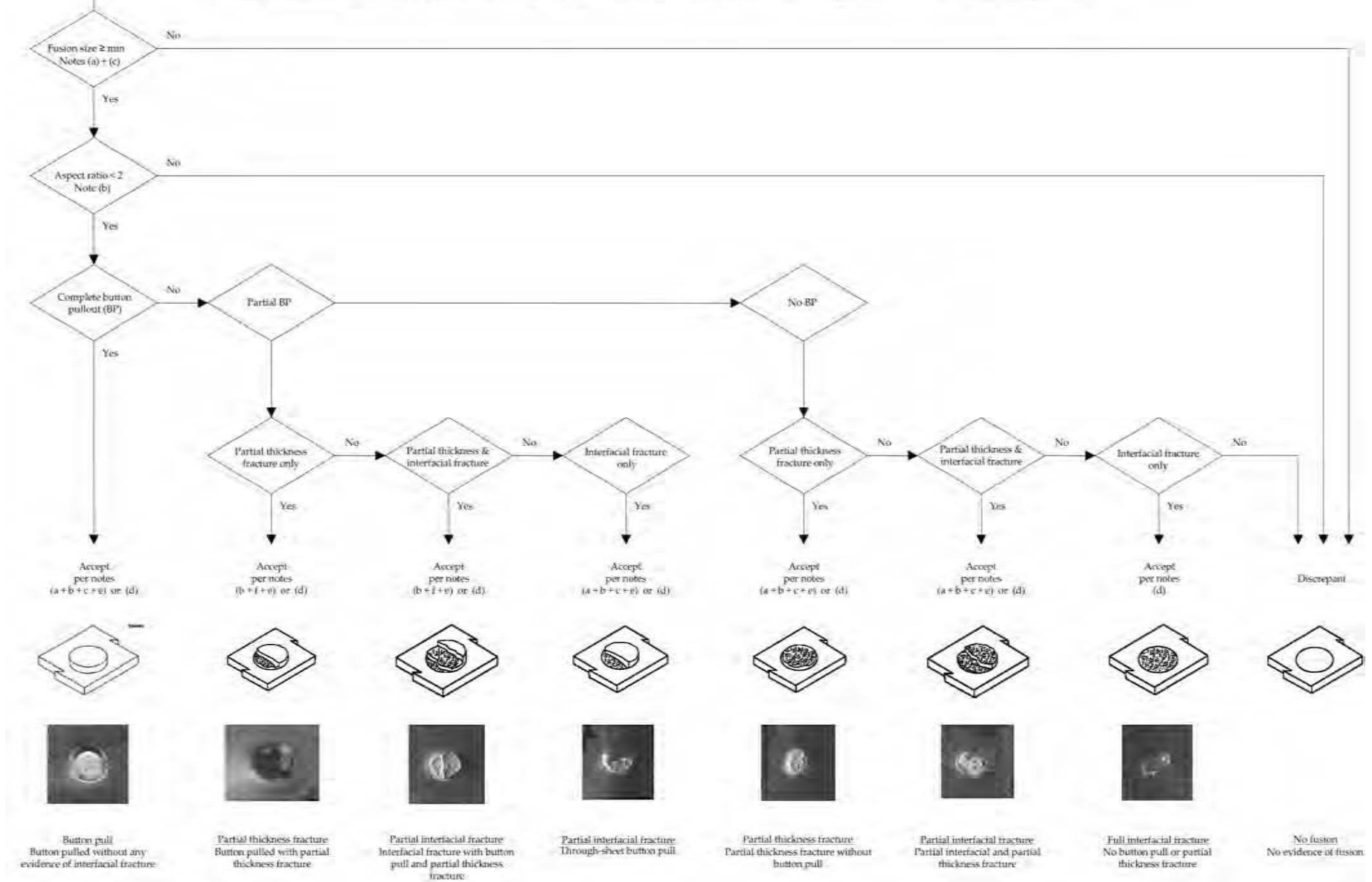


Fig. 14 Weld-quality assessment flow chart. Source: Ref 13

centered. The loading mode is altered if welds are not located at their designated locations, and the testing consistency may suffer as well.

U-Tension Test. A tensile load may be applied using a U-shaped specimen (Fig. 16). Such a specimen may create less deformation or distortion than that in a cross-tension test. Mounting a U-tension test specimen requires alignment of the hole/bolt, and spacers are generally needed to restrain a specimen. Certain formability is needed on the sheet material for it to be bent to the required radius without fracture.

In both cross-tension and U-tension tests, the specimen experiences unavoidable bending in the base metal during loading, which makes an accurate measurement of the weld tensile strength difficult. The low testing consistency, difficult mounting, and tedious specimen preparation make these tensile tests less popular than others, such as the tensile-shear test.

Tensile-Shear Test. Also commonly referred to as a tension-shear test, a tensile-shear test is the most commonly conducted test in weldability study. Compared with cross-tension and U-tension, the tensile-shear test has several advantages in specimen preparation and testing. A simple lap joint of two metal strips by a

single spot weld (Fig. 17), or occasionally by two or more welds, can be tested using standard tensile testing machines and grips. Because of the asymmetric nature of the testing specimens, bending of the base metal at the grips and rotation of the joint cannot be avoided during a tensile-shear test. This significantly affects the loading on the joint. An increasing portion of pulling load, and therefore a smaller portion of shear load, corresponds to the rotation of the joint. For specimens made of thick sheets, shimming is needed to avoid excessive bending of the base metal and the weld. Numerous studies, such as the one by Zhou et al. (Ref 15), have concluded that sufficiently wide specimens are required to minimize the influence from weld rotation. Their study also proved that a weld coupon length of 150 mm (6 in.) is sufficient for thin-sheet specimens.

In tensile-shear testing, the peak load is commonly monitored and used as the strength of the weld. A more complete description of weld quality needs information on the ductility of the joint, which can be described by the maximum displacement or the energy.

Combined Tension and Shear Test. Although the tensile and shear tests are intended to create tensile and shear loading modes, respectively, the actual loading is almost always a mixture of these two types of loads, in an uncontrollable manner. Efforts by Lee et al. have been made to purposely create a combined tensile and shear loading mode (Ref 16). In their study, simultaneous tensile and shear loadings can be applied, with control of the ratio of the two by varying the loading angle to the weld plane, as shown in Fig. 18 (Ref 16). There are pairs of holes on the lock plates that can be used to adjust the loading angles and create various mixtures of tensile and shear loadings. Similar to other tests, the weld should be centered with respect to the

mounting fixture to achieve the desirable loading mode. The testing mechanism shown in Fig. 18 has the flexibility of adjusting the location of the weld in the fixture by adding shimming plates of necessary thickness in the grips. By using this testing rig, it was found that the peak load a spot weld can withstand decreases with increase of the tensile component in a mixed tensile and shear loading, and the lowest strength was obtained when cross-tension loading was applied.

A less commonly conducted test on spot welds is the torsion test. Two types of torsional loading can be applied to a spot weldment. One is twisting a standard tension test specimen in which the angle of twist at failure is measured for the strength, in addition to the weld diameter and failure mode. Another so-called torsional shear test measures both strength and ductility through the ultimate torque required and the angle to destruction. In both tests, the weld diameter can be measured on separated sheets. The main drawback of a torsion test is the mounting of a specimen. To avoid excessive distortion, which is highly possible in a torsion test, a specimen must be tightly constrained. More details can be found in Ref 12.

Dynamic Mechanical Tests

Spot-welded joints in structures such as automobiles are generally under dynamic loading in service. Similar to that observed in testing of uniform specimens without a welded joint, the static strength of spot welds has certain implications for their dynamic performance, but there is no one-to-one correspondence, and extrapolation from static performance to dynamic behavior of spot welds could be erroneous and misleading. Dynamic testing of spot welds generally refers to fatigue tests in practice. Impact testing, which has significant implication for the crash-worthiness of automobiles, is rarely conducted on spot welds because of the complexity and low repeatability involved in the test. It has occasionally been conducted on welded structures (Ref 17).

Fatigue Tests. Vibration in welded structures, such as automobiles, imposes repetitive loading to the welded joints, and the process is called fatigue. The notchlike shape of a spot-welded joint makes it a stress raiser, which is undesirable for any mechanical loading, especially fatigue. The fatigue behavior of a spot-welded joint has several unique characteristics compared with other tests:

- Under small loading, failure may occur only after a large number of loading cycles.

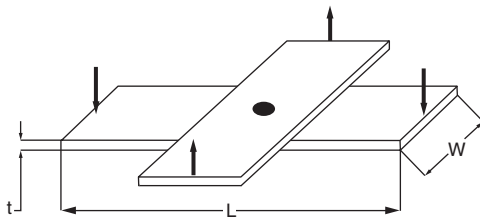


Fig. 15 Specimen and mounting fixture for a cross-tension test. Source: Ref 14

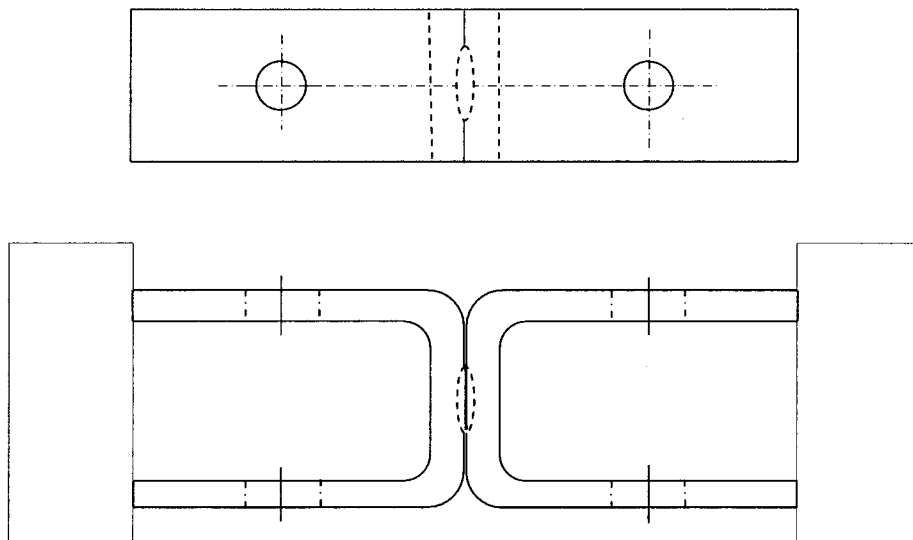


Fig. 16 U-tension test specimen. Source: Ref 1



Fig. 17 Tensile-shear test

- The failure loads are significantly lower than the static loading limits, which should be fully accounted for in structural design.
- A fracture surface usually has a brittle appearance; even static testing of the same weld renders a ductile appearance.

In practice, fatigue tests are usually conducted under constant loading ranges for simplicity. A number of factors must be taken into consideration, and certain precautions must be made in fatigue testing of spot welds. Standards and recommendations, such as the ISO standard for fatigue tests (Ref 18), which outlines the steps for fatigue testing of spot-welded joints, can be followed in testing. A common practice is to follow the ASTM International standards for fatigue testing of welded specimens (Ref 19). There are several issues that may affect the interpretation of fatigue testing and results, and they are discussed in the following.

Stress Concentration. Both the notchlike geometry around the edge of a weld nugget and the distributed strength in a weldment contribute to the stress concentration at a spot-welded joint. When loaded, the stress level at the notch can be several orders higher than at locations of a certain distance from the weld. A stress concentration, or even a singularity, exists at the vicinity of the weld. Stress distribution is also a strong function of material strength, which varies (often drastically) from the base metal to the nugget, as exhibited by the microhardness profiles in a weldment. Because a softer material would deform more than a harder one, given all conditions being equal, the stress level rises at the junction between these two parts. Similar phenomena are observed in a weldment.

Residual stresses are inevitable in a resistance spot weldment because of irreversible thermomechanical deformation during welding. There are three important aspects of residual stresses in characterizing stress distribution and understanding the effect of such stresses. The effect of residual stresses on the fatigue behavior of a spot weldment must be understood by considering the nature, amplitude, and location of the stresses. As in other types of loading, the nugget edge and the HAZ have the highest stress concentration, and the tensile residual stresses at these locations promote crack initiation and propagation, as observed by many researchers in fatigue testing. The residual stresses in a spot weldment are affected by many welding process-related factors. For instance, excessive heating induces large distortion and therefore high stresses. A properly constrained welding process, as discussed in Ref 10 and 12, can effectively minimize the distortion as well as residual stresses.

Specimen Preparation. Because of its simplicity, lap joint specimens are usually used in fatigue tests. However, a lap joint specimen can take very little compression without buckling. Care must be taken in selecting fatigue loading in accordance with the testing specimens. The ASTM International standards for fatigue testing of welded specimens (Ref 19) should be followed in preparing the specimens. Different-sized specimens impose different degrees of constraint onto the spot weld and affect deformation under loading. Therefore, the fatigue failure mode is a function of the specimen dimensions, similar to that observed in quasi-static tensile testing.

Loading. In fatigue testing of spot-welded joints, the loading can be force or moment.

There are a number of variables to be selected for a fatigue test: amplitude and range of loading, nature of loading, rate of loading, and number of cycles or repetitions. The types of loading commonly applied in fatigue testing of spot-welded joints include:

- Fluctuating tensile loading
- Fluctuating compressive loading
- Fluctuating loading, with maximum load tensile and minimum load compressive
- Completely reversed loading

Data Presentation. In fatigue testing a spot weldment, the fatigue life is usually expressed in terms of load versus cycles, or $L-N$ curves, instead of stress versus cycles. Similar to the information collected in fatigue testing a uniform specimen, the $L-N$ curve, range of loading, endurance limit, load ratio, cycling frequency, and criterion for termination of a test are usually reported.

Fracture Surface. A general fatigue fracture has a unique, characteristic appearance. Cracking usually starts from discontinuities, such as internal voids or inclusions, or locations of high stress concentration. Most fracture surfaces have a smooth appearance, even when the material is ductile, and it should not be confused with brittle fracture. Certain fatigue fracture characteristics, such as clamshell markings, may not be observed on spot-welded sheet specimens.

In a study by Ma et al. (Ref 8), the fatigue performance of spot welds of various sizes showed that weld size does not have much effect on fatigue life. The welds with expulsion appear to have a slightly lower fatigue limit.

Impact Test. The importance of impact performance of spot welds and spot-welded structures is obvious. However, because of the complexity, the relatively low reliability and repeatability, and the high cost, impact testing of spot welds is performed in very limited cases, and mostly on welded structures such as beams rather than single welds.

When properly instrumented, both tension and shear can be imposed during an impact test. There are several kinds of impact tests based on different mechanisms. Some of these tests, together with the testing specimens, can be found in AWS C1.1-66 (Ref 20), AWS D8.9-97 (Ref 13), or Ref 12. They are briefly discussed in the following.

Shear Impact Test. A modified pendulum-type impact testing machine is used for this type of loading. A simple conversion from potential energy to kinetic energy provides the impact loading by using a modified single-pendulum impact tester. It has the advantages of being simple to instrument, easy to prepare test specimens, and straightforward to interpret test results. The disadvantages are associated with the testing mechanism. For instance, the unrestrained specimen may experience large deformation, which can take a significant proportion of the measured impact energy. In

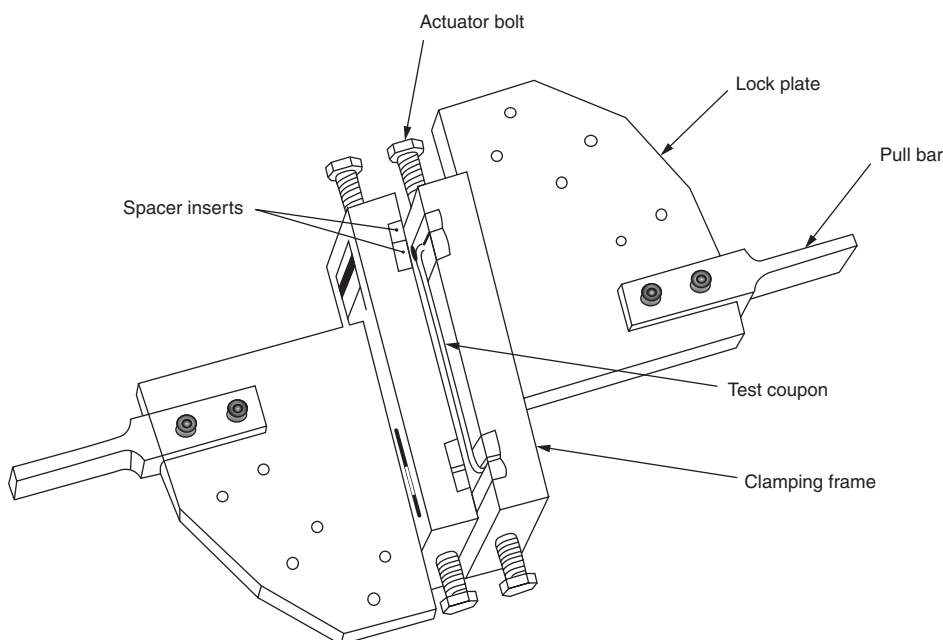


Fig. 18 Fixture for testing spot welds under simultaneous tension and shear loading. Source: Ref 16

general, it has fairly low accuracy and repeatability.

Drop Impact Test. By using test specimens as illustrated in Fig. 19, an impact tensile loading can be applied to a weld when the fixture is attached to a testing machine that provides rapid loading. Because bending of the plates and slippage of a specimen in the mounting fixture are difficult to avoid, and the energy absorbed by these two processes cannot be fully accounted for, the impact energy needed to fracture the spot weld is not accurately determined. Efforts have been made to stiffen the testing specimens to reduce bending, or minimize slippage by using serrated clamps.

Shear Impact Loading Test. This test, which is similar to the shear impact test, uses a pendulum-type impact tester. The fixturing mechanism and the U-shaped specimen (Fig. 20) make the spot weld under shear loading during impact. Although the U-shaped sections make it difficult for the sheet metal to deform, preparing such a specimen can be tedious, and specimen consistency as well as testing accuracy could be unsatisfactory.

Tension Impact Loading Test. This test uses the same type of U-section specimens and the same testing mechanism as a shear impact loading test. The only difference is that the impact loading is in tension. In addition to the difficulties in preparing the test specimens, the inevitable bending of the specimen when the spot weld is loaded in tension is a major source of inaccuracy in measurement.

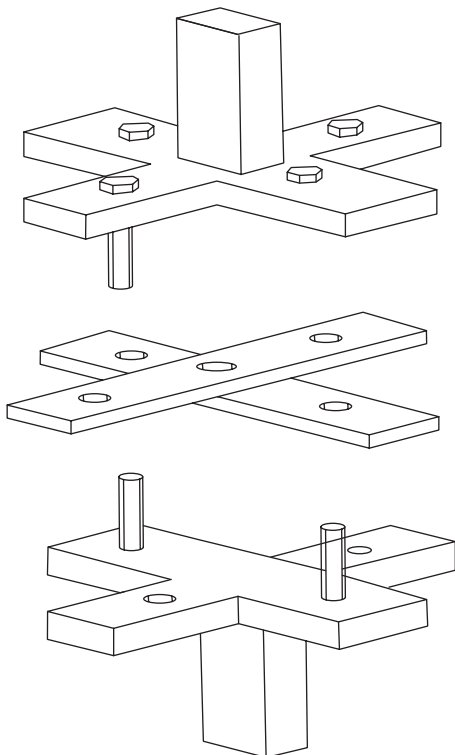


Fig. 19 Testing specimen for drop impact tests

Double-Pendulum Impact Test. All the aforementioned impact tests, except for the shear impact test, are complicated in specimen preparation and fixturing. The shear impact test, on the other hand, is simple in specimen and test preparation. The disadvantages of the shear impact test are also obvious, and efforts have been made to improve various aspects of specimen preparation, specimen mounting, and testing. A brief discussion of this test can be found in Ref 21 and 22. A novel impact testing mechanism has been developed using two pendulums for testing the impact strength of various joints, including resistance spot welds, loaded in either tension or shear. The basic working mechanism, specimens, and testing of this impact test are presented in this section.

As shown in Fig. 21, there are two pendulums on this device instead of one, as in a shear impact tester. A Z-shaped welded specimen (Fig. 22c) is mounted on one pendulum at one end and fixed to the machine base at the other end. The weld is placed at the center joining the two pieces of bent coupons. In the test, the impact energy input is defined by the initial position of the pendulum on the right side, adjustable by the weight and the angle θ_0 . The potential energy in this pendulum is converted into kinetic energy at the bottom when it hits the other pendulum to which the testing specimen is attached. The specimen, under the impact load, may or may not break. Its impact strength is measured by the impact energy absorbed by the specimen, through the maximum angles (θ_A and θ_B) of the pendulums after impact. A welded joint may not fracture if the predefined impact energy input is not sufficient, resulting in only a least estimate of its impact strength. The tester provides two types of loading to a joint: peeling and tensile-shear, and the specimens are shown in Fig. 22. In tensile-shear testing with this device, the specimen is restrained between the head of the pendulum on the left and the base of the tester. Little rotation is allowed in the sheets to minimize the impact energy consumed by sheet deformation and to maximize the proportion of the shear component in impact loading.

Force and displacement sensors can be installed on the tester to understand the detailed behavior of a welded joint under impact, in addition to the impact energy measured directly from the dial meters. Figure 23 shows the force and displacement profiles when a weld fails by

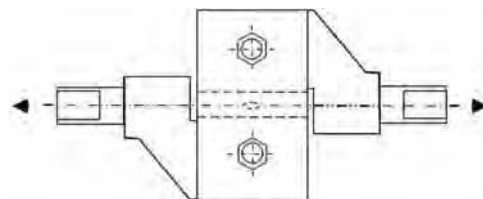


Fig. 20 One type of testing specimen for shear impact loading test

a weld pull-out. In general, the profiles can provide a more detailed account of weld impact strength than the impact energy from measurement of the angle read-outs. This is especially important when base-metal tearing is involved during testing. Good testing consistency has been observed using the tester on mild steels, high-strength steels under room and low temperatures (down to -60 °C, or -76 °F), and on self-piercing riveted aluminum joints.

Metallographic Examination

Some of the weld characteristics can only be revealed through metallographic examination. For instance, the weld size measured on a fractured weld may be drastically different from the actual size of the weld nugget, and it is influenced by the loading, property of the weldment, and others. A metallographic examination directly exposes the internal structure of a weld, such as the nugget size and shape, microstructures of various zones, internal defects, and so on.

A metallographic examination is usually performed on a specimen cut through a weld along one of the three planes shown in Fig. 24. For convenience, sectioning is usually done perpendicular to the coupon length (i.e., transverse direction), or plane A in Fig. 24. Because of the different constraint in electrical, thermal, and mechanical conditions in different orientations, the development of a weld nugget is not identical along planes A, B, and C in the figure. An example of the cross section of an AA5754



Fig. 21 Double-pendulum impact tester

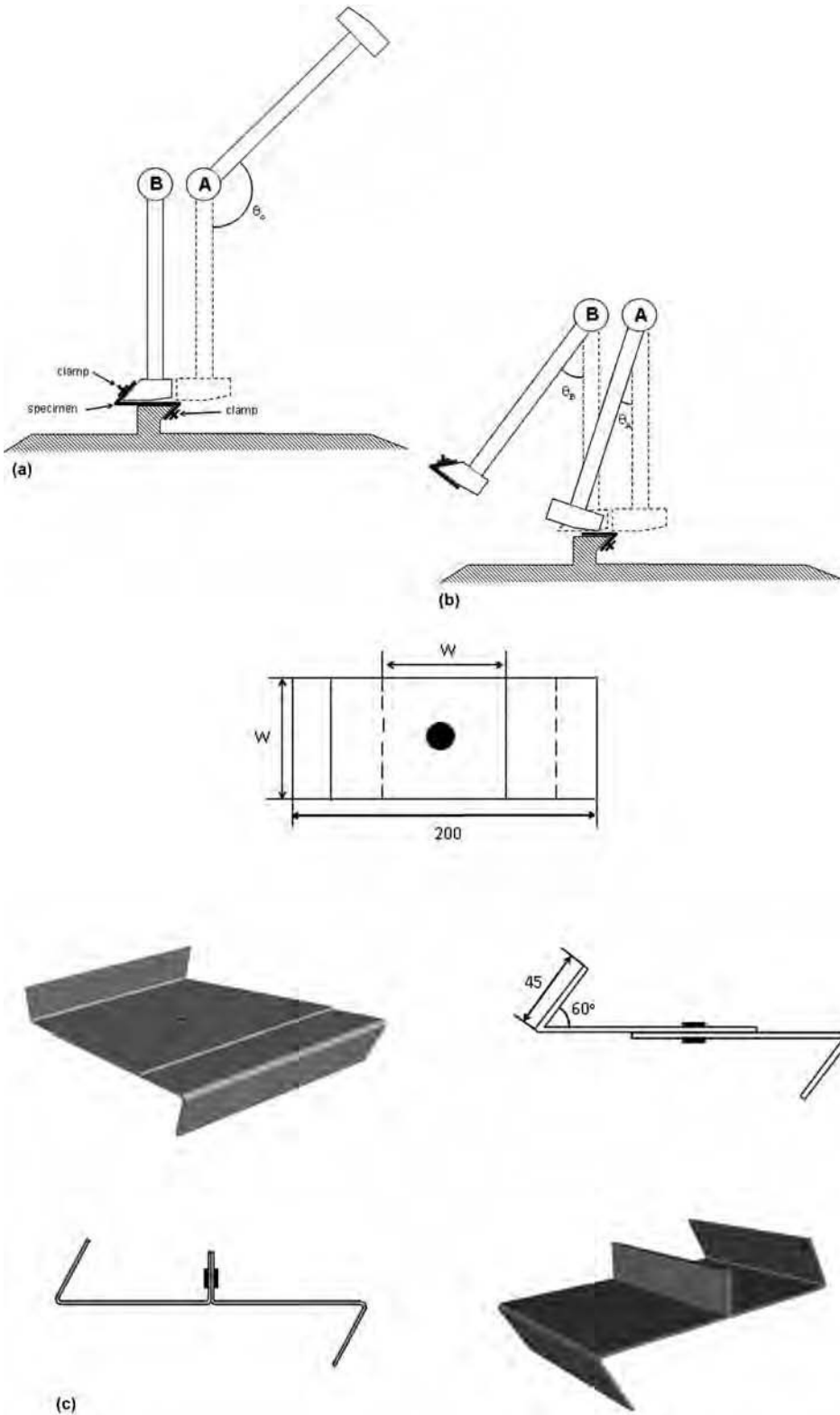


Fig. 22 Schematic diagram of testing procedure and specimen configuration for the double-pendulum impact test

weld along plane A is shown in Fig. 25(a). The weld nugget and some pores close to the center of the weld are clearly seen. When another weld, made under an identical condition as that of Fig. 25(a), is sectioned along the longitudinal direction, or plane B in Fig. 24, a weld of different shape and size appears, as in Fig. 25(b). In addition to the voids in the nugget, this cross section also reveals several liquation cracks in the HAZ. Such cracking is not visible in the transverse section of the weld, except a fine trace of crack in Fig. 25(a), which can be easily overlooked. The difference in cracking in these two sections is the result of different constraining conditions during welding, as discussed in detail in Ref 10. Occasionally, sectioning is done along the original faying interface, or plane C in Fig. 24. One advantage of such sectioning is that interfacial expulsion can be clearly observed, for instance, in a magnesium weld (Fig. 26). A large amount of ejected metal is visible outside of the weld area, through the liquid network of metals in the HAZ during welding (Ref 11).

Another common use of metallographic sectioning is for microhardness testing. The hardness value is usually measured along a diagonal direction across the base metal, the HAZ, and the nugget, with a constant spacing. In Fig. 27 (Ref 23), the indents, shown as dots in the figure, are the marks left from microhardness testing on a transverse cross section of a DP780 steel weld, with a distance of 0.38 mm (0.015 in.) between the indents (Ref 23). The measured microhardness values on welds of various material combinations are shown in Fig. 28 (Ref 14).

Nondestructive Testing

The advantages of nondestructive testing of spot welds are obvious. Such testing can be performed during welding, or on-line, through monitoring the process signals, or after a weld is made (off-line). Ultrasonic testing is the most common test in off-line evaluation of welds. Both on-line and off-line nondestructive evaluation methods of spot weld quality are discussed in this section.

Weld-Quality Monitoring Using Process Signals

Electric tip voltage, current, electrode force, and electrode displacement are commonly measured during resistance welding, and they generally correlate well with the welding process and weld quality. A typical data-acquisition system is shown in Fig. 29 (Ref 24).

Process Signals. Typical profiles of voltage, current, electrode force, and electrode displacement monitored in alternating current (ac) welding are shown in Fig. 30. When using high-magnitude ac welding, the strong induced magnetic field may corrupt the signals, and

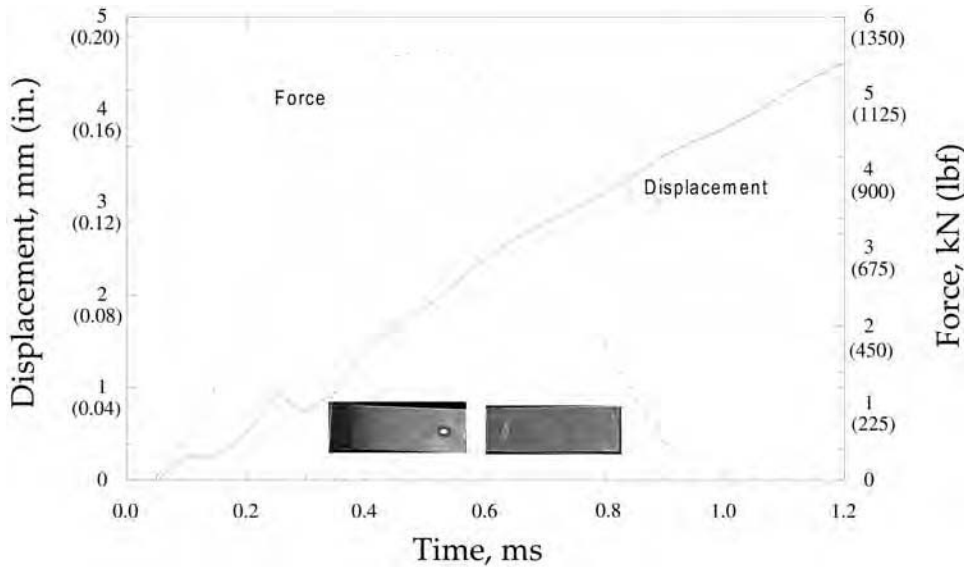


Fig. 23 Displacement and force profiles of impact for failure by button pull-out. Source: Ref 21

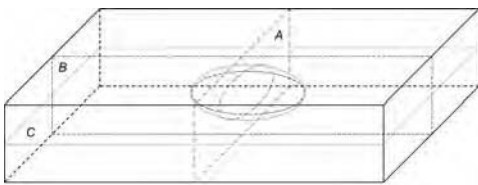
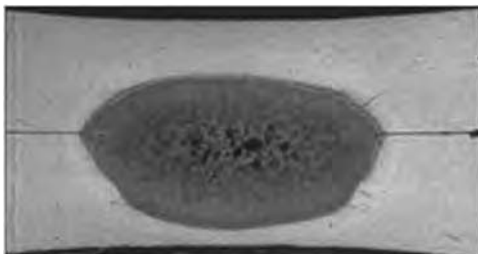
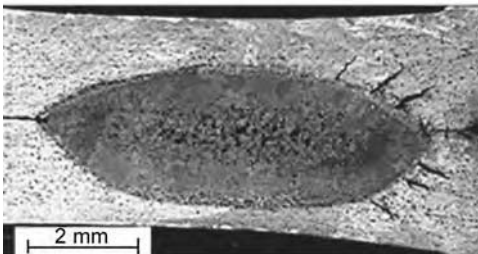


Fig. 24 Sectioning planes through the center of a weld



(a)



(b)

Fig. 25 Views of (a) transverse and (b) longitudinal sections of AA5754 welds. Source: Ref 7

certain treatment of the collected data, such as adaptive signal processing techniques, is needed (Ref 25).

The signals can be roughly classified as input variables and responses. The electric voltage

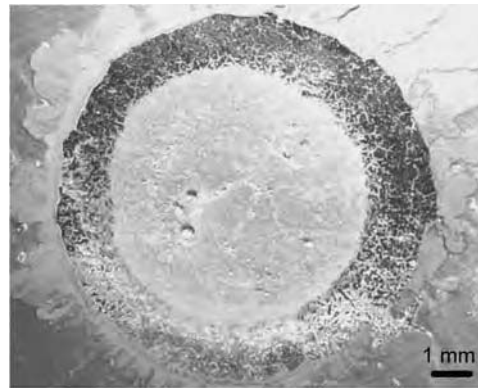


Fig. 26 Sectional view of an AZ91 weld along the original faying interface. Source: Ref 11

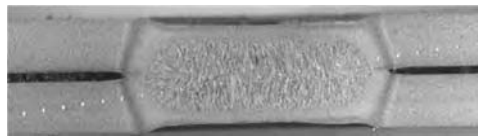


Fig. 27 Cross section of a DP780 steel weld with indentations from microhardness testing. Source: Ref 23

and current are obviously input to a welding process. However, they are affected, in general, by the welding process and possess the characteristics of response variables as well. For instance, the electric voltage, monitored during a normal welding process, as seen in Fig. 30(a), fluctuates as the electric resistance varies during welding and the electric current is controlled to be constant. Therefore, electric voltage is not a “pure” input. The dual characteristic of both input and response is more

evident for electrode force. As an input variable, its value is selected by the operator, but it is heavily influenced by thermal expansion and contraction, as seen in Fig. 30(c). Therefore, these input variables are responses as well, and clearly distinguishing inputs from responses may not be possible or necessary during resistance spot welding.

Electric Voltage. Depending on the welding control mechanisms, electric voltage for resistance welding can be either constant or variable. When the electric current is kept constant, the voltage varies with the dynamic resistance during welding. The voltage can be easily measured, because its level for resistance welding is fairly low. However, the collected signals are usually corrupted by the induced alternating magnetic field during ac welding, as shown in Fig. 30(a). The area of the wire loop of the voltage sensor should be minimized to reduce such an influence. Using a compensating loop is an effective means to approach this issue.

Electric Current. A very high electric current is usually needed in resistance spot welding, which demands an indirect measurement of its value. An induced voltage by the welding current, rather than the current itself, is measured, and as a result, the measurement may be polluted by process noises. For a direct current (dc) or a low-amperage ac, a resistive shunt method can be applied, in which the voltage across a known resistor is measured, and the current passing through the welding circuit can be derived. Because of inductance and resistance in the secondary loop, a welding current, either ac or mid-frequency dc, does not reach the designated value immediately after the current is switched on. Rather, it ramps up during the first few cycles of welding. As a result, the amount of heat may be less than calculated. This may not have much effect on the process or weld quality in steel welding, but it should be accounted for in welding aluminum or magnesium, because the welding time is usually very short for these alloys.

Dynamic resistance during resistance welding provides important information for both welding process and weld quality. It is generally measured through the electric voltage and current. This is a straightforward process when dc is used. However, care must be taken during ac welding because of the inductance in the secondary loop.

Because dynamic resistance is a strong function of the geometric and physical characteristics of a weldment, their changes during welding are directly reflected in the signals of the dynamic resistance measurement. As seen in Fig. 31, the dynamic resistance in welding a DP600 steel (Ref 24) shows initial melting of the faying interface (zone 2 in the figure), continued heating of the stack-up, more melting, and solidification. Expulsion, when it occurs, reduces weld thickness and increases the contact area in a short period of time. Therefore, it is usually revealed by a sudden drop in dynamic resistance.

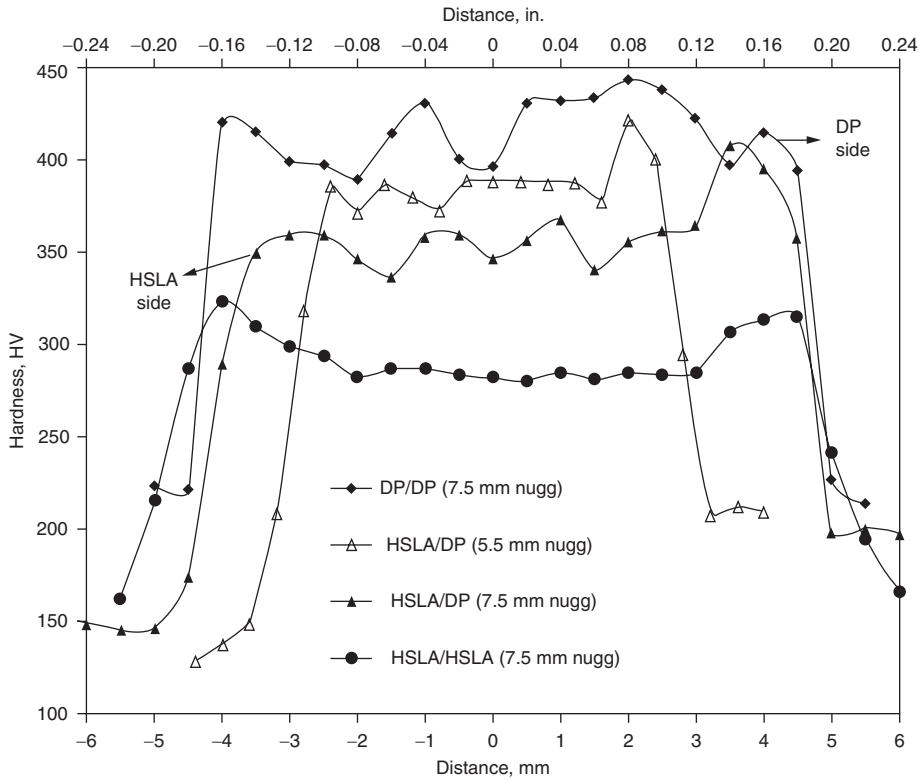


Fig. 28 Microhardness profiles of various material combinations. HSLA, high-strength, low-alloy; DP, dual phase. Source: Ref 14

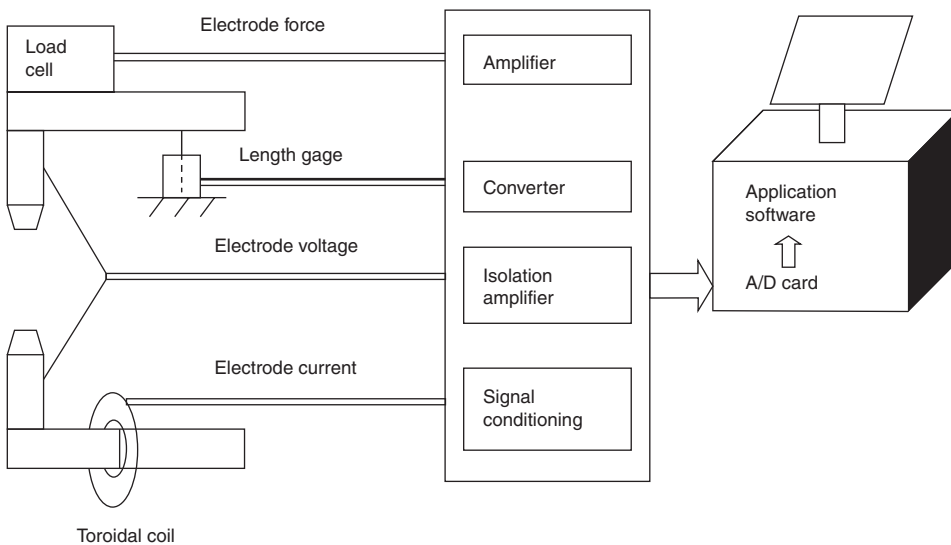


Fig. 29 Schematic of a typical data-acquisition system. A/D, analog/digital. Source: Ref 24

Electrode displacement is the result of expansion and contraction of a weldment along the electrode axis. They are the result of heating, melting, solidification, and cooling. However, electrode displacement can only serve as a qualitative, not quantitative, indicator of the welding process or weld quality, because the motion of an electrode is affected by more than one type of deformation in the weldment.

For instance, heating makes the weldment expand, yet it softens the solid material and makes it easier for the electrode to protrude into the weldment under the applied electrode force. The varying and nonuniform temperature and strength distributions in the weldment, the heating/cooling of the solid, the melting/solidification, along with constraint from the sides of the weld, make it difficult, if not

impossible, to quantitatively correlate the electrode displacement with the processes in the weldment.

Linear variable differential transformers and fiber-optic sensors are commonly used for displacement measurement in welding. The electrode displacement profile, measured using a fiber-optic sensor, is shown in Fig. 32. The increased distance between the electrodes corresponds to growth of the weldment thickness due to solid expansion and melting under heating. The measured electrode displacement is the result of two competing processes: an increasing electrode displacement corresponding to thermal expansion due to heating, and a decreasing electrode displacement due to softening of the weldment. The fluctuation in the displacement curve is the result of alternating cycles of heating (peaks in the displacement curve) and cooling (valleys in the curve). Other physical changes may also be revealed by the electrode displacement measurement. In Fig. 32, a large drop in displacement indicates expulsion, when a sudden loss of liquid metal reduces the distance between the electrodes. The magnitude of displacement drop may be used to describe the severity of expulsion.

Electrode Force. As an important input variable, electrode force creates necessary electric contact at the faying interface, contains the liquid metal to suppress expulsion, and provides a forging force to prevent porosity formation and cracking. Electrode force is usually applied in three stages in a typical welding cycle: touching, welding, and hold. Because it is measured by the reaction of the weldment to the electrodes, electrode force directly reflects the welding process and can be used to measure weld quality in a way similar to electrode displacement.

Figure 33 shows electrode force as a function of time in a welding cycle. When the electrodes touch the sheets, the electrode force may increase steadily or fluctuate, depending on the stiffness and damping properties of the sheet stack-up, the stiffness of the electrodes and welder, and so on. Such vibration may not affect weld formation if an electric current is applied after the electrodes are stabilized. However, an electric arc may be generated if the current is applied while the electrodes vibrate, and it may adversely influence weld quality. Controlling electrode force is an efficient way to suppress void formation and expulsion, and a large force is needed to create a large weld to balance the force from the liquid nugget (Ref 2).

Pneumatic cylinders are commonly used to drive electrodes. Therefore, electrode force is closely associated with the pressure change and follow-up characteristics of a cylinder. Other driving mechanisms, such as combined pneumatic and hydraulic systems, have been developed to control the electrode force in resistance welding. Electric servo-motor-based welders also provide the

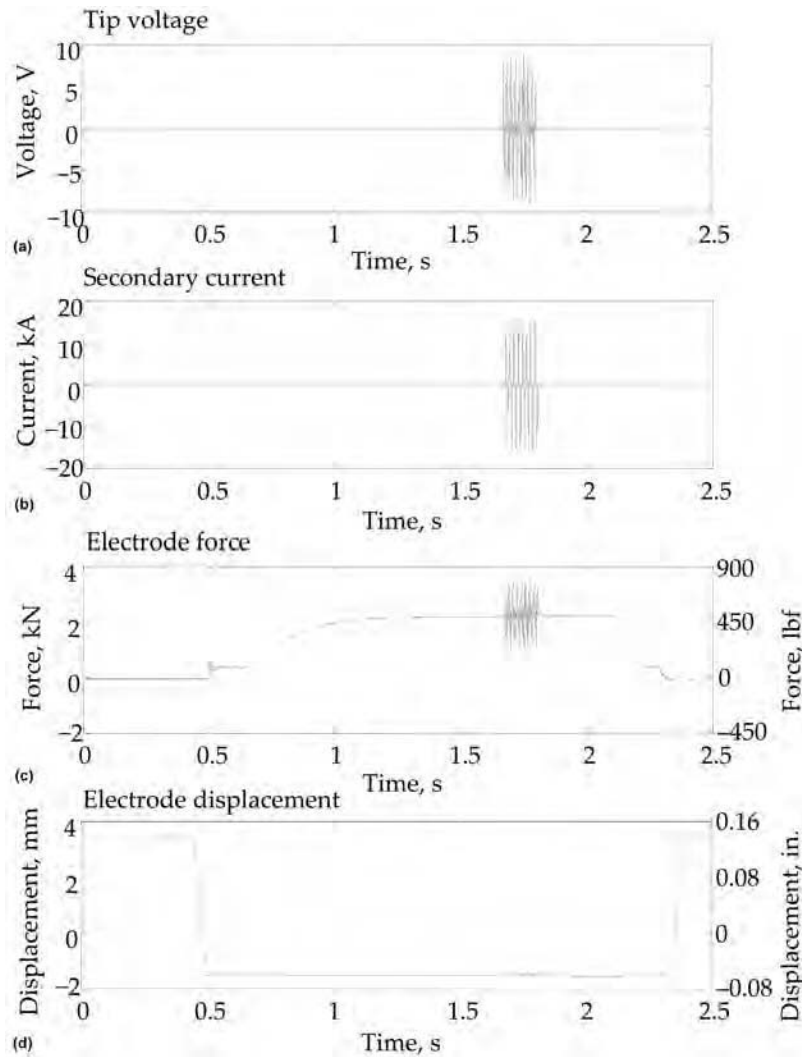


Fig. 30 Typical profiles of voltage, current, electrode force, and electrode displacement monitored in an alternating current welding

opportunity to alter electrode force during a welding cycle. Electrode force is usually measured using a strain-gage-based force sensor or a piezoelectric force sensor. It is important to realize that, as in measuring other signals during ac welding, the force signals could also be heavily corrupted by the induced voltage.

Ultrasonic Evaluation

The process signals discussed in the previous sections are important for on-line monitoring of the welding process and weld quality. However, they are generally of an indirect nature, and there is a lack of one-to-one correspondence between a monitored signal and the welding process. Therefore, the ability to use process signals for weld-quality monitoring is limited.

Ultrasonic inspection, on the other hand, has been quite mature in examining the internal structure of components. It has been applied to quality inspection of resistance spot welds as well, by providing a direct measurement of the structural characteristics of a weldment. Various ultrasonic inspection techniques currently used in resistance welding are briefly reviewed in this section.

The ultrasonic A-scan technique is also known as a ring-down technique. It is basically a plot of wave amplitude versus time (Fig. 34). When applied to a spot weldment, the ultrasound is reflected when it encounters an interface, back to the transducer. As a result, a series of echoes is formed. The location of a reflecting interface, determined by the echo positions on the time scale, is associated with the characteristics of a weldment.

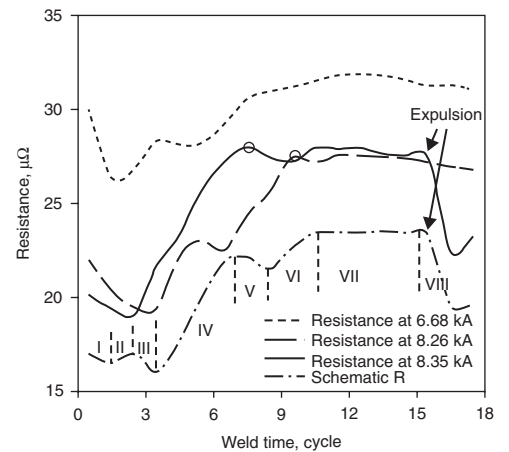


Fig. 31 Dynamic resistance profile in welding a DP600 steel. Source: Ref 24

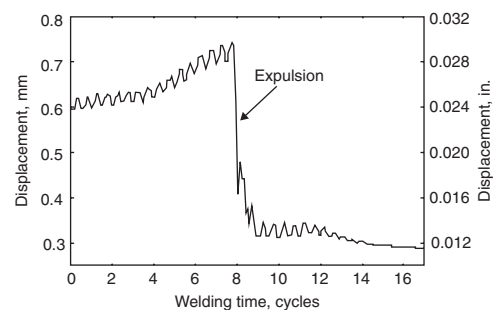


Fig. 32 Electrode displacement measured with a fiber-optic sensor during alternating current welding with a heavy expulsion. Source: Ref 6

The typically observed waveforms in using the ultrasonic A-scan technique for evaluating a resistance spot weld are illustrated in Fig. 34 (Ref 26).

The quality of a weld can be assessed by examining the features of the echo sequence in an ultrasonic A-scan. For a large weld of sufficient fusion at the faying interface, the ultrasonic wave passes through the faying interface and is reflected from the back surface of the stack-up. Figure 34(a) is the ultrasonic echo waveform for a good weld. In addition to the time intervals between the peaks corresponding to the time of flight of the reflected waves, a rapid attenuation is observed, resulting from the coarse microstructure in the fused part of the weld area. An acoustic beam onto a small weld is split into two parts, and the portion that is reflected by the unfused faying interfaces creates small, intermediate echoes, adding to those passing through the fused area (Fig. 34b).

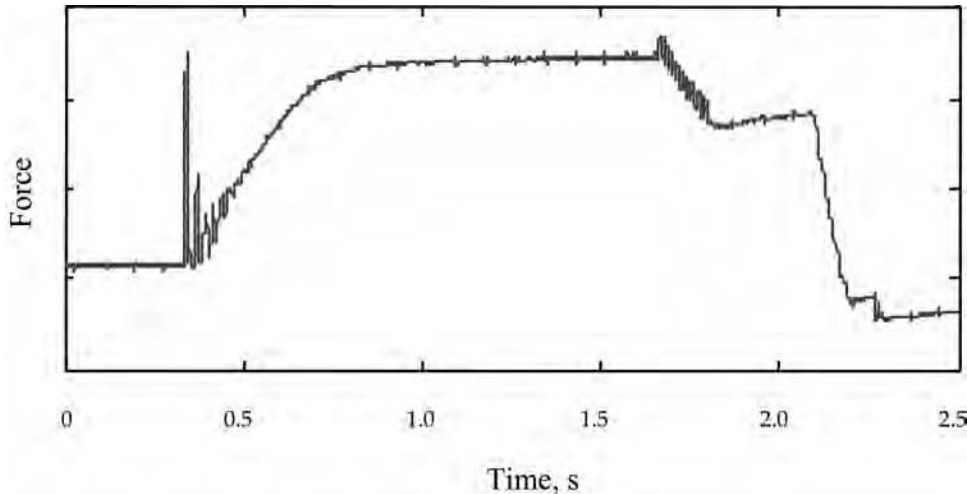


Fig. 33 Electrode force profile during welding

Therefore, the echoes obtained are influenced by the nugget size, relative to the probe diameter, and the position of the probe.

For a weld of insufficient fusion or a cold weld, the acoustic wave can pass through the faying interface if there is certain adhesion created by melting of the metals, such as the zinc coating in a hot-dipped galvanized steel or a small amount of base metal. The insufficient heating creates surface melting or a shallow weld with a fine microstructure, and therefore, little attenuation to the reflected beam results. Therefore, the echoes measured on a cold weld (Fig. 34c) have a lower attenuation than those in Fig. 34(a). When there is no adhesion at the faying interfaces, reflection occurs only within the upper plate, meaning no weld. Because there is no melting and therefore no structural changes, very slow attenuation is observed in such a weld (Fig. 34d).

In practice, the use of ultrasonic A-scan depends heavily on the operator's experience, as analyzed in a repeatability and reproducibility study (Ref 27). The large number of possibilities of welds in shape, size, microstructure, internal defect, surface topology of the top and bottom surfaces, and so on may affect the correct interpretation of the ultrasonic waveforms.

Ultrasonic B-Scan Technique. Although an A-scan image provides useful information based on the thickness and microstructure of a weldment through the distance between peaks, decay in the echo magnitude, and overall pattern of the acoustic waveform, the interpretation is generally operator-dependent. Many factors, such as probe size, axial and angular alignment of the probe with respect to the weld, and irregularities of a weld, affect the operator's interpretation of weld quality.

As a significant improvement to A-scan, ultrasonic B-scan overcomes many of the shortcomings of A-scan for weld-quality inspection. An ultrasonic B-scan image is a plot of elapsed pulse time (from reflections) versus the position

of the transducer along a line on the surface of the testpiece (Fig. 35). Echo intensity is not presented directly, as it is in A-scan inspection, but is often indicated semiquantitatively by the relative brightness and/or color of echo indications. An ultrasonic B-scan display can be likened to an imaginary cross section through the testpiece, where both front and back surfaces are shown in profile.

Unlike in A-scanning, in which the signals are collected with a stationary probe positioned on the top of the weld, the probe is moved across the weld surface in B-scanning. At each location, echoes are generated, as in an A-scan, from the interfaces between the top and back surfaces. A sequence of such echoes created when the probe slides along a line through the weld center on the top surface forms a B-scan image. A correctly constructed B-scan image is able to reveal the location and size of various geometric features of a weldment, including the indentation, nugget, voids and cracks, and degree of adhesion for distinguishing cold welds. A schematic B-scanner is shown in Fig. 36.

Various welds were generated and examined (Ref 28) by using a B-scan inspection system developed by Applied Metrics. The image of a good weld is shown in Fig. 37. On the top plate, the surfaces of the base metal are clearly distinguishable from that of the indentation from the rupture of continuous echoes of the top surface at the indentation walls. There is an undefined zone at the junction between the surfaces of the base metal and the indentation, resulting from a loss of signals at the inclined indentation wall on which the reflected acoustic beam does not directly reach the receiver. Such a region widens as echoes decay.

The echoes of the top plate can be used to accurately measure the thickness of the plate, which can also be used to calibrate the measurement of other thicknesses of the weldment, for example, weld thickness. The top surfaces of a weldment, that is, the surface of the base

metal and that of the indentation, are differentiated by B-scan. The difference is amplified by the different travel speeds of the ultrasonic beam in different media. The indentation area appears deeper than it is, relative to the top surface of the base metal, because it takes a longer time for the acoustic beam to travel through water. The indented surface also reflects the topology of the electrode and can be used as an indicator of the electrode condition. The echoes under the electrode impression (in the range of the indentation) provide information on the nugget width, weld thickness, and internal defects.

From an ultrasonic B-scan image, weld geometric attributes can be derived, and they usually comprise of the indentation width and depth, nugget width, weld thickness, projection of an internal discontinuity, trace of expulsion, degree of fusion, and the difference in grain structures between the fused area and other parts. Some examples of evaluating spot welds of various characteristics are shown in the following. A more complete discussion can be found in Ref 28.

Figure 38 shows the B-scan of a weld with an internal crack created by welding with electrodes of annular tips. The crack, which is parallel to the faying interface, is clearly visible at the center of the fused area in the ultrasonic image. It is noticeable that the relative width of the crack appears bigger than that observed in the corresponding metallographic sectional view (on the right). The reason for this is that when the probe moves toward the crack in the nugget, assumed from left to right, an echo from the crack is registered once the crack tip is encompassed by the ultrasound beam diameter at the depth of the crack, even when the crack tip is not yet at the center of the ultrasound beam, which is used as the location of the echoes. As a result, the crack appears earlier in the B-scan image than its actual physical location. Care should be exercised when quantitatively measuring the width of the crack.

A cold weld results when there is insufficient fusion at the faying interface. This is illustrated by very similar echoes from the weld area to those from the original faying interface, accompanied by a slight bending of the base metal due to thermomechanical deformation in an ultrasonic image of a cold weld (Fig. 39). Although all cold welds are the result of insufficient heating, the amount of fusion could be drastically different among them. In other words, they may have different degrees of "coldness." Some cold welds may have considerable strength, and others may behave like a "no-weld." The degree of coldness can be evaluated by ultrasonic B-scan through the color (strength) and thickness of the echoes of the faying interface in the image.

As seen in Fig. 39 for a cold weld, the B-scan image shows little difference in the weld area from the back surface of the top plate. The sectioning through plane C in Fig. 24 of the weldment reveals melting of the zinc coating as well

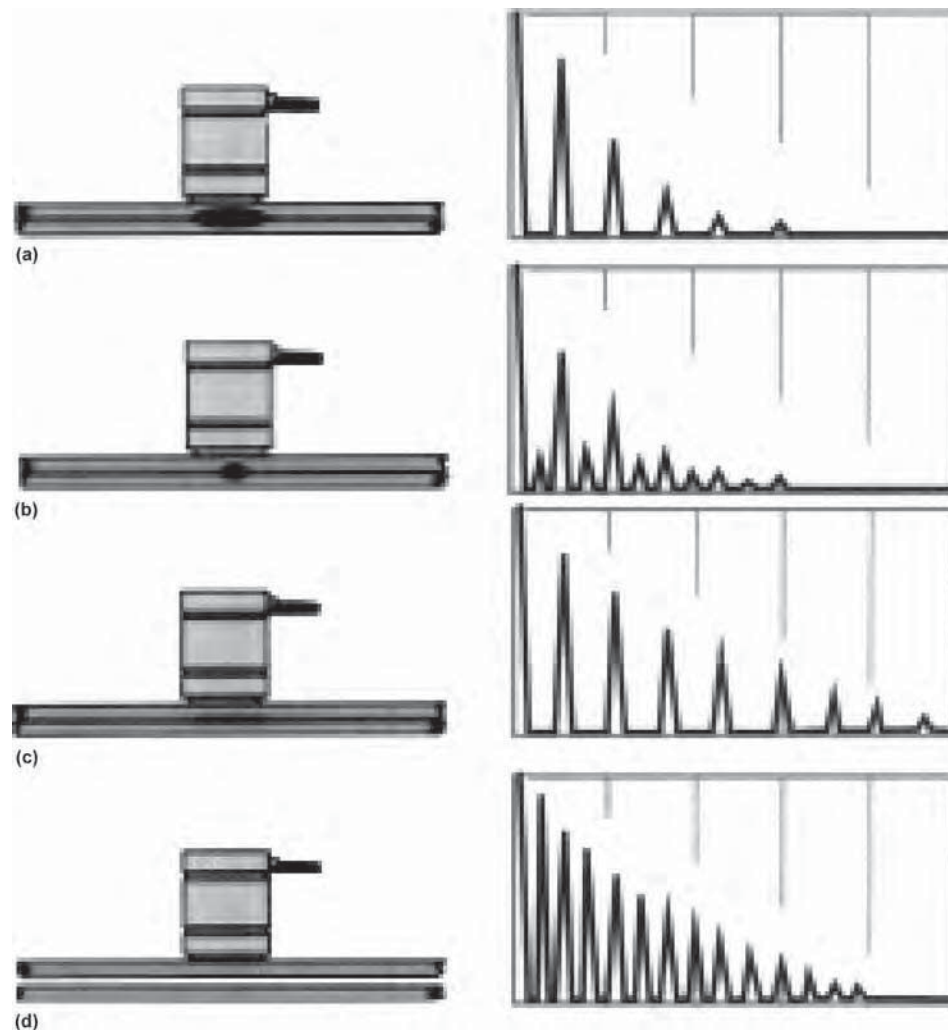
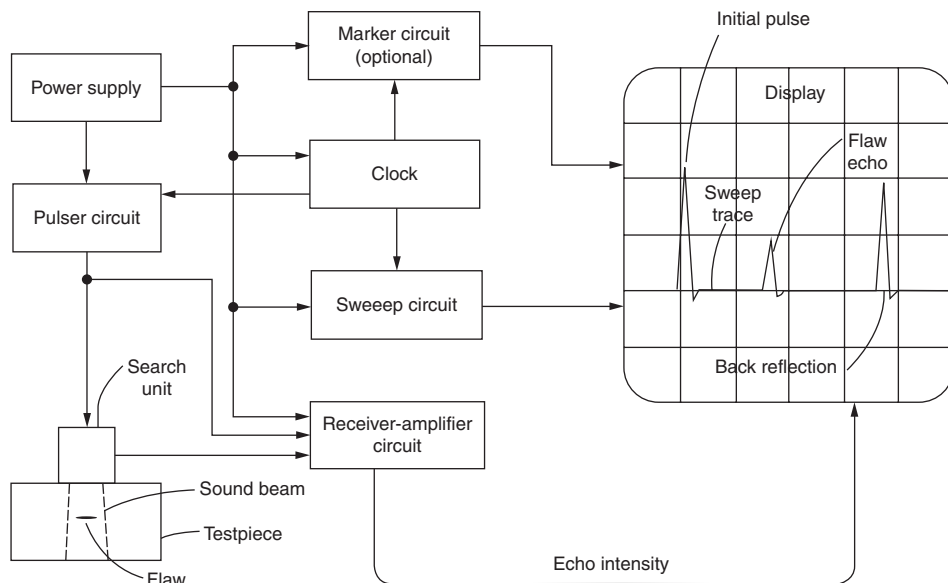


Fig. 34 Schematic of A-scan ultrasound and waveforms from A-scan ultrasounds of typical welds. See text for more information. (a) Good weld. (b) Reflection with unfused faying interfaces. (c) Cold weld. (d) No adhesion at the faying interfaces. Source: Ref 26

as some base metal at the center of the weld. In a B-scan image, the degree of fusion is reflected by the color, brightness, and thickness of the echoes. Increasing heat input, as observed in Ref 28, results in more base-metal melting and less degree of coldness. The corresponding changes in a B-scan image are that the colors of the echoes of the weld start to differ from those of the back surface of the top plate, and the echoes become thinner. For instance, the weld in Fig. 40 was made with 1000 A more current than that in Fig. 39, with more base-metal melting. The first echoes of the B-scan image of the weld are darker in color and thinner in thickness compared with that of less heat, because of less reflection from the original faying interface as more acoustic beam penetrates the interface, resulting from more fusion. The intensity of the echoes from the back surface of the weld, on the other hand, increases with brighter color. The difference between welds of different amounts of fusion is amplified by the attenuation of the signals, that is, the attenuated echoes. The attenuation rate of the hotter weld is higher, due to the coarse structure in the fused area.

In addition to ultrasonic A-scan and B-scan, arrays of ultrasonic probes are also used to obtain information on the in-plane attributes of a weld along the faying interface. These probes are currently in the development stage at a number of universities and industrial research laboratories.

In-Line Ultrasonic Test Monitoring. Besides off-line measurement of weld quality, attempts have also been made to use ultrasonic waves for on-line quality control. Generally, there are two different approaches for this purpose: the pulse-echo method and the through-transmission method. The former relies on analyzing the reflected echoes of ultrasound in a way similar to an A-scan (Ref 29). Difficulties may arise in interpreting the echoes, because the amplitude of the reflection and the time of flight are both strongly temperature dependent. The multiple interfaces, including the electrode-sheet interfaces, may complicate the interpretation. In the through-transmission method, the ultrasound signals are beamed from one side of the welding stack-up and received on the other side, as shown in Fig. 41 in the work by Kocimski et al. (Ref 30). The time of flight through a resistance spot welding setup was used to monitor weld quality at the moment the electric current was turned off. Because the transmission of the ultrasound through the weld stack-up is affected by the changes in the sheet metals, the difference in time of flight between two stages of welding, for example, before and after applying the welding current, can be used to evaluate the weld formed. The changes between the original and the welded stack-up due to welding, which are reflected in the ultrasound characteristics, include microstructure, adhesion at the faying interface, indentation, and temperature rise in the various media, including the cooling water, electrode, and weldment. Such changes are

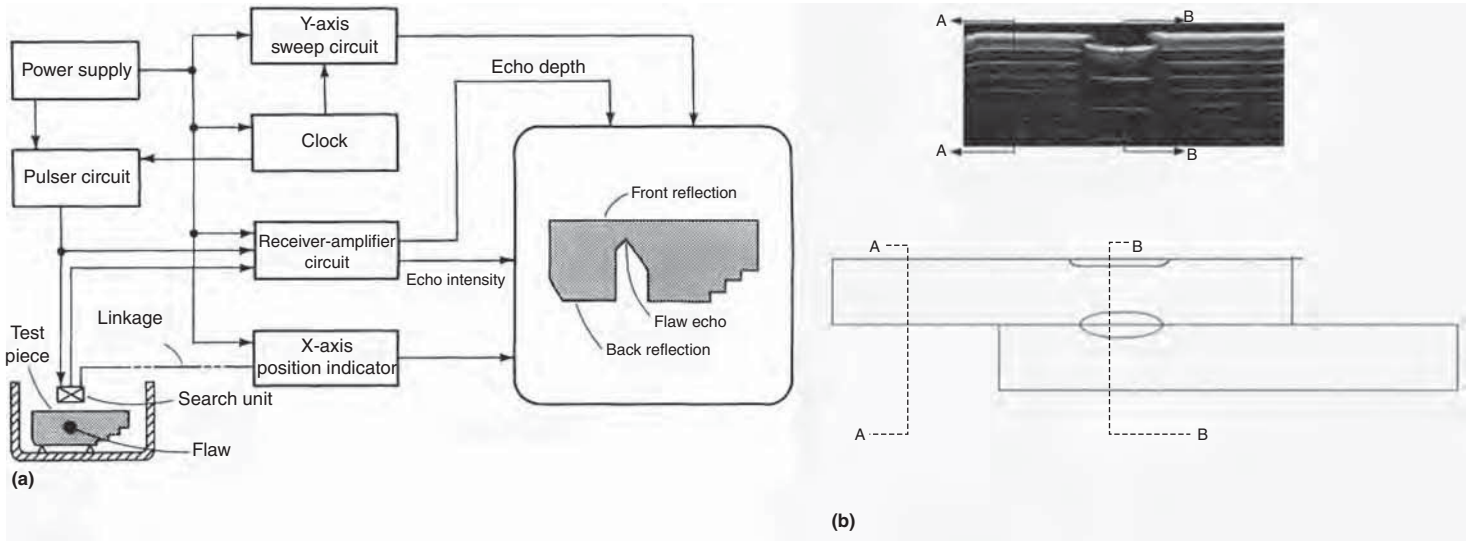


Fig. 35 (a) Schematic of B-scan ultrasound. (b) Example of B-scan image of a spot weld. Source: Ref 6

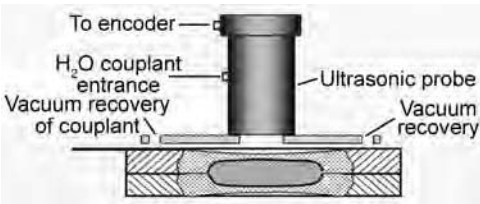


Fig. 36 Inspection system for B-scan ultrasound of spot welds

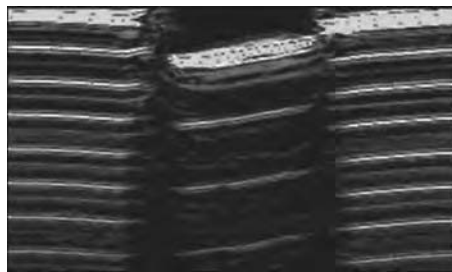


Fig. 37 B-scan image of a good weld

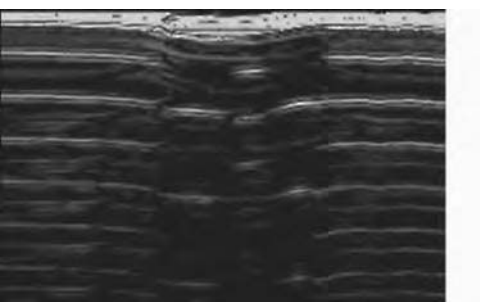


Fig. 38 Crack at the center of a low-carbon steel weld

reflected in the transmitted ultrasonic waves, and they are used to predict weld quality through a correlation between the quality and the changes in ultrasonic signals.

Because the received signals contain the contributions of all components in the path of ultrasonic wave propagation, it is necessary to isolate the portion resulting from fusion of the sheets. This requires an understanding of the temperature distribution in the setup. Finite-element modeling was used in the work by Kocimski et al. (Ref 30), and a good agreement with experimental results was obtained.

REFERENCES

1. "Recommended Practices for Automotive Weld Quality—Resistance Spot Welding," AWS D8.7, American Welding Society, Miami, FL, 2004
2. J. Senkara, H. Zhang, and S.J. Hu, Expulsion Prediction in Resistance Spot Welding, *Weld. J.*, Vol 83 (No. 4), 2004, p 123-s to 132-s
3. H.B. Lee, Y.S. Bang, J.L. Duval, and J.H. Han, "A Study on the Distortion Characteristic due to Spot Welding of

Body Structure Assembly for Passenger Car," SAE paper 2002-01-2002, Proceedings of the 2002 SAE International Body Engineering Conference and Automotive and Transportation Technology Conference, July 9–11, 2002 (Paris, France)

4. S.K. Khanna, X. Long, W.D. Porter, H. Wang, C.K. Liu, M. Radovic, and E. Lara-Curzio, Residual Stresses in Spot Welded New Generation Aluminium Alloys, Part A: Thermophysical and Thermomechanical Properties of 6111 and 5754 Aluminum Alloys, *Sci. Technol. Weld. Join.*, Vol 10, 2005, p 82–87
5. J.A. Khan, L. Xu, Y.J. Chao, and K. Broach, Numerical Simulation of Resistance Spot Welding Process, *Numer. Heat Transf., A*, Vol 37, 2000, p 425–446
6. H. Zhang and J. Senkara, *Resistance Welding: Fundamentals and Applications*, 1st ed., CRC/Taylor & Francis, 2006
7. J. Senkara and H. Zhang, Cracking in Multi-Spot Welding Aluminum Alloy AA5754, *Weld. J.*, Vol 79 (No. 7), 2000, p 194-s to 201-s
8. C. Ma, D.L. Chen, S.D. Bhole, G. Boudreau, A. Lee, and E. Biro, Microstructure

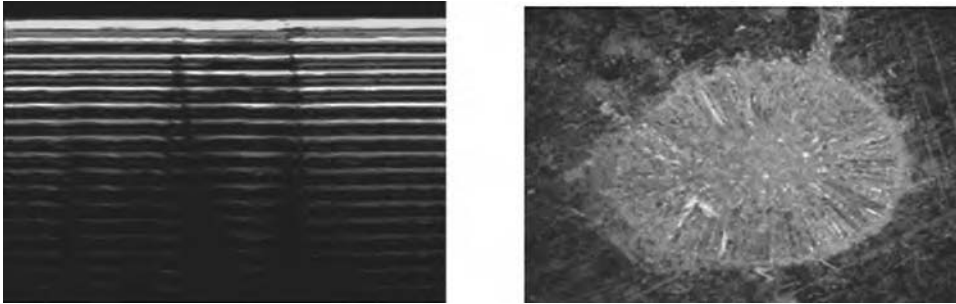


Fig. 39 B-scan and faying surface of a cold weld. Current = 5500 A

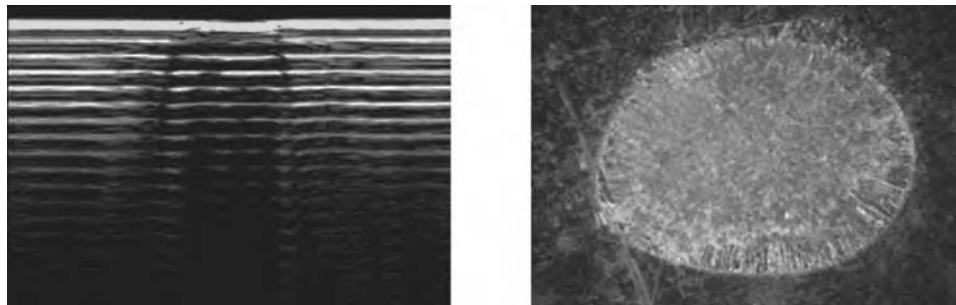


Fig. 40 B-scan and faying surface of a cold weld. Current = 6500 A

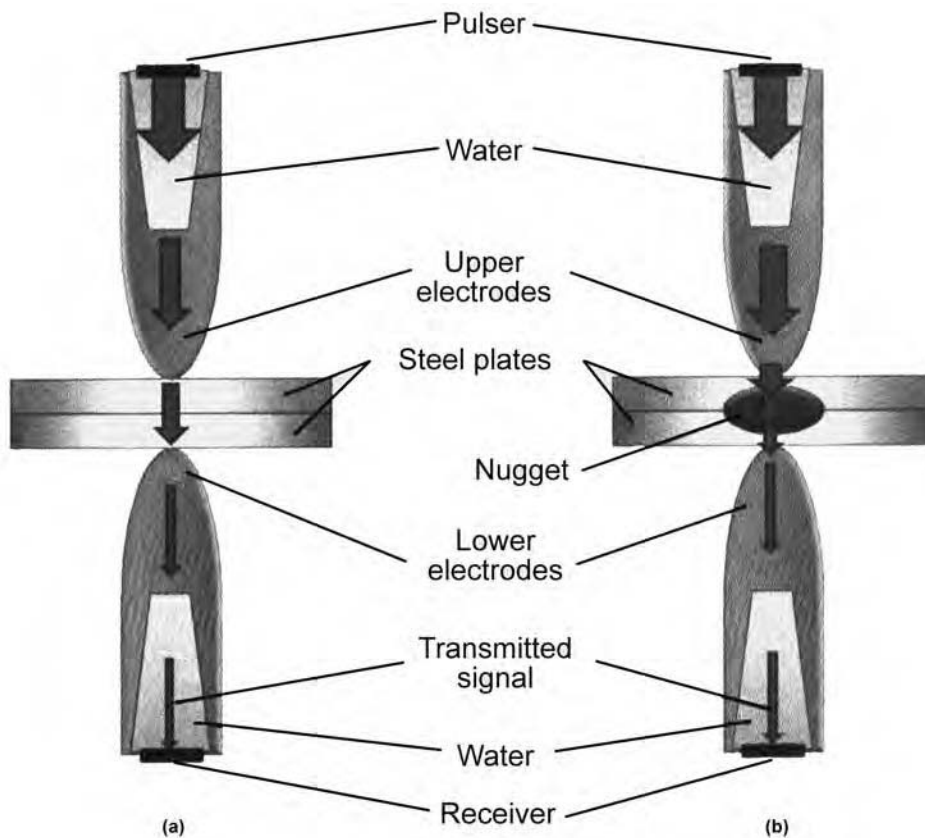


Fig. 41 Setup for in-line measurement of weld quality. (a) Before electric current is switched on. (b) After current is switched on

and Fracture Characteristics of Spot-Welded DP600 Steel, *Mater. Sci. Eng. A*, Vol 485, 2008, p 334–346

9. H. Luo, “New Joining Techniques for Magnesium Alloy Sheets,” M.S. thesis, Institute of Metal Research, Chinese Academy of Sciences, May 2008
10. H. Zhang, J. Senkara, and X. Wu, Suppressing Cracking in RSW AA5754 Aluminum Alloys by Mechanical Means, *ASME J. Manuf. Sci. Eng.*, Vol 124, 2002, p 79–85
11. H. Luo, C. Hao, J. Zhang, H. Chen, Z. Gan, and H. Zhang, Characteristics of Resistance Welding Magnesium Alloys AZ31 and AZ91, submitted to *Weld. J.*, in print Sept. 2011
12. H. Zhang and J. Senkara, *Resistance Welding: Fundamentals and Applications*, 2nd ed., CRC/Taylor & Francis, 2011
13. “Recommended Practices for Test Methods for Evaluating the Resistance Spot Welding Behavior of Automotive Sheet Steel Materials,” AWS D8.9, draft, American Welding Society, Miami, FL, 2005
14. M.S. Khan, S.D. Bhole, D.L. Chen, E. Biro, G. Boudreau, and J. van Deventer, Welding Behaviour, Microstructure and Mechanical Properties of Dissimilar Resistance Spot Welds between Galvannealed HSLA350 and DP600 Steels, *Sci. Technol. Weld. Join.*, Vol 14 (No. 7), 2009, p 616–625
15. M. Zhou, S.J. Hu, and H. Zhang, Critical Specimen Sizes for Tensile-Shear Testing of Steel Sheets, *Weld. J.*, Vol 78, 1999, p 305-s
16. Y. Lee, T. Wehner, M. Lu, T. Morrissett, E. Pakalnins, and C. Tsai, “Test of Resistance Spot Welds under Combined Tension and Shear,” Paper C2, SMWC VII, 1996
17. M. Avalle, L. Peroni, M. Peroni, and A. Scattina, Bi-Material Joining for Car Body Structures: Experimental and Numerical Analysis, *J. Adhes.*, Vol 86 (No. 5, 6), April 2010, p 539–560
18. “Resistance Spot Welding—Destructive Tests of Welds—Method for the Fatigue Testing of Spot Welded Joints,” International Standard, ISO/FDIS 14324, final draft, 2003
19. J.C. McMahon, G.A. Smith, and F.V. Lawrence, *Fatigue Crack Initiation and Growth in Tensile-Shear Spot Weldments*, STP 1058, H.I. McHenry and J. M. Potter, Ed., American Society for Testing and Materials, Philadelphia, 1990, p 47–77
20. “Recommended Practices for Resistance Welding,” AWS C1.1, American Welding Society, Miami, FL, 1966
21. H. Zhang, M. Zhou, and S.J. Hu, Impact Strength Measurement and a New Impact Tester, *J. Mech. Manuf.*, Vol 215, Part B, 2001, p 403–414
22. G. Karve and H. Zhang, “Impact Strength Measurement of Advanced High Strength Steel Welds,” Paper 5-3, *Proc. Sheet Metal Weld. Conf. XI* (Sterling Heights, MI), 2004

23. M.D. Tumuluru, "Effect of Post-Weld Baking on the Behavior of Resistance Spot Welds in a 780-MPa TRIP Steel," Paper 6-2, SMWC XI, 2004
24. C. Ma, S.D. Bhole, D.L. Chen, A. Lee, E. Biro, and G. Boudreau, Expulsion Monitoring in Spot Welded Advanced High Strength Automotive Steels, *Sci. Technol. Weld. Join.*, Vol 11 (No. 4), 2006, p 480–487
25. W. Li, S.J. Hu, and H. Zhang, "Signal Processing Issues in Resistance Spot Welding," p 3-2, Sheet Metal Welding Conference IX (Sterling Heights, MI), 2000
26. W. Roye, "Ultrasonic Testing of Spot Welds in the Automotive Industry," Special Issue No. SD 298, Krautkrämer GmbH & Co.
27. A. Shayan, H. Zhang, and Z. Gan, "Quality Test of AHSS Steel Spot Welds Using Ultrasonic Technique," Paper 3-2, SMWC XIV, 2010
28. H. Zhang, A.H. Jayatissa, and Z. Gan, "Monitoring Resistance Spot Welding Using Ultrasonic B-Scan Techniques," Submitted to *J. Mech. Manuf.*, Sept. 2011
29. A. Ambroziak, M. Korzeniowski, and P. Kustron, Investigations of Spot Welds Quality Based on Ultrasonic Techniques, *Sovremennyj Nauchnyj Vestnik, Matematika, Informatika*, No. 17, Technicheskie Nauki, Stroitel'stvo, 2007, p 32–41
30. J. Kocimski, P. Kustron, M. Korzeniowski, and A. Ambroziak, An Investigation of Ultrasonic Wave Behavior in Multilayered, Inhomogeneous Media of Resistance Spot Welding Set-Up, *Proc. Fifth Inter. Conf. Advances in Production Engineering* (Warsaw), 2010, p 264–270

High Energy Electron Beam and Laser Beam Welding

Introduction to High Energy Density Electron and

Laser Beam Welding	507
History of Electron Beams and Laser Beams	507
Properties of Electron and Laser Beams	509
Comparison between Electron and Laser Beam Welding	511

Electron Beam

Electron Beam Welding	514
Principles of Operation	514
Advantages	515
Limitations	516
Process Control	517
Operation Sequence and Preparation	517
Weld Geometry	519
Joint Design	519
Electron Beam Welding Machines	519
Safety	520

Design Considerations for Electron Beam Welding

Design Considerations for Electron Beam Welding	522
Weld Geometry	522
Joint Design	524
Special Joints and Welds	526
EBW in Vacuum	527
EBW in Nonvacuum	529
Tooling/Fixturing	531
Welding of Thin Metal	531
EBW of Thick Metal	532
Use of Filler Metal	533
EBW for Poorly Accessible Joints	534
Design for Scanning/Joint Tracking	535
Electron Beam Welding as a Repair Method	536
EBW Process Control Plans, Codes, and Specifications	538

Nontraditional Applications of Electron Beams

Nontraditional Applications of Electron Beams	540
Electron Beam Near-Net Shape Processing	540
Dynamic Beam Deflection Processing	544

Quality Control of Electron Beams and Welds

Quality Control of Electron Beams and Welds	548
Process Control of Essential Variables	548
Beam Diagnostic Tools for Determining Beam Focus	549
Quality Control	554

Laser Beam

Laser Beam Welding	556
Laser Beam Welding Advantages and Limitations	556
Laser Beam Welding Fundamentals and Process Physics	558
Process Selection	560
Health and Safety	566

Laser Beam Weld Design, Codes, and Quality Assessment ...	570
Design of Laser Beam Weld Joints	570
Laser Beam Weld Quality	572

Laser Beam Delivery Optics and Manufacturing

Economics	580
Optics for Beam Delivery	580
Manufacturing Economics	583

Laser Deposition Processes

Laser Deposition Processes	587
Laser Cladding	587
Near-Net Shape Processing	591

Laser Weld Quality Monitoring

Laser Weld Quality Monitoring	595
Overview of Laser Welding	595
Process Variables	597
Real-Time or In-Process Monitoring	599
Examples of Laser Weld Monitoring	601

Laser Cutting, Drilling, and Shock Peening

Laser Cutting, Drilling, and Shock Peening	606
Principles of Laser-Cutting Thermal Processes	606
Principles of Laser-Drilling Processes	619
Principles of Laser Shock-Peening Processes	621

Microjoining with Laser and Electron Beams

Microjoining with Laser and Electron Beams	625
Definition—What Is a Microweld?	625
Microscale Physical Phenomena	625
Process Description	628
Techniques and Applications	632
Future Trends	634

Introduction to High Energy Density Electron and Laser Beam Welding

J.W. Elmer, P.W. Hochanadel, K. Lachenberg, and T. Webber

HIGH ENERGY DENSITY BEAM WELDING refers to electron or laser processes where a beam of electrons or photons, respectively, can be focused to power densities high enough to melt and vaporize the metals being joined. The high power densities and associated metal vaporization can be used to produce welds with high depth-to-width aspect ratios, small heat-affected zones, and reduced distortion. In certain applications, high energy density beam welds can offer both high quality and cost-effectiveness when compared to other welding methods. Although there are many similarities between electron and laser welding techniques, there are also many significant differences. This article provides a brief history of electron and laser beam welding, discusses the properties of electrons and photons used for welding, and contrasts electron and laser beam welding by way of an introduction to the sections that follow, where each process is described separately. In addition, a section is included on the growing field of microjoining with electron and laser beams, which is becoming more important as miniaturization of components continues in the areas of microelectronics, implantable medical devices, sensors, optoelectronics, and micromechanical systems. Although many of the principles are the same between macro- and microjoining, when weld dimensions become less than a millimeter, spot size, beam control, and part manipulation become more challenging, joint preparation and cleanliness become more important, and not all of the material properties scale at the same rates. These factors bring new challenges to both the technological and metallurgical aspects of microjoints made by electron and laser beams.

History of Electron Beams and Laser Beams

The development of electron beams used for welding began in Europe in the mid- to late-1950s. In Germany around 1958, scientist

Karl-Heinz Steigerwald was conducting experiments on a transmission electron microscope and observed melting of the small samples as the beam current was increased (Ref 1, 2). About the same time in France, Dr. Jacques-Andre Stohr was looking to weld reactive materials with x-ray tube systems and began to develop electron beam welding through work carried out by the Commissariat Energie Atomique (CEA) (Ref 3–5). At the time, the science behind the production, acceleration, and focusing of electron beams in vacuum was well understood, so it was a relatively straightforward process to design and build systems large enough for welding practical materials once these initial ideas had germinated. The introduction of electron beam welding to manufacturing technology is important enough that one of the earliest electron beam welding machines from Steigerwald has been preserved and is on public display at the Deutsches Museum of Technology in Munich, Germany. By the early 1960s, high-voltage (125 to 150 kV) electron beam welding systems were being fabricated and sold by the Carl Zeiss Company in cooperation with Hamilton Standard, a division of United Technologies Corporation, and low-voltage (15 to 60 kV) systems by Sciaky SA through license agreement with CEA, which extended to Sciaky Brothers in the United States (Ref 3). These early machines were fabricated mostly for laboratory and limited commercial use. By the 1970s, electron beams became the welding method of choice for high-quality precision welds. The driving force for new developments during this time came mainly from the nuclear and aerospace industries, where 5 to 100 kW (7 to 130 hp) systems were developed for deep-penetration welding (Ref 2, 6). High-voltage systems, 150 to 200 kV, were developed to operate at less than 100 mA of beam current, while low-voltage systems, 30 to 60 kV, were developed to operate at higher beam currents of up to 1 A, with powers exceeding 50 kW (67 hp). The largest and most powerful electron beam welder to date was developed in Japan, reaching 300

kW (400 hp) at 600 kV, and was able to penetrate up to 305 mm (12 in.) of steel (Ref 7, 8).

Both high- and low-voltage electron beam welding systems were later integrated with computer numerical control systems using both fixed- and movable-head electron beam welding guns in the 1970s and 1980s to access greater commercial applications. Other advances in electron beam welding technology included out-of-vacuum welding systems, seam tracking, and beam rastering, which spurred new applications for heat treating, drilling, cutting, and cladding. Today (2011), electron beam welding is the method of choice for larger components that require welds to be made in vacuum, such as with reactive materials and hermetic vacuum sealing, and for welds with penetrations greater than approximately 12 mm (0.5 in.). Electron beam welding continues to evolve through the development of new applications, such as free-form fabrication with wire or powder filler metals (Ref 9), and rapid deflection optics to scan the beam in a way to allow a part to be simultaneously heat treated and welded with one beam, or allow multiple welds to be made using one beam (Ref 10, 11). In addition, electron beam diagnostics are being continually improved to provide a greater measure of quality control for electron beams that was not available in the past (Ref 12–14). These diagnostics are on par with diagnostics used for measuring power density distributions in continuous-wave laser beams and allow the two processes to be quantitatively compared. The number of electron beam welders appears to be approaching a steady-state value, where a rough estimated number of installed electron beam welders in the world is on the order of 2000 (Ref 3), which is approximately one-half the number of installed kilowatt-level high-power lasers used for welding (Ref 15).

While electron beam welding was being developed in the late 1950s and early 1960s for commercial applications, lasers were being invented and discovered in research laboratories in the United States. Many good articles exist on the early development of *lasers*, the

term first given to represent light amplification by stimulated emission of radiation by Gould in 1959 (Ref 16), so only a short introduction is provided here. The invention of the laser can be traced to the pioneering work performed in microwave electronics by A.L. Schawlow and C.H. Townes at Bell Laboratories for their work on infrared masers in 1958 (Ref 17). The first working laser, which was a solid-state flash-lamp-pumped synthetic ruby crystal laser that operated in a pulsed mode at $0.694 \mu\text{m}$ ($27 \mu\text{in.}$) wavelength, was developed in 1960 by Theodore Maiman at Hughes Research Laboratories (Ref 16). Shortly afterward, gas lasers based on helium and neon were developed at Bell Labs and were capable of being scaled to high powers due to easier heat management of the gas lasing medium (Ref 16). In 1962, semiconducting laser diodes were also developed at Bell Labs, further demonstrating the wide range of media capable of generating laser light (Ref 16).

Early lasers were not much more than laboratory curiosities, and it took more than a decade for their real commercial potential to be developed in consumer products, such as barcode scanners, compact disc players, laser pointers, laser printers, and materials processing applications. The majority of lasers used for welding today (2011) are either yttrium-aluminum-garnet (YAG) crystal solid-state lasers doped with neodymium or ytterbium, or CO_2 gas lasers. However, direct-diode lasers are now commercially available with high enough beam quality at high powers to be used for welding and other materials applications (Ref 18). The Nd:YAG and CO_2 lasers were both developed at Bell Laboratories in 1964, and although both operate in the infrared wavelength range, they have wavelengths that are an order of magnitude apart: 1060 nm ($42 \mu\text{in.}$) for Nd:YAG and $10,600 \text{ nm}$ ($420 \mu\text{in.}$) for CO_2 . This difference in wavelength results in different interactions with materials and requires different types of optics and laser delivery systems to be used for each. These differences, and the ease at which gas lasers were scaled up in the early years, led to CO_2 laser dominance of high-power laser applications, oftentimes competing with electron beams, while solid-state YAG lasers were used primarily for precision and low-power applications. By the early 1970s, CO_2 lasers had reached the 20 kW (27 hp) level, while flash-lamp-pumped Nd:YAG lasers were limited to only 400 W (0.5 hp) (Ref 19, 20). Today (2011), diode-pumped Nd:YAG lasers are available with powers up to 4 kW (5 hp), and direct-diode lasers are available with powers up to 10 kW (13 hp). The CO_2 lasers dominate the gas laser market and are commonly used for welding and cutting, with powers as high as 45 kW (60 hp) (Ref 21).

New-generation high-brightness lasers are being developed with ever-increasing powers. Disc lasers are now commercially available with powers up to 16 kW (21 hp), and fiber

lasers are available with powers up to 50 kW (67 hp) for military and commercial applications, with 200 kW (270 hp) powers planned for the near future (Ref 22). Note that the term *brightness* is used in this article as a descriptive term to refer to the quality of the laser beam, where higher brightness refers to higher-quality beams. These new-generation lasers use lasing media that are thin in at least one dimension so that heat can be removed from them efficiently. With less heating of the lasing media, higher-quality, higher-brightness beams are produced. In the case of disc lasers, the lasing crystal is a thin disk measuring only approximately 10 mm (0.4 in.) diameter and less than 1 mm (0.04 in.) thick. In the case of fiber lasers, the active lasing medium is a long, thin fiber only $10 \mu\text{m}$ (0.0004 in.) diameter.

High laser powers are now available from many suppliers, and after the overall power level for an application is established, the quality of the beam becomes the next important consideration. The quality of the beam affects how well the laser can be focused and delivered, and there are different ways to measure beam quality. One common measure of laser beam quality is the beam parameter product (BPP), which represents how tightly the beam can be focused under a limited divergence condition. The BPP is discussed in more detail later but is used in Fig. 1 to compare the beam quality of different types of lasers as a function of beam power up to their respective maximum

powers. Lower BPPs refer to more tightly focused and less divergent beams and are desired for precise cutting, deep keyhole welding, and long focal-length conditions. Diode lasers have the largest BPPs, which makes them most attractive for lower power density applications, where larger beam diameters and lower power densities are desired. Their high powers combined with large BPPs make them also very useful for nonwelding applications, such as large-area heat treating and cladding. Diode and flash-lamp-pumped Nd:YAG rod lasers are available from many sources with BPPs between 10 and 20 mm-mrad at the 4 kW (5 hp) level. These lasers, along with CO_2 lasers, have lower BPPs than diode lasers and dominated the laser welding and cutting market until solid-state disc and fiber lasers became commercially available. Disc lasers currently have BPPs on the order of 8 mm-mrad at the 8 kW (11 hp) level, while single-mode fiber lasers are now available with powers up to 10 kW (13 hp) and BPPs at the limit of diffraction for 1060 nm ($42 \mu\text{in.}$) beams of 0.37 mm-mrad . The CO_2 lasers below 10 kW can have similar diffraction-limited beam quality but have BPPs approximately 10 times as large as fiber lasers due to their longer wavelength. At power levels higher than 10 kW in CO_2 (up to 45 kW , or 60 hp) and fiber (up to 50 kW , or 67 hp), the BPP increases to the 6 to 8 mm-mrad range, because less-perfect multimode beams are required to generate these powers.

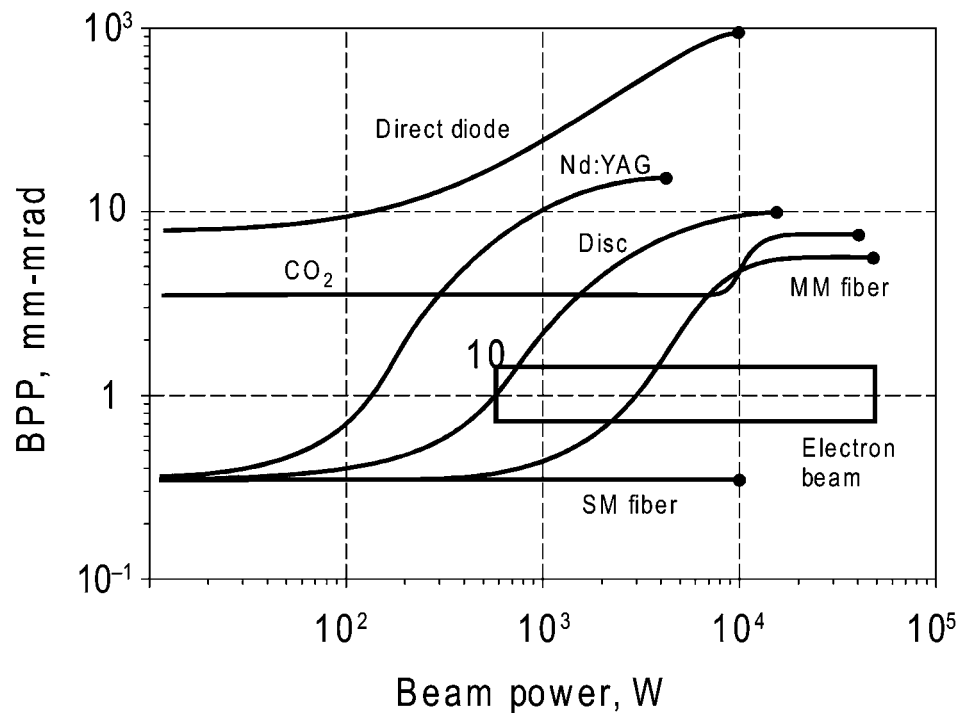


Fig. 1 Beam parameter product (BPP) plotted versus laser power up to the highest commercially available power levels for six different types of lasers. SM and MM refer to single-mode and multimode fiber lasers, respectively; Nd:YAG refers to neodymium: yttrium-aluminum-garnet laser. The estimated BPP range for electron beams is shown for comparison.

While the quality of laser beams is typically measured using the BPP, electron beam technology has not traditionally used the same convention, making it difficult to compare the two processes directly. However, estimates of electron beam quality can be made using diagnostic measurements of the beam power density distribution (Ref 23) and approximations of the beam divergence. Recent measurements of electron beams have been performed to determine the BPP of kilowatt-level electron beams, showing BPP values between 0.75 and 1.3 mm·mrad (Ref 11, 24, 25). This range is plotted in Fig. 1 for comparison with lasers, indicating that an equivalent BPP for electron beams is smaller than that of CO₂ lasers but larger than that of solid-state single-mode lasers. Additional work needs to be done to characterize electron beam quality using advanced diagnostics to determine the influence of operating voltage, cathode size and shape, and electron gun design on beam quality. However, it is clear that the recent increase in the quality and power of solid-state lasers has resulted in a large overlap of welding capabilities between CO₂ lasers, solid-state lasers, and electron beams, providing users with many options when selecting high energy density beam welding processes.

Properties of Electron and Laser Beams

Electron Beams

Electron beams are composed of electrons that are charged particles having a rest mass of 9.1×10^{-31} kg and can be accelerated in electron guns to relativistic velocities, giving them high kinetic energies. At 10 kV (13 hp), electrons travel at approximately 20% of the speed of light, while at 200 kV (270 hp) they travel at approximately 70% the speed of light (Ref 2, 26). The kinetic energy is the source of heat used for welding as the electrons in the beam rapidly slow down and deposit their energy into the substrate. The depth that the electrons penetrate into a substrate depends on the energy of the electron and the properties of material being welded and most importantly, is inversely related to the atomic number, Z . The penetration depth is often calculated using Carlo methods to account for multiple atomic collisions as the electrons continuously slow down (Ref 27). These calculations indicate that 150 kV (200 hp) electrons penetrate 10 to 100 μm (400 to 4000 $\mu\text{in.}$) in metals (Ref 26); thus, the majority of the electron energy is deposited in a rather thin surface layer. Electrons, being charged particles, interact with all types of matter, which places restrictions on how they are focused and delivered to the parts being welded. Unlike lasers, electron beam focusing is performed using magnetic lenses that do not function to the same degree of precision as optics for lasers. However, this magnetic lens

property does allow for dynamic adjustments of beam deflection and focus through computer control. Caution should also be used when working with magnetic and ferromagnetic materials and weld tooling so that the beam does not inappropriately deflect from the intended target. In addition, electron beams interact with gas molecules to the extent that a 100 kV (134 hp) beam will lose 90% of its energy after propagating through only 46 cm (18 in.) of air (Ref 26). Electron beam welding is therefore most typically performed under medium-to-high vacuum conditions of 13 to 0.13 mPa (10^{-4} to 10^{-6} torr) in large vacuum chambers to accommodate the welding of large structures (Ref 2, 6, 7). This vacuum environment is advantageous for welding materials that are reactive or refractory or require low levels of atmospheric contaminants. On occasion, electron beam welding is performed under non-vacuum conditions, but the beam must be kept very close to the surface of the part. Although the depth of the weld is significantly reduced compared to vacuum welding, numerous applications, particularly in the automotive industry, are found for out-of-vacuum electron beam welding (Ref 6, 28).

After electrons strike the substrate, they primarily lose their energy through elastic and inelastic scattering with atoms, causing the electrons to slow down as they deposit their energy into the material being welded (Ref 26, 27). In the process of slowing down, the electrons produce a spectrum of electromagnetic waves, particularly x-rays, which present a health and safety hazard that requires adequate shielding to protect the operator. Some of the electrons are backscattered from the surface, resulting in energy that is not deposited into the substrate. The fraction of backscattered electrons increases with atomic number, from approximately 0.1 for low- Z materials such as aluminum to nearly 0.5 for high- Z materials such as tantalum (Ref 2). Electrons can also be treated as waves instead of charged particles, according to the de Broglie equation $\lambda = h/p$, where λ is the wavelength of the electron, h is Planck's constant, and p is the electron momentum (mV) (Ref 29). Using this relationship and the relativistic velocity of the electrons to account for their increased mass at these speeds (Ref 29), the wavelength of electrons used for welding is smaller than atomic dimensions, ranging between $\lambda = 0.0123$ nm (0.0005 $\mu\text{in.}$) at 10 kV and $\lambda = 0.0025$ nm (0.0001 $\mu\text{in.}$) at 200 kV (Ref 29). These wavelengths are significantly less than photons used for laser welding, and this difference represents a fundamental difference between how electron and laser beams interact with materials.

Laser Beams

Lasers are devices that emit light (photons), typically in a narrow wavelength range (monochromatic) that is spatially coherent (in phase).

These properties allow lasers to be focused to much higher power densities than would be possible from incoherent multispectral light sources, giving lasers the ability to be used for a wide variety of materials processing applications, such as welding, cutting, drilling, and micromachining. Laser beams can be transported through air or inert gases and thus do not require the large vacuum chambers used for electron beam welding, which opens up a host of possibilities not readily accessible to electron beams. One of the most fundamental properties of laser beams is wavelength, which can vary from the ultraviolet to the visible and the near- and far-infrared regions of the electromagnetic spectrum. However, the majority of lasers used for welding have wavelengths close to either $\lambda = 1060$ nm (42 $\mu\text{in.}$) (solid-state lasers) or $\lambda = 10,600$ nm (420 $\mu\text{in.}$) (CO₂ lasers), representing a factor of 10^5 to 10^6 longer wavelengths than electron beams used for welding.

The minimum spot size of focused laser beams, and electron beams, operating under ideal conditions is ultimately limited by diffraction (Ref 29, 30). The minimum or diffraction-limited spot size for an ideal beam is given by $d_{\text{min}} = 2.44\lambda(f/x_c)$, where d_{min} is the smallest spot size of the laser beam, f is the focal length of the lens, and x_c is the coherence length of the beam taken to be the collimated beam diameter (Ref 30). Because the smallest-diameter spot is directly related to the wavelength of the beam, λ , smaller-wavelength electron beams can, in principle, be focused to many orders of magnitude smaller spot sizes than laser beams. However, the combination of the large size of the cathodes that emit the electrons, the comparatively poor quality of electron optics used for welding, and the mutual repulsion of electrons (space charge effect) prevents high-power electron beams used in welding from being focused to their diffraction limit. In fact, the sharpest focus conditions for most electron beam welders produce spot diameters on the order of 200 μm (0.008 in.) (Ref 12–14). On the other hand, high-power laser beams can be focused to diameters less than 100 μm (0.004 in.) for solid-state lasers with small f -number (ratio of focal length of lens to collimated beam diameter) optics (Ref 30). High-power CO₂ lasers, because of their longer wavelength, are at a disadvantage compared to solid-state lasers. However, their ability to produce Gaussian-like TEM₀₀ modes with low M^2 values (discussed later) at powers approaching 10 kW (13 hp) enables CO₂ lasers to maintain low BPPs and produce smaller spot sizes at high powers than Nd:YAG lasers, and similar spot sizes to fiber lasers at the 10 kW level.

Characterization and definition of laser beam propagation is important in order to compare different lasers and different optical configurations. This subject is discussed in many references and is detailed in ISO standard 11146 (Ref 31). A schematic drawing of the propagation of a laser beam is shown in Fig. 2, which

illustrates several important beam characteristics. As the beam is focused, the circular cross section, defined by either the second moment or 86% width (Ref 31), decreases in size as it converges to the waist of the beam where the sharpest spot occurs. The beam radius as a function of Z-axis position, $R(Z)$, reaches a minimum radius, R_o , at the beam waist. The Rayleigh length, Z_{RL} , is the Z-axis distance above or below the minimum beam radius, where the radius at that point, R_{RL} , increases by a factor of square root of 2, and the area of the beam is doubled. The beam diverges at a half-angle of θ in the far field, with the full beam angle of $\Theta = 2\theta$. The BPP is defined as the product of the half-width (beam radius) at the beam cross-over location and the beam divergence angle (BPP = θR_o) and has units of mm-mrad (Ref 31, 32). Note that the half-divergence angle, θ , is used and not the full-divergence angle for this calculation. The BPP is often used as a measure for comparing the quality of different laser beams and is a fundamental property of the beam and is not affected by the configuration of the output optics. Another common measure of the beam quality is M^2 , which is a dimensionless number defined as the ratio of the true BPP to the ideal BPP for a perfect Gaussian beam. It indicates how far the beam is from an ideal, diffraction-limited beam. Alternatively, K , which is defined as the reciprocal of M^2 ($K = 1/M^2$), is used as yet one more measure of beam quality, as a

matter of convenience. These definitions, and more details of beam quality, can be found in standard laser beam texts or beam-quality references (Ref 31).

Solid-state lasers operating at or near 1 μm (40 $\mu\text{in.}$) wavelength have rapidly evolved over the past decade from flash-lamp-pumped and diode-pumped rods to disk, fiber, and direct-diode lasers used for materials processing. These advances in technology have created commercial products with a wide variety of beam qualities and power levels, which are finding applications from low-brightness applications for welding of plastics, soldering, and brazing to high-brightness applications such as keyhole welding. Figure 3 plots these different regions on coordinates of BPP versus laser power, as redrawn and modified from Ref 18 to include keyhole welding, cutting, and drilling. Because the BPP is defined as the product of the beam radius at the beam waist with the far-field beam divergence, smaller numbers correspond to brighter beams that can be focused to higher power densities. More than 3 orders of magnitude of BPP are plotted in this figure, which cover a wide range of materials processing applications from large-area heat treating of metals at high powers without melting the substrate, to intense beams used for keyhole welding, cutting, and drilling. Although the regions of interest are only approximate and may vary by application, the overall plot is a useful starting point when considering the type

of laser and optical configurations required for a given job. Even though high-brightness lasers can be defocused to low-beam intensities, the higher cost of these systems may make less-expensive, lower-brightness lasers more cost-effective for selected applications.

Just as electron beams can be described in terms of either energy or wavelength using the de Broglie equation, so can laser beams. Because photons have no mass and travel at the speed of light, the relationship is simplified to $E = 1.240/\lambda$, where λ is in nm and E is in keV. Thus, the energy of a 1060 nm Nd:YAG laser beam is only 1.16 eV, and that for a 10,600 nm CO₂ laser is 0.116 eV, both being considerably smaller in energy than their electron beam counterparts. The lower energy and longer wavelengths of laser beams compared to electron beams results in significantly different beam/material interactions, particularly the fraction of energy that is absorbed by the substrate, which strongly depends on both the laser wavelength and the material properties (Ref 33). In addition, other factors, such as temperature, beam intensity, polarization, angle of incidence, alloy composition, surface roughness, oxide layers, and contamination, contribute to the absorption of laser beams (Ref 33).

Laser absorption increases as the wavelength decreases, and this factor is important when selecting the type of laser to use for a given application. The absorption for CO₂ lasers operating at 10,600 nm is 1/5 to 1/10 that of

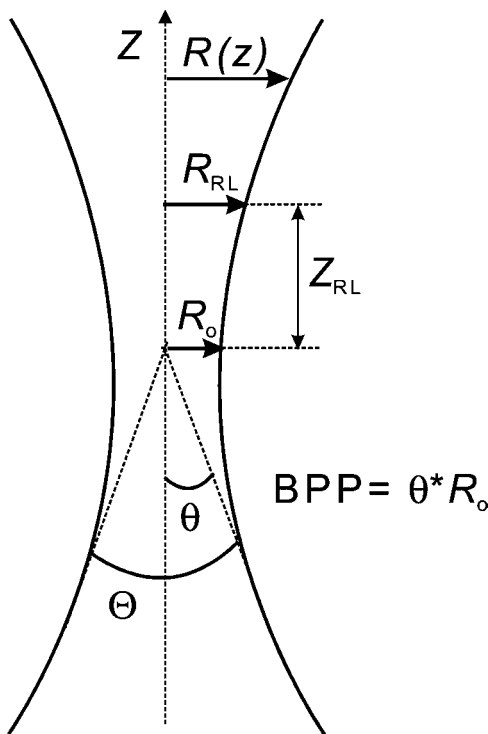


Fig. 2 Illustration of the propagation of a focused laser beam as the beam radius, $R(z)$, varies along the Z-axis. The beam parameter product (BPP) is a fundamental property of the beam and is a useful way to compare different laser beams.

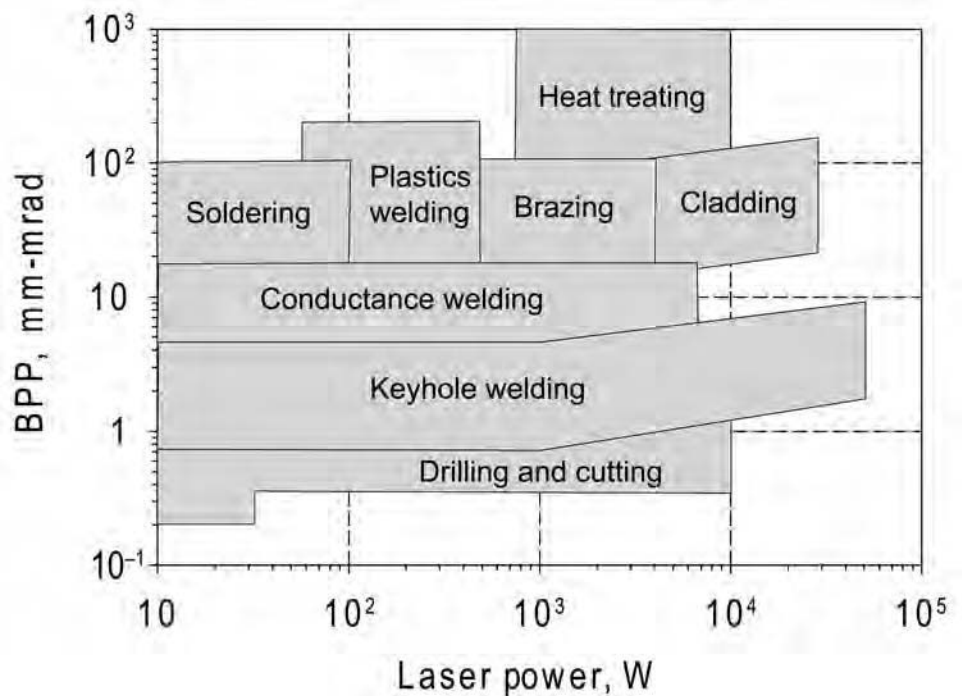


Fig. 3 Beam parameter product (BPP) plotted versus laser power, showing typical regions used for low- and high-brightness laser applications

solid-state lasers operating at 1060 nm on metal surfaces. Even for solid-state lasers with wavelengths of 1060 nm, the absorption is rather low. For example, absorption at 1060 nm is less than 0.5 for the highest-absorbing metals, such as titanium, and less than 0.05 for highly reflective materials, such as silver and gold, at room temperature (Ref 33). Significantly higher laser absorption on highly reflective metals such as gold and copper can be achieved by decreasing the wavelength into the green at 532 nm (21 μm) (Ref 34) or even lower wavelengths. These lasers are just now becoming commercially available in small packages with 10 W (0.01 hp)-level powers that are ideal for micro-electronic and small-component applications.

For material/laser combinations where the absorption is low, the fraction of energy not absorbed by the substrate is reflected and may or may not contribute to further heating of the material, depending on the weld geometry. The beam energy is absorbed in a very narrow surface layer because the photons interact only with electrons at these energy levels. This depth of penetration of the photons, or attenuation length, is inversely related to the material absorption coefficient, α . The penetration depth of the photons is on the order of 10^{-1} to 10^{-2} μm (4 to 0.4 μm) in metals, which is less than the wavelength of the laser beams. This shallow penetration is considerably smaller than that of electrons used for welding, which allows lasers to vaporize materials more easily, and is one reason why lasers are preferred over electron beams for precision cutting, drilling, scribing, marking, and micromachining.

Comparison between Electron and Laser Beam Welding

Beam quality measurements such as BPP are a good way to compare the brightness and focusing ability of different laser and electron beams. However, the power density, which is defined as the ratio of the absorbed power to the area of the beam, is the important parameter for determining how the beam will interact with a given material. High power density beam welding requires beams with power densities that exceed approximately 10^5 W/cm^2 (1.55×10^4 W/in^2), which is the level at which most metals will begin to vaporize rapidly beneath the beam (Ref 35). As the power density increases above this level, the rate of vaporization increases, producing deeper welds with little increase in the weld width. At a power density of 10^6 W/cm^2 (1.55×10^5 W/in^2), the depth-to width ratio of the weld can exceed 10 to 1. Further increases in power density above 10^7 W/cm^2 (1.55×10^6 W/in^2) can create such intense vaporization that metal is ejected from the keyhole, and the beam begins to enter a cutting rather than welding mode.

The power density is primarily controlled by the focal spot diameter and the beam power.

Figure 4 plots this relationship, showing the power required to achieve a given power density as a function of beam diameter. For example, to achieve a power density of 10^6 W/cm^2 (1.55×10^5 W/in^2), a 200 μm (0.008 in.) diameter beam only requires approximately 300 W (0.4 hp) of power, whereas a 1 mm (0.04 in.) diameter beam requires approximately 8 kW (11 hp) of power. Both laser and electron beams easily achieve the power density required for rapid vaporization and keyhole welding. To reach the higher power density limit of keyhole welding of 10^7 W/cm^2 (1.55×10^6 W/in^2), continuous beams of 5 kW (7 hp) would need to be focused to a diameter of approximately 250 μm (0.01 in.). This diameter and power combination has been easily achieved by electron beams for decades and is now being equaled, and surpassed, by solid-state lasers that can deliver these power levels through 100 μm (0.004 in.) diameter fibers with similar or smaller focused spot sizes, depending on the optics. These tightly focused laser beams now have the ability to produce power densities too high for welding and may need to be lowered in intensity by stepping up to larger-diameter fibers, using longer focal-length lenses, and/or defocusing the beam to produce acceptable welds.

When a beam interacts with a surface, not all of the beam power is absorbed by the substrate,

and one of the largest differences between laser and electron beams is the difference in absorption characteristics for lasers of different wavelengths and electron beams. Absorption of the beam is typically less for photons than electrons under most circumstances, and the differences can be large. Because the material must first absorb enough energy to melt before it can vaporize to form a keyhole, there is a power density level below which welding will not occur. This power level is highly dependent on the absorption as well as the thermophysical properties of the metal. While electrons instantly begin to penetrate the substrate and form a keyhole at 10^5 W/cm^2 (1.55×10^4 W/in^2), lasers may not if the reflectance is high enough to prevent a substantial portion of the beam from being absorbed. For electrons, where absorption is high, calculations show that materials with low thermal diffusivity, such as stainless steel and titanium alloys, will begin to melt at 5 to 10 times lower power densities than high-thermal-diffusivity metals such as copper and gold (Ref 7). For lasers, though, this threshold value may be as large as 2 orders of magnitude between high-reflectivity and high-conductivity metals or between low-conductivity and low-reflectivity metals (Ref 7). Pulsed lasers minimize the absorption problems at low powers by producing higher peak power densities than their

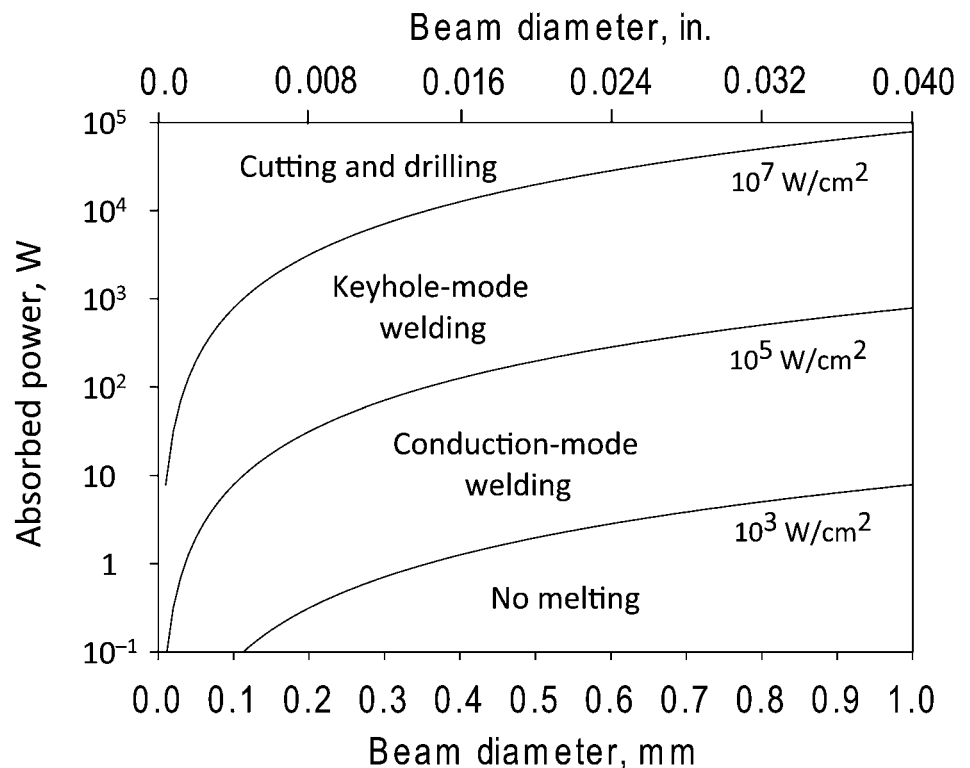


Fig. 4 Constant power density boundaries showing the relationship between the focused beam diameter and the absorbed beam power for approximate regions of keyhole-mode welding, conduction-mode welding, cutting, and drilling

continuous-wave counterparts, while maintaining the same average power. Electron beams can be pulse modulated for hole drilling, which is occasionally used for keyhole stability. However, pulse modulation does not increase the peak power density of electron beams and is not a technique used for initiating a keyhole in welds.

Travel speed plays the other major role in how the beam interacts with the substrate, because the energy density, rather than power density, is the parameter that ultimately controls the response of the material to the beam. The faster the beam moves, the less energy is deposited per unit length of weld, and the penetration decreases. The energy deposited per unit length of weld (J/mm) is defined by the beam power (W) divided by the travel speed of the weld (mm/s) and is one measure of how the travel speed influences weld behavior. Analytical solutions to heat-flow relationships in high power density welding (Ref 20, 36, 37) can be used to estimate the influence of welding speed on the threshold for surface melting and vaporization that leads to deep-penetration conditions, while more advanced models are continually evolving to predict the complicated relationships between welding variables and keyhole weld shape. These advanced numerical models use a coupled thermal-fluids approach to solve the equations of conservation of mass, momentum, and energy in three dimensions and must calculate the temperature distribution on the inside surface of the keyhole wall. In the case of lasers, multiple reflections of the beam off of the keyhole wall must be considered in how the keyhole is established and maintained (Ref 38). In the case of electron beams, the presence of welding in vacuum must be considered (Ref 39). More details about the numerical modeling of high power density beam welding can be found elsewhere in this Handbook.

A number of articles that compare laser and electron beam welding processes have been written. However, many of these comparisons are more than a decade old and have not kept pace with the recent advances in these technologies (Ref 40–45). Nevertheless, much of the reasoning behind the comparisons is still valid. For example, electrons require a vacuum to propagate the beam, and they generate large amounts of x-rays. Lasers, on the other hand, may require shielding gases, have higher reflectance, and present hazards in other ways. Concerning capital equipment and operating costs listed in some of these comparisons, it is important to note that the price per kilowatt of power has decreased significantly for lasers because higher average power lasers are being produced in more compact systems with smaller footprints and lower utility costs. Factoring in all the types of lasers used for welding and all the types of electron beam configurations creates too many variables to compare and contrast in this article. However, it is safe to say that either method will work well for many applications, but certain applications still

tend toward one method or the other. For deep-penetration welds over 12 mm (0.5 in.), for highly reflective metals, for welds on highly reactive materials that require vacuum conditions, and/or for welds that require hermetic sealing in vacuum, electron beams are most often the preferred method. Lasers, on the other hand, have more flexible delivery options and superior versatility that allow them to be directed into areas that are difficult to access with electron beams. This versatility allows lasers to be more easily configured and integrated into multiple-use workstations with associated potential cost-savings. Because lasers do not require vacuum operation, tooling is oftentimes simpler to fabricate and use, and production rates are oftentimes higher. In addition, lasers can be used to heat and melt non-electrically conductive materials, and they are not affected by magnetic or ferromagnetic base materials and tooling that tend to deflect and/or interfere with electron beams.

ACKNOWLEDGMENT

This work was performed under the auspices of the U.S. Department of Energy by Lawrence Livermore National Laboratory under Contract DE-AC52-07NA27344. This document was prepared as an account of work sponsored by an agency of the United States government. Neither the United States government nor Lawrence Livermore National Security, LLC nor any of their employees makes any warranty, expressed or implied, or assumes any legal liability or responsibility for the accuracy, completeness, or usefulness of any information, apparatus, product, or process disclosed, or represents that its use would not infringe privately owned rights. Reference herein to any specific commercial product, process, or service by trade name, trademark, manufacturer, or otherwise does not necessarily constitute or imply its endorsement, recommendation, or favoring by the United States government or Lawrence Livermore National Security, LLC. The views and opinions of authors expressed herein do not necessarily state or reflect those of the United States government or Lawrence Livermore National Security, LLC and shall not be used for advertising or product-endorsement purposes.

REFERENCES

1. K.J. Miller and T. Takenaka, "Electron Beam Welding," Welding Research Council Bulletin, No. 100, New York, 1964
2. S. Shiller, U. Heisig, and S. Panzer, *Electron Beam Technology*, John Wiley and Sons, 1982, English translation from German edition
3. K.H. Steigerwald, G. Sayegh, D. Powers, R. Bakish, O.K. Nazarenko, W. Dietrich, H. Irie, D. Wyatt, and D.V. Dobeneck, *An*

4. J.A. Stohr, *Fuel Elements Conference*, TID 7546, Book 1, Nov 1957 (Paris), U.S. Atomic Energy Commission, 1958, p 0–17
5. J.A. Stohr, CEA Sacley, Patent 1.41.535, Paris, 1956
6. M. Schwartz, "Electron Beam Welding," Welding Research Council Bulletin, No. 196, New York, 1974
7. Y. Arata, Ed., Development of Ultra High Energy Density Heat Sources and Their Application to Heat Processing, *Plasma, Electron and Laser Beam Technology*, The American Society for Metals, 1986, p 3–27
8. T.W. Eagar, Electron Beam and Laser Beam Welding in Japan, *Weld. J.*, Vol 57 (No. 7), 1986, p 19
9. K.W. Lachenberg and S. Stecker, "Manufacturing Advantages Using Electron Beam Welding/Free Form Fabrication (EBFFF)," AWS/Fabtech 2008 Conference, Oct 8, 2008 (Las Vegas Convention Center)
10. M. Mücke, All Welding Technologies AG, private communication, June 2009
11. U. Clauss, Fast Beam Deflection and Beam Quality—Keys to Economic High Quality Electron Beam Applications, Presented at the Second International Electron Beam Welding Conference, Fabtec Convention, Nov 2009 (Chicago, IL)
12. G.R. LaFlamme and D.E. Powers, Diagnostic Device Quantifies, Defines Geometric Characteristics of Electron Beams, *Weld. J.*, Vol 70 (No. 10), 1991, p 33–40
13. U. Diltthey and J. Weiser, Study of the "Tool" Electron Beam—Part 1: Comparison between the Arata Beam Test and Diabeam Beam Measurements, *Schweissen Schneiden*, Vol 47 (No. 5), 1995, p 339–345
14. T.A. Palmer and J.W. Elmer, Improving Process Control in Electron Beam Welding Using the Enhanced Modified Faraday Cup, *J. Manuf. Sci. Eng.*, Vol 130 (No. 4), 2008, p 041008
15. D. Belforte, PennWell Corporation, Tulsa, OK, private communication, Dec 2009
16. J.L. Bromberg, *The Laser in America 1950–1970*, MIT Press, 1991
17. A.L. Schawlow and C.H. Townes, Infrared and Optical Masers, *Phys. Rev.*, Vol 112 (No. 6), 1958, p 1940–1949
18. A. Eltze, "High Power Diode Lasers for Brazing, Welding, Cladding and Hardening," Presented at the Laser World of Photonics, June 2009 (Munich, Germany)
19. M. Schwartz, "Laser Welding and Cutting," Welding Research Council Bulletin, No. 167, New York, Nov 1971
20. D.T. Swift-Hook and A.E.F. Gick, Penetration Welding with Lasers, *Weld. J.*, Vol 52 (No. 11), 1973, p 492s–499s

21. M. Kido et al., "Development of 45-kW Laser Welding System for Continuous Finish Rolling," Nippon Steel Technical Report No. 89, 2004, p 91–95
22. V. Gaspontsev, V. Fomin, and A. Yusim, "Recent Progress in Scaling High Power Fiber Lasers at IPG Photonics," Presented at the 22nd Annual Solid State and Diode Laser Technology Review, July 2009 (Newton, MA)
23. T.A. Palmer, J.W. Elmer, K.D. Nicklas, and T. Mustaleski, Transferring Electron Beam Parameters Using the Enhanced Modified Faraday Cup, *Weld. J.*, Vol 86 (No. 12), 2007, p 388s–398s
24. C. Menhard and T. Löwer, The Electron Beam Geometry—Definition, Measurement, and Significance for the Welding Process, *Weld. Cutting*, Vol 8 (No. 3), 2009, p 138–142
25. M. Boyd and J. Vaja, unpublished research acquired on a 120 kV electron beam at the Atomic Weapons Establishment, Aldermaston, England, Dec 2009
26. A.C. Smith, Jr., E.E. Nolting, and W.M. Fawley, An Overview of the High Energy Electron Beam Science, *Conference Proceedings of High Energy Electron Beam and Welding and Materials Processing*, J. Danko and E. Nolting, Ed., American Welding Society, Sept 1992, p 1–41
27. T. Jenkins, W. Nelson, and A. Rindi, Ed., *Monte Carlo Transport of Electrons and Photons*, Plenum Press, 1987
28. Y. Arata, Ed., Some Fundamental Properties of Nonvacuum Electron Beams, *Plasma, Electron and Laser Beam Technology*, The American Society for Metals, 1986, p 71
29. D.B. Williams and C.B. Carter, *Transmission Electron Microscopy, A Textbook for Materials Science*, Plenum Press, 1996
30. K. Iga, *Fundamentals of Laser Optics*, Plenum Press, 1994
31. "Lasers and Laser-Related Equipment—Test Methods for Laser Beam Widths, Divergence Angles and Beam Propagation Ratios," BS EN ISO 11146-1: 2005, British Standard, 2005
32. R. Paschotta, *Encyclopedia of Laser Physics and Technology*, Vol 1, Wiley-VCH, Verlag GmbH & Co. KGaA, 2008
33. W.W. Duley, *Laser Processing and Analysis of Materials*, Plenum Press, 1983
34. M. Greenstein, Optical Absorption Aspects of Laser Soldering for High Density Interconnects, *Appl. Optics*, Vol 28 (No. 21), 1989, p 4595
35. *Welding Processes Part 2*, Vol 3, *Welding Handbook*, 9th ed., American Welding Society, 2007
36. P.G. Klemens, Heat Balance and Flow Conditions for Electron Beam and Laser Welding, *J. Appl. Phys.*, Vol 47 (No. 5), 1976, p 2165–2174
37. H.E. Cline and T.R. Anthony, Heat Treating and Melting Material with a Scanning Laser or Electron Beam, *J. Appl. Phys.*, Vol 48 (No. 9), 1977, p 3895–3900
38. R. Rai, J.W. Elmer, T.A. Palmer, and T. DebRoy, Heat Transfer and Fluid Flow during Keyhole Mode Laser Welding of Tantalum, Ti-6Al-4V, 304L Stainless Steel and Vanadium, *J. Phys. D, Appl. Phys.*, Vol 40, 2007, p 5753–5766
39. R. Rai, T.A. Palmer, J.W. Elmer, and T. DebRoy, Heat Transfer and Fluid Flow during Electron Beam Welding of 304L Stainless Steel Alloy, *Weld. J.*, Vol 88 (No. 3), 2009, p 54s–61s
40. R.C. Hanson, "High Energy Beam (EB/Laser) and Overview Comparison," First International Conference on Power Beam Technology, Sept 10–12, 1986, The Welding Institute—Brighton
41. Electron and Laser Beam Welding, *Proceedings of the International Conference I*, July 1986 (Tokyo, Japan), L'Institute International De La Soudure and The International Institute of Welding, Pergamon Press
42. D.E. Powers and G.R. LaFlamme, EBW vs. LBW—A Comparative Look at the Cost and Performance Traits of Both Processes, *Weld. J.*, Vol 67 (No. 3), 1988, p 25–31
43. P. Anderl, Comparison of Laser with Electron Beam Welding, *Chem.-Ing.-Tech.*, Vol 61 (No. 10), 1989, p 767–774, in German
44. R. Backish, Ed., *The Laser and the Electron Beam in Welding, Cutting and Surface Treatment State of the Art*, Bakish Materials Corporation, Englewood, NJ, 1991
45. C.O. Brown and C.M. Banas, High-Power Laser Beam Welding in Reduced-Pressure Atmospheres, *Weld. J.*, Vol 65 (No. 7), 1986, p 48–53

Electron Beam Welding*

P.W. Hochanadel, Los Alamos National Laboratory

J.W. Elmer, Lawrence Livermore National Laboratory

K. Lachenberg, Sciaky, Inc.

P. Burgardt and D.D. Kautz, Los Alamos National Laboratory

ELECTRON BEAM WELDING (EBW) is a high energy density beam welding process that is accomplished by bombarding the joint to be welded with an intense beam of electrons that have been accelerated up to velocities 0.3 to 0.7 times the speed of light at 30 to 200 kV, respectively. Some of the details were given in the article "Introduction to High-Energy Beam Welding" in this Volume. The instantaneous conversion of the kinetic energy of these electrons into thermal energy as they impact and penetrate into the workpiece on which they are impinging causes the workpiece surface(s) to melt and produces the weld-joint coalescence desired. Electron beam welding is used to weld any electrically conductive material that can be arc welded. Typically, the weld quality in most electron beam welded materials is equal to or superior to that produced by other welding processes.

Because the total kinetic energy of the electrons can be concentrated onto a small area on the workpiece, power densities as high as 10^8 W/cm² (10^7 W/in.²) can be obtained (Ref 1, 2). The high power density plus the extremely small intrinsic penetration of electrons in a solid workpiece causes an almost instantaneous local melting and vaporization of the workpiece material. This high power density characteristic can lead to keyhole formation. Keyhole-mode welding distinguishes EBW (and other high energy density processes) from other welding methods.

Principles of Operation

To illustrate the nature of an electron beam, Fig. 1 shows an electron beam weld being performed at a weld chamber pressure of approximately 13 mPa (1×10^{-4} torr). This figure illustrates that the electron beam has a small diameter, and the small beam diameter is retained over significant distances. The "beam" produces a visible glow that results from the

residual gas molecules that are excited by the electrons in the actual electron beam. This effect is reduced at lower pressures, where the glow is restricted to regions closer to the weld seam as vaporized metal atoms become ionized by the beam.

The electron beam is most often formed by a triode-style electron gun under high vacuum conditions, and a schematic of this is shown in Fig. 2. The triode assembly consists of a cathode, a heated source (emitter) of electrons that is maintained at some high negative potential; a grid cup, a specially shaped electrode that can be negatively biased with respect to the hot cathode emitter (filament); and an anode, a ground potential electrode through which the electron flow passes in the form of a collimated beam. The hot cathode emitter (filament) is made from a high-emission material, usually tungsten or tantalum, which is usually available in wire, ribbon, or sheet form. This emitter material is fabricated into the desired shape for being either directly or indirectly heated to the required emitting temperature of approximately 2500 °C (4500 °F). Other materials, such as lanthanum hexaboride (LaB₆), have also been used as filament material.

Diode-style electron guns have also been employed historically. In a diode gun, the specially shaped electrode (grid cup) is maintained at the same voltage as the emitter, thus making the diode gun a two-element (cathode and anode) device (Fig. 2). With this gun design, the flow of electrons cannot be adjusted by simply varying a grid voltage, as is done with triode guns, and beam current adjustments are usually accomplished by varying the operating temperature of the cathode emitter instead.

Electrons emitted from the surface of the filament are accelerated to a high velocity and shaped into a collimated beam by the electrostatic field geometry generated from the cathode/grid/anode configuration employed, thus producing a steady stream of electrons that

flows through an aperture in the ground plane anode. By varying the negative potential difference between the grid and cathode, this flow of electrons can be altered easily (i.e., the beam current control can also include gating "on/off" and ramping up/down to different levels), rapidly, and in a precisely controlled manner.

Once the electrons exit the anode, they receive the maximum energy input allowable from the operating voltage being applied to



Fig. 1 Photograph of an electron beam operating in an enclosed chamber maintained at a pressure of approximately 13 mPa (1×10^{-4} torr)

* Revised and updated from Electron-Beam Welding, *Welding, Brazing, and Soldering*, Vol 6, *ASM Handbook*, ASM International, 1993, p 254-261

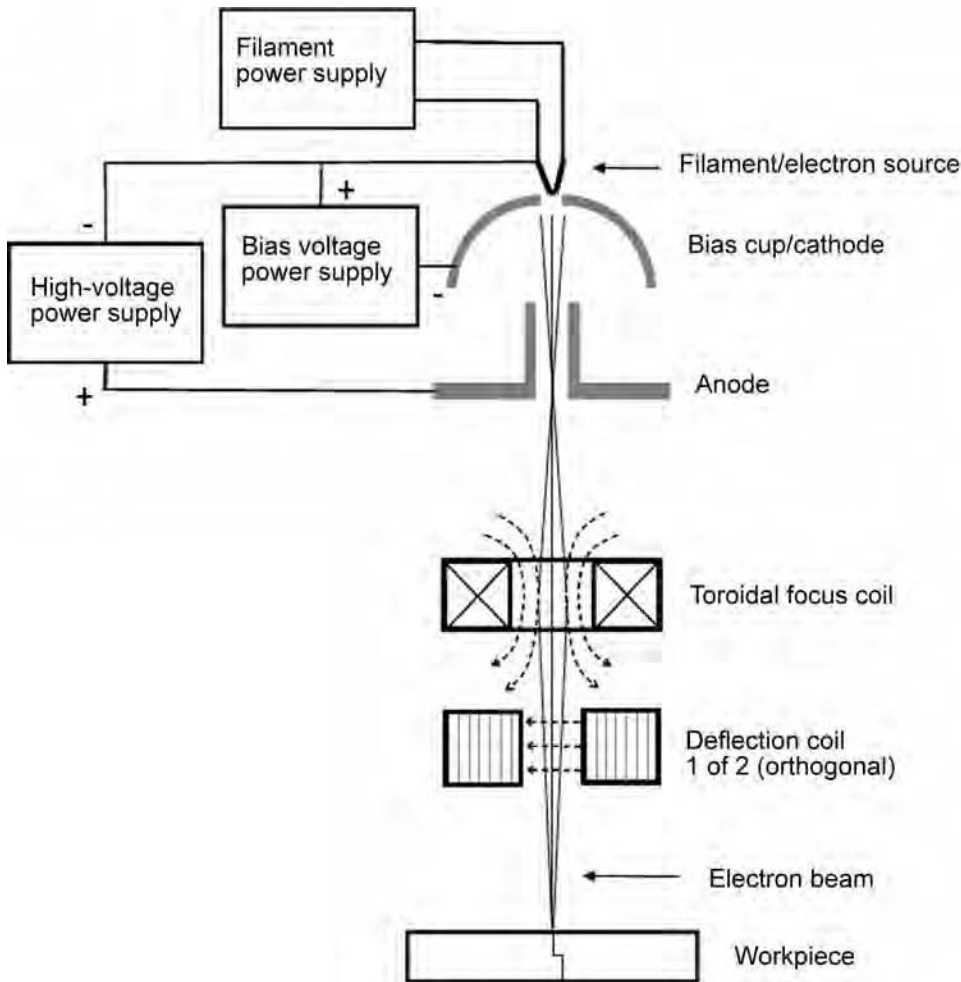


Fig. 2 Schematic drawing showing primary components of an electron beam welding head with a triode-style gun assembly

the gun. Electrons then pass down through the electron beam column assembly and into the field of an electromagnetic focusing coil (a magnetic lens). This focusing lens reduces the diameter of the electron beam as it continues in its passage and focuses the stream of electrons down to a much smaller beam cross section in the plane of the workpiece. This reduction in beam diameter increases the energy density, producing a very small, high-intensity beam spot. The size of the beam spot is one of the most important variables in EBW and is influenced by the EBW conditions, as is discussed later. In addition, an electromagnetic deflection coil (positioned below the magnetic lens) can be employed to "bend" the beam, thus providing the flexibility to move the focused beam spot. Figure 2 illustrates the main elements of the EBW head. As described previously and shown in Fig. 2, electrons are emitted from the cathode and are accelerated to high speed by the voltage between cathode and anode, thereafter maintaining a constant speed until they strike the workpiece.

The "gun" portion of an electron gun/column assembly generally is isolated from the welding chamber through the use of valves when desired, or by using vacuum dividers when employing medium or nonvacuum systems. The gun may be maintained in a vacuum on the order of 13 mPa (1×10^{-4} torr) when the welding chamber is vented to atmosphere (for access reasons). This level of vacuum in the gun region is needed to maintain gun component cleanliness, prevent filament oxidation, and impede high-pressure short circuiting between the cathode and the anode or the filament and the grid cup, known as gun arcing. Generally, electron guns are operated with applied voltages that vary from 30 to 200 kV, and they employ beam currents that range from 0.5 to 1500 mA. Electron beam welding equipment with power levels up to 30 kW is common. In addition, several units with power levels of up to 200 kW are commercially available for specialized applications (Ref 3). However, Osaka University developed a 300 kW system that used an electron gun with 600 kV (Ref 4).

Typically, high-vacuum EBW beams can be focused to spot sizes of approximately 0.25 mm (0.010 in.) in diameter, with a power density of about 10^7 to 10^8 W/cm² (10^6 to 10^7 W/in.²) (Ref 1, 2). This high level of beam spot intensity generates temperatures sufficient to vaporize almost any material, forming a vapor hole that penetrates deep into the workpiece. When this vapor hole is advanced along a weld joint, the weld is produced by three effects that occur simultaneously:

- The material at the leading edge of the vapor hole melts.
- This molten material flows around the sides of the vapor hole to the trailing edge.
- This continuous flow of molten material fills in the trailing edge of the advancing vapor hole and solidifies as the vapor hole moves forward to produce a continuous weld.

Originally, EBW was performed only under high-vacuum (≤ 13 mPa, or 1×10^{-4} torr, or lower pressure/higher vacuum) conditions; because an ambient vacuum environment was required to generate the beam, welding the part within the same clean atmosphere was considered beneficial. However, as the demand for greater part production increased, it was determined that the weld chamber vacuum level need not be as high as that needed for the gun region; ultimately, the need for any type of vacuum surrounding the workpiece was completely eliminated for some applications. Currently, three distinct modes of EBW are employed:

- High-vacuum (EBW-HV), where the workpiece is in an ambient pressure ranging from 0.13 to 133 mPa (10^{-6} to 10^{-3} torr)
- Medium-vacuum (EBW-MV), where the workpiece may be in a "soft" or "partial" vacuum ranging from 133 to 3.3×10^6 mPa (10^{-3} to 25 torr)
- Nonvacuum (EBW-NV), which is also referred to as atmospheric EBW, where the workpiece is at atmospheric pressure in air or protective gas

In EBW-MV and EBW-NV, the electron beam broadens more rapidly or scatters by excitation collisions of the electrons with gas molecules. In these applications, the electron beam gun region is maintained at a pressure of 13 mPa (10^{-4} torr) or lower through differential pumping.

Advantages

One of the prime advantages of EBW is the ability to make welds that are deeper and narrower than arc welds, with a total heat input that is much lower than that required in arc welding. This ability to achieve a high weld depth-to-width ratio eliminates the need for multiple-pass welds, as is required in arc welding. The lower heat input results in a narrow workpiece heat-affected zone and noticeably fewer thermal effects on the workpiece.

Another distinct advantage of EBW is the ability to produce very shallow penetration welds and deep penetration welds with the same equipment by simply manipulating the weld parameters. By manipulating the EBW parameters such as beam current and focusing current, the power density is easily changed from very low to very high power densities, which allows for such a wide range of weld penetrations in EBW. For example, when using lower power densities, the beam does not produce a deep vapor cavity and can act similar to an arc weld.

In EBW, a high-purity vacuum environment is generally used for welding, which results in freedom from impurities such as oxides and nitrides resulting from the welding process. In addition, this high-purity vacuum environment is particularly beneficial when welding refractory metals, because these materials are prone to embrittlement by interstitial atoms from the atmosphere, such as nitrogen and oxygen.

The process (or energy transfer) efficiency, which is defined as the power into the workpiece divided by the source power (or the proportion of the beam energy that is actually transferred to the workpiece) is well understood and relatively high for EBW processes. In EBW-HV, the process efficiency is expected to be quite high, because only a small fraction of the beam power is lost. The process efficiency of EBW has been reported as being at least 90% over a wide range of welding conditions and materials for EBW-HV (Ref 5, 6). In EBW-NV, the process efficiency has been reported to be between 60 and 80% at various welding conditions (Ref 6), which is explained by beam energy losses due to atmospheric scattering. For comparison, the energy transfer efficiency of CO₂ laser beam welding has been shown to vary from 20% to approximately 90%, depending on welding parameters, surface condition, plume control, and so on (Ref 7), while the energy transfer efficiency for neodymium: yttrium-aluminum-garnet laser spot welding was shown to be 40 to 80% for key-hole-mode spot welds and less than 50% for conduction spot welds (Ref 8).

The characteristics of EBW allow for the following:

- Minimizing distortion and shrinkage during welding
- Facilitating welding of most hardened or work-strengthened metals, frequently without significant deterioration of mechanical properties in the weld joint
- Facilitating welding in close proximity to heat-sensitive components or attachments
- Allowing for hermetic seal welding of evacuated enclosures while retaining a vacuum inside the component
- Permitting welding of refractory metals, reactive metals, and combinations of many dissimilar metals that are not easily joinable by arc welding processes

- Producing very shallow to very deep penetrations. Electron beam welds with penetrations of more than 250 mm (10 in.) in high-vacuum conditions have been reported (Ref 9, 10).
- Projecting the electron beam long distances, which allows otherwise inaccessible welds to be completed.

To demonstrate the flexibility of EBW in terms of welding depths, Fig. 3 shows both a shallow- and a deep-penetration weld cross section.

Limitations

The capital equipment costs for EBW generally are higher than those for conventional welding processes. The cost of joint preparation and tooling is also more than that encountered in arc welding processes, because the relatively small electron beam spot size that is used requires precise joint gap and position and the use of nonmagnetic tooling materials.

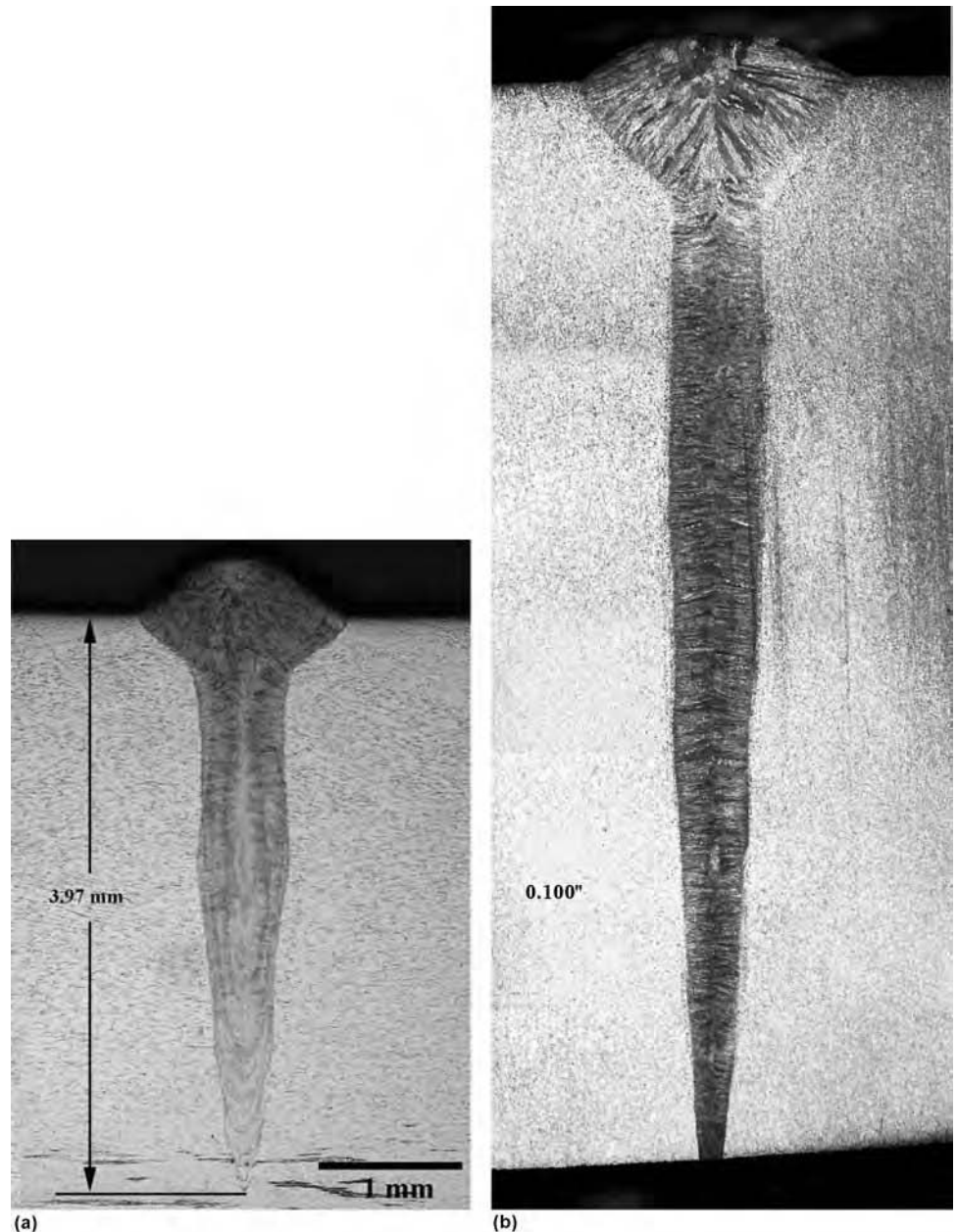


Fig. 3 Cross sections of electron beam welding using high-voltage welding equipment. (a) Shallow-penetration weld on 304L stainless steel with weld parameters of 100 kV, 10 mA, and a travel speed of 17 mm/s (0.7 in./s). Courtesy of T.A. Palmer, Applied Research Laboratory of Pennsylvania State University, State College, PA. (b) Deeper-penetration weld on superalloy 718 with weld parameters of 120 kV, 83 mA, and a travel speed of 8.5 mm/s (0.3 in./s). Courtesy of G. LaFlamme, PTR-Precision Technologies, Enfield, CT

For EBW-HV and EBW-MV, the vacuum chamber and related evacuation is a limitation as well. The available vacuum chamber capacities are limited; workpiece size is limited, to some degree, by the size of the vacuum chamber employed. Consequently, the production rate (as well as unit cost) is affected by the need to evacuate the chamber for each production load. Recent advances by EBW manufacturers have been in the area of throughput, and, as such, index tooling has allowed for greater throughput. In addition, the employment of medium vacuum and cryogenic refrigeration (Meissner coils) is used to decrease the vacuum evacuation time cycle and thus increase the throughput.

Although most of the aforementioned advantages and disadvantages generally are applicable to all modes of EBW, several do not specifically apply to EBW-NV. Nonvacuum EBW does not offer the advantage of a high-purity environment (unless some form of inert gas shielding is provided), and it is not subject to vacuum chamber limitations. Because welding is not done within the confines of a vacuum environment, the maximum practical “stand-off,” the working distance between the bottom of the electron beam column and the top of the workpiece, currently used on EBW-NV systems is limited to approximately 35 mm (1 3/8 in.). The maximum attainable penetration is currently limited to approximately 25 to 32 mm (1 to 1.25 in.) for 60 kW, 165 kV machines. These limitations, however, are offset by higher production rates.

Finally, although covered further in the “Safety” section later in this article, the generation of x-radiation, inherent in EBW, is also a consideration of this process because of the additional safety requirements required for workers’ safety.

Process Control

Basic variables employed for controlling the results of an electron beam weld include accelerating voltage, beam current, welding speed, focusing current (or “increments” of defocus), and standoff (cathode design, gun column assembly-to-workpiece) distance. The final beam spot size that is produced in the plane of the workpiece is determined by:

- Accelerating voltage
- Beam current
- Focusing current, which controls the focal length of the lens and resulting beam focus location
- Gun column assembly-to-workpiece distance
- Characteristics of the electron beam gun/column assembly (gun and electron optics)
- Vacuum level
- Filament design and peaking

Each of these variables, separately and jointly, affects final beam spot size. With the advent of electron beam characterization/profiling, the

output of power density has provided useful information to welding personnel who are interested in understanding the welding reproducibility and beam/material interactions (Ref 11, 12). This subject is covered in some detail in the article “Quality Control of Electron Beams and Welds” in this Volume.

Increasing the accelerating voltage or beam current increases the depth of penetration; the product of these two variables—the beam power—influences the amount of metal melted for a given exposure time. Increasing the welding speed—relative travel motion between beam spot and workpiece—without changing any other process variable reduces depth of penetration and correspondingly reduces weld width. Changing any of the other basic control variables to increase beam spot size, thereby lowering the beam spot intensity (e.g., reducing the power density), reduces depth of penetration and increases weld width, if welding speed is left unchanged.

Beam deflection can be used to change the impact angle of the beam (slightly) or to produce controlled patterns of beam oscillation to create greater beam spot size or other special effects. The beam may be oscillated in circular, elliptical, and linear oscillation patterns. The beam can also be pulsed to vary the average amount of power input per unit of time. Workpiece speed and, in certain instances, standoff distance are generally preset to a desired value. However, it is possible to vary these parameters during welding with the use of computerized numerical control (CNC) types of systems. The CNC electron beam welding systems allow for the beam current, standoff distance, and welding speed to be varied simultaneously, as required, throughout the welding process.

Finally, weld process modeling is an efficient means of understanding how changes in EBW parameters will potentially change resulting weld morphologies. Weld process modeling is an effective means of investigating potential changes in weld morphologies without actually welding several test pieces. However, this topic is out of the scope of this introductory article.

Operation Sequence and Preparation

Tooling and welding procedures for each EBW application are typically developed first on experimental workpieces. Details of the welding sequence vary somewhat, depending on equipment differences and application requirements. A typical sequence of steps required to make an electron beam weld is as follows:

1. Assemble and prepare work and fixtures for welding. This includes cleaning and may include demagnetizing, preheating, and tack welding.
2. Load fixtured work onto worktable or workholding mechanism in welding chamber (except for EBW-NV).

3. Start chamber evacuation (except for EBW-NV).
4. For EBW-HV and EBW-MV, after chamber pressure has been reduced to 13 to 1.3×10^4 mPa (10^{-4} to 10^{-1} torr), focus on a target block and set beam parameters. It is recommended that the beam diagnostics tool(s) are used here to characterize the electron beam. An example of beam diagnostics used is found in the literature (Ref 11, 12). A weld or scanning program may be called up.
5. Align joint to the beam position, using optical or electron-optical methods or through the use of a beam scanning program.
6. Set the travel speed.
7. Begin the welding sequence (ramp up/down); this usually is performed automatically but can be performed manually.
8. Terminate the welding cycle.
9. Allow work to cool sufficiently if made of reactive material, then admit air to the chamber and remove fixtured work.

Alignment of the joint with beam position for nonvacuum welding is slightly less critical than for vacuum EBW, because the beam spot size and weld width are slightly larger in nonvacuum welding.

Joint Preparation. A joint for EBW ordinarily has close-fitted, abutting, square-groove faces such as a butt or step joint (self-aligning butt joint) configuration, and filler metal is not typically used. Filler metal can be used if desired, as in EBW of dissimilar metals and alloys or alloys that have low weldability when welded autogenously, such as 6061 aluminum. Generally, the faces of the joint are machined to a surface roughness of 3.20 μm (125 $\mu\text{in.}$) or less.

Surface finish on the weld groove faces may not be critical, depending on part and joint design and the requirements for weld properties. Provided the surfaces can be properly cleaned to remove all contaminants, the roughness of the faying weld joint surfaces is not generally critical. If the surface roughness is such that contaminants such as machining fluids remain even after cleaning, then the resulting weld quality will suffer.

Joint Fit-Up. Unlike arc welding, where a gap is employed to accommodate filler material, in autogenously welded components in EBW, joint fit-up requires closely fitted, nearly parallel surfaces to enable the narrow electron beam to fuse base metal on both sides of the joint. The members of a joint to be melt-through welded also are closely fitted. Fit-up tolerance depends on work-metal thickness and joint design but is usually 0.13 mm (0.005 in.) or less. Joint gap is usually smaller for thin work metal and unbacked joints and may be only 0.05 mm (0.002 in.) maximum. Interference fits may be used where shrinkage can cause cracking, as in circular joints on hardenable metals. In some instances, the use of beam oscillation to increase the effective beam size can be used to accommodate larger gap sizes

or poorly fitting joints. More information is given in the subsequent article, "Design of Electron Beam Welds," in this Volume.

Cleaning. Workpiece surfaces must be properly cleaned for EBW. Inadequate surface cleaning of the workpiece can cause weld flaws such as cracking, porosity, blowouts, and so on and a deterioration of mechanical properties (as it would in other fusion welding processes). In EBW-HV and EBW-MV, inadequate cleaning of weld surfaces also adversely affects evacuation time and gun operational stability, as well as contributing to the rapid degradation of the oil used in the vacuum pumps.

Generally, workpiece material and quality requirements define the need for cleanliness and should be addressed during the manufacturing quality reviews.

Wire brushing generally is not recommended, because contaminants may become embedded in the metal surface. Solvent cleaning is preferred for cleaning electron gun components and workpiece parts. If workpieces are cleaned in chlorine or other halogen-containing compounds, residue from these compounds must be removed by another cleaning method (usually thorough washing in a solvent) before welding. Cleaning methods have been outlined in the AWS C7.1 document, "Recommended Practices for Electron Beam Welding" (Ref 13).

Fixturing Methods. Methods used for fixturing workpieces in EBW are similar to those used for gas tungsten arc welding of precision parts without the use of filler metal, except that clamping force is usually lower and all fixturing and tooling materials should be made of non-magnetic materials.

Because total heat input to the weld is much less in EBW than for arc welding for a given depth, and because the heat is highly localized, heavy fixturing, massive heat sinks, or water cooling is generally not needed. However, if welding near a particularly heat-sensitive material, then some method for heat removal may be necessary. C-clamps are sufficient for many parts. In some applications, clamping may be supplemented or replaced by small tack welds or by a shallow weld pass (sealing pass) over the joint; the penetration weld is completed later at full power.

For EBW-NV, general-purpose welding positioners are satisfactory. Locating and aligning mechanisms are of simpler design than for welding in a vacuum; accessibility and beam widths for nonvacuum welding do not require as much accuracy in tracking of the joint. Maintenance of work-handling equipment for EBW-NV is simplified because of its out-of-chamber location.

Demagnetization. Workpieces and welding fixtures should be made of nonmagnetic materials such as austenitic stainless steel, copper, magnesium, aluminum, and so on. If the fixturing is made of magnetic materials, then the fixtures should be demagnetized before welding. Residual magnetism may result from magnetic

particle testing, magnetic chucks, or electrochemical machining. Even a small amount of residual magnetism can cause beam deflection. Workpieces are usually demagnetized by placing them in a 60-cycle inductive field and then slowly removing them. Before welding, workpieces should be checked with a gaussmeter (or magnetometer). Acceptable gaussmeter readings vary from 5×10^{-5} T (0.5 G) for very narrow (highly critical) welds up to as much as 2×10^{-4} to 4×10^{-4} T (2 to 4 G) for relatively wide welds.

Evacuation. The time required to evacuate the work chamber of an in-vacuum EBW unit down to the desired ambient pressure depends on the chamber size used, type of pump employed, and level of vacuum required. In any production application, the actual evacuation time is also affected by a number of factors, including the cleanliness of the work chamber, the amount of water vapor (humidity) in the ambient air, and the workpiece assembly (material and shape of both weldment and fixturing). Electron beam welding equipment currently employs either computer or program logic controls, normally providing automatic vacuum valve sequencing.

For EBW-HV, the required vacuum is generally provided by a mechanical pump operating in conjunction with an oil-diffusion pump. Other pumps may be used, such as cryopumps or turbomechanical pumps, depending on machine requirements. Evacuation times of approximately 5 to 15 min are generally achievable in EBW-HV.

For partial-vacuum EBW, diffusion pumps are not needed for the weld chamber, and weld chamber pumping is accomplished strictly by mechanical pumping. For high-production EBW of small parts in a partial vacuum, evacuation times of less than a minute are achievable. Again, the actual evacuation time is affected by a number of factors and can vary considerably, depending on the particular production application.

Electron beam welding equipment manufacturers are able to provide details on evacuation requirements and typical evacuation times.

Preheat and Postheat. Most commonly welded metals can be processed with EBW methods, even in thick sections without preheating, because of the extremely narrow width of the fusion and heat-affected zones. Hardenable and difficult-to-weld metals may need to be preheated, especially for thick sections and in applications when the weld is restrained.

High-strength alloy steels and tool steels thicker than approximately 9.5 mm (0.375 in.) ordinarily must be preheated before EBW to prevent cracking. Deep circular welds, especially partial-penetration welds, in thick sections of carbon steel containing more than approximately 0.35% C usually require preheating. However, welds subject to less restraint, such as circumferential welds on cylindrical shapes, can be made on 13 mm (0.5 in.) thick 0.50% C steel without preheating.

Preheating, when required, can be done before the work is placed in the work chamber, provided the evacuation time is sufficiently short, thus allowing the work to remain at the sufficient preheat temperature. Selection of heating method depends on the size and shape of the work and the preheat temperature; a combination of methods can be used. Torch and furnace heating are widely used; induction and infrared-radiation heating are also used. On small parts or where distortion from localized heating is not a problem and where increased cycle time can be tolerated, heating is sometimes done with a defocused electron beam; this method can also be used to supplement other methods of heating. Preheating can also be performed in the chamber for crack-sensitive materials using high-intensity heat lamps. One of the most recent developments in EBW is rapid beam manipulation (usually in the megahertz range). The concept is to rapidly manipulate beam movement such that the beam is "time-shared" in multiple locations. This allows for the beam to preheat the workpiece, weld, and postweld heat treat the workpiece concurrently (in the same weld pass). These modern EBW systems, when using fast beam manipulation (or rapid deflection), may provide an in situ pre- or postweld heat treatment (Ref 14). Postheating used on EBW parts is most often accomplished by conventional means (i.e., stress relieving or tempering) after removing the work from the welding chamber.

Operating Conditions. Starting and stopping the weld usually require special consideration to avoid discontinuities in the weld at these points and possible melt-through and loss of metal.

One technique that is used to avoid these difficulties is to start the weld at full beam power on a starting tab of the work metal that is tightly fitted against one end of the joint, and to conclude the weld on a runoff tab at the other end of the joint. The use of starting and runoff tabs prevents underfill at the ends of the joint, which is caused by the introduction or exit of the beam. Workpieces can also be made oversized to provide extra material for starting and stopping. The tabs or the extra material can be machined off after welding. Starting and runoff tabs are used mainly in low-production operations.

Another technique is to start and stop the weld on the work, raising the current gradually (upslope) at the beginning of the weld and reducing it gradually (downslope) at the end of the weld. Upslope and downslope power may be used at controlled rates and time intervals, as established for a specific application, and can be programmed into the welding procedure. The use of upslope and downslope is of special value where the weld is a closed path, as in welding circular and circumferential joints.

The use of CNC and computer beam control allows the programming of the motion and upslope/downslope, which helps in the starting

and stopping of the welding sequence, especially in areas of the workpiece that contain corners. This type of controller is also capable of coordinating focus, beam current, and travel conditions to tailor welds with changing conditions such as geometry (thickness or changing joint configuration).

In many applications of closed-path welds, the weld can be started at full power, with downslope at the end providing a sufficiently gradual termination and a suitable distance of overlap. Downslope of current after overlapping the beginning of the weld on circular welds in thick sections of high-hardenability steels is critical to avoid porosity and cracking. Other parameters may also be adjusted to avoid these defects. Upslope is usually rapid; downslope is from a few degrees to a major portion of a revolution.

A "cosmetic pass" is made when needed to smooth or flatten the reinforcement of a weld that is irregular or too high. Such a pass is used to correct undercut or underfill. The beam is usually defocused, reduced in power, and/or manipulated using circle/elliptical beam deflection to reduce the intensity of the beam (or a combination of these three). Filler metal may also be added in making a cosmetic pass intended to correct undercut or underfill.

Weld Geometry

The shape of the parts to be welded and the corresponding joint designs are critical to the successful application of EBW in vacuum or at atmospheric pressures (nonvacuum). While minimum heat input and low thermal distortions are important advantages of EBW, the molten metal still shrinks as it solidifies. Shrinkage stresses may lead to microcracks if parts, due to design restrictions, are unable to shrink at corresponding rates and the joint volume is completely constrained. Additional information is available in the article "Design of Electron Beam Welds plus Codes" in this Volume.

Joint Design

Butt, step, corner, T-, lap, and edge joints can be made by the EBW process using square-groove or seam welds. Fillet welds, which are difficult to make with vacuum EBW, are readily made using EBW-NV. Square-groove welds require fixturing to maintain fit-up and alignment of the joint. They can, however, be self-aligning if a rabbeted joint design is used. Self-alignment is particularly important in batch loading the vacuum chamber for efficient work manipulation. The weld-metal area can be increased using a scarf joint, but fit-up and alignment of the joint are more difficult than with a square-groove weld. Most joints are designed to be welded in a single pass with full penetration or penetration to a specified depth.

The article "Design of Electron Beam Welds plus Codes" has further details on joint design.

Electron Beam Welding Machines

This brief review is aimed at introducing the potential user to some of the EBW equipment currently available. Further advances in the control and programming of these systems can be expected because of the likelihood of uninterrupted progress in the technology and intelligent process control.

As discussed earlier in this article, the EBW process is accomplished in three pressure-dependent zones, referred to as the three modes of EBW. The original mode is the "hard" or high-vacuum mode, in which welding is carried out in the pressure range of 0.13 to 130 mPa (10^{-6} to 10^{-3} torr). In the second mode, medium vacuum, welding is carried out in the pressure range of 130 to 3.3×10^6 mPa (10^{-3} to 25 torr). This mode is also referred to as "soft" or partial-vacuum EBW. The third mode is called nonvacuum or atmospheric, with welding carried out at atmospheric pressure.

All three modes employ an electron beam gun/column, a power supply with controls, one or more vacuum pumping systems, and work-handling equipment. In nonvacuum welding, while the workpiece is not placed in an evacuated work chamber, the electron beam gun/column must be in a vacuum environment. The electron gun in all three modes is held at a pressure of 13 mPa (10^{-4} torr) or less; otherwise, the high voltage required for the acceleration of the electrons could not be sustained, and the heated filament/cathode would be subject to high rates of oxidation.

Electron beam welding equipment comes in two basic designs: the low-voltage system, which uses accelerating voltages in the 30 to 60 kV range, and the high-voltage system, with accelerating voltages in the 100 to 200 kV range. Beam powers up to 100 kW are available with both high- and low-voltage equipment.

The lower-voltage machines operate at a higher current. Typically, 30 to 60 kV machines operate at a maximum beam current of 700 mA. The high-voltage machines of 150 kV typically operate at a maximum of approximately 170 mA. The higher-voltage machines produce a greater depth-to-width ratio of the weld nugget, with values up to 50 to 1. The higher-voltage machines can use a longer standoff distance than the low-voltage machines; however, low-voltage machines can employ articulated gun movement for greater weld joint access.

High- and low-voltage equipment is suitable for high- and medium-vacuum operations, while nonvacuum welding is carried out at higher voltages (150 to 200 kV) only. The nonvacuum, high-voltage systems generally are used for welding materials less than 25 mm (1 in.) thick. With low-voltage systems, the gun may be fixed in position on the chamber or may be mobile inside the chamber. With

high-voltage equipment, the gun is generally fixed in position on the chamber.

Figure 4 shows an available high-vacuum internal, movable gun system configuration. The boom arrangement is shown with a chamber size of 3.8 by 3.8 by 2.8 m (150 by 150 by 110 in.). This installation has a movable gun. Low-voltage, high-vacuum systems with movable guns are available with power ratings of 7.5 kW (60 kV, 125 mA) 15 kW (60 kV, 250 mA), 30 kW (60 kV, 500 mA), and 42 kW (60 kV, 700 mA).

Medium-vacuum machines are frequently special-purpose units tooled for particular assemblies. The medium-vacuum mode of EBW was initially employed to increase the production capacity of the process. This mode of application typically involves the use of a chamber custom-designed to provide a minimum of weld-zone volume that has to be evacuated during each part cycle (that is, a chamber envelope that is not much bigger in size than the particular workpiece to be welded plus any fixturing it may require). Recall that only a small volume needs to be evacuated (evacuation times of less than a minute). This, coupled with the fact that EBW-MV is normally performed in an ambient vacuum level of nominally 6.5×10^3 mPa (5×10^{-2} torr), allows for much higher throughput. To capitalize on the shorter processing times, further improvements in throughput may be realized by rapidly transporting parts into or out of the weld area on EBW-MV systems. One of the major applications of EBW-MV and EBW-NV is for automotive applications (Ref 15, 16).

With a smaller footprint becoming more of a necessity in some plants, newer machines are becoming "palletized." An example of a palletized machine is shown in Fig. 5. All of the components of the equipment are available on a movable pallet, such that the system is more of a "plug-and-play" system that can easily be



Fig. 4 Internal, movable gun configuration in a low-voltage, high-vacuum electron beam (EB) welding system with a boom manipulator. The photograph shows different motion configurations. Courtesy of Sciaky, Inc.

installed, leveled, and moved to new locations in a much more rapid fashion.

Large-chamber systems are available in both low- and high-voltage configurations. Figures 6 to 8 show large-chamber systems, and Fig. 9 shows a very large-chamber EBW system.

Computer control systems are currently available in many modern EBW systems, allowing for more complex configurations of components to be processed. Control of welding operations can be expanded to include joint locators, five-axis programmable contouring, and several digitizing provisions that can be actuated on the basis of information generated by the seam locator. Many EBW systems can also be adapted for electron beam heat treating applications.

Finally, most of the EBW system manufacturers will build custom systems to meet the needs of the customer. The equipment variations and configurations are nearly limitless, and, as such, are not covered in detail in this article.



Fig. 5 "Palletized," small-chamber electron beam welding system with all components (including high-voltage tank, vacuum system, and chamber) on a moveable platform. Courtesy of PTR- PTR Präzisionstechnik GmbH, Maintal

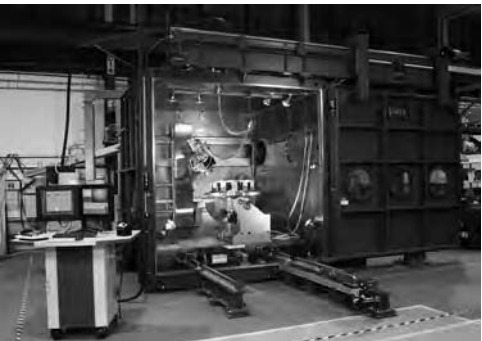


Fig. 6 Large-chamber, low-voltage electron beam welding system with movable gun. Courtesy of Sciaky, Inc.

Safety

Protection must be provided by equipment design and arrangement, and by safety precautions in EBW and related operations, against the usual hazards of welding and the special hazards of exposure to the high voltages involved in generating the electron beam, the beam itself (direct viewing of intense radiation emitted by molten weld metal can be harmful to eyesight and thus the beam operation should be viewed only through a filtered lens commonly used for arc welding), and radiation of x-rays produced by impingement of the beam on the work or other materials. From a safety standpoint, an accelerating voltage of less than

20 kV produces soft x-rays, while an accelerating voltage of more than 20 kV produces hard x-rays (Ref 1). Shielding against radiation is more demanding as the acceleration voltage increases. Suitable precautionary measures and safety issues are described and addressed in several documents (Ref 13, 17–19).

ACKNOWLEDGMENTS

This article first appeared as "Electron Beam Welding" in Volume 6 of *Metals Handbook*, 9th ed., published in 1983. Special thanks are extended to the ASM Committee on Electron Beam Welding (Edward A. Metzbowler, chair) that prepared the original article.

REFERENCES

1. H.B. Cary, *Modern Welding Technology*, 2nd ed., Prentice Hall, 1989, p 256
2. H. Schultz, Principles of Electron Beam Welding, *Second Electron Beam Processing Seminar Proceedings*, R. Silva, Ed., Universal Technology Corporation, Dayton, OH, 1972, p 3a1–3a48
3. Electron Beam Welding, Chap. 13, *Welding Processes, Part 2*, Vol 3 (9.3), *Welding Handbook*, 9th ed., American Welding Society, Miami, FL, 2007, p 452–502
4. Y. Arata, Development and Application of a Strong Focusing Electron Beam Gun with Multistage Electromagnetic Accelerating Units, *Plasma, Electron & Laser Beam Technology: Development and Use in Materials Processing*, American Society for Metals, 1986, p 95–104

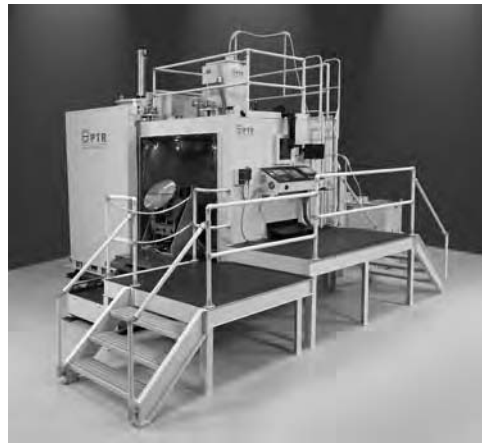


Fig. 7 Large-chamber, high-voltage electron beam welding system with fixed gun. Courtesy of PTR-Precision Technologies, Inc., Enfield, CT

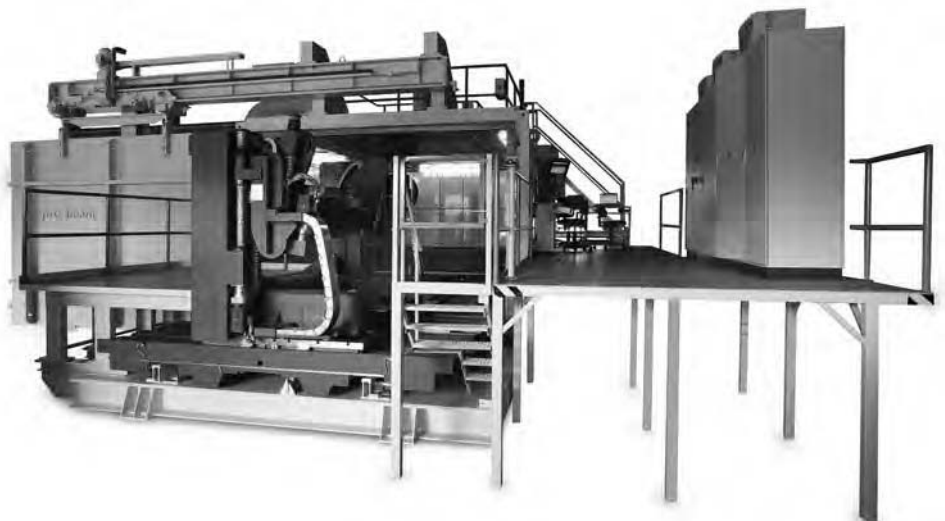


Fig. 8 Large-chamber, high-voltage electron beam welding system. Courtesy of pro-beam AG & Co. KGaA



Fig. 9 Very large-chamber, low-voltage electron beam welding machine (600 m³, 80 kV/40 kW machine). Courtesy of pro-beam AG & Co. KGaA

5. D.T. Swift-Hook and A.E.F. Gick, Penetration with Lasers, *Weld. J.*, Vol 52 (No. 11), 1973, p 492-s to 499-s
6. R. Peretz and H.G. Mayer, Parameter Correlations for Deep Penetration Welding with High Energy Focused Beams, *Opt. Lasers Eng.*, Vol 6, 1985, p 225–250
7. P.W. Fuerschbach, Measurement and Prediction of Energy Transfer Efficiency in Laser Beam Welding, *Weld. J.*, Vol 75 (No. 1), 1996, p 24-s to 34-s
8. J.T. Norris, C.V. Robino, M.J. Perricone, and D.A. Hirschfeld, Development of a Time-Resolved Energy Absorption Measurement Technique for Laser Beam Spot Welds, *Weld. J.*, Vol 89 (No. 4), 2010, p 75-s to 81-s
9. Y. Arata and M. Tomie, *JWRI 2*, Vol 1, 1973, p 17; *JWS*, Vol 9, p 78
10. Y. Arata, High Technology for Materials Processing Based on Welding, *Plasma, Electron & Laser Beam Technology: Development and Use in Materials Processing*, American Society for Metals, 1986, p 28–49
11. J.W. Elmer and A.T. Teruya, An Enhanced Faraday Cup for Rapid Determination of

- Power Density Distribution in Electron Beams, *Weld. J.*, Vol 80 (No. 12), 2001, p 288-s to 295-s
12. T.A. Palmer, J.W. Elmer, K.D. Nicklas, and T. Mustaleski, Transferring Electron Beam Welding Parameters Using the Enhanced Modified Faraday Cup, *Weld. J.*, Vol 86 (No. 12), 2007, p 388-s to 398-s
13. “Recommended Practices for Electron Beam Welding,” AWS C7.1M/C7.1:2011, AWS C7 Committee on High Energy Beam Welding and Cutting, American Welding Society, Miami, FL, in press
14. R. Zenker, Modern Thermal Electron Beam Processes—Research Results and Industrial Application, *Metall. Ital.*, April 2009, p 1–8
15. D. Powers and G. Schubert, Electron Beam Welding: A Useful Tool for the Automotive Industry, *Weld. J.*, Vol 79 (No. 2), Feb 2000, p 35–38
16. K.R. Schulze and D.E. Powers, EBW of Aluminum Breaks Out of the Vacuum, *Weld. J.*, Vol 83 (No. 2), Feb 2004, p 32–38
17. “Safety in Welding Cutting and Allied Processes,” ANSI Z49.1:2005, American Welding Society, Miami, FL
18. General Safety Standards for Installations Using Non-Medical X-Ray and Sealed Gamma Ray Sources, Energies up to 10 MeV, *NSB Handbook 114*, National Institute of Standards and Technology, Gaithersburg, MD
19. “Occupational Health Standards—Ionizing Radiation,” Occupational Safety and Health Administration (OSHA), Title 29, Chap. 17, Part 1910, Section 96, United States Government Printing Office, Washington, D.C.

Design Considerations for Electron Beam Welding*

Kenn Lachenberg, Sciaky, Inc.

Patrick Hochanadel, Los Alamos National Laboratory

John Elmer, Lawrence Livermore National Laboratory

ELECTRON BEAM WELDING (EBW) can produce deep, narrow, and almost parallel-sided welds with low total heat input and relatively narrow heat-affected zones in a wide variety of common and exotic metals. In many applications, a single pass is sufficient to weld the components. When initially used for industrial applications in the 1950s, EBW had to be performed totally in vacuum. In this form, EBW was primarily used because of its ability to reliably produce very high-quality welds in materials normally considered extremely difficult to join (for example, refractory metals, oxidizable metals, stainless steels, and superalloys). This made it ideally suited for use in aerospace, nuclear, and other similar (high-technology) manufacturing industries.

During the 1960s, the ability to employ the EBW process for medium-vacuum and nonvacuum welding tasks was developed. This increased production capacity helped make EBW more attractive to other businesses, such as the automotive and off-highway equipment industries, desiring to take advantage of the numerous joining benefits it provided. However, the use of EBW in these industries required that the applications be performed in a fairly high-volume production.

EBW is used to join not only difficult-to-weld materials but also common materials such as steel (≤ 150 mm, or 6 in., thick), aluminum (≤ 305 mm, or 12 in., thick), and copper (≤ 100 mm, or 4 in., thick) (Ref 1). These and other metals (in thicknesses ranging from foil to plate dimensions) can be welded by EBW. In addition, EBW can be used to join numerous combinations of dissimilar metals. See the Section "Electron Beam Welding" in this Handbook for a description of EBW systems and equipment.

Weld Geometry

The shape of the parts to be welded and the corresponding joint designs are critical to the successful application of EBW in vacuum or at atmospheric pressures (nonvacuum). Although minimum heat input and low thermal distortions are important advantages of EBW, the molten metal still shrinks as it solidifies. Shrinkage stresses may lead to microcracks if parts, due to design restrictions, are unable to shrink at corresponding rates and the joint volume is completely constrained.

Part Configuration

Whether a component is welded in a vacuum or at atmospheric pressure (nonvacuum), part configuration and the corresponding joint designs used are critical parameters in the successful application of EBW. A circular weld in the axial direction, for example, that joins a disk-shaped member (gear or cup) to a shaft (Fig. 1) may experience severe constraint. Such joints are practical in easily welded metals—those that are soft, have low yield points, and exhibit low shrinkage—but not in difficult-to-weld steels that have high strength and hardenability.

The difficulties encountered in welding shapes such as those shown in Fig. 1 are aggravated if the weld zone is broadened by defocusing the electron beam. This is a frequent problem if exact beam position cannot be controlled, either because of beam instability, magnetism of the parts, or excessive tolerances in tool fixtures.

Shrinkage stresses are better managed in radial welds, as shown in Fig. 2. The volume

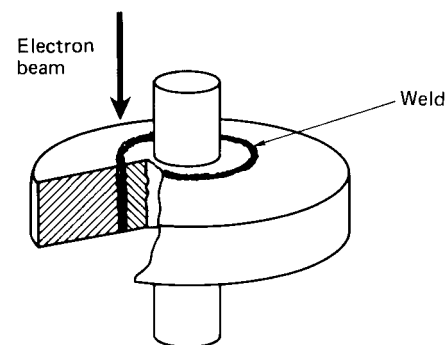


Fig. 1 Cutaway view showing location and penetration of a circular electron beam weld joining a disk-shaped component to a shaft

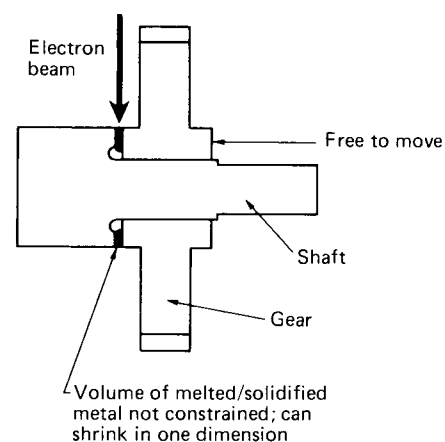


Fig. 2 Shrinkage stress in a radial weld

* Adapted from the article Procedure Development and Practice Considerations for Electron-Beam Welding, *Welding, Brazing, and Soldering*, Vol 6, *ASM Handbook*, ASM International, 1993, p 851-873

of molten metal is less constrained by the axial direction if the gear hub is allowed to move by using push fit and no restraints. The weld must also have root clearances—the weld zone must not extend into the shaft. Stresses are lower if the melt zone has parallel side boundaries. Triangular weld zones that are caused by broadened beams, uneven beam power distribution, or incomplete penetration have more complex stresses that may result in cracking.

The same principles of joint design discussed previously for joints between shafts and unlike members apply equally to T-joints and corner joints between plates. Figure 3 shows recommended and nonrecommended weld configurations. It is important in all welding methods, and essential in EBW (which is usually performed in a single pass), that constraints on the volume of the melt be avoided by self-aligning interlocking steps in the joint. In multilayer arc welds, the individual weld bead is less constrained in volume and shrinks from its surface downward. Functionally, it is not useful to make the cross section of the joint any less thick than the plates that are being joined. If two welds are made in succession, the second weld may be constrained by the first (Fig. 3), which may lead to solidification cracking. It is thus advisable to direct the beam at the joint parallel to the faying surfaces and to cause melting over the whole contact area.

Surface Geometry

Usually, EBW does not use or need filler wire. Therefore, V-grooves or large joint gaps are not required; in fact, too much of a gap could be detrimental to the process. Surface tension pulls some of the molten metal up the V-shaped or large gap surfaces so that it is no longer available to fill the space created by the keyhole that is generated by the moving beam. Voids remain in the actual joint plane (Fig. 4).

A step in the surfaces at the joint line is also undesirable. Any small lateral shift of the beam from the low to the high side, or vice versa, changes the penetration to some extent. In the extreme case, this shift may be equal to the height of the step, as shown in Fig. 5. On circular welds, with joint configurations similar to Fig. 5(a), a noncircular weld profile may develop with irregularities that can lead to uneven applied stresses. By contrast, a mere shift in the melt zone, as shown in Fig. 5(b), does not affect weld quality, as long as the entire joint line is consumed.

Configurations for Wide Welds

The high speed and autogenous nature of an electron beam weld can be advantageous when a wide weld (6.5 to 13 mm, or ¼ to ½ in.) is needed without great depth-to-width ratio. The electron beam can be deflected in a raster pattern and/or defocused to provide a wider beam energy distribution to facilitate a wider weld.

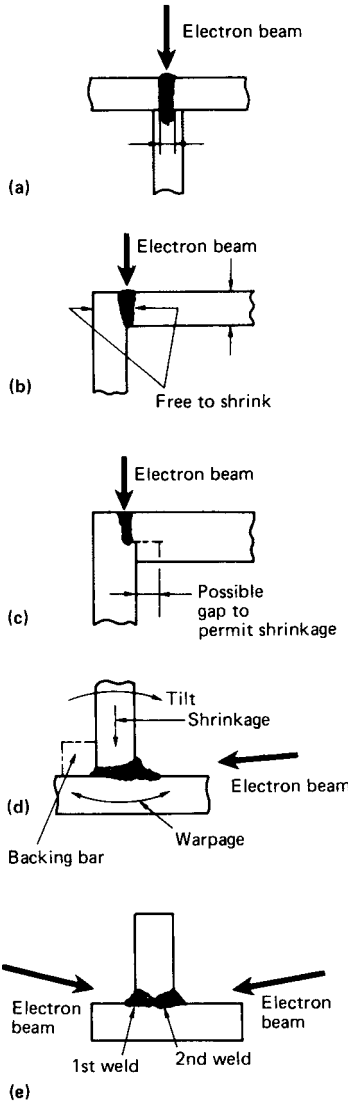


Fig. 3 Optimum versus least desirable weld configurations. (a) Not recommended—maximum confinement of molten metal, minimum joining cross section (arrows); wastes beam energy for melting, nonfunctional metal. (b) Most favorable—volume of melt not confined; maximum joining cross section (arrows). (c) Not recommended—maximum confinement of melt (unless gap is provided); joining cross section less than plate cross section. (d) Most favorable—minimum constraint and confinement of melt; minimum internal stresses; warpage can be offset by bending prior to welding; tilt can be offset by location of T-arm at less than 90° to base prior to welding. Fillet obtained by placing wire in right corner and melting it with the beam. (e) Not recommended—two successive welds; second weld is fully constrained by the first weld and shows strong tendency to crack.

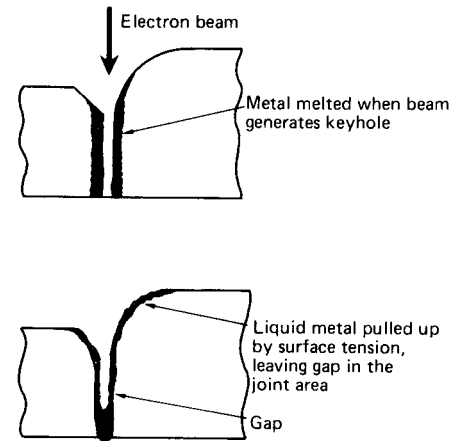


Fig. 4 Gap in joint plane created by surface tension

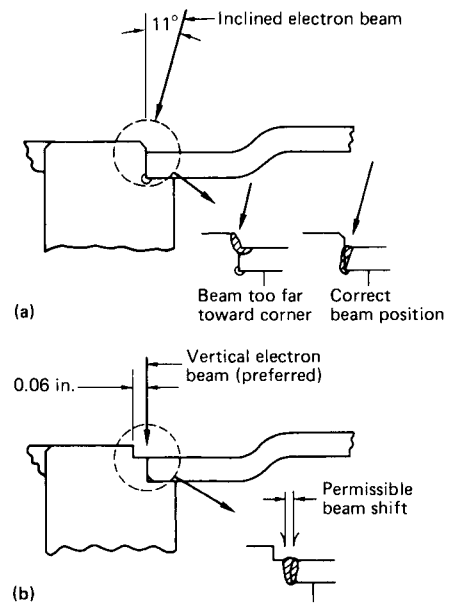


Fig. 5 Effect of beam and melt zone position on weld penetration. (a) Inclined electron beam. (b) Vertical electron beam

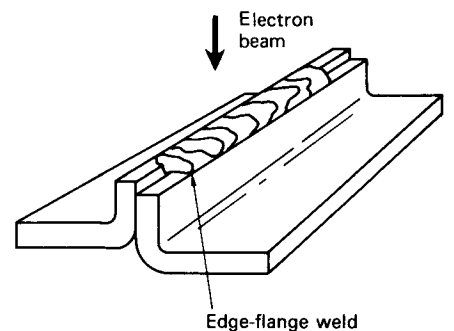


Fig. 6 Edge-flange weld typically used to join thin panels

A wider beam may need to be employed on some edge weld applications, as illustrated by the edge-flange weld in Fig. 6. For edge welds, changes in energy input per unit length and changes in power density affect only the amount of molten metal. Offset and gaps up to the thickness of the sheet to be joined can often be tolerated (Ref 2). In making an edge-flange

weld (Fig. 6), the same advantages exist, provided the flange is high enough. For joining thinner sheet that is tightly clamped, edge welds also can be made with the electron beam in the horizontal position.

The EBW process can tolerate and fill large gaps if sufficient sacrificial metal or wire feed is available to be melted by the beam (Fig. 7). If not, surface tension may pull whatever metal is melted to either side of the weld joint.

Melt-Zone Configuration

Welds with parallel sides are preferred over welds that are more triangular shaped (Fig. 8a). The parallel sided weld (Fig. 8b) shows minimum warpage and only transverse shrinkage when unconstrained. If there are constraints, the hindered warpage and shrinkage can cause internal stresses in the weld area. As a general rule, full penetration EB welds have a tendency to be more parallel than partial penetration welds that have a wider nail head and are tapered at the root.

Joint Design

Procedures which relate to the joint design, the material and its preparation, and the welding tooling are important factors that have a major influence on the weld quality and rate of production obtained. Various joint designs, including butt, corner, T-, lap, and edge joints,

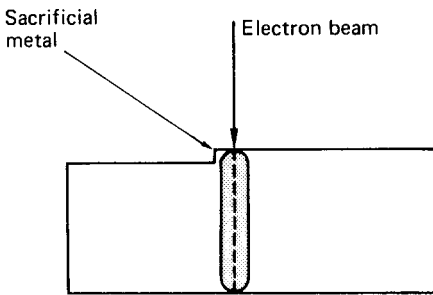


Fig. 7 Use of sacrificial metal to fill a large gap in a square-groove weld

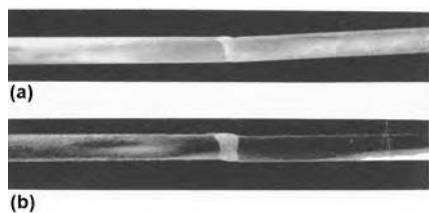


Fig. 8 Variation in beam velocity and subsequent warpage of 0.25 mm (0.10 in.) thick type 304 stainless steel joined by a butt weld. (a) Beam traverse, 7110 mm/min (280 in./min); triangular melt zone. (b) Beam traverse, 4190 mm/min (165 in./min); parallel-sided melt zone. Weld parameters: 12 kW beam power; 11.4 mm (0.45 in.) standoff; helium shielding gas

can be made by the EBW process using square-groove or seam welds. Square-groove welds require fixturing to maintain fit-up and alignment of the joint. They can, however, be self-aligning if a rabbeted joint design is used. Self-alignment is particularly important in batch loading the vacuum chamber for efficient work manipulation. Most joints are designed to be welded in a single pass with full penetration or penetration to a specified depth.

Figures 9 to 13 show the commonly used joint and weld types for EBW. Different joint

preparations, joint designs, and welding positions are used to meet special requirements. For preferred joint configurations and shrinkage stresses encountered in various joint designs, see the section on weld geometry for EBW in this article.

Welds in Butt Joints

Butt joints are the most common of the five basic joint types used in EBW. The basic square-groove weld, which is shown in Fig. 9(a) to (c),

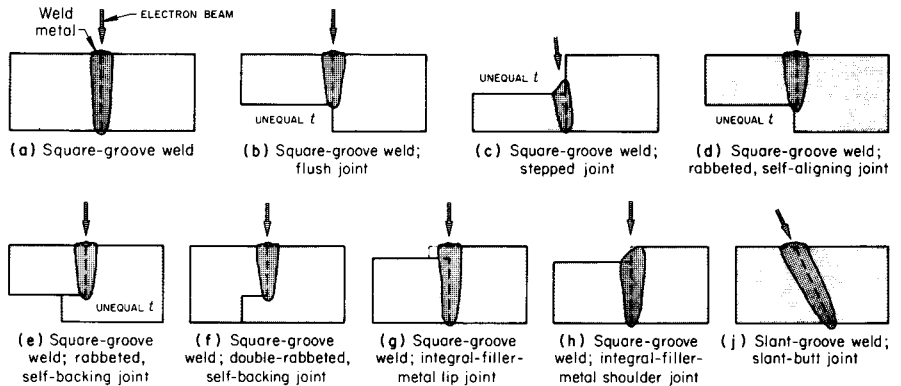


Fig. 9 Types of butt joints and welds typically generated by electron beam welding

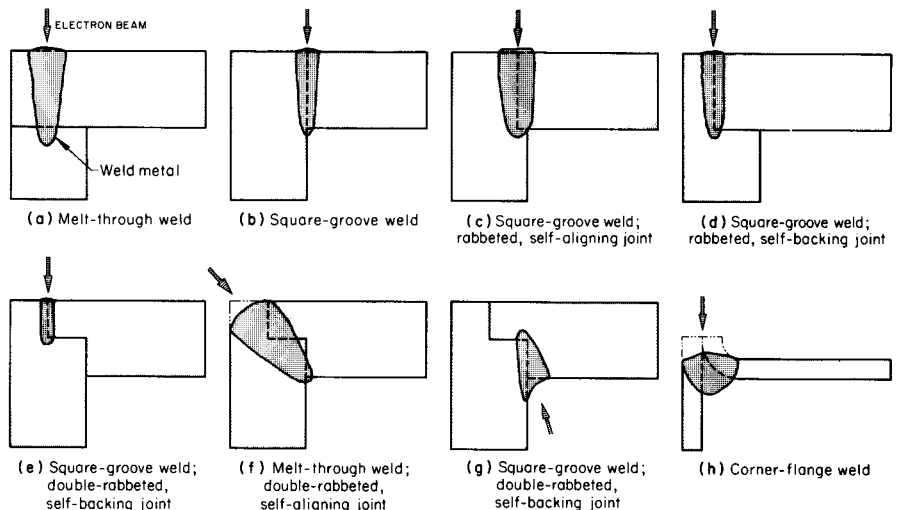


Fig. 10 Types of corner joints and welds typically obtained with electron beam welding

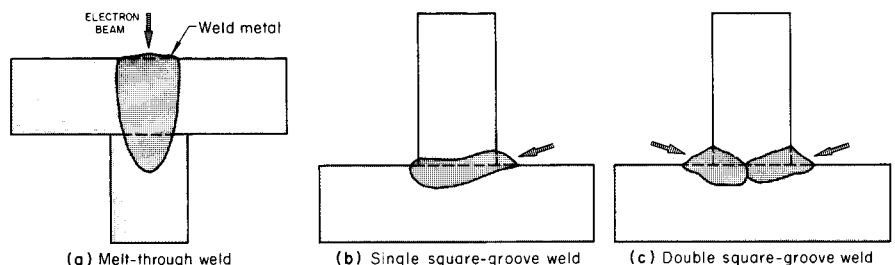


Fig. 11 Typical welds produced by electron beam welding of T-joints

needs only the simplest and least expensive joint preparation. It is suitable for either partial- or full-penetration welds. Good fit-up and external fixtures are needed. The flush joint (Fig. 9b) is preferred to the stepped joint (Fig. 9c) for joining unequal thicknesses, chiefly because control of conditions for making sound full-penetration welds is less critical than for the stepped joint. A wider beam is used in welding the stepped joint, and the beam angle must be carefully controlled to avoid scarfing the upper edge of the thicker member (angle too small) or missing the bottom of the joint (angle too large), especially if the thinner member is more than approximately 9.5 mm (3/8 in.) thick.

In Fig. 9(d), the joint is rabbeted to make it self-aligning, but the offset is small to avoid leaving an unwelded seam near the root of the weld (compare to Fig. 9e). In Fig. 9(d) to (g), the joints are self-aligning and may be self-fixturing in circular, circumferential, and certain other joint arrangements. In Fig. 9(e) and (f), the joints are both self-aligning and self-backing; each, however, leaves an unwelded seam near the root of the weld. Ideally, a slight gap should be incorporated at the nonwelded step portion at the joint shown in Fig. 9(f) to allow for weld shrinkage.

In Fig. 9(g) and (h), two ways are shown of providing integral and filler metal. The lip of the joint in Fig. 9(g) provides more filler metal than the shoulder of the joint in Fig. 9(h), but because it conceals the joint, a scribed line or other means for beam placement and for scanning must be provided before the welding operation can proceed.

The slant-groove weld (also called angular or scarf) shown in Fig. 9(j) is used in butt joints to facilitate fixturing. It is also used where limitations on the beam location prevent fusion for

the entire groove depth if the basic square-groove weld (Fig. 9a) were used. Greater weld depth, as measured parallel to the beam axis, is needed for full penetration of a given metal thickness than with the square-groove weld. This type of weld and variations of it are used both in butt joints and in corner joints.

A slant-but joint can also be welded with beam alignment set at 90° to the surface of the work. This beam angle permits the production of defect-free welds where fit-up is poor or where the joint opening is larger than can be tolerated when the beam is aligned with the groove. In a related type of weld, the joint has a square-groove preparation, and the beam is at an angle to the groove. This type of weld is used mainly under circumstances in which other types of welds would be hard to access.

Welds in Corner Joints

Eight types of electron beam welds frequently made in corner joints are shown in Fig. 10. Corner joints are second only to butt joints in frequency of use with EBW. Important differences between butt and corner joints are notch sensitivity and suitability for nondestructive testing. To compare alignment, self-fixturing, and the occurrence of portions of unwelded seam, see Fig. 9 and 10.

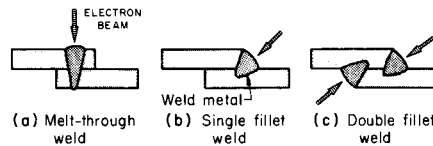


Fig. 12 Typical welds obtained by electron beam welding of lap joints

The two simplest and most economical welds in corner joints are the melt-through (Fig. 10a) and basic square-groove (Fig. 10b) welds. Neither is self-aligning or self-fixturing; manipulation of the work for the weld in Fig. 10(b) can be simplified by using a horizontal electron beam and corresponding work orientation (rotated 90° from the orientation shown). The melt-through weld (Fig. 10a), unless made with a fusion zone wide enough to eliminate the unwelded seam completely, is weaker than the square-groove weld and is notch sensitive. The corner-flange weld (Fig. 10h), usually made only on thin stock, requires precision forming of the 90° bend. Welds in corner joints are subject to high stress concentrations.

A corner joint weld and heat-affected zone (HAZ) of the electron beam process are compared with those of gas tungsten arc welding (GTAW) in Fig. 14. The joint designs differ between the two processes. For GTAW, multiple weld passes are required to fill the open-corner V-groove. For EBW, only a single weld pass may be required. However, because of

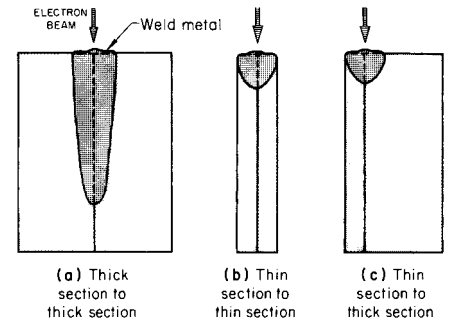
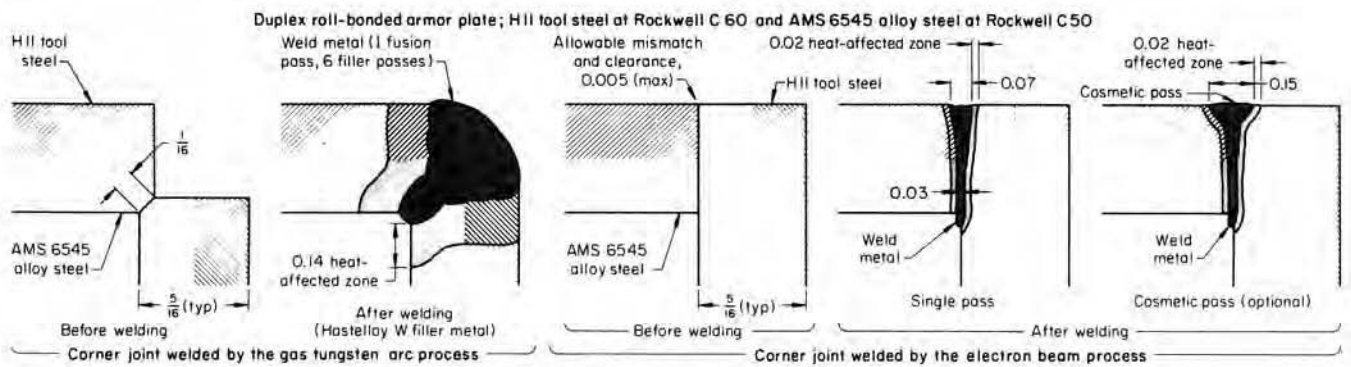


Fig. 13 Typical welds generated by electron beam welding of edge joints having components of equal and unequal section thicknesses



Joint type	Corner	Welding power:		Beam oscillation	None
Weld type	Square groove	Penetration pass	30 kV at 170 mA	Welding position	Flat
Machine capacity	30 kV at 500 mA	Cosmetic pass	19 kV at 95 mA	Welding speed:	
Vacuum chamber size	2845 × 760 × 1575 mm (112 × 30 × 62 in.)	Welding vacuum	1.3 mPa (10 ⁻⁵ torr)	Penetration pass	1525 mm/min (60 in./min)
Maximum vacuum	13 μPa (10 ⁻⁷ torr)	Pumpdown time	10 min	Cosmetic pass	815 mm/min (32 in./min)
Fixtures	Assembly jig; travel carriage	Beam focal point, penetration pass	At surface	Preheat and postheat	None

Fig. 14 Schematic of cross sections through corner joints and welds to show variation in the size of welds and heat-affected zone that are obtained with electron beam welding and gas tungsten arc welding

occasional undercutting, a second (cosmetic) pass may be used. Even when the second pass is used, the weld and the HAZ are much narrower than those created by arc welding. The effect of the cosmetic pass on the weld cross section is shown in Fig. 14; the machine settings for the defocused beam used to make the cosmetic pass are in the table with Fig. 14.

Welds in T-Joints

Three types of electron beam welds made in T-joints are shown in Fig. 11. The melt-through or blind weld (Fig. 11a), like melt-through welds in butt or corner joints, leaves an unwelded seam with resulting low strength, notch sensitivity, and corrosion susceptibility. Figure 11(b) shows another method for T-joint welding that may be best suited for thinner sections so that the entire joint is consumed with the weld. A joint clearance area may be employed, as shown in Fig. 15, to allow more unobstructed access to the T-joint area. The double-square-groove weld (Fig. 11c) is used primarily on sections 25 mm (1 in.) or more thick. For welds similar to Fig. 11(b) and (c), filler metal can be added.

Welds in Lap and Edge Joints

Three types of electron beam lap joint welds are shown in Fig. 12. An example of an EBW melt-through lap joint is illustrated on the rupture-disk assembly shown in Fig. 16. For this assembly, leak-tightness rather than high tensile strength is the objective. Originally, the components were joined in one pass by GTAW, using the design illustrated in the upper right corner of Fig. 16. A circular groove was cut in the nozzle wall to help localize the weld bead, which was made without filler metal. Light pressure was applied at both ends of the assembly to hold the parts in alignment for welding. However, the GTAW weld procedure resulted

in numerous rejects because of leaks due to excessive heat and disk burnback. To eliminate these difficulties, the operation was converted to EBW. Each assembly was fitted into a cylindrical receptacle or pot that was equipped with a hold-down ring that forced the periphery of the disks and caps into close alignment, as shown by the improved method of Fig. 16. A melt-through or lap weld was made, rather than an edge-flange weld at the periphery.

Three types of electron beam welds made in edge joints are shown in Fig. 13. Thick sections can be joined by deep, narrow square-groove welds (Fig. 13a). Shallow welds made with a low-power, partially defocused beam are used to join thin sections to each other or to thick sections, as shown in Fig. 13(b) and (c). Shallow edge welds can be made at high speed. Welds of this type are particularly useful on hermetically sealed assemblies, which may be designed for planned salvage by removal of the weld region and subsequent rewelding.

Butt Joints versus Corner and T-Joints

The concentration of bending stresses at the weld in corner and T-joints is sometimes

avoided by designing the work for a butt joint on a straight section near the corner or T (flange neck or welding neck construction). This principle of design is applicable also to butt joints between members having different thicknesses, and it can be applied to straight line, circular, and circumferential joints.

In welding such a joint in magnetic metals, if the beam path is too close to the corner, T, or shoulder, the beam may be deflected away from the metal that it passes near on its way to the joint, causing it to enter the work at an angle and possibly to miss the lower portion of the joint. To avoid this problem, the beam clearance should be 0.8 mm (0.030 in.) or more, depending on the height of the magnetic projection (Fig. 15).

Special Joints and Welds

Many variations of the basic joint and weld types described in the preceding section and illustrated in Fig. 9 through 16 are used to meet the needs of individual applications. Some of these special joints and welds are discussed as follows.

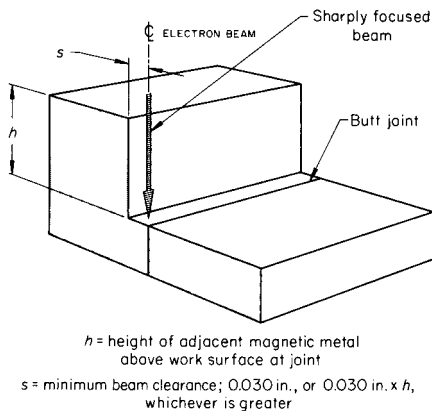
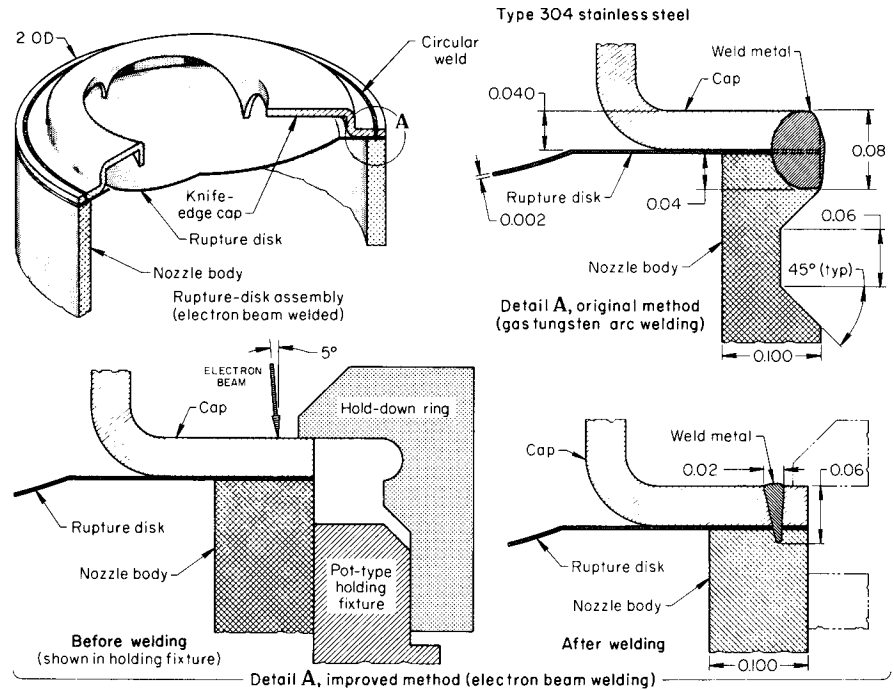


Fig. 15 Joint location and beam clearance for an electron beam welded butt joint near a projecting corner, T, or shoulder consisting of magnetic work metal



Joint type	Circular, three-piece corner	Welding vacuum	0.65 mPa (5×10^{-6} torr)
Weld type	Melt-through (spike)	Pumpdown time	10 min
Machine capacity	50 kV at 250 mA	Working distance	38 mm (1.5 in.)
Gun type	Diode; fixed during welding	Beam focal point	Sharp at work surface
Vacuum chamber	Steel: 1370 × 1220 × 1220 mm (54 × 48 × 48 in.) with full-width end doors	Beam spot size	~0.51 mm (~0.020 in.) diam
Fixtures	56-piece holding tool with individual rotation; table with x-y motion	Welding speed	2540 mm/min (100 in./min)
Welding power	26 kV at 16 mA	Number of passes	One, plus 30° downslope
		Setup time	48 min
		Production rate	44½ pieces/h

Fig. 16 Comparison of electron beam and gas tungsten arc welds applied to a type 304 stainless steel rupture disk assembly

Plug and Puddle Welds

Plug and puddle welds are usually made by manually (or automatically) manipulating the work under a fixed beam at low power. Filler metal used for plug welds is often preplaced at the weld site. Puddle welding is used mainly to fuse shallow defects together locally.

Multiple-Pass Welds

Most electron beam welds produce the desired penetration in a single pass. Tack welds and cosmetic or smoothing passes are not considered penetration passes. Welds several inches deep can be made in most metals in a single pass. Weld depth obtainable in a single pass can be nearly doubled by welding from both the face and the back of the work.

In a variation on straight-through two-pass welding from opposite sides, separate welds that meet or almost meet can be made at an angle of 90° to each other in a rabbeted square-groove joint.

Tangent-Tube Welds

Tangent-tube welds are longitudinal welds joining two parallel tangent tubes (or cylinders). The tubes may differ in size; the beam is perpendicular, or nearly so, to the common axial plane of the two tubes. Added filler metal may be used for reinforcement. Thinner-walled tubes can be joined more easily by EBW than by arc welding methods.

Three-Piece Welds

Welds can be made that join three or more pieces in which there is penetration in a single pass into all of the pieces. Many of the difficulties encountered in welding very thin metal or foil are eliminated by sandwiching it between two thicker sections.

Multiple-Tier Welds

Multiple-tier welds are welds made simultaneously in in-line, separated joints (usually butt joints) in a single pass of the electron beam. A more detailed discussion is given in the section of this article on multiple-tier welding.

Welds Using Integral Filler Metal

Welds using integral filler metal may be of the types shown in Fig. 9(g) and (h), in which an overhanging lip or a shoulder provides filler metal to a butt joint, or both members may be made thicker at the joint than elsewhere.

EBW in Vacuum

Most EBW is done in a vacuum environment where the maximum ambient pressure is less than 0.13 Pa (1×10^{-3} torr). Maintenance of this degree of vacuum is important because of the effect that ambient pressure has on both the beam and the weld produced. High-precision applications that require welding to be done in a high-purity environment to avoid contamination by oxygen or nitrogen are ideally suited for high-vacuum EBW (EBW-HV).

Electron beam welding in a medium vacuum (EBW-MV) is usually performed at a welding (work) chamber pressure of approximately 10 Pa (7.5×10^{-2} torr), or at a work chamber pressure ranging from 0.4 to 40 Pa (3×10^{-3} to 3×10^{-1} torr)—the total partial-vacuum region. The gun chamber, where the beam is generated, is held at 1.3 to 13 mPa (10^{-5} to 10^{-4} torr), as in high-vacuum welding. The chief advantage of welding in medium vacuum, compared with welding in high vacuum, is the short pumpdown time for the welding chamber; however, this benefit comes at the cost of a welding environment that is less pure.

In nonvacuum EBW (EBW-NV), where the ambient pressure is 10 MPa (760 torr) and above, the scattering dispersion of the beam increases so that the working distance and penetration are reduced significantly below values obtained in either high- or medium-vacuum processes. Electron beam dispersion characteristics and their effect on weld penetration at various pressures are shown in Fig. 17.

High-Vacuum Design Considerations

The high vacuum minimizes contamination of the molten weld zone by oxygen or other gas elements. Therefore, high-vacuum welding is best suited for metals that are reactive or refractory in nature, such as zirconium and titanium. Typical products include nuclear fuel elements, pressure vessels for rocket propulsion systems, special alloy jet engine components, and hermetically sealed vacuum devices. High depth-to-width weld ratios can be best achieved in high-vacuum conditions, thereby minimizing weld shrinkage and distortion.

Effect of Pressure on Beam. Under ambient high-vacuum conditions, the frequency of collisions between beam electrons and residual gas molecules is extremely low, and any dispersion (i.e., beam-broadening effect) that would result from such scattering collisions is minimal. However, because the frequency of scattering collisions increases with the density of gas molecules present, this effect becomes greater as the surrounding environment pressure is increased. Only at ambient pressure values below 0.13 Pa (1×10^{-3} torr) is the effect of scattering insignificant enough that the beam

can be held in sharp focus over distances of several feet (depending on the particular characteristics of the electron gun and electron optics being employed) to achieve maximum effectiveness in producing relatively deep, narrow welds.

The presence of a high vacuum in the work chamber protects the weld metal and the HAZ from oxidation and contamination by harmful gases, serving the same function as inert shielding gases in arc welding, while also degassing the weld. The nearly complete absence of gaseous impurities eliminates the serious contamination difficulties that are usually encountered when attempting to arc weld relative metals such as titanium and zirconium. The contamination of air (total concentration of gases present) is proportional to pressure, as shown in Table 1.

Width of Weld and Heat-Affected Zone.

Electron beam welds made in a high vacuum are narrower and have a narrower HAZ than comparable welds made in medium vacuum or at atmospheric pressure, and they are much narrower than the narrowest welds made in production welding by GTAW. The narrow width of the HAZ in hardenable steels and other hardenable alloys permits welding of these metals after heat treatment, in many instances without loss of strength.

Medium-Vacuum Design Considerations

The primary advantage to welding in a medium-vacuum environment is the reduced time for pumping the work chamber as compared to welding at high vacuum. The gun chamber, where the beam is generated, is held at 1.3 to 13 mPa (10^{-5} to 10^{-4} torr), as in high-vacuum welding. A diffusion or turbomolecular pump is required to provide this gun chamber vacuum; however, only a mechanical-type pump is required to evacuate the work chamber to the final partial-vacuum welding pressure desired, which typically ranges from 0.4 to 40 Pa (3×10^{-3} to 3×10^{-1} torr). The work chamber evacuation time ordinarily does not exceed 40 s for a general-purpose chamber (of approximately 0.11 m³, or 4 ft³). Accordingly, EBW-MV permits mass production of parts, using a chamber of minimum volume. Production rates for welding in medium vacuum depend on part design and other factors; maximum production rate is typically approximately 60 pieces per hour for general-purpose, manually operated equipment, and upwards of 600 pieces per hour for specially tooled automatic machines.

Effect of Pressure on Beam. Medium-vacuum welding is done at pressures with a considerable amount of residual gas molecules, as compared to high-vacuum conditions. The greater concentration of gas (approximately 100 parts per million) increases the collisions between the air and the beam of electrons,

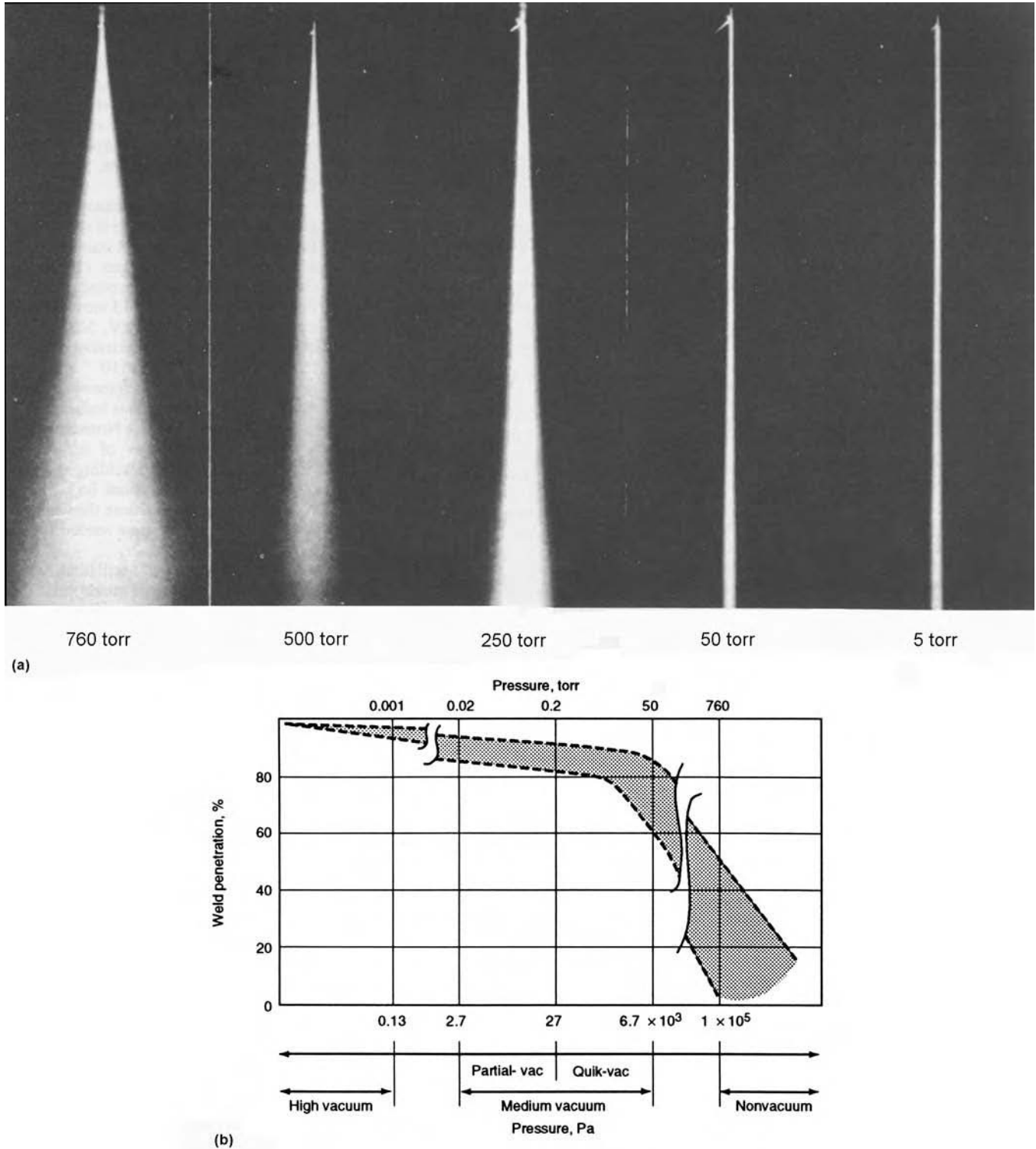


Fig. 17 Effect of pressure on beam intensity and resulting weld quality. (a) Dispersion patterns of electron beam at selected pressures. (b) Weld penetration as a function of ambient pressure level. Additional parameters, such as beam voltage, beam travel distance, and type of ambient gas used, can produce a wide range of values, thus accounting for the spread in the penetration data.

which results in a beam-broadening effect. This increases the beam diameter and decreases the power density, which results in welds that are generally greater in width and less in penetration

as compared to high-vacuum welds. Beam scattering from collisions with residual gas molecules begins to occur at ambient pressures above 0.13 Pa (1×10^{-3} torr). This scattering

effect reduces the maximum working distance that can be employed at these pressures for producing a similar electron beam weld to that obtained under high-vacuum conditions.

Width of Weld and Heat-Affected Zone. Electron beam welds made in a medium vacuum are wider and have a wider HAZ than comparable welds made in high-vacuum conditions. However, the medium-vacuum welds are still narrower than the narrowest welds made in production welding by GTAW. The effect of welding chamber pressure on penetration and weld shape is shown in Fig. 18 for welds made on type 304 stainless steel, using a beam length of 405 mm (16 in.) without changing focus. Maximum penetration, shown in Fig. 18, is approximately 13 mm (½ in.). Welding conditions are 150 kV, 30 mA, and 1525 mm/min (60 in./min). Penetration drops off rapidly at pressures of 13 Pa (10⁻¹ torr) or more at this beam length and at somewhat lower pressures when the beam path is longer.

General Vacuum Limitations

A major limitation in the use of high vacuum in the work chamber is the effect on unit production time, because of the need to pump the chamber down before each load is welded. Pumpdown time is typically approximately 3 min for a 0.85 m³ (30 ft³) chamber and 10 min for an 8.5 m³ (300 ft³) chamber. These pumpdown times are realistic only for a very clean and well-maintained system. In production, pumpdown may be nearly double the aforementioned times. The effect of this limitation on unit production time is reduced by welding a number of assemblies in each load and by keeping chamber size as small as possible. Small chambers specially designed for use with small workpieces have typical pumpdown times of 1 min (3.69 × 10⁶ mm³, or 225 in.³, chamber) and, in some cases, 15 s or less (1.0 × 10⁶ mm³, or 60 in.³, chamber).

A second major limitation in the use of high vacuum is that work size is limited by chamber dimensions. This limitation is sometimes circumvented by the use of a chamber bolt on threshold that facilitates special openings, and seals that permit oversize work to extend within a portable clamp-on extension chamber.

Vacuum Welding Conditions

Welding in high vacuum is done with low-voltage as well as high-voltage equipment. Beam voltage ranges from 15 to 185 kV; beam current, 2 to 1000 mA; and welding speed, 100 to 5000 mm/min (4 to 200 in./min) for most applications. However, higher welding speeds are typically used for

Table 1 Proportionality of weld pressure to contamination level in a vacuum chamber

Pressure		Gases, ppm
Pa	torr	
0.0013	10 ⁻⁵	0.01
0.13	10 ⁻³	1.3
13	10 ⁻¹	132
50	4 × 10 ⁻¹	500

special thin-section applications. The energy input to the work needed to produce a weld of the required depth of penetration and width is the basis for selecting the welding conditions.

Depth of penetration is increased by increasing the voltage or current for greater beam power, or by decreasing the welding speed. Table 2 lists approximate energy inputs per inch of weld length for making narrow single-pass electron beam welds 6.4 to 75 mm (0.25 to 3 in.) deep in the weldable alloys of copper, iron, nickel, aluminum, and magnesium. These values are intended to serve as guidelines for establishing conditions for welding work for which no previous experience is available. Energy-input requirements for specific applications depend on the alloy composition and special operating conditions, such as the use of beam oscillation or a defocused beam.

EBW in Nonvacuum

Unlike high- and medium-vacuum welding, EBW in nonvacuum can offer greater work-envelope capability. Welding at atmosphere may not include the limitations on work size that are imposed by the need to enclose the work in a vacuum chamber and the time needed for the chamber to pump down.

Explanation

In EBW-NV (workpiece out-of-vacuum), which is also referred to as atmospheric EBW,

the work to be welded is not enclosed in a vacuum chamber. Instead, it is welded at atmospheric pressure. A radiation-tight enclosure or chamber, similar to that used in high- or medium-vacuum EBW, surrounds the weld area. A vacuum, however, is not provided in this welding enclosure. A nonvacuum electron beam is generated at high vacuum in the same manner as in high- and medium-vacuum welding. It is focused down through a series of individually pumped stages, each connected to the other by concentrically aligned orifices, decreasing in diameter in the direction of increasing pressure; this differential pumping scheme provides the high vacuum (gun region) to atmospheric (workpiece region) pressure gradient necessary to allow the beam to pass down through the column and exit into the ambient atmosphere.

Operating Conditions

Conditions for nonvacuum welding differ substantially from those for welding in high or medium vacuum. Because beam dispersion increases in proportion to pressure and distance traveled, at pressures above the high-vacuum level, the nonvacuum beam becomes dispersed at relatively short travel distances.

To provide an electron beam of sufficient energy to minimize the scattering effect of collisions with residual gas molecules within the electron beam transfer column (i.e., the differentially

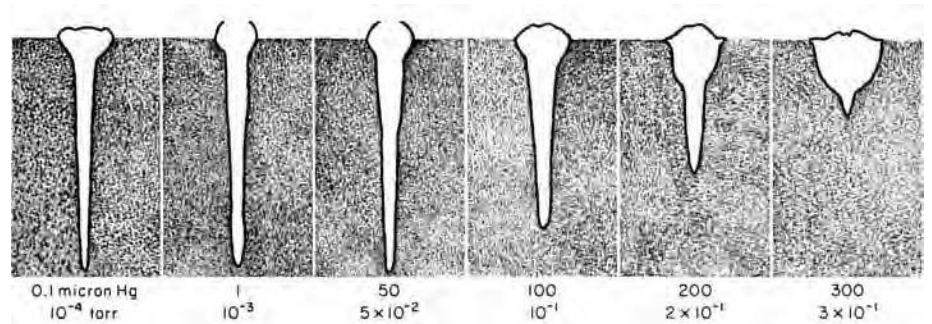


Fig. 18 Effect of welding-chamber pressure on penetration and weld shape for type 304 austenitic stainless steel

Table 2 Energy input at the weld for single-pass EBW in high vacuum for various depths of penetration

Depth of penetration		Energy input per weld length for indicated metal(a)									
		Cu		Fe		Ni		Al		Mg	
mm	in.	kJ/mm	kJ/in.	kJ/mm	kJ/in.	kJ/mm	kJ/in.	kJ/m	kJ/in.	kJ/mm	kJ/in.
6.35	0.25	0.3	0.7	0.2	5	0.2	4	0.1	2	0.04	1
12.7	0.50	0.6	0.15	0.4	10	0.3	8	0.2	5	0.1	3
19.1	0.75	1.0	0.25	0.7	18	0.6	15	0.3	8	0.2	5
25.4	1.00	1.5	0.37	1.1	27	0.9	22	0.5	13	0.3	8
38.1	1.50	2.4	0.62	1.8	46	1.5	39	0.9	23	0.6	15
50.8	2.00	3.4	0.87	2.7	68	2.4	60	1.4	35	0.9	22
63.5	2.50	4.4	112	3.5	90	3.1	80	1.9	47	1.1	29
76.2	3.00	5.4	137	4.4	112	3.9	100	2.3	59	1.4	36

(a) Values are approximate and apply to the commonly welded alloys of the metals. They are intended to serve as starting points for establishing conditions for making narrow welds. Energy input may vary substantially from these values in specific applications, depending on the composition of the alloy and special operating conditions. Energy input at weld = [(beam voltage) (beam current) 0.6]/welding speed, where energy input is in kJ/in.; beam voltage is in kV; beam current is in mA; and welding speed is in in./min.

pumped gun/column assembly), the applied gun voltage is held at a constant high value (typically from 150 to 200 kV). This also helps extend the work distance of the beam after it has exited the column and entered the ambient atmosphere. The practical working distance (standoff distance) for nonvacuum welding, as measured from the bottom of the final exit orifice to the top of the workpiece, ranges from 13 to 50 mm ($\frac{1}{2}$ to 2 in.), although some nonvacuum welding is performed at both shorter and longer standoff distances. With voltage held constant, beam current, working distance, and welding speed are selected to provide the required penetration and weld shape for a sound weld. Because it is usually desirable to keep working distance as short as possible and welding speed high, beam current is the primary control variable in nonvacuum welding.

The small size of the exit orifice on the electron gun makes it necessary to focus the beam at or very close to the exit orifice. Accordingly, it is not possible to vary weld characteristics to a significant degree by changing focus. Similarly, beam deflection and oscillation are not possible. The absence of these adjustment capabilities in nonvacuum welding may be a handicap, depending on material and weld-quality requirements.

The limitation on workpiece shape imposed by the need for a short working distance can be overcome to some degree by the use of electron gun nozzles specially designed to extend into restricted spaces. Filler metal is not ordinarily used except where necessary for weld reinforcement to produce the desired weld properties or to avoid cracking.

A stream of dry filtered air, or an inert shielding gas such as argon or helium, is passed across the weld region in the space between the work and the electron gun, or may be supplied through a special insert nozzle assembly that is part of the exit orifice and is designed to minimize entrance of welding vapors and other contaminants into the gun. Auxiliary inert-gas shielding is supplied where needed for complete protection of the molten weld metal and the HAZ from gaseous contaminants. Welds are sometimes made on carbon and alloy steel and other readily weldable metals without using shielding gas. However, shielding gas is often used, and helium is the preferred gas. Weld shape can be changed by varying the flow of helium.

Weld Shape, Penetration, and Heat Input

Nonvacuum electron beam welds are generally wider and more tapered than high-vacuum welds (medium-vacuum welds differ only slightly in shape from high-vacuum welds). EBW-NV is seldom deeper than 9.5 mm ($\frac{3}{8}$ in.). Welds having penetrations greater than 25 mm (1 in.) are not common and would require a significant reduction in welding speed and use of a helium shield to improve power density. Studies

made of nonvacuum welding of steel pipe showed that, at speeds of 2.5 to 25 m/min (100 to 1000 in./min), full-penetration welds could be made in metal twice as thick if helium shielding gas was used instead of air. Table 3 gives the results of this comparison in terms of welding speed for joining steel pipe 1.3 to 3.8 mm (0.050 to 0.150 in.) thick in air or in helium. Welding speeds were 2.16 to 2.24 times greater in helium as in air. Beam power used was 12 kW. Weld shrinkage across nonvacuum electron beam welds is generally less than half that of gas tungsten arc welds on the same work metal and thickness and is typically approximately twice that for high-vacuum electron beam welds.

Tooling

Tooling in nonvacuum electron beam welding is generally designed specifically for welding a particular assembly in mass production. Providing fixtures and equipment that permit welding at high speeds and efficient work handling is the key to obtaining high production rates and low cost. The work-handling equipment is at atmospheric pressure instead of in a

vacuum; hence, general-purpose welding positioners and related fixtures are usually satisfactory. Hold-down clamping devices can be simpler than those often needed for arc welding similar parts, because angular distortion or dihedral warpage is generally low. Locating and alignment mechanisms are simpler than for welding in a vacuum, because of their accessibility and because beams are wider and lower accuracy is required in tracking the joint.

Applications

Nonvacuum EBW is typically used in high-volume production of industrial components where the size or production rate precludes the need to weld in a vacuum environment. The applications include the production of transmission-train components, steering column jackets, die-cast aluminum intake manifolds, and catalytic converters. In addition, several appliance (and other consumer-related) items may also be produced using the EBW-NV process. Figure 19 shows a catalytic converter that was nonvacuum electron beam welded with the beam in a horizontal position.

Table 3 Speeds for nonvacuum full-penetration welding of carbon and low-alloy steel pipe at a beam power of 12 kW

Wall thickness		Welding speeds				Relative welding speed in helium(a)
		In air		In helium		
mm	in.	m/min	in./min	m/min	in./min	
1.27	0.050	10.6	417	22.9	900	2.16
2.03	0.80	6.12	241	13.4	528	2.20
2.54	0.100	4.75	187	10.5	412	2.21
3.81	0.150	3.00	118	6.68	264	2.24

(a) Based on welding speed in air being equivalent to 1.00

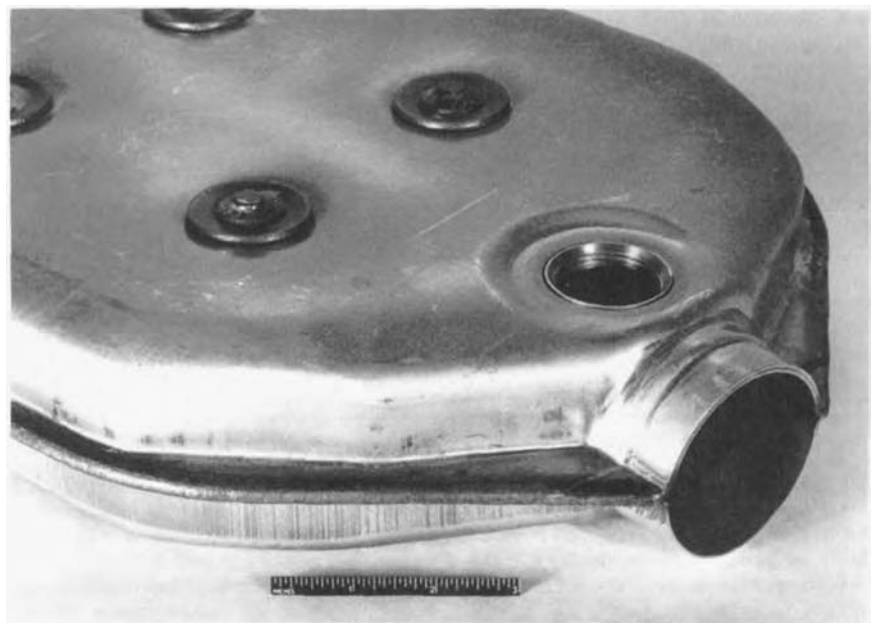


Fig. 19 Catalytic converter assembly consisting of seams joined by the nonvacuum electron beam welding process

Tooling/Fixturing

Because EBW is typically used in high-precision joining applications, special attention should be given to the tooling fixtures employed to grip or fasten the piece/part(s) to the work platen or manipulator. These considerations include the selection of the tooling material, the precision of the fixturing, and the reliability of the hardware. Furthermore, the design of tooling fixtures must take into account part distortion, part specifications, welding parameters, and the vacuum environment. Because EBW tooling may be used in a vacuum environment, tooling materials that outgas under vacuum conditions should be avoided. Also, when under vacuum, tight cavities or blind holes in the part fixturing may present a virtual leak condition that could add more time than desirable to pump down the weld chamber. Therefore, in tooling designs, unnecessary cavities should be avoided or properly vented.

Design for Heat-Input Control

Due to the high energy input of EBW that can serve to fuse metals with extreme melting temperatures, the tooling may need to be designed to withstand excessive heat buildup. To address this, heat sinks or chill bars may be employed as part of the tooling to better control the heat effects. Also to address the high heat input, refractory metal tooling may be used on the part contact surfaces. However, as a general rule, to avoid backspatter contamination in the welds, tooling is often made from the same material as the workpiece. Heat buildup can also cause excessive outgassing and distortion in the fixturing, which may impact joint alignment and weld repeatability.

Design for Weld Repeatability

Materials used for electron beam tooling should not induce magnetic fields in the weld region. Magnetic fields near the weld can cause the beam to deflect and not fully consume or altogether miss the weld joint. Ferritic steels used in electron beam tooling should be degaussed and the residual magnetism monitored. To minimize the development of electrostatic fields in the weld region (which can also influence beam positioning), avoid electrically insulating the tooling from the weldment to better facilitate a common electrical ground path.

Avoid the use of nonmetallics (ceramics, plastics, etc.) in tooling, and provide sufficient lateral pressure to minimize gapping during welding. When making girth welds on light-gage material, spring loading may be incorporated to allow for follow-up pressure. Maximum support and clamping close to the weld joint should be considered when welding sheet metal or light-gage material. Assuming that the tooling has the appropriate clamping

force and it does not present any stray movement of the electron beam, control system joint-tracking improvements over the years have paved the way for relaxing some of the precision requirements for part tooling.

Welding of Thin Metal

Electron beam welding can be advantageous for joints in which at least one member is made of thin metal. Applications include instrument parts, instrument enclosures, pressure or hermetic seals, diaphragms, encapsulations, electrical connectors, and electronic devices, of various metals. Even with the aid of the heat-sink capacity, heat input by arc welding often cannot be localized sufficiently and controlled closely enough to avoid damage to metal foil thickness. In some applications, using EBW instead of gas metal arc welding can eliminate excessive melting in thin materials.

Explanation and Ranges

Thin material (<2.4 mm, or $\frac{3}{16}$ in., and as thin as 0.025 mm, or 0.001 in.) can be successfully welded with EBW so long as proper parameters and part fit-up are incorporated. The joint area must be heated to melting temperatures in joining thin sections, just as in joining thick sections, but the rate of heat transfer away from the joint is much lower because of the reduced cross section. Hence, local heat buildup is greater, which increases weld width and decreases depth-to-width ratio. In addition, minimum beam spot size has a much greater effect on depth-to-width ratio in joining thin metal than in joining thick metal. The minimum usable beam spot size obtainable generally ranges from approximately 0.13 to 0.51 mm (0.005 to 0.020 in.) in diameter. Because of these conditions, depth-to-width ratio for full-penetration welds joining two sections thinner than approximately 2.4 mm ($\frac{3}{16}$ in.) usually does not exceed approximately 5 to 1 and may be less than 1 to 1.

When voltage, current, welding speed, and other variables have been optimized for a specific joint, use of a heat sink may still be necessary to avoid overheating thin material, depending on the base-metal properties (melting point, specific heat, and thermal conductivity) and metal thickness. Best results usually are obtained by the use of copper chill blocks machined to fit the workpiece closely at the joint area. Fixtures made of other metals may be effective as chill blocks if the contact area is sufficiently large and close to the heat source. Also, the joint gap for thinner parts becomes critical; typically, the thinner the material, the tighter the joint gap. As a general rule for thin materials, the fit-up should be as tight as possible and should never exceed 0.13 mm (0.005 in.).

Joining Thin Sections to Thick Sections

In joining thin sections to thick sections by EBW, the joint is usually designed so that the thick member serves as a heat sink for the thin member, and the point of beam impingement is slightly removed from the thin metal. When these precautions are taken, welding behavior and heat dissipation are generally the same as in welding thick sections under similar conditions. Depth of penetration in the thicker section is usually made only slightly greater than the thickness of the thin section.

Partial-Penetration Welds

The precise control of heat input obtainable in EBW permits partial-penetration welds having uniform depth to be made in metals as thin as or thinner than 0.25 mm (0.010 in.). Work-metal thickness must be uniform, and workpiece fixture arrangement and dimensions must be selected to provide a constant rate of heat loss adjacent to the path of the weld along its entire length, with special provisions made for weld starting and stopping. Beam power, focus, and workpiece travel speed must be closely regulated to minimize variation in penetration.

For the closest control of penetration, both beam power and focus can be regulated by sensitive, fast-response closed-loop servomechanisms or feedback controllers. Also, workpiece travel speed can be held within extremely narrow limits by precision, mechanical worktable, gun linear, or rotary-motion systems. To compensate automatically for the effect of any variation in voltage on focus, the control system regulating the beam focus can be coupled to the high- (accelerating) voltage supply to facilitate a rapid response time (typically less than 17 μ s).

Partial-penetration welds in thin metal are not subject to root voids, root porosity, or cold shuts, which are flaws frequently encountered in partial-penetration welds in thick metal, because such welds in thin metal have relatively low depth-to-width ratios and a wide-angle V-shape with a gently radiused bottom. Data on the relation of depth to width for high-vacuum partial-penetration welds in thin sections are given in Table 4. The ratio of depth to width is lower for the welds in the thinner sections. Penetration is from 50 to 85% of the work-metal thickness, and all welds are made with chill bars in intimate contact with the underside of the work at the weld location.

Depth of penetration generally varies 10 to 15% from a mean value for a work thickness of approximately 0.51 mm (0.020 in.), and the percentage variation is greater for welds in thinner metal. Accordingly, partial-penetration welds are not ordinarily made in metal of approximately 0.25 mm (0.010 in.) thickness.

Beam oscillation is sometimes used to smooth out variations in penetration, but such oscillation must be controlled closely to be effective.

EBW of Thick Metal

One of the major principal advantages of EBW is the capability to weld thick metals, including those with refractory and reactive material properties. Typically, EBW penetrations are considered thick as the weld depth approaches 25 mm (1.0 in.) or greater. For joining thick sections, EBW in a vacuum has a number of advantages over other welding processes. As in any welding process, the depth of penetration for a given output power level is dependent on the material type (melting temperature, density, etc.). However, because the majority of deep-penetration EBW is carried out in a vacuum environment, the vacuum level can also play a part in the obtainable weld depth.

Advantages/Disadvantages

For joining thick sections, EBW in a vacuum has three principal advantages over other welding processes:

- Much deeper penetration can be obtained in a single pass. Extremely narrow, only slightly tapered welds and a small HAZ can be produced.
- For joints on most weldable metals, no filler metal is needed. Where a filler metal is required, the quantity is usually very small.
- Joints have closely fitted parallel groove faces requiring no edge preparation, instead of V- or U-grooves.

Deep welds made in a vacuum are usually narrow; weld width for penetration deeper than 6.4 mm (¼ in.) is typically approximately ⅓ to ⅒ of the section thickness, except for a somewhat greater width at the crown of the weld. Welds may be either full or partial penetration. The disadvantages of EBW for joining thick metal may include equipment cost, size limitations imposed by the dimensions of the vacuum chamber in which the work must be placed, and the time needed for evacuating the chamber.

Effects of Pressure

Penetration capability is greatest for EBW-HV. The effect that welding pressure has on penetration of steel is shown in Table 5. A constant weld speed of 890 mm/min (35 in./min) and beam power of 7.5 kW from 150 kV/50 mA for high and medium vacuum, and 175 kV/43 mA for nonvacuum were used to obtain the data in Table 5.

Table 4 Relation of depth to width (*D/W*) for partial-penetration electron beam welds of thin sections in a high vacuum

Work metal(a)	Weld dimensions(a)						<i>D/W</i> for weld
	Thickness,		Depth, <i>D</i>		Width, <i>W</i> (b)		
	mm	in.	mm	in.	mm	in.	
Aluminum alloys							
6061-T6	0.13	0.005	0.008	0.003	0.38	0.015	0.2
5052	0.25	0.010	0.013	0.005	0.30	0.012	0.4
	0.51	0.020	0.43	0.017	0.38	0.015	1.1
Stainless steels							
17-4 PH	0.13	0.005	0.10	0.004	0.36	0.014	0.3
Type 301	0.25	0.010	0.15	0.006	0.28	0.011	0.5

(a) Chill tooling was in intimate contact with the underside of the work at the weld location. (b) Width of the weld at the crown, which was the greatest width for the gently radiused, wide-angle V-shaped welds

Table 5 Typical pressure and beam travel distance specifications required to obtain maximum weld penetration of steel(a)

Type of system	Ambient workpiece pressure		Beam travel distance		Maximum penetration	
	Pa	torr	mm	in.	mm	in.
High vacuum	0.013	1×10^{-4}	455	18	25	1
Medium vacuum	130	1	205	8	16	⅝
Nonvacuum	1.0×10^5	760	13	½	4.0	⅝ ₂

For 7.5 kW welds moving at 890 mm/min

Full-Penetration Welds

In welding carbon steel, single-pass, full-penetration, vacuum (high/medium) electron beam welds are made commercially in thicknesses up to approximately 100 mm (4 in.); production EBW-HV has been done on aluminum alloy plates 150 mm (6 in.) thick, and 230 mm (9 in.) thick aluminum alloy sections have been welded experimentally under near-optimum conditions.

Two-Pass Full-Penetration Welding

Penetration can be nearly doubled by making two passes, one on each side of the work, but cold shuts, voids, and porosity are encountered at the root of the second weld unless conditions are adjusted for the pass made on the second, or back, side. A broader second-side weld with a larger radius at the root helps to reduce the incidence and severity of these flaws.

Partial-Penetration Welding

Welds that do not penetrate completely through the work metal are satisfactory in many applications in welding thick metal; joint design and product requirements often rule out full penetration.

Effects of Gun Orientation (Vertical/Horizontal)

There are a number of EBW applications that, based on the geometry of the component and/or the working envelope of the vacuum chamber,

require the EBW gun to be in either the horizontal or the vertical position. Changing the gun orientation from vertical to horizontal and back can be done either through programmed control of a gun tilt mechanism (typically with internal moving gun systems) or by remounting the gun to another chamber port location (typically with external gun systems). However, with deep-penetration welding, the gun orientation may also play a part in minimizing weld defects such as porosity, cold shuts, or spiking.

Vapor pressure of the elements in the materials being welded, plays an important role in maintaining a weld-cavity keyhole EBW. However, a very important additional force tending to close the cavity is due to the surface tension. During heavy-penetration welding, the cavity is assumed to resemble a deep and narrow depression with liquid walls, and the force of gravity acting on the liquid metal in the keyhole may not overcome the surface tension forces when welding in the down-hand or vertical position. This may result in trapped gases or nonfused areas in the weld joint. Therefore, EBW of deep penetrations (typically welds >38 mm, or 1.5 in.) may be best performed horizontally. However, when welding in the near-horizontal configuration, a drip edge may be employed just below the weld seam to catch and prevent the molten weld from running out of the joint and leaving voids in the weld.

Problems and Flaws

In making vacuum electron beam welds 3.2 to 13 mm (⅛ to ½ in.) deep in weldable metals, weld quality is ordinarily equal to or better than

that of arc welds in the same metal. Special precautions are needed to avoid certain types of discontinuities, such as porosity, gas pockets, and cold shuts, in welds approximately 13 mm ($\frac{1}{2}$ in.) deep or deeper. Reducing the welding speed usually helps to reduce porosity and gas entrapment. Extreme care in cleaning the work metal may be necessary where the problem is severe. When flaws are found near the root of the weld, they can be avoided or minimized by any adjustment of welding conditions that broadens the weld and increases the radius of the weld at the root. Sometimes, the joint can be designed so that any root flaws are in a non-critical region, or in integral or separate backup metal that will be machined away after welding.

As in arc welding, cold shuts (incomplete fusion) are sometimes encountered at the root of a deep partial-penetration weld or of a full-penetration weld that has a poorly fitted backing strip. These discontinuities are troublesome because they are difficult to detect. Normally, they cannot be detected by radiographic methods. Ultrasonic testing can detect the larger cold shuts. Many cannot be observed on roughly polished macrosections of electron beam welds but require a metallographic polish and examination at high magnification for detection. Cold shuts can usually be avoided or minimized by reducing the welding speed or by otherwise changing conditions so as to broaden the weld and increase the radius of the weld at the root.

Poor fit-up or excessive joint gap can cause excessive shrinkage, underfill, undercut, voids, and cold shuts. Joint gap should not exceed 0.25 mm (0.010 in.) for narrow welds in most metals, although sound welds have been obtained using larger joint gaps by use of a procedure that increases the weld width.

Excessive mismatch can cause discontinuities of the same general types as poor fit-up; mismatch limits depend on joint design and dimensions and on operating conditions. Weld quality in joining thick sections is ordinarily unaffected by changes in surface roughness of the joint faces between approximately 1.60 to 2.50 μm (63 and 1000 $\mu\text{in.}$).

A problem that is unpredictable and inconsistent in making electron beam welds deeper than approximately 13 mm ($\frac{1}{2}$ in.) is arc-outs, or sudden failures of electron emission during welding. However, problems of arc-out can be decreased with routine gun cleaning and system maintenance. Work-metal composition and quality also influence arc-outs, which are more frequent in the welding of materials with low vaporization points, materials susceptible to outgassing in a vacuum, and materials that contain nonmetallic inclusions.

Use of Filler Metal

Fusion of closely fitted groove faces generally provides sufficient weld metal. If not, extra

metal can be provided by including extra stock thickness or integral shoulders or lips in the joint preparation. However, filler metal may be required where product requirements or other circumstances prevent the use of a joint preparation and welding conditions that will provide sufficient weld metal or chemistry.

Prevention and Cracking

Filler-metal (shim stock) additions can prevent cracking in electron beam welds in a crack-susceptible metal or combination of dissimilar metals. It may be needed even when joint design, fit-up, and operating conditions are selected to achieve minimum joint restraint and residual stress. In other applications, the use of preplaced filler metal can provide weld metal that is less brittle than would be obtained by welding a base metal (or metals) alone.

Among the base metals for which added filler metal is often required are heat treatable aluminum alloys 6061, 6063, and 6066, free-machining steels, and other free-machining alloys. Many combinations of dissimilar metals that are susceptible to cracking when welded directly, usually because of the formation of brittle intermetallic phases, can be electron beam welded with the aid of filler metal that has a composition compatible with both metals of the combination.

Preventing Porosity

The EBW of rimmed steel without filler metal ordinarily results in severe porosity in the weld, even when welding speed is slow and other conditions are selected to increase the time during which gas can escape from the molten weld metal. Inserting a filler metal that contains a deoxidizer, such as aluminum, manganese, or silicon, helps to minimize porosity.

Copper alloys C11000 (tough pitch copper) and other types of copper that do not contain residual deoxidizers also produce porous welds when joined without filler metal, but sound welds can be made with the aid of nickel filler metal or a deoxidizing filler metal.

Preplacement of Filler Metal

The technique most frequently used for the addition of filler metal in EBW, especially for deep welds, is preplacement. A shim of filler metal, usually of foil thickness, can be inserted between the groove faces when the joint is assembled for welding, or a wire or other suitable shape can be preplaced over the joint, being held in position by tack welding, if necessary.

Filler-Wire Feeding

Electrical or servo-operated filler-wire feeding systems that may be similar to wire-feed equipment used in GTAW are sometimes used

in the vacuum chamber. Usually, filler-wire feeding does not help in joining incompatible metals unless they are very thin.

The design of the wire-feeding nozzle and the technique with which it is used are important in guiding the wire so that it intercepts the weld pool. Any filler metal inserted into the beam path absorbs energy and affects penetration.

A prime consideration for proper implementation or use of wire feed relates to the precision of the wire-feed system itself. The unit must deliver the wire to a known location with a high degree of repeatability. The design of the wire-delivery system and welding technique demand that the energy beam and the incoming wire intercept at the same relative location over time. Inconsistency in the beam-to-wire alignment will result in irregular penetration and dilution of material in the fusion zone of the weld.

Wire-feed systems can be incorporated to provide edge buildup for repair of worn or damaged piece/parts. Many such applications exist in the jet engine and overhaul and repair industry. For example, during normal operation of a jet engine, various critical components undergo wear, for example, knife-edge seals, Z-notches, and vane surfaces. Because these expensive components are vital to maintaining the proper internal pressures required for the efficient operation of the engine, a repair procedure is developed to refurbish the worn component, which can represent a substantial cost-savings per engine.

Wire-Feeding Equipment

Several design features are desirable in a wire feeder for EBW. These include means of making positioning adjustments from outside the vacuum chamber during welding, such as changing the proximity of the nozzle to the weld pool, changing the angle of incidence between the workpiece and nozzle, and controlling the movement of the wire relative to the beam to ensure accurate interception. Figure 20 gives a view of a wire-feed system integrated with a moveable EBW gun.

A wire-feed system to be integrated in an electron beam welder must be capable of consistent and repeatable operation inside the weld chamber. These conditions include vacuum levels approaching 1 μtorr , x-ray bombardment associated with the process, metal vapor deposition, dissipation of radiant heat, and so on. Desirable characteristics for a wire-feed system of this type would include:

- Programmable closed-loop control of the wire-feed rate
- An x-, y-, z-positioning system for the wire nozzle, with jog capabilities
- Programmable automatic retraction of filler wire
- Forward and reverse jogging of the wire with positive drive rollers

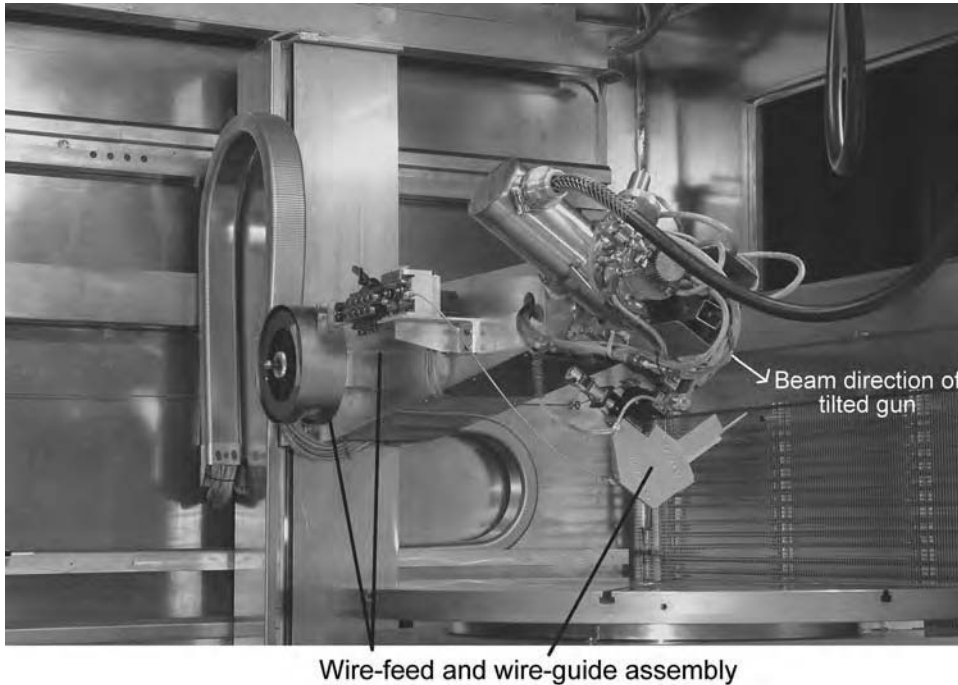


Fig. 20 Moveable electron beam welding gun assembly with wire-feed system. Courtesy of Sciaky, Inc.

- Control of the nozzle angle
- A wire-straightening system
- Easily changeable details to accommodate changing wire sizes

It is desirable to be able to control the timing so that wire feed can be started and stopped independently of the beam and table. A wire-feed servo system may be employed to precisely control the feed rate and timing to control the build size and to eliminate the sticking of the wire to the workpiece at the end of the weld. In some control systems, wire-feed synchronized pulsation with beam current may be employed to precisely control the heat input for fine buildup or special feature requirements. Also, an optical viewing system can enhance the wire-feed performance by allowing visual confirmation of the wire location relative to the joint or seam.

Welding Technique When Feeding Filler Wire

The wire-feed rate is usually set at approximately the same rate as the welding speed. Beam power must be sufficient to melt the wire as fast as it is fed. The wire diameter is selected so as to provide 1.25 times the volume of filler metal needed to fill the joint cavity. Where needed, backing strips or rings are used to prevent loss of molten weld metal.

The wire-feeding nozzle is normally held as close to the weld pool as possible without damage to the nozzle, and the wire is directed into the forward edge of the pool. The tip of the nozzle should be made of a heat-resistant

material, coated to prevent molten weld metal from inadvertently adhering to it. The nozzle is usually pointed in the direction of workpiece travel.

The filler metal can be deposited during the weld pass, using a low welding speed to allow time for the molten metal to fill the joint gap, but for deep welds it is better to deposit it in a separate pass. If cracking is a problem, another method used on thin metal is to deposit filler metal on the joint, and then make the welding pass to distribute the filler metal more effectively. Additional information on the wire-feed process and related equipment can be found in the section "Electron Beam Welding as a Repair Method" of this article.

Direct Manufacturing

A heavy-duty version of the wire-feed assembly previously described may be used with an EBW system to facilitate direct manufacturing (EBDM). Direct manufacturing uses the electron beam that impinges on the wire-fed alloy to build near-net shape metallic parts using a layer-by-layer additive process. Generally, part-path planning is executed through a software processing method, whereas a three-dimensional computer-aided design model is used to command the path of the beam and wire melt formations on a substrate plate until the desired near-net shape or geometry is formed (Ref 3). The substrate plate may be an integral part of the assembly, or it may later be machined away. This EBDM process using wire feed is also known as electron beam additive manufacturing and electron beam free-form

fabrication. For additional information with regard to these processes, refer to the section "Electron Beam Near-Net Shape Processing" in the article "Nontraditional Applications of Electron Beams" in this Volume.

EBW for Poorly Accessible Joints

There are attributes of EBW that facilitate welding of joint designs that are not easily accessible. This is primarily due to the beam diameter, directionality, and the broad capability to manipulate the beam in various orientations by both electromagnetic and mechanical means. However, as with other welding processes, there are weld component clearance requirements that must be taken into consideration.

Advantages

One of the advantages of EBW is the ability to reach into areas lying deep within narrow openings. This is possible because the electron beam has a small diameter, a long working distance, and, frequently, the ability to be projected at an angle. Many joints that are inaccessible for welding by other processes can be electron beam welded. This capability is used both in fabrication and in repair work and is especially useful in salvaging intricate castings.

Workpiece Requirements

For limited-access welding, the workpiece must satisfy three general requirements:

- The weld area must be on a line-of-sight path from the beam source.
- There must be sufficient sidewall clearance to avoid beam-fringe interference.
- The beam path must be free of magnetic fields.

Beam Characteristics

Beam characteristics that determine applicability of EBW to poorly accessible joints are beam diameter and the working distance, or effective beam length, available between the exit end of the beam transfer column and the work. These characteristics in turn depend on the beam power used, which is selected to produce the desired penetration, and on beam focus, which is influenced by the design of the gun, the chamber, and the focusing coil.

Sidewall Clearance

Parts intended for fabrication by EBW can often be designed with sufficient sidewall clearance for the beam power required. Where insufficient sidewall clearance exists in repair welding, lowering the beam power or slightly changing the angle of incidence of the beam

often avoids interference. In repair welding, tests should be made on simulated joints, using the same type of work metal and the required beam power, rather than risking damage to difficult-to-replace parts.

Where close sidewall clearances are involved, it is especially important to avoid magnetic fields, which can cause damage to the part by deflecting the beam. A test run on low power is commonly used to detect beam deflection; however, allowance must be made for the increase in deflection at full welding power. Magnetically soft materials with induced magnetism can usually be demagnetized with magnetic-particle inspection equipment or with degaussing coils.

Minimum beam clearance for making welds close to magnetic metal that projects above the work surface at the joint is given in Fig. 15.

Design for Scanning/Joint Tracking

The development of feedback servomechanisms for controlling variations in beam power and beam spot size, as well as in work travel and speed, permits EBW to be accurately controlled within tolerances of a few thousandths of an inch. Depending on machine characteristics, beam spots effective for most welding purposes can be set up in the range of 0.25 to 0.76 mm (0.010 to 0.030 in.) in diameter without difficulty. Assuming a very small beam variation, an application requiring a beam spot of only 0.25 mm (0.010 in.) diameter would require a means of holding the joint-to-beam coincidence with a runout of less than ± 0.13 mm (± 0.005 in.).

For welding with a 0.25 mm (0.010 in.) diameter beam, a pileup of manufacturing tolerances could easily cause the beam to miss the joint. Therefore, for most production purposes, scanning and joint location systems are necessary to better ensure the beam-to-weld joint alignment.

Accuracy of Beam Alignment

For external EBW gun systems, beam alignment is generally a matter of workpiece alignment, as even guns of the adjustable type are usually fixed during welding. For these systems, most joints are designed for simple path shapes—straight lines and circles—that can be adequately traced with precision-made carriages, cross-feeds, turntables, eccentric tables, and spindles. With internal moving gun systems, beam alignment accuracy is also dependent on the rigidity and performance of the motion mechanics that support, drive, and manipulate the gun. In either case, precision motion mechanics are required to hold the joint-to-beam alignment with an accuracy of ± 0.05 mm (± 0.002 in.) or better.

Scanning/Joint-Tracking Procedure

The workpiece is fixtured, and the joint is aligned for travel direction and is moved to its approximate location under the gun. The chamber is closed and pumped down to a vacuum sufficient for safe operation of the gun. A low-power beam is turned on and focused sharply on the workpiece surface. The specific power settings will vary with the working distance selected and the power ratings of the machine; however, they should be sufficient only to create a detectable spot without overheating the workpiece. All of this may be done through the selection of a scanning program.

The low-power beam is typically rastered at the same voltage as that used for welding and is made to sweep back and forth on the part surface at a right angle to the welding path; these settings are typically controlled automatically by the scanning program. The secondary emission feedback through the control system, which may be displayed on an oscilloscope or monitor, provides the operator with a beam-to-seam position displacement. The operator can then position the gun or the part to correct the alignment, or use the autocorrection feature if there is one. With autocorrection, servo drive direction and speed data can be defined or programmed to permit precise placement of the beam on the seam. If tooling is within acceptable tolerances, production parts ordinarily need only periodic scanning as a quality-control measure.

Joints that have a path that deviates from a straight line or circle usually require an automatic tracking device for EBW of production quantities. For small production lots, manual tracking, using a coordinate drive having separate controls, can sometimes be used. Whether the method is controlled manually or automatically, the motion required to generate the curve is usually imparted to the workpiece, although with precise moving gun motion mechanics, motion can be imparted to some guns.

Scanning Techniques

Scanning techniques vary in detail, depending on the type of equipment used as well as on joint design. It is not always necessary to position the beam spot precisely on the joint line. When welding dissimilar metals, dissimilar thicknesses of the same metal, or certain self-locating joints, it is often necessary to position the beam a short distance from the visible joint line. A corner edge or a scribed line can often serve as a reference, or measurement can be made with an optical grid.

Beam-to-seam alignment using secondary emission scanning systems may be more difficult for an operator to interpret when the joints are at an angle, near a projected corner, or stepped. However, with continued use with the special joint configuration, an operator can obtain

sufficient experience to use the scan signal to align the beam with the seam. Also, depending on the control system architecture, some later EBW systems may incorporate wave shaping or other signal conditioning that can filter scanned signals received from the gun antenna plate to increase scan performance. This type of scan-filtering system generally works in conjunction with the computer control system to autocorrect angular or unique joint configurations.

Scanning Problems

Some of the causes of excessive runout and other difficulties encountered during scanning are as follows:

- Poor joint design, inaccurate joint preparation
- Improper fit-up, inadequate fixturing
- Lack of precision in workpiece traversing mechanism
- Obstructions in the beam path
- Indistinct or undetectable joint line
- Beam deflection by electric or magnetic fields

The corrections required for mechanical discrepancies are self-evident; the effects of electric and magnetic fields may be less obvious.

The negatively charged electrons that comprise the electron beam constitute a negative space charge. When the electrons strike an insulated metal part, negative charges are built up, causing mutual repulsion between the part and the beam. By grounding the part, excess electrons are conducted away. To avoid unintentional deflection of the beam by nearby magnetic fields, workpieces, fixtures, and tooling components made of magnetic materials should be demagnetized before welding.

Optical Joint Locating

On newer machines, an optical system typically consists of a video camera that is directed toward the work and a monitor on which the image is displayed. On older EBW systems, such a system may consist of a horizontally mounted monocular or binocular telescope. For either case, internal illumination and reflecting mirrors are used to provide a line of sight coaxial with the beam path. Magnifying power may be 10 to 40 times, depending partly on working distance. High-precision alignment can be obtained.

There are two common methods of using this equipment. One method makes use of a low-power beam that is sighted on the workpiece surface. Using a calibrated grid, measurements to 0.025 mm (0.001 in.) can be made. In the other method, the beam is centered on a cross-hair reticle embodied in the viewing system. The beam is then turned off and the workpiece joint is moved into coincidence with the cross-hair, under internal illumination. The advantage of the latter method is that, after the beam is turned off, the chamber need no longer remain

under vacuum, and further alignment work can be done with the chamber opened, if necessary.

Before joint locating, the mirror surfaces (which are generally protected with glass shields within the internal optics system) should be cleaned, because vapor deposition takes place during welding. The frequency of cleaning may vary, depending on the amount of vapor created and the proximity of the weld. Typically, the glass shields can be removed for cleaning or replacement.

Electronic Scanning

The previous descriptions primarily refer to an electronic scanning system. For this device, the system displays the relationship on an oscilloscope or monitor. As previously mentioned, the equipment makes use of a low-power electron beam that is made to oscillate across the joint. The amplitude of the oscillation is sufficient to display the workpiece surface for a short distance on either side of the joint, as well as the joint line itself. At the point where the beam crosses the seam, a loss of reflected electrons at the antenna feedback signal enables the control to determine the seam location relative to the scan sweep (gun beam sweep) (Ref 4). Joint correction can be incorporated to provide accurate beam placement on the seam. Figure 21(a) shows a simplified view of an electronic scanning system; current systems incorporate more complex signal arrangements, but the overall concept is the same. Figure 21(a) shows the display condition for a beam centered exactly on the joint. The "V" represents the joint line, with the beam spot centered accurately; the two horizontal arms (of equal length with a centered beam) at the top of the "V" represent the adjacent workpiece surface. The broken lines above the work (at left in Fig. 21a) show the plane of oscillation; the wavy line along the joint in the same view shows the approximate amplitude of oscillation. If the beam location were displaced to the right of the joint, the display would look like Fig. 21 (b); an opposite-handed display would indicate displacement to the left. By the relative depth of the "V," the display also indicates the amount of joint separation from apparent zero to approximately 0.15 mm (0.006 in.). A joint mismatch of a few thousandths of an inch is indicated by the relative height of the horizontal arms. In setting up for electronic scanning (under vacuum), the work is provisionally aligned as for optical scanning, making sure that the joint line is parallel to the direction of travel.

Manual and Automated Joint Tracking

In manual tracking, the welding operator must closely observe the joint at the point where the weld is being made to anticipate any change in direction. The conditions best suited to this type of operation are as follows:

- A joint path consisting of a smooth curve
- Slow travel speed
- A low-power beam with oscillation, to form a weld as wide as possible.

The welding operator is capable of regulating two motions of the workpiece (or gun) by manually adjusting the remote controls of the travel mechanism. For a low heat input, to permit the use of the low welding speeds needed when manual tracking is used, beam pulsation can be combined with beam oscillation.

In automated joint tracking, mechanical, electromechanical, numerically controlled, and computerized systems are sometimes used for welding joints that deviate from straight lines or circles. The use of computerized numerical control has become highly prevalent in EBW equipment over the past decades. The capability of CNC for allowing the weld seam path of a part to be quickly "digitized" and "edited" makes it an ideal tool for programming and tracking the actual weld seam path (Ref 5). Axes position tables and autocorrection features may be implemented within the control system program to automatically scan, correct, collect, and store weld points along a joint path, to be subsequently run in a weld program.

Electron Beam Welding as a Repair Method

Restoration of worn or damaged components has traditionally been an important application for welding technology. Some repairs are approached by welding a new detail in the area requiring restoration. However, it is frequently more suitable and cost-effective to use a weld buildup process to restore the dimensions and structural integrity of the affected area.

Welding processes such as manual or automatic GTAW or gas metal arc welding (GMAW) have traditionally been used for this type of repair; these processes facilitate the addition of filler wire to accomplish a weld buildup. Although these processes enable efficient and relatively fast buildup of filler metal, they have the potential drawback of relatively high heat input, which may cause distortion when section thicknesses are small.

Explanation

The EBW process has been employed extensively for original equipment manufacturers mainly because of its ability to minimize or eliminate distortion on welded components through high weld speed, small HAZ, and small bead size. In the past, application of EBW for repair has been relatively limited, confined primarily to butt welding of repair insert details, penetration of parent metal (e.g., to eliminate a crack), or melting of preplaced filler wire. The matching of automatic wire-feed equipment to EBW equipment, however, has led to the development of a system that incorporates the inherent advantages of EBW systems and offers the additional capability of achieving a precise, multiple-pass weld buildup with minimum heat input. The addition of this capability has greatly increased the utilization of EBW as a repair mechanism.

Electron Beam Wire-Feed Process and Equipment for Repairs

Electron beam welding units used for weld buildup repairs are generally high-vacuum machines (13 mPa, or 10^{-4} torr). The availability of a highly controlled welding atmosphere is a

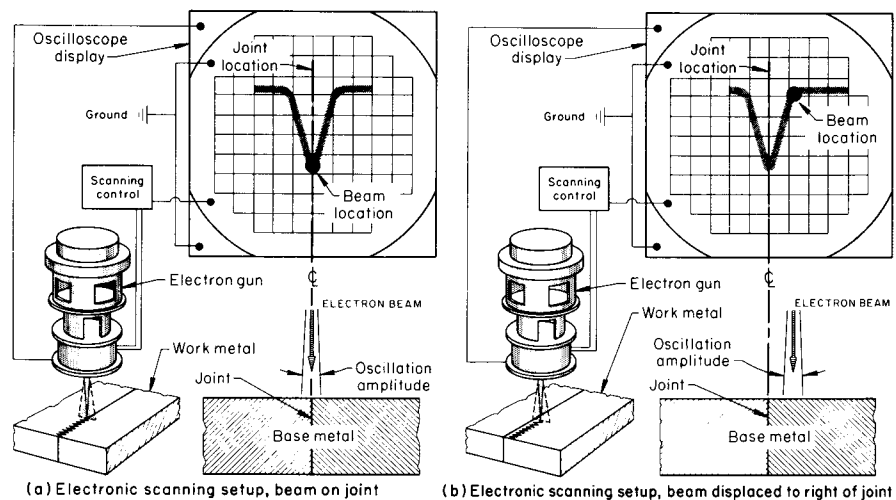


Fig. 21 Electronic scanning apparatus with cathode ray tube display to show alignment of electron beam relative to weld before welding operation is carried out. (a) Electron beam centered along length of joint. (b) Electron beam displaced from centerline of joint

distinct advantage for the electron beam process, particularly when welding reactive materials such as titanium. The EBW machines are typically equipped with signal generators or deflection control systems that oscillate and deflect the beam in the x - y directions. They are also capable of making circles and other geometric figures. Beam deflection frequency can be varied, and the beam can be focused above or below the point of impingement. Beam pulsing and modulation of the pulse are also possible. All these tools can be used in weld buildup repairs. Current electron beam vacuum chambers can accommodate parts exceeding 1525 mm (60 in.) in diameter. On the floor of the chamber is an x - y table; a rotary table is generally fixed to this table. The component to be repaired, typically a cylindrical ring or case, is fixtured to this rotary table. An automatic wire feeder delivers wire to the beam impingement point, enabling a continuous multiple-pass weld buildup when the component is rotated under the beam.

The wire-feed equipment is an adaptation of standard GTAW wire-feed equipment, and the technique is similar to that employed in cold wire circumferential automatic GTAW. The precision wire feeder delivers wire through a nozzle, which can be positioned in the x -, y -, and z -directions and which is visible in the coaxial optical or camera system of the EBW machine. Wire entry angle, nozzle position, wire speed, weld speed, accelerating voltage, focal position, deflection, and amperage are critical factors in EBW buildup. Both inside and outside surfaces can be restored, depending on the position of the wire feeder within the chamber.

A relatively small filler-wire diameter (≤ 0.89 mm, or 0.035 in.) typically is employed to attain a precise low-heat input and a weld buildup typically 1.0 to 1.3 mm (0.040 to 0.050 in.) wide and 2.54 to 7.62 mm (0.100 to 0.300 in.) high, although much larger buildups could possibly be attained by multiple applications of the process or larger wire (> 2.30 mm, or 0.090 in.), as used in EBDM. Electron beam weld buildup lends itself readily to automation, thereby opening the process to use by less skilled operators. On some machines, all parameters are preset. The operator merely lines the machine up on the surface to be welded and pushes the start button. The wire feeder automatically activates and adjusts itself to produce a smooth, precise buildup.

Application of Electron Beam Wire-Feed Process for Repairs

The electron beam wire-feed process has been applied primarily for restoration of worn or damaged gas turbine aircraft engine components, which are typically cylindrical in shape with diameters ranging from 100 to 1525 mm (4 to 60 in.), lengths from 25 to 915 mm (1 to 36 in.), and section sizes from 1.3 to 12.7 mm (0.050 to 0.500 in.). Repair of gas turbine engine components

has become increasingly attractive to commercial and military operators because of the cost and lead time involved in the procurement of spare parts. Repairs are typically conducted at 50 to 70% of the cost of a new component, with three to six times improvement in replacement time.

One of the key gas turbine engine component repairs is the restoration of the rotating labyrinth-type air seals used to maximize engine pressure gradients. As seals wear or are damaged, engine efficiency drops and fuel consumption rises. Hence, restoring minimal seal clearances has become increasingly attractive. Seal design is typically of the straight knife-edge or tapered knife-edge type (Fig. 22). Materials vary from iron-base alloys (AMS 6508 and A-286) to high-nickel alloys (Incoloy 901 and Waspaloy) to titanium alloys (Ti-6Al-4V, Ti-8Al-1Mo-1V, and Ti-6Al-2Sn-4Zr-2Mo).

Currently (2011), virtually all air seal restoration is done by welding. Gas tungsten arc welding, gas metal arc welding, and electron beam welding have all been successfully applied, depending on requirements of engine manufacturers, component design, material, and experience and equipment of repair stations. Prior to the establishment of the electron beam wire-feed process, utilization of the standard electron beam weld process for this type of repair was limited to competitive weld buildup processes (GTAW and GMAW) and was primarily applied where distortion and HAZ size were a primary concern.

Initial application of the standard electron beam process involved welding a machining ring onto a premachined pedestal on which the worn air seal was removed, as shown in Fig. 23a. The knife-edge configuration was then machined into the welded ring. Later, a splitting concept was introduced. In this procedure, an edge-rolled ring was assembled into a

shallow groove premachined into the pedestal top (Fig. 23b). Circumferential spike welds from each side welded the ring in place, and the ends of the split ring were radiused to blend the discontinuity in the ring. The wall thickness of the as-rolled ring was the finished thickness of the knife edge, typically approximately 0.25 mm (0.010 in.), and the outside diameter was finish machined after welding. Disadvantages of this weld buildup system include ring detail cost and the amount of postrepair machining required.

The application of the precision wire-feed electron beam process (Fig. 23c) to gas turbine seal repairs provides both the material application efficiency and cost advantages of weld buildup systems and the inherent low heat input and controlled atmosphere advantages of the EBW process. A typical automatic wire-feed electron beam air seal repair, applied to a compressor rotor spacer for a gas turbine engine, is shown in Fig. 24. This part is made from a titanium (Ti-6Al-4V) forging. The outside diameters of the knife edges wear in service, and the knife edges must be restored to maintain the proper tip clearance. The knife-edge material is machined close to the diameter of the pedestal; a weld buildup is made using Ti-6Al-4V titanium filler wire, and a new knife edge is machined. The multiple-pass technique typically deposits 0.25 to 0.38 mm (0.010 to 0.015 in.) of radial buildup per pass. Penetration of the HAZ below the pedestal top typically does not exceed 0.38 mm (0.015 in.). Because the entire weld buildup operation is performed in a vacuum, there is no weld metal or HAZ oxidation. Cost is minimized by the high speed of the EBW process, which substantially exceeds that of the standard GTAW buildup process.

Air seal repairs also are routinely performed on steel and nickel alloy parts. Experience with

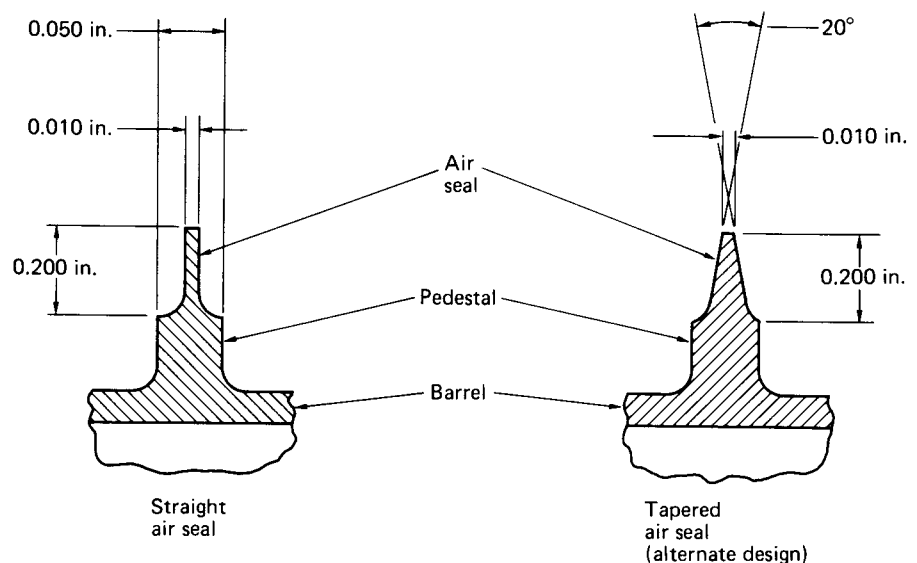


Fig. 22 Schematic comparing cross sections of straight and tapered air seals

nickel-base superalloys containing relatively high percentages of gamma prime that form hardening elements has shown these alloys to be crack-sensitive during welding or postweld heat treatment. Crack-free precision wire-feed EBW buildup repairs, however, are achieved when appropriate process parameters are used.

Quality-Assurance Testing

Quality-assurance testing is an integral part of all gas turbine engine repairs. The high degree of control inherent in the precision wire-feed electron beam repair process facilitates in-process control and quality assurance. Because of the high degree of control the electron beam process offers, process variables can be kept to a minimum. This built-up consistency tends to ensure a long-term high level of quality assurance.

Weld parameters are developed by the analysis of microsections of sample welds and by nondestructive testing. Once an acceptable process has been established for a component, a weld schedule is initiated and weld parameters are maintained. Any changes in equipment or process must be qualified by the analysis of new microsections. Quality of finished air seals is ensured by one or more of the following tests, depending on customer requirements:

- Visual
- Liquid penetrant
- Fluorescent magnetic particle
- X-ray
- Etch inspection

Future Applications for Repair

Although the most common application of the precision wire-feed electron beam buildup process has been in the repair of gas turbine engine air seals, the process is not limited to this type of application. Various other wear-restoration applications have been developed, including spline and groove buildups. Although the process is most efficiently used as a continuous multiple-pass process on cylindrical components, planar buildup can be achieved by using sequential weld pass patterns or oscillation. The process is also potentially applicable for new part manufacture

to enable a component to be machined from a smaller, less costly forging with selective electron beam buildup to provide material for specific structural features (for example, outside-diameter bosses on cylindrical cases).

With the advent of EBDM, there are many other potential applications for the repair of assemblies using this high-deposition wire-feed process. Applications for near-net shape repair of damaged or worn metal parts can consist of common or high-value metal alloy components on items such as airframes, landing gear, jet engines, guided missiles, and military vehicle parts. For additional information with regard to this process, refer to the section "Electron Beam Near-Net Shape Processing" in the article "Nontraditional Applications of Electron Beams" in this Volume.

EBW Process Control Plans, Codes, and Specifications

The applications that use EBW often include high-quality, high-precision components and specialty materials. Therefore, weld requirements are generally critical in nature, and process control plans, weld codes, and specifications may be required to achieve the ultimate goal of part performance.

Explanation

Control plans provide a written summary description of the systems used in minimizing process and product variation and how this information can be documented. The EBW process control plan (PCP) typically outlines all the product and procedural control operations implemented in the weld production process. A single PCP may apply to a group or family of welded products that are produced by the same process at the same source. Sketches, as necessary, may be attached to the PCP for illustration purposes.

In effect, the PCP describes the actions that are required at each phase of the EBW process, including receiving, in-process, outgoing, and periodic requirements to assure that all process outputs will be in a state of control. The PCP is maintained and used throughout the weld product life cycle. Early in the product life

cycle, its primary purpose is to document and communicate the initial plan for process control. Subsequently, it guides manufacturing in how to control the process and ensure product quality. Ultimately, the PCP remains a living document, reflecting the current methods of control and the measurement systems used, and is updated as systems and control methods are evaluated and improved. The PCP should be a central part of the supplier's overall process to meet

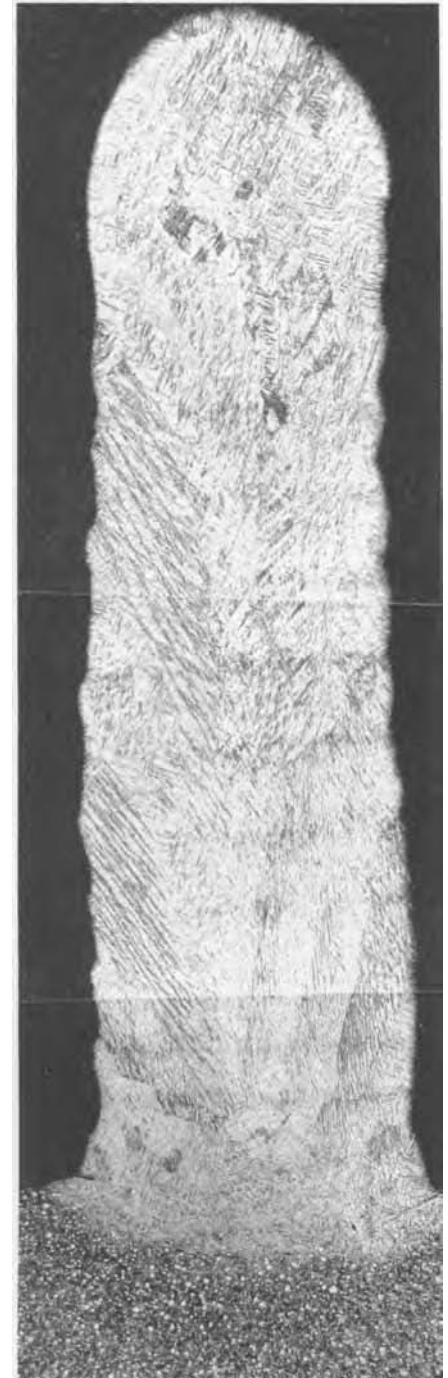


Fig. 24 Micrograph of a typical automatic wire-feed electron beam repair of an air seal. Original magnification: 15×

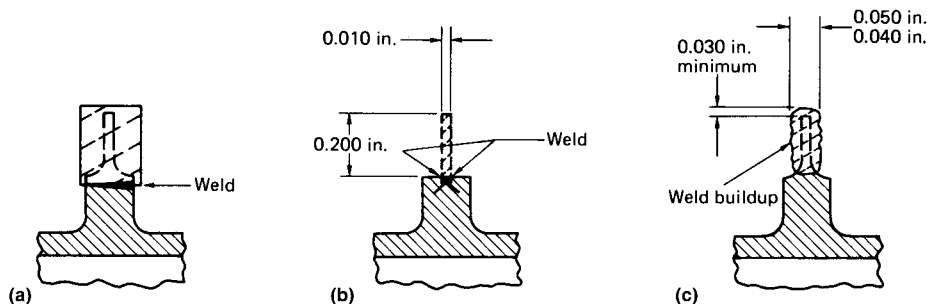


Fig. 23 Sequence of operations required for electron beam welding repair of an air seal. See text for details.

quality, cost, and delivery goals. The EBW process control plan may include the following:

- Verification of weld parameter settings on test samples
- Weld part cleaning requirements
- Part preparation for assembly
- Weld fixture details and loading requirements
- Weld vacuum requirements
- Preweld scanning and joint alignment procedures
- Weld program selection and identification of process characteristics
- Vacuum venting requirements
- Weld inspection and quality-control procedures
- Document certification and/or applicable procedure qualification record

The PCP may include a process flow chart, the applicable prequalified welding procedure specification, and weld rework, repair, and storage operations, if applicable. Almost all design, welding, fabrication, material, repair, testing, and inspection requirements are covered under governing organizations. For EBW, these include the American Welding Society (AWS), the Society of Automotive Engineers (SAE) International with the associated aerospace standards (AS), the American Society of Mechanical Engineers (ASME), and the Aerospace Material Standards (AMS). Even the Department of Defense has either adopted many of these codes or used them as a basis to develop their own codes, known as Mil-Specs. The codes are recognized by the American National Standards Institute (ANSI).

Weld Procedure Specifications

A welding procedure specification (WPS) is a formal document describing welding details to guide welders in the accepted procedures so that repeatable and trusted welding techniques and process parameters are used. A WPS should be developed for each material alloy and for each welding configuration used (Ref 6). Specific codes and/or engineering/welding societies are often the driving force behind the development of a company's WPS. The WPS may be supported by a welding procedure qualification record (WPQR), whereas the WPQR can provide a record of test welds performed to ensure that the procedure can produce acceptable welds. For EBW, typical items that should be recorded on a WPS include:

- Machine type (model/serial number)
- Electron beam gun type with gun component details (filament type/size, anode type/size, etc.)
- Process parameters and tolerances (accelerating voltage, beam current, beam focus, welding speed, gun-to-work-distances, beam deflection/oscillation values, etc.)
- Material details, such as base-metal type, filler type (if applicable), backing material (if applicable)
- Weld component characteristics (joint type, joint depth, fit-up gap, fixture type, etc.)

- Pre- and postheat treatment (if required)
- Other related welding requirements and techniques (part-cleaning method, gun angle, tack and cosmetic pass requirements, run-on/run-off tabs, vacuum level, etc.)

The WPS should contain sufficient details to enable any competent person to apply the information and produce a weld of acceptable quality for production. The amount of detail and level of controls specified on a WPS is dependent on the application and criticality of the joint to be welded.

Boiler and Pressure Vessel Codes

As with other welding codes, the Boiler and Pressure Vessel Code contains documents establishing legal obligations spelled out through laws and rules to be complied with whenever engaging in the manufacture of boilers and pressure vessels. The code covers requirements essential to guarantee public safety and reliability.

The ASME Boiler and Pressure Vessel Code (BPVC), which is issued once every three years, comprises a number of volumes that establish rules of safety governing the design, fabrication, and inspection of boilers and pressure vessels, including nuclear power systems. Section IX of the ASME BPVC relates to the qualification of welders, welding operators, and the procedures employed in welding in accordance with the code and the ASME B31 code for pressure piping. Section IX of the ASME BPVC establishes the basic criteria for welding (including EBW) and brazing in the preparation of requirements that affect procedure and performance for component manufacture when the maximum allowable working pressure exceeds 15 psi (1.03 bar). Also, welding variables are covered that are used in the preparation and qualification of the WPS.

Various Customer Quality Specifications

In most cases, quality standards are driven by a variety of customer-specific or general standards. These standards and specifications are used to provide consistent output quality to meet industrial and/or aerospace welding product requirements. For EBW, these quality specifications have been published by a number of committees and organizations, including the Aerospace Material Standards, the American Welding Society, General Electric, Pratt & Whitney, and Boeing.

The specifications serve to define the procedures for joining metals and alloys using the EBW process and to determine engineering and quality requirements for the production of these welds. The specifications may cover the requirements for weld joint design; written instructions for all preweld, weld, and postweld operations; inspection methods; and allowable limits. Also, process monitoring and control

plans may be implemented to assure fusion, process completion, and provisions for the certification and use of welding schedules, as well as the qualification of operators and equipment.

The general EBW specifications and the associated issuing groups are outlined as follows:

- AMS 2680, "Electron Beam Welding for Fatigue-Critical Applications," SAE International—Aerospace Material Specification
- AMS 2681, "Electron Beam Welding," SAE International—Aerospace Material Specification
- AWS C7-3, "Electron Beam Weld Process Specification," American Welding Society
- AWS D17.1, "Fusion Welding for Aerospace Applications," American Welding Society
- P8TF10, "Electron Beam Welding," GE Aircraft Engines
- PWA 16, "Arc, Gas, Electron Beam, Laser Beam and Inertia-Friction Welding," Pratt & Whitney
- RA1607-077, "Electron Beam Welding for ELV Requirements," Boeing North American, Inc.

At the time of this writing (2011), the aforementioned specifications are some of the most common relative to the EBW process; additional specifications may also apply on EBW or equipment contracts. Some older specifications may be superseded by later documents. For instance, the Aerospace Material Specification AMS-STD-1595, "The Qualification of Aircraft, Missile and Aerospace Fusion Welders," has been replaced by AWS D17.1. When conformance to one or more EBW specifications is stipulated in a contract, all provisions within the document may be required unless specifically listed or outlined as exempt by the contract authority.

REFERENCES

1. A. Sanderson and K.R. Nightingale, *Weld. J.*, April 1990, p 45
2. J.F. Lowry, J.H. Fink, and B.W. Schumacher, A Major Advance in High-Power Electron Beam Welding in Air, *J. Appl. Phys.*, Vol 47, 1976, p 95–106
3. K.W. Lachenberg, Precision Fabrication Layer by Layer, *Fabricator*, Vol 40 (No. 10), Oct 2010, p 46–47
4. R.C. Hanson, *Electron Beam Welding Equipment: Process Parameters, Limitations and Controls*, Sciaky Incorporated, p 8–10
5. J. Carrol and D.E. Powers, Automatic Joint Tracking for CNC-Programmed Electron Beam Welding, *Weld. J.*, Aug 1985, p 34–38
6. "Process Specification for Electron Beam Welding," AWS C7.3: 1999R, American Welding Society, July 12, 1999, p 10

Nontraditional Applications of Electron Beams

Kenn Lachenberg and Scott Stecker, Sciaky, Inc.,
Karen Taminger, NASA Langley Research Center,
Gary La Flamme, PTR-Precision Technologies, Inc.

SEVERAL SOLID FREEFORM FABRICATION TECHNIQUES developed over the past decade have the ability to produce structural metal parts directly from computer-generated designs (Ref 1, 2). These techniques also lend themselves to fabrication of unitized structures that reduce part count, decrease weight, reduce assembly time and cost, and improve structural efficiency, as compared to conventional fabrication and assembly methods.

Electron Beam Near-Net Shape Processing

This section covers the details for near-net shape processing using an electron beam (EB) generated from a fixed or moveable gun in a vacuum environment. The gun may be the same or similarly configured as that used for electron beam welding (EBW). As with EBW, the process environment is ideally suited to a wide range of aerospace materials, including many reactive and refractory alloys. The EB process offers unique advantages over other current available near-net shape processing methods in terms of power efficiency and deposition rate.

Process Description and Definitions

There are two main classes of EB deposition processes currently in use for near-net shape fabrication of three-dimensional (3-D) parts. These classes are based on the type of feedstock used and how it is delivered to the molten pool. One class uses a wire-feed-based feedstock method, and the other uses a powder-bed feedstock approach. Myriad other EB deposition processes also exist for depositing thin films, coatings, or performing surface modification and etching. These processes are typically used in the electronics and semiconductor industries and are generally focused on coverage of precise layers on a microscale (such as EB sputtering, physical vapor deposition, lithography,

EB-induced deposition, etc.). The focus of this article is restricted to the former, concentrating on the buildup of 3-D metallic components using an EB as the heat source and wire or powder feed as the material-delivery method.

Electron beam additive manufacturing (EBAM), electron beam free-form fabrication (EBFFF or EBF³), electron beam melting (EBM), and electron beam direct manufacturing (EBDM) are several of the acronyms used to describe various processes that correlate to the use of an EB power source for near-net shape processing. The majority of the EBAM, EBF³, and EBDM work performed has used wire as the feedstock, whereas powder primarily serves as the feedstock for EBM. In each case, 3-D EB deposition processing takes place by introducing metal feedstock into a molten pool that is created and sustained using a focus-controlled EB in a high-vacuum environment (1×10^{-4} torr or lower).

Electron beam additive manufacturing typically refers to a process where new material is added to a substrate to fabricate components. The term *additive manufacturing* has been used in the context of deposition of metallic and polymeric materials. In this article, *additive manufacturing* is used in the context of using metallic substrate and feedstock materials for the purpose of building up near-net-shaped components. For this process, the wire is directed toward the molten pool and melted by a focused EB. Parts are built up layer by layer by moving the EB and wire source across the surface of the underlying material, which is commonly referred to as the substrate, as shown in Fig. 1. The substrate material can become an integral part of the finished product. In this manner, free-standing shapes, or preforms, are generated without molds or dies. Conventional techniques then machine the component to the final part geometry (Ref 3). Depending on the wire size and the work envelope of the vacuum chamber, this process is well suited to building large assemblies or structures with high deposition rates (Ref 4). Bulk metal deposition at rates

in excess of 2500 cm³/h (150 in.³/h) as well as finer detailed deposition at lower deposition rates can be provided with the same piece of equipment, limited only by the positioning precision and wire-feed capabilities (Ref 5, 6).

Electron beam melting operates in a powder bed, tracing the part in a layer of powder with a high-energy EB and repeating for subsequent layers. In this case, the beam is steered magnetically and can be split into multiple beams running in a pattern to melt the layer of powder. While the layer is hot, the surrounding area is heated and a subsequent layer of powder is added. The heating of the surrounding area sinters the powder particulate, preventing material repulsion and improving the material quality of the down-facing surface. This specific process is typically used for small part fabrication (to fit within the powder bed), similar to standard industry practices in stereolithography (Ref 7).

Electron beam direct manufacturing can be considered a more generic term (no trademark) for the previously described EBAM, EBFFF/EBF³, and EBM processes. Although the majority of EBDM work performed has been with wire-additive processing using a substrate plate, the process term can be considered to include powder-based feedstock with or without substrate requirements. Therefore, the EBDM acronym is used in this article for general references to EB near-net shape processing.

Modeling/Tool-Path and Computer-Aided Design/Computer-Aided Manufacturing Tools

Regardless of the specific machine being used, the majority of components fabricated using EB deposition processes start with a 3-D model designed in a computer-aided design (CAD) environment. In this operation, the deposition path and process parameters are generated from the virtual 3-D model, which is typically executed by a real-time computer control. Any CAD package may be used to develop

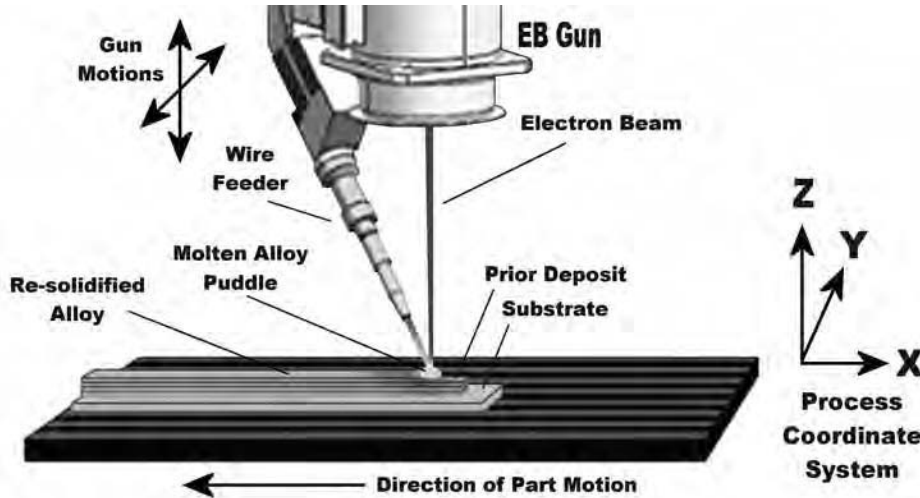


Fig. 1 Schematic diagram of the electron beam (EB) direct manufacturing process. Courtesy of Sciaky, Inc.

the solid model, as long as the data can be exported into a format that can be interpreted by the software that develops machine codes to build the components. Software may slice the solid model into layers and then generate a tool path to control the beam and motion system (depending on the EB deposition arrangement). Some systems can also take the computer-aided manufacturing outputs from standard CAD packages to develop the tool paths and output the results into standard G-code.

Thermal residual stresses are generated within parts built using EB deposition because of the thermal gradients induced between the baseplate at ambient temperature and the molten region below the EB. Thermal modeling can calculate the distribution of residual stresses, predict the distortion expected as a result of the EB deposition processes, and guide the processing parameters and tool paths to mitigate or minimize the generation of thermal residual stresses. Process modeling has also been performed to help guide the closed-loop control development and to help with understand the effects of processing parameters on the resulting geometry, microstructure, chemistry, and mechanical properties of the deposited material (Ref 8).

Process Quality and Control of Essential Variables

The EBDM process has numerous variables that control the resulting microstructures, chemistry, and shape of the deposit. These variables have been refined in the control system to make reproducible parts. There are much greater variances possible with the EB deposition systems where feedstock material is fed directly to the molten pool. Due to the challenges of feeding powder to the beam in a vacuum, only powder-bed systems have been

deployed with powder feedstock using EB; powder actively fed directly to the molten EB pool has not yet been demonstrated in production.

Wire-Feed Systems. For wire-feed systems, four of the most significant process variables that are easily controlled are the translation speed, wire-feed rate, beam power, and beam focus. The diameter of the wire feedstock is the controlling factor that determines the smallest detail attainable using this process. Fine-diameter wires may be used to add fine details, and larger-diameter wires can be used to increase deposition rate for bulk deposition (Ref 6). Due to spreading of the molten pool, a good rule of thumb for the smallest-width feature possible is on the order of $1\frac{1}{2}$ to 2 times the diameter of the wire. This general rule does not apply to the widest width possible; that is determined by the volume of wire being fed into the molten pool and sufficient power being delivered to melt large amounts of wire.

Multiple wire feeders have also been demonstrated to operate simultaneously, enabling either an increase in the volume of wire delivered to the molten pool or a functionally graded alloying where the alloy chemistry is changed over time. In this case, the width and depth of the layer being deposited is limited more by the ability to fully capture and melt wire being fed at a high wire-feed rate. For higher translation speed, the lower heat input and lower volume of wire being fed into the molten pool results in a smaller-diameter, shallower molten pool. This combined effect produces a decreasing taper in both the width and height of the deposit as the translation speed increases. The higher translation speed produces more rapid cooling and results in a homogeneous microstructure with smaller equiaxed grains (Ref 9).

Deposition rate in wire-feed systems is directly controlled by the wire-feed rate, but beam power and translation speed are also

important factors in defining the final dimensions of the deposited layer. Increasing the beam power and decreasing the translation speed increases the heat input into the part, resulting in a deeper and wider molten pool. The increased wire-feed rate adds more material to the molten pool, resulting in the greater deposition rate (Ref 9).

Powder-Bed Systems. In powder-bed processes, the diameter of the feedstock powder defines the minimum size of the layer and feature that can be produced using EB deposition. The layer thickness is controlled by the powder spreader when a new layer of powder is distributed after each previous layer of melting has been accomplished (Ref 7). The typical deposition rate for EB powder-bed processes is $60 \text{ cm}^3/\text{h}$ ($3.66 \text{ in.}^3/\text{h}$). The deposition rate is not readily changed in powder-bed processes, because the scan time with the EB is very short compared to the time consumed with spreading and leveling the powder layer.

Material Quality. Because the EBDM process is typically operated within a high-vacuum environment, this provides for an oxygen-free atmosphere, and secondary inert gases are not required to ensure the chemical integrity of the material. Furthermore, the quality of substrate and feedstock material may be traced for critical applications, and the degree of traceability would be specific to an end user's industry. At this writing (2011), a majority of the EBDM development work has been performed on aluminum and titanium alloys. However, a variety of weldable alloys can be processed using the EBDM processes, and new research on nonequilibrium processing is also being pursued on nonweldable alloys, functionally graded alloys, and selectively reinforced materials (Ref 10).

The EBDM process offers the potential for improved performance through control of microstructures and compositions at a much finer scale than parts machined from thick products. Typical thick sections have high degrees of microstructural inhomogeneity, leading to anisotropic mechanical properties. This is a direct result of differences in cooling rates and an inability to impart work evenly through a thick section. Working with smaller billets in conjunction with layer-additive processes can result in more optimal microstructural features, potentially improving the mechanical properties of the resultant part as compared to a similar part machined from a thick-section billet. Finally, compositional gradients offer improved performance and reduced cost by allowing grading from an inexpensive material for the bulk of the product to an expensive material at the surface for enhanced wear resistance, corrosion resistance, and so on (Ref 5).

Over the range of parameters tested for 2219 aluminum, resultant microstructures varied from a fine-grained, equiaxed grain structure to a solidification microstructure with larger grain sizes and dendritic growth. Representative microstructures for high and moderate heat

input (as influenced by the combination of translation speed, wire-feed rate, and beam power) are shown in Fig. 2 for as-deposited 2219 aluminum in the short-transverse plane of the deposit. The light-colored bands are dendrites that formed in the interpass region, where portions of a previous layer are remelted during deposition of a subsequent layer. Although dendrites can be seen contained within the grains, pervasive dendritic formation is minimal in the interpass regions of the deposit produced with the moderate heat input conditions (Ref 5).

Over the entire range of beam powers, translation speeds, and wire-feed rates tested, the deposits exhibited very little porosity, no cracking, and complete fusion between deposited layers. The chemical composition of the deposits compared with the starting 2219 aluminum wire feedstock confirmed that the alloy compositions were unaffected by the EBDM process. The tensile properties were also very consistent over a wide range of processing conditions. The results indicated that the EBDM process

provides a wide processing envelope from which 100% dense deposits can be made with useful mechanical properties. Refer to Fig. 3 to note the tensile properties of the EBDM-deposited 2219 aluminum as compared to typical handbook values for this material.

Experiments performed on Ti-6Al-4V resulted in the formation of large columnar grains growing epitaxially from the substrate, as shown in Fig. 4(a). At higher magnification, as shown in Fig. 4(b), α - β laths typical of the microstructures of α + β titanium alloys can be seen. Through rigorous process control, it has been demonstrated that the size of these columnar grains can be controlled by limiting the heat input during the deposition process (Ref 5).

As previously stated, following deposition, components are built near-net shape. Subsequent postdeposition processing steps may be required, depending on the requirements for the component. Final machining to provide surface finishes and precise geometry is required, as well as inspection for any internal flaws. Heat treatments

may also be performed, because the as-deposited materials tend to be in an annealed condition. Traditional heat treatment schedules used for forged materials, for stress relief, as well as for solutionized and aged conditions may be performed following deposition to achieve mechanical properties within approximately 5% of those of forged materials.

Process qualification may be required to adopt EBDM methods for select applications. This qualification requirement would be more evident for critical applications, such as those implemented in the aerospace industry. Aerospace Material Specification draft number 4999 was originally created for titanium alloy direct-deposited products using laser-additive manufacturing and has now been modified to allow alternate processes, including EBDM using wire (Ref 4). However, process qualification requirements may be the challenge preventing swift adaptation of the EBDM processes into numerous applications.

At this writing (2011), several efforts are underway to collect a database of material properties and to identify an appropriate process specification. Because the EB deposition processes tend to operate continuously in transient rather than steady-state thermodynamic conditions, maintaining consistent output parameters (such as molten pool width and depth and base temperatures) requires real-time monitoring and adjustments to one or more of the input parameters (beam power, scan speed, translation speed, wire-feed rate, etc.). This presents challenges in defining an applicable process specification, because the starting input parameters are actively modified throughout the deposition process.

Closed-loop control is being introduced into the market to provide the process with consistency to enable reproducibility from part to part, machine to machine, and day to day (Ref 8). After the process control has been translated into a process specification that can truly be representative of the conditions required to achieve a given end product, and the material database has proven that these

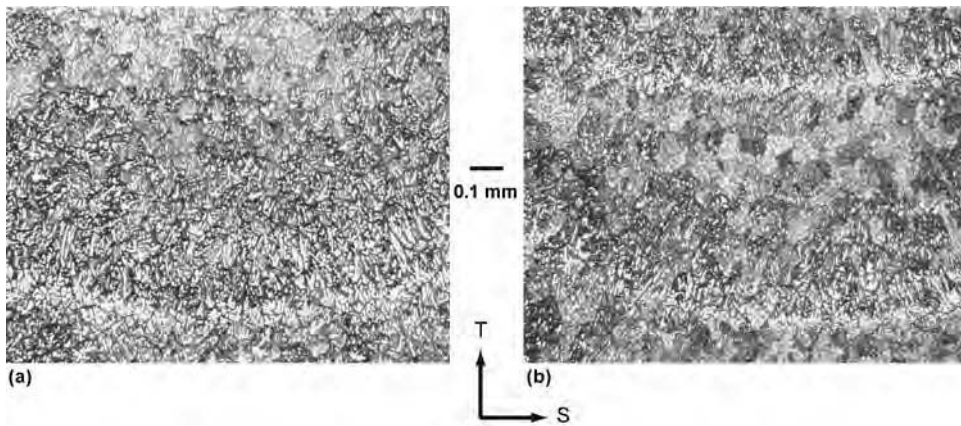


Fig. 2 Typical microstructures of 2219 aluminum deposit. (a) Dendrite growth in a deposit with high heat input and higher deposition-layer height. (b) Less dendrite growth and formation of equiaxed grain structure in the bulk deposit with more moderate heat input and a smaller deposition-layer height. Source: Ref 10. Courtesy of NASA Langley Research Center

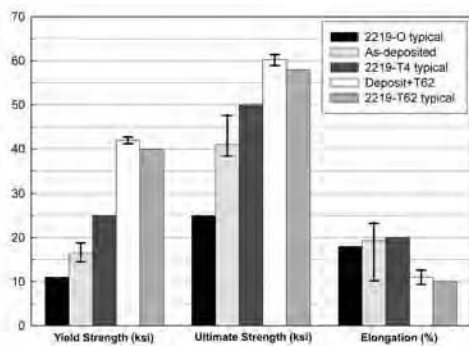


Fig. 3 Tensile properties at room temperature of electron beam free-form fabrication-deposited 2219 aluminum as compared to typical handbook values for 2219 aluminum sheet and plate. Source: Ref 6. Courtesy of NASA Langley Research Center

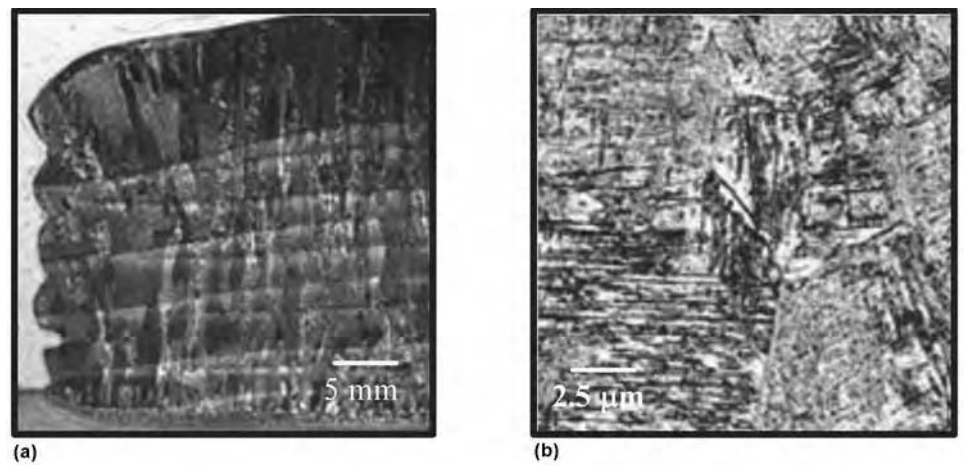


Fig. 4 Microstructures of electron beam free-form fabricated Ti-6Al-4V deposits. (a) Low magnification shows columnar grain structure in the longitudinal-short transverse plane. (b) High magnification shows α - β lath structure in the short-transverse plane.

conditions are reproducible, process qualification can be realized.

Certification efforts are currently underway to enable application of EB deposition parts to enter into service trials for the aerospace industry as structural aircraft components and in the medical industry as custom-designed medical implants (Ref 7). Within a short period of time after certification has been achieved, applications and uses may accelerate for components fabricated using the EB deposition processes.

General Applications (Target Parts and Applications)

Large-scale EB deposition processes such as EBDM are capable of producing large components directly on plate, rather than hogging-out large volumes of chips from a forging. Direct cost savings can also be realized through repair and salvage of parts, reduced machining time,

and reduced waste. Electron beam direct manufacturing can repair broken or out-of-tolerance parts at a fraction of the cost of remanufacturing. This can be particularly significant when there is a large investment, either in capital expenditures, high-value materials, or large amounts of time already invested in a part. The EBDM processes can build an entire structure or add detailed features to a simplified casting or forging. However, the replacement technology must be cost-competitive. Thus, issues such as high deposition rates, process efficiencies, process quality, and material compatibility are paramount to insertion of a new technology into a competitive metals-forming market. Implementing these processes can thereby reduce the material wasted during machining operations, reduce lead time and raw material costs by reducing billet sizes, and enable production of a generic, simplified part by conventional methods with the addition of specific details at a later time. Besides the raw material cost-savings, there is an ease in handling smaller billets of raw feedstock and the by-products or scrap produced from a less-extensively machined part (Ref 5).

Case Study. The following case study representing an aerospace component (structural chord) was explored to develop process techniques, feasibility, and proof of concept when compared to conventional manufacturing methods. In this example, the part integrity and economic models were analyzed to determine the viability of the process. This part was selected because of the high cost and lead times associated with obtaining Ti-6Al-4V, as well as the large mass of material that must be removed to produce the finished part. The CAD model was used to generate a computer numerical control (CNC) weld path offline, as shown in Fig. 5.

It was determined that a minimum of 5 mm (0.2 in.) excess material would be deposited such that a final net shape part could be machined from

the preform. A 150 mm × 1520 mm × 13 mm (6 in. × 60 in. × 0.5 in.) Ti-6Al-4V substrate plate was clamped to a work platen and processed using a moving-gun EBDM system. The preform was deposited at a rate of approximately 700 cm³/h (43 in.³/h). The parameters selected resulted in a single-pass buildup with approximate dimensions of 16 mm wide by 3 mm high (0.6 in. wide by 0.12 in. high). The preform shape was built to a height of 90 mm (3.5 in.). After thermal processing of the preform, it was machined to net size. Figure 6 depicts the chord in process and its final finished form.

A comparison of material volume is shown in Fig. 7, which depicts the material required for fabricating the chord with the EBDM approach as well as the “hog-out” method. It is easy to extrapolate that with nearly 80% more raw material required to fabricate the chord from the hog-out method, the EBDM method for fabrication would be proportionally less in costs for material and machining.

The actual cost of using the EBDM process depends on a few interrelated variables. These cost elements are associated with market pricing of raw materials, deposition rate, finish machining costs, and any required auxiliary services that may be necessary, such as thermal processing. Table 1 shows some relative cost percentages for each specific approach, with a net savings of over 40% that can be realized with the EBDM process.

The estimates assume the use of typical machining parameters for Ti-6Al-4V material. It should be noted that this estimate has been generated for comparison purposes and should not necessarily be construed as the only way to generate the subject part. The cost of raw materials is independent of the process and is driven by industry demand and availability. Deposition rates for titanium have been demonstrated up to 3996 cm³/h (244 in.³/h). It should be noted that

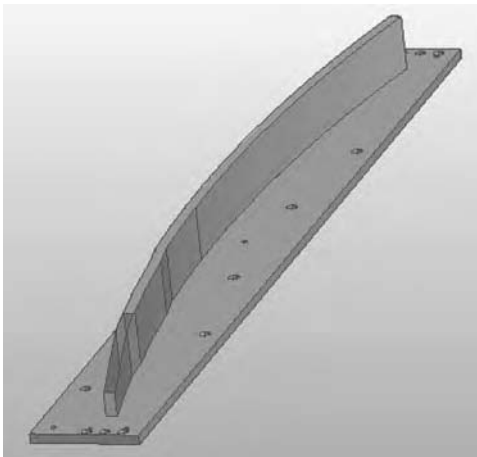


Fig. 5 Computer-aided design model of a target preform

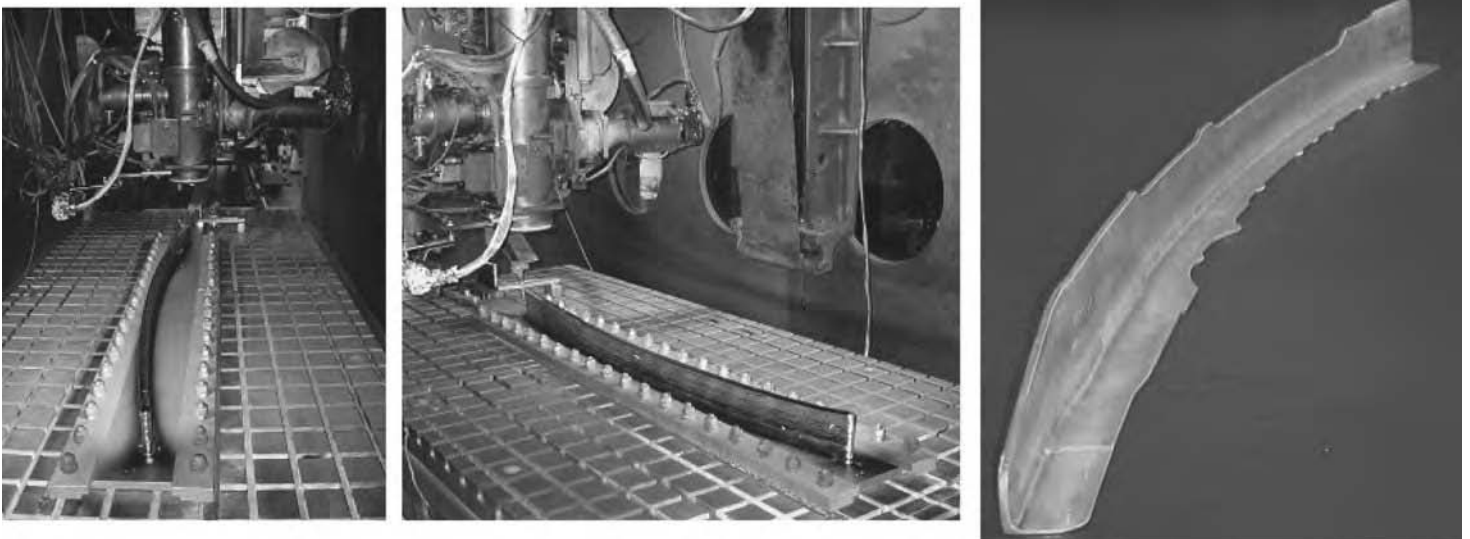


Fig. 6 Deposited chord preform and final part. Courtesy of Sciaky, Inc.

techniques to allow for higher deposition rates for EBDM are continually being refined.

Dynamic Beam Deflection Processing

General Description

Accelerated electrons travel through a vacuum in straight lines, as long as they are not affected by electric or magnetic fields. Magnetic or electromagnetic fields are used to intentionally deflect electrons from the straight flight path for various reasons, such as to focus the stream of electrons into a small beam spot with the help of a static field or to deflect the electron beam with a low-frequency (<1 kHz), low-amplitude dynamic field to influence the keyhole of the welding process. Lower-frequency and higher-amplitude deflection can be used for creating the weld without gun or part motion for making plug welds, for instance. High-frequency, dynamic fields (>100 kHz) are used to enhance traditional welding processes, typically consisting of one weld, by temporarily deflecting the EB out of the keyhole to perform another task, such as a second weld. In addition, the high frequency enables the creation of raster fields that can be used for heat treatment purposes as well.

Controlling Essential Variables

Dwell Time, Deflection, Accelerating Voltage, Beam Current, and Beam Focus. For fully CNC electron beam welders, all welding parameters are controlled by the welding

machine CNC and can be stored in the part program. The length of dwell time for the EB at each particular spot can be programmed and allows maximum process flexibility in terms of heat input into components.

A method for distributing the power of the EB over a surface to be pre- or post-heat treated or hardened consists of dividing the area into a number of points adequately spaced so that no hot spots exist when using a defocused beam. These locations may be spaced as required to obtain the necessary power density distribution, which is defined by the values of the accelerating voltage, beam current, and beam focus. The EB is successively positioned at each specific location, dwelled for a programmable time interval, and then translated at very high speed to the next coordinate point, producing a pattern that conforms to the contour requirements of the surface to be hardened or heat treated.

The beam deflection angles are determined by the working distance as a setup function and the distances of dwell points. As with traditional processes, the high (accelerating) voltage is typically held constant between 40 and 60 kV for low-voltage guns and 90 and 150 kV for high-voltage guns. The beam current can be changed in the part program if necessary. Fast beam deflections in combination with fast focus changes between dwell points enable the processing at different working distances.

Effective Power Density. The EB is capable of impinging power densities on the order of 3 MW/cm² (20 MW/in.²) when sharply focused for welding. However, this powerful energy concentration is easily controlled in power magnitude (accelerating voltage and beam current), power density (defocused beam), and beam position (computer-controlled deflection).

The extremely high power density in the EB focal spot combined with the constant transformation of beam energy into thermal energy in the high-90% range makes the process very flexible and robust at the same time. With an increasing spot size, achieved either through a defocused beam or the use of an increased deflection pattern, the beam power density can be continuously scaled down, to the point where a keyhole process turns into a conduction-mode welding process.

It is characteristic in dynamic beam deflection processes that the beam is moved or “shared” between different locations, in contrast to traditional processes where the beam impinges on one spot only. The extremely high-speed beam movement between points may be referred to as beam splitting or multibeam processing, because the speed of deflection makes the single beam appear to be more than one. In addition to the standard EBW parameters, the ratio of dwell time at each location influences weld penetration (or heat input) in such a way that the smaller the ratio in one spot, the shallower the resulting weld. The reduced power input per time at each dwell point can be compensated with an increased EB power. Also, depending on the speed of deflection, the beam power and focus can be dynamically changed to match the beam location to better tailor the power density of each spot.

For selective surface treatment, application of beam energy is such that the surface of the part is heated rapidly to a temperature just below the melting point (approximately 1480 °C, or 2696 °F, for steel) of the metal being hardened (Ref 11). Refer to Fig. 8 to note the graph of EB energy input as it applies to heat treating. As the thermal gradient becomes steeper, the surface temperature will tend to

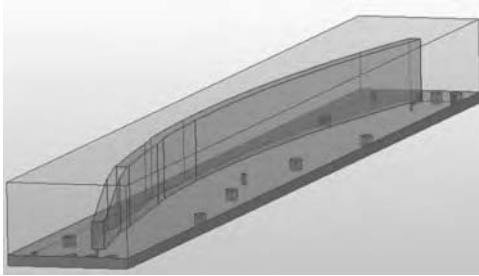


Fig. 7 Comparison of material volume for electron beam direct manufacturing (EBDM) buildup vs. hog-out

Table 1 Total relative percentage cost comparison case study for a chord

Cost summary in dollars	
Electron beam direct manufacturing (EBDM)	Hog-out/machining
Raw material (substrate plate): 8%	Raw material: 63%
EBDM deposition (includes cost of wire): 26%	...
Auxiliary processes (thermal processing): 14%	Finish machining: 37%
Finish machining: 8%	...
Total: 56%	Total: 100%

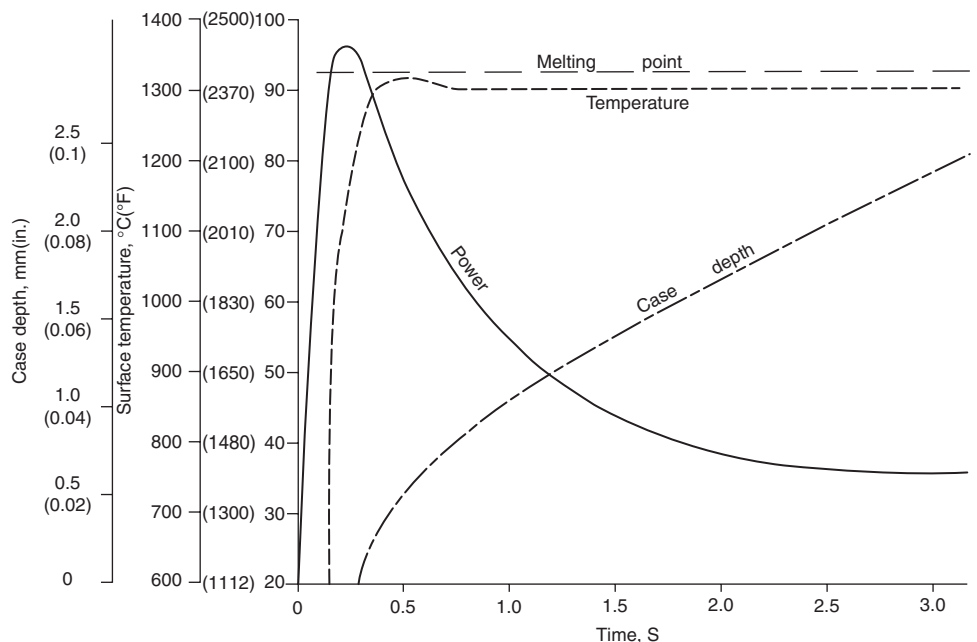


Fig. 8 Electron beam energy input for heat treating. Courtesy of Sciaky, Inc.

rise. This is countered to keep the surface temperature just under the melting point by decreasing the surface power density with respect to time. This is done to achieve the desired case depth by using the ability of the controls to rapidly adjust EB power for a specific duration. When the desired depth of austenite is prepared, the EB power is turned off. Extremely rapid heat flow to the interior of the part (self-quench) continues until the temperature is equalized throughout the workpiece. The cooling rate is rapid enough (in excess of 2200 °C/s, or 3960 °F/s) to exceed the critical cooling rate and convert the austenite to hard martensite. Transformation to martensite to achieve maximum surface hardness and case depth depends on several factors, such as the mass of the part, the percentage of carbon, and the initial condition of the base metal (normalized or quenched and tempered) (Ref 12).

General Pattern Designs

Split or Multibeam Processing. There are many EBW applications that involve two or more process steps, for example, a weld and a cosmetic pass to smooth the surface. Typically, they are carried out in series, one discrete process step after another, which requires long floor-to-floor cycle times. With the beam-splitting feature, it is possible to change from series to parallel processing, where two or more processes are executed at the same time with one EB (Fig. 9). Technically seen, one EB is switched between different locations with defined, multimillisecond-long dwell times. The length of dwell time influences weld

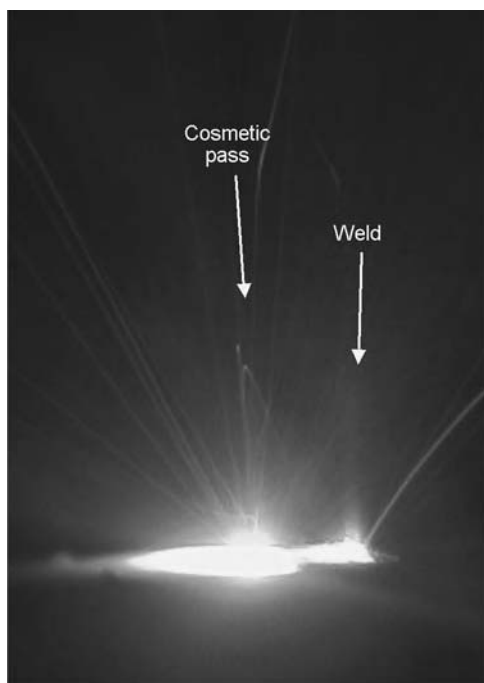


Fig. 9 Weld and cosmetic pass. Courtesy of PTR-Precision Technologies, Inc.

penetration in such a way that the longer the hold time in one location, the deeper the resulting weld. This means that weld penetrations are no longer influenced only by traditional parameters such as focus, beam power, and deflection pattern but also by the ratio of dwell time to nonimpinging time.

To provide maximum process flexibility, the dwell time can be programmed in the CNC for each individual beam position (Fig. 10). Process improvements with multipool welding depend on the particular application and often go beyond the shorter floor-to-floor production times. For example, multipool axial welding with four “simultaneous” weld pools on the same diameter balances the heat input much better than traditional processes with only one weld pool. The improved, balanced heat input results in a more balanced part distortion and, in addition, shortens cycle times.

High-Speed Raster Generation. The split or multibeam process requires only one dwell point for each individual melt puddle, such as welding and a cosmetic pass. If large numbers of dwell points are needed to form a grid for the purpose of heat treating selective surface areas, one or more predefined heat field with many dwell points must be preprogrammed as a raster. The individual dwell points of the raster (grid pattern) are programmed independently from each other in terms of location and dwell time. It allows precise control of temperature increases, temperature dwell times, and cooling rates. The high self-quenching rates, which are determined by material, mass, and geometry of the individual part, can be further influenced through timed thermal inputs after heating to accomplish nonlinear cooling rates with one or more heating cycles during quenching (Fig. 11).

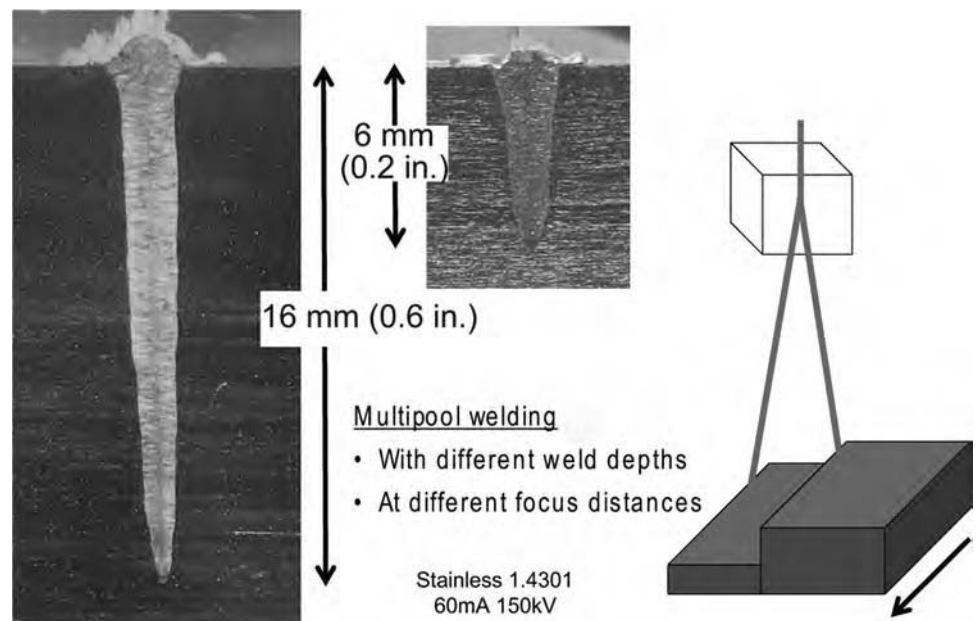


Fig. 10 Multipool welding with different focus and penetration. Courtesy of PTR-Precision Technologies, Inc.

The energy raster can be applied to the work surface using two distinct methods: static pattern (for fixed localized areas) or traveling pattern (for linear or circular stripping of larger surface areas). Surfaces can be flat, domed, or irregular, as in the case of gear teeth or splines. Line of sight between the workpiece and the EB gun is necessary, and demagnetization of parts is recommended (2.0 gauss or less) to ensure beam placement.

Applications of High-Frequency, Multibeam Processes

Selective Surface Treatment. The advantages of this selective heat treatment process are being used in mass production of camshafts. The EB equipment is used in automated, single-piece flow manufacturing lines to harden camshaft surfaces by deflecting an EB on a rotating part (Fig. 12). The self-quenching properties of the material are maintained through an extremely fast and localized temperature increase in the surface layer while maintaining the original room temperature underneath this heated layer. The extremely efficient self-quenching effect of the material is further influenced by the beam through a second heating pattern that is applied with a split beam shortly after the first heating pattern. This nonlinear cooling rate results in improved material characteristics and reduced wear of the camshaft surfaces compared to other heat treatment processes.

A cross section of a camshaft lobe made of pearlitic gray cast iron after heat treating and supercooling is shown in Fig. 13. For this camshaft, a beam pattern deflection technique was developed to optimize the heat treat pattern

density, which allowed four separate patterns to be independently varied on each of four camshaft lobes as the beam moved between the flat areas of the camshafts to the apex areas to provide a uniform heat profile around each camshaft lobe. Due to the pearlitic gray cast iron material, after heat treating, the camshafts were supercooled in liquid nitrogen (LN₂) to reduce the amount of retained austenite and to increase the hardness values from nominally R_C 55 to approximately R_C 60.

Other applications for selective surface heat treatment include camshaft followers, one-way clutch assemblies, rocker arms, and so on. Figure 14 shows a sketch of an EB gun with a heat treat pattern directed on the contact area of a rocker arm component to be hardened. This application is referred to as a static heat treat application because the beam pattern is rastered on the piece-part without moving the EB gun or the part. With the pattern raster applied for 1 s, a case depth of nominally 1 mm (0.04 in.) can be obtained on a cast iron contact area that would have a Rockwell hardness of approximately R_C 60. Also, unlike conventional heat treat methods such as induction or flame hardening, additional postoperative steps for

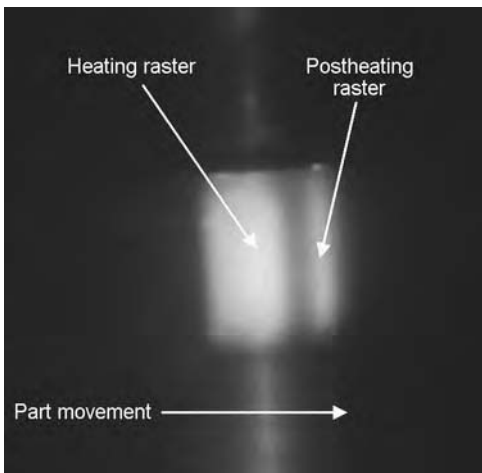


Fig. 11 Heat treatment for selective surface areas. Courtesy of PTR-Precision Technologies, Inc.

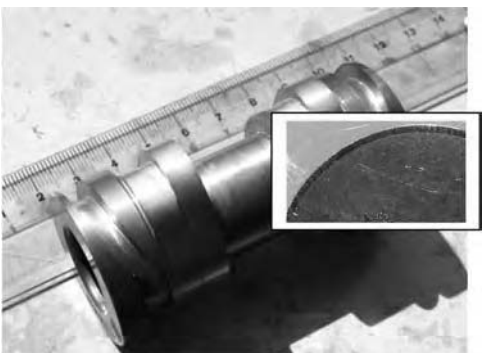


Fig. 12 Camshaft hardening. Material is 51CrV. Courtesy of PTR-Precision Technologies, Inc.

external quenching and finish grinding would be eliminated by processing this component using the EB surface treatment method. Figure 15 shows a cross section of a similar nodular cast iron rocker arm melt pad that produced a 0.6 mm (0.025 in.) deep white iron layer backed up by a 0.4 mm (0.016 in.) deep hardened zone. The white iron layer had a hardness value of R_C 64.

Multiple-Pool Welding with a Split Beam.

Two-pool welding is applied in mass production on radial welds. The disk-shaped damper assemblies are rotated underneath the EB, which switches back and forth from the outer to the inner joint, thereby welding both joints

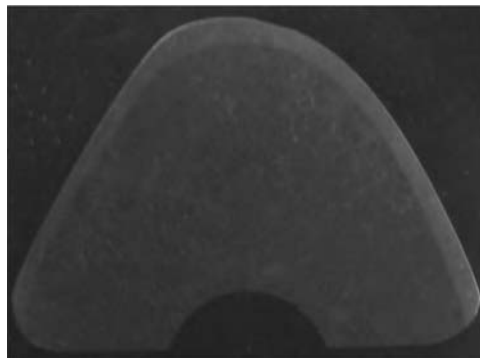


Fig. 13 Cross section of camshaft lobe. Material is pearlitic gray cast iron. Courtesy of Sciaky, Inc.

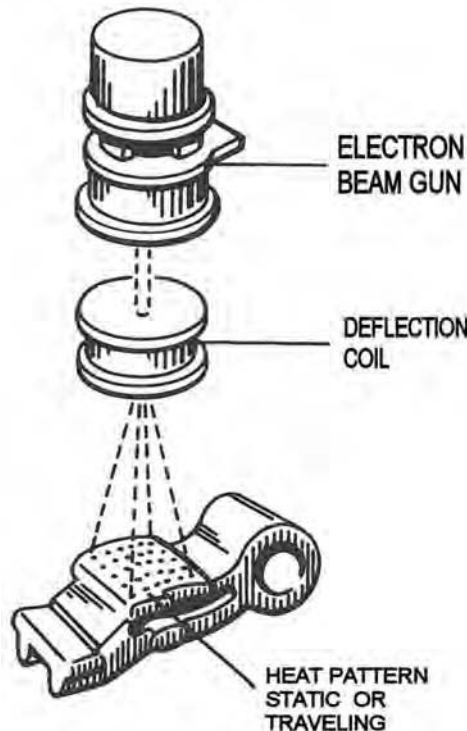


Fig. 14 Sketch of gun/coil and heat treat pattern on rocker arm assembly. Courtesy of Sciaky, Inc.

“quasi” at the same time (Fig. 16). The parallel processing of both joints shortens the floor-to-floor time compared to the traditional process, which performs in series, one weld after another.

Automotive transmission gear assemblies are conventionally welded with either the EB or laser process using a single-beam weld pool. This procedure typically requires the gear assembly to be tack welded first to maintain a balanced joint/stress configuration, and then the tack passes are overlapped with a single continuous weld pass. By contrast, in multipool welding, the components are welded at several points simultaneously along one and the same welding seam (Fig. 17), up to an overlapping portion in the area that already has been welded. With this approach, the welding time is reduced and the distortion is minimized because of the lower heat applied to the parts. The number of welding pools depends on the size and geometry of the part and on the deflection width of the EB.

It is important to note that the welding seam is not typically perpendicular to the surface with multipool EB welding. Therefore, the incidence angle of the EB and consequently the seam depend on the welding diameter of the welding circle and the distance between beam source and component (Ref 13). The weld seam may need to be configured to be directly in line with the beam trajectory, so that the weld consumes the joint (Fig. 18).

Pre- and Post-Heat Treating. Electron beam welding may employ leading or trailing deflected beams serving as additional heat regions around the weld. This may be done more frequently on materials that tend to

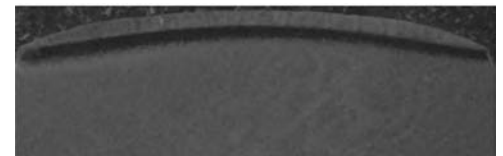


Fig. 15 Cross section of rocker arm contact area after heat treatment. Courtesy of Sciaky, Inc.

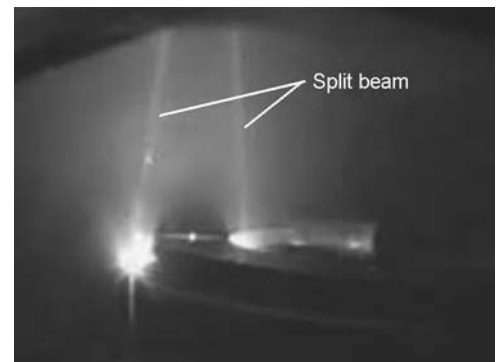


Fig. 16 Two-pool welding with one electron beam. Courtesy of PTR-Precision Technologies, Inc.

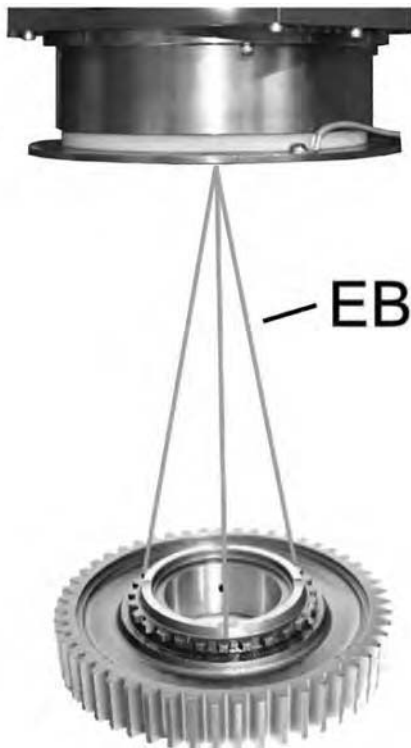


Fig. 17 Gear welding with three electron beams (EBs). Courtesy of Sciaky, Inc.

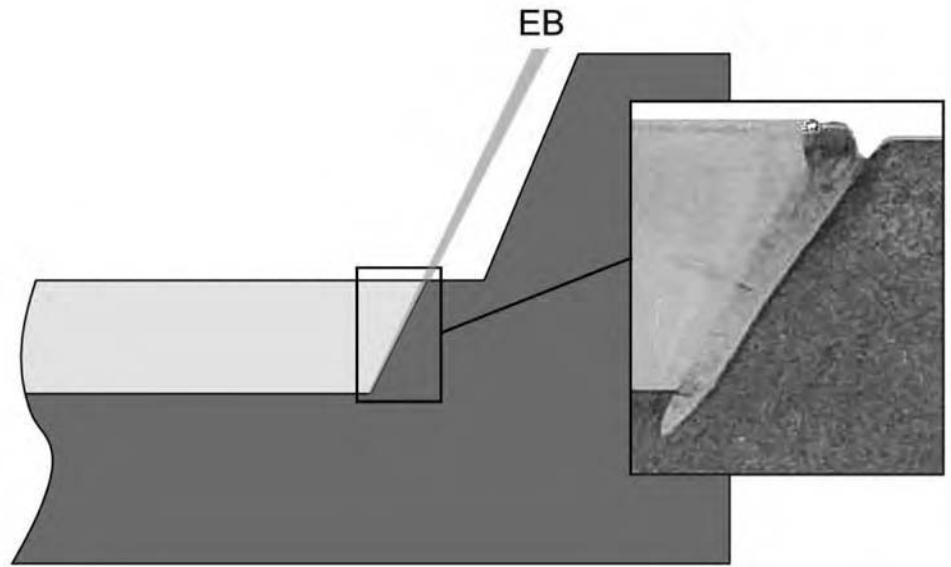


Fig. 18 Gear welding segment showing joint angle. EB, electron beam. Courtesy of Sciaky, Inc.

produce hot cracking with conventional welding methods. These additional pre- or post-heat treating beams would typically be defocused so as not to melt the piece-part, and they would serve to heat the surrounding areas of the weld to compensate for the large temperature gradient between the solidifying weld pool and the surrounding material. This compensation reduces the thermal stresses to better minimize crack formations in the weld.

REFERENCES

1. J.W. Sears, Direct Laser Powder Deposition—State of the Art, *Powder Materials: Current Research and Industrial Practices, Proceedings of the 1999 Fall TMS Meeting*, F.D.S. Marquis, Ed., Nov 1999, p 213–226
2. P.F. Jacobs, A Brief History of Rapid Prototyping and Manufacturing: The Growth Years, *2002 International Conference on Metal Powder Deposition for Rapid Manufacturing*, April 8–10, 2002 (San Antonio, TX), Metal Powder Industries Federation, p 5–8
3. S. Stecker, K.W. Lachenberg, H. Wang, and R.C. Salo, “Electron Beam Free Form Fabrication Technology,” IIW Doc. IV-911-06, IIW Comm. IV—Power Beam

- Processes, IIW Annual Assembly, Aug 2006 (Quebec City, Canada)
4. K.W. Lachenberg and S. Stecker, “Manufacturing Advantages Using Electron Beam Welding/Free Form Fabrication (EBFFF),” presented at AWS/Fabtech 2008 Conference, Oct 8, 2008 (Las Vegas, NV)
5. K.M.B. Taminger and R.A. Hafley, “Electron Beam Freeform Fabrication (EBF³) for Cost Effective Manufacturing,” NASA TM-2006-214284, March 2006
6. K.M.B. Taminger and R.A. Hafley, Electron Beam Freeform Fabrication: A Rapid Metal Deposition Process, *Proceedings of the Third Annual Automotive Composites Conference*, 2003
7. C.W. Fink, An Overview of Additive Manufacturing, Part II, *AMMTIAC Q.*, Vol 4 (No. 3), 2009
8. K.W. Lachenberg, Electron Beam Processing Using Wire-Feed, *Weld. J.*, Vol 90 (No. 1), Jan 2011, p 46–48
9. K.M.B. Taminger and R.A. Hafley, Characterization of 2219 Aluminum Produced by Electron Beam Freeform Fabrication, *13th Solid Freeform Fabrication Symposium*, Aug 4–8, 2002 (Austin, TX), p 482–489

10. V.R. Dave, “Electron Beam (EB)-Assisted Materials Fabrication,” Ph.D. thesis, Massachusetts Institute of Technology, Boston, MA, June 1995
11. C.A. Fiorletta and R.A. Ferry, *Electron Beam Heat Treating Selective Surface Hardening Process*, Sciaky Inc., p 13–16
12. R.C. Hanson, *Advances in E.B. Heat Treating Using Computer Modeled Heat Flow*, SAE Technical Paper Series 841102, p 1–5
13. R. Zenker, Modern Thermal Electron Beam Processes—Research Results and Industrial Application, *La Metall. Ital.*, April 2009, p 4–5

SELECTED REFERENCES

- K.M.B. Taminger, R.A. Hafley, and M.S. Domack, “Evolution and Control of 2219 Aluminum Microstructural Features through Electron Beam Freeform Fabrication,” Presented at the ICAA-10 meeting, Aluminum Alloys—Their Physical and Mechanical Properties, July 10–13, 2006 (Vancouver, Canada); *Aluminium Alloys 2006: Research Through Innovation and Technology—Proceedings of the Tenth International Conference on Aluminium Alloys*, Trans Tech Publications Ltd., July 2006, p 129–1304

Quality Control of Electron Beams and Welds

T.A. Palmer, Pennsylvania State University
P.W. Hochanadel, Los Alamos National Laboratory
K. Lachenberg, Sciaky, Inc.

THE ISSUE OF QUALITY CONTROL in electron beam (EB) welding is similar to that in other welding processes, where the primary goal is to consistently produce defect-free and structurally sound welds. Existing process controls in EB welding typically are directed at controlling the essential machine settings, which include the accelerating voltage, beam current, focus coil current, vacuum level, travel speed, and work distance (Ref 1). Additional quality-control checks are performed after the completion of the weld, with nondestructive evaluation (NDE) techniques, such as eddy current, radiography, or ultrasonic evaluation, to detect any potential defects in the components. An overview of the relevant NDE techniques is provided in *Nondestructive Evaluation and Quality Control*, Volume 17 of *ASM Handbook*, 1989.

A primary assumption in these existing process-control techniques is that the machine settings are highly accurate and reproducible and have a direct correlation with the resulting beam characteristics (Ref 2). Each of these machine settings is quantifiable and tightly controlled before and during the welding process, except for the focus coil current. This machine setting is used to define the focus condition of the beam, usually with respect to an operator-determined "sharp focus" setting. However, the actual beam characteristics, defined in terms of specific quantifiable parameters, such as the beam diameter and power density distribution, at this sharp focus setting can vary significantly with different operators, machines, and operating conditions.

The use of diagnostic tools for probing the beam characteristics has been growing over the last two decades with the development of several diagnostic tools (Ref 3–15). These beam probing techniques are based primarily on modifications to a traditional Faraday cup and use direct measurements of the EB current to obtain a profile of the beam energy distribution as the beam passes over an edge, slit, or pinhole. The resulting signal obtained as the beam passes over the edge or slit can provide

information about both the beam shape and size and the power density distribution. Several commercially available systems for measuring the EB characteristics over a range of powers have been developed and are in use (Ref 6–14).

In the following sections, common procedures for controlling the EB welding process are discussed. In addition to the control of the essential machine parameters, the introduction of closed-loop controls and diagnostic feedback systems in EB welding systems are also addressed. One quality-control tool fairly unique to EB systems interrogates the beam to produce a reconstruction of the power density distribution and provide additional information on the size and shape of the EB. Knowledge of these beam parameters can be used to improve process understanding and control. Based on existing practices, future directions for EB quality control are also discussed.

Process Control of Essential Variables

Like other common welding processes, the control of specific processing parameters is essential to controlling the process. In EB welding, the primary variables that are controlled include the accelerating voltage, beam current, focus coil current, vacuum level, travel speed, and work distance (Ref 1). These essential parameters are then verified prior to welding, in accordance with the requirements of the weld process specification and other relevant procedures with which the welder is required to comply. This documentation then becomes the basis for the quality-control paperwork that follows the welded component.

The majority of essential parameters are controlled primarily by using calibrated machine gage settings. In selected cases, the beam current can be measured through the use of a Faraday cup. A Faraday cup is an electrically conductive beam trap designed to contain and measure the beam current. In most cases

though, a Faraday cup is used only to confirm machine performance after maintenance and is not commonly used as a process-control tool. To maintain control over these machine settings, the calibration of the gages controlling these settings is performed at selected intervals to ensure that the machine output is consistent.

Calibration of the primary variables used in EB welding may be performed as follows:

1. The accelerating voltage may be verified using a calibrated voltage divider as the standard. The voltage divider reduces the high voltage (such as 150 kV) to a workable voltage (such as 1.5 or 15 V). This equipment is quite specialized and typically is used at the equipment manufacturing facility during the manufacture of new equipment or refurbishment of older equipment. Unless a serious anomaly occurs with the high-voltage system, this voltage is assumed to be fairly constant over the life of the equipment. Further details on calibration of the high voltage in EB welding can be found in the latest revision of ISO 14744-2 (Ref 16).
2. The beam current may be verified using a Faraday cup arrangement that contains a calibrated ground path resistor. Additional details can be found in the latest revision of ISO 14744-3 (Ref 17).
3. The focus position may be verified with a diagnostic tool such as the enhanced modified Faraday cup tool, provided the ground path resistor is calibrated. Details are given throughout this article.
4. The vacuum level is calibrated using a calibrated vacuum gage that is either calibrated or replaced at selected intervals based on the recommended schedule provided by the machine manufacturer.
5. The travel speed should be verified with a calibrated standard, such as a stopwatch. Typically, times are sufficiently long that this standard is sufficient. Some additional details can also be found in the latest revision of ISO 14733-4 (Ref 18).

6. The working distance is measured from a set location on each machine, typically the top of the welding chamber, and is easily verified with a calibrated standard-length measuring device, such as a calibrated tape measure or meterstick.

Modern control systems are commonly employed in EB welding systems to control these essential variables and to perform other desired quality-control functions. These modern systems employ a range of computerized controls to provide much-improved control of the essential parameters over that possible with older, open-loop, analog-based controls. Computer real-time processing, using feedback mechanisms, facilitates rigid command of critical process parameters. For EB welding, control circuitry that interfaces with the computer and the associated discrete supplies allows the gun power level (beam current, accelerating voltage, etc.) and effective energy density (beam focus, deflection, etc.) to be accurately maintained to specified requirements. Figure 1 shows a block diagram of a typical modern closed-loop gun control system. Additional feedback systems may be incorporated to control the part and/or gun motion mechanics to facilitate fully synchronized process and motion control.

Additional closed-loop systems allow for these improved controls to be further improved by both monitoring and altering the desired parameters. With these closed-loop systems, any observed changes in the weld shape or heat input can be mitigated by corresponding changes in the welding parameters to bring the desired properties back into target. Although this technology is in the early stages as of this writing (2011), these closed-loop systems will become an increasingly important tool in EB welding and other associated processes. For example, this type of closed-loop control is well suited for EB deposition processes. Because these processes tend to operate continuously in transient rather than steady-state conditions, the ability to maintain consistent output parameters requires real-time monitoring and adjustments to one or more input parameters.

In addition to monitoring the essential welding parameter settings, other in-process monitoring controls, based on phenomena resulting from the EB-material interaction, have been explored. Backscattered electrons, x-rays, and visible emitted light emanating from the weld region have been explored with varying amounts of success (Ref 2). These in-process observations can be used in a number of capacities, including employing it as an *in situ* seam

tracker, and allow a near-real-time diagnosis to be made as to whether the weld is proceeding as expected. Much like the closed-loop systems described earlier, these systems are currently not in widespread use, but as the supporting technologies mature further, they will become much more common.

Beam Diagnostic Tools for Determining Beam Focus

Process control of EB welding is based on control of machine settings, such as accelerating voltage, beam current, travel speed, and vacuum level. A variety of control systems are used to ensure that these machine settings are accurate and meet the process requirements. On the other hand, the focus coil current setting, which allows the operator to adjust the beam focus position in the weld chamber, is difficult to replicate, due to the manual nature in which the beam focus setting is controlled.

During focusing, the strength of the magnetic lens in the focus coils is manually adjusted by the operator to change the focal length of the magnetic focusing lens and to move the beam cross-over location in the work chamber. The focus coil current setting at which the cross-over

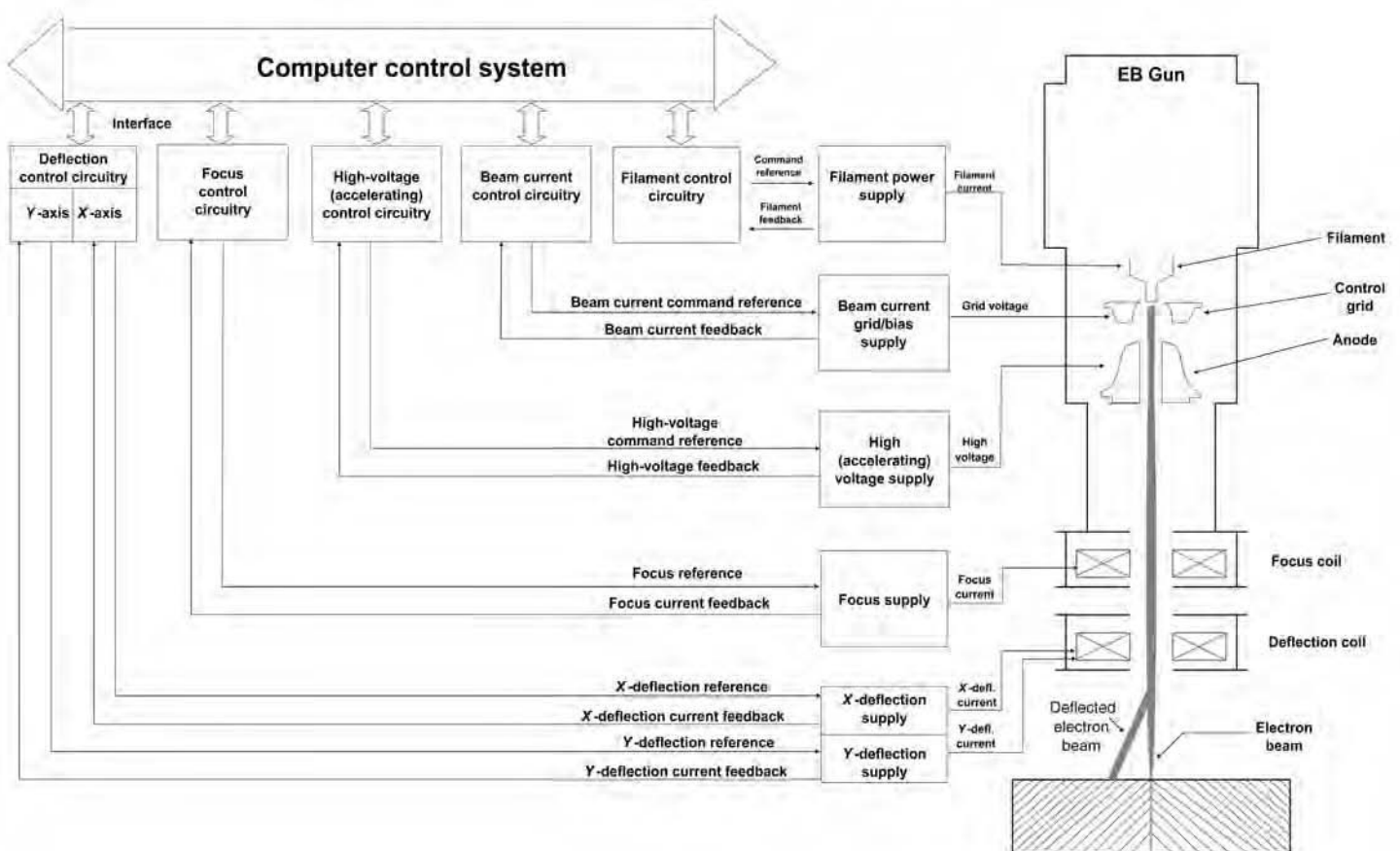


Fig. 1 Block diagram showing a typical modern closed-loop gun control system. EB, electron beam

point is located at the surface of the workpiece is referred to as the sharp focus setting. To determine the sharp focus setting, the operator directs the beam onto a high-melting-point target material, such as tungsten, and adjusts the focus coil current setting while observing the intensity of the light emitted from the target. When the emitted light reaches a maximum intensity, the beam is considered to be at sharp focus (Ref 1).

It is typical for the operator-determined sharp focus setting to be the only means for defining the beam properties. However, it is difficult to define and reproduce the sharp focus condition, and the reproducibility of a sharply focused beam at a given focus setting on even a single machine is not guaranteed. Various operators may interpret the brightest emission from the target material differently, resulting in different, operator-dependent definitions of sharp focus. In addition, changes in the sharp focus setting are commonly observed between evacuations of the work chamber. As a result, beams with different properties may be mistakenly used in the welding of potentially high-value components.

The inability to consistently control the beam properties and to define the focus condition in an easily quantifiable manner can be addressed through the use of beam diagnostic tools. This issue has been recognized for a number of years, resulting in the development of several rudimentary tools for characterizing the sharp focus condition of EBs. An early attempt at determining the sharp focus location for a given beam is embodied in the Arata beam (AB) test (Ref 4). In this test, an EB is run over a comb-shaped angled plate at a given travel speed. As the beam passes over the material, which is typically stainless steel, it either cuts or melts the thin vertical plates making up the comb-shaped angled plate, shown in a transverse orientation in Fig. 2 (Ref 4). The sharp focus location for the EB corresponds to the location where the width of the melted material is a minimum.

The AB test is designed to find the cross-over location of the EB for a given set of voltage, current, and focus coil current settings. This cross-over location corresponds to the sharp focus condition of the EB, where the minimum beam width is expected. After measuring the widths of the EB spots produced at each location on the AB test stand, the sharp focus position is correlated with the location where the narrowest weld is produced. Overall, the test is very similar in construction to the angled plate tests used in laser welding to determine the cross-over location for laser optics.

Even though the use of this test provides previously unavailable empirical data concerning the performance of the EB welder, it displays a number of drawbacks that limit its usefulness and applicability to production environments. For example, the test setup must be removed from the chamber to be analyzed, thus changing the conditions in the chamber and requiring an additional pump-down before welding. Also, the results of the AB test are only applicable for the welding conditions and materials with

which the test was conducted. Changes in the weld settings or materials will have an impact on the physical location of the beam cross-over. Therefore, any change in welding parameters or material will require additional testing, which can result in the need for a rather significant number of tests to be performed if multiple materials and welding conditions are needed. Finally, the results of the test reveal only the physical location of the beam sharp focus and nothing about the characteristics of the beam.

More modern techniques have begun to focus on the characterization of the beam produced by an EB welder rather than just identifying the beam cross-over location. To better understand the beam characteristics, techniques designed to directly probe the beam and provide quantitative information have been developed (Ref 5–14). These beam probing techniques include a rotating wire device and modifications to a traditional Faraday cup using either an edge, slit, or pinhole detection system (Ref 13). Each of these techniques uses a direct measurement of a portion of the EB current.

In the wire probing system, a small-diameter wire is passed or rotated through the beam, and the resulting beam current is measured. This system provides a means for measuring the beam current but is limited by the poor heat dissipation of the wire. Those systems that rely on the modification of a traditional Faraday cup are based on the capture of a selected portion of the beam intensity, from which a power density distribution can be computed. In the edge detection probing system, the beam is passed over the edge of a piece of electrically isolated refractory metal. As the beam passes over the edge, a portion of the beam current is obtained as a function of time, based on the speed that the beam is traversed. The current varies as the beam passes over the edge, resulting in a

beam profile from which energy density and beam width measurements can be made.

In the slit probing system, the beam is passed over a refractory metal containing a thin slit with a width typically in the range of 0.02 to 0.1 mm (0.0008 to 0.004 in.). Because the width of the slit is smaller than the width of the beam, a small portion of the beam current is captured in a Faraday cup as the beam is swept over the slit. The resulting signal obtained as the beam passes over the slit is similar to that obtained in the edge detection system and can provide information about the beam shape and size along the scan direction of the beam. In addition, the power density can be estimated from this measurement.

A pinhole detection system is based on principles similar to the slit probing system, but it uses a small hole instead of a slit to obtain profiles of the beam. In this system, the beam is rastered in both the x - and y -directions over a pinhole, usually less than 0.10 mm (0.004 in.) in diameter, producing a map of the power density distribution of the beam. Because the beam is continuously rastered over the pinhole to obtain a complete beam profile, precise beam control is required. Power density distribution can be measured with this technique, but it is limited because the technique has an inherently low signal-to-noise ratio.

Using the data obtained with these different systems, estimations of the sharp focus setting, the beam diameter, and the general beam profile can be made. However, because the edge and slit beam probing systems take only a single profile of the beam, it must be assumed that the beam is radially symmetrical and has a circular cross section for the results to be generally useful. While this assumption may be valid for typical sharp-focused beams, it is also known that beams can take on elliptical and

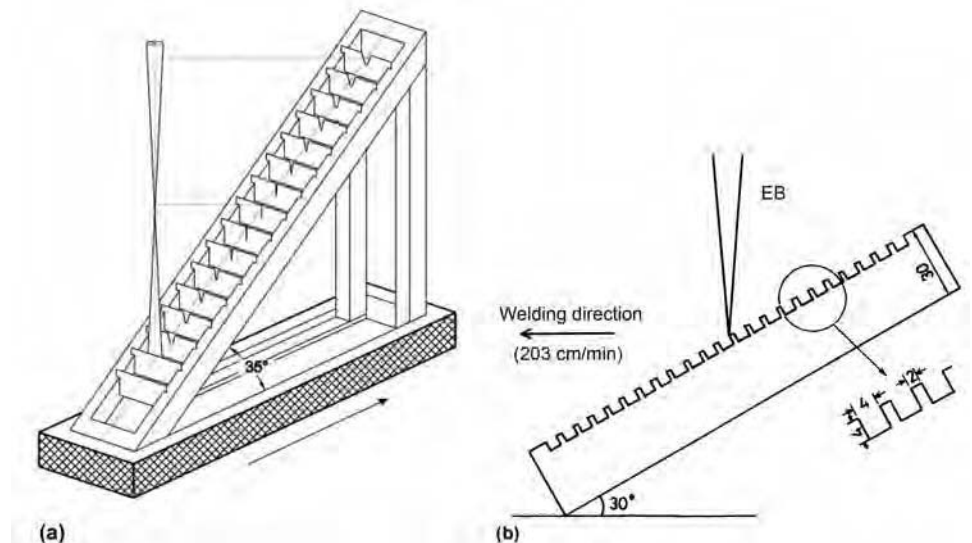


Fig. 2 Schematic diagrams showing the basics of the Arata beam test for measuring the electron beam (EB) focus position. Source: Ref 3, 4

noncircular shapes or power density distributions, especially when out of focus.

The use of diagnostic tools for probing these beam characteristics has been growing over the last two decades with the development of several diagnostic tools (Ref 4–14). These beam probing techniques are primarily based on modifications to a traditional Faraday cup and use direct measurements of the EB current to obtain a profile of the beam energy. Several diagnostic systems are commercially available and have been applied to the control of EB welding systems. These systems include the DIABEAM system from ISF-Aachen (Ref 5–8), the TWI slit probing system (Ref 13), and the enhanced modified Faraday cup tool developed at Lawrence Livermore National Laboratory (LLNL) (Ref 9–12). Even though each system uses a different method for obtaining data on the EBs that they are interrogating, they all rely on these same basic modifications to the traditional Faraday cup. All of the systems also rely on the rapid deflection of the beam, which allows the systems to be permanently placed in the EB chamber and used for a range of different characterization activities.

The DIABEAM system uses both a slit and a pinhole diaphragm to characterize beams up to powers of 100 kW. By employing both a slit and a pinhole, a rapid evaluation of the beam and a more in-depth analysis of the beam can be obtained. The TWI slit probing system uses multiple slits to probe the beam to estimate the focus, beam profile, beam asymmetry, beam current, and beam diameter. This system can be permanently attached to the EB welder and used to either characterize the machine or serve as a quality-control tool (Ref 13). Finally, the LLNL enhanced modified Faraday cup uses a series of 17 radial slits that interrogate the beam at a number of different angles, so that the resulting power density distribution can be reconstructed.

In addition to the diagnostic hardware described previously, specialized data-acquisition, signal-processing, and data-analysis software have been developed. The signal obtained by the diagnostic hardware is converted into a voltage drop across a known resistor and captured by a fast-sampling analog-to-digital converter before being transferred to the data-acquisition software. The resulting signal obtained as the beam passes over the edge or slit can provide information about both the beam shape and size and the power density distribution.

Computer tomography (CT) methods can be applied to multiple sets of data obtained through slit systems to produce a complete reconstruction of the beam profile. One method for producing a reconstruction of the beam is to take data from multiple slits positioned at various angles to obtain multiple slices of the beam. These multiple sets of data are reconstructed using CT algorithms (Ref 10–12) by first separating the individual beam profiles,

normalizing the areas under the peaks, filtering the data, creating a sinogram of the profiles, and reconstructing the power density distribution (Ref 10).

Once reconstructed, a number of measurements are made to characterize the size, shape, and power density distribution of the beam. The peak power density and two distribution parameters are the most used of these measurements. Figure 3 provides an illustration of how these parameters are determined. The first distribution parameter is the full width of the beam at one-half its peak power density (FWHM). This parameter represents the width at 50% of the beam peak power density. The second parameter is the full width of the beam measured at $1/e^2$ of its peak power density (FWe2). This parameter represents the width of the beam at 86.5% of the beam peak power density. Because the cross section of the measured beam is not always circular, the area of the beam at these two points is measured, and the diameter of a circle having the same area is used to represent both values. These approximations are good representations for most beams with generally circular cross-sectional shapes, such as the Gaussian-like distributions typically found near the sharp focus setting. The FWHM value is used to represent the beam width, while the FWe2 value is used to represent the beam diameter.

Application of Beam Diagnostics

The development of these various beam probing systems has led to the use of these tools in a number of different applications. Using the basic concepts described, several application areas, primarily involving machine characterization, weld parameter transfer, and weld quality control, can be pursued using diagnostic tools. It is shown in the following discussions that the use of beam diagnostics to monitor the beam characteristics provides a valuable quality-control tool and does much to improve the understanding of machine performance and beam characteristics.

Machine Characterization. The primary use of these EB diagnostic tools has been directed at characterizing individual machines and comparing the performance of different machines under similar operating conditions. A good example of the differences in beam characteristics for different machines has been obtained using the enhanced modified Faraday cup (EMFC) (Ref 14). In this study, the differences in the beams produced by two EB welders were characterized. Sharply focused beams were shown to display different shapes and peak power densities that vary by nearly 20% for the same welding parameters on two welders. Reconstructed beam profiles are shown in Fig. 4. The beams produced by each welder at the respective sharp focus settings vary both in shape and power density distribution. The

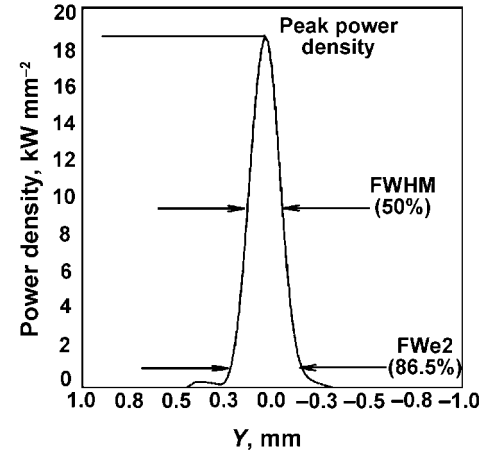


Fig. 3 A slice through the center of the reconstructed beam with the peak power density, full width at half maximum (FWHM), and full width at $1/e^2$ (FWe2) measurements indicated. Source: Ref 14

first welder (Fig. 4a) displays a slightly oblong shape and has the highest power densities located in the center of the beam. The power densities then decrease rather rapidly as the edges of the beam are approached. On the other hand, the second welder (Fig. 4b) produces a fairly round beam with a much more uniform peak power density distribution across the beam diameter and a less clearly defined hot spot in the center.

With knowledge of the respective beam characteristics for each welder, the correlation between the beam properties and the resulting weld pool size and shape can be examined. Autogenous welds are first made at the sharp focus setting of each welder on a 304L stainless steel sample at an accelerating voltage of 100 kV, a beam current of 10 mA, and a travel speed of 17 mm/s^{-1} (0.7 in./s). Figures 5(a) and (b) show the resulting weld cross sections produced by each welder.

Each welder produces similarly-shaped weld cross sections, showing keyhole-type behavior at the respective sharp focus settings. However, differences in the characteristics of sharply focused beams also result in differences in the measured depth and width of each weld. The measured weld depths produced at the respective sharp focus settings show a difference of 7%, with the second welder producing the deeper weld. Based on these observations, the higher peak power density weld shows the lower penetration. However, spiking, which is defined as a sudden increase in penetration above the average line of penetration at the root of the weld, is apparent on the weldment produced on the second welder. Unlike the cross section shown in Fig. 5(a), a rather large pore appears at the root of the weld shown in Fig. 5(b). The presence of root porosity such as this is indicative of spiking (Ref 19–23). In this case, the depth of the weld at both the top

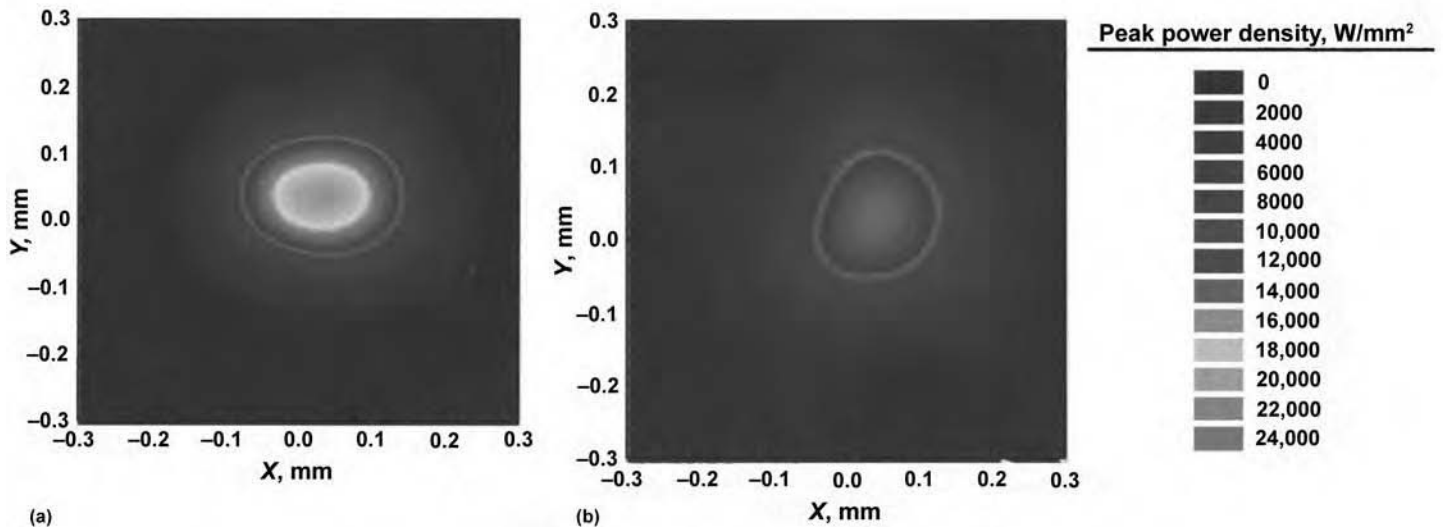


Fig. 4 Plots comparing reconstructed beams produced at sharp focus settings for 100 kV, 10 mA beams at a work distance of 229 mm (9 in.) on two different electron beam welders. Source: Ref 14

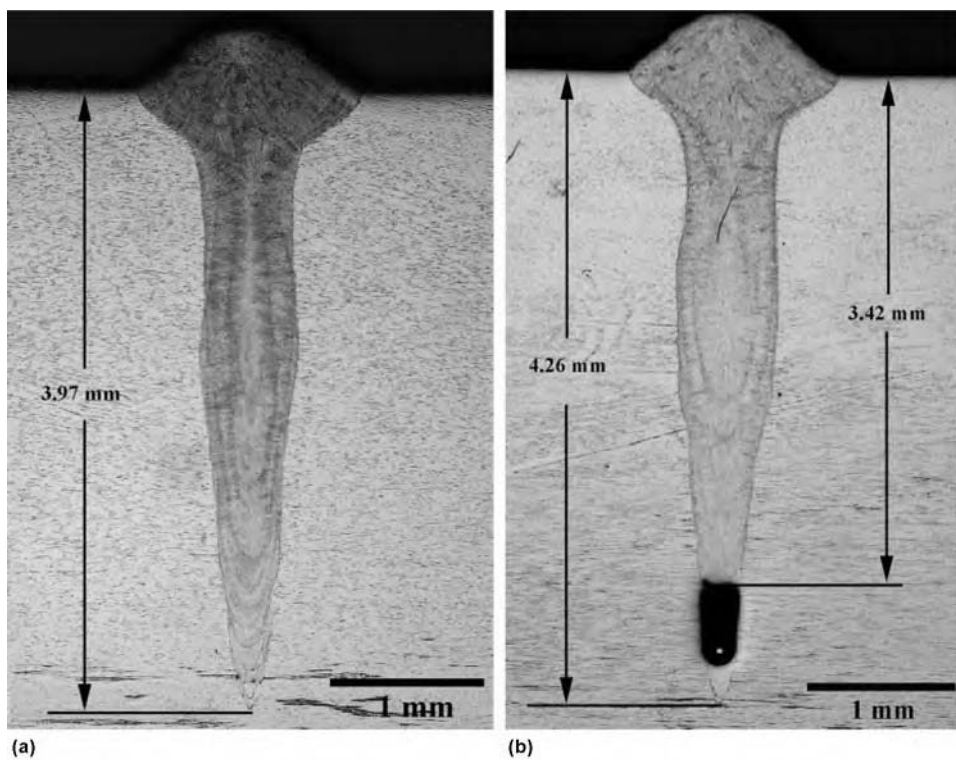


Fig. 5 Weld cross sections produced in 304L stainless steel samples at sharp focus setting for 100 kV, 10 mA beams at a work distance of 229 mm (9 in.) and travel speed of 17 mm/s^{-1} (0.7 in./s) on (a) welder 1 (peak power density = 520.0 kW/mm^{-2}) and (b) welder 2 (peak power density = 515.7 kW/mm^{-2}). Source: Ref 14

(3.42 mm) and bottom (4.26 mm) of the pore is measured, resulting in a 20% difference in the measured weld depth.

When the depth measurement is made at the top of the pore, the weld shown in Fig. 5(b) is 14% shallower than the weld shown

in Fig. 5(a). Other studies have indicated that beams with higher peak power densities produce deeper welds (Ref 24), especially when produced on the same equipment. When the depth at the top of the pore is taken into account, a shallower weld with a lower peak

power density beam is produced. A comparison of the peak power densities of the beams produced by the two machines shows a difference of 22%, while the depths of the two welds differ by 14% when taking into account the spiking. This difference is in agreement with prior observations of the peak power density weld-depth relationship.

The size and shape of the welds produced by each machine can also be affected by the different beam orientations and power density distributions, both of which are not detectable without the use of this diagnostic tool. First, the orientations of the beams vary, with the beam shown in Fig. 4(a) being more elongated along its x -axis, which corresponds to the direction of welding. The beam shown in Fig. 4(b), while not entirely circular, lacks the well-defined orientation of that shown in Fig. 4(a). Differences in the power density distribution and beam orientation lead to variations in how the EB energy interacts with the workpiece. As a result, differences in the weld dimensions are observed, even though the total power input is the same.

Weld Parameter Transfer. Based on the previous characterization of EB welding systems performed using these diagnostic tools, the ability to more efficiently transfer parameters between different machines can be accomplished. Until the development of these diagnostic tools, the inability to characterize and control the focus of EBs used for welding was a limiting factor in transferring welding parameters between different machines and different facilities. The process for transferring a set of EB welding parameters from one machine to another can be broken down into three consecutive steps: weld development, weld transfer, and production. Each of these categories includes a number of independent operations performed on a dedicated

development welder and one or more dedicated production welder(s). Significant redundancy is introduced into the development and transfer of these welding parameters. As a result, a series of costly and time-consuming weld development cycles are typically required before the transfer of a set of welding parameters is complete.

Using the data obtained with a given diagnostic system, estimations of the sharp focus setting, the beam diameter, the general beam profile, and the power density distribution can be made, assuming that the machine has been properly calibrated (Ref 25). Unlike existing qualitative methods based on the transfer of machine settings, a diagnostic tool-based procedure uses quantitative measurements of specific beam parameters, which can be correlated to the size and shape of the welds produced by the different welders.

To replicate the beam produced by a production welder on the development EB welding system, the beam is defocused. Reconstructions of the power density distribution for the defocused beam on the development welder and the sharp focused beam on the production welder are shown in Fig. 6 (a) and (b), respectively (Ref 25). With a +11 increment change in the focus coil current setting, the peak power density for the development welder decreases by 40%, and the FWHM and FWe2 values increase by approximately 22 and 28%, respectively. After the defocus correction is made to the beam produced by the development welding system, the resulting peak power density values vary by only approximately 2%, while the difference in the beam distribution parameters is 7% for the FWHM values and 4% for the FWe2 values. Even though the orientations of the beams differ, the power density distribution and general size of the beams produced by the two welding systems are very similar.

Cross sections of the welds made on the development and production welding systems using the beams described previously are shown in Fig. 7(a) and (b), respectively (Ref 25). In general, the two welds display similar depths, differing by only 0.30 mm (0.01 in.), or approximately 8%, with the weld produced by the development welding system being the deeper of the two. Even though the width of the beam produced by the production welding system is larger, the width of the weld produced by the development welding system, as measured at the top surface of the weld, is approximately 0.5 mm (0.02 in.) wider than that produced by the production welding system, corresponding to a difference of nearly 25%. This difference in width can be attributed, in part, to the orientation of the beam produced by the development welding system, which is elongated along the axis lying parallel to the direction of welding. On the other hand, the widths of the welds, as measured at the half-depth level, are fairly similar, varying by only approximately 10%.

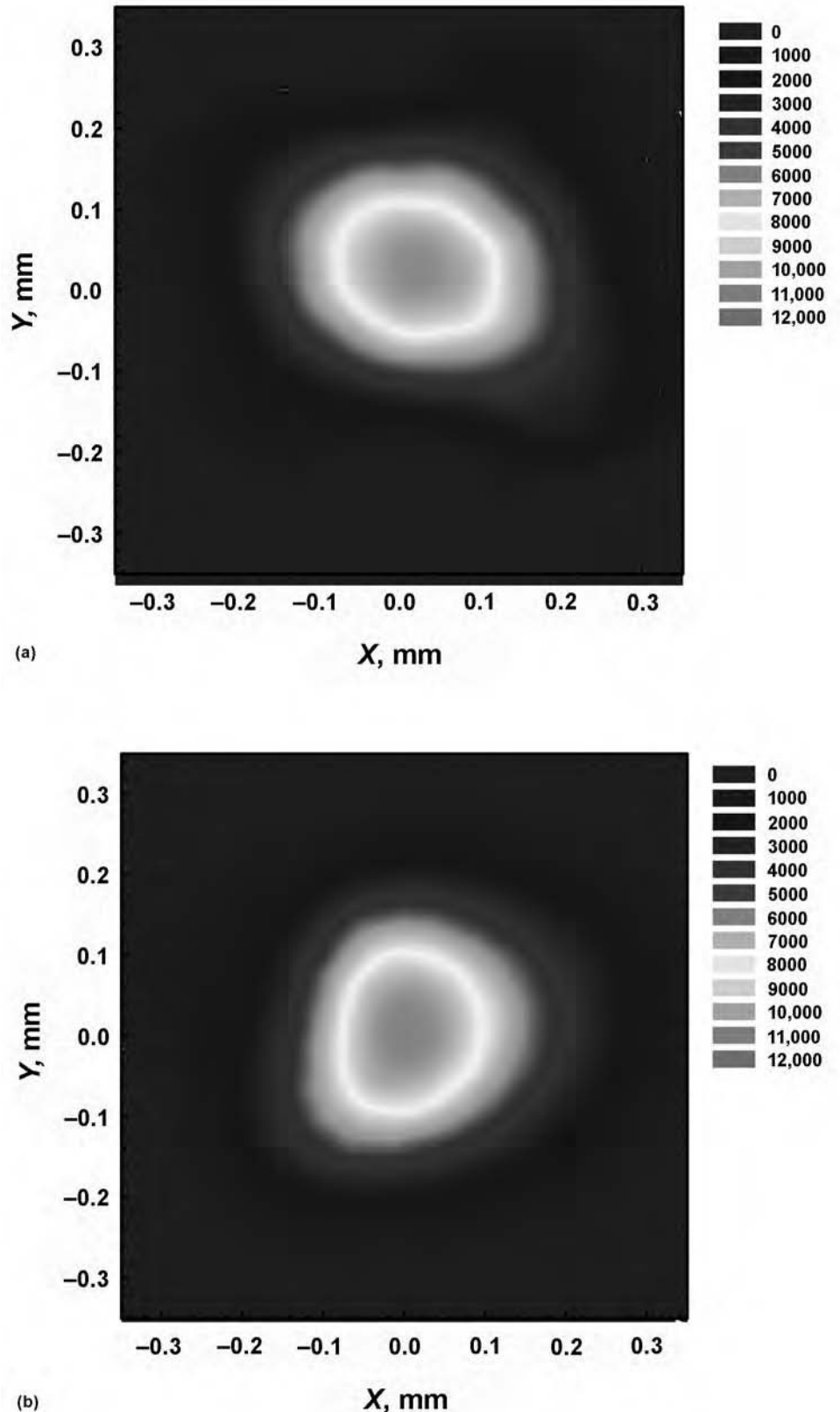


Fig. 6 Plots showing the reconstructed beams made at a constant voltage of 100 kV and current of 10 mA on (a) the development welding system at a defocus setting of +11 and a work distance of 210 mm (8.3 in.) (peak power density = 11.9 kW/mm²) and (b) the production welding system at the sharp focus setting and a work distance of 457 mm (18 in.) (peak power density = 11.6 kW/mm²). Source: Ref 25

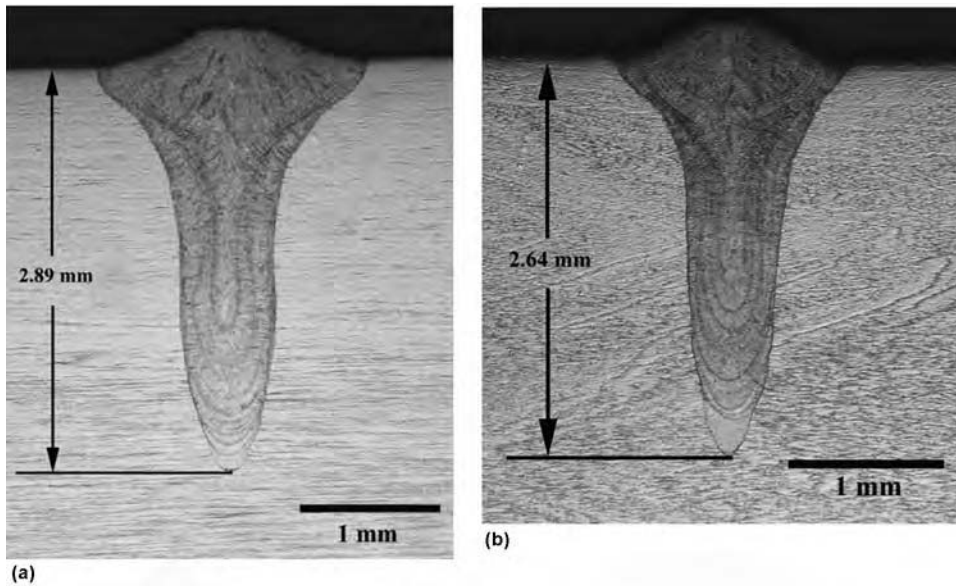


Fig. 7 Micrographs showing the weld cross sections in 304L stainless steel produced by (a) the development welding system at a work distance of 210 mm (8.3 in.) and a focus condition of +11 and (b) the production welding system at a work distance of 457 mm (18 in.) and at the sharp focus setting for 100 kV, 10 mA beams at a travel speed of 17 mm/s (0.67 in./s). Source Ref 25

The previous experiments show that it is possible to produce welds that are similar in shape and size by considering the differences in the performance of two machines determined through the use of the EMFC diagnostic tool. With this tool, the characteristics of the EB are quantified to a level that allows similar beams to be reproduced with ease on different welding systems. Using these results as a baseline, a procedure for the transfer of EB welding parameters between two machines can be adapted to specific needs. In any modified procedure, the EMFC diagnostic tool is integrated into each step of this procedure. Beginning with the weld development stage, the EMFC diagnostic tool provides a means for quantitatively characterizing the beam and ensuring that it exhibits the same characteristics each time it is used. During the transfer of weld parameters, the use of the EMFC diagnostic tool significantly streamlines the process by removing redundant test welds on each machine and minimizes the time and cost required to move a part from development to production. Therefore, traditional methodologies that rely on multiple test welds to transfer welding parameters from development to production can be replaced by a much more streamlined methodology that is based on a thorough knowledge of machine performance.

Quality Control

Process control with EB welding typically relies on the control of the machine settings during welding. These settings must fall within a set tolerance range for a weld to be considered acceptable. This tolerance range, as defined in the American Society of Mechanical Engineers (ASME) Boiler and Pressure Vessel code (Ref 26), can be rather wide, with beam current being allowed to vary by up to $\pm 5\%$, which allows for a rather significant amount of variability in the process parameters and the resulting beam characteristics. Even though this quality-control philosophy, termed the "goalpost" philosophy (Ref 27), can produce acceptable parts, there are no guarantees that the resulting components meet the nominal customer specifications.

More modern quality philosophies, such as the Taguchi loss function, recognize that customers desire the products to fall more consistently around the nominal specifications (Ref 27). From a process-control standpoint, the ultimate goal is to minimize these variations in the beam characteristics, particularly at the extremes of the tolerance band over the course of a production run, and for all of the parts to be near the nominal specifications. Enhanced process control is one means for meeting the ultimate goal of producing a product that meets customer expectations. In

EB welding, the integration of modern diagnostic tools provides a means for achieving this goal.

With beam diagnostic tools, these beam characteristics, including the peak power density and FWHM and FWE2 values, can be quantified on a regular basis. Previous work (Ref 28) has shown that machine performance, in terms of the measured beam characteristics, varies over time. Testing has shown that the variability of the beam characteristics can be measurably decreased with the use of a diagnostic tool. With the implementation of this diagnostic tool in the process-control procedures, variations in each of the measured beam parameters can be controlled at levels below $\pm 2.2\%$, which is smaller than the 5% tolerance band suggested by ASME for other welding parameters. Such an enhanced level of control allows product throughput to be increased by decreasing the number of rejected parts through the elimination of unexpected variations in beam characteristics (Ref 28).

The variation of the measured beam parameters for a single production run can be minimized with the integration of EB diagnostics into the process-control methodology. Such a powerful tool can have a significant impact on conventional process-control techniques for EB welding by incorporating previously unavailable quantitative information concerning the beam characteristics. With this new information, several areas should be explored further, and general improvement of available quality-control methods in EB welding will be realized. Three of these areas, primarily involving the enhanced process control afforded by this diagnostic tool, are addressed in the following discussion.

With the aid of beam diagnostic tools, allowable tolerance levels for the various beam parameters can be decreased in size. Currently, there is no standard accepted tolerance level for the beam characteristics measured by this diagnostic tool. In addition, maintaining tight control on the machine settings is not a sufficient guarantee of sufficient process control. By more tightly controlling the beam parameters, variations in the resulting weld properties can be diminished, and parts more closely meeting customer expectations can be produced more reliably and to increasingly stringent quality standards.

Secondly, by quantitatively characterizing the beam, the tighter beam requirements can lead to more imaginative joint designs. It is currently accepted in production environments that some level of postweld machining and rework is required for EB-welded components. Much of this rework is the result of the inability to provide adequate beam control in the absence of a beam diagnostic tool. As a result, joint geometries are designed to compensate for the lack of precision in beam control. With the

integration of beam diagnostic tools, joint geometries can be minimized and the need for follow-on machining reduced or even eliminated by guaranteeing consistent beam properties.

Finally, enhanced process knowledge gained through the use of this diagnostic tool can lead to higher levels of machine up-time and increased awareness of potential maintenance issues. Changes in the peak power density of the operator and diagnostic-determined sharp focus settings are good indications of the overall machine performance. For example, previous work has identified decreases in the peak power density measurements to correspond to a change in machine performance, which required unexpected maintenance. This degradation in performance would not be observed without the use of a diagnostic tool, which allowed the machine to be repaired before its degraded performance resulted in the fabrication of any unacceptable welds (Ref 28).

REFERENCES

1. "Recommended Practices for Electron Beam Welding," AWS C7.1M/C7.1:2004, American Welding Society, Miami, FL, 2004
2. P. Anderl and W. Scheffels, Process Control for Electron Beam Welding, *Weld. World*, Vol 30 (No. 5/6), 1992, p 138–144
3. U. Diltthey, A. Goumeniouk, O.K. Nazarenko, and K.S. Akopjantz, Mathematical Simulation of the Influence of Ion-Compensation, Self-Magnetic Field and Scattering on an Electron Beam during Welding, *Vacuum*, Vol 62, 2001, p 87–96
4. Y. Arata, Evaluation of Beam Characteristics by the AB Test Method, *Plasma, Electron, and Laser Beam Technology: Development and Use in Materials Processing*, Y. Arata, Ed., American Society for Metals, 1986, p 177–193
5. G.R. LaFlamme and D.E. Powers, Diagnostic Device Quantifies, Defines Geometric Characteristics of Electron Beams, *Weld. J.*, Vol 70 (No. 10), 1991, p 33–40
6. U. Diltthey and J. Weiser, Study of the Electron Beam "Tool." Part 2: Effects on the Welding Result, *Schweissen Schneiden*, Vol 47 (No. 7), 1995, p 558–564
7. U. Diltthey and J. Weiser, Study of the "Tool" Electron Beam—Part 1: Comparison between the Arata Beam Test and Diabeam Beam Measurement, *Schweissen Schneiden*, Vol 47 (No. 5), 1995, p 339–345
8. U. Diltthey, *New Developments in Advanced Welding*, N. Ahmed, Ed., CRC Press, Boca Raton, FL, 2005, p 198–228
9. J.W. Elmer and A.T. Teruya, An Enhanced Faraday Cup for Rapid Determination of Power Density Distribution in Electron Beams, *Weld. J.*, Vol 80 (No. 12), 2001, p 288s–295s
10. J.W. Elmer and A.T. Teruya, Fast Method for Measuring Power Density Distribution of Non-Circular and Irregular Electron Beams, *Sci. Technol. Weld. Join.*, Vol 3 (No. 2), 1998, p 51–58
11. J.W. Elmer, A.T. Teruya, and D.W. O'Brien, Tomographic Imaging of Noncircular and Irregular Electron Beam Current Density Distributions, *Weld. J.*, Vol 72 (No. 11), 1993, p 492s–505s
12. A. Teruya, J. Elmer, and D. O'Brien, System for the Tomographic Determination of the Power Distribution in Electron Beams, *The Laser and Electron Beam in Welding, Cutting, and Surface Treatment: State-of-the-Art 1991* (Englewood, NJ), Bakish Materials Corporation, p 125–140
13. O. Nello, Electron Beam Probing Systems—A Review, *TWI Bull.*, May/June 2001, p 38–40
14. T.A. Palmer and J.W. Elmer, Characterization of Electron Beams at Different Focus Settings and Work Distances in Multiple Welders Using the Enhanced Modified Faraday Cup, *Sci. Technol. Weld. Join.*, Vol 12 (No. 2), 2007, p 161–174
15. A. Lundback and H. Runnelmalm, *Sci. Technol. Weld. Join.*, Vol 10 (No. 6), 2005, p 717–724
16. "Welding—Acceptance Inspection of Electron Beam Welding Machines—Part 2: Measurement of Accelerating Voltage Characteristics," ISO 14744-2, latest revision, International Organization for Standardization (ISO), Geneva, Switzerland
17. "Welding—Acceptance Inspection of Electron Beam Welding Machines—Part 3: Measurement of Beam Current Characteristics," ISO 14744-3, latest revision, International Organization for Standardization (ISO), Geneva, Switzerland
18. "Welding—Acceptance Inspection of Electron Beam Welding Machines—Part 4: Measurement of Welding Speed," ISO 14744-4, latest revision, International Organization for Standardization (ISO), Geneva, Switzerland
19. R.E. Armstrong, *Weld. J.*, Vol 49 (No. 8), 1970, p 382s–388s
20. C.W. Weidner and L.E. Shuler, *Weld. J.*, Vol 52 (No. 3), 1973, p 114s–119s
21. G.L. Mara, E.R. Funk, R.C. McMaster, and P.E. Pence, *Weld. J.*, Vol 53 (No. 6), 1974, p 246s–251s
22. C.M. Weber, E.R. Funk, and R.C. McMaster, *Weld. J.*, Vol 51 (No. 2), 1972, p 90s–94s
23. H. Tong and W.H. Giedt, *Weld. J.*, Vol 49 (No. 6), 1970, p 259s–266s
24. T.A. Palmer, J.W. Elmer, K.D. Nicklas, T. Mustaleski, and P. Burgardt, unpublished research, 2004
25. T.A. Palmer, J.W. Elmer, K.D. Nicklas, and T. Mustaleski, Transferring Electron Beam Welding Parameters Using the Enhanced Modified Faraday Cup, *Weld. J.*, (Res. Suppl.), Vol 86 (No. 12), 2007, p 388s–398s
26. ASME Boiler and Pressure Vessel Code, Sections VIII and IX, American Society of Mechanical Engineers
27. P.J. Ross, *Taguchi Techniques for Quality Engineering: Loss Function, Orthogonal Experiments, Parameter and Tolerance Design*, McGraw-Hill Book Company, New York, 1988
28. T.A. Palmer and J.W. Elmer, Improving Process Control in Electron Beam Welding Using the Enhanced Modified Faraday Cup, *J. Manuf. Sci. Eng.*, Vol 130 (No. 4), 2008, p 041008

Laser Beam Welding*

Tim Webber, IPG Photonics
Thomas Lieb, L·A·I International
J. Mazumder, University of Michigan

LASER BEAM WELDING (LBW) uses a moving high-density coherent optical energy source called a laser as the source of heat. *Laser* is an acronym for light amplification by stimulated emission of radiation. The coherent nature of the laser beam allows it to be focused to a small spot, leading to high energy densities of 10^5 to 10^7 W/cm² (6×10^5 to 6×10^7 W/in.²). (See the article “Introduction to High Energy Density Electron and Laser Beam Welding” in this Volume for an introduction to the nature of laser beam radiation.)

Lasers have been promoted as potentially useful welding tools for a variety of applications. By 1965, a variety of laser systems had been developed for making microwelds in electronic circuit boards, inside vacuum tubes, and in other specialized applications where conventional technology was unable to provide reliable joining. Until the 1970s, however, laser welding had been restricted to relatively thin materials and low speeds, because of the limited continuous power available. Since then, the availability of high-power continuous-wave lasers has expanded the interest and use of lasers in welding applications (Fig. 1). High-power continuous-wave lasers include:

- Carbon dioxide (CO₂) lasers with wavelength of 10.6 μm
- Neodymium-doped yttrium-aluminum-garnet (Nd:YAG) lasers with wavelength of 1.064 μm (including both lamp-pumped and diode-pumped rod)
- Ytterbium-doped yttrium-aluminum-garnet (Yb:YAG) disc lasers with wavelength of 1.030 μm
- Yb: fiber lasers with wavelength of 1.070 μm

The ability of the laser to generate a power density greater than 10^6 W/cm² (6×10^6 W/in.²) is a primary factor for its potential in welding. Table 1 compares the energy consumptions and efficiencies of LBW with other major

welding processes. Numerous experiments have shown that the laser permits precision (that is, high-quality) weld joints rivaled only by those made with an electron beam (Ref 2).

Laser beams also are used for a number of industrial processes other than welding, including shock hardening, ablation, drilling and cutting, cladding, and transformation hardening. Figure 2 shows how the laser processing parameters interact for various industrial laser beam processes. Many of the other nonwelding applications of lasers are discussed in separate articles.

Laser Beam Welding Advantages and Limitations

Industrial applications of lasers have found that laser welding offers many advantages to conventional welding methods (Ref 3–5). These advantages include:

- Light is inertia-less (hence, high processing speeds with very rapid stopping and starting become possible).
- Focused laser light provides high energy density.



Fig. 1 Laser welding of automotive body assembly. Courtesy of PSA Peugeot Citroën

* Adapted from J. Mazumder, Laser-Beam Welding, *Welding, Brazing, and Soldering*, Vol 6, *ASM Handbook*, ASM International, 1993, p 262–269, and J. Mazumder, Procedure Development and Practice Considerations for Laser-Beam Welding, *Welding, Brazing, and Soldering*, Vol 6, *ASM Handbook*, ASM International, 1993, p 874–880

Table 1 Energy consumption and efficiency of laser beam welding relative to other selected welding processes

Welding process	Intensity of energy source		Joining efficiency, mm ² /kJ	Fusion-zone profile
	W/cm ²	W/in. ²		
Oxyacetylene	10 ² to 10 ³	6 × 10 ² to 6 × 10 ³	0.2–0.5	Shallow for single pass
Arc welding	5 × 10 ² to 10 ⁴	3 × 10 ³ to 6 × 10 ⁴	0.8–2(a) 2–3(b) 4–10(c)	Shallow for single pass
Plasma arc	10 ³ to 10 ⁶	6 × 10 ³ to 6 × 10 ⁶	5–10	Shallow at low-energy end. Deep penetration at high-energy end
Laser beam	10 ⁵ to 10 ⁷	6 × 10 ⁵ to 6 × 10 ⁷	15–25	Shallow at low-energy density range. Deep penetration at high-energy density range
Electron beam	10 ⁵ to 10 ⁸	6 × 10 ⁵ to 6 × 10 ⁸	20–30	Deep penetration

(a) Gas tungsten arc welding. (b) Gas metal arc welding. (c) Submerged arc welding. Source: Ref 1

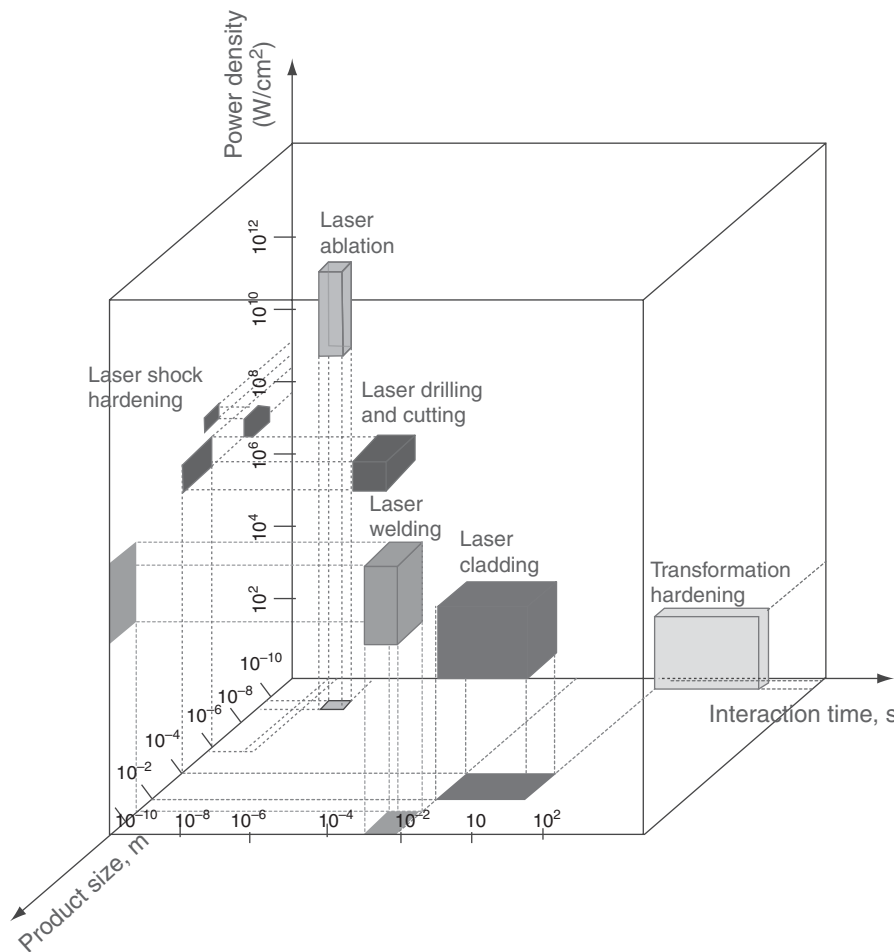


Fig. 2 Process map for various industrial laser beam processes

- Laser welding can be used under ambient atmospheric conditions or controlled gas-mix environments.
- Difficult-to-weld materials (for example, titanium, quartz, etc.) can be joined.
- Workpieces do not need to be rigidly held.
- No electrode or filler materials are required.
- range of weld geometry aspect ratios can be produced.
- Precise welds (relative to position, diameter, and penetration) can be obtained.
- Welds with little or no contamination can be produced.
- The heat-affected zone (HAZ) adjacent to the weld is very narrow.
- The laser beam can be directed a considerable distance from the laser source.
- Intricate shapes can be cut or welded at high speed using automatically controlled light-deflection techniques (remote welding, cutting).

- The laser beam can also be time-shared and/or energy-shared through the use of multiple optical paths.

Limitations of LBW include:

- Precise part fit-up and alignment are much more critical in laser welding than in ordinary arc welding, because the typical focal spot diameter for a laser beam range is small (ranging in size from 0.1 to 1 mm, or 0.004 to 0.04 in.).
- Laser welding equipment is almost 10 times more expensive than comparable power arc welding systems, although laser welding can provide much higher throughput relative to conventional arc welding, with economic advantage when a considerable amount of welding is to be done.
- The penetration depth obtained in laser welding is less than that observed in electron beam welding.

The penetration depth obtained in laser welding is less than that observed in electron beam welding, because the kinetic energy of electrons with rest mass (inertia) is greater than that of the photons (with zero rest mass) in the laser beam. For example, the maximum thickness of type 304 stainless steel plate that can be welded using a 77 kW CO₂ laser is 50 mm (2 in.) (Ref 6), whereas electron beam welding (EBW) can produce welds in type 304 stainless steel up to several inches in thickness. However, the penetration depth of EBW extends only a relatively short distance under atmospheric pressure. Welding under a vacuum is required to obtain optimum efficiency in EBW.

When the capital cost of LBW is compared to EBW, laser beam welding can be a cost-effective option, because no vacuum enclosure is necessary for LBW. A laser beam can propagate an appreciable distance through the atmosphere without serious attenuation or optical degradation, because of its coherent nature. Laser beam welding thus offers an easily maneuverable, chemically clean, high-intensity, atmospheric welding process with narrow HAZ and subsequent low distortion. Laser welding also can be conducted in controlled gas-mix environments (glove boxes) with locally applied inert gas shielding or no shielding, although the use of pressure-controlled environments increases the capital costs.

Peak penetration, A_{max} , is the maximum penetration in millimeters, where P is the incident laser power in watts and is defined by:

$$A_{max}(\text{mm}) \cong 2.5 \times 10^{-2} P^{0.7} \quad (\text{Eq 1})$$

Peak penetration (A_{max}) occurs at very slow speeds, and the weld is wide with respect to the depth. In terms of weld width (w) and depth (d), both conduction-mode welding ($w/d \geq 1$) and deep-penetration welding ($w/d < 1$) can be obtained with lasers.

Laser Beam Welding Fundamentals and Process Physics

Welding with laser beams is a process that takes place in a series of steps as the concentrated laser energy, in the form of electromagnetic energy, interacts with a material. The steps involved are inherently multidisciplinary, requiring knowledge from several branches of physics. A brief summary of the nature of laser beam interactions with materials and how heat is delivered from the beam into the part being welded is presented here. More detailed information on laser/material interactions can be found in the literature, such as by von Allmen (Ref 7) and those in the Selected References at the end of this article.

Laser interactions with metals are dominated by the effects of conduction (free) electrons at the metal surface. Absorption of the laser energy by these electrons occurs very rapidly, on the order of 10^{-13} s, and in a very shallow region of the metal surface, 10 to 100 nm, which is shorter than the wavelength of the laser. The photon energy is ~ 1.2 eV for Nd:YAG and 0.12 eV for CO₂ lasers, which is sufficient to excite the free electrons and give them excess kinetic energy. The excess kinetic energy is then transferred to the metal atoms through large numbers of elementary collisions and various energy-transfer mechanisms, creating heat as the excited electrons deposit their excess energy into the atomic lattice (Ref 7). This process of converting the laser energy into heat is called thermalization, and it produces a highly localized heat pulse on the surface of the metal where irradiation occurred. The thermalized heat can then macroscopically flow from this region into the remaining portion of the substrate, as described by classical heat-flow methods (conduction, convection, and radiation heat-transfer mechanisms).

During laser welding, the temperature rise must be sufficient to melt the surface, and during keyhole welding, the temperature rise must be sufficient to vaporize the substrate. Under the conditions where vapors are being created, the laser interaction becomes more complicated, because it must pass through this vaporized column to reach the metal surface. The hot vapor column becomes partially ionized and can absorb photons through interactions with the thermally excited atoms and through the ions or free electrons in the ionized plasma via a process known as bremsstrahlung absorption.

Bremsstrahlung absorption is defined as the process by which an inner-shell electron absorbs a photon and consequently realizes a higher energy state. Inverse bremsstrahlung (IB) absorption is the opposite effect, in which an electron emits a photon and descends to a lower energy state. These processes produce continuous absorption or emission spectra. The level of the free energy states at initiation and conclusion can take on any value. These spectra are quite similar to metallic spectra in that the

plasma can be either highly absorbing or highly reflecting, depending on its frequency.

The IB absorption is the means by which most of the power absorption within the plasma occurs. The degree to which IB occurs depends on the laser wavelength, the laser irradiation, and the molecular species in the plasma. It is an undesired effect because it partially blocks the laser beam and reduces the amount of energy that reaches the metal surface. Methods to minimize IB through plasma-suppression methods are discussed later in this article. It is important to note that free electrons must be present for the IB absorption mechanism to operate. These electrons can be created by thermionic emission through the vaporization of small flakes or protrusions on the metal surface. The prevalence of these flakes and other surface defects will significantly affect the threshold of plasma initiation. Once either of these mechanisms causes an electron cascade to begin, a plasma will form. The plasma will then be maintained by the IB absorption mechanism.

Modes of Laser Welding

Lasers are capable of both conduction-mode welding and deep-penetration welding.

Conduction-Mode Welding. Momentum transfer or convection dominates conduction-mode welding. High power density (10^5 to 10^7 W/cm², or 6×10^5 to 6×10^7 W/in.²) in laser welding produces a temperature gradient of the order of 10^6 K/cm (5×10^6 °F/in.), which in turn leads to surface-tension-driven thermocapillary flow (Marangoni convection) with surface velocities of the order of 1 m/s (Ref 8, 9).

Convection is the single most important factor affecting the geometry of the laser melt pool (that is, pool shape, aspect ratio, and surface ripples) and can result in defects such as variable penetration, porosity, and lack of fusion. Convection is also responsible for mixing, and it therefore affects the composition of the melt pool during laser welding. The pool configuration in conduction-mode laser welding is a function of the Prandtl number of the materials (Pr_m)—defined as the ratio of kinematic viscosity to molecular diffusivity (Ref 9). In materials with low Prandtl numbers (for example, aluminum with $Pr_m = 0.02$), the pool shape is more spherical and is dominated by conduction heat transfer. In contrast, a material with a high Prandtl number (for example, steel with $Pr_m = 0.1$) results in a pool shape that is shallow and wide, because it is dominated by the surface-tension-driven flow (Ref 9). Free surface deformation leading to defects such as undercuts is also influenced by convection. A small amount of surface reactant elements (for example, sulfur or oxygen) can change the convection direction. For most metals, thermocapillary flow drives the hot metal to the cold side (Fig. 3), but the addition of sulfur changes the sign of the temperature-dependence function of the surface tension and drives the liquid metal to the center of the pool.

Deep-Penetration-Mode Welding. The mechanism of deep-penetration welding by a laser beam is very similar to that encountered with an electron beam (that is, energy transfer is via “keyhole” formation) (Ref 10–12). This keyhole may be produced when a beam of sufficiently high power density causes vaporization of the substrate and the pressure produced by the vapor in the crater causes displacement of the molten metal upward along the walls of the hole (Fig. 4). This hole acts as a blackbody, aiding the absorption of the laser beam as well as distributing the heat deep in the material. The energy in most conventional welding processes is deposited at the surface of the workpiece and brought into the interior by conduction.

The conditions of energy and material flow during beam welding were investigated theoretically by Klemens (Ref 13). According to Klemens, the keyhole or cavity is formed only if the beam has sufficient power density. The keyhole is filled with gas or vapor created by continuous vaporization of wall material by the beam. This cavity is surrounded by liquid that, in turn, is surrounded by solid.

The flow of the liquid and the surface tension tend to obliterate the cavity, while the vapor, which is continuously generated, tends to maintain the cavity. There is a continuous flow of material out of the cavity at the point where the beam enters. For a moving beam, this keyhole achieves a steady state (that is, the cavity and the beam associated with the molten zone move forward at the speed set by the advance of the beam). The material lost by vaporization shows

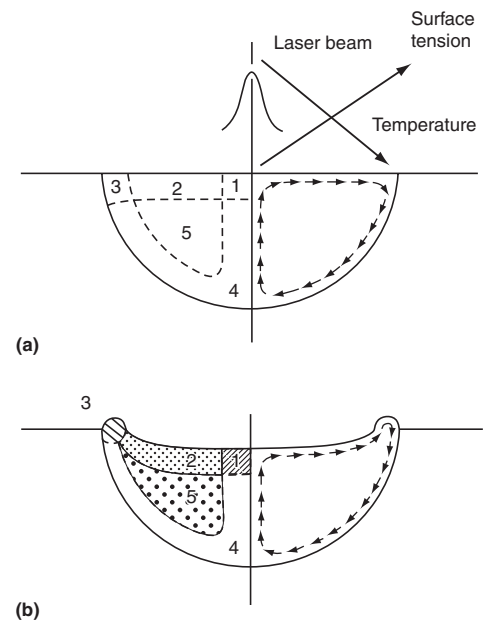


Fig. 3 Schematic showing effect of convection on laser beam welding melt pool configuration. (a) Spherical shape with flat surface typical of low- Pr_m materials. (b) Shallow and undercut free surface characteristic of high- Pr_m materials. Numbers in the figure identify specific regions: 1, stagnation flow region; 2, free surface boundary-layer region; 3, cooled corner region; 4, solid-liquid interface boundary-layer region; 5, isothermal inviscid core. Source: Ref 8

up as a depression in the solidified melt as porosity, as an inward deformation of the workpiece, or possibly as a combination of these effects. The requirement that sufficient vapor be produced to maintain a steady state leads to a minimum advance speed for a steady state. While the cavity moves through the solid and liquid material at a speed determined by the motion of the beam, materials must be moved continuously from the region ahead of the cavity to the region behind it. This is confirmed by the experimental work of Sickman and Morijn (Ref 14) and Arata et al. (Ref 15). Figure 5 shows how the laser beam interaction with the workpiece produces a keyhole plasma in the workpiece and a surface plasma above the workpiece. The relative positions of the HAZ, weld pool, and convection pattern within the weld are also shown.

An interesting experiment on the mechanism of deep-penetration welding with a continuous-wave CO₂ laser has been reported by Sickman and Marijn (Ref 14). It was conducted on transparent fused quartz so that the formation of the weld as a function of time could be photographed. The tip of the hole appears to bend toward the direction in which the workpiece is moving. This process is caused by the reflection of laser light from the leading edge of the hole. Material evaporated at this surface is effectively trapped by the cooler trailing edge. Thus, material is transported across the laser beam from the hot leading edge to the cooler trailing edge without significant ejection of material back out toward the beam. For welding speeds in the range of 10 to 45 mm/min (0.4 to 1.8 in./min), the depth of penetration was linearly related to welding speed. As expected, the minimum penetration was obtained at maximum welding speed.

Fluid flow during penetration welding was also studied by Arata et al. (Ref 15), using laser beam irradiation of low-viscosity glass at high temperature. High-speed photography of the phenomenon, taken at 8000 frames per second, clearly shows melt flow and the motion of the cavity. Molten fluid, which forms at the front wall of

the cavity, accelerates at an angle along the wall as it is driven by the forces of the turbulence generated by laser vaporization. In this process, a large vortex is formed behind the cavity near the weld surface. This vortex is considered to be the cause of the so-called “wine-glass” beads that are produced by the process.

The transport of material is mainly due to flow in the liquid. However, part of the material is transported in the vapor phase, and this vapor transport generates the excess pressure that drives the liquid flow.

Transport Phenomena (Heat, Momentum, and Mass)

Transport phenomena modeling is needed to estimate the weld pool size and cooling rate. The literature is abundant with sources describing one- to three-dimensional models for LBW and other laser processing. Steen and Mazumder (Ref 5) provide a detailed description of modeling of laser processing, although many practitioners still use the Rosenthal equation published in the early 1940s (Ref 16). It, of course, has a known error resulting from the point-source assumption used to derive the analytical solution, but it can be calibrated for a set of experiments using absorption coefficients to smooth out the errors created by the simplifying assumptions. To account for detailed process physics, numerical solution is needed. (See, for example, the article “Numerical Aspects of Modeling Welds” in this Volume.)

Process Parameters

The major independent process variables for laser welding include:

- Incident laser beam power
- Incident laser beam diameter
- Material-dependent absorptivity
- Traverse speed of the laser beam across the substrate surface

Parameters such as weld design, shielding gas, gap size for butt welds, and depth of focus with respect to the substrate also play important roles. These parameters are discussed in the section “Procedure Development” in this article.

The dependent variables are considered to be:

- Depth of penetration
- Microstructure and metallurgical properties of the laser-welded joints

The effects of some of the important variables are briefly discussed as follows.

Laser Beam Power. The depth of penetration with laser welding is directly related to the power density of the laser beam and is a function of incident beam power and beam diameter. For a constant beam diameter, penetration typically increases as the beam power is increased. Locke et al. (Ref 17) and Baardsen et al. (Ref 18) report that penetration increases almost linearly with incident laser power. It is generally observed that for LBW of a particular thickness, a minimum threshold power is required to initiate melting and form a weld pool.

Laser Beam Diameter. This parameter is one of the most important because it determines the power density. However, it is a challenge to measure for high-power laser beams. This difficulty is due partly to the nature of the beam diameter and partly to the definition of what is to be measured. A Gaussian beam diameter, d_G , can be defined as the diameter where the power has dropped to $1/e^2$ or $1/e$ of the central

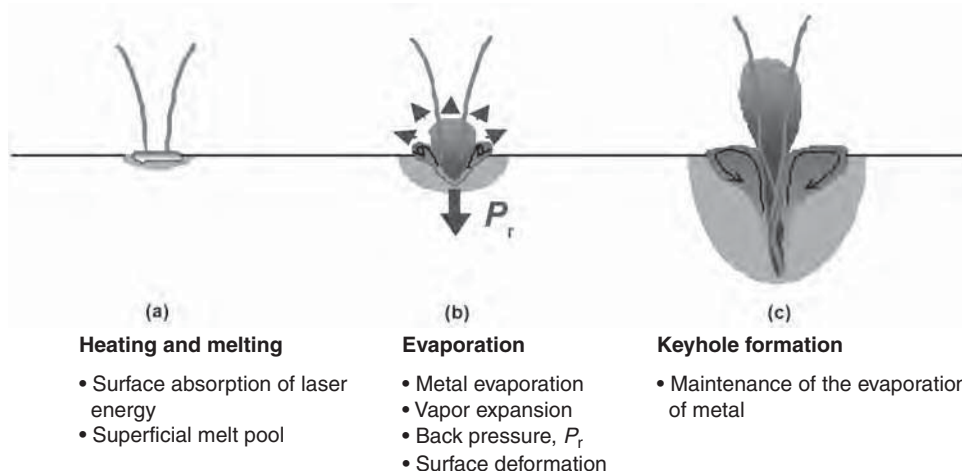


Fig. 4 Forming of a narrow and deep capillary of vapor, or a keyhole

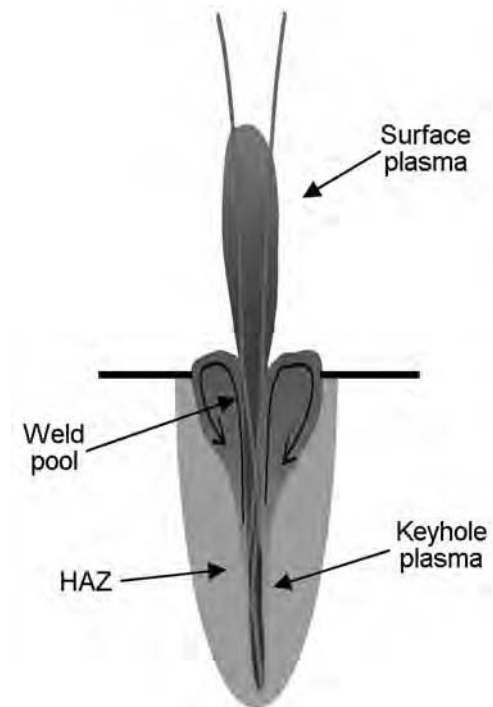


Fig. 5 Schematic of keyhole plasma and surface plasma. HAZ, heat-affected zone. Courtesy of Air Liquide

value. The beam diameter defined on the basis of $1/e^2$ of the central value contains more than 80% of the total power, whereas the power contained for $1/e$ beam definition is slightly over 60% (Ref 19). Therefore, the $1/e^2$ beam diameter is recommended.

Many techniques have been used to measure the beam diameter, but most are unsatisfactory in some respect. Single isotherm contouring techniques (for example, charring paper and drilling acrylic or metal plates) suffer because the particular isotherm they plot depends both on power and on exposure time. These techniques are also highly unlikely to coincide with either the $1/e$ or $1/e^2$ diameters. Multiple isotherm contouring techniques overcome these difficulties but are tedious to interpret. However, several commercial systems are now available that allow the direct measurement of the focused spot size and are discussed in the section "Procedure Development" in this article.

Absorptivity. The efficiency of LBW depends on the absorption of light energy by the workpiece. Any heat-transfer calculation for laser processing is based on the energy absorbed by the workpiece.

The infrared absorption of metal largely depends on the conductive absorption by free electrons. Therefore, absorptivity is a function of the electrical resistivity of the substrate material. Arata and Miyamoto (Ref 20) and McCay et al. (Ref 21) measured the absorptivity of polished surfaces of various materials and concluded that absorptivity is proportional to the square root of the electrical resistivity. This agrees closely with:

$$A = 112.2\sqrt{\rho_r} \quad (\text{Eq 2})$$

where A is the absorptivity, and ρ_r is the electrical resistivity ($\Omega \cdot \text{cm}$). A temperature-dependent relationship between the electrical resistivity and emissivity of the metal was derived by Bramson (Ref 22). Bramson's formula can be used for theoretical calculation of the absorptivity from the electrical resistivity because absorptivity is related to the emissivity. However, Bramson's formulas (Eq 3) will be valid only for metals without surface oxide layers (when heating occurs in a vacuum). The presence of an oxide layer will increase the absorptivity. The relationship between the emissivity and the electrical resistivity of a substrate for the perpendicular incidence of radiation of long wavelength derived by Bramson is:

$$\epsilon_\lambda = 0.365 \left[\frac{\rho_r(T)}{\lambda} \right]^{1/2} - 0.0667 \left[\frac{\rho_r(T)}{\lambda} \right] + 0.006 \left[\frac{\rho_r(T)}{\lambda} \right]^{3/2} \quad (\text{Eq 3})$$

where $\rho_r(T)$ is the electrical resistivity at absolute temperature, T , expressed in Ohm-centimeter ($\Omega \cdot \text{cm}$), and $\epsilon_\lambda(T)$ is the emissivity

of the substrate at temperature T (in $^\circ\text{C}$) for radiation having a wavelength λ (cm).

The estimated absorptivity for Ti-6Al-4V at 300°C (572°F) using Bramson's formula is approximately 15%. Experimental data published by Arata and Miyamoto (Ref 20) and Bramson (Ref 22) indicate that the absorptivities of aluminum, silver, and copper are between 2 and 3% and those of stainless steel (type 304), iron, and zirconium are below 15% even in the molten state. Reflection losses of this magnitude are significant. Therefore, when a sheet metal product form is welded, measures must be taken to avoid reflection losses. Applying an absorbent powder to the surface or forming an anodized film on the surface are two techniques that are considered to be very effective (Ref 21).

Absorptivity can also be increased by the use of reactive gases. Jorgensen (Ref 23) reported that the addition of 10% O_2 to an argon shielding gas gives an increase of up to 100% in welding depth. Jorgensen also found that gas flow had no significant effect on weld depth. However, an increase in depth was associated with a decrease in reflectivity, which was obtained by the addition of a small amount of oxygen.

Although metals are poor absorbers of infrared energy at room temperature, above a certain threshold, approximately 10^6 to 10^7 W/cm^2 (6×10^6 to 6×10^7 $\text{W}/\text{in.}^2$), energy transfer via the keyhole leads to much higher effective absorptivity. This occurs by multiple reflections within the keyhole, once a keyhole has formed. Because of this, the effective absorptivity increases rapidly and enables deep-penetration welding by the laser, despite the large convergence angles for laser beams relative to electron beams (Ref 21). However, the threshold energy required for keyhole formation in laser welding is higher than that required for an electron beam (1.5×10^5 W/cm^2 , or 9.5×10^5 $\text{W}/\text{in.}^2$) because of the poor absorptivity. Nevertheless, energy transfer by this keyhole mechanism permits the laser to provide efficient welding of even highly reflective materials (for example, aluminum) (Ref 24).

Traverse Speed. The correlation of penetration depth relative to welding speed with both LBW and EBW processes was studied by Duley (Ref 10) and Locke and Hella (Ref 17). The penetration in the laser weld is consistently less than that obtained with an electron beam, but the relative difference between the two penetration depths diminishes as the welding speed is increased. However, Duley (Ref 10) found this somewhat surprising because, as pointed out by Baardsen et al. (Ref 18), the time to form a void or keyhole depends on the illumination time for a particular area on the surface of the workpiece as the welding speed is increased. When this occurs, the average power dissipated in the sheet is expected to drop because the keyhole is no longer a completely effective trap for the incident laser radiation. For an electron

beam, absorptivity of the material is independent of the shape and extent of the keyhole. Hence, the total power dissipated in the workpiece is less dependent on the welding speed. However, Crafer (Ref 25) reports that the keyhole penetration threshold for laser beams or electron beams of radius 0.1 mm (0.004 in.) incident on a steel surface of thermal diffusivity $10 \text{ mm}^2/\text{s}$ ($0.4 \text{ ft}^2/\text{h}$) is achieved in 1 ms. This could be regarded as instantaneous. Again, for very low welding speeds, the penetration depth of laser welds becomes significantly less than that attainable with the electron beam. According to Locke et al. (Ref 17), this can be attributed to the formation of a plasma cloud, which attenuates the incident beam.

Process Selection

Laser beam welding is characterized by its low distortion and low specific energy input. It is an accurate, inertia-less method capable of high welding speeds for most materials, including many difficult-to-join materials. The process is often selected for high-volume, high-speed applications for joining materials/components that pose problems during arc welding, such as titanium alloys used for pacemakers. Often the selection criteria depend on economics, which is related to joining rate, welding speed, distortion, and postwelding treatment needs, among many other considerations. Another important consideration is whether the higher speeds can offset the higher initial capital costs within a reasonable time period. Low specific energy input is responsible for applications such as pacemakers, because it reduces the possibility of thermal damage of the sophisticated electronics contained in such devices. Some manufacturers of cigarette lighters are now using LBW as an alternative to resistance welding because of the lower porosity in laser welds.

Economics combined with the smaller HAZ and higher overall weld toughness associated with LBW makes it a popular joining method for high-volume automotive applications. For example, multiple pieces of different compositions are joined by LBW to form blanks for automobile body components such as side-frame panels. These blanks need considerable weld toughness to withstand the stresses induced during subsequent press forming operations. Weld geometry is another consideration for the selection of the process. Because a smaller volume of material is melted due to the low specific energy input, weld defects such as undercuts are also minimized. This is especially important for applications involving dissimilar workpiece thicknesses, which have a higher probability of undercuts.

Another example where the narrow HAZ combined with high welding speed makes LBW a preferred method is the welding of planetary gears used in automobile powertrains. Planetary gear teeth are so closely spaced that it

is difficult to access the weld joint without melting the neighboring gear teeth using conventional (arc) welding. This is one of the oldest LBW applications, and it is routinely carried out worldwide.

Metallurgical considerations are sometimes responsible for the selection of the LBW process. The characteristic low specific energy input for this process results in a higher cooling rate. Higher cooling rates are often needed to suppress precipitation of harmful intermetallic compounds (which may promote brittle fracture) during the solidification of the weld pool. This is an important criterion for welding of many nickel-base superalloys. For titanium alloys, a high cooling rate limits grain growth and oxidation during solidification, making it possible to weld titanium alloys outside a vacuum chamber with modest inert gas shielding. High cooling rates also help to avoid sensitization during welding of stainless steels. On the other hand, high cooling rates may cause problems in many ferrous alloys by promoting martensitic transformation and higher residual stresses; however, this is often balanced by the smaller size of the HAZ.

In many applications where resistance spot welding has been traditionally used, laser welding can offer many advantages, including single-side access and reductions in weight and costs by removing the tab needed in resistance welding. Tabs consist of extra material provided during the fabrication of the square frame in resistance welding that enable the electrodes to push the excess material together to complete the welding process. Adapting joint designs such as butt welding to the laser welding process eliminates the need for tabs. For example, up to 60 kg (130 lb) of steel can be saved from an automobile by replacing resistance spot welding with laser welding and taking advantage of the design flexibility (Ref 26).

Another key factor in the successful implementation of laser welding is the selection of the appropriate laser for a given application. An excellent source of laser beam device vendors is *Laser Focus World* buyer's guide, which is published annually (Ref 27) and is available online. Characteristics and parameters of commercial lasers available for welding are listed in Table 2. Carbon dioxide (CO₂) lasers with up to 25 kW power capacities and pulsed Nd:YAG lasers with up to 500 W peak power have been the workhorses for the industry until recently. The majority of the CO₂ laser applications involve lasers up to 6 kW. Recently, disc and fiber lasers have, in general, exceeded the power level of CO₂ lasers used in the welding industry.

In addition to welding speed and depth of penetration, which are the most important LBW attributes, the flexibility and precision of beam delivery are also important criteria for selecting LBW. Multi-axis workstations and robotics are already available in the market for

CO₂ laser applications. However, one of the major advantages of the 1 μm laser family (disc, fiber, and Nd:YAG laser) is its capability to deliver the energy through an optical fiber cable. Unfortunately, no fibers are yet available for CO₂ lasers with a 10.6 μm wavelength that are of a power level for welding metals. Much of the high-speed and deep-penetration welding is carried out with lasers with power in excess of 1 kW.

Continuous-wave 1 μm lasers can outperform CO₂ lasers with the same power capacity (Fig. 6). For materials with relatively high reflectivity, such as aluminum and copper, Nd:YAG, disc, and fiber lasers have better coupling, especially for conduction-mode welding, because of their shorter wavelength (1.06 μm). When conduction-mode welding of all materials, and even in keyhole welding of reflective material, care should be taken to prevent reflected energy from entering the beam-delivery system and/or impinging on beam-delivery hardware. Considerable damage can be done because a substantial percentage of the laser power can be reflected. A good guideline is to employ a beam angle 1.5 times the cone angle of the focused laser beam normal to the workpiece (Fig. 7).

Procedure Development

The key factor for procedure development is the selection of optimum independent and dependent process variables. The independent process variables for laser welding include incident laser beam power, incident laser beam diameter, traverse speed, absorptivity, shielding gas, depth of focus and focal position, and weld design and gap size. The important dependent variables are depth of penetration, microstructure and mechanical properties of laser-welded joints, and weld pool geometry. Detailed discussions of most of these variables are provided in Ref 1. They are discussed subsequently in view of their role in procedure development.

Power density is defined as the incident power per unit area. In any welding process, it is the power density that determines the depth of penetration and joining rate of the process, as much as the total power of the source. Therefore, beam diameter and spatial distribution of the laser beam energy play an extremely important role because they determine the area of incidence. Two other variables affecting the ultimate power density driving the welding process are absorptivity and plasma beam interaction, such as refraction. Position of focus with respect to the substrate and depth of focus of the beam also affect the power density and penetration depth.

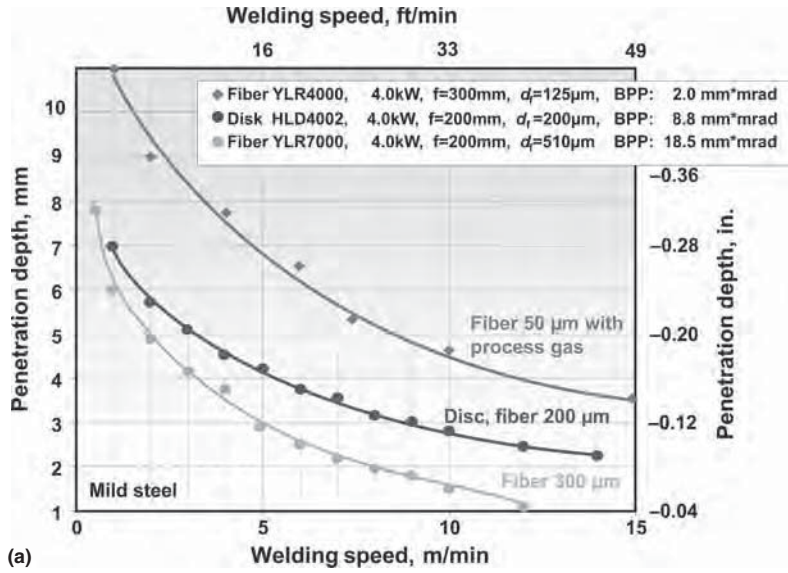
Spatial distribution of the energy is generally constant for a given laser, whereas absorptivity is a function of the substrate, its surface condition, and the laser beam wavelength. Therefore, the most common practice for process development with a given laser and material is the selection of focusing optics for optimum power density and working distance by controlling the beam diameter. Thus, a working knowledge of the focusing optics is important for an engineer developing the laser welding process. Important formulas related to the laser as a welding tool are summarized in following subsections dealing with process variables.

Interaction time is defined as the time a particular point on the substrate spends under the laser beam. In simple terms, it is the ratio of the beam diameter to the traverse speed. Strictly on the basis of heat transfer, one should account for the total time of heating and cooling at the point above the ambient temperature. This is, however, a much more difficult quantity to keep track of compared to the ratio of the traverse speed and beam diameter. Again, it is the interaction time that controls the weld pool profile, not the traverse speed alone. Laser welding procedure development involves the selection of optimum power density and interaction time after the selection of the laser.

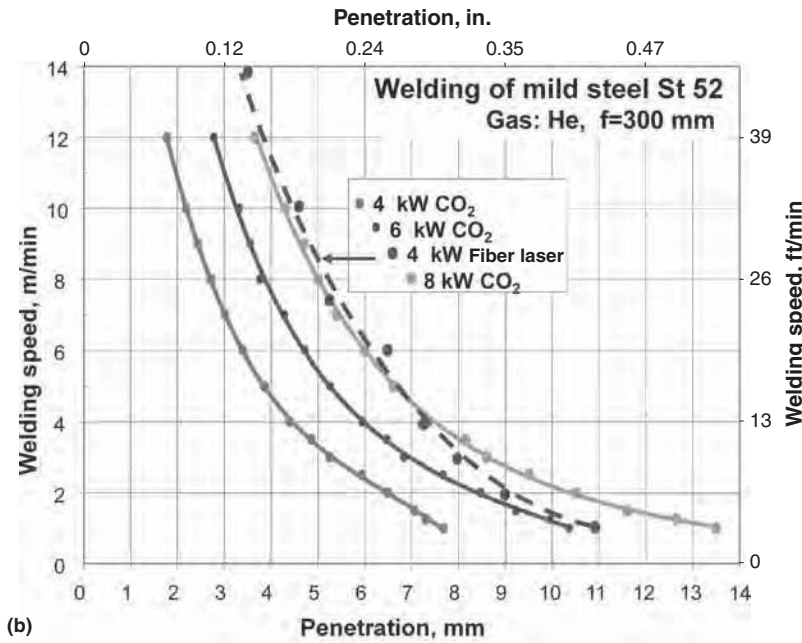
Table 2 Parameters for selected pulsed and continuous-wave lasers used for laser beam welding applications

Laser	Pulse length, ms	Pulse energy, J	Peak power, kW	Maximum weld thickness(a)		Welding speed	
				mm	in.	mm/s	in./min
Pulsed							
Ruby	3–10	20–50	1–5	0.13–0.50	0.005–0.020	1.2	3.0
Nd:glass	3–10	20–50	1–5	0.13–0.50	0.005–0.020	0.63	1.5
Nd:YAG(b)	3–10	10–100	1–10	0.13–0.60	0.005–0.025	2.1	5.0
CO ₂	5–20	0.1–10	1–5	0.13	0.005	1.2	3.0
Continuous wave							
Nd:YAG(b)	1.8	5.56	0.022	5.8	14.0
CO ₂ (direct current excited)	1	0.60	0.025	12.7	30.0
CO ₂ gas dynamic	20	19.0	0.750	21.2	50.0
CO ₂ gas dynamic	77	50.8	2.00	26.7	63.0
CO ₂ (radio-frequency excited)	5	10.0	0.4	10.8	25.6

(a) Data are for type 304 stainless steel. (b) Nd:YAG, neodymium: yttrium-aluminum-garnet



(a)



(b)

Fig. 6 Comparison of welding performance of (a) disc and fiber and (b) CO₂ lasers compared with 4 kw fiber laser. BPP, beam parameter product. Adapted from Ref 28

Laser beam power is one of the primary variables in determining the penetration depth in laser welding. For process development, the first action one should take is to calibrate the laser output power with the power delivered at the substrate. There is often a measurable loss due to the reflective and transmissive optics used to deliver the beam from the laser to the workpiece. Almost all commercial lasers are equipped with some kind of power-measuring device based either on a flowing-water

calorimeter where the full beam is dumped, or a solid-state detector where a fraction of the laser energy is continuously deposited. Additional calorimetric devices should be maintained to measure power at the workpiece for periodic calibration of output power with the power delivered at the weld pool.

For lasers with power in excess of a few hundred watts, water-cooled calorimeters are the most popular. For on-line monitoring, many multikilowatt systems also use precalibrated

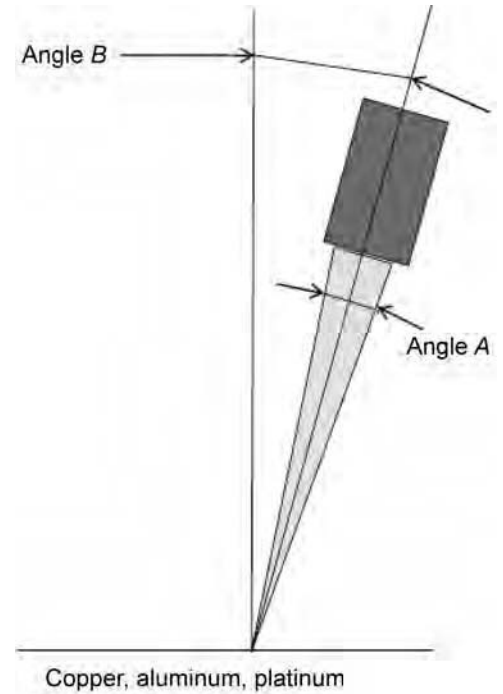


Fig. 7 Beam angle for welding reflective materials. Angle B is equal to 1.5 times angle A to minimize the risk of damaging the optics through back reflections.

solid-state detectors, usually behind one of the cavity mirrors that has a small leak of approximately 1% or less. Several vendors offer both types of power meters. In addition to the absolute power measurement, power density is also strongly influenced by beam diameter and beam mode (that is, the spatial distribution of energy, as described in the section “Laser Beam Spatial Distribution” in this article). Thus, beam diameter and beam mode also should be monitored to control power density.

Laser beam diameter is one of the most important variables because it determines the power density for a given total power. The focused beam diameter will also influence weld width, which is often an important weld requirement (Ref 29, 30). The spatial distribution of energy in the beam affects the focusing characteristics of the beam. For a Gaussian beam, the diameter is defined as $1/e^2$ of the central value (Fig. 8), and it contains almost 86% of the total power. The diffraction-limited focal spot size (d_{min} in mm) for such a Gaussian beam is given by the following relationship:

$$d_{min} = \frac{1.27f\lambda}{D} \tag{Eq 4}$$

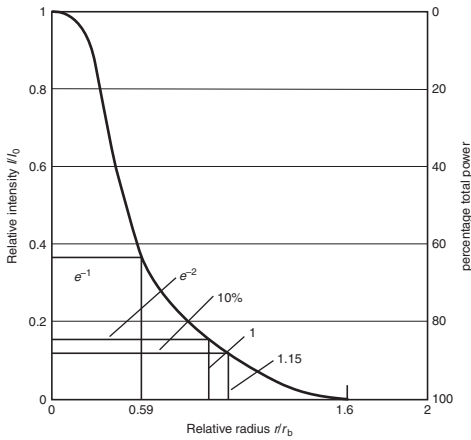


Fig. 8 Variation of relative intensity and percentage of total power with radius for a Gaussian beam. Source: Ref 19

where D is the unfocused beam diameter (in mm), f is the focal length (in mm) of the focusing optics, and λ is the wavelength (in mm) of the laser beam. Note that 1.27 is $4/\pi$. This is an ideal situation, and often the focused beam diameter will be larger due to aberrations and other imperfections in the focusing optics.

Light can be considered to take the form of a wave that can interfere constructively or destructively, depending on the phase angle between intersecting waves. Diffraction is one way that interference occurs with light, and it will occur when a beam is interrupted by an edge or aperture. A diffraction pattern will form of maximum and minimum light intensity. When a lens is introduced into the diffracted beam, the angle between each minimum can be approximated and thus the focused spot size. Diffraction-limited spot sizes for various types of laser beams can be estimated using the relationships given in Eq 5 to 7. For a rectangular beam with a plane wave front:

$$d_{\min} = \frac{2f\lambda}{D} \tag{Eq 5}$$

For a circular beam with a plane wave front:

$$d_{\min} = \frac{2.44f\lambda}{D} \tag{Eq 6}$$

For a multimode beam with a plane wave front—where the transverse electromagnetic mode (TEM) is described in indexing convention, TEM_{*m*} (as described in the following subsection on laser beam spatial distribution)—the diffraction-limited spot size is:

$$d_{\min} = \frac{2.44f\lambda}{D}(2m + n + 1) \tag{Eq 7}$$

For example, if a 25 mm (1 in.) TEM₀₁CO₂ laser beam is focused by a 100 mm (4 in.) focal-length lens, the diffraction-limited spot diameter is:

$$d_{\min} = \frac{2.44 \times 100 \times 10.6 \times 10^{-3}}{25} (2.0 + 1 + 1) = 0.21 \text{ mm}$$

However, as indicated earlier, these are estimates for the theoretically possible minimum spot size. One of the more useful means for evaluation of beam quality is the M^2 concept (Ref 5, 31). M^2 is the ratio of the divergence (θ) of the actual beam to that of a theoretical (ideal Gaussian) diffraction-limited beam:

$$M = \frac{\theta_{\text{Actual}}}{\theta_{\text{Gaussian}}}$$

The correlated beam diameter based on the M^2 concept is:

$$d_{\min}(\text{mm}) = \frac{4M^2f\lambda}{\pi D} \tag{Eq 8}$$

In this case, M must be measured at two known locations in the beam propagation path. This reinforces the point that a proper measurement technique for beam diameter is imperative for estimating the actual beam diameter and the power density.

There are several commercial systems now available for beam diameter measurement. Sasnett et al. (Ref 31) describe one system that is specifically designed for beam evaluation based on the M^2 concept. This instrument is capable of measuring the beam width within 0.5 μm accuracy in two mutually perpendicular transverse directions. Knife edges are used to scan the beam, and a set of lenses are traversed in the direction of the beam propagation to change the positions of the beam width. The measurement procedure and data acquisition and display are computer controlled.

Another commercial system is based on a hollow rotating needle, which samples the beam. This is based on the research carried out by Loosen et al. (Ref 32) and Lim and Steen (Ref 33), which resulted in the development of a laser beam analysis system based on a rotating needle that reflects part of the beam to a set of detectors.

Although beam quality related to the ideal Gaussian beam is a good starting point, there is evidence that for high-power laser processing, this characterization may not be sufficient (Ref 34). Spatial coherence and temporal and local fluctuations are generally ignored, but they do affect the processing behavior. Many European research groups are working on characterizing the beam in terms of the mode coherence coefficient, which is based on a set of suitable modes and averaged intensity distribution and which takes into account the partial coherence properties of the beam.

Another complication of high-power laser welding is interaction with the plasma column. Rockstroh et al. (Ref 35) found that free electrons in the plasma column cause absorption and refractions. For welding of aluminum with a CO₂ laser, as much as 30% of the energy is lost in the plasma, and the refracted beam diameter is 8% larger. This measurement is based on the

electron density measurement using the emission spectroscopy technique. This observation is subsequently supported by similar measurements by Lober et al. (Ref 36, 37). Complete characterization of beam diameter will require both measurement at the focal spot before processing and monitoring of the beam refraction during the process using spectroscopic techniques.

Laser Beam Spatial Distribution. Every laser resonator cavity, defined by the mirrors of the laser, has certain stable configurations of the electromagnetic field called modes. A well-defined mode has a definite spatial distribution for the laser beam. As evident from Eq 7, the mode affects the focused beam diameter and leads to higher spot size for a given $f\lambda$ focusing optics. The general convention for indexing a mode is TEM_{*m*} (transverse electromagnetic mode with m number of radial zero fields and n number of angular zero fields). TEM₀₀ is the ideal Gaussian beam and will provide the smallest focused spot and highest power density. Most of the fast axial-flow lasers offer a TEM₀₀ or TEM₀₁ beam. Most of the transverse-flow lasers offer TEM₀₁ (doughnut-shaped spatial distribution).

Intensity distribution for different modes can be calculated using the Hermite polynomial for rectangular coordinates and the LaGuerre polynomial for polar coordinates using the expressions for a TEM_{*m*} mode beam given in Eq 9 to 11. For a rectangular coordinate:

$$\sqrt{I_{mn}(x,y)} = \{H_m(\sqrt{2gx/R_b})H_n(\sqrt{2y/R_b})g \exp[-2r^2/R_b^2]\} \tag{Eq 9}$$

For a polar coordinate:

$$I_{mn}(r, \theta) = [L_m^n(2r^2/R_p^2)]^2 (\sqrt{2gr/R_0})^{2n} g \exp[-2^2/R_b^2] \cos^2 n\theta \tag{Eq 10}$$

For a Gaussian beam with TEM₀₀ mode:

$$I(\lambda) = \exp(-2r^2/R_b^2) \tag{Eq 11}$$

In Eq 9 to 11, x is a variable, r is the radial position, θ is the angular position of the beam, R_b is the beam radius at the $1/e^2$ point, H_m is the Hermite polynomial of order m , and L_m^n is the generalized LaGuerre polynomial.

A schematic of intensity distributions for different beam modes is shown in Fig. 9. For process development, the lowest-order mode available is the best choice for achieving the highest power density from a given power.

The position of focus with respect to the substrate surface influences the weld pool profile and penetration during laser welding. The optimum position for the focal point of the laser beam with respect to the substrate was investigated by Wilgoss (Ref 39). Figure 10 shows the transverse profiles generated by moving the focus point in 2.5 mm (0.1 in.) steps

perpendicular to the plane of the workpiece. The reported plate thickness for this study was 6 mm (0.25 in.). When the focal point was positioned deep inside the workpiece, a V-shaped weld resulted, necessitating more precise alignment than that for a parallel-side weld of the same cross section. When the beam was focused well above the level of the workpiece surface, a large “nail head” with a consequent loss of penetration was observed.

Wilgoss et al. (Ref 39) concluded that the optimum focus is approximately 1 mm (0.04 in.) below the level of the workpiece surface. This produced welds with little or no “nail head” and nearly parallel sides.

Engel (Ref 40) reported that for several metals, the optimum position of the focus is 1.25 to 2.5 mm (0.05 to 0.1 in.) below the surface. Research by Alexander (Ref 41) using a 10 kW laser and 1.9 mm (3/4 in.) thick AISI 1020 steel revealed that the optimum position of focus was 2 mm (0.08 in.) below the surface. When the beam was focused 4 mm (0.16 in.) below the surface, the depth of penetration was almost the same as that for the 2 mm (0.08 in.) focus depth. The general consensus is that the optimum position for the focal point is below the surface, but the exact distance is

dependent on the thickness of the workpiece and the laser power used.

Depth of focus is extremely important for welding thin-section materials because for a shallow depth of focus, the substrate comes in and out of the focal position due to thermal distortion. Depth of focus is defined as the distance over which the focus beam has the same approximate intensity. According to the Laser Institute of America, depth of focus is defined as the range over which the focus spot radius is increased by 5%. Based on this definition, the depth of focus (Z) is given by:

$$Z = \pm \frac{0.32\pi R_b^2}{\lambda} = \pm \frac{R_b^2}{\lambda} = \frac{2.33(F\lambda)^2}{\lambda} = 1.488F^2\lambda \quad (\text{Eq 12})$$

where F equals f/λ of the optics.

One can see from the previous expression that as the F number of the focusing optics increases, depth of focus also increases. However, this is also accompanied by an increased beam diameter and decreased power density. As a result, these variables must be optimized for each particular application.

Focus position can be taken from optics specification and/or instrumentation. Various empirical strategies can be employed to determine focus. A common practice in determining the focal position and depth of focus is to carry out a trial bead-on-plate weld on an inclined plate and use the position where the plasma seems to be the visually strongest. This is a quick, but not necessarily the most accurate, approach for establishing the focal position. Ultimately, the desired fusion-zone shape is obtained by adjusting focus position with respect to the initial focus determination and surface location.

There is some wisdom in developing a welding process where the work is being done at or approximately the depth of focus of the optics. It allows the maximum accommodation of

errors or variation in the Z -position. It is tempting to work outside the depth of focus when a larger image size is desired than an optics set can provide. Realize that sensitivity in spot size to Z -position change will be twice what it would be if the work is done within the depth of focus.

Absorptivity. The importance of absorptivity and its role in laser welding was discussed earlier. For deep-penetration welding with power densities exceeding 10^6 W/cm², keyhole formation leads to high absorption by trapping the beam inside the hole by total internal reflection. However, the absorption during the initial transient period is dependent on wavelength and surface conditions. There are several techniques to enhance the initial absorption (Ref 42). They include:

- Nonmetallic absorbent coatings
- Preheating
- Surface roughening
- Application of an electric field of the correct sign
- Periodic surface structure or induced grating structure

Surface periodic structure can be used to enhance absorption of the wavelength of interest, much like the use of optical gratings with spacing for preferential absorption of a certain wavelength of laser light.

Traverse Speed. The welding speed increases with increasing laser power to produce a constant penetration depth, as shown in Fig. 11. For a given thickness and power, a range of speed can be used to make successful welds. However, the fusion-zone size will increase with the decreased speed within that range. For process development, the nugget size or fusion-zone size and shape is often prescribed by the design engineer for strength considerations. The laser welding engineer needs to select an optimum combination of speed, power, and focus spot size to deliver the required nugget size.

Welding charts of speed versus power and the resulting weld penetration are useful to investigate and plan a welding solution. With CO₂ lasers, the task of generating a chart was a reasonable task for the equipment supplier, because there are usually a limited number of optical combinations available. With a given beam diameter and M^2 value, there exist only a few practical focal length lenses and resulting spot sizes to work with. Charts of weld performance can be produced for a few engineering alloys for a given laser make and model by the laser manufacturer's applications engineering staff. These kinds of charts do have a number of shortcomings, however. They are most often done for a bead-on-plate rather than a real weld joint. They are, at best, an estimate of the effect of process parameters on a resulting joint. The 1 μm laser family, in contrast, has available many combinations of optical components and configurations, providing a wide range of focus spot sizes and

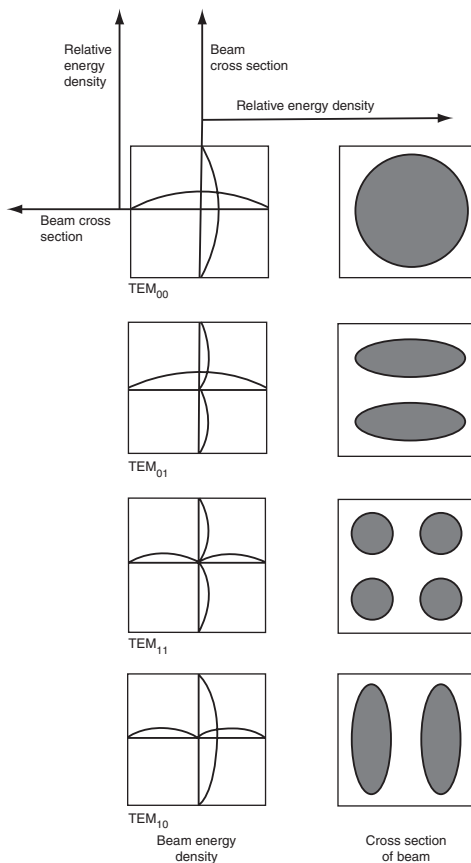


Fig. 9 Beam cross sections for four different transverse electromagnetic modes (TEM). Source: Ref 38

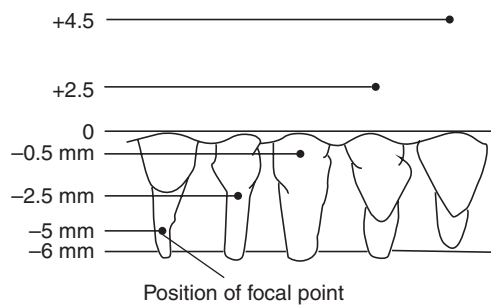


Fig. 10 Transverse profiles as a function of focus position for a laser-beam-welded type 310 stainless steel. Negative and positive numbers indicate position of the focal point below and above, respectively, the surface of the plate. Beam power, 5 kW; traverse welding speed, 16 mm/s (38 in./min). Source: Ref 39

F -numbers. Charting weld performance for every useful optical combination is simply too large an undertaking for the equipment manufacturer.

Laser welding efficiency has been found to be relatively consistent over a reasonable range of weld parameters (Ref 44, 45). It is also interesting to note that significant changes in alloy content, for example, between low-carbon steel and stainless steel, do not significantly impact laser welding efficiency. These facts, in the absence of a chart, allow a simple calculation to obtain an approximation of weld performance for a given set of weld parameters, provided a laser welding efficiency for the material is known.

Welding efficiency can be defined as the fraction of the amount of energy required to take a volume of metal from a base temperature to its melt temperature plus the heat of fusion energy required to melt the metal divided by the amount of energy actually used. This concept of welding efficiency must be differentiated from the concept of transfer efficiency. Arc welding processes have energy-transfer efficiencies of 70 to 90%; however, they only have welding efficiencies of 5 to 10% (Ref 12). Note that some authors use the term *melting efficiency* interchangeably with *welding efficiency*. This means the workpiece is heated by the transferred energy that did not produce a fusion zone. It is this excess heat that contributes to distortion and unwanted material transformation. The advantage of the laser is that energy-transfer efficiencies of 70 to 90% are found by the keyhole mechanism, but welding efficiency can be 30 to 60% (Ref 46–49). Substantially more of the laser energy transferred to the material generates fusion than occurs with arc welding processes.

Ream (Ref 44) defines laser welding efficiency, E , as “melt volume per unit of laser energy” in mm^3/kJ :

$$A_f V / P = E \quad (\text{Eq 13})$$

where A_f is the fusion-zone area in mm^2 , V is the traverse speed in mm/s , and P is the laser power on the workpiece in kW . Ream found that for both mild steel and stainless steel the value of E was 50 to 60 mm^3/kJ for a range

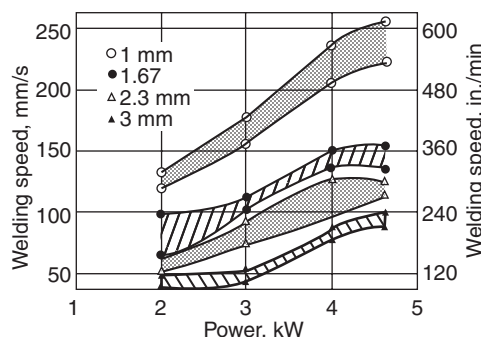


Fig. 11 Welding speed versus laser power for a 5 kW CO_2 laser. The base metal is Ti-6Al-4V. Source: Ref 43

of parameters and laser types. The work of Bermanns and Faerber (Ref 30) supported Ream's finding and also discovered that weld width is consistently inversely proportional to traverse speed. For example, at 3 kW and 50 mm/s (2 in./s) with a 100 μm focus spot, the weld width calculated from the 5.8 mm (0.2 in.) penetration and a fusion-zone area of 2.5 mm^2 (0.004 in.^2) is 0.43 mm (0.02 in.). At a welding speed of 167 mm/s (6.6 in./s), the weld width was 0.19 mm (0.007 in.). If it was desired to increase weld width, a question would be: What would the resulting weld look like if a 200 μm focused spot size was used with 3 kW? The assumption is that the weld width will increase by the spot size increase and the area of the welds will remain the same. A simple calculation reveals that the new weld width with a 200 μm focus spot will be 0.29 and 0.53 mm (0.01 and 0.02 in.) at 50 and 167 mm/s (2.0 and 6.6 in./s), respectively. The weld penetration will be 4.7 and 2.5 mm (0.2 and 0.1 in.), respectively. This calculated result is not an exact match, but it does agree with the chart in Fig. 12 that was generated from weld trials.

Plasma Suppression and Shielding Gas. The plasma produced during laser welding absorbs and scatters the laser beam. It is therefore necessary to remove or suppress plasma. The higher the power, the more clearly the phenomenon can be observed. This negative effect of plasma can be reduced by diluting it with injection of high-ionization-potential gas, such as helium, argon, nitrogen, and mixtures of these gases. Shielding gas may also be required to protect the hot resolidifying weld surfaces from oxidation. Both the composition and flow rate of the plasma suppression gas and shielding gas influence the depth of penetration (Ref 50, 51). In most literature, plasma suppression gas and shielding gas are referred to as shielding gas altogether.

Seaman (Ref 50) studied the role of shielding gas in high-power continuous-wave CO_2 laser welding. Weld cross sections made with various shielding gases and gas mixtures show a 60% difference in penetration. However, gases that permit the greatest penetration do not necessarily blanket (displace air from above the weld rapidly) the weld effectively at characteristically high laser welding speeds. This means that compromises are necessary to permit sound, deep-penetration laser welds (Ref 50).

The effect of the composition of the shielding gas on depth of penetration was studied by Seaman (Ref 50) and Rein et al. (Ref 51). Generally, helium is used as the shielding gas for high-power CO_2 laser welding. As shown in Fig. 13, helium seems to improve beam transmission, whereas argon can cause severe beam blockage (Ref 50). This is probably caused by the lower ionization potential of argon (15 eV) compared to that of helium (25 eV). The effects of air and CO_2 on beam transmission lie between the extremes represented by argon and helium (Fig. 14). Rein et al. (Ref 51) have shown that the addition of small quantities of

hydrogen, sulfur hexafluoride, and CO_2 to the helium enhances penetration at welding speeds below 40 mm/s (95 in./min).

The ionization potential of the shielding gas is not the only consideration for laser welding, especially at higher speeds. This is because gases with higher ionization potentials have lower atomic numbers and lower masses. These lighter gases are less effective in displacing air from the laser/material interaction area in the short time available in high-speed welding. Heavier gases are better able to displace air in a short time. Therefore, a mixture of heavier and lighter gases will result in optimum penetration. Figure 15 shows that as speed increases, the improvement resulting from the addition of a small amount of argon to helium (10% Ar and 90% He) becomes more noticeable. Newer studies found that it is even possible to replace helium with argon altogether by using appropriate new nozzle design technology that displaces the plasma away (Ref 52).

For mass-scale production, the cost of shielding gas is also an important consideration. Recently, Chrysler Corporation replaced helium with CO_2 for plasma suppression during laser welding (Ref 53). The shielding gas is delivered from the side at an angle to suppress the plasma and remove metal vapor from the interaction point. For 14 kW laser power, a welding speed of 20 m/min (65 ft/min), and a shielding gas flow rate of 40 L/min (85 ft^3/h), CO_2 shielding resulted in a wider weld nugget size, but the mechanical properties were acceptable. The cost of helium gas is much higher (e.g., approximately 5 times in 2011) than for CO_2 gas, and helium prices tend to be much more volatile. Therefore, for process development, there is room for optimization of gas selection. However, one should remember that the use of CO_2 gas for a CO_2 laser may cause problems for the concentric gas shield due to preferential absorption.

Proper implementation of a shielding gas for plasma suppression can also be applied for joining difficult-to-weld materials with volatile alloying elements such as aluminum alloy 5083. Blake and Mazumder (Ref 24) demonstrated that with a properly designed helium suppression jet, magnesium losses and porosity formation could be minimized during laser welding of 5083 aluminum alloy. The resulting weld had a tensile strength equal to its parent material. This demonstrates that for process development, shielding gas can also be used to control the chemistry and weld defects.

Plasma suppression/shield gas selection and implementation for the 1 μm laser family is less complex than for the 10.6 μm laser. The metal vapor above the weld does not absorb the shorter wavelength light to the degree it does the longer wavelength. The result is that less plasma is formed in the metal vapor to interrupt and disperse the focused beam. In general, industry uses argon for shielding welds made with 1 μm lasers (Ref 30).

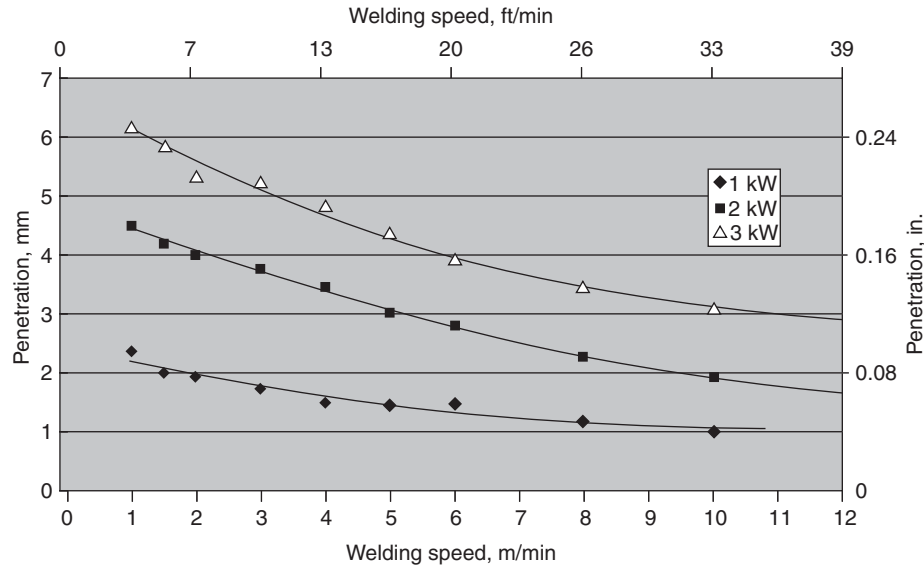


Fig. 12 Fiber laser welding performance for stainless steel. Weld penetration diagram for 200 μm spot size. Courtesy of IPG Photonics

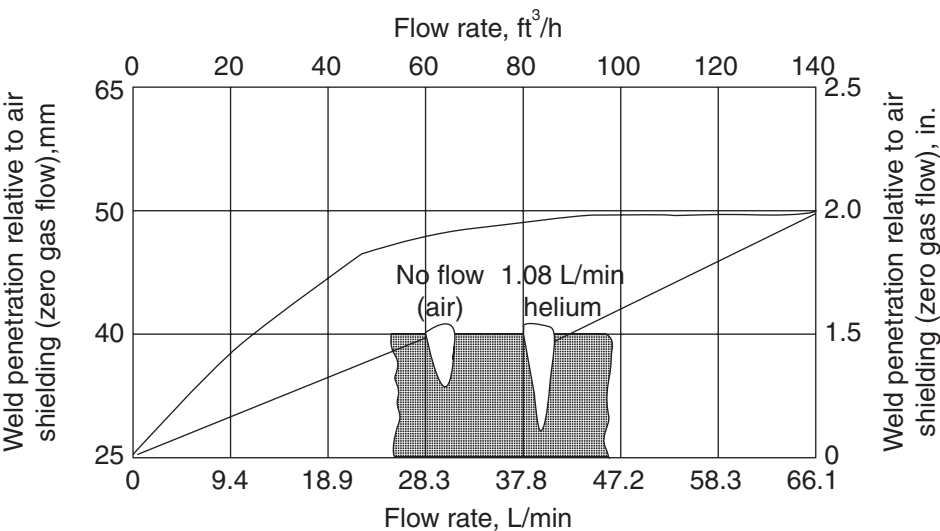


Fig. 13 Effect of shielding gas on depth of penetration during LBW of an austenite stainless steel. Laser power 15 kW. Travel speed, 25 mm/s (60 in./min). Source: Ref 38

Health and Safety

Laser beam welding hazards differ substantially from hazards encountered in other welding techniques. The primary wavelengths for lasers used in welding are invisible to the human eye. The hazards are not readily apparent, and inexperienced or unaware personnel may suffer permanent injury before the existence of hazardous conditions is recognized. For this reason, the United States Federal

Occupational Safety and Health Administration (OSHA), through its “Alliance” program, has fostered the adoption of the American National Standards Institute (ANSI) specification ANSI Z136 series as its enforcement text for laser workplace safety. ANSI Z136.1, “Safe Use of Lasers” (2007 or later edition), requires that each facility using lasers designates an individual as laser safety officer. This individual should be familiar with laser safety and ANSI Z136.1. The officer should implement a laser

safety management program, and, among other things, monitor the procurement, care, use, and disposal of lasers in the organization to ensure adherence to safe laser practice and the ANSI requirements. Because of the complexity of laser safety, this approach is virtually mandatory. The following brief review of laser safety is an introduction but, by itself, is not sufficient to ensure personnel safety.

Injury Hazards

Eye Hazards. Any laser beam capable of welding metals is also capable of causing serious damage to human tissue. Personnel exposure to the beam and any specularly reflected beam must therefore be prevented at all times. Certain lasers, however, are also capable of producing diffuse reflections that can cause permanent eye damage. Hence, viewing of the impact area of the laser beam or reflected beams also must be prevented. While wearing tested and marked laser protective eyewear is the minimum protection from this hazard, the preferred method for safeguarding is complete enclosure.

Enclosures can range from a simple sleeve between the laser optic and the part to be welded to fully automatic operations in enclosed rooms. The following are general guidelines:

- Laser enclosures (called protective housings in the pertinent safety and standards regulations) must be class I anywhere and everywhere the radiation is not needed for the function of the product. The enclosure must be opaque to the laser wavelength. When purchasing a complete system, including the enclosure, the manufacturer (usually the machine integrator) of that equipment must provide a certified laser product that incorporates all the necessary performance features. Any assembly which incorporates, or is intended to incorporate, a laser is itself a laser product. Therefore, automation and other machine integrators become laser product manufacturers when they marry the laser with other equipment and/or protective housings. Laser product manufacturers must certify and report their products to the Food and Drug Administration (FDA) prior to entry into commerce. The purchaser of complete certified products should see the certification label (nameplate) on the product and ask the supplier for the accession number, which is the FDA’s tracking number for reports filed.
- Protective enclosures built on site (not purchased as part of the system) must follow the performance requirements in 21 CFR 1040.10 and .11 and ANSI Z136.1 clause 4, “Control Measures.” The enclosure must be interlocked to prevent firing of the laser beam when personnel could be exposed.

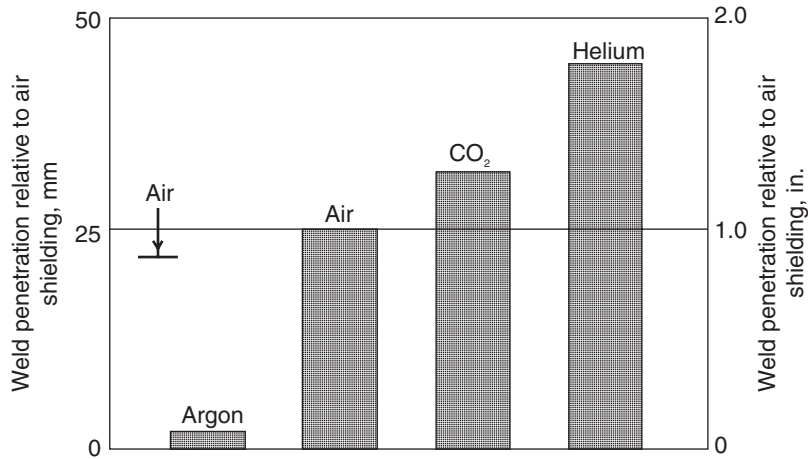


Fig. 14 Comparison of CO₂ laser weld penetration achieved with different shielding gases. Source: Ref 38

When the piece to be welded is a part of the enclosure, the interlocks should also prevent firing, unless the piece is in place. In the case of pulsed lasers, breaking of the interlocks should also discharge the stored energy into a dummy load.

- If the enclosure is large enough to walk in, the walk-in area is called the laser controlled area (LCA). Signs are required at access points to the enclosures in accordance with ANSI Z136.1. (If a complete system with a walk-in enclosure was purchased, it is called a walk-in workstation, and it must meet FDA Laser Policy 37 and ANSI Z136.1 clause 4.3.1.2.)
- Viewing of the weld area can be accomplished in several ways. Most common are viewing ports with filters and television monitors. For microwelding, microscopes should have filtered viewing optics or flip mirrors that permit either welding or viewing. (If a filtered port is installed separately from the certified product purchase, it must be labeled in accordance with ANSI Z136. If it is purchased as part of a certified product, the label is not required.)
- Alignment of laser welding systems should be accomplished using low-power lasers.

Laser welding can also be performed with personnel in attendance. When done in this manner, the hazard must be evaluated for each welding process using the ANSI standard. General requirements include:

- The laser welding area must be completely enclosed, and access must be restricted (see LCA requirements in ANSI Z136.1).
- In most cases, laser eye protection is required for all personnel in the area. The optical density of the eye protection must

be calculated to reduce the potential eye exposure to less than the maximum permissible exposure (MPE) level. In addition, much of the eyewear designed for laser protection will not afford protection from weld (plasma) radiation, so welding faceshields with AWS 3-5 may also be required. (Both protections are necessary together; some dual-purpose eyewear may be commercially available.)

- The welding beam must be carefully controlled and should still be enclosed to the greatest extent possible. There is no eyewear available that will withstand a direct viewing of the main multikilowatt beam. Even at powers below 1000 W, eye protection is likely to fail on exposure to the primary beam. Always avoid viewing angles that are at risk of line-of-sight viewing down the axis of the beam or its specular reflection.
- Compliance with personnel training requirements is exceedingly important.

Skin exposure to the primary beam obviously can result in thermal burns and must be prevented by complete enclosure and operator training. Even in attended operations where the operator is permitted to view the welding process, provision of partial enclosures to prevent personnel from placing any part of the body into the beam path is desirable.

The ANSI standard also prescribes MPE values for skin exposure. In the visible and near-infrared regions, these are much greater than the MPE values for the eyes; hence, a problem from excessive exposure due to diffuse reflections at these wavelengths rarely occurs. Excessive skin exposures in the ultraviolet and far-infrared regions are possible, however. Typically, ultraviolet exposures can be controlled with clothing of tightly woven material and

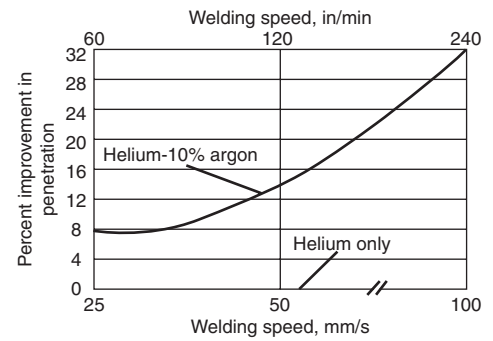


Fig. 15 Improvements in weld penetration resulting from the blanketing of a 10% argon addition to a helium shielding gas. Source: Ref 38

barrier creams applied to exposed skin. Harmful levels of ultraviolet light can also be generated by flash lamps; hence, covers should be kept in place. Harmful levels of ultraviolet are also generated by the weld process. Prolonged or repeated exposure to ultraviolet is a known carcinogen (causes cancer). The MPE limits for ultraviolet include limits in a single day and repeat exposures with any 24 hour period. Always protect eyes and skin from the laser and the weld radiation.

Associated Hazards

Electrical Hazards. All lasers used for welding employ high voltages capable of inflicting lethal electric shocks. Therefore, maintenance shall be performed only by personnel familiar with high-voltage safety procedures. (Accidents resulting in fatalities around lasers have all been by electrocution.)

Power supplies for high-power lasers contain capacitors capable of lethal shock even after initial discharge due to a phenomenon known as charge buildup. To facilitate safe maintenance access, the following provisions should be included:

- An automatic discharge and grounding circuit that is actuated when the laser is turned off
- Discharge and grounding interlocks on all access panels
- Grounding rods for manual verification of complete discharge. Safety glasses should be used, because explosion-like discharges are possible on partly charged capacitors.
- Grounding straps to short out capacitors to prevent charge buildup

In addition, all capacitors should be discharged and grounded before any work is performed on or near high-voltage components.

Control of laser performance usually requires switching of capacitors. Insulated switches that do not expose personnel to electric conductors are preferred. If switching requires work on

bus bars, the previously listed procedure should be followed, and the use of insulated tools should be considered. Cooling-water leaks are not acceptable, especially when electrical and cooling lines share the same umbilical.

Chemical Hazards. Laser welding generates metal fumes similar to other welding processes, and the hazard is largely dependent on the composition of the welded metals. Ventilation is required to meet OSHA standards and American Conference of Governmental and Industrial Hygienists threshold limit values. In high-power welding applications, fumes can be generated in sufficient quantities to make local exhaust ventilation, in addition to general room ventilation, both necessary and economical.

Harmful fumes of vapors can also be generated when laser energy is deposited in unwanted materials, such as breakdown of plastic enclosure materials due to laser exposure and failure of exotic lens materials due to thermal runaway. These conditions are best controlled by careful materials selection and monitoring of welder performance. Finally, laser optics cleaning agents may be toxic and flammable and should be handled accordingly.

Training, Medical Examinations, and Documentation. ANSI Z136.1 requires that training in the potential hazards and control measures be provided to operators, engineers, technicians, and maintenance and service personnel. Special training on subjects such as potential hazards (including biological effects), control measures, and applicable standards is required for the laser safety officer. A model safety and training program is outlined in Appendix A of the standard.

Routine medical surveillance of laser users is no longer mandated by the standard. However, an employer may wish to provide such for medical/legal reasons (that is, to document what eye damage existed prior to commencement of laser work and that no additional damage has occurred). Therefore, initial hiring or assignment exams and departure exams may still be a reasonable consideration.

Documentation may include:

- Listing of lasers, duration of use
- Results of hazard surveys and calculations of accessible laser radiation
- Interlock tests
- Laser use procedures
- Employees working in laser area
- Date and extent of employee training
- Dates and results of medical examinations (if any)
- Training and qualifications of laser safety officer

REFERENCES

1. J. Mazumder, Laser Welding, *Laser Materials Processing*, M. Bass, Ed., North Holland, Amsterdam, 1983, p 113–200
2. G. Verhaeghe and B. Dance, An Assessment of the Welding Performance of High-Brightness Lasers and a Comparison with In-Vacuum Electron Beams, *Proceedings of the Laser Institute of America's ICALEO 2008* (Temecula, CA), p 406–414
3. I.J. Spalding, Laser System Developments, *Phys. Bull.*, July 1971, p 402
4. Y.S. Arata and J. Miyamoto, *Technocrat*, Vol 11 (No. 5), 1978, p 33
5. W.M. Steen and J. Mazumder, *Laser Material Processing*, 4th ed., 2010, Springer, London
6. C.M. Banas, "Laser Welding to 100 kW," Report R76-912260-2, United Technologies, Feb 1977
7. M. von Allmen, Laser-Beam Interactions with Materials, *Springer Series in Materials Science 2*, 1987
8. J. Mazumder, *Opt. Eng.*, Vol 30 (No. 8), 1991, p 1208–1219
9. C.L. Chan, J. Mazumder, and M.M. Chan, *Metall. Trans. A*, Vol 15, 1982, p 2175
10. W.W. Duley, *CO₂ Lasers: Effects and Applications*, Academic Press, 1976, p 241
11. A.M. Maleka, Ed., *Electron Beam Welding Principles and Practice*, Welding Institute, McGraw-Hill, 1971, p 95–96
12. D.T. Swifhook and E.E.F. Gick, *Weld. J.*, 1973, p 492S–499S
13. P.G. Klemens, *J. Appl. Phys.*, Vol 47, 1976, p 2165–2174
14. J.G. Sickman and R. Morijn, *Phillips Res. Rep.*, Vol 23, 1968, p 375–376
15. Y. Arata, H. Maruo, I. Miyamoto, and Y. Inoue, "Dynamic Behavior of Laser Welding," IIW DOC IV/222/77, International Institute of Welding, 1977
16. D. Rosenthal and R. Schemerber, Thermal Study of Arc Welding, *Weld. J.*, Vol 17, 1938, p 208s
17. E.V. Locke and R.A. Hella, *IEEE J. Quant. Electron.*, Vol QE-10 (No. 2), Feb 1974, p 179–185
18. E.L. Baardsen, D.J. Schmatz, and R.E. Bisaro, *Weld. J.*, Vol 52, April 1973, p 227–229
19. J.E. Harry, *Industrial Application of Lasers*, McGraw-Hill, 1974
20. Y. Arata and I. Miyamoto, *Laser Focus*, Vol 3, 1977
21. M.H. McCay, T.D. McCay, A. Sedghinasab, and D.R. Keefer, *Laser Materials Processing III*, J. Mazumder and K. Mukherjee, Ed., Minerals, Metals and Materials Society, 1989
22. M.A. Bramson, *Infrared Radiation: A Handbook for Application*, Plenum Press, 1968
23. M. Jorgensen, *Met. Constr.*, Vol 12 (No. 2), Feb 1980, p 88
24. A. Blake and J. Mazumder, *ASME J. Eng. Ind.*, Vol 107 (No. 3), Aug 1985, p 275–280
25. R.C. Crafer, *Weld. Inst. Res. Bull.*, Vol 17, Feb 1976
26. F.A. DiPietro, Robotic Laser Welding Systems in the Automotive Industry, *Proceedings of Laser Systems Applications in Industry* (Torino, Italy), ATA, 1990, p 103–120
27. *Laser Focus World*, PennWell Publishing Company, Tulsa, OK, 1993
28. E. Beyer, "Fiber Laser Welding," ICALEO Special Presentation, Nov 9, 2006 (Orlando, FL)
29. T. Webber, Laser Welding: Efficient Weld Width Generation, *Proceedings of the Laser Institute of America's ICALEO '93*, Oct 24–28, 1993 (Orlando, FL), p 738–745
30. J. Bermanns and M. Faerber, *Facts About Laser Welding*, Linde Gas, Hollriegel-skreuth, Germany, p 18–19
31. M.W. Sasnett and T.F. Johnson, Jr., Laser Beam Diagnostics, *SPIE*, Vol 1414, 1991, p 21–32
32. P. Loosen, A. Drenker, G. Herziger, R. Kramer, and U. Sturm, Diagnostics of High Power Laser Beams, *SPIE Proc.*, Vol 1024, 1988
33. G.C. Lim and W.M. Steen, *J. Phys. E. Sci. Instrum.*, Vol 17, 1984, p 999–1007
34. G. Herziger, Laser Processing Research in Europe, *LAMP '92*, A. Matsunawa and S. Katayama, Ed., Japan High Temperature Society, 1992, p 23–28
35. T. Rockstroh and J. Mazumder, *J. Appl. Phys.*, Vol 61 (No. 3), 1987, p 917–923
36. R. Lober, "Spectroscopic Diagnostic of Argon-Aluminum Plasma during Laser-Metal Interaction," M.S. thesis, University of Illinois, 1989
37. R. Lober and J. Mazumder, *J. Phys. D: Appl. Phys.*, Vol 40 (No. 19), Oct 2007, p 5917–5923
38. E.A. Metzbowyer et al., Laser Beam Welding, *Welding, Brazing, and Soldering*, Vol 6, *Metals Handbook*, 9th ed., American Society for Metals, 1983, p 647–671
39. R.A. Wilgoss, J.H.P.C. Megaw, and J.N. Clark, *Weld. Met. Fab.*, March 1979, p 117
40. S.L. Engel, *Laser Focus*, Feb 1976, p 44
41. J. Alexander, "Penetration Studies in Laser and Arc Augmented Laser Welding," Ph.D. thesis, London University, 1982
42. W.W. Duley, Laser Surface Treatment of Metals, *NATO ASI Series E*, No. 115, C.W. Draper and P. Mazzoldi, Ed., Martinus Nijhoff Publishers, The Netherlands, 1986
43. J. Mazumder and W.M. Steen, *Met. Constr.*, Vol 12 (No. 9), 1980, p 423
44. S. Ream, Laser Welding Efficiency and Cost: CO₂, YAG, Fiber, and Disc, *Proceedings of the Laser Institute of America's ICALEO 2004* (Orlando, FL), p 28–32
45. S. Ream and E. Bachholzky, Analyzing Laser Butt Welding Efficiency, *12th International Congress (Laser '95)* (Munich, Germany), p 247s–256s
46. T. Webber, Laser Welding Melt Efficiency Comparison: CW and Q-

- Switched Nd:YAG, *Proceedings of the International Society for Optical Engineering*, Jan 1996 (San Jose, CA), p 162–169
47. M.H. Hablani, A Correlation of Welding Variables, *Proc. of the Fifth Symposium on Electron Beam Technology*, J.R. Moreley, Ed., Allied Electronics, Cambridge, MA, 1963, p 262–268
 48. L.M. Banas, High Power Laser Welding, *The Industrial Laser Annual Handbook*, D. Belforte and M. Levitt, Ed., Penwell, Tulsa, OK, 1986, p 69–86
 49. T.H. Kim, C.E. Albright, and S. Chang, Energy Transfer Efficiency in the Laser Welding Process, *J. Laser Appl.*, Jan–Feb 1990, p 23–28
 50. F. Seaman, “Role of Shielding Gas in Laser Welding,” Technical Paper MR77-982, Society of Manufacturing Engineers, Dearborn, MI, 1977
 51. R.M. Rein et al., Patent 1,448,740, United Kingdom, 1972
 52. K. Chouf, P. Lefebvre, G. Ballerini, and F. Briand, “New Nozzle for High Power CO₂ Laser Welding with Argon as Shielding Gas,” ICALEO (Anaheim, CA), 2010
 53. M. Ogle, Automotive Laser Application Workshop ‘93, Industrial Development

Division of University of Michigan, Ann Arbor, MI, 1993

SELECTED REFERENCES

- M. Born and E. Wolf, *Principles of Optics*, Pergamon Press, 1987
- L. Migliore, Ed., *Laser Materials Processing*, Marcel Dekker, New York and Basel, Switzerland
- W.M. Steen and J. Mazumder, *Laser Material Processing*, 4th ed., Springer, London, 2010
- O. Svelto, *Principles of Lasers*, Plenum Press, 1982
- J. Verdeyen, *Laser Electronics*, Prentice-Hall, 1989

Laser Beam Weld Design, Codes, and Quality Assessment*

J. Mazumder, University of Michigan
Tim Webber, IPG Photonics
Randolph Paura, Dynamic Laser Solutions

MOST WELD JOINT GEOMETRIES used in conventional fusion welding processes (for example, autogenous automatic gas tungsten arc welding or electron beam welding) are suitable for laser beam welding (LBW). However, it must be remembered that the laser beam is focused to a spot of a few hundred micrometers in diameter, and thus, fit-up tolerances and alignment requirements are also of that order of magnitude.

As with fusion welding processes, joints are designed to meet the design requirements of the weldment for structure, function (e.g., sealing), assembly, and so on. The high power density and the ability to achieve high-aspect-ratio (depth-to-width) welds offers distinct capabilities and advantages for joint design but imposes more stringent requirements on how the weld seam is presented to the laser beam. Some of the important joint geometries are illustrated in Fig. 1 and 2, and Table 1 summarizes joint selection criteria for a few categories of joint design. Different types of joint design reported for LBW were reviewed by Shewell (Ref 1).

Design of Laser Beam Weld Joints

Joint Preparation, Fit-Up, and Design

Butt Joint—Full-Penetration Type. Material to be laser welded does not need beveled edges. Sheared edges are acceptable if square and straight (Ref 2, 3). The fit-up tolerance should be within 15% of the workpiece thickness. Misalignment and out-of-flatness should be less than 25% of material thickness, as shown in Fig. 3(a), to keep the laser beam from

wandering. The transverse alignment should be kept within half of the focused beam diameter (Ref 4, 5). Clamping is recommended, and bucking is not troublesome except when welding material thinner than 0.25 mm (0.01 in.) (Ref 2).

Lap Joints. Air gaps severely limit penetration and welding speeds (Ref 2). Compressive clamping, as shown in Fig. 3(b), should be used to maintain a separation of less than 25% of the material thickness (Ref 3). For welding of dissimilar thicknesses, the thinner material should be placed on top to be welded to the thicker one (Ref 3). Lap joints require fusion width to generate weld strength. Laser type, optics, and weld parameter selections are made to generate weld width efficiently to meet design strength requirements (Ref 6). Caristan (Ref 7) also shows an unpeelable lap joint in which the faying surfaces are completely fused. (See the article “Laser Beam Welding” in this Volume for information regarding welding parameters and optics.)

Pulsed laser spot lap joints demand tighter tolerances than joints produced with continuous power laser welding. The maximum gap for ferrous and nickel alloys is 15% of the material thickness, and the gap must be less for higher-conductivity materials (Ref 1). Baranov et al. (Ref 8) studied the influence of gap size on the formation and strength of spot lap joints in laser welding. They reported that for laser spot lap joints of 0.4 mm (0.016 in.) thick steel and 0.33 mm (0.013 in.) thick nickel, a gap of up to 0.1 mm (0.004 in.) has little influence on joint strength, because there is almost no change in the diameter of the fusion zone. On the other hand, the shape of the weld pool changes with the gap size. It has also been observed that the presence of air in the gap

may lead to the formation of porosity and non-fusion (Ref 8). Micropores sometimes form in the fusion zone, and the number of pores and their size increase with increasing gap size.

Flange joints, as with butt joints, require straight, square edges, good fit-up, clamping, and precise transverse alignment. Flange joints are suitable for welding high-shrinking metals such as aluminum (Ref 2).

Kissing Welds. This type of joint is called a kissing weld because the weld pool forms where two pieces just “kiss.” This offers a small angle between the two parts that traps most of the energy of the laser beam. Very little (if any) pressure is required during welding, but the facing surfaces must fit well (Ref 1). A gap between the sheets will allow radiation to escape. This joint successfully joins thin foils in situations where spot welding would produce melt-through.

Polarization Effect on Kissing Weld. One of the unique advantages of a kissing weld is the ability to take advantage of the polarization behavior of the laser light. If the laser light is polarized perpendicular to the wall of the metal, the beam is preferentially reflected, and it delivers all the energy at the joint. This increases the joint efficiency considerably. This idea was originally proposed by Sepold in 1987 (Ref 9). Subsequently, this concept is used for laser welding of tube and pipe.

Wire Joints. The joint configurations for wires shown in Fig. 2 were developed by the electronics industry. For wire-to-wire joints, the two wires must share the incident laser energy. In a cross joint, for example, the laser beam should be directed at the intersection of the wires so that both wires are exposed directly to the beam.

* Adapted from J. Mazumder, Laser-Beam Welding, *Welding, Brazing, and Soldering*, Vol 6, *ASM Handbook*, ASM International, 1993, p 262–269, and J. Mazumder, Procedure Development and Practice Considerations for Laser-Beam Welding, *Welding, Brazing, and Soldering*, Vol 6, *ASM Handbook*, ASM International, 1993, p 874–880

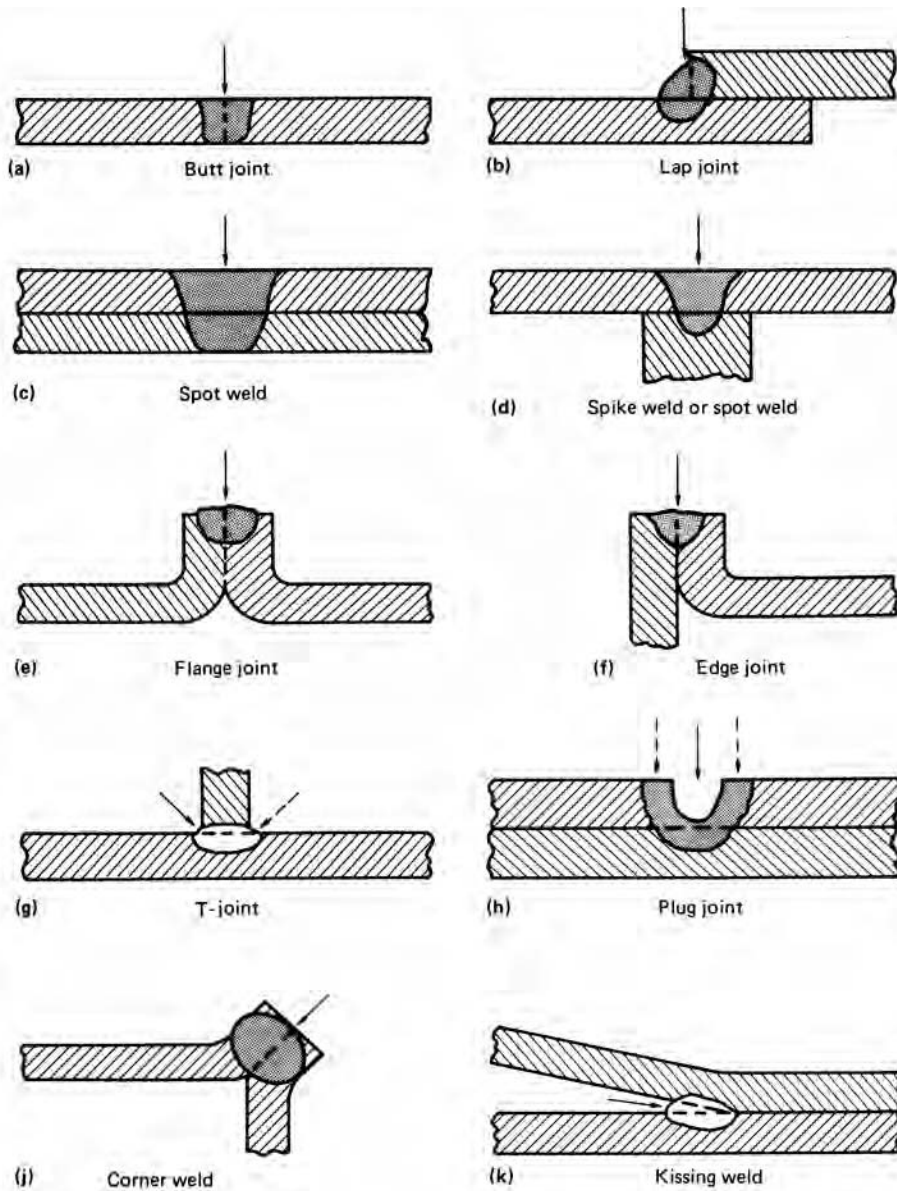


Fig. 1 Joint designs for laser beam welds on sheet metal. Arrows show direction of laser beam. Source: Ref 1

Use of Consumables and Special Welding Practices

Laser welding is ideal for autogenous welding. The main consumable for laser welding is the shielding gas. For thick-section welding, a filler wire can be used to make multipass welds. Sometimes filler metals (or injected powders) are used during laser welding to control the weld bead geometry. The most common use of filler metals, however, is to prevent undercutting. The use of filler materials to control the weld chemistry is also common. For example, insertion of aluminum foil during butt welding of semikilled steel results in a porosity-free sound weld. Vaporization losses during

laser welding of some alloys can be compensated for by the addition of filler materials or powder of desired composition. Energy consumption during LBW is lower with powder injection than with wire-fed filler metals. The wire surface reflects considerable amounts of energy and reduces the energy efficiency of the process.

As with arc welding processes, metallurgical considerations such as preweld and postweld heat treatments are also applicable to laser welding. Under special circumstances, it is possible to use the welding laser for pre- and post-heat treatments (Ref 10). The primary differences between LBW and other welding processes are the narrower heat-affected zone

associated with laser welds as well as the high cooling rates that result in higher localized residual stresses. These high cooling rates can be used beneficially for materials with brittle intermetallic phases. High cooling rate leads to extension of solid solubility and avoids brittle precipitates for many alloys.

Laser Welding of Engineering Alloys

Penetration Welding. The scope of technically and commercially feasible LBW applications has increased greatly since the demonstration of penetration welding using a multikilowatt continuous-wave CO₂ laser by Brown and Banas (Ref 11). Numerous experiments have shown that the laser produces precision weld joints of high quality in ferrous alloys, nickel alloys, and titanium alloys that are rivaled only by those made by electron beam welding. (See the articles in this Volume on electron beam welding.) Data describing the plate thickness of different laser-welded materials are given in Table 2.

Aluminum and its alloys have recently generated much interest in the laser welding community because of their potential application in the auto industry for their weight-reduction properties (Ref 13–18). During the 1970s and 1980s, aluminum alloys were reported to be rather difficult to weld due to the high initial surface reflections of 10.6 μm (417 $\mu\text{in.}$) radiation emitted by CO₂ lasers (Ref 3, 19–25). Surface coating often reduces this problem. Low melting point and relevant fluidity sometimes lead to “drop-through” problems, and thus, energy input is a critical parameter for laser welding. Another critical factor involving laser welding is the vaporization of alloying elements such as magnesium. Suppression of the plasma with a properly designed shielded gas nozzle can be used to avoid the loss of alloying elements (Ref 23). The other alternative is to use filler metal (Ref 16).

Although the welding of aluminum is difficult with LBW, it has already been demonstrated that, with proper precautions, welds having tensile strength equivalent to the parent materials can be obtained.

Steels. A great deal of laser welding research has been conducted on ferrous alloys. Most of the initial parametric studies were carried out on stainless steel (Ref 11, 25, 26). Stainless steel was investigated (Ref 26, 27) because of its importance in the power plant and chemical industries. Laser welding of rimmed steel sheet was evaluated for automotive applications by Baardsen et al. (Ref 28). High-speed LBW of tin plate and tin-free steel for container industries was reported by Mazumder and Steen (Ref 29). Results in HY-alloy steels were evaluated and reported by Banas (Ref 30) and by Metzbowler and Moon (Ref 20). Laser beam welding of modified 4340 alloy was reported by Seaman and Hella (Ref 31). Several other

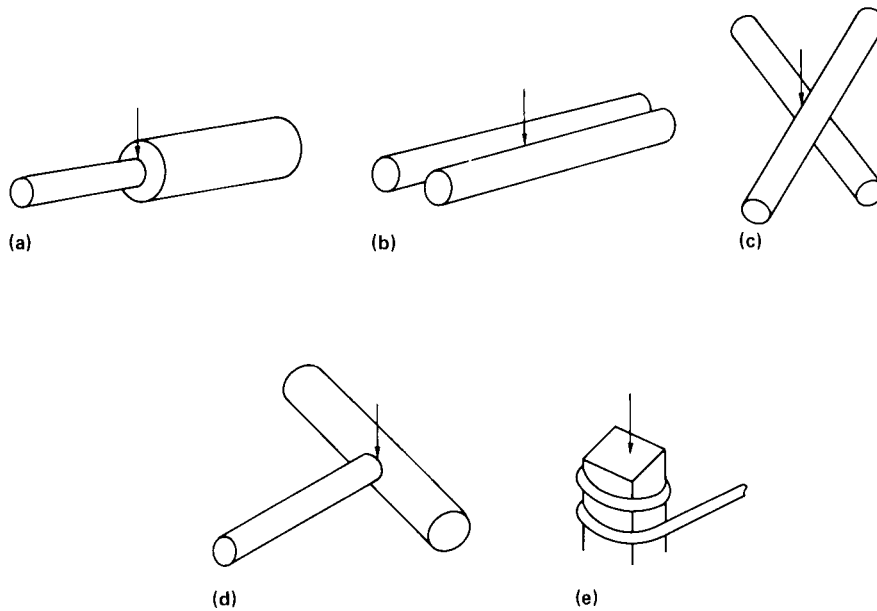


Fig. 2 Joint designs for laser beam welds on wire. Arrows show direction of laser beam. (a) Butt weld. (b) Round-to-round lap weld. (c) Cross-joint weld. (d) Spot weld for T-joint. (e) Terminal or lug weld

ferrous alloys that have been studied for the applicability of laser welding include X-80 Arctic pipeline steel (Ref 32), tanker construction steels (Ref 33), D-6ac low-alloy, ultrahigh-strength steel (Ref 34), and high-strength, low-alloy grade steels (Ref 34).

One of the earliest applications of LBW was for the welding of planetary gear assemblies for the automotive industry. Welding was carried out at 10 m/min (400 in./min) using a 5 kW laser. Subsequently, LBW was applied to produce automobile powertrain components. A most recent mass production application is in the production of the “body-in-white” tailored blank shown in Fig. 4. An LBW process developed by Fraunhofer Institute at Aachen that uses a polarized beam was applied by Krupp's Steel to produce steel pipe (Ref 35).

Titanium and Titanium Alloys. Until recently, the electron beam welding (EBW) technique has been the most popular method used to weld Ti-6Al-4V, which is the most widely used titanium material in the aerospace industry due to its remarkable strength-to-weight ratio. However, the deep penetration of EBW can be obtained only up to a short distance under nonvacuum conditions. For optimum efficiency, EBW must be carried out in an evacuated chamber (Ref 3). In contrast, CO₂ laser beams can be transmitted for appreciable distances through the atmosphere without serious attenuation or optical degradation. Even pulsed neodymium: yttrium-aluminum-garnet lasers (Fig. 5) can provide considerable penetration (Ref 37).

The application of the laser technique to a metal such as a titanium alloy, which is normally difficult to weld, is not only of direct interest to the aerospace and chemical

industries but also is of interest to those who need to weld chemically sensitive metals with complex temperature-dependent structures. The need for better joining methods for titanium and its alloys resulted in several investigations of LBW techniques over various power ranges (maximum 16 kW). A detailed review is available in Ref 12 and 38. Welding speeds in excess of 15 m/min (49 ft/min) were used to weld 1 mm (0.04 in.) thick Ti-6Al-4V with a 4.7 kW CO₂ laser, and materials up to 12.5 mm (0.492 in.) thick were joined using an 11 kW CO₂ laser.

Laser Beam Weld Quality

The American Welding Society has identified six weld process classes, which are defined according to their mechanisms (pressure, temperature, thermal energy delivery method) of achieving materials fusion/joining. These are:

- Gas welding
- Arc welding
- Resistance welding
- Solid-state welding
- Thermochemical welding
- Radiant energy welding (EBW, LBW)

In the radiant energy class, the continued increase of capabilities from such new laser technologies as the ytterbium:disc and ytterbium: fiber have made new welding process regimes possible due to the increase in:

- Output power
- Beam quality
- Electrical-optical conversion efficiency

Reduced cost of ownership, increased lifespan of the power supply, and corresponding reduced consumable and maintenance needs of these and other solid-state lasing technologies are bringing these new industrial laser power sources into more facilities and enabling greater production capacity and capabilities. Industrial lasers are opening new opportunities in manufacturing and are competing with and, in certain cases, replacing some established high-radiant welding power sources, such as the electron beam.

Given the high-energy beam delivery of both the electron beam and the laser to achieve the weld process, some weld quality specifications address both processes. Note that the actual equipment setup and associated health and safety concerns (regulations, codes, and consensus standards) will be different between these two processes, although the characteristics of the weld achieved can be very similar by virtue of the high-radiant-energy beam delivery to achieve the fusion joining process.

This section provides a definition of laser weld quality, surveys prominent laser weld quality specifications available to various industries, and discusses how quality is an important metric by which a company understands how its operations contribute to providing repeatable and reliable laser welds that meet the target value in performance and profitability.

Weld Quality Defined

In a broad sense, weld quality is defined as those measurable characteristics and features of the weld that allow the weldment to have the inherent integrity, functional performance, and, where necessary, appearance over the lifespan of the weldment.

With regard to the quality characteristics of the laser and electron beam weld, terms and definitions are important for determining process-tolerant parameters, for example, relating weld testing performance to weld parameters and procedures development.

For quality control of the weld process, in general, there are weld procedure specifications and weld quality specifications. These are derived by either referencing industry standard specifications or through an internal weld process and quality specification program, such as through proof-of-process work and design of experiments.

Weld quality characteristics can be categorized as geometrical, mechanical, or metallurgical. Quality characteristics include but are not necessarily limited to:

- *Geometrical:* Size and shape of the weld cross-sectional area, undercut, mismatch, concavity, convexity, continuity

Table 1 Joint design and considerations for use

Joint type	Applicability	Considerations for use	Design
Bull	Very commonly used in ferrous, other alloys having medium to high viscosity when molten	<ul style="list-style-type: none"> • Maximum allowable gap = $0.05 \times$ thickness • Beam/seam alignment requirement approx. $0.5 \times$ focus spot diameter • Joint strength dependent on degree of penetration and weld-metal strength 	
Bolt with backing	Commonly used with aluminum-bronze alloys and others with low viscosity when molten	<ul style="list-style-type: none"> • Consumable backings of same composition as base material most common • Root porosity found in partial-penetration laser welds may be removed by machining backing strip in some applications • Ceramic and nonconsumable (e.g., copper backings not usually applicable) 	
Lap welding	Commonly used in all materials	<ul style="list-style-type: none"> • Maximum allowable gap – $0.05 \times$ thickness of thinner member • Tolerant of beam/seam misalignment • Thin-on-top/thick-on-bottom joints easily accommodated • Thick-on-top/thin-on-bottom joints less desirable • Joint strength determined by weld-metal strength, weld width (multiple passes can increase joint strength) 	
Stake weld	Can produce 'blind welds' that are difficult or expensive to accomplish using arc processes	<ul style="list-style-type: none"> • Laser beam/web plate alignment tolerance dependent on web thickness, beam diameter • Maximum gap = $0.05 \times$ flange thickness • Joint strength determined by weld-metal strength and weld width (multiple passes can increase joint strength) 	
Edge weld	Usually applied in thinner gages where the laser weld bead consumes all or most of the thickness of both members	<ul style="list-style-type: none"> • Wide range of included angles possible with appropriate forming of edges (as illustrated) • Maximum gap = $0.05 \times$ thickness of thinner member • Joint strength dependent on degree of penetration and weld-metal strength • Determination of metal an important design strength consideration 	
"Skid" fillet weld	Full penetration possible with sufficient power	<ul style="list-style-type: none"> • Small beam centerline/flange angle (approx. 10° or less) • Maximum gap = $0.05 \times$ thickness of web plate • Beam/seam alignment approx. $0.5 \times$ focus spot diameter • Joint strength dependent on degree of penetration and weld-metal strength 	
Corner weld	Full penetration possible with sufficient power	<ul style="list-style-type: none"> • Beam/seam alignment (approx. $0.5 \times$ focus spot diameter) • Joint strength dependent on degree of penetration and weld-metal strength • Maximum gap = $0.05 \times$ thickness of web plate 	

- *Metallurgical:* Porosity, pinholes, cracks/cracking, heat-affected zone, penetration, slag
- *Mechanical:* Ultimate tensile and yield strengths, fatigue limits, elongation, cupping test (e.g., ball punch deformation); ASTM E 643

For process control, consideration should be given to documenting and establishing respective nominal values and bound values for the controllable aspects of the process, some of which are:

- *Laser:* Total power, focus optic arrangement (determining power density, spot size and caustic waist profile, depth of focus, angle of beam divergence), beam mode and quality, polarization, focal position with respect to workpiece

- *Process parameters:* Weld speed, sequencing of power for start and close of weld bead, shield gas selection and delivery (style, flow rate, volume)
- *Workpiece/tooling:* Weld joint presentation allowables (material mismatch, gap tolerances, focal position alignment tolerance with respect to weld seam)
- *Material properties:* Material thickness, material specifications (type), material surface conditions (e.g., oily, dry, scale, etc.)
- *Tooling:* Repeatability and reliability for presentation of the workpiece and the weld seam to the laser focus optics

When documenting and defining the weld procedures and qualification requirements within a facility or for a specific program/project, it is important to reference and define those terms employed.

Additional information can be found in Ref 39 to 42.

Weld Quality Assessment

The profile for the laser weld seam (cross-sectional geometry) can vary depending on the process parameters, optical configuration, and whether it is autogenous or augmented with metal inert gas, metal active gas, tungsten inert gas, plasma, other thermal power supplies, or filler wire.

Two elemental modes of LBW are conduction-limited and penetration (keyhole) welding. In the application of conduction-limited welding, as the name implies, the irradiance of the laser beam is sufficient to achieve melting of the base metal via absorption, but conduction of the thermal

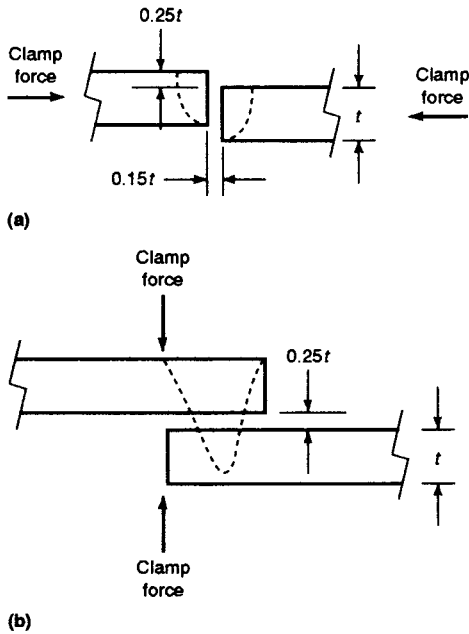


Fig. 3 Clamping and tolerances for (a) butt joint and (b) lap joint. Dimensions are in units of percent of material thickness, t . Source: Ref 3

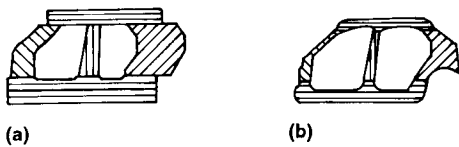


Fig. 4 Sequence of operations required to produce "body-in-white" tailored blank automotive bodies using laser beam welding. (a) Arrangement and welding of divided-type body panels before forming. (b) Tailored blank obtained after structural components have been formed in a press. Source: Ref 36

energy determines the melt pool shape (weld bead). As the laser beam irradiance increases and exceeds the capacity of the base metal to dissipate (conduct) the thermal energy, the temperature of the impinging material is elevated to its boiling point, where the material is vaporized. This process is dynamic, and the absorption level of the laser beam irradiance on the material increases as well as the metal vapor depth (Fig. 6a). The weld bead geometry of laser keyhole (penetration) welding is readily identified by the high aspect (depth/width) ratio of the weld seam (Fig. 6b).

Figure 7 illustrates changes of an autogenous laser weld profile, progressing from conduction-limited (left side of graph) to penetration (keyhole) welding (right side of graph). The transition from conduction to keyhole will occur at significantly different power densities, depending on materials and somewhat on shield gas type.

Table 2 Parameters for high-power laser beam welding relative to alloy type for bead-on-plate joints

Material	Type of joint	Thickness		Laser power, kW
		mm	in.	
Ship steel, grades A, B, C	Butt	28.6	1.125	12.8
	Butt	25.4	1.0	12.0
	Butt	19.0	0.75	12.0
	Butt	15.9	0.625	12.0
	Butt	12.7	0.50	12.0
	Butt	9.5	0.375	10.8
Low-alloy carbon steel	Tee	9.5–12.7	0.375–0.5	11.9
	Tee	9.5–12.7	0.375–0.5	7.5
AISI 1010	Beam plate	4	0.157	1.8(a)
	Butt	15.2	0.60	14
AISI 4130	Butt	19.0	0.75	14
Low-alloy high-strength steel, 300M	Butt	13.2	0.52	12
Arctic pipeline steel, X-80	Butt	6.4	0.25	15
D-6ac steel	...	12.5	0.49	10.6
HY-80	Butt	6.4	0.25	5.5
HY-130 steel	Butt	1.6	0.062	5.5
HY-180 steel (HP9-4-20)	...	1.6	0.062	10.5
...	...	16.3	0.64	5.5
Nickel-base alloy, Inconel 718	Butt	14.5	0.57	14
Stainless steel	...	6	0.24	17
AISI type 304	...	12.5	0.49	17
	...	17	0.67	17
...	...	16.5	0.65	17
...	...	3.8	0.15	11.5
...	...	5.6	0.22	11.5(b) 1.8(c)
...	...	8.9	0.35	8
...	...	20.3	0.8	20
...	...	12.7	0.5	20
...	...	50.8	2.0	77
AISI type 321	Butt	14.5	0.57	14
Aluminum alloy:	...	3.2, 6.4	0.125, 0.25	5.5
2219	Butt	6.4	0.25	5
2219	Butt	6.4	0.25	16
2219	Butt	6.4	0.25	7
5083	Butt	6.4	0.25	5.5
5456	Butt	3.2	0.125	8
5456	Butt	12.5	0.187	8
5456	Butt	12.5	0.49	...
Titanium alloy, Ti-6Al-4V	Butt	15.2	0.60	13.5
...	...	3	0.12	4.7
...	...	12.5	0.49	11

(a) Neodymium: yttrium-aluminum-garnet (Nd:YAG) laser. (b) CO₂ laser. (c) Continuous-wave Nd:YAG laser. Source: Ref 3, 12

The dimensions of the laser weld bead (cross section) are important components of weld quality specification. Dimensional features can include but are not necessarily limited to:

- Cross-sectional area
- Penetration depth
- Upper seam weld width
- Lower seam weld width

It is important that the weld quality specifications of an application identify appropriate nominal dimensional information of the laser weld profile. Figure 8 shows the difference in cross section between a conduction-limited laser weld and a penetration (keyhole) weld. Figure 9 shows how the dimensional shape of laser weld geometry can be quantified.

Because laser welding is a fusion process, the evaluation of weld quality is similar to other allied processes. Table 3 and Fig. 10 and 11 illustrate the common types of discontinuities

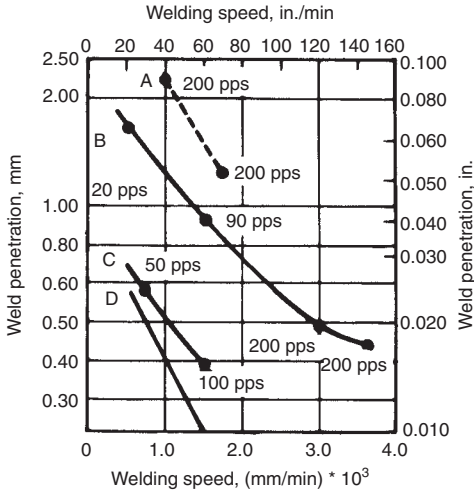
that are assessed for weld quality of an application.

Table 4 (Ref 45) identifies and compares discontinuities commonly (but not always) associated with various welding processes. The relative high power density applied for the fusion process of both electron beam and laser beam welding leads to them have similar weld defects, namely:

- Porosity
- Incomplete fusion
- Incomplete joint penetration
- Cracks

Standards and Specifications

There are a number of domestic and international organizations that develop codes, standards, and specifications for welding and allied processes as well as provide laser welding quality specifications and procedure



Curve	Welding mode	Average output, W	
		Pulsed	Continuous wave
A	Penetration	400	...
B	Conduction	400	...
C	Conduction	150	...
D	Conduction	...	400

Fig. 5 Plot of weld penetration versus welding speed of operation and average output for neodymium: yttrium-aluminum-garnet lasers at a wavelength of 1.06 μm. Source: Ref 37

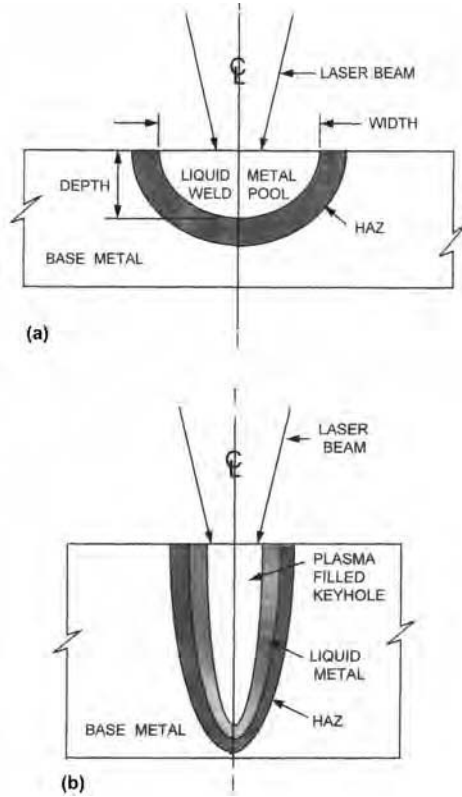


Fig. 6 Schematic diagrams of (a) conduction-limited and (b) penetration (keyhole) laser weld processes. HAZ, heat-affected zone. Source: Ref 43

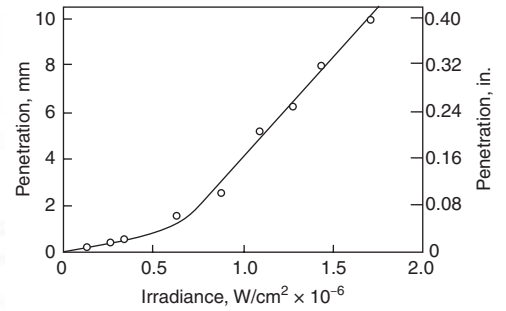


Fig. 7 Effect of irradiance on welding response. Source: Ref 43

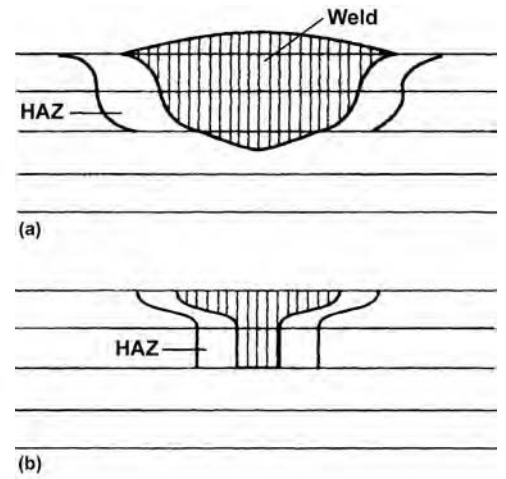


Fig. 8 Typical shapes of (a) conduction-limited and (b) penetration (keyhole) laser weld beads. HAZ, heat-affected zone. Source: Ref 43

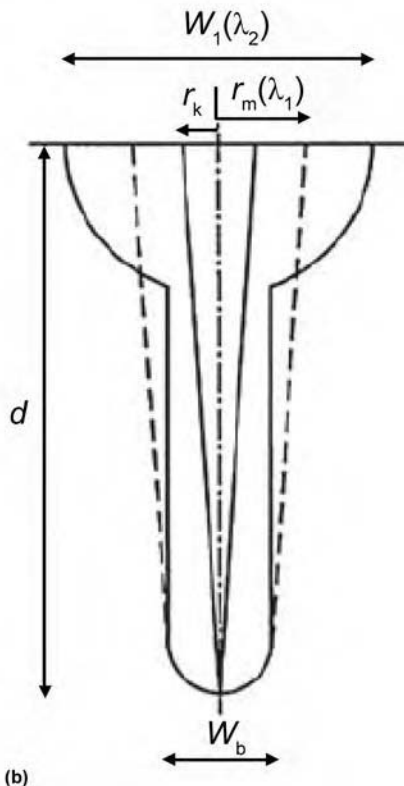


Fig. 9 (a) Actual cross section of a penetration (keyhole) laser weld. (b) Corresponding simplified geometry for calculating various weld dimensions. Source: Ref 44

documents. Several of the most active organizations and the standard or specification documents they have established are listed in Table 5. The organizations include:

- American Welding Society (AWS), www.aws.org
- American National Standards Institute (ANSI), www.ansi.org
- International Organization for Standardization (ISO), www.iso.org
- European Committee for Standardization (CEN), www.cen.eu
- SAE International (SAE), www.sae.org

REFERENCES

1. J.R. Shewell, *Weld Des. Fabr.*, June 1977, p 106
2. S.L. Engel, *Weld Des. Fabr.*, Jan 1978, p 62
3. M.M. Schwartz, *Metallurgical Joining Manual*, McGraw-Hill, 1979
4. J. Mazumder and W.M. Steen, *Met. Constr.*, Vol 12 (No. 9), 1980, p 423

Table 3 Common types of discontinuities

Type of discontinuity	Location (a)	Remarks
1 Porosity	WM	Porosity could also be found in the base metal and heat-affected zone (HAZ) if the base metal is a casting.
(a) Uniformly scattered
(b) Cluster
(c) Piping
(d) Aligned
(e) Elongated
2 Inclusion	WM, WI	...
(a) Slag
(b) Tungsten
3 Incomplete fusion	WM, WI	Weld metal between passes
4 Incomplete joint penetration	BM	Weld root
5 Undercut	WI	Adjacent to weld toe or weld root in base metal
6 Underfill	WM	Weld face or root surface of a groove weld
7 Overlap	WI	Weld toe or root surface
8 Lamination	BM	Base metal, generally near midthickness of section
9 Delamination	BM	Base metal, generally near midthickness of section
10 Seam and lap	...	Base-metal surface, generally aligned with rolling direction
11 Lamellar tear	BM	Base metal, near HAZ
12 Crack (includes hot cracks and cold cracks described in text)
(a) Longitudinal	WM, HAZ, BM	Weld metal or base metal adjacent to weld interface
(b) Transverse	WM, HAZ, BM	Weld metal (may propagate into HAZ and base metal)
(c) Crater	WM	Weld metal at point where arc is terminated
(d) Throat	WM	Parallel to weld axis. Through the throat of the fillet weld
(e) Toe	WI, HAZ	...
(f) Root	WI, HAZ	Root surface or weld root
(g) Underbead and HAZ	HAZ	...
13 Concavity	WM	Weld face or fillet weld
14 Convexity	WM	Weld face of a fillet weld
15 Weld reinforcement	WM	Weld face of a groove weld

(a) WM, weld-metal zone; BM, base-metal zone; HAZ, heat-affected zone; WI, weld interface. Source: Ref 45

5. J. Mazumder, "Laser Welding of Titanium and Tinplate," Ph.D. thesis, London University, 1978
6. T. Webber, Laser Welding: Efficient Weld Width Generation, *Proceedings of the Laser Institute of America's ICALEO '93 Conference*, Oct 24-28, 1993 (Orlando, FL), p 738-745
7. J.C.M. Caristan, Improved Laser Lap Welding of Galvanized Steel, *International Body Engineering Conference (IBEC), Body Assembly and Manufacturing Proceedings*, Sept 1997 (Stuttgart, Germany), p 88-93
8. M.S. Baranov, B.A. Vershok, I.N. Geinrikhs, and V.I. Privezenstev, *Weld. Prod.*, Vol 23 (No. 5), 1976, p 19
9. G. Sepold, R. Rothe, and K. Teske, *LAMP '87*, Y. Arata, Ed., Japan High Temperature Society, 1987, p 151-156
10. T. Webber, High Power CW Nd:YAG Laser Welding of High Carbon Steel with Pre- and Post-Weld Heat Treatment, *Proceedings of Fifth CISFFEL Conference*, June 1993 (La Baule, France), p 227-234
11. C.O. Brown and C.M. Banas, "Deep Penetration Laser Welding," AWS Annual Meeting, April 1971 (San Francisco)
12. J. Mazumder, Laser Welding, *Laser Materials Processing*, M. Bass, Ed., North Holland, Amsterdam, 1983, p 113-200
13. L. Rapp, C. Glumann, F. Dousinger, and H. Hügel, *Laser Treatment of Materials*, B.L. Mordike, Ed., DGM Informationsgesellschaft mbh, Germany, 1992, p 99-104
14. A.S. Brandson and T. Enders, *Laser Treatment of Materials*, B.L. Mordike, Ed., DGM Informationsgesellschaft mbh, Germany, 1992, p 117-124
15. H. Sakamoto, K. Shibata, and F. Dausinger, *Laser Treatment of Materials*, B.L. Mordike, Ed., DGM Informationsgesellschaft mbh, Germany, 1992, p 125-130
16. J. Berkman, S.K. Behler, and E. Beyer, *Laser Treatment of Materials*, B.L. Mordike, Ed., DGM Informationsgesellschaft mbh, Germany, 1992, p 151-156
17. A. Lang and H.W. Bergman, *Laser Treatment of Materials*, B.L. Mordike, Ed., DGM Informationsgesellschaft mbh, Germany, 1992, p 163-170
18. L.C. Mallory, R.F. Orr, and W. Wells, *Laser Materials Processing III*, J. Mazumder and K. Mukherjee, Ed., Minerals, Metals and Materials Society, 1989, p 123-134
19. R.C. Crafer, *Weld. Inst. Res. Bull.*, April 1976, p 17
20. E.A. Metzbowler and D.W. Moon, Mechanical Properties, Fracture Toughness, and Microstructures of Laser Welds of High Strength Alloys, *Proc. Conf. on Applications of Lasers in Materials Processing*, April 18-20, 1979 (Washington, D.C.)
21. D.B. Snow and E.M. Breinan, "Evaluation of Basic Welding Capabilities," United Technologies Research Center, July 1978

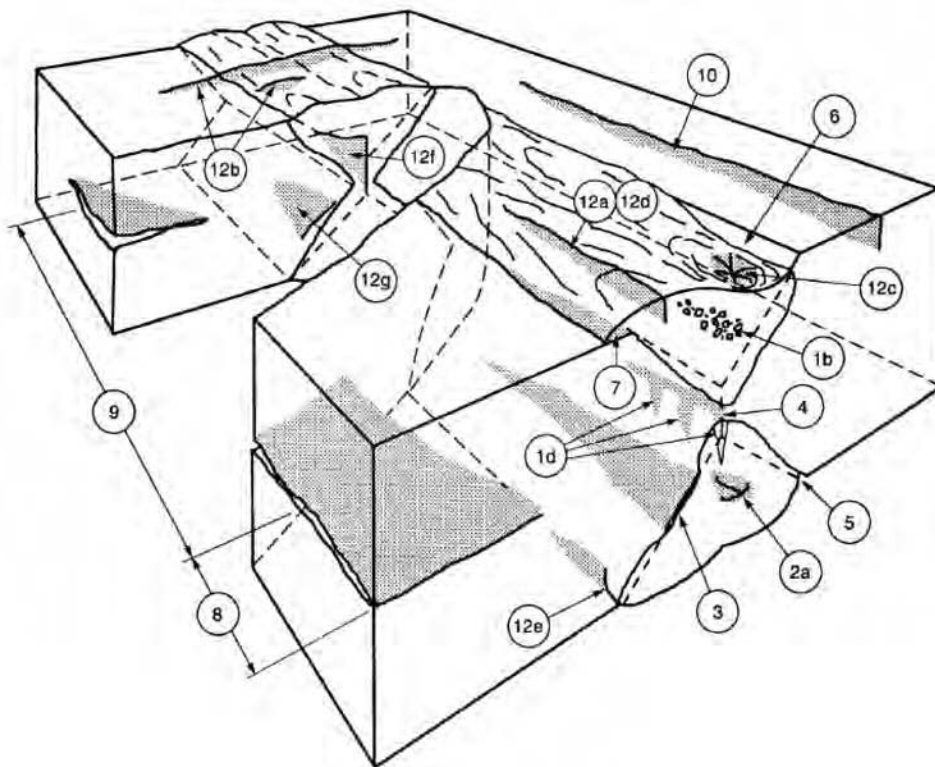


Fig. 10 Double V-groove weld in butt joint illustrating weld discontinuities. Numbers in circles refer to Table 3. Source: Ref 45

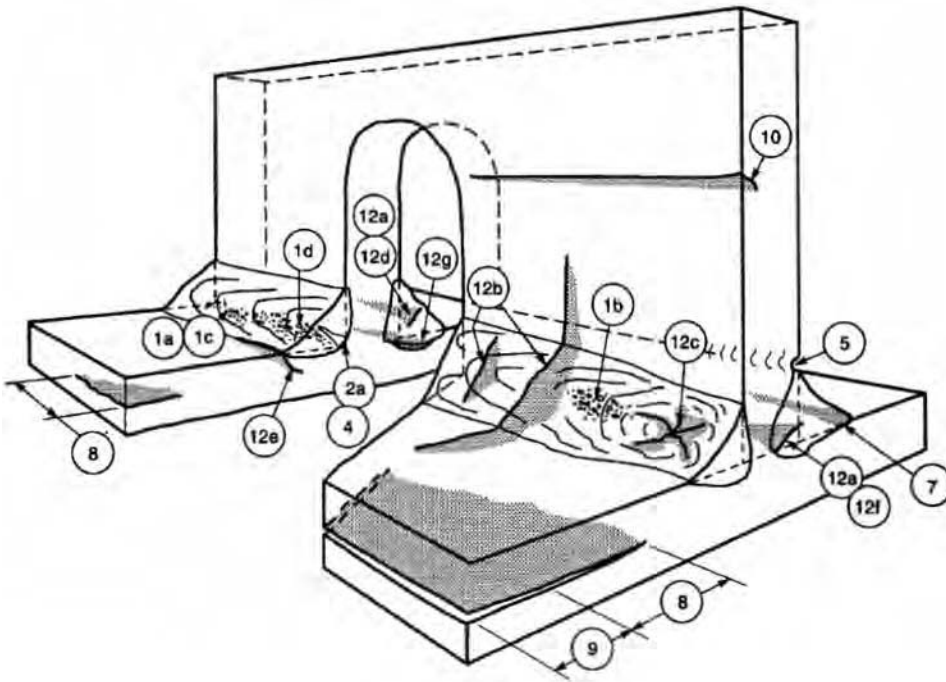


Fig. 11 Single-pass double-fillet weld in T-joint illustrating weld discontinuities. Numbers in circles refer to Table 3. Source: Ref 45

22. E.M. Breinan, C.M. Banas, and M.A. Greenfield, Laser Welding—The Present State of the Art, DOC IV-181-75, 11th Annual Meeting of the Welding Institute, July 6–12, 1975 (Tel Aviv), p 1–53
23. A. Blake and J. Mazumder, *ASME J. Eng. Ind.*, Vol 107 (No. 3), Aug 1985, p 275–280
24. D.W. Moon and E. Metzbower, *Weld. J.*, 1983, p 535–585
25. E.V. Locke and R.A. Hella, *IEEE J. Quant. Electron.*, Vol QE-10 (No. 2), Feb 1974, p 179–185
26. R.C. Crafer, Advances in Welding Processes, Paper 46, *Proc. Fourth Int. Conf.*, May 9–11, 1978 (Harrogate, Yorks, England), p 267–278
27. R.A. Wilgoss, J.H.P.C. Megaw, and J.N. Clark, *Weld. Met. Fab.*, March 1979, p 117–126
28. E.L. Baardsen, D.J. Schmatz, and R.E. Bisaro, *Weld. J.*, Vol 52, April 1973, p 227–229
29. J. Mazumder and W.M. Steen, Laser Welding of Steels Used in Car Making, *Weld. J.*, Vol 60 (No. 6), June 1981, p 19–25
30. C.M. Banas, “Laser Welding Developments,” *Proc. CEGB Int. Conf. on Welding*

Table 4 Discontinuities commonly encountered with welding processes

Welding process	Porosity	Slag	Incomplete fusion	Incomplete joint penetration	Undercut	Overlap	Cracks
Arc							
Stud welding (SW)	X	...	X	...	X	...	X
Plasma arc welding (PAW)	X	...	X	X	X	...	X
Submerged arc welding (SAW)	X	X	X	X	X	X	X
Gas arc tungsten welding (GTAW)	X	...	X	X	X	...	X
Electrode gas welding (EGW)	X	...	X	X	X	X	X
Gas metal arc welding (GMAW)	X	...	X	X	X	X	X
Flux cored arc welding (FCAW)	X	X	X	X	X	X	X
Shielded metal arc welding (SMAW)	X	X	X	X	X	X	X
Carbon arc welding (CAW)	X	X	X	X	X	X	X
Resistance							
Resistance spot welding (RSW)	X(a)	...	X	X	X
Resistance seam welding (RSEW)	X(a)	...	X	X	X
Projection welding (PW)	X	X	X
Flash welding (FW)	X	X	X
Upset welding (UW)	X	X	X
Oxyfuel gas							
Oxyacetylene welding (OAW)	X	...	X	X	X	X	X
Oxyhydrogen welding (OHW)	X	...	X	X	X
Pressure gas welding (PGW)	X	...	X	X
Solid state(b)							
Cold welding (CW)	X	X
Diffusion welding (DFW)	X	X
Explosion welding (EXW)	X
Forge welding (FOW)	X
Friction welding (FRW)	X
Ultrasonic welding (USW)	X
Other							
Electron beam welding (EBW)	X	...	X	X	X
Electroslag welding (ESW)	X	X	X	X	X	X	X
Induction welding (IW)	X	X
Laser beam welding (LBW)	X	...	X	X	X
Percussion welding (PEW)	X	X
Thermite welding (TW)	X	X	X	X

(a) Porosity in resistance welds is more properly called voids. (b) Solid state is not a fusion process, so incomplete joining is incomplete welding rather than incomplete fusion. Source: Ref 45

578 / High Energy Electron Beam and Laser Beam Welding

Table 5 Standards and specifications

Standard or specification	Remarks
American Welding Society (AWS), www.aws.org	
AWS A3.0M/A3.0:2010 Standard Welding Terms and Definitions; Including Terms for Adhesive Bonding, Brazing, Soldering, Thermal Cutting, and Thermal Spraying	This AWS standard is a glossary of the technical terms used in the welding industry. It establishes standard terms to aid in the communication of welding information. Because it is intended to be a comprehensive compilation of welding terminology, nonstandard terms used in the welding industry are also included. Alphabetical sequence
AWS C7.2:2010 Recommended Practices for Laser Beam Welding, Cutting, and Drilling	This document presents recommended practices for laser beam welding, cutting, and drilling. Its scope is limited to common applications of the subject processes. Process definitions, safe practices, general process requirements, and inspection criteria are provided.
AWS C7.4/C7.4M:2008 Process Specification and Operator Qualification for Laser Beam Welding	This specification on laser beam welding discusses applicable specifications, safety, requirements, fabrication, quality examination, equipment calibration and maintenance, approval of work, and delivery of work.
AWS B2.1/B2.1M: 2009 Specification for Welding Procedure and Performance Qualification	This specification provides the requirements for qualification of welding procedure specifications, welders, and welding operators for manual, semiautomatic, mechanized, and automatic welding. The welding processes included are electrogas welding, electron beam welding, electroslag welding, flux cored arc welding, gas metal arc welding, gas tungsten arc welding, laser beam welding, oxyfuel gas welding, plasma arc welding, shielded metal arc welding, stud arc welding, and submerged arc welding. Base metals, filler metals, qualification variables, welding designs, and testing requirements are also included.
AWS WHC3.14 Laser Beam Welding, Cutting and Associated Processes	Chapter 14 from <i>Welding Processes, Part 2</i> , Vol 3, <i>Welding Handbook</i> , 9th ed. has been selected by the AWS Product Development Committee. This chapter covers fundamentals of laser beam welding and cutting processes, modes of operation, and equipment. Other topics include laser beam welding operating systems, applications, joint design and preparation, weld quality, and the economics of using these processes. Similar information is presented for laser beam cutting, drilling, and related processes. The chapter concludes with a discussion on safety issues specific to laser beam operations and the safety codes that must be followed to provide the best working environment where lasers are in use.
Note: Subcommittee D8E Automotive Laser Welding	The D8 AWS/SAE Joint Committee on Automotive Welding is responsible for the development of AWS standards on all aspects of welding in the automotive industry. Laser weld quality specifications are currently in development by subcommittee D8E.
American National Standards Institute (ANSI), www.ansi.org	
ANSI Z136.1-2007 American National Standard for Safe Use of Lasers	The parent document and cornerstone of the Z136 series of laser safety documents, this standard provides recommendations for the safe use of lasers and laser systems that operate at wavelengths between 180 nm and 1 mm.
ANSI B11.21-2006 American National Standard for Machine Tools. Machine Tools Using Lasers for Processing Materials. Safety Requirements for Design, Construction, Care, and Use	This standard is part of the ANSI B11 series and pertains to the safety requirements for lasers used in machine tool applications as described in this document. It is limited to the requirements of safeguarding of personnel, installation, verification, operation, maintenance, training, and documentation for individual machines.
International Organization for Standardization (ISO), www.iso.org	
ISO 6520-1:2007 Welding and Allied Processes. Classification of Geometric Imperfections in Metallic Materials, Part 1: Fusion Welding	Serves as the basis for a precise classification and description of weld imperfections
ISO/TS 17845:2004 Welding and Allied Processes. Designation System for Imperfections	Gives a system for the designation of imperfections in welding and allied processes. It applies to metallic and nonmetallic materials (e.g., thermoplastics).
ISO 13919-1:1996 Welding. Electron and Laser Beam Welded Joints. Guidance on Quality Levels for Imperfections, Part 1: Steel	Gives guidance on quality levels of imperfections in electron and laser beam welded joints in steel. Three levels are given that refer to production quality.
ISO 13919-2:2001 Welding. Electron and Laser Beam Welded Joints. Guidance on Quality Levels for Imperfections, Part 2: Aluminum and Its Weldable Alloys	Gives guidance on quality levels of imperfections in electron and laser beam welded joints in aluminum and its weldable alloys. Three levels are given that refer to production quality.
ISO/TR 17671-6:2005 Welding. Recommendations for Welding of Metallic Materials, Part 6: Laser Beam Welding	Gives general guidance for laser beam welding of metallic materials in all forms (e.g., cast, wrought, extruded, forged) and associated processes
ISO 9956-11:1996 Specification and Approval of Welding Procedures for Metallic Materials, Part 11: Welding Procedure Specification for Laser Beam Welding	Revised by ISO 15609-4:2004
ISO 15609-4:2004 Specification and Qualification of Welding Procedures for Metallic Materials. Welding Procedure Specification, Part 4: Laser Beam Welding	Specifies requirements for the content of the welding procedure specification for laser beam welding processes, including overlay welding. It is not applicable to other processes for cladding (e.g., thermal spraying).
ISO 15614-11:2002 Specification and Qualification of Welding Procedures for Metallic Materials. Welding Procedure Test, Part 11: Electron and Laser Beam Welding	Specifies how a welding procedure specification for electron or laser beam welding is qualified by a welding procedure test
ISO 15616-1:2003 Acceptance Tests for CO ₂ Laser Beam Machines for High-Quality Welding and Cutting, Part 1: General Principles, Acceptance Conditions	...
ISO 15616-2:2003 Acceptance Tests for CO ₂ Laser Beam Machines for High-Quality Welding and Cutting, Part 2: Measurement of Static and Dynamic Accuracy	...
ISO 15616-3:2003 Acceptance Tests for CO ₂ Laser Beam Machines for High-Quality Welding and Cutting, Part 3: Calibration of Instruments for Measurement of Gas Flow and Pressure	...
ISO 22827-1:2005 Acceptance Tests for Nd:YAG Laser Beam Welding Machines. Machines with Optical Fiber Delivery, Part 1: Laser Assembly	Editor's note: This should also be applicable for other near-infrared laser power sources, such as the ytterbium:fiber and ytterbium:disc.
ISO 22827-2:2005 Acceptance Tests for Nd:YAG Laser Beam Welding Machines. Machines with Optical Fiber Delivery, Part 2: Moving Mechanism	Editor's note: This should also be applicable for other near-infrared laser power sources, such as the ytterbium:fiber and ytterbium:disc.
European Committee for Standardization (CEN), www.cen.eu	
EN 1011-6:2005 Welding. Recommendations for Welding of Metallic Materials. Laser Beam Welding	This European Standard gives general guidance for laser beam welding and associated processes of metallic materials in all forms of product (e.g., cast, wrought, extruded, forged).
EN 1011-6:2004 Welding. Recommendations for Welding of Metallic Materials. Electron Beam Welding	This document may be used for the electron beam welding of weldable metallic materials according to PD CR ISO 15608. It does not contain data on permissible stresses on weld seams or on the testing and evaluation of weld seams. Such data can either be seen from the relevant application standards or should be separately agreed between the contracting parties. A requirement for the application of this document is that the recommendations should be used by appropriately trained and experienced personnel.
SAE International (SAE), www.sae.org	
SAE AS7110/6D:2007 Nadcap Requirements for Laser Welding. This Aerospace Standard (AS) is to be used to supplement AS7110. In addition to the requirements contained in AS7110, the requirements contained herein shall apply to suppliers seeking Nadcap accreditation for laser welding.	SAE AS7110/6D:2007 revision work has been cancelled as of March 2010. The prior version, SAE AS7110/6C:2003, is available. Reference the SAE website for additional information.

- Res. Related to Power Plants, Sept 17–21, 1972 (Southampton, England)
31. F.D. Seaman and R.A. Hella, "Establishment of a Continuous Wave Laser Welding Process," IR-809-3 (1-10), report in Conference Proceedings AFML Contract F336 15-73-C5004, Oct 1976
 32. E.M. Breinan and C.M. Banas, Preliminary Evaluation of Laser Welding of X-80 Arctic Pipeline Steel, *WRC Bull.*, Dec 1971, p 201
 33. C.M. Banas and G.T. Peters, "Study of the Feasibility of Laser Welding in Merchant Ship Construction," Contract No. 2-36214, U.S. Dept. of Commerce, Final Report to Bethlehem Steel Corp., Aug 1974
 34. M. Yessik and D.J. Schmatz, "Laser Processing in the Automotive Industry," Paper MR74-962, SME, 1974
 35. E. Beyer, Fraunhofer Institute, Aachen, Germany, private communication, 1992
 36. F.A. DiPietro, Robotic Laser Welding Systems in the Automotive Industry, *Proceedings of Laser Systems Applications in Industry*, ATA (Torino, Italy), 1990, p 103–119
 37. H.L. Marshall, *Proc. SPIE*, Vol 86, 1976
 38. W.M. Steen and J. Mazumder, *Laser Material Processing*, 4th ed., Springer, London, 2010
 39. Weld Quality, Chap. 13, *Welding Science and Technology*, Vol 1, *Welding Handbook*, 9th ed., American Welding Society
 40. "Standard Welding Terms and Definitions, Including Terms for Adhesive Bonding, Brazing, Soldering, Thermal Cutting, and Thermal Spraying," A3.0M/A3.0:2010, American Welding Society
 41. *Jefferson's Welding Encyclopedia*, American Welding Society
 42. "Welding and Allied Processes. Nomenclature of Processes and Reference Numbers," EN ISO 4063, 2010
 43. *LIA Handbook of Laser Materials Processing*, Laser Institute of America, Magnolia Publishing Inc., p 319, 361, 367, 390
 44. C. Lampa, A. Kaplan, J. Powell, and C. Magnusson, An Analytical Thermodynamic Model of Laser Welding, *J. Phys. D: Appl. Phys.*, Vol 30, 1997, p 1293–1299
 45. "Guide for the Nondestructive Examination of Welds," B1.10:1999, American Welding Society, p 3, 4, 7, 12

SELECTED REFERENCES

The following resources, while not comprehensive, are provided as a reference for information regarding the laser weld process

of various materials employing a range of laser power sources, beam delivery, and focus optic arrangements. In identifying the characteristics and behavior of the laser weld process, these documents do touch upon the features and components of laser weld quality and its specification and quantification.

- M. Born and E. Wolf, *Principles of Optics*, Pergamon Press, 1987
- N.B. Dahotre and S.P. Harimkar, *Laser Fabrication and Machining of Materials*, Springer
- W.W. Duley, *Laser Welding*, John Wiley & Sons Inc.
- L. Migliore, Ed., *Laser Materials Processing*, Marcel Dekker, New York and Basel, Switzerland
- F.O. Olsen, *Hybrid Laser Arc Welding*, Technical University of Denmark, Denmark, CRC Press
- J.F. Ready and D.F. Farson, Ed., *LIA Handbook of Laser Materials Processing*, Laser Institute of America, Magnolia Publishing Inc.
- W.M. Steen and J. Mazumder, *Laser Material Processing*, 4th ed., Springer, London, 2010
- O. Svelto, *Principles of Lasers*, Plenum Press, 1982
- J. Verdeyen, *Laser Electronics*, Prentice-Hall, 1989

Laser Beam Delivery Optics and Manufacturing Economics

Tim Webber, IPG Photonics

LASER ENERGY is transmitted from the laser to the workpiece via a system of beam-delivery optics. The optical system can be an open system of mirrors or a fiber optic system. Properly designed beam-delivery optics are essential to the quality of the beam acting on the workpiece and to the economics of the manufacturing process.

Optics for Beam Delivery

The beams of the 1 μm wavelength family of industrial lasers can be directed to the workpiece by means of mirrors, the same way CO_2 laser beams are directed. Their advantage is to use a fiber optic beam delivery. Just a few ionic salts (ZnSe, ZnS, GaAs) have useful transmission properties in the 10.6 μm wavelength of the CO_2 laser for welding. The 1 μm wavelength, however, is transmissive to most materials that appear transparent to the eye, most importantly silica-base glass, SiO_2 . This glass can be drawn into a fiber that can flexibly transport considerable laser power over useful distances. Optical fibers have achieved intrinsic attenuation limits of 0.2 dB/km (Ref 1), which equates to 99.5% transmission over a kilometer. The damage threshold for fused silica has been found to be approximately 400 GW/cm^2 (Ref 2). This would suggest that up to 30 MW can be transmitted by a 100 μm core optical fiber without internal damage. The challenge is to be able to launch a useful amount of laser energy into an optical fiber, because the air-to-glass interface has a significantly lower damage threshold than the bulk material (Ref 3). Minute pits, scratches, and contamination on the fiber face (cross section) can act as sites for absorption of moisture and lead to material failure.

One method to circumvent this surface damage is to bond a fused silica cylinder to the fiber end (Ref 4). The laser light will diverge to a dramatically lower power density as it is emitted from the cylinder compared to the fiber. By applying an antireflection coating to the emission end of the cylinder, reflected losses can be reduced from approximately 4% to less than 1% at each end of the fiber cable. The photograph in Fig. 1 depicts a fiber optic cable connector using this technology.

An optical fiber propagates light down its length through the principle of total internal reflection. The numerical aperture (NA) is the solid angle over which the fiber optic can accept light. A fiber optic input NA will be the same as its output NA, provided that the fiber optic core/clad relationship remains constant. The NA is described by:

$$\text{NA} = ((n_1)^2 - (n_2)^2)^{1/2} \quad (\text{Eq 1})$$

or

$$\text{NA} = \sin \theta = n_1 \sin \theta' \quad (\text{Eq 2})$$

where n_1 is the refractive index of the core, n_2 is the refractive index of the clad, $n_1 \gg n_2$, $\theta' = \theta_c$, and $\theta_c = \cos^{-1} n_2/n_1$ is the critical angle for total internal reflection to occur.

The fused silica clad is doped to alter its refractive index, and the core is pure fused silica. The fiber optic types used by the 1 μm

wavelength family of industrial lasers for welding are shown in Fig. 2. The NA and core diameter of a stepped-index fiber optic cable are engineered to match the optical



Fig. 1 Fiber optic cable connector. Courtesy of IPG Photonics

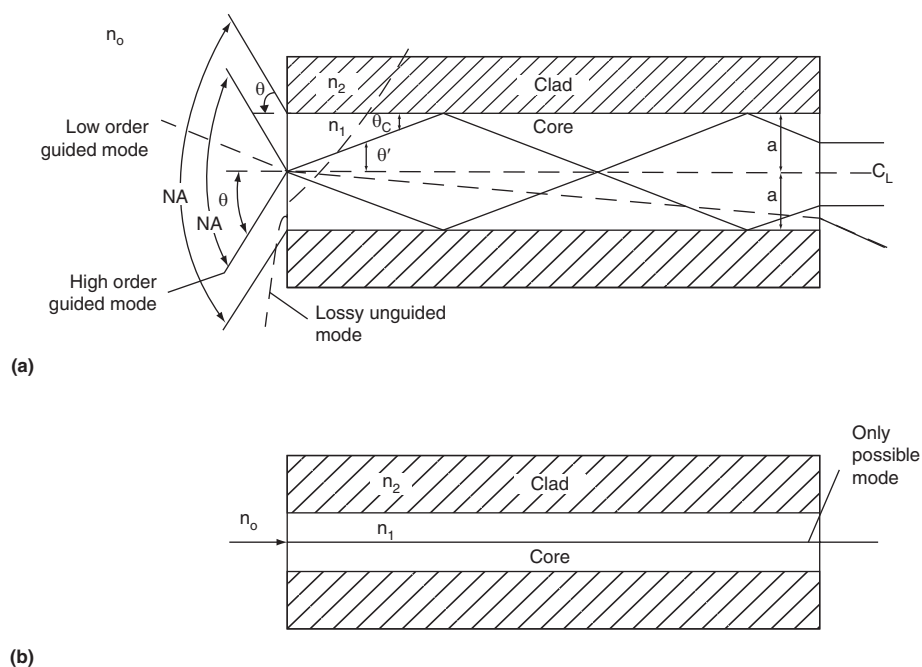


Fig. 2 (a) Multimode stepped-index and (b) single-mode optical fibers. Adapted from Ref 5

characteristics of the laser to which it is connected. There will be a practical lower limit of core diameter into which a laser of a given brightness can be launched successfully and reliably. The single-mode fiber optic is exclusive to the fiber laser.

Each laser provider will supply a family of compatible fiber cables with their product, or recommend a qualified accessory supplier. Fiber cables are specified primarily by their core diameter and length. Lengths of 10, 20, and 30 m (33, 66, and 98 ft) are typical. Stepped-index core diameters of 100, 200, 400, and up to 800 μm are used for welding. Fiber cables outside of these figures are available also but tend to be made to

order for custom specifications. The single-mode fiber and a 50 μm core stepped-index fiber optic are outputs of fiber lasers.

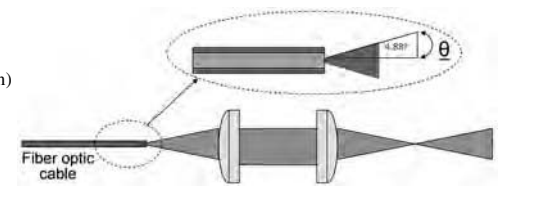
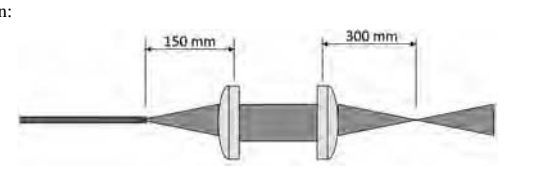
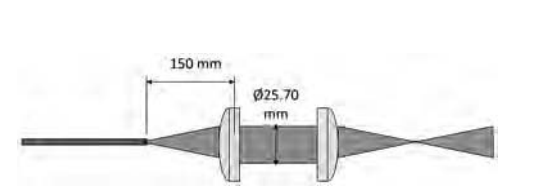
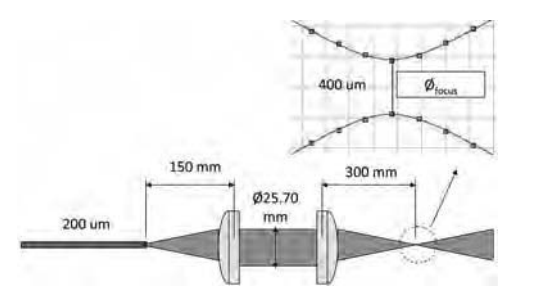
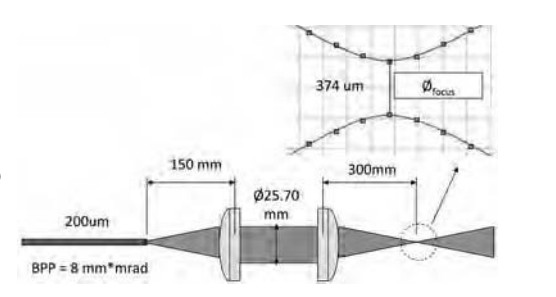
The cable will have a minimum bend radius specification provided by the supplier. This specification protects not only the fiber optic but also the cable protective coatings and armor jacket and prevents overstraining of the fiber cable connector.

The output of a fiber optic cable is imaged onto the work by careful selection of optical elements. These are shown schematically in Table 1 as single-lens elements, although multielement designs are often used. These lens elements can be reflective or transmissive. Collimator focal

lengths of 60, 75, 100, 120, 150, and 200 mm are common. Focus lenses range from 100, 125, 150, 200, 250, to 300 mm. Even longer focal lengths are used in remote welding (Ref 6). The economic availability of these optics provides considerable flexibility to the laser welding engineer to configure an optical solution specific to the task at hand. In contrast, CO₂ laser optics are limited in availability and impose constraints on the welding engineer.

A single-mode fiber laser uses a single-mode fiber to deliver its energy. The core diameter is approximately 10 μm and the NA is typically 0.065. These specifications are taken from the laser under consideration for the job. Using the relationships from Table 1, a fully corrected 60 mm collimator will produce a slightly less than 8 mm diameter beam. If a 120 mm focus lens is used, a 20 μm focus spot will be produced.

Table 1 Selection and configuration of optical elements for delivering laser beam from fiber optic cable to workpiece

Description	Optics configuration
<ul style="list-style-type: none"> • Half-angle numerical aperture (NA) of the emergent laser beam (depending on construction) is 0.084–0.090. • For working example, the emergent laser beam shall be taken as 0.085. • $NA = \sin(\theta) = 0.085$ • $\theta = 4.88^\circ$ 	
<p>Working example used in this document is based on:</p>	
<p>Spot size reproduction on the collimation lens can be determined as:</p>	
<ul style="list-style-type: none"> • $\phi_{spot, coll} = 2 \times f_{col} \times \tan(4.88) + \phi_{fiber}$ • For a 200 μm process fiber: $\phi_{spot, coll} = 2 \times 150 \times 0.085 + 0.200$ $= 25.70 \text{ mm}$ 	
<ul style="list-style-type: none"> • Optical determination of focus spot size: $\phi_{focus} = \phi_{fiber} \times f_{focus} / f_{collimation}$ $= 0.200 \times (300/150)$ $= 0.400 \text{ mm}$ $= 400 \mu\text{m}$ 	
<ul style="list-style-type: none"> • Beam quality determination of focus spot size: $\phi_{focus} = 4 \times f_{focus} \times BPP / \phi_{spot, coll}$ $= 4(300) \times (8/1000) / (25.7)$ $= 0.374 \text{ mm}$ $= 374 \mu\text{m}$ <p>(This compares well with the optical calculation.)</p>	

Design Considerations

The focal length of the collimator is constrained by the clear aperture of the optics used. For welding optics 25, 30, and 50 mm diameters are common specifications seen in product literature. Also, the designer must allow a safety factor. For a single-mode fiber optic, the beam has a Gaussian power density distribution profile. Measurements of the beam diameter to determine the NA are based on the outline that contains approximately 86.5% of the total beam power. See Fig. 3(a) and 4 for the case where $r/w = 1.0$ (r is the displacement off axis, and w is the laser spot size; units must be the same). This is also known as the $1/e^2$ profile. The designer must allow sufficient clear aperture for the power that resides outside the $1/e^2$ diameter of the calculated collimated beam diameter.

The stepped-index fiber optic output profile is sharply delineated (Fig. 3b). Significantly less safety factor is required compared to the single-mode case.

A very compact optical package can be designed where the collimator and focus lens sets are in close proximity. The only consideration regarding placement of the focus lens in relation to the collimator lens is the accuracy of collimation. The focus lens can be a considerable distance from the collimator, in a glove box perhaps, with a window between the respective lens elements to separate the atmospheres. In this case, a well-collimated beam is necessary.

Transmissive versus Reflective Lens Elements

Transmissive lenses absorb a percentage of the laser energy. The edges will be cooled, and some amount of thermal energy will be lost to convective heat transfer out of the surfaces. In a short amount of beam-on time, the center area of the lens will be at a higher temperature. A combination of thermal expansion and change in index of refraction caused by elevated temperature will change the focal length (Ref 7). Figure 5 schematically shows how thermal shift occurs.

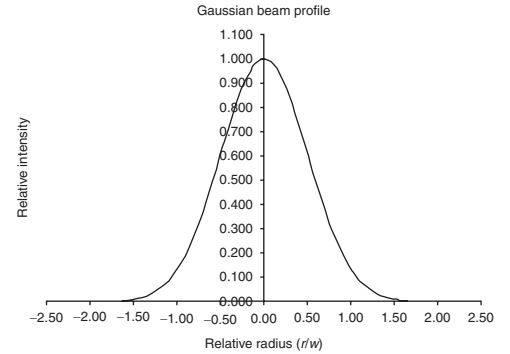
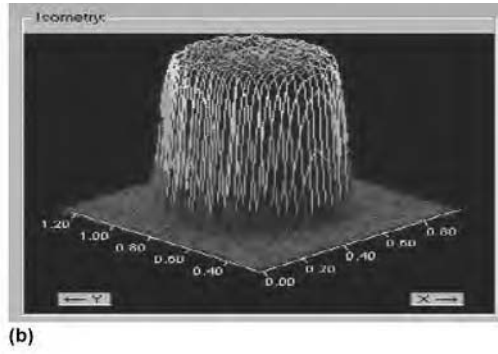
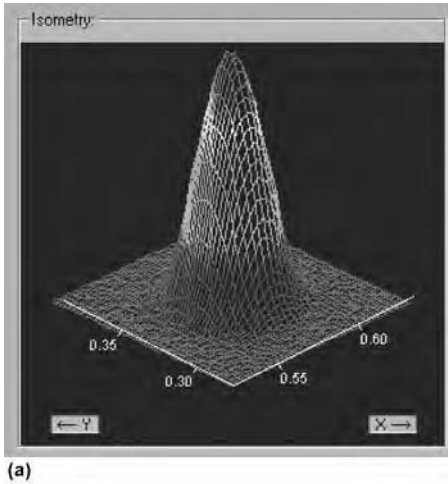


Fig. 4 Gaussian beam profile

Fig. 3 Output profiles for (a) single-mode fiber optic and (b) stepped-index fiber optic. Courtesy of IPG Photonics and Primes

The amount of focus shift may be small and inconsequential to the process, or it can be significant and troublesome. The amount of focus shift can be mitigated by careful selection of optical substrate materials and configuration (Ref 8). In some automated systems, the focus axis can be programmed to move to accommodate the focus shift. The use of reflective lens elements virtually eliminates focus shift. Figure 6 depicts focus assemblies for a fiber-delivered laser that uses 90° parabolic mirrors for both the collimator and the focus lens.

A valuable accessory to the 1 μm laser family is the beam switch (Fig. 7). In an energy-sharing situation, 100% of the laser power can be directed to one of several fiber optic cables. Two-, four-, and six-way switches are commonly offered by manufacturers. Fiber core sizes, lengths, and processes can be different from each port. Switch time is typically less than 0.1 s.

Energy sharing is where some percentage of the laser is directed down multiple ports at the same time. A hypothetical example of a situation where energy sharing may be used is on a part where three tack welds need to be placed on the circumference of a part and are equally spaced. Once these tack welds are made, the complete circumference weld is made with 100% power. The first three ports each deliver 33% of the laser power, and the fourth port delivers 100% of the laser power.

Optics for CO₂ Beam Delivery

The CO₂ beam is directed to the final focus optics by a combination of 90° turning mirrors (Fig. 8). The beam path is enclosed, sealed, and purged. A simple system may have only one turning mirror, or a complex system can have multiple mirrors with telescoping sections and rotating mirror sets that allow two- or three-dimensional processing envelopes to be addressed. A turning

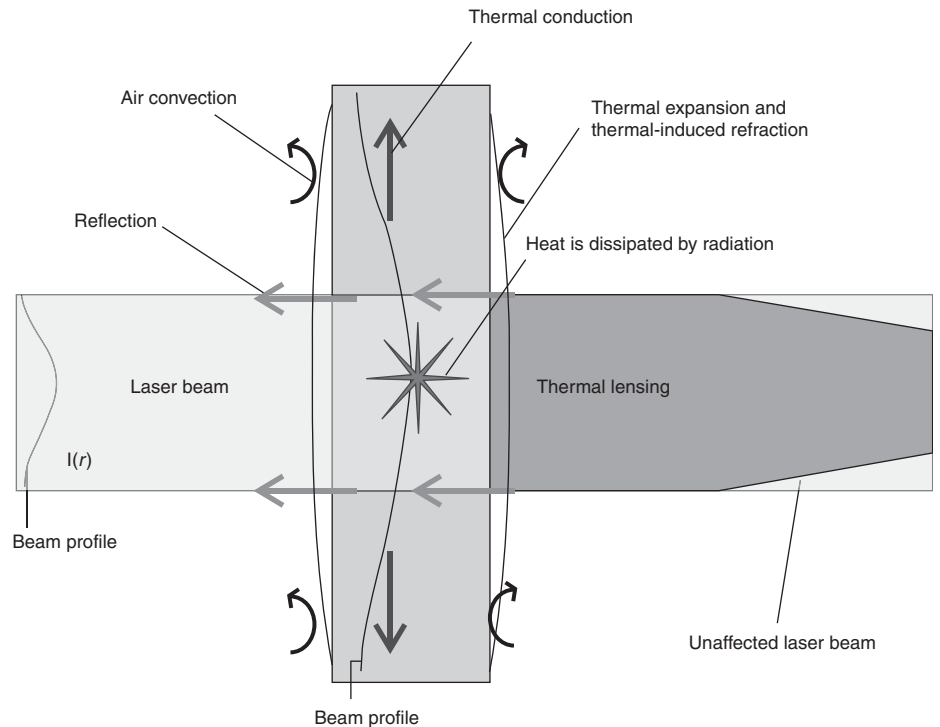


Fig. 5 Focus shift mechanism. Source: Ref 7

mirror has precision adjustments that allow very accurate alignment of the beam to be made to the beam-delivery path. The mechanical structure that supports the beam delivery must be quite stable and vibration free.

A telescope can be used provide more consistent optical results at the final focus optics as the beam path changes length. The beam properties from the laser mm-mrad product remain constant. A telescope expands the beam diameter a given factor; this then reduces beam divergence by the same factor.

The cleanliness of the beam path is critical to the propagation of the laser beam and to the life of the optical surfaces. The beam-delivery system and component supplier will specify the quality and volume of the purge gas. With a telescoping beam path, the purge supply volume must be such that it anticipates a telescoping section extension. The beam path pressure must not be allowed to go negative during this extension or ambient contamination may enter the beam delivery. The gas in the beam tube must not be stagnant. Turbulence must be maintained

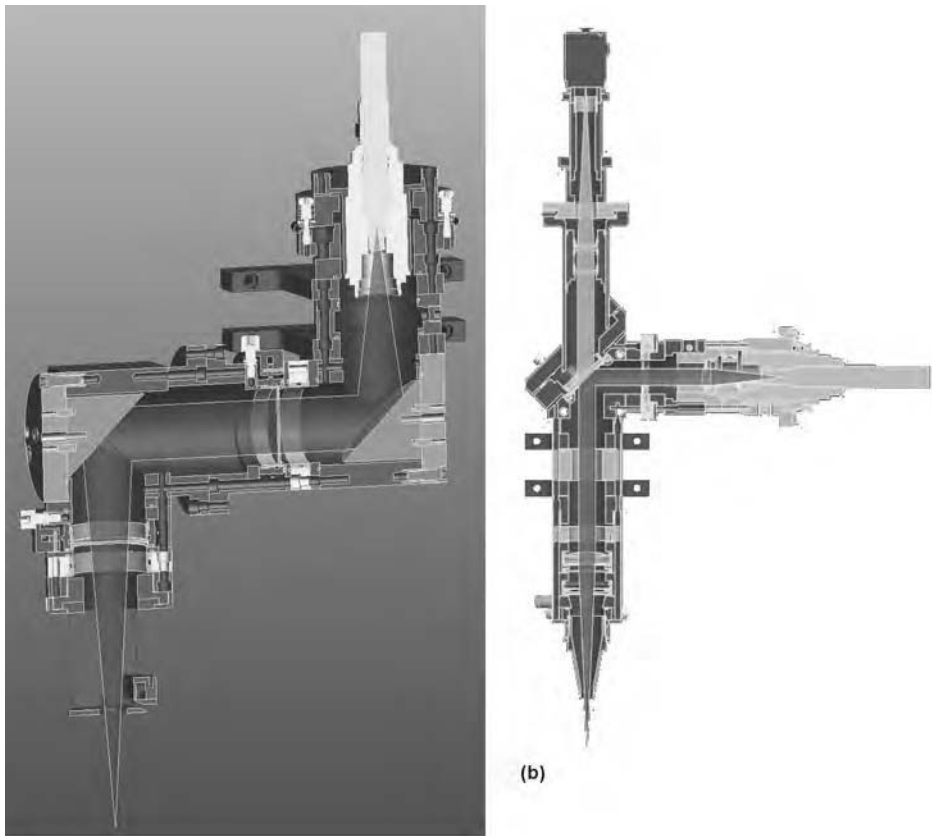


Fig. 6 (a) Reflective and (b) transmissive fiber optic focus assemblies with charge-coupled device camera. Courtesy of Laser Mechanisms

by the purge gas. Heating of the beam tube atmosphere by the passing laser beam will allow thermal gradients and local index of refraction changes. This effect will disrupt the beam propagation and beam properties (Ref 9, 10).

Manufacturing Economics

Engineers should expect to be asked two questions during a project or investigation: “Does it work?” followed quickly by “How much does it cost?” An engineer can turn to many resources for technical information. There are numerous technical conferences to attend and published proceedings to review. The most esoteric metallurgical effect often can be found fully documented. Reliable cost information, however, is much more difficult to determine, because this is the part of a study that does not get published. Having management shoot down a project with the argument “too expensive” is an unpleasant reality.

Project costs can be broken into two components: fixed costs and variable costs. Fixed costs comprise items such as the initial cost of the equipment, shipment, installation, and other such details. Variable costs are incurred with the operation and ongoing use of the equipment, such as electricity consumption, maintenance, consumables, and repair. The equipment provider will recommend a periodic maintenance schedule and the costs associated with it. Application-specific variable cost items will need to be identified by studies conducted prior to purchase. Repair costs are difficult to project because the source of a repair requirement can be well outside of the normal operation of the equipment.

The following two case studies review typical economic environments found in laser welding applications.

Case Study—1/M CO₂ versus Disc Laser Welding

A manufacturer has a product that is used in the aerospace and defense industries. This product requires a number of welding operations in its manufacture. The company relies on several job shops to provide electron beam, laser beam, and manual tungsten inert gas welding. All but one of the weld joints occur at sub-assembly stages so that the scheduling and transportation of the components is critical to the manufacturing process.

The company’s engineering department planned an evolution of this product that would be challenging to manufacture but would offer enhanced performance and features that the market was demanding. The change that impacts the welding operations is the use of electronics and rare-earth magnets in the product, which eliminates electron beam welding as an option for the final closing seam.

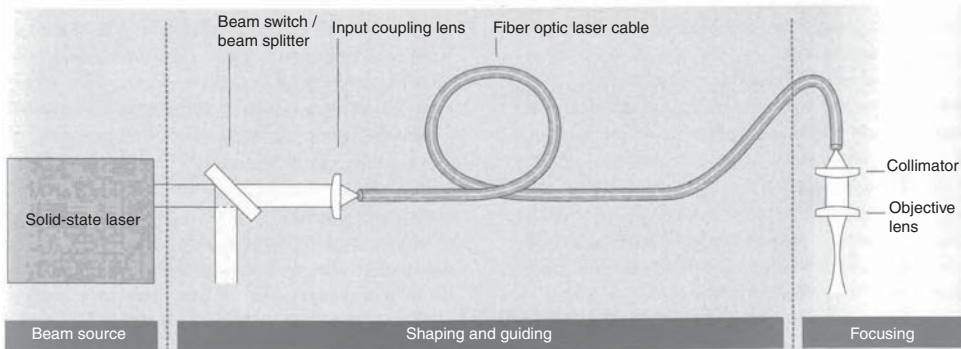


Fig. 7 Fiber optic beam delivery

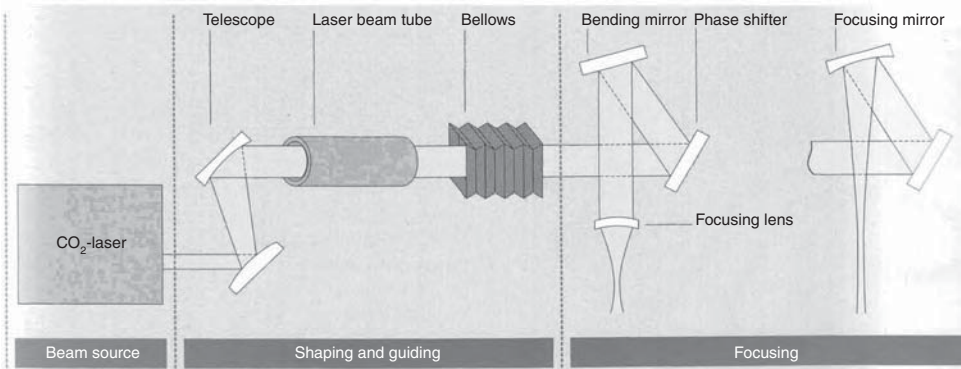


Fig. 8 CO₂ beam delivery

The sales group forecast that the new product would sell at a volume of 10,000 units the first production year and projected that the volume would grow at a rate of 20% per year for at least the first three years.

Historically, production schedule predictability has been unreliable. After reviewing operations, company management decided to target improving relationships with vendors, especially welding job shops, to better control production.

A sister division had a similar product in production but for a different market and application. This division's manufacturing strategy was also different, because they had considerable internal welding capability. The two divisions were combined, and the sister division's obsolete laser welding equipment was auctioned off. A considerable amount of manufacturing know-how and documentation were retained by the engineering staff. Records showed that their 2 kW CO₂ laser cost \$11.25/h average over the first five years of operation. This amount included maintenance parts, service parts, labor, laser resonator gas mix, and electricity. Service interventions increased operating costs 10% over the operating cost estimate provided by the equipment manufacturer. The beam delivery was all reflective except for a final focus lens of ZnSe, which was replaced approximately twice a month. Lens costs and other beam-delivery maintenance details, such as purge air filters, resulted in an operation cost of \$6.50/h. A significant service intervention occurred when a damaged air hose in the beam delivery was replaced with one that was not cleaned. The hose contaminated several optics that then needed to be replaced. It was estimated that an average of \$13.68/h of helium shield gas was used. The actual welding time was considered to be 24 min out of every hour.

A project was undertaken to determine the economics of bringing welding in-house and to develop a five-year plan. Of the weld joints that are used, two were identified as difficult and critical: the spider support weld and the closing seam weld. The economics will be established by the equipment selection to successfully weld these two joints. A volume of sample joints of each type were prepared for weld development. Part fixturing was designed and fabricated. Equipment vendors were identified and selected to do weld samples. It took several iterations of development to fully explore the capability of the equipment and to develop welds that met requirements.

The spider support weld joins four components with a circumferential weld, two of which are 304 stainless steel and the other two are 17-4 PH. The weld must have a minimum width of 1.5 mm (0.06 in.), and the fusion zone depth should be no more than 0.8 mm (0.03 in.).

The closing seam requires 4 mm (0.16 in.) weld penetration on a 125 mm (5 in.) diameter. The weld must be completed in less than 12 s to avoid thermal damage to internal components.

Mounting flanges, fixturing, and other external features restrict weld joint access. To produce this weld, the laser beam must have a minimum F-number of 12. The material in most configurations is 17-4 PH (focal length/beam diameter); however, Ti-6Al-4V also is used for special applications. Most of the weld studies were conducted on titanium to develop a safe shielding strategy.

CO₂ Laser Welding. The CO₂ laser vendor advocated using a controlled-atmosphere glove box for the closing seam weld. This solution seemed expensive, so instead, a simple welding chamber was designed and fabricated. The chamber closely contained the rotating part during welding and could be purged with helium. The laser beam entered the chamber through a port on top of the chamber, which was also used to vent the helium.

After a number of weld trials, it was found that the vendor's 3000 W laser could complete the closing seam at a rate of 2.5 m/min (8.2 ft/min) and exceed the required minimum with 5 mm (0.2 in.) weld penetration. The part was rotated at 6.36 rpm. The laser power was ramped up to 3000 W in 0.2 s to provide a smooth weld initiation. The dwell at 3000 W was 10.4 s to ensure weld overlap. The laser power was ramped down in 1.4 s to minimize the risk of generating a crater crack at the weld termination. The weld zone temperature did not exceed 100 °C (212 °F). The beam delivery used all reflective elements, and the final focus was F12. A purge of 30 s at a rate of 150 L/min (317.83 ft³/hr) ensured that the weld area was fully inert prior to welding. Helium use cost \$1.82/part.

The spider support weld proved to be a considerable challenge. The required weld aspect ratio was not obtainable. The solution was to join the four parts with three separate circumferential welds. Local shielding was quite

satisfactory at a rate of 25 L/min (53 ft³/hr) of helium, which amounted to a cost of \$0.36/part. Because this solution did not conform to the weld geometry that had a considerable history of reliable service, a full fatigue study would be required.

Disc Laser Welding. The closing seam was accomplished with a local shield gas lens and 25 L/min (53 ft³/hr) of argon. A 2000 W disc laser with welding optics having an F-number of 14 completed the weld to the required weld penetration, with a schedule that was identical to the CO₂ laser. This allowed for a close comparison between the two lasers. The argon cost \$0.04/part. After reviewing the shielding strategy required for helium, it was decided to try the purged chamber with argon. A flow rate of 25 L/min (53 ft³/hr) for 30 s worked well. This additional gas cost \$0.14/part, but it put the component at much less risk for oxygen contamination than the local shielding strategy.

The spider support weld was accomplished by positioning the weld optics out of focus so that a weld width of 1.5 mm (0.06 in.) was produced. Numerous combinations of laser power and weld speed were found that produced the required results. Argon at 25 L/min (7 gal/min) was again used.

Cost Comparison. Each laser vendor was requested to provide a five-year itemized operating cost estimate, shown in Table 2. Based on prior production experience, it is expected that one-third of every production minute will be welding time. During the remaining two-thirds of every production minute, the laser is in stand-by mode while parts are loaded and unloaded.

Also, facility management charges each department for floor utilization at a rate of \$15.75/m² per month. The beam delivery of

Table 2 Comparison of five-year estimate of operating costs for CO₂ and disc laser

Itemized operating	Estimated five-year operating cost		
	CO ₂ , 3 kW	Disc, 2 kW	
On time	20	20	
Off time	40	40	
Duty cycle	33%	33%	
\$/kW/h	\$0.09	\$0.09	
Hours/year	2000	2000	
Laser on, kW	50	12.5	
Chiller, kW	25	3.25	
Total power on, \$/h	6.75	1.42	
Laser standby, kW	2.5	0.5	
Chiller standby, kW	25	1.5	
Total standby, \$/h	2.48	0.18	
\$/h production	3.9	0.6525	Electricity consumption
Laser gas mix, \$/h	1.27		He, N ₂ , CO ₂
PM parts, \$/h	1.63	0.15	Resonator optics, filters
Service parts, \$/h	3.45	1.36	Mechanical, electrical parts
Chiller, \$/h	0.75	0.22	Filters, additives, clean water
Beam delivery, \$/h	0.25		Filters, dryer, and air compressor maintenance
Labor, \$/h	3.25	0.62	
Total	\$14.50	\$3.00	
Area, m ²	8.25	4.5	Laser, chiller, and beam delivery
Floor rate/month	\$15.75	\$15.75	\$/m ² per month
Per hour	\$0.78	\$0.42	
Total, \$/h	\$15.28	\$3.78	
Total, \$/min	\$0.25	\$0.06	

the CO₂ laser was given an area, while the fiber optic cable of the disc laser was not because it was routed overhead with the other power cables, control cables, and water cooling lines. The workstation design remained almost identical for each laser, except for accommodating minor differences in beam delivery.

Break-Even Analysis. The purchasing department provided a total cost from each laser vendor for the laser, chiller, and beam delivery. The calculated CO₂ laser total costs were \$185,000. The calculated disc laser total costs were \$215,000. Because the operating costs for the CO₂ laser were more than the disc laser, it is necessary to consider how part volume, *X* in Eq 3, impacts the economic decision. The closing seam weld costs were used to simplify the economic analysis according to Eq 3:

$$\begin{aligned} & (\text{CO}_2 \text{ fixed cost}) + (\text{Variable cost})X \\ & = (\text{Disc fixed cost}) + (\text{Variable cost})X \end{aligned} \quad (\text{Eq 3})$$

Solving Eq 3 with values taken from Table 2 gives:

$$\begin{aligned} & (\$185,000) + (\$1.82 + \$0.25)X \\ & = (\$215,000) + (\$0.14 + \$0.06)X \end{aligned}$$

$$X = 16,046$$

Thus, at part volumes greater than 16,043, the disc laser will cost less than the CO₂ laser. However, this part volume is not expected until well into the third production year (Ref 10).

Case Study—1/M Robotic Metal Inert Gas versus Robotic Laser Welding

An automotive parts manufacturer had a contract to supply in excess of 375,000 completed fabrications per year to a major auto company. The component is a resistance spot welded steel stamping design. The contract is up for renewal but has target cost reductions. The company considers this an opportunity for a new design that can improve performance, reduce weight, and enhance their profit margins as well as meet the target costs. Their customer will consider these design improvements as well as meet the cost targets in their vendor selection process.

The new design can be accomplished with robotic metal inert gas (MIG) or robotic laser welding. The resistance spot welded design was eliminated because of weight and limited corrosion resistance compared to other designs. The electrical costs of resistance spot welding were also substantially higher than the alternatives. Prototype parts were sent to various vendors of robotic MIG and robotic laser equipment for a review of the design and budgetary proposals

for systems with the required productivity. The company's manufacturing engineering team selected several vendors to engage in a more in-depth study, the purpose of which was to weld prototypes that would be used for structural, fatigue, and corrosion evaluation. The studies would also test weld joint design, fixturing requirements, and welding economics.

The selected laser system was configured with a two-way beam switch and two robots. The beam switch directs 100% of the laser power to the selected robot. Switch time is 0.10 s. This configuration allowed the full weld path to be reached by the two robots without part repositioning. The robots and fixtures were located such that load and unload occurred on one fixture while a part was being welded in the other fixture.

The robotic MIG system was configured such that load and unload occurred without incurring robot idle time. The fixtures were arranged so that multiple robots could address a set of loaded fixtures.

When the two studies were compared (Tables 3, 4), the laser-welded part had a weight advantage because of the absence of filler material, and thinner section components could be used because of less process-induced distortion and no risk of burn-through. Both processes produced favorable results in the evaluation of corrosion resistance and mechanical properties. The laser system had clear advantages for initial cost, operating cost, floor space requirements, and manpower requirements. However, the laser welding fixtures were heavier and more expensive than the MIG fixtures because they needed to hold the components more accurately and the mating surfaces needed to be forced into intimate contact prior to welding (Ref 11).

As the two case studies illustrate, there are subtle trade-offs between process parameters, component design, manufacturing efficiency, technological capability, and economics. Time spent conducting a rigorous evaluation of the trade-offs will pay dividends throughout the product manufacturing run.

ACKNOWLEDGMENT

Special thanks are given to Randolph Paura of Dynamic Laser Solutions, Fort Erie, Ontario, Canada, for his assistance in preparing graphics for this article.

REFERENCES

1. T. Miya, Y. Terunuma, T. Hosaka, and T. Miyashita, Ultimate Low-Loss Single-Mode Fiber at 1.55 μm, *Electron. Lett.*, Vol 15, Feb 1979, p 106–108

Table 3 Comparison of cost-effectiveness of metal inert gas (MIG) and laser welding systems

	MIG system	Laser system
Units per hour	90	90
Net units per year	375,840	422,820
Shifts per day	3	3
Hours per shift	7.25	7.25
Days per year	240	240
Uptime efficiency	80%	80%
Cycle time per unit	40	40
Equipment area, m ²	116	74.3
Operators	5	4
Robots	8	2
Tooling fixtures	10	2
Material added to laser weld, kg	None	0.24
Net part weight reduction/addition	Increase of 1.4 kg	Reduction of 1.1 kg
Equipment price excluding off-line, \$	3,012,000.00	2,600,000.00
Laser system equipment cost savings, \$		412,000.00

2. N. Neuroth, R. Hasse, and A. Knecht, *Damage in Laser Materials*, A.J. Glass and A.H. Guenther, Ed., NBS Spec. Pub. 356, 1971, p 3–14
3. J.H. Campbell et al., ICF Quarterly Report, Lawrence Livermore National Laboratory, Jan–March 1991, p 41
4. U.S. Patent 5,619,602, 1997
5. P. Klocek and G. Sigel, *Infrared Fiber Optics*, SPIE Optical Engineering Press, Bellingham, WA, 1989
6. D. Sabo, *The Evolution of Scanners for Remote Welding Applications*, ALAW, Plymouth, MI, 2007
7. T. Kugler, "Developments in All-Reflective High-Power 1 μm Laser Beam Delivery," Proceedings of the Laser Institute of America's ICALEO 2010 Conference (Anaheim CA)
8. S. Ream, W. Zhang, G. Firestone, and B. Victor, "Zinc Sulfide Optics for High Power Laser Applications," Proceedings of the Laser Institute of America's ICALEO 2007 Conference (Orlando, FL)
9. U.S. Patent 6,331,693
9. U.S. Patent 6,495,797
10. Case study based on information supplied by Mundt and Associates Inc., Scottsdale, AZ
11. Case study based on information supplied by Utica Enterprises Inc., Shelby Township, MI

586 / High Energy Electron Beam and Laser Beam Welding

Table 4 Cost comparison between robotic fiber laser and metal inert gas (MIG) welding systems

Laser welding sample: 4000 W fiber laser

Noncoated metal at 70% usage

		Cost per hour
Laser electrical power, 70% usage	$(14.4 \text{ kW/h}) \times (\$0.081/\text{kW/h}) =$	\$0.816
Chiller electrical power, 70% usage	$(13.2 \text{ kW/h}) \times (\$0.081/\text{kW/h})$	\$0.748
Chiller additive (deionized water)	$(32 \text{ L})(12.5 \text{ L})(8000 \text{ h})$	\$0.002
Assist gas	Not required	\$0.000
Cover slide	Not required	\$0.000
Exhaust system power	$(0.4 \text{ kW/h}) \times (\$0.085/\text{kW/h})$	\$0.034
Chiller and exhaust system filters	\$25/2000 h	\$0.013
Laser cell maintenance labor	4 h/1000 h operation) (\$55.00)	\$0.220
System spare parts	\$18,000/30,000 h operation	\$0.600
Total approximate operating cost per hour this application		\$2.43 per hour

Note: Chiller holds 168 L of tap water and approximately 32 L of deionized water.
Laser warranty: 2 years all parts and service

	90 units per hour
Laser consumption cost per unit	\$0.02704
Total parts per year	422,820
Total consumption cost per year	\$11,434.12

MIG welding sample: Based on 8 robotic MIG weld systems

		Cost per hour
MIG welding power, 60% usage	$(4.0 \text{ kW/h} \times 8 \text{ units}) \times (\$0.081/\text{kW/h}) \times 60\%$	\$1.56
MIG wire (450 kg drum), 8 required	$1 \text{ kg/h} \times 8 \times (\$2.40/\text{kg}) \times (60\% \text{ usage})$	\$6.93 (1 kg/h) \times (\$2.4/kg of MIG wire) \times (8 MIG welders) \times (60% usage/h)
Shielding gas bulk	$1 \text{ h}/1.72 \times 8 \times 0.6$	\$5.16 Cost per hour \times (8 MIG cells) at 60% usage
Exhaust ventilation power	$(0.4 \text{ kW/h}) \times (\$0.085/\text{kW/h}) \times 5 \text{ cells} =$	\$0.17
Exhaust system filters	\$45/2000 h	\$0.02
MIG maintenance labor	100 h/1000 h operation) (\$55.00)	\$5.50
Spare parts (tips and cleaner)	\$50/10 h operation	\$5.00
Total approximate operating cost per hour (at 60% continuous operation)		\$24.34 per hour

	90 units per hour
MIG consumption cost per unit:	\$0.27042
Total parts per year:	375,840
Total consumption cost per year:	\$101,634.24
Estimated consumption savings using fiber laser welding system per year:	\$90,200.12

Laser Deposition Processes

J.O. Milewski, Los Alamos National Laboratory
T. Palmer, Pennsylvania State University

LASER BEAMS provide a well-controlled heat source, both in terms of the power delivered and the spatial precision of the directed energy. The interaction of the laser beam with the material being processed is substantially different than that of other thermal processing methods, such as plasma spray, arc, or flame processing, offering distinct advantages over competing thermal processing methods used for material deposition. Numerous variants of the process are being developed that use a wide range of lasers, material delivery, motion, and control systems optimized for specific applications. The disadvantages of laser deposition processes include process cost and complexity, which must be considered during process selection and development.

The deposition of weld material on metallic substrates, commonly known as cladding, is an industrial process used to improve the corrosion resistance and wear resistance of common structural materials. This deposited material forms a coating on the substrate material that alters its surface properties and supplies a combination of desired properties not found in any one metal. When a cladding process is adopted, a base metal can be selected for cost or structural properties, and another metal added for surface protection or some other desired property, such as electrical conductivity. Common welding processes, such as gas metal arc, gas tungsten arc, or plasma transfer arc, have been adapted to deposit a range of corrosion- and wear-resistant materials in industrial applications. By using these welding-based processes, the thickness of the cladding can be made much heavier and more durable than that obtainable by electroplating. Other comparable coating technologies include thermal spray and plasma spray processes, which deposit thinner coatings than those possible with these arc-based processes. Unlike these coating technologies, welding-based deposition processes produce a metallurgical bond between the clad and substrate materials, because fusion of the clad material to the substrate occurs.

Laser deposition involves the articulation of a laser beam and the introduction of material into the beam path to fuse the material onto a substrate or into a functional shape. It can be

divided into two broad categories: cladding and near-net shape processing. Laser cladding has evolved from weld-metal deposition processes relying on the modification of an existing substrate surface or base component. Laser near-net shape processing has evolved from laser cladding or rapid prototyping technology of nonmetals to create complex parts or features without the reliance on a function substrate that remains integral to the part (Ref 1). A wide range of laser power sources with wavelengths between 1 and 10 μm are used. Articulation of the laser beam relative to the part ranges from simple linear or rotational movement to sophisticated computerized numerical control (CNC), computer-aided design and manufacturing (CAD/CAM) modeling, and programming. The materials being delivered are typically in powder or wire form and can range from metals to plastics, composites, and ceramics. The most common materials used are plastics for three-dimensional (3-D) models and those metals commonly processed by melting.

The primary advantages of using lasers is that of reduced heat input, providing metallurgical and geometric advantages, precision of the deposit, and economic advantages (speed, material savings, reduced product development time, etc.). These advantages must be assessed on a case-by-case basis with the understanding that a greater degree of process development and control may be required in comparison with more mature, better understood, and more widely applied conventional alternatives.

The application of lasers for deposition is a rapidly evolving field primarily driven by the rapid evolution of laser power sources. As the cost and complexity of lasers decrease, successful applications will continue to overtake existing well-established processing methods as well as develop new and unique applications. As with other competing processes, advances in process sensing, control, and modeling are being integrated to optimize process performance. In addition, research, development, and new applications continue to expand our understanding of the properties and performance of the deposited materials. A growing list of successful applications has demonstrated

substantial economic return and continues to justify further development of the technology.

Laser Cladding

Process Description

Laser cladding uses a high energy density laser heat source to deposit selected corrosion- or wear-resistant materials on structural material substrates. Historically, the development of high-power gas lasers led to the initial development of laser cladding processes in the late 1970s (Ref 2). In the 1980s, the process became more refined with improved system development and process understanding (Ref 3–9). Through this development work, laser cladding processes are now widely used in a range of industries, including the automotive, aerospace, energy exploration and production, medical, and marine industries.

The characteristics of the laser heat source give the laser cladding process several advantages over other arc-based cladding processes. For example, lasers are typically characterized as being highly monochromatic and coherent with a high degree of directionality, allowing the laser to be sharply focused to extremely high power densities, on the order of 10^{17} W/cm². These energy density levels far exceed those of other arc-based deposition processes but are similar to the electron-beam-based deposition process parameters. Because the laser is a high energy density heat source, the energy provided by the laser can be directed at a specific location on the substrate, resulting in a much lower overall heat input into the substrate than what is produced by an arc source. This low heat input level minimizes the impact of the process on the substrate material, thus allowing the process to be used in both thin- and thick-section parts.

In addition to the CO₂ systems with which the laser cladding process was developed and still are in common use, a number of other solid-state laser systems are becoming more widely used. The more common types of laser systems used in industry have been expanded to include not only CO₂ lasers but also solid-

state laser systems, such as neodymium: yttrium-aluminum-garnet (Nd:YAG) lasers, ytterbium: fiber lasers, and direct-diode lasers. With the increasing power available and decreasing costs of Nd:YAG, direct-diode, and fiber laser systems, these solid-state laser systems have become much more prominent in the development of new applications. These solid-state lasers also offer the benefit of increasing process flexibility and automation because of the ability of the laser energy to be directed through the use of fiber optic cables. Several examples of the industrial application of laser cladding include the repair of commercial aircraft gas turbines and the application of corrosion-, wear-, and oxidation-resistant coatings on shafts of drilling tools, engine valve seats, tool hardfacing, hydraulic pump components, and molds (Ref 10–17).

The laser cladding process produces a macrostructure similar to what is observed in arc-based cladding processes, albeit with smaller sizes for selected zones. Figure 1(a) shows a schematic diagram defining the structure of a laser clad and includes the clad metal, a mixed zone between the clad and substrate materials, a heat-affected zone in the substrate material, and the unaffected substrate base metal. These distinct regions display variations in properties, with the clad material imparting the desired surface properties on the material, and the mixed and heat-affected zones resulting from the interaction of the heat source and the clad material with the substrate. The small sizes of these

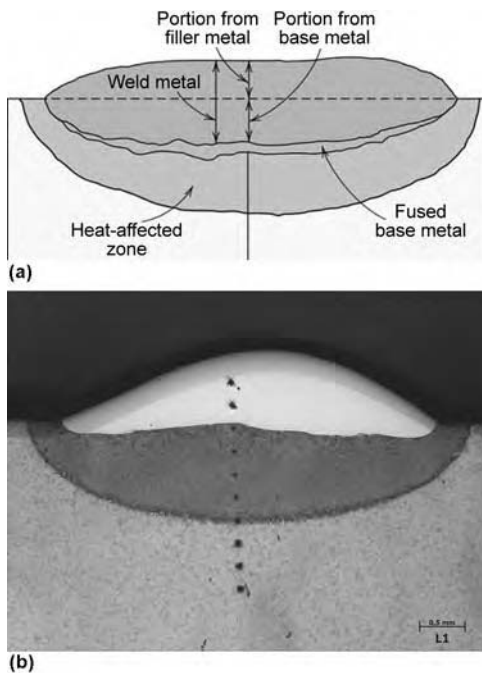


Fig. 1 (a) Schematic diagram of a laser cladding cross section with the primary structural regions identified. Adapted from Ref 10. (b) Underwater laser deposition. Base plate, type 304L stainless steel; layer 1, ER309L stainless steel. Courtesy of Westinghouse Electric Company, WEC Welding & Machining, LLC

two zones result in minimal impact of the cladding process on the substrate material. These different regions of a laser clad are shown in Fig. 1(b) for a 304L stainless steel deposit.

The resulting microstructures in each region of the clad macrostructure can be significantly different. Figures 2(a) and (b) show the microstructures present in the clad material and the mixed and heat-affected zones of an Inconel 625 laser clad made on a structural steel substrate. Figure 2(a) shows the dendritic structure formed in an Inconel 625 clad layer. Because the clad material has been melted and deposited on the substrate, it is primarily dendritic. The size and distribution of the dendrites will depend on the heating and cooling rates experienced during the laser cladding process. These thermal cycles will be dependent on the processing parameters, to include laser power and travel speed.

The thermal cycles produced by the laser cladding process will also have an impact on the underlying substrate material. Figure 2(b) shows the mixed and heat-affected zones formed in the structural steel substrate material during the laser cladding of Inconel 625. A gradient of microstructures appears as the distance from the clad metal interface is increased. The

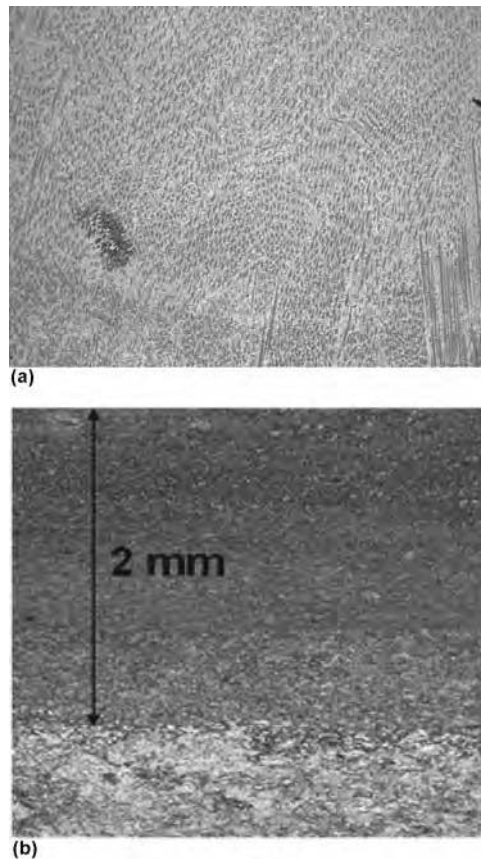


Fig. 2 Common microstructures observed in (a) the Inconel 625 laser-clad layer on high-strength steel and (b) the mixed and heat-affected zones. Courtesy of Applied Research Laboratory, Pennsylvania State University

common features of the heat-affected zone in a steel weld, to include the large and fine-grained regions caused by the heating and rapid cooling of the steel during the laser cladding process, are also present. Probably the most important consideration in examining this figure is the small size of the mixed and heat-affected zone. In Fig. 2(b), the heat-affected zone extends only approximately 2 mm (0.08 in.) from the clad metal interface. This small heat-affected zone is the result of the high energy density and low heat input characteristic of the laser cladding process.

Because a metallurgical bond is formed between the clad and substrate materials, some level of dilution between the clad material and the substrate material is expected. When viewing a laser-clad cross section, a region where the clad layer consumes some amount of the substrate material can be observed. This level of dilution can be defined geometrically across the cross section of the clad layer, with the amount of base metal consumed by the clad metal defining the level of dilution. In laser cladding, the extent of geometric dilution is typically rather small, usually not exceeding several millimeters in depth. Dilution levels in clads produced by arc-based processes are typically much larger, because these processes melt a much larger amount of substrate material.

Another means for measuring dilution levels involves the direct measurement of the chemical composition of the clad layer. Figure 3 shows a characteristic chemical composition profile of selected alloying elements measured across the depth of the clad material starting at the substrate interface for an Inconel 625 clad on a high-strength steel substrate. In this figure, the change in chemistry, primarily of the iron level, can be observed up to 2 mm (0.08 in.) into the clad layer. The presence of iron from the substrate material in the clad metal shows how the base metal is diluted into the clad material, resulting from the convection and transport of material caused by the laser cladding process. A measure of the level of dilution of the iron is the distance into the clad material needed for the iron level to reach the iron level present in the original clad material (just under 2 mm in Fig. 3). In laser cladding, this distance is significantly lower than what is observed in arc-based cladding processes, where additional clad layers are typically required to obtain the desired clad-metal chemistry.

Material Combinations

Laser cladding has been used to deposit a wide range of corrosion- and wear-resistant materials on compatible substrate materials. There are three main categories of materials and material combinations that are commonly deposited using laser cladding processes. These different material combinations include the deposition of a single corrosion- or wear-

resistant material on a structural material substrate, the formation of functionally graded or composite material structures (Ref 17, 18), and the fabrication of particulate composites containing high-melting-temperature particles (Ref 12, 13).

The deposition of corrosion- and wear-resistant materials on structural steel components is probably the most common use of laser cladding processes in industrial applications (Ref 12, 13). These materials are typically cobalt-base alloys, such as the Stellite family, for wear-resistant coatings (Ref 16); nickel-base alloys, such as the Inconel family, for corrosion-resistant applications; and iron-base alloys, such as austenitic and martensitic stainless steels, for both wear and corrosion applications. The laser deposition of coatings on magnesium (Ref 14), titanium (Ref 15), and aluminum components is also industrially relevant.

The selection of suitable material combinations is driven by material compatibility and similar thermal expansion coefficients between the clad and substrate materials. Metallurgical compatibility is one of the primary considerations. Because the clad and substrate materials will be fused together, alloy combinations that will result in the formation of undesirable intermetallic phases cannot be clad. For example, the deposition of cobalt-base alloys on titanium substrates is not recommended, because of the formation of these undesired intermetallic phases. It is worth noting, however, that the low levels of base-metal dilution prevalent in laser cladding, particularly at low heat inputs, can limit the formation of these undesired phases. This characteristic of the laser cladding process has led to the development of other additive manufacturing processes, which are discussed in later sections.

In addition to the deposition of these materials, laser cladding, particularly when using a powder precursor, allows for the production of composite microstructures. Two types of composite microstructures can be formed: graded microstructures and uniformly dispersed particulate microstructures. The low dilution levels prevalent in laser cladding processes allow for the formation of graded structures, such as those produced in aluminum-base and other compositionally graded materials (Ref 18, 19). This ability to functionally grade materials can lead to the development of materials with unique properties unobtainable through conventional processing routes. In wear-resistant applications, the addition of high-melting-temperature particles, such as WC, TiC, and other hard carbide materials, imparts the desired wear resistance to the surfaces of common structural materials, thus extending the usefulness of these materials in high-wear applications.

Process Characteristics

Laser cladding is a flexible process in which a range of process parameters can be varied to

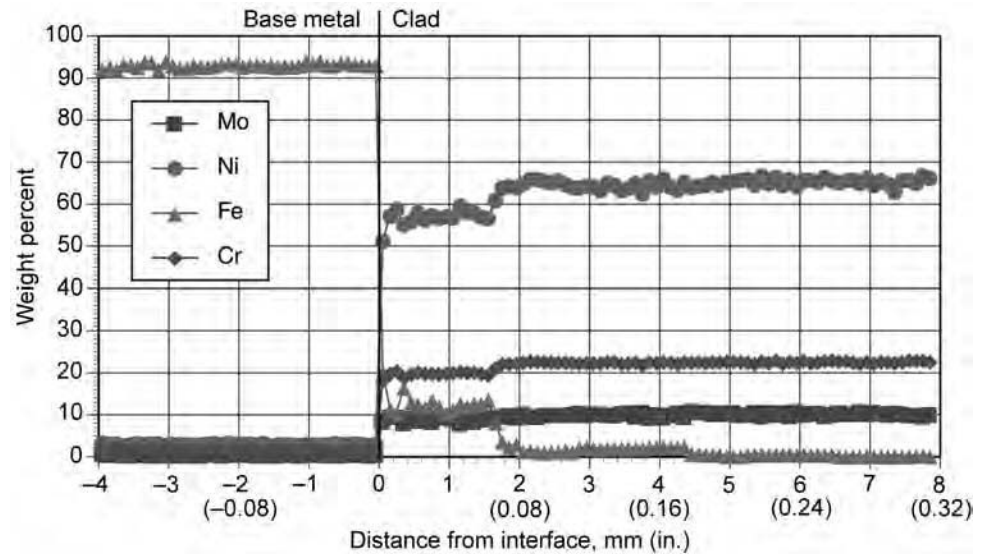


Fig. 3 Electron microprobe measurements made across the laser-clad/substrate interface in the laser cladding of Inconel 625 on a high-strength steel. Courtesy of Applied Research Laboratory, Pennsylvania State University

produce a wide array of different coating thicknesses and process efficiencies. Several of the important process parameters used in laser cladding include laser power, beam diameter, travel speed, clad material-introduction mode, and beam manipulation methods. The combination of these various process parameters can impact the types of materials deposited by the laser cladding process, the process efficiency as defined by the deposition rate of the clad material, the thickness of the coating, and the impact of the cladding process on the underlying substrate material.

Of these various processing parameters, the impact of different clad material-introduction modes, which are defined primarily by powder and wire feeding, and the impact of beam scanning are described subsequently. Depending on the laser power used and the mode of material introduction into the laser, the range of material deposition rates can span from very low rates of less than 0.5 kg/h (1 lb/h) to very high depositions that can reach levels approaching 15 kg/h (30 lb/h). The width of a clad pass can also be altered by the width and the scanning of the laser beams. In cases where the beam is scanned, clad pass widths can reach sizes of 25 mm (1 in.) or more, depending on the capabilities of the scanning optics. When a non-scanned beam is used, clad pass widths are the same size as the defocused laser beam, which is typically on the order of up to 5 mm (0.2 in.) or less.

Powder and Wire Feeding. In laser cladding processes, clad material can be deposited using either powder or wire feeding. Figures 4 (a) and (b) show schematic diagrams of powder-based and wire-based cladding, respectively. In both cases, the laser beam is directed at the powder or wire, which is then melted on the substrate surface. Each material-

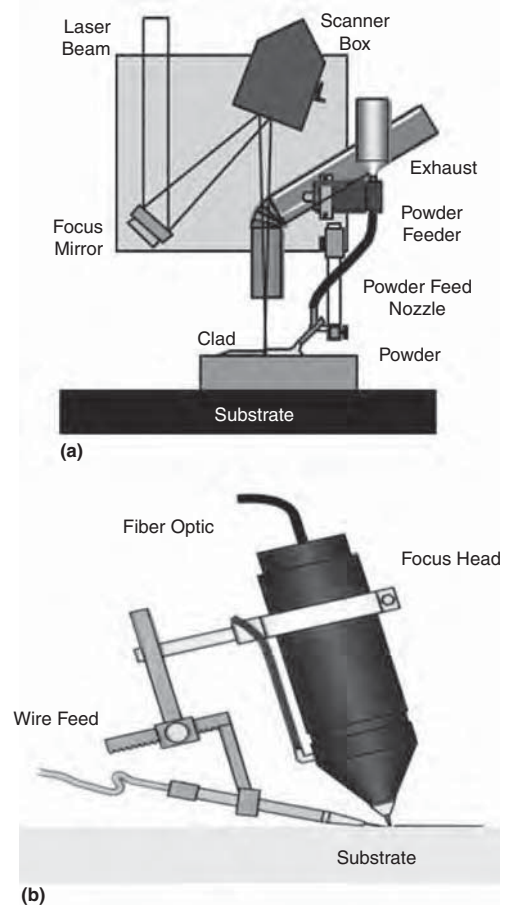


Fig. 4 Schematic diagrams showing (a) powder-fed and (b) wire-fed laser-cladding processes. Courtesy of Applied Research Laboratory, Pennsylvania State University

introduction mode, however, has unique properties, along with its characteristic advantages and disadvantages. This range of characteristics and different material-introduction modes increases the flexibility of the laser cladding process and makes it applicable to a range of applications, where different deposition rates are required or varying geometries must be processed.

When cladding with powder, the deposition of unique material combinations becomes possible, allowing for the fabrication of composite and graded structures. In addition, the use of powder allows for a range of deposition rates, with both low and high deposition rates being possible. For example, low-deposition-rate laser-clad layers can be produced with low heat inputs, resulting in minimal distortion and allowing for the deposition of thin clad layers. On the other hand, high-deposition-rate cladding is also possible, resulting in the deposition of thick clad layers on applications such as shafts or other components where thick corrosion- and wear-resistant coatings are needed. However, the use of powder feeding limits the cladding of components to specific geometries and welding positions, because some substrate configurations make it impossible to place the powder. Powder cladding is most often performed in the downhand or 1G position, so that the powder can be laid easily on the surface.

The use of wire-fed cladding is a technique that is finding wider use in the deposition of clads in repair and other unique applications. In many repair applications, the geometry and placement of the component may preclude the performance of the clad in a downhand position. Wire feeding

provides a means to easily introduce material into the laser beam without the issue of powder flowing out of the beam in a horizontal geometry. It is also possible to use commercially available filler-metal wire rather than powder, which may reduce issues with process qualification or the qualification of a new material for an existing application. Deposition rates, however, are limited with wire-fed cladding by the speed that the wire can be fed into a molten metal pool of limited size.

During powder-fed laser cladding, the powder can be introduced into the laser by either preplacing the powder in front of the advancing laser beam or by coaxially feeding the powder directly into the laser. Schematic diagrams of preplaced powder cladding and coaxially-fed powder cladding are shown in Fig. 4(a) and 5, respectively. These two different means of feeding the powder can be used to alter the deposition rates needed for specific applications. For example, when higher deposition rates or thicker coatings are desired, preplaced powder can be used instead of wire or coaxially-fed powder. By preplacing the powder in front of the advancing laser beam, more powder can be melted, thus maximizing the deposition rate.

Many of the advantages of the laser cladding process can be traced to the absorption of the laser energy by the preplaced powder bed (Ref 20). An analysis of the absorptivity of powder beds has shown that these powder beds are highly efficient absorbers of laser energy. As a result, only a small amount of laser energy reaches the substrate, thus minimizing the size of the mixed and heat-affected zones in the substrate material. This increased absorptivity is particularly prevalent in preplaced powder beds and is responsible for the low levels of dilution and minimal impact on the substrate material, even during high-power and high-deposition-rate laser cladding.

Coaxially-fed powder cladding, however, has limited capability for high deposition rates, because the amount of material to be deposited is limited by how much powder can be fed into the laser beam. As a result, this process typically produces much thinner coatings than those obtained using preplaced powder. This limited deposition rate also allows for the coaxially-fed powder process to produce more easily functionally graded structures and particulate material composites. The heat input into the part is also lower, thus minimizing the clad-metal dilution of the laser cladding process on

the substrate material to even lower levels. Along with these decreased dilution levels, the size of the heat-affected zone in the substrate material is also minimized.

Scanned versus Defocused Beams. During laser cladding, a defocused beam is typically used, because the goal of the process is to avoid excessive melting of the underlying substrate material. The beam diameter can vary from 1 to 5 mm (0.04 to 0.2 in.), depending on the laser power and the desired thickness and width of the clad layer. For coaxially-fed powder and wire-fed systems, the beam is defocused to provide a larger interaction area for the laser and the wire or streaming powder.

It is also possible to shape the laser beam into a desired shape. Beam-shaping optics are available to convert a circular beam into other shapes. For cladding, a linear heat source is used because it allows for a wider clad pass. Direct-diode lasers, which are becoming more widely available, can produce a linear heat source that will allow a wide clad pass to be deposited. The beam can also be scanned over a predetermined path to increase the size of the heat source. With the increased size of the heat source, a wider clad pass can be deposited.

Comparison with Arc Cladding Processes

Laser cladding is characterized by lower heat-input levels and lower base-metal dilution than widely used arc-based cladding processes. High-power laser systems also provide the ability to deposit large quantities of material at much higher travel speeds. A comparison between high-deposition laser cladding and several other common high-deposition-rate arc-based cladding processes is provided in Table 1. In this table, process parameters, such as deposition rate, travel speed, heat input, and base-metal dilution, and manufacturing considerations are compared for high-deposition-rate laser, pulsed gas metal arc, gas tungsten arc, submerged arc welding, and electroslag strip cladding processes.

A comparison of the processing parameters in Table 1 shows that the laser cladding process has a number of favorable characteristics when compared to other high-deposition-rate processes. In addition to the high deposition rate, the laser cladding process has high travel speeds and lower heat inputs than the other processes. These two characteristics make the laser cladding

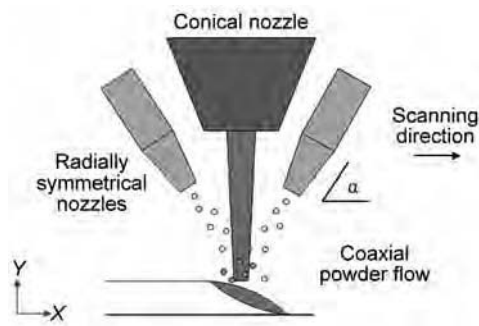


Fig. 5 Schematic diagram showing coaxially-fed powder laser cladding. Source: Ref 18

Table 1 Comparison of characteristics of laser and arc-based cladding processes

	Laser	Pulsed gas metal arc	Gas tungsten arc, hot wire and cold wire	Submerged arc welding	Electroslag strip cladding
Process parameter					
Deposition rate, kg/h (lb/h)	13–15 (25–30)	6 (12)	6–7 (12–13)	6–13 (12–25)	22 (44)
Travel speed, mm/min (in./min)	0.7–0.8 (18–20)	0.2–0.3 (6–8)	0.3–0.4 (7–9)	0.2–0.3 (6–8)	0.2 (6)
Heat input, kJ/mm (kJ/in.)	1.3 (33)	2.0 (51)	1.4–1.7 (36–42)	2.2 (56)	12 (300)
Base-metal dilution levels	Low	High (30%)	Moderate	High (30%)	Moderate
Size of heat-affected zone	Small	Large	Moderate	Large	Large
Manufacturing considerations					
Capital investment	High	Low	Low	Low	Moderate
Training and implementation	Moderate/high	High/low	High/low	High/low	High/low
Productivity/automation	High	Moderate	Moderate	Moderate	Moderate
Labor and material	Low	High	High	High	High

process attractive, particularly when considering the enhanced process efficiency afforded by the increased travel speed. The lower heat-input levels also minimize the impact on the substrate material, thus minimizing distortion and follow-on operations that may be required to bring the part back into specification.

When compared with manufacturing considerations of arc-based cladding processes, the laser cladding process has a number of advantages in terms of process control and improved product quality. For example, laser cladding produces lower levels of distortion in the product being clad than what is typically obtained in higher-heat-input arc cladding processes, which results in less postprocessing rework. The accuracy in the placement of the laser heat source also results in greater precision in the placement of the deposited material, which reduces postprocess machining. Laser cladding is also well suited to greater automation or mechanization, which improves process control. The reduced base-metal dilution leads to greater compositional control.

Future Directions for Laser Cladding

Because laser cladding is an additive process, it can be applied to a wide range of components as an advanced manufacturing process to overcome many of the shortcomings of other fabrication technologies and materials. Several benefits include the enhancement of corrosion and wear properties and improved thermal control. In addition, a reduction in production time, the production of functionally graded parts, and increased application to part repair and remanufacturing can be realized.

The application of corrosion- and wear-resistant coatings on structural materials using the laser cladding process is becoming more common with the introduction of new and more powerful laser systems. Laser cladding is commonly used in the manufacture of new components and the refurbishment of existing components. In addition, it is used increasingly for the repair of in-service components. An example of a laser-cladding-based repair process of aluminum components is shown in Fig. 6.

As described, the laser cladding process has great potential for a range of industrial applications. However, the utilization of laser cladding processes is limited because of its high cost, particularly of the laser power supply, and the limited process efficiency. With the increasing capabilities of the new-generation direct-diode, disc, and fiber lasers, process efficiencies can be improved, particularly as available laser powers continue to increase and costs decrease concurrently.

Near-Net Shape Processing

Process Characteristics

Near-net shape laser deposition processing features many attributes common to laser cladding when considering applications to metals or cermets. The range of metals processed and metallurgical properties of the deposited metals are often similar but may be affected by cooling rate or dilution by the substrate materials. As with laser cladding, materials commonly deposited range from aluminum-, iron-, nickel-, and

cobalt-base alloys to more exotic and difficult-to-process materials such as titanium alloys; refractory, reactive, or reflective metals; ceramics; and composites. Metals can be deposited up to 100% density, with properties ranging from those found in cast materials and, in some cases, even exceeding those of wrought material. In all cases, adequate and consistent material properties require the appropriate levels of verification during process development and prove-in. Near-net shape processing is differentiated easily from cladding when considering applications to plastics and ceramics. Another primary difference is the decreased reliance on a substrate component and the increased degree of process control and planning required to create a complex shape and to ensure that the desired properties of the deposit are met. Justification of the costs associated with the increased process complexity and development are being found in applications for low-volume, high-value-added components or with materials that are difficult to fabricate using conventional means. Early development of the technology is described in Ref 21 to 24. A comparison of the technology with other competing powder deposition processes and near-net shape processes is provided in Ref 25. A comprehensive review of the technology, including its historical evolution, is provided in Ref 26.

Process Applications

Three-dimensional prototype part models, offering form and fit testing, often are produced by using plastics and sintering layer by layer within a powder bed. Applications using plastics are well established and widely supported by vendors of equipment and commercial services. Functional material properties in metals may be obtained by either a powder bed method of deposition or direct injection of material into a molten pool and deposition along a traversed laser path to produce the desired shape. Each of these two methods has distinct advantages depending on the application.

Powder Bed Methods

Powder bed methods raster or direct the laser beam across a bed of powder material to selectively melt and fuse the material by turning the laser beam on and off. The powder bed is indexed downward, and a new layer of powder is applied and selectively fused layer by layer into a 3-D component; the process is shown schematically in Fig. 7. Process variants and trade names as of this writing (2011) include additive layer manufacturing, LaserCusing, selective laser sintering, and direct metal laser manufacturing.

Advantages of this method, when compared to direct powder injection, include relative process simplicity because the traversal paths are generally linear, and the x - and y -motion can be accomplished using laser beam rastering and an incremental z -axis motion. Powder



Fig. 6 Laser cladding repair of aluminum components. Courtesy of Naval Undersea Warfare Center Division, Keyport

delivery is accomplished using a layer-by-layer rolling technique to preplace new powder for successive laser paths. Planar slicing of the 3-D solid model uses software technology previously developed and refined for laser sintering of plastic models and offers a simplified programming and control interface. Dimensional accuracies of up to 0.1 mm (0.004 in.) and deposition rates of 2 to 20 cm³/h (0.12 to 1.2 in.³/h) may be achieved but are material-dependent. Support structures may or may not be required, depending on the geometry of the components being fabricated. Primary process parameters include laser power, laser spot size, raster speed, path overlap, planar z-step size, and powder type and size.

Disadvantages of this method include limitations of the processing chamber size and the inability to add near-net shape features to the existing base component for repair, refurbishment, or part modification. Full density of the deposited material may be more difficult to achieve than processes that maintain a larger molten pool.

Variants of the process include powder heating to increase deposition rates and powder recycling to reduce process waste. Full enclosure of the process within an inert chamber can offer class I isolation of the laser beam and containment of environmental and health hazards associated with powder processing. Multiple instances of the same part may be fabricated at the same time within the working envelope of the chamber. Complex internal structures are easily fabricated using this method. Applications include functional prototypes for use in the medical, defense, and space industry as well as applications for the tool and die industry, where complex cooling channels

may be easily formed within the deposited part. An example of direct metal laser sintering of a titanium structure for a competition bicycle is shown in Fig. 8.

Directed Powder Methods

Direct powder methods inject powder into the molten pool formed by the laser beam and produce a relative motion between the part or features being formed and the laser. Fusion of the deposit into adjacent and underlying material forms the near-net-shaped feature (Fig. 9). This method is an evolution of multipass 3-D laser cladding, with the primary differences related to the sophistication of powder delivery, process planning, and control. The process may be performed within a class I laser enclosure, an inert chamber, or in the open, with due consideration paid to hazards associated with the laser, powders, and associated motion system. The CNC motion or robotic motion and control are typical to the complex deposition paths required. Typically, the powder is delivered to the molten pool by inert gas through multiple jets within the laser head. Near-net shape cladding using wire feed is less suitable for laser net shape deposition because the articulation of wire feed into the molten pool limits the use of omnidirectional movement and out-of-position deposition. Process variants and trade names include DMD (direct metal deposition), LENS (laser-engineered net shape), solid freeform manufacturing, laser powder additive manufacturing, laser powder deposition, and LAM (laser additive manufacturing).

In comparison with conventional cladding methods, a near-net-shaped feature or part is

designed and the control sequence for deposition of the feature is planned using CAD/CAM or direct programming techniques. Deposition of the feature is begun on a substrate material that is either integral to the final part or is removed after deposition is complete. A high degree of sophistication may be incorporated within the deposited feature at the cost of more complicated process planning, refinement, and control. Trial and error is sometimes required to arrive at an acceptable deposit in terms of geometric shape, metallurgical considerations, and overall deposit morphology.

To reduce the complexity and speed to fabrication, a relatively simple substrate component may be fabricated by conventional means, with high-value-added features being added later using near-net shape laser deposition. Other high-value-added features may include the addition of intellectual property or specialty materials inappropriate for outsourcing. In other applications, entire parts may be fabricated or partially fabricated as modification to an existing CAD design and may be performed as in the case of complex shape repair or modification. Examples of a rebuilt turbocharger blade and a feed screw are shown in Fig. 10. Remanufacturing of components into a higher-value product is possible. In the case of repair or modification of existing components, the process has the potential of being applied in situ or on site, thus eliminating the need to transport large parts.

When compared to laser cladding of large objects, such as shafts and valve seats, small, precise features are formed at the expense of

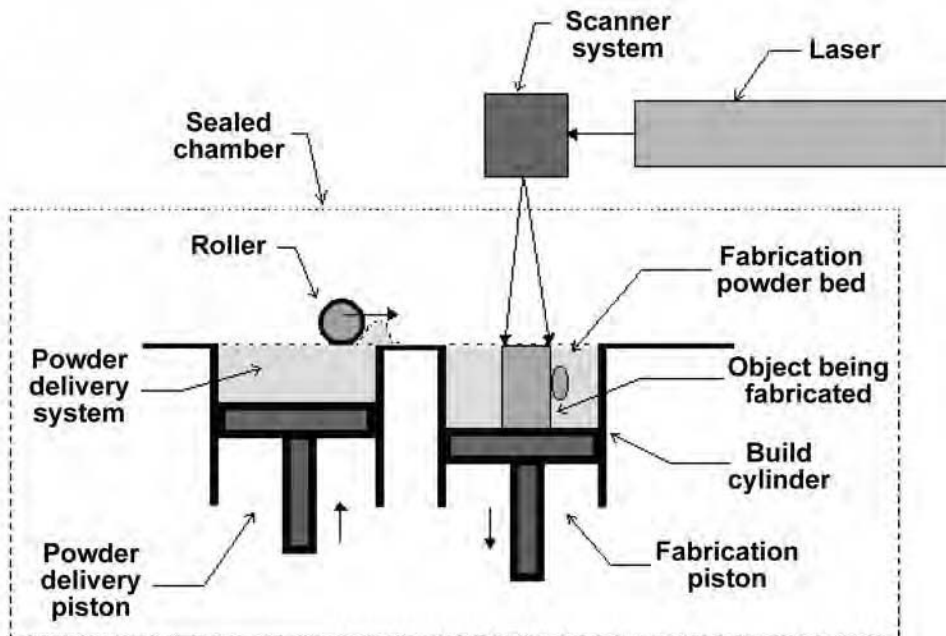


Fig. 7 Selective laser sintering. Courtesy of Castle Island Co.



Fig. 8 Direct metal laser sintering of a titanium structure for a competition bicycle. Courtesy of EOS

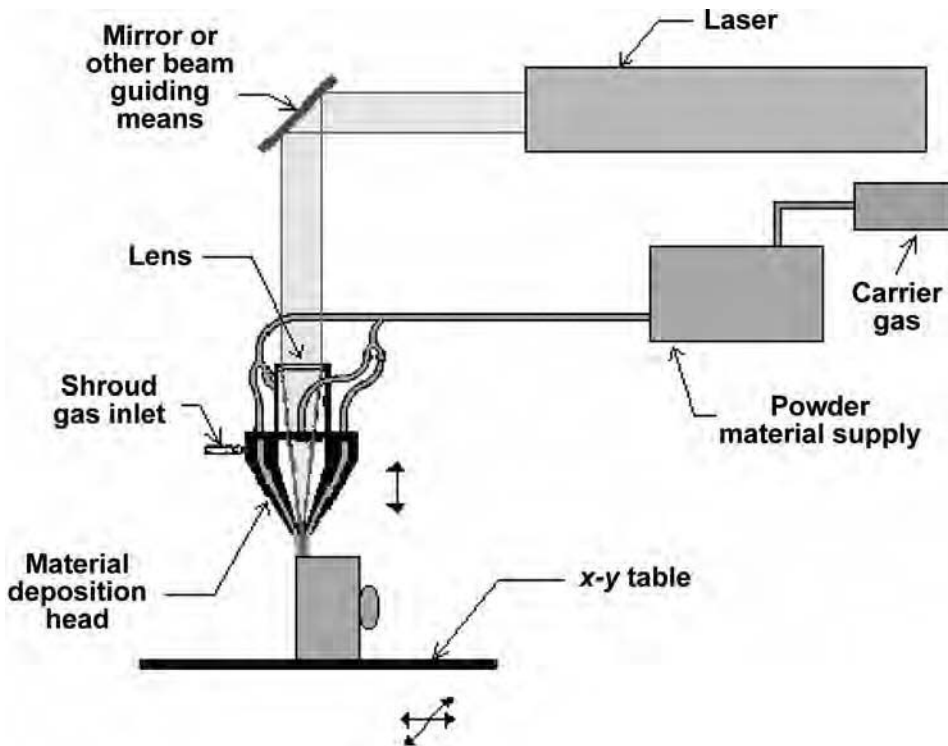


Fig. 9 Laser-engineered net shape process. Courtesy of Castle Island Co.

deposition rate but may result in materials savings. By the previous definition, the deposition of large titanium alloy backbone structures for aircraft that require extensive machining may be considered 3-D cladding, while repair or modification of turbine components, molds, or dies requiring less finishing may be considered near-net shape additions. Direct powder methods for near-net shape deposition use sophisticated powder-delivery systems and laser heads to allow the precise delivery of powder to the pool and laser focal region, allowing rapid omnidirectional movement and out-of-position deposits. The process is not limited to vertical deposition or gravity-assisted powder feed. The inert delivery gas is typically argon, although nitrogen or other gas mixes are possible.

In comparison with powder bed methods, directed powder methods are not limited by chamber size constraints. Switching powders or mixing powders to obtain functionally graded deposits is more easily facilitated with the use of multiple powder feeders, although precise control of powder mixing remains a technical challenge. Active control of a wider range of process control parameters is possible to optimize the quality, uniformity, and repeatability of the deposit and deposition rate at the cost of process complexity. As with welding or cladding, the resultant microstructure and properties of the deposit are highly dependent on the process parameters and fabrication environment. Qualification, standardization, and acceptance of the materials remain a challenge

when proposed for critical components such as those for aircraft, aerospace, or nuclear applications. To meet these standards, material properties must be duplicated across laser deposition platforms and vendor machines from one fabrication event to the next. Given the process sensitivity and the large number of variables to control, the need for real-time process control and sophisticated process planning is needed.

A 3-D solid model is often used as a starting point for both processes. The powder bed method will often create a tessellated shell structure and two-dimensional planar slices to produce profile and raster paths for the fusing of the powder bed. In addition, the directed powder method may use conventional CNC path-planning algorithms, such as those used for CNC milling. This technique can be used to create multiaxis deposition paths, increasing process flexibility at the cost of programming complexity. Adaptive sensing and control has been demonstrated for directed powder methods. To fully realize the optimization of all process parameters and the part itself, future systems may require rule-based or intelligent system integration of CAD, computer-aided engineering, finite-engineering analysis, CAM, and real-time control.

Variants of the process include multiple powder feeders and mixing to create functionally graded deposits and powder recycling to reduce process waste. Full enclosure of the process within an inert chamber can offer class I isolation of the laser beam and containment of environmental and health hazards associated with



(a)



(b)

Fig. 10 Examples of complex shapes fabricated by powder deposition. (a) Rebuild of the tip of a turbocharger blade. (b) Feed screw with welded-on Stellite layer. Stellite alloys are hard cobalt-chromium-base alloys. Reprinted with the permission of Sulzer Innotec, Winterthur, Switzerland

powder processing, but is not required. Multi-axis movement of the laser head out of a vertical orientation, such as typical with robotic or CNC articulation, creates the additional hazards of protecting personnel from class IV laser hazards. Multiple instances of the same part may be fabricated at the same time within the working envelope of the chamber. As with the powder bed method, complex internal structures are easily fabricated using this method. As with powder bed methods, dimensional accuracies of up to 0.1 mm (0.004 in.) are achievable, while deposition rates of 10 to 100 cm³/h (0.6 to 6 in.³/h) may be achieved but are material- and laser-dependent.

Process parameters include laser power, laser focal spot size, speed, path overlap, path step-up distance, and powder type and size. In

addition, other key parameters include powder feed rate, delivery gas type and flow rate, and nozzle configuration and orientation. Powder feed material considerations affecting precise and consistent delivery include powder morphology (spherical, angular, or agglomerated) and powder size, density, and purity. Substrate material considerations include degree of dilution, metallurgical compatibility, cleanliness, and other heat-sinking (thermal) or mechanical constraints that could lead to undesirable characteristics of the deposited material.

Future Directions for Near-Net Shape Processing

The future of near-net shape processing using laser powder fusing will benefit greatly by advances in laser cladding technology development, since those applications are likely to achieve greater near-term acceptance because of process simplicity and as direct replacement of existing cladding applications. Standardization and qualification of deposited materials will be driven by applications in the aerospace and nuclear industries, while the ability to create materials with uniquely designed properties will be driven by innovation. To fully realize the potential of near-net shape laser deposition, an entirely new set of tools will be required to fully integrate design through manufacturing. A new methodology is needed, from concept through computer-aided design, engineering, fabrication, and control, to fully optimize and use the many process parameters and to break free from conventional processing constraints. Challenges identified a decade ago, such as surface finish, accuracy, deposition rate, and control of residual stress and distortion, are being met through evolutionary changes to the processes, diagnostics, modeling, and control. Significant advances in the past decade have moved the technology out of universities and national laboratories and into industrial application. Future technology development (Ref 27) promises a greater pace of technology adoption and many new applications.

REFERENCES

1. B.K. Paul, A Review of Particulate Materials Processing in Additive Freeform Fabrication, *Rev. Part. Mater.*, Vol 4, 1996, p 105–120
2. D.S. Gnanamuthu, Laser Surface Treatment, *Opt. Eng.*, Vol 19 (No. 5), 1980, p 783–792
3. W.M. Steen and C.G.H. Courtney, Hardfacing of Nimonic 75 Using 2 kW Continuous-Wave CO₂ Laser, *Met. Technol.*, Vol 7 (No. 6), 1980, p 233–237
4. V.M. Weerasinghe and W.M. Steen, *Laser Cladding by Powder Injection*, IFS Ltd., 1983, p 125–132
5. V.M. Weerasinghe and W.M. Steen, *Laser Cladding by Powder Injection, Transport Phenomena in Materials Processing*, J. Mazumder, M.M. Chen, and C. Tucker, Ed., ASME, 1983, p 15–23
6. V.M. Weerasinghe and W.M. Steen, *Laser Processing of Materials (Laser Cladding with Pneumatic Powder Delivery)*, 1983, p 166–174
7. V.M. Weerasinghe and W.M. Steen, *Computer Simulation Model for Laser Cladding*, Vol 10, American Society of Mechanical Engineers, Production Engineering Division, 1983, p 15–23
8. L.J. Li and J. Mazumder, *Study of the Mechanism of Laser Cladding Processes*, Metallurgical Society of AIME, 1985, p 35–50
9. J. Mazumder, *State-of-the-Art Laser Materials Processing*, Vol 2 (No. 115), ASME, 1987, p 599–630
10. E. Toyserkani, A. Khajepour, and S. Corbin, *Laser Cladding*, CRC Press, Boca Raton, FL, 2005
11. W.D. Callister, Jr. and D.G. Rethwisch, *Materials Science and Engineering: An Introduction*, 8th ed., Wiley, 2010
12. M. Zhong and W. Liu, Laser Surface Cladding: The State of the Art and Challenges, *Proc. IMechE Part C: J. Mech. Eng. Sci.*, Vol 224, p 1041–1080
13. L. Pawlowski, Thick Laser Coatings: A Review, *J. Therm. Spray Technol.*, Vol 8 (No. 2), 1999, p 279–295
14. J.E. Gray and B. Luan, Protective Coatings on Magnesium and Its Alloys—A Critical Review, *J. Alloy. Compd.*, Vol 336, 2002, p 88–113
15. Y.S. Tian, C.Z. Chen, D.Y. Wang, and T. Q. Lei, Laser Surface Modification of Titanium Alloys—A Review, *Surf. Rev. Lett.*, Vol 12 (No. 1), 2005, p 123–130
16. G. Xu, M. Kutsuna, Z. Liu, and K. Yamada, Comparison between Diode Laser and TIG Cladding of Co-Based Alloys on the SUS403 Stainless Steel, *Surf. Coat. Technol.*, Vol 201, 2006, p 1138–1144
17. Y.T. Pei and J.Th.M. De Hosson, Functionally Graded Materials Produced by Laser Cladding, *Acta Mater.*, Vol 48, 2000, p 2617–2624
18. W. Ul Haq Syed, A.J. Pinkerton, Z. Liu, and L. Li, Coincident Wire and Powder Deposition by Laser to Form Compositionally Graded Material, *Surf. Coat. Technol.*, Vol 201, 2007, p 7083–7091
19. S. Wen and Y.C. Shin, Modeling of Transport Phenomena during the Coaxial Laser Direct Deposition Process, *J. Appl. Phys.*, Vol 108, 2010, p 044908
20. R.W. McVey, R.M. Melnychuk, J.A. Todd, and R.P. Martukanitz, Absorption of Laser Irradiation in a Porous Powder Layer, *J. Laser Appl.*, Vol 19 (No. 4), 2007, p 214–224
21. G.K. Lewis et al., Directed Light Fabrication of Near Net Shape Metal Components, *Advances in Powder Metallurgy and Particulate Materials—1996, Proceedings of the International Conference on Powder Metallurgy and Particulate Materials*, Metal Powder Industries Federation, Princeton, NJ, 1996, Section 15, p 65–76
22. J. Mazumder et al., Rapid Manufacturing by Laser Aided Direct Deposition of Metals, *Advances in Powder Metallurgy and Particulate Materials—1996, Proceedings of the International Conference on Powder Metallurgy and Particulate Materials*, Metal Powder Industries Federation, Princeton, NJ, 1996, Section 15, p 107–118
23. D.M. Keicher et al., Free Form Fabrication Using the Laser Engineered Net Shaping (LENS) Process, *Advances in Powder Metallurgy and Particulate Materials—1996, Proceedings of the International Conference on Powder Metallurgy and Particulate Materials*, Metal Powder Industries Federation, Princeton, NJ, 1996, Section 15, p 119–127
24. F.G. Arcella et al., Material Characterization of LaserCast Titanium, *Advances in Powder Metallurgy and Particulate Materials—1996, Proceedings of the International Conference on Powder Metallurgy and Particulate Materials*, Metal Powder Industries Federation, Princeton, NJ, 1996, Section 15, p 151–165
25. J. Sears, Development of Laser-Powder Additive Manufacturing for Industry Historical Perspective: Current and Future Applications, *Powder Materials: Current Research and Industrial Practices III*, D. S. Marquis, Ed., TMS, 2003
26. J. Mazumder and H. Qi, Fabrication of 3-D Component by Laser Aided Direct Metal Deposition, *Critical Review: Industrial Lasers and Applications*, J.T. Schriempf, Ed.; *Proceedings of SPIE*, Vol 5706, SPIE, Bellingham, WA, 2005
27. D.L. Bourell, M.C. Leu, and D.W. Rosen, *Roadmap for Additive Manufacturing*, University of Texas Austin, 2009

Laser Weld Quality Monitoring

Randolph Paura, Dynamic Laser Solutions

WELD QUALITY MONITORING is an integral part of manufacturing operations. In the early years of accelerated deployment of laser welding (pre-mid-1980s) in fully automated environments, it occurred to manufacturing engineers that there was no indication or display that told them that the laser beam had reached the part, let alone a quality weld had been produced. From investigations into the strategies and technologies to supply this information, it was found that emissions from the laser welding process could be detected and analyzed in such a way that weld quality could be ascertained to a useful degree (Ref 1–4). The integration of laser weld quality monitoring into the automated welding systems was found to be a useful and necessary addition to the existing quality program.

Laser weld inspection entails various monitoring options. This article reviews weld quality monitoring considerations for automotive materials (steel and aluminum), with a focus on photosensor technology. Radiative emission monitoring has seen considerable progress over the past years and can reliably determine weld quality. To establish a weld quality monitoring system with confidence and reliability, an appropriate selection of equipment, procedures, and people is required. Weld quality monitoring is part of a manufacturing strategy to ensure that weld defects are held to a very low number (for example, less than 5 parts per million). Working toward 0% product defects requires 100% laser weld inspection.

Numerous works are available regarding laser weld quality monitoring, and improvements in the process are continually being made. By understanding the elements of a quality weld, the weld process indicators and inspection options will provide the means for a company to select and implement the appropriate equipment. The goal is to maximize productivity, achieve and maintain confidence with the quality monitoring system, and reduce downtime for weld destruction inspections. As much as weld quality monitoring has been viewed as imprecise in the past, there are robust and reliable considerations available.

Overview of Laser Welding

Although other articles provide extensive details on laser welding, this section is a brief

review to establish the foundation for understanding the application of weld quality monitoring. Some basic process parameters are introduced first, followed by some application aspects related to automotive manufacturing. Laser welding of automotive frames and components has a demonstrated track record for operations efficiency and product optimization in Europe, with increasing levels of acceptance in North America.

Although laser welding is not a direct substitute for gas metal arc welding (GMAW) or resistance welding methods, laser welding does have benefits to offer for an automotive assembly. Most applications in the automotive industry center on the deep-penetration laser welding process, because it provides the speed necessary for economic justification. Benefits include:

- Contact-free processing
- High process speed (higher production rate or reduced floor space)
- Controlled heat input (smaller heat-affected zone)
- Joint geometry flexibility (single-sided accessibility, small flanges)
- Material process flexibility (metals, plastics)
- Process flexibility from one power source (heat treatment, cutting, welding)
- Process integration (potential to eliminate production steps)

- Process substitution (potential to alter production process steps)

The cost of a laser welding system is considerably higher than other traditional welding systems, but there has been a steady growth in applications for laser welding. This is due in part to the continuing improvements in power source reliability, laser power and beam quality, and power source diagnostics.

Laser Welding Process Description

Lasers produce coherent electromagnetic radiation that can be focused to a small spot size, resulting in a high power density. If the power input is greater than the heat dissipation capabilities of the material, melting occurs. At even greater power densities (above the critical or threshold limit), the material is vaporized, resulting in keyhole (or penetration) laser welding. (See the article “Laser Beam Welding” in this Volume for more details.)

Penetration (keyhole-mode) laser welding occurs when laser power density is above the vaporization threshold for the parent material (Fig. 1). Penetration (keyhole) welding is accomplished when the focused beam achieves a power

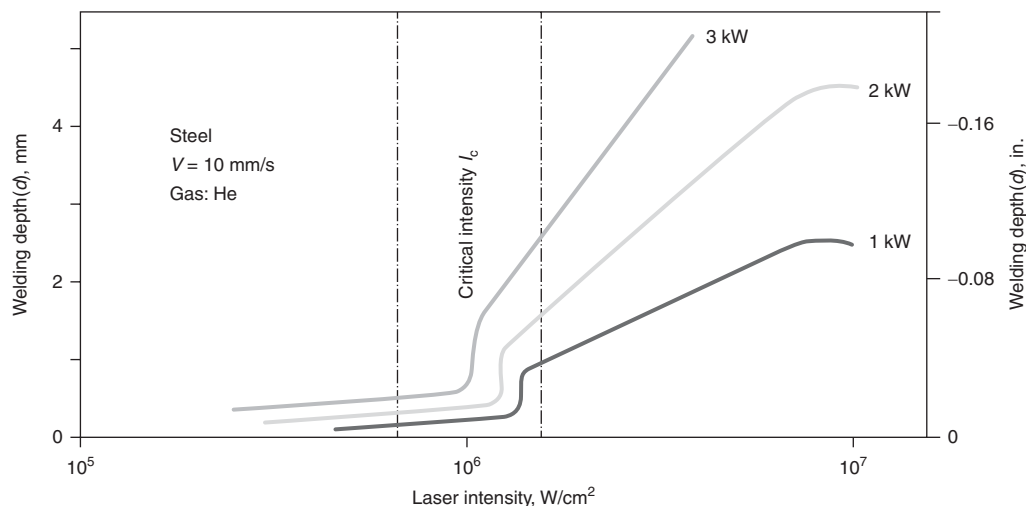


Fig. 1 Laser intensity and welding depth

density greater than the critical value ($\sim 10^6$ W/cm² for steels in atmosphere). With power levels above this threshold, vaporization of material is achieved, which allows for deeper and faster welding than can be accomplished with conduction-limited welding (Fig. 2). In laser welding for automotive components, welding speed is advantageous, and so most automotive applications concentrate on penetration laser welding.

Once a keyhole is produced, if the material and laser beam remain stationary, then a hole will be generated with no further results. Moving the focused laser beam relative to the workpiece to be welded produces the following actions:

- The material is partially vaporized and melted by the laser beam.
- The plasma plume generated is greater than the viscosity of the melt pool, forcing it away from the laser beam.
- As the beam proceeds through the material, the keyhole will collapse and a new one is generated.
- The collapsed keyhole (weld) solidifies as it cools.

The high energy density nature of the laser process then presents the following challenges:

- Ensuring the thermal gradient between the weld and the parent material is not excessive (which leads to cracking upon solidification)
- Excessive alloying elements are not lost in the weld through vaporization
- Controlling the size of the melt pool for the joint; too large or small results in poor weld quality (excess or insufficient heat input)

Understanding the material characteristics with appropriate laser weld equipment, configured for process tolerance, will result in welds that are able to meet specifications and, in turn, are dependable.

Penetration (Keyhole) Welding Process (Ref 5). Figure 3 is a schematic of the weld region from penetration laser welding. The laser beam is focused to provide sufficient power density above the critical threshold (10^6 to 10^7 W/cm²). For a 2 kW ytterbium (Yb): fiber, Yb:disc, or neodymium: yttrium-aluminum-garnet (Nd:YAG) (near-infrared) power supply, this equates to a focused beam diameter that is less than 0.5 mm (0.02 in.).

At this power density, the laser beam heats, melts, and vaporizes the steel in its path in a rapid manner. If no motion is introduced, all the metal is vaporized and a hole is “pierced” through the steel with no further action taking place. The laser beam is simply passing through the steel. By moving the laser beam along the weld joint, material is melted in the front half of the beam, with material solidifying along the trailing portion of the beam path.

To protect the molten metal from the atmosphere, a shielding gas is necessary, akin to the GMAW process, which is also referred to metal inert gas (MIG) welding. Common shielding gases for near-infrared laser welding are argon and/or helium. Helium is a common shield gas for CO₂ lasers, although argon may be successfully used for lower power levels (approximately <3 kW).

Various parameters influence the productivity and quality of the laser weld (Ref 6). Each must be assessed and addressed carefully:

- **Laser parameters:** Power (for pulsed laser beam welding, this should be either peak or average, pulse width, pulse repetition rate), beam mode, angle of divergence, focusing (includes spot size and caustic waist profile), polarization, focal position with respect to the workpiece surface
- **Process parameters:** Weld travel speed, shielding gas, weld joint gap
- **Workpiece/tooling:** Material(s), material thickness, workpiece surface (roughness, oxidation, cleanliness), workpiece properties, fixturing and tooling

Because laser welding is a high energy density process, the system requirements for quality and consistency are greater than with GMAW (also known as MIG welding).

In general, the high energy density allows for a rapid weld speed. Consequent to this, there is a small or narrow heat-affected zone. These features can be used to a great benefit when dealing with low-carbon steels. With high-carbon (or equivalent) steels, the rapid cooling of the weld zone can/will result in a hard/brittle weld. This can be overcome by reducing the weld speed or power density or by using other process parameter changes, such as dual-pass welding (one to preheat and one to weld). The result is that each weld application is unique and should be prototyped to verify the system requirements and the productivity capabilities.

Laser Weld Characteristics

Key Weld Quality Elements (Ref 7). The key weld quality elements include:

- **Weld penetration:** Readily verified with weld cross sections or visual inspection of the backside of full-penetration welded parts. Penetration depends on the cross-sectional size/shape of the weld.
- **Weld strength:** May be assessed by uniaxial tensile testing. The ultimate tensile and yield strength levels depend on the material, weld metallurgy, joint geometry, application of load, and weld-parent material interface.
- **Hardness and ductility:** Depends on material (s) welded, thermal experience during welding, and any postweld heat treatment/tempering

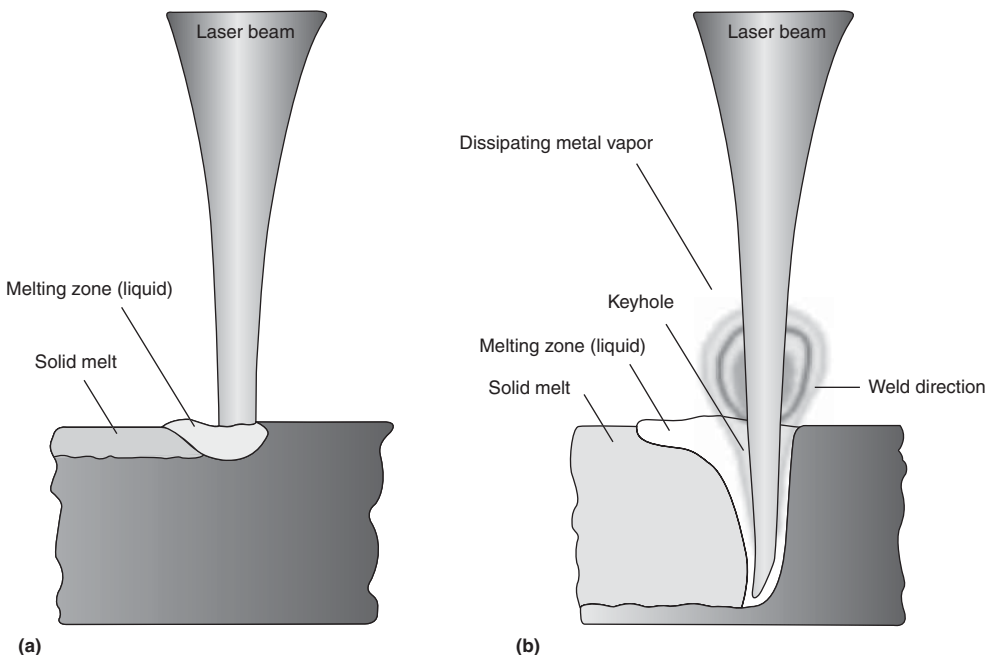


Fig. 2 Laser welding processes. (a) Conduction-limited laser welding. (b) Penetration (keyhole) laser welding

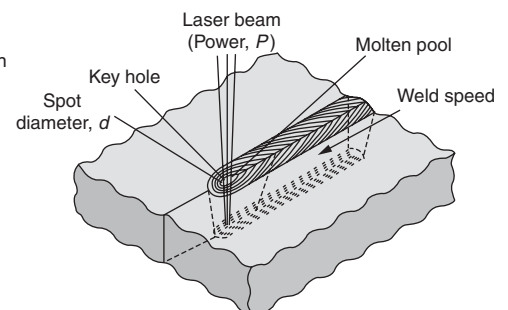


Fig. 3 Schematic of weld region from penetration laser welding

- **Cracking:** Although cracking is not desired, it may be allowed in certain cases, depending on the application of the weld (within limitations). If not allowed (as in welds subject to forming operations), relevant inspection methods are metallographic sectioning or nondestructive methods, such as visual, ultrasonic, dye penetrant, or radiographic inspection.
- **Undercutting:** Localized reduction in the weld cross section caused by metal flow into the weld joint
- **Porosity:** Voids can vary considerably within a weld. Like cracking, these are not desired (especially in stamping operations). The specifications should list the acceptable pore number/sizes allowed.
- **Hermeticity:** A weld providing a seal that encloses a volume will be subject to specifications such as a maximum leak rate and/or minimum burst pressure.
- **Cosmetics/appearance:** Can be quite subjective. Where welds are exposed and subject to postprocess operations (such as e-coating and/or painting), the visual appearance may be crucial from a customer-perception viewpoint.
- **Augmented laser weld process considerations:** Can enhance process tolerance and address metallurgical challenges (such as when welding certain aluminum alloys, high-carbon-content steels, or other alloys). Examples, which may include the use of cold or hot filler wire as appropriate to replace lost alloying elements, include hybrid welding, such as laser + MIG or laser + plasma, to extend the weld process tolerance window.

Figure 4 tables a schematic illustration of the different types of defects encountered when laser welding metallic materials (Ref 8).

Joint Configurations (Ref 9, 10). For laser-welded joints, gap tolerances are stricter than GMAW (MIG welding) joints, because the parent material is used for joint fusion with no filler wire added (except as may be required when welding aluminum). Gap limitations vary according to the joint configuration, as illustrated in Fig. 5.

Process Variables

The high beam energy and material interaction of the laser welding process gives rise to various parameters that affect the ability to achieve a quality weld. Grouping and understanding the various parameters that affect the quality of laser welds is necessary to configure a system that provides quality welds on a consistent basis. If parameters are fixed (with the equipment settings), then it is imperative that the quality of materials is maintained and there is process tolerance to allow for variations (within limits) that

will occur (with materials to be welded). Conversely, if adaptive controls are implemented, methods are needed to sense, interpret, calculate, and implement appropriate responses at a cycle rate that is greater than the process itself.

Defining the process parameters is essential in evaluating weld defects and monitoring weld quality. Details of the laser weld process have been the subject of various studies and discussions (Ref 11–13), but the depiction of a keyhole laser weld (Fig. 6) helps illustrate some basic elements of the process and the resulting weld. A more detailed description of the laser beam welding process is also found in the article “Laser Beam Welding” in this Volume.

By moving the laser beam along the weld joint, material is melted in the front half of the beam, with material solidifying along the trailing portion of the beam path. Surface tension of the molten metal helps to stop the melt flow, forming the weld pool behind the laser (Fig. 7).

To protect the molten metal from the atmosphere, a shielding gas is necessary, akin to the MIG welding process. Helium is a common or the first choice of shield gas for CO₂ lasers (10.6 μm). Argon and/or helium shielding gases are common for Yb: fiber lasers (1.07 μm), Yb: disc lasers (1.03 μm), or Nd-YAG lasers (1.064 μm).

Thermophysical properties (parent material) include:

- Absorptivity (an influencing factor to initiate keyhole welding)
- Melting point (influences required power level and weld speed for a given focused spot size)
- Surface tension (ability to form a weld joint; influences undercut and the molten material dynamics affecting penetration)
- Thermal conductivity (affects weld speed)
- Thermal diffusivity (affects weld size)
- Vapor pressure (affects stability of keyhole)
- Viscosity (affects stability of keyhole)









Defect	Explanation
 Cracks	Hot crack in the fusion zone or cold in the heat-affected zone
 Porosity and gas pores	Voids in the material: Spherical = gas bubbles Irregular = impurities
 Incomplete penetration	Not deep enough penetration
 Linear misalignment	The centerlines of two parts do not coincide.
 Lack of fusion	The two parts are not welded throughout the entire weld zone.
 Undercut Root sagging	Lack of material in upper weld zone Too much material in lower weld zone
 Reinforcement Root cavity	Too much material in upper weld zone Not enough material in lower weld zone
 Blowout	Crater formation on top surface

Fig. 4 Various types of defects that occur during laser welding. Source: Ref 8

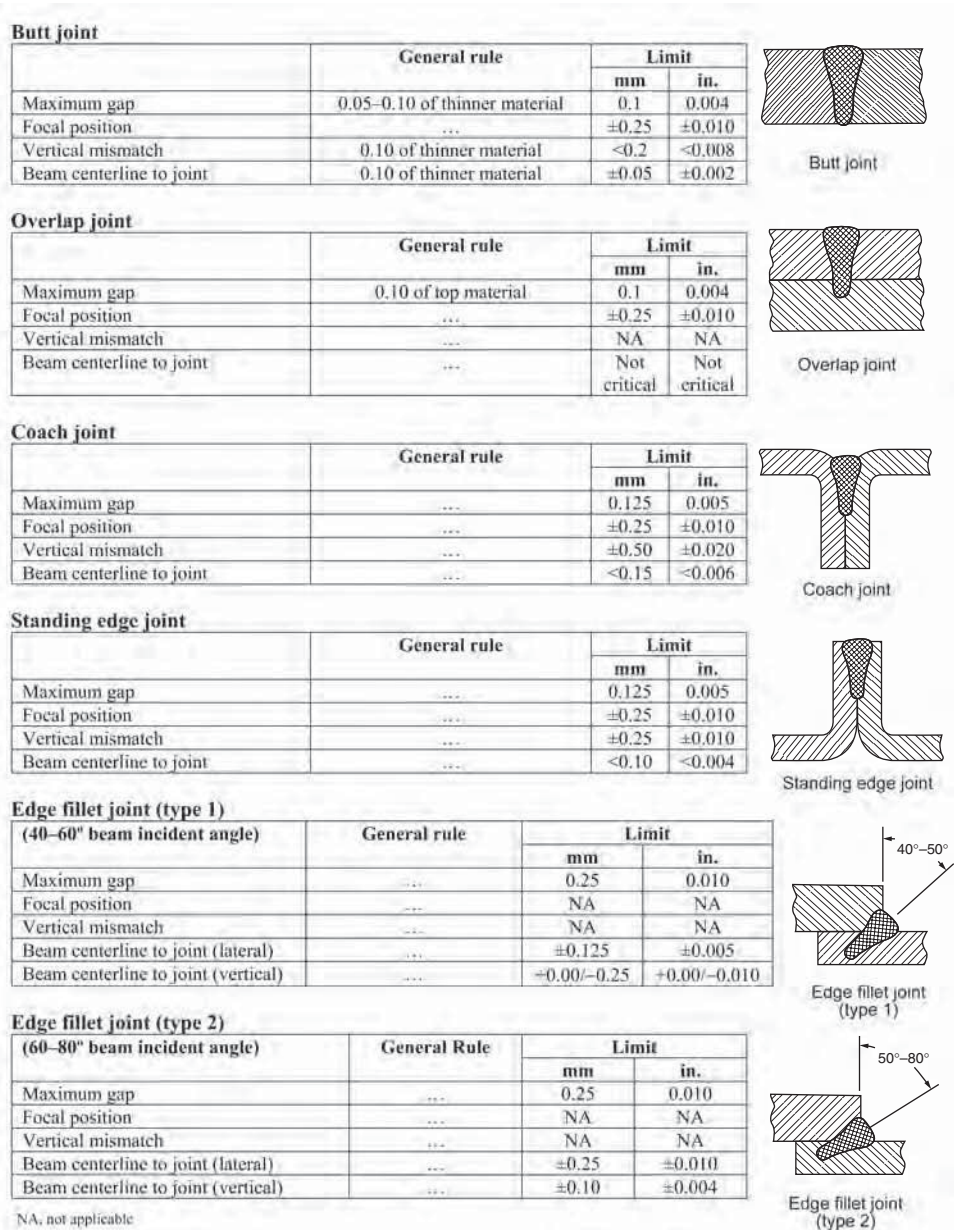


Fig. 5 Gap limitations vary according to the joint configuration for penetration (keyhole) laser welding.

- Loss of alloying elements (affects weld integrity and properties)

Process parameters (equipment configuration) include:

- Beam alignment (position relative to weld joint)
- Beam diameter (ability to bridge joint gaps)
- Beam focus position (influences weld profile)
- Beam irradiance (power density influences weld speed and depth of penetration)
- Joint geometry (affects allowable gap tolerances)
- Weld travel speed

- Shielding gap (influences plasma plume)
- Degree of process monitoring

Characteristic Laser Weld “Signals”

The product of the aforementioned parameters determines the behavior of the actual laser weld process, which, of itself, generates distinct signals (Fig. 8) that may be monitored. Knowing these characteristic signals and how they pertain to weld quality provides the means to achieve reliable weld quality monitoring. During the weld process, a portion of the laser light is reflected. Monitoring this energy level

can reveal if there is an excessive gap (little or no reflected energy) or poor coupling (excess reflection).

The creation and collapse of the keyhole when laser welding creates an acoustic signal (time dependence, frequency, and intensity) that has been used for weld quality monitoring. Acoustic signals generated from the laser weld process range from the audible (20 Hz to 20 kHz) and can extend to megahertz frequencies. Most useful information can be gathered over a smaller frequency range (20 to 100 kHz). The formation of metal vapor and plasma can be related to the actions of the melt pool and are characterized by acoustic frequencies generally less than 10 kHz. Hence, the core of acoustic emission (100 Hz to 20 kHz) relating to vaporization, plasma formation, instability, and mass motion of the melt pool in the keyhole is typically analyzed with quality monitoring (Ref 9).

The action of the molten pool and formation and collapse of the keyhole all generate structure-borne acoustic emissions that can be monitored as well. Structure-borne acoustic signals are generated by (Ref 12):

- Phase transformation of the parent material (solid-liquid) via the focused laser beam and conversely with the solidification of the weld pool
- Micromechanisms such as crack growth during phase transformation and subsequent cooling of the weld bead

The generation of metal vapor and subsequent plasma is another process indicator that can be monitored. Plasma conductivity (electron density) has been investigated as a diagnostic technique for weld quality monitoring (Ref 15, 16). An area that has received greater investigation is the spectral range of the electromagnetic radiation emission from the metal vapor/plasma plume. Monitoring this spectral range provides means to infer the quality of the laser weld process (immediately prior to keyhole collapse and molten pool solidification). Selective grouping of the spectral range monitoring provides more accurate means to analyze and infer weld quality. The metal vapor/plasma plume contains both ultraviolet and visible light electromagnetic radiation (1 to 700 nm).

The weld bead temperature can be measured with a near-infrared sensor, which can help assess weld quality. Spatter generated from the laser weld process also can be monitored for process consistency and stability with a near-infrared sensor.

Grouping the various radiative emissions from the keyhole and workpiece during laser welding helps to understand the greatest opportunity for data acquisition to analyze and infer weld quality. The chart in Table 1 (Ref 11) indicates radiative emission power (W) during laser welding of 1 mm (0.04 in.) steel with a 2.5 kW CO₂ laser (with 0.4 mm, or 0.016 in.,

spot size) at 60 mm/s (2.4 in./s). The infrared and ultraviolet spectra have the largest fraction of the radiated energy as possible signals for monitoring, supplemented by the visible spectrum, generated within the keyhole itself.

Real-Time or In-Process Monitoring

The quality of a welded component is determined by various means of weld inspection, process monitoring, and production control, depending on the required level of confidence determined by the functionality of the product and/or customer requirements. In the automotive sector, which typically requires a statistical probability of failure of components no greater than 5 parts per million, it is necessary to ensure that laser-welded components meet stringent quality requirements.

Monitoring methods include destructive testing and various nondestructive inspection methods common to other fusion welding processes. Real-time or in-process monitoring is also done with optical, acoustic, and/or charged-particle sensors. Real-time monitoring provides online validation and a database for monitoring process drift and deviations. Provided it does not interfere with production processes, real-time monitoring is becoming increasingly in demand as part of quality-assurance documentation. To be beneficial to production, a high degree of confidence must be statistically established to minimize the occurrence of both false positives and false negatives.

- Acoustic signals from the creation and collapse of the keyhole
- Electromagnetic signals from the laser weld process
- Imaging the weld after the keyhole (x-ray or other means)

An excellent review of sensor technology for weld quality monitoring can be found in Ref 17.

Acoustic Monitoring. Acoustic diagnostics is based on the premise that the behavior of good and bad welds generates a respective

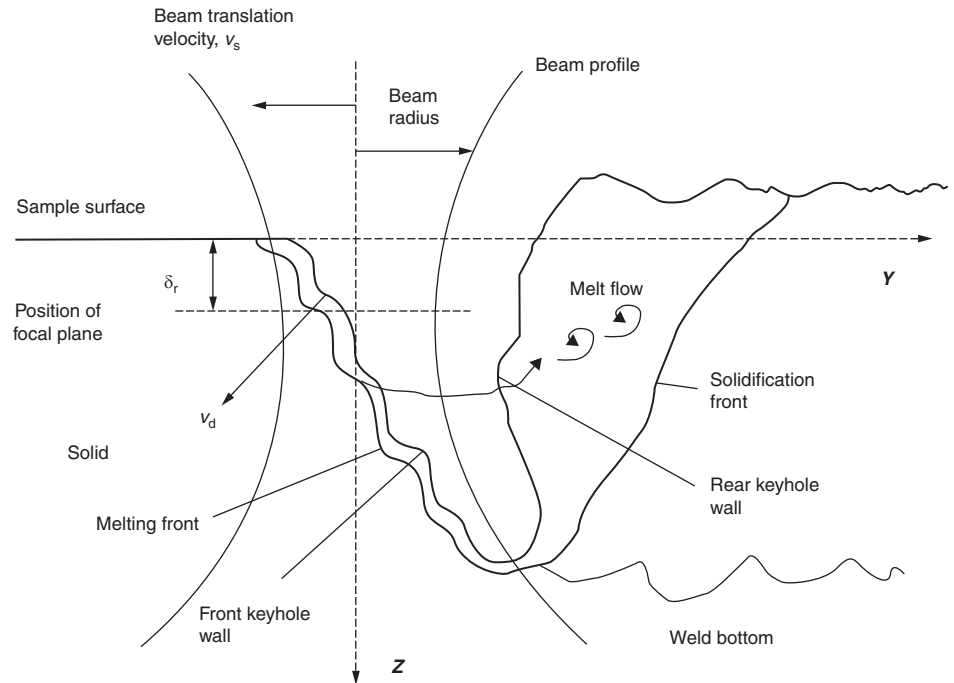


Fig. 7 Cross section of weld pool. Source: Ref 14

Sensors

The reliability of various signals generated by the laser weld process requires statistical process control methods to demonstrate their consistency and dependability to accurately qualify the various aspects/feature of the weld quality being monitored. Nondestructive, real-time monitoring of the laser weld has been explored in the following areas:

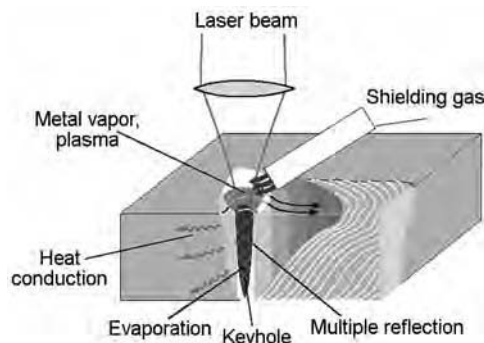


Fig. 6 Depiction of a keyhole laser weld structure. Courtesy of Precitec-Jurca

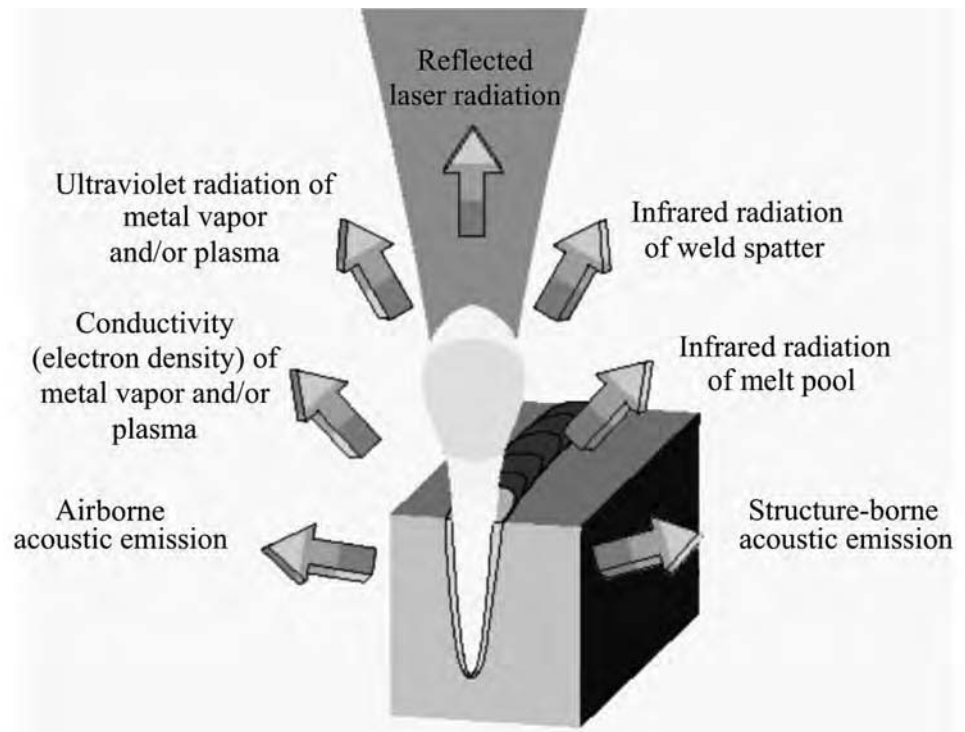


Fig. 8 Signals from a penetration (keyhole) laser weld

acoustic signal that can be translated (via fast Fourier transformations) to discern between acceptable and unacceptable welds. New methods for analyzing acoustic emissions (AE) have demonstrated great promise (Ref 18).

Acoustic emission can provide significant process data, because it has a high signal-to-noise ratio, is noncontact, and can be accomplished in real-time. When the frequency data are broken down into discrete bands, it is possible to determine the weld quality with a reasonable degree of reliability. Acoustic emission analysis can also be used to complement other weld quality monitoring systems. As with any process-monitoring system, AE-based analysis must demonstrate reliability and confidence to be solely relied upon for critical components.

Numerous articles and resources are available regarding acoustic monitoring of laser weld quality (Ref 19–27).

Electromagnetic Monitoring. Thermal emission monitoring is proving to be quite reliable, as shown by its implementation for laser welding of air bag deployment canisters. Using single to multiple sensors, with recorded data of acceptable welds and some “fuzzy logic,” these units provide a reliable means for real-time weld quality monitoring. Electromagnetic sensors measure discrete ranges of energy/intensity from the laser weld process. The most common sensors are:

- Ultraviolet for detection of the plasma plume intensity
- Infrared detection of keyhole molten metal
- Temperature detection of the weld bead behind the weld pool at the solid-liquid interphase
- Reflected laser power detection

These signals will vary over the course of a single weld length; hence, it is necessary to capture a “signature” of an acceptable weld and set boundaries, which identify acceptable upper and lower limits to these signals.

The relationship between the detected signals and the occurrence of welding faults at the surface of the weld has been proven in extended tests. Sensors such as these do not directly monitor the welding depth but process emissions, which are closely correlated to the welding depth.

A variety of material is available regarding various spectra of sensor analysis and their relationship to weld quality (Ref 28).

Electromagnetic acoustic transducers (EMATs) are rising quickly in the field of non-destructive testing/evaluation of welds. The principle of operation for this technology is based on establishing a magnetic field in a conductive material and subsequently imparting a high-frequency (radio-frequency, or RF) pulse by way of a coil above the same material. The RF pulse interacts with the magnetic field to produce a mechanical force in the elastic material, resulting in an acoustic pulse at the same frequency as the RF pulse (usually ultrasonic). All of this can be accomplished without any physical contact or coupling fluid with the test material. The height of the EMAT is approximately 1 mm (0.04 in.) above the test material, which then allows for ultrasonic inspection of materials (Ref 29). This technology shows promise for postweld process quality-control monitoring.

Weld Process Signals

Different materials generate different signals when being laser welded. Figure 9 (Ref 30) depicts the stability of the keyhole for three different metals, from a single sensor. Single-sensor monitoring of the complex laser weld process does not ensure absolute quality assurance. A combination of sensors provides the best means for confidence.

Process Monitoring and Weld Defects. Different process monitoring means have demonstrated the ability to determine specific laser weld defects as they occur. Table 2 illustrates what can be expected of the various sensors available (Ref 28, 31). The best means of ensuring real-time weld quality monitoring are those systems that use multiple sensors (more than one) in a relational basis, which then leads to how the benchmark data are first acquired for an acceptable weld and how the data are used.

Data-Acquisition Rate. The required data-acquisition rate is generally a function of the weld speed and desired “resolution” of signal information. Consider a weld speed of 100 mm/s (6.0 m/min, or 234 in./min), with a requirement that a failure size be no greater

than 0.5 mm (0.02 in.). This equates to a signal rate of 200 Hz. Analog photodiode detectors can reach upward of 1 kHz for a signal rate. It is important to ensure that the data-acquisition unit (computer) can receive and process multiple signal sources while maintaining the individual signal rate without a loss of information.

Selection of Weld Monitoring System

For a description of selection factors, the following describes considerations with regard to radiative emission monitoring of welding with an Nd:YAG laser. The working example assumes a photodiode-based system, with three sensors at the workpiece and an additional fourth sensor for monitoring the laser power delivered. A computer stores signal data and provides software for analysis.

Selection of Weld Monitoring Sensors. Figure 10 illustrates the arrangement of a single sensor for monitoring the weld process quality within a defined spectrum (as determined by the sensor selection and additional filters). The adjustable aperture determines the location of the field of view for the sensor, providing the ability to inspect the weld bead temperature behind the keyhole. The adjustable lens determines the field of view for the sensor. The arrangement shown is for a 90° Nd:YAG weld head (other configurations are possible).

Appropriate selection of sensors depends on the makeup of the emission spectrum for monitoring (Fig. 11). The example shown in Fig. 12 has three sensors that are used at the welding head. The temperature sensor (T) ranges from 1000 to 1800 nm and is located a few millimeters behind the weld pool, which avoids any influence that the Nd:YAG laser may have at 1064 nm, rather than examining the actual temperature of the keyhole itself.

The reflected radiation sensor (RR) has a narrow spectral response, ~1064 nm, because it is detecting the amount of back reflection during the weld process, which is aligned with the keyhole. The plasma sensor (P) has a limited spectral range of 440 to 500 nm to provide a signal “signature” that is specific to the behavior of the plasma plume during the keyhole welding process.

A working example of such is provided with the laser keyhole spot weld of titanium (Ref 32). Data collected by two sensors—reflected laser power and temperature—are plotted in Fig. 13 for a peak laser power of 1200 W over 10 ms. From the data plot, the stages are:

- The initial laser beam is reflected by the material, until enough energy has been absorbed to initiate a keyhole.
- Within 0.8 ms, the reflected laser power has reached its maximum, whereupon the heating phase of the material has translated into melting and vaporization.

Table 1 Emitted radiation power from keyhole region and workpiece during laser welding

Spectrum	Spectrum wavelength, nm	Emitted radiation			Keyhole proportion, %
		From workpiece, W	From keyhole, W	Total radiation, W	
Infrared	700–2000	0.152	4.787	4.940	96
Visible	400–700	0.006	1.739	1.745	99
Ultraviolet	1–400	0.003	8.120	8.124	99
Soft x-ray	1–10	0.000	0.000	0.000	...
All	1–2000	0.161	14.646	14.808	99

Source: Ref 11

- Beyond 0.8 ms, the reflected laser beam decreases as it becomes increasingly absorbed in the keyhole. Note the rise in the material temperature.

An energy balance between heat transfer and energy deposition is achieved at 6.8 ms, characterized by the nearly constant back reflection signal and temperature signal. At 10 ms, the laser beam is turned off, with a simultaneous drop in the temperature signal (but at a slower rate).

Data Acquisition. The weld process is monitored with three sensors at the weld head and an additional power sensor at the laser power source. Online process monitoring also is connected to a computer for the selection of weld-monitoring programs, reception of bad part signal(s), and weld-start and weld-end signals.

Software is needed to identify acceptable weld signatures and to discern unacceptable welds during operation. A statistically significant number of good welds can be input to the system when in “learn” mode, with each component identified for subsequent testing and evaluation against the signatures collected. With “fuzzy logic” applied by the software and a relatively stable laser weld process, the reference data can be acquired with as little as 6 samples, although 12 to 20 samples per signature would provide a greater degree of confidence.

When establishing the reference weld data, it is important to review and monitor the data collected against the test specimens. Accordingly, a matrix could be established and maintained between signature data and periodic destructive test specimens to ensure that an appropriate correlation is maintained and achieved. General Motors has a specification for laser weld quality assessment (GM 4485M) that provides an excellent benchmark for such tests in terms of:

- *Weld inspection:* Cracks, concavity, continuity, convexity, mismatch, undercut
- *Sectioning:* Microhardness, macrostructure and microstructure, pinholes, inclusions, cracks, porosity
- *Mechanical tests:* Cupping tests (Olsen), strength, ultimate tensile, yield strength, fatigue limits, elongation

Achieving confidence is necessary if weld process monitoring is to be implemented and relied upon. A program of destructive weld tests is necessary to ensure that what is monitored during the weld process actually results in a quality weld. The frequency of such tests can be reduced as any corrective actions/adjustments are made and confidence is gained in the system.

After completion of the “learning” function, upper and lower tolerance limits are established by the software for each signal. Where the weld process may be volatile (as with magnesium

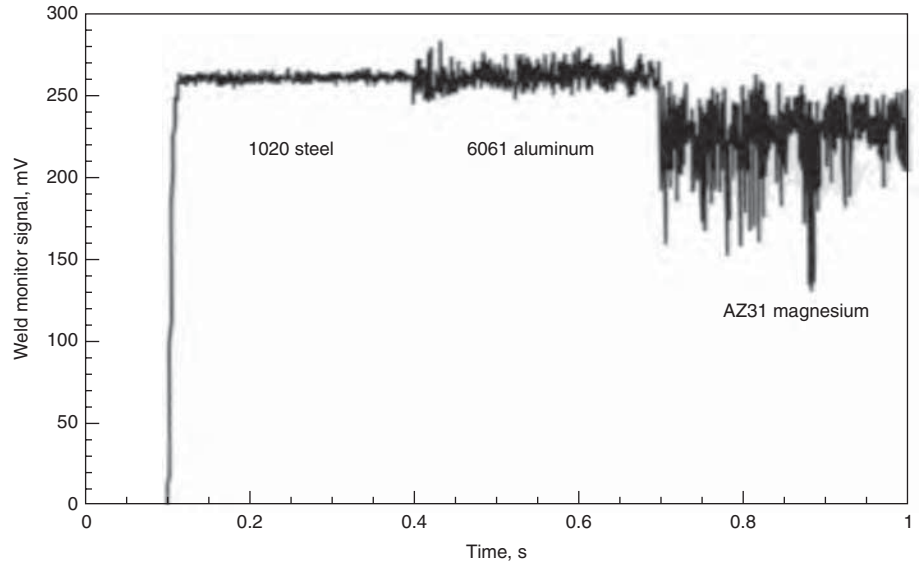


Fig. 9 Stability of the keyhole for three different metals (from a single sensor)

Table 2 Sensor capabilities in indicating weld features

Sensor	Feature	Weld characteristic/assessment(a)								
		Full/partial penetration	Penetration depth	Seam position	Lack of fusion	Focal position	Seam surface	Pores	Spatters	Cracks
Electro-optical with image processing	Melt pool	O	✓	✓	✓	✓	✓	O	✓	X
	Keyhole	O	✓	✓	✓	✓	✓	O	✓	X
Photodiodes for spectral density fluctuations	Weld spatter	O	✓	✓	✓	✓	✓	O	✓	X
	Plasma plume	✓	✓	O	✓	✓	✓	✓	✓	X
Microphones (acoustic)	Reflected laser power	✓	✓	O	✓	✓	✓	✓	✓	X
	Melt pool	✓	✓	O	✓	✓	O	X	✓	X
Capacitance diode	Airborne	✓	O	O	✓	✓	✓	O	O	X
	Structure-borne	✓	O	O	✓	O	✓	X	X	✓
Capacitance diode	Vapor conductivity (dc)	X	X	X	X	✓	X	X	X	X
	Vapor conductivity (ac)	✓	✓	O	✓	✓	✓	O	X	X

Note: dc, direct current; ac, alternating current. (a) ✓, possible; O, depends; X, not possible

welding), additional considerations are the amount total and clusters of signal spikes that may be allowed to exceed the tolerance bands, and/or “signal areas” that are allowed to exceed the nominal tolerance bands without affecting weld quality.

When in production mode, each signal then is evaluated to determine the probability of a characteristic failure. The group of signals (using a weighting function) is evaluated as a whole for the probability of an unacceptable weld.

Examples of Laser Weld Monitoring

The characteristic signal signatures from laser welding are useful in monitoring the welding process. Reference signals (with upper and lower boundaries) are established for key

variables such as keyhole temperature, applied laser power, and reflected laser power. A general example is illustrated in Fig. 14 (Ref 31), which depicts the temperature signal for Nd:YAG overlap welding of steel at 2000 W. The reference temperature signal was accomplished with laser power at 2000 W. Poor weld quality, indicated by the temperature signal outside of the bounded “good” range, is shown. Gap variations produced the out-of-range temperature signals.

Another example is monitoring of laser welding in the production of tailor-welded blanks (Ref 33). Tailor-weld blanks are a major application in automotive stamping operations. Production volumes are usually high, resulting in the need for 100% real-time quality-assurance monitoring. Because the laser weld bead is usually subject to drawing/formation in the subsequent stamping operation, quality must be assured.

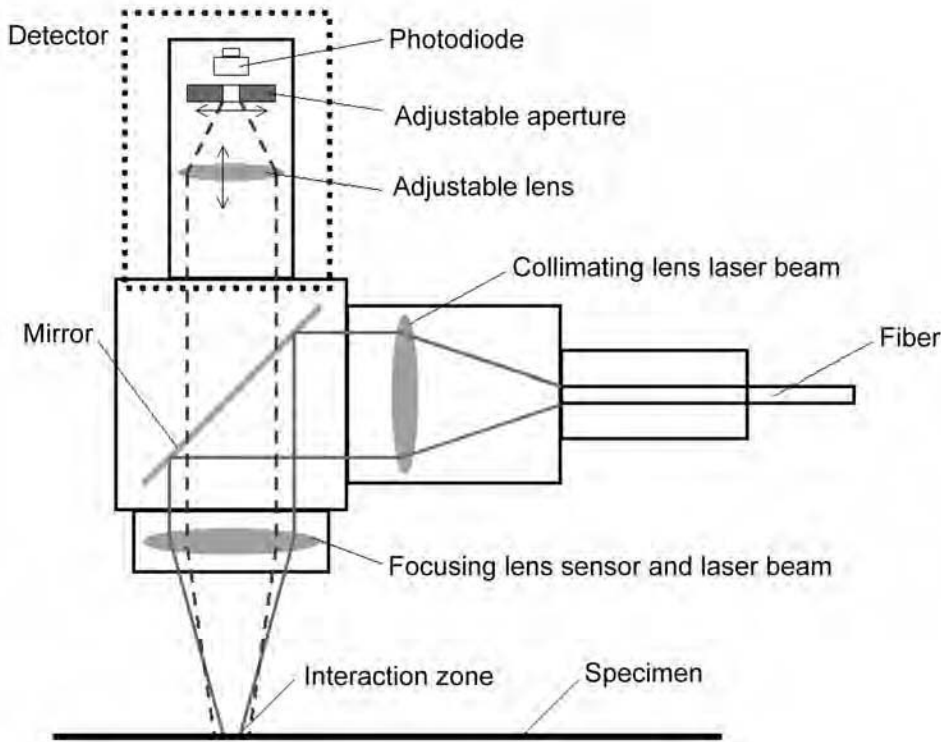


Fig. 10 Arrangement of a single sensor for monitoring the weld process quality within a defined spectrum. Courtesy of Precitec-Jurca

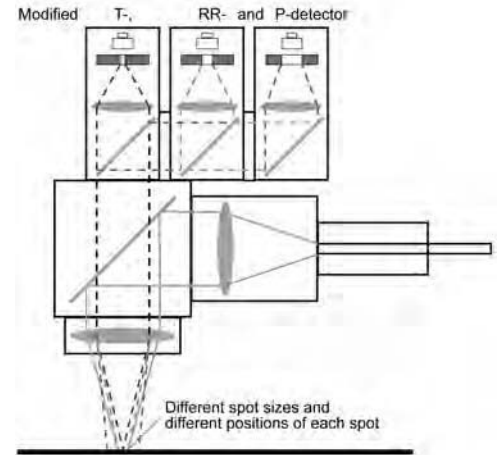


Fig. 12 Arrangement of sensors for monitoring temperature (T), reflected radiation (RR), and plasma (P)

The process problems that impact weld quality (to be detected by a weld quality monitoring system) include:

- Weld speeds on the order of 12 m/min (200 mm/s, or 472 in./min) and discontinuity sizes no greater than 0.5 mm (0.02 in.) equate to a detection rate of 400 Hz.
- Edge repeatability is critical. Weld edge mismatch, poorly trimmed edges, and improper clamping can lead to weld gaps that are too excessive to yield a quality weld.
- Hot dipped or galvanized zinc coatings and their variations may affect the baseline weld signature. In addition, they may introduce signal fluctuations that may or may not indicate an unacceptable weld.
- Variations of oil thickness on the steel to be welded may affect weld quality.
- Partial fusion must be detected, because this will affect the formability of the welded sheet for stamping operations.

Example: Real-Time Monitoring of Laser Welding in the Production of Tailor-Welded Blanks (Ref 28). This example illustrates various monitoring signatures for laser welding of 0.7 to 1.6 mm (0.03 to 0.06 in.) galvanized steel at 10 m/min (166 mm/s, or 393 in./min) with an Nd:YAG (3.4 kW) laser. Four sensors are used:

- Temp: Standard temperature sensor
- Plasma: Modified plasma sensor with 4 mm (0.16 in.) aperture
- Tempmod: Modified temperature sensor with 0.5 mm (0.02 in.) aperture
- HPTempmo: High-band-pass filtered sensor, as derived by the software from the Tempmod sensor data

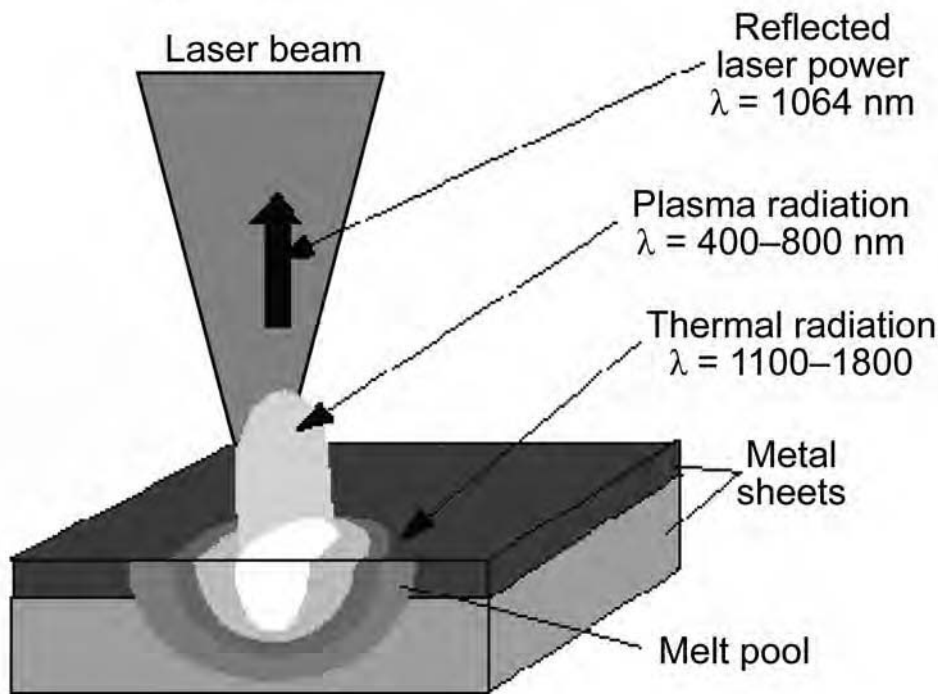


Fig. 11 Emitted spectrum from laser weld

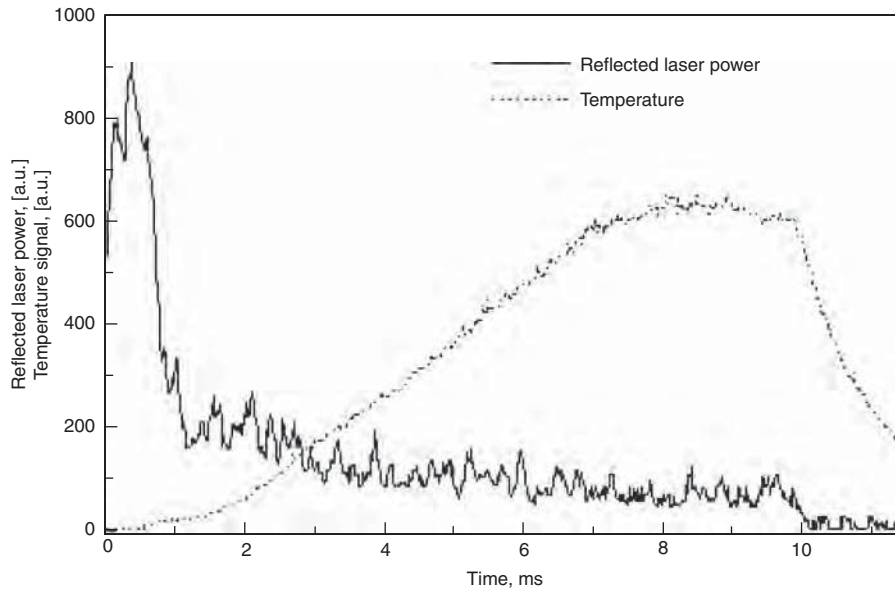


Fig. 13 Reflected laser power and temperature versus time

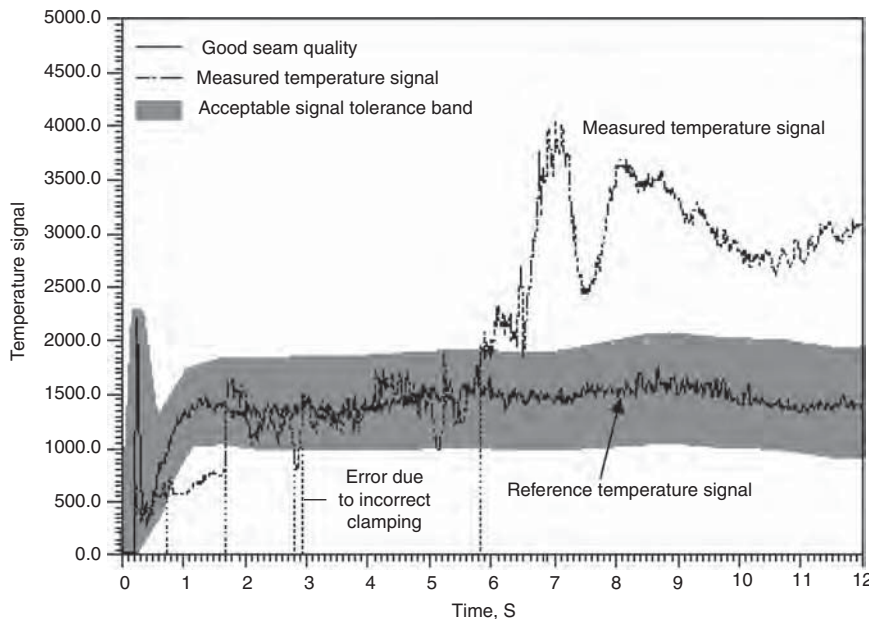


Fig. 14 Signals from overlap welding of steel at 2000 W with an Nd:YAG laser

The baseline or reference set of signatures for a good weld is shown in Fig. 15. Figure 16 depicts the signatures recorded (less the high-band-pass filter) for a weld that had two notches filed in the thicker sheet. This should have produced a weld fail condition, but the evaluation was not significant enough to do so.

Using the high-band-pass filtered sensor enables the software to determine a weld failure, as shown in Fig. 17. Two weld failures are noted over the length of the weld. The high-band-pass filter improves the ratio between noise and failure signature by approximately fivefold over the

unfiltered signal. In this example, other types of process variations that can be detected by monitoring with sensors include:

- Misalignment of the relative position of the focal point by 0.15 mm (0.006 in.) to the thinner sheet. This shift in relative location of the laser beam and weld seam was detected by the plasma and modified temperature sensors.
- Misalignment of the relative position of the focal point by 0.15 mm (0.006 in.) to the thicker sheet. Weld failure was detected only by the modified temperature sensor in this case.

ACKNOWLEDGMENTS

Many people have most graciously contributed to this article. Without their support and participation, this article would not have been possible:

- Tim Webber, IPG Photonics, Oxford, MA
- Frank Brennan, Trumpf, Plymouth, MI
- Rainer Uhlig, ABB, Fort Collins, CO
- Jim Cann, Rofin Sinar, Plymouth, MI
- Urban Widén, Permanova, Mölndal, Sweden
- Robert Borgstrom, Precitec, New Hudson, MI
- Scott Green, LT Ultra, New Hudson, MI
- Mike Fox, James Lafferty, and Ian Hastings, KTM Locks, Concord, Ontario, Canada
- Susan McKelvey and Dennis Nadeau, Rumble Laser Systems, Mississauga, Ontario, Canada

REFERENCES

1. T. Webber, Real-Time Laser Welding Quality Control System, *Society of Manufacturing Engineering Conference, Lasers in Manufacturing: SPOT '88*, May 1988 (Cleveland, OH), p IQ88-169 to IQ88-169-10
2. T. Webber, Real-Time Laser Welding Quality Control System, *Proceedings of the Laser Institute of America's ICALEO '87 Conference* (San Diego, CA), 1987, p 25-34
3. Method and Apparatus for Monitoring Laser Processes, U.S. Patent 4,663,513
4. T. Webber, Private meetings with D. Kolodziej, Ford Motor Company, 1985
5. D. Farson and R.F. Duhamel, Technology Review, *Ind. Laser Rev.*, March 1997
6. "Technical Information: Laser Welding," Trumpf, Feb 1994
7. T.R. Kugler, *LIA Handbook of Laser Materials Processing*, LIA, p 320-322
8. J. Karlsson and A.F.H. Kaplan, Analysis of a Fiber Laser Welding Case Study, Utilizing a Matrix Flow Chart, *Appl. Surf. Sci.*, Vol 257, 2011, p 4113-4122
9. W.W. Duley, *Laser Welding*, 1999, p 42-47
10. D. Havrilla, *Laser Welding Design and Process Fundamentals and Troubleshooting Guide*, p 55-56
11. P.D. Kapadia, R. Ducharme, C. Trayner, J.M. Dowden, K. Williams, and W.M. Steen, Radiative Emission in the Laser Welding of Thin Sheet Metals, *LIA Process Monitoring/Control*
12. S. Pathasarathi, P.A.A. Khan, and A.J. Paul, Intelligent Laser Processing of Materials, *LIA Process Monitoring/Control*
13. I. Miyamoto, K. Kamimuki, H. Mauro, K. Mori, and M. Sakamoto, In-Process Monitoring in Laser Welding of Automotive Parts, *LIA Process Monitoring/Control*

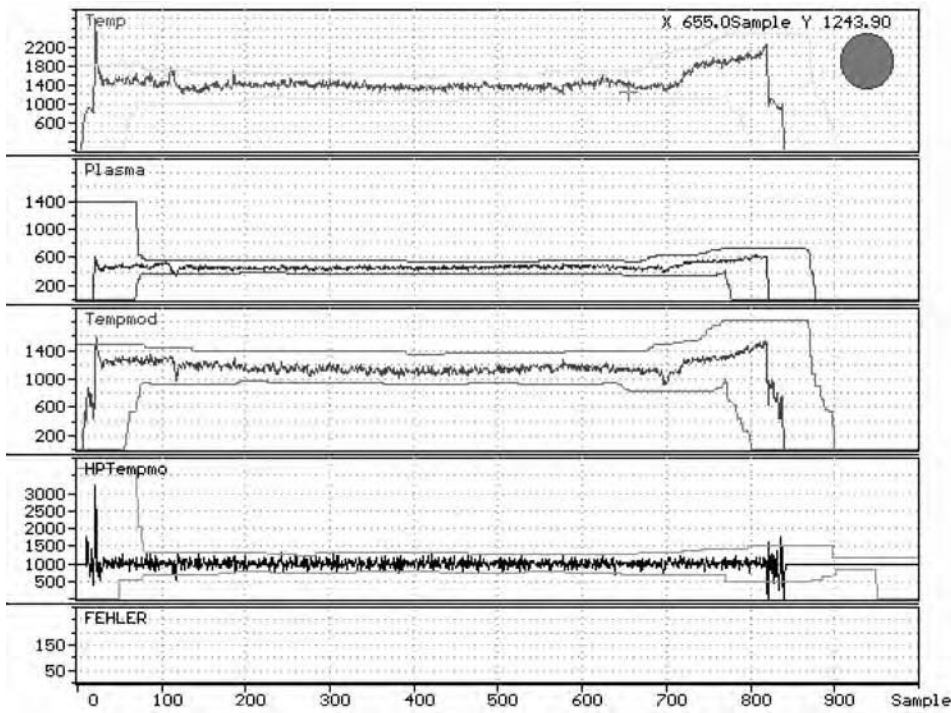


Fig. 15 Baseline or reference set of signatures for a good weld

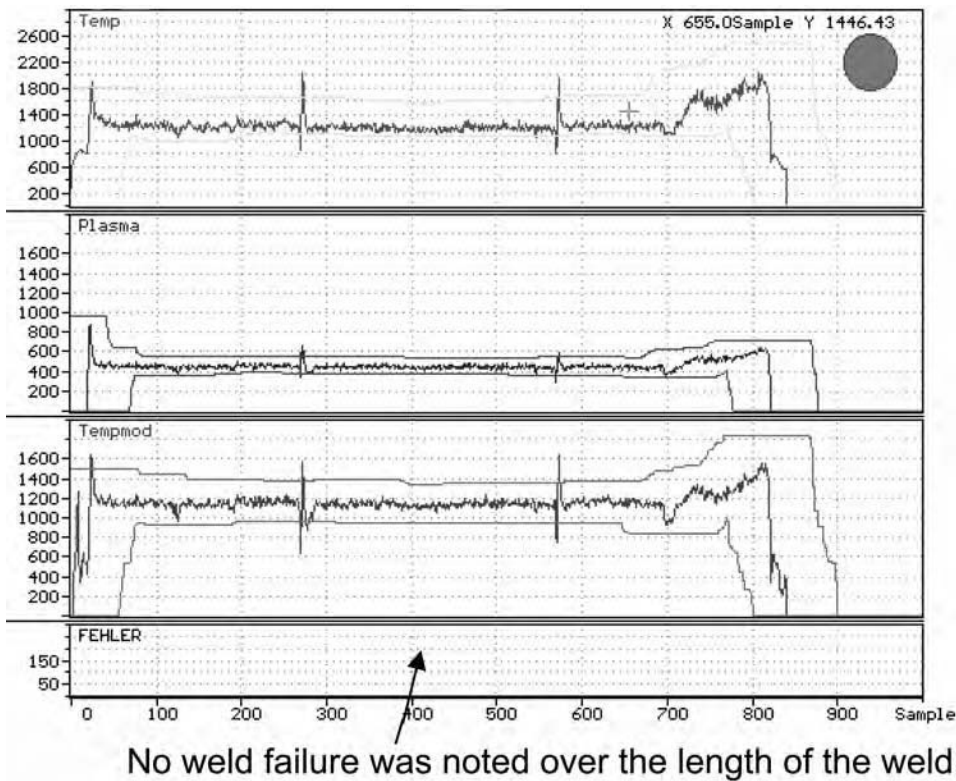


Fig. 16 Recorded signatures (without high-band-pass filter) for a weld that had two notches filed in the thicker sheet

14. V. Semak, "Laser Materials Interaction," Industrial Laser Processing Workshop, June 17, 1999
15. K. Shi, L. Li, W.M. Steen, et al., *Proceedings LAMP '92*, 1992, p 451
16. L. Li, W.M. Steen, and P. Modern, *Proceedings ICALEO '93*, 1993, p 372
17. A. Sun, E. Kannatey-Asibu, Jr., and M. Gartner, Sensor Systems for Real-Time Monitoring of Laser Weld Quality, *J. Laser Appl.*, Vol 11 (No. 14), Aug 1999
18. H. Zeng, Z. Zhou, Y. Chen, H. Luo, and L. Hu, Wavelet Analysis of Acoustic Emission Signals and Quality Control in Laser Welding, *J. Laser Appl.*, Vol 13 (No. 4), Aug 2001
19. M.A. Saifi and S.J. Vahaviolos, *IEEE J. Quant. Elec.*, Vol 12, 1976, p QE129
20. G. Habenicht, W. Stark, and R. Deimann, *Weld. Cutting*, Vol 10, 1991, p 37
21. J. Hanting and D. Aiqing, *Proceedings LAMP '92*, p 457
22. N.F.F. Willmott, R. Hibbard, and W.M. Steen, *Proceedings ICALEO '88*, 1988, p 109
23. C.E. Schou, V.V. Semak, and T.D. McKay, *Proceedings ICALEO '94*, 1994, p 41
24. D. Farson, K. Hillsley, J. Sames, et al., *Proceedings ICALEO '94*, 1994, p 86
25. M.C. Jon, *Weld. J.*, Vol 64, 1985, p 43
26. C. Hamman, H.G. Rosen, and B. Lassiger, *Proceedings SPIE 1132*, 1989, p 275
27. W.M. Steen and V.M. Weerasinghe, *Proceedings SPIE*, Vol 668, 1986, p 37
28. W.W. Duley, *Laser Welding*, John Wiley & Sons Inc., 1999
29. G.M. Light and J. Demo, An Evaluation of EMAT Technology for High-Temperature NDE, *NDTnet*, Vol 3 (No. 3), March 1998
30. K.H. Leong, Industrial Laser Processing Workshop, June 17, 1999
31. Precitec-Jurca, Info LWM900.pdf
32. M. Kogel-Hollacher, M. Jurca, C. Dietz, G. Janssen, and E.F. Dávila Lozada, "Quality Assurance in Pulsed Seam Laser Welding"
33. B. Kessler and B. Schürmann, Developments in In-Process Monitoring Techniques for Tailored Blank Welding, *Precitec*, 2001

SELECTED REFERENCES

- S.S. Charschan, *Guide to Laser Materials Processing*, Laser Institute of America, CRC Press, 1993
- W.W. Duley, *Laser Welding*, John Wiley & Sons Inc., 1999
- J. Griebisch, L. Schlichtermann, M. Jurca, S. Heissler, and D. Funk, On-Line Monitoring of Laser Welding, *Ind. Laser Rev.*, May 1997
- J. Griebisch, L. Schlichtermann, M. Jurca, W. Hoving, and C. Nillesen, Quality Assurance of Industrial Spot Welding with a Pulsed Nd:YAG-Laser, *Proc. of the Material Processing Conference ICALEO '96* (Detroit, MI), Laser Institute of America, 1996
- W.M. Steen, *Laser Material Processing*, Springer-Verlag, 1996

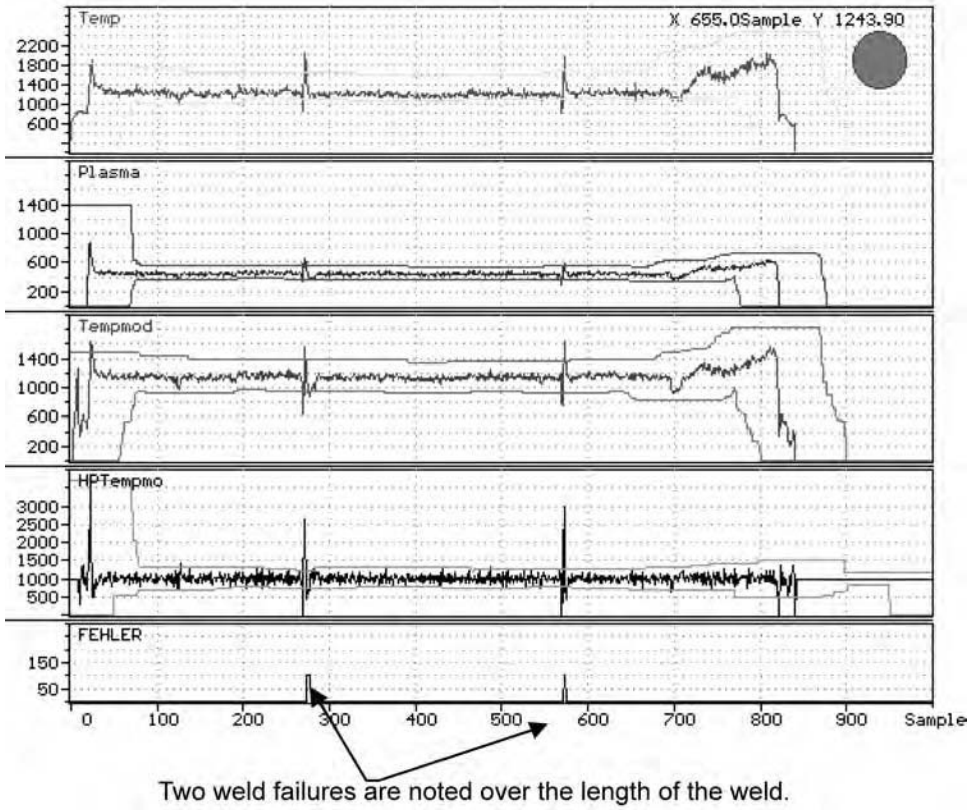


Fig. 17 Indications with high-band-pass filtered sensor

Laser Cutting, Drilling, and Shock Peening

Charles Caristan, Air Liquide Industrial U.S. LP

IT IS WELL KNOWN that *laser* is an acronym for light amplification by stimulated emission of radiation. In this 21st century era of manufacturing, it also has proven to stand for lean, agile, safe, efficient, and rapid. These attributes help the transition from manufacturing into a new era of “laserfacturing,” the art of manufacturing with industrial lasers, in which laser-cutting applications represent the overwhelmingly dominant share.

This article brings to light fundamentals about the field of laser cutting from an industrial manufacturing perspective. For more in-depth information, the book *Laser Cutting Guide for Manufacturing* (Ref 1) is an exhaustive review on the subject and should be useful to anyone in this field.

Principles of Laser-Cutting Thermal Processes

Laser cutting can be performed either by thermal processes or nonthermal ablation processes or sometimes by a weighted combination of both. The overwhelming majority of laser-cutting applications are for cutting of metals by thermal processes. Nonthermal vaporization processes for laser cutting are used mostly in microfabrication of nonmetallic materials with high peak power pulses of duration of the order of nanoseconds going into the femtoseconds pulse duration (Ref 2) and are still in development in macrofabrication of metals (Ref 3). For the purpose of this article, microfabrication describes a combination of subkilowatt laser power and small-sized workpieces or small-sized processed features, whereas macrofabrication describes multikilowatt laser processing, such as for metal cutting.

Thermal laser-cutting processes are high-spatial-definition derivatives from traditional thermal-cutting processes, such as plasma torches and flame torch cutting; all of these thermal-cutting processes consist of inputting heat on a workpiece faster than it can dissipate away through conduction, convection, and

radiative heat transfer. The resulting accumulation of heat energy raises the temperature of the workpiece material so as to melt and even vaporize it. In the case of laser cutting, the torch consists of a highly focused laser light beam that reaches power densities on the workpiece of more than 100 times that of sunlight on Earth. This creates extremely high power densities of light radiation that are being absorbed by the material, to the point of actually melting and even vaporizing metals almost instantaneously. Pressurized assist gas flows through the nozzle tip of the laser-cutting torch to flush away molten and vaporized material. The double action of this liquefaction and vaporization, added to the flushing action of the assist gas, enables metal removal by forming a void in the material along the cut path, called kerf (Fig. 1). The high spatial definition of laser cutting can be achieved thanks to the relative small size of the focused beam spot on the workpiece,

typically 0.25 to 0.50 mm (0.010 to 0.020 in.) in diameter, such as for multikilowatt lasers for macrofabrication. The width of the kerf is of the same order of magnitude as the diameter of the beam spot on the workpiece. Consequently, the benefits of lasers over traditional cutting tools include higher contour definition and precision, superior edge quality, faster cutting speeds, narrower heat-affected zone, and more efficient melting process.

Thermal laser-cutting processes are of two kinds: fusion cutting and oxidation cutting (Ref 4). In fusion cutting, the laser beam is the sole source of heat transferred to the workpiece. Generally, a low- to nonreactive neutral gas such as nitrogen (N_2) or, more rarely, an inert gas such as argon is used as the assist gas. In oxidation cutting, a reactive gas such as oxygen (O_2) is used as the assist gas. At high temperature, O_2 reacts exothermically with most metals and thus substantially adds heat

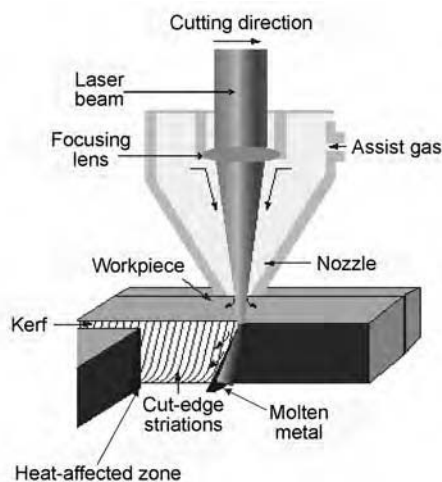


Fig. 1 Principle of laser-cutting thermal process. The laser beam is highly focused so as to input more heat per square inch than the workpiece can dissipate away by conduction, convection, or radiative heat transfer. The accumulation of heat causes the workpiece temperature to elevate, melting and vaporizing the metal. Pressurized assist gas flushes the molten and vaporized material away to form a void along the cut path, called kerf. Courtesy of BLM Group

to that brought by the laser source. With both processes, global purity of the assist gas, control of specific impurities, and even types of gas mixtures of the assist gas have a substantial impact on cutting performance.

Laser processing calls for specific methods associated with the particular nature and properties of laser lights. Figure 2 lists the key input and output process parameters; an exhaustive study of these key parameters and their cause-and-effect relationships can be found in Ref 1. The principal set-up parameters are illustrated in Fig. 3 and are discussed in greater detail in the following sections.

Laser Output

The laser beam is the source of light energy, which, when absorbed by workpiece materials, can produce changes such as raising their temperatures. From an operator's numerical control screen, it can be set by three main parameters: commanded power, P_c , which generally sets the peak power of the pulse; commanded pulse duty; and commanded pulsing frequency, as illustrated in Fig. 4. The frequency represents the number of pulses of output energy emitted per second. Pulse duty is the percent of on-time per pulse period. For example, a pulse that is 1 ms long with a 4 ms pulse period has a 25% duty cycle. A 100% duty corresponds to continuous wave output.

Most laser resonators are equipped with a power meter sensor internal to the laser source. This sensor measures an actual average output power, P_a , which can be compared with the calculated $P_{avg} = P_c \times \text{Duty}$. Any abnormally substantial discrepancy between P_a and P_{avg} should be investigated.

Even though it could be a function of the material type and thickness being cut, P_c is, with few exceptions, generally set at the maximum rated power capability of the laser resonator in use. Notable exceptions are when cutting mild steel with O_2 assist gas; for edge-quality reasons, it sometimes must be processed at reduced commanded power to better control the heat input on the material and to reduce gouging formation on the cut edges.

Moreover, the commanded power (P_c), duty, and frequency can be programmed to vary around their preset values as a function of the radius of curvature and angular profile of the feature being cut and as a function of the actual linear cutting speed. These variations are set by numerically preprogramming subroutines to adjust the linear feed rate (i.e., cutting speed) of the motion system of the machine and thus adjust the peak power, duty, and frequency as a function of the cut features and linear speed. Such adjustment enables better cut-edge quality by controlling the heat input, particularly in small features such as angular fins and small-radius features. For example, a machine designed with a motion system with a maximum mechanical acceleration rating of 1 G

(i.e., $9.8 \text{ m} \cdot \text{s}^{-2}$, the acceleration of gravity) will not be able to move with precision along a radius of curvature R at speed exceeding the square root of $(R \times 1 G)$. If the commanded

feed rate is above such value, the intelligent numerical control automatically overrides the commanded feed rate and slows down the motion system to the maximum speed

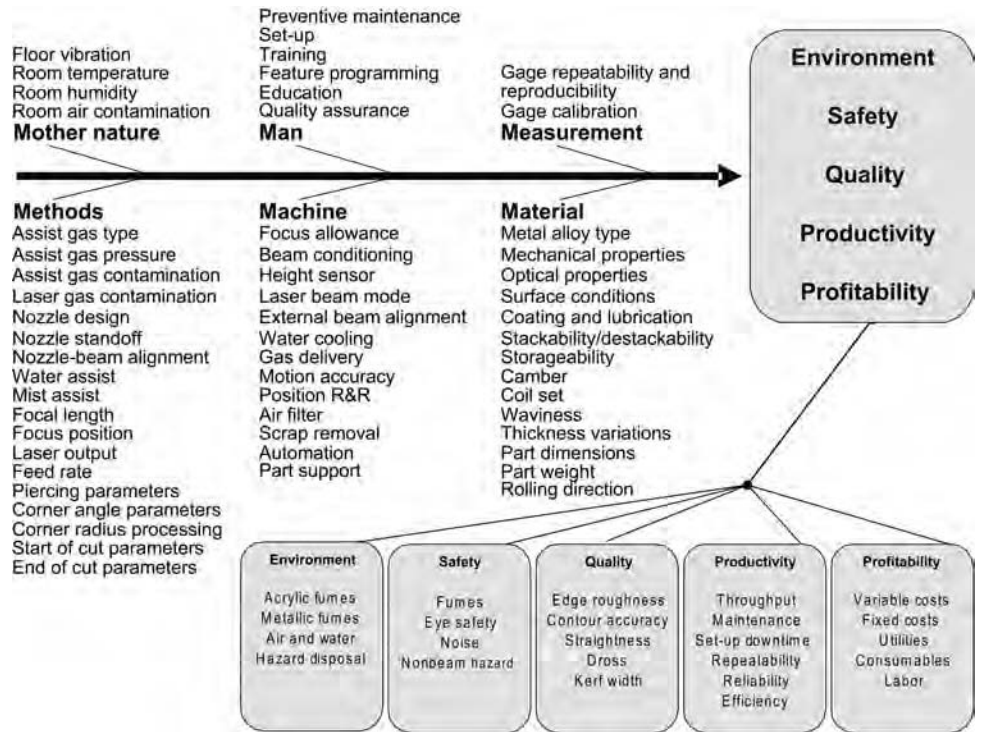
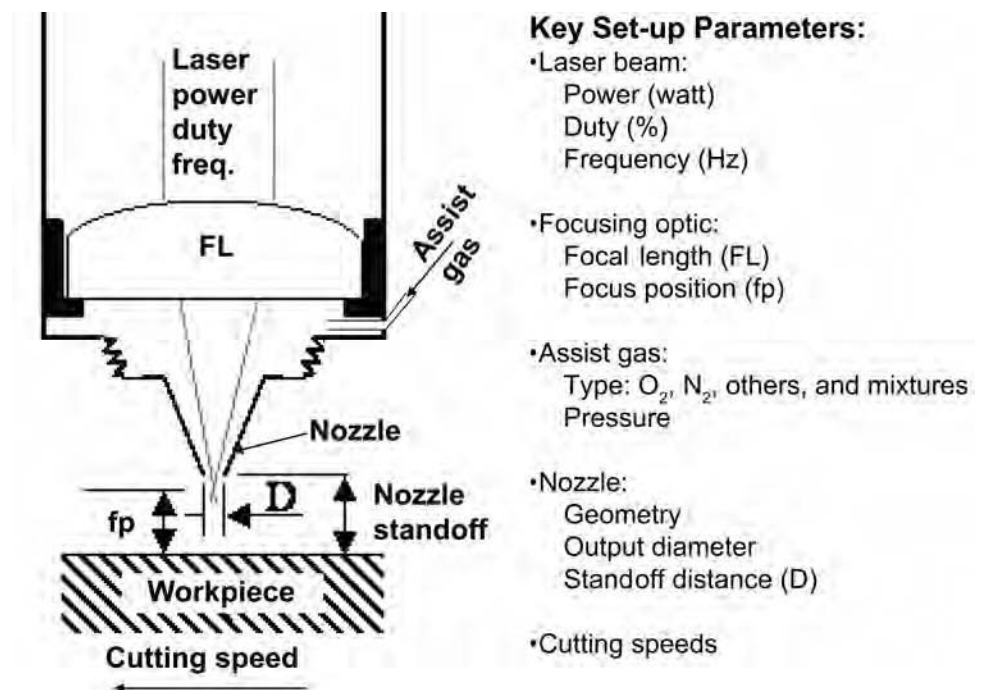


Fig. 2 Key process parameters for laser cutting. Inputs are categorized under the “6M” categories of Man, Machine, Method, Material, Measurement, and Mother Nature; outputs impact the environment, safety, quality, productivity, and profitability. See Ref 1 for a detailed discussion of the cause-and-effect relationship between inputs and outputs.



Key Set-up Parameters:

- Laser beam:
 - Power (watt)
 - Duty (%)
 - Frequency (Hz)
- Focusing optic:
 - Focal length (FL)
 - Focus position (fp)
- Assist gas:
 - Type: O_2 , N_2 , others, and mixtures
 - Pressure
- Nozzle:
 - Geometry
 - Output diameter
 - Standoff distance (D)
- Cutting speeds

Fig. 3 Primary set-up parameters for laser cutting

corresponding to the radius of curvature of the feature. When such a slowing down occurs, it becomes wise to override the commanded laser output by adjusting it correspondingly to avoid burning and other edge-quality defects caused by excessive localized heat input.

Piercing

Cutting generally starts either from an outer periphery of the part or from a hole that must be pierced through the part. Piercing can be achieved by using a single high-peak-power laser pulse or by “peck-piercing” with several pulses of energy needed to progressively drill through the workpiece. Sophisticated machine numerical control program functions even enable the peak power, pulse duty, and frequency to change by increments during piercing. Generally, either neutral gas such as N₂ or reactive gas such as, in most cases, O₂ is used to assist piercing; in some cases, a cross-jet of air knife between nozzle and workpiece may be necessary to flush recoiled metal fumes and spatters during piercing.

Piercing time can fluctuate significantly depending on surface conditions or change in material or piercing process. Newer machines incorporate sensors that can detect when piercing-through is completed, thus enabling the optimization of piercing cycle time. Example processing parameters for peck-piercing are given in Table 1.

Focusing Characteristics

For metal-cutting applications, focusing of the laser beam is generally achieved through a transmissive optic, that is, a focusing lens. Use of focusing mirrors is reserved for very high-power processes, because mirrors are more efficiently and uniformly water cooled than lenses, resulting in smaller temperature gradients across their irradiated area and less heat-induced distortion of their focusing characteristics, also referred to as thermal lensing (Fig. 5). On the other hand, at equal focal length, an aspheric lens introduces less aberration and less astigmatism than a mirror; as a consequence, a lens generally focuses to a smaller spot than a mirror. Finally, the use of a focusing mirror complicates the ability to provide back-up pressure for using co-axial assist gas flow. Additional transmissive window optics and/or ancillary nozzle arrangements have been developed to enable pressure buildup of assist gas flow upstream from the nozzle exit when using a focusing mirror arrangement.

For a CO₂ laser beam at 10.6 μm wavelength, focusing lenses are generally made of zinc selenide (ZnSe) material that can be either polished or diamond-turned into any free-form shape. On the other hand, for solid-state lasers such as yttrium-aluminum-garnet (YAG) lasers with 1.06 μm wavelength, disk lasers at 1.03

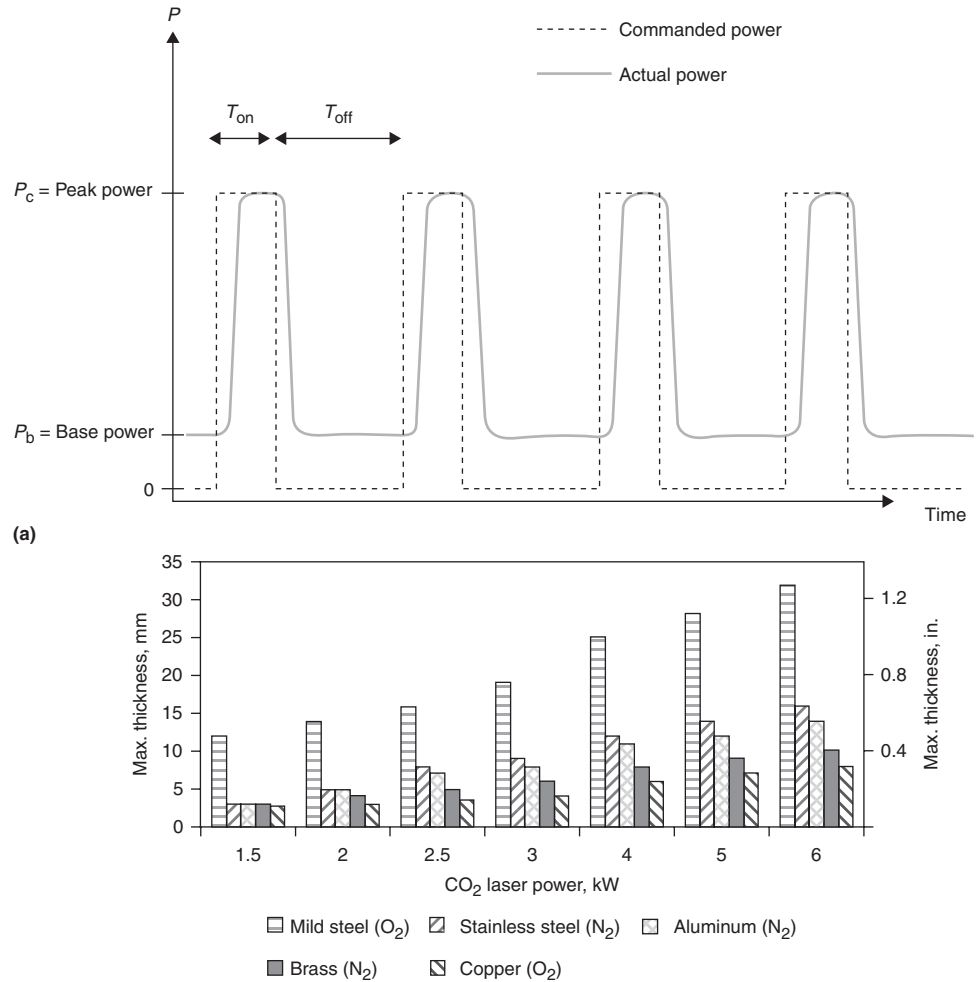


Fig. 4 (a) Example of power-time profile: commanded versus actual. Commanded power = P_c ; commanded frequency = $1/(T_{on} + T_{off})$; commanded duty = $T_{on}/(T_{on} + T_{off})$; calculated average power = $P_{avg} = P_b + (P_c - P_b) \times \text{Duty}$. (b) Maximum thickness cutting capability as a function of CO₂ laser power for various metal alloys

Table 1 Example of peck-piercing parameters on mild steel with a 2 kW peak power CO₂ laser, 190 mm (7.5 in.) focal length lens, and oxygen assist gas

Thickness	Initial	Initial	Frequency	Duty	Time between	Number of	Total piercing
mm in.	frequency, Hz	duty, %	increments, Hz	increments, %	increments, s	increments	time, s
6.5 ¼	10	20	1	1	0.1	10	3
12.5 ½	10	10	1	1	0.1	20	10

μm wavelength, and ytterbium-fiber lasers with 1.07 μm wavelength (all part of the “1 μm” laser family), focusing lenses are generally made of fused silica with special antireflecting coating. Other special coatings are being developed to compensate for thermal lensing and to reduce focus shifts (Ref 5). Fused silica (SiO₂) is turned to spherical shape by polishing, because it is too hard to be economically diamond-turned to free-form shapes. The radius of curvature of the lens shape determines its focal length. Alternatively, other materials such

as zinc sulfide (ZnS) can be used for focusing lenses for the aforementioned 1 μm lasers. As with ZnSe, ZnS can be diamond-turned into free-form shapes such as aspheric to reduce aberrations, toroidal to generate oblong focused beam spots, or bifocal optics (Fig. 6) to obtain a dual-focus effect for improved cutting speeds (Ref 6). Because of its superior thermal conductivity, a ZnS-made lens yields less thermal-lensing-induced focus shift. Table 2 compares mechanical, thermal, and optical properties of various materials for laser optics. The ZnS

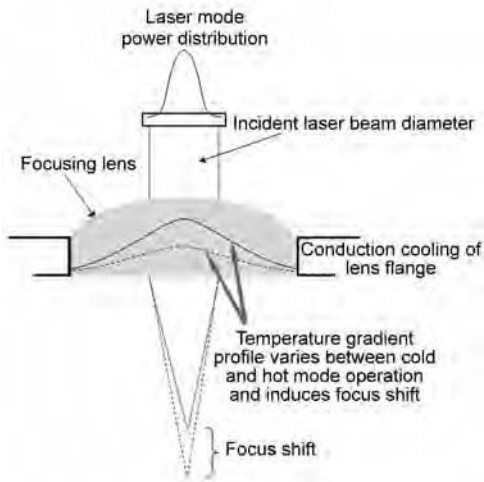


Fig. 5 Thermal lensing results in focus shift. The laser mode refers to the profile of power distribution across a laser beam; a Gaussian-like profile is depicted here. However, some industrial lasers exhibit a “doughnut” mode, which generally results in less focus shift.

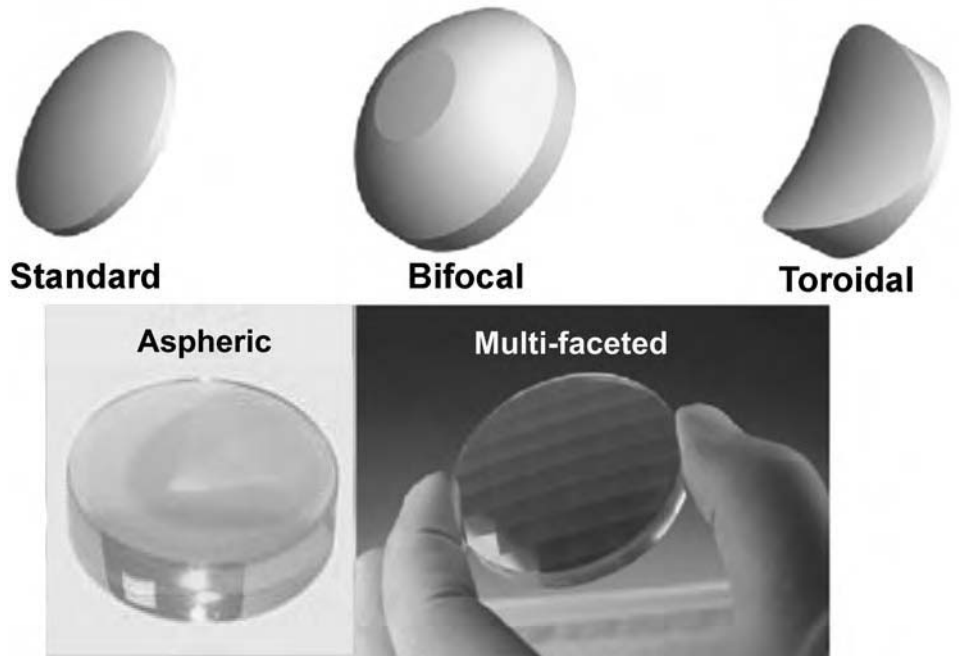


Fig. 6 Standard lenses have spherical curvatures that can be obtained by polishing. Aspheric, bifocal, toroidal, multifaceted, or other free-form curvatures can be achieved with diamond-turnable materials, such as zinc selenide for CO₂ lasers and zinc sulfide for solid-state lasers. Fused silica, often used for standard lenses with spherical curvatures for solid-state lasers, is too hard to be economically diamond-turned. Courtesy of II-VI Inc.

material yields better thermal properties than fused silica but has a light-scattering side effect that can require augmented cooling of the optics mount and assembly that absorbs the scattered light (Ref 7).

One important specification for a focusing lens is its thickness, which must be strong enough to sustain high-pressure assist gas. Lens manufacturers recommend and provide appropriate lens thicknesses based on the applications. Assuming a 90% clear-pressure aperture, a 38 mm (1.5 in.) diameter ZnSe lens of focal length between 125 and 190 mm (5 and 7.5 in.) and of 4 mm (0.160 in.) thickness can sustain approximately 120 psi (8 bar) pressure, whereas the same lens with a thickness of 8 mm (0.320 in.) can sustain almost 500 psi (35 bar). Typical industrial CO₂ laser-cutting systems have ZnSe focusing lenses of 38 mm (1.5 in.) diameter by 7.4 mm (0.29 in.) thick or 50 mm (2 in.) diameter by 9.7 mm (0.38 in.) thick.

Table 3 shows typical focal lengths chosen mostly as a function of workpiece thickness, whether for CO₂ laser systems or 1 μm laser systems.

Figure 7 describes a generic beam-delivery system having four optics of finite focal lengths, $f_1, f_2, f_3,$ and f_4 , which could be mirrors or lenses or any other kind of optical element, each characterized by at least one focal length. Folding mirrors with flat reflecting surfaces or simple transmissive windows are optics with infinite focal length.

Beam caustic (i.e., beam radius) downstream from the focusing lens is characterized by parameters such as focus diameter, 2^*w_{out} ; focus position, d_{out} , relative to the

Table 2 Properties of transmissive optics materials

For 1 μm wavelength compared to fused silica, multispectral zinc sulfide (MS ZnS) has a superior thermal conductivity to avert steep temperature gradient.

Properties	BK7	Fused silica	MS ZnS	ZnSe
Mechanical				
Density, g/cm ³	2.51	2.203	4.09	5.27
Poisson's ratio	0.208	0.17	0.27	0.28
Hardness, Knoop	610	500	150–165	105–120
Rupture modulus, dyne/cm ²	1.65×10^8	5.00×10^9	6.90×10^8	5.50×10^8
Young's modulus, dyne/cm ²	8.20×10^{11}	7.30×10^{11}	7.45×10^{11}	6.72×10^{11}
Thermal				
Linear expansion coefficient, $\times 10^{-6}/^\circ\text{C}$	7.1	0.55	6.5	7.57
Specific heat, J/g ^o C	0.858	0.703	0.527	0.356
Thermal conductivity, W/cm ^o C	0.0111	0.0138	0.272	0.18
Optical				
Scatter coefficient at 1.06 μm, /cm	ND	ND	<3%	<0.5%
Scatter coefficient at 0.6328 μm, /cm	ND	ND	<10%	<3%
Index of refraction at 1.06 μm	1.5066	1.4496	2.287	2.483
Temperature change of refractive index at 1.06 μm, $\times 10^{-6}/^\circ\text{C}$	1.2	11	42	70
Bulk absorption at 1.07 μm, /cm	~0.001	~0.0001	<0.0005	<0.001
K-values for lenses				
Plano/convex lens	0.07112	0.08994	0.02888	0.02849
Positive meniscus lens	0.06573	0.07792	0.02051	0.01758
Equiconvex lens	0.1029	0.11542	0.05494	0.05164

ND, not determined. Courtesy of II-VI Inc.

last downstream optic, f_1 ; and the Rayleigh range, Z_R . These parameters are bound by the following mathematical relationships for a laser beam of wavelength λ , of beam cross-sectional radius w_{in} , and of beam quality M^2 , knowing the optical path distances, d_1, d_2, d_3 , shown in Fig. 8, and distance d_{in} between the incident beam waist position and the first nonflat mirror optic, f_4 (for

detailed analytical derivations, see appendix B of Ref 1):

$$d_{out} = \frac{-\beta \delta - \alpha \gamma \frac{\pi^2 w_{in}^4}{M^2 \lambda^2}}{\delta^2 + \gamma^2 \frac{\pi^2 w_{in}^4}{M^2 \lambda^2}} \quad w_{out}^2 = \frac{w_{in}^2}{\delta^2 + \gamma^2 \frac{\pi^2 w_{in}^4}{M^2 \lambda^2}}$$

$$Z_R = \frac{\frac{\pi w_{in}^2}{M^2 \lambda}}{\delta^2 + \gamma^2 \frac{\pi^2 w_{in}^4}{M^2 \lambda^2}} \quad (\text{Eq 1})$$

$$W_{out}(z) = w_{out} \sqrt{1 + \left(\frac{z - d_{out}}{Z_R}\right)^2} \tag{Eq 2}$$

Parameters α , β , γ , and δ are analytical functions of d_{in} , d_3 , d_2 , d_1 , f_1 , f_2 , f_3 , and f_4 . In terms of units, α and δ are dimensionless, whereas β is proportional to a distance, and γ is inversely proportional to a distance. Generally, f_1 represents a focusing lens. For a CO₂ laser-beam-delivery system, f_3 and f_4 could represent collimator optics and f_2 a regular flat folding mirror. For a fiber-delivery optics system such as for YAG, disk, and fiber lasers, f_2 could be a collimating lens that receives the beam at the output of the delivery fiber, and $2 \cdot w_{in}$ is approximated to the diameter of the delivery fiber. Some optical elements have different optical properties in one plane versus another, in which case one can apply a different set of analytical formulas for the different planes. For CO₂ lasers, in the general case where one can approximate the

incident laser beam to a perfectly collimated beam, that is, with constant beam diameter along its optical propagation path, then the waist diameter $D = 2 \cdot w_{in}$ is approximately equal to the beam diameter incident on the focusing lens. The aforementioned equations can be used to determine the position and diameter of the focus point, simply by setting $d_{in} = d_3 = d_2 = d_1 = 0$ and $f_2 = f_3 = f_4 = \infty$. It yields $\alpha = 1$, $\beta = 0$, $\delta = 1$, $\gamma = -1/f_1$, and the following well-known approximations of Eq 1:

$$d_{out} = f_1 \quad w_{out} = \frac{M^2 \lambda f_1}{\pi w_{in}}$$

$$Z_R = \frac{M^2 \lambda f_1^2}{\pi w_{in}^2} \tag{Eq 3}$$

The beam quality factor, M^2 , is also called M-square or K or $1/k$; its absolute minimum theoretical value is 1. The factor M^2 is a measure of mode composition of a laser beam and also a proportional measure of its divergence once it exits

the cavity. For the 1 μm lasers, the beam quality is often evaluated in terms of the product of beam radius w_{in} at the waist position at the resonator exit by its beam natural divergence angle, θ , expressed in $\text{mm} \cdot \text{mrad}$ units rather than in dimensionless M^2 . A Rayleigh range, Z_R , represents a length around the beam waist, such as around the focus point of diameter $2 \cdot w_{out}$, within which the beam radius remains smaller than:

$$\sqrt{2} \cdot w_{out}$$

Z_R is representative of the depth of focus or tolerance to focus position of the process. The parameter w_{in} can be obtained from the laser manufacturer or measured with a precise digital beam analyzer or a more rudimentary-mode burn technique. $W_{out}(z)$ denotes the radius of the beam cross section as a function of optical distance z downstream from the last optic, f_1 : $W_{out}(d_{out}) = w_{out}$.

For most CO₂ laser machines, optical distances d_1 , d_2 , and d_3 vary with the cutting head position Z , Y , and X over the work envelope. Some CO₂ laser-cutting machine designs include an adjustable optical path retardation loop that maintains the total optical path length constant while position X , Y , and Z varies. This ensures constant focusing characteristics and, it is hoped, constant cutting performance regardless of the position on the work envelope. For solid-state 1 μm laser-cutting machines, the beam-delivery system is composed principally of a flexible fiber, which ensures a constant optical path length equal to the length of the beam-delivery fiber.

Figure 8 illustrates a near-perfect agreement between the calculated beam caustics using the analytical formulas of Eq 1 and the measured beam caustics using a digital beam scanning measurement analyzer. This near-perfect match illustrates the accuracy of these analytical formulas, which uniquely incorporate a dependency on the beam-quality parameter M^2 , without having to resort to complex integral calculation and software. Note that for 1 μm lasers, the beam-quality parameter is expressed as a beam parameter product (BPP) defined as the product of beam radius w at a waist position as the beam exits the resonator by beam divergence angle θ :

$$\text{BPP} = w \cdot \theta = \frac{\lambda M^2}{\pi} \tag{Eq 4}$$

Although the M^2 value, and thus the BPP, are dictated by intracavity design and cannot be altered once the beam exits the resonator cavity, multiple reflections inside a delivery fiber degrade the coherence property of the laser beam and thus its focusability. This degradation of coherence is equivalent to a multiplication of the M^2 and thus the BPP sometimes several folds. As an example, a 2 kW fiber laser delivered through a 100 μm diameter fiber could yield a BPP = 3 $\text{mm} \cdot \text{mrad}$, whereas the same laser coupled through a 150 μm diameter

Table 3 Typical effective focal lengths used in metal cutting

Maximum material thickness		CO ₂ laser system effective focal length		1 μm laser system effective focal length	
cm	in.	mm	in.	mm	in.
0.3	1/8	95	3.75	70	3
0.5	3/16	130	5	130	5
2.5	1	190	7.5	190	7.5
3.2	1/4	250	10

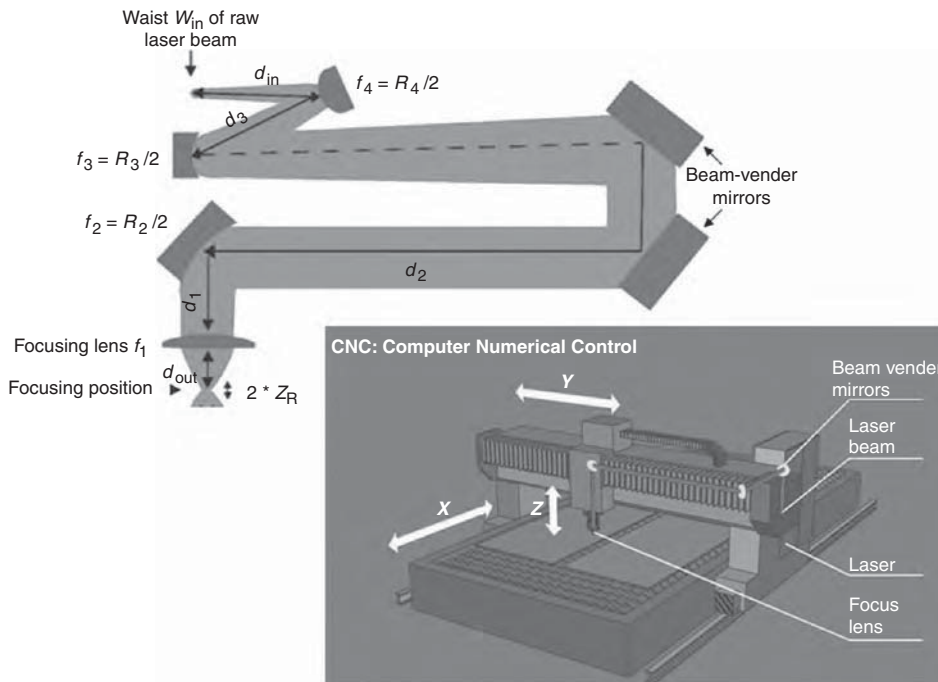


Fig. 7 Generic laser-beam-delivery system with up to four optics, f_1 , f_2 , f_3 , and f_4 , that have finite focal lengths. The system is representative of most industrial beam-delivery systems for CO₂ as well as solid-state lasers, even those with fiber optic delivery. A flat mirror, such as a standard beam-bender mirror, has an infinite focal length. The optical path distances represented, such as d_2 between f_2 and f_3 and, more moderately, d_1 between f_1 and f_2 , can vary during cutting.

delivery fiber would yield an equivalent BPP of $5 \text{ mm} \cdot \text{mrad}$ by the fiber exit.

Equation 4 shows that for focusability evaluation, the so-called f -number $= f_1/w_{in}$ ratio of focal length to incident beam diameter is more important than the focal length taken alone, regardless of the laser resonator type and characteristics. Table 4 shows typical values of BPP for industrial multikilowatt lasers.

A smaller f -number yields a smaller focus waist diameter, 2^*w_{out} , and a smaller Rayleigh range, Z_R . For best cutting capability, a maximized Rayleigh range is preferred for positioning tolerance, while a minimized diameter, 2^*w_{out} , is preferred for higher power density. These two conflicting requirements must lead to a delicate balance and choice of f -number as well as choice of laser resonator, characterized by M^2 (or BPP), λ , and indirectly by radius w_{in} . For applications aimed at high-speed cutting of thin sheets, preference can be given to

lasers having a small M^2 factor close to a diffraction limitation minimum value of 1 or, for a $1 \mu\text{m}$ laser, a BPP of approximately $0.34 \text{ mm} \cdot \text{mrad}$, whereas a larger M^2 factor, that is, larger BPP, yields larger Rayleigh length favorable to better cutting performance of thick gages. Figures 9 and 10 represent typical comparison results of laser-cutting performance for CO_2 lasers versus current state-of-the-art solid-state $1 \mu\text{m}$ lasers (disk and fiber types). The superiority of $1 \mu\text{m}$ lasers must be qualified within certain ranges, but it translates roughly into a ratio of almost 2 in power; that is, a 2 kW fiber or disk laser performance is generally compared to that of a 3 to 4 kW CO_2 laser. The following rules of thumb can be deduced for the current state-of-the-art at equal laser power:

- *Under oxygen assist gas:* The superiority of the fiber laser performance is limited to

gages thinner than approximately 4 mm (0.2 in.). Above 4 mm thickness, CO_2 lasers still produce superior edge quality and speed.

- *Under nitrogen assist gas:* The superiority of disk and fiber lasers for nitrogen-assisted fusion cutting of thinner gages is clear up to approximately 8 mm (0.3 in.) in thickness and actually grows dramatically for gages thinner than approximately 4 mm (0.2 in.), as is illustrated for both disk and fiber laser cutting in Fig. 9. However, as the thickness increases beyond 8 mm, the edge qualities in terms of dross and edge roughness, as well as the speed performance of $1 \mu\text{m}$ lasers, degrade much more rapidly than that of CO_2 lasers, leaving CO_2 lasers still the superior resonator type for cutting of such thick gages of mild steel, aluminum, and stainless steel with nitrogen assist gas. On the other hand, due to their shorter wavelength, $1 \mu\text{m}$ lasers are superior

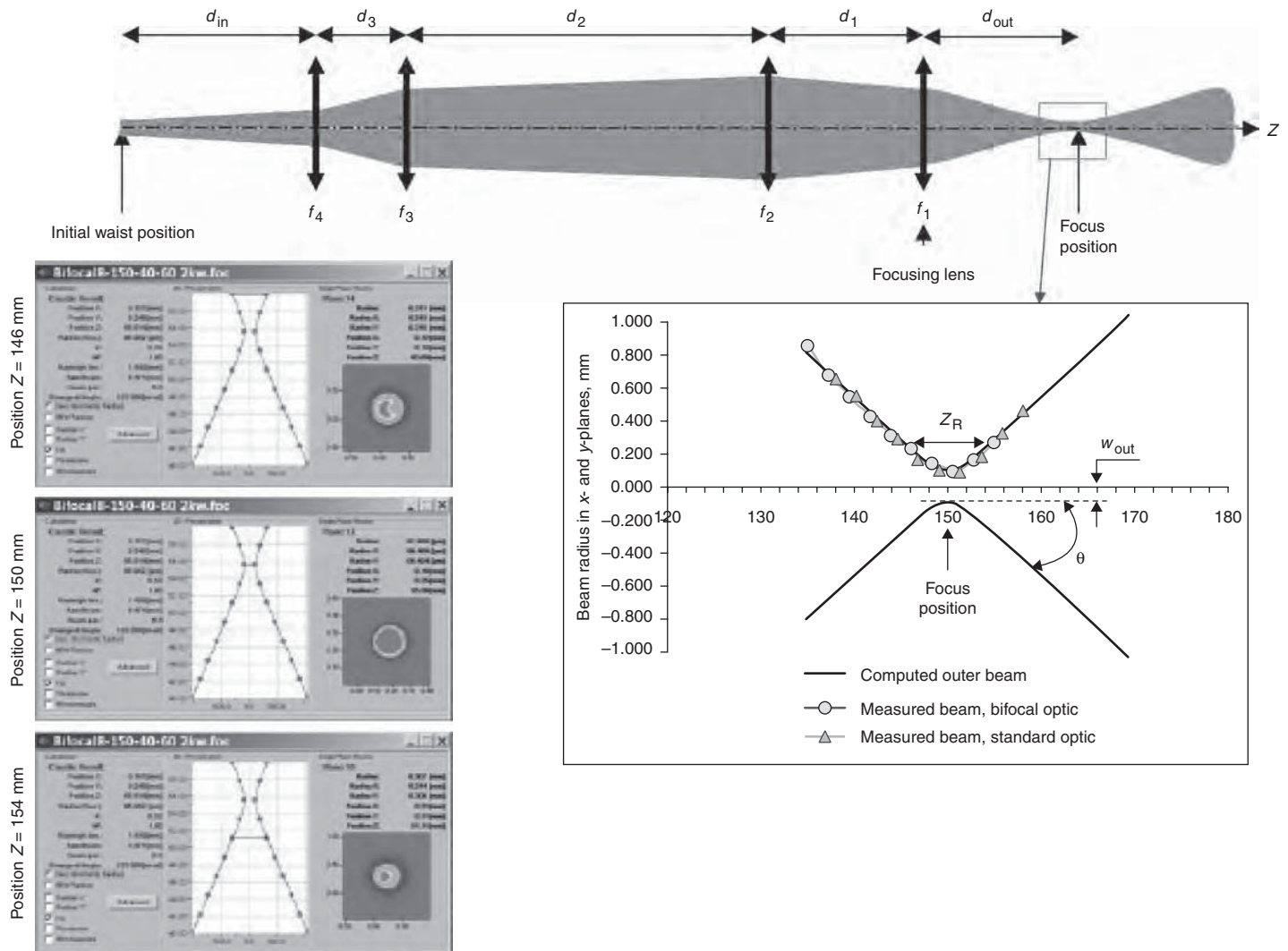


Fig. 8 Beam propagation caustics of diameter versus distance from the focusing lens. The top view represents the same generic beam-delivery system as in Fig. 7, with the optical path unfolded. The calculations with the analytical Eq 1 are in near-perfect agreement with measurements performed with a digital beam scanning analyzer (samples in left illustration) on bifocal and ordinary focusing lenses with focal length of 150 mm (6 in.), collimator lens of 120 mm (4 3/4 in.) focal length, and delivery fiber diameter of 150 mm (6 in.). The 5 kW fiber laser yielded a beam parameter product $= w \cdot \theta = 5 \text{ mm} \cdot \text{mrad}$ at the end of the delivery fiber.

to CO₂ lasers for cutting materials such as copper and brass.

Focus Position

Focus position (fp), defined in Fig. 3 and illustrated in Fig. 11, can be controlled by adjustment of the lens standoff distance between the focusing lens and the workpiece surface. This lens standoff can be adjusted manually during set-up or automatically by the power of a servo or stepping motor integrated inside the focusing head torch, without necessarily altering the nozzle standoff (Fig. 3); certain laser machines also use adaptive mirrors upstream from the focusing lens to dynamically control focus position. Such adaptive mirrors have curvature that can be altered by water pressure change or with piezoelectric actuators, which can change the focal length and thus change the diameter and divergence of the beam incident on the focusing lens and therefore change the characteristics d_{out} , W_{out} , and Z_R of the focus (Eq 1). For thin-gage cutting, the focus position is generally placed on the workpiece surface. For thick gage with O₂ assist gas, focus position may be placed above the workpiece surface for best edge quality in mild steel. For stainless steel and aluminum, cutting with N₂ assist gas and positioning the focus spot at least half way of the thickness below the surface are advantageous to reduce dross formation.

Assist Gas Types

There are four families of assist gas used for cutting purposes: pure reactive gases such

as oxygen; pure inert gases such as argon or helium; neutral gases such as nitrogen, which is not chemically reactive with a majority of metals and is a low-cost alternative to inert, rarer gases; and any combination of the first three kinds, such as air (20.9% O₂ + 78% N₂ + 1% Ar + traces of other elements). In some applications, additional mist or even a water shower assists laser cutting by cooling the workpiece. Table 5 summarizes the most common assist gas usages in industrial laser-cutting applications.

Gas Supply

Assist gases are supplied in three main modes adapted to the consumption rate of the manufacturing operation (Fig. 12):

- For low consumption rates, compressed gas cylinders that can be brought individually or in sets of 6 to 16 inside a plant are sufficient. A typical bank of 12 cylinders with nearly 3600 standard cubic feet (scf) total capacity of N₂ gas can supply between 3 and 4 hours of stainless steel cutting operation at 1000 standard cubic foot per hour (SCFH) flow rate if operating at approximately 50% duty; that is, actual cutting occurs only during 50% of the time, resulting in just under 1.8 h of cutting time. If a bank of cylinders contains the same volume of O₂, for low-pressure cutting of, for example, mild steel, it can supply approximately 32 hours of cutting operation at 100 SCFH if operating at approximately 50% duty.

- For high consumption rates of assist gas, bulk tanks are more suitable for high-volume storage of N₂, O₂, Ar, and H₂ in cryogenic liquid form rather than compressed gas. Table 6 gives liquid temperature and equivalent standard volumes of gas for 1 gal cryogenic liquid of the aforementioned molecules. Bulk tanks are generally stored outside the facility on a special foundation pad, with a vaporizer needed to transform the liquid into gas at pressure up to approximately 225 psi (15 bar) with ordinary bulk tanks and possibly up to 600 psi (40 bar) with more expensive bulk tanks designed for the higher-rated pressure. An optional boost pump or, as an alternative, a pumpless pressure booster system can help build up to 500 psi (35 bar) of supply pressure from an ordinary bulk tank. Although adding initial installation cost, bulk tanks enable much less cost per scft of gas than packs of compressed gas cylinders.
- Intermediate consumption rates can use transportable insulated cylinders containing cryogenic liquid gas, which can be installed inside a facility. As an alternative, an expanded-capacity pack of compressed gas cylinders at higher pressure (4500 psi, or 310 bar) can be used; each such 16-cylinder pack allows almost 9000 scft total capacity of N₂ gas.

Lasing gases are required only for gas lasers such as CO₂ lasers. Industrial CO₂ lasers can have either of two kinds of high-global-purity lasing gas supply requirements:

- The first kind requires individual cylinders of helium, nitrogen, and CO₂. These three gases are subsequently mixed in a proprietary mixture composition by a mixer internal to the laser machine. A turboblower internal to the laser machine circulates the lasing gas inside the cavity. To maintain high performance of the laser, the lasing gas that has degraded inside the cavity due to various chemical reactions is evacuated by a vacuum

Table 4 Typical values for equivalent beam parameter product $w \cdot \theta$ at the workpiece for industrial multikilowatt laser-cutting systems used in job shops and production environments

Diameters of delivery fiber are generally in the range of 100 μm for disk and fiber lasers and 600 μm for yttrium-aluminum-garnet (YAG) lasers.

	CO ₂ laser, mm · mrad	YAG laser lamp-pumped, mm · mrad	Fiber laser multimode, mm · mrad	Disk laser multimode, mm · mrad
Beam parameter product	8.5	30	3	4

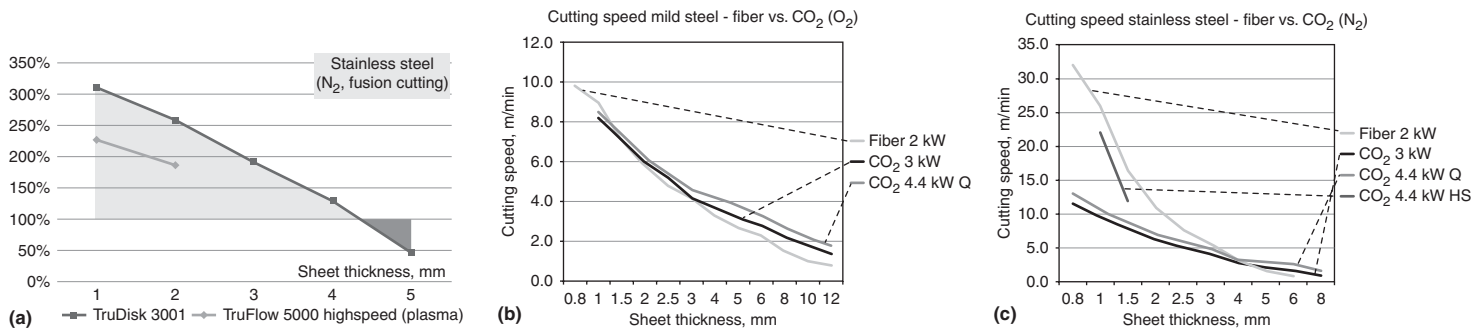


Fig. 9 Comparative scale between CO₂ laser and 1 μm laser-cutting systems. (a) Comparing 3 kW disk laser cutting with the 100% baseline of a 5 kW CO₂ laser for N₂-assisted fusion cutting of stainless steel. The disk laser yields superior speed performance up to approximately 4 mm (0.160 in.) thickness. Beyond 4 mm, CO₂ lasers are superior, in part because the edge quality of solid-state laser cutting degrades much more quickly than that of CO₂ laser cutting when thickness increases. Data courtesy of Trumpf Inc. (b) and (c) Comparing 2 kW fiber laser cutting with 3 and 4 kW CO₂ laser cutting. “Q” indicates dross-free cutting mode, whereas “HS” indicates high-speed cutting mode with the presence of plasma at the zone around the point of incidence of the beam on the workpiece, which may result in slight dross. (b) is with O₂ assist gas; (c) is with N₂ assist gas. Data courtesy of Bystronic Inc.

pump, and fresh, clean lasing gas is reinjected to compensate. This lasing gas refreshing can occur either continuously or by batched sequences.

- The second kind requires cylinders or cartridges filled with a specified premix of these same three gases, sometimes with added traces of CO and/or xenon and/or O₂, depending on the laser manufacturer. In some laser designs, the cartridge can last almost a year before needing a refill.

Gas Purity

Assist Gas Purity. Industrial-grade global purity of liquid oxygen assist gas is at least 99.5% at the tank or cylinder supply. The main impurities present in gaseous oxygen vaporized from liquid oxygen are nitrogen, water, and argon. Due to the closeness of the boiling temperatures of argon and oxygen (Table 6), argon is the most abundant impurity in industrial-grade liquid oxygen. Liquid oxygen can be further purified to reach the global-purity grade of 99.95% and above, by which one can expect substantial performance improvement to achieve a 10 to 40% increase in cutting speed, as reported in Ref 9 and 10 and represented in the experimental data of Fig.13.

Such significant range of performance improvement makes room available to share some of it between increasing cutting speed, increasing tolerance to focus position, and even improving the resulting cut-edge roughness quality.

The higher-purity oxygen at the supply source must be matched by an upgrade of the assist gas delivery system such that it preserves the higher purity all the way from the supply tank to the workpiece.

Industrial-grade global purity of liquid nitrogen exceeds 99.997%, which is largely sufficient for optimal laser-cutting performance.

Lasing Gas Purity. For industrial laser cutting of metals, CO₂ lasers are the only ones that consume lasing gases. The global purity of lasing gases is usually specified higher than industrial-grade gases. They yield a more efficient lasing mechanism and an appreciably longer life of consumables and nonconsumable components in the laser cavity. Higher-global-purity gas also yields higher peak power, better beam stability, and mode structure. Research aimed at ranking the relative impact of specific impurities on the laser performance found, for example, that addition of small quantities of carbon monoxide (CO) enhances the life of optics consumables by reducing the decomposition of CO₂ into CO and O₂. Some laser manufacturers specify a small, controllable quantity of CO in their CO₂ lasing mix. However, moisture and certain specific hydrocarbon molecules have unwelcome consequences and are also part of typical lasing gas specifications. For example, 10 ppm of

acetylene (C₂H₂) has as much negative effect on the laser efficiency as 10,000 ppm of methane (CH₄) (Ref 11). Water moisture (H₂O) is known to destabilize direct current and radio frequency discharges and accelerate degradation of the optical properties of cavity mirrors and lenses. Controlling specific impurities is more critical than controlling global purity. Laser gases are stored in specially segregated and dedi-

cated cylinders that should not be used even for the same molecules with lesser purity specifications, let alone other molecules. This is to prevent even residual ppm quantities of certain hydrocarbons from contaminating the high-global-purity lasing gas when the cylinder is filled. With some gas suppliers, the cylinders undergo special surface treatment aimed at limiting adsorption of any gas in the inside walls.

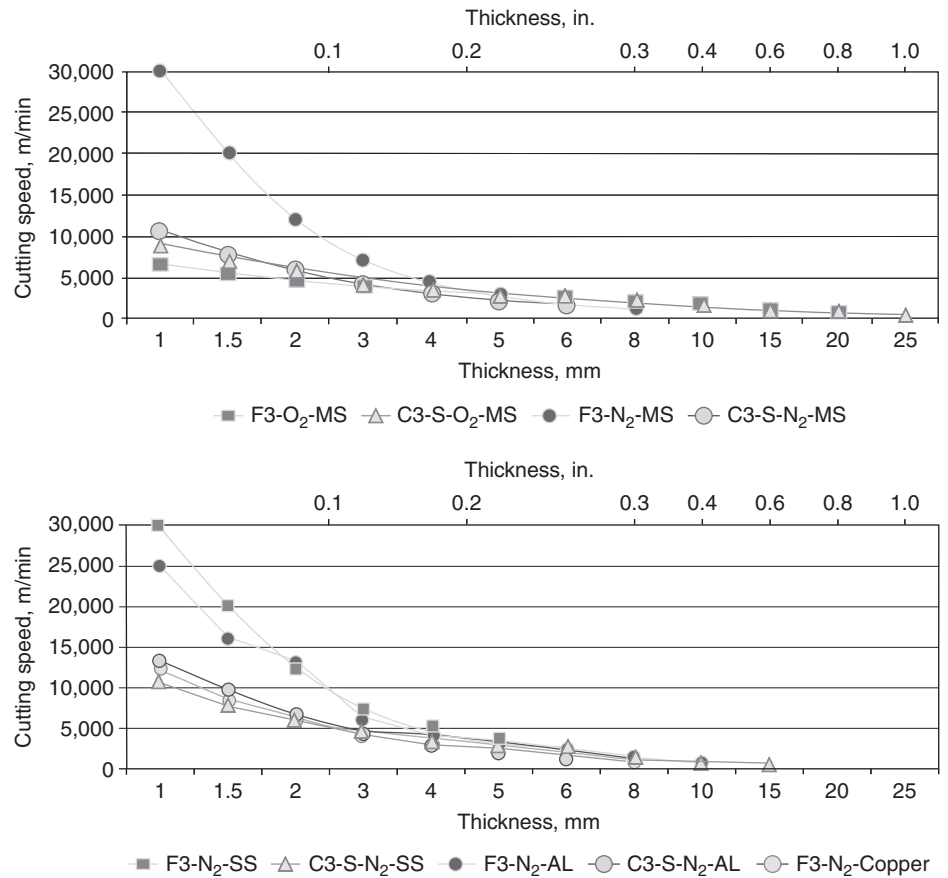


Fig. 10 Cutting speeds for tubes of various materials, with O₂ as well as N₂ assist gas and with CO₂ laser and fiber laser-cutting systems. F3 indicates 3 kW fiber laser, and C3.5 indicates 3.5 kW CO₂ laser; MS, mild steel; SS, stainless steel; and AL, aluminum. Courtesy of BLM Group

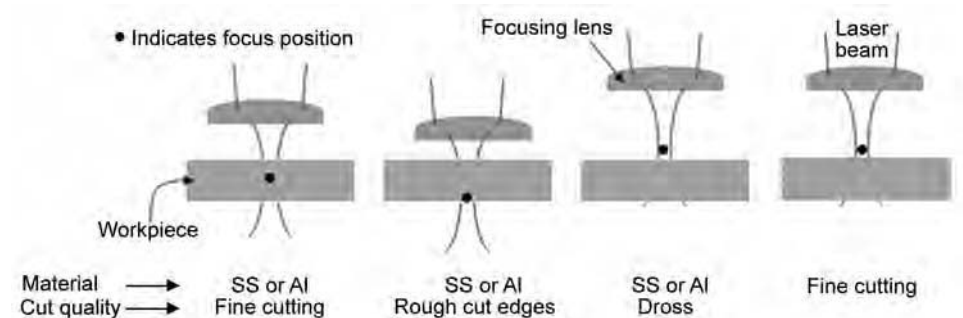


Fig. 11 Focus position comparison between multispectral with O₂ assist gas and stainless steel (SS) or aluminum (AL) with N₂ assist gas. Focus position when cutting with N₂ assist gas is preferably about halfway or more below the workpiece surface to yield a dross-free, fine-cut quality edge. With oxygen-assisted cutting, best cut-edge quality is obtained with the focus position at approximately 0.5 to 2 mm (0.02 to 0.08 in.) above the workpiece top surface.

Assist Gas Flow Rates

Flow dynamic through an orifice can be either in subsonic regime or supersonic regime. The transition from subsonic regime to supersonic regime occurs as soon as the following condition is realized:

$$\frac{P_0}{P_a} \geq \left(\frac{\gamma + 1}{2}\right)^{\frac{\gamma}{\gamma - 1}} \tag{Eq 5}$$

where P_0/P_a represents the ratio of stagnation absolute pressure, P_0 , in the cutting torch over the ambient atmospheric pressure, P_a , and γ is the ratio of specific heat coefficients for the flowing gas. At sea level, atmospheric pressure, P_a , is generally approximately 1 bar = 14.7 psi = 10^5 Pa. For O_2 and N_2 , $\gamma = 1.4$, and this condition means $P_0 > 0.89$ bar (13 psi, or 9×10^4 Pa) above atmospheric pressure.

The following “standard” volume flow rates of gas flowing through a nozzle circular orifice are derived analytically in appendix C of Ref 1. Here “standard” signifies that the volumes of gas are as if at atmospheric pressure and 273 K temperature, where one mole of any gas always occupies the same universal volume of 22.4 L:

$$\text{Subsonic volume flow rate} = \alpha \frac{P_0 D^2}{\sqrt{T_0}} \sqrt{\left(\frac{P_a}{P_0}\right)^{\frac{2}{\gamma}} - \left(\frac{P_a}{P_0}\right)^{\frac{\gamma+1}{\gamma}}}$$

$$\text{where } \alpha = \frac{\pi}{4} \sqrt{\frac{2\gamma}{Rm(\gamma-1)}} * CF \tag{Eq 6}$$

$$\text{Supersonic volume flow rate} = \beta \frac{P_0 D^2}{\sqrt{T_0}}$$

$$\text{where } \beta = \frac{\pi}{4} \sqrt{\frac{\gamma}{Rm} \left(\frac{2}{\gamma+1}\right)^{\frac{\gamma+1}{\gamma}}} * CF \tag{Eq 7}$$

where the molar mass, m , is in kilograms of the assist gas; $R = 8.314$ J/K · mol is the ideal gas constant; T_0 represents the temperature in Kelvin of the assist gas inside the cutting torch; D is the nozzle throat diameter in meters; and pressures P_a and P_0 are expressed in Pascals. With all variables and parameters expressed in International System (SI) units, CF is a unit conversion factor for the resulting volume flow rate; if the volume flow rate is expressed in SI units m^3/s , then $CF = 0.0224$; if in L/min, then $CF = 1344$; and if in standard cubic feet per hour (SCFH), then $CF = 2849.47$.

For a mixture of gas, such as air composed of approximately 21% O_2 + 78% N_2 + 1% Ar, γ and m are given theoretically by the following formulas in which x_i represents the molar fraction of gas i , and γ_i and m_i are the specific heat ratio and the molar mass, respectively, of gas i . Table 7 lists values for m and γ for various gases:

Table 5 Typical assist gas types used in industrial laser cutting of metals

Material	Assist gas	Applications
Mild steel	Low-pressure O_2	Most common for 2.67 mm (0.105 in.) and thicker
Mild steel	High-pressure N_2 , 5 to 20 bar	Mostly for high-speed cutting of thin sheets and to avoid oxide scales on steel cut edges
Stainless steel	High-pressure N_2 , 5 to 20 bar	Most common for stainless steel
Aluminum alloys	High-pressure N_2 , 5 to 20 bar	For special nonoxidized cut edge and/or thick plate requirement
Aluminum alloys	High-pressure air, 5 to 20 bar	Lower cost than pure N_2 but increases dross
Copper alloys	Low- to high-pressure O_2 , 1.5 to 12 bar	More efficient than air
Brass	Low- to high-pressure O_2 or N_2 , up to 20 bar	High-speed cutting of thin workpieces
Titanium alloys	High-pressure Ar, 3 to 10 bar	For aerospace applications, reactive O_2 and N_2 are avoided.
Nickel alloys	High-pressure N_2 , 3 to 10 bar	For aerospace and energy industries applications: slower cutting speed than with O_2 assist, but less dross and no edge oxidation

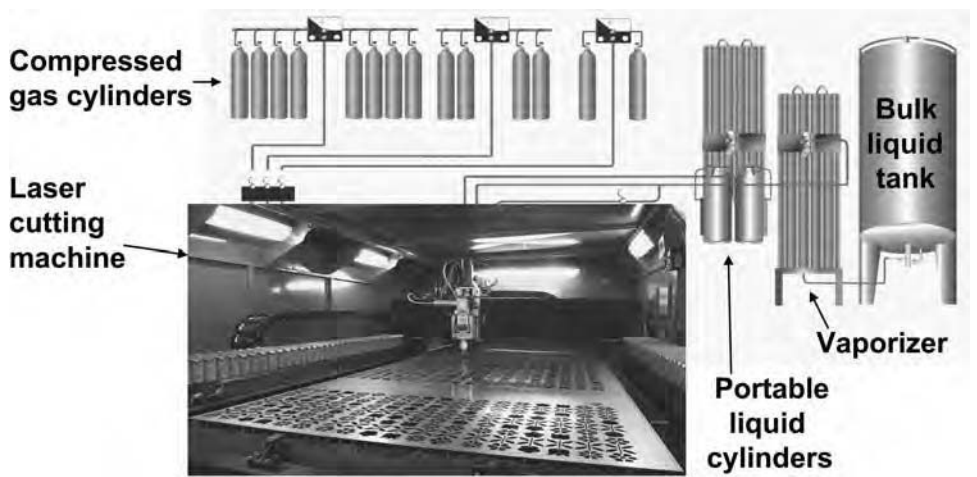


Fig. 12 Assist gases can be supplied in a bulk tank containing liquid cryogenic molecules or in transportable cylinders containing either compressed gases or liquid cryogenic molecules. Courtesy of Air Liquide

Table 6 Conversion data from 1 gal of cryogenic liquid molecules

A full, ordinary 1500 gal bulk tank can contain 5 U.S. tons (4590 kg) of liquid nitrogen, which is the equivalent of 139,000 scft of the same when vaporized in gas form at standard atmospheric pressure and temperature.

Molecules (1 gal of liquid = 3.785 L)	Boiling point at atmospheric pressure		Gas volume equivalent		Weight	
	°C	°F	nm ³ (a)	scft(a)	kg	lb
N_2	-196	-320	2.447	93.11	3.06	6.745
O_2	-183	-297	3.025	115.1	4.322	9.527
Ar	-185	-302	2.957	112.5	5.276	11.63
H_2	-252	-423	2.981	113.41	0.2679	0.5906
CO_2	-78	-109	1.9431	74.04	3.842	8.470
He	-269	-452	2.649	100.8	0.4728	1.042

(a) nm³ represents a normal cubic meter volume, and scft represents a standard cubic foot volume. In this context, the terms *standard* and *normal* are interchangeable because they equally refer to temperature condition of approximately 300 K and pressure of 1 bar for the gas volume considered. Source: Ref 8

$$\frac{1}{\gamma - 1} = \sum \frac{x_i}{\gamma_i - 1} \text{ and } m = \sum x_i * m_i \tag{Eq 8}$$

Example 1: Cutting Mild Steel. A 4 kW CO_2 laser cutting of 6.4 mm (¼ in.) mild steel uses a 190 mm (7.5 in.) focal length lens and O_2 assist gas at a cutting speed of 100 inches per minute (ipm) (255 cm/min), with a nozzle diameter of 2 mm (0.08 in.) and oxygen pressure of 0.7 bar (70 kPa) above atmospheric

pressure. The absolute pressure of 1.7 bar (170 kPa) is in the subsonic regime. The resultant consumption flow rate of oxygen is 116 SCFH. If the operator switches to a 3 mm (0.12 in.) nozzle at the same pressure, the flow rate would jump to 260 SCFH.

Example 2: Cutting Stainless Steel. A 4 kW CO_2 laser cutting of 1.5 mm (0.060 in.) stainless steel uses N_2 assist gas at a cutting speed of 400 ipm (10 m/min), with a nozzle diameter of 1.5

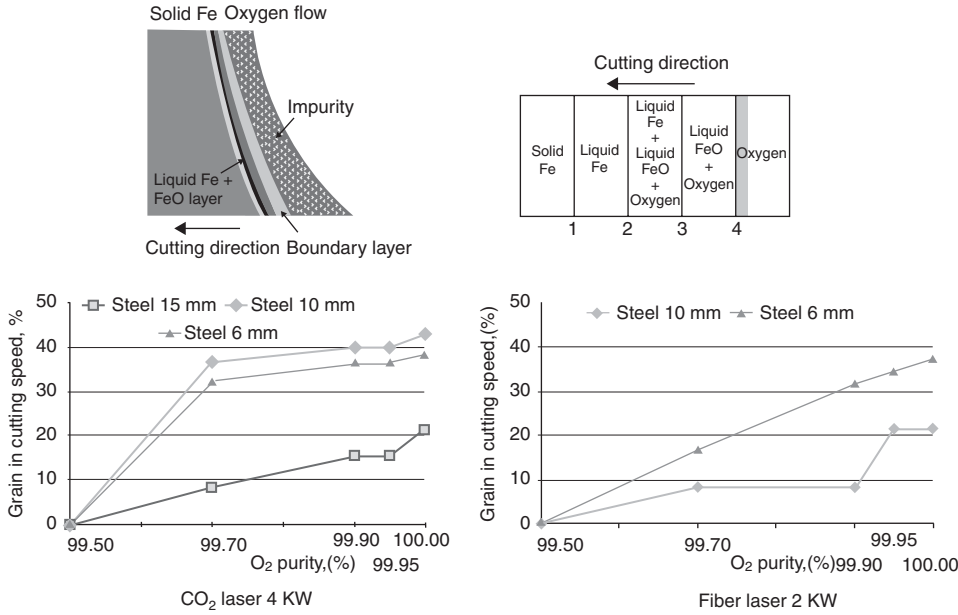


Fig. 13 Influence of oxygen assist gas purity on laser-cutting speed for CO₂ laser and fiber laser cutting of mild steel. Source: Air Liquide-CTAS Cutting and Welding R&D Laboratory

mm (0.060 in.) and nitrogen pressure of 13 bar (130 kPa) above atmospheric pressure. The absolute pressure of 14 bar (140 kPa) is in the supersonic regime. The resultant consumption flow rate of nitrogen is 577 SCFH. If the operator switches to a 3 mm (0.12 in.) nozzle at the same pressure, the flow rate would jump to 2308 SCFH.

Table 8 gives volume flow rates as a function of nozzle diameter and pressure for O₂ and N₂ assist gases. Yet another powerful piece of information that can be derived from these analytical formulas is the flow rate sensitivity to variations in pressure, temperature, and nozzle diameter by mathematically calculating the differentials. It allows for better understanding of repeatability and reproducibility challenges and can save some troubleshooting time: For the supersonic regime:

$$\frac{\Delta(\text{Flow rate})}{\text{Flow rate}} = \frac{\Delta P_0}{P_0} - \frac{1}{2} \frac{\Delta T_0}{T_0} + 2 \frac{\Delta D}{D} \quad (\text{Eq 9})$$

For the subsonic regime:

$$\frac{\Delta(\text{Flow rate})}{\text{Flow rate}} = F_0 * \frac{\Delta P_0}{P_0} - \frac{1}{2} \frac{\Delta T_0}{T_0} + 2 \frac{\Delta D}{D} + F_a * \frac{\Delta P_a}{P_a} \quad (\text{Eq 10})$$

where $F_0 + F_a = 1$ and F_0 varies from 1 at the limit of transition to the supersonic regime (Eq 5) to $+\infty$ at the no-flow limit when $P_0 = P_a$ (Ref 1). For most O₂-assisted laser cutting of mild steel, F_0 is typically of the order of 1.15. Generally, one assumes that P_a remains fairly constant, so $F_a * \Delta P_a \approx 0$.

Consequently, Eq 9 and 10 reveal that a 10% variation in nozzle diameter results in a 20%

variation in flow rate that will be noticed in the cutting performance. A typical nozzle size is 1 mm (0.040 in.); thus, a ± 0.1 mm (0.004 in.) variation in diameter, which is common and may appear negligible, has a substantial $\pm 20\%$ impact in flow rate equivalent to a 20% change in pressure. The way these nozzles are manufactured, whether their throat orifice is maintained clean and free of debris or residues, the dewpoint or the viscosity of the gas are factors that can impact the effective diameter, D , value and thus greatly influence the repeatability and reproducibility (R&R), particularly for smaller nozzle diameters.

Similarly, a temperature variation from -1 °C (30 °F, or 272 K) on a January morning to 38 °C (100 °F, or 311 K) on an August afternoon yields a 14% temperature difference and thus a 7% difference in flow rate. The key is to set up the system such that the process is tolerant enough so that a 7% variation will not affect R&R. It is also interesting to note that for O₂-assisted cutting occurring in the subsonic regime, the temperature of the kerf can be transferred to the gas inside the nozzle by radiation but also by conduction and convection when given the time. This may substantially increase the temperature of the gas in the nozzle after some duration of uninterrupted cutting time with subsonic assist gas flow; the impact on the cutting performance may be much more troublesome. However, when operating in the supersonic regime, conduction and convection heat cannot be transferred upstream in a supersonic flow; the only upstream heat-transfer mechanism in that case is limited to radiative heat transfer from the kerf to the nozzle.

Finally a 10% change in pressure could result in a 10% flow rate change in the supersonic

Table 7 Specific heat ratio of various potential elements of assist gases

Assist gas elements	γ	m , g
O ₂	1.40	32
N ₂	1.40	28
He	1.66	4
Ar	1.66	40
CO ₂	1.40	44
H ₂	1.40	2
H ₂ O	1.33	10
Air	1.40	29

Experimental data for γ can be found in Ref 12.

regime and slightly more than 10% in the subsonic regime.

Material Considerations

The majority of laser-cutting applications involve cutting of metals, which are mainly uncoated and coated mild steels, stainless steels, and aluminum alloys. Many steel makers, such as ArcelorMittal and US Steel in North America and Chubu Steel in Japan, have studied the effect of different alloying grades of steels on laser cut-edge quality (Ref 13). Penn et al. (Ref 14) compare in great detail the ability of various aluminum alloys, namely 6111-, 5754-, and 5182-series alloys, to be laser cut. The study recommends laser cutting of these automotive-grade aluminum alloy sheet metals instead of die blanking them for volume production of aluminum sheet blanking.

The following sections describe metallurgies and other key material considerations that impact laser-cutting performances and introduce examples of laser cutting of nonmetal materials.

Mild steels consist predominantly of iron with some small quantities of alloying elements, primarily carbon, manganese, silicon, phosphorus, sulfur, aluminum, and copper. From appliance panels and automobile body parts made with deep-drawable-quality mild steels to structural members made from high-strength steels, most steels used in consumer goods are low-carbon steels of commercial grade, drawing quality, or structural quality. Their compositions are between 0.05 and 0.40% C; manganese content is maintained between 0.25 and 0.50%, while phosphorus is kept under 0.035%, sulfur under 0.04%, and silicon under approximately 0.25%.

Generally speaking, steels on the low end of carbon content enable cutting at speeds up to 20% higher and of maximum thickness up to 20% thicker than steels on the high-end range of carbon content. Structural-quality steel with carbon content close to or higher than 0.40% is prone to microcracking along the cut edge. Under fatigue, those cracks can develop into full-fledged part failure in service. Heat treatment after cutting could be one way of fixing microcracking. It is interesting to note that such microcracking problems are actually more acute when using traditional mechanical cutting

Table 8 Flow rates in units of standard cubic feet per hour (SCFH) as a function of pressure and nozzle diameter for N₂ and O₂ assist gases (1 SCFH ≈ 0.47 L/min)

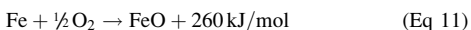
Gage reading			Flow rates, SCFH							
			Nozzle diameter, mm (in.)							
psi	bar	Pressure, psi	1 (0.040)	1.25 (0.050)	1.5 (0.060)	1.75 (0.070)	2 (0.080)	2.25 (0.090)	2.5 (0.100)	2.75 (0.110)
Nitrogen										
...	18.3	28.6	41.2	56.1	73.3	92.8	114.5	138.6
14.7	1	29.4	37	57	82	112	147	186	229	277
29.4	2	44.1	55	86	124	168	220	278	344	416
44.1	3	58.8	73	115	165	224	293	371	458	554
58.8	4	73.5	92	143	206	281	367	464	573	693
73.5	5	88.2	110	172	247	337	440	557	687	832
88.2	6	102.9	128	200	289	393	513	649	802	970
102.9	7	117.6	147	229	330	449	586	742	916	1109
117.6	8	132.3	165	258	371	505	660	835	1031	1247
132.3	9	147	183	286	412	561	733	928	1145	1386
147	10	161.7	202	315	454	617	806	1021	1260	1525
161.7	11	176.4	220	344	495	673	880	1113	1374	1663
176.4	12	191.1	238	372	536	730	953	1206	1489	1802
191.1	13	205.8	257	401	577	786	1026	1299	1604	1940
205.8	14	220.5	275	430	619	842	1100	1392	1718	2079
220.5	15	235.2	293	458	660	898	1173	1484	1833	2217
235.2	16	249.9	312	487	701	954	1246	1577	1947	2356
249.9	17	264.6	330	515	742	1010	1319	1670	2062	2495
264.6	18	279.3	348	544	783	1066	1393	1763	2176	2633
279.3	19	294	367	573	825	1122	1466	1856	2291	2772
294	20	308.7	385	601	866	1179	1539	1948	2405	2910
Oxygen										
6	0.41	20.7	23	36	52	71	92	117	144	175
7	0.48	21.7	24	38	54	74	97	123	151	183
8	0.54	22.7	25	40	57	78	101	128	158	192
9	0.61	23.7	26	41	59	81	106	134	165	200
10	0.68	24.7	28	43	62	84	110	139	172	208
11	0.75	25.7	29	45	65	88	115	145	179	217
12	0.82	26.7	30	47	67	91	119	151	186	225
13.083	0.89	27.783	32	51	73	99	130	164	202	245
29.4	2	44.1	51	80	116	157	206	260	321	389
44.1	3	58.8	69	107	154	210	274	347	429	519
58.8	4	73.5	86	134	193	262	343	434	536	648
73.5	5	88.2	103	161	231	315	411	521	643	778
88.2	6	102.9	120	187	270	367	480	607	750	907
102.9	7	117.6	137	214	309	420	549	694	857	1037
117.6	8	132.3	154	241	347	472	617	781	964	1167
132.3	9	147	171	268	386	525	686	868	1071	1296

means such as die blanking; for that reason, cutting of some advanced-strength steel hydroformed, closed-section products is preferably done with robotic laser cutting rather than with die trimming.

Electrical steels with higher levels of approximately 0.4% Si can be found in components such as transformer frames because of their increased electrical resistivity and higher thermal oxidation threshold. Such high levels of silicon result in approximately 20% reduction in cutting speed and the generation of more severe dross.

Manganese content as high as 0.5% and sulfur content as high as 0.04% also disrupt a laser-cutting process sufficiently to reduce cutting speed and worsen dross growth; such contents can be found in tool steels.

In the case of oxygen-assisted laser cutting of mild steel, an exothermic reaction between iron and oxygen occurs at approximately 1500 K (1225 °C, or 2240 °F) before metal melting starts:



This exothermic reaction can be equivalent in heat input to a CO₂ laser power of approximately

500 W added to a laser-material interaction zone the size of a typical focused laser beam spot, that is, approximately 250 μm in diameter for laser cutting. This heat input advantage enables a tremendous boost in cutting speed compared to cutting the same material with N₂ assist gas (Fig. 14). This advantage with O₂ gas is more prevalent with low laser power or with thicker gage. At high power and with thinner gages, faster speeds are achieved with N₂ assist gas than with O₂. Figures 15 and 16 illustrate the gas dynamic associated with O₂ and N₂ assist gases and their impact on the cutting process. When cutting with a 1 μm laser such as YAG, fiber, and disk lasers, the absorptivity of the 1 μm wavelength by a metal is several fold larger than that of a 10.6 μm wavelength of the CO₂ laser (Fig. 17). Consequently, with 1 μm laser cutting, the advantage of using oxygen assist becomes more modest than with oxygen-assisted CO₂ laser cutting.

One disadvantage of O₂-assisted laser cutting is that it generates iron oxide flakes that stick along the cut edge (Fig. 18). These flakes are composed of FeO in the core

and harder Fe₂O₃ on the outer layer. They are unwelcome contaminants for subsequent welding operations. These iron oxide flakes are also brittle and very easily crumble away from the cut edge into sand-sized particles and wear against tools and dies. The flaking-away action is obviously detrimental to most painting and stamping processes. One way to prevent formation of oxide flakes is to laser cut mild steel with N₂ assist gas. In particular, galvanized steels coated with either zinc- or aluminum-base coating are predominantly laser cut with N₂ assist gas. Because of the low-melting-temperature coating, dross forms when cutting coated steels; this dross can be minimized by slowing down the cutting speed. Typically, there is approximately a 20% difference in “production” cutting speed between bare steel less than 2 mm (0.08 in.) thickness and the same with a coating weight greater than approximately 80 g/m². Generally, no substantial difference is observed between the different galvanizing coating processes, that is, electrogalvanizing, hot dipped galvanizing, and galvannealing.

Stainless steels can contain up to approximately 18% Cr and 8% Ni by weight. They are highly resistant to corrosion due to a protective Cr₂O₃ film that naturally forms on its surface when exposed to free atmosphere. This Cr₂O₃ oxidation film also reduces the exothermic oxidation of iron with O₂, thus lowering the benefit of using O₂ assist gas compared to N₂. The Cr₂O₃ has a much higher melting temperature than iron, and during cutting, the same protective film of Cr₂O₃ solidifies around droplets of molten metal and sticks to the bottom edge of the kerf, thus creating stalactites called dross. Oxidation of nickel creates a black film coated on the dross ends (Fig. 19). To reduce dross, stainless steel is often laser cut with N₂ assist gas. The high pressure of N₂ assist gas requires large consumption of nitrogen and therefore increases processing costs. At equal laser power and equivalent cut-edge quality, the maximum thickness that can be cut dross-free for stainless steel is a little under half of that for mild steel. This has an impact on the cost of operation, as illustrated in Fig. 20.

Aluminum Alloys. After steels, aluminum and aluminum alloys are most significant in terms of industrial laser-cutting applications. Just as with stainless steel, aluminum is quickly oxidized when exposed to free atmosphere and forms an Al₂O₃ autoprotective surface film that prevents further corrosion penetration. This thin Al₂O₃ film oxidation also limits the benefit of oxidation with O₂-assisted laser cutting. Similarly, the same film is also responsible for dross formation because of the much higher melting temperature of 2300 K (2025 °C, or 3680 °F) for Al₂O₃ compared to only 950 K (675 °C, or 1250 °F) for aluminum. For these reasons, aluminum is mostly laser cut with compressed air or, most often, with N₂ assist gas for optimal quality.

Titanium and Nickel Alloys. The aerospace and energy industries represent some of the largest users of titanium alloys and nickel alloys, because these metals exhibit high toughness and high strength-to-weight ratio advantages over more common metals, including aluminum and steel. Nickel alloys such as Monel (66% Ni, 30% Cu), Inconel 600 (76% Ni, 15% Cr, 8% Fe), and Hastelloy (57% Ni, 16% Cr, 15% Mo, 6% Fe) are known for their high corrosion resistance under acid chemical environments and high temperature.

During oxygen-assisted thermal cutting, titanium reacts with O₂ in a highly exothermic reaction, and even with neutral gases such as N₂ in an environment at elevated temperatures above approximately 480 °C (895 °F). This highly reactive reaction of titanium can generate vigorous-to-explosive flame plumes detrimental to fine, intricate feature cutting. Cutting titanium alloys with an inert assist gas such as argon yields cutting speeds several fold slower than cutting with O₂ assist gas. Nickel alloys can be cut with N₂ assist gas for dross-free cut quality.

Copper Alloys. Lasers can cut copper in pure form or in alloy form, such as brass with zinc as the main alloying element of approximately 33%, or bronze with tin as the main alloying element of approximately 10% content. Copper alloys are difficult to laser cut because of a combination of high thermal conductivity (Table 9) and a high reflectivity to laser beams, particularly the higher wavelength (Fig. 17). Even though oxidation of copper by oxygen is moderately exothermic compared to steel oxidation, O₂ is still preferred over N₂ assist gas when laser cutting copper alloys because it yields significantly higher cutting speed. Figure 21 illustrates laser cutting of various metals, including copper

tubes with solid-state laser sources, thanks to better absorptivity of copper to the 1 μm wavelength.

Table 10 compares the heat energies needed to melt and vaporize a reference volume element of three materials: steel, aluminum, and stainless steel. These energies represent only a fraction of the laser beam energy needed, because most of it is wasted by reflection, transmission, conduction, convection, and radiation. In addition, other quality restrictions, such as edge smoothness and dross, or material properties, such as optical reflectivity, elevate the requirements for quality cutting beyond the plain heat energies input.

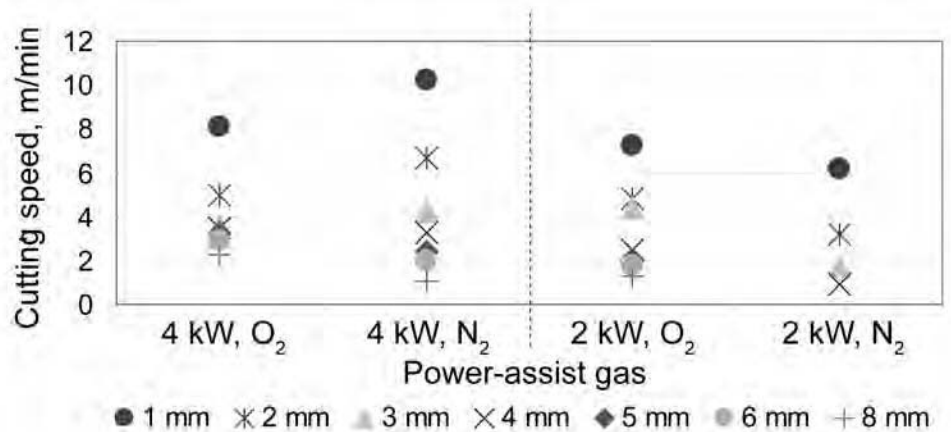


Fig. 14 Typical cutting speeds for N₂ versus O₂ at CO₂ laser powers of 4 kW versus 2 kW. The lower the power, the more O₂ contributes to speed. At high power, the higher the thickness, the larger the relative contribution of O₂ to speed; at thin gages, faster speeds are achieved with N₂ than with O₂.

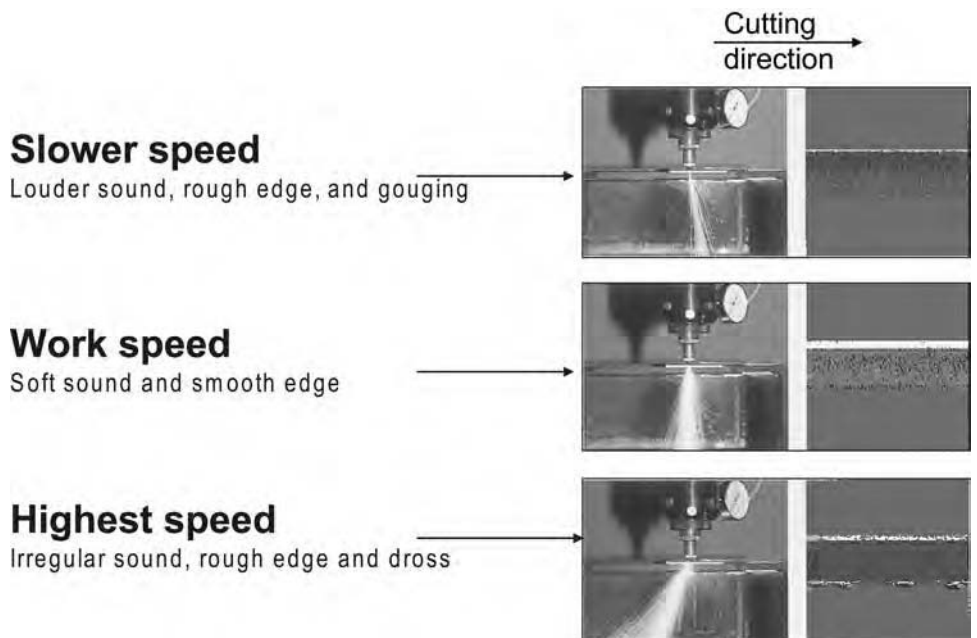


Fig. 15 Oxygen-assisted laser cutting showing the influence of cutting speed on cut quality. Courtesy of Air Liquide-CTAS Cutting and Welding R&D Laboratory

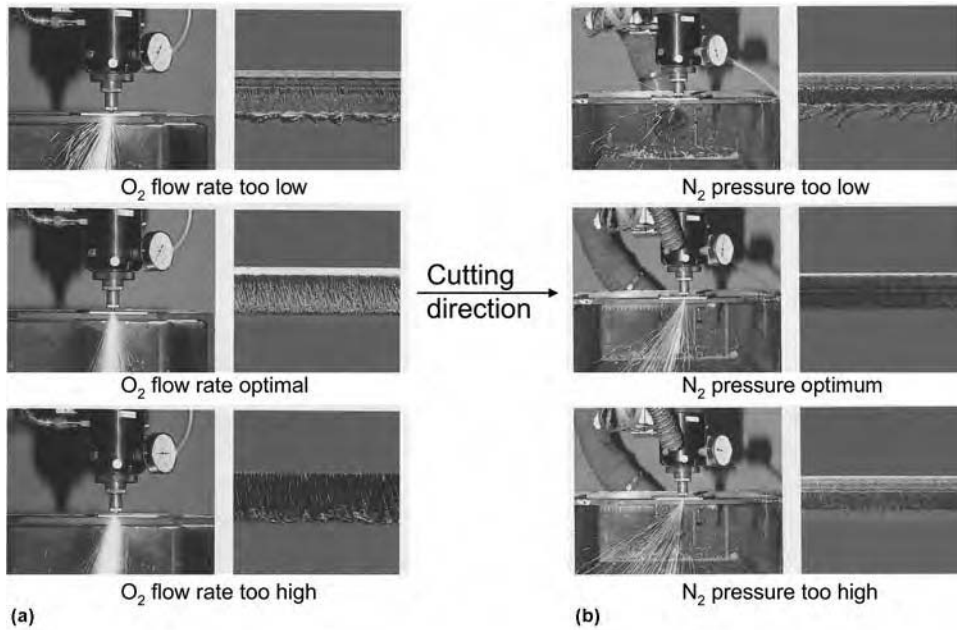


Fig. 16 Influence of gas pressure set-up on laser-cutting performance. (a) O₂ assist gas with mild steel. (b) N₂ assist gas with stainless steel. Courtesy of Air Liquide-CTAS Cutting and Welding R&D Laboratory

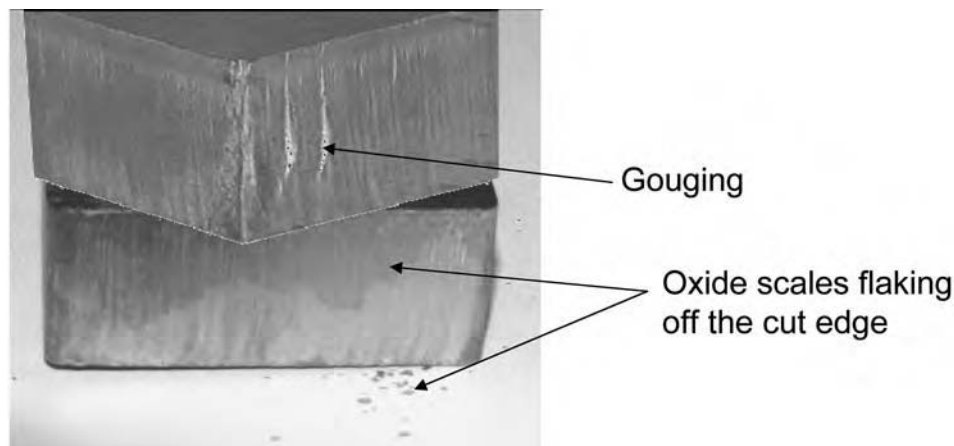


Fig. 18 Oxide scales cut with O₂ assist gas have a shiny, dark-blue appearance and flake off from the cut edge. They are detrimental to downstream painting and welding operations. Gouging leaves deep crevices that flare in the direction of the assist gas flow; they usually indicate excess heat from too much laser power or too much O₂ flow rate.

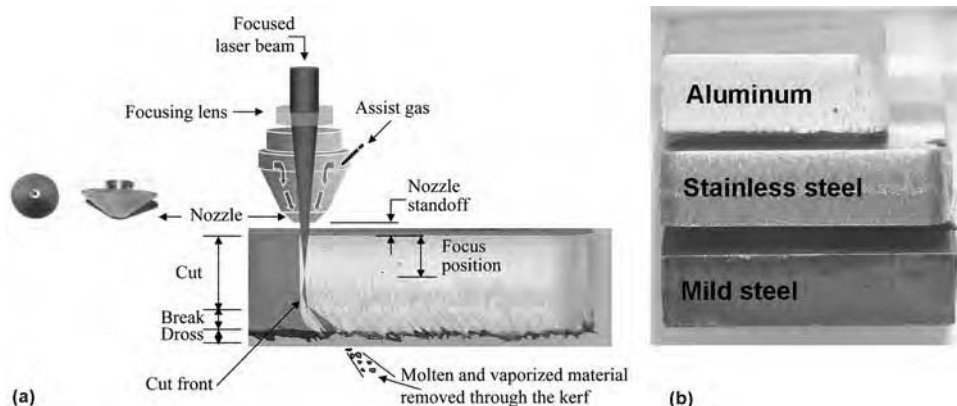


Fig. 19 (a) Features of edge quality for laser cutting. The striations observed on the cut-edge surface are indicative of a cut front line with three zones: a smoother cut area at the top, a rougher break area at the bottom, and a hanging dross area. For a high-quality cut, the break and the dross should be minimized or eliminated. (b) Dross-free, smooth cut edges for aluminum (cut with N₂ assist gas), stainless steel (cut with N₂ assist gas), and mild steel (cut with O₂ assist gas)

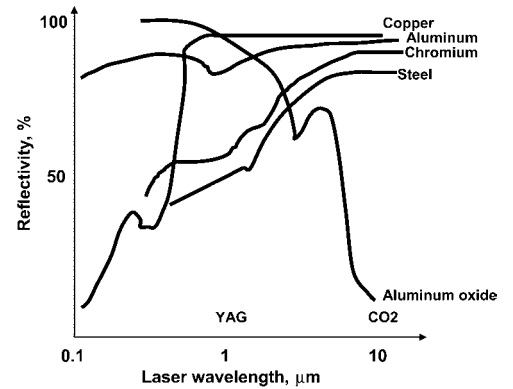


Fig. 17 Dependence of metal surface reflectivity on laser light wavelength. YAG, yttrium-aluminum-garnet. Data extracted from Ref 15

Wood, Plastics, and Synthetic Materials. Lasers can cut wood very effectively with O₂ assist gas. The die board industry is very vibrant, with over 5000 members in North America alone. Die boards are thick wood tools with narrow kerf cuts through which metal blades are inserted. These tools are used to cut cartons and papers, such as for the packaging used for pizza delivery and beer pack boxes (Fig. 22). Most die board cutting is still being done with routers. However, to enable more sophisticated three-dimensional blade inserts, laser cutting has become the manufacturing tool of choice, gaining market share versus all other wood-cutting technologies at a phenomenal growth rate. With a 2200 W CO₂ laser, 12.7 mm (½ in.) thick plywood material can be cut at a feed rate of 62 ipm (158 cm/min) using bifocal technology (Ref 19).

Lasers cut plastics, acrylic plastic sheets, synthetic materials, and even clothing fabrics in industrial applications. Just as for wood, adequate air filter systems are recommended to keep the atmosphere safe for operators. Because polyvinyl chloride can produce toxic chlorine vapors when cut with a thermal process, it is highly recommended that no thermal process be used to cut it.

Surface Conditions

Some metals coming out of hot rolled mills exhibit oxidation in the form of corrosion or, even worse, have oxide scale inclusions on their surfaces. These oxide inclusions have hardness and melting temperatures much higher than the base material; such differences in properties yield cutting defects, and set-up parameters must be readjusted. For these reasons, mill scales and corrosion are generally undesirable for laser cutting. Some steel materials are specified to be pickled and oiled to remove these and other surface contaminants; they yield a higher

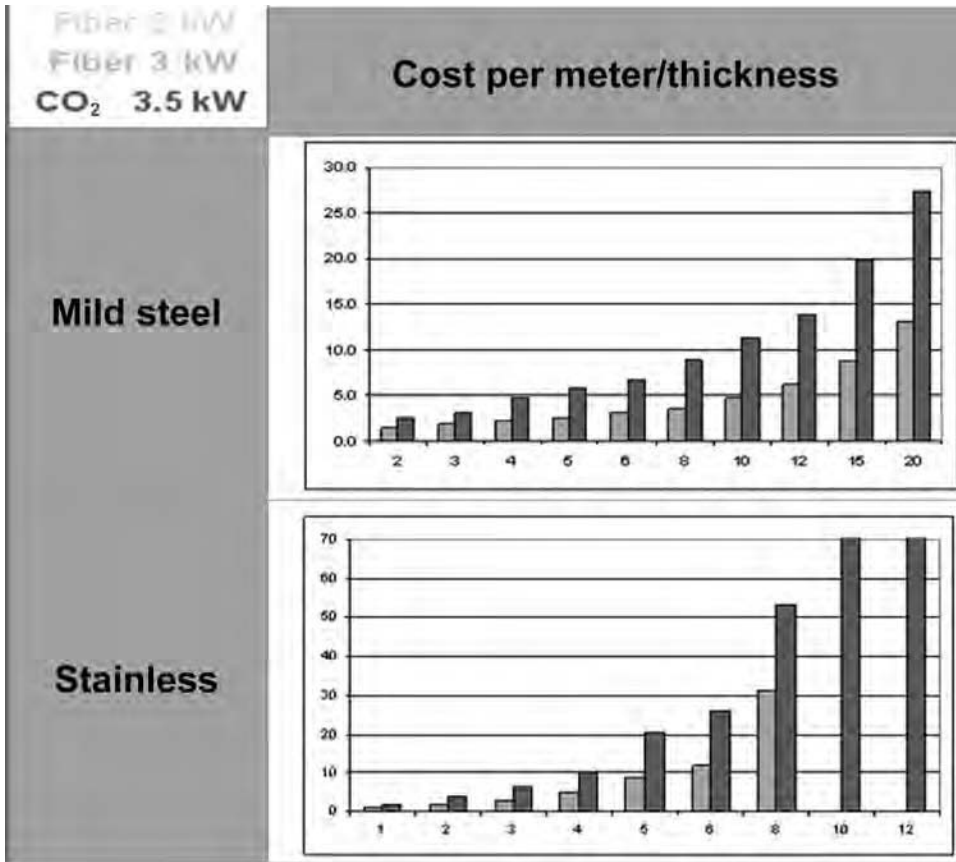


Fig. 20 Cost comparison for cutting of stainless steel and mild steel. Because high-pressure N₂ assist gas is required for cutting stainless steel, the cutting costs are approximately double those for cutting mild steel. Adapted from data courtesy of BLM Group

Table 9 Physical properties of common metals

Material	Thermal conductivity, W/(m · K)	Viscosity at melting temperature, 10 ⁻² poise	Melting temperature	
			K	°F
Mild steel	30	6.1	1810	2798
Stainless steel	17	...	1864	2896
Aluminum 6101, 7075 T6	218	4.5	873	2912
Aluminum 5456, 5083	117	4.5	873	2912
Copper	370	3.36	1356	1981
Brass	121	3.42	1193	1688
Inconel	17	...	1778	2741
Titanium	110	...	1943	3038
Chromium	26	0.684	2148	3407
Nickel	94	...	1726	2647

Source: Ref 16, 17

feed rate, more stable and repeatable cutting process, and better edge quality. Mill scales can also be shot blasted away with ceramic dust particles. However, the hard ceramic particles must be brushed away from the surface after shot blasting is completed.

Comparison between Laser and Traditional Cutting Processes

The various cutting technologies differ by their range of applications, process tolerances,

as well as variable and fixed costs (Ref 20). Table 11 summarizes the differences between three material-removal cutting technologies: laser cutting, water-jet cutting, and plasma cutting.

Principles of Laser-Drilling Processes

Laser drilling has been used in production for decades in the aerospace industry to drill

cooling-channel holes in aircraft engine turbine blades (Ref 18) (Fig. 23). In a typical nickel alloy aircraft engine turbine blade, laser-drilled cooling channels have diameters approximately 0.5 mm (0.02 in.) wide and can run as deep as 5 to 25 mm (0.2 to 1 in.). The cooling air from these holes is used to create a cold air-film layer across the surface of the turbine and to prevent combustion gases that are hotter than the melting temperature of the turbine material from directly contacting the turbine (Ref 21). Laser drilling also has applications in micromanufacturing, such as for drilling microholes of 0.1 mm (0.004 in.) diameter to depths exceeding 0.5 mm (0.02 in.) in surgical needles in the medical industry, and also in the semiconductor industry, such as for photovoltaic cells. The production of photovoltaic silicon film with thickness under 200 μm requires lasers to drill holes of diameter as small as 30 μm (Ref 22) at a rate of 20,000 holes per second. Galvano-scanner mirrors enable the synchronization of high-speed, high-acceleration positioning of the laser beam with high-frequency beam pulsing.

Drilling holes with lasers is done with two main techniques: percussion drilling and trepanning. Figure 24 illustrates examples of four drilling practices that derive from these two main techniques: single- and multiple-pulse percussion drilling, trepanning, and helical trepanning.

Percussion drilling is similar to the piercing process described to initiate laser cutting in that laser pulses of high energy create enough power density to almost instantaneously vaporize a certain volume of material. The amount of energy per volume of material to be vaporized can be written as:

$$E = \rho \left[\overbrace{C_{p-solid} (T_f - T) + L_f}^{Melt} + \overbrace{C_{p-molten} (T_v - T_f) + L_v}^{Vaporize} \right] \quad (Eq 12)$$

where ρ is the density of the material; C_p represents the specific heat for the solid and molten materials, respectively; L represents the latent heat for fusion and vaporization in accordance with the subscript; T_f and T_v are the fusion and vaporization temperatures, respectively; and T is the starting room temperature of the workpiece. It is known that C_p varies with temperature; for approximation purposes, Eq 12 includes the first-order approximation that C_{p-solid} is constant from room temperature, T, to T_f and that C_{p-molten} remains constant from melting point, T_f, to vaporization point, T_v. Table 10 lists comparative values of these parameters for steel, aluminum, titanium, and Inconel alloys; some variations are to be expected, depending on the nature and relative quantity of alloying elements and heat history.

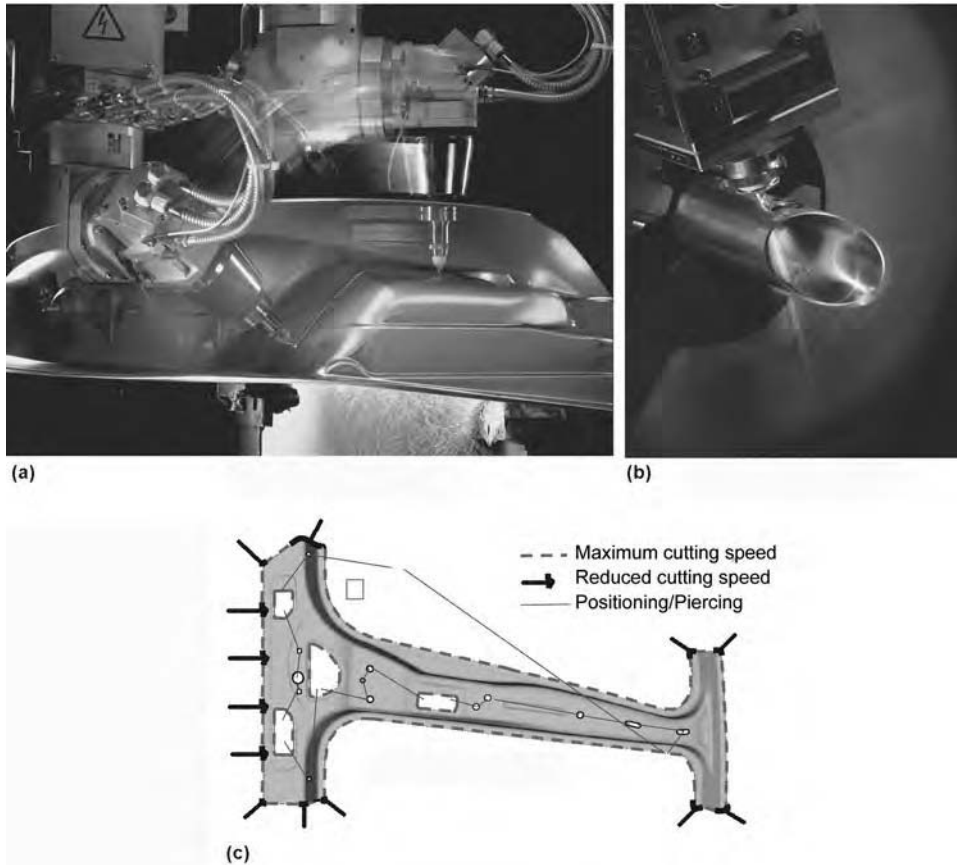


Fig. 21 (a) High-volume, three-dimensional (3-D) production CO₂ laser cutting of automobile steel components. Courtesy of Trumpf Inc. (b) Cutting of copper tubes with fiber laser. Courtesy of BLM Group. (c) B-pillar component illustrating guidelines for reducing speed and consequently adjusting power, required at small-radius features when performing 3-D cutting. Arrows show regions where cutting speed is reduced. Courtesy of Trumpf Inc.

Table 10 Estimated heat energy that must be absorbed by a metal workpiece to heat, melt, and vaporize a control kerf volume of 1 mm³ is tenfold larger than the heat energy to heat and melt the same control volume. Results can vary significantly from alloy to alloy but remain within the same order of magnitude.

Control kerf volume is 1 mm ³	Steel	Aluminum	Titanium	Inconel
Density (ρ), kg/m ³	7858	2700	4510	7900
Fusion temperature (T_f), K (°F)	1803 (2786)	933 (1220)	1941 (3034)	1673 (2552)
Vaporization temperature (T_v), K (°F)	3273 (5432)	2600 (4220)	3533 (5900)	3180 (5264)
Latent heat of fusion (L_f), J/kg	2.67×10^5	3.97×10^5	4.40×10^5	1.45×10^5
Latent heat of vaporization (L_v), J/kg	6.30×10^6	1.08×10^7	9.83×10^6	6.40×10^6
Specific heat for solid metal at room temperature (C_p), J/kg/K	460	963	658	462
Specific heat for molten metal at melting temperature (C_p), J/kg/K	627	1087	650	658
Heat energy to melt a control kerf volume, J	7.5	2.7	6.9	6.2
Heat energy to vaporize a control kerf volume, J	64.3	36.8	55.9	64.6

Source: Ref 16–18

For the single-pulse mode, a single pulse suffices to achieve the drilling depth required. In the multiple-pulse mode, each pulse digs progressively deeper into the material until the desired drilling depth is produced. If the workpiece is not drilled all the way through, the hole is called a “blind hole.” At each pulse, vaporized material is ejected out of the hole by recoil pressure (Fig. 25). The vapor ejection occurs at high speed under the recoil pressure from the

bottom of the hole in formation. Thanks to a Venturi effect, the vapor plume drains with it some molten metal droplets along the walls of the hole. These droplets resolidify into slag deposited on the workpiece surface and could potentially damage it.

With the percussion technique, the laser beam is kept in a stationary position relative to the workpiece. For the trepanning techniques, the laser beam is maneuvered by a numerically

controlled mechanism into a motion relative to the workpiece during the drilling process. The shape of this motion determines the shape of the drilled hole. Generally, the trepanning technique is used to drill holes that are larger than the laser beam spot diameter (Eq 1–3).

Typical lasers used for drilling are transverse excited atmospheric CO₂ lasers and Q-switched CO₂ lasers (10.6 μ m wavelength) (Ref 23), YAG lasers (1.064 μ m), fiber lasers (1.07 μ m), copper vapor lasers (0.511 and 0.578 μ m), and even excimer lasers (0.193 to 0.308 μ m) that can achieve drilling by ablation, used predominantly in nonmetals due to their short ultraviolet wavelength.

Table 12 illustrates examples of set-up parameters representative of drilling of various metals with a solid-state 1 μ m laser such as a YAG laser.

Hole Quality

When piercing to initiate laser cutting, the quality of the pierced hole is not very important. For most drilling applications, however, specific quality factors are generally imposed. For example, in applications where the drilled holes are channels for fluid dynamics, such as for turbine blades, or when they determine electrical efficiency, such as for solar cells, the following quality criteria may have to be kept under control for the laser-drilling process to be validated for production:

- Parallelism or taper of the walls of the drilled holes
- Variations in inside diameter or inside dimensions when not cylindrical along the depth of the hole
- Surface roughness inside the hole
- Presence of slag inside the walls of the hole
- Depth of a recast layer; the presence of microcracks developing from the recast layer
- Presence of resolidified metal droplets or other slag particles on the workpiece surface
- Degree of oxidation that can potentially be promoted at high temperature

In general, imposing quality factors negatively affects the throughput capability and quality process capability, C_{pk} , of a laser-drilling operation.

Ultrashort High-Energy Pulses for Laser Drilling

One method to increase the hole quality in terms of reducing or eliminating recast layers and slag projections is to use ultrashort pulsed laser beam output with high energy per pulse. Some of these lasers reach several Joules of energy per pulse, with pulse duration as low as a few femtoseconds. Consequently, under each pulse of several terawatt/cm² of power density, a volume of material instantaneously evaporates without giving time for conduction to heat the

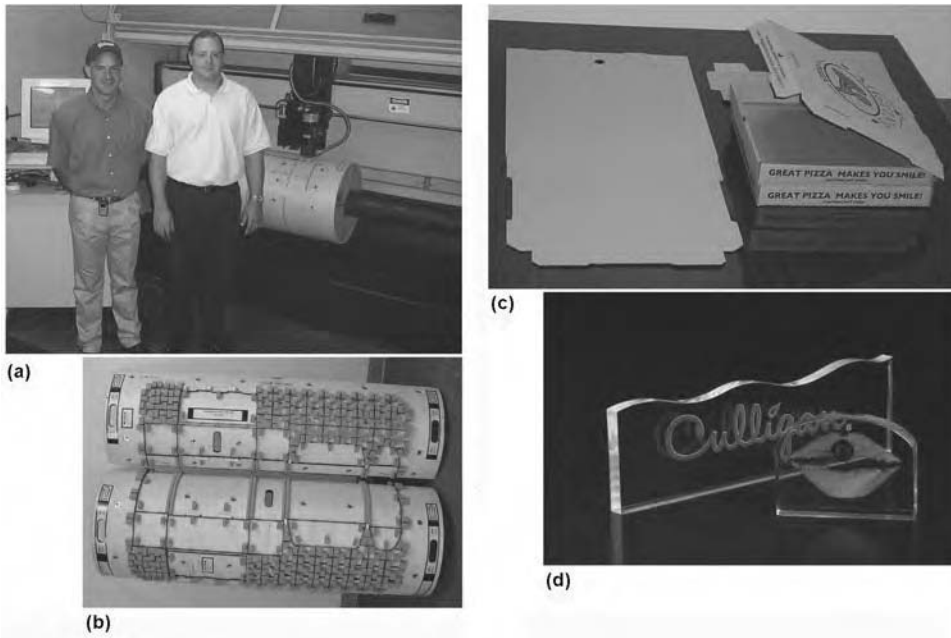


Fig. 22 (a) Cylindrical die board being laser-cut. (b) Ready-to-ship die board with steel rule blades inserted, and gray rubber pads with pressure-sensitive adhesives to prevent cardboard from sticking to the die after the cut. (c) Examples of corrugated boxes for pizza delivery cut with die board steel rule dies. (d) Acrylic plastic sheets can also be cut with lasers.

surrounding material. It generally results in the elimination of slag projections when laser drilling most materials and, in the case of drilling metals, the elimination of recast layers (Fig. 23). Such high irradiance could nevertheless damage the optical elements used in the beam-delivery system; indeed, the fused silica material used, for example, for lenses for solid-state lasers has a reported damage threshold of approximately the terawatt/cm² level.

Principles of Laser Shock-Peening Processes

Laser shock peening is a mechanical process intended to increase the fatigue and fretting resistance of a workpiece by producing a compressive residual stress within the material. A pulsed laser beam capable of being focused into high energy density per pulse creates a high-amplitude shock wave that propagates from the surface into the workpiece, to the point of plastically deforming layers of material and thereby inducing a residual compressive stress (Ref 25). In the laser shock process, the workpiece is generally coated or covered with a compound such as tape or paint; this compound

Table 11 Comparison between laser cutting, water-jet cutting, and plasma cutting

All values are approximate.

Parameter	Laser cutting	Water-jet cutting	Plasma/fine plasma cutting
Cutting process	High-power density light absorption heats up the material beyond its melting and vaporization points. Pressurized assist gas flushes molten and vaporized material through the kerf.	High-pressure water beam, with or without abrasive, "files" the material away. No or negligible heat is generated.	An electrical arc between electrode and workpiece ionizes a beam of pressurized gas to extreme temperatures (>15,000 K), which heats up the material beyond its melting point and flushes molten metal through the kerf.
Three-dimensional processing	No problems	Difficult and not recommended	No problems
Processed materials	All materials	All materials	Electrically conductive metals
Practical range of application metal thickness in the field	Metal thickness up to approximately 32 mm (1.25 in.). High-pressure assist gas can cut as thin as 0.8 mm (0.030 in.). Cutting of any nonmetal	Cutting of stone, ceramics, and up to 25 mm (1 in.) thick metals. Gages thinner than approximately 32 mm (0.125 in.) are difficult to process.	Preferable for metal thickness between 32 and 50 mm (0.125 and 2 in.)
Hardware consumables	Focusing lens, intra- and extracavity mirrors, nozzle tips	Nozzle and all high-pressure components, such as valves, hoses, and seals	All torch components (nozzles, electrodes)
Specialty consumables	Lasing gases: 10 L/h (for CO ₂ lasers only)	Abrasive: 36 kg/h (79 lb/h)	None
Fluid consumables	Assist gases: 15 bar N ₂ : 1000 SCFH(a) 1.5 bar O ₂ : 100 SCFH	Water: 60 L/h	Assist gases: 80 psi N ₂ = 500 SCFH(a) 80 psi O ₂ = 500 SCFH
Kerf width relative to laser-cut kerf width	1:1	3:1	4:1
Cut-edge quality	Cut surface will show a striated structure.	Sand-blasting appearance	Cut surface will show a striated structure; bevel-cut edges.
Metallurgical change in heat-affected zone (HAZ)	Deformation, tempering, and significant hardness changes may occur in the HAZ.	None	Deformation, tempering, and significant hardness changes may occur in the HAZ. Large-width HAZ
Eye safety	CO ₂ laser: laser safety glasses; 1 μm laser: total enclosure preferred	Standard safety glasses and protection against contact with high-pressure water jet are needed.	Safety glasses for electric arc processes
Noise safety	Low-decibel (dB) noise level	Above 85 dB, hearing protection required	Above 85 dB, hearing protection required
Waste	Cutting waste is mainly in the form of dust, requiring vacuum extraction and filtering.	Large quantities of cutting waste occur due to mixing water with cut material and abrasives.	Cutting waste is mainly in the form of dust, requiring vacuum extraction and filtering.

(a) SCFH, standard cubic feet per hour

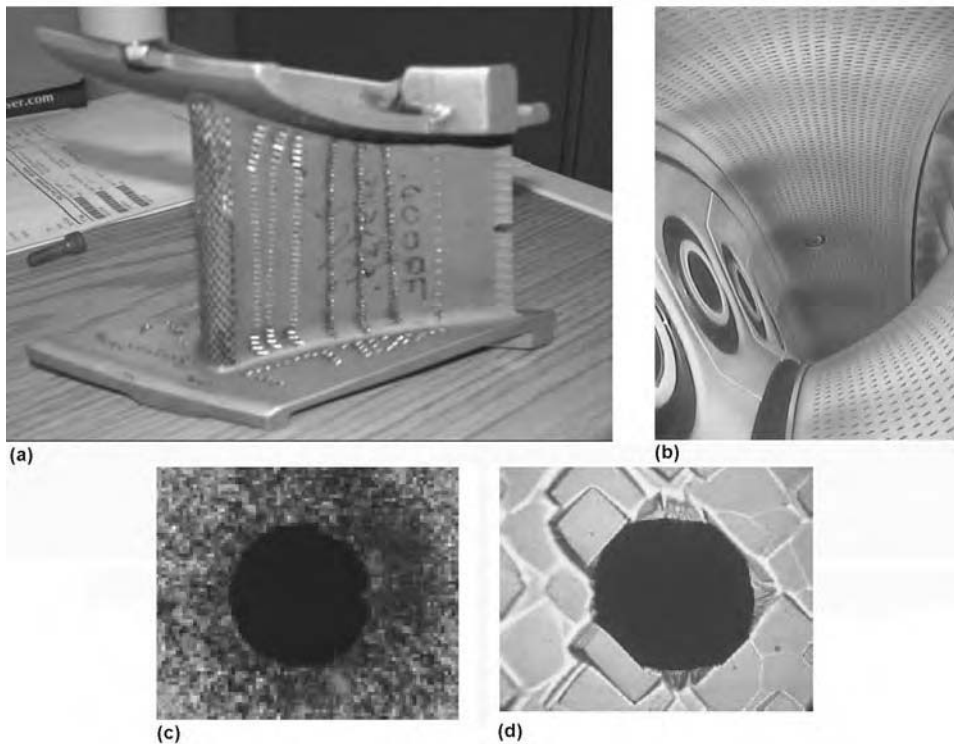


Fig. 23 Laser-drilling applications from macro to micro. (a) Turbine engine blades made of nickel alloy need drilled holes that serve as air-cooling channels to maintain their temperatures below melting temperature while in operation. Each hole is approximately 0.5 mm (0.02 in.) in diameter and 2.5 to 25 mm (0.10 to 1.0 in.) deep. Courtesy of GE. (b) A typical aircraft engine may have over 1 million drilled holes. Laser drilling is progressively displacing wire electric discharge machining as the preferred method for quality and throughput. Courtesy of GE. (c) The production of photovoltaic silicon film less than 200 μm thick requires lasers to drill holes with diameters as small as 30 μm at a rate of 20,000 holes per second. A galvano-scanner mirror enables the synchronization of high-speed, high-acceleration positioning of the laser beam with high-rate beam pulsing. The hole shown is 60 μm in diameter. Courtesy of Jenoptik. (d) Same hole as in (c) after etching. The etching process widens the hole diameter to 66 μm and affects the roundness. Courtesy of Jenoptik.

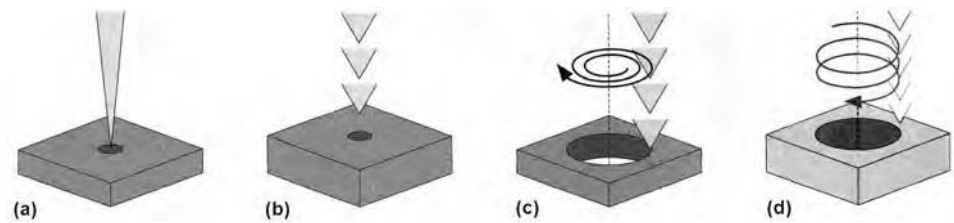


Fig. 24 Schematic representations of laser-drilling techniques. (a) Single-shot drilling. (b) Percussion drilling. (c) Trepanning drilling. (d) Helical drilling. Courtesy of Trumpf Inc.

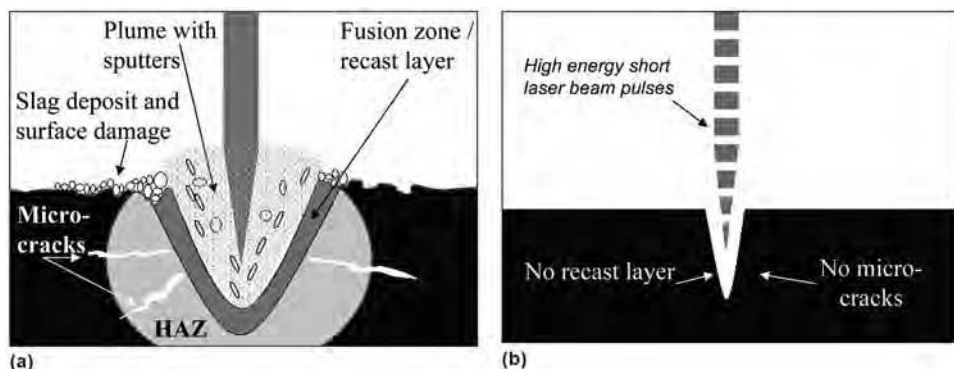


Fig. 25 Laser percussion drilling process. (a) Medium-energy, long pulses generate wide recast layers that can be a source of microcracks initiation sites in the Heat Affected Zone, HAZ. (b) High-energy, short pulses minimize and, in some cases, eliminate the recast layers and slag projections. Smaller-diameter holes can be produced than in (a).

becomes vaporized instantaneously by each laser pulse, resulting in high-temperature plasma and a shock wave (Fig. 26). A film of water flowing over the surface reflects the shock wave back into the workpiece to produce the compressive residual stress (Ref 26).

Figure 27 compares typical results of laser shock peening with traditional shot peening. Although the magnitude of the residual compressive stress is of the same order, the compressive stress generated by laser shock peening extends much deeper below the surface of the material, thus yielding greater fatigue resistance and even local strain hardening.

Typical lasers used are solid-state lasers, such as 1.05 μm wavelength neodymium-glass lasers with pulses as short as 15 to 30 ns and 50 J/pulse energy. Generally, the beam-delivery system of choice consists of mirrors and lenses rather than a fiber optic, so as to yield the maximum focusability possible.

REFERENCES

1. C.L. Caristan, *Laser Cutting Guide for Manufacturing*, SME Book Publishing, 2004
2. M. Kuhl, "From Macro to Micro—The Development of Laser Ablation," ICALEO, 2002
3. D. Petring, *More Productivity, Flexibility as Well as Energy Efficiency in Laser Cutting and Welding*, Fraunhofer ILT, Aachen, AKL, 2010
4. D. Petring, *Basic Description of Laser Cutting, LIA Handbook of Laser Materials Processing*, J.F. Ready, Ed., Laser Institute of America, Magnolia Publishing Inc., 2001
5. M. Scaggs and G. Haas, "Thermal Lensing Compensation Objective for Higher Power Lasers," White paper by Haas Laser Technologies, www.haaslti.com
6. C. Caristan and J. Finn, "Fiber Laser Cutting and Welding at Extreme Power—Extreme Speed," ICALEO (Orlando, FL), 2009
7. C. Caristan, "Advances in Optics for Efficient Laser Processing," *Materials Science & Technology* 2010, Oct 20, 2010 (Houston, TX)
8. *Gas Encyclopedia*, 2002 ed., Air Liquide, Elsevier Book Publishing, <http://encyclopedia.airliquide.com/encyclopedia.asp>
9. J. Powell, A. Ivarson, J. Kamalu, G. Broden, and C. Magnusson, "The Role of Oxygen Purity in Laser Cutting of Mild Steel," International Congress on Applications of Lasers and Electro-Optics (ICALEO), 1992
10. Z. Xiao, "Fiber Laser Cutting of Mild Steel," Master's thesis, Lappeenranta University of Technology, 2007
11. B. Marie, P. Van Der Have, and K.C. Roe, "Influence of Gaseous Impurities in the CO₂ Laser Cavity," International Congress

Table 12 Examples of set-up parameters for percussion laser drilling of various metals with a neodymium: yttrium-aluminum-garnet (Nd-YAG) laser

Material	Hole depth		Hole diameter		Pulse energy, J	Pulse duration, ms	Pulse frequency, Hz	Number of pulses needed for the depth
	mm	in.	mm	in.				
Inconel	10	0.4	0.9	0.04	15	0.5	10	70
Hastelloy	6	0.2	0.78	0.03	16.5	0.98	12	120
CrNi steel	2.2	0.09	0.03	0.001	0.07	0.1	35	350
Stainless steel	43	1.7	0.9	0.04	45	2	10	1200

Source: Extracted from Ref 24

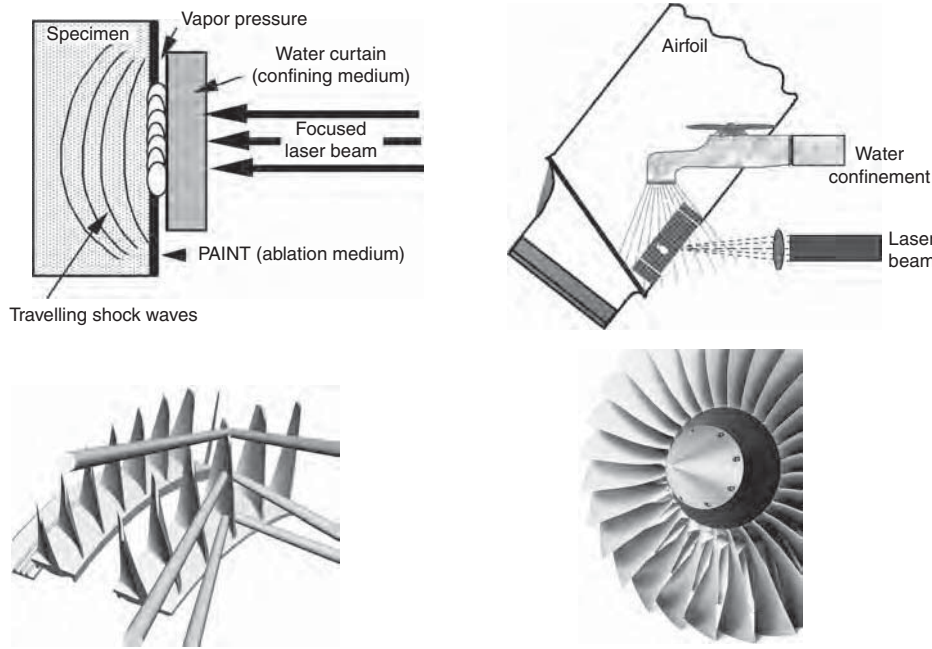


Fig. 26 Shock-peening principle. Step 1: Laser pulse creates a blast wave on the part surface. Step 2: Water across the surface forces blast energy into part. Step 3: Blast/acoustic wave imparts compressive residual stress. Step 4: Part surface is covered in sacrificial material or postprocessed. Courtesy of GE

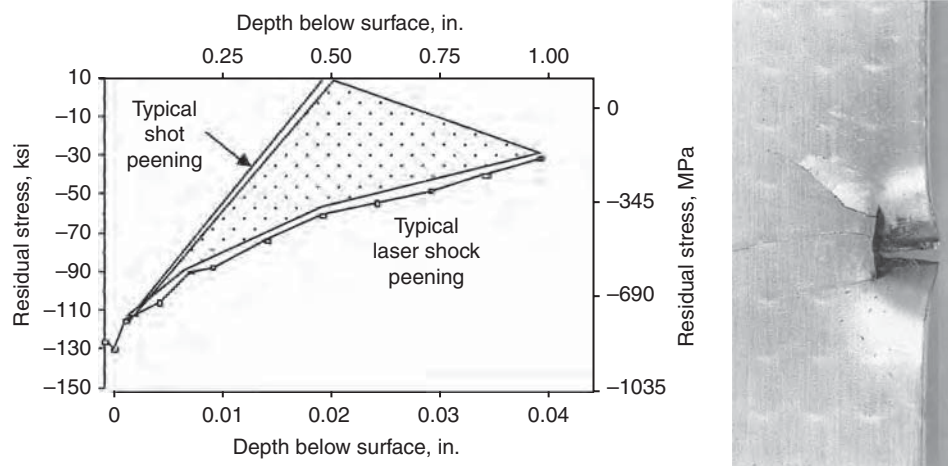


Fig. 27 Laser shock peening reduces residual stress much more efficiently than traditional shot-peening techniques. A titanium fan blade damaged by a foreign object (right) has 15 to 20 kksi high-cycle fatigue strength. A typical aircraft turbine engine runs at approximately 35 kksi. The blade treated with laser shock peening has 90 kksi strength, making it impervious to flying object damage. Courtesy of GE

on Applications of Lasers and Electro-Optics (ICALEO), 1988

- P.W. Atkins, *The Elements of Physical Chemistry*, W.H. Freeman and Company, New York, 1993
- M. Manohar, CO₂ Laser Beam Cutting of Steels: Material Issues, *J. Laser Appl.*, Vol 18 (No. 2), May 2006
- W. Penn, J. Clarke, and E. Quinn, High Speed Laser Blanking of Aluminum, *International Congress on Applications of Lasers and Electro-Optics (ICALEO)* (Dearborn, MI), 2000, p B1-B7
- R.W. Ohse, Laser Applications in Material Science and Technology: Materials Processing, Surface Modification and High-Temperature Property Measurement, *The Industrial Laser Annual Handbook*, D. Belforte and M. Levitt, Ed., Pennwell Books, 1990
- H.E. Boyer and T.L. Gall, Ed., *Metals Handbook Desk Edition*, American Society for Metals, 1985
- Materials and Applications, *Welding Handbook*, American Welding Society, 1996
- D. Zeng, "Annular Beam Shaping and Optical Trepanning," Ph.D. thesis, University of Central Florida, 2006
- C. Caristan, L. Stringer, K. Stringer, J. Zaiger, and J. Zaiger, Laser Cutting in Die-Board and Electronic Industries Using Bifocal Technology, *Laser Appl. Int.*, Fall 2005
- A. Julian, "Comparative Economics of Thermal Cutting Technologies," SME Technical Forum Seminar on Advanced Thermal Processing of Metal Sheets and Plates: Cutting, Welding and Inspection, The Ohio State University (Columbus, OH), June 2002
- T. Rockstroh, D. Scheidt, and C. Ash, Advances in Laser Drilling of Turbine Airfoils, *Ind. Laser Sol.*, Aug 2002
- K.-P. Stolberg, B. Kremser, S. Friedel, and Y. Atsuta, Systematic Optimisation of Process Parameters in Laser Drilling of 200 μm Photovoltaic Silicon Wafers Using New Kind of Nanosecond IR Lasers, *J. Laser Micro/Nanoeng.*, Vol 4 (No. 3), 2009
- A. Sugihashi, K. Hirano, M. Kido, and N. Hamada, "Study of Metal Drilling Characteristics with Q-Switched CO₂ Laser,"

624 / High Energy Electron Beam and Laser Beam Welding

- International Congress on Applications of Lasers and Electro-Optics, 2005
24. H. Rhode, *Drilling of Metals, LIA Handbook of Laser Material Processing*, J.F. Ready, Ed., Magnolia Publishing, 2001
25. A.H. Clauer, C.T. Walters, and S.C. Ford, The Effects of Laser Shock Processing on the Fatigue Properties of 2024-T3 Aluminum, *Lasers in Materials Processing*, ASM International, 1983, p 7
26. T.J. Rockstroh, "Cost Effective Laser Shock Processing Development at GE Aircraft Engines," International Congress on Applications of Lasers and Electro-Optics, 2005

Microjoining with Laser and Electron Beams

Gerald A. Knorovsky, Sandia National Laboratories

MICROJOINING with high energy density beams is both an old and a new subject. It is old, because some of the original work in both laser and electron beam welding was done with relatively low-power systems, and hence, the welds made were small. It is new in that the progress of miniaturization in industry has made the desire to make microjoints rapidly and reliably a current and exciting topic. In this article, the current state of microjoining with both electron and laser beams is summarized. Both techniques are still immature, so this article is somewhat forward-looking. Because both macroscale laser and electron beam welding are treated elsewhere in this Volume, differences are emphasized to minimize repetition. The reader is directed to those articles to obtain a basic understanding of each process at the macroscale.

Definition—What Is a Microweld?

For the purposes of this Volume, a microweld is defined as any weld that has at least one measured dimension (usually the thickness or diameter) less than 1 mm (0.04 in). Even though this value is a generous upper limit on weld size, it starts to distinguish between what has been known as microwelding for the past several decades, and which may more properly be called “milliwelding.” A stricter definition would reduce this upper limit by an order of magnitude to approximately 100 μm . Where possible in this article, examples are provided that adhere to the stricter definition. This definition goes a long way toward explaining the compelling attraction of the laser and electron beam processes for microscale welding. Simply put, it is their unique ability to precisely and controllably provide highly focused, high-power heat sources.

Microscale Physical Phenomena

To introduce the reader to phenomena that affect the melting, coalescence, and solidification needed for a successful microweld, this

section considers elementary physical processes such as heat and fluid flow. (The reader is directed to the lecture by Nobel Laureate E.M. Purcell, “Life at Low Reynolds Number,” for another, and unique, perspective of fluid dynamics and its consequences for microscopic life, Ref 1).

Transport

Energetics. To melt material either in a spot weld or along the path of a seam weld, a sufficient amount of energy must be deposited during the time that the beam dwells at each location. Assuming a fusion-zone volume approximated by a cube of 100 μm on a side for simplicity ($1 \times 10^{-3} \text{ mm}^3$) and noting that on the order of 10 J/mm^3 are required to melt typical metals (Ref 2), the input energy required (at 100% melting efficiency) is approximately 10 mJ. The local beam dwell period for a continuous or modulated beam seam weld can be approximated by the impinging beam diameter divided by the travel speed. At a dwell time of ~ 1 ms, equivalent to a typical small laser spotweld or one pulse of an overlapping spot laser seam weld at a travel speed of 50 $\mu\text{m}/1\text{ms}$ ($\sim 50 \text{ mm/s}$) (successive spots typically overlap by at least 50% in such welds), the beam power required would be 10 mJ/1 ms ($\sim 10 \text{ W}$).

Because highly focusable beam power sources (single-mode fiber lasers and small electron beam welders) of up to ~ 1 kW are presently available, quite fast travel speeds should be energetically possible. At 1 kW, still assuming a cubic fusion zone 100 μm on a side and its energy requirement of 10 mJ, the dwell time necessary is reduced to 10 mJ/1 kW = 10 μs , corresponding to a travel speed of 100 $\mu\text{m}/10 \mu\text{s}$ = 10 m/s (32.8 ft/s). Such speeds are not compatible with computer numerical control (CNC) table translation speeds, suggesting that laser scanner heads or magnetic lens electron beam rastering will be necessary to take advantage of the available power.

Diffusion Distances. The thermal diffusion distance (δ_t) corresponding to the beam dwell

time can be used to estimate the heat-affected zone (HAZ) size. The thermal diffusivity (α) of metals varies between 0.1 and $11 \times 10^{-5} \text{ m}^2/\text{s}$ (Ref 3), which gives the range of thermal diffusion distance in 10 μs , $\delta_t \sim (4 \cdot \alpha \cdot t)^{1/2}$ as 6 to 70 μm (Ref 4). In contrast, at the 5 ms dwell time typical for a small macroweld, the thermal diffusion range is 140 to 1500 μm . These time and size scales are important to consider when fixturing geometry and material choices are being made, and when HAZ thermal effects in microparts are being evaluated.

Thermal diffusion in the fusion zone is often overwhelmed by convective heat transfer. In simplified conduction-only models, the large effect of convection is often simulated by an “enhanced” thermal diffusivity, typically taken as 2 to 5 times greater than that of the solid state. This enhancement may be different in different directions (e.g., greater in the depth direction than the in-plane direction), to better simulate actual fusion-zone geometry depth-to-width ratios.

The mass diffusion coefficient for metals in the liquid state (Ref 5) is often approximated as $\sim 10^{-9} \text{ m}^2/\text{s}$, which is approximately 4 orders of magnitude less than the thermal diffusivity. Applying the same equation (using D_L rather than α and dwell times as given previously, the mass diffusion distance (δ_m) is calculated as $\sim 200 \text{ nm}$ for a 10 μs dwell time and $\sim 4 \mu\text{m}$ for 5 ms. This distance is useful when considering the expected distances over which compositional microsegregation may exist. Another factor influencing compositional homogenization in a dissimilar-metal fusion zone is convection, discussed in the following section.

Forces Acting on Microwelds

In the previous section, fluid convection was noted as providing enhanced thermal transport and affecting segregation in weld fusion zones. Because of these major effects, the various forces driving (and resisting) fluid flow are analyzed in more detail. After discussing each force, a summary tabulation is given,

highlighting which forces have enhanced importance in microwelds.

Driving Forces. Fluid flow in welds is driven by the force of gravity, viscous aerodynamic drag, the magnetohydrodynamic (Lorentz) force, surface-tension-driven forces (Marangoni flow), and the reaction force from rapid evaporation (Newton's second law).

Clearly, shielding-gas-driven viscous aerodynamic surface drag does not apply in the vacuum of an electron beam chamber, and because laser shielding gas flow is not driven by an arc plasma jet, nor does it apply for the laser beam case. (A more quantitative discussion of viscous shear forces in liquids, that is, a condensed fluid, is given in a later section, "Resisting Forces," in this article).

Current-driven magnetohydrodynamics (MHD) clearly does not apply in laser welding, because no electric current is present. Because the current density of an electron beam microwelder is low (even though its power density can be quite high, due to the few tens of kiloelectron volts, or keV accelerating voltage), MHD effects do not apply to electron beam microwelds either. (In gas tungsten arc welding, MHD effects start to predominate at currents beyond approximately 150 A, Ref 6, with an arc diameter of ~ 1 mm, corresponding to an order of magnitude estimate current density of ~ 150 A/mm². In the case of an electron beam microweld, the beam current is ~ 100 μ A, and the beam diameter is ~ 50 μ m, resulting in a current density of $\sim 100 \times 10^{-6}$ A/(50×10^{-3})² mm² = 0.04 A/mm², more than 3 orders of magnitude lower. For a more quantitative discussion of MHD effects, see Ref 7.)

Gravity generates two types of force in the fusion zone. The first is the buoyancy force on a submerged object (e.g., an inclusion, or bubble). Archimedes' principle states that this force is equal to the weight of the fluid displaced. The net force on the object must take into account that it may have weight also. Thus, the net force is given by $F_{\text{net}} = g\Delta\rho V$, where g is the gravitational acceleration, $\Delta\rho$ is the difference in density between the object of interest and the fluid it is immersed in, and V is the volume of the object. The buoyancy force is usually minor; however, it factors in when materials of significantly different densities are being welded, or when porosity is generated. Changes in fluid density are also created by either temperature gradients or by compositional gradients in an otherwise homogeneous fluid (i.e., local inhomogeneity, rather than a discrete object). The buoyancy force generated is proportional to volume. However, so is the mass of the volume of interest; thus, the acceleration is volume-independent.

The second gravity-induced force is the metallostatic head pressure, given by $p_m = g\rho h$, where h is the height and ρ is the density of the fluid column above the location of interest. This force scales with the vertical extent of the fusion zone. Given a concurrent relative increase in the effect of surface tension (see the next section), gravity-induced out-of-

position effects on the weld pool shape are expected to be minimal in beam microwelds.

Marangoni flow originates from the change in surface tension with temperature. It is a shear force and only acts at surfaces, although its consequences can dramatically influence fluid flow in a weld fusion zone (Ref 8). This driving force is calculated as:

$$\tau_M = d\sigma/dr = (d\sigma/dT)(dT/dr)$$

where σ is the liquid/vapor surface tension, T is the temperature, and r is the distance. Typical values for $d\sigma/dT$ range from approximately -0.3×10^{-3} N/m-K for a pure metal or 0.36×10^{-3} N/m-K (note the sign change) when a surface-active element is adsorbed on the surface (Ref 9). The flow is driven from the area of low surface tension toward that of high surface tension regardless of the sign of $d\sigma/dT$.

Estimating the magnitude of dT/dr in a macroweld as $dT/dr \sim 1200^\circ/0.005$ m (dT is approximated as the difference in boiling and melting temperatures, Ref 10), then $d\sigma/dr \sim \pm 70$ Pa (0.01 psi). Again, this is a shear stress and not a pressure, as in the normal case of capillarity. The magnitude of the shear stress, although small when the temperature gradient extends over centimeters, increases by 4 orders of magnitude and becomes quite appreciable when it extends over micrometers. Finally, because the surface tension temperature coefficient can be either positive or negative, the flow can be up or down the temperature gradient, causing significant changes in metal flow.

The last driving force to be considered is evaporative recoil-driven flow (Ref 11). Intense surface heating causes a high local evaporation rate, and the momentum of the evaporated metal atoms creates a reaction force that depresses the surface of the melt and may be sufficient to cause the formation of a cavity, or keyhole. With the formation of this cavity, the displaced liquid must flow elsewhere, often resulting in a raised crown around the molten-zone periphery and, in extreme cases, ejection of molten metal from the pool. This force is important for both laser and electron beam processes. For a given recoil pressure (evaporative force/unit area), the net overall effect with respect to size will depend on the resisting forces (the topic of the next section). Because the major resisting force will be surface tension, which increases at small size scales, the tendency to keyhole should be reduced or, alternatively, will need higher-intensity beams to achieve an equivalent (geometrically similar) behavior.

Resisting Forces. The previous section discussed driving forces; in this section, resisting forces are examined, of which the two most important are viscosity and capillary surface tension. They are also known as restoring, retarding, or dissipative forces.

The force due to viscosity is due to the inherent tendency of a fluid to resist being sheared and is given by:

$$\tau_{yx} = -\mu du_x/dy \quad (\text{Eq 1})$$

where τ_{yx} is the shear stress due to viscosity, u_x is the velocity in the x -direction (assumed to be the direction in which the shearing motion is occurring), and y is the other direction in the shear plane, normal to the shearing direction. (This same equation applies for the case of the aerodynamic viscous drag force mentioned in the previous section, "Driving Forces," except the viscosity coefficient scales with density and is thus several orders of magnitude smaller when viscous force due to a gaseous fluid is calculated, all other factors being constant.) This simple linear equation describes so-called Newtonian flow; other types of flow will raise the differential term to a power other than 1. Typical values of μ (the absolute viscosity) for molten metals are ~ 5 to 7×10^{-3} Ns/m² for molten iron and $\sim 1 \times 10^{-3}$ Ns/m² for molten aluminum (Ref 12). As an example, for fluid flow in the unmixed layer next to the solid HAZ of a steel macroscale weld, $du_x \sim 0.1$ m/s (0.3 ft/s) and $dy \sim 0.1$ mm (0.004 in.), resulting in $\tau_{yx} \sim 6$ Pa (0.0009 psi). In a microweld, the entire fusion zone may be smaller than the boundary-layer thickness noted previously. This implies that any flow in such a pool is close enough to a boundary to be strongly affected by it, implying that viscosity has an increased importance. Indeed, for microscale fusion zones, calculation of the Reynolds number ($\rho u_x D/\mu$), which gives the ratio of inertial to viscous force terms, shows it to be quite small, because it is proportional to the characteristic size D . For the aforementioned macroweld example, using data for steel, the Reynolds number is ~ 1000 ; by simply changing D to 0.1 mm, it drops to 10. With a decrease in velocity, it will decrease even more. Among other implications, low Reynolds number flows tend to exhibit little turbulence and do not mix very well (Ref 12); thus, dissimilar-material microwelds may be more inhomogeneous than a similar geometry but larger macroweld.

Surface tension (more correctly, the liquid/vapor surface energy) acts as a restraining force by attempting to minimize the surface area of a liquid/vapor interface. For a fluid with mean surface curvature κ , the surface tension generates an internal hydrostatic pressure p (also called the capillary pressure), given by:

$$p = \sigma\kappa \quad (\text{Eq 2})$$

Values of $\sigma \sim 0.5$ to 2 N/m (or N-m/m² = J/m²) are typical for liquid metals (Ref 13). The curvature, κ , of a surface is given by:

$$\kappa = (1/r_1 + 1/r_2) \quad (\text{Eq 3})$$

The two terms in the right side of the equation are the principal curvatures, that is, the curvatures of lines in the surface at the point of interest with the largest and smallest values. The curvature of a line is given by the inverse

of the radius of the circle that best approximates the line at the point of interest. (For a cylinder of radius r , the principal curvatures are $1/r$ and $1/\infty$; thus, the mean curvature is $1/r$. For a sphere of radius r , both principal curvatures are the same, $1/r$; thus, the mean curvature is $2/r$.) In a macroweld with a mean surface curvature equivalent to a surface radius of ~ 5 mm, the pressure created is ~ 400 Pa (~ 0.06 psi). Surface tension forces are increasingly important for microwelds because their magnitude increases linearly with surface curvature. Assuming that the applicable radii of liquid shapes on the fusion-zone surface scale with the overall size (i.e., geometrical similarity), surface tension effects will increase as the fusion-zone size decreases. If, instead of a 5 mm surface radius as mentioned previously, the surface radius is 5 μm , the capillary pressure will be 400 kPa (~ 4 atm). Because of the increased effect of surface tension relative to other forces in microwelds, one may expect that the surfaces of microwelds will be (relatively) smoother than macrowelds.

Other Forces. Thermal expansion and contraction act on the solid material surrounding the fusion zone and can produce sufficient force to create buckling or tearing, depending on whether the force is in compression or tension. Because the beam processes generally have a free liquid surface, the molten zone by itself can support relatively little stress. However, if contact between the parts being welded exists, and certainly after solidification, thermal stress/strain can be generated. The thermal expansion-induced stresses and strains created by melting are calculated in two steps (the constants used subsequently are for steel). First the linear expansion strain (per unit length of material) from ambient to the melting temperature is calculated from:

$$\epsilon_m = \alpha \Delta T_m$$

(This neglects the additional expansion upon melting.) Then, the stress needed to recompress back to the original length is calculated from:

$$\sigma_m = E \epsilon_m$$

where α is the average linear coefficient of thermal expansion, $\sim 10^{-5}$; ΔT is the temperature difference from ambient to melting, ~ 1500 °C (2730 °F); and E is Young's modulus, ~ 210 GPa (Ref 3). Substituting, $\epsilon_m \sim 0.015$ and $\sigma_m \sim 3$ GPa. Clearly, the linear elastic assumptions made are violated by this enormous stress, and plasticity and/or fracture will intervene. Further, none of the aforementioned factors are dependent on the size scale.

Even if the parts are not fully restrained and large forces are not generated, just the motion of parts expanding and contracting becomes of interest. Let a micropart be held a distance of 1 mm (0.04 in.) from the beam aim point, assumed to be at its edge. For simplicity, assume a linear temperature gradient from

ambient to the melting temperature is established from the clamping point to the edge where the beam impinges. The edge of the workpiece will move $\sim \epsilon_m/2 = 7.5$ μm , which is comparable to the beam diameter and which must be allowed for when programming the beam aim point.

Momentum effects can be due to pool sloshing, workpiece acceleration/deceleration, and impingement of material into the pool. In most instances, microbeam welds will be autogenous, so one can neglect this last source. The force due to pool sloshing can be estimated from:

$$f = dP/dt = d(mv)/dt \\ \sim 2 (\text{Pool mass} \times \text{Pool velocity}) \\ / (\text{Slosh period}/2)$$

where P is the momentum vector, m is the mass of the pool, v is the pool maximum velocity, and t is time. The factor of 2 comes from the reversal of motion, and the pool velocity is estimated from:

$$v \sim \text{Surface displacement (Peak-to-valley)} \\ / (\text{Slosh period}/2)$$

A hemispherical volume of steel of radius 1 mm (0.04 in.) has a pool mass of 0.3 g (0.01 oz.). With a surface displacement of ~ 0.2 mm (0.008 in.) and a period of 5 ms (Ref 14), the magnitude of f is calculated as ~ 20 mN. It has been found that the natural period of molten pools varies as the square root of the pool mass (Ref 14), and because the pool mass varies with the cube of the radius, the period should vary with the size to the $3/2$ power. It is assumed that the surface displacement exhibits geometric similitude with size. Combining, the aforementioned force equation is expressed in terms of size dependencies as:

$$f \sim \text{Mass} (\propto \text{Size}^3) \\ \times [\text{Displacement} (\propto \text{Size}^1)/\text{Period} (\propto \text{Size}^{3/2})] \\ / \text{Period} (\propto \text{Size}^{3/2}) \sim \text{Size}$$

While geometrical similitude predicts a linear size dependence for the surface displacement, elsewhere it is argued that surface tension will have a larger retarding effect at small size scales. Thus, a less-than-linear surface displacement dependence on size may be expected, in which case the size to the first power dependence predicted for sloshing force may be an overprediction. Data comparing surface velocities of millimeter-sized laser welds versus centimeter-sized gas tungsten arc welds seem to confirm a weak dependence on size, at least in macrowelds (Ref 15–17).

Forces due to external motion (i.e., a CNC stage accelerating the part through a sharp corner) are again given by $F = dP/dt$. For the case of a part accelerating around a corner, this transforms to:

$$f = mv^2/r$$

Assuming a 1 mm (0.04 in.) hemisphere fusion zone, a velocity of 25 mm/s (0.08 ft/s), and a radius of 0.1 mm (0.004 in.), the force on the pool calculates to be ~ 2 mN. For a 100 μm hemisphere microweld (keeping the same velocity and radius), the value decreases to 2 μN .

A compilation (Ref 18) of representative values for the forces/stresses described previously, contrasting macro and micro situations, is given in Table 1. Equivalency between stress/pressure and force assumes a 1 mm \times 1 mm area or 1 mm \times 1 mm \times 1 mm cube for macro forces and 10 μm \times 10 μm square or 10 μm \times 10 μm \times 10 μm cube for micro forces. The last column highlights the fact that surface-related stresses are extremely important in the microworld, and mass- or momentum-related stresses are more important in the macroworld.

Beam-Material Interactions

Typical welding laser photons and electron beam welder electrons interact differently with materials, losing their energy by way of differing physical mechanisms. Photons produced by a welding laser are ~ 1 eV energy (Ref 19) and react with the valence electrons of the workpiece, which are of comparable energy (Ref 20). This energy transfer is quantized (massless photons travel at only the speed of light, unlike electrons that can have variable velocity); hence, the photon loses all or none of its energy to a prospective target valence electron. The excited electrons in turn can give a part of their energy to other electrons or can emit a lower-energy photon. The net effect of these interactions results in a high metallic reflectivity for typical laser wavelength photons. Because the valence electrons are delocalized in metals and form a continuous layer at the surface, this interaction happens at the surface in the first atom layer or two; thus, the energy deposition is highly localized to the surface.

In contrast, the multi-keV electron beam welder electrons interact with the fields of the atom inner electrons (Ref 20). These scattering locations are more widely spaced; hence, the electrons can penetrate much deeper than photons into the lattice before interacting (micrometers of penetration instead of nanometers). Thus, the heating effect is more volumetric, although the surface heating is still quite appreciable. X-rays, back-scattered electrons, and secondary electrons that are also produced reduce the net energy input (especially for higher-atomic-number elements), but the energy-transfer efficiency for the electron beam is considerably higher than for a laser beam of comparable intensity.

With a sufficiently energetic beam (laser or electron), a keyhole may develop in the weld fusion zone; in macrowelds, the laser beam may reflect within the keyhole several times, multiplying the single-event absorption

Table 1 Macro versus micro comparison of forces acting on the weld pool

Force origin	Macro example magnitude: pressure/stress force	Micro example magnitude: pressure/stress force	Ratio of pressure/stress magnitudes: micro/macro
Driving forces			
Gravity metallostatic head	0.8 kPa (0.12 psi) 0.8 mN (0.0002 lb)	20 Pa (0.003 psi) 0.002 μN (5 × 10 ⁻¹⁰ lb)	0.025
Gravity buoyancy force (Δρg):			~1
Autogenous(a)	2 kN/m ³ , 20 mN (0.005 lb)	2 kN/m ³ , 2 μN (5 × 10 ⁻⁷ lb)	
Dissimilar(b)	50 kN/m ³ , 50 mN (0.01 lb)	50 kN/m ³ , 5 μN (1 × 10 ⁻⁶ lb)	
Aerodynamic shear stress	70–400 Pa (0.01–0.06 psi) 70–400 μN (0.00002–0.00009 lb)	70–400 Pa (0.01–0.06 psi) 7–40 pN (2 × 10 ⁻¹² to 9 × 10 ⁻¹² lb)	~1
Marangoni shear stress	70 Pa (0.01 psi) 70 μN (0.00002 lb)	0.7 MPa (101 psi) 70 μN (0.00002 lb)	10,000
Laser or electron beam driven evaporation	1.5–7 kPa (0.2–1.0 psi) 1.5–7 mN (0.0003–0.002 lb)	1.5–7 kPa (0.2–1.0 psi) 0.15–0.7 μN (3 × 10 ⁻⁸ to 2 × 10 ⁻⁷ lb)	~1
Resisting forces			
Liquid viscosity shear stress	6 Pa (0.0009 psi) 6 μN (1 × 10 ⁻⁶ lb)	6 Pa (0.0009 psi) 0.6 pN (1 × 10 ⁻¹³ lb)	~1
Surface tension pressure	2 kPa (0.3 psi) 2 mN (0.0004 lb)	200 kPa (30 psi) 20 μN (4 × 10 ⁻⁶ lb)	100
Other forces			
Thermal expansion (linear)	3 GPa (435 ksi) (ambient-to-molten) 3 kN (670 lb)	3 GPa (435 ksi) (ambient-to-molten) 0.3 N (0.07 lb)	~1
Pool sloshing	200 mN (0.04 lb)	20 μN (4 × 10 ⁻⁷ lb)	0.0001
Stage motion, centrifugal	40 mN (0.009 lb)	40 nN (9 × 10 ⁻⁹ lb)	0.000001

(a) Due to temperature gradient only in steel. (b) Due to compositional gradient only, aluminum vs. copper dissimilar-density combination. Source: Ref 19

efficiency by the number of reflections (Ref 21). This situation is not likely to occur in microjoining, where the limited part thickness will generally imply that if a keyhole is achieved, it will go all the way through the thickness, reducing the opportunity for multiple reflections. Thus, laser microwelds will probably exhibit lower energy-transfer efficiency than macrowelds.

Stability of the Keyhole. Because microwelds usually take place in parts that are thin, the typical microfusion zone is full penetration, and a simple surface energy analysis (Ref 22) of such a keyhole will yield some interesting conclusions relative to its stability. Assume that a cylindrical keyhole of radius r exists in a cylindrical spot weld fusion zone of radius R and depth h . The negative pressure created by surface tension on the cylindrical keyhole surface is given by σ/r , where σ is the liquid/vapor surface tension of the liquid. The evaporative recoil pressure generated by beam heating of the keyhole surface balances the surface tension force and keeps the keyhole open. The liquid/vapor surface area S of the fusion zone with keyhole is approximated by $S = 2\pi(R^2 - r^2 + rh)$. The change in surface area versus the keyhole radius is $dS/dr = 2\pi(h - 2r)$. The rate of change of dS/dr shifts from positive to negative when $h = 2r$. If $h > 2r$, equivalent to a relatively deep, small-diameter cavity, $dS/dr > 0$, which implies that a decrease in keyhole radius will result in a decrease in surface and hence surface energy. To preserve this keyhole, the evaporative recoil pressure must be present, or it will close up. On the other hand, if $h < 2r$, corresponding to a wider keyhole, dS/dr is negative, and the keyhole will decrease its energy by expanding, even without an

increase in recoil pressure, suggesting that it will not close up when the beam is shut off. This latter condition suggests that a lack of coalescence will occur, or that a drilling condition rather than a welding condition exists. Because only the depth-to-width ratio is critical, this stability analysis is independent of size scale.

In a previous paragraph, it was noted qualitatively that surface tension effects tend to decrease the tendency to keyhole as the size scale decreases. The aforementioned stability analysis shows in a more quantitative manner that the evaporative pressure needed to keep a keyhole open will increase inversely as the keyhole radius shrinks. The energy input/unit area of the keyhole surface will similarly need to increase to obtain a higher evaporation rate and hence recoil pressure.

Humping. When taking advantage of the high travel speeds afforded by the intense beams available from both laser and electron beam welders, the problem of weld bead surface morphology instability known as humping is likely to take place, as pictured in Fig. 1(b) (Ref 23). This is a result of rapid convective fluid flow created by the beam, together with convergent flow channels imposed by the solid/liquid (edge of fusion zone) and solid/vapor (keyhole interior surface) interfaces in the weld pool. For a given-sized weld pool, a smaller beam diameter creates a smaller keyhole, which in turn affords larger fluid channels, reducing the maximum flow velocity attained in the pool ($V \approx vd/(D - d)$, where V is the fluid flow velocity, v is the pool travel speed, and D and d are as pictured) and reducing the humping tendency, as shown in Fig. 1 (a) and (c).

Process Description

Suitable Equipment

As of this writing (2011), microjoining electron beam welders are just becoming commercially available. Most work to date has been done with converted scanning electron microscopes (SEMs), with the modifications ranging from simple substitution of the filament to a higher-current-capacity one (e.g., thoriated tungsten versus pure tungsten) and removal of the objective aperture, to actual modifications of the column, where beam-shaping apertures are modified to allow more current down the column. Small electron beam welders are commercially available, but they tend to be most useful at the less strict submillimeter definition of microscale rather than the strict sub-100 μm definition.

Minimally modified SEMs can produce ~1 W of beam power at beam diameters of ~10 μm, moderately modified SEMs can produce ~5 W at ~20 μm beam diameter, and small electron beam welders are capable of several hundred watts at ~100 μm beam diameter. The moderately modified SEMs and small electron beam welders also have much better beam and/or part motion controls, which are capable of producing actual seam welds, rather than being restricted to spot welds.

The situation with respect to laser micro-welding is much better, because the ability to produce diffraction-limited beams with sufficiently excellent optical elements and apertured beams has always been available, if expensive and inefficient. With the advent of kilowatt-power single-mode fiber lasers, obtaining diffraction-limited Gaussian beams has become almost routine, even employing conventional optics.

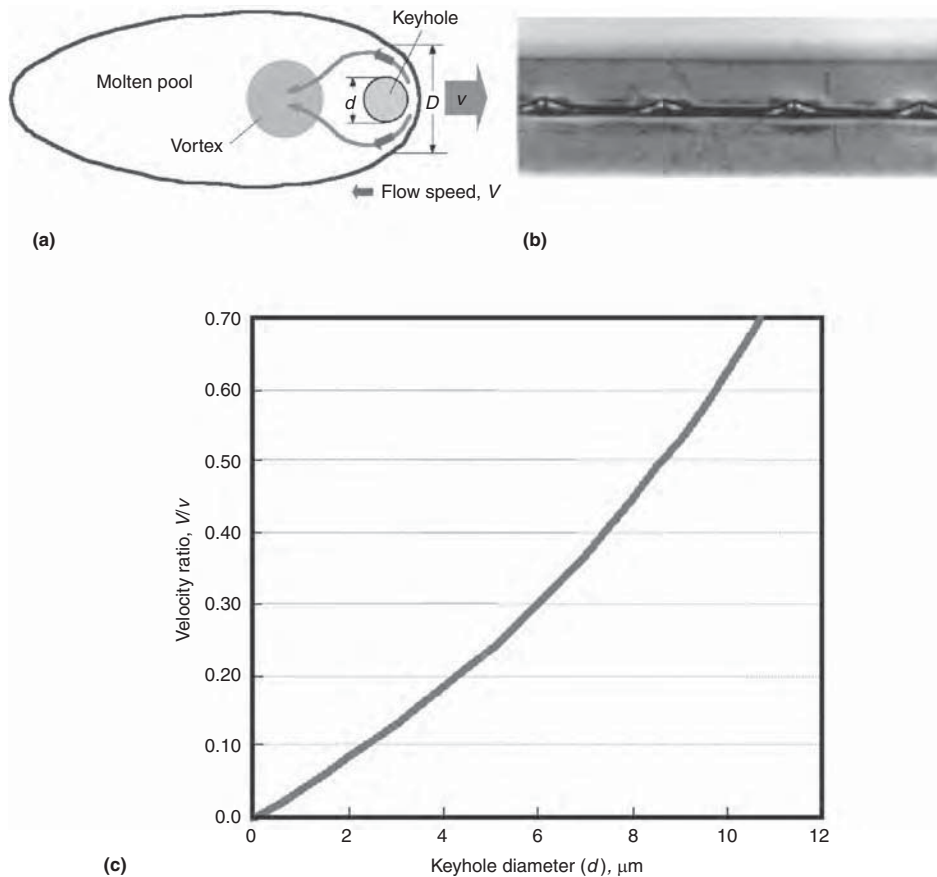


Fig. 1 (a) Schematic of fluid flow that encourages humping. (b) Example of a humped laser bead. (c) Velocity ratio calculated as a function of keyhole diameter, weld speed of 1 m/s (3.3 ft/s), and 40 μm thick stainless steel foil. Source: Ref 23

Spot Sizes. The optical diffraction limit and various lens aberrations set the smallest easily achievable beam diameter for visible and near-infrared wavelength lasers at $\sim 10 \mu\text{m}$ (Ref 24). In the case of electron beams, high-quality SEM or electron probe microanalysis instruments routinely focus their probe beams to a diameter $< 1 \text{ nm}$. The several-watt electron beams needed for microwelding cannot be focused as sharply as those used in electron microscopes (Ref 25); however, even for extremely sharply focused beams, electron absorption effects increase the beam/material interaction volume to a few-micrometer radius, which limits their effective minimum size, rather than the free-space focused beam diameter. Figure 2 shows a Monte Carlo calculation (Ref 26, 27) that simulates the path of electrons impinging on a solid. Thus, an effective minimum diameter of $\sim 10 \mu\text{m}$ is appropriate for electron microwelder beams as well as lasers, although this can be decreased if low accelerating voltages are used. (For comparison purposes, high-power electron beam or

multimode laser macrowelders typically employ beam diameters of ~ 0.5 to 1 mm, or 0.02 to 0.04 in., although they are capable of much smaller diameters, $< 0.1 \text{ mm}$, or 0.004 in.)

Beam Monitoring. Measurement of the beam size and current for microjoining electron beam systems is done with a Faraday cup, in the same manner as for large electron beam welders. (The Faraday cup is a standard piece of equipment for every SEM and transmission electron microscope, or TEM, as well.) The beam current is measured by directing the entire beam into the cup, and the size is measured by rastering it across either the edge of the Faraday cup aperture or across an electron-opaque element held above the cup, which may be a straight edge such as a razor blade. The time dependence of the energy reaching the cup may be used to imply the distribution of energy in the beam versus the position, although the assumption of radial symmetry is made. More sophisticated techniques involve traversing the beam in a circular path across a series of slits arranged in a radial

array. Computed tomography (CT) techniques can then be applied to reconstitute the beam-intensity distribution, without making any symmetry assumptions (Ref 28). The major difference between the micro-CT technique and the macro is that the slits used in the macrobeam technique are small with respect to the beam diameter, and this is not practical when the beam size is only 10 to 50 μm in diameter. An added differentiation of the beam energy versus time is thus required, which adds some experimental uncertainty, as does the decreased signal-to-noise levels when dealing with very small current beams.

For microlaser beams, as for the electron beam case, the techniques employed for macrolaser beams are still applicable, with some adaptation. Again, more care will be required to deal with ambient electrical noise, and more sensitive photon detectors may be required. Laser beam analysis systems with photodiode arrays of sufficient dimensional resolution are not yet available for focused beam use, so a defocused condition must be measured; however, with the advent of commercial high-resolution digital photography, higher-resolution arrays will undoubtedly become available in the near future, should demand arise. The simplest technique for macrolaser beam spot size determination—drilling a hole in a thin polymer film (typically 0.05 mm, or 0.002 in., thick Kapton polyimide, E.I. du Pont de Nemours and Company)—can be emulated at the microscale by using a thin graphite layer physically deposited onto a glass microscope slide. Fused silica may be necessary to avoid cracking of the glass if the laser beam is sufficiently energetic.

Both fiber laser and electron microbeams have excellent depth of focus. This capability will broaden the tolerance of both processes with respect to beam focus position.

Metallurgical Consequences

Effect on Cooling/Solidification Rates. The combination of fixturing needed to align and clamp microparts into intimate contact, plus the fact that melting temperatures do not scale with size, will tend to increase the temperature gradients seen by microparts during welding. This in turn will result in increased cooling rates compared to macrowelds. It is well known that rapid solidification can change the microstructures obtained when compared with those resulting from more sedate cooling rates. Examples include the changeover from ferritic to austenitic primary solidification in stainless steels (Ref 29), to more extreme cases where amorphous solids are formed rather than crystalline (Ref 30). In the case of stainless steels, the change to austenitic solidification can have negative weldability consequences relative to hot crack formation (Ref 31).

When cooling rates are increased, so are solidification rates. The ratio of gradient to

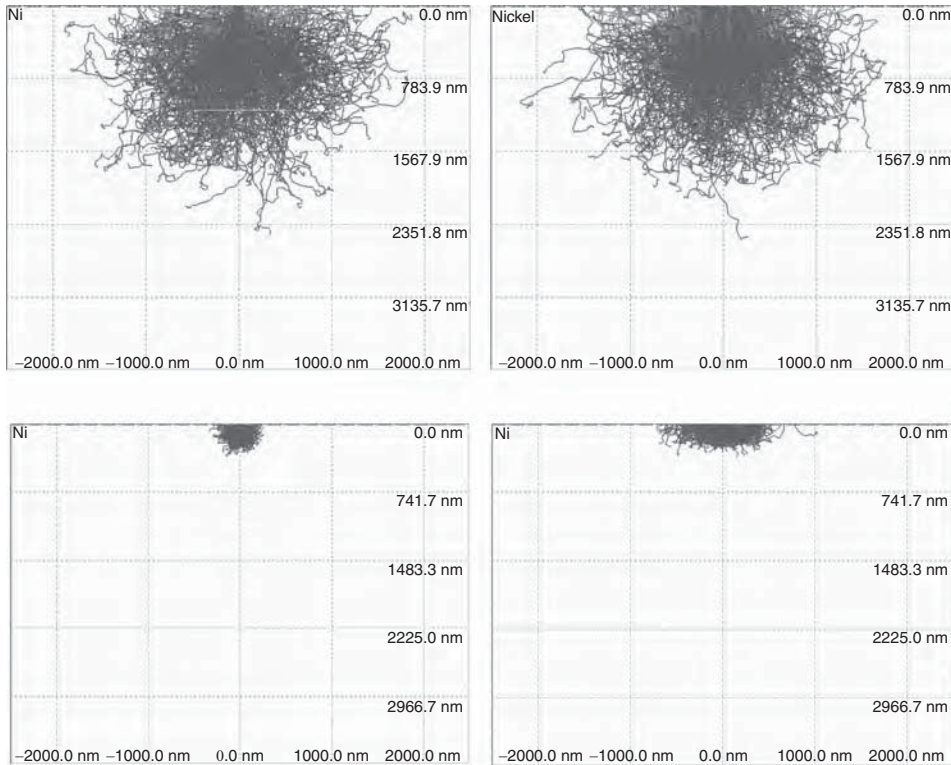


Fig. 2 Monte Carlo simulations of primary (blue, or gray in grayscale image) and backscattered (red, or black in grayscale image) electron beam paths for 30 keV (top) and 10 keV (bottom) beams of 100 nm (left) and 1 μm (right) diameter in pure nickel. Five hundred electron trajectories have been plotted. Source: Ref 26, 27

liquid/solid interface velocity, G/v , must be determined to predict whether plane front, cellular, or dendritic solidification will be favored in alloys being microwelded. Calculations (Ref 32) indicate that for both spot and seam laser microwelds, the G/v ratio decreases with size. The breakdown from a planar to a dendritic solidification interface occurs by the mechanism of constitutional undercooling, which involves solute partitioning at the interface, atomic diffusion of the solute, and convection in the molten pool. The condition for plane-front breakdown is given as $G/v < \Delta T_0/D$, where ΔT_0 is the temperature difference between the liquidus and solidus at the nominal composition of the material solidifying, and D is the diffusion rate of the alloy element in the liquid phase. For 304 stainless steel, calculations indicate that plane-front instability should be expected to occur in microwelds (Ref 33).

Because of solute partitioning between the liquid and solid, in alloy solidification a steady-state composition profile develops after an initial solidification transient, and a final transient often results in multiphase (eutectic or eutectic-like) terminal solidification. The initial transient length is given by $\delta_{tr} \sim 4D/vk$, where k is the partition coefficient (characteristic ratio of solidus to liquidus compositions over the solidification temperature interval). Using physical parameters appropriate to 304

stainless steel, the initial transient distance calculated is small, $<1 \mu\text{m}$. The terminal transient can be approximated by twice the excess composition buildup boundary layer ($\sim 4D/v$) (Ref 34) in front of a solidifying interface, $\sim 4(7.5 \times 10^{-9} \text{ m}^2/\text{s}/0.1 \text{ m/s}) = 3 \times 10^{-7} \text{ m}$, assuming a travel speed of 100 mm/s (0.3 ft/s). With faster travel speeds, the terminal transient will continue to decrease.

In cases of extremely rapid travel speed welds (several meters per second) using rastering/scanning techniques, it is conceivable to apply the absolute stability criterion posed by Mullins and Sekerka (Ref 35) and given by:

$$\lambda_i \sim 2\pi[(D\Gamma/v\Delta T_0)]^{1/2}$$

where λ_i is the critical wavelength below which perturbations will decay rather than grow because of surface energy, Γ is the Gibbs-Thomson coefficient ($= \sigma/\Delta s_f =$ surface tension/entropy of fusion per unit volume), and the other terms are as defined previously. While the value for λ_i is quite small ($\sim 0.025 \mu\text{m}$), it has been calculated that the limit will occur at solidification rates of $\sim 1 \text{ m/s}$ (3.3 ft/s) (Ref 34). At yet faster speeds, partition-less solidification may become possible. Models suggest that a velocity of $> 7.5 \text{ m/s}$ (24.6 ft/s) would be required in stainless steel alloys (Ref 36). No experimental evidence of either of these

phenomena are presently available. One speculates that the latter limit could be more easily achieved by microwelding of bulk metallic glasses, which tend to solidify to the amorphous state at more moderate cooling rates.

Diffusion-Limited Kinetics. A consequence of the extremely short dwell times/rapid cooling rates possible in microwelding is that diffusion-limited phase transformations may be suppressed, especially for those transformations that have incubation periods that are longer than the thermal cycle available. In particular, recrystallization and grain growth in the HAZ will probably not occur. If phase transformations do occur, the likelihood is that either short-range diffusion (massive) or diffusion-less (martensitic) mechanisms will be responsible.

Unmixed Zone. When etched metallographic sections of dissimilar-metal macroscale laser and electron beam welds are examined, fusion zones typically exhibit incomplete mixing as evidenced by a marbled structure. It is also very common to see dendritic solidification structures, and further, one often sees an unmixed resolidified layer at the boundary with the unmelted HAZ. The thickness of this unmixed zone varies with the welding process and is controlled by the viscosity of the fusion zone and the fluid flow conditions obtained at the solid/liquid interface. A typical thickness for this stagnant layer in a macroscopic arc weld can be on the order of a few tens of micrometers (Ref 37), that is, equivalent in size to the entire fusion zone of a microweld!

Ripples. Macro- and milliscale welds often exhibit a finely rippled (and sometimes surprisingly regular) surface topography, caused by solidification of waves of material “sloshing” back and forth due to the liquid pool resonant modes of motion. In microwelds, these effects are modified by the magnified effect of surface tension and the relative sizes of the mass and thermal diffusion distances. Smaller fusion zones have been determined to have higher resonant frequencies by several investigators.

For an object exhibiting sinusoidal motion given by $d = d_0 \sin(\omega t)$, where d is the instantaneous displacement, d_0 is the amplitude of the displacement, ω is the angular frequency ($2\pi f$, where f is frequency), and t is time, the velocity is given by the derivative of the displacement, and the acceleration (proportional to force, by way of $f = ma$) by the second derivative. The velocity is thus $v = \omega d_0 \cos(\omega t)$, and the acceleration is $a = -\omega^2 d_0 \sin(\omega t)$. The power expended is given by the product of the force and velocity, $P = -m\omega^3 d_0^2 \sin(\omega t) \cos(\omega t)$. Thus, for a given vibrational power level, P , $\omega^{3/2} d_0$ will be a constant, implying that higher-frequency vibrations will tend toward lower displacements, resulting in a less rippled surface, even without taking into account surface tension.

Surface Contamination. The most likely routes for contamination to enter a fusion zone are by way of pre-existing contaminated surfaces and gaseous contamination from inadequate shielding by inert gas or insufficient

vacuum. The latter will tend to be proportional to the instantaneous melted surface area exposed (contamination by adsorption of the HAZ and diffusion into the fusion zone may also occur but will be neglected). In a lap weld completely across two thin sheets of total thickness t , the surface area melted by a completely penetrated weld of uniform width w and length l is given by $A = 4lw + 2tw$. The volume of the weld is given by $V = ltw$. The surface-to-volume ratio is thus given by $A/V = (4lw + 2tw)/ltw$. Assuming that the length of the weld is greater than either the thickness or width, $A/V \sim 4lw/ltw = 4/t$. Thus, the surface-to-volume ratio will be inversely proportional to the weld thickness.

A form of self-contamination may occur from redeposition of vapors created by the high-intensity beam. In macrowelds, this layer is often removed with an alcohol swab; however, this will not be possible with microparts. Avoidance of keyhole formation may be necessary, and this will restrict the maximum power that may be employed. Indeed, given this restriction, the heat sinking applied by part fixturing may need to be carefully evaluated, or the acceptable window of power/travel speed may become quite small.

In addition to the development of pre- and postweld cleaning techniques, there will be an equal need to keep cleaned parts free from recontamination before (and after) welding. This will require attention to packaging and transport containers and processes. Laminar-flow clean benches or rooms will probably be necessary, as will be suitable training of personnel to use only clean utensils to handle microparts.

Fixturing and Process Controls

Fixtures. To produce reproducible microwelds, extreme emphasis must be placed on suitable fixturing. The two-dimensional nature of most microwelds implies that the thermal fields are laterally much more extensive than those typical of three-dimensional welds; thus, the relative length of material that may expand due to thermal effects is greater than for typical macrowelds. Furthermore, thin sheet materials are extremely sensitive to buckling when placed in compression; thus, the macroscopic tendency to clamp everything securely in place may not be sufficient to ensure a good microweld. It is already clear from pioneering work in Germany (Ref 38–40) that butt welds are extremely difficult to achieve, and lap, fillet, and edge welds will be much more practical. Such geometries inherently allow for some slippage of one part face-to-face with the other, reducing buckling tendencies. Similarly, cross-wire welds are more practical than in-line welds. Investigators have found that it is desirable to incorporate spring-loaded restraints, which allow for some motion of the parts being welded while keeping them in good thermal

contact. One advantage of laser welding over electron beam welding is that photon-transparent materials exist that may be used to physically clamp together the two parts being welded, while the laser beam is transmitted through the clamp material to the joint location. Fused silica has been successfully used as such a clamp (Ref 41).

Unfortunately, fixturing necessary to restrain parts and maintain intimate contact between them also impacts the thermal field and acts as a severe heat sink. Calculations show that such heat sinks may increase the heat-input requirement manyfold over that needed to just melt the materials of interest (Ref 18). Conversely, if no heat sinking is present, it may be very easy to overheat the parts being joined, because thermal diffusion to nearby boundaries does not take long for microscale parts (Ref 18). Methods of ensuring reproducible thermal contact will need to be developed.

Finally, for very small parts, it may become useful to employ heat-flow calculations that take into account the wave nature of heat flow, rather than the usual Fourier conduction equation (Ref 42).

Parameter Control Requirements. Another important factor in reproducible microwelds will be in precisely controlling the beam energy, travel speed, travel path, beam focus (spot size), and any pulsing or modulation applied to the beam.

Closed-loop process controls will need to employ high-bandwidth methods, because the characteristic times for microjoining processes will be quite short. Because it is likely that beam rastering will be employed rather than part motion, techniques to evaluate and correct pincushion/barrel distortion and astigmatism, when the beam is rapidly bent through large angles, will need to be instituted.

Another reason to employ closed-loop controls of beam energy is that heat sinking to part fixtures is generally not very reproducible and can have a major effect on the thermal history of the parts being welded. Electron beam microjoining may have an advantage over laser, simply because the feedback control methods will probably employ visual recognition techniques, and good imaging is inherent with the electron beam microprocess.

Beam Scanning versus Part Motion. One of the problems with microwelding is that, compared with photolithographic chemical methods used for microchip production (or even processes such as vapor-phase reflow soldering), it tends to be a serial process with relatively low productivity. The ability to rapidly scan/raster the beam offers at least a partial parallel processing option. It is possible to move both laser and electron beams with great rapidity (both are essentially momentum-less) and excellent reproducibility. Examples of such applications abound in the entertainment industry. Cathode ray tube devices have been around for many decades, and the ability to project rapidly changing images by way of micromirror

arrays is also a well-developed technology. Existing laser scanners generally employ dual-perpendicular-axis galvo-driven mirrors to provide beam scanning across an area, but because these are relatively high-momentum devices, they will no doubt give way to microelectromechanical systems (MEMS) or entirely solid-state methods in the future. Some examples of rapid-scan scenarios are given in a later section.

For the electron beam microwelder, the accelerating voltage can be readily controlled. This affords the possibility of controlling the relative penetration of the electrons and, consequently, the distribution of heat in extremely thin workpieces. When welding extremely thin materials in a lap weld configuration, if the penetration can be controlled to provide heating of both layers rather than just the top layer, improved coalescence may be promoted. Calculations (Ref 43) show that this effect is feasible with accelerating voltages in the range of 10 to 40 keV. The thickness where this effect operates ranges from just a few micrometers for nickel to $\sim 10 \mu\text{m}$ for silicon.

Postweld Metrology/Inspection

Visualizing and Measuring Microwelds. Microwelds can be difficult to see, let alone examine for conformance with requirements, simply because of their diminutive size. After all, $10 \mu\text{m}$ is only approximately 3 times the diameter of a human hair. For this reason, electron beam microwelding has a distinct advantage over laser microwelding, simply because SEM-like capability can be easily integrated into the welding system (assuming the welder is not a converted SEM to begin with). Otherwise, high-quality light optical or separate SEMs will be needed. Metrological calibration of such scopes will be needed to verify correct sizes. (Calibration of digitally-reconstituted images with high depth of field is still an active area of development as of this writing in 2011.)

Nondestructive Evaluation Micro-methods. Other nondestructive examination approaches similar to those employed for maintaining the quality control of microcircuits and MEMS devices are plausible. These could include hermeticity testing (although microvolumes being tested will need careful consideration of fine/gross leak testing time windows and care to not overpressurize and collapse them), ultrasonic probing (immersion C-mode scanning acoustic microscopy), and, of course, functional testing.

Handling. A remarkable feature of micropart handling is that it is sometimes difficult to release them once they have been picked up, due to residual magnetic, electrostatic, or stiction forces. Thus, handling tools will need to be provided that are capable of precise motion and positive, yet gentle holding, followed by an equally positive release. Alternatively, it may be necessary to hand off the parts from the manipulation tool to an active holding

device in the part holder. “Sticky” surfaces may suffice for part holders, but they must avoid transfer of deleterious contamination to clean surfaces to be welded.

Techniques and Applications

In the following section, examples of developmental welds employing laser and electron beam microwelding techniques are described.

Stationary Beam/Moving Workpieces

Moving the parts to be welded under a stationary beam is the conventional way in which laser and electron beam welds have been made. (Slight motion of the beam about its mean position, as in a circle, bar, or other geometrical shape pattern-generation positional modulation schemes, is allowed within this classification.)

The following examples of electron beam microspot and seam welds were accomplished with a moderately modified SEM (Ref 39). Another example, shown in Fig. 3, shows laser microwelding of stainless steel foil with a high-brightness fiber laser of moderate power. Thin stainless steel foils that ranged in thickness from 10 to 30 μm were welded successfully with 25 W at a travel speed of 1 m/s (3.3 ft/s). The beam was focused to $\sim 10 \mu\text{m}$ diameter (Ref 44, 45).

Particularly noted by the authors was that, while contact between the foils was needed to ensure coalescence of the two foils (Fig. 3b shows decoalescence when a gap is present and also shows humping in the top view of the two foils after disassembly, third panel from the left), heroic fixturing was not needed, because the condition for $dS/dr > 0$ was obtained.

Rapid Beam Rastering/Scanning

An alternative approach to holding the beam stationary while moving the workpieces is to reverse the roles. Both laser beams and electron beams are directed sources of energy and can be readily and rapidly steered by mirrors or magnetic lenses. Figure 4 shows schematically how a rapidly rastered electron beam (up to 800 m/s, or 2625 ft/s) can provide both productivity and quality enhancements (Ref 46). The two left figures schematically illustrate making multiple welds essentially simultaneously to

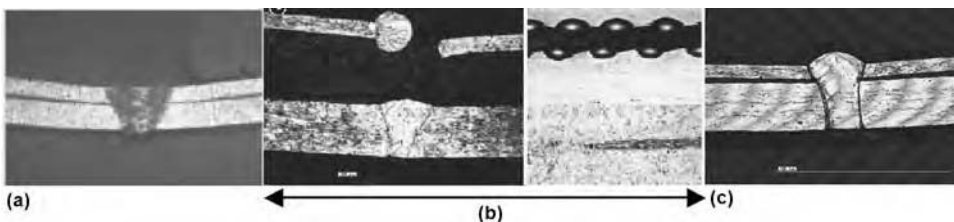


Fig. 3 Single-mode fiber laser lap welds in stainless steel foils of 10, 20, and 30 μm thicknesses. Source: Ref 44, 45

improve productivity. The right figure shows a gear being welded to a shaft with three simultaneous spots trisecting the weld circle, to simultaneously reduce distortion and improve productivity.

Figure 5 shows the results of combining either a local rotation or a transverse excursion with a larger circular travel path on a 30 μm foil of grade 1.4301 material (equivalent to grade 304 stainless steel) (Ref 46), a technique often used with electron beam macrowelders to reduce root spiking and surface roughness. In this case, the alternating step-function transverse excursion simulated generating three concentric traces, rather than just acting to broaden the beam. These bead-on-foil melt runs took several seconds and correspond to many retraces of the travel path, except for the trial on the far left, which corresponds to a conventional procedure where the heat source is localized and traces the weld path once, albeit with circular beam “weaving.” The second column of panels keeps the same relative speed of the two motions (100 to 1) but increases the overall rate tenfold, thus tracing the circle 10 times. The middle column takes a different approach, where the weaving is much slower than the large-diameter circular path travel speed ($\sim 1.6 \text{ m/s}$, or 5.2 ft/s), effectively presenting a 0.5 mm (0.02 in.) narrow circular heat source that is slowly changing its overall diameter. The next two columns adjust the ratio of the motions, with the fourth column slowing the circular path travel speed to 160 mm/s (0.5 ft/s) while increasing the diameter change rate tenfold, while the fifth column returns to the 1.6 m/s (5.2 ft/s) path velocity but increases the weave frequency in a manner to approximate a circular heat source but with significant width. The oscilloscope traces, taken at a constant beam persistence, show the temporal behavior of the beam for a time period of $\sim 30 \text{ ms}$. Highly retraced fusion pathways appear to accentuate grain-boundary grooving of the fused area and may not be useful.

Laser Spike Welding

Laser spike welding (Ref 47) is an attempt to deal with the difficulty of ensuring intimate contact in lap welds. In this technique, the initial laser power setting creates, by way of conduction-mode heating, a fully penetrated fusion zone in the upper layer; then, its power

is increased to a level that generates sufficient recoil force to drive the diaphragm-like pool into contact with the bottom layer. This recoil-force-driven contact must last for sufficient time for the upper pool to adhere to the bottom layer, either by causing superficial surface melting or by way of a brazelike adhesive bond. While the gap that may be bridged is only limited by the ability of the upper pool to extend without becoming unstable, the technique is limited by the bondability of the lower layer. If, for example, the lower layer is highly conductive, it may be difficult to heat it sufficiently to cause bonding via either melting or adhesion. Certainly, for the second mechanism, surface cleanliness will be critical. If the brazelike bonding approach can be made to work, this technique may be useful for joints between incompatible (intermetallic-compound-forming) dissimilar-metal pairs.

An example of the technique successfully applied to 250 μm thick X8CrNi1812 stainless steel foils is shown in Fig. 6. Gaps of up to 100% of the individual foil thickness were successfully bridged. With large gaps, the conical depression of the top surface may become objectionable; if so, a second cosmetic pass can be applied.

While developed as a spot welding technique, the approach may conceivably be applied to generate overlapping spot seam welds. The pulse profile duration of $\sim 20 \text{ ms}$ is not excessively long, so productivity should not suffer.

Because of the nonstandard pulse profile, which incorporates a delayed power spike, a laser with flexibly programmable pulse profiles will be required.

While not reported, an electron beam version of this technique should also be possible.

SHADOW Technique

SHADOW welding refers to a stepless, high-speed, accurate, and discrete one-pulse welding technique (Ref 48) that was developed to adapt laser macrowelding machines to the microweld. In this technique, a single pulse from a pulsed welding laser is translated rapidly along the parting surface of the parts to be joined, in effect tracing the entire weld seam path during the single pulse. Pulses retracing

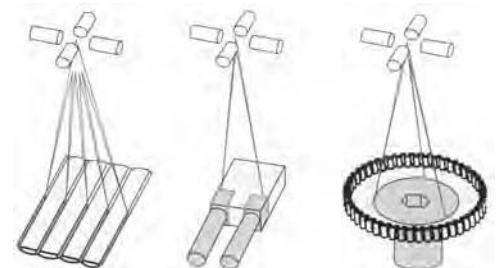


Fig. 4 Rapid beam rastering for productivity and quality improvement

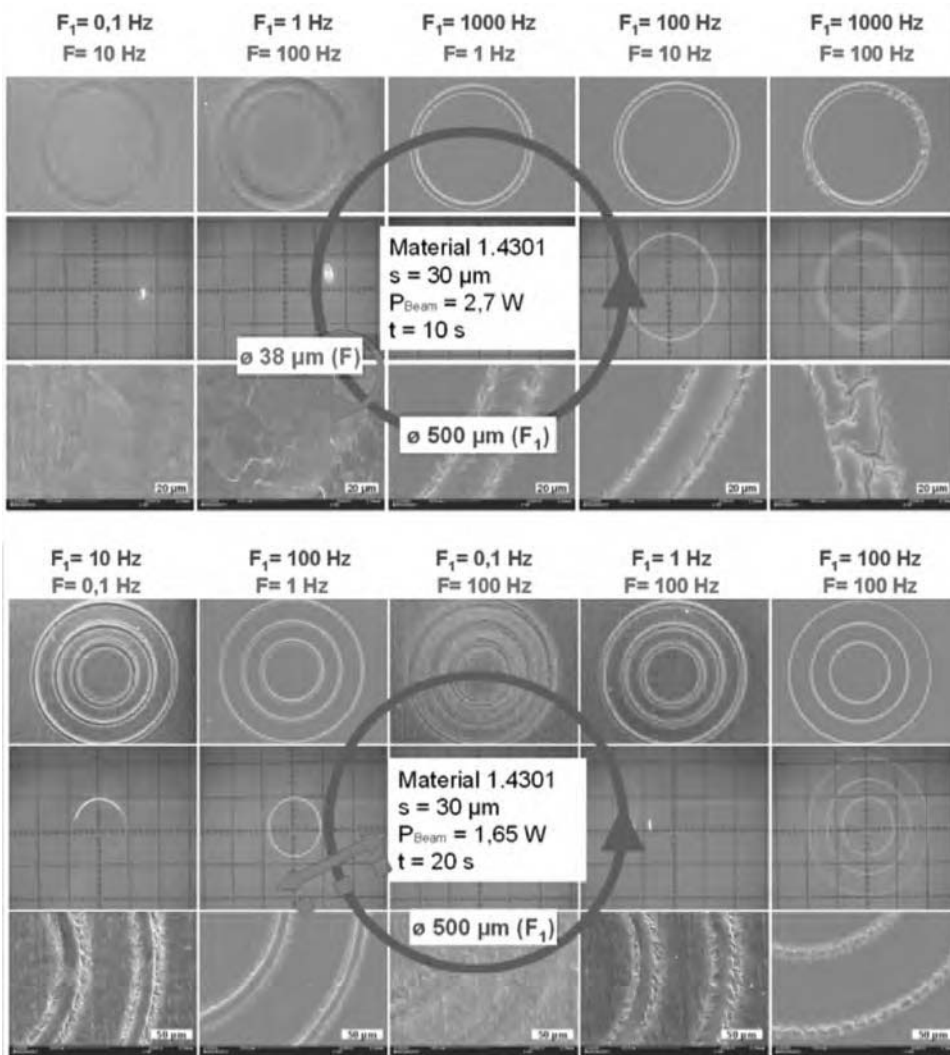


Fig. 5 Effect of relative frequency of modulation for circular (top) and alternating sign step-function bar-type (bottom) beam positional modulation relative to the overall path. Source: 46

the original pulse may also be added subsequently, perhaps using less power to stress relieve or heat treat the weld zone. Either the beam or the parts to be joined may be translated. For welds with circular symmetry, spinning the workpieces at a sufficient rotational speed is easy, although if the weld path is not circular, a galvo-directed beam scanner will be necessary. An early example of the technique in the production of mechanical time-piece parts is shown in Fig. 7. Advantages to the SHADOW technique over ordinary pulsed neodymium: yttrium-aluminum-garnet laser welding include a significant reduction in heat input (the rapid travel speed and single pulse have much higher melting efficiency than an overlapping pulse seam weld), less vapor re-deposition on the part, a smooth, ripple-free weld surface, and less angular distortion of the shaft, because the weld solidifies more or less simultaneously around the circumference, balancing the residual stresses.

Another example of the SHADOW technique in the production of miniature ball bearings is shown in Fig. 8.

In both of these examples, the laser beam was scanned on the part. In the example in Fig. 9, the part was rapidly rotated under the laser beam. The SEM image shows the exceptional weld surface smoothness achievable with this technique. The continuous seam also was found to aid in avoiding cracking by the high-strength steel pins used to pin the disks together.

Laser Droplet Welding

One of the major difficulties associated with microjoining is the inability to add filler material in a convenient manner. Generally, the only way to add filler is to incorporate a preplaced shim into the joint, and this is highly inconvenient when the parts are very small to start with. Thus, metallurgical incompatibilities that can

be solved with the addition of the appropriate filler prevent dissimilar pairings that are of industrial interest and importance. Laser droplet welding (Ref 51–54) is an approach that allows controlled addition of filler metal to micro-joints. Laser droplet welding has some similarities to laser spike welding described earlier. The process is described schematically in Fig. 10. An initial low laser power, P1, creates a molten droplet at the tip of an advancing wire. After a brief period of even lower power, P2, during which the droplet translates across the multilaser beam focus point, a high-power pulse, P3, vaporizes the wire behind the droplet, detaching and propelling the droplet by vapor-recoil force across a gap to the target location, where the droplet wets, spreads, and resolidifies. An example where droplets of pure nickel are used to join thin sheets of stainless steel is shown in Fig. 11, and an example where silver droplets are used to join a silver foil onto a silver-coated silicon substrate is shown in Fig. 12.

Electron Beam Microwelding Fixtures

Many issues of both fixturing and weld parameter choices are still to be resolved for microjoining. Research is being actively pursued to determine whether rapid beam rastering relative to a single microweld (e.g., breaking the beam path into segments and retracing the entire path rapidly, as in Fig. 5, etc.) may affect its development and reproducibility.

If beam microwelding processes are to successfully evolve from the development laboratory to the production floor, it is clear that much work remains. Some partial solutions to fixturing issues are given in examples in Ref 38 that are representative of electron beam microwelding scenarios (and they would be expected to be of equal use for laser microwelding). These examples were accomplished with a modified SEM capable of providing up to 6 W of power in a beam of $\sim 20 \mu\text{m}$ diameter.

One example describes fixturing for an in-line wire weld. As previously noted, cross-wire welds of small-diameter wires are much easier to accomplish than in-line geometry. However, when such an in-line geometry is necessary, it has been found useful to hold the wires together under a moderate axial pressure provided by spring loading of the clamping fixture (Ref 38). In the case of fillet seam welds, similar concerns with consistent thermal contact and foil buckling due to beam heating must also be addressed. It has been found useful to apply a lateral tensile preload to the substrate foil when fillet welding two foils together (Ref 38).

Attempts at making butt welds have been successful (Ref 38) with fixtures that employ an aluminum substrate support plate, a spring-loaded cover plate, and lateral spring-loaded clamps butting the two workpieces together. Thus, the adjustable fixturing restrains the workpieces against both in-plane

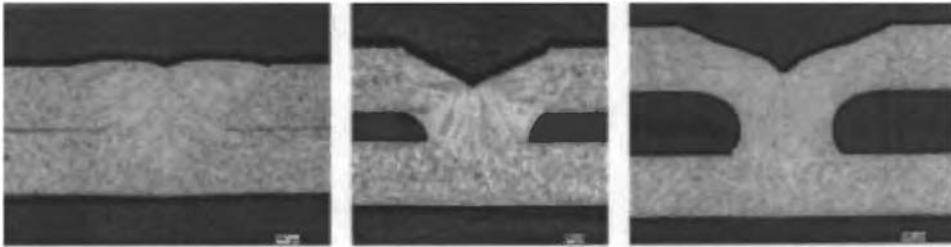
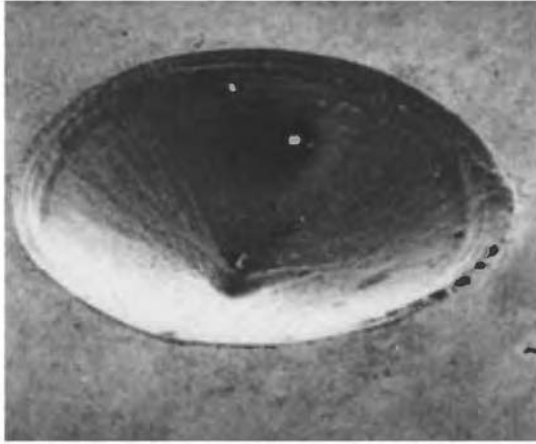


Fig. 6 Laser spike spot welding of 250 μm thick X8CrNi1812 stainless steel foils of varying gap. Top view and metallographic sections. Source: Ref 47

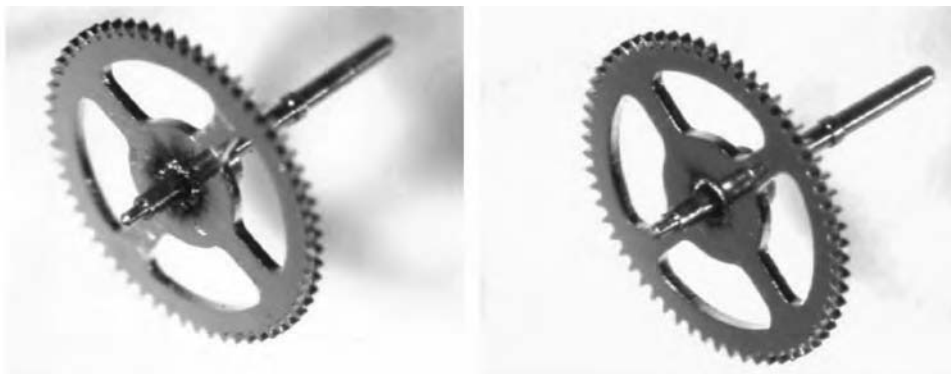


Fig. 7 Conventional overlapping spot-pulsed seam weld (left) compared to SHADOW weld (right) in a brass gear-to-steel shaft weld. 0.3 mm (0.01 in.) shaft diameter. Source: Ref 48

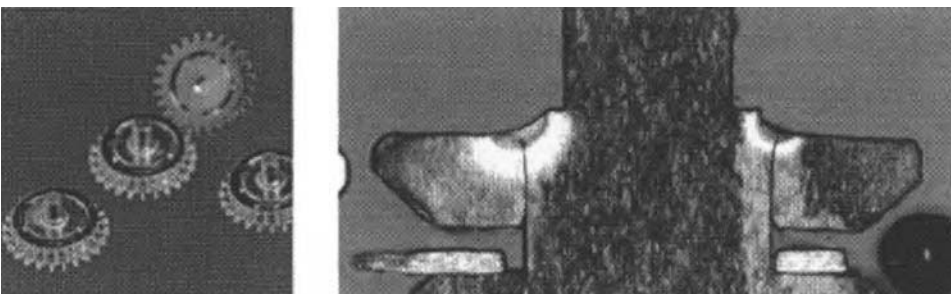


Fig. 8 SHADOW welding of miniature ball bearings. Inner cage diameter, 0.6 mm (0.02 in.); outer cage diameter, 3.0 mm (0.1 in.). Source: Ref 49

and out-of-plane motion, as well as provides thermal heat sinking.

Future Trends

In the previous sections, it has mostly been assumed that the beam microwelding processes are used as heat sources for autogenous welds. However, it is also possible that either the laser beam or the electron beam can be used to cause deposition of material from a vapor cloud directed in the vicinity of the gap to be joined (a quite rarefied cloud in the case of the nonlaser techniques). These techniques, laser-enhanced chemical vapor deposition and focused electron beam deposition by “cracking” of organometallic gases, have been demonstrated to effect repairs in microelectronic circuits (Ref 56).

Furthermore, the possibility of using ions, in addition to electrons and photons, also exists. (Ions are more effective at cracking the organometallic gases employed, although they alloy into the material deposited.) Focused ion beam (FIB) and focused electron beam (FEB) instruments available to the analytical community are being used regularly to cut and manipulate thin foils for examination by TEM instruments (Ref 57). As part of this technique, the FIB is used to cut thin specimens that are still attached by a narrow bridge of material, then a manipulation wand is spot welded to the foil by the FIB or FEB technique, and finally the thin bridges are cut away. Other investigators have shown that this technique can be used to create shapes and bonds in other geometries (Ref 58). The downside to the FIB/FEB technique is that it provides a very low deposition rate, and it can be difficult to bridge relatively wide gaps. Nevertheless, because the beams used can be very low current, they retain their extremely small-diameter focusing capability, such that nanometer-sized structures can be created. An example of such a deposit used to seal over etch holes left in a MEMS device is given in Fig. 13 (Ref 46).

As a concluding note, the difficulty of handling microparts has been noted repeatedly. It is interesting to speculate that processes such as laser shaping (and its electron beam analog) may be used to fold portions of lithographically-produced foil structures into proper alignment, which would then be welded together and finally cut away from the substrate to yield a final composite structure without ever having been handled, other than by the processing beam (Ref 59).

ACKNOWLEDGMENTS

Sandia National Laboratories is a multi-program laboratory managed and operated by Sandia Corporation, a wholly-owned subsidiary of Lockheed Martin Corporation, for the U.S. Department of Energy's National Nuclear

Security Administration under contract DE-AC04-94AL85000. The author would like to thank many colleagues and associates for contributing to this article, particularly Thorsten

Lower and colleagues at ProBeam AG, Thomas Dorfmueller and colleagues at the University of Aachen, and Isamu Miyamoto of Osaka University.

REFERENCES

1. E.M. Purcell, Life at Low Reynolds Number, *Am. J. Phys.*, Vol 45, 1977, p 3-11
2. K.K. Kelley, "Contributions to the Data on Theoretical Metallurgy, XIII," Bulletin 582, U.S. Bureau of Mines, USGPO, 1960
3. CenBase Materials Database, CenTOR Corporation, 1996
4. P.G. Shewmon, *Diffusion in Solids*, McGraw-Hill, NY, 1963, p 8
5. E. Saiz, R.M. Cannon, and A.P. Tomsia, "Atomic Transport at Liquid Metal/Al₂O₃ Interfaces," Key Engineering Materials, Defect and Diffusion Forum, 2001, www.osti.gov
6. P.F. Mendez and T.W. Eagar, Estimation of the Characteristic Properties of Weld Pool during High Productivity Arc Welding, *Mathematical Modelling of Weld Phenomena 5* (Graz, Austria), 1999, p 68
7. J. Szekely, *Fluid Flow Phenomena in Metals Processing*, Academic Press, New York, 1979
8. C.R. Heipleand and J.R. Roper, Mechanism for Minor Element Effect on GTA Fusion Zone Geometry, *Weld. J.*, Vol 61, 1982, p 97s-102s
9. P. Sahoo, T. DebRoy, and M.J. McNallan, Surface Tension of Binary Metal-Surface Active Solute Systems under Conditions Relevant to Welding Metallurgy, *Metall. Trans. B*, Vol 19, 1988, p 483-491
10. D.R. Lide, Ed., *CRC Handbook of Chemistry and Physics*, 84th ed., CRC Press, Boca Raton, FL, 2003
11. V. Semak and A. Matsunawa, The Role of Recoil Pressure in Energy Balance during Laser Materials Processing, *J. Phys. D: Appl. Phys.*, Vol 30 (No. 18), 1997, p 2541-2552

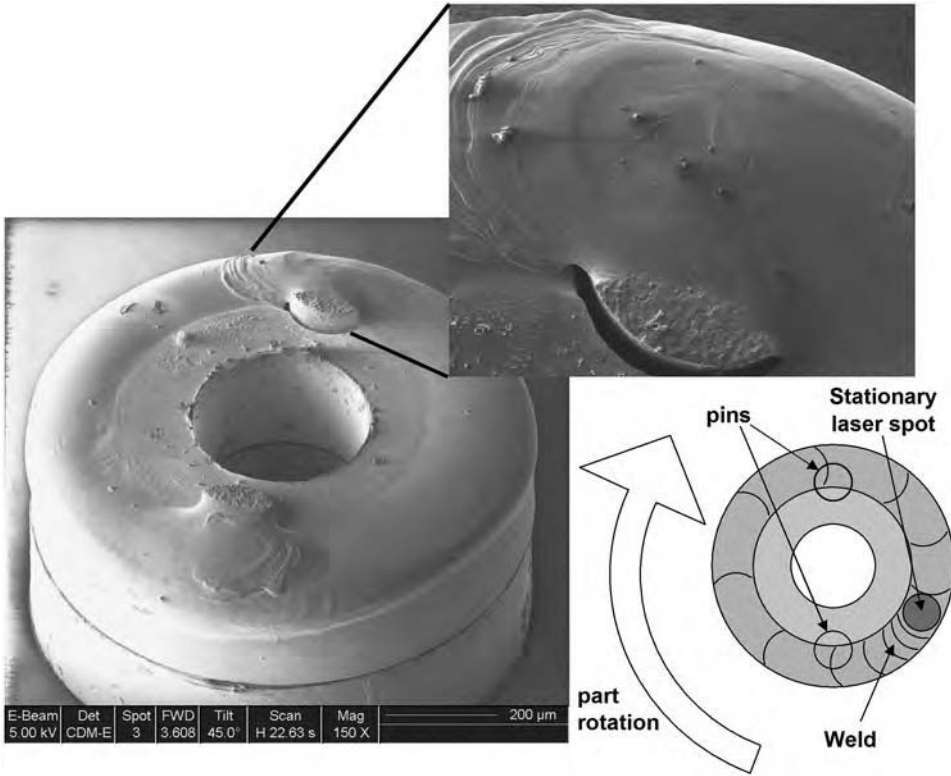


Fig. 9 SHADOW-like weld of tool steel-pinned lithographed, electroplated, and molded (LIGA) nickel parts rotated under single pulse from neodymium: yttrium-aluminum-garnet (Nd:YAG) laser. 1.3 revolutions during 10 ms and 15 J pulse. Source: Ref 50

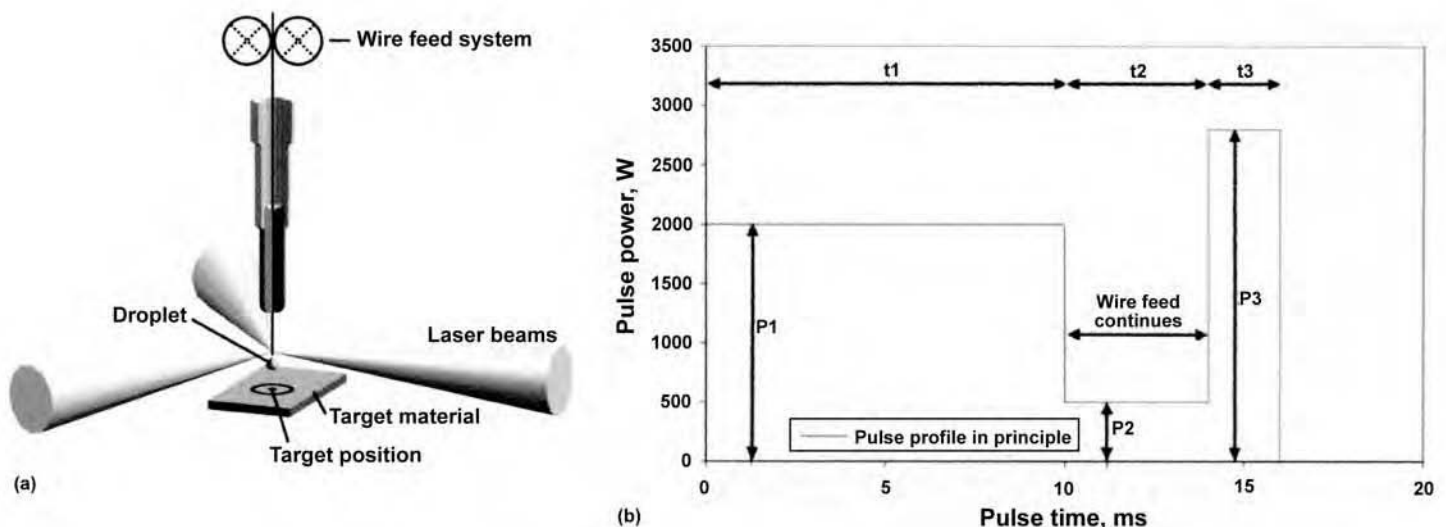


Fig. 10 Schematic description of laser droplet welding. (a) Physical arrangement. (b) Power level vs. time. Source: 52

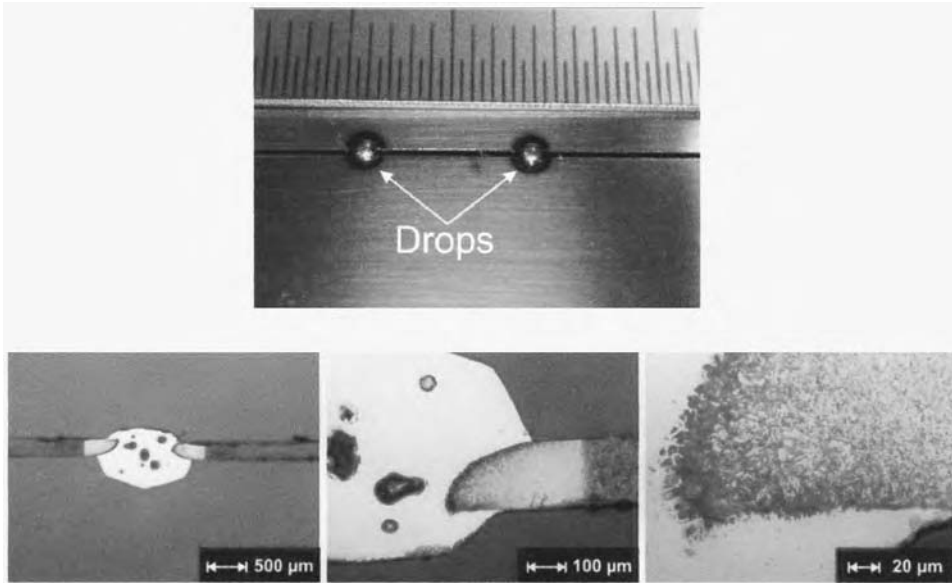


Fig. 11 Nickel droplets used to join foils of stainless steel, showing melting of stainless steel by the retained heat of the nickel droplet. Source: Ref 52

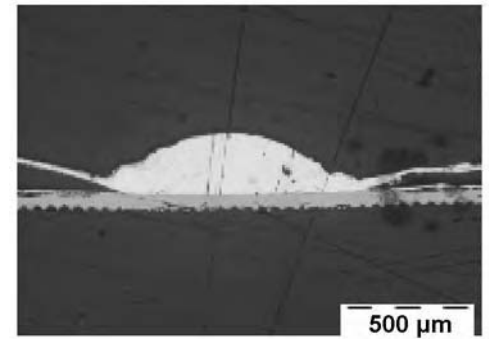


Fig. 12 Silver droplet used to join silver foil to silver-coated silicon substrate. Source: Ref 55

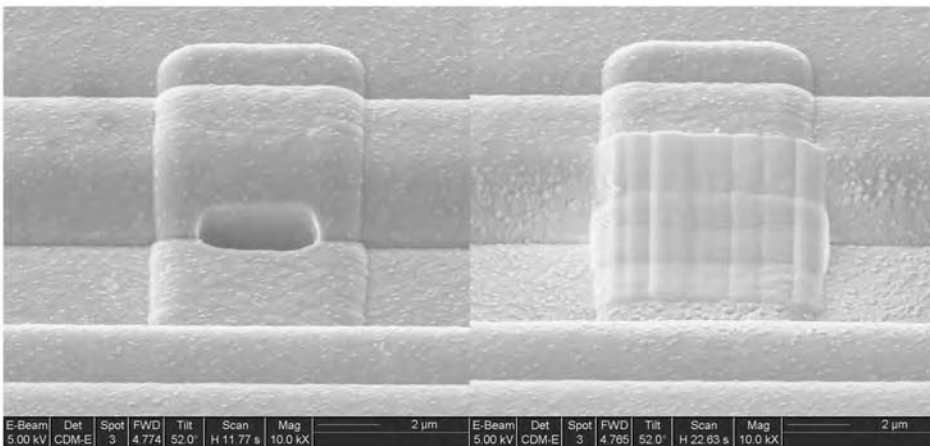


Fig. 13 Sealing patch on microelectromechanical systems-type peristaltic pump etch holes produced by focused ion beam deposition on silicon from a platinum-containing organometallic gas. Source: Ref 46

12. J. Szekely, *Fluid Flow Phenomena in Metals Processing*, Academic Press, New York, 1979, p 16, 19, 128
13. J.F. Lancaster, *The Physics of Welding*, 2nd ed., Pergamon Press, 1986
14. R.J. Renwick and R.W. Richardson, Experimental Investigation of GTA Weld Pool Oscillations, *Weld. J.*, Vol 62, 1983, p 29s–35s
15. H. Ki, P.S. Mohanty, and J. Mazumdar, Modeling of Laser Keyhole Welding: Part II, Simulation of Keyhole Evolution, Velocity, Temperature Profile, and Experimental Verification, *Metall. Mater. Trans. A*, Vol 33, 2002, p 1831–1842
16. A. Matsunawa, “Keyhole Dynamics in Laser Welding,” Technical Report, Lecture notes from a course given at ICALEO ‘99 (San Diego, CA), 1999
17. D.W. Walsh and W.F. Savage, The Mechanism of Minor Element Interaction in Autogenous Weld Pools, *Advances in Welding Science and Technology Conference Proceedings*, TWR ‘86, ASM International, 1986, p 59
18. G.A. Knorovsky and V.V. Semak, *Microjoining and Nanojoining*, Y. Zhou, Ed., Woodhead Publishing Limited, Cambridge, U.K., 2008, p 52–54, 72
19. J.W. Elmer, P.W. Hochenadel, K. Lachenberg, and T. Webber, Introduction to High Energy Density Electron and Laser Beam Welding, *Joining: Welding Fundamentals and Processes*, Vol 6A, *ASM Handbook*, ASM International, 2011
20. T. Löwer and C. Menhard, personal communication, Nov 2010
21. J. Milewski and E. Sklar, Modelling and Validation of Multiple Reflections for Enhanced Laser Welding, *Model. Simul. Mater. Sci. Eng.*, Vol 4, 1996, p 305–322
22. I. Miyamoto, Fundamentals of Laser Welding, *Proc. 26th Japan Laser Society Symposium*, Japan Laser Processing Society, Osaka, 1991, p 1–17 (in Japanese)
23. I. Miyamoto and G.A. Knorovsky, *Microjoining and Nanojoining*, Y. Zhou, Ed., Woodhead Publishing Limited, Cambridge, U.K., 2008, p 374–375
24. J.F. Ready, *Industrial Applications of Lasers*, Academic Press, New York, 1978, p 57–60
25. J.I. Goldstein, D.E. Newbury, D.C. Joy, C.E. Lyman, P. Echlin, E. Lifshin, L. Sawyer, and J.R. Michael, *Scanning Electron Microscopy and X-Ray Microanalysis*, Kluwer Academic/Plenum Publishers, New York, 2003, p 61–98
26. R. Gauvin, D. Drouin, and A.R. Couture, Casino v2.42, www.gel.usherbrooke.ca/casino/
27. D.C. Joy, *Monte Carlo Modeling for Electron Microscopy and Microanalysis*, Oxford University Press, New York, 1995, p 82
28. J.W. Elmer and A.T. Teruya, Fast Method for Measuring Power-Density Distribution of Non-Circular and Irregular Electron Beams, *Sci. Technol. Weld. Join.*, Vol 3, 1998, p 51
29. J.W. Elmer, “The Influence of Cooling Rate on the Microstructure of Stainless Steel Alloys,” Sc.D. thesis, MIT, Sept 1988
30. W. Klement, Jr., R.H. Willens, and P. Duwez, Non-Crystalline Structure in Solidified Gold-Silicon Alloys, *Nature*, Vol 187, 1960, p 869–870

31. V. Kujanpaa, N. Suutala, T. Takalo, and T. Moiso, Correlation between Solidification Cracking and Microstructure in Austenitic and Austenitic-Ferritic Stainless Steel Welds, *Weld. Res. Int.*, Vol 9, 1979, p 55–70
32. X. He, J.W. Elmer, and T. DebRoy, Heat Transfer and Fluid Flow in Microwelding, *J. Appl. Phys.*, Vol 97, 2005, p 084909
33. J.W. Elmer, Chapt. 7, “The Influence of Cooling Rate on the Microstructure of Stainless Steel Alloys,” Sc.D. thesis, MIT, Sept 1988, p 173
34. W. Kurz and D.J. Fisher, *Fundamentals of Solidification*, Trans Tech Publications LTD, Switzerland, 1986, p 165, 200
35. W.M. Mullins and R.F. Sekerka, *J. Appl. Phys.*, Vol 35, 1964, p 444
36. M.J. Aziz, Model for Solute Redistribution during Rapid Solidification, *J. Appl. Phys.*, Vol 53, 1982, p 1158–1168
37. W.A. Savage, Weldments: Physical Metallurgy and Failure Phenomena, *Proceedings of the Fifth Bolton Landing Conference*, R.J. Christoffel, E.F. Nippes, and H.D. Solomon, Ed., Aug 1978, General Electric Co. Technology Marketing Operation, Schenectady, NY, 1979, p 13
38. U. Reisgen and T. Dorfmueller, Developments in Micro-Electron Beam Welding, *Microsyst. Technol.*, Vol 14, 2008, p 1871–1877
39. G. Smolka, A. Gillner, L. Bosse, and R. Lützel, Micro Electron Beam Welding and Laser Machining—Potentials of Beam Welding Methods in the Microsystem Technology, *Microsyst. Technol.*, Vol 10, Springer, 2004, p 187–192
40. U. Dilthy and T. Dorfmueller, Micro Electron Beam Welding, *Microsyst. Technol.*, Vol 12, 2006, p 626–631
41. A.C. Lingenfelter, Laser Welding Thin Cross Sections, *First International Congress on Laser Advanced Materials Processing Conference (LAMP'87)* (Osaka, Japan), Laser Processing Society, 1987, p 211–216
42. A.F. Khadraw, A. Othman, and M.A. Al-Nimr, Transient Free Convection in a Vertical Microchannel as Described by the Hyperbolic Heat Conduction Model, *Int. J. Thermophys.*, Vol 26, 2005, p 905–918
43. G.A. Knorovsky, D.O. MacCallum, and M.T. Meyers, Selection of Parameters for μ E-Beam Welding, *Sci. Technol. Weld. Join.*, Vol 11 (No. 6), 2006, (electronic journal)
44. I. Miyamoto, S.-J. Park, and T. Ooie, High-Speed Microwelding by Single-Mode Fiber Laser, *Proceedings of the (Conference on) Laser Assisted Net Shape Engineering 4*, 2004, p 55–66
45. I. Miyamoto, S.-J. Park, and T. Ooie, Application of Single-Mode Fiber-Lasers to Novel Microwelding, *Proc. Fourth Laser Precision Microwelding*, Japan Laser Society, Nara, 2003, p 507–514
46. G.A. Knorovsky, T. Dorfmueller, U. Kilthey, and K. Woeste, *Microjoining and Nanoinforming*, Y. Zhou, Ed., Woodhead Publishing Limited, Cambridge, U.K., 2008, p 427, 451–452, 455–456
47. D.K. Dijken, W. Hoving, J.Th.M. De Hosson, Laser Penetration Spike Welding: A Microlaser Welding Technique Enabling Novel Product Designs and Constructions, *J. Laser Appl.*, Vol 15, 2003, p 11–18
48. A. Olowinsky, T. Kramer, N. Dumont, and H. Hanebuth, New Applications of Laser Beam Micro Welding, *Proceedings of ICALEO*, 2001
49. A. Gillner, A. Olowinsky, K. Klages, J. Gedicke, and F. Sari, High Precision and High Speed Laser Microjoining for Electronics and Microsystems, *Proc. SPIE*, Vol 6161, 2006, p 616102-1 to 616102-11
50. Sandia National Laboratories, unpublished internal research, Dec 2001
51. W. Hoving and B. Jahrsdörfer, Laser Droplet Weld, *Ein Innovatives Fuegeverfahren, Tagungsband Laser in der Elektronikproduktion & Feinwerktechnik, LEF 2001* (Meienbach, Bamberg), 2001, p 21–32
52. B. Jahrsdörfer, G. Esser, M. Geiger, and E. Govekar, Laser Droplet Weld—An Innovative Joining Technology Opens New Application Possibilities, *Photon Processing in Microelectronics II*, Vol 4977, SPIE, 2003
53. E. Govekar, J. Klemen, T. Kokalj, M. Schmidt, and M. Kastens, Progress in Laser Droplet Formation and Welding, *Laser in der Elektronikproduktion & Feinwerktechnik, LEF 2007*
54. B. Jahrsdörfer, B. Schmidt, and M. Geiger, Laser Droplet Welding and Its Potential for Joining Dissimilar Materials, *Proceedings of LANE2004*, p 651–659
55. E. Govekar, A. Jeric, M. Weigl, and M. Schmidt, *CIRP Ann., Manuf. Technol.*, Vol 58, 2009, p 205–208
56. D.L. Smith, *Thin Film Deposition: Principles and Practice*, McGraw-Hill, 1995, p 407
57. F.A. Stevie, R.B. Irwin, T.L. Shofner, S.R. Brown, J.L. Drown, and L.A. Giannuzzi, Plan View TEM Sample Preparation Using the Focused Ion Beam Lift-Out Technique, *AIP Conf. Proc.*, Vol 449, 1998, p 868
58. S. Reyntjens and R. Puers, A Review of Focused Ion Beam Applications in Microsystem Technology, *J. Micromech. Microeng.*, Vol 11, 2001, p 287–300
59. S. Yoshioka, T. Miyazaki, T. Misu, R. Oba, and M. Saito, Laser Forming of Thin Foil by a Newly Developed Sample Holding Method, *J. Laser Appl.*, Vol 15, 2003, p 96–100

Solid-State Welding Processes

Procedure Development and Practice Considerations for Inertia and Direct-Drive Rotary Friction Welding	641	Forge and Coextrusion Welding	701
Tooling	642	Forge Welding	701
Procedure Qualifications	642	Coextrusion Welding	702
Process Monitoring and Control of Rotary Friction Welding	646	Magnetic Pulse Welding	704
Background	646	Fundamental Theory	704
System Parameters	647	Equipment	705
Monitoring	648	Magnetic Pulse Welding Process	706
Control	652	Process Parameters	707
In-Process Quality Control	652	Mechanical Testing of Magnetic-Pulsed Welds	707
Development of Welding Procedures for Friction Stir Welding	654	Metallurgical Characterization of Magnetic-Pulsed Welds	707
Procedure and Procedure Development Requirements	655	Applications	708
Procedure Development	656	Safety Guidelines While Handling the MPW Setup	708
Procedure Qualification	661	Summary	709
Friction Stir Welding Tool Designs	664	Cold Welding	711
Friction Stir Welding Tool Materials	664	Bonding Mechanisms and Theoretical Modeling of Bond Strength	711
Friction Stir Welding Tool Geometry	666	Alternative Methods of Surface Preparation	712
Predicting and Measuring Tool Performance	672	Quality Control	713
Summary	673	Process Variants and Applications	713
Friction Surfacing	678	Roll Welding and Laser Roll Welding	717
Process Description	678	Roll Welding	717
Equipment	679	Laser Roll Welding	719
Applications	679	Laser Roll Welding of Dissimilar Metals	720
Diffusion Bonding	682	Ultrasonic Welding	725
Process Variants	682	Equipment and Process Parameters	725
Diffusion Bonding of Metals	683	Personnel Requirements	728
Diffusion Bonding of Oxide Ceramics (Ref 46)	685	Applications	729
Explosion Welding	690	Ultrasonic Additive Manufacturing	731
Overview of Process Attributes	690	Process Fundamentals	731
Procedure Development and Practice Considerations	691	Applications	733
Weld Characteristics	695	Equipment and Procedures	734
Manufacturing Process and Practice	697	Material Properties in UAM	735
Products and Applications	698	Quality Control	739
		Safety	740

Procedure Development and Practice Considerations for Inertia and Direct-Drive Rotary Friction Welding*

Revised by Tim Stotler, Edison Welding Institute

ROTARY FRICTION WELDING is a solid-state welding process that uses the compressive force of the workpieces that are rotating or moving relative to one another, producing heat and plastically displacing material from the faying surfaces, thereby creating a weld. Process variations include inertia, direct-drive, linear, and radial friction welding, as well as friction surfacing. This article provides information about practice considerations for the two most common variations: inertia and direct-drive friction welding.

Inertia welding obtains the heat needed for welding from stored rotational kinetic energy. Figure 1 depicts the parameter characteristics of the process. The inertia of the system is changed by either adding or removing flywheels from the rotating spindle that provides rotary motion and/or by changing the spindle speed.

After the inertial mass is set, the parts are loaded in the machine (one in the spindle and one in the fixture/tailstock). The spindle speed and welding forces are set to predetermined levels. The spindle is then accelerated to the set speed. After this speed is attained, the drive system is disengaged, allowing the flywheel (and the part in the spindle) to effectively coast. The stationary part is then brought into contact with the rotating part, under a preset applied force, causing frictional heating to begin. The flywheel is stopped by the transition of its kinetic energy into thermal energy (frictional heating) at the welding interface. This energy heats the part and allows forging to occur, displacing material at the interface. A second-stage force can also be used with inertia welding. This force is often referred to as an upset force and can be programmed to occur at any

point in the deceleration of the spindle speed or after the spindle has stopped.

Direct-drive friction welding differs from inertia welding, primarily in how the energy is delivered to the joint. Figure 2 depicts the characteristics of this process. Direct-drive friction welding, like inertia welding, has one of the parts loaded into a rotating spindle while the other is held stationary. However, the spindle has a fixed mass. To start the process, the spindle is set into motion at a constant speed. The

parts are then brought into contact under a low force (termed first friction force, or preheat force) and allowed to heat for a preset time or distance. In most applications, a higher welding force (termed second friction force, or welding force) is then applied, which increases the rate and amount of material extruded from the joint. The second friction force is also controlled through a preset time or distance. After the preset time or distance has been reached for the first two friction stages, the rotating spindle is

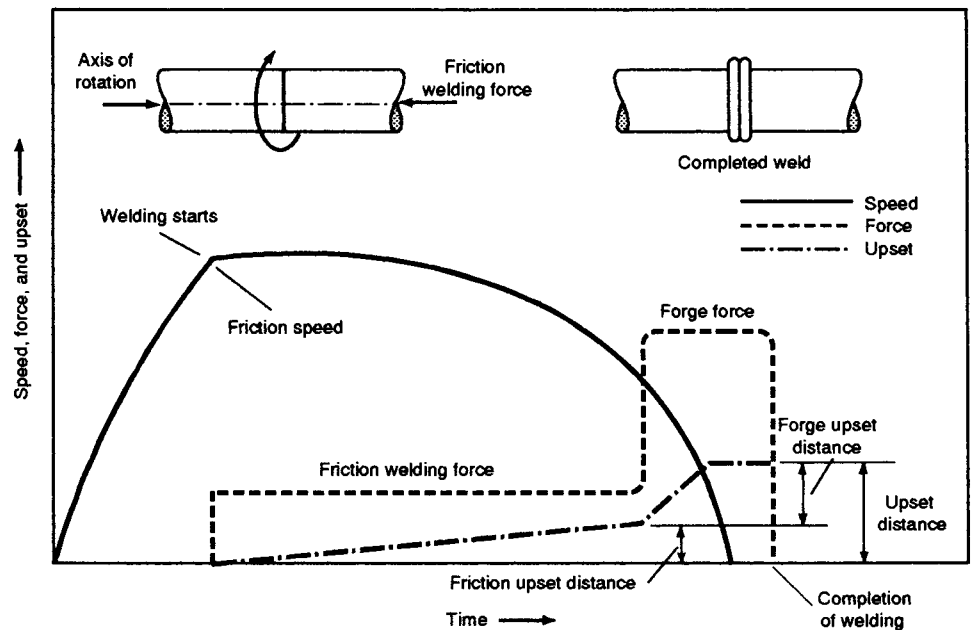


Fig. 1 Inertia welding parameter characteristics. Source: ANSI/AWS C6.1-89

* Revised from T. Stotler, Procedure Development and Practice Considerations for Inertia and Direct-Drive Friction Welding, *Welding, Brazing and Soldering*, Vol 6, ASM Handbook, ASM International, 1993, p 888-892

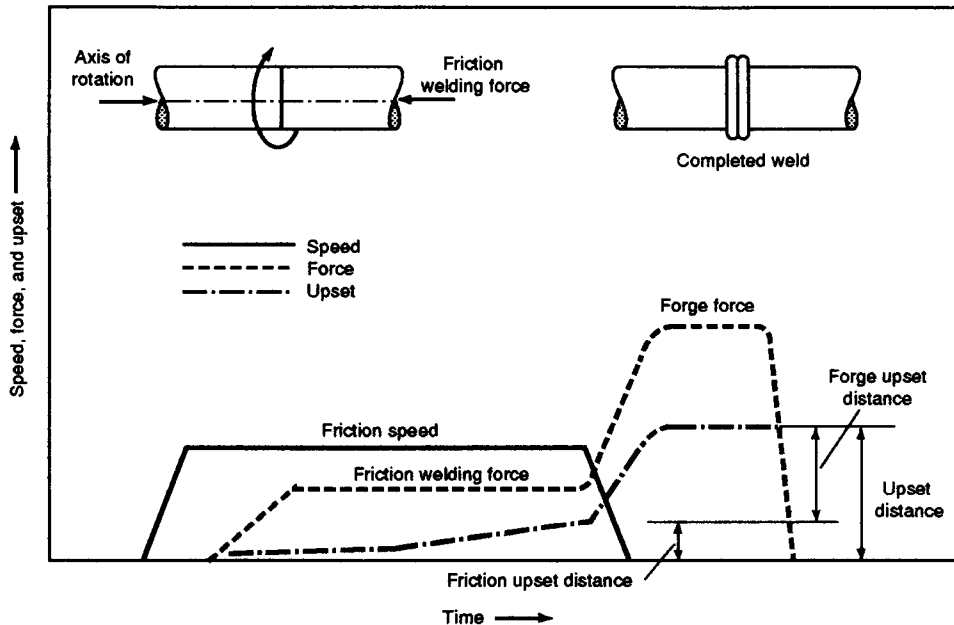


Fig. 2 Direct-drive friction welding parameter characteristics. Source: ANSI/AWS C6.1-89

brought to a stop using some type of braking mechanism. Braking is typically done via mechanical means (caliper-type brake) and/or an electric-type brake in the spindle drive motor. In most cases, a third increase in the welding force (usually referred to as the upset force) is applied at the start of or after braking has completed. This upset force acts to consolidate the joint. In contrast to inertia welding, where the microstructure at the interface reflects a rotational-type forging, direct-drive friction welding produces an axially forged microstructure in the weld. However, if braking times are increased, allowing the upset force to be applied while the spindle may still be rotating, some rotational-type forging can be obtained.

All friction welding processes induce a torque into the parts to be welded. This reaction torque induces work into the microstructure at the weld area and often has a distinct benefit to the strength of the joint. Typically, two torque peaks are induced on the workpiece: an initial peak when the parts are first brought into contact, and a final peak when the spindle decelerates to a stop. The first peak is related to developing a steady-state thermomechanical condition at the bondline. The final torque peak is associated with mechanical work as the part begins to cool. For inertia welds, this final torque peak induces a twisting-type feature to the microstructure that effectively refines the structure. For direct-drive friction welds, there is less of a twisting action to the microstructure. The level of this final torque peak is directly related to the rotating inertia of the spindle and the applied forces as the spindle decelerates. As a result, the final torque peak is

typically higher, and related refinements in microstructures are more commonly associated with inertia welding. Conversely, direct-drive systems typically both brake the spindle (removing energy from the system) and apply an upset force after the spindle has nominally stopped. As a result, the final torque peak is reduced compared to inertia welding. This lower final torque peak behavior often produces a microstructure that is more similar to that of a forged part, with little twisting to the structure.

While this second torque peak can be advantageous for improving local microstructures, a reduction in these values can be beneficial in certain applications. Such applications include those where the workpieces themselves are susceptible to damage with higher torque loads. For example, a thin-walled tube may buckle under a high final torque peak. Selection of a specific variant of friction welding, and the processing conditions used, must be based on the desired application, including component materials and resultant stiffness.

Tooling

Part of defining a set of welding parameters and then qualifying a procedure is careful consideration to the tooling design. Tooling includes all the items needed to safely counter the welding forces and torque loads imposed on the part, as well as the tooling needed to provide proper alignment between the parts to be welded. Misalignment of the two parts to be welded, caused by poor tooling design, is often found to be the cause of most friction weld defects. Misalignment of a tube-to-tube joint

can cause a reduction in the effective weld area. Tooling that is not sufficient to react the welding force(s) can prevent the weldment from reaching the desired level of force, also leading to a reduction in weld properties.

Tooling also refers to the items considered as consumables, although these items have very long lives. Tooling that makes contact with the parts to be welded has a finite life due to wear as the parts are loaded and unloaded from the machine. An environment where the volume of welds to be made causes the tooling to retain heat from part to part can also cause wear. Each particular joint design and welding rate will determine the frequency at which the tooling must be replaced. However, the frequency at which tooling changes occur should not be high enough to adversely affect the cost of the process. Wear of the tooling that contacts the part can also cause misalignment or other defects.

Procedure Qualifications

The following sections on welding parameter design and welding of different material family classes is intended to provide a baseline for initial development of a welding parameter set. Once a parameter set has been developed, along with the other necessary tooling and preweld and postweld processing needs related to the friction welding process, a welding procedure specification (WPS) is developed. American Welding Society (AWS) Document C6.2, "Specifications for Friction Welding of Metals," provides a guideline for development of a WPS. Included are guidelines for the three classes of welds and the type of testing necessary. Testing methods are also typically covered by AWS B4.0, "Standard Methods for Testing of Welds," unless otherwise indicated by the design needs of the weldment.

As part of the WPS, a process robustness testing procedure is also conducted. The process robustness defines the tolerance of the process to manufacturing variability that often occurs. Items included in the robustness definition could be each of the welding process variables, misalignment of the parts, part cleanliness, tooling wear, and so on. The levels at which each variable is tested are usually selected at the extreme upper and lower ends of each variable or at levels considered to be the allowable engineering design limits.

Welding Parameters

Inertia Welding Parameter Design. Differences in part geometry (bar-to-bar, tube-to-tube, bar-to-plate, and so on) affect the welding parameters. The calculation procedures described here are based on carbon steel. For a given alloy system, inertia welding spindle speeds are set within a specified range of surface velocities. Surface velocities for welding

carbon steels in all geometries typically range from 90 to 610 m/min (300 to 2000 ft/min). The actual spindle speed (rev/min) is calculated by:

$$\text{rev/min} = \frac{\chi S}{\pi \text{OD}} \tag{Eq 1}$$

where χ , the conversion factor, is 12 for the U.S. customary unit and 1000 for the metric SI unit, S is the surface velocity (m/min or ft/min), and OD is the outside diameter of the part (mm or in.).

For solid bars and a fixed welding force, lower surface velocities tend to reduce center heating. Center heating is not an issue for tube-type geometries, meaning there is greater flexibility in the surface velocities used. The effect of surface velocity on the heat pattern in a solid bar is shown in Fig. 3.

As mentioned previously, rotating flywheels are the source of energy for the inertia welding process. During the friction welding force stage where spindle deceleration occurs (Fig. 1), the process is characterized by a loss of material from the interface to the flash. Larger inertias prolong the welding cycle. The calculation of the flywheel energy that is needed to produce a weld depends on the surface velocity, material type, and joint geometry. As shown in Table 1 for a solid bar of low-carbon steel, the moment of inertia (expressed as wK^2 in mass units) is $0.18 \text{ kg} \cdot \text{m}^2$ ($4.2 \text{ lb} \cdot \text{ft}^2$). This is found by using Eq 2 and the approximate flywheel energy (E_T) of $63 \text{ N} \cdot \text{m/mm}^2$ ($30,000 \text{ ft} \cdot \text{lbf}$

in.²) for the inertia welding of low-carbon steels:

$$wK^2 = \frac{E_T C}{(\text{rev/min})^2} \tag{Eq 2}$$

where the value of C is 5873 for the U.S. customary unit and 182.4 for the SI unit, E_T is the total flywheel energy, and the (rev/min)² value is that for the spindle, which was calculated in Eq 1.

As mentioned previously, inertia welding has flexibility in how the welding force can be applied. Typically, a single force is used, but a second-stage force can be implemented (Fig. 1). The typical pressures for welding carbon steels range from 96.5 to 207 MPa (14 to 30 ksi). The second-stage force (forging force), which can vary from 1.5 to nearly 4 times the welding force, is usually determined through experimentation. The effect of the welding force on the size of the heat-affected zone is inverse to that of surface velocity. That is, welds made at low welding forces have heat-affected areas resembling those produced with high surface velocities (Fig. 3).

When designing an initial set of inertia welding parameters, the normal order of selection can be summarized as:

- Choose the desired spindle speed (rev/min)
- Calculate the total moment of inertia (wK^2) that is needed for the required energy level, E_T
- Choose the nearest available total moment of inertia (wK^2) level on the welding machine

- Recalculate the necessary spindle speed using the selected total moment of inertia (wK^2) that is available on the machine
- Calculate the necessary welding force (and upset force, if used)

Direct-Drive Friction Welding Parameter Calculations.

Similar to inertia welding, the same equation (Eq 1) is used for calculating the spindle rev/min value. Surface velocities for the direct-drive friction welding of carbon steels range from 76 to 182 m/min (250 to 600 ft/min), with tube joints requiring slightly higher surface velocities than joints using bars. Typical welding pressure values for carbon steels range from 83 to 166 MPa (12 to 24 ksi) for the second friction force and from 166 to 332 MPa (24 to 48 ksi) for the upset force. Although first friction forces vary, they are typically 10 to 20% of the second friction force. Examples of welding parameters for bar-to-bar and tube-to-tube direct-drive welds are shown in Table 2.

Table 1 Typical inertia welding conditions for low-carbon steel

Parameter	Value
Bar-to-bar	
Diameter, mm (in.)	25.4 (1)
Weld area, mm ² (in. ²)	506 (0.78)
Total moment of inertia, wK^2 , kg · m ² (lb · ft ²)	0.18 (4.2)
Speed	
Angular velocity, rev/min	5725
Surface velocity, m/min (ft/min)	460 (1500)
Total force, kN (lbf)	68.9 (15,500)
Approximate upset distance, mm (in.)	3.8 (0.150)
Tube-to-tube	
Outside diameter, mm (in.)	50.8 (2)
Inside diameter, mm (in.)	38.1 (1.5)
Weld area, mm ² (in. ²)	886 (1.37)
Total moment of inertia, wK^2 , kg · m ² (lb · ft ²)	1.23 (29.3)
Speed	
Angular velocity, rev/min	2875
Surface velocity, m/min (ft/min)	460 (1500)
Total force, kN (lbf)	91.7 (20,600)
Approximate upset distance, mm (in.)	5.1 (0.200)

Table 2 Typical direct-drive friction welding conditions for low-carbon steel

Parameter	Value
Bar-to-bar	
Diameter, mm (in.)	25.4 (1)
Weld area, mm ² (in. ²)	506 (0.785)
Speed	
Angular velocity, rev/min	1100
Surface velocity, m/min (ft/min)	88 (290)
Second friction force, kN (lbf)	35.6 (8000)
Upset force, kN (lbf)	71.2 (16,000)
Approximate upset distance, mm (in.)	4.6 (0.180)
Tube-to-tube	
Outside diameter, mm (in.)	50.8 (2)
Inside diameter, mm (in.)	38.1 (1.5)
Weld area, mm ² (in. ²)	886 (1.37)
Speed	
Angular velocity, rev/min	900
Surface velocity, m/min (ft/min)	143 (470)
Second friction force, kN (lbf)	48.9 (11,000)
Upset force, kN (lbf)	97.9 (22,000)
Approximate upset distance, mm (in.)	3.2 (0.125)

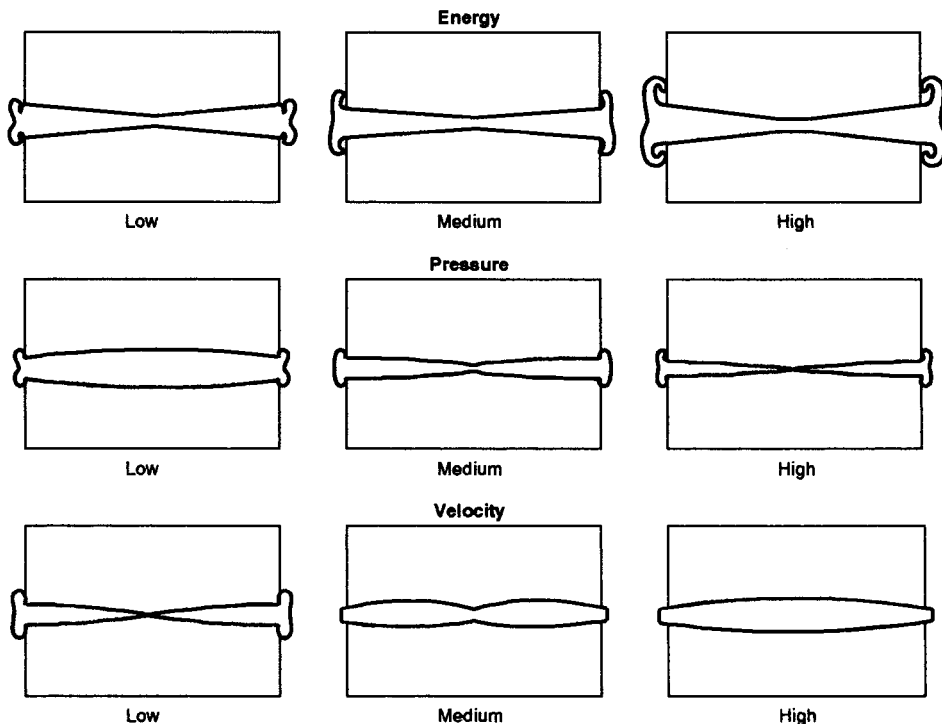


Fig. 3 Effect of welding variables on the heat pattern at the interface and flash formation of inertia welds. Source: AWS Welding Handbook

Steels

Carbon Steels. Generally, most metals that can be hot forged can readily be friction welded with either process variant. Carbon steels, which fall into this category, have been the fundamental basis of welding-parameter calculations for both inertia and direct-drive friction welding. Low- and medium-carbon steels are the easiest to weld and generally require no postweld heat treatments. Higher-carbon and alloyed steels can also be joined; however, a narrower welding-parameter window is often evident than for low-carbon steels. This is primarily due to the reduced forging characteristics of the higher-carbon steels. Steels that contain significant amounts of free-machining elements, such as lead, also can be friction welded. However, these free-machining elements can cause undesirable directional properties near the bondline and may also act as dry lubricants that reduce frictional heating. Heat treatable steels also can be friction welded. The rapid quenching of the weld area can present hardenability concerns, and a subsequent tempering or annealing procedure may be required. Hardenable steels such as these should be welded with parameters that increase the welding time in order to reduce the cooling rate.

Stainless steels are also commonly joined using either friction welding process. Austenitic and ferritic stainless steels are easily joined to each other and to themselves. Because the heat treatable stainless steels are sensitive to temperature and pressure, a postweld thermal treatment may be necessary to achieve the desired weld properties. Precipitation-hardenable stainless steels are often solution heat treated and aged after welding.

Welding parameters for stainless steels are similar to those used with carbon steels. Surface velocities for both bars and tubes fall within the same range as for carbon steels for both process variants. The flywheel energies, E_T , and welding forces for the inertia welding of stainless steels are typically 30 to 50% higher than those for carbon steels. The welding forces for both process variants are often 30 to 40% higher. Another factor relevant to the friction welding of stainless steel is the location of the weld when subjected to a corrosive environment. If possible, it should be located outside of the corrosive environment. In some instances, an increased corrosion rate occurs near the weld.

Nonferrous

Aluminum-Base Alloys. Aluminum alloys are commonly joined by friction welding. For inertia welding, rotational forging will form flow lines with radial patterns, as opposed to the straight flow patterns produced with direct-drive friction welding or flash welding. An advantage for direct-drive friction welding is that thin-walled aluminum tubes are somewhat easier to join. This result is from the ability to stop the rotation of the spindle before a forge force is applied, effectively reducing the final

torque peak. Because severe hot working of the two materials will occur, the heat-affected regions of aluminum friction welds are very narrow and have a fine-grained structure. In addition, the severe hot working leads to dynamic recrystallization at the interface.

Parameters for the inertia welding of aluminum alloys differ somewhat from those used for carbon steel. The differences are due to the higher thermal conductivity of these materials. The surface velocities used for welding aluminum alloys are approximately 30 to 50% higher than those used for carbon steel. Pressures for inertia welding are significantly lower than they are for carbon steels, ranging from 20 to 50% of those used for a similar-sized carbon steel part. The flywheel energy is from 20 to 50% of that for carbon steel. For direct-drive friction welding, the surface velocities are 10 to 50% higher than they are for carbon steel, depending on the type of aluminum alloy. Welding and upset pressures are typically 30 to 50% of those used for carbon steel.

Reactive and Refractory Metals. Of these classes of materials, the titanium alloys have been joined by friction welding the most frequently. For the inertia welding process, titanium alloys have flywheel energies that are similar to or slightly lower than those of steel. Surface velocities are typically at the higher end of the carbon steel scale, ranging from values that are equivalent to those used for carbon steel to values that are 40% greater. However, welding forces are lower, typically ranging from 30 to 40% of those used for welding carbon steel. This difference is attributed primarily to the lower thermal conductivity of titanium.

Work has been done using direct-drive friction welding for titanium, although to a lesser degree than inertia welding. The welding parameters for the direct-drive friction welding of titanium are similar to those of steel, with a slight reduction in the welding forces. Most friction-welded joints in titanium can be used in the as-welded condition. However, somewhat better tensile and fatigue properties are obtained if stress relieving or solution annealing and aging procedures are used.

Zirconium has properties that are very similar to those of titanium. Therefore, initial welding parameters should be based on the parameters for titanium.

Both friction welding processes can be used to join molybdenum and tungsten. Current applications include the friction welding of molybdenum and tungsten wires in drawing operations for the lighting industry. There is not a significant amount of friction welding information available for niobium and tantalum; however, it is expected that these alloys can be successfully welded.

Copper-, Nickel-, and Cobalt-Base Materials. Copper- and nickel-base alloys are commonly friction welded. Copper alloys are also typically used in a dissimilar-metal welding application with aluminum. For inertia welding, surface velocities are nearly twice those of carbon steel, because of the high thermal conductivity of

copper. Flywheel energies and welding forces are approximately 50% of those used for carbon steel.

For direct-drive friction welding, higher surface velocities would be required for copper, given its high thermal conductivity. Welding forces would also be lower, as they are for inertia welding.

Nickel-base alloys are routinely joined using the inertia welding process, specifically in the aerospace industry. Surface velocities are lower than those of steel, typically no higher than 50% of that for carbon steel. However, because of increased elevated-temperature properties, flywheel energies and welding forces are nearly double those required for carbon steels. After inertia welding, the joint in heat treatable nickel-base alloys is often subjected to a solution and aging treatment. This is needed to precipitate second-phase particles (that is, γ' and γ'') that have been taken back into solution by the thermal cycle of the weld.

For direct-drive friction welding, the surface velocities are approximately half those used for carbon steel, whereas welding forces are nearly double those used for carbon steel. The welding procedures for cobalt-base alloys are similar to those for nickel-base alloys.

Dissimilar Metals

In terms of process requirements for inertia or direct-drive friction welding of dissimilar-material combinations, the welding parameters typically tend to be closer to those used for the higher-strength material in the dissimilar combination. This results in a larger amount of upset from the lower-strength material. The higher-strength material may have little or no upset. As in any other joining process, the strength of the bond can be no higher than that of the lower-strength material. The combinations of metals that have been joined using the friction welding processes are shown in Fig. 4. Other combinations may be possible, with additional procedure development.

Two of the most common dissimilar joints produced using the friction welding processes are:

- Copper to aluminum
- Aluminum to steel or stainless steel

In such applications, some surface preparation may be required prior to joining. This preparation is to clean the surface just before welding and/or to prepare the interface with a specific joint geometry. In most cases where aluminum is used in a joint, a dry machining or chemical etching of the aluminum is preferred. As mentioned previously, a majority of the forging (material loss) will occur in the aluminum.

The joining of aluminum to ceramics can be done with friction welding. Steel has also been attached to ceramics using an aluminum interlayer. This is performed by first welding the steel to the aluminum, followed by welding the bimetal joint to the ceramic. Using an interlayer for applications such as this is common

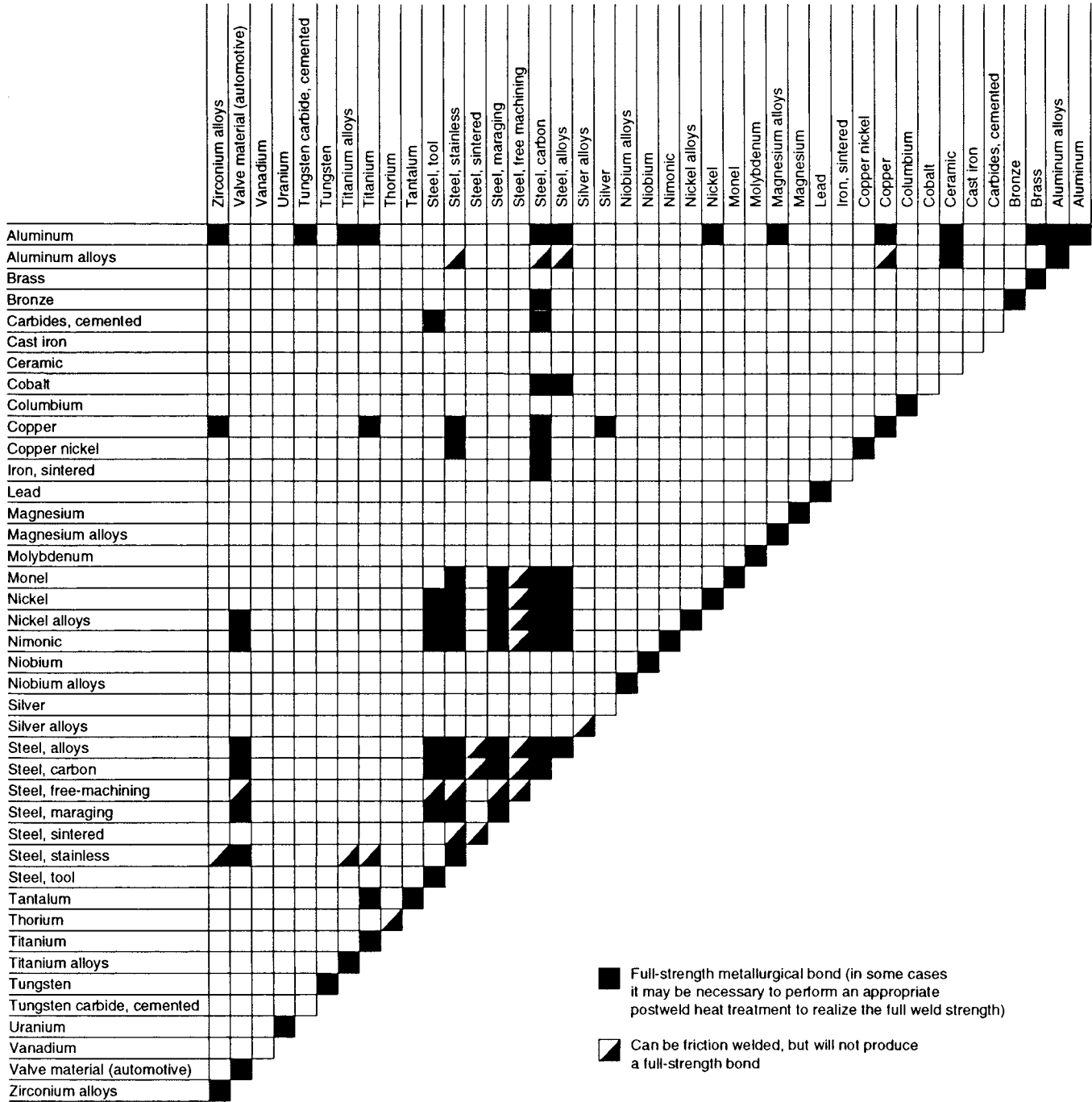


Fig. 4 Material combinations that are weldable by friction welding processes. List of alloys was compiled from available friction welding literature. Source: ANSI/AWS C6.1-89

when two incompatible materials are to be joined. The interlayer material must be selected on the basis of its ability to be forged and its compatibility with the two parent materials.

SELECTED REFERENCES

- *Metals Handbook*, 9th ed., Vol 6, American Society for Metals
- “Recommended Practices for Friction Welding,” ANSI/AWS C6.1-89, American Welding Society
- T. Stotler and J.E. Gould, “Inertia Welding of Steel to a Structural Ceramic,” 73rd AWS Meeting (Chicago, IL), American Welding Society, 1992
- A. Suzumura, T. Onzawa, A. Ohmori, and Y. Arata, “Friction Welding of Ceramics to Aluminum-Clad Steel,” Document III-890-87, 40th Annual Assembly of International Institute of Welding (Sofia, Bulgaria), IIW, 1987
- V.I. Vill, *Friction Welding of Metals*, American Welding Society, 1962
- *Welding Handbook*, 7th ed., Vol 3, American Welding Society
- *Welding Handbook*, 7th ed., Vol 4, American Welding Society
- *Welding Handbook*, 8th ed., Vol 2, American Welding Society
- *Welding Processes*, Part 2, *Welding Handbook*, 9th ed., Vol 3, American Welding Society

Process Monitoring and Control of Rotary Friction Welding

Daniel A. Hartman, Manufacturing Behavioral Science
Thomas J. Lienert, Los Alamos National Laboratory

THERE ARE A VARIETY of friction welding processes. Usually, they are characterized by the type of relative motion that is applied between the two components, including radial, orbital, angular reciprocating, linear reciprocating, or rotary. Two important variations of friction welding are friction surfacing and friction stir welding. These processes are sufficiently different from other traditional friction welding variants, that is, where two parts are rubbed together to achieve coalescence, and therefore are not discussed in this article. The most common method of friction welding uses rotary motion, in which one axially symmetric component, a stud, tube, or bar, is rotated with respect to a stationary component. Upon reaching a setpoint speed, the parts are brought together under pressure.

For a very short period after contact of the two parts, relative motion is accommodated by rubbing friction, which in turn causes heat generation. However, seizure occurs almost immediately at a radial position of 1/2 to 2/3 of the sample radius. In the seized region, relative motion is locally accommodated by high-strain-rate viscoplastic deformation of the material. This process results in the formation of a volume of deforming material shaped like a flat ring surrounding the seized region (Ref 1), and heat generation in this volume is then driven by viscoplastic deformation at high strain rates. At the time of initial seizure and formation of the deforming volume of material, rubbing of the interface continues for regions outside of the ring of material undergoing deformation. Subsequently, the ring of deforming material spreads radially inward and outward until the entire interface is replaced by a volume of deforming material (Ref 1). After this time, identification of a distinct interface between the two parts is not possible. If sufficient amounts of heat and pressure are applied, then the components will be forge-welded together by the time motion is arrested.

There are many advantages of friction welding as a production method. Generally speaking, friction welding is a highly robust and repeatable process. The process is capable of producing consistently identical welds and tolerates minor dimensional irregularities in the faying surfaces. The process parameters are easily controlled and well suited for automation and mass production. Welding cycles are measured in seconds as

compared to minutes for other more conventional methods, such as fusion welding. Because friction welding is a solid-state process, it is generally free from defects associated with solidification phenomena, including gas porosity and segregation. Filler metals, fluxes, and shielding gas are not required, which greatly simplifies the process. Finally, unlike fusion welding processes, friction welding is generally amenable to joining dissimilar metals.

This article reviews recent process monitoring and control developments in rotary friction welding. While the review focuses on rotary friction welding processes, the concepts outlined here are certainly applicable to other friction welding processes. The American Welding Society categorizes two basic variations of rotary friction welding as direct-drive friction welding (also commonly referred to as continuous-drive friction welding) and inertia friction welding (also commonly referred to as stored energy friction welding). Both methods employ high-velocity rotation and pressure to develop friction and heat at the faying surfaces to weld a rotatable part to a fixed part.

Background

Friction welding is a solid-state joining process that achieves coalescence of materials through compressive force and workpiece movement. During processing, heat generated by friction and high-strain-rate deformation softens the material surrounding the original faying surfaces, and the pressure causes displacement of this material in the radial direction as flash. The objective is to generate sufficient heat, soften the material around the interface, and plastically displace material and surface contaminants to form a solid-state weld. An important criterion to achieving a high-integrity metallurgical bond is to break up and expel the contaminated surface layers (oxides, lubricant, and adsorbed species). This process can be challenging with dissimilar materials when there is a substantial difference in material hardness.

Direct-drive friction welding employs a motor for continuously rotating one component. The system also includes a clutch and a brake. The brake is applied to control the deceleration phase.

Figure 1 illustrates the process parameter relationships during the evolution of a conventional direct-drive friction weld. The rotatable component to be welded is brought up to a setpoint speed while the other component is held stationary. (The technically correct term for speed is *angular velocity*, but the term *speed* is commonly used as standard terminology for friction welding parameters.) Upon reaching the required speed, the two components are brought together under moderate interface pressure. This action causes a rapid generation of heat and softening of material at the interface. Plasticized material and surface contaminants are expelled from the interface as flash. When the forging range of the material is reached, the motion is arrested by applying the brake. This is usually complemented with an increase in axial pressure (known as forge force) to forge the parts together.

Inertia friction welding (IFW) is a rotary friction welding process that employs a finite amount of stored energy in the form of a rotating flywheel. Figure 2 illustrates the process parameter relationships during the evolution of a conventional inertia friction weld. During processing, the rotating flywheel is accelerated to a spindle disengage speed. Upon reaching this speed, the drive motor is released by either disengaging from the spindle or applying zero torque to the spindle. The spindle decelerates naturally to the setpoint spindle speed, at which time the parts are brought together under an axial compressive force. (Speed control in inertia welding is difficult due to the massive flywheel and resulting inertia. Therefore, the common approach is to overshoot the preprogrammed speed and allow the spindle rotation to naturally decelerate to the desired setpoint.) As with direct-drive friction welding, heat generated by friction and high-strain-rate deformation softens the material surrounding the original faying surfaces, and the pressure causes displacement of this material in the radial direction as flash. The spindle rotationally decelerates at a rate dependent on the inertia, the energy losses inherent in the weld system, and the countervailing frictional weld torque due to the surface contact between the two workpieces. Upon reaching zero velocity, the weld controller initiates a cooling dwell period where weld pressure (or upset pressure) is maintained for a

predetermined period of time. An increase in force (forge force) is sometimes used to help improve the integrity of the weld (commonly referred to as a two-stage inertia friction weld). Generally, however, inertia friction welding uses a single weld pressure.

Unlike a typical direct-drive friction welding process where the rotational speed can be regulated, inertia friction welding is carried out at variable speed. The final upset is determined at the end of the cooling dwell period (and when the slide movement toward the spindle ceases). The

total upset can be calculated based on the difference between the upset zero position (at initial contact) and the upset final position. During inertia friction welding, the spindle is not under direct control of the motor drive, and upset is therefore determined by the process parameters and the natural characteristics of the weld itself, such as material properties, geometry, and surface finish. The upset that forms during the deceleration phase of a traditional inertia weld is uncontrolled, that is, the final upset is the response from an open-loop control process, and is therefore

subject to some inherent variability due to minor variability in the process parameters, surface irregularities of the two components, or minor variability in the material properties.

Table 1 lists the minimum required process parameters for controlling an inertia and direct-drive friction welding process. Referring to Fig. 1, at least seven parameters are required to control a conventional direct-drive friction welding process. In contrast, a conventional inertia friction welding process requires at least four parameters to accomplish the process (Fig. 2). The smaller number of parameters for the inertia welding process facilitates a simpler process development and optimization effort as compared to direct-drive friction welding (Ref 2).

The equipment for direct-drive and inertia machine tools is primarily the same. In general, a rotary friction welding machine tool consists of a drive motor for rotating a workpiece at high speed, a tailstock assembly for holding a stationary workpiece, a hydraulic ram for pressing the workpieces together, a hydraulic control system for controlling the force exerted by the ram, and an electrical control system for controlling the different phases of the weld process. Additionally, an inertia friction welding machine requires a flywheel for storing the rotational kinetic energy prior to engaging the rotating and nonrotating workpieces. The ability to store energy in the flywheel and thereby avoid using a continuous-drive motor during the friction weld phase makes the power requirements of inertia welding lower than the direct-drive process.

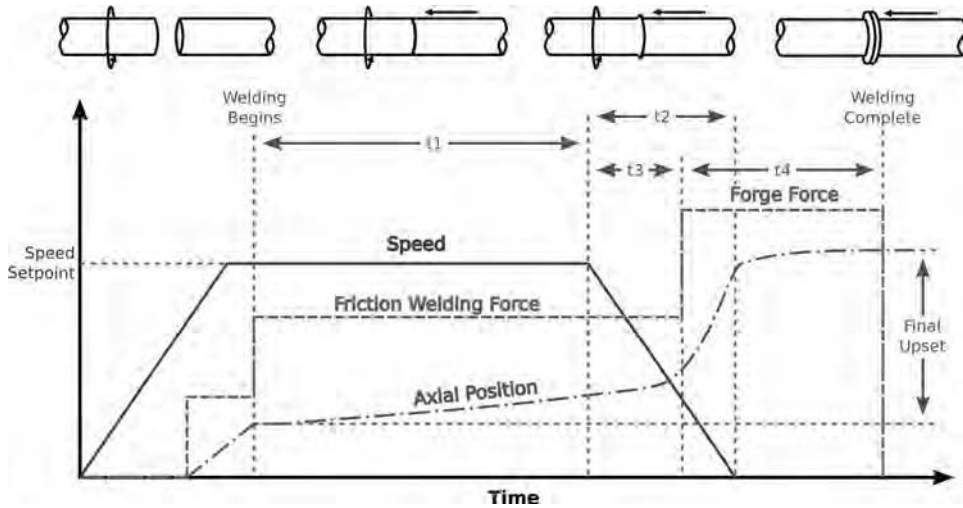


Fig. 1 Direct-drive friction welding relies on a continuous-drive motor and axial pressure to transfer energy to the common interface. First, the rotatable component to be welded is brought up to a setpoint speed while the other is held stationary. Upon reaching the required speed, the two components are brought together under moderate interface pressure. This causes a rapid generation of heat and softening of material at the interface. Plasticized material and surface contaminants are expelled from the interface as flash. When the forging range of the material is reached, the motion is arrested by applying the brake. This is usually complemented with an increase in axial pressure (known as forge force) to forge the parts together.

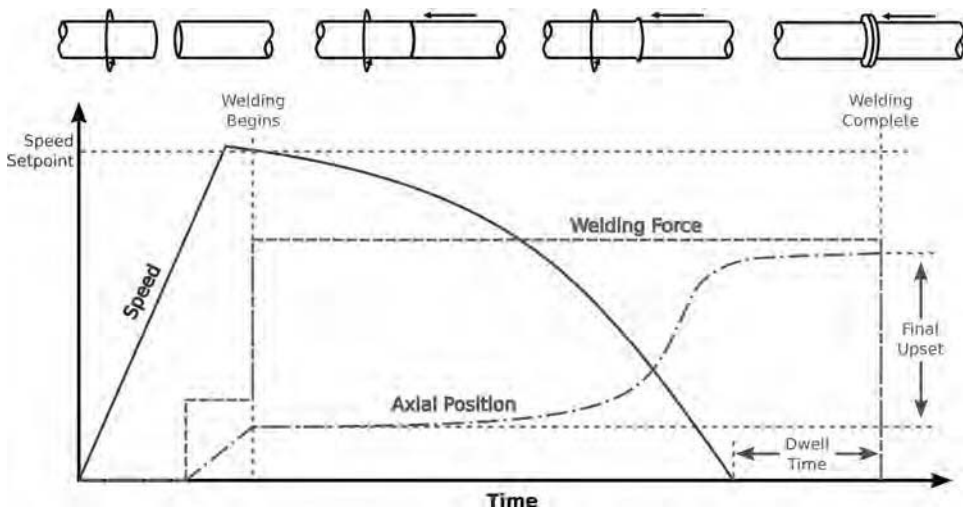


Fig. 2 Inertia friction welding relies on a finite amount of stored energy and axial pressure to transfer energy to the common interface. First, one workpiece is rotated while the other is held stationary. The inertial mass is accelerated to a preselected speed. The two workpieces are brought together under an axial compressive force. Rubbing of the faying surfaces generates local heating and softening of material at the interface. Plasticized material and surface contaminants are expelled as flash. The spindle rotationally decelerates at a rate dependent on the inertia, the frictional losses inherent in the weld system, and the countervailing frictional weld torque due to the surface contact between the two workpieces. Upon reaching zero velocity, the weld controller initiates a colling dwell period where weld pressure (or upset pressure) is maintained for a predetermined period of time.

System Parameters

The friction welding process is a tightly coupled system that is composed of the following:

- One rotating component
- One nonrotating component
- Electric motor and flywheel (for inertia) or electric motor and continuous-drive characteristics (for direct drive)
- Axial load and hydraulic response characteristics
- Dynamically evolving material response characteristics at the common interface

Decoupling such a complicated system is extremely difficult. However, mapping the

Table 1 Process parameters

Inertia	Direct drive
Speed	Speed
Welding force	Friction welding force
Inertia mass	Friction heating time, t_1
Dwell time	Delay time, t_3
	Deceleration time, t_2
	Forge force
	Forging time, t_4

The inertia friction welding process requires the selection of four independent parameters to accomplish the process, while the direct-drive friction welding process requires at least seven parameters to carry out the process.

friction welding process as a parameter space can help identify aspects of the process that must be explored in terms of process variability that can adversely affect product quality.

Figure 3 illustrates how the friction welding process can be separated into process and product attributes and follows the guidance provided in Ref 3. Process attributes are those aspects of the process that the welding engineer has control over. They include the indirect weld parameters (IWP), preselected parameters, workpiece parameters, and other influential aspects of the process. The product attributes, or direct weld parameters (DWP), represent the characteristics of the postwelded product.

The weld quality is characterized by the direct weld parameters and is affected to varying degrees by the coupled effects of the process attributes. Indirect weld parameters are parameters that can be modified in-process as part of an open- or closed-loop control procedure, while the preselected parameters remain fixed during the process, for example, the inertial mass. Finally, other factors that can affect weld quality include fixturing and workpiece alignment, machine maintenance and condition, hydraulic temperature, and the operator.

Once the preselected parameters are properly chosen, the quality of the weld can be controlled through proper selection and modification of the IWP. In general, the welding process presents the control engineer with two principal problems:

- In most cases, the relationship between the IWP and the DWP are non linear.
- The variables are highly coupled.

The job of the welding engineer is to determine a set of IWP that will produce the desired DWP. If the production floor conditions do not differ too much from the development environment, and the process and environmental variability is kept to a minimum, then the welding

operation can be expected to satisfy the post-process quality inspection procedures. Otherwise, human or computer intervention must provide the necessary feedback to make corrective actions in the welding equipment settings.

Monitoring and control of a manufacturing process falls within one of four categories:

- *Machine monitoring:* Machine monitoring involves measuring an indirect weld parameter before, during, and/or after the process and comparing the measured value to a setpoint. In general, if the measured value falls outside of some predetermined tolerance, then a machine fault is signaled.
- *Process monitoring:* Process monitoring involves measuring either direct weld parameters or key in-process physical behaviors. Comparing a measured direct weld parameter to a desired setpoint is usually straightforward. For example, a good first-order indicator of weld quality and process repeatability is the final upset. Most manufacturers use the final upset as a cursory indicator of process health and product quality. Extending this further, some machine tool manufacturers monitor the axial displacement rate, (the rate of change in length with respect to time) to gain a deeper understanding into the process performance. In general, however, in situ measurement of the direct weld parameters is difficult due to accessibility and instrumentation limitations. Consequently, in-process physical behaviors such as torque, strain, acceleration, audio, or acoustic emission are used to infer various direct weld parameters. Several examples are discussed in detail in the section “Monitoring” in this article.
- *Machine control:* Machine control extends machine monitoring by implementing a closed-loop control system on one or more indirect weld parameters. Two of the more common closed-loop controllers in rotary

friction welding are spindle speed control (particularly for direct-drive machine tools) and axial load control (controlling the thrust of the ram in response to a pressure control signal).

- *Process control:* Process control extends process monitoring by implementing a closed-loop control system on one or more direct weld parameters. For example, most modern inertia friction welding machine tools can now control the final upset, and recently friction welding machine tool manufacturers have demonstrated control of the axial shortening rate (or upset profile) by modulating pressure and/or drive torque.

Ideally, closed-loop control of the heat generated at the weld interface is of great interest and importance to controlling friction weld quality and joint strength. The peak joint temperature and the temperature profile within the weld region have a significant impact on material movement, flash formation, heat and deformation zones, and joint strength. Closely related to the temperature profile is the cooling rate, which directly influences the residual-stress state developed in the weld.

Monitoring the temperature at the weld interface is both difficult and impractical for a production welding environment. However, in-process physical behaviors, such as the rate of axial shortening, can be used to infer weld quality and have been used to control weld quality in certain friction welding machine tools. Other in-process physical behaviors, such as the stick-slip phenomenon, can be used to infer heat and material flow at the weld interface. Monitoring the torque, strain, or acceleration during friction welding can yield insight into the heat and material flow at the weld interface. It can also provide feedback to anomalous processing conditions, such as fixturing inconsistencies, workpiece misalignment, material chemistry variability, or surface irregularities or contamination.

Recent process monitoring and control advances are presented in the following two sections.

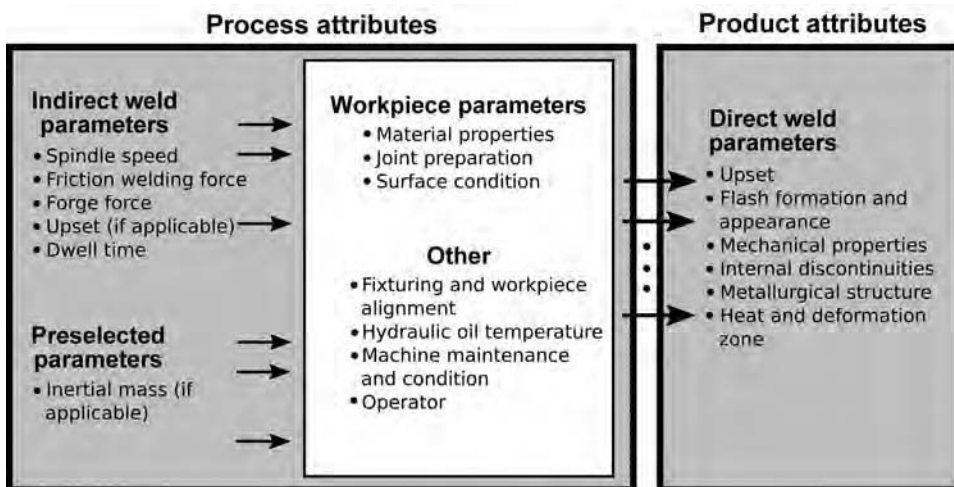


Fig. 3 The friction welding process can be separated into process and product attributes. The process attributes include those aspects of the process that the engineer has control over. The product attributes represent characteristics of the postwelded product.

Monitoring

Although friction welding is considered a highly robust and repeatable process, like all manufacturing processes, variability within the process can manifest itself as manufacturing flaws and product defects. Issues such as incoming material quality, workpiece surface finish and cleanliness, machine drift, and operator error can have a deleterious impact on the coalescence of the materials. In general, variability in the friction welding process is difficult to detect due to the inherent robustness of the process. Often, simple visual inspection or cursory examination of the process parameters reveals little information of the anomalous behavior or manufacturing flaw. In most cases, only large departures from the optimal process parameters or manufacturing conditions yield sufficient indications that there

is a problem with the process. Consequently, manufacturing flaws can potentially go undetected.

The application of postprocess destructive and nondestructive test methods is usually dictated by the standards required for the satisfactory service performance of the product. Destructive and nondestructive tests are an important part of the quality-control process that ensures products are safe. Traditionally, friction-welded parts tend to be difficult to inspect for the following reasons:

- Nondestructive test (NDT) methods normally detect gross disbands, leaving more subtle discontinuities, which could have a significant effect on fatigue life or joint fracture toughness. However, characterization of certain subtle aspects of discontinuities and macrostructures has been demonstrated for friction welds (Ref 4–7).
- The NDT methods are manually intensive, and the interpretation of their results is occasionally subjective and can be contradictory when viewed by different weld inspectors (Ref 8).
- Destructive postprocess inspection is time-consuming and costly. While the process provides reliable and quantitative assessment of the test weld, it imparts very little information about the process as a whole or any production welds in particular.

References in the open literature to nondestructive, in-process inspection date back over 50 years. The concept is not new, but the transition from research and development to commercialization has been slow up until

recently. The following sections present some of the more salient research efforts into nondestructive, in-process monitoring techniques for friction welding.

Weld Strength of Ferrous Alloys

A vein of noteworthy research into in-process quality control of friction welds was pursued by Wang and Oh. In Ref 9, Wang et al. demonstrated the feasibility of using acoustical emission (AE) as an in-process quality metric for inertia friction welding of ferrous metals. The authors correlated AE counts with joint strength for bar-to-bar (AISI 4140 to 1117 and 12L14) and tube-to-tube (AISI 1020 to 304SS) welds. The AE sensing was accomplished with a piezoelectric transducer attached directly to either the stationary chuck or the workpiece. For mild steels, the authors found two distinctive regions of AE: one during the welding process (A-zone) and the other during the cool-down portion of the weld cycle (B-zone).

The first burst of AE activity is due primarily to the plastic deformation of the material during the weld, whereas the second burst of AE activity is suspected to be a result of martensitic transformation. The authors showed relatively good correlation between the cumulative B-zone AE counts and the tensile breaking force (i.e., strength) for ferrous metals. However, their nonferrous (aluminum and copper) metal experiments resulted in no detectable B-zone AE activities, and hence, they were unable to determine weld strength.

In Ref 10 and 11, Oh et al. extended the data analysis portion of the experimental work conducted by Wang. The authors used the total

cumulative AE counts (A-zone counts + B-zone counts) as an in-process quality metric. In particular, they correlated weld strength with total cumulative AE counts and initial energy, total cumulative AE counts and total upset, and total cumulative AE counts and welding time (for direct-drive friction welding). The authors empirically derived an equation for tensile strength that can be used for in-process monitoring of friction weld strength. In Ref 12, Oh et al. correlated weld strength with IFW parameters (rotational speed, pressure, and inertia) and total cumulative AE counts. Oh et al. presented their final report (Ref 13) that correlates zone-A AE counts with weld strength.

Metallurgical Integrity of Dissimilar Metals

Friction-welded components made by joining aluminum to copper and stainless steel to copper are widely used in the electrical industry. In addition to a proper joint design and the selection of optimal welding parameters, surface preparation, including the surface finish and cleanliness prior to welding, can be critical for adequate metallurgical joint integrity. In Ref 14, Hartman et al. explored the feasibility of detecting inadequate surface preparation during IFW of stainless steel to copper.

The technique monitored the airborne audio data from the welding process using a novel, noncontact audio sensor. Four off-the-shelf electret microphones were mounted in an aluminum ring that surrounded the weld interface. The acoustic ring and an unwelded part are illustrated in Fig. 4.

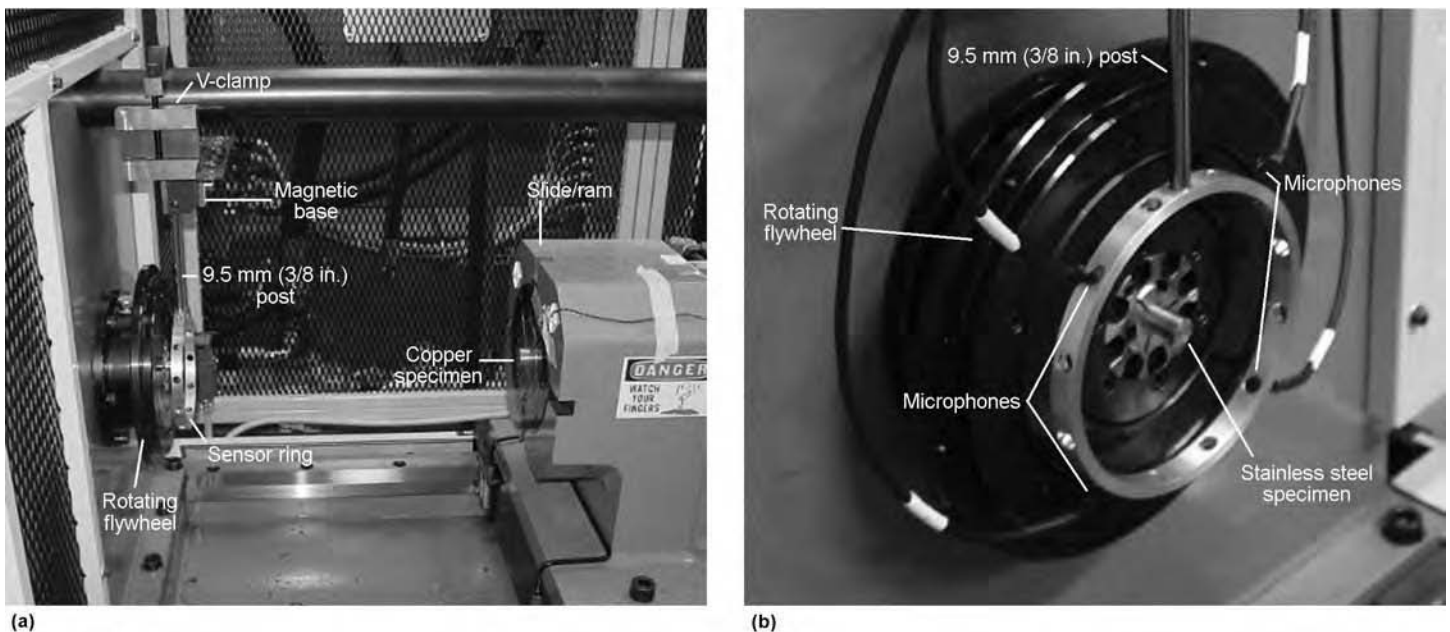


Fig. 4 The free-standing acoustic-ring assembly contains four equally-spaced microphones that surround the weld interface. For reference, a 12.7 mm (0.5 in.) diameter type 304L stainless steel bar is located in the rotating fixture of the inertia welding machine.

An experimental matrix was devised in which the resulting welds would fall into one of two bond integrity categories: acceptable or unacceptable. An acceptable weld is defined as one in which the majority of the interfacing surfaces are bonded. An unacceptable weld is defined as one in which no or little bonding at the surfaces exists.

The study welded 2.54 cm (1.0 in.) diameter oxygen-free high-conductivity copper bar to 1.27 cm (0.5 in.) diameter annealed type 304L stainless steel bar. Approximately three weeks before welding, each specimen was given a

preliminary finish cut to ensure a faying surface finish of 0.81 μm (32 $\mu\text{in.}$). The welding parameters remained constant throughout the investigation.

During the experimental welding portion of the investigation, the faying surfaces of selected copper specimens were machined immediately before welding while bathed in isopropyl alcohol. Others were welded as-is, that is, without further machining to remove surface oxidation that may have occurred while at ambient temperature and pressure for up to five weeks prior to welding. In all cases, the stainless steel was

rotated during the weld cycle, while the copper remained fixed.

Destructive testing of each weld was accomplished using an unguided bend test. The as-welded, full-sized specimens were tested. Following the fracturing of each specimen, image analysis was used to quantify the percent of bonded area. A total of 23 welds were considered in this study.

Although the experimental matrix was designed with only one variable in mind (surface preparation of the copper), three different bond integrity categories were generated:

- *Acceptable*: Bonded area is approximately 100%.
- *Conditional*: Bonded area is less than 100% but greater than 5%.
- *Unacceptable*: Bonded area is less than 5%.

Table 2 Unguided bend test results

Weld No.	Surface condition before welding	Bond quality	Bonded area, %
1–12	Freshly machined	Acceptable	100
13	Freshly machined	Conditional	80
14	Freshly machined	Conditional	70
15	Freshly machined	Conditional	69
16	Freshly machined	Conditional	67
17	Freshly machined	Conditional	54
18	Freshly machined	Conditional	26
19–23	Freshly machined	Unacceptable	0

Although the experimental matrix was designed with only one variable in mind (surface preparation of the copper), three different bond integrity categories were generated: acceptable, conditional, and unacceptable. The conditional welds were prepared in the same manner as the acceptable welds, which demonstrates the difficult and sensitive nature of joining these two materials. The weld numbers are ordered in the table for illustrative purposes, while the experimental matrix was conducted in a random order.

The conditional welds were prepared in the same manner as the acceptable welds, which demonstrates the difficult and sensitive nature of joining these two materials. Table 2 shows the results from the experimental matrix.

Figure 5 illustrates the typical flash and fracture surface for each category of weld. All specimens exhibited a symmetric flash with a light-golden color. The amount of upset (or reduction in length) was approximately

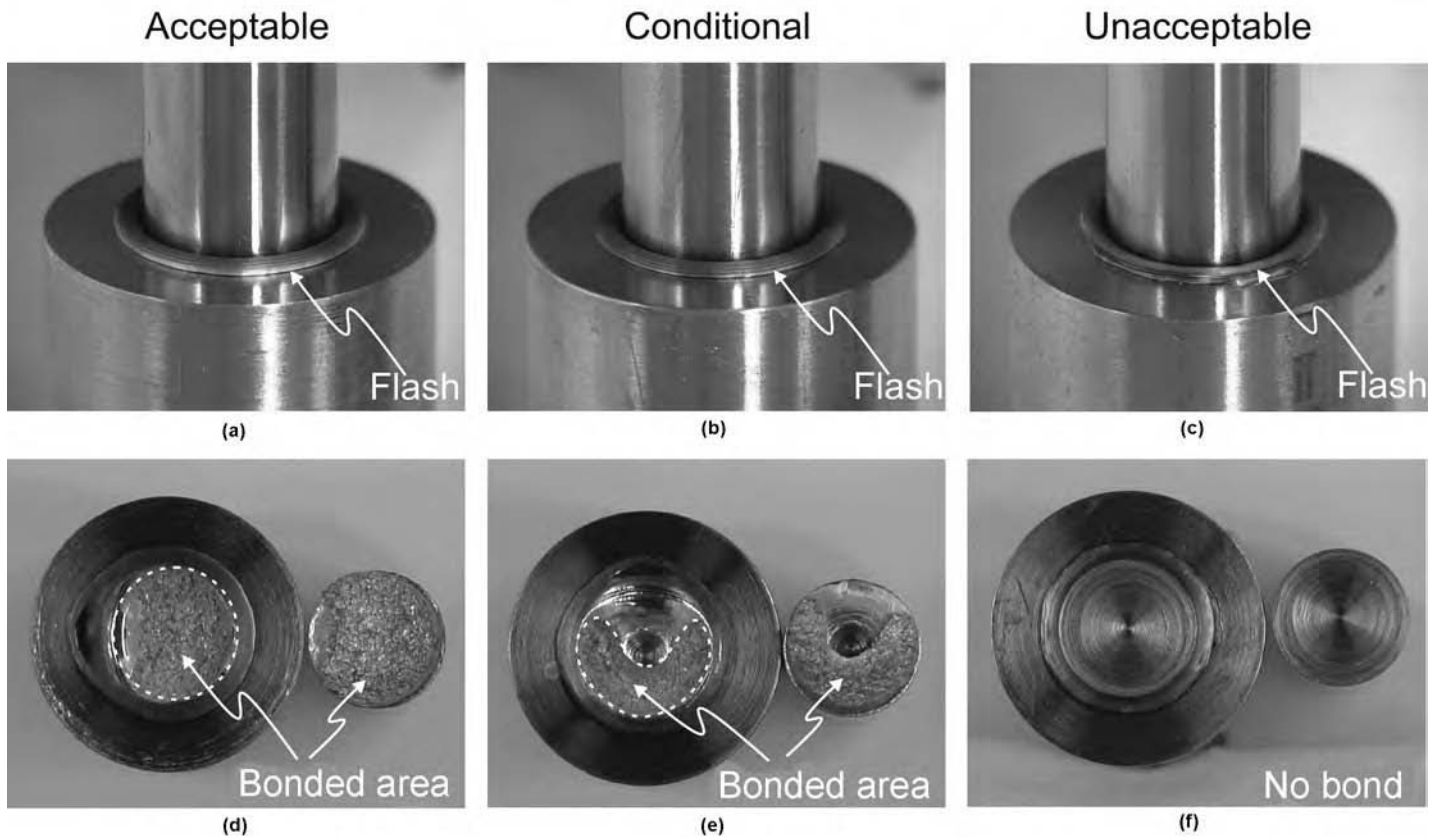


Fig. 5 The surface cleanliness of the copper was the only variable in the 23-weld experimental matrix, yet three different categories of bond quality were produced. All specimens exhibited a symmetric flash with a light-golden color. The amount of upset was approximately the same across all three categories. A total of 18 welds were freshly machined, while 5 welds were purposely left oxidized. All 5 oxidized welds yielded unacceptable bond quality, and 6 of the 18 freshly machined welds produced conditional bond quality. A conditional weld occurred intermittently even though the surface preparation was the same as an acceptable weld. The intermittent conditional bond quality demonstrates the difficult and sensitive nature of joining these two materials.

equal across all specimens and predominantly occurred in the copper. Moreover, the fact that the upsets were approximately equal, yet yielding acceptable, conditional, and unacceptable welds, suggests that upset alone is an insufficient measure of bond quality for this particular material combination.

A neural network was used to explore and discover structure within the audio data frequency content that may correlate with bond integrity. Due to the small experimental set, a single hold-out method was used to train and test the learning and classification capabilities of the neural network over a wide range of temporal and spatial aspects of the data. The results indicate that differences in the surface finish of the copper can be seen in the audio data.

Ferrite Formation of Stainless Steel Alloys

Austenitic stainless steels (γ -SSs) are widely used in chemical processing and petroleum refining applications due to their corrosion-resistance properties. Inertia friction welding is a solid-state joining process that can be used for welding a wide variety of components, and it generally works well for stainless steel alloys. The thermomechanical cycle experienced during IFW of some γ -SSs can lead to the formation of the body-centered cubic ferrite phase along the bondline. The presence of ferrite along the bondline can create concern regarding the mechanical and corrosion properties of the resulting weldment. In Ref 15 and 16, Hartman and Lienert investigate the feasibility of detecting the presence of ferrite during the microstructural evolution of IFW of three austenitic stainless steels.

Three stainless steels were chosen for this study: 310, 304, and 255. The 310 and 304 alloys are considered to be austenitic stainless steels, while the 255 alloy is a duplex (50% austenite and 50% ferrite) alloy. Five inertia friction welds were produced on 2.54 cm (1.0 in.) outside diameter tube samples (3.175 mm, or $\frac{1}{8}$ in., wall thickness) of each alloy using a Manufacturing Technology, Inc. model 90B machine. All welds used the same initial energy of approximately 15.3 kJ. Welds were made at three levels of forge pressure and three combinations of $\langle I \rangle$ (moment of inertia) and (revolutions per minute) to give the same initial energy.

A noncontact, audio-based, free-field microphone Brüel & Kjør-type 4939 was mounted several inches away from the weld zone and recorded the acoustic energy (in the form of sound pressure) that emanates from the friction welding process. The audio data were sampled at 50 kHz to account for potential signal content above a human's nominal audible sound sensitivity. The sensor sensitivity and the amplifier gain settings remained constant throughout the experimental effort. High-speed video was also collected synchronously with

the audio data in an attempt to correlate the audio data with the physical mechanisms of the IFW process.

The three alloys exhibited distinct acoustic signatures versus time. Examples of representative signatures are shown in Fig. 6 to 8. The audio data for the 255 alloy showed an initial small acoustic burst at the beginning of the weld cycle and remained relatively quiet thereafter. For the 304 alloy, acoustic bursts were found at the start and finish of each weld, with a quiet period in between. The 310 alloy exhibited the most energy of the three alloys, with acoustic content throughout the entire weld cycle and higher amplitude spikes at the start and finish.

For all three alloys, the amplitude and duration of the bursts and quiet periods varied

slightly with changes in welding parameters. For example, the amplitude and duration of the bursts increased with increasing pressure. The majority of the frequency content was found to be predominantly in the 20 to 25 kHz range.

In summary, the three alloys exhibit distinct acoustic signatures versus time that varied slightly with changes in welding parameters. The bursts appear to correlate temporally with features of the torque curve. The differences in acoustic signatures for welds made on the different alloys using identical welding conditions likely stem from differences in the acoustic, thermophysical, and thermomechanical properties between the alloys. This technique may prove useful for determining the phase balance of the weld region after welding and for predicting weld quality in situ.

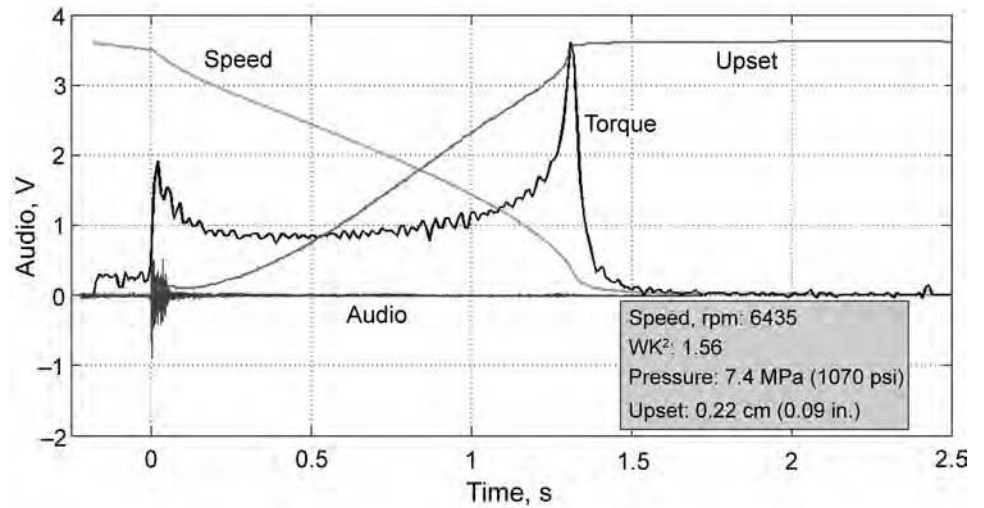


Fig. 6 The acoustic signature and machine data from a 255 dual-phase stainless steel alloy inertia friction weld. Most of the acoustic energy occurred during initial contact. The weld was relatively quiet thereafter.

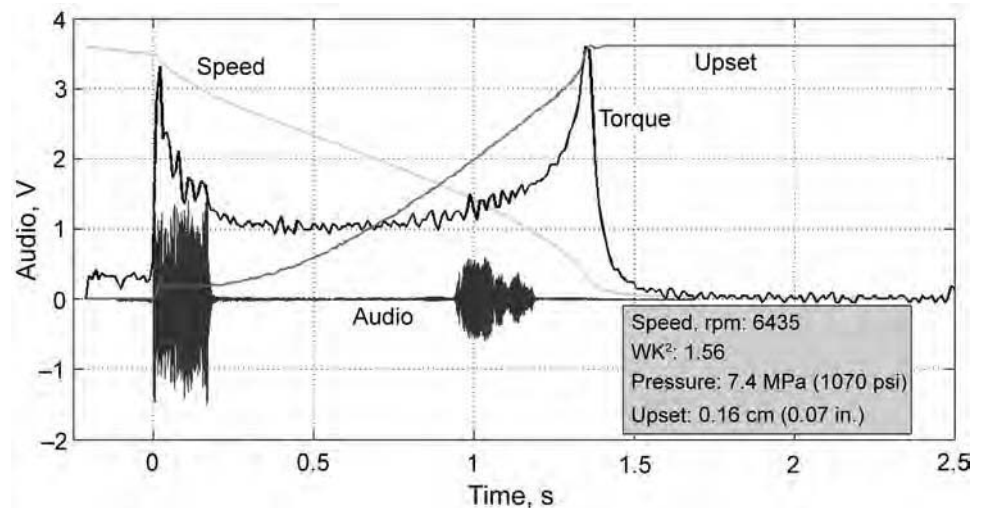


Fig. 7 The acoustic signature and machine data from a 304 stainless steel alloy inertia friction weld. The majority of the acoustic energy occurred at the beginning and end of the weld, with a quiet portion in between.

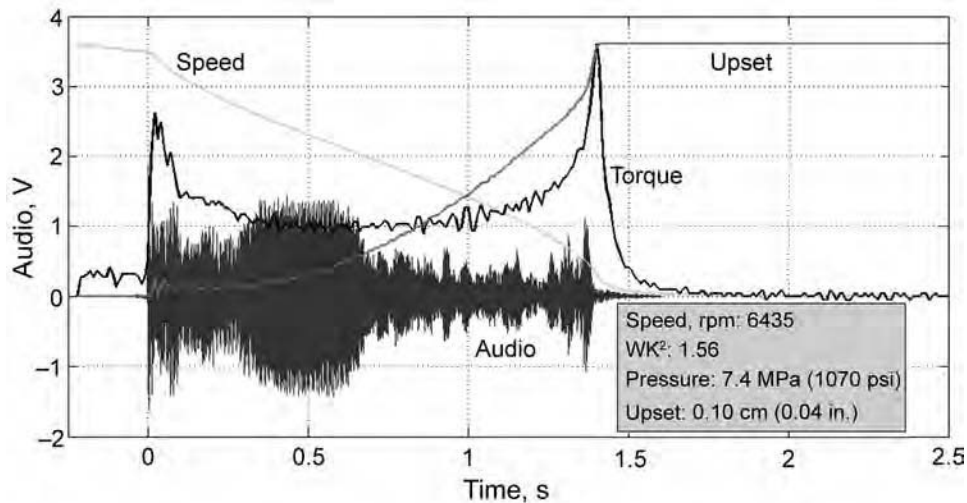


Fig. 8 The acoustic signature and machine data from a 310 stainless steel alloy inertia friction weld. The 310 stainless steel alloy generated the most acoustic energy of the three alloys. Unlike the 304 stainless steel alloy, this material exhibited a relatively loud burst of energy in the middle portion of the weld and was generally “noisy” throughout the entire process.

Control

Over the past 50 years, friction welding machine tools have seen an increase in precision and an overall improvement in machine control due to the introduction of high-performance embedded computers and micro-controllers for closed-loop feedback control and improvements in electric motors, servos, and encoders. The basic premise behind a friction welding machine control algorithm is to monitor and control the speed, pressure, and upset to provide assurance of the quality of the weld. Most machine tool controllers provide a fault indication should any of these values stray outside of some predetermined range within which a good quality weld can be assured.

Shortcomings that were once considered limitations of the friction welding process, such as control of the final rotational position of a rotating component with respect to the stationary workpiece or excessive tolerance in the final upset length, are now possible with high-precision sensing, fast-acting actuators, and closed-loop control algorithms. Yet, much of the work in machine and process control is proprietary. The specific details are closely guarded as secret intellectual property, which enables the machine tool manufacturers and certain end-users to maintain an advantage in a competitive market. Consequently, very little work is disclosed in the open literature.

Nevertheless, research and development in the area of process control is on-going by machine tool manufacturers and friction welding end-users (primarily aerospace companies). Improved control of the final upset length and rate-dependent control of the upset trajectory are now possible because of sophisticated

machine tool controllers that can manipulate a multiaxis machine element along a complex three-dimensional path at constant velocity. Research is also being performed in improving the weldability of dissimilar alloys by matching ductilities during welding through heating and/or cooling one component and/or the other.

In-Process Quality Control

The friction welding process usually lasts no more than a couple of seconds. During this time, a seasoned operator is listening to the process. After many years of experience, a knowledgeable operator can distinguish a “good” from a “bad” weld based strictly on the sound produced. The terms *good* and *bad* are commonly used on the production floor by the operator. In particular, the operator may say, “That was a good weld” or “That weld did not sound right.” From a manufacturing behavioral perspective, the operator is suggesting that the process did not generate the typical sounds to which he/she has grown accustomed. The terms *good* and *bad* are used loosely here to convey anomalous behavior and not to imply that the part is defective. Although the operator may be unable to articulate why the weld is different, he or she instinctively knows when the process sounds different. Unfortunately, these anecdotal observations carry little clout with process engineers and production floor managers.

The welding operator’s years of experience and intuitive knowledge about the process represents an undeveloped and largely overlooked aspect of manufacturing quality control. While time and resources are devoted to training and qualifying operators, calibrating and

qualifying machines, developing qualified procedures, and implementing sophisticated destructive and nondestructive test methods, in-process quality control remains absent from mainstream quality-control practices and exists only in isolated research and development activities. Generalizing upon and automating a human’s innate ability to sense, store, recall, and distinguish anomalous weld behavior can provide a significant leap forward in current manufacturing quality-control practices.

In-process quality control is based on the premise that most in-process physical behaviors of a manufacturing process can and should be regarded as process quality feedback. In-process monitoring relies on the systematic analysis and investigation of manufacturing behavior through controlled and naturalistic experimental observations and rigorous formulations. The end result is a nondestructive, in-process monitoring solution for manufacturing quality control. The in-process monitoring solution embodies a decision process and communication strategy for real-time, nondestructive, in-process manufacturing quality feedback.

The in-process monitoring research that was presented in the section “Monitoring” in this article was conducted with a narrow focus on a single process or product attribute:

- Correlate AE with joint strength
- Correlate audio with surface cleanliness and infer bond integrity
- Correlate audio with ferrite formation

The well-focused approach makes for a strong technical paper, but it overlooks the broader implications that in-process quality control can have on the current manufacturing quality-assurance and quality-control paradigm. From a more general perspective, monitoring the manufacturing behavior complements the current quality-control approaches that have already been engineered into a manufacturing process.

Traditional manufacturing quality-assurance and quality-control strategies prevent flaws from becoming defects by tightening tolerances and/or increasing postprocess destructive and nondestructive testing. However, the danger of experiencing a defect in-service can never be argued or strategized away. Machine tool manufacturers are continually improving machine control and tightening process tolerances in an effort to minimize process variability and to ensure high-quality product. In-process monitoring is a developing capability that has the potential to offset an overreliance on postprocess destructive and nondestructive testing. As in-process monitoring gains wider acceptance, the logical next step is for the machine tool manufacturer to implement closed-loop control on key in-process variables. Closed-loop control of key in-process variables will enhance the friction welding process robustness by sensing minor process variabilities and adjusting certain IWP to ensure compliance with the desired DWP.

REFERENCES

1. M. Rao and T.H. Hazlett, A Study of Mechanisms Involved in Friction Welding of Aluminum Alloys, *Weld. J.*, Vol 49 (No. 4), April 1970, p 181s–188s
2. K.K. Wang, Friction Welding, *Weld. Res. Counc. Bull.*, Vol 204, April 1975, p 1–21
3. G.E. Cook, Feedback and Adaptive Control in Automated Arc Welding Systems, *Met. Constr.*, Vol 13 (No. 9), Sept 1981, p 551–556
4. P.B. Nagy and L. Adler, Ultrasonic NDE of Solid-State Bonds: Inertia and Friction Welds, *J. Nondestruct. Eval.*, Vol 7, 1988, p 199–215
5. P.B. Nagy and L. Adler, Ultrasonic NDE of Solid-State Bonds, *Mater. Eval.*, Vol 50, 1992, p 1328–1337
6. P.B. Nagy, T.J. Lienert, L. Adler, and W.A. Baeslack III, Novel Nondestructive Evaluation Techniques for Inertia-Friction Welds in a SiC-Reinforced High-Temperature Aluminum Alloy, *Review of Progress in Quantitative Nondestructive Evaluation*. D.O. Thompson and D.E. Chimenti, Ed., Vol 14, Plenum Press, New York, NY, 1995, p 1545–1552
7. T.J. Lienert, P.B. Nagy, and W.A. Baeslack III, Ultrasonic Characterization of Microstructures in Inertia Friction Welds on SiC-Reinforced 8009 Aluminum, *Weld. J.*, Vol 77 (No. 1) Jan 1998, p 14s–28s
8. M. Lozev, “Validation of Current Approaches for Girth Weld Defect Sizing Accuracy by Pulse-Echo, Time-of-Flight Diffraction and Phased Array Mechanized Ultrasonic Testing Methods,” Tech. Rep. 45066CAP, Edison Welding Institute, 2002
9. K.K. Wang, G.R. Reif, and S.K. Oh, In-Process Quality Defection of Friction Welds Using Acoustic Emission Techniques, *Weld. J.* Vol 61 (No. 9), Sept 1982, p 312s–316s
10. S.K. Oh, A. Hasui, T. Kunio, and K.K. Wang, Effects of Initial Energy on Acoustic Emission Relating to Weld Strength in Friction Welding, *Trans. Jpn. Weld. Soc.*, Vol 13 (No. 2), Oct 1982, p 15–26
11. S.K. Oh, J.H. Oh, T.E. Jeon, and S. W. Oh, Development of Real-Time Quality Evaluation of Friction Welding by Acoustic Emission: Report 1, *Proceedings of the Fifth International Offshore and Polar Engineering Conference*, Vol 4, June 11–16, 1995 (The Hague, The Netherlands), The International Society of Offshore and Polar Engineers, p 163–168
12. S.K. Oh, J.H. Oh, and H.K. Chang, Development of Real-Time Quality Evaluation of Friction Welding by Acoustic Emission: Second Report, Effects of Welding Parameters on Weld Strength and AE, *Proceedings of the Sixth International Offshore and Polar Engineering Conference*, Vol 4, May 26–31, 1996 (Los Angeles, CA, USA), The International Society of Offshore and Polar Engineers, p 177–184
13. S.K. Oh, H.D. Park, and B.S. Lee, Development of Real-Time Quality Evaluation of Friction Welding by Acoustic Emission: Third Report, Effects of Initial AE Counts during Plastic Deformation in FRW, *Proceedings of the Seventh International Offshore and Polar Engineering Conference*, vol 4, May 25–30, 1997 (Honolulu, HI, USA), The International Society of Offshore and Polar Engineers, p 535–540
14. D.A. Hartman, M.J. Cola, V.R. Davé, N.G. Dozhier, and R.W. Carpenter, Non-destructive, In-Process Inspection of Friction Welding: An Investigation into a New Sensing Technique, *Trends in Welding Research, Proceedings of the Sixth International Conference*, H.B. Smartt, J.A. Johnson, and S.A. David, Ed., April 15–18, 2002 (Callaway Gardens, Georgia, USA), ASM International
15. D.A. Hartman, T.J. Lienert, W.L. Stellwag, Jr., M.J. Cola, V.R. Davé, I.E. Brazil, and J.D. Puskar, Acoustic Monitoring of Inertia Friction Welded Austenitic Stainless Steels: Initial Studies, *86th Annual AWS Convention, Abstracts of Papers*, Nov 13–18, 2005 (Chicago, IL)
16. T.J. Lienert, W.L. Stellwag, Jr., D.A. Hartman, R.E. Hackenberg, J.D. Puskar, and P.W. Hochenadel, Process Results and Microstructural Evolution of Inertia Friction Welded Austenitic Stainless Steels: Initial Studies, *86th Annual AWS Convention, Abstracts of Papers*, Nov 13–18, 2005 (Chicago, IL)

Development of Welding Procedures for Friction Stir Welding

Kevin J. Colligan, Concurrent Technologies Corporation

THE DEVELOPMENT of a welding procedure is one of the most important steps in implementation of a welding process in a production application. Procedure development can be systematically achieved by clearly defining the requirements of the procedure and the test plan, by executing the required testing and analyzing the results, and by fully documenting the testing performed and the results obtained. Successful procedures in similar materials can suggest a starting place for developing the welding tools and key process parameters for new procedures. By thoroughly testing and documenting procedures for friction stir welding (FSW), problems during production use of the process can be minimized by determining the robustness limits of the process, the properties of the welded joint, the required equipment capabilities, and the tool and fixture designs.

In its simplest form, the development of a welding procedure is simply a matter of determining the technical parameters that produce a sound weld in a given material. However, this is most often an insufficient basis for defining a procedure for production of commercial products. More commonly, development of a welding procedure involves establishing the robustness of the welding process, the properties of the welded joint, the required equipment capabilities, the tool and fixture designs, and the economic justification for using the procedure. The complexity of procedure development can also be increased by the requirements of applicable specifications or regulations based on the end use of the procedure, which may have special rules for testing and record keeping. The development of a welding procedure includes the process of discovering the technical parameters for consistently producing a sound weld, as well as the development and analysis of all of the necessary supporting data to satisfy the applicable requirements and to ensure the reliability of the procedure.

The route to commercial production for products involving a welding process can take many paths, but commonly it involves development of a preliminary product design, iteration between detail design and procedure development,

procedure qualification, work instruction development, and operator training and qualification. This article mainly concentrates on the development of procedures for FSW and touches on procedure qualification but does not address joint or product design and does not discuss the development of work instructions or other production qualification activities. It is also assumed that the reader has a working knowledge of FSW technology.

Procedure development is best viewed as an evolutionary process, where the welding process is initially demonstrated, evaluated, improved, tested further, and finally qualified for use. Iteration through these steps is common, as results of testing suggest new approaches. The development process may include the following steps:

- *Preliminary welding trials:* Show that a sound weld can be made
- *Systematic welding trials:* Explore the range of key process parameters
- *Robustness testing:* Evaluate welding performance subjected to procedure variability

These three sets of welding experiments are intended to optimize the welding process in an orderly way, minimizing the cost of procedure development by essentially learning to “crawl before walking.” This process also will help the introduction of a new welding process to the production environment by establishing reasonable expectations for each step of procedure development. The preliminary welding trials are not intended to yield optimum results, just a sound weld of any kind. Having done that, work can move on to systematically exploring key process parameters to find a combination of parameters that gives maximum joint performance. This can then be followed by tests to evaluate performance with some degree of production variability, such as joint misalignment. It should be noted that as these steps progress, there may be test results that indicate returning to an earlier step and making changes to the tool design or process parameters. For example, if the procedure is found to have very low

tolerance to joint-tracking errors (lateral offset of the joint relative to the tool), then the pin diameter may need to be increased and the preliminary and systematic welding trials repeated. More details on the overall process of procedure development are presented in Fig. 1 and in the paragraphs that follow.

The development of a welding procedure, starting with no prior experience with welding a given material, can be very challenging. Although FSW is a comparatively simple welding process, even a small number of process variables can quickly lead to a multitude of potential welding procedures. One objective of this article is to equip the reader with a summary of published procedures to suggest a starting point for new work. With this information in hand, the welding engineer may minimize the trial-and-error effort often associated with development of an FSW procedure. Preliminary welding trials are intended to simply demonstrate that sound welds can be produced. At this stage of the development, there may be a number of candidate welding tool designs that are evaluated, and one or more may yield acceptable results and be selected for follow-on testing.

Once a preliminary welding procedure has been demonstrated, the next phase of welding procedure development should be a process of systematically exploring the range of welding parameters to see their effect on basic joint properties appropriate to the end usage of the welded component. A detailed plan should be written, describing all of the detailed activities needed for optimizing the welded joint properties. Most often, these properties include tensile strength, yield strength, and ductility. Metallographic analysis is also useful for examination of the internal structure of the weld. Postweld aging or other treatments may also require development. After analyzing all of these various data, the welding engineer can select a welding procedure for producing test articles for more extensive testing, the results of which may influence the final detail design of the product.

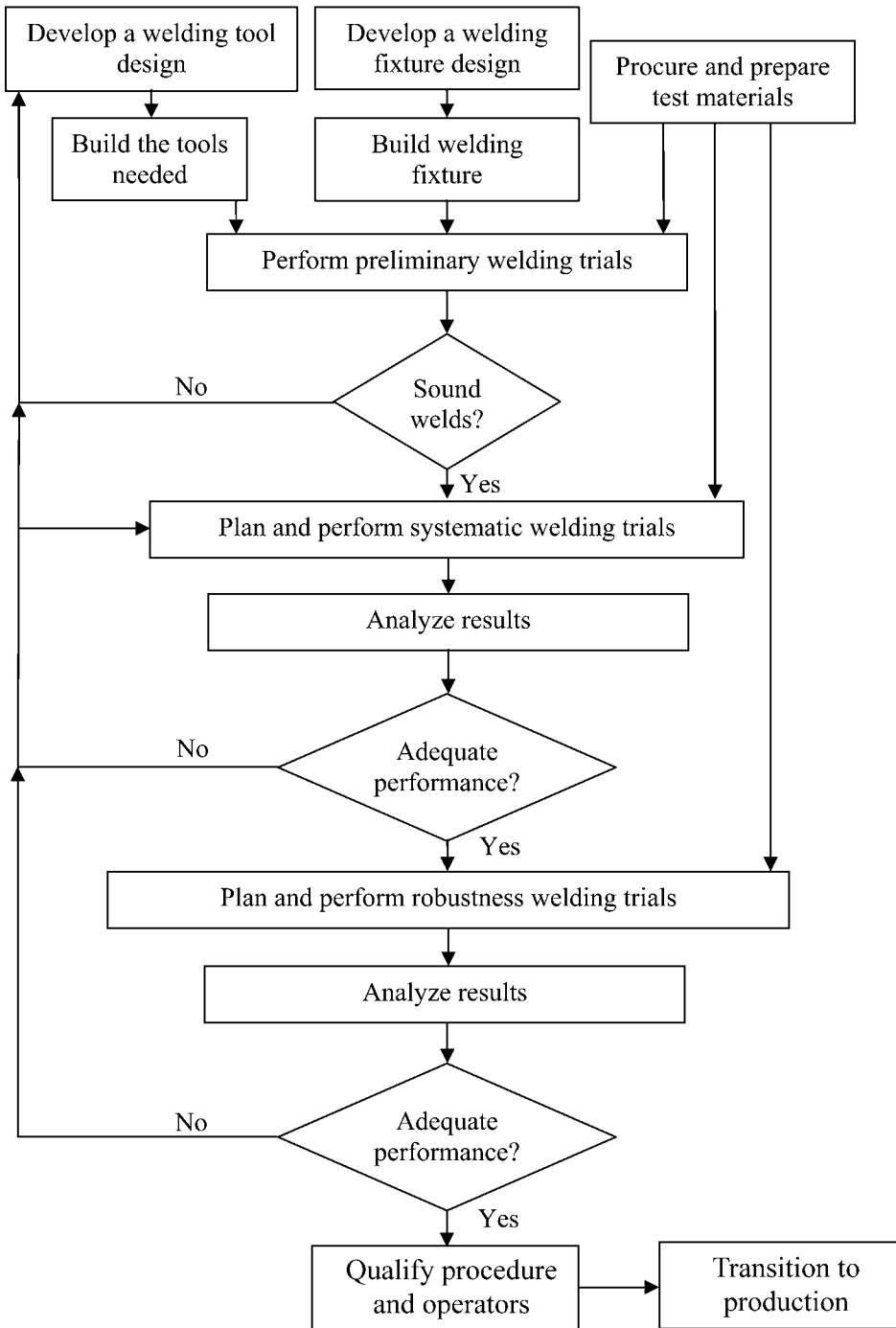


Fig. 1 Flowchart of welding procedure development steps

Robustness testing is intended to assess performance of the welding procedure when subjected to the process variability that inevitably occurs during production. The welding procedure parameters that are most subject to in-process variability are tested at the limits of their expected variation, confirming that the welding procedure is sufficiently robust. If any of these tests fail, the decision can be made to

improve the welding process, improve in-process controls, or both.

Prior to being finalized in many applications, such as safety- or mission-critical applications, the procedure will require formal qualification testing. Here, the weld procedure is used to produce welded materials and/or representative production parts and tested according to the rules established in published specifications

(Ref 1–5). Data from this testing provide assurance of the viability of the procedure for the associated application relative to accepted specifications. Assuming that these requirements are met, the procedure becomes accepted as a qualified procedure for use in production of the part.

This article details the development of a welding procedure, including the process of defining a preliminary procedure, the optimization of parameters, the development of supporting data, and other key features to ensure a successful procedure. The process of welding procedure qualification is also described, although this discussion must necessarily be generalized based on the variety of requirements for qualification from industry to industry and, over time, within an industry.

Procedure and Procedure Development Requirements

Clearly defining the associated requirements is an important first step in developing a welding procedure. For example, a welding procedure developed for an aerospace application, where safety of flight may be an issue, requires more testing than procedures developed for less demanding applications. By first defining the requirements for procedure development, adequate testing can be planned and efficiently executed, and the associated cost can be estimated in advance.

Important questions to ask during procedure development planning include the following:

- What is the alloy and its product form, temper, and thickness?
- What is the joint design? What is the geometry of the production part?
- What will be the condition of the workpiece material presented for welding? Will pre-weld processing be required, such as cleaning, oxide removal, edge trimming, and so on?
- Is there a required production rate for economic justification? Is there a known maximum acceptable cost per unit length of weld?
- What are the performance requirements for the joint? This should be broadly interpreted to include strength, ductility, fatigue performance, corrosion, toughness, and stress-corrosion cracking.
- What are the cosmetic requirements for the joint? Is it necessary to have a specific final surface condition?
- Is there a required welding tool life? Is there a known limitation on the cost of the welding tool?
- Will postweld aging or other treatment be required?
- Will formal qualification of the procedure be required? What are the requirements for the qualification? Will it be necessary to qualify using a production-representative

workpiece, or can test panels be used in the qualification?

- Will production welding be done on a known fixture, or will the fixture be designed later? Will it be possible to simulate the production welding fixture during procedure development?
- What style of FSW will be employed? Will it be conventional FSW, on a welding fixture with an anvil, or bobbin FSW, on a fixture with no anvil?
- What are the capabilities and limitations of the FSW equipment to be used for production?

A second step in developing a welding procedure is establishing what information is needed to completely define the procedure. The goal is to specify all of the important variables related to the process so that the qualified procedure can be replicated in production. Some specifications for welding refer to this list as essential elements (Ref 1). The following list provides a starting point for developing the essential elements for an FSW procedure, although the details of each procedure may require modification of this list:

- Base-metal specification (alloy, temper, product form)
- Base-metal thickness (nominal and range)
- Base-metal orientation relative to prior processing of the workpiece (for example, rolling direction)
- Joint design (joint type, allowable mismatch, allowable gap)
- Welding tool design (including material)
- Joint preparation (cleaning procedure, oxide removal procedure)
- Welding equipment (make and model of welding machine)
- Fixture design (anvil cross section and material, clamping arrangement and parameters)
- Welding parameters (spindle speed, travel speed, rotation direction, tool tilt angle, etc.)
- Welding tool pin length or length range for adjustable pin tools
- Tool axial position control method (load control or position control)
- Tool axial position relative to workpiece or anvil (such as the heel plunge depth or pin/anvil gap)
- Tool axial force (for axial load control method)
- Auxiliary heating or cooling method and parameters, if used
- Postweld processing (surface modification, heat treatment, etc.), if used

In developing a welding procedure, it is important to keep a record of all of the essential elements used for each weld, along with other suitable notes, so that the procedure can be reliably repeated. An example welding procedure record is shown in Table 1. The weld identification number can be used to refer to the welding procedure record. Using this type of form for each weld produced during process development should ensure

complete definition of the welding conditions and make procedure qualification and transition to production much easier.

Procedure Development

In this section, critical features of FSW tool design, initial process parameters, systematic welding trials, and robustness testing are discussed.

One of the most challenging aspects of FSW is the control of the welding tool depth in the workpiece. There are two aspects to this requirement. First, the welding tool shoulder contact with the workpiece surface must be regulated to give consistent heat generation and weld consolidation. Second, the welding tool pin depth must be controlled to maintain close proximity to the anvil,

a requirement for full penetration of the weld. Of course, this does not apply to bobbin-style FSW, in which the pin passes completely through the workpiece. For conventional, single-sided FSW, the maximum pin-to-anvil gap may be from 0.25 to 1.0 mm (0.010 to 0.040 in.), depending on the design of the pin and its ability to project plastic deformation beyond its end. The base-metal properties and other process conditions may also influence weld penetration. These tight tolerances on the pin-to-anvil gap make it clear that the relationship between the welding tool pin length and the workpiece thickness is a very important one.

The variables related to welding tool pin length and workpiece thickness are listed as follows and are shown schematically in Fig. 2 and 3:

Table 1 Example welding procedure record

Welding Procedure Record			
Description:			
		Material Data	
Weld ID		Advancing Side	Retreating Side
Equipment		Alloy	
Program		Lot	
Test Engineer		Temper	
Test Plan		Thickness	
Operator		Identification	
Date		Dimensions	
		Orientation	
Tool Data		Fixture Data	
Welding Tool ID		Fixture ID	
Tool Type		Clamp Spacing	
Shoulder Dia.	in	Clamp Pressure	psi
Shoulder Config.			
Pin Config.		Joint Preparation	
Thread Pitch	th/in		
Pin Dia.	in	Axial control mode	
Pin Length	in	Auxiliary heating	
Pin End Radius	in	Auxiliary cooling	
Joint Geometry			
Plunge Parameters		Notes	
Plunge Depth	in.		
Plunge Rate	in/min		
Spindle Speed	rpm		
Plunge Force	lbs.		
Dwell	s		
Tilt	deg		
Main Segment			
Plunge Depth	in		
Spindle Speed	rpm		
Travel Speed	in/min		
Plunge Speed	in/min		
Plunge Force	lbs		
Weld Length	in		
Tilt Angle	deg		
Termination			
Retract Rate	in/min		

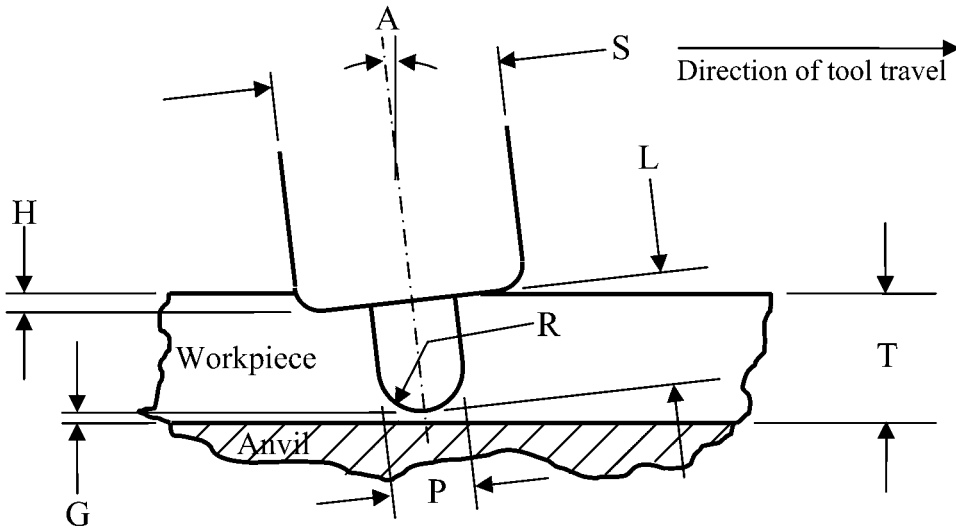


Fig. 2 Schematic of friction stir welding tool, anvil, and workpiece for spherical-tipped pin and tilted tool axis, side view. See text for an explanation of the variables.

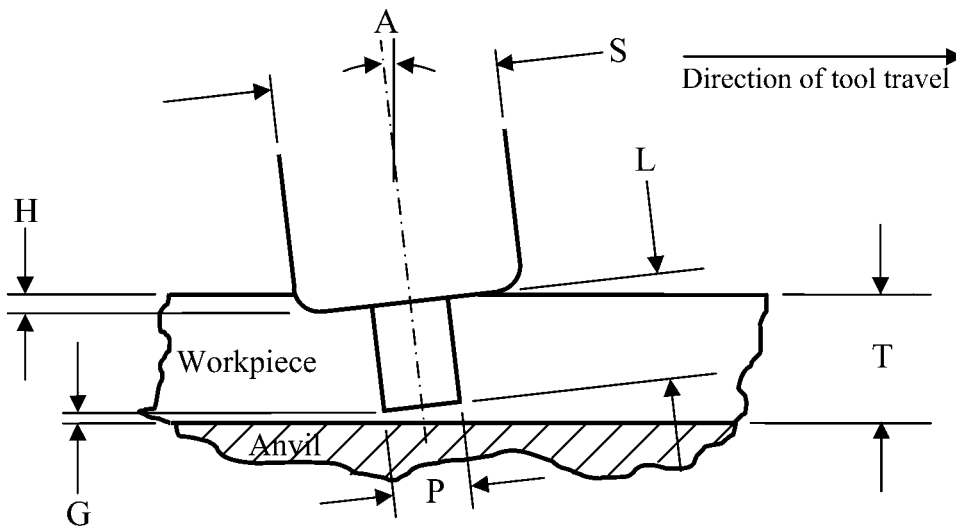


Fig. 3 Schematic of friction stir welding tool, anvil, and workpiece for flat-tipped pin and tilted tool axis, side view. See text for an explanation of the variables.

- A = tool tilt angle
- G = pin/anvil gap
- H = heel plunge depth
- L = pin length
- P = pin diameter
- R = pin tip radius
- S = shoulder diameter
- T = workpiece thickness

The equations for calculating the pin length, given the other variables, are presented as follows. For welding tools with a spherical tip, the pin length is calculated as:

$$L = R + \frac{T - G - H - R + \frac{S}{2} \sin A}{\cos A}$$

For a welding tool with an essentially flat tip, the pin length is calculated as:

$$L = \frac{T - G - H + (\frac{S}{2} - \frac{P}{2}) \sin A}{\cos A}$$

It should be noted that the radius for the spherical-tipped pin can be greater than half the diameter of the pin, as long as the lowest point of the pin tip is on the radius portion, not on the corner of the pin. In the latter case, which occurs when A is greater than $\sin^{-1}(P/2R)$, use the equations for the flat-tipped pin, counting the pin length as the distance from the shoulder to the corner of the pin, which does not include the length of the radius at the pin tip.

It should also be noted that in the equations for calculating the pin length, the heel plunge distance is a factor. However, the appropriate heel plunge depth for optimum weld performance is difficult to know without some preliminary welding experiments. A good starting point may be:

$$H = 0.7 * S * \sin A$$

For welding tools that are operated with the welding tool axis normal to the plane of the workpiece, the calculation of pin length is greatly simplified. These tools are operated with the shoulder surface flush to the workpiece surface, so the pin length is simply the workpiece thickness (T) minus the pin/anvil gap (G).

During procedure development, it is easiest to start with a known welding procedure in an alloy/thickness combination that is similar to the workpiece of interest. The list of welding procedures presented in Table 2 is the result of an analysis of published reports in which sound welds were described for aluminum alloys. Although the procedures may or may not be optimized, they were at least reported to produce sound welds. It is rare to find complete details related to welding procedures in the literature, so this summary covers publications where sufficient detail was given to afford a reasonable indication of how the welds were produced. The data in Table 2 can be used to learn about the design of welding tools. Dubourg and Dacheux (Ref 6) analyzed the literature and compiled welding procedures for FSW of aluminum materials between 1 and 8 mm (0.04 and 0.32 in.) in thickness. They reported statistical relations between workpiece thickness and shoulder diameter and between workpiece thickness and pin diameter. Following their approach, the data from Table 2 can be used in a similar way, as shown in Fig. 4 and 5. It is interesting that the relationship between workpiece thickness and shoulder diameters shows that when a broad range of workpiece thickness is analyzed, a bilinear relationship emerges, with the transition point being at approximately 8 mm (0.32 in.) thickness. This reflects the way in which heat generation by the shoulder plays a lesser role in thick-section FSW, because its ability to influence heating through the full material thickness diminishes with increasing workpiece thickness. These charts can be used to determine a starting point for the welding tool shoulder and pin diameters for a given workpiece thickness.

Once the welding tool shoulder and pin diameters are selected, other tool design features must be established (Ref 40). Welding tools for aluminum alloys typically include thread-shaped features that are designed to drive workpiece material away from the shoulder, toward the anvil, during welding. The pin design may also include flats or other reentrant features cut into the threaded profile, typically for the purpose of increasing transport of workpiece

Table 2 Procedures used in the production of sound friction stir welds in various aluminum alloys

Alloy and temper	Tool type	Shoulder diameter, in. (mm)	Pin diameter, in. (mm)	Workpiece thickness, in. (mm)	Plunge force or heel plunge depth	Tool rotational speed, rev/min	Tool travel speed, in./min (mm/s)	Tool tilt angle, deg	Ref
1050-H14	Pin: hardened steel Shoulder: hardened steel	0.787 (20)	0.224 (5.7)	0.236 (6)	not specified	400	2.36 (1)	not specified	7
1100-O	Pin: H13, cylindrical, threaded Shoulder: H13, smooth	0.750 (19.1)	0.250 (6.35)	0.250 (6.35)	not specified	1,200	23.00 (9.7)	not specified	8
2024-T3	Pin: cylindrical, threaded Shoulder: not specified	0.276 (7)	0.098 (2.5)	0.039 (1)	not specified	2,200	13.78 (5.8)	not specified	9
2024-T351	Pin: variable-gap bobbin, cylindrical, counter rotating threads, 3 flats Shoulders: scrolled	0.510 (13)	0.200 (5)	0.160 (4)	224–314 lb (1–1.4kN)	450	3.94 (1.7)	0	10
2024-T3	Pin: not specified Shoulder: not specified	0.906 (23)	0.323 (8.2)	0.276 (7)	not specified	360	7.80 (3.3)	not specified	11
2095-? (temper not specified)	Pin: cylindrical, threaded Shoulder: not specified	0.394 (10)	0.150 (3.8)	0.064 (1.63)	not specified	750	9.92 (4.2)	not specified	12
2195-T8	Pin: H13, TiN coated, cylindrical threaded, 0.8 threads/mm pitch Shoulder: H13, TiN coated, 7° concave	0.984 (25)	0.394 (10)	0.319 (8.1)	9892 lb (44kN)	390	7.80 (3.3)	2.5	13
2195-? (temper not specified)	Pin: frustum, threaded with three flats Shoulder: flat, scrolled	1.200 (30.5)	0.600 (15.2)	1.000 (25.4)	not specified	220	4.00 (1.7)	0	14
2219-T87	Pin: cylindrical, threaded, thread pitch of 1.27 mm (0.05 in.) Shoulder: double scrolled	1.200 (30.5)	0.500 (12.7)	0.250 (6.35)	6969 lb (31 kN)	150	4.49 (1.9)	0	15
2524-T351	Pin: cylindrical, threaded Shoulder: smooth, concave	0.799 (20.3)	0.279 (7.1)	0.250 (6.4)	9,500 lb (42.26 kN)	300	7.98 (3.38)	2.5	16
5052-O	Pin: cylindrical, threaded Shoulder: not specified	0.354 (9)	0.118 (3)	0.079 (2)	not specified	4,000	39.45 (16.7)	not specified	17
5083 (rolled plate)	Pin: cylindrical, threaded Shoulder: not specified	0.787 (20)	0.236 (6)	0.118 (3)	not specified	560	5.90 (2.5)	2	18
5083 (rolled plate)	Pin: cylindrical, threaded Shoulder: smooth, concave	0.787 (20)	0.236 (6)	0.236 (6)	not specified	800	2.36 (1)	2	19
5083-H131	Pin: MP159, frustum, threaded, three flat cuts, thread pitch of 0.055 in. (1.4 mm) Shoulder: H13 tool steel, flat, scrolled	1.650 (42)	0.600 (15.2)	1.000 (25.4)	9891 lbs (44kN)	250	5.00 (2.1)	0	20
5251-O, H34	Pin: MX-Triflute Shoulder: not specified	0.984 (25)	0.354 (9)	0.197 (5)	3,147 (14 kN)	500	19.68 (8.3)	not specified	21
5454-H22	Pin: cylindrical, threaded Shoulder: not specified	0.590 (15)	0.138 (3.5)	0.138 (3.5)	1,124–1,798 lb (5–8 kN)	1,500	7.80 (3.3)	not specified	22
5456-H116	Pin: frustum, threaded with 3 flats Shoulder: flat, scrolled	1.200 (30.50)	0.681 (17.3)	0.748 (19)	not specified	264	7.80 (3.3)	0	23
6N01-T6	Pin: not specified Shoulder: not specified	0.984 (25)	0.551 (14)	0.472 (12)	not specified	315	4.96 (2.1)	not specified	24
6005A-T6	Pin: cylindrical, threaded Shoulder: not specified	0.787 (20)	0.276 (7)	0.236 (6)	not specified	1,000	39.37 (16.67)	not specified	25
6061-T6	Pin: cylindrical, threaded Shoulder: not specified	0.551 (14)	0.138 (3.5)	0.157 (4)	not specified	1,600	13.50 (5.7)	3	26
6061-T651	Pin: threaded frustum Shoulder: not specified	0.512 (13)	0.157 (4)	0.157 (4)	not specified	1,600	15.80 (6.7)	not specified	27
6061-T6	Pin: WC, cylindrical, threaded, thread pitch of 0.98 mm (0.039 in.) Shoulder: H13, smooth	0.750 (19.1)	0.250 (6.35)	0.250 (6.35)	not specified	1,540	8.5 (3.6)	3	28
6082-T6	Pin: not specified Shoulder: not specified	0.591 (15)	0.236 (6)	0.236 (6)	not specified	2,000	39.37 (16.7)	not specified	29
6082-T6	Pin: frustum, threaded with 3 flats Shoulder: Smooth, concave	0.787 (20)	0.315 (8)	0.236 (6)	2,923 (13 kN)	600	12.79 (5.42)	1.5	30
6082-T6	Pin: “5651”, cylindrical, threaded Shoulder: smooth	0.512 (13)	0.197 (5)	0.236 (6)	not specified	1,900	27.56 (11.7)	2	31
6082-T6	Pin: frustum, threaded with 3 flats Shoulder: not specified	2.953 (75)	1.417 (36)	2.953 (75)	not specified	230	1.57 (0.67)	2	32
7050-T7451	Pin: H13 tool steel, cylindrical, threaded Shoulder: H13 tool steel	0.940 (24)	0.310 (8)	0.250 (6.35)	not specified	350	4.00 (1.7)	not specified	33
7050-T7451	Pin: cylindrical, threaded Shoulder: smooth, concave	0.800 (20.3)	0.280 (7.1)	0.250 (6.4)	8,205 lb (36.5 kN)	900	9.92 (4.2)	2.5	34
7075-T6	Pin: cylindrical, threaded Shoulder: smooth, concave	0.394 (10)	0.118 (3)	0.079 (2)	not specified	1500	78.74 (33.3)	not specified	35

(continued)

Table 2 (continued)

Alloy and temper	Tool type	Shoulder diameter, in. (mm)	Pin diameter, in. (mm)	Workpiece thickness, in. (mm)	Plunge force or heel plunge depth	Tool rotational speed, rev/min	Tool travel speed, in./min (mm/s)	Tool tilt angle, deg	Ref
7075-T6	Pin: frustum, threaded with 3 flats Shoulder: flat, double scrolled	0.402 (10.2)	0.187 (4.76)	0.126 (3.2)	2,158 lb (9.6 kN)	750	20.10 (8.5)	0	36
7075-T6	Pin: cylindrical, threaded, 6.1 mm (0.24 in.) long Shoulder: not specified	0.750 (19)	0.250 (6.35)	0.25 (6.35)	not specified	200	4.00 (1.7)	not specified	37
7449-TAF	Pin: threaded with 3 flats Shoulder: smooth	0.512 (13)	0.197 (5)	0.126 (3.2)	not specified	900	11.81 (5)	not specified	38
Bobbin welding procedures									
2139-T8	Pin: threaded Shoulder: scrolled	0.472 (12)	0.236 (6)	0.098 (2.5)	742 lb pinching force (3.3 kN)	600	11.81 (5.0)	0	39
2139-T8	Pin: threaded Shoulder: scrolled	0.472 (12)	0.236 (6)	0.138 (3.5)	944 lb pinching force (4.2 kN)	600	11.81 (5.0)	0	40
2198-T8	Pin: threaded Shoulder: scrolled	0.472 (12)	0.236 (6)	0.098 (2.5)	607 lb pinching force (2.7 kN)	600	7.87 (3.3)	0	41
2198-T8	Pin: threaded Shoulder: scrolled	0.472 (12)	0.236 (6)	0.138 (3.5)	674 pinching force (3.0 kN)	600	7.87 (3.3)	0	42
2199-T8	Pin: threaded Shoulder: scrolled	0.472 (12)	0.236 (6)	0.138 (3.5)	584 pinching force (2.6 kN)	600	7.87 (3.3)	0	43

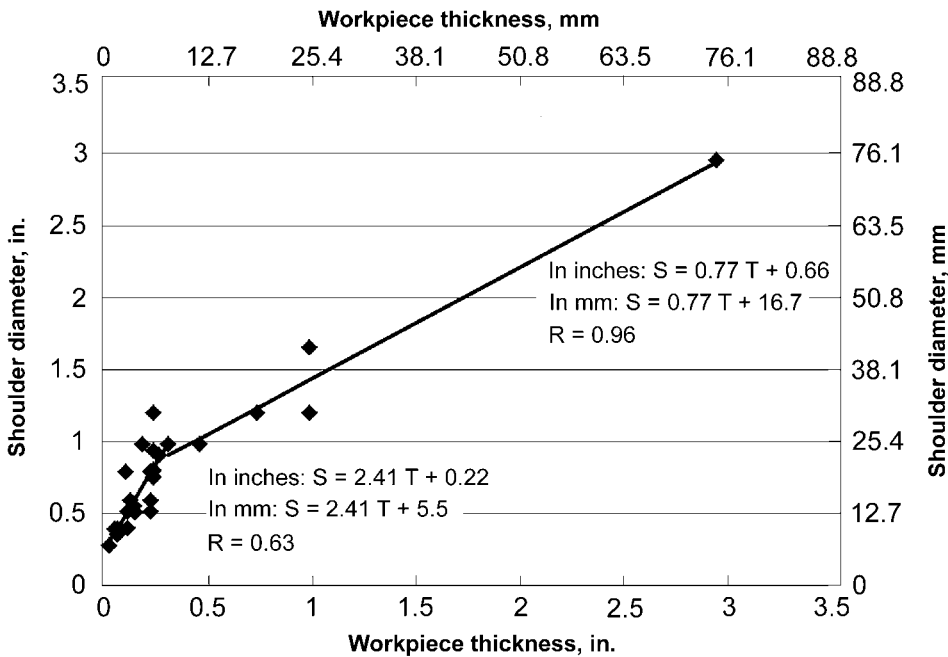


Fig. 4 Shoulder diameter as a function of workpiece thickness, from the literature

material around the pin and reducing in-plane resistance force against the pin. Welding tool shoulders may be essentially smooth and cupped inward slightly, or they may be flat, with spiral grooves designed to pull softened workpiece material toward the pin. The welding tool shoulder may also protrude in a tapered profile, which is embedded in the workpiece surface during welding (Ref 41).

Once the initial welding tool design is selected, it is necessary to choose starting

welding conditions for preliminary welding trials. Experience in adapting FSW procedures to untested workpieces has indicated that one way to extrapolate the spindle speed from an established procedure to one with a different welding pin diameter is to calculate the pin surface speed from a known procedure in a similar alloy, and then apply that pin surface speed to the present welding tool design. The data in Table 2 can be used to choose a similar alloy type, calculate the pin surface speed, and then

calculate a spindle speed for the tool design chosen. A reasonable travel speed can then be estimated by calculating the advance per revolution (travel speed divided by the spindle speed) for a similar welding procedure, and then multiplying this by the spindle speed calculated previously. This will give a good starting point for preliminary welding trials.

Procedure development often begins with a series of preliminary welds that are made for the purpose of exploring new tool designs and the reaction of the workpiece to the welding process. This is especially true for a completely new welding procedure, where there is limited experience with the material or tool design being used. Preliminary welds must be made in this case just to establish that a weld can be produced, before detailed plans can be developed.

Systematic welding trials are best carried out after a detailed plan is developed. The test plan should define the specific test welds to be made, the postweld testing to be performed, and all documentation requirements. The test plan should contain all of the details needed by welding engineers and technicians, including specific welding procedures, sketches of weld geometry, inspection requirements and procedures, cut plans for welded plates, specimen geometries, mechanical test procedures, and metallographic preparation details. Also, it is often useful to produce successive revisions of the test plan as results are obtained and new test requirements emerge. It may be helpful to use outline numbering in the various sections and paragraphs of the test plan, so that work instructions distributed to the various work areas can reference specific test plan paragraphs.

Systematic welding trials usually consist of making welds with different welding speeds and spindle speeds, at a minimum, and may

include evaluation of other process variables. Each test panel is then tested to characterize the weld produced. This testing may include nondestructive testing and should, at a minimum, include a detailed visual inspection. Test panels are then typically cut to produce a variety of test specimens, according to the test plan. Mechanical property tests could include root, face, or side bend testing and transverse tensile testing. Several specimens for each test type are normally tested to develop mean values for each weld. These specimens may be distributed along the length of a long weld or clustered at some region on the test panel. These specimens are often interspersed with specimens for metallographic preparation and inspection.

During systematic welding trials, it is helpful to consider each specific aluminum alloy as being able to tolerate increasing spindle speed only up to some maximum value, beyond which the transverse tensile strength begins to decrease. Increasing the spindle speed further will lead to volumetric defects internal to the weld, and still further increases in the spindle speed will lead to gross, surface-breaking defects and will be accompanied by an increasing in-plane force (resistance to travel) against the welding tool. The spindle speed yielding the maximum tensile strength can then be used to calculate the maximum pin surface speed that the alloy will tolerate. This surface speed can then be used to calculate the maximum spindle speed for other pin diameters.

Once the maximum spindle speed is determined for a given alloy, trials with different travel speeds can be tested. In non-heat-treatable alloys, such as the 5xxx-series aluminum alloys, tensile strength is not typically influenced by travel speed to a great extent, but in heat treatable aluminum alloys, strength often increases with increasing travel speed. This increase in strength continues to a maximum value, and then the strength begins to decrease with further increase in travel speed. As with the spindle speed trials, further increasing travel speed will ultimately lead to internal defects, then to gross, surface-breaking defects and to increasing in-plane force against the welding tool. The maximum travel speed with high tensile strength and good weld formation may then be further tested in follow-on trials.

The data analysis that accompanies systematic welding trials involves generating a summary of the information collected, looking for trends in the data, seeking explanations for observations, and developing conclusions about the best procedure to use in follow-on tests. Even if the systematic welding trials produced a procedure that is a clear “winner,” it is important to go through the data analysis to confirm and support preliminary conclusions formed during testing and to document the results of the trials.

If the welding system used for welding trials has a data collection package, it is often useful to plot the data from each weld in a systematic way so that the data from each weld can be

studied and compared to data from other welds in the series. This process may include producing charts that show travel speed and spindle speed as a function of time or position on the weld, and a chart that shows in-plane force, plunge force, and spindle torque as a function of time or position on the weld. Plotting as a function of position on the weld is helpful for isolating data generated at the locations where tensile specimens were cut for testing. It is also possible to plot weld power (heat generated per unit time) and specific energy (heat generated per unit length), using the following equations. See Table 3 for details of the associated units.

$$\text{Power} = 2 * \pi * \text{Torque} * \text{Spindle speed}$$

* Power units conversion

$$\text{Specific energy} = \frac{2 * \pi * \text{Torque} * \text{Spindle speed}}{\text{Travel speed}}$$

* Specific energy units conversion

Tensile test results should also be analyzed. It is a good idea to look at the fractured specimens from each weld and note the general failure location, the point of failure initiation, the appearance of the fracture surface, and any indications of defects that may have caused or influenced the fracture. The goal here is to determine if each tensile specimen represents the true transverse strength of a sound weld or if fracture was the result of some defect. Average values for tensile strength, yield strength, and elongation should also be calculated, along with the standard deviation of the test lot. For sound welds in aluminum alloys, the standard deviation should be very low; for example, it is common to see standard deviations for tensile and yield strength to be less than 7 MPa (1 ksi), and for elongation, less than 1%. These values may be slightly higher for 5xxx-series alloys. If fractures in any of the specimens are the result of a defect that can be attributed to incorrectly following the welding procedure, the weld should be repeated and retested. Tensile

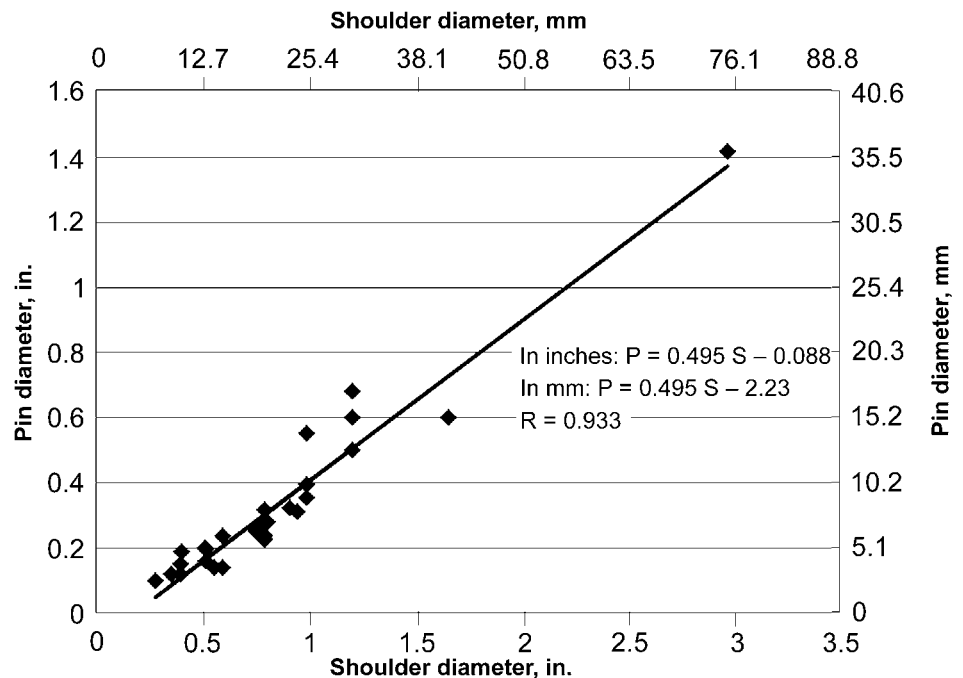


Fig. 5 Pin diameter as a function of shoulder diameter, from the literature

Table 3 Power and specific energy units conversion

Torque	Travel speed	Spindle speed	Units conversion	Energy units
ft-lb	in./min	rev/min	Power: 1 Specific energy: 1 Power: 0.00128 Specific energy: 0.00128 Power: 0.0226 Power: 0.0000303	Power: ft-lb/min Specific energy: ft-lb/in. Power: Btu/min Specific energy: Btu/in. Power: W Power: hp Power: J/min Specific energy: J/mm Power: W
N-m	mm/min	rev/min	Power: 1 Specific energy: 1 Power: 0.0167	Power: W Power: J/min Specific energy: J/mm Power: W

results should then be plotted as a function of the welding process parameters that were evaluated.

After completing systematic welding trials and establishing the preliminary welding procedure, it is often necessary to perform robustness testing, where the welding procedure is tested to evaluate materials produced with some degree of intentional variability in welding conditions. The goal is to determine how sensitive the welding procedure will be when encountering the inevitable in-process variation, discussed in the previous section. This testing may, for example, indicate that a lower travel speed, and hence production rate, is necessary to ensure reliable joint properties, given the anticipated variations in workpiece features and process execution. This testing may also include more detailed characterization of basic weld properties, such as toughness, corrosion, fatigue, and stress-corrosion cracking tests, as required by operational or performance specifications. The welding process parameters most likely to vary in-process are:

- Travel speed
- Spindle speed
- Workpiece thickness
- Plunge depth
- Plunge force
- Joint offset
- Joint gap
- Joint mismatch
- Tool geometry (wear)

Travel speed and spindle speed are two very important variables in FSW, and they typically experience a degree of normal variation in practice. However, most welding systems are capable of controlling these variables well enough that weld quality is not adversely affected. In spite of this, it is usually a good idea to implement a data collection system to log these values during production welding, as confirmation that the correct weld parameters were used and that machine performance was adequate throughout the weld.

Workpiece thickness is usually not subject to a significant amount of in-process variation when the workpiece is a machined component, but when rolled plate or extruded products are used in the as-received condition, thickness variation within a workpiece or between workpieces can be significant and can lead to poor FSW quality. As a result, careful attention must be paid to workpiece thickness variation in FSW. Typically, mill-produced aluminum materials are controlled by one or more specifications. One common specification that regulates geometry of aluminum mill products is ANSI H35.2 (Ref 42). This specification gives the allowable thickness variation for rolled and extruded products. Based on this or other applicable specifications, one can test the ability of the welding tool to produce sound welds at the limits of thickness variation. When the potential thickness variation is greater than the

welding tool design can handle, such as when the strength or ductility of the joint is reduced at the maximum material thickness condition, thickness measurement procedures can be specified, and welding tool pin length adjustment can be employed.

Welding tool plunge depth is also critical to producing a sound friction stir weld. The welding tool plunge depth can be expressed in terms of the heel plunge depth, the pin/anvil gap, or the depth of the tip of the welding tool relative to the workpiece surface, depending on the details of the control system used. Some welding systems employ absolute position control, relative to a fixed coordinate system. Others use relative position control, either relative to the anvil or relative to the workpiece surface, and still other systems may operate with no active axial position control, such as a system where the axis is set and locked during welding. Other welding systems may only operate in load control, where the plunge force is controlled and the welding tool depth varies in response to variation in local conditions. In any case, the depth of the welding tool in the workpiece is critical to ensure complete weld penetration and to ensure adequate surface forging by the shoulder. As a result, plunge depth must be monitored during welding. As with the travel speed and spindle speed, this variable should be recorded in a log file during production welding for the purpose of confirming that the welding tool tip was sufficiently close to the anvil at all times to achieve complete weld penetration.

In an FSW implementation that uses plunge force as the primary axial position control variable, plunge force variation is typically low enough that sound welds can be reliably produced. The larger issue is the variation in plunge depth that occurs as the welding system actuates the axial position to maintain constant plunge force, as discussed previously. In a process where the axial position is the primary control variable, the plunge force should be monitored to ensure that adequate consolidation of the crown surface of the weld is maintained. Review of the weld log file can give an indication of possible areas of the weld that may have defects from being insufficiently consolidated at the crown surface during welding due to low plunge force.

During welding, joint gap, offset, and mismatch errors can occur, either due to improper setup in advance of welding or due to shrinkage stress and welding forces during welding. It is often wise to evaluate the effect of these alignment errors on joint strength in order to know the limits of variability that can be tolerated. Gap tolerance can be evaluated by completing a weld or series of welds in specially designed test panels that have short, shallow notches cut into one side of the joint, as shown in Fig. 6. By testing several gap settings, joint strength as a function of gap can be determined. If the gap tolerance is too low, additional welds at a lower travel speed may provide a more robust

procedure. Similar tests can be done for offset errors and mismatch errors. Based on the results of these tests, an in-process monitoring scheme can be implemented to confirm joint alignment and joint gap, thus ensuring that these errors never result in excessive joint strength variation.

Finally, welding tool wear over time can result in variation in the welding process. The best way to account for tool wear is to complete life testing of the welding tool in production or in simulated production welds. Tool life can be determined by the point at which wear of the welding tool results in sufficient alteration of the tool that joint strength or other critical joint properties are adversely affected, or by catastrophic tool failure due to accumulated fatigue damage. In either case, a life test can indicate the practical life of a given welding tool design.

The results from the systematic welding trials and the robustness testing should then be collected and summarized for future reference and reported when formal qualification is required. Formal weld procedures can then be prepared for use in each application.

Procedure Qualification

Procedure qualification is the process by which a regulatory authority evaluates a welding procedure, performed by a contractor, and approves the use of the procedure in production of some deliverable item. Similarly, operator qualification is the process by which an individual is approved to execute a qualified welding procedure. Further, in some cases, regulatory authorities have set requirements for how production welding operations are to be carried out, such as requirements for detailed work instructions, in-process monitoring, and post-weld inspections and testing. In this section, some of the common features of procedure qualification are presented.

Typically, procedure qualification consists of the steps listed as follows, although there may be some variability in the process between specifications (Ref 1–5, 43):

1. Develop and document a welding procedure, with all supporting tests and evaluations

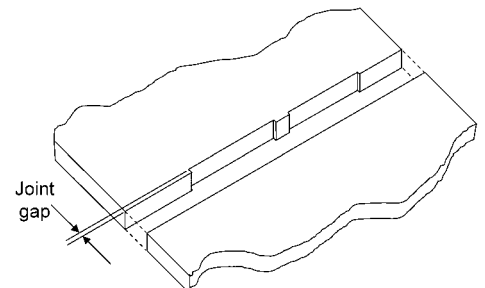


Fig. 6 Joint gap test panel schematic

2. Submit the procedure and supporting data for review
3. Demonstrate the procedure(s) being proposed and record all variables used
4. Test weldments(s) produced and collect test data
5. Present procedure and qualification test data for approval
6. Release the procedure for production use

In qualifying a welding procedure for FSW, given the relative newness of the process, it is important to communicate with the approval authority early in the planning process and to be well prepared for the qualification process. As the test plans for systematic welding trials and robustness testing are developed, they should be submitted to the approval authority to solicit their comments on the planned testing. This will help ensure that all appropriate tests are completed in advance of requesting formal procedure approval. After preparatory tests are completed, the test data should be submitted to the approval authority in advance or concurrently with a request to witness qualification welds.

REFERENCES

1. "Requirements for Welding and Brazing Procedure and Performance Qualification," NAVSEA Technical Publication S9074-AQ-GIB-010/248, 1995
2. "Specification for Friction Stir Welding of Aluminum Alloys for Aerospace Applications," AWS D17.3/D17.3M:2010, American Welding Society, 2010
3. "Specification for Welding Procedure and Performance Qualification," AWS B2.1:2000, American Welding Society, 2000
4. "Structural Welding Code—Aluminum," AWS D1.2/D1.2M:2003, American Welding Society, 2003
5. "Process Specification for Friction Stir Welding," PRC-0014, Revision C, National Aeronautics and Space Administration, 2007
6. L. Dubourg and P. Dacheux, "Design and Properties of FSW Tools: A Literature Review," Sixth International Symposium on Friction Stir Welding, Oct 10–13, 2006 (Saint-Sauveur, Canada)
7. B. Huneau, X. Sauvage, S. Marya, and A. Poitou, "Microstructure Evolution during Friction Stir Welding of Commercial Aluminum Alloys," *Friction Stir Welding and Processing III*, K.V. Jata, M.W. Mahoney, R.S. Mishra, and T.J. Lienert, Ed., TMS, Warrendale, PA, 2005, p 253–260
8. T.W. Nelson, B. Hunsaker, and D.P. Field, "Local Texture Characterization of Friction Stir Welds in 1100 Aluminum," First International Symposium on Friction Stir Welding, June 14–16, 1999 (Thousand Oaks, CA)
9. A.K. Shukla and W.A. Baeslack, "Effect of Process Conditions on Microstructure Evolution and Mechanical Properties of Friction Stir Welded Thin Sheet 2024-T3," Sixth International Symposium on Friction Stir Welding, Oct 10–13, 2006 (Saint-Sauveur, Canada)
10. T. Neumann, R. Zettler, P. Vilaca, J.F. Dos Santos, and L. Quintino, "Analysis of Self-Reacting Friction Stir Welds in a 2024-T351 Alloy," *Friction Stir Welding and Processing IV*, R.S. Mishra, M.W. Mahoney, T. Lienert, and K.V. Jata, Ed., TMS, Warrendale, PA, 2007, p 55–72
11. M.A. Sutton, B. Yang, A.P. Reynolds, and R. Taylor, "Microstructural Studies of Friction Stir Welds in 2024-T3 Aluminum," *Mater. Sci. Eng. A*, Vol 323, 2002, p 160–166
12. M.M. Attallah and H.G. Salem, "Effect of Friction Stir Welding Process Parameters on the Mechanical Properties of the As-Welded and Post-Weld Heat Treated AA2095," Fifth International Symposium on Friction Stir Welding, Sept 14–16, 2004 (Metz, France)
13. A.P. Reynolds and W. Tang, "Alloy, Tool Geometry, and Process Parameter Effects on Friction Stir Weld Energies and Resultant FSW Joint Properties," *Friction Stir Welding and Processing*, K.V. Jata, M.W. Mahoney, R.S. Mishra, S.L. Semiatin, and D.P. Field, Ed., TMS, Warrendale, PA, 2001, p 15–23
14. K.J. Colligan and S.K. Chopra, "Examination of Material Flow in Thick Section Friction Stir Welding of Aluminum Using a Stop-Action Technique," Fifth International Symposium on Friction Stir Welding, Sept 14–16, 2004 (Metz, France)
15. J.A. Querin, A.M. Davis, and J.A. Schneider, "Effects of Processing Parameters on Microstructure of the FSW Nugget," *Friction Stir Welding and Processing IV*, R.S. Mishra, M.W. Mahoney, T. Lienert, and K.V. Jata, Ed., TMS, Warrendale, PA, 2007, p 185–192
16. J. Yan, M.A. Sutton, and A.P. Reynolds, "Process-Structure-Property Relationship for Nugget and HAZ Regions of AA2524-T351 FSW Joints," Fifth International Symposium on Friction Stir Welding, Sept 14–16, 2004 (Metz, France)
17. Y.S. Sato, Y. Sugiura, and H. Kokawa, "Hardness Distribution and Microstructure in Friction Stir Welds of Aluminum Alloy 5052," Fourth International Symposium on Friction Stir Welding, May 14–16, 2003 (Park City, UT)
18. M.J. Peel, M. Preuss, A. Steuwer, M. Turcki, and P.J. Withers, "The Evaluation of the Mechanical Properties of AA5083 Friction Stir Welds by Electronic Speckle Pattern Interferometry," *Proceedings of the Sixth International Trends in Welding Research Conference*, April 15–19, 2002 (Pine Mountain, GA), ASM International, 2003
19. Z.W. Chen and R. Maginness, "Formation of Weld Zones during Friction Stir Welding of Aluminum Alloys," Fifth International Symposium on Friction Stir Welding, Sept 14–16, 2004 (Metz, France)
20. K.J. Colligan, J. Xu, and J.R. Pickens, "Welding Tool and Process Parameter Effects in Friction Stir Welding of Aluminum Alloys," *Friction Stir Welding and Processing II*, K.V. Jata, M.W. Mahoney, R.S. Mishra, and T. Lienert, Ed., TMS, Warrendale, PA, 2003, p 181–190
21. M. Strangwood, C.L. Davis, and M.M. Attallah, "Microstructural Development and Modelling in Friction Stir Welds of Strain-Hardenable Alloys," Fifth International Symposium on Friction Stir Welding, Sept 14–16, 2004 (Metz, France)
22. M. Gutensohn, G. Wagner, M. Endo, and D. Eifer, "Fatigue Behavior of Friction Stir Welded (FSW) Aluminum Joints," *Friction Stir Welding and Processing*, K.V. Jata, M.W. Mahoney, R.S. Mishra, S.L. Semiatin, and D.P. Field, Ed., TMS, Warrendale, PA, 2001, p 305–314
23. K.J. Colligan, "Description of a Pre-Rotation Defect in Friction Stir Welding of 5456 Aluminum," Eighth International Symposium on Friction Stir Welding, May 18–20, 2010 (Timmendorfer Strand, Germany)
24. H. Hori, S. Makita, T. Minamida, S. Watanabe, E. Anzai, and H. Hino, "Joint Strength of Thick Sheet Welded by Friction Stir Welding," Third International Symposium on Friction Stir Welding, Sept 27–28, 2001 (Kobe, Japan)
25. A. Simar, B. deMeester, Y. Brechet, and T. Pardoen, "Microstructural Evolution and Local Mechanical Properties Evolution Throughout Friction Stir Welds in Al 6005A," Sixth International Symposium on Friction Stir Welding, Oct 10–13, 2006 (Saint-Sauveur, Canada)
26. W.S. Chang, H.S. Bang, S.B. Jung, Y.M. Yeon, H.J. Kim, and W.B. Lee, "Joint Properties and Thermal Behaviors of Friction Stir Welded Age Hardenable 6061 Al Alloy," *Proceedings of Thermec 2003*, Part 4, July 7–11, 2003 (Leganes, Madrid, Spain), Trans Tech Publications, Switzerland, 2003, p 2953–2958
27. S. Lim, S. Kim, C.G. Lee, and S. Kim, "Tensile Behavior of Friction Stir Welded Al 6061-T651," *Metall. Mater. Trans. A*, Vol 35, Sept 2004, p 2829–2835
28. K.J. Colligan, "Dynamic Material Deformation during Friction Stir Welding of Aluminum," First International Symposium on Friction Stir Welding, June 14–16, 1999 (Thousand Oaks, CA)
29. L. Ekman, A. Norlin, and J. Backlund, "Evaluation of Weld Quality When Using Run-On/Run-Off Tabs in FSW," Second International Symposium on Friction Stir Welding, June 26–28, 2000 (Gothenburg, Sweden)

30. D. Gesto, V. Pintos, J. Vazquez, I. Villar, J. Rasilla, and S. Barreras, "6082-T6 Aluminum Alloy Welded by FSW and GMAW Processes for Marine Applications—A Comparative Study," Seventh International Symposium on Friction Stir Welding, May 20–22, 2008 (Awaji Island, Japan)
31. S. Kahl, "Fatigue Strength of Friction Stir Welds in Aluminum Alloy AA6082-T6," Eighth International Symposium on Friction Stir Welding, May 18–20, 2010 (Timmendorfer Strand, Germany)
32. M.M.Z. Ahmed, B.P. Wynne, R.M. Rainforth, and P.L. Threadgill, "An Investigation of Hardness, Microstructure and Crystallographic Texture in Thick Sectioned Friction Stir Welded AA6082," Seventh International Symposium on Friction Stir Welding, May 20–22, 2008 (Awaji Island, Japan)
33. B. London, M. Mahoney, W. Bingel, M. Calabrese, R.H. Bossi, and D. Waldron, "Material Flow in Friction Stir Welding Monitored with Al-SiC and Al-W Composite Markers," *Friction Stir Welding and Processing II*, K.V. Jata, M.W. Mahoney, R.S. Mishra, and T. Lienert, Eds., TMS, Warrendale, PA, 2003, p 3–12
34. A. Reynolds, W. Tang, Z. Khandkar, J.A. Khan, and K. Lindner, "Relationships between Weld Parameters, Hardness Distribution and Temperature History in Alloy 7050 Friction Stir Welds," *Sci. Technol. Weld. Join.*, Vol 10 (No. 2), 2005, p 190–199
35. L. Dubourg, R. Amargier, and M. Jahazi, "Relationship between FSW Parameters, Hardness, and Tensile Properties of 7075-T6 and 2098-T851 Similar Butt Welds," Seventh International Symposium on Friction Stir Welding, May 20–22, 2008 (Awaji Island, Japan)
36. J.E. Barnes, J. McMichael, and A. Reynolds, "Effects of Friction Stir Welding Defects on 7075 Joint Strength and Fatigue Life," Sixth International Symposium on Friction Stir Welding, Oct 10–13, 2006 (Saint-Sauveur, Canada)
37. D.P. Field, T.W. Nelson, Y. Hovanski, and D.F. Bahr, "Texture Effects on Corrosion Behavior of Friction Stir Welded 7075 Aluminum," *Friction Stir Welding and Processing*, K.V. Jata, M.W. Mahoney, R. S. Mishra, S.L. Semiatin, and D.P. Field, Eds., TMS, Warrendale, PA, 2001, p 83–91
38. J.D. Robson and L. Campbell, "Precipitate Evolution and Grain Size Modelling in Friction Stir Welding of AA7449," Eighth International Symposium on Friction Stir Welding, May 18–20, 2010 (Timmendorfer Strand, Germany)
39. F. Marie, B. Guerin, D. Deloison, D. Aliaga, and C. Desrayaud, "Investigation on Bobbin Tool Friction Stir Welding of 2000 Series Aluminum Thin Sheets," Seventh International Symposium on Friction Stir Welding, May 20–22, 2008 (Awaji Island, Japan)
40. D. Lohwasser and Z. Chen, Eds., Chap. 2, *Friction Stir Welding, from Basics to Applications*, Woodhead Publishing, Great Abington Cambridge, U.K., 2010
41. K.J. Colligan, "Tapered Friction Stir Welding Tool," U.S. Patent 6,669,075, Dec 30, 2003
42. "American National Standard Dimensional Tolerances for Aluminum Mill Products," ANSI H35.2-2006, The Aluminum Association, Inc., 2006
43. "Friction Stir Welding of Aluminum—General Requirements," ISO 25239, International Organization for Standardization

Friction Stir Welding Tool Designs

Carl D. Sorensen, Brigham Young University

A KEY DIFFERENTIATOR between friction stir welding (FSW) and other friction welding processes is the presence of a nonconsumable tool in FSW, often referred to as a pin tool to differentiate it from other tooling associated with the process. The pin tool used in FSW influences virtually every aspect of the process. Pin tool design affects the process loads, material flow, process-zone temperature, and weld quality. Tool design also has significant effects on tool life and tool cost. Historically, tool design has been a combination between art and science. As the understanding of the process matures, tool design has been coupled more closely with process behavior, and tool performance has increased correspondingly.

This article discusses materials for FSW pin tools, various tool geometries that have been used, designs for specific applications, predicting and measuring tool performance, and other considerations in FSW pin tool design.

Friction Stir Welding Tool Materials

Friction stir welding has been performed with a variety of pin tool materials. When welding materials with low softening temperatures (under approximately 600 °C, or 1110 °F), the range of materials that can be used is relatively large. However, when welding materials with higher softening temperatures, it can be a challenge to find appropriate tool materials. This section discusses the requirements for tool materials along with materials that have been successfully used in various FSW applications.

Tool Material Requirements

Friction stir welding is a challenging material application. The pin tool is surrounded by workpiece material at the softening temperature, which is typically between 80 and 95% of the absolute melting temperature of the workpiece (Ref 1). Friction stir welding tools also see significant process loads; on the order of 10,000 Newtons (N) of force along the tool axis and several thousand Newtons perpendicular to the tool axis are common (Ref 2, 3).

Table 1 summarizes the relationships between the classes of tool materials and the desired tool material characteristics.

Strength at Room Temperature and Process Temperature. Friction stir welding tools must be strong enough to support the process loads. This strength must exist both at room temperature (for the start of the weld) and at elevated temperature (for the major portion of the weld). For welding alloys such as 6061 in thicknesses under approximately 16 mm (0.6 in.), strength is typically not a major problem. For higher-strength alloys and thicker plates, strength can be a significant factor in the choice of FSW pin tool material.

Chemical Inertness at Elevated Temperature. Chemical interactions with the material to be welded can cause significant detrimental effects. Strong chemical adhesion of the workpiece and the tool can lead to reduced flow. Chemical wear can reduce the strength of tools. Tool material can contaminate the weld material. In some cases, incipient melting at the tool-workpiece interface is thought to lead to liquid metal embrittlement of the tool (Ref 4). To avoid all of these problems, tool materials that do not chemically react with the workpiece should be chosen.

Wear Resistance. Over an extended period of time, wear can change the shape of the tool and adversely affect the properties of the weld. In some cases, wear can lead to tool failure in a relatively short time. In other cases, wear particles of the tool material left behind in the weld can greatly reduce the properties of the weld, especially in fatigue (Ref 5). Therefore, tool materials should have a strong resistance to wear.

Fracture Toughness. Friction stir welding tools operate in a cyclic environment under high loads. To avoid failure, fracture toughness should be high. Fracture toughness has been a particular problem in tools for welding high-softening-temperature materials such as steels. Pure tungsten tools have low fracture toughness at room temperature, leading to failure on plunge (Ref 6). Ceramic and superabrasive tools tend to fail by fracture, rather than by wear. Higher fracture toughness is always a desirable characteristic for FSW tools.

Manufacturability. Many FSW tools have complex geometries, so manufacturability is a key aspect of tool material choice. Tools that can be worked with standard machines and processes are generally preferred over those that require special processing (e.g., grinding with superabrasive wheels). Nevertheless, if the performance of a difficult-to-manufacture material justifies the increased cost, such materials can be used for FSW tools in demanding applications.

Availability. To be feasible for a production process, the availability of the material should be high. Materials whose availability is limited will tend to have high cost or may be unavailable at any cost. For example, iridium was tried as a tool material for FSW of titanium alloys (Ref 7). Although it had most of the characteristics required for a tool material, availability of iridium is so limited that it could not be used as a commercially feasible tool material.

Cost. Friction stir welding tools are generally considered to be consumables. Therefore, the cost should be commensurate with this application (Ref 8). For some high-performance materials, the cost of a tool can exceed several

Table 1 Characteristics of typical friction stir welding tool materials

Material characteristic	Tool material class				
	Tool steels	Superalloys	Refractory metals	Carbides, cermets, and ceramics	Superabrasives
Room-temperature strength	Good	Excellent	Excellent	Excellent	Excellent
Process-temperature strength	Good	Very good	Excellent	Good	Excellent
Chemical inertness	Good	Very good	Good	Good	Excellent
Wear resistance	Good	Good	Very good	Good	Excellent
Fracture toughness	Very good	Very good	Very good	Good	Poor to good
Availability	Excellent	Very good	Very good	Very good	Very good
Cost	Excellent	Very good	Poor to acceptable	Good	Poor to acceptable

thousand dollars. Such expensive tools will have only limited applicability, where the value of the joint to be made is sufficiently high to support the tool cost.

Classes of Tool Materials

Various tool material classes have been used to perform FSW and processing. This section describes the general properties of each of the classes of tool materials.

Tool steels have been used for the large majority of FSW. The most commonly cited tool steel is H13 (Ref 9–26), which is used to weld most aluminum alloys, magnesium, lead, and other low-softening-temperature materials. H13 is an air-hardening, high-hot-strength tool steel with good thermal fatigue resistance and wear resistance (Ref 27). Other tool steels used include O1, D2, SKD61, Orvar Supreme, and Divar (Ref 28–33). The maximum-use temperature for oil- and water-hardening tool steels is approximately 500 °C (930 °F). Secondary-hardened tool steels can be used up to approximately 600 °C (1110 °F) (Ref 27).

Superalloys. Cobalt- and nickel-base superalloys have been used as materials for FSW tools in high-strength aluminum, copper, and thin steels. These alloys typically have excellent high-temperature deformation resistance. They are relatively available, serving as commercial alloys for aircraft engine components, and have moderate costs. Nimonic 105 has probably had the most use in welding copper (Ref 34). MP159 (a cobalt-base superalloy) has been used for welding high-strength aluminum alloys such as 7075 and 7050 (Ref 4, 35, 36). Some researchers have reported premature tool failure when used at high temperatures in these alloys, which was thought to be related to liquid metal embrittlement (Ref 4).

A custom cobalt-base alloy strengthened by $\text{Co}_3(\text{Al,W})$ precipitates has been tested for use in welding carbon steel and titanium alloys (Ref 37). It was tested with a relatively short probe (1.4 mm, or 0.06 in., in length) but was able to survive over 45 m (148 ft) in mild steel.

Limited reactivity was found with either steel or titanium. Its relatively low cost and high manufacturability make it a promising tool material for future testing.

Refractory metals are promising FSW tool materials for high-softening-temperature alloys because of their very high hot strength. Niobium and tantalum have high oxygen solubility at elevated temperatures, so they cannot be used for FSW in atmosphere (Ref 38). Molybdenum and tungsten have both been used for FSW of steel and titanium. Pure tungsten suffers from low room-temperature toughness (Ref 4, 39). W-25%Re, W-1%LaO₂, and Densimet have all been used for FSW of steel, titanium, and copper (Ref 40–48).

With the exception of tungsten-rhenium alloys, refractory metals have an acceptable price and availability. Due to a limited supply of rhenium, tungsten-rhenium alloys are extremely expensive. Refractory metals are limited in the geometries that can be used, because small features tend to wear away rapidly (Ref 49). The most common refractory metal tools have either no surface features or very gentle surface features.

Carbides and Ceramics. A variety of ceramics and carbides have been explored for use in FSW tools. Al₂O₃ and Si₃N₄ have outstanding strength, but their toughness is too low for successful use in FSW of steels. Cemented tungsten carbide (WC-Co) has been used for welding metal-matrix composites due to its high abrasion resistance (Ref 50). Cemented carbide has also been used for welding of steels (Ref 51). The use of cemented carbide for steels is limited by its relatively low hot strength.

Superabrasives are ceramic materials that have been processed in high-temperature, ultra-high-pressure (HT-UHP) presses. The most widely known superabrasive is synthetic diamond. It is used for FSW tools in the form of a sintered compact called polycrystalline diamond (PCD). The superabrasive most widely used in FSW is polycrystalline cubic boron nitride (PCBN). Because they must undergo an HT-UHP process, superabrasive materials

are fairly expensive. Manufacturability of superabrasive tools can be a challenge, because the primary method of machining is grinding with diamond abrasive wheels. Availability of the raw materials for superabrasives is excellent.

Polycrystalline diamond has been used in FSW of aluminum metal-matrix composites, where its superb hardness and wear resistance allow for extremely long tool life (Ref 52). It is also a candidate shoulder material for FSW of titanium. Polycrystalline diamond is not usable for FSW of steels because of its high reactivity with iron at elevated temperatures (Ref 53).

Polycrystalline cubic boron nitride has been used for FSW of a variety of high-softening-temperature materials. It has the lowest wear rate of all materials used for FSW in these alloys. However, the relatively low fracture toughness of PCBN generally leads to failure by fracture rather than by wear (Ref 39).

FSW Tool Material Applications

A variety of FSW tool materials have been used for welding various materials. Because the tool requirements vary with the material welded, the tool materials for each alloy class are discussed separately. Table 2 summarizes the tool materials used for each alloy class.

Aluminum Alloys. The bulk of FSW in aluminum alloys is performed with H13 steel tools, at least up to a thickness of 13 mm (0.5 in.). Other tool steels have been used, but H13 appears to be the workhorse of the aluminum FSW industry in moderate and low thicknesses (Ref 11–26). In greater thicknesses and with higher-strength 7xxx-series alloys, H13 probes can fail prematurely. In such applications, the cobalt-base alloy MP-159 is the most widely used tool material (Ref 4, 35, 36). For aluminum alloys, tool materials are generally considered to meet the primary needs, with tools often lasting for 1000 m (3300 ft) or more of welding.

Table 2 Tool materials used for welding various alloy classes

Material welded	Tool material class				
	Tool steels	Superalloys	Refractory metals	Carbides, cermets, and ceramics	Superabrasives (a)
Aluminum alloys	Most commonly used, typically H13	MP159 used for probes in 7xxx alloys	...	WC-Co	...
Magnesium alloys	Generally H13	WC-Co	...
Copper alloys	...	Nimonic 105 for probe, Inconel 718, Waspalloy	Densimet for shoulder, Mo, W-25Re	WC-Co	PCBN
Titanium alloys	Mo, W, W-Re, W-LaO ₂ , Mo-Re-HfC	WC-Co, but limited tool life	...
Stainless steels	W-Re (ferritic)	...	PCBN
Low-alloy steels	...	Co(Al,W) ₃	W-Re, W, Mo, W-Re-HfC	WC-Co	PCBN
Nickel alloys	WC-Co	PCBN
Metal-matrix composites	WC-Co	PCD
Thermoplastics	H13

(a) PCBN, polycrystalline cubic boron nitride; PCD, polycrystalline diamond

Magnesium alloys have been welded with both tool steel (H13) and WC-Co (Ref 54). The mechanical and thermal loads on the tool in welding magnesium are generally quite small, so the lower-strength tool materials work well. Perhaps the largest concern in FSW of magnesium is the tendency of the alloy to stick to the tool (Ref 55). Careful attention to tool surface finish helps provide successful results in FSW of magnesium alloys.

Copper and Copper Alloys. Copper has been tested with perhaps the widest range of tool materials of any alloy. Because FSW has been chosen as a joining technology for 50 mm (2.0 in.) thick welds in sealing canisters to contain nuclear waste in Sweden, a significant research program on FSW of thick-section copper has been carried out for several years. Seventeen different probe materials, including metals, cermets, ceramics, and superabrasives, were tested (Ref 56). Of these materials, Nimonic 90, Inconel 718, and Waspalloy were able to produce 3.3 m (11 ft) long welds. Nimonic 105 was able to produce welds 20 m (66 ft) in length with no visible damage. For these canister welds, Densimet was chosen as the shoulder material (Fig. 1). The PCBN tools have also been demonstrated to produce sound welds with good life in copper, aluminum bronze, and nickel-aluminum bronze (Ref 56, 57).

Titanium Alloys. Titanium and its alloys are particularly challenging to weld because of the high softening temperature, low thermal conductivity, and high reactivity of these alloys. Polycrystalline cubic boron nitride was tested and found to react with the titanium (Ref 58). Various tungsten alloys have been used to weld titanium alloys. W-1%LaO₂ has been shown to provide excellent results in welding beta and alpha-beta titanium alloys (Ref 59–62). A proprietary refractory metal alloy produced by General Electric and Edison Welding Institute has also shown promise in FSW of titanium. Although molybdenum alloys and W-25%Re survive the FSW process in titanium, the welds

made with these materials were of lower quality than those made with W-1%LaO₂ (Ref 63).

Stainless Steels. Ferritic stainless steels have been welded with both PCBN and refractory metal alloys (Ref 64–66). Both materials produce sound welds. Refractory metal tools currently have a higher thickness capability (approximately 18 mm, or 0.8 in.) than PCBN tools (approximately 8 mm, or 0.3 in.).

Austenitic stainless steels are much more challenging to weld than ferritic steels. Tool wear is a challenge in these alloys. Tools containing tungsten wear quite rapidly (Ref 67, 68). The PCBN tools wear less rapidly but still experience some wear. Smooth PCBN tools (Fig. 2) can sometimes lead to sigma-phase formation in FSW of 304L (Ref 69, 70). The PCBN tools with a convex scrolled shoulder and a stepped-spiral pin (Fig. 3) have been shown to eliminate sigma-phase formation (Ref 71). Thus, it appears that thread features may be necessary to achieve optimum properties in FSW of 304L. Polycrystalline cubic boron nitride has also been used to weld 316L and 2507 superduplex (Ref 39, 72). No tool materials have been found that successfully join AL-6XN superaustenitic stainless steel (Ref 73).

Low-Alloy Steel. Tungsten- and molybdenum-base tools have been used to successfully weld low-alloy steels, including W, W-25%Re, and W/Mo-Re-HfC alloys (Ref 74–78). Tools made from these alloys are typically hemispherical or truncated-cone probes with very small shoulders and smooth surfaces (Ref 79). Periodic redressing of the tool allows for an extended tool life.

A cobalt-base alloy containing Co₃(Al,W) precipitates has been shown to weld both low- and high-carbon steels (Ref 37). Although the alloy is only demonstrated for thin sheets (the probe length was 1.4 mm, or 0.06 in.), the

material looks promising due to its high availability, high manufacturability, and low cost.

Polycrystalline cubic boron nitride has been used to weld a variety of low- and high-alloy steels (Ref 80–83). Welds are generally of high quality, with good ductility and joint efficiencies greater than 90%. Tool wear is generally quite low in these alloys. Tool failure is generally due to fracture.

Nickel Alloys. Finding tool materials for welding of nickel alloys has been a significant challenge. WC-Co has been used to make welds in alloy 600 (Ref 84). Polycrystalline cubic boron nitride has been used to weld a variety of nickel alloys, including alloys 600, 718, 201, and 22 (Ref 39). Surface finish and mechanical properties are excellent, although tool life remains an issue in strengthened alloys.

Metal-Matrix Composites. The ceramic particles found in metal-matrix composites lead to excessive wear in FSW of these materials with tool-steel tools (Ref 85–87). More wear-resistant materials are needed. WC-Co has been demonstrated to allow FSW aluminum-base metal-matrix composite with 30 vol% SiC particles, with acceptable wear rates. A composite tool with a PCD shoulder and a WC-Co + PCD probe was demonstrated to weld aluminum metal-matrix composites with both SiC and B₄C, with no measurable wear (Ref 52).

Thermoplastics. The mechanical requirements for FSW of thermoplastics are similar to those for aluminum, although the temperatures are lower. H13 is generally used as a tool material for these applications. Friction stir welding of thermoplastics requires a stationary shoulder (Ref 88, 89) and has yet to find wide commercial application.

Friction Stir Welding Tool Geometry

Friction stir welding tools consist of a shoulder and a probe (or pin). The shoulder is larger in diameter than the probe and rides along the joint at or near the surface of the workpiece. The probe extends below the surface to approximately the maximum depth of the weld. It can

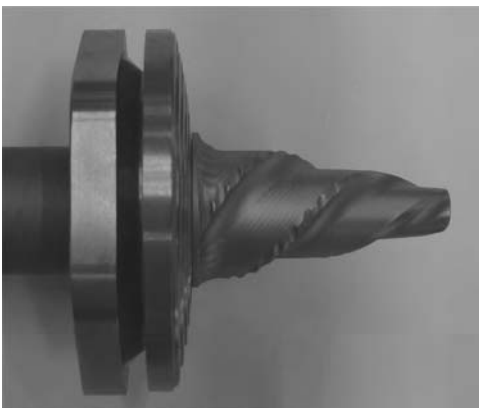


Fig. 1 Friction stir welding tool with convex scrolled shoulder of Densimet and MX Triflute probe of Nimonic 105. Source: Ref 34

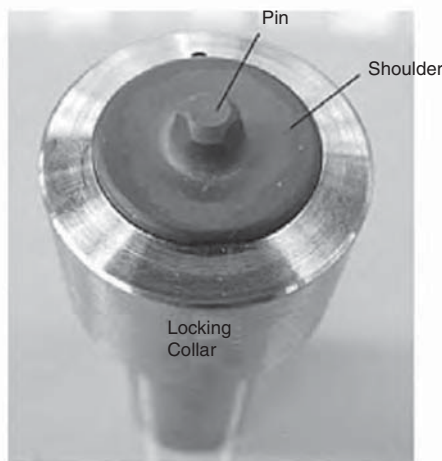


Fig. 2 Conventional geometry (smooth concave shoulder, cylindrical pin, three flats) used for welding ferrous alloys



Fig. 3 Convex scrolled shoulder and stepped-spiral pin geometry used for welding ferrous alloys

be convenient to consider the designs of each component of the tool separately.

Shoulder Designs

The shoulder of the pin tool has the primary function of containing the deformed material within the weld zone. It has a secondary function of generating frictional heat to soften the material ahead of the probe. However, the heat generated by the shoulder increases the top-to-bottom asymmetry of the through-thickness thermal profile. Therefore, current research is exploring the value of minimizing shoulder heating.

Shoulders have three fundamental geometries: concave, flat, and tapered or convex.

Concave Shoulder. The concave shoulder was the original shoulder used in FSW (Ref 90) (Fig. 4). The concave shoulder has the cross section of a hollow cone, with a cone angle of approximately 6 to 10° from the horizontal. The hollow cone provides a reservoir for material displaced by the probe during the plunge phase of FSW and serves to bring material back toward the probe to achieve full consolidation. The shoulders of concave shoulder pin tools are typically smooth, with no surface features of any kind.

Pin tools with concave shoulders must be operated with the tool axis tilted (typically between 2 and 5°) from the vertical, such that the trailing edge of the shoulder is lower than the leading edge. This facilitates consolidation of the weld, but making nonlinear welds with tilted tools requires a machine with at least four axes of motion in order to maintain the appropriate orientation of the tool.

Flat Shoulder. A major advantage of a pin tool with a flat shoulder is that the tool does not need to be tilted to complete the weld. The disadvantage of such a tool is that there is no inherent ability to move material from the edge of the shoulder toward the probe. Therefore, flat shoulders typically have scrolls or

other features designed to draw weld material toward the tool axis (Ref 91).

Scrolls can have a variety of shapes, but the most common shape used in flat-shoulder tools is a rectangular cross section, spiral scroll projecting from the flat surface of the shoulder (Fig. 5). The tools are typically run with the scrolls 0.3 to 0.8 mm (0.01 to 0.03 in.) below the surface of the workpiece. If the scrolls are deeper, excessive flash results. If the scrolls are shallower, there is typically insufficient consolidation.

Tools with narrow flat shoulders and no scrolls have been recently used to weld materials with high softening temperatures (Ref 92) (Fig. 6). However, in this application the tool must be tilted like a standard concave shoulder tool.

Tapered and Convex Shoulder. Flat-shoulder tools and, to a lesser extent, concave-shoulder tools must operate within a very narrow depth range. If the tool is too shallow, insufficient consolidation occurs. If the tool is too deep, excessive flash is generated. This means that the tool must follow the profile of the top surface of the workpiece.

In contrast, the end of the probe should remain a fixed distance from the anvil to assure a full-penetration weld. Therefore, for a fixed probe length, it is desirable to maintain a fixed

tool position regardless of the workpiece surface profile.

To solve this fundamental conflict, tapered- and convex-shoulder pin tools were developed (Ref 93, 94). In such tools, the outer radius of the shoulder is farther from the end of the probe than the inner radius of the shoulder. This allows the tool to create a successful weld over a range of thicknesses nearly equal to the taper in the shoulder (Fig. 7).

To keep the material properly constrained within the stir zone, tapered- and convex-shoulder tools need scrolls. In contrast with the scrolls on flat shoulders, scrolls on tapered and convex shoulders are typically much shallower.

Like flat-shouldered tools, convex- and tapered-shoulder tools can be run at zero tilt angles. However, unlike flat-shouldered tools, convex- and tapered-shoulder tools can be successfully run at a large range of plunge depths (Ref 94).

Tapered-shoulder tools were the initial tools in this class, and they work well. By allowing the cross section of the shoulder surface to have geometry other than a straight line, the performance of the tool can be tailored to a particular application. For example, a convex-shoulder tool can be designed that will have less variation in top surface width with plunge depth than a tapered-shoulder tool.

Tapered shoulders allowed the creation of fixed-gap bobbin tools, where two tapered shoulders were separated by a fixed-length probe (Fig. 8). The fixed-gap bobbin tool allows symmetric welding of plates with relatively inexpensive equipment, even in the presence of typical plate thickness variation.

Stationary Shoulder. If the shoulder is being used for only the primary purpose of containing material, there is no need to have the shoulder rotate with the probe. In such cases, a nonrotating or stationary shoulder can be used.

Stationary shoulders (Fig. 9) were first used in FSW of thermoplastics, where the rotating shoulder tended to fling material out of the stir zone. By moving to a stationary shoulder with



Fig. 5 Flat scrolled shoulder friction stir welding tool. Source: Ref 39

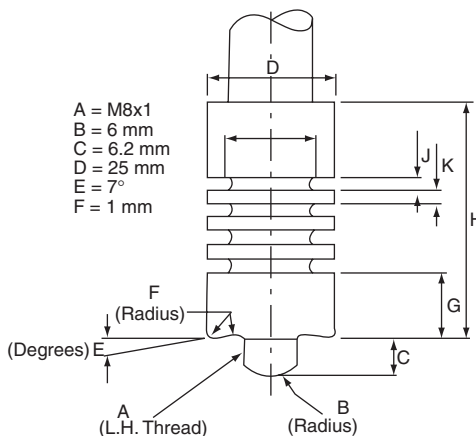


Fig. 4 Original tool design used by The Welding Institute to develop the friction stir welding process. Source: Ref 33



Fig. 6 Typical refractory metal tool geometries for welding of high-temperature materials. Source: Ref 92

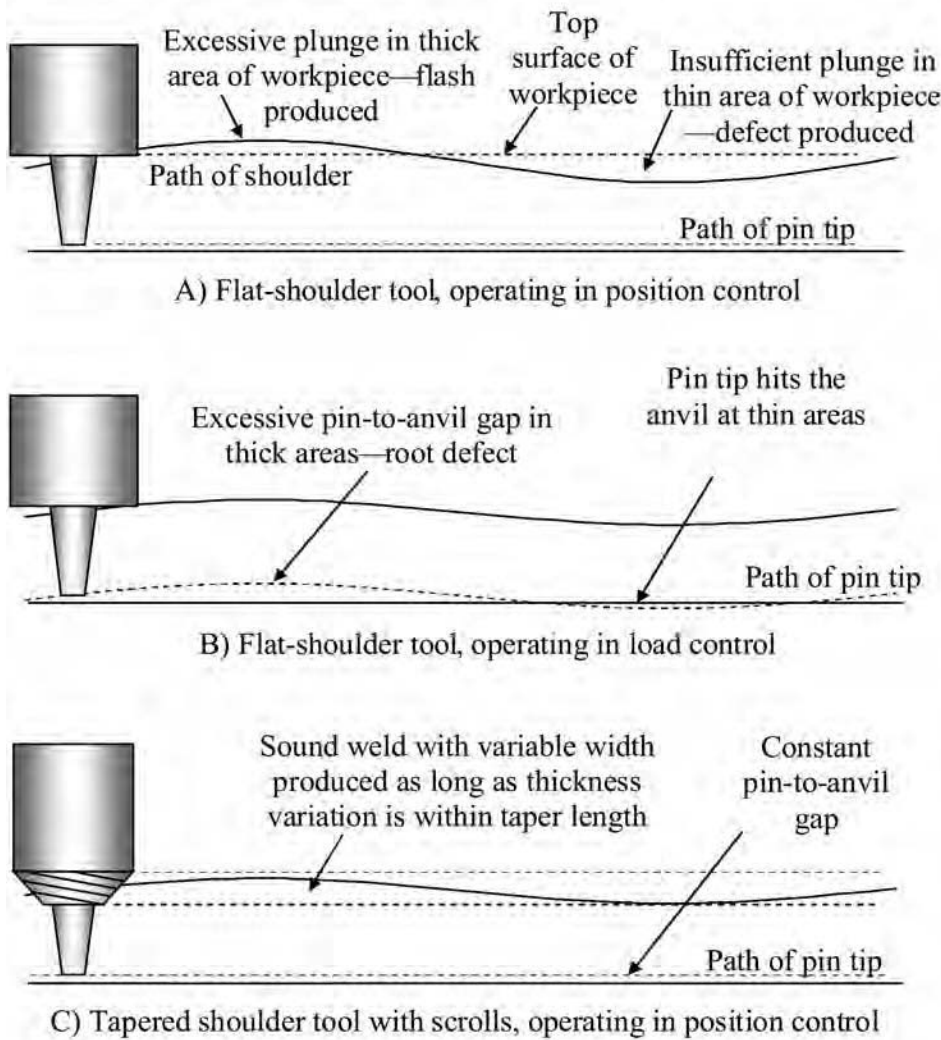


Fig. 7 Tapered-shoulder workpiece showing how a convex scrolled shoulder can accommodate variable workpiece thicknesses. Courtesy of Kevin Colligan, Concurrent Technologies Corporation

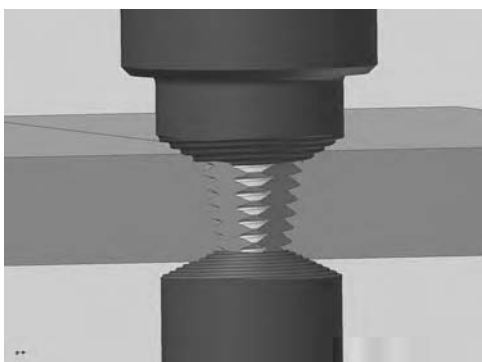


Fig. 8 Model of a fixed-gap bobbin tool with tapered scrolled shoulders. Workpiece material is removed for clarity. Courtesy of Kevin Colligan, Concurrent Technologies Corporation



Fig. 9 Stationary tool with heating cartridge embedded for use in friction stir welding of thermoplastics. Source: Ref 88

a heating cartridge embedded, the material was able to be both heated and contained (Ref 89). Stationary shoulders have also been applied in the welding of aluminum and titanium alloys. These shoulders have been used in butt

welding and fillet welding (Ref 96). Through proper design of the stationary shoulder, coupled with the addition of a feed wire, the surface profile of the weld can be controlled. For example, reinforcement can be added to a butt weld, or a radius can be added to a fillet weld. A stationary-shoulder weld can often be made with an exceptionally high-quality surface finish (Fig. 10).

One of the challenges in stationary-shoulder welding is preventing the weld material from entering the gap between the stationary shoulder and the rotating probe. This is typically accomplished through the use of very small clearances between the shoulder and the probe.

Probe Geometries

The purpose of the probe is to generate deformation and resultant heat and to facilitate the flow of the material in the stir zone. Various probe geometries and features have been used to accomplish these objectives.

Cylindrical. Probes used in the initial FSW experiments were typically cylinders with ends having a spherical radius (Ref 90) (Fig. 4). Later designs had a flat rather than round end.

Cylindrical probes have been used with various features. Smooth probes having no features have been used for experimental work (Ref 3), but their use in production work has been limited. The most common feature on cylindrical probes has been threads. Threads are generally constant-pitch, 60°, V-form threads.

When tool materials are difficult to thread, small flats have been used on a cylindrical probe to increase the heat generation in the stir zone (Ref 81). This is generally done with a symmetric series of flats at an angle to the tool axis. Three flats is a common number to use (Fig. 11).

Flutes have also been used in conjunction with threads on cylindrical pins, particularly for use in swept-spot welding. Such tools are discussed in the section on tools for specific processes.

Conical. Cylindrical tools perform well in relatively thin plate, but as plate thickness increases, the strength of a cylinder is insufficient, so tools with more strength at the top surface of the weld are desirable. The most common geometry used to accomplish this is a truncated cone or frustrum geometry. This geometry has a relatively narrow probe end to keep forces low and a relatively large probe base to keep probe strength high. Conical probes can be smooth or can use various features to improve metal flow and increase heat generation. The commonly-used features include threads, flats, and flutes, alone or in combination.

Smooth conical probes have been used for welding materials with high softening temperatures, particularly for tools made out of refractory metals (Ref 79).

Other. Some researchers have noticed that tools used to weld difficult materials, such as

materials with high softening temperatures or metal-matrix composites, deform rapidly in the early stages of welding. However, at later stages of welding, the tool deformation rate decreases. This has led these researchers to propose that the deformed probe geometries are optimal for the particular welding process.

In welding silica-reinforced aluminum with a threaded cylindrical steel probe (Ref 28–30), the probe wore near the root to greatly increase the root radius while slightly decreasing the probe radius (Fig. 12). The large radius was thought to contribute to the low wear rate.

In processing nickel-aluminum bronze with a stepped-spiral probe, the end of the probe was observed to shorten, leading to a beehive-shaped probe. It was thought that this probe shape provided an optimal trade-off between strength and slenderness.

Noncircular Cross Sections. Most FSW probes have generally circular cross sections. However, other geometries have sometimes been used. Probes with a generally polygonal cross section have been used in both butt and spot welding.

Perhaps the most widely used noncircular probe geometry is the Trivex (The Welding Institute) probe (Fig. 13). The Trivex probe is roughly triangular in shape (Ref 95, 97–99). Each of the triangular sides is a circular arc whose center is located at the opposite vertex.

The Trivex tool has a dynamic volume ratio of approximately 1.3, even without additional features being added. The Trivex tool has been found to reduce both axial and path-direction forces by approximately 20% compared to a cylindrical tool.

Probe Features

Probe features can generally be classified as threads, flats, or flutes. They serve to increase heat generation and to control the flow of the material around the pin. Flats and flutes interrupt the threads on the probe and may provide for better mixing of the weld material.

It has been proposed that a major purpose for probe features is to facilitate the transfer of weld metal from the leading edge of the weld to the trailing edge of the weld. The swept volume of the probe gives the minimum volume of the stir zone. The actual volume of the probe is the volume of the material that must be displaced. The dynamic volume ratio is the ratio of these two volumes. A smooth probe with a circular cross section has a dynamic volume ratio of 1.0. A typical cylindrical threaded probe has a dynamic volume ratio of 1.1. A probe with aggressive threads and flutes, such as the MX-Triflute (The Welding Institute), has a dynamic volume ratio of 2.6. High values of the dynamic volume ratio have been found to

lead to high weld travel speeds, particularly in thick-section welding (Ref 56).

Threads. Threaded conical pins have been reported with three different thread forms: V-threads, stepped-spiral threads, and threads with semicircular or other well-radiused root cross sections. The threads on the probe have two major purposes. First, they generate heat through forcing the deformation of the parent material. Second, they control the flow of the parent material in the vertical direction. For butt welds, the material is typically forced downward by the threads to achieve full-penetration welds. For lap and spot welds, the flow is adjusted to minimize the sheet-thinning defect.

Many of the threads used in FSW are standard V-form machine threads. These threads can be easily made from existing tools and provide the benefits of threads as mentioned previously. However, the sharp angle in the root of the thread provides a stress concentration that can lead to probe failure at high loads. They primarily load the material in shear parallel to the probe surface, so they provide less material deformation than other thread profiles.

To avoid the problems with stress concentrations at the root, threads with MX-type features have been designed (Fig. 14). These threads often have much steeper faces than the standard 60° V-thread (Ref 99). They also have generous radii at the root of the threads. This serves to

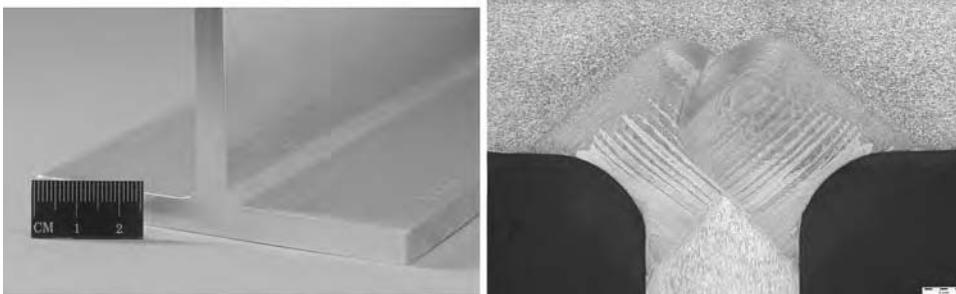


Fig. 10 Surface finish and weld profile possible with stationary-shoulder friction stir welding in fillet welding. Courtesy of Jonathan Martin, The Welding Institute



Fig. 11 Polycrystalline cubic boron nitride tool for welding ferrous alloys, showing a cylindrical probe with three flats. Source Ref 39

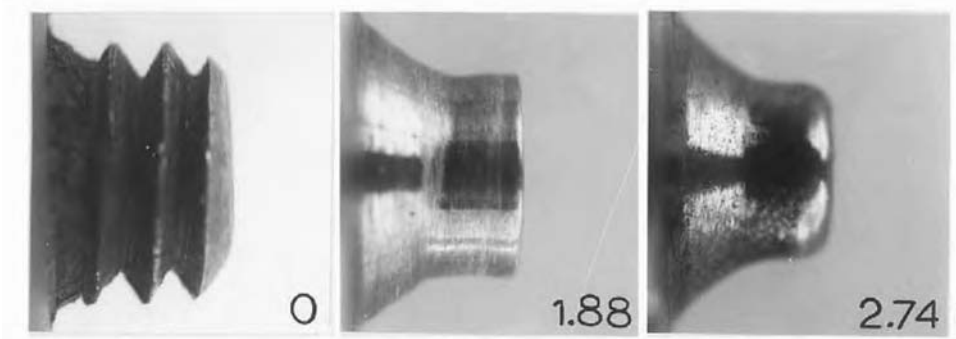


Fig. 12 Self-optimizing probe geometry resulting from wear in friction stir welding of 6061 + 20% Al_2O_3 with tool steel pin tool. Source: Ref 12

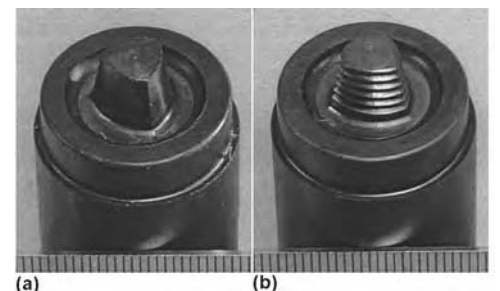


Fig. 13 Trivex tools with and without threads. Courtesy of The Welding Institute

extend tool life while increasing the dynamic volume ratio of the probe.

Stepped-spiral threads (Fig. 15) are often used on FSW probes, particularly for applications in higher-softening-temperature materials. Stepped-spiral threads have a cross section similar to a staircase, with a thrust surface parallel to the tool axis. Because the thrust surface is completely exposed to the workpiece material throughout the length of the probe, the volume of material effectively loaded by the probe is higher than for V-threads and MX threads. The dynamic volume ratio of stepped-spiral-threaded conical probes is between that for V-threaded and MX-threaded probes.

Flats are the least aggressive of the thread-interruption features. They slightly increase the dynamic volume ratio compared with threads alone. They also increase the heat-generation rate. The flat surfaces provide the equivalent of a machining tool with a large negative rake, which is inefficient for cutting but generates heat quite well.

To maximize strength, flats are generally produced in odd numbers (Ref 99). This allows the full radius of the probe to be available directly opposite the flat, thus providing the strongest possible probe for a given geometry.

Flats have not been demonstrated to have a major effect on facilitating vertical mixing of the material, but they do provide an increased rate of material flow from the advancing side to the trailing side. For a typical conical pin

with a standard V-thread form and three flats, the dynamic volume ratio is approximately 2.

In applications for aluminum and other alloys with low softening temperatures, flats are seldom used, because flutes give a higher dynamic volume ratio. However, in applications for steel and other high-softening-temperature alloys, flats are used because they can be readily made in hard tool materials and show reduced wear compared to flutes (Ref 81).

On conical probes, flats typically run parallel to the conical edge and extend the entire length of the probe. On cylindrical probes, flats are generally inclined with respect to the tool axis and cover only part of the probe length (Fig. 16).

Flutes are the most aggressive features that are typically created on FSW probes. They give the highest dynamic volume ratios, typically in the range of 2.6 (Ref 99). They are most often combined with threads when used for butt welding but have been used without threads for spot welding and lap welding.

To maximize probe strength, an odd number of flutes is generally used. Virtually all of the fluted tools described in the literature use three flutes.

The most common fluted tool described in the literature is the MX-Triflute tool, invented by The Welding Institute. This tool contains three flutes and MX threads and has been used in welding of aluminum alloys as well as copper (Ref 100).

In addition to their effect on dynamic volume ratio, which affects transport of material from the leading edge of the probe to the trailing edge, flutes can also affect the axial transport of material from the root of the probe to the end of the probe. Flutes can have any of the following characteristics (Ref 101) (Fig. 17):

- Additive, meaning that they move material in the same direction as the threads
- Neutral, meaning that they are aligned with the tool axis and have no effect on the axial material transport
- Subtractive, meaning that they move material in the opposite direction of the threads

For butt welding, an additive configuration is generally used. For lap and spot welding, a subtractive configuration is sometimes used to minimize sheet-thinning defects. Although neutral flutes have been tested, they do not appear to be in wide use.

Designs for Specific FSW Processes

Most FSW currently performed is butt welding using a pin tool with fixed geometry, as has been described previously. However, a number of processes vary from this typical practice. These processes require tool designs specific to the process.

Adjustable Probe Length. To accommodate workpieces with variable thickness, pin tools

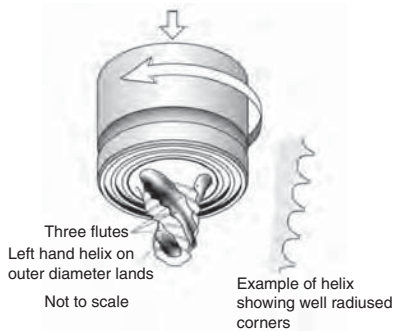


Fig. 14 Typical friction stir welding tool with an MX-Triflute probe. Source: Ref 38

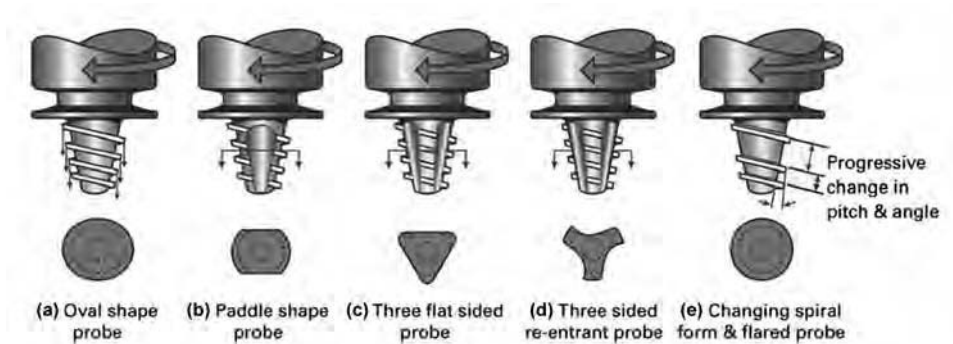


Fig. 16 Representative variations of the Whorl tool (The Welding Institute), including both flats and square threads. Source: Ref 38

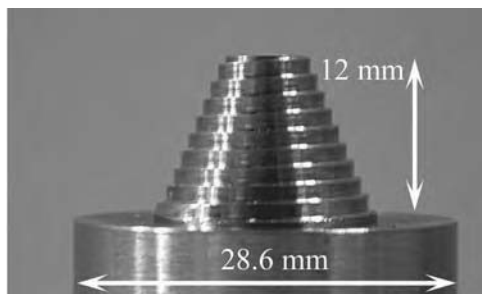


Fig. 15 Photograph of a conical probe with stepped-spiral threads. Source: Ref 38

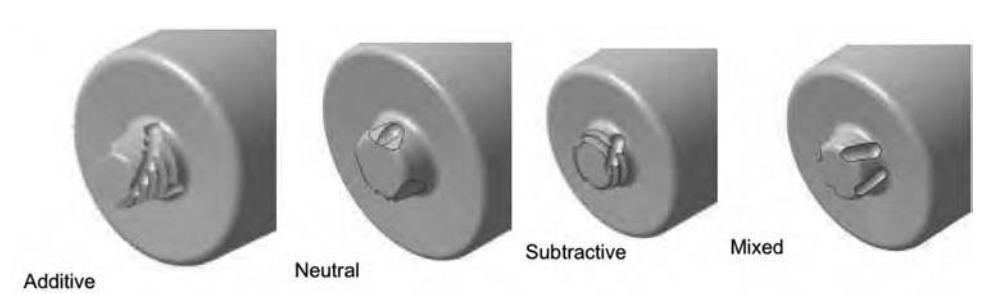


Fig. 17 Probe designs with various flute actions. Threads move material away from the shoulder; flutes have variable directions. Courtesy of Dwight Burford, National Institute for Aviation Research

with adjustable probe lengths have been developed (Ref 102, 103). These tools can also be used to eliminate the probe exit hole by gradually reducing the probe length to zero (Fig. 18). The main drawback to adjustable-probe welding is the necessity for more complex FSW machines to provide separate axes for the probe and the shoulder.

Welding with adjustable probe length requires a cylindrical probe geometry. Threads have been used with adjustable probes, as have flats, but flutes have not been reported in the literature.

Self-reacting welding (sometimes called bobbin tool) is an FSW process with no anvil. Instead, a rotating tool carries shoulders on both sides of the workpiece, with a probe that connects the two shoulders. This process minimizes the external forces required for FSW, because the two shoulders on opposite sides of the plate support the compressive loads required to forge the material in the stir zone. It also provides a way to weld without leaving a probe exit hole, because the tool can be run right off the edge of the parent metal.

Two versions of self-reacting welding have been implemented: adjustable gap and fixed gap. In adjustable-gap self-reacting FSW (Fig. 19), the lower shoulder is connected to

an adjustable probe while the upper shoulder is fixed to the machine spindle (Ref 104). By adjusting the probe length, the gap between the shoulders can be adjusted to compensate for part-thickness variations. Adjustable-gap self-reacting FSW requires machine capabilities equivalent to those for adjustable-probe FSW.

In fixed-gap self-reacting FSW, the gap between the upper and lower shoulders is fixed (Ref 105). Some form of convex or tapered shoulder is used to compensate for variations in part thickness. Any FSW machine is capable of fixed-gap self-reacting FSW. In fact, The Welding Institute has demonstrated fixed-gap self-reacting FSW on a computer numerical control milling machine (Ref 106).

Both forms of self-reacting FSW run at zero tool tilt and therefore require scrolled shoulders. Both forms carry the compressive load of the shoulders on the probe, so stresses in the probe are high. Both require cylindrical probes. In both cases, the probes are generally threaded and without flats or flutes, although flats have been used occasionally. The probe often contains left-hand threads on one end and right-hand threads on the other, to drive material flow toward the centerline of the workpiece.

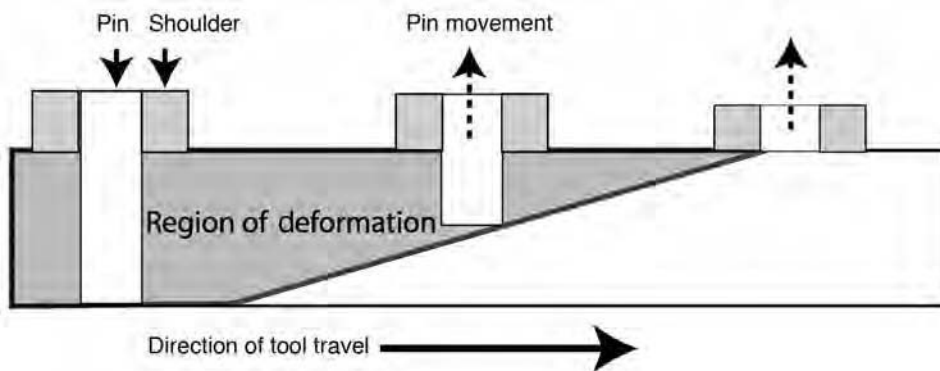


Fig. 18 Schematic showing how an adjustable probe can be extracted to eliminate an exit hole. Source: Ref 39



Fig. 19 Adjustable self-reacting (bobbin) pin tool used in friction stir welding of aluminum extrusions. Source: Ref 39

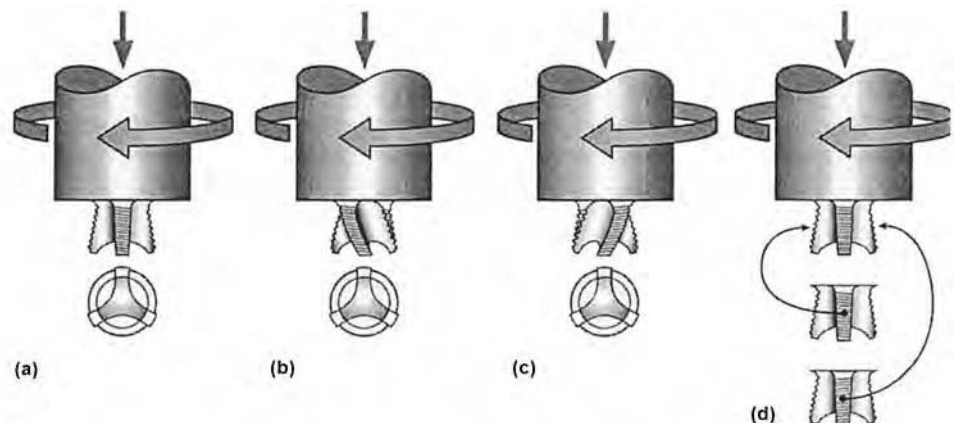


Fig. 20 Flared Triflute tool used for lap welding of aluminum. Source: Ref 39

Due to the high loads in the probe, self-reacting FSW has been demonstrated only on aluminum alloys.

Lap Welding. In lap welding, the original joint line is perpendicular to the tool axis. Standard FSW tool designs induce significant material flow parallel to the tool axis. For butt welding, this flow is vital because it allows the formation of full-penetration welds. In lap welding, this axial flow is problematic because it can create a displacement of the original joint into either the top or bottom workpiece. This displacement, known as a hooking defect or plate thinning, greatly reduces the strength of the lap joint (Ref 107).

To avoid the hooking defect, it is desirable to minimize the flow of material across the original joint. At the same time, to eliminate the original joint, it is necessary to have significant flow in the plane of the joint. This requires design of special probes for effective lap welding.

One very effective probe for lap welding is the flared probe. Flared probes are frustrums of cones that have a radius that is larger at the end of the probe than at the probe root. These tools, generally in the form of a Flared-Triflute tool (The Welding Institute) (Fig. 20), have been used effectively in lap welds for relatively thick aluminum (Ref 108). Flared-Triflute tools have been demonstrated to reduce process forces and reduce upper plate thinning by a factor of 4.

Refill Spot Welding. Refill friction stir spot welding (RFSSW) (Fig. 21) was developed by GKSS (Ref 109).

In RFSSW, a tool with three coaxial pieces having relative motion is used. The outer piece is a stationary clamp. The intermediate piece is a rotating shoulder that can also move axially relative to the clamp. The inner piece is a rotating probe that moves axially relative to the clamp and the shoulder. In RFSSW, the clamp is brought to the surface of the parts to be welded. The rotating probe is then extended into the cavity formed by the shoulder, the probe, and the clamp. Finally, the shoulder is extended

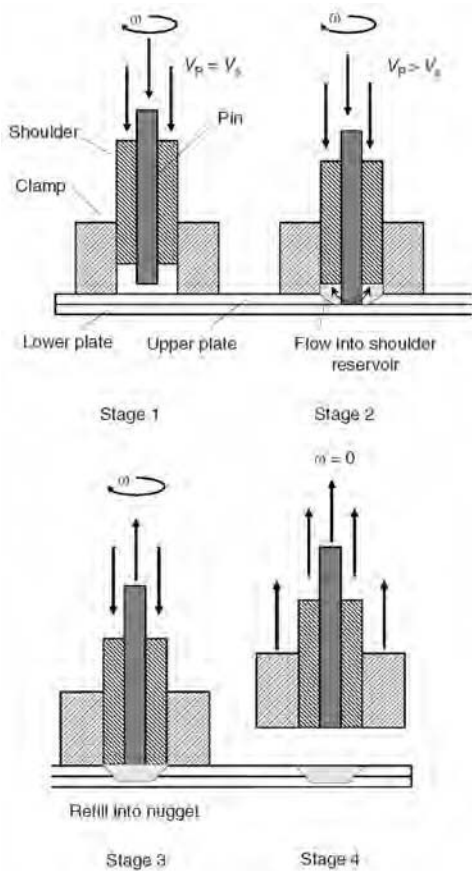


Fig. 21 Schematic diagram of refill friction stir spot welding process. Source: Ref 109

to the surface of the workpiece while the probe is retracted to the surface of the workpiece, leaving the final weld surface flush with the original surface of the workpiece.

Because of the need for axial motion while constraining the weld material, the probe geometry for RFSSW must be cylindrical. As with adjustable-probe FSW, threads have been used in RFSSW tools, but no flats or flutes have been reported in the literature.

Swept Spot Welding. Swept spot friction stir welding (SSFSW) is used to join thin sheets in a lap configuration. In SSFSW, a fixed-probe FSW tool is displaced into the upper sheet. The tool is then transformed through a relatively localized path to create a localized lap weld. The path can have various geometries, such as stitch welding, swing welding (Fig. 22), and Octaspot welding (Wichita State University) (Fig. 23) (Ref 101, 110, 111).

In each of these welding processes, the objective is to eliminate the oxide layer between the sheets to enable a metallurgical bond. A potential failure mode in SSFSW is the sheet-thinning or hooking defect, where the remnant oxide layer is displaced upward or downward from its original location, leading to reduced strength due to reduced sheet thickness.

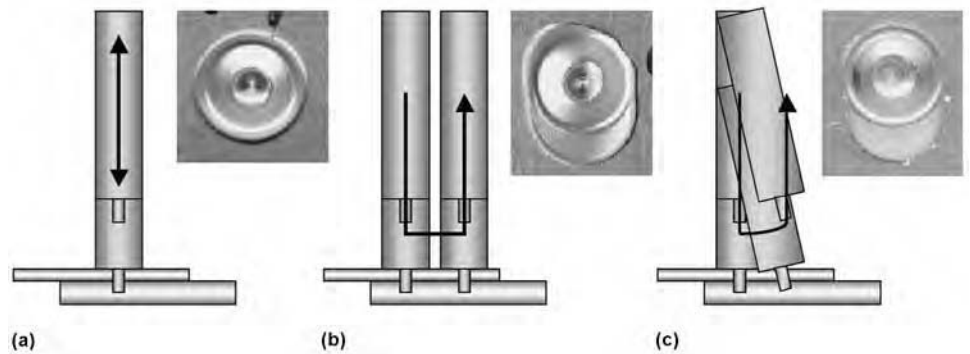


Fig. 22 Tool movement and view of finished spot for three variants of friction stir welding (FSW) spot welds. (a) Friction stir spot welding (sometimes called poke welding). (b) Stitch FSW. (c) Swing FSW. Source: Ref 110

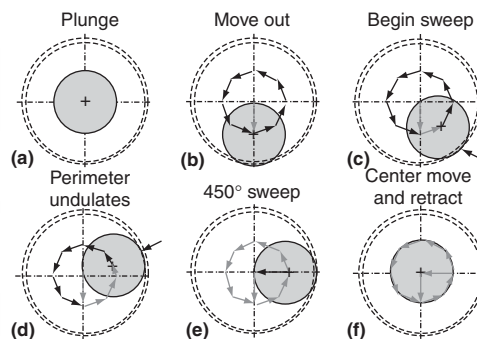


Fig. 23 Path moved by the tool in an Octaspot weld. Source: Ref 101

Control of vertical flow is important in SSFSW to minimize the sheet-thinning defect. Tools with cylindrical probes, threads, flats, and flutes have been used in SSFSW. Trivex tools have been found to provide improved spot weld strength.

Predicting and Measuring Tool Performance

At the present time (2011), design of pin tools for friction stir processing is as much art as science. Hypotheses concerning the effects of tool features on tool performance are difficult to prove, and tool design is accomplished more by judgment than by calculations. Efforts to improve this situation are proceeding through numerical modeling as well as through experimental investigations.

Modeling of Tool Features

Numerical modeling of the FSW process is a challenging task. It is a coupled thermomechanical process, with large gradients in both temperature and deformation. Furthermore, large plastic deformations are observed in the process. Thus, models are often used more to gain insight into the appropriate physics than to obtain an exact answer about the process.

Of particular challenge when modeling tool features is the fact that the threads are generally quite small compared to the dimensions of the probe, shoulder, and workpiece. A mesh that accurately captures the threads would be very large and lead to extremely long solution times. Thus, in most numerical models of FSW, the threads are not explicitly modeled. Instead, a boundary condition representing the effect of the threads is applied to the probe surface.

While this simplification makes sense from a modeling point of view, it makes it difficult to model the effects of the threads, because the boundary condition is an input to the model rather than an output.

Perhaps the most thorough numerical investigation of the effects of tool features has been carried out by Colegrove and Shercliff (Ref 95, 97). Using two- and three-dimensional computational fluid dynamics models, they explored a variety of probe profiles to examine the effects on material flow and probe-boundary conditions. To enable calculations in a reasonable time, they decoupled the thermal model from the flow model. The flow model was restricted to the region near the probe, and fine features on the tool, such as the threads on the probe, were ignored. It was expected that these were second-order effects.

The Colegrove and Shercliff model was effective in predicting the potential for defect formation with the Trivex tool and demonstrated increased axial flow in the Triflute tool (Fig. 24). Predicted force trends for both the Triflute and Trivex tools matched the experimental data, even though the absolute numerical values were significantly different.

Buffa et al. propose a method for designing optimal FSW tools through the application of a numerical model of the FSW process (Ref 113). Although the process seems sound, and the parametric exploration of the tool design space is appropriate, it appears that the model is too simple to provide reliable results.

The scientific design of FSW tools through predictive modeling is currently not technically feasible.

Experimental Observation of Tool Features

Experimental observation of the effects of features on tool performance is generally limited to single-point observations. For example, Colegrove and Shercliff compared the performance of Trivex and Triflute tools at various operating parameters. However, they compared only one version of the Trivex tool and one version of the Triflute tool.

The parametric exploration of FSW tools is a relatively new experimental technique. Yang et al. explored eight different tools in a parametric study of lap welding of magnesium (Ref 114). They identified that a triangular-shaped probe (Fig. 25) was superior to a round or pie-shaped probe, and that a small-diameter shoulder was superior to a large-diameter shoulder.

Sorensen and Nielsen completed a parametric exploration of convex scrolled-shoulder, stepped-spiral probe tools (Fig. 26) in FSW of AA7075 (Ref 94). They explored the effects of all the parameters used to design the tool in a screening design to identify the parameters that had a significant effect on process forces, spindle torque, and tool temperature. They identified probe angle, shoulder length, scroll radius, and scroll pressure angle as the most significant variables affecting the performance of the tool (Table 3). A follow-on response-surface study by Nielsen identified correlation functions to predict the process loads, torque, temperature, and defect formation as a function of tool design and operating parameters (Ref 115).

Although experimental studies such as these are time-consuming, at present they provide the best opportunity for quantifying the effects of tool design on the FSW process.

Summary

Much is known about the design of FSW tools. The design process is still somewhat empirical, but tool design can proceed on a rational basis. Tool materials can be chosen to be compatible with the material to be welded. Tool geometry and tool features can be chosen to achieve the desired weld characteristics. Modeling and experimentation have demonstrated the ability to assist in the selection of specific values for tool and operating parameters. Tools should be carefully designed to achieve the desired properties in the completed weld.

REFERENCES

1. W.J. Arbegast, Modeling Friction Stir Joining as a Metal Working Process, *Hot Deformation of Aluminum Alloys*, Z. Jin, Ed., TMS, 2003
2. H. Atharifar, D.C. Lin, and R. Kovacevic, Numerical and Experimental Investigations

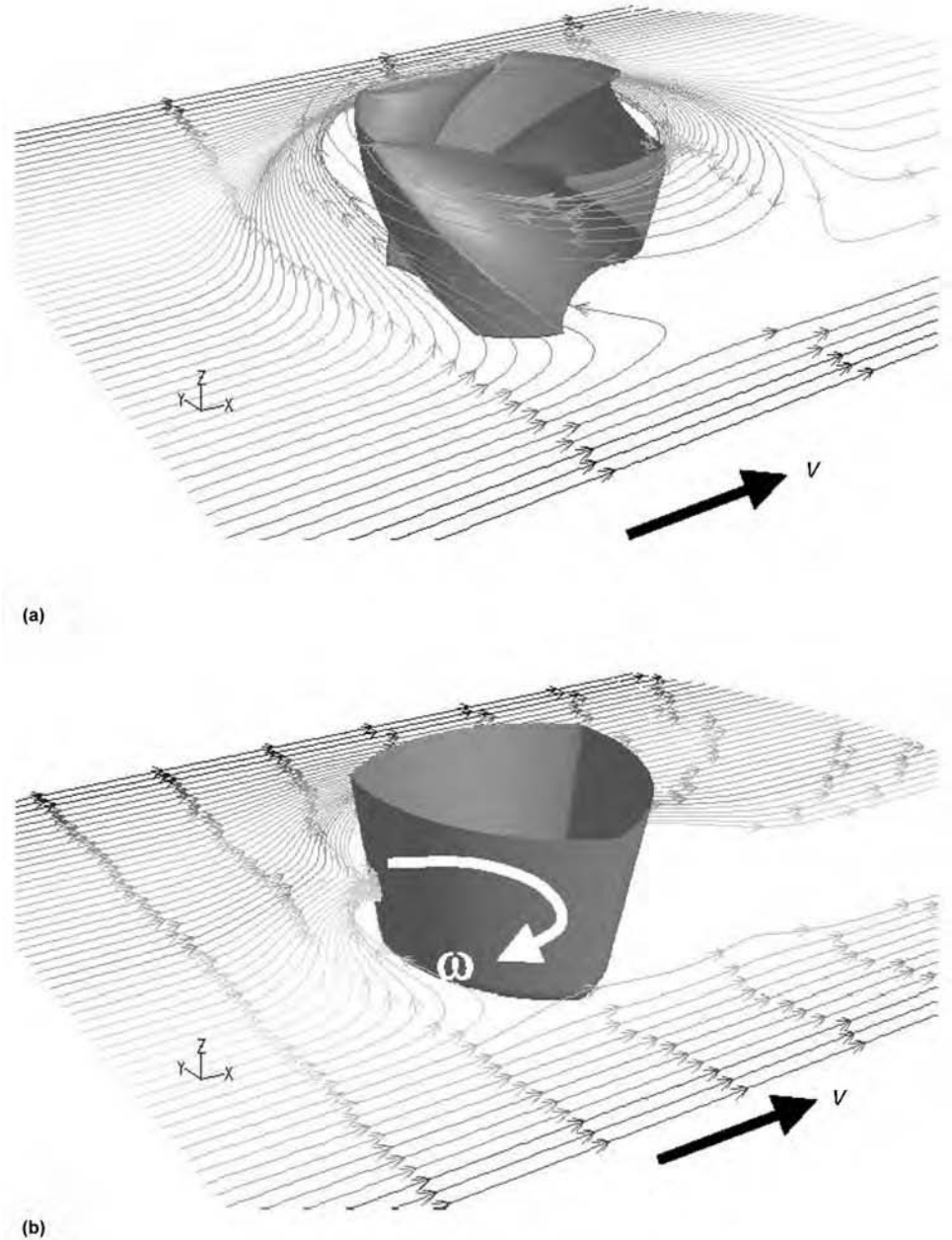


Fig. 24 Predicted streamlines around (a) Triflute and (b) Trivex probes. Flow is much less regular around the Trivex, which increases the likelihood of defect formation. Source: Ref 112

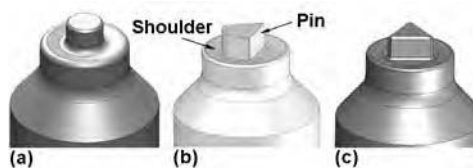


Fig. 25 Schematic representation of the variant spot welding tools used by Yang et al. Source: Ref 114

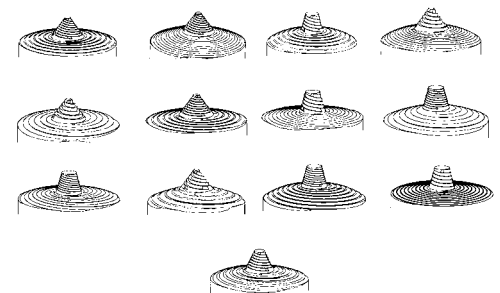


Fig. 26 Convex scrolled-shoulder, stepped-spiral probe tools explored in Plackett-Burman screening experiment. Source: Ref 94

Table 3 Most important parameters for determining various responses in the friction stir welding process

Parameter	Axial force	Longitudinal force	Lateral force	Spindle torque	Tool temperature
Cone angle	1
Shoulder curvature	1	2	...	1	1
Shoulder length	2	1
Spiral starts
Spiral height	3
Pressure angle	3	...	2	2	...
Scroll starts	4	...	4
Scroll radius
Land fraction

- on the Loads Carried by the Tool during Friction Stir Welding, *J. Mater. Eng. Perform.*, Vol 18 (No. 4), 2009, p 339–350
- C.D. Sorensen and A.L. Stahl, Experimental Measurements of Load Distributions on Friction Stir Weld Pin Tools, *Metall. Mater. Trans. B*, Vol 38 (No. 3), 2007, p 451–459
 - C. Standen, B.K. Jahsti, D.J. Medlin, and W.J. Arbegast, Liquid Metal Embrittlement of MP-159 Pin Tools, *Friction Stir Welding and Processing IV*, p 395–401
 - R. Schafrik and R. Sprague, Saga of Gas Turbine Materials, *Adv. Mater. Process.*, April 2004
 - R. Rai, A. De, H.K.D.H. Bhadeshia, and T. DebRoy, Review: Friction Stir Welding Tools, *Sci. Technol. Weld. Join.*, 2011
 - S.A. David, S.M. Packer, T.W. Nelson, and C.D. Sorensen, unpublished research
 - T. Leonhardt, Properties of Tungsten-Rhenium and Tungsten-Rhenium with Hafnium Carbide, *JOM*, Vol 61 (No. 7), 2009, p 68–71
 - M.A. Sutton, A.P. Reynolds, B. Yang, and R. Taylor, Mixed Mode I/II Fracture of 2024-T3 Friction Stir Welds, *Eng. Fract. Mech.*, Vol 70, 2003, p 2215–2234
 - M.A. Sutton, A.P. Reynolds, J. Yan, B. Yang, and N. Yuan, Microstructure and Mixed Mode I/II Fracture of AA2524-T351 Base Material and Friction Stir Welds, *Eng. Fract. Mech.*, Vol 73 (No. 4), 2006, p 391–407
 - R.S. Mishra and Z.Y. Ma, Friction Stir Welding and Processing, *Mater. Sci. Eng. A*, Vol 50 (No. 1–2), 2005, p 1–78
 - R.A. Prado, L.E. Murr, D.J. Shindo, and K.F. Soto, Tool Wear in the Friction-Stir Welding of Aluminum Alloy 6061 + 20% Al₂O₃: A Preliminary Study, *Scr. Mater.*, Vol 45 (No. 1), 2001, p 75–80
 - W.B. Lee, Y.M. Yeon, and S.B. Jung, Joint Properties of Friction Stir Welded AZ31B-H24 Magnesium Alloy, *Mater. Sci. Technol.*, Vol 19 (No. 6), 2003, p 785–790
 - N.A. Rodriguez, E. Almanza, C.J. Alvarez, and L.E. Murr, Study of Friction Stir Welded A319 and A413 Aluminum Casting Alloys, *J. Mater. Sci.*, Vol 40 (No. 16), 2005, p 4307–4312
 - H. Nami, H. Adgi, M. Sharifitabar, and H. Shamabadi, Microstructure and Mechanical Properties of Friction Stir Welded Al/Mg₂Si Metal Matrix Cast Composite, *Mater. Des.*, Vol 32 (No. 2), 2011, p 976–983
 - R.K.R. Singh, C. Sharma, D.K. Dwivedi, N.K. Mehta, and P. Kumar, The Microstructure and Mechanical Properties of Friction Stir Welded Al-Zn-Mg Alloy in As-Welded and Heat Treated Conditions, *Mater. Des.*, Vol 32 (No. 2), 2011, p 682–687
 - S. Rajakumar, C. Muralidharan, and V. Balasubramanian, Influence of Friction Stir Welding Process and Tool Parameters on Strength Properties of AA7075-T-6 Aluminium Alloy Joints, *Mater. Des.*, Vol 32 (No. 2), 2011, p 535–549
 - W.M. Thomas, E.D. Nicholas, E.R. Watts, and D.G. Staines, Friction Based Welding Technology for Aluminium, *Mater. Sci. Forum*, 2002, p 396–402, 1543–1548
 - C.Y. Lee, D.H. Choi, Y.M. Yeon, and S. B. Jung, Dissimilar Friction Stir Spot Welding of Low Carbon Steel and Al-Mg Alloy by Formation of IMCS, *Sci. Technol. Weld. Join.*, Vol 14 (No. 3), 2009, p 216–220
 - A. Elrefaey, M. Gouda, M. Takahashi, and K. Ikeuchi, Characterization of Aluminum/Steel Lap Joint by Friction Stir Welding, *J. Mater. Eng. Perform.*, Vol 14 (No. 1), 2005, p 10–17
 - T. Chen, Process Parameters Study on FSW Joint of Dissimilar Metals for Aluminum-Steel, *J. Mater. Sci.*, Vol 44 (No. 10), 2009, p 2573–2580
 - T.P. Chen and W.B. Lin, Optimal FSW Process Parameters for Interface and Welded Zone Toughness of Dissimilar Aluminium-Steel Joint, *Sci. Technol. Weld. Join.*, Vol 15 (No. 4), 2010, p 279–285
 - T. DebRoy and H. Bhadeshia, Friction Stir Welding of Dissimilar Alloys—A Perspective, *Sci. Technol. Weld. Join.*, Vol 15 (No. 4), 2010, p 266–270
 - U. Dressler, G. Biallas, and U.A. Mercado, Friction Stir Welding of Titanium Alloy TiAl6V4 to Aluminium Alloy AA2024-T3, *Mater. Sci. Eng. A*, Vol 526 (No. 1–2), 2009, p 113–117
 - M.P. Miles, Z. Feng, K. Kohkonen, B. Weickum, R. Steel, and L. Lev, Spot Joining of AA 5754 and High Strength Steel Sheets by Consumable Bit, *Sci. Technol. Weld. Join.*, Vol 15 (No. 4), 2010, p 325–330
 - C. Meran and V. Kovan, Microstructures and Mechanical Properties of Friction Stir Welded Dissimilar Copper/Brass Joints, *Materialwiss. Werkstofftech.*, Vol 39 (No. 8), 2008, p 521–530
 - G. Kennedy, R. Sprague, and R. Kennedy, *Tool Steels*, 5th ed., ASM International, 1998, p 219–250
 - R.A. Prado, L.E. Murr, D.J. Shindo, and J. C. McClure, Friction Stir Welding: A Study of Tool Wear Variation in Aluminum Alloy 6061-20% Al₂O₃, *Friction Stir Welding and Processing*, K.V. Jata, M.W. Mahoney, R.S. Mishra, S.L. Semiatin, and D.P. Field, Ed., TMS, 2001, p 105–116
 - R.A. Prado, L.E. Murr, A.R. Rivera, D.J. Shindo, K.F. Soto, G.J. Fernandez, and J. C. McClure, Tool Wear and Shape Optimization in the Friction-Stir Welding of Aluminum Metal-Matrix Composite, *Friction Stir Welding and Processing II*, K.V. Jata, M.W. Mahoney, R.S. Mishra, S.L. Semiatin, and T. Lienert, Ed., TMS, 2003, p 23–32
 - S.H. Kazi and L.E. Murr, Complex Flow Phenomena Associated with Friction-Stir Welding of Aluminum Alloys, *Friction Stir Welding and Processing*, K.V. Jata, M.W. Mahoney, R.S. Mishra, S.L. Semiatin, and D.P. Field, Ed., TMS, 2001, p 139–150
 - H. Fujii, Y. Takada, N. Tsuji, and K. Nogi, Friction Stir Welding of Ultrafine Grained Materials, *Proceedings of the Fifth International Conference on Friction Stir Welding*, Sept 14–16, 2004 (Metz, France), TWI, paper on CD
 - O.T. Midling and G. Rorvik, Effect of Tool Shoulder Material on Heat Input during Friction Stir Welding, *Proceedings of the First International Conference on Friction Stir Welding*, June 14–16, 1999 (Thousand Oaks, CA), TWI, paper on CD
 - P.A. Colegrove and H.R. Shercliff, Experimental and Numerical Analysis of Aluminum Alloy 7075-T7351 Friction Stir Welds, *Sci. Technol. Weld. Join.*, Vol 8 (No. 5), 2003, p 360–368
 - L. Cederqvist, C.D. Sorensen, A. Reynolds, and T. Oberg, Improved Process Stability during Friction Stir Welding of 5 cm Thick Copper Canisters through Shoulder Geometry and Parameter Studies, *Sci. Technol. Weld. Join.*, Vol 14 (No. 2), 2009
 - K.J. Colligan, J. Xu, and J.R. Pickens, Welding Tool and Process Parameter Effects in Friction Stir Welding of Aluminum Alloys, *Friction Stir Welding and*

- Processing II*, K.V. Jata, M.W. Mahoney, R.S. Mishra, S.L. Semiatin, and T. Lienert, Ed., TMS, 2003, p 181–190
36. S.P. Vaze, J. Xu, R.J. Ritter, K.J. Colligan, J.J. Fisher, Jr., and J.R. Pickens, Friction Stir Processing of Aluminum Alloy 5083 Plate for Cold Bending, *Mater. Sci. Forum*, Vol 426–432, 2003, p 2979–2986
 37. Y. Sato, M. Miyake, H. Kokawa, T. Omori, K. Ishida, S. Imano, S.H.C. Park, and S. Hirano, *Development of a Cobalt-Based Alloy FSW Tool for High-Softening-Temperature Materials*, John Wiley & Sons, Hoboken, NJ, 2011, p 3–9
 38. C.B. Fuller, Friction Stir Tooling: Tool Materials and Designs, *Friction Stir Welding and Processing*, R.S. Mishra and M.W. Mahoney, Ed., ASM International, 2007, p 7–35
 39. C.D. Sorensen and T.W. Nelson, Friction Stir Welding of Ferrous and Nickel Alloys, *Friction Stir Welding and Processing IV*, R.S. Mishra and M.W. Mahoney, Ed., ASM International, 2007, p 111–121
 40. M.W. Mahoney, W.H. Bingel, S.R. Sharma, and R.S. Mishra, Microstructural Modification and Resultant Properties of Friction Stir Processed Cast NiAl Bronze, *Mater. Sci. Forum*, Vol 426–432, 2003, p 2843–2848
 41. B. London, J. Fino, A. Pelton, C. Fuller, and M. Mahoney, Friction Stir Processing of Nitinol, *Friction Stir Welding and Processing III*, K.V. Jata, M.W. Mahoney, R. S. Mishra, and T.J. Lienert, Ed., TMS, 2005, p 67–74
 42. L. Christodoulou, W. Palko, and C. Fuller, Equipment and Processing Variables Affecting Friction Stir Processing of NiAl Bronze, *Friction Stir Welding and Processing III*, K.V. Jata, M.W. Mahoney, R.S. Mishra, and T.J. Lienert, Ed., TMS, 2005, p 57–66
 43. M.W. Mahoney, C.B. Fuller, W.H. Bingel, and M. Calabrese, Friction Stir Processing of Cast NiAl Bronze, *THERMEC 2006*, July 4–8, 2006 (Vancouver, Canada), TMS
 44. M.I. Khan, M.L. Kuntz, P. Su, A. Gerlich, T. North, and Y. Zhou, Resistance and Friction Stir Spot Welding of DP600: A Comparative Study, *Sci. Technol. Weld. Join.*, Vol 12 (No. 2), 2007, p 175–182
 45. B. Thompson and S.S. Babu, Tool Degradation Characterization in the Friction Stir Welding of Hard Metals, *Weld. J.*, Vol 89 (No. 12), 2010, p 256S–261S
 46. T. Weinberger, N. Enzinger, and H. Cerjak, Microstructural and Mechanical Characterisation of Friction Stir Welded 15-5PH Steel, *Sci. Technol. Weld. Join.*, Vol 14 (No. 3), 2009, p 210–215
 47. T. Liyanage, J. Kilbourne, A.P. Gerlich, and T.H. North, Joint Formation in Dissimilar Al Alloy/Steel and Mg Alloy/Steel Friction Stir Spot Welds, *Sci. Technol. Weld. Join.*, Vol 14 (No. 6), 2009, p 500–508
 48. P. Edwards and M. Ramulu, Effect of Process Conditions on Superplastic Forming Behaviour in Ti-6Al-4V Friction Stir Welds, *Sci. Technol. Weld. Join.*, Vol 14 (No. 7), 2009, p 669–680
 49. T.J. Lienert, W.L. Stellwag, Jr., B.B. Grimmer, and R.W. Warke, Friction Stir Welding Studies on Mild Steel, *Weld. J.*, Jan 2003, p 1-s to 9-s
 50. H.J. Liu, J.C. Feng, H. Fujii, and K. Nogi, Wear Characteristics of a WC-Co Tool in Friction Stir Welding of AC4A + 30 Vol%SiCP Composite, *Int. J. Mach. Tools Manuf.*, Vol 45 (No. 14), 2005, p 1635–1639
 51. C. Meran, V. Kovan, and A. Alptekin, Friction Stir Welding of AISI 304 Austenitic Stainless Steel, *Materialwiss. Werkstofftech.*, Vol 38, 2007, p 829–835
 52. T.W. Nelson, Friction Stir Welding of Aluminum MMC 6061-Boron Carbide, *Aeromat 2000*
 53. S. Gimenez, O. Van der Biest, and J. Vleugels, The Role of Chemical Wear in Machining Iron Based Materials by PCD and PCBN Super-Hard Tool Materials, *Diam. Relat. Mater.*, 2007
 54. C.Y. Lee, D.H. Choi, Y.M. Yeon, and S. B. Jung, Dissimilar Friction Stir Spot Welding of Low Carbon Steel and Al-Mg Alloy by Formation of IMCs, *Sci. Technol. Weld. Join.*, Vol 14 (No. 3), 2009, p 216–220
 55. Y. Yang, H. Dong, H. Cao, Y. Chang, and S. Kou, Liquefaction of Mg Alloys in Friction Stir Spot Welding, *Weld. J.*, 2008, p 167–177
 56. L. Cederqvist, FSW to Seal 50 mm Thick Copper Canisters—A Weld That Lasts for 100,000 Years, *Proceedings of the Fifth International Conference on Friction Stir Welding*, Sept 14–16, 2004 (Metz, France), TWI, paper on CD
 57. C.D. Sorensen, T.W. Nelson, S.M. Packer, and R.J. Steel, Innovative Technology Application in FSW of High Softening Temperature Materials, *Proceedings of the Fifth International Conference on Friction Stir Welding*, Sept 14–16, 2004 (Metz, France), TWI, paper on CD
 58. Y. Zhang, Y.S. Sato, H. Kokawa, S.H.C. Park, and S. Hirano, Stir Zone Microstructure of Commercial Purity Titanium Friction Stir Welded Using PCBN Tool, *Mater. Sci. Eng. A*, Vol 488 (No. 1–2), 2008, p 25–30
 59. P. Edwards and M. Ramulu, Identification of Process Parameters for Friction Stir Welding Ti-6Al-4V, *J. Eng. Mater. Technol. ASME*, Vol 132 (No. 3), 2010, p 031006
 60. P.D. Edwards and M. Ramulu, Investigation of Microstructure, Surface and Subsurface Characteristics in Titanium Alloy Friction Stir Welds of Varied Thicknesses, *Sci. Technol. Weld. Join.*, Vol 14 (No. 5), 2009, p 476–483
 61. P. Edwards and M. Ramulu, Peak Temperatures during Friction Stir Welding of Ti-6Al-4V, *Sci. Technol. Weld. Join.*, Vol 15 (No. 6), 2010, p 468–472
 62. A.P. Reynolds, E. Hood, and W. Tang, Texture in Friction Stir Welds of Timetal 21S, *Scr. Mater.*, Vol 52 (No. 6), 2005, p 491–494
 63. A.P. Reynolds, unpublished research, 2009
 64. W.M. Thomas, P.L. Threadgill, and E.D. Nicholas, Feasibility of Friction Stir Welding Steel, *Sci. Technol. Weld. Join.*, Vol 4 (No. 6), 1999, p 365–372
 65. K. Okamoto, S. Hirano, M. Inagaki, S.H.C. Park, Y.S. Sato, H. Kokawa, T.W. Nelson, and C.D. Sorensen, Metallurgical and Mechanical Properties of Friction Stir Welded Stainless Steels, *Proceedings of the Fourth International Symposium on Friction Stir Welding*, May 14–16, 2003 (Park City, UT), TWI, paper on CD
 66. S. Park, Y. Sato, H. Kokawa, K. Okamoto, S. Hirano, and M. Inagaki, Boride Formation Induced by PCBN Tool Wear in Friction-Stir-Welded Stainless Steels, *Metall. Mater. Trans. A*, Vol 40 (No. 3), 2009, p 625–636
 67. A.P. Reynolds, W. Tang, T. Gnaupel-Herold, and H. Prask, Structure, Properties, and Residual Stress of 304L Stainless Steel Friction Stir Welds, *Scr. Mater.*, Vol 48 (No. 9), May 2003, p 1289–1294
 68. A.P. Reynolds, M. Posada, J. DeLoach, M.J. Skinner, and T.J. Lienert, FSW of Austenitic Stainless Steels, *Proceedings of the Third International Symposium on Friction Stir Welding*, Sept 2011 (Kobe, Japan), TWI, paper on CD
 69. C.D. Sorensen and T.W. Nelson, Sigma Phase Formation in Friction Stirring of Iron-Nickel-Chromium Alloys, *Trends in Welding Research, Proceedings of the Seventh International Conference*, ASM International, 2005
 70. Y.S. Sato, T.W. Nelson, and C.J. Sterling, Recrystallization in Type 304L Stainless Steel during Friction Stir Welding, *Acta Mater.*, Vol 53, 2005, p 637–645
 71. C.D. Sorensen, T.W. Nelson, B.D. Nelson, and M. Abbasi, Tool Features and Extended Plasticity Mechanisms in FSW of 304L, *Proceedings of the International Society of Offshore and Polar Engineers 2011*, in press
 72. R.J. Steel, C.O. Pettersson, C.D. Sorensen, Y. Sato, C.J. Sterling, and S.M. Packer, Friction Stir Welding of SAF 2507 (UNS S32750) Super Duplex Stainless Steel, Paper PO346, *Proceedings of Stainless Steel World 2003*, KCI Publishing

73. M. Posada, J. DeLoach, A.P. Reynolds, and J.P. Halpin, Mechanical Property and Microstructural Evaluation of Friction Stir Welded AL-6XN, *Trends in Welding Research, Proceedings of the Sixth International Conference*, April 15–19, 2002 (Pine Mountain, GA), ASM International, p 307–311
74. M. Posada, J. DeLoach, A.P. Reynolds, M. Skinner, and J.P. Halpin, Friction Stir Weld Evaluation of DH-36 and Stainless Steel Weldments, *Friction Stir Welding and Processing*, TMS, 2001, p 159–171
75. R. Johnson, J. dos Santos, and M. Magnasco, Mechanical Properties of Friction Stir Welded S355 C-Mn Steel Plates, *Proceedings of the Fourth International Symposium on Friction Stir Welding*, May 14–16, 2003 (Park City, UT), TWI, paper on CD
76. T.J. Lienert, W. Tang, J.A. Hogeboom, and L.G. Kvidahl, Friction Stir Welding of DH-36 Steel, *Proceedings of the Fourth International Symposium on Friction Stir Welding*, May 14–16, 2003 (Park City, UT), TWI, paper on CD
77. P.J. Konkol, J.A. Mathers, R. Johnson, and J.R. Pickens, Friction Stir Welding of HSLA-65 Steel for Shipbuilding, *J. Ship Prod.*, Vol 19 (No. 3), Aug 2003, p 159–164
78. M. Posada, J. DeLoach, A.P. Reynolds, R. Fonda, and J. Halpin, Evaluation of Friction Stir Welded HSLA-65, *Proceedings of the Fourth International Symposium on Friction Stir Welding*, May 14–16, 2003 (Park City, UT), TWI, paper on CD
79. B. Thompson and S.S. Babu, Tool Degradation Characterization in the Friction Stir Welding of Hard Metals, *Weld. J.*, 2010, p 256–261
80. P. Konkol, Characterization of Friction Stir Weldments in 500 Brinell Hardness Quenched and Tempered Steel, *Proceedings of the Fourth International Symposium on Friction Stir Welding*, May 14–16, 2003 (Park City, UT), TWI, paper on CD
81. C.J. Sterling, T.W. Nelson, C.D. Sorensen, R.J. Steel, and S.M. Packer, Friction Stir Welding of Quenched and Tempered C-Mn Steel, *Friction Stir Welding and Processing II*, TMS, 2003, p 165–171
82. Z. Feng, Friction Stir Welding of API Grade X-65 Steel Pipe, *Annual AWS Conference* (Dallas, TX), American Welding Society, 2005
83. A. Ozekcin, H. Jin, J.Y. Koo, N.V. Bangaru, R. Ayer, and S. Packer, A Microstructural Study of Friction Stir Welded Joints of Carbon Steels, *ISOPE 2004*, May 23–28, 2004 (Toulon, France), International Society of Offshore and Polar Engineers
84. F. Ye, H. Fujii, T. Tsumura, and K. Nakata, Friction Stir Welding of Inconel Alloy 600, *J. Mater. Sci.*, Vol 41 (No. 16), p 5376–5379
85. R.A. Prado, L.E. Murr, K.F. Soto, and J. C. McClure, Self-Optimization in Tool Wear for Friction-Stir Welding of Al6061 + 20% Al₂O₃ MMC, *Mater. Sci. Eng. A*, Vol 349 (No. 1–2), 2003, p 156–165
86. G.J. Fernandez and L.E. Murr, Characterization of Tool Wear and Weld Optimization in the Friction-Stir Welding of Cast Aluminum 359 + 20% SiC Metal-Matrix Composite, *Mater. Charact.*, Vol 52 (No. 1), 2004, p 65–75
87. D.J. Shindo, A.R. Rivera, and L.E. Murr, Shape Optimization for Tool Wear in the Friction-Stir Welding of Cast Al359-20% SiC MMC, *J. Mater. Sci.*, Vol 37 (No. 23), 2002, p 4999–5005
88. S.R. Strand, C.D. Sorensen, and T.W. Nelson, Effects of Friction Stir Welding on Polymer Microstructure, *ANTEC 2003, Conference Proceedings*, May 2003 (Nashville, TN), Society of Plastics Engineers
89. C.D. Sorensen, T.W. Nelson, S. Strand, C. Johns, and J. Christensen, Joining of Thermoplastics with Friction Stir Welding, *ANTEC 2001, Conference Proceedings*, May 2001 (Dallas, TX), Society of Plastics Engineers
90. P.A. Colegrove, T. Hyoe, and H.R. Shercliff, 3-Dimensional CFD Modeling of Flow Round a Threaded Friction Stir Welding Tool Profile, *J. Mater. Process. Technol.*, Vol 169, 2005, p 320–327
91. C.J. Dawes and W.M. Thomas, Development of Improved Tool Designs for Friction Stir Welding of Aluminum, *Proceedings of the First International Conference on Friction Stir Welding*, June 14–16, 1999 (Thousand Oaks, CA), TWI, paper on CD
92. J.A. Querin, H.A. Rubisoff, and J.A. Schneider, Effect of Weld Tool Geometry on Friction Stir Welded Ti-6Al-4V, *Trends in Welding Research, Proceedings of the Eighth International Conference*, ASM International, 2009, p 108–112
93. K.J. Colligan and J.R. Pickens, Friction Stir Welding of Aluminum Using a Tapered Shoulder Tool, *Friction Stir Welding and Processing III* (Warrendale, PA), TMS, 2003, p 161–170
94. C. Sorensen and B. Nielsen, Exploring Geometry Effects for Convex Scrolled Shoulder, Step Spiral Probe FSW Tools, *Friction Stir Welding and Processing V*, TMS, p 85–92
95. P.A. Colegrove and H.R. Shercliff, Development of Trivex Friction Stir Welding Tool, Part 2: Three-Dimensional Flow Modeling, *Sci. Technol. Weld. Join.*, Vol 9 (No. 4), 2004, p 352–361
96. J.P. Martin, C. Stanhope, and S. Gascoyne, Novel Techniques for Corner Joints Using Friction Stir Welding, *Friction Stir Welding and Processing VI*, John Wiley & Sons, Hoboken, NJ, 2011, p 179–193
97. P.A. Colegrove and H.R. Shercliff, Development of Trivex Friction Stir Welding Tool, Part 1: Two-Dimensional Flow Modeling and Experimental Validation, *Sci. Technol. Weld. Join.*, Vol 9 (No. 4), 2004, p 345–351
98. P.A. Colegrove, T. Hyoe, and H.R. Shercliff, Development of the Trivex Friction Stir Welding Tool for Making Lap Welds, *Proceedings of the Fifth International Symposium on Friction Stir Welding*, Sept 2004 (Metz, France), TWI
99. Tool Technology—The Heart of Friction Stir Welding, *Connect*, No. 107, The Welding Institute, July-Aug 2000, p 3
100. L. Cederqvist, O. Garpinger, T. Hagglund, and A. Robertsson, Reliable Sealing of Copper Canisters through Cascaded Control of Power Input and Tool Temperature, *Friction Stir Welding and Processing VI*, R. Mishra, M.W. Mahoney, Y. Sato, Y. Hovanski, and R. Verma, Ed., John Wiley & Sons, Inc., Hoboken, NJ, 2011, p 49–58
101. K. Withar, J. Brown, and D. Burford, Swept FSSW in Aluminum Alloys through Sealants and Surface Treatments, *Friction Stir Welding and Processing VI*, 2011, p 417–424
102. R.J. Ding and P.A. Oelgoetz, Autoadjustable Pin Tool for Friction Stir Welding, U.S. Patent 5,893,507, April 13, 1999
103. R.J. Ding, Force Characterization on the Welding Pin of a Friction Stir Welding Retractable Pin-Tool Using Aluminum-Lithium 2195, *Proceedings of the Second International Conference on Friction Stir Welding*, June 26–28, 2000 (Gotheburg, Sweden), TWI, paper on CD
104. R.W. Carter, Auto-Adjustable Tool for Self-Reacting and Conventional Friction Stir Welding, U.S. Patent 6,758,832, 2004
105. K.J. Colligan and J.R. Pickens, Friction Stir Welding of Aluminum Using a Tapered Shoulder Tool, *Friction Stir Welding and Processing III*, p 161–170
106. P.L. Threadgill, M.M.Z. Ahmed, J.P. Martin, J.G. Perrett, and B.P. Wynne, The Use of Bobbin Tools for Friction Stir Welding of Aluminium Alloys, *Mater. Sci. Forum*, Vol 638–642, 2010, p 1179–1184
107. K.S. Miller, C.R. Tolle, D.E. Clark, C.I. Nichol, T.R. McJunkin, and H.B. Smartt, Investigation into Interface Lifting within FSW Lap Welds, *Trends in Welding Research, Proceedings of the Eighth International Conference*, p 133–139
108. W.M. Thomas, K.I. Johnson, and C.S. Wiesner, Friction Stir Welding—Recent

- Developments in Tool and Process Technologies, *Adv. Eng. Mater.*, Vol 5 (No. 7), 2003, p 485–490
109. C.D. Allen and W.J. Arbegast, "Evaluation of Friction Spot Welds in Aluminum Alloys," Paper 2005-01-1252, 2005 SAE World Congress (Detroit, MI), Society of Automotive Engineers, 2005
 110. H. Badarinarayan, F. Hunt, and K. Okamoto, Friction Stir Spot Welding, *Friction Stir Welding and Processing*, R.S. Mishra and M.W. Mahoney, Ed., ASM International, 2007, p 235–272
 111. K. Okamoto, F. Hunt, and S. Hirano, "Development of Friction Stir Welding Technique and Machine for Aluminum Sheet Metal Assembly," Paper 2005-01-1254, 2005 SAE World Congress (Detroit, MI), Society of Automotive Engineers, 2005
 112. H.R. Shercliff and P.A. Colegrove, Process Modeling, *Friction Stir Welding and Processing*, R.S. Mishra and M.W. Mahoney, Ed., ASM International, 2007, p 187–217
 113. G. Buffa, J. Hua, R. Shivpuri, and L. Fratini, Design of the Friction Stir Welding Tool Using the Continuum Based FEM Model, *Mater. Sci. Eng. A*, Vol 419, 2006, p 381–388
 114. Q. Yang, X. Li, K. Chen, and Y.J. Shi, Effect of Tool Geometry and Process Condition on Static Strength of a Magnesium Friction Stir Lap Linear Weld, *Mater. Sci. Eng. A*, Vol 528, 2011, p 2463–2478
 115. B. Nielsen, "Developing Response Surfaces Based on Tool Geometry for a Convex Scrolled Shoulder Step Spiral (CS4) Friction Stir Processing Tool Used to Weld AL 7075," M.S. thesis, Brigham Young University, 2009

Friction Surfacing*

FRICION WELDING, a solid-state (non-melting) joining process, relies on the presence of relative motion between the parts while they are being pressed together under an applied axial force to generate the thermomechanical conditions for welding. The process, in its simplest form, makes use of rotary motion. A modification of conventional friction welding makes it possible to deposit layers of metal onto a substrate, a metal-transfer method that is called friction surfacing.

Although surfacing by friction can be regarded as novel, the original concept was reported, and a patent application filed, in 1941 (Ref 1). The technology was dormant until the late 1950s, when the process was rediscovered by Russian workers (Ref 2) with a wide variety of applications that used the process at that time:

- Shaft reclamation (Ref 3)
- Hardfacing of agricultural parts (Ref 4)
- Reconditioning bushings of sliding friction bearings and roll trunnions (Ref 5–9)
- Hardfacing (Ref 10) and improving wear resistance in gas and oil equipment (Ref 11)

Currently, friction surfacing has been successfully developed and commercialized over the past decade. The process is used for corrosion- and wear-resistant coatings and for reclamation of worn engineering components. Friction surfacing can be considered as an alternative for fusion-based overlay coatings, such as coating stainless steel on low-carbon steel for corrosion protection, repair, or reclamation. The solid-state nature of the process retains or even improves the mechanical properties of the coating and eliminates alloy dilution associated with fusion.

Friction surfacing can deposit a wide variety of high-specification materials, with an ideal metallurgical bond, onto a range of metal substrates. Friction surfacing has been used to apply a metal coating onto a metal substrate, but the process is being explored for the deposition of metal coatings onto ceramic substrates (Fig. 1). This unique way of metallizing ceramics has potential uses in heat sinking applications on temperature-sensitive substrates and as tracks for providing electrical conductivity.

Friction surfacing can deposit a wide variety of dissimilar materials with a good metallurgical bond onto a range of substrates. Advantages include:

- Excellent bonding with no inclusions, porosity, or oxidation
- Dense, clean, and fine microstructures
- Deposition of nonweldable alloys
- No melting of materials, with negligible dilution and small localized heat-affected zone
- Automatic and highly repeatable process

Process Description

In the friction-surfacing process, a rotating consumable is brought into contact with a moving substrate, which results in a deposited layer on the substrate (Fig. 2). First, the consumable rod is rotated to the desired speed. Next, it is brought into contact, under an axial force, with the stationary substrate. An initial rubbing period is required to allow the generation of heat and a plasticized layer in the consumable (Fig. 3). Several seconds are required before this condition is achieved. Then, the substrate is traversed across the consumable, leav-



Fig. 1 Friction surfacing of an aluminum layer on an alumina substrate. Courtesy of The Welding Institute

ing a layer of deposited material. The deposit is characterized by a fine hot-worked microstructure, zero dilution, and a very strong bond with the substrate.

The width of the coating depends on the diameter of the consumable rod and is normally in the range of 0.9 times the rod diameter (Ref 12). The thickness of the deposited layer is influenced by the primary surfacing variables of rotational speed, axial force, substrate traverse rate, consumable diameter, and type of material. Generally, the fully bonded width of the deposit is approximately 1 to 3 mm (0.04 to 0.12 in.) less than the diameter of the consumable, with the extreme angles of the deposit being characterized by lack of bond. It is thought that this lack of bond is associated with nonuniform pressure distribution across the consumable, lack of restraint to the highly plasticized flowing material, and the reduced time in action seen at the outer edges as compared to the center of the consumable.

The deposit thickness in a single pass is considerably influenced by the type of consumable material. Materials that have good resistance to plastic deformation at elevated temperatures, such as the nickel-base alloys and the Stellite alloys, will only yield thicknesses of the order of 0.5 to 1 mm (0.02 to 0.04 in.). When austenitic stainless steel and carbon steels are used, the thickness increases to approximately 3 mm (0.12 in.). For materials with low strength at elevated temperature, such as aluminum and its alloys, thicknesses can approach 5 to 6 mm (0.20 to 0.24 in.).

Representative variables associated with friction-surfacing conditions are shown in Table 1. A typical deposit of austenitic stainless steel from a 25 mm (1 in.) diameter rod that has been laid down on mild steel by the friction-surfacing process is shown in Fig. 4(a). The layer is characterized by a uniformly rippled surface of consistent width and thickness. A transverse section reveals lack of bond at the edges and sound bond formation between the deposit and substrate, above the narrow, crescent-shaped, heat-affected zone in the latter (Fig. 4b). Figure 4(c) shows the microstructural features at the bond interface. It is important to remember that a uniform and smooth mushroom-shaped upset is continuously formed on

* Revised from E.D. Nicholas, Friction Surfacing, *Welding, Brazing, and Soldering*, Vol 6, *ASM Handbook*, ASM International, 1993, p 321–323.

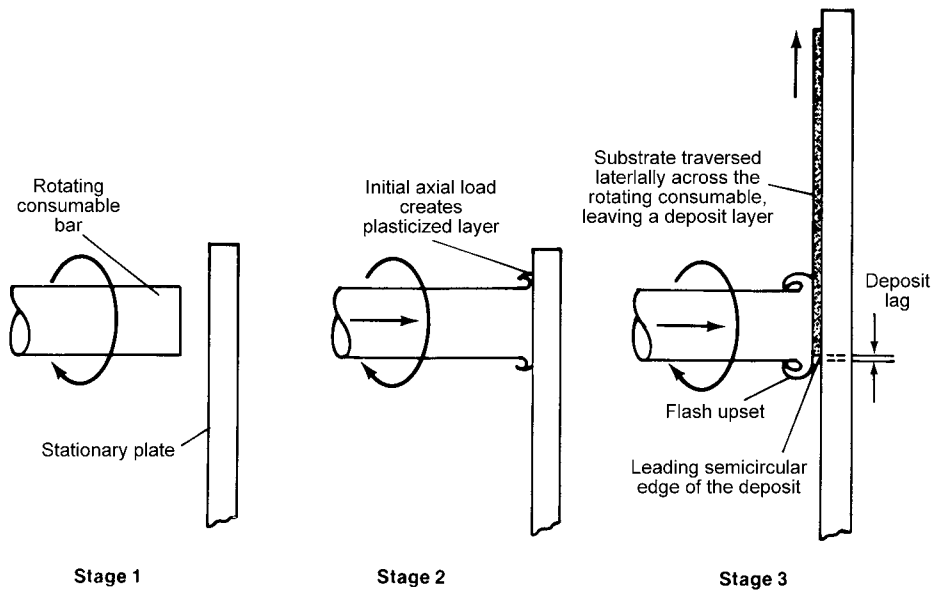


Fig. 2 Basic technique for friction surfacing

Table 1 Friction-surfacing parameters for selected material combinations

Combination	Consumable diameter		Rotation speed, rev/min	Applied force		Traverse rate	
	mm	in.		kN	10 ³ lbf	mm/s	in./s
Austenitic stainless steel to mild steel	25	1.0	550	50	11.3	5	0.20
Stellite 6 to austenitic stainless steel	20	0.8	330	50	11.3	2.5	0.10
Al-4Cu to Al-4Cu	25	1.0	780	17	3.8	4	0.16

the consumable rod during the surfacing operation.

If it is necessary to clad larger surface areas, then multiple side-by-side layers can be laid down. If thicker deposits are needed, then layers one on top of another can be used. If both approaches are called for, then interpass machining may be required to ensure sound adhesion properties.

Selection of process parameters for new coating materials or substrate geometries is typically by experimental development work. Most of the earlier works on friction surfacing focused on feasibility aspects of the process (Ref 13–15). Mathematical models of the process may facilitate process optimization. Current development activities include optimization models (Ref 12, 16, 17), process modeling (Ref 18), and the performance of friction-surfaced coatings (Ref 19).

Equipment

The process uses equipment that is similar to a machine tool, for which the surfacing conditions are preset. Therefore, the process can provide good reproducibility and is not dependent on operator skill. The earliest feasibility studies were conducted on a modified, continuous-drive, friction-welding machine (Ref 20).

Practical use necessitated increased surfacing capacity.

The ability to use converted machine tools offers a low-cost option in the technology of friction surfacing. For example, a milling machine (Ref 21) designed for the heaviest class of milling was used for longer deposition runs and larger-diameter components. Machines (such as in Fig. 5) are built dedicated to friction surfacing. In this example, the machine is particularly suited for longitudinal deposition. The table moves with 1575 mm (65 in.) of longitudinal travel and 725 mm (30 in.) of transverse travel at a lateral rate between 0.5 and 17 mm/s (0.02 and 0.68 in./s). Capabilities of this example include:

- Put down runs of 3 m (10 ft)
- Use consumables up to 70 mm (3 in.) in diameter
- Provide a range of rotation speeds from 250 to 1800 rev/min
- Develop axial forces up to a maximum of 180 kN (40.5×10^3 lbf)

The machine frame is designed to minimize deflection. Rotary manipulators (Fig. 6) can be used for circumferential deposition onto curved surfaces. A rotary table can be used for annular deposits on disks and flanges.

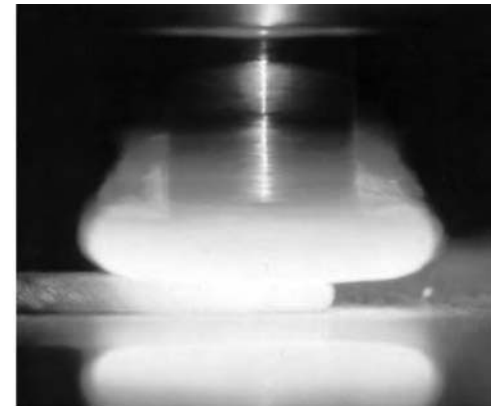


Fig. 3 Friction surfacing process of metal deposition as the substrate is being moved to the left. Courtesy of Frictec Ltd.

Applications

Initially, potential applications for this solid-state technique were in the cladding of localized areas. Typical examples include the anticorrosion surfacing of slide valve plates, the surfacing of the annular contact face of composite pipe flanges, the inlay cladding by suitable strategic materials in positions that suit bearings and seal-contact areas on shafts, and the cladding of the exposed regions of shafts that are used in pernicious environments. Hardfacing applications on cutting edges and agricultural tools were the early applications (Ref 11).

The available methods, in terms of surfacing and surface-treatment technology, are still being developed, particularly in the reclamation of worn parts and reconditioning of worn shafts. The process may increasingly accompany other solid-state, large-overlay techniques, especially with respect to localized repair and the reclamation of explosively clad and roll-bonded composite materials.

Various substrate geometries that have interesting potential for friction cladding are shown in Fig. 7. Shell banding may be another application, where suitably soft material is friction surfaced to the bodies of artillery shells (Ref 22). Other possibilities include the manufacture of specialized wear tiles (for sinter plant and quarrying equipment) and the in situ reclamation of worn railway points. Turbine blades, guillotine and shear blades, disk brakes, machine-tipped tools, and press tool dies are also considered to be potential friction-surfacing applications.

Friction surfacing has now been applied to a wide range of monolithic deposit/substrate combinations. There has been considerable success in producing high-strength bonding, fine-grained forged microstructures, and full homogeneity. A lack of porosity has also been attained, as have desirable surface properties, such as corrosion and wear characteristics that

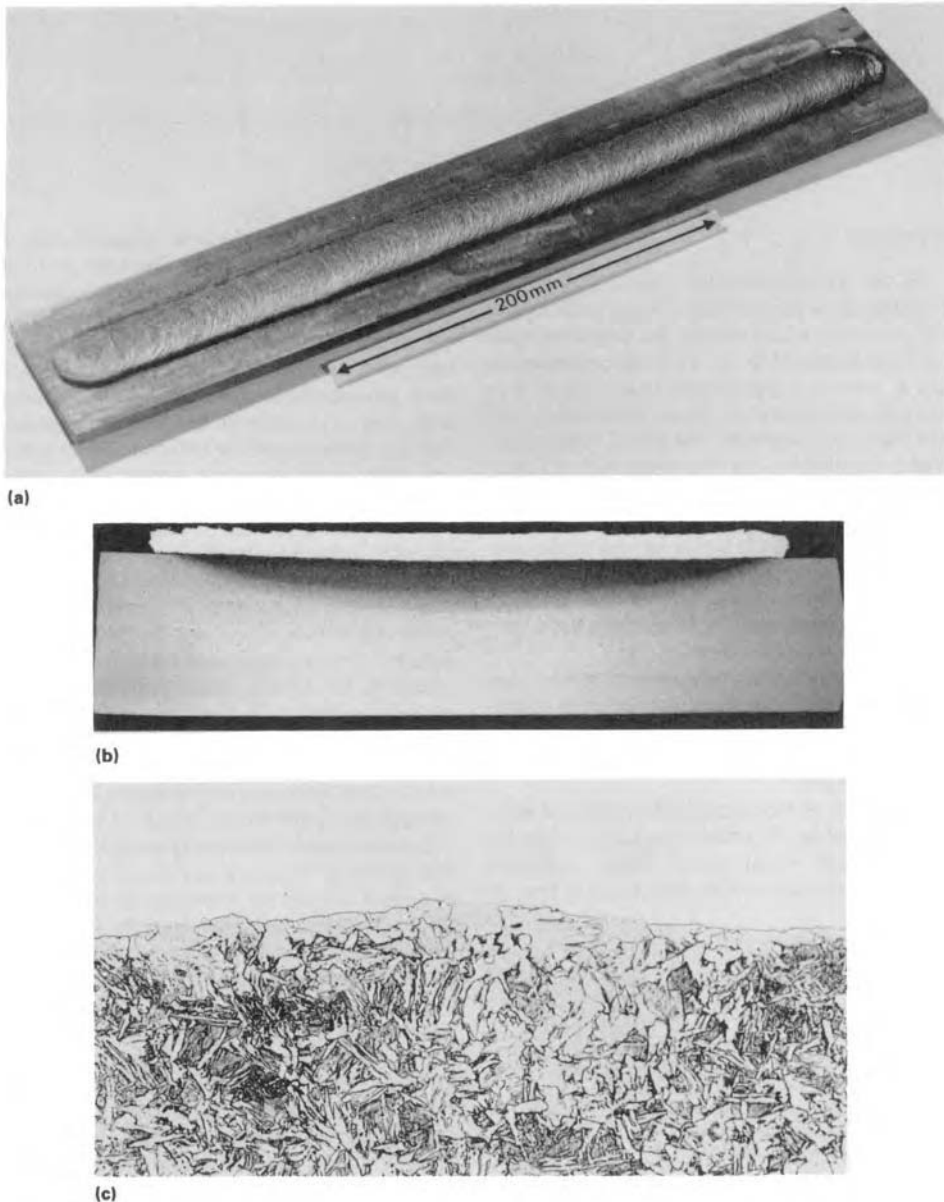


Fig. 4 Three views of 500 mm (20 in.) friction-surfaced deposit of austenitic stainless steel on mild steel. (a) View showing entire section. (b) Transverse section of deposit. (c) Microstructure at the deposit-substrate weld interface. Original magnification: 550 \times



Fig. 5 Commercial friction-surfacing machine. Courtesy of Blacks Equipment Ltd.

either equal or surpass the bar stock from which the deposit originated. Combinations include:

- Inco 625 to austenitic stainless steel
- Austenitic stainless steel to carbon steel
- Stellite 6 and 12 to austenitic stainless steel
- Hastelloy to austenitic stainless steel
- Ti-6Al-4V alloy to Ti-6Al-4V alloy
- Al-4Cu alloy to Al-4Cu alloy
- Hardfacing steels, such as D2 and H13, to medium-carbon steels

As noted, friction surfacing of metals on ceramic substrates is also a more recent area of development. For example, process research at The Welding Institute has used friction

surfacing to deposit aluminum with less than 50 μ m thickness onto an alumina substrate (Fig. 1). The technique also can be used to lay copper tracks on aluminum nitride and silicon carbide substrates.

REFERENCES

1. H. Klopstock and A.R. Neelands, "An Improved Method of Joining and Welding Metals," British patent specification 572,789, Application date, Oct 1941
2. E. Bishop, Friction Welding in the Soviet Union, *Weld. Met. Fabr.*, Oct 1960, p 408-410
3. Kh.A. Tyayar, Friction Welding in the Reconditioning of Worn Components, *Svar. Proizvod.*, Vol 1 (No. 10), 1959, p 3-24
4. R.I. Zakson and F.G. Turukin, Friction Welding and Hardfacing of Agricultural Machine Parts, *Avesta Svarka*, Vol 3, 1965, p 48-50
5. V.Ya. Kershenbaum and B.A. Averbukh, Special Features in the Friction Deposition of Bronze on Steel, *Avesta Svarka*, Vol 3, 1964, p 19-22
6. G.K. Schreiber, V.Ya. Kershenbaum, and S.G. Tkachenko, Influence of Friction Surfacing Conditions on Transition Layer Properties in Clad Metals, *Svar. Proizvod.*, Vol 9, 1971, p 32-33
7. V.Ya. Kershenbaum et al., Performance of Steel Bronze Bimetal Produced by Friction Surfacing, *Svar. Proizvod.*, Vol 7, 1972, p 29-30
8. V.Ya. Kershenbaum and B.A. Averbukh, Optimum Dimensions of Friction Surfaced Components, *Avesta Svarka*, Vol 5, 1972, p 64-66
9. B.A. Averbukh and A.L. Velinskii, Thermal Effects in Friction Surfacing, *Avesta Svarka*, Vol 11, 1975, p 29-31
10. E.I. Pluzhnikova, E.L. Demina, V.Ya. Kershenbaum, and G.K. Schreiber, Friction Facing of Cast Iron on Steel, translated from *Metalloved. Term. Obrab. Met.*, Vol 11, 1971, p 46-47
11. M.V. Nogik et al., Friction Hardfacing Steel with Stellite V3K, *Svar. Proizvod.*, Vol 8, 1970, p 16-17
12. V.I. Vitanov and I.I. Voutchkov, Process Parameters Selection for Friction Surfacing Applications Using Intelligent Decision Support, *J. Mater. Processing Technol.*, Vol 159, 2005, p 27-32
13. W.M. Thomas and S.B. Dunkerton, Friction Surfacing, *Weld. Inst. Res. Bull.*, Abington, U.K., Vol 25 (No. 10), 1984, p 327
14. W.M. Thomas, E.D. Nicholas, and S.W. Kallee, Friction Based Technologies for Joining and Processing, *TMS Friction Stir Welding and Processing Conference* (Indianapolis, IN), 2001, available at <http://www.twi.co.uk>

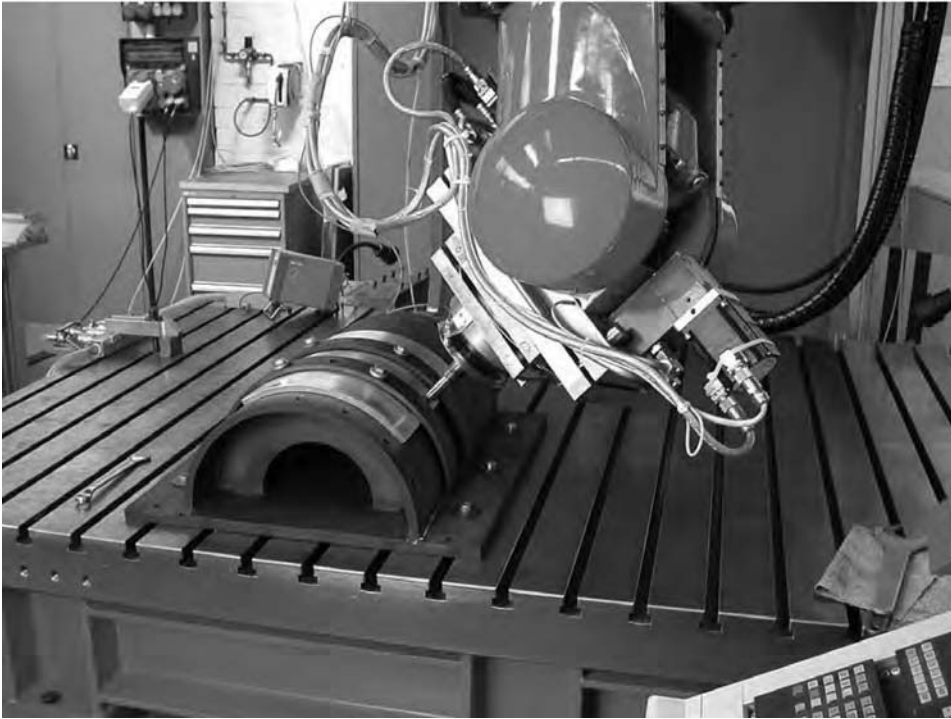


Fig. 6 Friction surfacing with rotary manipulators for deposition onto curved surfaces. Courtesy of GKSS Forschungszentrum

15. G. Madhusudhan Reddy and T. Mohandas, Friction Surfacing of Metallic Coatings on Steels, *Proceedings of the International Institute of Welding International Congress 2008*, Jan 2008 (Chennai, India), p 1197–1213
16. V.I. Vitanov, I.I. Voutchkov, and G.M. Bedford, Decision Support System to Optimize Frictec (Friction Surfacing) Process, *J. Mater. Process. Technol.*, Vol 107, 2000, p 236–234
17. I.I. Voutchkov, B. Jaworski, V.I. Vitanov, and G.M. Bedford, An Integrated Approach to Friction Surfacing Process Optimization, *Surf. Coat. Technol.*, Vol 141, 2001, p 26–33
18. X.M. Liu, Z.D. Zou, Y.H. Zhang, S.Y. Qu, and X.H. Wang, Transferring Mechanism of the Coating Rod in Friction Surfacing, *Surf. Coat. Technol.*, Vol 202, 2008, p 1889–1894
19. G. Madhusudhan Reddy, K. Srinivasa Rao, and T. Mohandas, Friction Surfacing: Novel Technique for Metal Matrix Composite Coating on Aluminium-Silicon Alloy, *Surf. Eng.*, Vol 25, 2009, p 25–30
20. W.M. Thomas, E.D. Nicholas, and S.B. Dunkerton, "Feasibility Studies into Surfacing by Friction Welding," TWI Research Report 236, The Welding Institute, April 1984
21. W.M. Thomas, Solid Phase Cladding by Friction Surfacing, *Proc. TWI International Symposium 18*, April 1988, p 18
22. E.D. Nicholas and W.M. Thomas, Metal Deposition by Friction Welding, *Weld J.*, Vol 65 (No. 8), Aug 1986, p 17–27

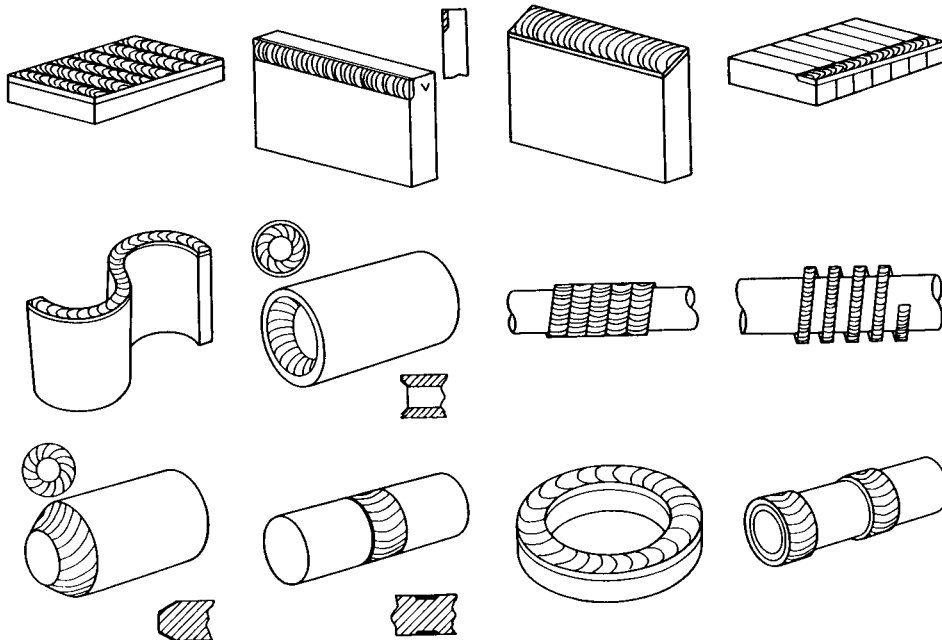


Fig. 7 Geometric arrangements for friction surfacing

Diffusion Bonding*

THE JOINING OF MATERIALS IN THE SOLID STATE can be an attractive alternative to fusion-welding processes. In fact, metals that are conventionally difficult to weld and combinations of dissimilar materials can only be welded using a solid-state process. The wide range of techniques that are available for solid-phase joining have various modes of heat and pressure application.

Diffusion welding represents one extreme within this range, in that it involves minimal pressurization but relatively high temperatures and long periods of time. In its simplest form, the process involves holding premachined and cleaned parts in intimate contact and then heating them in a protective atmosphere. As its name implies, diffusion has a major role in the joining of mating parts, although other mechanisms, such as microyielding and oxide dissolution, are also critical steps in successful welding.

The process of diffusion welding has been used for many years, although it did not attain industrial acceptance until the 1970s or 1980s, and then, only for specialized applications. A comprehensive, although somewhat dated, review of systems that have been successfully joined using diffusion welding is provided in Ref 1.

The specific advantages of the process include its ability to join most metals and some nonmetals in like or dissimilar combinations, the minimal amount of deformation that results, and the fact that the weld area is mostly independent of welding time. These advantages are offset by the need to machine parts to fairly tight tolerances on component fit-up, as well as on surface finish. However, the requirements that are generally specified can readily be achieved using standard machine shop practices.

Process Variants

Solid-Phase Process. The more-conventional form of diffusion welding uses uniaxial loading, which can be applied by dead weight, mechanical, pneumatic, or hydraulic means.

The applied load is such that macrodeformation of the parent material(s) does not have to be reached. Because deformation also depends on welding temperature, temperatures that range from 50 to 75% of the melting point are usually employed. Heat can be applied by radiant, induction, and either direct or indirect resistance heating. Most welding operations are performed in vacuum or inert gas atmospheres, although welding in air has been reported (Ref 2). When welding noble metals, the requirements for a clean atmosphere are less stringent, but protection can prevent parent-metal oxidation while maintaining a clean weld interface.

An examination of the proposed sequence of stages in diffusion welding (Ref 3, 4) emphasizes the importance of the original surface finish. In forming a bond, it is necessary for the two metal surfaces to come into atomic contact (Fig. 1). Hence, microasperities and surface contaminants must be removed from the bonding faces. The applied load first causes the plastic deformation of surface asperities, thereby reducing interfacial voids. Bond development then continues by diffusion-controlled mechanisms, including grain-boundary diffusion and power-law creep.

Premachined parts for uniaxial diffusion welding should have a surface finish of greater than $0.4 \mu\text{m}$ ($16 \mu\text{in.}$), roughness average (RA). Swabbing with acetone or petroleum ether, which should occur immediately prior to set-up in the welding machine, can suffice as a degreasing measure. Ultrasonic cleaning also has been used. Many researchers have examined the removal of oxide, prior to welding, by ion bombardment or other means. This can be applicable to certain metals if welding is to be carried out in the same vacuum chamber, or if the parts are in-vacuo coated with an oxide-resistant material. However, the additional cost and time involved in this procedure make it impractical for most industrial applications.

The liquid-phase process is applicable only to dissimilar-material combinations or to like materials in situations where a dissimilar-metal insert is used. Solid-state diffusional processes lead to the formation of a different phase at

the weld interface. The liquid-phase welding temperature is based on the temperature at which this phase (usually eutectic) melts. This thin layer of liquid spreads along the interface to form a joint at a lower temperature than the melting point of either of the parent metals. A reduction in welding temperature leads to the solidification of the melt. At the point where this phase is diffused into the parent metals, by holding at temperature, the process is known as

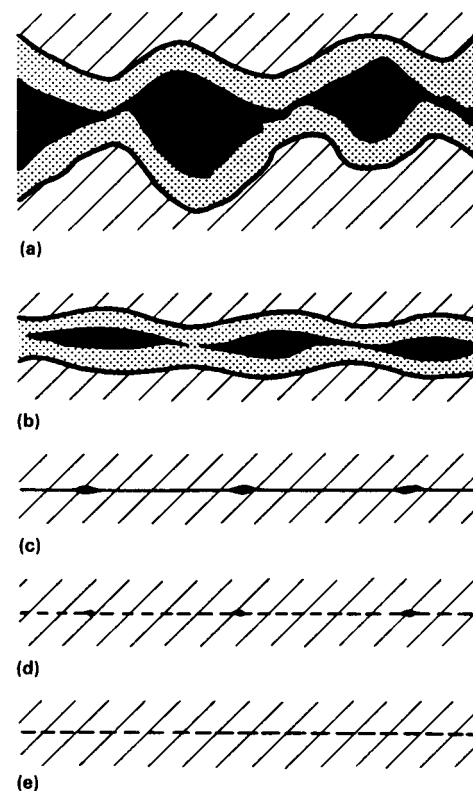


Fig. 1 Mechanism of diffusion welding. (a) Initial "point" contact and oxide contaminant layer. (b) After some "point" yielding and creep, a thinner oxide layer with large voids results. (c) After final yielding and creep, some voids remain with very thin oxide layer. (d) Continued vacancy diffusion eliminates oxide layer and leaves few small voids. (e) Completion of bonding

* Updated from S.B. Dunkerton, Procedure Development and Practice Considerations for Diffusion Welding, *Welding, Brazing, and Soldering*, Vol 6, *ASM Handbook*, ASM International, 1993, p 883-887

transient liquid-phase diffusion welding. The optimal welding time and temperature can be estimated by using the applicable phase diagram and solidification kinetics (Ref 5).

The **superplastic forming/diffusion welding** (SPF/DW) technique has been developed specifically within the aerospace industry. Its industrial importance is such that it is worthy of separate consideration. The process is used commercially for titanium and its alloys, specifically those that exhibit superplastic properties at elevated temperatures within defined strain-rate conditions (Ref 6–8). This process also has been successfully used for advanced aluminum alloys (Ref 9). Because the temperature and pressure conditions coincide with the conditions required for welding, the two processes have been combined into one manufacturing operation. See also the *ASM Handbook* articles “Superplastic Sheet Forming” (Ref 10) and “Forming of Titanium and Titanium Alloys” (Ref 11).

Hot Isostatic Pressing (HIP) is a solid-phase process that involves the application of a high-temperature, high-pressure gas to components. Isostatic pressurization allows the welding of more-complex geometries than the uniaxial welding process can handle.

A hot isostatic press consists of a furnace within a gas pressure vessel. Its size can range from a diameter of 100 mm (4 in.) to a diameter of 1.1 m (44 in.) and a height of 2.2 m (88 in.). Argon gas is typically used, and there is a need to encapsulate the bond interfaces to prevent the gas from entering the site of the bond. This is most often achieved by locating the specimen in an evacuated and sealed steel can, although various other means can be used as well.

The pressures associated with HIP welding are significantly higher than those used in uniaxial welding. However, because the pressure is isostatic, the level of deformation is extremely low. In addition, less premachining is required. Typical HIP cycles can last from 6 to 16 h, but because many components can be fitted into one furnace, the unit costs on large production runs can be low. Bryant (Ref 12) has developed a graphical procedure to determine the minimum pressure and temperature required for the HIP welding of several metals and alloys.

Diffusion Bonding of Metals

Steels

Diffusion Bonding of Carbon and Low-Alloy Steels. Although diffusion welding is applicable to this class of steels, industrial applications are limited. The process is used in situations where it is essential to avoid or minimize distortion and postweld machining, and for complicated geometries that involve internal features.

These steels are generally welded without the use of filler material (interlayer). The parts

themselves are machined to a good surface finish ($<0.4 \mu\text{m}$, or 16 $\mu\text{in.}$, RA surface roughness, and flat) and assembled in a heating unit such that force can be applied uniaxially or isostatically.

In terms of uniaxial diffusion welding, a wide range of bonding conditions have been shown to give sound joints, that is, temperatures of 900 to 1200 °C (1650 to 2190 °F), pressures of 5 to 14 MPa (0.7 to 2 ksi) and times of 5 to 120 min. Because the parameters are interdependent, as temperature increases, the load and/or time can be reduced and vice versa. Figure 2 depicts a typical cross section of a joint in 0.4% C steel, in which a layer of ferrite indicates the bond line of the sound bond that has formed.

Tensile strength develops as temperature/pressure/time increase. Parent-metal tensile strength is readily achieved; failure occurs away from the joint interface, even when welding is not complete. Work has shown that only 80% bonding is necessary to achieve the equivalent parent-metal strength (Ref 13). However, ductility and joint-line toughness require a greater level of bond integrity.

Joints made in 0.4% C steel and a 1Cr-0.25Mo alloy steel have shown low Charpy impact values, when compared with the parent steels (Ref 14, 15). With the 0.4% C steel, it is possible to improve the toughness properties by using a postweld normalizing heat treatment (equivalent to the thermally cycled and normalized parent material). However, although the chromium-molybdenum steel had an improved microstructure after a postweld quench and temper heat treatment, it still had low joint-line toughness. This indicates the greater difficulty in forming a sound joint as alloy content increases.

Therefore, when diffusion welding carbon and low-alloy steels, the final application and service requirements should be considered carefully. The process is useful in low-stress applications, but when impact toughness is required, the fitness of a particular steel for the specific purpose must be examined. For higher-carbon-content steels and low-alloy steels, a suitable postweld heat treatment is recommended to return the steel to its original

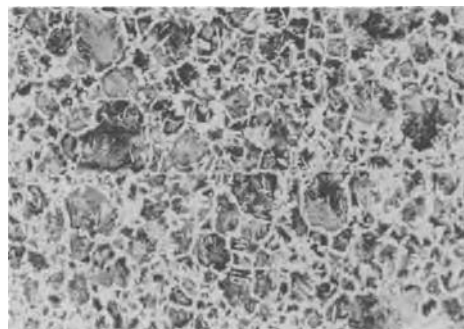


Fig. 2 Cross section of diffusion weld in 0.4% C steel. Original magnification: 50 \times

condition. However, it should be noted that some of the high temperatures referred to earlier ($\geq 1100 \text{ }^\circ\text{C}$, or 2010 °F) can cause significant grain coarsening.

The HIP welding of these steels also can be used when typical conditions involve a temperature of 1100 °C (2010 °F), a pressure of 100 MPa (14.5 ksi), and a bonding time of 4 h. Again, grain coarsening and the property considerations described previously must be reviewed.

Diffusion Bonding of High-Strength Steels. Although diffusion welding has not been widely applied to high-strength steels, it is a feasible process, and guidelines similar to those identified for carbon and low-alloy steels will apply. Because diffusion welding relies on microplastic yielding in the early stages of bonding, it is necessary to use parameters at the higher end of the ranges specified previously, that is, temperatures above 1000 °C (1830 °F) and pressures of 7 MPa (1 ksi) and above.

Although good tensile properties can be achieved, the as-bonded toughness will be low. In addition, a postweld heat treatment to restore the parent microstructure is recommended.

Diffusion Bonding of Stainless Steels. Stainless steels can be diffusion welded using conditions similar to those that are used for high-strength steels. These steels are normally covered by a thin adherent oxide (chromium oxide) that must be broken up and/or dissolved during the welding process. This is possible when higher temperatures and/or higher pressures are used. Alternatively, stainless steels can be welded in dry hydrogen, which will reduce the oxide film, or the oxide can be removed prior to welding. The latter measure has been accomplished by anodic cleaning of the steel surfaces, followed immediately by copper plating to protect the surfaces from reoxidation. Again, if a dry hydrogen atmosphere is used, then the copper oxide will be reduced during welding and a sound bond will be attained.

Although few property data are available on the diffusion welding of stainless steels, it is known that tensile strength is readily achieved, whereas toughness is more difficult. If high welding temperatures are employed, then it will generally be necessary to use a postweld heat treatment to restore properties.

Nonferrous Alloys

Diffusion Bonding of Aluminum-Base Alloys. Diffusion welding of aluminum alloys is difficult, because of the presence of a tenacious surface oxide film. The surface oxide can be disrupted by the use of large deformations and/or high temperatures in, for example, roll bonding. However, for low-deformation diffusion welding, interlayers of similar or dissimilar materials have been used. The specific

procedures to be followed for aluminum alloys vary, depending on the alloy system.

For Al-Mg-Si alloys (specifically, Al-0.6Mg-0.9Si-0.5Mn), diffusion welding without an interlayer has yielded tensile strengths of 145 MPa (21 ksi) for a welding temperature of 550 °C (1020 °F) (Ref 16). However, this does induce deformation of the components. It has been more attractive to use copper or silver interlayers, which can be applied as a coating or a foil. These interlayers can be used to provide a solid-state weld or a transient liquid-phase (eutectic) weld. Care must be taken to achieve the latter, to ensure that the heating rate is not so slow as to allow the interlayer to be diffused away before the eutectic temperature is reached. Solid-state diffusion welds made with either copper or silver have yielded joint strengths of 85 MPa (12 ksi) for bonding temperatures as low as 450 °C (840 °F).

More attention has been directed to the diffusion welding of alloys that are of interest to the aerospace industries, that is, 7010 (Ref 17), 7475 (Ref 18, 19), and 8090 (Ref 20–23). No clear guidelines exist as to the best practice for welding these alloys, because researchers have investigated many techniques and the results point in sometimes conflicting directions. Welding the alloys without an interlayer is possible, if disruption of the oxide can take place during welding. Some success has been achieved by welding the 7475 alloy with a “rough” surface (that is, brushed in air), by surface grinding the alloy in an argon atmosphere prior to welding, and by grit blasting with fine alumina particles followed by chemical cleaning in hot 30 wt% NaOH solution. Long welding times have been used for this material, and high strengths have been reported by welding at 515 °C (960 °F) under a load of 5 MPa (0.7 ksi) for 5 h, followed by a postweld heat treatment to T6 condition. In instances where interlayers have been used for this alloy system, the material that has shown the greatest promise is zinc.

Aluminum-lithium alloys are currently attracting great attention for applications in the aerospace industries. This is because lithium significantly increases the elastic modulus of aluminum, by approximately 6% for each wt% addition of lithium, and simultaneously decreases its density by 3%. For aerospace applications, improvements in specific modulus and strength can lead directly to weight savings. In addition, it has been shown that aluminum-lithium alloys can develop superplastic behavior after appropriate thermomechanical processing, which means that advantage can be taken of the SPF/DW procedures already established in this industry.

Superplastic forming after welding restricts the welding temperature that can be used. Ideally, the temperature should be lower than or equal to the superplastic temperature for the alloy. In addition, the welding time must be restricted to avoid grain growth in the parent

sheet, which could affect the superplastic-forming properties.

Aluminum-lithium alloys have been bonded with no interlayer and with interlayers of zinc, copper, zinc-copper, pure aluminum, and aluminum alloys. Surfaces have been prepared by a number of techniques, such as grinding with emery paper, shot peening, chemical etching, and degreasing. All techniques have shown some degree of success, but it is difficult to compare results, because the testing methods to achieve shear strength are varied. Generally, all of these welds require some form of post-weld heat treatment to restore properties (for example, solution treatment at 535 °C, or 995 °F, followed by quenching). A section through a diffusion weld containing a pure aluminum interlayer is shown in Fig. 3. The position of the original aluminum foil is discernible by the presence of spheroidal precipitates, similar in size and shape to those precipitated in the grain boundaries of the aluminum alloy.

To avoid surface contamination during heating to the welding temperature, greater care must be taken with the aluminum-lithium alloys, because of the reactivity of lithium. However, this reactivity is also claimed to make this alloy system somewhat easier to weld than other less-reactive aluminum alloys.

Diffusion Bonding of Reactive and Refractory Metals. The diffusion welding of titanium alloys is well documented, because of its commercial application and importance to the aerospace industry. Many titanium airframe structures are now manufactured using the SPF/DW process, which provides significant benefits through weight and cost savings. Typical examples include hot-air nozzles, landing-gear doors, intricately shaped housings, keel sections, and heat-exchanger ducts. Most of the detailed procedures for welding are commercially sensitive. The factors that are important are (Ref 24):

- Metallurgical condition of the starting material
- Characterization of the superplasticity of the material
- Surface cleanliness
- Tooling material and surface condition
- Welding atmosphere
- Forming and welding parameters
- Part geometry

The primary alloy that is used is Ti-6Al-4V. It has been established that commercially available sheet material containing an equiaxed, uniform, small grain size (preferably <10 μm, or 400 μin.) is suitable for superplastic forming. Conventional cutting processes are used for the preparation of sheet material, which is then subjected to an etching treatment prior to placement in the press. Although tooling is typically made of a 22Cr-4Ni-9Mn stainless steel with appropriate surface-parting compounds, ceramic-faced tooling has also been used. During the application of heat at

temperatures ranging from 900 to 930 °C (1650 to 1710 °F), argon gas provides a protective atmosphere that is also used, under pressure, to effect forming and diffusion welding. Tool-to-titanium sealing, to contain the forming/bonding pressure of 2 to 4 MPa (0.3 to 0.6 ksi), is of paramount importance to leakage prevention.

Multiple-sheet fabrication requires the application of a stop-off material (typically, yttria and a binder) after conventional titanium cleaning. The application of a stop-off material uses a silk-screen technique that allows complex patterns to be transferred to the sheet. The multiple-sheet pack is plumbed with stainless steel capillary tubes for internal gas pressurization (between the sheets), as opposed to single-sheet processing, where gas pressure access is achieved directly through tooling parts. The process allows formed titanium shapes that are far more complex than those produced by conventional forming methods. Parts can feature integral end flanges, deep beads, corner beads, and small-bend radii. In addition, compound contour; multiple, variable, hollow sections; and complex sandwich (including circular) structures with varying core configurations can be fabricated.

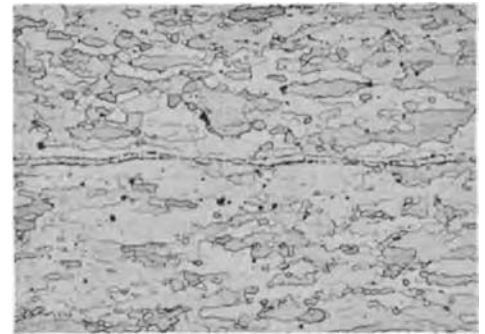


Fig. 3 Cross section of diffusion weld in aluminum-lithium alloy containing pure aluminum interlayer. Original magnification: 75×

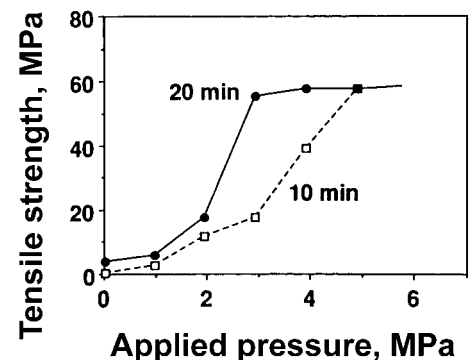


Fig. 4 Effect of applied pressure (for two bonding times) on the tensile strength of solid-state welds of CaO-stabilized ZrO₂, joined to itself using an interlayer of 5052 aluminum alloy. Source: Ref 50

Zirconium and its alloys also have been joined by diffusion welding, as have the refractory metals of tungsten, tantalum, niobium, and molybdenum (Ref 25).

Diffusion Bonding of Other Nonferrous Alloys. Other alloy systems have been diffusion welded but with few industrial applications. Copper bonds to itself readily, if the surface oxide can be disrupted, and temperatures ranging from 850 to 950 °C (1560 to 1740 °F) have been employed. Alternatively, a liquid-phase procedure that uses silver as an interlayer has been adopted to reduce welding times. The nickel- and cobalt-base alloys are bondable, but some alloy systems exhibit good high-temperature strength that inhibits the microyielding required for diffusion welding. Beryllium alloys also can be bonded at low temperatures (Ref 26).

The noble metals, such as gold, bond readily because of their very thin surface oxide. Gold, in particular, is often used as an interlayer material when welding temperatures are restricted, because bonds can be achieved at temperatures as low as 250 to 350 °C (480 to 660 °F), if the surfaces and atmosphere are clean.

Dissimilar-Metal Combinations

Diffusion Bonding of Dissimilar Ferrous Alloys. Dissimilar steel joints have not been extensively investigated in diffusion-welding research, primarily because it was initially believed that the process would mostly be used to join material combinations that were difficult to join by other, more-conventional methods. However, this is not strictly true, and in situations where multiple joints can be formed in one welding operation, the process can be economically viable for dissimilar steel joints.

The literature on steel includes the bonding of high-speed steels to carbon steels for prismatic cutting tools (Ref 27) and the joining of pure iron to a range of carbon steels (Ref 28). In this latter work, the bond tensile strength was greater than 430 MPa (62 ksi), which exceeds that of the weaker parent metal. A slight increase in tensile strength occurred with a decrease in welding temperature from 1000 to 900 °C (1830 to 1650 °F).

Diffusion Bonding of Dissimilar Nonferrous Alloys. Many combinations have been studied within this category, but the most common one uses aluminum as one of the parent materials (Ref 29–31). The diffusion welding of aluminum to copper and titanium results in the formation of intermetallic compounds at the bond interface. With copper, it has been found that the aluminum/copper intermetallic can reach 15 µm (600 µin.) in thickness before a reduction in the joint strength occurs (Ref 32). Also described in this work is the fact that the parent aluminum strength was not achieved, even before the excessive growth of the intermetallic, which suggests that full bonding can

be achieved only after the time necessary for extensive intermetallic formation. However, aluminum-to-titanium diffusion bonds can reach a tensile strength that is equal to that of the parent aluminum, and it is claimed that intermetallic thicknesses of up to 10 µm (400 µin.) can be tolerated (Ref 33). Again, an interlayer of silver can be used to promote bonding between the aluminum and titanium, such that the parent aluminum strength can be achieved in shorter welding times.

The aerospace and nuclear industries have driven the development of a wide variety of special alloy and dissimilar-metal combinations. Examples of materials that have been successfully joined include nickel-stainless steel (Ref 34), uranium-stainless steel (Ref 35), beryllium-nickel (Ref 36), beryllium-stainless steel (Ref 36), thorium dioxide dispersion-strengthened-nickel alloys (Ref 37), zirconium-steel (Ref 38), and copper-Monel (Ref 39).

Diffusion Bonding of Ferrous-to-Nonferrous Alloys. The joining of aluminum to steel has received a great deal of interest. This subject has been reviewed by Elliot and Wallach (Ref 40), who recognized that the two major problems associated with this metal combination are:

- The tenacious oxide layer on the aluminum, which, being stoichiometric and highly stable, inhibits weld formation
- The formation of brittle intermetallics, such as the FeAl₃ and Fe₂Al₅ types, at the joint interface

These problems are generally overcome by using interlayers, both to promote welding and to prevent the formation of brittle intermetallic compounds. Silver has been successfully used as an interlayer, either as a foil interlayer or applied by electroplating (Ref 41, 42), vapor deposition (Ref 43, 44), or sputter deposition (Ref 45) on one or both surfaces. Both solid- and liquid-phase joints have been produced, the latter of which involves melting of the aluminum-silver eutectic.

Other interlayer materials that have been examined include nickel and a multilayer system of zinc and silver. However, both of these have disadvantages. The nickel also forms brittle intermetallics with iron that inhibit joint strength. In the multilayer system, the zinc was found to erode the silver, thereby removing the diffusion barrier. In addition, aluminum and steel alloys can be diffusion welded without any interlayer by a careful evaluation of the process parameters and with a higher amount of aluminum deformation.

The diffusion welding of refractory metals to steels has been another major research area. Molybdenum has been welded directly to steel, but the formation of brittle intermetallics limits the strength of the joints. Lison and Stelzer (Ref 27) have investigated the interlayers required to give good joint properties for

this metal combination, based on metallurgical compatibility and the coefficients of thermal expansion. A complex multilayer system was devised, in which tantalum, vanadium, nickel, and copper were positioned in the following order: Mo-Ta-Ni-Cu-steel. Initially, the Mo-Ta-V combination was bonded at 1500 °C (2730 °F) for 40 min, whereas the remaining bonds were formed at 850 °C (1560 °F) in 20 min. The mechanical properties of such a joint are not given, but metallographic examination revealed full bond formation.

Diffusion Bonding of Oxide Ceramics (Ref 46)

Developments in gas-turbine and ceramic-engine technology have created an interest in the diffusion welding of ceramics to steels, because the low temperatures used for joining minimize the residual stresses created by thermal mismatch. Silicon nitride and zirconium oxide are two examples that have been successfully welded to steel using the diffusion welding process. Both ceramic-ceramic and ceramic-metal joints have been fabricated using diffusion bonding. Most of the work has been on ceramic-metal joints in which the metal portion of the joint is either a bonding material added to the interface between two ceramic components or is the second member of a bimaterial joint. The more extensively studied ceramic-metal joint is discussed first and in more detail. Ceramic-ceramic diffusion welding and a variation on this process in which ceramic powder compacts are simultaneously sintered and bonded (sinter-bonding process) are discussed at the end of this section.

Ceramic-Metal Joints

Two types of interaction have been observed in diffusion welding of ceramic-metal joints. In the first type, bonding, is driven by a decrease in surface energy as a new interface is formed to replace the two original surfaces. This physical interaction is indicated by an abrupt transition in microstructure between metal and ceramic at the interface. Examples of this type of bond include those between alumina welded under high vacuum to the metals aluminum, copper, nickel, platinum, and niobium (Ref 47, 48). However, under certain conditions of temperature and excess oxygen activity, reaction products can form at some of these interfaces (Ref 49). In the case of the Al₂O₃-Nb couple, a model system that has been extensively studied, a reaction layer does not occur at the interface because Al₂O₃ dissolves in the niobium (Ref 48). The driving force for the formation of the physical-type bond is the change

in surface energy (ΔG_s) as given by the Dupre equation:

$$\Delta G_s = (\gamma_c + \gamma_m) - \gamma_{cm} \quad (\text{Eq 1})$$

where γ_c and γ_m are the surface energies of the ceramic and metal, respectively, and γ_{cm} is the surface energy of the interface formed during joining. The change in surface energy (ΔG_s) is the same as the thermodynamic work of adhesion (W_{ad}), the energy required to separate a unit area of the bonded interface.

In the second type of solid-state bond between ceramics and metals, chemical reaction further lowers the energy of the system and increases the strength of the bond. Chemical reaction product layers are observed in the joints after welding. These reaction products generally cause stronger bonds; however, weakening of the joint may occur if the reaction products grow to excessive thicknesses during welding or in service. Diffusion welds between oxide materials and metals that result in the formation of interfacial reaction products are alumina with aluminum (although it is suggested in Ref 50 that the reaction is between aluminum and the SiO_2 in the alumina and not with the Al_2O_3 itself); aluminum and magnesium with SiO_2 and ZrO_2 (Ref 51) nickel and titanium with Al_2O_3 (Ref 52).

The temperature required for diffusion welding to occur usually ranges from 0.5 to 0.8 of the absolute melting point of either the ceramic, the metal being bonded to the ceramic, or an interlayer that is added at the interface to promote bonding. A wide range of applied pressures has also been used, ranging from 15 kPa to 200 MPa (3 psi to 29 ksi) and higher. The surface finish of the mating materials is also a critical variable, because the success of the process depends on the attainment of intimate interfacial contact. If all other variables are equal, the surface finish and pressure are related because rough surfaces require greater pressures to force the surfaces into contact for bonding. The observed effects of each of these variables (applied pressure, temperature, and surface finish) are discussed as follows.

Applied Pressure. Diffusion welding is usually performed under conditions in which at least one component undergoes plastic deformation under the applied load. The material that deforms may be the ceramic, the metal portion of a ceramic-metal joint, or an intermediate material placed in the joint. Klomp suggests that applied pressure is critical in solid-state bonding of oxygen-active metals to oxide materials (Ref 50). The applied pressure creates an active metal surface by plastic deformation of the surface oxide layer that usually inhibits bonding, thereby allowing contact between clean metal and the ceramic during the bonding process. Such behavior was clearly observed in a study conducted by Arata and Ohmori on the solid-state bonding of CaO-stabilized ZrO_2 to itself in vacuum using 0.5 mm (0.02 in.) thick

inserts of 5052 aluminum alloy (2.2 to 2.8 wt % Mg) (Ref 51). The surfaces of the ZrO_2 to be joined were polished with 1500-grade emery paper and degreased with acetone prior to bonding. The effect of bonding pressure on the room-temperature tensile strength of the joints is clearly shown in Fig 4. The bonding mechanism was described as a sequential process in which the oxide film on the aluminum alloy is broken, the alloy is forced into the pores of the zirconia, and finally the aluminum and magnesium of the alloy react with the grain-boundary phases of the zirconia and with the zirconia.

Bonding Temperature. Temperature is the most significant variable affecting the strength of diffusion-welded joints, yet the mechanisms involved in ceramic-ceramic or ceramic-metal diffusion welding have not been modeled. Formation of metal-metal joints (Ref 53, 54) are considered to involve the processes associated with pressure sintering, that is, plastic flow, creep deformation, and diffusion along surfaces and grain boundaries or through the bulk of a grain. If similar behavior occurs in joints containing ceramics, it can be concluded that increased temperature increases contact between the materials being joined by reducing their yield strengths, and increases the diffusion rates that control pore closure, grain growth, and chemical interactions.

The effect of temperature on mechanical deformation at the joint can be illustrated by the previously cited work of Arata and Ohmori (Ref 51). As shown in Fig 5, a 25-fold increase occurred in the room-temperature tensile strength of ZrO_2 to ZrO_2 welds (using 0.5 mm, or 0.02 in., thick inserts of 5052 aluminum alloy) when the bonding temperature was raised from 450 to 550 °C (840 to 1020 °F).

Similar behavior was observed by Nicholas and Crispin (Ref 55) in diffusion welding an alumina (97.5% Al_2O_3) to type 321 stainless steel using an aluminum interlayer, as shown in Fig 6. The effects of variations in welding parameters were determined in a series of experiments using a steel insert between standard ASTM F 19 testpieces. Fixed variables were: a 0.5 mm (0.02 in.) thick interlayer of commercial-purity aluminum at both alumina-steel interfaces, an applied pressure of 50 MPa (7.25 ksi), a time at temperature of 30 min (2 to 3 h heat-up time), and a vacuum of a few mPa. The bonding surfaces of the alumina testpieces were in the as-received, fired condition. Increasing the welding temperature from 496 to 625 °C (925 to 1155 °F) resulted in progressively stronger joints. In room-temperature tensile testing, the welds made at 625 °C (1155 °F) failed at the stainless steel-aluminum interface, while all others failed at the alumina-aluminum interface. These authors concluded that the relationship between fabrication temperature and the strengths of the joints which failed at the alumina-aluminum interface could be expressed as follows:

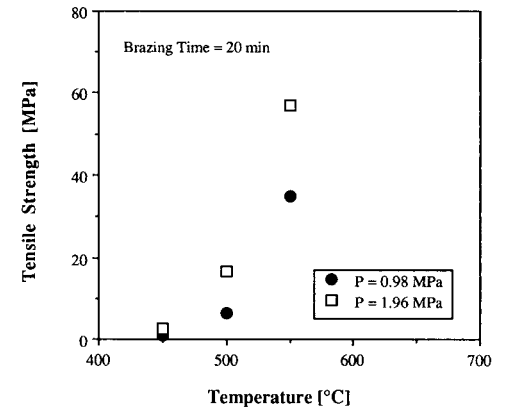


Fig. 5 Effect of bonding temperature on the room-temperature tensile strength of solid-state welds of CaO-stabilized ZrO_2 joined to itself using an interlayer of 5052 aluminum alloy. Source: Ref 51

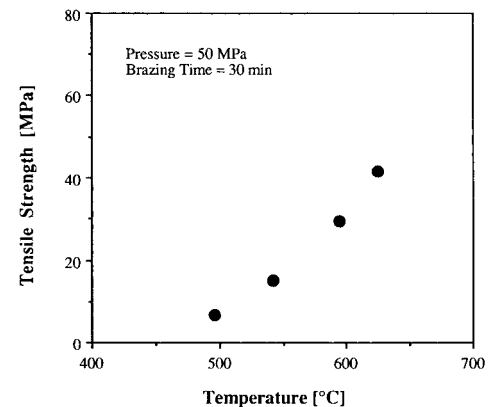


Fig. 6 The effect of bonding temperature on the room-temperature tensile strength of diffusion welds between alumina and type 321 stainless steel (made using an aluminum interlayer). Source Ref 55

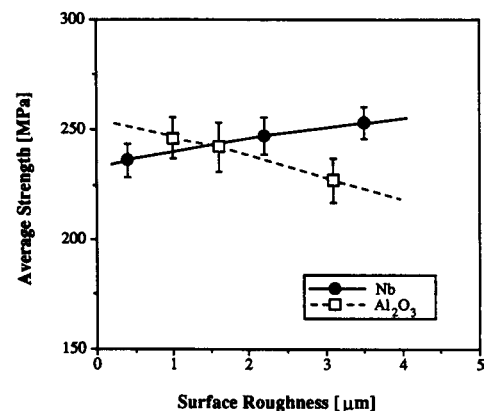


Fig. 7 The effect of the roughness of the surfaces of the materials being joined when alumina was diffusion welded to niobium. Source: Ref 59

$$\sigma = \sigma_0 \exp(-Q/RT) \quad (\text{Eq 2})$$

where σ is the failure stress, in MPa, of samples bonded for a fixed time, at a given applied pressure, over a range of temperatures. In this equation, σ_0 is a constant (3.14×10^6 MPa), Q is an apparent activation energy (83.3 kJ mol^{-1}) for the bonding process, R is the gas constant, and T is the absolute temperature. Derby (Ref 56) observed that the activation energy derived from the data in this study was approximately the same as the 80.3 kJ mol^{-1} reached in a similar study by Dawihl and Klinger (Ref 57). Derby compared these values with the activation energies for self-diffusion by lattice-, grain-boundary-, or surface-diffusion mechanisms and for vapor-phase transport in aluminum and alumina. Because of the close agreement with the published value for grain-boundary self-diffusion in aluminum (84 kJ mol^{-1}), Derby concluded that grain-boundary diffusion in the aluminum was the most probable bonding route in these welds.

Crispin and Nicholas also conducted a similar study on diffusion welding the same alumina (97.5% Al_2O_3) to itself using a 0.5 mm (0.02 in.) thick copper foil interlayer (Ref 52). Welding was conducted in vacuum (<10 mPa) at temperatures ranging from 600 to 950 °C (1110 to 1740 °F), a time at temperature of 30 min, and a pressure of 50 MPa (7.25 ksi), which was applied when the sample reached the bonding temperature. They concluded that the most obvious correlation in the experimental data was between average joint strength and fabrication temperature. The room-temperature tensile strengths of the ASTM F 19 alumina specimens increased from essentially no strength when welded at 600 °C (1110 °F) to a maximum of 54 MPa (7.8 ksi) when welded at 875 °C (1605 °F). Further increases in welding temperature led to decreases in joint strength. The samples welded at temperatures >700 °C (>1290 °F) failed within the alumina, but generally near to and influenced by the interface.

Surface Roughness. The effect of surface roughness on the strength of diffusion welds has been explored in several studies. In research by Derby (Ref 56), ASTM F 19 testpieces fabricated from alumina (99.5% Al_2O_3 , 0.5% MgO + CaO) were joined using a 0.5 mm (0.02 in.) thick interlayer of 99.99% aluminum, an applied pressure of 50 MPa (7.25 ksi), and a temperature of 600 °C (1110 °F). The atmosphere during bonding was not specified, but the bonding conditions were reported to be similar to those of Nicholas and Crispin, who used a vacuum of >10 mPa. Two surface conditions were investigated: a ground surface with an average surface roughness of 1.4 μm and average peak-to-valley height of 5 μm , and a polished surface with values of 0.4 μm and 1 μm , respectively. A postbonding heat treatment of 30 min at 400 °C (750 °F) in the bonding furnace was followed by a 4 h anneal at 200 °C (390 °F) in a furnace. The strength of the samples was negligible without these

thermal treatments. For both surface conditions the bond strength increased with time. However a maximum of only 20 MPa (2.9 ksi) after 40 min bonding time was reached in the ground specimens, while the strength of the lapped specimens reached an average strength of 32 MPa (4.6 ksi) after a 20 min bonding time. An interesting footnote to this study is that much stronger joints, with tensile strengths averaging 50 MPa (7.25 ksi), were achieved at bonding temperatures above the melting point of aluminum (660 °C, or 1110 °F).

Suganuma and co-workers investigated the solid-state bonding of an alumina (99.7 wt% Al_2O_3) to niobium (99.5 wt% pure) as a function of bond face grinding conditions (Ref 59). The bonding was done in a hot press under a vacuum of 2.7 mPa, at a temperature of 1500 °C (2730 °F) for 1 h, and an applied pressure of 20 MPa (2.9 ksi). The effects on room-temperature bond strength of three surface roughness conditions of both the alumina and the niobium were explored. The bonded specimens were ground to remove a 1.5 mm (0.06 in.) wide unbonded region that was sometimes present along the edges of the joint, and then cut into bars for four-point flexure testing. As in the study by Derby, these researchers concluded that significantly stronger joints resulted in welds made with the alumina having the smoothest surface (average surface roughness of 0.97 μm). However, as shown in Fig 7, the surface finish of the niobium had just the opposite effect; that is, the strongest bonds were produced with the roughest niobium (average surface roughness of 3.49 μm). In addition, the rough bond face on the niobium resulted in the elimination of the unjoined region at the edges of the original specimens. Both beneficial effects of niobium roughness were probably caused by plastic flow of the metal.

Ceramic-Ceramic Joints

As stated previously, diffusion welding is usually performed under conditions of temperature and pressure where at least one component plastically deforms under the applied load so that the surfaces to be joined are brought into intimate contact. Although the material that deforms in most cases is either the metal portion of a ceramic-metal joint, or an intermediate material placed in the joint, it may also be the ceramic. For example, Ellsner et al. reported weak joints when a coarse-grained alumina (grain size $\sim 18 \mu\text{m}$) was bonded to itself without an interlayer, because the ceramic was creep resistant and therefore resisted formation of an intimate interface (Ref 60). Conversely, bonds between the same coarse-grained alumina and an alumina with smaller grains ($\sim 1 \mu\text{m}$) were much easier to produce because the fine-grained material deformed much more readily. The flexure strength (test method not given) for joints between the two aluminas

reached a maximum value of 200 MPa (29 ksi) when welded at 1750 °C (3180 °F).

Scott and Tran studied the effect of the level of MgO sintering aid on diffusion welds in high-purity alumina (Ref 61). Dense, fine-grained alumina bodies (1 to 3 μm average grain size) were fabricated by pressureless sintering at 1500 °C (2730 °F), a series of compacts containing 0.0075, 0.075, or 0.75 wt% MgO. The sintered pellets were diffusion welded in a vacuum hot press at temperatures from 1200 to 1500 °C (2190 to 2730 °F) and applied pressures from 34 to 138 MPa (4.9 to 20 ksi). The bonded pellets were cooled to room temperature and then resintered in H_2 at 1875 °C (3405 °F) for 3 h for grain growth. As expected, the best results (as indicated by minimal interfacial porosity and grain growth across the original interface) were achieved at the higher temperatures and pressures. The study also showed that the level of MgO dopant in the alumina bodies had a significant effect on bond quality. Joints between samples with the highest level of MgO (0.75 wt%) had fewer interfacial voids and a much finer grain size. The lower dopant levels allowed exaggerated grain growth to occur, leaving porosity trapped in the large grains and at the interface.

The effect of the superplastic behavior of Y_2O_3 -stabilized tetragonal zirconia polycrystal ceramic (Y-TZP) on diffusion-bonded joints has been investigated by Nagano and coworkers (Ref 62). The materials included fine-grained alumina (99.9 wt% Al_2O_3 , 0.64 μm grain size), coarse-grained alumina (99.7 wt% Al_2O_3 , 5.87 μm grain size), Y-TZP (3 mol% Y_2O_3 , 0.59 μm grain size), and a series of Y-TZP/alumina composites with the alumina content ranging from 20 to 80 wt%, and grain sizes of approximately 1 μm . Bonding was conducted in air at temperatures ranging from 1450 to 1500 °C (2640 to 2730 °F) under an applied stress of

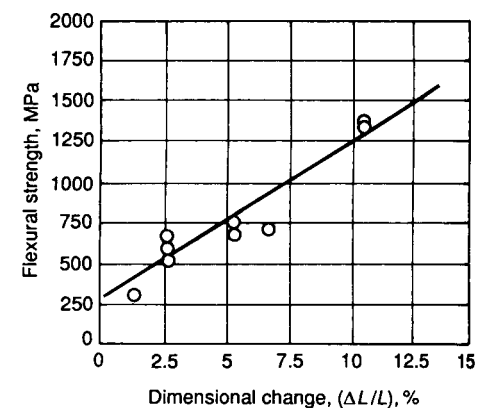


Fig. 8 Relationship between the degree of deformation and the strength of solid-state welds. A series of Y_2O_3 -stabilized tetragonal zirconia polycrystal ceramic/alumina composites containing 80 wt% ZrO_2 , 3 mol% Y_2O_3 , and 20 wt% Al_2O_3 were joined to each other at temperatures ranging from 1450 to 1500 °C (2640 to 2730 °F). Source: Ref 62

12.5 MPa (1.8 ksi). The welded samples were cut into bars that were tested in four-point bending at room temperature. They concluded that the strengths of the bonds increased with the degree of deformation during welding (Fig. 8), which resulted from higher bonding temperatures or increased amounts of the superplastic Y-TZP phase in at least one member of the joint. Flexural strengths greater than 1000 MPa (145 ksi) were achieved. Similar to Ellsner (Ref 60), they found that it was difficult to bond the coarse-grained alumina to itself, but that it was possible to bond the coarse-grained alumina to materials that were more readily deformed during welding, such as the 80% Al₂O₃-20% Y-TZP composite or the fine-grained alumina.

REFERENCES

- W.A. Owczarski and D.F. Paulonis, Application of Diffusion Welding in the USA, *Weld. J.*, Feb 1981, p 22-33
- O.S. Spanswick, Diffusion Bonding—A Case Study, Reprint R269/10/B4, *Weld. Inst. Res. Bull.*, The Welding Institute, 1984
- B. Derby and E.R. Wallach, Theoretical Model for Diffusion Bonding, *Met. Sci.*, Vol 16, Jan 1982, p 49-56
- B. Derby and E.R. Wallach, Diffusion Bonding: Development of Theoretical Model, *Met. Sci.*, Vol 18, Sept 1984, p 427-431
- I. Tuah-Poku, M. Dollar, and T.B. Massalski, A Study of the Transient Liquid Phase Bonding Process Applied to Ag/Cu/Ag Sandwich Joint, *Metall. Trans. A*, Vol 19, March 1988, p 675-686
- J. Pilling, The Kinetics of Isostatic Diffusion Bonding in Superplastic Materials, *Mater. Sci. Eng.*, Vol 100, 1988, p 137-144
- J. Pilling, D.W. Livesey, J.B. Hawkyard, and N. Ridley, Solid State Bonding in Superplastic Ti-6Al-4V, *Met. Sci.*, Vol 18, March 1984, p 117-122
- Y. Maehara, Y. Komizo, and T.G. Langdon, Principles of Superplastic Diffusion Bonding, *Mater. Sci. Technol.*, Vol 4, Aug 1988, p 669-674
- J. Pilling and N. Ridley, Solid State Bonding of Superplastic AA7475, *Mater. Sci. Technol.*, Vol 3, May 1987, p 353-359
- A.K. Ghosh and C.H. Hamilton, Superplastic Sheet Forming, *Metalworking: Sheet Forming*, Vol 14B, *ASM Handbook*, ASM International, 2006, p 345-366
- J. Beal, R. Boyer, and D. Sanders, Forming of Titanium and Titanium Alloys, *Metalworking: Sheet Forming*, Vol 14B, *ASM Handbook*, ASM International, 2006, p 656-669
- W.A. Bryant, A Method for Specifying Hot Isostatic Pressure Welding Parameters, *Weld. J.*, Dec 1975, p 433-s to 435-s
- C.E. Thornton and E.R. Wallach, Impact Strength of Steel Diffusion Bonds, *Met. Constr.*, July 1985, p 450R-455R
- S. Elliot, "Properties of Diffusion Bonds in a 0.4 C Steel," Report 131/1980, The Welding Institute, 1980
- S.B. Dunkerton, "Diffusion Bonding of a 0.4 Carbon Chromium/Molybdenum Steel," Report 178/1982, The Welding Institute, 1982
- A.E. Dray and E.R. Wallach, "Diffusion Bonding of Aluminium Alloys," Paper presented at International Conference on Diffusion Bonding (Cranfield, U.K.), 1987
- D.V. Dunford, C.G. Gilmore, and P.G. Partridge, "Effect of Silver Coating Thickness on the Shear Strength of Diffusion Bonded Clad Al-Zn-Mg (7010) Alloy," Paper presented at International Conference on Diffusion Bonding (Cranfield, U.K.), 1987
- N. Ridley et al., "Diffusion Bonding of Superplastic Aluminium Alloys," Paper presented at International Conference on Diffusion Bonding (Cranfield, U.K.), 1987
- D.W. Livesey and N. Ridley, Diffusion Bonding of Superplastic Aluminium Alloys Using a Transient Liquid Phase Interlayer (Zinc), *Diffusion Bonding 2*, Elsevier Applied Science, 1991
- R.A. Ricks et al., Development of Diffusion Bonding Techniques for Al-Li Base Alloy AA8090, *Diffusion Bonding 2*, Elsevier Applied Science, 1991
- H.M. Tensi and M. Wittman, Influence of Surface Preparation on the Diffusion Welding of High Strength Aluminium Alloys, *Diffusion Bonding 2*, Elsevier Applied Science, 1991
- D.V. Dunford, P.G. Partridge, and C.G. Gilmore, Diffusion Bonding of Al-Li 8090 Alloy, *Diffusion Bonding 2*, Elsevier Applied Science, 1991
- A. Urena and S.B. Dunkerton, "Diffusion Bonding of an Aluminium-Lithium Alloy (AA 8090)," Report 403/1989, The Welding Institute, 1989
- R.J. Rehder and D.T. Lovell, Process Development for Diffusion Welding Ti-6Al-4V, *Weld. J.*, May 1970, p 213-s to 218-s
- A.T. D'Annessa, The Solid-State Bonding of Refractory Metals, *Weld. J.*, May 1964, p 232-s to 240-s
- J.L. Knowles and T.H. Hazlett, High-Strength Low-Temperature Bonding of Beryllium and Other Metals, *Weld. J.*, Vol 49, July 1970, p 301-s to 310-s
- R. Lison and J.F. Stelzer, Diffusion Welding of Reactive and Refractory Metals to Stainless Steels, *Weld. J.*, Vol 58 (No. 10), 1979, p 306-314
- V.F. Shatinski et al., The Diffusion Bonding of Refractory Alloys to a Steel with a Decarburized Surface, *Weld. Prod.*, Vol 24 (No. 12), 1977
- E.R. Naimon, J.H. Doyle, C.R. Rice, D. Vigil, and D.R. Walmsley, Diffusion Welding of Aluminum to Stainless Steel, *Weld. J.*, Nov 1981, p 17-20
- P.D. Calderon, D.R. Walmsley, and Z.A. Munir, An Investigation of Diffusion Welding of Pure and Alloyed Aluminum to Type 316 Stainless Steel, *Weld. J.*, April 1985, p 104-s to 112-s
- C.H. Crane, D.T. Lovell, W.A. Baginski, and M.G. Olsen, Diffusion Welding of Dissimilar Metals, *Weld. J.*, Vol 46, p 23-s to 31-s
- T. Enjyo et al., Diffusion Welding of Copper to Aluminium, *Trans. JWRI*, Vol 8, 1979, p 77-83
- T. Enjyo et al., Diffusion Bonding of Aluminium to Titanium, *Trans. JWRI*, Vol 6 (No. 1), 1977, p 123-130
- G.R. Kamat, Solid-State Diffusion Welding of Nickel to Stainless Steel, *Weld. J.*, June 1988, p 44-46
- R.S. Rosen, D.R. Walmsley, and Z.A. Munir, The Properties of Silver-Aided Diffusion Welds Between Uranium and Stainless Steel, *Weld. J.*, Vol 65, April 1986, p 83-s to 92-s
- W. Feduska and W.L. Horigan, Diffusion Bonding of High-Temperature Alloys with Beryllium, *Weld. J.*, Jan 1962, p 28-s to 35-s
- T.J. Moore and K.H. Holko, Solid State Welding of TD-Nickel Bar, *Weld. J.*, Sept 1970, p 395-s to 409-s
- M.L. Wayman, R.R. Smith, and M.G. Wright, The Diffusion Bonding of Zr-2.5% Nb to Steel, *Metall. Trans. A*, Vol 17, March 1986, p 429-433
- J.T. Niemann, R.P. Sopher, and P.J. Rieppel, Diffusion Bonding Below 1000 °F, *Weld. J.*, Aug 1958, p 337-s to 342-s
- S. Elliot and E.R. Wallach, Joining Aluminium to Steel, Part 1—Diffusion Bonding, *Met. Constr.*, Vol 13 (No. 3), 1981, p 167-171
- J.W. Dini, Use of Electrodeposition to Provide Coatings for Solid-State Bonding, *Weld. J.*, Nov 1982, p 33-39
- J.W. Dini, W.K. Kelley, W.C. Cowden, and E.M. Lopez, Use of Electrodeposited Silver as an Aid in Diffusion Welding, *Weld. J.*, Jan 1984, p 26-s to 34-s
- C. Schalansky, Z.A. Munir, and D.L. Walmsley, An Investigation on the Bonding of Hot-Hollow Cathode Deposited Silver Layers to Type 304 Stainless Steel, *J. Mater. Sci.*, Vol 22, 1987, p 745-751
- P.S. Macleod and G. Mah, The Effect of Substrate Bias Voltage on the Bonding of Evaporated Silver Coatings, *J. Vac. Sci. Technol. II*, Vol 1, Jan/Feb 1974, p 119-121
- R.S. Rosen and M.E. Kassner, Diffusion Welding of Silver Interlayers Coated Onto Base Metals by Planar-Magnetron Sputtering, *J. Vac. Sci. Technol. A*, Vol 8 (No. 1), Jan/Feb 1990, p 19-29
- Adapted from A. Moorhead and H.-Ee Kim, Joining of Oxide Ceramics, *Ceramics*

- and Glasses, Vol 4, *Engineered Materials Handbook*, ASM International, 1991, p 511
47. J.T. Klomp, Ceramic and Metal Surfaces in Ceramic-to-Metal Bonding, *Ceramic Surfaces and Surface Treatments, British Ceramic Proceedings*, No. 34, R. Morrell and M.G. Nicholas, Ed., Shelton, Stoke-on-Trent, Staffs, U.K., 1984, p 249–259
 48. G. Elssner et al., Fracture of Ceramic-to-Metal Interfaces, *J. De Physique*, Vol 46, 1985, p C4-597 to C4-612
 49. M. Rühle and W. Mader, Structure and Chemistry of Metal/Ceramic Interfaces, *Designing Interfaces for Technological Applications: Ceramic-Ceramic, Ceramic-Metal Joining*, The European Colloquium, April 20–21, 1988 (Petten, The Netherlands), S.D. Peteves, Ed., Elsevier, London, 1989, p 145–195
 50. J.T. Klomp and A.J.C. VandeVen, Parameters in Solid-State Bonding of Metals to Oxide Materials and the Adherence of Bonds, *J. Mater. Sci.*, Vol 15, 1980, p 2483–2488
 51. Y. Arata and A. Ohmori, Studies on Solid State Reaction Bonding of Metal and Ceramic (Report I), *Trans. JWRI*, Vol 13, 1984, p 41–46
 52. H.J. DeBruin, A.F. Moodie, and C.E. Warble, Ceramic-Metal Reaction Welding, *J. Mater. Sci.*, Vol 7, 1972, p 909–918
 53. B. Derby and E.R. Wallach, *Met. Sci.*, Vol 16, 1982, p 49
 54. K. Nishiguchi and Y. Takahashi, Determination of Optimum Process Conditions in Solid Phase Bonding, by a Numerical Model, *Q. J. Jpn. Soc.*, Vol 3, 1985, p 65
 55. M.G. Nicholas and R.M. Crispin, Diffusion Bonding Stainless Steel to Alumina Using Aluminum Interlayers, *J. Mater. Sci.*, Vol 17 (No. 11), 1982, p 3347–3360
 56. B. Derby, The Influence of Surface Roughness on Interface Formation in Metal/Ceramic Diffusion Bonds, *Ceramic Microstructures '86*, J. Pask and A. Evans, Ed., Plenum, 1988, p 319–328
 57. W. Dawihl and E. Klinger, Mechanical and Thermal Properties of Welded Joints Between Alumina and Metals (in German), *Ber. Deutsch. Keram. Ges.*, Vol 46 (No. 12), 1969
 58. R.M. Crispin and M.G. Nicholas, Alumina-Copper Diffusion Bonding, *Ceram. Eng. Sci. Proc.*, Vol 10 (No. 11–12), 1989, p 1575–1581
 59. K. Suganuma, T. Okamoto, and M. Koizumi, Effect of Surface Grinding Conditions on Strength of Alumina/Niobium Joint, *Ceram. Eng. Sci. Proc.*, Vol 10 (No. 11–12), 1989, p 1919–1933
 60. G. Elssner et al., Microstructure and Mechanical Properties of Metal-to-Ceramic and Ceramic-to-Ceramic Joints, *Surfaces and Interfaces in Ceramic and Ceramic-Metal Systems*, J. Pask and A. Evans, Plenum Publishing, 1981, p 629–639
 61. C. Scott and V.B. Tran, Diffusion Bonding of Ceramics, *Am. Ceram. Soc. Bull.*, Vol 64 (No. 8), 1985, p 1129–1131
 62. T. Nagano, H. Kato, and F. Wakai, Diffusion Bonding of Zirconia/Alumina Composites, *J. Am. Ceram. Soc.*, Vol 73 (No. 11), 1990, p 3476–3480

Explosion Welding

Stephen Liu, Colorado School of Mines
John Banker and Curtis Prothe, Dynamic Materials Corporation

EXPLOSION WELDING (EXW), also known as explosive cladding, is accomplished by creating a high-velocity collision between two metal surfaces. The explosive detonation causes shock loading of one of the metals, the flyer plate, accelerating it downward and causing an oblique impact with the other metal, or base plate. It is necessary that this impact have sufficient energy to cause the colliding metal surfaces to flow hydrodynamically. Upon impact, conservation of momentum results in a reentrant jetting action and hydrodynamic flow of the faying metal surfaces. The jet is ejected outward from the collision apex, producing clean surfaces, being that it is comprised of the metal that was the prior effacing metal surface layers. The residual virgin metal surfaces are then forced together under high pressure, resulting in welding.

This phenomenon was first observed during World War I, when fragments from bombs or shells were found to be welded to surrounding metal structures (Ref 1). The first publication to recognize the potential for generating metallic welding by using explosively driven plates appeared in 1944 (Ref 2). The first EXW patent was issued in 1962 (Ref 3).

The two most beneficial attributes of EXW are:

- Dissimilar-metal systems can be welded, even when conventional fusion welding techniques are metallurgically inappropriate due to brittle intermetallic compound formation
- Large-area clad plates of almost any metal combination can be manufactured economically.

Applications of EXW are diverse and include the production of sandwiched metal for coinage (Ref 4), the production of titanium-to-stainless steel transition joints in the Apollo spacecraft (Ref 5), and production of explosion clad plates for industrial applications. The most common application of EXW is production of clad plates used in construction for pressure vessels for environments requiring superior corrosion resistance combined with high temperatures and/or pressures, such as chemical processes (Ref 6).

Several very good reviews of the EXW process have been published (Ref 7–11). A fundamental understanding of EXW involves a large number

of highly interactive variables (explosive detonation dynamics, dynamic materials deformation, metallurgical bonding, and more). Many of these interactive variables are defined in this article, and the references cited offer additional detail and explanation. Reliable models and predictive algorithms using numerical methods have been established, but, to a large extent, EXW is an empirical industrial technology practiced by experienced technologists. As such, much of the available knowledge relating to EXW is still based on experimental observation.

Since its origin in the 1960s, the EXW process has been shown to be a highly robust and reliable industrial welding technology. By 2010, there were well over 50 companies producing explosion-welded products worldwide. Combined annual industrial production is estimated to be in the range of 300,000 metric tons.

Overview of Process Attributes

Metallurgical Attributes. Because of the absence of heating, EXW products do not exhibit many of the metallurgical characteristics of fusion-welded, brazed, or hot rolled/forged products. Unlike those processes, in EXW (Ref 12–15):

- The component metals remain in their wrought states; continuous cast structures are not created.
- The microstructures, mechanical properties, and corrosion properties of the wrought parent components are not significantly altered.
- There are no bulk heat-affected zones.
- There is virtually no diffusion of alloying elements between components.
- The EXW interface is typically stronger than the weaker of the two parent components.

Metals Combinations. Explosion welding is an effective joining method for virtually any combination of metals. The only metallurgical limitation is that the component metals must exhibit sufficient ductility and fracture impact toughness to undergo the rapid deformation of the process without fracture. Generally accepted

limits are 10% elongation and 30 J (22 ft lb) Charpy impact energy minimum, respectively. Explosion welding is suitable for joining metals of the same type, for example, steel to steel, as well as metals with substantially different densities, melting points, and/or yield strengths, for example, tantalum to titanium alloys. The process is extensively used to join corrosion-resistant alloys to carbon or alloy steels. Table 1 shows a broad range of metal combinations that have been successfully welded using EXW. Most of the unproven combinations are considered to be weldable but have not been evaluated due to a lack of industrial or commercial need.

Explosion Welding Interface Morphology. Explosion welding is traditionally known for its wavy bond zone morphology (Fig. 1). However, the interface morphology can range from flat to turbulently wavy depending on the features needed from the interface and the welding process variables selected. Bond morphology is discussed in greater detail in the section “Weld Interface Morphology” in this article.

Size and Configuration Limitations. Explosion welding is appropriate for use over a broad range of sizes. It has been used for joining electronic components of widths less than 0.5 mm (0.020 in.) and for cladding plates up to 5 × 12 m (16 × 40 ft). Cladding metal thicknesses can range from 0.025 to 100 mm (0.001 to 4 in.), and base-metal thickness can range from 0.025 mm (0.001 in.) to over 1 m (40 in.). The size limits are generally mandated by component metal manufacturability and transportation requirements.

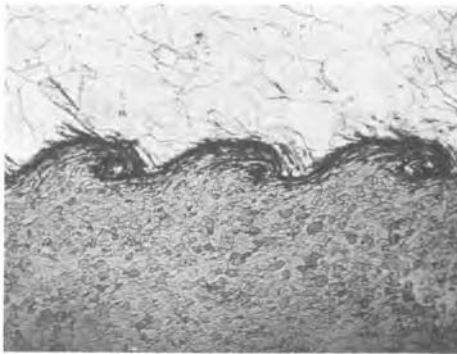
Explosion welding is limited to the welding of flat surfaces or coaxial cylindrical surfaces. This limitation results from the interface jetting mechanism, which is discussed in detail in later sections of this article. Explosion welding is ideally suited for joining large, flat areas, as in clad plate manufacture. When more complex components are the objective, a bimetal preform is typically produced by explosion welding in the plate or tube configuration, followed by hot or cold working to the end-product configuration.

Performance Characteristics and Process Reliability. The physical and mechanical performance features required of the EXW bond zone are determined by the product application.

Table 1 Commercial metals and alloys that have been successfully joined with explosion welding

Metal 1	Metal 2														
	Zr	Mg	Co alloys	Pt	Au	Ag	Nb	Ta	Ti	Ni alloys	Cu alloys	Al alloys	Stainless steels	Alloy steels	Carbon steels
Carbon steels	X	X	X	...	X	X	X	X	X	X	X	X	X	X	X
Alloy steels	X	X	X	X	X	X	X	X	X	X	X	...
Stainless steels	X	...	X	...	X	X	X	X	X	X	X	X	X
Aluminum alloys	X	X	X	X	X	X	X	X	X	X
Copper alloys	X	X	X	X	X	X	X	X
Nickel alloys	X	X	X	X	X	...	X	X	X	X
Titanium	X	X	X	X	X	X
Tantalum	X	X	...	X	X
Niobium	X	X
Silver	X
Gold
Platinum	X
Cobalt alloys	X
Magnesium	X	X
Zirconium	X

Source: Adapted from Ref 16

**Fig. 1** Bond zone pattern typical of explosion clad metals. Materials are type 304L stainless steel and carbon steel. Original magnification: 20 \times

In most cases, a direct weld between the two desired metals will achieve the required interface performance. However, with some combinations of metals, the required bond zone performance characteristics are best achieved with an interlayer between the two primary metals. For example, a titanium interlayer can be used to increase the performance temperature of an aluminum/copper weld, and a silver interlayer can be used to improve the leak tightness of an aluminum/stainless steel weld.

When EXW is performed by experienced technologists using metals in the appropriate metallurgical conditions, the process reliability is exceptionally high. The loss of product due to EXW process failure by well-established manufacturers is typically well under 0.1%.

Procedure Development and Practice Considerations

Explosion welding, like all other welding or joining processes, has a well-defined set of input parameters or conditions that must fall within certain limits for the desired weld quality to be achieved. Contrary to other joining processes, however, the EXW process occurs so rapidly (completed within a few microseconds) that there

is no time for in-process adaptive control or modification of the welding parameters or conditions. Therefore, a total quality joining approach must be taken to ensure that proper process parameters are applied and controlled to consistently achieve high-quality welds. The quality must be built into the preparation stages of the process materials and setups before welding takes place. It is necessary to be thoroughly familiar with every aspect of the process and the quality level that must be applied in order to ensure the consistent quality of the end-product weld (Ref 17).

This section provides a general overview of the important mechanistic aspects of EXW, the process-material interactions, and the critical aspects or parameters that must be controlled. The procedure for ensuring control is also discussed. This type of approach to setting and controlling process parameters is particularly important when explosion welding dissimilar or metallurgically incompatible metals. Metallurgically incompatible combinations, such as titanium and steel, aluminum and steel, and zirconium and steel, will form brittle intermetallic compounds at the explosion weld interface if excessive energies are used during welding. The intermetallic compounds result in poor-quality welds. Setting and controlling process parameters is also important when welding some of the newer advanced materials, which have little tolerance for parametric variations. To fully understand EXW and its control, it is helpful to know the general characteristics of the process, particularly the rates, pressures, and energies involved. The following are the general process parameters:

Traversal rate, m/s (ft/s)	2000–3000 (6600–9800)
Pressure, GPa (10 ⁶ psi)	1.5–6.0 (0.22–0.88)
Pressure time duration, μ s	5–20
Energy deposition/unit area, J/cm ² (Btu/ft ²)	100–300 (90–260)
Energy deposition rate, MJ/s (Btu/h)	20–90 (70 \times 10 ⁶ to 310 \times 10 ⁶)

By comparison, standard fusion welding processes will typically have traversal rates of a

fraction of a meter/second and energy depositions/unit area in the range of 10,000 to 30,000 J/cm² (9000 to 26,000 Btu/ft²). The low-energy input of EXW and the high interface propagation rate along the weld interface allow the weld to be made with an absolute minimum of thermal excursion and very limited heat-affected zone (HAZ).

To better explain the EXW process, some fundamental understanding of the several components of the process is discussed in the following sections. It is important to understand that these parameters are affected by the general geometric positioning relationship between the components to be welded. Two basic geometric configurations of the EXW process are commonly used: angle welding and parallel-plate welding. In the angle-welding configuration, the cladder plate is positioned at an angle relative to the base plate. Angle welding is limited to relatively small weld areas (weld length < 20 times cladder plate thickness), such as for seam welding or welding very small components. The parallel-plate geometry is much more commonly used. It is applicable for production of very large weld areas, typical of clad plate. Figure 2 presents a schematic of the parallel-plate EXW configuration.

Explosives and Explosive Detonation

The explosive is the energy source for the process. It releases its energy in a very specific manner during detonation. It is therefore necessary to first recognize how explosives detonate and how their energy is delivered to the flyer or cladder component. In almost all instances, the explosives used for EXW can be classified as nonideal. They do not detonate in a manner that can be easily defined by the physics equations-of-state typically used for extremely-high-velocity military or weapons explosives. This behavior results from the fact that these explosives are almost always granular in nature, with the primary ingredient typically being ammonium nitrate (NH₄NO₃). Other ingredients (for example, sensitizers,

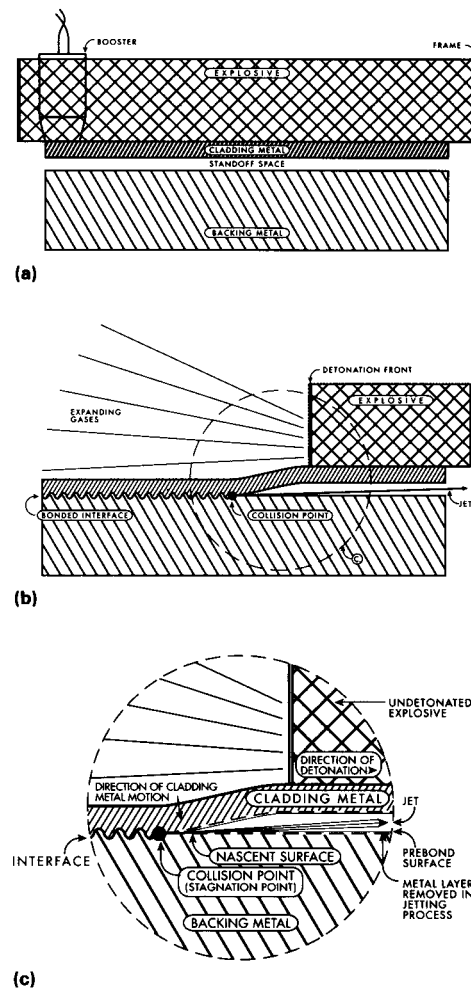


Fig. 2 Schematic showing mechanics of explosion welding. (a) Alignment of components to be joined before detonation. (b) Motion of components at detonation. (c) Close-up view of jet and wavy interface characteristic of explosion welding process

density control agents, and diluents) are then blended to produce an explosive that yields the desired detonation velocity, pressure, and duration of pressure.

The detonation characteristics of the explosive are controlled by its composition, particle size distribution, pour or packing density, layer thickness, confinement, moisture content, and, in some instances, age. The detonation performance of the explosive should be tailored to match the metals or alloy combinations being welded with respect to the density, thickness, and sonic or shock wave velocity of the flyer component, as well as the sonic velocity of the base component (if it is different from that of the flyer component).

Detonation is a progressive event that starts at the detonator and progresses into the undetonated explosive at a rate known as the detonation velocity. Within the detonation region (Fig. 3), the detonation front consists of an

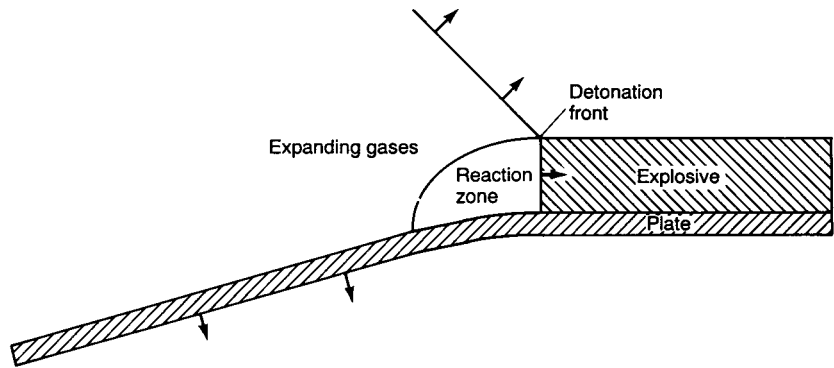


Fig. 3 Schematic showing detonation regions in a nonideal explosive and the associated acceleration of the flyer component

initial high-pressure shock wave intense enough to trigger the high-pressure chemical reaction that follows in the reaction zone. In an ideal explosive, the reaction goes almost instantaneously to completion; therefore, the reaction zone is extremely short (usually <1 mm, or 0.04 in.). In a nonideal explosive, however, the reaction zone is much longer (5 to 25 mm, or 0.2 to 1 in.) because the reaction takes longer to complete. While the pressure in the reaction zone of a nonideal explosive is much lower than that in the initial shock wave, it has a much longer duration in which the high-pressure gases in the zone can deliver their impulse to accelerate the flyer component. Behind the reaction zone is the third and final region of relatively low-pressure expanding gases, which contribute little, if any, to the impulse delivered to the acceleration of the flyer component. Each type of explosive has its characteristic detonation velocity, pressure, and duration factors that can be applied to predict the specific velocity, pressure, and duration for a given thickness and density of that explosive. For welding, it is usually desirable for nonideal explosives to detonate in the range of 2000 to 3000 m/s (6600 to 9800 ft/s). When the explosive is manufactured to exacting specifications, it is possible to control the detonation velocity within $\pm 2\%$ of the target terminal velocity. With nonideal explosives, however, such factors as start-up regions near the initiation point and predetonation compression due to the precursor shock wave in the flyer component ahead of the EXW collision front can cause nonsteady-state detonation conditions, which in turn can result in non-uniform weld quality.

Several important concepts pertaining to the explosive parameters, hydrodynamic flow, jetting, and metal properties were discussed earlier. The following discussion summarizes the criteria used to model the explosive bonding process.

Shock Effects and Explosive Parameters. Even though many different types of explosives have been used for EXW, those that have a broad range of low-detonation velocities are

the most appropriate, because of the deleterious effects of shock rarefaction. Shock fronts are described by a sharp discontinuity in pressure on one side of the transmitting medium where the violent motion that is due to high pressure is separated from a near-quiet state in the unaffected material. This condition can produce tensile stresses of sufficient magnitude to fracture the explosive weld. Shock waves are not pronounced unless the velocity of the shock front exceeds the sonic velocity of the transmitting medium. Sonic velocity is defined as:

$$U_s = \sqrt{\frac{E'}{\rho}} \quad (\text{Eq 1})$$

where U_s is the sonic velocity, E' is the appropriate elastic modulus, and ρ is the material density. If the shock wave propagation does not exceed the sonic velocity, then a broadening of the shock front occurs, and the magnitude of resultant stress and stress gradients is greatly reduced. Because most metals have a characteristic sonic velocity that ranges from 2000 to 6000 m/s (6600 to 20,000 ft/s), it is desirable to use explosives with detonation velocities within this range. Carpenter et al. (Ref 18) indicate that explosives with detonation velocities greater than 120% of the sonic velocity of the metal should not be used (Ref 19).

Detonation velocity is a characteristic of the type of explosive and has been shown to be directly proportional to the explosive density. This proportionality is shown in Eq 2, as derived empirically for nitroguanidine explosive (Ref 20):

$$V_d = 1440 + 4020\rho_e \quad (\text{Eq 2})$$

where V_d equals the detonation velocity, and ρ_e is the explosive density. The typical operating range for nitroguanidine is from 2000 to 5000 m/s (6600 to 16,000 ft/s), which corresponds to explosive densities that range from 0.14 to 0.9 g/cm³ (0.0051 to 0.033 lb/in.³).

The explosive pressure, P , is also proportional to the explosive density, ρ_e , as shown by the Bernoulli equation:

$$P \propto V_d^2 \rho_e \quad (\text{Eq 3})$$

Flyer plate velocities can be calculated from models similar to that presented by Gurney (Ref 21), who assumed that the driven metal was accelerated perpendicular to the direction of the detonation propagation and used a specific energy with a characteristic value for each explosive (the Gurney energy). Kennedy (Ref 22) gives a very good explanation of the Gurney model, along with several reconstructions of the Gurney equation, to account for changes in geometry. The equation that is applicable to the parallel gap explosive bonding technique is:

$$V_p^2 = 2E' \frac{3}{[1 + 5(\frac{m}{c}) + 4(\frac{m^2}{c^2})]} \quad (\text{Eq 4})$$

where V_p is the flyer plate velocity, E' is the Gurney energy, m is the flyer plate mass, c is the explosive mass, and m/c is the explosive load factor.

Once the flyer plate and detonation velocities are known, it is a simple matter to define the dynamic nature of the flyer plate bend angle through geometry. The following equation holds for the parallel gap geometry:

$$V_p = 2V_d \sin\left(\frac{\beta}{2}\right) \quad (\text{Eq 5})$$

where V_p and V_d are the velocities defined in Eq 4 and 5, respectively, and β is the flyer plate dynamic bend angle.

Equations 1 through 5, as well as an understanding of the metal physical-mechanical properties, are the basis for most models developed for EXW. These models are discussed as follows in general terms, beginning with a description of component acceleration, component collision, and jetting phenomena, followed by a description of welding and the methods used to define explosive parameter boundaries that will produce acceptable welds.

Component Acceleration

For EXW, the explosive is distributed over the top or exposed surface of the flyer component and is detonated such that the detonation front progresses in a grazing or tangential manner over the length of the flyer component. In doing so, the explosive delivers a specific level of impulse to the flyer component that causes it to be accelerated to a terminal bend angle, θ , and velocity, v_p , as shown in Fig. 2. For EXW, the acceleration region before terminal conditions are reached is the important region.

The acceleration of the flyer component actually results from the two separate zones of the detonation region in the explosive. First is the contribution of the high-pressure shock front

in the explosive. This imparts a high-pressure shock wave into the flyer component. The shock wave traverses back and forth, or rattles, between the opposite surfaces of the component, causing it to accelerate quickly in its early stages. The effects of this contribution diminish quickly and cause the component to reach only approximately 80% of the full-potential bend angle (Fig. 3) and velocity. As the effects of the shock component begin to diminish, the expanding high-pressure gas from the trailing reaction zone takes over and continues the acceleration more gradually until the terminal angle and velocity are obtained when the reaction is completed. This contribution (Fig. 4) plus the shock contribution yields the total impulse delivered to the flyer component. In an ideal explosive, nearly all of the acceleration comes from the extremely high pressure of the shock wave and very little from the trailing reaction zone; therefore, the primary (flyer) component reaches terminal conditions much more quickly with an ideal or near-ideal explosive.

The flyer component acceleration depends on the following parameters:

- Explosive pressure (shock and gas)
- Duration of the explosive pressure pulse
- Sonic or shock wave velocity of the flyer component
- Thickness of the flyer component
- Density of the component material

With the aforementioned variables, the acceleration characteristics of the flyer component can be calculated. In addition, techniques exist to directly measure the acceleration of a flyer component (Ref 23). Precise knowledge of the acceleration achieved for a specific flyer component/explosive combination is extremely important. It allows the exact standoff or separation distance to be set between the flyer and base components to obtain the required

collision angle and flyer component velocity in the next step of EXW (that is, the collision and welding step).

Component Collision. Once the accelerated flyer component crosses the standoff gap, it collides with the stationary base component. The exact collision angle and flyer component velocity achieved at the time of the collision will, of course, depend on the combination of the acceleration characteristics of the flyer component and the standoff distance selected for the system. The standoff distance is usually specified to ensure that the collision occurs while the flyer component is still undergoing acceleration, usually in its final stages.

The collision is characterized by:

$$v_p = 2v_c \sin\left(\frac{\theta}{2}\right) \quad (\text{Eq 6})$$

where v_p is the velocity of the flyer component or the relative velocity of the flyer and base components; v_c is the collision point velocity of the welding front, which also equals the detonation velocity, v_d , of the explosive; and θ is the collision angle. If any two of the aforementioned variables are known, it is then easy to calculate the third variable. The relative component velocity, v_p , at the time of the collision is very important in that it determines the equation-of-state pressure generated at the collision point. This pressure, which must be sufficient to generate hydrodynamic flow of both materials at the collision point, can be determined from the characteristic pressure versus plate (or particle) velocity for the material or materials being welded. Figure 5 shows a high pressure versus particle velocity plot for a similar material collision. Initially, the pressure required for dynamic yielding of the two materials being welded is calculated. This pressure is then located on the curve, and a mirror image of the curve is drawn through the selected pressure. The point at which the mirror-image curve

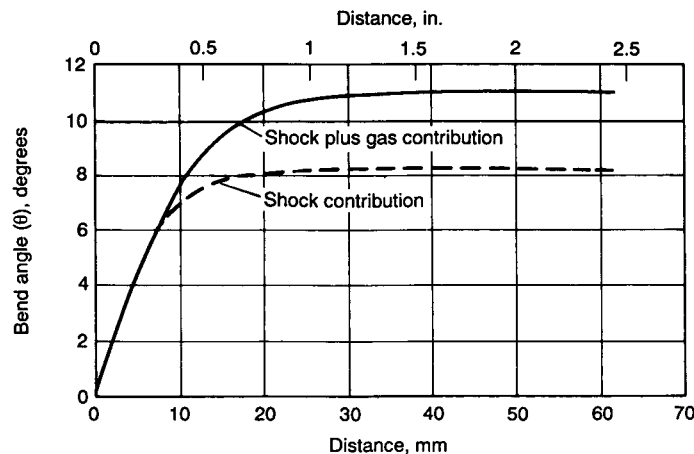


Fig. 4 Plot of flyer plate component bend angle versus distance to show contribution of shock wave and gas pressure to acceleration

intersects the zero pressure line or abscissa is the minimum flyer plate velocity necessary to obtain the desired pressure and accompanying dynamic flow and jetting necessary for welding to occur.

Jet Formation. During World War II, it was discovered that a hollowed explosive charge lined with metal could be used to produce a high-energy jet to perforate armor plate. Several investigators (Ref 24–26) have described the limiting conditions for the formation of jets in high-velocity collisions. Walsh et al. (Ref 25) indicated that a critical impact angle must be exceeded before jetting will occur. On the other hand, Cowan and Holtzman (Ref 26) indicated that for subsonic collisions, the elastic strength of the metal must be exceeded before jetting will occur. In both cases, jetting is described by a hydrodynamic flow of the metal surfaces. Walsh et al. presented equations based on this principle and the equations of state, which enable a calculation of the critical angle for jetting.

When the required minimum collision pressure, a minimum duration of the pressure pulse, and a minimum collision angle are obtained, the surfaces of the two materials being joined locally flow in the immediate region of the collision point. Because of the angular geometry of the collision, these surfaces at the collision point are forced to reverse their flow direction with severe shearing flow and to be ejected out ahead of the advancing collision point in the form of a fine fingerlike mist (that is, a jet) (Fig. 2). Under the extremely high hydrodynamic pressures involved, this jet, which consists of a combination of both parent materials, has an extremely high temperature. When the collision conditions of the weld are within an appropriate range (as discussed in a following section, “Parametric Limits for Welding”), most of the jet, with its attendant heat, is ejected out of the weld interface with little or no effect on the remaining weld zone. Of

greatest importance, however, is that the surface-scarfing action of the jet removes the surface layers containing the oxides and other contaminants that typically inhibit solid-state atom-atom contact. These clean surfaces allow the two metals to directly weld under the substantial residual pressure of the collision, which continues to act from some period of time on the two metals at the weld interface. This residual pressure on the interface after the collision also counteracts any reflected stress waves from separating the weld while it is forming.

Kowalick and Hay (Ref 27) reported an experimental technique to evaluate both the critical angle for jetting and the morphological changes in explosion welds resulting from changes in collision angle. The experimental setup consisted of the normal flyer plate arrangement used in the parallel gap technique, but with the base plate replaced by a half cylinder. Each welding trial produced continuously changing flyer plate collision angles that resulted in surface deformation and interface morphology variations. This analysis expanded upon the work of previous researchers by evaluating the geometry of fluid flow, jetting, and their effects on bond morphology.

Laminar fluid flow (low collision-point velocity and low Reynolds numbers) was correlated with direct bonding and a very flat bond interface. Turbulent fluid flow was separated into two regimes:

- At intermediate collision-point velocities, the flow was described by vortice formation into a von Karman vortex street and the production of a wavy bond interface.
- At high collision-point velocities, the flow was disturbed by a disordering of the jet wake, which led to a molten layer bond interface.

The micrographs on the right side of Fig. 6 show the relationship between detonation

velocity and wave morphology. The images on the left side show the similarity to fluid flow over a protuberance.

Selection of EXW Parameters

The preceding discussion introduced the primary variables used to predict EXW parameters. The following four conditions are used to define a window of acceptable welding parameters:

- Critical angle for jetting (Ref 28)
- Critical flow transition velocity (Ref 26, 27)
- Minimum flyer plate impact for jetting, based on analysis of the stress required to cause flow
- Maximum flyer plate impact for the limitation of weld defects, based on jet entrapment (Ref 26)

The critical angle for jetting is used to define the upper boundary for collision-point velocities. The lower limit in collision velocity is determined by the transition from laminar to turbulent flow, where turbulent flow is preferred (Ref 27). The other two limiting conditions are specified by using the physical and mechanical properties of the material to determine the maximum amount of energy required to either produce hydrodynamic flow (that is, overcome a critical shear stress) or avoid extensive melting. Once the correct set of explosive parameters has been determined by using either predictive models or an empirical approach, the production of explosively welded metal is a relatively simple task.

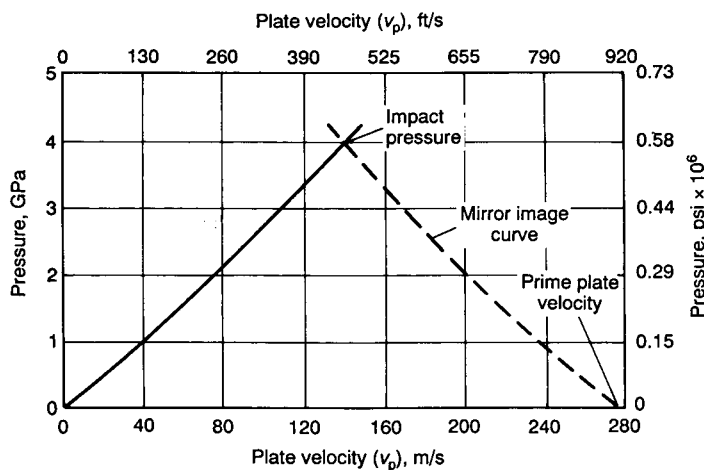


Fig. 5 Plot of high pressure versus particle velocity typically used to determine the flyer component velocity necessary to achieve dynamic yielding and welding

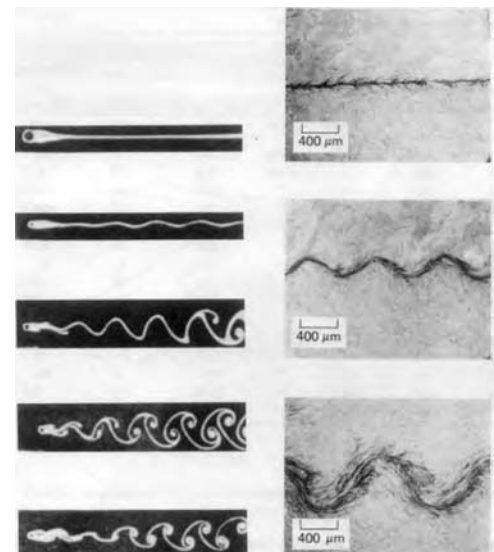


Fig. 6 Explosion welding interface exhibits patterns similar to flowing fluid, even though metals remain as solids. Right side shows explosion welding interface patterns; left side shows pattern of fluid flow around a pin. Velocity increases from top to bottom in both cases.

Parametric Limits for Welding. All the aforementioned considerations and an understanding of EXW and its controlling parameters can be assembled to produce a parametric envelope or window of parameters within which a high-quality explosion weld can be consistently produced. The basic concept of the boundaries defining the envelope has been advanced by several researchers (Ref 29–31).

A typical parametric envelope is defined by four distinct boundary segments (Fig. 7). The lower boundary (1) is controlled by the collision pressure and dwell time of the pressure pulse. The left boundary (2), although somewhat complicated, is primarily controlled by the sonic velocities of the two materials being welded. The right boundary (3) is controlled by the upper sonic-velocity limit at which a jet will form. It is almost never of concern because EXW is typically conducted at collision velocities significantly below this limit. The upper limit (4 or 4A) is primarily controlled by the kinetic-energy release generated at the collision point. In similar or metallurgically compatible combinations of metals or alloys, increasingly higher amounts of energy in this area of the envelope result in increasingly greater amounts of residual heat effects (for example, large melt pockets, interface voids, and a general degradation of the weld quality and properties). Therefore, this boundary (4) cannot be sharply defined in this instance. In metallurgically incompatible systems, however, this upper boundary (4A) becomes very sharply defined because it corresponds to the energy level at which a brittle intermetallic compound begins to form. Welding at or above this limit produces a weld that is typically brittle and can fail in service. Typically, this boundary is relatively close to the lower boundary (1), thus leaving a relatively small amount of latitude in collision parameters permissible to obtain a high-quality weld.

Each of the aforementioned boundaries can be calculated with relative accuracy for almost

all material combinations and thicknesses to be explosion welded. With these limits defined, the collision conditions must then be maintained to fall within the boundaries sufficiently away from the edges to allow for minor variations in the collision conditions during EXW. If this is accomplished, then a reproducible, high-quality explosion weld can always be expected and produced.

Weld Characteristics

Of particular importance is the nature or characteristics of the explosion weld itself. When properly made, it is, in essence, a solid-state bond or weld without any HAZ to degrade its strength, as is typical of all other heat-dependent welding or joining processes.

Weld Interface Morphology. Most EXW products exhibit the characteristic wavy interface shown in Fig. 1. However the morphology of an explosion weld can range from a flat interface to a highly turbulent wavy interface, depending on the explosive detonation rate and energy. Figure 6 shows the effect of increasing explosive detonation velocity on wave characteristics.

The flat or straight-line interface occurs only when the collision conditions are at or near the lower limits for jetting and welding. These conditions typically require very slow explosive detonation rates that are challenging to control to the precision needed for EXW; thus, weld reliability can be compromised. Although rarely used in production EXW, a flat interface exhibits features that can be beneficial in some specific unique applications.

Wave Formation. Abrahamson (Ref 32) examined the formation of surface deformations that were caused by a traveling jet using projectiles shot at thin metal targets, resulting in oblique impact. Two primary conclusions

drawn from this work were that the target metal deformation was a horizontal shear in the direction of impact and that the resultant wave peaks were deformed in such a pattern that they turned back in the direction opposite to impact. When the angle of impact was varied, two important responses occurred. First, below an impact angle of approximately 5° , no wave formation was observed. Second, as the angle of impact was increased above 5° , the amplitude and wavelength increased. The proposed mechanism for wave formation in high-velocity oblique impacts was based on subsonic or supersonic metal flow. Bahrani et al. (Ref 33) and Hunt (Ref 34) drew upon this hypothesis and proposed a physical description of wave formation in EXW, which included the following sequence of events:

- *Step 1:* Impact produces shear deformation in the stationary base plate, which results in a depression.
- *Step 2:* Conservation of volume criteria produces an upheaval of metal (a hump) ahead of the impact apex.
- *Step 3:* Hump interferes with the jet flow and produces an eddy in the jet, which traps molten material in the rear vortex.
- *Step 4:* Allowing for collision-point velocity causes a forward deformation of the hump and further jet turbulence, which again causes jet entrapment in the front vortex.

This wave formation, which has been the subject of considerable investigation (Ref 33, 34), results from the localized dynamic compression of the two metals in the region immediately adjacent to the collision point and weld interface. The compression causes localized bulk flow of the metals, which become unstable and make the weld interface oscillate above and below the theoretical plane of the interface. The size of the wave pattern is the one postwelding characteristic that can be used to determine the collision conditions used to make the weld and to allow for adjustments in subsequent welds of the same material type and thickness.

Wavelength. The wavelengths or frequency of the interfacial wave in an explosion weld is directly related to the thickness of the flyer or cladding plate and its angle of collision with the base plate (Ref 35), as shown in Fig. 8. For practical purposes, this relationship is relatively independent of the types or combinations of metals or alloys being welded. It also shows that the wave formation ceases at collision angles of 4° or less.

Wave Amplitude. The amplitude of the waves, on the other hand, is more difficult to predict. It depends on several factors, including the relative flow characteristics of the two metals being joined and the collision-point velocity of the EXW process. Control of the wave size, particularly the wavelength, is an important part of controlling several aspects of the explosion weld because:

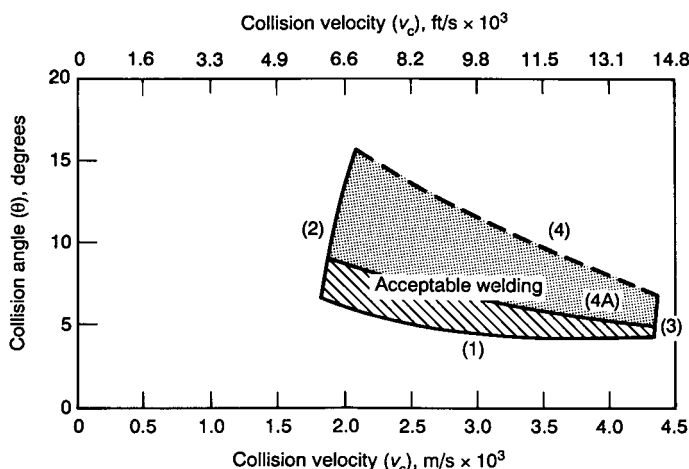


Fig. 7 Plot of collision angle versus collision velocity to obtain a typical explosion welding process parametric envelope for both similar- and dissimilar-metal combinations. See text for details.

- Wave size determines the amount of localized flow and work hardening in and adjacent to the explosion weld interface.
- Excessive collision energies and wave sizes can result in the formation of larger melt pockets on the front and back slopes of the waves, along with residual heat effects on the region in and adjacent to the weld interface, which will affect the mechanical properties of the weld (Fig. 6).

Interface Microstructure. As shown in Fig. 1, optical microscopy indicates no evidence of significant heating at the interface:

- No significant melt layers can be observed.
- There is significant cold work in the waves, and no recrystallization is evident.
- When examined by scanning electron microscopy, there is no evidence of diffusion of one metal into the other on either side of the interface.

Consequently, EXW is considered to be a cold welding process. Early researchers referred to it as a “solid-state electron-sharing bond” (Ref 26). Some researchers considered the interface to be similar in nature to a high-energy grain boundary.

Microstructural analysis of explosive bond zones has revealed several interesting results. Numerous metallurgical reactions have been reported:

- Extensive grain elongation in the direction of bonding, within several hundreds of micrometers of the bond interface, and measured elongations of several thousand percent (Ref 36)
- Residual dislocation densities on the order of 10^{11} cm^{-2} near the bond interface (Ref 36)
- Microtwinning has been observed (Ref 36, 37) in low-stacking-fault-energy metals (for example, copper).
- Recrystallization and recovery have been observed in bands on both sides of high-dislocation-density regions (Ref 38).
- Very little diffusion occurs across the bond interface (Ref 38).

These observations support the hypothesis, commonly held in the early years of the technology, that wave formation is a result of extreme metal deformation, and that bonding is a result of solid-state processes with very little diffusion.

Although the interface wave pattern can have significant effect on the EXW weld properties, it becomes increasingly apparent that the complex microstructures associated with the wave formation, not the wave pattern itself, determine the mechanical properties of the interface. In more recent years, transmission electron microscopy (TEM) studies have provided better insight into the nature of the interface and the bonding mechanism. These TEM studies indicate that very significant heating is occurring at the interface, but on a scale barely observable

with optical microscopy (Ref 39–41). These TEM studies indicate the presence of a thin interface reaction layer, 0.1 to 0.2 μm (3.9 to 7.9 $\mu\text{in.}$) thick. This layer appears to have been liquid at the time of formation, similar to the weld. Further, the studies report indications of an amorphous-like structure of the resolidified weld metal. This finding suggests that the time at elevated temperature is extremely short and the cooling rates are extremely fast. Other research data indicate that the metals are heated to the welding conditions and returned to well below the melting point in less than 20 μs . The result is a metastable metallurgical condition at the interface. The stable and deleterious phases that occur in most dissimilar-metal systems under equilibrium transformation conditions do not have time to form in explosion welds.

A comprehensive analysis of the characteristic features of the microstructures on the nanometer scale of explosive-welded components does not yet exist. The number of studies of this type has been severely limited by the high cost of TEM work and the relatively small budgets of the explosion cladding companies and research groups. It is estimated that less than twenty specimens were extensively analyzed

by TEM prior to 2008. Considering the area analyzed in a single TEM specimen, this is an extremely small sampling ratio. Modern nanoscale analytical capabilities are beginning to provide further knowledge of the interface. Figure 9 presents TEM data from work performed by Song and others at Max-Planck Institute in 2008 and 2009 (Ref 42).

Song et al. (Ref 43) has extensively analyzed a titanium-steel interface from the macrolevel to the nanometer level. They observed that the microstructure of the interface of an explosion weld can be characterized by four successive microstructures (Fig. 10). Figure 10 presents the hierarchical structure levels at the interface region of a titanium-to-steel interface. The macro-, meso-, and microlevels show structures that are similar to those that have been extensively investigated by others using optical microscopy. In discussion of the TEM analysis of the nanoscale interface, Song noted that “the extreme thermodynamic conditions associated with EXW cause formation of new, highly metastable crystal structures which, so far, were not reported in the crystallographic data bases. The very thin interface reaction layer (~ 100 to 300 nm) is the main, dominating component along the interface length that

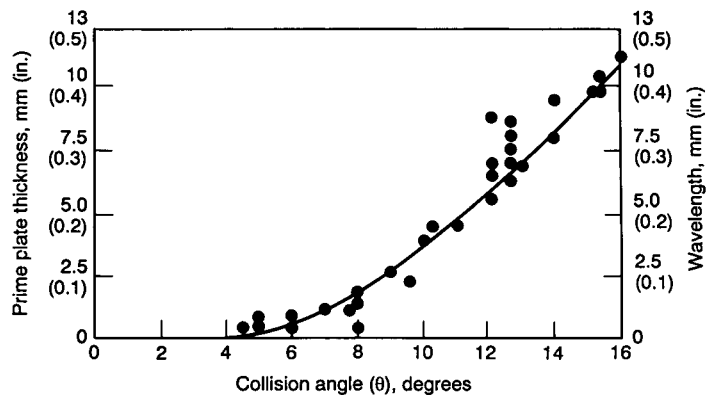


Fig. 8 Relationship of a function of collision angle wavelength to plate thickness

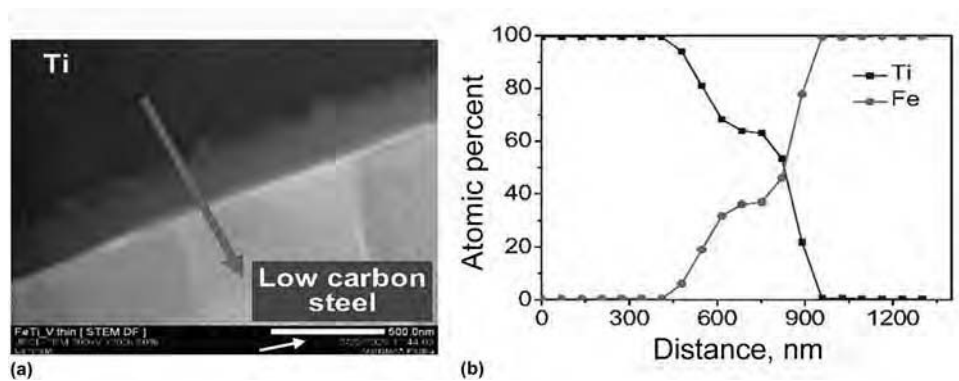


Fig. 9 (a) Transmission electron microscopy image of titanium/steel interface. Titanium and steel both exhibit wrought grain structures on either side of a narrow interface region (~ 200 nm wide). (b) Titanium and steel compositions across the interface region

ensures good macroscopic bonding between the joined components. Its formation is very complex and involves both mechanical alloying and solid-state reaction processes occurring at very high pressure, high local heating, and subsequent rapid cooling.” Today (2011), the explosion clad interface is frequently referred to as a very thin, hypercooled fusion weld.

Ongoing studies at Max-Planck Institute, Oak Ridge National Laboratory, Colorado School of Mines, and others are beginning to provide significantly more insight and understanding of the product and process.

Explosion Welding Interface Mechanical Properties. The interface strength is typically measured using the shear strength test of A264 and similar specifications. The shear strength of an EXW weld is typically greater than the strength of the weaker of the two parent metals (Fig. 11a). When through-thickness tensile strength is important, interface tensile strength is measured using either a ram tensile (in accordance with MIL-J-24445A specification) or a modified round tensile specimen (Fig. 11b). The work by Prothe et al. (Ref 44) measured the through-thickness tensile strength of the EXW interface and compared it with the shear strength of the same material. The test data demonstrated that the tensile strength of the interface was consistently greater than the shear strength. Because most EXW product is clad plate with a thin cladding layer, interface tensile strength cannot be easily measured. These data are significant from the design perspective, in that the shear strength, which can easily be measured, is an indicator of minimum interface tensile strength. The minimum interface permitted in ASTM International/American Society of Mechanical Engineers (ASME) specifications for stainless steel, nickel, titanium, and zirconium clad is 137 MPa (20,000 psi).

Manufacturing Process and Practice

Because of the unique safety and noise-vibration considerations, EXW is generally performed in relatively isolated facilities by companies specializing in explosives operations.

Safety and Regulations

Safety is of critical importance in the practice of EXW. Guidelines and regulations for the safe handling and transport of explosives are provided by the U.S. Bureau of Alcohol, Tobacco, and Firearms (Ref 45), the U.S. Department of Transportation in its Federal Motor Carrier Safety Regulations (Ref 46), and the Institute of Makers of Explosives Safety Library Publications (Ref 47). Licensing and regulations for the purchase, transport, manufacture, and use of explosives may vary significantly among states and municipalities. Depending on the types of explosives used, the detonation by-products may be subject

to environmental regulation. Potential practitioners of EXW operations should understand the safety standards and regulations before proceeding.

Noise and Vibration Abatement. The sound and ground vibration generated during EXW can be considerable. Common methods for noise abatement include performing the operation in a highly remote geographic location, in a mine or bunker, or in a specially designed blast chamber or vacuum chamber. Safety considerations vary among these options. Precautions must be taken to ensure that personnel are protected from shrapnel and facility deterioration.

Clad Plate Production

The following discussion describes the process for welding a two-component flat plate product (Fig. 12). Bimetal flat plate products are commonly produced to internationally accepted clad metal specifications:

- *ASME SA-263/A263*: Martensitic and ferritic stainless steel clad to carbon or alloy steel

- *ASME SA-264/A264*: Austenitic stainless steel clad to carbon or alloy steel
- *ASME SA-265/A265*: Nickel and nickel alloy clad to carbon or alloy steel
- *ASTM B 432*: Copper and copper alloy clad to steel
- *ASTM B 898*: Reactive and refractory metal clad plate (titanium, zirconium, tantalum)

Sizing Considerations. It is common practice to start with materials that are wider, longer, and thicker than required in the finished product to compensate for thinning and edge effects. In most situations, metals cannot be reliably bonded fully to the edges. Typically, allowances for edge nonbond are four to eight times the flyer plate thickness, depending on the combination of metals. Additionally, an area of nonbond is typical near the explosive initiator. The thickness of the component metals is reduced during surface preparation and bonding. Surface conditioning removes up to 0.75 mm (0.030 in.) from the thickness. During the bonding operation, the force vector parallel to the detonation causes a 1 to 2% increase in plate lateral dimensions; this change is

Scale	Macro	Meso	Micro	Nano
Microstructure				
Schematic				
Hierarchical structure unit	Plastically deformed base materials: different degree of accumulated strain in Ti and elongated steel grains	Wavy interface: wavelength of 540 μm and amplitude of 100 μm	Wave crest: different intermetallic phases, presence of microcracks	Thin interface reaction layer: two nanosize-grained components

Fig. 10 Hierarchical structure levels at the interface region of a titanium/steel clad. Source: Ref 43

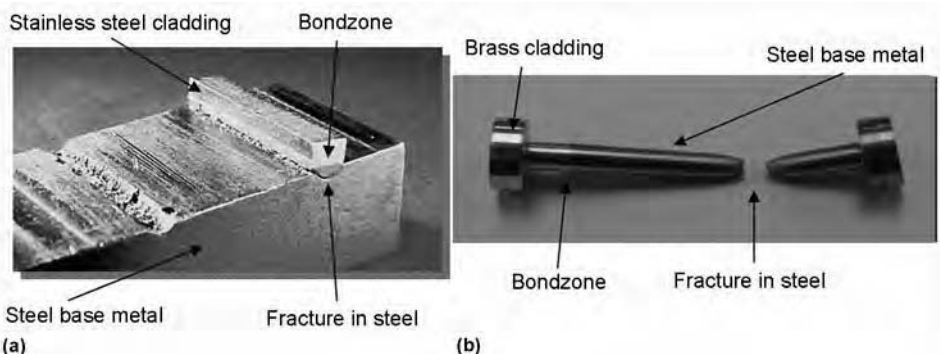


Fig. 11 Test specimens of explosion welding interface showing ductile failure in the parent steel. (a) Shear strength test. (b) Tensile strength test

accomplished by a corresponding reduction in thickness. The jetting of the metal surfaces during the bonding process causes only a thin layer to be removed, usually less than 0.05 mm (0.002 in.).

Surface Preparation and Assembly. The faying surfaces of the components are ground to achieve a smooth, pit-free finish of 1 to 3 μm (50 to 100 $\mu\text{in.}$). The plates are fixtured parallel while separated by a standoff gap. Methods for determining the standoff gap were presented in earlier sections of this article. Small standoff devices are required to bear the weight of the flyer plate and the explosive. Edge standoff devices are easily ejected from the system during bonding; therefore, material of construction is rarely critical. Internal standoff devices must be of sufficiently low mass to be removed by the jet, or must be located in trim regions. Some commonly used internal standoff materials are thin metal ribbons and foam blocks.

Explosive Loading and Welding. The explosive is placed on top of the flyer plate. The most commonly used explosives are granular or liquid and are typically contained within a simple box structure fabricated around the perimeter of the flyer plate. Initiating explosives are positioned in a suitable location on the plate surface. The required detonation range of EXW is below that of most commercially manufactured explosives. Consequently, most practitioners of EXW use proprietary explosive blends. Appropriate detonation characteristics can be achieved by specialized blending of commercial explosives such as Amatol, Dynamite, or ANFO.

The main explosive layer is initiated by a sequence of an electric blasting cap and a

high-explosive booster, causing a progressive detonation of the explosive, which creates the actions. The energy of welding typically creates sufficient deformation that flattening occurs (Fig. 2) and welds the plates together.

Postweld Processing. Most metal systems do not require postweld heat treatment to achieve the specified properties; however, some combinations provide superior properties if they are given a stress relief after bonding. For example, titanium/steel and zirconium/steel exhibit improved bond toughness after stress relief, and ferritic stainless steels exhibit an improvement in ductile-to-brittle transition temperature after stress relief.

Straightening is required prior to further processing. Flattening is performed with equipment of the same design used in plate and sheet manufacture.

Testing and inspection are performed as mandated by the product specifications. Ultrasonic inspection, typically performed using standard procedures such as ASTM A 578, is the most commonly accepted method for inspecting the bond continuity. Bond shear strength is normally measured using the test defined in ASTM A 264.

Because of the process edge effects, it is common practice to cut the product from a larger plate after bonding. The process options vary with the metal combinations and include oxyfuel gas cutting, plasma cutting, waterjet cutting, sawing, and machining. Finished plates are typically polished on the cladding side for cosmetic quality. Figure 13 shows typical clad plates after final processing.

Process Variants

Essentially the same approach can be used for producing multilayer products or cylindrical shapes:

- Multiple layers can be welded sequentially in a single operation; as many as 50 individual thin layers have been welded in a single event.
- Two-sided clad plates, with a heavy core metal, can be produced by simultaneously welding both sides using a vertical assembly.
- Two or more cylinders can be welded concentrically. The explosive is placed either inside of the cylinder or outside of the outer cylinder, depending on diameter and wall thickness.

Shop Welding Applications. Small, specialty EXW devices have been developed for a few unique shop applications. Explosion welding is used in heat exchanger shops for joining tubes to tubesheets and tube plugging. Explosion spot welding devices have also been used in limited commercial applications (Ref 48, 49).

Products and Applications

The largest industrial application of EXW is manufacture of large clad plates that are used in pressure vessels (Fig. 14), heat exchangers (Fig. 15), and electrochemical process applications (Ref 5, 42, 50, 51).

The dissimilar-metal welding features of EXW are made available to a broader industrial base through the concept of welding transition joints. Transition joint components are produced by explosion welders at their production facilities and then provided in the form of blocks, strips, or tubular couplings to equipment fabricators for use in the conventional welding of dissimilar metals (Fig. 16). Common applications are aluminum/steel (Ref 52), titanium/steel, aluminum/titanium (Ref 53), and aluminum/copper-nickel for shipboard construction; aluminum/copper and aluminum/steel for electrical contacts and buss systems (Ref 54); aluminum/stainless steel for cryogenic pipe couplings; titanium/stainless steel for aerospace and aircraft applications; and

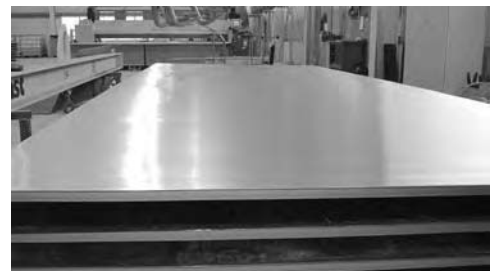


Fig. 13 Clad plates after final processing

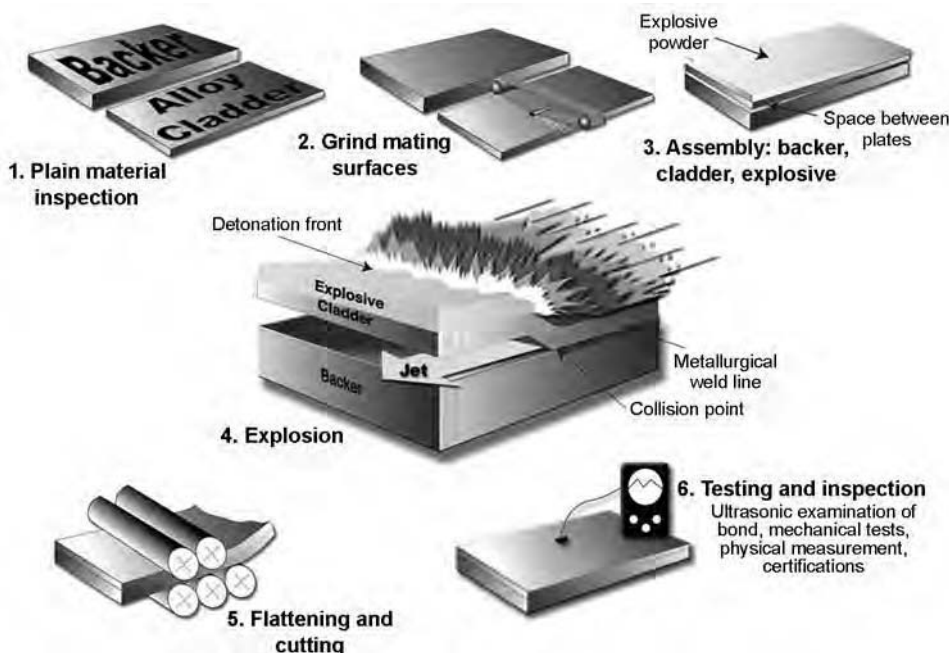


Fig. 12 Schematic of typical explosion clad plate manufacturing sequence

Kovar/copper and Kovar/aluminum for electronic packaging (Ref 55).

ACKNOWLEDGMENTS

This article includes adapted content from the following articles in *Welding, Brazing, and Soldering*, Vol 6, *ASM Handbook*, ASM International, 1993:

- J.G. Banker and E.G. Reineke, *Explosion Welding*, 1993, p 303–305
- V.D. Linse, *Procedure Development and Practice Considerations for Explosion Welding*, 1993, p 896–900
- R.A. Patterson, *Fundamentals of Explosion Welding*, 1993, p 160–164

REFERENCES

1. B. Crossland, *Explosive Welding of Metals and Its Application*, Clarendon Press, 1982
2. L.R. Carl, *Met. Prog.*, Vol 46, 1944, p 102
3. V. Philipchuk and F. LeRoy Bois, U.S. Patent 3,024,526, 1962
4. K. Richardson, *Explosion Welding: From Principle to Practice*, *Outlook*, Vol 25 (No. 1), 2004
5. V.D. Linse, R.H. Wittman, and R.J. Carlson, "Explosion Bonding," Report X68-10247, Battelle Memorial Institute
6. J. Banker, Try Explosion Clad Steel for Corrosion Protection, *Chem. Eng. Prog.*, July 1996
7. J.S. Rinehart and J. Pearson, *Explosive Working of Metals*, Pergamon Press, 1963
8. A.A. Ezra, *Principles and Practice of Explosive Metal Working*, Industrial Newspapers Limited, John Adams House, London, 1973
9. T.Z. Blazynski, *Explosive Welding, Forming and Compaction*, Applied Science Publishers, U.K., 1983
10. Young et al., *Explosion Welding*, Chap. 9, *AWS Handbook*, American Welding Society, 2010, p 304–331
11. J. Banker, Advances in Explosion Welding, Chap. 15, *The Handbook of Advanced Welding*, Woodhead Publishing Ltd., London, 2004
12. R.E. Savidge, Mechanical Properties of Explosion Clad Bonds of High Nickel Alloys on Low Alloy Steels and the Effect of Explosion Cladding on the Fracture Properties of the Steel, *Third International Conference on High Energy Rate Fabrication*, 1971, p 3.3.1
13. W. Lucas, J.D. Williams, and B. Crossland, Some Metallurgical Observations on Explosion Welding, *Second International Conference of the Centre for High Energy Forming*, 1969, p 8.1.2
14. S.H. Carpenter and M. Nagarkar, The Effects of Explosive Welding on the



Fig. 14 Titanium clad autoclave for nickel laterite leaching. Approximately 5 m diameter × 33 m long × (120 mm steel + 8 mm titanium)



Fig. 15 Shell and tube heat exchanger with titanium/steel clad tubesheets and covers

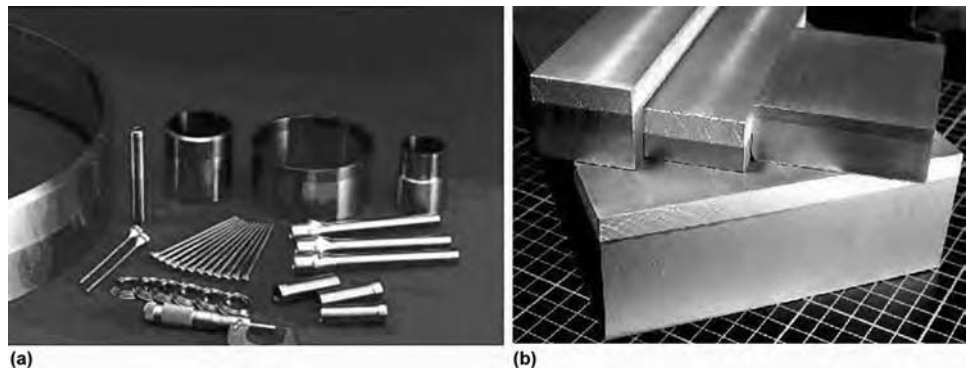


Fig. 16 Transition joints for joining dissimilar metals. (a) Tubular transition joints for welding dissimilar-metal pipes and tubes. (b) Transition joint blocks for dissimilar-metal electrical connections

- Kinetics of Metallurgical Reactions, *Third International Conference of the Centre for High Energy Forming*, 1971, p 3.4.1
15. L.F. Trueb, Microstructural Effects of Heat Treatment on the Bond Interface of Explosively Welded Metals, *Metall. Trans.*, Vol 2, Jan 1971, p 145
 16. R.L. O'Brien, Ed., *Welding Handbook*, Vol 2, 8th ed., American Welding Society, 1991, p 772
 17. V.D. Linse, Procedure Development and Process Considerations for Explosion Welding, *Welding, Brazing, and Soldering*, Vol 6, *ASM Handbook*, ASM International, 1993, p 896-900
 18. S. Carpenter, R.H. Wittman, and R.J. Carlson, Relationships of Explosive Welding Parameters to Material Properties and Geometry Factors, *Proc. First Int. Conf. of the Center for High Energy Forming*, June 1967, University of Denver, p 124
 19. A.A. Patterson, Fundamentals of Explosion Welding, *Welding, Brazing, and Soldering*, Vol 6, *ASM Handbook*, ASM International, 1993, p 160-164
 20. J. Groschopp, V. Heyne, and B. Hoffman, Explosively Clad Titanium Steel Composite, *Weld. Int.*, No. 9, 1987, p 879-883
 21. R.W. Gurney, "The Initial Velocities of Fragments from Bombs, Shells, and Grenades," Report 405, Ballistic Research Laboratory, 1943
 22. J.E. Kennedy, Explosive Output for Driving Metal, *Proc. Behavior and Utilization of Explosives in Engineering Design Conf.*, L. Davidson, J.E. Kennedy, and F. Coffey, Ed., ASME (New Mexico Section), 1972, p 109
 23. E.G. Smith, Jr. and V.D. Linse, The Acceleration Characteristics of Explosively Driven Flyer Plates, *Proc. Sixth Int. Conf. High Energy Rate Fabrication*, Sept 13-16, 1977 (Essen, West Germany)
 24. G. Birkhoff, D.P. MacDougall, E.M. Pugh, and G. Taylor, *J. Appl. Phys.*, Vol 19, 1948, p 563
 25. J.M. Walsh, R.G. Sheffler, and F.J. Willig, *J. Appl. Phys.*, Vol 24 (No. 3), 1953 p 349
 26. G.R. Cowan and A.H. Holtzman, *J. Appl. Phys.*, Vol 34 (No. 4), 1963, p 928
 27. J.F. Kowalick and D.R. Hay, *Metall. Trans.*, Vol 2, 1971, p 1953
 28. R.H. Wittman, "An Experimentally Verified Model Predicting Impact Welding Parameters," Thesis, University of Denver, 1975
 29. K.T. Christensen, N.S. Egley, and L. Atling, Explosive Welding of Tubes to Tube-Plates, *Proc. Fourth Int. Conf. Center for High Energy Forming*, July 9-13, 1973 (Vail, CO)
 30. R.H. Wittman, The Influence of Collision Parameters on the Strength and Microstructure of an Explosion Welded Aluminum Alloy, *Proc. Second Int. Symp., Use of Explosive Energy in Manufacturing Metallic Materials of New Properties*, Oct 9-12, 1973 (Marianske Lazne, Czechoslovakia)
 31. A.A. Deribas, Classification of Flows Appearing on Oblique Collisions of Metallic Plates, *Proc. Second Int. Symp., Use of Explosive Energy in Manufacturing Metallic Materials of New Properties*, Oct 9-12, 1973 (Marianske Lazne, Czechoslovakia)
 32. G.R. Abrahamson, *J. Appl. Phys.*, Vol 34 (No. 4), 1961, p 519
 33. A.S. Bahrani, T.G. Black, and B. Crossland, The Mechanics of Wave Formation in Explosive Welding, *Proc. R. Soc.*, Vol 296 (No. 1445), 1967, p 123-126
 34. J.N. Hunt, Wave Formation in Explosive Welding, *Philos. Mag.*, Vol 17 (No. 148), April 1968, p 669-680
 35. A.A. Deribas, Simulation of the Process in Wave Formation in Explosive Welding, *Combustion, Explosion and Shock Waves*, Vol 4 (No. 1), USSR, 1968
 36. L.F. Trueb, *J. Appl. Phys.*, Vol 34 (No. 4), 1968, p 928
 37. M.P. Bondar and V.M. Ogolikhin, Plastic Deformation in Bonding Zone Under Explosive Welding and Its Role in Bonding Formation, *J. Phys.*, C5 (No. 8-46), 1985, p C5-379 to C5-384
 38. W. Lucas, J.D. Williams, and B. Crossland, Some Metallurgical Observations on Explosive Welding, *Proc. Second Int. Conf. of Center for High Energy Forming*, 1969, p 8.1.1
 39. M. Hammerschmidt and H. Kreye, TEM Investigation of the Microstructure Affected by the Bonding Process during Oblique Collision of Metallic Surfaces, *Fifth International Symposium Explosive Working of Metals*, Oct 12-14, 1982, Gottwaldov, Czechoslovak Scientific and Technical Society
 40. A. Chiba, N. Minoru, and M. Yasuhiro, Microstructure of Bonding Interface in Explosively-Welded Clads and Bonding Mechanism, *Mater. Sci. Forum*, Vol 465-475, 2004, p 465-474
 41. M.C. Lafont, T. Masri, and A. Nobili, Recent Developments in Characterization of a Titanium-Steel Explosion Bond Interface, *Reactive Metals in Corrosive Applications Conference Proceedings*, J. Haygarth and J. Tosdale, Ed., Wah Chang, Albany, OR, 1997, p 89-98
 42. J. Banker, Explosion Cladding—An Enabling Technology for Zirconium in the Chemical Process Industry, *Zirconium Production & Technology: The Kroll Papers 1975 to 2010*, ASTM International, 2010
 43. J. Song, A. Kostka, M. Veehmayer, and D. Raabe, Hierarchical Microstructure of Explosive Joints: Example of Titanium to Steel Cladding, *Mater. Sci. Eng. A*, 2010
 44. C. Prothe and A. Vargo, Comparative Tensile Strength and Shear Strength of Detached Explosion Clad Products, *Proceedings of Corrosion Solutions Conference 2007*, Wah Chang Corporation, Albany, OR
 45. "ATF—Explosives Law and Regulations," Bureau of Alcohol, Tobacco, and Firearms, Department of the Treasury, June 1990
 46. "Federal Motor Carrier Safety Regulations," U.S. Department of Transportation, Federal Highway Administration, Feb 1991
 47. "Suggested Code of Regulations for the Manufacture, Transportation, Storage, Sales, Possession and Use of Explosive Materials," Institute of Makers of Explosives, Jan 1985
 48. L.G. Lazari, Explosive Welding and Its Practical Applications, *Weld. Rev.*, May 1988, p 74
 49. C. Toth and C. Prothe, Kinetic Spot Welding, *Proceedings of Corrosion Solutions Conference 2005*, Wah Chang Corporation, Albany, OR
 50. J. Banker, Hydrometallurgical Applications of Titanium-Clad Steel, *Proceedings 1999 Reactive Metals in Corrosive Applications Conference*, Sept 1999, Wah Chang Corp., p 99-104
 51. J. Laermans and J. Banker, Large Titanium Clad Pressure Vessels, Design, Manufacture and Fabrication Issues, *Corrosion Solutions Conference 2003*, Sept 2003, Wah Chang Corporation
 52. C.R. McKenney and J.G. Banker, *Explosion-Bonded Metals for Marine Structural Applications*, The Society of Naval Architects and Marine Engineers, Nov 1970, p 285-292
 53. M. Scaturro and J. Banker, Titanium for Secondary Marine Structures, *Titanium in Shipboard Applications*, ITA, Dec 1996
 54. J. Banker and A. Nobili, Aluminum-Steel Electric Transition Joints, Effects of Temperature and Time upon Mechanical Properties, *Light Metal 2002, Proceedings of TMS Conference*, Feb 2002, p 439-448
 55. H. Mansell, Hybrid Metal Packages by Explosion Bonding, *Hybrid Circuit Technol.*, Sept 1990, p 67

Forge and Coextrusion Welding

Revised by Paul S. Korinko, Savannah River National Laboratory

FORGE WELDING is a solid-state joining process in which the workpieces are heated to the welding temperature and then sufficient blows or force are applied to cause permanent deformation and bonding at the faying surfaces. It is most commonly applied to the butt welding of steels but is also used to laminate steels together, as in the manufacture of Damascus blades. It is an ancient process and has been dated as early as 2000 B.C. (Ref 1, 2).

Coextrusion welding is a solid-state process that produces a weld by heating two or more workpieces to the welding temperature and forcing them through an extrusion die. The process typically is conducted at elevated temperatures not only to improve welding but also to lower extrusion pressures. Some cold coextrusion welding of aluminum and copper has been performed. For hot coextrusion, the parts to be welded are often assembled in a can or retort that is designed with the appropriate leading taper and wall thickness to promote initiation of extrusion. For reactive metals, such as zirconium, titanium, and tantalum, the retort may be evacuated and sealed. Both forward and back coextrusion have been employed, but forward coextrusion is the usual mode. A principal advantage of coextrusion welding is that the high isostatic pressures associated with the process are favorable to the deformation welding of low-ductility alloys.

Forge Welding

Forge welding of ferrous materials is accomplished at very high homologous temperatures on the order of 0.8 to 0.9 of the melting temperature, which contrasts with hot pressure (thermocompression) welding of ductile face-centered cubic metals, which is normally performed at temperatures of less than one-half the melting temperature. The forge welding temperature is generally selected to be as high as possible with due consideration to avoiding such metallurgical problems as hot shortness, embrittlement, sensitization, and excessive grain coarsening. This limitation implies an understanding of the unique metallurgical problems of the alloy to be welded.

Forge welding can be completed either manually or automatically. For manual forge welds,

the process is as follows. The pieces to be joined are heated and forged into common joints (Fig. 1). The joint surfaces in Fig. 1 are slightly rounded or crowned to ensure that the centerline region of the components joined will be welded first to force any contaminants (for example, slag, dirt, or oxide) present on the surfaces out of the joint. The two pieces are fluxed with a material that will remove oxides and prevent further oxidation, and heated using a furnace, an oxyacetylene torch, or perhaps a clean-burning, slightly reducing fire of the type a blacksmith would use. The parts are heated to the desired temperature, that is, near white hot, and then hammered to the target thickness and thus joined. It is desirable to achieve the final dimensions in one or two heat cycles. If the joint has not been thinned sufficiently, then the joint is reheated and forged again. If the pieces have been overthinned, additional work is needed to bring the minimum dimension back.

Typical joint configurations used for automatic forge welding operations are shown in Fig. 2 (Ref 1). Hydraulic presses are typically employed to apply pressure. Presses are often highly automated, featuring microprocessor control of pressure and temperature cycles. Heat is applied locally to the joint area by multiple-tip oxyacetylene torches, resistance heating, or induction heating. Often, the oxyacetylene torches are oscillated to ensure uniformity of heating. In a closely related process, magnetically induced arc butt welding, the surfaces to be welded are heated by a rapidly rotating arc plasma. Generally, the process is conducted in the open air, with oxygen

partially occluded from the joint area by the initial contact of the faying surfaces. When employing oxyacetylene torches, a slightly reducing flame affords some atmospheric protection. Vacuum, inert, and reducing atmospheres have been used.

The normal welding sequence is:

1. Apply sufficient pressure to firmly seat the faying surfaces against one another.
2. Heat the joint to welding temperature.
3. Rapidly apply additional pressure to mechanically upset the weld zone.

Typical weld durations are 1 to 2 min. A less common procedure is to initially apply high pressure and permit deformation to occur during the heating cycle. Most forge welding employs sufficient pressure to upset the surface until the increase in the surface area is 125% or more. However, such high deformation tends to cause flow lines to bend toward the surface during upsetting. Consequently, alloys that contain significant stringers and inclusions may exhibit poor impact or fatigue properties when welded with high amounts of upset. This effect may be minimized by reducing the upset, which normally requires increasing welding temperature and/or time to ensure complete elimination of voids and surface oxide.

Forge welding is most commonly applied to carbon and low-alloy steels, with typical welding temperatures of approximately 1125 °C (2060 °F). Low-carbon steels can be used in the as-welded condition, but medium-carbon steels and low-alloy steels normally are given full heat treatments following welding. In those cases where full heat treatment is impractical

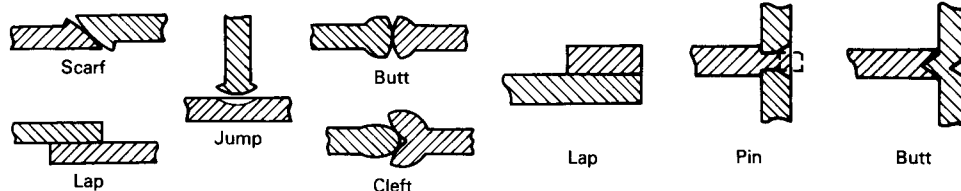


Fig. 1 Typical joint configurations used for manual forge welding applications. Source: Ref 1

Fig. 2 Recommended joint configurations used in automatic forge welding applications. Source: Ref 1

but hardening due to rapid cooling has occurred, induction heating may be used to temper the weld zone. Other metals welded by forge welding include high-alloy steels, nickel-base alloys, cobalt-base alloys, aluminum alloys, titanium alloys, and tungsten. Applications of this process include welding rods, bars, tubes, rails, aircraft landing gear, chains, and cans. The forge welding process is competitive with flash welding and friction welding.

The primary variables for forge welding are temperature, total deformation, and deformation rate (for automated forge welding). Of these parameters, temperature is usually the most important.

Forge welding can be used to weld high- and low-carbon steels together, as is done for decorative swords. The forging process allows uniform carbon distribution profiles to be generated while having the steel exhibit a patterned weld (Ref 3). In addition to the same base-metal weldments being made via forge welding, dissimilar metals such as aluminum and iron have also been joined. Control of the variables is important, and, as suggested previously, weld temperature is the critical variable for creating a successful weld joint (Ref 4).

Flux must be added when forge welding certain metals to prevent the formation of oxide scale. The flux and the oxides present combine to form a protective coating on the heated surfaces of the metal that prevents the formation of additional oxide and lowers the melting point of the existing oxide. The flux removes the native oxide and allows metallurgical bonding of these clean surfaces.

Silica sand and borax are two fluxes commonly used on steels. Silica sand can be used as a flux in the forge welding of low-carbon steel. The oxides of very-low-carbon steels (ingot irons) and wrought irons do not require fluxes because their oxides have low melting points. Borax, sprinkled on the workpiece while it is in the process of being heated, is commonly used in the forge welding of high-carbon steels because of its low fusion point (Ref 1).

Weld durations for resistance welding are very short (seconds) compared to those for forge welding where gas torches are employed. This is because heat is generated internally in resistance welding but externally with gas torches. Terms that are sometimes used synonymously with forge welding include pressure welding, upset welding, and solid-state resistance upset welding.

Coextrusion Welding

Coextrusion can be used to join materials from the same alloy family. A corrosion-resistant alloy can be joined with a less-expensive base alloy to provide the required chemical properties where needed without using monoliths of the typically more expensive corrosion-resistant alloy. Coextrusion welding can also replace

other fusion processes such as overlay welding for surface property enhancement.

In a similar process, extrusion welding has been used to butt weld tubes. The ends of the tubes are prepared for extrusion by beveling at a 45 to 60° angle to produce an overlapping joint (Fig. 3). The leading tube contains the female portion of the beveled joint and is the stronger of the two metals in dissimilar-metal joints. Extrusion press die angles of 30 to 35° are common. An advantage of extrusion welding over other methods of deformation butt welding of tubes is that there is no flash or upset to remove following extrusion.

Common Metals Welded. The most common metals welded by the coextrusion process include low-carbon steel, aluminum, aluminum alloys, copper, and copper alloys. Additional applicable materials include nickel, nickel-base alloys, zirconium, titanium, tantalum, and niobium.

Common coextrusion behaviors are illustrated in Fig. 4. The quality of the coextruded material can be affected by the arrangement of the materials being welded. In coextrusion of 304 stainless steel and carbon steel, having the core be 8 to 20% shorter than the sleeve for a coextruded pipe resulted in a more uniform extrudant with less material loss (Ref 6).

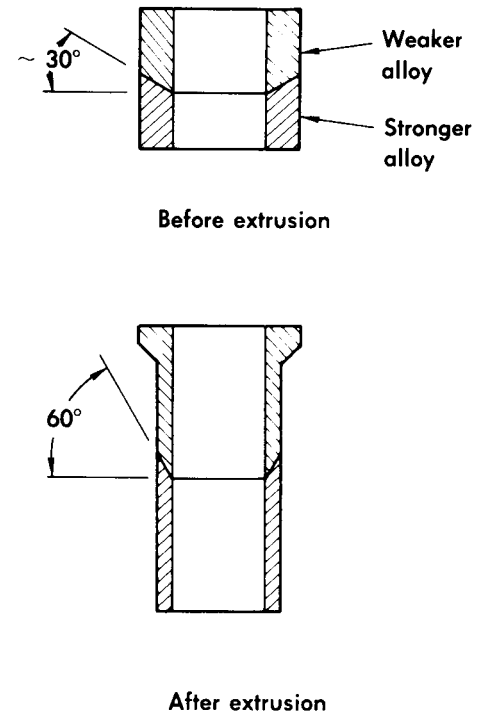


Fig. 3 Design for butt welding of tubes by extrusion

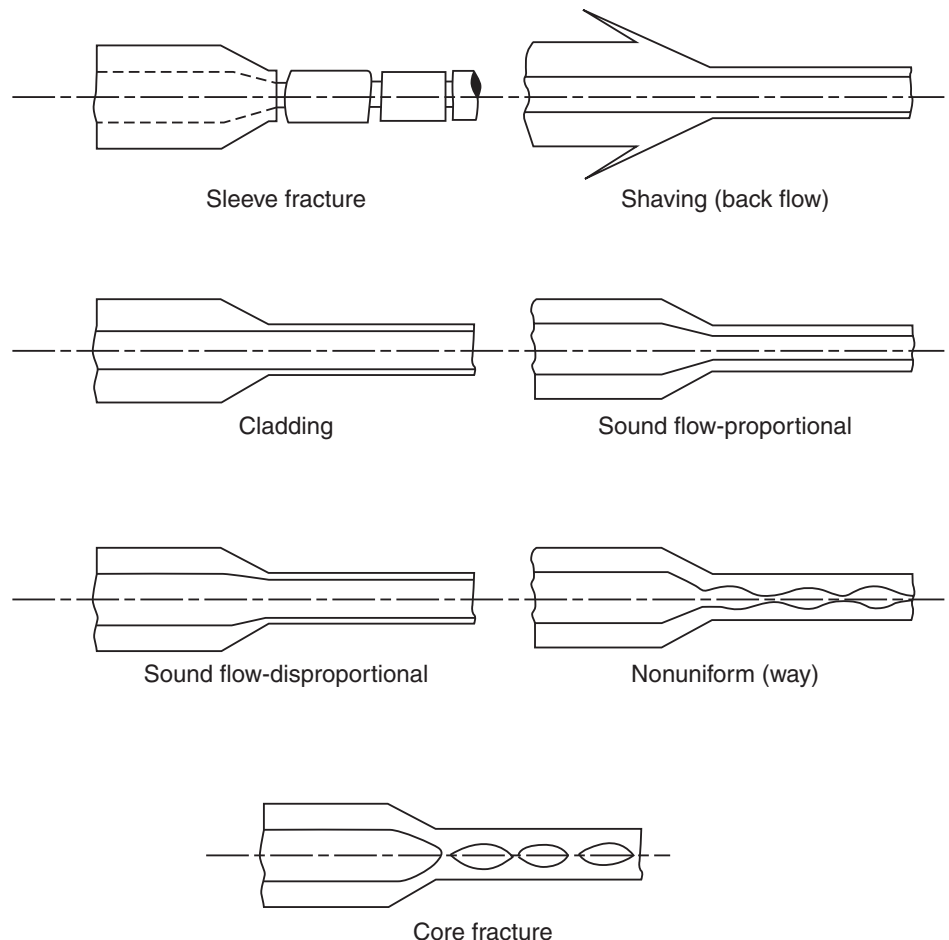


Fig. 4 Common coextrusion behaviors. Source: Ref 5

REFERENCES

1. R.L. O'Brien, Ed., *Welding Handbook*, 8th ed., Vol 2, American Welding Society, 1991, p 917–918
2. L. Griffing, Ed., *Welding, Cutting, and Related Processes*, Section 3, Part B, *Welding Handbook*, 6th ed., American Welding Society, 1971, p 61.4–61.9
3. J.D. Verhoeven and H.F. Clark, Carbon Diffusion between the Layers in Modern Pattern-Welded Damascus Blades, *Mater. Character.*, Vol 41, 1998, p 183–191
4. T.F. Kong, L.C. Chan, and T.C. Lee, Experimental Study of Effects of Process Parameters in Forge Welding Bimetallic Materials: AISI 316L Stainless Steel and 6063 Aluminum Alloy, *Strain*, Vol 45 (No. 4), Aug 2009, p 373–379
5. M.H. Apperley, C.C. Sorrell, and A. Crosky, *J. Mater. Process. Technol.*, Vol 102, 2000, p 193
6. M.E. Epler and W.Z. Misiolek, Novel Billet Design for Co-Extrusion of Ferrous Material Tubes, *Mater. Sci. Eng. A*, Vol 429, 2006, p 43–49

Magnetic Pulse Welding

Sachin D. Kore, Indian Institute of Technology, Guwahati, India
J. Imbert, Y. Zhou, and M. Worswick, University of Waterloo, Canada

WEIGHT-REDUCTION EFFORTS for automobiles require the joining of various light-weight metals, such as aluminum and magnesium alloys. Although welding is a well-known and widely accepted joining process, the welding of dissimilar and difficult-to-weld metals is a major challenge faced by the automobile and aerospace industries. Welding of dissimilar metals is difficult to perform by a fusion welding process, because of the differences in their melting temperatures as well as the intermetallic compounds formed in the weld, which result in unacceptable mechanical properties (Ref 1). Additional difficulties in welding aluminum arise from the high affinity of aluminum for oxygen and the resulting formation of aluminum oxide (Al_2O_3) layers on the surface, which in turn result in poor-quality welds. Solid-state techniques based on generating extremely high pressures to create welds between dissimilar metals have been developed, with explosive welding being the most studied. Solid-state welds require clean surfaces; in explosive welding, the impact of the materials achieves this by removing the surface oxide layers. Explosive welding is well suited for welding dissimilar and difficult-to-weld metals; however, because of cost and safety concerns, it has remained applicable mainly for low-production-volume applications. Magnetic pulse welding (MPW) is a solid-state welding technique that is potentially well suited for high-volume welding of dissimilar and hard-to-weld metals. A fast-emerging impact welding method similar to explosive welding, MPW produces a solid-state weld by creating contact at extremely high pressures and by removing the oxide layers through the velocity and angle of impact. Complete metallurgical bonding can be obtained by pressing the two nascent surfaces together at very high pressure to obtain a weld between the metals.

In this process, the sudden discharge of a capacitor bank through a coil of relatively few turns produces a strong transient magnetic field. If this field is coupled with a metal workpiece, an intense impulsive force acts on the material and accelerates it to a velocity of the order of 10^2 m/s (225 mph) in a few microseconds. Magnetic pulse welding is safer and more amenable to mass production than explosive welding,

because a capacitor bank replaces explosives as the energy source, making the process safer, more repeatable, and suitable for use with standard power grids.

Fundamental Theory

Two current-carrying conductors, when placed in close proximity, exert force on each other. If the current directions are the same on each conductor, an attractive force is induced on the conductors; if the current directions are opposite to each other, a repulsive force is induced. If the currents are of high intensity and high frequency, they will generate high forces. These intense repulsive forces are used to accelerate the materials for MPW.

The energy for the process is provided by a capacitor bank that is connected to a standard industrial power outlet. The capacitor bank is initially charged with a direct current power supply. To generate the forces required for welding, the charged capacitor bank is discharged through a coil, generating a high-frequency current with a damped sinusoidal profile. The current produces a transient magnetic field that interacts with the metal sheets that are to be welded, inducing eddy currents in them in the opposite direction of the ones in the coil. Finally, the interaction of the eddy currents with the magnetic field generates Lorentz forces (\mathbf{F}) on the work sheets that drive them away from the coil and toward each other. The Lorentz force (\mathbf{F}) is given by (Ref 2):

$$\mathbf{F} = \mathbf{J} \times \mathbf{B} \quad (\text{Eq 1})$$

where \mathbf{J} is the current density, and \mathbf{B} is the magnetic flux density.

Because the Lorentz forces depend on the current density, the higher the conductivity of the material, the higher the current density and thus the higher the induced forces. This makes materials with high conductivity better suited for the MPW process. Steels, for example, have relatively low conductivity, which, combined with their higher mass and strength, makes them less suitable for MPW. To weld low-electrical-

conductivity materials, a highly conductive and low-strength material, called the “driver,” is placed between the workpiece and the coil. The driver is accelerated by the Lorentz forces and, in turn, accelerates the workpiece.

The magnitudes of the induced Lorentz forces depend on the magnetic field acting on the workpiece. Ideally, all of the magnetic field is used to generate Lorentz forces. However, transient magnetic fields can penetrate conductors, and, if the conductor is thin enough, part of the magnetic field can “leak.” Alternating electric current flow mainly at the skin of the conductor, at an average depth called the ‘skin depth.’ It is defined as follows (Ref 2):

$$\delta = \sqrt{\frac{\rho}{\pi \mu_0 \mu_r f}} \quad (\text{Eq 2})$$

where ρ is the electrical resistivity of the workpiece, μ_0 is the permeability of the freespace = $4\pi \times 10^{-7}$, μ_r is the relative permeability, and f is the frequency.

In the case of sheet metal, the skin depth can be greater than the thickness, a condition that will cause “leaking” of the magnetic field and lower the efficiency of the process. It is desirable for MPW operations that the value of the frequency should be selected in such a way that the skin depth of the induced currents in the workpiece is less than its thickness. Under this condition, an appreciable amount of the magnetic field is confined within the thickness of the workpiece, and the diffusion of the field beyond it is reduced to a minimum value, thus increasing the efficiency of the welding process.

Magnetic pulse welding and techniques for performing it have been studied in detail by many researchers. Most of this research is performed using the forming and welding of tubes, because it is relatively easy to control the magnetic field for axisymmetric components such as tubes (Ref 3, 4). The parameters that determine weld quality in MPW are similar to those in explosive welding: critical impact angle, impact speed, and the presence of a wavy interface after welding (Ref 5–10). Magnetic pulse welding has been explored for welding similar- and dissimilar-metal tubes for structural applications (Ref 11–19).

Thus far, the MPW technique has been mainly studied and applied to tubular structures and has been much less studied for welding of flat sheets, because of the difficulties in designing coils and controlling the magnetic fields in flat sheet welding operations. However, Aizawa et al. (Ref 20–22), Kore et al. (Ref 23–28), and Zhang et al. (Ref 29) have reported the feasibility of MPW of flat sheets. Kore et al. (Ref 24, 25), in particular, have reported a detailed study of the effects of process parameters on the strength and width of magnetic pulse welds of aluminum-to-aluminum and aluminum-to-stainless steel sheets. Kore et al. (Ref 30) have also reported the feasibility of MPW of magnesium (AZ31) to aluminum (AA3003) flat sheets.

Equipment

An electromagnetic (EM) welding system comprises the equipment shown in Fig. 1, connected electrically to form a resistance (R), inductance (L), and capacitance (C), or RLC, circuit.

Because the current and frequency requirements are high for MPW, low inductance and resistance must be used in the power supply system, high-voltage switches, and transmission cables.

Work Coil

The work coil converts the electrical energy in the capacitors into magnetic energy, which is finally transformed to mechanical energy on the workpiece. It is the part of the RLC circuit through which a damped sinusoidal current of high magnitude is passed, producing the transient magnetic field necessary for the performance of the welding operation. Coils are an essential part of any EM welding process.

Depending on the EM metal-processing technique, such different types of coils as solenoidal, flat pancake, and bar coils can be used, as described subsequently (Ref 31, 32).

Solenoid Coils. A solenoidal coil is shaped like a helix and is used for processing axisymmetric components. These coils, depending on their operation, are further classified into two types:

- *Expansion coils:* These coils are used inside axisymmetric workpieces (i.e., tubes) to expand the workpiece, as shown in Fig. 2.
- *Compression coils:* When a solenoid coil is placed outside the axisymmetric workpiece (tube) to compress the tube, it is termed a compression coil, as shown in Fig. 3.

Flat Pancake Coil. A spirally wound coil, such as the one shown in Fig. 4, is often called a pancake coil. Such coils are used for material processing of flat sheets. These coils do not produce uniform magnetic fields and often have dead spots where the magnetic field and thus the induced forces are zero. These nonuniform magnetic fields lead to nonuniform force distributions that can cause significant problems when forming sheet metal; these nonuniform distributions must be taken into account in process design. Uniform pressure coils (or actuators, as they are called by their developers) have been proposed to solve these problems in some applications (Ref 33).

Bar coils are of simple design (Fig. 5) and are used to concentrate the current (and thus increase the current density) on specific areas of a workpiece. The increase in current density is achieved by reducing the cross-sectional area of the coils. The smaller cross-sectional area produces a more intense magnetic field and thus induces higher Lorentz forces on the workpiece area that is directly facing the coil. This type of coil is mainly used for concentrating the

repulsive force onto a localized area of the workpiece, to obtain high levels of deformation for welds in a particular area of the workpiece.

Capacitor Bank

Capacitor banks are energy-storage devices that are used to store electric energy and produce from it a high-frequency and high-intensity current pulse. The energy (E) stored in a capacitor bank is given by:

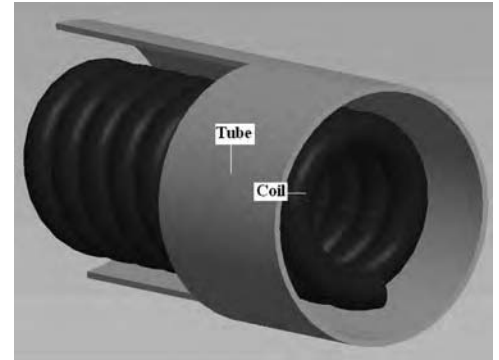


Fig. 2 Expansion coil

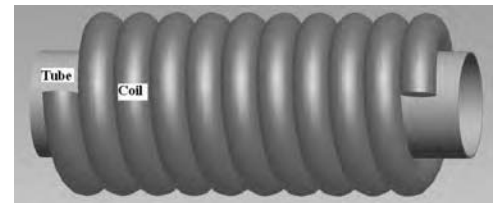


Fig. 3 Compression coil



Fig. 4 Flat pancake coil

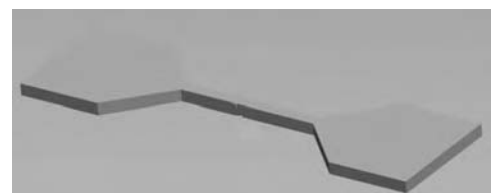


Fig. 5 Flat coil (bar)

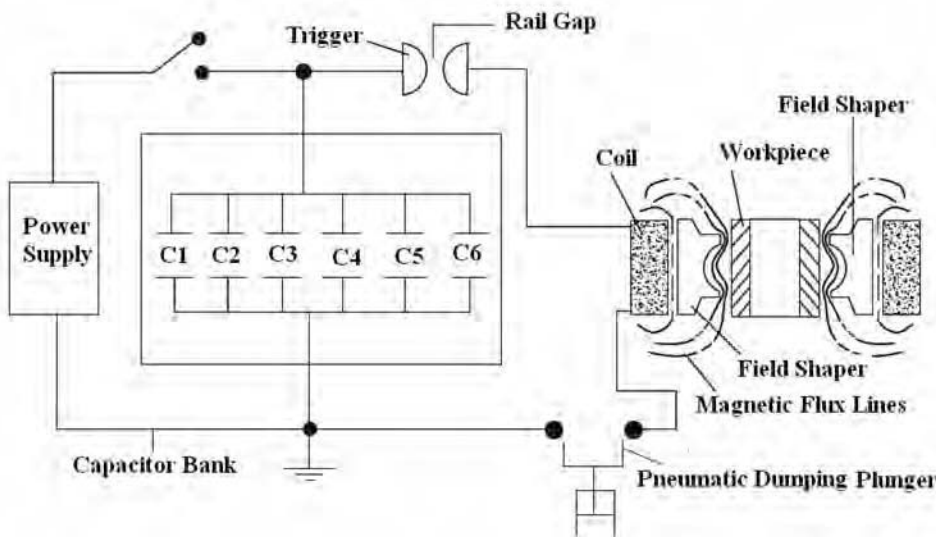


Fig. 1 Schematic of magnetic pulse welding equipment

$$E = \frac{1}{2} CV_0^2 \quad (\text{Eq 3})$$

where V_0 is the charging voltage, and C is the capacitance. The current pulse produced is in the form of a damped sinusoid (Fig. 6) (Ref 34).

The peak current produced by a capacitor bank is proportional to the charging voltage and the square root of the capacitance and inversely proportional to the square root of the inductance, as given by the following equation:

$$I_{\max} = V_0 \sqrt{\frac{C}{L_a}} \quad (\text{Eq 4})$$

where L_a is the inductance of the capacitor bank. The frequency of the current pulse produced is critical to the MPW process and is inversely proportional to the square root of the product of the capacitance and the inductance. The frequency is given by:

$$\omega = \sqrt{\frac{1}{L_a C}} = 2\pi f \quad (\text{Eq 5})$$

where f is the frequency. To determine the current pulse characteristics of a complete MPW, the inductance and capacitance of the system with the coil and workpiece included must be used. The capacitors can be connected in parallel, depending on the energy requirement for the material-processing operation.

High-Voltage Power Supply

Capacitors cannot be charged directly from a regular industrial alternating current power source, because direct current is required. The capacitor

bank must be charged from a variable-voltage power supply. Such a power supply consists of three basic elements: a step-up transformer, a rectifier, and a current-limiting device. It charges the capacitor by using a rectified current. The capacity of the power supply will depend on the requirements of the specific MPW operation.

High-Voltage Switches

Very high-speed switches, capable of withstanding high voltages, are required for MPW operations. Ignitrons, spark gap switches, or rail gap switches can be used to close the RLC circuit and produce the high-current pulse in the work coil. Ignitrons contain mercury and must be handled with care to meet all pertinent safety and environmental regulations.

Field Shapers

Field shapers are used to concentrate pressure at a specific location on the workpiece. They are also used to adapt large-diameter compression coils to smaller-diameter workpieces. Field shapers are essentially single-turn coils. They are inserted between the work coil and the workpiece; they receive their energy from the work coil and transfer it to the workpiece by induction (Ref 35). Thus, by using different sizes of field shapers, the same work coil can be used for job pieces of different diameters. However, field shapers must be electrically insulated from both the work coil and the workpiece. The use of field shapers increases the life of the coil by reducing the force acting on the coil.

The field shaper is inductively, rather than directly, coupled to a forming coil. Hence, the

efficiency of an EM welding or forming process that uses field shapers is lower than that in which only a forming coil is used. It is difficult to design a strong coil that can sustain the mechanical stress arising from Lorentz forces. By introducing a field shaper, the Lorentz forces can be shifted toward the region of greater mechanical strength of the coil (Ref 36, 37).

Additional Equipment

Other equipment that is helpful for MPW includes Rogowski coils (Ref 38) (to measure the current), accelerometers, load cells, and data-acquisition systems (to capture and analyze the signals obtained). High-speed cameras can be very useful, especially in the process development stage, in determining the deformation history of the workpieces and the location of arcing in the process.

Magnetic Pulse Welding Process

This section describes the MPW process and the critical parameters needed to obtain acceptable welds. Welding of axisymmetric sections is described first, followed by welding of flat sheet. Magnetic pulse welding of a tube to a solid core is shown in Fig. 7. In this case, a tube and a core that are to be welded are placed inside a coil. The outer tube is accelerated by the Lorentz forces induced on it by the coil, and it impacts the inner core (Ref 39–41). The impact pressure removes the oxides and surface contaminants and creates an atomic bond between the metals. Given the relative simplicity of the geometry, it is possible to estimate by both analytical and numerical methods the system inductance and EM pressure acting on the workpiece (Ref 5, 40).

Welding of sheet metal is substantially more difficult. A three-dimensional, flat rectangular, one-turn copper coil, such as the one shown in Fig. 8, can be used for MPW of similar- and dissimilar-metal sheets. The two sheets to be welded

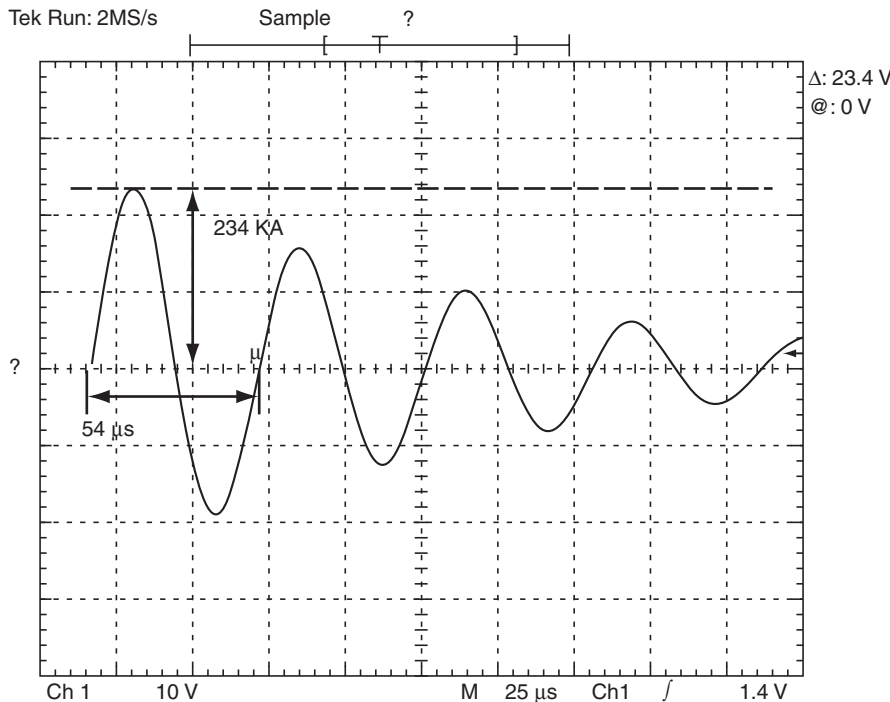


Fig. 6 Current waveform for an electromagnetic welding operation. Source: Ref 34

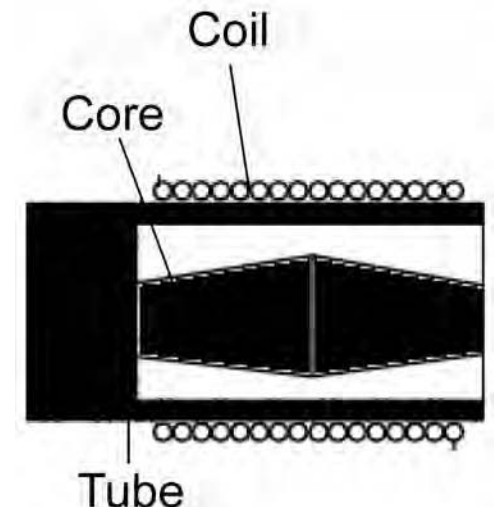


Fig. 7 Cross section of tubes with coil and core for magnetic impulse welding

are placed between the upper and lower halves of the coil. When the transient current flows through the coil, it produces a transient magnetic field that induces Lorentz forces on the sheets and thereby accelerates them toward each other at very high speeds. The sheets will then impact one another, producing the desired weld.

The web of the I-shaped cross section of the coil concentrates the current, increasing the current density, J , and thus resulting in increased Lorentz forces. The reduction of the cross-sectional area is limited by the strength of the coil, which is also subjected to induced forces. If the area is too narrow, it could deform or even break.

Process Parameters

The impact energy and hence the formation of a weld in MPW depend on equipment and workpiece parameters. Equipment parameters such as the inductance, capacitance, and resistance of the circuit and the energy storage capacity of the capacitor bank are critical to achieving a proper weld. They directly influence the amount of energy transferred to the sheet and the time in which this transfer occurs—factors that in turn determine the acceleration of the sheet and its velocity at impact. Increasing the discharge energy increases the magnetic field generated and thus increases the shearing strength and the width of the EM weld of aluminum-aluminum and aluminum-stainless steel sheets for a given standoff distance.

Most researchers have found that MPW has many similarities to explosive welding in the workpiece parameters, for example, the critical impact angle, the impact velocity needed for joining, and the wavy interface created after welding (Ref 9). The velocity acquired by the sheets prior to impact depends on the energy input, as discussed earlier, and on the distance between the workpieces, or standoff distance. If the standoff distance is too small, then the workpiece does not accelerate to the required speed; if it is too large, the sheet will start to decelerate prior to impact. The impact velocity is crucial, because the kinetic energy achieved by the sheets is converted into impact energy. For example, in MPW of aluminum-aluminum and aluminum-stainless steel sheets, for a given set of process parameters, the standoff distance has one optimal value that gives the maximum shearing strength and width of the weld (Ref 24, 25). For lower values of standoff distance, collision takes place before the sheets attain the maximum velocity, whereas for higher values, the velocity attained drops at the time of collision (Ref 24, 25). The conductivity, mass, and strength of the material will affect the workpiece velocity and will also have an effect on the weld.

Researchers have studied the MPW process experimentally, although continued work is required in the welding of flat sheets. Masumoto et al. (Ref 6) studied EM welding of similar- (aluminum-aluminum) and dissimilar-metal cores and tubes. Kojima et al. (Ref 10) also studied the effect of flow stress, collision velocity, and collision acceleration in EM welding. They

found that, like collision velocity, collision acceleration also affects the quality of electromagnetically welded joints. Kore et al. reported the effect of such process parameters as discharge energy, standoff distance, and coil shape on the strength and width of magnetic-pulsed welds of aluminum-to-aluminum and aluminum-to-steel sheets (Ref 24, 25).

Mechanical Testing of Magnetic-Pulsed Welds

Magnetic pulse welding samples that have been mechanically tested in tensile shear tests show two types of failures: failure at the weld interface and failure away from the weld in the base metal. The MPW samples prepared with a lower value of discharge energy or a nonoptimal standoff distance fail at the weld interface. Welds obtained at optimal values of discharge energy and standoff distance fail away from the weld in the base metal, exhibiting welds that are stronger than the base metal (Ref 24–26). Hardness testing of the weld interface has shown higher hardness values near the weld interface compared to the base metal (Ref 26). This phenomenon is due to the compression of grains at the weld interface. The testpieces cut from the center of the welds (along the length of the weld) of aluminum-aluminum and aluminum-stainless steel sheets exhibit greater shearing strength than the pieces cut from the edges (Ref 24, 25). This behavior is attributed to higher penetration of the magnetic field at the center and a change of current direction in the sheets at their edges, a circumstance that weakens the magnetic field developed at the edges and hence the impulse acting on the sheets.

Metallurgical Characterization of Magnetic-Pulsed Welds

The microstructure of the aluminum-aluminum weld obtained by MPW (Fig. 9) shows two weld zones: one with complete metal continuity and one with a no-weld zone at the center. Complete metal continuity without any waves, as shown in Fig. 9, is characteristic of a sound weld. Kore et al. (Ref 24) reported that the wavy pattern at the weld interface is due to interfacial instability at lower energy values or nonoptimal standoff distance. The weld shown was obtained at a discharge energy of 5.184 kJ, a voltage of 7.2 kV,

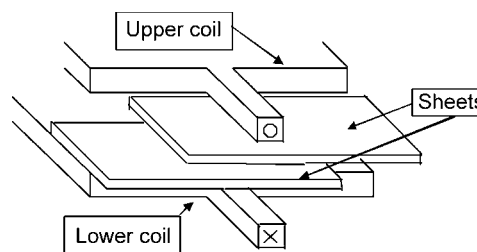


Fig. 8 Magnetic pulse welding of flat sheets. Source: Ref 34

a standoff distance of 2.5 mm (0.10 in.), and a weld width of 1.1 mm (0.04 in.). The effect of process parameters, including standoff distance, coil geometry, and energy, on width and shear strength of the weld is reported in the literature (Ref 24, 25).

The defect at the center of the weld, shown in Fig. 9, was caused by entrapped oxide at the center and rebounding of the sheet at the center. The complex deformation state at the interface is also a contributing factor to the existence of the defect.

Magnetic pulse welding of aluminum-iron and Al-SUS304 steel sheets has been reported in the literature (Ref 22, 25). The effect of process parameters such as standoff distance, coil geometry, and energy on the strength and width of the weld is reported by Kore et al. (Ref 25). For joining dissimilar sheets, researchers have driven aluminum sheet by using EM force, with the iron sheet kept stationary rather than driven (Ref 22). Kore et al. used an aluminum driver sheet to drive the electrically-poor-conductor stainless steel sheet. This approach doubled the energy of impact (Ref 25) and led to stronger magnetic-pulsed welds.

An image from the microstructure of aluminum that is pulse welded to stainless steel sheet (Fig. 10) shows a continuous weld from an area exactly under the coil area. The void observed

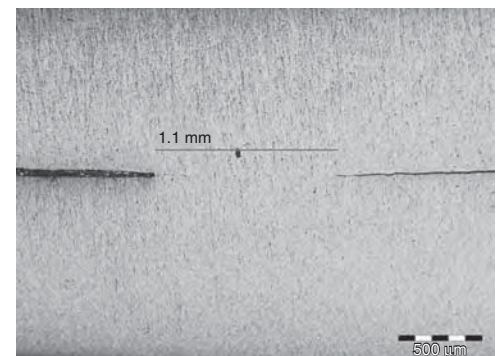


Fig. 9 Magnified view of an aluminum-to-aluminum weld zone from magnetic pulse welding. Source: Ref 34

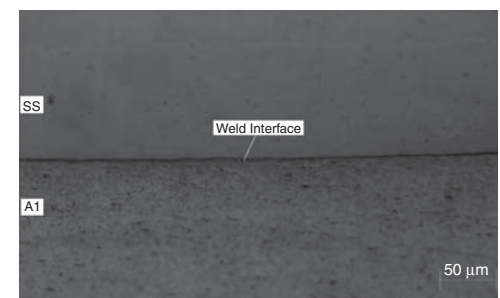


Fig. 10 Magnified view of an aluminum and stainless steel (SS) weld zone from magnetic pulse welding. Source: Ref 34

in the weld is at the edges, where the sheet is not directly under the coil.

A micrograph of the weld between two copper sheets joined by MPW is shown in Fig. 11. Metallographic study and scanning electron microscopy analysis of the EM weld has confirmed metal continuity between the two sheets. Copper is an ideal candidate for MPW because of its high electrical conductivity and relatively low strength.

Aluminum-lithium alloys can be welded using MPW without the aid of drivers; however, specific heat treatment cycles must be used to reduce their yield strength. A magnetic-pulsed weld of aluminum-lithium is shown in Fig. 12; the presence of a wavy interface is notable. This interface is due to surface irregularities present on the sheets and also due to insufficient impact energy to crush the irregularities and obtain a sound weld. Pulse welding of copper to stainless steel (Fig. 13, Ref 42) was done by using an aluminum driver to accelerate both the copper and stainless steel work sheets, with a capacitor discharge energy of 8.46 kJ. Pulse welding of aluminum to magnesium AZ31 sheets (Fig. 14) produced welds with no intermetallics at the weld interface (Ref 30), a condition that is very difficult to obtain by using conventional welding methods.

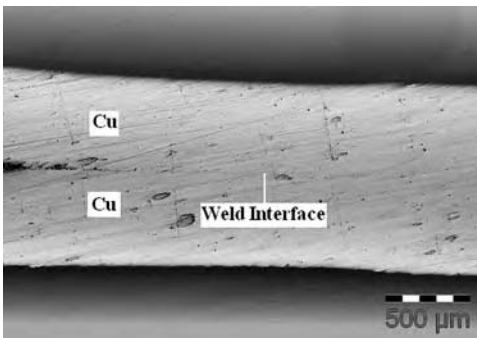


Fig. 11 Microstructural view of a copper-copper welded sample. Source: Ref 34

Applications

Magnetic pulse welding can be relatively easily applied to mass production, especially when compared to explosive welding, which is the more established impact-welding process. At the moment, MPW is more applicable to tubular structures than to flat sheets. Mechanical joining of tubular cross sections (e.g., torque rods) is already in use for high-volume production. Magnetic pulse welding can also be used for joining structural parts for underwater applications and automotive space frames (Ref 11–13), joining of aluminum cans and cap wafers to avoid heat-generated problems encountered in tungsten inert gas arc welding (Ref 13), and welding of dissimilar-metal tubes (Ref 5). It is also applicable to create bimetallic driver shafts for lightweight applications. Magnetic pulse welding has been used in nuclear projects to join copper reactor tubes to ceramic plugs (Ref 43).

Magnetic pulse techniques have been extensively studied and are accepted for welding of axisymmetric parts; studies have been done to improve the weld quality, to develop modeling capabilities, and to determine suitable applications. Unfortunately, as of this writing, no similar studies have been performed for the

welding of flat sheets or nonaxisymmetric parts, processes for which research is still required to obtain commercially viable processes. Designing coils to generate the desired EM force distributions is a major challenge. The key to developing proper coils is an understanding of how EM-driven sheets interact at the time of impact and how this interaction affects the welds. Many researchers have now concentrated their research in the field of MPW, due to the potential application of MPW to join flat sheets of dissimilar or hard-to-weld metals in automobile and aerospace components. Analyzing the process analytically is difficult; the development of proper numerical models will be crucial for the future implementation of MPW. The need to weld dissimilar and difficult-to-weld metals has made it essential to study such new joining techniques as MPW.

Safety Guidelines While Handling the MPW Setup

Given the high currents, voltages, and material speeds involved in MPW, special care must be taken when implementing this technique. The MPW process has three types of potential hazards: sonic, electrical, and mechanical. These hazards can be avoided by following proper safety measures. Some safety measures are suggested as follows, but they do not form a comprehensive list; each individual application has its own unique set of circumstances and safety precautions. All of the safety and operation guidelines provided by the equipment manufacturer should be followed. The following are suggested measures to follow when working with MPW:

- No operator should work alone.
- It should be ensured that the floor is nonconductive.
- Ear protection should be used against such sonic hazards as spark gap triggering, impact of the sheets, and the very loud sparks that occasionally result from the process.
- No one should be in close proximity to the welding area when the machine is discharged. This precaution is necessary to avoid injury from accidental flying of stray objects and from exposure to magnetic fields.
- The capacitor banks should always be kept shorted to ground when not in use.
- Interlocking between system covers, doors, and operating switches on the control panel can prevent accidental operation of control panel switches while people are working with the machine.
- Manual grounding via a grounding rod to ensure complete discharge of the capacitors should be employed before the machine is touched by an operator.
- Extreme precaution should be used when handling high-voltage equipment.

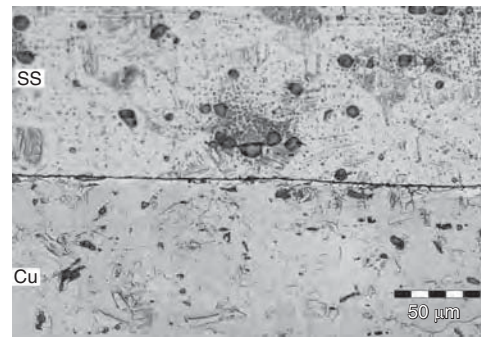


Fig. 13 Magnetic pulse welding of a copper-to-stainless steel (SS) weld. Source: Ref 34

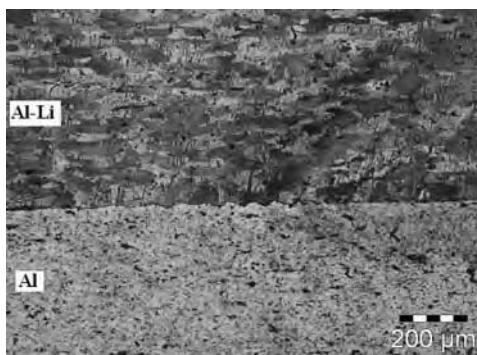


Fig. 12 Magnetic pulse welding of an aluminum-to-aluminum-lithium weld. Source: Ref 34

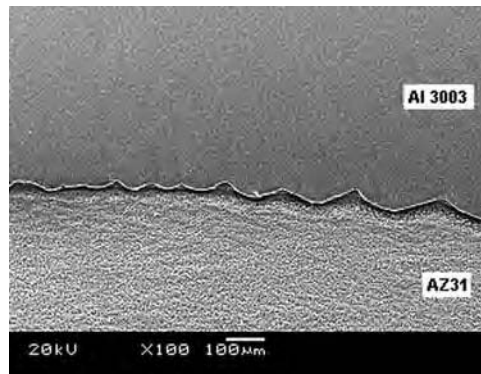


Fig. 14 Magnetic pulse welding of an aluminum-to-magnesium weld. Source: Ref 34

Summary

It is possible to use MPW to weld various similar- and dissimilar-metal combinations that are difficult to weld by conventional welding methods. Magnetic pulse welding has been shown to produce good-quality welds that are stronger than the base metal. Defects in the welds are usually due to the entrapment of oxides. Impact velocity and angle play a vital role for complete removal of oxides from the weld interface. The impact velocity will depend on the energy imparted to the workpiece by the coil, which depends on the parameters of the system. The conductivity of the materials is a critical parameter for MPW because, all else being equal, the higher the conductivity, the higher the Lorentz forces induced.

Currently, EM welding is more suitable for axisymmetric components, such as tubes, because it is easier to produce the coils and design the process for such components. Magnetic pulse welding has potential as a means of joining sheet metal parts; however, designing coils for joining sheets by using MPW is a challenging task that requires a better understanding of the process and the availability of numerical predictive capabilities. Detailed research must be carried out on the design of flat coils in order for sheet metal joining to develop efficient coils with long working lives. The MPW technique should be further studied as part of the wider efforts to reduce vehicle weight and fuel consumption.

REFERENCES

1. L. Agudo, D. Eyidi, C.H. Schmaranzer, E. Arenholz, N. Jank, J. Bruckner, and A.R. Pyzalla, Intermetallic Fe_xAl_y -Phases in a Steel/Al-Alloy Fusion Weld, *J. Mater. Sci.*, Vol 42 (No. 12), 2007, p 4205–4214
2. F.C. Moon, *Magneto Solid Mechanics*, John Wiley & Sons Inc., 1984
3. A.G. Mamalis, D.E. Manolacos, A.G. Kaldas, and A.K. Koumoutsos, Electromagnetic Forming and Powder Processing: Trends and Developments, *Appl. Mech. Rev.*, Vol 57 (No. 4), 2004, p 299–324
4. A. El-Azab, M. Garnich, and A. Kapoor, Modeling of the Electromagnetic Forming of Sheet Metals: State-of-the-Art and Future Needs, *J. Mater. Process. Technol.*, Vol 142, 2003, p 744–754
5. P. Zhang, "Joining Enabled by High Velocity Deformation," Ph.D. thesis, The Ohio State University, 2003
6. I. Masumoto, K. Tamaki, and M. Kojima, Electromagnetic Welding of Aluminum Tube to Aluminum or Dissimilar Metal Cores, *Trans. Jpn. Weld. Soc.*, Vol 16 (No. 2), 1985, p 110–116
7. M. Kojima and K. Tamaki, Electromagnetic Welding of Tubes, *Fifth International Symposium of the Japan Welding Society*, April 1990 (Tokyo), p 201–206
8. M. Kojima and K. Tamaki, Factors Affecting the Electromagnetic Welding of Aluminum Tube, *Trans. Jpn. Weld. Soc.*, Vol 19 (No. 1), 1988, p 35–43
9. M. Kojima, K. Tamaki, and T. Furuta, Effect of Collision Angle on the Result of Electromagnetic Welding of Aluminium, *Trans. Jpn. Weld. Soc.*, Vol 20 (No. 2), 1989, p 36–42
10. M. Kojima, K. Tamaki, J. Suzuki, and K. Sasaki, Flow Stress, Collision Velocity and Collision Acceleration in EM Welding, *Weld. Int.*, Vol 4, 1990, p 684–690
11. W.S. Hwang, N.H. Kim, H.S. Sohn, and J. S. Lee, Electromagnetic Joining of Aluminium Tubes on Polyurethane Cores, *J. Mater. Process. Technol.*, Vol 34, 1992, p 341–348
12. W.S. Hwang, J.S. Lee, N.H. Kim, and H.S. Sohn, Joining of Copper Tube to Polyurethane Tube by Electromagnetic Pulse Forming, *J. Mater. Process. Technol.*, Vol 37, 1993, p 83–93
13. H.G. Powers, Bonding of Al by the Capacitor Discharge Magnetic Forming Process, *Weld. J.*, June 1967, p 507–510
14. M. Marya and S. Marya, Interfacial Microstructures and Temperatures in Aluminum—Copper Electromagnetic Pulse Welds, *Sci. Technol. Weld. Join.*, Vol 9 (No. 6), 2004, p 541–547
15. A. Stern and M. Aizenshtein, Bonding Zone Formation in Magnetic Pulse Welds, *Sci. Technol. Weld. Join.*, Vol 7 (No. 5), 2002, p 339–342
16. M. Marya, S. Marya, and D. Priem, On the Characteristics of Electromagnetic Welds between Aluminum and Other Metals and Alloys, *Weld. World*, Vol 49, 2005, p 74–84
17. V. Shribman, A. Stern, Y. Livshitz, and O. Gafri, Magnetic Pulse Welding Produces High Strength Aluminum Welds, *Weld. J.*, Vol 81 (No. 4), 2002, p 33–37
18. M. Kimchi, H. Saho, W. Cheng, and P. Krishnaswamy, Magnetic Pulse Welding of Aluminum Tubes to Steel Bars, *Weld. World*, Vol 48, 2004, p 19–22
19. A. Ben-Artzy, A. Stern, N. Frage, and V. Shribman, *Sci. Technol. Weld. Join.*, Vol 13 (No. 4), 2008, p 467–471
20. T. Aizawa, K. Okogawa, M. Yoshizawa, and N. Henmi, Impulse Magnetic Pressure Seam Welding of Aluminium Sheets, *Impact Eng. Appl.*, 2001, p 827–832
21. T. Aizawa and K. Okogawa, Impact Seam Welding with Magnetic Pressure for Aluminium Sheets, *Mater. Sci. Forum*, Vol 465, 2004, p 231–236
22. T. Aizawa, Methods for Electromagnetic Pressure Seam Welding of Al/Fe Sheets, *Weld. Int.*, Vol 18 (No. 11), 2004, p 868–872
23. S.D. Kore, P.P. Date, and S.V. Kulkarni, Electromagnetic Welding of Aluminum Sheets, *AWS's Sheet Metal Welding Conference XII* (Livonia, MI), 2006, p 1–6
24. S.D. Kore, P.P. Date, and S.V. Kulkarni, Effect of Process Parameters on Electromagnetic Impact Welding of Aluminum Sheets, *Int. J. Impact Eng.*, Vol 34, 2007, p 1327–1341
25. S.D. Kore, P.P. Date, and S.V. Kulkarni, Electromagnetic Impact Welding of Aluminum to Stainless Steel Sheets, *J. Mater. Process. Technol.*, Vol 208 (No. 1–3), 2008, p 486–493
26. S.D. Kore, P.P. Date, S.V. Kulkarni, S. Kumar, D. Rani, M.R. Kulkarni, S.V. Desai, R.K. Rajawat, K.V. Nagesh, and D. P. Chakravarty, Electromagnetic Impact Welding of Cu to Cu Sheets, *Int. J. Mater. Form.*, Vol 3 (No. 2), 2010, p 117–121
27. S.D. Kore, P.P. Date, and S.V. Kulkarni, Numerical Modeling of Electromagnetic Welding, *Int. J. Appl. Electromagn. Mech.*, Vol 32 (No. 1), 2010, p 1–19
28. S.D. Kore, P.P. Date, S.V. Kulkarni, S. Kumar, D. Rani, M.R. Kulkarni, S.V. Desai, R.K. Rajawat, K.V. Nagesh, and D. P. Chakravarty, Electromagnetic Welding of Al-to-Al-Li Sheets, *J. Manuf. Sci. Eng.*, Vol 131, 2009, p 034502-1 to 03450-4
29. Y. Zhang, S.S. Babu, P. Zhang, E.A. Kenik, and G.S. Daehn, *Sci. Technol. Weld. Join.*, Vol 13 (No. 5), 2008, p 467–471
30. S.D. Kore, J. Imbert, M.J. Worswick, and Y. Zhou, Electromagnetic Impact Welding of Mg to Al Sheets, *Sci. Technol. Weld. Join.*, Vol 14 (No. 6), 2009, p 549–553
31. R. Davis and E.R. Austin, *Developments in High Speed Metal Forming*, Industrial Press Inc., 1970
32. H.M. Panshikar, "Computer Modeling of Electromagnetic Forming and Impact Welding," M.S. thesis, The Ohio State University, 2000
33. S. Golowin, M. Kamal, J. Shang, J. Portier, A. Din, G.S. Daehn, J.R. Bradley, K.E. Newman, and S. Hatkevich, Application of a Uniform Pressure Actuator for Electromagnetic Processing of Sheet Metal, *J. Mater. Eng. Perform.*, Vol 16 (No. 4), 2007, p 455–460
34. S.D. Kore, "Electromagnetic Welding of Flat Sheets," Ph.D. thesis, IIT Bombay, 2008
35. M.N. Wilson and K.D. Srivastava, Design of Efficient Flux Concentrators for Pulsed High Magnetic Fields, *Rev. Sci. Instrum.*, Vol 36 (No. 8), 1965, p 1096–1100

36. H. Suzuki, The Effect of a Field Shaper in EM Tube Bulging, *J. Mater. Process. Technol.*, Vol 15, 1987, p 229–240
37. Y.B. Kim and E.D. Platner, Flux Concentrator for High Intensity Pulsed Magnetic Fields, *Rev. Sci. Instrum.*, Vol 10, 1959, p 524–533
38. J.D. Ramboz, Machinable Rogowski Coil, Design and Calibration, *IEEE Trans. Instrum. Meas.*, Vol 45 (No. 2), 1996, p 445–448
39. G.R. Cowan, Mechanism of Bond Zone Wave Formation in Explosion Clad Metals, *Metall. Trans.*, Vol 2, 1971, p 3145–3155
40. P. Zhang and G. Daehn, Analysis of the Electromagnetic Impulse Joining Process with a Field Concentrator, *Numiform*, 2004, p 1253–1258
41. M. Kojima, Effect of Collision Angle on the Result of Electromagnetic Welding of Aluminium, *Trans. Jpn. Weld. Soc.*, Vol 20 (No. 2), 1989, p 36–42
42. S.D. Kore, P.P. Date, S.V. Kulkarni, S. Kumar, D. Rani, M.R. Kulkarni, S.V. Desai, R.K. Rajawat, K.V. Nagesh, and D.P. Chakravarty, Application of Electromagnetic Impact Technique for Welding Copper-to-Stainless Steel Sheets, *Int. J. Adv. Manuf. Technol.*, 2010
43. R.K. Rajawat, S.V. Desai, M.R. Kulkarni, D. Rani, K.V. Nagesh, and R. C. Sethi, Electromagnetic Forming—A Technique with Potential Applications in Accelerators, *Proceedings of APAC* (Gyeongju, Korea), 2004, p 187–189

Cold Welding

Niels Bay, Technical University of Denmark

COLD WELDING (also known as cold pressure welding) is a solid-phase welding process normally carried out at ambient temperature. A large number of metals can be joined, as illustrated in Fig. 1 (Ref 1).

To obtain bonding in cold welding, plastic deformation of one or both metals is required, implying that a basic parameter is the degree of deformation. This is normally expressed as the surface expansion, X , or the degree of surface exposure, Y :

$$X = \frac{A_1 - A_0}{A_0} \quad Y = \frac{A_1 - A_0}{A_1} \quad (\text{Eq 1})$$

where A_0 is the initial and A_1 the final interface area. Figure 2 shows the shear bond strength obtained in roll bonding of sheets in various combinations (Ref 2, 3), plotted as a function of Y , which equals the thickness reduction in rolling:

$$Y = r = \frac{t_0 - t_1}{t_0} \quad (\text{Eq 2})$$

A threshold surface exposure must be reached before bonding occurs. Beyond this threshold, which depends on the metal combination, the bond strength increases rapidly, with Y reaching a level corresponding to the strength of the weaker metal. This relationship between

	Ti	Cd	Be	Pd	Pt	Sn	Pb	W	Zn	Fe	Ni	Au	Ag	Cu	Al
Al															
Cu															
Ag															
Au															
Ni															
Fe															
Zn															
W															
Pb															
Sn															
Pt															
Pd															
Be															
Cd															
Ti															

Fig. 1 Combinations of metals that can be successfully cold welded (indicated by shaded box). Source: Ref 1

bond strength and surface exposure is fundamental to all cold welding processes, but the threshold surface expansion for a given metal combination is dependent on the type of forming process applied for cold welding. In the next section, a theoretical model explaining these phenomena is given based on metallographic studies and continuum mechanical analysis of the local plastic deformation in the weld interface.

Bonding Mechanisms and Theoretical Modeling of Bond Strength

Surface preparation before cold welding is of utmost importance. In most welding applications, surface preparation consists of degreasing followed by scratch brushing. Studies of the welded and subsequently fractured bonds in scanning electron microscopy (SEM) reveal the bonding mechanisms (Ref 4–6). The scratch brushing produces a hard, brittle surface layer that will crack when subjected to expansion (Fig. 3). At larger surface expansion (Fig. 4), virgin material is exposed, which extrudes through the cracks of the surface layer and meets similarly exposed surface area from the opposing metal. Figure 4(a and b) show the onset of extrusion at a surface exposure of $Y = 0.375$ but no visible bonds, whereas

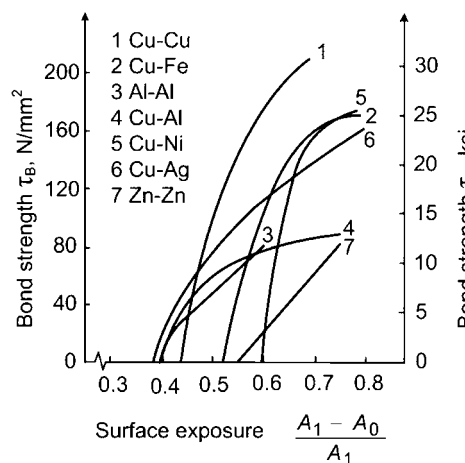


Fig. 2 Bond shear strength versus surface exposure/reduction in cold roll bonding. Source: Ref 2, 3

Fig. 4(c and d), representing a slightly larger surface exposure, $Y = 0.383$, show ductile fracture of bonds on the top of the extrudate. At higher surface exposure, $Y = 0.72$, as shown in Fig. 5, extended areas of base metal have been bonded, and the unwelded regions of brittle surface layer are confined to small isolated islands. The ratio σ_B/σ_0 between weld strength and base-metal strength in the deformed state is indicated in Fig. 4 and 5.

Figure 6 shows a schematic outline of the bonding mechanism and how contact area between the two rough, virgin surfaces will build

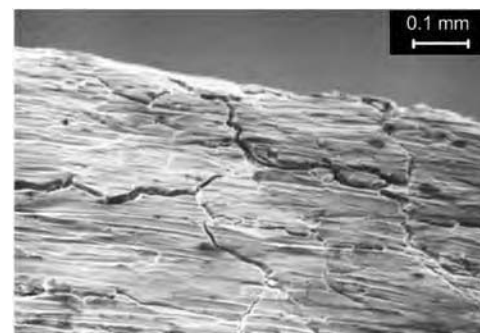


Fig. 3 Scratch-brushed and slightly deformed aluminum surface. $Y \approx 0$, no bonding

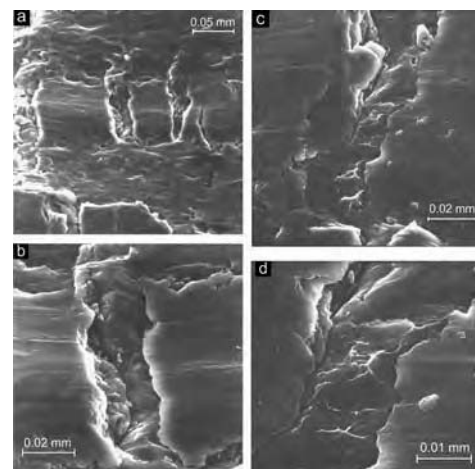


Fig. 4 Bonding surfaces after fracture. (a) and (b) $Y = 0.375$, $p/\sigma_0 = 1.9$, $\sigma_B/\sigma_0 = 0.02$. (c) and (d) $Y = 0.383$, $p/\sigma_0 = 2.0$, $\sigma_B/\sigma_0 = 0.09$. Source: Ref 7

up with increasing surface expansion and contact pressure, forming a metallic bond (Ref 6).

Later investigations have revealed that scratch brushing creates a surface partly consisting of a relatively thick, hard, and brittle cover layer (approximately 20 μm , or 800 $\mu\text{in.}$) and a surface partly covered only by a contaminant film of oxides and water vapor. Bonding in these areas occurs when the contaminant film, which is of the order of 10 to 100 nm (0.4 to 4 $\mu\text{in.}$), is thinned to fracture (Fig. 7). Based on the metallographic studies, a continuum mechanic model for the bond strength for cold welding of two similar materials as a function of surface exposure and normal pressure has been established (Ref 7):

$$\frac{\sigma_B}{\sigma_0} = (1 - \beta) \frac{p - p_E}{\sigma_0} + \beta \frac{Y - Y'}{1 - Y'} \cdot \frac{p}{\sigma_0} \quad (\text{Eq 3})$$

where σ_B is the weld strength, σ_0 is the flow stress of the material after deformation, $\beta = \psi_f^2$, ψ_f is the fraction of film layer to the total area of the scratch-brushed surface, p is the normal pressure at base-metal surfaces, p_E is the pressure required for extrusion through cracks of the cover layer, and Y' is the threshold surface exposure for contaminant film.

The first term in Eq 3 represents the contribution to the weld strength from the area where fracture of the brittle cover layer appears. This applies to zones where one or both of the mating surfaces has a brittle cover layer, which appears in a fraction:

$$\beta = \psi_f^2 \quad (\text{Eq 4})$$

where ψ_f is the fraction of film layer on the scratch-brushed surface, which is determined by measurements on scanning electron micrographs of scratch-brushed surfaces. For Al 99.5, it has been determined that $\psi_f = 0.645$, implying $\beta = 0.4$. The pressure, p_E , required for extrusion through cracks of brittle cover layer is a function of the crack width, that is, the surface exposure. The relationship, which is shown in Fig. 8, is

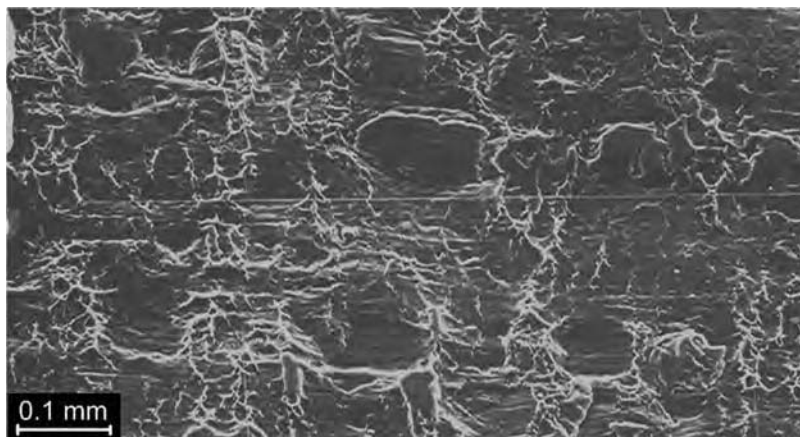


Fig. 5 Bonding surfaces after fracture. $Y = 0.72$, $p/\sigma_0 = 1.8$, $\sigma_B/\sigma_0 = 0.71$. Source: Ref 7

determined by plane-strain slipline analysis. The threshold surface exposure for contaminant film breakdown of scratch-brushed Al 99.5 has been determined to be $0.30 \leq Y' \leq 0.35$ by studying a number of SEM micrographs with different surface exposure to see at what level welds first appear (Ref 7).

Figure 9 shows the bond strength normalized with the flow stress of the deformed material, σ_B/σ_0 , versus the surface exposure with the normalized normal pressure, p/σ_0 , as a parameter for cold welding of scratch-brushed Al 99.5 ($\beta = 0.4$, $Y' = 0.35$). At low normal pressure, $p/\sigma_0 < 2.0$, welding is initiated when $Y > Y'$ by fracture of the contaminant film. For $p/\sigma_0 = 1.5$, there is a bend on the curve at $Y = 0.49$, corresponding to the starting point of extrusion through the cracks and weld formation between the segments of brittle surface layer. For $p/\sigma_0 > 2.0$, welding is initiated by fracture of the brittle layer, extrusion through the cracks, and weld formation in between the segments of brittle surface layer. The film fracture mechanism comes into action later, namely at $Y = Y'$. This explains the bend at $Y = 0.35$ of the curves for $p/\sigma_0 > 2.0$ (Fig. 9). Figure 10 shows a comparison of the theoretically calculated weld strength as a function of surface exposure for two different normal pressures, $p/\sigma_0 = 1.85$ and $p/\sigma_0 = 5.1$, respectively.

The model was later expanded to include cold welding of dissimilar metals and to take ductility of the cover layer into account (Ref 9). Figure 11(a) shows the theoretical as well as the experimental bond strength for cold roll bonding of aluminum-aluminum with one-sided, electroless nickel plating, whereas Fig. 11(b) shows the bond strengths for aluminum-mild steel with one-sided, electroless nickel plating on steel.

The proposed model for the bond strength is of a generic nature, applicable to different types of cold welding by processes such as rolling, indentation, extrusion, and drawing. The different cold welding processes are presented in the section "Process Variants and Applications" in

this article. In addition to metal combination, the threshold surface expansion is dependent on the type of forming process applied for cold welding, because this controls the normalized normal pressure, p/σ_0 .

Alternative Methods of Surface Preparation

Although scratch brushing is normally applied as the method of surface preparation, it has certain disadvantages. The bond strength obtained is variable, with rather large scatter caused by the rough surface treatment. Cold welding must be carried out as soon as possible after scratch brushing and within 10 min.

Systematic investigations of cold roll bonding aluminum-aluminum, aluminum-copper, copper-copper, and aluminum-mild steel, applying different methods of dressing the workpiece surfaces before cold welding, show that electrochemical and chemical (also called electroless) plating are good alternatives to scratch brushing (Ref 10). As an example, Fig. 12 shows the weld interface surface after fracture of roll-bonded aluminum-aluminum prepared by electroless nickel plating

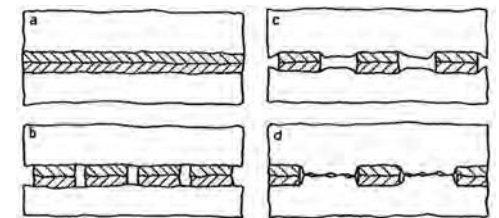


Fig. 6 Schematic outline of bonding mechanism. Source: Ref 6

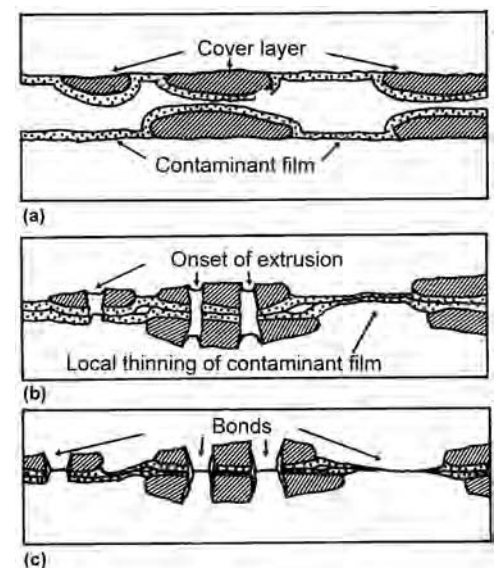


Fig. 7 Refined model for bonding mechanisms in cold welding. Source: Ref 8

of one of the two surfaces. Bonding is already obtained at a reduction $r = 0.35$, and at $r = 0.5$ extensive bonding is established in the cracks between the fragments of brittle cover layer.

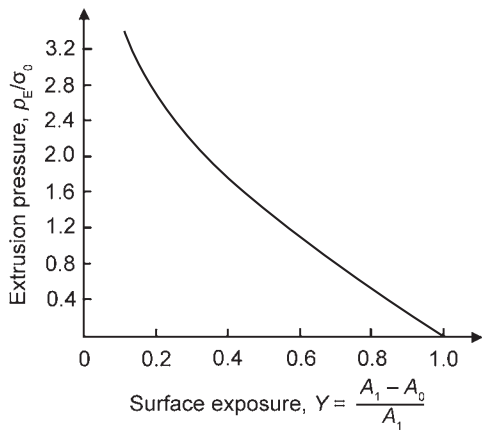


Fig. 8 Required pressure, p_E . Source: Ref 7

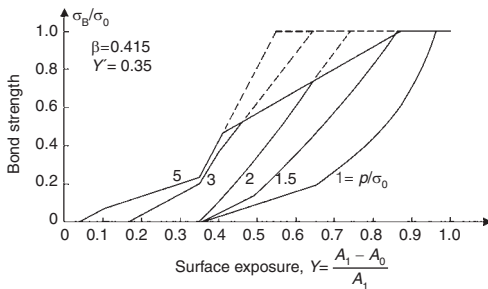


Fig. 9 Normalized bond strength versus surface exposure with normalized normal pressure as a parameter for scratch-brushed aluminum-aluminum. Source: Ref 7

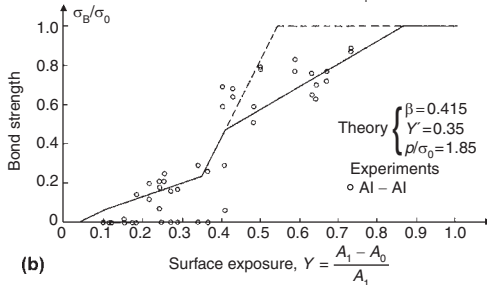
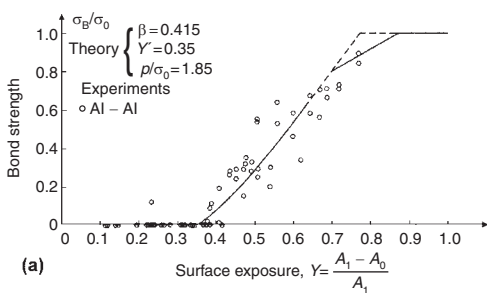


Fig. 10 Weld strength as a function of surface exposure for scratch-brushed aluminum-aluminum. (a) $p/\sigma_0 = 1.85$. (b) $p/\sigma_0 = 5.1$. Source: Ref 7

Figure 13 shows the weld strength in roll bonding aluminum-aluminum when adopting different methods of surface preparation. It is seen that electroless nickel plating leads to the earliest bond formation. Although anodizing of aluminum creates a very brittle cover layer, which is easily fractured by subsequent deformation, this surface-dressing method is not as efficient as nickel plating, electrochemically or electroless. This is due to the fragment size, which is substantially smaller than the one obtained by nickel plating. The optimum choice of surface preparation depends on the metal combination (Ref 9). Whereas electroless nickel plating is optimal for copper-copper and aluminum-aluminum, scratch brushing is the most efficient when cold roll bonding aluminum-copper and aluminum-mild steel.

Quality Control

The nature of the weld interface of a cold weld implies that nondestructive testing by, for example, ultrasonics is not applicable. The only way to test the quality is by destructive testing, implying that the surface preparation and subsequent cold welding should be handled with care to ensure good weld quality. Fingerprints on the scratch-brushed surfaces will have a detrimental effect on bond formation. This is due to the formation

of a thick contaminant film, which will impede bonding even in the areas uncovered after fracture of the cover layer.

Process Variants and Applications

A variety of metal-forming processes are suitable for production of cold welds. The following processes are most commonly applied in industry (Ref 8):

- Rolling
- Indentation
- Butt welding
- Extrusion
- Shear welding

Rolling

Roll bonding of two or more sheets is applied in a large variety of combinations. Evaporator plates for heat exchangers in aluminum and copper used in refrigerators (Fig. 14) and solar heat panels are made by roll bonding, applying stop-off ink prints to avoid bonding in the channels blown up after welding (Ref 12). Other roll bonding applications include compound plates of aluminum-copper and aluminum-stainless steel for cookware, aluminum-stainless steel

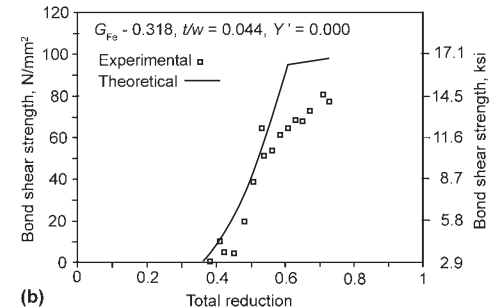
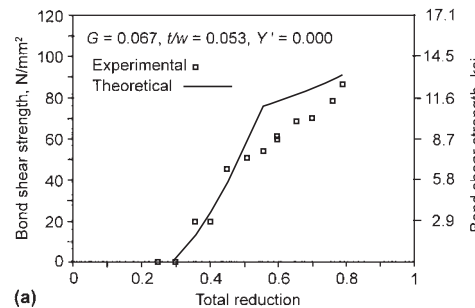


Fig. 11 Calculated and experimental weld shear strength as a function of reduction in roll bonding of (a) aluminum-aluminum with one-sided, electroless nickel plating and (b) aluminum-mild steel with electroless nickel plating on steel. Source: Ref 9

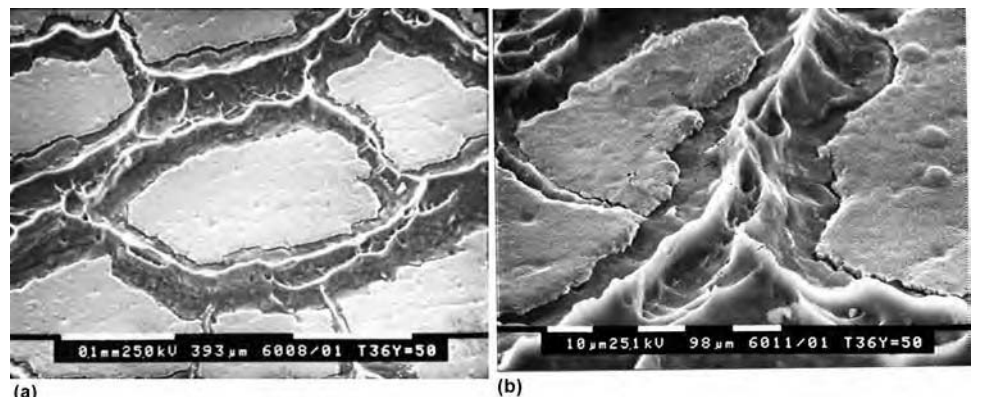


Fig. 12 Weld interface surface after fracture of roll-bonded electroless nickel-plated aluminum-aluminum. Source: Ref 11

for vehicle bumpers, copper-stainless steel-copper for architectural purposes, cupronickel-copper-cupronickel for coins, and nickel-stainless steel-copper and nickel-iron-nickel for button cell batteries (Ref 13, 14).

After the sheets are cleaned, they are roll bonded together, reducing thickness to approximately 20%. The roll bonding may be carried out at elevated temperature to facilitate deformation in the case of harder metal combinations. Subsequent heat treatment may be applied to improve bond strength by diffusion.

The AlSn and AlZn alloys are roll bonded to mild steel for use in automotive slide bearings (Fig. 15). In this application, asymmetrical rolling is performed using a three-high mill, with a small work roll contacting the softer aluminum

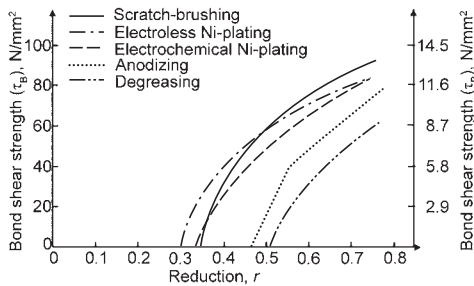


Fig. 13 Weld strength as a function of reduction and method of surface preparation for aluminum-aluminum roll bonding. Source: Ref 11



Fig. 14 Evaporator plate made by roll bonding aluminum-aluminum



Fig. 15 Roll-bonded and subsequently machined and formed half of an automotive slide bearing

alloy and the larger work roll, of the same size as the supporting roll for the smaller work roll, contacting the harder steel strip. In this way, the aluminum alloy is smeared out on the steel surface in a kind of shear welding operation.

Precious-metal contacts for the electronics industry are also manufactured by roll bonding. Base metals such as alloys of copper, aluminum, nickel, iron, and stainless steel with inlays of gold, silver, palladium, and tin are roll bonded for connectors, lead frames, and industrial electronics (Ref 15).

Indentation

Lap joining by local indentation in the two plates or bars to be welded is a common cold welding operation, normally carried out by small tool indentation (Fig. 16). Indentation may be done from both sides with opposing indenters (Fig. 16a) or from one side only using an indenter tool and a flat anvil (Fig. 16b). The indenters may be of round or rectangular cross section with a diameter or minimum cross section typically being one to three times the thickness of the sheets. The required thickness reduction is 50 to 90%. As shown in Fig. 16, the indenters are usually provided with a shoulder that controls the amount of deformation, minimizes distortion, and promotes welding in the peripheral area surrounding the indenter. In welding dissimilar metals, it is often necessary to increase the size of the indenter or to employ a flat anvil on the softer metal side. Lap joining is typically applied to join aluminum-aluminum, aluminum-copper, and copper-copper, including alloys for electricity supply. Copper terminals are bonded to aluminum windings for transformers in automotive starter motors. Figure 17 shows some examples of lap joints.

Butt Welding

Cold butt welding of wires, bars, or plates end-to-end is performed by securing the two workpieces in special clamps in such a way that

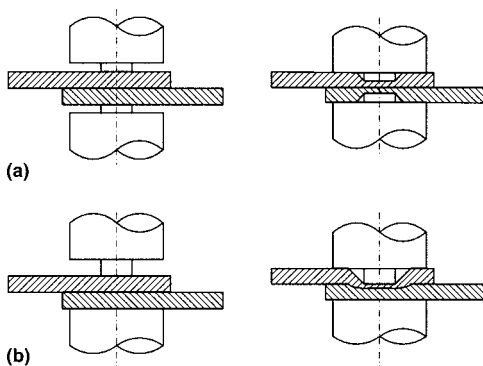


Fig. 16 Lap joining by small tool indentation. (a) Double-sided indentation. (b) Single-sided indentation. Source: Ref 16

a free length of the workpieces protrudes from the clamps (Fig. 18). The free ends are pressed together, and the axial upset results in plastic deformation of the projecting ends that moves the original, contaminated end surfaces into the flash, thus forming a strong bond between virgin surfaces in the welding region. To obtain a good bond, upsetting is performed two to six times. When welding aluminum-aluminum, aluminum-copper, and copper-copper, the weld

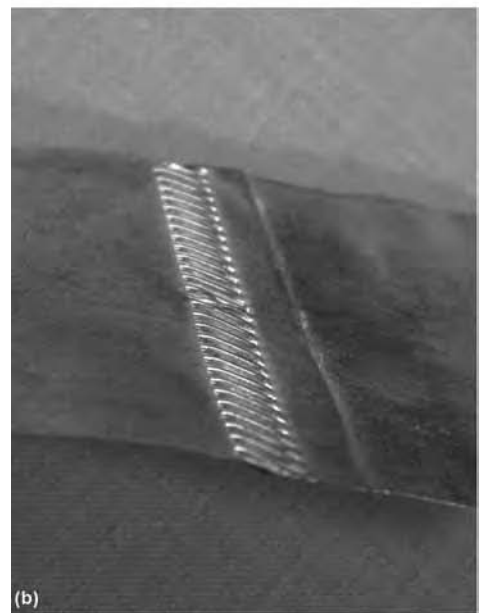
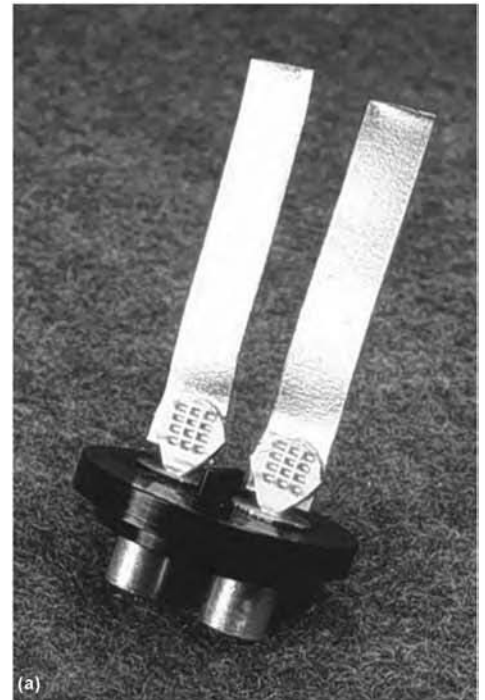


Fig. 17 (a) Lap-joined aluminum outlets for a condenser. (b) Lap-joined copper sheet with a thickness of 0.14 mm (0.006 in.)

strength is greater than the base-metal strength, and there is no increase of electrical resistance in the welds.

Cold butt welding is applied for joining wire ends in wire-drawing production. It is furthermore applied for joining electrical busbars, for example, when providing aluminum busbars with copper terminals (Fig. 19). Automotive aluminum wheel rims have also been manufactured by cold butt welding flat aluminum band, which is subsequently roll formed to the required profile shape. Machines for cold butt welding include small, manually operated machine tools for thin wire combination (0.07 to 2.0 mm, or 0.003 to 0.08 in.) and hydraulic machines for larger butt welds (Ref 17, 18).

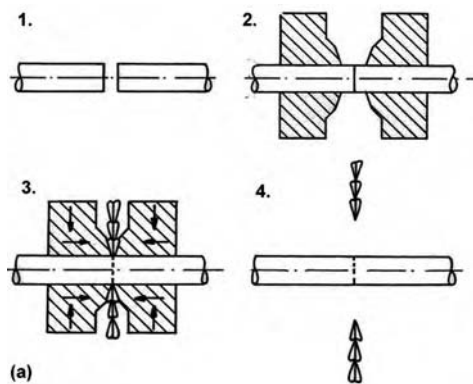


Fig. 18 (a) Schematic outline of cold butt welding with multiple upset. (b) Cold-butt-welded copper bar with a cross section of 3×5 mm (0.12×0.20 in.). Source: Ref 16

Extrusion

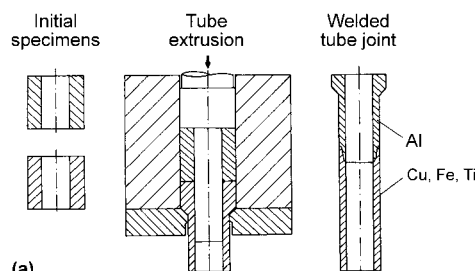
Tube transition joints of aluminum-stainless steel, aluminum-titanium, and zirconium-mild steel are manufactured for nuclear power and space technology by forward tube extrusion (Fig. 20a). The harder tube is placed nearest to the conical die opening. The punch is provided with a mandrel fitting the tube holes, thereby eliminating inward flow. Electronic devices and nuclear fuel elements are encapsulated by cold welding using an extrusion process, where the lid is joined to the can housing by an ironing operation (Fig. 20b).

Shear Welding

In several special cases, use of relative sliding between two surfaces in so-called shear welding has found application. Figure 21 (a-c) shows the principle of combining extruded aluminum profiles using a groove-and-tongue-like joint. The groove geometry ensures large local surface expansion, and the taper of the tongue ensures high normal-pressure in the interface, which, together with the shear deformation, establishes the conditions necessary for cold welding. This technique is applied for joining half-open aluminum extrusion profiles to closed sandwich constructions, as shown in Fig. 21(d). They are used for house construction as well as for stiffened panels for containers, trucks, vans, and ship sides. Figure 21(e) shows an air cooler assembled by the same technique (Ref 19, 20).



Fig. 19 Butt-welded and trimmed specimens. Aluminum-copper bars with cross sections of 5×15 mm (0.20×0.60 in.) and 10×100 mm (0.40×4.0 in.), respectively. Aluminum-aluminum sheet that is 0.3×35 mm (0.01×1.4 in.)

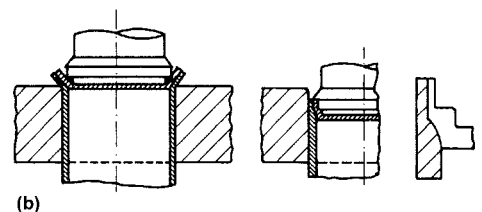


(a)

Cold weld riveting has been developed for welding aluminum sheet to aluminum frame profiles (Fig. 22). A hole is drilled through the sheet into the solid profile. An aluminum wire, oversized by 0.15 to 0.20 mm (0.006 to 0.008 in.), is forced into the hole, forming a cold shear weld along the hole side. The end of the wire is forged into a rivet head, using a pneumatic hammer. In this way, large roof and wall units have been mounted for industrial and public buildings.

REFERENCES

1. J. Wodara, Kaltpressschweissen, *Schweisstechnik*, Vol 15, 1965, p 411-415
2. L.R. Vaidyanath, M.G. Nicholas, and D.R. Milner, Pressure Welding by Rolling, *Br. Weld. J.*, Vol 6, 1959, p 13-28
3. K.J. McEwan and D.R. Milner, Pressure Welding of Dissimilar Metals, *Br. Weld. J.*, Vol 9, 1962, p 406-420
4. H. Eggers, E. Krause, and J. Ruge, Zum Mechanismus der Kaltpressschweissens—Bruchflächenuntersuchungen mit dem Rasterelektronenmikroskop, *Schweissen Schneiden*, Vol 22 (No. 6), 1970, p 241-244
5. J.A. Cave and J.D. Williams, The Mechanism of Cold Pressure Welding by Rolling, *J. Inst. Met.*, Vol 101, 1973, p 203-207
6. N. Bay, Cold Pressure Welding—The Mechanisms Governing Bonding, *J. Eng. Ind.(Trans. ASME)*, Vol 101, 1979, p 121-127
7. N. Bay, Mechanisms Producing Metallic Bonds in Cold Welding, *Weld. J., Res. Suppl.*, Vol 62, 1983, p 137s-142s
8. N. Bay, Cold Welding 1—Characteristics, Bonding Mechanisms, Bond Strength, *Met. Constr.*, Vol 18 (No. 6), 1986, p 369-372
9. W. Zhang and N. Bay, Cold Welding—Theoretical Modeling of the Weld Formation, *Weld. J., Res. Suppl.*, Vol 76 (No. 10), 1997, p 417s-420s
10. W. Zhang and N. Bay, Cold Welding—Experimental Investigation of the Surface



(b)

Fig. 20 (a) Forward tube extrusion of transition joints. (b) Encapsulation by ironing. Source: Ref 16

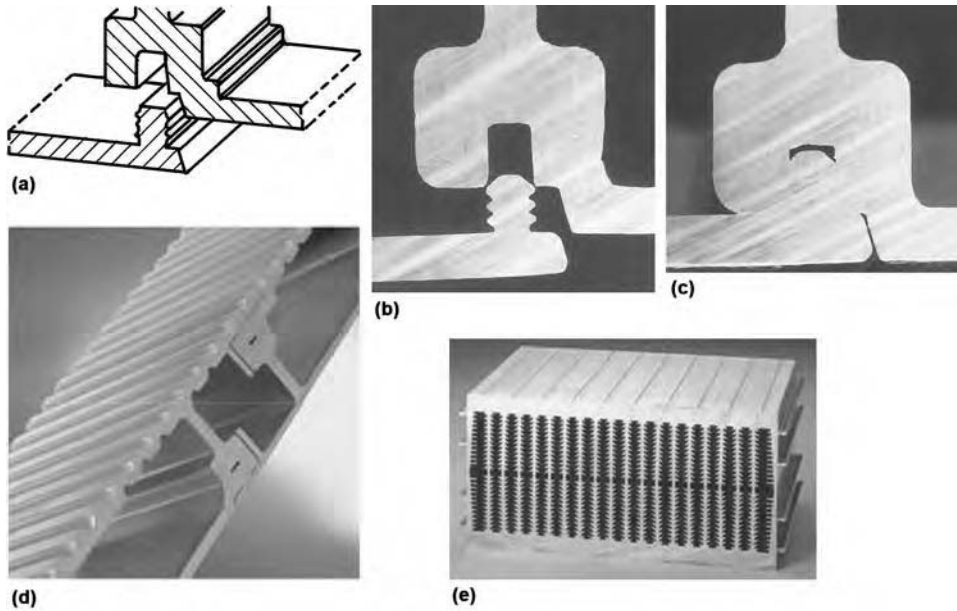


Fig. 21 (a) and (b) Extruded groove and tongue for shear welding. (c) Assembled joint. (d) Sandwich constructions assembled by shear welding of extruded aluminum profiles. (e) Air cooler. Courtesy of Honsel. Source: Ref 19, 20

- Preparation Methods, *Weld. J.*, Vol 76 (No. 8), 1997, p 326s–330s
11. C. Clemensen, O. Juelstorp, and N. Bay, Cold Welding 3—Influence of Surface Preparation on Bond Strength, *Met. Constr.*, Vol 18 (No. 10), 1986, p 625–629
 12. R.F. Tylecote, *The Solid Phase Welding of Metals*, Edward Arnold Publishers Ltd., London, 1968

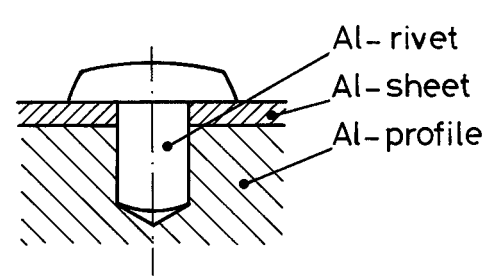


Fig. 22 Cold weld riveting joint. Source: Ref 16

13. “Clad Metal,” Engineered Materials Solutions, <http://www.emsclad.com>
14. Hitachi Cable, Ltd., <http://www.hitachicable.co.jp>
15. Technical Materials, Inc., <http://www.technicalmaterials.com>
16. N. Bay, Cold Welding—Part 2: Process Variants and Applications, *Met. Constr.*, Vol 18 (No. 8), 1986, p 486–490
17. BWE Ltd., <http://www.bwe.co.uk>
18. ECVV.com, http://www.ecvv.com/product_directory/cold-welding-machine.html
19. W. Linn, Linn Leichtmetall Consulting, personal communication, 2010
20. Honsel, <http://www.honsel.com>

Roll Welding and Laser Roll Welding*

Muneharu Kutsuna, Advanced Laser Technology Research Center Co., Ltd.

DISSIMILAR METALS in sheet or strip are joined for a variety of product applications. Domestic appliances such as electric frying pans and water boilers, for example, use combinations of dissimilar metals. Steel-aluminum sheet has structural application in automobiles and in antifriction parts such as cylinder liners and bushes. Dissimilar joining between steel and aluminum sheet also finds applications in liquefied natural gas storage tanks and steel supporting structure. Besides joining steel to aluminum to obtain higher strength than that of the base metals, other combinations of interest include:

- Steel to copper
- Steel to titanium
- Stainless steel to aluminum
- Galvanized steel to aluminum alloy
- Titanium to aluminum alloy

Joining for this purpose can be done in various ways, such as mechanical clinching, self-piercing riveting, adhesive bonding, diffusion bonding, explosion welding, friction welding, resistance spot welding, forge welding, and roll bonding.

This article describes two methods based on rolling of sheet. The first is roll welding, where two or more sheets or plates are stacked together and then passed through rolls until sufficient deformation has occurred to produce solid-state welds. The other process is laser roll welding, which is a hybrid process based on a thin-melting interface for a lap joint of dissimilar-metal sheets using a roller and one-sided laser heating.

Roll Welding

Two types of roll welding are common. In the first, the parts to be welded are merely stacked and passed through the rolls. The second method, usually termed pack rolling, involves sealing the parts to be rolled in a pack or sheath and then roll welding the pack assembly.

The first method is more generally employed in the cold welding of ductile metals and alloys.

Sometimes the stack to be welded is first tack welded at several locations to ensure alignment during rolling. Also, when using this method, the deformation during the first rolling pass must exceed the threshold for welding (typically greater than 60% for cold rolling) to keep the parts together. The required first pass reduction can be reduced by hot rolling, if the metals to be rolled can tolerate preheating without excessive oxidation. Once the first pass has been accomplished, the reduction per pass can be decreased, as is often desirable because roll-separating forces increase as the parts to be rolled become thinner. However, the nonuniform stress distribution that builds up during a sequence of very light passes can cause the weld to open up or "alligator." Therefore, the reduction for subsequent passes is generally a compromise between applying excessive separating forces and "alligatoring."

In pack roll welding, the parts to be welded are completely enclosed in a pack that is sealed (typically by fusion welding) and often evacuated to provide a vacuum atmosphere. This may be accomplished by a frame that surrounds the parts to be welded, which is sandwiched by two lids, or may simply consist of two covers formed to encapsulate the parts to be welded (Fig. 1). Semikilled or killed low-carbon steel is a common material for the pack but is not suitable for all alloy and temperature combinations. Although the preparation costs of pack roll welding are significant, the process has the following advantages:

- Provides atmospheric protection, which may be particularly important for reactive alloys such as those of titanium, zirconium, niobium, and tantalum
- Permits welding of complex assemblies involving several layers of parts.

A significant limitation of the process is that packs become difficult to process when their length exceeds several feet.

Titanium and titanium alloys are considerably more difficult to pack roll than are either steels or copper and aluminum alloys because most titanium alloys have very narrow working

temperature ranges. To overcome this problem, titanium alloys that are pack rolled are sometimes encased in a steel envelope, or can. The can is evacuated to minimize oxidation of the work metal, and it also serves to minimize heat loss to the relatively cold rolls upon deformation. The narrow working temperature range of titanium alloys makes the rolling of these materials labor-intensive. Rolling passes are done by hand on relatively small pieces, and many intermediate reheating steps are required. Some β -titanium alloys, however, are continuously rolled on hot and cold strip mills.

Nonpack rolling, of course, can employ continuous strip rolling. A seldom-used hybrid version of roll welding is to seal the edges of the parts to be welded by fusion welding prior to rolling. This method does not provide atmospheric protection to the outer surfaces, as in pack roll welding, but does occlude air from the more critical inner surfaces.

In roll welding, successful welding depends not only on the total amount of deformation but also on the pressure during rolling. A high isostatic pressure component during rolling is promoted by large reductions per pass, large roll diameters, and rough roll surfaces. A non-uniform distribution of normal stresses, referred

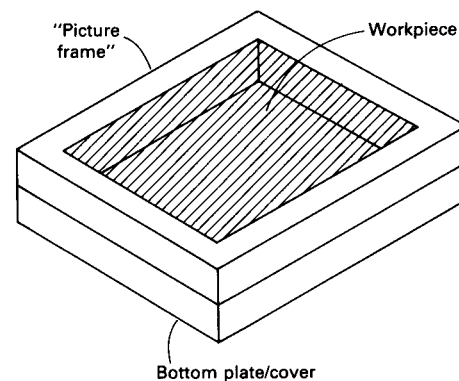


Fig. 1 Pack used for roll welding. The top cover, which would be welded in place before rolling, is not shown.

to as pressure hill effects, is caused by frictional and mechanical restraint and results in lower pressure near the outer edges of the parts being rolled. Therefore, rolling conditions must be such to ensure sufficient pressure near the edges to avoid weak welds in these regions.

Copper, aluminum, and their alloys are often cold roll welded. Hot rolling is applicable to a wide spectrum of alloys. Typically, hot rolling is performed above recrystallization temperatures. In practice, weldability is often improved by raising the temperature to the region where oxygen mobility becomes significant to promote oxide assimilation by diffusion. Also, welded assemblies are often postheat treated to cause recrystallization (in cold rolling), oxygen diffusion, and/or sintering. In welding dissimilar metals, selection of temperatures for rolling and postheating must take into consideration the possibility of intermetallic compound formation, eutectic melting, and/or porosity due to Kirkendall diffusion. The most common metals that are roll welded are low-carbon steels, aluminum and aluminum alloys, copper and copper alloys, and nickel. Low-alloy steels, high-alloy steels, nickel-base alloys, and titanium and titanium alloys have also been roll welded.

Roll-Welded Heat Exchangers

One of the more important applications of roll welding is the fabrication of heat exchangers. This process is used to fabricate flat solar collectors. In another method of heat-exchanger fabrication, three plates are stacked, with the middle plate containing the flow channels. The stacked plates are initially held together by tack fusion welds or resistance spot welds. This approach has been employed for both aluminum and steel heat exchangers. A second important application of this process is in the cladding of sheet metal products.

A principal application of roll welding is the production of heat-exchanger panels with flow tubes as an integral part of the composite. Millions of refrigerator evaporator plates have been formed by this process. A cross section of a similar application, solar collector panels, is illustrated in Fig. 2. Roll-welded heat-exchanger panels are most often made of aluminum, although copper and stainless steel panels have also been produced commercially.

The first major step in the production of roll-welded heat exchangers is to thoroughly clean the surfaces of the sheets to be joined by combinations of solvent cleaning, chemical cleaning, and wire brushing. Next, a stop-weld pattern is reproduced on one of the sheets that will later form the passageways in the heat exchanger. This is accomplished by transferring ink onto the surface by silkscreen processing. These stop-off inks contain materials such as graphite or titanium oxide.

The prepared plates are placed together and temporarily joined by spot welding to form a sandwich that is then roll welded, with at least

partial welding occurring during the first rolling pass. The sandwich sometimes is heated prior to this first rolling pass. Whether hot rolling or cold rolling is employed, the major reduction takes place in this first pass (50 to 80%). Subsequently, cold rolling may be employed to reduce the panel to final gage. Also, panels are generally given a postweld heat treatment. This heat treatment results in an annealed part and, particularly in the case of cold rolled panels, may improve the weld quality through recrystallization and diffusion. Finally, the passageways are formed by inflating them with air pressure while the sandwich is held between platens. The panel is then ready for trimming, additional forming, and painting, as required for the application.

The process has been used to produce heat exchangers for refrigerators, solar panels, poultry incubators, electronic equipment temperature controllers, industrial heat exchangers, and special applications such as thermal control of spacecraft. Modifications of the process permit as many as six sheets to be welded at one time and inclusion of passageways oriented along different principal directions at the different layers. Also, it is possible to produce panels where the passageways are expanded on one side only.

Cladding of Metals by Strip Roll Welding

The common early application of strip roll welding was the fabrication of bimetallic strips for thermostats. This remains an important application, with thermostats taking many complex forms and finding use in furnaces, color televisions, cars, and numerous industrial controls.

A key cladding application is the production of coins by the U.S. Mint. Silver shortages in the 1960s and 1970s resulted in the introduction of coins made from new materials. These coins required a unique set of properties for acceptance by the general public and use in automatic vending machines. Copper clad with cupro-nickel was found to meet these requirements (Fig. 3). The cladding process is relatively simple, although stringent in its requirement for surface preparation. Cladded strips are produced by continuous rolling, with the surfaces prepared just prior to rolling by processes such as wire brushing. Welding typically is accomplished in a single rolling pass. Subsequent heat treatments may be employed to improve the weld quality by processes such as sintering, diffusion, and recrystallization.

The starting material for the U.S. quarter is two outer layers of 75Cu-25Ni, each 1.2 mm (0.048 in.) thick, with an inner layer of pure copper that is 5.1 mm (0.20 in.) thick. To obtain good bond strength, the surfaces are chemically cleaned and wire brushed. The strips are then roll welded to a combined thickness of 2.29 mm (0.090 in.) (Fig. 4). A second rolling operation reduces the final thickness 1.36 mm (0.0535 in.). The strips thus undergo a total reduction of 82% (Ref 1).

Similar processing is applied to many new products, including electrical contacts, conductive springs, automotive windshield wiper sockets, automotive trim, clad cookware, wrap for underground cable, and electromagnetic shielding (Table 1).

Essentially all combinations of ductile metals and alloys can be clad by roll welding, although the oxides of some metals may make welding

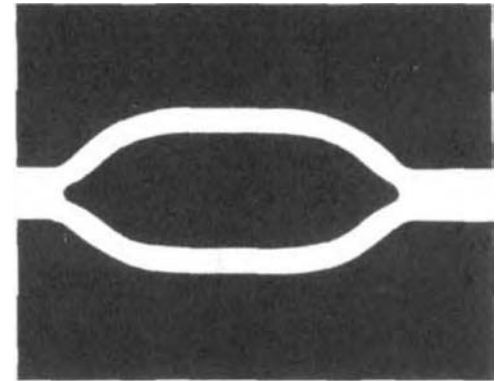


Fig. 2 Cross section of an aluminum solar collector panel produced by the roll welding process

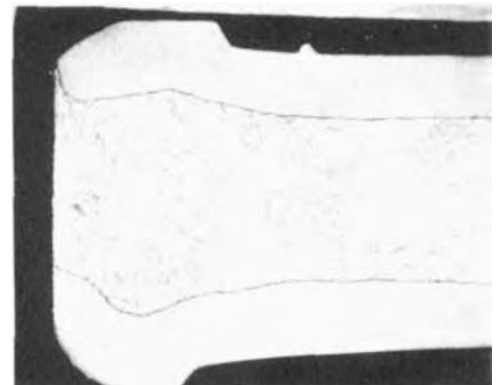


Fig. 3 Metallographic cross section of the edge of a cupronickel-clad copper coin

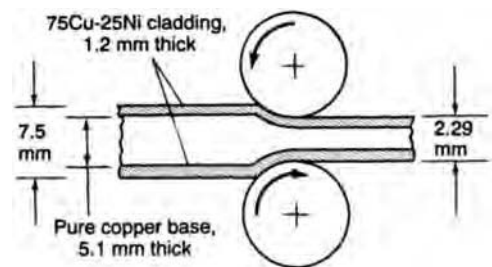


Fig. 4 Schematic showing 70% reduction in cross section of a U.S. Mint quarter coin (composed of an inside layer of pure copper sandwiched between two thin layers of cupronickel material) as it undergoes an initial roll welding operation. A second rolling operation further reduces the material to a final thickness of 1.36 mm (0.0535 in.) for a total reduction of 82%. Source: Ref 1

difficult and other combinations may suffer from intermetallic compound formation on heating. Most engineering metals and alloys can be processed into clad-laminate form, but some cannot (Table 2, Ref 2). One characteristic that makes some metals difficult or impossible to combine by deformation is low ductility. Such metals cannot be co-reduced to the extent necessary to achieve a metallurgical bond. Another characteristic that can cause problems is the tendency of some metals to form a tenacious oxide film that inhibits weld formation. Finally, some metals are thermally unstable; they form brittle intermetallic compounds when heated above a certain temperature. Those metals that are readily processed into clad laminates have opposite characteristics. They are ductile and easily cleaned of oxides, and they form no intermetallic

compounds. In most cases, when a metal is named, alloys of that metal also apply.

Laser Roll Welding

As noted, laser roll welding is a hybrid welding process—neither a fusion welding process nor completely a solid-state welding process. It is best described as a pressure welding process with a thin layer of melting from laser heating on one side of a lap joint. Using a roller and laser heating, it is typically used to join dissimilar-metal sheets. In the case of aluminum to steel with laser roll welding (Fig. 5), for example, the steel sheet is heated to 1300 °C (2370 °F) so that aluminum melts only near the interface with the steel.

The advantage of laser heating is the sharp focusing of energy for fast heating and cooling. Rapid heating and cooling minimizes the time for formation of brittle intermetallics by diffusion processes. The process of combining laser heating with roll bonding is intended to reach sufficient temperatures quickly, to form a bond while being pressed. Some basic process variables (Fig. 6) include laser power, travel speed, and roll pressure. By control of welding speed, laser power, and roll pressure, the interlayer thickness and formation of brittle intermetallic compounds can be minimized.

Different types of high-power lasers (on the order of 2 kW) can be used for laser roll welding of dissimilar-metal joints. A schematic of roll welding with a CO₂ laser is illustrated Fig. 5(a), and a setup with a fiber-optic laser

Table 1 Typical properties of common roll-welded clad laminates

Materials system	Composite ratio, %	Thickness		Width		Tensile strength		Yield strength		Elongation, %	Applications
		mm	in.	mm	in.	MPa	ksi	MPa	ksi		
Copper 10300/low-carbon steel	50:50	0.25–2.54	0.010–0.100	12.7–50	0.5–2	260(a)	38(a)	215(a)	31(a)	40(a)	Typically used for commutators in electric motors, replacing copper 10400. The lower conductivity of steel causes less heat loss during welding, resulting in faster, better-quality welds. The added strength of steel allows thickness reduction.
Deoxidized copper/carbon steel/deoxidized copper	5:90:5, 10:80:10, 15:70:15	0.25–2.54	0.010–0.100	≤610	≤24	420(b)	61(b)	250(b)	36(b)	35(b)	Used in heat exchangers, replacing brazing shim material. One-piece manufacturing eliminates separate shims and reduces assembly cost. Because no ferrous surfaces are exposed, no flux is needed.
Type 434 stainless/5052 aluminum	40:60	0.56–0.76	0.022–0.030	≤610	≤24	395	57	360	52	12	Widely used for automotive body moldings, drip rails, rocker panels, and other trim components, often replacing solid stainless steel or aluminum. Stainless steel provides bright appearance; the hidden aluminum base provides cathodic protection, corroding sacrificially to the body steel.
Copper 11000/1100 aluminum	50:50	0.51–2.54	0.020–0.100	50–510	2–20	180(c)	26(c)	12(c)	1.7	35(c)	Developed specifically for transition joints between copper and aluminum in refrigeration equipment. Usually used in the form of deep-drawn tubing.
C1008 steel/type 347 stainless steel/C1008 steel	43:10:45	0.36	0.014	305	12	393	57	195	28	35	Used in hydraulic tubing in vehicles, replacing terne-coated carbon steel tubing. The outer layer of carbon steel cathodically protects the stainless core of the tube, extending its life significantly.
Nickel 201/type 304 stainless steel/nickel 201	7.5:85:7.5	0.20–2.41	0.008–0.095	25–64	1–2.5	310	45	40	Used in formed cans for transistor and button cell batteries, replacing solid nickel at a lower cost.
Copper 10300/type 430 stainless steel/copper 10300	17:66:17, 20:60:20, 33:34:33	0.10–0.15	0.004–0.006	12.7–150	0.5–6	415(d)	60(d)	275	40	20(d)	Replaces heavier gages of copper and bronze in buried communications cable. The stainless steel provides resistance to gnawing by rodents, which is a serious problem in underground installations.
Phosphor bronze 51000/carbon steel/copper	10:85:5	0.38–1.52	0.015–0.060	≤610	≤24	455(e)	66(e)	435	63	16(e)	Used in automotive applications, such as windshield-wiper bearings. The bronze provides the bearing qualities, the steel provides strength, and the copper aids tooling life and provides corrosion resistance in service.

(a) In eighth-hard temper. (b) 10:80:10 material. (c) In three-quarter-hard temper. (d) 20:60:20 material. (e) In quarter-hard temper. Source: Ref 2

Table 2 Relative weldability of selected dissimilar metals and alloys roll welded into clad-laminate form

Base metal No. 1	Base metal No. 2																				
	Ag	Al	Al alloys	Au	Carbon steel	Co	Cu	Mn	Mn-Ni	Nb	Ni	Pt	Stainless steel	Steel	Sn	Ta	Ti	U	Zr		
Ag	A	B	B	
Al	A	C	B	C	B	B	B	...	B	C	
Alfesil	D	D	D	D	D	D	D	D	D	D	D	D	D	D	D	D	D	D	D	D	
Be	D	D	D	D	D	D	D	D	D	D	D	D	D	D	D	D	D	D	D	D	
Carbon steel	...	B	B	B	
Cu	A	B	...	A	B	B	B	A	B	B	A	A	B	B	...	B	...	
Mn	B	B	A	B	
Ni	...	B	...	A	A	B	...	B	A	
Nb	B	B	
Stainless steel	...	B	B	...	B	B	B	
Steel	B	A	B	B	
U	B

A, easy to weld; B, difficult but possible to weld; C, impractical to weld; D, impossible to weld. Source: Ref

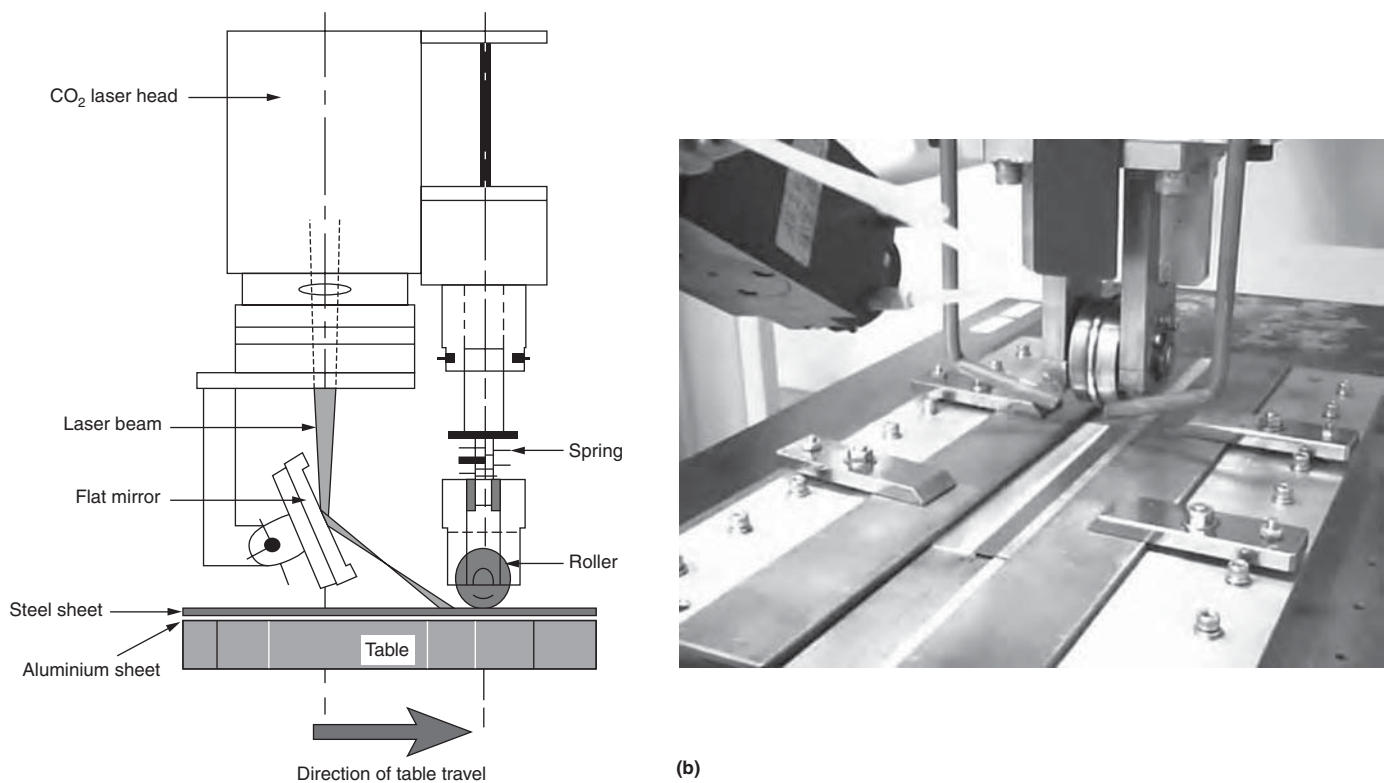


Fig. 5 Laser roll welding. (a) Schematic of laser roll welding process with aluminum and steel sheet. (b) Using a 2 kW fiber laser

is illustrated in Fig. 5(b). The diameter of the beam spot is approximately 3 by 5 mm (0.12 by 0.2 in.) on the metal sheet and 10 mm (0.4 in.) distance from the bottom of the roller. Incident angles of the laser beam were 45 μ m. CO₂ laser and 30 μ m. fiber laser, respectively.

Laser Roll Welding of Dissimilar Metals

Steel and Aluminum Sheet Joining

Fusion welding of aluminum to steel is impractical, because brittle intermetallic compounds such as FeAl₂, Fe₂Al₅, and FeAl₃ can

form during the melting and subsequent solidification. The reason for this is attributed to the great difference between their melting points (660 $^{\circ}$ C, or 1220 $^{\circ}$ F, for aluminum and 1538 $^{\circ}$ C, or 2800 $^{\circ}$ F, for iron), almost zero solid solubility in each other, and formation of brittle intermetallic compounds.

In the iron-aluminum system (Fig. 7), intermetallic compounds are grouped as iron-rich compounds (FeAl and Fe₃Al) and aluminum-rich compounds (FeAl₂, Fe₂Al₅, and FeAl₃). Mechanical properties of cast intermetallic compounds under compressive test are shown in Fig. 8. While the aluminum-rich intermetallic compounds are brittle, iron-rich intermetallic compounds show slight ductility and high

strength. The objective is to minimize formation of the brittle intermetallic compounds.

Although the complete elimination of brittle intermetallic compounds such as FeAl₃, FeAl₂, and Fe₂Al₅ is not possible due to their low free energy, their formation can be suppressed to some extent. Laser heating of the steel quickly reaches the temperature of the interface suitable to form ductile compounds such as FeAl and Fe₃Al (approximately 1250 $^{\circ}$ C, or 2280 $^{\circ}$ F). This results in melting of a very thin layer of aluminum—on the order of 10 μ m—at the interface. As this effect of laser heating is taking place, the heated zone is subjected to roll pressure to improve the contact area. This also helps in increasing the cooling rate, preventing

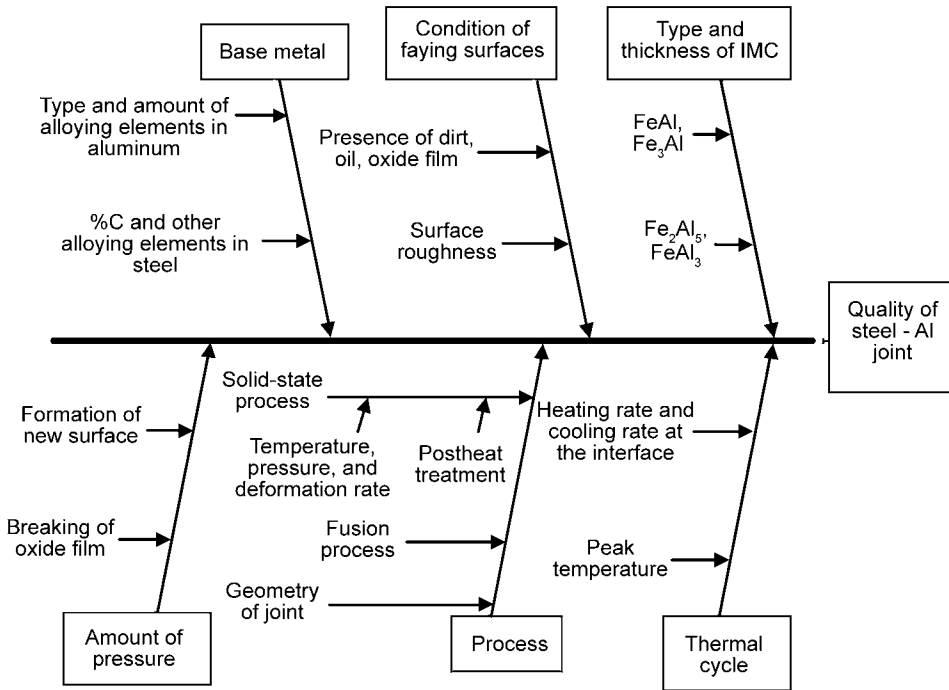


Fig. 6 Process parameter for laser roll welding. IMC, intermetallic compound

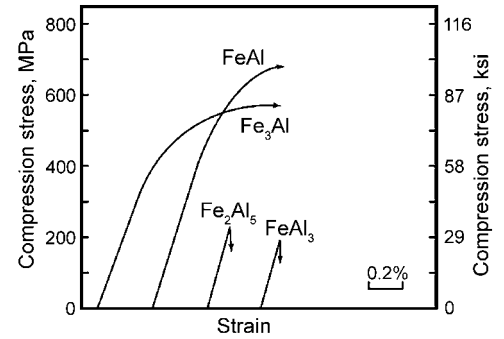


Fig. 8 Stress-strain curve in compressive test of iron-aluminum intermetallic compounds. Source: Ref 3

combined sections consisting of steel sheet with aluminum or aluminum alloy sheet. Attempts to use resistance spot welding with inserts for this purpose have already been made (Ref 3), with the major problem being the formation of brittle intermetallic compounds such as FeAl₃ and Fe₂Al₅ in the interface layer. It has also been reported that if the layer thickness of the intermetallic compound is limited to below 10 μm, the joint strength is improved (Ref 4).

In an example of laser roll welding, a low-carbon steel (JIS-SPCC, 0.12 C max, 0.5 Mn max, 0.04 P max, S 0.045 max) with a sheet thickness of 0.5 mm (0.02 in.) was joined with a 1 mm (0.04 in.) thick sheet of aluminum (A1050) and aluminum-magnesium alloy (A5052). A continuous-wave CO₂ laser was used to weld the steel sheet to the A5052 alloy, while a pulsed CO₂ laser was used to weld the steel sheet to the unalloyed aluminum sheet (A1050).

A lap joint was used, and the steel was placed on top of the aluminum to absorb the heat from the incident laser beam without melting and to conduct the heat to the interface. The overlap was 9 mm (0.36 in.), and the Gaussian beam was defocused to give an elliptical spot of 2.5 mm (0.10 in.) minor and 3.5 mm (0.14 in.) major diameter on the steel surface. A spring was used to press the joint against the table through the roll. Prior to joining, the faying surfaces of both sheets were cleaned ultrasonically to remove the hard aluminum oxide film, then treated with a brazing flux (KAIF₄: K₂AlF₅·H₂O) to prevent further oxidation.

Laser roll welding was conducted with varying travel speed, laser power, and roll pressure. The range of conditions was as follows:

- *Laser power:* 1.0 to ~2.0 kW
- *Travel speed:* 1.0 to 3.2 m/min (3.3 to 10.5 ft/min)
- *Beam spot diameter:* 3 to 5 mm (0.12 to 0.2 in.)
- *Roll pressure:* 100 to 200 MPa (14.5 to 29 ksi)
- *Shielding method:* Argon gas

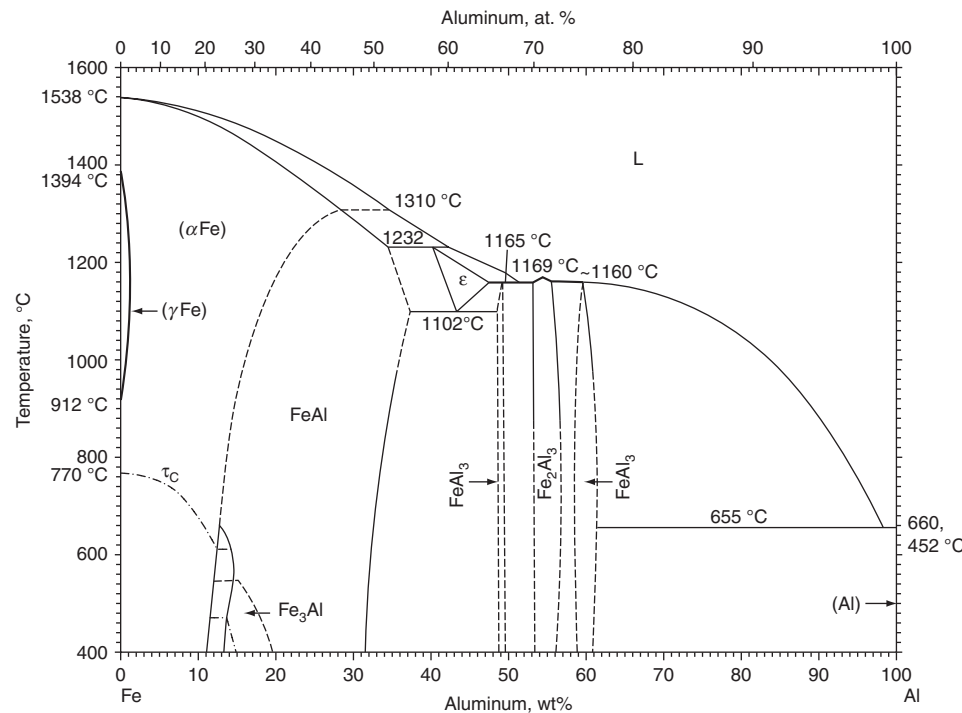


Fig. 7 Aluminum-iron phase diagram

further diffusion at the interface. Such conditions restrict the intermetallic compound layer thickness to thin levels. The existence of a thin interface layer containing some ductile compounds is favorable for improved joint strength.

Welding Uncoated Steel Sheet with Aluminum Sheet. Low-carbon steel and aluminum alloy sheet products are common in the automobile industry for structural components. For weight reduction, one method is to use

In addition to these parameters, pulsed laser welding is used to weld the unalloyed aluminum A1050, which enables more control of the heating and cooling rates by changing the pulse.

The joints were cut transversely to observe the macrostructure and microstructure. Macrostructure examples are shown in Fig. 9. Specimens were used to identify and estimate the intermetallic compounds through the interface layer by electron probe microanalysis (EPMA) with wavelength-dispersion analysis. Based on the EPMA results, the thickness of the interface layer was divided into ductile compounds (FeAl and Fe₃Al) and brittle compounds (FeAl₃ and Fe₂Al₅). The EPMA analysis showed that the interface layer consisted of brittle intermetallic compounds (FeAl₃ and Fe₂Al₅) on the aluminum side and ductile ones (FeAl and Fe₃Al) on the steel side. As the travel speed increased, the total thickness of the interface layer decreased with increasing thickness of the ductile compounds.

Thickness of the interface layer could be controlled by changing pressure values and interface temperature (by varying the laser power or travel speed). Increasing the power has the same effect as decreasing the speed, but if the power reaches high values, it will

cause melting of the steel sheet, and if it reaches low values, the heat input may not be sufficient to produce a bond. As for the pressure, it is necessary to increase the contact area for a short time after heating to allow the diffusion process to take place and help to increase the cooling rate of the joint by heat conduction.

Figures 10 and 11 illustrate the effect of travel speed on interface layer thickness and shear strength. By increasing the travel speed, the interface layer thickness decreases at the same time shear strength increases up to 33 MPa (4.8 ksi) for A1050 and to 56 MPa (8.1 ksi) for A5052. With higher speeds, the percentage of ductile compounds is relatively high, but the shear strength drops for fast travel speed, owing to insufficient temperature due to the lack of heat energy at the interface layer. To evaluate the formability of the joints, the Erichsen test was carried out and evaluated with different speeds, as shown in Fig. 12. The cupping height increases with speed until it reaches a maximum value, then starts to decrease almost in the same manner as the shear strength analysis.

Welding Galvanized Steel Sheet with Aluminum Sheet. Laser roll welding of dissimilar-metal-joint zinc-coated steel with 6000-series aluminum alloy (A6000) has also been

evaluated. Like the uncoated steel sheet, the following conclusions were observed:

- Increase in the travel speed of the table led to decrease in the thickness of the intermetallic compound layer at the interface. Increase in travel speed led to lowering of the peak temperature and shortening of the holding time more than 500 °C (900 °F) at the interface.
- It is suggested that the intermetallic compound layer formed is mainly brittle FeAl₃. Because the travel speed is faster than 0.6 m/min (2.0 ft/min), zinc is confirmed in the aluminum alloy.
- When the intermetallic compound layer was less than 10 μm, failure of the specimen occurred at the base metal of the zinc-coated steel in tensile shear test.

Steel and Titanium Sheet Joining

Fusion welding of steel and titanium is difficult because of generating the brittle intermetallic compound, but laser roll welding allows some control over the formation of intermetallic compounds. In the case of laser roll welding of titanium to steel, the eutectic phase between titanium and TiFe intermetallic compound is formed from the liquid phase at the interface above 1180 °C (2155 °F). The melting interface and interlayer should be controlled to obtain a ductile phase at the interlayer.

Pure titanium sheet (JIS H4600-TP340C) and low-carbon steel (JIS SPCC) sheet were used for joining. The dimension of the titanium sheet and the steel sheet were 40 by 200 by 0.5 mm (1.6 by 8 by 0.02 in.).

Process parameters are shown in Table 3. Travel speed varied from 1.2 to 1.7 m/min (3.9 to 5.6 ft/min). The steel surface exposed to the laser beam was coated with graphite

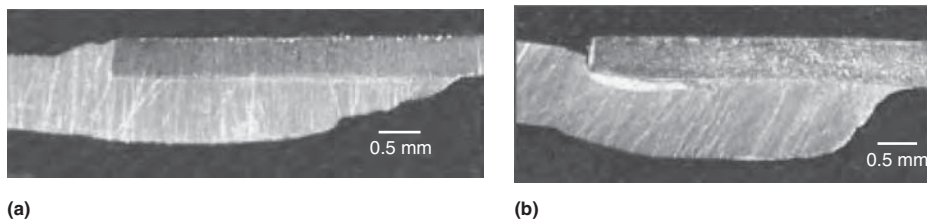


Fig. 9 Macrostructure samples from joints after laser roll welding of low-carbon steel sheet (JIS-SPCC) with (a) A1050 aluminum and (b) aluminum-magnesium alloy A5052. Laser power, welding speed, and roll pressure were: (a) 1.5 kW, 1.5 m/min (4.9 ft/min), and 150 MPa (22 ksi) for A1050, and (b) 1.5 kW, 2.2 m/min (7.2 ft/min), and 200 MPa (29 ksi) for A5052

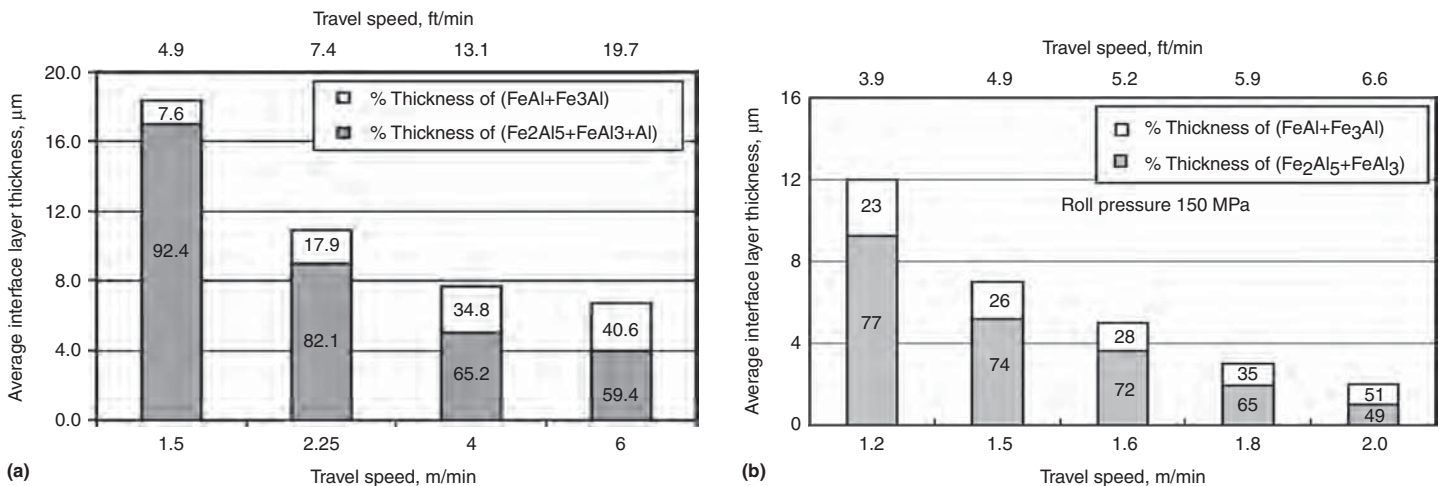


Fig. 10 Composition of intermetallic compounds in the interface layer. (a) SPCC-A1050 at 1.5 kW, 150 MPa (22 ksi). (b) SPCC-A5052 at 1.5 kW, 150 MPa (22 ksi)

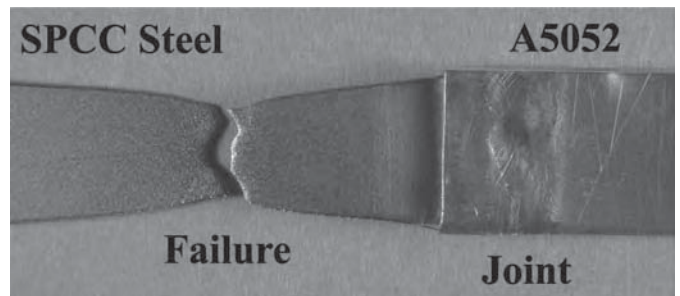
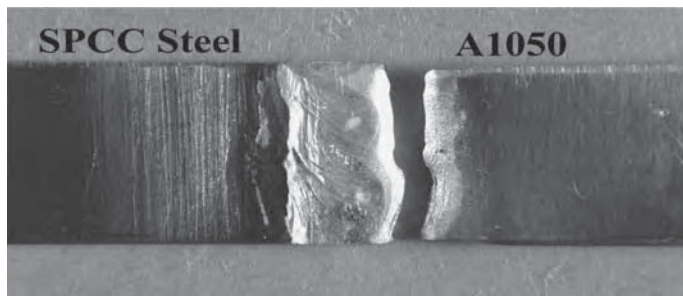
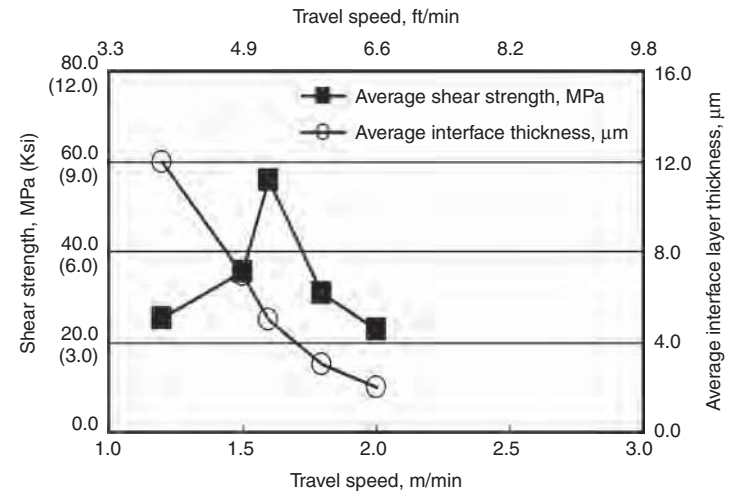
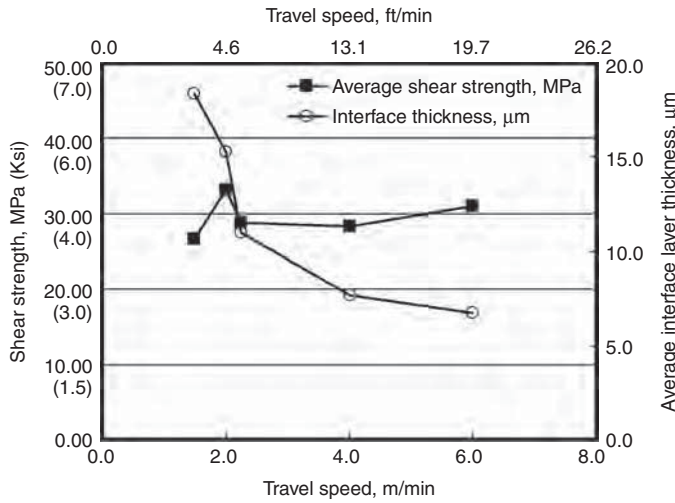


Fig. 11 Effect of travel speed on shear strength. (a) SPCC-A1050. (b) SPCC-A5052

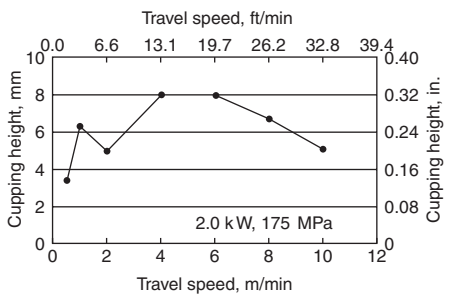
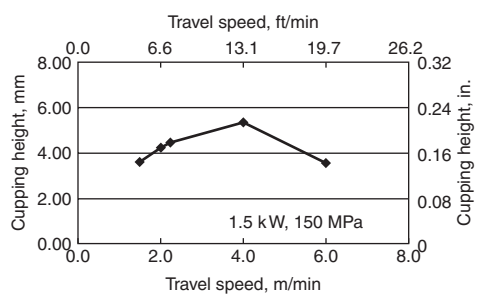
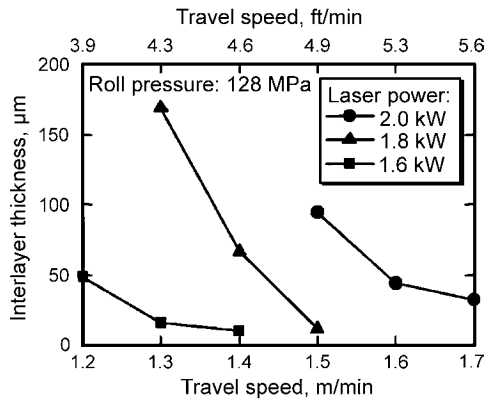


Fig. 12 Results of Erichsen test performed on laser roll-bonded joints. (a) A1050 at 1.5 kW, 150 MPa (22 ksi), 1.5 m/min (4.9 ft/min). (b) A5052 at 2.0 kW, 175 MPa (25 ksi), 2.0 m/min (6.6 ft/min)

Table 3 Process parameters in laser roll welding of commercially pure titanium with steel sheet

Type of laser	Pulsed CO ₂ laser
Laser power	1.6–2.0 kW
Duty cycles	80%
Frequency	150 Hz
Travel speed	1.2–1.7 m/min (3.9–5.6 ft/min)
Overlap width	3 mm (0.12 in.)
Roll pressure	76–128 MPa (11–18.5 ksi)
Center shielding gas	Ar: 25 L/min
Side shielding gas	Ar: 25 L/min



to increase the absorption of the laser beam. The faying surface was polished and degreased. Argon gas at the flow rate of 25 L/min was used for shielding of joints.

The effect of laser power and travel speed on interlayer thickness is shown in Fig. 13. Interlayer thickness decreases significantly from 170 to 10 μm as the travel speed is increased from 1.3 to 1.5 m/min (4.3 to 4.9 ft/min) at a laser power of 1.8 kW.

A tensile shear test was done to investigate the performance of the welded joint. Tensile shear specimens after testing of laser roll-welded joints are shown in Fig. 14. Some

specimens were broken at the interface (Fig. 14a), and others were broken in the base metal of the steel sheet (Fig. 14b). When the interlayer thickness was less than 25 μm, failure of the specimen occurred in the base metal of the steel sheet.

REFERENCES

1. S. Kalpakjian, *Manufacturing Processes for Engineering Materials*, Addison-Wesley, 1984, p 703–704

Fig. 13 Effect of power and speed on interlayer thickness

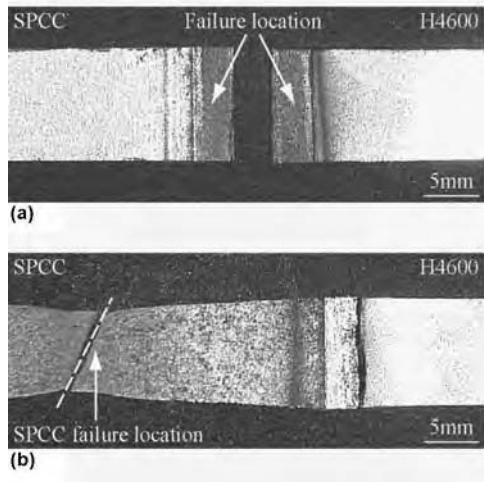


Fig. 14 Tensile shear specimens from steel-titanium joint after laser roll welding. (a) Failure at interface. (b) Failure in base metal of SPCC

2. R.G. Delagi, "Designing with Clad Metals," Metallurgical Materials Division of Texas Instruments, Inc.
3. M. Yasuyama, K. Ogawa, and T. Taka, Spot Welding of Aluminum and Steel Sheet with Insert of Aluminum Clad Steel Sheet—Part 1, *J. Jpn. Weld. Soc.*, Vol 14 (No. 2), 1996, p 314–320
4. C.E. Albright, The Fracture Toughness of Steel-Aluminum Deformation Welds, *Weld. J.*, Vol 60 (No. 11), 1981, p 207s–214s

Ultrasonic Welding

Janet Devine, Sonobond Ultrasonics Inc.

ULTRASONIC METAL WELDING is a solid-state welding process that produces coalescence through the simultaneous application of localized high-frequency vibratory energy and moderate clamping forces. Ultrasonic vibrations create frictional action between surfaces held together under pressure, dispersing oxides and contaminants to give metal-to-metal contact and bonding. Ultrasonic welding offers some advantages over other joining technologies in that it is a solid-state process with no melting; it can join dissimilar metals, weld thin sections to thicker sections, and weld through most oxides and surface oils; and it creates negligible odor and fumes. Ultrasonic welding requires no welding consumables, such as welding rods, fluxes, or solders; has modest space requirements; is environmentally friendly; has no arcs or sparks; and is cost-competitive.

Energy consumption is low when compared to resistance welding or self-piercing rivets. Weld times are short and equipment operation is similar to that needed for resistance welding, thus easing manufacturing acceptance.

The first ultrasonic welding patent for joining metals was awarded to AeroProjects in 1960, and the process has evolved to cover a wide range of applications. Most commercial applications involve nonferrous alloys. Although steel alloys can often be welded, there is a problem with the steel sticking to the welding tip after very few welds. Applications must be lap joints, not butt joints. The process has some welding thickness limitations, and generally the thinner sections are placed next to the welding tip, but the anvil tip side does not have the thickness limitation. The welding thickness limitation can be greatly extended by using a dual-head system in which the ultrasonic energy is introduced from both sides of the weldment.

Production applications include wire to wire and wire to terminals for wire harnesses for appliance, automotive, and the cable industry; buss bars; circuit breakers; contacts; ignition modules; motors; battery and capacitor foils; photovoltaic panels; passive solar heaters; heating, ventilation, and air conditioning (HVAC) tubing; and many others.

The advantages of ultrasonic welding include the ability to:

- Join metals without the heat of fusion, making it an efficient method, energy-wise
- Join dissimilar materials such as copper to aluminum
- Join thin materials to thick materials
- Join multiple layers of thin materials
- Provide strong joints with good thermal and electrical conductivity
- Require no filler materials or fluxes
- Require no special cleaning methods

Limitations include:

- Applications must be overlap joints, not butt welding.
- Materials are limited, for the most part, to nonferrous materials.
- Thickness of the top sheet is approximately 3 mm (0.12 in.) for aluminum and less for many other materials.
- Because the weld is generated by vibratory energy, there must be a gripping surface between the tooling and the parts that may deform the finished parts.

Equipment and Process Parameters

All ultrasonic systems include a power supply that converts line power to the high frequency and high voltage needed by a transducer or converter. The transducer transforms high-frequency electrical energy to vibratory energy because of its piezoelectric properties.

The transducer is incorporated in the welding head together with waveguides that transmit the energy to the welding tip or sonotrode. The tip is held against the desired weldment under pressure. The welding head may use pneumatic, hydraulic, or mechanical means to clamp the workpieces between the welding tip and an anvil or fixture that holds the parts to be welded in place in the desired configuration. Where large parts are to be joined with a series of spot welds, the anvil may be incorporated into a support frame or fixture, and the fixture can be moved by a robot in production use.

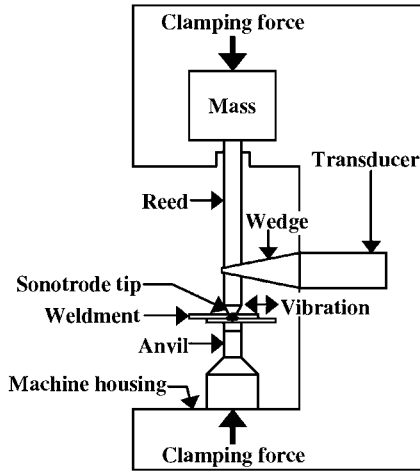
The most widely used frequency for operation is 20 kHz, which is a little beyond the range of human hearing, but there are also welders operating at 40 kHz and above. Because the waveguides are designed to be resonant at the operating frequency, the higher frequencies lead to smaller waveguides and limit the power capacity of the welder. For fine wire bonding, frequencies of 60 kHz and up are used because the parts are small and the power requirement is minimal.

Besides frequency, which is fixed for any particular machine, other parameters to be considered when selecting a suitable welder are power level and configuration. Larger sections require higher power levels and clamping force. For instance, spot welding of 1 mm (0.04 in.) thick aluminum alloy requires a minimum of 2500 W and approximately 150 N (34 lb) of clamping force. This power level would dictate a 20 kHz welder. Power and force can be controlled by the operator, so thinner weldments can be welded with the same machine, but the range of operation of a specific machine varies between manufacturers.

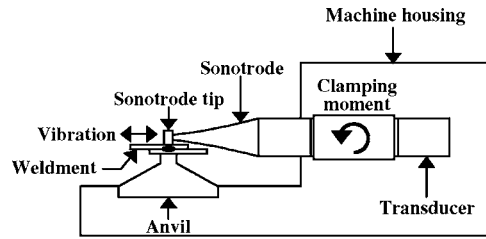
There are two basic designs: a wedge-reed system and a lateral-drive system (Fig. 1, 2). In the wedge-reed system, the transducer is attached to a reed that vibrates in flexure and is terminated by a heat treated steel tapered tip that fits into a cavity at the end of the reed. The lateral-drive system is an inline transducer, booster, and horn, where the welding tip may be integral with the horn or may be removable and held with a mechanical fastener.

In addition to the spot welders of Fig. 2, various welder configurations are available. These include a hand-guided weld gun used for spot welding or for closing and sealing copper tubes for HVAC assembly (Fig. 3) and a robot-controlled C-gun for welding automotive sheet metal assemblies, such as trunk lids or hoods (Fig. 4, 5). A continuous seam welder for foil welding is shown in Fig. 6.

Typically, welders use compressed air and a pneumatic cylinder with slide to bring the welder into location and apply the necessary clamping force. Machines are microprocessor controlled, and the operator can select and store job parameters from a control panel. Welds can



Wedge-reed system



Lateral-drive system

Fig. 1 Schematic depiction of wedge-reed and lateral-drive styles of ultrasonic welding heads

be controlled by time, by energy, or, if so equipped, by distance.

Wire welding requires that the wires to be bonded are gathered together in an anvil fixture with a slight pressure to prevent the wires from escaping from the intended weld area (Fig. 7). The most common application is the manufacture of wire harnesses for the transportation and appliance industries. Machines are available for welding wire bundles with cross-sectional area from 1 to 100 mm² (0.002 to

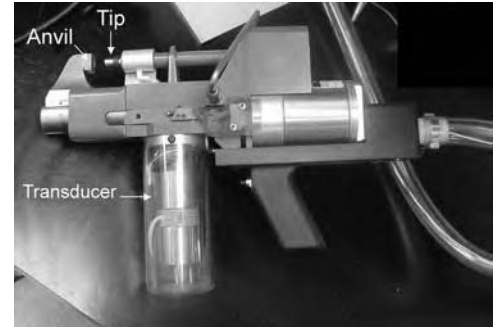


Fig. 3 Hand-guided portable ultrasonic welding gun with tooling to squeeze and seal copper tubing used in air conditioning systems and refrigerators

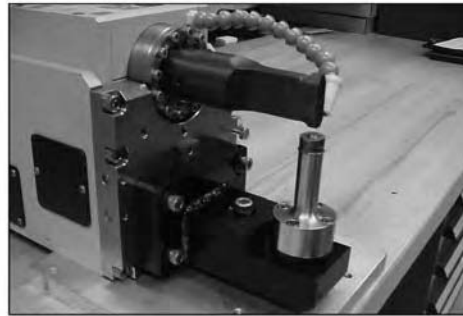


Fig. 2 Photographs of wedge-reed and lateral-drive styles of welding heads

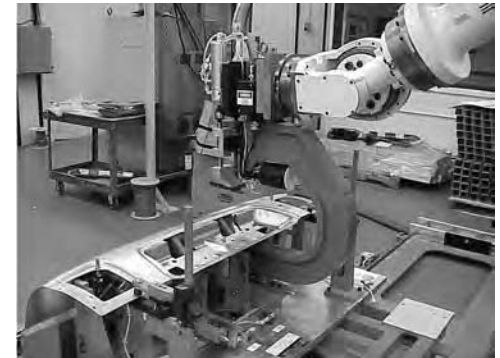


Fig. 4 C-frame ultrasonic welder on a robot arm welding a license plate holder to an aluminum automotive trunk lid

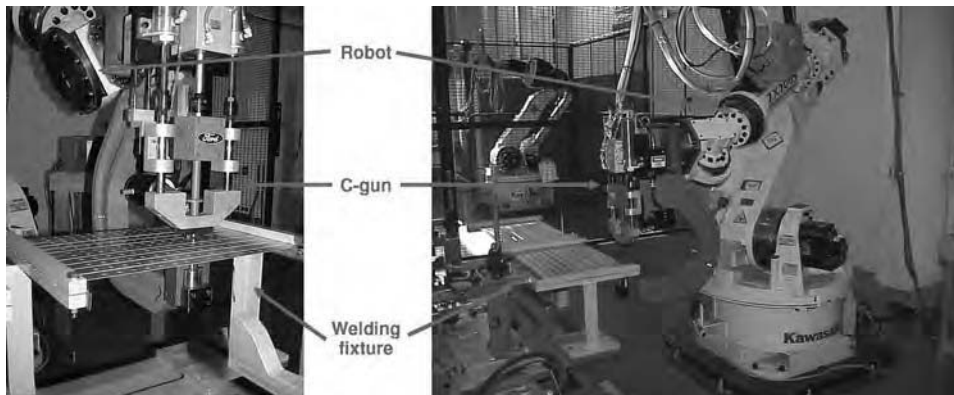


Fig. 5 C-frame ultrasonic welder on a robot arm programmed to make successive spot welds on coupons for a tip life study



Fig. 6 A 50 kHz ultrasonic rotating disk welder used to join foil to foil or foil to metallized glass in photovoltaic systems

0.156 in.²). Ultrasonically welded wire bundles should meet or exceed the Wire Harness Manufacturing Association's IPC/WHMA-A-620 specification (Ref 1).

Spot welds can be circular, elliptical, or ringlike in geometry, as dictated by the size and shape of the tip and anvil. The tip vibrates in a plane parallel to the interface and perpendicular to the clamping force holding the parts together; tip geometry is selected based on the parts to be bonded. Multiple spots can be made with a single tip, although there are size restraints on the weld area that can be successfully bonded in a single weld cycle. Weld time is typically 0.5 to 3.0 s for spot welding.

Applications include wire to terminal; battery terminals; battery foils; buss bars; circuit breakers; ignition modules; small motors; capacitors; heating, ventilation, and vacuum tubing; and aluminum body panels.

A recent study (Ref 2) conducted on welding of aluminum body parts used heat treated tool steel tips with a gripping surface geometry that successfully reduced the tendency for sticking between the tip and surface of aluminum alloys (Fig. 8). The study included some thermocouple and infrared temperature measurements at the weld location. The temperature recorded did not exceed 420 °C (790 °F)—well below the melting temperature of aluminum.

The same joint venture program included micrographs of the bond produced at increasing levels of energy to make the joint. The micrographs show the growth and progression of the weld at increasing energy levels (Fig. 9–11). Tensile testing of the test coupons typically resulted in a button pullout, with the parent metal breaking before the weld failed (Fig. 12, 13). Failure loads are given in Fig. 14 and Table 1. A comparison of fatigue life attained by ultrasonic welding and other joining methods is shown in Fig. 15.

Nondestructive testing included determination of the welded area by ultrasound. As shown in Fig. 16 and 17, there was a good correlation between the indicated bond area size and weld failure load, as expected. The automotive alloys included in this study are listed in Table 2.

Continuous seam welds are produced when a disk-shaped ultrasonically activated roller is rotated and traversed relative to the materials to be bonded. Typical uses include joining foil ends at rolling mills and joining aluminum interconnects to metalized glass for photovoltaic panels. Foil in the range of 0.004 to 0.12 mm (0.0002 to 0.004 in.) thickness is weldable with the high-frequency (typically 50 kHz), low-power systems. There are 20 kHz systems available for welding heavier materials, including passive solar panels up to approximately 0.2 mm (0.008 in.) thick.

Microelectronic welding of fine wires was the earliest of the commercially successful ultrasonic metal-welding applications and still

accounts for a large volume of industrial activity. Wire diameters range from less than 0.025 to 0.5 mm (0.0010 to 0.20 in.). Vibratory action at 60 kHz and higher removes surface contaminants, induces material flow, and permits a solid-state weld between the wire and metalized bond pad or leads on semiconductor packages.

A combination of ultrasonic and thermocompression bonding, known as thermosonic bonding, is also a popular technique. The ultrasonic welding is achieved on heated substrates, typically with interface temperatures from 100 to 200 °C (212 to 392 °F).

Surface condition of the materials to be welded does not present much of a problem

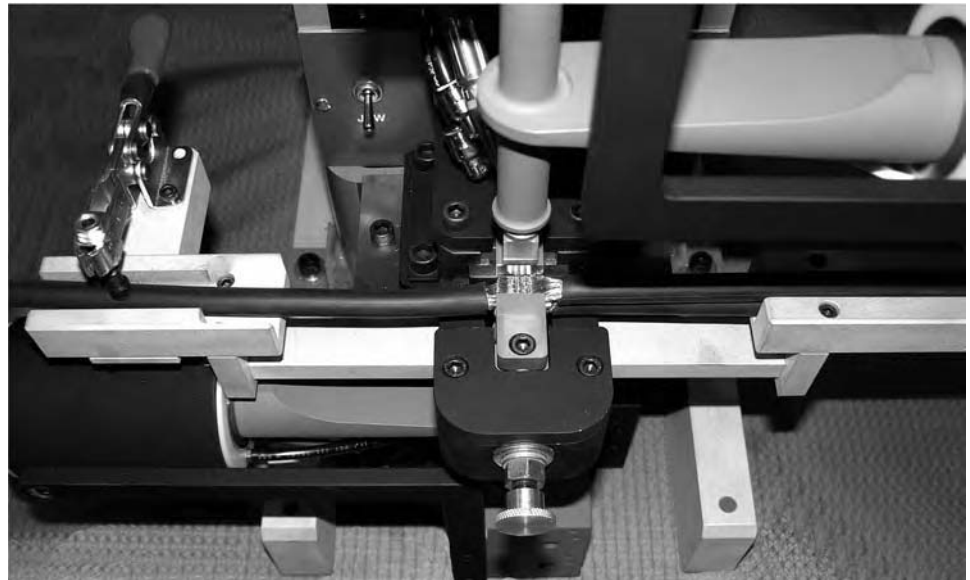
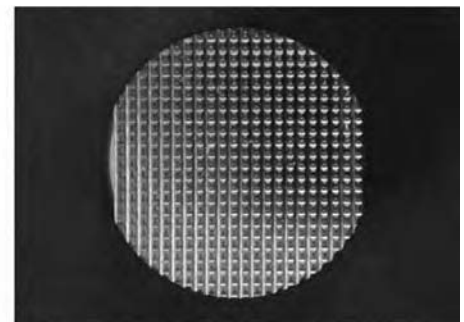


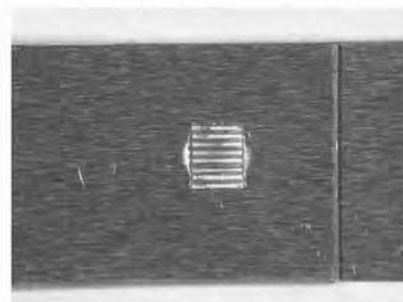
Fig. 7 Dual-headed 20 kHz wedge-reed style of ultrasonic welder capable of welding stranded wire bundles up to 100 mm² (0.16 in.²) in cross-sectional area, such as these three No. 2 American wire gage (AWG) wires



Tip gripping surface



Anvil gripping surface



Tip side of welded coupon

Fig. 8 Typical tip patterns for ultrasonic welding with good strength and minimum tip sticking when spot welding automotive aluminum

for most commonly welded materials, such as aluminum, copper, or brass alloys. These can usually be welded as-received from the mill or degreased with a common solvent or degreaser. Unless they are very thick, oxide coatings will

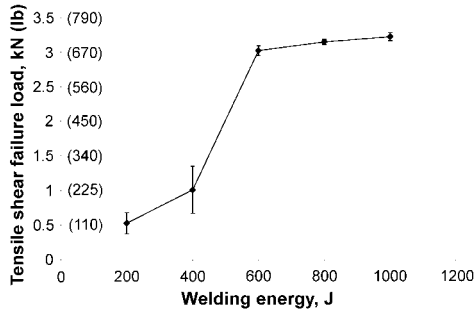


Fig. 9 Tensile shear strength of weld spots made at various energy levels showing weld strength increasing as the weld progresses, then leveling off at a strength level that gives a nugget when tensile tested to failure

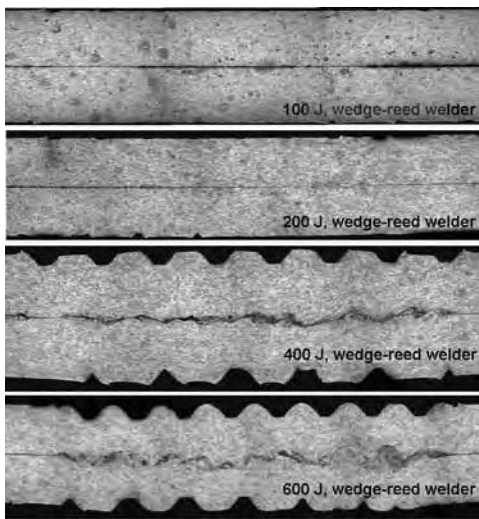


Fig. 10 Micrograph of 0.9 mm (0.04 in.) 6xxx aluminum sheet metal. At 100 and 200 J, there is very little perturbation at the weld interface. The 400 and 600 J energy levels show increased perturbation at the weld interface.

disperse during the process. Some types of coatings, for example, chemically deposited tin and low-temperature magnet wire coating, can be penetrated during the weld cycle. Heavy coatings of tin and high-temperature magnet coating may need to be mechanically abraded before effective welding is achievable.

Adhesive Bonding. A layer of adhesive placed between the panels to be welded is a technique known as weld bonding. It can be used to provide a watertight joint and also to increase the weld strength beyond that achieved with ultrasonic spot welding or with adhesive bonding alone. A paste adhesive or a fabric-supported adhesive can be used.

Control of Resonance. Complex workpieces or large parts may be induced to vibrate

by the ultrasonic system. This can cause fractures in the workpiece or in previously made welds, resulting in inconsistent weld quality. This effect can be minimized or eliminated by applying pressure in strategic locations on the fixture or by applying pressure circling the weld spot to isolate the section being welded from the vibration produced at the weld spot. Such a device is called a product clamp. The part being welded can also be clamped to a rugged fixture or anvil to dampen the tendency to vibrate. It is best to avoid light materials such as aluminum for fixturing; steel is the preferred material.

Welding Tooling. Preferred material for welding tips is high-quality heat treated tool steel. A precise fit is needed between the tip and the waveguides to ensure efficient transmission of the vibratory energy. The wedge-reed-type system uses a locking (Morse) taper between the tip and the vibrating reed; this provides a long life and an easily replaced and oriented weld tip. The lateral-drive system typically has a one-piece horn and tip that may have several weld surfaces, with rotation of the horn exposing a new surface.

Certain alloys, when welded, tend to stick to the tips. This was an issue with the referenced program (Ref 2) to weld aluminum automobile panels but was largely overcome by selection of tip geometry and welding parameters. As many as 100,000 welds were made with a single tip. The testing was set up to weld multiple spots on multiple strips, using a robot that could work repetitively to give the large numbers of welds required for the test, as shown in Fig. 5.

Welding and anvil tips typically have a cross-hatched or serrated pattern (Fig. 8) to prevent sliding between the tips and the weldment. A typical cross-hatched pattern for welding aluminum is approximately 0.5 mm (0.02 in.) peak to peak and 0.2 mm (0.008 in.) deep.



Fig. 11 Micrograph of 0.9 mm (0.04 in.) 6xxx aluminum sheet metal ultrasonically welded at 800 J, showing perturbation and intermixing at the weld interface. Physical deformation at the weld interface and at the tip and anvil interfaces occurs concurrently. Mechanical mixing occurs at the interface. Some deformation of grains occurs at the interfaces of the tip and anvil with the weldments, and there is no evidence of melting.



Painted welded coupons

Fig. 12 Typical lap shear coupons before tensile shear testing in 6xxx aluminum alloy preprepared for automotive study

Personnel Requirements

Operators of the ultrasonic welding process do not need elaborate or extensive training. Once the process parameters have been determined by a process engineer, the operator is only required to load the parts into a nest of supporting/locating anvil assembly, press the palm buttons or other starting device, and then unload the finished part. In-process monitoring can be performed either electronically by using a microprocessor or visually by the operator, which usually requires the operator to look at a power indication gage. The process engineer must work closely with the equipment manufacturer for guidance regarding tooling design and the selection of process parameters.

No arc, spark, or molten filler material is associated with ultrasonic welding, and no electrical current passes through the weldment. Because the welder is usually configured in a press form with moderately high forces, the normal precautions must be observed to ensure

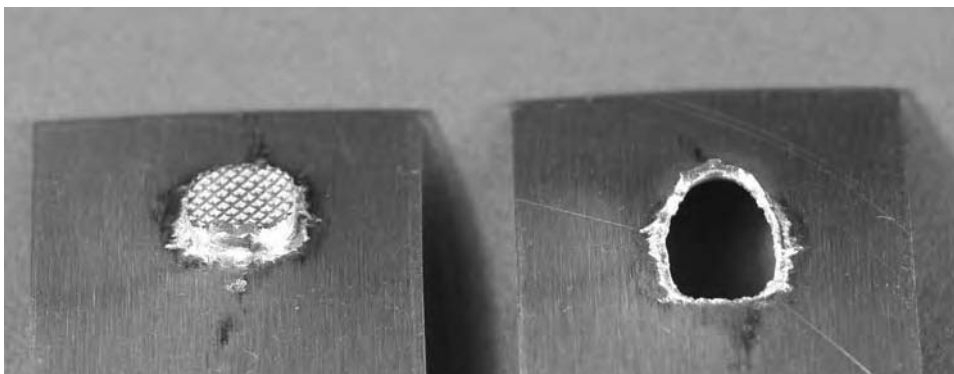


Fig. 13 Lap shear coupon after tensile shear testing, showing nugget tearout indicative of a good weld

Table 1 Typical lap shear failure loads of aluminum from 1 to 3 mm (0.04 to 0.12 in.) thick of particular interest to the automotive industry

1 mm (0.04 in.) 5754 to 1 mm (0.04 in.) 5754	2 mm (0.08 in.) 5754 to 2 mm (0.08 in.) 5754	3 mm (0.12 in.) 5754 to 3 mm (0.12 in.) 5754
2.8–3.0 kN (630–670 lb)	5.0–5.5 kN (1120–1240 lb)	7.5–8.5 kN (1690–1910 lb)

operator safety, that is, the use of anti-tie-down palm buttons or a similar provision to protect the hands of the operator. Another common consideration involves the high-frequency noise level produced by the ultrasonic vibration. In some instances, especially with the higher-power-level equipment, the noise exceeds the Occupational Safety and Health Administration (OSHA)-approved levels, and sound-deadening barriers or enclosures must be provided, or, at the least, operator hearing protection is required.

Applications

In addition to the spot welding of sheet metals, wire to wire and wire to terminals represent a large market for ultrasonic welders. The ultrasonic welds have good strength and electrical conductivity, there is no burning of the insulation, and no solder or other filler materials are required. Typical samples of stranded, braided, and solid wires, tinned and untinned, are shown in Fig. 18 to 20. A newly developing battery market requires the bonding of multiple layers of foil, and typical test samples are shown in Fig. 21.

REFERENCES

1. Specification IPC/WHMA-A-620, Wire Harness Manufacturers Association
2. U.S. National Institute of Standards and Technology, Advanced Technology Program 70NANB3H3015 from 2003–2007 in Joint Venture with Ford Motor Company, Edison Welding Institute, Branson Ultrasonics Corp., and Sonobond Ultrasonics Inc.

SELECTED REFERENCE

- J. Devine, Chap. 25, *Ultrasonic Welding, Welding Processes*, Vol 2, *Welding Handbook*, 8th ed., American Welding Society, 1991

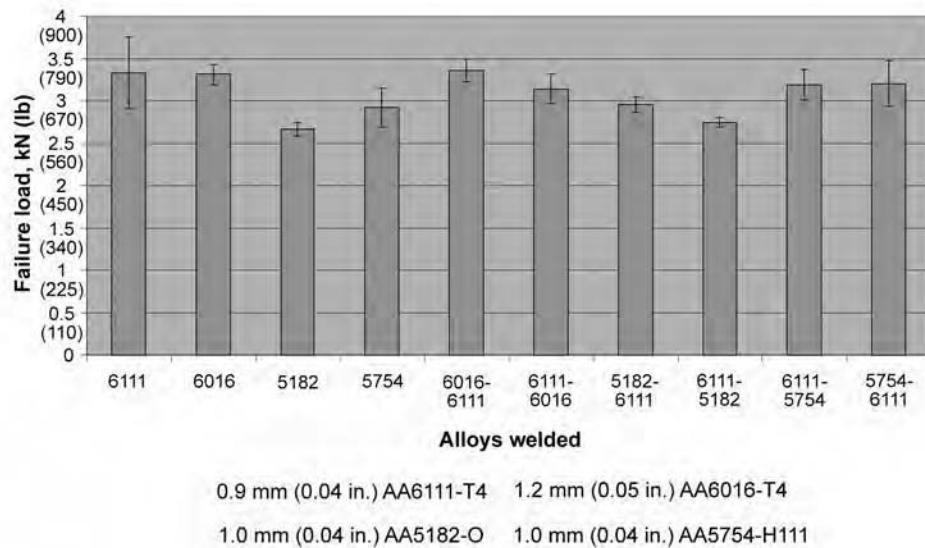


Fig. 14 Typical lap shear failure loads of ultrasonically spot-welded coupons of aluminum alloys of interest to the automotive industry

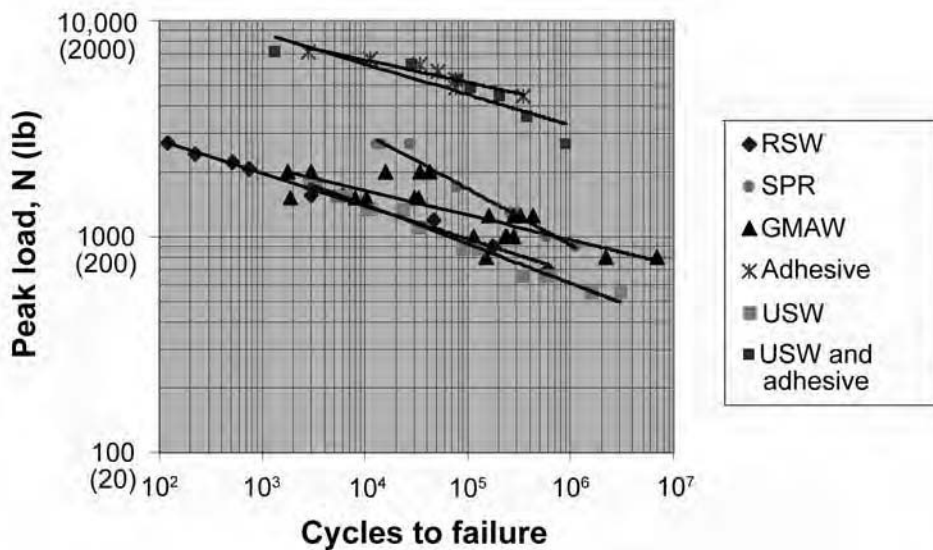


Fig. 15 Comparison of fatigue life of 0.9 mm (0.04 in.) aluminum panels (AA6111, $R = 0.1$) joined by resistance welding (RSW), self-piercing rivets (SPR), gas metal arc welding (GMAW), adhesive, ultrasonic welding (USW), and combined USW and adhesive

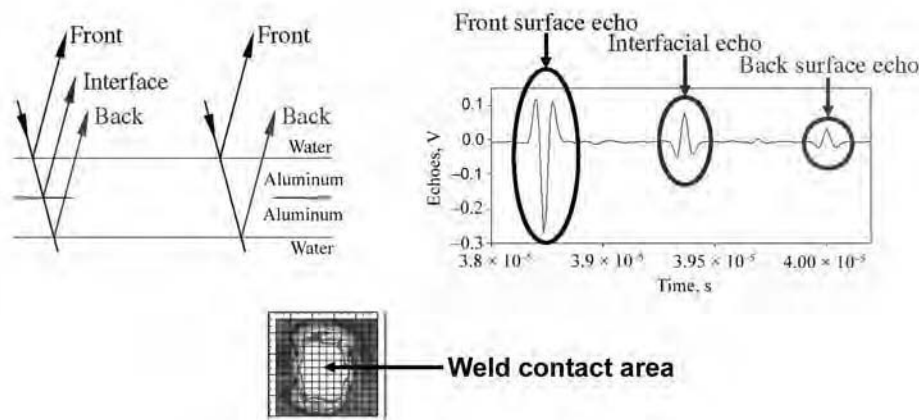


Fig. 16 Nondestructive testing using magnitude of ultrasound interface echo to measure weld contact area as an indication of weld quality

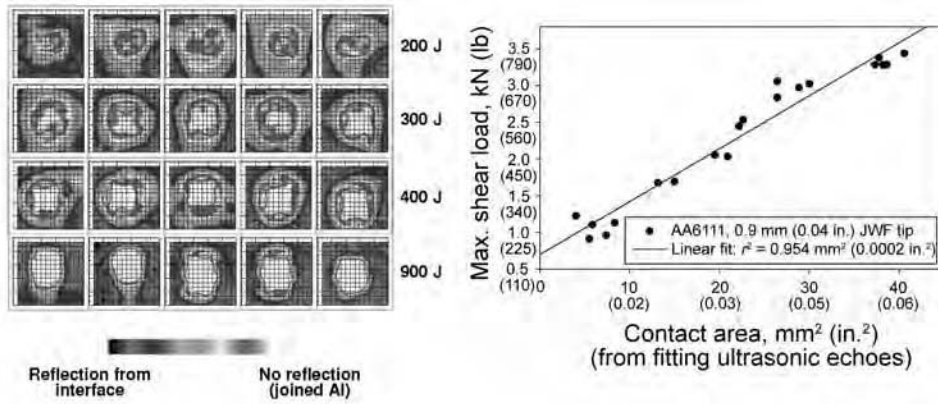


Fig. 17 Investigation of ultrasound as an effective nondestructive evaluation method by comparing indicated contact area and weld failure load. A good correlation was demonstrated.



Fig. 18 Ultrasonically welded bare and tinned copper wire, 1 to 30 mm² (0.002 to 0.05 in.²) cross-sectional area, for wire harness manufacture



Fig. 20 Single-point ground terminal that was ultrasonically welded using a special tooling package that gathers the wire for welding, then automatically folds over the strain-relief arms

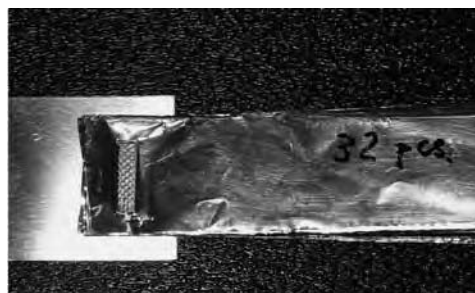


Fig. 21 Thirty-two layers of fine aluminum foil to aluminum plate; particularly of interest to battery manufacturers

Table 2 Aluminum alloys tested for ultrasonic weldability

Alloy	Typical gages
AA5182-O	0.9–3 mm (0.04–0.12 in.)
AA5754-H111	1–3 mm (0.04–0.12 in.)
AA6016-T4	1–1.5 mm (0.04–0.06 in.)
AA6111-T4	0.9–2 mm (0.04–0.08 in.)



Fig. 19 Heavy-gauge wire up to 100 mm² (0.16 in.²) cross-sectional area that was ultrasonically welded using a dual-headed wire welder (as shown in Fig. 7)

Ultrasonic Additive Manufacturing

Karl Graff, Edison Welding Institute

THE ULTRASONIC ADDITIVE MANUFACTURING (UAM) PROCESS consists of building up solid metal objects by ultrasonically welding successive layers of metal tape into a three-dimensional shape, with periodic machining operations to create the detailed features of the resultant object. The process has applications that include prototype metal parts, injection molding dies, composite materials, armor, embedded sensors and actuators, thermal management, and cladding.

Ultrasonic additive manufacturing is part of the broad field of additive manufacturing (AM), which has been defined by ASTM International (Ref 1) as "... the process of joining materials to make objects from 3-D model data, usually layer upon layer." The field of AM originated in 1987 with invention of the polymer-based stereolithography process, followed by selective laser sintering introduced in 1992. In the ensuing years, numerous other processes have been introduced, including metal-based processes that involve laser sintering/melting of various metal powder alloys and electron beam melting of metal powders (Ref 2, 3). The UAM process was introduced by Solidica in 2001 under the identification ultrasonic consolidation, a term that is still in use (Ref 4).

Process Fundamentals

The key features of the UAM process are shown in Fig. 1. Thus, Fig. 1(a) shows a rolling ultrasonic welding system, consisting of an

ultrasonic transducer, a booster, the (welding) horn, and a second "dummy" booster. The vibrations of the transducer are transmitted to the disc-shaped welding horn (which is sometimes also referred to as the sonotrode, a term used in ultrasonic metal welding) rolling in the x -direction, and from there to the tape-metal base, which creates an ultrasonic solid-state weld between the thin metal tape (shown as aluminum in the figure) and a base plate. The continuous rolling of the horn over the tape welds the entire tape to the plate. This is the essential building block of UAM.

By welding a succession of tapes, first side by side and then one on top of the other (but staggered so that seams do not overlap), it becomes possible to build a solid metal part, as shown in Fig. 1(b). Through the course of the build, there will be periodic machining operations, using an integrated computer numerical control (CNC) system, to add features to the part, as suggested by the slot in Fig. 1(b), to remove excess tape material and to true-up the topmost surface of the part. Thus, the process also involves subtractive as well as additive steps. Each of these key features is described further.

Ultrasonic Welding System

The ultrasonic welding system is driven by an ultrasonic transducer, similar in form to those used for ultrasonic metal and plastic welding and of piezoelectric construction operating at 20 kHz. The ultrasonic power capability of the transducer can

vary, depending on design, and has ranged from 1.5 kW to several kilowatts (where, for the latter, special two-transducer systems capable of delivering up to 9 kW have been developed). The entire series of components, transducer-booster-horn-booster, is designed to be acoustically resonant at the transducer operating frequency (of 20 kHz). The acoustic design principles are generally similar to those employed in conventional ultrasonic metal and plastic welding systems, except that the rolling sonotrode requires more complex acoustic analysis.

Not shown in the simplified Fig. 1 is that the welding horn is pressed against the tape and base plate with a static force, necessary to couple the ultrasonic vibrations into the tape. This static force is applied through bearings that are mounted on the boosters and designed and located so as not to dampen the vibrations of the ultrasonic system.

The disc-shaped welding horn is a solid, acoustically tuned shape designed to create a transverse vibration, shown by the arrow at the base of the disc in Fig. 1(a), which produces the weld between the tape and base plate or between the tape and a preceding tape layer. The nature of the transverse vibration and welding action is the same as occurs in conventional ultrasonic metal spot or seam welding. The amplitude of vibration is low, ranging from 20 to 50 μm (790 to 1970 $\mu\text{in.}$), peak to peak. The actual shape details of the welding horn vary for different systems, so the shape shown in Fig. 1(a) should be simply considered as a representative concept.

Ultrasonic Welding during UAM

The core of the UAM process is the formation of a solid-state bond between successive layers of tape under the ultrasonic vibrations of the rolling welding horn. The mechanism of the process is that the welding horn, having a roughened surface (typically achieved by an electrical discharge machining, or EDM, process), grips the top surface of the tape, causing it to move with the vibrations of the horn. This in turn creates a frictionlike action at the interface between the top tape and the lower tape to which it is being joined. The asperities of the

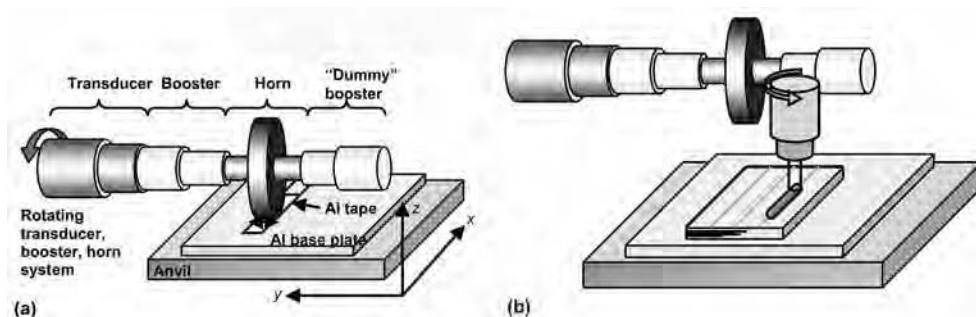


Fig. 1 Ultrasonic additive manufacturing (UAM) process. (a) UAM welding system. (b) Machining operation

opposing interface surfaces are sheared and plastically deformed during this process, disrupting and dispersing oxides and contaminants and permitting pure metal-to-metal contact of the nascent surfaces. Numerous microbonds form between the surfaces, which grow in bond area until all or nearly all of the opposing surfaces are completely bonded by a solid-state weld. This continuous process of rolling and welding results in the bonding of one tape to another tape.

The process just described in terms of UAM is simply that which occurs in ultrasonic metal welding, in particular, the process of ultrasonic seam welding—a solid-state process well known since the 1950s (Ref 5). It is worth emphasizing the solid-state nature of the process, which means that bonding has occurred without melting of the materials being joined.

A final word is in order on the aforementioned frictionlike nature of the process. Ultrasonic additive manufacturing is not a friction process (nor, for that matter, is ultrasonic spot or seam welding). At its initial stages, there is a transverse rubbing motion between opposing surfaces which, although oscillatory in nature, is similar to a frictional motion and thus easily understood as frictionlike. However, as the shearing-deformation process progresses, continuous bonds form across the interface, which grow in extent, leading from a frictionlike early relative motion to ultimate full bonding and fixing of the opposing surfaces.

Materials

The illustration of UAM in Fig. 1 shows the joining of aluminum tape to an aluminum base plate, and aluminum tape-to-tape bonding to form the solid part. In fact, a number of materials have been, or should be capable of being, bonded by UAM. Much of the early work with UAM focused on softer alloys, such as Al 1100, Al 3003, and Cu 1100. These alloys were known to be easily bonded by ultrasonic metal welding and were first choices for UAM. The bonding of a number of more-advanced alloys has been reported, including 316L stainless steel, commercially pure titanium, Ti-6V-4Al, and Al 6061-H18 as examples. The full scope of UAM-bondable materials is not yet known but will be ultimately governed by the basic ultrasonic weldability of various materials and combinations and by the levels of ultrasonic power that can be applied to the process to affect the bond.

The dimensions of the tape being welded are important material parameters. Typical dimensions of Al 3003 tape are 25 mm wide by 0.15 mm thick (approximately 1.0 by 0.006 in.). The width of the tape is governed by the width of the weld face of the horn, which is typically 25 mm. Thicknesses of aluminum and other tapes have ranged from 0.1 to 0.2 mm (0.004 to 0.008 in.). It is not presently known what maximum tape thicknesses will

be possible, but because this will be governed by the amount of tape mass that must be vibrated, it is ultimately expected to be governed by the ultrasonic power of the transducer. In some cases, tape is replaced by a thin sheet of metal foil, and bonding of the sheet is achieved by repeated, side-by-side passes of the welding horn.

As shown in Fig. 1(a), the first tape is welded directly to a base plate that is attached to a heavy anvil plate. The base plate is typically of the same alloy as the tapes being applied, because a sound bond of the first tape is essential to the subsequent layers. In some cases, a variation of alloy between base plate and tape is possible. Thus, Ti-6V-4Al may be bonded onto a commercially pure titanium plate, Al 1100 may be bonded to Al 3003, or Cu 1100 may be bonded onto an Al 3003 plate. The thickness of the plate may range from 1.5 to 12 mm (0.06 to 0.5 in.).

Welding Parameters

The key ultrasonic welding parameters are vibration amplitude, static force, and travel speed; in this sense, they are the same as those for the ultrasonic seam welding process. The vibration amplitude refers to that at the outer diameter of the horn at the tape surface. The amplitude can be set at different levels (i.e., micrometers peak to peak), with the range depending on the system design. A well-designed ultrasonic control system will then maintain the set amplitude throughout the welding process. Likewise, the role of the downward static force in ensuring good coupling and vibration transmission into the tape and base plate has been noted. Force levels again will depend on the overall UAM system design and the particular materials being welded and can range from 300 to 400 N (67 to 90 lbf) in low-power systems up to 20 kN (5 kips) for high-power UAM systems. The travel speed refers to the linear speed of the welding horn across the part and can range from 75 to 1000 cm/min (30 to 390 in./min), depending on system power and materials being welded.

While amplitude, force, and travel speed would be the standard welding parameters, with settings easily changed from trial to trial, the texture and material of the welding horn should also be considered a variable of the process and hence a settable parameter. Thus, the aggressiveness of the EDM-produced texture may be varied, depending on the hardness and thickness of the tape material. In welding 0.15 mm (0.006 in.) Al 3003, it is found that a titanium horn having a texture of 7 μm R_a will be satisfactory. Welding thin tapes may require a texture of 2 μm R_a . In cases involving extremely hard materials, or where tape thicknesses exceed the commonly used 0.15 mm, more aggressive textures, such as 14 or 21 μm R_a , may be required.

The material of the horn may also vary, depending on tape material. While titanium may suffice for bonding a soft aluminum alloy, the use of tool steels, such as AISI grade 18Ni, is needed in bonding titanium and stainless steel tapes.

A final adjustable welding parameter is that of preheat of the anvil and base plate. Also not shown in the simplified drawing of Fig. 1 is a rigid, heated platen that underlies the steel anvil plate. The purpose of the platen is to preheat the base plate to a given temperature level, for the purpose of assisting the welding under the ultrasonic vibrations. As previously noted, ultrasonic welding depends on achieving shearing and plastic deformation of asperities at the tape-tape interface. Preheating can modify the yield strength of materials and hence their deformability under ultrasonic vibrations. This effect is especially noticeable in the softer aluminum alloys. Hence, UAM systems have provisions for applying preheats that range from 21 to 260 °C (70 to 500 °F).

Process Consumables

Based on the preceding description of the UAM process, it should be evident that there are four primary consumables associated with its application:

- **Metal tape:** This is the primary process consumable, with the amount of tape, in terms of weight, being roughly proportional to the volume of the part being constructed. Allowance must be made, in such calculations, for the excess tape at the start and end of a tape layer due to the mechanized tape feeding and cutting hardware. This tape is always trimmed away in the machining operations and is thus excess. For some UAM systems, this may be on the order of 7.5 cm (3 in.) at each end, while other system designs have reduced this excess to 5.0 cm (2 in.) at each end. For a small part, for example, 50 cm³ (3.2 in.³), excess could approximate the net part volume. Increasingly large parts naturally result in a decreased percentage of excess material.
- **Obtaining metal tapes in the desired materials at the desired thicknesses and widths should be allowed for in any design process.** In some cases, this requires diligence in locating suppliers able to deliver at reasonable prices and schedules.
- **Base plate:** The base plate, on which the UAM build is made, is typically of the same alloy as the metal tapes being welded to it (note has been made that similar, but not identical, alloys may be used). The plate is subsequently machined away from the build and thus becomes a process consumable. The surface and thickness dimensions of the base plate play an obvious role in the resulting plate costs. The former will be related to the lateral dimensions of the part

being built and thus will directly depend on part design.

Plate thickness may also be a variable, with the practice here varying among various users of the process. In the interest of cost, some users adopt base plate thickness on the order of 4.7 mm ($\frac{3}{16}$ in.) and use a vacuum system to clamp the base plate to the anvil plate. Others prefer a thick plate, typically 12 to 13 mm (0.5 in.), bolted to the anvil plate. The view on this latter approach is that an absolutely solid base is needed on which to weld the many successive layers of material.

- *Ultrasonic tooling*: The welding horn must be considered a consumable. The continued welding of tapes will wear the textured surface of the horn, requiring resurfacing and EDM retexturing, and is thus one of periodic maintenance. After several such retextures, the outer diameter will have been sufficiently reduced such that the horn and

overall UAM system resonance is taken out of the control range of the ultrasonic power supply system. At this point, a replacement of the horn is necessary.

- *Machine tools*: Integral to the additive steps of UAM are the material-removal steps, by way of conventional machining processes, necessary to arrive at final part features. This means there must be allowance for maintenance and replacement of the various end mills used in the removal steps, with considerations being no different than those associated with conventional machining of solid materials and shapes.

Applications

The ability of UAM to build solid metal parts is a key capability of the process. Applications of the process, ranging from demonstrated and tested, to proof of concept, to simply envisioned,

are extensive, cutting across many industrial sectors, and include rapid prototyping, molding and stamping dies, production of composite and smart materials and structures, lightweight armor, thermal management systems, and cladding, as examples. These fields of application can be broken down into the following broad functional areas:

- Solid metal parts and materials
- Embedded channels
- Embedded materials
- Dissimilar materials

Some examples of UAM-fabricated parts are shown in Fig. 2. Thus, Fig. 2(a) is the mold (or cavity) component of an injection molding die, made from Al 3003 and approximately 100 by 150 by 20 mm (4 by 6 by 1 in.); the associated plastic part is also shown. Figures 2(b) and (c) show another unique UAM capability, that of creating embedded channels. As a part build

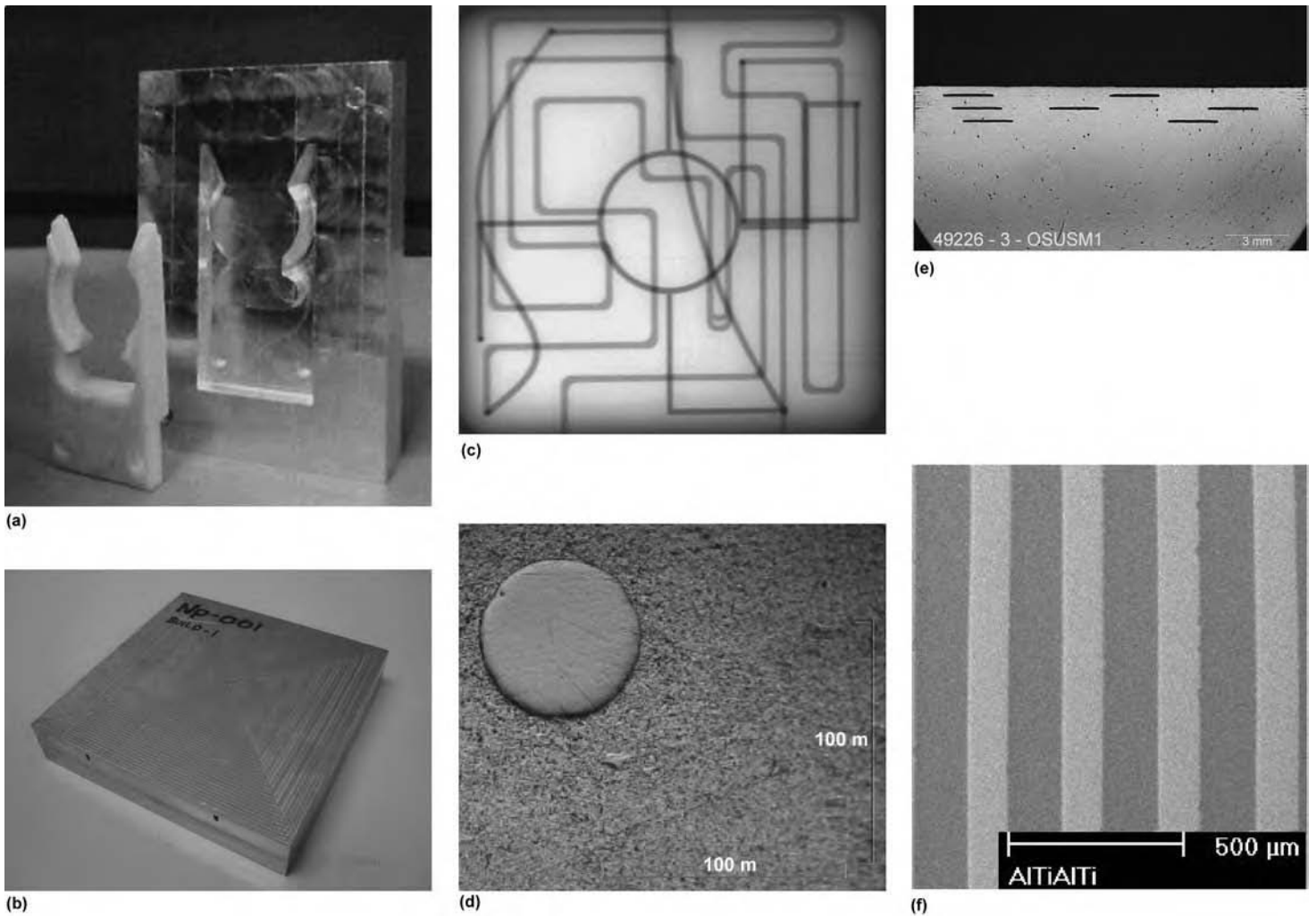


Fig. 2 Applications of ultrasonic additive manufacturing. (a) Injection molding die and part. Courtesy of Solidica Inc. (b) Plate with embedded channels. Courtesy of Edison Welding Institute. (c) X-ray of channel network in (b). Courtesy of Edison Welding Institute. (d) Embedded NiTi wire, 0.076 mm (0.003 in.) in diameter. Original magnification: 400 \times . Courtesy of The Ohio State University. (e) Embedded nickel tape, 2.5 mm wide by 0.1 mm thick (0.10 by 0.004 in.). Courtesy of The Ohio State University. (f) Titanium-aluminum composite. Courtesy of Solidica Inc.

progresses, open channels can be machined at one stage and then covered by the next welding stage(s). Thus, the apparently solid aluminum block, 100 by 100 by 13 mm (4 by 4 by 0.5 in.), in Fig. 2(b) is shown by x-ray in Fig. 2(c) to consist of a complex, multilevel, interconnected network of channels. Channel sizes can range from 2 mm (0.08 in.) down to 10 to 20 μm (390 to 790 $\mu\text{in.}$).

Yet another UAM capability is that of embedding materials within a metal matrix. This can take the form of tapes, wires, meshes, or fibers, as shown by the two examples in Fig. 2(d) and (e). The approach is to build the part to a desired height, lay down individual or multiple wires or tapes, and then weld the next tape layer, which covers and embeds the underlying wires/tapes. The UAM welding vibrations essentially soften and plasticize the tape material, causing it to flow about and firmly embed any underlying wires or fibers. Thus, Fig. 2(d) shows an embedded NiTi wire, while Fig. 2(e) shows embedded nickel tapes.

The ability of ultrasonic metal welding to bond dissimilar materials is well known (Ref 6), so it is not surprising that various material combinations are possible with UAM, an example of which is shown in Fig. 2(f), where a titanium-aluminum laminate has been formed by successively bonding aluminum and titanium sheets with a subsequent hot pressing operation.

As noted, numerous applications of UAM have been put forth in addition to those mentioned. These include rapid prototypes (e.g., models), direct part manufacture, repair (e.g., helicopter blades), casting (positives), injection mold die cooling blocks, computer system and solar panel heat sinks, microchannel reactors, metal-matrix composites, sensors and actuators based on embedded smart materials, cladding, and transition joints. It is expected that many of these applications will move up the manufacturing-readiness-level chain as higher-power UAM systems come on line that are capable of dealing with an increasing range of materials.

Equipment and Procedures

Two types of UAM systems for fabrication of parts are shown in Fig. 3. The system in Fig. 3(a) features a moving UAM gantry with a stationary base plate and integrated tape laying, tape cutting, and CNC machining. Because of the fixed base plate, this type of system has been found to be very suitable for research and development operations due to its flexibility. The Formation system in Fig. 3(b) features a fixed UAM and tape-laying module integrated into a CNC machining center, with a moving base plate. This type of system has been found to be very suitable for high-precision fabrication.

Hybrid software, known as RPCam, is used to control both the ultrasonic additive manufacturing process as well as the

CNC material-removal stage. Thus, the software instructs the machine on both depositing and removing material.

The steps in producing a part by the UAM process are shown in Fig. 4 and consist of the following, numbered in accordance with the figure:

1. The UAM process begins by generating a computer-aided design (CAD) model of the desired part in its final design format.

2. An initial graphics exchange specification (IGES) translation of the finalized CAD model is imported into RPCam.
3. Through a series of user interface features, RPCam evaluates the model to determine the most effective tape layouts, making adjustments to account for the number of tape layers and tape joints relative to edges and features (e.g., cutouts).
4. Adjustments to individual tape placement are then made to account for voids or

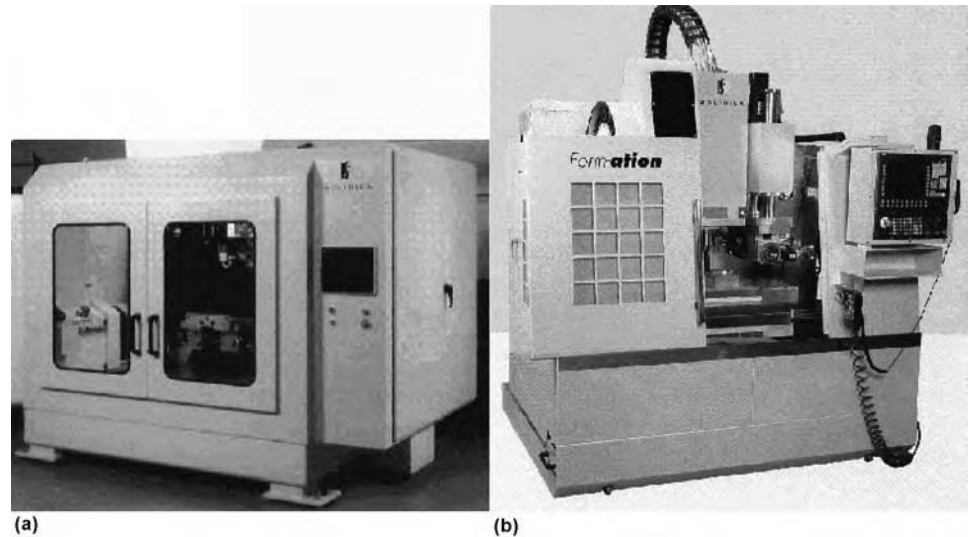


Fig. 3 Ultrasonic additive manufacturing (UAM) systems. (a) Solidica UAM Beta system. (b) Solidica, Formation system. Courtesy of Solidica Inc.

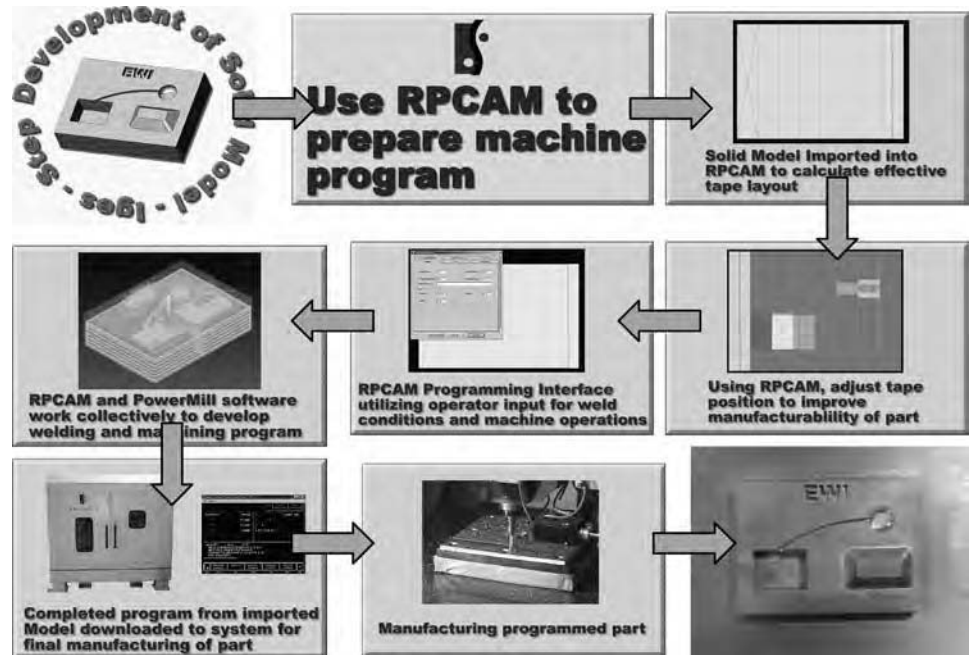


Fig. 4 The ultrasonic additive manufacturing process for producing a solid metal part. Photos 1, 3, 5, 6, and 9 courtesy of Edison Welding Institute; photos 2, 4, 7, and 8 courtesy of Solidica Inc.

- cavities that are designed into the part. The graphical interface allows the operator to shift the tape placement or weld position based on force.
5. Welding conditions, tape dimensions, and machining operations are imported into RPCam.
 6. RPCam and computer-aided manufacturing software (e.g., PowerMILL) interact to split the imported model into individual layers for creating the final welding and machining code.
 7. The finalized tool paths for welding and machining are then converted into G- and M-code commands that are imported into the main system controller for manufacturing of the part.
 8. Manufacturing of the part takes place.
 9. The final part is on the base plate, which is machined away, leaving the completed part.

In practice, the base plate of the material of the part to be fabricated is bolted to the anvil plate, and a “flat pass” milling operation serves to provide a true starting surface for tape layers. A single tape will then be fed under the weld horn and welded to the base plate, with some excess tape at either end of the weld necessary to allow for tape feed and cutting operations. The welding of the tape may comprise one to three steps, depending on the welding system and materials being used. Thus, a first “tack” pass may be used, under light welding parameters, to secure the tape in place. This will be followed by a welding pass, at full weld parameters, to completely weld the tape in place. In most cases, a tack pass incorporates a spot welding operation at the beginning and end to increase tape placement accuracy.

This process will be repeated as tapes are laid side by side across the base plate. Typically, the tapes are slightly overlapped (0.125 mm, or 0.005 in.) to ensure no gaps are present at the joints. The process is repeated for subsequent layers, making sure the joints between layers are staggered, in the manner of laying up bricks of a wall.

Every five to ten layers, a milling operation will be performed that trims off excess tape around the contour of the part, incorporates the desired features in the part, and again trues the top surface to flat for later tape welds.

This sequence of steps is repeated until the final part has been built on the base plate. The plate-part unit is then removed and the base plate machined away, leaving the desired fabricated part.

The sample part shown in CAD and final form in Fig. 4 also brings out the capability of UAM to achieve deep, narrow grooves and extremely sharp, deep corners—features that are challenging to conventional machining processes and often require recourse to supplemental EDM steps.

High-Power UAM Development. The UAM systems operating at 1.5 to 3.0 kW encounter some issues in seeking to bond

advanced materials, such as titanium alloys, stainless steels, some copper alloys, advanced aluminums, and nickel-base alloys. To a significant extent, these issues are related to the need for greater ultrasonic power in the bonding process. As noted in the description of UAM, making the ultrasonic bond depends on being able to shear and plastically deform opposing asperities. With increasing alloy strengths, greater interface shearing forces are required to bring about the necessary interface deformations, which directly require increased ultrasonic power. Likewise, the mass associated with increased tape thicknesses and/or widths requires increased ultrasonic power to be able to drive it in ultrasonic vibrations.

Developments are in progress for achieving greater ultrasonic power for UAM systems (Ref 7). These involve using two ultrasonic transducers, each of 4.5 kW or higher power, driving the ends of the welding horn in a push-pull arrangement that essentially adds the power of the individual units to the process. The ability of these power levels to bond stainless steel, titanium, and higher-strength aluminum alloys has been demonstrated.

Material Properties in UAM

The fundamental feature of UAM is the production of solid metal parts by way of ultrasonically welding together a succession of thin metal tapes or sheets. The metallurgical and mechanical properties of such parts must be determined to assess the range of materials and applications for which the process is suited. This is an active field of inquiry as new material systems are being investigated and modified and new UAM systems are being introduced.

Metallurgical Aspects of UAM Bonding

Metallurgical analysis of the interface between successive layers of tapes is critical to evaluating the nature and extent of UAM bonding, which, in turn, will relate to the mechanical properties of the parts.

By way of example, a metallurgical cross section of a build fabricated from 0.15 mm (0.006 in.) tape and taken from an interior cross section of a simple block build is shown in Fig. 5(b). The demarcation between the individual layers is evident, with some voids of unbonded regions along layer interfaces. To a significant extent, these voids are a result of the texturing on the surface of the weld horn. Thus, as the horn engages the top surface of a tape in making the ultrasonic weld, the horn texture is impressed on the tape surface. When the next layer of tape is laid down, the smooth bottom surface of the new tape is pressed against the textured top surface of the previous tape, resulting in voids at the interface (Ref 9). The welding action will smooth some of the

texture and plastically flow material into some of the void volume. Nevertheless, depending on the material being welded, the horn texture, and the power of the ultrasonic system, some voids may remain.

Metallurgical analysis of the underlying macro- and microstructures at the interface between successive layers of tapes is critical to evaluating the nature and extent of UAM bonding, which, in turn, will relate to the mechanical properties of the parts (Ref 10–16). Mechanical properties have also been related to the quality of bond at the interface between layers (Ref 8, 14). Optical microscopy is used to characterize the degree of bonding. Analysis of images taken with an optical microscope can provide a quantitative measure of the length of bonded regions. This measurement is often referred to as linear weld density (LWD) percentage (ratio of bonded region to length of interface). Certain literature quotes the same measurements in terms of linear void density (LVD), which is represented by $100\% - \text{LWD}$. An example LWD result (Ref 8) is shown in Fig. 5(a).

Thus, the LVD appears to vary across the height of the build (8.5 to 65.8 %). The corresponding optical microscopy image is shown in Fig. 5(b). By repeating this analysis over a large number of builds, it is possible to quantify the quality of the bonds made by the UAM process. Many authors have shown a direct correlation between peel strength of the bonds to the magnitude of LWD (Ref 10–16). In published literature, optimization of UAM process parameters has been driven by the desire to obtain higher LWD across the entire build volume. However, measures of LWD/LVD do not yield any of the critical microstructure information necessary to understand the fundamental bonding mechanisms.

Using a variety of characterization techniques, a number of researchers have accumulated extensive microstructure information at the bond interface (Ref 17–20). The work noted here covers the use of scanning electron microscopy and focused ion beam imaging, first reported by Johnson (Ref 17), and, more recently, the use of electron backscattered diffraction imaging and transmission electron microscopy to investigate the UAM bonding mechanism (Ref 18–20).

Some typical images from multiscale characterization of Al 3003 alloy UAM builds are now considered (Ref 19). The electron microscopy images from bottom, middle, and top of a typical build are shown in Fig. 6(a) to (c). The images from the bottom (Fig. 6a) and middle (Fig. 6b) regions did not show a sharp interface between adjoining tapes, which indicated that a metallurgical solid-state bond had been created. The grains at the interface zone were equiaxed in nature and quite different from that of elongated grains of the original Al 3003-H18 tapes. This indicates that the bond formation is associated with recrystallization. In addition to

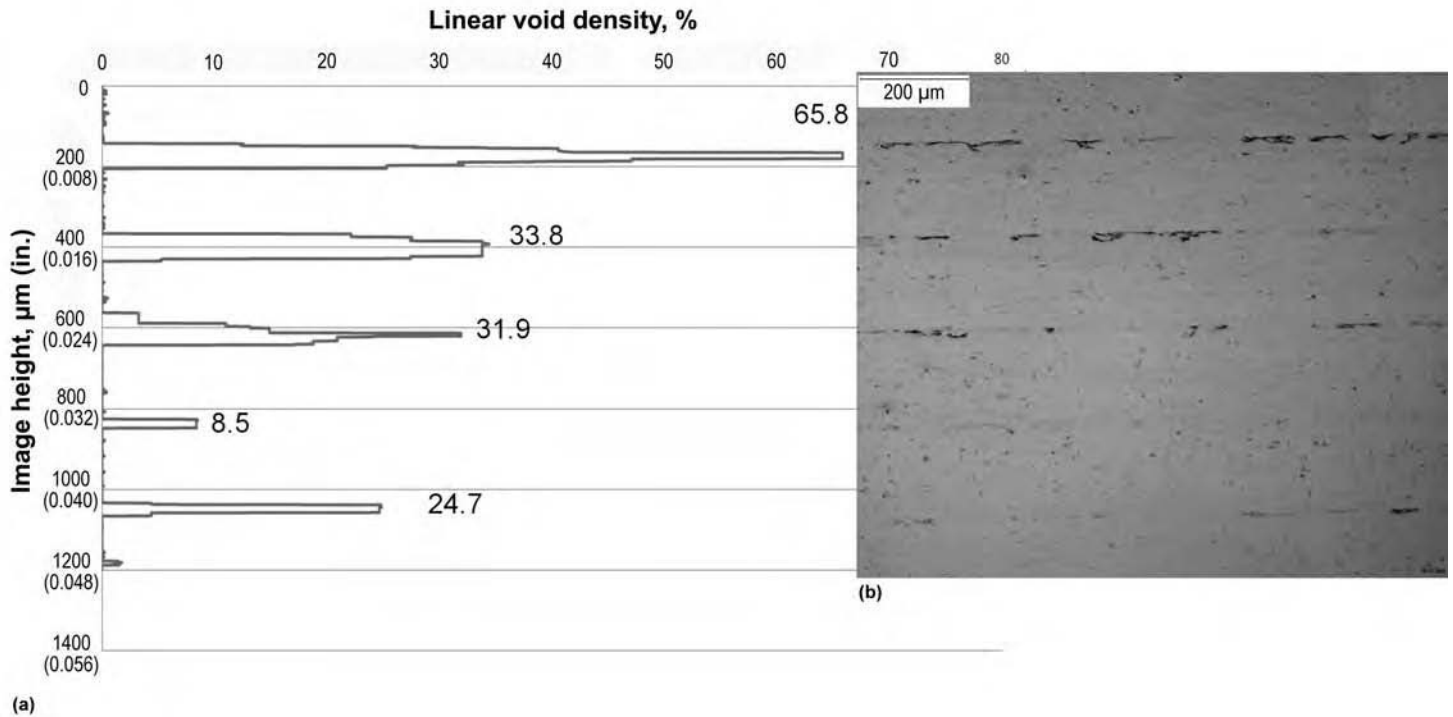


Fig. 5 (a) Plot of linear void density (LVD) versus five interfaces and (b) the corresponding optical image of interface number 5. The LVD point for each interface was taken at the high point, as shown in (a). Note: Linear void density is the inverse of linear weld density. Source: Ref 8

the equiaxed grains, fine Al-Mn-Fe-base intermetallics were observed in the samples along the grain boundaries and within the matrix grains. However, these intermetallics were present in the original Al 3003-H18 tapes and were not a consequence of the UAM process.

The interface microstructure from the top region (Fig. 6c) had certain unique features. The original interface location is identified from the sudden change in the grain structure. The microstructure in the $(n + 1)^{\text{th}}$ tape shows the original pancake structure, which transitions sharply to a coarse, recrystallized grain structure close to the original interface location. The microstructure from the n^{th} layer does not show any pancake structure but rather a more recrystallized structure. A survey of many samples from different regions also showed that the interface regions contained fine recrystallized grains (500 nm, or 20 $\mu\text{in.}$) with relatively low dislocation density and coarse grains (500 nm to 2 μm , or 20 to 80 $\mu\text{in.}$) with relatively high dislocation density, as shown by dark-field microscopy. The original foil, before consolidation, showed pancakelike grains, as expected, from as-rolled material. Dislocations were present, although at a much lower concentration than in the grains along interfaces after UAM processing.

In addition to the bonded region, transmission electron microscopy has been performed at the void regions. Oxide layers are found along the surface of the voids. These layers transition from nearly linear and continuous to

discontinuous and disbursed toward the welded region. It would be expected that intimate contact between the two aluminum regions would yield a stronger bond and increased mechanical strength compared to the region with a continuous oxide scale present.

Based on the aforementioned observations, microstructure evolution at the interface is considered to be the product of recrystallization, which is similar to that of hot working. This hypothesis is in agreement with microstructural observations from copper builds made with very high-power UAM samples (Ref 21).

Mechanical Properties of UAM Builds

The mechanical properties of UAM-fabricated parts and materials govern the range of applications for which the process may be used. A number of mechanical tests have been used to evaluate UAM bonding, including tensile testing, peel tests (Ref 10, 11, 13, 15), lap shear tests (Ref 10), push-pin tests (Ref 22), bulge tests (Ref 23), bend tests (Ref 24, 25), and microhardness and nanohardness tests (Ref 11, 26, 27). In parts with embedded fibers, fiber push-out testing to characterize bonding between the fiber and the matrix has also been reported (Ref 12). Fatigue tests are being developed for small specimen sizes involved in some UAM builds. Given the anisotropic nature of UAM-fabricated materials, in some cases, separate tests may be required for the various axes.

Referring to Fig. 1, it can be seen that anisotropy can arise from the direction of tape lay and welding. The rolling welding horn and the tape are oriented in the x -direction (the y -direction is at right angles to the x -direction in the plane of the plate, while z is perpendicular to the plane), so that the mechanical properties of a plate-type build will vary between the x - y in-plane and z -direction out-of-plane (or transverse) relative to the build plate. By fashioning appropriately dimensioned ASTM-type dog-bone samples, the mechanical properties of a build can be determined.

Thus, using the dog-bone specimen shown in Fig. 7 (middle), testing the transverse tensile strength of Al 3003 UAM builds generally reveals a behavior similar to that of a brittle material, as shown in Fig. 8(a). The specimens exhibit a linear force-displacement relationship prior to a sudden rupture while still within the elastic region (Ref 8). The ultimate tensile strength of transverse tensile specimens has been found to be approximately 15% of the solid parent material (Ref 8). However, scanning electron microscopy revealed that the fracture surfaces show ductile failure with microvoid coalescence. The absence of an appreciable macrolevel ductility in the load-displacement curves is attributable to the voids (or unbonded regions). These observations suggest that UAM does not reduce the inherent ductility of the material (Ref 8).

A lap shear specimen (Fig. 7, left) was used in testing the shear strength of UAM builds. A linear force-displacement relationship was

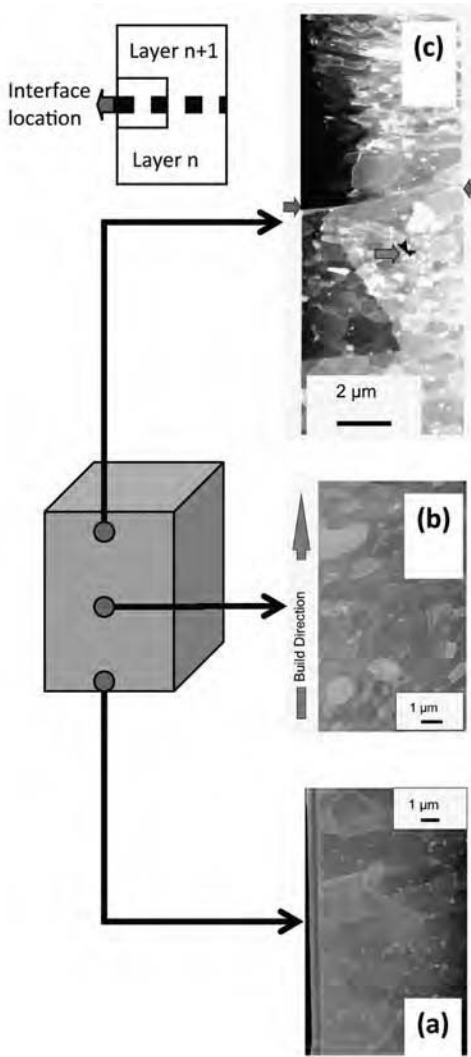


Fig. 6 Transmission electron microscopy (TEM) images. (a) Bright-field TEM image taken from an interface location with apparent good bonding. The interface cannot be determined easily, indicating potential recrystallization across the interface. Small, white Al-Mn-Fe intermetallics can be seen. (b) Another interface location again showing the difficulty in discerning the bond line. (c) A third interface location where the bond line can be determined, as pointed out by two opposing arrows. A third arrow points to a small void that appears to have migrated from the interface into the bulk of the material. Source: Ref 19

observed before sudden failure of the build along a tape interface, as shown in Fig. 8(b), similar to the behavior of the transverse tensile specimens (Ref 8). Ultimate shear strength of UAM builds was found to be approximately 50% of that of the solid parent material (Ref 8). Here again, a ductile failure mode was observed under the scanning electron microscope (Ref 8).

Longitudinal builds (Fig. 7, right) were then tested. As shown in Fig. 8(c), longitudinal test specimens behave as ductile materials during tensile tests. First, an initially linear elastic

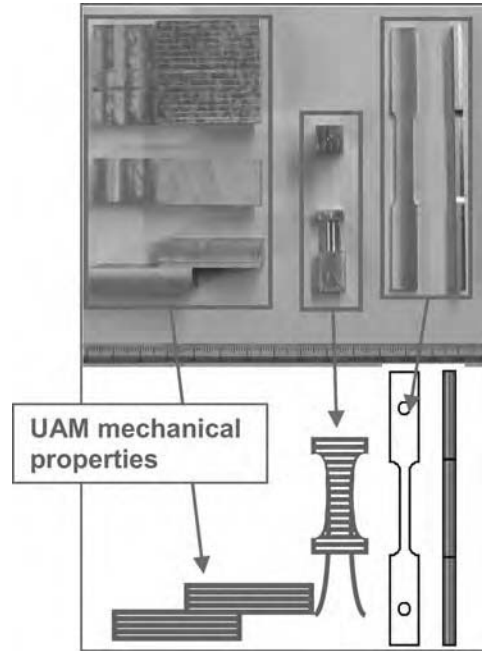


Fig. 7 Ultrasonic additive manufacturing (UAM) mechanical test specimens for shear (left), transverse tensile (middle), and longitudinal tensile (right) testing. Courtesy of The Ohio State University

region is observed, followed by a wide region of plastic deformation. Overall behavior of the longitudinal tensile specimens is similar to the solid parent material. However, the ultimate tensile strength is approximately 20% greater than the parent material, indicating that the foils are strengthened in the longitudinal direction during the UAM process.

It is noted that the aforementioned results were obtained from UAM builds fabricated using the same set of process parameters to bond Al 3003 tapes. By varying the process parameters, the strengths of the build could likely change. Further, the strengths could be different for other tape material.

Peel Testing. This is a method to evaluate how well a layer has bonded to another during UAM. The flap (or peel arm) of the tape extending outside of the weld is used to facilitate peeling of any given layer. A typical peel-testing apparatus (floating roller) (Ref 11, 28) is shown in Fig. 9(a), where the peel arm is loaded under tension to obtain a force-displacement curve, shown in Fig. 9(b). The maximum force encountered during peeling (highest resistance) provides a measure of the bond strength (Ref 11). Sometimes, the energy criterion (area under the force-displacement curve) is also used to characterize the degree of bonding (Ref 29). Depending on the strength of the bond, the force-displacement curves and fracture modes could be different (Ref 10, 13). The maximum peel force is then typically plotted as a function of vibration amplitude, normal force, and sonotrode travel speed to identify the effect of each of these parameters (Ref 10, 11).

In Al 3003 alloy UAM build, a 75% increase in amplitude, for instance, is reported to increase the peel force by approximately 25% (Ref 10). The peel test is also used in conjunction with LWD measurements to characterize bonding (Ref 9).

Peel tests provide a quick way of getting to the process window for UAM of a given material (Ref 9, 11, 13, 15). The test is fast, inexpensive, and requires very little sample preparation. Usually, a build consisting of two to three layers is adequate, compared to approximately 80 layers required for tensile testing. However, peel testing suffers from the disadvantage that it is primarily suited for determining the bonding strength of an adhesive (where peeling actually occurs) rather than the strength of welded joints. In the case of the latter, the tendency is more toward fracture (at the weakest region) than peeling, once good bonding has been achieved. Therefore, in well-bonded interfaces, failure can typically occur outside of the weld region, particularly at the transition between the weld and the peel arm, which is a region of stress concentration. Although such a fracture would signify a high degree of bonding, it may not be easy to quantify. Consequently, all well-bonded conditions may end up showing the same bond strength. Furthermore, the tests can only be comparative in nature, because correlating peel strength (peel force per unit width) to the more standard material strength parameters such as yield/tensile strength may also be difficult. The test can still serve as a rapid qualitative method to discriminate between poor and good bonding. Climbing drum peel test (Ref 30), T-peel test (Ref 31), and fixed-arm peel test (Ref 32) are other variants to the test.

Push-Pin Testing. This test, developed by Zhang, Deceuster, and Li (Ref 22), involves testing a UAM build under a compressive load applied normal to the layers (in the transverse direction). This is based on the premise that the overall strength of a laminated structure depends on the bond strength between individual layers (Ref 22). If the bonding between layers is poor, it can manifest as tensile loading between layers, pulling them apart and causing delamination (Ref 22). Alternatively, with good bonding, the layers may resist delamination and deform collectively until fracture. The test method is shown in Fig. 10(a) and can be performed on the Gleeble (Ref 22). The compressive force on the build layers is applied by means of a push rod that goes through the base plate and the build (Ref 22). The typical force-displacement curve obtained is shown in Fig. 10(b). As with peel testing, the maximum force or the deformation energy is considered to be a measure of the bond quality. Examination of fracture surfaces could also result in a correlation between the area of the bonded regions and LWD (Ref 22). However, unlike in peel or lap shear testing, a comparison of good versus better bonding could be very possible here. The force/energy values can be

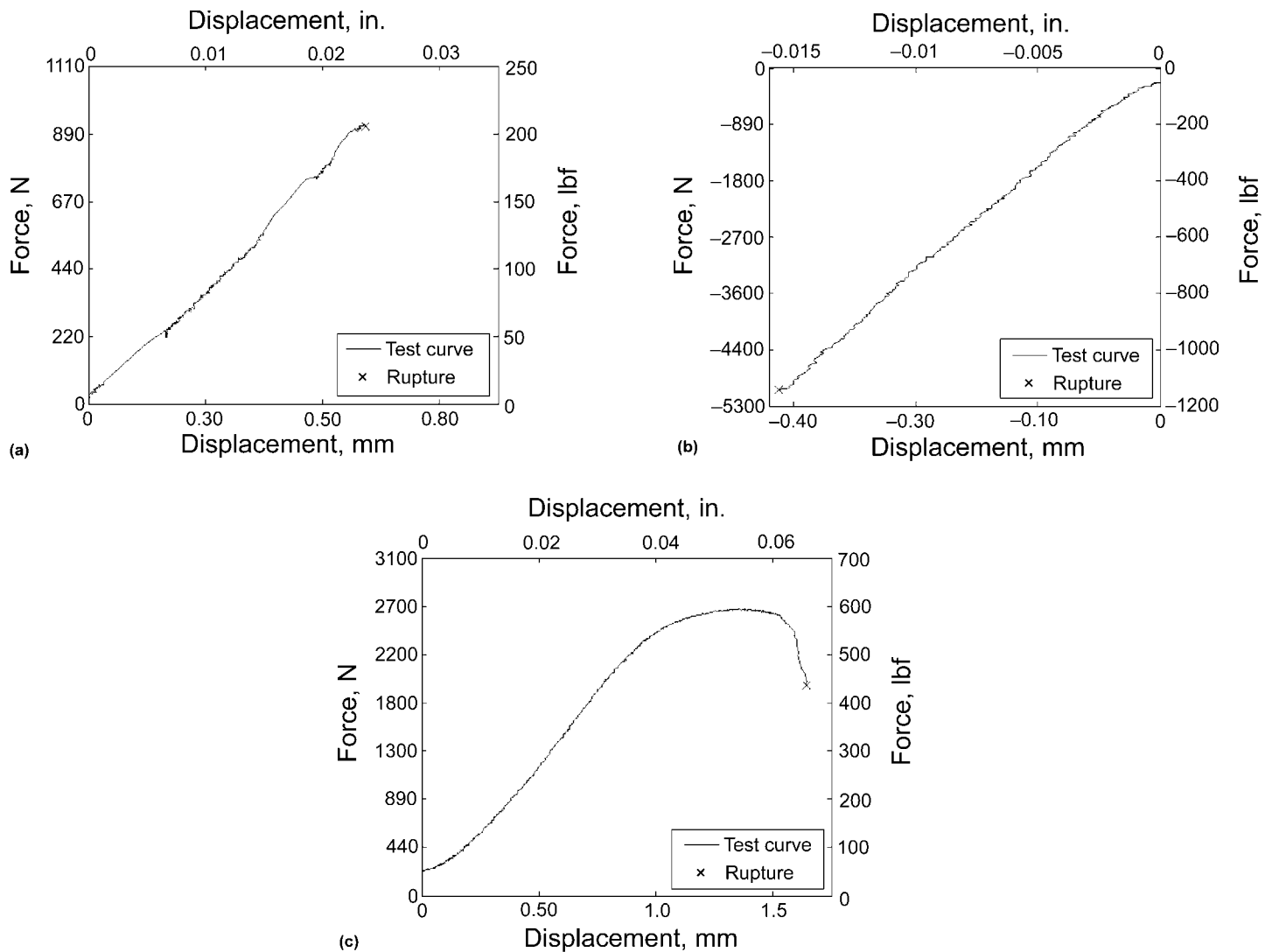


Fig. 8 Ultrasonic additive manufacturing mechanical testing force versus displacement plots for (a) transverse tensile, (b) shear, and (c) longitudinal tensile tests. Courtesy of The Ohio State University

correlated with the process parameters to identify the best processing conditions for a given material. Vibration amplitude has been reported (Ref 22) to have the maximum influence on bond strength. In Al 3003 alloy UAM build, the deformation force was observed to be nearly doubled with a 20% increase in amplitude, indicating much better bonding at higher amplitudes (Ref 22). When similar testing of a solid block of the same material is done, it may be possible to estimate the strength of the part built by UAM relative to a solid block.

Push-pin testing could represent the bulk transverse tensile strength of the build, but with much fewer layers than a regular tensile test. Thus, it is simpler, faster, and cost-effective, allowing for a large number of tests to be performed over a wide processing range. However, the deformation and fracture behavior could

depend on the geometry of the sample. Consequently, for a thicker sample (with a greater number of layers being tested), delamination may occur even in well-bonded structures.

Microhardness/Nanohardness Testing. These tests are done on UAM builds to observe any strain hardening or softening of the original tape material, both at the interfacial region as well as away from it. Depending on the material condition and processing, there could be hardening or softening at the interface (Ref 8, 11, 21). While an increase in microhardness of up to 12% has been reported in aluminum alloys (Ref 8, 11), a 23% decrease in microhardness was observed in copper (Ref 21). A linear correlation between interfacial hardness and bond strength has also been reported (Ref 27). Nanohardness testing close to the SiC fiber embedded in an Al 3003 alloy UAM

build is reported (Ref 27) to show a 46% increase in hardness in comparison to the starting foil.

Impact of High Power on Properties

Preliminary studies in applying higher levels of ultrasonic power have shown excellent promise as the basis for increasing the range of materials and applications for the UAM process. Using a very high-power “test bed” system (the bed had full ultrasonic UAM welding capabilities but did not have CNC machining or automatic tape feed), welds were made in several advanced materials, with results as shown in Fig. 11.

At higher levels of ultrasonic power, which also involve higher tool vibration amplitudes and static forces, it is found that interface voids,

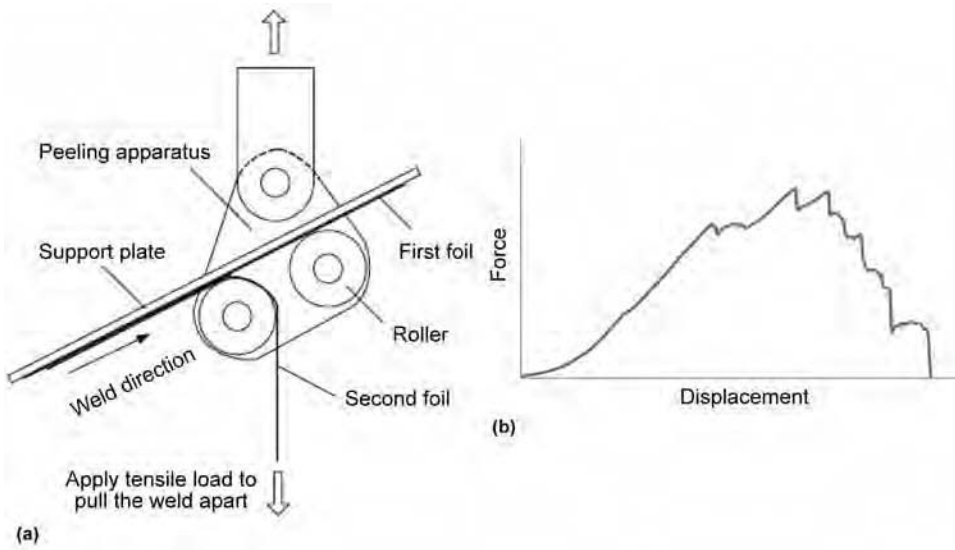


Fig. 9 Peel test applied to ultrasonic additive manufacturing builds. (a) Schematic of floating roller peel test. Source: Ref 10. (b) Typical peel test force-displacement curve

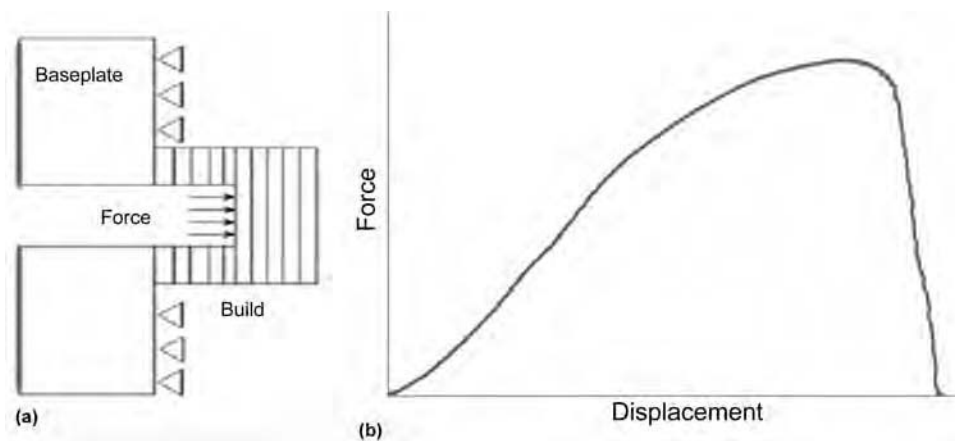


Fig. 10 Push-pin test applied to ultrasonic additive manufacturing. (a) Schematic of push-pin test. (b) Typical push-pin test force-displacement curve. Source: Ref 22

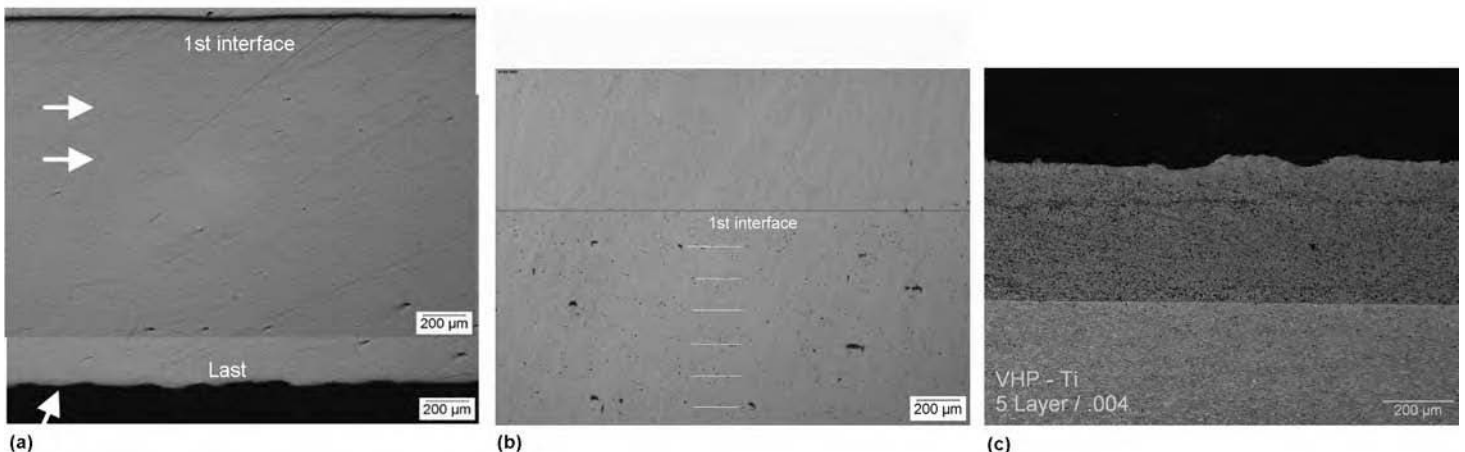


Fig. 11 Bonding of materials with very high-power ultrasonics. (a) Cu 1100, 12 layers of 1.5 mm (0.06 in.) thickness. Image inverted. (b) Al 6061, 1.5 mm (0.06 in.) thickness. Image inverted. (c) Titanium CP-4, 1.0 mm (0.04 in.) thickness. Courtesy of Edison Welding Institute

or any other readily apparent indications of lack of interface bond, are nearly absent, as seen in the examples in Fig. 11.

For example, bonding of Cu 1100 in Fig. 11 (a) shows 12 layers of 1.5 mm (0.06 in.) copper. Bond line interfaces are only faintly discernable at the given level of magnification; thus, the two parallel arrows locate one set of interfaces. (The lower-level shading discontinuity is an artifact of combining two photographic images.) Bonding in Al 6061 is shown in Fig. 11(b). The faint white horizontal lines locate the bond interfaces. While some voids can still be seen, there is a dramatic reduction in their number when compared to earlier results for Al 3003 (Fig. 5). Bonding of 1.0 mm (0.04 in.) thick titanium CP-4 tapes is shown in Fig. 11(c).

Quality Control

The objective, of course, is to produce a UAM-fabricated part or material having the desired level of quality as specified by the end-user service requirements. While these will obviously vary, the quality of the bond between tape layers would be expected to be common to most.

Assuming that a very high-power UAM set of RPCam-based weld process parameters have been developed for fabricating a given part or material, and that these have been validated by metallurgical and mechanical tests such as were described in the previous section, thus arriving at an acceptable quality level for the part/material, then considerations shift to maintaining quality levels while making large numbers of parts or carrying out continuous fabrication of materials.

The following are among those issues to be addressed in arriving at and maintaining UAM fabrication quality:

- *Design*: It is hardly unique to UAM to note that original design of the part will play a key role in its ultimate quality. Much of this will have to do with developing the RPCam program and assuring that the tape layouts are appropriate for the layout of edges, joints, and machined features.
- *System calibrations*: A variety of load cells, motion sensors, and ultrasonic units are integrated into a UAM system. Assuring that calibrations are kept current is critical. This likewise applies to the CNC machining equipment, for which there are several consensus American Society of Mechanical Engineers and International Organization for Standardization specifications.
- *Input materials*: For tapes, maintaining consistent chemistries, heat treat, dimensions, surface texture, and cleanliness specifications is a requirement. For the base plate, maintaining chemistries and heat treats is required. (Because the plate is typically machined to final size, incoming dimensions, texture, and cleanliness are less critical.)
- *Process monitoring*: Monitoring the running conditions of the system (forces, speeds, ultrasonic parameters, tape feeds) is recommended to maintain process consistency. In-process nondestructive evaluation (NDE) methods (e.g., infrared thermography) are not yet available on present UAM systems.
- *Postinspection*: In addition to visual inspections, NDE methods (e.g., ultrasonic inspection) may be used to verify bonding.
- *Tool texture*: In addition to simple visual inspection for evident wear, periodic surface roughness measurements should be made to determine if retexturing or replacement is required. The current practice for evaluating such textures is to conduct a three-dimensional surface microtexture measurement, a noncontact process based on white-light interferometry. Due to the graphical nature of this process, data recorded of the sonotrode in the as-cut condition can then be easily compared to that of a sonotrode having extended service.
- *Other maintenance*: Because it is basically a complex machine tool system, all maintenance procedures appropriate for such systems should be consistently followed.

Safety

The UAM system is basically a computer-controlled, robotic machine tool and must be treated with all of the cautions and safety considerations typically accorded such systems. This includes assuring that appropriate system safety interlocks are in place and fully operational. Allowance must also be made for the heated base plates present on some UAM systems.

ACKNOWLEDGMENTS

The contributions made to this chapter by Matthew Short of Edison Welding Institute and Dr. Suresh Babu, Dr. Sririman Ramanujam, and Dr. Marcelo Dapino of The Ohio State University are gratefully acknowledged.

REFERENCES

1. "Standard Terminology for Additive Manufacturing Technologies," F2792-09e1, ASTM International
2. T. Wohlers, "Wohlers Report—2009," Wohlers Associates, 2009
3. I. Gibson, D.W. Rosen, and B. Stucker, *Additive Manufacturing Technologies*, Springer, 2010
4. D.R. White, "Object Consolidation Employing Friction Joining," U.S. Patent 6,445,629, Oct 1, 2002
5. J. Devine, Ultrasonic Welding, *Welding, Brazing, and Soldering*, Vol 6, *ASM Handbook*, ASM International, 1993
6. K.F. Graff (Chapter Chair), Ultrasonic Welding, Chap. 8, *Welding Processes*, Vol 3, *AWS Welding Handbook*, 9th ed., The American Welding Society, 2007, p 263–302
7. M. Norfolk, "Development of a Very High Power Ultrasonic Additive Manufacturing System," Rapid/3-D Imaging 2010 Conference, May 18–20, 2010 (Anaheim, CA)
8. D.E. Schick, R.M. Hahnen, R. Dehoff, P. Collins, S.S. Babu, M.J. Dapino, and J.C. Lippold, Microstructural Characterization of Binding Interfaces in Aluminum 3003 Blocks Fabricated by Ultrasonic Additive Manufacturing, *Weld. J.*, Vol 89 (No. 5), 2010, p 105s–115s
9. D. Li and R. Soar, Influence of Sonotrode Texture on the Performance of Ultrasonic Consolidation Machine and the Interfacial Bond Strength, *J. Mater. Proc. Technol.*, Vol 209, 2009, p 1627–1634
10. C. Kong, R. Soar, and P. Dickens, Optimum Process Parameters for Ultrasonic Consolidation of 3003 Aluminum, *J. Mater. Proc. Technol.*, Vol 146, 2004, p 181–187
11. C. Kong, R. Soar, and P. Dickens, A Model for Weld Strength in Ultrasonically Consolidated Components, *J. Mech. Eng. Sci.*, Vol 219, 2004, p 83–91
12. Y. Yang, G.D. Janaki Ram, and B.E. Stucker, An Experimental Determination of Optimum Processing Parameters for Al/SiC Metal Matrix Composites Made Using Ultrasonic Consolidation, *Am. Soc. Mech. Eng.*, Vol 129, 2007, p 538–549
13. C. Kong, R. Soar, and P. Dickens, Characterization of Aluminum Alloy 6061 for the Ultrasonic Consolidation Process, *Mater. Sci. Eng. A*, Vol 363, 2003, p 99–106
14. J.D. Janaki Ram, Y. Yang, and B.E. Stucker, Effect of Process Parameters on Bond Formation during Ultrasonic Consolidation of Aluminum Alloy 3003, *J. Manuf. Syst.*, Vol 25, 2006, p 221–238
15. J. George and B.E. Stucker, Fabrication of Lightweight Structural Panels Through Ultrasonic Consolidation, *Virtual Phys. Prototyp.*, Vol 1, 2006, p 227–241
16. G.D. Janaki Ram, C. Robinson, Y. Yang, and B.E. Stucker, Use of Ultrasonic Consolidation for Fabrication of Multi-Material Structures, *Rapid Prototyp. J.*, Vol 13, 2007, p 226–235
17. K. Johnson, "Interlaminar Subgrain Refinement in Ultrasonic Consolidation," Ph.D. thesis, Loughborough University, Loughborough, U.K., 2008
18. B.L. Adams, C. Nylander, B. Aydelotte, S. Ahmadi, C. Landon, B.E. Stucker, and G.D. Janaki Ram, Accessing the Elastic-Plastic Properties Closure by Rotation and Lamination, *J. Acta Mater.*, Vol 56, 2008, p 128–139
19. R. Dehoff and S.S. Babu, Characterization of Interfacial Microstructures in 3003 Aluminum Alloy Blocks Fabricated by Ultrasonic Additive Manufacturing, *Acta Mater.*, Vol 58 (No. 13), 2010, p 4305–4315
20. E. Mariani and E. Ghassemieh, Microstructure Evolution of 6061 O Al Alloy during Ultrasonic Consolidation: An Insight from Electron Backscatter Diffraction, *Acta Mater.*, Vol 58 (No. 7), 2010, p 2492–2503
21. S.M. Ramanujam, S.S. Babu, and M. Short, Bonding Characteristics during Very High Power Ultrasonic Additive Manufacturing of Copper, *Scr. Mater.*, Vol 62, 2010, p 560–563
22. C. Zhang, A. Deceuster, and L. Li, A Method for Bond Strength Evaluation for Laminated Structures with Applications to Ultrasonic Consolidation, *J. Mater. Eng. Perform.*, 2009
23. I. Kaya, O.N. Cora, and M. Koc, Mechanical Behavior of UAM-Fabricated Al-Ti LMC Blanks, *Proceedings of the 2009 Ultrasonic Additive Manufacturing Symposium*, Oct 2009 (Columbus, OH)
24. A. Saadet and B. Semih, Bond Strength of Three Porcelains to Two Forms of Titanium Using Two Firing Atmospheres, *J. Prosth. Dentist.*, Vol 84, 2000, p 567–574
25. M. Kiyotaka, S. Noritoshi, K. Masayuki, and O. Kenichi, Nickel Monoaluminide Coating on Ultralow-Carbon Steel by Reactive Sintering, *Metall. Mater. Trans. A*, Vol 30, 1999, p 1605–1612
26. C. Doumanidis and Y. Gao, Mechanical Modeling of Ultrasonic Welding, *Weld. J.*, 2004, p 140S–146S
27. D. Li and R.C. Soar, Plastic Flow and Work Hardening of Al Alloy Matrices during Ultrasonic Consolidation Fiber Embedding Process, *Mater. Sci. Eng. A*, Vol 498, 2008, p 421–429

28. "Standard Test Method for Floating Roller Peel Resistance of Adhesives," D3167-03a, ASTM International, 2004
29. A.T. Nettles, E.D. Gregory, and J.R. Jackson, Using the Climbing Drum Peel Test to Obtain a GIC Value for Core/Face Sheet Bonds, *J. Comp. Mater.*, Vol 41, 2007, p 2863–2876
30. "Standard Test Method for Climbing Drum Peel for Adhesives," D1781-98, ASTM International
31. "Standard Test Method for Peel Resistance of Adhesives (T-Peel Test)," D1876-08, ASTM International
32. L.F. Kawashita, A.J. Kinloch, D.R. Moore, and J.G. Williams, The Influence of Bond Line Thickness and Peel Arm Thickness on Adhesive Fracture Toughness of Rubber Toughened Epoxy-Aluminium Alloy Laminates, *Int. J. Adhes. Adhes.*, Vol 28, 2008, p 199–210

Fundamentals of Weld Modeling

Introduction to Integrated Weld Modeling	745	Modeling of Metallurgical Microstructure Evolution	
Process Modeling	746	in Fusion Welding	797
Microstructure Modeling	748	The Internal State Variable Approach	797
Performance Modeling	754	Isokinetic Microstructure Models	798
Access and Delivery of Integrated Weld Process Models	756	Complex Microstructure Models Describing the Evolution of a	
Use of Optimization Methodologies	758	Particle Size Distribution	807
Concluding Remarks	759	Microstructure Modeling in the Context of Engineering	
		Design	813
		Acknowledgments	817
Modeling of Heat and Mass Transfer in Fusion Welding	766	Numerical Aspects of Modeling Welds	819
Important Considerations	766	Modeling of Welds	819
Mathematical Description	767	Geometry of Weld Models	820
Application to Fusion Welding Processes	775	Energy Equation and Heat Transfer	820
Mass Transfer in Weld Pool	780	Microstructure Evolution	825
Reliability of Models	785	Thermal Stress Analysis of Welds	826
Future Models	786	Fluid Flow in the Weld Pool	827
		Acknowledgment	828
Modeling of Thermal-Electrical-Mechanical Coupling in		Modeling of Thermomechanical Phenomena in Fusion Welding	830
Fusion Welding	789	Basic Principles and Heat Effects of Welding	830
Thermal Analysis	789	Required Material Properties and Measurement Techniques	831
Electrical Analysis	790	Analysis of Material Properties Input Data	832
Discretization of Sheet-Electrode Geometry for Numerical		Experimental Data for Validation of Thermal and Mechanical	
Modeling	790	Results	834
In-Process Growth of Electrode-Sheet Contact	790	Workflow for Thermomechanical Welding Simulation	835
Incorporation of Latent Heat	791		
Estimation of Contact Resistivity	791		
Results and Discussions	792		

Introduction to Integrated Weld Modeling*

Sudarsanam Suresh Babu, The Ohio State University

THE SCOPE of this article is to provide an overview of integrated weld modeling. It is not intended to provide a comprehensive review of integrated weld modeling activities in the literature but introduces methodology and relevant resources that can be accessed by the reader for further development, evaluation, and deployment.

Integrated weld modeling is an important activity that crosscuts many industries. In early 2000, the American Welding Society, Department of Energy, Edison Welding Institute, and industrial members from the heavy industry, aerospace, petroleum/energy, and automotive industries developed a research roadmap for the welding industry (Ref 1). The strategic goals for the welding industry by 2020 were identified to be the following:

- Increase the uses of welding by 25%, decrease the cost, and increase the productivity
- Enhance the process technology that allows for the use of welding across all manufacturing sectors
- Develop new welding technology along with new materials so that it can be used for all applications
- Assure that welding can be part of the six-sigma quality environment
- Increase the knowledge base of people employed at all levels of the welding industry
- Reduce energy use by 50% through productivity improvements

Although welding itself does not consume extensive energy, welding does play a critical role in the development and deployment of the materials for energy exploration, transfer, conversion, efficiency, and storage. The roadmap also identified that the engineering solutions for joining materials are not unique and do differ depending on the geometry, materials, and

applications. Due to this complexity of the problem, the development of joining technology for a given material is associated with extensive experimental trial-and-error optimization. To minimize this experimental approach, an integrated computational modeling was suggested as a solution (Fig. 1).

This leads to a fundamental question: Is it possible to develop physics-based computational models to describe the behavior of existing and

emerging materials subjected to joining processes? A review of the literature shows that the development of physics-based models is indeed challenging due to the complex interaction between physical processes during welding. Some of these physical processes include heat and mass transfer, phase transformations, electromagnetic phenomena, plastic strain, and reactions with the environment during welding/joining. Researchers, including Ashby (Ref 2),

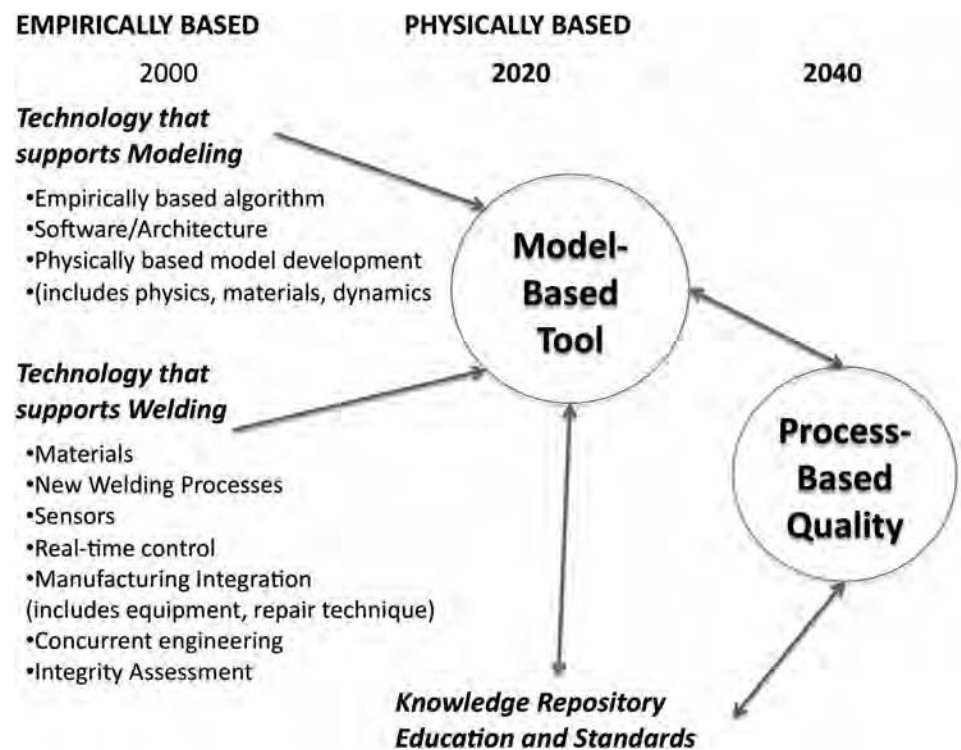


Fig. 1 Suggested roadmap for the development of a model-based tool in the year 2020 as a way of ensuring process-based quality by the year 2040

* Reprinted from Babu, S.S., Introduction to Integrated Weld Modeling, *Metals Process Simulation*, Vol 22B, *ASM Handbook*, ASM International, 2010, p 411-431.

Bhadeshia (Ref 3), Cerjak (Ref 4), David (Ref 5), DebRoy (Ref 6), Eagar (Ref 7), Easterling (Ref 8), Goldak (Ref 9), Grong (Ref 10), Kirkaldy (Ref 11), Koseki (Ref 12), Kou (Ref 13), Leblond (Ref 14), Matsuda (Ref 15), Rappaz (Ref 16), Szekely (Ref 17), Vitek (Ref 18), Yurioka (Ref 19), and Zacharia (Ref 20), developed a framework for linking thermo-mechanical histories to microstructure development and mechanical heterogeneity in welds. These developments can be summarized in the form of a schematic diagram (Ref 11) published by Kirkaldy (Fig. 2). According to this diagram, by integrating individual sub-models for heat, mechanical, and material models, one can predict the overall performance

of welded structures. The approach starts with a heat-transfer model that will simulate temperature distributions in three dimensions [$T = f(x, y, z, \text{time})$] as a function of process parameters and time. Thermal cycle data will be used by material models to predict the microstructure evolution and its impact on transient mechanical (σ - ϵ relations) properties. The transient changes in temperature and mechanical properties will be fed into a finite-element structural model to predict plastic strain distribution. This information allows for the prediction of final properties, residual stress, and distortion in a complex welded geometry. This interdisciplinary approach may appear simple; however, it

requires collaboration between experts in metallurgy, finite-element analysis, welding process, and computer science (Ref 21, 22). To a limited extent, this vision has become a reality by pioneering work in many organizations and commercial software companies (Ref 23–27).

It is noteworthy that the scope of this article is not to provide a comprehensive review of integrated weld modeling activities in the literature. It is designed to provide an overview of the methodology and relevant resources that can be accessed by the reader for further development, evaluation, and deployment. The reader is also referred to other articles within this Volume that describe modeling of inertia welding, diffusion bonding, and the additive manufacturing process. The reader is also referred to some of the series of conference proceedings titled *Mathematical Modeling of Weld Phenomena* (Ref 4, 28–34) as well as *Trends in Welding Research* conference proceedings published periodically by ASM International (Ref 35, 36). These conference proceedings provide a detailed progression of integrated weld modeling and its capability for a wide range of joining processes. In addition, the reader is also referred to three classic text-books related to modeling of welding processes (Ref 37–39). This article discusses some of the salient features of each subprocess model that is indicated as part of the integrated weld modeling shown in Fig. 2. Most of the materials presented in this review have been adopted from Ref 40.

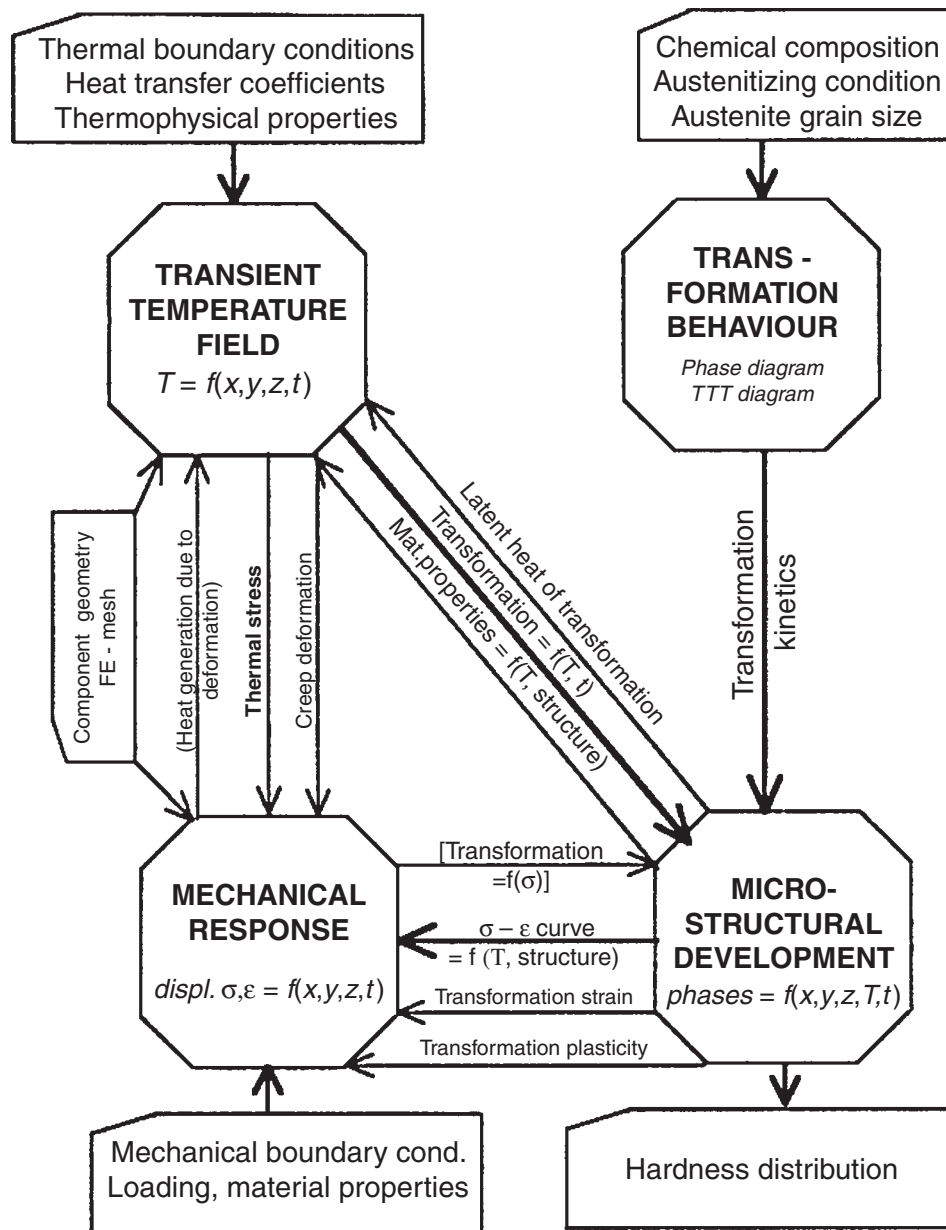


Fig. 2 Overview of integrated welding modeling methodology proposed by Kirkaldy (Ref 11) shows the importance of predicting transformation behavior and microstructural development as well as thermal and mechanical behavior

Process Modeling

The goal of process modeling is to predict weld pool shape, thermal cycles, and fluid flow conditions under transient (coordinate system fixed to the part) or steady-state (coordinate system moving with the welding heat source) conditions. This section discusses the fundamentals of the underlying physics and the methodologies to solve the same.

Underlying Physics and Methodologies

Modeling of Heat Transfer during Welding. Heat transfer in welding can be represented by equations of heat conduction in solids. For example, the spatial variation of the heating or cooling rate in a Cartesian coordinate can be related to the second derivative of the temperature gradients in x -, y -, and z -directions (Ref 39):

$$\frac{\partial T}{\partial t} = \frac{\lambda}{\rho c} \left[\frac{\partial^2 T}{\partial x^2} + \frac{\partial^2 T}{\partial y^2} + \frac{\partial^2 T}{\partial z^2} \right] = a \left[\frac{\partial^2 T}{\partial x^2} + \frac{\partial^2 T}{\partial y^2} + \frac{\partial^2 T}{\partial z^2} \right] \tag{Eq 1}$$

where T is temperature, t is time, λ is thermal conductivity, ρ is density, c is specific heat capacity, and a is the thermal diffusivity of the material being welded. With boundary

conditions imposed by the welding. Eq 1 can be solved for both transient and steady-state conditions of welding. A famous solution of the generic equation for steady-state distribution of temperature in a plate during arc welding was given by Rosenthal (Ref 41) as:

$$T\{x, R\} = T_0 + \frac{\eta VI}{2\pi\lambda} \left(\frac{1}{R}\right) \exp\left\{-\frac{v}{2a}(R+x)\right\}; R = \sqrt{x^2 + y^2 + z^2} \quad (\text{Eq 2})$$

where $T\{x, R\}$ is the temperature as a function of the radial distance (R) and distance (x) along the welding centerline, T_0 is the preheat or interpass temperature, V is the arc voltage, I is the welding current, v is the welding speed, a is the thermal diffusivity, and η is the arc efficiency. This solution is often referred as the Rosenthal equation and has been extensively used for obtaining approximate temperature isotherms during welding of plate as a function of process parameters. For example, Eq 2 was used to calculate the steady-state temperature distributions on a steel plate surface for two different welding speeds. The calculations (Fig. 3) show the formation of a teardrop-shaped weld pool with an increase in welding speed. The aforementioned distribution also can be used to calculate the heating and cooling rate. Equation 2 assumes a point heat source, which is not strictly applicable to arc welding heat sources. Modification of the previous equations for distributed heat sources has been attempted by many researchers. A review of the same can be seen in the book by Grong (Ref 39). In addition, this book also provides analytical solutions for other steady-state and transient welding cases.

Although analytical solutions provide a faster estimation, these solutions often ignore boundary conditions imposed by the geometries of a realistic welded structure. To address this limitation, finite-difference and finite-element formulations (Ref 42) have been developed. These formulations allow for both steady-state

and transient solutions (Ref 37). However, one of the biggest challenges in these formulations is to describe the heat flux into the weld pool. The extent and the distributions of heat flux determine the shape of the weld pool, peak temperature, and heating and cooling rates (Ref 43, 44). This challenge has been elegantly addressed by researchers from Goldak's group to distribute the power density within front and rear quadrants of the weld area. This methodology is schematically explained in Fig. 4. The power density distribution in the front quadrant is given by Eq 3:

$$q\{x, y, z, t\} = \frac{6\sqrt{3}f_f Q}{abc\pi\sqrt{\pi}} \exp\left\{\frac{-3x^2}{a^2}\right\} \exp\left\{\frac{-3y^2}{b^2}\right\} \exp\left\{\frac{-3[z + v(\tau - t)]^2}{c^2}\right\}; \text{front} \quad (\text{Eq 3})$$

$$q\{x, y, z, t\} = \frac{6\sqrt{3}f_r Q}{abc\pi\sqrt{\pi}} \exp\left\{\frac{-3x^2}{a^2}\right\} \exp\left\{\frac{-3y^2}{b^2}\right\} \exp\left\{\frac{-3[z + v(\tau - t)]^2}{c^2}\right\}; \text{rear} \quad (\text{Eq 4})$$

where Q is the energy input rate (in watts); the parameters a , b , and c are the dimensions that describe the ellipsoidal shape in x -, y -, and z -coordinates, respectively; τ is the lag factor; t is time, and f_f and f_r are the fractions of heat source deposited in the front and rear quadrant and are related to each other by Eq 5:

$$f_f + f_r = 1 \quad (\text{Eq 5})$$

By changing the dimensions of the a , b , c , f_f , and f_r values, it is possible to match most of the complex weld pool shapes that are observed in fusion welds. It is important to note that

these parameters must be obtained by the optimization procedure. For example, Kelly (Ref 45) must consider more than 2000 sets of such parameters to match the experimental weld pool size. In such calibration studies, it is often impossible to match all the experimental parameters, such as weld pool width, depth, curvature, and spatial variation of thermal cycles. Improvements to the aforementioned double ellipsoidal model are being pursued by many researchers (Ref 45). In this regard, it is important to understand fundamental reasons for such variations of the weld pool shape by using coupled heat- and mass-transfer models.

When the weld pool flux is calibrated using the double-ellipsoidal models, it is easier to describe steady and transient thermal cycles for complex welding conditions. An example of transient thermal simulation of laser cladding to build a nickel-base superalloy structure on a substrate is shown in Fig. 5 (Ref 46). The simulations were performed with

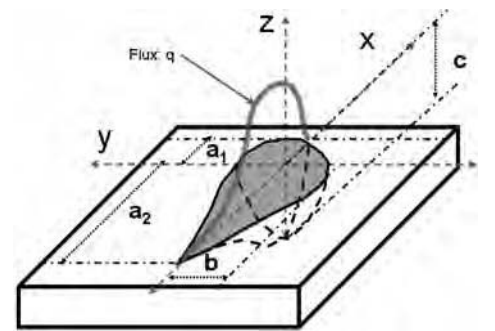


Fig. 4 Schematic of parameters used in describing the heat flux during welding. The reader is referred to Eq 3 and 4 in the text

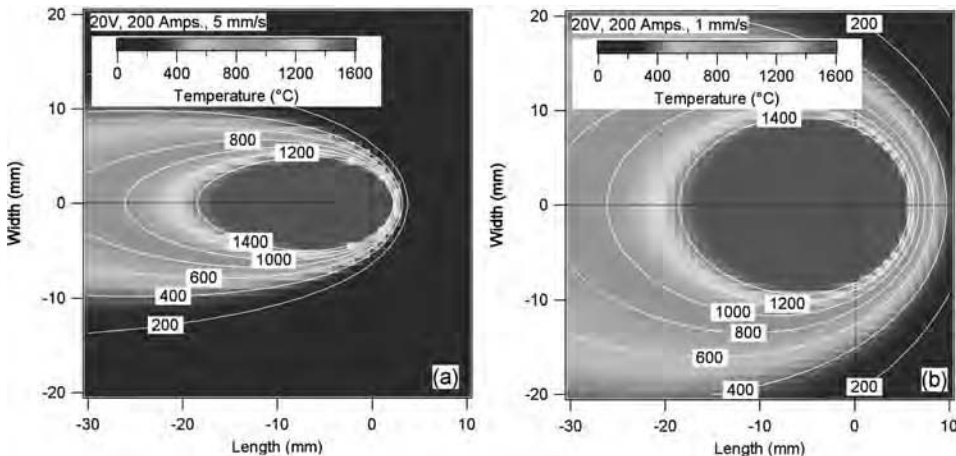


Fig. 3 Calculated temperature isotherms during welding of low-alloy steels are shown in image and contour plots. The plots demonstrate the change of weld pool shape with an increase in welding speed from 1 to 5 mm/s

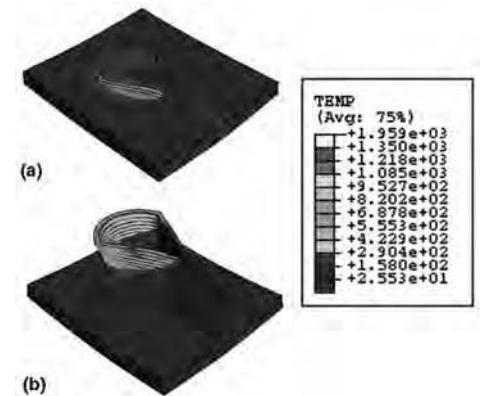


Fig. 5 Simulation of temperature transients while building a complex shape through the laser cladding process. (a) Thermal gradients are large at the early stage of cladding due to three-dimensional heat-transfer conditions. (b) With the buildup of sufficient layers, the heat-transfer condition changes to two dimensional. As a result, the thermal gradient is shallower. Such changes will affect the ensuing solidification and solid-state microstructure

commercial finite-element analysis software (ABAQUS) and user-defined subroutines. (Reference to any commercial software in this article does not imply endorsement of this software by the author or ASM International. Readers are requested to independently evaluate software for their own applications.) During the early stages of cladding, thermal simulations showed a small molten pool (Fig. 5a) due to the three-dimensional heat conduction mode. With the progress of the buildup, the heat conduction mode changes to two dimensional. As a result, the molten pool size increases, and there is remelting of the previous layers. The spatial and temporal variations of thermal cycles also change. These simulations demonstrated that for efficient laser cladding of the complex shapes shown in Fig. 5, the heat input must be changed based on local heat-transfer conditions. By coupling these thermal models with optimization software, it is possible to a priori design the path and heat input during laser cladding. The reader is referred to the article "Modeling of Laser-Additive Manufacturing Processes" in this Volume for more details.

Fluid Flow Modeling. As mentioned earlier, a complex weld pool shape develops due to heat transfer through conduction in the liquid and solid as well as convective transfer by way of electro-magnetic force, buoyancy forces, and shear stresses due to the spatial variation of surface tension with temperature. The effect of fluid flow on weld pool shape was initiated by the pioneering work of Kou (Ref 13), Zacharia (Ref 20), and DebRoy (Ref 6) and their collaborators. The underlying methodology relies on solving equations of energy and momentum conservation as well as continuity conditions. The first governing equation is the conservation of momentum:

$$\rho \nabla(V \cdot V) = -\nabla P + \mu \nabla(\nabla V) + (S_V - \rho \nabla \cdot (U_s V)) \quad (\text{Eq 6})$$

where ρ is density; V is the fluid flow velocity vector in the x -, y -, and z -directions, which is represented by u , v , and w ; respectively; U_s is the welding velocity; P is the effective pressure on the welding pool; and S_V is the source term that takes into account the buoyancy factor (S_b), Marangoni shear stress (τ_{mar}), and electro-magnetic force (Ref 13).

The buoyancy term (S_b) is described by $\rho g \beta (T - T_{\text{ref}})$, in which β is the thermal expansion coefficient at a temperature, T , with reference to a reference temperature (T_{ref}). The shear stress (τ) is given by $f_1 (d\gamma/dT) \nabla T$. In this relation, the parameter $d\gamma/dT$ is the variation of surface tension with temperature. This can take either positive or negative value and is shown to have large influence in the weld pool fluid flow conditions. The other parameter, f_1 , takes care of the reduction in shear stress near the mushy (mixture of liquid and solid) regions.

The second governing equation deals with the conservation of energy:

$$\rho \nabla(V \cdot h) = \nabla \cdot \left(\frac{k}{C_p} \nabla h \right) + S_1 + S_h - \rho \nabla \cdot (U_s h) \quad (\text{Eq 7})$$

where the total enthalpy of the material, h , is related to the sum of sensible heat and latent heat content, which takes into account the phase change (e.g., solid to liquid and liquid to solid); C_p is the specific heat; k is the thermal conductivity; S_h is a source term that takes into account the heat input from the welding source and convective and radiation heat loss; and S_1 is a source term that accounts for the latent heat of melting and the convective transport of latent heat. This term also takes care of the phase change during solidification. The aforementioned governing equations can be solved by numerical methods to calculate the spatial variation of fluid flow velocity (u , v , w) and temperature.

In the early 1990s, the previously mentioned methodologies were used on simple butt welds. In addition, the sensitivity of these calculations to the magnitudes of thermophysical properties was documented (Ref 47). Recently, the aforementioned methodology has been extended to fillet welds using coordinate transformation methods (Ref 48). The methodology to transform the fillet weld geometry in a real x , y , and z Cartesian coordinate system to a computational domain is shown in Fig. 6(a). After this coordinate transformation, the governing Eq 6 and 7 are solved in this domain. A typical result from such calculations is shown in Fig. 6(b). The plot shows the ability of fluid flow calculations to very effectively simulate the curvature of the welds as well as the penetration of the weld pool into the base materials. Comparisons of the calculated weld pool shapes to experimental weld shapes (Ref 49) are shown in Fig. 6(c). This example shows the predictive power of computational heat- and mass-transfer models. It is important to note that the change in weld pool shape shown in Fig. 6(c) also changes the spatial variation of cooling rates. As a result, the predictions of cooling rates are expected to be more accurate with the use of heat and fluid flow models. The fidelity of such calculations on the sensitivity of steel weld metal microstructure was demonstrated by Deb-Roy and his collaborators (Ref 50, 51).

Microstructure Modeling

The goal of microstructure modeling is to predict phase fractions as well as grain size in the heat-affected zone (HAZ) and weld metal region as a function of alloy composition and thermal cycles. Because thermal cycles are predicted by the process models described earlier, in this section, methods to predict the microstructures in the HAZ and weld metal are presented. The reader is also referred to a classic

textbook by Grong for in-depth treatment of this subject (Ref 10). In this section, the pioneering work done to predict the HAZ and weld metal microstructure in the early 1980s and 1990s is presented first. Later, the application of computational thermodynamic and kinetic models is also presented.

Prediction of HAZ Microstructure

Methods for predicting HAZ properties range from simple equations using the base material or weld metal chemistry to complex models that take many factors into account, including chemistry, initial grain size, heat input, and cooling rate. The overall goals and approaches are summarized schematically in Fig. 7. The approaches can be broadly classified into two main themes. In the first approach, the microstructure is not predicted explicitly; rather, the input parameters, such as base metal composition, microstructure, and welding process parameters, are related to one or more HAZ properties. In the second approach, the input parameters are used to calculate the HAZ microstructure and then are correlated with different properties. The historical development of these approaches is briefly discussed and is adopted from Ref 52.

First-generation approaches involve simple correlations between the steel composition and various properties, such as hardness, tensile strength, and cracking tendency. All of the formulas have a form of carbon equivalence that ignores the kinetics and does not consider the microstructure evolution explicitly (Ref 53). The second-generation methods (developed between the 1980s and the 1990s) build on the carbon equivalence formulas to consider the intricacies due to the peak temperature, initial precipitate type, cooling rates, and microstructure evolution. Yurioka et al. (Ref 54) have developed a carbon equivalent number (CEN):

$$\text{CEN} = C + A(C) \left(\frac{\text{Si}}{24} + \frac{\text{Mn}}{6} + \frac{\text{Cu}}{15} + \frac{\text{Ni}}{20} + \frac{\text{Cr} + \text{Mo} + \text{Nb} + \text{V}}{5} + 5B \right) \quad (\text{Eq 8})$$

where $A(C) = 0.75 + 0.25 \tan h \{20(C - 0.12)\}$.

The third-generation methods (developed between 1990 and 2000) started to focus on evaluating the HAZ microstructure with detailed thermodynamics and kinetics, because thermodynamic and kinetic models are generic and allowed for extrapolation to a wide range of steels. However, relating the microstructure to properties still relied on empirical correlations. Ion et al. (Ref 55) used a kinetic approach to predict the hardness and microstructure of weld HAZs. Their approach uses a modification of the Rosenthal equations (Ref 41) to provide a circular disc heat source rather than a point source. The hardness prediction is based on estimating the volume fractions of microstructural constituents (martensite, bainite,

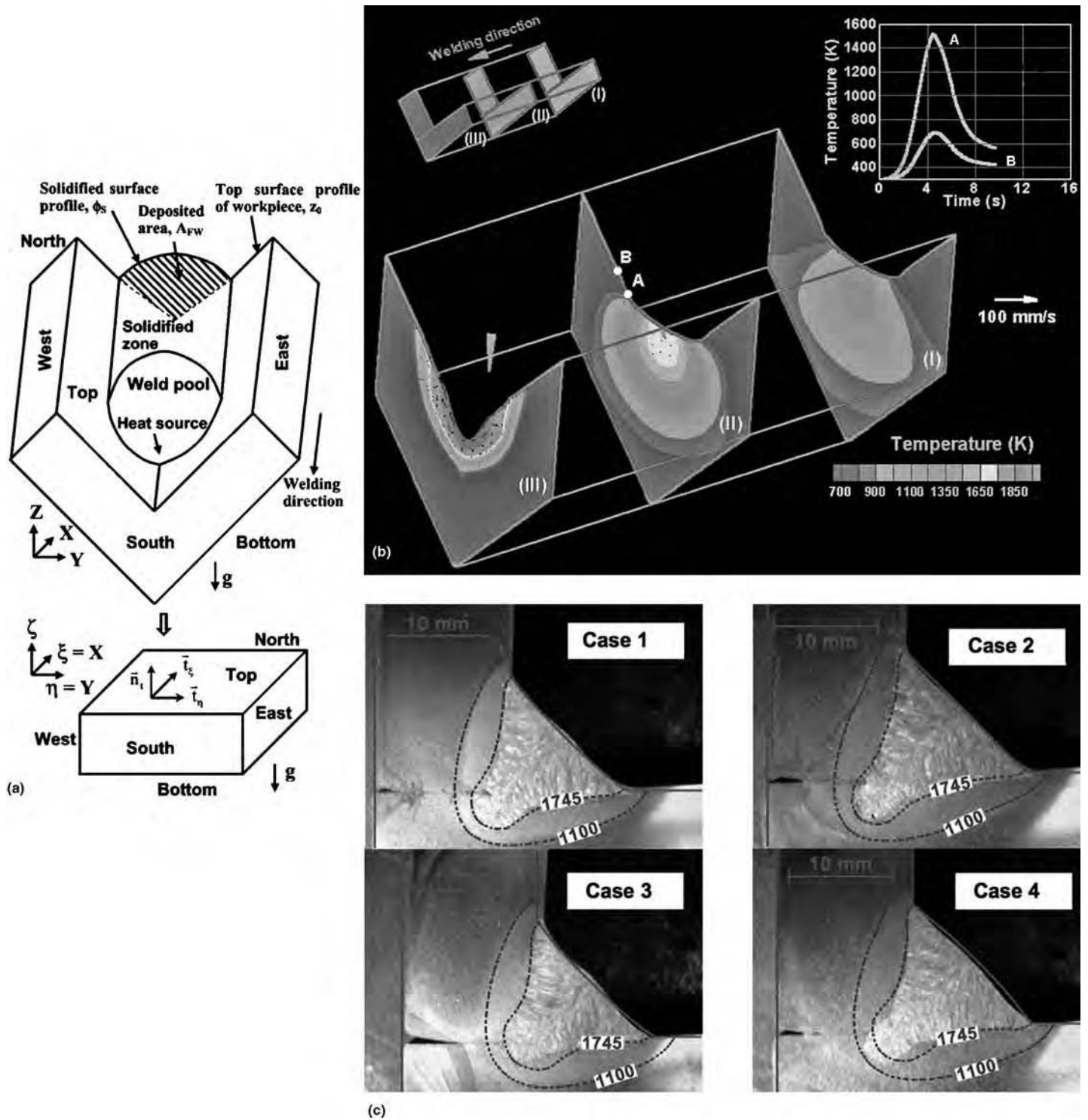


Fig. 6 (a) Technique to perform computational heat- and mass-transfer calculations for fillet welds using the coordinate transformation algorithm. (b) Typical result of such simulation shows the weld pool curvature as well as transients of temperature distributions. (c) Comparisons of predicted shape and size of the weld pool and the heat-affected zone for various welding process conditions show good agreement. Note the ability of these calculations to predict a change in curvature of the weld pool as one moves from top cap to the root of the weld. Such curvatures cannot be predicted without considering the fluid flow effects

ferrite, and pearlite) and using the rule of mixtures to approximate the hardness. The model takes into account many variables, including heat flow, austenite grain growth, precipitate dissolution and/or coarsening, and chemistry to predict the volume fraction of the

constituents. An example calculation is shown in Fig. 8. Using the model developed by Ion et al. (Ref 55), the microstructure and hardness of the HAZ for a given cooling rate (10 Ks^{-1}) and austenite grain size (50 m) for two different steels with 0.1 and 0.2 wt% C is shown. These

calculations show that a change in carbon content changes the HAZ microstructure from ferrite to a microstructure with predominantly martensite. In addition, the predictions also show an increase in hardness. Such calculations can be used to provide guidance for weld

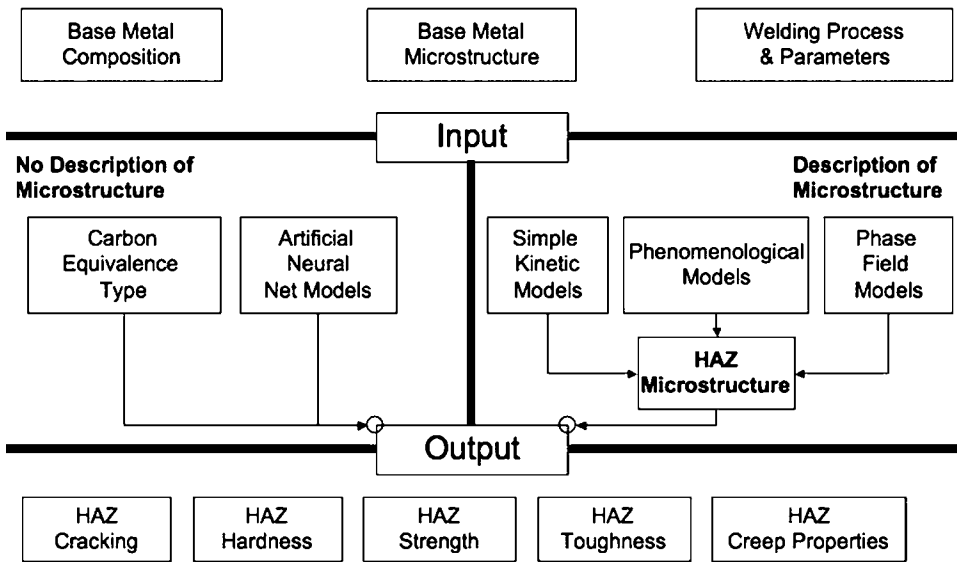


Fig. 7 Schematic illustration of various modeling methodologies to describe the heat-affected zone (HAZ) of steel welds

cooling rate control in the HAZ. An online version of these calculations is available (Ref 56).

Recently, prediction of HAZ microstructure and/or properties has relied on artificial neural networks (Ref 57) and detailed computational materials models coupled with either thermo-mechanical or fluid flow calculations. There has been much published literature that focuses on calculating the nucleation and growth of ferrite from austenite as a function of composition and cooling rate. These are essentially based on the calculation of time-temperature transformation diagrams and converting them to continuous cooling transformation diagrams (Ref 58). Advanced models that consider simultaneous formation of grain-boundary ferrite, Widmanstätten ferrite, pearlite, and bainite are also available (Ref 59). Some of these models are currently available in the form of public domain software (Ref 60). The models to predict microstructure evolution in the HAZ and weld metal region of age-hardening aluminum alloys can be found in the classic work of Myhr and Grong (Ref 61, 62). In this work, the dissolution of age-hardening precipitates and subsequent precipitation was described by isokinetic equations and assumed the additivity law.

In the previous treatments of microstructure evolution, in addition to phase transformation, an estimation of grain growth is important. For example, the steel microstructure predictions by equations given by Ion et al. (Ref 55) are sensitive to the prior austenite grain size. The austenite grain growth can be described by the following classic relationship:

$$\frac{dD}{dt} = nK \left[\frac{1}{D} - \frac{1}{\bar{D}_{\text{lim}}} \right]^{(1/n-1)} \quad (\text{Eq 9})$$

where D is the grain size (in micrometers); \bar{D}_{lim} is the limiting grain size (in micrometers), which is determined by the stability of the precipitates; and K and n are the rate constant and time exponent of grain growth, which depend on the materials and temperature, respectively. Therefore, if the composition and thermal cycle can be acquired from the steels and the welding parameters, the only thing needed for grain growth is the limiting grain size. In this article, the limiting grain size is determined by the pinning effect of precipitates (Ref 63):

$$\bar{D}_{\text{lim}} = k \frac{r}{f} \quad (\text{Eq 10})$$

where \bar{D}_{lim} is the limiting grain size; k is the Zener coefficient, which was first derived by Zener to be 0.75; r is the average radius of precipitates, with the unit of micrometers; and f is the volume fraction of precipitates. The limiting grain size is then related to stability (growth, coarsening, and dissolution) of grain-boundary pinning precipitates. Although, the aforementioned methodology has been extensively used, it does not provide morphological changes in grain shape and size. In this regard, pioneering work was done by Radhakrishnan et al. (Ref 64, 65) using Monte Carlo simulations. Using this methodology, thermal pinning of grain growth was also successfully simulated. This work has been pursued by other researchers to describe the HAZ grain growth in other alloy systems (Ref 66).

Prediction of Weld Metal Microstructure

The earliest models to calculate weld metal microstructure can be tracked to a classic paper

by Bhadeshia et al. (Ref 3) for steel welds. In this model, the sequential decomposition of the austenite phase into allotriomorphic ferrite (also known as grain-boundary ferrite), Widmanstätten ferrite, acicular ferrite, and martensite-austenite constituents is calculated. The basis of this model emanates from an ability to calculate the time-temperature transformation (TTT) diagram as a function of steel composition. The TTT diagrams are then converted into continuous cooling transformation (CCT) diagrams. Given an expression for the weld cooling curve and austenite grain size, the weld metal microstructure can be calculated using the flow chart shown in Fig. 9(a). Comparison of predicted microstructure and measured microstructure is shown in Fig. 9(b). The aforementioned model has been coupled with detailed heat- and mass-transfer models by DebRoy and his collaborators (Ref 50, 51). Microstructure development in the weld metal region of aluminum alloys (Ref 67) and nickel alloys (Ref 68) has been addressed through computational thermodynamics and kinetics, which are introduced in the next section (Ref 40).

Application of Computational Thermodynamics and Kinetics Tools

There are standard mathematical models to calculate multicomponent thermodynamics and diffusion-controlled growth of the product phase into a parent phase (Ref 69). A typical calculation of multicomponent equilibrium is demonstrated with the Fe-Cr-Ni system with liquid, δ -ferrite (body-centered cubic), and γ -austenite (face-centered cubic) phases at 1700 K (Fig. 10). Thin lines that go across the phase boundaries in this diagram correspond to tie lines. For further details on this subject, the readers are referred to other sections in this Handbook. In this section, application of these tools to weld metal microstructure prediction is described (Ref 40) for various reactions that happen as a function of high-to-low temperature during fusion welding.

Liquid-Gas Reactions. The prediction of weld metal composition in gas-shielded processes, including gas metal arc welding (GMAW) (Ref 70), gas tungsten arc welding (GTAW), laser beam welding, and low-pressure electron beam welding, has always remained a challenge due to competing phenomena with the arc, plasma, shielding gas, atmosphere, and consumables. For example, stainless steels with high nitrogen levels (Ref 71, 72) have been developed to reduce nickel concentration but still maintain an austenitic microstructure. However, predicting the amount of nitrogen that remains after GMAW or GTAW in these stainless steels as a function of welding parameters is indeed a challenge. Hertzman et al. (Ref 73, 74) concluded that the final nitrogen concentration is decided by the equilibrium

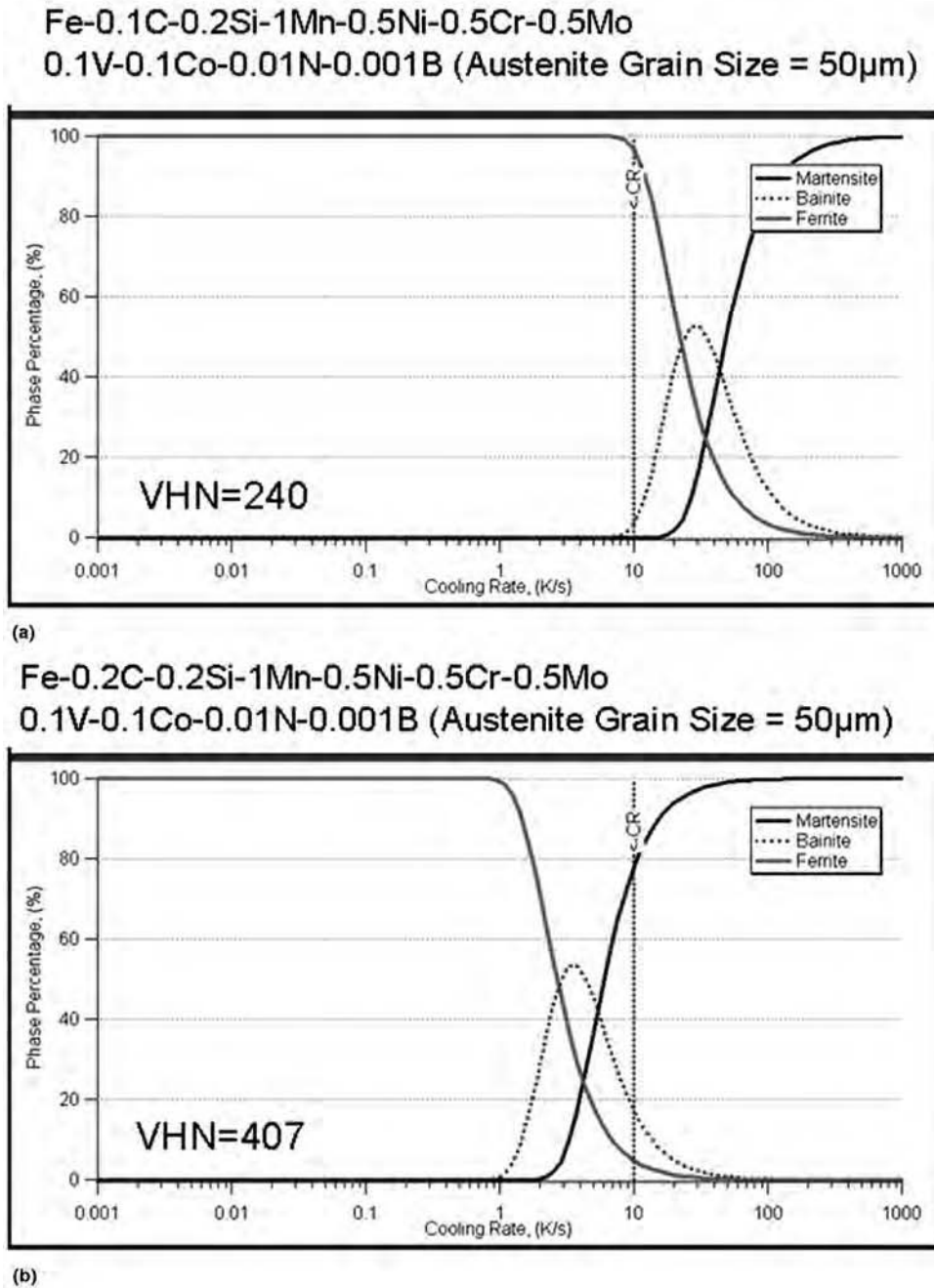


Fig. 8 Typical calculations of heat-affected zone microstructural constituent and hardness as a function of cooling rate. For a given low-carbon steel composition, (a) a slow cooling rate of 10 °C/s leads to a soft microstructure and (b) a faster cooling rate leads to a hard martensitic microstructure

between nitrogen activity and composition of the liquid metal after a critical time.

It is important to consider the effect of plasma environment, which may lead to enhanced nitrogen dissolution in steel welds. This phenomenon may play an important role at the early stages of nitrogen balance, as discussed by Hertzman et al. (Ref 73). Mundra and DebRoy (Ref 75), followed by Palmer and DebRoy (Ref 76), have developed models to

describe nitrogen dissolution (mono- and diatomic fashion) into liquid metal from the plasma environment. Enhanced nitrogen dissolution from laser plasma was leveraged by Babu et al. (Ref 77) to induce fine-scale carbonitrides during surface alloying of iron alloys. Similar to the kinetics of nitrogen dissolution (Ref 78–80), it is possible to describe the dissolution of oxygen (Ref 81) and hydrogen (Ref 82–84). Dissolved oxygen and sulfur (Ref 85)

have a major influence on the surface tension of liquid (γ_{surface}) and its variation with temperature ($d\gamma_{\text{surface}}/dT$). The sign and magnitude ($d\gamma_{\text{surface}}/dT$) has a large influence on the fluid flow characteristics in the weld pool (Ref 86, 87). In addition, evaporation from the weld pool has also been addressed by various researchers using thermodynamic and kinetic descriptions (Ref 88–90) and comprehensive heat- and mass-transfer models. Some preliminary efforts are also being made to predict the composition of the fume particles using the liquid-gas equilibrium (Ref 91).

Liquid-Slag Reactions. Most fusion welding processes encounter liquid and slag equilibrium, for example, shielded metal arc welding, submerged arc welding (SAW), and flux cored arc welding. There is a close similarity between these processes and steelmaking. As a result, ladle thermodynamics have been leveraged to describe liquid-slag equilibrium in welds. In the classic works of Mitra and Eager (Ref 92–94), thermodynamic theories were used to predict the final weld metal composition of SAW welds as a function of process, flux, and consumable characteristics. Many researchers considered interactions between flux/slag chemistry and consumables to evaluate final weld metal compositions (Ref 95–98) as well as the inclusion formation. As expected, these phenomenological theories were based on ladle thermodynamics (Ref 99).

Inclusion Formation. Inclusions that form in welds are either oxides, nitrides, carbides, sulfides, or a combination thereof. Certain oxide inclusions, with special characteristics, promote the formation of acicular ferrite (Ref 100, 101) during solid-state decomposition of austenite. Acicular ferrite is known to promote the toughness of welds. This beneficial effect of inclusion outweighs the deleterious effects on fracture initiation. Early work on predicting inclusion formation using ladle thermodynamics originated from many researchers, notably Olson, Liu, and Edwards (Ref 102), Thewlis (Ref 103), as well as Klukun and Grong (Ref 99). These researchers predicted that complex inclusions form due to sequential formation of oxides, including Al_2O_3 , SiO_2 , Ti_xO_y , MnO , and complex spinels. Even with the aforementioned classic work, the prediction of inclusion composition, size, number density, and type of surface oxide remained a challenge for some time. By coupling ladle thermodynamic theory, computational thermodynamics (Ref 104–106), and overall transformation kinetic theories (Ref 107–110), it is now possible to comprehensively predict inclusion characteristics. These models have also been extended to laser-surface alloying to predict dissolution of hard particles (Ref 111). These models have also been integrated with computational heat- and mass-transfer models (Ref 112–114). For example, Hong et al. evaluated the cyclic growth and dissolution of inclusions in a weld pool. The trajectory of the inclusion within a weld pool is shown in Fig. 11(a). This

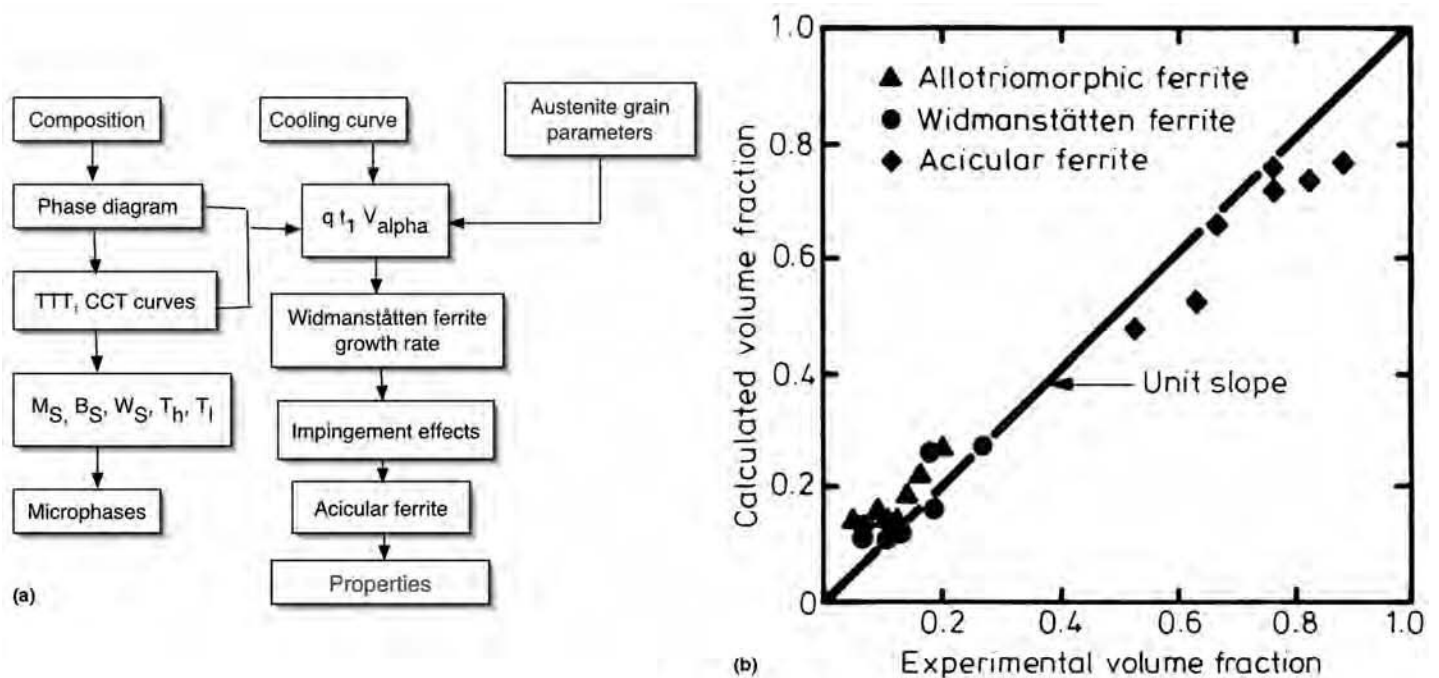


Fig. 9 (a) Overview of methodology developed by Bhadeshia et al. (Ref 3) to predict the microstructure constituent in the as-welded region of low-alloy steels. In contrast to the carbon equivalence formula, this model is based on quasi-chemical thermodynamics and kinetic equations. TTT, time-temperature transformation; CCT, continuous cooling transformation. (b) Comparison of predicted and measured microstructure in the as-welded region shows good agreement

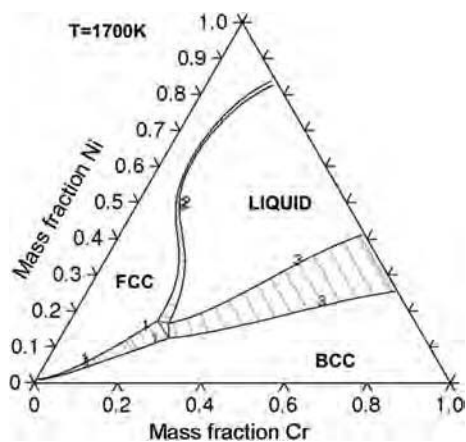


Fig. 10 Example of a calculated ternary phase diagram with tie lines and invariant triangles (three-phase equilibrium) in an Fe-Cr-Ni system at 1700 K. fcc, face-centered cubic; bcc, body-centered cubic

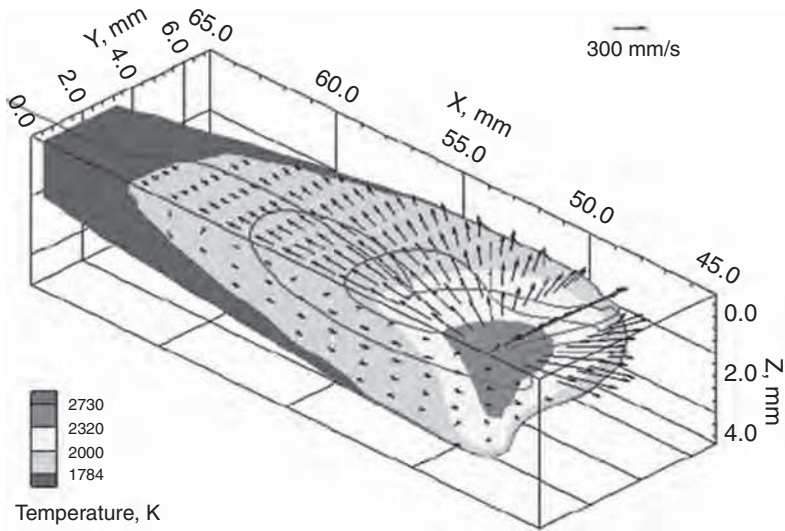
movement was calculated by using the fluid flow velocities (u , v , and w) calculated in x -, y -, and z -coordinates and by assuming no slip between the inclusion surface and liquid steel flow. The corresponding variation of temperature and the associated change in radius of the inclusion is shown in Fig. 11(b). Using such calculations and microstructure observations, the rapid rate of inclusion growth was rationalized based on a collision and coalescence mechanism (Ref 115).

Solidification. To comprehensively understand the weld metal microstructure, the following must be predicted:

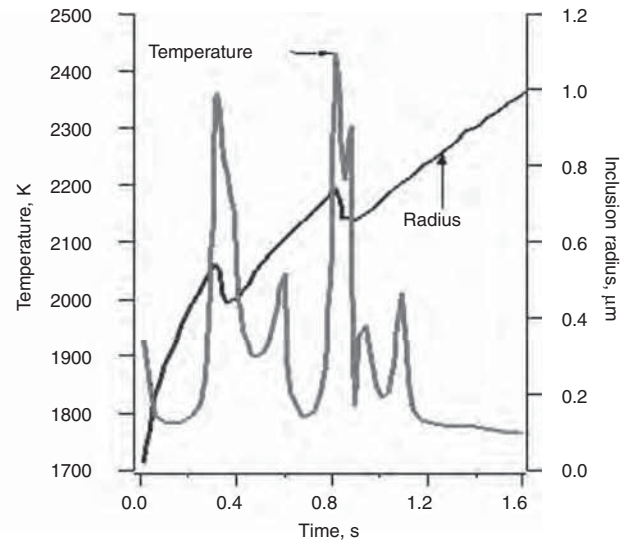
- First phase to form from the liquid
- Solidification temperature range ($\Delta T_{\text{equilibrium}} = T_L - T_s$)
- Extent of alloying element segregation
- Morphology of the solidification grains
- Cracking tendency
- Nonequilibrium solidification as a function of composition and cooling rates

A multicomponent thermodynamic phase diagram can be calculated using computational thermodynamics tools, and this information can be used to predict the first phase to form from liquid during welding (Ref 116–118). Using Scheil-Gulliver calculations, the non-equilibrium solidification range as well as the maximum extent of segregation can be predicted (Ref 119). It is important to note that equilibrium and Scheil-Gulliver calculations provide two extreme conditions of weld solidification. In nominal weld cooling rates, some extent of diffusion is expected in the solid phase. This must be considered in the Scheil-Gulliver calculations. Classic papers from Dupont's group (Ref 120–122) focus on using a modified form of the computational thermodynamics tools to evaluate the solidification path and also the microsegregation effect in similar and dissimilar metal welding conditions for a wide range of nickel-base and stainless steel alloys.

To track the solid-liquid interface, diffusion in both liquid and solid phases as a function of cooling rate must be considered. Early work on modeling the weld solidification rate was done by Koseki et al. (Ref 123, 124). With the introduction of sidewise dendrite growth models in DictTra software (Ref 69), weld solidification for a wide range of alloy systems and cooling rates can be done easily. With an increase in cooling rate, an increase in the liquid-solid interface velocity is expected. This may affect solute partitioning between the liquid and solid and induce morphological changes in the solidification microstructure. Often, this increase in the liquid-solid interface may also trigger a nonequilibrium phase selection during solidification. For example, in steels, a transition from ferrite (body-centered cubic) solidification and austenite (face-centered cubic) solidification may occur (Ref 125, 126) with an increase in the liquid-solid interface velocity. Using levitation melting methods, Koseki and Flemings (Ref 127) developed phase stability and growth velocity criteria to describe these transformations. Fukumoto and Kurz (Ref 128) used growth velocity considerations for the phase selection of austenite instead of ferrite during rapid cooling conditions, using interface-response function models. This is illustrated in Fig. 12. The selection of the ferrite or austenite phase is governed by its dendrite tip temperature. This temperature can be calculated using the interface-response function theories. The calculations show that for slow interface



(a)



(b)

Fig. 11 Prediction of inclusion size distribution in low-alloy steel welds by tracking the growth and dissolution of thousands of inclusions as they gyrate through the weld pool. (a) Trace of an inclusion as it traverses through the weld pool with different temperature regions, before being trapped by the advancing liquid-solid boundary. (b) Corresponding variation of temperature and the associated growth and dissolution of an inclusion. The calculations show that the observed inclusion diameters could be interpreted without invoking Ostwald ripening, which is typical of a stagnant molten pool

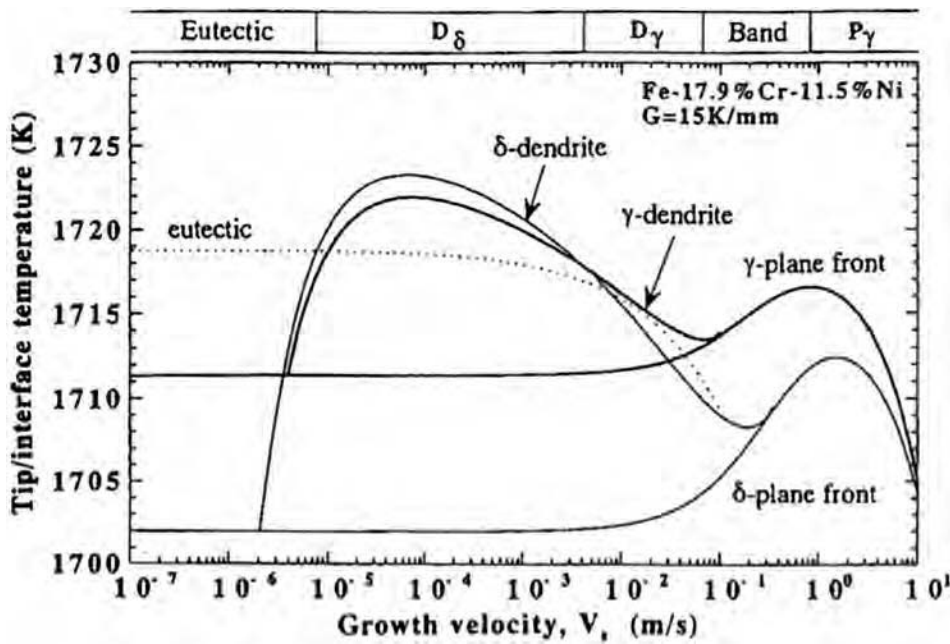


Fig. 12 Transition from body-centered cubic (bcc) to face-centered cubic (fcc) mode of solidification with an increase in the liquid-solid interface velocity. The calculations show that in an Fe-Cr-Ni weld, the bcc mode of solidification is preferred below 2×10^{-3} m/s, and the fcc mode of solidification is preferred at higher velocities. These plots are used to rationalize the transition from δ -ferrite to the austenite mode of solidification in laser welds. Source: Ref 127

velocities, the dendrite tip temperature of ferrite is always higher than that of austenite. Under this condition, only ferrite solidification is expected. However, above a critical velocity, the dendrite tip temperature of austenite is higher than ferrite. This condition will lead to the austenite mode of solidification. Using these

theories, the transition from ferrite to austenite solidification modes during laser welding was rationalized.

Solid-State Transformation. The role of various microalloying elements (Ref 129) on the HAZ microstructure in thermomechanical-controlled processing in low-alloy steels has

been evaluated with computational thermodynamics (CT) and computational kinetics (CK) tools. The ferrite-to-austenite transformation in stainless steel welds (Ref 130) was simulated for a condition that is close to limited partitioning of the substitutional condition, which is in between the paraequilibrium and local equilibrium conditions. The effect of retained austenite in the steel microstructure on the re-austenitization kinetics during heating was rationalized using a thermodynamic criterion (Ref 131). To design new steels with improved properties and weldability, CT and CK tools are very effective. For example, a transformation-induced plasticity (TRIP) steel with good welding and galvanizing performance was designed with CT and CK tools. In this work, carbon, silicon, and phosphorous concentrations were optimized, and the microstructure evolution during steel processing was modified (Ref 132, 133). Kaputaska et al. used CT tools to describe the stabilization of δ -ferrite in the HAZ of aluminum-base TRIP steels (Ref 134). Using CT tools, blast-resistant steels with good weldability (Ref 135) have been developed. The HAZ microstructure evolution in duplex stainless steel weld metal was modeled using overall transformation kinetic models based on CT tools. This work stressed the importance of nitrogen concentration on the stabilization of austenite (Ref 136). Similar work on duplex steels has been performed by other researchers (Ref 137). In addition, the effect of minor variations in boron was rationalized based on the CCT diagrams predicted by CT and CK tools (Ref 138). Barabash et al. (Ref 139) showed the dissolution of gamma-prime precipitate and its effect on dislocation activity in HAZ

regions. These interactions were rationalized based on transmission electron microscopy, synchrotron radiation, and computational thermodynamic calculations.

Kelly (Ref 45) used CT and CK tools to obtain the parameters for the Johnson-Mehl-Avrami-Kolmogorov model, which is then coupled with a thermal model for laser near-net shaping of Ti-6Al-4V alloys. Using this thermal-microstructure model, Kelly described the microstructure evolution as a function of the heating and cooling cycle. This model was used to describe the formation of various morphologies of $\alpha+\beta$, including the grain-boundary, colony, basketweave, massive, and martensitic microstructures. Similar approaches to describe microstructure gradients in multipass welds in steels were performed by Reed and Bhadeshia (Ref 140). In these analyses, the austenite formation and its effect on increasing the fraction of the reheated region was described by coupling heat-transfer models with thermodynamic and kinetic calculations (Ref 141). Extensive work has been done by Keehan et al. (Ref 142–146) to develop high-strength and high-toughness weld metal compositions that are based on bainite microstructure. These developments relied on CT and CK tools (Ref 147). The reliability of weld microstructure models and their relation to properties have been reviewed by Bhadeshia (Ref 148).

To address the stability of weldment structures during postweld heat treatment and service, CT and CK tools have been used. In certain 9Cr steels, the addition of boron leads to a fine distribution of $M_{23}C_6$ and an increase in creep resistance. Thermodynamic calculations showed that boron will segregate to martensite lath boundaries and increase the driving force of boride precipitation. These precursor phases will act as heterogeneous nucleation sites for boron containing $M_{23}C_6$ (Ref 149). Simultaneous transformation kinetic theories of carbide precipitation (Ref 150) and neural network models (Ref 151) have been used to develop creep-resistant weld metals. The nucleation and kinetics of chi, sigma, and secondary gamma (face-centered cubic) phases during aging of a super duplex stainless steel weld metal were investigated with experimental characterization and thermodynamic driving force calculations (Ref 152). Similar work has been performed by Sieurin et al. (Ref 153, 154) to describe the sigma-phase precipitation and reforming of austenite during isothermal and continuous cooling. Ramirez et al. (Ref 155) used analytical electron microscopy and thermodynamic modeling to evaluate secondary austenite formation and its interaction with Cr_2N precipitation. Another form of degradation in high-chromium stainless steel welds is the tendency for low-temperature embrittlement. This occurs due to the phase separation of chromium-rich and chromium-lean regions through a spinodal decomposition (Ref 156) and the subsequent precipitation of gamma phase. Many researchers have characterized this

decomposition using the atom probe technique and compared it with CT and CK tools (Ref 157). The CT and CK models also have been used for evaluating the stability of dissimilar material welds. One successful example is the prediction of carbon migration in dissimilar material welds (Ref 158, 159).

Performance Modeling

The goal of performance modeling relates to the prediction of weldability, geometrical distortion, and/or locked-in residual stresses as a function of material, restraint, process, and process parameters as well as service temperature.

Weldability Prediction

One of the main uses of numerical modeling is to predict the cracking tendency in welds. Weld solidification cracking is governed by severe restraints (stress/strain state) and the composition of the base metal (affects epitaxial growth) and the filler metal (affects the solidification range). To predict the solidification-cracking tendency in welds, there is a need to couple the CT and CK calculations with finite-element analysis that predicts the spatial variation of stress, strain, and temperature (Ref 160–164). This is explained with an example from the published literature.

There is a growing need to develop joining processes and process parameters for single-crystal nickel-base superalloys (Ref 165). During such a development cycle, autogenous welding experiments showed cracking (Fig. 13a) on only one side of the weld. Orientation imaging microscopy showed that the cracking was associated with the formation of stray grains on only one side of the weld (Fig. 13b). The reason for such asymmetrical cracking and grain structure evolution was rationalized with integrated process-microstructure models. The first step was to rationalize the dendrite growth velocities on the left and right side of the weld. The weld pool shape was modeled with a simple analytical heat-transfer equation (Ref 166). Using a geometric model (Fig. 13c) developed by Rappaz et al. (Ref 16), the spatial variation of the temperature gradient and dendrite growth velocity was calculated as a function of weld pool shape and crystallographic orientation of the single crystal. Next, these spatial variations of gradients and velocities were plotted (shown as triangular markers) on a processing map (Fig. 13d) that predicts the probability of stray grain formation. This map is developed using the constitutional supercooling theory for nucleation of new grains ahead of the growing liquid-solid interface. The comparison of these values showed that the tendency for the formation of stray grains is more on the right side of the weld. The formation of high-angle grain boundaries has been attributed as the cause for weld metal cracking (Ref 167).

Solidification cracking also requires mechanical driving force. Park et al. (Ref 162) integrated these material models with thermomechanical models to develop processing maps for cracking tendency due to stray grain formation. The processing map developed by Park et al. focused only on weld cracking for single crystals; however, in other polycrystalline alloys, the weldability evaluations must consider weld penetration, porosity formation, HAZ liquation, centerline grain formation, and solidification cracking.

Dye et al. (Ref 163) developed such weldability maps (Fig. 14) for nickel alloys using a different functional relationship between power and velocity. This map shows microstructural evolutions that impact weld penetration, tendency for porosity formation, HAZ liquation, solidification cracking, and center grain formation as a function of welding power and welding speed. For a given welding power, an increase in welding speed will lead to a reduction in weld penetration. An increase in welding power, more than needed for weld penetration, will lead to the formation of porosity. Similarly, with a large increase in power at the same velocity, the thermal gradient in the middle of the weld will be reduced. Under these conditions, the formation of centerline grains will be promoted. The overlaying of all these vulnerabilities leads to a small processing window where the welds can be made without undesirable defects. It is important to note that this optimum process parameter region will shift depending on the materials and thermomechanical conditions.

Residual Stress and Distortion Modeling

The reader is referred to Ref 168 for a comprehensive review of various methodologies and applications for processes and mechanisms of welding residual stress and distortion. In this section, some examples are presented to show the capability of numerical models to predict residual stress and distortion during welding.

Residual-Stress Prediction. The origin of residual stresses during materials processing is discussed in depth in a review by Withers (Ref 169). For in-depth understanding of the mechanics, the reader is also referred to a classic textbook by Masubuchi (Ref 170). Macroscopic residual stresses develop in welding due to localized plastic strain induced by a severe temperature gradient brought about by localized heat sources. The predictions of residual stresses are usually done by finite-element analyses in either two- or three-dimensional conditions. Most of these computational simulations are also performed in a sequential fashion, as explained subsequently. First, for a given set of geometry and welding process parameters, the thermal distribution is predicted. In the next step, using thermal distribution and the associated variation of mechanical properties, the localized plastic strain

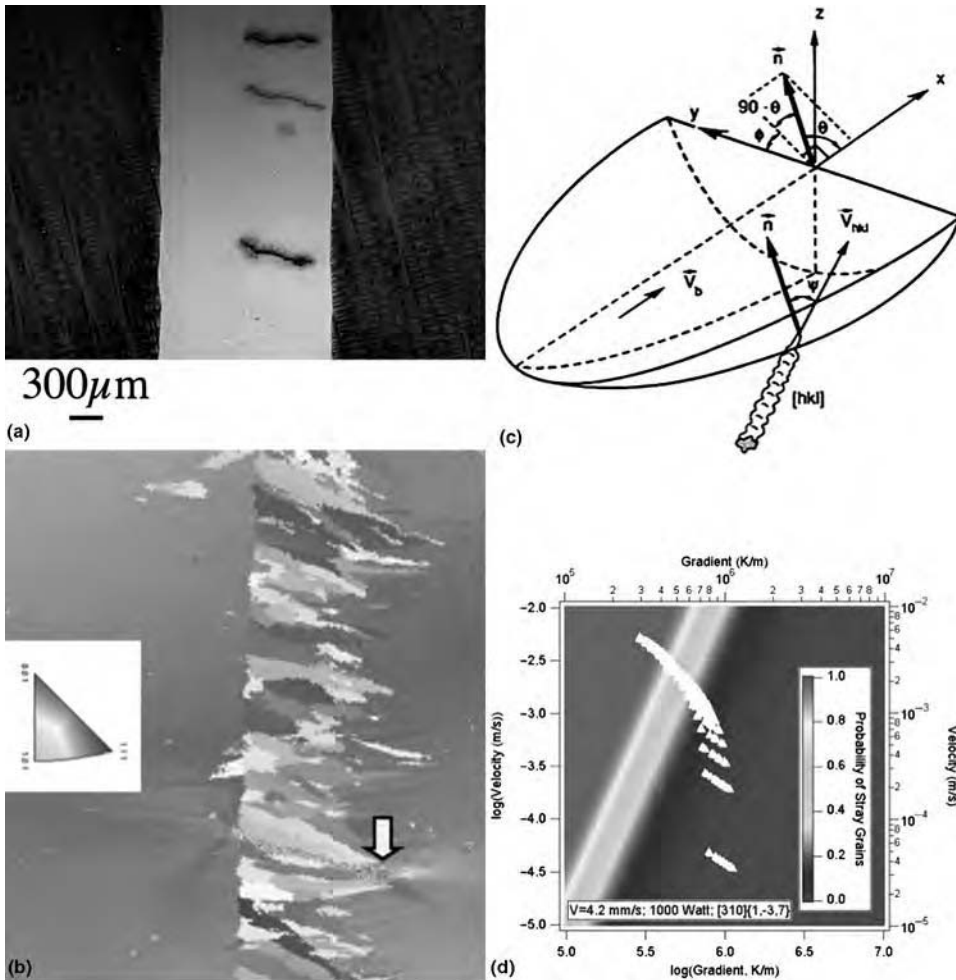


Fig. 13 (a) Optical micrograph of an autogenous gas tungsten arc weld made on a single-crystal nickel-base superalloy shows the transverse crack on only one side of the weld. (b) Orientation imaging microscopy showing the close correlation between the crack and the presence of high-angle stray grain boundaries. (c) Schematic illustration of a geometric model of the weld pool used for estimating the dendrite growth velocity as a function of welding speed. (d) Predicted tendency to form stray grains as a function of dendrite growth velocity and temperature gradients

distribution is predicted. Due to the mechanical equilibrium constraint, this localized plastic strain accumulation at high temperature leads to a distribution of locked-in elastic residual stresses. It is important to note that these predictions are sensitive to the boundary conditions used in the mechanical equilibrium calculations. For example, local constraints (clamps and fixtures) may affect the evolution of residual stress as well as postweld heat treatments such as temper-bead techniques (Ref 171, 172) and surface peening (Ref 173, 174). It has been demonstrated that the initial distribution of residual stress before the welding operation is important in the estimation of residual stress due to welding. For example, in automotive industries, the sheet metal forming process may induce a pattern of residual-stress distribution due to its inhomogeneous distribution of plastic strain (Ref 175). In addition, the postweld heat treatment affects the distribution of residual stress due to relaxation.

Residual stresses in welds can be measured by hole-drilling, x-ray diffraction, and neutron diffraction methods (Ref 169). The presence of residual stress has a large effect on fatigue life and stress-corrosion cracking. An example calculation of residual-stress prediction and experimental measurements using x-ray diffraction is shown in a steel weld (Fig. 15). The results (Ref 49) show that it is indeed possible to predict the distribution of residual stresses in welds with good accuracy. There has been a growing impetus to predict the effect of phase transformation on the magnitude of residual stresses in welds (Ref 176). This is partly driven by the need for the use of low-temperature-transformation wires to induce compressive residual stress near the toe of fillet welds to improve the fatigue life of welded components (Ref 49, 177).

Distortion Prediction. The distortion of the welded structure is essentially due to dimensional changes that occur during or after welding due to the imbalance of locked-in stresses.

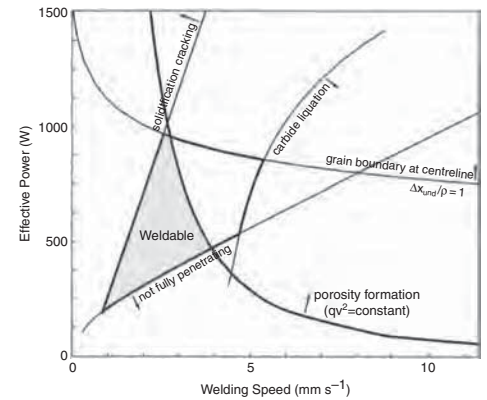


Fig. 14 Calculated weldability map showing the tendency for various weld-defect formations as a function of welding power and speed. Many of these phenomena, including liquation, are predicted using computational thermodynamics and computational kinetics tools. Source: Ref 162

The distortion simulation can be performed by finite-element analysis in three dimensions (Ref 23, 168, 178), with consideration of elastic and plastic strain accumulation during welding. However, the application of finite-element simulation to large-scale structures (e.g., ship superstructure) with consideration of detailed local welding process effects and constraints may become computationally expensive and time-consuming. In this regard, a simplified procedure that is based on applied plastic strain has been developed (Ref 179 to 181). A comparison of three-dimensional elastic-plastic analysis and the simplified plasticity strain method is shown in Fig. 16. The predicted distortions are comparable and prove the applicability of this technique to large-scale structures. This technique is very useful for consideration of buckling distortion in long welds on thin sheet structures. The technique was used to derive the process parameters for the transient thermal tensioning technique to minimize buckling distortion in ship panel structures (Ref 182).

Property Predictions

After the microstructural gradients, residual stress, and distortion conditions in a weld have been described, the next step is to predict the low- and high-temperature properties of the weld. Some of the methodologies are presented as follows.

Low-Temperature Properties. Relevant low-temperature properties for welds are hardness distributions, tensile properties, toughness, and fatigue properties. Hardness distributions in welds are often predicted using empirical equations, which relate the composition of the alloys and the microstructure. For steel welds, this is discussed in detail by Ion et al. (Ref 8) and Bhadeshia (Ref 148). Using these hardness models, Santella et al. (Ref 183) and Yuping et al. (Ref 184) predicted the performance of

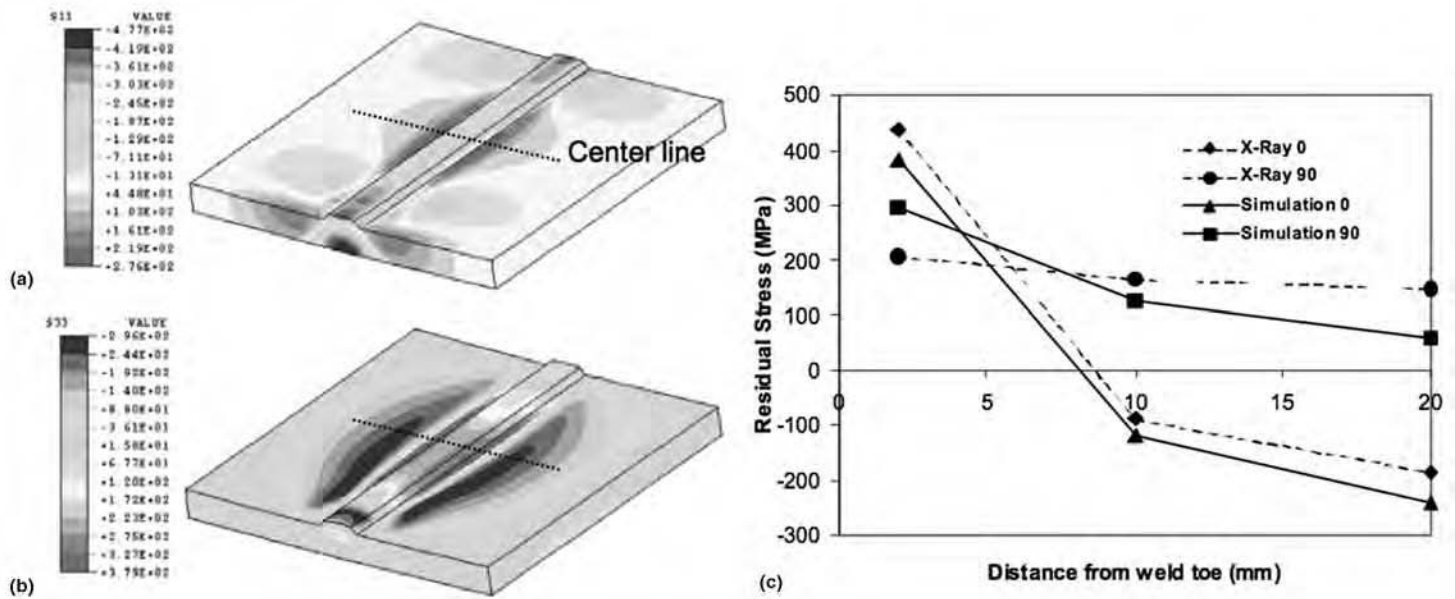


Fig. 15 Simulated residual stress in a butt weld in two directions: (a) perpendicular and (b) parallel to the welding direction. (c) The calculations are compared with the measurements by x-ray diffraction and show good agreement. Source: Ref 49

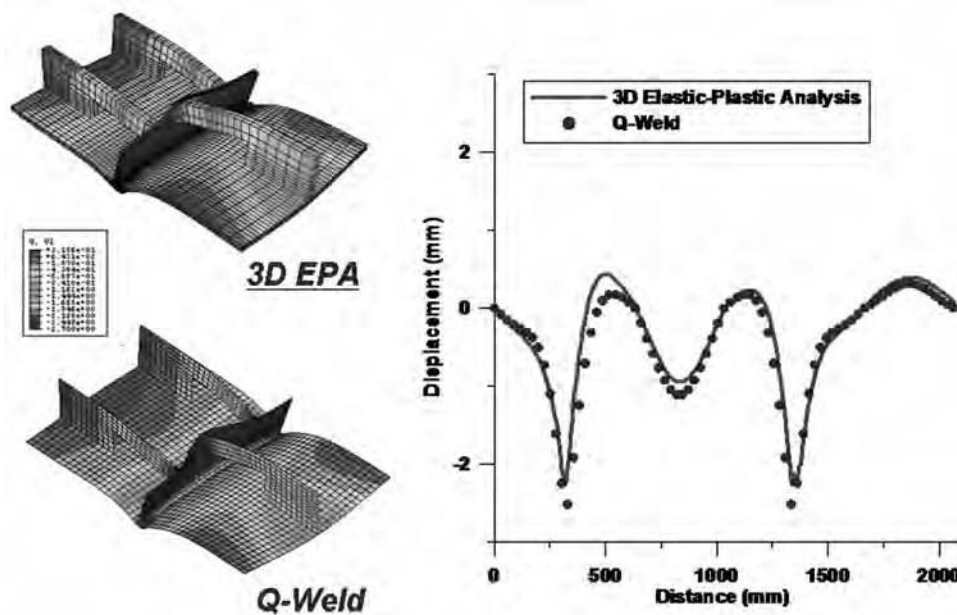


Fig. 16 Results from distortion modeling based on plasticity strain (Q-Weld) compared with fully three-dimensional coupled thermal elastic-plastic analysis (3D-EPA) model. The overall shape distortion (exaggerated) is comparable. In addition, the predicted displacement of the edges from the bottom plane is compared for both methods, demonstrating the applicability of the strain-based method for predicting the distortion of large-scale structures

steel spot welds. Similarly, the tensile properties of the welds are often predicted using additive law (Ref 185) and neural networks (Ref 151). An example of toughness prediction in steel weld metals, using artificial neural networks, is shown in Fig. 17. Using such maps, new filler metal compositions have been derived for low-temperature service (Ref 146). In welds, fatigue properties are often controlled by the crack propagation conditions. This is

partly because most of the welds often have submicroscopic features that provide an easy site for fatigue crack initiation. As a result, most of the research on prediction of fatigue-life estimation has relied on crack propagation conditions. Crack propagation is strongly affected by geometry (Ref 186) and the presence of compressive residual stresses (Ref 49, 171, 174, 175). An example calculation on the effect of tensile and residual stress is shown in

Fig. 18. The calculations indeed show an improvement of fatigue life near the toe of a fillet weld due to the presence of compressive residual stress. This has been experimentally evaluated by measurements (Ref 49).

High-Temperature Properties. The inherent creep properties of weld regions without the consideration of geometry can be predicted by using neural network models (Ref 148, 151, 187) or with hybrid models that consider the phase stability (Ref 188 to 190). It is also possible to develop detailed creep property calculations using detailed computational models, as described by To et al. (Ref 191). When the inherent properties are known, there is a need to map them to predict the creep life of structural components (Ref 192). Such calculations have become critical to evaluate the performance of welds made on new-generation high-chromium (P91) steels. These welds often show a soft zone in the HAZ. These regions will lead to localized reduction in creep strength. An example calculation of creep failure in the HAZ of a girth-welded pipe is shown in Fig. 19. In this model, different creep models (constitutive relations) were applied to the base metal and HAZ regions. In the next step, the damage accumulation in these regions was predicted for a given operating condition. These calculations have also been validated with experimental measurements.

Access and Delivery of Integrated Weld Process Models

The aforementioned examples clearly show that with an integrated weld-modeling framework,

it is possible to evaluate the welded structure, as envisioned by Kirkaldy (Ref 11). Some of the commercially available integrated weld-modeling software providers are listed in Table 1.

In addition, there are public domain software tools (Ref 193) that can be used for integrated modeling of welds. The listing of these resources is not an endorsement of the products, and readers are requested to make independent testing and evaluation for their own applications. It is important to note that this article did not include any reference to other forms of fusion welding (resistance, laser and electron beam) solid-state modeling techniques. There has been extensive work in this area, which is covered in other resources.

The discussions and references demonstrate that it is indeed possible to describe the weld properties in a wide range of alloy systems as a function of alloy composition and welding process parameters using integrated models. However, these models should be able to consider different processes (submerged, gas metal, gas tungsten, laser, etc.), process parameters, geometrical conditions (restraints, distortion), and mechanical integrity (residual stress, low- and high-temperature properties) in a simpler methodology. In addition, these integrated models should be seamlessly accessible to academic and industrial users. Although commercially available weld-modeling software exists (Table 1), it requires expertise in finite-element analysis as well as a computational and welding background. However, the presence of such expertise is often limited in small- and medium-scale industries. As a result, the use of computational weld mechanics has been widespread only in large-scale industries. To provide access to these models for small- and medium-scale industries, there is a need to develop methodologies for rapid deployment and easy-to-use applications.

To meet this crucial need, the E-WeldPredictor approach has been developed by researchers from the Edison Welding Institute (Ref 194). In this methodology, all of the expertise for developing and running a finite-element

analysis to calculate thermomechanical-metalurgical responses was ported into a supercomputing architecture. Simple, accessible, internet-based applications have been developed in collaboration with supercomputing expertise and have been deployed through a client-server computational architecture (Fig. 20). The steps are explained as follows.

First, the user provides the information for the welding processes. This allows the model to set the effective heat-transfer efficiency. In the next step, the user provides the overall geometry of the welding (pipe or plate) and the boundary conditions (thickness, diameter, and length). This information is used to set the overall simulation geometry within the finite-element software. In the next step, the user provides the detailed joint geometry (e.g., V- or J-groove). This information is used to calculate the extent of weld metal volume to be used for filling the void within the calculation framework. In the next step, the user provides the materials used for the base and filler metals. This information is used to calculate the microstructure and hardness. Currently, these material models do not consider the initial microstructure of the base metal, and a ferrite microstructure is assumed. In the next step, the user provides the information for heat input and geometry of the individual weld bead that will be used for filling up the joint. These parameters are then used to set the heat-flux conditions for simulating the weld pool (Ref 42). Finally, the model allows the user to check whether the intended weld geometry is indeed the one the user would like to consider. As soon as the user accepts and presses the submit button, the overall thermal-microstructure-mechanical model is evaluated in a sequential manner within a supercomputer architecture at the Ohio Supercomputing Center. The results of the calculations are formatted into a PDF and delivered to the user in an average time frame of 15 min. The

calculation time does increase with the number of beads. Currently, the E-WeldPredictor approach has been deployed for predicting microstructure, distortion, and residual stresses in pipe and plate welds for a wide range of steels. The reader is referred to the internet site listed in Ref 195 for more details and usage scenarios. In this section, a typical application of the tool for a case study to evaluate the use of X-65 steels instead of 2.25Cr-1Mo steels for a welded pipeline construction with the same filler and process parameters is discussed.

Case Study Evaluating Use of X-65 Steels

Case Study Involving Typical Use of the E-WeldPredictor Tool. While welding a 2.25Cr1Mo steel pipeline, a hard zone was observed in the HAZ. An ER70S6 filler wire was used in this situation. The focus of the case study was to substitute the 2.25Cr1Mo steels with traditional X-65 steels for the same process and filler wire conditions, without adverse effect in residual stress and distortion. The individual steps in running the simulations and input parameters are shown in Fig. 21. The results obtained based on these inputs are summarized in Fig. 22. The calculations indicated that there are no significant differences in the HAZ width, residual stress, or distortions by substitution of the 2.25Cr1Mo with the X-65 steel (Fig. 22). The most important difference was the formation of martensite in the HAZ of the 2.25Cr1Mo steels compared to a bainitic microstructure in the X-65 steels. This microstructural distribution is also reflected in the reduction of peak hardness in the HAZs of the X-65 steels. With this tool, the range of other process parameter and material combinations was evaluated, and some key conditions are

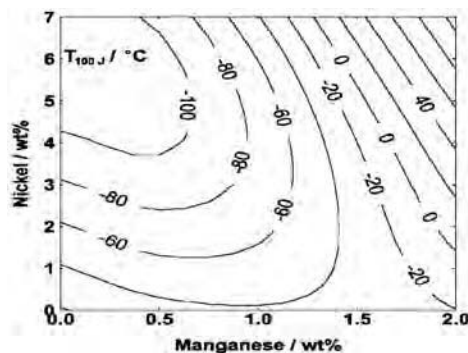


Fig. 17 Contour plot of Charpy toughness values, at a given temperature, as a function of manganese and nickel concentration constructed using an artificial neural network model. Such plots can be used to design welding consumables

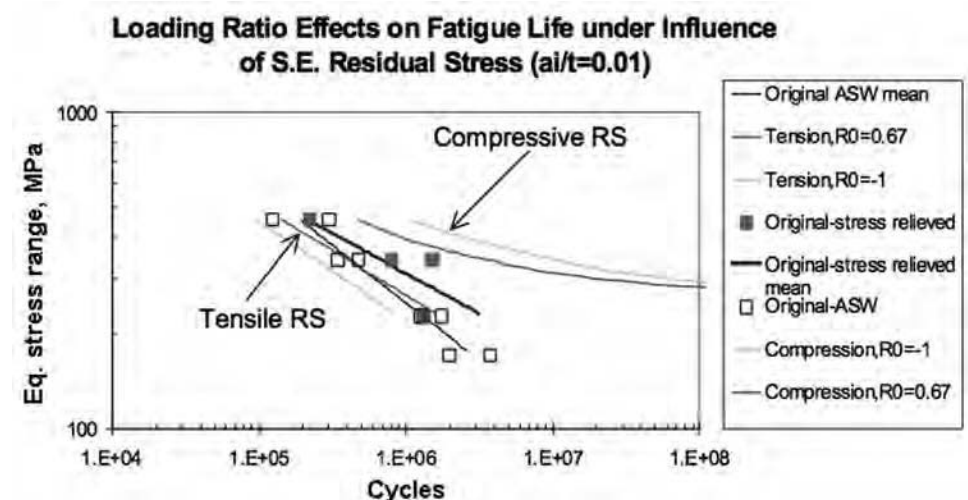


Fig. 18 Calculated increase in fatigue life predicted by the modification of residual stresses (RS) in the weld. Note that an order of magnitude or more increase in fatigue life is predicted due to the presence of compressive stress near the root of the weld. Source: Ref 49

Use of Optimization Methodologies

With the development of these integrated models, it is now possible to use the models as a virtual process design tool. Similar to experimental trial-and-error optimization, these models can be run over a wide range of process and material parameters. However, there are two challenges in the implementation of this. These are the inability of the models to do an exhaustive search and the lack of robust material parameters that describe the physical processes. In this regard, optimization methodologies have proved to be useful. Muruganath et al. (Ref 196) have used commercial optimization software so that optimum weld metal composition can be designed for maximizing the weld metal toughness. In this work, the exhaustive search of an artificial neural network model for weld metal toughness was avoided by using generic and stochastic optimization algorithms. The optimization exercise led to a weld metal composition that was in agreement with experimental measurements (Fig. 23). Although, in this exercise, the time for one set of calculations is not more than 10 s, the previously mentioned methodology proved the utility of the optimization tools. Recently, the aforementioned methodology was used to arrive at weld metal compositions that will maximize acicular ferrite in pipeline steel welds (Ref 197).

The previous example is based on a condition that a model for Charpy toughness is verified and validated. However, in certain conditions, the uncertainties of the modeling results are related to the parameters and constants used in the models. For example, in fluid flow simulation of arc welding, there arc uncertainties in the arc efficiency (η), arc radius (r^*), arc energy distribution parameter (d), effective thermal conductivity (k^*), and effective viscosity (μ) of the liquid metal. To predict the weld pool shape with greater accuracy, it is necessary to obtain these parameters by calibration with a limited number of experimental data. Similar to the earlier example, an exhaustive search of parameter space for these variables (η , r^* , d , k^* , and μ) is computationally impractical. To address this challenge, De and DebRoy (Ref 198) developed an elegant optimization methodology to derive these parameters using optimization algorithms. The algorithm evaluates various combinations of parameter space and tries to minimize an objective function that is a function of difference between the experimentally observed weld pool size and the predicted weld pool size. The progress of the optimization is shown in Fig. 24. As soon as, η , r^* , d , k^* , and μ are calibrated using the aforementioned method, the heat-transfer and fluid flow model can be used for a wide range of process parameters. The previously mentioned methodology has become a standard technique among weld-modeling researchers.

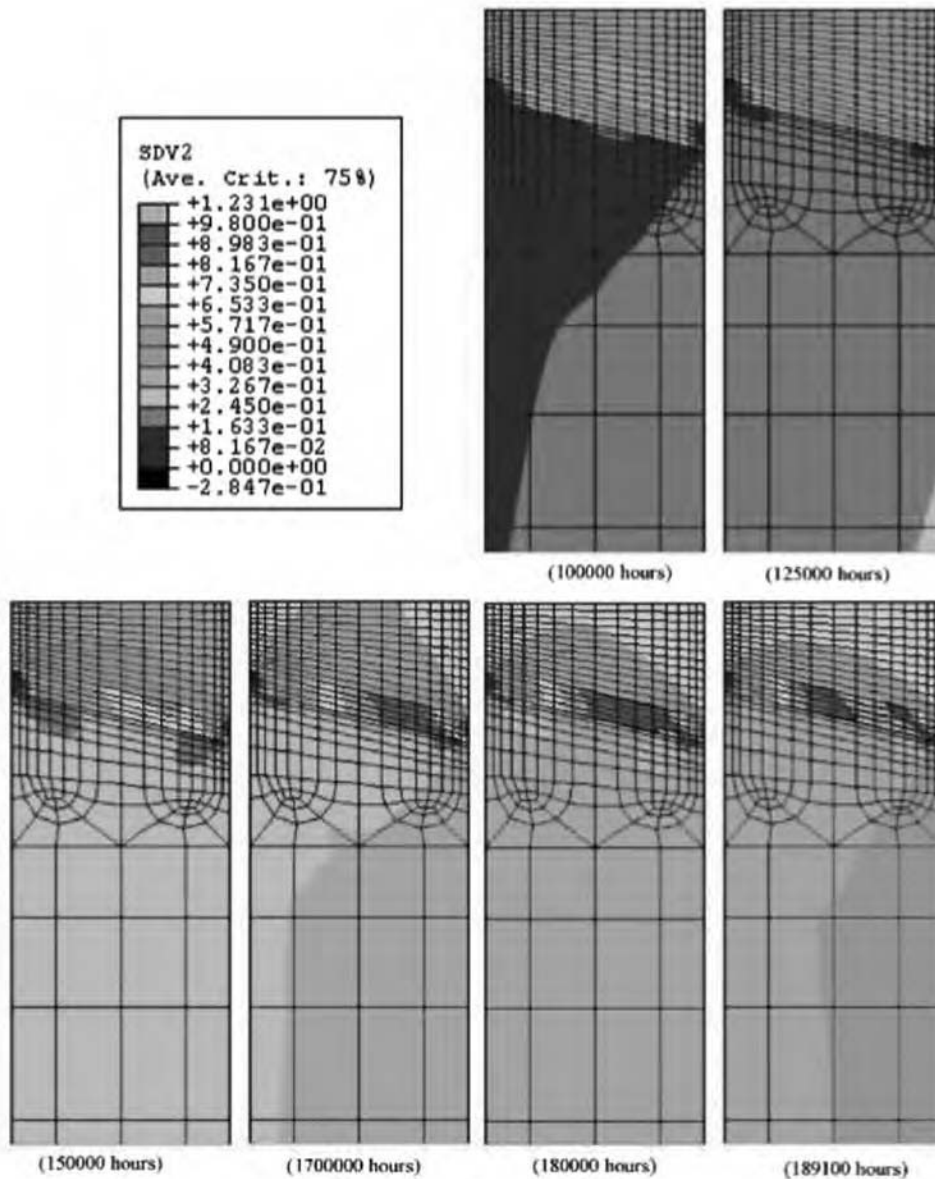


Fig. 19 Predicted accumulation of creep damage in the heat-affected zone of a chromium-molybdenum steel using constitutive equations as a function of service lifetime. Source: Ref 192

Table 1 Software tools for integrated weld modeling

Software	Internet link	Platform
SYSWELD	http://www.esi-group.com/products/welding	Desktop
VrWeld	http://goldaktec.com/vrweld.html	Desktop
VFT	http://www.battelle.org/	Desktop
WELDSIM	http://www.aws.org/wj/2008/05/wj200805/wj0508-36.pdf	Desktop
SORPAS	http://www.swantec.com/sorpas.htm	Desktop
E-WeldPredictor	http://calculations.ewi.org/VJP/	Internet

being considered for detailed experimental evaluations. It is important to note that this tool now can be used for seamlessly evaluating the process-material effects and satisfies the need identified earlier.

Currently, this tool is not comprehensive for a wide range of geometries (fillet welds), boundary

conditions (restraints), processes (resistance, laser, friction stir welding, etc.), alloy systems (aluminum, titanium, etc.), and performances (toughness, creep, fatigue, etc.). However, the framework can be modified for these needs with the development of submodels for these processes, materials, and performances (Fig. 21).

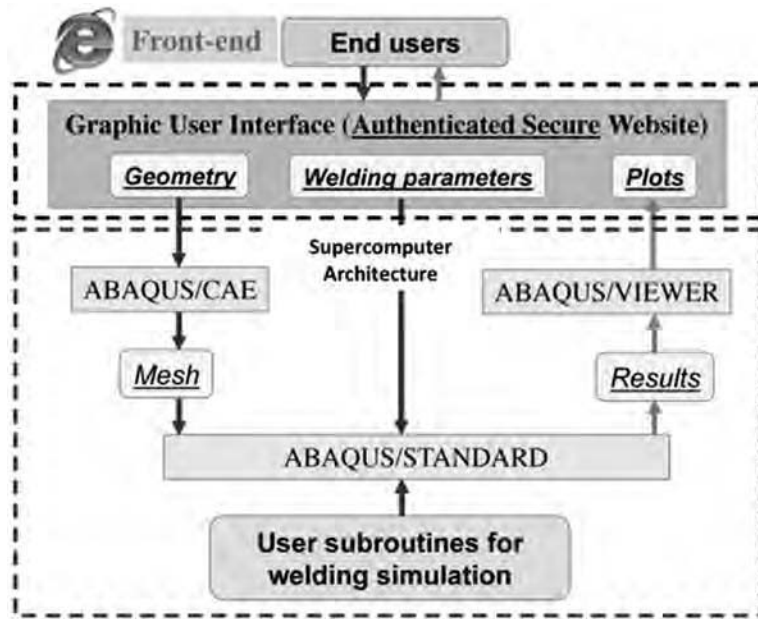


Fig. 20 Architecture for deploying computational weld mechanics models through internet technology and supercomputing architecture. This architecture allows for calculation of thermal cycle, microstructure, residual stress, and distortion within a single computer model

Concluding Remarks

The integrated weld process modeling methodology presented in this article is in alignment with the needs identified by the National Materials Advisory Board. In a report, integrated computational materials engineering is considered as a transformational discipline for improved competitiveness and national security (Ref 199). The integrated weld-modeling activity will be crucial for developing and deploying advanced materials in practical applications. Moreover, these tools will also accelerate the critical development and deployment of hybrid materials (Ref 200), which rely on a wide range of materials joined in a specific geometric shape and are expected to fill the holes in the material property space (Ref 201).

ACKNOWLEDGMENTS

The author would like to thank the collaboration with world-class researchers in the area of integrated computational weld modeling from The Pennsylvania State University, Oak Ridge National Laboratory, Caterpillar, Edison Welding Institute, Lincoln Electric Company, Engineering Mechanics Corporation of Columbus, Lawrence Livermore National Laboratory, BAM (Germany), and The Ohio State University. Many of the plots and graphs used in the article are derived from these collaborative works.

The author also acknowledges the permission to use various figures derived from the published work of international researchers in this area.

REFERENCES

1. Welding Technology Roadmap, U.S. Department of Energy, Sept 2000, <http://files.aws.org/research/roadmap.pdf>
2. M.F. Ashby and K.E. Easterling, A First Report on Diagrams for Grain Growth in Welds, *Acta Metall.*, Vol 30, 1982, p 1969–1978
3. H.K.D.H. Bhadeshia, L.-E. Svensson, and B. Grefott, A Model for the Development of Microstructure in Low-Alloy Steel (Fe-Mn-Si-C) Weld Deposits, *Acta Metall.*, Vol 33, 1985, p 1271–1283
4. H. Cerjak and K.E. Easterling, Ed., *Mathematical Modeling of Weld Phenomena*, The Institute of Materials, London, 1993
5. S.A. David and J.M. Vitek, Correlation between Solidification Parameters and Weld Microstructures, *Int. Mater. Rev.*, Vol 34, 1989, p 213–245
6. T. DebRoy and S.A. David, Physical Processing in Fusion Welding, *Rev. Mod. Phys.*, Vol 67, 1995, p 85–112
7. A.H. Dilawari, T.W. Eager, and J. Szekely, Analysis of Heat and Fluid Flow Phenomena in Electro Slag Welding, *Weld. J.*, Vol 57, 1978, p s24–s30
8. J. Ion and K.E. Easterling, Computer Modeling of Weld-Implant Testing, *Mater. Sci. Technol.*, Vol 1, 1985, p 405–411
9. D.F. Watt et al., An Algorithm for Modeling Microstructural Development in Weld Heat-Affected-Zones, A. Reaction—Kinetics, *Acta Metall.*, Vol 36, 1988, p 3029–3035
10. O. Grong, *Metallurgical Modeling of Welding*, *Materials Modeling Series*, The Institute of Materials, London, 1994
11. J.S. Kirkaldy, Diffusion-Controlled Phase Transformations in Steels—Theory and Applications, *Scand. J. Metall.*, Vol 20, 1991, p 50–61
12. T. Koseki et al., Numerical Modeling of Solidification and Subsequent Transformation of Fe-Cr-Ni Alloys, *Metall. Mater. Trans. A.*, Vol 25, 1994, p 1309–1321
13. S. Kou and Y.H. Wang, Computer Simulation of Convection in Moving Arc Weld Pools, *Metall. Trans. A—Phys. Metall. Mater. Sci.*, Vol 17, 1986, p 2271–2277
14. J.B. Leblond and J. Devaux, A New Kinetic Model for Anisothermal Metallurgical Transformations in Steels Including Effect of Austenite Grain Size, *Acta Metall.*, Vol 32, 1984, p 137–146
15. F. Matsuda, H. Nakagawa, and J. Lee, Numerical Analysis of Micro-Segregation during Welding, *Q. J. Jpn. Weld. Soc.*, Vol 9, 1991, p 85–92
16. M. Rappaz et al., Development of Microstructures in Fe-15Ni-15Cr Single Crystal Electron Beam Welds, *Metall. Trans. A.*, Vol 20, 1989, p 1125–1138
17. J. Szekely and G. Opreper, Transient Heat and Fluid Flow Phenomena in Arc Welding, *J. Met.*, Vol 35, 1983, p 49
18. J.M. Vitek, S.A. Vitek, and S.A. David, Numerical Modeling of Diffusion Controlled Phase Transformations in Ternary Systems and Application to the Ferrite to Austenite Transformation in the Fe-Cr-Ni System, *Metall. Mater. Trans. A.*, Vol 26, 1995, p 2007–2025
19. N. Yurioka et al., Determination of Necessary Preheating Temperature in Steel Welding, *Weld. J.*, Vol 62, 1983, p s147–s153
20. T. Zacharia et al., Weld Pool Development during GTA and Laser-Beam Welding of Type 304 Stainless Steel, 1. Theoretical Analysis, *Weld. J.*, Vol 68, 1989, p s499–s509
21. J.H. Hattel, Integrated Modeling in Materials and Process Technology, *Mater. Sci. Technol.*, Vol 24, 2008, p 137–148
22. J. Ronda and G.J. Oliver, Consistent Thermo-Mechano-Metallurgical Model of Welded Steel with Unified Approach to Derivation of Phase Evolution Laws and Transformation Induced Plasticity, *Comput. Methods Appl. Mech. Eng.*, Vol 189, 2000, p 361–417
23. SYSWELD, ESI Group, http://www.esi-group.com/products/welding-old/sysweld/sysweld_brochure.pdf
24. X.L. Chen et al., Achieving Manufacturing Quality and Reliability Using Thru-Process Simulation, *J. Phys. IV (France)*, Vol 120, 2004, p 793–800
25. VrWeld, Goldak Technologies Inc., <http://goldaktec.com/newsandevents.html>

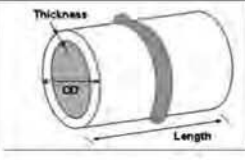
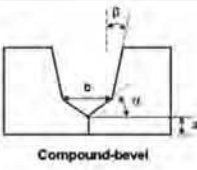
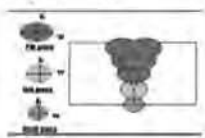
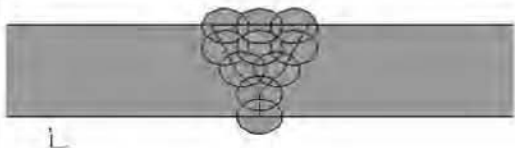
Input	Condition 1	Condition 2																																												
Weld Geometry		Outer diameter = 914 mm Wall thickness = 10 mm Length = 203 mm (8 inch)																																												
Joint Geometry		a = 2.54 mm (0.1 inch); b = 5.08 mm (0.2 inch); a = 45 deg; b = 30 deg																																												
Materials																																														
Base Metal Composition	X - 65: Fe - 0.07C - 0.19Si - 1.36Mn - 0.2Cr - 0Mo (wt.%)	2.25Cr1Mo: Fe - 0.15C - 0.30Si - 0.66Mn - 2.26Cr - 1.15Mo (wt.%)																																												
Filler Metal (ER70S6)	Fe-0.09C-0.5Si-1.1Mn (wt.%)	Fe-0.09C-0.5Si-1.1Mn (wt.%)																																												
Process	Gas Metal Arc Welding																																													
Process Parameters & Bead Shapes	<p>Welding Procedure</p>  <table border="1" data-bbox="625 955 812 1050"> <tr> <td colspan="4">Preheating Temperature</td> </tr> <tr> <td>302</td> <td>F</td> <td>150</td> <td>C</td> </tr> <tr> <td colspan="4">Post weld Temperature</td> </tr> <tr> <td>212</td> <td>F</td> <td>100</td> <td>C</td> </tr> </table> <table border="1" data-bbox="316 1113 812 1228"> <thead> <tr> <th>Plan</th> <th>Width (mm)</th> <th>Depth (mm)</th> <th>Conc. (A)</th> <th>Volume (cc)</th> <th>Grind Face (mm)</th> <th>Heat Input (kJ/in)</th> </tr> </thead> <tbody> <tr> <td>Root</td> <td>0.200</td> <td>0.150</td> <td>120.0</td> <td>14.0</td> <td>10.0</td> <td>10080</td> </tr> <tr> <td>Flt.</td> <td>0.200</td> <td>0.150</td> <td>120.0</td> <td>14.0</td> <td>10.0</td> <td>10080</td> </tr> <tr> <td>Fill</td> <td>0.200</td> <td>0.150</td> <td>120.0</td> <td>14.0</td> <td>10.0</td> <td>10080</td> </tr> </tbody> </table> <p>Conversion parameters: 1 ipm = 25.4 mm.min⁻¹; 1 inch = 25.4 mm</p>		Preheating Temperature				302	F	150	C	Post weld Temperature				212	F	100	C	Plan	Width (mm)	Depth (mm)	Conc. (A)	Volume (cc)	Grind Face (mm)	Heat Input (kJ/in)	Root	0.200	0.150	120.0	14.0	10.0	10080	Flt.	0.200	0.150	120.0	14.0	10.0	10080	Fill	0.200	0.150	120.0	14.0	10.0	10080
Preheating Temperature																																														
302	F	150	C																																											
Post weld Temperature																																														
212	F	100	C																																											
Plan	Width (mm)	Depth (mm)	Conc. (A)	Volume (cc)	Grind Face (mm)	Heat Input (kJ/in)																																								
Root	0.200	0.150	120.0	14.0	10.0	10080																																								
Flt.	0.200	0.150	120.0	14.0	10.0	10080																																								
Fill	0.200	0.150	120.0	14.0	10.0	10080																																								
Bead Locations																																														

Fig. 21 Table showing an overview of input parameters that can be considered by a computational weld mechanics model within the E-WeldPredictor architecture. Similar simulations can be performed by other models (Table 1); however, they require a dedicated workstation

Phenomena 5, The Institute of Materials, United Kingdom, 2001

32. H. Cerjak and H.K.D.H. Bhadeshia, Ed., *Mathematical Modeling of Weld Phenomena 6*, The Institute of Materials, United Kingdom, 2001
33. H. Cerjak, H.K.D.H. Bhadeshia, and E. Kozeschnik, Ed., *Mathematical Modeling of Weld Phenomena 7*, Verlag der Technischen Universität Graz, 2005
34. H. Cerjak, H.K.D.H. Bhadeshia, and E. Kozeschnik, Ed., *Mathematical Modeling of Weld Phenomena 8*, The Institute of Materials, United Kingdom, 2007
35. S.A. David, Ed., *Trends in Welding Research in the United States*, American Society for Metals, 1982
36. S.A. David, T. DebRoy, J.C. Lippold, H. B. Smartt, and J.M. Vitek, Ed., *Trends in Welding Research, Seventh International Conference Proceedings*, ASM International, 2006
37. J.A. Goldak and M. Akhlagi, *Computational Welding Mechanics*, Springer, 2005
38. D. Radjaj, *Welding Residual Stresses and Distortion: Calculation and Measurement*, DVS Verlag, Germany, 2003
39. O. Grong, *Metallurgical Modeling of Welding*, 2nd ed., The Institute of Materials, United Kingdom, 1997
40. S.S. Babu, Thermodynamic and Kinetic Models for Describing Microstructure Evolution during Joining of Metals and Alloys, *Int. Mater. Rev.*, Vol 54 (No. 6), 2009, p 333–367
41. D. Rosenthal, Mathematical Theory of Heat Distribution during Welding and Cutting, *Weld. J.*, Vol 20, 1941, p 220s–234s
42. J. Goldak, A. Chakravarti, and M. Bibby, A New Finite Element Model for Welding Heat Sources, *Metall. Trans. B*, Vol 15, 1984, p 299–305
43. S.M. Kelly and S.L. Kampe, Microstructural Evolution in Laser-Deposited Multilayer Ti-6Al-4V Builds: Part I. Microstructural Characterization, *Metall. Mater. Trans. A*, Vol 35, 2004, p 1861–1867
44. S.M. Kelly and S.L. Kampe, Microstructural Evolution in Laser-Deposited Multilayer Ti-6Al-4V Builds: Part II. Thermal Modeling, *Metall. Mater. Trans. A*, Vol 35, 2004, p 1869–1879
45. S.M. Kelly, “Thermal and Microstructure Modeling of Metal Deposition Processes with Application to Ti-6Al-4V,” Ph.D. thesis, Virginia Polytechnic Institute and University, Blacksburg, VA, 2004
46. Y. Yang, Edison Welding Institute, Columbus, OH, unpublished work
47. K. Mundra et al., Role of Thermophysical Properties in Weld Pool Modeling, *Weld. J.*, Vol 71, 1992, p s313–s320
48. W. Zhang, C.-H. Kim, and T. DebRoy, Heat and Fluid Flow in Complex Joints

26. O.R. Myhr and O. Grong, Utilizing a Predictive Tool for Designing Welded Aluminum Components, *Weld. J.*, May 2008
27. E-WeldPredictor, EWI, <http://calculations.ewi.org/vjp/EWeldPredictor.html>
28. H. Cerjak and H.K.D.H. Bhadeshia, Ed., *Mathematical Modeling of Weld Phenomena 2*, The Institute of Materials, United Kingdom, 1995

29. H. Cerjak and H.K.D.H. Bhadeshia, Ed., *Mathematical Modeling of Weld Phenomena 3*, The Institute of Materials, United Kingdom, 1997
30. H. Cerjak and H.K.D.H. Bhadeshia, Ed., *Mathematical Modeling of Weld Phenomena 4*, The Institute of Materials, United Kingdom, 1998
31. H. Cerjak and H.K.D.H. Bhadeshia, Ed., *Mathematical Modeling of Weld*












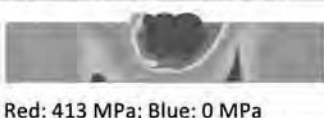
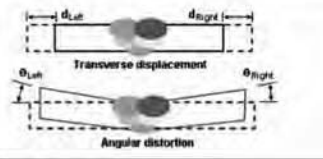
Results	X-65	2.25CrMo
Temperature Distribution Red: 1545 °C; Blue: 150 °C		 (a)
Ferrite Red: 100% Blue: 0%		 (b)
Bainite Red: 100% Blue: 0%		 (c)
Martensite Red: 100% Blue: 0%		 (d)
Hardness Distribution	 Red: 258 VHN; Blue: 127 VHN	 Red: 445 VHN; Blue: 127 VHN
Residual Stress (von-mises stresses)	 Red: 467 MPa; Blue: 0 MPa	 Red: 413 MPa; Blue: 0 MPa
Distortion		(e)
Transverse Displacement	Left 0.19; Right 0.07	Left 0.27; Right 0.08
Angular Distortion (deg)	Left 0.53; Right 0.54	Left 0.61; Right 0.63

Fig. 22 Results from E-WeldPredictor software for routine comparison of thermal cycle, microstructure, residual stress, and distortion as a function of two steel compositions

- during Gas Metal Arc Welding, Part I: Numerical Model of Fillet Welding, *J. Appl. Phys.*, Vol 95, 2004, p 5210–5219
- Z. Yang and H.W. Ludewig, "Virtual Welded-Joint Design Integrating Advanced Materials and Processing Techniques," Final technical report, DF-FC36-01ID14242, <http://www.osti.gov/bridge/purl.cover.jsp?purl=/862362-8Vmn0R/>, accessed on May 1, 2009
 - K. Mundra, T. DebRoy, S.S. Babu and S. A. David, Weld Metal Microstructure Calculations Form Fundamentals of Transport Phenomena in the Arc Welding of Low-Alloy Steels, *Weld. J.*, Vol 76, 1997, p S163–S171
 - Z. Yang and T. DebRoy, Modeling of Macro- and Microstructures of Gas Metal

- Arc Welded HSLA-100 Steel, *Metall. Mater. Trans. A*, Vol 30, 1999, p 483–493
- S. Fiore, S.S. Babu, and B. Glodowski, "Factors Controlling Microstructure and Properties of Steel Heat-Affected Zones—An Overview," unpublished research, 2009
 - J. Dearden and H. O'Neill, A Guide to the Selection and Welding of Low Alloy Structural Steel, *Trans. Inst. Weld.*, Vol 3, 1940, p 203–214
 - N. Yurioka, H. Suzuki, S. Ohshita, and S. Saito, Determination of Necessary Preheating Temperature in Steel Welding, *Weld. J. Res. Suppl.*, Vol 62 (No. 6), June 1983, p 147s–153s
 - J.C. Ion, K.E. Easterling, and M.F. Ashby, A Second Report of Diagrams of

- Microstructure and Hardness for Heat Affected Zones in Welds, *Acta Metall.*, Vol 32 (No. 11), 1984, p 1949–1962
- Edison Welding Institute, <http://calculations.ewi.org>
 - H.K.D.H. Bhadeshia, Neural Networks in Materials Science, *ISIJ Int.*, Vol 39, 1999, p 966–979
 - S.S. Babu and H.K.D.H. Bhadeshia, The Transition from Bainite to Acicular Ferrite in Reheated Fe-Cr-C Weld Deposits, *Mater. Sci. Technol.*, Vol 6, 1990, p 1005–1020
 - S.J. Jones and H.K.D.H. Bhadeshia, Kinetics of the Simultaneous Decomposition of Austenite into Several Transformation Kinetics, *Acta Mater.*, Vol 45 (No. 7), 1997, p 2911–2920
 - Materials Algorithm Project, University of Cambridge, United Kingdom, <http://www.msm.cam.ac.uk/map/mapmain.html>
 - O.R. Myhr and O. Grong, Process Modeling Applied to 6082-T6 Aluminum Weldments 1: Reaction Kinetics, *Acta Metall. Mater.*, Vol 39, 1992, p 2693–2702
 - O.R. Myhr and O. Grong, Process Modeling Applied to 6082-T6 Aluminum Weldments 2: Application of Model, *Acta Metall. Mater.*, Vol 39, 1992, p 2703–2708
 - C. Zener (quoted in C.S. Smith), Grains, Phases and Interphases; An Interpretation of Microstructure, *Trans. Metall. Soc.*, Vol 175, 1948, p 15–51
 - B. Radhakrishnan and T. Zacharia, Monte-Carlo Simulation of Grain-Boundary Pinning in the Weld Heat-Affected-Zone, *Metall. Mater. Trans. A*, Vol 26, 1995, p 2123–2130
 - B. Radhakrishnan and R.G. Thompson, Kinetics of Grain-Growth in the Weld Heat-Affected-Zone of Alloy-718, *Metall. Mater. Trans. A*, Vol 24, 1993, p 2773–2785
 - S. Mishra and T. DebRoy, Non-Isothermal Grain Growth in Metals and Alloys, *Mater. Sci. Technol.*, Vol 22, 2006, p 253–278
 - S.S. Babu et al., Solidification and Microstructure Modeling of Welds in Aluminum Alloys 5754 and 6111, *Sci. Technol. Weld. Join.*, Vol 6, 2001, p 31–40
 - S.S. Babu et al., Microstructural Development in PWA1480 Electron Beam Welds—An Atom Probe Field Ion Microscopy Study, *Appl. Surf. Sci.*, Vol 94/95, 1996, p 280–287
 - J.O. Andersson et al., Thermo-Calc and DicTra Computational Tools for Materials Science, *Calphad*, Vol 26, 2002, p 273–312
 - O. Grong and N. Christensen, Factors Controlling MIG Weld Metal Chemistry,

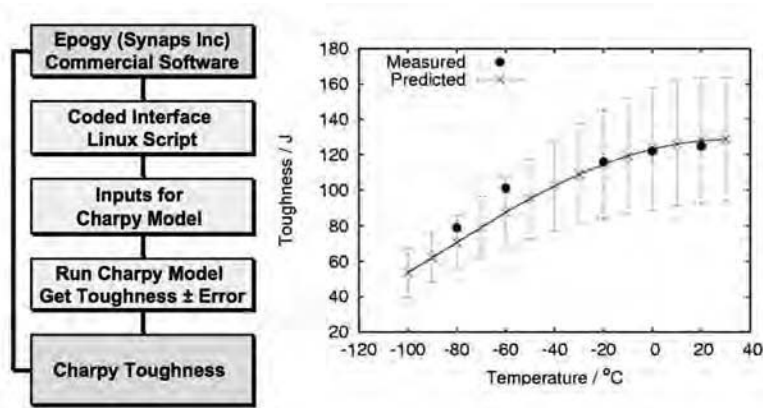


Fig. 23 Methodology used to optimize welding consumable composition. The methodology integrates commercial optimization software with a neural net model for weld metal toughness. The model predicted the optimized weld metal composition for maximizing toughness as a function of temperature. The model predictions are also compared with experimental measurements. The agreement shows the feasibility of optimization methodologies.

- Scand. J. Metall.*, Vol 12, 1983, p 155–165
71. M. Liljas and J.O. Nilsson, Development of Commercial Nitrogen-Rich Stainless Steels, High Nitrogen Steels '98, *Mater. Sci. Forum*, Vol 318 (No. 3), 1999, p 189–200
 72. V. Muthupandi et al., Effect of Nickel and Nitrogen Addition on the Microstructure and Mechanical Properties of Power Beam Processed Duplex Stainless Steel (UNS 31803) Weld Metals, *Mater. Lett.*, 2005, p 2305–2309
 73. S. Hertzman et al., Influence of Shielding Gas Composition and Welding Parameters on the N-Content and Corrosion Properties of Welds in N-Alloyed Stainless Steel Grades, *ISIJ Int.*, Vol 36, 1996, p 968–976
 74. S. Hertzman, The Influence of Nitrogen on Microstructure and Properties of Highly Alloyed Stainless Steels, *ISIJ Int.*, Vol 41, 2001, p 580–589
 75. K. Mundra and T. DebRoy, A General Model for Partitioning of Gases between a Metal and Its Plasma Environment, *Metall. Mater. Trans. A*, 1995, p 149–157
 76. T.A. Palmer and T. DebRoy, Physical Modeling of Nitrogen Partition between the Weld Metal and Its Plasma Environment, *Weld. J.*, Vol 75, 1996, p s197–s207
 77. S.S. Babu et al., Reactive Gas Shielding during Laser Surface Alloying for Production of Hard Coatings, *Surf. Coat. Technol.*, Vol 200, 2006, p 2663–2671
 78. M. Du Toit and P.C. Pistorious, Nitrogen Control during Arc Welding of Stainless Steel—Part 1: Experimental Observations, *Weld. J.*, Vol 82, 2003, p 219s–224s
 79. M. Du Toit and P.C. Pistorious, Nitrogen Control during Arc Welding of Stainless Steel—Part 2: A Kinetic Model for Nitrogen Absorption and Desorption, *Weld. J.*, Vol 82, 2003, p 231s–237s
 80. A. Gruszczyk, The Kinetics of Nitrogen Absorption by Arc-Melted Fe-C-Mn-Type Filler Metals, *Weld. J.*, Vol 83, 2004, p 94s–101s
 81. R.E. Francis, J.E. Jones, and D.L. Olson, Effect of Shielding Gas Oxygen Activity on Weld Metal Microstructure of GMA Welded Microalloyed HSLA Steel, *Weld. J.*, Vol 69, 1990, p s408–s415
 82. S.A. Gedeon and T.W. Eagar, Thermochemical Analysis of Hydrogen Absorption in Welding, *Weld. J.*, Vol 69, 1990, p s264–s271
 83. J.H. Kiefer, Effect of Moisture Contamination and Welding Parameters on Diffusible Hydrogen, *Weld. J.*, Vol 75, 1996, p s155–s161
 84. K. Mundra, J.M. Blackburn, and T. DebRoy, Absorption and Transport of Hydrogen during Gas Metal Arc Welding of Low Alloy Steel, *Sci. Technol. Weld. Join.*, Vol 2, 1997, p 174–184
 85. M.J. McNallan and T. DebRoy, Effect of Temperature and Composition on Surface Tension in Fe-Ni-Cr Alloys Containing Sulfur, *Metall. Trans. B*, Vol 4, 1991, p 557–560
 86. C.R. Heiple and J.R. Roper, Mechanism for Minor Element Effect on GTA Fusion Zone Geometry, *Weld. J.*, Vol 61, 1982, p S97–S102
 87. P. Sahoo, T. DebRoy, and M.J. McNallan, Surface Tension of Binary Metal—Surface Active Solute Systems under Conditions Relevant to Welding Metallurgy, *Metall. Mater. Trans. B*, Vol 19, 1988, p 483–491
 88. A. Powell, Mathematical Modeling of Vapor-Plume Focusing in Electron-Beam Evaporation, *Metall. Mater. Trans. A*, Vol 32, 2001, p 1959–1966
 89. K. Mundra and T. DebRoy, Calculation of Weld Metal Composition Change in High-Power Conduction Mode Carbon Dioxide Laser Welded Stainless Steels, *Metall. Mater. Trans. B*, Vol 24, 1993, p 145–155
 90. X. He, T. DebRoy, and P.W. Fuerschbach, Alloying Element Vaporization during Laser Spot Welding of Stainless Steel, *J. Phys. D—Appl. Phys.*, Vol 36, 2003, p 3079–3088
 91. J.W. Sowards, “Development of a Chromium Free Consumable for Joining Stainless Steels,” Ph.D. thesis, The Ohio State University, 2009
 92. U. Mitra and T.W. Eagar, Slag-Metal Reactions during Welding 1. Evaluation and Reassessment of Existing Theories, *Metall. Trans. B*, Vol 22, 1991, p 65–71
 93. U. Mitra and T.W. Eagar, Slag-Metal Reactions during Welding 2. Theory, *Metall. Trans. B*, Vol 22, 1991, p 73–81
 94. U. Mitra and T.W. Eagar, Slag-Metal Reactions during Welding 3. Verification of the Theory, *Metall. Trans. B*, Vol 22, 1991, p 83–100
 95. O. Grong, T.A. Siewert, G.P. Martins, and D.L. Olson, A Model for the Silicon-Manganese Deoxidation of Steel Weld Metals, *Metall. Trans. A*, Vol 17, 1986, p 1797–1807
 96. C.S. Chai and T.W. Eagar, Slag-Metal Equilibrium during Submerged Arc-Welding, *Metall. Trans. B*, Vol 12, 1981, p 539–547
 97. T. Lau, G.C. Weatherly, and A. McLean, The Sources of Oxygen and Nitrogen Contamination in Submerged-Arc Welding Using CaO-Al₂O₃ Based Fluxes, *Weld. J.*, Vol 64, 1985, p s343–s347
 98. M. Zinigrad, Computational Methods for Development of New Welding Materials, *Comput. Mater. Sci.*, Vol 37, 2006, p 417–424
 99. A.O. Klukun and O. Grong, Mechanisms of Inclusion Formation in Al-Ti-Si-Mn Deoxidized Steel Weld Metals, *Metall. Trans. A*, Vol 20, 1989, p 1335–1349
 100. H. Terashima and P.H.M. Hart, Effect of Aluminum on C-Mn-Nb Steel Submerged-Arc Weld Metal Properties, *Weld. J.*, Vol 63, 1984, p S173–S183
 101. H. Homma et al., Improvement of HAZ Toughness in HSLA Steel by Introducing Finely Dispersed Ti-Oxide, *Weld. J.*, Vol 66, 1987, p S301–S309
 102. F.C. Liao and S. Liu, Effect of Deoxidation Sequence on Carbon Manganese Steel Weld Metal Microstructures, *Weld. J.*, Vol 71, 1992, p S94–S103
 103. G. Thewlis and D.R. Milner, Inclusion Formation in Arc Welding, *Weld. J.*, Vol 56, 1977, p S281–S288
 104. K.C. Hsieh, S.S. Babu, and J.M. Vitek, Calculation of Inclusion Formation in Low-Alloy Steel Welds, *Mater. Sci. Eng. A*, Vol 215, 1996, p 84–91
 105. T. Koseki, S. Ohkita, and N. Yurioka, Thermodynamic Study of Inclusion

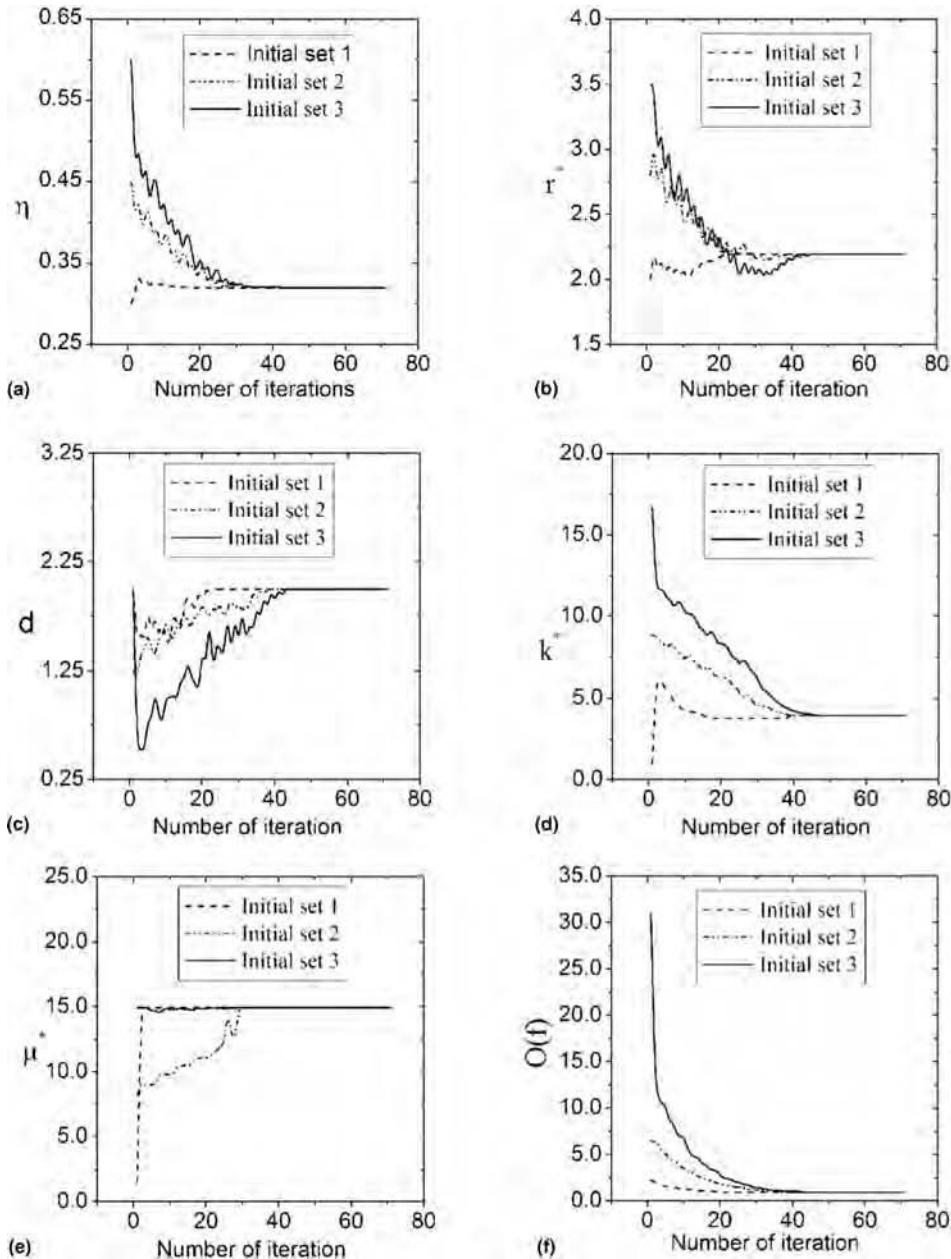


Fig. 24 Optimization methodology for arriving at parameters that are not possible or are difficult to measure. In this demonstration, uncertainty in the arc efficiency, arc radius, energy distribution parameter, effective thermal conductivity, and effective viscosity is reduced through optimization schemes.

- Formation in Low Alloy Steel Weld Metals, *Sci. Technol. Weld. Join.*, Vol 2, 1997, p 65–69
106. K. Ichikawa, T. Koseki, and M. Fuji, Thermodynamic Estimation of Inclusion Characteristics in Low Alloy Steel Weld Metals, *Sci. Technol. Weld. Join.*, Vol 2, 1997, p 231–235
107. S.S. Babu et al., Model for Inclusion Formation in Low Alloy Steel Welds, *Sci. Technol. Weld. Join.*, Vol 4, 1999, p 276–284
108. J. Lehmann, P. Rocabois, and H. Gaye, Kinetic Model of Non-Metallic Inclusions Precipitation during Steel Solidification, *J. Non-Cryst. Solids*, Vol 282, 2001, p 61–71
109. T. Hong and T. DebRoy, Time-Temperature-Transformation Diagrams for the Growth and Dissolution of Inclusions in Liquid Steels, *Scr. Mater.*, Vol 44, 2001, p 847–852
110. T. Hong and T. DebRoy, Nonisothermal Growth and Dissolution of Inclusions in Liquid Steels, *Metall. Mater. Trans. B*, Vol 34, 2003, p 267–269
111. S.S. Babu et al., Toward Prediction of Microstructural Evolution during Laser Surface Alloying, *Metall. Mater. Trans. A*, Vol 33, 2002, p 1189–1200
112. K. Mundra et al., Weld Metal Microstructure Calculations from Fundamentals of Transport Phenomena in the Arc Welding of Low-Alloy Steels, *Weld. J.*, Vol 76, 1997, p S163–S171
113. T. Hong, W. Pitscheneder, and T. DebRoy, Quantitative Modeling of Motion, Temperature Gradients, and Growth of Inclusions in Weld Pool, *Sci. Technol. Weld. Join.*, Vol 3, 1998, p 33–41
114. T. Hong et al., Modeling of Inclusion Growth and Dissolution in the Weld Pool, *Metall. Mater. Trans. B*, Vol 31, 2000, p 161–169
115. S.S. Babu et al., Coarsening of Oxide Inclusions in Low Alloy Steel Welds, *Sci. Technol. Weld. Join.*, Vol 1, 1996, p 17–27
116. J.M. Vitek et al., Welding of Single-Crystal Nickel-Based Superalloys, *Mathematical Modeling of Weld Phenomena 7*, H. Cerjak, H.K.D.H. Bhadeshia, and E. Kozeschnik, Ed., Technical University of Graz, 2005, p 235–250
117. J.M. Vitek et al., Analysis of Stray Grain Formation in Single-Crystal Nickel-Based Superalloy Welds, *Superalloys 2004*, K.A. Green, T.M. Pollock, H. Harada, T.E. Howson, R.C. Reed, J.J. Schira, and S. Walston, Ed., The Minerals, Metals & Materials Society, Warrendale, PA, 2004, p 459–466
118. S.N. Banovic, J.N. Dupont, and A.R. Marder, Dilution Control in Gas Tungsten Arc Welding Involving Super Austenitic Stainless Steels and Nickel Based Alloys, *Metall. Mater. Trans. B*, Vol 32, 2001, p 1171–1176
119. E.P. George, S.S. Babu, S.A. David, and B.B. Seth, IN-939 Based Superalloys with Improved Weldability, *Proceedings of BALTICA V* (Helsinki, Finland), 2001
120. D.F. Susan et al., A Solidification Diagram from Ni-Cr-Mo-Gd Alloys Estimated by Quantitative Microstructural Characterization and Thermal Analysis, *Metall. Mater. Trans. A*, Vol 37, 2006, p 2817–2825
121. J.N. Dupont, Mathematical Modeling of Solidification Paths in Ternary Alloys: Limiting Cases of Solute Redistribution, *Metall. Mater. Trans. A*, Vol 37, 2006, p 1937–1947
122. T.D. Anderson et al., Phase Transformations and Microstructure Evolution of Mo Bearing Stainless Steels, *Metall. Mater. Trans. A*, Vol 38, 2007, p 671–685
123. T. Koseki et al., Numerical Modeling of Weld Solidification of Austenitic Stainless Steels, *Proceedings of the Seventh International Symposium on Physical Simulations*, 1997, p 75–80
124. T. Koseki, H. Inoue, and A. Nogami, Prediction and Control of Weld Solidification in Steels and Ni-Base Alloys, *Trends in*

- Welding Research*, J.M. Vitek, S.A. David, J.A. Johnson, H.B. Smart, and T. DebRoy, Ed., ASM International, 1999, p 751–760
125. J.M. Vitek and S.A. David, Prediction of Non-Equilibrium Solidification Modes in Austenitic Stainless Steel Laser Welds, *Laser Materials Processing IV*, J. Mazumder, K. Mukerjee, and B.L. Modriks, Ed., TMS, Warrendale, PA, 1994, p 153–167
 126. W. Löser and D.M. Herlach, Theoretical Treatment of the Solidification Undercooled Fe-Cr-Ni Melts, *Metall. Trans. A*, Vol 23, 1992, p 1585–1591
 127. T. Koseki and M.C. Flemings, Solidification of Undercooled Fe-Cr-Ni Alloys: 3. Phase Stability in Chill Castings, *Metall. Mater. Trans. A*, Vol 28, 1997, p 2385–2395
 128. S. Fukumoto and W. Kurz, Solidification Phase and Microstructure Selection Maps for Fe-Cr-Ni Alloys, *ISIJ Int.*, Vol 39, 1999, p 1270–1279
 129. R. Lagneborg et al., The Role of Vanadium in Microalloyed Steels, *Scand. J. Metall.*, Vol 28, 1999, p 186–241
 130. J.M. Vitek, E. Kozeschnik, and S.A. David, Simulating the Ferrite to Austenite Transformation in Stainless Steel Welds, *Calphad*, Vol 25, 2001, p 217–230
 131. J.R. Yang and H.K.D.H. Bhadeshia, Re-Austenitization Experiments on Some High Strength Steel Weld Deposits, *Mater. Sci. Eng. A*, Vol 118, 1989, p 155–170
 132. L. Li et al., Design of TRIP Steel with High Welding and Galvanizing Performance in Light of Thermodynamics and Kinetics, *J. Iron Steel Res. Int.*, Vol 14, 2007, p 37–41
 133. L. Li et al., Effects of Alloying Element on the Concentration Profile of Equilibrium Phases in Transformation Induced Plasticity Steel, *J. Mater. Sci. Technol.*, Vol 19, 2003, p 273–277
 134. N. Kaputska et al., Effect of GMAW Process and Material Conditions on DP 780 and TRIP 780 Welds, *Weld. J.*, Vol 87, 2008, p 135–149
 135. A. Saha and G.B. Olson, Computer Aided Design of Transformation Toughened Blast Resistant Naval Hull Steels: Part I, *J. Comput.-Aided Mater. Des.*, Vol 14, 2007, p 177–200
 136. S. Hertzman et al., An Experimental and Theoretical Study of Heat Affected Zone Austenite Formation in Three Duplex Stainless Steels, *Metall. Mater. Trans. A*, Vol 28, 1997, p 277–285
 137. H. Lee et al., Effect of Tungsten Addition on Simulated Heat Affected Zone Toughness in 25%Cr Base Super Duplex Stainless Steels, *Mater. Sci. Technol.*, Vol 14, 1998, p 54–60
 138. S.S. Babu et al., Effect of Boron on the Microstructure of Low-Carbon Steel Resistance Seam Welds, *Weld. J.*, Vol 77, 1998, p 2495–2535
 139. O.M. Barabash et al., Evolution of Dislocation Structure in the Heat-Affected-Zone of a Nickel Based Single Crystal, *J. Appl. Phys.*, Vol 96, 2004, p 3673–3679
 140. R.C. Reed and H.K.D.H. Bhadeshia, A Model for Multipass Welds, *Acta Metall. Mater.*, Vol 42, 1994, p 3663–3678
 141. R.C. Reed, “The Characterization and Modeling of Multipass Weld Heat-Affected Zones,” Ph.D. thesis, University of Cambridge, United Kingdom, 1990
 142. E. Keehan et al., New Developments with C-Mn-Ni High Strength Steel Weld Metals, Part A—Microstructure, *Weld. J.*, Vol 85, 2006, p 200s–210s
 143. E. Keehan et al., New Developments with C-Mn-Ni High Strength Steel Weld Metals, Part B—Mechanical Properties, *Weld. J.*, Vol 85, 2006, p 218s–224s
 144. E. Keehan et al., Influence of Carbon, Manganese and Nickel on Microstructure and Properties of Strong Steel Weld Metals Part 1—Effect of Nickel Content, *Sci. Technol. Weld. Join.*, Vol 11, 2006, p 1–8
 145. E. Keehan et al., Influence of Carbon, Manganese and Nickel on Microstructure and Properties of Strong Steel Weld Metals Part 2—Impact Toughness Gain Resulting from Manganese Reductions, *Sci. Technol. Weld. Join.*, Vol 11, 2006, p 9–18
 146. E. Keehan et al., Influence of Carbon, Manganese and Nickel on Microstructure and Properties of Strong Steel Weld Metals Part 3—Increased Strength Resulting from Carbon Additions, *Sci. Technol. Weld. Join.*, Vol 11, 2006, p 19–24
 147. H.K.D.H. Bhadeshia et al., Coalesced Bainite, *Trans. Indian Inst. Met.*, Vol 15, 2006, p 689–694
 148. H.K.D.H. Bhadeshia, Reliability of Weld Microstructure and Property Calculations, *Weld. J.*, Vol 83, 2004, p 237s–243s
 149. P. Hofer et al., Atom Probe Field Ion Microscopy Investigation of Boron Containing Martensitic 9% Cr Steel, *Metall. Mater. Trans. A*, Vol 31, 2000, p 975–984
 150. D. Cole and H.K.D.H. Bhadeshia, Design of Creep-Resistance Steel Welds, *Proc. Mathematical Modeling of Weld Phenomena—V*, H. Cerjak and H.K.D.H. Bhadeshia, Ed., Institute of Materials, 2001, p 431–448
 151. H.K.D.H. Bhadeshia, Neural Networks in Materials Science, *ISIJ Int.*, Vol 39, 1999, p 966–979
 152. J.O. Nilsson et al., Structural Stability of Super Duplex Stainless Weld Metals and Its Dependence on Tungsten and Copper, *Metall. Mater. Trans. A*, Vol 27, 1996, p 2196–2208
 153. H. Sieurin et al., Sigma Phase Precipitation in Duplex Stainless Steel 2205, *Mater. Sci. Eng.*, Vol 444, 2007, p 271–276
 154. H. Sieurin and R. Sandstorm, Austenite Reformation in the Heat-Affected Zone of Duplex Stainless Steels, *Mater. Sci. Eng. A*, Vol 418, 2006, p 250–256
 155. A.J. Ramirez, S.D. Brandi, and J.C. Lippold, Secondary Austenite and Chromium Nitride Precipitation in Simulated Heat-Affected Zones of Duplex Stainless Steels, *Sci. Technol. Weld. Join.*, Vol 9, 2004, p 301–313
 156. J.M. Vitek et al., Low-Temperature Aging Behavior of Type-308 Stainless Steel Weld Metal, *Acta Metall. Mater.*, Vol 39, 1991, p 503–516
 157. F. Danoix and P. Auger, Atom Probe Studies of the Fe-Cr System and Stainless Steels Aged at Intermediate Temperature: A Review, *Mater. Charact.*, Vol 44, 2000, p 177–201
 158. V. Jan et al., Weld Joint Simulations of Heat-Resistant Steels, *Arch. Metall. Mater.*, Vol 49, 2004, p 469–480
 159. T. Helander et al., Structural Changes in 12-2.25 Cr Weldments—An Experimental and Theoretical Approach, *Mater. High Temp.*, Vol 17, 2000, p 389–396
 160. Z. Feng, T. Zacharia, and S.A. David, Thermal Stress Development in a Nickel Based Superalloy during Weldability Test, *Weld. J.*, Vol 76, 1997, p s470–s483
 161. Z. Feng et al., Quantification of Thermo-mechanical Conditions for Weld Solidification Cracking, *Sci. Technol. Weld. Join.*, Vol 2, 1997, p 11–19
 162. J.W. Park et al., Stay Grain Formation, Thermomechanical Stress and Solidification Cracking in Single Crystal Nickel Base Superalloy Welds, *Sci. Technol. Weld. Join.*, Vol 9, 2004, p 472–482
 163. D. Dye, O. Hunziker, and R.C. Reed, Numerical Analysis of the Weldability of Superalloys, *Acta Mater.*, 2001, p 683–697
 164. T. Bollinghaus and H. Herold, Ed., Section III, *Hot Cracking Phenomena in Welds*, Springer, p 185–245
 165. S.S. Babu et al., Joining of Nickel Base Superalloy Single Crystals, *Sci. Technol. Weld. Join.*, Vol 9, 2004, p 1–12
 166. J.M. Vitek, The Effect of Welding Conditions on Strain Grain Formation in Single Crystal Welds—Theoretical Analysis, *Acta Mater.*, Vol 53, 2005, p 53–67
 167. S. Mokadem, Laser Repair of Superalloy Single Crystals with Varying Substrate Orientations, *Metall. Mater. Trans. A*, Vol 38, 2007, p 1500–1510

168. Z. Feng, Ed., *Processes and Mechanisms of Welding Residual Stress and Distortion*, CRC Press, 2005
169. P.J. Withers, Residual Stress and Its Role in Failure, *Rep. Prog. Phys.*, Vol 70, 2007, p 2211–2264
170. K. Masubuchi, *Analyses of Welded Structures*, Pergamon Press, 1980
171. A. Saxena, Role of Nonlinear Fracture Mechanics in Assessing Fracture and Crack Growth in Welds, *Eng. Fract. Mech.*, Vol 74, 2007, p 821–838
172. N. Yurioka and Y. Horii, Recent Developments in Repair Welding Technologies in Japan, *Sci. Technol. Weld. Join.*, Vol 11, 2006, p 255–264
173. W. Sagawa et al., Stress Corrosion Cracking Countermeasure Observed on Ni-Based Alloy Welds of BWR Core Support Structure, *Nucl. Eng. Des.*, Vol 239, 2009, p 655–664
174. O. Hatamleh, A Comprehensive Investigation on the Effects of Laser and Shot Peening on Fatigue Crack Growth in Friction Stir Welded AA 2195 Joints, *Int. J. Fatigue*, Vol 31, 2009, p 974–988
175. W.J. Kang and G.H. Kim, Analyses of Manufacturing Effects on Fatigue Failure of an Automotive Component Using Finite Element Methods, *Fatigue Fract. Eng. Mater. Struct.*, Vol 32, 2009, p 619–630
176. M. Mochizuki and M. Toyoda, Strategy of Considering Microstructure Effect on Weld Residual Stress Analysis, *J. Press. Vessel Technol.*, Vol 129, 2007, p 619–629
177. A. Ohta et al., Superior Fatigue Crack Growth Properties in Newly Developed Weld Metal, *Int. J. Fatigue*, Vol 21, 1999, p s113–s118
178. D. Deng et al., Determination of Welding Deformation in Fillet-Welded Joint by Means of Numerical Simulation and Comparison with Experimental Measurements, *J. Mater. Proc. Technol.*, Vol 183, 2007, p 219–225
179. L. Zhang et al., Evaluation of Applied Plastic Strain Methods for Welding Distortion Prediction, *Trans. ASME*, Vol 129, 2007, p 1000–1010
180. G.H. Jung, A Shell-Element Based Elastic Analysis Predicting Welding-Induced Distortions for Ship Panels, *J. Ship Res.*, Vol 51, 2007, p 128–136
181. G.H. Jung and C.L. Tsai, Fundamental Studies on the Effect of Distortion Control Plans on Angular Distortion in Fillet Welded T-Joints, *Weld. J.*, Vol 83, 2004, p 213s–223s
182. J. Song et al., Sensitivity Analysis and Optimization of Thermo-Elastic-Plastic Processes with Applications to Welding Side Heater Design, *Comput. Meth. Appl. Mech. Eng.*, Vol 193, 2004, p 4541–4566
183. S.S. Babu et al., Modeling of Resistance Spot Welds: Process and Performance, *Weld. World*, Vol 45, 2001, p 18–24
184. Y.P. Yang et al., Integrated Computational Model to Predict Mechanical Behavior of Spot Weld, *Sci. Technol. Weld. Join.*, Vol 13, 2008, p 232–239
185. C.H. Young and H.K.D.H. Bhadeshia, Strength of Mixtures of Bainite and Martensite, *Mater. Sci. Technol.*, Vol 10, 1994, p 209–214
186. P. Dong, A Robust Structural Stress Method for Fatigue Analysis of Off-shore/Marine Structures, *J. Offshore Mech. Arctic Eng.—Trans. ASME*, Vol 127, 2005, p 68–74
187. H. Fujii et al., Prediction of Creep Rupture Life in Nickel Base Superalloys Using Bayesian Neural Network, *J. Jpn. Inst. Met.*, Vol 63, 1999, p 905–911
188. F. Brun et al., Theoretical Design of Ferritic Creep Resistant Steels Using Neural Network, Kinetics and Thermodynamic Models, *Mater. Sci. Technol.*, Vol 15, 1999, p 547–554
189. H.K.D.H. Bhadeshia, Performance of Neural Networks in Materials Science, *Mater. Sci. Technol.*, Vol 25, 2009, p 504–510
190. H.K.D.H. Bhadeshia, Mathematical Models in Materials Science, *Mater. Sci. Technol.*, Vol 24, 2008, p 128–136
191. A.C. To et al., Materials Integrity in Microsystems: A Framework for a Peta-Scale Predictive-Science-Based Multi-Scale Modeling and Simulation System, *Comput. Mech.*, Vol 42, 2008, p 485–510
192. J. Storesund et al., Creep Behavior and Life Time of Large Welds in 20 CrMoV 12 1—Results Based on Simulation and Testing, *Int. J. Pressure Vessel Piping*, Vol 83, 2006, p 875–883
193. Materials Algorithm Project, University of Cambridge, United Kingdom, <http://www.msm.cam.ac.uk/map/mapmain.html>
194. W. Zhang et al., Automatic Weld Modeling Based on Finite Element Analysis and High Performance Computing, *AWS Annual Meeting* (Chicago, IL), 2007
195. Edison Welding Institute, <http://calculations.ewi.org>
196. M. Muruganath et al., Optimization of Shielded Metal Arc Weldmetal for Charpy Toughness, *Weld. J.*, Vol 83, 2004, p 267s–276s
197. S.S. Babu and M. Muruganath, Computational Optimization of Weld Metal Composition for Maximizing Acicular Ferrite, *Proceedings of Eighth International Conference on Trends in Welding Research*, S.A. David, T. DebRoy, J.N. Dupont, T. Koseki, and H.B. Smartt, Ed., 2008 (Pine Mountain, GA), ASM International, 2009, p 568–574
198. A. De and T. DebRoy, Probing Unknown Welding Parameters from Convective Heat Transfer Calculation and Multivariable Optimization, *J. Phy. D*, Vol 37, 2004, p 140–150
199. *Integrated Computational Materials Engineering: A Transformational Discipline for Improved Competitiveness and National Security*, Committee on Integrated Computational Materials Engineering, National Research Council, 2008, <http://www.nap.edu/catalog/12199.html>
200. M.F. Ashby and Y.J.M. Brechet, Designing of Hybrid Materials, *Acta Mater.*, Vol 51, 2003, p 5801–5821
201. M.F. Ashby, Hybrids to Fill Holes in Material Property Space, *Philos. Mag.*, Vol 85, 2005, p 3235–3257

Modeling of Heat and Mass Transfer in Fusion Welding

Wei Zhang, Oak Ridge National Laboratory

Rohit Rai, Pennsylvania State University

Amit Kumar, ExxonMobil Upstream Research Company

Igor V. Kivitsun, E.O. Paton Electric Welding Institute of the National Academy of Sciences of Ukraine

IN FUSION WELDING, parts are joined together by melting and subsequent solidification. Although this principle is simple, complex transport phenomena take place during fusion welding, and they determine the final weld quality and performance (Ref 1–3). The heat and mass transfer in the weld pool directly affect the size and shape of the pool, the solidification microstructure, the formation of weld defects such as porosity and humping, and the temperature distribution in the fusion zone and heat-affected zone (HAZ). Furthermore, the temperature evolution affects the kinetics and extent of various solid-state phase transformations, which in turn determine the final weld microstructure and mechanical properties. The formation of residual stresses and distortion originates from the thermal expansion and contraction during welding heating and cooling, respectively.

As discussed elsewhere in this Handbook, experimental observation of weld pool dynamics is challenging. Nevertheless, valuable insights have been gained into the mechanisms of heat and mass transfer in the weld pool. Such understanding is crucial to the development of sound and robust mathematical models. Unlike the experimental approach that directly measures the temperature or molten metal flow velocity, the mathematical models describe the heat and mass transfer using a set of partial differential equations (PDEs). The models solve those PDEs using numerical methods such as the finite-volume method to calculate the temperature and velocity fields. Over the past decades, the models of heat and mass transfer have evolved from simple two-dimensional (2-D) steady-state models to complex three-dimensional (3-D) transient models considering the free surface flow under metal droplet impact. These models have significantly improved the current understanding of welding transport phenomena (Ref 4), including various driving forces for molten metal flow in the weld

pool, effect of shielding gas composition, dendrite microstructure during solidification, vaporization and loss of alloying elements, and formation of weld bead humping, just to name a few.

The heat and mass transfer in fusion welding is truly a broad, multidisciplinary topic (Ref 1–3). In the published literature, there exist a large amount of models employing different approaches and simplifications. With ever-increasingly sophisticated experimental tools for probing and theoretical understanding of heat and mass transfer, models are constantly enhanced to tackle complex transport phenomena. The main objective of the present article is to provide a comprehensive review and critical assessment of the current state of the art in numerical modeling of heat and mass transfer in fusion welding. The article is focused on the fusion welding processes that have been modeled extensively in the published literature. They include gas tungsten arc welding (GTAW), gas metal arc welding (GMAW), laser welding, electron beam welding, and laser-arc hybrid welding. Furthermore, the models are based on the solution of governing conservation equations for mass, momentum, energy, and chemical species. The calculated results from the heat and mass transfer models, especially the temperature evolution in the weldment, are crucial for the understanding of other aspects of fusion welding, including microstructure evolution, residual stresses, and distortion.

The article is organized as follows. First, the mathematical equations of mass, momentum, energy, and species conservation are provided. The boundary conditions for heat flux and the various driving forces for fluid flow are also discussed. Second, applications of heat transfer and fluid flow models to different welding processes are reviewed. The modeling of mass transport such as gas absorption and vaporization of alloying elements is also presented.

Finally, approaches to improve reliability of and reduce uncertainty in numerical models are discussed.

Important Considerations

It is important to recognize that state-of-the-art models are only as good as the mathematical equations that they are solving and the materials properties that they are using. Even for some of the phenomena for which mathematical descriptions of the underlying mechanisms are well established, the difficulty in obtaining converged numerical solutions for highly nonlinear problems may render the simulation impractical. Furthermore, theories and detailed mathematical descriptions are still evolving for some of the important phenomena due to the multiphysics nature of the welding processes and their nonlinear interactions (Ref 5).

A prerequisite for developing sound models is the theoretical understanding of the problem that will be modeled numerically. Several excellent textbooks and review papers can be found in the reference section of this article. Other articles in the present Handbook are also good sources.

Because of the complexity of fusion welding, simplifications and assumptions are generally required to make the simulation tractable. Different approaches have been developed to model the heat and mass transfer in fusion welding, and each approach has its own strengths and weaknesses. Some consideration for choosing the modeling approach is discussed in the following.

For arc welding, an important option of modeling of heat and mass transfer in the weld pool is whether to directly simulate the arc plasma. For simplicity, the majority of the models published in the literature rely on prescribing heat flux distribution on the weld pool surface instead of direct arc plasma simulation.

A Gaussian profile is typically used for the heat flux distribution (Ref 6). Clearly, this approach will fall short when answering questions such as how the shielding gas composition affects the nugget penetration. There are several published efforts aimed at coupling the arc plasma with the weld pool. However, those models are currently limited to relatively simple gas tungsten arc or gas metal arc spot welding (Ref 7).

Unlike stress models where the transient formulation is typically used, the weld pool model often employs the quasi-steady-state formulation. In this formulation, a coordinate system that is attached to the welding heat source is used, and the material flows through the calculation domain (Ref 8). The temperature and flow velocities at a spatial location do not change with time when viewed in the moving coordinate system. This formulation fits well the Eulerian method used to discretize the mathematical equations of conservation where the material flows through the mesh. The main advantage of the quasi-steady-state formulation is that it is very efficient, because it requires 1 to 2 orders of magnitude less computational power than the transient formulation. On the other hand, the quasi-steady-state formulation is limited to linear welding and cannot capture transient behaviors such as those encountered in weld start and stop. Obviously, the transient formulation is needed for situations where the detailed dynamics are important, for example, the droplet transfer to weld pool.

In the autogenous GTAW and conduction-mode laser or electron beam welding, the weld pool surface is assumed to be flat and its position is known. However, the weld pool surface can be severely deformed by the arc pressure and droplet impingement in arc welding and the recoil force due to vaporization in laser and electron beam welding. In those situations, the position of the weld pool surface must be determined as part of the simulation, a requirement that adds significant complexity to the numerical model. The transport equation with additional variables (such as volume of fluid) is solved in order to track the evolution of the weld pool surface. More details on the free surface flow are provided in the section "Free Surface Flow" in this article.

A practical choice is the software platform (commercial, in-house, or open source) on which the weld model will be developed. Commercial programs typically offer a complete package of preprocessing (especially mesh generation), solving, and postprocessing (especially visualization of results). User-defined functions (or subroutines) can be used for implementation of specific functionalities relevant to the weld model. The specific functionalities needed for weld modeling can sometimes be difficult to realize due to the limitations in user-defined functions. In-house code gives full control over the implementation of the numerical solver. At the same time, development and quality-assurance efforts can be much more demanding

for in-house code than for commercial software. Open-source codes may offer flexibility in accessing and modifying the underlying numerical solver without the need to reimplement the basic numeric functions. However, to date (2011), there seems to be little work on the application of open-source code for weld modeling in the published literature.

Once a converged numerical solution is obtained, the validity of simulated results must be carefully examined. Experimental validation can include the comparison between the calculated and measured fusion zone size and shape and temperature profiles. It can also be beneficial to compare the simulated results with the published work for similar welding conditions. Finally, it is noted that there are always uncertainties in the input parameters (such as arc efficiency) of a model. Inverse modeling, discussed later in the section "Reliability of Models," can be a useful tool to reduce the uncertainties and improve model reliability.

Mathematical Description

Governing Transport Equations

The transport equations are available in many standard textbooks (Ref 9, 10). In this section, a concise summary of the governing transport equations for weld heat and mass transfer is provided. It is noted that these equations are applicable to both the weld pool and the arc plasma. For clarity, the following discussion is for the weld pool heat and mass transfer. The specifics relevant to the arc plasma are presented in a later section.

If an incompressible, laminar, and Newtonian liquid flow is assumed in the weld pool, the circulation of liquid metal can be represented by the following momentum equation:

$$\rho \frac{\partial u_j}{\partial t} + \rho \frac{\partial (u_i u_j)}{\partial x_i} = \frac{\partial}{\partial x_i} \left(\mu \frac{\partial u_j}{\partial x_i} \right) + S_j \quad (\text{Eq 1})$$

where ρ is the density, t is the time, x_i is the distance along the i^{th} ($i = 1, 2, \text{ and } 3$) direction, u_j is the velocity component along the j^{th} direction, μ is the viscosity, and S_j is the source term for the j^{th} momentum equation, which is as follows:

$$S_j = -\frac{\partial p}{\partial x_j} - C \left(\frac{(1 - f_L)^2}{f_L^3 + B} \right) u_j + S_{e_j} + S_{b_j} \quad (\text{Eq 2})$$

where p is the pressure. In Eq 2, the first term on the right side is the pressure gradient. The second term represents the frictional dissipation in the mushy zone according to the Carman-Kozeny equation for flow through a porous media (Ref 11), where f_L is the liquid fraction, B is a very small computational constant introduced to avoid division by zero, and C is a constant accounting for the mushy-zone morphology. The third and fourth terms, S_{e_j} and S_{b_j} , correspond to the electromagnetic and

buoyancy source terms, respectively. Their calculations are discussed in the section "Boundary Conditions" in this article.

The following continuity equation is solved in conjunction with the momentum equation to obtain the pressure field:

$$\frac{\partial u_i}{\partial x_i} = 0 \quad (\text{Eq 3})$$

To track the weld pool liquid-solid interface, that is, the phase change, the enthalpy-porosity method is commonly used (Ref 11). In this method, the total enthalpy, H , is represented by a sum of sensible heat, h , and latent heat content, ΔH , that is, $H = h + \Delta H$. The sensible heat, h , is expressed as:

$$h = \int C_p dT$$

where C_p is the specific heat, and T is the temperature. The latent heat content, ΔH , is given as $\Delta H = f_L L$, where L is the latent heat of fusion. The liquid fraction, f_L , can be assumed to vary linearly with temperature for simplicity:

$$f_L = \begin{cases} 1 & T > T_L \\ \frac{T - T_S}{T_L - T_S} & T_S \leq T \leq T_L \\ 0 & T < T_S \end{cases} \quad (\text{Eq 4})$$

where T_L and T_S are the liquidus and solidus temperatures, respectively. Thus, the thermal energy transportation in the weld workpiece can be expressed by the following modified energy equation:

$$\rho \frac{\partial h}{\partial t} + \rho \frac{\partial (u_i h)}{\partial x_i} = \frac{\partial}{\partial x_i} \left(\frac{k}{C_p} \frac{\partial h}{\partial x_i} \right) + S_h \quad (\text{Eq 5})$$

where k is the thermal conductivity. The source term S_h is due to the latent heat content and is as follows:

$$S_h = -\rho \frac{\partial (\Delta H)}{\partial t} - \rho \frac{\partial (u_i \Delta H)}{\partial x_i} \quad (\text{Eq 6})$$

If the transport of species in the weld pool is of interest, the governing equation is as follows:

$$\rho \frac{\partial C_A}{\partial t} + \rho \frac{\partial (u_i C_A)}{\partial x_i} = \frac{\partial}{\partial x_i} \left(D_A \frac{\partial C_A}{\partial x_i} \right) + S_{rxn} \quad (\text{Eq 7})$$

where C_A is the concentration of species A (such as sulfur), D_A is the diffusion coefficient of species A in the molten metal, and S_{rxn} is the volumetric reaction rate (equal to zero if there is no chemical reaction).

Equations 1 through 7 are based on the transient formulation. As discussed previously, the quasi-steady-state formulation is extensively used in modeling heat and mass transfer in the weld pool because of its high efficiency. In the coordinate system that moves along with the heat source, the energy conservation equation can be rewritten as follows:

$$\rho \frac{\partial (u_i h)}{\partial x_i} = \frac{\partial}{\partial x_i} \left(\frac{k}{C_p} \frac{\partial h}{\partial x_i} \right) - \rho \frac{\partial (u_i \Delta H)}{\partial x_i} - \rho U_w \frac{\partial h}{\partial x_1} - \rho U_w \frac{\partial \Delta H}{\partial x_1} \quad (\text{Eq 8})$$

where U_w is the welding speed in direction 1. The last two terms in Eq 8 represent the convective heat transfer due to the bulk material flow through the calculation domain at the welding speed. Similar equations can be formulated for the momentum and species conservation equations, and the details are available elsewhere in the literature (Ref 6, 8, 12).

Boundary Conditions

Heat Transfer into the Weld Pool. As discussed earlier, the prescribed heat flux distribution is typically used for the simulation of heat transfer and fluid flow in the weld pool, because the direct modeling of arc plasma and its interaction with the weld pool currently remains a challenging effort. For arc welding, the following Gaussian profile has been widely used to describe the heat flux distribution at the weld top surface:

$$q(r) = \frac{f_d \eta VI}{\pi r_b^2} \exp\left(-f_d \frac{r^2}{r_b^2}\right) \quad (\text{Eq 9})$$

where q is the heat flux at a given location at the weld top surface, r is the distance between the specific location and the heat source center, f_d is a distribution factor, V and I are the arc voltage and current, respectively, η is the arc efficiency, and r_b is the arc radius. The values of f_d , η , and r_b depend on the particular welding conditions, including electrode tip angle, arc length, shielding gas composition, and so on. Although arc plasma models (described in the section "Welding Arc Plasma" in this article) are increasingly used to determine these values, the current practice still relies largely on empirical data. Among the three parameters, the efficiency value has a significant effect on the resulting shape and size of the weld pool and the temperature distribution in the HAZ. Kou has summarized the efficiencies of the heat sources in various welding processes (Ref 2). An empirical formula for estimating arc efficiency is developed by Arenas et al. (Ref 13) based on the experimental data of Tsai and Eagar (Ref 14):

$$\eta = 7.48 \frac{r_b^{0.63} R_c^2}{L^{0.8} IV} \quad (\text{Eq 10})$$

where L is the arc length (mm), I is the arc current (A), V is the arc voltage (V), and R_c is the effective arc radius (mm), which is related to the arc radius r_b by the equation $R_c = 2.13 r_b$.

As shown in Eq 9, f_d and r_b together define the shape of the Gaussian profile. Higher f_d and smaller r_b indicate a more constrained and intense arc for the same arc efficiency, and vice versa. In the literature, two typical values of f_d have been reported. The f_d value of 3.0 seems to be favored for laser welding, whereas the value of 0.5 is favored for arc welding. When comparing r_b values, it is important to know the f_d value, because it is their combined form:

$$r_b / \sqrt{f_d}$$

that defines the shape of the Gaussian distribution.

In GMAW, the molten metal formed from the consumable electrode can carry a substantial amount of heat, mass, and momentum into the weld pool. Transient models based on the interface-capturing approach have been used to directly simulate the impingement of individual droplets into the weld pool. An alternative method for describing the heat transfer by droplets is the placement of an imaginary cylindrical volumetric heat source in the weld pool underneath the arc (Ref 6, 15, 16). This simplified method is found to be effective in capturing finger penetration in the fusion zone of GMAW.

The Gaussian heat flux distribution given in Eq 9 is also used for conduction-mode laser and electron beam welding. Heat transfer in keyhole-mode laser and electron beam welding is much more complex. Similar to the handling of heat transfer from metal droplets in GMAW, heat transfer from the keyhole can be either simulated directly or approximated using a volumetric heat source. More details are given in the section "Application to Fusion Welding Processes" in this article.

Driving Forces for Fluid Flow. Figure 1 is a schematic drawing of various driving forces for fluid flow in a gas tungsten arc weld pool (Ref 2, 17). The equations for calculating those forces are discussed in the following.

The electromagnetic force (\vec{F}_{emf}), shown in Fig. 1(a), can be calculated as:

$$\vec{F}_{\text{emf}} = \vec{J} \times \vec{B} \quad (\text{Eq 11})$$

where \vec{J} is the current density vector, and \vec{B} is the magnetic flux vector. The following analytical expressions developed by Kou and Sun (Ref 18) are widely used to calculate the \vec{J} and \vec{B} fields in the workpiece:

$$J_z = \frac{I}{2\pi} \int_0^\infty \lambda J_0(\lambda r) \exp(-\lambda^2 \sigma_j^2 / 12) \frac{\sin h[\lambda(c-z)]}{\sin h(\lambda c)} d\lambda \quad (\text{Eq 12a})$$

$$J_r = \frac{I}{2\pi} \int_0^\infty \lambda J_1(\lambda r) \exp(-\lambda^2 \sigma_j^2 / 12) \frac{\cos h[\lambda(c-z)]}{\sin h(\lambda c)} d\lambda \quad (\text{Eq 12b})$$

$$B_\theta = \frac{\mu_m I}{2\pi} \int_0^\infty J_1(\lambda r) \exp(-\lambda^2 \sigma_j^2 / 12) \frac{\sin h[\lambda(c-z)]}{\sin h(\lambda c)} d\lambda \quad (\text{Eq 12c})$$

where J_z is the vertical component of the current density, I is the current, J_0 is the Bessel

function of zero order and first kind, r is the radial distance from the arc center, σ_j is the current radius of the arc, c is the thickness of the workpiece, z is the vertical distance from the top surface, J_r is the radial component of current density, J_1 is the first kind of Bessel function of first order, B_θ is the angular component of the magnetic field, and μ_m is the magnetic permeability of the material. Because the electrical current distribution is assumed to be axisymmetric, J_θ , B_r , and B_z are equal to zero. Recently, Kumar et al. (Ref 19) used a numerical integration method to calculate the current density in the workpiece and then calculate the magnetic field using the Biot-Savart law. Zhang et al. (Ref 20) solved the electrical potential and the magnetic vector potential conservation equations using the finite-volume method for a moving arc in orbital GTAW of an aluminum alloy tube.

Marangoni shear stress (i.e., the spatial gradient of surface tension) arises as a result of spatial variation of temperature and composition, which can be expressed as:

$$\tau = \frac{\partial \gamma}{\partial T} \frac{\partial T}{\partial r} + \frac{\partial \gamma}{\partial C} \frac{\partial C}{\partial r} \quad (\text{Eq 13})$$

where τ is the shear stress due to surface tension (γ), T is the temperature, r is the distance along the surface, and C is the concentration of surface active element. In most cases, the $\partial \gamma / \partial C$ term is zero, and the shear stress depends only on $\partial \gamma / \partial T$ and the spatial temperature gradient $\partial T / \partial r$ at the pool surface. A widely used expression for calculating $\partial \gamma / \partial T$ as a function of both temperature and composition was developed by Sahoo et al. (Ref 21):

$$\frac{\partial \gamma}{\partial T} = A - R\Gamma_s \ln(1 + K a_i) - \frac{K a_i}{(1 + K a_i)} \frac{\Gamma_s (\Delta H^0 - \Delta \bar{H}_i^M)}{T} \quad (\text{Eq 14})$$

where A is the $\partial \gamma / \partial T$ value for pure metal, Γ_s is the surface excess at saturation, K is the adsorption coefficient, a_i is the activity of species i in the solution, ΔH^0 is the standard heat of adsorption, and $\Delta \bar{H}_i^M$ is the partial molar enthalpy of mixing of species i in the solution. Equation 14 shows that the value of $\partial \gamma / \partial T$ can be dramatically altered if a small yet significant amount of surface active elements such as sulfur and oxygen is present in the weld pool. The effect of $\partial \gamma / \partial T$ on the fluid flow pattern is illustrated in Fig. 1(b) and 1(c). Computed patterns of weld pool fluid flow driven by Marangoni shear stress are provided in the GTAW section.

The Boussinesq approximation is typically used in the calculation of buoyancy-force-driven flow, shown in Fig. 1(d). The buoyancy force can be expressed as:

$$F_b = \rho g \beta (T - T_{\text{ref}}) \quad (\text{Eq 15})$$

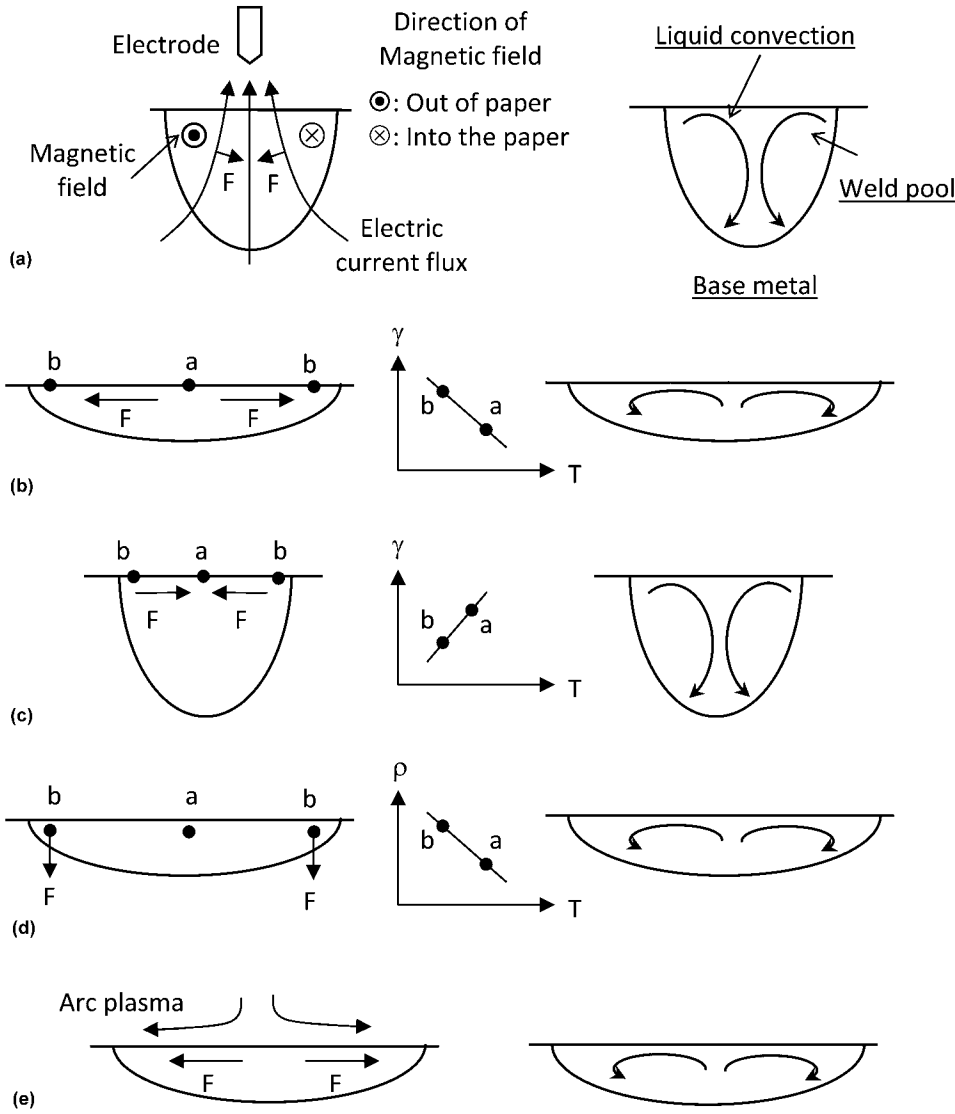


Fig. 1 Various driving forces and the resulting liquid convection in a gas tungsten arc weld pool. (a) Electromagnetic force. (b) Surface tension gradient force with negative $\partial\gamma/\partial T$. (c) Surface tension gradient force with positive $\partial\gamma/\partial T$. (d) Buoyancy force. (e) Plasma jet shear stress. The symbol γ is the surface tension, $\partial\gamma/\partial T$ is the temperature coefficient of surface tension, T is the temperature, ρ is the density, a and b are two locations in the weld pool, and F is the driving force. Adapted from Ref 17

where ρ is the density of liquid metal, g is the acceleration due to gravity, β is the thermal expansion coefficient, T is the temperature of the liquid metal, and T_{ref} is a reference temperature, often chosen to be the solidus temperature (T_S).

As shown in Fig. 1(e), the arc plasma moves outward at high speeds along the weld pool surface, which can exert an outward shear stress at the pool surface. It has been shown that the plasma shear stress may dominate both electromagnetic and surface tension gradient forces as the driving force for liquid convection when a long arc is used in GTAW (Ref 22). The arc plasma shear stress (τ_{ps}) is calculated based on Newton's law of viscosity:

$$\tau_{\text{ps}} = \mu_p \frac{\partial \vec{V}}{\partial \vec{n}} \quad (\text{Eq 16})$$

where μ_p is the viscosity of arc plasma, and the term $\partial \vec{V} / \partial \vec{n}$ represents the plasma flow velocity gradient in the direction normal to the weld pool surface. The calculation of the plasma shear stress using Eq 16 requires the direct simulation of arc plasma. As an alternative method, Cho (Ref 23) used an analytical solution of the wall shear stress produced by the normal impingement of a jet on a flat surface (Ref 24).

Turbulence

Due to the high energy density of the heat source in fusion welding, the top surface of

the weld pool experiences steep temperature gradients. The resulting strong surface tension gradients along with the other driving forces for fluid flow (electromagnetic, buoyancy, etc.) result in very high velocities in small weld pools (Ref 25–27). For example, surface velocities of the order of 1 m/s were measured by Ki et al. (Ref 27). Such high velocities in small confined spaces typically lead to turbulent weld pools. A criterion has been given by Atthey (Ref 28), based on weld pool width (w), maximum velocity (u_{max}), density (ρ), and viscosity (μ). The weld pool flow is turbulent if the following condition is met:

$$\text{Re} = \frac{\rho u_{\text{max}} w}{\mu} > 600 \quad (\text{Eq 17})$$

In a turbulent weld pool, the fluctuating velocity components increase the rates of heat and momentum transport in the weld pool. The enhanced rates of transport can be accounted for in the numerical model by taking “effective” values of viscosity and thermal conductivity (Ref 29). The turbulent thermal conductivity (k_t) is given as:

$$k_t = \frac{\mu_t C_p}{\text{Pr}_t} \quad (\text{Eq 18})$$

where μ_t is the turbulent viscosity, and Pr_t is the turbulent Prandtl number, which ranges between 0.7 and 0.9 (Ref 26, 30, 31). Various turbulence models are used to calculate the turbulent viscosity. Those models may be classified into categories depending on the number of equations that must be solved.

Zero-equation (or algebraic) turbulence models derive the turbulence characteristics from the average flow variables and do not require solution of additional equations. Although not as accurate as one-equation or two-equation models, they are simpler to use. According to mixing-length theory, the turbulent viscosity can be given as (Ref 26, 29):

$$\mu_t = \rho l_m u_m \quad (\text{Eq 19})$$

where μ_t is the density, l_m is the characteristic length scale for mixing, and u_m is the characteristic velocity. Several methods exist for the determination of l_m and u_m . One of the methods for calculating l_m is as follows (Ref 25, 29, 32):

$$l_m = \kappa y \left[1 - e^{-y^+ / A_0^+} \right] \quad (\text{Eq 20})$$

where $\kappa = 0.41$, and $A_0^+ = 26.0$:

$$y^+ = y \sqrt{\frac{\rho}{\mu} \left(\frac{\partial u}{\partial y} \right) \Big|_w}$$

where the term:

$$\left(\frac{\partial u}{\partial y} \right) \Big|_w$$

is the velocity gradient at the weld pool boundary.

One of the methods for determining u_m is given as:

$$u_m = l_m |\omega| = l_m \sqrt{\left(\frac{\partial v}{\partial x} - \frac{\partial u}{\partial y}\right)^2 + \left(\frac{\partial w}{\partial y} - \frac{\partial v}{\partial z}\right)^2} + \sqrt{\left(\frac{\partial u}{\partial z} - \frac{\partial w}{\partial x}\right)^2} \quad (\text{Eq 21})$$

where ω is vorticity (Ref 25, 29, 32).

A one-equation model solves a single partial differential equation for a turbulence variable. Prandtl's one-equation model (Ref 29), for example, solves an equation for the turbulent kinetic energy (k_t):

$$\rho \frac{\partial k_t}{\partial t} + \rho \frac{\partial(u_i k_t)}{\partial x_i} = \frac{\partial}{\partial x_i} \left(\mu + \frac{\mu_t}{\sigma_k} \frac{\partial k_t}{\partial x_i} \right) + G - \frac{C_\mu \rho k_t^{3/2}}{l} \quad (\text{Eq 22})$$

where G is the rate of generation of turbulence energy, and σ_k and C_μ are two model constants. The turbulent viscosity can be determined from k_t by the equation $\mu_t = \rho k_t^{1/2} l$, where l is the Kolmogorov length scale (Ref 29).

The two-equation models solve two partial differential equations for turbulence. Generally, one of the equations is for the turbulent kinetic energy. The other equation solves for another characteristic of the turbulent flow, such as the turbulent dissipation rate, ε (k - ε model), or the specific dissipation rate, ω (k - ω model). The k - ε model is frequently used for welding processes (Ref 15, 31, 33) and involves the solution of the following equations for turbulent kinetic energy, k_t , and dissipation rate, ε :

$$\rho \frac{\partial k_t}{\partial t} + \rho \frac{\partial(u_i k_t)}{\partial x_i} = \frac{\partial}{\partial x_i} \left(\mu + \frac{\mu_t}{\sigma_k} \frac{\partial k_t}{\partial x_i} \right) + G - \rho \varepsilon \quad (\text{Eq 23})$$

$$\rho \frac{\partial \varepsilon}{\partial t} + \rho \frac{\partial(u_i \varepsilon)}{\partial x_i} = \frac{\partial}{\partial x_i} \left(\mu + \frac{\mu_t}{\sigma_\varepsilon} \frac{\partial \varepsilon}{\partial x_i} \right) + \frac{C_1 \varepsilon G}{k_t} - \frac{C_2 \rho \varepsilon^2}{k_t} \quad (\text{Eq 24})$$

where σ_ε , C_1 , and C_2 are model constants. μ_t can be calculated from k_t and ε because $\mu_t = C_\mu \rho k_t^2 / \varepsilon$, where C_μ is another model constant.

Boundary Conditions for Turbulent Flow. To apply the k - ε model to simulate weld pool turbulence, the zero flux boundary condition is typically used at the top surface:

$$\frac{\partial k_t}{\partial z} \Big|_{z=0} = 0, \text{ and } \frac{\partial \varepsilon}{\partial z} \Big|_{z=0} = 0 \quad (\text{Eq 25})$$

where $z = 0$ corresponds to the top surface. Near the solid-liquid boundaries, turbulence dies down, and the effective values of viscosity

and thermal conductivity reach their molecular values. A computationally efficient way to model the behavior near the wall is through the use of wall functions (Ref 34). However in the enthalpy-porosity method, there is no explicitly defined boundary between the weld pool and the surrounding solid; hence, no boundary condition or wall function is imposed at the weld pool boundary (Ref 15). An alternative method is used by Hong et al. (Ref 31), in which one block of elements is always kept in the liquid phase and the other block of elements is always in the solid phase. The interface between the two blocks of elements conforms to the weld pool boundary by way of dynamic mesh remapping. At this clearly defined solid-liquid interface, boundary conditions for turbulent kinetic energy and dissipation rate are:

$$k_t = \frac{u_\tau^2}{\sqrt{C_\mu}} \quad (\text{Eq 26a})$$

$$\varepsilon = \frac{C_\mu^{3/4} k_t^{3/2}}{\lambda d_n} \quad (\text{Eq 26b})$$

where u_τ is a function of local velocity, d_n is the shortest distance from the solid-liquid boundary to the mesh node where the wall function is applied, and λ is a constant.

Free Surface Flow

From the computational fluid dynamics point of view, weld pool fluid flow phenomena fall into the class of flows with moving boundaries, especially the surface-tension-dominated free-surface flow regime. There are two major numerical approaches for free-surface-flow modeling: interface tracking and interface capturing (Ref 35). In the interface-tracking approach, a boundary-fitted moving mesh is used and the free surface shape is exactly tracked. Boundary conditions such as the heat flux and surface tension can be precisely applied at the free surface. However, this approach is not suited for problems involving the breakup or coalescence of fluids (such as the impingement of metal droplets into the weld pool). Unlike the interface-tracking approach, the interface-capturing method uses stationary grids to resolve the location of the free surface. Additional variables, such as the volume fraction of each fluid, are solved in conjunction with the continuity and momentum conservation equations. The free-surface location is then extrapolated based on the gradient of the volume fraction. The volume-of-fluid (Ref 36) and level-set (Ref 37) methods are two representative methods in the interface-capturing approach. Very fine grids are required in order to obtain sufficiently accurate representation of the interface. As a result, the calculation can be computationally intensive.

The published literature on weld pool models can be divided into three groups according to the handling of the free surface. First, in the simplest situation of autogenous GTAW and conduction-mode laser and electron beam welding without filler-metal addition, the weld pool free surface is assumed to be rigid and does not deform. In other words, the position of the weld pool free surface is known and there is no need to solve for the surface position. Second, in the quasi-steady formulation, the weld pool free surface position is unknown, but it does not vary with time. The interface-tracking approach can be used where the surface position is determined by solving a total surface energy minimization equation. This method can be applied to GTAW with and without filler metal and GMAW. Third, transient models based on the interface-capturing approach are used to calculate the evolution of weld pool free surface with time. These transient models are suitable for describing the dynamic impingement of metal droplets into the weld pool and the liquid-vapor interface evolution in laser keyhole welding. Results from each group of models are presented in the section "Application to Fusion Welding Processes" in this article.

Welding Arc Plasma

There are many approaches and models for numerical investigation of transport phenomena in electric arc plasma, as well as of its interaction with electrodes, for various arc welding processes (Ref 38–44). In the majority of the published models (Ref 38–43), the arc plasma is considered to comprise a single component, that is, atoms and ions of shielding or plasma gas, which is usually inert. In reality, arc plasma is multicomponent, because it contains atoms and ions of the evaporated material of electrodes along with the gas particles. Therefore, an adequate mathematical model of the welding arc must allow for the multicomponent nature of the arc plasma (Ref 44, 45). Such a model must have another important characteristic: self-consistency, which makes it possible to account for the interrelation of physical processes occurring at electrodes and in the near-electrode regions with processes occurring in arc column plasma. A recent review on metal vapor in the welding arc is provided in Ref 45.

A self-consistent mathematical model of energy, mass, and charge-transfer processes taking place in the anode region and the arc column plasma in GTAW and GMAW can be developed using an approach in which the near-anode plasma bulk is conditionally subdivided into three zones (Fig. 2) (Ref 39, 46, 47). The first zone directly adjoining the anode surface is a space charge layer (sheath), wherein the condition of quasi-neutrality of plasma is violated and the main potential drop between the plasma and anode surface is

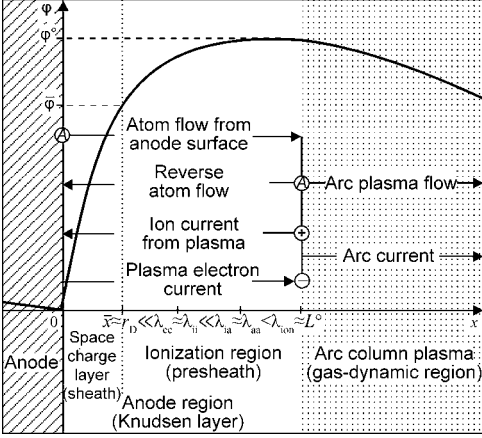


Fig. 2 Structure of near-anode plasma, scale lengths, flows of particles, and potential distribution in anode region of welding arc

formed. This layer can be considered as collisionless. The conditions for the sheath are:

- Pressure close to the atmospheric pressure
- Electron temperature (T_e) approximately 1 eV
- Thickness of this layer (\bar{x}), with a Debye radius (r_D) of approximately 10^{-8} m, which is much smaller than the characteristic lengths of free path (λ) (approximately 10^{-7} to 10^{-5} m) of the plasma particles (Ref 47)

The second zone is an ionization region of the nonisothermal quasi-neutral plasma (presheath), wherein the charged particles are generated by plasma electron ionization of the gas atoms desorbed from the metallic anode surface and of the evaporated metal atoms. The ions formed in this zone are accelerated toward the anode surface by the electric field, induced by more mobile electrons, and are recombined near the anode surface. Therefore, the condition of local ionization equilibrium is violated within this zone. Moreover, a marked change in the plasma potential takes place in the presheath, which can be comparable to its drop in the sheath. The third zone beginning outside the Knudsen layer, comprising the sheath and presheath, is a gas-dynamic region with a local thermodynamic equilibrium formed therein.

The self-consistent model of transport phenomena in welding arc includes two interrelated models: a model of the thermal, electromagnetic, gas-dynamic, and diffusion processes occurring in the multicomponent plasma of the arc column, and a model of the anode region. The thickness of Knudsen-layer boundary (L^0) is equal to several lengths of free path of the heavy particles (typically $L^0 < 10^{-4}$ m). Because L^0 is much smaller than the curvature radius of the anode surface (electrode metal droplet or weld pool), $R \sim 10^{-3}$ m, as well as characteristic scales in the arc column, the anode region can be assumed to be flat and infinitely thin. Therefore, the anode region is treated as a discontinuity surface in the self-consistent model, which makes it possible

to formulate boundary conditions at the anode surface required to solve the equations of the arc column model as well as to determine the characteristics of the thermal and dynamic effect of the welding arc on the droplet or weld pool surface.

Anode Region. To describe the processes occurring in the anode region of the arc with an evaporating anode, the plasma at the external boundary of this region is characterized by the following parameters: n_e^0 is the concentration of electrons; $n_{\alpha Z}^0$ is the concentration of atoms (charge number $Z = 0$) and ions ($Z = 1$) of the shielding gas (kind of particles $\alpha = g$), atoms ($Z = 0$), and ions ($Z = 1, 2$) of the metal vapor ($\alpha = m$); Ze is the ion charge; e is the elementary charge; T_e^0 is the electron temperature; T_h^0 is the temperature of the heavy particles, which is assumed to be identical for all kinds of atoms and ions but different from T_e^0 (i.e., this is a two-temperature plasma model); m_e is the electron mass; M_α is the masses of heavy particles (atoms and ions) of gas ($\alpha = g$) and metal ($\alpha = m$); and j_a is the electric current density at the anode surface. As noted previously, the anode region is considered as infinitely thin. Therefore, n_e^0 , $n_{\alpha Z}^0$, T_e^0 , T_h^0 , and j_a are specified at a given point on the anode surface, which is characterized by a local value of surface temperature (T_s).

It is assumed that all ions that go to the anode surface recombine there and return in the form of atoms, and that the current of electrons emitted by the anode is negligibly small, that is, that the electric current at the anode consists only of electrons and ions coming from the plasma. The current density at the anode surface is expressed as follows:

$$j_a = j_e - j_i (j_a > 0) \quad (\text{Eq 27})$$

where j_e is the electron current density and:

$$j_i = \sum_{\alpha=m,g;Z \geq 1} j_{\alpha Z}$$

is the total ion current density (for ions of all kinds and charge numbers).

Because the plasma potential is, as a rule, higher than that of the anode surface (Ref 39), electrons are decelerated by the electric field, and ions are accelerated toward the anode surface. In this case, the electron current density at the anode can be represented as (Ref 47):

$$j_e = \frac{1}{4} e n_e^0 v_{Te} \exp\left(-\frac{e\phi^0}{kT_e^0}\right) (\phi^0 > 0) \quad (\text{Eq 28})$$

where:

$$v_{Te} = \sqrt{\frac{8kT_e^0}{\pi m_e}}$$

is the thermal velocity of electrons at the external boundary of the anode region, k is the Boltzmann constant, and ϕ^0 is the plasma potential with respect to the anode surface (Fig. 2).

To determine the ion current, it is possible to use an approach based on the fact that the length of free path of ions relative to Coulomb collisions between them is much smaller than the length of their free path at collision with atoms and the ionization length (Fig. 2). This suggests that ions in the presheath are intensively maxwellized and acquire the common velocity. The value of the common velocity at the boundary between the presheath and the sheath is determined by the following equations (Ref 47):

$$\bar{V}_i \equiv V_i(\bar{x}) = \sqrt{\frac{\sum_{\alpha=m,g;Z \geq 1} k(ZT_e^0 + T_h^0)n_{\alpha Z}^0}{\sum_{\alpha=m,g;Z \geq 1} M_\alpha n_{\alpha Z}^0}} \quad (\text{Eq 29a})$$

$$\bar{V}_i = \frac{w^0}{2} \left[\sqrt{1 + \frac{4 \sum_{\alpha=m,g;Z \geq 1} k(ZT_e^0 + T_h^0)n_{\alpha Z}^0}{(w^0)^2 \sum_{\alpha=m,g;Z \geq 1} M_\alpha n_{\alpha Z}^0}} - 1 \right] \quad (\text{Eq 29b})$$

where w^0 is the vapor velocity at the Knudsen layer boundary. Equation 29(a) corresponds to the diffusion mode of evaporation (i.e., $w^0 \approx 0$), whereas Eq 29(b) corresponds to the convective mode of evaporation of the anode metal (i.e., $w^0 > 0$).

The concentration of charged particles at the sheath-presheath boundary can be determined from the following (Ref 46):

$$\begin{aligned} \bar{n}_e &\equiv n_e(\bar{x}) = n_e^0 \exp\left(-\frac{1}{2}\right); \bar{n}_{\alpha Z} \equiv n_{\alpha Z}(\bar{x}) \\ &= n_{\alpha Z}^0 \exp\left(-\frac{1}{2}\right), \alpha = m, g; Z \geq 1 \end{aligned} \quad (\text{Eq 30})$$

Then the ion currents to the anode surface for the diffusion mode of evaporation can be expressed as:

$$j_{\alpha Z} = Ze n_{\alpha Z}^0 \exp\left(-\frac{1}{2}\right) \bar{V}_i, \alpha = m, g; Z > 1 \quad (\text{Eq 31})$$

In the convective mode of evaporation of the anode, the $\exp(-1/2)$ term in Eq 30 and 31 is replaced by (Ref 47):

$$\exp\left[-\frac{(w^0)^2 \sum_{\alpha=m,g;Z \geq 1} M_\alpha n_{\alpha Z}^0}{8 \sum_{\alpha=m,g;Z \geq 1} k(ZT_e^0 + T_h^0)n_{\alpha Z}^0}\right] \left\{ 1 + \sqrt{1 + \frac{4 \sum_{\alpha=m,g;Z \geq 1} k(ZT_e^0 + T_h^0)n_{\alpha Z}^0}{(w^0)^2 \sum_{\alpha=m,g;Z \geq 1} M_\alpha n_{\alpha Z}^0}} \right\}^2$$

In Eq 28 through 31, the values of the electron and ion currents at the anode surface can be calculated. Then, the plasma potential (ϕ^0) relative to this surface or anode potential drop (U_a) can be calculated as follows:

$$U_a \equiv -\phi^0 = -\frac{kT_e^0}{e} \ln\left(\frac{e n_e^0 v_{Te}}{4[j_a + j_i]}\right) (U_a < 0) \quad (\text{Eq 32})$$

To calculate j_e , $j_{\alpha Z}$, and U_a , it is necessary to know temperatures T_e^0 and T_h^0 , as well as concentrations n_e^0 and $n_{\alpha Z}^0$ of the charged particles at the

external boundary of the anode region. Assuming that the multicomponent plasma in the arc column is in an ionization equilibrium state, the composition of the plasma can be determined by using the following system of equations (Ref 47).

The Saha equations allow for nonideality of plasma:

$$\frac{n_e^0 n_{\alpha Z+1}^0}{n_{\alpha Z}^0} = \left(\frac{2\pi m_e k T_e^0}{h^2} \right)^{3/2} \frac{2\theta_{\alpha Z+1}}{\theta_{\alpha Z}}$$

$$\exp \left[-\frac{e(U_{\alpha Z} - \Delta U_Z)}{k T_e^0} \right], \alpha = m, g; Z \geq 0 \quad (\text{Eq 33})$$

where h is the Planck's constant, $\theta_{\alpha Z}$ are the statistical sums for heavy particles of α -kind in charged state Z , $U_{\alpha Z}$ are the ionization potentials (for transfer of the α -kind particles from charged state Z to $Z + 1$), and:

$$\Delta U_Z = \frac{e(Z+1)}{r_D}$$

is the decrease of the ionization potential, where:

$$r_D = \left[k T_e^0 / 4\pi e^2 \left(n_e^0 + \frac{T_e^0}{T_h^0} \sum_{\alpha=m,g;Z \geq 1} (n_{\alpha Z}^0 Z^2) \right) \right]^{1/2}$$

The condition of plasma quasi-neutrality is given by:

$$n_e^0 = \sum_{\alpha=m,g;Z \geq 1} (n_{\alpha Z}^0 Z) \quad (\text{Eq 34})$$

The law of partial pressures is:

$$p = n_e^0 k T_e^0 + \sum_{Z \geq 0} n_{mZ}^0 k T_h^0 + \sum_{Z \geq 0} n_{gZ}^0 k T_h^0 - \Delta p \quad (\text{Eq 35})$$

where p is the plasma pressure near the anode and:

$$\Delta p = \frac{1}{6} \frac{e^2}{r_D} \left(n_e^0 + \sum_{\alpha=m,g;Z \geq 0} (n_{\alpha Z}^0 Z^2) \right)$$

is the decrease in pressure caused by plasma nonideality.

To close the system of Eq 33 through 35, the concentration of the metal vapor particles at the external boundary of the anode region is required. Detailed mathematical equations for determining the metal vapor concentration are provided elsewhere in the literature (Ref 46–48).

Consider now the energy-transfer processes occurring in the anode region of the electric arc. Heat flux, Q_a , from the near-anode plasma to the anode surface has the following form:

$$Q_a = Q_e + Q_i \quad (\text{Eq 36})$$

where Q_e and Q_i are the fluxes of potential and kinetic energy transferred with electrons and ions, respectively. For the convective mode of anode evaporation, the energy Q_v removed from the melt surface by the metal vapor flow

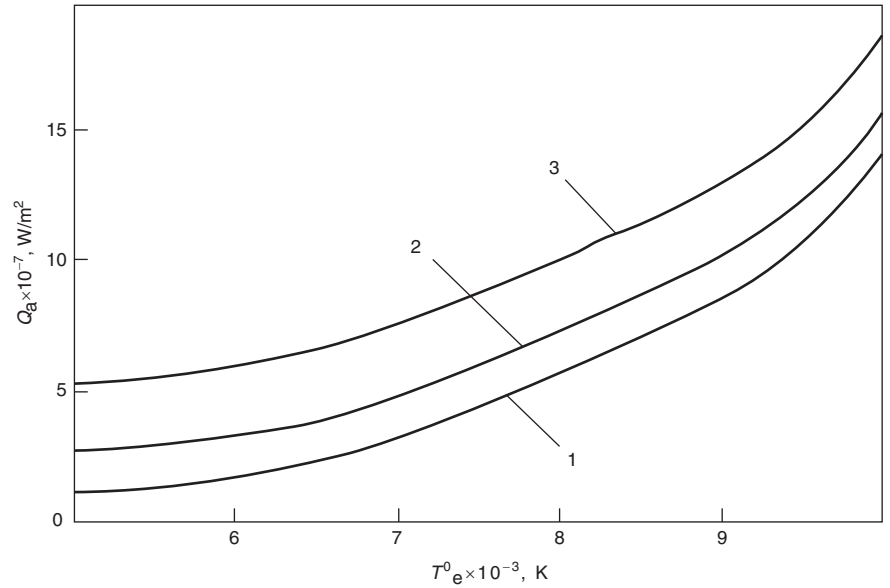
should be taken into account in the energy balance of the anode region:

$$Q_v = \sum_{Z \geq 0} n_{mZ}^0 v^0 \lambda_v \quad (\text{Eq 37})$$

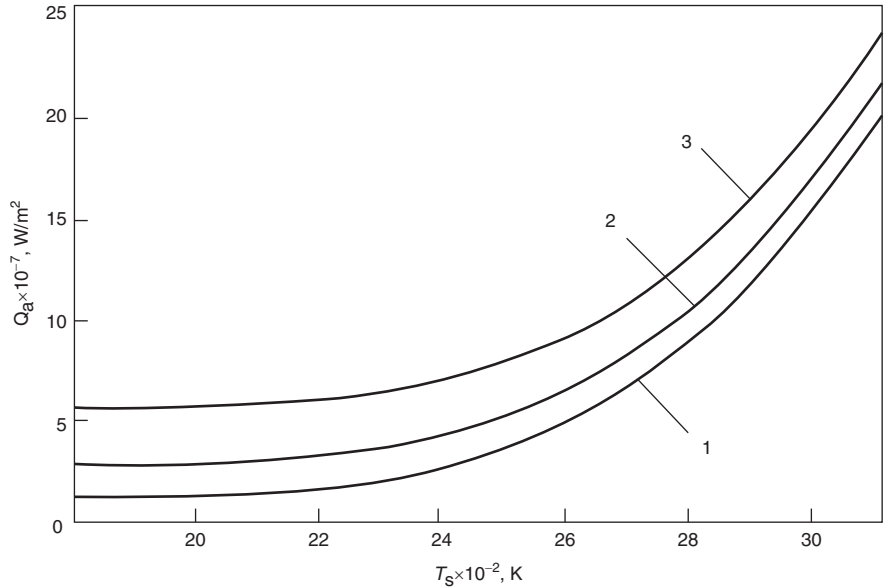
Details for the calculation of Q_e and Q_i are available elsewhere in the literature (Ref 46–48). Figures 3(a) and (b) show the calculation results for a heat flux to the anode characteristic of tungsten inert gas welding of steel in

argon. As indicated by the calculation results, the values of Q_a grow with increase of the electron temperature in the near-anode plasma, the current density at the anode, and the temperature of its surface.

Arc Column. A total of five governing transport equations are solved in the gas-dynamic region of the arc plasma (i.e., the arc column). The first two equations express the conservation of mass and momentum (see the section ‘‘Governing Transport Equations’’



(a)



(b)

Fig. 3 Heat flux to iron anode in argon arc vs. (a) electron temperature in anode region at $T_s = 2472$ K and (b) anode surface temperature at $T_e^0 = 7 \times 10^3$ K. Curve 1: $j_a = 2 \times 10^6$ A/m²; curve 2: 5×10^6 A/m²; and curve 3: 10^7 A/m²

for the expressions). The third equation expresses the conservation of electrical charge (ϕ), which is defined by Poisson's equation, $\nabla(\sigma \nabla \phi) = 0$, where σ is the electrical conductivity of the plasma. The fourth equation expresses the conservation of energy. Two equations are solved to determine the temperatures of electrons (T_e) and heavy particles (T_h). In an axisymmetric coordinate system, these two equations are expressed as follows:

$$n_e C_{pe} \left(\frac{\partial T_e}{\partial t} + v \frac{\partial T_e}{\partial r} + u \frac{\partial T_e}{\partial z} \right) = \frac{1}{r} \frac{\partial}{\partial r} \left(r \chi_e \frac{\partial T_e}{\partial r} \right) + \frac{\partial}{\partial z} \left(\chi_e \frac{\partial T_e}{\partial z} \right) + \frac{k}{e} \left\{ j_r \frac{\partial [5/2 - \delta] T_e}{\partial r} + j_z \frac{\partial [5/2 - \delta] T_e}{\partial z} \right\} + \frac{j_r^2 + j_z^2}{\sigma} - \psi - \beta(T_e - T_h) \quad (\text{Eq 38})$$

$$\rho C_p \left(\frac{\partial T_h}{\partial t} + v \frac{\partial T_h}{\partial r} + u \frac{\partial T_h}{\partial z} \right) = \frac{1}{r} \frac{\partial}{\partial r} \left(r \chi \frac{\partial T_h}{\partial r} \right) + \frac{\partial}{\partial z} \left(\chi \frac{\partial T_h}{\partial z} \right) + \beta(T_e - T_h) \quad (\text{Eq 39})$$

where C_{pe} is the specific heat of the electron gas, χ_e is the electron thermal conductivity, δ is the constant of thermal diffusion of the electrons, ψ is the energy losses due to radiation (in the approximation of an optically thin plasma), β is the coefficient of heat exchange between electrons and heavy particles, C_p is the specific heat of heavy particles, and χ is the thermal conductivity of the heavy particles.

The fifth and final governing transport equation expresses the conservation of species in the multicomponent plasma as:

$$\rho \left(\frac{\partial C_m}{\partial t} + v \frac{\partial C_m}{\partial r} + u \frac{\partial C_m}{\partial z} \right) = \frac{1}{r} \frac{\partial}{\partial r} \left(r \rho D_{m0} \frac{\partial C_m}{\partial r} \right) + \frac{\partial}{\partial z} \left(\rho D_{m0} \frac{\partial C_m}{\partial z} \right) + \frac{1}{r} \frac{\partial}{\partial r} \left(r \rho \left[\bar{D}_{m1} \frac{\partial C_{m1}}{\partial r} + \bar{D}_{m2} \frac{\partial C_{m2}}{\partial r} \right] \right) + \frac{\partial}{\partial z} \left(\rho \left[\bar{D}_{m1} \frac{\partial C_{m1}}{\partial z} + \bar{D}_{m2} \frac{\partial C_{m2}}{\partial z} \right] \right) \quad (\text{Eq 40})$$

where C_m is the relative mass concentration of the metal vapor in the arc column plasma, C_{m1} and C_{m2} are the relative mass concentrations of metal ions, and D_{m0} , D_{m1} , and D_{m2} are the coefficients of diffusion of atoms, single- and double-charged metal ions. In addition, $\bar{D}_{m1} = D_{m1} - D_{m0}$ and $\bar{D}_{m2} = D_{m2} - D_{m0}$.

To solve these governing transport equations in the arc plasma, it is necessary to specify the physical properties as well as the boundary conditions determined from the anode region

model discussed in the section "Welding Arc Plasma" in this article. Details are available in Ref 46 and 47. The previous discussion completes the description of the self-consistent mathematical model of energy, mass, and charge transfer in the arc column plasma and anode region of the welding arc for GTAW and GMAW in inert gas.

Cathode Region. Similar to the anode region, there exists a cathode sheath region between the cathode and the plasma. Lowke et al. (Ref 49) considered the principal heating mechanism due to the ion current at the tungsten cathode surface in GTAW. The ion current is assumed to be equal to the difference between the theoretical thermionic emission current and the electron current. No consideration is made of the space charge sheath at the cathode. Ion current heating at the cathode surface is also considered in the GTAW arc model by Goodarzi et al. (Ref 50). In their model, the current density distribution on the cathode surface was adjusted so that the total current entering was equal to the applied current. The cathode fall voltage was determined based on the assumption that the electrons were in a free fall across the cathode sheath.

In GMAW, the workpiece is typically the cathode, whereas the consumable electrode is the anode. Murphy et al. (Ref 51) calculated the heat flux at the cathode (workpiece) surface by taking into account the influence of the measured cathode sheath voltage in accelerating electrons to excite atoms and the work function of the workpiece material. In the GMAW arc model by Hu and Tsai (Ref 52), the conduction heat exchange between plasma and workpiece at the cathode surface was taken into account, whereas the thermal effect due to the cathode sheath was not considered.

From the previous discussion, it is evident that a significant challenge in modeling welding arc plasma arises from the anode and cathode regions. Models employing closed-form expressions for describing the anode and cathode regions have demonstrated their usefulness in studying the effect of shield gases and active flux on the resulting weld pool geometry. Detailed numerical modeling of transport phenomena in the anode and cathode regions will help further improve the current understanding of heat and mass transfer in the complex welding arc.

Numerical Solution

Grid (or mesh) generation is an important consideration in computing numerical solutions to the partial differential equations governing the welding process. The generation of a mesh is an important numerical issue; the type and quality of mesh can determine the success or failure of the numerical model in attaining a

converged and accurate solution. Computational fluid dynamics (CFD) requires the subdivision of the computational domain into a number of smaller elements or grid cells, and the discretized domain needs to have adequate spatial resolution. During weld pool modeling, sufficiently fine mesh should be used to provide an adequate resolution of the important flow features in the weld pool. For turbulence models, it is recommended that recirculation vortices or steep flow gradients within the viscous boundary layers be properly resolved through local refining.

When the geometry is simple and regular, the most straightforward approach is to employ an orthogonal grid in a Cartesian coordinate framework. This type of grid is generally called a structured mesh. Structured mesh can also be applied for a more complicated geometry by creating a nonorthogonal mesh with deformed body-fitted grids. In this method, grid cells still retain a regular element shape in the form of either a skewed rectangle in two dimensions or a distorted hexahedron in three dimensions. The advantage of such a mesh is that the connectivity is straightforward because cells adjacent to a given elemental face are identified by the indices, and the cell edges form continuous mesh lines that begin and end on opposite elemental faces. The disadvantage, particularly for more complex geometry, is the increase in grid nonorthogonality or skewness, which can generate physically unrealistic solutions upon the transformation of the governing equations. The transformed equations, which accommodate the nonorthogonality, contain additional terms acting as the link between the structured coordinate system (such as the Cartesian coordinate) and the body-fitted (curvilinear) coordinate system, thereby augmenting the cost of numerical calculations and difficulties in programming. Consequently, such a mesh may also affect the accuracy and efficiency of the numerical algorithm that is being applied. Block-structured or multiblock mesh is another special case of a structured mesh.

Another meshing approach is based on what is called unstructured mesh, in which the cells are allowed to be assembled freely within the computational domain. The most typical shapes of unstructured elements in three dimensions are tetrahedral and hexahedral cells. Unstructured meshes are well suited for handling arbitrary shape geometries, especially for domains having high-curvature boundaries. However, there are several disadvantages to unstructured mesh. If triangular or tetrahedral cells with high aspect ratio (very long and thin shape) are placed adjacent to the wall boundaries, this configuration may create large inaccuracies in the approximation of the diffusive fluxes. Other disadvantages are the extra bookkeeping effort required to handle the connectivity of elemental cells, and the more complex solution algorithms needed to solve the flow-field variables, each of

which may result in increased computing times and erode the gains in computational efficiency. In recent years, many commercial CFD codes have made available the capabilities to mesh the interior domain using polyhedral cells. Polyhedral meshing has tremendous advantages over tetrahedral meshing with regard to computational accuracy and efficiency. An important aspect of the unstructured mesh is the mesh quality, which can be measured by such factors as aspect ratio, skewness, and warp angle. For instance, large aspect ratios should always be avoided in weld pool regions, because they can degrade the solution accuracy and may result in poor convergence.

Methods for discretizing and solving the governing transport equations are discussed in many textbooks. The majority of the published heat and mass transfer models are based on the control volume method (and its variations, including finite-volume and finite-difference methods). An excellent textbook on the control volume method is provided by Patankar (Ref 10). With the recent advance in computation, the numerical solution of transport equations has been implemented into fairly sophisticated solvers. The availability of such solvers allows one to focus on the specifics relevant to weld transport phenomena without expending much effort on basic code development. See the section "Important Considerations" for a discussion of the choice of solvers.

Dimensional Analysis

Although a detailed numerical solution is required to describe weld pool transport phenomena, some simple formulas have been established based on dimensional analysis to correlate welding parameters (such as current) to resulting weld characteristics (such as penetration).

Robert and DebRoy (Ref 53) studied the Peclet (Pe) and Marangoni (Ma) numbers in conduction-mode laser spot welding of materials with diverse properties, such as gallium, pure aluminum, aluminum alloy 5182, pure iron, steel, titanium, and sodium nitrate. It was found that for materials with high Prandtl number (Pr), such as sodium nitrate, Pe and Ma were high, and heat was transported primarily by convection within the weld pool. The resulting welds were shallow and wide. For low-Pr materials, such as aluminum, Pe and Ma were low in most cases, and low Pe made the weld pool deep and narrow. The cross-sectional areas of stationary and low-speed welds could be correlated with welding conditions and material properties using dimensionless numbers, as shown in Fig. 4.

Arora et al. (Ref 54) studied the formation of wavy weld pool boundary using dimensionless numbers derived from the Buckingham π -theorem. Their calculations show that in metallic systems the wavy fusion-zone boundary forms at a Marangoni number greater than

26,000 and a Prandtl number less than 0.06 for dimensionless heat input greater than 20. The wavy boundary originates from the interaction of counterrotating liquid metal loops at high Marangoni numbers.

Tello et al. (Ref 55) developed a scaling law for estimating the weld penetration in GTAW involving high current and travel speed. As shown in Fig. 5, the predicted penetration using the scaling expression is consistent with the

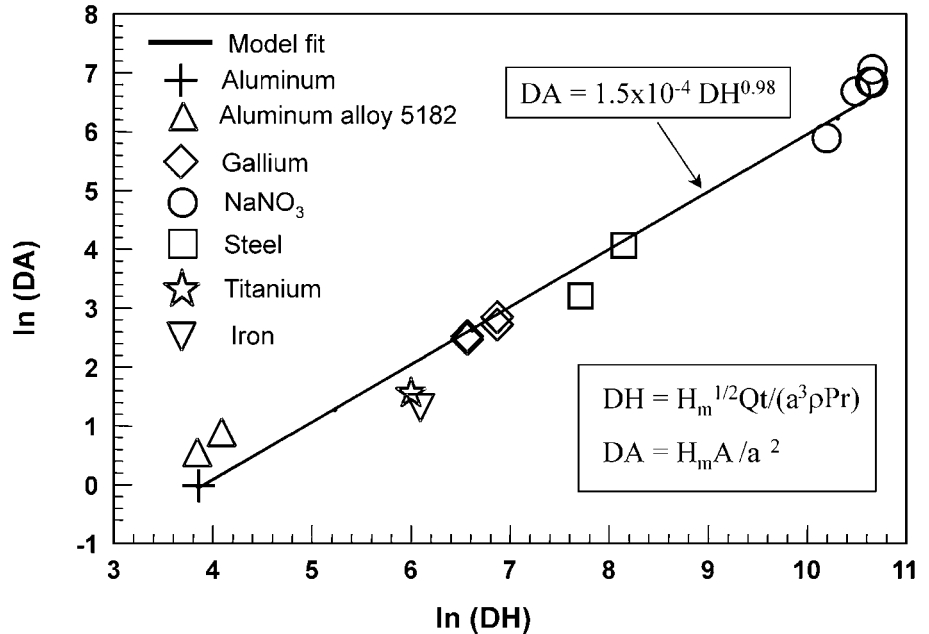


Fig. 4 Correlation between dimensionless cross-sectional area (DA) and dimensionless heat input (DH) for spot and low-speed laser welds. Adapted from Ref 53

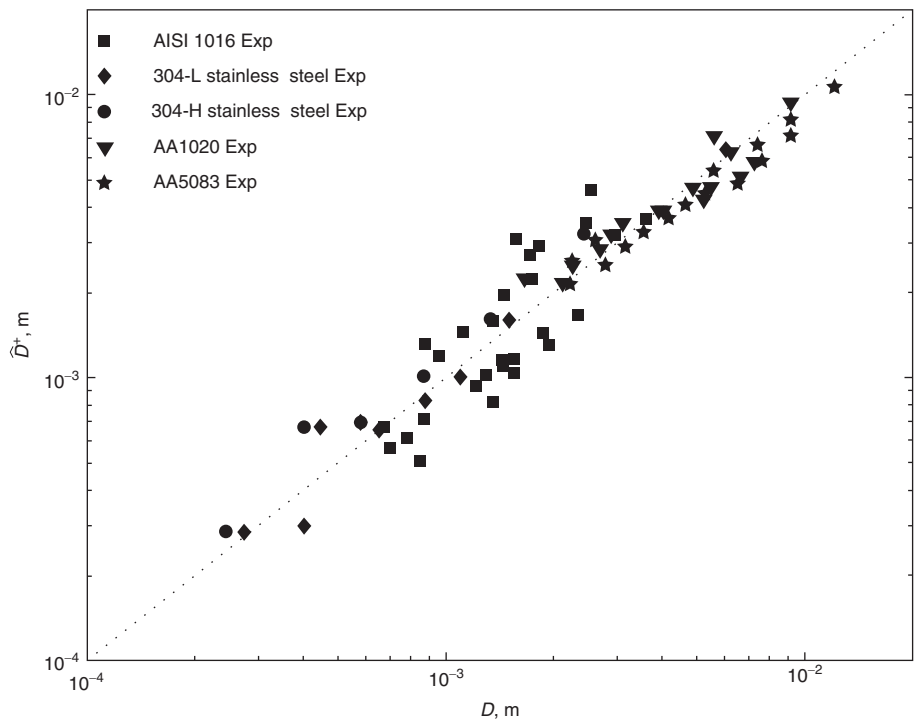


Fig. 5 Comparison between the corrected scaling law and experiments with different materials and process parameters. Adapted from Ref 55

experimental data for different materials and process parameters.

Application to Fusion Welding Processes

Heat and Mass Transfer in Arc Plasma

Figures 6(a) and (b) show the distributions of plasma temperature (within an isothermal plasma model) and plasma flow velocity in the arc plasma column calculated using the self-consistent modeling approach outlined previously. The GTAW is done in argon atmosphere with the following parameters: arc current (I) = 200 A, arc length (L_a) = 6.3 mm (0.25 in.), and temperature of the water-cooled anode surface (T_s) = 700 K.

Gas Tungsten Arc Welding

Among the various fusion welding processes, GTAW is perhaps the process most studied by numerical heat and mass transfer models. Some of the early models for GTAW include those developed by Oreper et al. (Ref 56), Kou and Sun (Ref 18), Zacharia et al. (Ref 57), Wu and Tsao (Ref 58), and Kanouff and Greif (Ref 59). Excellent review of those early models can be found in the papers by Matsunawa (Ref 22) and Jönsson et al. (Ref 60). This section summarizes some recent results on heat and mass transfer modeling for GTAW.

Mishra et al. (Ref 61) modeled gas tungsten arc butt welding of stainless steel plates containing different sulfur concentrations. The species conservation equation for sulfur is solved along with the governing equations of mass, momentum, and energy conservation. As shown in Fig. 7, both the simulated and experimental

results show significant shift of the fusion zone toward the low-sulfur steel. Flaring of the arc toward the low-sulfur side was found to be an important factor governing the shifting of the weld pool and the missed weld joint.

Lim et al. (Ref 62) calculated the fluid flow and heat transfer in a weld pool of nickel alloy Inconel 690 that is stirred by circular magnetic arc deflection. The arc stirring effect is modeled by considering an arc orbiting in a circle on the weld top surface. As a result, the heat flux, arc pressure, and electromagnetic force vary with time, depending on the center position of the arc. Numerical simulations predicted large changes in the temperature gradient accompanied by reversal of liquid/solid interface velocities (i.e., solidification and remelting) at a stirring frequency of 7 Hz.

Zhang et al. (Ref 63) modeled the transient heat transfer and fluid flow during gas tungsten arc spot welding of low-carbon steel. Figure 8 shows the evolution of calculated temperature and velocity fields in the workpiece, where the weld pool shape is defined by the solidus temperature isotherm. For clarity, only one-half of the weld is shown. Important solidification parameters, that is, the temperature gradient at the solidification front (G) and the solidification rate (R), are computed from the temperature data. The combination of solidification parameters G and R , that is, G/R and GR , were used to estimate the solidification morphology and substructure in a 1005 steel spot weld. A similar approach is used to study the solidification parameters in laser spot microjoining of 304 stainless steel by He et al. (Ref 64), linear GTAW of commercial pure aluminum (Ref 65), and conduction-mode laser and electron beam welding of single-crystal superalloy (Ref 66).

Hong et al. (Ref 31) showed that the weld geometry for 304 stainless steel, calculated

using a heat and fluid transport model along with the k - ϵ turbulence model, agreed with the experimental results (Fig. 9b). Assumption of laminar flow, on the other hand, resulted in overprediction of weld depth (Fig. 9a). Figure 9(c) shows the variation of the dimensionless viscosity, given as the ratio of turbulent and molecular viscosities, with location in the weld pool. Turbulence was stronger near the middle of the weld pool and decreased closer to the solid-liquid boundary. The enhancement of viscosity resulted in significant decrease in fluid velocities compared to calculations of the laminar flow model.

Gas Metal Arc Welding

Although the basic governing transport equations of heat and mass transfer are almost identical for GTAW and GMAW, the metal transfer in GMAW introduces additional complexities in the GMAW weld pool. Metal transfer in GMAW is a complex phenomenon of drop growth, neck formation, and detachment, and it can take place in three principal modes: globular, spray, and short-circuiting, depending on the welding conditions. The impingement of molten droplets onto the weld pool in GMAW greatly affects the shape of the free surface and the convective heat transfer in the weld pool. The deformed weld pool influences the current distribution in the arc and thus influences the heat and momentum fluxes transferred from the arc plasma to the weld pool. In addition, superheated metal droplets carry a significant amount of thermal and kinetic energy into the weld pool. The resulting weld pool is fairly deep at its root, and its geometry exhibits a characteristic “finger penetration” pattern (especially for the spray transfer mode). Due to complicated interactions among arc

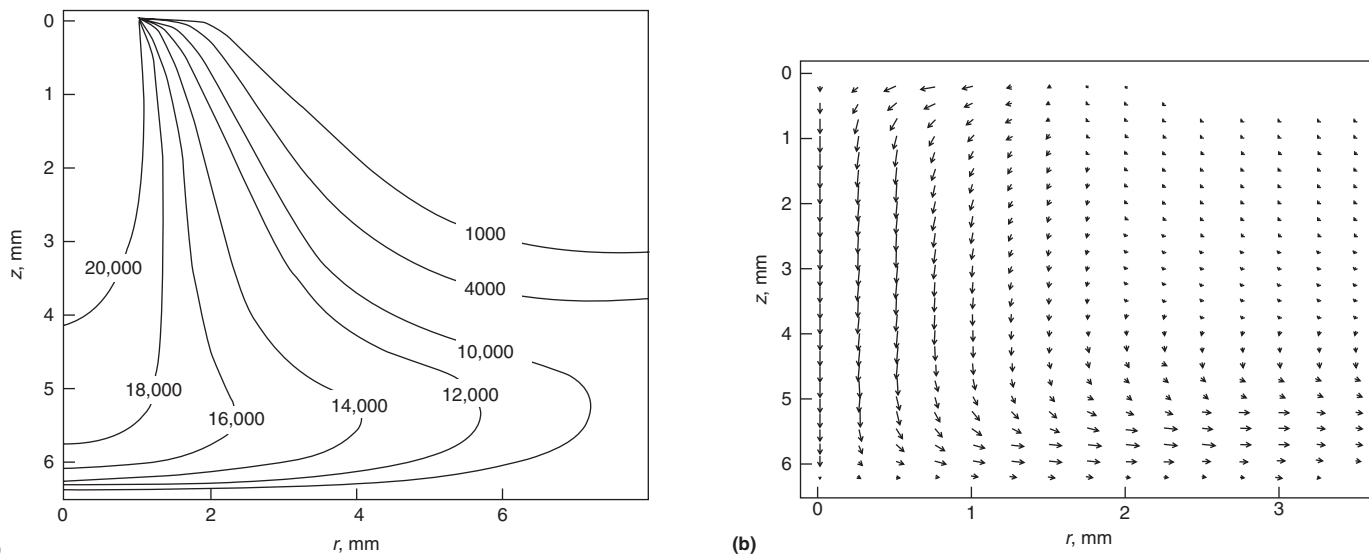


Fig. 6 (a) Plasma temperature distribution (in degrees K). (b) Plasma velocity distribution in argon arc. In (b), the maximum velocity magnitude is equal to 330 m/s (985 ft/s).

plasma, droplets, and weld pool, many existing numerical models only focus on one or two events of the GMAW process while simplifying the rest of the events. Depending on the physics incorporated in the models, the numerical models of GMAW can be classified into the following three groups.

The first group of numerical models focuses on understanding the mechanism of droplet formation. Among various models, the static force balance model (SFBM), dynamic force balance model (DFBM), and pinch instability theory (PIT) have been most widely used for metal transfer analysis (Ref 67–70). The SFBM predicts the detaching drop size by comparing the forces exerted on the drop in the globular mode (Ref 67–70). The forces affecting metal transfer are surface tension, electromagnetic, gravitational, and plasma drag forces. When the detaching force becomes greater than the attaching force, the drop detaches from the wire tip. Due to its static nature, the SFBM cannot take account of the effects of dynamic forces such as inertia. On the other hand, the DFBM includes the effect of inertial force. The PIT has been used for spray-mode analysis based on Rayleigh instability and provides the critical wavelength at which the current-conducting liquid cylinder breaks up (Ref 69, 70). All these

models provide useful closed-form equations to estimate the detaching drop size but fail to predict the drop size accurately in the high-current range. In the literature, other models have also been proposed to predict metal transfer more accurately. Nemchinsky (Ref 71) calculated the droplet shape affected by surface tension and electromagnetic force. Jones et al. (Ref 72) simulated the dynamic movement of a drop with a complex shape, including ellipsoids and tapered neck, calculating the spring and viscous damping forces and using correction factors; their calculations matched experimental results. Numerical techniques such as the volume-of-fluid (VOF) method have been employed to predict the drop profile and fluid flow within the drop (Ref 73–75). Choi et al. (Ref 74) showed that the pendant drop oscillates and the fluid flow within the drop affects drop detachment, which demonstrates that inertial force influences metal transfer. Haidar and Lowke (Ref 75) used an arc model to simulate the droplet formation in GMAW using VOF. The energy equation and the continuity, momentum, and current-conservation equations were solved for both the molten droplet and the surrounding plasma arc, and the shape of the droplet was predicted as a function of time. In their model, the fluid flow in the weld pool was not calculated, and only the heat conduction was considered.

The second group of models incorporates the effect of droplet and arc plasma by decoupling the physics and including the effect of these variables using boundary conditions. Yang and DeRoy (Ref 15) used the $k-\epsilon$ turbulence model to calculate the fluid flow inside a GMAW weld pool. They found that the dissipation of heat and momentum in the weld pool is significantly aided by turbulence. Figure 10 shows the distributions of turbulent viscosity, thermal conductivity, kinetic energy, and dissipation rate in the weld pool obtained by their model. Their modeling results show that the maximum values of these variables lie in the middle of the weld pool, and the values decrease progressively from the center to the periphery. This outcome is as expected, because the circulation of the molten metal is most intense near the surface, and the level of turbulence decreases progressively as the fluid approaches the solid surface. To model the heat carried by the droplets, they used the cylindrical volumetric heat source in the weld pool. In their model, the dimensions of the volumetric heat source were determined by such parameters as the drop size, shape, velocity, and frequency, using a model suggested by Kumar and Bhaduri (Ref 76). Although their model did not take into account the impinging force of the droplet on the free surface, the prediction of their model agreed well with the experimentally obtained fusion-zone geometry for several different welding conditions, as shown in Fig. 11. A similar cylindrical-heat-source approach was used later by Zhang et al. (Ref 25, 77). Kim and Na (Ref 78) presented a 3-D quasi-steady heat and fluid

flow analysis for the moving heat source of a GMAW process with a deformed free surface using boundary-fitted coordinates. Ushio and Wu (Ref 79) used a boundary-fitted nonorthogonal coordinate system to handle the largely deformed gas metal arc weld pool surface and predicted the weld pool dimensions. In those models, the heat delivered by the droplet was approximated by an internal heat-generation term, and the impact of droplets onto the weld pool was assumed to be a constant force acting on the surface. In other words, the actual droplet impinging process was not simulated. The dynamic change of the weld pool free surface was recently modeled by Wang and Tsai (Ref 80), Fan and Kovacevic (Ref 81), and Cao et al. (Ref 82) using the VOF method. All these models (Ref 80–82) assumed the droplets were already generated with a certain shape, volume, temperature, and initial velocity at a certain distance above the weld pool. The droplet was then accelerated to the weld pool by applying a drag force calculated from an empirical formula and an assumed plasma velocity. Recently, Hu et al. (Ref 83) developed a model to predict humping defects in GMAW. In their paper, they focused on weld pool dynamics and the formation of ripples, and they did not calculate the droplet generation. They found that during welding, a crater was opened as a result of droplet impingement, and its closeup was caused mainly by hydrostatic force. The crater open and closeup led to the “up-and-down” of the fluid level in the weld pool, as shown in Fig. 12. A ripple was formed as solidification proceeds in the welding direction. They concluded that the periodic impingement of droplets, weld pool dynamics, and solidification all contributed to the formation of ripples, and the “pitch” of the ripples depends on many welding parameters, including droplet size (electrode diameter), droplet momentum, drop frequency (wire-feed speed), welding speed, welding power (current and voltage), and others.

Models falling into the third group are more comprehensive in nature and incorporate the arc physics, droplet formation mechanism, and weld pool dynamics in an integrated manner. Very limited work is published in the open literature on this type of models. Hu and Tsai (Ref 43, 84) developed a model that simulates melting of the electrode, the droplet formation, detachment, transfer, and impingement onto the workpiece, and the transient flow in the weld pool. Their model predicted the crater and oscillations in the weld pool due to periodical droplet impingement. They calculated the current distribution in the droplet and workpiece through the coupling effect of the arc and the metal. In their model, the heat flux, arc pressure, and plasma shear stress are all obtained from the coupled arc domain. They found that the droplet transfer and the deformed weld pool surface have significant effects on the transient distributions of current density, arc temperature, and arc pressure, which are

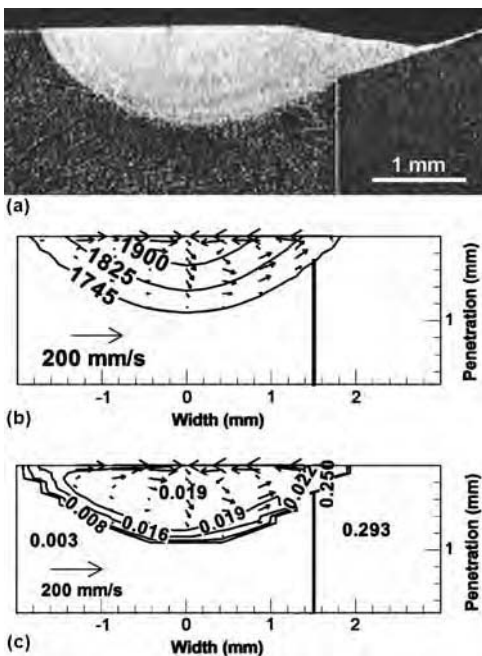


Fig. 7 (a) Experimental weld pool geometry. The vertical line shows the joint of the two plates. (b) Calculated temperature and velocity fields in the weld pool. The contours represent the temperatures in degrees Kelvin, and the vectors represent the liquid velocity. (c) The contours represent calculated sulfur concentrations in wt%. The sulfur concentration on the top surface and the bulk of the weld pool was approximately 0.019 wt%. Welding conditions: 100 A, 10.2 V, and 3.4 mm s⁻¹ welding speed. Adapted from Ref 61

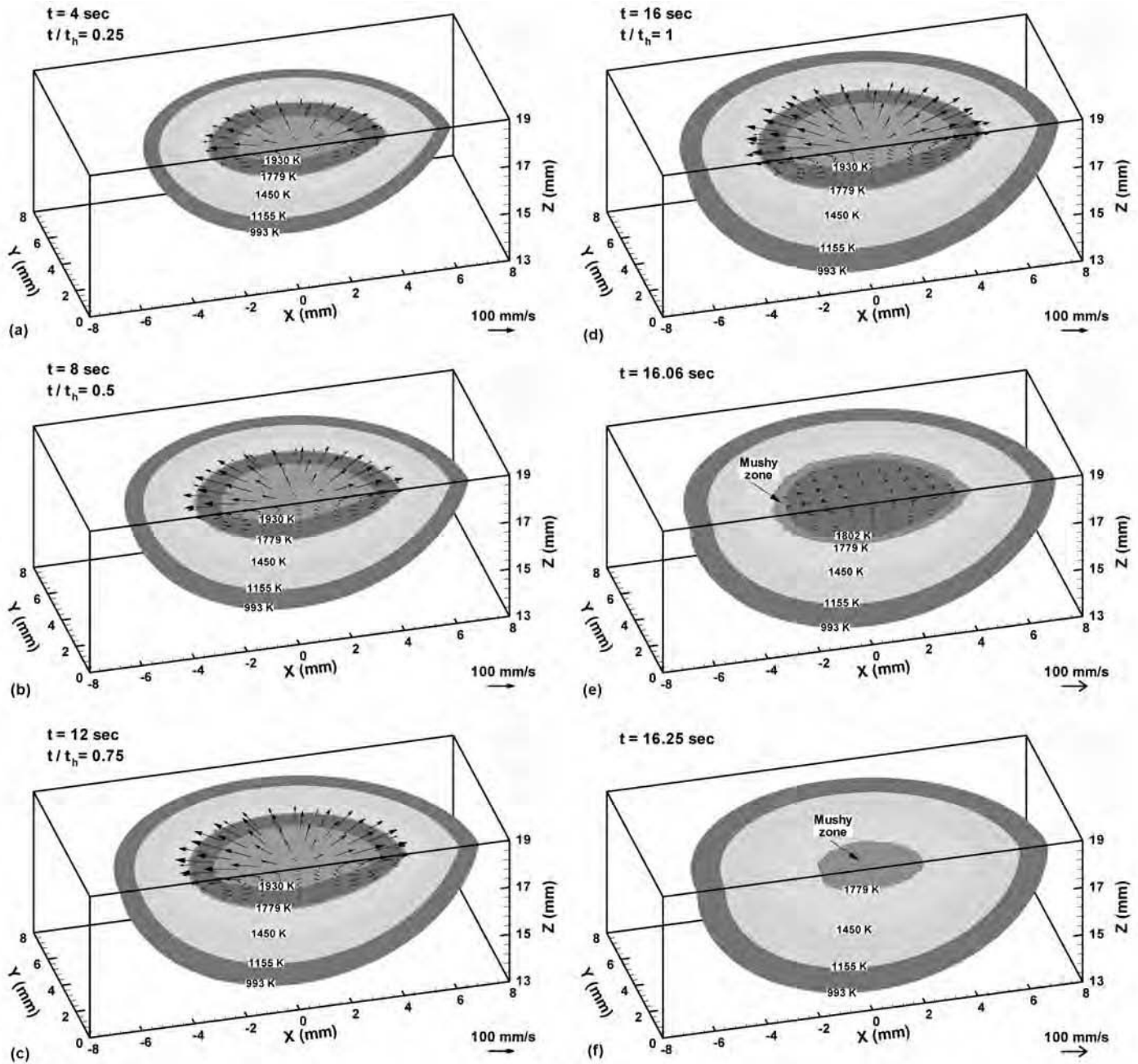


Fig. 8 Evolution of temperature and velocity fields at various times. Welding conditions: current = 120 A, voltage = 17.5 V, and arc on-time = 16 s. The velocities are represented by the arrows, while the temperatures are represented by the contours. Adapted from Ref 63

normally assumed to be constant Gaussian profiles. They also simulated the solidification processes of the electrode and weld pool after the arc is extinguished. Figure 13 shows the sequence of temperature distributions for droplet generation, detachment, transfer in the arc, impingement onto the weld pool, and weld pool dynamics (Ref 81). Modeling results show that a round droplet forms at the electrode tip and grows with time. Subjected to the arc pressure,

plasma shear stress, surface tension, and electromagnetic force, the detached droplet also changes its shape in the arc. The fluid flow in the detached droplet helps to mix the cold liquid in the droplet center with the hot liquid at the surface. Thus, a more uniform temperature distribution appears in the detached droplet than in the droplet hanging at the electrode tip. When the droplet hits the solid workpiece, it quickly spreads out on the workpiece, and

the droplet fluid is continually pushed downward and outward by arc pressure and arc shear stress, as shown in Fig. 13.

Laser Welding

When energy density of a laser or electron beam exceeds a threshold value, typically of the order of 10^5 W/cm², intense

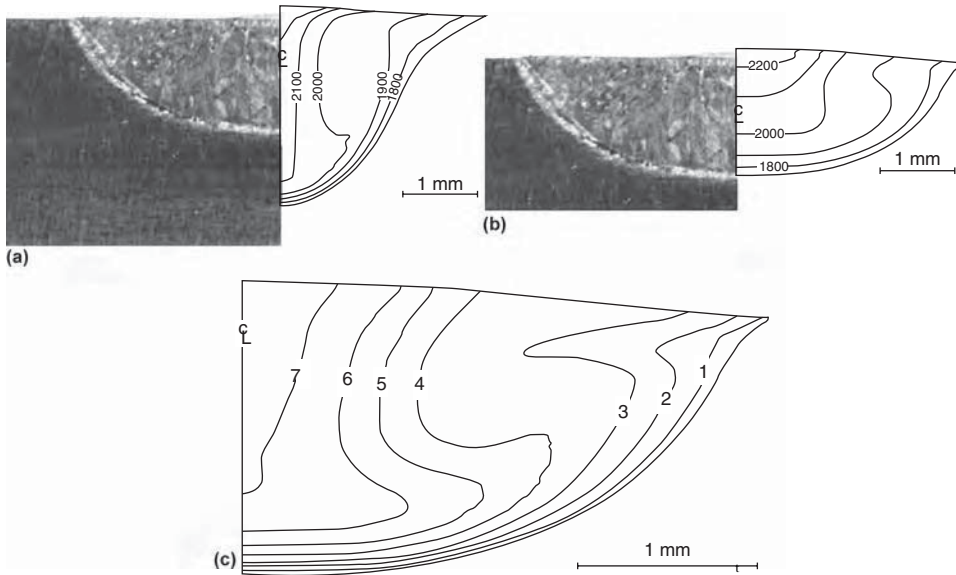


Fig. 9 Comparison of calculated and experimental weld geometries for 0.005 wt% S in 304 stainless steel assuming (a) laminar, (b) turbulent flow with k - ϵ model, and (c) dimensionless viscosity (μ/μ_0). Adapted from Ref 31

It is noted that keyhole-mode welding is a highly dynamic process and the keyhole exhibits complex fluctuations. Keyhole instability is an important issue that often leads to defects such as spiking and porosity. Comprehensive, transient numerical models have been developed to study the dynamic behavior of keyhole and related instabilities in LBW. They have provided valuable insight into the mechanisms of keyhole collapse and defect formation. On the other hand, quasi-steady-state models, which are very computationally efficient, have shown their usefulness in understanding the weld pool shape and temperature evolution in LBW of different engineering materials.

The earliest studies identified surface tension, vapor pressure, and hydrostatic force as the key factors influencing keyhole shape and penetration depth (Ref 85–87). An early pressure-balance model, proposed by Klemens (Ref 85), defined the equilibrium between the forces that tend to keep the keyhole open and those that try to close it:

$$p_0(z) = \frac{\gamma}{r(z)} + \rho gz \quad (\text{Eq 41})$$

where $p_0(z)$ is the difference between the pressure in the keyhole and the ambient pressure, γ is the surface tension, $r(z)$ is the keyhole radius at a depth z from the top surface, ρ is the density, and g is the acceleration due to gravity. The first term on the right is the surface tension pressure, and the second term is the hydrostatic pressure. The pressure inside the keyhole near the top surface equals the sum of surface tension pressure and ambient pressure, because the hydrostatic pressure becomes negligible. Immediately outside the keyhole, pressure is equal to the ambient pressure. Continuity of vapor pressure near the top surface requires that the surface tension pressure should become small. A trumpetlike flare (Ref 87) or a constriction (Ref 85) of the keyhole near the surface would ensure a large radius of curvature (hence small surface tension pressure) and continuity of vapor pressure. Kaplan (Ref 88) argued that heat transport in the keyhole-mode LBW was planar due to the constant wall temperature (equal to the boiling point of the alloy) and nearly vertical keyhole walls. His model considered the multiple reflections of laser beam inside the keyhole as well as the inverse bremsstrahlung absorption of the laser beam by the plasma.

With improvements in computational power, more comprehensive models of heat and mass transport in keyhole-mode welding were developed. Zhou et al. (Ref 89, 90) used the VOF method to model the keyhole dynamics and suggested that porosity may be avoided by controlling the laser pulse shape. Ki et al. (Ref 27, 91, 92) studied the transient evolution of the liquid-vapor interface using the narrow-band level-set method to transform the problem to a partial differential equation and simplify

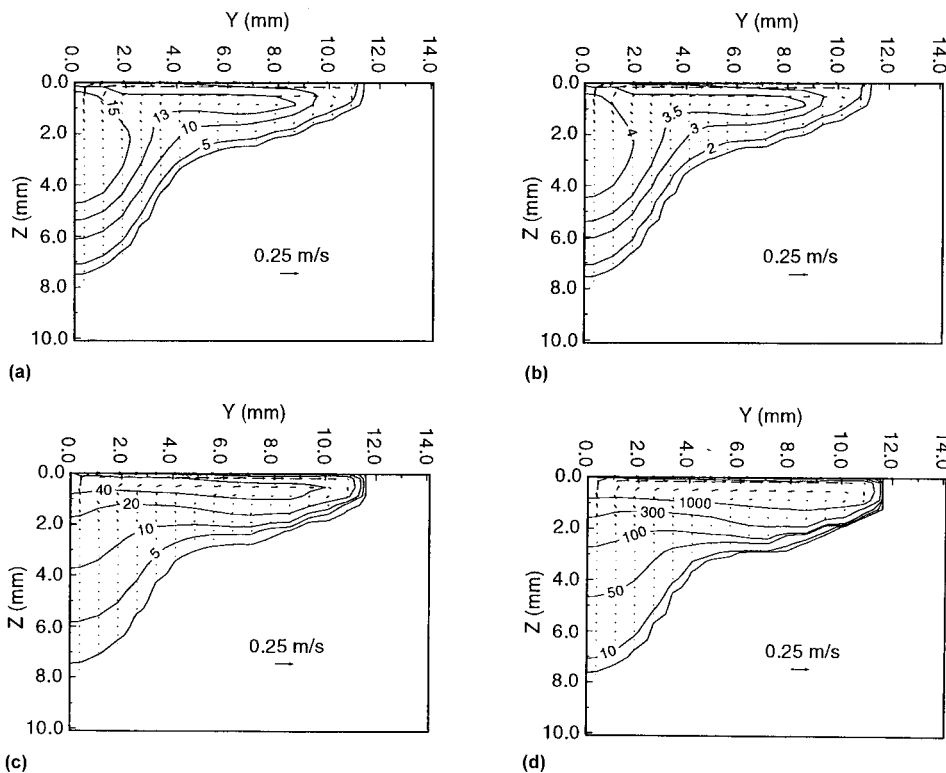


Fig. 10 Distribution of turbulent variables in the weld pool. (a) Dimensionless viscosity, μ/μ_0 . (b) Dimensionless thermal conductivity, k_e/k . (c) Turbulent kinetic energy, $\text{m}^2/\text{s}^2 \times 10^{-4}$. (d) Dissipation rate of turbulent kinetic energy, $\text{m}^2/\text{s}^3 \times 10^{-4}$. Adapted from Ref 15

vaporization of workpiece material results in formation of a deep and narrow vapor cavity (or keyhole) surrounded by liquid and solid metal. This section, and the next, focuses on this keyhole-mode welding. Modeling of laser

beam welding (LBW) done at relatively low energy densities is similar to the modeling of GTAW, which was previously discussed in the section “Gas Tungsten Arc Welding” in this article.

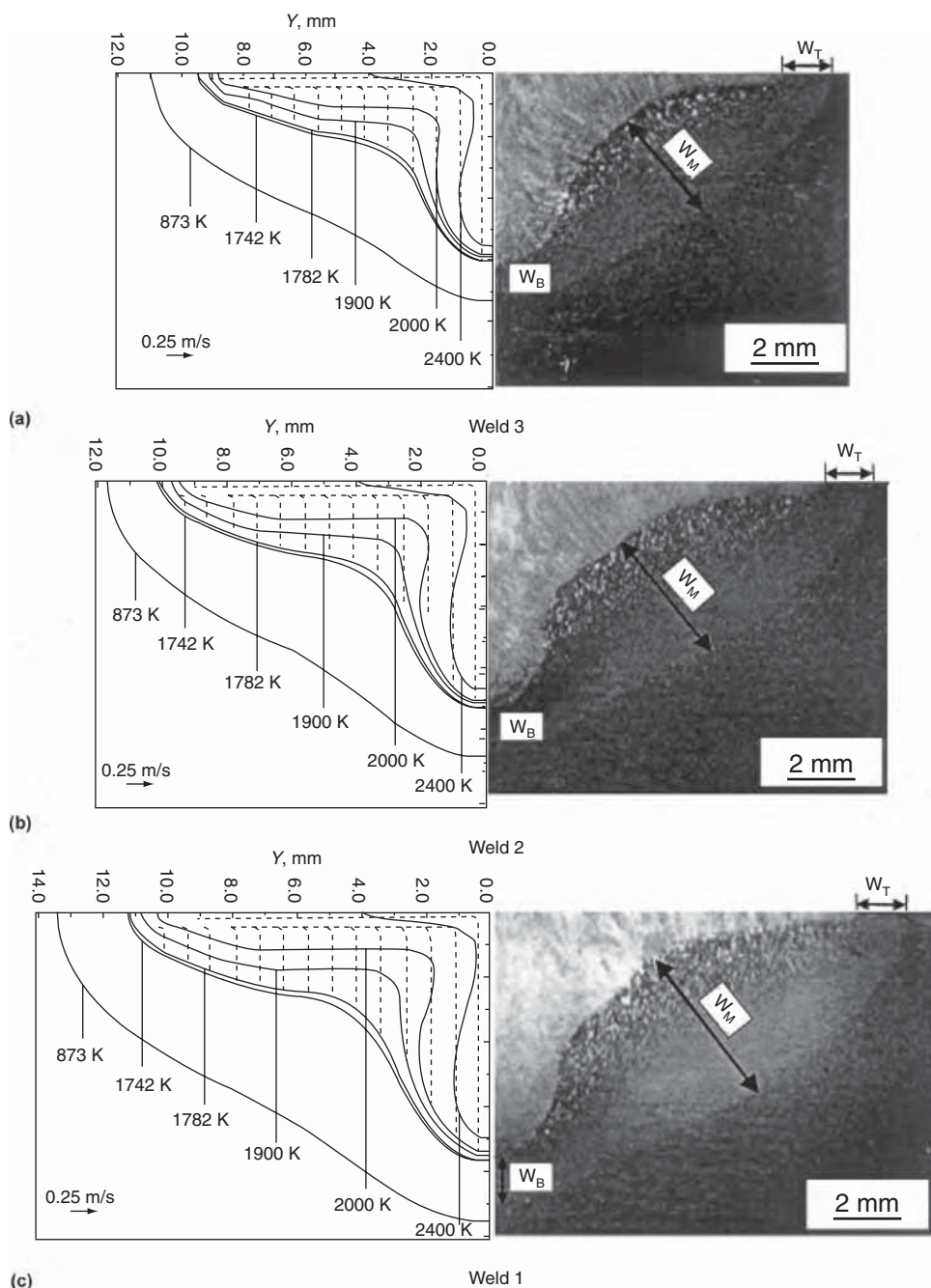


Fig. 11 Comparison of the calculated and experimental geometry of the fusion zone and the heat-affected zone (HAZ). The heat input per unit length for the three welds is (a) weld 3: 2.4 kJ/mm, (b) weld 2: 3.15 kJ/mm, and (c) weld 1: 3.94 kJ/mm. The symbols W_T , W_M , and W_B are the widths at the top, middle, and bottom of the HAZ, respectively. Adapted from Ref 15

the calculations of the surface curvature and the surface normal. A ray-tracing procedure was implemented to account for multiple reflections of the laser beam within the keyhole. The temporal evolution of the keyhole shape and temperature distribution for a steel weld made with a 4 kW laser beam of 0.5 mm (0.02 in.) beam diameter at 25 mm/s (1.0 in./s) welding speed is shown in Fig. 14. Due to the small time step required for convergence (10^{-6} s), the code

was optimized and parallelized to reduce the run time.

To reduce the computational requirements while preserving model accuracy, Rai et al. (Ref 25, 26) decoupled the keyhole calculation from the 3-D heat and fluid transport modeling. The keyhole profile was calculated using the energy balance at the liquid-vapor interface, which was assumed to be at a constant temperature. The calculations also considered multiple

reflections and plasma absorption in a manner similar to Kaplan's model (Ref 88). The 3-D temperature and velocity fields were subsequently calculated by solving the equations of conservation of mass, momentum, and energy coupled with a one-equation turbulence model based on Prandtl's mixing-length hypothesis. The model was validated for welding of several engineering materials, including aluminum alloys, steels, and titanium. Convection driven by surface tension gradients was found to significantly enhance the heat transport in the weld pool. A contrast in the weld pools of low-thermal-conductivity alloys such as steels and high-thermal-conductivity materials such as aluminum is apparent from Fig. 15. For low-thermal-conductivity materials, the greatly enhanced heat transport near the weld pool top surface results in a "nail-head" shaped weld. Such characteristic weld shape is usually absent in high-thermal-conductivity alloys because diffusive heat transport remains significant even in highly convective regions of the weld pool.

Electron Beam Welding

Although electron beam welding (EBW) is similar to LBW in many respects, there are some important differences in the two processes. The keyhole wall temperature at any depth in EBW or LBW can be estimated from the equilibrium temperature-pressure relation and the pressure-balance equation. In EBW, which is performed in a vacuum chamber, the increase of pressure with depth can result in significant corresponding increase in temperature (Ref 93, 94). However, in LBW, which is performed under atmospheric pressure, an increase in pressure results in a small temperature increase compared to that in EBW (Ref 25, 26, 85). Therefore, the assumption of constant keyhole wall temperatures commonly used in LBW models cannot be applied to EBW models.

Very few numerical heat and mass transfer models of keyhole-mode welding have focused on EBW. Elmer et al. (Ref 95) proposed heat conduction models based on distributed, point, and line heat sources. The choice of heat source depends on input power, power density, and depth-to-half-width ratio of welds. Wei and Chow (Ref 96) calculated keyhole wall temperatures based on a balance of surface tension and vapor pressure and found results comparable to the measurements of Schauer et al. (Ref 97). They also studied the effects of beam defocusing and alloying element vaporization on the keyhole shape on the assumption that the keyhole cross sections are circular. Their results (Fig. 16) showed that keyhole wall temperatures varied by approximately 600 K with depth and decreased with increasing concentration of alloying elements.

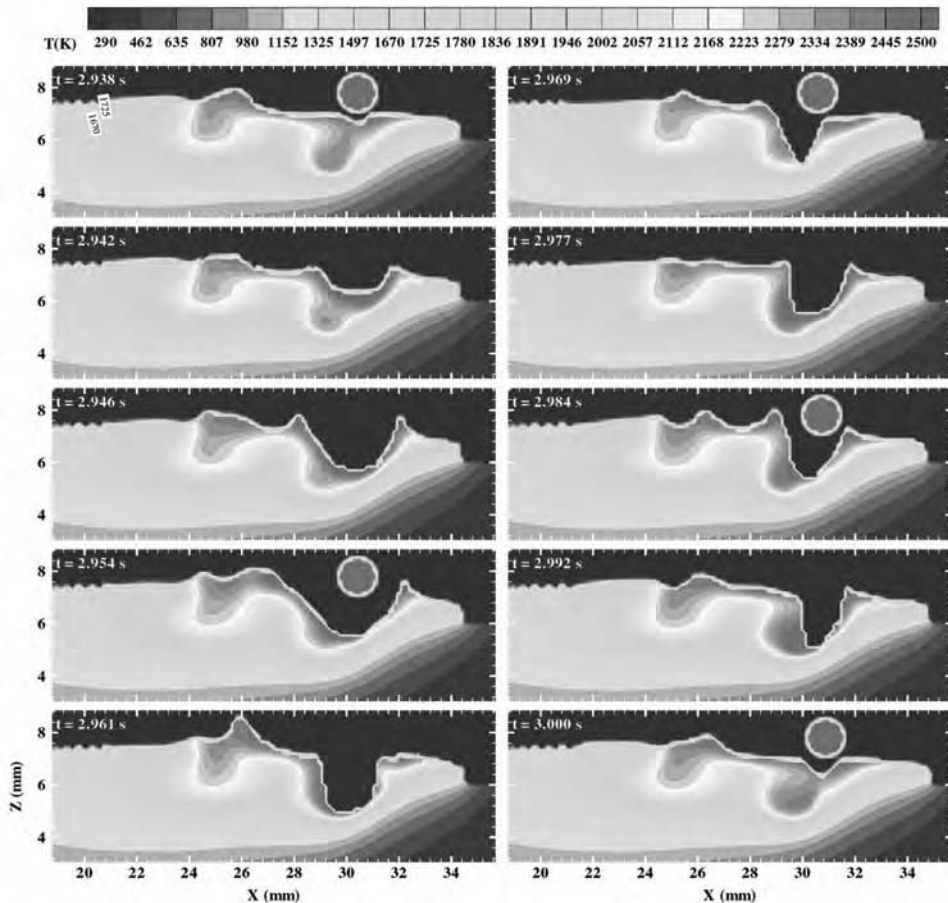


Fig. 12 Typical sequence showing the impinging of droplets, weld pool dynamics, and temperature distribution (side view). Adapted from Ref 83

A 3-D heat and mass transport model was developed by Rai et al. (Ref 93, 94) and tested for stainless steel and Ti-6Al-4V alloy welds by comparing the calculated weld geometries and thermal cycles with experimental results. The vapor pressure in the keyhole was calculated from the pressure balance at the keyhole walls, and the keyhole wall temperatures were calculated using the equilibrium pressure-temperature relationship. The 3-D model considered convection driven by surface tension gradients at the top surface and the keyhole walls, buoyancy, and turbulence. Figure 17 shows the variation of calculated keyhole pressure and wall temperatures with depth. Keyhole wall temperatures in EBW are lower than the normal boiling point of the alloy. As a result, lower wall temperatures are required in order to maintain the EBW keyhole, and penetration depth is greater compared to LBW (Fig. 18). However, due to the lower wall temperatures in EBW, less heat is transported in horizontal planes, and, as a result, welds are narrower than in LBW (Ref 93).

It is noted that compared to the work on keyhole dynamics in LBW, very little study has been done in EBW. Nevertheless, the keyhole

fluctuation and instability is an important issue in EBW. The results obtained using the quasi-steady-state model (Ref 93) provide a useful basis for developing future generations of comprehensive transient models to understand the keyhole dynamics in EBW.

Laser-Arc Hybrid Welding

The laser-arc hybrid welding process takes advantage of the benefits of both laser and arc welding, resulting in wide and deep welds in a single pass, with low distortion and residual stresses. As pointed out in an excellent review paper (Ref 98), the benefits of the laser-arc hybrid welding process mainly arise out of the physical interaction of the two heat sources. In situations where the laser and arc are separated by a distance at which no plasma interaction occurs, the process should be considered as tandem welding (Ref 99).

Laser-arc interactions are complex in hybrid welding. The synergistic interaction between the laser and the arc involve surface-heating interactions, stabilization of the arc cathode spot, and constriction of the arc plasma column (Ref 98). For simplicity, the majority of

published hybrid welding models to date do not consider the details of laser-arc interactions. Zhou and Tsai (Ref 100) developed a transient 2-D axisymmetric model to simulate the impingement of metal droplets into the weld pool containing a keyhole during laser-metal inert gas (MIG) hybrid welding. The laser-MIG hybrid weld pool was also simulated by Gao et al. (Ref 101). Unlike the model by Zhou and Tsai where the laser and arc are aligned coaxially, the laser and arc heat sources are separated at a horizontal distance of 4 mm (0.16 in.) in the model by Gao et al. Cho and Farson (Ref 102) developed a 3-D heat transfer and fluid flow model to evaluate the humping defect formation in CO₂ laser-GMAW hybrid welding. Cho et al. (Ref 103) developed 3-D transient simulations of CO₂ laser-GMAW hybrid welding for the laser trailing the arc. Their hybrid welding model is a combination of the arc welding model and the laser welding model, without any interactive effect between the two.

Ribic et al. (Ref 104, 105) assessed the arc-laser interactions in laser-GTAW hybrid welding. To match the predicted fusion-zone depth and width with the experimental data, the arc radius used in their 3-D heat transfer and fluid flow model was varied. The best-fit data show the arc radius must decrease to achieve the observed weld depth when the arc and laser are in close proximity.

In conclusion, laser-arc hybrid welding is one of the most challenging fusion welding processes to model numerically, because of the complexity of laser-arc interactions. Comprehensive mathematical description of such interactions is yet to be fully developed. The current generation of models has provided useful insights into the molten metal flow and heat transfer in hybrid welding. Those models will serve as a solid basis for the development of the next generation of models as understanding of laser-arc interactions improves.

Mass Transfer in Weld Pool

Nitrogen Absorption

Nitrogen is an important alloying element in modern steel chemistry, and its concentration can have significant effects on the mechanical and corrosion properties of weld metal. Many published data have shown that nitrogen absorption by the weld metal is enhanced above the equilibrium solubility of nitrogen predicted by Sievert's law. The existence of monatomic nitrogen dissociated from molecular nitrogen in the plasma is responsible for the enhancement of the nitrogen absorption in the low-nitrogen steel weld pool during arc welding (Ref 106).

Palmer and DebRoy (Ref 12) developed a comprehensive model for enhanced nitrogen dissolution in the weld metal during GTAW of iron. Their model works as follows. First,

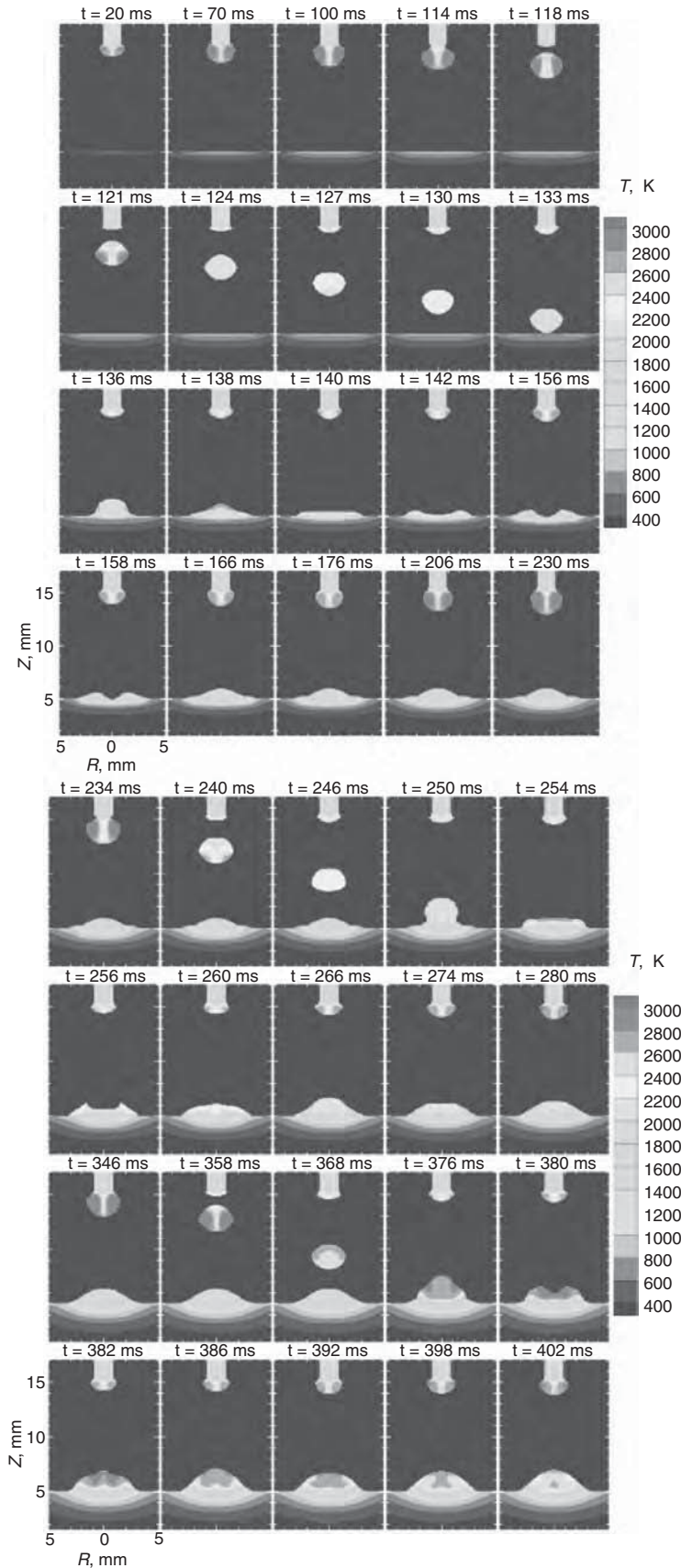


Fig. 13 Sequence of temperature distributions showing droplet generation, detachment, transfer in the arc, impingement onto the weld pool, and weld-pool dynamics. Adapted from Ref 84

monatomic nitrogen partial pressures are calculated as a function of the electron temperatures in the plasma phase. Second, nitrogen concentrations on the weld pool surface are calculated as a function of both the monatomic nitrogen partial pressure and the weld pool surface temperatures. Third, the model takes account of the fact that, once absorbed at the weld pool surface, nitrogen is transported predominantly by convection to the interior of the weld pool. The species conservation equation shown in Eq 7 is solved to obtain the distribution of nitrogen concentration in the weld pool, where the enhanced transport of nitrogen due to turbulence is modeled by increasing the nitrogen diffusion coefficient. Finally, nitrogen desorption is taken into account by placing a limit on nitrogen concentrations in the weld pool to define the concentration at which desorption occurs. As shown in Fig. 19, the modeling and experimental results are equivalent in magnitude for a given set of welding parameters and follow similar trends with changes in the nitrogen addition to the shielding gas.

Vaporization of Alloying Elements

During LBW of many important engineering alloys, an appreciable amount of alloying element vaporization takes place from the weld pool surface. As a consequence, the composition of the solidified weld pool is often significantly different from that of the alloy being welded. The composition change, in turn, can lead to significant changes in the microstructure and degradation of the mechanical and corrosion properties of the welds.

DebRoy et al. (Ref 107) combined the principles of gas dynamics and weld pool transport phenomena to calculate the rates of vaporization in CO₂ laser welding of pure iron and titanium. An extended method is used by He et al. (Ref 108) to study the composition change in 304 stainless steel weld metal during microjoining with short laser pulse. Two mechanisms for vaporization are considered. The first mechanism is the vaporization due to concentration gradient. For an element *i*, this diffusive vaporization flux (J_{ci}) can be calculated as:

$$J_{ci} = K_{gi} \left(M_i \frac{a_i P_i^0}{R T_i} - C_i^s \right) \quad (\text{Eq 42})$$

where K_{gi} is the mass transfer coefficient of element *i* between the weld pool surface and the shielding gas, M_i is the molecular weight of element *i*, a_i is the activity of element *i* in the liquid metal, P_i^0 is the equilibrium vapor pressure of element *i* over its pure liquid, R is the gas constant, T_i is the temperature on the weld pool surface, and C_i^s is the concentration of element *i* in the shielding gas.

The second mechanism is vaporization due to the pressure gradient. For element *i*, the vaporization rate due to this mechanism (J_{pi}) can be expressed as:

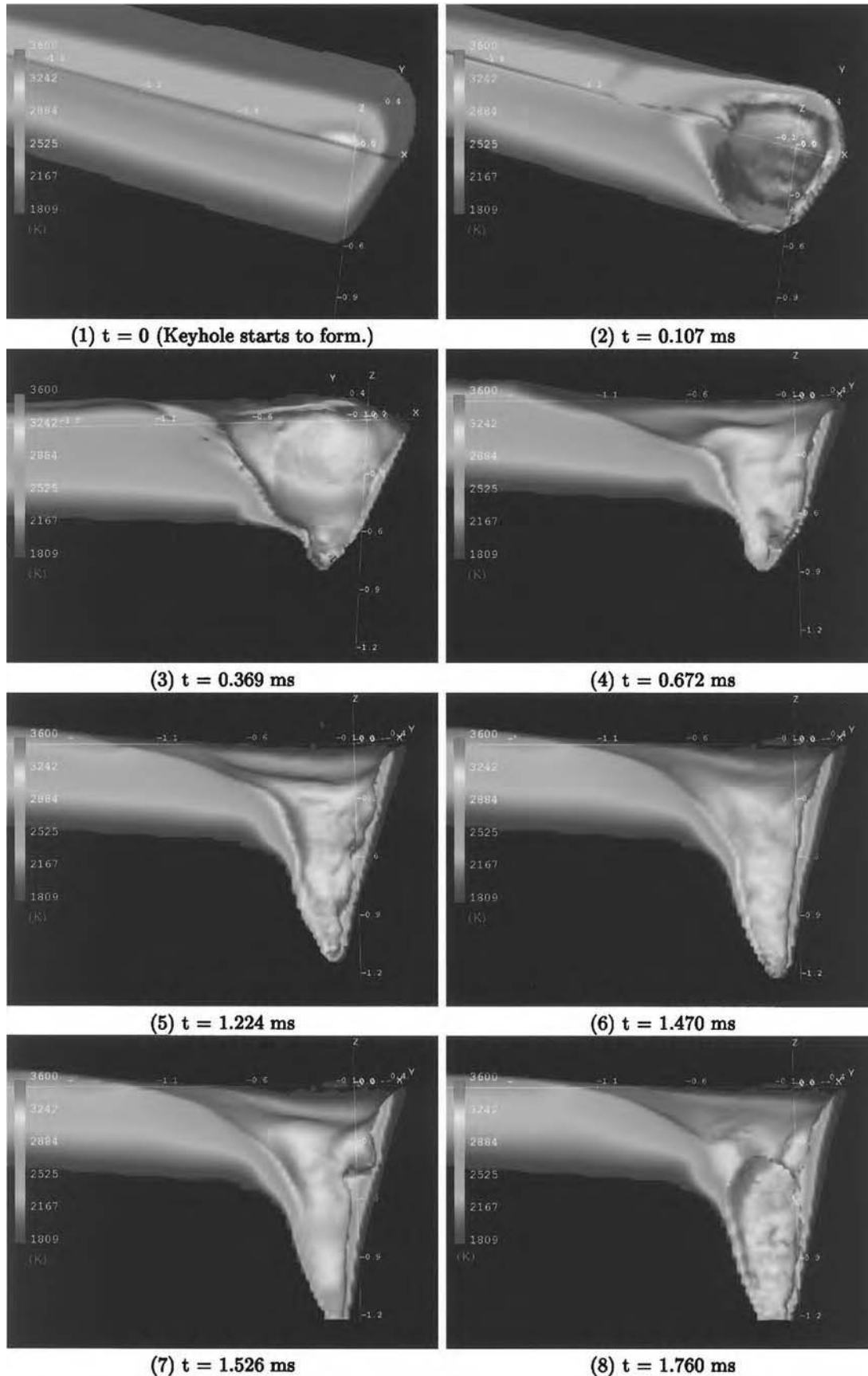


Fig. 14 Temporal evolution of keyhole shape and temperature distribution of a full-penetration keyhole weld. Laser power: 4 kW; welding speed: 25 mm/s (1.0 in./s); beam diameter: 0.5 mm (0.02 in.). Adapted from Ref 27

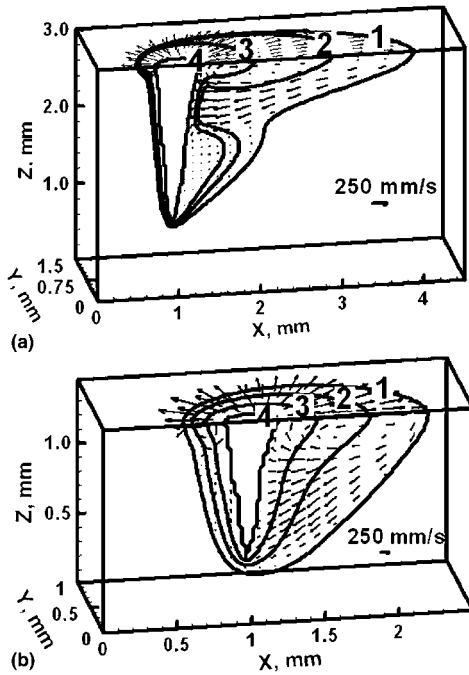


Fig. 15 Computed temperature and flow field for (a) SS 304L at 1000 W and 19 mm/s and (b) Al 5754 at 2600 W and 74.1 mm/s. For SS 304L, levels 1, 2, 3, and 4 correspond to 1697, 1900, 2100, and 3100 K, respectively. For Al 5754, levels 1, 2, 3, and 4 correspond to 880, 1100, 1400, and 2035 K, respectively. Adapted from Ref 25

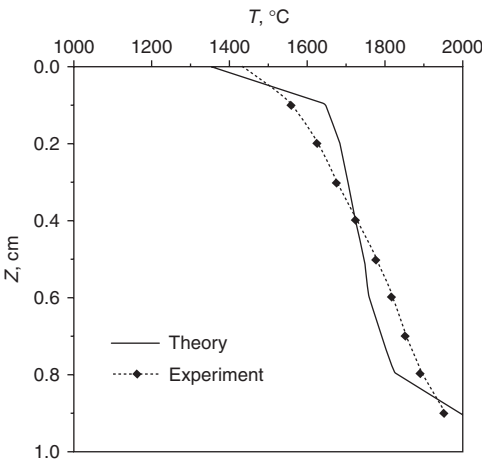


Fig. 16 Measured and calculated variation of keyhole wall temperatures with depth for Al 1100 alloy. Welding parameters: 4.34 kW, 8 mm/s (0.32 in./s), 0.005 rad divergence, -4 mm (-0.16 in.) defocus, and 0.7 mm (0.03 in.) focal spot size. Adapted from Ref 96, 97

$$J_{pi} = a_i \frac{P_i^0 M_i}{P_i M_v} J_p \quad (\text{Eq 43})$$

where P_i is the vapor pressure on the liquid surface, and M_v is the average molecular weight of

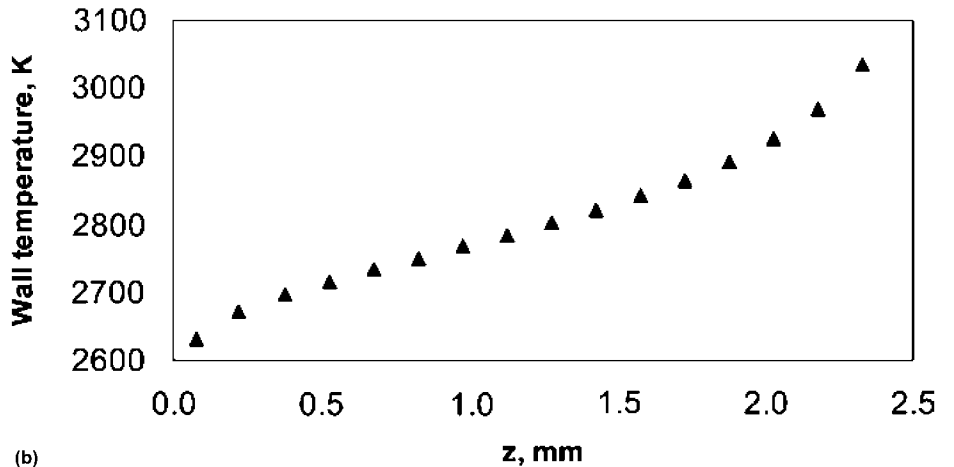
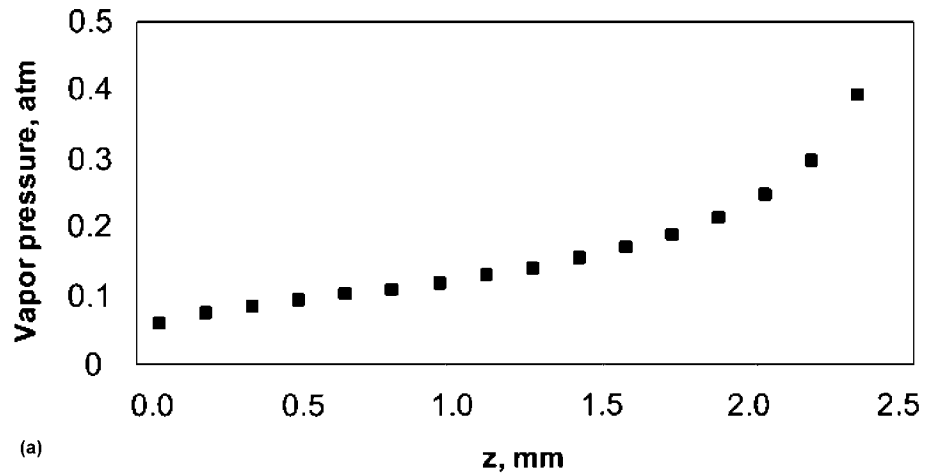


Fig. 17 Variation of (a) vapor pressure in the keyhole and (b) keyhole wall temperature, with depth for electron beam welding of Ti-6Al-4V at 550 W and 16.9 mm/s (0.67 in./s). $z = 0$ at the surface of the workpiece. Adapted from Ref 93

the vapor. J_p is determined by using the following equation:

$$J_p = \rho_v M S \quad (\text{Eq 44})$$

where ρ_v is the vapor density, M is the Mach number, and S is the speed of sound in the vapor. Details on the procedure for the calculation of vaporization flux using Eq 42 through 44 are available elsewhere (Ref 107, 108).

He et al. (Ref 108) calculated the weld-metal composition change in 200 μm deep 304 stainless steel microjoints fabricated using millisecond-long neodymium: yttrium-aluminum-garnet (Nd-YAG) laser pulses. The temperature profile on the weld pool surface is obtained by solving the energy and momentum conservation equations. Figure 20 shows a fair agreement between the experimental and computed concentration changes of the various alloying elements in a 304 stainless steel microjoint.

In high-power LBW, the peak temperatures on the weld pool surface often exceed the material boiling point. In such situations, the escaping vapor exerts a large recoil force on the weld pool surface. As a consequence, the molten metal may be expelled from the weld pool. He et al. (Ref 109) studied the liquid metal expulsion during laser spot welding of 304 stainless steel. By comparing the vapor recoil force with the surface tension force at the periphery of the liquid pool, their model predicted whether liquid metal expulsion would take place under various welding conditions. It is found that a higher laser power density and longer pulse duration significantly increased liquid metal expulsion during spot welding.

For arc welding, Murphy (Ref 45) reviewed various methods for the calculation of the production rate of metal vapor. Among those methods, the Clausius-Clapeyron equation is worth noting, which is expressed as:

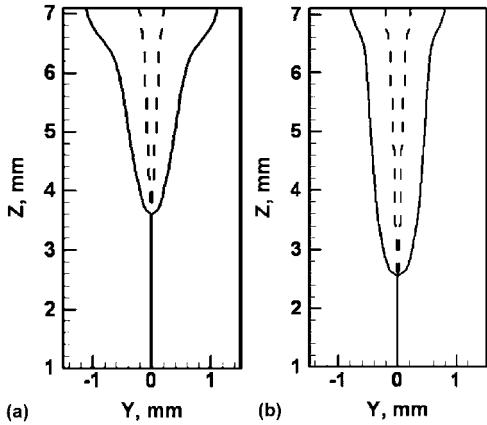


Fig. 18 Computed fusion-zone cross sections for Ti-6Al-4V welds at 1000 W and 17 mm/s (0.67 in./s). (a) Laser beam welding. (b) Electron beam welding. Adapted from Ref 93

$$P_{vap} = P_{atm} \exp \left[\frac{-H_{vap}}{R} \left(\frac{1}{T_1} - \frac{1}{T_b} \right) \right] \quad (\text{Eq 45})$$

where P_{vap} and P_{atm} are the vapor pressure and atmospheric pressure, respectively, H_{vap} is the molar heat of evaporation, T_1 is the temperature of the liquid metal, T_b is the boiling temperature of the metal at atmospheric pressure, and R is the ideal gas constant. In a unified numerical model taking into account the tungsten cathode, arc plasma, and weld pool, the Clausius-Clapeyron equation is used by Murphy et al. (Ref 51) to calculate the iron vapor concentration at the boundary between the arc and the weld pool. They found that the heat flux density and current density to the weld pool are reduced substantially by the presence of iron vapor in the helium arc. Tashiro et al. (Ref 110) simulated a series of processes from evaporation of metal vapor to fume formation from the metal vapor. They found that most of the fume was produced in the downstream region of the arc originating from the metal vapor evaporated mainly from the droplet in argon GMAW.

Dissimilar-Metal Welding

There are two approaches to modeling the mixing of dissimilar liquid metals in the weld pool, depending on the miscibility between the metals being joined. If the two metals are completely miscible, the species conservation equation (Eq 7) can be solved to obtain the concentration field. There is no interface between the two metals. This approach is used by Phani-kumar et al. (Ref 111) and Chakraborty (Ref 112) for a copper-nickel dissimilar couple and by Arghode et al. (Ref 16) for two aluminum alloys with different silicon contents. On the other hand, if the two metals are immiscible, the interface between them must be explicitly modeled. The models developed by Wei et al. (Ref 113) and Tomashchuk et al. (Ref 114)

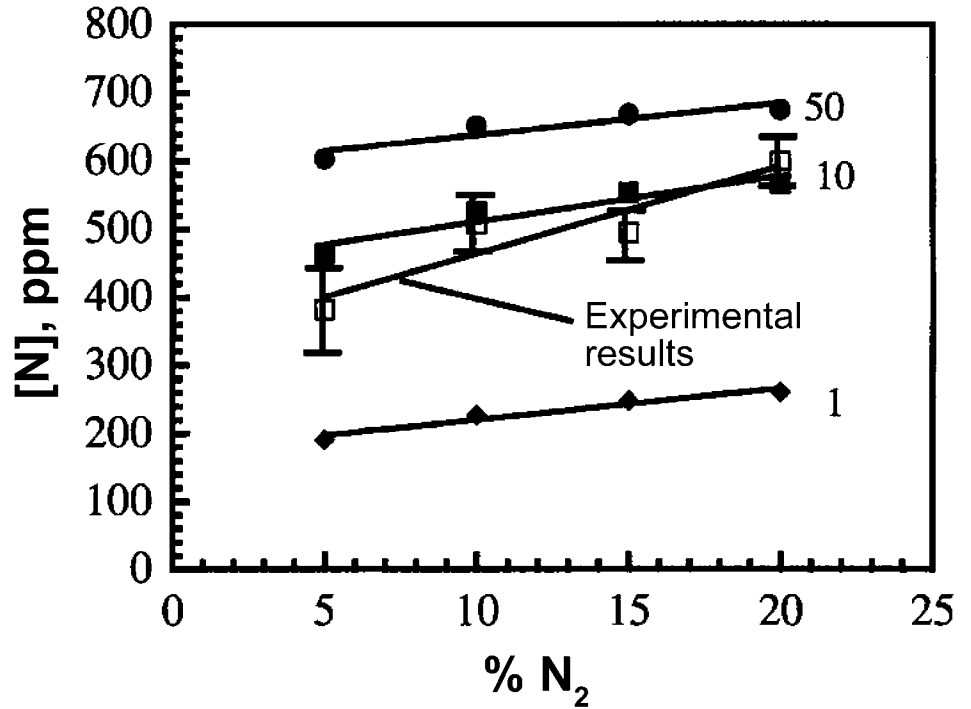


Fig. 19 Comparison between experimental nitrogen concentrations and modeled results for several mass transport enhancement factors at electron temperatures between 3250 and 3000 K for a nitrogen supersaturation level of 75% at a travel speed of 8.5 mm/s (0.33 in./s). Adapted from Ref 12

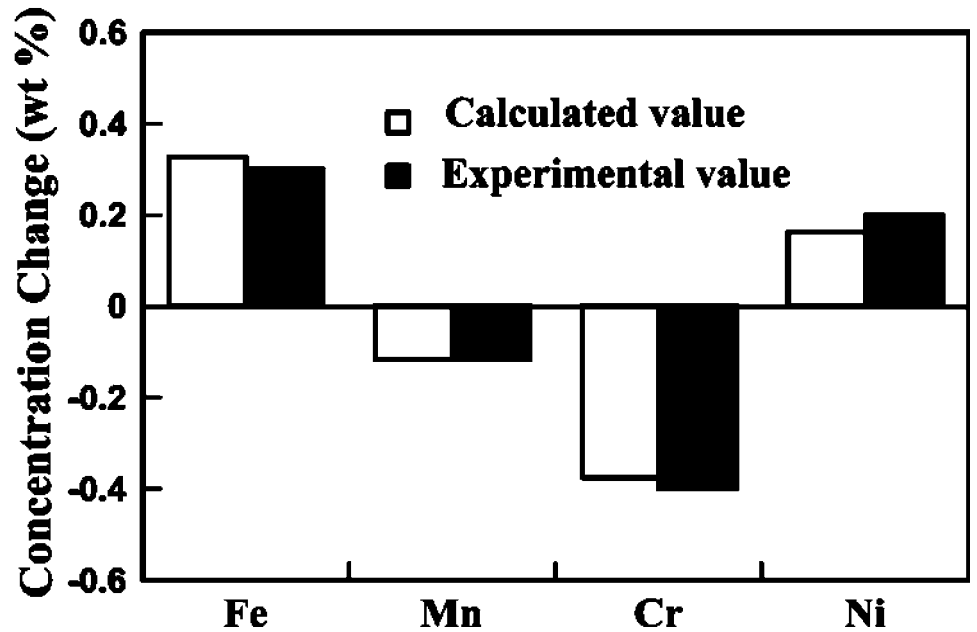


Fig. 20 Comparison between calculated and experimentally determined composition change of 304 stainless steel. Laser power: 1067 W; pulse duration: 3 ms; and beam radius: 0.225 mm (0.009 in.). Adapted from Ref 108

are based on the second approach. Salient features of the aforementioned models are summarized as follows.

Wei and Chung (Ref 113) developed a transient 2-D model to simulate the Marangoni flow

in a weld pool during conduction-mode laser welding of two dissimilar metals. The equations for conservation of mass, momentum, and energy are solved for the dissimilar-metal mixture, with properties assigned weights based on

the volume fractions of each metal. The two metals are immiscible, and the interface between them is tracked using the VOF method. The predicted weld pool depth is found to be consistent with the experimental data for welding of copper to iron under different welding speeds. Figure 21 shows an agreement between the predicted and observed weld pool shapes in welding of copper to nickel.

Phanikumar et al. (Ref 111) developed a 3-D transient model to solve heat transfer and fluid flow conservation during conduction-mode laser welding of copper to nickel. Because they considered the copper-nickel system, which exhibits complete miscibility in both liquid and solid states, in their model the species conservation equation is solved to obtain the concentration field. They found that the weld pool shape becomes asymmetric even when the heat source is symmetrically applied on the two metals forming the couple. Using a similar approach, Chakraborty (Ref 112) studied the effects of turbulence on molten pool transport in a copper-nickel dissimilar couple. The turbulent transport model, based on a high-Reynolds-number k - ϵ model, shows that the turbulent mass diffusivity is approximately 10^7 to 10^8 times greater than molecular mass diffusivity, which results in better mixing between two dissimilar molten metals than the laminar transport model. The species distribution obtained from the turbulent transport model is shown to be in better agreement with the experimental data than that obtained from the laminar transport model.

Arghode et al. (Ref 16) developed a 3-D transient model for linear GMAW of two aluminum alloys with different silicon contents. In this model, the silicon concentration in the liquid metal is obtained by solving the species conservation equation. The effect of molten droplet addition to the weld pool is simulated using a cavity model, in which the droplet heat and species addition to the molten pool are considered as volumetric heat and species sources, respectively, and distributed in an imaginary cylindrical cavity within the molten pool. The Scheil equation is used to correlate the temperature to the liquid fraction, given the local silicon concentration in the binary aluminum-silicon system.

Tomashchuk et al. (Ref 114) developed a 2-D model for dissimilar copper-steel electron beam welds. The calculation domain corresponds to the horizontal plane of the weld, where a predefined circular keyhole is introduced as an interior boundary with constant wall temperatures set as the vaporization temperatures. The copper and steel are treated as immiscible, and their interface is captured using the level-set method.

Reliability of Models

Although numerical heat transfer and fluid flow models have provided significant insights

about fusion welding processes and welded materials, several model input parameters cannot be easily prescribed from fundamental principles (Ref 115–119). As a result, the calculated outputs of these models do not always agree with the experimental results. One valuable solution to this problem is the inverse modeling technique, a new research paradigm that is generally used to find the value of uncertain process variables using a limited volume of experimental data (Ref 115–131).

The purpose of inverse modeling is to quantitatively study the unknowns in the models. Figure 22 shows the difference between commonly used numerical models and the inverse models. In inverse modeling, both measured values and corresponding calculated quantities are required to estimate the values of uncertain input parameters. Because most inverse problems cannot be solved analytically, computational methods play a fundamental role (Ref 120–124). This is especially true for welding problems, which are invariably complex and nonlinear.

In the inverse modeling technique, the phenomenological models that govern the physics of the problem are generally called forward models, and the problem of solving them is called a direct problem. These models are then coupled with optimization algorithms to minimize an objective function representing the error between calculated outputs and the desired or experimentally obtained outputs. In the optimization problem, the uncertain model parameters are treated as control variables, and the objective function is related to a degree of fit (or misfit) between the model predictions and the experimentally observed data. Generally, a least-squares error function is used as an objective function, because it accounts for both positive and negative residuals without letting them cancel each other out, as would be the case if a simple summation form were used. Constraints enter the problem through physical restrictions on the values that can be considered for the fitted (i.e., optimal) parameters. Inverse modeling is an iterative process in which the optimization algorithm first starts the calculation by running the phenomenological model using the initial guessed values of uncertain input parameters. The optimization algorithms minimize the error between the predicted and the experimentally observed variable values by considering the sensitivity of these variables to each of the uncertain parameters. The calculation is repeated until the objective function reaches the prescribed tolerable value.

Several optimization techniques are available to estimate the values of uncertain input parameters. The most common methods include quasi-Newton methods, steepest ascent/descent methods such as Levenberg-Marquardt (LM) and conjugate gradient (CG), and global optimization algorithms such as genetic algorithms and simulated annealing (Ref 117, 123, 124, 131). Global optimization techniques are stochastic in nature and therefore typically have

slower rates of convergence. Furthermore, they require much higher numbers of runs of the forward model, if the initial starting values are not close to the optimal values. On the other hand, local optimization algorithms such as LM or CG methods may have difficulty in finding the global optimal values of uncertain parameters. Another disadvantage of using a local optimization technique is that the solution at which it arrives depends on the starting solution (Ref 116). Obviously, the combination of both local and global optimization approaches is promising in finding the robust optimal parameters.

One of the main issues in parameter estimation is that the models are overparameterized relative to the amount of information that is available to calibrate them (Ref 122–124). This problem arises when the model output being observed is not uniquely responsive to the parameter being estimated, for example, when errors in two different parameters cancel each other out in affecting the model response. However, measurements having systematic errors do not cancel each other with averaging. Therefore, the minimum value of the objective function is subject to systematic errors associated with experiments, measurement techniques, and the assumptions used in the heat transfer and fluid flow numerical model. During parameter estimation, it is generally assumed that the errors in the experimental data are independent and normally-distributed random variables with means of zero and constant variances. By performing a statistical analysis, it is possible to assess the accuracy of the calculated values of uncertain input parameters (Ref 121–124). If the errors are Gaussian in distribution, the minimization of the chi-square norm can be used for testing the accuracy of the parameters. Furthermore, confidence intervals for individual parameters and joint confidence region should be calculated to check the robustness of calculated values (Ref 123).

The inverse problem is much more difficult to solve than the direct problem because it is typically ill-posed in the sense that small perturbations in the observed parameters/functions may amplify into large changes in the

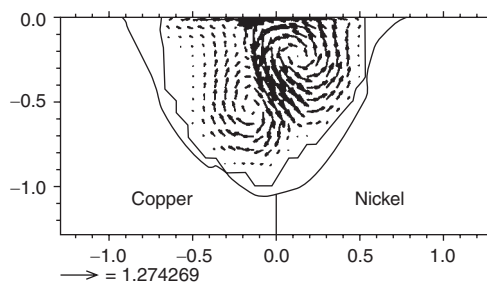


Fig. 21 Comparison between theoretical prediction and experimental observation of the fusion-zone shapes in welding copper to nickel with CO_2 laser. It is noted that the copper and nickel are treated as immiscible in the simulation. Adapted from Ref 113

corresponding solutions (Ref 126, 127) (i.e., the problem is ill-conditioned). This ill-conditioned problem requires special numerical techniques to stabilize the results of the calculations. In the LM method, the ill-conditioned nature of the inverse problem is alleviated by using an iterative procedure and adding a damping parameter to the coefficient of the diagonal sensitivity matrix. The damping parameter is made large in the beginning of the iterations, because the problem is generally ill-conditioned in the region around the initial guess used for the iterative procedure, which can be quite far from the exact parameters. A very small step is taken in the direction of the negative gradient. The damping parameter is then gradually reduced as the iteration procedure advances. The CG method differs from the LM method principally in the calculation of the search step size and the direction of descent. In the iterative procedure of the conjugate gradient method, at each iteration a suitable step size is taken along a direction of descent to minimize the objective function. The direction of the descent is obtained as a linear combination of the negative gradient direction in the current iteration and the direction of the descent in the previous iteration. This linear combination is such that the resulting angle between the direction of descent and the negative gradient direction is less than 90° and the minimization of the objective function is assured.

If the inverse problem involves the estimation of only a few unknown parameters, the use of an ordinary least-squares norm can be stable (Ref 121, 124). However, if the estimation of a large number of parameters is involved, excursion and oscillation of solutions may occur. One approach to reduce such instabilities is to use the procedure called Tikhonov's regularization, which modifies the least-square norm by the addition of a term having a regularization parameter and a whole-domain zeroth-order regularization term (Ref 128). Instabilities in the solution can be alleviated by proper selection of the regularization parameter (Ref 123).

The optimization schemes are computationally intensive because they require multiple runs of the forward model. The efficiency of these techniques is defined by the number of direct problem runs needed to find the values of uncertain input parameters. In the literature on the application of inverse modeling to welding processes, forward models have been simplified for the convenience of the computation. As a result, such applications to date have been largely based on rather simple heat conduction equations (Ref 132, 133), often using Rosenthal's analytical solution of heat conduction equation, which completely ignores convection in the weld pool. The primary focus of those works was to determine the distribution of heat flux at the workpiece surface exposed to an arc or a laser beam from measured temperatures at several monitoring locations in the solid region. Recently, researchers (Ref 116–

119,134–136) have developed inverse models to calculate such unknown input parameters as arc efficiency, effective thermal conductivity, and effective viscosity for transport-phenomena-based modeling of different fusion welding processes. Kumar and DebRoy (Ref 117) calculated the values of arc efficiency and enhancement factors for thermal conductivity and viscosity in a gas metal arc fillet welding process using a limited set of experimental data. Their results show that the arc efficiency increases slightly with increasing input power and decreasing wire-feeding rate (Fig. 23). This behavior is consistent with the fact that with a decrease in wire-feed rate, less power is consumed in melting the wire and more heat is available to the workpiece for the same heat input rate. Their results also show that the enhancement factor for thermal conductivity and viscosity increases with an increase in heat input per unit length. Using the values of

unknown parameters determined by an inverse modeling approach, good agreement was obtained between the model predictions and the experimental data of weld bead dimensions for various welding conditions. Their work shows that the reliability of the numerical heat transfer and fluid flow calculations in the weld pool can be significantly improved by including a suitable optimization model to determine the uncertain welding parameters from a limited volume of experimental data on weld dimensions.

Future Models

Over the past decades, significant progress has been made in the numerical modeling of heat and mass transfer in fusion welding. The numerical models have greatly expanded the quantitative understanding of weld transport

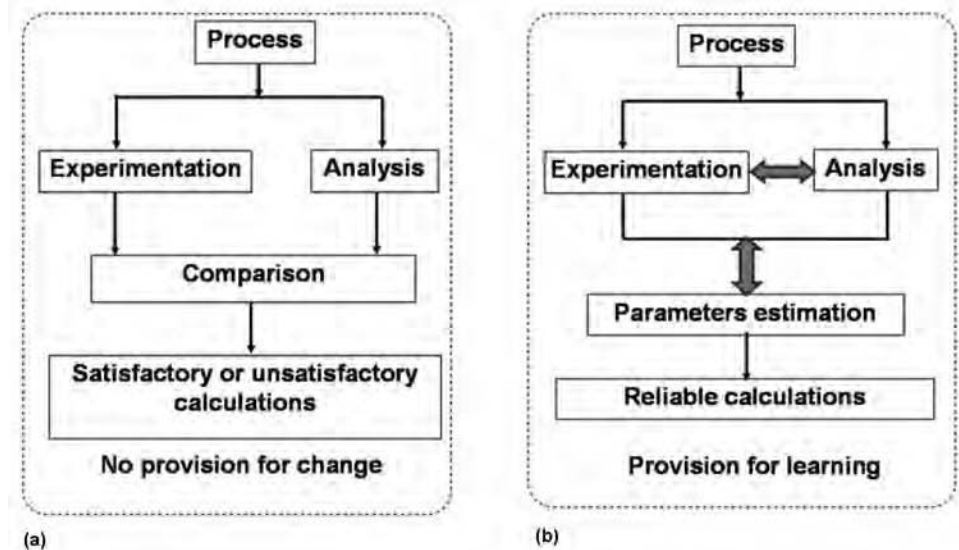


Fig. 22 (a) Common paradigm and (b) new paradigm of inverse modeling. Adapted from Ref 116

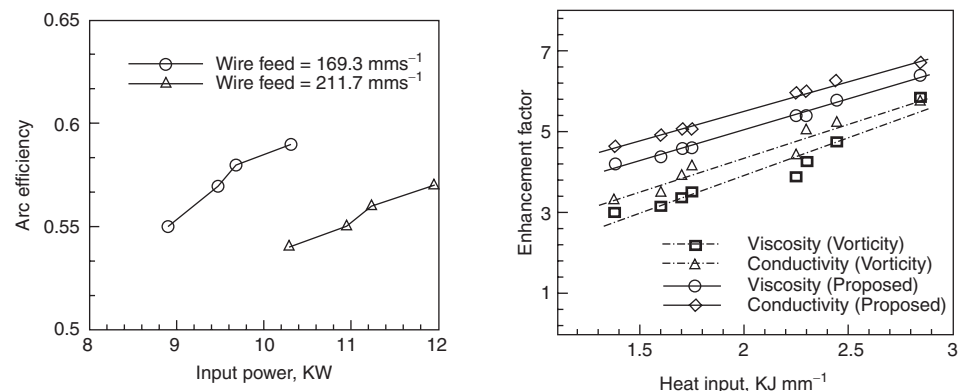


Fig. 23 (a) Computed values of arc efficiency. (b) Enhancement factor for thermal conductivity and viscosity using estimated values of unknown parameters for different welding conditions. Adapted from Ref 117

phenomena, including the formation of a wavy fusion-zone boundary, mixing in the weld pool of dissimilar metals, the effect of shield gas composition on heat transfer from arc plasma to weld pool, keyhole dynamics in laser welding, droplet impingement into the weld pool in GMAW and laser-GMAW hybrid welding, and much more. Such quantitative knowledge is essential for achieving the goal of science-based control of composition, structure, and properties for fusion welding.

Development of the next generation of heat and mass transfer models will benefit from progress in the following two areas. First, an improved fundamental understanding of weld transport phenomena is of importance. For instance, a more comprehensive and detailed mathematical description of heat and mass transfer in hybrid welding is achievable only with improved understanding of laser-arc interactions. To this end, experimental observations of welding transport phenomena are crucial. Furthermore, in view of the complexities of welding processes, numerical models must be tested by well-designed experiments. Second, advanced numerical algorithms (such as those for tracking free surface evolution) and parallel computing are needed.

A final emphasis is placed on the integration of models. A good example is the recent development of the unified model combining the arc plasma and the weld pool, which serves as an ever-increasingly sophisticated tool for improved understanding of the complex weld transport phenomena. Furthermore, the heat and mass transfer models enable the accurate prediction of temperature evolution in the workpiece. Such temperature history is a prerequisite for the calculation of the microstructural changes and the residual stresses and distortion during fusion welding. The integration of heat and mass transfer models with microstructure models and thermal-stress models is essential for intelligent process control and optimization to produce structurally sound and reliable welds (Ref 137).

ACKNOWLEDGMENTS

The authors would like to express their sincere appreciation to Prof. T. DebRoy of the Pennsylvania State University and Prof. P. Mendez of the University of Alberta for their valuable comments.

REFERENCES

1. S.A. David and T. DebRoy, *Science*, Vol 257, 1992, p 497
2. S. Kou, *Welding Metallurgy*, 2nd ed., John Wiley & Sons, Hoboken, NJ, 2003
3. Ø. Grong, *Metallurgical Modeling of Welding*, 2nd ed., The Institute of Materials, London, 1997
4. S. Kou, *Proceedings of Sixth Trends in Welding Research*, 2003, p 104–111
5. P. Dong, *Proceedings of Sixth Trends in Welding Research*, 2003, p 815–825
6. W. Zhang, C.-H. Kim, and T. DebRoy, *J. Appl. Phys.*, Vol 95, 2004, p 5210
7. F. Lago, J.J. Gonzalez, P. Fretton, and A. Gleizes, *J. Phys. D: Appl. Phys.*, Vol 37, 2004, p 883–897
8. K. Mundra, T. DebRoy, and K.M. Kelkar, *Numer. Heat Transf. A*, Vol 29, 1996, p 115–129
9. R.B. Bird, W.E. Stewart, and E.N. Lightfoot, *Transport Phenomena*, 1st ed., John Wiley & Sons, New York, 1960
10. S.V. Patankar, *Numerical Heat Transfer and Fluid Flow*, Hemisphere Publishing Corp., New York, 1982
11. A.D. Brent, V.R. Voller, and K.J. Reid, *Numer. Heat Transf. A*, Vol 13, 1988, p 297
12. T.A. Palmer and T. DebRoy, *Metall. Mater. Trans. B*, Vol 31, 2000, p 1371
13. M. Arenas, V.L. Acoff, and N. El-Kaddah, *Mathematical Modelling of Weld Phenomena 5*, IOM Communications, 2001, p 39
14. N.S. Tsai and T.W. Eager, *Metall. Trans. B*, Vol 16, 1985, p 841
15. Z. Yang and T. DebRoy, *Metall. Mater. Trans. B*, Vol 30, 1999, p 483
16. V.K. Arghode, A. Kumar, S. Sundarraj, and P. Dutta, *Numer. Heat Transf. A*, Vol 53, 2008, p 432–455
17. W. Zhang, "Probing Heat Transfer, Fluid Flow and Microstructural Evolution during Fusion Welding of Alloys," Ph.D. dissertation, Pennsylvania State University, 2004
18. S. Kou and D.K. Sun, *Metall. Trans. A*, Vol 16, 1985, p 203–213
19. A. Kumar and T. DebRoy, *J. Appl. Phys.*, Vol 94, 2003, p 1267
20. W. Zhang, C. Conrardy, and I. Harris, *Proceedings of Seventh Trends in Welding Research*, 2006, p 79–84
21. P. Sahoo, T. DebRoy, and M.J. McNallan, *Metall. Trans. B*, Vol 19, 1988, p 483
22. A. Matsunawa, *Proceedings of Third Trends in Welding Science and Technology*, 1993, p 3–16
23. M.H. Cho, "Numerical Simulation of Arc Welding Process and Its Application," Ph. D. dissertation, The Ohio State University, 2006
24. D.J. Phares, G.T. Smedley, and R.C. Flagan, *J. Fluid Mech.*, Vol 418, 2000, p 351–375
25. R. Rai, G.G. Roy, and T. DebRoy, *J. Appl. Phys.*, Vol 101, 2007, p 11
26. R. Rai, J.W. Elmer, T.A. Palmer, and T. DebRoy, *J. Phys. D: Appl. Phys.*, Vol 40, 2007, p 5753–5766
27. H. Ki, P.S. Mohanty, and J. Mazumder, *Metall. Mater. Trans. A*, Vol 33, 2002, p 1831–1842
28. D.R. Atthey, *J. Fluid Mech.*, Vol 98, 1980, p 787–801
29. B.E. Launder and D.E. Spalding, *Lectures in Mathematical Models of Turbulence*, Academic Press, NY, 1972
30. R.T.C. Choo and J. Szekely, *Weld. J.*, Vol 73, 1994, p 25s–31s
31. K. Hong, D.C. Weckman, A.B. Strong, and W. Zheng, *Sci. Technol. Weld. Join.*, Vol 7, 2002, p 125–136
32. D.C. Wilcox, *Turbulence Modeling for CFD*, DCW Industries, California, 1993
33. J. Jaidi and P. Dutta, *Sci. Technol. Weld. Join.*, Vol 9, 2004, p 407–414
34. T.J. Craft, S.E. Gant, H. Iacovides, and B. E. Launder, *Numer. Heat Transf. B*, Vol 45, 2004, p 301–318
35. W. Shyy, *Computational Fluid Dynamics with Moving Boundaries*, Taylor & Francis, Washington D.C., 1996
36. C.W. Hirt and B.D. Nichols, *J. Comput. Phys.*, Vol 39, 1981, p 201
37. S.J. Osher and R.P. Fedkiw, *Level Set Methods and Dynamic Implicit Surfaces*, Springer, New York, 2002
38. J. Jenista, J.V.R. Heberlein, and E. Pfender, *IEEE Trans. Plasma Sci.*, Vol 25, 1997, p 883–890
39. H.A. Dinulescu and E. Pfender, *J. Appl. Phys.*, Vol 51, 1980, p 3149–3157
40. J.J. Lowke, R. Morrow, and J. Haidar, *J. Phys. D: Appl. Phys.*, Vol 30, 1997, p 2033–2042
41. J. Haidar, *J. Phys. D: Appl. Phys.*, Vol 32, 1999, p 263–272
42. H.G. Fan and R. Kovacevic, *J. Phys. D: Appl. Phys.*, Vol 37, 2004, p 2531–2544
43. J. Hu and H.L. Tsai, *Int. J. Heat Mass Transf.*, Vol 50, 2007, p 833–846
44. M. Tanaka, K. Yamamoto, S. Tashiro, K. Nakata, M. Ushio, K. Yamazaki, E. Yamamoto, K. Suzuki, A.B. Murphy, and J.J. Lowke, *Weld. World*, Vol 52, 2008, p 82–88
45. A.B. Murphy, *J. Phys. D: Appl. Phys.*, Vol 43, 2010, p 434001
46. I.V. Krivtsun, *Paton Weld. J.*, No. 3, 2001, p 2–9
47. I.V. Krivtsun, V.F. Demchenko, and I.V. Krikent, *Paton Weld. J.*, No. 6, 2010, p 2–9
48. C.J. Knight, *AIAA J.*, Vol 17, 1979, p 519–523
49. J.J. Lowke, M. Tanaka, and M. Ushio, *J. Phys. D: Appl. Phys.*, Vol 38, 2005, p 3438
50. M. Goodarzi, R. Choo, and J.M. Toguri, *J. Phys. D: Appl. Phys.*, Vol 30, 1997, p 2744–2756
51. A.B. Murphy, M. Tanaka, K. Yamamoto, S. Tashiro, J.J. Lowke, and K. Ostrikov, *Vacuum*, Vol 85, 2010, p 579–584
52. J. Hu and H.L. Tsai, *J. Appl. Phys.*, Vol 100, 2006, p 053304
53. A. Robert and T. DebRoy, *Metall. Mater. Trans. B*, Vol 32, 2001, p 941
54. A. Arora, G.G. Roy, and T. DebRoy, *Scr. Mater.*, Vol 60, 2009, p 68–71
55. K. Tello, U. Duman, and P. Mendez, Scaling Laws for the Welding Arc, Weld Penetration and Friction Stir Welding,

- Proceedings of Eighth Trends in Welding Research*, 2009, p 172–181
56. G.M. Oreper, T.W. Eagar, and J. Szekely, *Weld. J.*, Vol 62, 1983, p 307–312
 57. T. Zacharia, A.H. Eraslan, and D.K. Aidun, *Weld. J.*, Vol 67, 1988, p 18s–27s
 58. C.S. Wu and K.C. Tsao, *Eng. Comput.*, Vol 7, 1990, p 241
 59. M. Kanouff and R. Greif, *Int. J. Heat Mass Transf.*, Vol 35, 1992, p 967–979
 60. P.G. Jönsson, J. Szekely, R.T.C. Choo, and T.P. Quinn, *Model. Simul. Mater. Sci. Eng.*, Vol 2, 1994, p 995
 61. S. Mishra, T.J. Lienert, M.Q. Johnson, and T. DebRoy, *Acta Mater.*, Vol 56, 2008, p 2133–2146
 62. Y.C. Lim, X. Yu, J.H. Cho, J. Sosa, D.F. Farson, S.S. Babu, S. McCracken, and B. Flesner, *Sci. Technol. Weld. Join.*, Vol 15, 2010, p 583
 63. W. Zhang, G.G. Roy, J.W. Elmer, and T. DebRoy, *J. Appl. Phys.*, Vol 93, 2003, p 3022
 64. X. He, P.W. Fuerschbach, and T. DebRoy, *J. Phys. D: Appl. Phys.*, Vol 36, 2003, p 1388–1398
 65. A. Farzadi, S. Serajzadeh, and A.H. Kokabi, *Mater. Sci. Technol.*, Vol 24, 2008, p 1427
 66. T.D. Anderson, J.N. DuPont, and T. DebRoy, *Acta Mater.*, Vol 58, 2010, p 1441–1454
 67. J.C. Amson, *Br. Weld. J.*, Vol 41, 1962, p 231–239
 68. J.C. Allum, *J. Phys. D: Appl. Phys.*, Vol 18, 1985, p 1431–1446
 69. Y.S. Kim and T.W. Eagar, *Weld. J.*, Vol 72, 1993, p 269s–278s
 70. J.H. Choi, J. Lee, and C.D. Yoo, *J. Phys. D: Appl. Phys.*, Vol 34, 2001, p 2658–2664
 71. V.A. Nemchinsky, *J. Phys. D: Appl. Phys.*, Vol 27, 1994, p 1433–1442
 72. L.A. Jones, T.W. Eagar, and H.J. Lang, *J. Phys. D: Appl. Phys.*, Vol 31, 1998, p 107–123
 73. S.K. Choi, C.D. Yoo, and Y.S. Kim, *Weld. J.*, Vol 77, 1998, p 38s–44s
 74. S.K. Choi, C.D. Yoo, and Y.S. Kim, *J. Phys. D: Appl. Phys.*, Vol 31, 1998, p 207–215
 75. J. Haidar and J.J. Lowke, *J. Phys. D: Appl. Phys.*, Vol 29, 1996, p 2951–2960
 76. S. Kumar and S.C. Bhaduri, *Metall. Mater. Trans. B*, Vol 25, 1994, p 435–441
 77. W. Zhang, C.-H. Kim, and T. DebRoy, *J. Appl. Phys.*, Vol 95, 2004, p 5220
 78. J.W. Kim and S.J. Na, *Trans. ASME, J. Eng. Ind.*, Vol 116, 1994, p 78–85
 79. M. Ushio and C.S. Wu, *Metall. Mater. Trans. B*, Vol 28, 1997, p 509–516
 80. Y. Wang and H.L. Tsai, *Int. J. Heat Mass Transf.*, Vol 44, 2001, p 2067–2080
 81. H.G. Fan and R. Kovacevic, *Metall. Mater. Trans. B*, Vol 30, 1999, p 791–801
 82. Z. Cao, Z. Yang, X.L. Chen, *Weld. J.*, Vol 83, 2004, p 169s–176s
 83. J. Hu, H. Guo, and H. L. Tsai, *Int. J. Heat Mass Transf.*, Vol 51, 2008, p 2537–2552
 84. J. Hu and H.L. Tsai, *Int. J. Heat Mass Transf.*, Vol 50, 2007, p 808–820
 85. P.G. Klemens, *J. Appl. Phys.*, Vol 47, 1976, p 2165–2174
 86. D.E. Swift-Hook and A.E.F. Gick, *Weld. J.*, Vol 52, 1973, p 492s
 87. J.G. Andrews and D.R. Atthey, *J. Phys. D: Appl. Phys.*, Vol 9, 1976, p 2181–2194
 88. A. Kaplan, *J. Phys. D: Appl. Phys.*, Vol 27, 1994, p 1805–1814
 89. J. Zhou, H.L. Tsai, and T.F. Lehnhoff, *J. Phys. D: Appl. Phys.*, Vol 39, 2006, p 5338–5355
 90. J. Zhou and H.L. Tsai, *Trans. ASME, J. Heat Transf.*, Vol 129, 2007, p 1014–1024
 91. H. Ki, P.S. Mohanty, and J. Mazumder, *J. Laser Appl.*, Vol 14, 2002, p 39–45
 92. H. Ki, P.S. Mohanty, and J. Mazumder, *Metall. Mater. Trans. A*, Vol 33, 2002, p 1817–1830
 93. R. Rai, P. Burgardt, J.O. Milewski, T.J. Lienert, and T. DebRoy, *J. Phys. D: Appl. Phys.*, Vol 42, 2009, p 025503
 94. R. Rai, T.A. Palmer, J.W. Elmer, and T. DebRoy, *Weld. J.*, Vol 88, 2009, p 54s–61s
 95. J.W. Elmer, W.H. Giedt, and T.W. Eagar, *Weld. J.*, Vol 69, 1990, p 167s–176s
 96. P.S. Wei and Y.T. Chow, *Metall. Trans. B*, Vol 23, 1992, p 81–90
 97. D.A. Schauer, W.H. Giedt, and S.M. Shintaku, *Weld. J.*, Vol 57, 1978, p 127s–133s
 98. B. Ribic, T.A. Palmer, and T. DebRoy, *Int. Mater. Rev.*, Vol 54, 2009, p 223
 99. A. Mahrleand and E. Beyer, *J. Laser Appl.*, Vol 18, 2006, p 169–180
 100. J. Zhou and H.L. Tsai, *J. Phys. D: Appl. Phys.*, Vol 42, 2009, p 095502
 101. Z. Gao, Y. Wu, and J. Huang, *Int. J. Adv. Manuf. Technol.*, Vol 44, 2009, p 870–879
 102. M.H. Cho and D.F. Farson, *Weld. J.*, Vol 86, 2007, p 253s–262s
 103. W.-I. Cho, S.-J. Na, M.-H. Cho, and J.-S. Lee, *Comput. Mater. Sci.*, Vol 49, 2010, p 792–800
 104. B. Ribic, R. Rai, and T. DebRoy, *Sci. Technol. Weld. Join.*, Vol 13, 2008, p 683
 105. B.D. Ribic, R. Rai, T.A. Palmer, and T. DebRoy, *Proceedings of Eighth Trends in Welding Research*, 2009, p 313–320
 106. W. Dong, H. Kokawa, S. Tsukamoto, Y.S. Sato, and M. Ogawa, *Metall. Mater. Trans. B*, Vol 35, 2004, p 331
 107. T. DebRoy, S. Basu, and K. Mundra, *J. Appl. Phys.*, Vol 70, 1991, p 1313
 108. X. He, T. DebRoy, and P.W. Fuerschbach, *J. Appl. Phys.*, Vol 96, 2004, p 4547
 109. X. He, J.T. Norris, P.W. Fuerschbach, and T. DebRoy, *J. Phys. D: Appl. Phys.*, Vol 39, 2006, p 525–534
 110. S. Tashiro, T. Zeniya, K. Yamamoto, M. Tanaka, K. Nakata, A.B. Murphy, E. Yamamoto, K. Yamazaki, and K. Suzuki, *J. Phys. D: Appl. Phys.*, Vol 43, 2010, p 434012
 111. G. Phanikumar, P. Dutta, and K. Chattopadhyay, *Metall. Mater. Trans. B*, Vol 35, 2004, p 339
 112. N. Chakraborty, *Appl. Therm. Eng.*, Vol 29, 2009, p 3618–3631
 113. P.S. Wei and F.K. Chung, *Metall. Mater. Trans. B*, Vol 31, 2000, p 1387
 114. I. Tomashchuk, P. Sallamand, J.M. Jouvard, and D. Grevey, *Comput. Mater. Sci.*, Vol 48, 2010, p 827–836
 115. A. Kumar, W. Zhang, C.H. Kim, and T. DebRoy, *Weld. World*, Vol 49, 2005, p 32–48
 116. A. Kumar, “Tailoring Defect Free Fusion Welds Based on Phenomenological Modeling,” Ph.D. dissertation, Pennsylvania State University, 2006
 117. A. Kumar and T. DebRoy, *J. Phys. D: Appl. Phys.*, Vol 38, 2005, p 127–134
 118. A. Kumar, S. Mishra, J.W. Elmer, and T. DebRoy, *Metall. Mater. Trans. A*, Vol 36, 2005, p 15–22
 119. A. Kumar and T. DebRoy, *Int. J. Heat Mass Transf.*, Vol 47, 2004, p 5793–5806
 120. J.V. Beck, B. Blackwell, and C.R. St. Clair, *Inverse Heat Conduction: Ill-Posed Problems*, Wiley International, New York, 1985
 121. J.V. Beck and K.J. Arnold, *Parameter Estimation in Engineering and Science*, John Wiley and Sons, New York, 1977
 122. M.N. Ozisik and H.R.B. Orlande, *Inverse Heat Transfer: Fundamentals and Applications*, Taylor and Francis, New York, 2000
 123. Y. Bard, *Nonlinear Parameter Estimation*, Academic Press, New York, 1974
 124. J. Dennis and R. Schnabel, *Numerical Methods for Unconstrained Optimizations and Non-Linear Equations*, Prentice Hall, 1983
 125. N. Tikhonov, *Soviet Math. Dokl.*, Vol 4, 1963, p 1035–1038
 126. N. Tikhonov, *Soviet Math. Dokl.*, Vol 4, 1963, p 1624–1627
 127. N. Tikhonov, *J. Eng. Phys.*, Vol 29, 1975, p 816–820
 128. O.M. Alifanov, *High Temp.*, Vol 15, 1977, p 498–504
 129. O.M. Alifanov, *Inverse Heat Transfer Problems*, Springer-Verlag, New York, 1994
 130. O.M. Alifanov, *J. Eng. Phys.*, Vol 26, 1974, p 471–476
 131. R. Fletcher and C.M. Reeves, *Comput. J.*, Vol 7, 1964, p 149–154
 132. R.W. Fonda and S.G. Lambrakos, *Sci. Technol. Weld. Join.*, Vol 7, 2002, p 177–181
 133. V.A. Karkhin, V.V. Plochikhine, and H. W. Bergmann, *Sci. Technol. Weld. Join.*, Vol 7, 2002, p 224–231
 134. A. De and T. DebRoy, *Sci. Technol. Weld. Join.*, Vol 11, 2006, p 143–153
 135. A. De and T. DebRoy, *J. Appl. Phys.*, Vol 95, 2004, p 5230–5239
 136. R. Nandan, S. Mishra, and T. DebRoy, *Proceedings of Mathematical Modeling of Weld Phenomena 8*, 2007, p 505–530
 137. T. DebRoy and S.A. David, *Rev. Mod. Phys.*, Vol 67, 1995, p 85

Modeling of Thermal-Electrical-Mechanical Coupling in Fusion Welding

A. De, IIT Bombay

THE RESISTANCE SPOT WELDING PROCESS involves heating two or more metallic sheets under high-amperage current for a short duration through a pair of copper electrodes that hold the sheets under compressive force. The compressive force ensures adequate contact for the current to flow through the metallic sheets. Localized resistive heating at the contacting interface of the sheets results in melting, which, on solidification, provides a joint in the form of a spot. Throughout the welding process, the molten metal remains enclosed by the surrounding solid material supported by the electrode force. Thus, the process poses a heat-transfer-dominated problem that influences and is also affected by the electrical current flow and thermomechanical deformation along the contacting interfaces, which decide the overall current-carrying region. A coupled thermal-electrical-mechanical analysis is thus ideal for quantitative understanding of the process based on scientific principles.

A host of two-dimensional axisymmetric heat-transfer models using the finite-difference method were reported to compute the temperature field during spot welding of uncoated steels, considering uniform current density distribution (Ref 1–5). Coupled thermal-electrical simulation models were reported next, based on finite-difference (Ref 6, 7) and finite-element methods (Ref 6–17) that could also consider nonuniform current density distribution. Coupled electrical-thermal-mechanical models are also attempted to analyze resistance spot welding based on the finite-element method (Ref 18, 19). In short, numerical models are established as an effective route to carry out the coupled thermal-electrical and thermal-mechanical analyses in resistance spot welding. These numerical models have generally considered temperature-dependent material properties while the latent heat during melting and solidification is often neglected. Most of these models have considered the variation of contact resistance along the electrode-sheet and sheet-sheet interfaces based on experimentally measured data reported in independent literature (Ref 20–26). There are relatively fewer

attempts to model the spot welding process with spherical tip electrodes, considering the incremental change in electrode-sheet contact diameter during weld time (Ref 6, 18, 19). This article outlines a general approach to develop a coupled electrical-thermal-mechanical analysis to analyze the resistance spot welding process.

Thermal Analysis

The problem of heat flow in resistance spot welding is primarily a case of heat conduction associated with melting and subsequent solidification. Although the nature of heat flow is three-dimensional, a two-dimensional axisymmetric model is sufficient due to the circular cross section of the electrode that applies both electrical current and compressive force (Fig. 1). The merit of the axisymmetric formulation is that the symmetry with respect to θ , the azimuthal angle, considers the variation in heat transfer and current flow in radial (r) and vertical (z) directions only. The governing equation for transient state heat conduction in a cylindrical coordinate system, considering no variation of temperature with respect to the θ -axis, can be stated as (Ref 27–30):

$$\frac{1}{r} \frac{\partial}{\partial r} \left(rk \frac{\partial T}{\partial r} \right) + \frac{1}{r} \frac{\partial}{\partial z} \left(rk \frac{\partial T}{\partial z} \right) + \dot{Q} = sC \frac{\partial T}{\partial t} \quad (\text{Eq 1})$$

where \dot{Q} refers to the rate of resistive heat generation per unit volume, r and z are radial and axial coordinates, T and t refer to temperature and time variables, and s , C , and k refer to density, specific heat, and thermal conductivity of the material, respectively. The electrode internal surfaces in contact with cooling water (e.g., lines GH and HK in Fig. 2) can be considered to remain at ambient temperature. The external surfaces of the electrode can be considered as adiabatic because these are far away from the zone of resistive heating (Ref 27–30). Alternately, convective heat loss from the exterior electrode surfaces can be modeled by specifying a lumped surface heat-transfer coefficient, h_c , which is often estimated

as $h_c = 2.4 \cdot 10^{-3} \cdot \varepsilon \cdot T^{1.61}$, where ε is the emissivity of copper, and T is the temperature variable.

The term \dot{Q} in Eq 1 is evaluated using Ohm's law as (Ref 11, 28):

$$\mathbf{J} = \frac{1}{\rho} \mathbf{E} \quad (\text{Eq 2})$$

where \mathbf{J} is the current density vector, \mathbf{E} is the electric field intensity vector, and ρ is the electrical resistivity. Considering a small current-conducting cylinder of cross-sectional area ΔA and of length Δl (as shown in Fig. 3), the

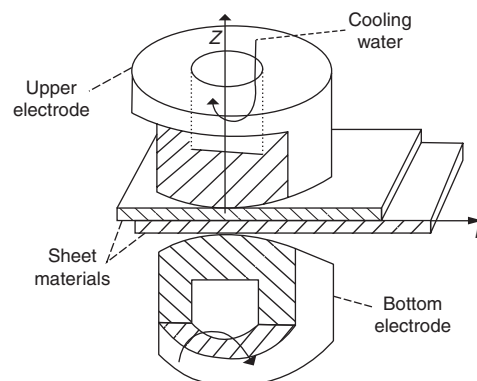


Fig. 1 Schematic view of the sheet-electrode in a cylindrical coordinate system

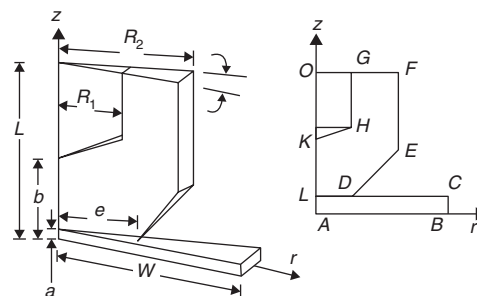


Fig. 2 Cross-sectional view of one quadrant of the sheet-electrode system

current flow, ΔI , through the cylinder and the potential drop, ΔU , across the cylinder can be stated as (Ref 11):

$$\Delta I = J \cdot \Delta A \tag{Eq 3}$$

$$\Delta U = E \cdot \Delta l \tag{Eq 4}$$

So, the rate of heat generated per unit volume can be written as:

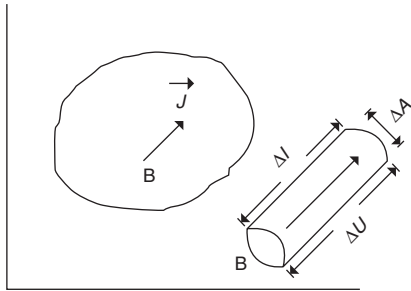
$$\dot{Q} = \frac{\Delta I \cdot \Delta U}{\Delta A \cdot \Delta l} = \rho(\mathbf{J} \cdot \mathbf{J}) \tag{Eq 5}$$

The dot product term, $(\mathbf{J} \cdot \mathbf{J})$, in Eq 5 can be simplified further by presuming the current paths to be predominantly axial ($J_z \approx J$, as indicated in Fig. 4) due to smaller sheet thickness in comparison to the electrode-sheet contact diameter. The term \dot{Q} can thus be evaluated as:

$$\dot{Q} = \rho \cdot J^2 \tag{Eq 6}$$

Electrical Analysis

Like heat-transfer analysis, the current conduction through the sheet-electrode can be analyzed in two-dimensional, axisymmetric form using cylindrical coordinates, assuming no variation of electric potential in the θ -direction. The governing equation for a steady-state current conduction can be expressed in terms of electrical potential, ϕ , as (Ref 11, 27–30):



$\Delta U =$ Voltage drop across the cylinder

Fig. 3 Schematic view of a circular current-conducting conduit

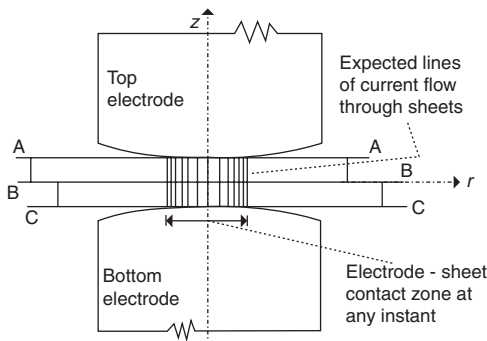


Fig. 4 Schematic view of current flow lines

$$\frac{1}{r} \frac{\partial}{\partial r} \left(r \frac{1}{\rho} \frac{\partial \phi}{\partial r} \right) + \frac{1}{r} \frac{\partial}{\partial z} \left(r \frac{1}{\rho} \frac{\partial \phi}{\partial z} \right) = 0 \tag{Eq 6}$$

where ρ is the electrical resistivity. Considering Fig. 2, the primary boundary condition for the current-conduction analysis can be considered as:

$$\frac{1}{\rho} \frac{\partial \phi}{\partial n} + J = 0 \text{ on surface } FG \tag{Eq 7}$$

where J denotes the applied current density on the top surface of the electrode, and n depicts normal to the surface. The other boundary condition is the assumption that no current loss occurs from the electrode surface to the atmosphere.

Discretization of Sheet-Electrode Geometry for Numerical Modeling

Figures 5(a) and (b) show the schematic views of typical sheet-electrode geometry with curved electrodes and the zone of analysis that can be considered for symmetric sheet thicknesses, respectively. The zone of analysis can be divided into a finite number of ring-shaped isoparametric rectangular elements (Fig. 6)

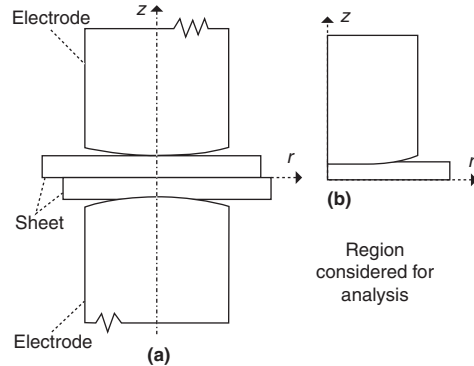


Fig. 5 (a) Sheet-electrode system with curved-face electrodes. (b) Zone of analysis

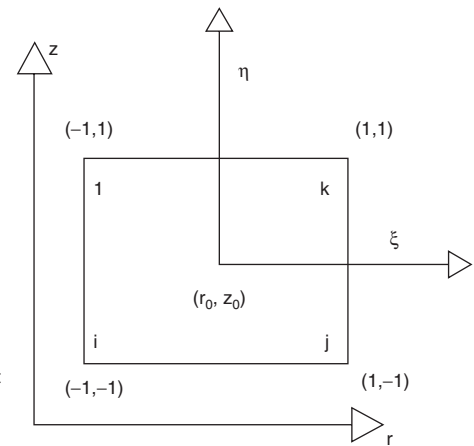


Fig. 6 Four-node isoparametric elements

with, whenever necessary, triangular cross sections to account for the curved boundary. Any variable, ϕ (e.g., temperature or potential), within a discrete element can be defined as:

$$\phi(r, z) = \sum_{i=1}^{\ell} N_i \phi_i \tag{Eq 8}$$

where ℓ is the number of nodes of an element, and N_i is the appropriately defined nodal shape function (often referred to as the interpolation function) (Ref 31).

In-Process Growth of Electrode-Sheet Contact

Figures 7(a) and (b) schematically present how the contact area along the electrode-sheet interface can grow, in particular for a curved-face electrode, during weld time because of thermo-elastic-plastic deformation. The coupled thermo-elastic-plastic behavior of the sheet and electrode materials in resistance welding can be described using the static equilibrium equation:

$$\frac{\partial \sigma_{ij}}{\partial x_j} + f_i = 0 \tag{Eq 9}$$

considering $\sigma_{ij} = \sigma_{ji}$ where σ_{ij} refers to the stress tensor, x_j refers to the Cartesian coordinate system, and f_i is the body force and can be neglected.

The constitutive equation in thermo-elastic-plastic deformation must be considered in an incremental manner as:

$$d\sigma_{ij} = 2Gd\epsilon_{ij} + \gamma\delta_{ij}d\epsilon_{ij} - (3\gamma + 2G)\alpha\delta_{ij}(T - T_r) - \left\{ \frac{9G^2 \sigma_{ij}^d \sigma_{kl}^d d\epsilon_{kl}}{\bar{\sigma}^2 (E_T + 3G)} \right\} \tag{Eq 10}$$

where the strain tensor, ϵ_{ij} , the deviatoric stress components, σ_{ij}^d , and the equivalent stress, $\bar{\sigma}$, are expressed as:

$$\epsilon_{ij} = \frac{1}{2} \left(\frac{\partial u_i}{\partial x_j} + \frac{\partial u_j}{\partial x_i} \right) \tag{Eq 11}$$

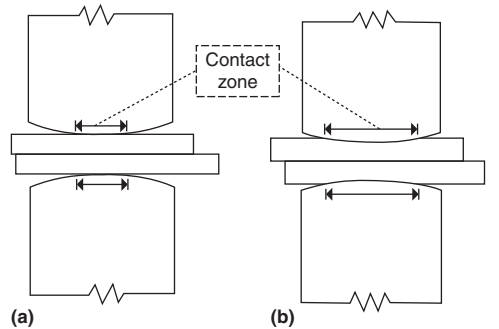


Fig. 7 Schematic view of in-process growth of the electrode-sheet contact zone

$$\sigma_{ij}^d = \sigma_{ij} - \frac{1}{3}(\sigma_{ii} + \sigma_{jj} + \sigma_{kk}) \quad (\text{Eq 12})$$

$$\bar{\sigma} = \left(\frac{3}{2} \sigma_{ij}^d \sigma_{ij}^d \right)^{1/2} \quad (\text{Eq 13})$$

In Eq 10, E_T is the local slope of the stress versus plastic strain behavior of the material in the elastic-plastic regime, G and γ are expressed respectively as:

$$G = E/2(1 + \nu)$$

and

$$\gamma = \nu E / \{ (1 + \nu)(1 - 2\nu) \}$$

where E is the elastic modulus, ν is Poisson's ratio, and α is the linear coefficient of thermal expansion (or contraction). Lastly, $\delta_{ij} = 0$ for $i \neq j$ and $\delta_{ij} = 1$ for $i = j$. The incremental strain, $d\epsilon_{ij}$, is computed as:

$$d\epsilon_{ij} = d\epsilon_{ij}^{el} + \delta_{ij} (d\epsilon_{ij}^{pl} + d\epsilon_{ij}^{th})$$

where $d\epsilon_{ij}^{el}$, $d\epsilon_{ij}^{pl}$, and $d\epsilon_{ij}^{th}$ are the elastic, plastic, and thermal strain components, respectively. It is noteworthy that the plastic and the thermal strains are volumetric in nature. Moreover, cooling of the fusion zone or heat-affected zone can be associated with a phase transformation that will contribute to an additional volumetric strain in terms of dilation as:

$$\{d\epsilon_{ij}^d\} = C_1 (\Delta V / V) (\sigma_{ij} / \bar{\sigma})$$

where σ_{ij} is the applied stress, $\bar{\sigma}$ is the yield stress of the parent phase before transformation, ΔV is the volume change associated with phase change, and V is the volume of the parent phase.

The solution of Eq 9, neglecting body force (i.e., $f_i = 0$) and considering the constitutive equations in incremental form (Eq 10), further requires the application of boundary conditions and external loads. Considering a typical axisymmetric sheet-electrode geometry in resistance welding (Fig. 2), a zero axial displacement can be applied along AR and a symmetric displacement boundary condition should be applied along AO that will further eliminate the chance of rigid body movement when the electrode force will be applied along GF .

The solution of the final displacement and stress fields in the sheet-electrode system, considering the aforementioned phenomena, is, however, a real challenge primarily due to the uncertain nature of the mechanical behavior and properties of sheet materials at high temperature. An analytical approach is often followed to estimate the sheet-sheet and electrode-sheet contact area in a simple manner. At any particular time instant, the total electrode force, P , is considered to be supported by the sheet surface in contact to the electrode face as (Ref 27–30):

$$P = \int_0^{r_c} \sigma_y(T) 2\pi r dr \quad (\text{Eq 14})$$

where r_c is the radius of the projected area of the contact surface (Fig. 8) along the interface, and $\sigma_y(T)$ is the temperature-dependent flow stress. To incorporate this, a thin layer of elements (size 0.1 by 0.1 mm, or 0.004 by 0.004 in.) is considered along the electrode-sheet and sheet-sheet interfaces. At the beginning of each time step, r_c along an interface is estimated with $\sigma_y(T)$ evaluated at the average temperature, T_{av} , prevailing along the corresponding interface (Ref 27–30).

Incorporation of Latent Heat

The latent heat of melting and solidification can be included in the heat-transfer simulation through an increase or decrease in the specific heat of the material. The specific heat, C , is expressed as:

$$\begin{aligned} C &= C_1 \quad \text{for } T \leq T_S \\ C &= C_2 \quad \text{for } T \geq T_L \\ C &= C_m = [\lambda / (T_L - T)] + (C_1 + C_2) / 2 \quad \text{for } T_S \leq T \leq T_L \end{aligned} \quad (\text{Eq 15})$$

where λ is the latent heat, and T_S and T_L are the solidus and liquidus temperatures. For an element of volume undergoing phase change, the specific heat can be estimated as a weighted average of the associated specific heats, that is, C_1 and C_m (for solid to mushy state or the reverse), C_m and C_2 (for mushy to liquid state or the reverse), or C_1 , C_m , and C_2 (for a jump from solid to liquid state or the reverse) (Ref 27–30).

Estimation of Contact Resistivity

Greenwood proposed a generic relation to estimate electrical resistance between two contacting flat metallic surfaces (Ref 32, 33):

$$R = \frac{\rho}{nk} + \frac{\rho}{\pi n_a^2} \sum_{i \neq j} \frac{1}{S_{ij}} \quad (\text{Eq 16})$$

where nk is the number of spots formed by contacting surface asperities, $(r_a)_i$ is the radius of an i^{th} spot, ρ is the material electrical resistivity, and S_{ij} is the distance between i^{th} and j^{th} spots that were considered to be neighbors. The second term in Eq 16 accounts for the constriction resistance arising out of the tendency of the current flow lines to become crowded toward the conducting spots only. In actual practice, it is difficult to use Eq 16, and Holm proposed a more workable relation to estimate contact resistance (Ref 34):

$$R = \frac{\rho_1 + \rho_2}{2} \sqrt{\frac{H_m}{P_m}} \quad (\text{Eq 17})$$

where ρ_1 and ρ_2 are the bulk material electrical resistivities of two contacting materials, H_m is the Meyer's hardness number of the softer

material, and P_m is the applied pressure. Babu et al. proposed to calculate the unit area contact resistance, R_{CA} (in Ωm^2) as (Ref 13):

$$R_{CA} = (\rho_1 + \rho_2) \left[\frac{1}{4} \left(\frac{\pi \sigma_{YS}}{\eta F_P} \right)^{1/2} + \frac{3\pi}{16\eta^{1/2}} \right] \quad (\text{Eq 18})$$

where η is the contacting asperity density (m^{-2}), σ_{YS} is the yield strength of the softer material in contact, and F_P is the uniform contact pressure based on the apparent contact area. Babu et al. showed that the contacting asperity densities (η) can be determined experimentally as a function of the ratio of F_P and σ_{YS} . For typical aluminum alloys, an exponential decay of contact resistance as a function of temperature is also proposed (Ref 10):

$$R_k(T) = \frac{\alpha R_0}{\beta^{(T-T_0)/(T_L-T_0)}} \quad (\text{Eq 19})$$

where $R_k(T)$ is the temperature-dependent contact resistance, R_0 is the initial value of the contact resistance at room temperature, α and β are factors depending on the type of sheet metal and their surface coatings, T_L is the liquidus temperature of the sheet metal, T_0 is the ambient temperature, and T is the variable temperature. The distribution of contact resistivity along the sheet-sheet and electrode-sheet interfaces can further be estimated based on the discretized geometry used for the numerical modeling:

$$(\rho_k)_i = (R_k(T) \cdot A/h)(A/A_i) \quad (\text{Eq 20})$$

where $(\rho_k)_i$ is the contact resistivity of the i^{th} contact element, A is the cross-sectional area of the contact zone, and A_i and h are the cross-sectional area and height of the i^{th} contact element, respectively. The net resistivity of the i^{th} contact element $(\rho)_i$ is:

$$(\rho)_i = (\rho_k)_i + (\rho_b)_i \quad (\text{Eq 21})$$

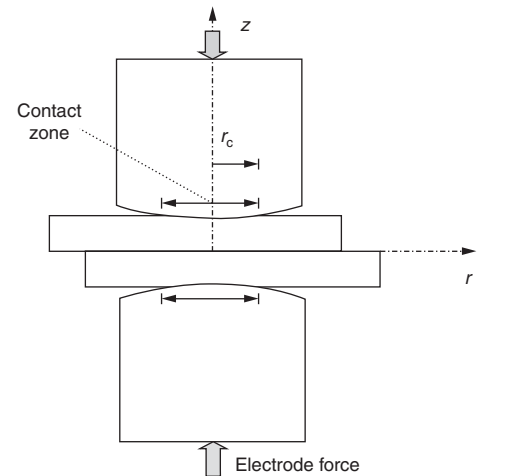


Fig. 8 Anticipated sheet-electrode contact zone at any time instant

where $(\rho_b)_i$ is the temperature-dependent bulk resistivity of the i^{th} element.

Results and Discussions

Figures 9(a) and (b) show the discretized geometry of a typical sheet-electrode system and its zoomed view, showing primarily four-node quadrilateral and a few three-node triangular elements, especially along the curved electrode boundary. The sheet thickness confirms to 0.88 mm (0.03 in.). The discretized geometry is made finer along the interfaces and coarser away from the interfaces, because the temperature and current density gradients are expected to be negligible in the bulk electrode.

Figures 10(a) to (d) show the computed temperature fields at different time instants corresponding to a welding current of 7.0 kA and an electrode force of 2.2 kN. The temperature-dependent material properties of low-carbon steel, which are used in the model calculations, are reported elsewhere (Ref 29, 30). The red-colored zone ($>1500^\circ\text{C}$, or 2730°F) depicts the simulated weld nugget, and its extent along the axial and radial directions shows the penetration and radius of the weld nugget, respectively. The computed nugget diameter increases from 4.8 mm (0.2 in.) at 50 ms to 5.4, 6.0, and 6.3 mm (0.21, 0.24, and 0.25 in.) at 100, 150, and 200 ms, respectively. The computed nugget penetration increases from 0.4 mm (0.016 in.) at 50 ms to 0.45 mm (0.018 in.) at 100 ms and remains unchanged at higher weld time. The computed electrode-sheet contact diameter increases from 4.0 mm (0.16 in.) at 50 ms to 4.90, 5.7, and 6.0 mm (0.19, 0.22, and 0.24 in.) at 100, 150, and 200 ms, respectively. An initial contact resistance of $250\ \mu\Omega$ is considered along the sheet-sheet interface for all the calculations.

Figures 11(a) and (b) show the increase in computed weld nugget dimensions with the increase in welding current. For example, as the welding current increases from 6.5 to 7.5 kA, the computed values of nugget diameter, penetration, and electrode-sheet contact diameter increase from 4.8 to 6.4 mm (0.19 to 0.25 in.), 0.2 to 0.41 mm (0.01 to 0.02 in.), and 5.2 to 6.0 mm (0.2 to 0.24 in.), respectively.

Figures 12(a) and (b) show the influence of electrode force on the computed weld dimensions. As the electrode force increases from 2.2 to 3.0 kN, the computed values of nugget diameter, penetration, and electrode-sheet contact diameter decrease from 6.8 to 4.8 mm (0.27 to 0.19 in.), 0.6 to 0.2 mm (0.02 to 0.01 in.), and 6.4 to 5.2 mm (0.25 to 0.20 in.), respectively. The resistive heating in the sheet-electrode system is directly proportional to the weld time and to the square of welding current. Hence, the increase in weld nugget dimensions with increase in weld time and welding current is expected. With increasing electrode force, the effective contact area along

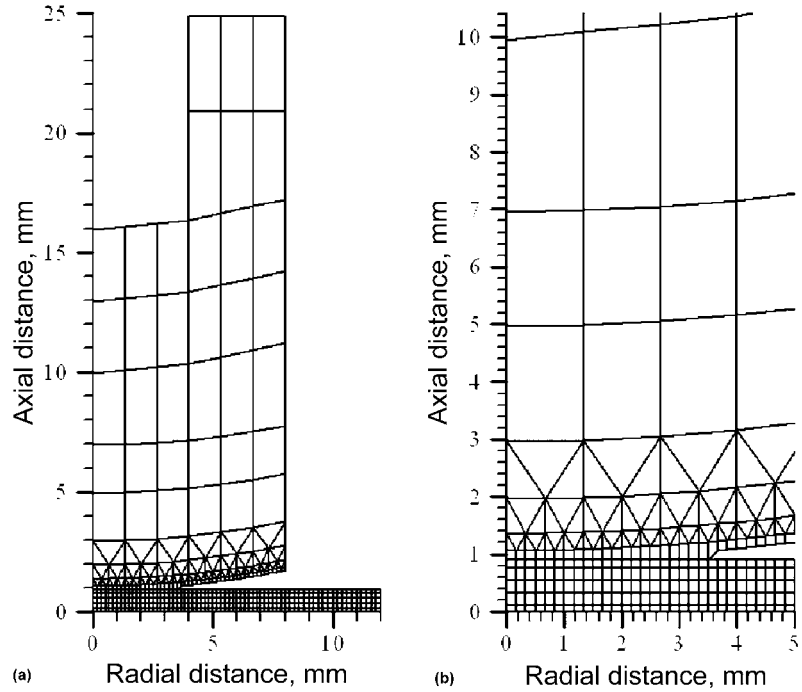


Fig. 9 Discretized sheet-electrode geometry with spherical tip electrodes. (a) Complete geometry. (b) Zoomed view of elements across contact areas

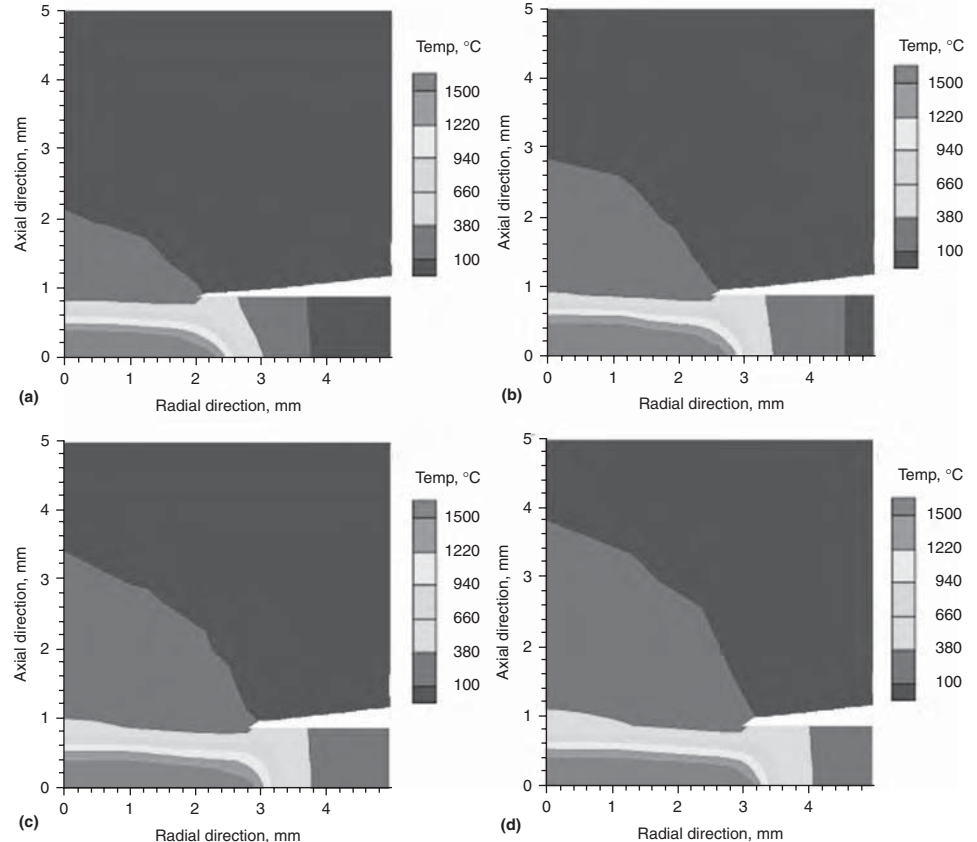


Fig. 10 Computed temperature isotherm of the sheet-electrode geometry (zoomed section) at (a) 50, (b) 100, (c) 150, and (d) 200 ms at current = 7.0 kA and force = 2.2 kN

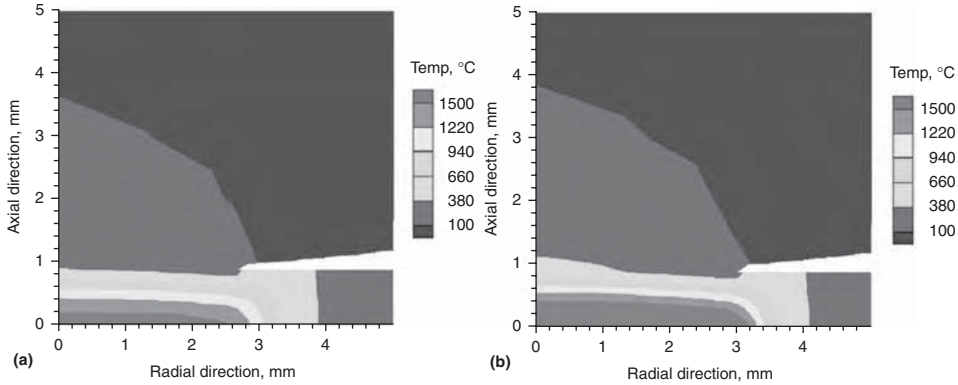


Fig. 11 Computed temperature isotherm in sheet-electrode system at (a) 6.5 and (b) 7.5 kA. Other welding parameters: electrode force = 2.2 kN and weld time = 200 ms

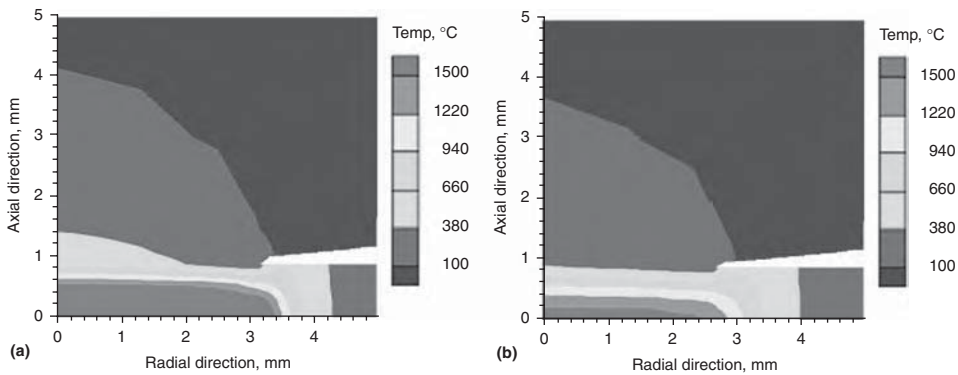


Fig. 12 Computed temperature isotherm in sheet-electrode system at (a) 2.2 and (b) 3.0 kN. Other welding parameters: welding current = 7.0 kA and weld time = 200 ms

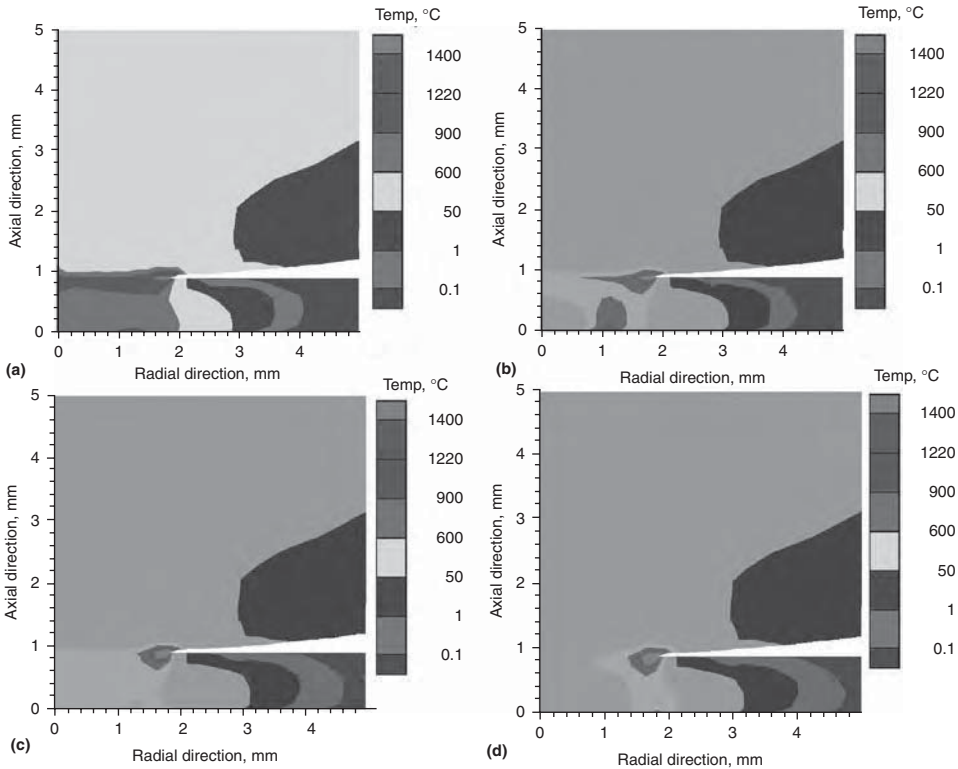


Fig. 13 Isocontours depicting computed current density distribution (A/mm^2) in the sheet-electrode geometry at (a) 5, (b) 20, (c) 40, and (d) 60 ms. Other welding parameters: welding current = 7.0 kA and electrode force = 2.2 kN

the electrode-to-sheet interface increases, thereby reducing the effective current density for a given value of welding current. Smaller current density reduces resistive heating, and thus, melting and subsequent weld nugget dimensions are reduced as the electrode force increases.

Figures 13(a) to (d) show the computed current density distribution in the sheet-electrode geometry at different time instants corresponding to a welding current of 7.0 kA and electrode force of 2.6 kN. The current density is at its highest at the edge of the electrode-sheet interface due to the change in cross section from the larger electrode diameter to the smaller electrode-sheet contact zone. Figures 13(a) to (d) also indicate the variation in the nature of the current density distribution in the sheet material at different weld times. An increase in temperature increases bulk material (for steel) resistivity while decreasing contact resistance. As a result, the current density distribution, which is inversely proportional to the net electrical resistivity, changes in a complex manner with increase in weld time.

The estimation of the electrode-to-sheet and the sheet-to-sheet contact diameters is essential for accurate calculation of current density distribution, subsequent resistive heating, and final temperature distribution in the sheet-electrode geometry. Figures 14(a) to (d) show the calculated variation of normal stress along the sheet-sheet and the electrode-sheet interfaces for various combinations of welding current and electrode force at a time instant of 5 ms. These calculations are done using a commercial finite-element software (ANSYS 10.0) following thermal-elastic-plastic analyses. The vertical dotted lines in each of these figures indicate the radius of the corresponding contact zone, that is, either electrode to sheet (referred to as E-S) or sheet to sheet (referred to as S-S). The negative values of stresses on the vertical axis refer to compressive stresses and vice versa. Figures 13(a) to (d) indicate that the magnitude of the compressive normal stresses is the maximum at the center of both the sheet-sheet and the electrode-sheet contact zones. The normal electrode-sheet contact stress is initially compressive and becomes tensile in nature at a certain distance away from the center. It is assumed that the perfect contact holds (both along the electrode-sheet and the sheet-sheet) up to this point, where the normal stress changes from compressive to tensile.

A comparison of Fig.14(a) and (b) shows that at a constant electrode force of 2.2 kN, as welding current increases from 7.0 to 8.0 kA, the S-S contact diameter increases from 6.5 to 6.8 mm (0.26 to 0.27 in.) while the E-S contact diameter remains nearly the same. A similar comparison of Fig.14(a) and (c) indicates that for a welding current of 7.0 kA, an increase in electrode force from 2.0 to 3.0 kN increases E-S and S-S contact diameters from 4.0 to 4.5 mm (0.16 to 0.18 in.) and 6.5 to 7.3 mm (0.26 to 0.29 in.), respectively. An overall

comparison of Fig.14(a) to (d) clearly indicates that the computed values of both E-S and S-S contact diameters are sensitive to both the electrode force and the welding current.

The numerically computed values of the E-S and S-S contact diameters are compared with

the corresponding analytically estimated values (Eq 14) in Fig.15(a) to (c). Although the nature of the computed values of the E-S and S-S contact diameters is nearly the same, the analytically estimated values are slightly underpredicted. This can possibly be attributed

to the simple one-dimensional nature of the analytical relation (Eq 14). In reality, a complex state of stress prevails along the interfaces that can certainly be captured more accurately through a full-fledged thermal-elastic-plastic analysis. Figures 15(a) to (c) also indicate that an analytical estimation of the E-S and S-S contact diameters as proposed through Eq 14 can be sufficiently reliable.

A comparison of the experimentally measured weld nugget dimension with the corresponding computed values is shown in Fig. 16(a) and (b) and in Fig. 16(c) and (d), respectively. The weld nugget boundary in the experimentally measured macrographs is indicated by a white line. The computed weld nugget is presumed to be the zone within the sheet material enclosed by the melting temperature isotherm (1500 °C, or 2730 °F). These figures clearly show that the weld dimensions can be estimated to a fair degree of accuracy using numerical models based on scientific principles.

Estimation of the peak temperature, weld thermal cycle, cooling rate, and the duration through which the weld fusion zone and heat-affected zone remain beyond some critical temperature are requisite to design weld schedules for optimum weld joint mechanical properties. From this point of view, the numerical models can serve as an efficient, off-line design tool. Figures 17(a) and (b) show the calculated weld thermal cycles during spot welding in steel sheets (0.88 mm, or 0.035 in., thickness) corresponding to two different welding currents. In these figures, the thermal cycles are drawn for four different positions along the weld nugget midplane: the center point (A), a point (B) residing approximately midway between the center and the periphery of the weld nugget, a point (C) that is almost at the edge of the weld nugget or fusion zone, and lastly, a point (D) that is within the heat-affected zone.

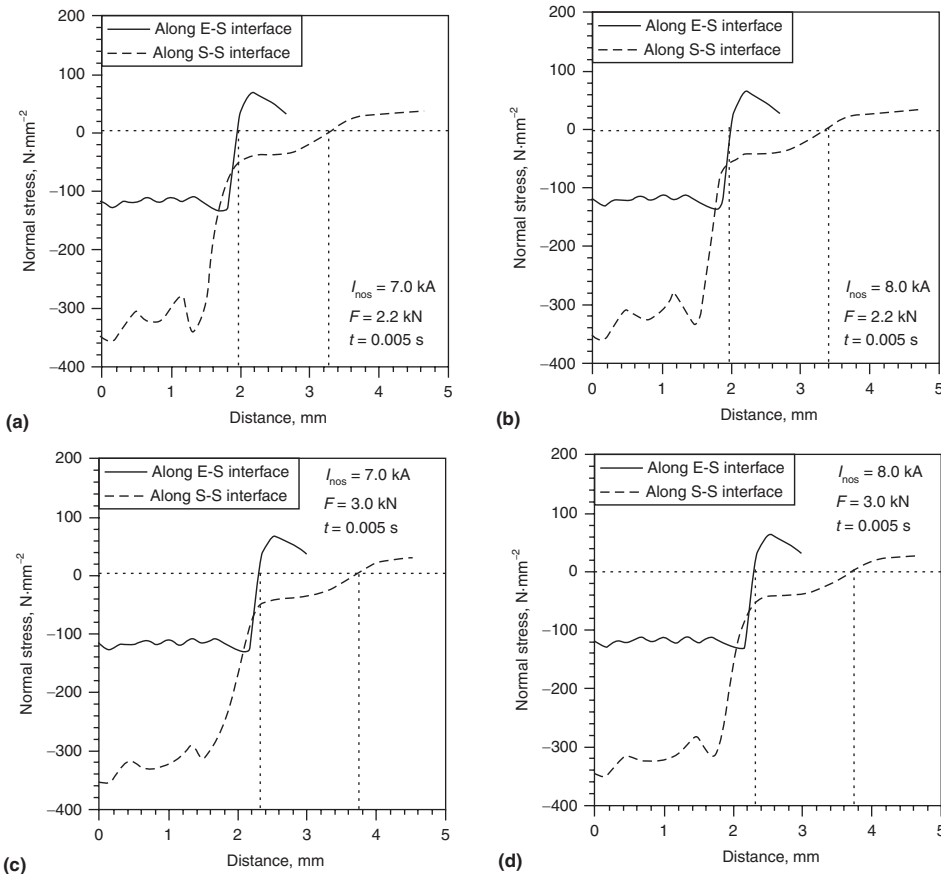


Fig. 14 Computed variations in electrode-to-sheet (E-S) and sheet-to-sheet (S-S) interface diameters at a specific time instant (0.005 s) for different combinations of welding current and electrode force. The thermal-elastic-plastic analyses are performed in ANSYS 10.0.

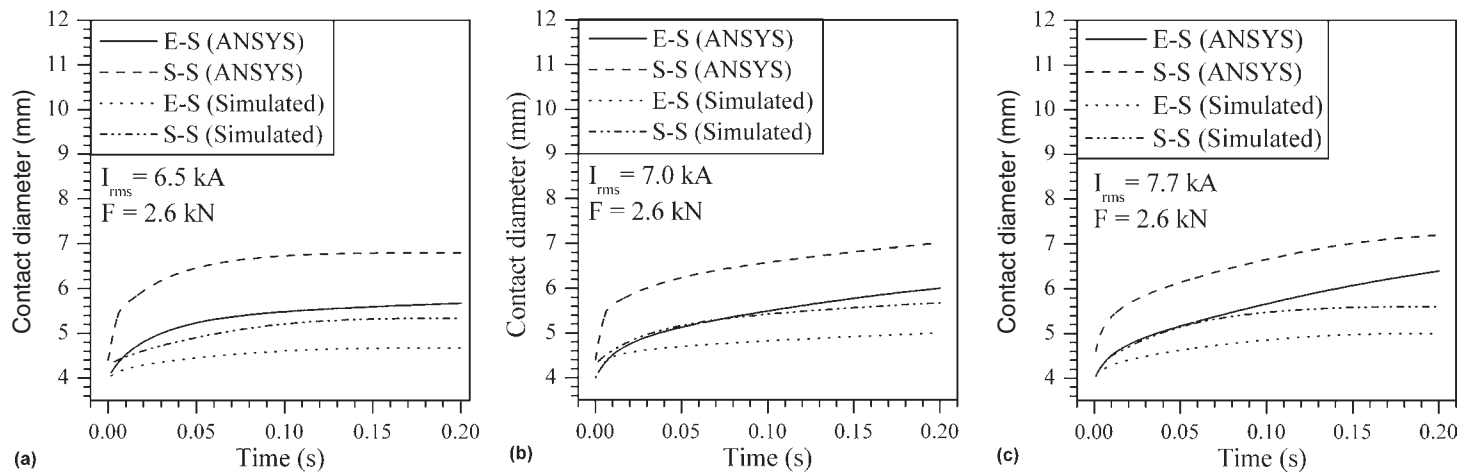


Fig. 15 Comparison of computed values of electrode-to-sheet (E-S) and sheet-to-sheet (S-S) contact diameters using ANSYS 10.0 with corresponding analytically estimated values for different combinations of welding current and electrode force

Figures 17(a) and (b) show that the rates of both heating and cooling increase toward the center of the weld nugget (fusion zone). The points within the fusion zone are observed to start cooling within the later part of the weld time, even if the welding current is on. The cooling rate is comparatively slower until the welding current is on (up to 0.2 s), and thereafter, a rapid cooling rate is observed. The point (D) within the heat-affected zone shows a smaller peak temperature and lower cooling rate. At a relatively higher welding current of 7.5 kA (Fig. 17b), the peak temperature at the center of the weld nugget (A) is slightly higher. The point (D) within the heat-affected zone exhibits a nearly constant temperature region at the later part of the weld time at higher welding current. This can possibly be attributed to a competitive effect between slow resistive heating and simultaneous conduction heat transfer to surrounding regions at point (D). The peak temperature of the point (D) within the heat-affected zone seems to remain unaltered for a change in welding current from 6.7 to 7.5 kA. It is also apparent from both Fig.17(a) and (b) that higher weld time at a constant current setting will simply delay the cooling with no appreciable increase

in the peak temperature. This can be attributed to the competitive effect between the slower resistive heating at the later part of weld time and simultaneous conduction heat transfer to the surrounding regions. The thermal cycles can be used further for more detailed and fundamental understanding of the metallurgical and mechanical properties of the weld and the surrounding heat-affected zone.

The organized efforts toward development of comprehensive numerical models have enriched the quantitative understanding of coupled thermal-electrical and thermal-electrical-mechanical phenomena involved in resistance welding processes. In particular, the increased availability of commercial software based on the finite-element method has enabled a greater number of welding researchers to develop such models. Although such commercial software generally facilitates coupled field analysis that is helpful to undertake coupled thermal-electrical and thermal-elastic-plastic phenomena, a linking of the two to provide a fully coupled electrical-thermal-elastic-plastic analysis has remained a challenge. At present, various user-defined schemes are followed to establish a link between the coupled thermal-electrical

and thermal-elastic-plastic analyses in a sequential manner such that the computed temperature field due to nonuniform current density from the former can be used to compute thermal-elastic-plastic displacement and stress fields from the latter. Provision of exclusive elements that can handle a fully coupled electrical-thermal-elastic-plastic analysis primarily for the resistance welding process in the commercial finite-element-method-based software is possibly a future solution.

REFERENCES

1. H.S. Cho and Y.J. Cho, A Study of Thermal Behavior in Resistance Spot Welds, *Weld. J.*, Vol 68 (No. 6), 1989, p 236–244
2. Z. Han, J. Orozco, J.E. Indacochea, and C.H. Chen, Resistance Spot Welding: A Heat Transfer Study, *Weld. J.*, Vol 68 (No. 9), 1989, p 363s–371s
3. P.S. Wei and C.Y. Ho, Axisymmetric Nugget Growth during Resistance Spot Welding, *ASME J. Heat Transf.*, Vol 112 (No. 2), 1990, p 309–316
4. P.S. Wei and C.Y. Yeh, Factors Affecting Nugget Growth with Mushy-Zone Phase Change during Resistance Spot Welding, *ASME J. Heat Transf.*, Vol 113 (No. 8), 1991, p 643–649
5. T. Yamamoto and T. Okuda, A Study of Spot Welding of Heavy Gauge Mild Steel, *Weld. World*, Vol 9 (No. 7/8), 1971, p 234–255
6. K. Nishiguchi and K. Matsuyama, Influence of Current Wave Form on Nugget Formation Phenomena when Spot Welding Thin Steel Sheets, *Weld. World*, Vol 25 (No. 11/12), 1987, p 222–244
7. A.H. Neid, The Finite Element Modeling of Resistance Spot Welding, *Weld. J.*, Vol 63 (No. 4), 1984, p 123–132
8. C.L. Tsai, O.A. Jammal, J.C. Papritan, and D.W. Dickinson, Modeling of Resistance Spot Weld Nugget Growth, *Weld. J.*, Vol 71 (No. 2), 1992, p 47–54
9. C.L. Tsai, J.C. Papritan, D.W. Dickinson, and J.C. Papritan, Analysis and Development of a Real-Time Control Methodology in Resistance Spot Welding, *Weld. J.*, Vol 70 (No. 12), 1991, p 339s–351s
10. M.J. Greitmann and K. Rother, Numerical Simulation of the Resistance Spot Welding Process Using Spotwelder, *Mathematical Modeling of Weld Phenomena 4* (Graz, Austria), 1997, p 531–544
11. O.P. Gupta and A. De, An Improved Numerical Modeling for Resistance Spot Welding Process and Its Experimental Verification, *ASME J. Manuf. Sci. Eng.*, Vol 120, 1998, p 246–252
12. T. Dupuy and S. Ferrasse, Influence of the Type of Current and Material Properties on Resistance Spot Welding Using a Finite Element Method, *Fifth International Conference on Trends in Welding Research*

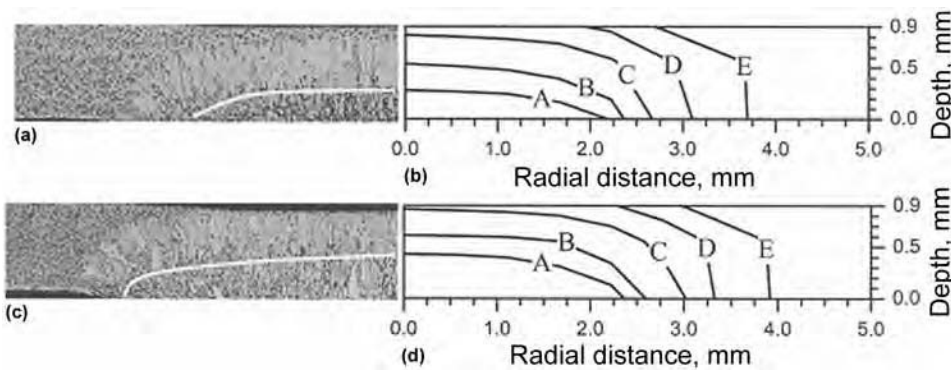


Fig. 16 Comparison of computed values of weld dimensions with the corresponding measured weld macrographs. The letters in (b) and (d) refer to temperature contours: A, 1500 °C (2730 °F); B, 1200 °C (2190 °F); C, 873 °C (1603 °F); D, 500 °C (930 °F); E, 300 °C (570 °F). Weld time and electrode force in (a) to (d) correspond to 200 ms and 3.0 kN, respectively. Welding current is 6.5 kA for (a) and (b), and 8.6 kA for (c) and (d).

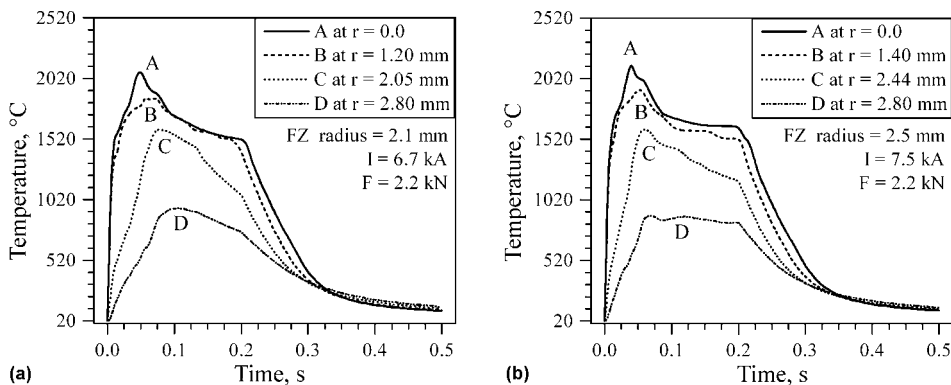


Fig. 17 Computed thermal cycle (time-temperature plot) in steel at two different welding currents. The electrode force and weld time are constant as 2.2 kN and 200 ms, respectively. FZ, fusion zone

- (Pine Mountain, GA), ASM International, 1998, p 610–615
13. Z. Feng, J.E. Gould, S.S. Babu, M.L. Santella, and B.W. Riemer, An Incrementally Coupled Electrical-Thermal-Mechanical Model for Resistance Spot Welding, *Fifth International Conference on Trends in Welding Research* (Pine Mountain, GA), ASM International, 1998, p 599–604
 14. H. Huh and W.J. Kang, Electrothermal Analysis of Electric Resistance Spot Welding Process by a 3-D Finite Element Method, *J. Mater. Process. Technol.*, Vol 63 (No. 1–3), 1997, p 672–677
 15. R.J. Bowers, C.D. Sorensen, and T.W. Eagar, Electrode Geometry in Resistance Spot Welding, *Weld. J.*, Vol 69 (No. 2), 1990, p 45s–51s
 16. H.S. Chang and H.S. Cho, A Study on the Shunt Effect in Resistance Spot Welding, *Weld. J.*, Vol 69 (No. 8), 1990, p 308s–317s
 17. U. Dilthey, H.C. Bohlmann, V. Sudnik, V. Erofeev, and R. Kudinov, Calculation of Welding Areas and Numerical Simulation of the Resistance Spot Welding Process, *Schweissen Schneiden*, Vol 52 (No. 1), 2000, p 18–23
 18. J. Khan, L. Xu, and Y.J. Chao, Prediction of Nugget Development during Resistance Spot Welding Using Coupled Thermal-Electrical-Mechanical Model, *Sci. Technol. Weld. Join.*, Vol 4 (No. 4), 1999, p 201–207
 19. X. Sun and P. Dong, Analysis of Aluminum Resistance Spot Welding Processes Using Coupled Finite Element Procedures, *Weld. J.*, Vol 79 (No. 12), 2000, p 216s–221s
 20. F.J. Studer, Contact Resistance in Spot Welding, *Weld. J.*, Vol 18 (No. 10), 1939, p 374s–380s
 21. R.F. Tylecote, Spot Welding, Part II: Contact Resistance, *Weld. J.*, Vol 20 (No. 12), 1941, p 591s–602s
 22. W.F. Savage, E.F. Nippes, and F.A. Waswell, Static Contact Resistance of Series Spot Welds, *Weld. J.*, Vol 56 (No. 11), 1977, p 365–370
 23. M.M. Vogler and S.D. Sheppard, Electrical Contact Resistance under High Loads and Elevated Temperatures, *Weld. J.*, Vol 72 (No. 6), 1993, p 231s–238s
 24. P.H. Thornton, A.R. Krause, and R.G. Davies, Contact Resistances in Spot Welding, *Weld. J.*, Vol 75 (No. 12), 1996, p 402s–412s
 25. P.H. Thornton, A.R. Krause, and R.G. Davies, Contact Resistances of Aluminum, *Weld. J.*, Vol 76 (No. 8), 1997, p 331s–341s
 26. E. Criton and J.T. Evans, The Effect of Surface Roughness, Oxide Film Thickness and Interfacial Sliding on the Electrical Contact Resistance of Aluminium, *Mater. Sci. Eng. A*, Vol 242, 1998, p 121–128
 27. A. De and L. Dorn, Computer Simulation of Resistance Spot Welding Process, *Mathematical Modeling of Weld Phenomena 7* (Graz, Austria), 2003
 28. A. De, Finite Element Modeling of Resistance Spot Welding of Aluminum with Spherical Tip Electrodes, *Sci. Technol. Weld. Join.*, Vol 7 (No. 2), 2002, p 119–124
 29. A. De, L. Dorn, and K. Momeni, Proving the Role of Instantaneous Current Waveform in Numerical Modeling of Resistance Spot Welding, *Sci. Technol. Weld. Join.*, Vol 20 (No. 3), 2005, p 325–334
 30. A. De, K. Momeni, M.P. Thaddeus, and L. Dorn, Influence of Machine Specific Instantaneous Current Wave Form on Resistance Spot Welding Process, *J. Manuf. Sci. Eng., Trans. ASME*, Vol 128 (No. 3), 2006, p 668–676
 31. O.P. Gupta, *Finite and Boundary Element Methods in Engineering*, Oxford & IBH, New Delhi, 1999
 32. J.A. Greenwood and J.B.P. Williamson, Contact of Nominally Flat Surfaces, *Proc. R. Soc. (London) A*, Vol 295, 1966, p 300–319
 33. J.A. Greenwood, Constriction Resistance and the Real Area of Contact, *Br. J. Appl. Phys.*, Vol 17, 1966, p 1621–1632
 34. R. Holm, *Electrical Contacts: Theory and Application*, 4th ed., Springer-Verlag, Berlin/Heidelberg/New York, 1967

Modeling of Metallurgical Microstructure Evolution in Fusion Welding

Ole Runar Myhr, Hydro Aluminium and Norwegian University of Science and Technology
Øystein Grong, Norwegian University of Science and Technology

MODELING OF THE MICROSTRUCTURE EVOLUTION is a rapidly expanding field of research. In particular, the integration of microstructure modeling with the detailed process histories available from modern finite-element analyses represents an increasingly important field of industrial applications. Even though microstructure models are readily available, they usually cannot be applied directly to welding problems because they tend to describe ideal conditions, such as isothermal heat treatment, often applied to ideal materials, such as pure metals or binary alloys (Ref 1). Before such ideal models can be used for welding processes, they must be recast mathematically so they can handle nonisothermal heat treatments. For this purpose, the internal state variable method is particularly well suited. The general method and its simplification for single-parameter models, in which the microstructure evolution may be treated as an “isokinetic” reaction, are outlined in the section “The Internal State Variable Approach” in this article.

In the section “Isokinetic Microstructure Models,” the general methods described in the previous section are applied to diffusional transformations in fusion welding, covering particle dissolution, growth, and coarsening of precipitates in the heat-affected zone (HAZ). Examples of applications of the methods include grain-boundary liquation in Al-Zn-Mg alloys and coarsening of TiN precipitates during steel welding. In this section, the evolution of the grain structure in the HAZ following recrystallization and grain growth is also dealt with, and isokinetic solutions are derived.

The internal state variable method is not restricted to single diffusion mechanisms but can even be used to capture transformations that occur sequentially (i.e., in succession) or in parallel during a weld thermal cycle, as described by an example from welding of duplex stainless steel in the section “Isokinetic Microstructure Models” in this article. However, this concept fails when attempting to

model welding as part of a multistage process chain, under which the transformation has a strong memory of the past process steps. This is typically the case for precipitation reactions occurring during heat treatment and welding of age-hardening aluminum alloys, where the detailed thermal history affects the evolution of the precipitate structure. In this case, nucleation, growth, and coarsening (and likewise dissolution) must be modeled as coupled processes within a single physical framework, as outlined in the section “Complex Microstructure Models Describing the Evolution of a Particle Size Distribution” in this article.

Finally, in the case studies presented in the section “Microstructure Modeling in the Context of Engineering Design,” the microstructure models are exploited in engineering design to optimize the load-bearing capacity of welded aluminum components.

The Internal State Variable Approach

There is a wide spectrum of modeling approaches available for predicting microstructure evolution in metals and alloys during welding, including empirical and statistical methods. Even though such methods can be useful for many problems, they usually require a considerable amount of experimental data to capture the behavior of the process, without offering substantial predictive power. This is particularly true if the chemical composition is varied (Ref 1).

Alternatively, the internal state variable method, as originally proposed by Richmond (Ref 2), can be applied to predict nonisothermal transformation behavior, as experienced in welding. This method offers a good compromise between the many conflicting requirements for broad application to industrial process modeling and offers useful predictive capability when calibrated to experimental data. Provided that the microstructure evolution is

captured mathematically in terms of the differential variation of the state variables with time, these may be integrated stepwise through any process history, using an appropriate numerical procedure. Usually, this computation can occur independently of the prediction of the thermal history itself, unless the microstructure evolution is strongly coupled to the macroscopic response.

General Methodology

A microstructure may be described by many different state variables; choosing the most relevant depends on the problem (Ref 1). Typical examples of state variables in the context of microstructure evolution are the mean grain size in single-phase alloys, the particle size and volume fraction in multiphase alloy systems, and the fraction of recrystallized grains in work-hardened and annealed materials. Collectively, the microstructural state variables are termed S_i .

State Variable Formulation. At the most general level for a thermally controlled process, the evolution of microstructure can be described by a simultaneous set of differential equations for each of the independent state variables, S_i (Ref 1):

$$\frac{dS_1}{dt} = h_1(S_1, S_2, \dots, T) \quad (\text{Eq 1a})$$

$$\frac{dS_2}{dt} = h_2(S_1, S_2, \dots, T) \quad (\text{Eq 1b})$$

where T is the instantaneous temperature. Given a process temperature history $T(t)$, these equations may be solved (usually numerically) to give the evolution of the state variables.

Most commonly, the instantaneous values are fed into a response equation for some dependent quantity, such as flow stress, σ (Ref 1):

$$\sigma = h_3(S_1, S_2, \dots) \quad (\text{Eq 2})$$

In some cases, it may be the final values of the state variables that are required, either when these are the output of interest or if they are to become the starting values for a subsequent processing step. For fully coupled problems, in which a significant quantity of heat is released by the microstructural change (as in solidification), $T(t)$ will itself depend on the material state. Then, the evolution laws must be solved simultaneously with the temperature history, including a further differential equation for temperature (Ref 1):

$$\frac{dT}{dt} = h_4(S_1, S_2, \dots, T) \quad (\text{Eq 3})$$

An important feature of a “true” state variable model of the form given by Eq 1 is that it does not depend on previous thermal history or microstructure; that is, given the instantaneous values of the state variables, their evolution in the next time increment is uniquely defined by these values and the current temperature alone.

Many important problems of microstructural evolution in thermal processing can be described by single-state variable models. In this case, it is sometimes possible to obtain closed-form solutions that include the temperature dependence of the reaction. Such a reaction is termed isokinetic, and the conditions under which it applies are examined subsequently. If a single-state parameter microstructure model is not isokinetic, or if there are two or more state variables besides temperature, then the solutions will be thermal path dependent.

Definition of an Isokinetic Reaction. The solution of a single internal state variable problem involving the evolution of a specific microstructural feature can be greatly simplified if the evolution law is isokinetic. Nonisothermal process histories can then readily be treated in a single computational step, by invoking the concept of the kinetic strength of the thermal cycle with respect to microstructure evolution. Broadly speaking, a reaction is said to be isokinetic if the increments of transformation in infinitesimal isothermal time steps are additive. Christian (Ref 3) defines this mathematically by stating that a reaction is isokinetic if the evolution equation for some state variable X may be written in the form:

$$\frac{dX}{dt} = \frac{G(X)}{H(T)} \quad (\text{Eq 4})$$

where $G(X)$ and $H(T)$ are arbitrary functions of X and T , respectively.

Equation 4 is a first-order (separable) differential equation that can be integrated as follows:

$$\int_0^X \frac{dX}{G(X)} = \int_0^t \frac{dt}{H(T)} \quad (\text{Eq 5})$$

The integral on the right side is termed the kinetic strength of the thermal cycle with

respect to the evolution of variable X . If the state variable X is a dimensionless parameter, the function $H(T)$ becomes a time constant that includes the temperature dependence of the reaction. In that case, the right side of Eq 5 reduces to the well-known Scheil integral (Ref 4):

$$I = \int_0^t \frac{dt}{t^*} \quad (\text{Eq 6})$$

where $t^* = t_r \exp(Q_d/RT)$ is the temperature-dependent time constant.

In the context of diffusional transformations, a direct consequence of Eq 5 is that the reaction is uniquely defined by a single C-curve, as shown schematically in Fig. 1. This C-curve represents the time taken to reach a given fraction $X = X_c$ under isothermal conditions. Under isokinetic conditions, the total time to reach $X = X_c$ during continuous cooling is simply obtained by adding the fractions of temperature-weighted time until the kinetic strength integral is equal to unity.

Isokinetic Microstructure Models

The majority of phase transformations that take place in alloys are diffusional and are preceded by thermally activated movements of atoms across a concentration gradient (Ref 5, 6). Of particular importance in relation to welding are precipitation reactions that are induced by a change in temperature of an alloy with a fixed bulk composition. If the precipitates form from a supersaturated solid solution, three major processes are involved (Ref 7–9): nucleation, growth, and coarsening. In the following, the additivity concept and the more general internal state variable formalism are applied to establish a basis for modeling nonisothermal diffusional transformations.

Particle Dissolution

Traditionally, the additivity concept has been associated with diffusion-controlled growth (Ref 3, 4, 10–13). Although growth and dissolution are not conjugate processes (Ref 14), the state variable formalism implies that the additivity concept is equally applicable to particle dissolution, because the phenomenon has its common origin in the form of the controlling differential evolution equation rather than the reaction mechanism itself.

The invariant size solutions of Whelan (Ref 15) provide a good starting point for a discussion of additivity and isokinetic behavior in relation to particle dissolution. These solutions are based on the assumption that the particle/matrix interface is stationary; that is, the diffusion field has no memory of the past position of the interface. It follows that the original rate laws describing dissolution of platelike and spherical precipitates are not strictly isokinetic, because time is also embedded in the

solutions. Still, they can be recast into isokinetic solutions according to the definition given previously by proper manipulation of the constitutive equations and subsequent substitution of variables.

Platelike Precipitates. In the case of platelike precipitates embedded in an infinite matrix, a flux balance at the particle/matrix interface leads to the following expression for the dissolution rate (Ref 15):

$$\frac{dB}{dt} = -\frac{k}{2} \sqrt{\frac{D}{\pi t}} \quad (\text{Eq 7})$$

where B is the half-thickness of the plate, and $k = 2(C_1 - C_0)/(C_p - C_1)$. This is not a strict state variable evolution equation, because time, t , enters on the right side, implying the time from the start of dissolution. Integrating Eq 7 gives:

$$B = B_0 - \frac{k}{\sqrt{\pi}} \sqrt{Dt} \quad (\text{Eq 8})$$

where B_0 is the initial half-thickness of the plate at time $t = 0$. Equation 8 can be rewritten in a dimensionless form by introducing the scaled particle volume fraction, $f/f_0 = B/B_0$, and a time constant, t_1^* , for complete dissolution:

$$\frac{f}{f_0} = 1 - \left(\frac{t}{t_1^*}\right)^{1/2} \quad (\text{Eq 9})$$

The next step is to introduce a chosen reference state to allow all unknown material constants to be replaced by a single time constant, t_{r1} , for the dissolution reaction. This time constant can be readily determined by calibration against experimental data. At the chosen reference temperature, T_r , the total time required for complete particle dissolution, t_{r1} , is given by:

$$t_{r1} = \frac{\pi}{D_r} \left(\frac{B_0^2}{k_r}\right)^2 \quad (\text{Eq 10})$$

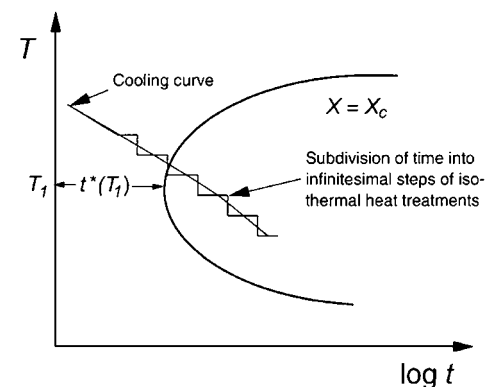


Fig. 1 Schematic illustration of the principles of additivity, according to the theory advanced by Scheil. Source: Ref 1

where k_r and D_r refer to the values of k and D at the reference temperature, and B_0^* refers to a reference plate thickness. The time constant t_1^* at any other temperature may be found by appropriate scaling of k_r and D_r . Similarly, for any other plate thickness in the initial material, the time constant is scaled with respect to B_0 . Hence, in general, the time constant t_1^* is defined as:

$$t_1^* = t_{r1} \left(\frac{k_r}{k} \right)^2 \left(\frac{B_0}{B_0^*} \right)^2 \left(\frac{D_r}{D} \right) \quad (\text{Eq 11})$$

The time constant therefore contains all material- and temperature-dependent parameters.

By differentiating Eq 9 with respect to time, ff_0 can, after some manipulation, be expressed in terms of the Scheil integral, as follows (Ref 1):

$$\frac{f}{f_0} = 1 - \left(\int_0^t \frac{dt}{t_1^*} \right)^{1/2} \quad (\text{Eq 12})$$

Then, in the isothermal case, this clearly yields the original form of Eq 9. However, the appearance of the Scheil integral in Eq 12 shows that the reaction also is additive in the general sense defined by Christian (Ref 3), which makes it applicable to a wide range of thermal treatments under conditions where this solution is valid.

Spherical Precipitates. A similar flux balance for spherical precipitates leads to the following expression for the dissolution rate at a constant temperature (Ref 15):

$$\frac{dr}{dt} = -\frac{kD}{2r} - \frac{k}{2} \sqrt{\frac{D}{\pi t}} \quad (\text{Eq 13})$$

The $1/r$ term on the right side of Eq 13 stems from the steady-state part of the diffusion field, while the term $1/\sqrt{t}$ arises from the transient part. Because of the complex form of this equation, it is not possible to arrive at a closed analytical solution that can serve as a basis for establishing a valid nonisothermal rate law. However, if the transient part of the diffusion field is neglected, it is possible to proceed as before and to obtain a closed analytical solution for the variation of the particle radius, r , with time (Ref 14–16):

$$r^2 = r_0^2 - kD_r t \quad (\text{Eq 14})$$

This simplified solution is valid when $t > 100r_0^2/\pi D$.

Equation 14 can be manipulated and rewritten in a dimensionless form analogous to that done in the one-dimensional case. By introducing the scaled volume fraction $ff_0 = (r/r_0)^3$ and the corresponding time constant t_2^* for the reaction, the following is obtained (Ref 1):

$$\frac{f}{f_0} = \left(1 - \frac{t}{t_2^*} \right)^{3/2} \quad (\text{Eq 15})$$

where the time constant for complete dissolution is given by:

$$t_2^* = t_{r2} \left(\frac{k_r}{k} \right) \left(\frac{D_r}{D} \right) \left(\frac{r_0}{r_0^*} \right)^2 \quad (\text{Eq 16})$$

taking t_{r2} equal to:

$$t_{r2} = \frac{(r_0^*)^2}{k_r D_r} \quad (\text{Eq 17})$$

Similarly for platelike precipitates, Eq 15 can be expressed in terms of the Scheil integral (Ref 1):

$$\frac{f}{f_0} = \left(1 - \int_0^t \frac{dt}{t_2^*} \right)^{3/2} \quad (\text{Eq 18})$$

Although Eq 18 is derived on the basis of the steady-state part of the diffusion field around the particles, the preceding analysis shows that the additivity concept is readily applicable to particle dissolution. The salient point appears to be the form of the isothermal starting equation, which must be simple enough to allow substitution of time with the primary state variables f and T in the nonisothermal rate law. Again, a slight modification of the rigorous form of state variable evolution law is required, in that the evolution law also depends on the initial values of f and r .

Case Study: Grain-Boundary Liquefaction in Al-Zn-Mg Weldments. As a first example of applications of the principles outlined earlier, consider grain-boundary liquation, which may occur if the constituent phases situated at the boundaries do not dissolve before the eutectic temperature is reached (Ref 17).

This phenomenon can be modeled by assuming that dissolution occurs within a sphere surrounding each particle. This means that the dissolution can be predicted by combining Eq 18 with an appropriate heat flow model, as described in Ref 17. It is then possible to calculate the degree of particle dissolution occurring during single-pass butt welding of Al-Zn-Mg alloys for different starting conditions (Ref 17). The results are summarized in Fig. 2. Figure 2(a) shows a sketch of the temperature-time pattern within the subsolidus region of the HAZ during welding. It follows that points located close to the solidus isotherm are most liable to grain-boundary liquation because the heating rate increases with decreasing distance from the fusion boundary. The process diagram in Fig. 2(b) has axes of weld energy input, q_0/vd , and precipitate (plate) thickness, $2B_0$, and displays contours of $ff_0 = 0$ for various positions within the subsolidus region. Each of these contours defines the condition for achieving full particle dissolution at 475 °C (887 °F) during heating

to the indicated peak temperatures. Above the field boundaries, the risk of local melting is small, because the dissolution process is completed before the eutectic temperature is reached. Similarly, crossing these lines means that the melting reaction will be triggered, because remnants of the particles exist at the grain boundaries when the eutectic temperature of 475 °C (887 °F) is reached.

Particle Coarsening

When dispersed particles have some solubility in the matrix in which they are contained, there is a tendency for the smaller particles to dissolve and for the matter in them to precipitate on larger particles. The driving force for the reaction is provided by the consequent reduction in the total interfacial energy, and ultimately, only a single large particle would exist within the system (Ref 5).

Coarsening Kinetics. The classical theory for particle coarsening was developed independently by Lifshitz and Slyozov (Ref 18) and by Wagner (Ref 19). According to their analysis, the kinetics is controlled by volume diffusion through the matrix. Provided that no solute is lost to the surrounding matrix during the process (i.e., $df/dt = 0$), the time dependence of the mean particle radius, r , may be written as (Ref 18, 19):

$$r^3 - r_0^3 = \frac{c_1 t}{T} \exp\left(-\frac{Q_d}{RT}\right) \quad (\text{Eq 19})$$

where r_0 is the initial particle radius, Q_d is the activation energy for particle coarsening (here taken equal to the activation energy for diffusion of the less mobile constituent element), and c_1 is a kinetic constant.

Equation 19 can be written in a dimensionless form by introducing:

$$X = \frac{r^3 - r_0^3}{r_0^3} = \frac{c_1 t}{r_0^3 T} \exp\left(-\frac{Q_d}{RT}\right) \quad (\text{Eq 20})$$

Let t_{r3} denote the time taken to reach a certain value $X = X_c$ at a chosen reference temperature, $T = T_r$. Then:

$$X_c = \frac{c_1 t_{r3}}{r_0^3 T_r} \exp\left(-\frac{Q_d}{RT_r}\right) \quad (\text{Eq 21})$$

Dividing Eq 20 by Eq 21 gives:

$$\frac{X}{X_c} = \frac{t T_r}{t_{r3} T} \exp\left[\frac{Q_d}{R} \left(\frac{1}{T_r} - \frac{1}{T}\right)\right] \quad (\text{Eq 22})$$

Based on Eq 22, it is possible to define the time constant for the system:

$$t_3^* = t_{r3} \frac{T}{T_r} \exp\left[\frac{Q_d}{R} \left(\frac{1}{T_r} - \frac{1}{T}\right)\right] \quad (\text{Eq 23})$$

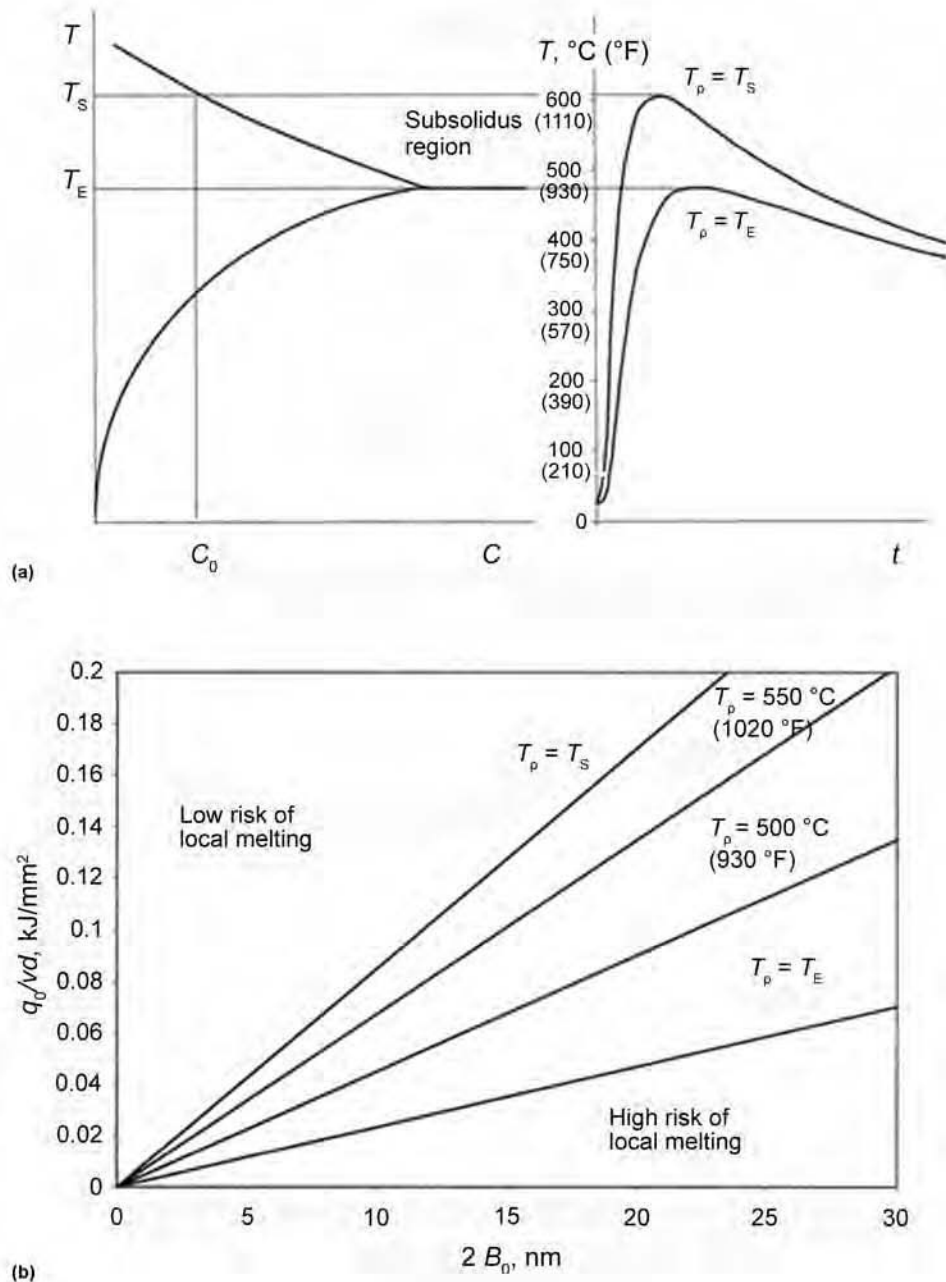


Fig. 2 Conditions for local melting during single-pass butt welding of Al-Zn-Mg extrusions. (a) Schematic representation of the temperature-time pattern within the subsolidus region of the weld heat-affected zone. (b) Process diagram showing contours of $f/f_0 = 0$ for various positions within the subsolidus region. Source: Ref 1, 17

which leads to the following expression for X :
$$\frac{dX}{dt} = \frac{X_c}{t_3^2} \tag{Eq 25}$$
 and
$$X = X_c \frac{t}{t_3^2} \tag{Eq 24}$$

Isokinetic Solution. Equation 24 provides a more general description of the original Lifshitz-Slyozov-Wagner (LSW) equation. To obtain the desired isokinetic solution, Eq 24 must first be rewritten in a differential form, followed by independent integration of the left and right sides:

$$X = X_c \int_0^t \frac{dt}{t_3^2} \tag{Eq 26}$$

From Eq 26, $X = X_c$ when the value of the Scheil integral is equal to unity. Thus, in the nonisothermal case, the total time to reach X_c

is obtained simply by adding the fractions of time to reach this stage isothermally until the sum is equal to unity.

Case Study: Coarsening of TiN during Steel Welding. The isokinetic coarsening law can be used to predict the extent of particle coarsening that occurs within the HAZ during welding of titanium-microalloyed steels. Details of the calculations can be found in Ref 20.

Problem Description. The situation is described in Fig. 3. The problem of interest here is to calculate the size of the TiN precipitates in different positions from the fusion boundary. This requires quantitative information about the weld thermal program (via a heat flow model) along with data for the coarsening kinetics of TiN in low-alloy steels (Ref 20). Coarsening of TiN may, in turn, lead to extensive austenite grain growth within the high-peak-temperature regions of the HAZ, with consequent formation of undesirable (low-toughness) microstructures such as upper bainite and Widmanstätten ferrite during the γ -to- α transformation.

Coarsening Behavior. By calculating the value of the Scheil integral at discrete points across the HAZ, the diagram in Fig. 4 can be constructed. In these calculations, it is assumed that coarsening occurs within small volume elements, where the length scale is considerably less than the actual HAZ thermal gradient. It is evident from this figure that significant coarsening of the precipitates occurs within the HAZ during welding, particularly in regions close to the fusion boundary where the peak temperature of the thermal cycle is high. Moreover, a comparison with relevant microstructure data shows that the predicted increase in the particle size is in fair agreement with experimental observations (Ref 20, 21). This suggests that the kinetics described by the classic LSW model is the dominant coarsening mechanism for TiN under the prevailing circumstances.

Recrystallization

Recrystallization of a cold-worked metal is a thermally activated transformation characterized by the nucleation and growth of new strain-free grains. The reaction is driven by the stored energy in the cold-worked matrix, and the reaction kinetics is a function of both the nucleation rate and the growth rate. Recrystallization leads to the formation of nearly defect-free crystallites and the subsequent growth of these into the surrounding structure (Ref 22, 23).

In welding, recrystallization may occur in the HAZ in positions where the peak temperature during the weld thermal cycle has been sufficiently high. The resulting recrystallized grain structure may impair the structural integrity of the weld, because of the associated reduction in strength and fracture toughness (Ref 24, 25).

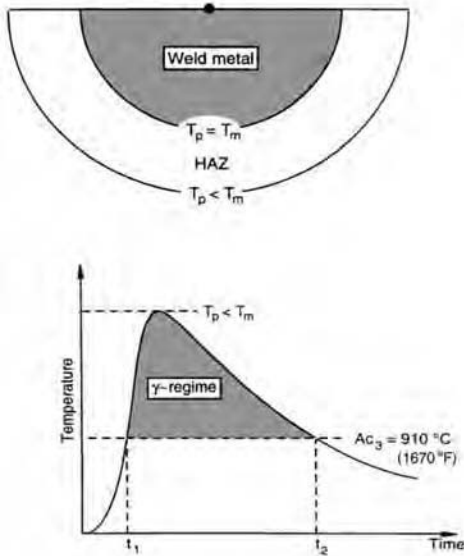


Fig. 3 Schematic diagrams showing some characteristic isothermal contours and the resulting time-temperature pattern within a weld heat-affected zone (HAZ). Source: Ref 1, 20

Recrystallization kinetics can be solved isothermally or isokinetically.

Isothermal Solution. By assuming a constant and isotropic growth rate and random spatial distribution of nucleation sites, the volume fraction of a transformed material, X_{rex} , can be described by an Avrami type of equation (Ref 26, 27):

$$X_{\text{rex}} = 1 - \exp(-t/\tau)^n \quad (\text{Eq 27})$$

where the temperature dependence of the time constant, τ , is given as (Ref 27, 28):

$$\tau = \tau_0 \exp(Q_{\text{app}}/RT) \quad (\text{Eq 28})$$

taking Q_{app} equal to the apparent activation energy for recrystallization.

Let t_{r4} denote the time taken to reach a certain value $X_{\text{rex}} = X_r$ at a chosen reference temperature, $T = T_r$. Then:

$$X_r = 1 - \exp(-t_{r4}/\tau)^n \quad (\text{Eq 29})$$

Combining Eq 27 to 29 gives:

$$X_{\text{rex}} = 1 - (1 - X_r)^{(t/t_{r4})^n} \quad (\text{Eq 30})$$

where t_4^* is given as:

$$t_4^* = t_{r4} \exp\left[\frac{Q_{\text{app}}}{R} \left(\frac{1}{T} - \frac{1}{T_r}\right)\right] \quad (\text{Eq 31})$$

Equation 30 provides a more general description of the original Avrami equation and is the basis for the isokinetic solution presented as follows.

Isokinetic Solution. To obtain the desired isokinetic solution, Eq 30 must first be rewritten in

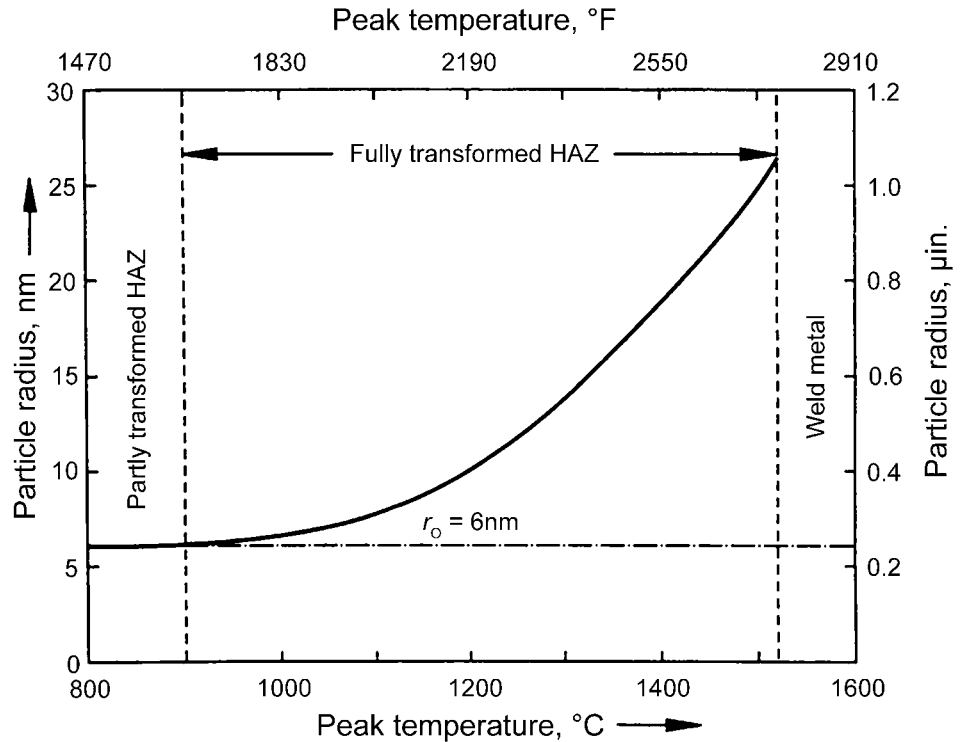


Fig. 4 Predicted coarsening behavior of TiN during steel welding. HAZ, heat-affected zone. Adapted from Ref 1, 20

a differential form and then the left and the right sides independently integrated. This gives:

$$X_{\text{rex}} = 1 - (1 - X_r)^{I/n} \quad (\text{Eq 32})$$

where I is the Scheil integral, defined as:

$$I = \int_0^t \frac{dt}{t_4^*} \quad (\text{Eq 33})$$

Case Study: Recrystallization during Welding of Aluminum Alloys. The isokinetic recrystallization law can be used to predict the extent of recrystallization that occurs within the HAZ during welding of predeformed wrought aluminum-magnesium alloys.

Problem Description. The problem of interest here is to calculate the fraction recrystallized in different positions in the HAZ. This requires quantitative information about the weld thermal program (by means of an analytical heat flow model) along with data for the recrystallization kinetics for the actual aluminum alloy.

To illustrate the recrystallization behavior during welding of aluminum-magnesium alloys, a set of mutually consistent kinetic data have been obtained by reexamining the experimental data reported by Sarrazin (Ref 28). In this case, $T_r = 673$ K (400 °C, or 750 °F), $t_{r4} = 4.7$ s, $X_r = 0.63$, $Q_{\text{app}} = 183$ kJ/mol, and $n = 1.23$ are deemed to be representative of work-hardened AA5086 in the H24 condition.

Recrystallization Behavior. By calculating the value of the Scheil integral at discrete points across the HAZ, the fraction recrystallized can be obtained as a function of the distance from the weld centerline, as illustrated in Fig. 5(a). These plots show a comparison between calculated and measured fractions of recrystallized grains following welding. Figure 5(b) shows similar plots for hardness, where the predicted fractions recrystallized from Fig. 5(a) are converted to hardness by means of a simple regression formula. It follows that significant softening takes place within the HAZ during welding of this specific aluminum alloy. The inclination to recrystallization during welding is even more clearly revealed in Fig. 6, which displays contours of constant fraction recrystallized X_{rex} in q_0/vd (alternatively $\Delta t_{3/2}$) and T_p space. Based on this diagram, it can be concluded that recrystallization of the high-peak-temperature regions of the HAZ cannot readily be avoided but will occur even at very low values of q_0/vd representative of laser and electron beam welding.

Grain Growth

A general problem associated with welding of metals and alloys is the instability of the matrix grain structure following coarsening or dissolution of the pinning grain-boundary precipitates (Ref 1). Depending on the circumstances, this may lead to either normal or

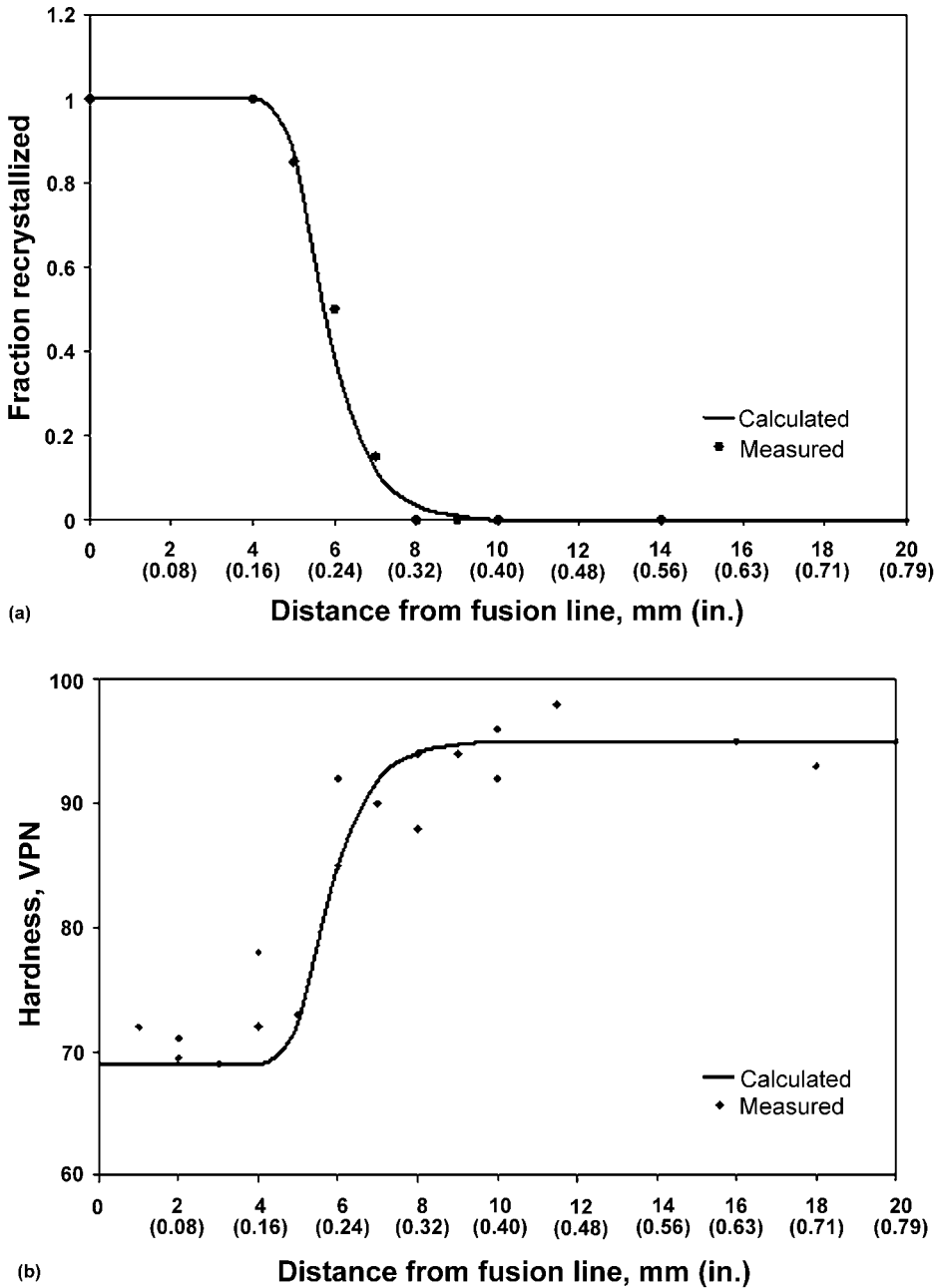


Fig. 5 Comparison between measured and predicted recrystallization behavior following welding of preformed AA5086-H24. (a) Fraction of recrystallized grains vs. distance from fusion line. (b) Hardness vs. distance from fusion line. Adapted from experimental data from Ref 28

abnormal grain growth. Normal grain growth is a thermally activated process driven by the reduction in the grain-boundary surface energy. Physically, it occurs by growth of the larger grains at the expense of the smaller ones, which tend to shrink.

Grain Growth Kinetics. A common observation in metals and alloys is that the size distributions of grain aggregates during normal growth become equivalent when the measured grain size parameter, g , is normalized (scaled)

by the time-dependent average of this metric, \bar{g} . This means that grain structures are completely characterized, in a statistical sense, by simple probability functions of the standard deviation of the distribution together with the time dependence of the average-sized scale, \bar{g} .

In its simplest form, the fundamental rate law describing the change in \bar{g} with time and temperature under various grain-boundary pinning conditions can be written as (Ref 29):

$$\frac{d\bar{g}}{dt} = M_0^* \exp\left(-\frac{Q_{app}}{RT}\right) \left[\frac{1}{\bar{g}} - \frac{1}{\bar{g}_{lim}}\right]^{(1/n)-1} \quad (\text{Eq 34})$$

where n is the time exponent for grain growth (≤ 0.5), M_0^* is a mobility term (with the dimension $m^{1/n}/s$), Q_{app} is the apparent activation energy for grain growth, and \bar{g}_{lim} is the limiting grain size, which, according to Hellman and Hillert (Ref 30), is given as:

$$\bar{g}_{lim} = \frac{8r}{9f} \quad (\text{Eq 35})$$

The form of Eq 34 shows that the rate of grain growth depends on the current value of the three primary state variables, \bar{g} , T , and \bar{g}_{lim} , where the latter is a group parameter that incorporates two other variables (i.e., the particle radius, r , and the volume fraction, f).

Dimensionless Evolution Equation. Equation 34 can be written in a dimensionless form by introducing the scaled state variables $X = \bar{g}/\bar{g}_0$ and $Y = \bar{g}_{lim}/\bar{g}_0$, where \bar{g}_0 is equal to the initial grain size of the material at time $t = 0$. After substitution and some manipulation, the following equation is obtained (Ref 1):

$$\frac{dX}{dt} = \frac{1}{t_5^*} \left[\frac{1}{X} - \frac{1}{Y}\right]^{(1/n)-1} \quad (\text{Eq 36})$$

where t_5^* is the time constant for the reaction, defined as:

$$t_5^* = t_{r5} \exp\left(\frac{Q_{app}}{RT}\right) \quad (\text{Eq 37})$$

taking $t_5^* = \bar{g}_0^{1/n}/M_0^*$.

Based on Eq 36, a number of special solutions can be derived that apply to normal grain growth under various grain-boundary pinning conditions. Some of these are presented as follows.

Grain Growth in the Absence of Pinning Precipitates. In the absence of grain-boundary pinning precipitates, $f = 0$, $\bar{g}_{lim} \rightarrow \infty$, and $1/Y = 0$. Under such conditions, Eq 36 becomes a first-order separable differential equation, which can be integrated as follows (Ref 1):

$$X = \left[1 + \frac{1}{n} \int_0^t \frac{dt}{t_5^*}\right]^n \quad (\text{Eq 38})$$

This solution again contains the Scheil integral, which shows that the governing evolution equation is isokinetic in the general sense defined by Christian (Ref 3).

Grain Growth in the Presence of Stable Precipitates. If grain growth occurs in the presence of stable precipitates (e.g., oxide inclusions in steel weld metals) (Ref 20), the state variable representing the limiting grain size becomes constant and independent of temperature (i.e., $Y = Y^*$). In the limiting case where $n = 0.5$, Eq 36 yields the following closed isokinetic solution:

$$-XY^* - (Y^*)^2 \ln\left(1 - \frac{X}{Y^*}\right) + Y^* + (Y^*)^2 \ln\left(1 - \frac{1}{Y^*}\right) = \int_0^t \frac{dt}{t_5^*} \quad (\text{Eq 39})$$

from which the mean grain size can readily be obtained. In other cases ($n < 0.5$), numerical integration methods must be employed to evaluate X .

It follows from Eq 39 that the grain-growth inhibiting effect of the precipitates is very small during the initial stage of the growth process in situations where $\bar{g}_0 \ll \bar{g}_{lim}$, corresponding to $X \ll Y^*$. Under such conditions, the grains will coarsen at a rate comparable with that observed for free grain growth, as described by Eq 38. The grain-coarsening process gradually retards as the matrix grain size increases, until it comes to a complete stop when X approaches Y^* .

Grain Growth in the Presence of Growing Precipitates. If grain growth occurs in the presence of growing precipitates, \bar{g}_{lim} will no longer be constant but will evolve with time. In the limiting case of pure particle coarsening, an approximate isokinetic solution for Y can be found by substituting Eq 19 into Eq 35. Taking Y^0 equal to the value of Y at time $t = 0$:

$$Y = \left[(Y^0)^3 + \int_0^t \frac{dt}{t_6^*} \right]^{1/3} \quad (\text{Eq 40})$$

where

$$t_6^* = t_{r6} \frac{T}{T_r} \exp\left(\frac{Q_d}{RT}\right) \quad (\text{Eq 41})$$

and

$$t_{r6} = \frac{9^3 f^3 (\bar{g}_0)^3 T_r}{8^3 c_2} \quad (\text{Eq 42})$$

Under nonisothermal conditions, Eq 36 and 40 must be solved in a fully coupled manner to obtain the actual grain size, using inputs from a separate heat flow model. However, the situation becomes much simpler if heat treatment is instead carried out isothermally, due to the fact that the time constants t_5^* and t_6^* then only differ from each other by a constant factor, $m = t_5^*/t_6^*$ (Ref 20, 31). It follows that the extent of grain growth depends on the initial value of m . If m is large, the grain-boundary precipitates will completely outgrow the matrix grains, leading to a grain-coarsening behavior quite similar to the one observed during free grain growth. Conversely, at small m values, the drag exerted by the particles becomes appreciably larger, which ultimately brings about a complete stop in the grain-growth process when X approaches Y . This type of response is characteristic of a system containing stable precipitates, as defined by Eq 39.

Grain Growth in the Presence of Dissolving Precipitates. An analogous situation exists if

the grain-boundary precipitates dissolve during heat treatment. Under such conditions, the scaled limiting grain size increases from its initial value $Y = Y^0$ at $t = 0$ toward infinity, as shown in Ref 20 and 31:

$$Y = \frac{(Y^0)^3}{(Y^0)^2 - \int_0^t \frac{dt}{t_7^*}} \quad (\text{Eq 43})$$

where t_7^* is the time constant for the reaction, which, according to Eq 17, may be written as:

$$t_7^* = \left(\frac{9\bar{g}_0}{8f}\right)^2 \frac{1}{kD} \quad (\text{Eq 44})$$

In the isothermal case, the ratio between the time constants t_5^* and t_7^* becomes constant and equal to m^* . From this it can be seen that the stability of the second-phase particles is sensitive to variations in the proportionality constant, m^* . Normally, the precipitates will exert a drag on the grain boundaries as long as they are present in the metal matrix. However, when the dissolution process is completed, the matrix grains are free to grow without any interference from precipitates. This means that the grains, after prolonged heat treatment, will coarsen at a rate that is comparable with free grain growth. Conversely, if the dissolution process is more sluggish (conforming to small m^* values), the grain-growth behavior becomes similar to that predicted from Eq 39, which applies to a system containing stable precipitates.

Grain Growth in Welding of Structural Steels. Welding diagrams similar to the one

shown in Fig. 6 for recrystallization are also very useful for grain growth, because they summarize the effect of the important process variables on the austenite grain evolution in a quantitative manner. At the same time, they provide a good overall indication of the grain-growth behavior of various grades of steel during welding. The welding diagrams presented in the following sections are constructed on the basis of the nonisothermal grain-growth models described previously in combination with analytical heat flow models (Ref 20).

Titanium-microalloyed steels are widely used in welded structures. From a thermodynamic standpoint, additions of small amounts of titanium to steel would be expected to impede austenite grain coarsening during welding by virtue of its ability to form stable nitrides even at high temperatures.

The response of titanium-microalloyed steels to the temperature history in the limiting case of thick-plate welding is shown in Fig. 7. This diagram reveals that the presence of finely dispersed TiN particles in the base material will retard austenite grain growth within certain regions of the HAZ during welding. However, because particle coarsening is a physical phenomenon occurring at temperatures well below the equilibrium solvus of the precipitates, the problem cannot be eliminated. This means that a coarse-grained region will always form adjacent to the fusion boundary, even at very low heat inputs, as indicated by the nomograms in Fig. 7.

Niobium-Microalloyed Steels. This class of steel is used for a variety of applications,

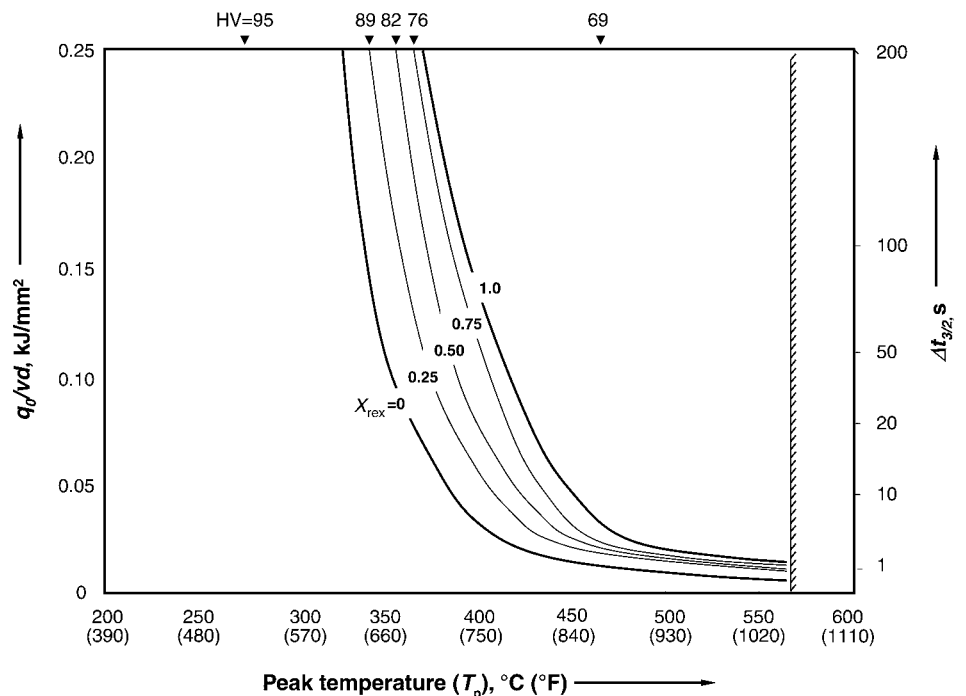


Fig. 6 Computed heat-affected zone recrystallization diagram for thin-plate welding of predeformed AA5086-H24 showing contours of X_{rex} for various combinations of q_d/v_d and T_p

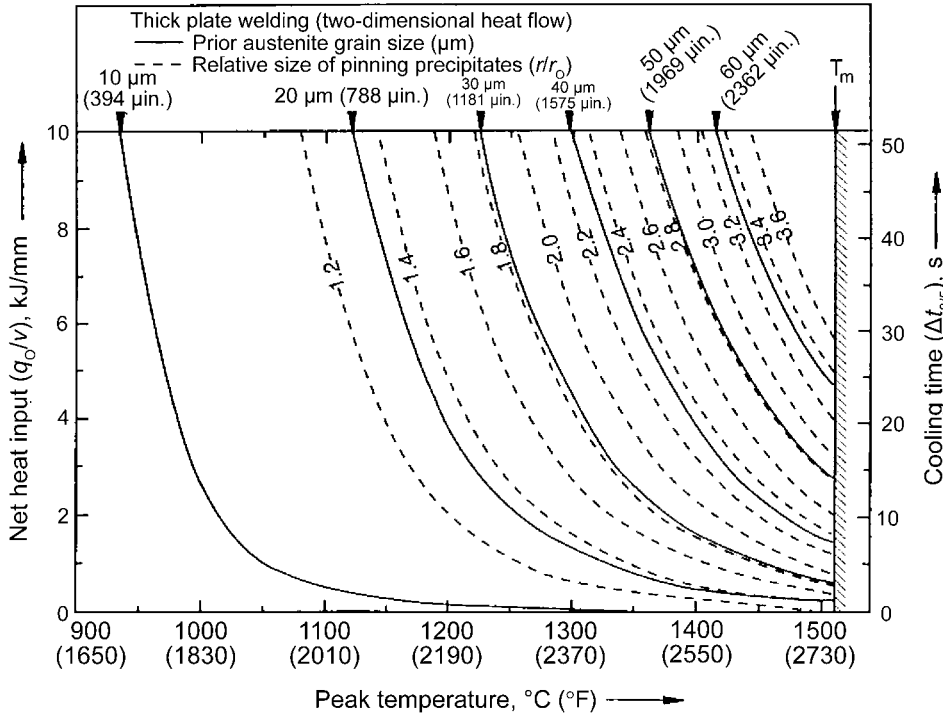


Fig. 7 Computed heat-affected zone grain-growth diagram for thick-plate welding of a titanium-microalloyed steel. Source: Ref 1, 20

including shipbuilding, pressure vessels, oil platforms, and bridges. The steels contain small amounts of microalloying elements, such as niobium, vanadium, and aluminum, which, during thermomechanical processing, combine with carbon and nitrogen to form fine dispersions of grain-boundary pinning precipitates. They are readily weldable but suffer from severe HAZ grain coarsening due to dissolution of the carbonitrides at elevated temperatures (Ref 20, 21, 32).

It is evident from the nomograms in Fig. 8 that considerable austenite grain coarsening occurs during welding of niobium-microalloyed steels because of dissolution of the grain-boundary pinning precipitates. On average, the HAZ austenite grain size adjacent to the fusion boundary is four to six times larger than that observed for titanium-microalloyed steels, as shown previously in Fig. 7. This gives rise to a high HAZ hardenability, which facilitates formation of low-temperature transformation products such as martensite and bainite during cooling (Ref 20).

Coupled Reactions in Duplex Stainless Steel Weldments

In duplex stainless steel weldments, the microstructure evolution occurs in a coupled manner. In the model by Hemmer and Grong (Ref 33), this is handled mathematically by assuming that the reactions occur in series

(i.e., succession) rather than in parallel, which allows a one-way exchange of inputs and outputs between the various submodels.

Problem Description. Referring to Fig. 9, the important reactions that must be modeled are the dissolution of austenite during heating, subsequent grain growth in the delta-ferrite regime, and finally, the decomposition of delta ferrite to austenite during cooling.

Due to the complexity of the rate phenomena involved, a differential formulation of the underlying diffusion problems is required, based on the internal state variable approach. However, a significant reduction in the programming and computational effort can be achieved if the solutions are rewritten in a closed (isokinetic) form, as described previously in the section “Definition of an Isokinetic Reaction” in this article. In the present treatment, the temperature dependence of the reactions is captured mathematically in terms of the Scheil integral (i.e., Eq 6), which represents the kinetic strength of a given thermal cycle with respect to microstructure evolution. In a calibrated form, these solutions yield results that are within 10% of the values calculated from the corresponding differential evolution equations. Further details are given in Ref 33.

Dissolution of Austenite. As shown in Fig. 9, dissolution of austenite occurs during the initial heating leg of the thermal cycle and is well described by the following equation (Ref 33):

$$\frac{f}{f_0} = 1 - \left[\int_{t=0}^{t_1} \frac{dt}{t_{8d}^*} \right]^{1/2} \tag{Eq 45}$$

where f and f_0 are the current and the initial volume fraction of austenite in the material, respectively, while t_{8d}^* is the time constant for the reaction, defined as:

$$t_{8d}^* = t_{r8d} \left(\frac{C_{\delta,i}^r - C_{\delta}^r}{C_{\delta,i}^r - C_{\delta}^r} \right)^2 \frac{(C_{\gamma} - C_{\delta,i})(C_{\gamma} - C_{\delta,i})}{(C_{\gamma}^r - C_{\delta,i}^r)(C_{\gamma}^r - C_{\delta,i}^r)} \left(\frac{x_{\gamma}}{x_{\gamma}^r} \right)^2 \exp \left[\frac{Q_d}{R} \left(\frac{1}{T} - \frac{1}{T_{r1d}} \right) \right] \tag{Eq 46}$$

In a real welding situation, full dissolution of the austenite phase will occur within the high-peak-temperature region of the HAZ. This requires a separate treatment of the austenite formation on subsequent cooling. Conversely, within the partly reverted region, back diffusion of nitrogen leads to renewed growth of the parent austenite phase during cooling, which tends to reverse the previous dissolution process and restore the original phase balance. Still, this is a very delicate problem to handle mathematically, because a differential formulation of the nitrogen flux balance is required. However, as shown in Ref 33, a simple isokinetic solution can be found if the phase transformation is split into two different subreactions:

$$\frac{f}{f_0} = 1 - \left[\int_{t=0}^{t_1} \frac{dt}{t_{8d}^*} \right]^{1/2} + \left[\int_{t_1}^{t_2} \frac{dt}{t_{8g}^*} \right]^{1/2} \tag{Eq 47}$$

taking

$$t_{8g}^* = t_{r8g} \left(\frac{C_m^r - C_{\delta,i}^r}{C_m^r - C_{\delta,i}^r} \right)^2 \frac{(C_{\gamma} - C_m)(C_{\gamma,i} - C_{\delta,i})}{(C_{\gamma}^r - C_m^r)(C_{\gamma,i}^r - C_{\delta,i}^r)} \left(\frac{x_{\gamma}}{x_{\gamma}^r} \right)^2 \exp \left[\frac{Q_d}{R} \left(\frac{1}{T} - \frac{1}{T_{r1g}} \right) \right] \tag{Eq 48}$$

The first term on the right side of Eq 47 represents the contribution from the initial dissolution that occurs during heating, while the latter term includes the subsequent growth of the parent austenite phase on cooling. Note that the integration limit, t_1 , refers to the time at which the interface concentration, $C_{\delta,i}$, drops below the matrix concentration, C_m , during cooling. This defines the onset of the transient growth period.

Delta-Ferrite Grain Growth. In general, growth of the delta-ferrite grains will occur both during and after the decomposition of the austenite phase. In the former case, the extent of grain growth is determined by the rate of austenite dissolution and is well described by the following equation (Ref 33):

$$\bar{g}_{\delta} = 2 \left[\frac{x_{\gamma}}{f_0} - x_i \right] \tag{Eq 49}$$

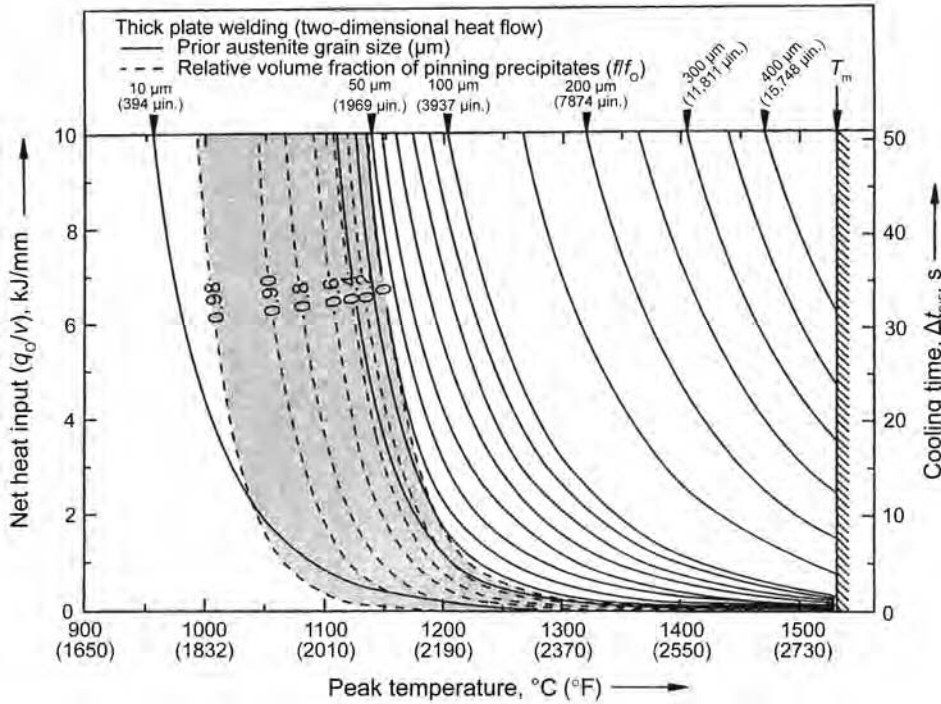


Fig. 8 Computed heat-affected zone grain-growth diagram for thick-plate welding of a niobium-microalloyed steel. Source: Ref 1, 20

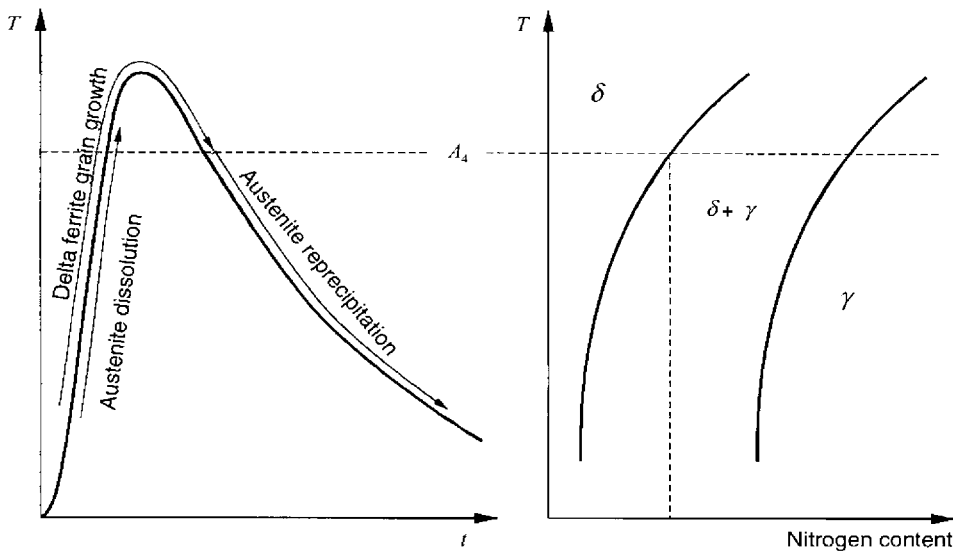


Fig. 9 Schematic representation of the heat-affected zone microstructure evolution during welding of duplex stainless steels. Source: Ref 1, 33

where x_i and x_γ are the current and initial half-thickness of the austenite plates, respectively, while \bar{g}_δ is the mean delta-ferrite grain size.

Normal grain growth takes place within the fully reverted region of the weld HAZ and is conveniently described by an isokinetic solution of the form (Ref 33):

$$Z = \frac{(\bar{g}_\delta)^{1/n} - (\bar{g}_{\delta,0})^{1/n}}{(\bar{g}_{\delta,0})^{1/n}} = Z_r \int_{t_1}^{t_2} \frac{dt}{t_0^*} \quad (\text{Eq 50})$$

where n is the time exponent for grain growth, Z_r is the value of Z at the chosen reference time $t = t_{r9}$ and temperature $T = T_{r2}$, and t_0^* is the time constant for the reaction defined as:

$$t_0^* = t_{r9} \exp \left[\frac{Q_{app}}{R} \left(\frac{1}{T} - \frac{1}{T_{r2}} \right) \right] \quad (\text{Eq 51})$$

The resulting delta-ferrite grain size can then be found by solving Eq 50 with respect to \bar{g}_δ :

$$\bar{g}_\delta = \left[\bar{g}_{\delta,0}^{1/n} (1 + Z) \right]^n \quad (\text{Eq 52})$$

where $\bar{g}_{\delta,0}$ is the initial delta-ferrite grain size following complete dissolution of the austenite phase (equal to $2x_\gamma/f_0$).

Delta-Ferrite Decomposition. During the cooling leg of the thermal cycle, delta ferrite starts to decompose to austenite below the A_4 temperature, as shown in Fig. 9. As a starting point, the delta-ferrite grains are assumed to be spherical (with a radius $r = r_\delta$). Under such conditions, the austenite phase will start to grow from the outside of the sphere and toward the center. If the cooling rate is sufficiently high that soft impingement due to nitrogen depletion can be neglected (as in electron beam welding), the thickness $r_\delta - r_i$ of the austenite layer is given by the following three-dimensional isokinetic solution (Ref 33):

$$s_i = \sqrt{\frac{1}{3} r_i^2 + \frac{2}{3} r_\delta^2} - r_\delta = s_i^r \left(\int_{t_1}^{t_2} \frac{dt}{t_0^*} \right)^{1/2} \quad (\text{Eq 53})$$

where s_i^r is the value of s_i at the chosen reference time $t = t_{r10}$ and temperature $T = T_{r3}$, and t_0^* is the time constant for the reaction defined as:

$$t_0^* = t_{r10} \left(\frac{C_0^r - C_{\delta,i}^r}{C_0 - C_{\delta,i}} \right)^2 \frac{(C_{\gamma,i} - C_{\delta,i}) (\bar{C}_\gamma - C_0)}{(C_{\gamma,i}^r - C_{\delta,i}^r) (\bar{C}_\gamma^r - C_0^r)} \exp \left[\frac{Q_d}{R} \left(\frac{1}{T} - \frac{1}{T_{r3}} \right) \right] \quad (\text{Eq 54})$$

To quantify the extent of delta-ferrite decomposition occurring during welding, it is necessary to convert the current value of r_i into an equivalent volume fraction of austenite. For the spherical grain morphology assumed in the model, the volume fraction of austenite is simply given by Ref 33:

$$f = \frac{\frac{4}{3} \pi r_\delta^3 - \frac{4}{3} \pi r_i^3}{\frac{4}{3} \pi r_\delta^3} = \frac{r_\delta^3 - r_i^3}{r_\delta^3} \quad (\text{Eq 55})$$

Case Study: Application to Electron Beam Welding. The direct coupling between the various microstructure models is illustrated in Fig. 10, which shows the calculated microstructure evolution in two different positions within the HAZ. Considering the fully reverted region (Fig. 10a), the austenite dissolves completely during the heating leg of the thermal cycle. This process is succeeded by free delta-ferrite grain growth and partial decomposition of the delta ferrite to austenite during cooling below the A_4 temperature. In the partly reverted region of the HAZ (Fig. 10b), the austenite dissolution

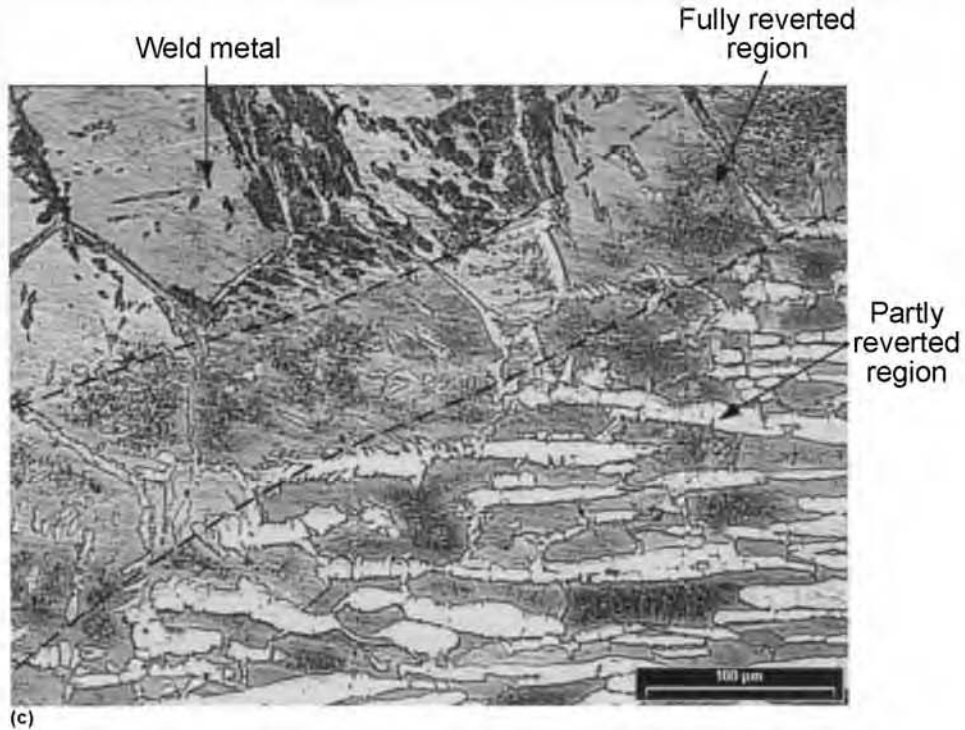
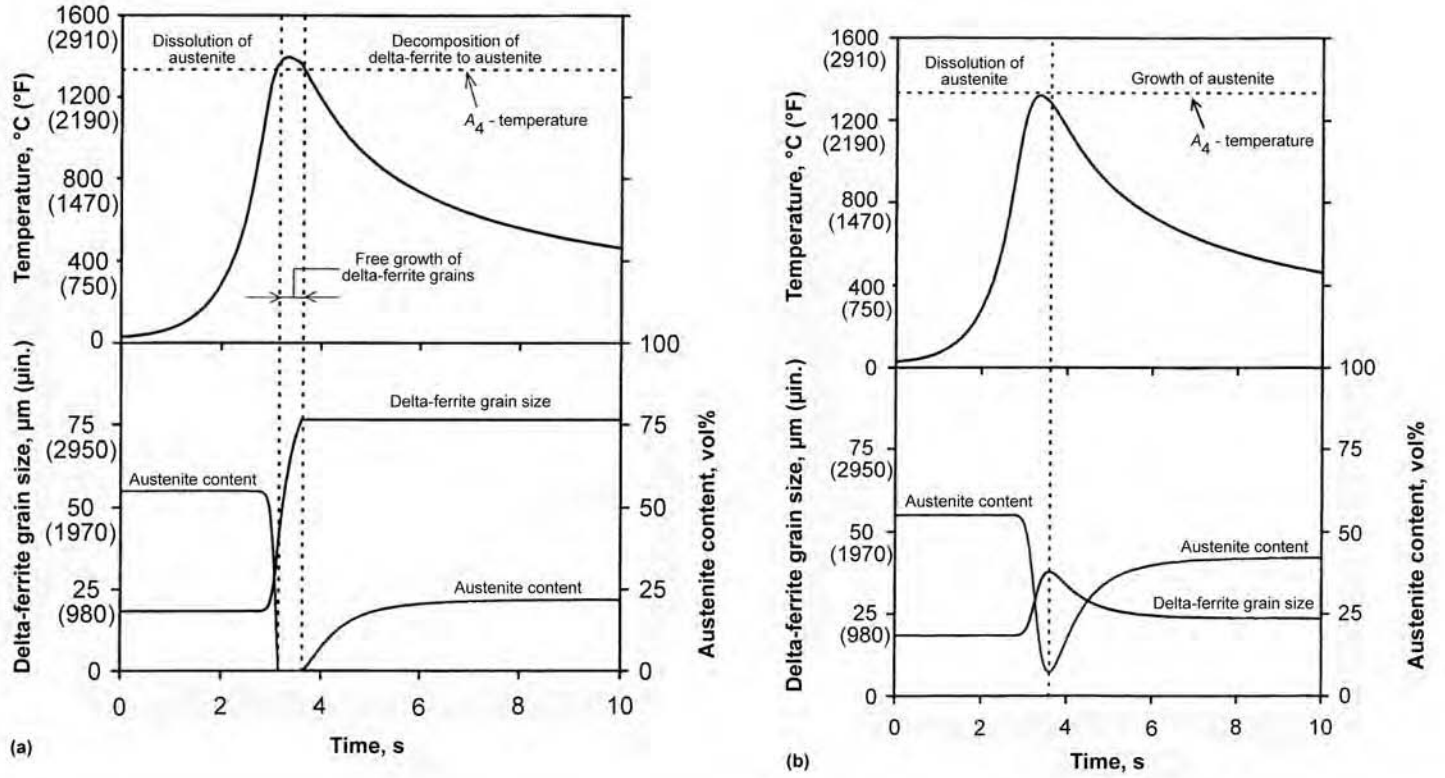


Fig. 10 Examples of outputs from the process model for duplex stainless steels showing details of the microstructure evolution at various locations within the weld heat-affected zone (HAZ). (a) Fully reverted region. (b) Partly reverted region. (c) Optical micrograph showing the sharp boundary between the fully and partly reverted regions of the weld HAZ. Source: Ref 1, 33

is incomplete, and hence, extensive growth of the austenite occurs on cooling due to back diffusion. This retransformation explains why the boundary between the two regions during electron beam welding is quite sharp with no indication of the previous austenite dissolution, as illustrated by the optical micrograph in Fig. 10(c).

Summary of Isokinetic Solutions

In the previous sections, the versatility of the internal state variable approach in modeling of nonisothermal transformations for various materials and processes has been demonstrated. In cases where the reaction is isokinetic and the temperature dependency can be captured mathematically in terms of the Scheil integral (i.e., Eq 6), simple analytical solutions exist that are quick and easy to implement and are accessible to most users. Table 1 summarizes the various analytical solutions presented in the previous sections, showing that a wide range of processes can be described by the same type of equation based on the Scheil integral formulation.

Complex Microstructure Models Describing the Evolution of a Particle Size Distribution

So far, only reactions that involve a single diffusion mechanism (e.g., dissolution or coarsening of precipitates) have been considered. Although these represent idealized cases, the isokinetic models can be applied to a wide range of problems that are relevant to thermal processing of metals and alloys. However, they fail when the diffusion problem is more complicated and requires a full description of the particle size distribution as well. For example, this is the case during industrial heat treatment and welding of age-hardening aluminum alloys, because the transformation has a strong memory of the past process steps due to interactions between different groups or classes of particles that form at various temperatures (Ref 34). In the following, a numerical solution is presented, capable of handling nucleation, growth, and coarsening, and likewise dissolution, of hardening precipitates in Al-Mg-Si alloys during aging, welding, and postweld heat treatment (PWHT). By coupling this to a separate strength model for shearing and bypassing of particles by dislocations, the evolution of the macroscopic yield stress at room temperature can be calculated at each time step.

Microstructural Changes during Heat Treatment and Welding of Al-Mg-Si Alloys

During artificial aging, a high density of fine, needle-shaped β'' particles form uniformly in

the matrix, as shown in Fig. 11(a), which is the dominating hardening phase in T6 heat treated Al-Mg-Si alloys (Ref 35). However, because these precipitates are thermodynamically unstable in a welding situation, the smallest ones will start to dissolve in parts of the HAZ where the peak temperature has been above, say 250 °C (480 °F), while the larger ones will continue to grow (Ref 36). Close to the weld fusion line, full reversion of the β'' particles is achieved (Ref 20, 35, 37). At the same time, coarse, rod-shaped β' precipitates may form in the intermediate-peak-temperature range between 250 and 480 °C (480 and 900 °F), as indicated in Fig. 11(b). In the model, these refer to the largest particles in the distribution, which will grow rapidly in the presence of the abundant solute being supplied from the small, dissolving β'' precipitates.

If welding is succeeded by a PWHT reprecipitation of hardening, β'' particles will take place within the high-peak-temperature regions of the weld HAZ, as shown in Fig. 11(c). The extent to which this occurs depends on both the matrix vacancy concentration and the level of magnesium and silicon in solid solution, according to classic nucleation theory (Ref 20). Accordingly, the reprecipitation would be expected to be most extensive in the fully reverted region close to the weld fusion line, owing to the combined effect of a high solute content and a high concentration of quenched-in vacancies. Conversely, the renewed β'' formation will be suppressed in parts of the HAZ where the peak temperature is lower, because the aluminum matrix in these regions will be depleted with respect to vacancies and solute. This eventually leads to the development of a permanent soft region within the weld HAZ after PWHT, in agreement with experimental observations (Ref 38, 39).

If this simplified description of the microstructure evolution is accepted, it is possible to simulate the sequence of precipitation and reversion reactions occurring during artificial aging, welding, and PWHT of age-hardening Al-Mg-Si alloys, along the lines indicated by Myhr and Grong (Ref 34). A brief description of the basic features of the model is given as follows.

Precipitation Model

The precipitation model consists of the following three components:

- A nucleation model, which predicts the number of stable nuclei that form at each time step
- A rate law, which calculates either the dissolution or growth rate of each discrete particle size class
- A continuity equation, which keeps record of the amount of solute being tied up in the precipitates

A brief summary of the main constitutive equations is given subsequently. Further details are given in Ref 34, 38, and 39.

Nucleation Law. Following classic nucleation theory, the nuclei form as a result of localized compositional fluctuations that occur statistically within the supersaturated matrix. The nucleation rate, j , during artificial aging and welding is conveniently expressed as follows when the effect of quenched-in vacancies on the nucleation rate is included in the expression (Ref 39):

$$j = j_0 \exp \left[\frac{-\Delta H_v}{R} \left(\frac{1}{T_p} - \frac{1}{T_{ss}} \right) \right] \exp \left[- \left(\frac{A_0}{RT} \right)^3 \left(\frac{1}{\ln(\bar{C}/C_e)} \right)^2 \right] \exp \left(- \frac{Q_d}{RT} \right) \quad (\text{Eq 56})$$

where j_0 is a pre-exponential term, A_0 is a parameter related to the potency of the heterogeneous nucleation sites in the parent material (with the units J/mol), Q_d is the activation energy for diffusion, \bar{C} is the mean solute content in the matrix, C_e is the equilibrium solute content in the matrix (given by the phase diagram), ΔH_v is the enthalpy of vacancy formation in aluminum, and T_{ss} is the solutionizing temperature, which corresponds to the chosen input value of j_0 (i.e., 530 °C, or 985 °F). In practice, j_0 and A_0 must be determined experimentally for a specific family of alloys within the Al-Mg-Si system (Ref 35, 36), while Q_d and ΔH_v can be obtained from literature data (Ref 35).

The simple form of Eq 56 makes it easy to implement in a numerical code. At the same time, the nucleation law is sufficiently relevant and comprehensive to facilitate modeling of coupled welding and PWHT operations, as described previously, because the vacancy concentration established in the former operation is embedded in the expression via the T_p term, representing the peak temperature of a specific HAZ position. Although this analytical formulation of the nucleation problem means that a consideration of diffusion and annihilation of vacancies at grain boundaries and incoherent particle/matrix interfaces during subsequent cooling/reheating is neglected, it is thought to be a reasonable approximation in the context of the model being developed.

Rate Law. The next step is to invoke the growth model. When a particle with radius r and solute concentration C_p is introduced into the system, it will either dissolve or grow, depending on whether the solute concentration in the matrix at the particle/matrix interface, C_i , exceeds \bar{C} or not. The rate at which this occurs can be expressed as (Ref 40):

$$v = \frac{dr}{dt} = \frac{\bar{C} - C_i}{C_p - C_i} \frac{D}{r} \quad (\text{Eq 57})$$

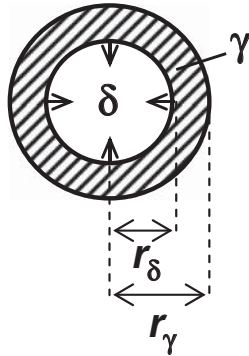
Table 1 Summary of various isokinetic solutions containing the Scheil integral

Material	Process	Solution	Expression for t^* , s	Source
Aluminum/steel	Particle dissolution	Plates	Eq 11	Ref 1, 20
		Spheres	Eq 16	
Aluminum/steel	Coarsening		Eq 23	Ref 1, 20
Aluminum	Recrystallization		Eq 31	...
Steel	Grain growth (no pinning precipitates)		Eq 37	Ref 1
Steel	Grain growth in the presence of stable precipitates		Eq 37	Ref 1
Steel	Grain growth in the presence of growing precipitates		Eq 37, 41	Ref 1
Steel	Grain growth in the presence of dissolving precipitates		Eq 37, 44	Ref 1, 31
Duplex stainless steel	Dissolution and growth of austenite		Eq 46, 48	Ref 1, 33

(continued)

Table 1 (continued)

Material	Process	Solution	Expression for r^* , s	Source
Duplex stainless steel	Delta-ferrite decomposition	$s_i = \sqrt{\frac{1}{3}r_i^2 + \frac{2}{3}\frac{r_\delta^3}{r_i} - r_\delta^2} = s_i^r \left(\int_{r_i}^{r_\delta} \frac{dr}{r_{i0}} \right)^{1/2}$ <p>where $s_i = r_\delta - r_i$ and $f = \frac{\frac{4}{3}\pi r_\delta^3 - \frac{4}{3}\pi r_i^3}{\frac{4}{3}\pi r_\delta^3} = \frac{r_\delta^3 - r_i^3}{r_\delta^3}$</p>	Eq 54	Ref 1, 33



Precipitates: -small β^{II} -larger β^{II} -coarse β^I

is divided into a series of small “radius” elements, each with a size Δr . Analogous to the diffusion problem, the growth or dissolution of particles that occurs during a small time increment, Δt , can be regarded as a flux of matter in or out of the elements. Let J denote the particle flux, while N is the number density of particles within Δr . A mass balance then gives (Ref 34, 38):

$$\frac{\partial N}{\partial t} = -\frac{\partial J}{\partial r} + S \tag{Eq 59}$$

where the source term, S , describes the formation of new particles at each time step Δt . In the context of diffusional transformations, S is equal to the nucleation rate, j .

The particle flux, J , through the volume element is, in turn, given by the following equation (Ref 34, 38):

$$J = N v \tag{Eq 60}$$

where v is the growth or dissolution rate of a particle defined by Eq 57.

Hence, the governing evolution equation may be written as (Ref 34, 38):

$$\frac{\partial N}{\partial t} = -\frac{\partial(Nv)}{\partial r} + S \tag{Eq 61}$$

Moreover, if the particle size distribution is continuous, the mean solute concentration in the matrix can be expressed as (Ref 34, 38):

$$\bar{C} = C_0 - (C_p - \bar{C}) \int_0^\infty \frac{4}{3}\pi r^3 \phi dr \tag{Eq 62}$$

where ϕ is the size distribution function.

Note that Eq 62 is simply a mass balance relating the amount of solute tied up in particles to the amount of the solute drained from the matrix.

Numerical Solution. To calculate the values of N at discrete grid points, the particle size

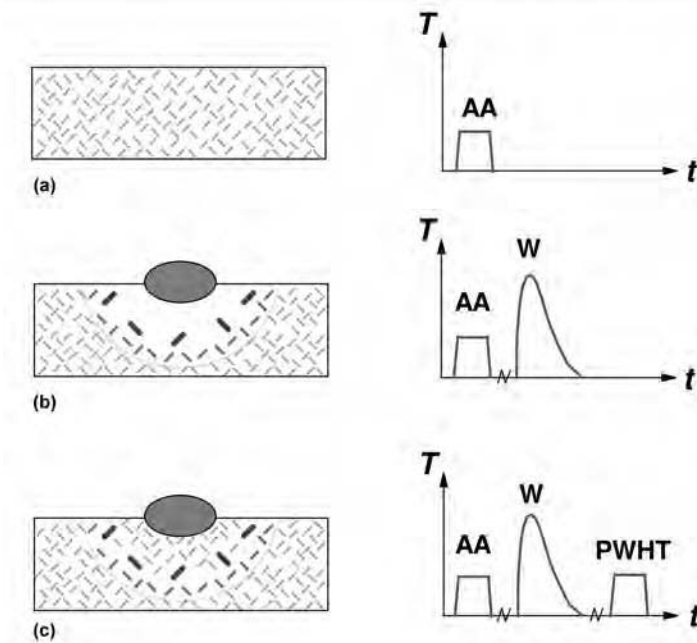


Fig. 11 Schematic diagrams showing the microstructure evolution during multistage thermal processing of Al-Mg-Si alloys involving heat treatment and welding. AA, artificial aging; W, welding; PWHT, postweld heat treatment. The outer boundary of the heat-affected zone is indicated by the semicircles in the diagrams. Adapted from Ref 36, 38

Based on the Gibbs-Thomson equation, it is then possible to obtain an explicit expression for the critical radius, r^* , of a particle that will neither grow nor dissolve (Ref 34, 38):

$$r^* = \frac{2\gamma_i V_m}{RT} \left(\ln \left(\frac{\bar{C}}{C_c} \right) \right)^{-1} \tag{Eq 58}$$

where γ_i is the particle/matrix interfacial energy, and V_m is the molar volume of the precipitates.

Because r^* depends on the current value of C_c , the thermal stability of the precipitates is sensitive to changes in the temperature during heat treatment. It follows that reheating promotes particle dissolution, whereas cooling or isothermal annealing favors nucleation, growth, and coarsening in a successive manner.

Inclusion of the Particle Size Distribution. The control volume approach is used to capture the flux balance for a distribution of particles. As a starting point, the particle distribution

distribution is divided into small intervals $[r_i, r_{i+1}]$. The continuity equation (Eq 62) may then be written as (Ref 34, 38):

$$\bar{C} = C_0 - (C_p - \bar{C}) \sum_i \frac{4}{3} \pi r_i^3 N_i \quad (\text{Eq 63})$$

where $N_i = \phi_i \Delta r_i$. From Eq 63, the particle volume fraction, f , can be calculated, taking $f = (C_0 - \bar{C}) / (C_p - \bar{C})$ as a first approximation.

Consider now a small grid-point configuration that is isolated from the particle size distribution, as shown in Fig. 12. This is delimited by dashed lines at "w" and "e," which represent the west and east boundaries, respectively. To obtain equations for N at discrete grid points, one starts by integrating the governing evolution equation over the control volume. By ignoring the source term S , Eq 61 gives (Ref 34, 38):

$$\int_w^{e} \int_t^{t+\Delta t} \frac{\partial N}{\partial t} dt dr = - \int_w^{e} \int_t^{t+\Delta t} \frac{\partial(Nv)}{\partial r} dr dt \quad (\text{Eq 64})$$

The integral on the left side of Eq 64 is equal to (Ref 34, 38):

$$\int_w^{e} \int_t^{t+\Delta t} \frac{\partial N}{\partial t} dt dr = (N_p - N_p^0) \Delta r \quad (\text{Eq 65})$$

while the right-side integral is given by (Ref 34, 38):

$$\int_w^{e} \int_t^{t+\Delta t} \frac{\partial(Nv)}{\partial r} dr dt = ((Nv)_e - (Nv)_w) \Delta t \quad (\text{Eq 66})$$

The velocities v_e and v_w at each control volume interface can be calculated from Eq 57. By combining Eq 64 to 66, the equations for discrete grid points can be cast into the following standard form (Ref 34, 38):

$$a_p N_p = a_E N_E + a_W N_W + a_p^0 N_p^0 \quad (\text{Eq 67})$$

The values of the coefficients a_p , a_E , a_W , and a_p^0 depend on the directions of the interface

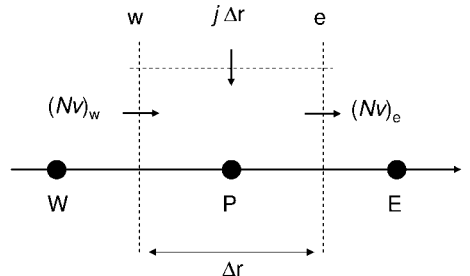


Fig. 12 Grid-point configuration used in the finite-difference model showing particle fluxes entering and leaving a control volume. Adapted from Ref 34, 38

velocities, as described in Ref 34. Finally, the desired number densities are obtained by solving the set of mutually dependent equations of the form defined by Eq 67, using a standard Gaussian elimination method (Ref 34, 41).

Microstructure Evolution during Multistage Thermal Processing

In the following, the process model described in the previous section is applied to predict the microstructure evolution in Al-Mg-Si alloys during multistage thermal processing involving heat treatment and welding.

Evolution of Precipitate Structure during Artificial Aging. Referring to Fig. 11(a), the first process stage to model is artificial aging. Figure 13 shows examples of outputs from the model following prolonged artificial aging at 180 °C (355 °F) for an Al-Mg-Si alloy with a nominal composition close to AA6082 (i.e., approximately 0.9 wt% Si and 0.6 wt% Mg). Because the incubation period during nucleation is disregarded, the nucleation rate is seen to be fairly constant over an appreciable period of time, as illustrated in Fig. 13(a). The nucleation rate then drops quickly due to solute depletion, as \bar{C} approaches C_e . This coincides, in time, with the observed peak in the particle number density. Moreover, a comparison with Fig. 13(b) shows that the nucleation period is accompanied by rapid growth of the particles during the early stages of the aging process, which gradually shifts to pure coarsening when r^* approaches \bar{r} . At the entry of the coarsening period, the characteristic Lifshitz-Slyozov-Wagner (LSW) distribution is obtained (Ref 18, 19), as shown by the plots in Fig. 13(c).

Precipitate Structure in the HAZ Following Artificial Aging, Welding, and PWHT. As schematically illustrated in Fig. 11(b) and (c), the precipitate structure formed during artificial aging changes significantly during the subsequent welding and PWHT operations. These changes are readily captured by the model, as shown in Fig. 14, where predicted microstructure quantities are compared with corresponding quantities obtained from measurements carried out on Gleeble simulated weld HAZs of AA6005. Figures 14(a) and (b) show how the particle number density and mean particle size, respectively, vary with distance from the centerline. Because the distance from the centerline is directly related to the peak temperature, the corresponding T_p values are indicated by the upper abscissae in the graphs for comparison. During reheating of the peak-aged material, the smallest particles will be unstable and dissolve, while the largest ones will grow. As seen from the curves presented, the microstructure model adequately captures this behavior. If weld simulation is accompanied by a subsequent PWHT, full reprecipitation of the hardening particles takes place within the high-peak-temperature region

of the specimen, where both the vacancy concentration and the solute level are inherently high.

Figure 15 shows the predicted sequence of reactions occurring during artificial aging, welding, and PWHT for a fixed position in the HAZ where the peak temperature has been 350 °C (660 °F), conforming to the partially reverted region. Figure 15(a) summarizes the thermal history, where the peak temperature within the weld HAZ is seen to reach 350 °C during welding. Figure 15(b) shows the nucleation rate, j , and the corresponding change in the particle number density, N_v , as a function of time. During artificial aging, N_v reaches the peak value after approximately 1.25 h before it starts to level off as the nucleation rate, j , drops and the combined growth and coarsening regime is entered. It follows from Fig. 15(c) that this regime is characterized by a steady increase in the mean particle radius, \bar{r} , with time. At the same time, the particle volume fraction, f , increases, leading to a gradual decrease in the matrix solute content until the equilibrium concentrations of magnesium and silicon are reached after long times at the actual aging temperature.

During subsequent welding, the microstructure within the partly reverted HAZ changes dramatically over a very short period of time. Although the nucleation rate, j , again increases, reheating to $T_p = 350$ °C (660 °F) implies that both N_v and f drop initially as a result of particle dissolution. This change is accompanied by rapid growth of some of the largest particles within the distribution, taking advantage of the abundant solute being supplied from the dissolving precipitates. Thus, when the final PWHT stage is entered, neither the solute content nor the vacancy concentration within the partly reverted HAZ is high enough to promote extensive precipitation of new hardening β'' particles. Instead, the remaining particles will continue to grow, mainly by consumption of excess solute. This is observed by the almost constant value for N_v in Fig. 15(b) along with the monotonic increase in \bar{r} and f in Fig. 15(c), both during welding and subsequent PWHT.

Yield Strength Model

For predictions of the structural integrity of weldments, it is not the precipitate structure, as such, but rather the macroscopic room-temperature yield stress that is of main concern. However, due to the intimate connection between the precipitate structure and the yield stress of age-hardening aluminum alloys, the yield stress can be estimated when the particle size distribution is known (Ref 35). This is done by coupling some key precipitate parameters extracted from the particle size distribution to a separate strength model for shearing and bypassing of particles by dislocations, as shown subsequently. This, in turn, allows the evolution of the macroscopic yield stress at room

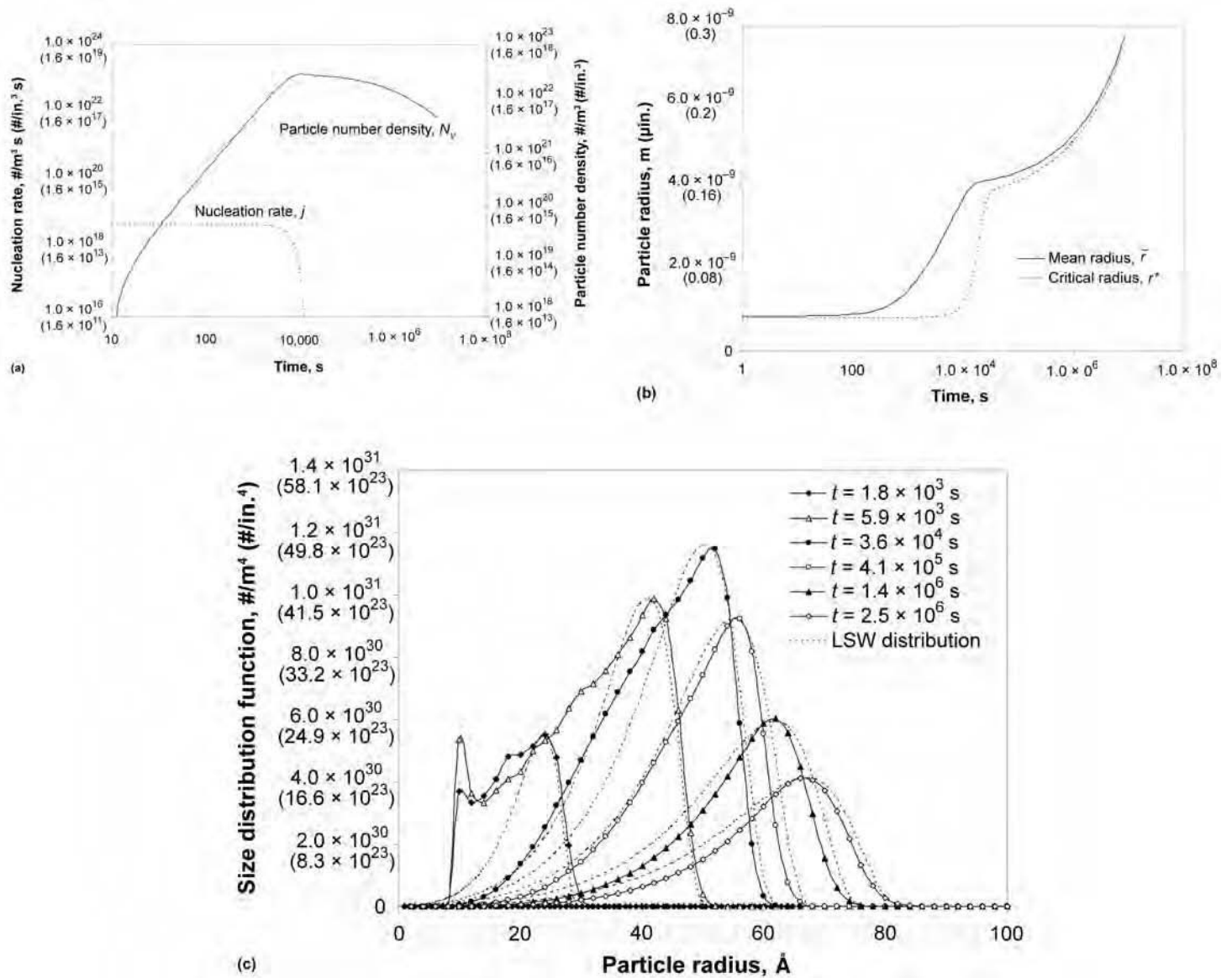


Fig. 13 Examples of outputs from the precipitation model following prolonged artificial aging at 180 °C (355 °F). (a) Change in nucleation rate, j , and particle number density, N_v , with time. (b) Increase in the mean particle radius, \bar{r} , and the critical radius, r^* , with time. (c) Snapshots of the particle size distribution at different aging times. The corresponding Lifshitz-Slyozov-Wagner (LSW) distributions are indicated by the broken curves in the graph for comparison. Source: Ref 34

temperature to be calculated at each time step during heat treatment and welding.

For age-hardening aluminum alloys, the following contributions are of importance: precipitation hardening due to shearing and bypassing of particles by dislocations, σ_p , and solid-solution hardening effects, σ_{ss} (Ref 42–45).

Precipitation Hardening. The relationship between the macroscopic yield strength, σ_p , and the mean obstacle strength, \bar{F} , can be written as (Ref 45):

$$\sigma_p = \frac{M\bar{F}}{bl} \quad (\text{Eq 68})$$

where M is the Taylor factor, b is the magnitude of the Burgers vector, and l is the mean

effective particle spacing in the slip plane along the bending dislocation.

Assuming a monodisperse system of spheres, the effective particle spacing, l , in the slip plane can be expressed in terms of the mean particle size, \bar{r} , the particle volume fraction, f_v , and the mean obstacle strength, \bar{F} , using the Friedel formalism (Ref 46), as done in Ref 45. Substituting this expression for l into Eq 68 gives (Ref 36):

$$\sigma_p = \frac{M}{b^2\sqrt{G}} \sqrt{\frac{N_v\bar{r}}{\beta}} \bar{F}^{3/2} \quad (\text{Eq 69})$$

where G is the shear modulus of the aluminum matrix, and β is a constant close to 0.5.

In the general case, where the alloy contains a mixture of weak (shearable) and strong (non-shearable) particles, the mean obstacle strength is conveniently defined as:

$$\bar{F} = \frac{\sum_i N_i F_i}{\sum_i N_i} \quad (\text{Eq 70})$$

where N_i is the number density of particles that belongs to a given-size class r_i , and F_i is the corresponding obstacle strength.

In practice, the parameter F_i will be a function of the particle radius, r_i . For weak particles, it is a fair approximation to assume that F_i is proportional to the particle radius as long

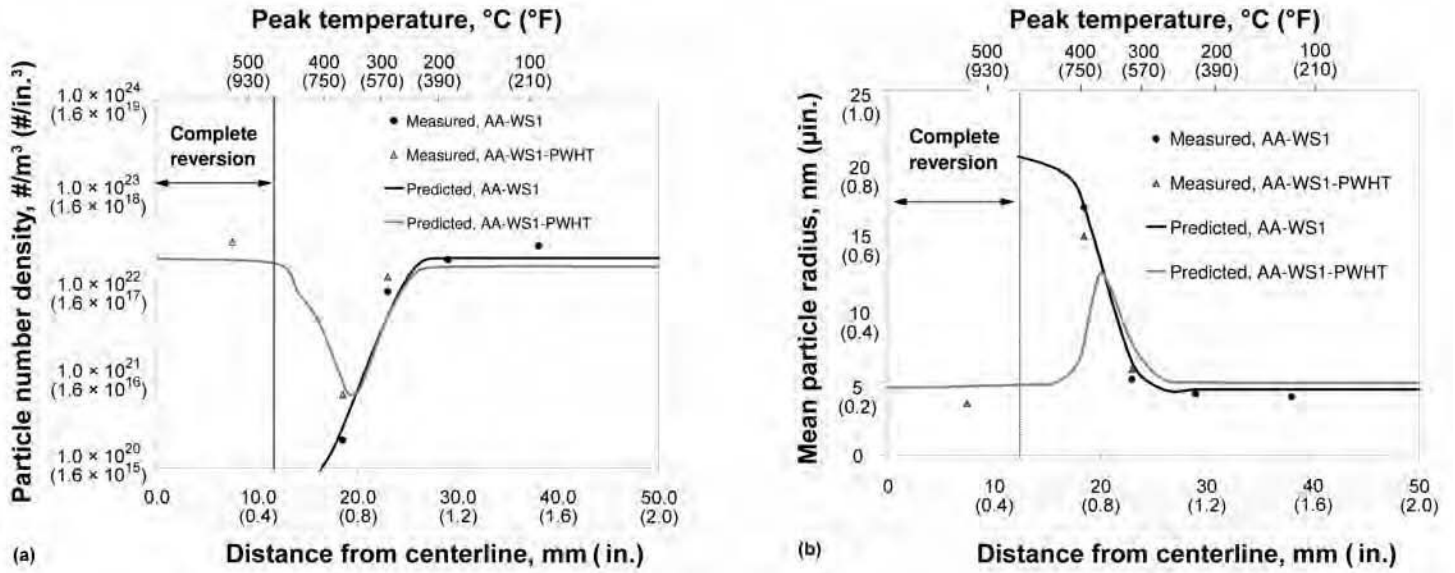


Fig. 14 Comparison between observed and predicted microstructural stability of Gleeble simulated specimens after various thermal treatments. (a) Variation in particle number density, N_v , with distance from centerline of specimen. (b) Variation in mean particle radius, \bar{r} , with distance from centerline of specimen. PWHT, postweld heat treatment. Source: Ref 36

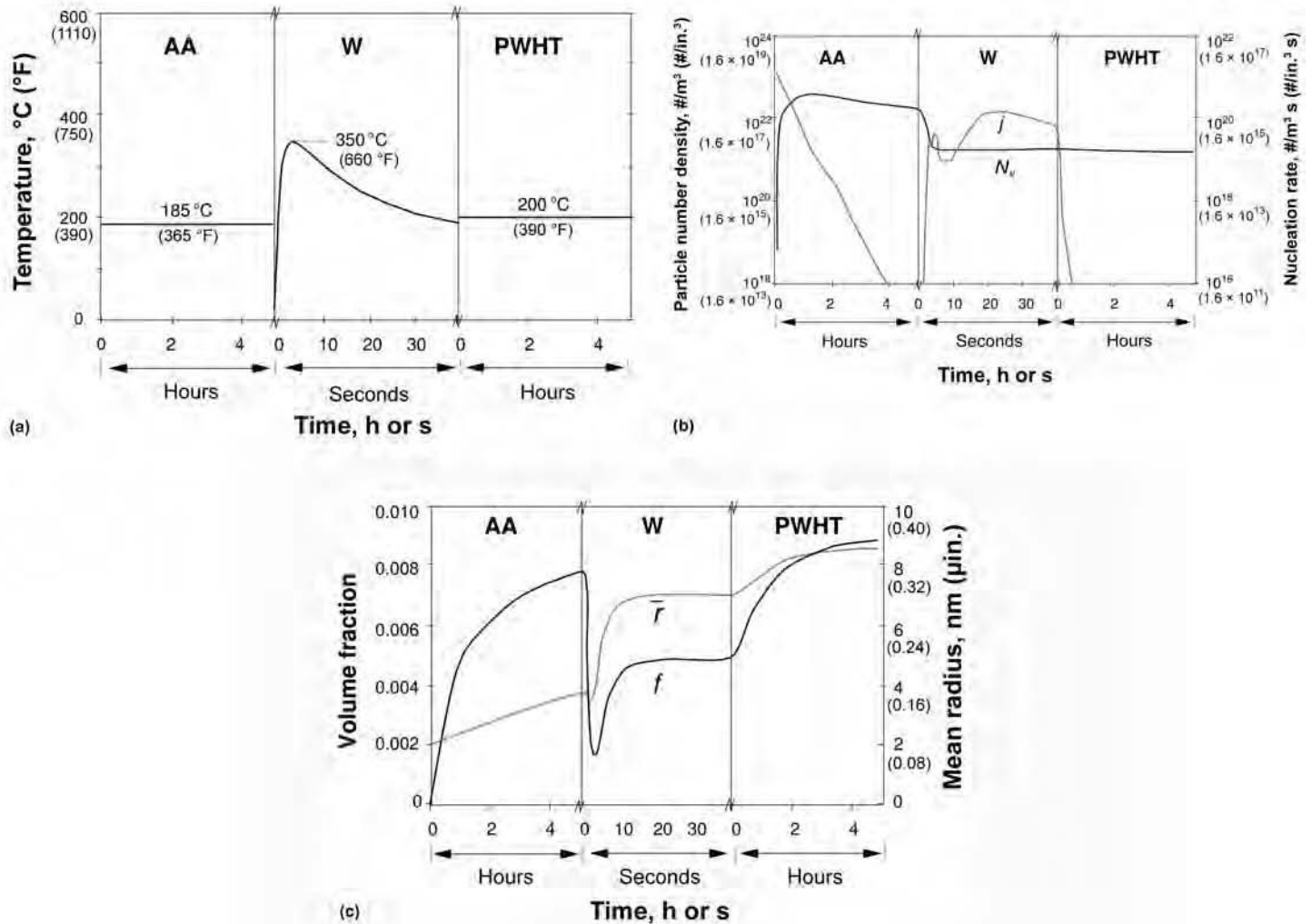


Fig. 15 Industrial case study showing the sequence of reactions occurring during artificial aging (AA), welding (W), and postweld heat treatment (PWHT) of 5 mm (0.2 in.) AA6005 plate material. (a) Record of thermal history. (b) Predicted change in particle number density, N_v , and nucleation rate, j , with time. (c) Predicted change in mean particle radius, \bar{r} , and volume fraction, f , with time. Source: Ref 36

as r_i is smaller than the critical radius for shearing, r_c (Ref 35, 45, 47):

$$\bar{F}_i = 2\beta G b^2 \left(\frac{r_i}{r_c} \right) \quad (\text{Eq 71})$$

Conversely, for strong (nonshearable) particles, characterized by $r_i > r_c$, the obstacle strength, F_i , will be constant and independent of r_i (Ref 35, 45, 47):

$$\bar{F}_i = 2\beta G b^2 \quad (\text{Eq 72})$$

Solid-Solution Hardening. In age-hardening aluminum alloys, elements such as magnesium, silicon, and copper give rise to considerable solid-solution strengthening. Provided that the contribution from each element is additive, the solid-solution hardening potential of the alloy, σ_{ss} , can be expressed as (Ref 46, 48):

$$\sigma_{ss} = \sum_j k_j C_j^{2/3} \quad (\text{Eq 73})$$

where C_j is the concentration of a specific alloying element in solid solution, and k_j is the corresponding scaling factor.

Overall Yield Strength. In alloys where several strengthening mechanisms are operative at room temperature, it is reasonable to assume that the individual strength contributions can be added linearly. Thus, taking σ_i equal to the intrinsic yield strength of pure aluminum, the resulting expression for the overall macroscopic yield strength, σ_y , becomes:

$$\sigma_y = \sigma_i + \sigma_{ss} + \sigma_p \quad (\text{Eq 74})$$

Equations 69 to 74 represent the important link between precipitation structure and strength, because they convert the relevant output parameters from the precipitation model into an equivalent room-temperature yield stress. An example application is presented in Fig. 16, which shows the evolution of the resulting room-temperature yield stress, σ_y , as well as the individual contributions from solid-solution hardening, σ_{ss} , and precipitation hardening, σ_p , respectively, to the total strength level for the case study previously presented in Fig. 15. During artificial aging, σ_p increases at the expense of σ_{ss} , because nucleation and growth of the β'' particles give rise to substantial precipitation hardening. This, in turn, leads to a corresponding increase in σ_y , although the aluminum matrix becomes drained with respect to solute, thereby reducing σ_{ss} .

Moreover, a comparison between Fig. 15(b) and 16 reveals that the observed drop in σ_p and σ_y during welding arises from the corresponding drop in the particle number density, N_v , because of particle dissolution. It follows that the small increase in σ_{ss} is not sufficient to compensate the softening that occurs due to particle reversion, resulting in a local room-temperature yield strength of approximately 155 MPa (23 ksi) after

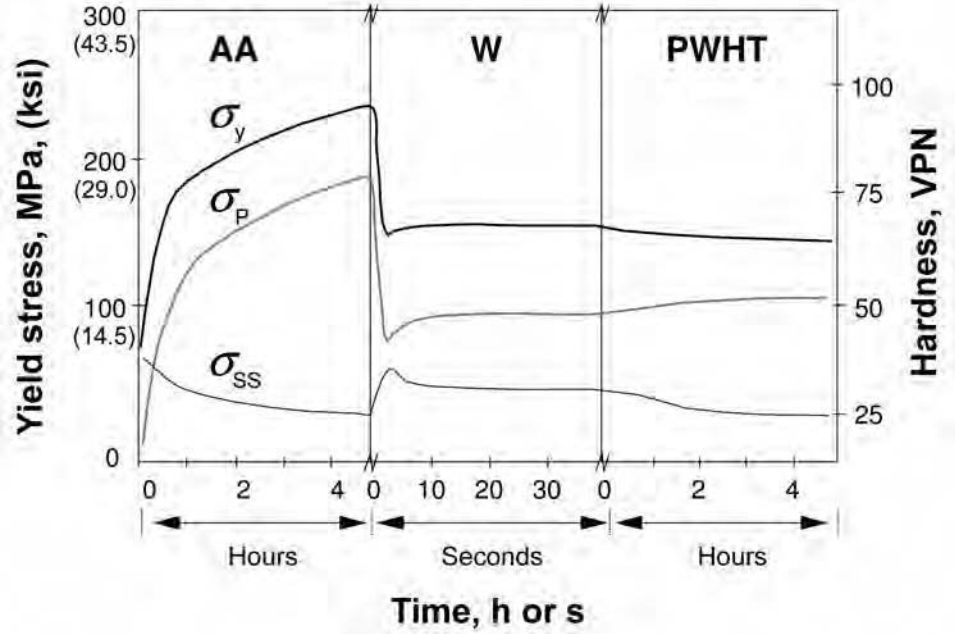


Fig. 16 Predicted change in overall room-temperature yield stress, σ_y , and individual strength components solid-solution hardening, σ_{ss} , and precipitation hardening, σ_p , with time for the industrial case study presented in Fig. 15. The ordinate to the right in the diagram indicates the corresponding hardness level. AA, artificial aging; W, welding; PWHT, postweld heat treatment. Source: Ref 36

completion of the welding operation. Finally, because the combination of a low solute content and a reduced vacancy concentration implies that the resulting aging response of the partly reverted region is weak, this leads to a permanent strength loss in the HAZ after PWHT.

Microstructure Modeling in the Context of Engineering Design

In the following, the microstructure model for age-hardening Al-Mg-Si alloys, presented in the previous section, is exploited in engineering design to optimize the load-bearing capacity of welded aluminum components.

In welding of age-hardening aluminum alloys and particularly artificially aged Al-Mg-Si alloys such as AA6082-T6, HAZ softening is of particular concern. In engineering design, this strength loss must be taken into consideration, both the total width of the reduced strength zone and the corresponding minimum strength level.

Calculation of the Design Stress

To illustrate how the design stress depends on the minimum strength level and reduced strength zone width, the two idealized loading conditions are considered more in detail. If the loading is perpendicular to the weld, the nominal stress, σ_{\perp} , is given as (Ref 49):

$$\sigma_{\perp} = \frac{P}{A} = \frac{P}{d w} \quad (\text{Eq 75})$$

where P is the tensile or compressive force being applied perpendicular to the axis of the weld, and A is the cross section of the joint (equal to the plate thickness, d , times the width, w , of the component).

Provided that the HAZ is also the softest part of the weld, and yielding is not permitted during service, the design stress, σ_{\perp} , cannot exceed the minimum HAZ yield stress, σ_{\min} . This, in turn, imposes a restriction on the design stress, $\sigma_{\perp} \leq \sigma_{\min}$. Hence, the metallurgical parameter, σ_{\min} , has a direct physical meaning in engineering design and is the key parameter determining the joint strength when the loading is perpendicular to the weld.

Similarly, if the loading is parallel to the weld, Mazzolini (Ref 49) introduces the so-called reduced cross-sectional area, A_{red} , as a basis for calculating the design stress, σ_{\parallel} , which, according to the definitions in Fig. 17, can be written as:

$$A_{\text{red}} = A - 2y_{\text{red}}^{\text{eq}} d(1 - \beta) \quad (\text{Eq 76})$$

where A is the total cross-sectional area of the joint (including the weld reinforcement), $y_{\text{red}}^{\text{eq}}$ is the equivalent half-width of the reduced strength zone (including the weld metal) of strength σ_{\min} , while β is a metallurgical efficiency factor that takes into account the degree of softening occurring due to welding ($\beta \leq 1$).

Thus, provided that yielding is not permitted during service, β is equal to the ratio between the minimum HAZ yield stress, σ_{\min} , and the base-metal yield stress, σ_b :

$$\beta = \frac{\sigma_{\min}}{\sigma_b} \tag{Eq 77}$$

Similarly, the equivalent half-width of the reduced strength zone, $\Delta y_{\text{red}}^{\text{eq}}$, of strength σ_{\min} can be calculated by considering the idealized yield strength profile shown in Fig. 17 and solving the integral (Ref 39):

$$\Delta y_{\text{red}}^{\text{eq}} = \frac{\int_{y_m}^{\infty} (\sigma_b - \sigma(y)) dy}{(\sigma_b - \sigma_{\min})} \tag{Eq 78}$$

where the lower integration limit, y_m , refers to the fusion boundary of the weld, and the upper integration limit, y_{tot} , refers to the total half-width of the reduced strength zone as defined in Fig. 17.

Note that Eq 78 is conservative in the sense that it just considers the HAZ yield strength profile and ignores the strength contribution from the weld metal.

In the following, the previously described precipitation and yield strength models for Al-Mg-Si alloys are combined with thermal field calculations obtained from WELDSIM, which is a general-purpose finite-element code for welding (Ref 37, 38, 50). By this means, the complete HAZ yield stress distributions can be calculated, from which the desired design parameters σ_{\min} and $\Delta y_{\text{red}}^{\text{eq}}$ may be extracted.

Process Diagrams for Al-Mg-Si Butt Welds

Figure 18 shows the predicted local yield stress distribution across the HAZ following welding and subsequent natural aging of butt welds of AA6082-T6 for various combinations of q_0/vd , h , and d . Note that if steel backing is used, the plate thickness, d , must also be specified to uniquely define the HAZ thermal program. It is evident from these plots that the critical parameters controlling the joint strength depend on complex interactions between

several process variables that are not accounted for in the current design codes for aluminum weldments (Ref 51, 52). The most important variables, in addition to the alloy composition and initial temper condition, are the applied heat input during welding, the heat-transfer coefficient between the aluminum plate and the steel backing, as well as the extent of natural aging occurring after welding.

Figure 19, which applies to butt welding of AA6060-T6, AA6005-T6, and AA6082-T6, respectively, shows predicted design parameters σ_{\min} and $\Delta y_{\text{red}}^{\text{eq}}$ being defined previously in Fig. 17 for different combinations of q_0/vd , h , and d . Note that the curves for $h = 0$ are not limited to a specific plate thickness, as opposed to those in Fig. 19(b), which hold for 2 mm (0.08 in.) sheet material only. As expected, the design parameters are seen to depend both on the applied heat input during welding as well as on the actual value of the heat-transfer coefficient between the aluminum plate and the steel backing. The absolute value of σ_{\min} is, in turn, determined by the alloy composition, which represents a third option that can be exploited in engineering design. However, for a given alloy composition, minimization of the HAZ strength loss will require that the q_0/vd ratio is kept as low as possible during welding. At the same time, the aluminum plate should be properly clamped to the steel backing (if this is practically feasible) to make sure that the excess heat from the fusion zone is effectively transferred to the steel plate and not allowed to diffuse into the HAZ.

Optimization of the Load-Bearing Capacity of Welded Aluminum Structures

Until now, only predictions involving the yield stress were considered because this property is usually the most critical in engineering design. However, for complex nonlinear finite-element simulations of the load-bearing capacity of welded structural members, complete

stress-strain curves are required in all positions of the solution domain. As illustrated in Fig. 20, such curves can be obtained by using output from the precipitation model to calculate the yield stress, as described in the section ‘‘Yield Strength Model’’ in this article, and the rate of work hardening during plastic deformation by invoking an appropriate work-hardening model.

In age-hardening aluminum alloys, the work-hardening behavior is controlled by the so-called geometric slip distance and the corresponding volume fraction of nonshearable Orowan particles in addition to the solute content, which determines the rate of dynamic recovery (Ref 53). In practice, all of these parameters can be extracted from the predicted particle size distribution.

A brief outline of the work-hardening model developed for Al-Mg-Si alloys is given subsequently. Further details are given in Ref 53.

Work-Hardening Model. In the work-hardening model presented subsequently, the total dislocation density, ρ_t , is taken equal to the sum of the geometrically necessary dislocations, ρ_g , and the statistically stored dislocations, ρ_s . The geometric slip distance, λ_g , is a measure of how far the dislocations move before they are stored around particles that are dispersed within the matrix material. This storage of dislocations is necessary to obtain compatibility between the two phases during deformation. The parameter λ_g is therefore a characteristic of the microstructure and is related to the type and distribution of the hardening precipitates in the material. According to Ashby (Ref 54), the geometrically necessary dislocations will dominate if the geometric slip distance, λ_g , is smaller than the corresponding slip distance for statistical storage of dislocations, λ_s , as measured from the length of the slip lines in the work-hardened material. In the other extreme, when $\lambda_g > \lambda_s$, their contribution to the total dislocation density becomes negligible and can be ignored.

To establish a useful work-hardening model for commercial Al-Mg-Si alloys, it is necessary to convert the current values of the dislocation densities into an equivalent room-temperature flow stress, σ . Because the Ashby approach (Ref 54) is based on the assumption that the two dislocation densities can be added linearly in stress-strain space, their total contribution to the net flow stress, $\Delta\sigma_d = \sigma - \sigma_y$, is given by the following equation:

$$\Delta\sigma_d = \sigma - \sigma_y = \alpha M G \mathbf{b} \sqrt{\rho_t} = \alpha M G \mathbf{b} \sqrt{\rho_s + \rho_g} \tag{Eq 79}$$

where α is a constant with a numerical value close to 0.3, M is the Taylor factor, G is the shear modulus, and \mathbf{b} is the magnitude of the Burgers vector.

The form of Eq 79 suggests that the work-hardening behavior of Al-Mg-Si alloys can be captured mathematically by considering the

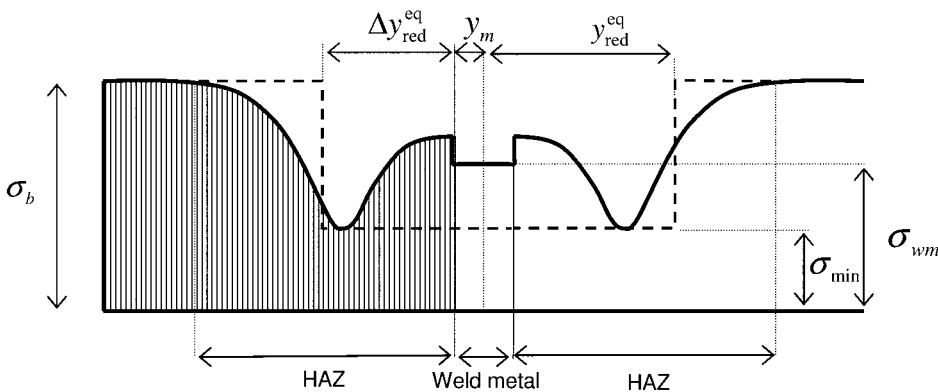


Fig. 17 Schematic diagram showing the yield strength profile across an AA6082-T6 butt weld following complete natural aging. The equivalent half-widths of the reduced strength zones, $y_{\text{red}}^{\text{eq}}$ and $\Delta y_{\text{red}}^{\text{eq}}$, of minimum strength, σ_{\min} , are defined to the right and left in the diagram, respectively. HAZ, heat-affected zone. Adapted from Ref 39

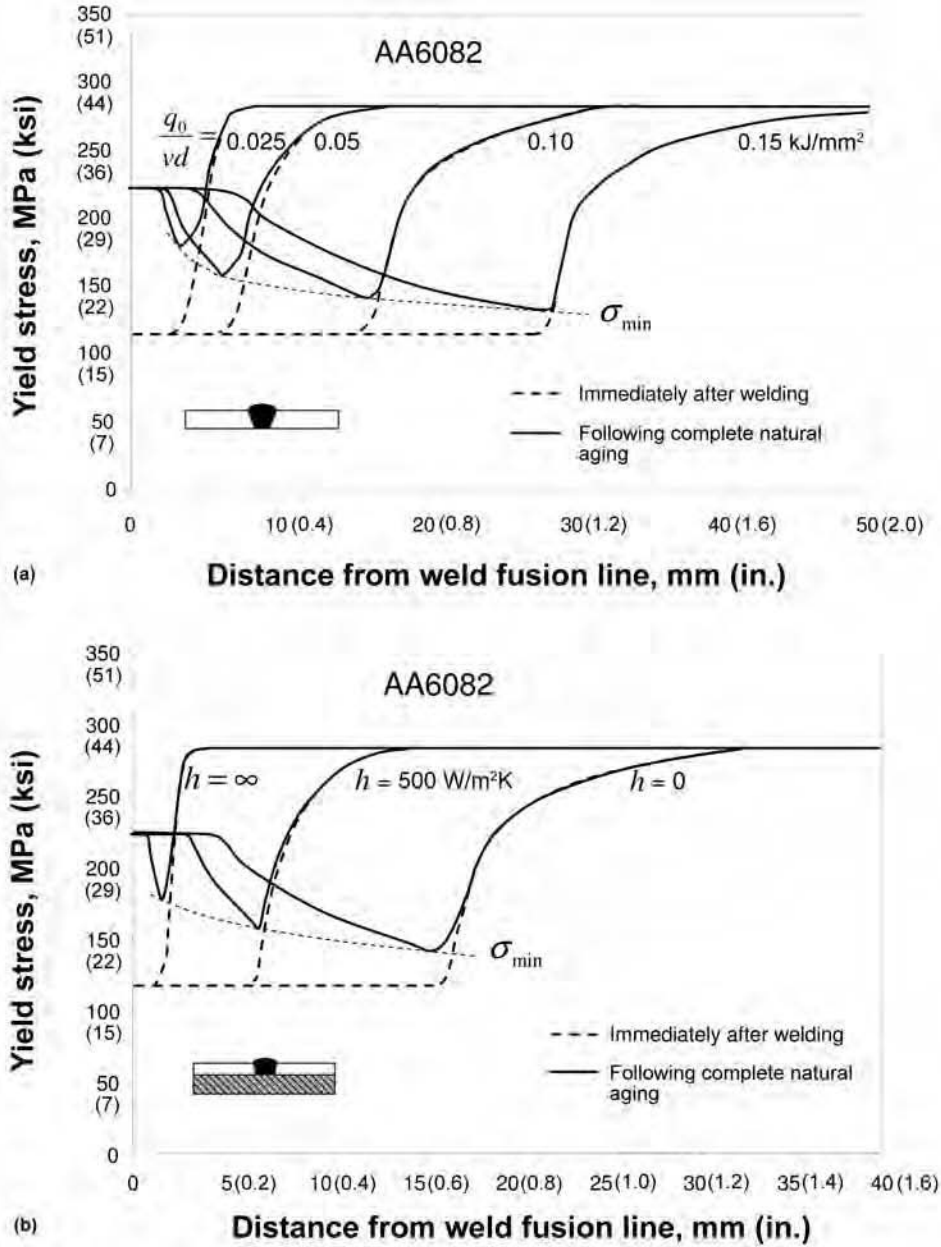


Fig. 18 Predicted heat-affected zone (HAZ) yield strength profiles for single-pass butt welds of AA6082-T6 immediately after welding and following complete natural aging. (a) Effect of the applied heat input, q_0/vd , on the HAZ yield strength distribution for $h = 0$ (adiabatic surfaces, no heat loss to the surroundings). (b) Effect of the heat-transfer coefficient, h , on the HAZ yield strength distribution for $q_0/vd = 0.1$ kJ/mm². Note that the two curves for $h = 500$ W/m²K and $h = \infty$, respectively, apply specifically to butt welding of 2 mm (0.08 in.) sheet material. Source: Ref 39

net contribution from dislocation hardening, $\Delta\sigma_d$, using ρ_s and ρ_g as the independent internal variables of the system.

Contribution from Shearable Particles and Alloying Elements in Solid Solution. Experiments have shown that the work-hardening behavior of Al-Mg-Si alloys in the naturally aged (T4) condition is essentially similar to that in the as-quenched (W10) condition (Ref 53). Hence, in the context of the model developed, no distinction is made between small shearable particles in the form of Guinier-Preston zones

(or clusters) and atoms in solid solution. This means that the balance between statistical storage and dynamic recovery of dislocations in both types of matrix materials is conveniently described by the evolution equation proposed by Kocks (Ref 55, 56):

$$d\rho_s = (k_1 \rho_s^{1/2} - k_2 \rho_s) d\varepsilon_p \quad (\text{Eq 80})$$

where k_1 is a constant being characteristic of the material under consideration, whereas the

k_2 parameter, which determines the rate of the dynamic recovery during plastic deformation, depends on the solute content of the alloy.

For Al-Mg-Si alloys, k_2 is well described by the following analytical expression (Ref 53):

$$k_2 = k_1 \frac{\alpha M G \mathbf{b}}{k_3 (\hat{C}_{\text{Mg}})^{3/4}} \quad (\text{Eq 81})$$

where k_3 is a characteristic material constant, while \hat{C}_{Mg} is a weight parameter that takes into account the combined effect of magnesium and silicon on the resulting rate of dynamic recovery. The expression for \hat{C}_{Mg} is (Ref 53):

$$\hat{C}_{\text{Mg}} = \bar{C} + 0.5C_{\text{Si}}^{\text{eff}} \quad (\text{Eq 82})$$

where \bar{C} is the mean concentration of magnesium in the aluminium matrix (given by Eq 63 in the precipitation model), and $C_{\text{Si}}^{\text{eff}}$ is the corresponding silicon concentration following a correction for the amount of silicon being tied up as coarse $\alpha\text{-Al}_{15}(\text{FeMn})_3\text{Si}_2$ particles in the alloy (Ref 35).

Contribution from Nonshearable Orowan Particles. The density of geometrically necessary dislocations, ρ_g , in a dispersion-strengthened material is interrelated to the geometric slip distance, λ_g , and the imposed shear strain, γ , through the following relationship (Ref 53):

$$\rho_g = \rho_g^{\text{ref}} \frac{\lambda_{g,o}^{\text{ref}} \gamma}{\lambda_{g,o} \gamma^{\text{ref}}} \quad (\text{Eq 83})$$

where $\lambda_{g,o}$ specifically refers to the geometric slip distance of hardening precipitates in Al-Mg-Si alloys that fulfill the Orowan criterion.

Because the accumulation of dislocation loops around the precipitates (and thus ρ_g) cannot increase without limit, as predicted by Eq 83, ρ_g will, in practice, saturate at some given (critical) plastic strain, $\varepsilon_p = \varepsilon_c$. This threshold strain depends, in turn, on the volume fraction, f_o , of the dispersed Orowan particles (Ref 54). Taking $\varepsilon_c = \varepsilon_c^{\text{ref}}$ when $f_o = f_o^{\text{ref}}$ for the chosen reference alloy, a rational expression for ε_c is (Ref 53):

$$\varepsilon_c = \left(\frac{f_o^{\text{ref}}}{f_o} \right) \varepsilon_c^{\text{ref}} \quad (\text{Eq 84})$$

Overall Stress-Strain Response. Eventually, after integration and some manipulation of the resulting analytical solutions, the following analytical expressions for the relationship between $\Delta\sigma_d$, ρ_s , ρ_g , and $\rho_{g,s}$ are derived (Ref 53):

$$\Delta\sigma_d = \alpha M G \mathbf{b} \sqrt{\left(\frac{k_1}{k_2} \right)^2 \left(1 - \exp\left(-\frac{k_2 \varepsilon_p}{2} \right) \right)^2 + \rho_{g,s}^{\text{ref}} \frac{\lambda_{g,o}^{\text{ref}} \varepsilon_p}{\lambda_{g,o} \varepsilon_c^{\text{ref}}}} \quad (\text{Eq 85})$$

when $\varepsilon_p < \varepsilon_c$

and

$$\Delta\sigma_d = \alpha M G b \sqrt{\left(\frac{k_1}{k_2}\right)^2 \left(1 - \exp\left(-\frac{k_2 \varepsilon_p}{2}\right)\right)^2 + \rho_{f,s}^{\text{ref}} \frac{\lambda_{g,o}^{\text{ref}} \varepsilon_c}{\lambda_{g,o} \varepsilon_c^{\text{ref}}}}$$

when $\varepsilon_p \geq \varepsilon_c$ (Eq 86)

where the actual value of ε_c is given by Eq 84.

Expressions for $\lambda_{g,o}$ and f_o . Following calibration, the present work-hardening model relies solely on outputs from the precipitation model. In addition to the mean matrix solute content, \bar{C} , the two other microstructure

parameters that control the work-hardening behavior of Al-Mg-Si alloys are the geometric slip distance, $\lambda_{g,o}$, and the corresponding volume fraction, f_o , of nonshearable Orowan particles in the matrix material. Both parameters can be extracted from the predicted particle size distribution. Let the Orowan particles be characterized by their radius $r_o > r_c$, where r_c is the critical particle radius for dislocation bypassing, analogous to that done in the yield strength model (Ref 35, 36). Then $\lambda_{g,o}$ and f_o are readily calculated from the following expressions (Ref 53):

$$\lambda_{g,o} = \left(8 \sum_{r=r_o}^{r=\infty} r_i^2 N_i\right)^{-1} \quad (\text{Eq 87})$$

$$f_o = \frac{4\pi}{3} \sum_{r=r_o}^{r=\infty} r_i^3 N_i \quad (\text{Eq 88})$$

where N_i is the number of particles per unit volume within the size class r_i .

Application of the Combined Precipitation, Yield Stress, and Work-Hardening Model.

As an example, the combined precipitation, yield stress, and work-hardening model outlined in Fig. 20 is used to optimize the load-bearing capacity of a welded aluminum component that has been subjected to a series of thermal and mechanical operations during fabrication. As a starting point, the thermal module in WELDSIM (Ref 37, 38, 50) is used to predict the temperature field resulting from the welding, including the peak-temperature distribution in the HAZ shown in Fig. 21(a). The calculated thermal history is input to the combined precipitation, yield stress, and work-hardening model, which calculates the full stress-strain curves for all positions within the solution domain, including the three positions labeled "A," "B," and "C" in Fig. 21(a). These curves are shown in Fig. 21(b). It follows that each region yields a unique stress-strain response, where position "B" corresponds to the softest part of the HAZ.

Finally, a commercial finite-element code (Ref 58) is used to simulate the load-bearing capacity of the welded component, subjected to the loading situation shown in Fig. 22(a). These simulations are carried out using a shell-based modeling approach in which the predicted stress-strain curves for each position of the solution domain correspond to the mechanical model (Ref 57). The resulting predicted load-displacement curves are shown in Fig. 22(b). It follows that a change in the alloy

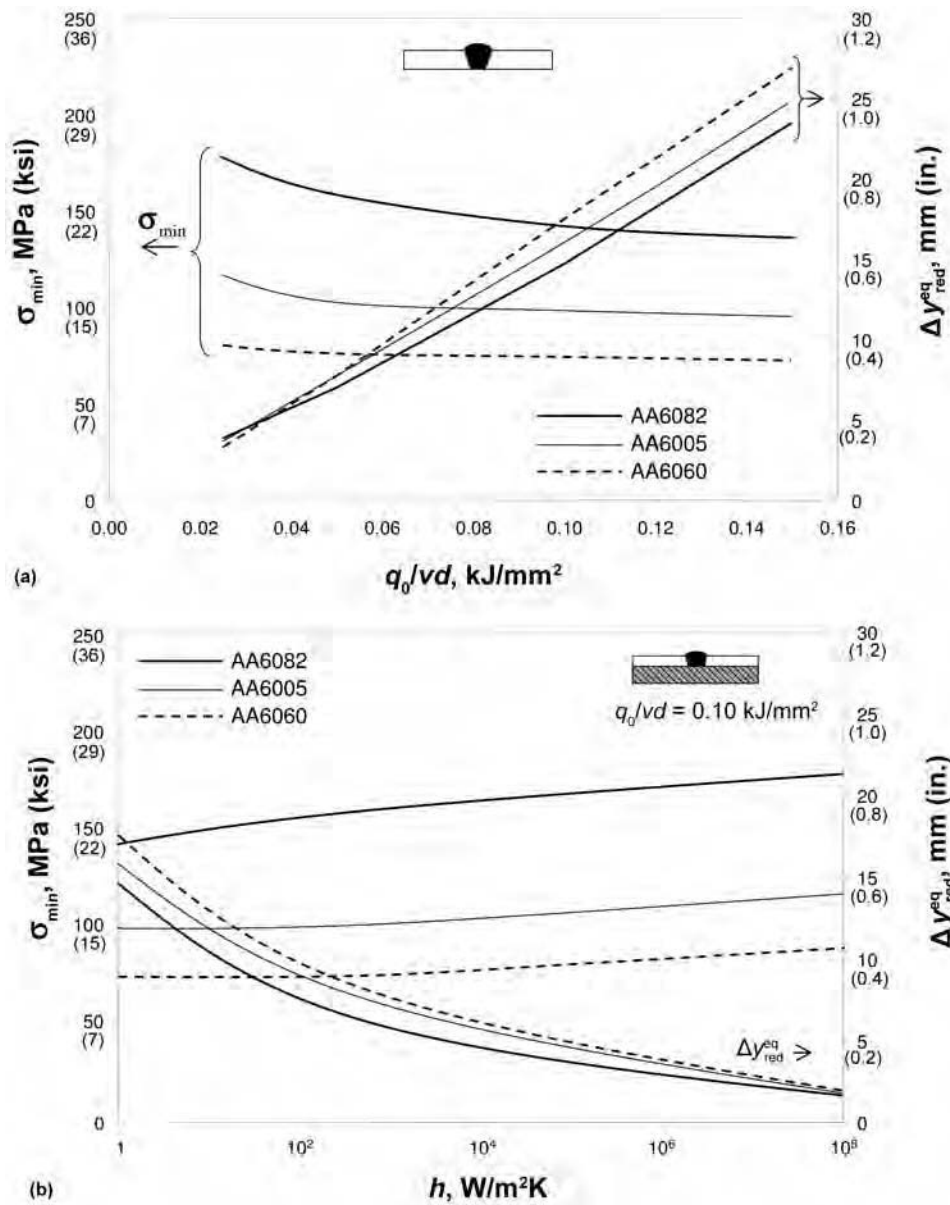


Fig. 19 Predicted process diagrams for Al-Mg-Si butt welds showing the variation in the design parameters σ_{min} and Δy_{red}^{eq} with q_0/vd and h for the alloys AA6060-T6, AA6005-T6, and AA6082-T6 following complete natural aging. (a) Effects of the applied heat input, q_0/vd , on the heat-affected zone (HAZ) softening behavior for $h = 0$ (adiabatic surfaces, no heat loss to the surroundings). (b) Effects of the effective heat-transfer coefficient, h , on the HAZ softening behavior for a fixed heat input, q_0/vd , of 0.1 kJ/mm² and a plate thickness, d , of 2 mm (0.08 in.). Source: Ref 39

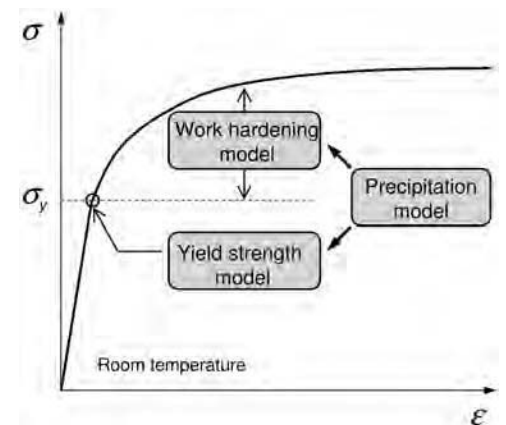


Fig. 20 Schematic diagram showing the coupling between the precipitation, yield strength, and work-hardening models developed for Al-Mg-Si alloys. Source: Ref 53

composition from a soft AA6060 to a medium-strength AA6082 alloy results in a significant increase in the predicted ultimate load.

These simulation results are interesting, both from an academic and practical point of view, because they illustrate in a quantitative manner how the present modeling approach can be used

to optimize the load-bearing capacity of welded aluminum structural components simply by manipulating the alloy composition and the applied heat treatment schedules.

Acknowledgments

The authors acknowledge the financial support provided by the Norwegian Research Council and Hydro Aluminium through SIM-Lab, the Centre for Research-Based Innovation at the Norwegian University of Science and Technology, Trondheim, Norway.

REFERENCES

1. Ø. Grong and H.R. Shercliff, Microstructural Modelling in Metals Processing, *Prog. Mater. Sci.*, Vol 47, 2002, p 163–282
2. O. Richmond, *Proc. Int. Conf. Aluminium Technology '86*, The Institute of Materials, London, U.K., 1986, p 615–625
3. J.W. Christian, *The Theory of Phase Transformations in Metals and Alloys—Part I*, Pergamon Press, Oxford, U.K., 1975
4. E. Scheil, *Anlaufzeit Der Austenitumwandlung*, *Arch. Eisenhüttenwes.*, Vol 8, 1935, p 565–567
5. D.A. Porter and K.E. Easterling, *Phase Transformations in Metals and Alloys*, Van Nostrand Reinhold, Wokingham, U. K., 1981
6. R.D. Doherty, in *Physical Metallurgy*, 3rd ed., R.W. Cahn and P. Haasen, Ed., North-Holland Physics Publ., Amsterdam, 1983

7. J.E. Burke and D. Turnbull, Recrystallization and Grain Growth, *Prog. Met. Phys.*, B. Chalmers, Ed., Pergamon Press, London, 1952, p 220–292
8. G.W. Greenwood, The Growth of Dispersed Precipitates in Solutions, *Acta Metall.*, Vol 4, 1956, p 243–248
9. M.E. Fine, *Phase Transformations in Condensed Systems*, MacMillan, New York, 1964
10. M.J. Avrami, Kinetics of Phase Change I: General Theory, *J. Chem. Phys.*, Vol 7, 1939, p 1103–1102; Vol 8, 1940, p 212–224; Vol 9, 1941, p 177–184
11. J.W. Cahn, The Kinetics of Grain Boundary Nucleated Reactions, *Acta Metall.*, Vol 4, 1956, p 449–459
12. J.T. Staley, Quench Factor Analysis of Aluminium Alloys, *Mater. Sci. Technol.*, Vol 3, 1987, p 923–933
13. L.A. Wierszykowski, The Effect of the Thermal Path to Reaction Isothermal Temperature on Transformation Kinetics, *Metall. Trans. A*, Vol 22, 1991, p 993–999
14. H.B. Aaron, D. Fainstein, and G.R. Kotler, Diffusion-Limited Phase Transformations: A Comparison and Critical Evaluation of the Mathematical Approximations, *J. Appl. Phys.*, Vol 41, 1970, p 4404–4410
15. M.J. Whelan, On the Kinetics of Particle Dissolution, *Metal. Sci. J.*, Vol 3, 1969, p 95–97
16. J. Ågren, Kinetics of Carbide Dissolution, *Scan. J. Metall.*, Vol 19, 1990, p 2–8

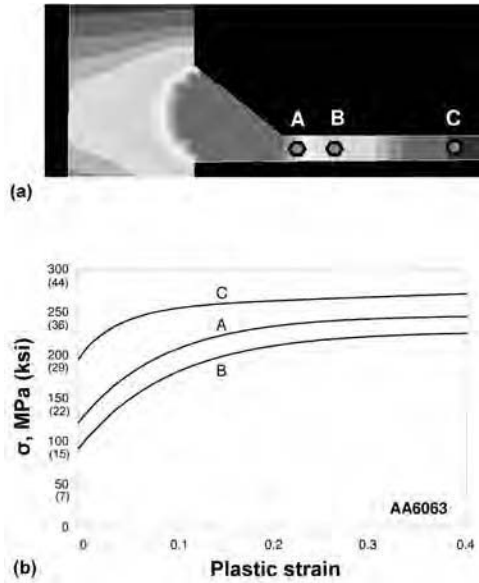


Fig. 21 Outputs from the coupled numerical simulations of the welding case referred to in the text. (a) Predicted peak-temperature, T_p , distribution during gas metal arc welding. (b) Calculated stress-strain curves for the three positions labeled “A,” “B,” and “C” in (a). Source: Ref 53, 57

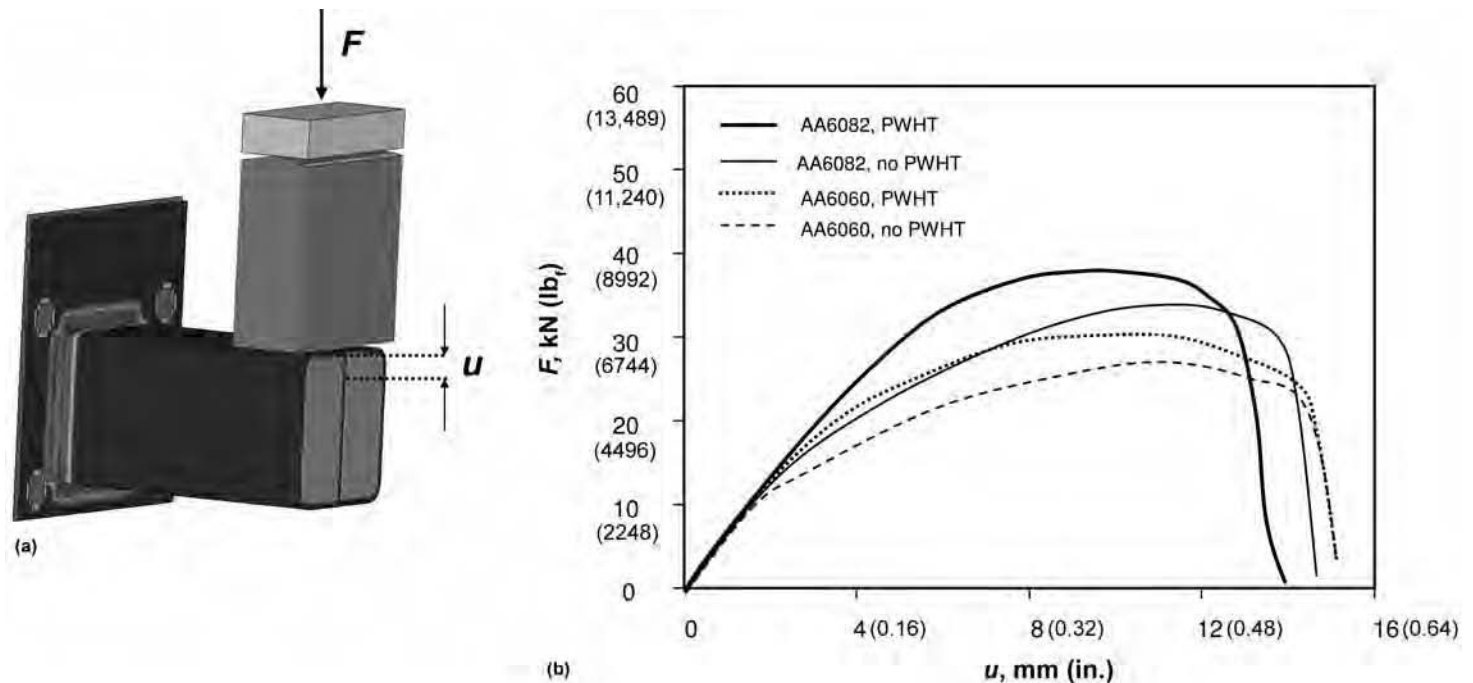


Fig. 22 Summary of results from the experimental and numerical case study. (a) Shell model of the component demonstrating the spatial variation of the initial yield stress. (b) Predicted load-displacement curves for alloys AA6060 and AA6082. PWHT, postweld heat treatment. Source: Ref 57

17. B.I. Bjørneklett, Ø. Grong, O.R. Myhr, and A.O. Kluken, Modelling of Grain Boundary Liquation in Al-Zn-Mg Weldments, *Sci. Technol. Weld. Join.*, Vol 4 (No. 3), 1999, p 161–169
18. J.M. Lifshitz and V.V. Slyozov, The Kinetics of Precipitation from Supersaturated Solid Solutions, *J. Phys. Chem. Solids*, Vol 19, 1961, p 35–50
19. C. Wagner, Theorie Dealtering Von Niederschlagen Durch Umlösen, *Z. Electrochem.*, Vol 65, 1961, p 581–591
20. Ø. Grong, *Metallurgical Modelling of Welding*, 2nd ed., The Institute of Materials, London, U.K., 1997
21. J.C. Ion, K.E. Easterling, and M.F. Ashby, A Second Report of Microstructure and Hardness for Heat-Affected Zones in Welds, *Acta Metall.*, Vol 32, 1984, p 1949–1962
22. J.E. Hatch, *Aluminium—Properties and Physical Metallurgy*, American Society for Metals, 1984
23. G.E. Dieter, *Mechanical Metallurgy*, 3rd ed., McGraw-Hill Book Company, New York, 1986
24. G. Mathers, *The Welding of Aluminium and Its Alloys*, Woodhead Publishing Ltd. and CRC Press LLC, 2002, p 31–35
25. A.M. Gokhale, N.U. Deshpande, and D.K. Denzer, Characterization of Fracture Path and Its Relationship to Microstructure in Wrought Aluminium Alloys, *Proc. Fourth Int. Conf. on Aluminium Alloys*, Vol 1, Sept 11–16, 1994 (Atlanta, GA), 1994, p 685–692
26. R.W. Cahn, *Physical Metallurgy, Recovery and Recrystallization*, R.W. Cahn, Ed., North Holland Publishing Company, Amsterdam, 1970, p 1151–1154
27. J.D. Verhoeven, *Fundamentals of Physical Metallurgy*, John Wiley & Sons, New York, 1975, p 325–354
28. E. Sarrazin, “Modélisation du Soundage d’Alliages d’Aluminium,” Ph.D. thesis, Ecole Polytechnique, Palaiseau, France, 1995
29. H. Hu and B.B. Rath, On the Time Exponent in Isothermal Grain Growth, *Metall. Trans.*, Vol 1, 1970, p 3181–3184
30. P. Hellman and M. Hillert, On the Effect of Second-Phase Particles on Grain Growth, *Scand. J. Metall.*, Vol 4, 1975, p 211–219
31. I. Andersen and Ø. Grong, Analytical Modeling of Grain Growth in Metals and Alloys in the Presence of Growing and Dissolving Precipitates, *Acta Metall. Mater.*, Vol 43, 1995, p 2673–2688
32. M.F. Ashby and K.E. Easterling, A First Report on Diagrams for Grain Growth in Welds, *Acta Metall.*, Vol 30, 1982, p 1969–1978
33. H. Hemmer, Ø. Grong, and S. Klokkehaug, A Process Model for the Heat-Affected Zone Microstructure Evolution in Duplex Stainless Steel Weldments, Part II: Application to Electron Beam Welding, *Metall. Mater. Trans. A*, Vol 31, 2000, p 1035–1048
34. O.R. Myhr and Ø. Grong, Modelling of Non-Isothermal Transformations in Alloys Containing a Particle Distribution, *Acta Mater.*, Vol 48, 2000, p 1605–1615
35. O.R. Myhr, Ø. Grong, and S.J. Andersen, Modelling of the Age Hardening Behavior of Al-Mg-Si Alloys, *Acta Mater.*, Vol 49, 2001, p 65–75
36. O.R. Myhr, Ø. Grong, H.G. Fjær, and C.D. Marioara, Modelling of the Microstructure and Strength Evolution in Al-Mg-Si Alloys during Multistage Thermal Processing, *Acta Mater.*, Vol 52, 2004, p 4997–5008
37. O.R. Myhr, S. Klokkehaug, Ø. Grong, H.G. Fjær, and A.O. Kluken, Modelling of Microstructure Evolution, Residual Stresses and Deformations in 6082-T6 Aluminium Weldments, *Weld. J.*, Vol 77 (No. 7), 1998, p 286–292
38. O.R. Myhr, Ø. Grong, S. Klokkehaug, and H.G. Fjær, Modelling of the Microstructure and Strength Evolution during Ageing and Welding of Al-Mg-Si Alloys, *Mathematical Modelling of Weld Phenomena 6*, H. Cerjak, Ed., The Institute of Materials, 2002, p 337–363
39. O.R. Myhr and Ø. Grong, Novel Modelling Approach to Optimisation of Welding Conditions and Heat Treatment Schedules for Age Hardening Al Alloys, *Sci. Technol. Weld. Join.*, Vol 14 (No. 4), 2009, p 621–632
40. H.B. Aaron, D. Fainstain, and G.R. Kotler, Diffusion-Limited Phase Transformations: A Comparison and Critical Evaluation of the Mathematical Approximations, *J. Appl. Phys.*, Vol 41, 1970, p 4404–4410
41. S.V. Patankar, *Numerical Heat Transfer and Fluid Flow*, Hemisphere Publishing Corporation, Washington, 1980
42. H.R. Shercliff and M.F. Ashby, A Process Model for Age Hardening of Aluminium Alloys—I. The Model, *Acta Metall.*, Vol 38, 1990, p 1789–1802
43. H.R. Shercliff and M.F. Ashby, A Process Model for Age Hardening of Aluminium Alloys—II. Applications of the Model, *Acta Metall.*, Vol 38, 1990, p 1803–1812
44. A. Deschamps and Y. Brechet, Influence of Predeformation and Aging in an Al-Zn-Mg Alloy—I. Microstructure Evolution and Mechanical Properties, *Acta Mater.*, Vol 47, 1999, p 281–292
45. A. Deschamps and Y. Brechet, Influence of Predeformation and Aging of an Al-Zn-Mg Alloy—II. Modelling of Precipitation Kinetics and Yield Stress, *Acta Mater.*, Vol 47, 1999, p 293–305
46. J. Friedel, *Dislocations*, Pergamon Press, Oxford, U.K., 1964
47. J. Gerold, *Dislocations in Solids*, Vol 4, North Holland Publ. Co., Amsterdam, The Netherlands, 1979
48. F.R.N. Nabarro, *Theory of Crystal Dislocations*, Oxford University Press, Oxford, U.K., 1967
49. M.F. Mазzolari, *Aluminium Alloy Structures*, 2nd ed., E & FN Spon, London, U.K., 1995
50. H.G. Fjær, O.R. Myhr, S. Klokkehaug, and E.J. Holm, Advances in Aluminium Weld Simulations Applying WELDSIM, *Proc. 11th International Conference on Computer Technology in Welding*, Dec 2001 (Columbus, OH), 2001
51. “Structural Use of Aluminium, Part 1. Code of Practice for Design,” BS 8118, 1991
52. “Design of Aluminium Structures, Part 1.1: General Rules,” Eurocode 9, ENV 1999-1-1, CEN/TC 250/SC 9, 1998
53. O.R. Myhr, Ø. Grong, and K.O. Pedersen, A Combined Precipitation, Yield Strength and Work Hardening Model for Al-Mg-Si Alloys, *Met. Trans. A*, Vol 41 (No. 9), 2010, p 2276–2289
54. M.F. Ashby, The Deformation of Plastically Non-Homogeneous Materials, *Philos. Mag.*, Vol 21, 1970, p 399–424
55. U.F. Kocks, Laws for Work-Hardening and Low-Temperature Creep, *J. Eng. Mater. Technol.*, Vol 98, 1976, p 76–85
56. H. Meckling and U.F. Kocks, Kinetics of Flow and Strain-Hardening, *Acta Metall.*, Vol 29, 1981, p 1865–1875
57. O.R. Myhr, Ø. Grong, O.G. Lademo, and T. Tryland, Optimizing Crash Resistance of Welded Aluminium Structures, *Weld. J.*, Vol 88 (No. 2), 2009, p 42–45
58. *LS-DYNA Keyword User’s Manual*, Vol I and II, Version 960, Livermore Software Technology Corp., 2001

Numerical Aspects of Modeling Welds*

John Goldak and Mahyar Asadi, Carleton University
Lennart Karlsson, Luleå University of Technology

THE DESIGN OF A STRUCTURE that achieves its highest performance levels with the least chance of failure can be facilitated by the mathematically based prediction modeling of weld behavior in a variety of circumstances. One aspect of a weldment that can be predicted with remarkable accuracy, given certain data, is the transient temperature field. Distortion also can be predicted with considerable accuracy. Although residual stresses and microstructure predictions are less accurate, they are still useful.

At the present time, some aspects of the arc and the weld pool are difficult to predict. Although the prediction of specific defects can be difficult, the conditions that make it likely for specific kinds of defects to form can be predicted. This situation is similar to that of predicting weather conditions that suggest a high risk of tornadoes, but not being able to predict individual tornadoes.

Reality, Models, and Mathematics. Like cartoons, mathematics is not real. Yet, even in cartoons, some relationship to reality is nearly always intended. To understand either cartoons or mathematics, every individual must define his own relationship to reality.

Unlike cartoons, mathematics has two fundamental pillars. A set of axioms, which are sometimes called assumptions, laws, primitives, or other terms, is assumed to be given and to be true. When these assumptions or axioms are combined in ways that obey a strict logic, results remain true, that is, for the purposes of mathematics, rather than for the real world. The meaning of the axioms, as interpreted in the real world, is irrelevant to mathematics. For example, given a sphere of radius r , mathematicians can prove that volume equals $(4\pi r^3)/3$. Whether any particular ball can actually be described or approximated as a sphere of radius r is not a question that mathematics considers. In fact, one cannot prove that the formula for the volume of a sphere is correct by measuring the volume of balls. Rather, the exercise is a matter of judgment and

interpretation for those who are interested in the volume of a real ball.

This example is presented in order to show that the confusion and controversy that occur in the modeling of welds and other areas arises from a failure to separate mathematics that are correct from mathematics that represent a useful model for a particular weld. Although this point is often not understood, those who can appreciate it are able to use models more effectively.

Modeling of Welds

The first assumption should be that the weld has been specified, and therefore, all information needed to produce the real weld has been given. This includes the geometry of the welded structure and the weld joint, the composition of the base and weld metal, the distribution of input energy, the preheat temperature, the welding path and speed, the hydrogen content in the arc, the start time and start position of each weld pass, the fixtures, and other factors. It is usually assumed that the transient temperature field is the most critical field, in the sense that if this temperature field is wrong, then the predictions of the model are likely to be wrong. It is also most critical in the sense that different welds usually have different temperature fields. After computing the transient temperature field, the evolution of microstructure in the heat-affected zone and the fusion zone is computed. Then the thermal stress, strain, distortion, and residual stress are computed. The next objective, which is a current research issue, is to predict the mechanical properties of the weldment, including fracture toughness, ductile-brittle transition temperature, and the probability that defects will occur. The ultimate objective is to predict the manufacturing cost and the reliability of both the weld and the welded structure.

Computational weld mechanics described in algorithmic notation comprises the following steps:

- Define the geometry, material properties, heat inputs, boundary conditions such as thermal convection, and mechanical support
- Compute the transient temperature field
- Compute the evolution of microstructure. If latent heats of transformation are to be included, then the transient temperature and evolution of microstructure become an iterative problem.
- Compute the displacement; strain and stress fields, including the effects of temperature and microstructure on material properties; thermal expansion; and phase transformations. Usually, a thermoelastoplastic stress-strain relationship is used. The displacement or distortion can significantly impact the cost of welding.
- Estimate material properties of the weldment, the probability of defects, and the risk of failure due to fatigue, ductile or brittle failure, and corrosion. Although very little research has been published on this step, it is clearly an important objective of computational weld mechanics.

The results of such an analysis are shown in Fig. 1 to 5. It has been assumed that the weld

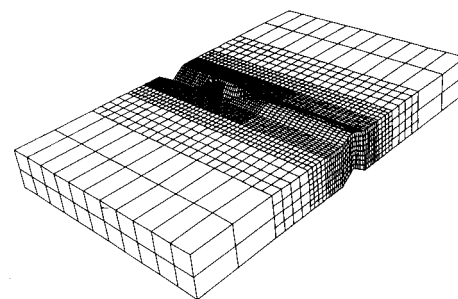


Fig. 1 Finite-element mesh for a weld described in a Eulerian reference frame. Note that filler metal is added. The weld pool, which is not shown, is not needed in this analysis because the temperature is prescribed at the weld-pool boundary. The mesh is finest just in front of the weld pool.

Energy Equation and Heat Transfer

The conservation of energy is the fundamental principle that underlies all thermal analysis, including that of welds. In the simplest terms, it states that while energy can be added or extracted, no energy can be created or destroyed in the domain being analyzed. The essential material behavior for heat conduction is that a flux of energy, q ($J/m^2 \cdot s$), flows from hot regions to cold regions under the influence of a temperature gradient, ∇T , and the thermal conductivity of the material, κ :

$$q = -\kappa \nabla T \quad (\text{Eq 1})$$

The energy required to change the temperature of a material is defined by another material property, the specific heat, C_p , or enthalpy, H , of a material. The enthalpy is defined with respect to a reference temperature, T_{ref} , as:

$$H(T) = \int_{T_{\text{ref}}}^T C_p dT \quad (\text{Eq 2})$$

In terms of the enthalpy, thermal flux, and a distributed heat-source term, S ($J/m^3 \cdot s$), the energy equation in differential form is:

$$H - \nabla \cdot q - S = 0 \quad (\text{Eq 3})$$

or, in terms of temperature, it is:

$$\rho C_p T - \nabla \cdot (-\kappa \nabla T) - S = 0 \quad (\text{Eq 4})$$

This is a parabolic partial differential equation. The essential parts of any such equation are the boundary conditions, the initial conditions, and the parameters such as specific heat, C_p , thermal conductivity, κ , and heat source per unit volume, S . The boundary conditions can be either essential (prescribed temperature) or natural (prescribed thermal fluxes) for all time. The part of the boundary on which essential boundary conditions are prescribed is called $\partial\Omega_D$, whereas the part of the boundary on which natural boundary conditions are prescribed is called $\partial\Omega_N$. These two parts must make up the entire boundary, and they must not overlap at any point, that is, at no point can both be essential and natural. In mathematical terms, this is expressed as $\partial\Omega = \partial\Omega_D \cup \partial\Omega_N$ and $\partial\Omega_D \cap \partial\Omega_N = \emptyset$. The essential boundary condition is:

$$T(x, t) = F_D(x, t), \quad x \in \partial\Omega_D, t > 0 \quad (\text{Eq 5})$$

and the natural boundary condition is:

$$q(x, t) = F_N(x, t), \quad x \in \partial\Omega_N, t > 0 \quad (\text{Eq 6})$$

The initial conditions describe the distribution of temperature or enthalpy at all points in the interior of the domain, Ω , at time zero:

$$T(x, t) = F_{\text{init}}(x), \quad x \in \Omega, t = 0 \quad (\text{Eq 7})$$

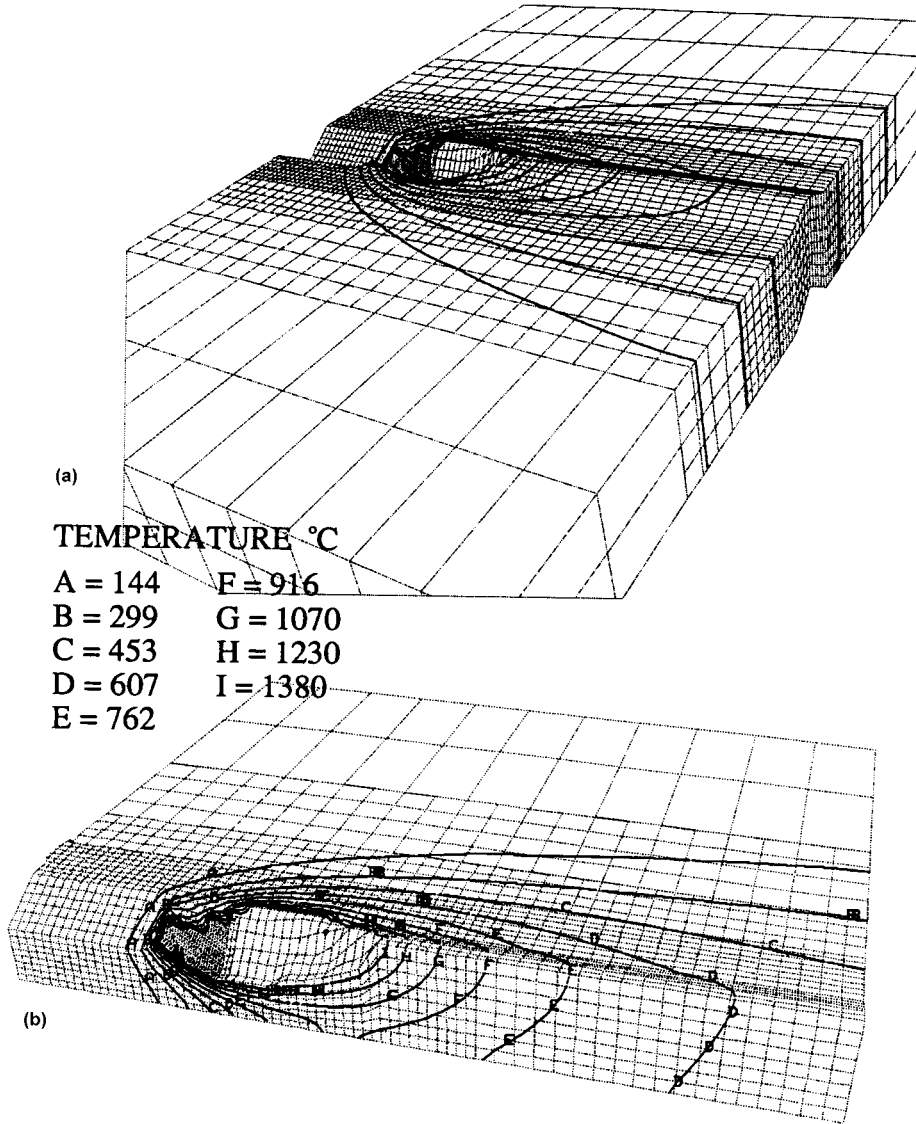


Fig. 2 Temperature contours of a weld in low-carbon steel. (a) For whole mesh. (b) For the region around the weld pool

pool is characterized by known data. The weld pool behavior has not been predicted. In order to predict weld pool behavior, most researchers would assume that the distribution of thermal flux, the current density, and the velocity and pressure in the arc are known data. With these data, they would solve the conservation of mass, momentum, and energy to compute the temperature, velocity, and pressure fields in the weld pool and the position of the weld-pool liquid-solid and liquid-plasma interfaces.

The proceedings of recent conferences in computational weld mechanics are now embodied in the literature (Ref 1–4).

Geometry of Weld Models

Most computational models have analyzed bead-on-plate welds, because of their

simple geometry. In addition to bead-on-plate welds, this discussion considers V-groove welds, girth welds, and branch welds on pipes (Fig. 1–9). The geometry specifies the region of space that is to be analyzed. This region is called the domain, Ω , and its boundary is denoted $\partial\Omega$. To analyze the weld, the geometry will usually be represented by a finite-element mesh. Because temperature, stress, and strain change rapidly near the weld, it is useful to use a fine mesh near the weld for resolution and accuracy. However, a coarse mesh is preferred at a site far from the weld, in order to reduce computational costs without unduly sacrificing accuracy or resolution. For this reason, it is desirable to have the ability to grade the mesh or to adaptively refine and coarsen a finite-element mesh for analyzing welds (Ref 5).

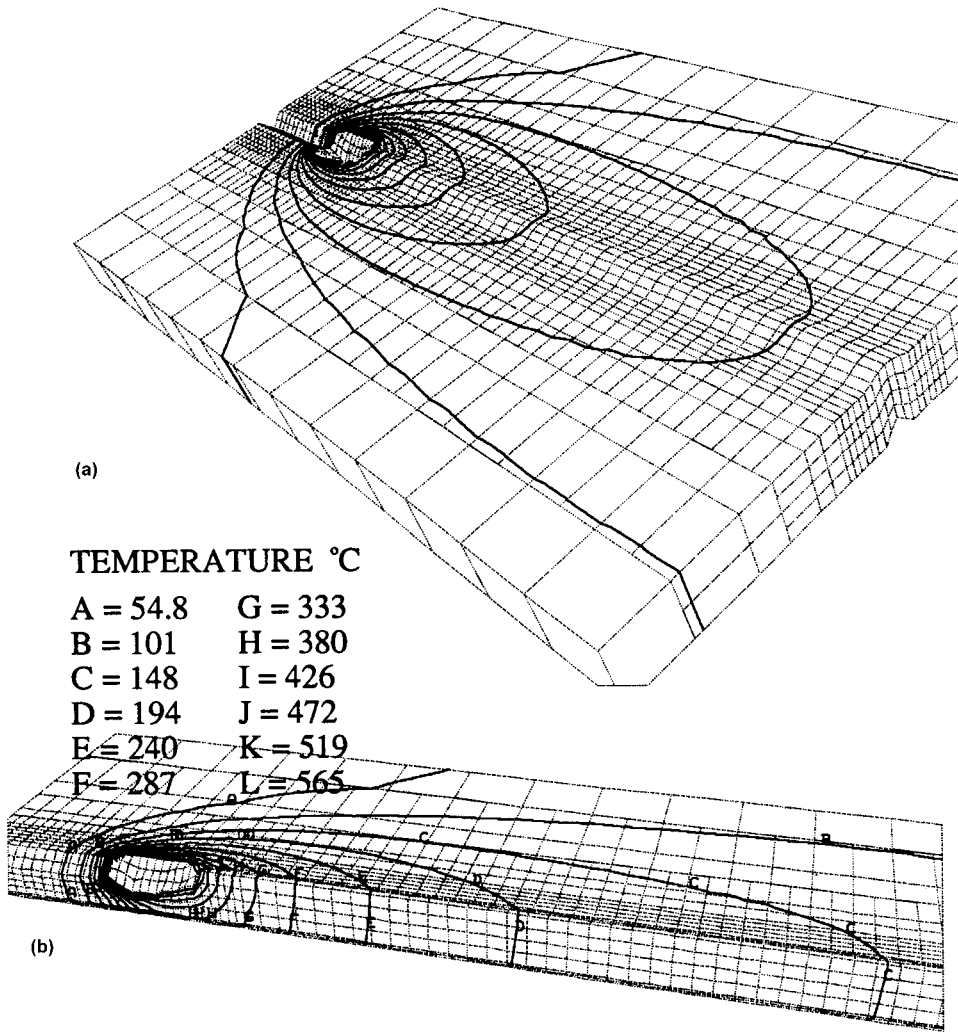


Fig. 3 Temperature contours of a weld in aluminum alloy. (a) For whole mesh. (b) For the region around the weld pool. Because the thermal diffusivity of aluminum is higher than steel, the mesh can be coarser, particularly in front of the weld pool.

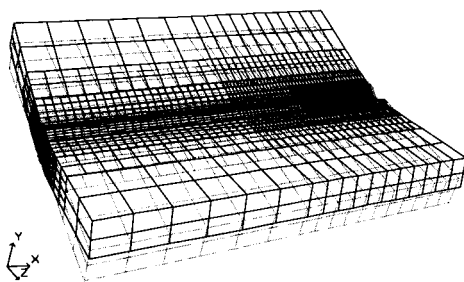


Fig. 4 Distortion (magnified by a factor of 2) of a steel plate

If the latent heat of phase transformations is to be considered, then the initial distribution of the density of each phase, ρ_i , is also needed:

$$\rho_i(x, 0) = \rho_{init}(x), \quad x \in \Omega, t = 0 \quad (\text{Eq 8})$$

The known functions, that is, data, are F_D , F_N , F_{init} , and ρ_{init} .

To include the effect of phase transformations, such as liquid to solid and the decomposition of austenite in low-alloy steels, it would be necessary to have equations describing the evolution of each phase. However, this has not been included in this energy equation. The latent heat of solid-state transformations, such as austenite to ferrite in steel, has a detectable effect on the temperature field, but it is not large. To date, this effect has not played an important role in the thermal analysis of welds.

Solving the Energy Equation. The energy equation defined previously can now be solved for a specific welding situation. Finite-element methods (FEMs) have been the method of choice for stress analysis. Finite-difference methods (FDMs) have been the method of choice for fluid flow. Whether the FDM or FEM method is best is an old argument. In rough terms, FEM has been used more frequently for complex geometries and for stress analysis, whereas FDM has been used

more frequently for fluid-flow analysis. However, FDM can be used for complex geometries that use body-fitted coordinates. Some have argued that FDMs are computationally more efficient than FEMs. The computational efficiency depends on the implementation. There is no fundamental reason why one method should have a computational advantage. The FEM is used here because of its familiarity and because it is better established for stress analysis.

The FDM directly discretizes the partial differential equation by approximating derivatives with finite-difference expressions. The FEM transforms the partial differential equation to an integral form and then approximates the integrals. A Green's identity is usually used to reduce the degree of the highest derivative from order two to order one. In addition, it introduces the natural boundary conditions in a natural and elegant manner. The resulting integrals are approximated by a finite set of basis functions, usually piecewise polynomials. The piecewise polynomials can be interpreted as being defined by choosing a mesh of elements and nodes. Within each element, a polynomial is chosen for each node. Usually, it has a value of 1 for its node and a value of 0 at all other nodes in the element.

These basis functions can be used to interpolate the temperature field by using the value of the temperature at each node. For example, if the (x,y) nodal coordinates of a triangle are $(1,0)$, $(0,1)$, $(0,0)$, and the basis functions for a triangle are chosen to be $\phi_1(x,y) = x$; $\phi_2(x,y) = y$; and $\phi_3(x,y) = 1 - x - y$, then the temperature at any point (x,y) in the element can be expressed as:

$$T(x, y) = \phi_1(x, y)T_1 + \phi_2(x, y)T_2 + \phi_3(x, y)T_3 \\ = \sum_{i=1}^3 \phi_i(x, y)T_i \quad (\text{Eq 9})$$

where T_i is the temperature at node i . Note that if distorted triangles are used, then understanding the mathematics becomes more complex, because the polynomial basis functions are distorted into rational functions. If the distortion is excessive, then the basis functions can become singular. However, distorted elements do not make FEM programs more difficult to use, as long as the distortion is not excessive.

To solve the energy equation defined previously, FEM can be interpreted as minimizing a potential, solving a variational problem, projecting an exact solution from an infinite dimensional space onto a finite dimensional space, or finding the best approximation to the exact solution in the finite dimensional space in some least-squares sense. All of these interpretations lead to the same set of ordinary differential equations, which can then be converted to the same set of algebraic equations in order to solve:

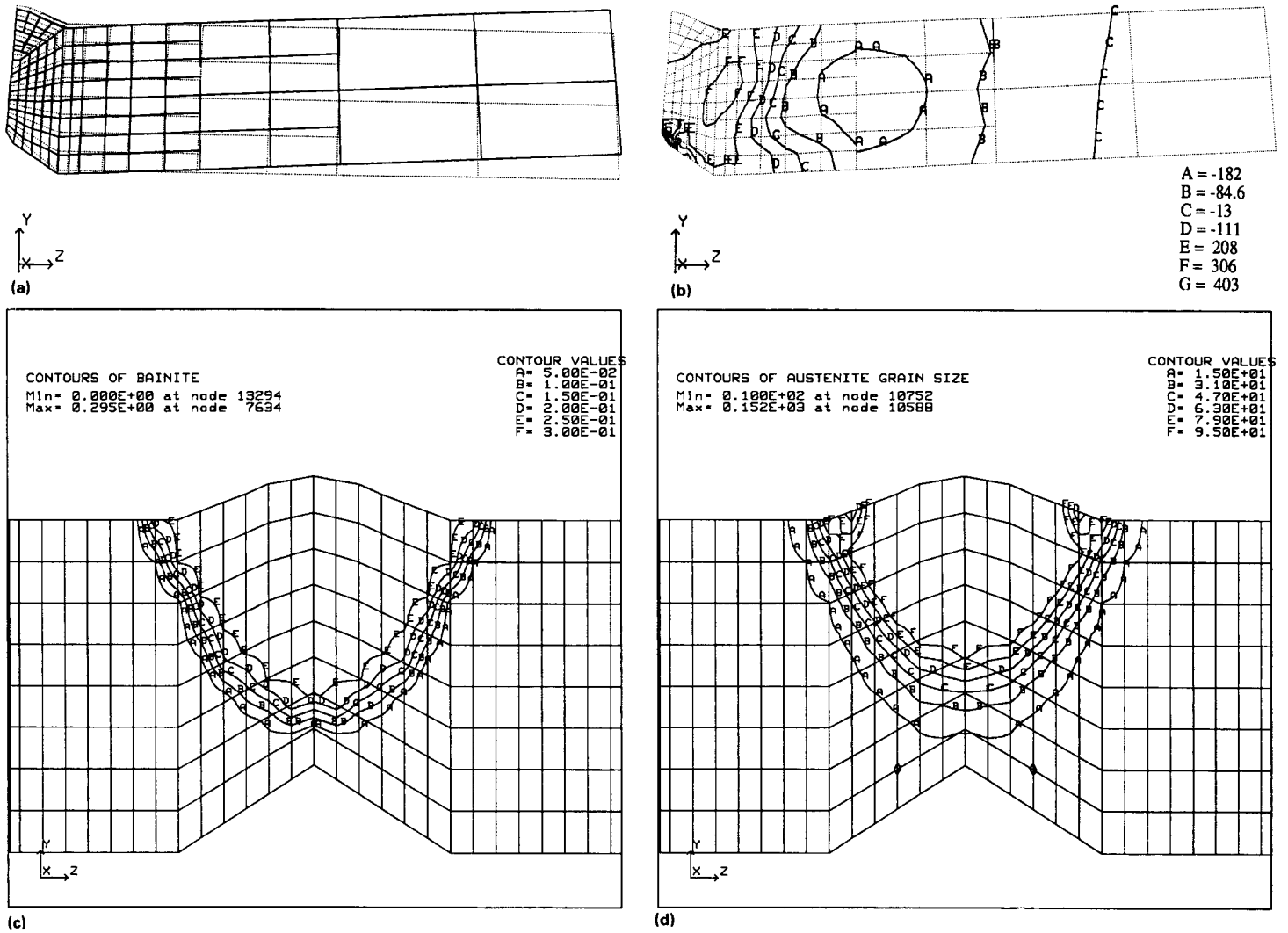


Fig. 5 (a) Distortion of weld shown in a cross section. Note the rigid body motion of the region far away from the weld nugget. (b) Contours of the longitudinal residual-stress component, σ_{xx} . Note that the maximum stress is not located at the surface. (c) Contours of fraction of bainite at end of weld; maximum fraction of bainite is just under 0.3. (d) Contours of prior-austenite grain size at the end of weld

$$\left(\bar{C}_p \frac{G}{\delta} + \theta K\right) \Delta T = S^1 - K T^1$$

$$-\bar{N}(U) H^1 \rightarrow K_{\text{eff}} \Delta T = b_{\text{eff}} \quad (\text{Eq 10})$$

where \bar{C}_p is the specific heat per unit volume, G is the gram matrix, δ is the length of the time step, θ is a parameter that determines the time-integration method, $\Delta T = T^3 - T^1$ is the increment in the temperature in this time step, S^1 is the nodal load vector that is due to external thermal loads, $\bar{N}(U) H^1$ is the nodal load vector that is due to advection evaluated at the beginning of the time step, K_{eff} is the effective stiffness matrix, and b_{eff} is the effective load vector.

For a detailed presentation of FEM theory, refer to any textbook on the subject, such as Ref 6 to 8. Space constraints here do not allow a more detailed explanation.

Because commercially competitive FEM programs typically require hundreds of man-years to write, as well as special expertise, it is assumed that most readers will choose not to write an FEM program, but will use an FEM program written by others. When choosing an FEM program, four main issues should be considered: functionality, computational efficiency, ease of use, and ease of learning. Because most of the costs of analysis are in preparing data and training, the latter two issues are nearly as important as functionality.

Convection, Radiation Boundary Conditions, and Contact Conductance. Given a body at temperature T immersed in a fluid at temperature T_{amb} , convection assumes that a thermal boundary layer exists with conductance, h ($\text{J}/\text{m}^2 \cdot \text{s} \cdot ^\circ\text{C}$), such that the

temperature difference across the boundary layer causes a flux, q ($\text{J}/\text{m}^2 \cdot \text{s}$), given by:

$$q_{\text{con}} = h(T - T_{\text{amb}}) \quad (\text{Eq 11})$$

If the fluid is flowing with velocity, v , and pressure, p , over a plate with a Prandtl number, Pr , and a Reynolds number, Re , then the convection coefficient can be estimated to be:

$$h = 0.332 \frac{k}{\lambda} \text{Re}^{1/3} \text{Pr}^{1/3} \quad (\text{Eq 12})$$

Given a body at temperature T radiating to a body at temperature T_{amb} , radiation assumes an emissivity and Stefan-Boltzmann constant, σ ($\text{J}/\text{m}^2 \cdot \text{s} \cdot \text{K}^4$), such that the temperature difference causes a flux, q ($\text{J}/\text{m}^2 \cdot \text{s}$), given by:

$$q_{\text{rad}} = \epsilon \sigma (T^4 - T_{\text{amb}}^4) \quad (\text{Eq 13})$$

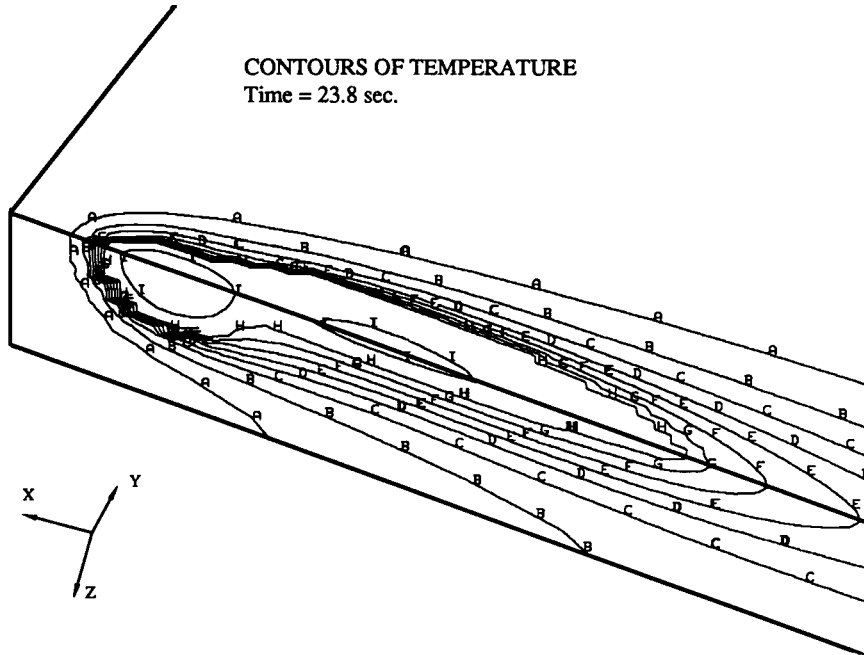


Fig. 6 Temperature isotherms near the weld pool in Barlow's weld. Note that contour "I" has two pools: one under the arc and one in the region behind the arc. This heat source was modeled as a prescribed-temperature region.

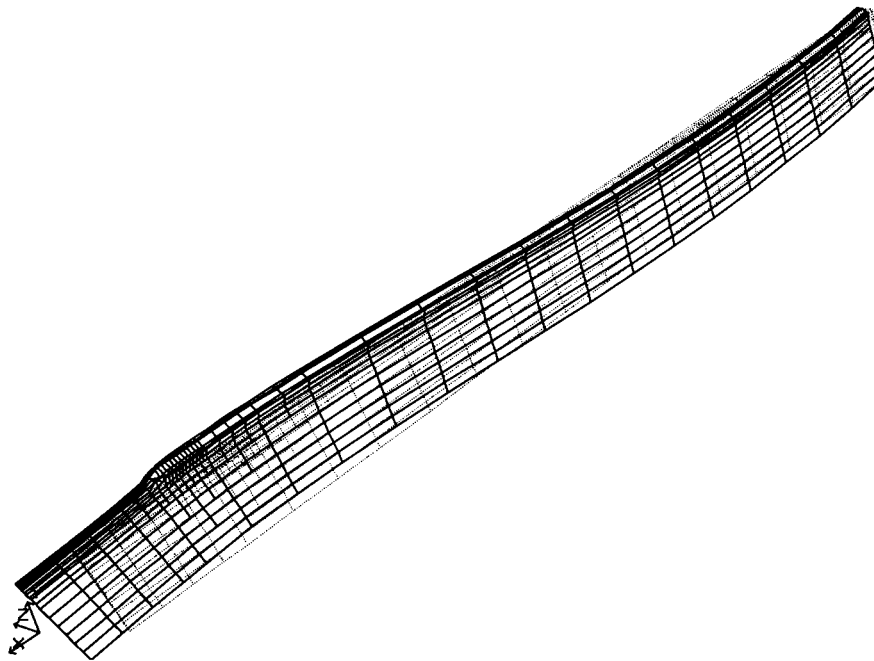


Fig. 7 Distortion of a bar being welded. Note the change of curvature. Near the weld pool, the center of curvature is below the bar. Far behind the weld pool, the center of curvature is above the bar.

This is usually linearized as:

$$q_{rad} = \epsilon \sigma (T^2 + T_{amb}^2)(T + T_{amb})(T - T_{amb}) \equiv h_{rad}(T - T_{amb}) \quad (\text{Eq 14})$$

Then, the effects of radiation and convection can be combined into a single effect if the

ambient temperatures are equal. Of course, the ambient temperature for convection and radiation need not be equal.

In an FEM program, this boundary condition is applied by specifying the values of the convection coefficient and the ambient temperature at the nodes on this part of the boundary.

The program computes a contribution to the nodal thermal load and the stiffness matrix.

Modeling the Heat Source in a Weld. Rosenthal (Ref 9) and Rykalin (Ref 10) modeled the heating effect of the arc traveling on a thick plate as a point source; that is, they assumed that all the energy is input into a point. In an FEM model, this could be approximated by specifying a thermal load at a node shared by very small elements.

It is worth exploring the difference between the FEM approximation and the Rosenthal solution for the point source. The most notable difference is that the temperature at the point source is infinite in the Rosenthal solution, whereas it is finite in the FEM approximation. The explanation is that in the Rosenthal solution, a finite amount of energy is being put into zero volume at the point. This causes an infinite temperature. In the FEM approximation, a finite amount of energy is being put into the elements containing the node, which is the point source. Because these elements have a finite volume, the temperature is finite.

If the temperature is plotted near the point source, the Rosenthal solution varies exponentially with position. The FEM solution has a polynomial dependence on position that comes from the polynomial basis functions. If the finite-element mesh size goes to zero, then the FEM approximation to the Rosenthal solution becomes more accurate.

Rosenthal and Rykalin chose a point source, not because they believed the arc was of zero size, but because it enabled them to solve the energy equation. Their solution was a useful approximation at points that were sufficiently accurate far from the arc. With the FEM, there is no advantage in choosing a point source. It is preferable to use a more-accurate approximation to the energy distribution in the arc.

Pavelic et al. (Ref 11) used a truncated Gaussian distribution of a prescribed flux in a circular disk moving with the arc over the weld joint. This can be accurate as long as the arc does not suppress the weld-pool surface too much and convection effects in the weld pool are not too large. If the arc-pool surface depression is large and/or if the velocity in the weld pool is large, then it can be more accurate to model the heat input, not as a distributed flux but as a distributed power density heat source that defines the heat input per unit volume per unit time at each point in the weld-pool region.

Goldak et al. (Ref 12) proposed a truncated Gaussian distributed heat source in a double-ellipsoid region. More-complex weld-pool shapes can be approximated by superimposing distributed heat sources.

Various phenomena can be introduced into these heat-source models, such as radiation, evaporation, and latent heat of fusion. However, it is useful to perform the following thought experiment to clarify their role. Assume that the exact temperature field is known as a function of time. Now, prescribe

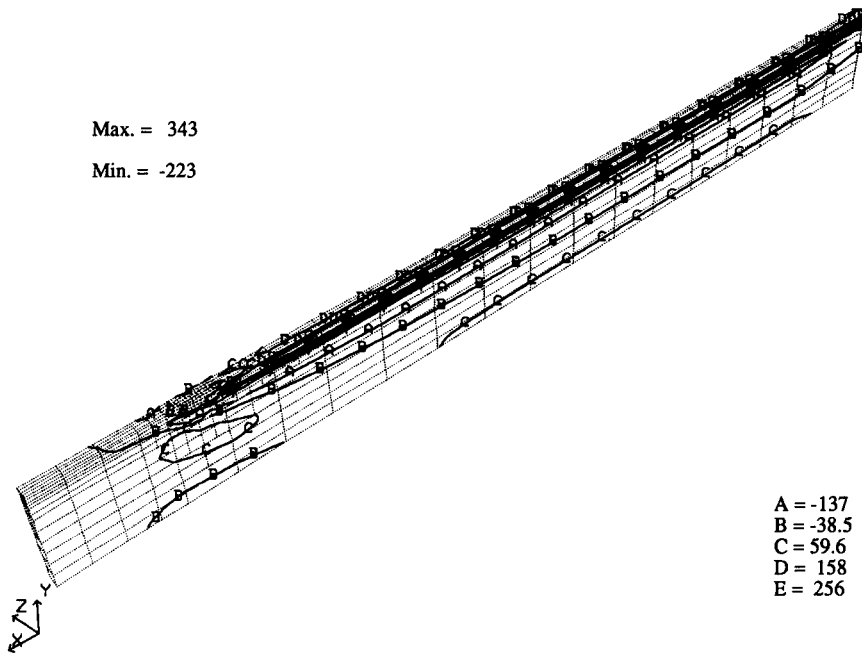


Fig. 8 Contours of the longitudinal stress for the weld shown in Fig. 7

TEMPERATURE °C

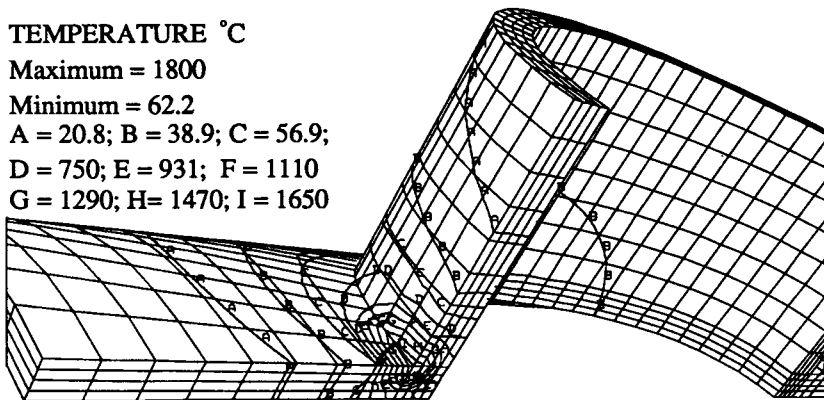
Maximum = 1800

Minimum = 62.2

A = 20.8; B = 38.9; C = 56.9;

D = 750; E = 931; F = 1110

G = 1290; H = 1470; I = 1650



TEMPERATURE °C

Maximum = 1800

Minimum = 62.2

A = 20.8; B = 38.9; C = 56.9;

D = 750; E = 931; F = 1110

G = 1290; H = 1470; I = 1650

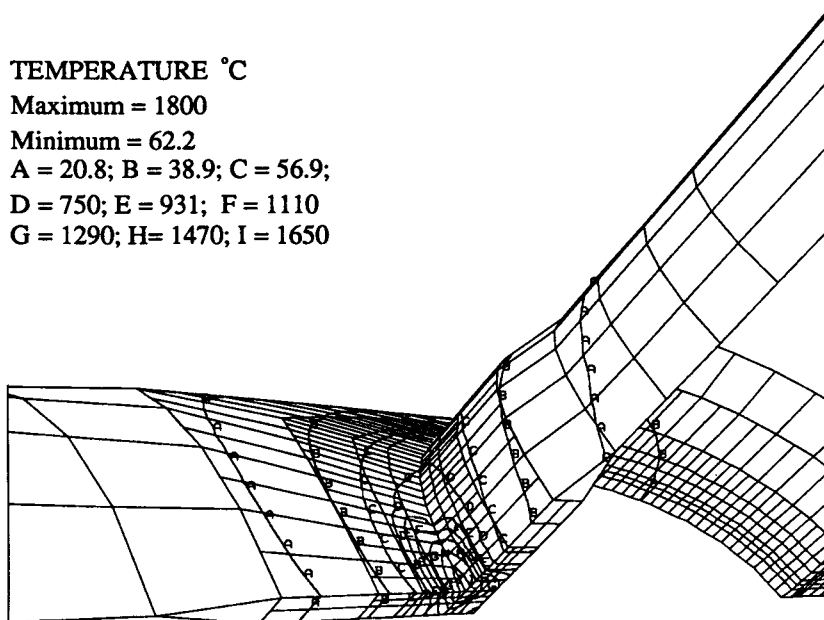


Fig. 9 Cutaway views of a branch pipe or T-joint weld. Top figure uses only eight node bricks. Note that the temperature gradient through the thickness of the pipe is negligible, except near the weld pool. The mesh in the bottom figure uses thermal shell elements and is both more accurate and more efficient.

that temperature field in the FEM equation. The reaction at each node is the nodal thermal load, which includes the net effect of all such phenomena. This can be for any shape of weld pool. Therefore, these phenomena can be included implicitly in the distributed heat source model, if desired, or they can be treated separately. If they are treated separately, then the definition and value of the distributed heat source should be changed accordingly.

Prescribed-Temperature Heat Source. If an estimate of the temperature in the weld pool is available, then it is often more convenient to model the heat source by prescribing the temperature in the weld-pool region (Ref 13). For example, the temperature on the surface of the weld pool and a cross section of the weld nugget could be measured. The liquid-solid interface could be assumed to be at or slightly below the solidus temperature. Then, nodes in the weld-pool region could have their temperatures prescribed. The reactions at these nodes would be the prescribed nodal thermal load that produces the same temperature distribution. Thus, the prescribed-temperature heat-source model and the prescribed distributed thermal load heat source are equivalent in the sense that either can be used to produce the same temperature solution. The experience of the authors has shown that estimating the prescribed-temperature distribution is much easier than estimating the distributed heat source, particularly for complex weld-pool shapes. For example, the authors were not able to estimate a distributed power density source that could model the weld shown in Fig. 6, whereas modeling this weld with a prescribed-temperature source was not difficult.

Material versus Spatial Reference Frames. Although Rosenthal used a spatial reference frame, most FEM analyses of welds have used a material reference frame. A spatial frame is fixed in space, and any space can be chosen. Rosenthal chose a space that was tied to the arc. It may be easiest to visualize this as an arc that is fixed in space, where the plate being welded moves under the arc through the spatial mesh. It is equally valid to imagine the plate fixed in one space and the arc fixed in a second space. In this case, Rosenthal used the second space.

A material reference frame defines the configuration of the body either at some point in time (usually, time zero) or at the beginning of each time step. The displacement field defines the mapping from the reference configuration to the configuration of the body at any other time. Imagine that each node in a finite-element mesh is associated with a material point. The node and its associated material point move through space as a function of time. This defines a material reference frame.

Most FEM analyses of welds have used a material reference frame, also called a Lagrangian reference frame, in which the heat source moves as a function of time. However, because the FEM is discretized in time, the usual FEM analysis is equivalent to a series of spot welds. If the time steps are sufficiently small so that

the distance the heat source moves in one time step is sufficiently small, such as half its diameter, then the effect of this discretization need not be excessive. If the time step is so large that the heat source moves more than, say, three times its diameter, for example, then the difference between the computed and measured temperature field will be large.

The use of a spatial frame, which is often called a Eulerian frame, avoids this problem. However, it introduces an advective term into the FEM equation. This term is nonlinear, and the usual formulation leads to an asymmetric set of equations to solve. Recently, Gu (Ref 14) implemented the Eulerian formulation and demonstrated its advantages (Fig. 1–5). The spatial frame enables longer time steps to be taken as the weld approaches steady state.

Transient versus Steady State. In a spatial frame that is tied to the heat source, the temperature near the arc of a long weld parallel to the prismatic axis of a prismatic body soon reaches a steady state. Indeed, the Rosenthal solution is an example of such a steady state. The weld pool typically reaches steady state in one to three weld-pool lengths. A rough guide is that any isotherm will approach the steady state in one to three isotherm lengths. Thus, lower temperatures require longer times and longer lengths to reach steady state. In analyzing long prismatic welds, computational efficiency can be gained by analyzing the steady state. Leblond et al. (Ref 15) and Gu (Ref 14) provide details, and the results of a steady-state analysis are shown in Fig. 1 to 5.

Modeling the Addition of Filler Metal. Bead-on-plate welds can have the simplest geometry and meshes, and they can exploit symmetry to reduce computing costs. When joint details are included, the mesh is somewhat more difficult to create. If welds are not on the symmetry plane, then symmetry cannot be exploited and the computational cost increases. These difficulties are minor, when compared with the difficulties of modeling the addition of filler metal. The first models used a material reference frame, created a mesh, and then turned on or activated those elements to which filler metal was added as they filled (Ref 14, 16). When it is applicable, a spatial frame offers a more-elegant approach, because the weld pool can be fixed or varied slowly, as desired (Ref 14) (Fig. 6). Figures 2 and 3 show the transient temperature field in a groove weld with added filler metal.

Microstructure Evolution

Microstructure strongly affects the material behavior and hence constitutive parameters, such as thermal conductivity, specific heat, and Young’s modulus. Volume changes associated with phase changes, such as austenite to ferrite, can cause large strains. For these

reasons, microstructure can have a dominant effect in the stress analysis of a weld.

This discussion is limited to welds in low-alloy steels. The phase, or equilibrium, diagram identifies the phases that are present, their composition, and the fraction of each phase present in a steel as a function of alloy composition, temperature, and pressure. Because as many as 10 alloying elements can be significant in low-alloy steel, the phase diagram could be in a space of 11 dimensions. To make this more tractable, this discussion uses pseudobinary iron-carbon diagrams. As functions of composition, the Ae_3 (austenite to austenite-ferrite line) and Ae_1 (eutectoid) temperatures are of particular interest when analyzing the decomposition of austenite.

At each temperature, the system tends to equilibrium. Phases that are unstable tend to transform to stable phases. Although the direction is largely controlled by thermodynamics, the rate is largely governed by kinetics. Following Kirkaldy (Ref 17), it is assumed that the decomposition of austenite into ferrite, pearlite, and bainite can be described by ordinary differential equations of the form:

$$\frac{df}{dt} = B(G, T)f^m(1 - f)^p \tag{Eq 15}$$

where $(1 - f)$ is the fraction of austenite; f is the fraction of the transformation product, for example, ferrite; the function $B(G, T)$ reflects the influence of grain size, undercooling, the alloy and temperature dependence of the solute diffusivity, and the phase fractions that are present; and m and p are parameters of the alloy system. This is essentially the model that was developed by Henwood et al. (Fig. 10). It was used to compute the microstructures in the heat-affected zone (HAZ) of the problems analyzed in Ref 19. Vandermeer (Ref 20) has proposed a modification to include the effect of carbon accumulation in the austenite during the transformation.

Austenite grain growth in the HAZ is computed from the ordinary differential equation:

$$\frac{dG}{dt} = \frac{1}{2G}ke^{-Q/RT} \tag{Eq 16}$$

where G is the austenite grain size, k is a parameter, Q is the activation energy, R is the

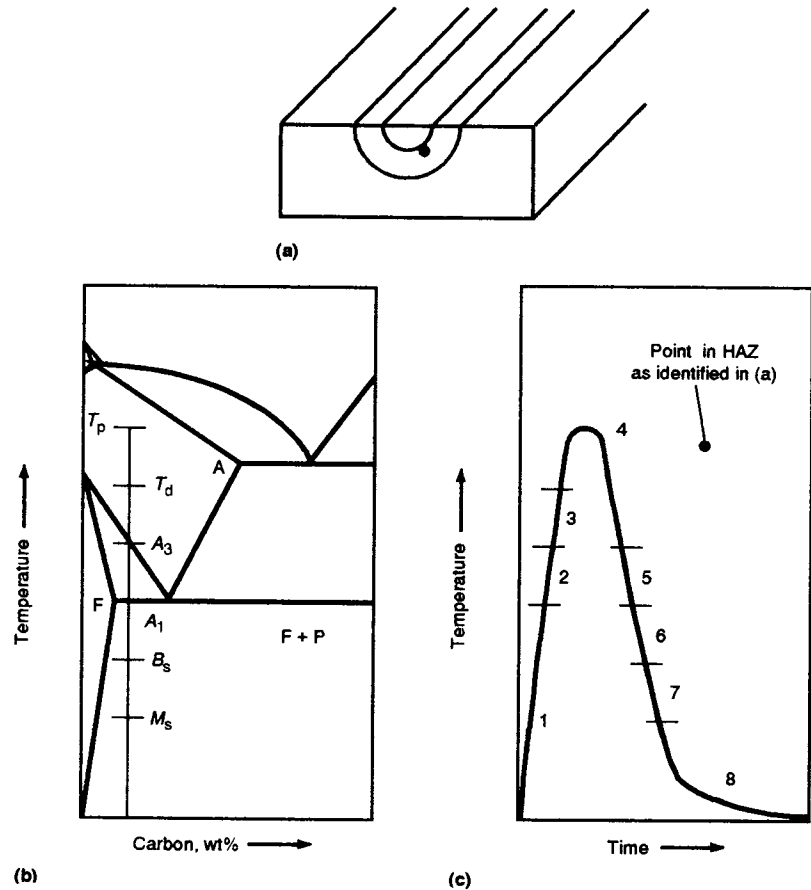


Fig. 10 (a) Schematic cross section of a bead-on-plate weld, identifying a point in the heat-affected zone (HAZ). (b) Iron-carbon phase diagram, identifying the cooling path and critical temperatures. (c) Thermal cycle, identifying the regions that must be considered when implementing the microstructure algorithm. Source: Ref 18

universal gas constant, and T is the absolute temperature. The grain size of austenite has a dominant effect on the hardenability of steel and hence the decomposition of austenite. The authors suspect that errors in the predicted austenite grain size are a significant cause of errors in the evolution of microstructure in the HAZ. In particular, this grain size is the average grain size. The equation was developed for grain growth in annealing essentially homogeneous regions. In a heterogeneous HAZ with steep temperature gradients across single grains, it is not clear that this equation is appropriate (Ref 21).

The aforementioned microstructure models, with the exception of that proposed by Vandermeer, do not consider the composition of each phase or the composition changes that are due to solute diffusion between phases. They only consider the composition of the system. Phase fractions are density functions that specify the mass fraction of a phase per unit volume. Grain size is also a density function. Thus, there is no representation of the microstructure and no capability to draw the microstructure being analyzed.

Thermal Stress Analysis of Welds

Stress analysis deals with the equilibrium of forces, the kinematics of deformation, and the relationship between deformation and force. The existence of a stress tensor field, a strain tensor field, a displacement vector field, and a constitutive relationship between stress and strain are assumed. The conservation of momentum is the fundamental conservation law.

From another viewpoint, the equilibrium of forces is expressed by the conservation of momentum and the definition of the stress tensor, σ , the traction vector, τ , and the body force, b , in the differential equation:

$$\nabla \cdot \sigma + b = m\ddot{x} \quad (\text{Eq 17})$$

In welding, it is typical to assume that the inertial forces are negligible, that is, $m\ddot{x} \approx 0$. This implies that the rate of change of loads is small, relative to the time required for a stress wave to propagate across the domain and for a stress wave to decay.

The solvability equations require the integrals of the external forces, that is, the traction vector, τ , and the body force, b , to be in equilibrium with themselves:

$$\int_{\Omega} b \, d\Omega + \int_{\partial\Omega} \tau \, d\Omega = 0 \quad (\text{Eq 18})$$

Whether or not the deformed body is rigid, the external forces must be in equilibrium.

The kinematics or deformation is described by the displacement and strain fields. For a total displacement field, $[u, v, w]^T = [u(x, y, z, t), v(x, y, z, t), w(x, y, z, t)]^T$, at the point (x, y, z, t) , the Green's strain is defined as:

$$\epsilon = \frac{\nabla u + \nabla u^T + \nabla u^T \nabla u}{2} \quad (\text{Eq 19})$$

where ∇u is the deformation gradient:

$$\nabla u = \begin{bmatrix} \frac{\partial u}{\partial x} & \frac{\partial v}{\partial x} & \frac{\partial w}{\partial x} \\ \frac{\partial u}{\partial y} & \frac{\partial v}{\partial y} & \frac{\partial w}{\partial y} \\ \frac{\partial u}{\partial z} & \frac{\partial v}{\partial z} & \frac{\partial w}{\partial z} \end{bmatrix} \quad (\text{Eq 20})$$

The Green's strain is a symmetric tensor. It measures the change in distance between points in the neighborhood of a point caused by the deformation.

The material properties are described by the constitutive, or stress-strain, relationship, $\sigma = D\epsilon$, where D is the fourth-order tensor that maps the elastic strain tensor to the stress tensor. Thermodynamic arguments require D to be symmetric positive definite. For isotropic elastic materials, D is defined by two constants, such as Young's modulus and Poisson's ratio.

Most FEM analyses of welds have used an additive decomposition of the total strain rate into elastic, thermal, plastic, and transformation plasticity strain rates:

$$\dot{\epsilon}^{\text{Tot}} = \dot{\epsilon}^{\text{Elas}} + \dot{\epsilon}^{\text{Therm}} + \dot{\epsilon}^{\text{Plas}} + \dot{\epsilon}^{\text{TransPlas}} \quad (\text{Eq 21})$$

Plasticity theory and numerical algorithms based on the multiplicative decomposition of the deformation gradient $\mathbf{F} = \mathbf{F}^e \mathbf{F}^p$ were developed in the period 1985 to 1994 (Ref 22). This theory is better suited to finite strain analyses. Although the creep strain rate could be included, the authors are not aware of published studies of creep in the modeling of welds, to date.

Equation 18 is an elliptic partial differential equation. Boundary conditions are an essential part of any such equation, and they can be either essential (prescribed displacement) or natural (prescribed traction). They must be prescribed for all time. The part of the boundary on which essential boundary conditions are prescribed is called $\partial\Omega_D$, whereas the part of the boundary on which natural boundary conditions are prescribed is called $\partial\Omega_N$. These two parts must make up the entire boundary, and they must not overlap at any point. In mathematical terms, this is expressed as $\partial\Omega = \partial\Omega_D \cup \partial\Omega_N$ and $\partial\Omega_D \cap \partial\Omega_N = 0$. The essential boundary condition is:

$$u(x, t) = F_D(x, t), \quad x \in \partial\Omega_D, t > 0 \quad (\text{Eq 22})$$

The natural boundary condition is:

$$\tau(x, t) = F_N(x, t), \quad x \in \partial\Omega_N, t > 0 \quad (\text{Eq 23})$$

Although an elliptic boundary value problem does not have initial conditions, initial data describing the distribution of the displacement, strain, or stress can be specified at all points in the interior of the domain, Ω , at time zero:

$$\begin{aligned} \sigma(x, t) &= F_{\text{init}}(x), \quad x \in \Omega, t = 0 \\ \epsilon(x, t) &= F_{\text{init}}(x), \quad x \in \Omega, t = 0 \\ u(x, t) &= F_{\text{init}}(x), \quad x \in \Omega, t = 0 \end{aligned} \quad (\text{Eq 24})$$

If microstructure evolution is considered, then only the macroscopic (average) stress, strain, and displacement fields will be considered. In other words, the variations in the fields, below some length scale, are averaged or ignored. This is inherent in a finite-element mesh, because an FEM analysis cannot detect spatial frequencies higher than those captured by the polynomials in the mesh.

Given the transient temperature-rate field in a weld, the thermal volumetric strain rate is:

$$\begin{aligned} \dot{\epsilon}^{\text{Therm}} &= \bar{\alpha} T \\ \delta t \dot{\epsilon}^{\text{Therm}} &\approx \Delta \epsilon^{\text{Therm}} = \alpha \Delta T \\ \bar{\alpha} &= \alpha + \frac{d\alpha}{dT} (T - T_{\text{ref}}) \end{aligned} \quad (\text{Eq 25})$$

The coefficient of thermal expansion, α , is a property of the material.

If the stress, body force, traction, strain, and displacement fields are sufficiently smooth, then this is a well-posed problem and the mathematics is well understood. The aforementioned continuum mechanics problem can be solved by an FEM approximation. In particular, the total strain rate is approximated by:

$$\dot{\epsilon}^{\text{Tot}} = B\dot{u} \quad (\text{Eq 26})$$

where \dot{u} is the nodal displacement rate or velocity, and B is the discrete symmetric gradient operator.

Examples of stress analysis of welds are shown in Fig. 7 and 8. For a general reference on continuum mechanics and stress analysis, refer to Ref 23 and 24.

Transformation Plasticity. Although the transformation of austenite to ferrite, pearlite, bainite, and martensite causes only a small effect on the temperature field, it can have a major effect on the stress field. This arises through the phenomenon of transformation plasticity (Ref 25, 26). The rate of transformation of austenite, \dot{Z} ; the deviatoric stress, τ_{ij} , and constant, K , that includes the volume change associated with the phase change; and the yield strength all determine a contribution to the strain rate and strain increment, given by:

$$\dot{\epsilon}_{ij}^{\text{TransPlas}} = K \tau_{ij} \dot{Z} \quad \Delta \epsilon_{ij}^{\text{TransPlas}} = \int_{t_1}^{t_2} K \tau_{ij} \dot{Z} d\xi \quad (\text{Eq 27})$$

This effect is greatest in high-strength steels such as HY-80 because the decomposition of austenite occurs at lower temperatures, where the volume change associated with the phase change is largest (Fig. 11). In addition, plastic deformation that occurs after the phase transformation is complete tends to hide or blur the effects of transformation plasticity. When the transformation occurs closer to room temperature, the effects of transformation are blurred

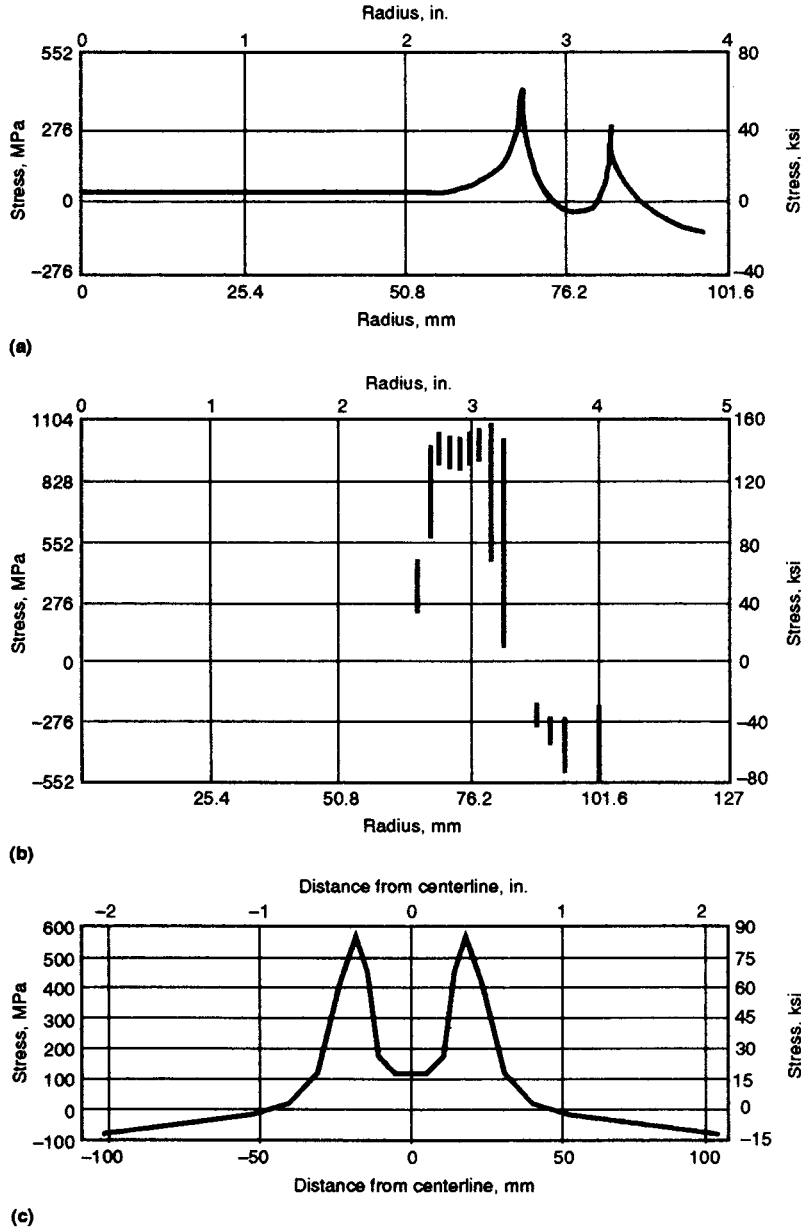


Fig. 11 (a) Experimental data published by Corrigan (Ref 27) for the residual stress in an HY-130/150 weld. (b) Predicted values of residual stress, published by Hibbitt and Marcal (Ref 28), who ignored the austenite-to-martensite transformation in their finite-element method (FEM) analysis of the residual stress. (c) Predicted values of longitudinal residual stress, as predicted by FEM analysis of Oddy (Ref 26), who has taken into account the effects of the phase transformation and transformation plasticity. Clearly, the effects of the phase transformation dominate the stress analysis in this case.

the least. In lower-strength steels and higher weld heat inputs, the transformation of austenite tends to occur nearer the eutectoid temperature, and the effect on the final residual-stress state is less pronounced.

Because the transformation plastic strain rate strongly affects the deviatoric stress, and because the deviatoric stress strongly affects the transformation plastic strain rate, the integration of Eq 27 requires some care in order to avoid instability. Details are provided in (Ref 26).

Stress Analysis near the Weld Pool. At temperatures below 800 to 1200 °C (1470 to 2190 °F) in steel welds, it has often been assumed that the viscous strain, or creep, rate can be neglected in welds, because the time at high temperatures is relatively short. If this assumption is accepted, then the material can be modeled as a thermoelastoplastic material. The theory for this is rather well accepted. Above some temperature, it is expected that the viscous strain, or creep, rate will become important, possibly becoming the dominant

deformation mechanism, in which case the material would behave as a viscoelastoplastic material. The theory for this behavior is not well established.

When a solid melts, the material changes from elastic behavior to a viscous fluid. This change is reflected in the Deborah number. It has been argued that even at the melting point, the crystal maintains a yield strength of the order of 5 MPa (0.7 ksi). When it melts, the yield stress drops to zero. Matsunawa (Ref 29) estimated that the viscosity of a liquid increases by a factor of 2×10^{13} upon solidification. The essence of elastic behavior is the existence of a reference state with zero stress. In a crystal, this reference state is crystal lattice. A liquid has no such reference state. Thus, there is a profound change in the physical behavior and the relevant mathematics upon melting. To deal with the change, the liquid and solid regions are typically considered as separate problems. On the interface, the temperature and the traction are continuous.

Because the authors do not know of any careful stress analysis in this temperature range for welds, this problem is left open.

Stress Analysis of Welds in Thin-Walled Structures. The use of plate and shell FEM elements can reduce cost and improve numerical accuracy significantly (Ref 30, 31). These elements usually assume that those stress components that project onto the normal-to-the-midsurface plane are zero, that is, s_{zz} , s_{xz} , and s_{yz} are 0 if the z -axis is normal to the midsurface. In heat-transfer analysis, the projection of the temperature gradient onto the midsurface normal plane is assumed to be 0, that is, $\partial T/\partial z = 0$. This is usually an excellent approximation, except near the intersection of surfaces, such as a pipe T-joint. It can be a good approximation of near-deep-penetration electron-beam and laser-beam welds but is usually not accurate near arc weld pools. Figure 9 shows an example of a weld that would not be accurately approximated by shell elements near the weld pool. Except in such regions, shell and plate elements can be effective. Combining shell and brick elements often provides the best approximation.

Fluid Flow in the Weld Pool

Thus far, weld pool data, that is, an adequate approximation of size, shape, and position, have been known as functions of time. Either the weld pool temperature or the power density and thermal flux distribution also have been known as functions of time. To predict weld penetration, solidification mode and microstructure, and other phenomena that are sensitive to the weld-pool physics, such as hot cracking and the stress and strain near the weld pool, it is necessary to model the weld pool. The model should predict the temperature, pressure, and velocity distribution in the weld pool, as well as the position of the liquid-solid and

liquid-plasma boundaries. It is also desirable to predict the current density, velocity, and pressure fields in the arc. Matsunawa (Ref 29) presents an excellent review of weld-pool analyses.

The major forces that drive convection in the weld pool are electromagnetic, gravitational or buoyancy, surface tension, and aerodynamic drag. The electromagnetic and gravitational forces act on the interior of the weld pool, whereas the surface tension and aerodynamic drag forces act on the surface, producing a traction force.

The conservation of mass, or continuity, equation for an incompressible liquid in the weld pool is:

$$\nabla \cdot \mathbf{v} = 0 \quad (\text{Eq 28})$$

The conservation of momentum in the interior of the weld pool in spatial coordinates is:

$$\rho \dot{\mathbf{v}} + \rho \mathbf{v} \cdot \nabla \mathbf{v} + \nabla p + \nabla \cdot \boldsymbol{\mu} \nabla \mathbf{v} + \mathbf{J} \times \mathbf{B} + \mathbf{f} \quad (\text{Eq 29})$$

where ρ is the density, and p is the pressure. The boundary conditions on the weld pool and arc interface are the traction that is due to the gradient in the surface tension, $-(\partial\gamma)/(\partial T)\nabla_s T$, and the traction, τ_D , that is due to drag from the velocity of the plasma:

$$\boldsymbol{\sigma} \cdot \mathbf{n} = -\mu \dot{\mathbf{e}} \cdot \mathbf{n} = -\frac{\partial\gamma}{\partial T} \nabla_s T + \tau_D \quad (\text{Eq 30})$$

where \mathbf{n} is the direction normal to the weld pool and arc interface, and the gradients are gradients in the surface. On the interface between the weld pool and solid, the velocity is zero, and the traction vector is continuous. The pressure must be specified at one point in the weld pool. When dealing with an incompressible fluid, it is important to remember that the pressure is not a thermodynamic variable but a constraint to enforce incompressibility.

The conservation of energy in the interior of the weld pool in spatial coordinates is:

$$\rho \frac{\partial H}{\partial t} + \rho \mathbf{v} \cdot \nabla H = \nabla \cdot \boldsymbol{\kappa} \nabla \mathbf{v} + \mathbf{f} \quad (\text{Eq 31})$$

The velocity in the energy equation is determined from the momentum and continuity equation. The thermal flux from the arc is prescribed on the weld pool and arc interface. With these data, the energy equation determines the position of the liquid-solid interface. With a new temperature distribution, the momentum equation is solved. If this iteration procedure converges, then the result is said to be a solution.

The mathematical nature of the aforementioned equations that model the weld pool and their numerical solution is significantly more difficult than those needed to model the behavior of welds below, say, 0.7 of the melting temperature. The physics is also more difficult. Most analyses of the weld pool have used either finite-difference or finite-volume methods.

They have achieved interesting results and have done much to clarify the physics of the weld pool. However, in Matsunawa's view (Ref 29), the capability to accurately predict weld-pool shape and size is still limited. See Ref 30 and the references therein for more recent research on weld-pool modeling. Continued progress in weld-pool modeling is needed and can be expected.

Acknowledgment

The financial support of the National Science and Engineering Research Council is gratefully acknowledged.

REFERENCES

1. S.A. David, T. DeRoy, J.N. DuPont, T. Koseki, and H.B. Smartt, Ed., Technology and Engineering, *Trends in Welding Research, Proceedings of the Eighth International Conference*, June 2–5, 2008 (Callaway Gardens Resort, Pine Mountain, GA), ASM International, 2009
2. L. Karlsson, Ed., *Mechanical Effects of Welding, IUTAM Symposium* (Luleå, Sweden), International Union of Theoretical and Applied Mechanics, June 1991
3. H. Cerjak, H.K.D.H. Bhadeshia, and N. Enzinger, Ed., *Ninth International Seminar on Numerical Analysis of Weldability*, Sept 28–30, 2009 (Graz-Seggau, Austria)
4. T.H. North, Ed., *Proc. Int. Institute of Welding Congress on Joining Research*, Chapman and Hall, July 1990, p 69–82
5. M. McDill, A. Oddy, and J. Goldak, An Adaptive Mesh-Management Algorithm for Three-Dimensional Automatic Finite Element Analysis, *Can. Soc. Mech. Eng.*, Vol 15 (No. 1), 1991
6. K.J. Bathe, *Finite Element Procedures in Engineering Analysis*, Prentice-Hall, 1982
7. C. Johnson, *Numerical Solution of Partial Differential Equations by the Finite Element Method*, Cambridge Press, 1987
8. T.J.R. Hughes, *The Finite Element Method: Linear and Static and Dynamic Finite Element Analysis*, Prentice-Hall, 1987
9. D. Rosenthal, The Theory of Moving Sources of Heat and Its Application to Metal Treatments, *Trans. ASME*, Vol 68, 1946, p 849–865
10. R.R. Rykalin, Energy Sources for Welding, *Welding in the World*, Vol 12 (No. 9/10), 1974, p 227–248
11. V. Pavelic, R. Tanbakuchi, O.A. Uyehara, and P.S. Myers, Experimental and Computed Temperature Histories in Gas Tungsten-Arc Welding Thin Plates, *Weld. J. Res. Suppl.*, Vol 48, 1969, p 295s–305s
12. J.A. Goldak, A. Chakravarti, and M.J. Bibby, A New Finite Element Model for Welding Heat Sources, *Trans. AIME*, Vol 15B, June 1984, p 299–305
13. J. Goldak, M.J. Bibby, and M. Gu, Heat and Fluid Flow in Welds, *Proc. Int. Institute of Welding Congress on Joining Research*, T.H. North, Ed., Chapman and Hall, July 1990, p 69–82
14. M. Gu and J. Goldak, Steady State Thermal Analysis of Welds with Filler Metal Addition, *Can. Metall. Q.*, Vol 32, 1993, p 49–55
15. J.B. Leblond, Three-Dimensional Simulation of a Laser Surface Treatment through Steady State Computation in the Heat Source's CoMoving Frame, *Proc. Modeling of Casting, Welding and Advanced Solidification* (Davos, Switzerland), TMS, Sept 1990
16. R.I. Karlsson and B.L. Josefson, Three Dimensional Finite Element Analysis of Temperature and Stresses in Single-Pass Butt Welded Pipe, *J. Pressure Vessel Technol.* (Trans. ASME), Vol 11 (No. 2), Feb 1990, p 76–84
17. J.S. Kirkaldy and D. Venoguplan, *Phase Transformations in Ferrous Alloys*, A.R. Marder and J.L. Goldenstein, Ed., AIME, 1984, p 125–148
18. C. Henwood, M.J. Bibby, J.A. Goldak, and D.F. Watt, Coupled Transient Heat Transfer-Microstructure Weld Computations, *Acta Metall.*, Vol 36 (No. 11), 1988, p 3037–3046
19. M. Gu and J. Goldak, Modelling the Evolution of Microstructure in the Heat-Affected Zone, *Can. Metall. Q.*, Vol 32 (No. 4), 1993, p 351–362
20. R.A. Vandermeer, Modeling Diffusional Growth during Austenite Decomposition to Ferrite in Polycrystalline Fe-C Alloys, *Acta Metall.*, Vol 38 (No. 12), 1990, p 2461–2470
21. D.G. Tecco, The Effects of Micro-Alloy Level over the Kinetics of Grain Growth in Low-C HSLA Heat-Affected Zones, *Proc. Int. Trends in Welding Research* (Gatlinburg, TN), S. David and J. Vitek, Ed., ASM International, June 1992
22. J.C. Simo, Numerical Analysis of Classical Plasticity, *Handbook for Numerical Analysis*, Vol IV, P.G. Ciarlet and J.J. Lions, Ed., Elsevier, Amsterdam, 1998
23. L.E. Malvern, *Introduction to the Mechanics of a Continuous Medium*, Prentice-Hall, 1969
24. M.E. Gurtin, *An Introduction to Continuum Mechanics*, Academic Press, 1981
25. J.B. Leblond, G. Mottet, and J.C. Devauz, A Theoretical and Numerical Approach to the Plastic Behavior of Steels during Phase Transformations—I. Derivation of General Relations, *J. Mech. Phys. Solids*, Vol 34 (No. 4), 1986, p 395–409
26. A.S. Oddy, J.A. Goldak, and J.M. McDill, Numerical Analysis of Transformation Plasticity in 3D Finite Element Analysis of Welds, *Euro. J. Mech.*, Vol 9 (No. 3), 1990, p 253–263

27. D.A. Corrigan, "Thermomechanical Effects in Fusion Welding of High Strength Steels," Ph.D. thesis, Massachusetts Institute of Technology, 1966
28. H.D. Hibbit and P.V. Marcal, A Numerical Thermo-Mechanical Model for the Welding and Subsequent Loading of a Fabricated Structure, *Comput. Struct.*, Vol 3, 1973, p 1145-1174
29. A. Matsunawa, Modeling of Heat and Fluid Flow in Arc Welding, *Proc. Int. Trends in Welding Research* (Gatlinburg, TN), S. David and J. Vitek, Ed., ASM International, June 1992
30. L. Lindgren and L. Karlsson, Deformations and Stresses in Welding of Shell Structures, *Int. J. Num. Meth. Eng.*, Vol 25, 1988, p 635-655
31. M. Gu, J. Goldak, and K. Haaland, Mixing Thermal Shell and Brick Elements in FEA of Welds, *Proc. Offshore Mechanics and Arctic Engineering Conference* (Stavanger, Norway), ASME, June 1991

Modeling of Thermomechanical Phenomena in Fusion Welding

C. Schwenk, BAM—Federal Institute for Materials Research and Testing, Berlin, Germany

THE LONG-TERM TARGET in the processing industry is to fully cover the production process—from the raw material, through the individual fabrication steps, to the end product—in the form of a so-called virtual process chain. A continuous simulation of all relevant fabrication segments is necessary to achieve a reduction of development and fabrication costs but more importantly, an optimization of the products and all fabrication procedures. An essential link in this virtual process chain is welding simulation, because of the central position of welding in the process chain.

Welding simulation enables early statements to be made regarding the thermomechanical phenomena in fusion welding, that is, mainly the welding-specific temperature fields, distortions, and residual stresses in components. Therefore, simulation helps to minimize the number of iteration loops currently required in the development process by adopting the simultaneous engineering concept. In addition, it provides information that can only be gained experimentally with disproportionately high expenditure or sometimes not at all, for example, transient evolution of thermal strains in the overall component during the ongoing process. Hence, simulation provides a basis for specific identification of the causes of welding-induced distortion and residual-stress conditions, thereby permitting a structured approach to component and process optimization.

Basic Principles and Heat Effects of Welding

A particularly significant potential application of welding simulation is seen in the engineering services market. Increasingly, large corporate groups (original equipment manufacturers) delegate the development of individual components to industry suppliers (in most cases, small- and medium-sized enterprises), to whom a time-saving and cost-efficient development process is of vital interest because of sharply increasing requirements and

international competition. Welding simulation can make valuable contributions to assist them; some industrial application examples are given in Ref 1. For trouble-free communication with the customers, a defined and generally applicable guideline for execution, analysis, and postprocessing is imperative to assure reliability and relevance of the calculation results. Furthermore, a defined mode for displaying results will provide a basis for effective comparison of various computation projects. Such certainty is essential to both the potential customers and the respective contractors. It helps to encourage a wide application of welding simulation and hence to fully exploit the potential of this powerful computational method. While being covered by various welding simulation tools that are designed for fast and easy prediction of the heat effects of welding via special modeling approaches, these aspects are not generally covered for transient three-dimensional (3-D) numerical welding simulation because of the complexity of the application and the necessary user experience. For differentiating the applicability of various welding simulation methods as well as unifying the prerequisites and steps to be taken in simulation, normative codes are required as a reference for the user. Standardized documents do not yet exist in this field; to address this topic, some work has recently been done to create a standardized guideline for verification and validation (Ref 1) as well as for a common workflow for welding simulation (Ref 2, 3).

The procedure explained in the following sections is valid for a specific aspect of welding simulation—the 3-D transient approach—in order to obtain high-quality results. It relates to the simulation of line welds produced by fusion welding processes such as arc or beam welding as well as by respective process combinations. It presupposes the occurrence of a quasi-stationary process regime that is reached during welding. A further prerequisite is that the nonstationary regimes at the weld start and end must be reproducible and fit for the simulation. Such simulations deal with the subdomain

of structure simulation (Fig. 1), which serves to calculate the thermomechanical phenomena in fusion welding, namely the structural temperature field and the ensuing distortions and stresses, also referred to as computational weld mechanics (Ref 4). It additionally concerns individual aspects of materials simulation if phase transformation of the material is taken into account, which implies that couplings between structure and material simulation are well within the scope of the procedure.

The following sections refer to 3-D transient (time-dependent) numerical welding simulations. Furthermore, the recommendations given for deviations and limits are true for possible high-quality results. Depending on the application case and the intended conclusions of a simulation task, a lower accuracy may sometimes be sufficient to obtain the simulation statements required, so that it is possible to deviate from the prespecified details in order to save time and effort, which must be decided by the user. For special calculation tasks, an even higher accuracy may be needed, for example, for calculation of phenomena in the direct vicinity of the weld pool, such as cracking behavior. With the current state-of-the-art in commercially available welding simulation software, various tasks can already be modeled not only in a research environment but also with industry-related applications (Ref 1, 6).

This article concentrates on the necessary basics for such simulations and gives an overview of the specific aspects to be considered for such a simulation project. These include the required material properties, the experimental data needed for validation of the simulation results, the simplifications and assumptions as a prerequisite for modeling, and finally the thermomechanical simulation itself. The article concludes with some information about the sensitivity of the material properties data with respect to the simulation results, providing hints about the central challenge of having the right material properties at hand for a specific simulation task.

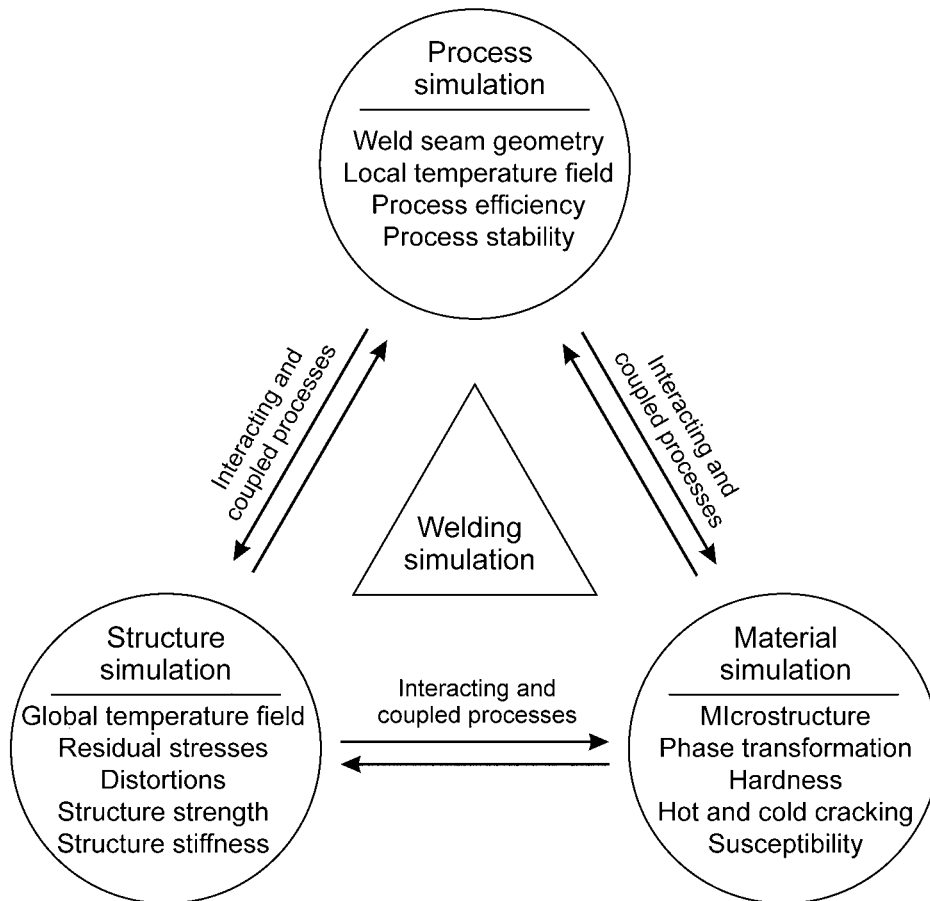


Fig. 1 Subdomains of welding simulation showing the main target and coupling factors. Adapted from Ref 5

Required Material Properties and Measurement Techniques

One of the most important challenges of a high-quality simulation of the thermomechanical phenomena in fusion welding is the lack of temperature- and phase-dependent material properties that are needed as input data. For most modern alloys, these data are not yet available from the supplier or in the literature. Consequently, an experimental determination of the values is often required in order to obtain high-quality simulation results. One remaining aspect is the inevitable scatter of the experimental data, especially at relatively high temperatures. These uncertainties can have major effects on the subsequently calculated temperatures and distortions (Ref 7–9). Furthermore, the correct measurement of the necessary properties is a demanding task with respect to time, costs, and accuracy, especially at elevated temperatures and for alloys with phase transformation. Some measurement techniques that are suitable for this task, as well as the corresponding equipment, are described in this section.

As previously stated, the numerical welding simulation requires a wide range of material

properties as input data. Considering the temperature field calculation, the required thermophysical properties are:

- Density, ρ
- Specific heat capacity, C_p
- Thermal conductivity, λ

Instead of the specific heat capacity and density, the enthalpy of the alloy can also be used, because of the mathematical relationship of these properties, which is described in detail in Ref 10. Information about the application of enthalpy in welding simulation can also be found in Ref 11. For calculation of distortions and stresses, the required thermomechanical properties are:

- Yield strength, $R_{p0.2}$
- Hardening behavior
- Young's modulus, E
- Thermal expansion, α
- Poisson's ratio, ν

All of these properties must be expressed with temperature dependencies from room temperature to the solidus temperature and above. The calculated temperatures can easily reach

values of 2500 °C (4530 °F) and more, and the numerical approach presupposes available data for all the temperatures that occur. From an experimental point of view, measurement at these temperatures is usually extremely difficult or even impossible, especially for the thermomechanical properties. A common practical compromise is to measure properties from room temperature to approximately 0.8 T_{Solidus} of the alloy. In addition to this wide temperature range, alloys with phase transformation must identify phase dependencies (e.g., ferrite, austenite, bainite, martensite), including the continuous cooling transformation (CCT) diagram.

The measurement of the required material properties involves a thermophysical and a thermomechanical part. During all experiments, one must take care that the rising temperatures do not affect the surface of the material. To prevent scaling that can influence the accuracy of optical detection methods, all measurements should be done under an inert atmosphere. For the thermophysical data, one special aspect must be taken into account. The material used in the automotive industry, as well as in other industries, is often coated (galvanized) with zinc to prevent corrosion. These coatings must be removed prior to measurement, because a clean and matte surface is necessary for correct measurement of the thermal diffusivity, $k(T)$, using a laser flash method. The density and specific heat capacity can be determined using commercially available equipment and standard specimen preparation. After the experiments, a calculation of the thermal conductivity as input for the simulation is done using the gathered data in combination with Eq 1:

$$\lambda(T) = k(T) \cdot \rho(T) \cdot C_p(T) \quad (\text{Eq 1})$$

Measurement of thermomechanical material properties must be done with consideration of two important aspects that are characteristic for welding. Depending on the welding technique and the specimen thickness, the heating and cooling rates can be very high. While the heating rate has a direct influence on the strain rates and therefore the yield strength and hardening behavior of the material, the cooling rate is an important factor for the phase-transformation effects of an alloy and the corresponding thermal expansion.

Tensile tests for the determination of the yield strength and hardening behavior must be executed with both a quasi-static and at least one higher strain rate. This is necessary in order to reflect the influence on the mechanical properties caused by the higher strain rates, as mentioned previously. The value for the expected higher strain rate can be approximated by using Eq 2:

$$\dot{\epsilon} = \alpha(T) \cdot \dot{T} = \alpha(T) \cdot \frac{\Delta T}{\Delta t} \quad (\text{Eq 2})$$

For example, the temperature rate for laser beam welding with high power and velocity

can easily reach $\dot{T} = 4000\text{K/s}$ ($7200\text{ }^\circ\text{F/s}$). With an assumed averaged thermal expansion coefficient of $\alpha_{st} = 1.3 \times 10^{-5}/\text{K}$ ($7.2 \times 10^{-6}/^\circ\text{F}$) for steel and $\alpha_{al} = 2.5 \times 10^{-5}/\text{K}$ ($1.4 \times 10^{-5}/^\circ\text{F}$) for aluminum alloys, the strain rates during laser beam welding can be estimated to values of $\dot{\epsilon}_{st} = 0.05/\text{s}$ and $\dot{\epsilon}_{al} = 0.1/\text{s}$ in correspondence with literature values (Ref 12). These values must be adapted to the welding technique that is to be simulated and are also the values that should be considered for tensile tests with higher strain rates. For other processes, such as gas metal arc welding (GMAW) or tungsten inert gas (TIG) welding, different heating rates are typical.

In the measurement setup of a tensile test at elevated temperatures, some special characteristics must be known that are based on specific thermomechanical effects which only occur under special conditions. Here, in particular, the Portevin-LeChatelier effect is of interest because it can cause a stress-strain behavior that is somewhat different than the overall behavior of the alloy.

At certain alloy-dependent conditions with a special combination of specimen temperature and given strain rate, metallurgical effects can cause problems with machine usage while running in force-control mode. In such cases, the measured curves can show a steplike behavior because of the Portevin-LeChatelier effect, where the atomic diffusion in the material has the same velocity as the movement of the dislocations. The movement of the dislocations is locked, resulting in fluctuation of the material flow and stiffness of the specimen. This leads to difficulties in the force control of the testing machine, observable in the tensile test plots as a high scatter in the recorded curves, as shown in Ref 13, and can be overcome using the distance-control mode. Consequently, the testing machine should be run in distance-control rather than force-control mode for all tensile tests at elevated temperatures.

The Young's modulus of the alloys should not be derived from tensile test results. Especially with rising temperatures and higher strain rates, the gradient at the beginning of the data curves normally shows very high scatter. Instead of using tensile test results (which are the basis of the original definition of Young's modulus), this value can be measured much more accurately with an ultrasonic device based on monitoring the signal after an ultrasonic excitation of the material. This approach yields good results even for high temperatures. Nevertheless, the extracted values should be cross-checked later with available tensile test results up to approximately $0.5 T_{\text{Solidus}}$ of the considered alloy. The temperature-dependent measurement of Poisson's ratio is not necessary when doing a distortion calculation because the influence on the results is negligible, and a room-temperature value is sufficient for a welding simulation (Ref 7, 13).

As stated, the cooling rates have a direct influence on the phase-transformation behavior

and the corresponding thermal expansion. This fact must be accounted for in the measurement of the thermal expansions, that is, the dilatometric curves of the alloys. One typical parameter for the weldability of alloys is the cooling time between temperatures of 800 and $500\text{ }^\circ\text{C}$ (1470 and $930\text{ }^\circ\text{F}$), the so-called $t_{8/5}$ time. During high-power welding processes with a concentrated heat input, such as laser beam welding, extremely low $t_{8/5}$ times of less than a second are possible and must also be reached in the experiments. As for the tensile tests, the welding technique has a significant influence on the cooling rates, too, and leads to different $t_{8/5}$ times, for example, for GMAW or TIG processes. More information about the measurement of dilatometric curves and the analysis of the generated data can be found in the next section.

While the correct measurement of the material properties data is one very important task for a welding simulation project, it is nevertheless only the first part of generating a dataset suitable for simulation of the thermomechanical phenomena in fusion welding. The second part consists of the plausibility check of the monitored raw data as well as comparison with scatter bands of comparable alloys from published literature or previously executed experiments. This second part is explained in the following section.

Analysis of Material Properties Input Data

One necessary step after the experimental determination of the material properties

necessary for the simulation task is the analysis of these data to ensure the correctness of the measurements and to check their appropriateness for a numerical welding simulation. This is important because the material property data have a strong and direct influence not only on the result quality but also on the convergence behavior of the numerical calculation and, as a result, on the overall computation time (Ref 14).

The cross check of the measurement data with scatter bands from literature values is shown exemplarily in Fig. 2 for the specific heat capacity of three alloys; further information about the alloy contents and the material characteristics can be found in Ref 14. Both the austenitic steel H400 (EN 1.4376) and the dual-phase steel DP-W 600 (EN 1.0936) are well within the scatter bands for high-alloy steel and mild steel, respectively. The data show only minor scatter; the progression of the graphs is smooth. The curve for Ecodal 608 (EN-AW 6181, AlMgSi alloy group with precipitation hardening) shows some characteristics that must be investigated. The general behavior is consistent with the data for pure aluminum and AlMgSiCu taken from Ref 15 and 16. Nevertheless, the deviations in certain temperature intervals are significant.

The local minimum in the temperature range between 200 and $300\text{ }^\circ\text{C}$ (390 and $570\text{ }^\circ\text{F}$) is caused by an extensive precipitation of Mg_2Si particles and the subsequent dissolution. Analyses show that this local minimum of the specific heat capacity has only small effects on the calculated temperature field and the following macroscopic mechanical behavior and can be neglected (Ref 13). As stated previously, such local effects in the material data curves

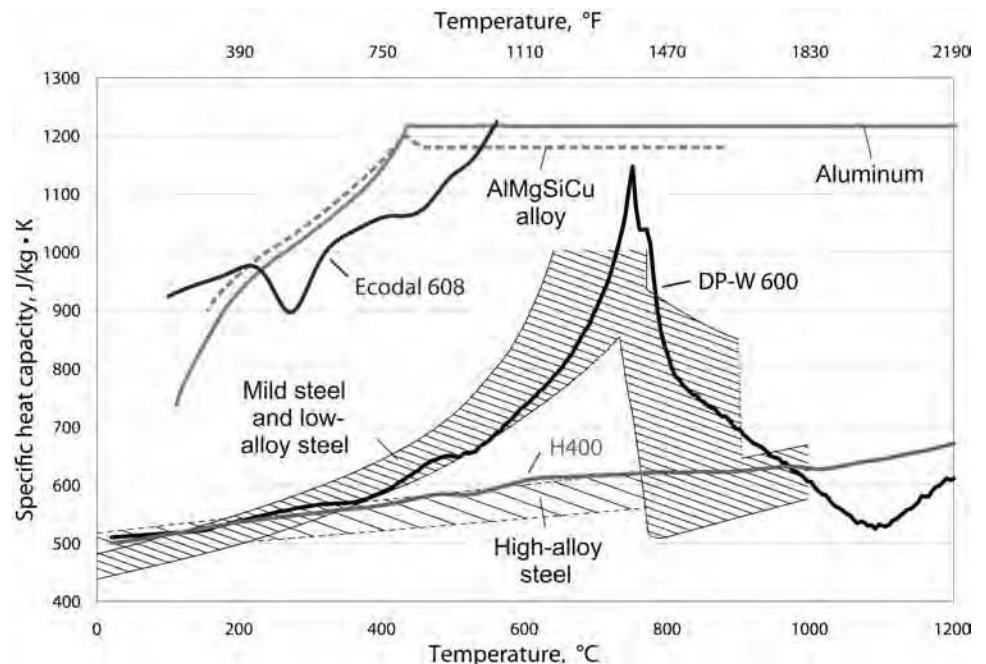


Fig. 2 Comparison of experimentally determined specific heat capacity, C_p , and literature values. Adapted from Ref 5, 15, 16

can have a major effect on the convergence and computation time. Other examples for a similar nonlinear behavior are the specific heat capacity peak of the phase transformation or the latent heat of fusion. If the peaks must be considered in the material dataset because their influence cannot be neglected, one possible solution is to stretch extremely steep or step-wise peaks over a slightly larger temperature interval. The effects on the result quality are negligible, but the convergence behavior is much improved in most cases; that is, depending on the steepness of the gradient, a factor of up to 2 to 3 (typical values of approximately factor 1.5) in the calculation time can be observed.

As stated in the description of the measurement techniques, the strain-rate effect during tensile tests can be significant due to the high strain rates during welding. The combined effect of the temperature and the strain rate on the yield strength can be checked in accordance with Eq 3, proposed by Makhnenko (Ref 17):

$$\frac{\sigma_y(T)}{\sigma_{y,0}(T)} = \left(\frac{\dot{\epsilon}}{\dot{\epsilon}_0}\right)^{m(T)} \quad (\text{Eq 3})$$

Here, the parameters are the yield strength $\sigma_y(T)$ at temperature T and strain rate $\dot{\epsilon}$, as well as the yield strength $\sigma_{y,0}(T)$ at the quasi-static strain rate $\dot{\epsilon}_0$. The temperature- and alloy-dependent exponent, $m(T)$, is a measure for the dependence of the yield strength $\sigma_y(T)$ during a variation of the strain rates. A high value of the exponent $m(T)$ stands for a high dependency of the yield strength from the strain rate.

Figure 3 shows the extracted measurement data in comparison with literature values from

Makhnenko (Ref 17). In Fig. 3(a), the strain-rate influence for the dual-phase steel DP-W 600 becomes significant for temperatures above 500 °C (930 °F), while the yield strength of the austenitic steel H400 is independent of the strain rate up to 700 °C (1290 °F). The values for Ecodal 608 (Fig. 3b) show that the strain-rate effect becomes visible for temperatures above 300 °C (570 °F). The information gathered using Eq 3 indicates that the tensile tests at elevated temperatures must be executed with different strain rates for temperatures above 500 °C (930 °F) for DP-W 600, 700 °C (1290 °F) for H400, and 300 °C (570 °F) for Ecodal 608.

The thermal expansion of a specimen undergoing high heating and cooling rates is normally measured with a special dilatometric device, for example, a Gleeble machine. Here, $t_{8/5}$ times of approximately 3 s for a thin-sheet metal specimen can be reached with passive cooling via the clamping devices. In contrast, the extremely low $t_{8/5}$ times of less than a second during laser beam welding necessitate an active cooling that can be done using a direct inert gas spray on the specimen. As shown in the following paragraphs, this behavior results in challenges for optical measurement of the lateral contraction of the specimen and leads to deviations in the monitored dilatometric curves. The thermal expansion experiments must be conducted with a variation of the $t_{8/5}$ time in order to monitor the phase transformation correctly and to obtain the correct temperature intervals of the transformation. The appearance of a small hysteresis between both cycles, caused by the very short heating and cooling of the specimen, is normal and, in most cases, inevitable.

The experimental raw data for thermal expansion are shown exemplarily for DP-W 600 in Fig. 4(a). Monitoring of the thermal expansion was done with a laser-based optical device to record both the expansion in the longitudinal direction of the specimen and the perpendicular longitudinal axis. The heating branch of the curves shows no noteworthy deviations for all four measurements. In contrast, in the cooling branch between 900 and 400 °C (1650 and 750 °F), the curves for all cooling times except $t_{8/5} = 3.1$ s are deviated. The reason is that active cooling of the specimen with inert gas causes flickering effects, that is, an optical deviation of the gas flow due to steep changes in the temperature of the gases, resulting in a different refraction index. While necessary to reach the high cooling rates, here the cooling gas interferes with the optical measurement of the specimen.

Therefore, for use in numerical simulation, the cooling branches of the curves achieved with active cooling must be corrected using the general characteristic of the $t_{8/5} = 3.1$ s curve with passive cooling. Coming from the high-temperature region of the curve, the gradient of the austenite expansion coefficient can be elongated until transformation takes place at approximately 400 °C (750 °F) (Fig. 4b). These corrected curves can now also be used to evaluate the required transformation temperatures A_{r1} and A_{r3} for the correct description of the CCT behavior. Using the standardized method in Ref 18 leads to the derived values given in Fig. 4(b).

The exemplary analysis of the measurement data gives an overview of the possible scatter of the material properties. A detailed

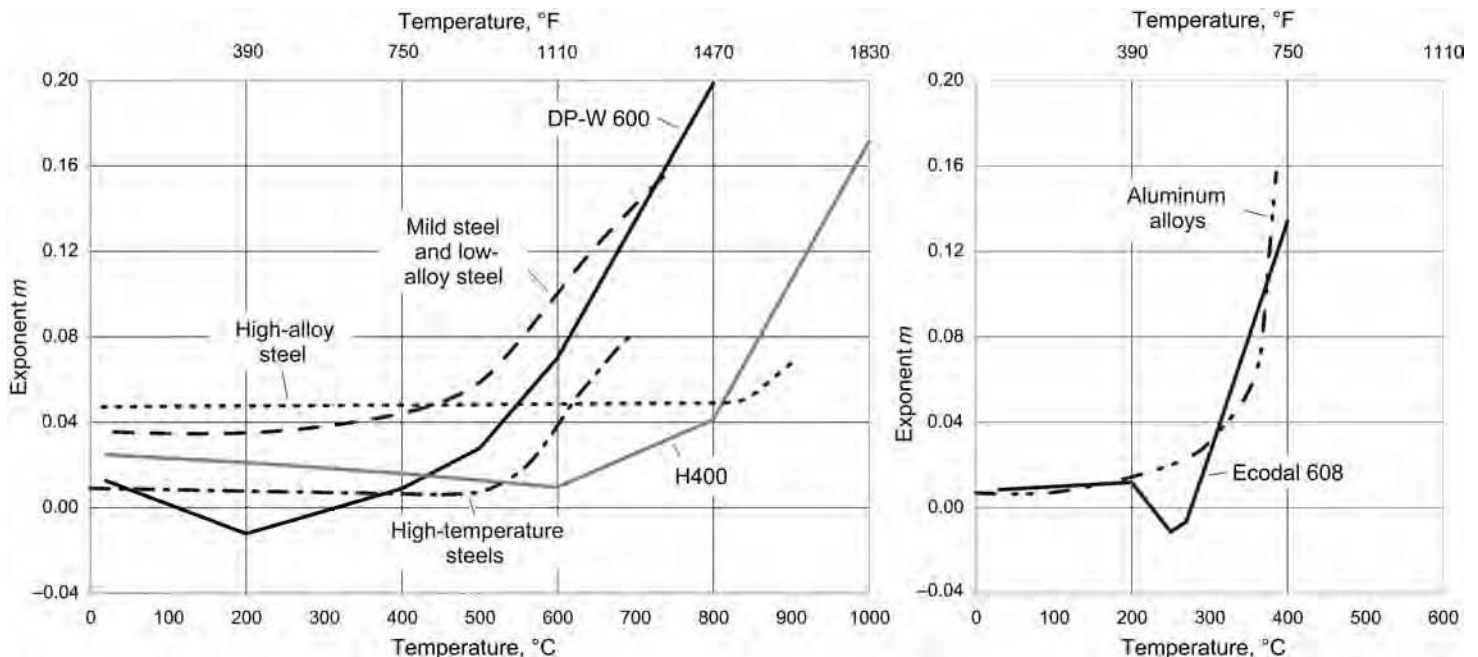


Fig. 3 Comparison of exponent m for measured data and literature values in (a) steels and (b) aluminum alloys. Adapted from Ref 17

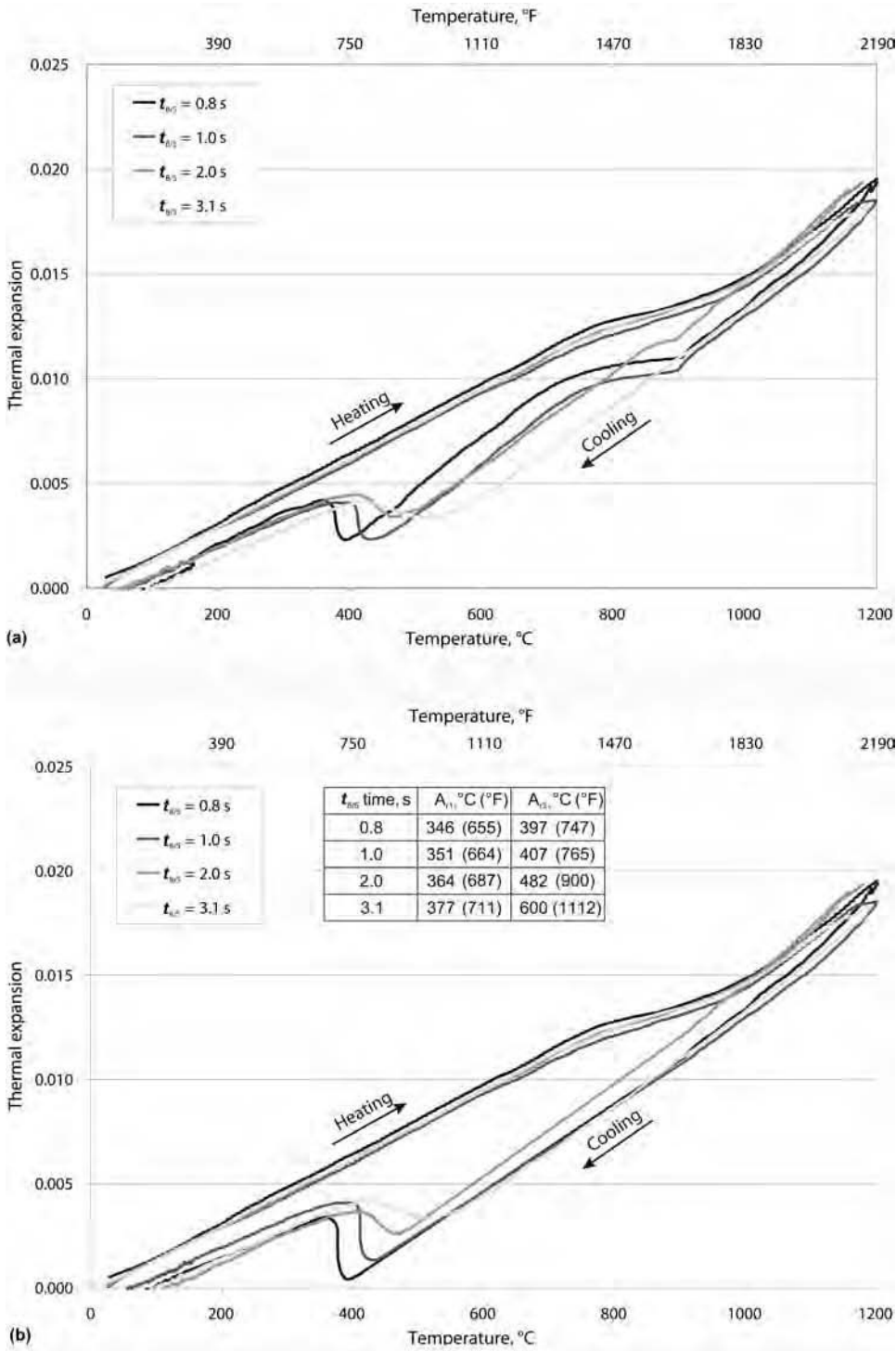


Fig. 4 Measured thermal expansion for DP-W 600 for various $t_{8/5}$ times. (a) Raw data. (b) Corrected curves for high cooling rates and transformation temperatures. Adapted from Ref 18

plausibility check of the data is needed to derive a high-quality material property dataset from the raw data of the measurements and is strongly recommended. The analysis methods help to identify possible systematic measurement errors. The temperature-dependent

thermophysical and thermomechanical material properties for three different alloys are given as a result of the preceding measurements and plausibility checks and are represented in a ready-to-use format for a numerical welding simulation in Ref 14.

Experimental Data for Validation of Thermal and Mechanical Results

Based on the current state-of-the-art in welding simulation, experimental validation of calculated results is imperative for the attainment of high-accuracy results (Ref 4, 5). This is also stated in a recently developed guideline about the execution and documentation of a numerical welding simulation (Ref 3). A missing validation and an unsuitable result display often make it impossible to judge the result quality and therefore transfer the conclusions to other tasks and make good use of the research results, or to compare them with similar analyses. Consequently, the presented workflow includes some general rules and specific aspects about how to validate a simulation and how to display the results. For the scope pointed out in the beginning, respective experimentally-determined data are required. Generally, it must be ensured that the experiments as well as the measurements are conducted based on the state-of-the-art and that the experimental result is not influenced more than a minimum degree by the measurements.

Temperature Field. For the experimental validation of the temperature field calculation, the basic required information is the 3-D weld pool geometry, that is, the cross section transverse to the welding direction and the weld pool length on the top and bottom sides of the specimen, respectively. For all cases, a quasi-stationary process regime is a prerequisite. Whereas the molten and heat-affected zone areas and shapes transverse to the welding direction can be determined directly from macrosections, the measurement of the weld pool length is more sophisticated. Possible direct measurement methods are digital images taken by a high-speed video camera or by thermal imaging techniques, but, in most cases, an indirect measurement is done with thermocouples by way of the temperature cycles. Here, a time-dependent measurement of the component temperatures in the direct weld vicinity for at least two points in linear arrangement transverse to the welding direction is adequate to allow mapping of the temperatures and temperature gradient. The data recording should start shortly before running the welding process and last until the specimen has completed cool-down to ambient temperature. This is normally done at the specimen top side and, if necessary, at the specimen bottom side, for example, when the thickness of the specimen leads to a temperature gradient in the thickness that is not negligible. During all thermocouple measurements, at least 50% of the solidus temperature in °C of the investigated material should be reached at the nearest measuring spot. Thermocouples with a wire diameter that is compatible with the welding process and a scanning frequency that permits reliable mapping of the peak and the achieved maximum temperature in the temperature-time history must be used.

Distortion. An experimental validation of the component distortions and residual stresses is needed to ensure the correct behavior of the thermomechanical part of the simulation model. The specimen support and the clamping conditions of the real part must be resembled in the simulation model as well. To have information for validating the general qualitative behavior of the welding simulation model, a time-dependent measurement of the welding distortions is needed for later comparison with the calculated results. It should run for the entire welding time and the following cooling time until reaching nearly ambient temperature, parallel to the temperature field measurements. A measurement of the longitudinal and transverse distortions is always necessary; it is strongly recommended for the angular distortions. Any rigid body displacements should be avoided beforehand or taken out of the calculation with the help of differential measurements, respectively. Examples of common measuring techniques are inductive displacement transducers or optical methods such as the 3-D gray-level correlation method. Additionally, coordinate-measuring machines can be used to monitor the status before and after welding; this is often done for special reference points or mounting dimensions of industrial parts.

Residual Stresses. The component residual stresses are the second aspect of the validation of thermomechanical simulation results. In comparison with the calculated distortions, they offer additional information about the simulation result quality. Whereas the calculated distortions of a welded specimen may be qualitatively and quantitatively satisfactory while neglecting the phase-transformation behavior of a material, the residual-stress state normally is strongly dependent on the transformation characteristics of an alloy. This is especially true for the local areas near the weld seam. Consequently, validation of the residual-stress state ensures a high-quality simulation result. The measurement of the residual stresses must be done after a complete cooling of the specimen to room temperature. To map the stress gradient in the weld seam and heat-affected zone, at least three points in linear arrangement transverse to the welding direction are recommended. Here, both the longitudinal and transverse directions should be considered. Possible measurement techniques are the hole-drilling method or diffraction methods such as x-ray, synchrotron, or neutron diffraction (Ref 19). An additional measurement using strain gages is also possible and can provide valuable transient information of the thermal strains. The information is also summarized in Table 1.

Workflow for Thermomechanical Welding Simulation

The major challenge in modeling of thermomechanical phenomena in fusion welding is to meet the industrial requirements for welding

simulation software (Ref 1). On one hand, in-house codes or multipurpose finite-element analysis products, such as ANSYS, Abaqus, or Marc, are very flexible and enable simulation, with various degrees of complexity, of most welding processes. Nevertheless, the prerequisite expert knowledge and the computational costs increase exponentially with the complexity of the simulation. On the other hand, special simulation software, such as Sysweld, has been designed with a particular focus on welding. In such programs, many tools are available, for example, a tool to consider solid-state transformations or a tool for the heat source, and so on. This software is very powerful and enables good results in a reasonable calculation time. However, it is mainly implemented in research institutions; a wide industrial application is not yet established. In most cases, the time to solution, that is, the preprocessing, calculation, and postprocessing times, hinder an industrial application. Even with a short calculation time, the pre- and postprocessing times can last up to several weeks for a single simulation task. A friendly and intuitive user interface could decrease the time significantly and make possible an industrial application of welding simulation (Ref 6). (For a summary of simulation programs for welding and other metals processing applications, see Appendix A, “Software for Computational Materials Modeling and Simulation,” in *Metals Process Simulation*, Vol 22B, of *ASM Handbook*, 2010.)

The general workflow for a welding simulation, according to the stated approach, is shown in Fig. 5. It consists of the experimental and material properties data, setup of the simulation, temperature field, calculation of the distortions and stresses, and finally, postprocessing in combination with cross-checking of the results. All single steps are explained in detail in the following sections.

A simplified phenomenological heat-source model is normally used to represent the heat

of the welding process. Because this model is not a process model but an abstract parameterized mathematical model, it must be calibrated in an iterative way so that the resulting temperature field and fusion zone fit well with the experimental data (Ref 21). Good agreement with the simulated and experimental thermal results is a prerequisite to achieving a high-quality mechanical simulation of distortions (Ref 5). The implementation of welding simulation in the automotive sector, a key industry for the application of various production simulation approaches, has been investigated in Ref 22. Some examples for automotive welded assemblies are a front axle carrier (Ref 23), rear axle carriers (Ref 24, 25), a gear wheel (Ref 26), and some fuel injector components (Ref 27, 28), which have been investigated with various techniques, software, and accuracy.

Setup of Simulation, Simplifications, and Assumptions

A complete, self-consistent welding simulation that includes all relevant physical aspects is not yet available, although various mathematical descriptions are available for different aspects of welding (Ref 5, 29, 30). However, many couplings are still unknown or not described mathematically, and incorporation of all aspects would result in a very complicated model that is not realistically solvable. Furthermore, the available computational capacities would be limiting for such a complex and demanding task. However, not all aspects must be known with absolute certainty for reliable calculation and clarification of individual effects (Ref 4, 31, 32). Welding simulations using finite elements have the ability to separate the influence of the various metallurgical parameters and their effect on the calculated results.

To assess the relevance and quality of the achieved simulation results, a detailed description of essential information about the entire

Table 1 Experimental data for validation

Information	Explanatory notes
Weld pool geometry	Information about the three-dimensional geometry of the weld pool—mainly cross section and length on top and bottom sides
Component temperatures in weld vicinity	Time-dependent measurement starting shortly before running the welding process and until completed cooling to room temperature Measurement at two or more points, in linear arrangement transverse to the welding direction, for mapping of the temperature gradient Measurement at the specimen top side; if needed, at the specimen bottom side as well At least 50% of the solidus temperature in °C of the investigated material should be reached.
Component distortions	Time-dependent measurement starting shortly before running the welding process and until completed cooling to room temperature Measurement of longitudinal and transverse distortion is always necessary; measurement of angular distortion is strongly recommended. Additional measurement of reference points or mounting dimensions is recommended. Rigid body displacements should be avoided or taken out of the calculation with the help of differential measurements.
Component residual stresses	Measurement after completed cooling of the component at three points (at least) in linear arrangement transverse to the welding direction to allow mapping of the stress gradient Additional transient measurement of the thermal strains using strain gages is also advisable. Longitudinal and transverse directions should be considered. Measurements should be carried out specifically in the weld vicinity and directly in the weld.

simulation is indispensable. The essential information concerns the exact designation of the welding process to be simulated, relevant simplifications and assumptions for the desired results, applied boundary conditions, material properties used, and heat sources, in addition to general information about the simulation project, such as the software package and version as well as solver settings that deviate from the standard, with a brief explanation.

Simplifications and Assumptions. The simplifications and assumptions that were made for the simulation task should be given in the order of their importance. In most cases, there are simplifications of the welded part geometry, for example, deviations between the ideal computer-aided design geometry and the real part because of production processes or the observed weld reinforcement after welding. This also includes the possible use of a partial model while taking advantage of mirror or rotational symmetry to save computation time. Finally, the relevant information about the meshed model should be given, namely, the number of nodes and elements applied, with the element base function or element type and the minimum element length in the areas where the maximum thermal and mechanical loads are applied. An overview picture plus zoomed pictures of important regions, such as a more dense mesh in the weld seam area, complete the data (Fig. 6). One important aspect is the possible influence of the mesh structure on the calculation results; here, the correct meshing strategy has a big influence on both the calculation time and result quality (Ref 33, 34).

Two other very important aspects are the consideration of previous process steps, such as primary forming or metal shaping, which have an influence on the residual-stress state, and assumptions made for the material properties, such as homogeneous and isotropic characteristics or neglect of segregations. The information about the consideration of the given real physical processes and their couplings, such as the neglect of weld pool fluid flow or the neglect of keyhole formation during laser beam welding, is also important. Further data referring to potential simplifications can be found in the literature (Ref 7, 32, 33, 35).

Boundary Conditions. Considering the boundary conditions used in the simulation, there are several important pieces of information to be stated. For the thermal aspects, the respective ambient temperature is needed. Furthermore, consideration of the conductive, convective, and radiative heat transfer between individual components and fixtures in the modeled system as well as across the system boundaries must be given to ensure a consistent heat transport and cooling behavior in the model. From the mechanical point of view, the boundary conditions include the support of the specimen and the applied clamping conditions with respect to the clamping position and area, clamping and unclamping time, and clamping force, which can be modeled in different ways,

for example, as a spring constant at individual nodes or with complex contact algorithms.

Material Properties. The thermophysical and thermomechanical material properties and the corresponding transformation behavior are a central aspect of a qualitatively-high welding simulation. The exact designation of the real alloy used in the experiments, for example, the alloy number and the actual chemical composition, as well as the material dataset used in the simulation must be mentioned. The simulation dataset is especially important because it is common to take an available dataset for a

comparable alloy and adapt the data to the special alloy in the experiment by using some additional measurements of the actual material. Information about the temperature dependence and, when applicable, the phase-transformation behavior is required, including the CCT diagram as well as the solidus temperature, which is necessary for validation of the transverse weld pool geometry. An indication of the reference source of the material characteristics or a graphical and tabular representation, respectively, of the material properties data is strongly recommended; see Ref 14 for an example.

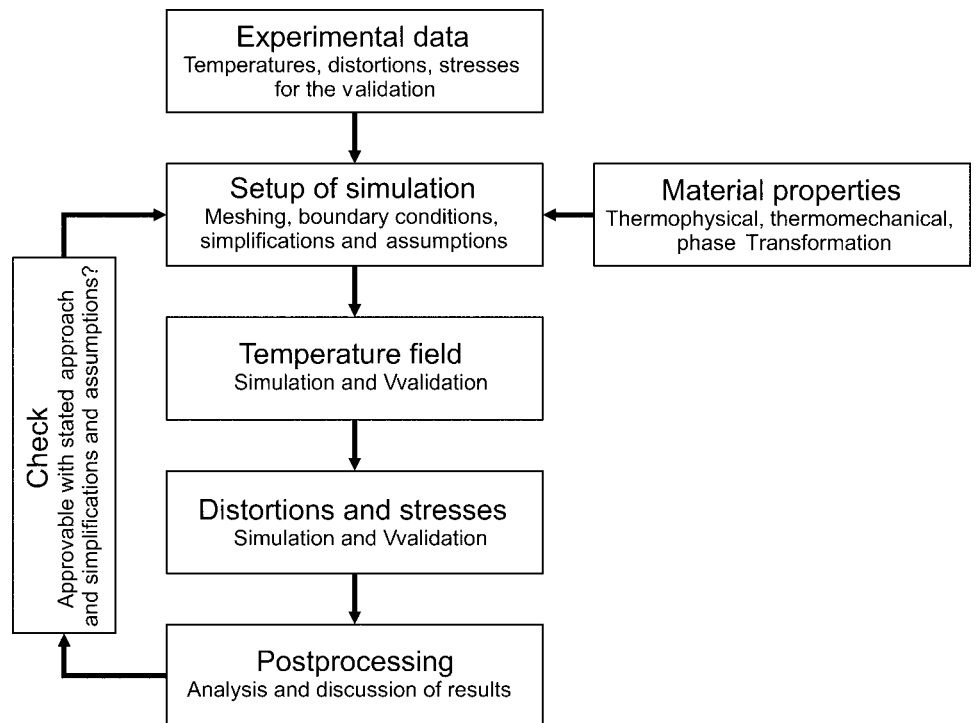


Fig. 5 General workflow for a transient, three-dimensional numerical welding simulation of the temperature field, distortions, and stresses. Adapted from Ref 20

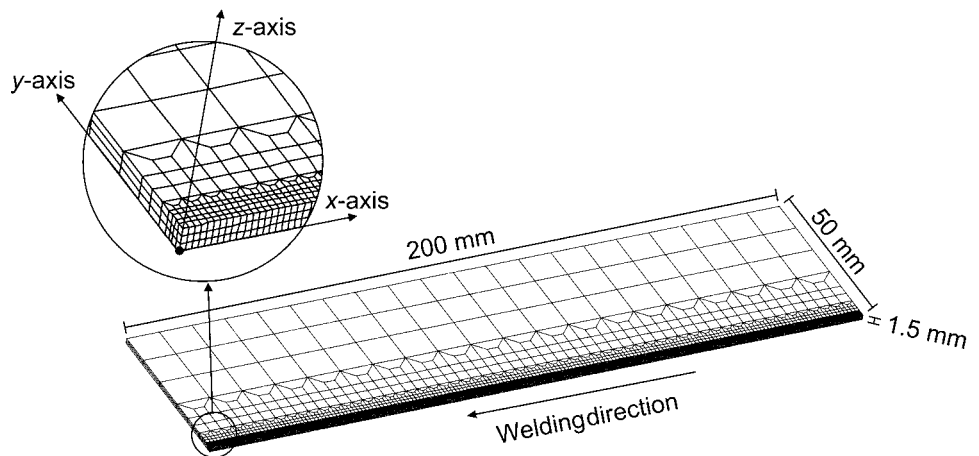


Fig. 6 Example for the correct display of the meshed simulation model. Half model, sheet thickness = 1.5 mm (0.06 in.), approximately 15,000 nodes and 20,000 elements. Closeup of weld seam area is shown at left. Adapted from Ref 20

If the investigated alloy undergoes a phase transformation during heating and cooling, this effect can be integrated in welding simulations. In such a case, a thermal-metallurgical calculation is first completed using the thermal properties of the material, the calculated temperature field derived and validated from the welding experiments, and the CCT behavior formalized mathematically. The thermal-metallurgical calculation data are then used as an input to the mechanical calculation, which determines stresses and strains according to the transient and spatial distribution of the previously calculated temperatures in the model. It is noted that this one-way coupling, also referred to as weak coupling, does not account for the effect of stress on phase-transformation behavior. Furthermore, there is no interaction between the latent heat generated by solid-state phase transformations and the calculated temperature field. More detailed information about phase-transformation models and the influence of material property data on simulation results can be found in the literature (Ref 7–9, 36–45).

Heat Source. Finally, the applied heat source resembling the real heat input of the validation experiments must be given. There are different types of heat sources available that are sometimes combined to match the validation data; here, the most important fact is the statement of the approach that was chosen for the current task. A summary of the given aspects can be found in Table 2.

General Aspects

Based on the state-of-the art, the welding temperature field generation may be accomplished in various ways. A manual iterative approach may be adopted for heat-source parameter fitting. Alternatively, automated procedures may be drawn upon, as described in Ref 46 to 49. Both the numerical and analytical computational methods are basically equivalent with specific regard to the result. The correct spatial and transient representation of the real temperature field of welding is solely essential in any such approach. For validation of the simulation and representation of the calculated results, the following general aspects should be observed.

The values that are given and discussed should preferably be in SI units, and given rules of current standards regarding the graphical display must be respected (Ref 50). For every value that will be compared, the exact measuring point and time must be stated for a clear correlation of the position in the component as well as the simulation results, for example, the distance to the weld seam center for thermocouples. An interpolation between the nodes of the meshed model may be necessary. In the actual comparison, the positions for evaluation of the experiment and simulation must coincide in the range of experimental data scatter. Additionally, all scales and ranges of values that are important for the representation must be

indicated, especially the overall specimen dimensions, plate thickness for macrosections, and ranges of values for contour plots. In case of low absolute values, a scaling factor is often used for better visualization in the representation of the calculated results, for example, the overall distortion. This factor must be given if applicable.

For all comparisons of experimental and simulation data, the values must be displayed in a common chart. This is especially required for the weld pool geometry, temperature cycles, transient behavior of the distortions, and residual stresses. Details for each individual aspect are given in the following sections. Any time-

dependent data should be given with adequate resolution of both the time domain of actual welding and the time domain of subsequent cooling to at least 100 °C (212 °F) in order to display any deviations.

The differences between calculated results and measured data must be given in absolute numbers in an order of magnitude consistent with the value and may additionally be expressed as a percentage. When an experimentally determined scatter band is represented, the indication of the deviation may be omitted if the calculated results lie within the respective scatter band. See Table 3 for a summary.

Table 2 Setup of the simulation

Information	Explanatory notes
Welding process	Exact designation of the welding process to be simulated
Simplifications of geometry	Details on accomplished simplifications of geometry compared to the real component and their implementation in component mesh generation
Indication of applied symmetry boundary conditions	Use of a partial model to save computation time for mirror or rotational symmetry
Generation of the component mesh	Overview and detail meshes of the weld area and further relevant areas, where appropriate Indication of the number of nodes and elements as well as the applied element base function or element type Indication of the minimum element edge length in the area of maximum load, i.e., normally the weld area
Consideration of previous process steps	Details on the consideration of the component history and the associated influences on the component
Simplifications of the material	Details on simplifications and assumptions concerning the material characteristics for the simulation
Applied material characteristics	Exact alloy designation or material number, respectively, of the materials used for the simulation Indication of the temperature dependence and, where applicable, the phase dependence, including time-temperature transformation diagram as well as solidus temperature Indication of the reference source of the material characteristics or graphical and tabular representations, respectively, of data required for the simulation
Consideration and couplings of physical processes	Details on considered physical phenomena as well as applied couplings between them
Thermal boundary conditions	Indication of the ambient temperature Consideration of the conductive, convective, and radiative heat transfer between individual components and fixtures in the modeled system as well as across the system boundaries
Mechanical boundary conditions	Details on the support of the specimen and the applied clamping condition with respect to the position, area, clamping and unclamping time, and clamping force
Applied heat source	Statement about the chosen approach for the heat source
General information	Applied software and version number

Table 3 General aspects for validation and result display

Information	Explanatory notes
Indication of the position and time of the measured values	Exact measuring point and time must be stated for a clear correlation of the position in the component and the model
Position for evaluation of the experiment and simulation	Position for evaluation of the experiment and simulation must coincide in the range of scatter of the experimental data. Interpolation nodes of the meshed model may be necessary.
Indication of the scales and ranges of values	All scales and ranges of values that are important for the representation must be indicated.
Indication of any applied increase factor in the representation	In case of low absolute values, the applied scaling factor used for better visualization must be given.
Plotting of measured values and simulation results in a common chart	Plotting of simulation results and measured values in a common diagram for direct comparison
Representation of time dependencies	Time-dependent data must be given with adequate resolution for both the time of actual welding and the cooling time to at least 100 °C (212 °F).
Indication of differences between calculated results and measured data	Differences between calculated results and measured data must be given in absolute numbers in an order of magnitude consistent with the value and may additionally be expressed as a percentage. When an experimentally determined scatter band is represented, indication of the deviation can be abandoned, if the calculated results lie within the respective scatter band.

Temperature Field Simulation

In the given approach for modeling of thermomechanical phenomena in fusion welding, the temperature field simulation is the first step. For validation of the temperature field simulation and representation of the calculated results, the following factors should be observed.

Temperature Deviations. Two main aspects must meet the quality requirements: the temperature cycles, with the corresponding temperature gradient in the direct vicinity of the weld seam, and, at the same time, with identical heat-source parameters, the weld pool geometry. The first step is the check of the ambient temperature in the simulation, which must match the experiments. Any deviations must be justified. The correct calculation of the temperature increase from the moving heat source is, in most cases, not a challenge and normally shows very little deviation. For the maximum temperature, there are several aspects that must be considered. First, the maximum time step must be small enough to generate a well-developed peak; that is, the peak must be covered by several data points. Second, a comparison between the measured and calculated maximum temperatures should not exceed a deviation of 50 K (90 °F). Considering the cooling behavior, the difference between the relevant temperature gradients in the measurements and calculation, for example, $t_{8/5}$ or $t_{12/9}$ time, and so on, depending on the material and the application, should be less than 10%.

Weld Pool Geometry. Representation of the weld pool geometry is the second important aspect when validating the temperature field calculations. To have all the important information at hand, it is valuable to have a representation of the calculated weld pool geometry in the form of a contour plot, along with the solidus temperature. A comparative representation in one graph, showing the calculated weld pool geometry in the left half and the macrosection in the right half, combined with a marking of the weld pool contour, helps to judge the result quality. The scaling of both pictures should be identical to that of the macrosection from the experiment. The maximum deviation of the weld pool area or the characteristic weld seam shape, respectively, should generally not exceed 10%. An example picture for the temperature field validation is shown in Fig. 7. An alternative display method, in the case of asymmetric weld pool geometry, is a marking of the weld pool contour in the macrosection and a plot of the identical contour in the representation of the calculated weld pool geometry. Additionally, for both cases, an indication of the weld pool area in the cross section in mm^2 as well as the deviations between experiment and simulation (e.g., for penetration depth, weld width on the top and bottom sides, and so on) should be given in the accompanying descriptive text or in a table. Table 4 is a summary of the statements.

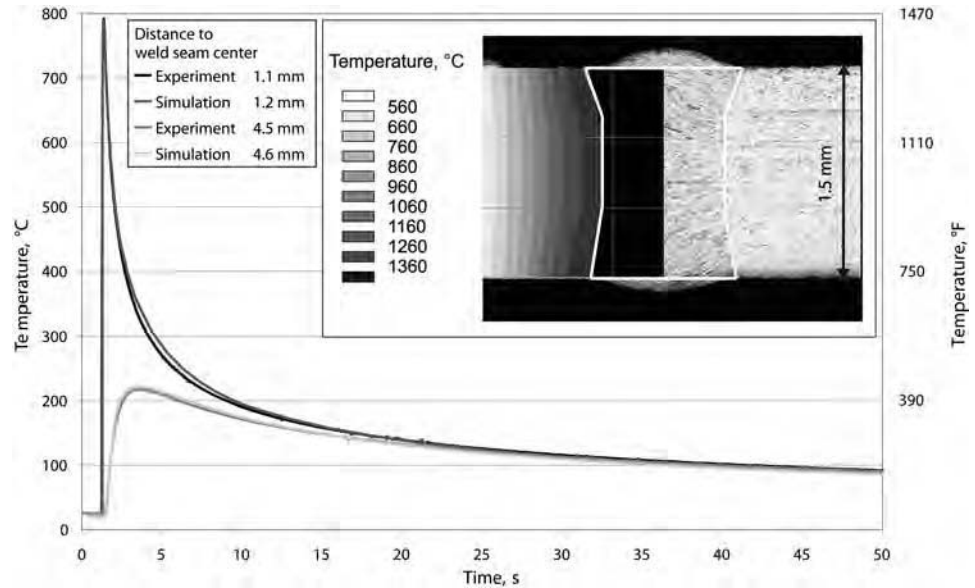


Fig. 7 Example for correct display of temperature field validation. H400 (EN 1.4376), 3 kW neodymium: yttrium-aluminum-garnet laser beam bead-on-plate weld, sheet thickness = 1.5 mm (0.06 in.), $v_{\text{weld}} = 6.5$ m/min (256 in./min). Adapted from Ref 20

Table 4 Validation and result display of the temperature field calculation

Information	Explanatory notes
Room temperature	Comparison between measured room temperature and room temperature entered into the simulation
Maximum temperature of the temperature-time histories	Comparison between measured and calculated maximum temperatures of the temperature-time histories Maximum deviation should not exceed 50 K (90 °F)
Temperature gradient during cooling to room temperature	Comparison between the relevant temperature gradients in the measurements and the calculation Maximum deviation should be less than 10%.
Representation of the weld pool geometry	Representation of calculated weld pool geometry in the form of a contour plot along with solidus temperature as an isotherm Comparative representation in one graph Scaling identical to macrosection from the experiment Maximum deviation of the weld pool area or characteristic weld formation parameters is 10%.

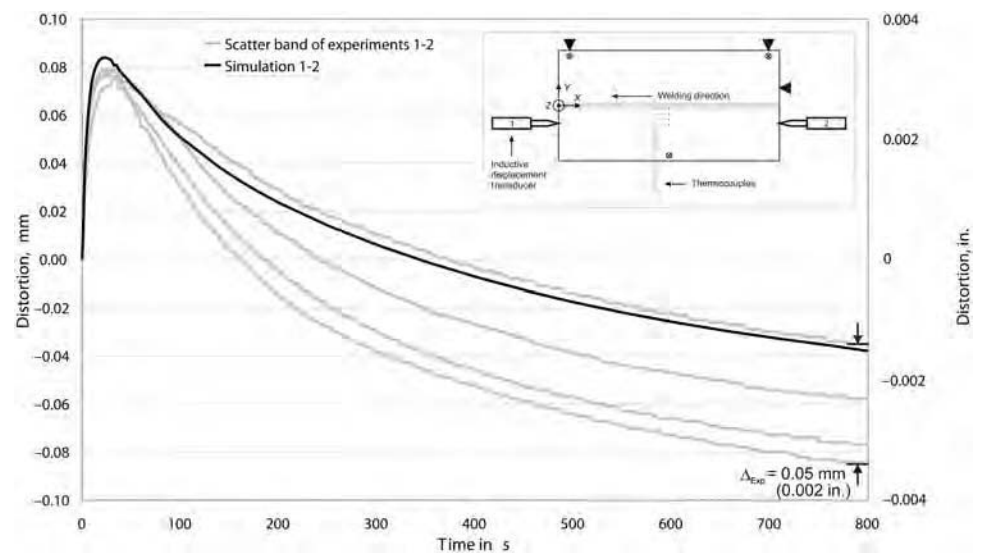


Fig. 8 Example for correct display of longitudinal distortion validation. H400 (EN 1.4376), 3 kW neodymium: yttrium-aluminum-garnet laser beam bead-on-plate weld, sheet thickness = 1.5 mm (0.06 in.), $v_{\text{weld}} = 6.5$ m/min (256 in./min). Adapted from Ref 20

Table 5 Validation and result display of the distortion calculation

Information	Explanatory notes
Quantitative value after completed cooling to room temperature	Comparison of calculated and measured distortion
Shape of the quality profile	Plotting of the time-dependent calculated and measured distortions in a common diagram

Mechanical Simulation

Distortion calculation is the second step in the approach for modeling of thermomechanical phenomena in fusion welding. Here, the qualitative and quantitative aspects of the results must be compared. Hence, the necessary information is the calculated quantitative value of the distortion in the longitudinal, transverse, and angular directions or the change of specific points in the model, such as distances between reference points. Additionally, the qualitative behavior of these distortions over time in an appropriate diagram, together with experimental data as stated in the general rules section, is important for the validation of the correct general distortion behavior of the simulation model. Figure 8 shows an example for the display of distortion results. The summary for the aspects is given in Table 5.

Residual Stress. The completion of a numerical welding simulation includes not only the temperature and distortion behavior but also the accompanying thermal and residual stresses. If these stresses are used for validation, the following aspects will be observed. A prerequisite for an analysis of the calculated residual stresses is an admissible position for evaluating the data. Because of possibly false calculated stresses in node areas with obstruction of individual or all degrees of freedom, any evaluation in the direct vicinity of modeled fixtures or clamping should be avoided.

The quantitative value of the residual stresses in the observed directions after completed cooling of the component to room temperature is best visualized in a diagram showing the distance to the weld seam or component edges; see Fig. 9 for an example. The determination of the values must be done analogously to the restraint conditions prevailing at the time of measurement during the experiment, that is, any clamping or unclamping of the specimen. In these diagrams, the weld seam area should be marked if appropriate in order to give information about the position and size of the weld seam and heat-affected zone area in combination with the stresses.

For both the measured values and the simulation, the local resolution attained in each case must be taken into account. This resolution is dependent on various factors, such as the measuring-dot diameter in x-ray residual-stress

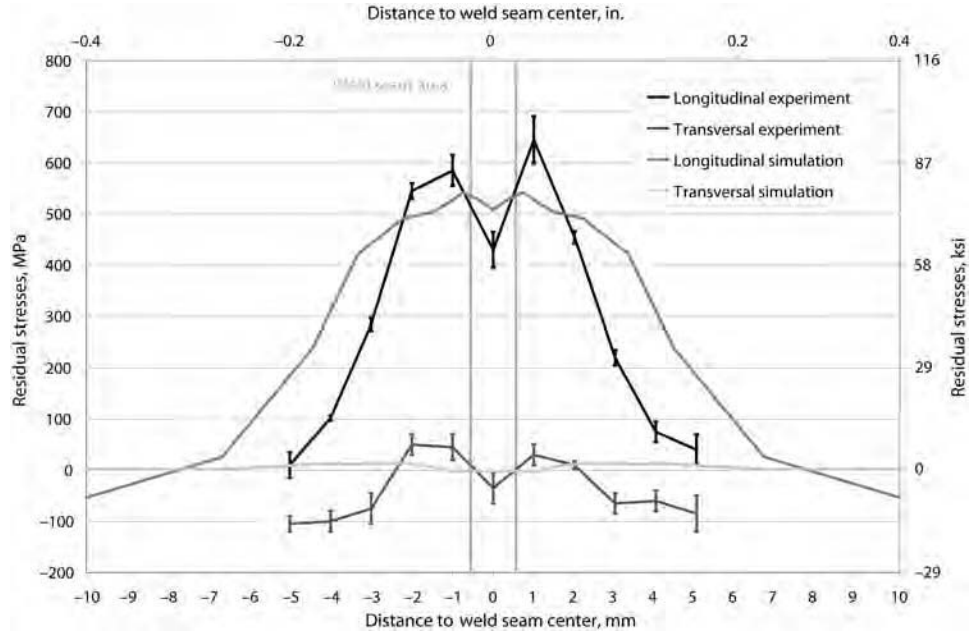


Fig. 9 Example for correct display of residual-stress validation. H400 (EN 1.4376), 3 kW neodymium: yttrium-aluminum-garnet laser beam bead-on-plate weld, sheet thickness = 1.5 mm (0.06 in.), $v_{weld} = 6.5$ m/min (256 in./min). Adapted from Ref 20

Table 6 Validation and result display of the residual-stress calculation

Information	Explanatory notes
Position for evaluation of residual stresses in the simulation	Any evaluation of the calculated residual stresses in the vicinity of fixtures should be avoided. Weld area must be marked in the representation.
Quantitative value after completed cooling to room temperature	Residual stresses in longitudinal and transverse directions to the weld after completed cooling of the component to room temperature Determination of the values analogously to the restraint prevailing at the time of measurement during the experiment
Consideration of the local resolution	For both the measured values and the simulation, the local resolution (measuring point or element size) attained in each case must be taken into account.

analysis, the drill hole diameter and strain gage measuring surface in the application of the hole-drilling method, or the element edge length in the simulation. Table 6 shows a summary of the information.

REFERENCES

1. S.S. Babu, G. Sonnenberg, C. Schwenk, J. Goldak, H. Porzner, S.P. Khurana, W. Zhang, and J. Gaylor, How Can Computational Weld Mechanics Help Industry?, *Weld. J.*, Vol 89 (No. 1), 2010, p 40–45
2. D. Tikhomirov and C. Schwenk, Efficient Numerical Welding Simulation Through Standardization, *Weld. Cut.*, Vol 9 (No. 5), 2010, p 292–295
3. “Numerical Welding Simulation—Execution and Documentation—Part 1: Overview,” DIN SPEC 32534-1, Deutsches Institut für Normung e.V. DIN, 2011
4. D. Radaj, A. Lundbäck, and L.-E. Lindgren, Verification and Validation in Computational Welding Mechanics, *Mathematical*

5. D. Radaj, *Fachbuchreihe Schweißtechnik*, Vol 143, *Eigenspannungen und Verzug beim Schweißen: Rechen und Meßverfahren*, DVS-Verlag, Düsseldorf, 2002
6. W. Perret, R. Thater, U. Alber, C. Schwenk, and M. Rethmeier, Approach to Assess a Fast Welding Simulation in an Industrial Environment—Application for an Automotive Welded Part, *Int. J. Auto. Technol. (IJAT)*, in publication
7. C. Schwenk, M. Rethmeier, K. Dilger, and V. Michailov, Sensitivity Analysis of Welding Simulation Depending on Material Properties Value Variation, *Mathematical Modelling of Weld Phenomena*, Vol 8, H. Cerjak, H.K.D.H. Bhadeshia, and E. Kozeschnik, Ed., Verlag der Technischen Universität Graz, 2007, p 1107–1128
8. J. Caron, C. Heinze, C. Schwenk, M. Rethmeier, S.S. Babu, and J. Lippold, Sensitivity Analysis of Martensite

Modelling of Weld Phenomena, Vol 8, H. Cerjak, H.K.D.H. Bhadeshia, and E. Kozeschnik, Ed., Verlag der Technischen Universität Graz, 2007, p 1039–1051

- Transformation Temperature with Respect to Numerical Calculation of Welding-Induced Residual Stresses, *Mathematical Modelling of Weld Phenomena*, Vol 9, H. Cerjak and N. Enzinger, Ed., Verlag der Technischen Universität Graz, 2010, p 215–238
9. J. Caron, C. Heinze, C. Schwenk, M. Rethmeier, S.S. Babu, and J. Lippold, Effect of Continuous Cooling Transformation Variations on Numerical Calculation of Welding-Induced Residual Stresses, *Weld. J.*, Vol 89 (No. 7), 2010, p 151–160
 10. V.A. Karkhin, H. Pesch, A.S. Ilin, A. Prikhodovsky, V. Plochikhine, M. Makhutin, and H.-W. Zoch, Effects of Latent Heat of Fusion on Thermal Processes during Welding, *Mathematical Modelling of Weld Phenomena*, Vol 7, H. Cerjak, H.K.D.H. Bhadeshia, and E. Kozeschnik, Ed., Verlag der Technischen Universität Graz, 2005, p 39–62
 11. L.-E. Lindgren, Finite Element Modeling and Simulation of Welding, Part 2: Improved Material Modeling, *J. Therm. Stresses*, Vol 24, 2001, p 195–231
 12. D. Bru, J. Devaux, J.M. Bergheau, and D. Pont, Influence of Material Properties at High Temperatures on the Modelling of Welding Residual Stress and Deformation State, *Mathematical Modelling of Weld Phenomena*, Vol 3, H. Cerjak and H.K.D. H. Bhadeshia, Ed., The Institute of Materials, London, 1997, p 456–463
 13. C. Schwenk, “FE-Simulation des Schweißverzugs laserstrahlgeschweißter dünner Bleche—Sensitivitätsanalyse durch Variation der Werkstoffkennwerte,” Ph.D. thesis, *BAM-Dissertationsreihe*, Vol 26, Technical University of Berlin, Berlin, 2007
 14. C. Schwenk and M. Rethmeier, Temperature Dependent Material Properties for Welding Simulation—Measurement, Analysis, Exemplary Data, *Weld. J.*, in review
 15. F. Richter, Die wichtigsten physikalischen Eigenschaften von 52 Eisenwerkstoffen, *Stahleisen-Sonderberichte*, Vol 8, Verlag Stahleisen mbH, Düsseldorf, 1973
 16. F. Richter, Physikalische Eigenschaften von Stählen und ihre Temperaturabhängigkeit—Polynome und Graphische Darstellungen, *Stahleisen-Sonderberichte*, Vol 10, Verlag Stahleisen mbH, Düsseldorf, 1983
 17. W.I. Makhnenko, “Calculation Methods for the Investigation of the Kinetics of Welding Residual Stresses and Deformations,” Kiev, 1976 (in Russian)
 18. Aufstellung von Zeit-Temperatur-Umwandlungsschaubildern für Eisenlegierungen, *Stahl-Eisen-Prüfblätter (1680)*, Verlag Stahleisen GmbH, Düsseldorf, 1990
 19. T. Kannengiesser, S.S. Babu, Y. Komizo, and A. Ramirez, Ed., *In-Situ Studies with Photons, Neutrons and Electrons Scattering*, Springer-Verlag, Berlin Heidelberg, 2010
 20. C. Schwenk and M. Rethmeier, Structured Approach for a Transient 3-D Numerical Welding Simulation, *Mathematical Modelling of Weld Phenomena*, Vol 9, H. Cerjak and N. Enzinger, Ed., Verlag der Technischen Universität Graz, 2010, p 901–917
 21. D. Weiß, K.H. Christensen, and L.K. Kristensen, Computerised Calibration of Thermal Welding Models, *Mathematical Modelling of Weld Phenomena*, Vol 8, H. Cerjak, H.K.D.H. Bhadeshia, and E. Kozeschnik, Ed., Verlag der Technischen Universität Graz, 2007, p 469–484
 22. M.F. Zaeh, L. Papadakis, and W. Rauh, Realisation of the Virtual Process Chain Forming—Welding on Whole Assembled Automotive Body Components by Means of Shell Elements, *Mathematical Modelling of Weld Phenomena*, Vol 8, H. Cerjak, H.K.D.H. Bhadeshia, and E. Kozeschnik, Ed., Verlag der Technischen Universität Graz, 2007, p 537–554
 23. C. Hackmair, E. Werner, and M. Pönisch, Application of Welding Simulation for Chassis Components within the Development of Manufacturing Methods, *Comput. Mater. Sci.*, Vol 28, 2007, p 540–547
 24. B. Saint-Germain, “Etude Expérimentale et Numérique des Distorsions de Structure Mécano-Soudées,” Ph.D. thesis, Ecole Centrale des Arts et Manufactures, École Centrale Paris, 2006
 25. A. Grün, G. Heckeler, and M. Hügel, Analysis of Distortion and Residual Stresses for the Welded Side Component of a Rear-Axle Carrier, *DVS-Berichte*, Vol 214, 2001, p 118–121
 26. C. Schwenk, M. Rethmeier, and K. Dilger, Analysis of the Transient Deformation Behaviour and Numerical Optimisation of an Electron Beam Welded Gearwheel, *Mathematical Modelling of Weld Phenomena*, Vol 8, H. Cerjak, H.K.D.H. Bhadeshia, and E. Kozeschnik, Ed., Verlag der Technischen Universität Graz, 2007, p 1155–1166
 27. M. Rethmeier, O. Voss, I. Decker, H. Wohlfahrt, and R. Kocik, Numerical Calculation of Temperature Load and Distortion during Welding of Circumferential Weld Seams, *Mathematical Modelling of Weld Phenomena*, Vol 6, H. Cerjak and H.K.D.H. Bhadeshia, Ed., Institute of Materials, London, 2002, p 685–701
 28. H. Shirai, M. Mochizuki, and M. Toyoda, “Reduction of Welding Deformation by Split Laser Beams in Automobile Parts,” *IHW Doc. X-1618-07*, 2007
 29. D. Radaj, *Fachbuchreihe Schweißtechnik*, Vol 141, *Schweißprozesssimulation: Grundlagen und Anwendungen*, DVS-Verlag, Düsseldorf, 1999
 30. C.S. Wu, *Welding Thermal Processes and Weld Pool Behaviors*, CRC Press/Taylor & Francis Group, 2011
 31. K. Mundra, T. DebRoy, T. Zacharia, and S.A. David, Role of Thermophysical Properties in Weld Pool Modelling, *Weld. J.*, Vol 9, 1992, p 313
 32. L.-E. Lindgren, Modelling for Residual Stresses and Deformations due to Welding—Knowing What Isn’t Necessary to Know, *Mathematical Modelling of Weld Phenomena*, Vol 6, H. Cerjak, Ed., The Institute of Materials, London, 2002, p 491
 33. T. Schenk, I. Richardson, M. Kraska, and S. Ohnimus, Modelling Buckling Distortion of DP600 Overlap Joints Due to Gas Metal Arc Welding and the Influence of the Mesh Density, *Comput. Mater. Sci.*, Vol 46 (No. 4), 2009, p 977–986
 34. T. Schenk and C. Schwenk, Material Response of GMA Welded 1 mm Thick DP600 Overlap Joints, *Sci. Technol. Weld. Join.*, Vol 15 (No. 7), 2010, p 567–574
 35. D. Radaj, Integrated Finite Element Analysis of Welding Residual Stress and Distortion, *Mathematical Modelling of Weld Phenomena*, Vol 6, H. Cerjak and H.K.D. H. Bhadeshia, Ed., The Institute of Materials, London, 2002, p 469–489
 36. C. Heinze, A. Kromm, C. Schwenk, T. Kannengiesser, and M. Rethmeier, Welding Residual Stresses Depending on Solid-State Transformation Behaviour Studied by Numerical and Experimental Methods, *Mater. Sci. Forum*, Vol 681, 2011, p 85–90
 37. J. Goldak, A. Chakravarti, and M. Bibby, A New Finite Element Model for Welding Heat Sources, *Metall. Trans. B*, Vol 15, 1984, p 299–305
 38. O. Voß, “Untersuchung relevanter Einflußgrößen auf die numerische Schweißsimulation,” Ph.D. thesis, Technical University Braunschweig, 2001
 39. S.S. Babu, Thermodynamic and Kinetic Models for Describing Microstructure Evolution during Joining of Metals and Alloys, *Int. Mater. Rev.*, Vol 54 (No. 6), 2009, p 333–367
 40. J.B. LeBlond and J. Devaux, A New Kinetic Model for Anisothermal Metallurgical Transformations in Steels Including Effect of Austenite Grain Size, *Acta Metall.*, Vol 32, 1984, p 137–146
 41. W.A. Johnson and R.F. Mehl, Reaction Kinetics in Process of Nucleation and Growth, *Trans. AIME*, Vol 135, 1939, p 416–458
 42. M. Avrami, Kinetics of Phase Change I: General Theory, *J. Chem. Phys.*, Vol 7, 1939, p 103–112
 43. M. Avrami, Kinetics of Phase Change II: Transformation-Time Relations for Random Distribution of Nuclei, *J. Chem. Phys.*, Vol 8, 1940, p 212–224
 44. M. Avrami, Kinetics of Phase Change III: Granulation, Phase Change, and Microstructure, *J. Chem. Phys.*, Vol 9, 1941, p 177–184
 45. D.P. Koistinen and R.E. Marburger, A General Equation Prescribing the Extent of the Austenite-Martensite Transformation

- in Pure Iron-Carbon Alloys and Plain Carbon Steels, *Acta Metall.*, 1959, p 59–60
46. P.V. Jeberg, “Automatic Process Optimised Weld Planning of Full Penetration I-Joint GMA Welding,” Ph.D. thesis, Aalborg University, 2005
47. A. Kumar and T. DebRoy, Tailoring Fillet Weld Geometry Using Genetic Algorithm and a Neural Network Trained with Convective Heat Flow Calculations, *Weld. J.*, Vol 86 (No. 1), 2007, p 26–33
48. C.V. Goncalves, L.O. Vilarinho, A. Scotti, and G. Guimaraes, Estimation of Heat Source Efficiency and Thermal Efficiency in GTAW Process by Using Inverse Techniques, *J. Mater. Proc. Technol.*, Vol 172, 2006, p 42–51
49. A. Pittner, D. Weiss, C. Schwenk, and M. Rethmeier, Methodology to Improve Applicability of Welding Simulation, *Sci. Technol. Weld. Join.*, Vol 13 (No. 6), 2008, p 496–508
50. ISO 80000 Family: “Quantities and Units,” partially available and under ongoing development by IEC TC 25

Reference Information

Safe Welding Practices	845	Summary of Fusion Welding Processes	870
Safety Management	845	Weldability of Ferrous and Nonferrous Alloys	874
Protection of the Work Area	846	Preheat and Postweld Heat Treatment Temperatures for	
Personal Protective Equipment	848	Selected Steels	878
Protection Against Fumes and Gases	850	Glossary of Terms	882
Safe Handling of Compressed Gases	855	Abbreviations	892
Protection Against Electromagnetic Radiation	858	Metric Conversion Guide	895
Electrical Safety	858	Index	897
Fire Prevention and Protection	860		
Explosion Prevention	861		
Process-Specific Safety Considerations	861		
Safety in Robotic Operations	866		
Welding Fuels and Shielding Gases	869		

Safe Welding Practices*

American Welding Society

HEALTH AND SAFETY CONSIDERATIONS are paramount in all welding, cutting, brazing, and related processes. No activity is satisfactorily completed if personal injury or property damage occurs. This article presents an overview of the rules, regulations, and techniques that are implemented to minimize the safety hazards associated with welding, cutting, and allied processes. It examines safety management, the protection of personnel and the work area, process-specific safety considerations, and robotic safety.

The limited scope of this discussion precludes an exhaustive examination of the health and safety considerations related to all welding processes, particularly those involving sophisticated technology. Additional safety and health information relating to the various welding processes is presented in the American National Standard “Safety in Welding, Cutting, and Allied Processes,” ANSI Z49.1 (Ref 1), and in *Safety and Health Fact Sheets* (Ref 2), the latter of which is available electronically at <http://www.aws.org>. (At the time of the preparation of this article, the referenced codes and other standards were valid. If a code or other standard is cited without a date of publication, it is understood that the latest edition of the document referred to applies. If a code or other standard is cited with the date of publication, the citation refers to that edition only, and it is understood that any future revisions or amendments to the code or standard are not included; however, as codes and standards undergo frequent revision, the reader is encouraged to consult the most recent edition.) Further process-specific information is published in *Welding Processes*, Volume 2 of the American Welding Society’s (AWS) *Welding Handbook*, 8th edition (Ref 3). The reader is encouraged to consult these sources and others listed in the References and Selected References at the end of this article.

Safety Management

According to estimates made by the U.S. Department of Labor, Occupational Safety and Health Administration (OSHA), over 30 million U.S. workers are potentially exposed to one or more chemical hazards from approximately 650,000 hazardous chemical products in the workplace. As these numbers increase with the growing workforce and the introduction of hundreds of new products annually, this situation poses a serious problem for exposed workers and their employers (Ref 4). Of these workers, an estimated 562,000 are at risk for exposure to chemical and physical hazards associated with welding, cutting, brazing, and related activities. Risks include injury from explosion, asphyxiation, electrocution, falling and crushing, and weld flash (burn to the eyes) as well as health hazards associated with over-exposure to fumes, gases, or radiation produced or released during welding and related activities. These include lung disease, heavy metal poisoning, and metal fume fever, among others (Ref 5).

The “Occupational Safety and Health Act” of 1970 (Ref 6) was promulgated to ensure safe and healthy working conditions for all workers by providing for the transmission of information, training, education, and research in the field of occupational health and safety. OSHA’s current standards for welding, cutting, and brazing in general industry and construction are based on the 1967 American National Standards Institute (ANSI) standard Z49.1 and the National Fire Protection Association’s (NFPA) “Standard for Fire Prevention in Use of Cutting and Welding Processes,” NFPA 51B-1962 (Ref 7). Although these standards have undergone several revisions, the OSHA rules presented in the latest edition of Subpart Q of Title 29 of *Code of Federal Regulations (CFR) 1910* (Ref 8) have not been updated.

Management Support

In compliance with the provisions of Title 29 CFR 1910, management must demonstrate its commitment to personnel safety and health by providing direction and support to an effective safety and health program. Management must clearly state safety guidelines and require that everyone—including management—follow safe practices consistently.

Moreover, in accordance with the provisions originally established in ANSI Z49.1:1967 and NFPA 51B:1962, management must designate approved areas where welding and cutting operations can be performed safely. When welding operations must be performed elsewhere, management must assure that proper safety procedures are established and followed to protect personnel and property. (The term *management* refers to “all persons who are responsible for welding operations such as owners, contractors, and others,” as defined in Ref 1.)

Management is also responsible for ensuring that only approved welding, cutting, and allied equipment is used in the workplace. This equipment includes torches, regulators, welding machines, electrode holders, and personal protective devices. Management must provide adequate supervision to ensure that all equipment is properly used and maintained (Ref 1).

Contractors hired by management to perform welding operations must employ trained, qualified personnel. Management must inform contractors about any hazardous conditions that may be present in the work area.

Hazard Communications

The “Hazard Communication Standard,” 29 CFR 1910.1200 (Ref 4), which is included in the “Occupational Safety and Health Act,” requires employers to inform personnel of potential hazards in the workplace and provide

* This article is reprinted by permission of the American Welding Society from *Welding Science & Technology*, Vol 1, *Welding Handbook*, 9th ed., American Welding Society, Miami, FL, 2001. It was prepared by the Welding Handbook Chapter Committee on Safe Practices, consisting of D.G. Scott, Consultant, Chair; K.L. Brown, The Lincoln Electric Company; M. Cooper, Premier Industries; R.C. DuCharme, Consultant; R.F. Gunow, Vacmet, Inc.; J.D. McKenzie, Emhart Automotive; C.F. Padden, Consultant; D.K. Roth, RoMan Manufacturing, Inc. (affiliations circa 2011).

training regarding the safe handling of hazardous materials. This standard addresses physical hazards, such as flammability and the potential for explosion, as well as acute and chronic health hazards. The "Hazard Communication Standard" requires that all chemicals produced, imported, or used in U.S. workplaces be evaluated and that hazard information be transmitted to affected employers and exposed employees by means of precautionary information on containers and material safety data sheets (MSDSs) and training (Ref 4).

The "Hazard Communication Standard" identifies many welding consumables as hazardous materials. When welders (in this article, the term *welder* is intended to include all welding and cutting personnel as well as brazers and solderers) and other equipment operators are properly taught safe practices, they work more safely and cause fewer accidents. Users must be trained to read and understand all safety documentation before work begins. This documentation includes precautionary information, such as that presented in Fig. 1, and the manufacturers' safety instructions for the use of materials and equipment, including MSDSs.

Material safety data sheets, which manufacturers, suppliers, and importers are required to provide customers under the "Hazard Communication Standard," 29 CFR 1910.1200 (Ref 4), identify products that could cause health hazards and provide information on each hazardous chemical, including its physical and chemical characteristics, potential effects, and recommendations for protective measures. Material safety data sheets also provide the permissible exposure

limit established by OSHA, another exposure limit such as the threshold limit value established by the American Conference of Governmental Industrial Hygienists (ACGIH), or any other limit recommended by the manufacturer.

All employers, including those who use welding consumables, must make applicable MSDSs readily available to their employees as well as train them to read and understand their contents. The MSDSs used in the welding industry contain important information about the ingredients in welding electrodes, rods, and fluxes; the composition of fumes that may be emitted during use; and means to protect the welder and others from potential hazards. A sample MSDS is presented in Fig. 2.

Training

As mandated by the provisions of the "Occupational Safety and Health Act," thorough and effective training is an essential aspect of a safety program. Therefore, in addition to providing access to all applicable government and industry standards, management must ensure that all personnel are properly trained in the safe operation and maintenance of all equipment. For example, personnel must be instructed to position themselves away from gases or fume plumes while performing welding or cutting operations. (The term *fume plume* refers to the smokelike cloud containing minute solid particles that arises directly from the area of melting metal. Unlike gases, fumes are metallic vapors that have condensed to a solid. They are often associated with a chemical reaction such as oxidation.)

Personnel must also be trained to recognize safety hazards in all situations and environments. If they are to work in an unfamiliar situation or environment, they must be thoroughly briefed on the potential hazards involved. For example, welders who work in confined areas that are poorly ventilated must be thoroughly trained in the proper ventilation practices and be cognizant of the adverse consequences of not using them (see the section "Welding in Confined Spaces" in this article). Moreover, employees should be trained to question their supervisors before initiating any type of welding or cutting operation if they believe that the safety precautions for a given task are inadequate or misunderstood.

In sum, training must be provided to ensure that all personnel have knowledge of the safety rules that apply for the practices of welding and circumstances they may encounter in the workplace and are familiar with the risks and consequences that may arise should these rules be ignored or violated.

Protection of the Work Area

Good housekeeping is essential in ensuring safe and healthy working conditions. Welders

and supervisors must keep work areas and locations such as passageways, ladders, and stairways clean and clear of obstructions. Because welders shield their vision with necessary eye protection, and those passing by a welding station must shield their eyes from the flame or arc radiation, vision is limited. Because eye protection interferes with their vision, welders and passersby can easily trip over objects on the floor. Therefore, management must lay out the production area so that gas hoses, cables, mechanical assemblies, and other pieces of equipment do not cross walkways or interfere with routine tasks.

Safety rails, harnesses, or lines must also be provided to keep workers away from restricted, potentially hazardous areas and prevent falls, whether work is being carried out at floor level or in an elevated location.

Hazard Notification and the Positioning of Equipment

In accordance with ANSI Z49.1:1999, notification signs should be posted to designate welding areas where eye protection must be worn. Because unexpected events such as fire and explosions can occur in industrial environments, all escape routes must be identified and kept clear to allow for an orderly, rapid, and safe evacuation (Ref 1).

Thus, materials and equipment must not be stored in evacuation routes. Equipment, machines, cables, hoses, and other apparatus should always be situated in such a manner so as not to present a hazard to personnel in passageways, on ladders, or on stairways. If an evacuation route must be blocked temporarily, the employees who normally use that route must be informed of the obstructions and trained to use another route to evacuate the premises.

Machinery Safeguarding

All personnel must be protected from injuries that may be caused by the machinery and equipment they operate as well as other machinery operating in the work area. Inasmuch as welding helmets and dark filter lenses restrict vision, welders may be more susceptible than other workers to injury from unseen, unguarded machinery. Therefore, moving components and drive belts must be equipped with guards to prevent physical contact. Rotating and automatic welding machines, fixtures, and welding robots must also be outfitted with appropriate guards or sensing devices to prevent operation when personnel are in the hazard area.

During the repair of machinery by means of welding or brazing, the power supply to the machine must be disconnected, locked out, and tagged out to prevent inadvertent operation and injury. (When a piece of machinery is locked out, a locking device that prevents the switch, valve, or other mechanism from being

<p>WARNING:</p> <p>PROTECT yourself and others. Read and understand this information.</p> <p>FUMES AND GASES can be hazardous to your health.</p> <p>ARC RAYS can injure eyes and burn skin.</p> <p>ELECTRIC SHOCK can KILL.</p> <ul style="list-style-type: none"> • Before use, read and understand the manufacturer's instructions, Material Safety Data Sheets (MSDSs), and your employer's safe practices. • Keep your head out of fumes. • Use enough ventilation, exhaust at the arc, or both to keep fumes and gases from your breathing zone and the general area. • Wear correct eye, ear, and body protection. • Do not touch live electrical parts. • See American National Standard ANSI Z49.1, <i>Safety in Welding, Cutting, and Allied Processes</i>, published by the American Welding Society, 550 N.W. LeJeune Rd., Miami, Florida 33126; and OSHA <i>Safety and Health Standards</i>, available from the U.S. Government Printing Office, Superintendent of Documents, P.O. Box 371954, Pittsburgh, PA 15250-7954. <p style="text-align: center;">DO NOT REMOVE THIS INFORMATION</p>
--

Fig. 1 Minimum precautionary information for arc welding processes and equipment. Adapted from Ref 1

MATERIAL SAFETY DATA SHEET

(Welding Consumables and Related Products Conforms to the Requirements of OSHA's 29 CFR 1900.1200)

Section 1—IDENTIFICATION	
Manufacturer/Supplier Name	Telephone No.
Address	Date
Trade Name	
Product Type	

Section 2—HAZARDOUS* INGREDIENTS		
IMPORTANT! This section covers the materials from which this product is manufactured. The fumes and gases produced during welding with (normal use of)** this product are covered by Section 3.		
Ingredient***	Approximate Weight %**	Exposure Limit
		Source (1) OSHA (2) ACGIH TLV (3) Mfr. Recommendation
*The term "hazardous" should be interpreted as a term required and defined in the OSHA Hazard Communication Standard (29 CFR Part 1910.1200) and does not necessarily imply the existence of any hazard. **Optional ***Ingredient means the chemical name or common name, chemical abstract service (CAS) registry number (optional), or any other information that reveals precise chemical designation of the substance.		

Section 3—PHYSICAL AND CHEMICAL CHARACTERISTICS
Not applicable (<i>appearance information may be included</i>).

Section 4—FIRE AND EXPLOSION HAZARD DATA
Nonflammable. Welding arc and sparks, however, can ignite combustibles and flammable products. See guideline reference ANSI Z49.1.

Section 5—REACTIVITY DATA
Hazardous Decomposition Products Welding fumes and gases cannot be classified simply. The composition and quality of both are dependent upon the metal being welded and electrodes used. Other conditions which also influence the composition and quantity of the fumes and gases to which workers may be exposed include: coatings on the metal being welded (such as paint, plating, or galvanizing), the number of welders, the volume of the work area, the quality and amount of ventilation, the position of the welder's head with respect to the fume plume, the presence of contaminants in the atmosphere (such as chlorinated hydrocarbon vapors from cleaning and degreasing activities). When the electrode is consumed, the fume and gas decomposition products generated are different in percent and form from the ingredients listed in Section 2. Decomposition products of normal operation include those originating from the volatilization, reaction, or oxidation of the materials shown in Section 2, plus those from the base metal, coatings, etc., as noted above. Reasonably expected fume constituents of this product would include: (insert fume composition). Reasonably expected gaseous constituents of this product would include: (insert gas composition). Ozone and nitrogen oxides may be formed by the radiation from the arc. One recommended way to determine the composition and quantity of fumes and gases to which workers are exposed is to take an air sample inside the welder's helmet if worn or in the worker's breathing zone. See ANSI/AWS F.1.1 and ANSI/AWS F.1.2.

Section 6—HEALTH HAZARD DATA
Threshold Limit Value: The ACGIH recommended limit for Welding Fume NOC (Not Otherwise Classified) is 5 mg/m ³ . ACGIH-1995 (or latest date) preface states "These values are not fine lines between safe and dangerous concentrations and should not be used by anyone untrained in the discipline of industrial hygiene." See Section 5 for specific fume constituents.
Effects of Overexposure Welding may create one or more of the following health hazards: FUMES AND GASES can be dangerous to your health. Short-term (acute) overexposure to welding fumes may result in discomfort such as: metal fume fever, dizziness, nausea, or dryness or irritation of the nose, throat, or eyes and may aggravate pre-existing respiratory conditions, e.g., asthma or emphysema. Long-term (chronic) overexposure to welding fumes can lead to siderosis (iron deposits in the lungs) and may affect pulmonary function. Manganese overexposure can affect the central nervous system resulting in impaired speech and movement. The primary entry route for welding fumes and gases is by inhalation. ARC RAYS can injure eyes and burn skin. ELECTRIC SHOCK can kill. Before use, read and understand the manufacturer's instructions, Material Safety Data Sheets (MSDSs), and your employer's safety practices. Keep your head out of the fumes. Use enough ventilation, exhaust at the arc, or both, to keep fumes and gases from your breathing zone and the general area. Wear correct eye, ear, and body protection. Do no touch live electrical parts.
Emergency and First Aid Procedures Call for medical aid. Employ first aid techniques recommended by the American Red Cross.
Carcinogenicity: NTP? IARC Monographs? OSHA Regulated?

Section 7—PRECAUTIONS FOR SAFE HANDLING AND USE/APPLICABLE CONTROL MEASURES
Read and understand the manufacturer's instructions and the precautionary label on the product. See American National Standard Z49.1 (<i>Safety in Welding, Cutting, and Allied Processes</i>) and OSHA Publication (29 CFR 1910) for more detail on many of the following.
Ventilation Use enough ventilation, local exhaust at the arc, or both, to keep the fumes and gases from the worker's breathing zone and the general area. Train the welder to keep his head out of the fumes. Keep exposures as low as possible.
Respiratory Protection Use respirable fume respirator or air supplied respirator when welding in confined space or where local exhaust or ventilation does not keep exposure below the recommended exposure limit.
Eye Protection Wear helmet or use face shield with correct shade of filter lens. Provide protective screens and flash goggles, if necessary, to shield others. As a rule of thumb, start with a shade that is too dark to see the weld zone. Then go to the next lighter shade which gives sufficient view of the weld zone.
Protective Clothing Wear hand, head, and body protection which help to prevent injury from radiation, sparks, and electrical shock. See ANSI Z49.1. At a minimum this includes welder's gloves and a protective face shield, and may include arm protectors, aprons, hats, shoulder protection, as well as dark substantial clothing. Train the welder not to touch live electrical parts and to insulate himself from work and ground.
Procedure for Cleanup of Spills or Leaks Waste Disposal Method—Prevent waste from contaminating surrounding environment. Discard any product, residue, disposable container, or liner in an environmentally acceptable manner, in full compliance with federal, state, and local regulations. STEPS TO BE TAKEN IF MATERIAL IS RELEASED OR SPILLED: not applicable.

Fig. 2 Sample material safety data sheet. Adapted from Ref 9

opened has been installed. When a piece of machinery is tagged out, a tag reading "DANGER" or "WARNING" along with a short message has been attached to the locking device. The message includes the name and contact information of the person who is responsible for the lock out of the machinery.) Welders assigned to work on equipment whose safety devices are disengaged should fully understand

the hazards involved and the steps necessary to avoid accidental injury.

If the pinch points on resistance welding machines, robots, automatic arc welding machines, fixtures, and other mechanical equipment are not properly guarded, they can result in serious injury. To avoid injury with such equipment, a machine should be activated only when the workers' hands are at safe locations.

Otherwise, the pinch points must be suitably guarded mechanically. During equipment maintenance, pinch points should be blocked to prevent them from closing in case of equipment failure. In very hazardous situations, an observer should be stationed to prevent the power from being turned on during maintenance. The topic of the protection of personnel servicing automatic equipment is addressed in Ref 10 and 11.

Metalworking equipment should be carefully safeguarded so as to prevent welders from accidentally falling into or against it while working.

Protective Booths

According to the provisions of ANSI Z49.1:1999, workers and others in areas adjacent to welding and cutting areas must be protected from radiant energy and hot spatter by flame-resistant screens or shields or by suitable eye and face protection and protective clothing. Appropriate radiation-protective, semitransparent materials are permissible. Operations permitting, workstations should be separated by noncombustible screens or shields. Protective booths with semitransparent shielding are shown in Fig. 3. Booths and screens should permit air circulation at floor level as well as above the screen (Ref 1).

Wall Reflectivity

In areas where arc welding or cutting is routinely performed, the walls and nearby reflective surfaces must be painted with a finish having low reflectivity of ultraviolet (UV) radiation, such as those formulated with titanium dioxide or zinc oxide (Ref 12). Color pigments may be added, provided they do not increase reflectivity. The use of pigments that are based on powdered or flaked metals is not recommended, because these reflect a large amount of UV radiation. As an alternative, welding curtains can be used to minimize reflectivity (Ref 1).

Public Exhibitions and Demonstrations

Persons conducting exhibits and public demonstrations of arc or oxyfuel gas welding or cutting processes are responsible for the safety of demonstrators and the public. All welding and welding-related equipment used in trade shows and other public events must be installed by or under the supervision of a qualified individual at a site that is located and designed to ensure viewing safety. (The term *qualified person* denotes “a person who by reason of training, education, and experience is knowledgeable in the operation to be performed and is competent to judge the hazards involved,” according to Ref 1.) Electric cables and hoses must be routed away from the audience to avoid possible electric shock or tripping hazards. Exhibitors must also provide protection against fires from fuels, combustibles, and overheated apparatus and wiring. Fire extinguishers must be on hand, and combustible materials must be removed from the area or shielded from flames, sparks, and molten metal (Ref 1).

Appropriate protection for demonstrators, observers, and passersby is mandatory. Overexposure to welding fumes and gases must be controlled by the use appropriate ventilation. Individuals must also be shielded from flames, sparks, molten metal, and harmful radiation. A protective, moveable, transparent screen can be used to permit the audience to observe a welding operation under safe viewing conditions. After welding is completed, the screen can be moved to allow the audience to observe the completed weld (Ref 1).

Personal Protective Equipment

The use of personal protective equipment (PPE) is required by OSHA to reduce the risks of exposure to hazards when administrative measures are not feasible or effective in reducing these risks. Employers are required to identify all potential hazards in the workplace and determine whether PPE should be used to protect workers. Title 29 CFR 1910.132 stipulates that employers must establish general procedures, in the form of a PPE program, to provide employees protective equipment and training in how to use it (Ref 13).

Of particular importance in the welding industry are burns, a serious potential hazard during all welding, brazing, soldering, and cutting operations. Operators and others in the work area must always wear eye, face, hand, foot, and body protection to prevent burns from UV and infrared radiation, sparks, and spatter.

Eye, Face, and Head Protection

Protective equipment for the eyes, face, and head must be used by employees who perform tasks that may produce dust, flying particles, or molten metal; those who are exposed to extreme heat, physical or chemical irritants, or intense radiation and light, such as that created by welding arcs and lasers; and those who may be struck on the head by tools or falling objects.

The PPE for the eyes, face, and head includes welding helmets (Ref 14), face shields, welding goggles, and spectacles (Ref 15). In accordance with the specifications of ANSI Z49.1:1, the bodies of welding helmets and shields must be composed of material that is noncombustible, thermally and electrically insulating, and opaque to radiation. The lenses in helmets, shields, and goggles must have protective outer covers to protect the wearer from welding spatter. To protect against flying debris, lift-front helmets must incorporate inner impact-resistant safety lenses or plates (Ref 1).

Filter lenses must be selected in accordance with the ultraviolet, luminous, and infrared transmittance requirements specified in “Practice for Occupational and Educational Eye and Face Protection,” ANSI Z87.1 (Ref 15). The shade used must be in accordance with “Lens Shade Selector,” ANSI/AWS F2.2 (Ref 16). Table 1 presents suggested shade numbers of filter lenses for various welding, brazing, soldering, and thermal cutting processes.

Individuals who have special eye conditions should consult a health care provider for specific information about the use of protective equipment. Contact lens use is permitted, provided lenses are worn in combination with the appropriate safety eyewear, except when the industrial environment presents the probability of exposure to intense heat, significant chemical splash, an extremely particulate atmosphere, or where such use is prohibited by specific regulation (Ref 2).



Fig. 3 Protective screens between workstations

Table 1 Guide for shade numbers

Process	Electrode size		Arc current, A	Minimum protective shade	Suggested shade number (comfort)(a)
	mm	in.			
Shielded metal arc welding	2.5	Less than 3/32	Less than 60	7	...
	2.5-4	$\frac{3}{32}$ - $\frac{5}{32}$	60-160	8	10
	4-6.4	$\frac{5}{32}$ - $\frac{1}{4}$	160-250	10	12
	6.4	More than 1/4	250-550	11	14
Gas metal arc and flux cored arc welding	Less than 60	7	...
	60-160	10	11
	160-250	10	12
	250-500	10	14
Gas tungsten arc welding	Less than 50	8	10
	50-150	8	12
	150-500	10	14
Air carbon arc cutting	Less than 500	10	12
	500-1000	11	14
Plasma arc welding	Less than 20	6	6-8
	20-100	8	10
	100-400	10	12
	400-800	11	14
Plasma arc cutting	Less than 300	8	9
	300-400	9	12
	400-800	10	14
Torch brazing	3 or 4
Torch soldering	2
Carbon arc welding	14

	Plate thickness		Suggested shade number (comfort)(a)
	mm	in.			
Oxyfuel gas welding	Under 3.2	Under 1/2	4 or 5
	3.2 to 12.7	to 1/2	5 or 6
	Over 12.7	Over 1/2	6 or 8
Oxygen cutting	Under 25	Under 1	3 or 4
	25 to 150	1 to 6	4 or 5
	Over 150	Over 6	5 or 6

(a) As a rule of thumb, the user should start with a protective shade that is too dark to see the weld zone. Then, a lighter shade that provides sufficient visibility of the weld zone without going below the minimum number can be selected. In oxyfuel gas welding or cutting, in which a torch produces a high-yellow light, it is desirable to use a filter lens that absorbs the yellow or sodium line in the visible light of the (spectrum) operation. (b) These values apply where the arc is clearly seen. Experience has shown that lighter filters may be used when the arc is hidden by the workpiece. Adapted from Ref 1

Process-Specific Requirements. Specific PPE requirements for the common welding process are discussed as follows. These processes include arc welding and cutting, oxyfuel gas welding and cutting, submerged arc welding, torch brazing and soldering, and resistance welding, among others.

Arc Welding and Cutting. To protect against arc rays, sparks, and spatter, welding helmets or hand shields that have appropriate filter lenses and cover plates must be used by welders, welding operators, and nearby personnel when viewing a welding arc. Protective eyewear must also be used during all arc welding and cutting operations. Worn under the welding helmet during arc welding activities, this eyewear must have full, conforming side shields to protect against potentially hazardous rays or the flying particles generated by grinding or chipping operations. Protective eyewear with clear or colored lenses may be used, depending on the intensity of the radiation that personnel may be exposed to from adjacent welding or cutting operations while their welding helmets are raised or removed (Ref 1).

Oxyfuel Gas Welding and Cutting and Submerged Arc Welding. Safety goggles with filter lenses and full, conforming side shields

must be worn while performing operations using the oxyfuel gas welding and cutting processes.

During submerged arc welding operations, an arc welding helmet is not needed because the arc is covered by flux and is therefore not readily visible. However, because the arc occasionally flashes through the flux covering the arc zone, the operator should wear safety goggles at all times.

Resistance Welding and Other Processes. Personnel engaged in resistance, induction, salt bath, dip, and infrared processes must wear safety spectacles and a face shield to protect their eyes and face from spatter. Filter lenses are not necessary but may be used for comfort.

In resistance welding and other processes that may produce sparks and spatter, suitable protection against flying sparks must be provided. Protective devices include shields made of a suitable fire-resistant material or approved personal protective eyewear. However, because resistance welding operations vary, each operation must be evaluated individually with respect to the use of PPE.

Torch Brazing and Soldering. Safety spectacles with appropriate filter lenses and with or without side shields are recommended for use during the performance of torch brazing and soldering. As with oxyfuel gas welding and



Fig. 4 Typical protective clothing for arc welding

cutting, a bright yellow flame may be visible during torch brazing and soldering. Therefore, filters similar to those used for oxyfuel gas welding and cutting should be used for torch brazing and soldering operations.

Hand, Foot, and Body Protection

Protective gloves, sturdy shoes or boots, and heavy clothing like that shown in Fig. 4 should be worn to protect the whole body from

welding sparks, spatter, and radiation (Ref 1). Hand and arm injuries that may occur in the welding industry include burns, bruises, abrasions, cuts, and chemical exposure. To protect the hands, sturdy, flame-resistant gloves made of leather or other suitable material must always be worn during welding, cutting, and related processes. Dry leather gloves in good condition not only protect the hands from burns and abrasion but also provide insulation from welding current electrical shock. Gloves with special linings should be used to protect against high radiant energy.

The specifications for protective footwear are found in the American National Standard "Personal Protection—Protective Footwear," ANSI Z41 (Ref 17). This standard specifies requirements with respect to toe and metatarsal protection, impact and compression resistance, sole puncture resistance, conductivity, and static dissipation.

Body protection shields welding personnel from intense heat; splashes of molten metal; impacts from materials, machinery, and tools; hazardous chemicals; and radiation. Clothing treated with nondurable flame-retardant chemicals must be retreated as recommended by the manufacturer. Welding personnel should avoid wearing any clothing or shoes made of synthetic or plastic materials, which can melt and may cause severe burns. Outer clothing should be kept reasonably free of oil and grease, especially in an oxygen-rich atmosphere. Cuffless pants and covered pockets are recommended to avoid spatter or spark entrapment. Pockets should be emptied of flammable materials, and cuffless pant legs should be worn outside of shoes. A cap providing protection for the hair is recommended. In addition, flammable hair preparations such as hair spray should not be used (Ref 1).

Special protective clothing must be worn by personnel performing overhead welding or when special circumstances warrant additional protection. This clothing includes aprons, leggings, suits, capes, sleeves, and caps, all of which must be made of durable, flame-resistant materials (Ref 1).

Hearing Protection

Hearing loss is one of the leading occupational illnesses in the United States. Occupational exposure to excess noise is a recognized stressor that can affect both behavior and physical well being. Excessive noise, particularly continuous noise at high levels, can cause temporary or permanent full or partial hearing loss as well as hypertension. To protect workers from exposure to excessive noise, OSHA regulates allowable noise exposure levels in "General Industry Standards," Title 29 CFR 1910.95 (Ref 8).

In welding, cutting, and allied operations, noise may be generated by the process or the equipment, or both (Ref 18). Air carbon arc

and plasma arc cutting tend to have high noise levels. Engine-driven generators sometimes emit a high noise level, as do some high-frequency and induction welding power sources. Therefore, appropriate noise-limiting devices should be used to protect against possible hearing loss. Properly fitted, flame-resistant earplugs should also be worn when sparks or hot spatter could land in the ears.

Respiratory Protection

In areas where natural or mechanical ventilation is not adequate (see the section "Ventilation" in this article), respiratory protective equipment must be used (Ref 19). When the use of respiratory protective equipment is required by the job, a program must be established to identify and implement the appropriate equipment.

Either dust/mist/fume respirators or any of the new series of respirators approved by National Institute for Occupational Safety and Health (NIOSH) can be used for protection against metal fumes as long as the proper respirator type (e.g., half-mask, full-face, or powered air respiratory protection) is selected based on the calculated hazard ratio for the contaminant of concern. (According to Ref 20, NIOSH promulgated 42 CFR 84 in July 1995, which modified the requirements for particulate—dust/mist and dust/mist/fume—respirators. The dust/mist and dust/mist/fume classifications were replaced by nine new classes of respirators, categorized as the N-, R-, and P-series. The N-series respirators are not resistant to oils, which can degrade the filter media. The R-series respirators are more resistant to oils, while the P-series are significantly more resistant to oils. Production of the previous series of respirators ceased in July 1998, although distributors were allowed to sell either series until supplies were depleted, and OSHA and the Mine Safety and Health Administration, or MSHA, have allowed their use as long as they are available and properly maintained.) A powered air-purifying respirator is shown in Fig. 5.

Some welding materials (fluxes, welding rods, and residual cleaning and degreasing compounds, for example) may contain harmful materials or release gases and vapors for which filter respirators do not provide adequate protection. In these cases, a chemical cartridge/particulate, gas mask/particulate, or airline respirator should be used. As a general rule, a NIOSH-approved air-supplied respirator should be the only choice as adequate protection when the contaminants themselves or their concentrations have not been identified (Ref 20).

It is also important to note that according to the "Respiratory Protection Standard," OSHA 29 CFR 1910.134, respirators must not be passed from one worker to another without sanitizing the equipment (Ref 1). According to NIOSH, the service life of all filters is limited



Fig. 5 Powered air respiratory protection

by considerations of hygiene, damage, and breathing resistance. All filters should be replaced whenever they are damaged or soiled or they cause noticeably increased breathing resistance (Ref 21).

Considering that protection against fumes and gases is essential in the field of welding and its allied processes, this topic is discussed in greater length in the following section.

Protection Against Fumes and Gases

Many welding and welding-related processes generate gases and fumes that may be harmful. Fumes are composed of airborne particles of base metal, welding consumables, or coatings that may be present on the workpiece. Welders, welding operators, and all others in the work area must therefore be protected from overexposure to fumes and gases produced during welding, brazing, soldering, and cutting operations. The term *overexposure* is defined as exposure that may pose a health risk and exceeds the permissible limits specified by a government agency such as OSHA in Title 29 CFR 1910.1000 or other recognized authority, such as the ACGIH in its 1999 publication *TLVs and BEIs: Threshold Limit Values for Chemical Substances and Physical Agents, Biological Exposure Indices* (Ref 22).

The potential short- and long-term health effects of overexposure to welding fumes and gases can include nausea, headache, dizziness, dermatitis, chronic or acute systemic poisoning,

metal fume fever, pneumoconiosis, irritation of the respiratory tract, and possibly cancer.

Proper ventilation (see the section "Ventilation" in this article) usually provides protection against excess exposure. When exposure would exceed permissible limits with the available ventilation, respiratory protection must be used. Fume protection must be provided not only for the welding and cutting personnel but also for others in the area. It is important to note that individuals who have special health problems may have unusual sensitivity that requires even more stringent protection than that specified by a recognized authority.

Exposure Factors

Many factors contribute to the amount of fume exposure that may occur during arc welding. The most important factor is the position of the welder's head with respect to the fume plume. When the head is in such a position that the fume envelops the face or helmet, exposure levels can be very high. Thus, welders must be trained to keep their heads to one side of the fume plume. In some cases, the work can be positioned so the fume plume rises to one side.

Welding personnel can also reduce fume exposure by the kind of welding helmet they wear. The extent to which the helmet curves under the chin toward the chest affects the amount of fume exposure. However, it is important to note that the welding helmet alone is not considered an adequate respiratory protection device.

The amount of fume exposure also depends on the kind of ventilation used. Ventilation may be local, in which case the fumes and gases are extracted near the point of welding, or general, in which case the air from a portion of the shop is changed or filtered. The appropriate type of ventilation to use depends on the welding process, the material being welded, and other shop conditions. Adequate ventilation is necessary to maintain the personnel's exposure to fumes and gases within the recommended limits.

The size of the welding or cutting work area is also important. As a rule, fume exposure inside a tank, pressure vessel, or other confined area tends to be higher than that which occurs in a high-bay fabrication area. The size of the work area also affects the background fume level, which depends on the number and type of welding stations, type of ventilation, and the duty cycle for each station.

The type of base metal being welded influences both the constituents and the amount of fume generated. Surface contaminants or coatings may contribute significantly to the potential fume hazards. Paints containing lead and platings containing cadmium emit hazardous fumes during welding and cutting. Galvanized material emits zinc fume.

Sources of Fumes and Gases

Fumes and gases are usually a greater concern in arc welding than in oxyfuel gas welding, cutting, or brazing. Welding arcs may generate a larger volume of fume and gas, and a greater variety of materials are usually involved in arc welding. Special concerns related to arc welding and cutting, resistance welding, and oxyfuel gas welding and cutting are discussed in the following paragraphs.

Arc Welding and Cutting Fumes and Gases. The fumes and gases produced during arc welding and cutting operations are not simple to classify. Their composition and quantity depend on a number of factors. These include the welding process employed, the composition of the base metal, the consumables used, the coatings on the workpiece (e.g., paint, galvanizing, or plating), and the contaminants in the atmosphere (e.g., halogenated hydrocarbon vapors resulting from cleaning and degreasing activities), among others (Ref 1).

In welding and cutting, fume is a product of the vaporization, oxidation, and condensation of the components in the consumable and, to some degree, the base metal. The electrode, rather than the base metal, is usually the major source of fume. However, significant fume constituents can originate from the base metal if this contains alloying elements or is covered with a coating that is volatile at elevated temperatures. The composition of the fume usually differs from the composition of the electrode or consumable. The products of the volatilization, reaction, or oxidation of the consumables are reasonably expected fume constituents, as is material from base metals, coatings, and atmospheric contaminants.

Various gases are also generated during welding. Some are a product of the decomposition of fluxes and electrode coatings. Others are formed by the action of arc heat or UV radiation emitted by the arc on atmospheric constituents and contaminants. Still others may come from the external gas shielding that is an inherent part of some welding processes. Potentially hazardous gases include carbon monoxide, oxides of nitrogen, ozone, and phosgene, or other decomposition products of chlorinated hydrocarbons, as well as fluorides. Helium and argon, although chemically inert and nontoxic, can cause asphyxia and dilute the atmospheric oxygen concentration to harmfully low levels. Carbon dioxide and nitrogen can also cause asphyxiation.

Welding arcs, especially gas-shielded arcs using high levels of argon and helium, emit UV radiation. Ultraviolet radiation can produce ozone from the oxygen in the surrounding air, even at some distance from the UV source. Photochemical reactions between this UV radiation and chlorinated hydrocarbons can result in the production of phosgene and other decomposition products. Welding arcs can also produce carbon monoxide and nitrogen oxides. Arc heat is responsible for the formation of nitrogen

oxides from atmospheric nitrogen. Hence, nitrogen oxides may be produced by a welding arc or other high-temperature heat sources. Carbon monoxide forms when an arc decomposes carbon dioxide and inorganic carbonate compounds. Levels can be especially significant when carbon dioxide is used as the shielding gas.

The quantity and chemical composition of air contaminants vary substantially from process to process due to the wide range of variables inherent in each process. During arc welding, the arc energy and temperature depend on the process and the welding variables used in that process. Therefore, fumes and gases are generated in varying degrees in different welding operations.

Consequently, reliable estimates of fume and gas composition cannot be made without considering the nature of the welding process and chemical system being examined. For example, aluminum and titanium are normally arc welded in an atmosphere of argon or helium or a mixture of the two gases. The arc creates relatively little fume but may emit intense UV radiation that can produce ozone. The inert gas shielded arc welding of steels also creates a relatively low fume level.

However, the arc welding of steel in oxidizing environments generates considerable fume and can produce carbon monoxide and oxides of nitrogen. These fumes generally consist of discreet particles of complex oxides containing iron, manganese, silicon, and other metallic constituents, depending on the alloy system involved. Chromium and nickel compounds are found in fumes when stainless steels are arc welded. Some covered and flux cored electrodes are formulated with fluorides. The fumes associated with these electrodes can contain significantly more fluorides than oxides.

The generation rate of fumes and gases during the arc welding depends on numerous variables, including the following:

- Welding current
- Arc voltage and length
- Mode of metal transfer
- Shielding gas
- Welding process
- Consumables

These variables are interdependent and can have a substantial effect on total fume generation. They are examined in detail as follows.

Welding Current. Although fume-generation rates generally increase with welding current, the increase varies depending on the process and the type of electrode used. Certain covered, flux cored, and solid wire electrodes exhibit a disproportional increase in the fume-generation rate with increasing current. Several studies have shown that fume-generation rates with covered electrodes are proportional to the welding current raised to a power (Ref 23). For E6010 electrodes, the exponent is 2.24, whereas for E7018 electrodes, it is 1.54.

The relationship between flux cored and solid electrode fume-generation rates and the welding current is more complex. Welding current levels affect the type of metal droplet transfer. As a result, fume-generation rates can decrease with increasing current until a minimum is reached. At this point, fume generation increases in a somewhat proportional fashion.

An increase in current can also increase the emission of UV radiation from the arc. Therefore, the generation of gases formed photochemically by this radiation (e.g., ozone) can be expected to increase as the welding current is increased. Measurements of ozone concentration during gas metal arc and gas tungsten arc welding have shown such behavior.

Arc Voltage and Length. Arc voltage is directly related to arc length. For a given arc length, there is a corresponding arc voltage. The voltage is mostly dependent on the type of electrode, welding process, and power supply used. In general, increasing the arc voltage (arc length) increases the fume-generation rate for all open arc welding processes. The levels of generation differ somewhat for each process and electrode type.

Mode of Metal Transfer. When steel is joined by means of gas metal arc welding using a solid wire electrode, the resulting mode of metal transfer depends on the current and voltage used. At a low welding current and voltage, short-circuiting transfer takes place; that is, droplets are deposited during short circuits between the electrode and molten weld pool. As the current and voltage are increased, the mode of metal transfer changes to the globular type, in which large globules of metal are projected across the arc into the weld pool. At high currents and with argon-base shielding, the mode of transfer shifts to spray mode, in which fine metal droplets are serially propelled rapidly across the arc.

The fume-generation rate also appears to follow a transition. The fume rate is relatively high during short-circuiting transfer because of arc turbulence. As the transition current is approached in an argon-rich shielding gas, the fume rate decreases and then increases again as spray transfer is achieved. In the spray region, the rate of fume generation is proportional to the welding current.

It has been shown, moreover, that the use of pulsed arc transfer during gas metal arc welding results in the generation of significantly less welding fume as compared to conventional gas metal arc welding. This mode of transfer produces a controlled droplet size with a lower average welding current. Thus, the use of this mode can be an effective way of reducing and controlling exposure to welding fume emissions, particularly when implemented in conjunction with local exhaust ventilation that has been properly designed for the application (Ref 24).

For other welding processes, the type of metal transfer varies little with current and

voltage. In these cases, fume generation is approximately proportional to the changes in current.

Shielding gas must be used in gas metal arc welding. It is also required in flux cored arc welding when certain electrodes are used. The type of shielding gas used affects both the composition of the fume and its generation rate. It also affects the kind of gases found in the welding environment. For example, the fume-generation rate is higher with carbon dioxide shielding than with argon-rich shielding. The rate of fume formation with argon-oxygen or argon-carbon dioxide mixtures increases with the oxidizing potential of the mixture.

For welding processes in which inert gas shielding is used—gas tungsten arc or plasma arc welding, for example—the fume-generation rate varies with the type of gas or gas mixture. More fume can be generated with helium than with argon shielding.

By-product gases also vary with the composition of the shielding gas. The rate of formation of ozone depends on the wavelengths and intensity of the UV rays generated in the arc. Ozone is more commonly found with argon-rich gases than with carbon dioxide. Nitrogen oxides are present in the vicinity of any open arc process, and carbon monoxide is commonly found around carbon dioxide-shielded arcs.

Welding Process. Studies conducted on the relative fume-generation rates of the consumable electrode processes for welding on mild steel have shown definite trends. Considering the ratio of the weight of fumes generated per weight of metal deposited, covered electrodes and self-shielded flux cored electrodes produce the most fume. Gas shielded flux cored electrodes produce less fume, whereas solid wire electrodes produce an even lower amount. The submerged arc welding process consistently produces the lowest amount of fumes because the fume is captured in the flux and slag cover.

Consumables. Within a specific process, the fume rate depends on the composition of the consumables. Some components of covered and flux cored electrodes are designed to decompose and form protective gases during welding. Hence, they generate relatively high fume levels.

Many constituents of covered and flux cored electrodes are proprietary. Therefore, two electrodes with identical AWS classifications may have substantially different fume-generation rates because they are produced by two different manufacturers. One way that can be used to compare electrodes is to obtain the MSDS for the product composition to determine specific fume-emission characteristics.

Resistance Welding Fumes and Gases. In resistance welding, fumes and gases as well as airborne particulates can be generated by the materials being welded and the electrodes used. Adequate ventilation must be provided to maintain exposure levels below the allowable limits set by CFR Title 29, Chapter XVII, Part 1910.

For more information on resistance welding fumes and gases, the reader is encouraged to consult Section 10 of "Recommended Practices for Resistance Welding," AWS C1.1M/C1.1:2000 (Ref 25).

Oxyfuel Gas Welding and Cutting Fumes and Gases. The temperatures encountered in oxyfuel gas welding and cutting are lower than those found in electric arc processes. Consequently, the quantity of fumes emitted is normally lower. The gases formed are the reaction products of fuel-gas combustion and of the chemical reactions between the gases and other materials present. The fumes emitted are the reaction products of the base metals, coatings, filler metals, fluxes, and the gases being used. In the oxyfuel gas cutting of steel, the fumes produced are largely oxides of iron.

Fume constituents that present a greater hazard may be expected when coatings such as galvanizing, paint primers, or cadmium plating are present. The gases of greatest concern include oxides of nitrogen, carbon monoxide, and carbon dioxide. Oxides of nitrogen may be present in especially large amounts during the oxyfuel gas cutting of stainless steels using either the chemical flux or the iron powder process.

Ventilation

The bulk of fumes emitted during welding and cutting consists of small particles that remain suspended in the atmosphere for a considerable length of time. Thus, the concentration of fume in a closed area can build up over time, as can the concentration of any gas evolved or used in the process. Many particles eventually settle on the walls and floor. However, because fume is produced faster than it settles, fume concentration must be controlled by ventilation.

Adequate ventilation is the key to fume and gas control in the welding environment (Ref 1). Ventilation is adequate when fumes and gases are kept from breathing zones and the general area. Natural, mechanical, or respirator ventilation must be provided for all welding, cutting, brazing, and related operations. The ventilation must ensure that concentrations of hazardous airborne contaminants are maintained below recommended levels. These levels must be no higher than the allowable levels specified by OSHA or other recognized authority.

Welders must always take precautions to keep their breathing zone away from the fume plume, even when a sampling of the atmosphere indicates that the concentrations of contaminants do not exceed permissible limits. Air movement should always flow laterally from either side of the welder. Lateral airflow makes it easier for the welder to keep out of the plume and to keep fumes and gases out of the welding helmet. Air should not blow toward the face or back of the welder because it may force the fume into the breathing zone (Ref 1).

Many ventilation methods are available. They range from natural convection to localized devices, such as air-ventilated welding helmets. Additional ventilation methods include natural ventilation; general area mechanical ventilation; overhead exhaust hoods; portable local exhaust devices; downdraft, crossdraft, and water tables; and extractors built into the welding equipment.

General ventilation occurs naturally outdoors and indoors when the shop doors and windows are open. In most cases, general ventilation is more effective in safeguarding personnel in adjacent areas than in protecting the welders in the immediate area. According to CFR Title 29 CFR 1910 (Ref 26), when all of the following conditions are present, natural ventilation often keeps contaminant concentrations within permissible levels:

- A work area of more than 284 m³ (10,000 ft³) for each welder is provided.
- Ceiling height is above 5 m (16 ft).
- Welding is not performed in a confined area.
- The general welding area is free of partitions, balconies, or other structural barriers that significantly obstruct cross ventilation. (In this case, the term *general welding area* refers to a building or a room in a building, not a welding booth or screened area used to provide protection from welding radiation.)
- Toxic materials with low permissible exposure limits are not deliberately present as constituents (the employer should refer to the MSDS).

When natural ventilation is insufficient, fans may be used to force and direct the required amount of air through a building or work room.

The effectiveness of general ventilation, whether natural or forced, is dependent on the design of the system. Ventilation introducing fresh air and exhausting contaminated air must be arranged in work areas so that the welding fumes and gases are carried away, not concentrated in dead zones. In some cases, the fresh air supply may be located so that incoming fresh air provides the required protection for the welders and personnel in the general area. If this is not possible, general mechanical ventilation may need to supplement local ventilation to keep the background level of airborne contaminants at acceptable levels.

Local Ventilation. Although general ventilation can be used to control contamination levels in the work area, it does not usually provide sufficient local ventilation to protect personnel. Local exhaust ventilation is usually the most effective way of providing protection at workstations. Local ventilation, which provides efficient, economical fume control, can be accomplished with various methods, including the following:

- Fixed open or enclosing hood
- Moveable hood with a flexible duct

- Crossdraft or downdraft table
- Water table
- Gun-mounted fume-removal equipment

The fixed open or enclosing hood has at least a top and two sides. It must have sufficient airflow and velocity to keep contaminant levels at or below permissible limits (Ref 22). The movable hood, with a flexible duct, is positioned by the welder as close to the point of welding as practicable. This hood should allow sufficient airflow to produce a maximum velocity of 30 m/min (100 ft/min) in the zone of welding. An air velocity of 31 m/min (100 ft/min) will not disturb the torch gas shield during gas shielded arc welding if adequate shielding gas flow rates are used. Higher air velocities may disturb the gas shield and render it less effective. This method of providing local ventilation is shown in Fig. 6.

Air flow requirements range from 4 m³/min (150 ft³/min), when the hood is positioned 100 to 150 mm (4 to 6 in.) from the weld, to 17 m³/min (600 ft³/min) at 250 to 300 mm (10 to 12 in.) from the weld. These requirements are particularly applicable for bench work but may be used for any location, provided the hood is moved as required.

Another method of achieving local ventilation is the crossdraft or downdraft table. A crossdraft table is a welding bench with the exhaust hood placed to draw air laterally across the table. A downdraft table has a grill as a work surface and an exhaust hood below that draws the air downward and away from the welder's head.



Fig. 6 Movable hoods positioned near the welding arcs

The water table is another technique used to provide local ventilation of the work area. Used for oxyfuel gas and plasma arc cutting operations, this cutting table fills with water to near to the bottom or in contact with the bottom surface of the workpiece. A great deal of the fume that emerges from the cut is captured in the water.

Gun-mounted fume-removal equipment, often used with self-shielded flux cored arc welding, extracts the fumes at the point of welding, creating an almost smokeless environment. The exhaust rate must be set so that it does not interfere with the shielding gas pattern provided by the welding process. Virtually all the fume produced by the flux cored arc welding process can be collected using a gun-mounted fume-removal device. A fume-extracting torch for gas metal arc welding is shown in Fig. 7.

Where permissible, air cleaners that can efficiently collect submicron particles may be used to recirculate a portion of ventilated air that would otherwise be exhausted. However, it is important to note that some air cleaners do not remove gases. Therefore, the filtered room air must be monitored to prevent the accumulation of harmful gas concentrations.

Special Ventilation Situations

Some situations are potentially more hazardous than routine welding circumstances. Situations requiring special ventilation include welding in a confined space or welding with certain materials. These are discussed in the following sections.

Welding in Confined Spaces. The terms *confined spaces* and *permit-required confined space* are employed by OSHA to refer to those workspaces that hinder employees' activities while entering, performing operations, or exiting, and those spaces that both hinder employees' activities and pose health or safety hazards, respectively (Ref 27). The American National Standard "Safety in Welding, Cutting, and Allied Processes," ANSI Z49.1:1999, defines the term as a small or restricted space in which poor ventilation may exist due to the



Fig. 7 Fume-extracting gas metal arc welding torch. Courtesy of Abicor Binzel

size or shape of the space (Ref 1). Welding personnel who work in confined spaces are apt to be exposed to serious health and safety hazards, such as asphyxiating or flammable atmospheres. Examples of confined spaces are small rooms, furnaces, ship compartments, reactor vessels, and storage tanks.

Ventilation in confined spaces must ensure sufficient oxygen for life support. In addition, it must keep airborne contaminants at or below the recommended limits in breathing atmospheres and prevent the accumulation of flammable mixtures (Ref 28). Inasmuch as ventilation must also prevent the occurrence of oxygen-enriched atmospheres, oxygen levels should remain between 19.5 and 23.5% per volume (natural air contains approximately 21% oxygen by volume). Only clean, respirable air must be used for ventilation; the use of pure oxygen, other gases, or mixtures of gases for ventilation purposes is prohibited (Ref 1).

Without an adequate supply of the proper concentration of oxygen, welders may asphyxiate, become unconscious, and possibly die without apparent warning symptoms. It should be noted that in confined areas, oxygen-enriched atmospheres—especially those with more than 25% oxygen—also pose other hazards. Materials that burn normally in air may flare up violently in such atmospheres. Therefore, clothing may burn fiercely; oil- or grease-soaked clothing or rags may catch fire spontaneously; and paper may flare into flame, all of which may cause severe or even fatal burns.

Confined areas must be tested for toxic or flammable gases and vapors and adequate oxygen supply prior to entry and during occupancy. The tests should be conducted with instruments approved by the U.S. Mine Safety and Health Administration (MSHA). It is also advisable that a continuous monitoring system with audible alarms be used. It is important to note that these same safety precautions apply to other areas as well. Gases that are heavier than air—argon, methylacetylene-propadiene, propane, and carbon dioxide, for example—may accumulate in pits, tank bottoms, low areas, and near floors. Gases that are lighter than air—helium and hydrogen, for example—may accumulate in tank tops, high areas, and near ceilings (Ref 1).

If proper ventilation cannot be ensured, personnel lacking the proper training and PPE must never enter the confined work area. The welders, cutters, and other personnel who do work in such areas must wear an approved positive-pressure air-supplied breathing apparatus that is self-contained. (Air-supplied respirators and hose masks must be approved by MSHA or other recognized agency.) They must also have an emergency air supply lasting at least 5 min in the event that the main air source fails. Another person wearing similar safety equipment should also be present. When work is carried out in confined areas in atmospheres that are immediately hazardous to life and health, attendants knowledgeable in rescue procedures

must be stationed outside of the area. Each attendant must have his or her own self-contained breathing device (Ref 1).

Besides testing atmospheric conditions, workers in confined space must take additional precautions. Because compressed gas cylinders could leak gases or volatiles, they must be located outside confined areas. Welding power sources must also be placed outside of any confined space to reduce the hazard of electric shock and asphyxiation from engine exhaust. Personnel must be able to exit quickly in the event of an emergency. Those using safety belts and lifelines must ensure that this equipment is worn properly so that it does not become entangled or jammed while they are attempting to exit (Ref 1).

The operation of brazing furnaces also poses potential hazards. These furnaces, which are a type of confined space, use a variety of atmospheres (vacuum, inert gas, flammable gas, or flammable gas combustion products, for example) to exclude oxygen. Thus, among the hazards presented are the accumulation of hazardous fumes or gases in the work area, the development of explosive mixtures of flammable gas and air, and the asphyxiation of personnel (Ref 1).

Welding of Containers and Piping. The welding or cutting of containers and vessels also presents special risks. (In accordance with Ref 29, the following types of containers require specialized safety considerations: containers that can be entered by personnel; containers that have held radioactive substances; containers that have held compressed gases; containers that have held explosive substances; ship tanks, bunkers, or compartments; gasometers or gas holders for natural and manufactured gases; outside, above-ground vertical petroleum storage tanks; and containers holding flammable substances that must be repaired while in service. For safe practices specific to these container types, the reader is advised to consult the latest edition of this standard and any other applicable regulatory and industry-specific codes and guidelines.) Fires, explosions, and health hazards can result if the objects contain combustible, reactive, or toxic materials. Thus, the precautions for confined spaces must be observed. All containers should be considered unsafe for welding and cutting unless they are judged clean or rendered safe by a qualified person. Additionally, the immediate area outside and inside the container should be cleared of all obstacles and hazardous

materials (Ref 26, 29). When repairing a container in place, the welder must never allow hazardous substances released from the floor or the soil beneath the container to enter. The required personal and fire protection equipment must also be available, serviceable, and in position for immediate use.

One method used to weld containers safely involves filling the container with an inert medium such as water, gas, or sand. When using water, the level should be kept to within a few inches from the welding point. The space above the water should be vented to allow the heated air to escape. When employing inert gas, the responsible individual must know how to produce and maintain a safe atmosphere during welding, including the percentage of inert gas required in the tank to prevent fire or explosion.

Gases generated during welding must be discharged safely and in an environmentally friendly manner in accordance with government rules and regulations. This is especially important when welding inside containers, where workers must prevent pressure buildup. When needed, testing for gases, fume, and vapors should be conducted periodically to ensure that recommended limits are maintained during welding.

Low-Allowable-Limit Materials. Certain materials sometimes present in consumables, base metals, coatings, or atmospheres for welding, cutting, or brazing operations have permissible exposure limits at or below those specified by the authority having jurisdiction. These constituents include antimony, arsenic, barium, beryllium, cadmium, chromium, cobalt, copper, lead, manganese, mercury, nickel, selenium, silver, and vanadium (Ref 1). Table 2 presents the base and filler metals that may release some of these materials in fume during welding, cutting, and allied operations.

The manufacturer's MSDSs, which should be supplied, can be consulted to determine if any of these materials are present in the welding filler metals and fluxes being used. It is best to remember, however, that hazardous materials may also be present in base metals, coatings, or other sources in the work area. Radioactive materials under the jurisdiction of the Nuclear Regulatory Commission require special consideration.

When any of these materials is encountered as a designated constituent in welding, brazing, or cutting operations, special precautions must be taken to ensure that atmospheric

Table 2 Possible hazardous materials emitted during welding or thermal cutting

Base or filler metal	Emitted metals or their compounds
Carbon and low-alloy steels	Chromium, manganese, vanadium
Stainless steels	Chromium, manganese, nickel
Manganese steels and hardfacing materials	Chromium, cobalt, manganese, nickel, vanadium
High-copper alloys	Beryllium, chromium, copper, lead, nickel
Coated or plated steel or copper	Cadmium(a), chromium, copper, lead, nickel, silver

(a) When cadmium is a constituent in a filler metal, a precautionary label must be affixed to the container or coil. Source: Ref 1

contaminants remain at or below permissible levels for human exposure. Unless atmospheric tests under the most adverse conditions establish that exposure is within acceptable concentrations, certain precautions are necessary—both indoors and outdoors. Whenever any materials with a low allowable limit are encountered in indoor operations, local exhaust mechanical ventilation must be used. When beryllium is encountered indoors, respiratory protection in addition to local exhaust ventilation is essential. In confined spaces, local exhaust ventilation and respiratory protection must be used, and all personnel in adjacent areas must be similarly protected (Ref 1).

Additionally, personnel must refrain from consuming food in areas where fumes contain materials with very low allowable exposure limits. To prevent the ingestion of these contaminants, welding personnel should also practice good personal hygiene, such as washing their hands before touching food.

Fluorine and Zinc Compounds. The inhalation of the fumes and gases from fluorine compounds can be hazardous. These compounds can also burn the eyes and skin on contact. Thus, local mechanical ventilation or respiratory protection must be provided when welding, brazing, cutting, or soldering operations in confined areas involve fluxes, coatings, or other material containing fluorine compounds.

In open spaces, the need for local exhaust ventilation or respiratory protection against fluorine compounds depends on the circumstances. Local exhaust ventilation is not necessary when air samples taken in breathing zones indicate that all fluorides are within allowable limits. However, local exhaust ventilation is always desirable when fluorine compounds are used in fixed-location or stainless steel production welding.

Zinc compounds, which may be present in consumables, base metals, or coatings, can produce nausea, dizziness, or metal fume fever (sometimes referred to as Galo fever). Therefore, the same safety procedures for fumes containing fluorine compounds also apply to fumes containing zinc compounds.

Cleaning Compounds. Inasmuch as cleaning compounds may be hazardous or flammable, they often require special ventilation precautions. The manufacturer's instructions should be carefully followed before welding or cutting on cleaned materials (Ref 1).

Chlorinated Hydrocarbons. Degreasing or cleaning involving chlorinated hydrocarbons must be carried out in an area where the vapors from these operations are prevented from entering the atmosphere in the vicinity of the molten weld metal or the welding arc. When these vapors enter the atmospheres of arc welding operations, a reaction produces highly toxic phosgene gas, which has an irritating, objectionable odor. Low levels of exposure can cause nausea, dizziness, and weakness, whereas high exposure levels can cause serious health impairment or even death (Ref 1).

Cutting of Stainless Steel. Because stainless steel contains chromium and nickel compounds, the fume emitted during cutting operations may be hazardous. Symptoms of overexposure to fumes containing these compounds may include headaches, nausea, and dizziness. Therefore, when cutting stainless steel using oxyfuel gas, gas shielded arc, or plasma arc cutting, local mechanical ventilation should be implemented to remove the fumes emitted. In underwater plasma arc cutting, the water captures most of the fume.

Air Sampling and Measurement of Exposure

When ventilation is questionable, the only manner in which to ensure that airborne contaminant levels are within the allowable limits is to take air samples of the breathing zone. When an operator's actual on-the-job exposure to welding fume and gases is to be sampled, the guidelines provided in "Methods for Sampling Airborne Particulates Generated by Welding and Allied Processes," ANSI/AWS F1.1 (Ref 19), must be adhered to. This document describes the techniques used to obtain an accurate breathing zone sample of welding fume for a particular welding operation. Both the amount and composition of the fume can be determined in a single test using the method described. Multiple samples are recommended for increased accuracy, one of which must be collected inside the welder's helmet, if one is worn.

The ACGIH and OSHA have established allowable limits of airborne contaminants, referred to as threshold limit values (TLVs) or permissible exposure limits, respectively. The TLV is the concentration of an airborne substance to which most workers may be repeatedly exposed, day after day, without adverse effect. The threshold limit value-time weighted average (TLV-TWA) is used to adapt TLVs to normal workplace conditions. The TLV-TWA is the time-weighted average airborne substance concentration to which nearly all personnel may be repeatedly exposed without adverse effect during a normal 8 h workday or 40 h workweek. TLV-TWA values should be used as a general guide for controlling health hazards, not as a sharp, clear division between safe and hazardous concentrations of airborne substances. Revised annually, the TLVs may or may not correspond to OSHA's permissible exposure limits for the same materials. In many cases, current ACGIH values for welding materials are more stringent than OSHA levels.

Safe Handling of Compressed Gases

The gases used in welding and cutting operations are packaged in containers that are referred to as cylinders (Ref 30). The gas cylinders used in welding operations contain gas that

is pressurized at approximately 17,237 kPa (2500 psig) or higher. Gases at these pressures must be handled properly to prevent damage to the cylinders. Mishandling may result in leaks or explosions, causing damage, injury, or death (Ref 1).

Only cylinders constructed and maintained in accordance with U.S. Department of Transportation (DOT) specifications can be used in the United States. The use of other cylinders is illegal and may be extremely hazardous. Cylinders requiring periodic retest under DOT regulations may not be filled unless the retest is current (Ref 31).

Filling Cylinders and Mixing Gases

According to the provisions of ANSI Z49.1:1999 (Ref 1) and "Safe Handling of Gas in Containers," CGA P-1-1999 (Ref 31), cylinders may be filled only by the owner or individual authorized by the owner. Mixing gases and filling one cylinder from another are hazardous; therefore, the mixing and transfilling should not be attempted by anyone who is not qualified and authorized to perform this activity. Combustible or incompatible combinations of gases must never be mixed in cylinders (Ref 1).

Labeling

Before using gas from a cylinder, welding personnel must carefully read the label, which provides the chemical or trade name of the contents in accordance with regulations. The label is the only proper notice of the cylinder's contents. Other means of marking—including cylinder color, banding, or shape—must not be used because they may vary among manufacturers, geographical areas, or product lines and could be misleading. If the label is illegible or no label is affixed to the cylinder, the contents must not be used and the cylinder must be returned to the supplier (Ref 1).

Storage and Usage

Gas cylinders and other containers must be stored in accordance with all state and local regulations and the appropriate standards issued by OSHA and the Compressed Gas Association (CGA). Safe handling and storage procedures are discussed in detail in the CGA's *Handbook of Compressed Gases* (Ref 30) and "Safe Handling of Gas in Containers," CGA P-1 (Ref 31).

Numerous precautions must be taken in the use and storage of gas cylinders. Cylinders must be stored in areas where they are protected against tampering and exposure to extreme temperatures. Storage temperatures must not fall below $-30\text{ }^{\circ}\text{C}$ ($-20\text{ }^{\circ}\text{F}$) or exceed $52\text{ }^{\circ}\text{C}$ ($125\text{ }^{\circ}\text{F}$). They must also be stored at an adequate distance from welding activities to prevent exposure to slag, sparks, or flames;

alternatively, fire-resistant shields must be used. The rough handling of gas cylinders should be avoided; therefore, cylinders must be protected from bumps, falls, falling objects, and weather and must never be dropped. In addition, cylinders must be stored away from passageways, elevators, or stairs where they may be struck, knocked over, or damaged by vehicles.

Cylinders containing acetylene and liquefied gas must always be stored and used in the upright position. Other cylinders are preferably stored and used in the upright position. Moreover, cylinders must always be secured to prevent them from falling during storage and use. During transport by motor vehicle, they must be secured according to U.S. DOT regulations. During lifting, they must be hoisted using the proper cradle or platform, not electromagnets or slings. Any of these exposures, misuses, or abuses could cause damage to cylinders and severe consequences (Ref 1, 31).

Due to the inherent risks of fire and explosion, gas cylinders must never be welded. Cylinders must never be used as work rests or rollers. Moreover, they must not be allowed to become part of an electrical circuit, because arcing may result. Cylinders containing the shielding gases used in conjunction with arc welding must not be placed where they may become part of an electrical circuit. To prevent arcing or interference with valve operation, items such as electrode holders, welding torches, cables, hoses, or tools must not be stored on gas cylinders. Arc-damaged gas cylinders may leak or rupture, thereby injuring and possibly killing anyone nearby (Ref 1).

Many cylinders have a valve protection cap to protect the cylinder valve. This cap should always be in place except when the cylinder is in use. The cylinder should never be lifted by the valve protection cap, because the threads that secure these protection caps may not be capable of supporting the full weight of the cylinder. The caps should always be threaded completely onto the cylinder and hand-tightened.

Gas Withdrawal. Many gases in high-pressure cylinders are filled to pressures of 13,790 kPa (2000 psig) or more. Unless the equipment to be used with a gas is designed to operate at full-cylinder pressure, an approved regulator must be used to reduce pressure by withdrawing gas from a cylinder or manifold. Simple needle valves should never be used. A pressure-relief or safety valve that is rated to function at less than the maximum allowable pressure of the welding equipment should also be employed as a backup in case the regulator fails. The valve is designed to prevent equipment failure at pressures in excess of working limits. The equipment involved in the withdrawal of gas from cylinders is discussed in more detail as follows.

Cylinder Valves. Valves on cylinders containing high-pressure gas, particularly oxygen, must always be opened slowly. If the valves are opened too rapidly, the high temperature associated with adiabatic recompression can

occur. In the case of oxygen, the heat can ignite the valve seat, which, in turn, may cause the metal to melt or burn. To avoid injury, welding personnel must open the cylinder valve outlet while standing to one side of the outlet, not in front of it.

Before a gas cylinder can be connected to a pressure regulator or a manifold, the valve outlet must be cleaned of dirt, moisture, and other foreign matter by wiping it with a clean, oil-free cloth. Then, to prevent dirt or dust from entering the regulator, the valve is opened for an instant and closed immediately—a procedure known as cracking the cylinder valve. Fuel gas cylinders must never be cracked near sources of ignition (i.e., sparks and flames), in confined spaces, or while operators are smoking. In addition, before a regulator is connected to a gas cylinder, the regulator must be drained of gas pressure. After shutting down the operation, the cylinder valve must be closed (Ref 1).

The outlet threads on cylinder valves are standardized for specific gases so that only regulators or manifolds with similar threads can be attached (Ref 32). Preferably, the valves on low-pressure fuel gas cylinders should be opened using no more than one turn. This usually provides adequate flow and allows the valve to be closed quickly in the event of an emergency. In contrast, high-pressure cylinder valves must usually be opened fully to backseat the packing and prevent packing leaks during use.

The cylinder valve should be closed after each cylinder use and when returning an empty cylinder to the supplier. This prevents hazardous gas leaks that may develop and remain undetected while the cylinder is unattended. It also prevents the back flow of contaminants into the cylinder. It is advisable to return cylinders to the supplier with approximately 172 kPa (25 psi) of contents remaining. This practice prevents possible contamination of the cylinder by the atmosphere during shipment.

Pressure-relief devices are intended to protect cylinders that are subjected to a hostile environment, such as fire or other source of heat that may raise the pressure within the cylinders. These safety mechanisms are designed to relieve the pressure in gas cylinders to within safe limits. Only trained personnel are allowed to adjust cylinder pressure-relief devices. The available types of pressure-relief devices, their maintenance, and application are addressed in “Pressure-Relief Device Standards—Part I: Cylinders for Compressed Gases,” CGA S-1.1 (Ref 33).

Regulators. A pressure-reducing regulator must always be used when withdrawing gas from cylinders for use in welding or cutting operations. All gas regulators must meet the requirements specified in “Standard for Gas Pressure Regulators,” CGA E-4 (Ref 34), and other code regulations.

Pressure-reducing regulators must be used only for the gas and pressure specified on the label affixed to the cylinder, although the

cylinder valve outlet threads may be the same as those on other gas cylinders. Threaded connections should never be forced onto the regulator. An improper fit between the gas cylinder and the regulator or between the regulator and hose constitutes an improper—and unsafe—combination of devices. Before a cylinder is used, all threads and the regulator connection glands must be inspected for dirt or damage. If a hose or cylinder connection leaks, the connection must not be forced with excessive torque. Damaged regulators and components must be repaired by properly trained mechanics or returned to the manufacturer for repair.

A suitable valve or flowmeter should be used to control gas flow from a regulator. The regulator internal pressure must be drained before the regulator is connected or removed from a gas cylinder or manifold. An adapter must not be used to change the cylinder connection, because this increases the risk of using an inappropriate or contaminated regulator. For instance, gases that are contaminated with oil can deposit an oily film on the internal parts of the regulator. This film can contaminate oil-free gas or, in the case of oxygen, can cause fire or explosion. Further details are specified in CGA’s “Standard Connections for Regulator Outlets, Torches, and Fitted Hose for Welding and Cutting Equipment,” CGA E-1 (Ref 35).

Manifold Piping Systems. A manifold is used when gas is needed without interruption or at a higher delivery rate than can be supplied from a single cylinder. A manifold and its components must be leaktight and designed for a specific gas and operating pressure. The components of the manifold must be used for the gas and pressure for which they are approved only. Oxygen and fuel gas manifolds must meet additional specific design and safety requirements (Ref 36).

Manifold piping systems must incorporate an appropriate overpressure relief valve unless the system is specifically designed and constructed to withstand full cylinder or tank pressure. A pressure-relief device should be sufficient to prevent the overpressurization of the weakest element of the system. To be effective, a pressure-relief device such as a relief valve or bursting disc must be isolated from other protective devices (such as another relief valve) and located in every section of the system that may be exposed to the full force of the supply pressure. However, welding personnel should beware of relying solely on pressure-reducing regulators. Some pressure regulators have integral safety-relief valves designed for the protection of the regulator only. These alone should not be relied on to protect the downstream system, however.

In cryogenic piping systems, relief devices must be located in every section of the system that could trap liquefied gas. Upon warming, such liquids vaporize to gas, and in a confined area, gas pressure can increase dramatically. Pressure-relief devices protecting fuel-gas piping systems or other hazardous gas systems

must vent gas in safe locations. Piping and fittings for manifolds carrying acetylene or methylacetylene-propadiene (MPS) must not consist of any unalloyed copper or alloys containing 70% or more copper. Acetylene and MPS react with copper under certain conditions to form unstable copper acetylide, a compound that may detonate under shock or heat.

In addition, each fuel gas cylinder lead should incorporate a back flow check valve and a flash arrester. Back flow check valves should also be installed in each line at each station outlet where both fuel gas and oxygen are provided for a welding, cutting, or preheating torch. Back flow check valves must be examined periodically for tightness in accordance with the manufacturer's instructions (Ref 37).

Oxygen

Although oxygen is nonflammable, it vigorously accelerates combustion in flammable materials. Therefore, oxygen cylinders and liquid-oxygen containers must be stored away from combustibles and fuel-gas cylinders. Oil, grease, and combustible dusts may spontaneously ignite on contact with pure oxygen. Hence, all manifold systems and apparatus manufactured expressly for oxygen service must be kept free of any combustibles. Oxygen valves, regulators, and apparatus must never be lubricated with oil. If lubrication is required, the type of lubricant and the method of applying the lubricant should be specified in the manufacturer's literature. If these indications are not specified, the device should be returned to the manufacturer or authorized representative for service. Valves, piping, or system components not expressly manufactured for oxygen service must be cleaned and approved for oxygen service before use in an operation (Ref 38).

It is also important to note the difference between pure oxygen and air. Pure oxygen supports combustion much more vigorously than air, which contains only 21% oxygen. Thus, pure oxygen should never be used as a substitute for compressed air; otherwise, raging fires and explosions may occur. For example, pure oxygen must never be used to power compressed air tools, which are typically lubricated with oil. Similarly, pure oxygen must never be used to blow dirt from workpieces and clothing, which are also often contaminated with oil, grease, or combustible dust. Only clean clothing should be worn when working with oxygen systems. In addition, pure oxygen must never be used to ventilate confined areas. This would create an oxygen-rich atmosphere that could be ignited by a chemical reaction or separate ignition energy in conjunction with a fuel.

Information regarding special procedures for oxygen cylinders is provided in Section 10 of ANSI Z49.1:1999 (Ref 1). Additional information is available in "Oxygen," CGA G-4 (Ref 39), and "Torch Standard for Welding and Cutting," CGA E-5 (Ref 40).

Fuel Gas

Fuel gases commonly used in oxyfuel gas welding and cutting are acetylene, MPS, natural gas, propane, and propylene. Hydrogen is also used in a few applications. Gasoline, which vaporizes in the torch, is sometimes used as a fuel for oxygen cutting. These gases should always be referred to by name, not by the generic term *gas*. The rate of withdrawal of fuel gases from cylinders must never surpass that recommended by the manufacturer (Ref 1).

Acetylene and MPS require special precautions. Acetylene possesses the lowest explosive limit of all the fuel gases. When acetylene is stored in cylinders, it is dissolved in a solvent so that it can be safely maintained under pressure. In the free state, acetylene must never be used at pressures higher than 103 kPa (15 psig) because it can decompose with explosive violence. Moreover, neither acetylene nor MPS should be used in contact with silver, mercury, or alloys containing 70% or more copper. These gases react with these metals to form unstable compounds that may detonate under shock or heat. For this reason, the valves on fuel gas cylinders must never be opened to clean the valve outlet near possible sources of flame ignition or in confined areas (Ref 41).

Hydrogen also requires special attention. Hydrogen flames may be difficult to see or invisible. Because of this lack of visibility, the torch and flame should be handled with extreme care because the body, clothes, or combustibles may easily be exposed to hydrogen flames.

Fuel gases used for brazing furnace atmospheres must be burned or vented to a safe location. Before filling a furnace or retort with fuel gas, the equipment must first be purged with a nonflammable gas, such as nitrogen or argon, to prevent the formation of an air-fuel mixture that could explode.

Preventing Fuel-Gas Fires. Fuel-gas systems can cause fire hazards. Most fuel gases in cylinders are in liquid form or dissolved in liquids. Therefore, gas cylinders should always be used in the upright position to prevent liquid surges into the system.

One source of fire in welding and cutting is the ignition of leaking fuel by sparks or spatter. The best procedure for avoiding fire from a fuel gas or liquid is to prevent leaks in the manifold system. All fuel systems should be checked carefully for leaks upon assembly and at frequent intervals thereafter. Fuel-gas cylinders should frequently be examined for leaks, especially at fuse plugs, safety devices, and valve packing.

If a leak is discovered around the valve of a fuel gas cylinder, the packing nut must be tightened or the valve must be closed (Ref 1). If the fuel leak cannot be stopped, the cylinder should be removed by trained fire personnel to a safe location outdoors. The supplier should also be notified. A warning sign should be posted, and no smoking or other sources of ignition should be permitted in the area. In case of fire, the fire

alarm should be activated, and trained fire personnel should be summoned immediately.

One of the most effective means of controlling a fuel fire is to shut off the fuel valve, if accessible. A fuel gas valve should never be opened beyond the point necessary to provide adequate flow, which is usually no more than one turn of the handle. This practice makes it possible for the valve to be shut off quickly in an emergency. If the immediate valve controlling the burning gas is inaccessible, another upstream valve may cut off the flow of gas.

A small fire near a cylinder safety device or valve can be controlled using water, wet cloths, or fire extinguishers. If a large fire at a fuel-gas cylinder occurs, the fire alarm should be sounded, and all personnel should be evacuated from the area. The cylinder should be kept wet and cool by fire personnel with a heavy stream of water. It is usually better to allow the fire to continue to burn and consume all issuing gas rather than attempt to extinguish the flame. Otherwise, although the flames have been extinguished, the escaping gas may reignite, with explosive violence (Ref 1).

Shielding Gas

Argon, helium, nitrogen, and carbon dioxide and their mixtures in cylinders and manifold systems are used for shielding with some welding processes. All of these, except carbon dioxide, are used as brazing atmospheres. These gases are odorless and colorless, and they can displace the air needed for breathing. For this reason, confined areas filled with these gases must be well ventilated before personnel are permitted to enter.

Should there be any question regarding the presence of these gases in a work area, the area must be monitored for adequate oxygen concentration with an oxygen analyzer. If an analyzer is not available, air-supplied respirators must be worn by personnel entering the area. In addition, containers filled with these gases must not be placed in confined spaces, as pointed out previously (see the section "Welding of Containers and Piping" in this article).

Cryogenic Liquids

Cryogenic cylinders and tanks are used to store at very low temperatures those liquids that evaporate at room temperature. The cryogenic liquids used for commercial purposes include oxygen, nitrogen, and argon, although other gases may also be handled similar to cryogenic liquids. The cylinders and tanks used for storing cryogenic liquids are usually double-walled. They are evacuated and insulated between the walls. Designed to keep temperatures low and minimize heat increase, these liquid-gas containers hold a greater amount of gas for a given volume than high-pressure gas cylinders.

For safety, these containers must be handled carefully. They must always be maintained in an upright position and transported only in cylinder-handling trucks specifically designed for the transport of these containers. In addition, they must not be rolled on a bottom edge, as is often done with high-pressure cylinders. Overpressurization could cause an explosion.

If these cylinders are handled improperly, the inner or outer cylinder wall can rupture, causing a loss of vacuum and a rapid rise of internal pressure. When this occurs, the cylinder protective devices are designed to activate, allowing the contents to escape. These cylinder protection devices must never be tampered with.

A visible frosting on the container exterior is a sign of damage to the internal walls or fittings. Whenever this frosting appears, the gas supplier must be notified, and personnel should keep clear until the frost disappears. Generally, when the frost disappears, the contents have evaporated and any internal pressure has been relieved.

Cryogenic liquid, which is a gas at room temperature, evaporates before exiting the cylinder by passing through a vaporizer system, warming the gas to atmospheric temperature. In some cases, however, the user may want to withdraw the contents in liquid form. Should this extremely cold liquid contact the skin, it may cause burns similar to those caused by hot substances. Contact with the liquid can also result in severe frostbite. Therefore, to prevent bodily contact from these cold liquids, users must wear protective clothing. An adequate face shield and loose-fitting insulated gloves that can be quickly removed in case of an exposure emergency are essential.

The properties of many materials at room temperature change drastically at cryogenic liquid temperatures. Many metals, including carbon steel, and most elastomers, such as rubber, become extremely brittle. When cryogenic liquids are to be withdrawn from cylinders, the transfer line must be made of materials that maintain satisfactory properties at these low temperatures.

It is also important to note that liquid oxygen may react with explosive violence on contact with asphalt or similar bituminous materials. Thus, liquid oxygen must not be allowed to come into contact with these materials. Liquid-oxygen tanks must always be installed on concrete pads—never on asphalt or similar bituminous materials.

Further information on this topic is provided in "Safe Handling of Cryogenic Liquids," P-12 (Ref 42), "Safe Handling of Liquefied Nitrogen and Argon," CGA AV-5 (Ref 43), and "Standard for Cryogenic Liquid Transfer Connections," CGA V-6 (Ref 44).

Protection Against Electromagnetic Radiation

Electromagnetic fields, UV radiation, and infrared radiation are produced by most arc

welding and cutting processes as well as by electron beam welding; laser beam welding; and torch welding, cutting, brazing, or soldering. Although radiation is invisible, it can inflict injury. The most common injuries resulting from exposure to radiation are skin burns and eye damage.

Two types of radiation—ionizing and non-ionizing—can be produced during welding operations. Ionizing radiation, produced by electron beam welding, can be maintained within acceptable levels with shielding around the welding area. During the grinding of thoriated tungsten electrodes for gas tungsten arc welding, a local exhaust system must be used to prevent the inhalation of the dust, which is radioactive. Respiratory protection should also be used, if necessary. Otherwise, users should follow the instructions on the manufacturer's MSDS for the thoriated tungsten electrode. Protection against nonionizing radiation includes the use of safety glasses with UV protective side shields in addition to a welding helmet with the correct filter plate. In addition, the skin must be protected with adequate hand and body PPE, as specified by ANSI Z49.1:1999 (Ref 1, 2).

Electrical Safety

Most welding and cutting operations employ some type of electrical equipment. For example, even oxyfuel gas cutting machines use motor drives, controls, and various other electrical systems. In the absence of precautionary measures, personnel may be injured or even killed by electric shock in welding and cutting operations. Some electrical accidents, such as those caused by lightning, are unavoidable; however, the majority can be avoided with the proper training and safety precautions.

A good safety training program in electrical safety is essential. Before working with any electrical application, employees must be fully instructed in electrical safety by a competent professional. As a minimum, this training should include the points covered in part II of ANSI Z49.1:1999 (Ref 1).

Electric shock occurs when an electric current of sufficient magnitude passes through the body. The severity of the shock depends primarily on the amount of current, the duration and path of flow, and the individual's state of health. The amount of current depends upon the applied voltage, which causes the current to flow, and the resistance of the body path. The frequency of the current may also be a factor when alternating current (ac) is involved.

Currents greater than approximately 5 mA are considered primary shock currents because they are capable of causing direct physiological harm. Steady-state currents less than 5 mA are considered secondary shock currents, which are capable of causing involuntary muscular reactions without normally causing direct physiological harm. Most people begin to feel a

tingle from the current at 0.5 mA; therefore, this point is referred to as the perception threshold.

Sources of Electric Shock

Electric shock can originate from natural sources or from equipment. Shock from natural sources is exemplified by that caused by lightning-induced voltage surges in power distribution systems. Even earth grounds can attain high potential relative to true ground during severe transient phenomena due to power line faults or lightning strikes, although such circumstances are rare. Most electrical equipment can present a hazard of shock if improperly installed, used, or maintained. Thus, for purposes of safety, all equipment must be installed, operated, maintained, and repaired by qualified personnel. Worn, damaged, or inappropriate cables must not be used.

In welding and cutting activities, most electrical equipment is powered from ac sources of 115 to 575 V or by engine-driven generators. Most welding operations require less than 100 V. Some arc cutting methods use power sources that operate at more than 400 V, while electron beam welding machines operate at up to approximately 150 kV. These levels warrant precautions because fatalities can result even with equipment that operates at less than 80 V.

In the welding industry, most instances of electric shock occur because of accidental contact with bare or poorly insulated conductors. Therefore, welders must take precautions against contacting bare elements in the welding circuit and primary circuits.

When performing welding operations in electrically hazardous conditions, personnel must take special care to prevent electric shock. Examples of electrically hazardous conditions are wet or damp areas; restricted work areas that force personnel to work in an uncomfortable position, making contact with conductive parts; and areas in which contact with conductive elements is likely (Ref 1).

Water or moisture typically reduces electrical resistance, often creating more severe electrical hazards. When arc welding or cutting in damp or wet conditions—including conditions creating heavy perspiration—welding personnel must wear dry, nonconductive gloves and clothing in good condition to prevent electrical shock. Welders should also be protected from electrically conductive surfaces, including the earth, by means of rubber-soled shoes or an insulating layer such as a rubber mat or dry wooden board, which is preferred. Under such hazardous conditions, welders can also employ a semiautomatic direct current (dc) power source, a dc manual shielded metal arc power source, or an arc welding power source with reduced voltage control. The use of these power sources can reduce the possibility of electric shock.

When welders are required to work in a cramped kneeling, sitting, or lying position,

they should implement the same precautions discussed previously. The hazards posed by making contact with conductive elements can be minimized by insulating the parts in the operator's vicinity (Ref 1).

As a general safety precaution, rings and other jewelry should be removed before welding, to decrease the possibility of electric shock.

Equipment Selection

In addition to the use of proper clothing and body protection, operators can reduce the possibility of electric shock by selecting and using the proper equipment. Operators should use the correct equipment designed for each job and situation. All equipment must meet the applicable standards, such as "Transformer-Type Arc Welding Machines," UL 551 (Ref 45), and other standards issued by the National Electrical Manufacturers Association, such as "Electric Arc Welding Power Sources," ANSI/NEMA EW 1 (Ref 46).

As previously mentioned, if a significant amount of welding and cutting work is performed under electrically hazardous conditions, the use of automatic machine controls that reduce the no-load (open-circuit) voltage to a safe level is recommended. When special welding and cutting processes require open-circuit voltages higher than those specified in ANSI/NEMA EW 1 (Ref 46), adequate insulation and operating procedures must be provided to protect personnel from these higher voltages.

Installation

Personnel installing electrical equipment must follow the requirements of the National Fire Protection Association's (NFPA) "National Electric Code (NEC)," ANSI/NFPA 70 (Ref 47), and other local codes. These codes describe necessary disconnects, fusing, and the different types of incoming power lines, among other topics. All electrical equipment should be installed in an area that is clean and dry. If installation in a clean, dry area is not possible, the equipment should be adequately safeguarded from dirt and moisture.

Terminals for welding leads and power cables must be shielded from accidental contact with personnel or metal objects, such as vehicles and cranes. Connections between welding leads and power supplies may be guarded utilizing dead-front construction using receptacles for plug connections, terminals located in a recessed opening or under a nonremovable hinged cover, insulating sleeves, or other equivalent mechanical means (Ref 1).

Grounding

The workpiece and the frame or chassis of all electrically powered machines must be placed or connected to a good electrical ground, such as a grounded metal floor or platen. They can

also be connected to a properly grounded building frame or other satisfactory ground. Special radio-frequency grounding may also be necessary for arc welding machines equipped with high-frequency arc-initiating devices and arc stabilizers (Ref 46). Chains, wire ropes, cranes, hoists, and elevators must never be used as grounding connectors or as carriers of welding current (Ref 1).

It is important to note that the work lead is not the grounding lead. The work lead connects the work terminal on the power source to the workpiece. A separate lead is required to ground the workpiece or power source work terminal. Thus, great care must be taken when connecting the grounding circuit to avoid double-grounding. Otherwise, the welding current may flow through a connection intended only for grounding, and the welding current may be of higher magnitude than the grounding conductor can safely carry.

Portable control devices such as push buttons must not be connected to circuits having operating voltages above approximately 120 V. Exposed metal parts on portable control devices operating on circuits above 50 V must be grounded by a grounding conductor in the control cable. Controls using intrinsically safe voltages below 30 V are recommended.

Connections and Cables

Electrical connections must be tight and clean to prevent local heating; therefore, they must be checked periodically. Magnetic work clamps must be free of an accumulation of metal particles and spatter on contact surfaces. Coiled welding leads should be spread out before use to avoid overheating and damage to the insulation. When jobs alternately require long and short leads, insulated cable connectors should be used so that the idle lengths can be disconnected when they are not needed (Ref 1).

Equipment, cables, fuses, plugs, and receptacles must be used within their current-carrying and duty-cycle capacities. The operation of apparatuses above the current rating or the duty cycle causes overheating and the rapid deterioration of insulation and other parts. When welding with short leads or low voltages, or both, the actual welding current may be higher than that shown by the indicators on the welding machine. General-purpose welding machines are likely to render high currents when they are used with processes that use low arc voltage, such as gas tungsten arc welding.

Welding lead cable should be flexible and designed especially for the rigors of welding service. The insulation on cables used with high voltages or high-frequency oscillators must provide adequate protection. The cable manufacturer's recommendations and precautions must be followed. Cable insulation must be maintained in good condition, and cables must be repaired or replaced promptly when necessary.

Operation

To ensure overall safe operation, welding personnel must be knowledgeable of the codes and standards related to their responsibilities. Personnel must have access to written rules governing the safe operation of equipment. These rules must be strictly followed (Ref 1).

Welders must not allow the energized metal parts of electrodes, electrode holders, or torches to touch their bare skin or any wet apparel. Electrode holders must not be cooled by immersion in water, and electrode-holder insulation must be kept in good condition. Before using water-cooled welding guns or holders, welders must inspect them for any water leaks and condensation, which would compromise safety. In addition, welders must not drape or coil the welding leads around their bodies (Ref 1).

During operation and work interruptions, welding circuits must be de-energized to avoid electric shock while the electrode, torch, or gun is being changed or adjusted. The only exception is shielded metal arc welding, during which the welding circuit need not be de-energized while electrodes are changed. However, when the circuit is energized in shielded metal arc welding, covered electrodes must be changed with dry welding gloves, never with bare hands. De-energizing a circuit is always desirable for optimum safety, even with covered electrodes (Ref 1).

At the end of an operation or when leaving the workstation for an appreciable time, operators must turn a welding machine off. Similarly, when the machine is to be moved, the input power supply must be disconnected at the source. When equipment is not in use, exposed electrodes must be removed from the holder to eliminate the hazard of accidental electrical contact with workers or conducting objects. Semiautomatic welding guns must be placed so that the gun switch cannot be operated accidentally (Ref 1).

Modification and Maintenance

Defective electrical equipment or safety hazards must be reported to the supervisor as soon as these are identified. Faulty equipment must not be used until it has been serviced by authorized personnel and its safety has been assured. Only qualified personnel are permitted to modify and maintain electrical equipment. Welding machines require numerous modification and maintenance procedures. Typical procedures are listed below (Ref 1):

- Commutators on rotating welding machines must be kept clean to prevent excessive arcing.
- Rectifier welding machines must be inspected frequently for accumulations of dust or lint that may interfere with ventilation.
- Louvers and internal electrical coil ventilating ducts require inspection for the accumulation of dust and lint.

- Welding machines may be blown out occasionally with clean, dry, compressed air at low pressure unless prohibited by the manufacturer. Adequate safety precautions, such as the proper eye protection, must be observed.
- The use of air filters in the ventilating systems of electrical components is not recommended unless these are provided by the welding machine manufacturer. If used, filters should be inspected as recommended by the manufacturer, because the reduction of air flow from dust accumulating on the air filter can cause internal components to overheat and fail altogether.
- Machines that have become wet must be thoroughly dried and properly retested before being operated.
- All input connections must be checked.
- All grounding connections must be verified.

Multiple-Arc Welding Operations

Increased hazard of electrical shock exists when several welders are working on a large metal structure, such as a building frame or ship, that is part of the return welding circuits. Proper electrical contact must exist at all joints in the structure. Sparking or heating at any point in the structure renders it unsuitable as a return circuit.

When two or more welders working on the same structure are likely to touch the exposed parts of more than one electrode holder simultaneously, the welding machines must be connected to minimize the hazard of shock. Ideally, all dc welding machines should be connected with the same polarity. A test lamp or voltmeter can be used to determine whether the polarities are matched. It is also preferable to connect all single-phase ac welding machines to the same phase of the supply circuit with the same instantaneous polarity. These precautions minimize the potential difference in polarity between electrode holders.

In some cases, the preferable connections may not be available. Welding may require both dc polarities, or supply circuit limitations may necessitate the distribution of ac welding machines among the phases of the supply circuit. In these cases, the no-load voltage between electrode holders or welding guns may be twice the normal voltage. Because of the increased voltage, the welders and other personnel in the area must be instructed to avoid simultaneous contact with more than one electrode holder, welding gun, or installed electrode (Ref 1).

Special Precautions for Pacemaker Wearers

Inasmuch as pacemakers are electrical in operation, their functioning may be compromised by the presence of the strong electromagnetic fields

produced by electric arc welding and cutting. Therefore, the wearers of pacemakers or other electronic equipment vital to life must consult a physician and the manufacturer regarding possible hazards before performing these operations.

Pacemaker wearers who have been cleared to perform welding and cutting activities must observe special precautions. Welding current settings higher than necessary should not be used by pacemaker wearers. Welding cables should be kept close together and positioned to one side of the welder. Repeated, short spurts of welding should be avoided; 10 s should be allowed to transpire between welds. Pacemaker wearers should not work alone and must stop welding and seek immediate medical attention if they feel ill (Ref 2).

Fire Prevention and Protection

Most precautions against electrical shock are also applicable to the prevention of electrical equipment fires, which may be caused by overheating electrical components, sparks, or spatter from welding or cutting operations, or the mishandling of fuel in overheated engine-driven equipment. For engine-driven equipment, fuel systems must be in good condition. Otherwise, the ignition system, electrical controls, spark-producing components, or engine heat may start a fire. Leaks must be repaired promptly. Engine-driven machines must be turned off before refueling, and any fuel spills should be wiped up and fumes allowed to dissipate before the engine is restarted.

In most welding, cutting, and allied processes, a high-temperature heat source is present. Open flames, electric arcs, molten metal, sparks, and spatter are ready sources of ignition. Sparks and spatter can pass through or lodge in cracks, holes, and other small openings in floors and walls, often causing fires. Because sparks can travel up to 10.7 m (35 ft) from their source and fall much greater distances, floors must always be free of combustible materials for a radius of at least 10.7 m (35 ft) around the work area (Ref 2).

Without the proper protective shields, welding or cutting too close to combustibles increases the risk of fire. The materials most commonly ignited are combustible floors, roofs, partitions, and building contents including trash, wood, paper, textiles, plastics, chemicals, and flammable liquids and gases. Outdoors, the most common combustibles are dry grass and brush.

The best protection against fire is to perform welding and cutting away from combustibles in specially designated areas or noncombustible enclosures. Combustibles should always be removed from the work area. Combustibles that cannot be removed from the area, including combustible walls, ceilings, doorways, windows, cracks, and other openings, should be covered with tight-fitting flame-resistant material. Alternatively, the work area itself can be

enclosed with portable flame-resistant screens. Combustible floors must be protected with damp sand, sheet metal, or water. If water is used, measures must be taken to protect personnel from experiencing electric shock. Appropriate fire-extinguishing equipment must be available for immediate use in the work area (Ref 1).

Personnel should refrain from welding or cutting in atmospheres that contain hazardously reactive or flammable gases, liquids, vapor, or dust. Moreover, heat should not be applied to a container that has held an unidentified substance or combustible material or to a work-piece covered with an unidentified substance or flammable coating (Ref 2).

The fuel for engine-driven equipment must be carefully stored and handled. The equipment manufacturer's instructions should be followed because the fuels and vapors commonly found in welding and cutting areas are combustible and can be explosive under some conditions. Examples of such fuel gases are acetylene and propane. All fuel-gas cylinders, hoses, and apparatus must be carefully inspected for leaks. Welders must also be alert for the traveling vapors of flammable liquids. Vapors are often heavier than air and can travel along floors and in depressions for a considerable distance from the location where the flammable liquid is stored. In addition, light vapors can travel along ceilings to adjacent rooms.

When welding or cutting material on or adjacent to a metal wall, ceiling, or partition, heat that is conducted through the metal can ignite combustibles on the opposite side. Therefore, combustibles on the other side of the barrier must be moved to a safe location. If this cannot be accomplished, a fire watcher (see the section "Fire Watchers" in this article) must be stationed to monitor the combustibles.

Welding, brazing, or cutting must not be performed on any material having a combustible coating or internal structure. This is the case with certain walls, ceilings, floors, and platforms. Moreover, hot scrap or slag must not be placed in containers holding combustible materials. After the operation has been completed, the work area should be inspected for fires for at least 30 min. Personnel should be alert for conditions that may warrant an extension of this period. Supervisory personnel should also inspect the area before leaving.

Fire Watchers

According to the provisions of ANSI Z49.1:1999 (Ref 1) and "Fire Prevention during Welding, Cutting, and Other Hot Work," NFPA 51B (Ref 48), fire watchers—qualified personnel who are trained in fire detection, the fire-reporting process, and emergency rescue procedures—must be situated in areas where welding or cutting operations are being performed and where a fire may start. Fire watchers must also be posted when any of the following are present:

- Combustibles within 10.7 m (35 ft) of welding or cutting operations
- Wall or floor openings that expose combustible materials within a radius of 10.7 m (35 ft)
- Metal walls, ceilings, roofs, or pipes adjacent to which materials that are likely to ignite by means of radiation or conduction are located
- Ship work that poses a fire hazard to an adjacent compartment

Fire watchers are allowed to perform additional duties, provided these do not distract them from detecting fires.

Hot-Work Authorization

When welding, cutting, or similar hot-work operations are to be performed in an area not designated for these activities, the hot-work authorization system is used to alert area supervisors to the extraordinary hazard of fire. (The term *hot work* is defined in Ref 1 as “any work involving burning, welding, or similar operations capable of initiating fires or explosions.”) The authorization, which is usually written, should incorporate a checklist of safety precautions, including an inspection of fire extinguishers; the establishment of fire watches, if necessary; a search for flammable materials; and safety instructions for area personnel who are not involved in the hot work (Ref 1).

Explosion Prevention

When certain gases, vapors, and dusts are mixed with oxygen or other elements in certain proportions, they can cause explosions and fires. The heat, sparks, and spatter produced during welding and related activities may cause otherwise low-volatile materials to produce flammable vapors. All of these materials must be kept in leaktight containers or be well removed from the work area.

Welding, brazing, soldering, or cutting activities should never be carried out in an atmosphere containing flammable material. Personnel must also refrain from placing any operating equipment that can produce heat or sparks near these flammables. Inasmuch as some welding operations involve the risk of explosion, personnel must always wear proper PPE.

Containers must be vented before applying heat. Heat must not be applied to a container that has held an unknown material, a combustible substance, or a substance that may form flammable vapors upon the application of heat (Ref 29). The container must first be thoroughly cleaned or filled with an inert gas. In addition, heat should never be applied to a workpiece covered by an unknown substance or to a substance that may form flammable or toxic vapors when heated.

Process-Specific Safety Considerations

Broad safety guidelines for most welding, cutting, brazing, or soldering processes have been addressed earlier. The precautions and procedures unique to particular processes are discussed in this section. All applicable precautions and guidelines discussed subsequently must be considered as part of a safety program in the workplace.

Oxyfuel Gas Welding and Cutting

Acetylene, MPS, natural gas, propane, propylene, and hydrogen are commonly used in oxyfuel gas welding and cutting. In addition, gasoline is sometimes used as a fuel for oxygen cutting. As mentioned previously, these fuels should always be referred to by name, not by the generic term *gas*.

Oxygen equipment—including cylinders and pipelines—must not be used interchangeably with any other gas. Failure to comply with this measure may result in spontaneous combustion or explosion as a result of the contamination of the oxygen apparatus with combustible substances (Ref 1).

Torches. Only welding and cutting torches that have been approved by the authority with jurisdiction must be used in oxyfuel gas welding and cutting operations. Oxyfuel gas torches must meet appropriate government regulations and the requirements stipulated in “Torch Standard for Welding and Cutting,” CGA E-5 (Ref 40). Torches should be kept in good working order and serviced at regular intervals by the manufacturer or qualified technicians. A torch must be used only with the fuel gas for which it was designed. The fuel-gas and oxygen pressures should be those recommended by the torch manufacturer. Torches must be inspected for leaking before lighting, and frequent leak testing should be performed when the equipment has been employed in such a way as to induce leaks (Ref 1).

To minimize the hazard of burns on the hands and fingers, the manufacturer’s recommendations must be followed when lighting and extinguishing the torch. The torch should be lighted only with a friction lighter, pilot light, or similar ignition source. Matches, cigarette lighters, or welding arcs must never be used as a source of ignition. The manufacturer’s specifications must also be followed regarding the sequencing of operations while lighting, adjusting, and putting out torch flames (Ref 1).

Hoses. Only those hoses that have been specified for use in oxyfuel gas welding and cutting systems may be used. Hoses used in oxyfuel gas service must be manufactured in accordance with the standard “Specifications for Rubber Welding Hose,” ANSI/RMA IP-7 (Ref 49). Hoses must be in good condition and free of oil and grease. Worn, leaking, defective hoses must be repaired or replaced.

In the United States, red hose with left-hand threaded fittings is typically used for fuel gas, while green hose with right-hand threaded fittings is used for oxygen. (Hose connections must comply with requirements stipulated in Ref 35.) To permit color recognition and ensure adequate ventilation, when parallel lengths of hose are strapped together, no more than 100 mm (4 in.) of any 300 mm (12 in.) section of hose should be taped. The hose colors used internationally are specified in “Welding—Rubber Hoses for Welding, Cutting, and Allied Processes,” ISO 3821 (Ref 1, 50).

Only the proper ferrules and clamps should be used to secure hose to fittings. Long runs of hose should be avoided. Excess hose should be coiled to prevent kinks and tangles, but it should not be wrapped around cylinders or cylinder carts while in use.

Backfire and Flashback. The term *backfire* refers to the momentary retrogression of the flame back into the torch tip, causing the tip flame to disappear and then reappear. This is accompanied by a pop or bang, depending on the size of the tip. In severe cases, the hot combustion products within the tip may be forced back into the torch and even the hoses. Backfires occasionally ignite the inner liner of the hose and result in burnthrough of the hose wall, especially when using oxygen. Such backfires can result in injury. In addition, when the hose ruptures, the gases flow out of the tube into the atmosphere until the valve at the tank is closed.

The term *flashback* describes a phenomenon that is usually characterized by a whistling or squealing sound. Flashback is initiated by a backfire in which the flame continues to burn inside the equipment instead of being re-established at the tip. This causes a very rapid internal heating that can easily destroy the equipment. This rapid heating may also cause sparks to issue from the tip. Flashback should be extinguished by turning off the torch valves as quickly as possible. Different manufacturers recommend shutting off either the fuel or oxygen first, but the most important concern is to shut both valves quickly.

Backfires and flashbacks are not ordinarily a concern when the manufacturer’s instructions have been followed. When they do occur, the operator allowed the tip to become overheated by flame backwash, forcing the tip into the work, or providing insufficient gas flow for the size of the tip. If frequent backfires or flashbacks occur, the work should be stopped, and the equipment or operation should be investigated.

To prevent backfires and flashbacks, hose lines should always be purged before oxyfuel gas equipment is lighted. Purging flushes out any combustible oxygen-fuel or air-fuel gas mixtures in the hoses. Hoses are purged by opening either the fuel or the oxygen valve on the torch and allowing the gas to flow for several seconds to clear the hose of any possible gas mixtures. That valve is then closed, and

the other valve is opened to allow the other gas to flow for a similar period. The purge stream must not be directed toward any flame or other source of ignition. Torches must not be purged in confined areas because accumulated, highly concentrated gas may explode.

Hose-Line Safety Devices. When they are installed and operating properly on hose lines, reverse-flow check valves and flashback arrestors can prevent the reverse flow of gases and flashbacks into hoses. These safety devices must be used, inspected, and maintained strictly in accordance with the manufacturer's instructions and recommendations (Ref 1).

Regulators. Pressure-reducing regulators must be approved according to the specifications of "Standard for Gas Pressure Regulators," CGA E-4 (Ref 34). These regulators must be used for the gases and pressures specified on their labels only. Inlet connections must be made in accordance with *Compressed Gas Cylinder Valve Outlet and Inlet Connections*, ANSI/CGA V-1 (Ref 32), and all connections must be inspected for leaktight performance before use. Regulators must not be used interchangeably among designated gas applications. To minimize the possibility of fire, oxygen regulators must be drained of gas before they are connected to a manifold or a cylinder, and valves must always be opened slowly (Ref 1).

Shutdown Procedures. When oxyfuel gas operations are finished, the equipment must always be completely shut down, with the gas pressures drained from the system and all cylinder supply valves closed. The equipment must not be left unattended until the shutdown has been completed.

Ventilated Storage. Oxyfuel gas cylinders or equipment connected to cylinders must always be stored in well-ventilated areas, rather than in confined areas, such as unventilated cabinets. Even small gas leaks in confined areas can create mixtures that may cause disastrous explosions. For the same reason, gas cylinders should never be transported in enclosed vehicles, particularly in closed vans or the trunks of automobiles.

Arc Welding and Cutting

The potential hazards of arc welding and cutting, discussed in detail earlier, necessitate precautions that must be followed. Potential hazards encountered in arc welding and cutting include electric shock, asphyxiation, fumes and gas, infrared and UV radiation, burns, fire, explosion, and noise. Noise levels during arc cutting operations can be very high, and prolonged exposure can cause hearing impairment. A certified safety specialist or industrial hygienist can be consulted to measure occupational exposure levels in the work area and make recommendations. Whenever necessary, approved ear protection, such as ear plugs or muffs, must be provided for operators and others in the area.

Plasma arc cutting is a particularly noisy process and one that also emits a great deal of fume. Two common accessories can be used in the mechanized plasma arc cutting of plate to aid in fume and noise control. One method is the water table, discussed earlier in the section "Local Ventilation." This is a cutting table filled with water to the bottom surface of the plate or above the plate. In the latter case, cutting is done under water using a special torch to minimize noise and reduce radiation. The high-speed gases emerging from the plasma jet produce turbulence in the water, consequently trapping most fume particles in the water.

Another accessory designed to reduce noise is the water muffler, a nozzle attached to a special torch body that produces a curtain of water around the front of the torch. The water muffler is always used in conjunction with a water table. The combination of a water curtain at the top of the plate and a water table contacting the bottom of the plate encloses the arc and creates a noise-reducing shield, attenuating noise by roughly 20 dB. These accessories should not be confused with cutting variations using water injection or water shielding, however.

Resistance Welding

When selecting resistance welding equipment, personnel safety must be a consideration. All equipment must be installed by qualified personnel under the direction of a technical supervisor in accordance with the "Electrical Standard for Industrial Machinery," NFPA 79 (Ref 51) and the "National Electric Code," NFPA 70 (Ref 47) or its equivalent. Operators must be properly trained to operate all resistance welding equipment safely.

Machinery Safeguarding. Devices that initiate a resistance welding operation—push buttons, foot switches, retraction, and dual-schedule switches on portable guns, for example—must be arranged or guarded to prevent inadvertent activation (Ref 1). One or more emergency stop buttons must be provided on all welding machines that require three or more seconds to complete a sequence and have mechanical movements that can be hazardous to personnel if the guards are removed. It should be verified that the installation and use of these emergency stop buttons do not in themselves create additional hazards (Ref 1).

Stationary Equipment. All gears, chains, operating linkages, and belts used with welding equipment must be guarded in accordance with ANSI safety standards for mechanical power transmission devices. It is crucial that the operator's hands be kept away from the point of operation. On stationary single-ram welding machines, an appropriate device must be used to prevent the hands from making contact with the point of operation during the machine cycle unless the size of the workpiece, its configuration, or fixture keeps both of the operator's

hands away from the point of operation. Appropriate safety apparatus includes latches, two-handed controls, machine guards, or fixtures to prevent the hands from passing under the point of operation, and presence-sensing equipment. Similar precautions must be taken if the operator's hands must pass under the point of operation during a multigun welding machine operation (Ref 1).

Portable Equipment. All suspended portable welding gun equipment, except the gun assembly, must be fail-safe. It must incorporate a support system that is capable of withstanding the total impact load in case any component of the supporting system should fail. Cables, chains, and clamps are satisfactory support system components (Ref 1).

Moving holder mechanisms on portable welding equipment require additional precautions. A moving holder mechanism that enters the gun frame must be designed to ensure that no sharp shear points could cause injury to fingers. If shear points are present, appropriate guarding must be provided. If adequate guarding from shear cannot be accomplished, the use of two handles—one for each hand—is permitted, provided each handle has one or two operating switches at appropriate holding points. These handles and operating switches must be positioned a safe distance away from any shear or pinch point to prevent contact when the hands are on the controls (Ref 1).

Electrical Considerations. All external weld-initiating control circuits must operate at or below 120 V ac for stationary equipment. Portable equipment must operate at or below 36 V ac root mean square. In addition, resistance welding equipment and control panels containing capacitors used for stored-energy resistance welding involving high voltages (above 550 V ac) must be suitably insulated and protected by complete enclosures. All doors on this equipment must have suitable interlocks and contacts wired into the control circuit. These interlocks or contacts must be designed to interrupt power and short circuit all capacitors when the panel is open. As an added safety measure ensuring absolute discharge of all capacitors, a manual switch or suitable positive device must be installed in addition to the mechanical interlocks or contacts. It is important to note that because the panel box itself is considered an enclosure, the capacitors inside it require no additional protection when all other safety requirements have been met (Ref 1).

To prevent unauthorized access to live portions of equipment, all electrical resistance welding equipment must be locked or interlocked, including all doors and access panels on resistance welding machines and remote control panels that are accessible at floor level. A door or access panel is considered locked when a key, wrench, or other instrument is required to open it. Control panels that are located on overhead platforms or in separate rooms must be locked, interlocked, or guarded

by a physical barrier or a sign, except when the equipment is undergoing service. In addition, panel doors must always be closed (Ref 1).

On large welding machines that have a platen, electrically interlocked safety apparatus such as pins, blocks, or latches must be provided when the platen or the head can move. When activated, this safety device must break the energizing circuit. The device itself must prevent movement of the platen or head under static load. Although more than one device may be required, depending on the machine size or accessibility, each device alone must be capable of sustaining the full static load involved (Ref 1).

To ensure the safety of personnel in the area, protection from flying sparks and molten metal must be provided by a guard of suitable fire-resistant material or approved protective eye-wear. For flash welding equipment, flash guards of suitable fire-restraint material must be provided to control flying sparks and molten metal. In addition, for proper electrical safety, resistance welding equipment must have appropriate grounding. The welding transformer secondary may be grounded by either permanent grounding of the welding secondary circuit or by connecting a grounding reactor across the secondary winding with reactor tap(s) to ground. As an alternative on stationary machines, an isolation contactor can be arranged to open both sides of the line to the primary of the welding transformer (Ref 1).

It is important to remember that because resistance welding operations vary, each operation must be evaluated individually to provide proper protection.

High-Frequency Welding

Injuries from high-frequency welding power, especially at the upper range of welding frequencies, tend to produce severe localized surface tissue damage. These injuries are not likely to be fatal, however, because the current flow is shallow and does not penetrate deeply into the body.

On the other hand, high-frequency welding generators, which emit lethal voltages ranging from 400 to 20,000 V in either low or high frequency, can cause fatal injuries. Thus, proper care and safety precautions must be taken while working on high-frequency welding generators and their control systems. Units must be equipped with safety interlocks on access doors and with automatic safety grounding devices to prevent equipment operation when access doors are open. The equipment must not be operated with the panels or high-voltage covers removed or with the interlocks and grounding devices blocked. (This equipment should not be confused with high-frequency arc stabilization equipment, which is used in gas tungsten arc welding.)

The output high-frequency primary leads must be encased in metal ducting and should

not be operated in the open. Induction coils and contact systems must always be properly grounded for operator protection. High-frequency currents are more difficult to ground than low-frequency currents, and grounding lines must be kept short and direct to minimize inductive impedance. The magnetic field from the output system must not induce heat in adjacent metallic sections, which could cause burns or fires.

High-frequency welding stations often emit a loud, steady whine that can cause permanent hearing loss. Ear protection is essential under these circumstances.

Electron Beam Welding

The standards "Recommended Practices for Electron Beam Welding," ANSI/AWS C7.1 (Ref 52), and "Safety in Welding, Cutting, and Allied Processes," ANSI Z49.1 (Ref 1), stipulate general safety requirements that must be followed strictly at all times while performing electron beam welding. The primary hazards associated with electron beam welding equipment are electric shock, x-radiation, fumes and gases, and damaging visible radiation. Thus, precautionary measures must be taken at all times. These hazards are discussed as follows.

Electric Shock. Electron beam welding machines operate at voltages that are much higher than those employed in other welding processes. Electron beam equipment is typically operated at voltages above 20 kV. These voltages can cause fatal injury regardless of whether the machine is labeled as being a low-voltage or a high-voltage device. Even though the manufacturers of electron beam welding equipment produce machines that are well insulated against high voltage, precautions must be taken with all systems when high voltage is present. The manufacturer's instructions should be followed for proper equipment operation and maintenance.

The x-radiation generated by electron beam welding machines is produced when electrons traveling at high velocity collide with matter. The majority of x-rays are produced when the electron beam impinges upon the workpiece. Substantial amounts are also produced when the beam strikes gas molecules or metal vapor in the gun column and work chamber. Producers and users must follow procedures that adhere to regulations established by Underwriters Laboratories and OSHA, providing firm rules for permissible x-ray exposure levels.

Electron beam welding and cutting equipment must be properly shielded to block out x-radiation or reduce it to acceptable levels (Ref 1). The steel walls of the chamber are generally adequate protection in systems up to 60 kV, assuming proper design. High-voltage machines use lead lining to block x-ray emission beyond the chamber walls. Lead glass windows are employed in both high- and low-voltage electron beam systems. The shielded

vacuum chamber walls normally provide adequate protection for the operator.

If a system does not have a vacuum, a radiation enclosure must be provided to assure the safety of the operator and others in the work area. Instead of lead, thick walls of high-density concrete or other similar material may be used, especially for large radiation enclosures on non-vacuum installations. Special safety precautions should also be implemented to prevent personnel from accidentally entering or becoming trapped inside the enclosure during equipment operation.

A complete x-ray radiation survey of the electron beam equipment should always be made at the time of installation and at regular intervals thereafter. This survey must be conducted by qualified technicians to ensure initial and continued compliance with all radiation regulations and standards applicable to the site where the equipment is installed. The results should be documented and posted (Ref 1).

Fumes and Gases. Nonvacuum and medium-vacuum electron beam systems can produce ozone and oxides of nitrogen in harmful concentrations as well as other types of airborne contaminants in concentrations above acceptable levels. Therefore, adequate area ventilation must reduce the concentrations of airborne contaminants around the equipment to within permissible exposure limits. Proper exhausting techniques should also be employed to maintain permissible residual concentrations in the area.

High-vacuum electron beam chambers are unlikely to produce ozone and oxides in harmful concentrations because of the small amount of air in the chamber.

Personnel must consult the pertinent MSDSs before welding unfamiliar material or using unfamiliar cleaning products (Ref 1).

Visible Radiation. Because the electron beam welding process produces visible, UV, and infrared (IR) radiation, direct viewing of the process can be hazardous to the eyesight. Therefore, adequate optical protection must be provided against UV and IR radiation by the installation of leaded glass in the viewing ports. In addition, visible light must be reduced to a comfortable level by means of the appropriate filters (Ref 1).

Laser Beam Welding and Cutting

The basic hazards associated with laser operation are eye damage, including burns of the cornea or retina, or both; skin burns; electrical shock; respiratory system damage from hazardous materials emitted during operation; and chemical hazards, including contact with cryogenic coolants.

Laser manufacturers are required to qualify their equipment with the U.S. Bureau of Radiological Health. Electrical components must comply with the standards issued by the National Electrical Manufacturers Association.

The use of lasers is governed by OSHA requirements. In all cases, the “American National Standard for Safe Use of Lasers,” ANSI Z136.1, should be adhered to (Ref 53). In addition, a laser safety officer (LSO)—responsible for the protection of personnel and the enforcement of laser safety regulations—must be present at all installations performing laser welding and cutting (Ref 2).

Eye and Skin Hazards. Laser beams can readily inflict eye injury. With laser beams operating at visible or near-infrared wavelengths, even a 5 mW beam can inflict retinal damage. Thus, the use of safety glasses is essential. Glasses appropriate to the specific laser system must be used. Safety glasses substantially transparent to visible light but opaque to specific laser beam outputs are available. Selective filters for ruby, neodymium: yttrium-aluminum-garnet (Nd:YAG), and other laser systems are also available. Ordinarily, transparent materials such as glass are opaque to longer infrared wavelengths, such as those produced by carbon dioxide lasers, so clear safety glasses with side shields may be used with these systems. In this case, the only light reaching the eye is from the incandescence of the workpiece. Nevertheless, plasma generation at high powers can cause extreme brilliance, so filter lenses should be used for viewing the operation.

According to the specifications of ANSI Z136.1 (352), laser protective eyewear—whether plain or prescription—must be labeled with the optical density and the wavelengths for which protection is provided. This standard also requires that protection be afforded against secondary radiation. Protection against UV light, which may leak into the work area, should also be provided by the eyewear (Ref 2).

To prevent skin burns, welding personnel must always avoid all contact with laser beams. The burns these produce can be deep and very slow to heal. All laser beams used for welding and cutting are visible only when they impinge on a solid, so workers must take special precautions to avoid accidental exposure. As a preventive measure, the laser beams can be enclosed, or a safety device can be used to prevent operation of the beam unless its path is unobstructed.

Electrical Hazards. Because lasers have high voltages and large capacitor storage devices, the possibility of lethal electric shock is always present during laser beam welding. Hazards range from those inherent in any conventional electrical power source to those common to lasers in general and those unique to the particular laser beam welding and cutting process. As a general precaution, electrical system enclosures should have appropriate interlocks on all access doors and provisions for discharging capacitor banks before entry. All laser equipment should also be appropriately grounded. The manufacturer’s recommended safety procedures must be followed at all times.

Respiratory Hazards. Although the fumes and gases produced during laser beam welding

and cutting are often not visible, they pose potentially serious respiratory hazards. Hazardous products may be generated from the interaction of the beam and the workpiece, making adequate ventilation and exhaust provisions for laser work areas necessary. For example, the plastic materials used for “burn patterns” to identify beam shape and distribution in high-power carbon dioxide laser systems can generate highly toxic vapors if irradiated in an oxygen-lean atmosphere. In deep-penetration welding, fine metal fume can arise from the joint. In addition, intense plasma generation can produce ozone.

The LSO must ensure that all laser-generated air contaminants are characterized in accordance with applicable regulations. When exposure exceeds acceptable levels as established by Title 29 CFR 1910, Subpart Z and the applicable ACGIH standards, the LSO may require the implementation of control measures such as exhaust ventilation systems, respiratory protection, or process isolation (Ref 53).

Chemical Hazards. Many hazardous chemicals and gases are used in laser welding and cutting operations. These include toxic or corrosive gases such as chlorine, fluorine, hydrogen chloride, and hydrogen fluoride. Cryogenic gases can cause injuries due to freezing because of their extremely low temperatures. Safety hazards are also associated with the use of laser dye compounds. Manufacturers’ MSDSs should always be consulted, and appropriate measures must be taken to ensure personnel safety in all cases.

Friction Welding

The risks posed by friction welding include mechanical hazards, heat, and spatter. To minimize the risk of injury, friction welding machines should be equipped with appropriate mechanical guards and shields. They should also have two-hand operating switches and electrical interlocks to prevent machine operation when the operator or others have access to the work area, rotating drive, or force system.

Friction welding machines are similar to machine tool lathes in that one workpiece is rotated by a drive system, and to hydraulic presses in that one workpiece is forced against the other. Thus, operating personnel should wear the eye protection and safety apparel that is commonly used for machine tool operations. Also, the applicable OSHA standards should be strictly observed.

Explosion Welding

Explosives and explosion devices are an integral part of explosion welding. If these devices are misused, they can cause injury, death, property damage, and destruction. Although these materials are inherently hazardous, safe practices can minimize the risks associated with

their handling. For this reason, explosive materials must be used only by trained personnel who are experienced in their safe handling.

Handling and safety procedures must comply with all applicable federal, state, and local regulations. The U.S. Bureau of Alcohol, Tobacco, and Firearms; the Hazardous Materials Regulation Board of the U.S. Department of Transportation; OSHA; and the Environmental Protection Agency have federal jurisdiction on the sale, transport, storage, and use of explosives. Many state and local governments require a blasting license or permit, and some cities have special requirements for explosives.

Other organizations also provide safety education for the handling of explosives. The Institute of Makers of Explosives distributes educational publications to promote the safe handling, storage, and use of explosives. The NFPA also provides recommendations for the safe manufacture, storage, handling, and use of explosives (Ref 54).

Ultrasonic Welding

Ultrasonic welding may pose the risk of mechanical hazards, electric shock, heat, and burns. In high-power ultrasonic equipment, high voltages are present in the frequency converter, the welding head, and the coaxial cable connecting these components. Thus, the equipment should not be operated when its panel doors are open or its housing covers are removed. Door interlocks are normally installed to prevent the introduction of power to the equipment when its high-voltage circuitry is exposed. Because the cables are fully shielded, they should present no hazard if properly connected and maintained.

Because of the hazards associated with clamping force, operators must not place hands or arms in the vicinity of the welding tip when the equipment is energized. In accordance with OSHA regulations, the equipment must have two palm buttons for manual operation. These must be pressed simultaneously to initiate a weld cycle, and both must be released before the next cycle can begin. For automated systems in which the weld cycle is sequenced with other operations, protective guards should be installed to protect operators. As a further precaution, the welding stroke can be set to the minimum that is compatible with workpiece clearance.

Thermite Welding

Thermite welding is a process that uses the thermochemical reaction between metal oxide and aluminum to produce the heat to form a weld. Moisture in the thermite mix, whether in storage, in the crucible, or on the workpieces, can rapidly emit steam during the chemical reaction for thermite welding. This may cause the ejection of molten metal from the crucible. To minimize the risk of steam formation, the

thermite mix should be stored in a dry place, the crucible should be dry, and moisture should not be permitted to enter the system prior to or during welding.

The preheating required for the thermite process should be carried out using the safety precautions applicable to oxyfuel gas equipment and operations. The work area should be free of materials that may be ignited by sparks or small particles of molten metal. The area should also be well ventilated to prevent the buildup of fumes and gases from the thermite reaction. Starting powders and rods should be protected against accidental ignition.

Personnel should use appropriate PPE to shield against hot particles or sparks. Full-face shields with filter lenses for eye protection, headgear, gloves, and safety boots should be used. Clothing should not have pockets or cuffs that may catch hot particles.

Brazing and Soldering

The hazards encountered in brazing and soldering operations are similar to those associated with the welding and cutting processes (Ref 55). Personnel and property must be protected against gases, fumes, hot materials, electrical shock, radiation, and chemicals (Ref 56, 57). Because hazardous materials may be present in the fluxes, filler metals, coatings, and atmospheres used in brazing, the MSDSs should be consulted as a prerequisite to any job.

Hazardous and Explosive Gases and Fumes. Brazing and soldering operations may be performed at temperatures that induce some elements in the filler metal to vaporize into fumes and gases. Some of these elements are hazardous. These include cadmium, beryllium, zinc, mercury, and lead. Thus, it is essential that adequate ventilation be provided to protect personnel from inhaling the gases and fumes emitted during brazing or soldering. Brazing fluxes may also contain chemical compounds of fluorine, chlorine, and boron. These compounds are harmful if they are inhaled or come into contact with the eyes or skin. Ventilation methods used to avoid these hazards were described earlier (see the section "Ventilation" in this article).

Flammable gases, such as combusted fuel gas, hydrogen, and disassociated ammonia, are sometimes used as atmospheres for furnace brazing operations. Before introducing such atmospheres, the furnace or retort must be purged of air by safe procedures recommended by the furnace manufacturer. These gases may emanate from furnace purging and brazing operations. Thus, adequate area ventilation must exhaust and discharge explosive or hazardous gases to a safe location. Local environmental regulations should be consulted when designing the exhaust system.

In dip brazing and soldering, the parts to be immersed in the bath must be completely dry. Any moisture on the parts instantly creates

steam. The expanding steam may then cause an explosion, expelling the contents of the dip pot and creating a serious burn hazard. If supplementary flux is necessary, it must be adequately dried to remove all moisture and water of hydration to prevent the hazard of explosion.

Solder Flux. Some fluxes, such as rosin, petrolatum, and reaction types, emit considerable smoke, the amount depending on the soldering temperature and the duration of heating. Other fluxes emit fumes that are hazardous if inhaled in large quantities. The prolonged inhalation of halides and some of the newer organic fluxes must be avoided. Aniline fluxes and some of the other amines also emit harmful fumes that can cause dermatitis. The fluorine in flux is also hazardous to health. It causes skin burns and can be fatal if ingested.

The ACGIH has established the safe TLV for the decomposition products of rosin-core solder at 0.1 mg/m³ aliphatic aldehydes, measured as formaldehyde. Suitable ventilation must be provided to meet this requirement. When ventilation is insufficient to reduce contaminants or the implementation of ventilation is not feasible, personnel must use the appropriate approved respiratory protective equipment.

Thermal Spraying

All thermal spraying processes involve the deposition of molten metallic or nonmetallic materials to coat an object. These processes use modifications of oxyfuel, arc, and plasma energy sources to create the high temperatures and projectile velocities required to perform spray operations. These operations present safety hazards to all individuals in the work area. Thus, the safe practices described previously for these processes should be implemented when conducting thermal spraying activities with similar equipment. However, thermal spraying generates dust and fumes to a greater degree. Additional information may be found in Ref 58.

Those involved with and in the proximity of thermal spraying operations must take precautions against dust, fire, electrical shock, arc radiation, fumes and gases, and noise. Thermal spray operators must be protected with the proper eye, respiratory, and bodily protection. Appropriate protective clothing required for a thermal spraying operation will vary with the

size, nature, and location of the work performed.

Dust. Finely divided airborne solids, especially metal dusts, must be treated as an explosive and inhalation hazard. Therefore, the dust produced during thermal spraying must be adequately vented out of spray booths. Instead of bag and filter collectors, a water-wash wet collector is recommended to collect spray dust. Good housekeeping in the work area prevents the accumulation of metal dusts, particularly on rafters, the tops of booths, and in floor cracks. Paper, wood, oily rags, and other combustibles that could cause a fire in the spraying area should be removed before the equipment is operated. Clothing should be fastened tightly around the wrists and ankles to keep dusts from contacting the skin. When personnel work in confined areas, they should wear flame-resistant clothing and gloves.

Electrical Shock. The high voltages used in the thermal spraying processes increase the hazard of electrical shock. Thus, general safety precautions for the avoidance of electric shock must be implemented to protect personnel.

Radiation. Because thermal spraying processes generate both UV and infrared radiation, helmets, hand shields, face shields, or eye protection must be used to protect the eyes, face, and neck at all times. Safety goggles must be worn to avoid eye damage and burns. Table 3 presents a guide for the selection of the proper filter shade number for viewing specific spraying operations.

The intense UV radiation of plasma and electric arc spraying can cause skin burns through normal clothing. Thus, the protection against radiation that is used during arc spraying is practically the same as that employed for arc welding at equivalent current levels.

Fumes and Gases. Most thermal spraying operations require operators to wear adequate respiratory protection. The nature, type, and magnitude of the fume and gas exposure determine which respiratory protective device should be used. All devices used must be approved by MSHA, NIOSH, or other recognized authority.

Noise. Thermal spraying operations generate noise in high decibel ranges. Consequently, noise control programs must be implemented in accordance with Title 29 CFR 1910.95. In addition, operators and others in the area should

Table 3 Recommended eye filter plates for thermal spraying operations

Operation	Filter shade numbers
Wire flame spraying (except molybdenum)	5
Wire flame spraying of molybdenum	5-6
Flame spraying of metal powder	5-6
Flame spraying of exothermics or ceramics	5-8
Plasma and arc spraying	9-12
Fusing operations	5-6

Note: When cadmium is a constituent in a filler metal, a precautionary label must be affixed to the container or coil. Refer to Section 9 of Ref 1.
Source: Adapted from Ref 3

wear earmuffs or properly fitted soft rubber earplugs.

Adhesive Bonding

Because corrosive materials, flammable liquids, and hazardous substances are commonly used in adhesive bonding, adequate safety precautions must be observed in compliance with all federal, state, and local regulations, including "Air Contaminants," Title 29 CRF 1900.1000.

Safety Facilities. Management must properly supervise manufacturing operations to ensure that proper safety procedures, protective devices, and protective clothing are employed. Areas in which adhesives are handled should be separated from those in which other operations are performed. In addition to being equipped with the proper fire protection equipment, these areas should have ventilating facilities, a first-aid kit, a sink with running water, and an eye shower or rinse fountain. To ensure proper ventilation, ovens, presses, and other curing equipment should be individually vented to remove fumes. Vent hoods should be provided at mixing and application stations.

All personnel should also practice good personal hygiene. They should be instructed in the proper procedures to prevent skin contact with solvents, curing agents, and uncured base adhesives. Showers, wash bowls, mild soaps, clean towels, refatting creams, and protective equipment should be available. Curing agents on hands should be cleaned off with soap and water. Resins should be removed with soap and water, alcohol, or a suitable solvent. Solvents should be used sparingly; following use, they should be washed off with abundant soap and water. If an allergic reaction or burning occurs, prompt medical attention should be sought.

Personal Protective Equipment. While working with potentially hazardous adhesives, personnel must wear plastic or rubber gloves at all times. Contaminated gloves should never touch objects that others may touch with their bare hands. Instead, these gloves should be discarded or cleaned using procedures that remove the particular adhesive. Cleaning may require solvents, soap and water, or both. The hands, arms, face, and neck should be coated with a commercial barrier ointment or cream, which provides short-term protection and makes adhesives easier to wash off the skin.

Full-face shields should be worn for eye protection whenever the possibility of splashing exists. Otherwise, glasses or goggles should be worn. In case of irritation, the eyes should be flushed immediately with water and then promptly treated by a physician.

Protective clothing should be worn at all times by those who work with adhesives. Shop coats, aprons, or coveralls may be suitable, and they should be cleaned before reuse.

Flammable and Hazardous Materials. To prevent fires during the storage and use of flammable materials such as solvents, these hazardous materials must be stored in tightly sealed drums and issued in suitably labeled safety cans. Solvents and flammable liquids must not be used in poorly ventilated confined areas. When solvents are used in trays, safety lids should be provided. Flames, sparks, or spark-producing equipment must not be permitted in the area where flammable materials are being handled. In addition, fire extinguishers should be readily available.

Factors to be considered in identifying the types of precautionary measures that should be implemented while working with hazardous materials include the frequency and duration of exposure, the degree of hazard associated with a specific adhesive, the solvent or curing agent used, the temperature at which the operations are performed, and the potential evaporation surface area exposed at the workstation.

For most personnel, preventing skin contact with an adhesive should be an adequate safety measure. It is mandatory that protective equipment, barrier creams, or both be used to avoid skin contact with certain types of formulations. However, others may suffer severe allergic reactions produced by direct contact with or the inhalation or ingestion of phenolics, epoxies, and most catalysts and accelerators. The eyes or skin may become sensitized over a long period of time even though no signs of irritation are visible. Once personnel become sensitized to a particular adhesive, they may no longer be able to work in its vicinity because of allergic reactions.

Proper safety rules must be observed to prevent the careless handling of adhesives and thereby prevent exposure to hazardous materials. For example, personnel performing adhesive bonding with potentially hazardous materials should avoid contact tools, door-knobs, light switches, or other objects that may become contaminated.

Safety in Robotic Operations

The hazards associated with robotic welding, cutting, and allied process are those generally related to equipment (e.g., faulty power sources, protective devices, control circuits, and so on), installations (human errors during setup, ergonomics, maintenance, mounting, positioning, loose objects, and so forth), and the robot system itself or its interaction with other equipment and persons (e.g., moving components that cause trapping or crushing, hazardous atmospheres, inadvertent operation, and so forth) (Ref 59).

Personnel must be safeguarded against hazards during all stages of robotic system implementation—design and development, installation and integration, verification, operation, and maintenance. Safeguarding is the

responsibility of those involved in all of these stages. In addition, the user must ensure that all personnel are trained in robotic system operation and that the appropriate safeguarding devices are installed and functioning. Awareness signals (signs, lights, floor markers, horns, and beepers, for example) and barriers should be used in conjunction with safeguarding devices (Ref 59).

The welding process equipment may have specific additional safety requirements regarding barriers, guarding, and precautionary labels. The safety requirements of the welding process that is performed by the robotic system must be implemented. In addition, the testing and startup of robots and robotic systems must be performed according to the specifications of "American National Standard for Industrial Robots and Robot Systems—Safety Requirements," ANSI/RIA R15.06-1999 (Ref 59).

Inasmuch as robotic installations vary significantly from application to application, they must be scrutinized individually for specific safety hazards. During the design stage and again upon completing the final configuration and setup of an installation, the user or integrator must perform a risk assessment of the installation. This assessment involves a task and hazard identification as well as a risk estimation. The selection of the appropriate safeguards is based on the information collected and documented as part of the risk assessment (Ref 59).

Among the safeguarding devices that may be used to protect personnel are barriers; two-hand controls; and presence-sensing devices, including area scanning systems, single and multiple safety beams, safety mats, and safety light curtains or screens (Ref 59). Figure 8 shows several typical robotic installations.

With respect to personnel training, the user must ensure that individuals who program, teach, operate, or maintain robots are properly trained in the tasks performed by the robot, the hazards presented by the system, health and safety procedures, and the purpose and function of safeguarding devices. Training must include general and emergency workplace safety procedures, industry codes and standards, vendor safety information, and lockout and tag-out procedures. Maintenance personnel must be trained in emergency operations as well as in the hazards related to process variables and materials, preventive maintenance, troubleshooting, faulty safety devices, and communication systems. Retraining is required to ensure safe operation following personnel or system changes or an accident (Ref 59).

For detailed information regarding the safety regulations governing robotic operations, the reader is encouraged to consult the "American National Standard for Industrial Robots and Robot Systems—Safety Requirements," ANSI/RIA R15.06-1999, the primary industry standard (Ref 59).

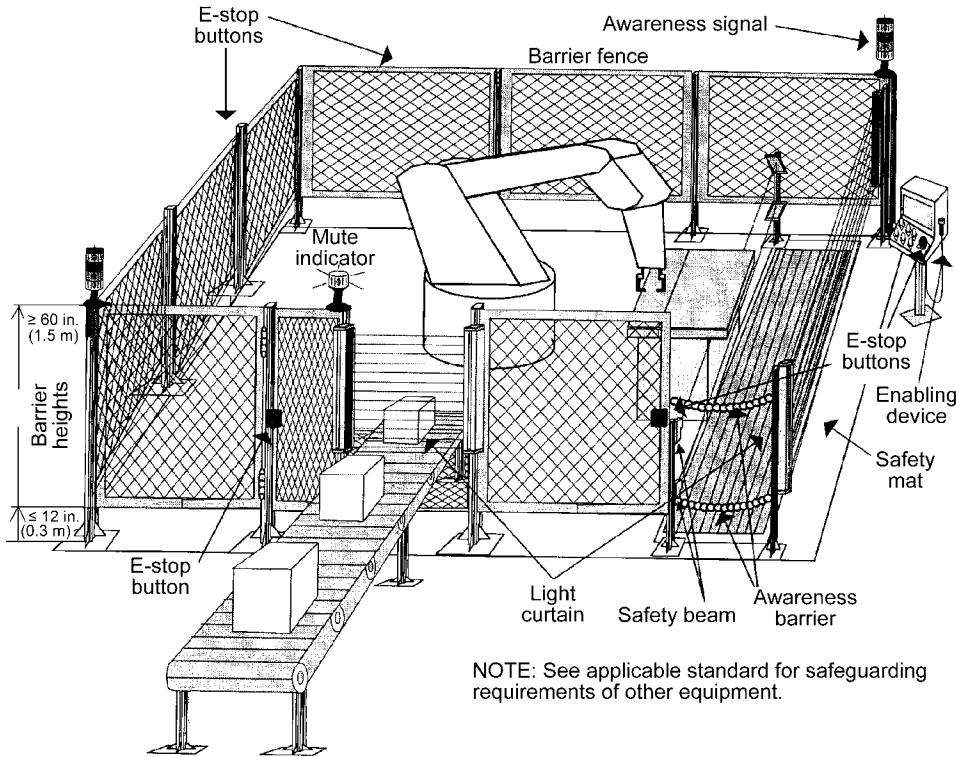


Fig. 8 Typical robotic cell with safeguarding devices. Adapted, with permission, from Ref 59

REFERENCES

- American National Standards Institute Accredited Standards Committee Z49, "Safety in Welding, Cutting, and Allied Processes," ANSI Z49.1:1999, American Welding Society, Miami, FL, 1999
- American Welding Society Project Committee on Labeling and Safe Practices, *Safety and Health Fact Sheets*, 2nd ed., American Welding Society, Miami, FL, 1998, <http://www.aws.org>
- R.L. O'Brien, Ed., *Welding Processes*, Vol 2, *Welding Handbook*, 8th ed., American Welding Society, Miami, FL, 1991
- "OSHA Fact Sheet 93-26, Hazard Communication Standard," 29 CFR 1910.1200, Occupational Health and Safety Administration, 1993
- Welding, Cutting, and Brazing*, Occupational Safety and Health Administration, 1999
- "Occupational Safety and Health Act," Public Law 91-596, 91st Congress, Superintendent of Documents, U.S. Government Printing Office, Washington, D.C., 1970
- "Standard for Fire Prevention in Use of Cutting and Welding Processes," NFPA 51B:1962, National Fire Protection Association, Quincy, MA, 1962
- "Occupational Safety and Health Standards for General Industry," Title 29 CFR 1910, Subpart Q, *Code of Federal Regulations* (CFR), Occupational Safety and Health Administration, Superintendent of Documents, U.S. Government Printing Office, Washington, D.C., 1999
- Guidelines for the Preparation of Material Safety Data Sheets for Welding Consumables and Related Products*, National Electrical Manufacturers Association, Rosslyn, VA, 1997
- "Performance Criteria for the Design, Construction, Care, and Operation of Safeguarding when Referenced by the Other B11 Machine Tool Safety Standards," ANSI B11.19-1990 (R1997), Association for Manufacturing Technology, McLean, VA, 1997
- "Machine Tools—Manufacturing Systems/Cells—Safety Requirements for Construction, Care, and Use," ANSI B11.20-1991 (R1997), Association for Manufacturing Technology, McLean, VA, 1997
- O.A. Ullrich and R.M. Evans, *Ultraviolet Reflectance of Paint*, American Welding Society, Miami, FL, 1976
- Assessing the Need for Personal Protective Equipment: A Guide for Small Business Employers*, OSHA 3151, Occupational Safety and Health Administration, 1997
- "American National Standard for Industrial Head Protection," ANSI Z89.1-1997, American National Standards Institute, Safety Equipment Association, Arlington, VA, 1997
- "Practice for Occupational and Educational Eye and Face Protection," ANSI Z87.1-1989, American National Standards Institute, American Society of Safety Engineers, Des Plaines, IL, 1989
- American National Standards Institute/American Welding Society Committee on Safety and Health, "Lens Shade Selector," ANSI/AWS F2.2-89(R), American Welding Society, Miami, FL, 1989
- "Personal Protection—Protective Footwear," ANSI Z41-1999, American National Standards Institute, National Safety Council, Itasca, IL, 1999
- American Welding Society Committee on Safety and Health, *Arc Welding and Cutting Noise*, American Welding Society, Miami, FL, 1979
- American Welding Society Committee on Fumes and Gases, "Methods for Sampling Airborne Particulates Generated by Welding and Allied Processes," ANSI/AWS F1.1-92, American Welding Society, Miami, FL, 1992
- National Institute for Occupational Safety and Health (NIOSH), Letter to publisher, May 9, 2000
- NIOSH Respirator User Notice, *NIOSH Guide to Selection and Use of Particulate Respirators (Certified under 42 CFR84)*, Publication No. 96-101, National Institute for Occupational Safety and Health, U.S. Department of Health and Human Services, 1997, <http://www.cdc.gov/niosh/userguid.html>
- TLVs and BEIs: Threshold Limit Values for Chemical Substances and Physical Agents in the Workroom Environment*, American Conference of Governmental Industrial Hygienists, Cincinnati, OH, 1999
- American Welding Society Committee on Safety and Health, *Fumes and Gases in the Welding Environment*, American Welding Society, Miami, FL, 1979
- M. Wallace, D. Landon, A. Echt, and R. Song, "Control Technology Assessment for the Welding Operations at Vermeer Manufacturing, Pella, Iowa," Report 214-15a, National Institute for Occupational Safety and Health, Division of Physical Sciences and Engineering, Cincinnati, OH, 1998
- American Welding Society Committee on Resistance Welding, "Recommended Practices for Resistance Welding," AWS C1.1M/C1.1:2000, American Welding Society, Miami, FL, 2000
- "Title 29—Labor," *Code of Federal Regulations (CFR)*, Chapter XVII, Parts 1901.1 to 1910.1450, Occupational Safety and Health Administration, Superintendent of Documents, U.S. Government Printing Office, Washington, D.C., 1999
- Confined Spaces*, Occupational Safety and Health Administration, 1999
- "Safety Requirements for Confined Spaces," ANSI Z117.1-1995, American

- National Standards Institute, American Society of Safety Engineers, Des Plaines, IL, 1995
29. American Welding Society Committee on Labeling and Safe Practices, "Recommended Safe Practices for the Preparation for Welding and Cutting of Containers and Piping," ANSI/AWS F4.1-94, American Welding Society, Miami, FL, 1994
 30. *Handbook of Compressed Gases*, 4th ed., Compressed Gas Association, Kluwer Academic, Boston, MA, 1999
 31. "Safe Handling of Gas in Containers," CGA P-1-1999, Compressed Gas Association, Arlington, VA, 1999
 32. *Compressed Gas Cylinder Valve Outlet and Inlet Connections*, 7th ed., ANSI/CGA V-1, Compressed Gas Association, Arlington, VA, 1994
 33. "Pressure-Relief Device Standards—Part I: Cylinders for Compressed Gases," CGA S-1.1-1994, Compressed Gas Association, Arlington, VA, 1994
 34. "Standard for Gas Pressure Regulators," CGA E-4-1994, Compressed Gas Association, Arlington, VA, 1994
 35. "Standard Connections for Regulator Outlets, Torches, and Fitted Hose for Welding and Cutting Equipment," CGA E-1-1994, Compressed Gas Association, Arlington, VA, 1994
 36. "Design and Installation of Oxygen-Fuel Gas Systems for Welding, Cutting, and Allied Processes," NFPA 51, National Fire Prevention Association, Quincy, MA, 1997
 37. "Hose Line Flashback Arrestors," Technical Bulletin TB-3, Compressed Gas Association, Arlington, VA, 1998
 38. "Cleaning Equipment for Oxygen Service," G4.1-1996, Compressed Gas Association, Arlington, VA, 1996
 39. "Oxygen," CGA G-4, Compressed Gas Association, Arlington, VA, 1996
 40. "Torch Standard for Welding and Cutting," CGA E-5-1998, Compressed Gas Association, Arlington, VA, 1998
 41. "Acetylene," CGA G-1-1998, Compressed Gas Association, Arlington, VA, 1998
 42. "Safe Handling of Cryogenic Liquids," P-12-1993, Compressed Gas Association, Arlington, VA, 1993
 43. "Safe Handling of Liquefied Nitrogen and Argon," CGA AV-5-1986, Compressed Gas Association, Arlington, VA, 1986
 44. "Standard for Cryogenic Liquid Transfer Connections," CGA V-6-1993, Compressed Gas Association, Arlington, VA, 1993
 45. "Transformer-Type Arc Welding Machines," UL 551-1998, Underwriters Laboratories, Northbrook, IL, 1998
 46. "Electric Arc Welding Power Sources," EW 1-1988, National Electrical Manufacturers Association, Rosslyn, VA, 1988
 47. "1999 National Electric Code," NFPA 70, National Fire Protection Association, Quincy, MA, 1999
 48. "Fire Prevention during Welding, Cutting, and Other Hot Work," NFPA 51B, National Fire Protection Association, Quincy, MA, 1999
 49. "Specifications for Rubber Welding Hose," ANSI/RMA IP-7, Rubber Manufacturers Association, Washington, D.C., 1999
 50. "Welding—Rubber Hoses for Welding, Cutting, and Allied Processes," ISO 3821:1998, International Organization for Standardization, Geneva, Switzerland, 1998
 51. "Electrical Standard for Industrial Machinery," NFPA 79, National Fire Protection Association, Quincy, MA, 1997
 52. American Welding Society Committee on High Energy Beam Welding and Cutting, "Recommended Practices for Electron Beam Welding," AWS C7.1:1999, American Welding Society, Miami, FL, 1999
 53. "American National Standard for Safe Use of Lasers," Z136.1-1993, American National Standards Institute, Laser Institute of America, Orlando, FL, 1993
 54. "Explosive Materials Code," NFPA 495, National Fire Protection Association, Quincy, MA, 1996
 55. American Welding Society Committee on Brazing and Soldering, Chapt. 6, *Brazing Handbook*, American Welding Society, Miami, FL, 2007
 56. "Standard for Ovens and Furnaces," NFPA 86, National Fire Protection Association, Quincy, MA, 1999
 57. "Industrial Furnaces Using Vacuum as an Atmosphere," NFPA 86D, National Fire Protection Association, Quincy, MA, 1999
 58. American Welding Society Committee on Thermal Spraying, *Thermal Spraying: Practice, Theory, and Application*, American Welding Society, Miami, FL, 1985
 59. "American National Standard for Safety Requirements for Industrial Robots and Robot Systems," ANSI/RIA R15.06-1999, American National Standards Institute, Robotic Industries Association, Ann Arbor, MI, 1999

SELECTED REFERENCES

- American Welding Society Safety and Health Committee, *Effects of Welding on Health*, 10 vol, American Welding Society, Miami, FL, 1979–1998
- *Arc Welding Safety*, American Welding Society, Miami, FL, 1988
- "Control of Gas Hazards on Vessels," NFPA 306, National Fire Prevention Association, Quincy, MA, 1997
- "LP-Gas Code," NFPA 58, National Fire Protection Association, Quincy, MA, 1998
- N. McManus, *Safety and Health in Confined Spaces*, American Conference of Governmental and Industrial Hygienists, Cincinnati, OH, 1999
- "Occupational Safety and Health Standards for Construction, Code of Federal Regulations (CFR)," Title 29 CFR 1926, Subpart J, Occupational Safety and Health Administration, Superintendent of Documents, U.S. Government Printing Office, Washington, D. C., 1999
- J. Rekus, *Complete Confined Spaces Handbook*, American Conference of Governmental Industrial Hygienists, Cincinnati, OH, 1994
- "Respiratory Protection," ANSI Z88.2-1992, American National Standards Institute, Lawrence Livermore National Laboratory, Livermore, CA, 1992
- *Safety and Health in Arc Welding and Cutting*, National Institute for Occupational Safety and Health, Cincinnati, OH, 1976
- "Safe Welding and Cutting Practices in Refineries, Gasoline Plants, and Petrochemical Plants," Publ. 2009, American Petroleum Institute, Washington, D.C., 1995
- *Seguridad en la Soldadura por Arco*, American Welding Society, Miami, FL, 1988 (Spanish-language version of *Arc Welding Safety*)
- R.B. Stuart and C. Moore, *Safety and Health on the Internet*, 2nd ed., American Conference of Governmental Industrial Hygienists, Cincinnati, OH, 1998
- *Ventilation: A Manual of Recommended Practice*, 23rd ed., Publication 2002, American Conference of Governmental Industrial Hygienists, Cincinnati, OH, 1998
- "Welding of Pipelines and Related Facilities," API 1104, American Petroleum Institute, Washington, D.C., 1999

Welding Fuels and Shielding Gases

Table 1 Properties of fuel gases

Property	Acetylene	Hydrogen	Methane	Methyl acetylene propadiene	Propane	Propylene	Natural gas
Symbol	C ₂ H ₂	H ₂	CH ₄	CH ₃ C:CH (MPS)	C ₃ H ₈ (LP gas)	C ₃ H ₆ (PRY)	MET
Molecular weight	26.036	2.016	16.042	40.07	44.094	42.078	Similar to methane
Specific gravity of gas (air = 1)	0.91	0.069	0.55	1.48	1.56	1.48	0.56
Specific volume of gas (at 60°F and 1 atm), ft ³ /lb	14.5	192.0	23.6	8.85	8.6	9.5	23.6
Specific gravity of liquid	0.576	0.507	0.527	...
lb/gal of liquid at 60°F	4.80	4.25	4.38	...
Density of gas, lb/ft ³	0.0680	0.0052	0.0416	0.113	0.115	0.105	0.0424
Boiling point (at 1 atm)							
°F	-119.2	-422.9	-258.6	-9.6	-43.8	-53.9	-161
°C	-84	-252	-161	-23.1	-42.1	-47.7	-107
Flame temperature (neutral)							
In oxygen, °F	5,600	4,800	5,000	5,300	4,600	5,250	4,600
In oxygen, °C	3,100	2,650	2,775	2,925	2,550	2,900	2,550
In air, °F	4,700	4,000	3,525	3,200	3,840	3,150	3,525
In air, °C	2,600	2,200	1,950	1,760	2,100	1,730	1,950
Ratio of oxygen to fuel gas required for combustion	1 : 1	0.5 : 1	1.75 : 1	2.5 : 1	3.5 : 1	4.5 : 1	2 : 1
Ratio of air to fuel gas required for combustion	11.9	2.38	9.52	21.83	24.30	21.83	10.04
Gross heat of combustion							
Btu/lb	21,600	52,800	23,000	21,000	21,500	22,000	24,000
Btu/ft ³	1,500	344	1,000	2,500	2,500	2,400	1,000
Flammable limits in air (by volume), %	2.5–81	4–75	5.3–15	2.4–11.7	2.2–9.5	2.0–10.3	5.3–14

Source: Ref 1

Table 2 Summary of shielding gases and mixtures and their use

Shielding gas	Gas reaction	GMAW and FCAW(a)	GTAW and PAW(b)
Pure gases			
Argon (Ar)	Inert	Nonferrous	All metals
Helium (He)	Inert	Nonferrous	Al, Mg, Cu, and alloys
Carbon dioxide (CO ₂)	Oxidizing	Mild and low-alloy steels, some stainless steels	Not used
Two-component mixtures			
Argon mixtures			
Ar + 20–50% He	Inert	Al, Mg, Cu, and alloys	Al, Mg, Cu, and alloys
Ar + 1–2% CO ₂	Oxidizing	Stainless and low-alloy steels	Not used
Ar + 3–5% CO ₂	Oxidizing	Mild, low-alloy, and stainless steels	Not used
Ar + 20–30% CO ₂	Slightly oxidized	Mild and low-alloy steels, some stainless steels	Not used
Ar + 2–4% He	Reducing	Not used	Nickel and alloy and austenitic stainless steels
Helium mixtures			
He + 25% Ar	Inert	Al and alloys, Cu and alloys	Al and alloys, Cu and alloys
CO ₂ mixtures			
CO ₂ + up to 20% O ₂	Oxidizing	Mild and low-alloy steels	Not used
CO ₂ + 3–10% O ₂	Oxidizing	Mild and low-alloy steels	Not used
Three-component mixtures			
Helium mixtures			
He + 75% Ar + 25% CO ₂	Inert	Stainless steel and low-alloy steels	Not used
Argon mixtures			
CO ₂ + 3–10% O ₂ + 15% CO ₂	Oxidizing	Mild steels	Not used

(a) GMAW, gas metal arc welding; FCAW, flux cored arc welding. (b) GTAW, gas tungsten arc welding; PAW, plasma arc welding

REFERENCE

1. H.B. Cary, *Modern Welding Technology*, 2nd ed., Prentice Hall, 1989

Summary of Fusion Welding Processes

Table 1 Fusion welding and cutting processes

Process	Heat source	Power source and polarity	Mechanics	Shielding or cutting agent	Typical applications		Industrial use
					Metals	Thickness range	
Electroslag welding	Resistance heating of liquid slag	Alternating or direct current	Automatic; joint set up vertically; weld pool and slag contained by water-cooled shoes; filler wire fed into slag pool and melted by resistance heating; no arc	Slag	Carbon, low-alloy and high-alloy steel	50 mm (2.0 in.) and upward	Welding thick sections for press frames, pressure vessels, shafts, etc.; foundry and steelworks applications; general engineering
Submerged arc welding	Arc	Alternating or direct current	Automatic or semi-automatic; arc maintained in cavity of molten flux formed from granular material	Slag and self-generated gas	Carbon, low-alloy, and high-alloy steels; copper alloys	1 mm (0.04 in.) and upward (but generally over 10 mm, or 0.4 in.)	Downhand or horizontal vertical joints suitable for automatic welding; boilers, pressure vessels, structural steel; horizontal joints in storage tanks
Manual metal arc welding (coated electrodes)	Arc	Alternating or direct current; electrode positive or negative	Short lengths of wire coated with flux; manual operation	Slag and self-generated gas	All engineering metals and alloys except pure Cu, precious metals, low-melting and reactive metals	1 mm (0.04 in.) and upward	All fields of engineering
Gas metal arc welding (flux cored wire)	Arc	Direct current; electrode positive	Flux is enclosed in tubular electrode of small diameter; automatic or semi-automatic; wire fed continuously through a gun with or without a gas shield	Slag and gas, either self-generated or from external source (normally CO ₂)	Carbon steel	1 mm (0.04 in.) and upward	Sheet metal welding; general engineering
Gas metal arc welding (solid wire)	Arc	Direct current; electrode positive	As above but using solid wire; free-flight metal transfer	Argon or helium, argon-O ₂ or argon-CO ₂	Nonferrous metal; carbon, low-alloy or high-alloy steel	2 mm (0.08 in.) and upward	Welding of high-alloy and nonferrous metals; pipe welding; general engineering
	Arc	Direct current; electrode positive	As above but in short-circuiting metal-transfer mode	Argon-O ₂ , argon-CO ₂ , or CO ₂	Carbon and low-alloy steel	1 mm (0.04 in.) and upward	Sheet metal; root pass in pipe welding; positional welding
	Pulsed arc	Direct current; electrode positive; 50–100 Hz pulse superposed on low background current	Pulse detaches drop at electrode tip and permits free-flight transfer at low current	Argon, argon-O ₂ , or argon-CO ₂	Nonferrous metals; carbon, low-alloy, and high-alloy steels	1 mm (0.04 in.) and upward	Positional welding of relatively thin carbon or alloy steel
Gas welding	Oxyacetylene flame	...	Manual; metal melted by flame and filler wire fed in separately	Gas (CO, H ₂ , CO ₂ , H ₂ O)	Carbon steel, copper, aluminum, zinc, and lead; bronze welding	Sheet metal and pipe up to approx. 6 mm (0.24 in.)	Sheet metal welding, small-diameter pipe
Gas cutting	Oxyacetylene/oxygen flame	...	Oxygen jet injected through flame oxidizes and ejects metal along the cutting line	Oxygen	Carbon and low-alloy steel	...	Cutting and bevelling plate for welding; general engineering applications
Gas tungsten arc welding	Arc	Alternating current with stabilization for aluminum, magnesium, and alloys; direct current; electrode negative for other metals	Manual or automatic arc maintained between nonconsumable tungsten electrode and work; filler wire fed in separately	Argon, helium, or argon-helium mixtures	All engineering metals except Zn and Be and their alloys	1 to approx. 6 mm (0.04 to 0.24 in.)	Nonferrous and alloy steel welding in all engineering fields; root pass in pipe welds
Pulsed gas tungsten arc welding	Arc	Direct current; electrode negative with low-frequency	Low-frequency pulse allows better control over weld pool behavior; high-frequency pulse improves arc stiffness	Argon	As above	1 to approx. 6 mm (0.04 to 0.24 in.)	Automatic gas temperature welding of tubes or tubes to tubesheets to improve consistency of penetration or

(continued)

Table 1 (continued)

Process	Heat source	Power source and polarity	Mechanics	Shielding or cutting agent	Typical applications		Industrial use
					Metals	Thickness range	
		(1 Hz) or high-frequency (1 kHz) current modulation					(high frequency) prevent arc wander
Plasma welding	Arc	Direct current; electrode negative	As for gas tungsten arc, except that arc forms in a chamber from which plasma is ejected through a nozzle; improved stiffness and less power variation than gas tungsten arc welding	Argon, helium, or argon-hydrogen mixtures	As above	Usually up to approx. 1.5 mm (0.6 in.)	Normally low-current application where gas tungsten arc lacks stiffness; also used at higher currents in keyholing mode for root runs
Plasma cutting	Arc	Direct current; electrode negative	As for welding but higher current and gas flow rates	Argon-H ₂	All engineering metals	1 mm (0.04 in.) and upward	Used particularly for stainless and nonferrous metal but also carbon and low-alloy steel
Stud welding	Arc	Direct current; electrode negative for steel, positive for nonferrous	Semiautomatic or automatic; arc drawn between tip of stud and work until melting occurs and stud then pressed onto surface; weld cycle controlled by timer	Self-generated gas plus ceramic ferrule around weld zone	Carbon, low-alloy, and high-alloy steel; aluminum; nickel and copper alloys require individual study	Stud diameters up to approx. 25 mm (1.0 in.)	Shipbuilding, railway, and automotive industries; pressure vessels (for attaching insulation); furnace tubes and general engineering
Spot, seam, and projection welding	Resistance heating at interface of lapped joint	Alternating current; transformer with low-voltage, high-current output	Lapped sheet clamped between two copper electrodes and welded by means of high-current pulses; weld may be continuous (seam) or intermittent (spot and projection)	Self-shielded plus water for resistance welding Mo, Ta, and W	All engineering metals except Cu and Ag; Al requires special treatment	Sheet metal up to approx. 6 mm (0.24 in.)	Automobile and aircraft industries; sheet metal fabrication in general engineering
Electron beam welding	Electron beam	Direct current; 10–200 kV; power generally in range 0.5–10 kW; workpiece positive	Automatic welding carried out in vacuum; beam of electrons emitted by cathode focused on joint; no metal transfer	Vacuum (~10 ⁻⁴ mm Hg)	All metals except where excessive gas evolution and/or vaporization occurs	Up to approx. 25 mm (1.0 in.) normally but may go to 100 mm (4.0 in.)	Nuclear and aerospace industries; welding and repair of machinery components such as gears
Laser welding	Light beam	None	As for electron beam except different energy source	Helium	As for electron beam	Up to 10 mm (0.4 in.)	Potentially as for electron beam; cutting nonmetallic materials
Thermit welding	Chemical reaction	None	A mixture of metal oxide and aluminum is ignited, forming a pool of superheated liquid metal, which then flows into and fuses with the joint faces.	None	Steel, austenitic CrNi steel, copper, copper alloys, steel-copper joints	Normally up to 100 mm (4.0 in.)	Welding rails and copper conductors to each other and to steel

Source: Ref 1

Table 2 General characteristics of arc welding processes

Characteristic	Arc welding processes				
	Shielded metal	Flux cored	Submerged	Gas metal	Gas tungsten
Part (assembly)					
Material	All but Zn	All steels	All steels	All but Zn	All but Zn
Preferred material	Steels	Low-C steels	Low-C steels	Steels; non-heat-treatable Al; Cu	All but Zn
Thickness, minimum, mm	(1.5)3	1.5	5	0.5	0.2
Single pass maximum	8–10	3–6	40	5	5
Multiple pass maximum	>25	>15	>200	>25	>6
Unequal thickness	Difficult	Difficult	Very difficult	Difficult	Difficult
Distortion(a)	A–B	A–C	A–B	B–C	B–C
Jigging needed	Minimum	Minimum	Full	Variable	Variable
Deslagging for multipass	Yes	Yes	Yes	No	No
Current					
Type	Alternating or direct	Direct (reverse polarity)	Alternating or direct	Direct (reverse polarity)	Alternating or direct (straight polarity)
Volts(b)	40 or 70 ↓	40 or 70 ↓	25–55	20–40 or 70 ↓	60–150
Amperes	30–800	30–800	300–2500	70–700	100–500
Cost					
Equipment(a)	D	B–D	B–C	B–C	B–C
Labor(a)	A	A–D	B–D	A–C	A–C
Finishing(a)	A–B	A–C	A–C	B–D	B–E
Production					
Operator skill(a)	A	A–D	C–D	A–D	A–D
Welding rate, m/min	(1–6 kg/h)	0.02–1.5	0.1–5	0.2–15	0.2–1.5
Operation	Manual	All	Automatic	All	All

Note: Values in parentheses may be obtained by special techniques. (a) Comparative ratings, with A indicating the highest value, E the lowest. (b) Down arrow indicates dropping voltage. Source: Ref 2

Table 3 Process selection guide for arc welding carbon steels

Usability	Cost factors	Weld-metal quality	Effect on base metal	General comments
Shielded metal arc welding (SMAW):				
Very adaptable, all-position process. Can be used outdoors. Gives excellent joint accessibility. Very portable. Can be used on carbon steels down to 18 gage. Joint preparation is required on thicknesses over 3.2 mm (1/8 in.). Unlimited upper thickness, but other processes (GMAW, FCAW, or SAW) are usually more economical.	A low-deposition-rate process (up to 9 kg/h, or 20 lb/h) with low deposit efficiency (typically 65%). Low operator factor. Equipment cost is low and spare parts are minimal. Welding speeds are generally low. Housekeeping is required to deslag and dispose of flux and electrode stubs.	Strongly dependent on the skill of the welder. Lack of fusion or slag inclusions are potential problems. The relatively small beads usually result in a high percentage of refining in multipass welds, and very good toughness is achievable with some electrodes.	Low heat inputs can cause rapid heat-affected zone (HAZ) cooling. Flux coatings are a potential source of hydrogen.	Very versatile, low-cost process. Especially strong on nonroutine or repair jobs. Usually not economical on standard thick welds or on repetitive jobs that can be mechanized
Gas metal arc welding (GMAW):				
An all-position process in the short-arc or pulsed mode. Moderately adaptable, but use limited outside where loss of shielding is possible. Usable on steel down to <0.25 mm (0.010 in.) thick. Above 4.8 mm (3/16 in.), requires joint preparation. No upper limit of plate thickness	Deposition rates (to 16 kg/h, or 35 lb/h) are higher than SMAW. Deposition efficiency (90–95%) and operator factor (typical 50%) are also higher. Equipment and spare parts cost are moderate to high (pulsed-arc power supplies are higher cost). Welding speeds are moderate to high (buried-arc CO ₂ can weld at over 2540 mm/min, or (100 in./min). Cleanup is minimal.	Very good quality. Porosity or lack of fusion can be a problem. Less tolerant of rust and millscale than flux-using processes. Very good toughness is achievable.	Generally a low-hydrogen process	Relatively versatile. Equipment more costly, complex, and less portable than SMAW. Easily mechanized. A clean process with higher deposition rates and efficiencies than SMAW
Flux cored arc welding (FCAW):				
All-position process. Equipment similar to GMAW, but self-shielded version has better portability and is usable outdoors. Minimum plate thickness is 18 gage. Self-shielded material above 6.4 mm (1/4 in.) requires joint preparation. With CO ₂ shielding, materials above 13 mm (1/2 in.) require joint preparation. There is no upper limit on plate thickness.	Deposition rates (up to 18 kg/h, or 40 lb/h) are higher than GMAW. Deposition efficiencies (80–90%) are lower, but operator factors (50%) are similar to GMAW. Equipment cost is moderate. Good out-of-position deposition rates can be achieved with conventional power sources. Welding speeds are moderate to high. Slag and spatter removal and disposal is required.	Good quality. Weld metal toughness is fair to good (best with basic electrodes). Slag inclusions are a potential problem.	Flux core can contribute hydrogen.	Relatively versatile (self-shielded version can be used outside). Higher deposition rates than GMAW (higher fumes also). Welds easily out-of-position. Readily mechanized
Gas tungsten arc welding (GTAW)/plasma arc welding (PAW):				
An all-position process with fair joint accessibility. Limited outdoor use. Can weld very thin material in all positions; GTAW—<0.13 mm (0.005 in.) min thickness, joint prep. over 3.2 mm (1/8 in.), PAW—<0.13 mm (0.005 in.) min thickness, joint prep. over 6.4 mm (1/4 in.). No upper limit on thickness but other processes are more efficient	Low deposition rates (up to 5.4 kg/h, or 12 lb/h) but high deposition efficiency (99%). If automated, the operator factor is high. Equipment and spare parts cost is moderate to high, depending on complexity (PAW is slightly more expensive). Cleanup is generally unnecessary due to no flux or spatter.	High quality but requires clean plate. Excellent toughness possible due to small bead size (high refined weld metal, finer grain size)	A low-hydrogen process. Low heat inputs can cause rapid HAZ cooling.	Extremely good welds in all positions. Requires more preparation. Low deposition rates limit process to thinner plates.
Submerged-arc welding (SAW):				
Limited to flat and horizontal position. Semiautomatic version has some adaptability, but process is most often mechanized and has limited portability. Minimum material thickness is 1.6 mm (1/16 in.) (mechanized). Joint preparation is required on material above 13 mm (1/2 in.) thick. The process lends itself to welding thick materials.	Deposition rates are very high (over 45 kg/h, or 100 lb/h, with multiwire systems). Deposition efficiency is 99%, but that does not include the flux (a 1:1 flux-to-wire ratio is common). Because the process is usually mechanized, operator factors are high. Cost is moderate for single-wire systems. High welding speeds are achievable. Higher housekeeping costs result from the need to handle the slag and unfused flux.	Very good. Good weld-metal toughness is possible. Handles rust and millscale well with proper flux selection. High-dilution process	Higher heat inputs can result in large HAZ and possible deterioration of baseplate properties (especially quenched and tempered plate). Flux is a source of hydrogen.	A high-deposition, high-penetration process, but thin material can be welded at high speeds. Easily mechanized. Natural for welding thicker plates. Housekeeping and position limitation can be a problem.

(continued)

Table 3 (continued)

Usability	Cost factors	Weld-metal quality	Effect on base metal	General comments
Electrogas welding (EGW)/electroslag welding (ESW):				
Limited to vertical or near-vertical. O.K. outside. Fair portability. Used on plate 9.5 to 102 mm (¾ to 4 in. thick).	High joint-completion rate. High deposition efficiency (solid wires 99%, cored wires lower). High operator factor. High equipment and set-up costs	Large columnar grain structure results in only fair toughness. High dilution of baseplate (up to 35% for EGW, up to 50% for ESW)	High heat input results in large HAZ and grain growth. Not recommended for quenched and tempered steels unless reheat treatment is to be done. Slow weld cooling allows hydrogen to escape weld area.	High joint-completion rate but limited to vertical. Used mainly on long, vertical welds. High heat input can limit baseplates.
Stud arc welding:				
All-position. O.K. outside. Fair portability. Used on plate 1.0 mm (0.04 in.) and above. No joint preparation required	Equipment cost is moderate.	Minimal weld size. Usually fine-grained due to fast cooling. Weld structure is as-cast.	Causes rapid cooling of HAZ	Specialized process for attaching studs to steel plate. Usually more economical than drilling and tapping

REFERENCES

1. J.F. Lancaster, *Metallurgy of Welding*, 5th ed., Chapman & Hall, 1993
 2. J.A. Schey, *Introduction to Manufacturing Processes*, 2nd ed., McGraw-Hill, 1987

Weldability of Ferrous and Nonferrous Alloys

WELDABILITY refers to the ease of welding a material under the imposed fabrication conditions to perform satisfactorily during service. All metals can be welded to themselves by at least one of the fusion welding processes.

A fusion weld cannot be made between dissimilar metals unless they have metallurgical solubility; otherwise, brittle compounds may form. Solid-state welding processes, which do not involve melting and solidification, are suited

to welding dissimilar metals or joining heat-sensitive alloys such as precipitation-hardening aluminum alloys. Tables 1 to 4 summarize the general weldability of ferrous and nonferrous alloys by common fusion welding processes.

Table 1 General weldability of specific metals and alloys by arc welding processes

Base metals welded	Welding processes					
	Shielded metal arc	Gas tungsten arc	Plasma arc	Submerged arc	Gas metal arc	Flux cored arc
Aluminum	C	A	A	No	A	No
Copper-base alloys						
Brasses	No	C	C	No	C	No
Bronzes	A	A	B	No	A	No
Copper	C	A	A	No	A	No
Copper nickel	B	A	A	No	A	No
Nickel silver (Cu-Ni-Zn)	No	C	C	No	C	No
Iron						
Cast, malleable nodular	C	No	No	No	C	No
Wrought iron	A	B	B	A	A	A
Lead	No	B	B	No	No	No
Magnesium	No	A	B	No	A	No
Nickel-base alloys						
Inconel	A	A	A	No	A	No
Nickel	A	A	A	C	A	No
Monel	A	A	A	C	A	No
Precious metals	No	A	A	No	No	No
Steels						
Low-carbon steel	A	A	A	A	A	A
Low-alloy steel	B	B	B	B	B	B
High- and medium-carbon steel	C	C	C	B	C	C
Alloy steel	C	C	C	C	C	C
Stainless steel (austenitic)	A	A	A	A	A	B
Tool steels	No	A	A	No	No	No
Titanium	No	A	A	No	A	No
Tungsten	No	B	A	No	No	No
Zinc	No	C	C	No	No	No

Metal or process rating: A, recommended or easily weldable; B, acceptable but not best selection or weldable with precautions; C, possibly usable but not popular or restricted use or difficult to weld; No, not recommended or not weldable. Source: Ref 1

Table 2 Weldability of cast irons

Weld processes(a)		Procedure	Remarks
Gray cast iron	MMA, MIG, TIG, oxyacetylene. Filler rods 3.5C-3Si-0.6P	Ferritic gray irons are readily welded, but complex irons are difficult to weld. Increasing silicon above 2% also decreases weld-ability. Preheat to 400–600 °C (750–1110 °F) or to 1000 °C (1830 °F) with 60/40 brass filler (bronze welding). Preheat to avoid hard, brittle deposit. Difficult to machine unless preheated. Prone to cracking—cool slowly and/or stress relieve at 600 °C (1110 °F) when hot. Can alsopeen when red hot	Complications in weld-metal and heat-affected zones. Massive free carbide and martensite in weld deposit. Welding used in repair of castings and production of welded assemblies. Filler materials are cast iron, low-carbon steel, nickel-base alloys, copper-base alloys
Ductile irons	Most fusion processes	Welding should be done on fully annealed material. Composition affects weld quality. For MIG, a 60Ni-4Fe filler is best. Preheat to 250 °C (480 °F). Interpass 80–100 °C (175–212 °F).	(b)
Malleable cast iron (ferritic and pearlitic)	Use low-hydrogen rods. Can be successfully brazed or soldered	Preheat or other procedures to minimize heat buildup. Heat concentration should be held to a minimum. Very important to clean before welding to avoid porosity and low joint strength	(b) Welding not recommended
Chilled and white cast irons			
Corrosion-resistant cast irons (high Si, high Cr, high Ni) and heat-resistant cast irons		Welding confined to minor repair of castings subject to availability of filler materials. For more extensive welding, properties of material should be determined.	(b)
Iron-nickel-chromium heat-resisting alloys (e.g., PH Incoloy, 800, 802, 901)	TIG most widely used, especially in thin sections. Also manual arc (<12 mm, or 0.5 in., thickness) is used. MIG is employed where TIG is not practical. Submerged arc is employed for thick sections, provided a suitable flux is available. Fillers are employed to produce weld metal of similar composition to the base metal.	Heat input kept low. Rapidly cool to maintain weld ductility. Precipitation-hardenable alloys containing Al, Ti, Ni are very difficult to weld. Can obtain high joint efficiency up to 2.5 mm (0.10 in.) thickness. Sensitive to cracking and require preweld and postweld heat treatment and selection of most suitable filler material. Solid-solution-strengthened alloys are more easily welded.	Usual range of temperature, 1200–1400 °C (2190–2550 °F). Limits the selection of filler materials and possible pre- and postweld treatment

(a) MMA, manual metal arc; MIG, metal inert gas; TIG, tungsten inert gas. (b) Cast irons are less weldable than carbon steel owing to higher carbon and silicon content leading to lower ductility. More metallurgical complications occur in weld metal and heat-affected zones. Massive free carbide and martensite occur in weld deposit. Filler materials are cast iron, low-carbon steel, nickel-base alloys, copper-base alloys. With MIG, base wire electrodes of low-carbon steel and nickel-base alloys are also used. Adapted from Ref 2

Table 3 Weldability of steels

Steel type	Preheat, °C (°F)	Interpass, °C (°F)	Hold cool, °C (°F)	Postweld, °C (°F)	Remarks
Mild steel	Excellent weldability—no precautions necessary with rutile and basic electrodes
Vanadium steel	Low-carbon-grade electrodes. Minimum heat input 30 kJ/mm (760 kJ/in.) for 30 mm (1.2 in.) thickness, unless preheating or low-hydrogen electrodes are employed
C-Mn steel (0.15–0.025 C)	100–200 (212–390)	For thick sections, low-hydrogen electrode, high heat input, and preheat. For thin sections, no preheat required
C-Mn steel (<0.2 C, <1.4 Mn)	100–250 (212–480)	For thick sections, low-hydrogen electrode, high heat input, preheat. For thin sections, no preheat required
Medium-carbon steel	250–350 (480–660)	High heat input. Low-hydrogen electrodes
High strength, low alloy, low carbon (HSLA)	250–300 (480–570)	High heat input. Low-hydrogen electrodes
Carbon-molybdenum	150–300 (300–570)	650–700 (1200–1290)	Filler as parent metal
Medium carbon and low alloy	200–350 (390–660)	200–350	...	550–600 (1020–1110)	Filler rod lower carbon than parent metal. Make test welds with highly hardenable low-alloy steels
Chromium-molybdenum steels	250–300 (420–570)	Normalize 870–980 (1600–1800) Temper 680–770 (1260–1420) Anneal 840–900 (1545–1650) Stress relieve 700–730 (1290–1350)	Filler as parent metal, but lower Cr. Postweld treatment depends on properties.
Cryogenic steels (9Ni, 5Ni)	Electrodes 50Ni-16Cr/Fe, electrodes 25Cr-20Ni Fe-25Cr-12Ni Fe. Preheat/postweld not required up to 50 mm (2.0 in.) thickness
Martensitic stainless steels (AISI 410, AISI 420)	250 (480) 250 (480)	250–350 (480–660) 250–350 (480–660)	80–100 (175–212) 150–180 (300–355)	700–750 (1290–1380) 700–750 (1290–1380)	No special precautions if C <0.1%. Austenitic fillers or fillers for matching strength. Require preheat to avoid H ₂ cracking. Tendency to harden when cooled from high temperatures
Martensitic stainless 440	Welding not recommended
Ferritic stainless steels	200 (390)	Anneal after welding 700–850 (1290–1560)	Limited transformation to martensite via austenite can occur. Grain growth. Two factors reduce

(continued)

Adapted from Ref 2

876 / Reference Information

Table 3 (continued)

Steel type	Preheat, °C (°F)	Interpass, °C (°F)	Hold cool, °C (°F)	Postweld, °C (°F)	Remarks
Precipitation-hardened stainless steel alloy W	ductility. Most weldable grades contain Al, Nb to retain ferrite Good weldability. If joint strength not required equal to parent metal, use 18Cr-8Ni-type filler. For precipitation-hardened joint, use similar composition and precipitate harden after welding.
Precipitation stainless steel types: 17-4 PH, 15-5 PH, 17-7 PH, 15-7 Mo	650–870 (1200–1600) then refrigerate or cold work	Good weldability. Weld in annealed condition. Filler depends on mechanical properties required. Can be precipitation-hardened stainless steel. Postweld treatment precipitates carbides and martensite.
Austenitic stainless steels (301, 302)	Arc welding not recommended. Flash welding possible
Austenitic stainless steel types: 303, 304 L, 304, 305, 309, 310, 314, 316, 321, 347	Not recommended	950–1150 (1740–2100) If undertaken—or stress relieve below 650 °C (1200 °F) (to avoid weld decay)	Excellent weldability. Filler materials of similar composition but higher alloy content. Weld cracking is avoided by ensuring that the weld contains 5–10% ferrite. Weld decay (chromium carbide precipitation) leads to loss of corrosion resistance. Minimized by C <0.03% or add Nb, Ti (stabilized steel) and pay regard to postweld heat treatment. Heat-affected zone liquation cracking: Low energy input. Fine grain size. Ferrite ≥5%
Maraging steels	Age after welding at 500 °C (930 °F)	Soft martensite matrix. No risk of decarburization, distortion, or cracking. Very poor weldability

Adapted from Ref 2

Table 4 Weldability of nonferrous metals

Material	Welding processes(a)	Preheat, °C (°F)	Postweld, °C (°F)	Remarks
Aluminum alloys				
Series 1000, pure Al	MIG, TIG, gas resistance, laser	Thick sections only	Most welds left in as-welded condition	Readily weldable, sheets and pressings
Series 2000, Al-Cu	Resistance	Thick sections only	As welded or(b)	Not normally fusion welded
Series 3000, Al-Mn	MIG, TIG, gas resistance, laser	Thick sections only	As welded	Readily weldable, building and transport applications
Series 4000, Al-Si	MIG, TIG, resistance, gas, laser	Thick sections only	As welded	Not normally welded
Series 5000, Al-Mg	MIG, TIG, resistance, gas, laser	Thick sections only	As welded	Readily weldable, high-strength welded applications
Series 6000, Al-Mg-Si	Resistance, MIG, TIG	Thick sections	As welded or reheated(b)	Widely welded but welds have low strength and care must be taken to avoid cracks
Series 7000, Al-Zn-Mg	Resistance, MIG, TIG	Thick sections	As welded or reheated(b)	Can be welded, structures with high mechanical strength through age hardening
Series 8000, Al-Li	MIG, TIG, laser, electron beam	Thick sections	As welded or reheated(b)	Can be welded, careful choice of filler wire to avoid cracking
Copper and copper alloys				
Tough pitch copper, deoxidized copper	MIG, TIG, electron beam, resistance, MIG, MMA	For arc welding, preheat thick sections up to 700 °C (1290 °F) and conserve heat with insulating blanket	...	Difficult to weld—high-temperature weakness, porosity, low weld ductility(c)
High-conductivity copper	MIG, TIG, electron beam, resistance, MIG, MMA	Same as tough pitch Cu	...	More suitable for welding, especially with copper fillers(c)
Brass (<20% Zn)	MIG, TIG	250–400 (480–750)	Stress relief	Good weldability
Brass (20% <Zn <40%)	Resistance	250–400 (480–750)	...	Excessive zinc or 2% Pb gives hot shortness (weld-metal cracking). Zinc causes porosity. Use oxidizing conditions
High-tensile brass (additions Pb-Fe + Al)	...	250–400 (480–750)	...	Susceptible to lead and sulfur embrittlement. Aluminum impedes coalescence of liquid metal
Phosphor bronze (Cu5–8%Sn)	TIG, resistance, MIG, electron beam	Heavy sections 175–290 °C (350–555 °F)	Peen at 480–500°C (895–930 °F) then rapid cool for maximum ductility	Relatively good weldability
Gunmetal (5–10%Sn,2–5%Zn)	TIG, resistance, MIG, electron beam	Same as phosphor bronze	Same as phosphor bronze	Hot cracks and porosity (avoid overheating or joint stressing). Greater than 2% Pb gives hot shortness
9% Sn	Resistance good, arc welding fair	Welding not recommended at or above 9% Sn
Silicon bronzes (Cu3%Si1%Mn)	TIG, MIG, resistance	Preheat 20–65 °C (70–150 °F)	...	Can be welded by arc, resistance methods. Avoid stressing joints. Filler as parent metal

(continued)

(a) MIG, metal inert gas; TIG, tungsten inert gas; MMA, manual metal arc (b) Heat treatable aluminum alloys may be re-heat treated after welding. (c) If metal of identical composition is not required, use fillers of silicon or phosphor bronze or brazing. (d) Strong reactivity of refractory metals requires thorough protection. Weld pool is prone to recrystallization and low ductility.

Table 4 (continued)

Material	Welding processes(a)	Preheat, °C (°F)	Postweld, °C (°F)	Remarks
Aluminum bronzes (Cu-5%Al, Cu-10% Al, 5%Fe, 5%Ni)	TIG, resistance, MIG, electron beam	20–150 (70–300)	...	Good weldability
Nickel silver (10–18%Ni, 25%Zn)	TIG, resistance	20–110 (70–230)	Not required	Good weldability
Cupronickel (Cu-10NiFe, Cu-30NiFe)	TIG, MIG, MMA	Not normally required	Not required	Readily weldable, argon gas
Copper beryllium (1.0–2.75% Be, 2.5–0.2% Ni)	Electron beam	Increasing beryllium decreases weldability. Poor heat conductors. Toxic fumes
Nickel alloys				
Commercial-purity nickel, nickel-copper (Monels), nickel-molybdenum-chromium (Hastelloys), nickel-chromium (Inconel 600, 625)	TIG, MIG, manual arc, electron beam	Not normally required	Necessary to avoid intergranular corrosion	Solution-hardened nickel alloys: low-ductility temperature range; avoid stressing welds. Particularly susceptible to hot shortness with Pb, S. Danger of oxide formation. Generally good weldability. Generally more viscous than steel except Hastelloys. This should be allowed for in joint designs.
Nickel-chromium-cobalt-aluminum-titanium (Nimonic)	TIG, MIG	Anneal in inert atmosphere before welding	Resolution treat and age after welding (some alloys can be solution treated before and aged after welding)	Precipitation-hardened alloys. Susceptible to heat-affected zone cracking
Titanium alloys				
Commercially pure grades and alpha alloys	TIG, MIG, electron beam, resistance pressure, flash butt	Weld in annealed condition	Stress relieve 400–650 °C (750–1200 °F)	Highly reactive, requires good shielding. No filler is used below 2.5 mm (0.10 in.) thickness. Otherwise parent metal or commercial-purity titanium is used.
Ti-6Al-4V	TIG, electron beam, resistance pressure, flash butt		2 h at 538 °C (1000 °F) Complete aging during stress relief	
Air-hardenable alloys (Ti-4Al-4Mo-0.5Si-2.4Sn, Ti-2.25Al-1.1Sn-Si, Ti-2.25Al-1.1Sn-5Zr-Si, Ti-6Al-5Zn-Mo-Si, Ti-6Al-6V-2Sn)				Air-hardenable alloys. Welding not recommended
Ti-13V-11Cr-3Al beta alloy	Electron beam, resistance pressure, flash butt		Cold work and fully reheat treat	Low-strength welds, ductile as welded
Other alloys				
Lead and zinc-lead alloys	Gas resistance, TIG			Equal to base metal in corrosion resistance and strength. Lead easy, Pb-Sb more difficult. Zinc difficult. Fillers of parent metal
Molybdenum and tungsten alloys	Electron beam, TIG	150 (300) for TIG-welded tungsten alloy		Brittle—avoid restraint on joints. 0.05% oxygen in argon arc. Grain growth occurs(d)
Niobium, tantalum, tantalum alloys with up to 15% Hf, Mo, W, Re	TIG, electron beam		Stress relieve 1 h at 816 °C (1500 °F)	Broadly similar to titanium. Can weld tantalum alloys to give very high room-temperature bend strength(d)
Zirconium	TIG	Weld in annealed condition	Stress relieve 400–650 °C (750–1200 °F)	Zirconium requires even better protection (chamber) than titanium(d)
Beryllium	Electron beam pressure welding, TIG			Brittle—avoid restraint on joints. 0.05% oxygen TIG. Grain growth occurs. Satisfactory joints obtainable
Magnesium	TIG, resistance	Heat thin sections to prevent cracking 260–380 °C (500–715 °F) depending on alloy recommendations	Stress relieve anneal wherever possible, particularly when likely to be exposed to wet or corrosive environments	Weldable but prone to stress corrosion in alloys containing aluminum. Ce, Th are used in MgZnZr alloy to improve weldability. Welding of alloys containing zinc only satisfactory with thorium or rare earth additions

(a) MIG, metal inert gas; TIG, tungsten inert gas; MMA, manual metal arc (b) Heat treatable aluminum alloys may be re-heat treated after welding. (c) If metal of identical composition is not required, use fillers of silicon or phosphor bronze or brazing. (d) Strong reactivity of refractory metals requires thorough protection. Weld pool is prone to recrystallization and low ductility.

REFERENCES

1. K.G. Budinski, *Engineering Materials: Properties and Selection*, 4th ed., Prentice-Hall, 1992
2. N. Waterman and M. Ashby, *The Materials Selector*, 2nd ed., Vol 1, Chapman and Hall, 1997, p 704–707, 709

Preheat and Postweld Heat Treatment Temperatures for Selected Steels

Table 1 Recommended preheat and interpass temperatures for selected carbon steels

AISI- SAE steel specifi- cations	Carbon range(a), %	Recommended welding condition									
		Thickness range		Minimum preheat and interpass temperature				Postweld heat treatment			
				Low hydrogen		Other than low hydrogen		Desirable or optional	Temperature range		Peening may be necessary
		mm	in.	°C	°F	°C	°F		°C	°F	
1008, 1010, 1011, 1012, 1013	Within specification	≤50 >50 to 100	≤2 >2 to 4	Ambient(b) 38	Ambient(b) 100	Ambient(b) 65	Ambient(b) 150	Optional Optional	590–675 590–675	1100–1250 1100–1250	... Yes
1015, 1016	Within specification	≤50 >50 to 100	≤2 >2 to 4	Ambient(b) 38	Ambient(b) 100	Ambient(b) 93	Ambient(b) 200	Optional Optional	590–675 590–675	1100–1250 1100–1250	... Yes
1017, 1018, 1019	Within specification	≤50 >50 to 100	≤2 >2 to 4	Ambient(b) 38	Ambient(b) 100	Ambient(b) 121	Ambient(b) 250	Optional Optional	590–675 590–675	1100–1250 1100–1250	... Yes
1020, 1021, 1022, 1023	Within specification	≤50 >50 to 100	≤2 >2 to 4	Ambient(b) 93	Ambient(b) 200	38 149	100 300	Optional Optional	590–675 590–675	1100–1250 1100–1250	... Yes
1024, 1027	0.18–0.25	≤25 >25 to 50 >50 to 100	≤1 >1 to 2 >2 to 4	Ambient(b) 38 93	Ambient(b) 100 200	38 93 149	100 200 300	Optional Optional Optional	590–675 590–675 590–675	1100–1250 1100–1250 1100–1250 Yes
	0.25–0.29	≤13 >13 to 25 >25 to 50 >50 to 100	≤½ >½ to 1 >1 to 2 >2 to 4	10 65 121 149	50 150 250 300	65 149 149 177	150 300 300 350	Optional Optional Optional Optional	590–675 590–675 590–675 590–675	1100–1250 1100–1250 1100–1250 1100–1250 Yes
1025	Within specification	≤25 >25 to 50 >50 to 100	≤1 >1 to 2 >2 to 4	Ambient(b) Ambient(b) 38	Ambient(b) Ambient(b) 100	38 38 93	100 100 200	Optional Optional Optional	590–675 590–675 590–675	1100–1250 1100–1250 1100–1250 Yes
1026, 1029, 1030	0.25–0.30	≤25 >25 to 50 >50 to 100	≤1 >1 to 2 >2 to 4	Ambient(b) 38 93	Ambient(b) 100 200	38 93 149	100 200 300	Desirable Desirable Desirable	590–675 590–675 590–675	1100–1250 1100–1250 1100–1250	... Yes Yes
	0.31–0.34	≤13 >13 to 25 >25 to 50 >50 to 100	≤½ >½ to 1 >1 to 2 >2 to 4	Ambient(b) 38 93 121	Ambient(b) 100 200 250	38 93 149 177	100 200 300 350	Desirable Desirable Desirable Desirable	590–675 590–675 590–675 590–675	1100–1250 1100–1250 1100–1250 1100–1250 Yes Yes
1035, 1037	Within specification	≤13 >13 to 25 >25 to 50 >50 to 100	≤½ >½ to 1 >1 to 2 >2 to 4	Ambient(b) 38 93 149	Ambient(b) 100 200 300	38 93 149 205	100 200 300 400	Desirable Desirable Desirable Desirable	590–675 590–675 590–675 590–675	1100–1250 1100–1250 1100–1250 1100–1250 Yes Yes
1036, 1041	0.30–0.35	≤13 >13 to 25 >25 to 50 >50 to 100	≤½ >½ to 1 >1 to 2 >2 to 4	38 65 121 149	100 150 250 300	93 149 149 177	200 300 300 350	Desirable Desirable Desirable Desirable	590–675 590–675 590–675 590–675	1100–1250 1100–1250 1100–1250 1100–1250 Yes Yes
	0.36–0.40	≤13 >13 to 25 >25 to 50 >50 to 100	≤½ >½ to 1 >1 to 2 >2 to 4	65 93 149 177	150 200 300 350	93 149 177 205	200 300 350 400	Desirable Desirable Desirable Desirable	590–675 590–675 590–675 590–675	1100–1250 1100–1250 1100–1250 1100–1250 Yes Yes
	0.41–0.44	≤13 >13 to 25 >25 to 50 >50 to 100	≤½ >½ to 1 >1 to 2 >2 to 4	93 149 177 205	200 300 350 400	149 177 205 230	300 350 400 450	Desirable Desirable Desirable Desirable	590–675 590–675 590–675 590–675	1100–1250 1100–1250 1100–1250 1100–1250 Yes Yes
1038, 1039, 1040	0.34–0.40	≤13 >13 to 25 >25 to 50	≤½ >½ to 1 >1 to 2	38 93 121	100 200 250	93 149 177	200 300 350	Desirable Desirable Desirable	590–675 590–675 590–675	1100–1250 1100–1250 1100–1250 Yes

(continued)

(a) Ranges are inclusive. (b) Ambient above –12 °C (10 °F). (c) Due to lead content, manufacturing operations involving elevated temperatures in the range of those encountered in gas cutting or welding should be carried out with adequate ventilation. (d) Hold at temperature for 1 h after welding is completed. Source: Ref 1

Table 1 (continued)

AISI- SAE steel speci- fications	Recommended welding condition										
	Carbon range(a), %	Thickness range		Minimum preheat and interpass temperature				Postweld heat treatment			Peening may be necessary
				Low hydrogen		Other than low hydrogen		Desirable or optional	Temperature range		
		mm	in.	°C	°F	°C	°F		°C	°F	
1042, 1043	0.41–0.44	>50 to 100	>2 to 4	149	300	205	400	Desirable	590–675	1100–1250	Yes
		≤13	≤½	65	150	121	250	Desirable	590–675	1100–1250	...
		>13 to 25	>½ to 1	93	200	149	300	Desirable	590–675	1100–1250	...
		>25 to 50	>1 to 2	149	300	177	350	Desirable	590–675	1100–1250	Yes
		>50 to 100	>2 to 4	205	400	230	450	Desirable	590–675	1100–1250	Yes
		≤13	≤½	93	200	149	300	Desirable	590–675	1100–1250	Yes
1044, 1045, 1046	Within specification	>13 to 25	>½ to 1	121	250	149	300	Desirable	590–675	1100–1250	Yes
		>25 to 50	>1 to 2	149	300	177	350	Desirable	590–675	1100–1250	Yes
		>50 to 100	>2 to 4	205	400	230	450	Desirable	590–675	1100–1250	Yes
		≤13	≤½	149	300	177	350	Desirable	590–675	1100–1250	Yes
1048, 1049, 1050, 1052, 1053	Within specification	>13 to 100	>½ to 4	205	400	230	450	Desirable	590–675	1100–1250	Yes
		≤25	≤1	93	200	149	300	Desirable	590–675	1100–1250	Yes
		>25 to 50	>1 to 2	149	300	177	350	Desirable	590–675	1100–1250	Yes
1108, 1109, 1110	Within specification	≤50	≤2	Ambient(b)		Not recommended		Optional	590–675	1100–1250	...
		>50 to 100	>2 to 4	38	100	Not recommended		Optional	590–675	1100–1250	Yes
1116, 1117, 1118, 1119	Within specification	≤25	≤1	Ambient(b)		Not recommended		Optional	590–675	1100–1250	...
		>25 to 100	>1 to 4	93	200	Not recommended		Optional	590–675	1100–1250	Yes
1132, 1137, 1139, 1140, 1141, 1144, 1145, 1146, 1151	0.27–0.30	≤13	≤½	10	50	Not recommended		Optional	590–675	1100–1250	...
		>13 to 25	>½ to 1	38	100	Not recommended		Desirable	590–675	1100–1250	...
		>25 to 50	>1 to 2	93	200	Not recommended		Desirable	590–675	1100–1250	Yes
		>50 to 100	>2 to 4	121	250	Not recommended		Desirable	590–675	1100–1250	Yes
		≤13	≤½	38	100	Not recommended		Desirable	590–675	1100–1250	...
		>13 to 25	>½ to 1	65	150	Not recommended		Optional	590–675	1100–1250	...
	0.31–0.35	>25 to 50	>1 to 2	121	250	Not recommended		Desirable	590–675	1100–1250	Yes
		>50 to 100	>2 to 4	149	300	Not recommended		Desirable	590–675	1100–1250	Yes
		≤13	≤½	38	100	Not recommended		Desirable	590–675	1100–1250	...
		>13 to 25	>½ to 1	65	150	Not recommended		Optional	590–675	1100–1250	...
		>25 to 50	>1 to 2	121	250	Not recommended		Desirable	590–675	1100–1250	Yes
		>50 to 100	>2 to 4	149	300	Not recommended		Desirable	590–675	1100–1250	Yes
0.36–0.40	≤13	≤½	65	150	Not recommended		Desirable	590–675	1100–1250	...	
	>13 to 25	>½ to 1	93	200	Not recommended		Desirable	590–675	1100–1250	...	
	>25 to 100	>1 to 4	149	300	Not recommended		Desirable	590–675	1100–1250	Yes	
	≤13	≤½	93	200	Not recommended		Desirable	590–675	1100–1250	...	
	>13 to 25	>½ to 1	149	300	Not recommended		Desirable	590–675	1100–1250	...	
	>25 to 100	>1 to 4	177	350	Not recommended		Desirable	590–675	1100–1250	Yes	
1132, 1137, 1139, 1140, 1141, 1144, 1145, 1146, 1151	0.41–0.45	≤13	≤½	93	200	Not recommended		Desirable	590–675	1100–1250	...
		>13 to 25	>½ to 1	149	300	Not recommended		Desirable	590–675	1100–1250	...
		>25 to 100	>1 to 4	177	350	Not recommended		Desirable	590–675	1100–1250	Yes
	0.45–0.50	≤13	≤½	149	300	Not recommended		Desirable	590–675	1100–1250	...
		>13 to 25	>½ to 1	205	400	Not recommended		Desirable	590–675	1100–1250	...
		>25 to 100	>1 to 4	230	450	Not recommended		Optional	590–675	1100–1250	Yes
1211, 1212, 1213, 1215, B1111, B1112, B1113	Within specification	≤50	≤2	Ambient(b)		Not recommended		Optional	590–675	1100–1250	...
		>50 to 100	>2 to 4	38	100	Not recommended		Optional	590–675	1100–1250	Yes
		≤50	≤2	Ambient(b)		Not recommended		Optional	590–675	1100–1250	...
12L13 (c), 12L14(c)	Within specification	>50 to 100	>2 to 4	38	100	Not recommended		Optional	590–675	1100–1250	Yes
		≤13	≤½	121	250	Not recommended		Desirable	550–565	1025–1050	...
1330, 1335, 1340, 1345	0.27–0.33	>13 to 25	>½ to 1	149	300	Not recommended		Desirable	550–565	1025–1050	...
		>25 to 50	>1 to 2	177	350	Not recommended		Desirable	550–565	1025–1050	Yes
		≤13	≤½	149	300	Not recommended		Desirable	550–565	1025–1050	...
		>13 to 25	>½ to 1	205	400	Not recommended		Desirable	550–565	1025–1050	...
		>25 to 50	>1 to 2	205	400	Not recommended		Desirable	550–565	1025–1050	Yes
		≤13	≤½	177	350	Not recommended		Desirable	550–565	1025–1050	...
	0.38–0.43	>13 to 25	>½ to 1	230	450	Not recommended		Desirable	550–565	1025–1050	...
		>25 to 50	>1 to 2	290(d)	550(d)	Not recommended		Desirable	550–565	1025–1050	Yes
		≤13	≤½	205	400	Not recommended		Desirable	550–565	1025–1050	...
		>13 to 25	>½ to 1	260(d)	500	Not recommended		Desirable	550–565	1025–1050	...
		>25 to 50	>1 to 2	315	600(d)	Not recommended		Desirable	550–565	1025–1050	Yes
		≤25	≤1	Ambient(b)		Ambient(b)		Optional	590–675	1100–1250	...
1513, 1518,	≤0.20	>25 to 50	>1 to 2	Ambient(b)		38	100	Optional	590–675	1100–1250	...
		>50 to 100	>2 to 4	38	100	93	200	Optional	590–675	1100–1250	Yes

(continued)

(a) Ranges are inclusive. (b) Ambient above –12 °C (10 °F). (c) Due to lead content, manufacturing operations involving elevated temperatures in the range of those encountered in gas cutting or welding should be carried out with adequate ventilation. (d) Hold at temperature for 1 h after welding is completed. Source: Ref 1

Table 1 (continued)

AISI- SAE steel specifi- cations	Carbon range(a), %	Recommended welding condition											
		Minimum preheat and interpass temperature						Postweld heat treatment					
		Thickness range		Low hydrogen		Other than low hydrogen		Desirable or optional	Temperature range		Peening may be necessary		
		mm	in.	°C	°F	°C	°F		°C	°F			
1522, 1525	0.21–0.25	≤25	≤1	Ambient(b)		38	100	93	200	Optional	590–675	1100–1250	...
		>25 to 50	>1 to 2	38	100	93	200	Optional	590–675	1100–1250	
		>50 to 100	>2 to 4	93	200	149	300	Optional	590–675	1100–1250	...	Yes	
1513, 1518, 1522, 1525	0.26–0.29	≤13	≤½	10	50	65	150	Optional	590–675	1100–1250	
		>13 to 25	>½ to 1	65	150	149	300	Optional	590–675	1100–1250	
		>25 to 50	>1 to 2	1165	250	149	300	Optional	590–675	1100–1250	
		>50 to 100	>2 to 4	149	300	177	350	Optional	590–675	1100–1250	...	Yes	
1524, 1526, 1527	≤0.25	≤25	≤1	10	50	38	100	Optional	590–675	1100–1250	
		>25 to 50	>1 to 2	38	100	93	200	Optional	590–675	1100–1250	
		>50 to 100	>2 to 4	93	200	149	300	Optional	590–675	1100–1250	...	Yes	
	0.26–0.29	≤25	≤1	65	150	121	250	Desirable	590–675	1100–1250	
		>25 to 50	>1 to 2	121	250	149	300	Desirable	590–675	1100–1250	
		>50 to 100	>2 to 4	149	300	177	350	Desirable	590–675	1100–1250	...	Yes	
1536, 1541	≤0.35	≤13	≤½	38	100	93	200	Desirable	590–675	1100–1250	
		>13 to 25	≤½ to 1	65	150	149	300	Desirable	590–675	1100–1250	
		>25 to 50	>1 to 2	121	250	149	300	Desirable	590–675	1100–1250	...	Yes	
		>50 to 100	>2 to 4	149	300	177	350	Desirable	590–675	1100–1250	...	Yes	
	0.36–0.40	≤13	≤½	65	150	93	200	Desirable	590–675	1100–1250	
		>13 to 25	>½ to 1	93	200	149	300	Desirable	590–675	1100–1250	
		>25 to 50	>1 to 2	149	300	177	350	Desirable	590–675	1100–1250	...	Yes	
		>50 to 100	>2 to 4	177	350	205	400	Desirable	590–675	1100–1250	...	Yes	
	0.41–0.44	≤13	≤½	93	200	149	300	Desirable	590–675	1100–1250	...	Yes	
		>13 to 25	>½ to 1	149	300	177	350	Desirable	590–675	1100–1250	
		>25 to 50	>1 to 2	177	350	205	400	Desirable	590–675	1100–1250	...	Yes	
		>50 to 100	>2 to 4	205	400	230	450	Desirable	590–675	1100–1250	...	Yes	
1547, 1548	0.43–0.52	≤13	≤½	149	300	177	350	Desirable	590–675	1100–1250	
		>13 to 100	>½ to 4	205	400	230	450	Desirable	590–675	1100–1250	...	Yes	

(a) Ranges are inclusive. (b) Ambient above –12 °C (10 °F). (c) Due to lead content, manufacturing operations involving elevated temperatures in the range of those encountered in gas cutting or welding should be carried out with adequate ventilation. (d) Hold at temperature for 1 h after welding is completed. Source: Ref 1

Table 2 Recommended preheat and interpass temperatures for heat treatable steels

Steel designation	Preheat and interpass temperature range for indicated section thickness(a)					
	At ≤13 mm (≤½ in.)		At 13–25 mm (½–1 in.)		At 25–50 mm (1–2 in.)	
	°C	°F	°C	°F	°C	°F
Low-alloy steels						
1330	175–230	350–450	205–260	400–500	230–290	450–550
1340	205–260	400–500	260–315	500–600	315–370	600–700
4023	≥40	≥100	95–150	200–300	120–170	250–350
4028	95–150	200–300	120–175	250–350	205–260	400–500
4047	205–260	400–500	230–290	450–550	260–315	500–600
4118	95–150	200–300	175–230	350–450	205–260	400–500
4130	150–205	300–400	205–260	400–500	230–290	450–550
4140	175–230	350–450	230–290	450–550	290–345	550–650
4150	205–260	400–500	260–315	500–600	315–370	600–700
4320	95–150	200–300	175–230	350–450	205–260	400–500
4340	290–345	550–650	315–370	600–700	315–370	600–700
4620	≥40	≥100	95–150	200–300	120–175	250–350
4640	175–230	350–450	205–260	400–500	230–290	450–550
5120	≥40	≥100	95–150	200–300	120–175	250–350
5145	205–260	400–500	230–290	450–550	260–315	500–600
8620	≥40	≥100	95–150	200–300	120–175	250–350
8630	95–150	200–300	120–175	250–350	175–230	350–450
8640	120–175	250–350	175–230	350–450	205–260	400–500
Ultra high-strength steels						
AMS 6434	175–230	350–450	230–290	450–550	260–315	500–600
300M	290–345	550–650	290–345	550–650	315–370	600–700
D-6a	230–290	450–550	260–315	500–600	290–345	550–650
H11 mod	315–540	600–1000	315–540	600–1000	315–540	600–1000
H13	315–540	600–1000	315–540	600–1000	315–540	600–1000
HP 9-4-20	(b)	(b)	(b)	(b)	(b)	(b)
HP 9-4-30	(b)	(b)	(b)	(b)	(b)	(b)
AF 1410	(b)	(b)	(b)	(b)	(b)	(b)
HY-180	(b)	(b)	(b)	(b)	(b)	(b)

(a) Data are for low-hydrogen welding processes and low-hydrogen filler metals. (b) Preheating not required

Table 3 Recommended preheat and postweld heat treatment of steel pressure vessel and pipe welds

ASTM specification	Grade	Thickness		Minimum preheat and interpass temperature		Maximum tensile strength		Postweld heat treatment temperature range(a)	
		mm	in.	°C	°F	MPa	ksi	°C	°F
Pressure vessel plate steel									
A 203 (Ni alloy steel)	A	(b)	(b)	120	250	(c)	(c)	595–635	110–1175
	B	(b)	(b)	120	250	(c)	(c)	595–635	1100–1175
	D	(b)	(b)	150	300	(c)	(c)	595–635	1100–1175
	E	(b)	(b)	150	300	(c)	(c)	595–635	1100–1175
	F	(b)	(b)	150	300	(c)	(c)	595–635	1100–1175
A 204 (Mo alloy steel)	...	<12.5	<0.5	10	50	485	70	595–720	1100–1325
				80	175	>485	>70	595–720	1100–1325
				80	175	(c)	(c)	595–720	1100–1325
A 302 (Mn-Mo, Mn-Mo-Ni)	A; B	<12.5	<0.5	10	50	485	70	595–720	1100–1325
				80	175	>485	>70	595–720	1100–1325
				80	175	(c)	(c)	595–720	1100–1325
				80	175	(c)	(c)	595–720	1100–1325
				80	175	(c)	(c)	595–720	1100–1325
A 353 (9% Ni)	...	(b)	(b)	10	50	(c)	(c)	550–585	1025–1085
				10	50	415	60	595–745	1100–1375
A 387 (Cr-Ni)	11; 12	<12.5	<0.5	10	50	415	60	595–745	1100–1375
				120	250	415	60	595–745	1100–1375
				120	250	>415	>60	595–745	1100–1375
				150	300	415	60	675–760	1250–1400
				205	400	>415	>60	675–760	1250–1400
Pipe									
A 333	3	(b)	(b)	150	300	(c)	(c)	595–635	1100–1175
				120	250	(c)	(c)	595–635	1100–1175
				10	50	(c)	(c)	550–585	1025–1085
A 335	P1	<12.5	<0.5	10	50	485	70	595–720	1100–1325
				80	175	>485	>70	595–720	1100–1325
				80	175	(c)	(c)	595–720	1100–1325
				150	300	415	60	675–760	1250–1400
				205	400	>415	>60	675–760	1250–1400
				10	50	415	60	595–745	1100–1375
				120	250	415	60	595–745	1100–1375
				120	250	>415	>60	595–745	1100–1375
				150	300	415	60	675–760	1250–1400
				205	400	>415	>60	675–760	1250–1400
A 672	H75; H80	<12.5	<0.5	10	50	485	70	595–720	1100–1325
				80	175	>485	>70	595–720	1100–1325
				80	175	(c)	(c)	595–720	1100–1325
				80	175	(c)	(c)	595–720	1100–1325
				80	175	(c)	(c)	595–720	1100–1325

(a) For more detailed specifications and requirements on postweld heat treating, heating rates, and localized heat treatment, refer to specifications such as: ASME VIII, Division I, Section UW and UC-56; ASME/ANSI B31.1, Chapter V, Sections 131, 132, 330, and 331; or British Specification BS2633, Sections 18 and 22. (b) All available sizes per ASTM International specifications. (c) Values vary with size.

REFERENCE

1. R.D. Stout, *Weldability of Steels*, 4th ed., Welding Research Council, 1987, p 420–426

Abbreviations

Å	angstrom	DCEN	direct current, electrode negative
ac	alternating current	DCEP	direct current, electrode positive
Ac ₁	temperature at which austenite begins to form during heating	DFB	diffusion brazing
Ac ₃	temperature at which transformation of ferrite to austenite is completed during heating	DFW	diffusion welding
Ae _{cm} , Ae ₁ , Ae ₃	equilibrium transformation temperatures in steel	diam	diameter
AISI	American Iron and Steel Institute	DIN	Deutsche Industrie-Normen (German Industrial Standards)
AMS	Aerospace Material Specification	DPH	diamond pyramid hardness
ANSI	American National Standards Institute	DTA	differential thermal analysis
AOD	argon-oxygen decarburization	<i>e</i>	natural log base, 2.71828; charge of an electron
API	American Petroleum Institute	EB	electron beam
Ar _{cm}	temperature at which cementite begins to precipitate from austenite on cooling	EBC	electron beam cutting
Ar ₁	temperature at which transformation to ferrite or to ferrite plus cementite is completed on cooling	EBW	electron beam welding
Ar ₃	temperature at which transformation of austenite to ferrite begins on cooling	EDM	electrical discharge machining
ASME	American Society of Mechanical Engineers	EDXA	energy-dispersive x-ray analysis
ASTM	American Society for Testing and Materials	EGW	electrode gas welding
at.%	atomic percent	ELI	extra-low interstitial
atm	atmospheres (pressure)	emf	electromotive force
AWS	American Welding Society	EPA	Environmental Protection Agency
bal	balance	EPFM	elastic-plastic fracture mechanics
bcc	body-centered cubic	EPRI	Electric Power Research Institute
bct	body-centered tetragonal	Eq	equation
C	cementite; coulomb	ESW	electroslag welding
<i>C</i>	heat capacity	et al.	and others
CAC	carbon arc cutting	ETP	electrolytic tough pitch
CAC-A	air carbon arc cutting	eV	electron volt
CAD/CAM	computer-aided design/computer-aided manufacturing	EXB	exothermic brazing
CAW	carbon arc welding	exp	base of the natural logarithm
CAW-G	gas carbon arc welding	EXW	explosion welding
CAW-S	shielded carbon arc welding	<i>f</i>	frequency
CBN	cubic boron nitride	FCAW	flux cored arc welding
CCD	charge-coupled device	fcc	face-centered cubic
CCT	continuous cooling transformation	fct	face-centered tetragonal
CE	carbon equivalent	FEA	finite-element analysis
cgs	centimeter-gram-second (system of units)	FEM	finite-element method
cm	centimeter	Fig.	figure
cP	centipoise	FRW	friction welding
CP	commercially pure	FS	furnace soldering
cSt	centiStokes	ft	foot
CTE	coefficient of thermal expansion	FW	flash welding
CTOD	crack tip opening displacement	g	gram
CVD	chemical vapor deposition	<i>g</i>	acceleration due to gravity
CVN	Charpy V-notch (impact test or specimen)	gf	gram force
<i>D</i>	diameter	GMA	gas metal arc
<i>da/dN</i>	fatigue crack growth rate	GMAC	gas metal arc cutting
dB	decibel	GMAW	gas metal arc welding
DB	diffusion bonding; dip brazing	GPa	gigapascal
DBTT	ductile-to-brittle transition temperature	GTA	gas tungsten arc
dc	direct current	GTAC	gas tungsten arc cutting
		GTAW	gas tungsten arc welding
		h	hour
		<i>h</i>	Planck's constant (6.626×10^{-27} erg · s)
		H	Henry
		<i>H</i>	enthalpy; hardness; magnetic field
		HAZ	heat-affected zone

HB	Brinell hardness	MO	multiple operator
hcp	hexagonal close-packed	MPa	megapascal
HHC	hot-hollow cathode	mpg	miles per gallon
HIC	hydrogen-induced cracking	mph	miles per hour
HIP	hot isostatic pressing	MRR	material removal rate
HK	Knoop hardness	ms	millisecond
hp	horsepower	M _s	temperature at which martensite starts to form from austenite on cooling
HR	Rockwell hardness (requires scale designation, such as HRC for Rockwell C hardness)	mV	millivolt
HREM	high-resolution electron microscopy	MV	megavolt
HSLA	high-strength, low-alloy (steel)	N	Newton
HSS	high-speed steel(s)	N	number of cycles; normal solution; normal force
HTLA	heat-treatable low-alloy (steel)	NACE	National Association of Corrosion Engineers
HV	Vickers hardness	NASA	National Aeronautics and Space Administration
Hz	hertz	NDE	nondestructive evaluation
<i>I</i>	intensity; electrical current	NEC	National Electric Code
IGA	intergranular attack	NEMA	National Electrical Manufacturers Association
IGSCC	intergranular stress-corrosion cracking	NIST	National Institute of Standards and Technology
IIW	International Institute of Welding	nm	nanometer
IMO	International Maritime Organization	No.	number
in.	inch	OAW	oxyacetylene welding
IPTS	International Practical Temperature Scale	OCV	open-circuit voltage
IR	infrared	Oe	oersted
IRS	infrared soldering	OFG	oxyfuel gas
IS	induction soldering	OFW	oxyfuel gas welding
ISCC	intergranular stress-corrosion cracking	ORNL	Oak Ridge National Laboratory
ISO	International Organization for Standardization	OSHA	Occupational Safety and Health Administration
J	joule	oz	ounce
k	equilibrium distribution coefficient	p	page
<i>k</i>	thermal conductivity; Boltzmann constant	P	pearlite
K	Kelvin	Pa	pascal
kg	kilogram	PAW	plasma arc welding
kgf	kilogram force	PEEM	photoemission electron microscopy
<i>K_{1c}</i>	plane-strain fracture toughness	pH	negative logarithm of hydrogen-ion activity
<i>K_{ISCC}</i>	threshold stress intensity to produce stress-corrosion cracking	PH	precipitation hardenable; precipitation hardening
km	kilometer	PID	proportional-integral-differential
kN	kilonewton	PM	planar magnetron
kPa	kilopascal	ppb	parts per billion
ksi	kips (1000 lbf) per square inch	ppm	parts per million
kV	kilovolt	ppt	parts per trillion
kW	kilowatt	PRE	pitting resistance equivalent
L	longitudinal, liter	psi	pounds per square inch
lb	pound	psia	pounds per square inch absolute
lbf	pound force	psig	gage pressure (pressure relative to ambient pressure) in pounds per square inch
LBW	laser beam welding	PSTM	photon scanning tunneling microscopy
LCL	lower control limit	PW	projection welding
LEED	low-energy electron diffraction	PWAA	postweld artificial aging
LEFM	linear elastic fracture mechanics	PWHT	postweld heat treatment
LME	liquid metal embrittlement	PWM	pulse width modulation
LMP	Larson-Miller parameter	Q&T	quenched and tempered
ln	natural logarithm (base <i>e</i>)	R	roentgen
LNG	liquefied natural gas	<i>R_a</i>	surface roughness in terms of arithmetic average
log	common logarithm (base 10)	RA	rosin fully activated; roughness average; reduction in area
m	meter	RE	rare earth
mA	milliampere	Ref	reference
MC	metal carbide	REF	relative erosion factor
MeV	megaelectronvolt	rf	radio frequency
<i>M_f</i>	temperature at which martensite formation finishes during cooling	RH	relative humidity
mg	milligram	RMA	rosin mildly activated
Mg	megagram (metric tonne, or kg × 10 ³)	rms	root mean square
MIC	microbiologically influenced corrosion	RPF	relative potency factor
min	minute; minimum	rpm	revolutions per minute
mL	milliliter	<i>R_q</i>	rms (root mean square) roughness
mm	millimeter	RS	resistance soldering

894 / Reference Information

RSA	rosin superactivated	T	tesla
RSEW	seam welding	<i>T</i>	temperature
RSW	resistance spot welding	TB	torch brazing
RT	room temperature	tcp	topologically close-packed
RW	resistance welding	TEM	transmission electron microscope/microscopy
RWMA	Resistance Welder Manufacturers Association	TGA	thermogravimetric analysis
s	second	TGSCC	transgranular stress-corrosion cracking
S	siemens	TIG	tungsten inert gas (welding)
SAE	Society of Automotive Engineers	TMCP	thermomechanically controlled process
SAM	scanning acoustic microscope/microscopy	TS	torch soldering
SAW	submerged arc welding	TTT	time-temperature transformation
SCC	stress-corrosion cracking	TW	thermit welding; thermite welding
SEM	scanning electron microscope/microscopy	UNS	Unified Numbering System
SHE	standard hydrogen electrode	USW	ultrasonic welding
SI	Système International d'Unités	UTS	ultimate tensile strength
SIR	surface insulation resistance	UW	upset welding
SLAM	scanning laser acoustic microscope/microscopy	<i>v</i>	velocity
SLEEM	scanning low-energy electron microscopy	V	volt
SMA	shielded metal arc	VIM-VAR	vacuum induction melted-vacuum arc remelted
SMAW	shielded metal arc welding	vol	volume
SPA-LEED	spot profile analysis-low-energy electron diffraction	vol%	volume percent
SPC	statistical process control	VPPA	variable polarity plasma arc
SQC	statistical quality control	W	watt
SRA	stress-relief annealing	WI	wettability index
SSW	solid-state welding	WRC	Welding Research Council
STA	solution treated and aged	WS	wave soldering
STEM	scanning transmission electron microscope/microscopy	WSN	weld set number
STM/S	scanning tunneling microscopy/spectroscopy	wt%	weight percent
SUS	Saybolt universal seconds (viscosity)	XPS	x-ray photoelectron spectroscopy
Sv	sievert	yr	year
SW	stud arc welding	Z	atomic number
<i>t</i>	thickness; time		

Officers and Trustees of ASM International (2010–2011)

Mark F. Smith

President and Trustee
National Laboratories

Christopher C. Berndt

Vice-President and Trustee Swinburne University
of Technology

Frederick J. Lisy

Immediate Past President and Trustee
Orbital Research Incorporated

Stanley C. Theobald

Managing Director & Secretary
ASM International

Robert J. Fulton

Treasurer and Trustee
Hoeganaes Corporation (retired)

Riad I. Asfahani

United States Steel Corporation

Mufit Akinc

Iowa State University

Sunniva R. Collins

Swagelok

Diana Essock

Metamark Inc.

David U. Furrer

Pratt & Whitney

Robert Hill, Jr.

President Solar Atmospheres, Inc.

Richard Knight

Drexel University

John J. Letcavits

AEP

Vilupanur A. Ravi

California State Polytechnic University
Student Board Members

Kathryn (Katie) S. Czaja

University of Connecticut

Emily J. Kuster

Iowa State University

Indranil Lahiri

Florida International University

Members of the ASM Handbook Committee (2010–2011)

Craig D. Clauser

Chair 2010–
Member 2005–
Craig Clauser Engineering Consulting Incorporated

Joseph W. Newkirk

Vice Chair 2010–
Member 2005–
Missouri University of Science and Technology

Kent L. Johnson

Immediate Past Chair 2010–
Member 1999–
Materials Consulting and Engineering, Ltd.

Viola L. Acoff (2005–)

University of Alabama

Scott W. Beckwith (2010–)

BTG Composites Inc

Rodney R. Boyer (2010–)

Boeing Company

Lichun Leigh Chen (2002–)

Umicore Technical Materials North America

Sarup K. Chopra (2007–)

Consultant

Craig V. Darragh (1989–)

The Timken Company (ret.)

Jon L. Dossett (2006–)

Consultant

Alan P. Druschitz (2009–)

University of Alabama-Birmingham

Gerald S. Frankel (2010–)

The Ohio State University

David U. Furrer (2006–)

Pratt & Whitney

Larry D. Hanke (1994–)

Materials Evaluation and Engineering Inc

Jeffrey A. Hawk (1997–)

National Energy Technology Laboratory

Kang N. Lee (2010–)

Rolls Royce Corporation

Dale E. Newbury (2010–)

National Inst. of Standards

Robert P. O'Shea, Jr. (2008–)

Baker Engineering and Risk Consultants

Toby V. Padfield (2004–)

ZF Sachs Automotive of America

Cynthia A. Powell (2009–)

National Energy Technology Laboratory

Thomas E. Prucha (2010–)

American Foundry Society

Prasan K. Samal (2010–)

North American Höganäs

Jeffrey S. Smith (2009–)

Material Processing Technology LLC

George Vander Voort (1997–)

Consultant, Struers

Michael K. West (2008–)

South Dakota School of Mines and Technology

Chairs of the ASM Handbook Committee

J.F. Harper

(1923–1926) (Member 1923–1926)

W.J. Merten

(1927–1930) (Member 1923–1933)

L.B. Case

(1931–1933) (Member 1927–1933)

C.H. Herty, Jr.

(1934–1936) (Member 1930–1936)

J.P. Gill

(1937) (Member 1934–1937)

R.L. Dowdell

(1938–1939) (Member 1935–1939)

G.V. Luerssen

(1943–1947) (Member 1942–1947)

J.B. Johnson

(1948–1951) (Member 1944–1951)

E.O. Dixon

(1952–1954) (Member 1947–1955)

N.E. Promisel

(1955–1961) (Member 1954–1963)

R.W.E. Leiter

(1962–1963) (Member 1955–1958, 1960–1964)

D.J. Wright

(1964–1965) (Member 1959–1967)

J.D. Graham

(1966–1968) (Member 1961–1970)

W.A. Stadler

(1969–1972) (Member 1962–1972)

G.J. Shubat

(1973–1975) (Member 1966–1975)

R. Ward

(1976–1978) (Member 1972–1978)

G.N. Maniar

(1979–1980) (Member 1974–1980)

M.G.H. Wells

(1981) (Member 1976–1981)

J.L. McCall

(1982) (Member 1977–1982)

L.J. Korb

(1983) (Member 1978–1983)

T.D. Cooper

(1984–1986) (Member 1981–1986)

D.D. Huffman

(1986–1990) (Member 1982–2005)

D.L. Olson

(1990–1992) (Member 1982–1988, 1989–1992)

R.J. Austin

(1992–1994) (Member 1984–1985)

W.L. Mankins

(1994–1997) (Member 1989–)

M.M. Gauthier

(1997–1998) (Member 1990–2000)

C.V. Darragh

(1999–2002) (Member 1989–)

Henry E. Fairman

(2002–2004) (Member 1993–2005)

Jeffrey A. Hawk

(2004–2006) (Member 1997–)

Larry D. Hanke

(2006–2008) (Member 1994–)

Kent L. Johnson

(2008–2010) (Member 1999–)

Craig D. Clauser

(2010–) (Member 2005–)

List of Contributors

- Lee Allgood**
The Lincoln Electric Company
- Mahyar Asadi**
Carleton University, Ottawa, Ontario,
Canada
- Sudarsanam Suresh Babu**
The Ohio State University
- John Banker**
Dynamic Materials Corporation
- Niels Bay**
Technical University of Denmark
- O.W. Blodgett**
The Lincoln Electric Company
- S.D. Brandi**
Escola de Politecnica da USP, São Paulo,
Brazil
- P. Burgardt**
Los Alamos National Laboratory
- Charles Caristan**
Air Liquide Industrial U.S. LP
- Harvey R. Castner**
Edison Welding Institute
- Anil Chaudhary**
Applied Optimization
- Kevin J. Colligan**
Concurrent Technologies Corporation
- Chris Conrardy**
Edison Welding Institute
- George E. Cook**
Vanderbilt University
- Glenn Daehn**
The Ohio State University
- Amitava De**
Indian Institute of Technology, Bombay,
India
- P.S. De**
Missouri University of Science and
Technology
- Tarasankar DebRoy**
Pennsylvania State University
- David R. DeLapp**
Vanderbilt University
- Janet Devine**
Sonobond Ultrasonics Inc.
- David Dewees**
Equity Engineering Group
- Ray Dixon**
Consultant
- John N. DuPont**
Lehigh University
- Thomas W. Eagar**
Massachusetts Institute of Technology
- J.W. Elmer**
Lawrence Livermore National
Laboratory
- David Farson**
The Ohio State University
- E. Friedman**
Westinghouse Electric Corporation
- Sean Gleeson**
Edison Welding Institute
- S.S. Glickstein**
Westinghouse Electric Corporation
- John Goldak**
Carleton University, Ottawa, Ontario,
Canada
- Jerry E. Gould**
Edison Welding Institute
- Karl Graff**
Edison Welding Institute
- Oystein Grong**
Norwegian University of Science and
Technology, Trondheim, Norway
- Ian D. Harris**
Edison Welding Institute
- D.A. Hartman**
Manufacturing Behavioral Science
- P.W. Hochanadel**
Los Alamos National Laboratory
- J. Ernesto Indacochea**
University of Illinois At Chicago
- J. Imbert**
University of Waterloo, Ontario, Canada
- Kent Johnson**
Materials Consulting and Engineering, Ltd.
- Lennart Karlsson**
Luleå University of Technology, Luleå,
Sweden
- D.D. Kautz**
Los Alamos National Laboratory
- Menachem Kimchi**
Edison Welding Institute
- Gerald A. Knorovsky**
Sandia National Laboratories
- Steve Knostman**
Hobart Brothers
- Sachin D. Kore**
Indian Institute of Technology, Bombay,
India
- Paul S. Korinko**
Savannah River National Laboratory
- Sindo Kou**
University of Wisconsin
- Igor V. Krivtsun**
E.O. Paton Electric Welding Institute,
National Academy of Sciences of Ukraine,
Kiev, Ukraine
- Amit Kumar**
Exxon Mobil Upstream Research
Company
- N. Kumar**
Missouri University of Science and
Technology
- Muneharu Kutsuna**
Advanced Laser Technology Research
Center Co. Ltd.
- K. Lachenberg**
Sciaky Inc.
- Samuel G. Lambrakos**
Naval Research Laboratory
- Leijun Li**
Utah State University
- Victor Li**
Portland State University
- Thomas Lieb**
LAI International
- T.J. Lienert**
Los Alamos National Laboratory
- John C. Lippold**
The Ohio State University
- Stephen Liu**
Colorado School of Mines

Mehran Maalekian
The University of British Columbia,
Vancouver, British Columbia, Canada

Donald F. Maatz, Jr.
RoMan Engineering Services

Bruce Madigan
Montana Tech, The University of Montana

R. P. Martukanitz
Applied Research Laboratory, Pennsylvania
State University

Robert Matteson
Taylor-Winfield Technologies Inc.

J. Mazumder
Univeristy of Michigan

Aaron D. Mazzeo
Massachusetts Institute of Technology

Michael T. Merlo
RevWires LLC, A Heico Wire Group
Company

Robert W. Messler, Jr.
Rensselaer Polytechnic Institute

P. Michaleris
Pennsylvania State University

J.O. Milewski
Los Alamos National Laboratory

R.S. Mishra
Missouri University of Science and
Technology

William Mohr
Edison Welding Institute

Pierre Montmitonnet
Ecole des Mines

Tom Morrisett
RoMan Engineering Services

Ole Runar Myhr
Hydro Aluminium, Raufoss, Norway

Jeong Na
Edison Welding Institute

Kotobu Nagai
National Institute of Metals (Japan)

T.A. Palmer
Pennsylvania State University

Randolph Paura
Dynamic Laser Solutions

Warren Peterson
Edison Welding Institute

Curtis Prothe
Dynamic Materials Corporation

Joseph Puskar
Sandia

Rohit Rai
Pennsylvania State University

Roger Reed
University of Birmingham

Charles V. Robino
Sandia

Michael Santella
Sandia

C. Schwenk
BAM - Federal Institute for Materials
Research and Testing, Berlin, Germany

Hugh Shercliff
Cambridge University

Thomas Siewert
NIST (retired)

Carl D. Sorenson
Brigham Young University

Tim Stotler
Edison Welding Institute

J.Q. Su
Missouri University of Science and
Technology

R.D. Thomas, Jr.
R.D. Thomas and Company

Evgueni Todorov
Edison Welding Institute

Chon L. Tsai
United Ship Design and Development
Center, Taipei

Murali D. Tumuluru
United States Steel Corporation

Brian M. Victor
Edison Welding Institute

John. M Vitek
Oak Ridge National Laboratory

Wesley Wang
Esab Welding & Cutting Products

Tim Webber
IPG Photonics

Perry White
Edison Welding Institute

M. Worswick
University of Waterloo, Ontario,
Canada

Yu-Ping Yang
Edison Welding Institute

Chunbo (Sam) Zhang
Utah State University

Hongyan Zhang
University of Toledo

Wei Zhang
Oak Ridge National Laboratory

Y.M. Zhang
University of Kentucky and Adaptive
Intelligent Systems LLC

Norman Y. Zhou
University of Waterloo, Ontario,
Canada

Metric Conversion Guide

This Section is intended as a guide for expressing weights and measures in the Système International d'Unités (SI). The purpose of SI units, developed and maintained by the General Conference of Weights and Measures, is to provide a basis for worldwide standardization of units and measure. For more information on metric conversions, the reader should consult the following references:

- *The International System of Units*, SP 330, 1991, National Institute of Standards and Technology. Order from Superintendent of Documents, U.S. Government Printing Office, Washington, DC 20402-9325
- *Metric Editorial Guide*, 5th ed. (revised), 1993, American National Metric Council, 4340 East West Highway, Suite 401, Bethesda, MD 20814-4411
- "Standard for Use of the International System of Units (SI): The Modern Metric System," IEEE/ASTM SI 10-1997 Institute of Electrical and Electronics Engineers, 345 East 47th Street, New York, NY 10017, USA
- *Guide for the Use of the International System of Units (SI)*, SP811, 1995, National Institute of Standards and Technology, U.S. Government Printing Office, Washington, DC 20402

Base, supplementary, and derived SI units

Measure	Unit	Symbol	Measure	Unit	Symbol
Base units			Base units		
Amount of substance	mole	mole	Force	newton	N
Electric current	ampere	A	Frequency	hertz	Hz
Length	meter	m	Heat capacity	joule per kelvin	J/K
Luminous intensity	candela	cd	Heat flux density	watt per square meter	W/m ²
Mass	kilogram	kg	Illuminance	lux	lx
Thermodynamic temperature	kelvin	K	Inductance	henry	H
Time	second	s	Irradiance	watt per square meter	W/m ²
			Luminance	candela per square meter	cd/m ²
			Luminous flux	lumen	lm
Supplementary units			Supplementary units		
Plane angle	radian	rad	Magnetic field strength	ampere per meter	A/m
Solid angle	steradian	sr	Magnetic flux	weber	Wb
			Magnetic flux density	tesla	T
Derived units			Derived units		
Absorbed does	gray	Gy	Molar energy	joule per mole	J/mol
Acceleration	meter per second squared	m/s ²	Molar entropy	joule per mole kelvin	J/mol · K
Activity (of radionuclides)	becquerel	Bq	Molar heat capacity	joule per mole kelvin	J/m · K
Angular acceleration	radian per second squared	rad/s ²	Moment of force	newton meter	N · m
Angular velocity	radian per second	rad/s	Permeability	henry per meter	H/m
Area	square meter	m ²	Permittivity	farad per meter	F/m
Capacitance	farad	F	Power, radiant flux	watt	W
Concentration (of amount of substance)	mole per cubic meter	mol/m ³	Pressure, stress	pascal	Pa
Current density	ampere per square meter	A/m ²	Quantity of electricity, electric charge	coulomb	C
Density, mass	kilogram per cubic meter	kg/m ³	Radiance	watt per square meter steradian	W/m ² · sr
Does equivalent, does equivalent index	sievert	Sv	Radiant intensity	watt per steradian	W/sr
Electric charge density	coulomb per cubic meter	C/m ³	Specific heat capacity	joule per kilogram kelvin	J/kg · K
Electric conductance	siemens	S	Specific energy	joule per kilogram	J/kg
Electric field strength	volt per cubic meter	V/m	Specific entropy	joule per kilogram kelvin	J/kg · K
Electric flux density	coulomb per square meter	C/m ²	Specific volume	cubic meter per kilogram	m ³ /kg
Electric potential, potential difference, electromotive force	volt	V	Specific volume	cubic meter per kilogram	m ³ /kg
Electric resistance	ohm	Ω	Surface tension	newton per meter	N/m
Energy, work, quantity of heat	joule	J	Thermal conductivity	watt per meter kelvin	W/m · K
Energy density	joule per cubic meter	J/m ³	Velocity	meter per second	m/s
Entropy	joule per kelvin	J/K	Viscosity, dynamic	pascal second	Pa · s
			Viscosity, kinematic	square meter per second	m ² /s
			Volume	cubic meter	m ³
			Wavenumber	1 per meter	1/m

896 / Reference Information

Conversion factors

To convert from	to	multiply by	To convert from	to	multiply by	To convert from	to	multiply by
Angle			Heat input			Pressure (fluid)		
degree	rad	1.745 329 E - 02	J/in.	J/m	3.937 008 E + 01	atm (standard)	Pa	1.013 250 E + 05
Area			kJ/in.	kJ/m	3.937 008 E + 01	bar	Pa	1.000 000 E + 05
in. ²	mm ²	6.451 600 E + 02	Impact energy per unit area			in. Hg (32 °F)	Pa	3.386 380 E + 03
in. ²	cm ²	6.451 600 E + 00	ft.lbf/ft ²	J/m ²	1.459 002 E + 01	in.Hg (60 °F)	Pa	3.376 850 E + 03
in. ²	m ²	6.451 600 E - 04	Length			lbf/in. ² (psi)	Pa	6.894 757 E + 03
ft ²	m ²	9.290 304 E - 02	Å	nm	1.000 000 E - 01	torr (mm Hg, 0 °C)	Pa	1.333 220 E + 02
Bending moment or torque			μin.	μm	2.540 000 E - 02	Specific heat		
lbf · in.	N · m	1.129 848 E - 01	mil	μm	2.540 000 E + 01	Btu/lb · °F	J/kg · K	4.186 800 E + 03
lbf · ft	N · m	1.355 818 E + 00	in.	mm	2.540 000 E + 01	cal/g · °C	J/kg · K	4.186 800 E + 03
kgf · m	N · m	9.806 650 E + 00	in.	cm	2.540 000 E + 00	Stress (force per unit area)		
ozf · in.	N · m	7.061 552 E - 03	ft	m	3.048 000 E - 01	tonf/in. ² (tsi)	Mpa	1.378 951 E + 01
Bending moment or torque per unit length			yd	m	9.144 000 E - 01	kgf/mm ²	Mpa	9.806 650 E + 00
lbf · in./in.	N · m/m	4.448 222 E + 00	mile, international	km	1.609 344 E + 00	ksi	Mpa	6.894 757 E + 00
lbf · ft/in.	N · m/m	5.337 866 E + 01	mile, nautical	km	1.852 000 E + 00	lbf/in. ² (psi)	Mpa	6.894 757 E - 03
Current density			mile, U.S. statute	km	1.609 347 E + 00	MN/m ²	Mpa	1.000 000 E + 00
A/in. ²	A/cm ²	1.550 003 E - 01	Mass			Temperature		
A/in. ²	A/mm ²	1.550 003 E - 03	oz	kg	2.834 952 E - 02	°F	°C	5/9 · (°F - 32)
A/ft ²	A/m ²	1.076 400 E + 01	lb	kg	4.535 924 E - 01	°R	°K	5/9
Electricity and magnetism			ton (short, 2000 lb)	kg	9.071 847 E + 02	K	°C	K - 273.15
gauss	T	1.000 000 E - 04	ton (short, 2000 lb)	kg × 10 ³ (a)	9.071 847 E - 01	Temperature interval		
maxwell	μWb	1.000 000 E - 02	ton (long, 2240 lb)	kg	1.016 047 E + 03	°F	°C	5/9
mho	S	1.000 000 E + 00	Mass per unit area			Thermal conductivity		
Oersted	A/m	7.957 700 E + 01	oz/in. ²	kg/m ²	4.395 000 E + 01	Btu · in./s · ft ² · °F	W/m · K	5.192 204 E + 02
Ω · cm	Ω · m	1.000 000 E - 02	oz/ft ²	kg/m ²	3.051 517 E - 01	Btu/ft · h · °F	W/m · K	1.730 735 E + 00
Ω circular-mil/ft	μΩ · m	1.662 426 E - 03	oz/yd ²	kg/m ²	3.390 575 E - 02	Btu · in./h · ft ² · °F	W/m · K	1.442 279 E - 01
Energy (impact, other)			lb/ft ²	kg/m ²	4.882 428 E + 00	cal/cm · s · °C	W/m · K	4.184 000 E + 02
ft · lbf	J	1.355 818 E + 00	Mass per unit length			Thermal expansion(b)		
Btu (thermochemical)	J	1.054 350 E + 03	lb/ft	kg/m	1.488 164 E + 00	in./in. · °C	m/m · K	1.000 000 E + 00
cal (thermochemical)	J	4.184 000 E + 00	lb/in.	kg/m	1.785 797 E + 01	in./in. · °F	m/m · K	1.800 000 E + 00
kW · h	J	3.600 000 E + 06	Mass per unit time			Velocity		
W · h	J	3.600 000 E + 03	lb/h	kg/s	1.259 979 E - 04	ft/h	m/s	8.466 667 E - 05
Flow rate			lb/min	kg/s	7.559 873 E - 03	ft/min	m/s	5.080 000 E - 03
ft ³ /h	L/min	4.719 475 E - 01	lb/s	kg/s	4.535 924 E - 01	ft/s	m/s	3.048 000 E - 01
ft ³ /min	L/min	2.831 000 E + 01	Mass per unit volume (includes density)			in./s	m/s	2.540 000 E - 02
gal/h	L/min	6.309 020 E - 02	g/cm ³	kg/m ³	1.000 000 E + 03	km/h	m/s	2.777 778 E - 01
gal/min	L/min	3.785 412 E + 00	lb/ft ³	g/cm ³	1.601 846 E - 02	mph	km/h	1.609 344 E + 00
Force			lb/ft ³	kg/m ³	1.601 846 E + 01	Velocity of rotation		
lbf	N	4.448 222 E + 00	lb/in. ³	g/cm ³	2.767 990 E + 01	rev/min (rpm)	rad/s	1.047 164 E - 01
kip (1000 lbf)	N	4.448 222 E + 03	lb/in. ³	kg/m ³	2.767 990 E + 04	rev/s	rad/s	6.283 185 E + 00
tonf	kN	8.896 443 E + 00	Power			Viscosity		
kgf	N	9.806 650 E + 00	Btu/s	kW	1.055 056 E + 00	poise	Pa · s	1.000 000 E - 01
Force per unit length			Btu/min	kW	1.758 426 E - 02	stokes	m ² /s	1.000 000 E - 04
lbf/ft	N/m	1.459 390 E + 01	Btu/h	W	2.928 751 E - 01	ft ² /s	m ² /s	9.290 304 E - 02
lbf/in.	N/m	1.751 268 E + 02	erg/s	W	1.000 000 E - 07	in. ² /s	mm ² /s	6.451 600 E + 02
Fracture toughness			ft · lbf/s	W	1.355 818 E + 00	Volume		
ksi√in.	Mpa√m	1.098 800 E + 00	ft · lbf/min	W	2.259 697 E - 02	in. ³	m ³	1.638 706 E - 05
Heat content			ft · lbf/h	W	3.766 161 E - 04	ft ³	m ³	2.831 685 E - 02
Btu/lb	kJ/kg	2.326 000 E + 00	hp (550 ft · lbf/s)	kW	7.456 999 E - 01	fluid oz	m ³	2.957 353 E - 05
cal/g	kJ/kg	4.186 800 E + 00	hp (electric)	kW	7.460 000 E - 01	gal (U.S. liquid)	m ³	3.785 412 E - 03
			Power density			Volume per unit time		
			W/in. ²	W/m ²	1.550 003 E + 03	ft ³ /min	m ³ /s	4.719 474 E - 04
						ft ³ /s	m ³ /s	2.831 685 E - 02
						in. ³ /min	m ³ /s	2.731 177 E - 07

(a) kg × 10³ = 1 metric ton or 1 megagram (Mg). (b) Preferred expression is 10⁻⁶/F as length units are unnecessary.

Policy on Units of Measure

By a resolution of its Board of Trustees, ASM International has adopted the practice of publishing data in both metric and customary U.S. units of measure. In preparing this Handbook, the editors have attempted to present data in metric units based primarily on *Système International d'Unités* (SI), with secondary mention of the corresponding values in customary U.S. units. The decision to use SI as the primary system of units was based on the aforementioned resolution of the Board of Trustees and the widespread use of metric units throughout the world.

For the most part, numerical engineering data in the text and in tables are presented in SI-based units with the customary U.S. equivalents in parentheses (text) or adjoining columns (tables). For example, pressure, stress, and strength are shown both in SI units, which are pascals (Pa) with a suitable prefix, and in customary U.S. units, which are pounds per square inch (psi). To save space, large values of psi have been converted to kips per square inch (ksi), where 1 ksi = 1000 psi. The metric tonne ($\text{kg} \times 10^3$) has sometimes been shown in megagrams (Mg). Some strictly scientific data are presented in SI units only.

To clarify some illustrations, only one set of units is presented on artwork. References in the accompanying text to data in the illustrations are presented in both SI-based and customary U.S. units. On graphs and charts, grids corresponding to SI-based units usually appear along the left and bottom edges. Where appropriate, corresponding customary U.S. units appear along the top and right edges.

Data pertaining to a specification published by a specification-writing group may be given in only the units used in that specification or in dual units, depending on the nature of the data. For example, the typical yield strength of steel sheet made to a specification written in customary U.S.

units would be presented in dual units, but the sheet thickness specified in that specification might be presented only in inches.

Data obtained according to standardized test methods for which the standard recommends a particular system of units are presented in the units of that system. Wherever feasible, equivalent units are also presented. Some statistical data may also be presented in only the original units used in the analysis.

Conversions and rounding have been done in accordance with IEEE/ASTM SI-10, with attention given to the number of significant digits in the original data. For example, an annealing temperature of 1570 °F contains three significant digits. In this case, the equivalent temperature would be given as 855 °C; the exact conversion to 854.44 °C would not be appropriate. For an invariant physical phenomenon that occurs at a precise temperature (such as the melting of pure silver), it would be appropriate to report the temperature as 961.93 °C or 1763.5 °F. In some instances (especially in tables and data compilations), temperature values in °C and °F are alternatives rather than conversions.

The policy of units of measure in this Handbook contains several exceptions to strict conformance to IEEE/ASTM SI-10; in each instance, the exception has been made in an effort to improve the clarity of the Handbook. The most notable exception is the use of g/cm^3 rather than kg/m^3 as the unit of measure for density (mass per unit volume).

SI practice requires that only one virgule (diagonal) appear in units formed by combination of several basic units. Therefore, all of the units preceding the virgule are in the numerator and all units following the virgule are in the denominator of the expression; no parentheses are required to prevent ambiguity.

Glossary of Terms*

A

activated rosin flux A rosin-base flux containing an additive that increases wetting by the solder.

actual throat The shortest distance between the weld root and the face of a fillet weld.

adhesive bonding A materials joining process in which an adhesive is placed between the faying surfaces. The adhesive solidifies to produce an adhesive bond.

air carbon arc cutting (AC-A) An arc cutting process that melts base metals by the heat of a carbon arc and removes the molten metal by a blast of air.

arc blow The deflection of an electric arc from its normal path because of magnetic forces.

arc brazing (AB) A brazing process that uses an arc to provide the heat. See *carbon arc brazing*.

arc cutting (AC) A group of cutting processes that melt the base metal with the heat of an arc between an electrode and the base metal.

air cutting gun (gas metal arc cutting) A device used in semiautomatic, machine, and automatic arc cutting to transfer current, guide the consumable electrode, and direct the shielding gas.

arc force The axial force developed by an arc plasma.

arc gouging An arc cutting process variation used to form a bevel or groove.

arc oxygen cutting A nonstandard term for *oxygen arc cutting*.

arc seam weld A seam weld made by an arc welding process.

arc spot weld A spot weld made by an arc welding process.

arc spraying (ASP) A thermal spraying process using an arc between two consumable electrodes of surfacing materials as a heat source and a compressed gas to atomize and propel the surfacing material to the substrate.

arc strike A discontinuity consisting of any localized remelted metal, heat-affected metal, or change in the surface profile of any part of a weld or base metal resulting from an arc.

arc welding (AW) A group of welding processes that produces coalescence of metals by heating them with an arc, with or without

the application of pressure, and with or without the use of filler metal.

arc welding electrode A component of the welding circuit through which current is conducted and which terminates at the arc.

arc welding gun A device used in semiautomatic, machine, and automatic arc welding to transfer current, guide the consumable electrode, and direct the shielding gas.

as-welded The condition of weld metal, welded joints, and weldments after welding, but prior to any subsequent thermal, mechanical, or chemical treatments.

autogenous weld A fusion weld made without the addition of filler metal.

automatic welding Welding with equipment that performs the welding operation without adjustment of the controls by a welding operator. The equipment may or may not load and unload the workpieces. See also *machine welding*.

B

back bead A weld bead resulting from a back weld pass.

backfire The momentary recession of the flame into the welding tip or cutting tip followed by immediate reappearance or complete extinction of the flame.

back gouging The removal of weld metal and base metal from the other side of a partially welded joint to facilitate complete fusion and complete joint penetration upon subsequent welding from that side.

backhand welding A welding technique in which the welding torch or gun is directed opposite to the progress of welding.

backing A material or device placed against the back side of the joint, or at both sides of a weld in electroslag and electrogas welding, to support and retain molten weld metal. The material may be partially fused or remain unfused during welding and may be either metal or nonmetal.

backing bead A weld bead resulting from a backing pass.

backing filler metal A nonstandard term for *consumable insert*.

backing pass A weld pass made for a backing weld.

backing ring Backing in the form of a ring, generally used in the welding of pipe.

backing shoe A nonconsumable backing device used in electroslag and electrogas welding.

backing weld Backing in the form of a weld.

backstep sequence A longitudinal sequence in which weld passes are made in the direction opposite to the progress of welding.

back weld A weld made at the back of a single-groove weld.

balling up The formation of globules of molten brazing filler metal or flux due to lack of wetting of the base metal.

base material The material to be welded, brazed, soldered, or cut. See also *base metal* and *substrate*.

base metal The metal to be welded, brazed, soldered, or cut. See also *base material* and *substrate*.

bead weld A nonstandard term for *surfacing weld*.

bevel An angular edge preparation.

bevel angle The angle formed between the prepared edge of a member and a plane perpendicular to the surface of the member.

bevel groove weld A type of groove weld.

bit That part of the soldering iron, usually made of copper, that actually transfers heat (and sometimes solder) to the joint.

blacksmith welding A nonstandard term for *forge welding*.

block sequence A combined longitudinal and cross-sectional sequence for a continuous multiple-pass weld in which separated increments are completely or partially welded before intervening increments are welded.

blowhole A nonstandard term for *porosity*.

bond See *bonding force*, *covalent bond*, *mechanical bond*, and *metallic bond*.

bond coat (thermal spraying) A preliminary (or prime) coat of material that improves adherence of the subsequent spray deposit.

bonding force The force that holds two atoms together. It results from a decrease in energy as two atoms are brought closer to one another.

bond line The cross section of the interface between thermal spray deposits and substrate, or between adhesive and adherend in an adhesive bonded joint.

bottle A nonstandard term for *gas cylinder*.

boxing The continuation of a fillet weld around a corner of a member as an extension of the principal weld.

braze A weld produced by heating an assembly to the brazing temperature using a filler metal having a liquidus above 450 °C (840 °F) and below the solidus of the base metal. The filler metal is distributed between the closely fitted faying surfaces of the joint by capillary action.

braze interface The interface between filler metal and base metal in a brazed joint.

brazement An assembly whose component parts are joined by brazing.

brazier One who performs a manual or semiautomatic brazing operation.

braze welding A welding process variation in which a filler metal, having a liquidus above 450 °C (840 °F) and below the solidus of the base metal, is used. Unlike brazing, in braze welding the filler metal is not distributed in the joint by capillary action.

brazing (B) A group of welding processes that produce coalescence of materials by heating them to the brazing temperature in the presence of a filler metal having a liquidus above 450 °C (840 °F) and below the solidus of the base metal. The filler metal is distributed between the closely fitted faying surfaces of the joint by capillary action.

brazing alloy A nonstandard term for *brazing filler metal*.

brazing filler metal The metal that fills the capillary joint clearance and has a liquidus above 450 °C (840 °F) but below the solidus of the base metals.

brazing operator One who operates machine or automatic brazing equipment.

brittle nugget A nonstandard term used to describe a faying plane failure in a resistance weld peel test.

bronze welding A nonstandard term for *braze welding*.

buildup A surfacing variation in which surfacing metal is deposited to achieve the required dimensions. See also *buttering*.

burner A nonstandard term for *oxygen cutter*.

burning A nonstandard term for *oxygen cutting*.

burn through A nonstandard term for excessive melt through or a hole.

burn through weld A nonstandard term for a *seam weld* or *spot weld*.

buttering A surfacing variation that deposits surfacing metal on one or more surfaces to provide metallurgically compatible weld metal for the subsequent completion of the weld. See also *buildup*.

butt joint A joint between two members aligned approximately in the same plane.

button That part of a weld, including all or part of the nugget, that tears out in the destructive testing of spot, seam, or projection welded specimens.

butt weld A nonstandard term for a weld in a butt joint.

C

carbon arc brazing (CAB) A brazing process that produces coalescence of metals by heating them with an electric arc between two carbon electrodes. The filler metal is distributed in the joint by capillary action.

carbon arc cutting (CAC) An arc cutting process that severs base metals by melting them with the heat of an arc between a carbon electrode and the base metal.

carbon arc welding (CAW) An arc welding process that produces coalescence of metals by heating them with an arc between a carbon electrode and the base metal. No shielding is used. Pressure and filler metal may or may not be used.

carbonizing flame A nonstandard term for *reducing flame*.

caulk weld A nonstandard term for *seal weld*.

chain intermittent weld An intermittent weld on both sides of a joint in which the weld increments on one side are approximately opposite those on the other side.

chamfer A nonstandard term for *bevel*.

chemical flux cutting (FOC) An oxygen cutting process that severs base metals using a chemical flux to facilitate cutting.

chill ring A nonstandard term for *backing ring*.

clad brazing sheet A metal sheet on which one or both sides are clad with brazing filler metal.

coalescence The growing together or growth into one body of the materials being welded.

coated electrode A nonstandard term for *covered electrode*.

coating density A nonstandard term for *spray deposit density ratio*.

coextrusion welding (CEW) A solid-state welding process that produces coalescence of the faying surfaces by heating and forcing base metals through an extrusion die.

cold crack A crack that develops after solidification is complete.

cold soldered joint A joint with incomplete coalescence caused by insufficient application of heat to the base metal during soldering.

cold welding (CW) A solid-state welding process in which pressure is used at room temperature to produce coalescence of metals with substantial deformation at the weld. See also *diffusion welding*, *forge welding*, and *hot pressure welding*.

complete fusion Fusion which has occurred over the entire base metal surface intended for welding and between all adjoining weld beads.

complete joint penetration A penetration by weld metal for the full thickness of the base metal in a joint with a groove weld.

complete penetration A nonstandard term for *complete joint penetration*.

concavity The maximum distance from the face of a concave fillet weld perpendicular to a line joining the weld toes.

cone The conical part of an oxyfuel gas flame next to the orifice of the tip.

constricted arc (plasma arc welding and cutting) A plasma arc column that is shaped by a constricting nozzle orifice.

consumable insert Preplaced filler metal that is completely fused into the joint root and becomes part of the weld.

contact resistance (resistance welding) Resistance to the flow of electric current between two workpieces or an electrode and a workpiece.

contact tube A device that transfers current to a continuous electrode.

convexity The maximum distance from the face of a convex fillet weld perpendicular to a line joining the weld toes.

copper brazing A nonstandard term for brazing with a copper filler metal.

cored solder A solder wire or bar containing flux as a core.

corner-flange weld A flange weld with only one member flanged at the joint.

corner joint A joint between two members located approximately at right angles to each other.

corona (resistance welding) The area sometimes surrounding the nugget of a spot weld at the faying surface which provides a degree of solid-state welding.

CO₂ welding A nonstandard term for *gas metal arc welding*.

covalent bond A primary bond arising from the reduction in energy associated with overlapping half-filled orbitals of two atoms.

covered electrode A composite filler metal electrode consisting of a core of a bare electrode or metal-cored electrode to which a covering sufficient to provide a slag layer on the weld metal has been applied. The covering may contain materials providing such functions as shielding from the atmosphere, deoxidation, and arc stabilization and can serve as a source of metallic additions to the weld.

crack A fracture type discontinuity characterized by a sharp tip and high ratio of length and width to opening displacement.

crater A depression at the termination of a weld bead.

cutting attachment A device for converting an oxyfuel gas welding torch into an oxygen cutting torch.

cutting blowpipe A nonstandard term for cutting torch.

cutting nozzle A nonstandard term for *cutting tip*.

cutting tip The part of an oxygen cutting torch from which the gases issue.

cutting torch (arc) A device used in air carbon arc cutting, gas tungsten arc cutting, and plasma arc cutting to control the position of the electrode, to transfer current, and to control the flow of gases.

cutting torch (oxyfuel gas) A device used for directing the preheating flame produced by the controlled combustion of fuel gases and to direct and control the cutting oxygen.

cylinder manifold A multiple header for interconnection of gas or fluid sources with distribution points.

D

defect A discontinuity or discontinuities that by nature or accumulated effect (for example, total crack length) render a part or product unable to meet minimum applicable acceptance standards or specifications. This term designates rejectability. See also *discontinuity* and *flaw*.

deposit (thermal spraying) A nonstandard term for *spray deposit*.

deposited metal Filler metal that has been added during welding.

deposition efficiency (arc welding) The ratio of the weight of deposited metal to the net weight of filler metal consumed, exclusive of stubs.

deposition efficiency (thermal spraying) The ratio of the weight of spray deposit to the weight of the surfacing material sprayed, usually expressed in percent.

deposition sequence A nonstandard term for *weld pass sequence*.

depth of fusion The distance that fusion extends into the base metal or previous pass from the surface melted during welding.

diffusion bonding A nonstandard term for *diffusion brazing* and *diffusion welding*.

diffusion brazing (DFB) A brazing process that produces coalescence of metals by heating them to brazing temperature and by using a filler metal or an *in situ* liquid phase. The filler metal may be distributed by capillary action or may be placed or formed at the faying surfaces. The filler metal is diffused with the base metal to the extent that the joint properties have been changed to approach those of the base metal. Pressure may or may not be applied.

diffusion welding (DFW) A solid-state welding process that produces coalescence of the faying surfaces by the application of pressure at elevated temperature. The process does not involve macroscopic deformation, melting, or relative motion of the workpieces. A solid filler metal may or may not be inserted between the faying surfaces. See also *cold welding*, *forge welding*, and *hot pressure welding*.

dilution The change in chemical composition of a welding filler metal caused by the admixture of the base metal or previous weld metal in the weld bead. It is measured by the percentage of base metal or previous weld metal in the weld bead.

diode laser A semiconductor laser. A p-n junction semiconductor with a resonator cavity that is capable of emitting electromagnetic radiation in the wavelength range of 0.180 μm to 1 mm, by radiative recombination in the semiconductor.

diode pumped solid state (DPSS) laser: also known as DPSSL, employs diodes to pump/excite the solid state lasing gain medium

such as a ruby crystal, a Neodymium doped Yttrium Aluminum Garnet (Nd:YAG) crystal, a Ytterbium doped silica core fiber (Yb: fiber) or a Ytterbium doped Yttrium Aluminum Garnet crystal (Yb:YAG) thin disk laser

dip brazing (DB) A brazing process using the heat furnished by a molten chemical or metal bath. When a molten chemical bath is used, the bath may act as a flux. When a molten metal bath is used, the bath provides the filler metal.

dip soldering (DS) A soldering process using the heat furnished by a molten metal bath which provides the solder filler metal.

direct current electrode negative (DCEN) The arrangement of direct current arc welding leads in which the workpiece is the positive pole and the electrode is the negative pole of the welding arc.

direct current electrode positive (DCEP) The arrangement of direct current arc welding leads in which the workpiece is the negative pole and the electrode is the positive pole of the welding arc.

direct current reverse polarity A nonstandard term for *direct current electrode positive*.

direct current straight polarity A nonstandard term for *direct current electrode negative*.

discontinuity An interruption of the typical structure of a weldment, such as a lack of homogeneity in the mechanical, metallurgical, or physical characteristics of the material or weldment. A discontinuity is not necessarily a defect. See also *defect* and *flaw*.

double-bevel-groove weld A type of groove weld.

double-flare-bevel-groove weld A weld in grooves formed by a member with a curved surface in contact with a planar member.

double-flare-V-groove weld A weld in grooves formed by two members with curved surfaces.

double-J-groove weld A type of groove weld.

double-square-groove weld A type of groove weld.

double-U-groove weld A type of groove weld.

double-V-groove weld A type of groove weld.

double-welded joint A fusion-welded joint that is welded from both sides.

downhand A nonstandard term for *flat position*.

drag (thermal cutting) The offset distance between the actual and straight line exit points of the gas stream or cutting beam measured on the exit surface of the material.

E

edge-flange weld A flange weld with two members flanged at the location of welding.

edge joint A joint between the edges of two or more parallel or nearly parallel members.

edge weld A weld in an edge joint.

edge weld size The weld metal thickness measured at the weld root.

effective throat The minimum distance minus any convexity between the weld root and the face of a fillet weld.

electric arc spraying A nonstandard term for *arc spraying*.

electric bonding A nonstandard term for surfacing by thermal spraying.

electric brazing A nonstandard term for *arc brazing* and *resistance brazing*.

electrode See *welding electrode*.

electrode extension For gas metal arc welding, flux cored arc welding, and submerged arc welding, the length of unmelted electrode extending beyond the end of the contact tube.

electrode force The force between the electrodes in making spot, seam, or projection welds by resistance welding.

electrode holder A device used for mechanically holding the electrode while conducting current to it.

electrode indentation (resistance welding) The depression formed on the surface of workpieces by electrodes.

electrode lead The electrical conductor between the source of arc welding current and the electrode holder.

electrogas welding (EGW) An arc welding process that produces coalescence of metals by heating them with an arc between a continuous filler metal electrode and the work. Molding shoes are used to confine the molten weld metal for vertical position welding. The electrodes may be either flux cored or solid. Shielding may or may not be obtained from an externally supplied gas or mixture.

electron beam cutting (EBC) A cutting process that uses the heat obtained from a concentrated beam composed primarily of high-velocity electrons which impinge upon the workpieces; it may or may not use an externally supplied gas.

electron beam gun A device for producing and accelerating electrons. Typical components include the emitter (also called the filament or cathode), which is heated to produce electrons via thermionic emission; a cup (also called the grid or grid cup); and the anode.

electron beam welding (EBW) A welding process that produces coalescence of metals with the heat obtained from a concentrated beam composed primarily of high-velocity electrons impinging on the joint.

electroslag welding (ESW) A welding process that produces coalescence of metals with molten slag that melts the filler metal and the surfaces of the workpieces. The weld pool is shielded by this slag, which moves along the full cross section of the joint as welding progresses. The process is initiated by an arc that heats the slag. The arc is then extinguished by the conductive slag, which is kept molten by its resistance to electric current passing between the electrode and the workpieces.

end return A nonstandard term for *boxing*.

erosion (brazing) A condition caused by dissolution of the base metal by molten filler metal resulting in a reduction in the thickness of the base metal.

explosion welding (EXW) A solid-state welding process that affects coalescence by high-velocity movement together with the workpieces produced by a controlled detonation.

F

face reinforcement Weld reinforcement at the side of the joint from which welding was done. See also *root reinforcement*.

faying surface That mating surface of a member that is in contact with or in close proximity to another member to which it is to be joined.

ferrite number An arbitrary, standardized value designating the ferrite content of an austenitic stainless steel weld metal. It should be used in place of percent ferrite or volume percent ferrite on a direct replacement basis.

fiber laser: a solid state laser in which the active (lasing) medium is a doped optical fiber. See also **diode pumped solid state laser**

filler metal The metal to be added in making a welded, brazed, or soldered joint. See also *brazing filler metal, consumable insert, solder, welding electrode, welding rod, and welding wire*.

filler wire A nonstandard term for *welding wire*.

fillet weld A weld of approximately triangular cross section joining two surfaces approximately at right angles to each other in a lap joint, T-joint, or corner joint.

fillet weld break test A test in which the specimen is loaded so that the weld root is in tension.

fillet weld leg The distance from the joint root to the toe of the fillet weld.

fillet weld size For equal leg fillet welds, the leg lengths of the largest isosceles right triangle that can be inscribed within the fillet weld cross section. For unequal leg fillets, the leg lengths of the largest right triangle that can be inscribed within the fillet weld cross section.

fillet weld throat See *actual throat, effective throat, and theoretical throat*.

firecracker welding A variation of the shielded metal arc welding process in which a length of covered electrode is placed along the joint in contact with the workpieces. During the welding operation, the stationary electrode is consumed as the arc travels the length of the electrode.

fish-eye A discontinuity found on the fracture surface of a weld in steel that consists of a small pore or inclusion surrounded by an approximately round, bright area.

flame cutting A nonstandard term for *oxygen cutting*.

flame propagation rate The speed at which a flame travels through a mixture of gases.

flame spraying (FLSP) A thermal spraying process in which an oxyfuel gas flame is the source of heat for melting the surfacing material. Compressed gas may or may not

be used for atomizing and propelling the surfacing material to the substrate.

flange weld A weld made on the edges of two or more members to be joined, usually light gage metal, at least one of the members being flanged.

flange weld size The weld metal thickness measured at the weld root.

flare-bevel-groove weld A weld in a groove formed by a member with a curved surface in contact with a planar member.

flare-V-groove weld A weld in a groove formed by two members with curved surfaces.

flash Material that is expelled from a flash weld prior to the upset portion of the welding cycle.

flash butt welding A nonstandard term for *flash welding*.

flash coat A thin coating usually less than 0.05 mm (0.002 in.) in thickness.

flash welding (FW) A resistance welding process that produces coalescence at the faying surfaces of a butt joint by a flashing action and by the application of pressure after heating is substantially completed. The flashing action, caused by the very high current densities at small contacts between the parts, forcibly expels the material from the joint as the parts are slowly moved together. The weld is completed by a rapid upsetting of the workpieces.

flat position The welding position used to weld from the upper side of the joint; the face of the weld is approximately horizontal.

flaw A near synonym for discontinuity but with an undesirable connotation. See also *defect and discontinuity*.

flux brightening (soldering) Fusion of a metallic coating on a base metal.

flux Material used to prevent, dissolve, or facilitate removal of oxides and other undesirable surface substances.

flux cored arc welding (FCAW) An arc welding process that produces coalescence of metals by heating them with an arc between a continuous filler metal electrode and the work. Shielding is provided by a flux contained within the tubular electrode. Additional shielding may or may not be obtained from an externally supplied gas or gas mixture. See also *flux cored electrode*.

flux cored electrode A composite filler metal electrode consisting of a metal tube or other hollow configuration containing ingredients to provide such functions as shielding atmosphere, deoxidation, arc stabilization, and slag formation. Minor amounts of alloying materials may be included in the core. External shielding may or may not be used.

flux cover (metal bath dip brazing and dip soldering) A layer of molten flux over the molten filler metal bath.

flux oxygen cutting A nonstandard term for *chemical flux cutting*.

forehand welding A welding technique in which the welding torch or gun is directed toward the progress of welding.

forge welding (FOW) A solid-state welding process that produces coalescence of metals by heating them in air in a forge and by applying pressure or blows sufficient to cause permanent deformation at the interface. See also *cold welding, diffusion welding, hot pressure welding, and roll welding*.

friction welding (FRW) A solid-state welding process that produces coalescence of materials under compressive force contact of workpieces rotating or moving relative to one another to produce heat and plastically displace material from the faying surfaces.

furnace brazing (FB) A brazing process in which the workpieces are placed in a furnace and heated to the brazing temperature.

furnace soldering (FS) A soldering process in which the workpieces are placed in a furnace and heated to the soldering temperature.

fused spray deposit (thermal spraying) A self-fluxing spray deposit that is subsequently heated to coalescence within itself and with the substrate.

fusion The melting together of filler metal and base metal (substrate), or of base metal only, which results in coalescence. See also *depth of fusion*.

fusion face A surface of the base metal that will be melted during welding.

fusion welding Any welding process that uses fusion of the base metal to make the weld.

fusion zone The area of base metal melted as determined on the cross section of a weld.

G

gap A nonstandard term for *joint clearance and root opening*.

gas brazing A nonstandard term for *torch brazing*.

gas cutter A nonstandard term for *oxygen cutter*.

gas cutting A nonstandard term for *oxygen cutting*.

gas cylinder A portable container used for transportation and storage of a compressed gas.

gas gouging A nonstandard term for *oxygen gouging*.

gas laser A laser in which the lasing medium is a gas.

gas metal arc cutting (GMAC) An arc cutting process in which metals are severed by melting them with the heat of an arc between a continuous filler metal electrode and the workpiece. Shielding is obtained entirely from an externally supplied gas.

gas metal arc welding (GMAW) An arc welding process that produces coalescence of metals by heating them with an arc between a continuous filler metal electrode and the workpieces. Shielding is obtained entirely from an externally supplied gas.

gas pocket A nonstandard term for *porosity*.

gas regulator A device for controlling the delivery of gas at some substantially constant pressure.

gas shielded arc welding A general term used to describe *flux cored arc welding* (when gas shielding is employed), *gas metal arc welding*, and *gas tungsten arc welding*.

gas torch A nonstandard term for cutting torch and welding torch.

gas tungsten arc cutting (GTAC) An arc cutting process in which metals are severed by melting them with an arc between a single tungsten electrode and the workpiece. Shielding is obtained from a gas.

gas tungsten arc welding (GTAW) An arc welding process that produces coalescence of metals by heating them with an arc between a tungsten electrode (nonconsumable) and the workpieces. Shielding is obtained from a gas. Pressure may or may not be used, and filler metal may or may not be used.

gas welding A nonstandard term for *oxyfuel gas welding*.

globular transfer (arc welding) The transfer of molten metal in large drops from a consumable electrode across the arc. See also *short circuiting transfer* and *spray transfer*.

gouging The forming of a bevel or groove by material removal. See also *arc gouging*, *back gouging*, and *oxygen gouging*.

groove angle The total included angle of the groove between the workpieces.

groove face That surface of a joint member included in the groove.

groove radius The radius used to form the shape of a J- or U-groove weld.

groove weld A weld made in a groove between the workpieces.

groove weld size The joint penetration of a groove weld.

groove weld throat A nonstandard term for *groove weld size*.

ground connection An electrical connection of the welding machine frame to the earth for safety. See also *workpiece connection* and *workpiece lead*.

ground lead A nonstandard term for *workpiece lead*.

gun See *air cutting gun*, *arc welding gun*, *electron beam gun*, *resistance welding gun*, *soldering gun*, and *thermal spraying gun*.

H

hammer welding A nonstandard term for *cold welding* and *forge welding*.

hard solder A nonstandard term for silver-base brazing filler metals.

heat affected zone That portion of the base metal that has not been melted, but whose mechanical properties or microstructure have been altered by the heat of welding, brazing, soldering, or cutting.

high frequency resistance welding A group of resistance welding process variations that uses high frequency welding current to

concentrate the welding heat at the desired location.

horizontal fixed position (pipe welding) The position of a pipe joint in which the axis of the pipe is approximately horizontal, and the pipe is not rotated during welding.

horizontal position (fillet weld) The position in which welding is performed on the upper side of an approximately horizontal surface and against an approximately vertical surface.

horizontal position (groove weld) The position of welding in which the weld axis lies in an approximately horizontal plane and the weld face lies in an approximately vertical plane.

horizontal rolled position (pipe welding) The position of a pipe joint in which the axis of the pipe is approximately horizontal, and welding is performed in the flat position by rotating the pipe.

hot crack A crack that develops during solidification.

hot pressure welding (HPW) A solid-state welding process that produces coalescence of metals with heat and application of pressure sufficient to produce macrodeformation of the base metal. Vacuum or other shielding media may be used. See also *diffusion welding* and *forge welding*.

hydrogen brazing A nonstandard term for any brazing process that takes place in a hydrogen atmosphere.

I

impulse (resistance welding) A group of pulses occurring on a regular frequency separated only by an interpulse time.

inclined position The position of a pipe joint in which the axis of the pipe is at an angle of approximately 45° to the horizontal, and the pipe is not rotated during welding.

inclined position (with restriction ring) The position of a pipe joint in which the axis of the pipe is at an angle of approximately 45° to the horizontal, and a restriction ring is located near the joint. The pipe is not rotated during welding.

included angle A nonstandard term for *groove angle*.

induction brazing (IB) A brazing process in which the heat required is obtained from the resistance of the workpieces to induced electric current.

induction soldering (IS) A soldering process in which the heat required is obtained from the resistance of the workpieces to induced electric current.

induction welding (IW) A welding process that produces coalescence of metals by the heat obtained from the resistance of the workpieces to the flow of induced high frequency welding current with or without the application of pressure. The effect of the high frequency welding current is to concentrate the welding heat at the desired location.

inert gas A gas that normally does not combine chemically with the base metal or filler metal. See also *protective atmosphere*.

inert gas metal arc welding A nonstandard term for *gas metal arc welding*.

inert gas tungsten arc welding A nonstandard term for *gas tungsten arc welding*.

infrared brazing (IRB) A brazing process in which the heat required is furnished by infrared radiation.

infrared soldering (IRS) A soldering process in which the heat required is furnished by infrared radiation.

intergranular penetration The penetration of a filler metal along the grain boundaries of a base metal.

interpass temperature In a multipass weld, the temperature of the weld metal before the next pass is started.

iron soldering (INS) A soldering process in which the heat required is obtained from a soldering iron.

J

J-groove weld A type of groove weld.

joint The junction of members or the edges of members which are to be joined or have been joined.

joint clearance The distance between the facing surfaces of a joint. In brazing, this distance is referred to as that which is present before brazing, at the brazing temperature, or after brazing is completed.

joint efficiency The ratio of the strength of a joint to the strength of the base metal, expressed in percent.

joint penetration The depth a weld extends from its face into a joint, exclusive of reinforcement.

joint root That portion of a joint to be welded where the members approach closest to each other. In cross section, the joint root may be either a point, a line, or an area.

joint type A weld joint classification based on the five basic arrangements of the component parts such as butt joint, corner joint, edge joint, lap joint, and T-joint.

K

kerf The width of the cut produced during a cutting process.

L

lamellar tear A terracelike fracture in the base metal with a basic orientation parallel to the wrought surface. It is caused by the high stress in the thickness direction that results from welding.

land A nonstandard term for *root face*.

lap joint A joint between two overlapping members in parallel planes.

laser A device that produces a concentrated coherent light beam by stimulating electronic or molecular transitions to lower energy levels. Laser is an acronym for light amplification by stimulated emission of radiation.

laser beam cutting (LBC) A thermal cutting process that severs materials by melting or vaporizing them with the heat obtained from a laser beam, with or without the application of gas jets to augment the removal of material.

laser beam welding (LBW) A welding process that produces coalescence of materials with the heat obtained from the application of a concentrated coherent light beam impinging upon the joint.

lead burning A nonstandard term for the welding of lead.

liquation The separation of a low melting constituent of an alloy from the remaining constituents, usually apparent in alloys having a wide melting range.

locked-up stress A nonstandard term for *residual stress*.

longitudinal crack A crack with its major axis orientation approximately parallel to the weld axis.

M

machine welding Welding with equipment that performs the welding operation under the constant observation and control of a welding operator. The equipment may or may not load and unload the workpieces. See also *automatic welding*.

macroetch test A test in which the specimen is prepared with a fine finish and etched to give a clear definition of the weld.

manual welding A welding operation performed and controlled completely by hand. See also *automatic welding*, *machine welding*, and *semiautomatic welding*.

mask (thermal spraying) A device for protecting a substrate surface from the effects of blasting or adherence of a spray deposit.

mechanical bond (thermal spraying) The adherence of a spray deposit to a roughened surface by the mechanism of particle interlocking.

melt-through Visible root reinforcement produced in a joint welded from one side.

metal arc cutting (MAC) Any of a group of arc cutting processes that serves metals by melting them with the heat of an arc between a metal electrode and the base metal. See also *gas metal arc cutting* and *shielded metal arc cutting*.

metal cored electrode A composite filler metal electrode consisting of a metal tube or other hollow configuration containing alloying materials. Minor amounts of ingredients and fluxing of oxides may be included. External shielding gas may or may not be used.

metal electrode A filler or nonfiller metal electrode used in arc welding or cutting that consists of a metal wire or rod that has been manufactured by any method and that is either bare or covered.

metallic bond The principal bond that holds metals together and is formed between base metals and filler metals in all welding processes. This is a primary bond arising from

the increased spatial extension of the valence electron wave functions when an aggregate of metal atoms is brought close together. See also *bonding force* and *covalent bond*.

metallizing A nonstandard term for *thermal spraying*.

metallurgical bond A nonstandard term for *metallic bond*.

metal powder cutting (POC) An oxygen cutting process that severs metals through the use of powder, such as iron, to facilitate cutting.

MIG welding A nonstandard term for *flux cored arc welding* and *gas metal arc welding*.

mixing chamber That part of a welding or cutting torch in which a fuel gas and oxygen are mixed.

molten weld pool A nonstandard term for *weld pool*.

multiport nozzle (plasma arc welding and cutting) A constricting nozzle containing two or more orifices located in a configuration to achieve a degree of control over the arc shape.

N

neutral flame An oxyfuel gas flame in which the portion used is neither oxidizing nor reducing. See also *oxidizing flame* and *reducing flame*.

nontransferred arc (plasma arc welding and cutting, and plasma spraying) An arc established between the electrode and the constricting nozzle. The workpiece is not in the electrical circuit. See also *transferred arc*.

nozzle A device that directs shielding media.

nugget The weld metal joining the workpieces in spot, roll spot, seam, or projection welds.

nugget size (resistance welding) The diameter of a spot or projection weld or width of a seam weld measured in the plane of the faying surfaces.

O

orifice gas (plasma arc welding and cutting) The gas that is directed into the torch to surround the electrode. It becomes ionized in the arc to form the plasma and issues from the orifice in the torch nozzle as the plasma jet.

oven soldering A nonstandard term for *furnace soldering*.

overhead position The position in which welding is performed from the underside of the joint.

overlap The protrusion of weld metal beyond the weld toes or weld root.

overlap (resistance seam welding) The portion of the preceding weld nugget remelted by the succeeding weld.

overlaying A nonstandard term for *surfacing*

oxidizing flame An oxyfuel gas flame having an oxidizing effect due to excess oxygen. See also *neutral flame* and *reducing flame*.

oxyacetylene welding (OAW) An oxyfuel gas welding process that produces coalescence

of metals by heating them with a gas flame or flames obtained from the combustion of acetylene with oxygen. The process may be used with or without the application of pressure and with or without the use of filler metal.

oxyfuel gas cutting (OFC) A group of cutting processes used to sever metals by means of the chemical reaction of oxygen with the base metal at elevated temperatures. The necessary temperature is maintained by means of gas flames obtained from the combustion of a specified fuel gas and oxygen. See also *oxygen cutting*.

oxyfuel gas spraying A nonstandard term for *flame spraying*.

oxyfuel gas welding (OFW) A group of welding processes that produces coalescence by heating materials with an oxyfuel gas flame or flames, with or without the application of pressure, and with or without the use of filler metal.

oxygas cutting A nonstandard term for *oxygen cutting*.

oxygen arc cutting (AOC) An oxygen cutting process used to sever metals by means of the chemical reaction of oxygen with the base metal at elevated temperatures. The necessary temperature is maintained by an arc between a consumable tubular electrode and the base metal.

oxygen cutter One who performs a manual oxygen cutting operation.

oxygen cutting (OC) A group of cutting processes used to sever or remove metals by means of the chemical reaction between oxygen and the base metal at elevated temperatures. In the case of oxidation-resistant metals, the reaction is facilitated by the use of a chemical flux or metal powder. See also *chemical flux cutting*, *metal powder cutting*, *oxyfuel gas cutting*, *oxygen arc cutting* and *oxygen lance cutting*.

oxygen cutting operator One who operates machine or automatic oxygen cutting equipment.

oxygen gouging An application of oxygen cutting in which a bevel or groove is formed.

oxygen grooving A nonstandard term for *oxygen gouging*.

oxygen lance A length of pipe used to convey oxygen to the point of cutting in oxygen lance cutting.

oxygen lance cutting (LOC) An oxygen cutting process used to sever metals with oxygen supplied through a consumable lance. The preheat to start the cutting is obtained by other means.

oxygen lancing A nonstandard term for *oxygen lance cutting*.

oxyhydrogen welding (OHW) An oxyfuel gas welding process that produces coalescence of materials by heating them with a gas flame or flames obtained from the combustion of hydrogen with oxygen, without the application of pressure and with or without the use of filler metal.

P

parallel welding A resistance welding secondary circuit variation in which the secondary current is divided and conducted through the workpieces and electrodes in parallel electrical paths to simultaneously form multiple resistance spot, seam, or projection welds.

parent metal A nonstandard term for *base metal*.

partial joint penetration Joint penetration that is intentionally less than complete.

penetration A nonstandard term for *joint penetration* and *root penetration*.

percussion welding (PEW) A welding process that produces coalescence at the faying surface using the heat from an arc produced by a rapid discharge of electrical energy. Pressure is applied percussively during or immediately following the electrical discharge.

pilot arc (plasma arc welding) A low current continuous arc between the electrode and the constricting nozzle to ionize the gas and facilitate the start of the welding arc.

plasma arc cutting (PAC) An arc cutting process that severs metal by melting a localized area with a constricted arc and removing the molten material with a high velocity jet of hot, ionized gas issuing from the constricting orifice.

plasma arc welding (PAW) An arc welding process that produces coalescence of metals by heating them with a constricted arc between an electrode and the workpiece (transferred arc) or the electrode and the constricting nozzle (nontransferred arc). Shielding is obtained from the hot, ionized gas issuing from the torch which may be supplemented by an auxiliary source of shielding gas. Shielding gas may be an inert gas or a mixture of gases. Pressure may or may not be used, and filler metal may or may not be supplied.

plasma metallizing A nonstandard term for *plasma spraying*.

plasma spraying (PSP) A thermal spraying process in which a nontransferred arc of a plasma torch is utilized to create a gas plasma that acts as the source of heat for melting and propelling the surfacing material to the substrate.

plenum chamber (plasma arc welding and cutting, and plasma spraying) The space between the inside wall of the constricting nozzle and the electrode.

plug weld A weld made in a circular hole in one member of a joint, fusing that member to another member. A fillet-welded hole is not to be construed as conforming to this definition.

polarity See *direct current electrode negative* and *direct current electrode positive*.

porosity Cavity type discontinuities formed by gas entrapment during solidification.

postheating The application of heat to an assembly after welding, brazing, soldering, thermal spraying, or thermal cutting. See also *postweld heat treatment*.

postweld heat treatment Any heat treatment after welding.

powder cutting A nonstandard term for *chemical flux cutting* and *metal powder cutting*.

precoating Coating the base metal in the joint by dipping, electroplating, or other applicable means prior to soldering or brazing.

preform Brazing or soldering filler metal fabricated in a shape or form for a specific application.

preheat A nonstandard term for *preheat temperature*.

preheat current (resistance welding) An impulse or series of impulses that occur prior to and are separated from the welding current.

preheat temperature A specified temperature that the base metal must attain in the welding, brazing, soldering, thermal spraying, or cutting area immediately before these operations are performed.

pressure-controlled welding A resistance welding process variation in which a number of spot or projection welds are made with several electrodes functioning progressively under the control of a pressure-sequencing device.

pressure gas welding (PGW) An oxyfuel gas-welding process that produces coalescence simultaneously over the entire area of faying surfaces by heating them with gas flames obtained from the combustion of a fuel gas and oxygen and by the application of pressure, without the use of filler metal.

pretinning A nonstandard term for *precoating*.

procedure qualification The demonstration that welds made by a specific procedure can meet prescribed standards.

procedure qualification record (PQR) A document providing the actual welding variables used to produce an acceptable test weld and the results of tests conducted on the weld to qualify a welding procedure specification.

process A grouping of basic operational elements used in welding, cutting, adhesive bonding, or thermal spraying.

projection welding (PW) A resistance welding process that produces coalescence by the heat obtained from the resistance to the flow of the welding current. The resulting welds are localized at predetermined points by projections, embossments, or intersections.

protective atmosphere A gas or vacuum envelope surrounding the workpieces used to prevent or facilitate removal of oxides and other detrimental surface substances.

puddle A nonstandard term for *weld pool*.

pull gun technique A nonstandard term for *backhand welding*.

pulse (resistance welding) A current of controlled duration of either polarity through the welding circuit.

R

random intermittent welds Intermittent welds on one or both sides of a joint in which the weld increments are made without regard to spacing.

reaction flux (soldering) A flux composition in which one or more of the ingredients reacts with a base metal upon heating to deposit one or more metals.

reaction stress A stress that cannot exist in a member if the member is isolated as a free body without connection to other parts of the structure.

reducing atmosphere A chemically active protective atmosphere which at elevated temperature will reduce metal oxides to their metallic state.

reducing flame A gas flame having a reducing effect due to excess fuel gas. See also *neutral flame* and *oxidizing flame*.

reflowing A nonstandard term for *flow brightening*.

reflow soldering A nonstandard term for a soldering process variation in which preplaced solder is melted to produce a soldered joint or coated surface.

residual stress Stress present in a member that is free of external forces or thermal gradients.

resistance brazing (RB) A brazing process in which the heat required is obtained from the resistance to electric current flow in a circuit of which the workpiece is a part.

resistance butt welding A nonstandard term for *flash welding* and *upset welding*.

resistance seam welding (RSW) A resistance welding process that produces coalescence at the faying surfaces of overlapped parts progressively along a length of a joint. The weld may be made with overlapping weld nuggets, a continuous weld nugget, or by forging the joint as it is heated to the welding temperature by resistance to the flow of the welding current.

resistance soldering (RS) A soldering process in which the heat required is obtained from the resistance to electric current flow in a circuit of which the workpiece is a part.

resistance spot welding (RSW) A resistance welding process that produces coalescence at the faying surfaces of a joint by the heat obtained from resistance to the flow of welding current through the workpieces from electrodes that serve to concentrate the welding current and pressure at the weld area.

resistance welding (RW) A group of welding processes that produces coalescence of the faying surfaces with the heat obtained from resistance of the work to the flow of the welding current in a circuit of which the work is a part, and by the application of pressure.

resistance welding electrode The part(s) of a resistance welding machine through which the welding current and, in most cases, force are applied directly to the work. The

electrode may be in the form of a rotating wheel, rotating bar, cylinder, plate, clamp, chuck, or modification thereof.

resistance welding gun A manipulatable device to transfer current and provide electrode force to the weld area (usually in reference to a portable gun).

reverse polarity A nonstandard term for *direct current electrode positive*.

roll welding (ROW) A solid-state welding process that produces coalescence of metals by heating and by applying sufficient pressure with rolls to cause deformation at the faying surfaces. See also *forge welding*.

root A nonstandard term for *joint root* and *weld root*.

root bead A weld that extends into or includes part or all of the joint root.

root edge A root face of zero width. See also *root face*.

root face That portion of the groove face adjacent to the joint root.

root gap A nonstandard term for *root opening*.

root opening The separation at the joint root between the workpieces.

root penetration The depth that a weld extends into the joint root.

root radius A nonstandard term for *groove radius*.

root reinforcement Weld reinforcement opposite the side from which welding was done.

root surface The exposed surface of a weld opposite the side from which welding was done.

S

scarf joint A form of butt joint.

seal coat Material applied to infiltrate the pores of a thermal spray deposit.

seal weld Any weld designed primarily to provide a specific degree of tightness against leakage.

seam weld A continuous weld made between or upon overlapping members, in which coalescence may start and occur on the faying surfaces, or may have proceeded from the outer surface of one member. The continuous weld may consist of a single weld bead or a series of overlapping spot welds. See also *arc seam weld* and *resistance seam welding*.

secondary circuit That portion of a welding machine that conducts the secondary current between the secondary terminals of the welding transformer and the electrodes, or electrode and workpiece.

self-fluxing alloys (thermal spraying) Surfacing materials that wet the substrate and coalesce when heated to their melting point, without the addition of a flux.

semiautomatic arc welding Arc welding with equipment that controls only the filler metal feed. The advance of the welding is manually controlled.

series welding A resistance welding secondary circuit variation in which the secondary current is conducted through the workpieces and electrodes or wheels in a series electrical

path to simultaneously form multiple resistance spot, seam, or projection welds.

set down A nonstandard term for *upset*.

shadow mask A thermal spraying process variation in which an area is partially shielded during thermal spraying, thus permitting some overspray to produce a feathering at the coating edge.

sheet separation (resistance welding) The gap surrounding the weld between faying surfaces, after the joint has been welded in spot, seam, or projection welding.

shielded metal arc cutting (SMAC) A metal arc cutting process in which metals are severed by melting them with the heat of an arc between a covered metal electrode and the base metal.

shielded metal arc welding (SMAW) An arc welding process that produces coalescence of metals by heating them with an arc between a covered metal electrode and the workpieces. Shielding is obtained from decomposition of the electrode covering. Pressure is not used, and filler metal is obtained from the electrode.

shielding gas Protective gas used to prevent atmospheric contamination.

short circuiting transfer (arc welding) Metal transfer in which molten metal from a consumable electrode is deposited during repeated short circuits. See also *globular transfer* and *spray transfer*.

shoulder A nonstandard term for *root face*.

shrinkage stress A nonstandard term for *residual stress*.

shrinkage void A cavity type discontinuity normally formed by shrinkage during solidification.

silver alloy brazing A nonstandard term for brazing with a silver-base filler metal.

silver soldering A nonstandard term for brazing with a silver-base filler metal.

single-bevel-groove weld A type of groove weld.

single-flare-bevel-groove weld A weld in a groove formed by a member with a curved surface in contact with a planar member.

single-flare-V-groove weld A weld in a groove formed by two members with curved surfaces.

single impulse welding A resistance welding process variation in which spot, projection, or upset welds are made with a single impulse.

single-J-groove weld A type of groove weld.

single-port nozzle A constricting nozzle containing one orifice, located below and concentric with the electrode.

single-square-groove weld A type of groove weld.

single-U-groove weld A type of groove weld.

single-V-groove weld A type of groove weld.

single-welded joint A fusion welded joint that is welded from one side only.

skull The unmelted residue from a liquated filler metal.

slag inclusion Nonmetallic solid material entrapped in weld metal or between weld metal and base metal.

slot weld A weld made in an elongated hole in one member of a joint fusing that member to another member. The hole may be open at one end. A fillet weld slot is not to be construed as conforming to this definition.

slugging The act of adding a separate piece or pieces of material in a joint before or during welding that results in a welded joint not complying with design, drawing, or specification requirements.

soft solder A nonstandard term for *solder*.

solder A filler metal used in soldering that has a liquidus not exceeding 450 °C (840 °F).

soldering (S) A group of welding processes that produces coalescence of materials by heating them to the soldering temperature and by using a filler metal having a liquidus not exceeding 450 °C (840 °F) and below the solidus of the base metals. The filler metal is distributed between the closely fitted faying surfaces of the joint by capillary action.

soldering gun An electrical soldering iron with a pistol grip and a quick heating, relatively small bit.

soldering iron A soldering tool having an internally or externally heated metal bit usually made of copper.

solder interface The interface between filler metal and base metal in a soldered joint.

solid-state welding (SSW) A group of welding processes that produces coalescence at temperatures essentially below the melting point of the base metal without the addition of a brazing filler metal. Pressure may or may not be used.

spacer strip A metal strip or bar prepared for a groove weld and inserted in the joint root to serve as a backing and to maintain the root opening during welding. It can also bridge an exceptionally wide root opening due to poor fit.

spit A nonstandard term for *flash*.

split pipe backing Backing in the form of a pipe segment used for welding round bars.

spool A filler metal package consisting of a continuous length of welding wire in coil form wound on a cylinder (called a barrel) which is flanged at both ends. The flange contains a spindle hole of smaller diameter than the inside diameter of the barrel.

spot weld A weld made between or upon overlapping members in which coalescence may start and occur on the faying surfaces or may proceed from the outer surface of one member. The weld cross section (plan view) is approximately circular. See also *arc spot weld* and *resistance spot welding*.

spray deposit The coating or layer of surfacing material applied by a thermal spraying process.

spray deposit density ratio (thermal spraying) The ratio of the density of the spray deposit to the theoretical density of a surfacing material, usually expressed as a percent of theoretical density.

spray transfer (arc welding) Metal transfer in which molten metal from a consumable electrode is propelled axially across the arc in small droplets. See also *globular transfer* and *short circuiting transfer*.

square-groove weld A type of groove weld.

stack cutting Thermal cutting of stacked metal plates arranged so that all the plates are severed by a single cut.

staggered intermittent weld An intermittent weld on both sides of a joint in which the weld increments on one side are alternated with respect to those on the other side.

standoff distance The distance between a nozzle and the workpiece.

stick electrode A nonstandard term for *covered electrode*.

stick electrode welding A nonstandard term for *shielded metal arc welding*.

stickout A nonstandard term for *electrode extension*.

stopoff A material used on the surfaces adjacent to the joint to limit the spread of soldering or brazing filler metal.

straight polarity A nonstandard term for *direct current electrode negative*.

stranded electrode A composite filler metal electrode consisting of stranded wires that may mechanically enclose materials to improve properties, stabilize the arc, or provide shielding.

stress relief cracking Intergranular cracking in the heat affected zone or weld metal that occurs during the exposure of weldments to elevated temperatures during postweld heat treatment or high temperature service.

stress relief heat treatment Uniform heating of a structure or a portion thereof to a sufficient temperature to relieve the major portion of the residual stresses, followed by uniform cooling.

stringer bead A type of weld bead made without appreciable weaving motion. See also *weave bead*.

stub The short length of welding rod or consumable electrode that remains after its use for welding.

stud arc welding (SW) An arc welding process that produces coalescence of metals by heating them with an arc between a metal stud, or similar part, and the other workpiece. When the surfaces to be joined are properly heated, they are brought together under pressure. Partial shielding may be obtained by the use of a ceramic ferrule surrounding the stud. Shielding gas or flux may or may not be used.

stud welding A general term for joining a metal stud or similar part to a workpiece. Welding may be accommodated by arc, resistance, friction, or other processes with or without external gas shielding.

submerged arc welding (SAW) An arc welding process that produces coalescence of metals by heating them with an arc or arcs between a bare metal electrode or electrodes and the workpieces. The arc and molten

metal are shielded by a blanket of granular, fusible material on the workpieces. Pressure is not used, and filler metal is obtained from the electrode and sometimes from a supplemental source (welding rod, flux, or metal granules).

substrate Any material to which a thermal spray deposit is applied.

surface expulsion Expulsion occurring at an electrode-to-workpiece contact rather than at the faying surface.

surfacing The application by welding, brazing, or thermal spraying of a layer or layers of material to a surface to obtain desired properties or dimensions, as opposed to making a joint.

surfacing material The material that is applied to a base metal or substrate during surfacing.

surfacing metal The metal that is applied to a base metal or substrate during surfacing. See also *surfacing material*.

surfacing weld A weld applied to a surface, as opposed to making a joint, to obtain desired properties or dimensions.

sweat soldering A soldering process variation in which two or more parts that have been precoated with solder are reheated and assembled into a joint without the use of additional solder.

synchronous timing (resistance welding) The initiation of each half cycle of welding transformer primary current on an accurately timed delay with respect to the polarity reversal of the power supply.

T

tacker A nonstandard term for a tack welder.

tack weld A weld made to hold parts of a weldment in proper alignment until the final welds are made.

theoretical throat The distance from the beginning of the joint root perpendicular to the hypotenuse of the largest right triangle that can be inscribed within the cross section of a fillet weld. This dimension is based on the assumption that the root opening is equal to zero.

thermal cutting (TC) A group of cutting processes that melts the base metal. See also *arc cutting*, *electron beam cutting*, *laser beam cutting*, and *oxygen cutting*.

thermal spraying (THSP) A group of processes in which finely divided metallic or non-metallic surfacing materials are deposited in a molten or semimolten condition on a substrate to form a spray deposit. The surfacing material may be in the form of powder, rod, or wire. See also *arc spraying*, *flame spraying*, and *plasma spraying*.

thermal spraying gun A device for heating, feeding, and directing the flow of a surfacing material.

thermal stress Stress resulting from nonuniform temperature distribution.

thermit crucible The vessel in which the thermit reaction takes place.

thermit mixture A mixture of metal oxide and finely divided aluminum with the addition of alloying metals as required.

thermit mold A mold formed around the workpieces to receive the molten metal.

thermit reaction The chemical reaction between metal oxide and aluminum that produces superheated molten metal and a slag containing aluminum oxide.

thermit welding (TW) A welding process that produces coalescence of metals by heating them with superheated liquid metal from a chemical reaction between a metal oxide and aluminum, with or without the application of pressure. Filler metal is obtained from the liquid metal. (*Note:* The *ASM Handbook* uses the spelling "thermite welding.")

thermocompression bonding A nonstandard term for *hot pressure welding*.

throat of a fillet weld See *actual throat*, *effective throat*, and *theoretical throat*.

throat of a groove weld A nonstandard term for *groove weld size*.

TIG welding A nonstandard term for *gas tungsten arc welding*.

finning A nonstandard term for *precoating*.

T-joint A joint between two members located approximately at right angles to each other in the form of a T.

toe crack A crack in the base metal at the toe of a weld.

torch brazing (TB) A brazing process in which the heat required is furnished by a fuel gas flame.

torch soldering (TS) A soldering process in which the heat required is furnished by a fuel gas flame.

torch tip See *cutting tip* and *welding tip*.

transferred arc (plasma arc welding) A plasma arc established between the electrode and the workpiece.

transverse crack A crack with its major axis oriented approximately perpendicular to the weld axis.

twin carbon arc brazing A nonstandard term for *carbon arc brazing*.

U

U-groove weld A type of groove weld.

ultrasonic coupler (ultrasonic soldering and ultrasonic welding) Elements through which ultrasonic vibration is transmitted from the transducer to the tip.

ultrasonic soldering A soldering process variation in which high frequency vibratory energy is transmitted through molten solder to remove undesirable surface films and thereby promote wetting of the base metal. This operation is usually accomplished without a flux.

ultrasonic welding (USW) A solid-state welding process that produces coalescence of materials by the local application of high frequency vibratory energy as the workpieces are held together under pressure.

underbead crack A crack in the heat affected zone generally not extending to the surface of the base metal.

undercut A groove melted into the base metal adjacent to the weld toe or weld root and left unfilled by weld metal.

underfill A depression on the weld face or root surface extending below the adjacent surface of the base metal.

upset Bulk deformation resulting from the application of pressure in welding. The upset may be measured as a percent increase in interface area, a reduction in length, a percent reduction in lap joint thickness, or a reduction in cross wire weld stack height.

upset butt welding A nonstandard term for *upset welding*.

upset distance The total loss of axial length of the workpieces from the initial contact to the completion of the weld. In flash welding, the upset distance is equal to the platen movement from the end of flash time to the end of upset.

upset welding (UW) A resistance welding process that produces coalescence over the entire area of faying surfaces or progressively along a butt joint by the heat obtained from the resistance to the flow of welding current through the area where those surfaces are in contact. Pressure is used to complete the weld.

V

vacuum brazing A nonstandard term for various brazing processes that take place in a chamber or retort below atmospheric pressure.

vertical position The position of welding in which the weld axis is approximately vertical.

vertical position (pipe welding) The position of a pipe joint in which welding is performed in the horizontal position and the pipe may or may not be rotated.

V-groove weld A type of groove weld.

W

wave soldering (WS) An automatic soldering process where workpieces are passed through a wave of molten solder. See also *dip soldering*.

wax pattern (thermit welding) Wax molded around the workpieces to the form desired for the completed weld.

weave bead A type of weld bead made with transverse oscillation.

weld A localized coalescence of metals or nonmetals produced either by heating the materials to the welding temperature, with or without the application of pressure, or by the application of pressure alone, with or without the use of filler metal.

weldability The capacity of a material to be welded under the imposed fabrication conditions into a specific, suitably designed structure and to perform satisfactorily in the intended service.

weld axis A line through the length of the weld, perpendicular to and at the geometric center of its cross section.

weld bead A weld resulting from a pass. See also *stringer bead* and *weave bead*.

weld bonding A resistance spot welding process variation in which the spot weld strength is augmented by adhesive at the faying surfaces.

weld brazing A joining method that combines resistance welding with brazing.

weld crack A crack located in the weld metal or heat affected zone.

welder One who performs manual or semiautomatic welding operation.

welder performance qualification The demonstration of a welder's ability to produce welds meeting prescribed standards.

weld face The exposed surface of a weld on the side from which welding was done.

welding A materials joining process used in making welds.

welding blowpipe A nonstandard term for welding torch.

welding current The current in the welding circuit during the making of a weld.

welding cycle The complete series of events involved in the making of a weld.

welding electrode A component of the welding circuit through which current is conducted and that terminates at the arc, molten conductive slag, or base metal. See also *arc welding electrode*, *flux cored electrode*, *metal cored electrode*, *metal electrode*, *resistance welding electrode*, and *stranded electrode*.

welding ground A nonstandard term for *workpiece connection*.

welding leads The workpiece lead and electrode lead of an arc welding circuit.

welding machine Equipment used to perform the welding operation; for example, spot welding machine, arc welding machine, and seam welding machine.

welding operator One who operates machine or automatic welding equipment.

welding position See *flat position*, *horizontal fixed position*, *horizontal position*, *horizontal rolled position*, *inclined position*, *overhead position*, and *vertical position*.

welding procedure The detailed methods and practices involved in the production of a weldment. See also *welding procedure specification*.

welding procedure specification (WPS) A document providing in detail the required variables for a specific application to ensure repeatability by properly trained welders and welding operators.

welding rod A form of welding filler metal, normally packaged in straight lengths, that does not conduct electrical current.

welding sequence The order of making the welds in a weldment.

welding tip That part of an oxyfuel gas welding torch from which the gases issue.

welding torch (arc) A device used in the gas tungsten and plasma arc welding processes to control the position of the electrode, to transfer current to the arc, and to direct the flow of shielding and plasma gas.

welding torch (oxyfuel gas) A device used in oxyfuel gas welding, torch brazing, and torch soldering for directing the heating flame

produced by the controlled combustion of fuel gases.

welding wheel A nonstandard term for *resistance welding electrode*.

welding wire A form of welding filler metal, normally packaged as coils or spools, that may or may not conduct electrical current depending upon the welding process with which it is used. See also *welding electrode* and *welding rod*.

weld interface The interface between weld metal and base metal in a fusion weld, between base metals in a solid-state weld without filler metal or between filler metal and base metal in a solid-state weld with filler metal, and in a braze.

weld line A nonstandard term for *weld interface*.

weldment An assembly whose component parts are joined by welding.

weld metal That portion of a weld that has been melted during welding.

welder A nonstandard term for *welder*.

weld pass A single progression of welding or surfacing along a joint or substrate. The result of a pass is a weld bead, layer, or spray deposit.

weld pass sequence The order in which the weld passes are made.

weld penetration A nonstandard term for *joint penetration* and *root penetration*.

weld pool The localized volume of molten metal in a weld prior to its solidification as weld metal.

weld puddle A nonstandard term for *weld pool*.

weld reinforcement Weld metal in excess of the quantity required to fill a joint. See also *face reinforcement* and *root reinforcement*.

weld root The points, as shown in cross section, at which the back of the weld intersects the base metal surfaces.

weld size See *edge weld size*, *fillet weld size*, *flange weld size*, and *groove weld size*.

weld tab Additional material on which the weld may be initiated or terminated.

weld throat See *actual throat*, *effective throat*, and *theoretical throat*.

weld toe The junction of the weld face and the base metal.

wetting The phenomenon whereby a liquid filler metal or flux spreads and adheres in a thin continuous layer on a solid base metal.

wiped joint A joint made with solder having a wide melting range and with the heat supplied by the molten solder poured onto the joint. The solder is manipulated with a hand-held cloth or paddle so as to obtain the required size and contour.

work connection A nonstandard term for *workpiece connection*.

work lead A nonstandard term for *workpiece lead*.

workpiece The part being welded, brazed, soldered, or cut.

workpiece connection The connection of the workpiece lead to the workpiece.

workpiece lead The electrical conductor between the arc welding current source and the workpiece connection.

INDEX

<u>Index Terms</u>	<u>Links</u>		
2-D Axisymmetric model	780		
2-D FE models, USW	202		
2-D Small- and large deformation analysis	149		
2-D Versus 3-D analyses	153		
2-D/3-D Applied plastic strain methods	152		
2T Bend test	139		
3-D EB deposition processing	540		
3-D FE models, USW	202		
3-D Gray-level correlation method	835		
3-D Heat and fluid transport modeling	779	780	
3-D Laser cladding	592		
3-D Small- and large deformation analysis	149		
3-D Solid model	592		
3-D Transient approach	830		
3-D Transient (time-dependent) numerical welding simulations	830		
3-D/3-D Applied plastic strain methods	153		
22Cr-4Ni-9Mn Stainless steel	684		
 A			
ABAQUS	835		
ABAQUS subroutines	203		
ABAQUS/Explicit	195		
Abbreviations	892		
Absorption characteristics (lasers)	511		
Ac mode	18	45	346
Acetylene (C ₂ H ₂)			
chemically driven fusion welding	14	15	
fire prevention and protection	860		
fuel gas	857		
lasing gas purity	613		
oxyfuel gas welding and cutting	861		
safe welding practices	856	857	
Acicular ferrite	130	133	751

Index Terms**Links**

Acoustic emission (AE)	600	649		
Acoustic emission technique	227			
Acoustic monitoring	599			
Acoustic softening	203			
Activated rosin flux	882			
Actual throat	882			
Adams, Comfort	245			
Adaptive control (use of term)	290			
Adaptive Lagrangian-Eulerian technique (ALE)	190			
Additive manufacturing (AM)	540	732		
Adherends	5	6		
Adhesion	6			
Adhesive	5			
Adhesive bonding				
definition of	882			
overview	6			
USW	727			
Advance per revolution (APR)	195			
Advanced high-strength steel (AHSS)	416	417	420	421
	448			
Aeroprojects	725			
Aerospace applications	140			
CDSW	392			
EXW	698			
FSW tool materials	665			
FW	449			
GTAW with a PEC	357			
integrated weld modeling	745			
laser-drilling	620			
NI-139 compound	357			
SPF/DW process	708			
USW	201			
Aerospace Material Specification draft				
number 4999	542			
Aerospace Material Standards (AMS)	539			
Ag-5wt%Cu alloy	112			
Agglomerated fluxes	49			
Air carbon arc cutting (AC-A)	849	882		

Index Terms**Links**

Air compressor, built-in	281		
Air cutting gun (gas metal arc cutting)	882		
Air seal repairs	537		
Air-cooled welding guns	331		
Aircraft industry	29		
Al ₂ O ₃	175	371	617
Alclad alloys	482		
Alliance program	566		
Allied processes	13		
Alligatoring	442	717	
Allotriomorphic	129		
Allotriomorphic ferrite	131	133	
Alloy AL-6XN	117		
Alloy steels			
EXW	690		
FRW	183		
Alternating current (ac)	278		
Aluminothermic reactions	16		
Aluminum			
arc welding	246		
butt welding	78		
case studies	70		
cold roll welding	718		
complex joint geometries	78		
EGW	376		
ESW	376		
FRW	183		
HAZ	162		
joining	29		
laser welding of	571		
PW	426		
RSEW	482		
spot welding	421		
square-groove weld	162		
start and stop in welding	76		
studs	381		
wide-lap seam welding	444		

Index Terms**Links**

Aluminum alloys			
5182-series	615		
5754-series	615		
6111-series	615		
7050Al-T651	198		
7050Al-T76	198		
7050-T651	196	197	
7075Al	198	199	
AA1100	197		
AA2024	482		
AA2195	197		
AA5754	465	473	488
AA6061	197	533	
AA6063	197	533	
AA6066	533		
AA6111	473		
AA7075	197	482	673
Alclad alloys	482		
Al-Li-Cu	198		
AZ31	199		
cold roll welding	718		
EBW	532		
EDBM-deposited 2291 aluminum	542		
FRW	644		
FSW tool applications	665		
full-penetration welds	532		
laser cutting	615	617	
laser welding of	571		
liquation cracking	139		
PW	426		
RSEW	482		
seam welding	444		
texture	197		
UAW	733		
weldments	139		
wide-lap seam welding	444		
Aluminum-base alloys	426	644	683
Aluminum-lithium alloys	684	708	

Index Terms**Links**

Amatol	697			
American Conference of Governmental and Industrial Hygienists threshold limit values	568			
American Conference of Governmental Industrial Hygienists (ACGIH)	846	855	865	
American National Standard for Industrial Robots and Robot Systems— Safety Requirements	866			
American National Standards Institute (ANSI)				
EBW	863			
EBW specifications	539			
H35.2	661			
LBW	566			
Z41 850				
Z49.1	301	845	863	
Z49.1:1	848			
Z49.1:1967	845			
Z49.1:1999	846	848	853	855
857	860			
Z49.1-99	358			
Z87.1	848			
Z136	566	567		
Z136.1	327	566	567	568
	864			
Z136.1 clause 4.3.1.2.	567			
American Society of Mechanical Engineers (ASME)	260	539		
American Society of Mechanical Engineers (ASME) Boiler and Pressure Vessel code	554			
American Welding Society (AWS)				
A5.1	304			
A5.3	304			
A5.4	304			
A5.5	304			
A5.6	304			
A5.11	304			
A5.13	304			

Index Terms**Links**

American Welding Society (AWS) (<i>Cont.</i>)			
A5.20	333		
A5.21	304		
A5.22	334		
A5.29	333		
C6.2	642		
filler-metal specification	351		
integrated weld modeling	745		
master chart	13		
rotary friction welding	646		
SMAW electrodes	303		
Standard Welding Procedure Specifications	260		
weld process classes	572		
welding and allied processes	13		
Ammonium nitrate (NH ₄ NO ₃)	691		
AMS 2680	539		
AMS 2681	539		
AMS-STD-1595	539		
AMS-W-6858A	427		
ANFO	697		
Angle welding	691		
Angular distortion	162		
Angular friction welding	24	25	
Angular velocity	646		
Annular-projection welding	209	214	430
Annular-projection welds	424		
Anode	17		
arc welding	242		
EBW	514		
GTAW	250		
ANSI/AWS			
A5.9	339		
A5.14	339		
A5.17	339		
A5.23	339		
A5.23/A5.23M	339		
C7.1	863		
F2.2	848		

Index Terms**Links**

ANSI/AWS (<i>Cont.</i>)				
Z49.1	284	307	317	353
ANSI/CGA V-1	862			
ANSI/NEMA EW 1	859			
ANSI/NFPA 70	859			
ANSI/RIA R15.06- 1999	866			
ANSI/RMA IP-7	861			
ANSYS	835			
ANSYS 10.0	793			
Appliance industry, CDSW	392			
Applied Metrics	499			
Applied plastic (inherent) strain	152			
Arata beam (AB) test	550			
Arbegast's flow-partitioned model	195			
Arc blow				
definition of	882			
GMAW	84			
GTAW	346			
power sources (arc welding)	278			
SAW	337	340	343	
SMAW	307			
SW	385			
Arc brazing (AB)	882			
Arc cutting (AC)	882			
Arc force	253	302	311	318
	882			
Arc gouging	266	267	272	882
Arc oxygen cutting	882			
Arc physics				
GMAW	254			
GTAW	249			
Arc plasma	296			
Arc power	37			
Arc radiation				
GMAW	317			
GTAW	353			
HLAW	327			
safe welding practices	846	865		

Index Terms**Links**

Arc radiation (<i>Cont.</i>)			
SAW	335	343	
Arc seam weld	882		
Arc sensing	287		
Arc spot weld	767	775	882
Arc spraying (ASP)	882		
Arc stabilizers	45	51	
Arc strike	84	882	
Arc tracer spectroscopy	289		
Arc transfer efficiency	37		
Arc voltage control (AVC)	357		
Arc welder	305		
Arc welding			
fundamentals			
arc, nature of	242		
arc shielding	242		
limitations, overcoming	243		
overview	241		
heat source, modeling of	36		
heat utilization efficiency	33		
historical development			
commercial arc welding (USA)	244		
electrodes	245		
new welding methods	244		
overview	243		
postwar developments	247		
rapid advance, years of	246		
slow growth, era of	245		
World War I	245		
modes of	17		
overview	241		
power sources. <i>See</i> Power sources (arc welding)			
processes			
consumable electrode arc welding	18		
nonconsumable electric arc welding	18		
overview	18		
processes, characteristics of	871		
Arc welding (AW)	882		

Index Terms

Links

Arc welding electrode	304	882		
Arc welding gun	882			
<i>See also</i> welding guns				
Arc welding process control				
control of arc welding.				
adaptive control	290			
distributed, hierarchical control	291			
intelligent control	290			
multivariable control	291			
overview	290			
introduction	285			
modeling	289			
overview	285			
sensing				
acoustical signals	289			
arc sensing	287			
arc tracer spectroscopy	289			
imaging optics	288			
nonimaging optics	287			
temperature measurements	288			
ultrasonic techniques	289			
system parameters	286			
system requirements	285			
Arc welding processes, definition of flow-partitioned model	16			
Arc welding processes, design				
considerations for	266			
appendix	273			
Arc-assisted laser welding	322			
Arc-augmented laser welding	321			
ArcelorMittal	615			
Arc-outs	533			
Argon	18			
arc welding	242			
FCAW	330			
GTAW	251	350		
shielding gases	296	297	298	597
Armor plate	246			
Artificial intelligence	290			

<u>Index Terms</u>	<u>Links</u>	
Asbestos	49	
ASME Boiler and Pressure Vessel Code (BPVC)	539	
Assist gases (laser cutting)	612	613
ASTM A 264	697	
ASTM A 578	697	
ASTM G48 test	120	
As-welded		
definition of	882	
EGW	365	
ESW	376	377
low-carbon steels	701	
RSW	439	
titanium friction welded joints	644	
A-TIG	355	
Atomic bonding	217	
Atomic hydrogen	165	
Atoms (welding)	7	
Austenite	134	
Austenite grain growth	126	
Austenitic stainless steels	115	319
Austin Company, The	245	
Autogenous weld		
beam welding	551	
definition of	882	
dilution in fusion welding	115	118
GTAW	351	
laser welding	571	
PAW	361	
single-crystal nickel-base superalloys	754	
Automatic voltage compensation (AVC)	407	
Automatic welding		
definition of	882	
FCAW	330	331
historical development	246	
SAW	335	
self welding practices	846	
SMAW	304	

Index Terms

Links

Automatic welding (<i>Cont.</i>)		
weld joint design	267	
Automatic welding heads	243	
Automobile industry	4	29
CDSW	392	
FCAW	330	
flange-joint lap seam welds	444	
frequent electrode tip dressing	463	
FW	449	
high-frequency, multibeam processes	546	
integrated weld modeling	745	
LBW	572	
PW	427	
RSW	415	
USW	201	
welding simulation	835	
AWS 3-5	567	
AWS A5.XX	361	
AWS B4.0	642	
AWS C1.1-66	493	
AWS C1.1M/ C1.1:2000	852	
AWS C1.1M/C1:2000	427	
AWS C7.1	518	
AWS C7-3	539	
AWS D1.1	269	
AWS D17.1	539	
AWS D17.2	427	
AWS D8.1M:2007	427	
AWS D8.7	487	
AWS D8.9:2000	427	
AWS D8.9:2002	427	
AWS D8.9-97	493	
AWS/SAE D8.9M	470	
Axial grains	100	
B		
Back bead	882	
Back gouging	272	882

Index Terms**Links**

Back weld	882			
Back-diffusion	107			
Backfire	861	882		
Backhand welding	882			
Backing	265	267	286	321
	362	882		
Backing bars	272	350	375	
Backing bead	882			
Backing filler metal	882			
Backing pass	882			
Backing ring	882			
Backing shoe	882			
Backing weld	882			
Backscattered electrons	509	549	627	
Backstep sequence	882			
Bad	652			
Balling up	882			
Ball-to-sheet welds	425			
Banded feature	189			
Bar coils	705			
Base material	9	882		
Base metal	487	882		
Base-metal zone	55			
Basicity index	47	338		
Bead weld	882			
Bead-on-plate welding	77	251		
Beam parameter product (BPP)	508	510	610	
Beam spot	515	531		
Beam switch	582	585		
Beam welding	39			
Bearing maintenance	481			
Bell Laboratories	508			
Bend test				
2T bend test	139			
guided-bend tests	263			
UAM	736			
unguided	650			
Beryllium alloys	685			

Index Terms**Links**

Beryllium copper alloys	483			
Bevel	882			
Bevel angle	11	271	882	
Bevel groove weld	267	882		
Beveled joints	336			
Biot-Savart law	768			
Biringuccio, Vannoccio	243			
Bit	882			
Blacksmith welding	882			
Blind holes	531			
Block sequence	882			
Blowhole	377	882		
Bobbin tool	671			
Body-centered cubic (bcc) b phase	140			
Bond	882			
Bond line				
DB	219	683		
definition of	882			
metallographic inspection	433			
PW	432			
resistance butt welding	398			
solid-state resistance welding	209	210	211	215
	216			
stage III: interface migration	220			
UAM	739			
Bonded fluxes	49			
Bonding force	882			
Bondline strain	171	175	177	209
Bottle	883			
Boussinesq approximation	768			
Boxing	883			
Brasses	15	483	484	
Braze	883			
Braze interface	883			
Braze joints	10			
Braze welding	10	883		
Brazement	883			
Brazer	883			

Index Terms**Links**

Brazing (B)	9	25	883	
Brazing alloy	25	883		
Brazing filler	11			
Brazing filler metal	883			
Brazing furnaces	26	854		
Brazing operator	883			
Brightness (use of term)	508			
Brittle fracture	163	184	493	561
Brittle nugget	883			
Brody-Flemings model	107			
Bronze welding	883			
Bronzes	483	484		
Buckling distortion	162	165		
Buildup	883			
Built-up beams	162			
Bulge test	736			
Bulk resistivity	423	426	792	
Buoyancy force	89	626	748	768
Burn through	249	883		
Burn through weld	883			
Burner	883			
Burning	883			
Butt joints				
versus corner and T-joints (EBW)	526			
definition of	266	883		
EBW	524			
general design aspects	10	11		
grooves, recommended				
proportions for	273			
HLAW	325			
LBW design	570			
PAW	362			
Butt weld	272	448	668	702
	883			
Butt welding				
CW	714			
GMAW	319			

Index Terms**Links**

Butt welds				
Al-Mg-Si alloys	814			
RW	398			
SAW	336			
Buttering	883			
Butt-lap joints	10			
Button	883			
C				
Cables	412			
Cadmium telluride (CdTe) detectors	222			
Calcium fluoride (CaF ₂)	371			
Cantilever hooks	6			
Capacitive discharge (CD)	213	402	403	429
Capacitor bank	705			
Capacitor discharge stud welding (CDSW)	391			
Carbides				
continuous heating transformation diagrams	125			
EGW	377			
FSW tool designs	665			
inclusion formation	44	751		
similar materials, joining	181			
solid-state transformations	373			
welding fundamentals	16			
Carbon				
sensitivity to	132			
solid-state resistance welding	210			
Carbon additions	110			
Carbon arc air scarfing	281			
Carbon arc brazing (CAB)	883			
Carbon arc cutting (CAC)	883			
Carbon arc welding (CAW)	883			
Carbon dioxide (CO ₂) lasers				
focusing characteristics	608	609	610	
HLAW	325			
laser deposition processes	587			
LBW	556	561	564	572

Index Terms**Links**

Carbon dioxide (CO ₂) lasers (<i>Cont.</i>)				
ROW	719			
wood cutting	618			
Carbon dioxide, shielding gases	296			
Carbon equivalent (CE)	126	132	307	443
Carbon equivalent (C _{eq})	421			
Carbon equivalent number (CEN)	748			
Carbon monoxide(CO)	613			
Carbon segregation	210			
Carbon steel flux cored electrodes	330			
Carbon steels				
A36	116			
DB	683			
FCAW	331			
FRW	183	644		
preheat and interpass temperatures	878			
process selection guide	872			
Carbonizing flame	883			
Carl Zeiss Company	507			
Carman-Kozeny equation	767			
Cartesian coordinate	4	746	748	773
	790			
Cartesian coordinate system	4			
Cast iron				
solid-state transformations	129			
weldability of	875			
Cathode	17			
arc welding	242			
EBW	514			
Caulk weld	883			
Ceramic arc shields	383			
Ceramics				
adhesive bonding	7			
aluminum	644			
brazing	10	13	26	
copper	666			
copper alloys	666			
EBW	22			

Index Terms**Links**

Ceramics (<i>Cont.</i>)		
electron beam tooling	531	
exothermic reactions	16	
FRW	644	
FSW	181	665
FSW tool designs	665	
joining processes (overview)	3	5
laser deposition processes	587	591
mechanical joining	5	
metallizing	678	
nonfusion (solid-state) welding	24	
oxide ceramics	685	
RW	397	
shielding the weld	350	
soldering	10	13
solid-state welding	25	
ultrasonic testing	222	
UW	201	
welding	9	11
CFR Title 29 CFR 1910	852	
Chain intermittent weld	883	
Chamfer	450	883
Charpy V-notch (CVN)	133	330
Chemical applications	287	
Chemical flux cutting (FOC)	883	
Chemically compatible	4	
Chicago Bridge and Iron Company	246	
Chill	11	
Chill ring	883	
Chill zone	96	97
Chisel tests	446	
Chubu Steel	615	
Chuck	385	
Clad brazing sheet	883	
Cladding. <i>See also</i> Laser deposition processes		
3-D laser cladding	592	
coaxially-fed powder cladding	590	

Index Terms**Links**Cladding (*Cont.*)

explosive cladding. <i>See</i> Explosion welding (EXW)				
GMAW	319			
laser cladding	103	592	594	747
	748			
weld cladding	264			
Clausius-Clapeyron equation	783			
Clyne-Kurz model	108			
CMSX-4	104	105		
CO ₂ beam delivery	582			
CO ₂ effects, surface tension	92			
CO ₂ gas lasers	508	509	510	
CO ₂ laser welding	584			
CO ₂ laser-GMAW hybrid welding	780			
CO ₂ welding	883			
Coalescence	883			
Coated electrode	883			
Coated steels				
dross formation	616			
mash seam welding	482			
organic	447			
RSEW	440	443	445	446
RSW	415	420		
seam welding current	480			
steels	421			
terne-coated	478			
zinc-coated	413	420	471	
Coating density	883			
Coaxially-fed powder cladding	590			
Cobalt-base alloys				
DB	685			
FRW	644			
Coextrusion welding (CEW)	701	702	883	
Coffin, Charles	243			
Cold crack	883			
Cold cracking	134	453		
Cold Metal Transfer (CMT)	257			
Cold pressure welding. <i>See</i> Cold welding (CW)				

Index Terms**Links**

Cold shuts	531	532	533
Cold soldered joint	883		
Cold weld			
HFRW	462		
NDE detection	462		
quality control	713		
resistance welding processes	462		
resistance-welded joints	490	499	
Cold weld effect	225		
Cold weld riveting	715		
Cold welding (CW)			
applications	713		
bond strength, modeling	712		
bonding mechanisms	711		
definition of	883		
indentation	714		
nonfusion (solid-state) welding	24		
overview	711		
process variants			
butt welding	714		
cold weld riveting	715		
extrusion	715		
indentation	714		
rolling	713		
shear welding	715		
quality control	713		
surface preparation, alternative			
methods	712		
Cold wire feeding	352		
Colegrove and Shercliff model	672		
Collet	385		
Color pigments	848		
Columnar-to-equiaxed transition (CET)	103	104	
Combination welder	305		
Combustion synthesis reactions	16		
Combustion synthesis welding processes	14		
Commissariat Energie Atomique (CEA)	507		
Complete fusion	264	327	542
			883

<u>Index Terms</u>	<u>Links</u>			
Complete joint penetration	270	883		
Complete penetration	375	883		
Compound scanning technique	226			
Compressed Gas Association (CGA)				
CGA AV-5	857			
CGA AV-6	857			
CGA E-1	856			
CGA E-4	856	857	862	
CGA E-5	857	861		
CGA P-1-1999	855			
Computational fluid dynamics (CFD)	147	773	774	
Computational kinetics (CK)	753			
Computational thermodynamics (CT)	753			
Computational weld mechanics	757	819	830	
Computed tomography (CT)	629			
Computer beam control	518			
Computer tomography (CT)	551			
Computer-aided design and manufacturing (CAD/CAM) modeling	587	592	593	
Computer-aided design (CAD)	540	734		
Computerized numerical control (CNC)				
EBW	517	518	536	
electron beams, nontraditional applications	543			
laser deposition processes	587	593		
split or multibeam processing	545			
UAM	732			
Concavity	326	327	601	883
Conduction mode	21			
Conduction-mode electron beam welds	90			
Cone				
definition of	883			
FSW	187			
FSW tool designs	666	667		
GMAW	84			
GTAW	251	253		
LBW	561			
solid-state resistance welding	213	214		

Index Terms**Links**

Cone (<i>Cont.</i>)				
welding processes	14	15		
Confined spaces	853			
Conjugate gradient (CG)	785			
Constant current (CC) control	407			
Constant current/constant voltage (CC/CV)	279			
Constant shear	190	235		
Constant voltage (CV)	255	277		
Constitutional liquation	128			
Constitutional supercooling	60	96	99	100
	103	754		
Constricted arc (plasma arc welding and cutting)	883			
Consumable electrode arc welding	18			
Consumable electrodes	18			
Consumable insert	264	265	883	
Contact resistance (resistance welding)	883			
Contact tip to work distance (CTWD)	337			
Contact tube	18	883		
Contact-tip-to-work distance	340			
Continuous cooling transformation (CCT) diagram	750	830	832	837
Continuous dynamic recrystallization (CDRX)	198	199		
Continuous heating transformation diagrams	125			
Continuous seam welds	727			
Control circuit	411			
Convexity	883			
Cooling shoes	365			
Copper				
DB	685			
FSW tool applications	666			
PW	427			
RSEW	483			
seam welding	444			

Index Terms**Links**

Copper alloys			
C11000	533		
DB	685		
FRW	644		
FSW tool applications	666		
laser cutting	617		
PW	427		
RSEW	483		
seam welding	444		
Copper brazing	883		
Copper vapor lasers	620		
Cored solder	883		
Corner joint	11	883	
Corner joints			
definition of	267		
EBW	525		
grooves, recommended proportions for	274		
Corner-flange weld	525	883	
Corona (resistance welding)	142	883	
Cosmetic pass	519		
Coulomb forces	7		
Coulomb's friction	190		
Coulomb's friction law	203		
Covalent bond	883		
Covered electrode	245	883	
Covered electrode welding.			
<i>See</i> Shielded metal arc welding (SMAW)			
Covered "stick" electrode	242		
Cr ₂ O ₃	50	617	
Crack	55	883	
Crack propagation	143	268	756
Crack tip opening displacement (CTOD)	135		
Crater	242	883	
Creep			
creep resistance	139	233	332
DB	682	686	687
integrated weld modeling	756		
weld pool	827		

Index Terms

Links

Creep, soft-interlayer solid-state welds	330			
Creep resistance	139	233	332	754
Crimps	6			
Crossdraft table	853			
Cross-tension strength (CTS)	417			
Cross-tension test	416	490	492	
Cross-wire welding	209	424	432	
Curie temperature	457			
Current range test	433			
Cutting attachment	883			
Cutting blowpipe	883			
Cutting nozzle	883			
Cutting tip	883			
Cutting torch (arc)	883			
Cutting torch (oxyfuel gas)	883			
CV transformer	279	280		
CV/pulse mode	84			
Cylinder manifold	884			

D

Damping	401			
Davy, Sir Humphrey	243			
de Benardos, Nikolas	243			
de Meritens, Auguste	243			
Deborah number	827			
Deep-penetration-mode welding	558			
DeepTIG for GTAW	355			
DeepTIG PEC	356			
Defects				
definition of	884			
design aspects in prevention of				
lamellar tearing	268			
overview	268			
solidification cracks	268			
tunnel defect	223			
Deformation				
2-D small- and large deformation				
analysis	149			

Index Terms**Links**

Deformation (<i>Cont.</i>)			
3-D small- and large deformation			
analysis	149		
DB	218		
plastic	24	204	
USW	202	204	
Degaussing coils	535		
Dendrite core compositions	107		
Dendrite spacing	105	107	
Densimet	666		
Deoxidation	44		
Department of Defense	539		
Department of Energy	745		
Deposit (thermal spraying)	884		
Deposited metal	47	884	
Deposition efficiency (arc welding)	884		
Deposition efficiency (thermal spraying)	884		
Deposition sequence	884		
Depth of fusion	298	314	884
Design for joining (use of term)	10		
Destructive testing	713		
Destructive testing (resistance-welded joints)			
dynamic mechanical tests			
fatigue tests	492		
impact test	493		
overview	492		
manual testing	490		
metallographic examination	494		
overview friction law	489		
quasi-static mechanical tests			
combined tension and shear test	492		
cross-tension test,	490	492	
tensile-shear test	492		
U-tension test	492		
Deutsches Museum of Technology	507		
Device	3		
DIABEAM system	551		
DictTra software	752		

<u>Index Terms</u>	<u>Links</u>		
Die burns	450		
Diffraction			
EBW	149		
electron backscattered diffraction imaging	735		
focused laser beams	509		
laser beam diameter	563		
laser beams	509		
laser micro-welding	628		
of neutrons	160		
residual stresses, measuring	755		
spot size	629		
thermomechanical phenomena in fusion welding	835		
TOFD technique	226		
Diffusion	7		
Diffusion bonding (DB)	884		
ceramic-ceramic joints	687		
ceramic-metal joints			
applied pressure	686		
bonding temperature	686		
overview	685		
surface roughness	687		
creep	682	686	687
dissimilar-metal combinations			
ferrous alloys	685		
ferrous-to-nonferrous alloys	685		
nonferrous alloys	685		
interface aids	220		
mechanism of			
overview	218		
stage I: microasperity deformation	218		
stage II: diffusion-controlled mass			
transport	219		
stage III: interface migration	220		
surface roughness	219		
noble metals	685		
nonferrous alloys			
aluminum-base alloys	683		
beryllium alloys	685		

Index Terms**Links**

Diffusion bonding (DB) (<i>Cont.</i>)			
cobalt-base alloys	685		
copper alloys	685		
nickel-base alloys	685		
reactive metals	684		
refractory metals	684		
overview	24	217	682
oxide ceramics	685		
oxides, surfaces containing	218		
process	217		
process variants			
HIP	683		
liquid-phase process	682		
solid-phase process	682		
SPF/DW technique	683		
steels			
carbon	683		
high-strength	683		
low-alloy	683		
stainless steels	683		
Diffusion brazing (DFB)	884		
Diffusion welding (DFW)	24	884	
<i>See also</i> Diffusion bonding (DB)			
Dilution	884		
Dilution (fusion welding)			
fusion zone composition and	115		
fusion-zone microstructure and properties			
overview	119		
stainless steel, deposition on carbon or			
low-alloy steel	119		
superaustenitic stainless steels, joining	119		
introduction	115		
welding parameters, influence of	117		
Dimensionless groups	67		
Diode laser	884		
Diode pumped solid state (DPSS) laser	884		
Diode-pumped Nd:YAG lasers	508		
Dip brazing (DB)	884		

<u>Index Terms</u>	<u>Links</u>		
Dip pot	26		
Dip soldering (DS)	884		
Direct current electrode negative (DCEN)			
arc stabilizers	45		
definition of	884		
GMAW	309		
GTAW	36	37	
PAW	359		
polarity	313		
SMAW	302		
Direct current electrode positive (DCEP)			
definition of	884		
GMAW	38	255	309
GTAW	36	250	
HLAW	324		
PAW	359		
polarity	313		
SMAW	302		
spray transfer	311		
Direct current reverse polarity (DCRP)	17	19	884
Direct current straight polarity (DCSP)	17	884	
Direct metal deposition (DMD)	592		
Direct weld parameters (DWP)			
arc welding process control	286		
modeling	289		
rotary friction welding	646		
Direct-diode lasers	588	590	
Direct-drive rotary friction welding			
dissimilar materials	644		
nonferrous			
aluminum-base alloys	644		
cobalt-base materials	644		
copper-base materials	644		
nickel-base materials	644		
reactive metals	644		
refractory metals	644		
overview	641		

Index Terms**Links**

Direct-drive rotary friction welding (<i>Cont.</i>)		
parameter qualification	643	
procedure qualifications	642	
steels		
carbon steels	644	
stainless steels	644	
tooling	642	
Direct-drive welding	24	25
Directed-energy fusion welding		
EBW	22	
LBW	23	
overview	21	
Disc laser welding	584	
Disc lasers	508	
Discontinuity	189	884
Discontinuous dynamic recrystallization (DDRX)	198	199
Disk laser	325	561
Distortion.		
fusion welding	151	
integrated weld modeling	754	
joint control	11	
modeling of thermomechanical phenomena in fusion welding	835	839
residual stresses and. <i>See</i> Residual stresses and distortion		
weld joint design	268	
welding	256	
Double-bevel-groove weld	884	
Double-Electrode GMAW	257	
Double-ellipsoid heat-input model	146	
Double-ellipsoid model	149	
Double-flare-bevel-groove weld	884	
Double-flare-V-groove weld	884	
Double-J-groove weld	884	
Double-square-groove weld	884	
Double-U-groove weld	884	
Double-V-groove weld	884	

Index Terms**Links**

Double-welded joint	884			
Dovetail-and-groove joints	6			
Downdraft table	853			
Downhand	388	532	590	884
Downslope power	518	519		
Downslope time	466			
DP 600 steel	470			
DP 780 steel	495			
DP-W 600	832	833		
Drag (thermal cutting)	884			
Drag angle	323			
Drop (use of term)	83			
Droplets				
detachment	256			
ESW	367			
FCAW	330			
GMAW	83	256		
laser droplet welding	633			
temperature	85			
transfer modes	83			
velocity	85			
Dross formation	612	616		
Dry welding	307			
Dual-feed (push-pull) feed units	315			
Dube ´ scheme	129			
Ductility				
bend test	490			
combined tension and shear test	492			
CW	712			
DB steels	683			
EGW	377			
EXW	690			
FOW	701			
FRW	182			
GTAW	345			
guided-bend tests	263			
hot cracking	453			
lamellar tearing	268			

Index Terms**Links**

Dual-feed (push-pull) feed units (<i>Cont.</i>)			
laser weld characteristics	596		
low-alloy steels	666		
nickel-base superalloys	140		
nonfusion pressure welding	24		
PW	426	433	
ROW	719		
spot welding	420		
tensile-shear test	492		
titanium alloys	143		
UAM	875		
underwater welding	307		
weld nugget	488	489	
Duty cycle	278		
Dynamic beam deflection processing			
design patterns			
high-speed raster generation	545		
split or multibeam processing	545		
essential variables, controlling			
accelerating voltage	544		
beam current	544		
beam focus	544		
deflection	544		
dwell time	544		
power density	544		
high-frequency, multibeam processes			
multiple-pool welding with a split beam	546		
pre- and post-heat treating	546		
selective surface treatment	545		
overview	544		
Dynamic force balance model (DFBM)	776		
Dynamic recovery (DRV)	199		
Dynamically recrystallized zone	196		
Dynamite	697		
E			
Ecodal	608	832	833
Eddy current	223	227	

Index Terms**Links**

Edge joints				
definition of	267	884		
EBW	526			
Edge preparation				
back gouging	272			
backing bars	272			
methods	272			
overview	271			
root faces	272			
spacer bars	272			
Edge projection welding	209			
Edge projection welds	215			
Edge weld	487	488	523	884
Edge weld size	884			
Edge-flange weld	523	526	884	
Edge-to-sheet welds	424			
Edison Welding Institute				
(EWI)	355	666	745	757
Effective throat	325	884		
Einstein equation	33			
Electric arc fusion welding				
arc welding	17			
arc welding processes	18			
modes of	17			
overview	16			
resistance welding processes	19			
Electrical circuit	411			
Electrical stickout (ESO)	337	340		
Electrode coating	303			
Electrode extension	313			
Electrode “follow” behavior	401			
Electrode force	464			
Electrode holder	303			
Electrodes				
arc welding	242			
ESW	371			
GTAW	349			
PAW	360			

Index Terms**Links**

Electrodes (<i>Cont.</i>)				
PW	429			
RSEW	483			
RSW	414			
Electrogas welding (EGW)				
aluminum	376			
carbon steels	375			
castings, joining	376			
castings, repairing	376			
dissimilar metal joining	376			
low-alloy steels	375			
multipass	375			
nickel-base alloys	376			
overview	18	19	365	374
problems				
fusion zone	376			
hydrogen cracking	377			
PMZ	377			
PWHT	377			
temper embrittlement	377			
weld distortion	377			
shielding gases	374			
stainless steel alloys	376			
structural steels				
heavy machinery	376			
overview	375			
pressure vessels	375			
shipbuilding	375			
titanium	376			
tool and die surfacing and welding	376			
Electroless nickel	220			
Electroless plating	712			
Electromagnetic	5			
Electromagnetic (Lorentz) stirring	92			
Electromagnetic acoustic transducers				
(EMATs)	600			
Electromagnetic acoustic transduction				
technology	227			

Index Terms

Links

Electromagnetic arc oscillation				
system	287			
Electromagnetic induction	223			
Electromagnetic monitoring	600			
Electromagnetic radiation				
high-frequency welding	461			
LBW	595	598		
PAW	364			
protection against	858			
Electron beam additive manufacturing (EBAM)	540			
Electron beam direct manufacturing				
(EBDM)	534	540	541	543
Electron beam evaporation	230			
Electron beam free-form fabrication				
(EBFFF or EBF ³)	540			
Electron beam melting (EBM)	540			
Electron beam near-net shape processing				
additive manufacturing	540			
EBDM	540			
general applications (target paths and applications)				
case study	543			
overview	543			
melting	540			
modeling/tool-path and computer aided design/				
computer-aided manufacturing tools	540			
process description and definitions	540			
process quality and control of essential variables				
material quality	541			
overview	541			
power-bed systems	541			
process qualification	542			
wire-feed systems	541			
Electron beam welding, design considerations				
boiler and pressure vessel codes	539			
customer quality specifications	539			
filler metal				
direct manufacturing	534			
filler metal, preplacement of	533			

Index Terms

Links

Electron beam welding, design considerations (*Cont.*)

filler wire, technique when feeding	534
filler-wire feeding	533
overview	533
porosity, preventing	533
prevention and cracking	533
wire-feeding equipment	533
high-vacuum design consideration	
overview	527
pressure, effect on beam	527
width of weld and HAZ	527
joint design	
butt joints	524
butt joints versus corner and T-joints	526
corner joints	525
edge joints	526
integral filler metal, welds using	527
lap joints	526
multiple-pass welds	527
multiple-tier welds	527
overview	524
plug welds	527
puddle welds	527
tangent-tube welds	527
three-piece welds	527
T-joints	526
medium-vacuum design consideration	
overview	527
pressure, effect on beam	527
width of weld and HAZ	529
nonvacuum	
applications	530
explanation	529
heat input	530
operating conditions	529
overview	529
penetration	530
tooling	530

Index Terms

Links

Electron beam welding, design considerations (<i>Cont.</i>)	
weld shape	530
overview	522
PCP	538
poorly accessible joints	
advantages	534
beam characteristics	534
overview	534
sidewall clearance	534
workpiece requirements	534
repair method, EBW as a	
electron-beam wire-feed process for repairs,	
application of	537
explanation	536
future applications	538
overview	536
quality-assurance testing	538
scanning/joint tracking, design for	
automatic joint tracking	536
beam alignment, accuracy of	535
electronic scanning	536
manual joint tracking	536
optical joint locating	535
overview	535
problems	535
procedure	535
techniques	535
thick metal	
advantages	532
disadvantages	532
flaws	532
full-penetration welds	532
gun orientation (vertical/horizontal)	532
overview	532
partial-penetration welding	532
pressure, effect of	532
problems	532
two-pass full-penetration welds	532

Index Terms

Links

Electron beam welding, design considerations (*Cont.*)

thin metal, welding

explanation	531
overview	531
partial-penetration welds	531
ranges	531

tooling/fixtures

heat-input control, design for	531
overview	531
weld repeatability, design for	531

in vacuum

vacuum limitation	529
vacuum welding conditions	529

weld geometry

melt-zone configuration	524
overview	522
part configuration	522
surface geometry	523
wide weld configurations	523

WPS	539
-----	-----

Electron beam welding (EBW)

See also High energy density beam welding

advantages	515
equipment cost	32
fluid flow phenomena	
keyhole fluid flow	92
overview	92
heat and mass transfer modeling	779
joint design	519
limitations	516
operation principles	514
operation sequence and preparation	
cleaning	518
demagnetization	518
evacuation	518
fixturing methods	518
joint fit-up	517
joint preparation	517

Index Terms**Links**

Electron beam welding (EBW) (<i>Cont.</i>)		
operating conditions	518	
overview	517	
postheat	518	
preheat	518	
overview	22	514
penetration depth	74	
process control	517	
safety	520	
weld geometry	519	
welding machines	519	
Electron beams and welds, quality control		
beam diagnostics, application of		
machine characterization	551	
overview	551	
quality control	554	
weld parameter transfer	552	
beam focus, beam diagnostic tools for	549	
essential variables, process control of	548	
NDE	548	
overview	548	
Electron gun/column assembly	515	
Electron probe microanalysis (EPMA)	115	722
Electrons	509	
Electroslag welding (ESW)		
aluminum	376	
carbon steels	375	
castings, joining	376	
castings, repairing	376	
CO ₂ shielding gas	365	
constitutive equations		
travel rate	368	
voltage	368	
welding current	368	
dissimilar metal joining	376	
EGW, differences between	365	
electrodes	371	
fluxes		

Index Terms**Links**

Electroslag welding (ESW) (<i>Cont.</i>)			
electrical resistivity	371		
fluidity	371		
metallurgical compatibility	371		
overview	370		
fusion zone compositional effects			
electrochemistry	373		
overview	372		
thermochemistry	372		
low-alloy steels	375		
multipass	375		
nickel-base alloys	376		
overview	18	19	365
power density	31		
process			
heat flow conditions	365		
magnetic field coupling	367		
metal transfer	367		
out-of-position (nonvertical) ESW	367		
weld pool morphology	367		
weld pool penetration	367		
process development			
electroslag surfacing	374		
high-productivity electroslag			
processes	373		
NGI-ESW	374		
slag bath and electrode, temperature			
relations between	369		
solidification structure	373		
solid-state transformations	373		
stainless steel alloys	376		
structural steels			
heavy machinery	376		
overview	375		
pressure vessels	375		
shipbuilding	375		
thermal cycle equations	369		
titanium	376		

Index Terms**Links**

Electroslag welding (ESW) (<i>Cont.</i>)			
tool and die surfacing and welding	376		
weld metal inclusions	373		
Electrostatic	5		
Embossed projections	209		
Embossed-projection welding	209	425	
Emergency Fleet Corporation	245		
End tabs	55		
Enderlein Electric Welding Company	244		
Energy-source intensity	29		
Enhanced modified Faraday cup (EMFC)	551	554	
<i>See also</i> Faraday cup			
Enthalpy	14		
Environmental Protection Agency	864		
Equiaxed zone	99	101	102
Equilibrium	43		
Equilibrium lever law	105	106	
Erichsen test	722	723	
Eulerian flow representation	190		
Eulerian method	767		
European Committee for Standardization (CEN)	575		
Evacuation	518		
Evaporative recoil-driven flow	626		
E-WeldPredictor approach	757		
E-WeldPredictor tool	757		
Excimer lasers	620		
Exothermic reactions	14		
Explosion welding (EXW)			
applications	690	698	
clad plate production			
assembly	698		
explosive loading	698		
metal specifications	697		
overview	697		
postweld processing	698		
process variants	698		
sizing considerations	697		

Index Terms

Links

Explosion welding (EXW) (<i>Cont.</i>)			
surface preparation	698		
welding	698		
component acceleration			
component collision	693		
jet formation	694		
overview	693		
definition of	885		
explosive detonation	692		
explosive parameters	692		
explosives	691		
geometric configurations	691		
HAZ	691		
manufacturing process and practice			
noise abatement	697		
regulations	697		
safety	697		
vibration abatement	697		
overview	24	25	690
parameters, selection of			
overview	694		
parametric limits	695		
practice considerations	691		
procedure development	691		
process attributes			
configuration limitations	690		
explosion welding interface morphology	690		
metallurgical attributes	690		
metals combinations	690		
performance characteristics	690		
reliability	691		
size limitations	690		
products	698		
shock effects	692		
shop welding applications	698		
weld characteristics			
interface mechanical properties	697		
interface microstructure	696		

Index Terms**Links**Explosion welding (EXW) (*Cont.*)

wave amplitude	695		
wave formation	695		
wavelength	695		
weld interface morphology	695		
Explosive cladding. <i>See</i> Explosion welding (EXW)			
Expulsion	215	432	450
Expulsion weld	210		
Extrusion			
arc welding	245		
CEW	701		
CW	712	715	
definition of	7		
FSW	195		
solid-projection welding	423		
solid-state welding	172	174	176
welding	702		
EXX10 stick-electrode welding	243		

F

Face reinforcement	885		
Faraday cup	550	629	
<i>See also</i> Enhanced modified Faraday cup (EMFC)			
Fast follow-up heads	212	428	
Fast-fill electrode	247		
Fatigue, weld joint design	268		
Fatigue fracture	165	493	
Fatigue tests	446	492	736
Fatigue-crack initiation	55		
Faying surface			
definition of	885		
RSW	41		
FDA Laser Policy 37	567		
Fe-10Al-5Cr alloy	108		
Fe-18Cr-11.3Ni (wt%) alloy	113		
Federal Communications Commission (FCC)	461		

<u>Index Terms</u>	<u>Links</u>			
Feedback control	290			
Ferrite (body-centered cubic) phase	488			
Ferrite number	138	885		
Ferrous alloys				
weld strength	649			
weldability of	874			
Ferrules	383			
Fiber laser	325	561	620	885
Fiber push-out testing	736			
Filler materials				
308 stainless steel	116			
brazing	9			
EBW	533			
ER70S6	757			
ESW	373			
GTAW	351			
HLAW	326			
IN622	119			
IN625	119			
IN686	110	111	119	120
soldering	9	26		
tungsten	18			
Filler metal	885			
welding personnel, qualification of	265			
welding qualification tests	264			
Filler wire	18	885		
Fillet weld	885			
Fillet weld break test	885			
Fillet weld leg	885			
Fillet weld size	885			
Fillet weld throat	885			
Fillet welding	149	162		
Fillet welds				
definition of	267			
design considerations				
fillet versus groove weld	270			
overview	269			
throat size	269			

Index Terms**Links**

Fillet welds (<i>Cont.</i>)				
weld placement	270			
weld size	269			
out-of-plane distortion	162			
SAW	336			
throat size	269			
weld size	269			
welding qualification tests	261	263		
Finger weld penetration	311			
Finite-difference methods (FDMs)	821			
Finite-element (FE) analysis				
soft-interlayer solid-state welds	235			
USW	201			
Finite-element method (FEM)	231	234	821	823
	826			
Finite-element modeling (FEM)	190			
Firecracker welding	306	885		
Fisheye	885			
Flame cutting	158	272	305	885
Flame propagation rate	885			
Flame spraying (FLSP)	885			
Flame temperatures, oxyfuel gas				
welding (OFW)	16			
Flange joints				
grooves, recommended proportions for	274			
LBW design	570			
Flange weld	523	525	885	
Flange weld size	885			
Flange-joint lap seam welds	444			
Flare-bevel-groove weld	885			
Flare-V-groove weld	885			
Flash	384	885		
Flash (use of term)	380			
Flash butt welding	885			
<i>See also</i> Flash				
welding (FW)				
Flash coat	885			

Index Terms**Links**

Flash welding (FW)	21	885
description of	397	
failure origins		
cold cracks	453	
hot cracks	453	
incomplete fusion	453	
poor weld contours	453	
porosity	453	
flash butt welding	448	
introduction	448	
overview	448	
process steps		
flashing stage	450	
preweld preparation	450	
PWHT	450	
upsetting (forging) stage	450	
processing equipment		
auxiliary equipment	452	
clamping dies	452	
controls	452	
fixtures	452	
overview	450	
state-of-the-art welding unit components	452	
UW	448	
Flashback	861	
Flash-lamp-pumped Nd:YAG lasers	508	
Flat pancake coil	705	
Flat position	83	885
Flat spots	210	
Flats	670	
Flats at the tip	215	
Flaw	223	885
Flow brightening (soldering)	885	
Fluid flow phenomena		
EBW	92	
keyhole fluid flow	92	
keyhole fluid flow, instability in	93	
GMAW	93	

Index Terms

Links

Fluid flow phenomena (*Cont.*)

GTAW

experimental observations	90
high current, effects of	92
numerical simulations	91
overview	89
poor penetration, controlling	92
surface-tension-driven fluid flow model	89
variable penetration, controlling	92

LBW

keyhole fluid flow	92
keyhole fluid flow, instability in	93
overview	92
mass transport in the arc	89
overview	89

SAW

transport equations	94
---------------------	----

Fluid flow velocities	89
-----------------------	----

Fluorite	49
----------	----

Flutes	667	668	669	670
	671	672		

Flux	18	885
------	----	-----

Flux cored arc welding (FCAW),	885
--------------------------------	-----

See also Power sources (arc welding)

advantages	330
------------	-----

applications	330
--------------	-----

base metals

carbon steels	331
---------------	-----

low-carbon steels	331
-------------------	-----

nickel-base alloys	332
--------------------	-----

stainless steels	332
------------------	-----

disadvantages	330
---------------	-----

electrode classification

carbon electrodes	333
-------------------	-----

low-alloy steel electrodes	333
----------------------------	-----

nickel-base electrodes	334
------------------------	-----

stainless steel electrodes	334
----------------------------	-----

electrode diameters	333
---------------------	-----

Index Terms**Links**

Flux cored arc welding (FCAW) (<i>Cont.</i>)				
electrode manufacture	332			
equipment				
automatic	331			
fume-removal	331			
mechanized	331			
semiautomatic	330			
fluxes				
electrode formulation example	52			
fluorides	51			
formulation	50			
negative interactions	51			
overview	49			
positive interactions	52			
self-shielded wires	50			
GMAW	245			
heat source, modeling of	39			
overview	18	329		
process features				
gas-shielded flux cored process	329			
self-shielded flux cored arc welding	330			
shielding gases	298			
wires	49			
Flux cored electrode	242	247	332	353
	885			
Flux cover (metal bath dip brazing and dip soldering)	885			
Flux oxygen cutting	885			
Flux TIG	355			
Flux welding processes	39			
Flux-cored arc welding (FCAW)	18			
Fluxes				
agglomerated fluxes	49			
arc welding	242			
basicity index	47			
bonded fluxes	49			
equilibrium parameters	43			
ESW	370			

Index Terms**Links**Fluxes (*Cont.*)

FOW	702		
fused fluxes	49		
granular	246		
overview	43		
oxygen, effect of			
inclusion formation	44		
overview	43		
pyrochemical reactions, metal transferability			
during	45		
shielding gas	46		
reground	338		
safe welding practices	865		
SAW	49	335	337
slag viscosity	48		
SMAW formulation			
alloy modification	48		
binding agents	48		
pyrochemical kinetics	47		
slag detachability	49		
slag formation	49		
slipping agents	48		
types			
FCAW	49		
SAW	49		
SMAW	49		
Flywheel			
energy	181		
speed	181		
Focused electron beam (FEB)	634		
Focused ion beam (FIB)	634		
Food and Drug Administration (FDA)	566		
Forehand welding	885		
Forge welding (FOW)	243	701	885
<i>See also</i> Solid-state welding (SSW) processes			
Formation system	734		
Fourier transform	85		

Index Terms

Links

Fracture toughness	
austenite grain growth	126
CVN tests	263
FSW tool designs	664
high-frequency welding	457
NDT	649
PCBN	665
qualification tests	262
recrystallization	800
RSW	418
titanium alloys	140
weld modeling	819
Frequency converter	405
Friction	4
nonfusion (solid-state) welding	24
ultrasonic welding (USW)	204
Friction stir welding (FSW)	
defects	
defect formation	191
defect formation, simulation of	195
overview	191
theoretical models	193
types	191
friction	190
material flow	
analytical modeling	189
coupled numerical modeling	190
experimental aspects	188
numerical modeling	189
overview	188
microstructural features	
cross section	196
dynamic recrystallization	198
microstructural evolution	198
nugget zone, grain size in	196
precipitate distribution	197
texture	197
overview	186

Index Terms

Links

Friction stir welding (FSW) (*Cont.*)

strain	195
strain rate	195
thermal aspects	
heat source estimation	187
overview	186
temperature management	186
temperature prediction:	
analytical approach	187
temperature prediction:	
numerical approach	188

Friction stir welding (FSW) tool designs

overview	664
probe features	
flats	670
flutes	670
overview	669
threads	669
probe geometries	
conical	668
cylindrical	668
noncircular cross sections	669
other	668
stationary shoulder	668
shoulder designs	
concave shoulder	667
flat shoulder	667
overview	667
stationary shoulder	667
tapered and convex shoulder	667
specific FSW processes, designs for	
adjustable probe length	670
lap welding	671
refill spot welding	671
self-reacting welding	671
swept spot welding	672
summary	673
tool geometry	666

Index Terms

Links

Friction stir welding (FSW) tool designs (*Cont.*)

tool material application

aluminum alloys	665
copper	666
copper alloys	666
low-alloy steel	666
magnesium alloys	666
MMCs	666
nickel alloys	666
stainless steels	666
thermoplastics	666
titanium alloys	666

tool material requirements

availability	664
chemical inertness at elevated temperature	664
cost	664
fracture toughness	664
manufacturability	664
overview	664
strength at process temperature	664
strength at room temperature	664
wear resistance	664

tool materials, classes of

carbides	665
ceramics	665
refractory metals	665
superabrasives	665
superalloys	665
tool steels	665

tool performance, predicting and measuring

overview	672
tool features, experimental observation of	673
tool features, modeling	672

Friction stir welding (FSW), welding procedures

ANSI H35.2	661
mechanical property tests	660
overview	654

Index Terms

Links

Friction stir welding (FSW), welding procedures (<i>Cont.</i>)			
procedure development	656		
procedure development requirements	655		
procedure qualification	661		
procedure requirements	655		
tensile tests	660		
Friction surfacing			
applications	679		
equipment	679		
overview	678		
process description	678		
Friction welding (FRW)	885		
banded feature	189		
dissimilar materials, problems welding			
brittle-phase formation	184		
differential thermal expansion	184		
joint interfaces	183		
low-melting-phase formation	183		
dissimilar metals, joining			
carbon steels and alloy steels	183		
overview	182		
stainless steels to other metals	183		
metallurgical parameters	181		
overview	24	25	179
process parameters			
friction heating, mechanisms of	179		
overview	179		
quality, factors influencing	179		
similar materials, joining	181		
technology			
direct drive welding	180		
inertia-drive welding	180		
overview	180		
Frustrum geometry	668		
<i>Fulagar</i>	245		
Full width of the beam at one-half its			
peak power density (FWHM)	551	553	

Index Terms

Links

Full width of the beam measured at 1/e2 of its peak power density (FWe ²)	551	553	554
Full-penetration groove welds, tests for			
CVN tests	263		
guided-bend tests	263		
overview	262		
tension tests	262		
Fume plume	846		
Furnace brazing (FB)	885		
Furnace soldering (FS)	885		
Fused fluxes	49		
Fused silica (SiO ₂)	608		
Fused spray deposit (thermal spraying)	885		
Fusion	885		
Fusion cutting	606	611	612
Fusion face	885		
Fusion welding	885		
chemically driven	14		
dilution in. <i>See</i> Dilution (fusion welding)			
energy-source intensity	29		
heat flow. <i>See</i> Fusion welding, heat flow in			
heat flow, factors influencing.			
<i>See</i> Fusion welding, factors			
influencing heat flow			
nucleation considerations			
application	98		
nucleation theory	97		
overview	97		
pool shape	99		
process fundamentals	29		
thermomechanical effects.			
<i>See</i> Fusion welding, thermomechanical			
effects			
Fusion welding, complex welding operations			
advanced boundary conditions	78		

Index Terms

Links

Fusion welding, complex welding operations (<i>Cont.</i>)	
groove welding	
joint geometries, complex	78
joint geometries, simple	77
overview	75
start and stop in welding	
case studies	77
overview	76
transient heating period, duration of	76
temperature-dependent material properties	
latent heat of fusion	75
thermal conductivity	76
volumetric heat capacity	76
Fusion welding, factors influencing	
heat flow	
bead-on-plate welding	69
complex welding operations. <i>See</i> Fusion welding, complex welding operations	
distributed heat sources	
fast-moving high-power source	72
general solution	71
overview	71
peak temperature distribution	72
introduction	
arc efficiency factors	67
fusion welding processes	67
metal and alloys, thermal properties of	67
line source solution, analogy with	
overview	74
penetration depth, coupling of models and predictions of	74
moving keyhole	
overview	73
temperature distribution	73
moving point and line sources	
medium-thick-plate model	69
thick-plate model	68

Index Terms

Links

Fusion welding, factors influencing		
heat flow (<i>Cont.</i>)		
thin-plate model	68	
overview	67	
pseudo-steady-state temperature		
distribution		
case studies	70	
heat flow mode	69	
isothermal contours	69	
overview	69	
Fusion welding, heat flow in		
engineering materials, thermophysical		
properties of	65	66
engineering solutions and empirical		
correlation		
cooling rate	59	
example: cooling rate for location at distance		
y (mm) from centerline	63	
example: solidification rate	64	
example: welding of 5 mm thick low-carbon		
steels	61	
example: welding of 6 mm thick low-carbon		
steels	62	
general solutions	58	
heat-flow equations, practical		
application of	61	
modified temperature solution	60	
peak temperature	60	
solidification rate	60	
general approach	56	
literature review	56	
mathematical formulations		
boundary conditions, other	58	
conduction equation	57	
heat-source formulation	57	
surface heat loss	57	
overview	55	
parametric effects		

Index Terms

Links

Fusion welding, heat flow in (*Cont.*)

material type	64
overview	64
welding speed	64
thermally related welding problems	56
welding control	56
welding distortion	56
welding engineering problems	55
welding metallurgy	55
welding thermal process	55

Fusion welding, modeling of heat and mass

transfer	
boundary conditions	
fluid flow, driving forces for	768
weld pool, heat transfer into	768
considerations (important)	766
dimensional analysis	774
dissimilar-metal welding	784
free surface flow	770
fusion welding processes	
EBW	779
GMAW	775
GTAW	775
laser welding	777
laser-arc hybrid welding	780
future models	786
mathematical description	767
model reliability	785
numerical solution	773
overview	766
transport equations	767
turbulence	
one-equation model	770
overview	769
turbulent flow, boundary conditions for	770
two-equation models	770
zero-equation (or algebraic) turbulence	
models	769

Index Terms

Links

Fusion welding, modeling of heat and mass transfer (<i>Cont.</i>)		
weld pool, mass transfer in		
alloying elements, vaporization of	781	783
nitrogen absorption	780	
welding arc plasma		
anode region	771	
arc column	772	
cathode region	773	
overview	770	
Fusion welding, modeling of metallurgical microstructure evolution		
Al-Mg-Si alloys	807	
Al-Mg-Si butt welds	814	
complex microstructure models (evolution of particle size distribution)	807	
design stress	813	
duplex stainless steel weldments, coupled reactions in		
austenite, dissolution of	804	
case study: application to EBW	805	
delta-ferrite decomposition	805	
delta-ferrite grain growth	804	
isokinetic solutions	807	
overview	804	
problem description	804	
engineering design	813	
grain growth		
dimensionless evolution equation	802	
grain growth kinetics	802	
overview	801	
structural steels	803	
internal state variable approach		
general methodology	797	
isokinetic reaction, definition of	798	
state variable formulation	797	
isokinetic microstructure models.		
<i>See</i> Isokinetic microstructure models		

Index Terms

Links

Fusion welding, modeling of metallurgical microstructure evolution (<i>Cont.</i>)		
multistage thermal processing		
artificial aging	810	
HAZ, precipitate structure following artificial aging	810	
HAZ, precipitate structure following PWHT	810	
HAZ, precipitate structure following welding	810	
overview	797	
precipitation model		
nucleation law	807	
numerical solution	809	
overview	807	
particle size distribution, inclusion of rate law	809	809
welded aluminum structures		
combined precipitation, yield stress, and work-hardening model, application of	816	
overview	814	
work-hardening model	814	
yield strength model		
overall yield strength	813	
overview	810	
precipitation hardening	811	812
solid-solution hardening	813	
Fusion welding, modeling of thermal-electrical mechanical coupling		
contact resistivity, estimation of	791	
discussions	792	
electrical analysis	790	
electrode-sheet contact, in-process growth	790	
latent heat, incorporation of	791	
numerical modeling, sheet-electrode geometry for	790	

Index Terms

Links

Fusion welding, modeling of thermal-electrical mechanical coupling (<i>Cont.</i>)	
overview	789
results	792
thermal analysis	789
Fusion welding, modeling of thermomechanical phenomena in	
general aspects	837
material properties input data	832
material properties, required	831
measurement techniques	831
mechanical simulation	
distortion calculation	839
residual stress	839
overview	830
temperature field simulation	
temperature deviations	838
weld pool geometry	838
thermal and mechanical results, validation of	
distortion	835
overview	834
residual stresses	835
temperature field	834
thermomechanical welding simulation, workflow	
assumptions	836
boundary conditions	836
heat source	837
material properties	836
overview	835
setup	835
simplifications	836
welding, basic principles	830
welding, heat effects	830
Fusion welding processes, summary of	870
Fusion welding, thermomechanical effects	
distortion	
2-D versus 3-D analyses	153
2-D/3-D applied plastic strain methods	152

Index Terms

Links

Fusion welding, thermomechanical effects

distortion (*Cont.*)

3-D/3-D applied plastic strain methods 153

applied plastic strain methods 152

initial plate straightness, effect of 153

overview 151

mathematical formulations

heat-input models 149

material models 149

multipass welding 149

solid-state transformations 149

thermal transport 147

thermoelastoplasticity 148

overview 146

residual stress 149

residual stress, formation of 146

three-bar analogy 146

Fusion welds

grain structure 99

weld solidification.

See Weld solidification (fusion welds)

Fusion welds, substructure formation

application 101

CET 103

constitutional supercooling 100

overview 100

single crystals 103

solute redistribution during solidification

binary models 105

multicomponent alloys, modeling of 110

ternary models 109

substructural scale, factors affecting 105

Fusion zone 122 377 885

Fuzzy logic 290 291 600 601

G

Gadolinium 108 109

Galo fever 855

Index Terms**Links**

Galvano-scanner mirrors	619	622	631
Gap	167	885	
Gas brazing	885		
Gas cups	253		
Gas cutter	885		
Gas cutting	266	885	
Gas cylinder	885		
Gas density	297		
Gas gouging	885		
Gas laser	885		
Gas metal arc cutting (GMAC)	885		
Gas metal arc welding (GMAW)	885		
<i>See also</i> Power sources (arc welding)			
acoustical signals	289		
advantages	309	318	
applications			
components	319		
industries	319		
joints	319		
material types	319		
arc climb	257		
arc length/voltage control	255		
consumables	313		
cooling rate (empirical equation)	59		
disadvantages	318		
dry welding	307		
electromagnetic arc oscillation system	287		
equipment	314		
overview	318		
power sources	318		
shielding gases	319		
welding torches	318		
fluid flow phenomena	93		
free surface flow (weld modeling)	770		
GTAW, differences between	254		
heat and mass transfer modeling	775		
heat input control	257		
heat source, modeling of	38		

Index Terms

Links

Gas metal arc welding (GMAW) (*Cont.*)

heat transfer.

See Gas metal arc welding (GMAW),

heat transfer

hybrid laser GMAW

316

hybrid plasma GMAW

316

hyperbaric welding

307

limitations

309

liquid-gas reactions

750

mass transfer. *See* Gas metal arc welding

(GMAW), mass transfer

mass transport in the arc

89

metal transfer

256

metal-transfer control

257

narrow-groove GMAW

316

overview

18

254

309

318

personnel

health issues

320

safety issues

320

skill level

320

training

320

postwar developments

247

principles of operation

arc length regulation

309

globular transfer

310

metal transfer, modes of

310

overview

309

pulsed spray

312

short-circuiting transfer

310

spray transfer

311

procedure

inspection requirements

319

process operating

319

troubleshooting

319

weld quality control

319

procedure development

85

process parameters

arc voltage

313

Index Terms

Links

Gas metal arc welding (GMAW) (<i>Cont.</i>)		
electrode extension	313	
overview	312	
polarity	313	
travel angle	313	
welding current	312	
process variations	316	
reciprocating wire feed short-circuit		
GMAW	316	
safety considerations	317	
shielding gases	298	
short arc power sources	280	
static force balance	257	
tandem GMAW	316	
variable polarity GMAW	316	
weld modeling	768	
weld modeling, arc column	772	
weld modeling, cathode region	772	
welding arc plasma (weld modeling)	770	
welding speed, effect of	64	
wire melting	255	
Gas metal arc welding (GMAW), heat transfer		
overview	82	83
partitioning of	83	
Gas metal arc welding (GMAW), mass transfer		
acoustic signals	85	
droplet temperature	85	
droplet transfer modes	83	
droplet velocity	85	
electrical signals	85	
overview	82	
Gas metal arc welding (GMAW) torch	326	
Gas pocket	885	
Gas purity	297	
Gas regulator	886	
Gas shielded arc welding	264	886
<i>See also</i> Plasma arc welding (PAW)		

Index Terms

Links

Gas shielding	249	251
<i>See also</i> Shielding gases		
Gas supply (laser cutting)		
assist gases	612	
lasing gases	612	
Gas torch	14	886
Gas tungsten arc cutting (GTAC)	886	
Gas tungsten arc welding (GTAW). <i>See also</i> Power sources (arc welding).		
acoustical signals	289	
adaptive control	290	
advantages	345	
applications	345	
arc physics		
anode	250	
arc column	251	
arc length control	253	
cathode tip shape, effect of	251	
electrode regions	249	
flow structure	252	
gas shielding	249	
overview	249	
polarity	249	
shielding gas composition, effect of	251	
arc tracer spectroscopy	289	
DCEN	298	
definition of	886	
dry welding	307	
equipment		
electrode selection	349	
electrode tip shape	350	
filler metals	351	
power supplies	347	
torch construction	349	
welding inserts	351	
fluid flow phenomena		
experimental observations	90	
high current, effects of	92	

Index Terms

Links

Gas tungsten arc welding (GTAW) (<i>Cont.</i>)		
numerical simulations	91	
overview	89	
poor penetration, controlling	92	
surface-tension-driven fluid flow model	89	
variable penetration, controlling	92	
fluid flow velocities	89	
free surface flow (weld modeling)	770	
heat and mass transfer modeling	775	
heat source, modeling of	36	
historical development	246	
hyperbaric welding	307	
limitations	345	
liquid-gas reactions	750	
mass transport in the arc	89	
modeling	289	
operation, principle of		
alternating current	346	
arc polarity	346	
overview	346	
overview	18	344
power supplies		
high frequency	349	
overview	347	
safety considerations		
arc radiation	353	
electrical shock	353	
explosion	353	
fire	353	
fumes/gases	353	
overview	353	
shielding gases	298	
argon	350	
backup purge	351	
gas flow rates	350	
gas purity	350	
helium	350	
shielding the weld	350	

Index Terms**Links**

Gas tungsten arc welding (GTAW) (<i>Cont.</i>)		
single crystals	105	
temperature measurements	288	
weld modeling, arc column	772	
weld modeling, cathode region	772	
welding arc plasma (weld modeling)	770	
welding procedures		
automatic and robotic welding (A/R)		
GTAW	352	
current range	351	
current type	351	
filler-metal feeding	352	
manipulation	351	
overview	351	
Gas tungsten arc welding with		
penetrating-enhancing compounds		
advantages/disadvantages	355	
applications	357	
A-TIG	355	
DeepTIG for GTAW	355	
DeepTIG PEC	356	
equipment	356	
Flux TIG	355	
GTAW with a PEC	355	
GTAW-DeepTIG process	355	
operation, principles of	355	
overview	355	
penetration-enhanced GTAW process	355	
personnel	357	
procedure	356	
Gas welding	886	
Gas-shielded arc welding	385	
Gas-shielded flux cored wires	330	
Gaussian distribution	823	
Gaussian function		
GMAW	38	
GTAW	37	251
high-energy-density welding	40	

Index Terms**Links**

Gaussian profile	767	768		
G-code	541			
General Electric Company	243	539	666	
General Motors	601			
Geometric dynamic recrystallization	198			
Gibbs-Thompson parameter	112	630	809	
Globular (use of term)	83			
Globular transfer (arc welding)	83	256	310	886
GM 4485M	601			
Gold	685			
Good (use of term for welds)	652			
Gouging	16	886		
Grain coarsening	142			
Grain growth				
austenite	125	133	825	
bonding temperature	686			
continuous heating transformation diagrams	125			
DB	684			
estimation of	750			
FSW	199			
fusion welds	96			
grain-boundary pinning	126	372		
HAZ	134	366	488	630
	805			
metallurgical microstructure evolution,				
modeling,	797	801		
pool shape influence on	99	100		
thermal pinning	126			
titanium alloys	561			
titanium oxide steels	133			
weld modeling	825	826		
welding metallurgy	55			
Grain structure, solid-state welding (SSW)				
processes	174			
Grain-coarsened zone (GC HAZ)	134			
Gravity welding	306			
Groove angle	886			
Groove face	270	886		

Index Terms**Links**

Groove joint	162	270	317	324
	325	527		
Groove preparation welds				
assembly, joint preparation after	271			
bevel angles	271			
double-groove weld joints	271			
included angles	270			
overview	270			
root openings	271			
Groove radius	886			
Groove weld				
angular distortion	162			
definition of	886			
reaction stresses	160			
residual welding stresses	160			
SAW	336			
stress distributions	160			
Groove weld size	886			
Groove weld throat	886			
Groove welding				
joint geometries, complex	78			
joint geometries, simple	77			
Groove-welded butt joints	261			
Ground connection	886			
Ground lead	886			
Grounding lines	461			
Gun	886			
Gun welders				
J-type	414			
S-type	414			
Gurney energy	693			
Gurney equation	693			
H				
H13 tool steel	665	666		
H400	832			
Hamilton Standard	507			
Hammer welding	886			

Index Terms**Links**

<i>Handbook of Compressed Gases</i>	855		
Hard solder	886		
Hard-surfacing welding procedures	264		
Hastelloy	617		
Hazardous Materials Regulation			
Board	864		
Heat affected zone (HAZ)	886		
austenitic grain growth	825		
EBW	23	527	
EGW	375	377	
ESW	365	366	
EXW	691		
FRW	182	196	197
fusion welding	33	55	56
girth-welded pipe	756		
integrated weld modeling	748		
LBW	23	557	560
microjoining	625		
PW	426		
resistance-welded joints	486	488	
RSW	416		
underwater welding	307		
X-65 steels	757		
Heat sink	11		
Heat source, modeling of			
FCAW	39		
flux welding processes	39		
GMAW	38		
GTAW	36		
high-energy-density welding	39		
overview	35		
RSW	40		
SAW	39		
simplified modeling	36		
SMAW	39		
Heat treatable steels, preheat and interpass			
temperatures	880		

Index Terms**Links**

Heating, ventilation, and air conditioning		
(HVAC) tubing	725	
Heat-source distribution	37	
Heavy equipment industries	330	
HeliArc process	246	
Helical trepanning	620	
Helium		
GTAW	252	350
shielding gases	297	298
Hems	6	
Hermeticity	597	631
High energy density beam welding		
electron and laser beam welding, comparison		
between	511	
electron beams		
historical development	507	
properties	509	
laser beams		
historical development	507	
properties	509	
overview	507	
High frequency resistance welding (HFRW)		
advantages	458	
applications	458	
cold weld	462	
definition of	886	
equipment	459	
fundamentals	457	
HAZ	457	
inspection	461	
limitations	458	
NDE	461	
overview	456	
personnel	461	
quality control	462	
safety	461	
High-brightness lasers	508	
High-energy-density welding	39	

<u>Index Terms</u>	<u>Links</u>			
High-frequency (HF) circuit	348			
High-frequency RW	397			
High-frequency spark discharges	243			
High-strength low-alloy (HSLA) steels	127	416	420	
High-strength steels (HSS)				
DB	683			
DP 600 steel	470			
DP 780 steel	495			
DP-W 600 steel	832	833		
welding current range	416			
High-temperature, ultra-high-pressure (HT-UHP) presses	665			
High-vacuum (EBW-HV)	515	516	517	518
	527			
Hold time	466			
Horizontal fixed position (pipe welding)	886			
Horizontal position (fillet weld)	886			
Horizontal position (groove weld)	886			
Horizontal rolled position (pipe welding)	886			
Hot cable	241			
Hot crack	886			
Hot cracking				
fusion welding	55			
FW	453			
Hot dipped galvanized (HDGI) coatings	420			
Hot dipped galvanized (HDGA) coating	420			
Hot isostatic pressing (HIP)	683			
Hot pressure welding (HPW)	24	886		
Hot spots	442			
Hot wire feeding	352			
Hot work	861			
Hot-hollow cathode (HHC)	230	234	235	236
HSLA-100 steels	133			
Hughes Research Laboratories	508			
Humping	321	327	628	780

Index Terms

Links

Hybrid laser arc welding (HLAW)	
advantages	321
applications	321
consumables	
consumable parts	326
filler-metal consumables	326
defects, sources of	
concavity	327
incomplete fusion	327
incomplete penetration	327
overview	326
porosity	326
root humping	327
undercut	327
disadvantages	321
equipment	
GMAW sources	326
hybrid welding head	326
laser sources	325
motion systems	326
hybrid welding head	
GMAW torch	326
laser-focusing optics	326
inspection	327
joint designs	
joint gap	325
joint mismatch	325
joint thickness	325
overview	324
operating modes	321
overview	321
process description	322
penetration-mode	322
stabilization-mode	322
process separation	
GMAW current	324
GMAW polarity	324
GMAW voltage	324

Index Terms

Links

Hybrid laser arc welding (HLAW) (*Cont.*)

laser power	323			
process orientation	323			
shielding gas	324			
wire feed speed	324			
quality control	327			
safety				
electrical hazards	327			
eye hazards	327			
fume hazards	327			
overview	327			
skin hazards	327			
training	327			
welding parameters				
overview	322			
process orientation	323			
travel speed	323			
Hybrid processes	10			
Hybrid welding.				
<i>See</i> Hybrid laser arc welding (HLAW)				
Hydrogen				
fusion welding	14			
shielding gases	296	297		
Hydrogen bonding	6			
Hydrogen brazing	886			
Hydrogen embrittlement				
residual stresses	160			
soft-interlayer solid-state welds	236			
Hydrogen-induced cracking (HIC)	128	134	165	342
	377			
Hydrogen-induced cracks	165			
Hyperbaric welding	307			

I

Ideal explosive	692			
Imaging optics	288			

Index Terms

Links

Impact tests (resistance-welded joints)		
double-pendulum test	494	
drop impact test	494	
overview	493	
shear impact loading test	494	
shear impact test	493	
tension impact loading test	494	
Impeders	460	
Impulse (resistance welding)	886	
Inactive elements	149	
Inclined position	886	
Inclined position (with restriction ring)	886	
Included angle	209	886
Inclusion formation	44	
Incoloy 901	537	
Inconel 600	617	
Inconel 625	588	
Inconel 718	140	666
Indentation (cold welding)	714	
Indirect weld parameters (IWP)		
arc welding process control	286	
modeling	289	
rotary friction welding	646	
Induction brazing (IB)	886	
Induction soldering (IS)	886	
Induction welding (IW)	886	
Inductive “skin” effect	431	
Inert gas	886	
Inert gas metal arc welding	886	
Inert gas tungsten arc welding	886	
Inertia friction welding (IFW)	646	651
Inertia rotational friction welding	24	25
Inertia welding		
dissimilar materials	644	
nonferrous		
aluminum-base alloys	644	
cobalt-base materials	644	
copper-base materials	644	

Index Terms

Links

Inertia welding (<i>Cont.</i>)	
nickel-base materials	644
reactive metals	644
refractory metals	644
overview	641
parameter design	642
procedure qualifications	642
steels	
carbon steels	644
stainless steels	644
tooling	642
Infrared (IR) point source	288
Infrared brazing (IRB)	886
Infrared soldering (IRS)	886
Initial graphics exchange specification (IGES)	734
Initial plate straightness, effect of	153
In-line destructive weld testing	418
Innershield process	247
In-service repair	4
Integral interlocks. <i>See</i> Integral mechanical attachment	
Integral mechanical attachment	6
Integrated weld modeling	
case study: X-65 steels	757
computational thermodynamics	
inclusion formation	751
liquid-gas reactions	750
liquid-slag reactions	751
solidification	752
solid-state transformation	753
concluding remarks	759
creep	756
distortion prediction	754
E-WeldPredictor tool	757
HAZ microstructure, prediction of	748
kinetics tools	
inclusion formation	751
liquid-gas reactions	750

Index Terms**Links**

Integrated weld modeling (<i>Cont.</i>)			
liquid-slag reactions	751		
solidification	752		
solid-state transformation	753		
microstructure modeling	748		
models, access and delivery	756		
optimization methodologies	758		
overview	745		
performance modeling	754		
physics and methodologies			
fluid flow modeling	748		
heat transfer, modeling	746		
process modeling	746		
property predictions			
high-temperature properties	756		
low-temperature properties	755		
residual-stress			
overview	754		
prediction	754		
weld metal microstructure, predictions of	750		
weldability prediction	754		
Interatomic bonding	171	172	176
Intercritically reheated grain-coarsened (ICGC) zone	134	135	
Interfacial contact	29	220	686
Interference	5		
Intergranular penetration	886		
Internal joule heating. See Resistance welding (RW)			
International Annealed Copper Standard (IACS)	445		
International Electrotechnical Commission (IEC)			
IEC 60529	284		
IEC 60934-1	284		
International Institute of Welding (IIW)	83	129	
International Standards Organization (ISO)	414	415	

Index Terms

Links

Interpass temperature	128	886
Interrupted (periodic impulse) current	479	
Inverse modeling	785	
Inverter power supplies	347	
Ionic salts	580	
IR camera (vision-based digital)	288	
Iron, forge welding (FOW)	243	
Iron soldering (INS)	886	
Iron-base alloys		
A-286	537	
AMS 6508	537	
ISF-Aachen	551	
ISO 11146	509	
ISO 14733-4	548	
ISO 14744-2	548	
ISO 14744-3	548	
ISO 3821	861	
Isokinetic microstructure models		
overview	798	
particle coarsening		
case study: coarsening of TiN during		
steel welding	800	
coarsening kinetics	799	
isokinetic solution	800	
overview	799	
particle dissolution		
case study: grain-boundary liquation in		
Al-Zn-Mg weldments	799	
overview	798	
platelike precipitates	798	
spherical precipitates	799	
recrystallization		
case study: recrystallization during welding of		
aluminum alloys	801	
overview	800	
recrystallization kinetics	801	
Isokinetic reaction, definition of	798	

Index Terms

Links

J

Jackson, C.E	249	
JBK-75 stainless steel	91	92
Jerk	403	
J-groove weld	267	886
Johnson-Mehl-Avrami-Kologoromov model	754	
Joining processes		
adhesive bonding	6	
brazing	9	
design aspects		
joint design	11	
overview	10	
hybrid processes	10	
introduction	3	
joining, need for	3	
materials joining		
chemical forces	5	
dissimilar materials, compatibility of	4	
mechanical forces	4	
overview	4	
physical forces	5	
mechanical joining		
integral mechanical attachment	6	
mechanical fastening	5	
overview	5	
soldering	9	
summary	11	
variant processes	10	
welding	7	
Joint		
definition of	886	
use of term	266	
Joint clearance	526	886
Joint design		
accessibility	11	
alignment	11	
distortion control	11	
location	11	

Index Terms**Links**Joint design (*Cont.*)

orientation	11	
unequal section thickness	11	
use of term	11	
welding qualification tests	264	
Joint efficiency	6	886
Joint penetration	270	886
Joint root	886	
Joint type	886	
Joint-line remnant (JLR) defect	191	
Joule effect	399	401

K

Kerf	606	886		
Keyhole				
description of	21			
EBW	92	514	779	
fluid flow	92			
fluid flow, instability in	93			
formation	92			
fusion welding	73			
HLAW	322	327		
laser weld quality monitoring	596			
LBW	778			
microjoining	628			
PAW	360	361		
penetration (keyhole) welding process	596			
Keyhole formation				
absorptivity	564			
avoidance of	631			
deep-penetration-mode welding	558			
EBW	514			
LBW	836			
vapor pressure	40	92	93	532
	597	778		
Keyhole mode welding	39			
Kissing welds	570			
Kjellborg, Oscar	245			

Index Terms**Links**

Knudsen-layer boundary	771			
Knurl drive	438	445	477	
Kurz, Giovanola, Trivedi (KGT) model	103	113		
L				
Lack of penetration (LOP)	223			
Ladle thermodynamics	751			
Lamellar tear	886			
Lamellar tearing	267	268	269	
Land	325	886		
Lap joints	11	261	267	526
	886			
Lap seam weld	439	444		
Lap seam welding				
mash seam weld	444			
metals welded	443			
overview	441			
weld, cooling	443			
weld force	443			
wheel geometry	443			
wheel maintenance	443			
Lap welding	670	671	673	
Lap welds	336	351	398	632
	671			
Laplace transformation solution methods	402			
Lap-shear test	416	736		
Laser	23	886		
Laser additive manufacturing (LAM)	592			
Laser beam cutting (LBC)	887			
Laser beam delivery optics				
CO ₂ beam delivery	582			
design considerations	581			
overview	580			
transmissive versus reflective lens				
elements	581			
Laser beam manufacturing economics				
case study: CO ₂ versus disc laser welding				
break-even analysis	585			

Index Terms**Links**

Laser beam manufacturing economics (<i>Cont.</i>)	
CO ₂ laser welding	584
cost comparison	584
disc laser welding	584
overview	583
case study: robotic metal inert gas versus	
robotic laser welding	585
overview	583
Laser beam weld codes	574
Laser beam weld joints, design of	
consumables, use of	571
engineering alloys	
aluminum	571
aluminum alloys	571
penetration welding	571
steels	571
titanium	572
titanium alloys	572
joint preparation, fit-up, and design	
butt joint—full penetration type	570
flange joints	570
kissing welds	570
lap joints	570
wire joints	570
overview	570
special welding practices	571
Laser beam weld quality assessment	
assessment	573
defined	572
overview	572
Laser beam welding (LBW)	
advantages	556
associated hazards	
chemical hazards	568
electrical hazards	567
conduction-mode welding	558
deep-penetration mode welding	558
definition of	887

Index Terms

Links

Laser beam welding (LBW) (*Cont.*)

documentation	568		
equipment cost	32		
fluid flow phenomena			
keyhole fluid flow	92		
keyhole fluid flow, instability in	93		
overview	92		
fundamental and process physics	558		
health	566		
heat and mass transfer modeling	777		
injury hazards			
eye hazards	566		
skin exposure	567		
limitations	557		
liquid-gas reactions	750		
medical examinations	568		
overview	22	23	556
procedure development			
absorptivity	564		
interaction time	561		
laser beam diameter	562		
laser beam power	562		
laser beam spatial distribution	563		
laser welding efficiency	565		
plasma suppression	565		
power density	561		
shielding gas	565		
traverse speed	564		
process parameters			
absorptivity	560		
laser beam diameter	559		
laser beam power	559		
traverse speed	560		
process selection	561		
safety	566		
training	568		
transport phenomena (heat, momentum, and mass)	559		

Index Terms**Links**

Laser cladding	103	592	594	747
	748			
<i>See also</i> Laser deposition processes				
Laser controlled area (LCA)	567			
Laser cutting				
assist gas flow rates				
example: cutting mild steel	614			
example: cutting stainless steel	614			
overview	614			
assist gas types	612			
focus position	612			
focusing characteristics	608			
gas purity				
assist gas	613			
lasing gas	613			
gas supply				
assist gases	612			
lasing gases	612			
laser and traditional cutting processes,				
comparison between	619			
laser output	607			
material considerations				
aluminum alloys	617			
copper alloys	617			
mild steels	615			
nickel alloys	617			
overview	615			
plastics	618			
stainless steels	617			
synthetic materials	618			
titanium alloys	617			
wood	618			
overview	606			
piercing	608			
surface conditions	618			
thermal processes, principles of	606			
<i>Laser Cutting Guide for Manufacturing</i>	606			

Index Terms

Links

Laser deposition processes	
laser cladding	
arc cladding, comparison with	590
future directions for	591
material combinations	588
powder cladding	589
process characteristics	589
process description	587
scanned versus defocused beams	590
wire feeding	589
near-net shape processing	
applications	591
characteristics	591
directed powder methods	592
future directions for	594
powder bed methods	591
overview	587
Laser droplet welding	633
<i>Laser focus World</i> buyer' guide	561
Laser hybrid welding. <i>See</i> Hybrid laser arc welding (HLAW)	
Laser roll welding	
dissimilar metals	
galvanized steel sheet with aluminum sheet	722
steel and aluminum sheet metal	720
uncoated steel sheet with aluminum sheet	721
introduction	717
overview	719
steel and titanium sheet joining	722
Laser shock-peening	621
Laser spike welding	632
Laser weld quality monitoring	
acoustic monitoring	599
electromagnetic monitoring	600
EMATs	600
examples	

Index Terms**Links**

Laser weld quality monitoring (<i>Cont.</i>)		
overview	601	
real-time monitoring of laser welding		
in production of tailor-welded		
blanks	602	
in-process monitoring	599	
laser weld characteristics		
joint configurations	596	
weld elements	596	
laser welding, overview of	595	
laser welding process description	595	
overview	595	
penetration (keyhole) welding		
process	596	
process variables		
laser weld “signals”	598	
overview	597	
real-time monitoring	599	
sensors	599	
weld monitoring system, selection of		
data acquisition	601	
sensors	600	
Laser-arc hybrid welding	766	780
Laser-assisted arc welding	322	
LaserCusing	591	
Laser-drilling		
hole quality	620	
overview	619	
ultrashort high-energy pulses	620	
Laser-engineered net shape (LENS)	592	
Laser-GMAW hybrid welding	780	785
Laser-metal inert gas (MIG) hybrid welding	780	
Lasers (use of term)	507	
Lasing gases	612	
Latent heat of fusion	75	
Lateral-drive system	725	
Lawrence Livermore National Laboratory		
(LLNL)	551	

Index Terms**Links**

Lazy “S”	191		
Lead burning	887		
Ledeburite	129		
Lenticular structure	143		
Levenberg-Marquardt (LM)	785		
Lichtenberg, G.	243		
Lifshitz-Slyozov-Wagner (LSW) equation	800	810	
Lift	382		
Light amplification by stimulated emission of radiation (laser)	606		
Lincoln Electric Company, The	244	245	247
Linear (reciprocating) friction welding	24	25	
Linear (vibration) friction welding	24	25	
Linear void density (LVD)	735		
Linear weld density (LWD)	205	735	
Liquation cracking	139	377	
Liquidation	887		
Local brittle zones (LBZs)	135	136	
Local thermodynamic equilibrium (LTE)	252		
Locked out	846		
Locked-up stress	887		
Locking (Morse) taper	728		
London Naval Treaty (1930)	246		
Longitudinal crack	887		
Longitudinal distortion	162		
Longitudinal stresses	160		
Lorentz force. guide	92	626	
Lorentzian curve	251		
Low-alloy nickel-base alloys	427		
Low-alloy steels			
DB	683		
FSW tool applications	666		
HAZ	753		
Low-carbon steel welds	161		
Low-carbon steels			
FCAW	331		
RSEW	474		
SAE 1005	474		

Index Terms**Links**Low-carbon steels (*Cont.*)

SAE 1010	474
SAE 1015	474
stress-relieving treatments	164
studs	381

Low-pressure electron beam welding	750
------------------------------------	-----

M

Machine welding	887
-----------------	-----

Macroetch test	887
----------------	-----

Maglay process	374
----------------	-----

Magnesium

aluminum alloys	139	184
-----------------	-----	-----

aluminum studs	381
----------------	-----

diffusion welds	686
-----------------	-----

electrode tip shape	350
---------------------	-----

fluxes	51
--------	----

FSW	189
-----	-----

FSW tool designs	673
------------------	-----

FW	448
----	-----

GTAW	249	347	349
------	-----	-----	-----

HAZ	489
-----	-----

laser deposition	589
------------------	-----

laser roll welding	721
--------------------	-----

metallographic examination	495
----------------------------	-----

Magnesium (continued)

metallurgical compatibility	371
-----------------------------	-----

metallurgical microstructure evolution, modeling	810	813	815
--	-----	-----	-----

MPW	704	705	708
-----	-----	-----	-----

PMZ	487
-----	-----

recrystallized grain size	196	199
---------------------------	-----	-----

RSEW	445
------	-----

RW	406	482
----	-----	-----

shielding gases	350	565
-----------------	-----	-----

three-dimensional (3-D) lobe diagrams	473
---------------------------------------	-----

tool steels	665	666
-------------	-----	-----

vacuum welding conditions	529
---------------------------	-----

vaporization	571
--------------	-----

<u>Index Terms</u>	<u>Links</u>		
Magnesium, arc welding	246		
Magnesium alloys			
AZ31D	489		
FSW tool applications	666		
Magnetic pulse welding (MPW)			
additional equipment	706		
applications	708		
capacitor bank	705		
EM welding system	705		
equipment	705		
field shapers	706		
fundamental theory	704		
high-voltage power supply	706		
high-voltage switches	706		
mechanical testing	707		
metallurgical characterization	707		
overview	704		
power system	705		
process			
overview	706		
parameters	707		
Rogowski coils	706		
safety guidelines	708		
summary	709		
work coil			
bar coils	705		
flat pancake coil	705		
overview	705		
solenoid coils	705		
Magnetically-impelled arc butt welding (MIAB)	18		
Magnetohydrodynamics (MHD)	626		
Maiman, Theodore	508		
Management (use of term)	845		
Manganese			
AHHS	420		
EBW	533		
EGW	377		
ESW	371	372	373

Index Terms**Links**Manganese (*Cont.*)

FCAW	330			
fluxes	45	47	48	49
	53	338		
fumes/gas hazard	353	554	851	
fusion welding	115	116		
laser cutting	616			
mild steels	615	616		
oxidation potential	300			
RSW	421			
safe welding practices	854			
SAW	49			
shielding gases	296			
steel electrodes	314			
steels	126	127		
Manual metal arc (MMA) welding	137			
Manual welding	252	887		
Marangoni (Ma) numbers	13	774		
Marangoni convection	89	94		
Marangoni flow	626			
Marangoni shear stress	768			
Marc	835			
Marine applications	287	357	375	
Martensite	134			
Martensite (body-centered tetragonal) phase	488			
Mash seam welding	438	439	444	474
	482			
Mask (thermal spraying)	887			
Material safety data sheets (MSDSs)	846			
Mathematical axioms	819			
Mathematical Modeling of Weld Phenomena	746			
Maximum permissible exposure (MPE) level	567			
Mechanical bond (thermal spraying)	887			
Mechanical compatibility	4			
Mechanical fastening	5			
Mechanical interlocking	7			
Mechanical stress relieving	163			
Mechanical system	411			

Index Terms**Links**

<i>Mechanics Handbook</i> (Enderlein)	244			
Medium-frequency direct current (MFDC)				
controls	407			
Medium-vacuum (EBW-MV)	515	517	518	519
	527			
Melt-in mode	21			
Melting efficiency (use of term)	565			
Melt-through	270	887		
Meredith, Russell	344			
Mesh generation	773			
Metal arc	243			
Metal arc cutting (MAC)	887			
Metal cored electrode	887			
Metal electrode	887			
Metal inert-gas (MIG) welding	247			
Metal powder cutting (POC)	887			
Metal-induced embrittlement	236			
Metallic bond	26	712	887	
Metallizing	678	887		
Metallurgical bond	26	887		
Metal-matrix composites (MMCs)				
FRW	181			
FSW tool applications	666			
Methane (CH ₄)	613			
Method of images	71			
Methylacetylene-propadiene (MPS)	857			
Metric conversion guide	895			
Meyer Werft GmbH	322			
Meyer's hardness number	793			
Microalloyed steels	127			
Microelectronic welding	727			
Microhardness testing	736	738		
Microjoining				
beam-material interactions				
humping	628			
keyhole stability	628			
overview	627			
electron beam microwelding fixtures	633			

Index Terms

Links

Microjoining (<i>Cont.</i>)	
fixtures	631
future trends	634
laser droplet welding	633
laser spike welding	632
metallurgical consequences	
cooling/solidification rates,	
effect on	629
diffusion-limited kinetics	630
ripples	630
surface contamination	630
unmixed zone	630
microscale physical phenomena	625
microweld, definition of	625
microwelds	
driving forces	626
other forces	626
overview	625
resisting forces	626
overview	625
postweld metrology/inspection	
handling	631
microwelds, visualizing and measuring	631
NDE micromethods	631
process controls	
beam scanning versus part motion	631
parameter control requirements	631
process description	
beam monitoring	629
spot sizes	629
suitable equipment	628
rapid beam rastering/scanning	632
SHADOW technique	632
stationary beam/moving workpieces	632
transport	
diffusion distances	625
energetics	625
Microlap joints	362

Index Terms**Links**

Microphases	130			
Microwelding	24			
Midfrequency direct current (MFDC)	411	429	463	
MIG welding	887			
<i>See also</i> Gas metal arc welding (GMAW)				
Mild steels				
AE	649			
cross-wire welding	432			
double-pendulum test	494			
FCAW	332			
GMAW	311			
laser cutting	615			
PW	426			
SMAW	303			
Military applications	287			
Mil-Specs	539			
MIL-W-6858D	427			
Mine Safety and Health Administration, (MSHA)	850			
Mirrors				
adaptive	612			
cavity	613			
CO ₂ beam delivery	582			
EBW	535			
focusing	608			
folding	609			
Galvano-scanner mirrors	619	622	631	
hybrid welding head	326			
LBW	562	563	567	612
optics for beam delivery	580			
parabolic	582			
rapid beam rastering/scanning	632			
Mixing chamber	887			
Mode of metal transfer	310			
Molten weld pool	17	887		
Molybdenum				
AHHS	420			
DB	683	685		

Index Terms**Links**Molybdenum (*Cont.*)

electrodes	483			
ESW	372	373		
FCAW	319	320		
FRW	644			
FSW tool designs	665			
GMAW	319			
high-frequency welding	459			
high-temperature chromium-molybdenum steels	332			
low-alloy steels	666			
multicomponent alloys, modeling of	110	111		
RW	400	401		
shielding gases	350			
solid-state welding processes	644			
superaustenitic stainless steels (joining)	120			
titanium alloys	666			
weld solidification	107			
Monel	617			
Monte Carlo simulation	126	629	750	
Multicomponent alloys, modeling	110			
Multipass welding				
ESW and EGW	375			
LBZ	136			
thermomechanical effects	149			
transverse shrinkage	162			
Multiple-pass welds	23	247	338	355
	515	527		
Multiple-tier welds	527			
EBW	527			
Multiport nozzle (plasma arc welding and cutting)	887			
Mushrooming	405	414	463	
N				
Nail head	564			
Nanohardness testing	736	738		

<u>Index Terms</u>	<u>Links</u>		
Narrow-gap improved electroslag welding (NGI-ESW)	374		
Narrow-lap welding. <i>See</i> Mash seam welding			
National Electric Code (NEC)	284	859	
National Electrical Manufacturers Association	858		
National Fire Protection Association (NFPA) 70, Article 630	284		
National Fire Protection Association's (NFPA) 51B	317	860	
51B-1962	845		
NFPA 79	862		
safe welding practices	859		
National Institute for Occupational Safety and Health (NIOSH)	850		
National Joint Council	355		
National Materials Advisory Board	759		
Nd:YAG lasers	325	561	600
Near-net shape processing			
applications	591		
characteristics	591		
directed powder methods	592		
future directions for	594		
powder bed methods	591		
Neodymium: yttrium-aluminum-garnet (Nd:YAG) laser pulses	783		
Neodymium: yttrium-aluminum-garnet (Nd:YAG) lasers	588		
Neodymium-doped yttrium-aluminum-garnet (Nd:YAG) lasers	556		
Neural networks	290		
Neutral flame	15	887	
Newton's law of viscosity	768		
Newton's second law of motion	402		
Nickel			
copper nickels	484		
DB	685		
seam welding	444		

Index Terms**Links**

Nickel alloys				
FSW tool applications	666			
laser cutting	617			
seam welding	444			
Nickel-base alloys				
alloy 600	332			
alloy 625	319	332		
DB	685			
EGW	376			
ESW	376			
FCAW	332			
FRW	644			
IN622	115			
IN625	115	117		
Nickel-base filler metal (IN686)	110	111	119	120
Nickel-base superalloys	139	538		
Ni-Cr-Mo-Gd alloys	108	109		
Nimonic 90	666			
Niobium	644	685		
Nitrogen, shielding gases	297			
Nitrogen absorption (weld modeling)	780			
Nitroguanidine explosive	692			
Noble metals	682	683		
Nonconsumable electric arc welding	18			
Nonconsumable electrodes	18			
Noncontinuous cooling transformation (CCT)				
diagram	122	123		
<i>Nondestructive Evaluation and Quality</i>				
<i>Control</i> , Volume 17 of ASM				
<i>Handbook</i> 1989	548			
Nondestructive evaluation (NDE)				
EBW	548			
HLAW	327			
rotary friction welding	649			
solid-state welds. <i>See also</i> Solid-state				
welds, NDE				
eddy current	223			
radiography	222			

Index Terms**Links**

Nondestructive evaluation (NDE) (<i>Cont.</i>)		
ultrasound	222	
UAM	738	
USW	727	
Nondestructive testing	495	
arc welding	247	
CW	713	
EBW	525	538
EMATs	600	
FSW	659	
resistance welded joints	492	
rotary friction welding	652	
RSEW	446	
RW	446	
UAM	736	
USW	727	729
UW	454	
Nondestructive testing (resistance-welded joints)		
dynamic resistance	496	
electric current	496	
electric voltage	496	
electrode displacement	497	
electrode force	497	
overview	495	
process signals	495	
ultrasonic evaluation		
in-line ultrasonic test monitoring	500	
overview	498	
ultrasonic A-scan technique	498	
ultrasonic B-scan technique	499	
Nonequilibrium	122	
constitutional liquation	128	
fusion welding	5	56
integrated weld modeling	752	
nonweldable alloys	541	
solidification	109	
solid-state	122	
weld solidification	96	105

Index Terms**Links**

Nonequilibrium lever rule	44	106		
Nonequilibrium solidification	109			
Nonferrous alloys law of viscosity				
DB second law of motion	683			
weldability of	874			
Nonferrous metals, weldability of	876			
Nonfusion (solid-state) welding				
diffusion welding/bonding	24			
EXW	25			
FRW	25			
nonfusion pressure welding	24			
overview	24			
solid-state deposition welding	25			
USW	25			
Nonfusion pressure welding	24			
Nonideal explosive	692			
Nonimaging optics	287			
Nonisothermal quasi-neutral plasma (presheath)	771			
Nonthermionic (or field) emission	250			
Nontransferred arc (plasma arc welding and cutting, and plasma spraying)	887			
Nonvacuum (EBW-NV)	515	516	517	519
	527	529	530	
Norway iron	245			
Nozzle				
definition of	887			
ESW	372			
Nozzle orifice				
GMAW	318	319		
PAW	359	360	363	364
Nuclear industries	594	685		
Nucleation-based theory	233			
Nugget size (resistance welding)	887			
Nugget zone	196	197	198	
Nuggets				
definition of	887			
solid-state resistance welding	209	210		
Nut welding	431			

Index Terms

Links

O

Occupational Safety and Health Act of 1970	845			
Occupational Safety and Health Administration (OSHA)				
29 CFR 1910, Subpart Q	461			
29 CFR 1910.1200	845			
29 CFR 1910.134	850			
chemical hazards	568			
explosive welding	864			
HFRW	461			
laser beam hazards	566			
permissible exposure limits	855			
safety management	845			
ultrasonic welding	864			
USW	729			
Octaspot welding	672			
Off time	466			
Ohio Supercomputing Center	757			
Ohm's law	397			
Olsen ball tests	446			
Olszewski, Stanislav	243			
One-way coupling	837			
Open-source codes	767			
Orbital friction welding	24	25		
Organic coated steels	447			
Orifice				
EBW	529	530		
gas. <i>See</i> Plasma gas				
GMAW	318	319		
laser cutting	614			
PAW	300	359	360	363
Orifice gas (plasma arc welding and cutting)	300	319	359	887
Orowan particles	814	815	816	
Ostwald ripening	127			
Out-of-plane distortion	162			
Oven soldering	887			
Overexposure	850			
Overhead position	887			

<u>Index Terms</u>	<u>Links</u>			
Overlap	218	887		
Overlaying	339	473	754	887
Oxidation cutting	606	611	612	
Oxide ceramics, diffusion bonding of				
ceramic-ceramic joints	687			
ceramic-metal joints	685			
applied pressure	686			
bonding temperature	686			
surface roughness	687			
overview	685			
Oxides, diffusion bonding	218			
Oxidizing flame	15	887		
Oxyacetylene flame	15			
Oxyacetylene welding (OAW)				
definition of	887			
development of	241			
equipment cost	32			
heat utilization efficiency	33			
overview	14			
power density	31			
Oxyfuel gas cutting (OFC)	887			
Oxyfuel gas spraying	887			
Oxyfuel gas welding (OFW)				
definition of	887			
flame temperatures	16			
heat source	35			
overview	14			
Oxygas cutting	887			
Oxygen				
safe welding practices	857			
shielding gases	296	297		
Oxygen, effect of				
inclusion formation	44			
interactions	91			
overview	43			
pyrochemical reactions, metal transferability				
during	45			
shielding gas	46	92		

Index Terms**Links**

Oxygen arc cutting (AOC)	887			
Oxygen cutter	887			
Oxygen cutting (OC)	887			
Oxygen cutting operator	887			
Oxygen gouging	887			
Oxygen grooving	887			
Oxygen lance	887			
Oxygen lance cutting (LOC)	887			
Oxygen lancing	887			
Oxyhydrogen welding (OHW)	557	887		
P				
P8TF10	539			
Pacemaker wearers	860			
Paper-covered electrode	245			
Parallel welding				
definition of	888			
RSW	413			
Parallel-plate welding	691			
Parent metal	25	888		
Partial differential equations (PDEs)	766			
Partial joint penetration	888			
Partially melted zone (PMZ) law	139	377	487	
Partially mixed zone (PMZ)	116	119		
Partial-penetration groove welds	263			
Particle coarsening	799			
Paste weld. <i>See</i> Cold weld				
Paton Welding Institute	355			
Pavlecka, V.H.	344			
Peak temperature				
fusion welding	60	72		
HAZ	123			
weldment	60			
Peak temperature-cooling time (PTCT)				
diagram	124			
Peck-piercing	608			
Peclet (Pe) numbers	774			
Peel test	205	433	736	737

Index Terms**Links**

Peltier effect	398	399	401
Penetration	888		
Penetration (keyhole) welding process	596		
Penetration depth	74		
Penetration-enhancing compound (PEC)	355		
Perception threshold	858		
Percussion drilling	619		
Percussion welding (PEW)			
definition of	888		
overview	20		
Permit-required confined spaces	853		
Personal protective equipment (PPE)	848		
eye, face, head protection	848		
hand, foot, body protection	849		
hearing protection	850		
process-specific requirements	849		
respiratory protection	850		
Philips Research Laboratories	318		
Phosphorus	220		
Photovoltaic silicon film	619	622	
Physical compatibility	4		
Pilot arc (plasma arc welding)	318	319	359
	888		
Pin tool	664		
Pin tools	656	664	667
	672		670
Pin-and-tenon welds	424		
Pinch instability theory (PIT)	776		
Pinch points	390	421	847
Pinhole detection system	550		
Pipe welder	305		
Pipe welds	881		
Planar-magnetron (PM) sputtering	230	234	
Plasma	242		
Plasma arc cutting (PAC)	888		
Plasma arc welding (PAW)			
advantages	360		
applications	361		

Index Terms

Links

Plasma arc welding (PAW) (<i>Cont.</i>)				
components	362			
definition of	888			
disadvantages	360			
equipment				
electrodes	360			
overview	360			
plasma (orifice)	361			
shielding gases	361			
welding torches	360			
joints	362			
keyhole mode	359	360		361
melt-in mode (microplasma mode)	359			
microplasma (melt-in-mode)	361			
operation, principles of				
current modes	359			
operating modes	359			
overview	359			
overview	18	21		359
personnel requirements				
health issues	364			
safety issues	364			
skill level	364			
training	364			
procedures				
inspection	363			
process operating procedure	363			
troubleshooting	363			
weld quality control	363			
shielding gases	300			
Plasma gas	300	319		360
	363	770		
Plasma gas metal arc welding. <i>See</i> Gas metal arc welding (GMAW)				
Plasma metal inert gas (MIG) welding. <i>See</i> Gas metal arc welding (GMAW)				
Plasma metallizing	888			
Plasma spraying (PSP)	888			

Index Terms**Links**

Plastic deformation				
nonfusion pressure welding	24			
USW	204			
Plastic interlocks	6			
Plastic zone sizes	143			
Plastics				
laser cutting	618			
use of term	3			
Plastics welding	25			
Plenum chamber (plasma arc welding and cutting, and plasma spraying)	888			
Plug welds				
definition of	888			
EBW	527			
grooves, recommended proportions for	274			
residual stresses	160			
UW	455			
welding qualification tests	261	263		
Plunge	382			
PM sputter deposition	230	231	234	235
Poisson's ratio	204	609	791	826
	831	832		
Polarity				
arc welding	17			
DCEN	313			
DCEP	313			
definition of	888			
GMAC	313			
Polycrystalline cubic boron nitride (PCBN)	665	666		
Polycrystalline diamond (PCD)	665			
Polyhedral meshing	774			
Polymers, use of term	3			
Pool shape, fusion welding	99			
Porosity				
aluminum	483			
arc welding	246			
arc welding processes	268			
butt welding	571			

Index Terms**Links**Porosity (*Cont.*)

conduction-mode welding	558			
DB	210	215	220	687
definition of	888			
EBW	375	518	519	531
	532	533		
FCAW	329	330		
fluid-flow phenomena	93			
fluxes	43			
friction surfacing	678	679		
FSW	186			
FW	450	453		
GMAW	18	313	318	319
GTAW	346	350		
H LAW	326			
lap joint	570			
laser weld	597	601		
LBW	558	559	560	565
	626			
PAW	362			
PW	430	432	436	
qualification tests	264			
resistance welded joints	497			
rotary friction welding	646			
ROW	718			
RW	397	418	421	428
	471			
SAW	337	343	344	
shielding gases	297			
slag viscosity	48			
SMAW	306			
solid-state welds	224			
spray transfer	311			
SW	383			
two-pass full-penetration welding	532			
ultrasonic testing	289			
weld modeling	766	778		
weld quality	573	574		

<u>Index Terms</u>	<u>Links</u>			
Postheating	888			
Postweld heat treatment (PWHT)				
Al-Mg-Si alloys	807			
cracking	140			
definition of	888			
EGW	377			
fusion welding	136			
FW	450			
nickel-base superalloys	140			
welding qualification tests	264			
Powder cutting	888			
Power density				
arc welding process control	285			
fusion welding	30			
Power factor	280			
Power sources (arc welding)				
characteristics				
inverter-based power sources	279			
overview	277			
power factor	280			
power source efficiency	280			
with single-phase ac input voltage	278			
three-phase input machines	279			
multiple arc (multiple operator)				
multiple dc+ welders	282			
overview	281			
resistance grid systems	281			
overview	277			
selection considerations	283			
short arc GMAW	280			
Prandtl number (Pr)	558	769	774	821
	822			
Precoating. ratio		888		
Preform	543	888		
Preheat	62	888		
Preheat current (resistance welding)	888			
Preheat temperature	62	888		
Pressure gas welding (PGW)	577	888		

Index Terms**Links**

Pressure hill effects	717		
Pressure-controlled welding	888		
Pretinning	888		
Primary bonds	7	9	
Primary rectified dc	429		
Primer	7		
Procedure qualification	260	888	
Procedure qualification record (PQR)	260	265	888
Process	3	888	
Process control plan (PCP)	538		
Product clamp	728		
Productivity, use of term	241		
Projected (use of term)	83		
Projection weld nuts/studs/screws	424		
Projection welding (PW)			
advantages	425		
annular-projection welds	424		
ball-to-sheet welds	425		
cross-wire welding	424	432	
defects, sources of	432		
definition of	888		
edge-to-sheet welds	424		
embossed-projection welding	423		
equipment			
electrode followup	428		
electrode parallelism	428		
electrodes	429		
overview	428		
power supply types	428		
welder stiffness	428		
history			
embossed-projection welding	425		
modern projection welding	425		
solid-projection welding	425		
inspection	433		
introduction	423		
limitations	426		
material property effects			

Index Terms**Links**Projection welding (PW) (*Cont.*)

aluminum	426		
aluminum alloys	426		
copper	427		
copper alloys	427		
low-alloy nickel-base alloys	427		
overview	426		
stainless steels	427		
steels	426		
titanium alloys	427		
overview	20	423	
personnel	430		
pin-and-tenon welds	424		
process fundamentals	427		
process requirements	430		
projection weld nuts/studs/screws	424		
quality control			
current range test	433		
feedback controller systems	433		
overview	432		
peel test	433		
projection set-down	433		
shear- or normal-type tensile tests	433		
torque test	433		
recommended practices	427		
resistance mash welds	424		
safety	434		
solid-projection welding	423		
solid-state resistance welding	209		
solid-steel projection welding			
annular-projection welding	430		
cross-wire welding	432		
nut welding	431		
specifications	427	435	437
steel embossed-projection welding			
dissimilar-thickness joints	430		
heavy-gage sheet steels	430		
thin-gage sheet	430		

Index Terms**Links**

Projection welds		
electrical characteristics, effect of	213	
RW	398	
system mechanical dynamics,		
effect of	211	
Protective atmosphere	46	888
Protective housings	566	
Puddle	888	
Puddle welds	527	
Pull gun technique	888	
Pulse (resistance welding)	888	
Pulse welding (PW)	277	708
Pulse/constant-voltage (CV) mode	84	
Pulsed arc control	257	
Pulsed gas tungsten arc welding procedure	137	
Pulsed Nd:YAG lasers	561	
Pulsed spray	312	
Pulsed spray source waveforms	315	
Pulse-echo technique	223	
Pulse/pulse mode	84	
Pumpdown time	527	529
Pure input	496	
Pure iron	93	
Push angle	323	
Push-pin testing	736	737
Push-pin-type test	205	
Push-pull welding	413	
PWA 16	539	
PWA 1480	103	
Pyrochemical reactions		
ac mode	45	
arc stabilizers	45	
DCEN mode	45	
delta quantity	45	
delta quantity, changes in flux		
composition with	45	
<i>Pyrotechnia</i> (Biringuccio)	243	

Index Terms**Links****Q**

Qualification procedures	260
Qualified person	848
Quasi-steady state	55
Quiet elements	149

R

RA1607-077	539			
Radial friction welding	24	25		
Radiation				
arc	353			
brazing and soldering	865			
EBW	517	529	863	
electromagnet radiation	858			
GMAW	38	317	327	
GTAW	36	288	353	
high-frequency welding	461			
HLAW	327			
LBW	23	520	556	
NDE, solid-state welds	222			
PAW	364			
radiography	222			
safe welding practices	845	848	850	863
	865			
SAW	335	343		
THSP	865			
x-radiation	863			
Radiation, EBW	520			
Radio frequency (RF) pulse	600			
Radiography	222	223		
Radiused (contoured) wheels	439			
Random intermittent welds	888			
Raoultian behavior	175			
Rapid beam manipulation	518			
Rayleigh instability	776			
Rayleigh length/range	510	609	610	611
Reactance	412			

Index Terms**Links**

Reaction flux (soldering)	888		
Reaction stress	888		
Reactive metals	644	684	
Reducer	11		
Reducing atmosphere	298	416	888
Reducing flame	15	701	888
Reference information			
abbreviations	892		
ferrous and nonferrous alloys, weldability of			
arc welding processes	874		
cast irons	875		
nonferrous alloys	876		
steels	875		
fusion welding processes	870		
glossary	882		
metric conversion guide	895		
shielding gases	869		
steels, preheat and postweld treatment			
temperatures			
carbon steels	878		
heat treatable steels	880		
pipe welds	881		
steel pressure vessel, abbreviations			
welding fuels	869		
Refill friction stir spot welding (RFSSW)	671		
Reflected radiation sensor (RR)	600		
Reflow soldering	888		
Reflowing	888		
Refractory metals			
FRW	644		
FSW tool designs	665		
Reground fluxes	338		
Repair welding	307		
Repelled (use of term)	83		
Residual stress			
definition of	888		
integrated weld modeling	754		

Index Terms

Links

Residual stress (*Cont.*)

modeling of thermomechanical phenomena in fusion welding	839
thermomechanical effects of fusion welding	149
thermomechanical phenomena in fusion welding, modeling of	835

Residual stresses and distortion

analyses of	159
brittle fracture	163
buckling distortion	162
built-up beams, longitudinal distortion column	162
compressive loading, buckling under	165
distortion (weldments)	161
environmental effects	165
fatigue fracture	165
fillet welds, out-of-plane distortion	162
formation	158
groove weld reaction stresses	160
residual welding stresses	160
stress distributions	160
groove weld, angular distortion	162
low-carbon steel welds	161
measuring	159
overview	158
plug weld	160
residual stresses, changes in	162
service behavior	162
square-groove weld, transverse shrinkage	162
stress-relieving treatments	164
thermal stresses and metal movements metal movement	159
overview	158
residual stresses, equilibrium condition of	159
thermal stresses	158

Index Terms**Links**

Residual stresses and distortion (<i>Cont.</i>)			
ultrahigh-strength steels	161		
welded shape	160		
weldments, thermal treatment of			
postweld thermal heat treatments	165		
preheat	165		
Resistance	412		
Resistance brazing (RB)	888		
Resistance butt welding	171	216	888
Resistance mash welds	424		
Resistance seam welding (RSEW)			
advantages	439		
aluminum			
electrodes	483		
equipment	483		
overview	482		
aluminum alloys			
electrodes	483		
equipment	483		
overview	482		
bearing maintenance	481		
coated steels	446		
copper			
electrodes	483		
equipment	483		
overview	483		
copper alloys			
beryllium copper alloys	483		
bronzes	484		
copper nickels	484		
low- and high-zinc brasses	484		
overview	483		
definition of	438	888	
electrodes	477		
electrodes, selection of			
class 1 copper	445		
class 2 copper	445		
class 3 copper	445		

Index Terms**Links**Resistance seam welding (RSEW) (*Cont.*)

class 20 copper	445		
shapes	446		
sizes	445		
lap seam welding			
mash seam weld	444		
metals welded	443		
overview	441		
weld, cooling	443		
weld force	443		
wheel geometry	443		
wheel maintenance	443		
limitations	440		
low-carbon steels			
overview	474		
part fit-up	475		
surface preparation	475		
mash seam welding	482		
nonferrous alloys	482		
overview	20	21	438
procedure development	473		
process applications			
lap seam weld	439		
mash seam weld	439		
process control	446		
processing equipment	444		
roll spot welding	482		
stainless steels			
overview	474		
part fit-up	475		
surface preparation	475		
testing	480		
types			
flange-joint lap seam welds	444		
lap seam weld	444		
weld quality	446		
welding machines			
electrode drives	445		

Index Terms

Links

Resistance seam welding (RSEW) (<i>Cont.</i>)	
electrode force	445
gear drive	445
knurl drive versus friction drive	445
movable carriages	445
overview	444
support	445
workpiece drives	445
welding machines, types	
circular	445
longitudinal	445
portable	445
universal	445
welding parameters	
current	480
electrode force	478
speed	479
time	479
Resistance soldering (RS)	888
Resistance spot welding (RSW)	
advantages	409
applications	
aluminum, spot welding	421
overview	419
steels, spot welding	420
uncoated steels, spot welding	419
zinc-coated steels, spot welding	420
DB	684
definition of	888
disclaimer	422
equipment	
overview	411
power supplies	411
secondary impedance	412
evaluation methods	416
heat source, modeling of	40
machine construction	
gun welders (J-type)	414

Index Terms

Links

Resistance spot welding (RSW) (<i>Cont.</i>)		
gun welders (S-type)	414	
overview	413	
pedestal-type welding machines	413	
portable welding guns	413	
MFDC	411	
on-line nondestructive testing	409	
overview	20	409
process description	409	
safety	421	
single-weld configurations	412	
spot welding variables		
heating, effect of weld spacing on	466	
surface finish	466	
weld lobe diagrams	469	
weld time	465	
welding current	463	
welding machine	469	
welding or electrode force	464	
welding schedules development	467	469
surface condition		
oil coatings, effect of	415	
overview	415	
oxide, effect of	415	
rust, effect of	415	
scale, effect of	415	
surface preparation	415	
two-weld configurations		
overview	412	
parallel welding	413	
push-pull welding	413	
series welding	413	
weld integrity		
acceptable, criteria for	417	
in-line destructive weld testing	418	
overview	416	
visual examination	416	
welding behavior evaluation		

Index Terms**Links**

Resistance spot welding (RSW) (<i>Cont.</i>)			
metallographic characterization	416		
welding current range	416		
welding electrodes			
coolant parameters	415		
maintenance	414		
overview	414		
shapes	415		
welding qualification tests	261		
Resistance Welder Manufacturers' Association			
(RWMA)	400	427	452
Resistance welding electrode	888		
Resistance welding gun	889		
Resistance Welding Manual	427		
Resistance Welding Manufacturers Alliance			
(RWMA)	411		
Resistance welding power supplies and			
controls			
duty selection	408		
equipment selection	404		
heat input	404		
newer systems	407		
overview	404		
rectification systems, older	405		
secondary rectification systems	405		
single-phase dc systems	405		
single-phase systems	405		
three-phase primary rectification system	406		
Resistance welding, procedure development			
and practice considerations			
overview	463		
seam welding procedure development. See			
Resistance seam welding (RSEW)			
spot welding variables			
heating, effect of weld spacing on	466		
surface finish	466		
weld lobe diagrams	469		
weld time	465		

Index Terms

Links

Resistance welding, procedure development and practice considerations (<i>Cont.</i>)		
welding current	463	
welding machine	469	
welding or electrode force	464	
welding schedules development	467	469
Resistance welding (RW)		
definition of	16	888
electrode "follow" behavior	401	
fundamentals, overlooked	398	
overview	397	
processes	19	397
Resistance Welder Manufacturers' Association's (RWMA)	400	
thermoelectric effects		
example: automotive	400	
example: battery terminal	400	
interfacial resistance, effect of	401	
Joule effect, contribution of	399	
overview	398	
Peltier effect	398	
Peltier effect, contribution of	399	
Thomson effect	399	
welds, types of		
butt welds	398	
projection welds	398	
seam welds	398	
spot welds	398	
Resistance-welded joints, evaluation and quality control		
destructive testing	489	
dynamic mechanical tests		
fatigue tests	492	
impact test	493	
overview	492	
manual testing	490	
metallographic examination	494	
nondestructive testing	494	

Index Terms

Links

Resistance-welded joints, evaluation				
and quality control (<i>Cont.</i>)				
overview	486			
process signals, weld-quality control using				
dynamic resistance	496			
electric current	496			
electric voltage	496			
electrode displacement	497			
electrode force	497			
process signals	495			
quality attributes	489			
quasi-static mechanical tests				
combined tension and shear test	492			
cross-tension test	490	492		
tensile-shear test	492			
U-tension test	492			
structural attributes				
imperfections	487			
internal characteristics	488			
spot welds	486			
<i>See also</i> Spot welds				
ultrasonic evaluation Association				
in-line ultrasonic test monitoring	500			
overview	498			
ultrasonic A-scan technique	498			
ultrasonic B-scan technique	499			
Resistivity	19			
Resonance	403	727	728	733
Retained austenite	134			
Reverse polarity	249	346	889	
<i>See also</i> Direct current electrode positive (DCEP)				
Reynold's number	626	694	822	
Ripples	630			
RLC circuit	705	706		
Robotic metal inert gas versus robotic laser welding	585			

Index Terms**Links**

Robotic torch orientation detection and control	287			
Robustness testing	655			
Rogowski coils	706			
Roll pressure welding	24			
Roll spot welding	482			
Roll welding (ROW)				
alligatoring	717			
cold roll welding	718			
definition of	889			
hot rolling	718			
overview	717			
pack rolling	717			
roll-welded heat exchangers	718			
strip roll welding	718			
Rolling (cold welding)	713			
Root	11	889		
Root bead	323	326	327	889
Root edge	889			
Root face	270	272	889	
Root gap	268	889		
Root humping	327			
Root opening	11	271	889	
Root penetration	191	889		
Root radius. (RWMA)	889			
Root reinforcement	311	889		
Root surface	889			
Rosenthal equation	747	748		
Rosenthal solution	823			
Rosenthal thick-plate solution	68	188		
Rosenthal thin-plate solution	68			
Rotary friction welding.				
<i>See also</i> Direct-drive rotary friction welding; Inertia welding				
description of	641			
Rotary friction welding, process monitoring and control of				
background	646			

Index Terms

Links

Rotary friction welding, process monitoring and control of (<i>Cont.</i>)				
categories	648			
control	652			
in-process control	652			
monitoring				
dissimilar metals, metallurgical integrity				
of	649			
ferrous alloys, weld strength of	649			
overview	648			
stainless steel a, ferrite formation of	651			
overview	646			
system parameters	647			
Rotating arc sensors	287			
Routers	618			
Royal Institute of England	243			
RPCam	734	735	739	740
Runoff tab	518			

S

Safe welding practices. <i>See also</i> Safety considerations				
adhesive bonding				
flammable materials	866			
hazardous materials	866			
personal protective equipment	866			
safety facilities	866			
air sampling	855			
arc welding and cutting	862			
brazing and soldering				
hazardous/explosive gases and fumes	865			
overview	865			
solder flux	865			
compressed gases				
cryogenic liquids	857			
cylinder valves	856			
filling cylinders	855			
fuel gas	857			

Index Terms

Links

Safe welding practices (*Cont.*)

fuel-gas fires, preventing	857
gas withdrawal	856
labeling	855
manifold piping systems	856
mixing gases	855
overview	855
oxygen	857
pressure-relief devices	856
regulators	856
shielding gas	857
storage/usage	855
electrical safety	
cables	859
connections	859
electric shock, sources of	858
equipment selection	859
grounding	859
installation	859
modification/maintenance	859
multiple-arc welding operations	860
operation, principles of	859
overview	858
pacemaker wearers, special precautions	860
electromagnetic radiation	858
electron beam welding	
fumes and gases	863
overview	863
visible radiation	863
x-radiation	863
explosion prevention	861
fire prevention and protection	
fire watchers	860
hot-work authorization	861
overview	860
friction welding	
explosion welding	864
overview	864

Index Terms

Links

Safe welding practices (<i>Cont.</i>)	
thermite welding	864
ultrasonic welding	864
fumes and gases, protection against	
exposure, measurement of	855
exposure factors	851
overview	850
fumes and gases, sources of	
arc welding/cutting operations	851
cutting fume and gases	852
oxyfuel gas welding	852
welding current	851
high-frequency welding	863
laser beam welding and cutting	
chemical hazards	864
electrical hazards	864
eye hazards	864
overview	863
respiratory hazards	864
skin hazards	864
overview	845
oxyfuel gas welding and cutting	
backfire	861
flashback	861
hose-line safety devices	862
hoses	861
oxygen equipment	861
regulators	862
shutdown procedures	862
torches	861
ventilated storage	862
personal protective equipment (PPE)	
eye, face, head protection	848
hand, foot, body protection	849
hearing protection	850
process-specific requirements	849
respiratory protection	850
process-specific safety considerations	861

Index Terms

Links

resistance welding	
electrical considerations	862
machinery safeguarding	862
overview	862
robotic operations	866
safety management	
hazard communications	845
management support	845
overview	845
training	846
thermal spraying	
dust	865
electrical shock	865
fumes and gases	865
noise	865
overview	865
radiation	865
ventilation	
general ventilation	853
local ventilation	853
overview	852
ventilation, special situations	
chlorinated hydrocarbons	855
cleaning compounds	855
confined spaces, welding in	853
containers, welding of	854
fluorine compounds	855
low-allowable limit materials	854
piping, welding of	854
stainless steel, cutting	855
zinc compounds	855
work area, protection of	
equipment, positioning	846
hazard notification	846
machinery safeguarding	846
overview	846
protective booths	848
public demonstrations	848

Index Terms**Links**

resistance welding (<i>Cont.</i>)				
public exhibitions	848			
wall reflectivity	848			
<i>Safety and Health Fact Sheets</i>	845			
Safety considerations. <i>See also</i> Safe welding practices				
EBW	520			
EXW	697			
GMAW	317			
HFRW	461			
HLAW	327			
LBW	566			
MPW	708			
PAW	364			
PW	434			
RSW	421			
SAW	343			
SMAW	307			
SW	390			
UAM	740			
Saha equations	772			
Satoh test	134			
Scan sweep (gun beam sweep)	536			
Scanning acoustic microscopy (SAM)	226			
Scanning electron microscope (SEM)				
CW	711			
microjoining	628	631	632	
Scar	525			
Schaeffler diagram	119			
Schawlow, A.L	508			
Scheil equation	111			
eutectic fraction calculations	109			
fusion welding	106	107		
inclusion formation	44			
multicomponent alloys, modeling of	110			
Scheil-Gulliver calculations	752			
Sciaky SA	507			
Scratch brushing	172	711	712	713

Index Terms**Links**

Scrolls	667		
Seal coat	889		
Seal weld	889		
Seam welds			
definition of	889		
RW	398		
welding qualification tests	261		
Secondary circuit	85	889	
Secondary rectified dc	429		
Seebeck coefficient	401		
Self-fluxing alloys (thermal spraying)	889		
Self-organizing, fuzzy logic weld			
penetration controller	290		
Self-propagating high-temperature synthesis			
reactions	16		
Self-reacting welding	671		
Self-shielded flux cored arc welding	301		
Self-shielded flux cored wires	330		
Semiautomatic arc welding	889		
Semiautomatic guns	243		
Semiconductor diode lasers	325		
Series welding			
definition of	889		
RSW	413		
Set down	432	889	
Shadow mask	889		
SHADOW technique	632		
Shear welding	715		
Shear-tension strength (STS)	417		
Shear-tension test	416		
Sheet separation (resistance welding)	482	487	889
Shell banding	679		
Shielded metal arc cutting (SMAC)	889		
Shielded metal arc welding (SMAW).			
<i>See also</i> Power sources (arc welding)			
applications	303		
cooling rate (empirical equation)	59		
definition of	889		

Index Terms

Links

Shielded metal arc welding (SMAW) (*Cont.*)

dry welding	307	
electrodes		
aluminum	304	
aluminum alloy	304	
copper alloy	304	
deposition rates	304	
mild and low-alloy steel-covered	304	
nickel alloy	304	
overview	303	
stainless steel-covered	304	
suffix symbols	304	
surfacing welding electrodes	304	
fluxes	49	
alloy modification	48	
binding agents	48	
pyrochemical kinetics	47	
slag detachability	49	
slag formation	49	
slipping agents	48	
heat source, modeling of	39	
hyperbaric welding	307	
liquid-slag reactions	751	
overview	18	302
preheating	306	
procedures	305	
process		
advantages	302	
base-metal thickness	302	
equipment	302	
limitations	302	
overview	302	
weld quality	302	
welding circuit	302	
repair welding	307	
safety considerations	307	
slag viscosity	48	
underwater welding		

Index Terms

Links

Shielded metal arc welding (SMAW) (*Cont.*)

dry welding	307
overview	307
wet welding	307

variations

firecracker welding	306
gravity welding	306

welder training	305
-----------------	-----

welding schedules	304
-------------------	-----

Shielding

arc welding	246
-------------	-----

GTAW	249
------	-----

welding qualification tests	264
-----------------------------	-----

Shielding gas

consumable electrode arc welding	18
----------------------------------	----

definition of	889
---------------	-----

fluxes	46
--------	----

GMAW	314
------	-----

GTAW	252
------	-----

nonconsumable electrode arc welding	18
-------------------------------------	----

oxygen	92
--------	----

sulfur	92
--------	----

Shielding gases

argon	597
-------	-----

basic properties

dissociation	296
--------------	-----

gas purity	297
------------	-----

overview	296
----------	-----

reactivity/oxidation potential	296
--------------------------------	-----

recombination	296
---------------	-----

blends

argon	297
-------	-----

helium	297
--------	-----

hydrogen	297
----------	-----

nitrogen	297
----------	-----

oxygen	297
--------	-----

blends, accuracy of	297
---------------------	-----

CO ₂ lasers	597
------------------------	-----

Index Terms**Links**Shielding gases (*Cont.*)

EGW	374			
FCAW				
argon/carbon dioxide	298			
carbon dioxide	298			
fume generation	300			
GMAW	319			
argon	298			
argon-helium	298			
argon-oxygen	298			
carbon dioxide	298			
helium	298			
three-gas blends	298			
GTAW	350			
argon	298			
argon-helium	298			
argon-hydrogen	298			
helium	298			
helium	597			
H LAW	324			
LBW	565	571		
mechanical properties, influence on	300			
mixtures and uses	869			
Nd-YAG lasers	597			
overview	296			
PAW	300	361		
plasma arc welding (PAW)				
high-current ($\leq 100A$) PAW	300			
low-current ($< 100A$) PAW	300			
self-shielded flux cored arc welding	301			
summary of	869			
Yb: disc lasers	597			
Yb: fiber lasers	597			
Shock	402			
Shocking	402			
Short arc (GMAW-S) power supplies	280			
Short-circuiting transfer (arc welding)	83	84	256	310
	889			

Index Terms**Links**

Short-cycle stud arc welding	385		
Shot blasting	619		
Shoulder	180	889	
Shrinkage stress			
definition of	889		
EBW	522		
Shrinkage void	268	426	889
Shunting	466		
Siemund-Wienzell Electric Welding			
Company	244		
Silica-base glass SiO ₂	580		
Silicon chips	3		
Silicon-controlled rectifier (SCR)			
contactors	452		
Silver	685		
<i>See also</i> Soft-interlayer solid-state welds			
Silver alloy brazing	889		
Silver soldering	889		
Simplified plasticity strain method	755		
Single crystals (fusion welding)	103		
Single impulse welding	430	889	
Single-bevel-groove weld	889		
Single-flare-bevel-groove weld	889		
Single-flare-V-groove weld	889		
Single-J-groove weld	889		
Single-pass weld (HAZ)			
austenite grain growth	126		
continuous heating transformation diagrams	125		
grain-boundary pinning	127		
microstructural zones	123		
partially melted zone	127		
PTCT diagrams	124		
thermal pinning	125		
unmixed zone	127		
Single-port nozzle	889		
Single-square-groove weld	889		
Single-U-groove weld	889		
Single-V butt joints	319	362	

Index Terms**Links**

Single-V-groove weld	889			
Single-welded joint	889			
Sinusoidal ac welding	278			
Skull	889			
Slag				
ESW	369	372		
SAW	338			
SMAW	302			
Slag detachability	49			
Slag entrapment	341			
Slag formation	43	49	242	
Slag inclusion	51	289	306	341
	371	889		
Slag viscosity	48			
Slag-metal reaction temperature	43			
Slavianoff, N.G	243			
Slit probing system	550			
Slot weld	261	263	264	889
Slugging	889			
Snap-fits	6			
Society of Automotive Engineers (SAE)				
International	539			
Soft solder	889			
Soft-interlayer solid-state welds				
interlayers, environmentally induced				
failure of	236			
microstructure				
as-deposited coatings	230			
solid-state-welded interlayers	230			
multiaxial loading	236			
overview	230			
shear loading				
microstructure, effect of	235			
time-dependent failure	235			
tensile loading				
base-metal properties, effect of	233			
interlayer fabrication method,				
effect of	234			

Index Terms**Links**

Soft-interlayer solid-state welds (<i>Cont.</i>)				
overview	231			
stress, effect of interlayer thickness				
on	231			
time-dependent failure	232			
Solder	889			
Solder interface	889			
Soldering (S)	9	25	26	889
Soldering gun	889			
Soldering iron	889			
Solenoid coils				
compression coils	705			
expansion coils	705			
Solidification cracking	341	426		
Solidification cracks	268			
Solid-projection welding	425			
Solid-state deposition welding	24	25		
Solid-state lasers	325	510	621	
Solid-state microelectronic devices	3			
Solid-state resistance welding				
bonding mechanisms	210			
conclusions	215			
geometric effects	213			
mechanical/heat transfer balances	210			
overview	209			
projection welds, effect of electrical				
characteristics	213			
projection welds, effect of system mechanical				
dynamics	211			
PW	209			
summary analysis	215			
Solid-state switches	452			
Solid-state transformations				
aluminum alloys	139			
multipass weldments, fusion zone in	137			
multipass weldments, HAZ in	134			
nickel-base superalloys	139			
overview	122			

Index Terms

Links

Solid-state transformations (*Cont.*)

single-pass weld, fusion zone of

carbon sensitivity 132

titanium oxide steels 133

transformations 129

transient weld stresses 134

weld-metal toughness 133

single-pass weld, HAZ of

austenite grain growth 126

continuous heating transformation

diagrams 125

grain-boundary pinning 127

microstructural zones 123

partially melted zone 127

PTCT diagrams 124

thermal pinning 125

unmixed zone 127

stainless steels 137

titanium alloys 140

transformation behavior, factors

affecting 122

Solid-state welding (SSW) 889

Solid-state welding (SSW) processes

contacting surfaces, extension of 172

contaminated areas, separation of 172

grain structures, realignment for bonding 174

interfacial structure, breakdown of 176

mechanisms 171

containment displacement/interatomic

bonding 172

overview 171

oxides/contaminates, thermal dissolution

of 175

processes 171

processes, comparison of 176

summary 176

Solid-state welds, NDE

examples

Index Terms**Links**

Solid-state welds, NDE (<i>Cont.</i>)				
eddy current	227			
radiography (x-ray)	223			
ultrasound	224			
NDE fundamentals				
eddy current	223			
radiography	222			
ultrasound	222			
overview	222			
Solute diffusivity	101	103	105	107
	113	825	889	
Solute redistribution				
binary models	105			
multicomponent alloys, modeling of	110			
ternary models	109			
Space charge layer (sheath)	770			
Spacer bars	272			
Spacer strip	889			
Speed (use of term for friction welding)	646			
Spinels	49	751		
Spit	889			
Split pipe backing	889			
Spool	309	889		
Spool-type guns	315			
Spot size				
fusion welding	32			
HLAW	323			
Spot welding. <i>See</i> Resistance spot welding (RSW)				
Spot welds				
base metal	487			
definition of	889			
HAZ	486			
indentation depth	487			
indentation width	487			
PMZ	487			
RSEW	438			
RW	398			

Index Terms**Links**

Spot welds (<i>Cont.</i>)				
USW	727			
weld nugget	486			
welding qualification tests	263			
Spray (use of term)	83			
Spray deposit	889			
Spray deposit density ratio (thermal spraying)	889			
Spray transfer (arc welding)				
definition of	890			
GMAW	13	256	311	
Springs	212			
Sputtering	230			
Square butt joint	325			
Square-groove welds				
definition of	267	890		
transverse shrinkage	162			
welds	266			
Square-grooved butt joints	362			
Square-wave-type power supplies	278			
Squeeze time	465			
SQUID system	227			
SS-7 compound	356	357		
Stack cutting	890			
Staggered intermittent weld	890			
Stainless steel alloys				
EGW	376			
ESW	376			
ferrite formation	651			
FRW	183	184		
integrated weld modeling	752			
LBW	630			
rotary friction welding	651			
Stainless steels	304	234	474	560
304L	235	551	588	
DB	683			
deposition on carbon or low-alloy steel	119			

Index Terms**Links**

Stainless steels (<i>Cont.</i>)		
dilution	119	
FCAW	332	
FRW	183	644
FSW tool applications	666	
laser cutting	617	
PW	427	
RSEW	474	
safe welding practices	855	
seam welding	444	
studs	381	
types	474	
weldments	137	
X8CrNi1812 (foils)	632	
Standard (use of term)	614	
Standard cubic foot per hour (SCFH)	612	
Standoff distance	309	890
Static force balance model (SFBM)	776	
Steel		
electrical steels	616	
laser cutting	615	
laser welding of	571	
spot welding	420	
start and stop in welding	76	
uncoated steels	421	
zinc-coated steels	420	
Steel pressure vessel	881	
Steel welding. <i>See also</i> Shielded metal		
arc welding (SMAW)		
case studies	70	
Steels		
DB	683	
weldability of	875	
Steigerwald, Karl-Heinz	507	
Stepless, high-speed, accurate, and discrete		
one-pulse welding technique		
(SHADOW)	632	
Stick electrode	242	890

Index Terms**Links**

Stick electrode welding	243	890		
Stickout	309	890		
Stiffeners	162			
Stirred nugget zone	196			
Stitch welding	398	672		
Stohr, Jacques- Andre	507			
Stopoff	890			
Stored-energy seam welding machines	444			
Straight polarity	249	890		
<i>See also</i> Direct current electrode negative (DCEN)				
Strain/strain rate (FRW)	195			
Strakes	362			
Stranded electrode	890			
Streaming transfer	84			
Stress relief cracking	890			
Stress relief heat treatment	890			
Stress-corrosion cracking (SCC)				
environmental effects	165			
residual stresses	160			
soft-interlayer solid-state welds	236			
Stress-relieving treatments	164			
Stringer bead	70	71	77	890
Stub	306	890		
Stuck weld. <i>See</i> Cold weld				
Stud arc welding (SW)	381			
overview	18	380		
Stud welding. <i>See also</i> Stud arc welding (SW)				
definition of	890			
Stud welding gun	380	386		
Stud welds	264			
Studs	381			
Subcritically reheated				
grain-coarsened (SCGC) zone	134	135		
Submerged arc plug welds	336			
Submerged arc welding (SAW)	335			
<i>See also</i> Power sources (arc welding)				
basicity index	47			

Index Terms**Links**

Submerged arc welding (SAW) (<i>Cont.</i>)				
cooling rate (empirical equation)	59			
definition of	890			
fluid flow phenomena	94			
fluxes	49	337		
grooves for joints, recommended proportions	276			
heat source, modeling of	39			
liquid-slag reactions	751			
overview	18	19	335	
shielding gas	46			
Substrate	10	890		
Sulfur	90	616		
Superabrasives	665			
Superalloys				
differential thermal expansion	184			
EBW	522			
electron beam wire-feed process	537			
FSW tool designs	665			
GTAW	345			
LBW	561			
nickel-base superalloys	139			
partially melted zone	128			
single-crystal nickel-base superalloys	665			
solid-state upset welding	454			
Superaustenitic stainless steel				
AL-6XN	115	117		
CN3MN	110	120		
Superaustenitic stainless steels (joining)	119			
Supercooling				
CET	103			
dendrite solidification	44	288	630	
dendrite tip undercooling	96	105	111	113
dendritic growth rate	103			
high-energy-density welding	96			
nucleation process	97	98	99	
rapid solidification	111			

Index Terms**Links**

Supercooling (<i>Cont.</i>)			
single-crystal FW	106		
substructure formation	101		
weld solidification (fusion welds)	99		
Supercritically reheated grain-refined (SCGR)			
zone	135		
Superplastic forming (SPF)	217		
Superplastic forming/diffusion welding			
(SPF/DW) technique	683		
Surface adsorption	6		
Surface contamination	29		
Surface expulsion	426	487	890
Surface tension			
CO ₂ , effect on	92		
oxygen, effect on	93		
Surface Tension Transfer (STT)	257		
Surfacing	16	890	
Surfacing material	890		
Surfacing metal	890		
Surfacing weld	890		
Sweat soldering	890		
Swedish iron	245		
Swept spot friction stir welding (SSFSW)	672		
Swing welding	672		
Synchronous timing (resistance welding)	890		
Synthetic diamond	665		
Synthetic materials, laser cutting	618		
Sysweld	835		
T			
Tabs	561		
Tack weld	890		
Tack welder	305		
Tacker	890		
Tagged out	847		
Tailor-weld blanks	601	602	
Tangent-tube welds	527		
Tantalum	644	685	

Index Terms**Links**

Taxonomy	13			
Tee joints	11			
Temper embrittlement	377			
Tensile testing	388	418	596	660
	686	736		
Tensile-shear test	489	492	494	707
	723			
Tetrahedral meshing	774			
Theoretical throat	890			
Thermal cutting (TC)	890			
Thermal cycle simulator (TCS)	124			
Thermal pinning	125			
Thermal soak-backs	215			
Thermal spraying gun	890			
Thermal spraying (THSP)	10	890		
Thermal stress	55	890		
Thermal transport models	147			
Thermionic emission	250			
Thermit crucible	890			
Thermit mixture	890			
Thermit mold	890			
Thermit reaction	890			
Thermit welding (TW)	16	890		
Thermocompression bonding	727	890		
Thermocouples	289			
Thermoelastoplasticity	148			
Thermomechanical processing (TMP)	141			
Thermomechanically affected zone (TMAZ)	196	197		
Thermoplastics	666			
Thermosonic gold ball bonding	201			
Thinnest outer sheet (TOS)	442			
Thomson, Elihu	245	397	448	
Thomson, William	399			
Thomson effect	250	399	401	
Thoriated electrodes				
GTAW	349			
PAW	360			

<u>Index Terms</u>	<u>Links</u>		
Threads (threaded conical pins)	669		
Three-bar analogy	146		
Three-dimensional (3D) elastic-plastic analysis	755		
Three-dimensional (3-D) models	587		
Three-dimensional (3-D) moving-source models	146		
Three-dimensional (3-D) objects	201		
Three-dimensional (3-D) parts	540		
Three-dimensional (3-D) transient models	766		
Three-piece welds	527		
Threshold limit values (TLVs)	855		
Threshold limit value-time weighted average (TLV-TWA)	855		
Throat depth	405	441	
Throat gap	405		
Throat of a fillet weld	890		
Throat of a groove weld	890		
Through-the-arc sensing. <i>See</i> Arc sensing			
TIG welding. <i>See also</i> Gas tungsten arc welding (GTAW)			
definition of	890		
Time-of-flight diffraction (TOFD) technique	226		
Time-temperature transformation (TTT) diagram	750		
Tinning	890		
Titanium			
arc sensing	287		
EGW	376		
ESW	376		
FRW	183	644	
laser welding of	572		
pulsed-current GMAW	287		
ROW	717		
Titanium alloys	542	572	708
aerospace applications	140		
DB	217		

Index Terms**Links**

Titanium alloys (<i>Cont.</i>)				
FSW tool applications	666			
laser cutting	617			
laser welding of	572			
PW	427			
ROW	717			
Ti-6Al-2Sn-4Zr-2Mo	537			
Ti-6Al-4V	235	537	542	543
	572	684		
Ti-8Al-1Mo-1V	537			
weldments	140			
Titanium nitride (TiN)	127			
Titanium oxide steels	133			
Title 21 CFR 1040.10	566			
Title 21 CFR 1040.11	566			
Title 29 CFR 1900.1000	866			
Title 29 CFR 1910	845			
Title 29 CFR 1910, Subpart Z	864			
Title 29 CFR 1910.1000	850			
Title 29 CFR 1910.132	848			
Title 29 CFR Chapter XVII, Part 1910	852			
T-joints				
aluminum	78			
definition of	267	890		
EBW	526			
grooves, recommended proportions for	275			
Toe angle	323			
Toe crack	890			
Tool steels	665			
Top hat	40			
Torch brazing (TB)	849	890		
Torch soldering (TS)	849	890		
Torch tip	861	890		
Torque test	433			
Torsion locks	6			
Touch-and-withdraw method	243			
Townes, C.H	508			
Trace elements	89	90	92	355

<u>Index Terms</u>	<u>Links</u>			
Trailer shield	352			
Transferred arc (plasma arc welding)	890			
Transistors	3			
Transmission electron microscopy (TEM)	131	629	696	
Transverse crack	755	890		
Transverse electromagnetic mode with m number (TEM _{mm})	563			
Transverse excited atmospheric CO ₂ lasers	620			
Transverse shrinkage	162			
Transverse stresses	160			
Travel angle	313			
Travel speed				
GMAW	313			
high energy density beam welding	512			
SAW	343			
Trepanning	619	620		
Triflute tool	672	673		
Trivex tool	672	673		
Truncated cone	214	414	415	432
	666	668		
Tungsten				
electrodes	249			
FSW tool materials	665			
gas tungsten arc welding (GTAW)	18			
Tungsten inert-gas (TIG) process	246.			
<i>See also</i> Gas tungsten arc welding (GTAW);				
Gas tungsten arc welding with penetrating-enhancing compounds				
Tungsten inert-gas (TIG) welding	832			
Tunnel defect	223			
Turbulence	769			
TWI slit probing system	551			
Twin carbon arc brazing	890			
Two-dimensional (2- D) steady-state models	766			
Two-layer temper-bead procedure	137			

Index Terms

Links

U

U-groove welds	267	890
UL 551	858	
Ultimate tensile strength (UTS)	231	
soft-interlayer solid-state welds	232	
Ultrahigh-strength steels		
4130	160	
D-6a	160	
H13	160	
residual stresses and distortion	161	
Ultrashort high-energy pulses		
(laser drilling)	620	
Ultrasonic additive manufacturing (UAM)		
equipment	734	
high power, impact of	738	
high-power development	735	
material properties in		
mechanical properties of builds	736	
metallurgical aspects	735	
microhardness/nanohardness testing	738	
overview	731	
procedures	734	
process consumables		
base plate	732	
machine tools	733	
metal tape	732	
ultrasonic tooling	733	
process fundamentals	731	
push-pin testing	737	
quality control	739	
safety	740	
ultrasonic welding during		
applications	733	
consumables	732	
materials	732	
overview	731	
welding parameters	732	
ultrasonic welding system	731	

Index Terms**Links**

Ultrasonic A-scan technique	498			
Ultrasonic B-scan technique	499			
Ultrasonic consolidation (UC)	201			
Ultrasonic soldering	890			
Ultrasonic spectroscopy	226			
Ultrasonic welding (USW)	725			
bond formation, mechanisms for	206			
bond strength	205			
friction	204			
heat generation				
friction coefficient	203			
surface heat	203			
volume heat	203			
material behavior				
plastic deformation	202			
thermomechanical hardening rules	202			
overview	24	25	201	725
thermomechanical processes, governing				
equations	202			
wedge-reed system	725			
yield rule	202			
Ultrasound				
acoustic emission technique	227			
compound scanning technique	226			
electromagnetic acoustic transduction				
technology	227			
linear phased array	223			
matrix phased array	223			
SAM	226			
solid-state welds	222	224		
TOFD technique	226			
ultrasonic spectroscopy	226			
Ultraviolet (UV) light	327			
Ultraviolet (UV) radiation	848	851	852	
Unaltered grain-coarsened (UAGC) zone	135			
Underbead crack	890			
Undercooling, fusion welding	99			
Undercut	298	891		

Index Terms**Links**

Undercutting			
corner joint welds	526		
definition of	597		
electroslag overlays	368		
filler metals, effect of	671		
fluid flow phenomena	89		
joining process	11		
Maglay process	374		
magnetic field, effect on	368		
shielding gases	297		
Underfill	518	891	
Underwater welding	307		
Underwriters Laboratories	863		
United Technologies Corporation	507		
Unzipping	442		
Upper bainite	131		
Upset			
definition of	891		
rotary friction welding	646	648	650
Upset butt welding	891		
Upset distance	891		
Upset welding (UW)	453		
definition of	891		
description of	397	453	
versus flash welding	448	453	
Upsetting	171		
Upslope power	518		
Upslope time	466		
U.S. Bureau of Alcohol, Tobacco, and Firearms	864		
U.S. Department of Transportation (DOT)	855	864	
U.S. Mine Safety and Health Administration (MSHA)	854		
U.S. Mint	718		
U.S. Navy	245	246	357
U.S. Steel	615		
U-tension test	492		

Index Terms**Links****V**

Vacuum brazing	891			
Vacuum environment	509			
van der Waals bonding	6			
Vanadium	685			
Vapor pressure				
EBW	532			
fluxes	45			
fusion welding	116			
keyhole formation	40	92	93	532
	597	778		
laser weld quality monitoring	597			
SAW	49			
weld modeling	779	780		
welding processes (overview)	15			
Vaporization				
alloying elements	781	783		
arc outs	533			
arc welding process control	285			
directed-energy fusion welding	21	22		
EBW	514			
ESW	371			
flux	783			
high-energy-density welding	39			
keyhole formation	778	779		
laser cutting	606			
laser weld quality monitoring	595	596	598	600
LBW	507	511	512	558
	559			
losses	571			
manganese loss due to	45			
mass transport, modeling	767			
penetration-mode HLAW	322			
PW copper/copper alloys	427			
safe welding practices	851			
weld modeling	785			
Variable polarity plasma arc (VPPA)				
welding process	359	361	362	364

Index Terms**Links**

Variable-voltage power supply	706		
Variant processes	10		
Venturi effect	620		
Vertical position	265	891	
Vertical position (pipe welding)	891		
V-groove weld	267	891	
Vibration, ultrasonic welding	203		
Virtual process chain	830		
Voids			
DB	218	219	220
FRW	191		
MPW	707		
RSW	416		
shrinkage void	268	428	889
soft-interlayer solid-state welds	230		
solid-state welds	223		
UAM	734	736	
Volume-of-fluid (VOF) method	776		
Volumetric solid-state phase transformations	147		
von Mises plastic strain	204		
von Mises stress			
fusion welding	149		
soft-interlayer solid-state welds	231	232	
von Mises yield condition	149		
von Mises yield criterion	202		
W			
Walk-in workstation	567		
Waspalloy	537	666	
Watanabe number	377		
Water moisture (H ₂ O)	613		
Water muffler	862		
Water table	853		
Water-cooled welding guns	331		
Watts (W)	35		
Wave soldering (WS)	891		
Waveform-controlled welding. <i>See</i> Pulse welding (PW)			

Index Terms**Links**

Wax pattern (thermit welding)	891			
WC-Co	666			
Weak coupling	837			
Wear parameters	287			
Weave bead	264	891		
Wedge-reed system	725			
Weld	891			
Weld (use of term)	266			
Weld axis	262	891		
Weld bead				
definition of	891			
heat source, modeling of	39			
Weld bonding	10	11	471	728
	891			
Weld brazing	10	11	891	
Weld cladding	264			
Weld crack	891			
Weld crater/weld finger	71	72		
Weld face	269	891		
Weld line	159	891		
Weld lobe diagrams				
3-D lobe diagrams	473			
electrode force, effect of	471			
overview	469			
probabilistic boundaries	472			
process variables, influence of	470			
Weld metal	267	891		
Weld pass	64	891		
Weld pass sequence	891			
Weld penetration	11	891		
Weld pool				
alloy additions	48			
arc welding	243			
creep	827			
definition of	891			
fusion welding	31			
oscillation sensing	287			
oxygen, effect of	44			

Index Terms**Links**

Weld pool (<i>Cont.</i>)				
solidification rate	60			
vibrations	288			
Weld puddle	31	891		
Weld reinforcement	78	165	311	530
	836	891		
Weld root	224	891		
Weld size	269	891		
Weld solidification cracking	754			
Weld solidification (fusion welds)				
grain structure	99			
microstructural features				
overview	96			
solidification parameters	97			
nucleation considerations				
application	98			
nucleation theory	97			
overview	97			
rapid solidification	111			
substructure formation. See Fusion welds,				
substructure formation				
Weld tab	891			
Weld throat	268	891		
Weld time				
downslope time	466			
hold time	466			
off time	466			
squeeze time	465			
upslope time	466			
weld time	465			
Weld toe	50	268	322	323
	891			
Weldability	874	891		
Welder	846	891		
Welder performance qualification	891			
Welding. <i>See also</i> individual types; Joining				
processes				
aluminum	71			

Index Terms

Links

Welding (*Cont.*)

annular projection welding	209	
bead-on-plate welding	69	
cross-wire welding	209	
definition of	891	
direct-drive FRW	180	
edge projection welding	209	
embossed projection welding	209	
groove welding		
joint geometries, complex	78	
joint geometries, simple	77	
inertia-drive FRW		
axial pressure versus peripheral velocity	181	
flywheel energy	181	
overview	180	
peripheral velocities	181	
metal movement during	159	
overview	7	
parallel welding	413	
push-pull welding	413	
series welding	413	
steel	70	
thermal stresses during	158	
Welding blowpipe	891	
Welding current		
definition of	891	
ESW	368	
GMAW	312	
RSW	416	
RW	463	
safe welding practices	851	
SAW	340	
Welding cycle	183	891
Welding distortion		
fusion welding	151	
angular change	151	154
buckling distortion	151	154
in-plane distortion	151	

Index Terms**Links**

Welding distortion (<i>Cont.</i>)				
longitudinal bending (bowing or camber distortion)	151	154		
longitudinal shrinkage	151	154		
out-of-plane distortion	151			
rotational distortion	151	154		
transverse shrinkage	151	154		
heat flow	56			
Welding efficiency (use of term)	565			
Welding electrode	17	891		
Welding force	464			
Welding fuels	869			
Welding ground	891			
Welding guns				
air-cooled	331			
arc (definition of)	882			
arc welding	247	287	342	
electro servo welding gun	465			
FCAW	330	331		
GMAW	309	313	314	
LBW	507			
portable	413			
RSW	411	412	413	414
	420			
safe welding practices	859	860	862	
semiautomatic	859			
stud welding	380	383	386	
ultrasonic	726			
water-cooled	331	859		
Welding inserts	351			
Welding interface	641	690	694	697
	891			
Welding leads	859	891		
Welding machine				
definition of	891			
Resistance welding	469			
Welding metallurgy	55			
Welding operator	265	343	536	891

Index Terms**Links**

Welding personnel, qualification of				
codes and standards	260			
overview	260	265		
performance qualification tests	265			
Welding position	51	891		
Welding procedure	11	891		
Welding procedure qualification record (WPQR)	539			
Welding procedure record	656			
Welding procedure specifications (WPS)	260 891	265	539	642
Welding procedures, qualification of				
codes and standards	260			
overview	260			
procedure qualification, limitations on purpose of	264 260			
qualification documentation	265			
qualification of				
qualification tests	260			
special qualification tests	262			
responsibility for the task	260			
standard tests	263			
Welding processes				
brazing	25			
classification of	13			
directed-energy fusion welding	21			
electric arc fusion welding	16			
fusion welding, chemically driven	14			
introduction	13			
nonfusion (solid-state) welding	24			
soldering	25	26		
Welding rod	891			
Welding schedules	304			
Welding sequence	359 519	450 701	451 891	517
Welding slag	43			
Welding tip	725	891		

Index Terms**Links**

Welding torches				
Arc	891			
GTAW	348			
oxyfuel gas	891			
PAW	360			
Welding wheel	891			
Welding wire	18	46	319	891
The Welding Institute of the United Kingdom	186			
Weldment				
cooling rate	59			
definition of	891			
distortion	161			
parametric effects				
material type	64			
overview	64			
welding speed	64			
peak temperature	60			
RSW	40			
welding distortion	56			
Weldments. <i>See also</i> welding				
distortion in	161			
residual stresses and distortion, analyses of	159			
solid-state transformations. <i>See</i> Solid-state transformations				
thermal treatment				
postweld thermal heat treatments	165			
preheat	165			
Weld-metal (WM) zone	55			
Weld-metal quench effect	307			
Weldor	891			
Weld-puddle motion	37			
Welds. <i>See also</i> Arc welding processes, design				
considerations for; individual types				
advancing side	186			
composite zone	127			
partially melted zone	127			

Index Terms**Links**

Welds (<i>Cont.</i>)			
retreating side	186		
thermal stress analysis of	826		
true heat-affected zone	127		
unmixed zone	127		
Welds, numerical aspects of modeling			
energy equation and heat transfer	820		
microstructure evolution	825		
modeling	819		
overview	819		
reality, models, and mathematics	819		
thermal stress analysis	826		
WELDSIM	75	816	
Wet welding	307		
Wetting	50	891	
Widmanstätten ferrite	131	750	
Widmanstätten side plates	130		
Widmanstätten structure	143		
Wine glass beads	559		
Wiped joint	891		
Wire joint, LBW design	570		
Wire melting, GMAW	255		
Wire probing system	550		
Wire welding			
cross-wire welding	424	432	
FCAW	19	300	
fume generation	301		
GMAW	18		
self-shielded flux cored arc welding	301		
solid projection welding	209		
solid-state welding processes	726		
Wood, laser cutting	618		
Work connection	891		
Work lead	859	891	
Workpiece	15	891	
Workpiece connection	891		
Workpiece lead	891		
WRC-1992 diagram	137	139	140

Index Terms**Links****X**

X-65 steels	757	
X-radiation	517	863

Y

Y ₂ O ₃ -stabilized tetragonal zirconia polycrystal ceramic (Y-TZP)	687			
YAG lasers	620			
Yb: fiber lasers	556			
Yellow brasses	484			
Young's modulus	609	627	825	826
	831	832		
Ytterbium: fiber lasers	588			
Ytterbium-doped yttrium-aluminum-garnet (Yb:YAG) disc lasers	556			
Yttrium-aluminum-garnet (YAG) crystal solid-state lasers	508			
Yttrium-aluminum-garnet (YAG) lasers, focusing characteristics	608			

Z

Zener coefficient	750			
Zigzag line	191			
Zinc	685			
Zinc sulfide (ZnS)	608			
Zirconium	644	685		
absorptivity	560			
aluminum welds	103			
CD stud welding	391			
CW	715			
DB oxide ceramics	685			
DB process	218			
dissimilar ferrous alloys	685			
electrodes	349			
EXW	691	697		
fluxes	45			
FOW	701	702		

Index Terms**Links***Zirconium (Cont.)*

gas purity	297		
GTAW	345		
high-vacuum welding	527		
HLAW modulus		321	322
joints	362		
PAW	361		
postweld processing	698		
ROW	717		
welding parameters	644		